Bioconjugate Chemistry

COMMUNICATION

pubs.acs.org/bc

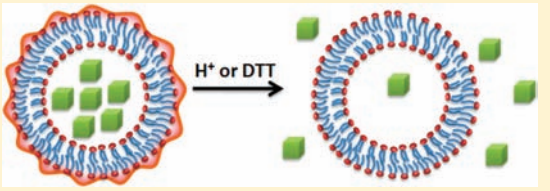
Controlled Release from Cleavable Polymerized Liposomes upon Redox and pH Stimulation

Shiyong Zhang and Yan Zhao*

Department of Chemistry, Iowa State University, Ames, Iowa 50011-3111, United States

Supporting Information

ABSTRACT: A gallate derivative with three propargyl groups was coupled to palmitoyl oleoyl phosphoethanolamine (POPE). The resulting anionic lipid was formulated with common lipids such as palmitoyl oleoyl phosphatidyl choline (POPC) to form large unilamellar vesicles (LUVs). Polymerization of the LUVs was accomplished by the Cu(I)-catalyzed click reaction between the propargyl groups and the azide groups in the cross-linker. When the cross-linker contained a disulfide or ketal group, the resulting polymerized liposomes depolymerized and released entrapped contents upon the addition of a reducing thiol or under weakly acidic conditions. The click reaction allowed simultaneous multivalent surface functionalization during cross-linking, making these cleavable polymerized liposomes (CPLs) potentially very useful in the delivery and controlled release of pharmaceutical agents.



An ideal drug-delivery vehicle unloads its contents only at the target site. Liposomes have many of the desired features of "smart" drug-delivery systems including large encapsulating capacity, ease of surface decoration, and biocompatibility.[1−7] A number of liposomal drug formulations have been approved by FDA and numerous others are undergoing clinical trials.[1−7] In recent years, there has been growing interest in developing liposomes that release their contents under specific stimuli including pH,[5,8−19] enzymes,[20−23] temperature,[24] redox signals,[25−27] and light.[12,28−32] The majority of the reported methods focus on the design of responsive lipids. Typically, the stimulus triggers changes in the lipid structure and, in turn, causes destabilization and leakage of liposomes.

An important challenge faced by liposomal delivery lies in the stability of the noncovalently assembled structures. Formation of liposomes is driven by hydrophobic interactions among the lipid tails. After entering the vascular system, liposomes are destabilized through the loss of lipid molecules to hydrophobic entities such as biomembranes and plasma proteins, resulting in premature leakage of entrapped contents. Many approaches have been developed to improve liposomal stability, including tuning of membrane fluidity, incorporation of cholesterol, and surface protection with poly(ethylene glycol).[1−7] More recently, cholesterol-derived lipids[33,34] and polymers[35] were found to be particularly effective at enhancing liposomal stability.

Polymerization of liposomes, whether near the headgroup or in the lipid tails, can stabilize the structure as well.[36−40] Although some polymerized liposomes are known to survive harsh treatment including dehydration and rehydration, their usage in clinical drug delivery is hampered by the poor biocompatibility of the polymerized materials. Whereas most lipids used in common liposomal formulations are bio-originated and thus fully biodegradable, the polymerized materials, often connected by carbon−carbon bonds, are macromolecules very difficult to degrade.

In this paper, we report a simple method to prepare cleavable polymerized liposomes (CPLs). Our approach combines the simplicity of polymerization-derived stabilization with the flexibility of small-molecule lipids. Our method can be easily applied to common lipid formulations to create liposomes with controlled-release properties under biologically relevant conditions. The chemistry employed to polymerize the liposomes permits facile conjugation of the liposomes with functional ligands such as fluorescent labels, making it convenient to track the fate of the liposomes.

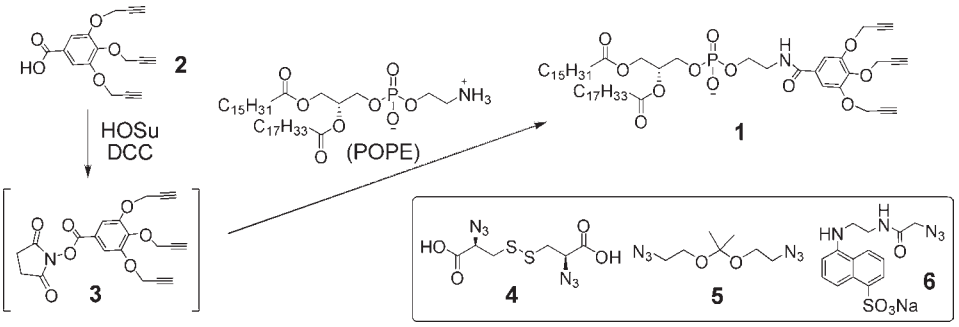
Polymerizable lipid **1** is a derivative of common POPE lipid. As shown by Scheme 1, a propargylated gallic acid (**2**) was activated by *N*-hydroxysuccinimide (HOSu). The resulting activated ester (**3**) reacted with the amino group of POPE in the presence of diisopropylethylamine to afford **1**. The product was purified by column chromatography and characterized by ^{1}H and ^{13}C NMR spectroscopy, as well as mass spectrometry. The three propargyl groups of **1** are included for polymerizing the liposomes by azide-containing cross-linkers such as **4** and **5** through the highly efficient click reaction (i.e., the 1,3-dipolar cycloaddition between terminal alkyne and azide). The high-yield, selectivity, and outstanding tolerance of functional groups of the click reaction[41−43] enabled its numerous applications in biolabeling,[44,45] surface modification,[46] dendrimer synthesis,[47−49] and polymer formation.[46] Click chemistry has also been applied to liposomes in recent years,[35,50−55] but mostly for their conjugation with ligands or functional labels.

Received: July 21, 2010
Revised: December 29, 2010
Published: March 15, 2011

ACS Publications © 2011 American Chemical Society

dx.doi.org/10.1021/bc1003197 | *Bioconjugate Chem.* 2011, 22, 523–528

Scheme 1. Synthesis of Cross-Linkable Lipid 1



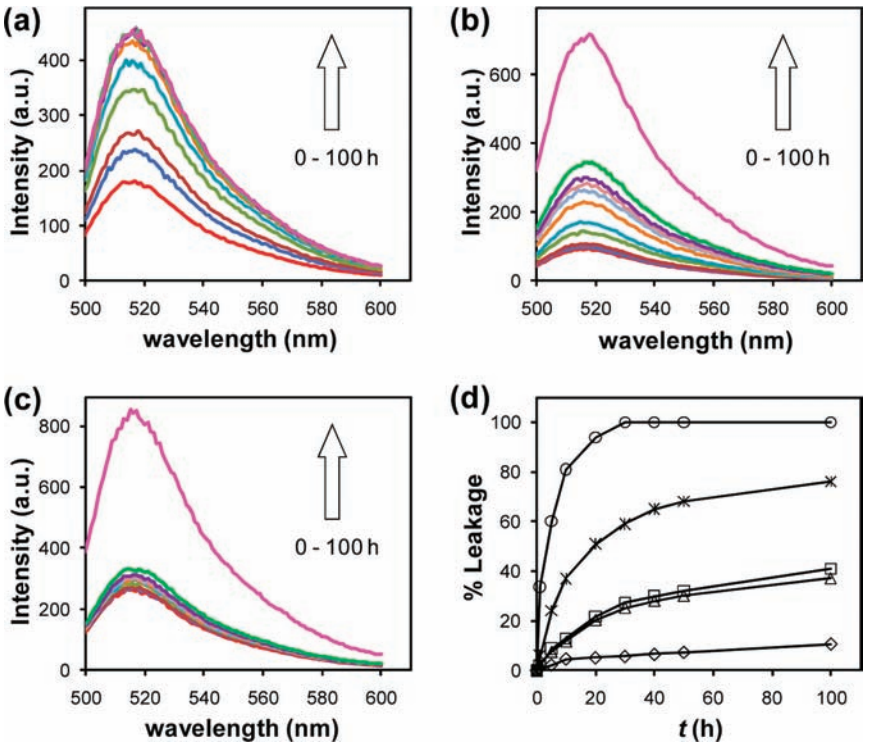


Figure 1. Fluorescence spectra of CF-containing LUVs prepared with (a) **1**, (b) 1:1 [**1**]/[POPC], and (c) POPC at ambient temperature. $[CF]_{initial}$ = 50 mM in 10 mM HEPES buffer. [NaCl] = 0.1 M. The spectra were recorded at 0, 0.5, 1, 5, 10, 20, 30, 40, 50, and 100 h after the liposomes were prepared. (d) Percent leakage of CF from LUVs prepared with different lipid formulations. [**1**]/[POPC] = 1:0 (○), 2:1 (×), 1:1 (□), 1:2 (△), 0:1 (◇).

Lipid **1** could be easily formulated with POPC to form liposomes. We employed the well-established carboxyfluorescein (CF) leakage assay[56] to understand the effect of lipid formulation on liposomal stability. Briefly, CF was trapped inside large unilamellar vesicles (LUVs) at a concentration (50 mM) that gave significant self-quenching. Any leakage of the dye would dilute the probe and enhance its fluorescence. Figure 1a−c shows the fluorescence spectra of several CF-containing LUVs over a period of 100 h. The spectra in violet were recorded at the end of the 100 h after 1% Titron X-100 aqueous solution was added to lyse the liposomes. The spectrum after Triton addition thus corresponded to 100% leakage and the percent leakage of CF at different times was calculated accordingly and summarized in Figure 1d.[57] From the leakage profile, we can easily see that, by itself, **1** did not make very stable liposomes—the majority of CF leaked out in 10−20 h (Figure 1d, ○). The stability of the liposomes improved significantly when **1** was formulated with POPC. The liposomes with **1**/POPC = 1:1 or 1:2, for example, retained over 60% of the dye at 100 h.

The POPC LUVs leaked very little even at 100 h (Figure 1c). Because polymerized liposomes are expected to be more stable than unpolymerized ones, the normal CF assay might not be sensitive enough for their characterization. A common way to speed up the leakage is to apply an osmotic gradient across the membranes.[33,58−60] Indeed, the LUVs with [**1**]/[POPC] = 1:1 lost all the entrapped CF in 5 M NaCl in only 12 h (Figure 2a, ▲), whereas the same lost <40% after 100 h when the buffer contained 0.1 M NaCl (Figure 1d, □). An increase of POPC in the formulation stabilized the liposomes (Figure 2a), as it did without the osmotic stress. Note that, in all the assays, the leakage

dx.doi.org/10.1021/bc1003197 |*Bioconjugate Chem.* 2011, 22, 523–528

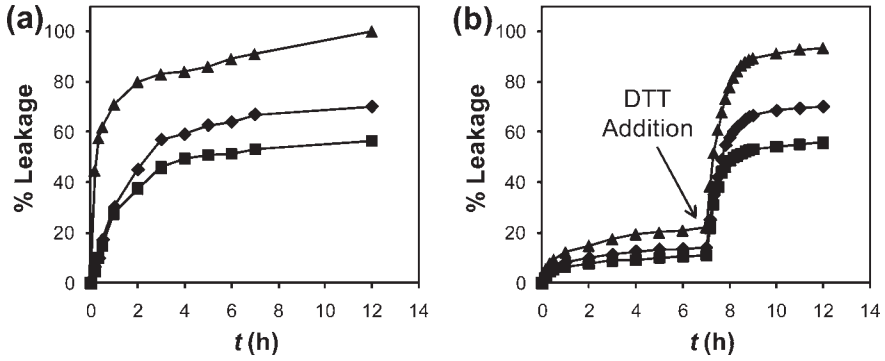


Figure 2. Percent leakage of CF from LUVs (a) before and (b) after polymerization. [CF] = 50 mM in 10 mM HEPES buffer. [NaCl] = 5 M; [**1**]/[POPC] = 1:1 (▲), 1:2 (♦), and 1:5 (■); DTT = dithiothreitol.

was fast initially and leveled off afterward. This was a reasonable result. The exchange of water and/or salt probably occurred when the dye escaped from the liposomes. As the osmotic pressure decreased across the lipid membranes, the driving force for leakage became smaller over time.

Polymerization of the LUVs was accomplished by $CuCl_2$/sodium ascorbate in the presence of 1.5 equiv of cross-linker **4**.[61] The stoichiometry was chosen because **1** contained three alkynyl groups and **4** two azides. The organic HEPES buffer was found to interfere with the click reaction and a white precipitate formed when Cu(II) salt was added to the buffer. Assuming the precipitate was a complex between copper ions and the organic amine HEPES, we added 4 equiv of *N,N,N′,N″,N″*-pentamethyldiethylenetriamine (PMDETA), a water-soluble amine known to complex with the copper catalyst used in the click reaction.[62] The click reaction indeed proceeded smoothly (vide infra) without any precipitation. The experimental details are given in the Supporting Information.

We polymerized liposomes with three different formulations —[**1**]/[POPC] = 1:1, 1:2, and 1:5. Liposomes with higher POPC are more stable according to Figure 1d but would give a lower degree of polymerization. As expected, polymerization suppressed the CF leakage to a large extent in all three liposomes. Instead of 50−90% leakage prior to polymerization (Figure 2a), the cross-linked LUVs displayed 10−20% leakage when placed in 5 M NaCl solution before dithiothreitol or DTT was added (Figure 2b). It was surprising, however, that the relative stability of the three liposomes (■ > ♦ > ▲) stayed the same, and the most polymerized liposomes (▲) were the least stable among the three. Polymerization clearly improved the liposomal stability, but it was puzzling that the degree of polymerization did not correlate with the stability. Possibly, the sensitivity toward osmotic pressure derived partly from the ionic nature of lipid **1** (which would not change upon polymerization). Figure 1d indicates that neutral POPC is far more resistant to leakage than the anionic **1**. Regardless of the exact reason for the retained order of stability, the result was actually quite desirable. For any practical applications, one would rather not have to use a lot of a specially synthesized lipid to improve stability.

The disulfide-containing cross-linker (**4**) permitted the cleavage of the polymerized liposomes with a commonly used reducing thiol, DTT. Because thiol concentration reaches 10 mM in the cytosol and is only about 10 μM in the plasma, the disulfide−thiol conversion is widely used for cellular delivery.[63] Thiol-triggered release is also useful for delivering anticancer drugs because the thiol concentration could be seven times higher near some tumors than in normal tissues.[64]

To our gratification, DTT (ca. 0.3 mM) was able to completely reverse the effect of polymerization on the CF leakage. Fast leakage started as soon as the thiol was added and the leakage profiles were nearly identical to those before the polymerization (compare Figures 2a and 2b after DTT addition). In our method, the copper catalyst was added after the formation of the liposomes and the water-soluble copper catalyst should not permeate the bilayers easily. Polymerization, as a result, was anticipated to occur predominantly on the external leaflets of the bilayers. Such a configuration is beneficial from the viewpoint of release, as it is certainly easier to cleave the disulfide bonds in the external leaflets than those in the interior by external stimuli.

For the polymerized LUVs, mass spectrometry indeed revealed high M.W. species (Figure 1S, Supporting Information). Nonetheless, since there was no guarantee that all polymeric species ionized to the same extent, the peaks in the MS might not accurately represent the polymerized lipids. To better understand the click polymerization, we took advantage of the reversible nature of the cross-linkage and studied the depolymerized LUVs to probe the cross-linking density. This method was used previously to characterize similar, click-cross-linked materials.[61] The depolymerized LUVs were obtained after the CPLs ([**1**]/[POPC] = 1:1) were incubated with 0.3 mM DTT for 24 h and were then immediately analyzed by ESI-MS. Although we could not assign every single peak due to the complexity of the system, two major peaks in the mass spectrum were identified as **7** (m/z = 1229.59) and **8** (m/z = 1276.60). We did not detect any significant amount of **9** (m/z = 1424.62). Thus, the MS results indicated that the majority of lipid **1** underwent two cycloadditions and some reacted only once under our experimental conditions.

There could be several reasons why the click reaction did not result in high cross-linking density. The click reaction was performed in fairly dilute liposomal solutions, with [**1**] = 0.26 mM. Since both the liposomes and the cross-linked **4** were anionic, it could be difficult for the cross-linker to access the alkynyl groups of the anionic **1**. Moreover, because of the hydrophobicity of the propargylated gallate, the alkynyl groups could be buried within the hydrophobic membranes instead of being exposed to the aqueous phase. Finally, electrostatic interactions among the lipids demanded that the anionic **1** be dispersed as far from one another as possible in the matrix of POPC. All of these could have contributed to the low cross-linking density of the CPLs. It should be noted, nevertheless, that

dx.doi.org/10.1021/bc1003197 |*Bioconjugate Chem.* 2011, 22, 523–528

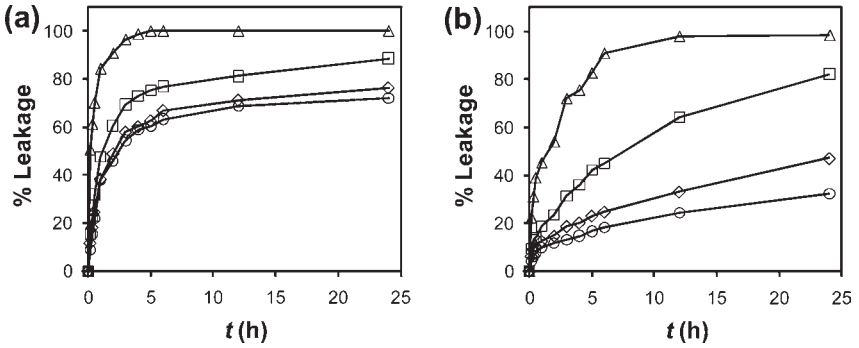
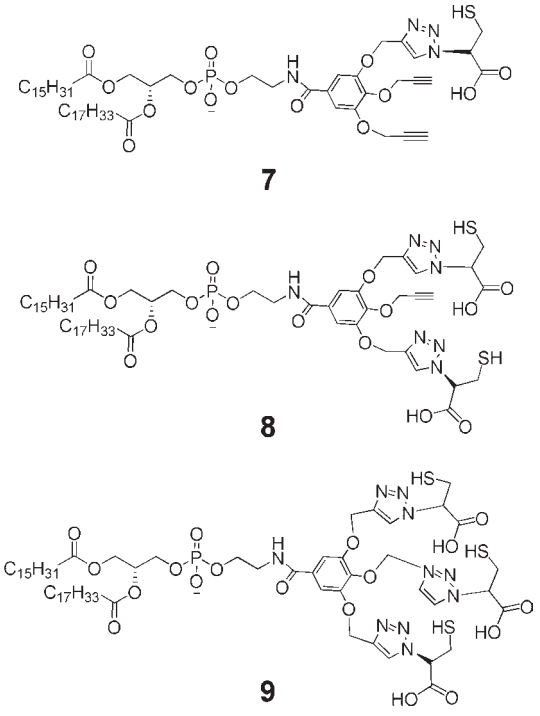


Figure 3. Percent leakage of ANTS/DPX from LUVs (a) before and (b) after polymerization. [ANTS/DPX] = 12.5/45 mM in 5 mM TES buffer. [**1**]/[POPC] = 1:2; [NaCl] = 5 M; pH = 7.0 (○), 6.0 (◊), 5.0 (□), and 4.0 (△).



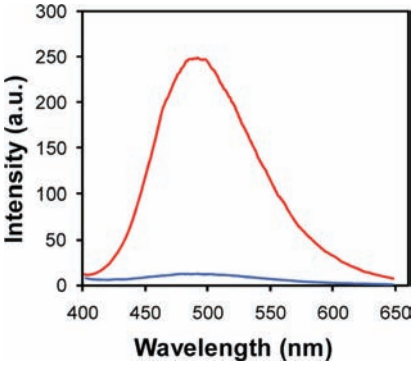


Figure 4. Fluorescence spectra of click-labeled LUVs (red) and the control LUVs (blue) after gel permeation chromatography (λ_{ex} = 345 nm). The control LUVs were prepared exactly the same as the click-labeled LUVs except that no copper catalyst was added in the process. [**1**]/[POPC] = 1:2.

the leakage assays suggested that the low cross-linking density might not be a bad result at all—even though the CPLs were significantly more stable than the unpolymerized materials, the release started as soon as the cleavage agent was added.

The outstanding tolerance of the click reaction made it easy to incorporate cross-linkers sensitive to other stimuli. Cross-linker **5**, for example, contained a ketal bond that could hydrolyze easily under acidic conditions. Acid-triggered release is important to many delivery applications. Endocytotic delivery often exploits the higher acidity of endosomes compared to cytosols.[65] Cancerous and inflammatory tissues are also known to be more acidic than normal tissues.[66−68] We prepared CPLs with a composition of [**1**]/[POPC] = 1: 2 with a slightly modified procedure. Cross-linker **5** was not soluble in water; we thus could not add the cross-linker to preformed liposomal solution. Instead, we mixed **1**, POPC, and **5** together during lipid film formation and prepared LUVs with **5** already in the lipid bilayers. Polymerization was accomplished by Cu(I) catalysts added to the aqueous solution.

We could not use the CF leakage assay for acid-triggered release because of its acid-sensitivity.[15] Instead, we employed the ANTS/DPX assay, known to work well under acidic conditions.[69,70] ANTS is a fluorescent dye and quenched strongly by DPX. When trapped together inside the liposomes, the pair gives little fluorescence. Leakage of one or both compounds reduces the concentration-dependent quenching and can be easily detected.

The ANTS/DPX assay worked well for both unpolymerized liposomes and the CPLs. As shown by Figure 3a, leakage occurred readily when the LUVs was subjected to the 5 M NaCl osmotic stress. In general, the fastest leakage took place within the first 5 h of time and leveled off afterward. Polymerization changed the release profiles significantly. The polymerized liposomes had considerably higher stability at pH 7 (Figure 3b, ○). Whereas the unpolymerized LUVs lost over 70% of the probes after 24 h, the CPLs only lost ∼30%. As the solution became more acidic, the effect of polymerization disappeared gradually. At pH 6 (◊), for example, the 24 h leakage was ∼50% and 80% for the polymerized and unpolymerized LUVs, respectively. When the solution pH decreased further to 5 (□) and 4 (△), polymerization no longer affected the 24 h leakage, but the initial rates of release, judged by the slopes of the curves in the early stage of the assays, were clearly smaller for the polymerized liposomes.

Covalent labeling of the liposomes was extremely easy with our method. As a proof of concept, compound **6** (Scheme 1) was prepared by a one-step reaction from a commercially available probe (see Supporting Information for details). Cross-linking and fluorescent labeling occurred simultaneously when **4** and **6** were added together during polymerization. After gel permeation

dx.doi.org/10.1021/bc1003197 |*Bioconjugate Chem.* 2011, 22, 523–528

chromatography (GPC) over Sephadex G-50 resins, the CPLs emitted much more strongly than the control liposomes, in which no catalyst was added (Figure 4). GPC separates molecules by their sizes. Without cross-linking, most of the dye was removed from the control liposomes during chromatography. The weak emission from the control LUVs (Figure 4, blue) probably came from physically adsorbed **6**.

In summary, polymerization of liposomes is an effective strategy to improve their stability. Introduction of multiple "clickable" functionalities on the headgroup of the lipid and the subsequent click polymerization with cleavable cross-linkers such as **4** and **5** create novel CPLs that readily depolymerize under biologically relevant conditions. In contrast to conventional free radical polymerization, the click reaction retained the benefits of polymerization (i.e., enhanced stability) without the problem of polymer-related poor biodegradability. The simplicity of the synthesis, the facile implementation of the technique in common liposome formulations, and the convenient multivalent surface modification make this method highly attractive in the controlled release and delivery of pharmaceutical agents.

■ ASSOCIATED CONTENT

Supporting Information. Entire experimental section including synthesis and characterization of the compounds, liposome preparation, and leakage assays. This material is available free of charge via the Internet at http://pubs.acs.org.

■ AUTHOR INFORMATION

Corresponding Author

*To whom correspondence should be addressed. Phone: 515-294-5845. Fax: 515-294-0105. E-mail: zhaoy@iastate.edu.

■ ACKNOWLEDGMENT

NSF (CHE-0748616 and DMR-1005515) for supporting the research.

■ REFERENCES

(1) New, R. R. C. (1990) *Liposomes: a practical approach*; IRL Press; Oxford University Press: Oxford.

(2) Philippot, J. R.; Schuber, F. (1995) *Liposomes as tools in basic research and industry*; CRC Press: Boca Raton.

(3) Gregoriadis, G. (2007) *Liposome technology*, 3rd ed.; Informa Healthcare: New York.

(4) Drummond, D. C., Meyer, O., Hong, K., Kirpotin, D. B., and Papahadjopoulos, D. (1999) Optimizing liposomes for delivery of chemotherapeutic agents to solid tumors. *Pharmacol. Rev. 51*, 691–743.

(5) Guo, X., and Szoka, F. C., Jr. (2003) Chemical approaches to triggerable lipid vesicles for drug and gene delivery. *Acc. Chem. Res. 36*, 335–341.

(6) Allen, T. M., and Cullis, P. R. (2004) Drug delivery systems: entering the mainstream. *Science 303*, 1818–22.

(7) Drummond, D. C., Noble, C. O., Hayes, M. E., Park, J. W., and Kirpotin, D. B. (2008) Pharmacokinetics and in vivo drug release rates in liposomal nanocarrier development. *J. Pharm. Sci. 97*, 4696–740.

(8) Yatvin, M. B., Kreutz, W., Horwitz, B. A., and Shinitzky, M. (1980) pH-sensitive liposomes: Possible clinical implications. *Science 210*, 1253–5.

(9) Thomas, J. L., and Tirrell, D. A. (1992) Polyelectrolyte-sensitized phospholipid-vesicles. *Acc. Chem. Res. 25*, 336–342.

(10) Chu, C. -J., Dijkstra, J., Lai, M. -Z., Hong, K., and Szoka, F. C. (1990) Efficiency of cytoplasmic delivery by pH-sensitive liposomes to cells in culture. *Pharm. Res. 7*, 824–34.

(11) Kirpotin, D., Hong, K. L., Mullah, N., Papahadjopoulos, D., and Zalipsky, S. (1996) Liposomes with detachable polymer coating: Destabilization and fusion of dioleoylphosphatidylethanolamine vesicles triggered by cleavage of surface-grafted poly(ethylene glycol). *FEBS Lett. 388*, 115–118.

(12) Gerasimov, O. V., Boomer, J. A., Qualls, M. M., and Thompson, D. H. (1999) Cytosolic drug delivery using pH- and light-sensitive liposomes. *Adv. Drug Delivery Rev. 38*, 317–338.

(13) Drummond, D. C., Zignani, M., and Leroux, J. −C. (2000) Current status of pH-sensitive liposomes in drug delivery. *Prog. Lipid Res. 39*, 409–60.

(14) Zhu, J., Munn, R. J., and Nantz, M. H. (2000) Self-cleaving ortho ester lipids: A new class of pH-vulnerable amphiphiles. *J. Am. Chem. Soc. 122*, 2645–2646.

(15) Guo, X., and Szoka, F. C., Jr. (2001) Steric stabilization of fusogenic liposomes by a low-pH sensitive PEG-diortho ester-lipid conjugate. *Bioconjugate Chem. 12*, 291–300.

(16) Guo, X., MacKay, J. A., and Szoka, F. C., Jr. (2003) Mechanism of pH-triggered collapse of phosphatidylethanolamine liposomes stabilized by an ortho ester polyethyleneglycol lipid. *Biophys. J. 84*, 1784–95.

(17) Zhang, J. X., Zalipsky, S., Mullah, N., Pechar, M., and Allen, T. M. (2004) Pharmaco attributes of dioleoylphosphatidylethanolamine/cholesterylhemisuccinate liposomes containing different types of cleavable lipopolymers. *Pharmacol. Res. 49*, 185–198.

(18) Fattal, E., Couvreur, P., and Dubernet, C. (2004) Smart" delivery of antisense oligonucleotides by anionic pH-sensitive liposomes. *Adv. Drug Delivery Rev. 56*, 931–46.

(19) Sawant, R. M., Hurley, J. P., Salmaso, S., Kale, A., Tolcheva, E., Levchenko, T. S., and Torchilin, V. P. (2006) SMART" drug delivery systems: Double-targeted pH-responsive pharmaceutical nanocarriers. *Bioconjugate Chem. 17*, 943–949.

(20) Meers, P. (2001) Enzyme-activated targeting of liposomes. *Adv. Drug Delivery Rev. 53*, 265–72.

(21) Davidsen, J., Jorgensen, K., Andresen, T. L., and Mouritsen, O. G. (2003) Secreted phospholipase A(2) as a new enzymatic trigger mechanism for localised liposomal drug release and absorption in diseased tissue. *Biochim. Biophys. Acta, Biomembr. 1609*, 95–101.

(22) Andresen, T. L., Jensen, S. S., Kaasgaard, T., and Jorgensen, K. (2005) Triggered activation and release of liposomal prodrugs and drugs in cancer tissue by secretory phospholipase A2. *Curr. Drug Delivery 2*, 353–62.

(23) Sarkar, N., Banerjee, J., Hanson, A. J., Elegbede, A. I., Rosendahl, T., Krueger, A. B., Banerjee, A. L., Tobwala, S., Wang, R., Lu, X., Mallik, S., and Srivastava, D. K. (2008) Matrix metalloproteinase-assisted triggered release of liposomal contents. *Bioconjugate Chem. 19*, 57–64.

(24) Rosoff, M. (1996) *Vesicles*; Marcel Dekker: New York.

(25) Tang, F., and Hughes, J. A. (1998) Introduction of a disulfide bond into a cationic lipid enhances transgene expression of plasmid DNA. *Biochem. Biophys. Res. Commun. 242*, 141–145.

(26) Zalipsky, S., Qazen, M., Walker, J. A., 2nd, Mullah, N., Quinn, Y. P., and Huang, S. K. (1999) New detachable poly(ethylene glycol) conjugates: Cysteine-cleavable lipopolymers regenerating natural phospholipid, diacyl phosphatidylethanolamine. *Bioconjugate Chem. 10*, 703–7.

(27) Ong, W., Yang, Y., Cruciano, A. C., and McCarley, R. L. (2008) Redox-triggered contents release from liposomes. *J. Am. Chem. Soc. 130*, 14739–44.

(28) Zhang, Z. -Y., and Smith, B. D. (1999) Synthesis and characterization of NVOC-DOPE, a caged photoactivatable derivative of dioleoylphosphatidylethanolamine. *Bioconjugate Chem. 10*, 1150–2.

(29) Shum, P., Kim, J. -M., and Thompson, D. H. (2001) Phototriggering of liposomal drug delivery systems. *Adv. Drug Delivery Rev. 53*, 273–84.

(30) Bisby, R. H., Mead, C., and Morgan, C. G. (2000) Active uptake of drugs into photosensitive liposomes and rapid release on UV photolysis. *Photochem. Photobiol. 72*, 57–61.

(31) Bisby, R. H., Mead, C., and Morgan, C. G. (2000) Wavelength-programmed solute release from photosensitive liposomes. *Biochem. Biophys. Res. Commun. 276*, 169–73.
(32) Kobuke, Y., and Ohgoshi, A. (2000) Supramolecular ion channel containing trans-azobenzene for photocontrol of ionic fluxes. *Colloids Surf., A 169*, 187–197.
(33) Huang, Z., and Szoka, F. C., Jr. (2008) Sterol-modified phospholipids: Cholesterol and phospholipid chimeras with improved biomembrane properties. *J. Am. Chem. Soc. 130*, 15702–12.
(34) Huang, Z., Jaafari, M. R., and Szoka, F. C., Jr. (2009) Disteroylphospholipids: Nonexchangeable lipids and their application to liposomal drug delivery. *Angew. Chem., Int. Ed. 48*, 4146–9.
(35) Lee, S. -M., Chen, H. M., O'Halloran, T. V., and Nguyen, S. T. (2009) Clickable" polymer-caged nanobins as a modular drug delivery platform. *J. Am. Chem. Soc. 131*, 9311–9320.
(36) Mueller, A., and O'Brien, D. F. (2002) Supramolecular materials via polymerization of mesophases of hydrated amphiphiles. *Chem. Rev. 102*, 727–57.
(37) Ringsdorf, H., Schlarb, B., and Venzmer, J. (1988) Molecular architecture and function of polymeric oriented systems - models for the study of organization, surface recognition, and dynamics of biomembranes. *Angew. Chem., Int. Ed. Engl. 27*, 113–158.
(38) Fendler, J. H., and Tundo, P. (1984) Polymerized surfactant aggregates - characterization and utilization. *Acc. Chem. Res. 17*, 3–8.
(39) Higashi, N., Adachi, T., and Niwa, M. (1990) A novel 2-dimensional photopolymerization at an oriented bilayer surface - effective molecular-weight control using membrane state and chain transfer. *Macromolecules 23*, 1475–1480.
(40) Fukuda, H., Diem, T., Stefely, J., Kezdy, F. J., and Regen, S. L. (1986) Polymer-encased vesicles derived from dioctadecyldimethylammonium methacrylate. *J. Am. Chem. Soc. 108*, 2321–2327.
(41) Rostovtsev, V. V., Green, L. G., Fokin, V. V., and Sharpless, K. B. (2002) A stepwise Huisgen cycloaddition process: Copper(I)-catalyzed regioselective "ligation" of azides and terminal alkynes. *Angew. Chem., Int. Ed. 41*, 2596–2599.
(42) Kolb, H. C., Finn, M. G., and Sharpless, K. B. (2001) Click chemistry: Diverse chemical function from a few good reactions. *Angew. Chem., Int. Ed. 40*, 2004–2021.
(43) Finn, M. G., Kolb, H. C., Fokin, V. V., and Sharpless, K. B. (2008) Click chemistry - Definition and aims. *Prog. Chem. 20*, 1–4.
(44) Link, A. J., Vink, M. K. S., and Tirrell, D. A. (2004) Presentation and detection of azide functionality in bacterial cell surface proteins. *J. Am. Chem. Soc. 126*, 10598–10602.
(45) Baskin, J. M., Prescher, J. A., Laughlin, S. T., Agard, N. J., Chang, P. V., Miller, I. A., Lo, A., Codelli, J. A., and Bertozzi, C. R. (2007) Copper-free click chemistry for dynamic in vivo imaging. *Proc. Natl. Acad. Sci. U.S.A. 104*, 16793–7.
(46) Iha, R. K., Wooley, K. L., Nyström, A. M., Burke, D. J., Kade, M. J., and Hawker, C. J. (2009) Applications of orthogonal "click" chemistries in the synthesis of functional soft materials. *Chem. Rev. 109*, 5620–5686.
(47) Wu, P., Feldman, A. K., Nugent, A. K., Hawker, C. J., Scheel, A., Voit, B., Pyun, J., Frechet, J. M., Sharpless, K. B., and Fokin, V. V. (2004) Efficiency and fidelity in a click-chemistry route to triazole dendrimers by the copper(i)-catalyzed ligation of azides and alkynes. *Angew. Chem., Int. Ed. 43*, 3928–32.
(48) Helms, B., Mynar, J. L., Hawker, C. J., and Frechet, J. M. (2004) Dendronized linear polymers via "click chemistry. *J. Am. Chem. Soc. 126*, 15020–1.
(49) Ornelas, C., Ruiz Aranzaes, J., Cloutet, E., Alves, S., and Astruc, D. (2007) Click assembly of 1,2,3-triazole-linked dendrimers, including ferrocenyl dendrimers, which sense both oxo anions and metal cations. *Angew. Chem., Int. Ed. 46*, 872–7.
(50) O'Neil, E. J., DiVittorio, K. M., and Smith, B. D. (2007) Phosphatidylcholine-derived bolaamphiphiles via click chemistry. *Org. Lett. 9*, 199–202.
(51) Hassane, F. S., Frisch, B., and Schuber, F. (2006) Targeted liposomes: Convenient coupling of ligands to preformed vesicles using "click chemistry. *Bioconjugate Chem. 17*, 849–854.
(52) Ramakrishnan, B., Boeggeman, E., and Qasba, P. K. (2007) Novel method for in vitro O-glycosylation of proteins: Application for bioconjugation. *Bioconjugate Chem. 18*, 1912–1918.
(53) Smith, M. D., Sudhahar, C. G., Gong, D., Stahelin, R. V., and Best, M. D. (2009) Modular synthesis of biologically active phosphatidic acid probes using click chemistry. *Mol. Biosyst. 5*, 962–972.
(54) Jølck, R. I., Berg, R. H., and Andresen, T. L. (2010) Solid-phase synthesis of PEGylated lipopeptides using click chemistry. *Bioconjugate Chem. 21*, 807–810.
(55) Frisch, B., Hassane, F. S., and Schuber, F. (2010) Conjugation of ligands to the surface of preformed liposomes by click chemistry. *Methods Mol. Biol. 605*, 267–77.
(56) New, R. R. C. (1990) *Liposomes: A practical approach*, pp 131−134, Oxford University Press, Oxford.
(57) Because the trapping efficiencies for CF by different LUVs were not always the same, the end intensity also differed.
(58) Allen, T. M., and Cleland, L. G. (1980) Serum-induced leakage of liposome contents. *Biochim. Biophys. Acta 597*, 418–426.
(59) Mönkkönen, J., Liukkonen, J., Taskinen, M., Heath, T. D., and Urtti, A. (1995) Studies on liposome formulations for intraarticular delivery of clodronate. *J. Controlled Release 35*, 145–154.
(60) Lasic, D. D., and Barenholz, Y. (1996) *Handbook of nonmedical applications of liposomes*, pp 105−111, CRC Press, Boca Raton.
(61) Zhang, S. Y., and Zhao, Y. (2010) Facile synthesis of multivalent water-soluble organic nanoparticles via "surface clicking" of alkynylated surfactant micelles. *Macromolecules 43*, 4020–4022.
(62) Golas, P. L., Tsarevsky, N. V., Sumerlin, B. S., and Matyjaszewski, K. (2006) Catalyst performance in "click" coupling reactions of polymers prepared by ATRP: Ligand and metal effects. *Macromolecules 39*, 6451–6457.
(63) Saito, G., Swanson, J. A., and Lee, K.-D. (2003) Drug delivery strategy utilizing conjugation via reversible disulfide linkages: role and site of cellular reducing activities. *Adv. Drug Delivery Rev. 55*, 199–215.
(64) Russo, A., DeGraff, W., Friedman, N., and Mitchell, J. B. (1986) Selective modulation of glutathione levels in human normal versus tumor-cells and subsequent differential response to chemotherapy drugs. *Cancer Res. 46*, 2845–2848.
(65) Mellman, I., Fuchs, R., and Helenius, A. (1986) Acidification of the endocytic and exocytic pathways. *Annu. Rev. Biochem. 55*, 663–700.
(66) Helmlinger, G., Schell, A., Dellian, M., Forbes, N. S., and Jain, R. K. (2002) Acid production in glycolysis-impaired tumors provides new insights into tumor metabolism. *Clin. Cancer Res. 8*, 1284–1291.
(67) Trevani, A. S., Andonegui, G., Giordano, M., López, D. H., Gamberale, R., Minucci, F., and Geffner, J. R. (1999) Extracellular acidification induces human neutrophil activation. *J. Immunol. 162*, 4849–4857.
(68) Engin, K., Leeper, D. B., Cater, J. R., Thistlethwaite, A. J., Tupchong, L., and Mcfarlane, J. D. (1995) Extracellular pH distribution in human tumors. *Int. J. Hyperthermia 11*, 211–216.
(69) Smolarsky, M., Teitelbaum, D., Sela, M., and Gitler, C. (1977) Simple fluorescent method to determine complement-mediated liposome immune lysis. *J. Immunol. Methods 15*, 255–265.
(70) Ellens, H., Bentz, J., and Szoka, F. C. (1984) pH-Induced destabilization of phosphatidylethanolamine-containing liposomes: role of bilayer contact. *Biochemistry 23*, 1532–8.

Supporting Information

Controlled Release from Cleavable Polymerized Liposomes upon Redox and pH Stimulation

Shiyong Zhang and Yan Zhao*

Department of Chemistry, Iowa State University, Ames, Iowa 50011-3111, USA

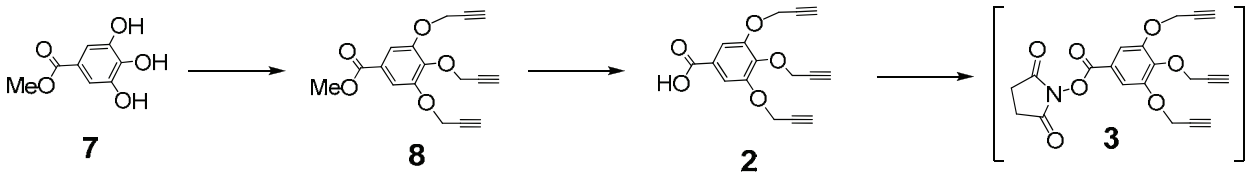
General Method

All reagents and solvents were of A.C.S.-certified grade or higher, and were used as received from commercial suppliers. Millipore water was used in all aqueous experiments. All glassware and syringes were dried in an oven at least overnight prior to use. NMR spectra were recorded on a BRUKER DRX-400 or a VARIAN VXR-400 spectrometer. ESI-MS was performed on a FINNIGAN TSQ700 mass spectrometer. Fluorescence spectra were recorded at ambient temperature on a VARIAN Cary Eclipse Fluorescence spectrophotometer.

Caution: *Small organic azides are potentially explosive* and must be handled with care and avoid high temperatures, particularly in concentrated forms and/or in large quantities.

Synthesis

Scheme 1S



Methyl 3,4,5-Triproparyloxybenzoate (8).[1] A mixture of methyl 3,4,5-trihydroxybenzoate (**7**, 1.84 g, 10 mmol), propargyl bromide (80% wt in toluene, 3.4 mL, 31 mmol), K_2CO_3 (5.53 g, 40 mmol), and 18-crown-6 (13.2 mg, 0.05 mmol) in acetone (50 mL) was heated to reflux for 24 h. The solid was removed by filtration and the acetone was removed by rotary evaporation. Water (50 mL) was added and the mixture was extracted with CH_2Cl_2. The organic phase was dried over Na_2SO_4 and the solvent was removed *in vacuo* to give the desired product as a white powder (2.63 g, 88 %). ^{1}H NMR (400 MHz, $CDCl_3$, δ): 7.47 (s, 2H), 4.83-4.80 (m, 6H), 3.91 (s, 3H), 2.53 (s, 2H), 2.46 (s, 1H).

3,4,5-Triproparyloxybenzoic Acid (2). Compound **8** (2.63 g, 8.8 mmol) was dissolved in MeOH (100 mL). A solution of 2 M LiOH (22 mL) in water as added. The reaction mixture was stirred at room temperature for 12 h and monitored by TLC. The solvent was removed by rotary evaporation and HCl (2.0 M) was added to the mixture to adjust the pH ≈ 2. The mixture was extracted with EtOAc. The organic phase was dried over Na_2SO_4 and the solvent was removed *in vacuo* to afford **2** as a white powder (2.22 g, 89%). ^{1}H NMR (400 MHz, DMSO-*d6*, δ): 7.38 (s, 2H), 4.89 (d, *J* = 2.4 Hz, 4H), 4.72 (d, *J* = 2.4 Hz, 2H), 3.62 (t, *J* = 2.0 Hz, 2H), 3.48 (t, *J* = 2.4 Hz, 1H).

Lipid 1. Compound **2** (284 mg, 1.00 mmol), *N*-hydroxysuccinimide (115.1 mg**,** 1.00 mmol), and 1,3-dicyclohexylcarbodiimide (DCC, 206.3 mg, 1.00 mmol) were dissolved in 10 mL of CH_3CN. The mixture was stirred at room temperature for 6 h. The precipitate was removed by filtration and the filtrate evaporated to dryness, affording compound **3** as a light yellow powder (377.5 mg, 99%). A portion of this compound (27.9 mg, 0.0731 mmol), diisopropylethylamine (61 μL, 0.348 mmol), and 1-palmitoyl-2-oleoyl-*sn*-glycero-3-phosphoethanolamine (POPE, 50 mg in 2

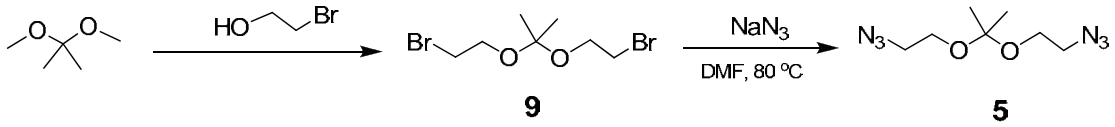
[1] Camponovo, J.; Ruiz, J.; Cloutet, E.; Astruc, D. *Chem.–Eur. J.* **2009**, *15*, 2990–3002.

mL $CHCl_3$, 0.0696 mmol) were dissolved in 4 mL of CH_3Cl_3/MeOH (2:1, v/v). The mixture was stirred at room temperature for 24 h. The solvents were removed by rotary evaporation and the product was purified by preparative TLC with $CHCl_3$/MeOH = 7/1 as the developing solvents to give a viscous liquid (37.5 mg, 55%). ^{1}H NMR (400 MHz, $CDCl_3/CD_3OD$ = 1:1, δ): 7.30 (s, 2H), 5.33 (b, 2H), 5.3 (b, 1H), 4.79-4.76 (m, 6H), 4.33-4.31 (m, 1H), 4.11-4.06 (m, 1H), 3.96-3.92 (m, 4H), 3.59 (s, 2H), 2.69 (s, 2H), 2.58 (s, 1H), 2.26 (b, 4H), 1.99 (d, *J* = 5.2 Hz, 4H), 1.55 (b, 4H), 1.23 (s, 48H), 0.86 (t, *J* = 6.0 Hz, 3H). ^{13}C NMR (100 MHz, CD_3OD, δ): 175.0, 174.95, 174.66, 152.96, 141.23, 130.99, 130.90, 109.23, 79.90, 79.40, 77.58, 77.02, 63.78, 61.14, 58.27, 55.88, 43.87, 35.25, 35.06, 33.24, 30.99, 130.83, 30.79, 30.65, 30.64, 30.53, 30.43, 30.38, 30.35, 28.33, 26.17, 23.91, 14.65, 13.32. ESI-MS (*m/z*): [M^-], calcd for $C_{55}H_{85}NO_{12}P^-$ 983, found 983.

Compound 4.[2] Triflic anhydride (1.3 mL, 10 mmol) was added over 5 min to a mixture of sodium azide (2.1 g, 10 mmol) in H_2O (10 mL) and CH_2Cl_2 (15 mL) at 0 °C. After the mixture was stirred for 3 h, the organic phase was separated. The aqueous layer was extracted with CH_2Cl_2 (2 × 10 mL). The combined organic phases were cooled by an ice bath and washed once with saturated Na_2CO_3 and added to a solution of L-cystine (0.24 g, 1 mmol), K_2CO_3 (0.41 g, 3 mmol), and $CuSO_4 \cdot 5H_2O$ (5.0 mg, 0.02 mmol) in H_2O (10 mL) and CH_3OH (10 mL). The mixture was stirred at room temperature overnight. The organic solvents were removed by rotary evaporation. The aqueous slurry was diluted with H_2O (50 mL) and acidified to pH 6 with concentrated HCl. The mixture was diluted with 0.25 M pH 6.2 phosphate buffer (100 mL) and extracted with EtOAc (4 × 50 mL) to remove the sulfonamide byproduct. The aqueous phase was then acidified to pH 2 with concentrated HCl and extracted with EtOAc (5 × 50 mL). The combined organic phases were dried ($MgSO_4$), and concentrated *in vacuo* to give a light yellow oil (34 mg, 12%). ^{1}H NMR (400 MHz, CD_3OD, δ): 4.37-4.34 (m, 2H), 3.30-3.28 (m, 2H), 3.08-3.02 (m, 2H); ^{13}C NMR (100 MHz, CD_3OD, δ): 172.73, 63.03, 41.78; High resolution EI-MS (*m/z*): calcd for $C_6H_8N_6O_4S_2$, 292.0048; found 292.0053.

[2] Lundquist, J.T., Pelletier, J. C. *Org. Lett.* **2001**, *3*, 781-783.

Scheme 2S



9 **5**

Compound 9. A mixture of 2-bromoethanol (5.0 mL, 6.6 mol), 2,2-dimethoxypropane (4.0 mL, 3.0 mol), benzene (16 mL), and *p*-toluenesulfonic acid (5.0 mg) were placed into a 50 mL round-bottomed flask fitted with a fractional distillation head. The mixture was heated with an oil bath. When the fraction at 62–65 ^{o}C started to distill, the oil bath was removed and the mixture was cooled to room temperature. A solution of sodium methoxide (0.1 g) in methanol (2 mL) was added rapidly under stirring. The distillation was resumed and the fraction at 80–83 ^{o}C was collected. The crude product was a 50:50 mixture of 2-bromoethanol and the desired product, as indicated by ^{1}H NMR spectroscopy, and was used in the next step without further purification.

Compound 5. A mixture of crude **9** (2.32 g, ca. 5.6 mmol), sodium azide (5.2 g, 80 mmol), and DMF (20 mL) was stirred at 80 °C for 10 h. The mixture was poured into water and the mixture was extracted with hexane (3 × 50 mL). The combined organic phases were washed with brine, dried over anhydrous Na_2SO_4, and concentrated *in vacuo* to give a yellow oil (0.87 g, 73%). ^{1}H NMR (400 MHz, $CDCl_3$, δ): 3.66 (t, J = 4.0 Hz, 4H), 3.39 (t, J = 4.0 Hz, 4H), 1.40 (s, 6H).

Preparation of CF-Containing LUVs. A solution of POPC (3.0 mg, 0.004 mmol) and lipid **1** (3.9 mg, 0.004 mmol) in chloroform (0.3 mL) was placed in a 10 mL test tube and dried under a stream of nitrogen. The residue was dried further under high vacuum overnight. The resulting lipid film was hydrated in 10 mM HEPES buffer (0.3 mL, 50 mM CF, 10 mM NaCl, pH = 7.4) for 30 min with occasional vortexing. The opaque dispersion was subjected to ten freeze–thaw cycles. The resulting mixture was extruded twenty-nine times through a polycarbonate filter (diameter = 19 mm, pore size = 100 nm) at room temperature using an Avanti Mini-Extruder. A portion (0.1 mL) of the liposome solution was passed through a column of Shepadex G-50 using 10 mM HEPES buffer (pH = 7.4) containing 107 mM NaCl as the eluent. The liposome fractions were combined and diluted to 5.0 mL with the same HEPES buffer. The concentration of the total phospholipids in the stock solution was 5.3×10^{-4} M.

Polymerization of LUVs. To the liposome solution (1 mL), cross-linker **4** (10 μL of 0.04 M aqueous solution, 0.4 μmol), Cu-complex (10 μL of 0.053 M aqueous solution, 0.53 μmol),[3] and sodium ascorbate (10 μL of 27 mg/mL aqueous solution, 1.4 μmol) were added. The reaction mixture was slowly stirred at room temperature for 24 h. A portion (0.2 mL) of the CPLs solution was passed through a column of Shepadex G-50 using 10 mM HEPES buffer (pH = 7.4) containing 107 mM NaCl as the eluent. The liposome fractions were combined and diluted to 5.0 mL with the same HEPES buffer. The concentration of the total phospholipids in the stock solution was 2.12×10^{-5} M. Our experiments showed that the minute amount of copper ions in the reaction mixture did not affect the results of the leakage assays if the leakage experiment was performed immediately after the click polymerization.

CF Leakage Assay. An aliquot (40.0 μL) of the above liposomal solution was added to 1.96 mL of 10 mM HEPES buffer (pH = 7.4) containing the appropriate concentration of NaCl.[4] The lipid concentration in the sample was 4.8 μM. The fluorescence emission at 520 nm (λ_{ex} = 492 nm) was measured overtime. At the end of the assay, 40 μL of Triton X-100 (1%) was added, disrupting the vesicles and releasing the remaining CF (100% release). The percent leakage at any given time was calculated using Eq. (1), in which I_0 and I_t are the initial and intermediate emission intensity, respectively.

$$\% \text{ leakage} = (I_t - I_0)/(I_\infty - I_0) \times 100 \quad (1)$$

Preparation of ANTS/DPX-Containing LUVs. A typical procedure is as follows. A solution of POPC (4.0 mg, 0.0053 mmol) and lipid **1** (2.7 mg, 0.0027 mmol) in chloroform (0.3 mL) was placed in a 10 mL test tube and dried under a stream of nitrogen. The residue was dried further under high vacuum overnight. The resulting lipid film was hydrated in 5 mM TES buffer (12.5 mM ANTS, 45.0 mM DPX, 20 mM NaCl, pH = 7.0) for 30 min with occasional vortexing. The opaque dispersion was subjected to ten freeze–thaw cycles. The resulting mixture was extruded twenty-nine times through a polycarbonate filter (diameter = 19 mm, pore size = 100 nm) at room temperature using an Avanti Mini-Extruder. A portion (0.1 mL) of the liposome solution

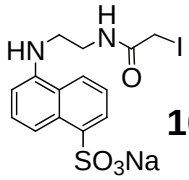
[3] The preparation of the stock solution of the Cu-complex is as follows: To a 3 mL aqueous solution of $CuCl_2$ (71.3 mg, 0.53 mmol) was added 3 mL of an aqueous solution of PMDETA (442 μL, 2.1 mmol). The resulting blue solution was stirred for 2 h and then diluted to 10 mL with water. The concentration of the Cu-complex in the stock solution was 0.053 M.

[4] The concentration of NaCl was 107 mM for the 100 h assay and 5 M for the accelarated assay.

was passed through a column of Shepadex G-50 using 5 mM TES buffer (pH = 7.0) containing 100 mM NaCl as the eluent. The liposome fractions were combined and diluted to 5.0 mL with the same TES buffer. The concentration of the total phospholipids in the stock solution was 5.3×10^{-4} M.

ANTS/DPX Leakage Assay. An aliquot (100 μL) of the above liposomal solution was added to 1.90 mL of the appropriate buffer.[5] The fluorescence emission at 510 nm (λ_{ex} = 353 nm) was measured overtime. After 24 h, 40 μL of Triton X-100 (1%) was added, disrupting the vesicles and releasing the remaining CF (100% release). The percent leakage at any given time was calculated using equation (1).

Polymerization and Labeling of LUVs. A solution of POPC (4.0 mg, 0.0053 mmol) and lipid **1** (2.7 mg, 0.0027 mmol) in chloroform (0.3 mL) was placed in a 10 mL test tube and dried under a stream of nitrogen. The residue was dried further under high vacuum overnight. The resulting lipid film was hydrated in 10 mM HEPES buffer (0.3 mL, 50 mM CF, 10 mM NaCl, pH = 7.4) for 30 min with occasional vortexing. The opaque dispersion was subjected to ten freeze–thaw cycles. The resulting mixture was extruded twenty-nine times through a polycarbonate filter (diameter = 19 mm, pore size = 100 nm) at room temperature using an Avanti Mini-Extruder. The resulting liposome solution was diluted to 4 mL with the same buffer. The concentration of **1** in the stock solution was 6.75×10^{-4} M. Separately, a commercially available dye, 1,5-I-AEDANS (**10**, 4.3 mg, 0.010 mmol), was allowed to react with sodium azide (1.0 mg, 0.12 mmol) in water (1 mL) for 12 h. Aliquots of the resulting solution (10 mM, 14 μL, 0.14 μmol), cross-linker **4** (10 μL of 20 mg/mL aqueous solution, 0.675 μmol), Cu-complex (10 μL of 0.034 M aqueous solution, 0.34 μmol),[3] and sodium ascorbate (10 μL of 27 mg/mL aqueous solution, 1.4 μmol) were added to the liposomal solution (1 mL). After 24 h, the mixture was passed through a column of Sephadex G-50 with 10 mM HEPES buffer (107 mM NaCl, pH=7.4) as the eluent. The liposome fractions were combined and diluted to 5.0 mL with the same HEPES buffer. A portion (2.5 mL) or the resulting solution was placed in a plastic cuvette for fluorescence measurement (λ_{ex} = 345 nm). The control LUVs were prepared exactly the same as the click-labeled LUVs except that no copper catalyst and sodium ascorbate were added in the process.



10

[5] pH = 7.0: 5 mM TES, 100 mM NaCl; pH = 6.0: 10 mM PBS, 5 M NaCl; pH = 5.0: 10 mM acetate, 5 M NaCl; pH=4.0: 10 mM acetate, 5 M NaCl.

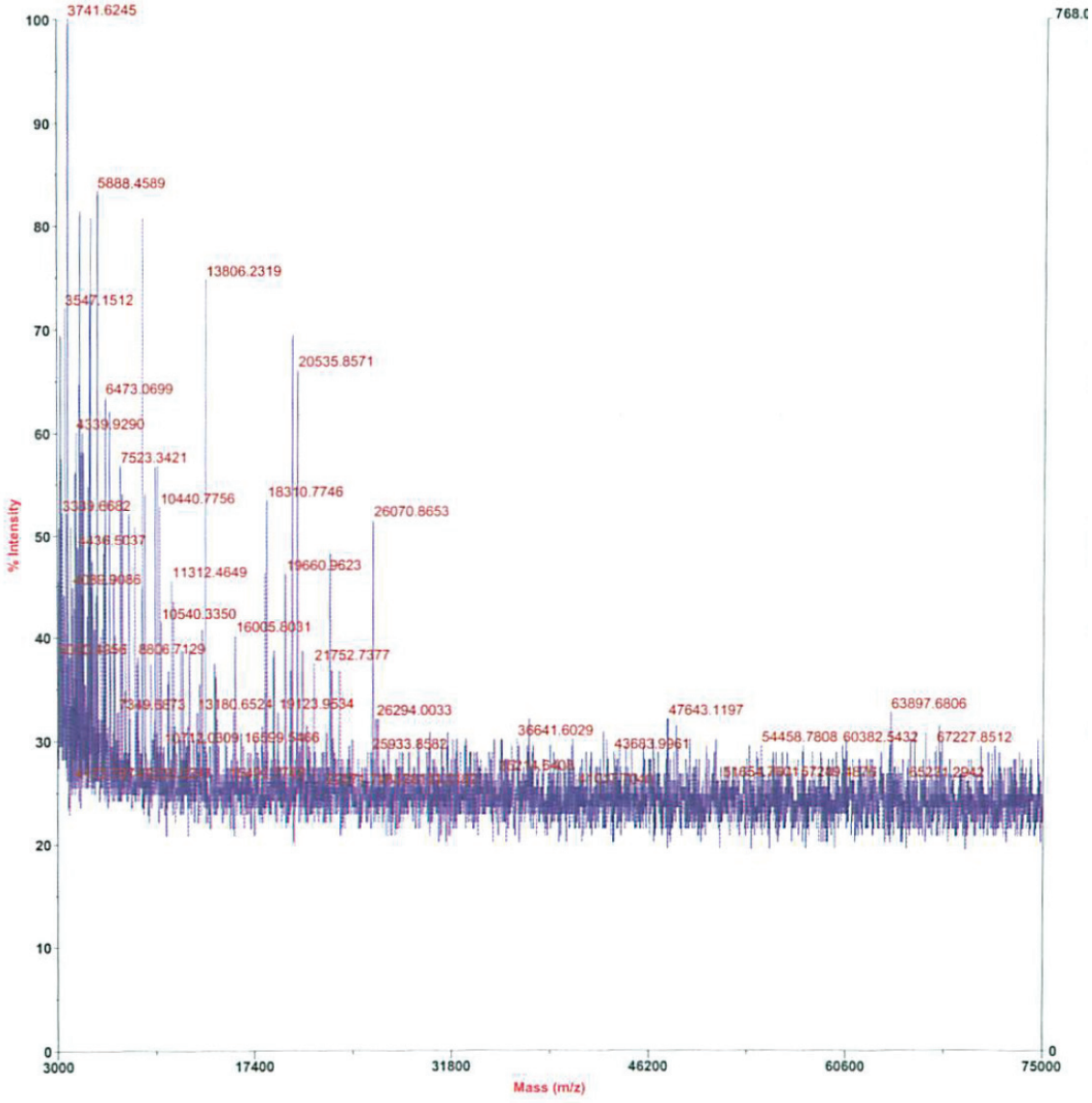


Figure 1S. MALTI-TOF mass spectrum of the CPLs prepared with [**1**]/[POPC] = 1:1.

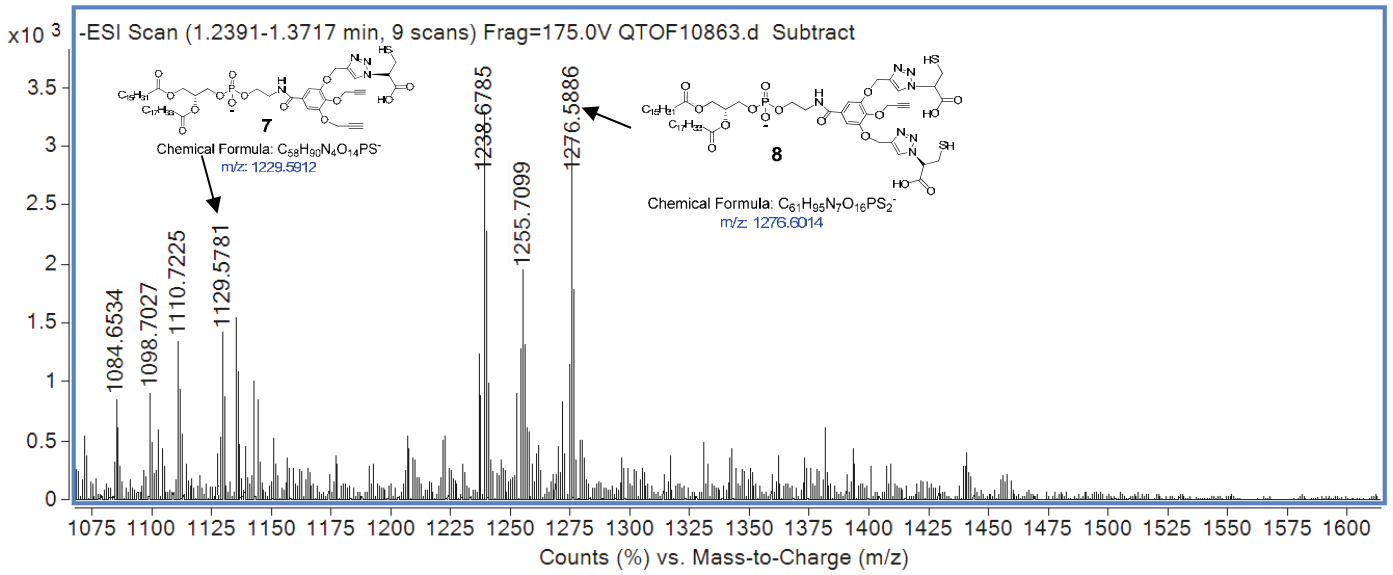
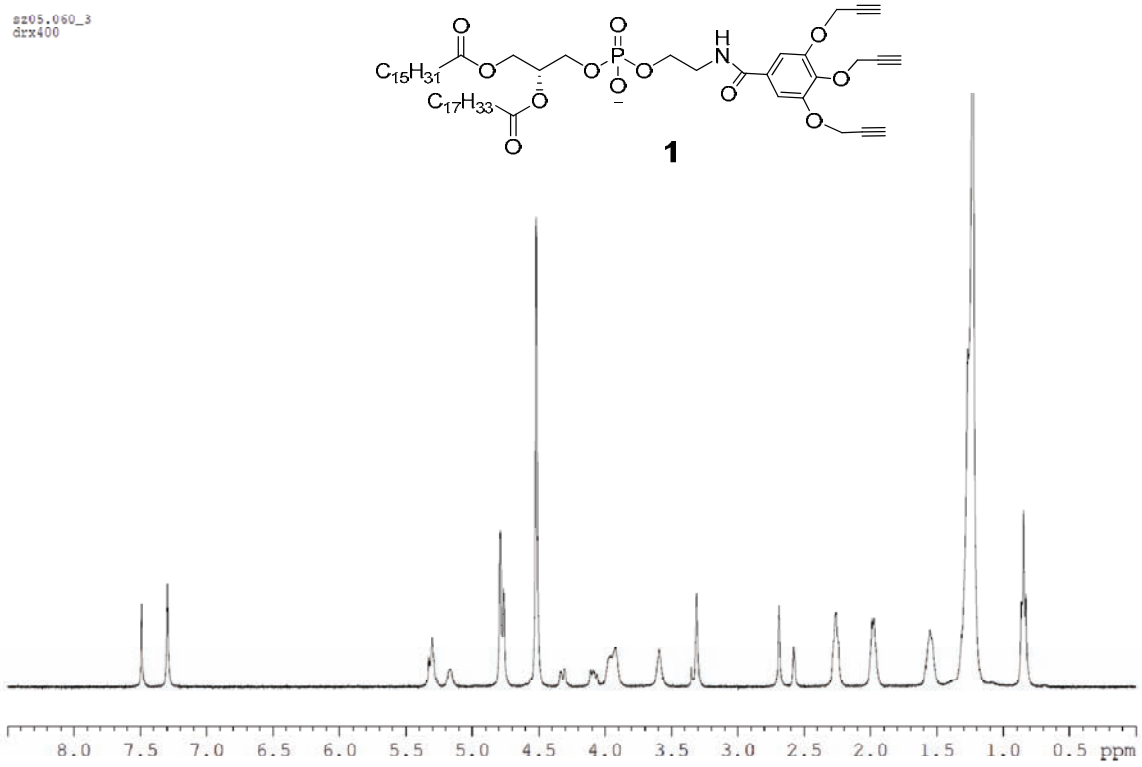
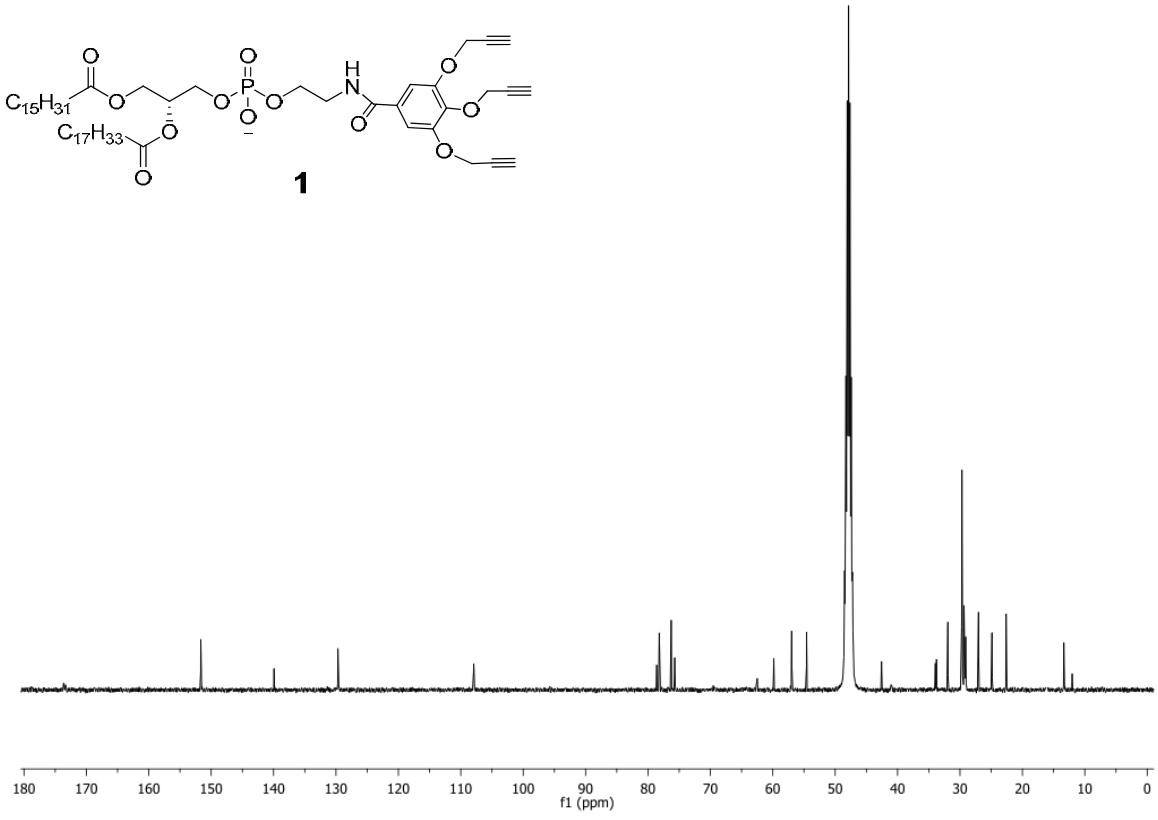
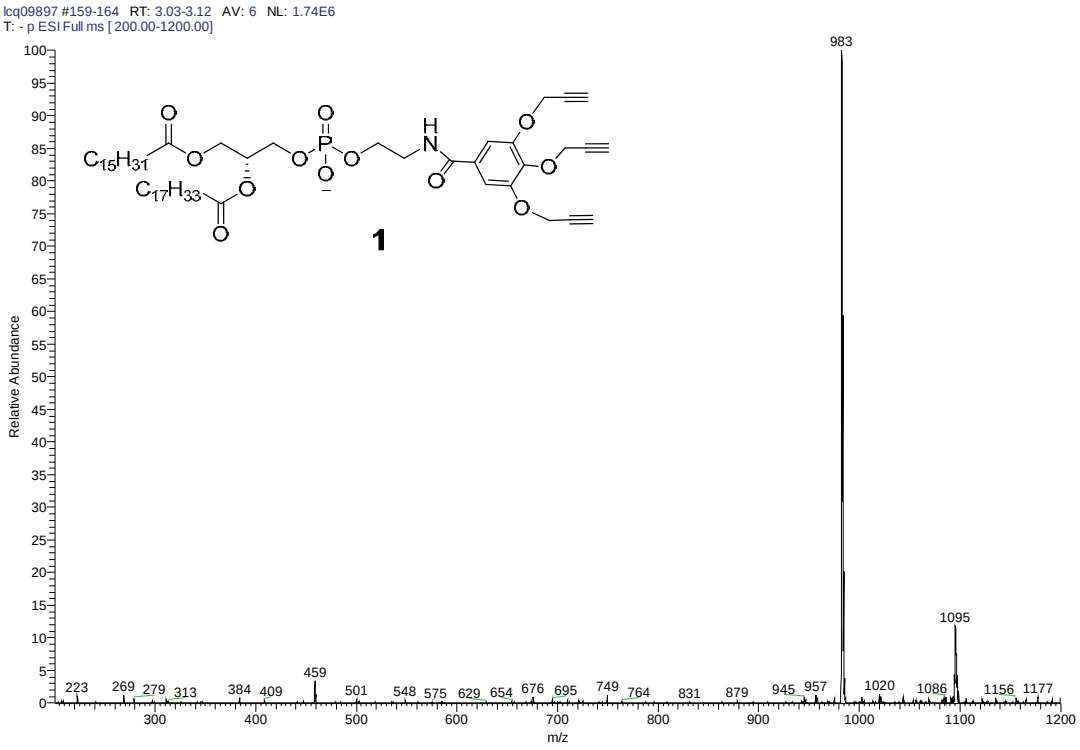
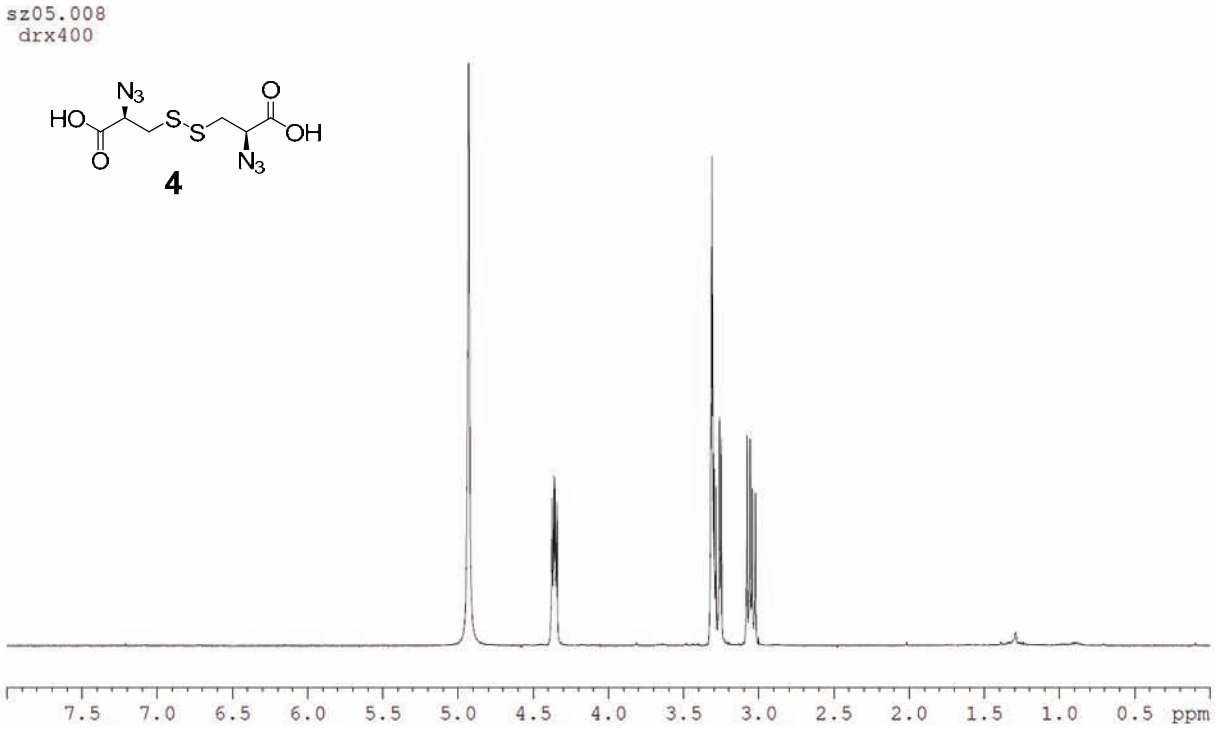


Figure 2S. ESI mass spectrum of the depolymerized CPLs. Depolymerization was accomplished by incubation of the CPLs with 0.3 mM of DTT for 24 h at room temperature.

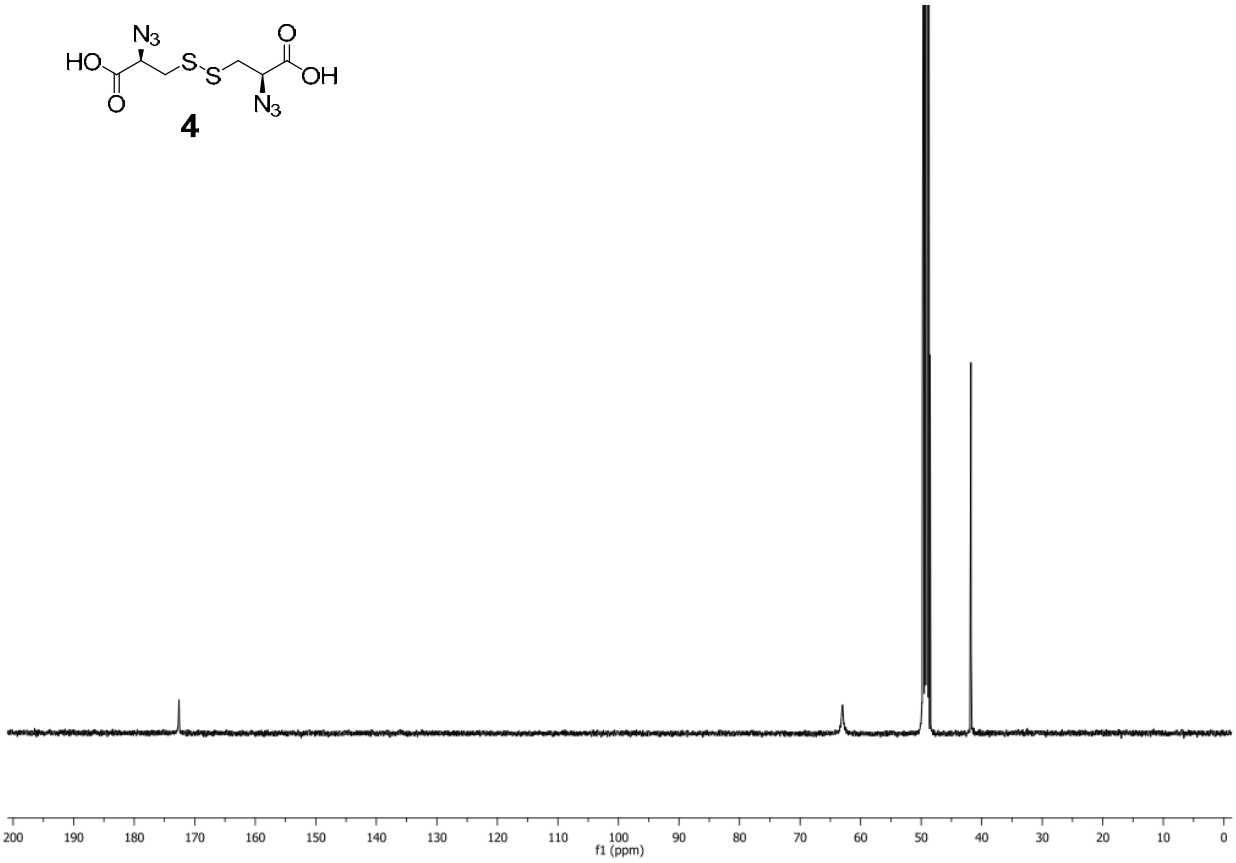

sz05.060_3
drx400
1
8.0 7.5 7.0 6.5 6.0 5.5 5.0 4.5 4.0 3.5 3.0 2.5 2.0 1.5 1.0 0.5 ppm


1
180 170 160 150 140 130 120 110 100 90 80 70 60 50 40 30 20 10 0
f1 (ppm)

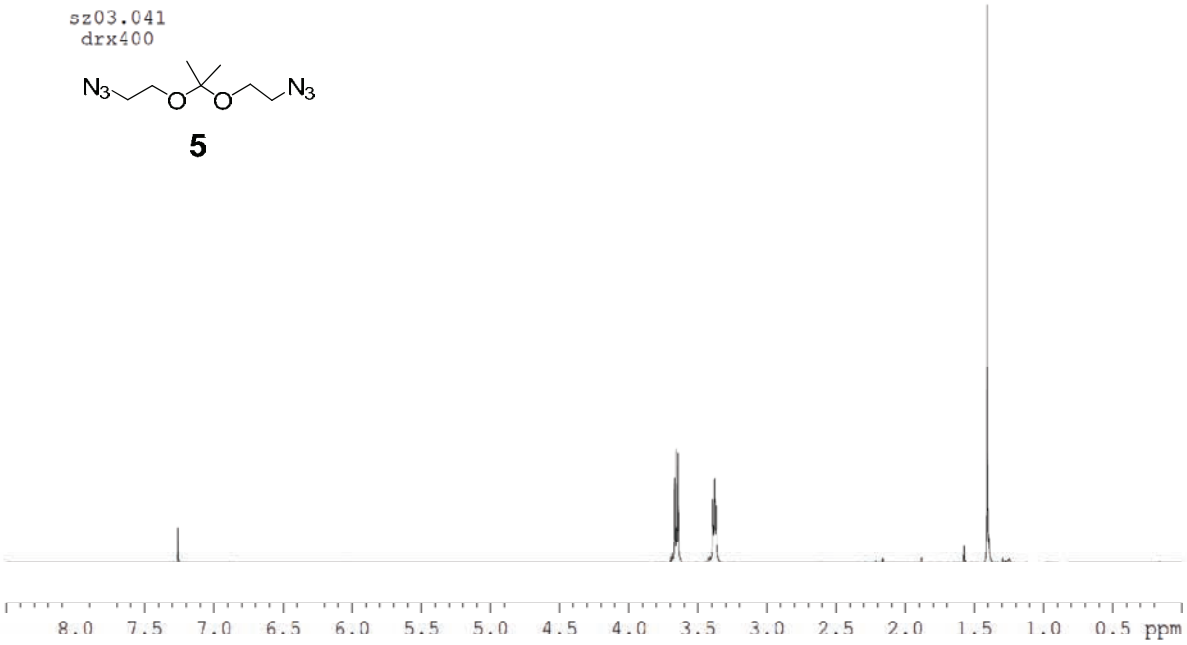

lcq09897 #159-164 RT: 3.03-3.12 AV: 6 NL: 1.74E6
T: - p ESI Full ms [200.00-1200.00]
Relative Abundance
m/z
983
1095
459
1
C15H31
C17H33


sz05.008
drx400
4
7.5 7.0 6.5 6.0 5.5 5.0 4.5 4.0 3.5 3.0 2.5 2.0 1.5 1.0 0.5 ppm

4


200
190
180
170
160
150
140
130
120
110
100
90
80
70
60
50
40
30
20
10
0
f1 (ppm)

5


sz03.041
drx400
8.0
7.5
7.0
6.5
6.0
5.5
5.0
4.5
4.0
3.5
3.0
2.5
2.0
1.5
1.0
0.5
ppm

Bioconjugate Chemistry

COMMUNICATION

pubs.acs.org/bc

Glycated AAV Vectors: Chemical Redirection of Viral Tissue Tropism

Eric D. Horowitz,[†] Marc S. Weinberg,[†] and Aravind Asokan*[,†,‡,§]

[†]Gene Therapy Center

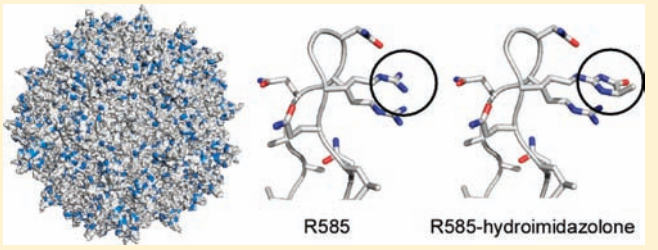
[‡]Department of Genetics

[§]Molecular and Cellular Biophysics Program

University of North Carolina at Chapel Hill

Supporting Information

ABSTRACT: A chemical approach for selective masking of arginine residues on viral capsids featuring an exogenous glycation reaction has been developed. Reaction of adeno-associated viral (AAV) capsids with the α-dicarbonyl compound, methylglyoxal, resulted in formation of arginine adducts. Specifically, surface-exposed guanidinium side chains were modified into charge neutral hydroimidazolones, thereby disrupting a continuous cluster of basic amino acid residues implicated in heparan sulfate binding. Consequent loss in heparin binding ability and decrease in infectivity were observed. Strikingly, glycated AAV retained the ability to infect neurons in the mouse brain and were redirected from liver to skeletal and cardiac muscle following systemic administration in mice. Further, glycated AAV displayed altered antigenicity demonstrating the potential for evading antibody neutralization. Generation of unnatural amino acid side chains through capsid glycation might serve as an orthogonal strategy to engineer AAV vectors displaying novel tissue tropisms for gene therapy applications.



Protein engineering tools have played a central role in understanding structure-function correlations of viruses.[1,2] The application of site directed mutagenesis to elucidate the structural basis of virus-receptor interactions is particularly noteworthy in this regard.[3,4] Altering virus-receptor interactions by selective incorporation of unnatural amino acids or chemical masking of amino acid residues, exposed on the viral capsid surface, could greatly expand the ability to discover receptor footprints on viral capsid surfaces, as well as design new viral vectors and vaccines.

Several studies exploring the genetic incorporation of unnatural amino acids and/or chemoselective ligation to viral capsids have been reported.[5] For instance, viral capsids containing unnatural amino acids with alkyne,[5] azide,[5] or aminophenyl[6] side chains have been generated for coupling of drugs and/or targeting ligands. Synthetic strategies for chemoselective ligation to naturally occurring amino acid residues such as Lys, Glu, Cys, Trp, and Tyr on the surface of viral capsids have also been developed.[7−11] However, the application of such chemistries toward reengineering viruses for gene delivery remains unexplored thus far.

In the current study, we focused on exploiting the naturally occurring chemical reaction involving α-dicarbonyl compounds with proteins, which leads to the formation of advanced glycation end-products (AGE).[12] We hypothesized that methylglyoxal, an intermediate of the Maillard reaction, will selectively form adducts with the guanidinium side chain of surface-exposed Arg residues on viral capsids (Scheme 1). The reaction proceeds readily in aqueous solution and has been shown to predominantly modify Arg residues in various proteins with high efficiency. Proteomic analysis of Arg adducts has previously demonstrated the formation of dihydroxyimidazolidines followed by subsequent rearrangement into hydroimidazolones.[13,14]

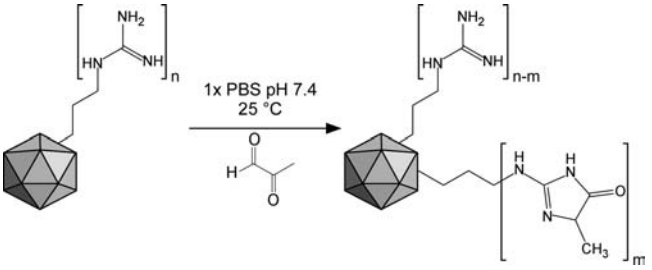
AAV is a small nonenveloped ssDNA virus that is rapidly gaining momentum as a vector in human gene therapy applications.[15] The AAV capsid is composed of 60 capsid protein subunits assembled in icosahedral symmetry ($T = 1$). Each capsid protein subunit contains a β-barrel core with long loops between the β-strands that create striking surface features. Surface spikes located at the threefold symmetry axes are most prominent and have been implicated in receptor binding and cell entry. The remarkable plasticity of the AAV virion shell has been demonstrated through extensive mutagenesis studies.[15]

Of several strains isolated to date, AAV serotype 2 is the most studied and binds to its primary receptor heparan sulfate using a basic cluster of amino acids (R484, R487, K532, R585, and R588) located at the threefold axis of symmetry.[16,17] Previous site-directed mutagenesis studies have demonstrated the critical role played by this continuous basic patch in cell surface recognition as well as liver tropism in mice.[18,19] In particular, mutation of Arg

Received: November 1, 2010
Revised: February 8, 2011
Published: March 09, 2011

ACS Publications © 2011 American Chemical Society

Scheme 1. Glycation of AAV Vectors with Methylglyoxal



residues within this basic cluster has been shown to confer muscle tropism. However, the potential for generating atypical tissue tropisms through the latter approach is restricted by the ability to only incorporate naturally occurring amino acids with limited side chain diversity.

We hypothesized that an orthogonal approach based on selective chemical masking of Arg residues with α-dicarbonyl compounds would enable display of unnatural amino acid residues with diverse functional groups on the AAV capsid surface. Such modification of amino acid side chains might enable design of viral vectors displaying atypical tissue tropisms. As proof of principle, we chose methylglyoxal (MGO), a highly reactive compound derived from glycolysis and known for its propensity to form Arg and Lys adducts.[14] It should be noted that chemical conjugation to Lys residues on AAV2 capsids are routinely carried out and demonstrate no adverse effect on capsid infectivity.[20]

Overnight reaction of AAV2 with methylglyoxal at neutral pH produced glycated AAV vectors. Characterization of the glycated vectors was carried out using MALDI-TOF/MS of trypsin-treated capsid proteins. Rationale for such analysis is based on earlier observations that altered tryptic digestion of glycated proteins enables proteomic analysis of MGO adducts.[13] Tryptic fragments obtained from the major AAV capsid protein subunit (VP3; Genbank# AAC03779.1) were subject to MALDI-TOF/MS analysis. Peak signals were normalized to that of a peptide fragment located within the capsid interior[16] containing residues L299 through K309 (m/z = 1375.7), which are expected to remain unmodified when subject to glycation. Analysis of mass spectra using the MASCOT search engine revealed a decrease in peak signal intensities corresponding to peptide fragments containing Arg residues and, to a lesser extent, Lys residues (Supporting Information). Specifically, the MGO-derived hydroimidazolone adduct is expected to add 54 m/z units to the modified peptide fragment. New peak signals, observed between m/z 2400 and 2600 were specifically assigned to peptide fragments containing hydroimidazolone adducts at R585 and R459 positions (Figure 1a). Computation of the ratio of peak signal intensities pertaining to the latter residues before and after glycation indicates that 29.5% of R585 and 58.9% of R459 residues are glycated. Although the latter results indicate the potential formation of mixtures of variably glycated capsids and are semiquantitative in nature, we have optimized chemical modification of AAV vectors to consistently generate the same phenotype (Supporting Information). Moreover, the aforementioned results are in agreement with earlier studies and corroborate the notion that surface-exposed Arg residues on proteins are preferred targets for glycation.[13,14]

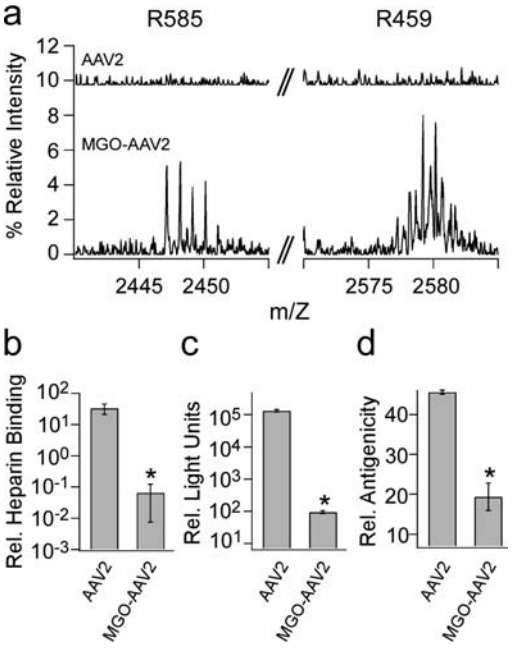


Figure 1. (a) Tryptic digestion of chemically modified AAV2 VP3 capsid proteins demonstrates two preferred sites for Arg adduct formation. The increase in signal at m/z 2446.1 and 2577.2 corresponds to the hydroimidazolone adduct at R585 and R459 positions within the peptides 566-TTNPVATEQYGSVSTNLQRGNR-588 (expected adduct m/z = 2446.173) and 448-TNTPSGTTTQSRLQFSQAGAS-DIR-471 (expected adduct m/z = 2577.231), respectively. (b) Solid-phase binding assay of unmodified and glycated AAV2 capsids to heparin-coated plates. Binding is relative to the charge neutral dextran. (c) In vitro infectivity assay of unmodified and glycated AAV2 in HEK293 cells (10 000 viral genomes/cell). (d) Solid-phase binding assay of unmodified and glycated AAV2 capsids to plates coated with the monoclonal antibody A20. Binding is relative to an isotype-matched antibody control. Error bars represent standard deviation (n = 3). Asterisks represent statistical significance ($p < 0.05$). Additional experimental details available in Supporting Information.

The ability of glycated AAV2 to bind heparin was determined using a streptavidin-coated 96-well assay plate coated with biotinylated heparin. Binding was determined using Q-PCR and binding to biotinylated dextran was utilized as a control. Glycated AAV2 capsids display a significant loss ($p < 0.05$) in heparin binding ability in comparison with unmodified AAV2 capsids (Figure 1b). Further, MGO-modified AAV2 vectors demonstrate an approximately 1000-fold decrease in gene transfer efficiency in HEK293 cells (Figure 1c). These results corroborate the notion that glycated AAV2 is unable to bind its cognate attachment receptor, heparan sulfate.[21] Of the five residues (R484, R487, K532, R585, and R588) located within the heparan sulfate receptor footprint, R585 or R588 has been shown to be indispensable for heparin binding and infectivity.[18,19] Taken together with MS data, the aforementioned results suggest that conversion of the guanidinium side chain of R585 into the hydroimidazolone derivative likely disrupts the heparan sulfate footprint on the AAV2 capsid surface. It should also be noted that, although glycation of R459 was observed, this residue has not been implicated in heparin binding or infectivity.[18,19]

Another observation supporting the chemical masking of arginine residues within surface-exposed domains is the altered antigenicity of glycated AAV2 vectors. Using a solid-phase

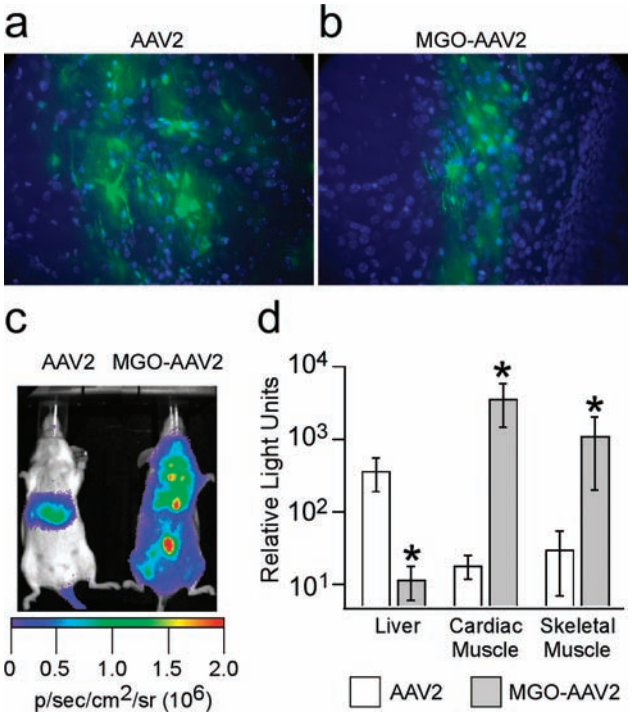


Figure 2. Epifluorescence images of neuronal GFP expression in 40 μm brain sections obtained from BALB/c mice injected intracranially with 7.5×10^8 (a) untreated AAV2 and (b) MGO-treated AAV2 vectors. Brain sections were taken 2 weeks post-injection and stained with DAPI prior to imaging. (c) Live animal bioluminescent images of BALB/c mice ($n = 3$) injected with untreated and MGO-treated AAV2 vectors. Mice were injected via tail vein at a dose of 5×10^{10} viral particles. Mice were imaged 4 weeks post-injection. Changes in luciferase expression patterns indicate altered tissue tropism profiles and are represented on a rainbow scale. (d) Luciferase expression from untreated and MGO-treated AAV2 vectors in different tissue lysates. Relative light units represent luciferase transgene expression and levels are normalized to tissue mass. Error bars represent standard deviation ($n = 3$). Asterisks represent statistical significance ($p < 0.05$). Additional experimental details available in Supporting Information.

binding assay, we determined that MGO-modified AAV2 vectors showed a >2-fold decrease in binding to a prototypical monoclonal antibody (A20), which recognizes intact AAV2 capsids (Figure 1d). An isotype matched antibody served as control. These results indicate the potential for glycated AAV vectors to evade pre-existing neutralizing antibodies in the human population.[22]

Despite demonstrating decreased infectivity *in vitro*, glycated AAV2 capsids infect neurons as efficiently as untreated AAV2 following intracranial injection into the mouse brain (Figure 2). Taken together with the altered antigenicity described earlier, these results suggest that glycated AAV2 vectors might be well suited for CNS gene transfer applications. Further, bioluminescent images of mice obtained following intravenous (tail vein) administration of glycated AAV2 show expansion of viral tissue tropism beyond the liver to other systemic organs (Figure 2c). Quantitation of luciferase expression in tissue lysates reveals approximately 100-fold higher transgene expression levels in cardiac and skeletal muscle with MGO-treated AAV2 in comparison with untreated AAV2 vectors (Figure 2d). In addition, a concomitant decrease in transgene expression within the liver (over 10-fold) is observed. These results demonstrate the feasibility of chemical redirection of AAV2 capsids from liver to muscle tissue and corroborate a similar transduction profile obtained by mutagenesis of R585/R588 residues within the heparan sulfate footprint.[19,23]

In conclusion, the aforementioned studies validate the notion that selective chemical masking of Arg residues with α-dicarbonyl compounds can serve as an orthogonal approach to reengineer viral surface topology and consequently, antigenicity, receptor usage and tissue tropism. This initial study is one of the first to demonstrate the feasibility of displaying unnatural hydroimidazolone side chains on viral capsids. A broad range of α-dicarbonyl compounds ranging from glyoxal to oxo-(7-oxoacetyl-9*H*-fluoren-2-yl)-acetaldehyde are currently being explored for formation of diverse Arg adducts on AAV capsids. An increase in complexity of the α-dicarbonyl side chain may allow generation of novel tissue tropisms, while simultaneously enabling design of AAV vectors capable of evading neutralizing antibodies. This chemical approach represents a new dimension in viral capsid engineering and is likely to impact viral vector design for human gene therapy applications.

■ ASSOCIATED CONTENT

Supporting Information. Experimental methods for virus production, reaction conditions, mass spectroscopic analysis, solid phase binding, in vitro transduction assays, and live animal studies. This material is available free of charge via the Internet at http://pubs.acs.org.

■ AUTHOR INFORMATION

Corresponding Author

*Corresponding author. Aravind Asokan, Ph.D., Gene Therapy Center 4101, Thurston-Bowles Building CB7352, University of North Carolina, Chapel Hill, NC 27599-7352. Phone: 919-843-7621. Fax: 919-966-0907. E-mail: aravind@med.unc.edu.

■ ACKNOWLEDGMENT

We would like to thank Jana Phillips, Kelli Bryant, and Swati Yadav for their assistance with animal studies and Q-PCR. We would also like to thank Drs. Jude Samulski and Nagesh Pulicherla for helpful comments. The aforementioned studies were funded by grants (awarded to A.A.) from NIH (R01HL089221, R01HL089221-S2) and the American Heart Association.

■ REFERENCES

(1) Kwon, I., and Schaffer, D. V. (2008) Designer gene delivery vectors: Molecular engineering and evolution of adeno-associated viral vectors for enhanced gene transfer. *Pharm. Res. 25*, 489–499.

(2) Law, L. K., and Davidson, B. L. (2005) What does it take to bind CAR?. *Mol. Ther. 12*, 599–609.

(3) Racaniello, V. R. (1996) Early events in poliovirus infection: Virus-receptor interactions. *Proc. Natl. Acad. Sci. U. S. A. 93*, 11378–11381.

(4) Cotmore, S. F., and Tattersall, P. (2007) Parvoviral host range and cell entry mechanisms. *Adv. Virus Res. 70*, 183–232.

(5) Strable, E., and Finn, M. G. (2009) Chemical modification of viruses and virus-like particles. *Curr. Top. Microbiol. Immunol. 327*, 1–21.

(6) Carrico, Z. M., Romanini, D. W., Mehl, R. A., and Francis, M. B. (2008) Oxidative coupling of peptides to a virus capsid containing unnatural amino acids. *Chem. Commun. (Camb.)* (10), 1205–1207.

(7) Wang, Q., Lin, T., Johnson, J. E., and Finn, M. G. (2002) Natural supramolecular building blocks. cysteine-added mutants of cowpea mosaic virus. *Chem. Biol. 9*, 813–819.

(8) Hooker, J. M., Kovacs, E. W., and Francis, M. B. (2004) Interior surface modification of bacteriophage MS2. *J. Am. Chem. Soc. 126*, 3718–3719.

(9) Antos, J. M., and Francis, M. B. (2004) Selective tryptophan modification with rhodium carbenoids in aqueous solution. *J. Am. Chem. Soc. 126*, 10256–10257.

(10) Meunier, S., Strable, E., and Finn, M. G. (2004) Crosslinking of and coupling to viral capsid proteins by tyrosine oxidation. *Chem. Biol. 11*, 319–326.

(11) Barnhill, H. N., Reuther, R., Ferguson, P. L., Dreher, T., and Wang, Q. (2007) Turnip yellow mosaic virus as a chemoaddressable bionanoparticle. *Bioconjugate Chem. 18*, 852–859.

(12) Rabbani, N., and Thornalley, P. J. (2008) The dicarbonyl proteome: Proteins susceptible to dicarbonyl glycation at functional sites in health, aging, and disease. *Ann. N.Y. Acad. Sci. 1126*, 124–127.

(13) Brock, J. W., Cotham, W. E., Thorpe, S. R., Baynes, J. W., and Ames, J. M. (2007) Detection and identification of arginine modifications on methylglyoxal-modified ribonuclease by mass spectrometric analysis. *J. Mass Spectrom. 42*, 89–100.

(14) Lo, T. W., Westwood, M. E., McLellan, A. C., Selwood, T., and Thornalley, P. J. (1994) Binding and modification of proteins by methylglyoxal under physiological conditions. A kinetic and mechanistic study with N alpha-acetylarginine, N alpha-acetylcysteine, and N alpha-acetyllysine, and bovine serum albumin. *J. Biol. Chem. 269*, 32299–32305.

(15) Mitchell, A. M., Nicolson, S. C., Warischalk, J. K., and Samulski, R. J. (2010) AAV's anatomy: Roadmap for optimizing vectors for translational success. *Curr. Gene Ther. 10*, 319–340.

(16) Xie, Q., Bu, W., Bhatia, S., Hare, J., Somasundaram, T., Azzi, A., and Chapman, M. S. (2002) The atomic structure of adeno-associated virus (AAV-2), a vector for human gene therapy. *Proc. Natl. Acad. Sci. U. S. A. 99*, 10405–10410.

(17) Levy, H. C., Bowman, V. D., Govindasamy, L., McKenna, R., Nash, K., Warrington, K., Chen, W., Muzyczka, N., Yan, X., Baker, T. S., and Agbandje-McKenna, M. (2009) Heparin binding induces conformational changes in adeno-associated virus serotype 2. *J. Struct. Biol. 165*, 146–156.

(18) Opie, S. R., Warrington, K. H., Jr, Agbandje-McKenna, M., Zolotukhin, S., and Muzyczka, N. (2003) Identification of amino acid residues in the capsid proteins of adeno-associated virus type 2 that contribute to heparan sulfate proteoglycan binding. *J. Virol. 77*, 6995–7006.

(19) Kern, A., Schmidt, K., Leder, C., Muller, O. J., Wobus, C. E., Bettinger, K., Von der Lieth, C. W., King, J. A., and Kleinschmidt, J. A. (2003) Identification of a heparin-binding motif on adeno-associated virus type 2 capsids. *J. Virol. 77*, 11072–11081.

(20) Lee, G. K., Maheshri, N., Kaspar, B., and Schaffer, D. V. (2005) PEG conjugation moderately protects adeno-associated viral vectors against antibody neutralization. *Biotechnol. Bioeng. 92*, 24–34.

(21) Summerford, C., and Samulski, R. J. (1998) Membrane-associated heparan sulfate proteoglycan is a receptor for adeno-associated virus type 2 virions. *J. Virol. 72*, 1438–1445.

(22) Calcedo, R., Vandenberghe, L. H., Gao, G., Lin, J., and Wilson, J. M. (2009) Worldwide epidemiology of neutralizing antibodies to adeno-associated viruses. *J. Infect. Dis. 199*, 381–390.

(23) Asokan, A., Conway, J. C., Phillips, J. L., Li, C., Hegge, J., Sinnott, R., Yadav, S., DiPrimio, N., Nam, H. J., Agbandje-McKenna, M., McPhee, S., Wolff, J., and Samulski, R. J. (2010) Reengineering a receptor footprint of adeno-associated virus enables selective and systemic gene transfer to muscle. *Nat. Biotechnol. 28*, 79–82.

Glycated AAV Vectors: Chemical Redirection of Viral Tissue Tropism

Eric D. Horowitz, Mark S. Weinberg and Aravind Asokan

Supporting Information

Methods

Chemicals and reagents. Methylglyoxal (MGO) was purchased from Acros Organics (Morris Planes, NJ) as a 40% wt/v solution and was used without further purification. Streptavidin-coated and protein A-coated plates were purchased from Pierce Scientific and used as received. Biotinylated dextran (Biotium Inc., Hayward, CA) and biotinylated heparin (Invitrogen, Carlsbad, CA) were dissolved in dH_2O to a concentration of 10 μg/mL before use. Luciferin for *in vitro* luciferase assays (Promega, Madison, WI) and *in vivo* live animal imaging (Caliper Life Sciences, Hopkinton, MA) were diluted in phosphate-buffered saline (PBS, pH 7.4) as required.

Virus production and purification. Adherent human embryonic kidney (HEK293) cells were grown in Dulbecco's Modified Eagle Medium supplemented with 10% fetal bovine serum, penicillin, streptomycin, and amphotericin B. Cells were grown at 37 ˚C and 5% CO_2. AAV2 vectors packaging either a firefly luciferase gene driven by chicken β-actin promoter (CBA-Luc) or a self-complementary GFP gene driven by the cytomegalovirus promoter (CMV-GFP) were produced using the triple plasmid transfection method as described previously.[1] Viral titers, which ranged from 5×10^{11} vg/mL to 2×10^{12} vg/mL, were determined using Q-PCR.

AAV glycation and mass spectrometric analysis. AAV2 CBA-Luc capsids in 1× PBS were mixed with MGO at 4 mM. Reactions were allowed to proceed at room temperature for 20 hrs. Similarly untreated virus was also allowed to sit at room temperature for 20 hrs. Reactions were then dialyzed against 1× PBS for 5 hrs at 4 ˚C. Virus was then used immediately afterwards without additional freeze-thaws.

For mass spectroscopic analysis of glycated viral particles, 5×10^{10} glycated particles were first separated by SDS/PAGE (10% Bis/Tris). Viral proteins were visualized using Brilliant Blue R-250 Coomassie stain (Bio-Rad, Hercules, CA). The VP3 band visualized at 60 kDa was excised and subjected to in-gel tryptic digestion (Applied Biomics, Hayward, CA). After peptide extraction and desalting the digested peptides were spotted on a MALDI source and separated by MALDI/TOF/TOF. Fragments were then identified using the NCBI MASCOT database. All peak intensities were normalized to an internal peptide fragment.

Solid phase binding assays. Solid phase binding studies were performed by binding either biotinylated heparin or biotinylated dextran (10 μg/mL) to a streptavidin-coated 96-well plate. After washing the plate of unbound heparin and dextran, reacted and unreacted AAV2 CBA-Luc (1×10^9 vg) was allowed to bind to the plates for 60 minutes at 37 ˚C. After thorough washing with PBS, bound virus was degraded using proteinase K and was quantified by Q-PCR amplification of the vector genome. Dextran binding served as a control for non-specific binding.

Similarly, antibody recognition was determined by binding A20 (1μg/mL) or Rabbit antihuman (1 μg/mL) antibodies to a protein A-coated 96-well plate. After washing the plate of unbound antibody, reacted and unreacted AAV2 CBA-Luc (1×10^9 vg) was allowed to bind to the plates for 60 minutes at 37 ˚C. After thorough washing with PBS, bound virus was degraded using proteinase K and was quantified by Q-PCR amplification of the vector genome. The isotype-matched rabbit antihuman antibody binding served as a control for non-specific binding.

Transduction assays. Transduction efficiency was determined by adding glycated AAV2 CBA-Luc to HEK293 cells in a 96-well plate at 10,000 viral genomes per cell. Transgene expression was determined by luminometric analysis using a Perkin Elmer Victor luminometer 18 hrs post infection.

Animal Studies. Housing and handling of BALB/c mice used in the current study were carried out in compliance with National Institutes of Health guidelines and approved by IACUC at University of North Carolina-Chapel Hill (protocol #09–117). Unreacted or glycated AAV2 CBA-Luc were administered intravenously in a volume of 200 μl PBS. Luciferase expression in animals was imaged using a Xenogen IVIS-Lumina imaging system (Caliper Life Sciences, Hopkinton, MA) after intraperitoneal injection of luciferin substrate (120 mg/kg; Nanolight). Image analysis was carried out using the Living Image software. Luciferase transgene expression in various tissue types was determined using a luminometric assay (Promega, Madison, WI) from tissue lysates and normalized per μg of protein determined by Bradford assay. Vector genome copy numbers were determined by Q-PCR after extraction of genomic DNA at different time intervals from various tissue types using a DNeasy kit (Qiagen, Valencia, CA).

For vector infusions into the mouse brain, animals were anesthetized with isofluorane and placed into a stereotaxic frame. Using a 32-gauge stainless steel injector and a Fisher Scientific infusion pump, mice (n=4) received 0.5 μl per hemisphere (total of 7.5×10^8 vg) of AAV2 CMV-GFP (right hemisphere) and the glycated AAV2 (left hemisphere) into the striatum (bregma +0.5 mm, lateral +/-1.5 mm, vertical -4.0 mm based on a brain atlas over 5 min. The injector was left in place for 3 min after infusion to allow diffusion from the injector. Two weeks after intracerebral injection, animals received an overdose of avertin (0.2 mL/10g of a 1.25% solution, intraperitoneally) and were perfused transcardially with ice-cold sodium phosphate-buffered saline (PBS pH 7.4), followed by 4% paraformaldehyde in phosphate buffer (PB, pH 7.4). After brains were post-fixed 24 hours at 4°C in the paraformaldehyde–PB, 40 μm coronal sections were cut using a vibrating blade microtome and subjected to immunohistochemical processing for GFP.

Statistical Analysis. All statistical analyses were performed using a two-tailed, unpaired Student's t-test. All error bars represent standard deviation (n=3).

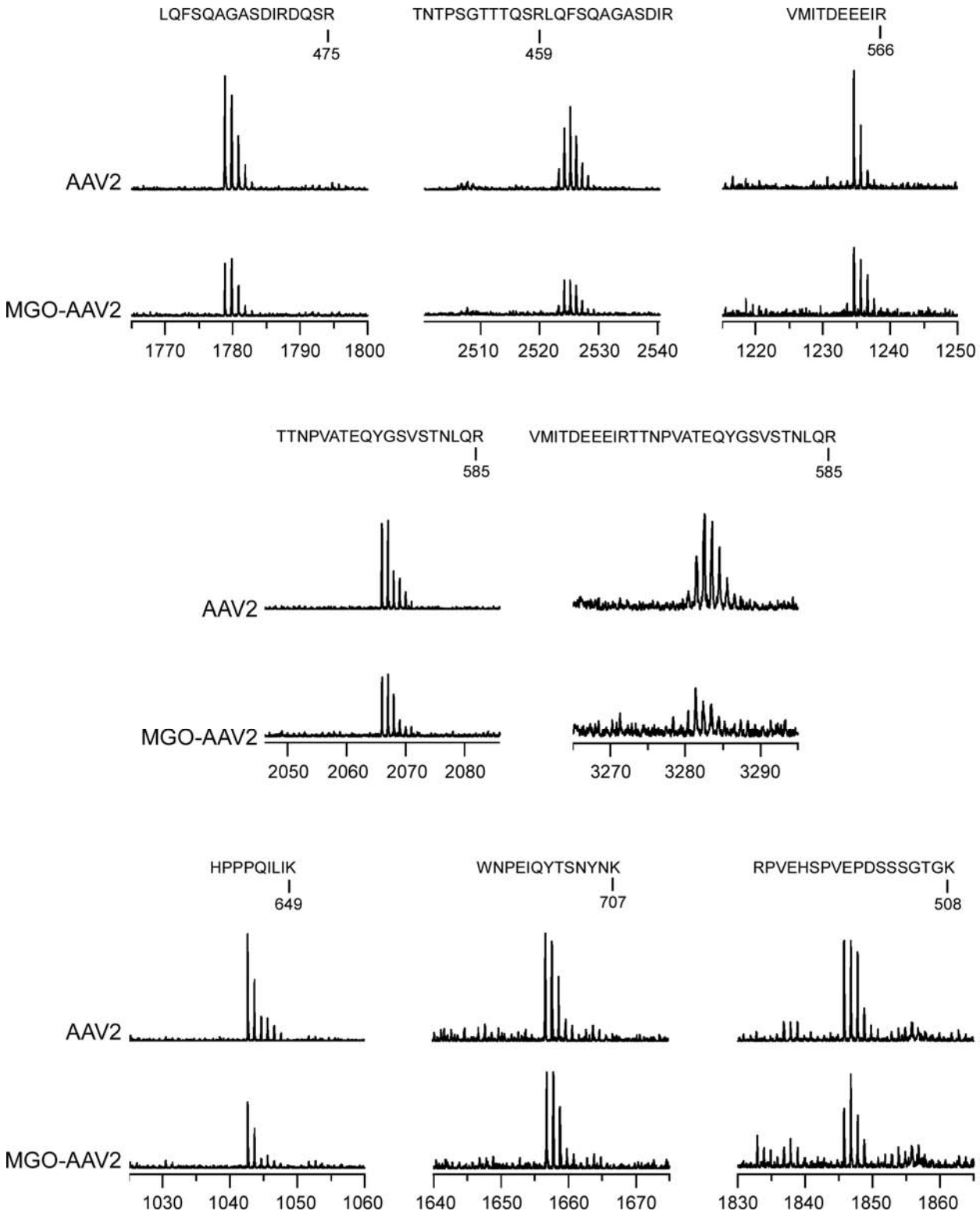


Figure S1. Analysis of MS peaks corresponding to peptide fragments which decrease tryptic digestion after glycation. Loss of tryptic digestion corresponds to the chemical modification of the terminal positively charged residue.

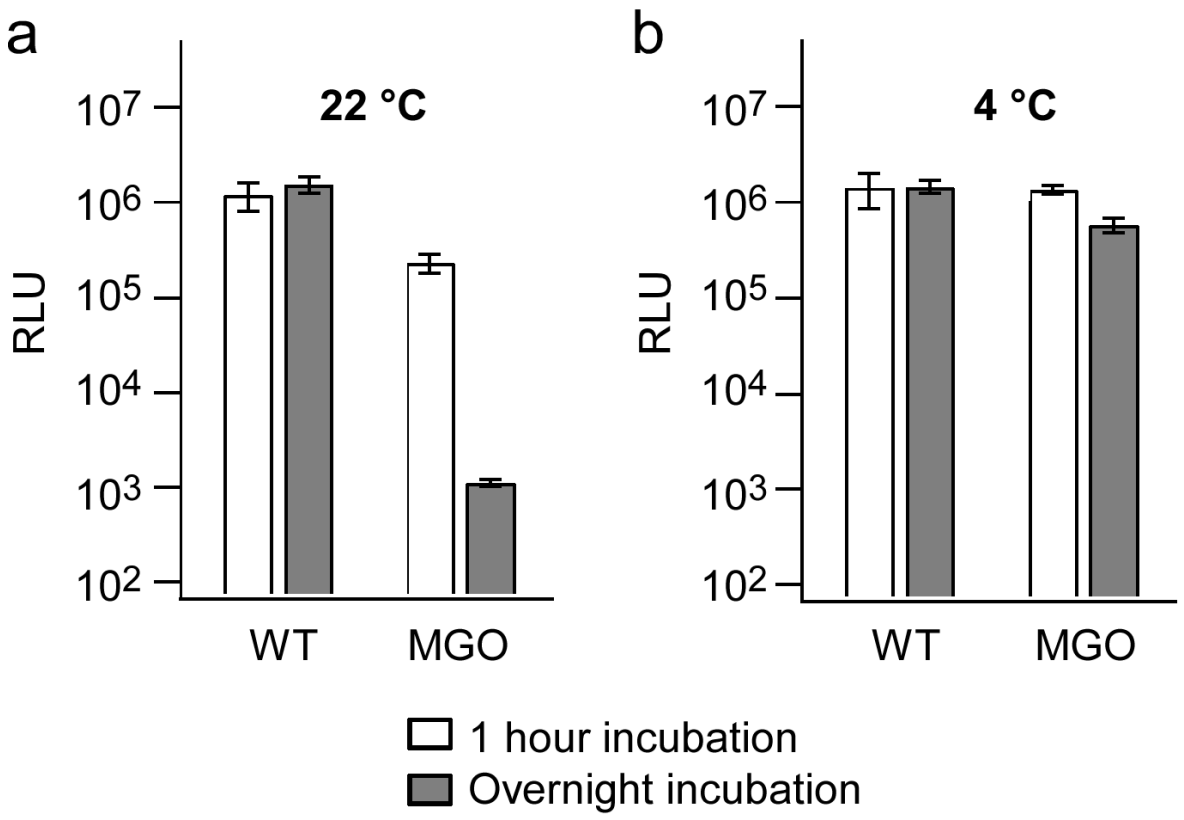


Figure S2. Optimization of glycation reaction. Glycation reactions were performed at two different time points 1 hr or overnight. Reactions were also performed at either a) 22 ˚C or b) 4 ˚C. Extent of glycation was determined by loss of infectivity on HEK293 cells (MOI = 10,000).

References

(1) Grieger, J. C.; Choi, V. W.; Samulski, R. J. *Nat. Protoc.* 2006, *1*, 1412-1428.

Bioconjugate Chemistry

COMMUNICATION

pubs.acs.org/bc

LNA for Optimization of Fluorescent Oligonucleotide Probes: Improved Spectral Properties and Target Binding

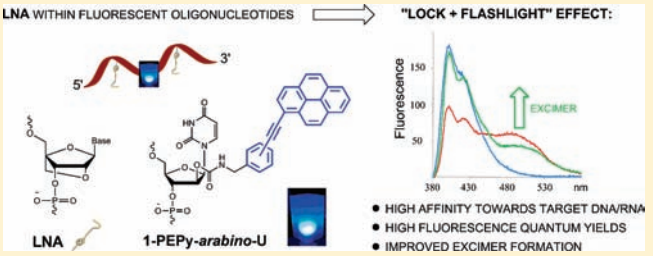
Irina V. Astakhova,[†] Alexey V. Ustinov,[‡] Vladimir A. Korshun,[‡] and Jesper Wengel*[,†]

[†]Nucleic Acid Center, Department of Physics and Chemistry, University of Southern Denmark, DK-5230 Odense M, Denmark

[‡]Shemyakin-Ovchinnikov Institute of Bioorganic Chemistry, Miklukho-Maklaya 16/10, 117997 Moscow, Russia

Supporting Information

ABSTRACT: Mixmer LNA/DNA fluorescent probes containing the 1-(phenylethynyl)pyrene fluorophore attached to 2′-*arabino*-uridine were synthesized and studied. The conjugates displayed significantly higher hybridization affinity to target DNA, increased fluorescence quantum yields of single-stranded oligonucleotides and their duplexes, and improved ability to form an interstrand excimer compared to analogous non-LNA probes.



INTRODUCTION

DNA- and RNA-derived fluorescent probes of various constructs that result in clear fluorescence signals upon binding to targets constitute a paradigm for modern, relatively inexpensive, and sequence-specific, homogeneous detection of nucleic acids.[1,2] For effective nucleic acid targeting, high-affinity and sequence-specific synthetic oligonucleotides (ONs) are required. Locked nucleic acid (LNA, Chart 1) is a synthetic nucleotide analogue[3−7] that provides high-affinity and selective recognition of cDNA and RNA.[8−13] High-affinity LNA/DNA ONs containing different fluorescent dyes have recently been applied for single-nucleotide polymorphism (SNP) analysis,[9−13] real-time PCR,[14−16] FISH analysis,[17−20] and other applications.[21,22] In all these assays, fluorescent LNA/DNA probes were superior in thermal affinity (T_m values increased up to 8 °C per one LNA monomer incorporation measured in a medium salt buffer) and in SNP discrimination of target sequences, when compared to the analogues DNA probes.

Another important aspect of fluorescent ON probes is suitable fluorescent dyes or dye pairs that are sensitive, photostable, and relatively inexpensive. Most fluorescent LNA/DNA probes reported so far have contained terminally attached fluorescent dyes of the xanthene or cyanine families (e.g., FAM, JOE, HEX, Cy5, etc.), which signal hybridization by fluorescence effect of choice (e.g., by dye-quencher proximity or by light-up effect of a single dye).[23−30] However, being exposed into the medium, these dyes did not allow more informative studies of biomolecules and their segments, or of their specific interactions.

Fluorescent ONs containing polyaromatic hydrocarbons (PAHs) are alternative probes for nucleic acid studies which due to the PAH electronic $\pi-\pi^*$ structure sense even minor changes in their microenvironment by fluorescence.[31] Among various PAH dyes, pyrene is of increased interest because of the long lifetime of its excited state and its ability in π-stacking, resulting in exciplex and excimer formation.[31] The main disadvantage of the pyrene label is its low quantum yields within biomolecules and relatively short absorption and emission wavelengths crossing the autofluorescence region of cells. Recently, the 1-(phenylethynyl)pyrene fluorophore (1-PEPy, Chart 1) was introduced as a refined alternative to parent pyrene with advantages of increased absorption, bathochromic shift of the absorption and emission maxima, and increased fluorescence quantum yield within biomolecules.[32−35] Previously, we attached the 1-PEPy fluorophore to 2′-*arabino*-uridine via a carbamate linker and showed the utility of this modification for detection of nucleic acid hybridization.[36] Even though 1-PEPy attached to DNA exhibited short excited lifetime (0.96−2.40 ns), the dye was able to form inter- and intrastrand excimers.[36] On the other hand, we observed that internal 1-PEPy modification, i.e., 1-PEPy attached to an internal 2′-*arabino*-uridine monomer, significantly reduced thermal stabilities of DNA duplexes (T_m values decreased by 3−8 °C per one modification in a medium salt buffer) which can become an obstacle for its utility.[36] The negative effect of 1-PEPy on probe affinity can be reduced by incorporation of two or more LNA nucleotides into ONs. However, recent structural investigations of LNA/DNA ONs have showed that, being a RNA mimic, LNA nucleotides significantly change duplex geometry by decreasing the B-type character of double-stranded DNA toward intermediate A/B-type.[8−13] Therefore, we propose that the effect of LNA within ONs on spectral properties of any PAH label can be significant and need to be studied in detail.

We herein evaluate ONs having the 1-PEPy label attached to 2′-*arabino*-uridine via a carbamate linker in combination with LNA nucleotides. We report synthesis, thermal denaturation,

Received: November 16, 2010
Published: March 14, 2011

 © 2011 American Chemical Society

Chart 1. Structures of LNA, 1-PEPy, Modified Phosphoramidites 1[36] and 2[36] and the Corresponding Monomers X and Y

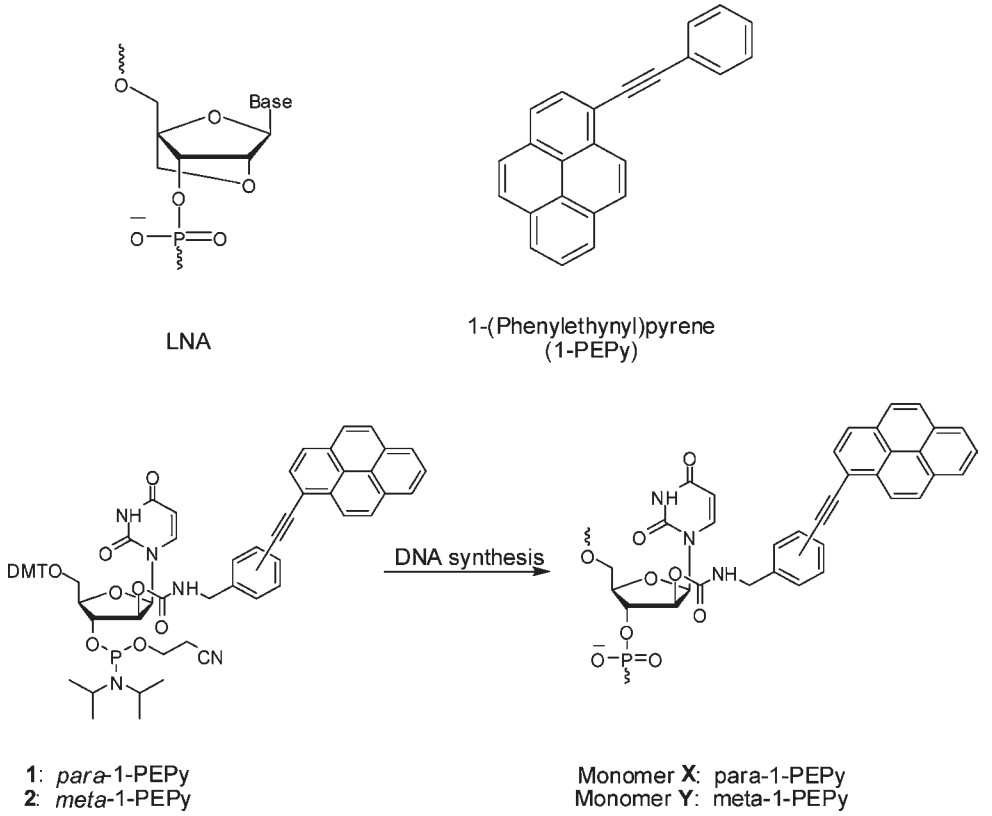


Table 1. ONs Used in This Study and Thermal Stabilities of Modified Duplexes[a]

#	Sequence, 5′→3′	#	Sequence, 5′→3′
ON1	ATT TGA GCC TGG GAG	**ON8**	ATT XGA GCC TGG GAG
ON2	CTC CCA GG^{Me}C^{L} X ^{Me}C^{L}A AAT	**ON9**	AYT TGA GCC TGG GAG
ON3	CTC CCA GG^{L}C XCA^{L} AAT	**ON10**	ATY TGA GCC TGG GAG
ON4	CTC CCA G^{L}GC XCA A^{L}AT	**ON11**	ATT YGA GCC TGG GAG
ON5	CTC CCA^{L} GGC XCA AA^{L}T	**ON12**	CTC CCA GGC TCA AAT
ON6	AXT TGA GCC TGG GAG	**ON13**	CTC CCA GGC XCA AAT
ON7	ATX TGA GCC TGG GAG		

#	Schematic structure	T_m, °C	ΔT_m*, °C	ΔT_m**, °C
ON2:ON1		58.0	0.0	+8.0
ON3:ON1		57.0	-1.0	+7.0
ON4:ON1		62.0	+4.0	+12.0
ON5:ON1		59.0	+1.0	+9.0
ON13:ON1		50.0	-8.0	–

[a] A^{L}, G^{L}, and ^{Me}C^{L} denote LNA adenin-9-yl, guanin-9-yl, and 5-methylcytosin-1-yl monomers, respectively. Melting temperatures were measured in a medium salt buffer using 1.0 μM concentrations of ONs. The blue and gray droplets represent monomer X and LNA monomers, respectively. ΔT_m* and ΔT_m** values were calculated relative to unmodified double-stranded DNA **ON12:ON1** (T_m = 58.0 °C) and 1-PEPy modified LNA-free double-stranded DNA **ON13:ON1** (T_m = 50.0 °C), respectively.

and spectral studies of these resulting 1-PEPy-labeled LNA/DNA probes, and demonstrate how incorporation of LNA can improve both binding affinity and spectral properties of fluorescent ON probes.

dx.doi.org/10.1021/bc1005027 |*Bioconjugate Chem.* 2011, 22, 533–539

Table 2. Spectroscopic and Photophysical Properties of Modified ONs and Duplexes[a]

#	λ^{abs}_{max}, bands I, II (nm)	λ^{fl}_{max} (nm)	τ_1 (ns)	S_1 (%)	τ_2 (ns)	S_2 (%)	$\langle\tau_f\rangle$ (ns)	Φ_f
ON2	394, 371	402	0.75	32	2.68	68	2.06	0.25
ON2:ON1	390, 370	402	0.63	38	2.46	62	1.76	0.24
ON3	395, 373	402	0.79	27	2.86	73	2.30	0.39
ON3:ON1	391, 372	404	0.68	40	2.76	60	1.93	0.26
ON4	393, 370	401	1.05	11	2.87	89	2.67	0.63
ON4:ON1	390, 367	403	0.82	7	2.81	93	2.67	0.76
ON5	396, 373	402	0.66	20	2.70	80	2.29	0.34
ON5:ON1	390, 370	402	0.67	26	2.68	74	2.15	0.32
ON13	397, 372	405	0.60	35	2.50	65	1.83	0.16
ON13:ON1	391, 370	405	0.90	44	2.68	56	1.89	0.23

[a] Absorption and steady-state fluorescence emission spectra measured in a medium salt buffer using 0.1−1.0 μM concentrations of ONs. λ^{abs}_{max} and λ^{fl}_{max} are absorption and fluorescence maxima, respectively; τ_1 and τ_2 are two fluorescence lifetime components; S_1 and S_2 are contribution of τ_1 and τ_2 components in percentages; average fluorescence lifetime $\langle\tau_f\rangle$ is calculated using equation: $\langle\tau_f\rangle = \Sigma S_i\tau_i / \Sigma S_i$.[26]

RESULTS AND DISCUSSION

Initially, we prepared four different ONs having the 1-PEPy fluorophore (monomer **X**)[36] and two LNA nucleotides[3−7] in four different relative positions (Table 1; **ON2**−**ON5**). Synthesis of the modified ONs was performed using phosphoramidite derivative **1**[36] and commercially available LNA phosphoramidites.[3−7] Additionally, compounds **1** and **2**[36] were utilized to prepare six complementary sequences to **ON2**−**ON5** having monomers **X** and **Y** positioned near the 5′-end (Table 1; **ON6**−**ON11**). The latter was done in order to study 1-PEPy interstrand excimer formation within DNA duplexes. Finally, we prepared the LNA-free fluorescent probe **ON13**, which was used as a reference to verify the effect of LNA on 1-PEPy properties. The sequence of **ON13** was equivalent to the one that was previously used to investigate 1-PEPy-2′-*arabino*-uridine attached to DNA.[36] All modified oligonucleotides were prepared using standard protocols except for extended coupling times (10 min) for the phosphoramidites of monomers **X** and **Y**, and for LNA phosphoramidites. Moreover, we observed better coupling yields of the phosphoramidite reagents **1** and **2** using 0.6 M pyridine hydrochloride in MeCN as activator in comparison with standard 1*H*-tetrazole in MeCN (99% vs 89−90%, respectively). All modified ONs were purified by RP-HPLC and their identities and purities were confirmed by MALDI-MS and IC-HPLC, respectively.

First, we investigated the binding of **ON2**−**ON5** and **ON13** to DNA by UV thermal denaturation experiments using a medium salt buffer (100 mM NaCl, 10 mM Na-phosphate, 0.1 mM EDTA, pH 7.0), and compared the data to the unmodified and **X**-labeled references **ON12**:**ON1** and **ON13**:**ON1**, respectively (Table 1). Insertion of the two LNA monomers completely neutralized the destabilizing effect of 1-PEPy-2′-*arabino*-uridine (Table 1, T_m and ΔT_m data for **ON2**−**ON5**). Interestingly, the specific positioning of the LNA monomers along the probe sequences had a remarkable effect on T_m values as well. The highest duplex stabilization by LNAs was observed for the duplex **ON4**:**ON1** having LNA monomers separated by two nucleotides from the 1-PEPy (ΔT_m = +12.0 °C compared to **ON13**:**ON1**).

Next, we evaluated spectroscopic and photophysical properties of the 1-PEPy-containing LNA/DNA conjugates (Table 2). Steady-state fluorescence emission spectra were recorded in a medium salt buffer using an excitation wavelength of 360 nm. Generally, all spectra exhibited a typical 1-PEPy-monomer emission of the 1-PEPy dye in the region 380−480 nm with $\lambda^{fl}_{max} \sim$ 400 nm. The insertion of LNA monomers into **ON2**−**ON5** did not significantly affect either absorption or fluorescence emission wavelengths of the 1-PEPy dye. Next, fluorescence quantum yields Φ_f of single-stranded **ON2**−**ON5** and their duplexes Φ_f = 16−76% were approximately 160−390% higher than those for **ON13** and also remarkably higher that typical quantum yields of pyrene label attached to DNA. We propose that the high quantum yields of 1-PEPy within LNA/DNA conjugates might result from combination of two factors: (1) short fluorescence lifetime of 1-PEPy and (2) shielded positioning of the 1-PEPy fluorophore within the polar groove environment preventing interactions of the fluorophore with quenchers of fluorescence such as medium, oxygen, and nucleobases. As it was demonstrated for the fluorescent pyrene label attached directly to 2′-amino-LNA,[37,38] this specific positioning can be achieved due to structural alterations within the duplexes induced by the LNA nucleotides. The high fluorescence quantum yields of the 1-PEPy-LNA/DNA significantly decrease probe detection limits, which is of high importance for biological studies and biomedical assays.

However, the high Φ_f values of conjugates **ON2**−**ON5** (0.25−0.63) were only slightly affected by hybridization with complementary unmodified DNA. Additionally, slightly increased average fluorescence lifetimes of the 1-PEPy dye within LNA-containing ONs and duplexes compared to the references **ON13** and **ON13**:**ON1** were observed. Moreover, even in presence of the two RNA-mimicking LNA nucleotides still two fluorescent excited states of the 1-PEPy were observed, and both had fluorescence lifetimes and contribution values of the same range as **ON13**. This implies that insertion of the LNA nucleotides remarkably affects positioning of the fluorophore within the probes and increase their fluorescence quantum yields without affecting basic photophysical characteristics of the dye, such as the number of fluorescent excited states and their lifetimes.

Remarkably high Φ_f values were observed for both single-stranded **ON4** and its duplex **ON4**:**ON1** in which 1-PEPy and LNAs were separated by two nucleotides (Table 2). Such high fluorescence quantum yields of the dye within a single-stranded conjugate are quite surprising and may result from LNA-induced formation of a secondary structure in **ON4** preventing quenching interaction of the fluorophore. The formation of a preorganized structure by **ON4** was also suggested by the more structured CD

dx.doi.org/10.1021/bc1005027 |*Bioconjugate Chem.* 2011, 22, 533–539

spectra obtained for single-stranded **ON4** compared to the CD spectra of LNA/DNA probes **ON2**, **ON3**, and **ON5**, and reference probe **ON13** (Figure 1 in Supporting Information).

To further investigate how the 1-PEPy can be protected from quenchers of fluorescence within single-stranded LNA/DNA, molecular models were built (Figure 2). They showed that stacked structures from two spatially accessible G:C base pairs allow placing of 1-PEPy in a cave isolating it from quenching by the buffer medium, oxygen, or nucleobases (Figure 2C,D).

Next, pyrene excimer fluorescence ($\lambda^{fl}_{max} \sim 480$ nm) is proven to be a useful tool for structural studies in biochemistry and molecular biology as "probing of proximity" since the excimer signal is observed when the two pyrenes display some degree of coplanarity and are positioned within a distance less than 4 Å.[31,39−41] Previously, pyrene attached to the sugar part of different nucleosides formed interstrand excimers being located in "+2 zipper",[42−44] "+1 zipper,[37,43,44] or "−1 zipper"[37,45] modes (for description of the "zipper" nomenclature, see caption of Table 3). Recently, we also confirmed weaker inter- and intrastrand excimers formed by 1-PEPy, although it has such a short excited lifetime (<2.5 ns).[36]

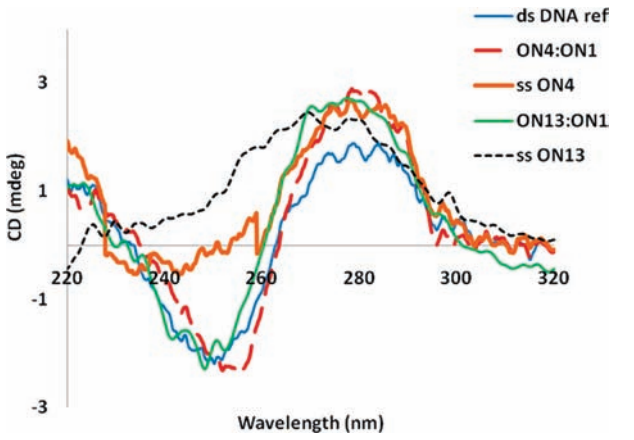


Figure 1. CD spectra of modified single-stranded (ss) oligonucleotides **ON4** and **ON13** and their duplexes with cDNA **ON1**. Double-stranded DNA reference (ds DNA ref) represents the corresponding unmodified duplexes of the same sequence. The spectra were recorded in a medium salt buffer at 19 °C using 1.5 μM concentration of complementary strands.

Herein, we have investigated the influence of LNA nucleotides on interstrand excimer formation between 1-PEPy fluorophores of different geometries (*meta*- and *para*-isomers, Chart 1) being incorporated into "+2-", "+3-", and"+4-zipper" constructs (Table 3). We used excimer-to-monomer fluorescence intensity ratio, I_{500}/I_{402}, as the excimer formation criterion, which was measured to be approximately 0.1 in the absence of excimer emission. Next, in the case of excimer formation the 1-PEPy dyes showed a broad emission band around λ^{fl}_{max} 500 nm (Figure 3) and I_{500}/I_{402} ratios of more than 12% (Table 3). As expected, the excimer-to-monomer fluorescence intensity ratio I_{500}/I_{402} was highly sensitive to the location of additional LNA monomers along the sequence. Hybridization of the probes **ON2** and **ON3** containing LNA close to the 1-PEPy with modified complementary strands **ON6**−**ON11** resulted in effective excimer formation for both *para*- and *meta*-1-PEPy dyes. The excimer signal for both 1-PEPy-isomers was also remarkably improved compared to the LNA-free complexes (Table 3, I_{500}/I_{402} values = 12−80% for **ON2** and **ON3**, compared to I_{500}/I_{405} = 15−45% for analogues **ON13**), and it always increased in order "+4 zipper" < "+3 zipper" < "+2 zipper". No excimer signal was detected only for the "zipper" complexes formed by **ON4** (Figure 3). The complete absence of excimer emission in these complexes suggests that the 1-PEPy moieties cannot come into close proximity, probably due to unfavorable orientations of the fluorophores upon duplex formation. Finally, all duplexes of **ON5** with **ON6**−**ON11** exhibited the same I_{500}/I_{402} values as those observed in the absence of LNA (I_{500}/I_{405} = 20−50%). We presume that the LNA modifications in **ON5** are positioned too far from the fluorophore to affect its microenvironment and

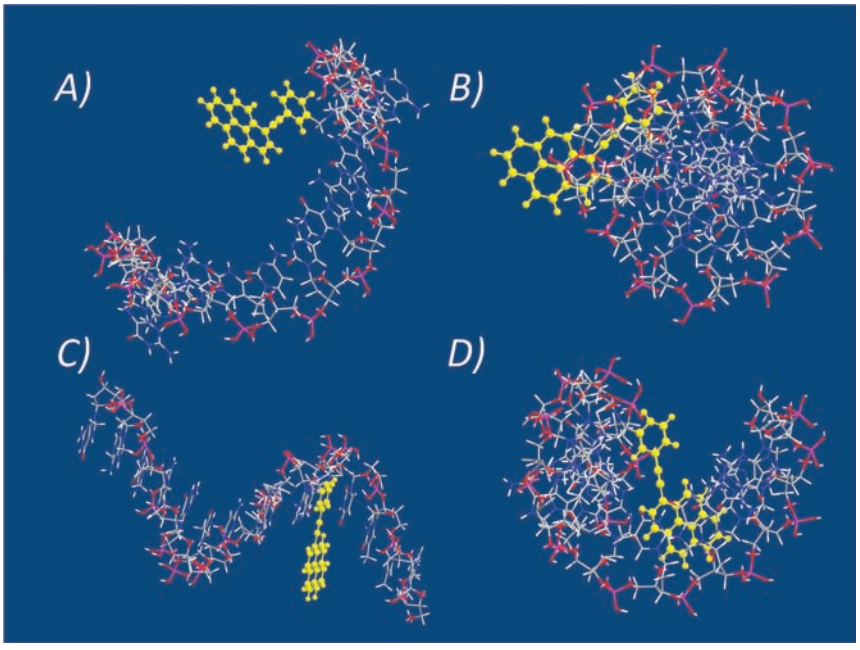
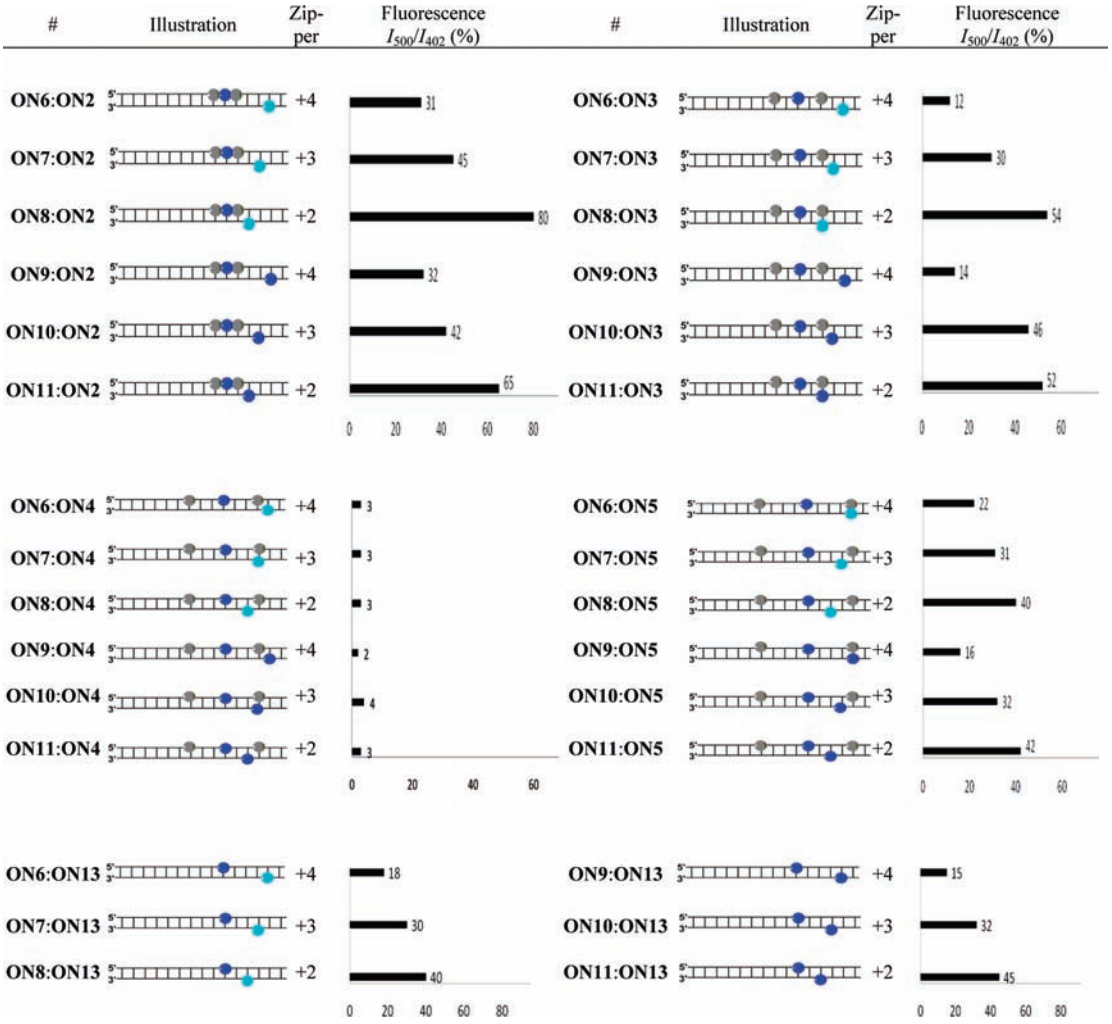


Figure 2. Truncated representations of the lowest energy structure obtained from molecular modeling of single-stranded oligonucleotides **ON2** (view from side (A) and top (B)) and **ON4** (C,D). 1-PEPy residue is shown in yellow.

Table 3. Fluorescent Properties of Modified Duplexes Having LNA Monomers and *para*- and *meta*-1-PEPy Pairs located in "+2", "+3", and "+4 Zipper" Modes[a]



[a] For the conditions of fluorescence measurements, see Figure 3 and the Supporting Information. [b] The "zipper" nomenclature defines arrangements of modified duplexes containing monomers in both complementary strands. An "*n* zipper" describes the arrangement of two modified nucleotides of interest, positioned in opposite strands of a DNA duplex. The number *n* indicates the distance in base pairs between the two nucleotides. If *n* is positive, the two modified monomers are positioned relatively toward the 5′-end of the two strands, and if *n* is negative, the two modified monomers are positioned relatively toward the 3′-ends of the two strands.

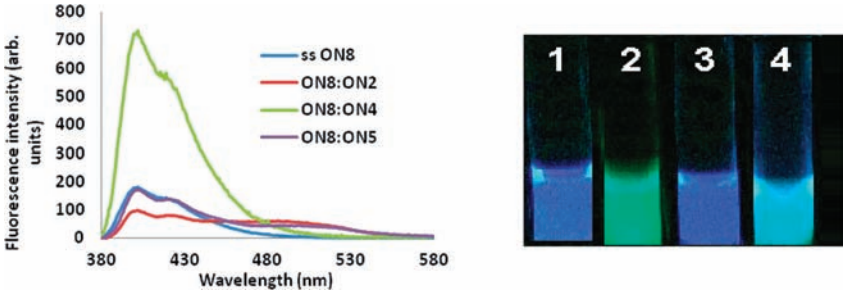


Figure 3. (left) Representative steady-state fluorescence emission spectra of 0.2 μM duplexes having 1-PEPy monomers in both complementary strands in a medium salt buffer using λ_{ex} 360 nm. (right) Photographs of the fluorescence emission in a medium salt buffer: the buffer (negative control, vial 1); **ON8**:**ON2** (vial 2); **ON8**:**ON4** (vial 3), and **ON8**:**ON5** (vial 4). Photographs were taken with a digital camera using a laboratory UV-lamp (λ_{ex} = 365 nm) and 2.0 μM concentration of complementary strands.

therefore have no impact on fluorescence properties of the probes.

Increased 1-PEPy-excimer formation induced by the neighboring LNA nucleotides was additionally monitored by the

change in fluorescence color of the probes upon excitation with a standard laboratory UV-lamp. An intensive excimer emission signal at $\lambda^{fl}_{max} \sim 500$ nm by the complex **ON8**:**ON2** resulted in a green color of its solution (Figure 3, vial 2, I_{500}/I_{405} = 80%), while an increasing predominance of 1-PEPy-monomer emission led to cyan and blue fluorescence of **ON8**:**ON5** and **ON8**:**ON2** solutions, respectively (Figure 3, vials 3−4, I_{500}/I_{405} = 40% and 5%, respectively).

In conclusion, synthesis and spectral properties of fluorescent oligonucleotides containing combinations of a microenvironment sensitive dye, 1-PEPy, and two LNA nucleotides in different positions relative to the fluorophore have been reported. We observed that insertion of the LNA nucleotides into the probes resulted in high binding affinity to cDNA and improved fluorescence quantum yields. Moreover, incorporation of two LNA monomers into neighboring positions of the 1-PEPy modification resulted in significant improvement of excimer formation (I_{500}/I_{405} = up to 80%) compared to the LNA-free reference. Besides, the possibility of stable secondary structure formation by single-stranded probes reported herein is an important detail, which has to be considered while designing fluorescent LNA/DNA probes. Overall, increased fluorescence quantum yields, increased tendency to form excimers, and the ability to modulate binding affinity without modifying the actual sequence makes such fluorescently labeled LNA/DNA probes promising constructs for nucleic acid based diagnostics and studies.

■ ASSOCIATED CONTENT

Supporting Information. Experimental procedures, CD spectra of single-stranded conjugates **ON2**, **ON3**, **ON5**, and of their duplexes with a cDNA strand. This material is available free of charge via the Internet at http://pubs.acs.org.

■ AUTHOR INFORMATION

Corresponding Author

*Corresponding author. E-mail: jwe@ifk.sdu.dk, Tel: +45-6550-2510, Fax: +45-6550-4385.

■ ACKNOWLEDGMENT

We thank The Sixth Framework Programme Marie Curie Host Fellowships for Early Stage Research Training under contract number MEST-CT-2004-504018. The Danish National Research Foundation is thanked for funding the Nucleic Acid Center. V. A. K. and A. V. U. were supported by the Molecular and Cellular Biology Program of the presidium of Russian Academy of Sciences and Dynasty Foundation.

■ REFERENCES

(1) Demidov, V. V. (2003) Earrings and padlocks for the double helix: topological labeling of duplex DNA. *Trends Biotechnol. 21*, 148–151.

(2) Tyagi, S., and Kramer, F. R. (1996) Molecular beacons: probes that fluoresce upon hybridization. *Nat. Biotechnol. 14*, 303–308.

(3) Singh, S. K., Nielsen, P., Koshkin, A. A., and Wengel, J. (1998) LNA (locked nucleic acids): synthesis and high- affinity nucleic acid recognition. *Chem. Commun.* 455–456.

(4) Koshkin, A. A., Singh, S. K., Nielsen, P., Rajwanshi, V. K., Kumar, R., Meldgaard, M., Olsen, C. E., and Wengel, J. (1998) LNA (locked nucleic acids): synthesis of the adenine, cytosine, guanine, 5-methylcytosine, thymine, and uracil bicyclonucleoside monomers, oligomerisation, and unprecedented nucleic acid recognition. *Tetrahedron 54*, 3607–3630.

(5) Obika, S., Nanbu, D., Hari, Y., Andoh, J., Morio, K., Doi, T., and Imanishi, T. (1998) Stability and structural features of the duplexes containing nucleoside analogues with a fixed *N*-type conformation, 2′-*O*,4′-*C*-methyleneribonucleosides. *Tetrahedron Lett. 39*, 5401–5404.

(6) Koshkin, A. A., Nielsen, P., Meldgaard, M., Rajwanshi, V. K., Singh, S. K., and Wengel, J. (1998) LNA (locked nucleic acid): an RNA mimic forming exceedingly stable LNA:LNA duplexes. *J. Am. Chem. Soc. 120*, 13252–13253.

(7) Bondensgaard, K., Petersen, M., Singh, S. K., Rajwanshi, V. K., Wengel, J., and Jacobsen, J. P. (2000) Structural studies of LNA:RNA duplexes by NMR: conformations and implications for RNase H activity. *Chem.—Eur. J. 6*, 2687–2695.

(8) Petersen, M., and Wengel, J. (2003) LNA: a versatile tool for therapeutics and genomics. *Trends Biotechnol. 21*, 74–81and references cited therein.

(9) Jacobsen, N., Bentzen, J., Meldgaard, M., Jacobsen, M. H., Fenger, M., Kauppinen, S., and Skouv, J. (2002) LNA-enhanced detection of single nucleotide polymorphism in the apolipoprotein E. *Nucleic Acids Res. 30*, e100.

(10) Simeonov, A., and Nikiforov, T. T. (2002) Single nucleotide polymorphism genotyping using short, fluorescently labelled locked nucleic acid (LNA) probes and fluorescence polarization detection. *Nucleic Acids Res. 30*, e91.

(11) Brugè, F., Littarru, G. P., Silvestrini, L., Mancuso, T., and Tiano, L. (2009) A novel real time PCR strategy to detect SOD3 SNP using LNA probes. *Mutat. Res. 669*, 80–84.

(12) Johnson, M., Haupt, L., and Griffiths, L. R. (2004) Locked nucleic acid (LNA) single nucleotide polymorphism (SNP) genotype analysis and validation using real-time PCR. *Nucleic Acids Res. 32*, e55.

(13) Ameziane, N., Arar, K., Lamoril, J., Breniere-Schaff, S., and Prost, D. (2004) Application of locked nucleic acids and real-time PCR methodology to detection of the V249I polymorphism of the CX3CR1 chemokine receptor. *Preclinica 2*, 275–278.

(14) Goldenberg, O., Landt, O., Schumann, R. R., Göbel, U. B., and Hamann, L. (2005) Use of locked nucleic acid oligonucleotides as hybridization/FRET probes for quantification of 16S rDNA by real-time PCR. *BioTechniques 38*, 29–30.

(15) Costa, J.-M., Ernault, P., Olivi, M., Gaillon, T., and Arar, K. (2004) Chimeric LNA/DNA probes as a detection system for real-time PCR. *Clin. Biochem. 37*, 930–932.

(16) Josefsen, M. H., Löfström, C., Sommer, H. M., and Hoorfar, J. (2009) Diagnostic PCR: comparative sensitivity of four probe chemistries. *Mol. Cell. Probes 23*, 201–203.

(17) Silahtaroglu, A. N., Tommerup, N., and Vissing, H. (2003) FISHing with locked nucleic acids (LNA): evaluation of different LNA/DNA mixmers. *Mol. Cell. Probes 17*, 165–169.

(18) Silahtaroglu, A., Pfundheller, H., Koshkin, A., Tommerup, N., and Kauppinen, S. (2004) LNA-modified oligonucleotides are highly efficient as FISH probes. *Cyt. Genome Res. 107*, 32–37.

(19) Thompsen, R., Nielsen, P. S., and Jensen, T. H. (2005) Dramatically improved RNA in situ hybridization signals using LNA-modified probes. *RNA 11*, 1745–1748.

(20) Kubota, K., Ohashi, A., Imachi, H., and Harada, H. (2006) Improved in situ hybridization efficiency with locked-nucleic-acid-incorporated DNA probes. *Appl. Environ. Microbiol. 72*, 5311–5317.

(21) Jacobsen, N., Fenger, M., Bentzen, J., Rasmussen, S. L., Jacobsen, M. H., Fenstholt, J., and Skouv, J. (2002) Genotyping of the apolipoprotein B R3500Q mutation using immobilized locked nucleic acid capture probes. *Clin. Chem. 48*, 657–660.

(22) Elmén, J., Lindow, M., Schütz, S., Lawrence, M., Petri, A., Obad, S., Lindholm, M., Hedtjärn, M., Hansen, H. F., Berger, U., Gullans, S., Kearney, P., Sarnow, P., Straarup, E. M., and Kauppinen, S. (2008) LNA-mediated microRNA silencing in non-human primates. *Nature 452*, 896–899.

(23) Moch, H. (2004) Genomic alterations in renal tumours: what have we learned in the era of comparative genomic hybridization? *Pathology 36*, 51–57.

(24) Ragoussis, J. (2009) Genotyping technologies for genetic research. *Annu. Rev. Genomics Hum. Gen. 10*, 117–133.

(25) Lopez, M. F., Mikulskis, A., Golenko, E., Herick, K., Spibey, C. A., Taylor, I., Bobrow, M., and Jackson, P. (2003) High-content proteomics: Fluorescence multiplexing using an integrated, high-sensitivity, multiwavelength charge-coupled device imaging system. *Proteomics 3*, 1109–1116.

(26) Graves, P. R., and Haystead, T. (2002) A Molecular biologist's guide to proteomics. *Microbiol. Mol. Biol. Rev. 66*, 39–63.

(27) Prinz, A., Reither, G., Diskar, M., and Schultz, C. (2008) Fluorescence and bioluminescence procedures for functional proteomics. *Proteomics 8*, 1179–1196.

(28) Singer, R. H. (2003) RNA localization: visualization in real-time. *Curr. Biol. 13*, R673–675.

(29) Paul, C. P. (2005) Subcellular distribution of small interfering RNA: directed delivery through RNA polymerase III expression cassettes and localization by in situ hybridization. *Methods Enzymol. 392*, 125–145.

(30) Blower, M. D., Feric, E., Weis, K., and Heald, R. (2007) Genome-wide analysis demonstrates conserved localization of messenger RNAs to mitotic microtubules. *J. Cell. Biol. 179*, 1365–1373.

(31) Lakowicz, J. R. (2006) *Principles of Fluorescence Spectroscopy*, 3th ed., pp 86 and 225, Chapters 3 and 6, Springer, Singapore.

(32) Korshun, V. A., Prokhorenko, I. A., Gontarev, S. V., Skorobogatyi, M. V., Balakin, K. V., Manasova, E. V., Malakhov, A. D., and Berlin, Yu. A. (1997) New pyrene derivatives for fluorescent labeling of oligonucleotides. *Nucleosides Nucleotides 16*, 1461–1464.

(33) Dioubankova, N. N., Malakhov, A. D., Shenkarev, Z. O., and Korshun, V. A. (2004) Oligonucleotides containing new fluorescent 1-phenylethynylpyrene and 9,10-bis(phenylethynyl)anthracene uridine-2′-carbamates: synthesis and properties. *Tetrahedron 60*, 4617–4626.

(34) Malakhov, A. D., Skorobogatyi, M. V., Prokhorenko, I. A., Gontarev, S. V., Kozhich, D. T., Stetsenko, D. A., Stepanova, I. A., Shenkarev, Z. O., Berlin, Yu. A., and Korshun, V. A. (2004) 1-(Phenylethynyl)pyrene and 9,10-bis(phenylethynyl)anthracene, useful fluorescent dyes for DNA labeling: excimer formation and energy transfer. *Eur. J. Org. Chem.* 1298–1307.

(35) Maeda, H., Maeda, T., Mizuno, K., Fujimoto, K., Shimizu, H., and Inoye, M. (2006) Alkynylpyrenes as improved pyrene-based biomolecular probes with the advantages of high fluorescence quantum yields and long absorption/emission wavelengths. *Chem.—Eur. J. 12*, 824–831.

(36) Astakhova, I. V., Malakhov, A. D., Stepanova, I. A., Ustinov, A. V., Bondarev, S. L., Paramonov, A. S., and Korshun, V. A. (2007) 1-Phenylethynylpyrene (1-PEPy) as refined excimer forming alternative to pyrene: case of DNA major groove excimer. *Bioconjugate Chem. 18*, 1972–1980.

(37) Astakhova, I. V., Korshun, V. A., and Wengel, J. (2008) Highly fluorescent conjugated pyrenes in nucleic acid probes: (phenylethynyl)-pyrenecarbonyl-functionalized locked nucleic acids. *Chem.—Eur. J. 14*, 11010–11026.

(38) Hrdlichka, P. J., Babu, B. R., Sørensen, M. D., Harrit, N., and Wengel, J. (2005) Multilabelled pyrene-functionalized 2′-amino-LNA probes for nucleic acid detection in homogeneous fluorescence assays. *J. Am. Chem. Soc. 127*, 13293–13299.

(39) Birks, J. B. (1975) Excimers. *Rep. Prog. Phys. 38*, 903–974.

(40) Winnik, F. M. (1993) Photophysics of preassociated pyrenes in aqueous polymer solutions and in other organized media. *Chem. Rev. 93*, 587–614.

(41) Lehrer, S. S. (1997) Intramolecular pyrene excimer fluorescence: A probe of proximity and protein conformational change. *Methods Enzymol. 278*, 286–295.

(42) Dioubankova, N. N., Malakhov, A. D., Stetsenko, D. A., Gait, M. J., Volynsky, P. E., Efremov, R. G., and Korshun, V. A. (2003) Pyrenemethyl *ara*-uridine-2′-carbamate: a strong interstrand excimer in the major groove of a DNA duplex. *ChemBioChem 4*, 841–847.

(43) Hrdlicka, P. J., Kumar, T. S., and Wengel, J. (2005) Targeting of mixed sequence double-stranded DNA using pyrene-functionalized 2′-amino-alpha-L-LNA. *Chem. Commun.* 4279–4281.

(44) Kawai, K., Yoshida, H., Takada, T., Tojo, S., and Majima, T. (2004) Formation of pyrene dimer radical cation at the internal site of oligodeoxynucleotides. *J. Phys. Chem. B 108*, 13547–13550.

(45) Hrdlicka, P. J., Babu, B. R., Sørensen, M. D., and Wengel, J. (2004) Interstrand communication between 2′-*N*-(pyren-1-yl)methyl-2′-amino-LNA monomers in nucleic acid duplexes: directional control and signalling of full complementarity. *Chem. Commun.* 1478–1479.

LNA for optimization of fluorescent oligonucleotide probes: improved spectral properties and target binding

Irina V. Astakhova, Alexey V. Ustinov, Vladimir A. Korshun, and Jesper Wengel

SUPPORTING INFORMATION

S2. Experimental procedures.

S5. CD spectra of single-stranded conjugates **ON2**, **ON3** and **ON5**, and of their duplexes with complementary DNA strand (Figure S1).

S6. References.

EXPERIMENTAL PROCEDURES

General. 3′-*O*-(*N*,*N*-Diisopropylamino-2-cyanoethoxyphosphinyl)-5′-*O*-(4,4′-dimethoxytrityl)-2′-*O*-[3(4)-(pyren-1-ylethynyl]phenylmethylaminocarbonyl)uracil-1-*β*-D-arabinofuranosides **1** (*1*) and **2** (*1*), 5-(pyrene-1-ylethynyl)-2-deoxyuridine (*2*) were prepared as described; LNA phosphoramidites were obtained from commercial supplier (Exiqon).

Synthesis and purification of modified oligonucleotides. Oligonucleotide (ON) synthesis was carried out on a Perseptive Biosystems Expedite 8909 instrument in 200 nmol scale using manufacturer's standard protocols, except for increased coupling time for modified phosphoramidies **1** and **2** (*1*) and LNA phosphoramidites (*3*–*7*) (10 min using 0.6 M pyridine hydrochloride or 1*H*-tetrazole in MeCN as activator, respectively). Coupling yields based on the absorbance of the dimethoxytrityl cation released after each coupling were approximately 99% for modified phosphoramidites **1** and **2**, LNA phosphoramidites, and unmodified DNA phosphoramidites. Cleavage from solid support and removal of nucleobase protecting groups were performed using standard conditions (32% aqueous ammonia for 12 h at 55 ºC). Unmodified DNA/RNA strands were obtained from commercial suppliers and used without further purification, while all the modified ONs were purified by DMT-ON RP-HPLC using Waters Prep LC 4000 equipped with Xterra MS C18-column (10 μm, 300 mm × 7.8 mm). Elution was performed starting with an isocratic hold of A-buffer for 5 min followed by a linear gradient to 55 % B-buffer over 75 min at a flow rate of 1.0 mL/min (A-buffer: 95% 0.1 M NH_4HCO_3, 5% CH_3CN; B-buffer: 25% 0.1 M NH_4HCO_3, 75% CH_3CN). RP-purification was followed by detritylation (80% aq. AcOH, 20 min), precipitation (abs. EtOH, -18 ºC, 12 h) and washing with abs. EtOH three times. The identity and purity of ONs were verified by MALDI-TOF mass spectrometry (recorded on an Applied Biosystems Voyager-DE STR spectrometer) and IC-HPLC, respectively. Measured masses $[M-H]^-$ of the ONs (calculated masses *m/z* for $[M-H]^-$): **ON2**: 4938 (4941); **ON3**: 4913 (4913); **ON4**: 4910 (4913); **ON5**: 4912 (4913); **ON6**: 5006 (5005); **ON7**: 5006 (5008); **ON8**: 5006 (5006); **ON9**: 5006 (5006); **ON10**: 5006 (5006); **ON11**: 5006 (5006); **ON13**: 4776 (4774).

UV-visible absorption and thermal denaturation studies. UV-visible absorption spectra and thermal denaturation experiments were performed on a Perkin Elmer Lambda 35 UV/VIS Spectrometer equipped with PTP 6 (Peltier Temperature Programmer) element in a medium salt buffer (100 mM sodium chloride, 10 mM sodium phosphate, 0.1 mM EDTA, pH 7.0). Concentrations of ONs were calculated using the following extinction coefficients (OD_{260}/μmol): G, 10.5; A, 13.9; T/U, 7.9; C, 6.6; **X**, 17.3; **Y**, 20.0. ONs (1.0 μM each strand) were thoroughly mixed, denaturated by heating and subsequently cooled to the starting temperature of experiment. Thermal denaturation temperatures (T_m values, ºC) were determined as the maxima of the first derivative of the thermal denaturation curves (A_{260} vs. temperature). Reported T_m values are an average of two measurements within ± 1.0 ºC.

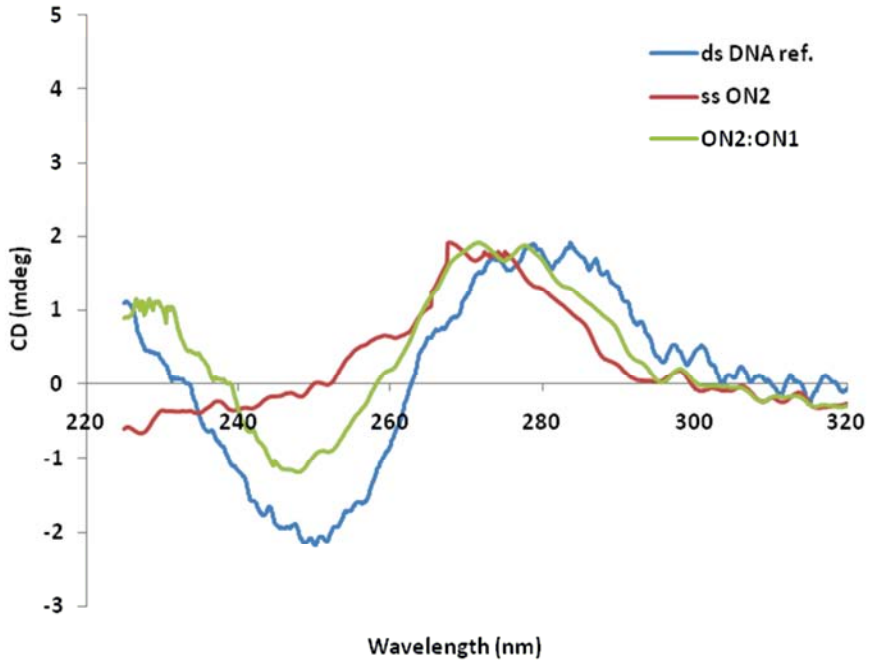
Fluorescence steady-state emission studies, and quantum yield and fluorescence lifetime determinations. Fluorescence spectra were obtained in a medium salt buffer (see above) using a PerkinElmer LS 55 luminescence spectrometer equipped with a Peltier temperature controller using an excitation wavelength of 360 nm, excitation slit of 4.0 nm, emission slit of 2.5 nm, scan speed of 120 nm/min and 0.2 μM concentrations of the single-stranded probe or the corresponding duplex. The fluorescence quantum yields (Φ_f) were measured by the relative method (*8*) using 5-(pyrene-1-ylethynyl)-2-deoxyuridine (Φ_f 0.45) (*2*) in abs. EtOH as a standard. The optical density of the solutions in a 1-cm quartz cuvette at the excitation wavelength did not exceed 0.1. The values of Φ_f were corrected with the refractive index of the solvent; the measured refractive indexes of abs. ethanol and phosphate buffer were 1.361 and 1.334 at 20 ºC, respectively. Fluorescence lifetimes were determined by the method of time-correlated single-photon counting using a PRA model 3000 nanosecond lifetime fluorometer. The parameters of the fluorescence decays were analyzed using T900 software (Edinburgh Instruments). The samples used in quantum yield and lifetime fluorescence measurements were not degassed; concentrations were 3.0×10^{-6} M.

CD measurements. CD spectra were recorded on a JASCO J-815 CD Spectrometer equipped with CDF 4265/15 temperature controller. Samples for CD measurements were prepared as described for the

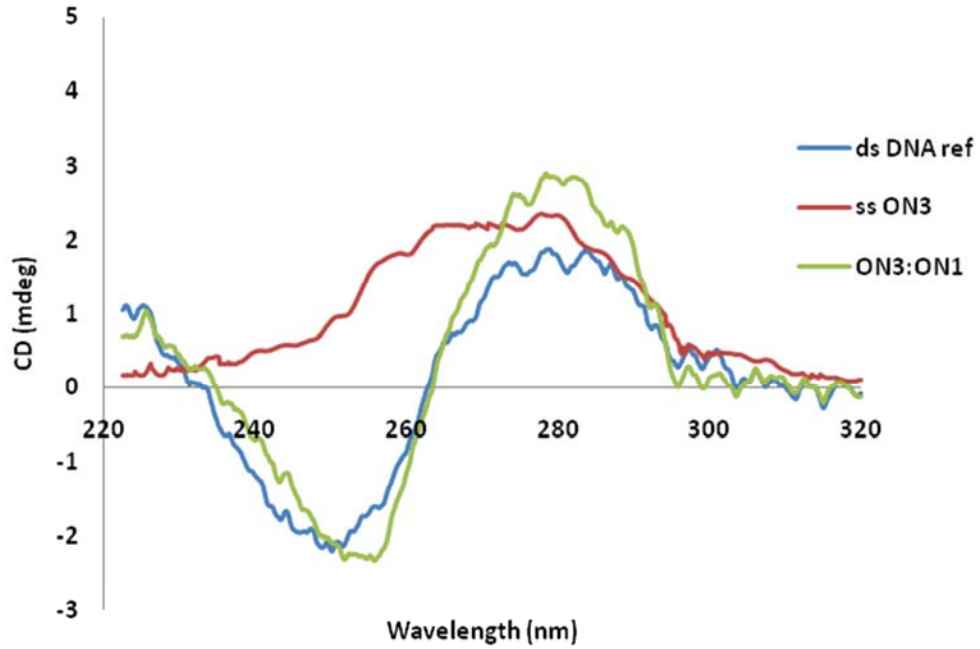
thermal denaturation studies section except that a concentration of 1.5 μM of the two complementary ONs was used. Quartz optical cells with a path-length of 0.5 cm were used.

Molecular modelling. ON4 was built in standard B-type helical geometry and further analyzed by MacroModel V9.1 (*9*). When doing this the structure of **ON4** was minimized using the Polak–Ribiere conjugate gradient method, the all-atom AMBER force field (*10–11*), and the GB/SA solvation model (*12*) as implemented in MacroModel V9.1. Non-bonded interactions were treated with extended cut-offs (van der Waals 8.0 Å and electrostatics 20.0 Å). The minimized structures were then (using the same constraints as described above) submitted to 3 ns of stochastic dynamics (simulation temperature 300 K, time step 2.2 fs, SHAKE all bonds to hydrogen), during which 300 structures were sampled and subsequently minimized.

A)


ds DNA ref.
ss ON2
ON2:ON1
CD (mdeg)
Wavelength (nm)
5
4
3
2
1
0
-1
-2
-3
220
240
260
280
300
320

B)


ds DNA ref
ss ON3
ON3:ON1
CD (mdeg)
Wavelength (nm)
5
4
3
2
1
0
-1
-2
-3
220
240
260
280
300
320

C)

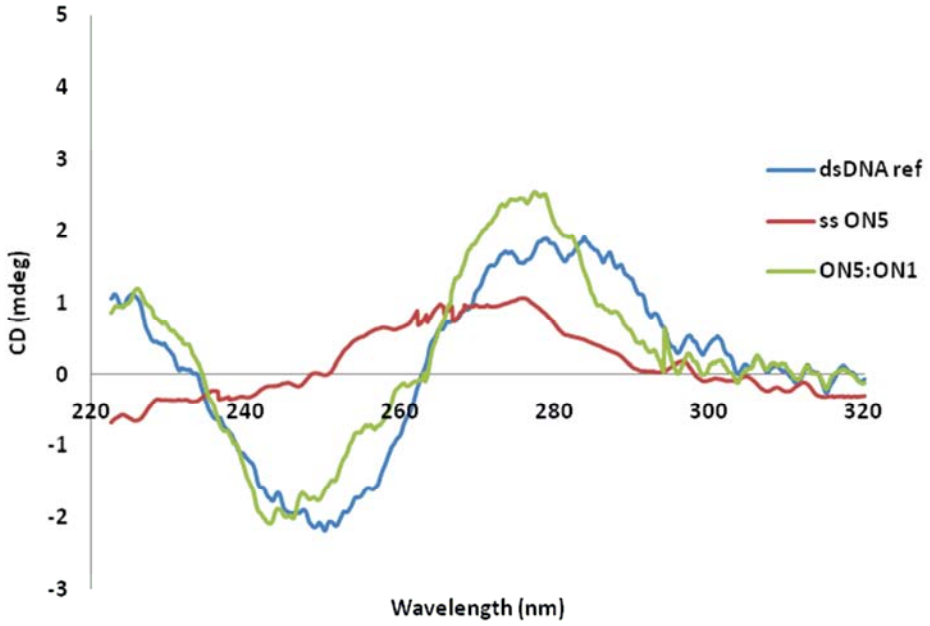


Figure S1. CD spectra of modified ONs and of duplexes. The spectra were recorded in medium salt buffer at 19 ºC using 1.5 μM concentration of strands. dsDNA ref = unmodified DNA duplex reference **ON12**:**ON1**.

References

(1) Astakhova, I. V., Malakhov, A. D., Stepanova, I. A., Ustinov, A. V., Bondarev, S. L., Paramonov, A. S., and Korshun, V. A. (2007) 1-Phenylethynylpyrene (1-PEPy) as refined excimer forming alternative to pyrene: case of DNA major groove excimer. *Bioconjugate Chem. 18*, 1972–1980.

(2) Korshun, V. A., Manasova, E. V., Balakin, K. V., Prokhorenko, I. A., Buchatskii, A. G., and Berlin, Yu. A. (1996) 5-(1-Pyrenylethynyl)-2'-Deoxyuridine, a Novel Fluorescent Nucleoside Analogue. *Russ. J. Bioorg. Chim. 22*, 807–809.

(3) Koshkin, A. A., Singh, S. K., Nielsen, P., Rajwanshi, V. K., Kumar, R., Meldgaard, M., Olsen, C. E., and Wengel, J. (1998) LNA (Locked Nucleic Acids): Synthesis of the Adenine, Cytosine, Guanine,

5-Methylcytosine, Thymine, and Uracil Bicyclonucleoside Monomers, Oligomerisation, and Unprecedented Nucleic Acid Recognition. *Tetrahedron 54*, 3607–3630.

(4) Obika, S., Nanbu, D., Hari, Y., Andoh, J., Morio, K., Doi, T., and Imanishi, T. (1998) Stability and structural features of the duplexes containing nucleoside analogues with a fixed *N*-type conformation, 2′-*O*,4′-*C*-methyleneribonucleosides. *Tetrahedron Lett. 39*, 5401–5404.

(5) Koshkin, A. A., Nielsen, P., Meldgaard, M., Rajwanshi, V. K., Singh, S. K., and Wengel, J. (1998) LNA (Locked Nucleic Acid): An RNA Mimic Forming Exceedingly Stable LNA:LNA Duplexes. *J. Am. Chem. Soc. 120*, 13252–13253.

(6) Bondensgaard, K., Petersen, M., Singh, S. K., Rajwanshi, V. K., Wengel, J., and Jacobsen, J. P. (2000) Structural Studies of LNA:RNA Duplexes by NMR: Conformations and Implications for RNase H Activity. *Chem. Eur. J. 6*, 2687–2695.

(7) Astakhova, I. V., Korshun, V. A., and Wengel, J. (2008) Highly Fluorescent Conjugated Pyrenes in Nucleic Acid Probes: (Phenylethynyl)pyrenecarbonyl-Functionalized Locked Nucleic Acids. *Chem. Eur. J. 14*, 11010–11026.

(8) Lakowicz, J. R. (2006) Principles of Fluorescence Spectroscopy, 3th Ed., Springer, Singapore.

(9) *MacroModel*, version 9.1 (2005). Schrödinger, LLC, New York, NY.

(10) Weiner, S. J., Kollman, P. A., Case, D. A., Singh, U. C., Ghio, C., Alagona, G., Profeta, S., and Weiner, P. J. (1984) A new force field for molecular mechanical simulation of nucleic acids and proteins. *J. Am. Chem. Soc. 106*, 765–784.

(11) Weiner, S. J., Kollman, P. A., Nguyen, D. T., and Case, D. A. (1986) An All Atom Force Field for Simulations of Proteins and Nucleic Acids. *J. Comput. Chem.* 7, 230–252.

(12) Still, W. C., Tempczyk, A., Hawley, R. C., and Hendrickson, T. (1990) Semianalytical treatment

of solvation for molecular mechanics and dynamics. *J. Am. Chem. Soc. 112*, 6127–6129.

Bioconjugate Chemistry

COMMUNICATION

pubs.acs.org/bc

Development of a Cell-Selective and Intrinsically Active Multikinase Inhibitor Bioconjugate

Stefan Harmsen,[†] M. Emmy M. Dolman,[†] Zoltan Nemes,[†] Marie Lacombe,[‡] Bálint Szokol,[§] János Pató,[§] György Kéri,[§,∥] László Orfi,[§] Gert Storm,[†] Wim E. Hennink,[†] and Robbert J. Kok*[,†]

[†]Department of Pharmaceutics, Utrecht Institute of Pharmaceutical Sciences, Utrecht University, Universiteitsweg 99, 3584 CG Utrecht, The Netherlands

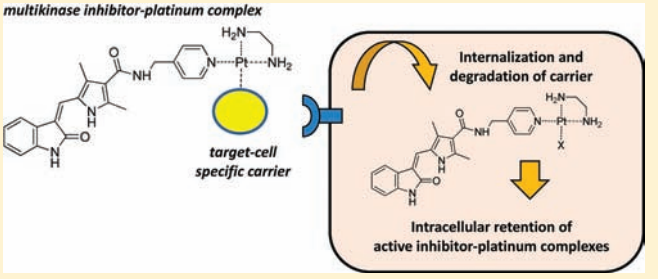
[‡]Kreatech Biotechnology BV, Amsterdam, The Netherlands

[§]Vichem Chemie, Budapest, Hungary

[∥]Pathobiochemistry Research Group of Hungarian Academy of Sciences and Semmelweis University, Budapest, Hungary

Supporting Information

ABSTRACT: Multikinase inhibitors are potent anticancer drugs that simultaneously intervene in multiple related signaling cascades, thus being capable of blocking salvage pathways that may play a role in the development of drug resistance. Multikinase inhibitors are increasingly evaluated for indications other than cancer, but long-term safety risks dictated by off-organ toxicities of these agents may prevent their safe and effective use. Here, we describe a new approach in which platinum coordination chemistry is applied for the development of a cell-selective multikinase inhibitor bioconjugate. The platinum(II) kinase inhibitor bioconjugate was designed to be active with the linker attached to the inhibitor and displayed improved activity by enhanced cell specificity as well as enhanced intracellular retention, thereby prolonging its pharmacological activity. In addition, the utilized platinum-based linkage technology potentiated the inhibitory activity of the multikinase inhibitor. These features in combination with carrier-mediated uptake in the target cells may revolutionize dosing regimens and safety profiles of (multi)kinase inhibitors.



In recent years, kinase inhibitors have emerged as highly successful anticancer drugs. Initially designed to inhibit specific protein kinases such as BCR-ABL (e.g., imatinib), later multikinase inhibitors (e.g., sunitinib) were developed to concomitantly interrupt multiple distinct signaling pathways. Apart from cancer therapy, multikinase inhibitors are currently increasingly investigated for less life-threatening diseases as well; i.e., sunitinib has been shown to potently ameliorate liver cirrhosis[1] and chronic airway inflammation,[2] while the related oxindole-based intedanib (BIBF-1120) shows potential in the treatment of idiopathic pulmonary fibrosis.[3] A point of concern, however, is the safety profile of multikinase inhibitors.[4] The most commonly reported multikinase inhibitor related toxicities include rash, diarrhea, and nausea, while long-term toxicities include fatigue, hypothyroidism, and even cardiotoxicity.[5,6] Although these off-target toxicities are more acceptable in cancer therapy, they complicate long-term use of these agents in chronic, less life-threatening illnesses.

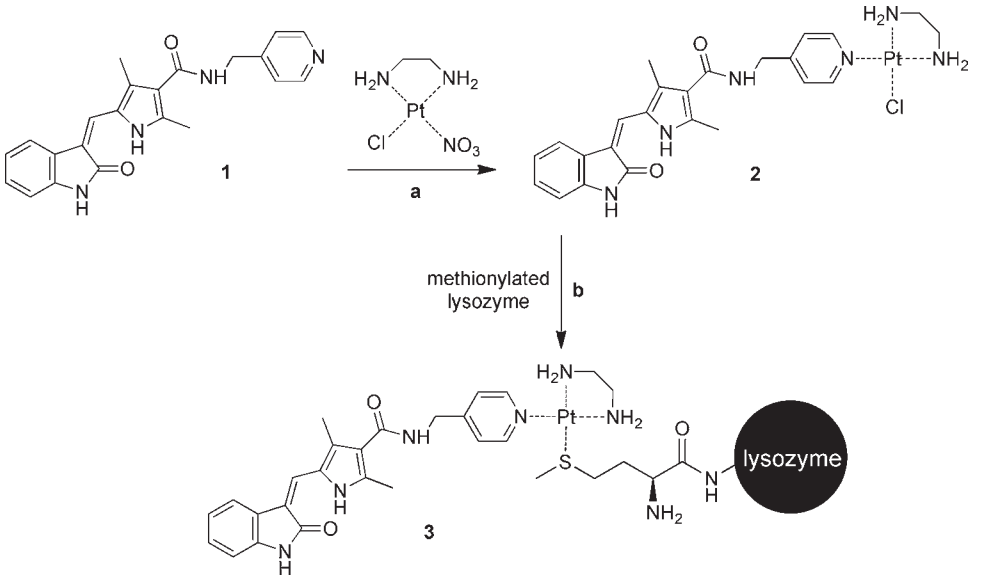
To address these safety issues, we developed a multikinase inhibitor bioconjugate that accumulates in disease-inflicted organs in a target cell-selective manner by recognition of surface-exposed receptors that facilitate internalization. This approach permits lower drug dosages due to increased drug accumulation at the designated pathological tissue while avoiding uptake in healthy tissues and, thus, decreases the risk of off-organ toxicities. Furthermore, the uptake into specific cell types within the targeted organ will greatly improve the specificity profile of such cellular targeted drugs. We have previously demonstrated that renal tubular cells can be targeted with drug−lysozyme conjugates.[7] In the present study, we will use this type of drug−protein conjugate as the platform technology for a new type of intrinsically active multikinase inhibitor bioconjugates.

The linkage of the multikinase inhibitor to its carrier was achieved by the platinum(II)-based Universal Linkage System (ULS, Scheme 1). This bioinorganic linker afforded a straightforward linking protocol and also ensured the formation of a conjugate that can be dissociated within cells by competitive displacement of the platinum ligands by endogenous thiols such as glutathione (GSH). Since previous studies had demonstrated that drug−platinum conjugate linkages have a very long intracellular half-life after in vivo accumulation in target tissues, we now have designed a new class of kinase inhibitor−platinum

Received: December 13, 2010
Revised: March 19, 2011
Published: March 28, 2011

ACS Publications © 2011 American Chemical Society

Scheme 1. Synthesis of a Platinum Coordinated Multikinase Inhibitor Bioconjugate[a]



[a] The multikinase inhibitor **1** is complexed with monochloromononitrate−(ethylenediamine)platinum(II) (ULS) via binding to the pyridine nitrogen. The resulting drug−platinum complex **2** is conjugated to methionyl groups in lysozyme, yielding **3**. Reagents and conditions: (a) DMF, 37 °C, 84.0% of **2**; (b) 0.02 M tricine/sodium nitrate buffer, pH 8.5, 72% of **3**. DMF = *N*,*N*-dimethylformamide.

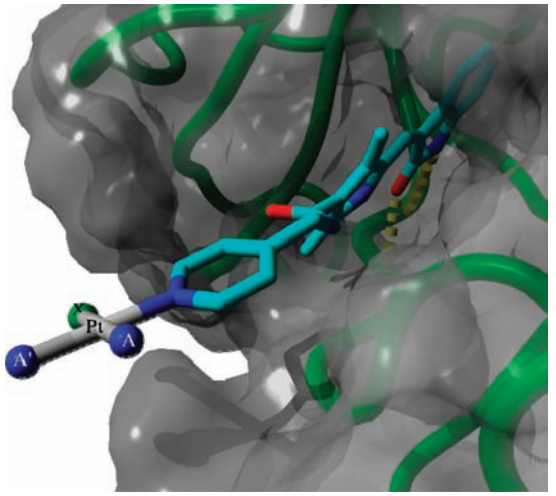


Figure 1. Illustration of the square-planar multikinase inhibitor−platinum complex **2** (as depicted in Scheme 1) bound to the ATP-binding pocket of the protein kinase c-KIT. The 4-(amidomethyl)pyridine is sticking outward permitting binding to the platinum(II) atom and leaving enough space to accommodate a drug carrier at position X. Ethylenediamine is complexed at position A and A′.

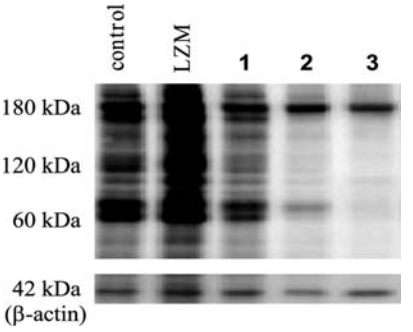


Figure 2. Pharmacologic activity of multikinase inhibitors. Cell lysate of immortalized proximal tubular cells (HK-2) was preincubated with equimolar amounts (2 μM) of **1**, **2**, **3**, unconjugated lysozyme (LZM), or water (control) and activated with ATP. Phosphorylation was detected with an antibody raised against phosphorylated tyrosine residues (pY-20). While **1** showed only some inhibitory effects on total tyrosine phosphorylation, significant inhibitory effects were observed with **2** and **3**. β-Actin was used as loading control.

adducts that can bind into the ATP pocket of kinases when platinum is still bound to the parent drug. Such an approach infers that the ULS linker and the pending cell-specific carrier are conjugated to the multikinase inhibitor via a functional group that protrudes from the ATP pocket.

Therefore, we first investigated how oxindole-based multikinase inhibitors generally are oriented inside the active site of their target kinases. Analysis of published protein structures cocrystallized with oxindole-based inhibitors revealed that the oxindole pharmacophore scaffold binds deeply within the ATP-binding pocket[8,9] with the pyrrolylmethylidenyl and the pending side groups oriented toward the outside. Next, we synthesized an oxindole-based inhibitor **1** with a 4-(amidomethyl)pyridine side chain[10] that permitted complexation to the platinum(II)-based linker. As shown in Figure 1, the multikinase inhibitor **1** binds to the ATP-binding site of its target kinase while leaving enough space to accommodate the platinum-based ULS linker and even a drug carrier at the X position without directly disrupting inhibitor−kinase interactions. We therefore postulated that this type of inhibitor−platinum complex could be used as intrinsically active, target cell-selective conjugates. Complexation of **1** with ULS (monochloromononitrate−(ethylenediamine)platinum(II)) for 4 h at 37 °C in the dark afforded complex **2** (84.0%). Finally, **2** was coupled to the prototypic drug-carrier protein lysozyme

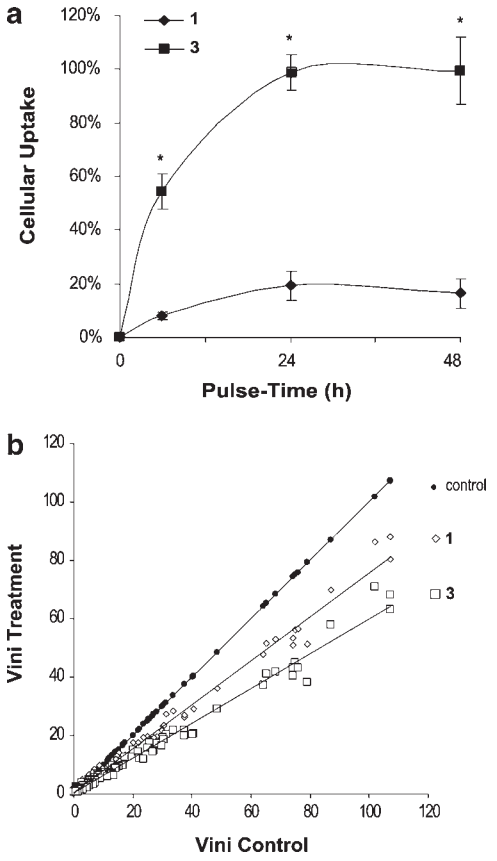


Figure 3. (a) Cellular uptake of multikinase inhibitors in renal tubular cells. Uptake was determined by incubating HK-2 cells with 10 μM **1** or **3** for different time intervals (pulse time). Maximal uptake of cellular targeted complex **3** was set at 100%. Significance was determined for each time point versus $t = 0$ h (*, $P < 0.05$). (b) Pharmacological profile of inhibitors in HK-2 cells. A flow-through tyrosine kinase peptide array was used to determine the inhibitory activity of **1** and **3**. Peptide phosphorylation was detected in real time with a monoclonal antiphosphotyrosine antibody (pY-20) coupled to FITC. Data were expressed as Vini (initial linear rate of tyrosine residue phosphorylation) and ranked based on strongest pY inhibition compared to control. The slope of the plotted curves is a measure for pan-tyrosine pY inhibition (control slope = 1).

(LZM), which is a low-molecular weight protein that selectively accumulates in renal proximal tubular cells. The molar coupling ratio of **2** to LZM was determined to be 0.9:1.

We evaluated whether platinum coordination affected the pharmacological activity of **1** by spiking freshly prepared human proximal tubular cell lysate with 2 μM concentration of **1**, of the intermediate complex **2**, or of conjugate **3** and analyzing total tyrosine kinase phosphorylation in the lysate. Interestingly, **2** and **3** inhibited tyrosine phosphorylation more potently than **1** (Figure 2). As anticipated, these results demonstrate that the multikinase inhibitor−lysozyme conjugate is intrinsically active and, second, that the platinum(II)-based ULS positively contributes to the pharmacological activity of **1**, most likely through electrostatic interactions of the platinum(II) scaffold with electron donating groups within the target protein(s).

Next, we investigated the capability of target cells to internalize **3**. Lysozyme is freely filtered through the glomerular barrier into the tubular lumen and is reabsorbed by proximal tubular cells via megalin and cubilin receptor-mediated endocytosis.[7] We

Table 1. Strongest Inhibited Tyrosine-Peptide Residues by 3 on the Tyrosine Kinase PamTyrChip Peptide Array

	protein (p-site)	(pathological) function
1	PI3K (p85 Y607)	cell motility/proliferation
2	PDGFRβ (Y579/581)	cell proliferation, cell migration, differentiation
3	paxillin (Y31/33)	focal adhesion, cell mobility, and differentiation
4	paxillin (Y118)	focal adhesion, cell mobility, and differentiation
5	pecam-1 (Y713)	endothelial marker (CD31)
6	EphrinA7 (Y608/Y614)	often overexpressed in invasive tumors
7	c-FES (Y713)	cell migration
8	VEGFR2 (Y996)	angiogenesis
9	CDK2 (Y15/19)	cell cycling/proliferation
10	RASA1 (Y460)	implicated in linking PDGFR signaling to RAS-GAP mitogenicity

studied drug uptake in immortalized human proximal tubular cells (HK-2), a cell line that can be used for in vitro testing of uptake of megalin ligands.[11] We exposed these cells to 10 μM **1** or **3** for different time intervals and determined absolute intracellular drug accumulation. As shown in Figure 3a, the uptake of **3** reached a steady state after 24 h. Moreover, the intracellular drug accumulation in the cells treated with **3** was 5 times higher than in cells treated with **1**.

We additionally determined which intracellular kinases were affected by treatment with **1** and **3** by means of a flow-through tyrosine kinase peptide array.[12] We observed that **3** was more potent than **1** (Figure 3b). Interestingly, the most inhibited peptide residues (Table 1) correspond with proteins that are either direct targets of similar oxindole-based kinase inhibitors sunitinib and indetanib[13−15] (vascular-endothelial growth factor receptor (VEGFR)-2, platelet-derived growth factor receptor (PDGFR)-β) or lie downstream of these receptors (phosphoinositol-3-kinase (PI3K), paxillin, Ras p21 protein activator (RASA1), cyclin-dependent kinase (CDK)-2, and c-FES). These kinases play important roles in pathophysiological processes like angiogenesis, cell adhesion, and migration, processes that underlie pathologies such as arteriosclerosis, rheumatoid arthritis, and fibrosis.

To further evaluate whether platinum complexation or bioconjugation would affect the inhibitory activity of compound **1** toward its target kinases, we evaluated the inhibitory activity of **1**, **2**, and **3** against recombinant PDGFRβ and c-KIT. As shown in Figure 4 and Table 2, complexation of platinum with **1** did not affect the inhibitory activity of **1** against PDGFRβ and increased the inhibitory activity against c-KIT 3-fold. Interestingly, **1** and **2** were as potent as the clinically approved oxindole-based multikinase inhibitor sunitinib (Table 2). Conjugation to LZM slightly decreased the inhibitory activity toward both kinases, which might be due to steric hindrance of the relatively large LZM homing ligand. This part of the conjugate will be degraded into smaller peptide fragments upon internalization and hence will not interfere with the kinase inhibitory activity of compound **2**.

To study the effect of drug conjugation on drug efflux, a pulse-chase experiment was conducted. HK-2 cells were exposed for 24 h to **1** or **3**, after which the cells were allowed to efflux in blank

dx.doi.org/10.1021/bc1005637 |*Bioconjugate Chem.* 2011, 22, 540–545

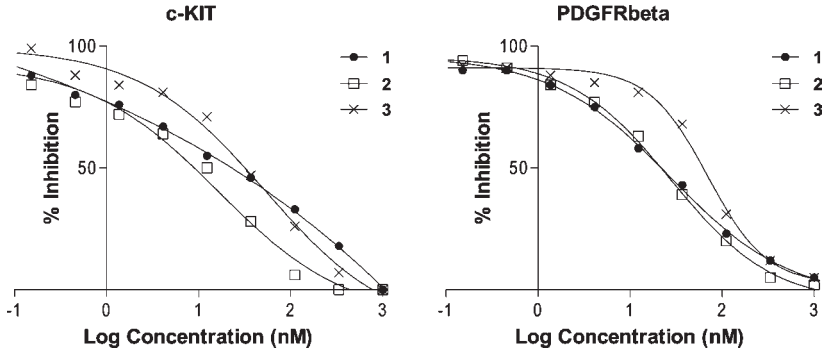


Figure 4. IC_{50} determinations of compounds **1**, **2**, and **3** against recombinant c-KIT and PDGFRβ. Radiometric protein kinase assays were performed with the indicated compounds at various concentrations (0.03−1000 nM). Kinase inhibition was plotted as (%) of total kinase activity (control).

Table 2. IC_{50} for Compounds 1, 2, 3 and the Reference Compound Sunitinib against c-KIT and PDGFRβ

	c-KIT IC_{50} (nM)	PDGFRβ IC_{50} (nM)
1	51	16
2	17	16
3	76	48
sunitinib	23	14

medium (chase time t = 2, 24, 48 h). As shown in Figure 5a, cells treated with **1** rapidly cleared the drug (<2 h), while in the cells treated with **3**, the drug was still detectable after 48 h. Because of its rapid intracellular turnover rate, it is expected that the lysozyme part of the drug conjugate (**3**) is fully degraded within 48 h. In addition, since **1** is rapidly cleared from the cell, we conclude that the oxindole inhibitor is still attached to platinum. In turn, complex **2** could be attached to degradation residues of the lysozyme such as methionine but could also have competitively reacted with GSH or other strong electron-donating-group-rich molecules such as thiol/methionine-rich proteins, thereby creating an intracellular depot of **2′** (representing any metabolite of **2** that is formed by binding at the X-position) from which **1** is slowly released. To verify whether intracellular processing affects the pharmacological activity of **3**, the total tyrosine phosphorylation state was determined in the chased cells. Figure 5b shows that **1** significantly decreased the total endogenous phosphorylation status, but because of its rapid clearance, no significant decrease could be observed 24 and 48 h after exposure. In contrast, treatment with equimolar amounts of **3** produced sustained inhibition on total endogenous tyrosine-residue phosphorylation of >10% for up to 48 h, confirming the presence of pharmacological active **2′** in the cells. These results demonstrate that complexation of **1** to platinum positively alters the efflux kinetics of this multikinase inhibitor without adversely affecting its pharmacological activity.

Taken together, the complexation of platinum to the oxindole-based multikinase inhibitor **1** did not affect its pharmacological activity but additionally provided superior cellular kinetics compared to the free drug. Although the use of platinum as a linker would probably raise questions concerning safety, we have shown that drug−ULS complexes are by far less toxic than the prototypical platinum drug *cis*-diamminedichloroplatinum (CDDP).[16,17] Apart from platinum,[18] several other transition metals such as ruthenium,[19] osmium,[20] iridium,[21] and iron[22] have been complexed to kinase inhibitors without adversely affecting

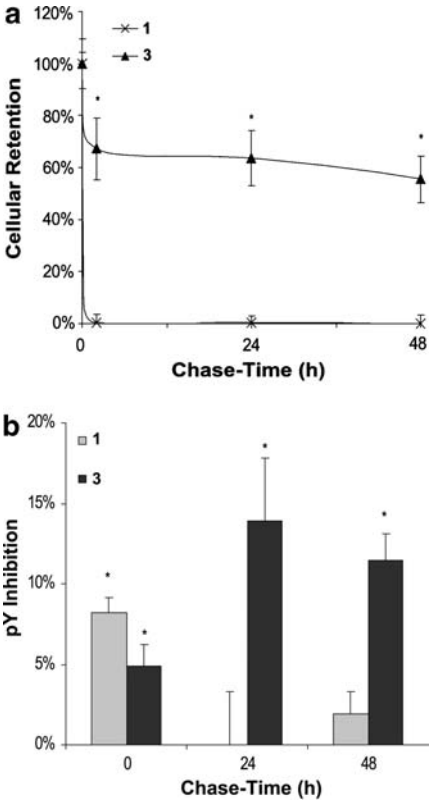


Figure 5. (a) Effect of platinum-based conjugation on cellular retention. Proximal tubular cells (HK-2 cells) were incubated for 24 h (pulse time) with equimolar amounts (10 μM) of **1** or **3**, after which cells were allowed to efflux in blank medium for 0, 24, or 48 h (chase time). Values were normalized to the absolute **1** or **3** levels at t = 0 h (100%) and expressed as % cellular retention. Significance of cellular retention was determined by comparing the intracellular concentration at different time points with the intracellular concentration at t = 0 h (∗, $P < 0.05$). (b) Inhibitory effect of **1** and **3** on the intracellular phosphorylation of tyrosine residues (pY). HK-2 cells were exposed for 24 h (pulse time) with **1** (10 μM) or **3** (10 μM). After the pulse time, the incubation medium was replaced with blank medium (t = 0). At t = 0, 24, and 48 h (chase time) the endogenous pY state was determined by immunostaining of phosphorylated proteins with the anti-pY antibody pY-20. Total pY signal of treated cells was normalized to total pY signal of control cells and expressed as percentage pY inhibition (0% in control cells) (∗, $P < 0.05$).

their pharmacological activity. However, a major difference between these compounds and the now reported platinum

dx.doi.org/10.1021/bc1005637 |*Bioconjugate Chem.* 2011, 22, 540–545

complex is that platinum served as a linker for attachment to a cell-selective carrier and as part of the pharmacophore of the multikinase inhibitor. Organometallic chemistry opens new opportunities in kinase inhibitor drug discovery, as well as in drug delivery research.[23−25] One or more (kinase inhibiting) drugs can be bound to a transition metal center, while drug carriers such as antibodies, peptides, or proteins can be coordinated at another metal ligand-binding site. When properly designed, these complexes will provide intrinsically active-site-selective drug bioconjugates. This could reduce off-target toxicities and eventually enable the clinical use of drugs with currently unfavorable safety or pharmacokinetic profiles.

In conclusion, we have developed an intrinsically active multikinase inhibitor bioconjugate in which platinum not only enabled straightforward linkage but also contributed to improved retention of the multikinase inhibitor in the target cells, thereby prolonging the pharmacological activity of the delivered compound. The developed cell-selective multikinase inhibitor bioconjugate may eventually provide a safe and efficient way to administrate such agents in less life-threatening diseases without inducing dose-limiting off-organ toxicities.

■ ASSOCIATED CONTENT

Supporting Information. Experimental procedures. This material is available free of charge via the Internet at http://pubs.acs.org.

■ AUTHOR INFORMATION

Corresponding Author
*Phone: +31-620275995. E-mail: r.j.kok@uu.nl.

■ ACKNOWLEDGMENT

This work was supported financially by the European Framework Program FP6 (Grant LSHB-CT-2007-036644). Dr. R. W. Sparidans, Dr. E. E. Moret, and Dr. R. Ruijtenbeek are kindly acknowledged for performing the MS analyses and support with molecular modeling and kinase peptide array analyses, respectively.

■ REFERENCES

(1) Tugues, S., Fernandez-Varo, G., Munoz-Luque, J., Ros, J., Arroyo, V., Rodes, J., Friedman, S. L., Carmeliet, P., Jimenez, W., and Morales-Ruiz, M. (2007) Antiangiogenic treatment with sunitinib ameliorates inflammatory infiltrate, fibrosis, and portal pressure in cirrhotic rats. *Hepatology 46*, 1919–1926.

(2) Huang, M., Liu, X., Du, Q., Yao, X., and Yin, K. S. (2009) Inhibitory effects of sunitinib on ovalbumin-induced chronic experimental asthma in mice. *Chin. Med. J. (Engl.) 122*, 1061–1066.

(3) Antoniu, S. A., and Kolb, M. R. (2010) Intedanib, a triple kinase inhibitor of VEGFR, FGFR and PDGFR for the treatment of cancer and idiopathic pulmonary fibrosis. *IDrugs 13*, 332–345.

(4) Hartmann, J. T., Haap, M., Kopp, H. G., and Lipp, H. P. (2009) Tyrosine kinase inhibitors—a review on pharmacology, metabolism and side effects. *Curr. Drug Metab. 10*, 470–481.

(5) Mego, M., Reckova, M., Obertova, J., Sycova-Mila, Z., Brozmanova, K., and Mardiak, J. (2007) Increased cardiotoxicity of sorafenib in sunitinib-pretreated patients with metastatic renal cell carcinoma. *Ann. Oncol. 18*, 1906–1907.

(6) George, S. (2007) Sunitinib, a multitargeted tyrosine kinase inhibitor, in the management of gastrointestinal stromal tumor. *Curr. Oncol. Rep. 9*, 323–327.

(7) Dolman, M. E., Harmsen, S., Storm, G., Hennink, W. E., and Kok, R. J. (2010) Drug targeting to the kidney: advances in the active targeting of therapeutics to proximal tubular cells. *Adv. Drug Delivery Rev. 62*, 1344–1357.

(8) Gajiwala, K. S., Wu, J. C., Christensen, J., Deshmukh, G. D., Diehl, W., DiNitto, J. P., English, J. M., Greig, M. J., He, Y. A., Jacques, S. L., Lunney, E. A., McTigue, M., Molina, D., Quenzer, T., Wells, P. A., Yu, X., Zhang, Y., Zou, A., Emmett, M. R., Marshall, A. G., Zhang, H. M., and Demetri, G. D. (2009) KIT kinase mutants show unique mechanisms of drug resistance to imatinib and sunitinib in gastrointestinal stromal tumor patients. *Proc. Natl. Acad. Sci. U.S.A. 106*, 1542–1547.

(9) Mohammadi, M., McMahon, G., Sun, L., Tang, C., Hirth, P., Yeh, B. K., Hubbard, S. R., and Schlessinger, J. (1997) Structures of the tyrosine kinase domain of fibroblast growth factor receptor in complex with inhibitors. *Science 276*, 955–960.

(10) Sun, L., Liang, C., Shirazian, S., Zhou, Y., Miller, T., Cui, J., Fukuda, J. Y., Chu, J. Y., Nematalla, A., Wang, X., Chen, H., Sistla, A., Luu, T. C., Tang, F., Wei, J., and Tang, C. (2003) Discovery of 5-[5-fluoro-2-oxo-1,2-dihydroindol-(3*Z*)-ylidenemethyl]-2,4-dimethyl-1*H*-pyrrole-3-carboxylic acid (2-diethylaminoethyl)amide, a novel tyrosine kinase inhibitor targeting vascular endothelial and platelet-derived growth factor receptor tyrosine kinase. *J. Med. Chem. 46*, 1116–1119.

(11) Fretz, M. M., Dolman, M. E., Lacombe, M., Prakash, J., Nguyen, T. Q., Goldschmeding, R., Pato, J., Storm, G., Hennink, W. E., and Kok, R. J. (2008) Intervention in growth factor activated signaling pathways by renally targeted kinase inhibitors. *J. Controlled Release 132*, 200–207.

(12) Hilhorst, R., Houkes, L., van den Berg, A., and Ruijtenbeek, R. (2009) Peptide microarrays for detailed, high-throughput substrate identification, kinetic characterization, and inhibition studies on protein kinase A. *Anal. Biochem. 387*, 150–161.

(13) Hilberg, F., Roth, G. J., Krssak, M., Kautschitsch, S., Sommergruber, W., Tontsch-Grunt, U., Garin-Chesa, P., Bader, G., Zoephel, A., Quant, J., Heckel, A., and Rettig, W. J. (2008) BIBF 1120: triple angiokinase inhibitor with sustained receptor blockade and good antitumor efficacy. *Cancer Res. 68*, 4774–4782.

(14) Laird, A. D., Vajkoczy, P., Shawver, L. K., Thurnher, A., Liang, C., Mohammadi, M., Schlessinger, J., Ullrich, A., Hubbard, S. R., Blake, R. A., Fong, T. A., Strawn, L. M., Sun, L., Tang, C., Hawtin, R., Tang, F., Shenoy, N., Hirth, K. P., McMahon, G., and Cherrington (2000) SU6668 is a potent antiangiogenic and antitumor agent that induces regression of established tumors. *Cancer Res. 60*, 4152–4160.

(15) Mendel, D. B., Laird, A. D., Xin, X., Louie, S. G., Christensen, J. G., Li, G., Schreck, R. E., Abrams, T. J., Ngai, T. J., Lee, L. B., Murray, L. J., Carver, J., Chan, E., Moss, K. G., Haznedar, J. O., Sukbuntherng, J., Blake, R. A., Sun, L., Tang, C., Miller, T., Shirazian, S., McMahon, G., and Cherrington, J. M. (2003) In vivo antitumor activity of SU11248, a novel tyrosine kinase inhibitor targeting vascular endothelial growth factor and platelet-derived growth factor receptors: determination of a pharmacokinetic/pharmacodynamic relationship. *Clin. Cancer Res. 9*, 327–337.

(16) Prakash, J., Sandovici, M., Saluja, V., Lacombe, M., Schaapveld, R. Q., de Borst, M. H., van Goor, H., Henning, R. H., Proost, J. H., Moolenaar, F., Keri, G., Meijer, D. K., Poelstra, K., and Kok, R. J. (2006) Intracellular delivery of the p38 mitogen-activated protein kinase inhibitor SB202190 [4-(4-fluorophenyl)-2-(4-hydroxyphenyl)-5-(4-pyridyl)1*H*-imidazole] in renal tubular cells: a novel strategy to treat renal fibrosis. *J. Pharmacol. Exp. Ther. 319*, 8–19.

(17) Moreno, M., Gonzalo, T., Kok, R. J., Sancho-Bru, P., van Beuge, M., Swart, J., Prakash, J., Temming, K., Fondevila, C., Beljaars, L., Lacombe, M., van der Hoeven, P., Arroyo, V., Poelstra, K., Brenner, D. A., Gines, P., and Bataller, R. (2010) Reduction of advanced liver fibrosis by short-term targeted delivery of an angiotensin receptor blocker to hepatic stellate cells in rats. *Hepatology 51*, 942–952.

(18) Williams, D. S., Carroll, P. J., and Meggers, E. (2007) Platinum complex as a nanomolar protein kinase inhibitor. *Inorg. Chem. 46*, 2944–2946.

(19) Zhang, L., Carroll, P., and Meggers, E. (2004) Ruthenium complexes as protein kinase inhibitors. *Org. Lett. 6*, 521–523.

(20) Maksimoska, J., Williams, D. S., Atilla-Gokcumen, G. E., Smalley, K. S., Carroll, P. J., Webster, R. D., Filippakopoulos, P., Knapp, S.,

Herlyn, M., and Meggers, E. (2008) Similar biological activities of two isostructural ruthenium and osmium complexes. *Chemistry 14*, 4816–4822.

(21) Wilbuer, A., Vlecken, D. H., Schmitz, D. J., Kraling, K., Harms, K., Bagowski, C. P., and Meggers, E. (2010) Iridium complex with antiangiogenic properties. *Angew. Chem., Int. Ed. 49*, 3839–3842.

(22) Spencer, J., Mendham, A. P., Kotha, A. K., Richardson, S. C., Hillard, E. A., Jaouen, G., Male, L., and Hursthouse, M. B. (2009) Structural and biological investigation of ferrocene-substituted 3-methylidene-1,3-dihydro-2*H*-indol-2-ones. *Dalton Trans. 14*, 918–921.

(23) Gasser, G., Ott, I., and Metzler-Nolte, N. (2011) Organometallic anticancer compounds. *J. Med. Chem. 54*, 3–25.

(24) Chavain, N., and Biot, C. (2010) Organometallic complexes: new tools for chemotherapy. *Curr. Med. Chem. 17*, 2729–2745.

(25) Hillard, E. A., and Jaouen, G. (2011) Bioorganometallics: future trends in drug discovery, analytical chemistry, and catalysis. *Organometallics 30*, 20–27.

Supporting Information

Development of a Cell-Selective and Intrinsically Active Multikinase Inhibitor Bioconjugate

Stefan Harmsen, M.E. (Emmy) M. Dolman, Zoltan Nemes, Marie Lacombe, Bálint Szokol, János Pató, György Kéri, László Őrfi, Gert Storm, Wim E. Hennink, and Robbert J. Kok

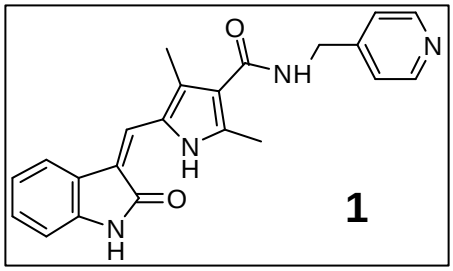
1. Materials and Methods

All chemicals used in this study were of analytical grade or equivalent and obtained from Sigma Aldrich (Zwijndrecht, the Netherlands) and used without further purification unless otherwise stated. The multikinase inhibitor precursor (*Z*)-2,4-dimethyl-5-((2-oxoindolin-3-ylidene)methyl-1*H*-pyrrole-3-carboxylic acid was synthesized by Vichem Chemie (Budapest, Hungary). Universal Linkage System™ (monochloro-mononitrato(ethylenediamine)platinum(II)) was provided by Kreatech (Amsterdam, the Netherlands). HPLC grade acetonitrile (ACN), methanol (MeOH), isopropanol (IPA), formic acid (FA) and *N,N'*-dimethylformamide (DMF) which was dried over molecular sieve before use were purchased from Biosolve (Valkenswaard, the Netherlands). Products were characterized by $^{1}H/^{195}Pt$ NMR and LC-MS/MS. $^{1}H/^{195}Pt$ NMR spectra were recorded on a Varian Gemini (300 MHz; 298 K; Varian Associates Inc., NMR Instruments, Palo Alto, CA) NMR spectrometer. The LC-MS/MS equipment consisted of an Accela pump and autosampler and a TSQ Quantum Ultra quadrupole mass spectrometer with heated electrospray ionization (Thermo Fisher Scientific, San Jose, CA, USA). Data were recorded on and the system was controlled by a Dell Precision T3400 personal computer, equipped with the Thermo Fisher Xcalibur software (version 2.07). 5-µl injections were made on an Aquity UPLC® BEH C18 column (30 × 2.1mm × 1.7 µm; Waters, Milford, USA) with the corresponding VanGuard pre-column (5 × 2.1mm × 1.7 µm; Waters, Milford, USA). Column temperature was maintained at 40˚C and the autosampler was maintained at 4˚C. A 20-90% gradient of solvent B over 2.5 min with a 0.5 ml/min flow rate was used. Solvent A consisted of 0.1% (v/v) formic acid in water and solvent B of methanol. The eluate was totally led into the electrospray probe, oriented at "+1" in the X-, at "1" in the Y- and at "C" in the Z-direction, from 0.7 min after injection. Electrospray (ESI+) settings were a 4000 V spray voltage, 350°C capillary and vaporizer temperatures and a 1.0 mTorr argon collision pressure. The mass resolution was set at 0.7 full with at half height (unit resolution) for both separating quadrupoles.

2. Molecular Modeling of an oxindole-based inhibitor in the ATP-binding pocket of c-KIT

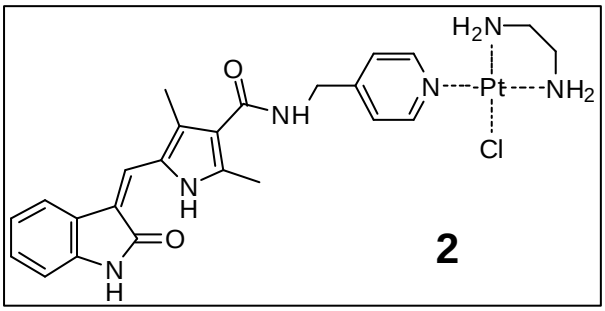
YASARA (www.yasara.org; version 10.6.1) was used to evaluate how oxindole-based multikinase inhibitors generally bind to their targets. Therefore, protein structures co-crystallized with either sunitinib (3G0E) or intedanib (3C7Q) were downloaded from www.pdb.org and their orientation in the binding pocket of their target kinases was studied. YASARA was additionally used to generate a graphic representation of how compound **2** would bind to c-KIT by modification of the structure used in 3G0E.

3. Synthesis of the multikinase inhibitor (1), multikinase inhibitor platinum complex (2) and drug-lysozyme conjugate (3)



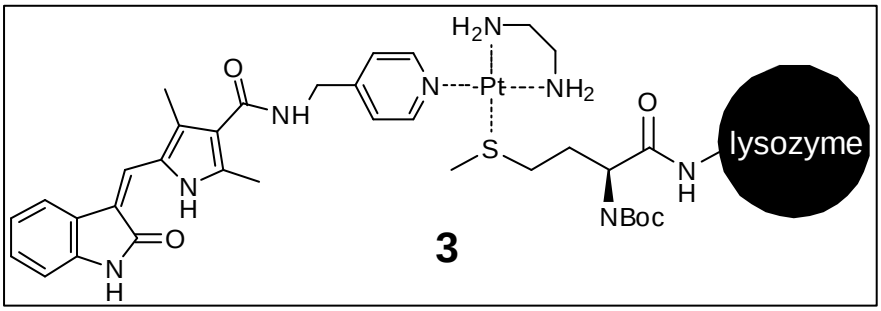
Synthesis of multikinase inhibitor (1) ((*Z*)-2,4-dimethyl-5-((2-oxoindolin-3-ylidene)methyl)-*N*-(pyridin-4-ylmethyl)-1*H*-pyrrole-3-carboxamide)

Compound **1** was synthesized according to methods described by Sun *et al*[1]. In brief, (*Z*)-2,4-dimethyl-5-((2-oxoindolin-3-ylidene)methyl-1*H*-pyrrole-3-carboxylic acid (1.0 g, 3.5 mmol) was suspended in 40 ml dry DMF and 4-(aminomethyl)pyridine (0.38 g, 3.5 mmol), EDC (0.81 g, 4.2 mmol), HOBt (0.57 g, 6.0 mmol) and triethylamine (0.74 ml, 5.3 mmol) were added to the suspension and stirred at 50^{o}C for 72 hours. The solvent was removed under reduced pressure and the residue was taken up with water and the product was filtered off yielding compound **1** (0.72 g, 54%). ^{1}H NMR (300 MHZ, DMF-d_7): δ (ppm): 10.87 (s, 1H, NH); 8.55 (d, 2H, 2CH, ^{3}J=4.2 Hz); 8.11 (t, 1H, NH); 7.85 (d, 1H, CH, ^{3}J=7.6 Hz); 7.79 (s, 1H, CH); 7.41 (d, 2H, 2CH, ^{3}J=5.0 Hz); 7.18 (t, 1H, CH, ^{3}J=7.6 Hz); 7.02 (t, 1H, CH, ^{3}J=7.6 Hz); 6.97 (d, 1H, CH); 4.60 (d, 2H, CH_2, ^{3}J=6.1); 2.56 (s, 3H, CH_3); 2.55 (s, 3H, CH_3). MS (ESI^{+}) calcd. for $C_{22}H_{20}N_4O_2H^{+}$ $[M+H]^{+}$ 373, detected 373.



Synthesis of multikinase inhibitor platinum(II) complex (2)

Compound **1** (15.0 mg, 40.3 μmol) was reacted with monochloro-mononitrato (ethylenediamine)platinum(II) (Universal Linkage System (ULS)^{TM}- nitrate; 14.2 mg , 40.3 μmol) in DMF for 2 hours at 37^{o}C to yield compound **2** (23.1 mg, 83.4%). ^{195}Pt NMR (300 MHz, DMF-d_7) -2492 ppm (N3PtCl). ^{1}H NMR (300 MHz, DMF- d_7): δ (ppm): 10.91 (s, 1H, NH); 8.80 (d, 2H, 2CH, ^{3}J=5.6 Hz); 8.23 (t, 1H, NH); 7.86 (d, 1H, CH); 7.81 (s, 1H, CH); 7.62 (d, 2H, 2CH, ^{3}J=6.2 Hz); 7.19 (t, 1H, CH, ^{3}J=7.7 Hz); 7.04 (t, 1H, CH, ^{3}J=7.4 Hz); 7.00 (d, 1H, CH); 6.31 (s, 2H, NH_2), 5.89 (s, 2H, NH_2); 4.69 (d, 2H, CH_2,^{3}J=5.7 Hz); 2.58 (s, 3H, CH_3); 2.57 (s, 3H, CH_3); 1.56 (t, 2H, CH_2); 1.29 (s, 2H, CH_2).MS (ESI^{+}) calcd. for $C_{24}H_{28}N_6O_2HPtCl$ $[M+H]^{+}$ 663, detected 663 $[M+H]^{+}$.



Conjugation of a multikinase inhibitor platinum(II) complex to methionylated lysozyme (3)

Methionylated lysozyme was synthesized as previously described by Fretz *et al.*[2]. Compound **2** (15.5 mg, 23.3 μmol) was reacted with methionylated lysozyme (112.1 mg, 7.8 μmol overnight in 0.02 M tricine/sodium nitrate buffer (pH 8.5). The product was purified by dialysis (molecular weight cut-off 10,000 Da) against ultrapure water (MilliQ, Millipore, Bedford, MA, USA) and lyophilized. MS (ESI^{+}) calcd. for

$C_{24}H_{28}N_6O_2HPt$-LZM $[M+H]^+$ 14930, detected 1493.0 $[M+H]^{10+}$ and 1357.2 $[M+H]^{11+}$ corresponding with 14930 $[M+H]^+$. Conjugation efficiency was determined as described previously[2]. Liberated **1** was quantified in samples containing **3** incubated overnight at 80°C in the presence of the strong platinum ligand thiocyanate (SCN; 0.5 M) thereby competitively displacing compound **1** from ULS by HPLC-photodiodearray (PDA) analysis at 431 nm. The HPLC system consisted of a Waters 717 autosampler, Waters 600 pumps and a Waters 2996 Photodiode Array Detector (Waters, Milford, USA). Data were recorded with Empower software (version2.0; Waters). 50-µl injections were made on SunFire™ C18 column (150 × 4.6mm × 5 µm; Waters). Gradient elution according to table S1 at 1 ml/min was used with solvent A consisting of 5 % ACN in water + 0.1 % TFA (w/w) and solvent B of 0.1 % TFA (w/w) in ACN. The molar coupling ratio was determined to be 0.9:1 (drug-ULS:LZM). ChemDraw Ultra 12.0 was used to prepare draw the above molecular structures and those in scheme 1.

Table S1

t [min]	%B
0	0
25	80
26	100
33	100
34.5	0

4. Determination of intrinsic activity

Cell lysate was prepared by lyzing serum-starved HK-2 cells using mammalian protein extraction reagent (M-PER) containing protease and phosphatase inhibitors (Thermo Fischer Scientific, Etten-Leur, the Netherlands). Protein concentrations were determined using the BCA protein determination assay (Thermo Fischer Scientific). HK-2 cell lysate (0.1 mg/ml) was pre-incubated with equimolar amounts of **1**, **2** complex, or the **3** drug conjugate at room temperature for 30 minutes. Phosphorylation was initiated by adding 1 µM ATP in Abl kinase assay buffer (50 mM Tris–HCl [pH

7.5], 10 mM $MgCl_2$, 1 mM ethyleneglycoltetraacetic acid (EGTA), 2 mM dithiothreitol (DTT), and 0.01% Brij-35). The reaction mixture was incubated at 37°C for 60 minutes. Phosphorylation was terminated by adding reducing sample buffer (Invitrogen, Breda, the Netherlands) containing a final concentration of 40 mM DTT and 0.1% (w/v) SDS. Total protein (10 μg) was separated by SDS-polyacrylamide gel electrophoresis using NuPage novex 4-12% bis-tris gradient gels (Invitrogen, Breda, the Netherlands). Proteins were electroblotted onto Immobilon P polyvinylidenefluoride (PVDF) membranes (Millipore). After blocking (1 hour at RT) with 3% (w/v) BSA in tris-buffered saline containing 0.1% (v/v) Tween-20, the membranes were incubated for 1 hour at RT with a murine monoclonal anti-phosphotyrosine (pY) primary antibody (pY-20; 1:500; Abcam, Cambridge, UK) coupled to horse radish peroxidase (HRP). β-actin (1:10000; AC-15; Abcam, Cambridge, UK) was used as a loading control. The proteins were visualized by a chemiluminescence-based detection reagent (SuperSignal West Femto; Thermo Fischer Scientific, Etten-Leur, the Netherlands) and band density was determined on a Gel Doc XRS Imaging system with Quantity One analysis software (Bio-Rad, Hercules, CA, USA).

5. Cellular uptake and retention

Cell culturing

The human kidney proximal tubular cell line HK-2 (ATCC, LGC Standards, Middlesex, UK) was cultured in Dulbecco's Modified Eagle's Medium (DMEM) containing 3.7 g/L sodium bicarbonate, 1.0 g/L glucose, supplemented with 10% (v/v) fetal bovine serum, penicillin (100 U/L), streptomycin (100 μg/mL) and amphotericin B (0.25 μg/mL) at 37°C with 5% CO_2 in humidified air. All cell culture related media were obtained from PAA Laboratories GmbH (Pasching, Austria).

Cellular uptake

HK-2 cells (1.5×10^4 cells/well) were seeded onto 96-well plates. Cells were serum-starved overnight before the uptake experiments were initiated. Cellular uptake was studied by incubating the HK-2 cells with **1** (10 μM) or **3** (10 μM) for different time

intervals (t=0, 1, 2, 3, 24, 48, 72 h) at 4°C (only 1, 2, 3 h) or 37°C. Uptake was determined by measuring the cellular optical density (OD) at 431 nm of **1** and 700 nm (reference wavelength) with a Versamax microplate reader (Molecular Devices, Sunnyvale, CA, USA). Values were normalized to the number of living cells (as determined with an Alamar Blue assay). The obtained data were analyzed and processed with Microsoft Excel (figure 3a).

Cellular retention

Cellular retention was studied by incubating serum-starved HK-2 cells (1.5×10^4 cells/well) with either 10 μM **1** or 10 μM **3**. After 24 h (indicated as t = 0 h), cells were washed thrice with phosphate buffered saline (PBS) and medium was replaced with blank serum-free DMEM medium every 24 hours. Cellular retention was determined by measuring the cellular $OD_{431/700}$ (normalized to the number of living cells (Alamar Blue). The obtained data were analyzed and processed with Microsoft Excel (figure 4a).

6. Cellular activity

PamChip® Peptide microarray

A microarray-based multiplex method with real-time detection was used to determine the inhibitory activity of **3** on the phosphorylation of peptide substrates that correspond with human proteins. In brief, HK-2 cell lysate (prepared from lysis with MPER) spiked with **1** (2 μM) or **3** (2 μM) were incubated on a tyrosine kinase PamChip® microarray (PamGene International BV, 's-Hertogenbosch, the Netherlands) with 10 μM ATP at 30°C in a total volume of 25 μL. Just prior to the incubations, the PamChip was blocked with 2% (w/v) BSA in water and washed three times with Abl kinase assay buffer. After application onto the array, the incubation mixture was pumped up and down through the array for 152 cycles at a rate of 2 cycles per minute. Peptide phosphorylation was detected with a monoclonal murine anti-phosphotyrosine primary antibody (pY-20) coupled to FITC. Images of each array were taken every fifth cycle.

Data generated on PamChip peptide microarrays were analyzed with Bionavigator software (PamGene). The software quantifies signal intensity in each spot and its background, calculates signal minus background[3]. The obtained data was ranked based on strongest pY inhibition compared to control, and graphics were prepared with Microsoft Excel (figure 3b).

IC_{50} determination

IC_{50} determinations of the compounds **1**, **2** and **3** against platelet derived growth factor receptor (PDGFR)-β and c-KIT were performed by SignalChem (Richmond, Canada). In brief, protein kinase assays were performed in duplicate at room temperature for 30 min in a final volume of 25 µL containing ~10-20 nM recombinant kinase, peptide substrate (0.2 µg/µL), 5 µM ^{33}P-ATP (0.04 µCi; PerkinElmer, Waltham, MA, USA), and the indicated compounds at concentrations ranging from 0.03 nM-1000 nM in kinase buffer. After the incubation period, the assay was terminated by spotting 10 µL of the reaction mixture onto Multiscreen phosphocellulose P81 plate. The Multiscreen phosphocellulose P81 plate was washed 3 times 15 minutes in a 1% phosphoric acid solution. The radioactivity on the P81 plate was counted in the presence of scintillation fluid in a Trilux scintillation counter. The data was analyzed with Prism 5.0 (Graphpad Software Inc, La Jolla, CA, USA).

In-cell Western blotting

After incubation, cells were washed thrice with ice-cold PBS and were fixed with 3% (v/v) formaldehyde (Sigma Aldrich) for 15 minutes. Cells were permeabilized by washing five times with 0.1% (v/v) triton X-100 (Sigma Aldrich) in PBS for 5 minutes and blocked for 1 h with 3% (w/v) BSA. After blocking, cells were incubated with a horseradish peroxidase coupled primary antibody raised against phosphorylated tyrosine residues (pY-20; Abcam, Cambridge, UK). After 1 h, cells were washed thrice with PBS and phosphorylation was visualized with a chemiluminescence-based detection reagent (SuperSignal West Femto; Pierce, Rockford, IL, USA). The signal intensities were determined on a Gel Doc XRS Imaging system with Quantity One

analysis software (Bio-Rad, Hercules, CA, USA). The obtained data were analyzed with Microsoft Excel (figure 4b).

7. References

1) Sun, L., Liang, C., Shirazian, S., Zhou, Y., Miller, T., Cui, J., Fukuda, J. Y., Chu, J. Y., Nematalla, A., Wang, X., Chen, H., Sistla, A., Luu, T. C., Tang, F., Wei, J., and Tang, C. (2003) Discovery of 5-[5-fluoro-2-oxo-1,2- dihydroindol-(3Z)-ylidenemethyl]-2,4- dimethyl-1H-pyrrole-3-carboxylic acid (2-diethylaminoethyl)amide, a novel tyrosine kinase inhibitor targeting vascular endothelial and platelet-derived growth factor receptor tyrosine kinase. *J Med Chem* 46, 1116-1119.

(2) Fretz, M. M., Dolman, M. E., Lacombe, M., Prakash, J., Nguyen, T. Q., Goldschmeding, R., Pato, J., Storm, G., Hennink, W. E., and Kok, R. J. (2008) Intervention in growth factor activated signaling pathways by renally targeted kinase inhibitors. *J Control Release 132*, 200-207.

(3) Hilhorst, R., Houkes, L., van den Berg, A., and Ruijtenbeek, R. (2009) Peptide microarrays for detailed, high-throughput substrate identification, kinetic characterization, and inhibition studies on protein kinase A. *Anal Biochem 387*, 150-161.

Bioconjugate Chemistry

COMMUNICATION

pubs.acs.org/bc

Supramolecular Complexing of Membane Siglec CD22 Mediated by a Polyvalent Heterobifunctional Ligand that Templates on IgM

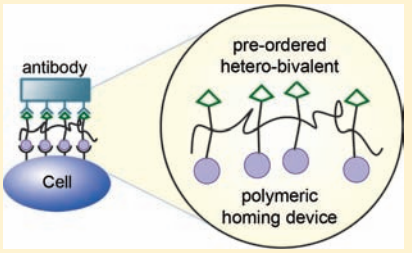
Lina Cui,[†] Pavel I. Kitov,[†] Gladys C. Completo,[‡] James C. Paulson,[‡] and David R. Bundle*[,†]

[†]Department of Chemistry, Alberta Ingenuity Centre for Carbohydrate Science, University of Alberta, Edmonton, Alberta, Canada

[‡]Department of Chemical Physiology, The Scripps Research Institute, 10550 North Torrey Pines Road, La Jolla, California 92037, United States

Supporting Information

ABSTRACT: We report the synthesis and *in vitro* evaluation of a multivalent homing device, a polymer which contains preordered pendant groups with dual specificity, a trisaccharide moiety, which is specific for the siglec CD22, and an antibody specific hapten, nitrophenol. The device efficiently attracts antihapten IgM to the surface of human lymphoma B cells as well as to CD22-conjugated magnetic beads by mediating the formation of a ternary complex on the surface of the target.



Directing neutralizing proteins such as antibodies to pathogenic agents using heterobifunctional ligands that contain binding fragments for both receptors has emerged as a promising therapy against cancer,[1−5] viral or bacterial infection,[6−16] and Alzheimer's disease.[17] Surface-bound receptors and oligomeric proteins that possess multiple unidirectional binding sites can bind multiple copies of heterobifunctional ligands, allowing the other head groups to attract their cognate proteins to form supramolecular ternary complexes.[18] Due to saving of binding entropy, the efficiency of the ligand binding to its target can be enhanced by several orders of magnitude, while the templating protein can perform additional effector functions.[8,14,15]

Our efforts are directed to application of supramolecular templating to cancer immunotherapy. CD22, a member of the siglec family of glycan-binding proteins, is expressed on the B cell surface as a key regulator of signaling[19] and has been identified as a target for immunotherapy (B cell depletion therapy) to treat B cell lymphomas and autoimmune diseases.[20] However, targeting CD22 using its glycan ligands is challenging due to the low intrinsic affinity that CD22 exhibits for its native ligands (NeuAcα(2−6)Galβ, $K_d \approx 0.2$ mM). Additionally, CD22 is glycosylated with the self-ligand and these *cis* interactions mask the ligand binding sites.[21,22]

Previously, we reported heterobifunctional ligands, which comprise CD22 ligand, NeuAcα(2−6)Galβ(1−4)GlcNAc, modified at the C-9 position of neuraminic acid with biphenyl carbonylamido (BPC) substituent, which is known to increase the affinity for CD22 by a factor of 100.[21] The heterodimer of this ligand with a nitrophenol (NP) moiety was able to overcome receptor-masking *cis* interactions and dock anti-NP antibodies to B cell.[23] We sought to develop an efficient way to construct polyvalent heterobifunctional ligands and to evaluate the influence of polyvalency on the ligand-mediated assembly of supramolecular immune complexes on cell membrane (Figure 1).

We have previously found that the supramolecular templating effect is not observed when the two binding functionalities are independently distributed on a polymer scaffold.[16] In order to mediate the formation of ternary complexes, the pendant ligands must be arranged as heterobifunctional units on the polyvalent scaffold; hence, we designed a homing device comprising 5 major components: a mulvalent scaffold, polyacrylamide (PAA); a spacer, tri(ethylene glycol) derivative; a bifurcation unit, selectively protected lysine; and 2 specific ligands, trisaccharide and nitrophenol.

Compound **1** (Figure 2) was assembled by sequential elaboration of polyacrylamide (Scheme 1). First, a spacer was introduced by trans-amination of PAA. To the resulting polymeric amine an orthogonally protected glycine derivative (Boc and Fmoc) was attached to provide a bifurcation fragment, which permits sequential installation of two different ligands. Removal of Fmoc protection followed by acylation of the liberated amine with the NHS ester of 4-hydroxy-3-nitrophenylacetic acid yielded polymer **6**. After removal of Boc, the second amine was capped as propargyloxycarbamoyl **7**. The trisaccharide ligand **8** was synthesized chemo-enzymatically as previously reported[24] and incorporated into the polymer *via* copper(I)-catalyzed Huisgen cyclization to give the desired polyvalent heterobifunctional ligand **1**.

To evaluate the ability of the polyvalent ligand **1** to drive complex formation between IgM and CD22 on B cells, human

Received: December 17, 2010
Revised: March 15, 2011
Published: March 15, 2011

ACS Publications © 2011 American Chemical Society

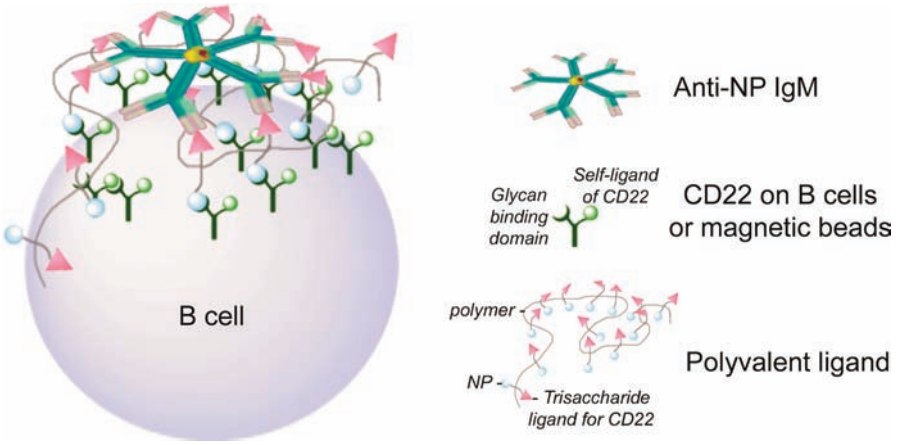


Figure 1. Assembly of immune complex of IgM and CD22 mediated by a polyvalent heterobifunctional ligand.

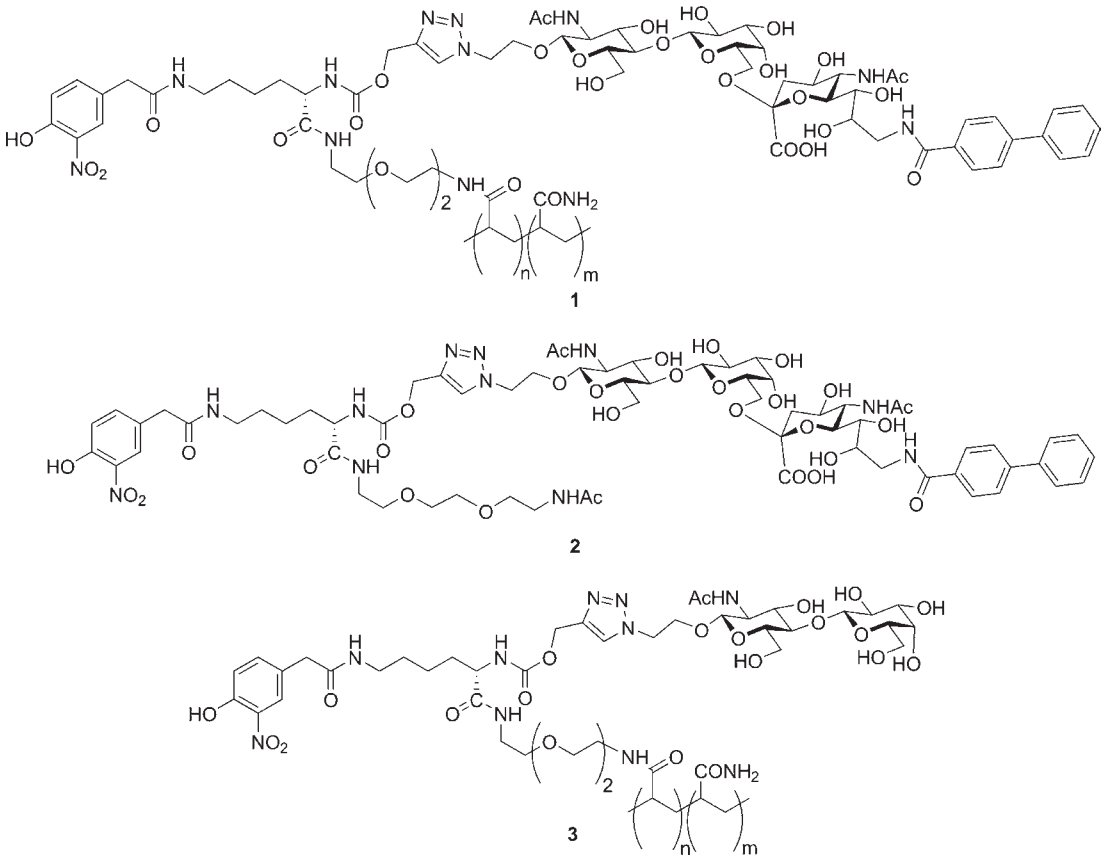


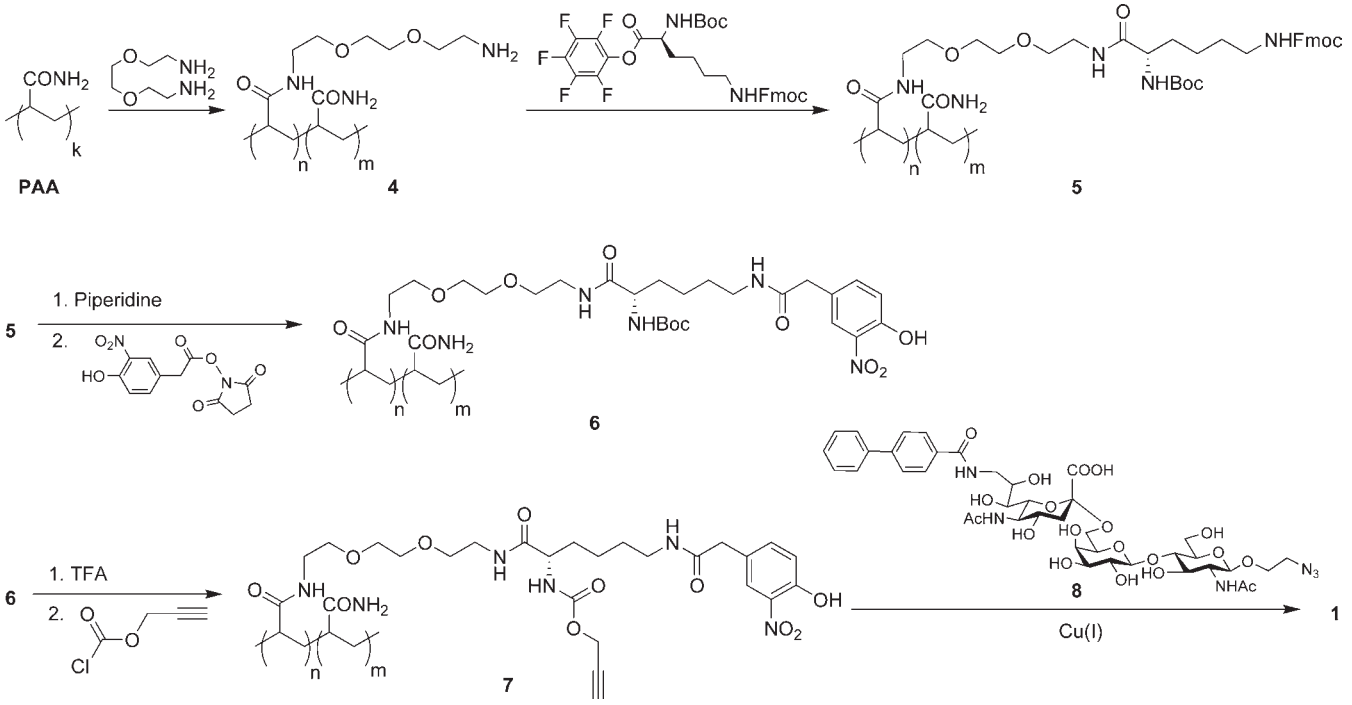
Figure 2. Structures of polyvalent heterobifunctional ligand **1**, its unimeric control ligand **2**, and its polyvalent LacNAc control ligand **3**.

lymphoma cells (BJAB) were incubated with anti-NP IgM at fixed concentration (10 μg/mL), and polyvalent ligand **1**, its unimeric analogue **2**, then stained with FITC-labeled anti-IgM antibody, and analyzed by flow cytometry. As shown in Figure 3, only in the presence of ligand **1** (at all tested concentrations higher than 0.04 μg/mL) was anti-NP IgM associated with B cells. In comparison, only background fluorescence was observed for the unimeric ligand **2**. In separate experiments, the polyvalent LacNAc control (compound **3**), lacking the terminal neuraminic acid moiety, showed no binding to the BJAB cells (not shown). This is consistent with our previous observations that, although the longer linker between the ligand and antigen (NP) reduces the ability of the heterobivalent ligand to mediate formation of a ternary complex between two multivalent proteins due to the loss of conformational entropy,[23] it still allows templating on anti-NP-IgM when presented on a polymeric scaffold.[15] If confirmed by further examples, this effect may have important implications for the design of multivalent heterobifunctional homing devices.

Complex formation between IgM and CD22 on B cells was concentration dependent for polyvalent ligand **1** and, as expected, was described by a bell-shaped curve (Figure 3b). The binding peaked at 2.5 μg/mL of ligand **1** and became inhibitory at higher concentrations, presumably due to saturation of one or

dx.doi.org/10.1021/bc100579d |*Bioconjugate Chem.* 2011, 22, 546–550

Scheme 1. Synthesis of Polyvalent Heterobifunctional Ligand 1



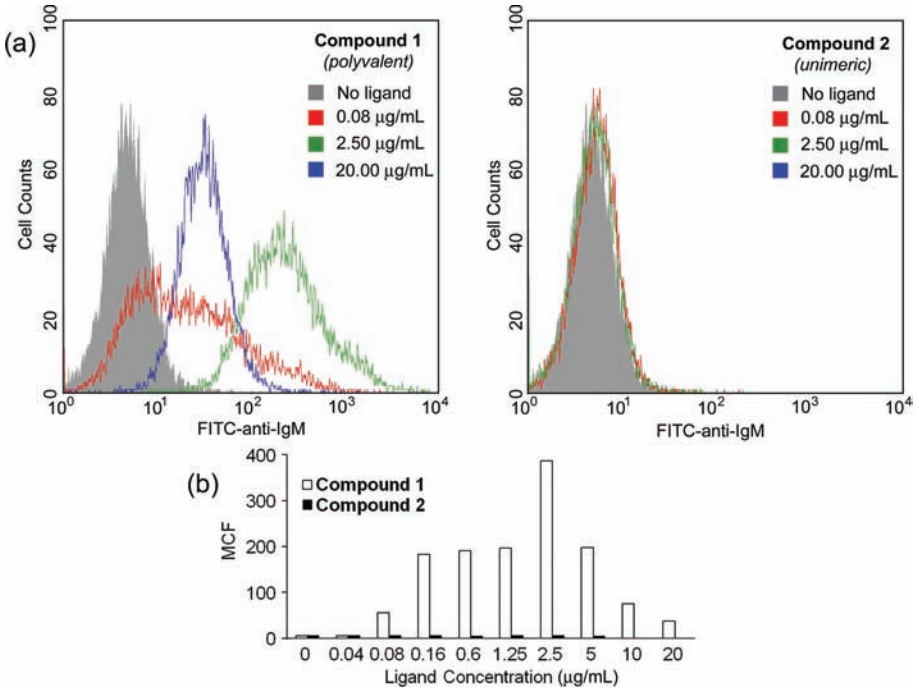


Figure 3. Binding of anti-NP IgM to CD22 on BJAB cells. Formation of IgM-CD22 complex was assessed by incubating BJAB cells with ligands at various concentrations and FITC labeled anti-NP IgM at 10 μg/mL, staining with FITC-anti-IgM, and measuring cell fluorescence by flow cytometry. (a) Histograms of cells treated with polyvalent ligand **1** (left) and unimeric ligand **2** (right). (b) Comparison of mean channel fluorescence (MCF) of cell samples treated with **1** and **2** at various concentrations.

both proteins by the ligand. Such dose dependence is typical for cross-linked complexes and was previously observed by us[23] and others.[25,26]

To eliminate cell-related effects such as ligand-mediated endocytosis and lateral mobility of CD22 in the cell membrane, we also evaluated complex formation using magnetic beads with immobilized CD22 (Figure 4). Anti-NP IgM and magnetic beads were incubated with ligand **1** at various concentrations at both 37 and 4 °C, and the beads were treated with FITC-anti-IgM antibody and analyzed using flow cytometry. The results agreed

dx.doi.org/10.1021/bc100579d |*Bioconjugate Chem.* 2011, 22, 546–550

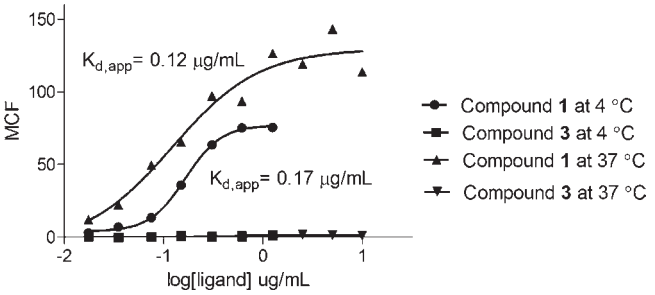


Figure 4. Avidity of complex formation mediated by ligands **1** and **3** was analyzed by titrating ligands in the presence of CD22 immobilized on magnetic beads and FITC labeled anti-NP IgM (5 μg/mL) and measuring bead fluorescence by flow cytometry. Mean channel fluorescence (MCF) is plotted against ligand concentration.

well with the experiments performed on B cells. Complex formation was a dose-dependent process at both temperatures, and more IgM were associated with magnetic beads with the increase of the concentration of ligand **1** until a plateau was reached. Neither the polyvalent control lacking the CD22 ligand (compound **3**) nor the monovalent compound **2** (not shown) supported binding of the anti-NP antibody to beads. The apparent K_d values were found to be 0.12 μg/mL (0.024 nM per pendant ligand) and 0.17 μg/mL (0.034 nM per pendant ligand) at 37 and 4 °C, respectively. This represents a 5000-fold (at 37 °C) and 200-fold (at 4 °C) higher binding affinity over the best univalent ligand identified previously.[23]

More interestingly, the polymeric heterobifunctional ligand exhibited significantly positive binding entropy with little temperature dependency (very similar K_d's at different temperatures) (Figure 4). This is in sharp contrast with previously examined unimeric ligands, which showed a 10- to 20-fold decrease in affinity when temperature increased from 4 to 37 °C due to faster dissociation at higher temperature.[23] Considering mainly the entropic nature of the multivalency effect, which reduces entropy loss upon complex formation (smaller value of ΔS term in binding energy), the weak dependence of the apparent binding constants on temperature for multivalent ligands is expected. Binding of carbohydrate ligands to lectins is often accompanied by a large favorable enthalpy change (ΔH), which is partially offset by an almost equally large unfavorable entropy term ($-T\Delta S$) resulting in low net change in free energy.[27] Multivalent presentation leads to the decrease in absolute value of both thermodynamic terms per pendant ligand with entropy term changing faster.[28] It has also been shown that ΔS can even change the sign and become positive for polymeric ligands.[29] In accord with higher avidity, an increase in net binding of IgM to the beads was observed at 37 °C, which can be attributed to a reduced rate of dissociation and more IgM retention after washing steps as discussed previously in our report on unimeric heterobifunctional ligands.[23]

In conclusion, we report a polymer-based heterobifunctional ligand as a potent homing device that redirects antibodies to cell-surface receptors that are overexpressed on lymphoma B cells. These data suggest new applications of polymeric drugs in targeted cancer therapy that together with other properties, such as enhanced permeability and retention (EPR) effect and prolonged retention in the circulatory system, render them attractive as potential therapeutics.

■ ASSOCIATED CONTENT

Supporting Information. Details of experimental procedures. This material is available free of charge via the Internet at http://pubs.acs.org.

■ AUTHOR INFORMATION

Corresponding Author

*Correspondence should be addressed to Prof. David Bundle, Department of Chemistry, Alberta Ingenuity Centre for Carbohydrate Science, University of Alberta, Edmonton, Alberta, Canada. Phone: (+1) 780 492 8808. E-mail: dave.bundle@ualberta.ca.

■ ACKNOWLEDGMENT

We thank Dr. Ryan T. McKay (NANUC, Edmonton) for his help in characterization of compound **1** using 800 MHz NMR and Dr. Norihito Kawasaki for his kind assistance in preparation of the manuscript. This work was supported by Alberta Ingenuity Centers Program and NIH grants GM60938 and AI16165).

■ REFERENCES

(1) Carlson, C. B., Mowery, P., Owen, R. M., Dykhuizen, E. C., and Kiessling, L. L. (2007) Selective tumor cell targeting using low-affinity, multivalent interactions. *ACS Chem. Biol. 2*, 119–127.

(2) Owen, R. M., Carlson, C. B., Xu, J. W., Mowery, P., Fasella, E., and Kiessling, L. L. (2007) Bifunctional ligands that target cells displaying the alpha$_v$beta$_3$ integrin. *ChemBioChem. 8*, 68–82.

(3) Murelli, R. P., Zhang, A. X., Michel, J., Jorgensen, W. L., and Spiegel, D. A. (2009) Chemical control over immune recognition: a class of antibody-recruiting small molecules that target prostate cancer. *J. Am. Chem. Soc. 131*, 17090–17092.

(4) Popkov, M., Gonzalez, B., Sinha, S. C., and Barbas, C. F. (2009) Instant immunity through chemically programmable vaccination and covalent self-assembly. *Proc. Natl. Acad. Sci. U.S.A. 106*, 4378–4383.

(5) Lu, Y. J., Sega, E., Leamon, C. P., and Low, P. S. (2004) Folate receptor-targeted immunotherapy of cancer: mechanism and therapeutic potential. *Adv. Drug Delivery Rev. 56*, 1161–1176.

(6) Bertozzi, C. R., and Bednarski, M. D. (1992) Antibody targeting to bacterial-cells using receptor-specific ligands. *J. Am. Chem. Soc. 114*, 2242–2245.

(7) Bertozzi, C. R., and Bednarski, M. D. (1992) A receptor-mediated immune-response using synthetic glycoconjugates. *J. Am. Chem. Soc. 114*, 5543–5546.

(8) Liu, J. Y., Zhang, Z. S., Tan, X. J., Hol, W. G. J., Verlinde, C., and Fan, E. K. (2005) Protein heterodimerization through ligand-bridged multivalent pre-organization: Enhancing ligand binding toward both protein targets. *J. Am. Chem. Soc. 127*, 2044–2045.

(9) Krishnamurthy, V. M., Quinton, L. J., Estroff, L. A., Metallo, S. J., Isaacs, J. M., Mizgerd, J. P., and Whitesides, G. M. (2006) Promotion of opsonization by antibodies and phagocytosis of Gram-positive bacteria by a bifunctional polyacrylamide. *Biomaterials 27*, 3663–3674.

(10) Shokat, K. M., and Schultz, P. G. (1991) Redirecting the immune-response — ligand-mediated immunogenicity. *J. Am. Chem. Soc. 113*, 1861–1862.

(11) Naicker, K. P., Li, H. G., Heredia, A., Song, H. J., and Wang, L. X. (2004) Design and synthesis of alpha Gal-conjugated peptide T20 as novel antiviral agent for HIV-immunotargeting. *Org. Biomol. Chem. 2*, 660–664.

(12) Perdomo, M. F., Levi, M., Sallberg, M., and Vahlne, A. (2008) Neutralization of HIV-1 by redirection of natural antibodies. *Proc. Natl. Acad. Sci. U.S.A. 105*, 12515–12520.

(13) Parker, C. G., Domaoal, R. A., Anderson, K. S., and Spiegel, D. A. (2009) An antibody-recruiting small molecule that targets HIV gp120. *J. Am. Chem. Soc. 131*, 16392–16394.

(14) Solomon, D., Kitov, P. I., Paszkiewicz, E., Grant, G. A., Sadowska, J. M., and Bundle, D. R. (2005) Heterobifunctional multivalent inhibitor-adaptor mediates specific aggregation between Shiga toxin and a pentraxin. *Org. Lett. 7*, 4369–4372.

(15) Kitov, P. I., Lipinski, T., Paszkiewicz, E., Solomon, D., Sadowska, J. M., Grant, G. A., Mulvey, G. L., Kitova, E. N., Klassen, J. S., Armstrong, G. D., and Bundle, D. R. (2008) An entropically efficient supramolecular inhibition strategy for Shiga toxins. *Angew. Chem., Int. Ed. Engl. 47*, 672–676.

(16) Kitov, P. I., Mulvey, G. L., Griener, T. P., Lipinski, T., Solomon, D., Paszkiewicz, E., Jacobson, J. M., Sadowska, J. M., Suzuki, M., Yamamura, K. I., Armstrong, G. D., and Bundle, D. R. (2008) In vivo supramolecular templating enhances the activity of multivalent ligands: A potential therapeutic against the Escherichia coli O157 AB(5) toxins. *Proc. Natl. Acad. Sci. U.S.A. 105*, 16837–16842.

(17) Gestwicki, J. E., Crabtree, G. R., and Graef, I. A. (2004) Harnessing chaperones to generate small-molecule inhibitors of amyloid beta aggregation. *Science 306*, 865–869.

(18) Kitov, P. I., Sadowska, J. M., Mulvey, G., Armstrong, G. D., Ling, H., Pannu, N. S., Read, R. J., and Bundle, D. R. (2000) Shiga-like toxins are neutralized by tailored multivalent carbohydrate ligands. *Nature 403*, 669–672.

(19) Crocker, P. R., Paulson, J. C., and Varki, A. (2007) Siglecs and their roles in the immune system. *Nat. Rev. Immunol. 7*, 255–266.

(20) Browning, J. L. (2006) B cells move to centre stage: novel opportunities for autoimmune disease treatment. *Nat. Rev. Drug Discovery 5*, 564–576.

(21) Collins, B. E., Blixt, O., Han, S. F., Duong, B., Li, H. Y., Nathan, J. K., Bovin, N., and Paulson, J. C. (2006) High-affinity ligand probes of CD22 overcome the threshold set by cis ligands for binding, endocytosis, and killing of B cells. *J. Immunol. 177*, 2994–3003.

(22) Han, S., Collins, B. E., Bengtson, P., and Paulson, J. C. (2005) Homomultimeric complexes of CD22 in B cells revealed by protein-glycan cross-linking. *Nat. Chem. Biol. 1*, 93–97.

(23) O'Reilly, M. K., Collins, B. E., Han, S., Liao, L., Rillahan, C., Kitov, P. I., Bundle, D. R., and Paulson, J. C. (2008) Bifunctional CD22 ligands use multimeric immunoglobulins as protein scaffolds in assembly of immune complexes on B cells. *J. Am. Chem. Soc. 130*, 7736–7745.

(24) Kaltgrad, E., O'Reilly, M. K., Liao, L. A., Han, S. F., Paulson, J. C., and Finn, M. G. (2008) On-virus construction of polyvalent glycan ligands for cell-surface receptors. *J. Am. Chem. Soc. 130*, 4578–4579.

(25) Sulzer, B., and Perelson, A. S. (1997) Immunons revisited: binding of multivalent antigens to B cells. *Mol. Immunol. 34*, 63–74.

(26) Stone, J. D., Cochran, J. R., and Stern, L. J. (2001) T-cell activation by soluble MHC oligomers can be described by a two-parameter binding model. *Biophys. J. 81*, 2547–2557.

(27) Dam, T. K., and Brewer, C. F. (2002) Thermodynamic studies of lectin-carbohydrate interactions by isothermal titration calorimetry. *Chem. Rev. 102*, 387–429.

(28) Dam, T. K., Roy, R., Das, S. K., Oscarson, S., and Brewer, C. F. (2000) Binding of multivalent carbohydrates to concanavalin A and *dioclea grandiflora* lectin. *J. Biol. Chem. 275*, 14223–14230.

(29) Otsuka, I., Blanchard, B., Borsali, R., Imberty, A., and Kakuchi, T. (2010) Enhancement of plant and bacterial lectin binding affinities by three-dimensional organized cluster glycosides constructed on helical poly(phenylacetylene) backbones. *ChemBioChem 11*, 2399–2408.

SUPPORTING INFORMATION

Supramolecular Complexing of Membane Siglec CD22 Mediated by a Polyvalent Heterobifunctional Ligand that Templates on IgM

Lina Cui,[†] Pavel I. Kitov,[†] Gladys C. Completo,[‡] James C. Paulson,[‡] and David R. Bundle[*,†]

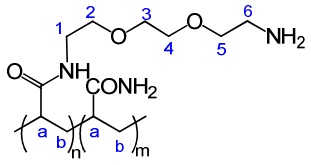
[†]*Department of Chemistry, Alberta Ingenuity Centre for Carbohydrate Science, University of Alberta, Edmonton, AB, T6G 2G2 Canada, and* [‡]*Department of Chemical Physiology, The Scripps Research Institute, 10550 N. Torrey Pines Road, La Jolla, California 92037*

General Methods. All reagents and solvents were purchased from Sigma-Aldrich (reagent grade) and used as supplied unless otherwise noted. TLC plates were visualized by ultraviolet light (254 nm), or charred with ethanolic solution of ninhydrin or sulfuric acid containing anisaldehyde. High performance liquid chromatography (HPLC) was performed using a Waters 2487 Dual λ UV absorbance detector and separations were done on a Beckman C_{18} silica column. ^{1}H NMR spectra were recorded at 600 MHz or 800 MHz. First order chemical shifts are reported in δ (ppm) referenced to external acetone (0.1% v/v) at δ2.225. Signals in ^{1}H spectra were assigned with the aid of two dimensional COSY, HMQC and HMBC spectra. For some signals in ^{1}H NMR spectra, the coupling patterns were reported as multiplets due to high order coupling or signal overlap.

IgM Binding to BJAB Cells. BJAB cells were suspended in RPMI medium supplemented with 10% FBS and 50 μM 2-mercaptoethanol at 4×10^6 cells/mL containing anti-NP IgM at 10 μg/mL. Ligands were diluted to various concentrations in RPMI medium at 50 μL/sample. Aliquots of 50 μL of the cells were added to the ligand dilutions, followed by incubation at 4 °C for 7 h. Cells were then washed with 0.2 mL of HBSS/BSA containing 100 nM ligand and then incubated with FITC-labeled anti-IgM antibody (10 ug/mL) for 30 min on ice. After washing, the cells were analyzed by BD FACS Calibur Flow Cytometer using CellQuest software.

IgM Binding to CD22-Fc Magnetic Beads. hCD22-Fc, which comprises a chimera of the constant fragment of a human IgG fused to the C-terminus of the extracellular portion of CD22, was immobilized onto Protein A-conjugated magnetic beads (Dynal Biotech) by adding 5 mL of culture supernatant containing hCD22-Fc chimera to 20 μL of bead slurry and incubating overnight at 4 °C with end-over-end rotation. Beads were isolated by exposure to a magnet, washed three times with HBSS/BSA, and then resuspended in 200 μL of HBSS/BSA. Aliquots of 2 μL of beads were added to 2 μL of anti-NP IgM (5 μg/mL in HBSS/BSA) containing the various concentrations (0.0175-10.0 μg/mL, obtained by 2-fold dilutions) of ligand, for a final volume of 100 μL. Incubation was done for at least 14 h at 4 °C or 37 °C to allow complex formation to reach equilibrium. Beads were then isolated and washed with 300 μL of HBSS/BSA. Beads were then incubated for 30 min at 4 °C in 100 μL of HBSS/BSA containing FITC-anti-IgM to detect bound IgM. Beads were isolated and washed with 300 μL of HBSS/BSA and then resuspended in 200 μL of the same buffer and analyzed by a FACS Calibur Flow Cytometer using CellQuest software. Curves were generated by nonlinear regression analysis of the data using the equation for log (agonist) versus response-variable slope in GraphPad Prism software (Version 5.0a).

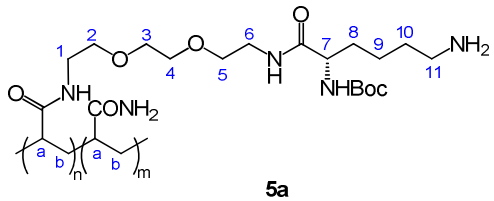
Synthetic procedures.



4

2-[2-(2-aminoethoxy)ethoxy]ethylamidopolyacrylamide (4)

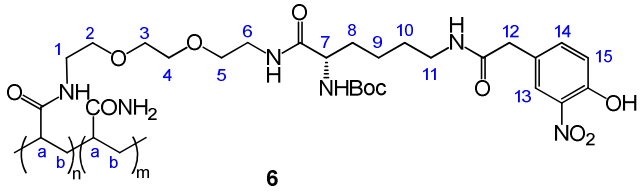
To a solution of polyacrylamide (10.0 g, *M.W.* ~ 40 kDa) in water (100 mL) was added 2,2'-(ethylenedioxy)bis(ethylamine) (100 mL). The reaction mixture was heated at 80 °C for 15 min, and was immediately cooled in an ice bath. The solution was then dialyzed and lyophilized to obtain the desired product as a white foam: ^{1}H NMR (600 MHz, D_2O): δ 3.75 (app. s, 2H, H-2), 3.75-3.68 (m, 4H, H-3, H-4), 3.63 (app. s, 2H, H-5), 3.39 (app. s, 2H, H-1), 3.21 (app. s, 2H, H-6), 2.40-2.05 (m, H-a), 1.85-1.40 (m, H-b).



5a

2-{2-[2-(N_α-Boc-lysine)amidoethoxy]ethoxy}ethylamidopolyacrylamide (5a)

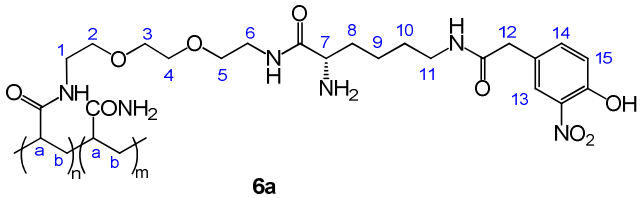
Aminated polymer **4** (510 mg) was dissolved in buffer (pH 8.0, 10 mL), and a solution of Fmoc-Lys(Boc)-OPfp (312 mg, 3 eq.) in DMF (20 mL) was added to obtain a semitransparent mixture, which was then stirred for 18 h at r.t. and a white precipitate formed, which disappeared after sonication. TLC was used to monitor the reaction using ninhydrin stain. Disappearance of red spot on TLC indicated formation of compound **5**. Then piperidine (3 mL, 10 %) was added when the solution turned clear. A new white precipitate began to form gradually after 5 min and progressed until the reaction mixture turned into a gel. The reaction tube was centrifuged and the supernatant solution was dialyzed. Lyophilization gave the product **5a** as a white foam: ^{1}H NMR (600 MHz, D_2O): δ3.95 (app. s, 1H, H-7), 3.76 (app. s, 2H, H-5), 3.22 (app. s, 2H, H-6), 3.06 (m, 2H, H-11), 2.40-2.00 (m, H-a), 1.87 (app. s, 2H, H-8), 1.85-1.35 (m, H-b, H-9, H-10), 1.42 (s, 9H, Boc).



6

2-{2-{2-[N_α-Boc-N_ε-(4-hydroxy-3-nitro-phenyl)acetamido-lysine]amidoethoxy}-ethoxy}ethylamidopolyacrylamide (6)

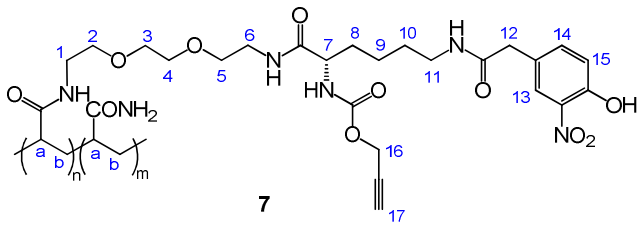
To a solution of **5a** (40 mg) in buffer (pH 8.0, 2 mL) and DMSO (0.2 mL) was added 4-hydroxy-3-nitrophenylacetyl-hydroxysuccinimide ester (Biosearch Technologies, 12 mg, 3 eq.). The reaction mixture was stirred for 18 h at r.t. to give a clear bright orange solution, which was dialyzed to produce a faint yellow solution. Upon lyophilization, a yellow foam product was obtained. ^{1}H NMR (600 MHz, D_2O): δ8.02 (s, 1H, H-13), 7.57 (m, 1H, H-14), 7.20 (m, 1H, H-15), 4.25 (m, 1H, H-7), 3.02 (app. s, 2H, H-12), 2.40-2.00 (m, H-a, H-8), 2.00-1.30 (m, H-b, H-9, H-10), 1.42 (s, 9H, Boc).



6a

2-{2-{2-[N_ε-(4-hydroxy-3-nitro-phenyl)acetamido-lysine]amidoethoxy}ethoxy}ethyl-amidopolyacrylamide (6a)

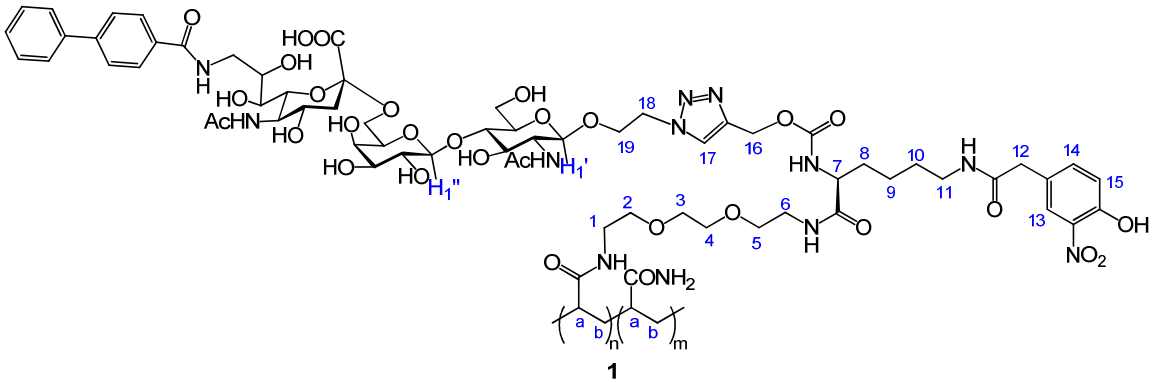
Polymer **6** (39 mg) was dissolved directly in TFA (2 mL) and was stirred at r.t. for 30 min. The reaction was quenched by diluting with water (2 mL) and neutralizing carefully with sodium carbonate powder. The bright yellow solution was then dialyzed and lyophilized to give the product as a yellow foam. ^{1}H NMR (600 MHz, D_2O): δ8.02 (s, 1H, H-13), 7.59 (app. s, 1H, H-14), 7.19 (app. s, 1H, H-15), 4.26 (app. s, 1H, H-7), 2.97 (app. s, 2H, H-12), 2.40-2.00 (m, H-a, H-8), 2.00-1.30 (m, H-b, H-9, H-10).



7

2-{2-{2-[N_ε-(4-hydroxy-3-nitro-phenyl)acetamido-N_α-propargyloxycarbonyl-lysine]-amidoethoxy}ethoxy}ethylamidopolyacrylamide (7)

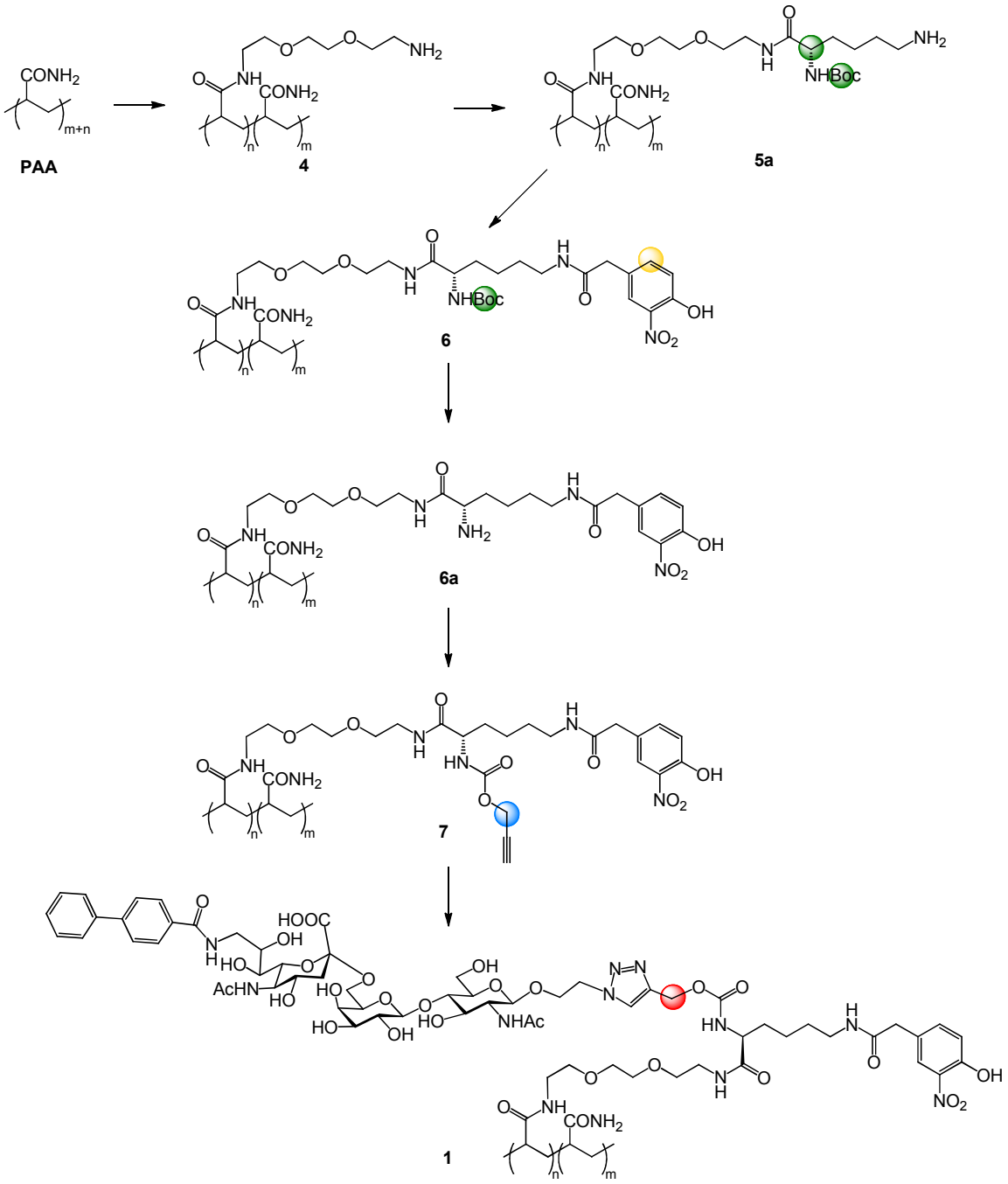
Amino polymer **6a** (34 mg) was dissolved in water (2 mL) and sodium carbonate powder was added to adjust the pH to 10. Propargyl chloroformate (8.4 μL, 10 eq.) was added with vigorous stirring until the oily beads disappeared. TLC staining indicated disappearance of primary amine. Another portion of propargyl chloroformate (8.4 μL, 10 eq.) was added to ensure the complete capping of the amino groups. The resulting solution was close to neutral as indicated by pH paper, and was dialyzed. Lyophilization gave the product as a yellow foam. ^{1}H NMR (600 MHz, D_2O): δ8.03 (s, 1H, H-13), 7.59 (app. s, 2H, H-14), 7.20 (app.s, 2H, H-15), 4.66 (app. s, 2H, H-16), 4.26 (app. s, 1H, H-7), 3.10 (app. s, 2H, H-12), 2.90 (s, 1H, H-17), 2.80-2.00 (m, H-a, H-8), 2.00-1.30 (m, H-b, H-9, H-10).



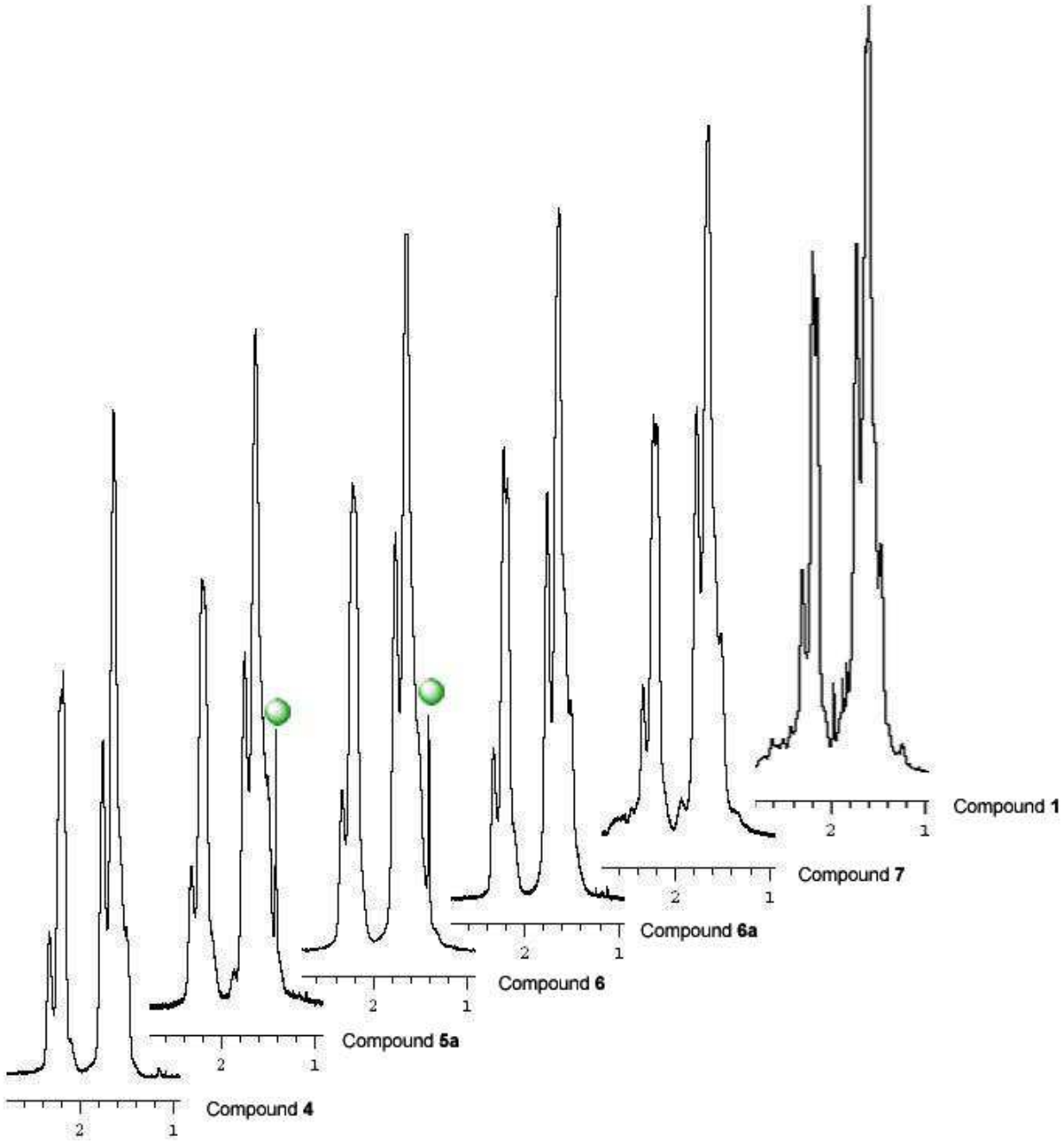
1

Polyvalent heterobifunctional ligand 1

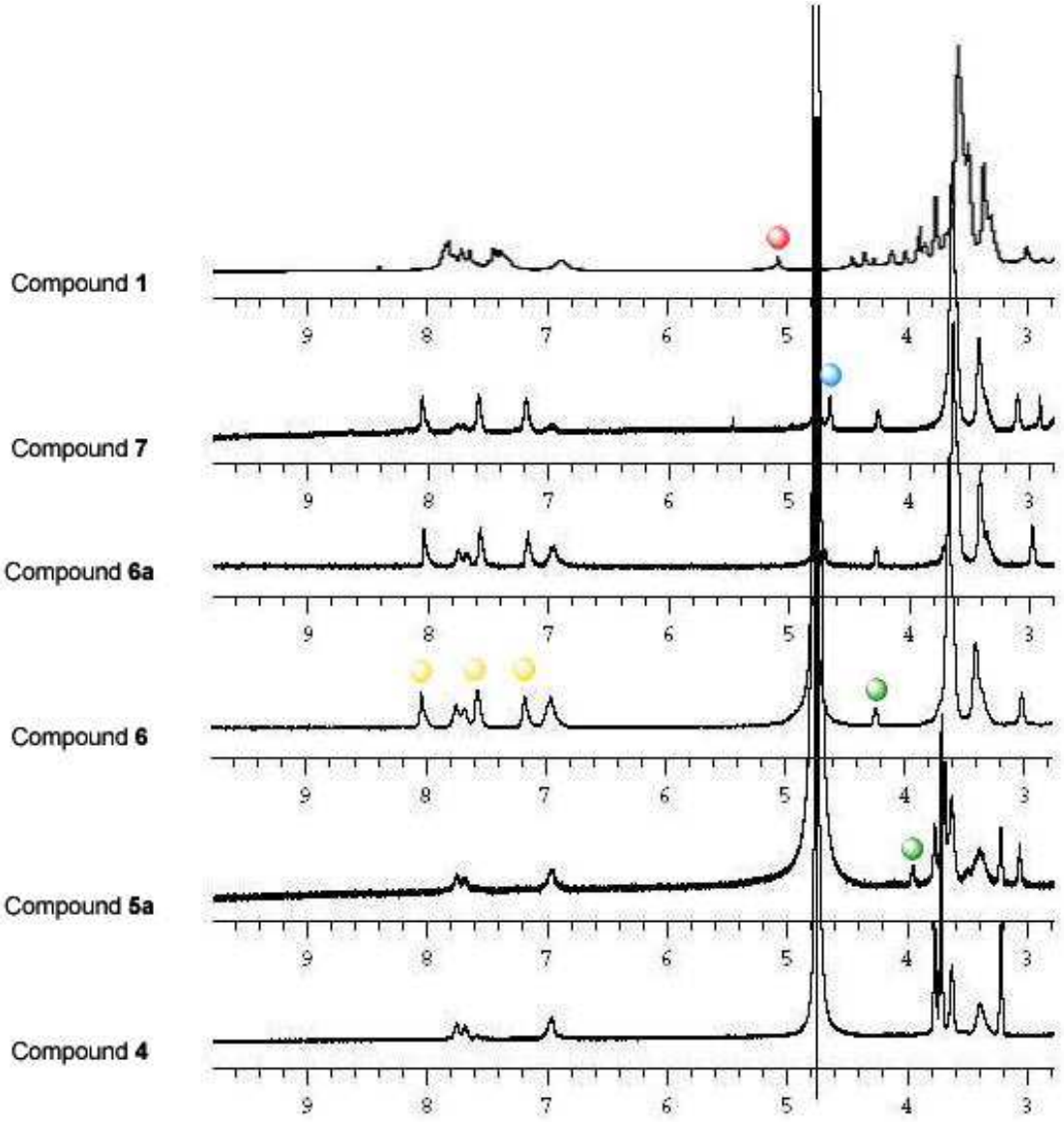
A mixture of **7** (10 mg), ^{BPC}Neu5Ac-α-(2-6)-Gal-β-(1-4)-GlcNAc-$OCH_2CH_2N_3$ (**8**, 4.5 mg, 2 eq.), and copper powder (30 mg) in water (0.5 mL) was degassed, and a Cu(I)-bathophenanthroline solution (25 μL, 0.04 M) was added. The reaction was allowed to proceed for 40 h at room temperature, and ethylenediamine (50 μL) was added to displace the copper ions chelated with the polymer. The solution was then dialyzed, and lyophilization gave the product as a yellow foam. ^{1}H NMR (600 MHz, D_2O): δ 7.90-6.60 (m, H-17, H-13, H-14, H-15), 5.10 (s, 2H, H-16), 4.50 (app. s, 2H, H-18), 4.36 (m, 2H, H-1′, H-1″) 4.30 (app. s, 1H, H-7), 2.90-0.60 (m, H-a, H-b, H-8, H-9, H-10).



S1: *The synthetic scheme for polyvalent heterobifunctional ligand **1**. The circles in different colors indicate the signature protons of each compound.*



S2: *NMR spectra of polymer backbone of compounds **1** to **7**.*



S3: *Ligand region in NMR spectra of compounds **1** to **7**. The circles in different colors indicate the resonances of the signature protons in each compound.*

Removal of Boc group to restore the amino functionality in compound **6a** was confirmed by the missing peak at δ_H 1.42 ppm in the NMR spectrum (S1, S2, green circle). Formation of compound **7** was verified by the new peak at δ_H 4.66 ppm, representing the propargyl protons (S1, S3, blue circles). Emergence of the proton resonance at δ_H 5.10 ppm in the NMR spectrum of compound **1** suggested the successful formation of the triazole ring via "click chemistry" between azido and alkynyl compounds (S1, S3, red circles).

Bioconjugate Chemistry

COMMUNICATION

pubs.acs.org/bc

Bioconjugation of L-3,4-Dihydroxyphenylalanine Containing Protein with a Polysaccharide

Niraikulam Ayyadurai,[†] Nadarajan Saravanan Prabhu,[†] Kanagavel Deepankumar,[†] Yoon Jung Jang,[‡] Nataraj Chitrapriya,[‡] Eunjung Song,[§] Nahum Lee,[§] Seog K. Kim,[‡] Byung-Gee Kim,[§] Nagasundarapandian Soundrarajan,[∥] Sungu Lee,[∥] Hyung Joon Cha,[⊥] Nediljko Budisa,[#] and Hyungdon Yun*[,†]

[†]School of Biotechnology

[‡]Department of Chemistry

Yeungnam University, Gyeongsan, South Korea

[§]School of Chemical and Biological Engineering, Seoul National University, Seoul, South Korea

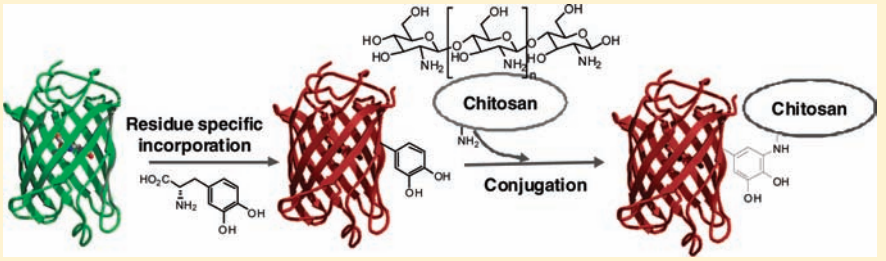
[∥]Department of Chemical Engineering, Pusan National University, Busan, South Korea

[⊥]Department of Chemical Engineering, Pohang University of Science and Technology, Pohang, South Korea

[#]Department of Biocatalysis, Technische Universität Berlin, Germany

Supporting Information

ABSTRACT:



We describe the simple bioconjugation strategy in combination of periodate chemistry and unnatural amino acid incorporation. The residue specific incorporation of 3,4-dihydroxy-L-phenylalanine can alter the properties of protein to conjugate into the polymers. The homogeneously modified protein will yield quinone residues that are covalently conjugated to nucleophilic groups of the amino polysaccharide. This novel approach holds great promise for widespread use to prepare protein conjugates and synthetic biology applications.

Protein conjugation plays an important role in the development of effective vaccines, affinity matrices, drug delivery systems, and functional hydrogels.[1] These conjugations occur commonly in nature, but experimentally it is difficult to prepare or adapt such biochemical approaches. Chemical activation of polysaccharide and proteins during the conjugation step is complex and also technically difficult. Generally, protein conjugation methods rely on chemoselective modification of canonical amino acids of the protein.[2] To date, several approaches such as simple absorption and protein trapping with gel matrix or through covalent linkage have been used in preparing the bioconjugates.[3,4] Among them, the most common and frequently employed approach is covalent linkage. Covalent linkages typically occur through amine coupling of lysines and sulfhydryl coupling of cysteine residues of protein.[5,6] Cysteine is relatively a rare amino acid, and its thiol group can undergo disulfide exchange to form mixed disulfides, which is very important in preserving protein structure and function. Although amine coupling of lysine residues is considerably more prevalent in bioconjugation studies, it should be noted that reagents used for lysine modification can additionally modify the N termini of proteins.[5] Therefore, it is a challenging goal to modify these residues. Furthermore, modification of these residues through chemical reactions is reversible, slow, and also inefficient.[7] In general, approaches for the site-specific modification of canonical amino acid and finding ideal chemical candidate molecules that precisely modify the side chains for bioconjugation is highly challenging. Recently, protein−polysaccharide conjugates were achieved through tyrosinase mediated oxidation of tyrosine in the recombinant protein to form a reactive *ortho*-quinone. Further, bioconjugation was achieved through the nonenzymatic reaction of the nucleophilic amino groups of the polymer with

Received: January 4, 2011
Revised: February 18, 2011
Published: March 04, 2011

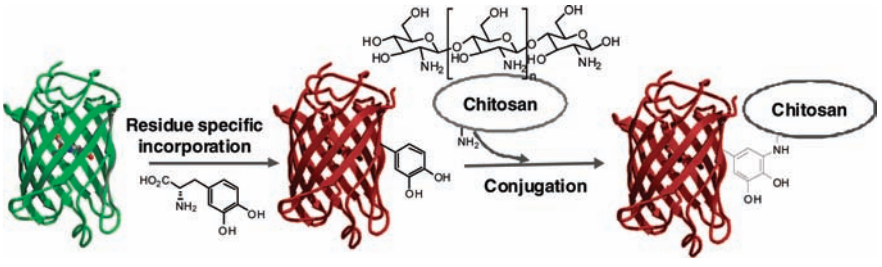
ACS Publications © 2011 American Chemical Society

electrophilic *ortho*-quinones of the protein.[8] This method was successfully used for fabricating biological samples and in developing a novel microdevice which investigates how bacteria communicate with each other for enhancing their resistance toward drugs.[9] However, in this approach it is very difficult to maintain specificity, monitor product formation, and remove the enzymes after the reaction.

Since preparing conjugates is a difficult process, a new bioconjugation reaction is currently of high interest to develop a systematic approach for coupling a specific protein of interest with polysaccharide targets. In an effort to establish a valuable protein−polysaccharide complex, we aimed to replace the tyrosine amino acid of recombinant protein with 3,4-dihydroxy-L-phenylalanine (L-DOPA). DOPA is an important neurotransmitter biosynthesized naturally in humans by tyrosinase-catalyzed oxidation of tyrosine in a melanin biosynthetic pathway, and by tyrosine hydroxylase in brain for catecholamine neurotransmitter biosynthesis. It also play an important role in adhesive and cross-linking property of mussel adhesive proteins.[10] Recently, genetic incorporation of L-DOPA was achieved through a site specific suppression method, and it is significantly used in exploring protein−protein interaction.[11,12] However, the practical importance of this method is still limited by low protein yields due to cellular toxicity.[13] On the other hand, DOPA has also been incorporated into proteins by in vitro protein synthesis and solid-phase peptide synthesis.[14] Here, we demonstrate the successful in vivo incorporation of L-DOPA in a residue specific manner, which also enables development of an efficient and improved bioconjugation strategy (Scheme 1).

This improved bioconjugation method will facilitate the synthesis of homogeneously modified protein with reactive chemical groups that can be utilized to create novel protein−polysaccharide complexes. DOPA-enriched recombinant proteins are selectively oxidized by periodate to form an *ortho*-quinone intermediate which is then subsequently attacked by the amino groups of chitosan resulting in a nonenzymatic cross-linking reaction through Michael addition.[14] To evaluate the scheme shown above, we chose green fluorescent protein (GFP) as a model protein since its functional and spectral properties were well-studied and characterized.[15] Our current GFP variant contains eight tyrosine residues which will be replaced with L-DOPA through an in vivo incorporation method. The detailed sequence information about the GFP variant used in the study was mentioned in Table S1 (Supporting Information). Chitosan, an aminopolysaccharide, is selected as a target polysaccharide for the bioconjugation reaction. It is an attractive material in the biomedical field and has a wide range of applications in drug delivery, gene therapy, and tissue engineering due to its high biocompatibility and biodegradability properties.[16] This polysaccharide molecule contains primary amino groups, which are nucleophilic and undergo reactions with a variety of electrophiles such as aldehyde and quinones. In this study, we expressed our recombinant protein by replacing tyrosine residues with unnatural amino acid L-DOPA by the selective pressure incorporation (SPI) method, which is a highly efficient method to express protein with high yield.[17] It enables the simple residue specific incorporation of unnatural amino acids into different recombinant proteins.[18] Cells containing recombinant GFP were expressed in minimal medium containing the 20 natural amino acids, 19 amino acid lacking tyrosine, and 19 amino acids plus L-DOPA and subjected to the SDS-PAGE analysis. Since oxidation of L-DOPA leads to the formation of highly toxic quinone moiety,[19] we performed a series of optimization experiments with different reducing agents such as dithiothreitol (DTT) and L-ascorbic acid at various concentrations. To verify whether the reducing agent selectively plays any role in L-DOPA incorporation, crude bacterial lysates were subjected to gel electrophoresis. The band intensity of the DOPA protein expressed in the presence of the reducing agent was comparable with that of the band expressed in the absence of the reducing agent. This result suggests that the reducing agent played little or no effect in the expression and efficiency of L-DOPA incorporation into GFP (Figure 1a). Furthermore, GFP and GFPdopa were purified on a Ni-NTA affinity column and gel permeation chromatography (GPC) by AKTA Explorer FPLC system in the absence of reducing agent at 4 °C, respectively (Supporting Information Figure S1). The purification yield of GFPdopa was approximately 32 mg/L, which was similar to that of wild type GFP (34 mg/L). Interestingly, incorporation of L-DOPA into GFP altered the spectral properties; a distinct 19 nm red shift was observed in the emission peak (530 nm) when compared with the GFP protein (511 nm) and a distinct 11 nm shift was observed in the excitation peak (512 nm) compared to the GFP protein (501 nm) (Figure 1c). This shift might be due to the presence of additional hydroxyl group (electron donor) of L-DOPA when compared with L-tyrosine (Y66), which alters the chromophore chemistry. Further, to identify that L-DOPA was incorporated into the GFP protein, we employed a redox staining method using nitroblue tetrazolium (NBT) which detects proteins containing *o*-catechols, like DOPA, after their separation by SDS-PAGE and western transfer to the polyvinylidene membranes.[20] This staining method confirmed the presence of L-DOPA only in the GFPdopa (Supporting Information Figure S2). Next, we investigated that this replacement occurred specifically in place of tyrosine, which is further confirmed by LC-MS/MS and ESI-MS

Scheme 1. Schematic Representation of the Proposed Approach for Bioconjugation of L-DOPA Containing Protein with a Polysaccharide



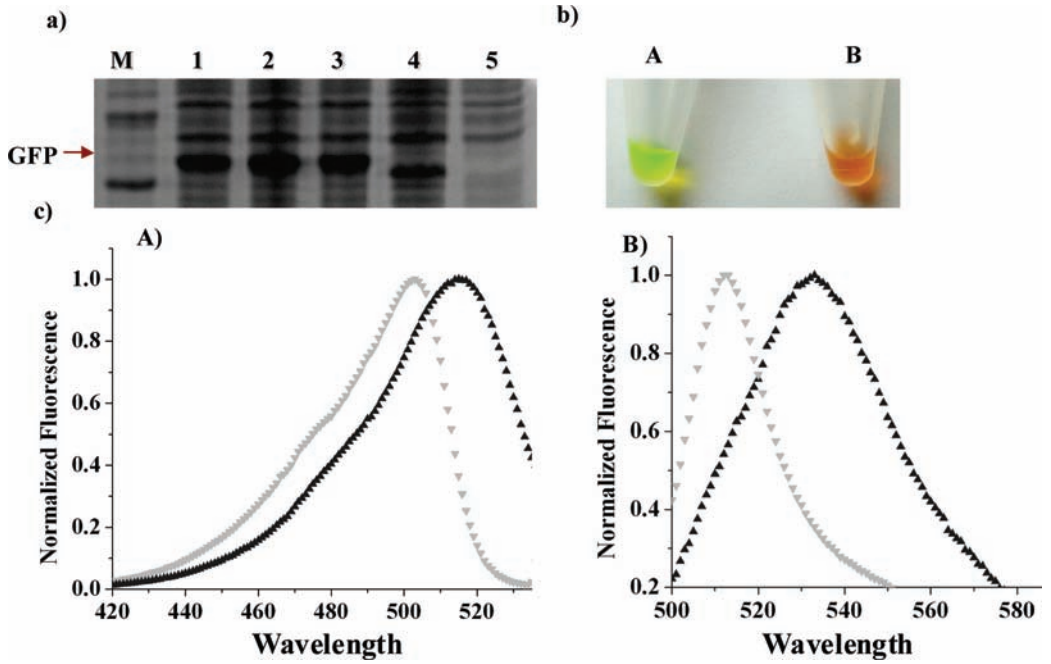


Figure 1. (a) Polyacrylamide gel electrophoresis of protein labeled with L-DOPA. The labeled proteins are indicated by an arrow. Lane M: protein ladder (Promega prestained Ladder). Lane 1: positive control (expressed with all 20 canonical amino acid). Lane 2: test (expressed with 19 amino acid plus L-DOPA). Lane 3: test 1 (expressed with 19 amino acid plus L-DOPA with L-ascorbic acid). Lane 4: test 2 (expressed with 19 amino acid plus L-DOPA with DTT). Lane 5: negative control (expressed only with 19 amino acids). (b) Purified GFP shows the green native color (A) and GFPdopa shows changed color (B). (c) Normalized fluorescence excitation spectrum (A), emission spectrum (B) of GFP (▼), and GFPdopa (▰).

(Supporting Information Table S2 and Figure S3), and the efficiency is >90%.

The successful design and confirmation of a protein with a novel L-DOPA moiety further allowed us to prepare functional protein−polysaccharide complexes. To substantiate the reaction outlined in Scheme 1, purified GFP and GFPdopa was treated with sodium periodate ($NaIO_4$) and incubated with chitosan at room temperature. We could observe the slight fluorescence reduction in GFP and GFPdopa (less than 10%) during $NaIO_4$ treatment; however, the amount of reduction is negligible (Supporting Information Figure S4−S5). Initially, we have evaluated the pH dependency of GFP and GFPdopa. The GFP-chitosan conjugation efficiency was estimated by using the intensity of the fluorescence at different conditions such as precipitation, washing, and resolubilization (Supporting Information). It indicates that GFP and GFPdopa fluorescence also depends on the pH of the environment (Supporting Information Figure S6) and also well correlated with the earlier report about the effect of pH on GFP.[15] On the basis of the observation, pH 6.0 was selected for estimating fluorescence in the conjugation experiment. Initially, individual proteins were pretreated with periodate to convert DOPA into an *ortho*-quinone intermediate. After conjugation, chitosan was precipitated by raising the pH of solution to basic. Subsequently, the pellet and supernatant retrieved after centrifugation were subjected to fluorescence analysis and the relative amounts of proteins that conjugated successfully were assessed. As shown in Figure 2, fluorescence was almost exclusively observed (only 10% reduction was observed) in the supernatant of GFP, GFPdopa not treated with $NaIO_4$, and $NaIO_4$ treated GFP. Such a 10% reduction of fluorescence might be due to the $NaIO_4$ effect on the protein. In contrast, a strong reduction in fluorescence was observed in $NaIO_4$ treated GFPdopa. To measure the relative amount of protein conjugated with chitosan, we compared the initial fluorescence with the fluorescence retained in supernatants. On the basis of fluorescence intensity of the supernatant, efficiency of conjugation between GFPdopa and chitosan in the presence of $NaIO_4$ was around 90%. GFP and GFPdopa pellets obtained by centrifugation were washed with PBS buffer to remove physically bound proteins and then resolubilized in aqueous acetic acid solution (Supporting Information). A strong fluorescence appeared in the resolubilized pellet of $NaIO_4$ treated GFPdopa−chitosan conjugates. A modest level of fluorescence was observed in $NaIO_4$ treated GFP reacted with chitosan; it may be due to unspecific binding of the protein rather than the GFP−chitosan bioconjugation (Figure 2a). Similarly, we observed a little fluorescence in the GFPdopa−chitosan conjugates, which are prepared in the absence of $NaIO_4$. This little fluorescence may be due to the nonspecific binding of GFPdopa with chitosan during precipitation. This observation clearly indicates that cross-linking occurred specifically between the DOPA-containing protein and chitosan only in the presence of periodate. To be specific, the fluorescence results suggest that >90% of the initial fluorescence of GFPdopa was in the pellet after $NaIO_4$ activation, whereas 10% when GFP treated with $NaIO_4$ had occurred by physical entrapment. This demonstrates that conjugation of GFPdopa with chitosan occurs only through the quinone moiety rather than the canonical amino acids. Strong evidence that the quinone containing GFPdopa can be conjugated to chitosan is provided in Figure 2b. The cast chitosan films were incubated with GFP and GFPdopa in the presence and absence of $NaIO_4$ (Supporting Information). These treated films were observed to have a relatively significant increase in absorbance at wavelengths above 350 nm. Control films incubated with or without protein show little absorbance above

dx.doi.org/10.1021/bc2000066 |*Bioconjugate Chem.* 2011, 22, 551–555

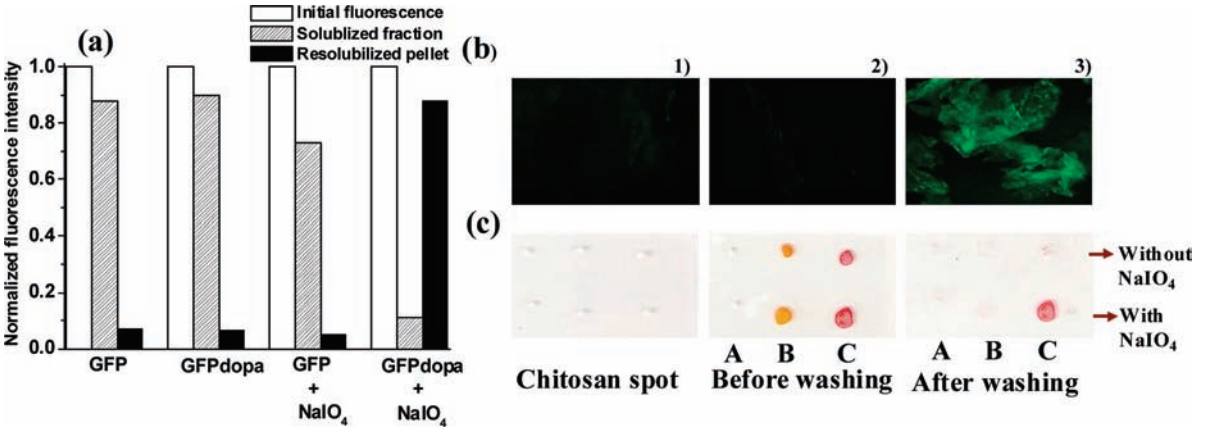


Figure 2. (a) Fluorescence analysis of periodate initiated conjugation of GFPdopa with chitosan (see Supporting Information for the detailed experimental conditions). (b) Fluorescence microscopic analysis of chitosan hydrogel and each set of images obtained under identical conditions. (1) Chitosan. (2) Chitosan conjugated with $NaIO_4$ treated GFP. (3) Chitosan conjugated with $NaIO_4$ treated GFPdopa. (c) Protein spot assay. A: chitosan. B: GFP. C: GFPdopa.

350 nm, and the films incubated with the GFP protein, $NaIO_4$, show no increased absorbance above 350 nm. Increased absorbance in the UV−vis range was identified in chitosan films incubated with $NaIO_4$ treated GFPdopa protein, which provide the evidence for quinone mediated reaction (Supporting Information Figure S7). It indicates that $NaIO_4$ selectively generates the quinone from the GFPdopa and facilitates the assembly onto the chitosan. To evaluate our currently developed bioconjugation method, proteins were further conjugated to chitosan hydrogels under heterogeneous conditions. Chitosan hydrogels were prepared as described earlier[8] (see Scheme S1 in Supporting Information). After the hydrogel preparation, $NaIO_4$ solution was spread onto the surface and treated with GFP and GFPdopa protein, respectively. After incubation, to remove nonspecifically bound proteins hydrogels were thoroughly washed with PBS buffer and imaged using a fluorescence microscope. Hydrogel samples were prepared for fluorescence analysis and each set of images obtained under identical condition. As expected, the hydrogel treated with the GFPdopa protein in the presence of $NaIO_4$ had a high level of fluorescence, whereas gels treated with chitosan and GFP in the presence of $NaIO_4$ has no significant fluorescence (Figure 2b). Interestingly, the initial bioconjugation study with chitosan solution shows around 10% physical entrapment of protein. However, in the bioconjugation study with hydrogel, we could not observe such physical entrapment of GFPdopa protein on chitosan.

This indicates that the nonspecific binding of GFPdopa protein is higher with chitosan solution when compared to the chitosan hydrogel. This is due to the interior physical entrapment of proteins by chitosan, which occurred when the pH was raised for precipitation. During the washing step, the nonspecifically bound protein onto chitosan surface could be easily removed, but the proteins which are trapped in the interior are very difficult to remove in the washing process. On the other hand, in the case of the bioconjugation reaction with hydrogel and spot assay, binding occurs only on the surface of the chitosan, and these nonspecifically bound GFP and GFPdopa proteins could be removed during the washing step. Next, we utilized this current strategy to develop the protein spot. For this purpose, we prepared chitosan on glass side, and further, quinone containing GFPdopa was covalently assembled onto the chitosan surface (Figure 2c) (Supporting Information Figure S8). Binding was quantified densitometrically using the *Scion Image* PC software package. Densitometric analysis revealed the high abundance binding of GFPdopa protein with chitosan coated in the glass slide (Supporting Information, Figure S8).

In conclusion, we developed a simple, efficient, and facile method to prepare bioconjugates by activating protein genetically encoded with L-DOPA, which allows it to be covalently coupled with chitosan. This is the first report that demonstrates the effective protein−polysaccharide bioconjugation through a combination of periodate mediated oxidation chemistry and genetic code engineering. The combination of biochemical conjugation with selective cross-linking chemistry will provide an alternative approach for the assembly of proteins onto the patterned surfaces. This approach can be used to explore the role of the adhesive and cross-linking nature of DOPA in mussel adhesive protein, which can be used in developing novel biosensor and in synthetic biology applications.

■ ASSOCIATED CONTENT

Supporting Information. Full experimental procedures, protein purification, LC MS/MS analysis, bioconjugation reaction. This material is available free of charge via the Internet at http://pubs.acs.org.

■ AUTHOR INFORMATION

Corresponding Author

*To whom correspondence should be addressed. Phone: +82-53-810-3044, FAX: +82-53-810-4769, E-mail: hyungdon@ynu.ac.kr.

■ ACKNOWLEDGMENT

This research was supported by the Basic Science Research Program through the National Research Foundation of Korea (2010-0006343) and the 21C Frontier Microbial Genomics & Applications Center Program (M102KK010019-08K1101-01930) funded by the Ministry of Education, Science and Technology, Korea.

REFERENCES

(1) Reddy, S. T., Swartz, M. A., and Hubbell, J. A. (2006) Targeting dendritic cells with biomaterials: developing the next generation of vaccines. *Trends Immunol. 27*, 573–579.

(2) Aslam, M., and Dent, A. *Bioconjugation. Protein Coupling Techniques for Biomedical Sciences*, Grove's Dictionaries Inc., New York, 1998.

(3) Lutz, J. F., and Börner, H. G. (2008) Modern trends in polymer bioconjugates design. *Prog. Polym. Sci. 33*, 1–39.

(4) Chalker, J. M., Bernardes, G. J. L., Lin, Y. A., and Davis, B. G. (2009) Chemical modification of proteins at cysteine: opportunities in chemistry and biology. *Chem. Asian J. 4*, 630–640.

(5) Sletten, E. M., and Bertozzi, C. R. (2009) Bioorthogonal chemistry: fishing for selectivity in a sea of functionality. *Angew. Chem., Int. Ed. 48*, 6974–6998.

(6) Younggyu, K., Sam, O. H., Gassman, N. R., Korlann, Y., Landorf, E. V., Collart, F., and Weiss, S. (2008) Efficient site-specific labeling of proteins via cysteines. *Bioconjugate Chem. 3*, 786–791.

(7) Pawlowski, A., Kallenius, G., and Svenson, S. B. (2000) Preparation of pneumococcal capsular polysaccharide-protein conjugate vaccines utilizing new fragmentation and conjugation technologies. *Vaccine 18*, 1873–1880.

(8) Wu, H., Shi, X., Tsao, C., Lewandowski, A. T., Fernandes, R., Hung, C., DeShong, P., Kobatake, E., Valdes, J. J., Payne, G. F., and Bentley, W. E. (2009) Biofabrication of antibodies and antigens via IgG-binding domain engineered with activatable pentatyrosine pro-tag. *Biotechnol. Bioeng. 103*, 231–236.

(9) Fernandes, R., Roy, V., Wu, H. C., and Bentley, W. E. (2010) Engineered biological nanofactories trigger quorum sensing response in targeted bacteria. *Nat. Nanotechnol. 5*, 213–217.

(10) Messersmith, P. B. (2008) Multitasking in tissues and materials. *Science* 319–1767.

(11) Alfonta, L., Zhang, Z., Uryu, S., Loo, J. A., and Schultz, P. G. (2003) Site-specific incorporation of a redox-active amino acid into proteins. *J. Am. Chem. Soc. 125*, 14662–14663.

(12) Umeda, A., Thibodeaux, G. N., Zhu, J., Lee, Y., and Zhang, Z. J. (2009) Site-specific protein cross-linking with genetically incorporated 3,4-dihydroxy-L-phenylalanine. *ChemBioChem 25*, 1302–1304.

(13) Lepthien, S., Merkel, L., and Budisa, N. (2010) In vivo double and triple labeling of proteins using synthetic amino acids. *Angew. Chem., Int. Ed. 49*, 5446–5450.

(14) Liu, L. B., Burdine, L., and Kodadek, T. (2006) Chemistry of periodate-mediated cross-linking of 3,4-dihydroxylphenylalanine containing molecules to proteins. *J. Am. Chem. Soc. 128*, 15228–15230.

(15) Tsien, R. Y. (1998) The green fluorescent protein. *Annu. Rev. Biochem. 67*, 509–544.

(16) Ta, H. T., Dass, C. R., and Dunstan, D. E. (2008) Injectable chitosan hydrogels for localized cancer therapy. *J. Controlled Release 126*, 205–208.

(17) Link, A. J., and Tirrell, D. A. (2005) Reassignment of sense codons in vivo. *Methods 36*, 291–298.

(18) Moroder, L., and Budisa, N. (2010) Synthetic biology of protein folding. *ChemPhysChem 11*, 1181–1187.

(19) Brien, P. J. (1991) Molecular mechanisms of quinone cytotoxicity. *Chem. Biol Interact. 80*, 1–41.

(20) Rodgers, K. J., Hume, P. M., Dunlop, R. A., and Dean, R. T. (2004) Biosynthesis and turnover of DOPA-containing proteins by human cells. *Free Radical Biol. Med. 37*, 1756–1759.

Supporting Information

Bio-conjugation of L-3, 4-dihydroxyphenylalanine containing protein with a polysaccharide

Niraikulam Ayyadurai[a], Nadarajan Saravanan Prabhu[a], Kanagavel Deepankumar[a], Yoon Jung Jang[b], Nataraj Chitrapriya[b], Eunjung Song[c], Nahum Lee[c], Seog K. Kim[b], Byung-Gee Kim[c], Nagasundarapandian Soundrarajan[d], Sungu Lee[d], Hyung Joon Cha[e], Nediljko Budisa[f] and Hyungdon Yun[a]*

[a]Dr. N. Ayyadurai, N. Saravanan Prabhu, K. Deepankumar, Prof. H. Yun*
School of Biotechnology
Yeungnam University
Gyeongsan, South Korea. E-mail: hyungdon@ynu.ac.kr

[b]Dr. Y. J. Jang, Dr. N. Chitrapriya, Prof. S. K. Kim
Department of chemistry
Yeungnam University, Gyeongsan
South Korea

[c]E. Song, N. Lee, Prof. B. G. Kim
School of Chemical and Biological Engineering
Seoul National University, South Korea.

[d]N. Soundrarajan, Prof. S. G. Lee
Department of Chemical Engineering
Pusan National University
South Korea

[e]Prof. Hyung Joon Cha
Department of Chemical Engineering
Pohang University of Science and Technology
South Korea

[f]Prof. N. Budisa
Department of Biocatalysis,
Technische Universität Berlin, Germany

[*] Corresponding author

Materials

PCR reagents, T4 DNA ligase and restriction endonucleases were purchased from Promega (Madison, WI, USA). The isopropyl-D-thiogalactopyranoside (IPTG) was purchased from sigma chemicals (St. Louis, MO, USA). The host bacterium *Escherichia coli* strain XL1-blue (Stratagene, CA, USA) was used for plasmid DNA preparation, in this study. *E. coli* cells with plasmids were grown aerobically in Luria-Bertani (LB) broth (Difco Laboratories, Detroit, Michigan, USA) or on LB agar plate, supplemented with appropriate antibiotics for the selection of transformants. Natural amino acids, unnatural amino acid 3, 4-dihydroxy-L-phenylalanine (L-DOPA) and chitosan were purchased from Sigma (St. Louis, MO, USA). The nickelnitrilotriacetic acid (Ni-NTA) affinity column was purchased from Qiagen (Valencia, CA, USA). *E.coli* strain JW2581 tyrosine auxotroph was obtained from *E. coli* Genetic Stock Centre, Yale University, New Haven, USA and plasmid pQE-80 L was obtained from Qiagen (Valencia, CA, USA).

Construction of plasmids and strains

The DNA manipulations were performed according to the procedures described by Sambrook and Russel.[1] The PCR reaction (50 µl) contains 10 pM of each primer, 50 ng of template DNA, 1X Taq DNA polymerase buffer, 1 U of *Taq* DNA polymerase (Promega, Madison, WI, USA), 0.2 mM of each deoxyribonucleotide triphosphates and 1.5 mM $MgCl_2$. Amplification was performed in a DNA thermal cycler (Master Gradient thermal cycler, Eppendorf, Hamburg, Germany) programmed for an initial denaturation (94 ºC for 1 min) followed by 30 cycles of 1 min at 94ºC, 1 min at 60ºC and 0.5 min at 72ºC with an extension at 72ºC for 10 min. pQE-60 bearing GFPhs2 containing eight tyrosine residues was constructed by cloning it in the pQE-80 L using *BamH*1 and *Hind*III restriction enzymes.[2] The constructed pQE80-GFPhs2 (hereafter it will be mentioned as GFP) plasmid was transformed into *E. coli* JW2581 tyrosine auxotroph for the production of recombinant natural and unnatural recombinant proteins. All these constructs were sequenced and confirmed for their target protein sequence.

Incorporation of L-DOPA into recombinant protein and SDS-PAGE analysis

The above mentioned constructs were grown in M9 minimal medium supplemented with 0.4% (w/v) of glucose, 0.1 mM of $CaCl_2$, 1.0 mM of $MgSO_4$, 35 µg/mL of thiamine, 20 amino acids (40 mg/L), and appropriate antibiotics. When an optical density of the culture reaches 0.8 to 1.0 at 600 nm, then its centrifuged for 10 min (5,000 rpm) at 4 °C. The cell pellets were washed twice with 0.9% (w/v) of NaCl solution. The cells were then resuspended in M9 minimal medium supplemented with 19 amino acids (40 mg/L) lacking tyrosine. The resuspended cells were added to different test tubes containing M9 minimal medium containing L-tyrosine (40 mg/L) as a positive control, L-DOPA (1 mM) as a test. Reducing agent such as DTT (concentration varied from 100 to 500 µM) and ascorbic acid (concentration varied from 1 to 10 mM) at different concentrations was added to

medium supplemented with L-DOPA. After incubating at 37^0C for 10 min, 1 mM of IPTG was added to induce the protein expression. The cells were harvested finally after 6 hrs of induction and OD_{600} was measured. The harvested cells by centrifugation were stored at -70°C until further use. Cell lysis was carried out by using BugBuster protein extraction kit (Novagen) followed by sonication. Briefly, collected cell pellet corresponding to 1 mL of culture was resuspended in 100 µl of lysis buffer, incubated at room temperature for 10 min., and centrifuged at 9000g, 4ºC for 20 min. The supernatant was saved as a soluble protein fraction, and analyzed by SDS-PAGE (12% acrylamide gel).

Table S1. Amino acid sequences of the GFP. The GFP expressed as recombinant protein contains a hexahistidine tag sequence of the vector pQE80L (MRGSHHHHHHGF) was appended to the N-terminus of each protein for Ni-NTA purification.

	10	20	30	40
GFP	MSKGEELFTG	VVPILVELDG	DVNGHKFSVR	GEGEGDATNG
GFPdopa				

	50	60	70	80
GFP	KITLKLICTT	GKLPVPWPTL	VTTCG**Y**GVQC	FAR**Y**PDHMKR
GFPdopa			**Y***	**Y***

	90	100	110	120
GFP	HDFFKSAMPE	G**Y**VQERTISF	KDDGTFKTRA	EVKFEGDTIV
GFPdopa		**Y***		

	130	140	150	160
GFP	NRIKLKGIDF	KEDGNILGHK	LE**Y**NFNSHNK	**Y**ITADKQKNG
GFPdopa			**Y***	**Y***

	170	180	190	200
GFP	IKANFKIRHN	VEDGSVQLAD	H**Y**QQNTPIGD	GPRLLPDNH**Y**
GFPdopa			**Y***	**Y***

	210	220	230
GFP	LSTQSVILED	PNEKRDHMVL	HEFVTAAGITHGMDEL**Y**K
GFPdopa			**Y***

Y* represents the L-DOPA incorporation site

Protein purification

The pQE80-GFP in *E. coli* tyrosine auxotroph was grown to OD_{600} of 0.6 in 100 mL M9 medium, induced with 1 mM IPTG for 6 hrs and pelleted. Purification of recombinant proteins were performed by using Ni-NTA HisBind Resin (Novagen). Further Histag purified samples were subjected to gel permeation chromatography (GPC) purification by AKTA Explorer FPLC system containing Superdex 75 HR column at 4 °C.

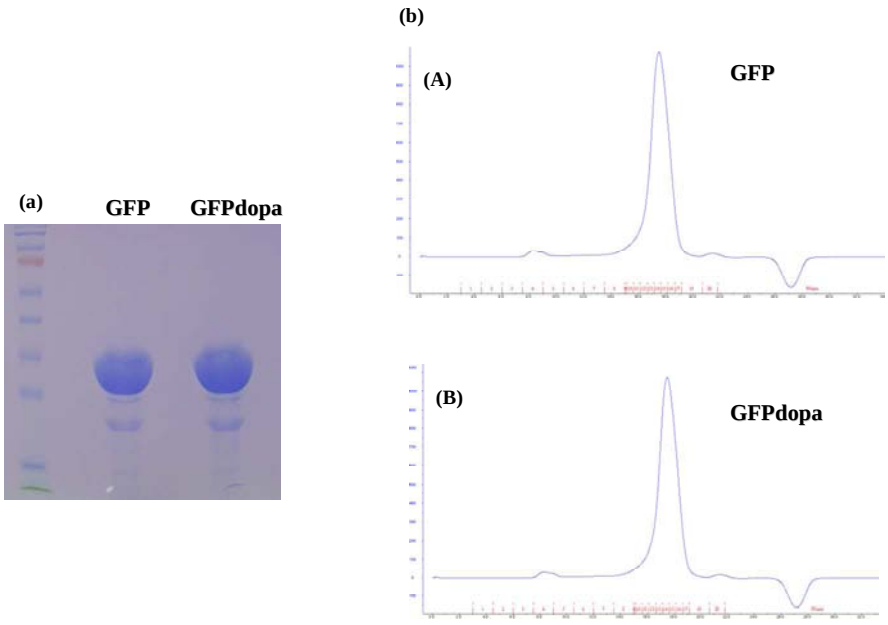


Figure S1. (a) GFP and GFPdopa proteins were purified by nickel affinity chromatography column (b) Gel permeation chromatography of purified GFP and GFPdopa proteins. GFP (A) and GFPdopa (B) proteins were applied to a gel permeation column and eluted with PBS (100 mM NaH_2PO_4, 500 mM NaCl, pH 6.8) at 0.75 mL/min. at 4°C. For each run, 1 mL of 5 mg/mL protein was injected. The elution pattern was monitored by measuring the absorbance at 280 nm.

Protein quantification and fluorescence analysis

Absorption spectrum and quantification of proteins were measured as describe elsewhere. Fluorescence spectra (2 μM protein samples were excited at 470 nm by using excitation/emission slits of 5.0 nm) were recorded on a JASCO FP-777 spectrofluorimeter equipped with digital software.

Redox-cycling staining of DOPA containing proteins

The GFP containing tyrosine and GFPdopa containing L-DOPA was obtained as described in the previous section. GFP and GFPdopa were blotted electrophoretically onto poly vinylidene difluoride membrance (PVDF) and visualized by staining the membrane with nitroblue tetrazolium (NBT). The membrane was incubated in the NBT staining solution (2 M sodium glycinate, 0.24 mM NBT, pH 10.0) in dark room for 3 h.

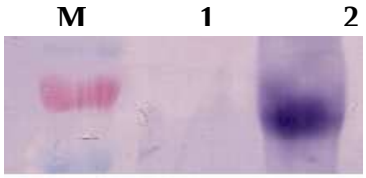


Figure S2. Detection of DOPA incorporation in GFP variants by redox-cylcing staining. Approximately equal amounts (12.5µg) of each of the purified samples were separated on SDS-PAGE gel and stained by NBT. Protein Ladder (Promega prestained Ladder); Lane 1: Positive control (expressed with 19 amino acid plus L-tyrosine); Lane 2: test (expressed with 19 amino acid plus L-DOPA (residue specific incorporation)).

In-gel digestion

Samples were resolved by SDS-PAGE and stained with Colloidal Coomassie blue R250 solution (ProteomeTech Inc. Korea). Protein in-gel digestion was performed with modifications as described previously[3]. Gel bands were sliced into 1 mm^3 cubes and washed twice with 50 mM ammonium bicarbonate containing 50% acetonitrile. Protein reduction and alkylation were performed consecutively with 10 mM DTT in 50 mM ammonium bicarbonate for 1 h at 56 °C and then with 10 mM acrylamide in 50 mM ammonium bicarbonate for 45 min at room temperature, respectively. Gel pieces were washed twice with 50 mM ammonium bicarbonate, 50% acetonitrile, dehydrated with 100% acetobitrile, and dried in a speed vac. The dried gel pieces were rehydrated with 20 ng µL-1 sequencing grade trypsin (Promega, CA, USA) in 50 mM ammonium bicarbonate and incubated overnight at 37 °C. Supernatants were transferred to fresh tubes, and the remaining peptides in gel slices were extracted by sonicating with 50% acetonitrile in 5% TFA in water bath for 40 min. The extracts were combined, dried about 2 µL and desalted using a GeLoader tip column packed with POROSR2/R3 (Applied Biosystems, CA, USA) and the eluted peptides were subjected to mass spectrometric analysis.

Nano LC-MS/MS

Tryptic digests were separated by an Ultimate nanoLC systems including the FAMOS autosampler and Switchos column switching valve (LC-Packings, Amsterdam, The Netherlands) and on-line analyzed by a QSTAR Mass spectrometer (Applied Biosystems, CA, USA) with a nanospray interface as described.[4] Peptide binding was occurred in a 2 cm 200 μm ID self-packed column Zorbax 300SB-C18, 5μm (Agilent) with 5% acetonitrile in 0.1% formic acid with a flow rate 4 μL /min for 10 min. The bound peptides were separated in a 15 cm fused silica emitter (75 μm ID) in-house packed with the same resin, eluted with 5 – 50 % (v/v) acetonitrile in 0.1 % formic acid over 45 min at a flow rate of 0.2 μL /min. MS/MS spectra were acquired in an automated switching mode tandem mass spectrometer with m/z-dependent set of collision offset values.

Peptide identification via MASCOT database search

The mass spectral data were processed into peak lists with Analyst QS (version 1.1; Applied Biosystems) and searched against GFP protein sequences using in-house Mascot server (version 2.1, matrix Sciences, UK). The initial mass tolerance in MS mode was set to 0.3 Da and MS/MS mass tolerance was 1 Da. Two tryptic missed cleavages were allowed and L-DOPA (Y^{*}) were searched as variable modifications. The candidate peptides whose probability MOWSE scores are significant ($p<0.05$) were considered and selected. The MS/MS spectra of selected peptides were manually validated as well.

Table S2. List of peptide amino acid sequences of samples observed by ESI-MS/MS.

Amino acids	Obseved mass (Da)	Calculated mass (Da)	Ions score¥	Sequence
Wild-type GFP				
181 - 206	949.4257	2845.3379	143	R.HNVEDGSVQLADHYQQNTPIGDGPVR.L
207 - 226	1156.5345	2311.1332	122	R.LPDNHYLSTQSVILEDPNEK.R
228 - 250	872.0356	2613.2355	126	R.DHMVLHEFVTAAGITHGMDELYK.
GFPdopa				
181 - 206	955.7592	2864.2848	105	R.HNVEDGSVQLADHY*QQNTPIGDGPVR.L
207 - 226	776.6923	2327.1281	36	R.LPDNHY*LSTQSVILEDPNEK.R
228 - 250	662.2860	2645.2253	71	R.DHMVLHEFVTAAGITHGMDELY*K.

Y* represents Tyr⟶ DOPA substitution in GFPdopa protein.

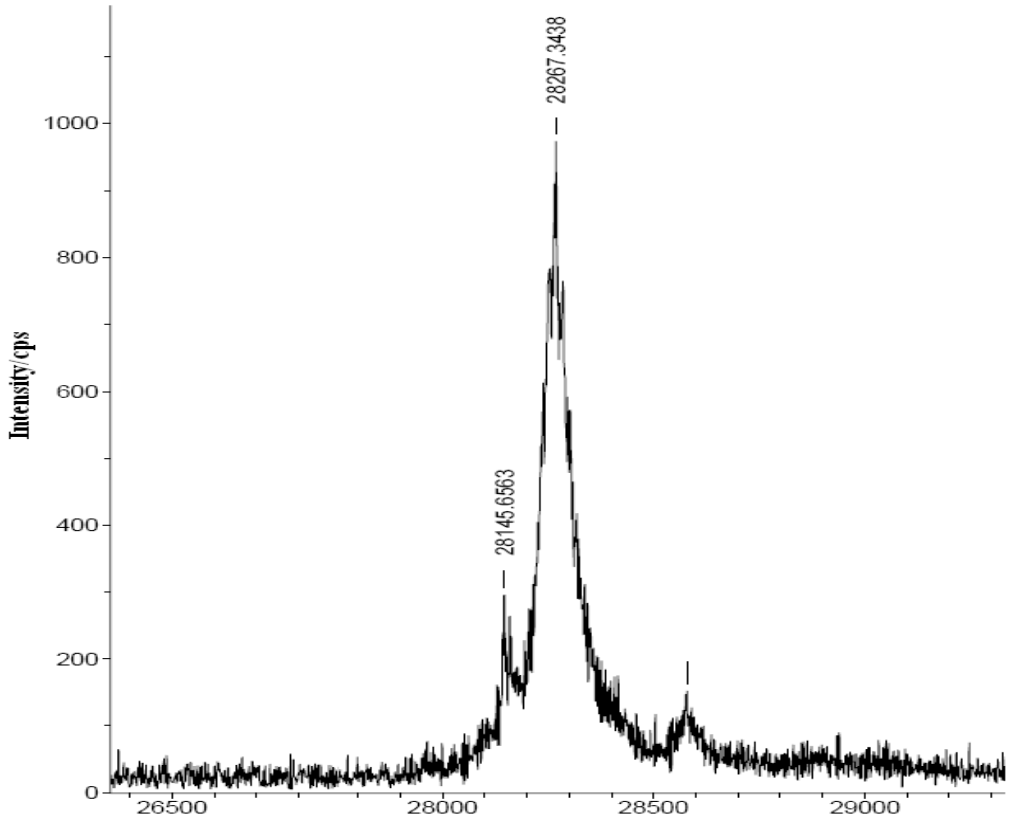


Figure S3. ESI-MS analysis of GFPdopa. ESI-MS profile showed the match with calculated mass (28274.7) with found mass (28267.3) for the incorporation of L-DOPA and minor side peak matched the GFP mass (28145.7).

Bioconjugation reaction of genetic code engineering protein with chitosan

A concentrated chitosan solution was prepared by adding 1.6 g chitosan to 100 ml of cold 0.25 N HCl with vigorous stirring and kept at 4°C overnight. After stirring overnight, the undissolved materials were removed by filtration. This chitosan solution was diluted and the pH was slowly raised to 5.8–6.0 by adding 1M NaOH. This pH was selected to balance chitosan's solubility and maintain the protein stability. Solutions (pH 6.0) were prepared with GFP and GFPdopa protein (30µg/mL) either in the absence (controls) or presence (samples) of sodium periodate (1mM) and mixed with chitosan (0.7% w/v). After five hours incubation at room temperature, conjugant's were precipitated by raising the pH with phosphate buffer (pH >7) and centrifuged to measure the fluorescence of the supernatant. In all the steps such as precipitation, washing, and resolubilization, the sample pH was adjusted to 6.0 and fluorescence was estimated by Jasco Fluorescence spectrophotometer. The pellet was washed several times with PBS buffer to remove physically bound protein and then resolubilized in aqueous acetic acid solution (0.5 v/v %) (**Figure S4).**

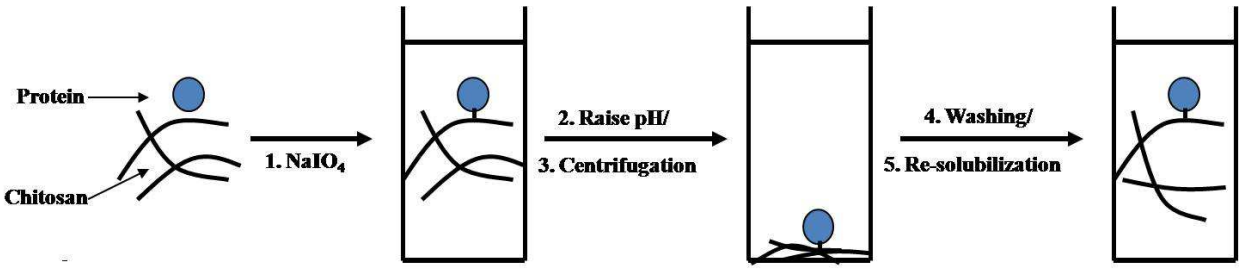


Figure S4. Schematic representation of the periodate mediated protein-polysaccharide conjugation

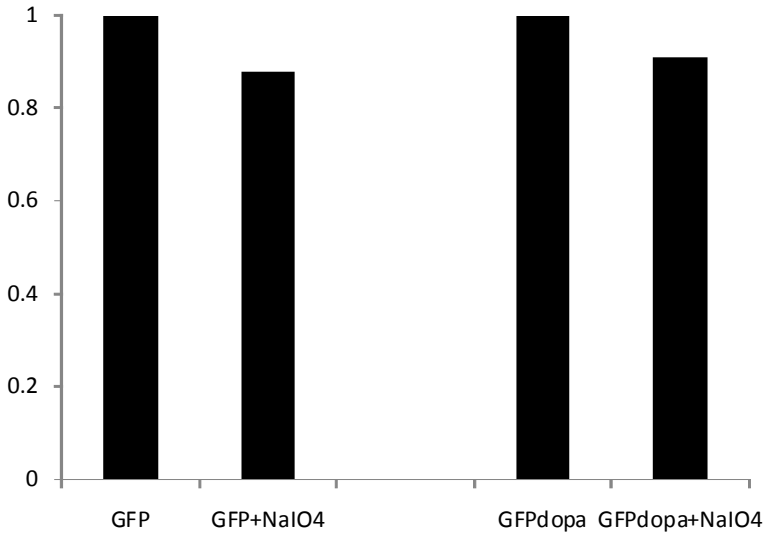


Figure S5. Effect of periodate on GFP and GFPdopa proteins (in the absence of chitosan)

Effect of pH on GFP and GFPdopa protein

The pH of the proteins was adjusted from 3 to 11, with MOPS buffer, in increments of 1 pH unit.[3] The fluorescence emission of each protein was recorded using Jasco Fluorescence spectrophotometer.

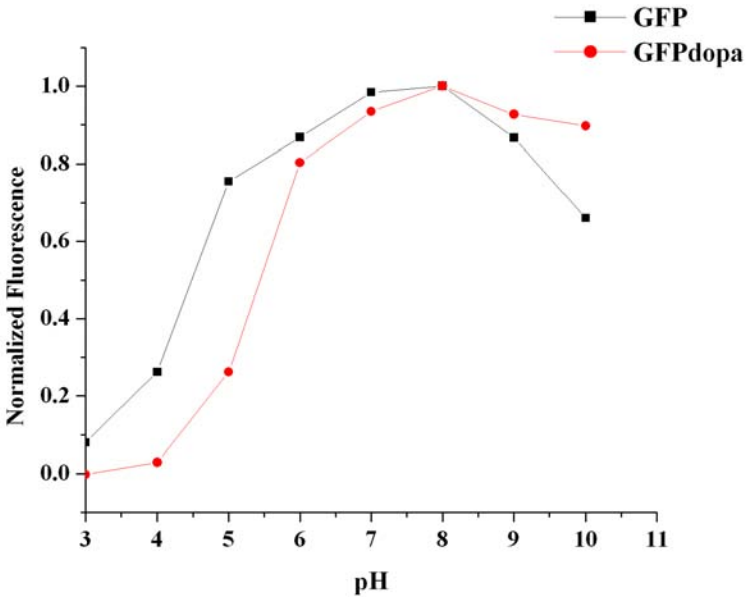


Figure S6. Effect of pH on GFP and GFPdopa proteins

Preparation of chitosan film and GFPdopa conjugation

For chitosan film conjugation study, chitosan films were prepared by pouring 0.5% chitosan solution into a small Petri dish and then dried overnight at 45°C. Then these chitosan films were neutralized with NaOH for 30 min and washed several times with 0.01M PBS. Further, the chitosan films were then peeled from the Petri dish and a UV-Vis spectrum was measured[5]. The conjugation reactions were then performed by incubating the chitosan films with the combination of GFP (30 µg/ml) and GFPdopa (30 µg/ml) and $NaIO_4$ (1mM) solution for 1 h. The resulting films were rinsed several times with PBS and to obtain UV spectra the glass slides were placed in the spectrophotometer perpendicular to the light-path such that the light passed directly through the film. The difference between the UV-Vis spectrums provides the absorbance GFP and GFPdopa on chitosan films.

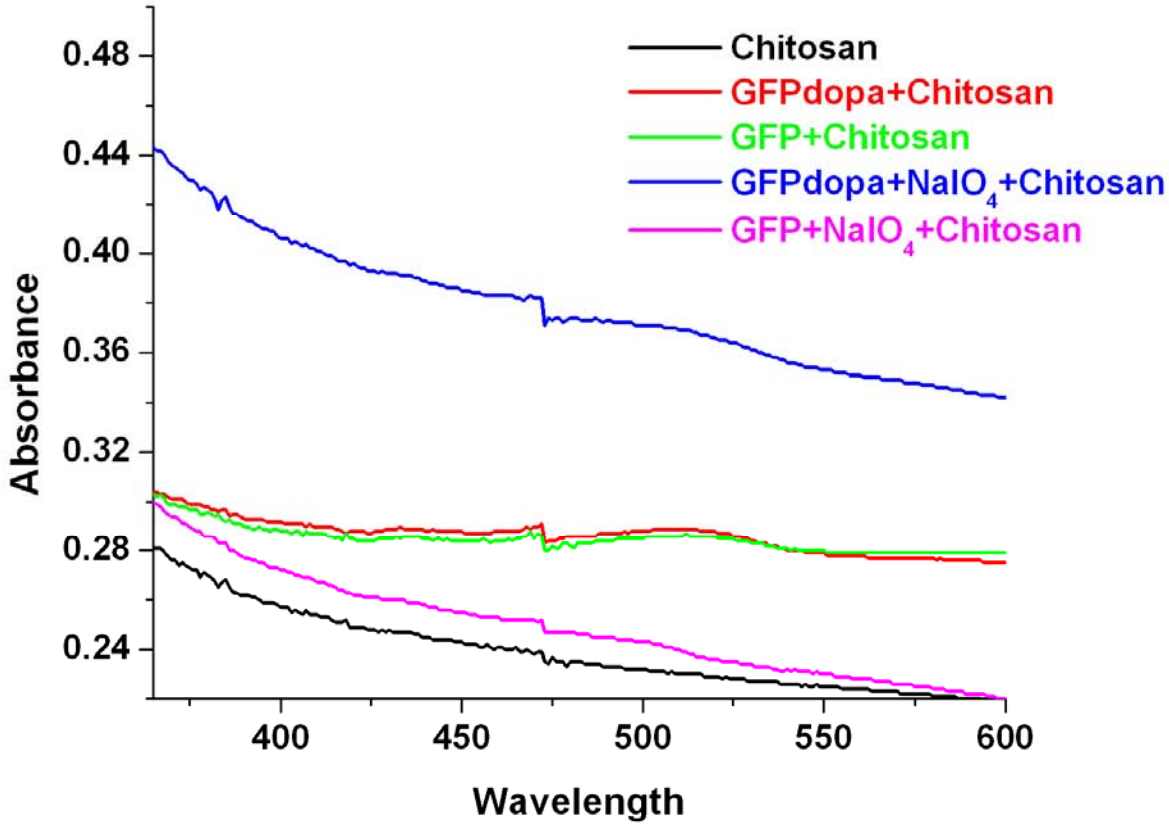


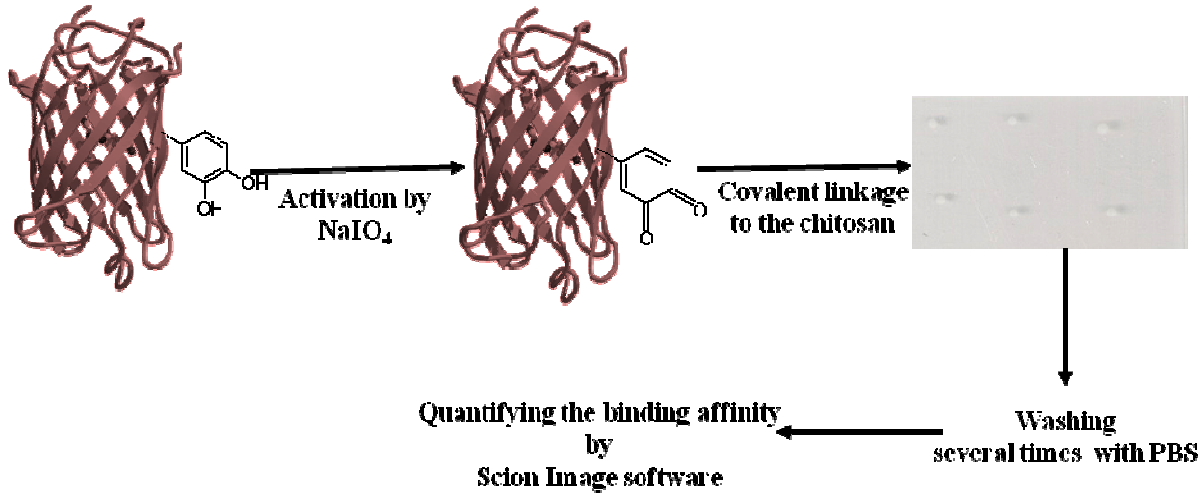
Figure S7. GFP and GFPdopa bioconjugation with chitosan film

Preparation of hydrogels and fluorescence microscopy analysis

Chitosan hydrogels were prepared by pouring 10 ml of 2% chitosan solution into a small Petri dish and then dish was immersed in a caustic solution (1 M NaOH). After gel formation, the gels were washed extensively with water and PBS buffer. GFP and GFPdopa proteins (2 ml at 40µg/ml) treated with 1 mM $NaIO_4$ were spread on the surface of the chitosan hydrogel. The solution was incubated at room temperature for 5 hrs to cross link with chitosan hydrogel. After cross linking, gels were thoroughly washed with PBS buffer to remove the unspecific binding of proteins. Images were obtained on a Zeiss Axiovert 200 fluorescence microscope with mercury vapour lamp illumination and FITC and Cy3 filter sets. Images were captured on a Hamamatsu ORCA-ER grey scale digital camera using simple PCI software. For colour panels in figure 2 separate grey scale images were taken with FITC and Cy3 filter sets with the auto exposure setting in simple PCI. The grey scale images were combined and false colored using Corel Draw. The images were taken with a gain of 255 and an exposure of 0.0125 seconds.

Fabrication of well type chitosan

Well-type chitosan arrays were fabricated by dropping 0.5% chitosan solution into a glass slides and then dried overnight at 45°C. The chitosan films were neutralized with NaOH for 30 min and washing several times with 0.01M PBS. Further, conjugation reactions were then performed by incubating the chitosan spots with the combination of GFP (30 µg/ml) and GFPdopa (30 µg/ml) with $NaIO_4$ (1mM) solution for 1 h. The resulting films were rinsed several times with PBS and Scanned. The images were imported as TIFF file and densitometry analysis was carried out using Scion Image package (Scion Corp., Frederick, MD).



Scheme S1. Fabrication of GFPdopa protein into chitosan by stepwise method.

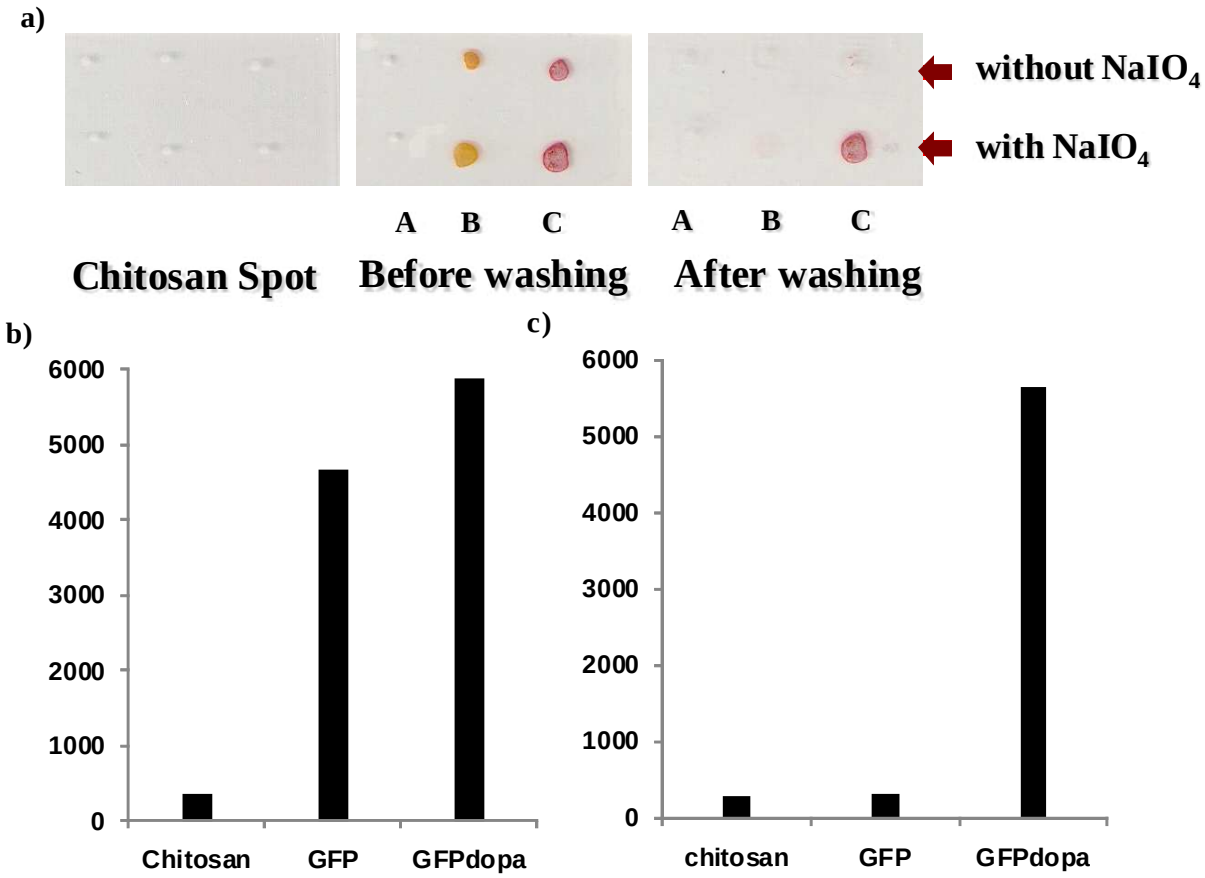


Figure S8. Densitometry analysis of well type chitosan array. a) Fluorescence analysis of periodate initiated conjugation of GFP with chitosan by stepwise method. Chitosan spot (A), Chitosan treated with GFP (B), Chitosan treated with GFPdopa (C). b) Densitometry analysis of chitosan, GFP and GFPdopa before washing with PBS solution , c) Densitometry analysis of chitosan, GFP and GFPdopa after washing with PBS solution.

Reference

1. J. Sambrook, E. Fritsch, T. Maniatis, *Molecular Cloning: A Laboratory Manual.* 2nd ed., Cold spring harbor laboratory press, Cold spring harbor, NY, USA, **1989.**

2. N. Soundrarajan, N. Ayyadurai, N. Budisa, L. Merkel, G. Raghunathan, S. Sriram,E. Song, B.G. Kim, H. Yun, S. G. Lee, *Chembiochem* (In review).

3. A. Goulding, S. Shrestha, K. Dria, E. Hunt, S. K. Deo, *Protein Eng.* **2010,** *21*, 101.

4. M. A. Marti-Renom, A. Stuart, A. Fiser, R. Sanchez, F. Melo, A. Sali, *Annu. Rev. Biophys. Biomol. Struct.* **2000,** *29*, 291.

5. Wu, H., Shi, X., Tsao, C., Lewandowski, A. T., Fernandes, R., Hung, C., DeShong, P., Kobatake, E., Valdes, J. J., Payne, G. F., and Bentley, W. E. *Biotech. Bioeng.*, **2009,** *103*, 231-236.

Bioconjugate Chemistry

ARTICLE

pubs.acs.org/bc

Cellular Trafficking and Photochemical Internalization of Cell Penetrating Peptide Linked Cargo Proteins: A Dual Fluorescent Labeling Study

Michael P. Gillmeister,[*,†,‡] Michael J. Betenbaugh,[†] and Paul S. Fishman[‡,§]

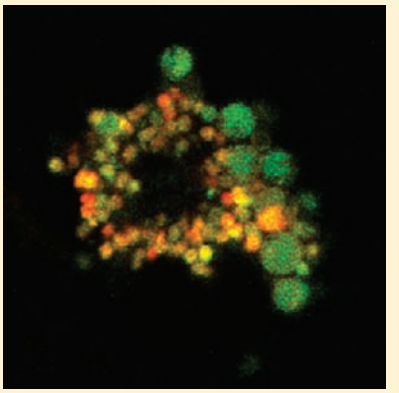
[†]Department of Chemical and Biomolecular Engineering, Johns Hopkins University, Baltimore, Maryland 21218, United States

[‡]Research Service, Veterans Affairs Maryland Health Care Service, Baltimore, Maryland 21201, United States

[§]Department of Neurology, University of Maryland School of Medicine, Baltimore, Maryland, United States

Supporting Information

ABSTRACT: Initial cellular uptake of cell penetrating peptide (CPP) linked macromolecules is usually endosomal, with passage from endosome to cytosol a major limitation to efficient delivery. To gain a better understanding of the passage of the CPP-linked proteins, we studied the uptake and localization of CPP-linked proteins that contained two different forms of fluorescent markers, GFP protein and chemically conjugated tetramethylrhodamine, in living cells. Rhodamine labeled TAT-GFP was internalized in multiple cell lines including HEK293, N18-RE-105, hippocampal slices, and human neural progenitor cells and showed predominantly endosomal localization of both fluorescent markers. Cytosolic localization of some rhodamine label was detected to suggest that some of the GFP label had exited from the endosome. However, quantification of the distribution of the rhodamine and GFP label indicated that the protein location was primarily endosomal and that the distribution of TAT-GFP was not significantly different than that of an exclusively endosomal localized exogenous protein (tetanus toxin fragment C - TTC). As a result, photochemical internalization (PCI) was evaluated and caused a significant quantitative redistribution of cellular fluorescence of rhodamine and GFP labels to demonstrate increased cytosolic delivery of GFP. While rhodamine-labeled TAT-GFP showed cytosolic delivery with exposure to specific wavelengths of fluorescent illumination, a similarly labeled GFP fusion protein containing the membrane binding domain of TTC did not mediate PCI in N18-RE-105 cells.



INTRODUCTION

Internalization and delivery of cargo proteins from the extracellular fluid across biological membranes and into the cytosol can be accomplished by attaching cationic peptides to the macromolecule of interest. Such peptides are the functional regions responsible for the ability of certain natural and recombinant proteins to enter into a cell and have been termed cell-penetrating peptides (CPPs) or protein transduction domains (PTDs). When fused with a number of potential therapeutics for delivery into the cell, these peptides greatly increase the traffic of desired therapeutics into cytosolic targets within the cell. Protein transduction domains have been used to translocate small cargo such as peptides and oligonucleotides, as well as larger cargo such as DNA complexes and full-length proteins. Although these peptides have been extensively studied and reviewed, some aspects of their efficiency are not yet fully resolved [1,2] (for other reviews, see refs 3−7). Among the different cell penetrating peptides, perhaps the most well-studied include a small domain from HIV transactivating transcriptional activator, TAT(47−57). Other well-studied natural and synthetic CPPs include penetratin from *Drosophila* Antennapedia, transportan (a chimeric peptide), VP22 from Herpes simplex virus type 1, and polyarginine.[8] The efficiency of uptake and the ability to translocate across a cell membrane varies with several factors including cargo, cell type, and type of cell penetrating peptide.[9,10]

Although initial studies suggested that these peptides and their cargo passed directly through the plasma membrane into the cytosol, most studies have shown delivery by protein transduction with a predominant endosomal vesicle localization. While the most widely accepted mechanism for cytosolic entry is the clathrin- and receptor-independent, lipid raft-dependent macropinocytosis,[9,11] many previous studies relied on post-mortem imaging of fixed cells.[12] Later studies including imaging of living cells showed that methanol[13] or paraformaldehyde[14] fixation changed the distribution of CPP-cargo proteins suggesting that cytosolic labeling in earlier studies may have been artifactual. Also, while initial work in the cell penetrating peptide field showed highly efficient delivery of peptides,[15] subsequent work utilizing the fusion of cell penetrating peptides to larger cargo proteins decreased the efficiency in the delivery and cytosolic

Received: October 18, 2009
Revised: February 15, 2011
Published: March 15, 2011

ACS Publications © 2011 American Chemical Society

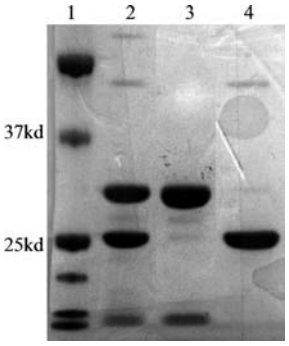


Figure 1. Cleavage and second purification of TAT-GFP from GST. Proteins run on 10% Bis-Tris Gel with MOPS running buffer and stained with SimplyBlue Safestain Coomassie Stain. Lane 1: Molecular Weight Standards. Lane 2: GST and TAT-GFP mixture after cleavage. Lane 3: TAT-GFP in wash. Lane 4: GST in elution.

distribution of CPP-cargo proteins.[16] Finally, much of the initial work with protein transduction cargo was done with denatured protein.[2] Later studies showed that natured protein was able to enter cells with only a slightly decreased transduction efficiency and that total denaturation was not necessary to translocate a cargo protein.[17] The use of fluorescent cargo proteins such as GFP, however, introduced the possibility of artifactual underestimation of cytosolic translocation, since denaturation of such proteins leads to elimination of their native fluorescence. While there have been many studies of mechanisms, the efficiency of cytosolic transfer of the cell penetrating peptides and protein cargoes in many studies has been far from optimal. Tracking the transduction of full length protein delivery by means of two fluorophores, one of which would fluoresce despite denaturation, would allow for the clarification of these issues of efficiency of translocation of CPP-linked cargo proteins.

It is generally accepted that the exit of protein from the endosome into the free cytosol is the primary limitation for protein transduction-based delivery using TAT and other similar peptides. Photochemical internalization (PCI) is one of several strategies to facilitate the cytosolic release of cargo molecules trapped within endocytic vesicle membranes [18−20]. PCI uses a photosensitizer, often based on porphyrin structure, which localizes to endosomal membranes and, when exposed to light, activates the release of cargo contained in the vesicle by forming reactive oxygen species which rupture the membrane.[21,22] Photochemical internalization, an offshoot of photodynamic therapy, has been primarily used for delivery of plasmid genes,[23−25] cytotoxic proteins,[26−29] and adenovirus.[30,31] PCI has also recently been used to deliver siRNA[32] and CPP-small nucleic acid combinations.[33]

The current study attempts to clarify some of the issues regarding transduction of CPP-linked cargo protein, particularly the efficiency of movement from the endosomal compartment into the cellular cytosol, using cargo that contains both a fluorescent protein and a small nonprotein fluorophore. To estimate efficiency of cytosolic transfer from endosomes, the cellular distribution of the test cargo GFP protein with TAT as a CPP was quantified and compared to the distribution of a similarly labeled protein, the binding domain of the heavy chain of tetanus toxin, fragment C (TTC), known to undergo only endosomal internalization without membrane translocation.[34] The distribution of fluorescent proteins after PCI was also evaluated, as this process appears to alter distribution of endosomal localized exogenous proteins.

EXPERIMENTAL PROCEDURES

Plasmid Construction and Expression of Recombinant Proteins. In order to create and express the recombinant proteins TAT-GFP and TTC-GFP, the following strategies were employed. The oligonucleotides for the TAT(47−57) sequence (YGRKKRRQRRR) were synthesized and purified by the Biopolymer Laboratory of the University of Maryland at Baltimore. The annealed oligos were cloned into the *Bam*HI-*Eco*RI sites of the pGEX6P-3 (GE Healthcare, Piscataway, NJ) expression vector. Primers were used to amplify EGFP from the pEGFP-1 vector (Clontech, Palo Alto, CA) and cloned into the *Eco*RI-*Sal*I site of the pGEX6P-3 TAT construct. cDNA for TTC (tetanus toxin fragment C) was a gift of Dr. Neil Fairweather of Imperial College, London, U.K. EGFP DNA fragments were amplified by PCR for cloning into the pGEX4T-3 bacterial expression vector. The TTC PCR primers were designed with a *Bam*HI site and a *Bgl*II-NotI site. The EGFP primers were designed with a *Bgl*II site and a NotI site. The fragments were then cloned into the respective sites. All constructs were sequenced to determine that fragments were in frame and there were no mutations generated.

The bacterial clones containing the plasmids were cultured at 37 °C to an OD600 of 0.6. The cultures were moved to 25 °C and induced with a final concentration of 1 mM IPTG (isopropyl-β-D-thiogalactopyranoside, Invitrogen) and incubated overnight. After incubation, the cultures were centrifuged and the cell pellets resuspended in 1× PBS (phosphate buffered saline) with 10 mg/mL lysozyme (Sigma), sonicated, and centrifuged. The GST-linked recombinant proteins were purified from the soluble fraction using glutathione sepharose, dialyzed against 1× PBS, cleaved overnight with PreScission Protease for TAT-GFP and thrombin for TTC-GFP, and the desired proteins purified away from GST using glutathione sepharose (Figure 1).

Preparation of Fluorescent Labeled Proteins. Rhodamine-labeled fusion proteins (Rh-TAT-GFP and Rh-TTC-GFP) were generated using a FluoReporter Tetramethylrhodamine Protein Labeling kit according to the manufacturer's protocol (Molecular Probes) followed by dialysis in 1× PBS at 5 times molar ratios of rhodamine to protein. Across multiple labelings, an average of 3 rhodamine groups were attached per molecule of TAT-GFP at a labeling efficiency of 60% and 3.7 rhodamine groups per molecule of TTC-GFP at a labeling efficiency of 74% as measured by a standard fluorescence curve in a Perkin-Elmer VICTOR.

Cell Culture and Exposure to Test Proteins. *HEK 293* cells were plated in 2 well Lab-Tek Chamber Coverglass slides at 40 000 cells/mL in MEM containing 10% fetal bovine serum, 2 mM L-glutamine, and pen/strep (Invitrogen, Carlsbad, CA) and allowed to expand for 3 days before treatment. N18-RE-105 cells were plated in chamber slides at 20 000 cells/mL in DMEM containing 10% fetal bovine serum, HAT supplement, and pen/strep (Invitrogen, Carlsbad, CA) and allowed to grow for 3 days before treatment. Hippocampi of postnatal day 7 rats were dissected free and 300-μm-thick slices cut using a McIlwain tissue chopper under aseptic conditions. Slices were placed on filter inserts (Millipore) in six-well dishes in maintenance medium (Invitrogen, Carlsbad, CA; 33.3% basal medium Eagle, 33.3% Hank's buffered saline solution, 33.3% horse serum, 25 mM D-glucose, 2 mM L-glutamine) and maintained for 7 days

dx.doi.org/10.1021/bc900445g |*Bioconjugate Chem.* 2011, 22, 556–566

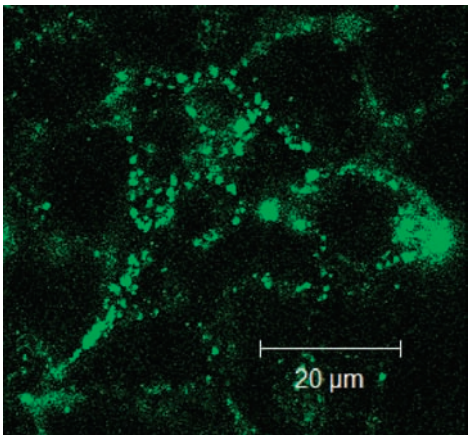


Figure 2. Confocal fluorescent microscopy of HEK 293 culture of TAT-GFP transduced cells. HEK 293 cells were incubated with 75 μg of TAT-GFP for 24 h, washed three times in media, and imaged live using a 40× objective.

before treatment. Human neural progenitor cells (hNPCs, Lonza) were plated in chamber slides at a density of 40 000 cells/well using a combination of hNPC starting medium [35] and 5% horse sera in MEM and allowed to expand for 7 days before treatment. All cultures were maintained at 37 °C in a 5% CO_2 humidified incubator.

Cells were given a complete media change before being treated with test proteins in reduced 4% sera media (HEK 293 and N18 RE-105), maintenance medium (slices), or starting medium (hNPCs) (2.5 μM TAT-GFP, 1.0 μM TTC-GFP). After 0.5, 2, 24, or 48 h, cells were washed 3 times with 1 mL media and immediately imaged.

Confocal Microscopy. Fluorescence was detected on a Zeiss LSM 510 laser scanning confocal microscope. Images were taken with a Zeiss Plan-apochromat 63×/1.4 oil DIC objective. Fluorophores were excited with an argon laser at 488 nm for GFP and a HeNe laser at 543 nm for rhodamine. Emission was filtered through a 505−530 BP filter and a 585 LP filter, respectively. Channels were collected in multitrack scan mode to prevent crosstalk between fluorophores. Pinholes were set to equate optical slice thicknesses. Fluorescence intensity histograms, pixel quantitation, and mean fluorescence intensities were analyzed with LSM (Carl Zeiss, Inc.) and *Slidebook 4.2* (Intelligent Imaging Innovations) software. Quantitative comparison of the distribution of fluorescence intensity was utilized as a reflection of cytosolic (diffuse, uniform) versus vesicular (punctate, highly nonuniform) distribution of the fluorescent protein as derived from previous studies.[36−38] Photochemical internalization was performed under the conventional fluorescence mode by exposing cultures continuously to the fluorescent light source through a TRITC filter for 0.5 to 5 min, followed immediately by imaging.

RESULTS

Cellular Distribution of TAT-Linked Proteins. Initial experiments with recombinant TAT-GFP demonstrated that at all time points of incubation evaluated (0.5, 2, 24, 48 h) the vast majority of labels in HEK 293 cells had a punctate cellular distribution consistent with an endocytic vesicle distribution (Figure 2). In order to determine if TAT-GFP had escaped into the cytosol, similar studies were performed with rhodamine labeled TAT-GFP (Figure 3). GFP fluorescence was excited at 488 nm, while rhodamine was excited at 543 nm. The distribution of pattern GFP fluorescence from Rh-TAT-GFP was similar to that of TAT-GFP to indicate that the localization of this protein was not altered by the rhodamine labeling process (Figure 3A). Comparison of cellular cytosolic GFP fluorescence to baseline background cell-free levels did not reveal a high GFP cytosolic signal. However, the rhodamine fluorescence in Figure 3B appeared to have nonzero levels of cytosolic fluorescence between the brightly labeled endosomic vesicles as compared to cell-free background areas. The amount of rhodamine fluorescence is shown for a larger selection of cells at lower magnification in Figure 3D. In order to evaluate the amount of rhodamine fluorescence, the average rhodamine fluorescence levels were quantified in the cytosolic regions excluding endosomes and compared to background fluorescence levels as shown in Figure 3E. These findings indicate that there was a quantitative increase in rhodamine labeling in the cytosol for the Rh-TAT-GFP protein to suggest that some TAT-GFP may have localized to the cytosol.

Delivery of an Endosomal Localized Control Labeled Protein. In order to confirm that cytosolic rhodamine fluorescence after Rh-TAT-GFP transduction did not represent dissociation of the rhodamine moiety from the fusion protein, similar studies were performed using a rhodamine-labeled protein with known endosomal uptake but without membrane translocation capacity.[39] A rhodamine labeled form of the binding domain of tetanus toxin (TTC) fused to GFP was created. This GFP fusion protein was expressed in a similar manner to the TAT-GFP protein. This protein was also rhodamine labeled at equal per molecule ratios of protein to fluorophore. Analysis of the cellular distribution of rhodamine labeled TTC-GFP served as an endosomally localized control. Shown in Figure 4 is an image of Rh-TTC-GFP transduction in N18-RE-105 neuroblastoma cells. These cells were used because they express surface ganglioside compositions similar to normal brain tissue and are well-known to bind tetanus toxin.[40,41] Rh-TAT-GFP also transduced N18-RE-105 cells in similar distribution patterns seen in HEK 293 cells (not shown). As shown in Figure 4A, the green GFP labeling appears less broadly distributed as compared to Figure 3A and is limited more to punctate structures consistent with endosomes. The red rhodamine fluorescence chemically conjugated to the TTC-GFP molecules is seen in Figure 4B and is also limited more to endosomal vesicular labeling. The Rh-TTC-GFP protein fluorescence was also examined at lower magnification as shown in Figure 4D. The red fluorescence also appears to be limited to endosomes, consistent with the restricted distribution of Figure 4A and B and significantly less distributed than the rhodamine fluorescence of Figure 3D. Unlike Rh-TTC-GFP, Rh-TAT-GFP transduced N18-RE-105 cells with the similar wide distribution pattern seen in HEK 293 cells (data not shown). Average rhodamine fluorescence levels were quantified in the cytosolic regions excluding endosomes and compared to background fluorescence levels shown in Figure 4E. The cytosolic rhodamine fluorescence levels for Rh-TTC-GFP were not significantly above background.

Quantification of Distribution of Cellular Fluorescence after Incubation with Fluorescent Proteins. The frequency distribution of pixel fluorescent intensity has been used to quantify the degree to which a fluorophore has endosome (nonuniform) versus cytosolic (uniform) distribution.[36−38,42]

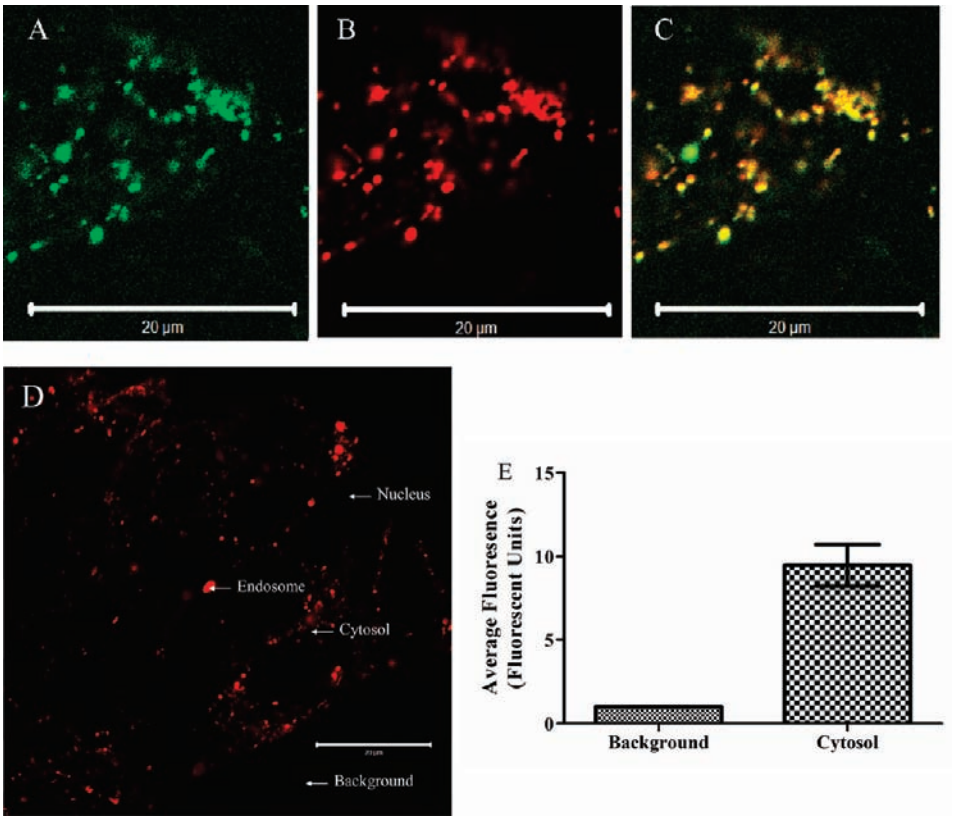


Figure 3. Dual-labeled rhodamine-TAT-GFP in HEK 293 cells. Cells were incubated with 75 μg of Rh-TAT-GFP for 24 h, washed three times in media, and imaged live using a 63× objective: (A) GFP, (B) rhodamine, (C) merge, (D) wide rhodamine field, and (E) average fluorescence units. Scale Bar 20 μm.

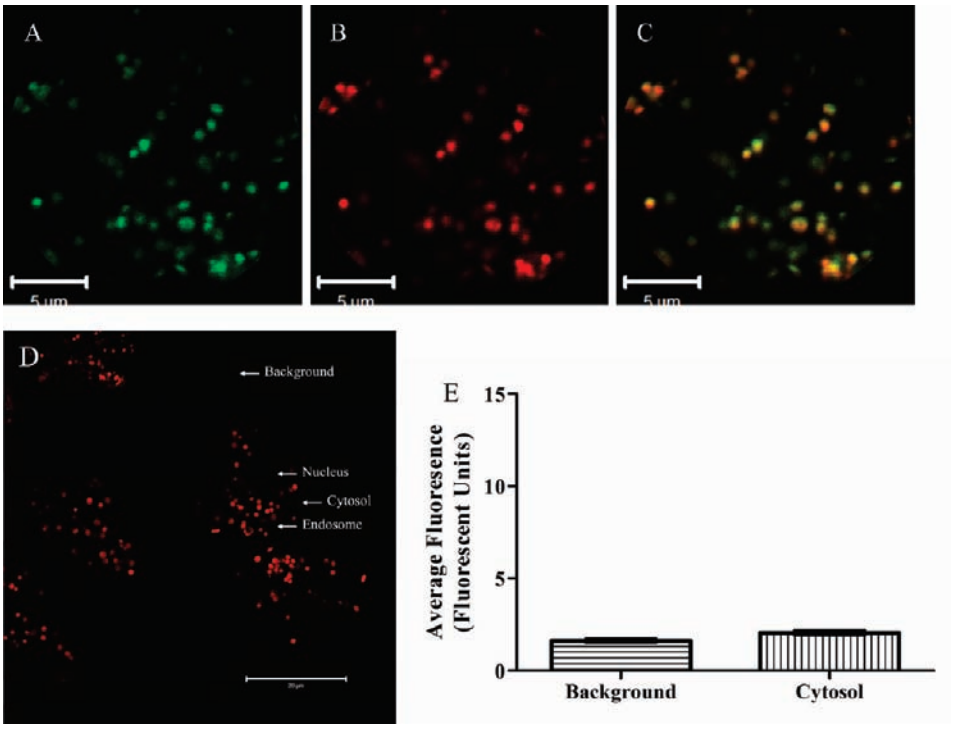


Figure 4. Rhodamine labeled TTC-GFP in N18-RE-105 Neuroblastoma cells. Both GFP (A) and rhodamine (B) fluorescence are localized exclusively to punctate structures consistent with the known endosomal localization of TTC linked proteins. Both moieties show completely overlapping distributions (C) with no detectable cytosolic rhodamine fluorescence demonstrating a stable linkage between the two chromophores without dissociation of the rhodamine moiety. (D) Wide rhodamine field. (E) Average fluorescence units. (A−C) Scale Bar 5 μm. (D) Scale Bar 20 μm.

dx.doi.org/10.1021/bc900445g |*Bioconjugate Chem.* 2011, 22, 556–566

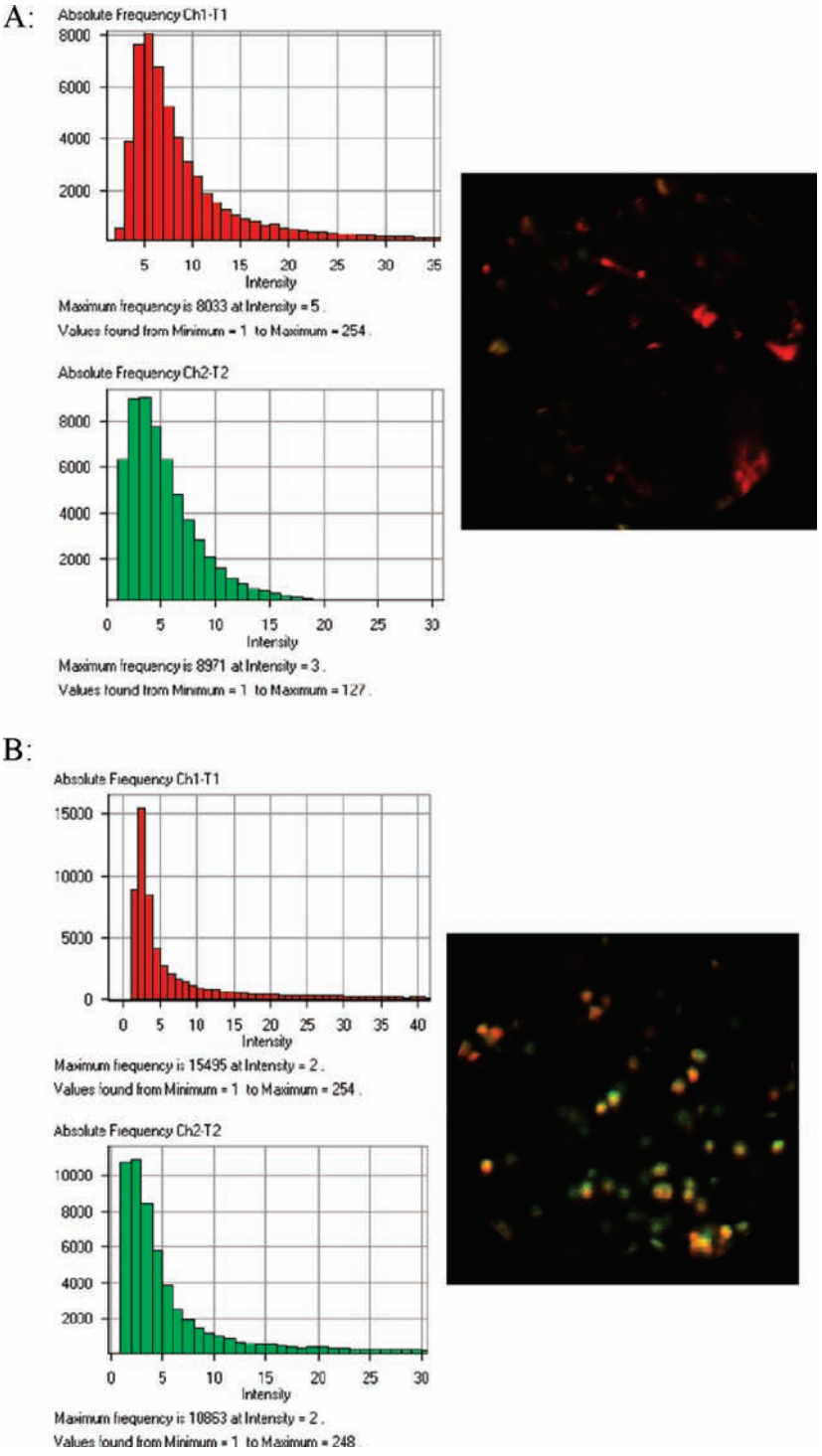


Figure 5. Rh-TAT-GFP (A) and Rh-TTC-GFP (B) taken with equal gain and comparable average fluorescence show similar frequency distributions of fluorescence. Distribution of fluorescence and uniformity from TAT-GFP is not quantitatively different than total endosomal labeled TTC-GFP, in spite of the qualitative cytosolic difference in red fluorescence between the two proteins. Images 20 μm across.

A narrow distribution of fluorescence frequency with a low average fluorescence is a sign of nonuniformity and punctate labeling. In such cases, fluorescent signal is localized primarily in small compartments and the majority of pixel intensities within the cytoplasm are zero or baseline. When little to no protein is distributed throughout the cytosol, the maximum number of the pixels is measured as zero or baseline fluorescence. A wide distribution of fluorescence frequency with a higher average fluorescence implies uniformity and an increased delivery of protein throughout the cytoplasm. Fluorescence intensities in Rh-TAT-GFP and Rh-TTC-GFP exposed cells were compared. Proteins were conjugated and cells were treated such that the total average fluorescence per cell was comparable between the two proteins. Shown in Figure 5 are the frequency distributions

dx.doi.org/10.1021/bc900445g |*Bioconjugate Chem.* 2011, 22, 556–566

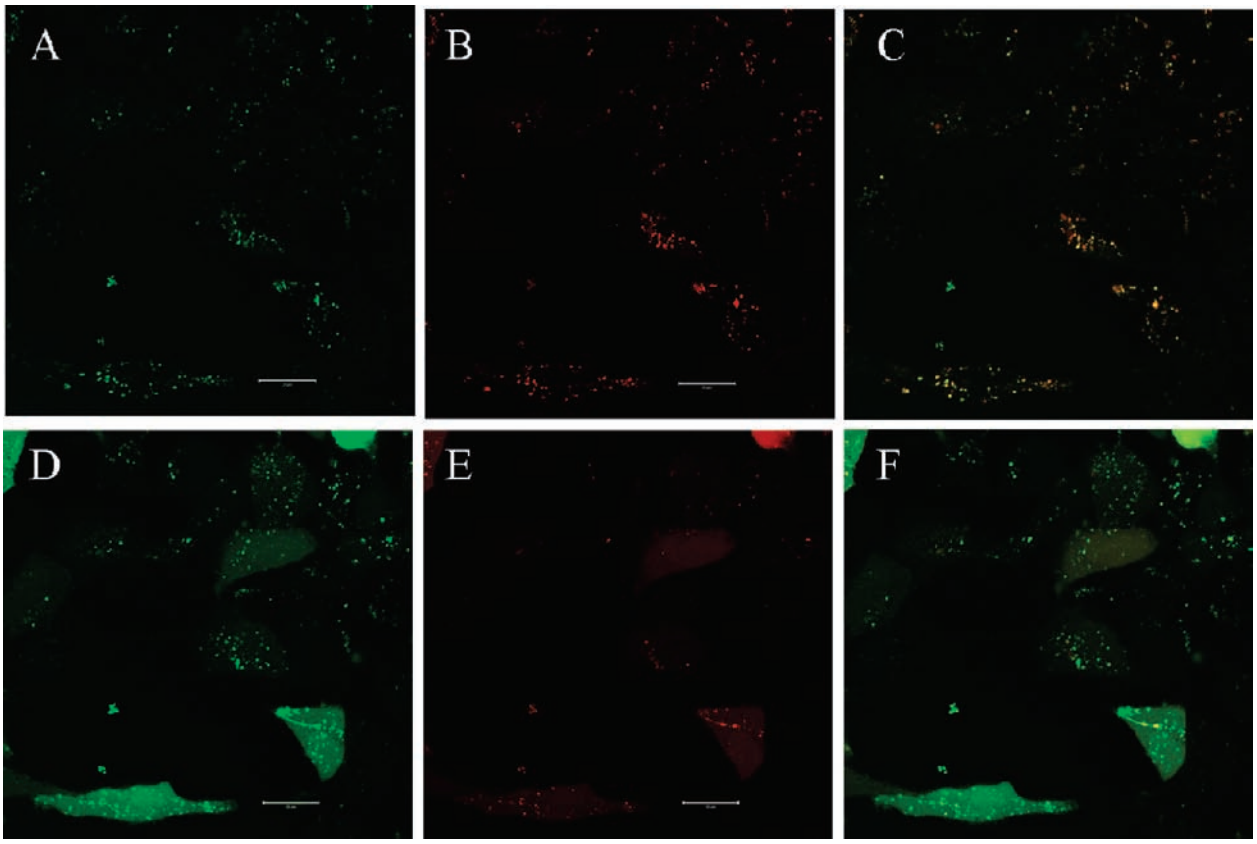


Figure 6. Protein transduction and photochemical internalization of rhodamine labeled TAT-GFP in HEK 293. (A−C): Preinternalization: (A) GFP, (B) rhodamine, (C) merge. (D−F): Post-photochemical internalization: (A) GFP, (B) rhodamine, (C) merge. Scale bar 20 μm.

of fluorescent intensity measurements per pixel in selected fields in Rh-TAT-GFP (A) and Rh-TTC-GFP (B) transduced cells. Both red (rhodamine) and green (GFP) distributions showed a maximum intensity frequency near baseline levels for both Rh-TAT-GFP and Rh-TTC-GFP. Analysis of Rh-TTC-GFP incubated control cells (Figure 5B) showed a predictable distribution with the majority of pixels measured as little to no intensity representing blank cytosol in between endosomes. Although there was a slight increase in the maximum frequency point from 2 units per pixel for rhodamine labeld TTC-GFP (Figure 5B) to 5 units per pixel for rhodamine labeled TAT-GFP (Figure 5A), the change in the fluorescent distribution was not deemed to be statistically significant. Taken together, the images and fluorescent distributions of Rh-TAT-GFP and Rh-TTC-GFP suggest a qualitative difference in distribution and localization of the TAT transduced cargo within the cytosol compared to the TTC transduced cargo, but little to no quantitative difference in overall uniformity. These results are in agreement with previous studies suggesting that endosomal escape of TAT proteins is a highly inefficient process.

Photochemical Internalization. In view of the very limited transfer of TAT labeled protein from endosomes, a method to enhance escape of fluorescent labeled proteins from endosomes was explored. Interestingly, when viewed under a fluorescent light source microscope rather than a confocal laser, the rhodamine labeled TAT-GFP underwent a redistribution of fluorescence within the cell. This phenomenon has been referred to as photochemical internalization (PCI) or photoacceleration of protein release. After one to two minutes of exposure to fluorescent light using the TRITC (red emission) filter, individual endosomes appeared to release the encapsulated cargo.

Several different cell lines were examined for both the ability to internalize and transduce TAT linked cargo protein as well as undergo photochemical internalization using the conjugated rhodamine as a photosensitizer. As seen earlier, HEK 293 cells were transduced with the TAT cell penetrating peptide. Shown in Figure 6A−C is another example of the distribution of TAT transduced GFP in this cell line before photochemical internalization. Figure 6A shows the fluorescence from the initial GFP, primarily localized in vesicles or endosomes. Figure 6B shows the red fluorescence from the conjugated rhodamine to the TAT-GFP protein. After exposure to a fluorescent light source, the HEK 293 cells underwent photochemical internalization and were imaged in Figure 6D−F. Visible are intact endosomes which have not yet undergone photochemical internalization as well as fluorescence which has filled the entire cell. In contrast to previous evaluation of cells transduced with Rh-TAT-GFP, extensive green (GFP) and red (rhodamine) florescence are visible after photochemical internalization throughout the cytosol. A time-lapse movie of photochemical internalization of Rh-TAT-GFP in HEK 293 cells was taken with images every 500 ms following the red rhodamine fluorescence (Supporting Information S.1). This video shows how cells do not undergo PCI immediately or at the same time. Also, it shows that individual endosomes, often those with the highest fluorescence in the cell, open to fill the cell with fluorescence. When a cell underwent PCI, the fluorescence was visible and expanding away from the bright point of fluorescence representing the endosome.

Not every endosome appeared to open, and rarely, multiple endosomes in one cell underwent PCI; at most, two endosomes have been observed opening per cell.

In vitro cultures of embryonic rat hippocampal slices were incubated with Rh-TAT-GFP and assessed for photochemical internalization. This model system not only contains neuronal and astrocytic cell types, but has substantial thickness (100−200 μm) compared to isolated cell cultures. Rh-TAT-GFP successfully transduced cells in this hippocampal slice culture system. Again, labeling was primarily localized in endosomes before photochemical internalization (Figure 7A−C). After exposure to fluorescent light with the TRITC filter, cells in the slice underwent PCI (Figure 7D−F).

The third cell system in which TAT transduction and photochemical internalization was tested was human neural progenitor cells (hNPCs) from Lonza. Rh-TAT-GFP successfully transduced cells in this system and labeling was again primarily localized to endosomes before photochemical internalization (Figure 8A−C). hNPCs transduced with Rh-TAT-GFP were also susceptible to PCI (Figure 8D−F) and underwent significant redistribution of fluorescence in the cells. Axon-like areas and cell projections previously unlabeled with endosomes or cytosolic rhodamine-TAT-GFP were brightly visible after PCI redistribution. Pre- and post-PCI cells were analyzed similar to the comparison between Rh-TAT-GFP and Rh-TTC-GFP distributions. Figure 8G,H shows fluorescent intensity frequencies of Rh-TAT-GFP transduction in hNPCs pre-PCI. This distribution was similar to that seen in Figure 5A with low maximum frequency values. However, after undergoing photochemical internalization, the frequency distributions of fluorescent intensities shift significantly with the maximum well above the baseline intensity (Figure 8I,J). Indeed, the red rhodamine fluorescence maximum shifts 5-fold from 5 in Figure 8G to 26 in Figure 8I. These findings show that a majority of pixels in a photochemically internalized cell are filled with greater fluorescence and protein than those in a nonphotochemically internalized cell. As expected, the sum of the fluorescence intensities for rhodamine is roughly equivalent pre- and post-PCI. The green GFP fluorescence distribution undergoes a similar shift of maximum fluorescence between Figure 8H and J; however, the sum of total cell fluorescence intensities for GFP increased 1.5-fold after PCI.

To investigate the possible mechanism underlying PCI and assess the importance of the TAT domain on this process, the exposure of Rh-TAT-GFP was compared to our exclusively endosomally controlled Rh-TTC-GFP treated cells. Figure 9A−C shows an example of an HEK 293 cell which had undergone PCI from exposure to the TRITC filter for 0.5 min. Fluorescence filled the entire cell profile, more resembling a DNA transfected cell rather than a protein transduced cell. However, the majority of the visible endosomes had not released their encapsulated proteins. Similar results were obtained with the N18-RE105 cells (data not shown). This phenomenon could not be reproduced with the FITC (green emission) filter. Furthermore, no photochemical internalization was observed when cells treated with Rh-TTC-GFP were exposed to a fluorescent light source with either TRITC or FITC filter. Figure 9D−F shows an image of an N18-RE105 cell incubated with Rh-TTC-GFP after exposure to the fluorescent light source for 5 min with no detectable cytosolic GFP or rhodamine. After 10 min of fluorescence exposure, Rh-TTC-GFP-incubated cells still did not show any signs of undergoing photochemical internalization, in spite of an intensity of fluorescence exposure sufficient to cause photobleaching.

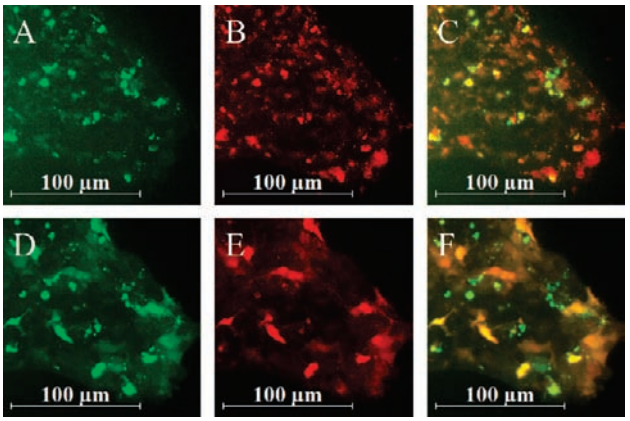


Figure 7. Protein transduction and photochemical internalization of Rh-TAT-GFP in hippocampal slices. (A−C) Preinternalization: (A) GFP, (B) rhodamine, (C) merge. (D−F) Post-photochemical internalization: (A) GFP, (B) rhodamine, (C) merge.

DISCUSSION

Protein transduction with cell penetrating peptides has been problematic due to the low efficiency of transductions. Some studies utilizing cargo proteins could not reproduce the cytosolic transfer seen with CPPs without a cargo protein,[16] and movement of target proteins across cell membranes was felt to be a postfixation artifact in other studies.[13,14] However, many studies of CPP-linked cargo proteins have demonstrated a biologic effect on a cytosolic or nuclear target, providing strong evidence of endosomal escape. In this study, the localization of a fusion protein containing both a widely used cell penetrating peptide, TAT from HIV−I, and a widely used labeled cargo protein (GFP) was imaged using live cell microscopy. This method eliminates the possibility of fixation-related artifactual change in cellular distribution of fluorescence. In order to control for possible artifactual underestimation of cargo protein translocation due to GFP denaturation, the GFP cargo protein was labeled with a small organic fluorescent dye—rhodamine.

There was a small change in the rhodamine fluorescence for cells transduced with Rh-TAT-GFP as compared to the endosomally localized control protein Rh-TTC-GFP. It is possible that the rhodamine could have been released from the TAT penetrating peptide and diffused into the cytoplasm. However, this same diffusion would have also been expected for the TTC peptide, and that was not evident even though the TTC peptide is larger than TAT. Taken together, the images and fluorescent distributions of Rh-TAT-GFP and Rh-TTC-GFP suggest that endosomal escape of TAT-linked proteins may occur to a slight degree. Nonetheless, this result confirms previous studies that the great majority of Rh-TAT-GFP remains trapped within endosomes.

The findings of the current study are consistent with previous studies where cell penetrating peptides could enhance the physiological effect of a cargo protein even without morphologic evidence of cytosolic transfer. Highly potent cargo proteins such as enzymes or transcription factors could easily have biologic activity at cytosolic levels below the threshold of fluorescence detection. In general, part of the misunderstanding of protein transduction stems from studies showing either negative

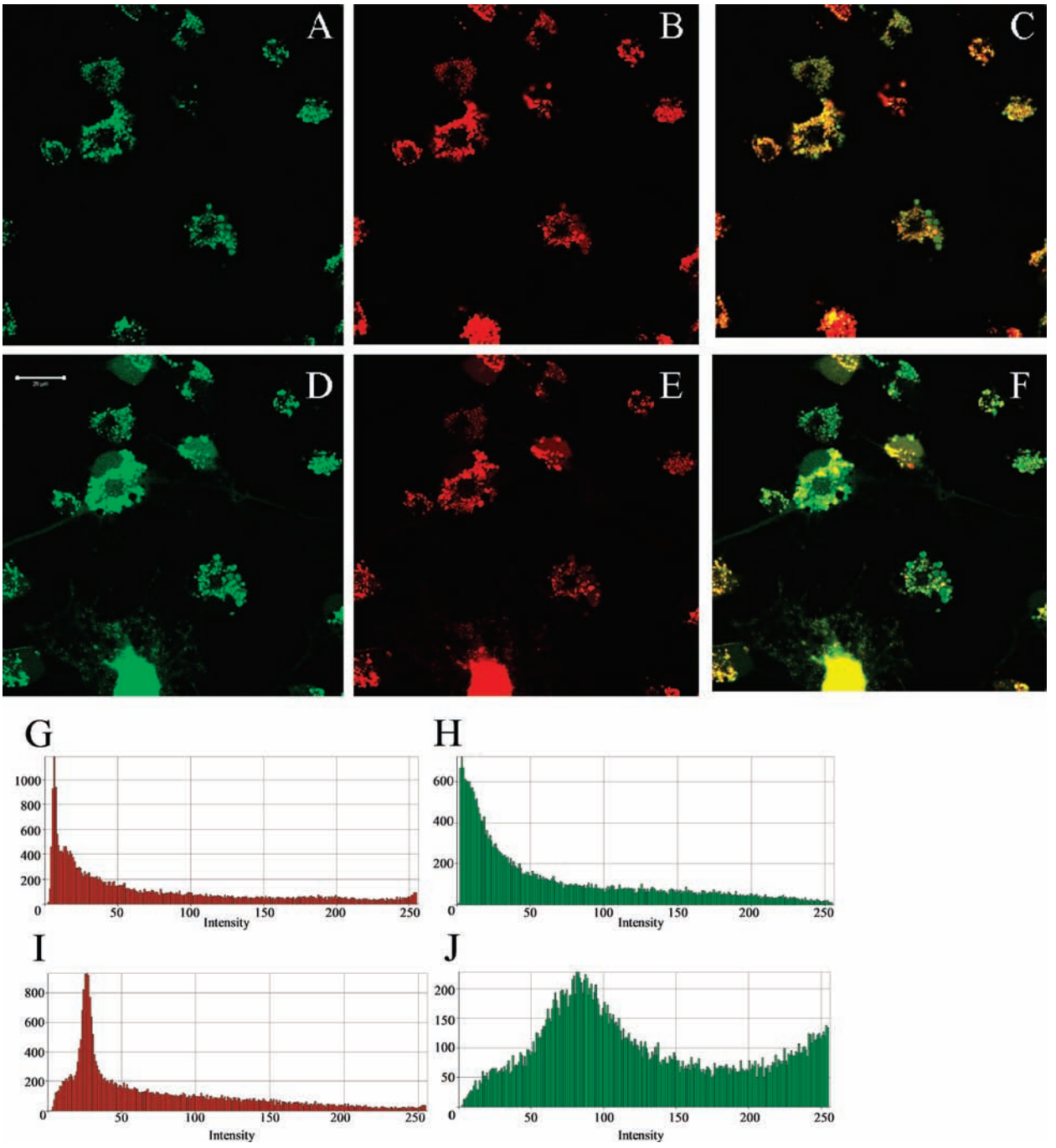


Figure 8. Protein transduction and photochemical internalization of Rh-TAT-GFP in human neural progenitor cells (Lonza) imaged with equal gain and comparable average fluorescence. (A−C) Preinternalization: (A) GFP, (B) rhodamine, (C) merge. (D−F) Postphotochemical internalization: (D) GFP, (E) rhodamine, (F) merge. (G−J) Fluorescence distributions showed change in intensity frequency maximum upon photochemical internalization. Total green fluorescence increased while total red total fluorescence was constant. (G) Rhodamine Pre-PCI; (H) GFP Pre-PCI; (I) Rhodamine Post-PCI; (J) GFP Post-PCI. Scale Bar 20 μm.

morphologic or positive physiological results, making estimation of efficiency of cytosolic transfer difficult. For example, TAT-Zfx[43] and TAT-HOXB4[44] showed an effect on hematopoetic stem cell expansion, where positively TAT-Zfx transduced cells were identified using FACS, which does not distinguish between intracellular protein localized in endosomal or cytosolic compartments. The study of TAT-HOXB4 assessed total cellular protein also without further subcellular localization. Constitutively active heat shock transcriptional factor 1 expressed as HSF1(+)-TAT was shown to upregulate HSP70 expression.[45] Total cellular HSF1(+)-TAT was assessed with immunoblot assay, while cytosolic HSF1(+)-TAT was detected with a highly sensitive luciferase reporter assay rather than localized with a direct morphologic method. In these examples, much of the total cellular protein likely remained trapped in endosomes, while a small proportion of protein released into the cytosol, although capable of a physiological effect, may well have been below the limits of detection with conventional fluorescent visualization.

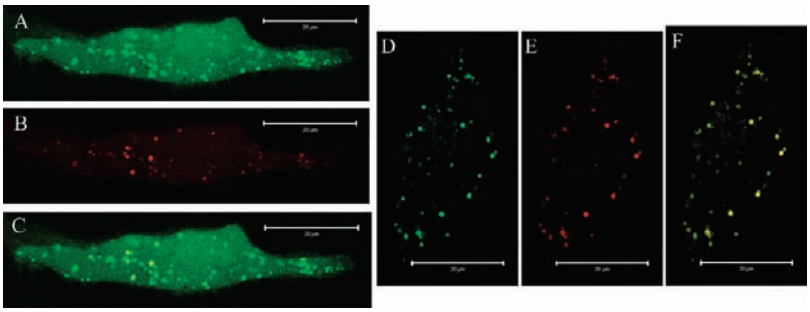


Figure 9. Photochemical internalization with chemically conjugated fluorophores occurs with TAT but not TTC linked cargo. (A−C) Cell treated with Rh-TAT-GFP after 0.5 min exposure to fluorescent light. (D−F) Cell treated with Rh-TTC-GFP after 5 min exposure to fluorescent light. Scale bar 20 μm.

Our study and previous studies indicate that, although cell penetrating peptide mediated translocation of a cargo protein into the cytosol appears to occur at least on a limited scale, a method that can potentially substantially improve the efficiency of endosomal escape of CPP-linked cargo proteins would be highly advantageous. Photochemical internalization (PCI) represents such a method. Both striking morphologic and quantifiable differences were observed in distribution of Rh-TAT-GFP after PCI.

In the current study, photochemical internalization was mediated with rhodamine as the photosensitizer directly conjugated to the cargo protein. This was accomplished using a simple procedure with inexpensive and readily available reagents in contrast to previous methods.[46−51] Direct conjugation of the photosensitizer to the cargo protein is preferable for both scientific and practical reasons. This method allowed observations regarding the relationship of the endosomal membrane to the photosensitizer. Previous studies have suggested the importance of the localization of the photosensitizer within the endocytic vesicles.[52] In this study, only a cargo protein possessing a CPP domain was able to mediate PCI, while a cargo protein similarly labeled but possessing a membrane binding domain (TTC-GFP) was not. The TAT cell-penetrating peptide appeared to allow for close integration of conjugated rhodamine into the membrane and subsequent PCI, while the surface receptor, neuronal ganglioside-bound TTC, did not. This study suggests a degree of intimacy between the photosensitizing agent and the endosomal membrane previously unappreciated and required to mediate this process.

These observations also suggest that PCI using a sensitizer directly linked to the cargo protein may cause oxidative injury in a very restricted location. Although few studies have assessed cell viability after PCI, it is a potentially toxic process requiring oxidative membrane damage.[53] Use of a photosensitizer linked only to the cargo protein may help limit oxidative injury to cargo-laden endosomes. In the current studies, there was no clearly evident effect on cell viability. However, studies need to be undertaken to more definitively track the effect of PCI on cell survival. The design of our experiments using actively proliferating cells for relatively short-term incubation periods is not suitable for assessment of the effect of PCI on cell viability. Future studies will be needed to optimize the conditions for PCI for both cargo delivery and cell viability before PCI can be considered an operational delivery method. The speed at which cells underwent photochemical internalization was affected by the intensity of the fluorescent light using neutral density filters, the amount of exposure time to fluorescent light, and the degree of labeling of the protein with rhodamine. Higher intensity light and the higher molar ratio of rhodamine to proteins decreased the exposure time necessary before PCI began to occur. This also suggests that the potential toxic effects of free radical generation of PCI may be further controllable. Thus, PCI could become a viable tool for use with proteins which have limited penetration into the cytosol with conventional CPP transduction and require relatively high cytosolic concentrations for their biologic effects.

■ ASSOCIATED CONTENT

Supporting Information. Video of photochemical internalization. Time-lapse video of photochemical internalization of Rh-TAT-GFP in HEK 293 cells. Images were taken every 500 ms with constant exposure to the 543 nm red rhodamine excitation with a conventional fluorescence light source. This material is available free of charge via the Internet at http://pubs.acs.org.

■ AUTHOR INFORMATION

Corresponding Author

*Tel 1-410-605-7000 x 6491; fax 1-410-605-7906; e-mail mpg@jhu.edu.

■ ACKNOWLEDGMENT

This work was supported by a REAP Fellowship by the VA Research Service and the Maryland Stem Cell Research Fund.

■ REFERENCES

(1) Murriel, C. L., and Dowdy, S. F. (2006) Influence of protein transduction domains on intracellular delivery of macromolecules. *Expert Opin. Drug Delivery 3*, 739–46.

(2) Nagahara, H., Vocero-Akbani, A. M., Snyder, E. L., Ho, A., Latham, D. G., Lissy, N. A., Becker-Hapak, M., Ezhevsky, S. A., and Dowdy, S. F. (1998) Transduction of full-length TAT fusion proteins into mammalian cells: TAT-p27Kip1 induces cell migration. *Nat. Med. 4*, 1449–52.

(3) Deshayes, S., Morris, M. C., Divita, G., and Heitz, F. (2005) Cell-penetrating peptides: tools for intracellular delivery of therapeutics. *Cell. Mol. Life Sci. 62*, 1839–49.

(4) Zorko, M., and Langel, U. (2005) Cell-penetrating peptides: mechanism and kinetics of cargo delivery. *Adv. Drug Delivery Rev. 57*, 529–45.

(5) Futaki, S. (2005) Membrane-permeable arginine-rich peptides and the translocation mechanisms. *Adv. Drug Delivery Rev. 57*, 547–58.

(6) Brooks, H., Lebleu, B., and Vives, E. (2005) Tat peptide-mediated cellular delivery: back to basics. *Adv. Drug Delivery Rev. 57*, 559–77.

(7) Chauhan, A., Tikoo, A., Kapur, A. K., and Singh, M. (2007) The taming of the cell penetrating domain of the HIV Tat: myths and realities. *J. Controlled Release 117*, 148–62.

(8) Gupta, B., Levchenko, T. S., and Torchilin, V. P. (2005) Intracellular delivery of large molecules and small particles by cell-penetrating proteins and peptides. *Adv. Drug Delivery Rev. 57*, 637–51.

(9) Jones, S. W., Christison, R., Bundell, K., Voyce, C. J., Brockbank, S. M., Newham, P., and Lindsay, M. A. (2005) Characterisation of cell-penetrating peptide-mediated peptide delivery. *Br. J. Pharmacol. 145*, 1093–102.

(10) Saalik, P., Elmquist, A., Hansen, M., Padari, K., Saar, K., Viht, K., Langel, U., and Pooga, M. (2004) Protein cargo delivery properties of cell-penetrating peptides. A comparative study. *Bioconjugate Chem. 15*, 1246–53.

(11) Wadia, J. S., Stan, R. V., and Dowdy, S. F. (2004) Transducible TAT-HA fusogenic peptide enhances escape of TAT-fusion proteins after lipid raft macropinocytosis. *Nat. Med. 10*, 310–5.

(12) Ryu, J., Han, K., Park, J., and Choi, S. Y. (2003) Enhanced uptake of a heterologous protein with an HIV-1 Tat protein transduction domains (PTD) at both termini. *Mol. Cells 16*, 385–91.

(13) Lundberg, M., and Johansson, M. (2001) Is VP22 nuclear homing an artifact?. *Nat. Biotechnol. 19*, 713–4.

(14) Richard, J. P., Melikov, K., Vives, E., Ramos, C., Verbeure, B., Gait, M. J., Chernomordik, L. V., and Lebleu, B. (2003) Cell-penetrating peptides. A reevaluation of the mechanism of cellular uptake. *J. Biol. Chem. 278*, 585–90.

(15) Reynolds, F., Weissleder, R., and Josephson, L. (2005) Protamine as an efficient membrane-translocating peptide. *Bioconjugate Chem. 16*, 1240–5.

(16) Maiolo, J. R., Ferrer, M., and Ottinger, E. A. (2005) Effects of cargo molecules on the cellular uptake of arginine-rich cell-penetrating peptides. *Biochim. Biophys. Acta 1712*, 161–72.

(17) Caron, N. J., Torrente, Y., Camirand, G., Bujold, M., Chapdelaine, P., Leriche, K., Bresolin, N., and Tremblay, J. P. (2001) Intracellular delivery of a Tat-eGFP fusion protein into muscle cells. *Mol. Ther. 3*, 310–8.

(18) Dietze, A., Selbo, P. K., Prasmickaite, L., Weyergang, A., Bonsted, A., Engesaeter, B., Hogset, A., and Berg, K. (2006) Photochemical internalization (PCI): a new modality for light activation of endocytosed therapeuticals. *J. Environ. Pathol. Toxicol. Oncol. 25*, 521–36.

(19) Berg, K., Selbo, P. K., Weyergang, A., Dietze, A., Prasmickaite, L., Bonsted, A., Engesaeter, B. O., Angell-Petersen, E., Warloe, T., Frandsen, N., and Hogset, A. (2005) Porphyrin-related photosensitizers for cancer imaging and therapeutic applications. *J. Microsc. 218*, 133–47.

(20) Hogset, A., Prasmickaite, L., Selbo, P. K., Hellum, M., Engesaeter, B. O., Bonsted, A., and Berg, K. (2004) Photochemical internalisation in drug and gene delivery. *Adv. Drug Delivery Rev. 56*, 95–115.

(21) Berg, K., Prasmickaite, L., Selbo, P. K., Hellum, M., Bonsted, A., and Hogset, A. (2003) Photochemical internalization (PCI)--a novel technology for release of macromolecules from endocytic vesicles. *Oftalmologia 56*, 67–71.

(22) Berg, K., Selbo, P. K., Prasmickaite, L., Tjelle, T. E., Sandvig, K., Moan, J., Gaudernack, G., Fodstad, O., Kjolsrud, S., Anholt, H., Rodal, G. H., Rodal, S. K., and Hogset, A. (1999) Photochemical internalization: a novel technology for delivery of macromolecules into cytosol. *Cancer Res. 59*, 1180–3.

(23) Ndoye, A., Bouali, S., Dolivet, G., Leroux, A., Erbacher, P., Behr, J. P., Berg, K., Guillemin, F., and Merlin, J. L. (2004) Sustained gene transfer and enhanced cell death following glucosylated-PEI-mediated p53 gene transfer with photochemical internalisation in p53-mutated head and neck carcinoma cells. *Int. J. Oncol. 25*, 1575–81.

(24) Prasmickaite, L., Hogset, A., Engesaeter, B. B., Bonsted, A., and Berg, K. (2004) Light-directed gene delivery by photochemical internalisation. *Expert Opin. Biol. Ther. 4*, 1403–12.

(25) Ndoye, A., Merlin, J. L., Leroux, A., Dolivet, G., Erbacher, P., Behr, J. P., Berg, K., and Guillemin, F. (2004) Enhanced gene transfer and cell death following p53 gene transfer using photochemical internalisation of glucosylated PEI-DNA complexes. *J. Gene Med. 6*, 884–94.

(26) Fretz, M. M., Hogset, A., Koning, G. A., Jiskoot, W., Storm, G. (2007) Cytosolic delivery of liposomally targeted proteins induced by photochemical internalization. *Pharm. Res.*

(27) Selbo, P. K., Sivam, G., Fodstad, O., Sandvig, K., and Berg, K. (2000) Photochemical internalisation increases the cytotoxic effect of the immunotoxin MOC31-gelonin. *Int. J. Cancer 87*, 853–9.

(28) Yip, W. L., Weyergang, A., Berg, K., Tonnesen, H. H., and Selbo, P. K. (2007) Targeted delivery and enhanced cytotoxicity of cetuximab-saporin by photochemical internalization in EGFR-positive cancer cells. *Mol. Pharm. 4*, 241–51.

(29) Weyergang, A., Selbo, P. K., and Berg, K. (2006) Photochemically stimulated drug delivery increases the cytotoxicity and specificity of EGF-saporin. *J. Controlled Release 111*, 165–73.

(30) Engesaeter, B. O., Tveito, S., Bonsted, A., Engebraaten, O., Berg, K., and Maelandsmo, G. M. (2006) Photochemical treatment with endosomally localized photosensitizers enhances the number of adenoviruses in the nucleus. *J. Gene Med. 8*, 707–18.

(31) Engesaeter, B. O., Bonsted, A., Berg, K., Hogset, A., Engebraten, O., Fodstad, O., Curiel, D. T., and Maelandsmo, G. M. (2005) PCI-enhanced adenoviral transduction employs the known uptake mechanism of adenoviral particles. *Cancer Gene Ther. 12*, 439–48.

(32) Oliveira, S., Fretz, M. M., Hogset, A., Storm, G., and Schiffelers, R. M. (2007) Photochemical internalization enhances silencing of epidermal growth factor receptor through improved endosomal escape of siRNA. *Biochim. Biophys. Acta 1768*, 1211–7.

(33) Shiraishi, T., and Nielsen, P. E. (2006) Enhanced delivery of cell-penetrating peptide-peptide nucleic acid conjugates by endosomal disruption. *Nat. Protoc. 1*, 633–6.

(34) Francis, J. W., Bastia, E., Matthews, C. C., Parks, D. A., Schwarzschild, M. A., Brown, R. H., Jr., and Fishman, P. S. (2004) Tetanus toxin fragment C as a vector to enhance delivery of proteins to the CNS. *Brain Res. 1011*, 7–13.

(35) Ebert, A. D., McMillan, E. L., and Svendsen, C. N. (2008) Isolating, expanding, and infecting human and rodent fetal neural progenitor cells. *Current Protocols in Stem Cell Biology*; John Wiley & Sons: New York, 2007; p 2, Chapter 2, Unit 2D.

(36) Woodburn, K. W., Vardaxis, N. J., Hill, J. S., Kaye, A. H., and Phillips, D. R. (1991) Subcellular localization of porphyrins using confocal laser scanning microscopy. *Photochem. Photobiol. 54*, 725–32.

(37) Soultanakis, R. P., Melamede, R. J., Bespalov, I. A., Wallace, S. S., Beckman, K. B., Ames, B. N., Taatjes, D. J., and Janssen-Heininger, Y. M. (2000) Fluorescence detection of 8-oxoguanine in nuclear and mitochondrial DNA of cultured cells using a recombinant Fab and confocal scanning laser microscopy. *Free Radic. Biol. Med. 28*, 987–98.

(38) Fink, C., Morgan, F., and Loew, L. M. (1998) Intracellular fluorescent probe concentrations by confocal microscopy. *Biophys. J. 75*, 1648–58.

(39) Francis, J. W., Hosler, B. A., Brown, R. H., Jr., and Fishman, P. S. (1995) CuZn superoxide dismutase (SOD-1):tetanus toxin fragment C hybrid protein for targeted delivery of SOD-1 to neuronal cells. *J. Biol. Chem. 270*, 15434–42.

(40) Rogers, T. B., and Snyder, S. H. (1981) High affinity binding of tetanus toxin to mammalian brain membranes. *J. Biol. Chem. 256*, 2402–7.

(41) Staub, G. C., Walton, K. M., Schnaar, R. L., Nichols, T., Baichwal, R., Sandberg, K., and Rogers, T. B. (1986) Characterization of the binding and internalization of tetanus toxin in a neuroblastoma hybrid cell line. *J. Neurosci. 6*, 1443–51.

(42) Avignolo, C., Bagnasco, L., Biasotti, B., Melchiori, A., Tomati, V., Bauer, I., Salis, A., Chiossone, L., Mingari, M. C., Orecchia, P., Carnemolla, B., Neri, D., Zardi, L., and Parodi, S. (2008) Internalization via Antennapedia protein transduction domain of an scFv antibody toward c-Myc protein. *Faseb J. 22*, 1237–45.

(43) Xu, C., Zhang, Y., and Jiang, H. (2009) Ex vivo expansion of hematopoietic stem cell by fusion protein TAT-Zfx. *Biochem. Biophys. Res. Commun. 379*, 771–4.

(44) Krosl, J., Austin, P., Beslu, N., Kroon, E., Humphries, R. K., and Sauvageau, G. (2003) In vitro expansion of hematopoietic stem cells by recombinant TAT-HOXB4 protein. *Nat. Med. 9*, 1428–32.

(45) Hou, Y., and Zou, J. (2009) Delivery of HSF1(+) protein using HIV-1 TAT protein transduction domain. *Mol. Biol. Rep.*

(46) Lackey, C. A., Press, O. W., Hoffman, A. S., and Stayton, P. S. (2002) A biomimetic pH-responsive polymer directs endosomal release and intracellular delivery of an endocytosed antibody complex. *Bioconjugate Chem. 13*, 996–1001.

(47) Chen, T., McIntosh, D., He, Y., Kim, J., Tirrell, D. A., Scherrer, P., Fenske, D. B., Sandhu, A. P., and Cullis, P. R. (2004) Alkylated derivatives of poly(ethylacrylic acid) can be inserted into preformed liposomes and trigger pH-dependent intracellular delivery of liposomal contents. *Mol. Membr. Biol. 21*, 385–93.

(48) Stayton, P. S., El-Sayed, M. E., Murthy, N., Bulmus, V., Lackey, C., Cheung, C., and Hoffman, A. S. (2005) 'Smart' delivery systems for biomolecular therapeutics. *Orthod. Craniofac. Res. 8*, 219–25.

(49) Kyriakides, T. R., Cheung, C. Y., Murthy, N., Bornstein, P., Stayton, P. S., and Hoffman, A. S. (2002) pH-sensitive polymers that enhance intracellular drug delivery in vivo. *J. Controlled Release 78*, 295–303.

(50) Cheung, C. Y., Murthy, N., Stayton, P. S., and Hoffman, A. S. (2001) A pH-sensitive polymer that enhances cationic lipid-mediated gene transfer. *Bioconjugate Chem. 12*, 906–10.

(51) Michiue, H., Tomizawa, K., Wei, F. Y., Matsushita, M., Lu, Y. F., Ichikawa, T., Tamiya, T., Date, I., and Matsui, H. (2005) The NH2 terminus of influenza virus hemagglutinin-2 subunit peptides enhances the antitumor potency of polyarginine-mediated p53 protein transduction. *J. Biol. Chem. 280*, 8285–9.

(52) Prasmickaite, L., Hogset, A., and Berg, K. (2001) Evaluation of different photosensitizers for use in photochemical gene transfection. *Photochem. Photobiol. 73*, 388–95.

(53) Moan, J., and Sommer, S. (1985) Oxygen dependence of the photosensitizing effect of hematoporphyrin derivative in NHIK 3025 cells. *Cancer Res. 45*, 1608–10.

Bioconjugate Chemistry

ARTICLE

pubs.acs.org/bc

Improved Targeting of Ligand-Modified Adenovirus as a New Near Infrared Fluorescence Tumor Imaging Probe

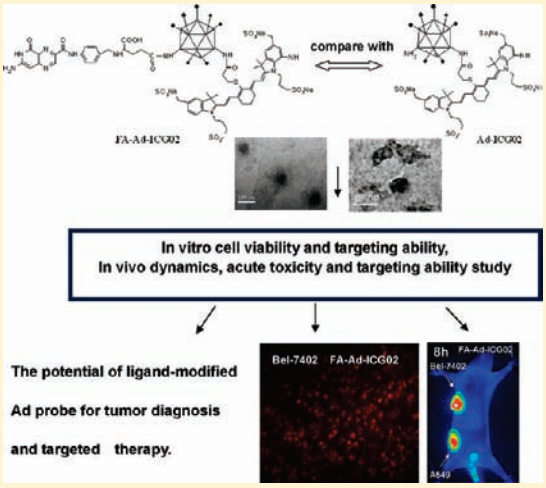
Lingling Shan,[†] Jianpeng Xue,[†] Jing Guo,[†] Zhiyu Qian,[‡] Samuel Achilefu,[§] and Yueqing Gu*[,†]

[†]Department of Biomedical Engineering, School of Life Science and Technology, China Pharmaceutical University, Nanjing 210009, China

[‡]Department of Biomedical Engineering, School of Automation, Nanjing University of Aeronautics and Astronautics, Nanjing 210017,China

[§]Department of Radiology, School of Medicine, Washington University, St. Louis, Missouri, United States

ABSTRACT: E1/E3-deleted Adenovirus 5 (Ad.5) possesses a great potential in gene therapy because of its high efficacy in gene transfer and low toxicity. Studies have shown that Coxsackie-Adenovirus receptor (CAR) is the determinant factor for the targeting of Adenovirus vectors. To extend the natural targeting of Ad to low CAR expressing tumors, we covalently attached folic acid (FA) to E1/E3-deleted Ad.5 capsids. Near-infrared (NIR) fluorescent dye ICG-Der-02 was subsequently conjugated with FA-Ad particles for in vivo imaging. The cell experiments and acute toxicity studies demonstrated the low toxicity of FA-Ad-ICG02 to normal cell/tissues. The dynamic behavior and targeting ability of FA-Ad-ICG02 to different tumors were investigated by NIR fluorescence imaging. In vitro and in vivo studies demonstrated its high targeting capability to CAR or FR positive tumors. The results support the potential of using ligand-modified Ad probe for tumor diagnosis and targeted therapy.



INTRODUCTION

Adenovirus (Ad) vectors have received extensive clinical evaluation and constitute a quarter of all gene therapy trials,[1] because of their relatively high efficacy in accomplishing gene transfer in vivo. As a gene carrier, Ad vectors do not insert their genome into the host chromosome. In particular, the gene depleted adenovirus lacks replication potential. Thus, it possesses low immunogenicity and low toxicity compared with other virus carriers.[2] In addition, Ad features high infection ability compared with other nonvirus particles,[3] which allows a more effective drug delivery to tumor cells overexpressing the Ad receptor.

With the recent heightened interest in materials science and molecular medicine, Ad vectors are now finding new applications as carriers and delivery system for macromolecules other than DNA.[4] Ad capsids are particularly amenable to modifications, allowing the use of Ad as a more functional vehicle for delivering imaging agents and drugs to target tissue. Researchers have successfully modified different sites on the Ad capsids with diverse reporter agents and drugs, such as magnetic resonance imaging contrast agents,[5,6] radiation sensitizers,[7] paramagnetic nanoparticles,[8] and antigenic peptides for vaccines.[9,10]

Serotype 5 adenovirus (Ad.5) is routinely used as a vector for gene transfer.[11] However, the targeted delivery and infectivity of Ad.5 is dependent on high expression of Coxsackie adenovirus receptor (CAR). Although the CAR receptor is usually over-expressed on tumor cells, many tumor types have low levels of this receptor,[12,13] thereby limiting therapeutic gene transduction in such tumors.[14] Furthermore, the inherent hepatic tropism of intravascularly administered Ad vectors hinder targeted delivery to alternative organs or disease sites.[15] In addition, immune responses to Ad vectors represent a major limitation to their use in vivo, particularly when repeated administration is required to maintain a long-term sustainable effect.[16] To overcome the above limitations, numerous strategies have been developed to modify Ad tropism and enhance its targeting ability to pathological sites. These surface engineering strategies often involve genetic modification of Ad capsids,[17,18] physical modification of adaptive molecules,[19] and chemical modification by covalent conjugation.[20,21] Increasingly, more targeting ligands are chemically modified to Ad capsids surface for targeted delivery. Such modifications could also have the added benefit of reducing the immune response, and thus to minimize the vector-related toxicity.

Received: May 30, 2010
Revised: February 14, 2011
Published: March 14, 2011

ACS Publications © 2011 American Chemical Society

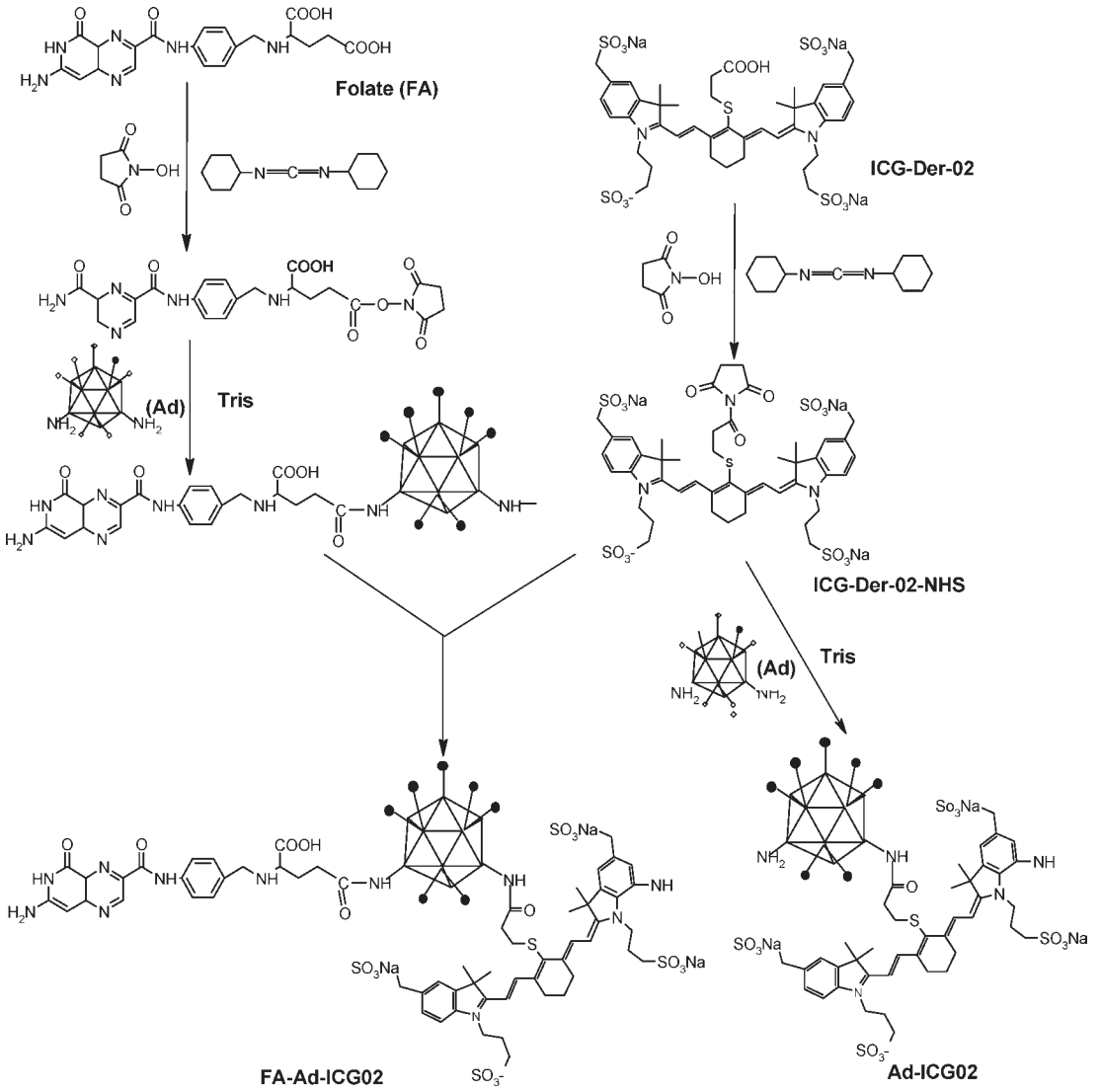


Figure 1. Synthetic scheme and structures of FA-Ad-ICG02 and Ad-ICG02 probes.

One of the fully characterized ligands for selective delivery of imaging or therapeutic agents to tumor cells is the vitamin folic acid (FA).[22,23] Uptake of FA into cells is mediated by the folic acid receptor (FR), and the binding of FA to FR initiates receptor-mediated endocytosis and internalization of FA.[24] Normally, the expression of FR on normal tissue and cells is low, whereas the demand for FA increases during cellular activation and proliferation in malignant tumors.[25] Indeed, FR expression is upregulated on a variety of human tumors, including cancers of the colon, kidney, liver, testis, brain, lung, and myelocytic blood cells.[26,27] Thus, FA has been studied as a promising targeting ligand for cancer detection, imaging, and treatment.[28] In our previous work, we demonstrated the targeting of FA-labeled compounds to different tumors with upregulated FR expression.[29,30] In this study, we covalently attached FA to the Ad capsid to enhance the tumor targeting ability of Ad particles for optical imaging.

Biomedical optics is a rapidly expanding imaging field with direct applications in cellular biology, pharmacology, and disease diagnosis.[31,32] In particular, near-infrared (NIR) fluorescence imaging possesses many advantages as a noninvasive technique for real-time in vivo monitoring of biological information in living subjects without the use of ionizing radiation.[33,34] The wavelength of NIR light ranges from 700 to 900 nm. This spectral window minimizes the high absorption of light by intrinsic chromophores such as hemoglobin and water, which allows light to penetrate in deeper tissue relative to visible light. To harness this transparent imaging window, many NIR fluorescent dyes have been developed and used for tumor detection in vitro and in vivo.[35] Among them, indocyanine green (ICG) is a widely used organic dye in optical imaging. This dye is approved for human use by the U.S. FDA. For this reason, many research groups have focused on the synthesis of ICG derivatives for in vivo imaging.[36−38] We have synthesized a variety of ICG derivatives and developed different types of NIR imaging systems for noninvasive in vivo imaging research. In this study, we used one of our hydrophilic ICG derivative (ICG-Der-02) to label FA-modified Ad (FA-Ad-ICG02) for NIR tumor imaging. We studied the dynamic behavior of the material in nude mice and demonstrated the tumor targeting capability of FA-Ad-ICG02 probe in mice bearing different tumor cell lines.

dx.doi.org/10.1021/bc100245t |*Bioconjugate Chem.* 2011, 22, 567–581

EXPERIMENTAL PROCEDURES

Materials and Apparatus. E1- and E3-deleted Ad particles were purchased from Sino Geno Max Co (Beijing, China). FA (MW 441.4), *N*,*N*′-Dicyclohexylcarbodiimide (DCC), *N*-hydroxysuccinimide (NHS), 3-(4,5-dimethylthialzol-2-yl)-2,5-diphenyltetrazolium bromide (MTT), RPMI 1640, fetal bovine serum (FBS), penicillin, streptomycin, and trypsin-EDTA were purchased from commercial sources. ICG-Der-02 (MW 995) was prepared in our laboratory. All reagents used in this study were certified analytical reagent grade.

Spectral measurements were recorded on a UV−vis spectrophotometer (JH 754PC, Shanghai, China) was used to record the absorbance measurements and a PHS-25 pH meter was used to determine the pH values. Sephadex G-25 was used to purify the products and a microscope equipped with a mercury vapor lamp, appropriate excitation and emission filters, a camera, and ACT1/DXM1200F software were used for recording images.

An NIR imaging system was used for real-time fluorescence imaging of the probe's distribution in animal subjects. This in-house built imaging system has been reported previously.[29,30] Briefly, the NIR imaging system is composed of an excitation laser (λ = 765.9 nm, NL-FC-2.0−763 laser light), a highly sensitive NIR CCD camera (PIXIS 512B), and an 800 nm long pass filter for capturing fluorescence from the tissue. A second 808 nm laser was used as background light to obtain the profile of the animal.

Synthesis of Folic Acid-Ad-Near Infrared Fluorescence Probe (FA-Ad-ICG02). FA and ICG-Der-02 were conjugated to the surface lysines on Ad capsid to form FA-Ad-ICG02 conjugate. The complex FA-Ad-ICG02 was synthesized in four steps, as shown in Figure 1. First, FA was reacted with DCC/NHS (molar ratio of FA:DCC:NHS is 1:1.2:2) in anhydrous dimethyl sulfoxide (DMSO, 2.5 mL) and the mixture was stirred in the dark for 6 h at 50 °C. The residue was removed by filtration under reduced pressure, and the activated FA was extracted with anhydrous acetone. Second, 1 mg of ICG-Der-02 in 100 μL DMSO was activated with EDC and NHS (molar ratio of ICG-Der-02:EDC:NHS is 1:1.5:1.5) at room temperature in the dark for 3 h. Third, the activated FA was dissolved in 2 mL of Tris buffer (10 mM, pH 8.0) and the Ad vectors were adjusted to a concentration of 2×10^8 plaque-forming units (pfu/mL) in 1 mL (4.74×10^9 VP/mL). The two solutions were then mixed in the above buffer (molar ratio of FA:Ad is 10^5:1).[39,40] After 3 h at −4 °C, the reaction mixture was purified by filtration over a Sephadex G-25 column equilibrated with Tris buffer (10 mM, pH 8.0) to remove unconjugated Ad and FA fragments. Last, the purified mixture was added to the above activated ICG-Der-02 (molar ratio of FA-Ad:ICG-Der-02 is 1:10^5) in Tris buffer (10 mM, pH 8.0). After 3 h, the reaction mixture was purified by filtration over a Sephadex G-25 column equilibrated with Tris buffer (10 mM, pH 8.0) to remove unconjugated FA-Ad and ICG-Der-02 fragments. The resulting product was stored at −20 °C. A similar method described above was used to synthesize the control Ad-ICG02. To determine the approximate number of viral particles (VP) per mL, the equation below was used. Tris buffer (10 mM, pH 8.0) was used as a blank.[40]

$$\text{VP/mL} = A_{260} \times \text{dilution factor} \times 10^{12}$$

Characterization of Folic Acid-Ad-Near Infrared Fluorescence Probe (FA-Ad-ICG02). The synthesized FA-Ad-ICG02 was evaluated by spectroscopic measurements at 365 nm, 260 nm, and 780 nm, which are the absorption peaks of FA, Ad, and ICG-Der-02, respectively. The influence of Ad particles on the absorption peaks of FA, Ad, and ICG-Der-02 were investigated by comparing the absorption spectra of FA, Ad, FA-Ad, and FA-Ad-ICG02. The modified number of FA molecules to the primary amino groups of viral particles was calculated by subtracting the unreacted FA from the initial total FA. The unreacted FA was obtained by following the recovery method (n = 4). The regression equation of the standard curve was obtained by dissolving different amounts of pure FA in Tris buffer (10 mM, pH 8.0). Different initial FA ratios (10^0−10^7 pmol) in FA-Ad-ICG02 particles (molar ratio of FA:Ad:ICG-Der-02 is 10^0−10^7:1:10^5) were used to optimize incorporated FA numbers in the Ad particle formulation for in vivo imaging. The number of particles generating the brightest fluorescence in tumor tissue (Bel-7402) was used as the optimal FA bonding number. The number of Ad particles for different initial FA was fixed at 2×10^8 pfu/mL (4.74×10^9 VP/mL). Accordingly, the amount of ICG-Der-02 for different initial FA ratio was fixed at 1 mg. The labeled numbers of ICG-Der-02 molecules were evaluated by UV−vis absorption spectroscopic at 780 nm (Tris buffer, pH 8.0).

In addition, the successful conjugation of FA to Ad was further confirmed by sodium dodecyl sulfate polyacrylamide gel electrophoresis (SDS-PAGE).

Characteristics of Size and Morphology. The size and morphology of Ad, Ad-ICG02, and FA-Ad-ICG02 were measured by Mastersizer 2000 Laser Particle Size Analyzer.

Cell Culture and in Vitro Study. The human cell lines A549 (lung cancer), Bel-7402 (hepatocellular carcinoma cells), U87MG (glioblastoma cancer), and HELF (human embryonic lung fibroblast cell line) were all purchased from ATCC. These cell lines have been used for cytotoxicity and in vitro targeting studies.[41−43] All the cell lines were cultured at 37 °C in a humidified atmosphere containing 5% CO_2 in DMEM and RPMI1640 medium supplemented with 10% fetal bovine serum, 100 U/mL penicillin, and 100 μg/mL streptomycin.

Assessments of CAR and FA Receptor Expression Level. The three tumor cell lines (A549, Bel-7402, U87MG) were used to evaluate receptor expression. The expression levels of CAR and FA receptors were assessed by reverse transcriptase PCR. Briefly, total RNA was extracted from freshly isolated A549, Bel-7402, and U87MG tumor cells using RNeasy Kit. RNA (3 μg) from each cell line was converted into cDNA with Superscript III reverse transcriptase. Subsequently, 1.0 μL cDNA was used for PCR amplification with CAR-specific primers: sense, 5′-AAAAAGCCAAAGGGGAAACTG-3′, and antisense, 5′-TGAGCGCTAGAGCAAGCAAAG-3′. The product length was 669 base pair (bp). The cDNA (1.0 μL) was used for PCR amplification using FOL-specific primers: sense, 5′-ACACCAGCCAGGAAGCCCATA-3′, and antisense, 5′-GAGCAGCCACAGCAGCATTAG-3′. The product length was 563 bp. The product (5 μL) was used for 2% agarose gel electrophoresis.

In Vitro Cytotoxicity of FA-Ad-ICG02. To evaluate the cytotoxicity of FA modified Ad and Ad itself, MTT assay was conducted on different cell lines (tumor cell A549, Bel-7402, U87MG; and nontumor cell lines HELF) by following standard protocols.[44] Cells were plated at a density of 2×10^3 cells/well in 96-well plates and subsequently infected for 24 h with Ad, Ad-ICG02, and FA-Ad-ICG02 at a wide range of multiplicity of infection (m.o.i.) from 0.01 to 1000 pfu/cell. Every moi was

tested in 6 wells. Five days after infection, each well was replaced and the cells were washed three times with Dulbecco's phosphate buffered saline (PBS, pH 7.0) before addition of 180 μL of fresh DMEM and 20 μL of MTT solution (5 mg/mL). After incubation for another 4 h, the medium containing MTT was carefully removed from each well and 150 μL of DMSO was added to dissolve the formed crystals. The optical density (OD) was measured at 595 nm with a multiwell plate reader. The cell viability was calculated by the following equation:

$$\text{viable cells } (\%) = (\text{OD}_{\text{treated}}/\text{OD}_{\text{control}}) \times 100\%$$

where $\text{OD}_{\text{treated}}$ was obtained in the presence of Ad, Ad-ICG02, and FA-Ad-ICG02; $\text{OD}_{\text{control}}$ was obtained from the incubation medium.

Cellular Uptaken of FA-Modified Ad in Tumor Cells. To investigate the tumor cell targeting of Ad vector and FA-modified Ad vector, the Ad and FA-Ad vectors were labeled with visible fluorescent dye Rhodamine B (RhB) for microscopy. A visible dye was used because our fluorescence microscope is not equipped with NIR imaging capability. The labeling process was conducted by a similar method used for the synthesis of FA-Ad-ICG02 probe described above. The initial molar ratio of FA:Ad:RhB is 10^5:1:10^5, and the labeled molecules of Rhodamine B were calculated based on the fluorescence emission spectroscopic at 578 nm (Tris buffer, PH 8.0).

Cells (1×10^4) were seeded in 24-well plates and incubated in culture medium overnight. The cells were washed twice with PBS (pH 7.0) and suspended in 150 μL of fresh DMEM and RPMI1640 medium. Ad or FA-Ad vector (20 μL; 1×10^5 pfu; m.o.i.:10 pfu/cell) was added into each well. After incubating for 1 h at 37 °C, the cells were washed twice with PBS and suspended in binding buffer. The cells were directly visualized by fluorescence microscopy (40× objective magnification).

Cell cytometry was used to further quantify the uptake of FA-Ad-RdB and Ad-RdB into the tumor cells (Bel-7402, A549, and U87MG). Briefly, 5×10^5 cells were seeded in 6-well plates and incubated in culture medium overnight. The cells were washed twice with PBS (pH 7.0) and suspended in 200 mL of fresh RPMI1640 and DMEM mediums. Subsequently, 50 μL of 5×10^6 pfu Ad-RhB and FA-Ad-RhB (m.o.i.:10 pfu/cell) were added into each well. After incubating for 1 h at 37 °C, the cells were washed twice with PBS and detached by trypsin (0.25%), followed by centrifugation at 1000 rpm for 5 min. The medium was discarded and the cells were resuspended in 500 μL of PBS. The cell suspension was immediately analyzed by a flow cytometry.

To evaluate the effect of NHS on the ability of Ad infection, the same amount of Ad-RhB was added into 6-well plates (Bel-7402), with and without NHS solution (molar ratio of Ad-RhB:NHS is 1:10^5). After incubating for 1 h at 37 °C, the cells were washed twice with PBS and detached by trypsin (0.25%), followed by centrifugation at 1000 rpm for 5 min, and the medium was discarded. The cells were resuspended in 500 μL of PBS and immediately analyzed by a flow cytometry.

Animal Experiments. Athymic nude mice and normal (Kunming) mice were purchased from Charles River Laboratories (Shanghai, China). All animal experiments were carried out in compliance with the Animal Management Rules of the Ministry of Health of the People's Republic of China (document no. 55, 2001) and the guidelines for the Care and Use of Laboratory Animals of China Pharmaceutical University.

Acute Toxicity Test in Mice. The acute toxicity of the Ad, Ad-ICG02, and FA-Ad-ICG02 probes to animal subjects were investigated on the normal mice. Briefly, 80 Kunming mice (aged 3−4 weeks, weighed 18−22 g, equal number of male and female subjects) were divided into 10 groups, including the control group (n = 8, 4 males and 4 females in each group), three normal dose group (1×10^{10} pfu/kg of Ad defined as normal dose, n = 8 for each probe), 25× dose group ($25 \times 1 \times 10^{10}$ pfu/kg, $n = 8 \times 3$), and 50× dose group ($50 \times 1 \times 10^{10}$ pfu/kg, $n = 8 \times 3$). Different doses of the above probes (Ad, Ad-ICG02, and FA-Ad-ICG02), 0.2 mL 1×10^{10} pfu/kg, 0.2 mL 2.5×10^{11} pfu/kg, and 0.2 mL 5×10^{11} pfu/kg, were injected by tail vein into the different groups of mice. Mice in the control group were given PBS buffer in the same volume (0.2 mL). Blood was drawn from the eye socket at the 24 h, 48 h, and 2 week time points after injection. The serum biochemical parameters including aspartate aminotransferase (AST) and alanine aminotransferase (ALT) indexes of the blood samples were examined. Finally, the mice were sacrificed 2 weeks postinjection and the livers were excised for histopathology. The pathological changes of liver tissue from different groups of mice were assessed and compared.

Dynamics and Biodistribution of FA-Ad-ICG02 in Normal Nude Mice. Normal nude mice were used for the investigation of the dynamics of FA-Ad-ICG02 probe (n = 5). FA-Ad-ICG02 probe (0.2 mL, 1×10^{10} pfu/kg) was administered into the bloodstream of the subject mice through tail vein injection. Fluorescence imaging was acquired with our NIR imaging system using the method we reported previously.[29] A series of images were collected from mice and the background images were taken for each mouse prior to injection. To confirm the biodistribution of FA-Ad-ICG02 probes in different organs obtained from the NIR imaging, the mice were sacrificed at 8 h postinjection. Different organs were separated and washed by saline and assembled for ex vivo fluorescence imaging.

In Vivo Tumor Models. To investigate the targeting ability of the probes, three types of tumor models were established. Briefly, Bel-7402 (with high FR expression and low CAR expression) and A549 (with high CAR expression and FR negative expression) were implanted in the upper and lower axillary fossa in the same mouse of group I (n = 10). U87MG with intermediate expression in both FR and CAR were implanted in the upper left axillary fossa in the another group of mice (n = 5).

In Vivo Study. As the tumors grew up to a diameter of 0.4−0.6 cm, the mice were immobilized for in vivo optical imaging. Ad-ICG02 or FA-Ad-ICG02 (0.2 mL, 1×10^{10} pfu/kg) was injected into each mouse cohort. Imaging was performed with the NIR imaging system in a dark room. A series of images were collected at specific time intervals during 48 h postinjection. The accumulation of the probes in tumors was compared among different groups of mice. To quantify the targeting ability of the different probes in different tumors, the average fluorescence intensity in tumor regions was acquired by selecting the region of interests (ROI) and compared with normal muscle tissue.[45,46] Tumor to normal tissue contrast ratios (T/N) were calculated by using the ROI functions of *Living Image* software.

Statistical Analysis. All data are reported as the mean ± SD of n independent measurements. Statistical analysis was performed by using Student's t-test with statistical significance assigned for P value of <0.05.

RESULTS

Synthesis and Characterization of FA-Ad-ICG02 Probes. FA-Ad-ICG02 and Ad-ICG02 were synthesized by following the

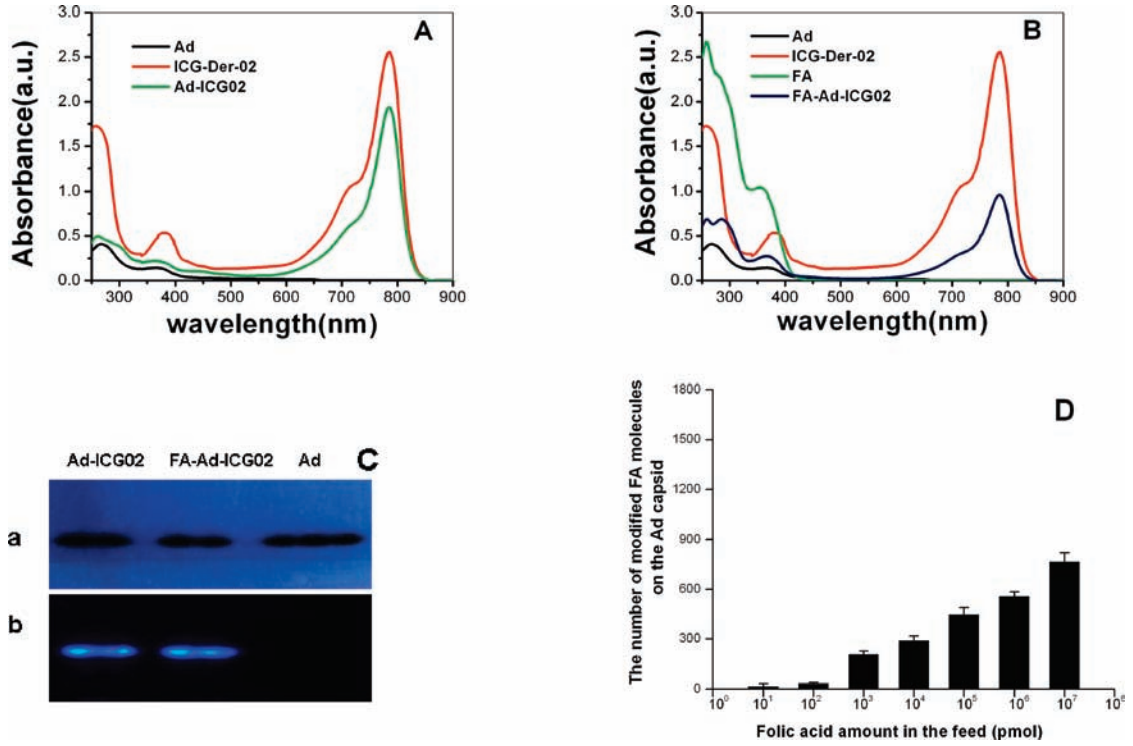


Figure 2. Characterization of FA-modified Ad probes. (A) Absorption spectra of synthesized Ad-ICG02 probe and Ad and ICG-Der-02 dye. The absorption peaks of Ad-ICG-02 overlaps the peaks of Ad and ICG-Der-02 at 260 and 780 nm, indicating the successful conjugation of Ad-ICG02. (B) Absorption spectra of FA-Ad-ICG02 probe, Ad, FA-Ad, and ICG-Der-02 dye. The absorption peaks at 260, 365, and 780 nm represent absorption of Ad, FA, and ICG-Der-02, respectively, indicating the successful preparation of FA-Ad-ICG02. (C) Gel electrophoresis further confirmed the successful synthesis of FA-Ad-ICG02 and Ad-ICG02. The fluorescence of ICG-Der-02 can be observed from the band of purified Ad-ICG02 and FA-Ad-ICG02 using NIR imaging system. (D) Number of modified FA molecules on the Ad capsid at different initial FA ratios. A total of 2×10^8 pfu/mL of Ad (4.74×10^9 VP/mL) was used for the modification. The number of modified FA molecules on the surface of Ad was determined by using the recovery method. The data are represented as mean ± standard deviation (SD), $n = 4$.

procedures described in the Experimental Section, as shown in Figure 1. The purified FA-Ad-ICG02 and Ad-ICG02 were evaluated by UV absorption spectrum analysis in the same Tris buffer with pH 8.0, as shown in Figure 2A and B. The absorption spectra of FA-Ad-ICG02 and Ad-ICG02 displayed all of the absorption peaks of the constituent components (Ad, FA, and ICG-Der-02 at 260, 365, and 780 nm, respectively) in the complex, indicating the successful conjugation of FA-Ad-ICG02 and Ad-ICG02. Successful FA-Ad-ICG02 and Ad-ICG02 conjugation was further confirmed by gel electrophoresis, as shown in Figure 2C. In addition, the fluorescence of ICG-Der-02 was observed from the band of purified Ad-ICG02 and FA-Ad-ICG02 under the NIR imaging system, which further demonstrated that the dye ICG-Der-02 was attached to the Ad particles.

To quantify the number of FA molecules to the amino groups of Ad surface, the recovery method was strictly followed in the calculation of unreacted FA based on the regression equation of the standard curve $Y(\mathrm{OD}) = 0.0544X\ (\mu\mathrm{g/mL}) + 0.1757$ ($r = 0.9998$). The linear rang of the standard curve was from 0.079 to 48.61 μg/mL. The relationship between the fraction of covalently bound and initial FA molecules is shown in Figure 2D. For the different initial ratios of 10^4:1, 10^5:1, and 10^6:1, the modified FA molecules were 289 ± 29, 448 ± 42, and 557 ± 28 per Ad ($n = 4$), respectively. The results indicates that the number of FA molecules conjugated to the surface amine groups of Ad particles increased with an increase in the amount of initial FA (Figure 2D).

The optimal number of FA molecule modified Ad particles is highly desirable to attain high accumulation of FA-Ad-ICG02 in tumors. From the in vivo experiment conducted with a different number of covalent FA molecules per Ad, it was found that the 448 ± 42 molecules of FA to per Ad, which was prepared from the initial FA to Ad ratio of 10^5:1 (pmol), showed the highest fluorescence signal in Bel-7402 tumors by the in vivo NIR imaging. Thus, Ad with 448 ± 42 molecules of FA modification was selected for all the experiments.

Similarly, the number of labeled ICG-Der-02 molecules on the surface of Ad was calculated by UV−vis and was found to be 293 ± 56 molecules per Ad ($n = 4$).

The size and morphology of Ad particles before and after modification were measured by LPSA and TEM, as shown in Figure 3A−C. The effective diameters of Ad, Ad-ICG02, and FA-Ad-ICG02 ($n = 4$) were 84.1 ± 18.6, 83.4 ± 15.3, and 81.8 ± 16.4 nm, respectively. No significant difference was observed between the Ad particles. Further, the morphologies of the three particles (Ad, Ad-ICG02, FA-Ad-ICG02) were obtained by negatively staining TEM images (Figure 3A−C). The results indicate that some aggregation occurred in the Ad particles itself (Figure 3A) and the chemical modification of Ad with ICG-Der-02 (Figure 3B) or FA (Figure 3C) resulted in highly monodisperse particles.

Cytotoxicity of FA-Ad-ICG02 Probe. MTT assay was used to quantify cell viability on the 4 human cell lines used in this study in the presence of FA-Ad-ICG02.[47] The results are displayed in

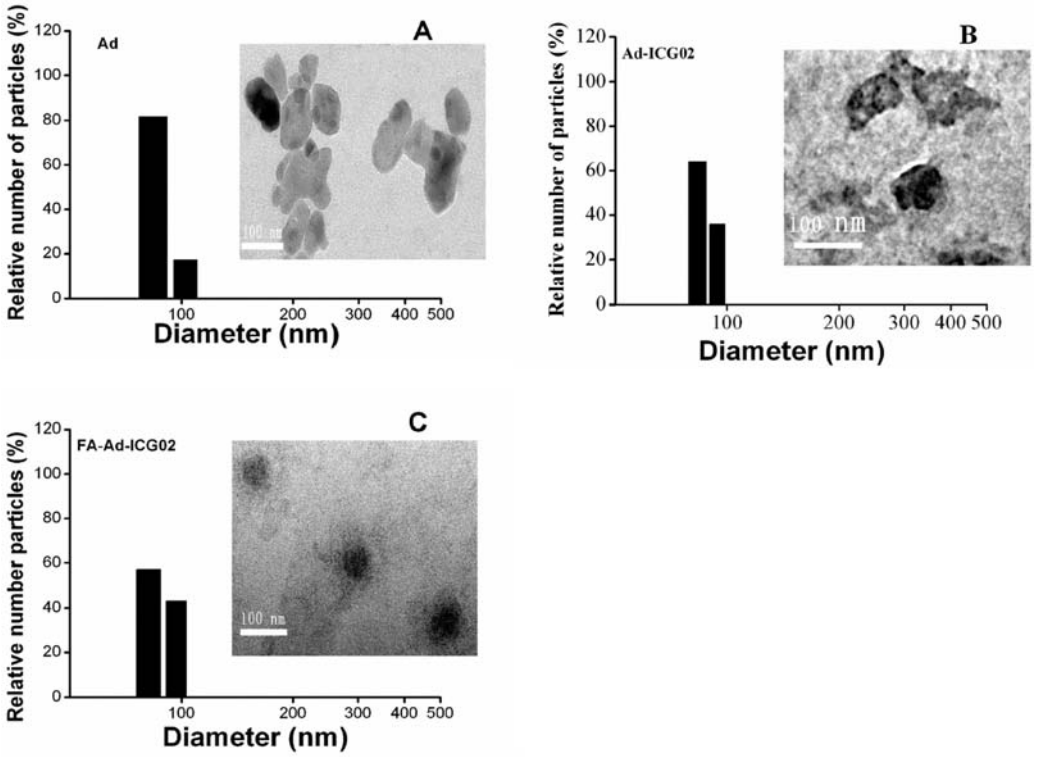


Figure 3. Size and morphology of Ad and modified particles were measured by LPSA and TEM. (A) The diameter of Ad was 84.1 ± 18.6 nm; the negative staining TEM picture shown some aggregation occurred in the Ad particles itself. (B)The diameter of Ad-ICG02 was 83.4 ± 15.3 nm. (C) The diameter of FA-Ad-ICG02 was 81.8 ± 16.4 nm. The negatively stained TEM images of FA-Ad-ICG02 showed that the Ad particles were well dispersed as individual particles with spherical shape.

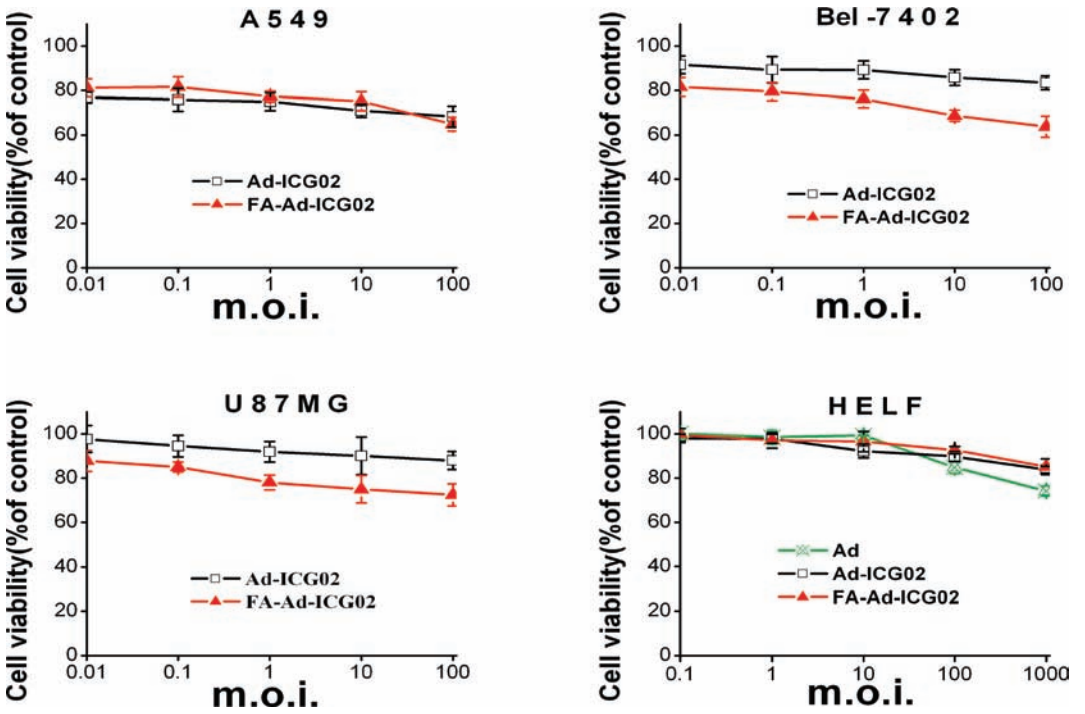


Figure 4. In vitro cytotoxicity of FA-Ad-ICG02. Cells at a density of 1×10^4 cells/well cultured in 96-well plates were infected with the indicated viruses in a wide range of m.o.i. Five days later, the cell viability was examined by MTT assay. Data showed that there is no obvious negative effect of FA-Ad-ICG02 on normal cells.

Figure 4. The cytotoxicity assay show that FA-Ad-ICG02 displayed very low toxicity to normal cells (HELF human embryonic lung fibroblast cell line) even at higher m.o.i. Cell viability was about 75% in FA-positive cells infected with

dx.doi.org/10.1021/bc100245t |*Bioconjugate Chem.* 2011, 22, 567–581

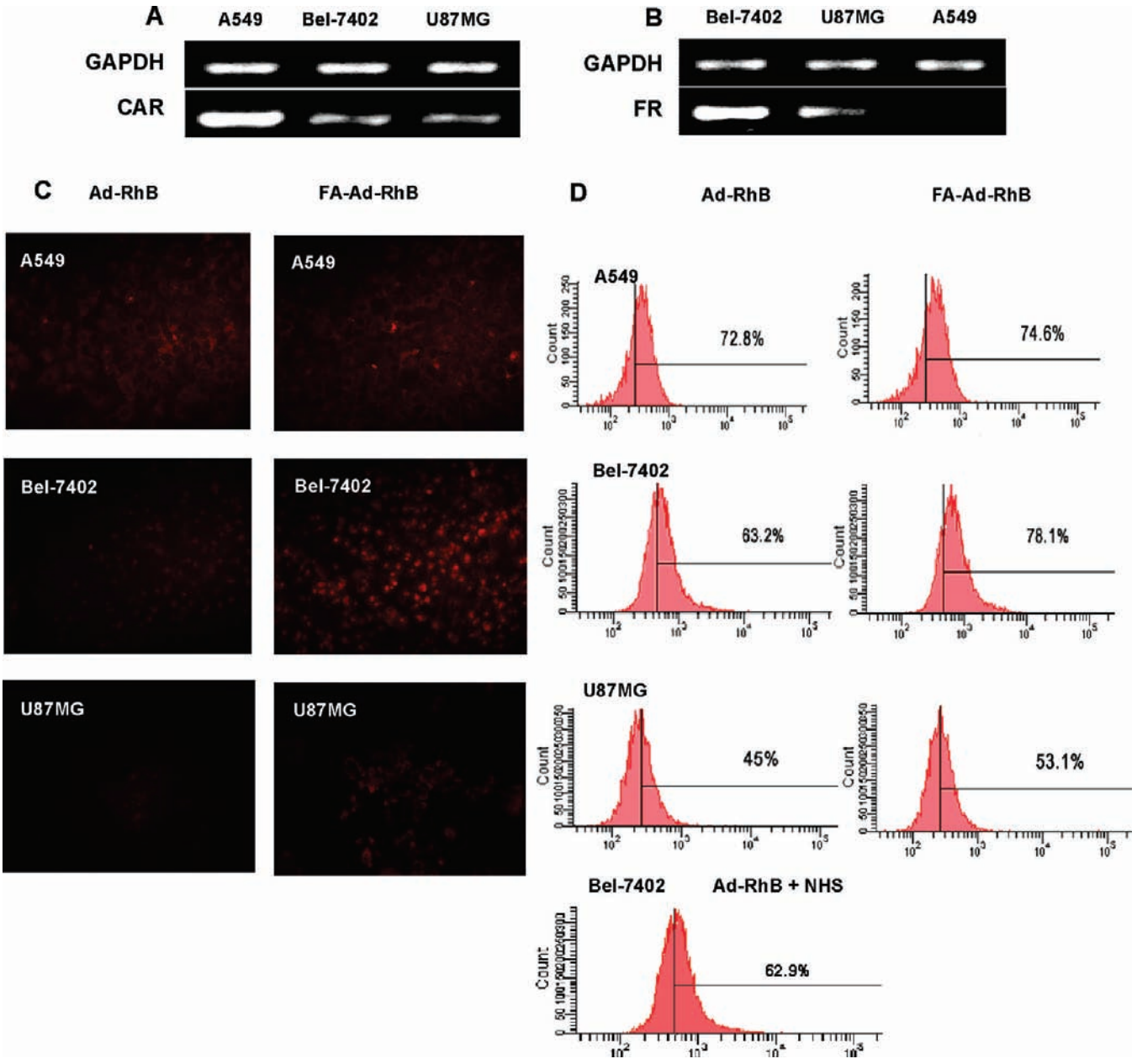


Figure 5. Targeting capability of FA-Ad particles in three different tumor cell lines compared to Ad particles. (A) mRNA levels of CAR on the three different tumor cells were determined by reverse transcriptase PCR. The CAR expression follows the order A549 > Bel-7402 > U87MG. (B) mRNA levels of FR was determined by reverse transcriptase PCR. The FA receptor expression follows the order Bel-7402 > U87MG >A549. (C) Targeting ability of FA-Ad-RhB and Ad-RhB particles in A549, Bel-7402, and U87MG cells imaged with a fluorescence microscope. FA-Ad-RhB and Ad-RhB were significantly retained in CAR overexpressed A549 cell lines. FA-Ad-RhB showed increased uptake in Bel-7402 and U87MG tumor lines (with low CAR expression and high FR expression) compared to Ad-RhB particles. (D) Flow cytometric analysis of FA-Ad-RhB and Ad-RhB particles in A549, Bel-7402, and U87MG cell lines. FA-Ad-RhB and Ad-RhB particles were taken into A549 cell lines at about 74.6% and 72.8%. FA-Ad-RhB showed increased uptake in Bel-7402 and U87MG cells (78.1% and 53.1%) compared to Ad (63.1% and 45.0%). Flow cytometric analysis of the effect of NHS on the infection of Ad particles to the tumor cell line. There is no obvious difference between Ad-RhB and mixture (Ad-RhB and NHS) (63.2%, 62.9%).

FA-Ad-ICG02 at m.o.i. of 1 pfu/cell but more than 90% in normal cells infected with these viruses at m.o.i. of 10 pfu/cell. The results demonstrated that FA-Ad-ICG02 displayed low cytotoxicity to all cells. More significantly, there is no obvious negative effect on normal cells, suggesting that the particles are safe for use in living systems.

In Vitro Cell Targeting. The FA-Ad-ICG02 was selectively retained in FA-positive (Bel7402 and U87MG) cells and CAR-positive (A549) cells at very low m.o.i. To explain the receptor mediated targeting of FA-modified Ad vectors to different tumors, A549, Bel-7402, and U87MG tumor cells with different CAR and FA receptor expression levels were first investigated by reverse transcriptase PCR, as shown in Figure 5A and B. The CAR receptor expression was found to decrease in the following order, A549 > Bel-7402 > U87MG, while the FA receptors expression follows the order Bel-7402 > U87MG >A549.

dx.doi.org/10.1021/bc100245t |*Bioconjugate Chem.* 2011, 22, 567–581

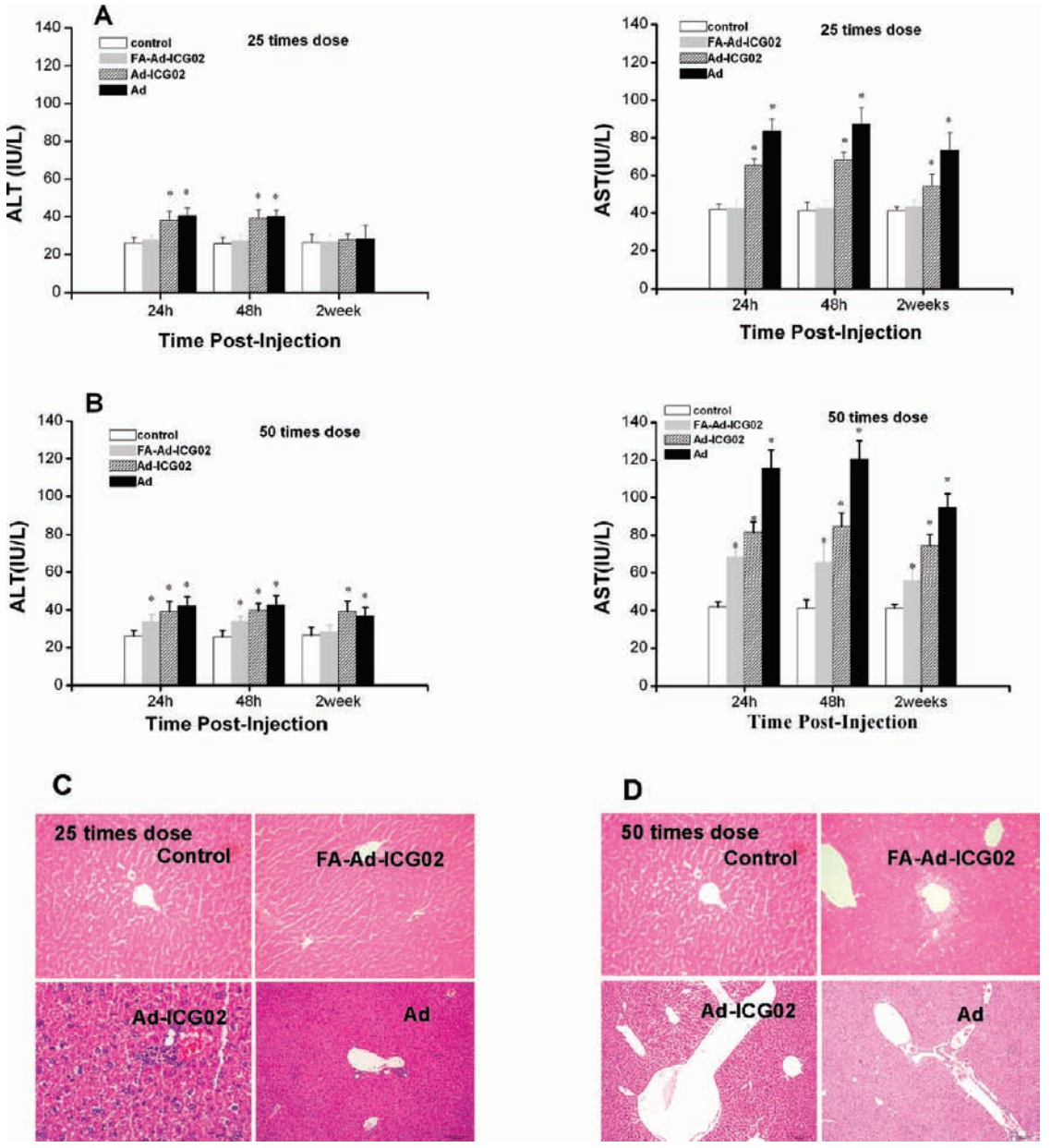


Figure 6. Acute toxicity of Ad, Ad-ICG02, and FA-Ad-ICG02 assessed on normal mice. (A) For the group treated with the 25× dose, the serum AST and ALT levels were significantly elevated after administration of Ad-ICG02 or Ad probes and peaked at about 24 and 48 h postinjection. Administration of FA-Ad-ICG02 did not induce any significant change in AST and ALT levels in mice. (B) AST and ALT levels in mice treated with a 50× dose were significantly elevated after injection of Ad or Ad-ICG02. The administration of FA-Ad-ICG02 probe at the 50× dose also caused a significant increase in both AST and ALT ($p < 0.05$). (C) Tissue sections of liver excised from the mice 2 weeks after administration of Ad, Ad-ICG02, and FA-Ad-ICG02 at 25× dose. No histologic change was observed in control and FA-Ad-ICG02 treated mouse groups. The liver tissue showed slight spotty necrosis and nuclear fission after administration of Ad-ICG02 or Ad particles (image magnification is 200×). (D) Tissue sections of liver excised from the mice 2 weeks after administration of Ad, Ad-ICG02, and FA-Ad-ICG02 at 50× dose. More than 90% of mice in the Ad and Ad-ICG02 treated groups showed hepatic tissue with slight spotty necrosis, nuclear fission, and venectasia under higher than normal doses. About 60% of the mice in the FA-Ad-ICG02 probe injected group exhibited different levels of toxicity, such as slight degree of inflammatory, spotty necrosis, and edemas diffusely distributed in the hepatic lobule (image magnification is 200×).

To visualize cellular uptake of FA-Ad and Ad, FA-Ad-RhB and Ad-RhB particles were, respectively, incubated in the above three tumor cell lines at 37 °C for 1 h. The number of RhB molecules was calculated based on fluorescence emission spectroscopic, which was found to be 312 ± 49 molecules per Ad particle ($n = 4$). The cellular uptake of these probes in cell lines was imaged by fluorescence microscopy and the results are shown in Figure 5C. FA-Ad and Ad particles were significantly retained in the CAR overexpressed A549 cells. The nonmodified Ad showed little uptake in the tumor lines with low CAR expression (Bel-7402 and U87MG). However, FA-Ad displayed increased uptake to FR overexpressed tumor cells (Bel-7402 and U87MG) compared to Ad. To determine the levels of cellular uptake of FA-Ad and Ad, flow cytometry data of

dx.doi.org/10.1021/bc100245t |*Bioconjugate Chem.* 2011, 22, 567–581

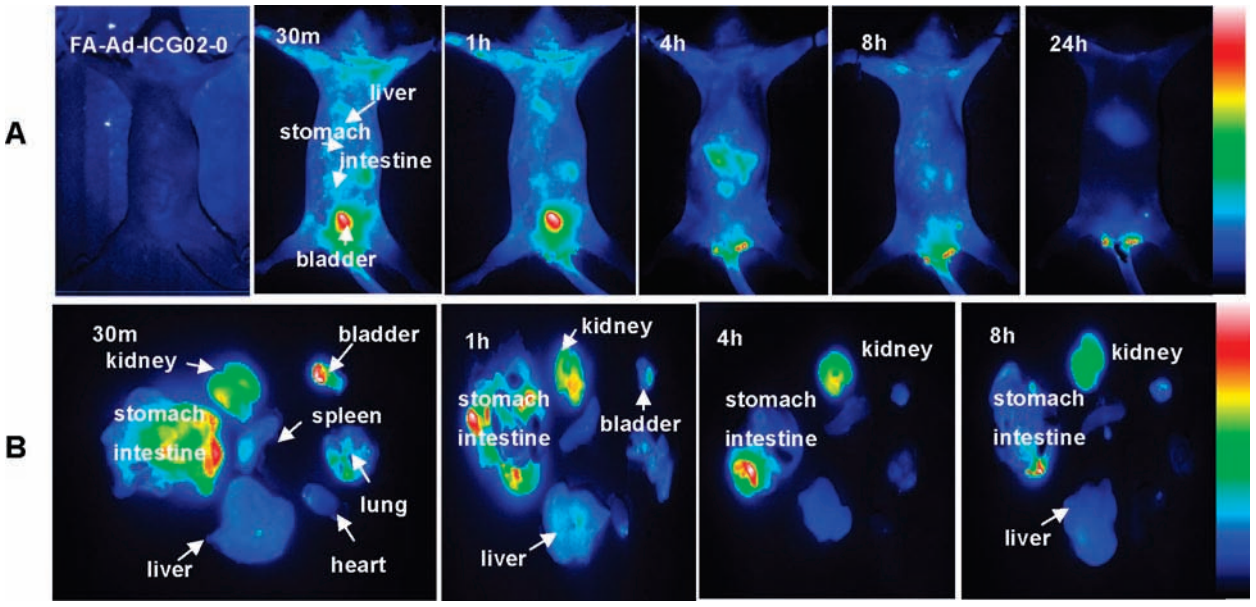


Figure 7. Dynamics of FA-Ad-ICG02 in normal nude mice monitored by NIR imaging system. (A) In vivo noninvasive monitoring of FA-Ad-ICG02 in mice within 24 h. Images show that the probe first accumulated in the liver and then cleared into the gastrointestinal and kidney−bladder pathway, respectively. (B) Fluorescence image of FA-Ad-ICG02 on the main organs excised from the mice within 8 h. Images show that the fluorescence accumulated in the liver gastrointestinal, kidney, and bladder after 1 h, which confirmed the real-time imaging data monitored with a noninvasive NIR imaging system.

FA-Ad-RhB and Ad-RhB were acquired, as shown in Figure 5D. Flow cytometry analysis indicated FA-Ad and Ad particles were taken in A549 cells at about 74.6% and 72.8%, respectively. FA-Ad in Bel-7402 and U87MG cells were retained at 78.1% and 53.1%, respectively, while Ad was retained in Bel-7402 and U87MG at about 63.2% and 45.0%, respectively. This finding suggests that FA modification enhanced the targeting capability of Ad particles to tumors overexpressing FR. The uptake levels of Ad particles in the three tumor cells are consistent with their mRNA levels.

To verify whether NHS affects the infection of Ad particle into tumor cells, the mixture of Ad-RhB and NHS was incubated with Bel-7402 cells. Flow cytometry analysis showed about 62.9% uptake of the particles (Figure 5D). There is no obvious difference between this mixture and Ad-RhB (63.2%), implying that NHS has no effect on the infection of Ad particles.

Acute Toxicity of the Probes on Normal Mouse Model. The acute toxicity of Ad, Ad-ICG02, and FA-Ad-ICG02 was assessed on normal mice. The biochemical parameters AST and ALT levels at 24 h, 48 h, and 2 weeks postinjection are shown in Figure 6. For the group treated with 25× of the normal dose (Figure 6A), serum AST and ALT were significantly elevated after injecting Ad-ICG02 or Ad probes. Peak levels were attained at about 24 h postinjection, while the administration of FA-Ad-ICG02 did not induce significant change of AST and ALT levels in the mice. Similarly, serum biochemical parameters AST and ALT were slightly elevated in the mice receiving a 50× dose after injection of Ad or Ad-ICG02 (Figure 6B). However, the administration of FA-Ad-ICG02 probe at 50× dose caused significant increase in both AST and ALT, suggesting some toxic effects at this high 50× dose. The above results suggest that the toxic effect only occurred in the high dosage of Ad particles, and ligand modified Ad could minimize liver toxicity compared with the nonmodified Ad.

To further evaluate the toxicity of Ad, FA-Ad-ICG02, and Ad-ICG02 on the animals, the main target organ, liver, was excised for pathology. Figure 6C,D is the representative tissue sections from different mouse groups. About 70% of the 25× dose group injected with Ad or Ad-ICG02 particles showed hepatic injury by 2 weeks, as evidenced by slight spotty necrosis and nuclear fission. More than 90% of mice in the Ad and Ad-ICG02 groups treated with 50× dose showed hepatic injury in the form of slight spotty necrosis, nuclear fission, and venectasia. As expected, the administration of FA-Ad-ICG02 did not render any significant pathologic changes at a 25× dose. No histological difference was observed in the control, normal dose, and 25× dose groups (Figure 6C) after FA-Ad-ICG02 injection. Moreover, 60% of the mice in the 50× dose group exhibited different levels of toxicity, such as slight degree of inflammatory, spotty necrosis, and edema that were diffusely distributed in the hepatic lobule (Figure 6D).

Dynamics of FA-Ad-ICG02 in Normal Nude Mice. To better understand the physiological behavior of FA-Ad-ICG02 probe, the dynamics of FA-Ad-ICG02 was first investigated in normal nude mice ($n = 5$) prior to using the tumor bearing mice. These mice were injected with FA-Ad-ICG02 probe (0.2 mL, 1×10^{10} pfu/kg) and monitored for 24 h. Representative images are shown in Figure 7A. The fluorescent probe FA-Ad-ICG02 initially spread in the whole body at about 30 min postinjection and gradually appeared in the excretion organs such as the liver, gastrointestinal system, and bladder. As the fluorescent probe in the liver gradually washed out in the first 8 h, the signal in the gastrointestinal organ and the bladder increased, as shown in the 8 h image (Figure 7A). At 24 h postinjection, the fluorescent probe has mostly cleared from the body. Typical of cyanine dyes, the probe probably entered liver and was subsequently transported to the gastrointestinal system. Another fraction of the probe was excreted by the kidney−bladder pathway.

dx.doi.org/10.1021/bc100245t |*Bioconjugate Chem.* 2011, 22, 567–581

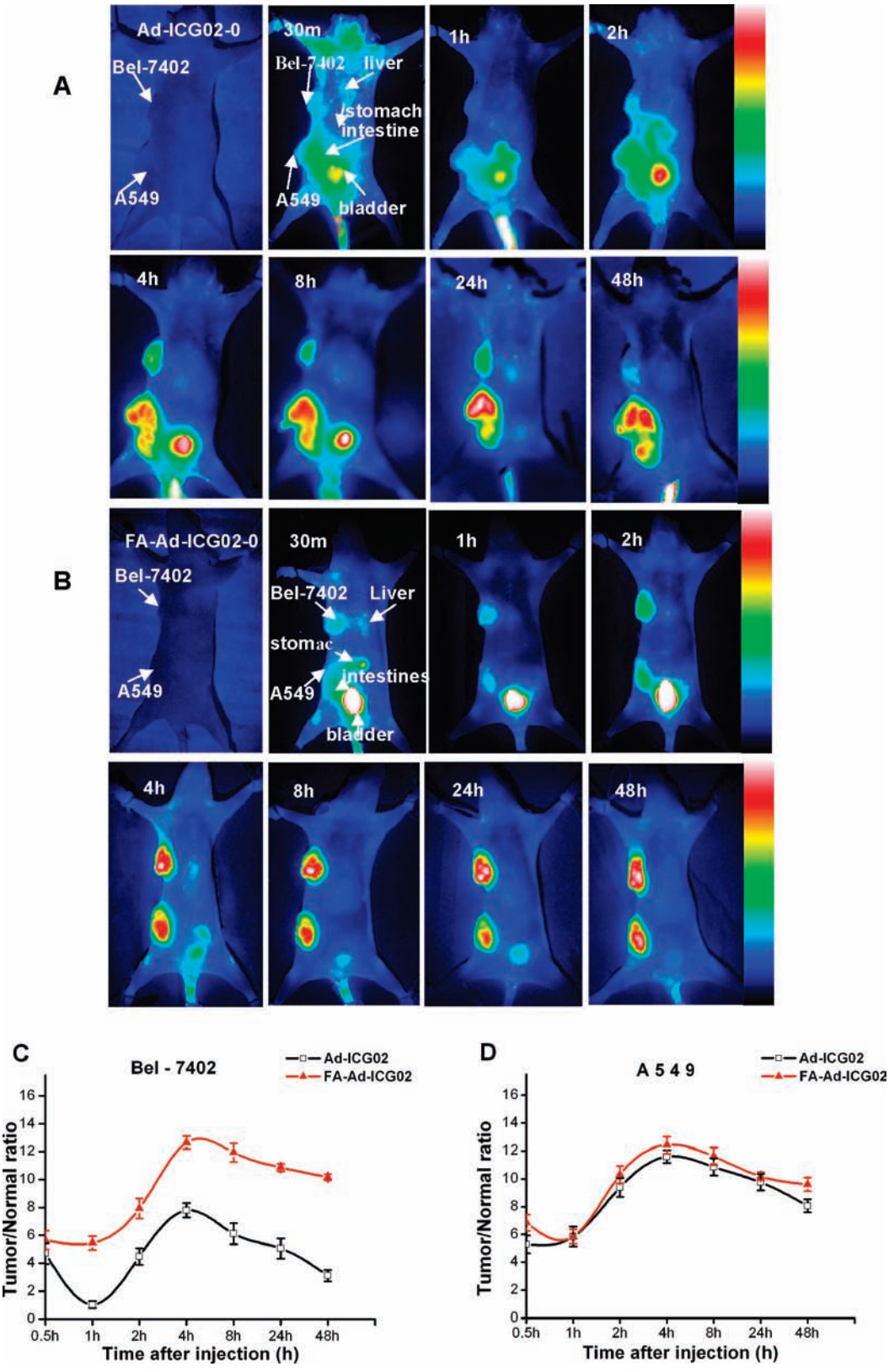


Figure 8. Tumor-targeting capability of FA-Ad-ICG02 and Ad-ICG02 in nude mice bearing Bel-7402 and A549 tumor xenograft monitored by NIR images system. (A) Fluorescence images of the mouse after administration of Ad-ICG02 within 48 h. Ad-ICG02 probe was targeted to CAR overexpressed A549 tumor and weak signal was displayed in the low CAR but high FR expressing Bel-7402 tumors. (B) Fluorescence images of the mouse after administration of FA-Ad-ICG02 within 48 h. FA-Ad-ICG02 displayed strong targeting capability to both A549 and Bel-7402. (C) Time courses of tumor-to-normal tissue (T/N) ratio in Bel-7402 tumor for Ad-ICG02 and FA-Ad-ICG02 probes. Statistical analysis indicates that there is a significant difference of T/N ratio in the Bel7402 tumors between the two probes ($p < 0.05$). (D) Time courses of tumor-to-normal tissue (T/N) ratio in A549 tumor. There is no significant difference in A549 tumors ($p > 0.05$). The data are represented as mean ± standard deviation (SD), $n = 5$/group.

dx.doi.org/10.1021/bc100245t |*Bioconjugate Chem.* 2011, 22, 567–581

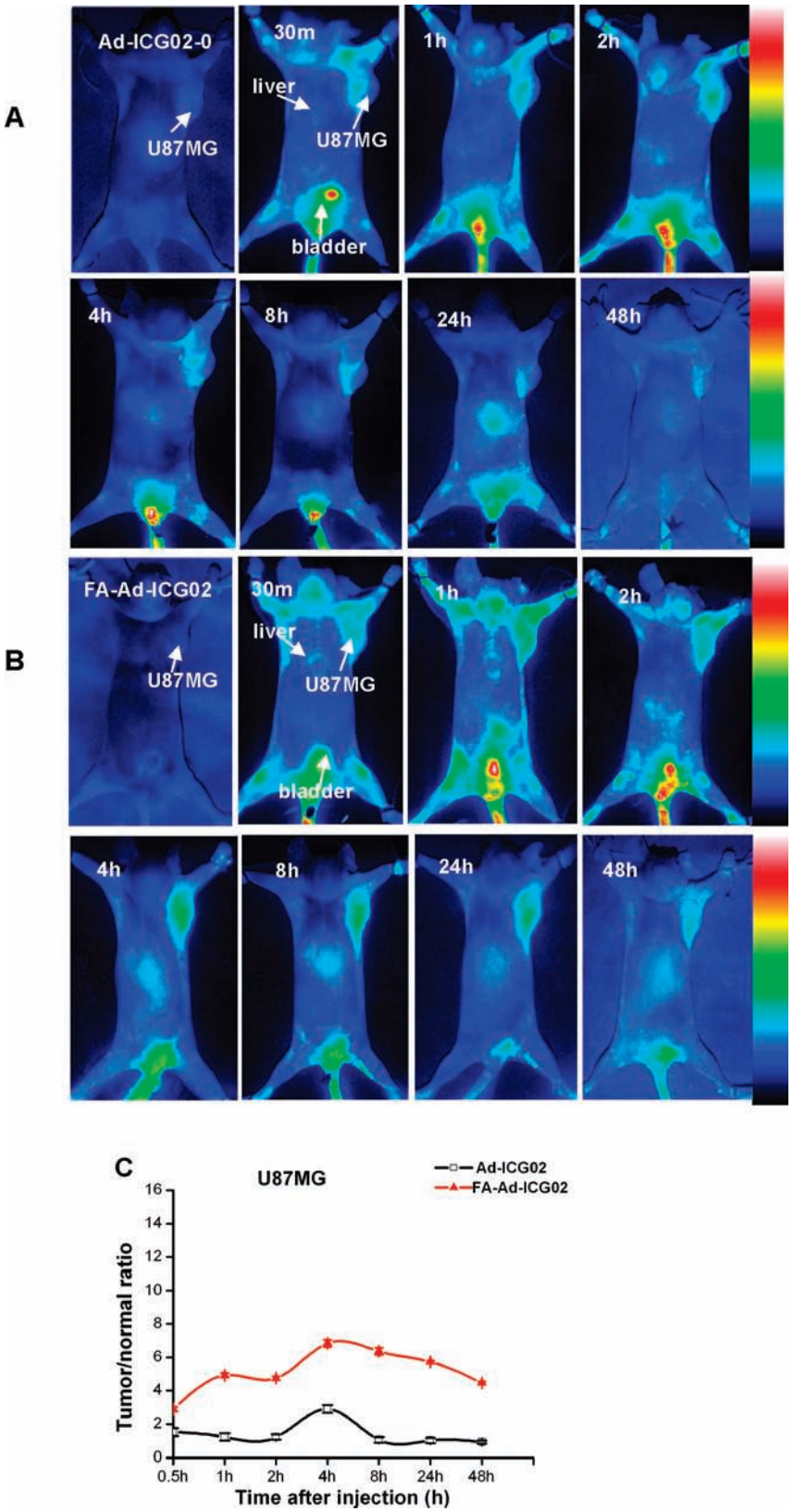


Figure 9. Tumor targeting capability of FA-Ad-ICG02 and Ad-ICG02 in nude mice bearing U87MG tumor xenograft monitored by NIR images system. (A) Fluorescence images of the mouse after administration of Ad-ICG02 within 48 h. Ad-ICG02 probe was poorly retained in U87MG tumor. (B) Fluorescence images of the mouse after administration of FA-Ad-ICG02 within 48 h. FA-Ad-ICG02 displayed a strong targeting capability to U87MG. (C) Time courses of tumor-to-normal tissue (T/N) ratio in U87MG tumor for Ad-ICG02 and FA-Ad-ICG02 probes. Statistical analysis indicates that there is a significant difference of T/N ratio in U87MG tumors for the two probes ($p < 0.05$). The data are represented as mean ± standard deviation (SD), $n = 5$/group.

dx.doi.org/10.1021/bc100245t |*Bioconjugate Chem.* 2011, 22, 567–581

To obtain detailed information about the probe's distribution in the main organs, the mice were sacrificed and the organs removed at 30 min, 1 h, 4 h, and 8 h ($n = 5$). Figure 7B shows the uptake of the fluorescent probes in representative organs ex vivo. Consistent with the in vivo observation, the fluorescent probe was first dispersed in all the organs and gradually moved to liver. At about 4 h, the probes were mainly observed in kidney and gastrointestinal system before clearing through urine and feces.

In Vivo Tumor Targeting Study. To investigate the tumor targeting capability of FA-Ad-ICG02 and Ad-ICG02, Bel-7402 and A549 cells that overexpress FA and CAR receptors, respectively, were used. The Bel-7402 and A549 cells were injected in the left axillary fossa and lower flank, respectively ($n = 10$). The in vivo distribution of the probes at specific time points was recorded with our NIR imaging system. Representative images are shown in Figure 8A and B. Similar to the profiles of the dynamics study described above, the probes were initially distributed all over the body and subsequently cleared by the hepatobiliary and renal pathways. However, the tumor sites were identifiable within one hour postinjection of the probes. Over time, the probe increasingly accumulated in the tumors and the fluorescence intensity peaked at about 4 h. For CAR receptor-positive A549 tumors, both Ad-ICG02 and FA-Ad-ICG02 displayed strong tumor-targeting capability, which further confirmed that CAR is the primary receptor for Ad. For Bel-7402 with FR overexpression, the FA-Ad-ICG02 probe showed higher targeting capability than Ad-ICG02, which is consistent with our previous findings. The bright fluorescence signal gradually disappeared after one week (data not shown).

To quantify the targeting ability of the probes, fluorescence intensity was analyzed by using ROI. The dynamics of the signals in tumors are depicted in Figure 8C and D. Fluorescence intensity ratio between Bel-7402 tumor and normal tissue (T/N) was 1.04 ± 0.24 at 1 h post injection of Ad-ICG02, reaching a peak at 4 h post injection (7.78 ± 0.51) and slowly declining to 3.11 ± 0.39 by 48 h (Figure 8C). In contrast, Bel-7402 tumor-bearing mice intravenously injected with FA-Ad-ICG02 probe showed a T/N ratio of 5.44 ± 0.49 after 1 h, and a peak uptake at 4 h reached 12.65 ± 0.48. Fluorescence intensity ratio between A549 tumor and normal tissue (T/N) was 5.83 ± 0.72 at 1 h after injection of Ad-ICG02 probe; a peak at 4 h reached 11.59 ± 0.46, and slowly declined to 8.06 ± 0.46 by 48 h (Figure 8D). Similarly, FA-Ad-ICG02 probe in A549 tumor bearing mice showed a T/N ratio of 5.84 ± 0.50 after 1 h, and a peak at 4 h reached 12.41 ± 0.61. Statistical analysis indicated a significant difference of T/N ratio in Bel-7402 tumors for the two probes ($p < 0.05$). There is no significant difference in the A549 tumors ($p > 0.05$). NIR images of mice with Bel-7402 and A549 tumor xenografts after injection of FA-Ad-ICG02 probe showed good fluorescence intensity and fast tumor targeting in vivo from 0.5 to 48 h.

To further explore the targeting capability of FA-Ad-ICG02 and Ad-ICG02, nude mice bearing U87MG tumor in the right axillary fossa were used. As shown in Figure 5A and B, U87MG displayed a relatively low expression in CAR and slightly higher level of FA receptor. Figure 9A and B shows two representative series of NIR images after administration of Ad-ICG02 and FA-Ad-ICG02, respectively. Fluorescence signal was clearly visualized in the U87MG tumor as early as 2 h for FA-Ad-ICG02 conjugate. Compared with FA-Ad-ICG02, Ad-ICG02 probe showed less targeting ability to U87MG tumor. Thus, the T/N tissue contrast ratio was less than that of FA-Ad-ICG02 probe (Figure 9C). The T/N ratio for FA-Ad-ICG02 probe peaked at about 4 h (6.84 ± 0.21), and the peak of Ad-ICG02 manifested at about 4 h (2.92 ± 0.23). Statistical analysis indicated the significant difference of T/N ratio existed in U87MG tumors for the two probes ($p < 0.05$). The results indicated that the targeting ability of FA-Ad-ICG02 probe to U87MG is stronger than that of Ad-ICG02 probe, which further confirms that FA modification can enhance the targeting ability of Ad to tumors with low CAR expression and high FA expression.

DISCUSSION

In this study, adenovirus capsids were covalently conjugated with FA ligands to extend the targeting ability of Ad particles to tumors with low CAR expression. To visualize the distribution of Ad in a living animal, the NIR fluorescence dye, ICG-Der-02, was subsequently attached to the Ad capsids. The number of FA incorporation to the Ad surface was calculated by following the recovery method (Figure 2D).The successful conjugation of FA-Ad-ICG02 was confirmed by the absorption and fluorescence spectra and electrophoresis (Figure 2A−C). It was previously reported that chemical modification of the Ad surface may alter their tropism and reduce infectivity because of the inherent CAR-mediated cellular uptake mechanism.

To modulate CAR binding and extend the applicability of the Ad particles, we chose FA for reasons given in the Introduction. In this configuration, it is important to incorporate an optimal number of FA per Ad particle for maximizing tumor targeting ability while substantially reducing normal tissues toxicity. In this study, the initial FA to Ad ratio was optimized to approximately 1×10^5 FA moieties per Ad particle, as shown by the in vivo imaging data. This corresponds to 448 ± 42 molecules of FA modification on the Ad surface (Figure 2D), which is similar to previously reported information.[40]

After chemical conjugation, the size and morphology of FA-Ad-ICG02 remained unchanged (Figure 3A−C). The TEM images of FA-Ad-ICG02 showed that the Ad particles were well dispersed as individual particles with spherical shape. However, in this study, FA was used as a cancer targeting moiety for Ad particles. The results reveal that FA-Ad-ICG02 could be delivered in more specific manner to target cells and tissues without undergoing a CAR-mediated viral infection mechanism. Our study demonstrates that retargeting of Ad particles is feasible by conjugating an appropriate targeting moiety on the surface, while maintaining high specific infection. The dynamics and biodistribution of FA-Ad-ICG02 in normal mice were traced by using NIR imaging system. The clearance profile of the functionalized Ad particles used in this study is consistent with that of Ad itself.[48−50]

Ad vector is a powerful tool in gene therapy. Immune toxicity of Ad is the key factor hindering the practical application of Ad particle.[51−53] Although E1- and E3-deleted Ad vector have defective replication abilities, innate and adaptive immune responses are still the main concern for the real application, especially when repeated administration is required.[54,55] Thus, toxicity study is crucial for the potential applications of new particles.

In this study, we assessed the toxicity of the probes in vitro and in vivo investigation. As in previous studies, MTT assay was conducted on different cell lines to evaluate the toxicity of the new probes (Figure 4). The results indicate that FA-Ad-ICG02 can selectively kill CAR and FA-positive cancer cells at low m.o.i.

There is no obvious toxicity to the normal cell (HELF). In the FA-Ad-ICG02 probe, the FA moiety is vitamin B_{11}, which is known to play an important role in DNA synthesis.[56,57] ICG-Der-02 is a derivative of ICG, approved by the U.S. FDA for human use.[58,59] Ad has the selective infectious ability to the specific cells. Our results confirmed that Ad has low infection to the cells without Ad specific receptors. Thus, the probe FA-Ad-ICG02 is relatively nontoxic to normal cells.

To further investigate the in vivo toxicity and acute toxicity, we studied these factors using conventional procedures. The liver expresses high levels of CAR, and it is the main target organ of toxicity.[60,61] Thus, pathologic status of liver and blood chemistry indexes was examined after intravenous administration of Ad, FA-Ad-ICG02, and Ad-ICG02 particles in normal mouse models. All data demonstrated that there was no obvious hepatotoxicity after injection of the three probes within the normal dose. The hepatotoxicity occurred at high doses of Ad and Ad-ICG02 injection, with significant increase of AST and ALT in 25× and 50× doses. However, the FA modified Ad FA-Ad-ICG02 did not induce any change even in the 25× dose. The cytotoxicity only occurred in the 50× high dose of FA-Ad-ICG02. The histologic examination showed that a small inflammation was observed in the 50× dose group (Figure 6). No obvious histologic changes were found, including focal necrosis, degeneration, and fibrosis in normal and 25× doses. These data suggest that even high doses of FA-Ad-ICG02 were not sufficient to cause damage to normal tissues compared to the nonmodified Ad.

The in vitro and in vivo toxicity studies indicate that FA-Ad-ICG02 is less toxic than Ad, which is consistent with a previous finding.[62] Usually, chemical modification of Ad particles could diminish the innate immune response due to the change of CAR dependent tropism. FA modification altered the tropism and thus decreased the Ad infection to liver cells. The in vivo imaging and pathological pictures also demonstrated the lower accumulation and reduced damage of FA modified Ad to the liver than that of Ad itself. Consequently, the modification to Ad may regulate the pharmacokinetics or part of the liver response, as reported in the literature.[40] The modified Ad has great potential for clinic application.

The primary purpose of this study is to extend the targeting ability of Ad to broad tumor types. FA was modified to the Ad capsids to improve the targeting of Ad to FA receptor over-expressed tumors except for the Ad specific tumors. In vitro studies in cell lines with different CAR and FA receptor expression (Figure 5A,B) showed that the targeting ability of Ad itself correlated with CAR expression, which corroborates other literature reports that infection of Ad is initiated by high-affinity binding of the fiber protein to CAR receptor.[63,64] Ad and FA-modified particles have almost identical infectivity in high expression CAR and FA negative cells (A549, Figure 5C,D). Differences were found in the low CAR expressing and FA-positive cells (Bel-7402 and U87MG, Figure 5C,D). The results showed that FA-modified Ad exhibited a relatively high targeting ability when compared with Ad particles in low CAR expressing and FA-positive cells. This suggests that FA-modified Ad infected Bel-7402 or U87MG cells via the dual recognition of CAR and FA receptors. The extent of enhancement in infectivity is consistent with the cell-surface FA expression level.

In vivo targeting capability of FA-Ad-ICG02 was investigated on different tumor bearing nude mouse models. Figures 8 and show that FA-Ad-ICG02 rapidly accumulates in tumors (Bel-7402 and U87MG), reaching the peak after 4 h postadministration. A significant amount of FA-Ad-ICG02 accumulated in the FA-positive and low CAR expressing tumor cells compared to Ad-ICG02. These results indicate that the tumor imaging ability of the probe correlated well with the receptor expression levels (Figure 5A and B), which is consistent with the in vitro experiments. In vitro and in vivo experiments all demonstrated that CAR is the primary receptor. FA modification could improve the targeting of Ad to low CAR and FA-positive tumors. FA-Ad-ICG02 can be used to enhance the ratio of tumor to normal tissue. Although the accelerated clearance of the modified Ad under repeated administration was reported,[16] the enhanced targeting ability and long retention time of the probes in the tumor site (one week) implies the possibility of sustained antitumor drug release to the tumors. This feature will decrease the need for repeated administration of the probe.

Ligand modification of the Ad surface is a more straightforward and versatile method than genetic modification of Ad surface with cell-recognizable proteins such as antibodies. Based on our results, we can deduce that Ad could be targeted to other tumor lines by chemically conjugating with the appropriate ligands. With the low toxicity of E1/E3-deleted Ad, FA-Ad-ICG02 probe has great potential for early tumor diagnosis and gene therapy.

In our previous studies, we have shown that the NIR molecular imaging technique is a useful tool to trace the dynamics of different probes in small animals.[29,30,47,65] This approach provides rapid, convenient, noninvasive, real-time, and inexpensive assays to monitor the distribution, magnitude, and duration of tumor targeting probes. In this study, the tool once again demonstrated its powerful ability in drug development.

CONCLUSIONS

In this study, FA was successfully conjugated to E1/E3-deleted Ad capsids (FA-Ad), which extended the targeting capability to low CAR expressing tumors. NIR fluorescent dye ICG-Der-02 was subsequently attached to the Ad (FA-Ad-ICG02) for in vivo fluorescence imaging. In vitro and in vivo studies demonstrated that the targeting capability of FA-Ad-ICG02 correlated well with the different receptor expression levels. CAR was shown to be the primary receptor of FA-Ad-ICG02 and FA modification enhanced the T/N tissue ratio in the CAR-negative and FR-positive tumors (Bel-7402, U87MG). The systemic toxicity study demonstrated the selective toxicity of FA-Ad-ICG02 to tumor tissue and low toxicity to normal tissues. The chemical modification of Ad decreased its toxicity. All the results support the hypothesis that the targeting capability of Ad could be extended to other Ad nonspecific tumors by chemical modification of the corresponding ligands. The modified E1/E3-deleted Ad has great potential for early tumor diagnosis and targeted therapy.

AUTHOR INFORMATION

Corresponding Author

*Author to whom correspondence should be addressed: Yueqing Gu, Ph.D., China Pharmaceutical University. Tel: 86-25-83271046. Fax: 86-25-83271249. E-mail: cpuyueqing@163.com.

ACKNOWLEDGMENT

The authors are grateful to Natural Science Foundation Committee of China (NSFC30672015, NSFC30700779,

NSFC30800257, NSFC30970776, NSFC 81000666, NSFC31050110123, and NSFC81071194), the Ministry of Science and Technology (2009ZX09310-004) for their financial supports.

REFERENCES

(1) Singh, R., and Kostarelos, K. (2009) Designer adenoviruses for nanomedicine and nanodiagnostics. *Trends. Biotechnol. 27*, 220–229.

(2) McConnell, M. J., and Imperiale, M. J. (2004) Biology of adenovirus and its use as a vector for gene therapy. *Hum. Gene. Ther. 15*, 1022–1033.

(3) Ewert, K., Slack, N. L., Ahmad, A., Evans, H. M., Lin, A. J., Samuel, C. E., and Safinya, C. R. (2004) Cationic lipid-DNA complexes for gene therapy: understanding the relationship between complex structure and gene delivery pathways at the molecular level. *Curr. Med. Chem. 11*, 133–149.

(4) Everts, M., Saini, V., Leddon, J. L., Kok, R. J., Stoff-Khalili, M., Preuss, M. A., Millican, C. L., Perkins, G., Brown, J. M., Bagaria, H., Nikles, D. E., Johnson, D. T., Zharov, V. P., and Curiel, D. T. (2006) Covalently linked Au nanoparticles to a viral vector: potential for combined photothermal and gene cancer therapy. *Nano Lett. 6*, 587–591.

(5) Anderson, E. A., Isaacman, S, Peabody, D. S., Wang, E. Y., Canary, J. W., and Kirshenbaum, K. (2006) Viral nanoparticles donning a paramagnetic coat: conjugation of MRI contrast agents to the MS2 capsid. *Nano Lett. 6*, 1160–1164.

(6) Huh, Y. M., Lee, E. S., Lee, J. H., Jun, Y. W., Kim, P. H., Yun, C. O., Kim, J. H., Suh, J. S., and Cheon, J. (2007) Hybrid nanoparticles for magnetic resonance imaging of target-specific viral gene delivery. *Adv. Mater. 19*, 3109–3112.

(7) Adam, J. F., Biston, M. C., Rousseau, J., Boudou, C., Charvet, A. M., Balosso, J., Estève, F., and Elleaume, H. (2008) Heavy element enhanced synchrotron stereotactic radiotherapy as a promising brain tumor treatment. *Phys. Med. 24*, 92–97.

(8) Allen, M., Bulte, J. W., Liepold, L., Basu, G., Zywicke, H. A., Frank, J. A., Young, M., and Douglas, T. (2005) Paramagnetic viral nanoparticles as potential high-relaxivity magnetic resonance contrast agents. *Magn. Reson. Med. 54*, 807–812.

(9) Liniger, M., Zuniga, A., and Naim, H. Y. (2007) Use of viral vectors for the development of vaccines. *Expert Rev. Vaccines 6*, 255–266.

(10) Clarke, J. M., Morse, M. A., Lyerly, H. K., Clay, T., and Osada, T. (2010) Adenovirus vaccine immunotherapy targeting WT1-expressing tumors. *Expert Opin. Biol. 10*, 875–873.

(11) Dash, R., Dmitriev, I., Su, Z. Z., Bhutia, S. K, Azab, B., Vozhilla, N., Yacoub, A., Dent, P., Curiel, D. T., Sarkar, D., and Fisher, P. B. (2010) Enhanced delivery of mda-7/IL-24 using a serotype chimeric adenovirus (Ad.5/3) improves therapeutic efficacy in low CAR prostate cancer cells. *Cancer Gene. Ther. 17*, 447–456.

(12) Hemminki, A., Kanerva, A., Liu, B., Wang, M., Alvarez, R. D., Siegal, G. P., and Curiel, D. T. (2003) Modulation of Coxsackie adenovirus receptor expression for increased adenoviral transgene expression. *Cancer Res. 15*, 847–853.

(13) Wakayama, M., Abei, M., Kawashima, R., Seo, E., Fukuda, K., Ugai, H., Murata, T., Tanaka, N., Hyodo, I., Hamada, H., and Yokoyama, K. K. (2007) E1A, E1B double-restricted adenovirus with RGD-fiber modification exhibits enhanced oncolysis for CAR-deficient biliary cancers. *Clin. Cancer Res. 13*, 3043–3050.

(14) Bergelson, J. M., Cunningham, J. A., Droguett, G., Kurt-Jones, E. A., Krithivas, A., Hong, J. S., Horwitz, M. S., Crowell, R. L., and Finberg, R. W. (1997) Isolation of a common receptor for Coxsackie B viruses and adenoviruses 2 and 5. *Science 275*, 1320–1323.

(15) Coughlan, L., Vallath, S., Saha, A., Flak, M., McNeish, I. A., Vassaux, G., Marshall, J. F., Hart, I. R., and Thomas, G. J. (2009) In vivo retargeting of adenovirus type 5 to alphavbeta6 integrin results in reduced hepatotoxicity and improved tumor uptake following systemic delivery. *J. Virol. 83*, 6416–6428.

(16) Wu, H., Dmitriev, I., Kashentseva, E., Seki, T., Wang, M., and Curiel, D., T. (2002) Construction and characterization of adenovirus serotype 5 packaged by serotype 3 hexon. *J. Virol. 76*, 12775–12782.

(17) Li, J., Le, L., Sibley, D. A., Mathis, J. M., and Curiel, D. T. (2005) Genetic incorporation of HSV-1 thymidine kinase into the adenovirus protein IX for functional display on the virion. *Virology 338*, 247–258.

(18) Shashkova, E. V., May, S. M., Doronin, K., and Barry, M. A. (2009) Expanded anticancer therapeutic window of hexon-modified oncolytic adenovirus. *Mol. Ther. 17*, 2121–2130.

(19) Singh, R., Tian, B., and Kostarelos, K. (2008) Artificial envelopment of nonenveloped viruses: enhancing adenovirus tumor targeting in vivo. *FASEB. J. 22*, 3389–3402.

(20) Eto, Y., Yoshioka, Y., Asavatanabodee, R., Kida, S., Maeda, M., Mukai, Y., Mizuguchi, H., Kawasaki, K, Okada., N., and Nakagawa, S. (2009) Transduction of adenovirus vectors modified with cell-penetrating peptides. *Peptides 30*, 1548–1552.

(21) Destito, G., Yeh, R., Rae, C. S., Finn, M. G., and Manchester, M. (2007) Folic acid-mediated targeting of cowpea mosaic virus particles to tumor cells. *Chem. Biol. 14*, 1152–1162.

(22) Sega, E. I., and Low, P. S. (2008) Tumor detection using folate receptor-targeted imaging agents. *Cancer Metastasis Rev. 27*, 655–664.

(23) Arote, R. B., Hwang, S. K., Lim, H. T., Kim, T. H., Jere., D., Jiang, H. L., Kim, Y. K., Cho, M. H., and Cho, C. S. (2010) The therapeutic efficiency of FP-PEA/TAM67 gene complexes via folate receptor-mediated endocytosis in a xenograft mice model. *Biomaterials 31*, 2435–2445.

(24) Leamon, C. P., and Low, P. S. (1991) Delivery of macromolecules into living cells: A method that exploits folate receptor endocytosis. *Proc. Natl. Acad. Sci. U.S.A. 88*, 5572–5576.

(25) Okarvi, S. M., and Jammaz, I. A. (2006) Preparation and in vitro and in vivo evaluation of technetium-99m-labeled folate and methotrexate conjugates as tumor imaging agents. *Cancer Biother. Radiopharm. 21*, 49–60.

(26) Chapkin, R. S., Kamen, B. A., Callaway, E .S., Davidson, L. A., George, N. I., Wang, N., Lupton, J. R., and Finnell, R. H. (2009) Use of a novel genetic mouse model to investigate the role of folate in colitis-associated colon cancer. *J. Nutr. Biochem. 20*, 649–655.

(27) Retnakumari, A., Setua, S., Menon, D., Ravindran, P., Muhammed, H., Pradeep, T., Nair, S., and Koyakutty, M. (2010) Molecular-receptor-specific, non-toxic, near-infrared-emitting Au cluster-protein nanoconjugates for targeted cancer imaging. *Nanotechnology 5*, 055103.

(28) Ke, J. H., Lin, J. J., Carey, J. R., Chen, J. S., Chen, C. Y., and Wang, L. F. (2010) A specific tumor-targeting magnetofluorescent nanoprobe for dual-modality molecular imaging. *Biomaterials 31*, 1707–1715.

(29) Liu, F., Deng, D., Chen, X., Qian, Z., Achilefu, S., and Gu, Y. (2010) Folate-polyethylene glycol conjugated near-infrared fluorescence probe with high targeting affinity and sensitivity for in vivo early tumor diagnosis. *Mol. Imaging Biol.*Epub ahead of print.

(30) Zhang, J., Deng, D., Qian, Z., Liu, F., Chen, X., An, L., and Gu, Y. (2010) The targeting behavior of folate-nanohydrogel evaluated by near infrared imaging system in tumor-bearing mouse model. *Pharm. Res. 27*, 46–55.

(31) Pierce, M. C., Javier, D. J., and Richards-Kortum, R. (2008) Optical contrast agents and imaging systems for detection and diagnosis of cancer. *Int. J. Cancer 123*, 1979–1990.

(32) Keramidas, M., Josserand, V., Righini, C. A., Wenk, C., Faure, C., and Coll, J. L. (2010) Intraoperative near-infrared image-guided surgery for peritoneal carcinomatosis in a preclinical experimental model. *Br. J. Surg. 97*, 737–743.

(33) Keramidas, R., Tung, C. H., Mahmood, U., and Bogdanov, A., Jr. (1999) In vivo imaging of tumors with protease-activated near-infrared fluorescent probes. *Nat. Biotechnol. 17*, 375–378.

(34) Hsu, A. R., Hou, L. C., Veeravagu, A., Greve, J. M., Vogel, H, Tse, V., and Chen, X. (2006) In vivo near-infrared fluorescence imaging of integrin alphavbeta3 in an orthotopic glioblastoma model. *Mol. Imaging Biol. 8*, 315–323.

(35) Ogawa, M., Regino, C. A., Choyke, P. L., and Kobayashi, H. (2009) In vivo target-specific activatable near-infrared optical labeling of humanized monoclonal antibodies. *Mol. Cancer Ther. 8*, 232–239.

(36) Björnsson, O. G., Murphy, R., and Chadwick, V. S. (1982) Physiochemical studies of indocyanine green (ICG): absorbance/concentration relationship, pH tolerance and assay precision in various solvents. *Experientia 38*, 1441–1442.

(37) Zou, P., Xu, S., Povoski, S. P., Wang, A., Johnson, M. A., Martin, E. W., Jr., Subramaniam, V., Xu, R., and Sun, D. (2009) Near-infrared fluorescence labeled anti-TAG-72 monoclonal antibodies for tumor imaging in colorectal cancer xenograft mice. *Mol. Pharmaceutics 6*, 428–440.

(38) Xiao, W., Yao, N., Peng, L., Liu, R., and Lam, K. S. (2009) Near-infrared optical imaging in glioblastoma xenograft with ligand-targeting alpha3 integrin. *Eur. J. Nucl. Med. Mol. Imaging 36*, 94–103.

(39) Leopold, P. L., Ferris, B., Grinberg, I., Worgall, S., Hackett, N. R., and Crystal, R. G. (1998) Fluorescent virions: dynamic tracking of the pathway of adenoviral gene transfer vectors in living cells. *Hum. Gene. Ther. 9*, 367–378.

(40) Oh, I. K., Mok, H., and Park, T. G. (2006) Folate immobilized and PEGylated adenovirus for retargeting to tumor cells. *Bioconjugate Chem. 17*, 721–727.

(41) Schumacher, A., Horvat, S., Woischwill, C., Wolff, G., and Witt, C. (2009) Co-expression of p21 (Waf1/Cip1) in adenovirus vectors improves expression of a second transgene. *Gene Ther. 16*, 574–578.

(42) Wang, W., Jin, B., Li, W., Xu, C. X., Cui, F. A., Liu, B., Yan, Y. F., Liu, X. X., and Wang, X. L. (2009) Targeted antitumor effect induced by hTERT promoter mediated ODC antisense adenovirus. *Mol. Biol. Rep. 30*, 176–181.

(43) Yong, R. L., Shinojima, N., Fueyo, J., Gumin, J., Vecil, G. G., Marini, F. C., Bogler, O., Andreeff, M., and Lang, F. F. (2009) Human bone marrow-derived mesenchymal stem cells for intravascular delivery of oncolytic adenovirus Delta24-RGD to human gliomas. *Cancer Res. 69*, 8932–8940.

(44) Mueller, H., Kassack, M. U., and Wiese, M. (2004) Comparison of the usefulness of the MTT, ATP, and calcein assays to predict the potency of cytotoxici agents in various human cancer cell lines. *J. Biomol. Screen. 9*, 506–515.

(45) Gao, J., Chen, K., Xie, R., Xie, J., Yan, Y., Cheng, Z., Peng, X., and Chen, X. (2010) In vivo tumor-targeted fluorescence imaging using near-infrared of non-cadmium quantum dots. *Bioconjugate Chem. 21*, 604–609.

(46) Cheng, Z., Wu, Y., Xiong, Z., Gambhir, S, S., and Chen, X. (2005) Near-infrared fluorescent RGD peptides for optical imaging of integrin alphavbeta3 expression in living mice. *Bioconjugate Chem. 16*, 1433–1441.

(47) Zhang, J., Chen, H., Xu, L., and Gu, Y. (2008) The targeted behavior of thermally responsive nanohydrogel evaluated by NIR system in mouse model. *J. Controlled Release 131*, 34–40.

(48) Johnson, M., Huyn, S., Burton, J., Sato, M., and Wu, L. (2006) Differential biodistribution of adenoviral vector in vivo as monitored by bioluminescence imaging and quantitative polymerase chain reaction. *Hum. Gene. Ther. 17*, 1262–1269.

(49) Awasthi, V., Meinken, G., Springer, K., Srivastava, S. C., and Freimuth, P. (2004) Biodistribution of radioiodinated adenovirus fiber protein knob domain after intravenous injection in mice. *J. Virol. 78*, 6431–6438.

(50) Liu, Q., and Muruve, D. A. (2003) Molecular basis of the inflammatory response to adenovirus vectors. *Gene Ther. 10*, 935–940.

(51) Danielsson, A., Elgue, G., Nilsson, B. M., Nilsson, B., Lambris, J. D., Tötterman, T. H., Kochanek, S., Kreppel, F., and Essand, M. (2010) An ex vivo loop system models the toxicity and efficacy of PEGylated and unmodified adenovirus serotype 5 in whole human blood. *Gene Ther. 17*, 752–762.

(52) Lubaroff, D. M., Konety, B. R., Link, B., Gerstbrein, J., Madsen, T., Shannon, M., Howard, J., Paisley, J., Boeglin, D., Ratliff, T. L., and Williams, R. D. (2009) Phase I clinical trial of an adenovirus/prostate-specific antigen vaccine for prostate cancer: safety and immunologic results. *Clin. Cancer Res. 15*, 7375–7380.

(53) Zaiss, A. K., Machado, H. B., and Herschman, H. R. (2009) The influence of innate and pre-existing immunity on adenovirus therapy. *J. Cell. Biochem. 108*, 778–790.

(54) Ohashi, M., Yoshida, K., Kushida, M., Miura, Y., Ohnami, S., Ikarashi, Y., Kitade, Y., Yoshida, T., and Aoki, K. (2005) Adenovirus-mediated interferon alpha gene transfer induces regional direct cytotoxicity and possible systemic immunity against pancreatic cancer. *Br. J. Cancer 93*, 441–449.

(55) Smith, J. S., Xu, Z., and Byrnes, A. P. (2008) A quantitative assay for measuring clearance of adenovirus vectors by Kupffer cells. *J. Virol. Methods 147*, 54–60.

(56) Ebisch, I. M., Thomas, C. M., Peters, W. H., Braat, D. D., and Steegers-Theunissen, R. P. (2006) The importance of folate, zinc and antioxidants in the pathogenesis and prevention of subfertility. *Hum. Reprod. Update 13*, 163–174.

(57) Bistulfi, G., Vandette, E., Matsui, S., and Smiraglia, D. J. (2010) Mild folate deficiency induces genetic and epigenetic instability and phenotype changes in prostate cancer cells. *BMC Biol. 21*, 8–6.

(58) Herbort, C. P. (2009) Fluorescein and indocyanine green angiography for uveitis. *Middle East Afr. J. Ophthalmol. 16*, 168–187.

(59) Ebisch, R. D., Jr., and Pascarella, A. (2010) Retinal angiomatous proliferation successfully treated with indocyanine green dye-enhanced photocoagulation. *Ophthalmic Surg. Lasers Imaging*Epub ahead of print.

(60) Lozier, J. N., Csako, G., Mondoro, T. H., Krizek, D. M., Metzger, M. E., Costello, R., Vostal, J. G., Rick, M. E., Donahue, R. E, and Morgan, R. A. (2002) Toxicity of a first-generation adenoviral vector in rhesus macaques. *Hum. Gene. Ther. 13*, 113–124.

(61) Shayakhmetov, D. M., Gaggar, A., Ni, S., Li, Z. Y., and Lieber, A. (2005) Adenovirus binding to blood factors results in liver cell infection and hepatotoxicity. *J. Virol. 79*, 7478–7491.

(62) Koizumi, N., Yamaguchi, T., Kawabata, K., Sakurai, F., Sasaki, T., Watanabe, Y., Hayakawa, T., and Mizuguchi, H. (2007) Fiber-modified adenovirus vectors decrease liver toxicity through reduced IL-6 production. *J. Immunol. 178*, 1767–1773.

(63) McDonald, D., Stockwin, L., Matzow, T., Blair, Zajdel, M. E, and Blair, G. E. (1999) Coxsackie and adenovirus receptor (CAR)-dependent and major histocompatibility complex (MHC) class I-independent uptake of recombinant adenoviruses into human tumor cells. *Gene Ther. 6*, 1512–1519.

(64) Kim, M., Zinn, K. R., Barnett, B. G., Sumerel, L. A., Krasnykh, V., Curiel, D. T., and Douglas, J. T. (2002) The therapeutic efficacy of adenoviral vectors for cancer gene therapy is limited by a low level of primary adenovirus receptors on tumor cells. *Eur. J. Cancer 38*, 1917–26.

(65) Chen, H., Wang, Y., Xu, J., Ji, J., Zhang, J., Hu, Y., and Gu, Y. (2008) Non-invasive near infrared fluorescence imaging of CdHgTe quantum dots in mouse model. *J. Fluoresc. 18*, 801–811.

Bioconjugate Chemistry

ARTICLE

pubs.acs.org/bc

Investigation of Polymer and Nanoparticle Properties with Nicotinic Acid and *p*-Aminobenzoic Acid Grafted on Poly(ε-caprolactone)-Poly(ethylene glycol)-Poly(ε-caprolactone) via Click Chemistry

Jiraphong Suksiriworapong,[†] Kittisak Sripha,[‡] Jörg Kreuter,[§] and Varaporn Buraphacheep Junyaprasert*[,†]

[†]Department of Pharmacy

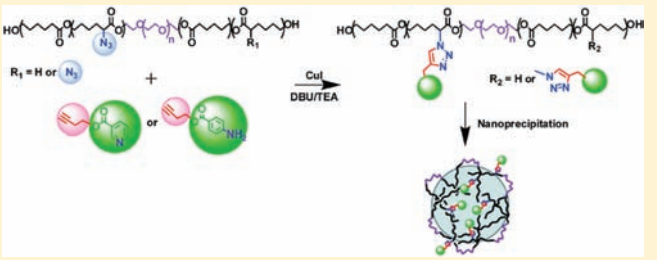
[‡]Department of Pharmaceutical Chemistry

Faculty of Pharmacy, Mahidol University, Bangkok 10400, Thailand

[§]Institute of Pharmaceutical Technology, Goethe-University, Max-von-Laue-Str. 9 (Biozentrum), D-60438 Frankfurt am Main, Germany

Supporting Information

ABSTRACT: In this study, the grafting of nicotinic acid and *p*-aminobenzoic acid (PABA) onto poly(ε-caprolactone)-poly(ethylene glycol)-poly(ε-caprolactone) was performed by Huisgen's 1,3-dipolar cycloaddition, also known as click chemistry. Concentrations used for grafting were 0.10, 0.20, and 0.30 molar ratios with respect to caproyl units. The grafted copolymers were successfully obtained at all ratios as confirmed by NMR, GPC, and FT-IR. According to the DSC results, the polymorphisms of these grafted copolymers were mostly changed from semicrystalline to amorphous depending on the type and the amount of grafting compounds. TGA thermograms showed different thermal stabilities of the grafted copolymers compared to the original copolymers. Cytotoxicity results from HUVEC models suggested that the toxicity of grafted nanoparticles increased with the molar ratios of grafting units. Due to differences in molecular structure between nicotinic acid and PABA, physicochemical properties (particle size and surface charge) of grafted copolymer nanoparticles were substantially different. With increasing molar ratio of the grafting units, the particle size of blank nanoparticles tended to increase, resulting from an increase in the hydrophobic fragments of the grafted copolymer. Ibuprofen was chosen as a model drug to evaluate the interaction between grafted copolymers and loaded drug. After ibuprofen loading, the particle size of the loaded nanoparticles of both grafted copolymers increased compared to that of the blank nanoparticles. Significant differences in loading capacity between nicotinic acid and PABA grafted copolymer nanoparticles were clearly shown. This is most likely a result of different compatibility between each grafting compound and ibuprofen, including hydrogen bond interaction, π−π stacking interaction, and steric hindrance.



INTRODUCTION

Over the past decades, the fabrication of copolymers of poly(ε-caprolactone) (PCL) and poly(ethylene glycol) (PEG) has been extensively developed to adapt their physicochemical and mechanical properties to much wider applications in pharmaceutical and medical fields.[1−12] PCL is a semicrystalline, hydrophobic, and biodegradable polymer, while PEG exhibits hydrophilic, crystalline, nontoxic, and biocompatible polymer properties.[13] The copolymer of these two materials can overcome the limitation of PCL after administration into the body by the stealth properties of the hydrophilic segment of PEG.[14] Therefore, this copolymer contributes to improvement of both properties and applications. To develop biomaterials for their use for novel drug delivery systems, one of the methods involves modification of the polymers by the attachment of attractive functional groups. Several reports have established the attachment of various functional groups such as hydroxyl, amino, and carboxylic acid groups onto the main polymer chain by different methods.[15] However, the aforementioned processes frequently exhibit several drawbacks such as incomplete conversion,[16] multiple synthesis steps,[17,18] and intra- and intermolecular transesterifications during the process of attachment.[19] Recently, the straightforward reaction for the grafting of functional groups along PCL has been successfully performed through "click chemistry" using versatile, easy, and mild conditions.[20−22] Riva et al.[23] reported successful grafting of benzoate, triethyl ammonium bromide, and poly(ethylene oxide) on PCL backbone by this reaction. In addition, Lee et al.[24,25] demonstrated the grafting of hexyne and proline to the methoxyPEG-*co*-PCL backbone and, recently, grafting of hexyne, decyne, and benzoate to the PEG-*co*-$(PCL)_2$ backbone. However, to the best of our knowledge, the grafting of pharmacologically active molecules along

Received: June 14, 2010
Revised: January 20, 2011
Published: March 04, 2011

ACS Publications © 2011 American Chemical Society

dx.doi.org/10.1021/bc100270m | *Bioconjugate Chem.* 2011, 22, 582–594

the PCL-PEG-PCL backbone with various amounts of grafting units has not been established.

Most drugs on the market are sparingly water soluble principally due to the presence of heterocyclic and aromatic rings in their structures. Nicotinic acid and *p*-aminobenzoic acid (PABA) are two examples of sparingly water soluble drugs which have been investigated for their pharmacological actions and safety in biological systems.[26−31] As per consideration of the structure of these two compounds, the *para*-amino group on the aromatic benzene ring of PABA contributes to the acidic, protic, and hydrogen bonding donor properties.[32,33] The nitrogen atom in the pyridine ring of nicotinic acid, on the other hand, will serve as base and hydrogen bond acceptor. Previously, it was found that the different structures and properties of these two drugs affected the ease of the grafting reaction onto the PCL backbone and the properties of grafted copolymer.[34] From this finding, it is expected that similar effects would occur in the case of the amphiphilic PCL-PEG-PCL copolymer. Furthermore, the grafting compounds (herein referred to nicotinic acid and PABA) on the polymer may potentially influence nanoparticle formation and their properties, especially drug loading capacity and entrapment efficiency. In addition, it is of interest to investigate the contribution of interaction between the grafted copolymer and encapsulated drugs on drug loading capacity and entrapment efficiency.

Ibuprofen (IBU) is a common nonsteroidal anti-inflammatory drug that is being used worldwide. Its molecular structure consists of a phenyl ring, an alkyl group, and a carboxylic acid group. With the availability of its phenyl ring, IBU may form $\pi-\pi$ bonds with other aromatic rings. In addition, a carboxylic group may form hydrogen bonds with both hydrogen bond donors and acceptors presented on the polymer backbone. Such properties make this drug suitable as a model drug for our investigation.

Therefore, this study aimed toward synthesizing the randomly grafted PCL-PEG-PCL with nicotinic acid and PABA by Huisgen's 1,3-dipolar cycloaddition reaction, also known as "click chemistry". The reaction was performed according to our previously published method.[34] The effects of varied concentrations of the grafting compounds on physicochemical and thermal properties of the copolymer backbone were also investigated. After synthesis, all grafted copolymers were used to prepare nanoparticles. To ascertain its potential use in humans, all nanoparticle preparations were tested for their cytotoxicity. Subsequently, the effects of the grafting compounds on nanoparticle formation and properties including particle size, zeta potential, and drug loading capacity were evaluated.

EXPERIMENTAL PROCEDURES

Materials. ε-Caprolactone (CL; Aldrich, USA) was dried over calcium hydride for 48 h followed by distillation prior to use. *p*-Aminobenzoic acid (PABA) (Aldrich, USA) and nicotinic acid (Ajax Finechem, Australia) were used without purification. 3-Butyn-1-ol, copper (I) iodide (CuI), 1,8-diazabicyclo[5.4.0] undec-7-ene (DBU), stannous (II) octanoate ($Sn(Oct)_2$), dimethylsulfoxide (DMSO), L-glutamine, and fetal bovine serum (FBS) were purchased from Sigma-Aldrich Chemicals, USA. *N, N*-Dicyclohexylcarbodiimide (DCC), 4-dimethylaminopyridine (DMAP), and MTT (3-(4,5-dimethyl-2-thiazolyl)-2,5-diphenyl-2*H*-tetrazoliumbromide) were purchased from Fluka Chemie, Germany. α-Chloro-ε-caprolactone (ClCL) was synthesized according to the previous report.[34] Poly(ethylene glycol) (M_w 4000 g/mol, PEG_{4000}) from Fluka Chemie, Germany, was purified by precipitation from chloroform solution with diethyl ether. Sodium azide was purchased from Fisher Scientific UK Limited, United Kindom. Dichloromethane (CH_2Cl_2), diethyl ether, dimethylformamide (DMF), and tetrahydrofuran (THF) were dried over molecular sieve 4 Å. Milli-Q water was used by purification with a Synergy (Millipore, France). Iscove's Modified Dulbecco Medium (IMDM) was obtained from Biochrom AG, Germany. Penicillin/streptomycin (Hoechst, Germany), sodium dodecyl sulfate (SDS) (MP Biochemicals, Germany), trypsin (Difco, Germany) and other organic solvents were used as received. Human umbilical vein endothelial cells (HUVECs) were isolated from human umbilical cord donated from Nordwest Krankenhaus (Nordwest Hospital, Germany). Acetonitrile and methanol were of HPLC grade from Merck, Germany. Glacial acetic acid (100%) was purchased from VWR International S.A.S., France.

Synthesis of PCL-*co*-PEG_{4000}-*co*-PCL Grafted with Nicotinic Acid and PABA. *Synthesis of Nicotinic Acid and PABA, 3-Butynyl Esters.* Prior to the Huisgen's 1,3-dipolar cycloaddition, azide pendants on polymer and terminal alkyne derivatives of model compounds are generally required for functionalization. Thus, but-3-ynyl nicotinate and but-3-ynyl-4-aminobenzoate were synthesized by esterification of acidic model compounds, nicotinic acid and PABA, and 3-butyn-1-ol using DCC and DMAP as catalysts as previously reported.[34] Briefly, known amounts of DCC and DMAP were dissolved in CH_2Cl_2 followed by the addition of an acidic compound. After stirring at room temperature for 30 min, 3-butyn-1-ol was introduced, and the reaction was conducted under argon atmosphere at room temperature for 24 h. The precipitate was filtered out, and the solvent was evaporated under reduced pressure. The crude product was purified by column chromatography on silica gel with the mobile of hexane (Hex), ethyle acetate (EtOAc), and CH_2Cl_2 (1:2:2) for but-3-ynyl nicotinate and Hex and EtOAc (1:1) for but-3-ynyl-4-aminobenzoate. The characteristics of the synthesized derivatives were assigned to their structures and agreed well with the previous report.[34]

But-3-ynyl nicotinate (1). ^{1}H NMR (DMSO-d_6): δ = 2.65 (m, 2H, CH_2C≡CH), 2.86 (t, J = 2.61 Hz, 1H, C≡C*H*), 4.35 (t, J = 6.48 Hz, 2H, COCH_2), 7.57 (m, 1H, pyridine), 8.28 (td, J = 7.96 Hz, 1H, pyridine), 8.80 (s, 1H, pyridine), 9.08 (s, 1H, pyridine).

But-3-ynyl-4-aminobenzoate (2). ^{1}H NMR ($CDCl_3$): δ = 2.04 (t, J = 2.5 Hz, 1H, C≡C*H*), 2.65 (td, J = 6.8, 2.6 Hz, 2H, CH_2C≡CH), 4.09 (s, 2H, NH_2), 4.38 (t, J = 6.8 Hz, 2H, COCH_2), 6.6 (d, J = 8.5 Hz, 2H, benzene), 7.88 (d, J = 8.5 Hz, 2H, benzene).

Synthesis of P(ClCL-ran-CL)-co-PEG_{4000}-co-P(ClCL-ran-CL) (P(ClCLCL)-PEG-P(ClCLCL)). The required amounts of ClCL and CL (Table 1) were added to the mixture of PEG_{4000} (0.8 g, 0.2 mmol) and $Sn(Oct)_2$ (81 mg, 0.2 mmol) in a dried round-bottom flask. The mixture was melted at room temperature under vacuum for 15 min. The reaction was initiated in an oil bath at 120 °C under argon atmosphere and conducted for 24 h. The copolymer was collected and dried under vacuum after precipitation of chloroform solution in cold Hex.

Synthesis of P(N_3CL-ran-CL)-co-PEG_{4000}-co-P(N_3CL-ran-CL) (P(N_3CLCL)-PEG-P(N_3CLCL)). The substitution reaction of chloride pendant by sodium azide was performed as reported elsewhere.[23] Briefly, 5 mL of copolymer solution in dry DMF

dx.doi.org/10.1021/bc100270m |*Bioconjugate Chem.* 2011, 22, 582–594

Table 1. Fed Composition of Copolymerization of ClCL and CL

copolymers	fed molar ratio of [ClCL]	fed weight (g)	
		ClCL	CL
0.10 P(ClCLCL)-PEG-P(ClCLCL)	0.10	0.29	2.05
0.20 P(ClCLCL)-PEG-P(ClCLCL)	0.20	0.59	1.82
0.30 P(ClCLCL)-PEG-P(ClCLCL)	0.30	0.89	1.60

containing 2.0 g of copolymer (1 equiv of chloride pendant) was stirred with sodium azide (1.02 equiv) overnight under argon atmosphere at room temperature in the dried flask. The mixture was dried under reduced pressure and redissolved in toluene to precipitate the coincident salt. The remaining precipitate was centrifuged at 4000 rpm for 15 min. The collected supernatant was evaporated under reduced pressure to collect the purified copolymer.

Typical Click Chemistry Reaction. Using the reaction of copper-catalyzed Huisgen's 1,3-dipolar cycloaddition, the 3-butynyl ester derivatives of nicotinic acid and PABA were grafted onto the P(N_3CLCL)-PEG-P(N_3CLCL) backbone at 0.10, 0.20, and 0.30 molar ratios based on caprolactone repeating units. The reaction was conducted according to our previous experiment.[34] Briefly, azide tethered amphiphilic copolymer solution (1.2 g, 1 equiv of azide) in 10 mL of dry THF was transferred into dried reaction flask followed by the ordered addition of butynyl ester derivative of model compound (1.5 equiv), CuI (0.2 equiv), and base (0.2 equiv). Under atmospheric argon, the reaction was stirred in a thermostated bath under temperature controlled at 40 °C. After 4 h reaction, the solution was precipitated in cold Hex and the collected copolymer was dried in a vacuum desiccator for another 24 h.

Polymer Characterization. *Typical Characterization Methods for Synthesis of Grafted Copolymers.* ^{1}H NMR spectra were recorded in $CDCl_3$ or DMSO-d_6 at 300 or 500 MHz in the FT mode with Bruker Avance 300 apparatus at 25 °C. Infrared spectra were recorded with Jasco FT-IR-4100 spectroscopy. Number- and weight-average molecular weights (M_n and M_w, respectively) were measured by a Waters 150-CV gel permeation chromatograph equipped with refractive index detector. THF was used as the mobile phase at a flow rate of 1 mL/min. Two columns of PLgel 10 μm mixed B were calibrated with polystyrene standards in the MW range 4490−1 112 000 g/mol.

Thermal Property Analysis by Differential Scanning Calorimetry (DSC) and Thermal Gravimetric Analysis (TGA). TGA was carried out with a TGA 7 Perkin-Elmer thermogravimetric analyzer at 10 °C/min. DSC was performed using a DSC 7 Perkin-Elmer differential scanning calorimeter calibrated with indium. Glass transition and melting temperatures (T_g and T_m, respectively) were measured according to running conditions: the sample was quenched to −80 °C, heated to 100 °C (first heating), cooled down to −80 °C, and heated again to 100 °C (second heating). Thermograms were recorded during the second heating cycle at 20 °C/min.

Formation of Nanoparticles. Fifty milligrams of grafted copolymer were dissolved in 5 mL of THF. The polymer solution was added dropwise to 8 mL of Milli-Q water under magnetic stirring (1000 rpm) at room temperature. The solvent was removed under reduced pressure. The final volume was adjusted by Milli-Q water to the initial volume. The nanoparticle suspension was filtered through a cellulose acetate membrane with a pore size of 0.45 μm to eliminate any aggregates. One milliliter of nanoparticle suspension was poured into 2 mL vials. After lyophilization for 48 h, the weight of the lyophilized powder was recorded. In the case of IBU-loaded nanoparticles, 10 mg of drug was initially added with the copolymers in the THF solution, and the nanoparticles were prepared as previously described.

Characterization of Nanoparticles. *Particle Size and Zeta Potential Analysis.* The average particle diameter and size distribution of particles were analyzed by photon correlation spectroscopy (PCS) using a Zetasizer 3000 HSA (Malvern, UK). The samples were measured after dilution with Milli-Q water. The surface charge of the nanoparticles was determined by zeta potential analysis with a Zetasizer 3000 HSA (Malvern, UK) after dilution in Milli-Q water. All measurements were performed with a HeNe laser at the wavelength of 633 nm, a 90° angle, and a temperature of 25 °C.

Cytotoxicity Testing of Nanoparticles. The cytotoxicity of grafted amphiphilic nanoparticles was evaluated by the MTT assay. HUVECs at passage 3−5 were cultured in IMDM solution supplemented with 1% penicillin/streptomycin, 2% glutamine, 3% bicarbonate solution, 15% FBS, and 0.1% fibroblast growth factor. A 50 μL of cells suspension at a density of 3×10^5 cells/mL was seeded in a 96-well plate and incubated at 37 °C in an atmosphere of 5% CO_2 for 24 h. Afterward, 50 μL of culture medium containing the nanoparticle dispersion was added to yield the final concentration of nanoparticles in the range 0.01−1.56 mg/mL, and the cells were then incubated for another 24 h. Subsequently, the cells were incubated with MTT solution (25 μL) for 24 h. After an SDS solution was added and incubated for 6 h to dissolve the metabolized formazan crystal, the absorbance of solution was measured and recorded at 560 and 620 nm. The difference in absorbance was calculated and expressed as % cell viability. The cells incubated with only medium were used as cell control and defined as 100% cell viability.

Drug Loading and Entrapment Efficiency Evaluation. The nanoparticle suspension was centrifugally filtered at 16 000 rpm for 10 min through Microcon Ultracel YM-30 tube (MW cutoff 30 000 Da) (Millipore, USA). The amount of drug in the filtrate was analyzed by HPLC. The lyophilized powder was dissolved in the mobile phase and ultrasonicated for 30 min. The precipitate was centrifuged at 16 000 rpm for 10 min. The supernatant was collected for quantitative analysis by HPLC. The amount of drug entrapped in nanoparticles was calculated from the different amounts of drug found in the lyophilized powder and that in the filtrate. Drug loading (% DL) and entrapment efficiency (% EE) were calculated according to eqs 1 and 2 as follows:

$$\%\ \text{Drug Loading} = \frac{\text{Amount of drug in lyophilized nanoparticles}}{\text{Amount of lyophilized nanoparticles}} \times 100 \quad (1)$$

dx.doi.org/10.1021/bc100270m |*Bioconjugate Chem.* 2011, 22, 582–594

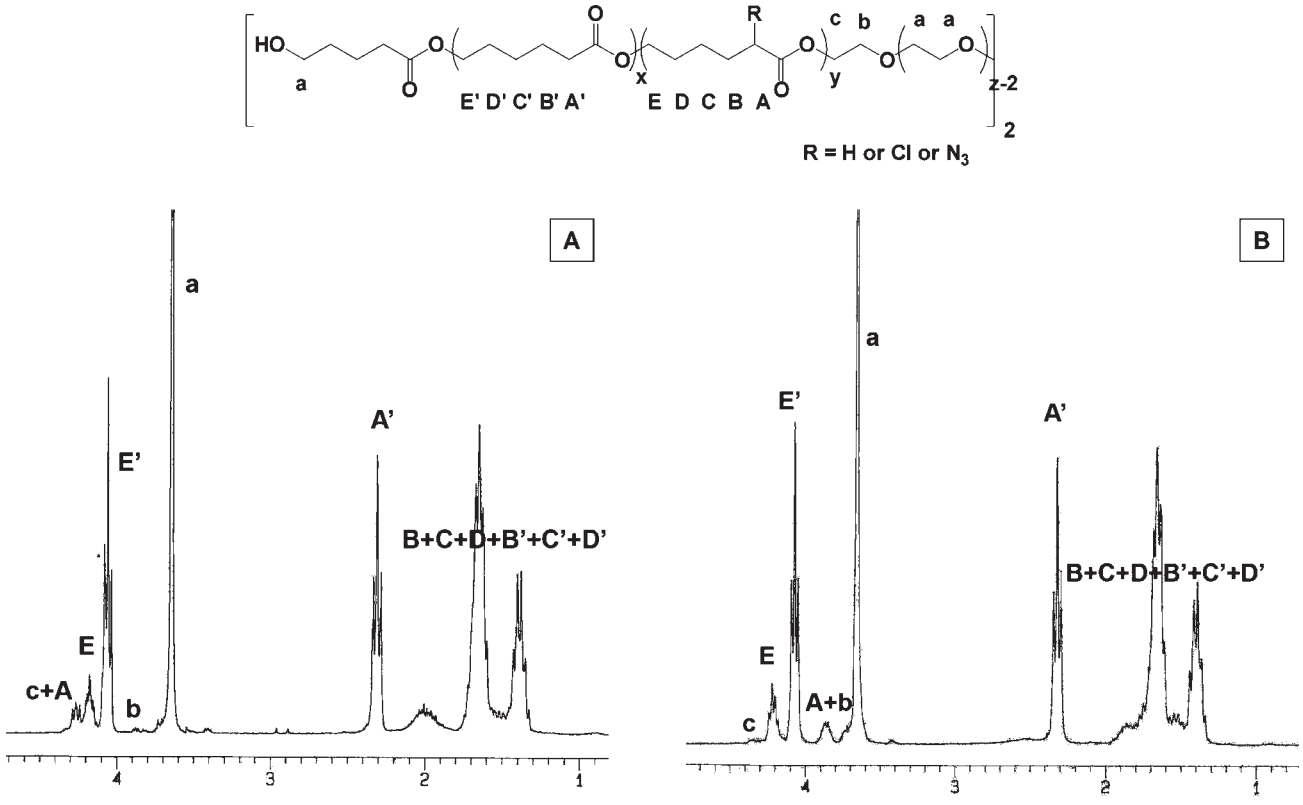


Figure 1. ^{1}H NMR spectra of P(ClCLCL)-PEG-P(ClCLCL) (A) and P(N_3CLCL)-PEG-P(N_3CLCL) (B), respectively.

$$\%\ \text{Entrapment Efficiency} = \frac{\text{Amount of drug in lyophilized nanoparticles}}{\text{Initial amount of drug added}} \times 100 \quad (2)$$

HPLC Measurement for Quantitative Analysis of Drug Loaded. IBU was quantitatively analyzed by HPLC (Shimadzu, Japan) consisting of an autoinjector SIL-10A (Shimadzu), a pump (Shimadzu LC-10AD), and a UV detector (Shimadzu SPD-10AV). This drug was eluted through a reverse-phase Hypersil ODS column, 5 μm particle size, 250 × 4.6 mm (Thermo Scientific, USA) using the mixture of methanol: water: acetonitrile: acetic acid (35:55:10:1) as a mobile phase at a flow rate of 1.4 mL/min. The peak area was calculated at wavelength of 264 nm using a calibration curve over the range 2.5−40 μg/mL.

Statistical Analysis. Results were recorded as mean ± SD of at least three measurements. The one way ANOVA with the Scheffe test applied post hoc for paired comparisons was performed to compare multiple groups. All analyses were performed using the SPSS program (*SPSS 13.0* for Windows), and differences were considered to be significant at a level of p-value < 0.05.

RESULTS AND DISCUSSION

Synthesis of P(ClCL-*ran*-CL)-*co*-PEG$_{4000}$-*co*-P(ClCL-*ran*-CL) (P(ClCLCL)-PEG-P(ClCLCL)). In order to graft the desired compounds on the PCL-PEG-PCL backbone, the chloride pending PCL-PEG-PCL was initially fabricated at the various ratios and further converted to the azide pending copolymer. P(ClCLCL)-PEG-P(ClCLCL) at molar ratios of 0.10, 0.20, and 0.30 relative to caproyl unit was successfully fabricated by ring-opening polymerization using PEG$_{4000}$ as an initiator and Sn(Oct)$_2$ as a catalyst (Scheme 1). The yield of all copolymers was higher than 80%. The M_n of the synthesized copolymers was calculated from the NMR spectrum (Figure 1A) according to eqs 3−6 as previously reported with some modification.[5,35] The molar ratios of ClCL units with respect to caproyl unit (F^a_{ClCL}) and polymer chain (F^b_{ClCL}) were calculated using eqs 7 and 8, respectively. All molecular parameters are listed in Table 2.

$$M_{n,\text{NMR}} = M_{n,CL} + M_{n,CICL} + M_{n,PEG} = 114x + 148.5y + 44z \quad (3)$$

$$\frac{2(x-1)}{I_{A'}} = \frac{4}{I_b} \quad (4)$$

$$\frac{3(y-1)+4}{(I_{A+cEE'} - I_{A'})} = \frac{4}{I_b} \quad (5)$$

$$\frac{4(z-2)+4}{I_a} = \frac{4}{I_b} \quad (6)$$

$$F^a_{\text{ClCL}} = \frac{\frac{1}{3}[I_{A+cEE'} - I_{A'} - I_b]}{\frac{1}{3}[I_{A+cEE'} - I_{A'} - I_b] + \frac{1}{2} I_{A'}} \quad (7)$$

dx.doi.org/10.1021/bc100270m |*Bioconjugate Chem.* 2011, 22, 582–594

Scheme 1. Typical Procedure for Grafting of Heterocyclic and Aromatic Model Drugs along PCL-PEG-PCL

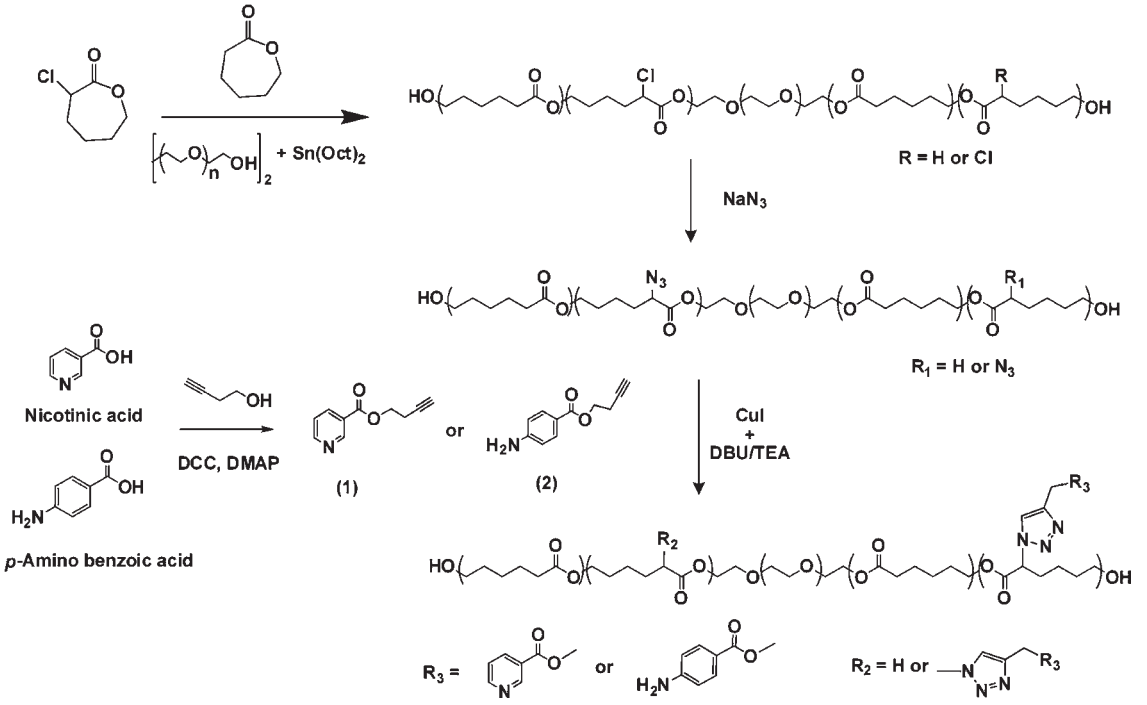


Table 2. Molecular Characteristic Results of P(ClCLCL)-PEG-P(ClCLCL) and P(N_3CLCL)-PEG-P(N_3CLCL) Copolymers

copolymers	F^a_{C1CL} or $F^a_{N_3CL}$		F^b_{ClCL} or $F^b_{N_3CL}$		% yield	$M_{n,theo}$[d]	$M_{n,NMR}$[c]	$M_{n,GPC}$[e]	M_w/M_n[e]	T_g (°C)	T_m (°C)
	calculated[c]	theoretical	calculated[c]	theoretical							
P(C1CLCL)-PEG-P(C1CLCL)											
0.10P(C1CLCL)-PEG-P(C1CLCL)	0.07	0.10	0.04	0.05	88.66	15745	16300	7437	1.8	-[f]	34
0.20P(C1CLCL)-PEG-P(C1CLCL)	0.17	0.20	0.09	0.10	83.62	16090	15800	6466	2.0	−59	31
0.30P(C1CLCL)-PEG-P(C1CLCL)	0.25	0.30	0.14	0.15	87.64	16435	15000	6748	1.8	−55	30
P(N_3CLCL)-PEG-P(N_3CLCL)											
0.10P(N_3CLCL)-PEG-P(N_3CLCL)	0.12	0.10	0.06	0.05	84.14	15810	15458	7014	1.8	-[f]	42
0.20P(N_3CLCL)-PEG-P(N_3CLCL)	0.21	0.20	0.11	0.10	78.78	16200	14200	5612	1.9	−51	42
0.30P(N_3CLCL)-PEG-P(N_3CLCL)	0.30	0.30	0.15	0.15	73.33	16630	12160	5721	1.8	−52	38

[a] Molar ratio of ClCL or N_3CL units calculated based on caproyl unit. [b] Molar ratio of ClCL or N_3CL units calculated based on polymer backbone. [c] Determined by ^{1}H NMR spectroscopy. [d] $M_{n,theo} = \{([CL]/[PEG_{4000}]) \times 114\} + \{([ClCL \text{ or } N_3CL]/[PEG_{4000}]) \times M_{ClCL \text{ or } N3CL}\} + M_{n,PEG4000}$ (where [CL] and [ClCL or N_3CL] are the molar concentration of CL and ClCL or N_3CL, respectively. [PEG_{4000}] is the molar concentration of PEG_{4000} (initiator), $M_{ClCL \text{ or } N3CL}$ is the molecular weight of ClCL or N_3CL, respectively, and $M_{n,PEG4000}$ is the number-average molecular weight of PEG_{4000}). [e] Determined by GPC. [f] No peak observed.

$$F^b_{ClCL} = \frac{\frac{1}{3}[I_{A+cEE'} - I_{A'} - I_b]}{\frac{1}{3}[I_{A+cEE'} - I_{A'} - I_b] + \frac{1}{2}I_{A'} + \frac{1}{4}I_a} \quad (8)$$

where $I_{A'}$ is the integral of methylene proton of CL unit at 2.30 ppm, $I_{A+cEE'}$ is the integral of protons of ClCL unit in the range 4.00−4.25 ppm and methylene proton in PEG end unit at 4.23 ppm, I_a is the integral of methylene proton in PEG unit at 3.65 ppm, I_b is the integral of methylene proton in PEG end unit at 3.90 ppm, and x, y, and z are the corresponding repeating number of CL, ClCL, and PEG units, respectively.

From Table 2, the $M_{n,NMR}$ values of P(ClCLCL)-PEG-P(ClCLCL) were in agreement with the theoretical values. However, the $M_{n,GPC}$ values of the copolymers from GPC results were less than those from NMR. It could be attributed to the change in hydrodynamic volume of P(ClCLCL)-PEG-P(ClCLCL) bearing hydrophilic and hydrophobic segments. Another reasonable explanation is that the molecular weight of this amphiphilic copolymer was calculated relative to the hydrophobic poly(styrene) standard whose intrinsic viscosity is tremendously different from that of this copolymer.[36,37] However, the values of the molar ratios of substituted chloride (F^a_{ClCL} and F^b_{ClCL}) were consistent with the theoretical values (Table 2).

Synthesis of P(N_3CL-*ran*-CL)-*co*-PEG_{4000}-*co*-P(N_3CL-*ran*-CL) (P(N_3CLCL)-PEG-P(N_3CLCL)). P(N_3CLCL)-PEG-P(N_3CLCL) was obtained by the substitution reaction between P(ClCLCL)-PEG-P(ClCLCL) and sodium azide at room temperature prior to

dx.doi.org/10.1021/bc100270m |*Bioconjugate Chem.* 2011, 22, 582–594

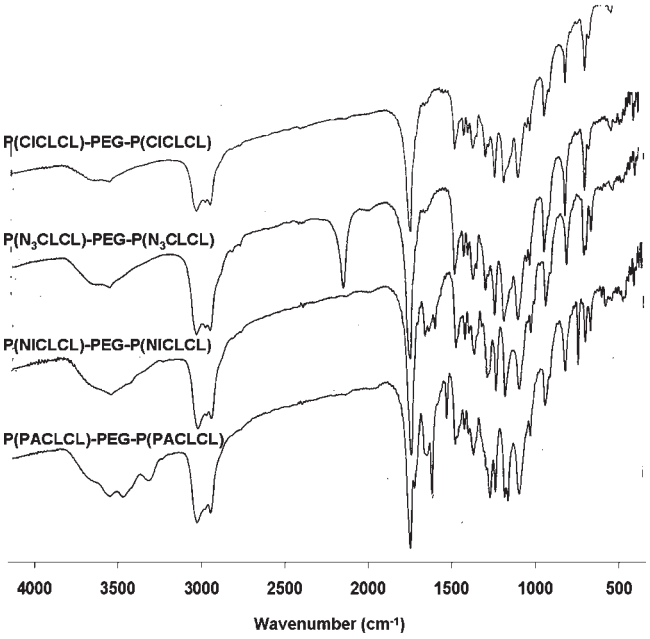


Figure 2. FT-IR spectra of P(NICLCL)-PEG-P(NICLCL) in the presence of DBU and P(PACLCL)-PEG-P(PACLCL) in the presence of TEA in comparison with P(ClCLCL)-PEG-P(ClCLCL) and P(N_3CLCL)-PEG-P(N_3CLCL).

grafting the selected molecules (Scheme 1). The conversion was complete after overnight reaction. As monitored by FT-IR, the characteristic peak of azide at 2100 cm^{-1} was apparent (Figure 2). ^{1}H NMR spectrum (Figure 1B) confirmed the complete conversion as seen by the entire disappearance of methyne proton peak (C*H*Cl) at 4.25 ppm and the presence of azide peak (C*H*N_3) at 3.85 ppm. The M_n of P(N_3CLCL)-PEG-P(N_3CLCL) was calculated from the NMR spectrum (Figure 1B) according to eqs 9−12 as previously reported with some modification.[5,23,35] The molar ratios relative to caproyl unit ($F^a_{N_3CL}$) and polymer backbone ($F^b_{N_3CL}$) were calculated according to eqs 13 and 14, respectively. The other molecular parameters are illustrated in Table 2.

$$M_{n,NMR} = M_{n,CL} + M_{n,N_3CL} + M_{n,PEG} = 114x + 155y + 44z \quad (9)$$

$$\frac{2(x-1)}{I_{A'}} = \frac{4}{I_c} \quad (10)$$

$$\frac{(y-1)+4}{I_{A+b}} = \frac{4}{I_c} \quad (11)$$

$$\frac{4(z-2)+4}{I_a} = \frac{4}{I_c} \quad (12)$$

$$F^a_{N_3CL} = \frac{(I_{A+b} - I_c)}{(I_{A+b} - I_c) + \frac{1}{2} I_{A'}} \quad (13)$$

$$F^b_{N_3CL} = \frac{(I_{A+b} - I_c)}{(I_{A+b} - I_c) + \frac{1}{2} I_{A'} + \frac{1}{4} I_a} \quad (14)$$

where $I_{A'}$ is the integral of methylene proton of CL unit at 2.30 ppm, I_{A+b} is the integral of methyne proton of N_3CL unit at 3.85 ppm and methylene proton in PEG end unit at 3.90 ppm, I_a is the integral of methylene proton in PEG unit at 3.65 ppm, I_c is the integral of methylene proton in PEG end unit at 4.23 ppm, and x, y, and z are the corresponding repeating number of CL, N_3CL, and PEG units, respectively.

The $M_{n,NMR}$ values of P(N_3CLCL)-PEG-P(N_3CLCL) were in agreement with the theoretical values. However, $M_{n,GPC}$ was lower than $M_{n,NMR}$ as previously discussed for P(ClCLCL)-PEG-P(ClCLCL). The molecular weight of P(N_3CLCL)-PEG-P(N_3CLCL) was decreased as compared to P(ClCLCL)-PEG-P(ClCLCL) due to a consequence of the hydrodynamic volume change in the substitution of chloride by azide.[23] The molar ratios of substituted azide ($F^a_{N_3CL}$ and $F^b_{N_3CL}$) agreed well with the theoretical values. The % conversion of chloride to azide was almost 100% indicating the completeness and feasibility of the reaction.

Grafting of Model Compounds along P(N_3CL-*ran*-CL)-*co*-PEG$_{4000}$-*co*-P(N_3CL-*ran*-CL) by Click Reaction. The 3-butynyl ester derivatives of two model compounds (nicotinic acid and PABA) were attached onto the backbone through copper-catalyzed Huisgen's 1,3-dipolar cycloaddition reaction using CuI and DBU as catalysts at 40 °C for 4 h (Scheme 1). The FT-IR spectra confirmed the conversion as the azide peak at 2100 cm^{-1} completely disappeared, while the presence of triazole peak at 1610 cm^{-1} was observed (Figure 2). Additionally, the characteristic peak of azide (C*H*N_3) at 3.85 ppm in NMR spectrum also disappeared and the methyne proton peak of triazole ring was observed at 7.70 ppm (Figure 3). From the NMR spectrum, the molar ratios of the grafting model compound based on the caproyl unit and polymer chain ($F^a_{grafted\text{-}CL}$ and $F^b_{grafted\text{-}CL}$, respectively) were calculated from the integration of the methyne proton of the grafted CL unit at 5.30 ppm (I_A, Figure 3) and the methylene proton of CL unit at 2.30 ppm (I_D, Figure 3) according to eqs 15 and 16, respectively.

$$F^a_{grafted\text{-}CL} = \frac{I_A}{\frac{1}{2} I_D + I_A} \quad (15)$$

$$F^b_{grafted\text{-}CL} = \frac{I_A}{\frac{1}{2} I_D + I_A + \frac{1}{4} I_H} \quad (16)$$

The calculation of grafting efficiency was made by the molar ratios of N_3CL unit and grafting unit using the characteristic methyne protons close to azide at 3.85 ppm and triazole ring at 5.30 ppm in the NMR spectra, respectively. Under this condition, the grafting efficiency of all copolymers was in the range 73−85%, depending on the type and amount of grafting compounds. In addition, the grafting molar ratios ($F^a_{grafted\text{-}CL}$ and $F^b_{grafted\text{-}CL}$) were in agreement with the theoretical values (Table 3).

Nicotinic Acid (P(NICLCL)-PEG-P(NICLCL)). The grafting of nicotinic acid (heterocyclic model compound) also was achieved. In addition to the apparent characteristic peak of triazole (Figure 3A), the peak of methyne proton close to azide at 3.85 ppm disappeared totally, and a peak at 5.30 ppm corresponding to the peak of methyne proton of caproyl unit adjacent to triazole ring was observed. The peaks at 7.45, 8.30, 8.70, and 9.25 ppm were assigned as the characteristic peaks of the proton in the pyridine ring of the

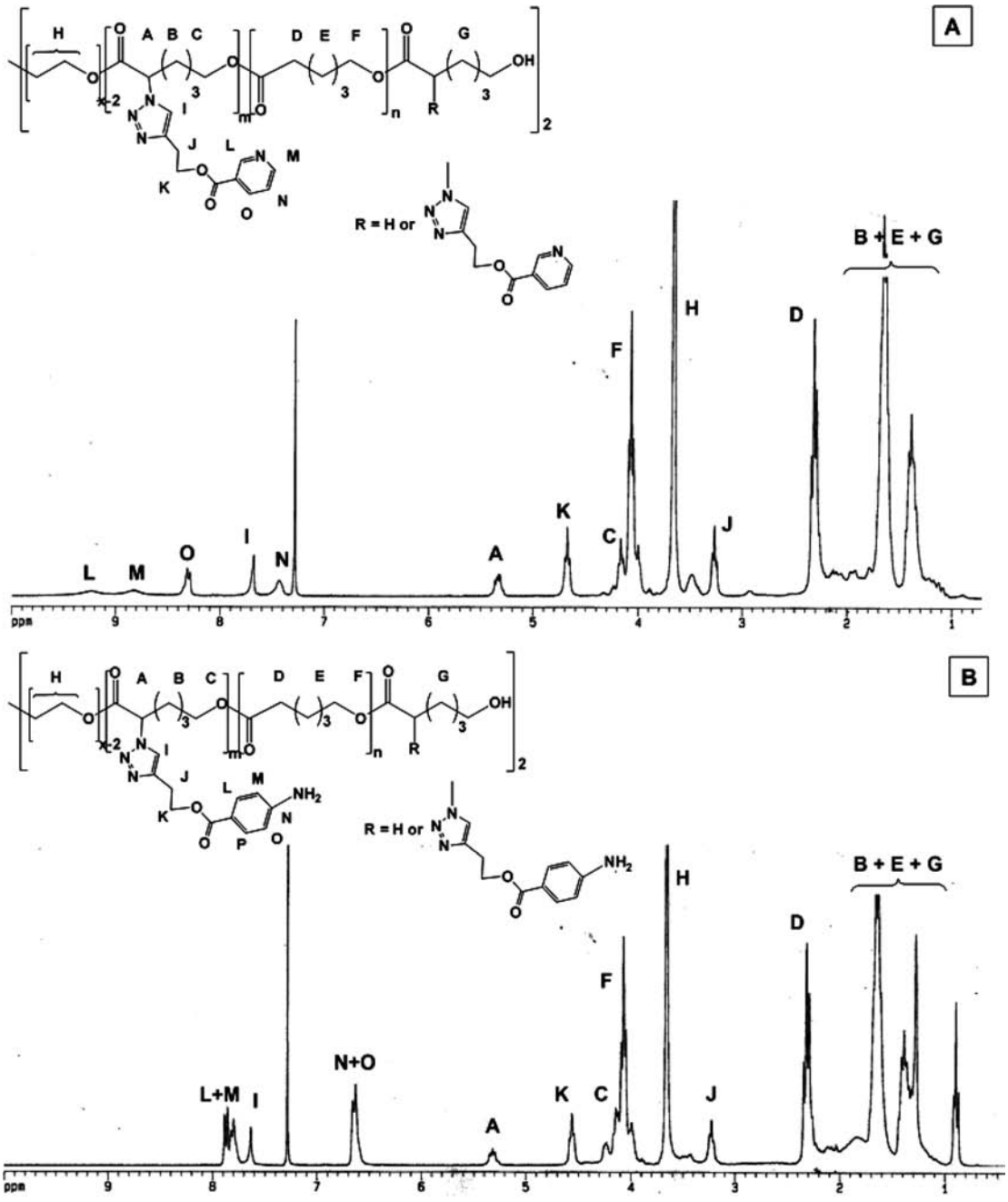


Figure 3. ^{1}H NMR spectra of P(NICLCL)-PEG-P(NICLCL) (A) and P(PACLCL)-PEG-P(PACLCL) (B) using DBU and TEA as base, respectively.

nicotinic acid molecule. Moreover, C═C stretching at 1590 cm^{-1} and C═N stretching at 1625 cm^{-1} were observed and contributed to the overlapping between the triazole and the pyridine ring of nicotinic acid (Figure 2). From $M_{n,GPC}$ values (Table 3), the molecular weight of the grafted copolymers was increased as compared to those of P(N_3CLCL)-PEG-P(N_3CLCL) (Table 2). The molecular weight distribution was narrower than those of the original polymers. The GPC chromatograms of most grafted copolymers (Figure 4A) revealed a unimodal peak indicating no degradation of the polymer chain. However, the GPC chromatogram of **0.30**P(NICLCL)-PEG-P(NICLCL) showed a small shoulder peak which may suggest slight degradation.

PABA (P(PACLCL)-PEG-P(PACLCL)). On the basis of our previous study,[34] it was notable that the aniline group induces the chain degradation under this condition, particularly that in presence of the strong base, DBU, leading to an occurrence of intra- and intermolecular transesterifications. In addition, in the case of hydroxyl group of propargyl alcohol,[23] the resulting grafted copolymers underwent a chain degradation when using DBU as base in the reaction. The extent of degradation appeared to be less with the use of triethylamine (TEA) instead of DBU. Therefore, TEA was used in this study for the grafting of PABA. Similarly to the grafting of nicotinic acid, the reaction was complete after 4 h under this condition. This successful approach could be visualized by the presence of the characteristic methyne proton of the triazole ring at 7.65 ppm and the benzene ring of PABA at 6.65 and 7.85 ppm, respectively (Figure 3B). In addition, the FT-IR spectrum showed the peaks of N−H

dx.doi.org/10.1021/bc100270m |*Bioconjugate Chem.* 2011, 22, 582–594

Table 3. Molecular Characteristic Results of P(NICLCL)-PEG-P(NICLCL) and P(PACLCL)-PEG-P(PACLCL) Copolymers and Nanoparticles

grafted copolymers[a]	$F^b_{\text{grafted-CL}}$ calculated[d]	$F^b_{\text{grafted-CL}}$ theoretical	$F^c_{\text{grafted-CL}}$ calculated[d]	$F^c_{\text{grafted-CL}}$ theoretical	$M^e_{n,GPC}$	M_n/M_w[e]	T_g(°C)	T_m (°C)	size (nm)	polydispersity index (PDI)	zeta potential (mV)
P(NICLCL)-PEG-P(NICLCL)											
0.10P(NICLCL)-PEG-P(NICLCL)	0.09	0.10	0.04	0.05	11981	1.6	−50	40	77 ± 10	0.192 ± 0.032	−9.6 ± 1.3
0.20P(NICLCL)-PEG-P(NICLCL)	0.17	0.20	0.09	0.10	6435	1.7	−47	39	82 ± 8	0.104 ± 0.024	−5.9 ± 1.4
0.30P(NICLCL)-PEG-P(NICLCL)	0.25	0.30	0.12	0.15	5807	1.6	−43	32	120 ± 25	0.099 ± 0.023	−17.3 ± 2.0
P(PACLCL)-PEG-P(PACLCL)											
0.10P(PACLCL)-PEG-P(PACLCL)	0.08	0.10	0.04	0.05	10211	1.5	−34	37	194 ± 37	0.208 ± 0.075	−12.3 ± 1.5
0.20P(PACLCL)-PEG-P(PACLCL)	0.16	0.20	0.09	0.10	9948	1.7	−25	[f]	129 ± 2	0.276 ± 0.006	−11.8 ± 1.4
0.30P(PACLCL)-PEG-P(PACLCL)	0.28	0.30	0.13	0.15	9269	1.4	−22	[f]	148 ± 27	0.210 ± 0.009	−10.8 ± 0.8

[a] Abbreviations: NI = nicotinic acid, PA = PABA. [b] Molar ratio of grafting unit calculated based on carproyl unit. [c] Molar ratio of grafting unit calculated based on polymer backbone. [d] Determined by ^{1}H NMR spectroscopy. [e] Determined by GPC. [f] No peak observed.

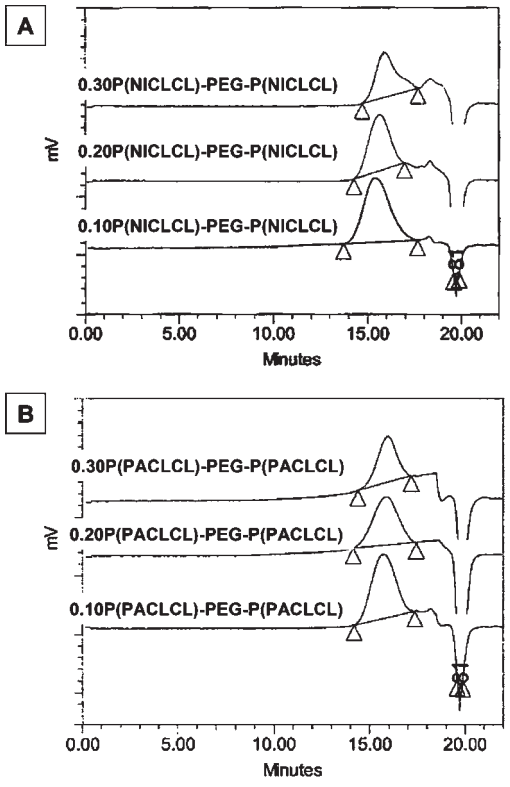


Figure 4. GPC chromatograms of P(NICLCL)-PEG-P(NICLCL) (A) using DBU as base and P(PACLCL)-PEG-P(PACLCL) (B) using TEA as base, respectively.

stretching at 3400 cm^{-1} and C═O stretching at 1725 cm^{-1} of PABA. The peaks of C═N stretching at 1626 cm^{-1} of the triazole ring and C═O stretching at 1725 cm^{-1} of the polyester polymer were also observed (Figure 2). At 0.10 and 0.20 molar ratios, the PABA grafted copolymers showed no degradation similar to the nicotinic acid grafted copolymers as supported by increasing $M_{n,GPC}$ values and narrowing molecular weight distribution (Table 3). Unlike the nicotinic acid grafted copolymers at 0.30 molar ratios, the PABA grafted copolymers showed no degradation as seen from the unimodal peak in the GPC chromatogram (Figure 4B).

Thermal Properties of Copolymers and Grafted Copolymers. The thermal properties of the grafted copolymers were evaluated by DSC and TGA because these properties may affect the rate of drug release from the polymeric carriers. The T_g and T_m values of all copolymers are illustrated in Tables 2 and 3. As shown in Table 2, the T_g values of P(N_3CLCL)-PEG-P(N_3CLCL) and P(ClCLCL)-PEG-P(ClCLCL) tended to increase as compared to those of the unsubstituted copolymer (PCL-PEG-PCL, $T_g \approx -60$ °C[38]). In the case of T_m, both chloride- and azide-substituted copolymers revealed a lower T_m than that of the unsubstituted material (PCL-PEG-PCL, $T_m \approx 55$ °C [38]). With increasing percent substitution, a trend in reduction of T_m values was observed. However, P(N_3CLCL)-PEG-P(N_3CLCL) provided a higher melting temperature than those of P(ClCLCL)-PEG-P(ClCLCL) at all ratios.

In the case of grafting nicotinic acid (heterocyclic model) and PABA (aromatic model) (Table 3), T_g was also recorded for all grafted copolymers. Both grafting model compounds showed an effect on thermal properties. Particularly with the grafting PABA, this effect was more pronounced than the grafting with nicotinic acid at all ratios. The heterocyclic compound yielded a lower T_g than the aromatic model, and T_g increased when the number of grafting units increased in both cases. In the case of the melting point, T_m of the nicotinic acid grafted copolymers decreased gradually with increasing number of grafting units. On the contrary, at 0.20 and 0.30 molar ratios of PABA, it did not yield a T_m indicating that PABA had more influence on crystallinity of the polymer backbone than the nicotinic acid at the same ratio. From the results, it can be concluded that grafting heterocyclic and aromatic models reduced the crystallinity of polymer. This might

dx.doi.org/10.1021/bc100270m |*Bioconjugate Chem.* 2011, 22, 582–594

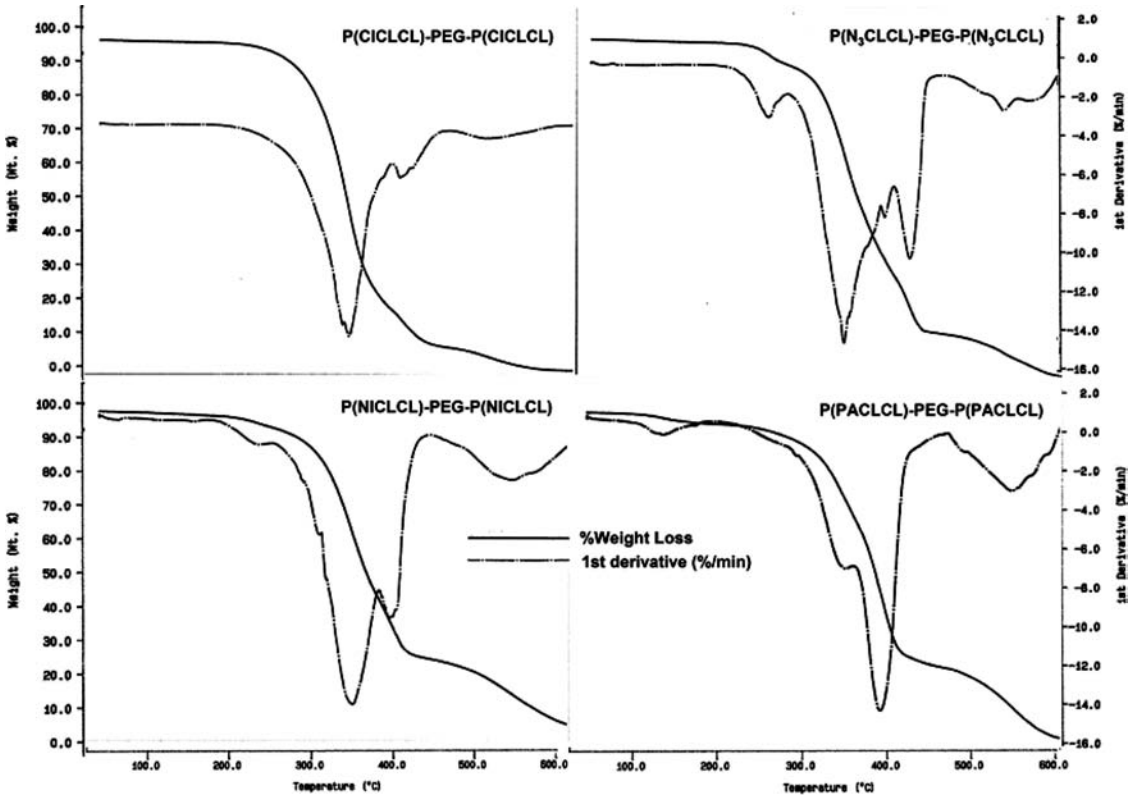


Figure 5. Thermal gravimetric diagrams of P(ClCLCL)-PEG-P(ClCLCL), P(N_3CLCL)-PEG-P(N_3CLCL), and P(NICLCL)-PEG-P(NICLCL) using DBU as base, and P(PACLCL)-PEG-P(PACLCL) using TEA as base, respectively.

be due to the fact that the sterically hindered molecule interrupted the orientation of the polymer chain and thus restricted the crystallization of polymer chain. The reduction of the crystallinity may affect the permeability of drug through the matrix of copolymer when forming the micro- and nanoparticulate systems.

The thermal stability of the grafted amphiphilic copolymers depends on the intrinsic properties of the materials, which is essential for practical use. To investigate the thermal degradation of the grafted copolymers, a TGA analysis was performed (Figure 5). It was found that P(ClCLCL)-PEG-P(ClCLCL) initially underwent thermal degradation at 250 °C similar to the degradation of poly(ClCL)[39] and had the inflection point at around 330 °C. The main degradation pattern was similar to PCL-PEG-PCL as previously reported by Gou et al.[1] However, a small peak of degradation at 400 °C was observed which may be attributed to the decomposition of the PEG segment at this high temperature.[37] Therefore, ClCL and CL were randomly copolymerized, since only one inflection point was detected in the main degradation curve. In the case of P(N_3CLCL)-PEG-P(N_3CLCL), the first step was attributed to the initial rupture of azide (N−N_2) starting at the temperature around 200 °C.[40,41] The last two steps of thermal decomposition were observed similar to those of P(ClCLCL)-PEG-P(ClCLCL). According to the thermograms of heterocyclic and aromatic grafted PCL-PEG-PCL, the small degradation peaks were observed at 240 °C for P(NICLCL)-PEG-P(NICLCL) and 140 °C for P(PACLCL)-PEG-P(PACLCL) with respect to about 9.4% and 6.5%, respectively. These results were consistent with the molar ratio of grafting unit along the whole polymer backbone. The first step degradation was supposed to be a consequence of the decomposition of grafting units. The main degradation peaks of grafted copolymers were observed at different temperatures, which were around 340 and 490 °C for P(NICLCL)-PEG-P(NICLCL) and P(PACLCL)-PEG-P(PACLCL), respectively, depending on the composition of copolymer. The last pattern of thermal degradation was typically detected corresponding to the degradation of PEG segment. However, further details are required to ascertain the underlying mechanism.

From these results, it can be concluded that grafting could change the polymer backbone from the semicrystalline to amorphous form, thus altering the thermal properties. With an increase in the molar ratios of grafting units, the copolymers became more amorphous. In addition, the grafting molecules affected the thermal stability of the copolymer.

Nanoparticle Formation with Grafted Amphiphilic Copolymers. Nanoparticles were prepared from heterocyclic and aromatic models grafted copolymers, and the effect of the different properties of the grafted copolymer on nanoparticle formation was studied. It was found that all nanoparticles prepared from P(NICLCL)-PEG-P(NICLCL) were significantly smaller than those from P(PACLCL)-PEG-P(PACLCL) (Table 3 and Figure 6). With both grafting compounds, the particle size of nanoparticles increased with increasing amounts of grafting untis (p-value < 0.05) except for **0.10**P(PACLCL)-PEG-P(PACLCL), whereas the size distribution tended to be smaller for P(NICLCL)-PEG-P(NICLCL) (p-value > 0.05). Indeed, it has been stated in general that the hydrophobic domain of amphiphilic copolymers has an effect on the formation of nanoparticles and micelles.[42−44] As the hydrophobic portion of the polymer chain increased, the size of particles became larger. In this study, the grafting heterocyclic ring of nicotinic acid

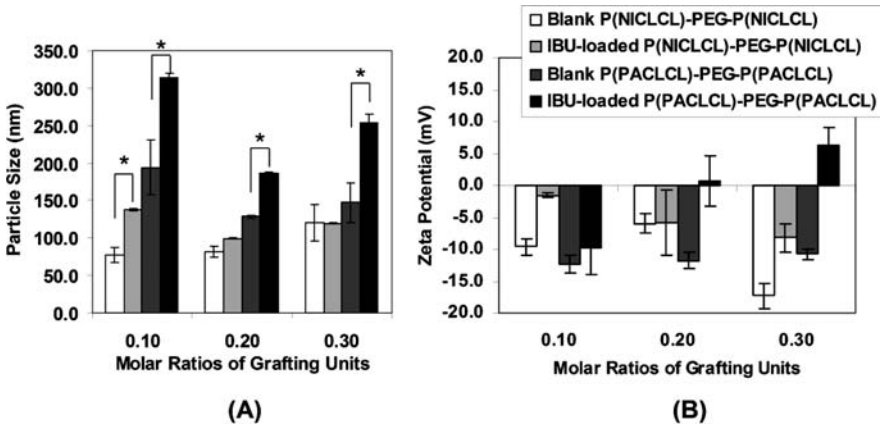


Figure 6. Particle size (A) and zeta potential (B) of blank and IBU-loaded nanoparticles (*p-value < 0.05).

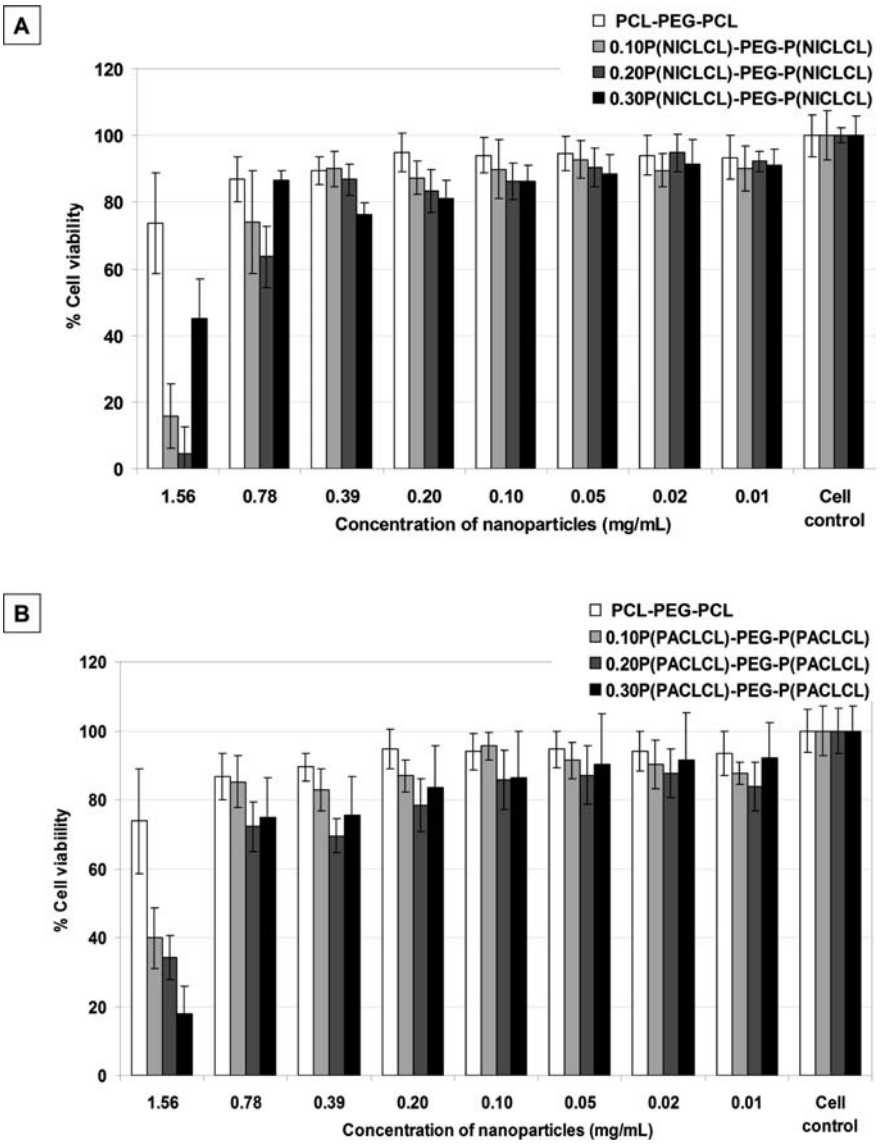


Figure 7. Cytotoxicity results of P(NICLCL)-PEG-P(NICLCL) and P(PACLCL)-PEG-P(PACLCL) nanoparticles at all molar ratios of grafting units compared to PCL-PEG-PCL nanoparticles.

and aromatic ring of PABA increased hydrophobicity of the polymer chain. In the case of **0.10**P(PACLCL)-PEG-P(PACLCL), the larger particles were observed owing to secondary aggregation. It has been stated that the secondary aggregates were a

dx.doi.org/10.1021/bc100270m |*Bioconjugate Chem.* 2011, 22, 582–594

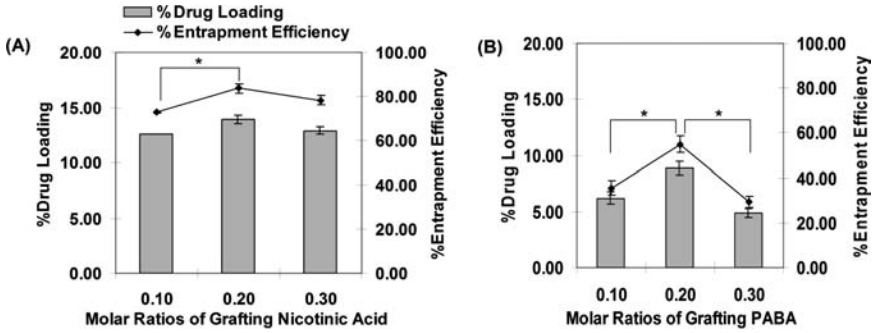


Figure 8. % Drug loading (column) and % entrapment efficiency (diamond) after incorporation with IBU into P(NICLCL)-PEG-P(NICLCL) (A) and P(PACLCL)-PEG-P(PACLCL) (B) nanoparticles (*p-value < 0.05).

consequence of hydrophobic−hydrophobic or van der Waals interactions between exposed cores from hydrophobic fragments of randomly grafted copolymer. Once the exposed cores are in close contact with water, they aggregate to large particles.[45,46] This could be confirmed by the bimodal peak observed in the PCS size distribution curve based on volume, whereas a unimodal peak was observed in the PCS size distribution curve based on intensity. The particle size shown in Table 3 was based on the intensity of the scattering light; therefore, the particle size of **0.10**P(PACLCL)-PEG-P(PACLCL) was the average diameter of two groups referring to individual nanoparticles and the secondary aggregates.

Considering the surface charge of nanoparticles (Table 3 and Figure 6), all nanoparticles of grafted copolymers showed more negative charge on their surface compared to the PCL-PEG-PCL nanoparticles which had a charge of almost zero (data not shown). This could be due to some grafted material present on the outer surface of the nanoparticles.

Cytotoxicity of Nanoparticles. To ascertain the safety of the grafted copolymers, all grafted copolymers were tested for their cytotoxicity using HUVECs. In order to avoid the use of organic solvents, the self-assembled nanoparticles were prepared and tested for their toxicity. These results are presented in Figure 7. It was observed that the PCL-PEG-PCL nanoparticles were toxic to HUVECs at the concentration of 1.56 mg/mL. The cytotoxic concentrations of **0.10**P(NICLCL)-PEG-P(NICLCL) and **0.10**P(PACLCL)-PEG-P(PACLCL) nanoparticles were found at 0.78 and 1.56 mg/mL, respectively. The increasing molar ratios of grafting nicotinic acid and PABA decreased the toxic concentration. The percent cell viability of **0.30**P(NICLCL)-PEG-P(NICLCL) at 0.78 mg/mL was higher than that at 0.39 mg/mL probably due to the variations in cells. From the results, it can be deduced that **0.10**P(PACLCL)-PEG-P(PACLCL) nanoparticles showed a similar toxicity compared to the PCL-PEG-PCL nanoparticles, whereas **0.10**P(NICLCL)-PEG-P-(NICLCL) nanoparticles showed a higher toxicity to HUVECs. In addition, the toxicity of the grafted nanoparticles increased when the molar ratios of grafting units increased.

IBU-Loaded Grafted Amphiphilic Nanoparticles. As stated earlier, the different structure between heterocyclic and aromatic models may affect the drug entrapment efficacy of the nanoparticles. In the present study, IBU was chosen as a model drug to investigate the effect of different structures and amount of grafting compounds on the loading efficiency of these nanoparticles. After encapsulation of drug in nanoparticles, the particle sizes of all grafted nanoparticles became larger as compared to the blank nanoparticles except for **0.30**P(NICLCL)-PEG-P(NICLCL) nanoparticles, for which the change in particle size was not significant (p-value > 0.05) (Figure 6A).

Concerning the efficiency of these carriers (Figure 8), the percentages of drug loading (% DL) and drug-entrapment (% EE) were evaluated. At all ratios of P(NICLCL)-PEG-P(NICLCL), the amount of IBU loaded into the nanoparticles was significantly higher than that into the nanoparticles prepared from P(PACLCL)-PEG-P(PACLCL) (p-value < 0.05). This result could be explained by the interaction between drug and grafting compounds of polymer. As mentioned previously, both nicotinic acid and PABA possibly interact with loaded drug by either $\pi-\pi$ stacking interaction or hydrogen bonding. In the case of $\pi-\pi$ stacking interaction from the aromatic ring, the extent of electron delocalization in the aromatic ring is in the following order: aniline of PABA > benzene of IBU > pyridine of nicotinic acid. The amino group of PABA mesomerically donates electrons to benzene ring, which is more predominant than electron withdrawal by the inductive effect of the nitrogen atom. Meanwhile, the nitrogen atom in the pyridine ring of nicotinic acid profoundly withdraws electrons leading to the localization of the electron in the pyridine ring and then showing a stronger basic effect. According to this fact, this $\pi-\pi$ stacking interaction in terms of electron charge transfer may be slightly involved because the benzene ring of IBU acts as an electron donor to the pyridine ring of nicotinic acid but as an electron acceptor for the aniline ring of PABA. Finally, the benzene ring of IBU can likely be in contact in planar formation with the aromatic ring of each compound.[47] In the case of hydrogen bonding, a hydroxyl group of carboxylic acid of IBU is more active than a carbonyl group due to the electron resonance between both groups of carboxylic acid of IBU. Thus, the carboxylic acid of IBU acts as a hydrogen bond donor rather than as an acceptor. By comparison of the pyridine ring of nicotinic acid and the aniline group of PABA with regard to the carboxylic acid of IBU, the hydrogen bonding thus predominantly occurs between the hydrogen bond donor of carboxylic acid of IBU and the hydrogen bond acceptor of the nitrogen atom in the pyridine. From the FT-IR results, it indicated that IBU formed hydrogen bonds with the pyridine ring of nicotinic acid grafted on the copolymer (data not shown). On the other hand, this bonding between IBU and PABA did not occur, since the amino group of PABA could donate electrons to the benzene ring indicating that it acted as a hydrogen bond donor. According to the proposed interaction between drug and copolymer, it was expected that % DL and % EE should increase with the molar ratios of grafting units. From the results, it was found that % DL and % EE increased with the increasing molar ratios of grafting units (p-value < 0.05) except for 0.30 molar

ratios of grafting units. The similar reduction in % DL and % EE of both nicotinic acid and PABA grafting at 0.30 molar ratios was observed probably because the steric hindrance of the grafting unit at 0.30 molar ratio might limit the drug encapsulation.

Regarding the zeta potential of the prepared nanoparticles (Figure 6B), it was found that the loaded nanoparticles displayed smaller zeta potential values to those of the blank nanoparticles. For all grafting of P(NICLCL)-PEG-P(NICLCL), increasing the molar ratios of grafting units led to less negative zeta potentials of the loaded nanoparticles. In contrast, at 0.20 and 0.30 molar ratios of P(PACLCL)-PEG-P(PACLCL), the reversal of the charges to positive was observed. It is well-known that the zeta potential can be employed as an overall charge measured at the shear plane of the particles. It is affected by the molecules surrounding the surface of particles, which may deposit directly on the outer particle surface or be present in the water closely to this surface. Therefore, the decrease in zeta potential might be caused by solubilized IBU in water, since the solubility of IBU is pH-dependent.[48] At the pH of Milli-Q water (~6.0−6.5), IBU dissolves in ionized form (solubility at pH 6.0 = 0.23 mg/mL[48]) in the dispersion medium. Due to the lower drug encapsulation of the drug-loaded P(PACLCL)-PEG-P(PACLCL) nanoparticles, the ionized IBU might be more available in the dispersion medium compared to that of P(NICLCL)-PEG-P(NICLCL). Therefore, more ionized molecules, especially protons of ionized IBU, might surround the surface of P(PACLCL)-PEG-P(PACLCL) nanoparticles and consequently led to the positive charge of the loaded nanoparticles at 0.30 molar ratio of grafting units.

CONCLUSIONS

The modification of grafting heterocyclic and aromatic models (nicotinic acid and PABA) along PCL-PEG-PCL with various molar ratios of grafting units was successfully achieved through copper-catalyzed Huisgen's 1,3-dipolar cycloaddition. The difference in the molecular structure of grafting compounds influenced the feasibility of the grafting reaction and the physicochemical and thermal properties of the copolymers. In addition, the nanoparticles prepared from the grafting compounds exhibited different characteristics in terms of particle size, surface charge, drug loading capacity, and entrapment efficiency depending on the different interaction between the grafting compounds and drug molecules. The toxicity study of grafted nanoparticles demonstrated the safety of the grafted nanoparticles at 0.10 molar ratios of grafting units up to the concentration of 0.78 mg/mL. The toxicity of grafted nanoparticles increased with the molar ratios of grafting units. According to the present study, it can be concluded that the grafting of interesting compounds onto biodegradable polymers could modify the physicochemical and thermal properties of the copolymer and also the characteristics of nanoparticles including particle size, surface properties, and drug loading capacity.

ASSOCIATED CONTENT

Supporting Information. PCS size distribution curves of blank and IBU-loaded P(PACLCL)-PEG-P(PACLCL) nanoparticles based on intensity and volume. Scanning electron microscopy photograph of blank **0.10**P(PACLCL)-PEG-P(PACLCL) nanoparticles. This material is available free of charge via the Internet at http://pubs.acs.org.

AUTHOR INFORMATION

Corresponding Author

*To whom correspondence should be addressed. Tel/Fax: +66-2-644-8694, E-mail: pyvbp@mahidol.ac.th (Varaporn Buraphacheep Junyaprasert).

ACKNOWLEDGMENT

Financial supports from the Thailand Research Fund (TRF) through the Royal Golden Jubilee Ph.D. Program (grant no. PHD/0189/2547) and the Thai Research Fund and Commission of Higher Education, Thailand, for the research funding (RMU5180019) are gratefully acknowledged. The authors are very pleased to acknowledge the National Metal and Materials Technology Center (MTEC, Pathumthani, Thailand) for the GPC experiment. The authors thank Denise Klassert, Ph.D. student, Frankfurter Stiftung für Krebskranke Kinder, Frankfurt am Main, Germany, for assistance with the cytotoxicity study and Assist. Prof. Dr. Surakit Nathisuwan, Department of Pharmacy, Faculty of Pharmacy, Mahidol University, Thailand, for his useful suggestions.

REFERENCES

(1) Gou, M., Qian, Z., Wang, H., Tang, Y., Huang, M., Kan, B., Wen, Y., Dai, M., Li, X., Gong, C., and Tu, M. (2008) Preparation and characterization of magnetic poly(ε-caprolactone)-poly(ethylene glycol)-poly(ε-caprolactone) microspheres. *J. Mater. Sci. Mater. Med. 19*, 1033–1041.

(2) Vroman, B., Mazza, M., Fernandez, M. R., Jerome, R., and Preat, V. (2007) Copolymers of ε-caprolactone and quaternized ε-caprolactone as gene carriers. *J. Controlled Release 118*, 136–44.

(3) Park, E. K., Kim, S. Y., Lee, S. B., and Lee, Y. M. (2005) Folate-conjugated methoxy poly(ethylene glycol)/poly(ε-caprolactone) amphiphilic block copolymeric micelles for tumor-targeted drug delivery. *J. Controlled Release 109*, 158–168.

(4) Huang, M. J., Gou, M. L., Qian, Z. Y., Dai, M., Li, X. Y., Cao, M., Wang, K., Zhao, J., Yang, J. L., Lu, Y., Tu, M. J., and Wei, Y. Q. (2008) One-step preparation of poly(ε-caprolactone)-poly(ethylene glycol)-poly(ε-caprolactone) nanoparticles for plasmid DNA delivery. *J. Biomed. Mater. Res., Part A 86A*, 979–986.

(5) Liu, C. B., Gong, C. Y., Huang, M. J., Wang, J. W., Pan, Y. F., Zhang, Y. D., Li, G. Z., Gou, M. L., Wang, K., Tu, M. J., Wei, Y. Q., and Qian, Z. Y. (2008) Thermoreversible gel-sol behavior of biodegradable PCL-PEG-PCL triblock copolymer in aqueous solutions. *J. Biomed. Mater. Res., Part B 84*, 165–75.

(6) Vroman, B., Ferreira, I., Jerome, C., Jerome, R., and Preat, V. (2007) PEGylated quaternized copolymer/DNA complexes for gene delivery. *Int. J. Pharm. 344*, 88–95.

(7) Li, R., Li, X., Xie, L., Ding, D., Hu, Y., Qian, X., Yu, L., Ding, Y., Jiang, X., and Liu, B. (2009) Preparation and evaluation of PEG-PCL nanoparticles for local tetradrine delivery. *Int. J. Pharm. 379*, 158–166.

(8) Lee, J. S., Go, D. H., Bae, J. W., Jung, I. K., Lee, J. W., and Park, K. D. (2007) Synthesis and characterization of heparin conjugated Tetronic-PCL copolymer for protein drug delivery. *Curr. Appl. Phys. 7S1*, e49–52.

(9) Remant Bahadur, K., Bhattarai, S., Aryal, S., Khil, M., Dharmaraj, N., and Kim, H. (2007) Novel amphiphilic triblock copolymer based on PPDO, PCL, and PEG: Synthesis, characterization, and aqueous dispersion. *Colloids Surf., A 292*, 69–78.

(10) Zhou, S., Deng, X., and Yang, H. (2003) Biodegradable poly(ε-caprolactone)-poly(ethylene glycol) block copolymers: characterization and their use as drug carriers for a controlled delivery system. *Biomaterials 24*, 3563–3570.

(11) Peng, C.-L., Shieh, M.-J., Tsai, M.-H., Chang, C.-C., and Lai, P.-S. (2008) Self-assembled star-shaped chlorin-core poly(ε-caprolactone)-poly(ethylene glycol) diblock copolymer micelles for dual chemo-photodynamic therapies. *Biomaterials 29*, 3599–3608.

(12) Zhang, Y., Tang, L., Sun, L., Bao, J., Song, C., Huang, L., Liu, K., Tian, Y., Tian, G., Li, Z., Sun, H., and Mei, L. (2010) A novel paclitaxel-loaded poly(ε-caprolactone)/Poloxamer 188 blend nanoparticle overcoming multidrug resistance for cancer treatment. *Acta Biomater. 6*, 2045–2052.

(13) Wei, X., Gong, C., Gou, M., Fu, S., Guo, Q., Shi, S., Luo, F., Guo, G., Qiu, L., and Qian, Z. (2009) Biodegradable poly(ε-caprolactone)-poly(ethylene glycol) copolymers as drug delivery system. *Int. J. Pharm. 381*, 1–18.

(14) Vonarbourg, A., Passirani, C., Saulnier, P., and Benoit, J.-P. (2006) Parameters influencing the stealthiness of colloidal drug delivery systems. *Biomaterials 27*, 4356–4373.

(15) Trollsas, M., Lee, V. Y., Mecerreyes, D., Lowenhielm, P., Moller, M., Miller, R. D., and Hedrick, J. (2000) Hydrophilic aliphatic polyesters: Design, synthesis, and ring-opening polymerization of functional cyclic esters. *Macromolecules 33*, 4619–4627.

(16) Rieger, J., Bustele, K. V., Lecomte, P., Detrembleur, C., Jérôme, R., and Jérôme, C. (2005) Versatile functionalization and grafting of poly(ε-caprolactone) by Michael-type addition. *Chem. Commun.* 274–276.

(17) Lecomte, P., Riva, R., Schmeits, S., Rieger, J., Butsele, K. V., Jérôme, C., and Jérôme, R. (2006) New prospects for the grafting of functional groups onto aliphatic polyesters. Ring-opening polymerization of α- or γ-substituted ε-caprolactone followed by chemical derivatization of the substituents. *Macromol. Symp. 240*, 157–165.

(18) Pitt, C. G., Gu, Z.-W., Ingram, P., and Hendren, R. W. (1987) The synthesis of biodegradable polymers with functional side chains. *J. Polym. Sci., Part A: Polym. Chem. 25*, 955–966.

(19) Riva, R., Lenoir, S., Jérôme, R., and Lecomte, P. (2005) Functionalization of poly(ε-caprolactone) by pendant hydroxyl, carboxylic acid and epoxide groups by atom transfer radical addition. *Polymer 46*, 8511–8518.

(20) Lutz, J.-F., and Zarafshani, Z. (2008) Efficient construction of therapeutics, bioconjugates, biomaterials and bioactive surfaces using azide-alkyne "click" chemistry. *Adv. Drug Delivery Rev. 60*, 958–970.

(21) Vsevolod, V. R., Luke, G. G., Valery, V. F., and Sharpless, K. B. (2002) A stepwise Huisgen cycloaddition process: copper(I)-catalyzed regioselective "ligation" of azides and terminal alkynes. *Angew. Chem., Int. Ed. Engl. 41*, 2596–2599.

(22) Hein, C. D., Liu, X. M., and Wang, D. (2008) Click chemistry, a powerful tool for pharmaceutical sciences. *Pharm. Res. 25*, 2216–30.

(23) Riva, R., Schmeits, S., Jérôme, C., Jérôme, R., and Lecomte, P. (2007) Combination of ring-opening polymerization and "Click Chemistry": Toward functionalization and grafting of poly(ε-caprolactone). *Macromolecules 40*, 796–803.

(24) Lee, R.-S., and Huang, Y.-T. (2008) Synthesis and characterization of amphiphilic block-graft MPEG-*b*-(PαN$_3$CL-*g*-alkyne) degradable copolymers by ring-opening polymerization and click chemistry. *J. Polym. Sci., Part A: Polym. Chem. 46*, 4320–4331.

(25) Lee, R.-S., and Huang, Y.-T. (2009) Synthesis and characterization of amphiphilic triblock-graft PEG-(b-PαN$_3$CL-g-Alkyne)2 degradable copolymers. *J. Polym. Res.*

(26) Safeer, R. S., and Lacivita, C. L. (2000) Choosing drug therapy for patients with hyperlipidemia. *Am. Fam. Physician 61*, 3371–3382.

(27) Pahan, K. (2006) Lipid-lowering drugs. *Cell. Mol. Life Sci. 63*, 1165–1178.

(28) Farmer, J. (2009) Nicotinic acid: A new look at an old drug. *Curr. Artheroscler. Rep 11*, 87–92.

(29) Iinuma, I., Uyama, S., Uenoyama, K., and Sakaguchi, T. (1961) PABA (*p*-aminobenzoic acid) as a possible therapeutic agent for glaucoma. I. *Nippon Ganka Gakkaizasshi 65*, 1463–1467.

(30) Jakobsen, J., Pedersen, A. N., and Ovesen, L. (2003) Para-aminobenzoic acid (PABA) used as a marker for completeness of 24 h urine: effects of age and dosage scheduling. *Eur. J. Clin. Nutr. 57*, 138–142.

(31) Bingham, S., and Cummings, J. H. (1983) The use of 4-aminobenzoic acid as a marker to validate the completeness of 24 h urine collections in man. *Clin. Sci. (London) 64*, 629–35.

(32) (1983) *p*-Aminobenzoic acid, in *The Merck Index* (Windholz, M., and Budavari, S., Eds.) pp 62−3, Merck & Co., Inc., New Jersey.

(33) Kern, C. J., Antoshkiw, T., and Maiese, M. R. (2002) p-Aminobenzoic acid and its sodium salt. *Anal. Chem. 20*, 919–922.

(34) Suksiriworapong, J., Sripha, K., and Junyaprasert, V. B. (2010) Synthesis and characterization of bioactive molecules grafted on poly(ε-caprolactone) by "click" chemistry. *Polymer 51*, 2286–2295.

(35) Huang, M. J., Gou, M. L., Qian, Z. Y., Dai, M., Li, X. Y., Cao, M., Wang, K., Zhao, J., Yang, J. L., Lu, Y., Tu, M. J., and Wei, Y. Q. (2007) One-step preparation of poly(ε-caprolactone)-poly(ethylene glycol)-poly(ε-caprolactone) nanoparticles for plasmid DNA delivery. *J. Biomed. Mater. Res., Part A 86A*, 979–986.

(36) Lucke, A., Teβmar, J., Schnell, E., Schmeer, G., and Göpferich, A. (2000) Biodegradable poly(D,L-lactic acid)-poly(ethylene glycol)-monomethyl ether diblock copolymers: structures and surface properties relevant to their use as biomaterials. *Biomaterials 21*, 2361–2370.

(37) Zhang, Y., Wang, C., Yang, W., Shi, B., and Fu, S. (2005) Tricomponent diblock copolymers of poly(ethylene glycol)-poly(ε-caprolactone-co-lactide): Synthesis, characterization and loading camptothecin. *Colloid Polym. Sci. 283*, 1246–1252.

(38) Bogdanov, B., Vidts, A., Van Den Buicke, A., Verbeeck, R., and Schacht, E. (1998) Synthesis and thermal properties of poly(ethylene glycol)-poly(ε-caprolactone) copolymers. *Polymer 39*, 1631–1636.

(39) Lenoir, S., Riva, R., Lou, X., Detrembleur, C., Jérôme, R., and Lecomte, P. (2004) Ring-opening polymerization of α-chloro-ε-caprolactone and chemical modification of poly(α-chloro-ε-caprolactone) by atom transfer radical processes. *Macromolecules 37*, 4055–4061.

(40) FazlIoglu, H., and Hacaloglu, J. (2002) Thermal decomposition of glycidyl azide polymer by direct insertion probe mass spectrometry. *J. Anal. Appl. Pyrolysis 63*, 327–338.

(41) Ero, M. S., and Güven, O. (1996) Thermal decomposition of poly(glycidyl azide) as studied by high-temperature FTIR and thermogravimetry. *J. Appl. Polym. Sci. 61*, 201–206.

(42) Jones, M.-C., and Leroux, J.-C. (1999) Polymeric micelles - a new generation of colloidal drug carriers. *Eur. J. Pharm. Biopharm. 48*, 101–111.

(43) Zhang, N., Guo, S. R., Li, H. Q., Liu, L., Li, Z. H., and Gu, J. R. (2006) Synthesis of three types of amphiphilic poly(ethylene glycol)-*block*-poly(sebacic anhydride) copolymers and studies of their micellar solutions. *Macromol. Chem. Phys. 207*, 1359–1367.

(44) Shin, G. I., Kim, Y. S., Lee, M. Y., Cho, S. C., and Kiel, Y. S. (1998) Methoxy poly(ethylene glycol)/ε-caprolactone amphiphilic block copolymeric micelle containing indomethacin.: I. Preparation and characterization. *J. Controlled Release 51*, 1–11.

(45) Allen, C., Maysinger, D., and Eisenberg, A. (1999) Nano-engineering block copolymer aggregates for drug delivery. *Colloids Surf., B 16*, 3–27.

(46) La, S. B., Okano, T., and Kataoka, K. (1996) Preparation and characterization of the micelle-forming polymeric drug indomethacin-incorporated poly(ethylene oxide)-poly(β-benzyl L-aspartate) block copolymer micelles. *J. Pharm. Sci. 85*, 85–90.

(47) Gung, B. W., Wekesa, F., and Barnes, C. L. (2008) Stacking interactions between nitrogen-containing six-membered heterocyclic aromatic rings and substituted benzene: Studies in solution and in the solid state. *J. Org. Chem. 73*, 1803–1808.

(48) Jiang, B., Hu, L., Gao, C., and Shen, J. (2005) Ibuprofen-loaded nanoparticles prepared by a co-precipitation method and their release properties. *Int. J. Pharm. 304*, 220–230.

Supporting information

Investigation of Polymer and Nanoparticle Properties with Nicotinic Acid and *P* Aminobenzoic Acid Grafted on Poly(ε-caprolactone)-Poly(ethylene glycol)-Poly(ε-caprolactone) via Click Chemistry

Jiraphong Suksiriworapong[†], Kittisak Sripha[‡], Jörg Kreuter[§], Varaporn Buraphacheep Junyaprasert[†*]

[†] Department of Pharmacy, Faculty of Pharmacy, Mahidol University, Bangkok 10400, Thailand

[‡] Department of Pharmaceutical Chemistry, Faculty of Pharmacy, Mahidol University, Bangkok 10400, Thailand

[§] Institute of Pharmaceutical Technology, Goethe-University, Max-von-Laue-Str. 9 (Biozentrum), D-60438 Frankfurt am Main, Germany

*** To whom correspondence should be addressed:**

Tel/Fax: +66-2-644-8694, E-mail: pyvbp@mahidol.ac.th (Varaporn Buraphacheep Junyaprasert)

Table of contents

Figure S1. PCS Size Distribution Curves of Blank and IBU-Loaded 0.10P(PACLCL)-PEG-P(PACLCL) Nanoparticles Based on Intensity (Left Panel) and Volume (Right Panel).

Figure S2. PCS Size Distribution Curves of Blank and IBU-Loaded 0.20P(PACLCL)-PEG-P(PACLCL) Nanoparticles Based on Intensity (Left Panel) and Volume (Right Panel).

Figure S3. PCS Size Distribution Curves of Blank and IBU-Loaded 0.30P(PACLCL)-PEG-P(PACLCL) Nanoparticles Based on Intensity (Left Panel) and Volume (Right Panel).

Figure S4. Scanning Electron Microscopy Photograph of Blank 0.10P(PACLCL)-PEG-P(PACLCL) Nanoparticles.

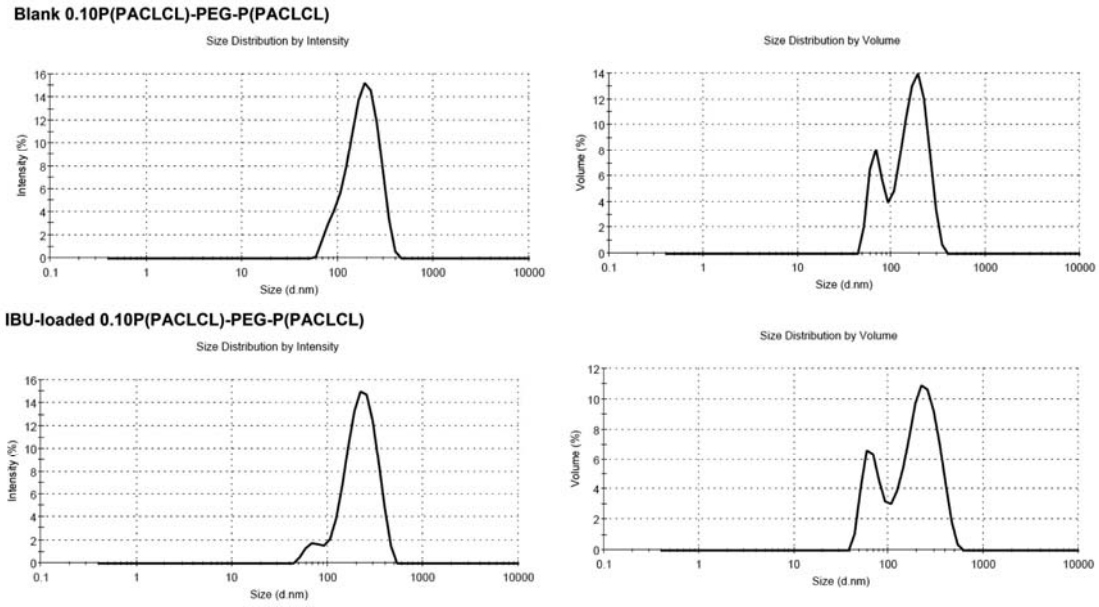


Figure S1. PCS Size Distribution Curves of Blank and IBU-Loaded 0.10P(PACLCL)-PEG-P(PACLCL) Nanoparticles Based on Intensity (Left Panel) and Volume (Right Panel).

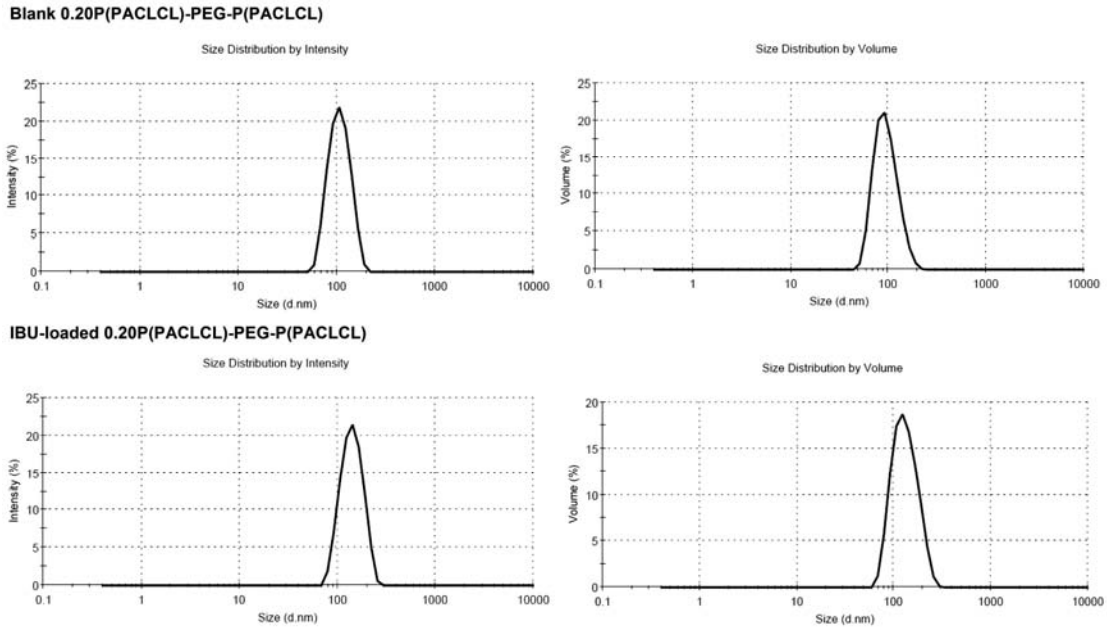


Figure S2. PCS Size Distribution Curves of Blank and IBU-Loaded 0.20P(PACLCL)-PEG-P(PACLCL) Nanoparticles Based on Intensity (Left Panel) and Volume (Right Panel).

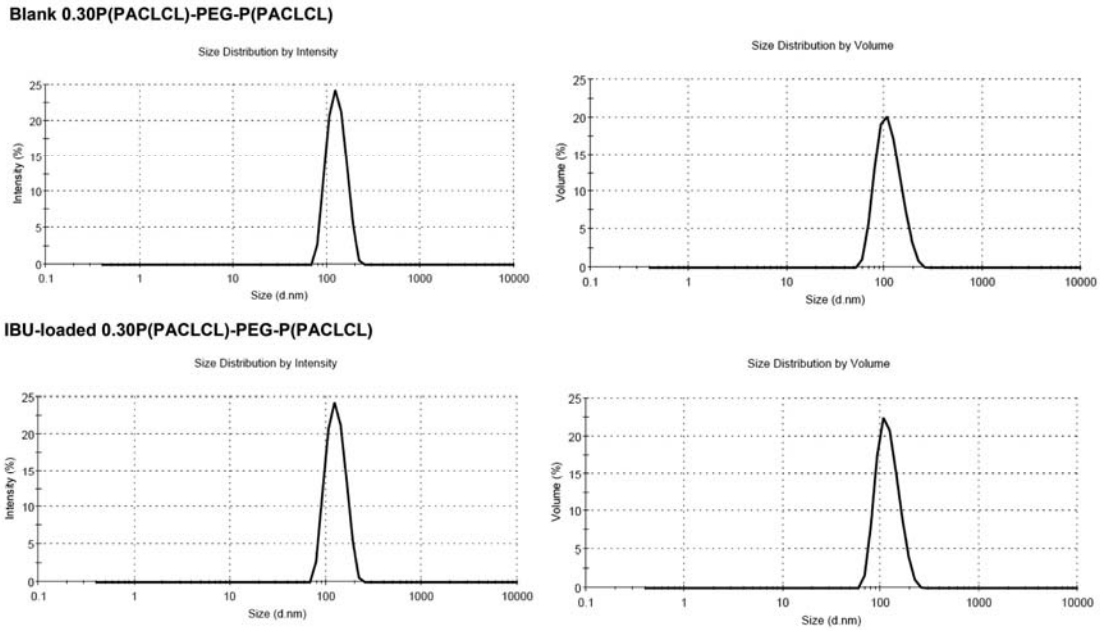


Figure S3. PCS Size Distribution Curves of Blank and IBU-Loaded 0.30P(PACLCL)-PEG-P(PACLCL) Nanoparticles Based on Intensity (Left Panel) and Volume (Right Panel).

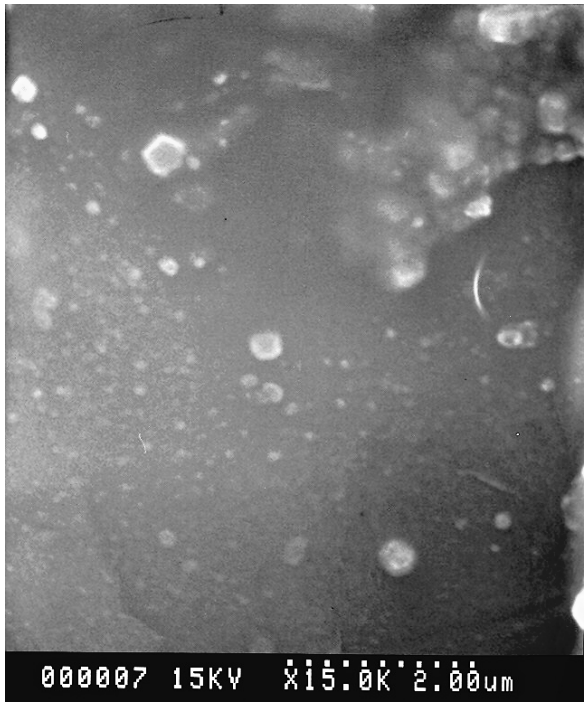


Figure S4. Scanning Electron Microscopy Photograph of Blank 0.10P(PACLCL)-PEG-P(PACLCL) Nanoparticles.

Bioconjugate Chemistry

ARTICLE

pubs.acs.org/bc

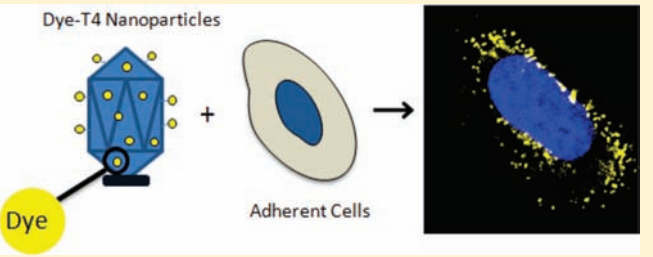
Engineered T4 Viral Nanoparticles for Cellular Imaging and Flow Cytometry

Kelly L. Robertson, Carissa M. Soto, Marie J. Archer, Onyekachi Odoemene, and Jinny L. Liu*

Contributed from the Center of for Bio/Molecular Science and Engineering, Naval Research Laboratory, 4555 Overlook Avenue SW, Washington, DC 20375, United States

Supporting Information

ABSTRACT: Viruses are of particular interest as scaffolds for biotechnology applications given their wide range of shapes and sizes and the possibility to modify them with a variety of functional moieties to produce useful virus-based nanoparticles (VNPs). In order to develop functional VNPs for cell imaging and flow cytometry applications, we used the head of the T4 bacteriophage as a scaffold for bioconjugation of fluorescent dyes. Bacteriophage T4 is a double-stranded DNA virus with an elongated icosahedron head and a contractile tail. The head is ~100 nm in length and ~90 nm in width. The large surface area of the T4 head is an important advantage for the development of functional materials since it can accommodate significantly larger numbers of functional groups, such as fluorescent dyes, in comparison with other VNPs. In this study, Cy3 and Alexa Fluor 546 were chemically incorporated into tail-less T4 heads (T4 nanoparticles) for the first time, and the fluorescent properties of the dye-conjugated nanoparticles were characterized. The T4 nanoparticles were labeled with up to 19 000 dyes, and in particular, the use of Cy3 led to fluorescent enhancements of up to 90% compared to free Cy3. We also demonstrate that the dye-conjugated T4 nanoparticles are structurally stable and that they can be used as molecular probes for cell imaging and flow cytometry applications.



INTRODUCTION

Recently, the use of viral nanoparticles (VNPs) as materials for biotechnology applications has gained interest given their biocompatibility, the diversity of shapes and sizes, and the possibility to tailor their surface characteristics.[1−4] VNPs produced from plant and animal viruses and bacteriophages have been used in biosensing, imaging, vaccine development, and drug and gene delivery.[3−7] Of these, bacteriophages (or phages) are among the most promising candidates as scaffolds in biotechnology applications due to their robust nature and unique display system, which enables the expression of a wide variety of peptides and polypeptides rendering diverse surface functionality.[3,8,9] The phage head varies in shape and size from micrometer-size in the filamentous type (fd, M13) to a few hundred nanometers in the spherical (PhiX174, G4, S13) and icosahedral type (T7, T4, MS2) and the tail, when present, can be contractile or flexible.[3,10,11] Bacteriophage T4 has several characteristics that distinguish it from other phage species and make it an ideal scaffold for biotechnology applications. For instance, it has a flexible and unique display system[12−14] that has been demonstrated to display peptides and full-length proteins on the viral capsids. Combining this feature with the possibility to engineer its morphology[15] significantly increases the range of functional materials that can be devised. In addition, when functionalized through chemical conjugation, the large surface area of the head allows a higher loading capacity and spatial distribution of the functional groups, which presumably leads to higher sensitivity.[16] The size and shape are also advantageous, because it has been demonstrated that cellular uptake occurs preferentially with spherical particles with sizes between 70 and 100 nm over elongated ones even with the same dimensions.[17]

Figure 1a presents a schematic representation of bacteriophage T4 consisting of an icosahedral head, a contractile tail, and tail fibers, while Figure 1b shows the concept of a T4 nanoparticle obtained through genetic engineering. Deletion of the tail and its fibers results in nanoparticles with dimensions of ~100 × ~90 nm^2,[18,19] which can be functionalized with fluorescent dyes using standard bioconjugation techniques.

Bacteriophage T4 has been proven useful in sensor probes[20−22] and vaccine carriers,[23−25] and the use of tail-less T4 nanoparticles (T4 NPs) as detection elements has been suggested,[26] yet no practical applications have been reported to date. We previously used atomic force microscopy to examine the variables that influence tail-less T4 NP assembly on surfaces.[19] In the work presented here, we demonstrate, for the first time, the use of T4 NPs as fluorescent probes for cellular imaging and flow cytometry applications. The properties of the T4 NP give it the potential of becoming a viable scaffold for biomaterial applications, but we are currently limited by the scarcity of information on its surface chemistry. The large size of the T4 head makes it

Received: August 10, 2010
Revised: January 4, 2011
Published: March 04, 2011

 © 2011 American Chemical Society

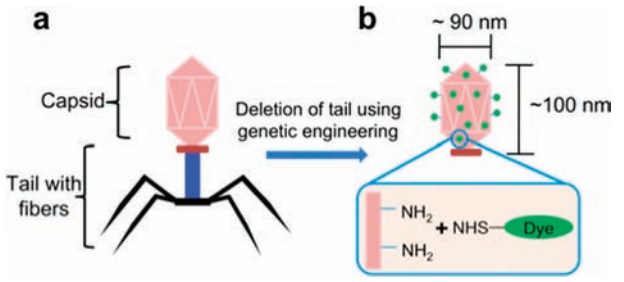


Figure 1. Experimental strategy for probe synthesis. (a) Schematic representation of bacteriophage T4. (b) Schematic representation of a tail-less T4 NP obtained by deletion of the tail using genetic engineering; functional T4 NPs can be developed by incorporating fluorescent dyes using standard bioconjugation techniques.

difficult to grow single crystals for X-ray crystallography at a resolution sufficient for determining the exact location of amino acids on the surface. The most current structure available comes from cryo-electron microscopy at a 2.2 nm resolution.[27] Thus, to further demonstrate its potential as an addressable nanobuilding block and understand its surface chemistry, the reactivity of the surface amines was investigated. While lysine groups are typically used to couple biomolecules due to their abundance and well-known chemistry, other amines may be available for conjugation as well. The total number of lysines on the T4 head is 32 303 (Supporting Information Table S1).

In the work presented here, we selected Cy3 and Alexa Fluor 546 as model dyes and characterized their performance on the T4 NP. These two fluorophores, while sharing similar excitation/emission spectra, have been reported to exhibit strikingly different performance characteristics, which are thought to be due, in part, to their molecular properties, but also to their neighboring interactions.[28,29] It is therefore relevant to understand their behavior on the T4 scaffold under a particular set of experimental conditions. Chemical bioconjugation of organic dyes has been utilized to prepare fluorescent probes using plant viruses such as cowpea mosaic virus (CPMV),[16,30−33] turnip yellow mosaic virus (TYMV),[34] tobacco mosaic virus (TMV),[35,36] and potato virus X (PVX);[37] however, there are fewer examples of the use of bacteriophages as scaffolds for this purpose.[38] In plant viruses containing small capsids, such as CPMV and TMV (30 and 28 nm in diameter, respectively), the number of dyes that can be incorporated is limited by the surface area of the capsids and corresponding reactivities of solvent-accessible amino acids on the virus surface. Precise control of the spacing between the dyes becomes more critical within this limited surface area in order to avoid dimer formation and quenching of the dyes.[32] While TMV with its "hollow-rod" shape has a larger surface area, the chemical conjugation is cumbersome, since commonly used residues, such as lysines, are not exposed on the surface.[35,39] PVX on the other hand has an elongated capsid (~500 nm × 18 nm), and even with this significantly larger surface area, the maximum number of dyes incorporated is only 1600 per capsid through primary amine modification.[37]

Here, we demonstrate that more than 1.9×10^4 dyes can be incorporated on a single T4 NP; to our knowledge, this is the highest number of dyes incorporated onto a single VNP. Our results also show that the T4 probes are so efficient that even those with dye numbers as low as 350 dyes per particle give good fluorescence intensities for *in vitro* applications. In addition, the dye-T4 NPs can be used to visualize cells and remain inside cells for at least 72 h.

EXPERIMENTAL SECTION

Purification of Tail-Less T4 Head Scaffolds. T4 K10 (38^- 51^-*denA*$^-$ *denB*$^-$), a kind gift from Dr. Lindsay Black at University of Maryland at Baltimore Medical School, was first propagated in the suppressor *Escherichia coli* host strain, CR63, to obtain the infectious phages. The infectious phages were then used to produce noninfectious tail-less T4 nanoparticles (T4 NPs) using the nonsuppressor host *E. coli* strain, Rosetta, modified from a previous procedure.[40] In brief, Rosetta grown in M9S (OD_{600} = 0.5) supplemented with 1/3 volume of Luria Broth were infected with K10 phage at a multiplicity of infection (MOI) = 3, followed by a repeated infection after 9 min and continued incubation for 2 h at 37 °C. Cells were spun down at 10 000 *g* for 10 min and resuspended in 50 mM potassium phosphate (pH 7.5) supplemented with 10 mM $MgCl_2$ and 2 mM $CaCl_2$; $CHCl_3$ (1/20 of total volume), DNase I (40 μg/mL), RNase I (50 μg/mL), and 0.4 μg of PMSF (phenylmethanesulfonylfluoride or phenylmethylsulfonyl fluoride) were then added to the cell suspension and the cells were gently shaken at 37 °C for 1−2 h. The cell debris was removed by spinning at 15 000 *g* for 30 min. The cell lysate containing the head scaffolds was concentrated through a Microcon YM-100 membrane according to the manufacturer's procedure (Millipore Corp, MA). The membrane was then washed 3−6 times with 50 mM potassium phosphate buffer, pH 7.5, supplemented with 10 mM $MgCl_2$ (50 KP/10 $MgCl_2$) and 0.1% sodium azide. The T4 NPs were then purified by gel filtration with Superose 6 (GE Healthcare Biosciences, NJ). The flowthrough and eluted fractions were then assessed using a 1.2% Tris-acetate agarose gel stained with either ethidium bromide or Coomassie blue.

Dye Conjugation. Tail-less T4 NP solutions in 50 KP/10 $MgCl_2$ and 0.1% sodium azide were desalted using a pre-equilibrated HiTrap Desalting Column (GE Healthcare Biosciences, Piscataway, NJ) and eluted fractions were analyzed by UV−vis spectroscopy (Cary 5000, Varian). The second 1.5 mL elution contained most of the T4 NPs. For the reaction optimization experiments, T4 NPs were reacted with fluorescein-5-isothiocyanate (FITC; Invitrogen, Carlsbad, CA) and Alexa Fluor 488 sulfodichlorophenol ester (Alexa488-SDP ester, Invitrogen) in various buffer conditions. When developing an optimally fluorescent dye-T4 NP, 9.0×10^{10} K10 heads (9 μg of protein) in 10% DMSO (Sigma-Aldrich, St. Louis, MO) were reacted with Cy 3 Mono NHS ester (Cy3-NHS; GE Healthcare Biosciences) or Alexa Fluor 546-NHS ester (Alexa 546-NHS; Invitrogen, Carlsbad, CA). Molar ratios of dye to T4 NP lysines were 0.1 (for Alexa Fluor 546 only), 0.6, 1.1, 1.5, 2.0, 2.8, 5, 10, 13, and 20. Prior to the addition of DMSO and dye, T4 NPs in 50 KP/10 $MgCl_2$ were incubated on ice for 5 min after which DMSO was added slowly with gentle mixing. Then, corresponding amounts of 10 μg/μL NHS-Cy3 or NHS-Alexa Fluor 546 in DMSO were added, and the mixture was vortexed. T4 NPs were kept at a concentration of 5.8×10^{11} particles/mL in the reaction mix, and the mixture was incubated at room temperature in the dark for 16 h. From these reactions, we obtained a series of samples containing a different number of dyes per T4 NP.

Dye-labeled T4 NPs were loaded separately into a Superose 6 prep grade (GE Healthcare Biosciences) column pre-equilibrated in 50 KP/10 $MgCl_2$/0.1% sodium azide. Individual 1 mL elutions were collected and analyzed by gel electrophoresis, atomic force microscopy, and UV−vis spectroscopy. For gel electrophoresis, 10 μL of unmodified and dye-labeled T4 NPs were loaded into a 1.2% agarose gel. The gel was visualized without staining using HP Scanjet 5590 scanner. DNA and protein visualization was also performed on the same gel using ethidium bromide and Coomassie blue staining, respectively. Images from

ethidium bromide staining were obtained using UVP Bio Doc-It system, a UV transilluminator. Coomassie blue stained images were captured by the HP scanner.

Spectroscopic Measurements. UV−vis spectroscopy was performed to determine the amount of T4 NPs and dye present in the reaction samples. Protein concentration was determined using a Bradford assay according to the manufacturer's procedure (Bio-Rad, Hercules, CA), and the number of T4 NPs per sample was then determined using the relationship that 1 mg of purified NPs is equivalent to 9.70×10^{12} tail-less T4 heads. The amount of Cy3 and Alexa 546 in the T4 solution was determined from absorbance at 550 and 555 nm, respectively, and by a standard curve produced using each free dye. UV−vis measurements were performed using Varian Cary-5000 UV−vis−near-IR spectrometer with Cary Win UV Scan Application v 3.00 software.

Fluorescence spectroscopy was also carried out to determine the fluorescence intensity (F.I.) of dye-T4 NPs. The Cy3-T4 and Alexa 546-T4 NPs were excited at 550 nm. The measurements were taken on a Cary Eclipse fluorescence spectrophotometer. To calculate the percentage of fluorescent enhancement, the following equation was used: ([dye-T4 complex F.I.] − [F.I. of free dye])/[dye-T4 complex F.I.] × 100.

Atomic Force Microscopy (AFM). For AFM characterization, 5 μL of the unmodified or dye-labeled T4 NPs were sonicated for 5−10 s, deposited on freshly cleaved mica, and kept in a humid environment at room temperature for 12 h. After adsorption of the T4 NPs onto the mica surface, the substrates were allowed to dry at room temperature, carefully rinsed with Milli-Q water, and allowed to dry at room temperature once more. Unmodified and conjugated T4 NPs were characterized using a Multimode scanning probe microscope (Veeco Instruments, Plainview, NY, USA) operated under tapping mode in air with a silicon cantilever (Nanoscience Instruments, Phoenix, AZ), 125 mm long, with an apex curvature radius of 5−6 nm, a resonant frequency of 300 kHz, and a spring constant of 40 N/m. The scanning rate was 0.5 Hz, at 0° angle. Image processing was performed using Research NanoScope II software ve 7.20. All images were filtered using the flattening built-in tool from NanoScope II software. Length and height values of the nanoparticles were obtained by utilizing the built-in tool for cross section analysis.

Cell Culture. A549 (American Type Culture Collection) lung cancer epithelial cells were grown at 37 °C under 5% CO_2 atmosphere in Dulbecco's modified Eagle's medium (DMEM), supplemented with 10% fetal bovine serum (FBS) (Cellgro, VA) and 1% (v/v) penicillin/streptomycin (Sigma, CA), and detached from culture flasks using trypsin-ethylenediamine-tetraacetic acid (EDTA) (Cellgro, VA). After the cells were harvested, they were counted and seeded onto microscope slides, 6-well tissue culture treated plates, or 24-well tissue culture treated plates and allowed to attach overnight.

Confocal Microscopy. A549 cells on microscope slides were treated with the dye-T4 NPs at varying times and concentrations in DMEM supplemented with 1% penicillin/streptomycin. The cells were then washed three times for 5 min each with 1 × PBS (phosphate buffered saline). The cells were fixed with 4% paraformaldehye in 1 × PBS for 15 min and then washed twice with 1 × PBS. The cells were then stained with 500 μM 4′,6-diamidino-2-phenylindole (DAPI) in 1 × PBS for 5 min and washed three times with 1 × PBS. Confocal microscopy was performed using a Nikon Eclipse TE2000 Confocal Imaging System, λ_{exe} = 402 nm (DAPI) and 561 (Cy3/Alexa 546). Images were taken with a 60× objective and are of integrated *Z*-stacks with 8 steps, 0.8 μm step size, and 10 averages per step.

Flow Cytometry. A549 cells on 24-well tissue culture plates were treated with 1×10^5 dye-T4 NPs per cell and analyzed at 4, 8, and 24 h. Following incubation, the cells were washed twice with 1 × PBS and harvested with trypsin−EDTA. The cells were then washed once with 1 × PBS and treated with a Live/Dead Fixable Far Red Dead Cell Stain Kit (Invitrogen, CA) according to the manufacturer's protocols. Following staining, the cells were washed twice in 1 × PBS, resuspended in 1 × PBS, and run on an Accuri C6 flow cytometer using standard lasers and filters for PE (FL-2) and APC (FL-4). For each sample, 2×10^4 events were collected in a gate corresponding to the cell population. To determine the percentage of live cells, a scatter plot showing the intensity of the Live/Dead reagent (FL-4) vs forward scatter (FSC) was gated for the population with the lowest fluorescence (live cells). The percentage of cells positive for the dye-T4 NPs was calculated using the histogram subtraction tool on FSC Express v 3.

Cell Tracking. A549 cells on 6-well tissue culture treated plates were treated for 6 h with 1×10^5 A546-T4 NPs per cell. The cells were then washed two times with 1 × PBS and harvested with trypsin−EDTA every 24 h up to 96 h. After harvesting, the cells were washed once with 1 × PBS and resuspended in 1 × PBS for counting and flow cytometry. The Nexcelom Cellometer Vision (Nexcelom, MA) with an optics module for Alexa 546 (VA-595−501) was used to count and measure the percentage of cells that contained A546-T4 NPs. Each time point was done in triplicate.

RESULTS AND DISCUSSION

Conjugation of Dyes on T4 NPs. The T4 phage head offers a spherical viral capsid that is similar in geometry to other widely used viral nanoparticles, but with the advantage of having a larger surface area for functionalization with dyes, proteins, antibodies, and inorganic nanoparticles. Large spherical viral capsids offer well-defined geometry, are relatively rigid, and offer better spatial distribution of conjugated functional groups. In order to create a noninfectious nanoparticle (NP) for various biomedical applications, the T4 bacteriophage was expressed without the tail (Figure 1b). The tail-less T4 NPs were purified from *E. coli*, and 3 mg T4 NPs/L of bacteria was recovered with >90% purity.

We then used the purified T4 NPs to explore the accessibility of the amine groups to dye modification. There is no information about the location or accessibility of the individual amino acids on the T4 NPs; therefore, by determining the number of reactive amines one can assess its utility for the applications presented here and as a potential scaffold for further chemical conjugation with antibodies, proteins, and targeting molecules.

Reaction conditions were selected based on the stability of the T4 NP and the reactivity of dyes in the selected conditions. In general, reactions carried out in buffer alone resulted in an average of 10× lower reactivity in comparison to reactions carried out in 90:10 buffer to DMSO, due to the enhanced solubility of the dye in DMSO. In addition, including $MgCl_2$ (1, 2, or 10 mM) in the reaction buffer enhanced the stability of T4 and did not affect the reactivity of the dyes. In early optimization reactions, fluorescein-5-isothiocyanate (FITC) and Alexa Fluor 488 sulfodichlorophenol ester (Alexa488-SDP ester) were compared to determine the level of reactivity of the T4 NP amines in different buffer conditions. Both dyes have similar spectral characteristics, which facilitates the comparison of UV−visible data when determining number of dyes per T4 NP. FITC is known to provide reasonable specificity toward the ε-amine of lysine,[30,41] while Alexa 488-SDP ester reacts with all primary amines in a similar manner as common NHS-ester dyes. By comparing FITC with Alexa 488-SDP, one can derive conclusions about the availability of amines on the T4 surface.

FITC demonstrated low labeling efficiency when the reaction was performed in the optimal T4 NP buffer (50 mM potassium

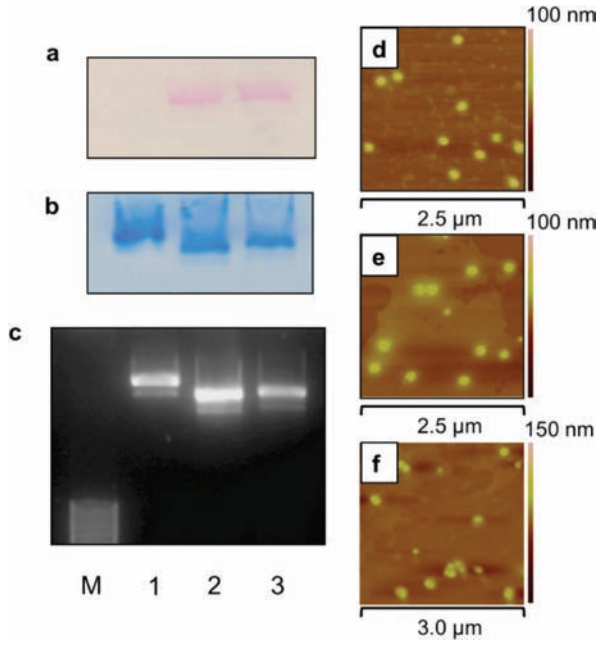


Figure 2. Characterization of the T4 NPs. Left: Agarose gel of T4 NPs visualized under (a) visible light with no staining, (b) UV irradiation after ethidium bromide staining, (c) visible light after Coomassie blue staining. Lane M: DNA marker. Lane 1: Unlabeled-T4 NP control. Lane 2: Alexa 546-T4 NP. Lane 3: Cy3-T4 NP. Right: Atomic force microscopy (AFM) topographical images of (d) unlabeled-T4 NPs, (e) Cy3-T4 NPs, (f) Alexa 546-T4 NPs. For AFM, 1.5×10^9 particles were deposited on freshly cleaved mica.

phosphate pH 7.5, 10 mM $MgCl_2$, 10% DMSO) instead of the manufacturer's recommended buffer (100 mM sodium bicarbonate, pH 9.0, 10% DMSO). However, the Alexa 488-SDP reacted similarly in both the optimal T4 NP buffer and its recommended buffer (100 mM sodium bicarbonate, pH 8.3, 10% DMSO). In order to compare the relative reactivity of FITC and Alexa 488-SDP ester, a series of reactions were performed in the recommended buffers for each dye. Our results showed a 30% higher load of Alexa 488 in comparison to FITC (data not shown). This result indicates that the SDP ester is labeling additional amines in comparison to FITC, presumably α-amines, since FITC is known to provide reasonable specificity toward ε-amines of lysines. On the basis of this information, for our current studies we used NHS ester-dyes, which are similar in reactivity to the SDP ester, but are available in a wider variety of dyes with different spectral characteristics. Cy3 NHS ester and Alexa Fluor 546 NHS ester dyes were reacted with T4 NPs at various molar ratios of dye to lysine to produce NPs with a range of dyes/virus (D/V).

Characterization of Dye-T4 NPs. To analyze the electrophoretic mobility and structural integrity of the T4 NPs after dye attachment and corresponding purification, the NPs were analyzed using agarose gel electrophoresis and atomic force microscopy (AFM). Figure 2 shows three views of an agarose gel that allows us to characterize different aspects of the Dye-T4 NPs. In Figure 2a, the gel has not been stained and the pink bands correspond to the dye conjugated on the NP. This indicates that the dye is coupled to the NP, since the band is running at the position expected for the unlabeled-T4 NP. Free dye, which is expected to run at a position closer to the bottom of the gel, was not observed, demonstrating the efficient purification of the dye-T4 NPs from free dye. Figure 2b shows a gel stained with ethidium bromide. The major band under UV irradiation indicates that the DNA is inside an intact NP. Figure 2c shows an agarose gel stained with Coomassie blue, which stains the intact T4 NPs. The fact that the bands in lanes 2 and 3 correspond to the same bands in all three visualization methods indicates that indeed the dyes are coupled to intact T4 NPs. When comparing the electrophoretic mobility of the unlabeled-T4 NP control (lane 1) and the dye-T4 NPs (lanes 2−3), it can be observed that the dye-T4 NPs have a net charge of higher negative character than the control, since both complexes ran farther into the agarose gel. This effect has been observed in the past with fluorescent dyes and is most likely due to the addition of negative charges associated with the binding of the dyes.[42] Both Cy3 and Alexa Fluor 546 NHS esters have a net negative charge (Supporting Information Figure S1) and eliminate one positive charge upon reacting with each amine group on the T4 surface.

In addition to the agarose gel, atomic force microscopy (AFM) topographical images were used to examine the structural features of the unlabeled and dye-labeled T4 NPs. Figure 2d−f shows that the T4-NPs with defined shapes and borders are well-dispersed. Cross-sectional analysis found that the average length of the unlabeled nanoparticle is 169 ± 14 nm, which is larger than the predicted length of 119.5 nm from the cryo-EM model.[43] Its average height is 39 ± 3 nm, half of what was predicted from cryo-EM (Figure 2d). The difference in length is mainly due to both virus collapsing and AFM tip effect; however, the differences in height of the T4 NPs prepared here can be explained by the loss of DNA from the NP during preparation. According to our solution spectroscopic analysis of the T4 NPs, 10% of the capsids still contain DNA. The empty NPs are collapsed to half of the original height during drying for AFM measurements and therefore are most likely flattened on the surface, which may also extend the length. Slight differences in the different labeled T4 NPs are most likely caused by varying degrees of collapse and flattening.

Overall, the height and length measurements of the unlabeled and dye-T4 NPs are comparable. The observed shape and close values of the average length and height between the unmodified and the modified T4 NPs indicate that the capsid withstands the conditions used for the chemical conjugation and purification. The relevance of assessing the structural stability of the T4 NPs after modification finds its rationale in the possible effects that dimethylsulfoxide (DMSO) can have on the cellular membrane and protein denaturation.[44,45] Although this solvent is widely used in many biology and molecular biology processes, DMSO can denature protein complexes such as the T4 NP. In the present study, the DMSO concentration was kept at 10%; however, we observed significant degradation of the scaffold at higher concentrations of DMSO (data not shown). This degradation is usually evident under AFM imaging as a layer of debris consisting of small clusters of material of irregular shape and size, as well as the presence of DNA. While other spherical virus capsids are less stable in the absence of DNA or RNA, the T4 NPs are stable under our reaction conditions as shown by gel electrophoresis and AFM.[46]

Spectroscopic Properties of Dye-T4 NPs. UV−vis measurements were taken of the Cy3-T4 and Alexa-T4 NPs and compared to spectra from the free dyes and unlabeled T4 NPs. Figure 3 shows T4 NP samples labeled with Cy3 and Alexa 546. The 260−280 nm peaks in the T4 spectra represent the

absorbance of the viral genomic DNA inside the T4 NP and the capsid proteins, respectively, while the peaks in the visible region represent the dye absorbance. There is a small red shift (5 nm) in absorption maxima of the Cy3 upon conjugation to the T4 NP, which is known to indicate cyanine dye−protein coupling.[47] Alexa 546-T4 NPs also show a slight shift in the dye absorbance compared to free Alexa 546, which is typical of other Alexa fluorophores.[48]

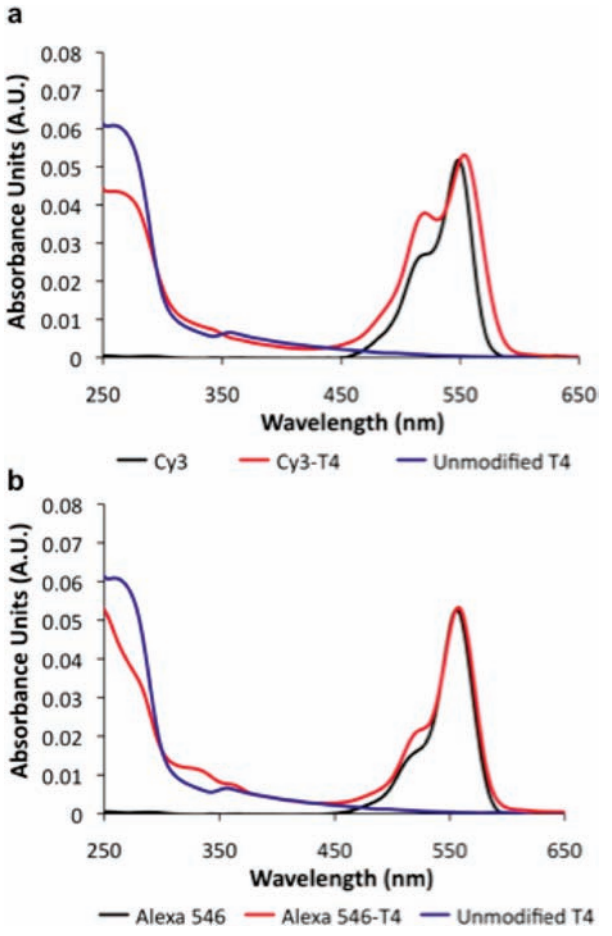


Figure 3. UV−vis spectra showing (a) Cy3 NHS ester (black), T4 NP after conjugation with Cy3 (red), and T4 NP (blue); (b) Alexa 546 NHS ester (black), T4 NP after conjugation with Alexa 546 (red), and T4 NP (blue). Absorbance is normalized relative to dye concentration.

Dye per Virus (D/V) Measurements. The absorbance measurements taken at the dye wavelengths for each dye-T4 NP sample along with the number of NPs present in each sample were used to calculate the D/V. As the molar excess of dyes to lysines was increased, the D/V increased up to 1.9×10^4 Alexa 546 dyes at 20 dyes to T4 NP lysines (Supporting Information Figure S2). This D/V ratio is 2 orders of magnitude higher than other isocosahedral viruses, such as CPMV[30] and 1 order of magnitude higher than the maximum D/V on the rod-shaped potato virus X and tobacco mosaic virus.[35,37] This high degree of labeling is possible due to the large number of amine groups present on the T4 NP (Supporting Information Table S1).

Fluorescence Properties of Dye-T4 NPs. Fluorescence emission of the dye-T4 complexes was studied as a function of D/V. As shown in Figure 4a and Supporting Information Table S2, fluorescence emission increases as the number of dyes in the Cy3-T4 is increased up to 715 D/V (orange line Figure 4a); beyond that point. fluorescence decreases as the number of dyes increases presumably due to quenching. In contrast, for the Alexa546-T4 series (Figure 4b) the best fluorescence output is obtained at 2166 D/V (orange line). To further analyze this phenomenon, the individual samples were compared to corresponding free dye in solution. Figure 5 shows the fluorescence enhancement obtained from the dye−T4 complexes calculated relative to a comparable amount of free dye in solution. All of the Cy3-T4 NPs examined showed enhanced fluorescence vs free Cy3 dye (Figure 5a) indicating that conjugation to the T4 changes the fluorescence characteristics of the dye. However, the enhancement of the Cy3-T4 NPs decreases linearly as the number of D/V increases (r = 0.99). In contrast, most of the Alexa546-T4 NPs examined show quenched fluorescence (negative enhancement) compared to free Alexa 546, and the effect is only linear up to 1500 D/V (r = 0.97 for Figure 5b, red squares only). Fluorescence enhancement has been observed previously in cyanine dyes and is caused by an increase in quantum yield, which is highly dependent upon solvent polarity and viscosity.[32,49,50] Upon binding to the T4, the Cy3 experiences a loss in conformational freedom, as well as a decrease in

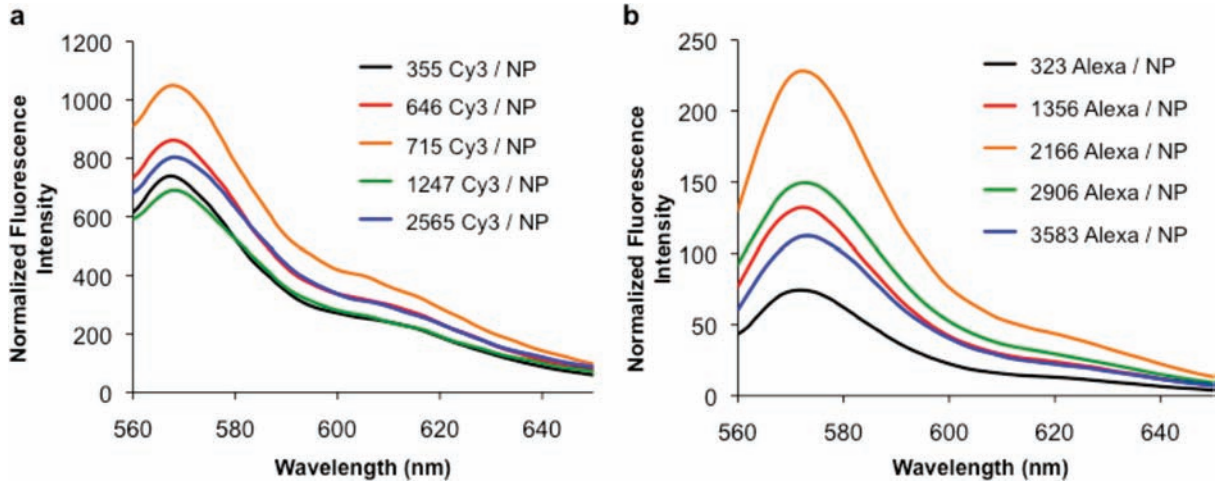


Figure 4. Fluorescence emission of dye-T4 NPs. Samples were excited at 550 nm and data were normalized relative to the number of unmodified T4 NPs: (a) Cy3-T4 samples, (b) Alexa 546-samples.

dx.doi.org/10.1021/bc100365j |*Bioconjugate Chem.* 2011, 22, 595–604

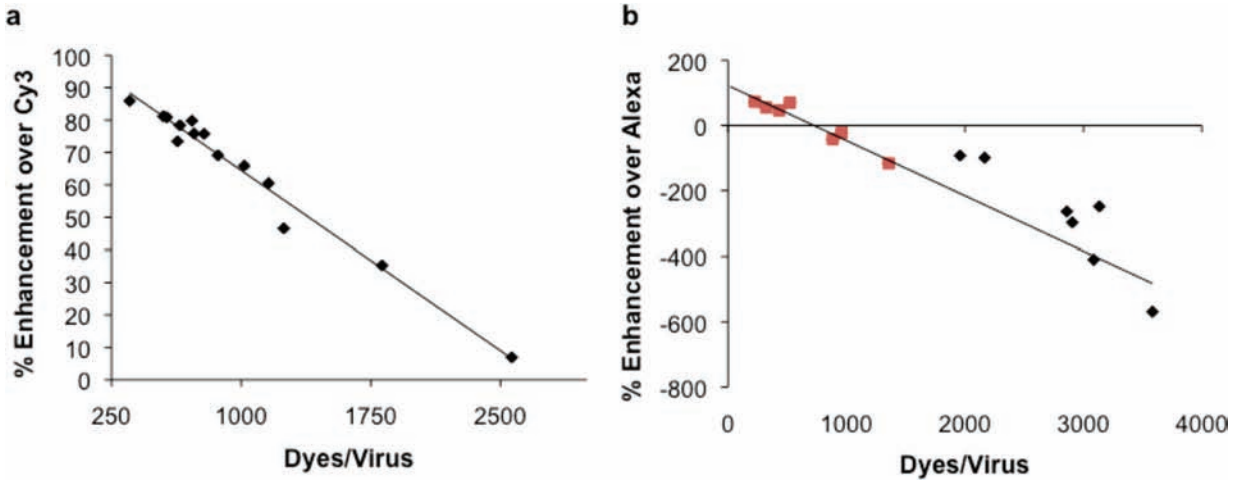


Figure 5. Fluorescence enhancement of dye-T4 NPs. Fluorescence enhancement of dye-T4 NPs as a function of dyes/virus calculated relative to free dye. Emissions of the Cy3-T4 and Alexa 546-T4 NPs were measured at 570 and 575 nm, respectively: (a) Cy3-T4 series; (b) Alexa 546-T4 series. Percentage of fluorescent enhancement is defined as follows: ([dye-T4 complex F.I.] − [F.I. of free dye])/[dye-T4 complex F.I.] × 100.

polarity at the site of binding, both leading to an increase in quantum yield.[50] Fluorescence enhancement in Alexa dyes has not been observed previously to our knowledge and may be due to energy transfer from the protein amino acids to the Alexa dye.

While fluorescence enhancement is occurring in Cy3 and to a lesser extent Alexa 546 when they are bound to the T4 NP, fluorescence quenching is causing the decreases in fluorescence at higher D/V in both dyes. Quenching can arise from dye−dye interactions and is often accompanied by a change in the absorption spectrum of the dye.[51,52] Evidence of dye−dye interactions (such as stacking or aggregate formation) can be observed in the absorption spectra of the Cy3 labeled T4 NP in Figure 3a. The free Cy3 dye has an absorption maximum at 555 nm with a shoulder at 520 nm. When the dye is bound to the T4 NP, there is an increase in the 520 nm peak in relation to the 555 nm peak. This increase in absorbance at 520 nm or blue shift can be attributed to nonfluorescent dimer formation.[50,51] A blue-shifted absorption band also appears to a lesser extent in the Alexa 546-T4 absorbance spectra and has been observed in Alexa dyes previously.[28,53] Dye−dye interactions are highly dependent on the location of the dyes on the virus, and while we have no information on the location of the dyes, the large surface area of the T4 NPs most likely prevents certain dye−dye quenching that would be observed with smaller VNPs.

Dye−protein interactions also cause quenching by photon-induced electron transfer (PET) and have been known to play a role in the quenching of Alexa dyes.[54] PET occurs when an excited dye molecule (donor) transfers its excited-state electron to another molecule (acceptor) when they are in close van der Waals contact. Recently, Chen et al. found that certain Alexa dyes were found to be quenched by interactions with tryptophan, tyrosine, methionine, and histidine residues.[54]

Dye-T4 NPs as Molecular Probes. The high fluorescence output and biocompatibility of dye-T4 NPs make them ideal molecular probes for cellular imaging and flow cytometry. To explore their application as molecular probes, the cellular uptake was explored using the lung cancer cell line, A549. Confocal microscopy was used to qualitatively investigate the interaction between the dye-T4 NPs and A549 cells at different incubation times (Figure 6). A549 cells were treated with Cy3-T4 (786 D/V) or Alexa 546-T4 NPs (2282 D/V) at a ratio of 1 cell to 10^5 T4 NPs. The nuclei were visualized by DAPI staining (blue), and the dye-T4 NPs are shown as small yellow spots distributed though the cell interior. Both dye-T4 NPs, Cy3-T4 and Alexa 546-T4 NPs, were clearly visible inside cells after 4, 8, and 24 h (Figure 6a−f). Unmerged and brightfield images of Alexa-546-T4 NP at 24 h incubation (Figure 6c) are shown in Figure S3 (Supporting Information).

The cellular uptake was also explored by flow cytometry, which can be used to separate and quantitatively measure fluorescently labeled cell populations using different molecular probes. We measured the cellular uptake by examining the change in fluorescence between the dye-T4 treated cells and the untreated cells. Figure 7a,b shows that a clear shift is present when cells are treated with both dye-T4 NPs in comparison to untreated cells. Furthermore, the results from the flow cytometry measurements were used to quantitatively measure the uptake of the dye-T4-NPs into cells at different time points. The percentage of cells positive for dye-T4 NPs was determined by subtracting the treated histograms from the untreated. Our results indicate that the percentage of cells that are positive for dye-T4 NPs is greater than 50% at all time points, suggesting that the uptake of T4 NP is quite efficient in our treatment condition. We also used flow cytometry to determine the cell viability after cellular uptake of dye-T4 NPs by staining both treated and untreated cells with a live/dead stain. More than 92% of the cells containing the dye-T4 NPs were alive compared with >95% of untreated cells (data not shown). This suggests that dye-T4 NPs have low cytotoxicity, even after 24 h. The ability to use dye-T4 NPs for flow cytometry opens the possibility of a number of applications including cell tracking, mechanistic studies, and immunoassays.

Aside from lung cancer cells, tail-less T4 NPs were also found to enter into noncancerous primary cultured cells, such as human endothelial cells, liver cells, and murine astrocytes in vitro (data not shown). While eukaryotic cells are not their natural hosts, coliphages along with their hosts are mammals' symbiots in the intestines and some phages may pass through the membrane and circulate in the blood system. Thus, T4 may adapt to the mammalian environment and likely interacts with eukaryotic

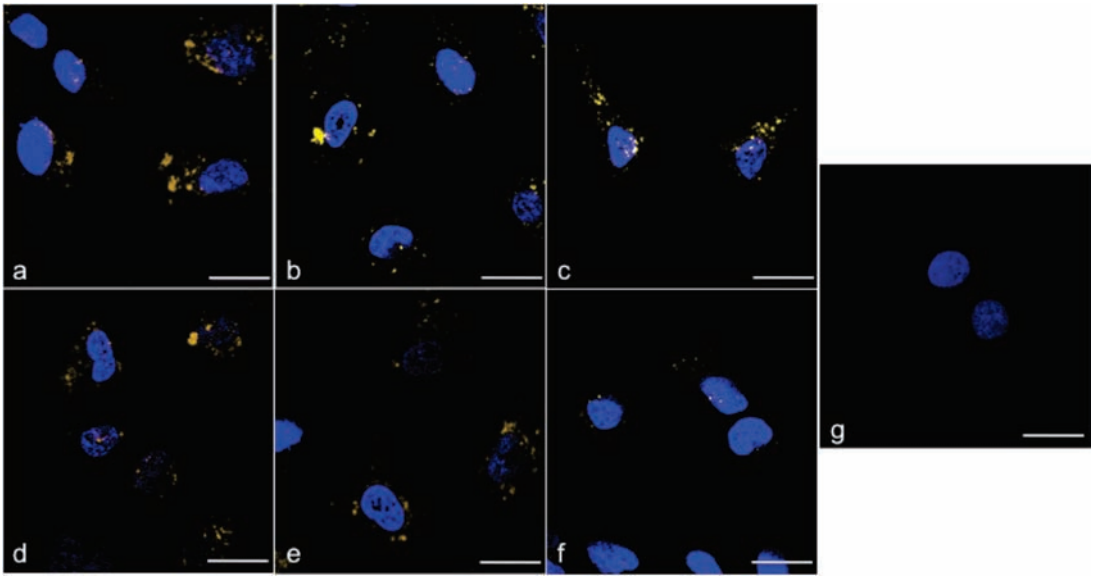


Figure 6. Confocal microscopy images of A549 cells after uptake of dye-T4 NPs at different time points. Uptake of Alexa 546-T4 NPs (2282 D/V): (a) 4 h after incubation, (b) 8 h, (c) 24 h. Uptake of Cy3-T4 NPs (786 D/V) after incubation at (d) 4 h, (e) 8 h, and (f) 24 h. (g) Untreated cells, negative control. Imaging was performed under 60× magnification. The scale bar is 10 μm.

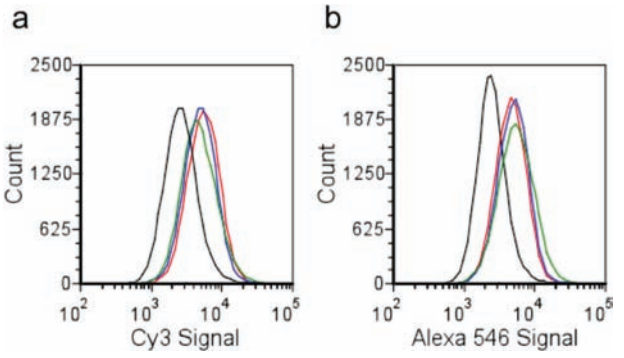


Figure 7. Flow cytometry histograms of A549 cells treated (a) Cy3-T4 NP (786 D/V) and (b) Alexa-T4 NP (2282 D/V) at different time points after incubation, 4 h (red), 8 h (blue), and 24 h (green); untreated cells after 24 h incubation are used as negative control (black line).

cells. It is believed that the interaction with eukaryotic cells is determined by the head surface protein contents and membrane proteins. Therefore, the uptake of dye-T4 by eukaryotic cells may be specific through certain molecular interactions. Some evidence suggests that bacteriophage T4 interacts with cancer cells in vitro by binding to integrin β3 through the Lys-Gly-Asp (KGD) amino acid motif, a homologue to Arg-Gly-Asp (RGD), within the minor capsid protein, gp24.[55] Likewise, our purified T4 NPs may preferentially bind and enter integrin $\beta3^+$ A549 and noncancerous primary cultured cells, possibly through receptor mediated endocytosis. We are currently investigating the cellular uptake mechanisms of dye-T4 NPs.

Interestingly, besides interacting with integrin β3, a nonessential head protein, Hoc, may also help to generate immune response by presenting phage T4 to macrophage and dendritic cells, through its three tandem immunoglobulin like domains.[56] This suggests that macrophage and dendritic cells may also preferentially take up dye-T4 NPs.

Table 1. Cell Proliferation Tracking over Time

time[a]	% positive[b]	total cells
0	93	81 900
24	84.2	105 700
48	24.8	161 000
72	4.6	382 600
96	1.4	1 105 000

[a] Time following 6 h T4 NP treatment. [b] % positive for A546 T4 NP as determined by Cellometer fluorescence measurements.

Cell Tracking. The ability to fluorescently label cells and track their proliferation can be useful in a variety of in vitro and in vivo studies. To explore this application for T4 NPs, we treated A549 cells with A546-T4 (2962 D/V) for 6 h and allowed the cells to grow for up to 96 h following treatment. A cell counter equipped with a fluorescence module was used to measure the number of cells and percentage of cells positive for T4-NPs. Table 1 shows that, as the cells divided and the number of total cells increased, the percentage of cells positive for A546-T4 NP decreased (Table 1). After 96 h, the percentage of cells positive for A546-T4 NPs decreased to 1.4%, a level equal to the background from untreated cells. We were also able to visualize this effect by taking images of the counted cells and observed a decrease in cellular fluorescence over time (Supporting Information Figure S4). When comparing the treated cells to untreated cells, there is no significant decrease in proliferation in dye-T4 NP treated cells (data not shown).

The fluorescence of the cells was also measured by flow cytometry. Figure 8 shows that, over time, as the cells proliferate, the fluorescence of the cell population decreases and the population becomes more heterogeneous (Figure 8). This supports the hypothesis that, over time, the fluorescence signals will decrease due to the dilution of A546-T4 NPs to newly divided cells. Our results demonstrate that the internal dye-T4 can

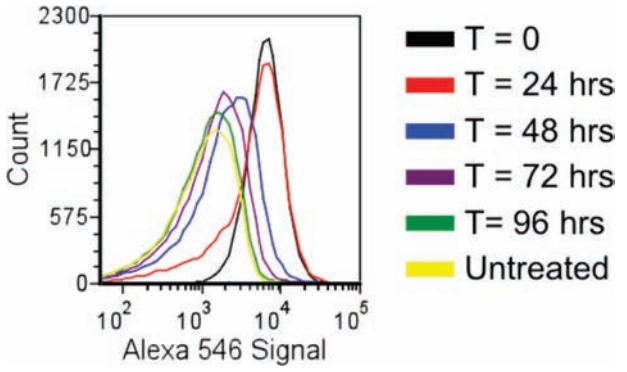


Figure 8. Flow cytometric detection of cell proliferation over time following A546-T4 NP treatment.

remain inside A549 cells for at least 72 h and dye-T4 NPs can be used to quantitatively track cellular proliferation.

CONCLUSIONS

We have successfully developed a novel viral nanoparticle, using tail-less T4 heads, as scaffolds for dye attachment, and moreover, the resulting fluorescent Cy3-T4 and Alexa 546-T4 can serve as molecular probes for cellular imaging and flow cytometry. Large surface areas and protein contents of T4 NPs give the tail-less T4 NPs more functional groups and more flexibility for dye conjugation than other viruses. The structure and size of dye-T4 NPs are close to that of unlabeled T4 NPs, and the T4 NPs are intact and stable after conjugation and purification. For the first time, we conclusively demonstrated that T4 enters eukaryotic cells using our dye-T4 NPs. Dye-T4 NPs can stay inside A549 cells at least 72 h and serve as ideal molecular probes for tracking cells, since cellular uptake of dye-T4 NPs can be clearly visualized by fluorescent microscopy, and cells positive for dye-T4 uptake can be distinguished and quantified by flow cytometry. The dye-T4 NPs can be used as a tool to understand in detail the molecular mechanisms of cell entry and the fate of the T4-NPs within cells. We are currently focusing on investigating this topic and the effect of surface modification on uptake into eukaryotic cells.

Besides using dye-T4 for in vitro studies, it is also possible to use dye-T4 NPs as *in vivo* molecular probes, although the chemical or genetic modification strategies for more surface functionalization with target ligands and chemicals are required.[6,7] The ability to conjugate the large surface area of the T4 NPs with up to 19 000 dyes/virus implies that the surface can be loaded with a variety of functionalities by using the available reactive amines. This functionalization capability will be useful in vivo when adding labels such as poly(ethylene glycol) (PEG) to prevent blood clearance, target antigens to ensure delivery to tumor tissues, and a large number of fluorescent dyes for highly fluorescent nanoprobes.

ASSOCIATED CONTENT

Supporting Information. A table containing T4 head proteins and total lysine amines; a table containing maximum fluorescence intensities for a selection of dye-T4 nanoparticles; the structure for Cy3 and Alexa 546; measurement of the number of dye/virus to the molar excess of dyes over T4 NPs; and additional cell images from confocal microscopy and Cellometer. This material is available free of charge via the Internet at http://pubs.acs.org.

AUTHOR INFORMATION

Corresponding Author

*E-mail: jinny.liu@nrl.navy.mil; phone: 202-404-6122; fax: 202-767-9594.

ACKNOWLEDGMENT

We would like to thank Dr. Lindsay Black from University of Maryland for his kind gift of T4 K10. O. O. wants to thank the National Science Foundation (Grant # DMR-0648917) for financial support. We also thank Drs. James Delehanty and Jing Zhou for their review of this manuscript. This work was supported by the Office of Naval Research. The opinions and assertions contained herein are the private ones of the authors and are not to be construed as official or reflecting the views of the Department of the Navy or the military at large.

REFERENCES

(1) Singh, P., Gonzalez, M. J., and Manchester, M. (2006) Viruses and their uses in nanotechnology. *Drug Dev. Res. 67*, 23–41.

(2) Fischlechner, M., and Donath, E. (2007) Viruses as building blocks for materials and devices. *Angew. Chem., Int. Ed. 46*, 3184.

(3) Mao, C., Liu, A., and Cao, B. (2009) Virus-based chemical and biological sensing. *Angew. Chem., Int. Ed. 48*, 6790–6810.

(4) Li, K., Nguyen, H. G., Lu, X., and Wang, Q. (2010) Viruses and their potential in bioimaging and biosensing applications. *Analyst 135*, 21–27.

(5) Lee, L. A., and Wang, Q. (2006) Adaptations of nanoscale viruses and other protein cages for medical applications. *Nanomed.: Nanotechnol., Biol., Med. 2*, 137–149.

(6) Manchester, M., and Singh, P. (2006) Virus-based nanoparticles (VNPs): Platform technologies for diagnostic imaging. *Adv. Drug Delivery Rev. 58*, 1505–1522.

(7) Steinmetz, N. F. (2010) Viral nanoparticles as platforms for next-generation therapeutics and imaging devices. *Nanomed.: Nanotechnol., Biol., Med. 6*, 634–641.

(8) Petrenko, V. A., and Vodyanoy, V. J. (2003) Phage display for detection of biological threat agents. *J. Microbiol. Methods 53*, 253–262.

(9) Paschke, M. (2006) Phage display systems and their application. *Appl. Microbiol. Biotechnol. 70*, 2–11.

(10) Ackermann, H. W., DuBow, M. S., Jarvis, A. W., Jones, L. A., Krylov, V. N., Maniloff, J., Rocourt, J., Safferman, R. S., Schneider, J., Seldin, L., Sozzi, T., Stewart, P. R., Werquin, M., and Wunsche, L. (1992) The species concept and its application to tailed phages. *Arch. Virol. 124*, 69–82.

(11) Ackermann, H. W., and Nguyen, T. M. (1983) Sewage coliphages studied by electron microscopy. *Appl. Environ. Microbiol. 45*, 1049–1059.

(12) Ren, Z. J., Lewis, G. K., Wingfield, P. T., Locke, E. G., Steven, A. C., and Black, L. W. (1996) Phage display of intact domains at high copy number: a system based on SOC, the small outer capsid protein of bacteriophage T4. *Protein Sci. 5*, 1833–1843.

(13) Ren, Z.-j., and Black, L. W. (1998) Phage T4 SOC and HOC display of biologically active, full length proteins on the viral capsid. *Gene 215*, 439–444.

(14) Jiang, J., Abu-Shilbayeh, L., and Rao, V. B. (1997) Display of a PorA peptide from *Neisseria meningitidis* on the bacteriophage T4 capsid surface. *Infect. Immunol. 65*, 4770–4777.

(15) Onorato, L., Stirmer, B., and Showe, M. K. (1978) Isolation and characterization of bacteriophage T4 mutant preheads. *J. Virol. 27*, 409–426.

(16) Wu, C., Barnhill, H., Liang, X., Wang, Q., and Jiang, H. (2005) A new probe using hybrid virus-dye nanoparticles for near-infrared fluorescence. *Opt. Commun. 255*, 366–374.

(17) Chithrani, B. D., Ghazani, A. A., and Chan, W. C. W. (2006) Determining the size and shape dependence of gold nanoparticle uptake into mammalian cells. *Nano Lett. 6*, 662–668.

(18) Olson, N. H., Gingery, M., Eiserling, F. A., and Baker, T. S. (2001) The structure of isometric capsids of bacteriophage T4. *Virology 279*, 385–391.

(19) Archer, M. J., and Liu, J. L. (2009) Bacteriophage T4 nanoparticles as materials in sensor applications: variables that influence their organization and assembly on surfaces. *Sensors 9*, 6298–6311.

(20) Gervais, L., Gel, M., Allain, B., Tolba, M., Brovko, L., Zourob, M., Mandeville, R., Griffiths, M., and Evoy, S. (2007) Immobilization of biotinylated bacteriophages on biosensor surfaces. *Sens. Actuators B 125*, 615–621.

(21) Goodridge, L. Bacteriophage linked immunosorbent assay for rapid, sensitive detection of multiple analytes; U. S. Patent 20070054292 A1; 2007.

(22) Shabani, A., Mohammed, Z., Beatrice, A., Marquette, C. A., Lawrence, M. F., and Mandeville, R. (2008) Bacteriophage-modified microarrays for the direct impedimetric detection of bacteria. *Anal. Chem. 80*, 9475–9482.

(23) Ren, Z. J., Tian, C. J., Zhu, Q. S., Zhao, M. Y., Xin, A. G., Nile, W. X., Ling, S. R., Zhu, M. W., Wu, J. Y., Lan, H. Y., Cao, Y. C., and Bi, Y. Z. (2008) Orally delivered foot-and-mouth disease virus capsid protomer vaccine displayed on T4 bacteriophage surface: 100% protection from potency challenge in mice. *Vaccine 26*, 1471–1481.

(24) Wu, J., Tu, C., Yu, X., Zhang, M., Zhang, N., Zhao, M., Nie, W., and Ren, Z. (2007) Bacteriophage T4 nanoparticle capsid surface SOC and HOC bipartite display with enhanced classical swine fever virus immunogenicity: A powerful immunological approach. *J. Virol. Methods 139*, 50–60.

(25) Rao, V. B. Methods and compositions comprising bacteriophage nanoparticles; WO 2005/058006 A2; 2005.

(26) Mattson, T. L. Inviable virus particles as scaffolds for constructing flexible detection systems; U. S. Patent 20020025515 A1; 2002. USA

(27) Fokine, A., Chipman, P. R., Leiman, P. G., Mesyanzhinov, V. V., Rao, V. B., and Rossmann, M. G. (2004) Molecular architecture of the prolate head of bacteriophage T4. *Proc. Natl. Acad. Sci. U.S.A. 101*, 6003–6008.

(28) Berlier, J. E., Rothe, A., Buller, G., Bradford, J., Gray, D. R., Filanoski, B. J., Telford, W. G., Yue, S., Liu, J., Cheung, C. -Y., Chang, W., Hirsch, J. D., Beechem, J. M., Haugland, R. P., and Haugland, R. P. (2003) Quantitative comparision of long-wavelength Alexa Fluor dyes to Cy dyes: Fluorescence of the dyes and their bioconjugates. *J. Histochem. Cytochem. 51*, 1699–1712.

(29) Panchuk-Voloshina, N., Haugland, R. P., Bishop-Steward, J., Bhalgat, M. K., Millard, P. J., Mao, F., Leung, W.-Y., and Haugland, R. P. (1999) Alexa dyes, a series of new fluorescent dyes that yield exceptionally bright, photostable conjugates. *J. Histochem. Cytochem. 47*, 1179–1188.

(30) Wang, Q., Kaltgrad, E., Lin, T., Johnson, J. E., and Finn, M. G. (2002) Natural supramolecular building blocks: Wild-type cowpea mosaic virus. *Chem. Biol. 9*, 805–811.

(31) Soto, C. M., Blaney, K. M., Dar, M., Khan, M., Lin, B., Malanoski, A. P., Tidd, C., Rios, M. V., Lopez, D. M., and Ratna, B. R. (2009) Cowpea mosaic virus nanoscaffold as signal enhancement for DNA microarrays. *Biosens. Bioelectron. 25*, 48–54.

(32) Soto, C. M., Blum, A. S., Vora, G. J., Lebedev, N., Meador, C. E., Won, A. P., Chatterji, A., Johnson, J. E., and Ratna, B. R. (2006) Fluorescent signal amplification of carbocyanine dyes using engineered viral nanoparticles. *J. Am. Chem. Soc. 128*, 5184–5189.

(33) Soto, C. M., Martin, B. D., Sapsford, K. E., Blum, A. S., and Ratna, B. R. (2008) Toward single molecule detection of Staphylococcal Enterotoxin B: Mobile sandwich immunoassay on gliding microtubules. *Anal. Chem. 80*, 5433–5440.

(34) Barnhill, H. N., Reuther, R., Ferguson, L. P., Dreher, T., and Wang, Q. (2007) Turnip yellow mosaic virus as a chemoaddressable bionanoparticle. *Bioconjugate Chem. 18*, 852–859.

(35) Schlick, T. L., Ding, Z., Kovacs, E. W., and Francis, M. B. (2005) Dual-surface modification of the tobacco mosaic virus. *J. Am. Chem. Soc. 127*, 3718–3723.

(36) Bruckman, M. A., Kaur, G., Lee, A. L., Xie, F., Sepulveda, J., Breitenkamp, R., Zhang, X., Joralemon, M., Russell, T. P., Emrick, T., and Wang, Q. (2008) Surface modification of tobacco mosaic virus with "click" chemistry. *ChemBioChem 9*, 519–523.

(37) Steinmetz, N. F., Mertens, M. E., Taurog, R. E., Johnson, J. E., Commandeur, U., Fischer, R., and Manchester, M. (2010) Potato virus X as a novel platform for potential biomedical applications. *Nano Lett. 10*, 305–312.

(38) Li, K., Chen, Y., Li, S., Nguyen, G. H., Niu, Z., You, S., Mello, C. M., Lu, X., and Wang, Q. (2010) Chemical modification of M13 bacteriophage and its application in cancer cell imaging. *Bioconjugate Chem. 21*, 1369–1377.

(39) Demir, M., and Stowell, M. H. B. (2002) A chemoselective biomolecular template for assembling diverse nanotubular materials. *Nanotechnology 13*, 541–544.

(40) Lin, H., Rao, V. B., and Black, L. W. (1999) Analysis of capsid portal protein and terminase functional domains: Interaction sites required for DNA packaging in bacteriophage T4. *J. Mol. Biol. 289*, 249–260.

(41) Chatterji, A., Ochoa, W. F., Paine, M., Ratna, B. R., Johnson, J. E., and Lin, T. (2004) New addresses on an addressable virus nanoblock uniquely reactive Lys residues on cowpea mosaic virus. *Chem. Biol. 11*, 855–863.

(42) Huang, S., Wang, H., Carroll, C. A., Hayes, S. J., Weintraub, S. T., and Serwer, P. (2004) Analysis of proteins stained by Alexa dyes. *Electrophoresis 25*, 779–784.

(43) Fokine, A., Bowman, V. D., Battisti, A. J., Li, Q., Chipman, P. R., Rao, V. B., and Rossman, M. G. (2007) Cryo-electron microscopy study of bacteriophage T4 displaying antrax toxin proteins. *Virology 367*, 422–427.

(44) Notman, R., Noro, M., O'Malley, B., and Anwar, J. (2006) Molecular basis for dimethylsulfoxide (DMSO) action on lipid membranes. *J. Am. Chem. Soc. 128*, 13982–13983.

(45) Yu, Z.-W., and Quinn, P. J. (1994) Dimethyl sulfoxide: a review of its applications in cell biology. *Biosci. Rep. 14*, 259–281.

(46) Roos, W. H., and Wuite, G. J. L. (2009) Nanoindentation studies reveal material properties of viruses. *Adv. Mater. (Weinheim, Ger.) 21*, 1187–1192.

(47) Buschmann, V., Weston, K. D., and Sauer, M. (2003) Spectroscopic study and evaluation of red-absorbing fluorescent dyes. *Bioconjugate Chem. 14*, 195–204.

(48) Anderson, G. P., and Nerukar, N. L. (2002) Improved fluoroimmunoassays using the dye Alexa Fluor 647 with the RAPTOR, a fiber optic biosensor. *J. Immunol. Methods 271*, 17–24.

(49) Mujumdar, R. B., Ernst, L. A., Mujumdar, S. R., Lewis, C. J., and Waggoner, A. S. (1993) Cyanine dye labeling reagents: Sulfoindocyanine succinimidyl esters. *Bioconjugate Chem. 4*, 105–111.

(50) Gruber, H. J., Hahn, C. D., Kada, G., Riener, C. K., Harms, G. S., Ahrer, W., Dax, T. G., and Knaus, H.-G. (2000) Anomalous fluorescence enhancement of Cy3 and Cy3.5 versus anomalous fluorescence loss of Cy5 and Cy7 upon covalent linking to IgG and noncovalent binding to avidin. *Bioconjugate Chem. 11*, 696–704.

(51) West, W., and Pearce, S. (1965) The dimeric state of cyanine dyes. *J. Phys. Chem. 69*, 1894–1903.

(52) West, W., Pearce, S., and Grum, F. (1967) Stereoisomerism in cyanine dyes-meso-substituted thiacarbocyanines. *J. Phys. Chem. 71*, 1316–1326.

(53) Cox, W. G., Beaudet, M. P., Agnew, J. Y., and Ruth, J. L. (2004) Possible sources of dye-related signal correlation bias in two-color DNA microarray assays. *Anal. Biochem. 331*, 243–254.

(54) Chen, H., Ahsan, S. S., Santiago-Berrios, M. E. B., Abruna, H. D., and Webb, W. W. (2010) Mechanisms of quenching of Alexa fluorophores by natural amino acids. *J. Am. Chem. Soc. 132*, 7244–7245.

(55) Dabrowska, K., Opolski, A., Wietrzyk, J., Switala-Jelen, K., Boratynski, J., Nasulewicz, A., Lipinska, L., Chybicka, A., Kujawa, M.,

Zabel, M., Dolinska-Krajewska, B., Piasecki, E., Weber-Dabrowska, B., Rybka, J., Salwa, J., Wojdat, E., Nowaczyk, M., and Gorski, A. (2004) Antitumor activity of bacteriophages in murin experimental cancer models caused possibly by inhibition of B3 integrin signaling pathway. *Acta Virol. 48*, 241–248.

(56) Bateman, A., Eddy, S. R., and Mesyanzhinov, V. V. (1997) A member of the immunoglobin superfamily in bacteriophage T4. *Virus Genes 14*, 163–165.

Supporting Information

for

Engineered T4 viral nanoparticles for cellular imaging and flow cytometry

Kelly L. Robertson, Carissa M. Soto, Marie J. Archer, Onyekachi Odoemene, and Jinny L. Liu

Table S1. Gene products and numbers of potential reactive amine groups on T4 NP scaffolds.

Gene Product	Copy #/NP	Lysine #/copy	Total Lysine #
gp 20	12	39	468
Hoc[1]	155	22	3410
Soc[2]	810	8	6480
gp 23*	930	22	20460
gp 24*	55	27	1485
Total amines from Lysine side chain			**32303**

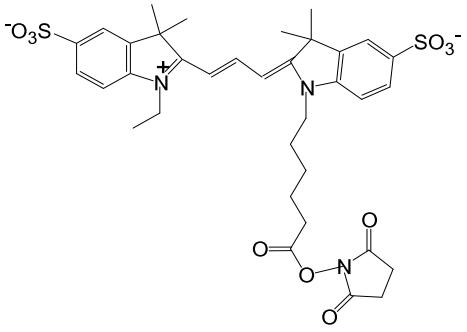
[1] Hoc stands for highly immunogenic outer capsid protein.
[2] Soc stands for small outer capsid protein.
*N-terminus cleaved gene product (gp) in T4 mature NPs.

Table S2. Dyes/Virus vs. maximum fluorescence intensity

Cy3-T4		Alexa 546-T4	
Cy3-T4	Fluorescence at 570 nm[A]	Alexa 564-T4	Fluorescence at 575 nm[B]
355	727	323	73
551	840	431	82
571	860	523	168
632	685	884	141
646	860	959	146
716	1019	1472	123
728	868	1356	129
866	807	1959	210
1159	845	2167	224
1247	672	2282	148
1816	808	2860	162
2565	793	2906	151
		3087	125
		3134	185
		3583	110

[A] – Collected using high PMT setting
[B] – Collected using medium PMT setting

a



b

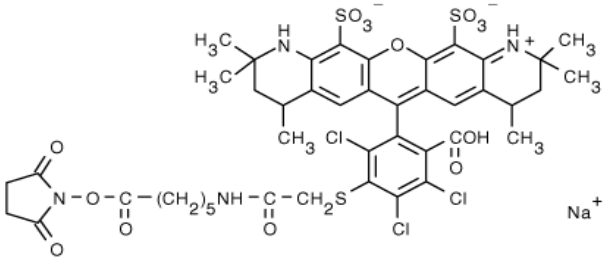


Figure S1. Chemical structures of (a) Cy3 NHS ester dye (49) and (b) Alexa Fluor NHS ester (www.invitrogen.com).

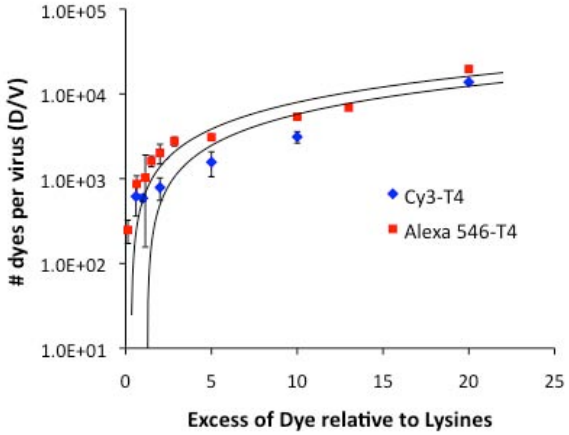


Figure S2. Dye/virus vs the molar excess of dyes over T4 NPs. Cy3 NHS ester (blue diamonds) and Alexa Fluor® 546 NHS ester (red squares). Different concentrations of dye NHS ester was mixed with same amount of the T4 NPs. The reaction volume was 125 µL for all the samples.

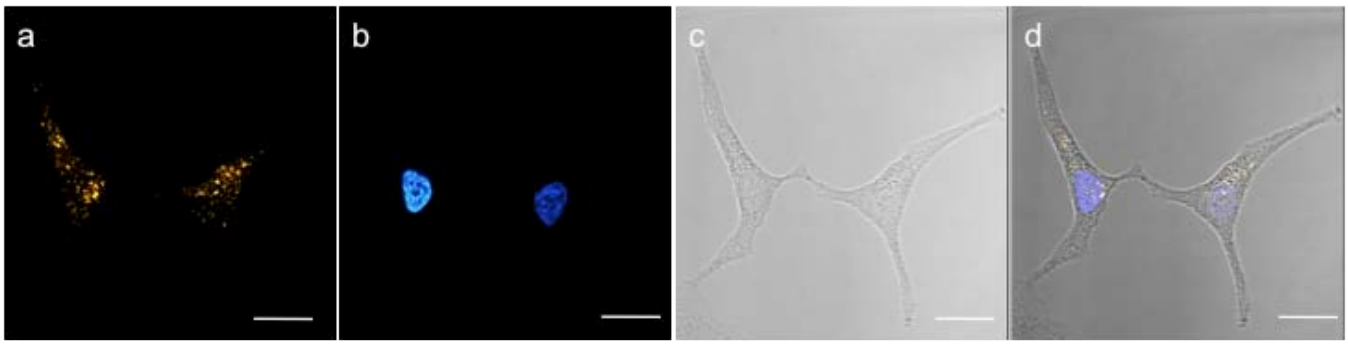


Figure S3: Confocal microscopy images of A549 cells after uptake of Alexa-T4 NPs at 24hrs. (a) Alexa 546 excitation (b) DAPI excitation (c) Brightfield (d) Merge of a-c. Imaging was performed under 60x magnification. The scale bar is 10 µm.

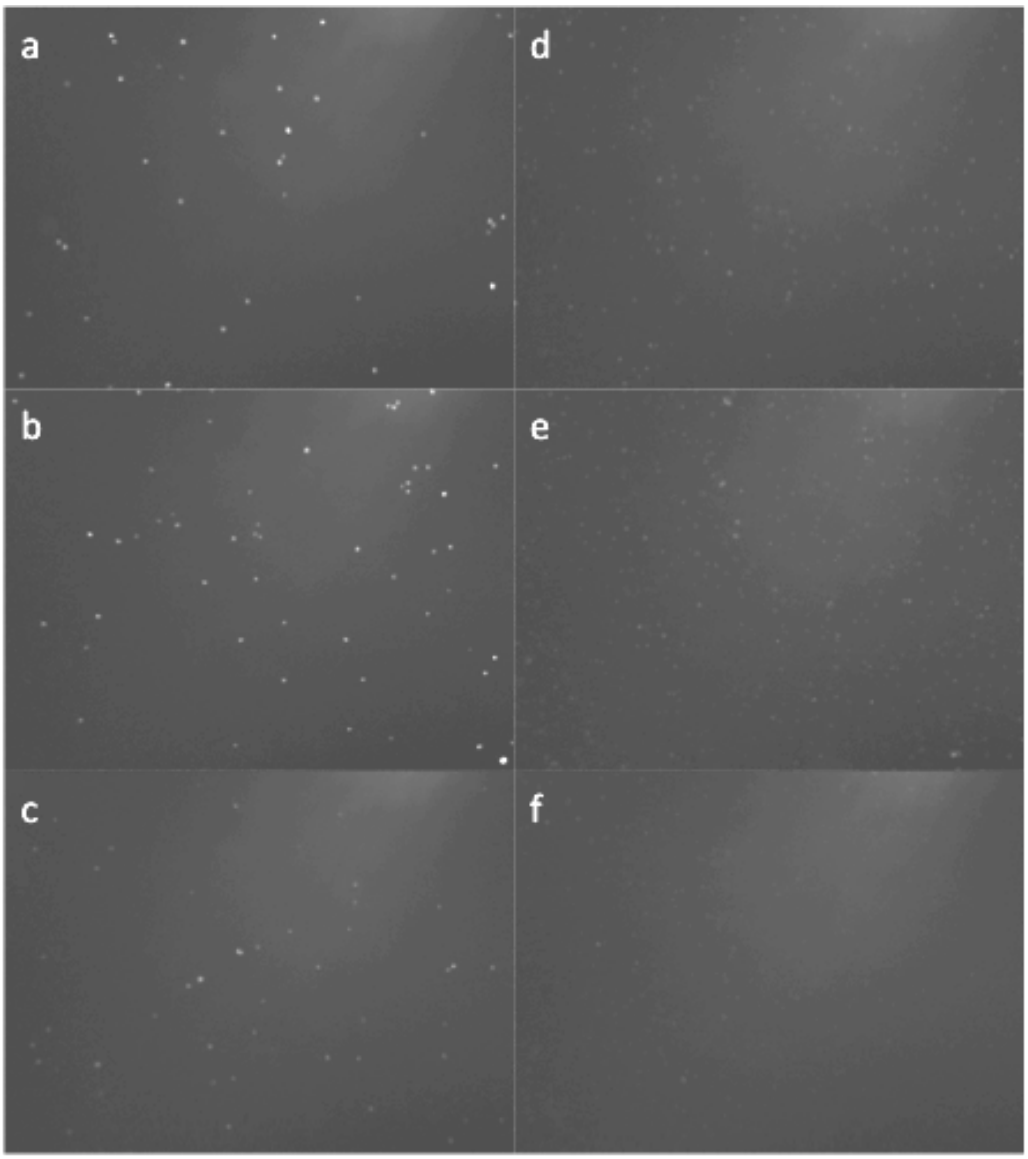


Figure S4: Cellometer Vision images of A549 cells treated with Alexa 546-T4 NPs at 1 x 10^5 NP/cell for 6hrs. After washing, the cells were incubated up to 96 hrs and measured on the Cellometer every 24hrs. a) immediately following incubation, b) 24 hrs, c) 48 hrs, d) 72 hrs, e) 96 hrs, f) Untreated.

Bioconjugate Chemistry

ARTICLE

pubs.acs.org/bc

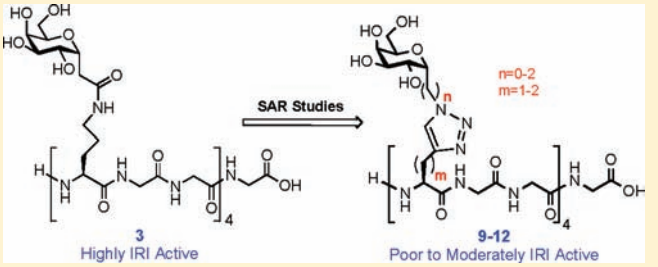
Synthesis of C-Linked Triazole-Containing AFGP Analogues and Their Ability to Inhibit Ice Recrystallization

Chantelle J. Capicciotti, John F. Trant, Mathieu Leclère, and Robert N. Ben*

Department of Chemistry, D'Iorio Hall, 10 Marie Curie, University of Ottawa, Ottawa, Ontario, Canada, K1N 6N5.

Supporting Information

ABSTRACT: C-Linked antifreeze glycoprotein (C-AFGP) analogues have been shown to have potent ice recrystallization inhibition (IRI) activity. However, the lengthy synthesis of these compounds is not amenable to large-scale preparation for the many commercial, industrial, and medical applications that exist. This paper describes the synthesis of triazole-containing AFGPs using a convergent solid-phase synthesis (SPS) approach in which multiple carbohydrate derivatives are coupled to a resin-bound synthetic peptide in a single step. Modified "Click" conditions using dry DMF as solvent with catalytic Cu(II), sodium ascorbate, and microwave radiation afforded the synthesis of AFGP analogues **9**−**12** in 16−54% isolated yield. Compound **9** demonstrated no IRI activity, while compounds **10**, **11**, and **12** were moderate inhibitors of ice recrystallization. These results suggest that, while the triazole group is a structural mimetic of an amide bond, the amide bond in C-AFGP analogue **3** is an essential structural feature necessary for potent IRI activity.



INTRODUCTION

Antifreeze glycoproteins (AFGPs) are found in many deep sea Teleost fish and serve to protect these organisms against cryoinjury and death. This is accomplished by inhibiting the growth of ice crystals *in vivo*—a phenomenon referred to as thermal hysteresis (TH). AFGPs are also potent inhibitors of ice recrystallization, and it has been recently hypothesized that this property would be beneficial for a cryoprotectant.[1] Cryopreservation experiments have been performed with AFGPs, but thermal hysteresis activity has been shown to cause significant cellular damage at temperatures below the thermal hysteretic gap,[2,3] thus ensuring that these compounds will not be further developed as cryoprotectants. However, AFGP analogues possessing "custom-tailored antifreeze activity" (i.e., are potent inhibitors of ice recrystallization but do not possess TH activity) have great potential as cryoprotectants that is presently unrealized.

During the past decade, our lab has been actively designing and synthesizing C-linked analogues of the native AFGP (C-AFGPs) in an effort to better understand their interactions at the ice−bulk water interface. Towards this end, we have reported the synthesis of several C-AFGP analogues (e.g., **3** and **5**) that exhibit potent ice recrystallization inhibition (IRI) activity but display no TH activity and have tremendous potential as novel cryoprotectants (Figure 1).[4,5] Structure−function studies on these C-AFGPs have questioned the functional importance of the amide bond in **3** for IRI activity. For instance, when the amide bond is removed as in C-serine analogue **5**, IRI activity is retained.[5] In contrast, other studies have shown that activity is significantly decreased when the length of the amide bond-containing side chain in **3** was either lengthened or shortened (Figure 1).[6] Molecular dynamics (MD) simulations and variable temperature (VT) NMR experiments suggest that the IRI activity of **3** is attributed to an unusual conformation in which the carbohydrate moiety folds back over the peptide chain creating a hydrophobic pocket. It was hypothesized that this "pocket" disrupts the ordering of water molecules in the primary hydration shell of the galactose moiety, resulting in IRI activity.[6] However, it is not known whether the amide bond in these analogues is an important structural feature necessary for this activity. One manner in which to probe the importance of this linkage is to utilize a suitable isostere. The 1,4-disubstituted triazole has been shown by Wong and co-workers to be an isostere of a *Z*-amide bond (Figure 2).[7,8] Furthermore, the mild, highly efficient copper-catalyzed Huisgen cycloaddition for the preparation of triazoles has facilitated their use in many biologically significant molecules.[9−19]

Prior syntheses of C-AFGPs by our laboratory have utilized a traditional linear synthesis requiring the preparation of a glycosylated amino acid prior to solid-phase synthesis (SPS). This approach can be lengthy and expensive.[20,21] Alternatively, convergent methodologies have been reported for the synthesis of glycoconjugates in which several carbohydrates are simultaneously coupled to the resin-bound peptide.[22−24] Two convergent syntheses of triazole-containing AFGP analogues have been reported. A triazole-containing proline AFGP analogue was

Received: September 2, 2010
Revised: March 14, 2011
Published: April 01, 2011

ACS Publications © 2011 American Chemical Society

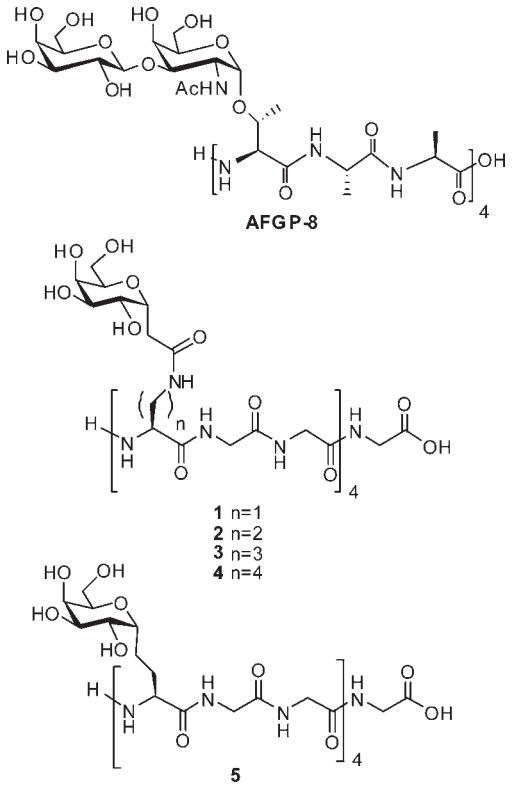


Figure 1. Previously prepared C-linked *C*-AFGP analogues.

synthesized in a solution-phase approach through coupling of an acetylenic carbohydrate derivative and an azido peptide using 10−20% $CuSO_4$ and 25−50% sodium ascorbate at 80 °C in the presence of microwaves.[25] In another approach, three AFGP peptoids (**6**, **7**, and **8**, shown in Figure 3) were prepared by coupling azido sugars with a resin-bound acetylenic peptoid using excess CuI and sodium ascorbate in anhydrous DMF and DIPEA.[26] On the basis of this precedent, we sought to prepare triazole-containing AFGP analogues of **3** using "Click" chemistry in a convergent solid-phase approach. The structures of these analogues (**9**−**12**) are shown in Figure 4. The goal of this study is to understand the functional importance of the amide bond in the side chain of *C*-AFGP analogue **3**.

EXPERIMENTAL PROCEDURES

General Methods and Materials. All anhydrous reactions were performed in flame-dried glassware under a positive pressure of dry argon. Air- or moisture-sensitive reagents and anhydrous solvents were transferred with oven-dried syringes or cannulae. All flash chromatography was performed with E. Merck silica gel 60 (230−400 mesh). All solution-phase reactions were monitored using analytical thin layer chromatography (TLC) with 0.2 mm precoated silica gel aluminum plates 60 F254 (E. Merck). Components were visualized by illumination with a short-wavelength (254 nm) ultraviolet light and/or staining (ceric ammonium molybdate, potassium permanganate, or orcinol stain solution). Dry-vacuum chromatography was carried out according to the protocol outlined by Pedersen and Rosenbohm.[27] All solvents used for anhydrous reactions were distilled. Tetrahydrofuran (THF) was distilled from sodium/benzophenone under nitrogen. Dichloromethane (DCM), triethylamine,

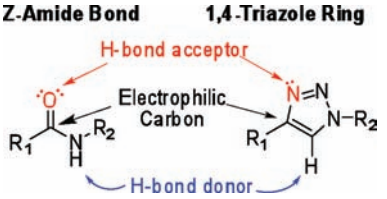


Figure 2. Electronic similarities between a Z-amide bond and a 1,4-disubstituted triazole ring.

and diisopropylethylamine (DIPEA) were distilled from calcium hydride. *N,N*-Dimethylformamide (DMF) was stored over activated 4 Å molecular sieves under argon. ^1H (400 or 500 MHz) and ^{13}C NMR (100 or 125 MHz) spectra were recorded at ambient temperature on a Bruker Avance 400, Bruker Avance 500, or Varian Inova 500 spectrometer. Deuterated chloroform ($CDCl_3$), methanol (CD_3OD), or water (D_2O) were used as NMR solvents. Chemical shifts are reported in ppm downfield from trimethylsilane (TMS) or the solvent residual peak as an internal standard. Splitting patterns are designated as follows: s, singlet; d, doublet; t, triplet; q, quartet; m, multiplet; and br, broad. Low resolution mass spectrometry (LRMS) was performed on a Micromass Quatro-LC Electrospray spectrometer with a pump rate of 20 μL/min using electrospray ionization (ESI), a Voyager DE-Pro matrix-assisted laser desorption/ionization-time-of-flight (MALDI-TOF) (Applied Biosystem, Foster City, CA) mass spectrometer operated in the reflectron/positive-ion mode with DHB in 20% EtOH/H_2O as the MALDI matrix, or a Bruker Microflex MALDI-TOF mass spectrometer with DHB in 20% acetonitrile/H_2O as the MALDI matrix. Analytical and preparatory scale RP-HPLC were carried out with Varian Polaris C-18 columns on a Varian Prostar HPLC system equipped with a variable wavelength detector (ProStar 330 PDA). Desalting was accomplished using C18 solid-phase extraction cartridges (Discovery, Supelco) using 40% acetonitrile in water for elution of glycopeptides. All yields are unoptimized.

Circular Dichroism. CD spectra of the glycopolymers **9**−**12** were obtained using a Jasco model *J*-810 automatic recorder spectropolarimeter interfaced with a Dell computer. All of the measurements were performed in quartz cells with 1.0 cm path length. Spectra were obtained with a 1.0 nm bandwidth, a time constant of 2 s, and a scan speed of 50 nm/min. Eight scans were added to improve the signal-to-noise ratio, and baseline corrections were made against each sample. All of the spectra were recorded between 190 and 300 nm, and all of the CD experiments were performed in doubly distilled H_2O at pH 7.4. Data obtained from CD spectroscopy were converted into molar ellipticities (deg cm^2 dmol^{-1}). Glycopeptide secondary structures were estimated using the deconvolution software *CD Pro*. The data from each spectrum were analyzed using three different deconvolution programs: SELCON3, CDSSTR, and CONTINLL. Of these three programs, SELCON3 and CONTINLL gave the most consistent results. IBASIS 5 was used as the set of reference proteins; it contains 37 proteins with α-helix, β-structure, polyproline II, and unordered conformations with optimal wavelengths of 185−240 nm.[6]

Thermal Hysteresis (TH) Assay. Nanoliter osmometry was performed using a Clifton nanoliter osmometer (Clifton Technical Physics, Hartford, NY), as described by Chakrabartty and Hew.[28] All of the measurements were performed in doubly distilled water. Ice crystal morphology was observed through a

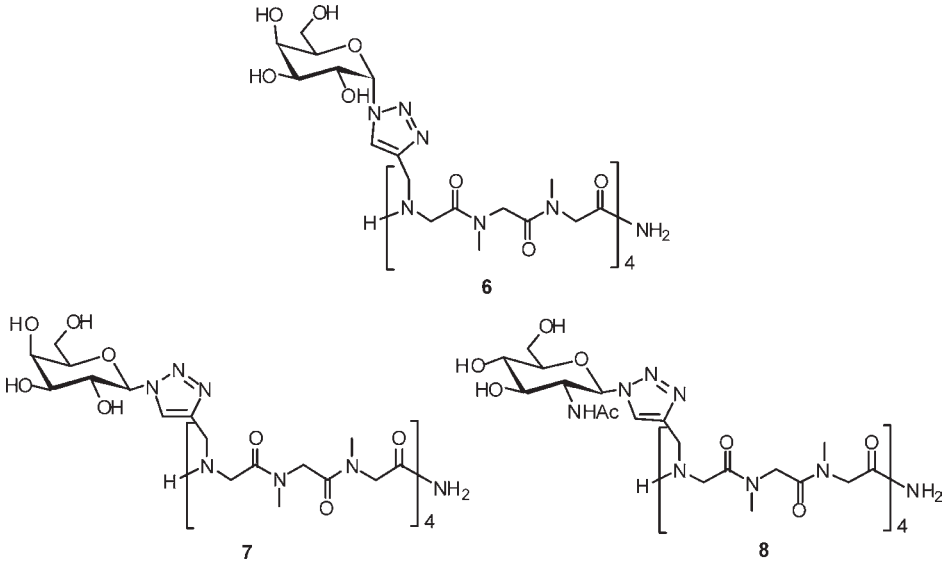


Figure 3. Triazole-containing peptoid analogues synthesized by Norgren et al.

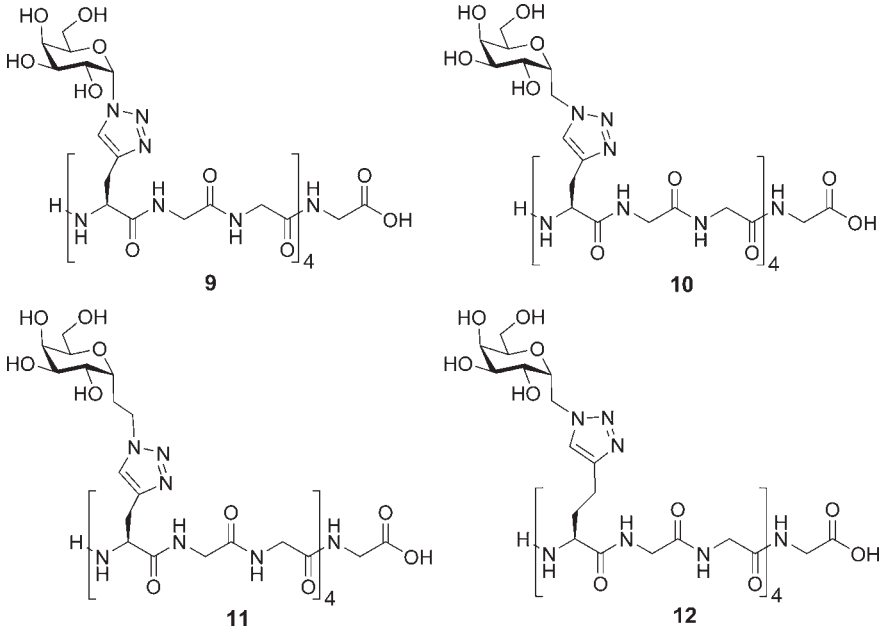


Figure 4. Proposed structures of triazole-containing AFGP analogues.

Leitz compound microscope equipped with an Olympus 20× (infinity-corrected) objective, a Leitz Periplan 32× photo eyepiece, and a Hitachi KPM2U CCD camera connected to a Toshiba MV13K1 TV/VCR system. Still images were captured directly using a Nikon CoolPix digital camera.

Ice Recrystallization Inhibition (IRI) Assay. Sample analysis for IRI activity was performed using the "splat cooling" method as previously described.[1] In this method, the analyte was dissolved in phosphate buffered saline (PBS) solution and a 10 μL droplet of this solution was dropped from a micropipet through a 2-m-high plastic tube (10 cm in diameter) onto a block of polished aluminum precooled to approximately −80 °C. The droplet froze instantly on the polished aluminum block and was approximately 1 cm in diameter and 20 μm thick. This wafer was then carefully removed from the surface of the block and transferred to a cryostage held at −6.4 °C for annealing. After a period of 30 min, the wafer was photographed between crossed polarizing filters using a digital camera (Nikon CoolPix 5000) fitted to the microscope. A total of three images were taken from each wafer. During flash freezing, ice crystals spontaneously nucleated from the supercooled solution. These initial crystals were relatively homogeneous in size and quite small. During the annealing cycle, recrystallization occurred, resulting in a dramatic increase in ice crystal size. A quantitative measure of the difference in recrystallization inhibition of two compounds X and Y is the difference in the dynamics of the ice crystal size distribution. Image analysis of the ice wafers was performed using a novel domain recognition software (DRS) program.[29]

dx.doi.org/10.1021/bc100394k |*Bioconjugate Chem.* 2011, 22, 605–616

This processing employed the Microsoft Windows Graphical User Interface to allow a user to visually demarcate and store the vertices of ice domains in a digital micrograph. The data was then used to calculate the domain areas. All data was plotted and analyzed using Microsoft *Excel*. IRI activity is reported as a ratio of the mean grain size (MGS) of ice crystals in the presence of the solute divided by the mean grain size (MGS) of ice crystals in a control solution of phosphate buffered saline (PBS). Small ratios indicate high levels of ice recrystallization inhibition.

***N*-[[(9*H*-Fluoren-9-ylmethoxy)carbonyl]amino]-L-propargylglycine allyl ester (13).** In a flame-dried round-bottom flask with 4 Å molecular sieves, Fmoc-L-Propargylglycine (338 mg, 1.01 mmol) was dissolved in anhydrous DCM (7 mL) under argon atmosphere. HBTU (460 mg, 1.2 mmol) was added and the mixture was stirred for 20 min. Allyl alcohol (347 μL, 5.1 mmol) was added, followed by a dropwise addition of DIPEA (355.5 μL, 2.04 mmol). The reaction was stirred at room temperature for 16 h. Upon consumption of starting material, the reaction was diluted with DCM, filtered through a Celite pad, and washed with 10% HCl, $NaHCO_3$, and brine successively. The final product was purified by dry vacuum chromatography (DVC) to yield 326 mg of a white powder (86% yield). ^{1}H NMR (400 MHz, $CDCl_3$): δ_{ppm} 7.77 (d, 2H, J = 7.5 Hz), 7.61 (d, 2H J = 7.4 Hz), 7.40 (t, 2H, J = 7.5 Hz), 7.32 (ddd, 2H, J = 7.5, 4.3, 1.1 Hz), 5.92 (ddd, 1H, J = 16.4, 10.8, 5.6 Hz), 5.66 (d, 1H, J = 8.1 Hz), 5.36 (dd, 1H, J = 17.2, 0.8 Hz), 5.28 (dd, 1H, J = 10.4, 0.9 Hz), 4.70 (dd, 2H, J = 2.7, 1.3 Hz), 4.61−4.54 (m, 1H), 4.40 (d, 2H, J = 7.2 Hz), 4.25 (t, 1H, J = 7.2 Hz), 2.82 (dd, 2H, J = 4.5, 2.6 Hz), 2.08 (t, 1H, J = 2.4 Hz). ^{13}C NMR (100 MHz, $CDCl_3$): δ_{ppm} 170.0, 155.6, 143.8, 143.7, 141.3, 131.3, 127.7, 127.1, 125.1, 120.0, 119.0, 72.0, 67.3, 66.4, 52.4, 47.1, 22.8. ESI-MS m/z calcd for $C_{23}H_{21}NO_4$ $[M+H]^+$: 376.154; $[M+Na]^+$: 398.137. Found: 376.14, 398.12.

2,3,4,6-Tetra-*O*-acetyl-α-D-galactopyranosyl Azide (14). 2,3,4,6-Tetra-*O*-acetyl-β-D-galactopyranosyl chloride[30] (4.68 g, 12.8 mmol) was dissolved in 15 mL of HMPA. Sodium azide (2.5 g, 38.4 mmol) was added and the reaction was stirred vigorously for 16 h at ambient temperature. The mixture was poured into an ice−water mixture and the solid was collected by filtration and washed with water. The product was recrystallized from ether and petroleum ether to yield 4.3 g of white crystals (89% yield). Characterization data are consistent with that reported previously in the literature.[31] ^{1}H NMR (400 MHz, $CDCl_3$): δ_{ppm} 5.67 (d, 1H, J = 3.9 Hz), 5.46 (dd, 1H J = 2.9, 1.2 Hz), 5.25 (dd, 1H, J = 10.8, 3.0 Hz), 5.20 (dd, 1H, J = 10.8, 3.9 Hz), 4.37 (dd, 1H, J = 6.5, 6.5 Hz), 4.12 (dd, 2H, J = 6.5, 4.4 Hz), 2.15 (s, 3H), 2.11 (s, 3H), 2.06 (s, 3H), 2.00 (s, 3H). ^{13}C NMR (100 MHz, $CDCl_3$): δ_{ppm} 170.4, 170.1, 170.0, 169.8, 86.7, 68.6, 67.6, 67.4, 67.2, 61.5, 20.67, 20.64, 20.60, 20.5. ESI-MS m/z calcd for $C_{14}H_{20}N_3O_9$ $[M+H]^+$: 374.12; $[M+Na]^+$: 396.10. Found: 374.09, 396.02.

1-Azido-2-(2,3,4,6-tetra-*O*-acetyl-α-D-galactopyranosyl) ethane (16). 2-(2,3,4,6-Tetra-*O*-acetyl-α-D-galactopyranosyl) acetaldehyde[5] (2.5 g, 6.7 mmol) was added to a round-bottom flask purged with argon and cooled to 0 °C. 70 mL of MeOH was then added followed by sodium borohydride (983 mg, 26 mmol) and the reaction was stirred for 40 min when TLC (1:1 hexanes:ethyl acetate) analysis showed consumption of starting material. The reaction was then quenched with 4 mL of acetic acid and the solvent was removed *in vacuo*. Following evaporation, the product was dissolved in ethyl acetate and washed successively with 10% HCl, sodium bicarbonate, and brine to yield 2.6 g of crude oil. The product was sufficiently pure to be used directly in the next transformation.

A round-bottom flask was cooled to 0 °C in an ice bath. Crude 2-(2,3,4,6-tetra-*O*-acetyl-α-D-galactopyranosyl)ethanol (2.6 g, 6.7 mmol) and methanesulfonylchloride (2.1 mL, 26.8 mmol) were then added to the flask and dissolved in 33 mL of pyridine (0.2 M). The reaction was stirred at 0 °C for 1.5 h. Once complete, the reaction was diluted with ethyl acetate and was washed successively with saturated aqueous copper(II) acetate, 10% HCl, saturated sodium bicarbonate, and brine. The organic layer was then dried with magnesium sulfate and the solvent removed *in vacuo* to yield a slightly brown solid. This crude product (2.2 g) was used directly without any further purification.

The crude mesylate (2.2 g, 4.8 mmol) was dissolved in 20 mL of DMF under argon. Sodium azide (760 mg, 11.7 mmol) was added and the reaction was stirred vigorously at room temperature overnight. The mixture was then poured into an ice−water mixture and the solid was filtered out and washed with water. Flash chromatography (7:3 ethyl acetate:hexanes) followed by recrystallization from ether and hexanes yielded 1.6 g (68.2% over three steps) of **16** as a pure white powder. Characterization data are consistent with that reported previously in the literature.[32] ^{1}H NMR (400 MHz, $CDCl_3$): δ_{ppm} 5.42 (dd, 1H, J = 3.1, 3.1 Hz), 5.25 (dd, 1H, J = 8.7, 4.7 Hz), 5.18 (dd, 1H, J = 8.7, 3.3 Hz), 4.34−4.32 (m, 2H), 4.09 (ddd, 2H, J = 7.8, 5.9, 3.4 Hz), 3.43−3.41 (m, 2H), 2.12 (s, 3H), 2.10 (s, 3H), 2.07 (s, 3H), 2.05 (s, 3H), 1.99−1.87 (m, 1H), 1.75−1.65 (m, 1H). ^{13}C NMR (100 MHz, $CDCl_3$): δ_{ppm} 170.6, 170.0, 169.8, 169.7, 69.0, 68.9, 68.2, 67.9, 67.2, 61.2, 47.7, 26.0, 20.8, 20.8, 20.7. ESI-MS m/z calcd for $C_{16}H_{23}N_3O_9$ $[M+H]^+$: 402.151; $[M+Na]^+$: 424.133. Found: 402.13, 424.11.

(2,3,4,6-Tetra-*O*-acetyl-α-D-galactopyranosyl)methyl Azide (24). Azido sugar **24** was synthesized according to a modified procedure[33] as indicated in Scheme 1 in the Supporting Information. Spectral data are consistent with previously published data. ^{1}H NMR (400 MHz, $CDCl_3$): δ_{ppm} 5.44 (dd, 1H, J = 3.3, 3.3 Hz), 5.27 (dd, 1H, J = 8.4, 4.6 Hz), 5.22 (dd, 1H, J = 8.4, 3.2 Hz), 4.39 (m, 2H), 4.25 (ddd, 1H, J = 8.0, 4.5, 3.4 Hz), 4.11 (dd, 1H, J = 11.7, 4.7 Hz), 3.63 (dd, 1H, J = 13.5, 8.8 Hz), 3.24 (dd, 1H, J = 13.5, 3.7 Hz), 2.12 (s, 3H), 2.11 (s, 3H), 2.07 (s, 3H), 2.06 (s, 3H). ^{13}C NMR (100 MHz, $CDCl_3$): δ_{ppm} 170.7, 169.8, 169.6, 169.5, 70.8, 69.8, 67.7, 67.5, 66.9, 60.7, 48.3, 20.67, 20.66, 20.59. ESI-MS m/z calcd for $C_{15}H_{21}N_3O_9$ $[M + K]^+$: 426.091. Found: 426.12.

(2*S*)-1-Allyl-2-[[(9*H*-Fluoren-9-ylmethoxy)carbonyl]amino]-3-(4-(2,3,4,6-tetra-*O*-acetyl-α-D-galactopyranosyl)-2,3,4-triazol-1-yl)-propanoate (15). Compounds **13** (10 mg, 0.027 mmol) and **14** (10 mg, 0.027 mmol) were dissolved in 200 μL of the organic solvent and 150 μL of water in a 3 mL culture tube. A 0.2 M cupric acetate solution (25 μL, 0.005 mmol) was then added and the reaction was sealed with a septum. The tube was flushed with argon for 10 min and then placed in a 40 °C oil bath. A 0.4 M sodium ascorbate solution (25 μL, 0.01 mmol) was added and the reaction was stirred until completion (for a maximum of 6 h). The reaction mixture was then cooled to room temperature, diluted with ethyl acetate, and washed with water and brine. Solvent was removed *in vacuo* and the crude product was purified by preparative TLC (6:4 ethyl acetate:hexanes). ^{1}H NMR (400 MHz, $CDCl_3$): δ_{ppm} 7.76 (d, 2H, J = 7.5 Hz), 7.61 (t, 2H, J = 7.3 Hz), 7.40 (ddd, 2H, J = 7.4, 7.4, 3.3 Hz), 7.37−7.29 (m, 3H), 6.38 (d, 1H, J = 6.1 Hz), 6.16 (dd,

1H, J = 10.7, 3.3 Hz), 5.97−5.86 (m, 1H), 5.85 (d, 1H, J = 8.2 Hz), 5.65 (d, 1H, J = 3.1 Hz), 5.46 (dd, 1H, J = 10.8, 6.0 Hz), 5.35 (d, 1H, J = 17.1 Hz), 5.27 (d, 1H, J = 10.4 Hz), 4.73 (ddd, 1H, J = 8.2, 5.2, 5.2 Hz), 4.64 (d, 2H, J = 5.6 Hz), 4.60 (dd, 1H, J = 6.4, 6.4 Hz), 4.39 (d, 2H, J = 7.1 Hz), 4.24 (dd, 1H, J = 7.0, 7.0 Hz), 4.10 (dd, 1H, J = 11.3, 6.6 Hz), 4.00 (dd, 1H, J = 11.3, 6.5 Hz), 3.32 (d, 2H, J = 5.1 Hz), 2.19 (s, 3H), 2.01 (s, 3H), 1.95 (s, 3H), 1.88 (s, 3H). ^{13}C NMR (100 MHz, $CDCl_3$): δ_{ppm} 170.6, 170.6, 170.3, 170.0, 169.4, 155.9, 143.8, 143.7, 142.0, 141.3, 141.2, 131.4, 127.8, 127.1, 127.1, 125.1, 124.5, 120.0, 119.2, 81.7, 70.5, 67.7, 67.5, 67.2, 67.2, 66.2, 61.2, 53.4, 47.1, 28.0, 20.61, 20.61, 20.6, 20.3. ESI-MS m/z calcd for $C_{37}H_{40}N_4O_{13}$ $[M+H]^+$: 749.2665; $[M+Na]^+$: 771.2490. Found: 749.22, 771.20.

(2*S*)-1-Allyl-2-[[(9*H*-fluoren-9-ylmethoxy)carbonyl]amino]-3-(4-(2,3,4,6-tetra-*O*-acetyl-α-D-galactopyranosylethyl)-2,3,4-triazol-1-yl)-propanoate (17). Compounds **13** (10 mg, 0.027 mmol) and **16** (11 mg, 0.027 mmol) were treated with the same conditions as the preparation of **15**. The crude product **17** was purified by preparative TLC (7:3 ethyl acetate: hexanes). ^{1}H NMR (400 MHz, $CDCl_3$): δ_{ppm} 7.76 (d, 2H, J = 7.5 Hz), 7.59 (t, 2H, J = 7.4 Hz), 7.40 (t, 2H, J = 7.4 Hz), 7.37 (s, 1H), 7.31 (t, 2H, J = 7.5, 7.5 Hz), 5.94 (d, 1H, J = 8.9 Hz), 5.89 (m, 1H), 5.41 (t, 1H, J = 2.8, 2.8 Hz), 5.32 (d, 1H, J = 17.1 Hz), 5.25 (dd, 1H, J = 10.4, 1.1 Hz), 5.20 (d, 1H, J = 4.5 Hz), 5.17 (dd, 1H, J = 8.7, 3.1 Hz), 4.73 (dd, 1H, J = 13.3, 5.4 Hz), 4.66 (d, 2H, J = 5.7 Hz), 4.46 (ddd, 1H, J = 12.9, 7.9, 4.8 Hz), 4.41−4.27 (m, 4H), 4.23 (dd, 1H, J = 7.2, 7.2 Hz), 4.19−4.13 (m, 1H), 4.11−4.02 (m, 2H), 3.31 (d, 2H, J = 4.9 Hz), 2.31−2.17 (m, 1H), 2.10 (s, 3H), 2.07 (s, 6H), 2.03 (s, 3H). ^{13}C NMR (100 MHz, $CDCl_3$): δ_{ppm} 170.8, 170.6, 169.9, 169.7, 169.7, 156.0, 143.8, 143.8, 142.7, 141.2, 141.2, 131.6, 127.7, 127.1, 125.2, 125.2, 122.8, 120.0, 118.7, 77.5, 77.2, 76.9, 69.2, 68.6, 68.0, 67.7, 67.1, 66.1, 61.1, 53.5, 47.1, 46.4, 28.1, 27.1, 20.77, 20.74, 20.71, 20.63. ESI-MS m/z calcd for $C_{39}H_{44}N_4O_{13}$ $[M+H]^+$: 777.2978. Found: 777.21.

General Method for Peptide Synthesis. The syntheses of the peptides were carried out using an Advanced Chem Tech Apex 396 automated peptide synthesizer (40 wells), equipped with a dual-arm system and argon atmosphere controlled from an IBM PC using *Advanced Chem Tech* v 1.6 software. Preloaded Fmoc-Gly-Wang or Fmoc-Ala-Wang resins were swollen in DMF for 1 h followed by filtration, and then were subjected to 20% piperidine in DMF twice successively for 30 min. Peptide couplings were performed using standard conditions for Fmoc solid-phase synthesis using HCTU as coupling agent.[34] Following the coupling of each residue, deprotection of the Fmoc moiety was accomplished by treatment with 20% piperidine in DMF. Between each deprotection and coupling, and after every coupling, the beads were shaken 4 times with 4 mL of DMF followed by filtration. Upon completion of the synthesis, the beads were washed extensively with DMF (6 × 4 mL), MeOH (6 × 4 mL), DCM (6 × 4 mL), hexanes (6 × 4 mL), and ethanol (3 × 6 mL) and then removed from the synthesizer and stored in a desiccator under vacuum in the presence of P_2O_5 until required. A small amount of the peptide was cleaved from the resin for characterization using 92.5:5:2.5 (v/v/v) TFA:triisopropylsilane:water. The peptides were purified using reversed-phase HPLC (ramp from 0% to 18% acetonitrile in water over 5 min followed by isocratic flow for 25 min) unless stated otherwise.

Resin-Supported Peptide 18. Peptide **18** was prepared using 100 mg of Wang resin using standard Fmoc-based SPS protocols.[34] 5 mg of resin was directly cleaved and the crude peptide was purified through preparatory TLC (30% water in methanol) to yield 0.8 mg of **18** as a white powder (91% based on resin loading). ^{1}H NMR (400 MHz, D_2O): δ_{ppm} 3.94−3.78 (m, 5H), 3.59 (d, 2H, J = 1.35 Hz), 2.64 (d, 2H, J = 3.23 Hz, 2H), 2.36 (t, 1H, J = 2.21). ^{13}C NMR (100 MHz, D_2O): δ_{ppm} 171.4, 171.32, 171.31, 168.9, 76.2, 74.4, 51.4, 42.6, 42.4, 42.3, 21.0. ESI-MS m/z calcd for $C_{11}H_{16}N_4O_5$ $[M+H]^+$: 285.1199. Found: 285.072.

Resin-Supported Peptide 20. Peptide **20** was prepared using 115 mg of Wang resin using standard Fmoc-based SPS protocols.[34] 18 mg of resin was cleaved directly and purified by reversed-phase HPLC to yield 3.0 mg of **20** as a white powder in 78% yield (based on resin loading). ^{1}H NMR (400 MHz, D_2O): δ_{ppm} 7.40−7.15 (m, 5H), 4.60 (dd, 1H, J = 8.2, 6.6 Hz), 4.30 (q, 1H, J = 7.3 Hz), 4.19 (t, 1H, J = 6.1 Hz), 3.91 (q, 2H, J = 16.9 Hz), 3.11 (dd, 1H, J = 13.9, 6.5 Hz), 2.96 (dd, 1H, J = 13.9, 8.3 Hz), 2.84 (td, 2H, J = 3.3, 2.9 Hz), 2.52 (t, 1H, J = 2.7 Hz), 1.33 (d, 3H, J = 7.3 Hz). ^{13}C NMR (125 MHz, D_2O): δ_{ppm} 176.7, 173.2, 171.0, 169.3, 136.8, 129.9, 129.4, 127.8, 83.2, 75.1, 55.4, 52.0, 49.3, 42.869, 42.861, 37.9, 21.7. ESI-MS m/z calcd for $C_{19}H_{24}N_4O_5$ $[M+H]^+$: 389.182; $[M+Na]^+$: 411.164. Found: 389.19, 411.17.

Resin-Supported Peptide 23. Peptide **23** was prepared using 115 mg of Wang resin according to standard Fmoc-based SPS protocols.[34] 10 mg of resin was cleaved directly and purified by reversed-phase HPLC to yield 1.8 mg of **23** as a white powder in 70% yield (based on resin loading). ^{1}H NMR (400 MHz, D_2O): δ_{ppm} 4.58 (m, 3H), 4.29 (t, 1H, J = 5.9 Hz), 4.19−3.79 (m, 18H), 2.93 (dd, 2H, J = 5.9, 2.8 Hz), 2.76 (bd, 6H, J = 6.1 Hz), 2.60 (t, 1H, J = 2.5 Hz), 2.46 (t, 3H, J = 2.4 Hz). ^{13}C NMR (125 MHz, D_2O): δ_{ppm} 172.7, 171.8, 171.5, 171.3, 168.8, 79.2, 76.2, 74.3, 72.2, 52.4, 52.3, 51.3, 42.5, 42.4, 42.2, 20.8. ESI-MS m/z calcd for $C_{38}H_{49}N_{13}O_{14}$ $[M+H]^+$: 912.3595; $[M+Na]^+$: 934.3420. Found: 912.34, 934.32.

Resin-Supported Peptide 25. Peptide **25** was prepared using 150 mg of Wang resin using standard Fmoc-based SPS protocols with amino acid **26** (Scheme 3b).[34] 20 mg of resin was directly cleaved and the crude peptide was purified by reversed-phase HPLC (isocratic flow with 10% acetonitrile in water for 5 min followed by a linear gradient from 10% to 60% acetonitrile in water) to yield 4.1 mg of **25** as a white powder in 48% yield (based on resin loading). ^{1}H NMR (500 MHz, D_2O, presaturation on HOD): δ_{ppm} 4.36 (m, 3H), 3.90−3.75 (m, 17H), 3.60 (s, 2H), 2.28−2.09 (m, 12H), 1.91 (m, 4H), 1.80 (m, 4H). ^{13}C NMR (125 MHz, D_2O): δ_{ppm} 176.4, 174.2, 174.2, 174.1, 171.9, 171.8, 171.7, 171.6, 171.5, 170.9, 83.3, 82.6, 70.8, 70.3, 52.9, 52.8, 52.8, 52.6, 43.1, 42.5, 42.4, 42.3, 29.3, 29.2, 14.4, 13.9. ESI-MS m/z calcd for $C_{42}H_{58}N_{13}O_{14}$ $[M+H]^+$: 968.42. Found: 968.76.

(*S*)-2-(9-Fluorenylmethoxycarbonylamino)-hex-5-ynoic Acid (26). Amino acid **26** was synthesized as indicated in Scheme 2 in the Supporting Information. ^{1}H NMR ($CDCl_3$/CD_3OD 2/1, 400 MHz): δ_{ppm} 7.71 (d, 2H, J = 7.6 Hz), 7.58 (dd, 2H, J = 7.1, 3.9 Hz), 7.35 (t, 2H, J = 7.6 Hz), 7.27 (t, 2H, J = 7.6 Hz), 4.35 (m, 3H), 4.18 (t, 1H, J = 6.8 Hz), 2.24 (m, 2H), 2.09 (m, 1H), 2.01 (t, 1H, J = 2.6 Hz), 1.86 (m, 1H). ^{13}C NMR ($CDCl_3$/CD_3OD 2/1, 100 MHz): δ_{ppm} 173.9, 156.7, 143.8, 143.7, 141.2, 141.2, 127.7, 127.0, 125.0, 119.8, 82.6, 77.5, 69.3, 66.9, 53.0, 47.1, 30.9, 14.9. ESI-MS m/z calcd for $C_{21}H_{19}NO_4$ $[M + Na]^+$: 372.12. Found: 372.24.

General Protocol for the Solid-Phase Organic Synthesis Microwave "Click" Reaction. A CEM Mars X Microwave System with 300 W maximum power and quartz reaction vessels

was used for these reactions. The resin supported peptide was initially stirred in DMF for 30 min under argon. Five equivalents of azide per mole of alkyne and 0.2 equiv of cupric acetate per mol of alkyne were added and the solution was degassed under argon. 0.4 equivalents of sodium ascorbate per mole of alkyne was then added and the stirbar was removed. The flask was sealed under argon and placed in the microwave and run under the following conditions: 2 min ramp to 90 °C then held at 15% power for 1.5 h. The solvent was then drained, and the beads were washed extensively with 1:1 water:isopropanol followed by 4 × 4 mL DMF, 4 × 4 mL MeOH, 4 × 4 mL DCM, and finally 4 × 4 mL hexanes. The beads were then stirred in 4 mL of 92.5:5:2.5 TFA:triisopropylsilane:water cleavage cocktail to remove the product off the resin. Solvent was evaporated at ambient temperature. The residue was washed with ether (4 × 5 mL), then dissolved in a solution of 0.01 M sodium methoxide in methanol with a drop of water and stirred for 1.5 h at room temperature. TFA was added until the pH of the solution was adjusted to 6. The mixture was evaporated to dryness, desalted, and resuspended in water and purified by reversed-phase HPLC.

Glycopeptide 21. Resin-supported **20** (80 mg, 0.046 mmol) was treated as per the general procedure described above with **14** (85.2 mg, 0.23 mmol), cupric acetate (1.7 mg, 0.0093 mmol), and sodium ascorbate (3.4 mg, 0.017 mmol). Purification by reversed-phase HPLC (1% acetonitrile in water for 12 min followed by a linear gradient from 1% acetonitrile in water to 10% acetonitrile in water over 28 min followed by a linear gradient from 10% acetonitrile in water to 98% acetonitrile in water over 40 min) yielded 16.7 mg of **21** as a white powder (61% based on resin-loading). ^{1}H NMR (500 MHz, D_2O): δ_{ppm} 8.01 (s, 1H), 7.38−7.15 (m, 5H), 6.26 (s, 1H), 4.69−4.56 (m, 1H), 4.51−4.42 (m, 1H), 4.35−4.15 (m, 2H), 4.13−3.96 (m, 3H), 3.89−3.75 (m, 2H), 3.70−3.56 (m, 2H), 3.33−3.09 (m, 3H), 3.04−2.95 (m, 1H), 1.33−1.18 (m, 3H). ^{13}C NMR (125 MHz, D_2O): δ_{ppm} 179.4, 171.8, 170.860, 170.7, 136.6, 129.1, 128.6, 1267.0, 74.9, 69.2, 68.7, 66.8, 61.1, 54.8, 54.2, 46.5, 42.4, 36.7, 17.5. ESI-MS m/z calcd for $C_{25}H_{35}N_7O_{10}$ $[M + H]^+$: 594.25. Found: 594.42.

Glycopeptide 22. Resin-supported **20** (24 mg, 0.0137 mmol) was treated as per the general procedure described above with **16** (27.5 mg, 0.0685 mmol), cupric acetate (0.5 mg, 0.0028 mmol), and sodium ascorbate (1 mg, 0.0051 mmol). Purification by reversed-phase HPLC (2% acetonitrile in water for 9 min followed by a linear gradient from 2% acetonitrile in water to 40% acetonitrile in water over 30 min) yielded 6 mg of **22** as a white powder (70% based on resin-loading). ^{1}H NMR (500 MHz, D_2O): δ_{ppm} 7.76 (s, 1H), 7.27−7.09 (m, 5H), 4.37 (dd, 2H, J = 14.0, 6.3 Hz), 4.18 (t, 1H, J = 6.3 Hz), 4.02 (dd, 1H, J = 14.3, 7.0 Hz), 3.76−3.85 (m, 3H), 3.74 (d, 1H, J = 1.6 Hz), 3.66−3.58 (m, 2H), 3.55 (d, 2H, J = 5.8 Hz), 3.18 (d, 1H, J = 6.3), 3.07 (dd, 1H, J = 13.9, 5.4 Hz), 2.87 (dd, 1H, J = 13.9, 9.3 Hz), 2.30−1.99 (m, 2H), 1.19 (d, 3H, J = 7.2 Hz). ^{13}C NMR (125 MHz, D_2O): δ_{ppm} 171.9, 170.4, 169.0, 162.8, 136.4, 129.2, 128.6, 127.0, 72.1, 69.5, 68.7, 67.6, 60.9, 54.8, 52.6, 47.0, 42.2, 36.9, 26.6, 24.6, 17.2. ESI-MS m/z calcd for $C_{27}H_{39}N_7O_{10}$ $[M+H]^+$: 622.284; $[M+Na]^+$: 644.266. Found: 622.15, 644.18.

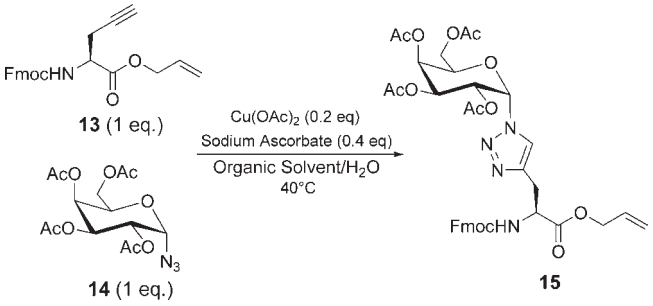
Glycopeptide 9. Resin-supported **23** (60 mg 0.026 mmol) was treated as per the general procedure described above with **14** (190 mg, 0.51 mmol), cupric acetate (3.8 mg, 0.020 mmol), and sodium ascorbate (8.2 mg, 0.041 mmol). Purification by reversed-phase HPLC (1% acetonitrile in water for 12 min followed by a linear gradient from 1% acetonitrile in water to 10% acetonitrile in water over 28 min followed by a linear gradient from 10% acetonitrile in water to 98% acetonitrile in water over 40 min) yielded 9 mg of **9** as a white powder (20% based on resin loading). ^{1}H NMR (500 MHz, D_2O): δ_{ppm} 7.83 (s, 4H), 6.12 (d, 4H, J = 5.9 Hz), 4.33 (d, 4H, J = 10.1 Hz), 4.17 (dd, 4H, J = 10.0, 6.3 Hz), 3.93 (m, 5H), 3.86−3.71 (m, 17H), 3.60−3.47 (m, 12H), 3.18−2.98 (m, 12H). ^{13}C NMR (125 MHz, D_2O): δ_{ppm} 173.2, 173.0, 172.0, 171.9, 171.83, 171.76, 171.3, 171.28, 171.22, 171.1, 148.8, 125.3, 85.2, 74.8, 69.3, 68.7, 67.0, 61.1, 53.2, 53.16, 53.14, 46.57, 42.59, 42.2, 27.1, 26.9, 26.8, 26.7, 26.65, 26.59, 25.1, 23.7. MALDI-TOF MS m/z calcd for $C_{62}H_{93}N_{25}O_{34}$ $[M + Na + H]^{2+}$: 877.814. Found: 877.8.

Glycopeptide 10. Resin-supported **23** (70 mg 0.030 mmol) was treated as per the general procedure described above with **24** (94 mg, 0.24 mmol), cupric acetate (6.5 mg, 0.036 mmol), and sodium ascorbate (13 mg, 0.072 mmol). Purification by reversed-phase HPLC (1% acetonitrile in water for 12 min followed by a linear gradient from 1% acetonitrile in water to 10% acetonitrile in water over 28 min followed by a linear gradient from 10% acetonitrile in water to 98% acetonitrile in water over 40 min) yielded 25 mg of **10** as a white powder (45% based on resin loading). ^{1}H NMR (500 MHz, D_2O): δ_{ppm} 7.73 (s, 4H), 4.53 (m, 4H), 4.24 (s, 4H), 3.93 (m, 5H), 3.88−3.63 (m, 28H), 3.59−3.56 (m, 5H), 3.54−3.38 (m, 12H), 3.13−2.97 (m, 8H). ^{13}C NMR (125 MHz, D_2O): δ_{ppm} 171.4, 171.3, 171.2, 171.1, 171.1, 171.0, 170.9, 129.8, 122.6, 74.7, 74.6, 74.5, 72.5, 69.5, 69.4, 69.2, 68.7, 68.6, 68.4, 67.1, 60.8, 45.74, 45.70, 45.6, 42.6, 42.4, 42.3, 42.2, 27.2, 27.13, 27.09, 27.02. MALDI-TOF MS m/z calcd for $C_{66}H_{101}N_{25}O_{34}$ $[M + H]^+$: 1788.69. Found: 1788.6.

Glycopeptide 11. Resin-supported **23** (40 mg 0.017 mmol) was treated as per the general procedure described above with **16** (136 mg, 0.34 mmol), cupric acetate (2.5 mg, 0.0136 mmol), and sodium ascorbate (5.5 mg, 0.0275 mmol). Purification by reversed-phase HPLC (2% acetonitrile in water for 9 min followed by a linear gradient from 2% acetonitrile in water to 40% acetonitrile in water over 30 min) yielded 17 mg of **11** as a white powder (54% based on resin loading). ^{1}H NMR (500 MHz, D_2O): δ_{ppm} 7.84 (s, 1H), 7.76 (s, 3H), 4.62−4.51 (m, 4H), 4.40−4.32 (m, 9H), 4.26 (t, 1H, J = 6.40 Hz), 3.92−3.70 (m, 24H), 3.63 (dd, 12H, J = 10.1, 3.0 Hz), 3.58−3.53 (m, 8H), 3.25 (d, 2H, J = 6.2 Hz), 3.21−2.96 (m, 6H), 2.24−2.10 (m, 4H), 1.95−2.10 (m, 4H). ^{13}C NMR (125 MHz, D_2O): δ_{ppm} 173.0, 172.0, 171.87, 171.80, 171.69, 171.42, 171.4, 171.36, 171.32, 171.19, 169.8, 169.3, 126.2, 126.1, 72.2, 72.1, 72.0, 69.6, 68.8, 67.7, 65.8, 61.0, 54.4, 53.8, 53.3, 52.7, 47.0, 46.95, 46.91, 42.6, 42.6, 42.3, 42.2, 27.9, 27.2, 27.0, 26.9, 26.8, 26.6, 24.6, 22.2. MALDI-TOF MS m/z calcd for $C_{70}H_{109}N_{25}O_{34}$ $[M]^+$: 1843.76. Found: 1843.8.

Glycopeptide 12. Resin-supported **25** (25 mg, 0.011 mmol) was treated as per the general procedure described above with **24** (85 mg, 0.22 mmol), cupric acetate (1.6 mg, 0.009 mmol), and sodium ascorbate (3.6 mg, 0.018 mmol). Purification by reversed-phase HPLC (isocratic 1% acetonitrile in water for 10 min followed by a linear gradient from 1% acetonitrile in water to 30% acetonitrile in water over 30 min) yielded 3.3 mg of **12** as a white powder (16% based on resin loading). ^{1}H NMR (500 MHz, D_2O, presaturation on HOD): δ_{ppm} 7.71 (br s, 4H), 4.31 (s, 4H), 4.17 (s, 3H), 4.08−3.43 (m, 51H), 2.65 (m, 8H), 2.05−1.77 (m, 8H). ^{13}C NMR (125 MHz, D_2O): δ_{ppm} 174.2, 171.8, 171.0, 124.0, 96.4, 74.8, 72.5, 69.6, 68.7, 67.1, 60.8, 52.8, 45.5, 43.1, 42.5,

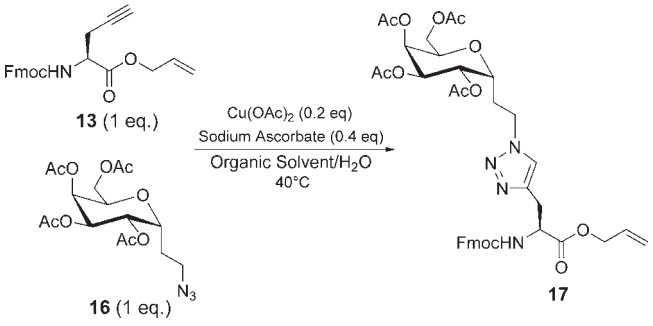
Table 1. Optimization of Solution-Phase "Click" Coupling



	organic solvent	solvent composition (% organic)	reaction time (hrs)	% conversion[a]
1	*t*-BuOH	50	5	81
2	DMF	50	4	76
3	NMP	50	3	>98
4	Dioxane	50	1	95
5	THF	50	0.5	>98
6	THF	75	0.75	>98
7	THF	80	0.25	>98
8	THF	90	0.5	>98
9[b]	THF	90	0.25	>98

[a] Conversions calculated based upon analysis of crude reaction mixture using ^{1}H NMR. [b] Reaction carried out with **5** equiv of azide.

Table 2. Optimization of Solvent Conditions Using a Primary Azido Sugar



	organic solvent	solvent composition (% organic)	reaction time (hrs)	conversion[a]
1	DMF	50	0.25	78
2	NMP	50	0.5	>98
3	Dioxane	50	0.5	>98
4	THF	50	0.5	>98

[a] Conversions calculated based upon analysis of crude reaction mixture using ^{1}H NMR.

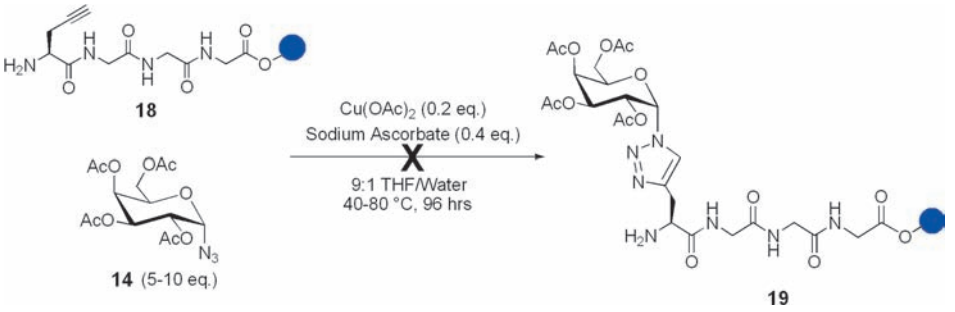
42.3, 30.1, 20.9. MALDI-TOF MS *m*/*z* calcd for $C_{70}H_{109}N_{25}O_{34}$ $[M + Na]^+$: 1866.7. Found: 1867.5.

RESULTS AND DISCUSSION

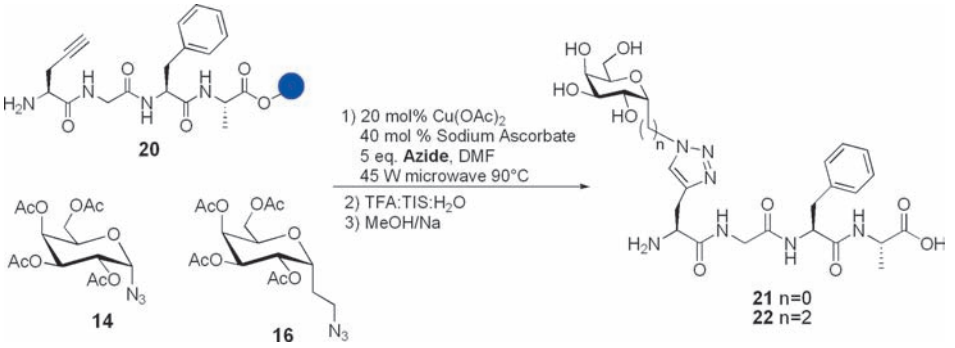
Several modifications to the original "Click" reaction conditions for solid-phase applications have been reported.[16,17,35−39] We sought to utilize solvents that would permit reaction conditions with sub-stoichiometric amounts of copper and also facilitate swelling of the solid-phase resin. As a result, a number of organic solvents capable of swelling Wang resin were examined for the solution-phase reaction between alkyne **13** and azido sugar **14** before applying the conditions to the solid-phase synthesis of triazole-containing *C*-AFGP analogues.[40] The reaction between **13** and **14** was investigated using aqueous mixtures (50%) of *N*-methyl morpholine (NMP), tetrahydrofuran (THF), *N*,*N*-dimethyl formamide (DMF), dioxane and *tert*-butanol (Table 1). All of these solvents have excellent swelling properties for Wang resin except for *tert*-butanol, which swells resins poorly.[40] Under typical Sharpless reaction conditions

dx.doi.org/10.1021/bc100394k |*Bioconjugate Chem.* 2011, 22, 605–616

Scheme 1. Solid-Phase Synthesis of a Triazole-Linked Glycopeptide Using Optimized Conditions



Scheme 2. Microwave Assisted Solid-Phase Synthesis of Triazole-Linked Glycopeptides



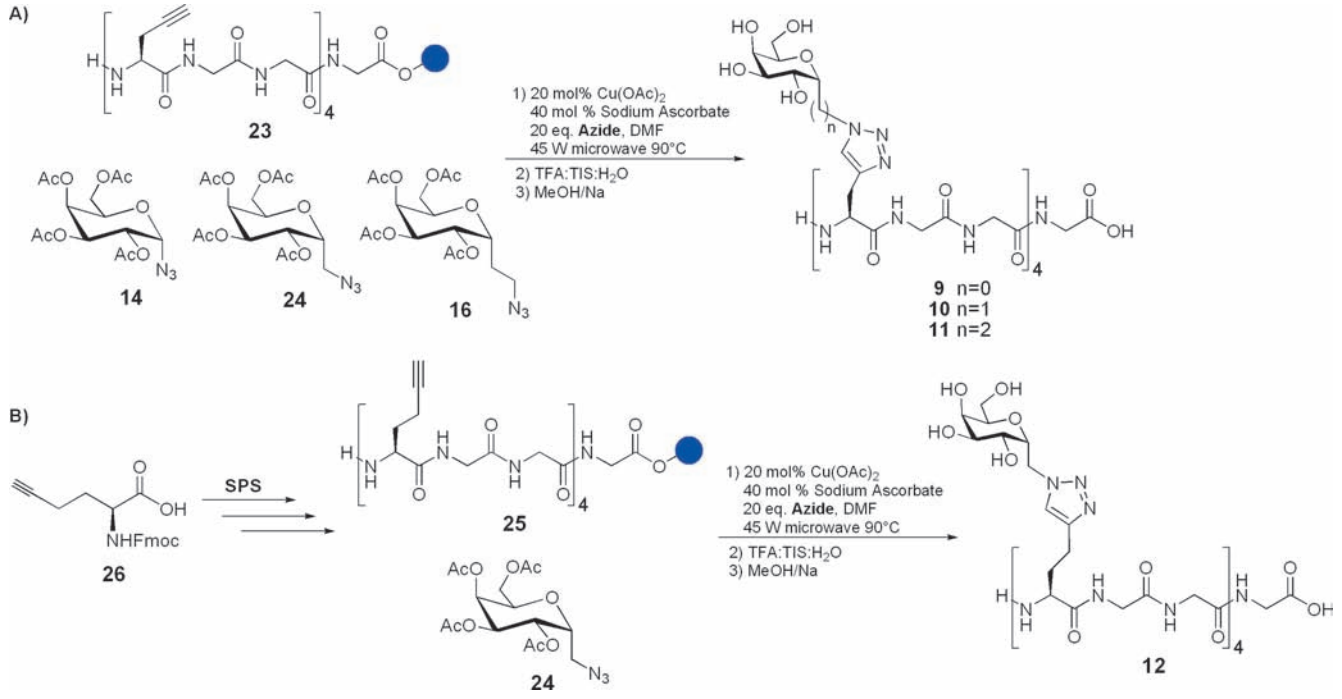
using *tert*-butanol,[11] **15** was formed, but reaction conversion was only 81% after 5 h (Table 1, entry 1). DMF resulted in only 76% conversion after 4 h (entry 2), while NMP resulted in complete conversion after 3 h (entry 3). In contrast, dioxane afforded 95% conversion after only 1 h (entry 4). However, the best results were obtained when THF was employed, with complete conversion after only 30 min (entry 5).

These solvent mixtures were also applicable with other azide substrates (Table 2). For instance, reaction of alkyne **13** with azido sugar **16** yielded similar results to those described above, but reaction times were generally shorter. When DMF was used as a cosolvent, glycoconjugate **17** was obtained in 78% conversion after only 15 min (Table 2, entry 1), as opposed to 76% conversion in 4 h for glycoconjugate **15** prepared from azido sugar **14** (Table 1, entry 2). Quantitative conversions for **17** were also obtained within 30 min when NMP, dioxane, and THF were employed (Table 2, entries 2−4). Overall, THF yielded the best results, showing it to be an ideal solvent for the solution-phase coupling regardless of the structure of the azide substrate.

As stated previously, a solvent system with minimal water content is desirable for solid-phase applications to ensure an efficient swelling of the resin. However, an aqueous component is necessary to dissolve the sodium ascorbate and facilitate reduction of Cu(II) to Cu(I).[9,41] Hence, the efficiency of the solution-phase Click reaction of alkyne **13** with azido sugar **14** was repeated using a decreased percentage of water in THF (Table 1, entries 6−9). Surprisingly, decreasing the water content had no effect upon conversions and reaction times were still less than one hour (entries 6−8). However, the reaction time could further be reduced to 15 min without decreasing reaction conversion by using a 10% water/THF solvent system in the presence of 5 equiv of azide (entry 9).

With optimized solution-phase results in hand, the solid-phase synthesis of a triazole-linked glycopeptide was attempted (Scheme 1). Initial attempts to couple resin-supported peptide **18** using the optimized conditions (10% water in THF, 0.2 equiv of $Cu(OAc)_2$, 0.4 equiv of sodium ascorbate) with azido sugar **14** (5 equiv) failed. Even upon heating the reaction for 96 h at 80 °C or adding 10 equiv of azido sugar **14**, the reaction still failed to yield glycopeptide **19**. Given the precedent for microwave accelerated Click couplings on solid-phase resins,[42] we investigated whether glycopeptide formation would occur in the presence of microwaves. Similar conditions were then attempted for the microwave accelerated "Click" coupling, but peptide **20** (Scheme 2) was utilized instead of **18**. Peptide **20** bearing a phenylalanine residue was selected, as the strong UV absorbance of this residue would facilitate purification by HPLC and anhydrous THF was used as the solvent. Consequently, resin-supported peptide **20** was reacted with azido sugar **14** in anhydrous THF, utilizing 0.2 equiv of $Cu(OAc)_2$, 0.4 equiv of sodium ascorbate, and microwave heating (300 W) for 2 h. Analysis by MALDI mass spectrometry of the crude reaction mixture failed to show a trace of product. However, when the solvent was changed to anhydrous DMF trace quantities of glycoconjugate **21** were detected after 2 h (the product was cleaved from the resin prior to analysis). By decreasing the power to 45 W, the reaction went to completion after only 1.5 h and glycoconjugate **21** was obtained in 61% yield after cleavage from the resin and subsequent deprotection and purification by reversed-phase HPLC (Scheme 2). Similarly, when resin-supported peptide **20** was reacted with azido sugar **16** under these

Scheme 3. Microwave Assisted Solid-Phase Synthesis of Glycopeptides 9−12



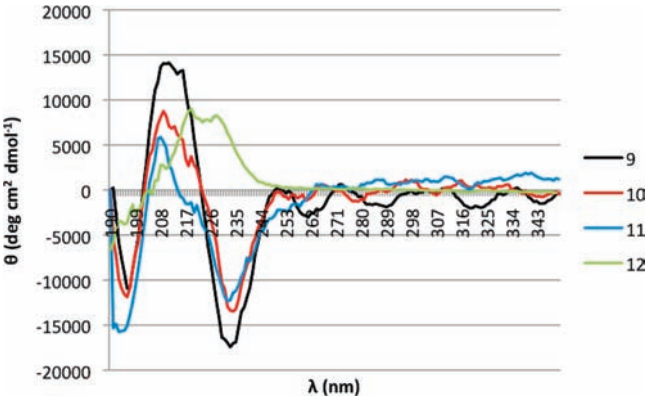


Figure 5. CD spectrum of glycopeptides **9**−**12**. All spectra were acquired at 22 °C, with a concentration of 43 μM. CD data has been normalized for concentration and number of chromophores.

reaction conditions, glycopeptide **22** was obtained in 70% isolated yield after cleavage from the resin, deprotection, and purification by reversed-phase HPLC.

With this promising result, the convergent syntheses of triazole-containing *C*-AFGP glycopeptides **9**, **10**, **11**, and **12** were attempted. Glycosyl azide **14** and resin-supported peptide **23** (prepared under standard Fmoc solid-phase coupling conditions) were subjected to microwave heating in DMF with 0.2 equiv of $Cu(OAc)_2$ and 0.4 equiv of sodium ascorbate (Scheme 3a). Glycoconjugate **9** was obtained in 20% isolated yield following cleavage from the Wang resin, deprotection, and purification by reversed-phase HPLC. Similarly, reaction of azido sugar **24** with resin-supported peptide **23** yielded glycopeptide **10** (45% yield), and when azido sugar **16** was utilized, glycopeptide **11** was obtained in 54% yield. Glycosyl azide **24** was also reacted with resin-supported peptide **25** (prepared under standard Fmoc solid-phase coupling conditions utilizing amino acid **26**) under the microwave "Click" conditions described above, and glycopeptide **12** was obtained in 16% yield (Scheme 3b).

Table 3. Analysis of Secondary Structure for Glycopeptides 9−12

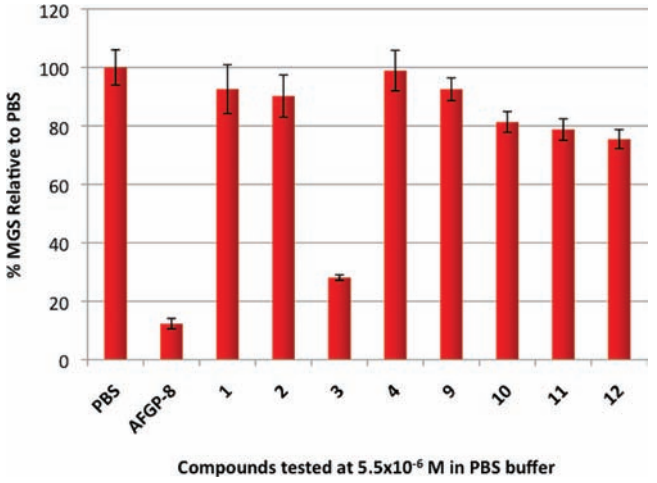
	α helix	β sheet	β turn	poly proline type 2	random coil
9	0.011	0.2975	0.1435	0.1225	0.4275
10	0.022	0.2505	0.1445	0.1125	0.469
11	0.0135	0.2855	0.1345	0.107	0.4555
12	0	0.358	0.093	0.193	0.356

Triazole-containing AFGP analogues **9**−**12** were first examined for TH activity using a nanoliter osmometer.[28] This instrument is regarded as the "gold standard" for assessing thermal hysteresis. All four *C*-AFGP analogues were found to exhibit no thermal hysteresis activity. Furthermore, no dynamic ice shaping was evident indicating there was no interaction with the ice surface, a result consistent with the lack of thermal hysteresis activity in previously reported ornithine analogues **1**−**4**.[4,6] Analysis of solution conformation using circular dichroism (CD) spectroscopy (Figure 5 and Table 3) suggests that the predominant secondary structure in solution is random coil with β-sheet being the next likely solution structure for glycopeptides **9**−**12**. This is consistent with the solution conformation reported for AFGP-8 and other *C*-AFGP analogues studied by our laboratory[2,4,43] and suggests that the lack of TH activity is not due to the fact that AFGP analogues **9**−**12** adopt different solution conformations compared to the native AFGP.

The triazole-containing *C*-AFGP analogues **9**−**12** were also screened for their ability to inhibit ice recrystallization (IRI

dx.doi.org/10.1021/bc100394k |*Bioconjugate Chem.* 2011, 22, 605–616

Chart 1. IRI Activity of *C*-Linked AFGP Analogues[a]



[a]PBS represents a positive control for ice recrystallization.

activity) using a splat cooling assay.[1,29] Chart 1 shows the IRI activity of triazole-containing *C*-AFGP analogues **9**−**12**, native AFGP-8, and previously synthesized *C*-AFGP analogues **1**−**4** (the latter contain an amide bond in the side chain).[6,44] In this assay, a phosphate buffered saline (PBS) solution is utilized as a positive control for ice recrystallization; thus, bars smaller than PBS indicate the ability to inhibit ice recrystallization. All samples have been normalized to PBS. As evident from Chart 1, triazole-containing AFGP analogue **9** failed to exhibit IRI activity. AFGP analogue **9** is closely related to peptoid AFGP analogue **6** (published by Norgren et al.) which also failed to exhibit IRI activity.[26] AFGP analogue **6** contains *N*-methyl glycine instead of glycine in the polypeptide backbone; however, the nature of the anomeric linkage, total length of the side chain, and the position of the triazole within the side chain are identical to those of AFGP analogue **9**. While these analogues did not inhibit the recrystallization of ice, the results are consistent with the suggestion that IRI activity is sensitive to the length of the side chain bearing the carbohydrate moiety. Similar results have been reported by our laboratory in analogues that contain an amide bond in the side

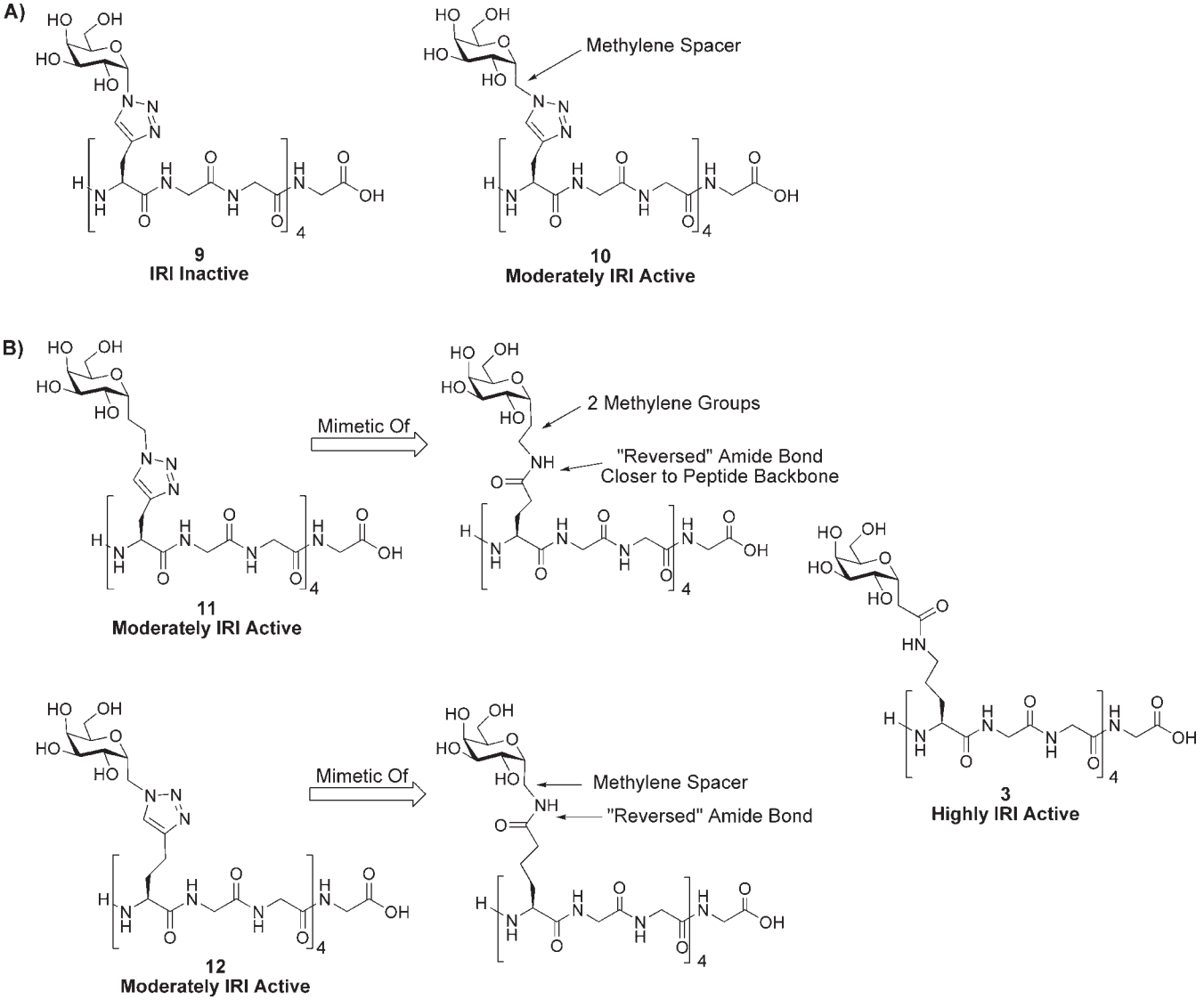


Figure 6. The presence of a hydrophobic methylene spacer and "reversed" directionality of the triazole moiety in AFGP analogues **9**−**12**.

dx.doi.org/10.1021/bc100394k |*Bioconjugate Chem.* 2011, 22, 605–616

chain instead of a triazole.[6] For instance, as the side chain of IRI active *C*-AFGP analogue **3** is shortened (compounds **1** and **2**) or lengthened (compound **4**) IRI activity is lost.[6]

Triazole-containing AFGP analogue **9** is also a close analogue of *C*-AFGP analogue **1**, which did not possess IRI activity. There are two key structural changes in AFGP analogue **9** relative to **1**. First, the triazole moiety has been employed to mimic the amide bond in **1**. Second, the orientation of the triazole in the side chain mimics an amide bond that is "reversed" in its orientation compared to **1**. These structural modifications in **9** do not restore IRI activity since this analogue failed to inhibit ice recrystallization. However, the fact that the lengths of the side chains in **9** and **1** are the same supports the hypothesis that the distance between the carbohydrate moiety and the peptide backbone is important for IRI activity.

Some of the most IRI active *C*-AFGP analogues prepared by our laboratory possess a methylene group between the carbohydrate moiety and the amide bond in the side chain. It has been proposed that the hydrophobic nature of this group is an important structural feature in *C*-AFGP analogue **3**. This methylene group is absent in triazole-containing AFGP analogue **9**. Interestingly, when this group is present as in triazole-containing *C*-AFGP analogue **10** (Figure 6a), the glycoconjugate is a moderate inhibitor of ice recrystallization, validating its importance.[6] Triazole-containing *C*-AFGP analogue **11** has two methylene groups incorporated between the carbohydrate moiety and the triazole linkage. This glycoconjugate has similar IRI activity as triazole-containing analogue **10**, further validating the importance of a hydrophobic group in the spacer close to the carbohydrate.[6] *C*-AFGP derivative **11** is also a close analogue of potent ice recrystallization inhibitor *C*-AFGP analogue **3**. However, **11** is not as active as **3**. The number of atoms between the carbohydrate moiety and the polypeptide backbone in analogues **3** and **11** is the same. However, the triazole moiety in **11** mimics an amide bond that has the directionality "reversed" relative to **3**. Furthermore, the position of the triazole linker in the side chain of **11** is different than the position of the amide bond in **3** (Figure 6b). The triazole linker in *C*-linked AFGP **11** is actually one atom closer to the polypeptide backbone than the amide bond in **3**. This structural modification is detrimental to IRI activity as analogue **11** is much less active than analogue **3**.

Triazole-containing *C*-AFGP analogue **12** is also a close analogue of **3** with the exception of the orientation of the triazole moiety. The orientation of the triazole mimics an amide bond that is "reversed" relative to **3** (Figure 6b). However, the length of the side chain between the carbohydrate and the peptide backbone, as well as the position of the triazole linker within this side chain, is the same (shown in Figure 6b). While triazole-containing analogue **12** exhibited moderate IRI activity, it is much less active than *C*-AFGP analogue **3**. These results indicate that while the presence of a hydrophobic methylene spacer and the length of the side chain bearing the triazole (or amide) linkage directly affect IRI activity, the amide bond in **3** is an essential structural feature necessary for potent IRI activity.

CONCLUSIONS

In summary, the synthesis of a series of triazole-containing AFGP and *C*-AFGP analogues has been reported. These compounds were prepared using a convergent solid-phase synthesis approach. "Click" chemistry conditions using Cu (II) (20 mol %) and sodium ascorbate as the *in situ* reductant in dry DMF in the presence of microwaves were utilized. Triazole-containing AFGP analogue **9** failed to exhibit IRI activity, while analogues **10**, **11**, and **12** exhibited moderate IRI activity. The results of this study suggest that substitution of the amide bond in *C*-AFGP analogue **3** with a triazole moiety is detrimental to IRI activity. In addition, a hydrophobic component (i.e., methylene spacer) close to the carbohydrate residue as well as the length of the side chain bearing the triazole (or amide) linkage is also important. This result is consistent with earlier findings by our laboratory. Molecular dynamics simulations and variable temperature NMR studies are currently being performed on analogues **10**, **11**, and **12** in an effort to elucidate how the methylene spacer and position of the triazole linker are influencing orientation of the carbohydrate residue. The results of these studies will be reported in due course.

ASSOCIATED CONTENT

Supporting Information. Synthetic procedures for azido sugar **24**, amino acid **26**, and ^{1}H and ^{13}C spectra are available for all characterized compounds. This material is available free of charge via the Internet at http://pubs.acs.org.

AUTHOR INFORMATION

Corresponding Author
*rben@uottawa.ca.

ACKNOWLEDGMENT

R.N.B. acknowledges NSERC, CBS, and CFI for financial support. J.F.T. holds an NSERC PGS-D.

REFERENCES

(1) Knight, C. A., Hallett, J., and DeVries, A. L. (1988) Solute effects on ice recrystallization: An assessment technique. *Cryobiology 25*, 55–60.

(2) DeVries, A. L., Komatsu, S. K., and Feeney, R. E. (1970) Chemical and physical properties of freezing point-depressing glycoproteins from Antarctic fishes. *J. Biol. Chem. 245*, 2901–2908.

(3) Bouvet, V., and Ben, R. N. (2003) Antifreeze glycoproteins: structure, conformation, and biological applications. *Cell Biochem. Biophys. 39*, 133–144.

(4) Czechura, P., Tam, R. Y., Dimitrijevic, E., Murphy, A. V., and Ben, R. N. (2008) The importance of hydration for inhibiting ice recrystallization with *C*-linked antifreeze glycoproteins. *J. Am. Chem. Soc. 130*, 2928–2929.

(5) Liu, S., and Ben, R. N. (2005) *C*-linked galactosyl serine AFGP analogues as potent recrystallization inhibitors. *Org. Lett. 7*, 2385–2388.

(6) Tam, R. Y., Rowley, C. N., Petrov, I., Zhang, T., Afagh, N. A., Woo, T. K., and Ben, R. N. (2009) Solution conformation of *C*-linked antifreeze glycoprotein analogues and modulation of ice recrystallization. *J. Am. Chem. Soc. 131*, 15745–15753.

(7) Tron, G. C., Pirali, T., Billington, R. A., Canonico, P. L., Sorba, G., and Genazzani, A. A. (2008) Click chemistry reactions in medicinal chemistry: applications of the 1,3-dipolar cycloaddition between azides and alkynes. *Med. Res. Rev. 28*, 278–308.

(8) Brik, A., Alexandratos, J., Lin, Y. C., Elder, J. H., Olson, A. J., Wlodawer, A., Goodsell, D. S., and Wong, C. H. (2005) 1,2,3-Triazole as a peptide surrogate in the rapid synthesis of HIV-1 protease inhibitors. *ChemBioChem 6*, 1167–1169.

(9) Rostovtsev, V. V., Green, L. G., Fokin, V. V., and Sharpless, K. B. (2002) A stepwise Huisgen cycloaddition process: copper(I)-catalyzed regioselective ligation of azides and terminal alkynes. *Angew. Chem., Int. Ed. 41*, 2596–2599.

(10) Tornøe, C. W., Christensen, C., and Meldal, M. (2002) Peptidotriazoles on solid phase: [1,2,3]-triazoles by regiospecific copper(I)-catalyzed 1,3-dipolar cycloadditions of terminal alkynes to azides. *J. Org. Chem. 67*, 3057–3064.

(11) Kolb, H. C., Finn, M. G., and Sharpless, K. B. (2001) Click chemistry: diverse chemical function from a few good reactions. *Angew. Chem. Intl. Ed. 40*, 2004–2021.

(12) van Dijk, M., Rijkers, D. T. S., Liskamp, R. M. J., van Nostrum, C. F., and Hennink, W. E. (2009) Synthesis and applications of biomedical and pharmaceutical polymers via Click chemistry methodologies. *Bioconjugate Chem. 20*, 2001–2016.

(13) Amblard, F., Cho, J. H., and Schinazi, R. F. (2009) Cu(I)-catalyzed Huisgen azide-alkyne 1,3-dipolar cycloaddition reaction in nucleoside, nucleotide, and oligonucleotide chemistry. *Chem. Rev. 109*, 4207–4220.

(14) Karskela, M., Helkearo, M., Virta, P., and Lönnberg, H. (2010) Synthesis of oligonucleotide glycoconjugates using sequential Click and oximation ligations. *Bioconjugate Chem. 21*, 748–755.

(15) Bera, S., Zhanel, G. G., and Schweizer, F. (2010) Evaluation of amphiphilic aminoglycoside-peptide triazole conjugates as antibacterial agents. *Bioorg. Med. Chem. Lett. 20*, 3031–3035.

(16) Pourceau, G., Meyer, A., Vasseur, J.-J., and Morvan, F. (2009) Synthesis of mannose and galactose oligonucleotide conjugates by bi-click chemistry. *J. Org. Chem. 74*, 1218–1222.

(17) Jølck, R. I., Berg, R. H., and Andresen, T. L. (2010) Solid-phase synthesis of PEGylated lipopeptides using click chemistry. *Bioconjugate Chem. 21*, 807–810.

(18) Meldal, M., Tornøe, C. W., Nielsen, T. E., Diness, F., Le Quement, S. T., Christensen, C. A., Feldthusen Jensen, J., Worm-Leonhard, K., Groth, T., Bouakaz, L., Wu, B., Hagel, G., and Keinicke, L. (2010) Ralph F. Hirschmann award address 2009: Merger of organic chemistry with peptide diversity. *Pept. Sci. 94*, 161–182.

(19) Oh, S., Jang, H. J., Ko, S. K., Ko, Y., and Park, S. B. (2010) Construction of a polyheterocyclic benzopyran library with diverse core skeletons through diversity-oriented synthesis pathway. *J. Comb. Chem. 12*, 548–558.

(20) Tachibana, Y., Matsubara, N., Nakajima, F., Tsuda, T., Tsuda, S., Monde, K., and Nishimura, S.-I. (2002) Efficient and versatile synthesis of mucin-like glycoprotein mimics. *Tetrahedron 58*, 10213–10224.

(21) Tachibana, Y., Fletcher, G. L., Fujitani, N., Tsuda, S., Monde, K., and Nishimura, S.-I. (2004) Antifreeze glycoproteins: elucidation of the structural motifs that are essential for antifreeze activity. *Angew. Chem., Int. Ed. 43*, 856–862.

(22) Ozawa, C., Hojo, H., Nakahara, Y., Katayama, H., Nabeshima, K., Akahane, T., and Nakahara, Y. (2007) Synthesis of glycopeptide dendrimer by a convergent method. *Tetrahedron 63*, 9685–9690.

(23) Conroy, T., Jolliffe, K. A., and Payne, R. J. (2009) Efficient use of the Dmab protecting group: applications for the solid-phase synthesis of *N*-linked glycopeptides. *Org. Biomol. Chem. 7*, 2255–2258.

(24) Kutterer, K. M. K., Barnes, M. L., and Arya, P. (1999) Automated, solid-phase synthesis of *C*-neoglycopeptides: coupling of glycosyl derivatives to resin-bound peptides. *J. Comb. Chem. 1*, 28–31.

(25) Miller, N., Williams, G. M., and Brimble, M. A. (2009) Synthesis of fish antifreeze neoglycopeptides using microwave-assisted "Click" chemistry. *Org. Lett. 11*, 2409–2412.

(26) Norgren, A. S., Budke, C., Majer, Z., Heggemann, C., Koop, T., and Sewald, N. (2009) On-resin Click-glycoconjugation of peptoids. *Synthesis* 488–494.

(27) Pedersen, D. S., and Rosenbohm, C. (2001) Dry vacuum column chromatography. *Synthesis* 2431–2434.

(28) Chakrabartty, A., and Hew, C. L. (1991) The effect of enhanced α-helicity on the activity of a winter flounder antifreeze polypeptide. *Eur. J. Biochem. 202*, 1057–1063.

(29) Jackman, J., Noestheden, M., Moffat, D., Pezacki, J. P., Findlay, S., and Ben, R. N. (2007) Assessing antifreeze activity of AFGP 8 using domain recognition software. *Biochem. Biophys. Res. Commun. 354* 340–344.

(30) Ibatullin, F. M., and Selivanov, S. I. (2002) Reaction of 1,2-trans-glycosyl acetates with phosphorus pentachloride: new efficient approach to 1,2-trans-glycosyl chlorides. *Tetrahedron Lett. 43*, 9577–9580.

(31) Szilágyi, L., and Györgydeák, Z. A. (1985) ^{13}C-N.M.R investigation of glycosyl azides and other azido sugars: stereochemical influences on the one-bond ^{13}C-^{1}H coupling constants. *Carbohydr. Res. 143*, 21.

(32) Podlipnik, C., Velter, I., La Ferla, B., Marcou, G., Belvisi, L., Nicotra, F., and Bernardi, A. (2007) First round of a focused library of cholera toxin inhibitors. *Carbohydr. Res. 342*, 1651–1660.

(33) Aldhoun, M., Massi, A., and Dondoni, A. (2008) Click azide-nitrile cycloaddition as a new ligation tool for the synthesis of tetrazole-tethered *C*-glycosyl α-amino acids. *J. Org. Chem. 73*, 9565–9575.

(34) Chan, W. C., and White, P. D. (2000) Basic procedures, in *Fmoc Solid Phase Peptide Synthesis: A Practical Approach* (Chan, W. C., and White, P. D., Eds.) pp 41−76, Oxford University Press, Oxford.

(35) Löber, S., Rodriguez-Loaiza, P., and Gmeiner, P. (2003) Click linker: efficient and high-yielding synthesis of a new family of SPOS resins by 1,3-dipolar cycloaddition. *Org. Lett. 5*, 1753–1755.

(36) Turner, R. A., Oliver, A. G., and Lokey, R. S. (2007) Click chemistry as a macrocyclization tool in the solid-phase synthesis of small cyclic peptides. *Org. Lett. 9*, 5011–5014.

(37) Gasser, G., Hüsken, N., Köster, S. D., and Metzler-Nolte, N. (2008) Synthesis of organometallic PNA oligomers by click chemistry. *Chem. Commun. 31*, 3675–3677.

(38) Singh, I., Vyle, J. S., and Heaney, F. (2009) Fast, copper-free click chemistry: a convenient solid-phase approach to oligonucleotide conjugation. *Chem. Commun. 32*, 3276–3278.

(39) Sharma, P., and Moses, J. E. (2010) Ethynyldiisopropylsilyl: a new alkynylsilane protecting group and "click" linker. *Org. Lett. 12*, 2860–2863.

(40) Santini, R., Griffith, M. C., and Qi, M. (1998) A measure of solvent effects on swelling of resins for solid phase organic synthesis. *Tetrahedron Lett. 39*, 8951–8954.

(41) Bock, V. D., Hiemstra, H., and van Maarseveen, J. H. (2006) Cu^{I}-catalyzed alkyne-azide "Click" cycloadditions from a mechanistic and synthetic perspective. *Eur. J. Org. Chem.* 51–68.

(42) Bouillon, C., Meyer, A., Vidal, S., Jochum, A., Chevolot, Y., Cloarec, J.-P., Praly, J.-P., Vasseur, J.-J., and Morvan, F. (2006) Microwave assisted "Click" chemistry for the synthesis of multiple labeled-carbohydrate oligonucleotides on solid support. *J. Org. Chem. 71* 4700–4702.

(43) Raymond, J. A., Radding, W., and DeVries, A. L. (1977) Circular dichroism of protein and glycoprotein fish antifreezes. *Biopolymers 16*, 2575–2578.

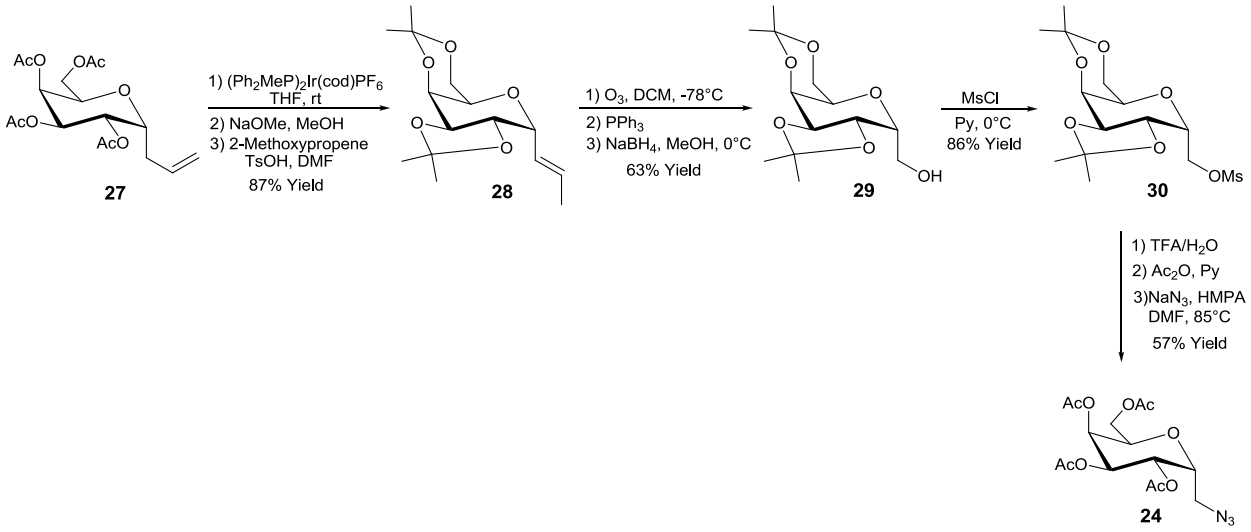
(44) Eniade, A., Purushotham, M., Ben, R., N., Wang, J. B., and Horwath, K. (2003) A serendipitous discovery of antifreeze protein-specific activity in *C*-linked antifreeze glycoprotein analogs. *Cell Biochem. Biophys. 38*, 115–124.

Supporting Information:

Synthesis of *C*-Linked Triazole-Containing AFGP Analogues and Their Ability to Inhibit Ice Recrystallization

*Chantelle J. Capicciotti, John F. Trant, Mathieu Leclère, Robert N. Ben**

University of Ottawa, Department of Chemistry, D'Iorio Hall, 10 Marie Curie, Ottawa, ON, Canada, K1N 6N5



Scheme 1. Synthesis of azido sugar **24**.

***E*-1-(2,3;4,6-di-*O*-isopropylidene-*α*-D-galactopyranosyl)-prop-1'-ene (28)**

Alkene **27**[1] was isomerized according to the procedure by Patnam.[2] (1,5-Cyclooctadiene)-bis-(methyldiphenylphosphine) Iridium (I) hexafluorophosphate (150 mg, 0.177 mmol) was suspended in 5 mL of THF under nitrogen with vigorous stirring. Hydrogen was bubbled into the mixture until the suspension dissolved giving a yellow solution. The solution was then flushed with Argon for 10 minutes and transferred via cannula into a flask containing **27** (2.31 g, 6.2 mmol) dissolved in THF. The reaction was stirred for 12 hours until complete conversion was observed by NMR. The solution was then concentrated under reduced pressure to yield 2.6 g of a crude yellow gel that was used without further purification.

The crude product was dissolved in 20 mL of a 0.1 M solution of sodium methoxide in methanol. The reaction was stirred for 1.5 hrs at room temperature whereupon DOWEX 50WX8 (50-100 mesh) ion exchange resin was added until the pH of the solution was neutral. The solution was filtered and concentrated to dryness to yield 1.3 g of a crude white solid which was used without any further purification.

The crude solid (1.3 g, 6.37 mmol) was dissolved in dry DMF under Argon with stirring. *Para*-toluenesulfonic acid monohydrate (100 mg, 0.525 mmol) was added followed by a dropwise addition of 2-methoxypropene (2.9 mL, 30 mmol). The reaction mixture was stirred for forty minutes. Upon complete consumption of starting material 500 μL of triethylamine was added and the solution was concentrated to dryness. The product was purified by flash chromatography (8:2 hexanes:ethyl acetate) to yield 1.53 g of **28** (87% yield over 3 steps). ^{1}H NMR (500 MHz, $CDCl_3$): δ_{ppm} 5.88 (dqd, 1H, J = 15.8, 6.4, 1.6 Hz), 5.60 (ddq, 1H, J = 15.8, 5.2, 1.6), 4.86 (t, 1H, J = 5.3 Hz), 4.45 (bs, 1H), 4.27 (dd, 1H, J = 9.9, 5.6 Hz), 4.09 (dd, 1H, J = 12.9, 2.1 Hz), 3.90 (dd, 1H, J = 12.9, 1.4 Hz), 3.67 (dd, 1H, J = 9.9, 2.9 Hz), 3.38 (dd, 1H, J = 3.2, 1.7 Hz), 1.74 (ddd, 3H, J = 6.5, 1.6, 1.6 Hz), 1.47 (s, 3H), 1.46 (s, 3H), 1.44 (s, 3H), 1.41 (s, 3H); ^{13}C NMR (100 MHz, $CDCl_3$): δ_{ppm} 131.3, 123.3, 110.0, 98.5, 75.2, 74.4, 70.9, 67.7, 63.5,

[1] Liu, S., and Ben, R. N. (2005) *C*-linked galactosyl serine AFGP analogues as potent recrystallization inhibitors. *Org. Lett.* 7, 2385-2388.
[2] Patman, R., Juárez-Ruiz, J.M., and Roy, R. (2006) Subtle stereochemical and electronic effects in iridium-catalyzed isomerization of C-allyl glycosides. *Org. Lett.* 8, 2691-2694.

63.5, 29.3, 26.7, 26.5, 18.5, 18.3. ESI-MS *m/z* calcd for $C_{15}H_{24}O_5$ $[M + NH_4]^+$: 302.19. Found: 302.19.

(2,3;4,6-di-*O*-isopropylidene-α-D-galactopyranosyl)methanol (29)

Compound **28** (430 mg, 1.51 mmol) was dissolved in 5 mL of DCM and cooled to -78º C. Ozone was bubbled through the solution until a blue colour persisted. The solution was then flushed with Nitrogen for 10 minutes until it became clear. Triphenylphosphine (800 mg, 3.05 mmol) was added and the reaction was allowed to warm to ambient temperature over 12 hours and then concentrated to dryness. The residue was immediately dissolved in methanol (10 mL) and cooled to 0 ºC. Sodium borohydride (340 mg, 9.0 mmol) was added portion wise and the reaction was stirred for 2 hrs. The reaction mixture was filtered through Celite and concentrated under reduced pressure. The residue was re-dissolved in ethyl acetate and washed sequentially with saturated sodium bicarbonate and brine, then dried with magnesium sulfate, filtered and concentrated *in vacuo*. The product was purified by flash chromatography (6:4 ethyl acetate: hexanes) to yield 261 mg of **29** as a clear oil (63% over 2 steps). ^{1}H NMR (400 MHz, $CDCl_3$): δ_{ppm} 4.55 (td, 1H, *J* = 7.9, 5.9 Hz), 4.52-4.50 (m, 1H), 4.38 (dd, 1H, *J* = 10.1, 6.0 Hz), 4.12 (dd, 1H, *J* = 13.1, 2.2 Hz), 3.95 (dd, 1H, *J* = 13.0, 1.5 Hz), 3.93-3.85 (m, 2H), 3.81 (dd, 1H, *J* = 10.1, 2.9 Hz), 3.40 (dd, 1H, *J* = 3.2, 1.6 Hz), 1.50 (s, 3H), 1.49 (s, 3H), 1.48 (s, 3H), 1.44 (s, 3H); ^{13}C NMR (100 MHz, $CDCl_3$): δ_{ppm} 110.3, 98.6, 75.5, 74.2, 70.3, 67.3, 64.5, 63.3, 58.7, 29.2, 26.6, 18.4. ESI-MS *m/z* calcd for $C_{13}H_{22}O_6$ $[M + Na]^+$: 297.13. Found: 297.17.

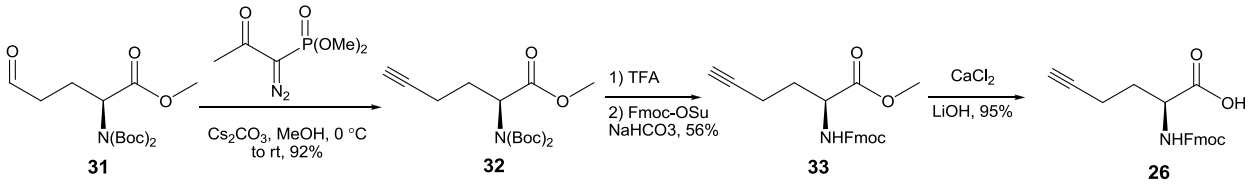
(2,3;4,6-di-*O*-isopropylidene-α-D-galactopyranosyl)methyl methanesulfonate (30)

Alcohol **29** (600 mg, 2.2 mmol) was dissolved in pyridine (12.5 mL) and cooled to 0 ºC. Methanesulfonyl chloride (620 µL, 8 mmol) was added dropwise and the mixture was stirred for 5 hours at 0 ºC. Upon complete consumption of starting material the reaction was diluted with DCM (50 mL) and washed twice with 10 % HCl (50 mL) and $NaHCO_3$ then dried with magnesium sulfate, filtered, and concentrated to yield 662 mg of **30** (86% yield) as a clear colourless oil. ^{1}H NMR (400 MHz, $CDCl_3$): δ_{ppm} 4.70-4.61 (m, 2H), 4.51-4.48 (m, 1H), 4.35 (d, 1H, *J* = 10.0 Hz), 4.34 (dd, 1H, *J* = 15.7, 5.5 Hz), 4.13 (dd, 1H, *J* = 13.2, 2.1 Hz), 3.90 (dd, 1H, *J* = 13.2, 1.4 Hz), 3.61 (dd, 1H, *J* = 10.2, 2.8 Hz), 3.53 (dd, 1H, *J* = 3.1, 1.8 Hz), 3.09 (s, 3H), 1.48 (s, 3H), 1.46 (s, 3H), 1.45 (s, 3H), 1.40 (s, 3H); ^{13}C NMR (100 MHz, $CDCl_3$): δ_{ppm} 110.8, 98.7, 74.5, 74.3, 69.2, 67.1, 64.7, 64.3, 63.2, 38.6, 29.2, 26.6, 26.5, 18.4. ESI-MS *m/z* calcd for $C_{14}H_{24}O_8S$ $[M + H]^+$: 353.12. Found: 353.16.

(2,3,4,6-Tetra-*O*-acetyl-α-D-galactopyranosyl)methyl azide (24)

Mesylate **30** (660 mg, 1.8 mmol) was dissolved in TFA (4 mL) and H_2O (1 mL) at room temperature. The reaction was stirred for 10 minutes and pyridine (10 mL) was added and solvent was removed *in vacuo*. The residue was immediately re-dissolved in pyridine (5 mL) and acetic anhydride (5 mL) and stirred for 4 hours. Solvent was removed *in vacuo* then the flask was flushed with Argon and the residue re-dissolved in DMF (1.5 mL). HMPA (500 µL) and sodium azide (400 mg, 6.1 mmol) were added and the reaction was heated to 85ºC for 12 hours. The solution was diluted with DCM, and washed sequentially with 10% HCl, saturated $NaHCO_3$, and brine. The organic layer was dried with magnesium sulfate, filtered, and concentrated. The final product was purified by DVC (100% hexanes to 100% ethyl acetate in 5% intervals) to yield 457 mg of residue that was recrystallized from diethyl ether/hexanes to yield 373 mg of **24** as a white crystalline solid (57% yield over 3 steps). Spectral data is consistent with previously published

data.[3] ^{1}H NMR (400 MHz, $CDCl_3$): δ_{ppm} 5.44 (dd, 1H, *J* = 3.3, 3.3 Hz), 5.27 (dd, 1H, *J* = 8.4, 4.6 Hz), 5.22 (dd, 1H, *J* = 8.4, 3.2 Hz), 4.39 (m, 2H), 4.25 (ddd, 1H, *J* = 8.0, 4.5, 3.4 Hz), 4.11 (dd, 1H, *J* = 11.7, 4.7 Hz), 3.63 (dd, 1H, *J* = 13.5, 8.8 Hz), 3.24 (dd, 1H, *J* = 13.5, 3.7 Hz), 2.12 (s, 3H), 2.11 (s, 3H), 2.07 (s, 3H), 2.06 (s, 3H); ^{13}C NMR (100 MHz, $CDCl_3$): δ_{ppm} 170.7, 169.8, 169.6, 169.5, 70.8, 69.8, 67.7, 67.5, 66.9, 60.7, 48.3, 20.67, 20.66, 20.59. ESI-MS *m/z* calcd for $C_{15}H_{21}N_3O_9$ $[M + K]^+$: 426.091. Found: 426.12.



Scheme 2. Synthesis of amino acid **26**.

(S)-Methyl 2-{(tert-butoxy)-N-[(tert-butyl)oxycarbonyl]- carbonylamino}-hex-5-ynoate (32).

Aldehyde **31**[4] (1.9 g, 5.5 mmol) and dimethyl (1-diazo-2-oxopropyl)phosphonate (1.58 g, 8.25 mmol) were dissolved in 20 mL of dry MeOH. The solution was cooled to 0 ºC and Cs_2CO_3 (2.51 g, 7.7 mmol) was added in one portion. The mixture was warmed to room temperature and stirred for 3 hrs. The solution was concentrated and partitioned with ether and water (100 mL each). The organic layer was successively washed with water and brine, dried over Na_2SO_4 and concentrated. The crude product was redissolved in 100 mL of petroleum ether and the cloudy solution was filtered through a pad of Celite. Evaporation of the solvent afforded 1.80 g of **32** (95% yield) as a colorless oil. ^{1}H NMR ($CDCl_3$, 400 MHz): δ_{ppm} 4.98 (dd, 1H, J = 9.0, 5.0 Hz), 3.69 (s, 3H), 2.41-2.19 (m, 3H), 2.06 (m, 1H), 1.94 (t, 1H, J = 2.6 Hz), 1.47 (s, 18H). ^{13}C NMR (CDCl3, 100 MHz): δ_{ppm} 171.0, 151.9, 83.3, 83.2, 69.1, 57.2, 52.2, 29.3, 28.0, 15.7. ESI-MS *m/z* calcd for $C_{17}H_{27}NO_6$ $[M + Na]^+$: 364.17. Found: 364.30.

(*S*)-methyl 2-(9-fluorenylmethoxycarbonylamino)-hex-5-ynoate (33).

To a cold (0 ºC) solution of **32** (1.8 g, 5.3 mmol) in 5 mL of DCM was added dropwise 5 mL of TFA. The solution was warmed to room temperature and stirred until TLC (9:1 petroleum ether:ethyl acetate) showed disappearance of the starting material. The crude mixture was then concentrated and co-evaporated with toluene (3 x 20 mL) and dried under high vacuum for several hours. The crude material was re-dissolved in 2:1 dioxane:water (45 mL) and was cooled to 0 ºC. $NaHCO_3$ (1.7 g, 21.2 mmol) and Fmoc-OSu (1.96 g, 5.8 mmol) were successively added and the mixture was warmed to room temperature and stirred overnight. Dioxane was evaporated and the aqueous layer was extracted with ethyl acetate. The organic layer was then washed with water and brine, dried over Na_2SO_4 and concentrated. Purification of the crude by flash chromatography (3:1 DCM:Petroleum ether, followed by pure DCM) afforded 1.08 g of **33** (56%

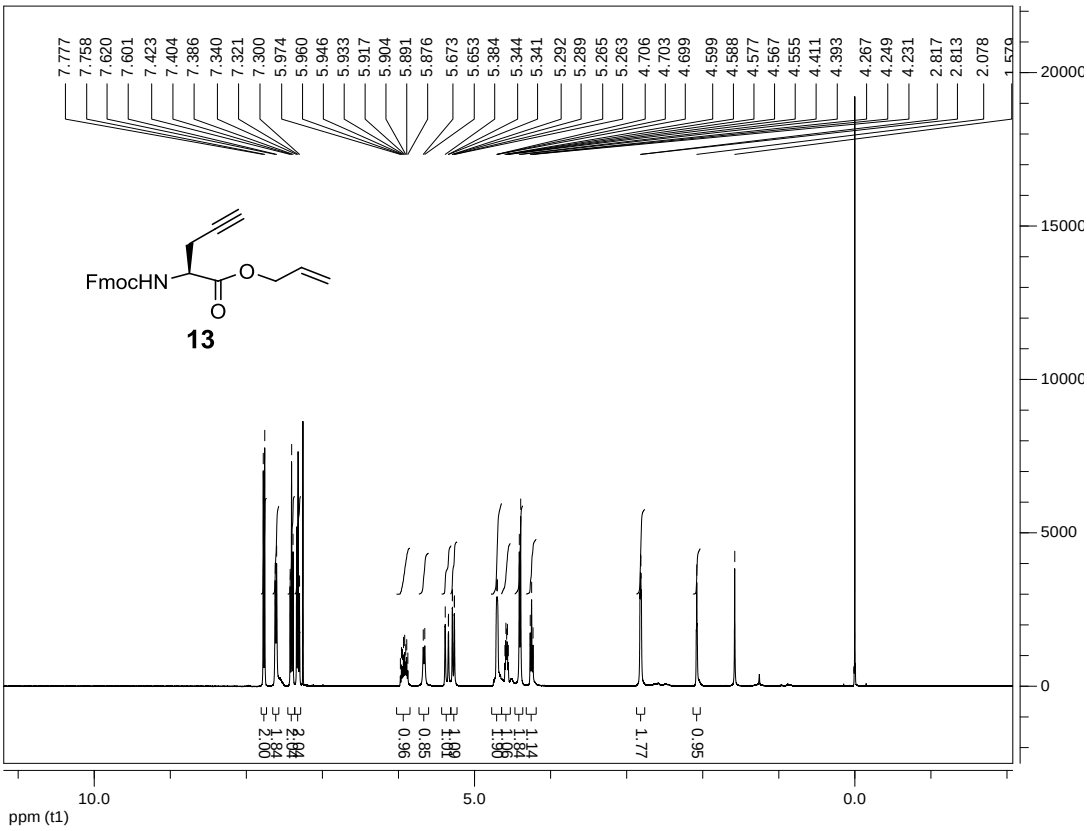
[3] Aldhoun, M., Massi, A., and Dondoni, A. (2008) Click Azide−Nitrile Cycloaddition as a New Ligation Tool for the Synthesis of Tetrazole-Tethered *C*-Glycosyl α-Amino Acids. *J. Org. Chem.* 73, 9565-9575.

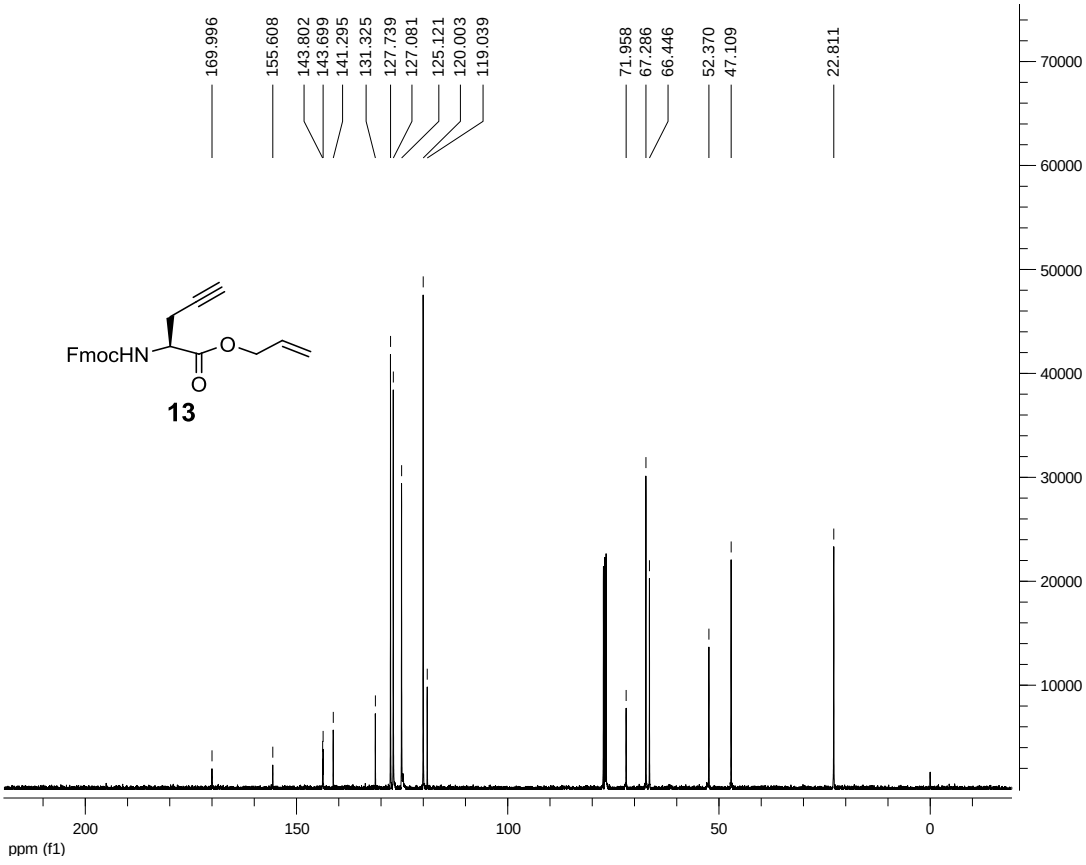
[4] Padrón J. M., Kokotos G., Martín T., Markidis T., Gibbons W. A., and Martín, V. S. (1998) Enantiospecific synthesis of α-amino acid semialdehydes: a key step for the synthesis of unnatural unsaturated and saturated α-amino acids. *Tetrahedron Asymmetry*. 9, 3381-3394.

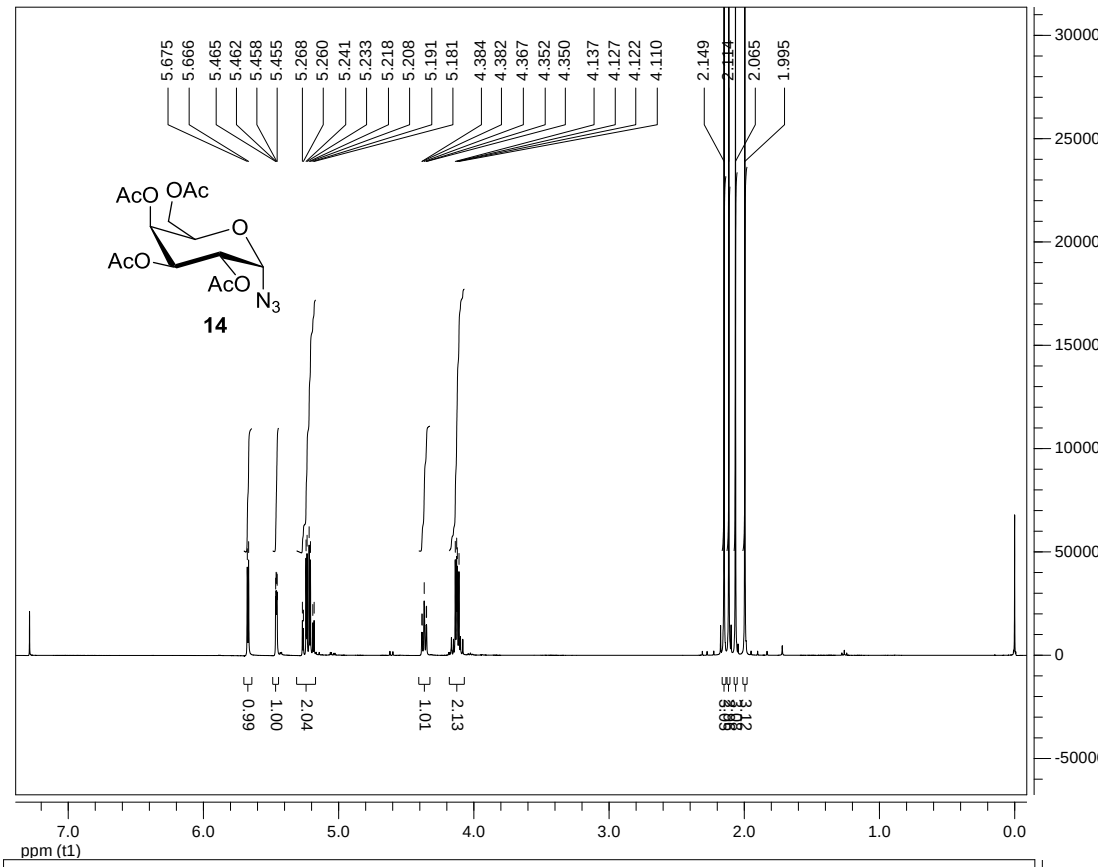
yield over 2 steps) as a white solid. ^{1}H NMR ($CDCl_3$, 400 MHz) : δ_{ppm} 7.75 (d, 2H, J = 7.4 Hz), 7.59 (dd, 2H, J = 7.2, 3.2 Hz), 7.38 (t, 2H, J = 7.4 Hz), 7.30 (t, 2H, J = 7.5 Hz), 5.44 (d, 1H, J = 8.0 Hz), 4.48 (m, 1H), 4.40 (d, 2H, J = 7.0 Hz), 4.21 (t, 1H, J = 7.0 Hz), 3.74 (s, 3H), 2.26 (m, 2H), 2.13 (m , 1H), 1.99 (t, 1H, J = 2.4 Hz), 1.92 (m, 1H). ^{13}C NMR ($CDCl_3$, 100 MHz): δ_{ppm} 172.4, 155.9, 143.9, 143.7, 141.4, 141.3, 127.8, 127.1, 125.1, 120.0, 82.7, 77.3, 69.5, 67.0, 53.2, 52.6, 47.2, 31.3, 14.8. ESI-MS *m/z* calcd for $C_{22}H_{21}NO_4$ $[M + Na]^+$: 386.14. Found: 386.25.

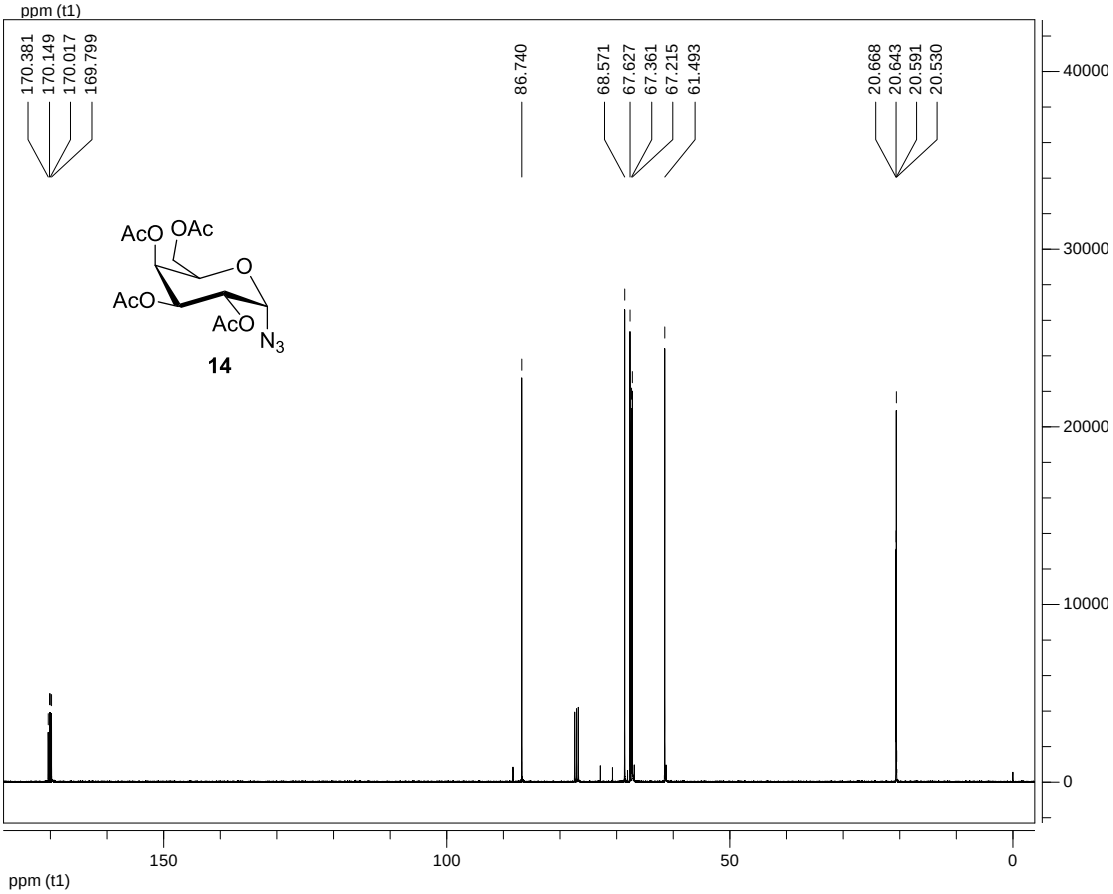
(*S*)-2-(9-fluorenylmethoxycarbonylamino)-hex-5-ynoic acid (26).

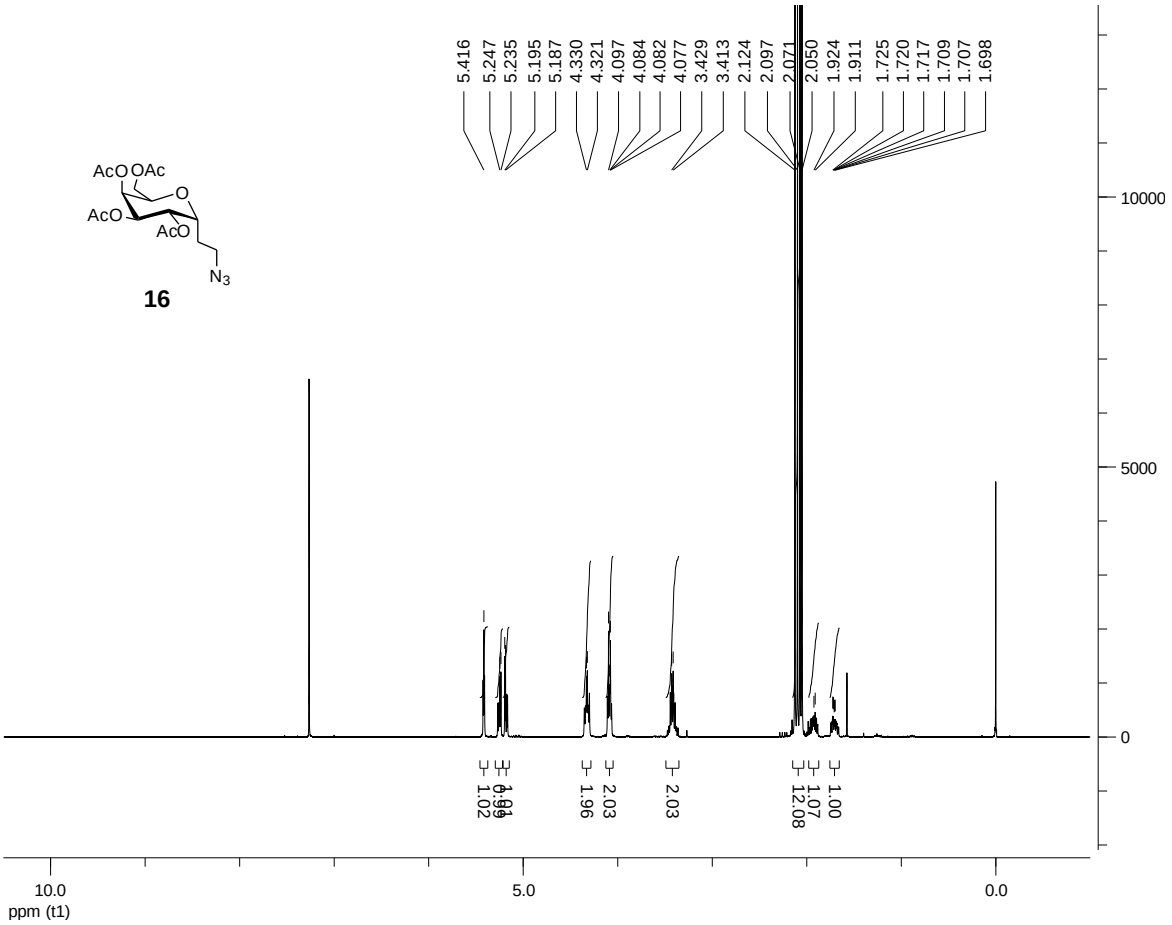
To a solution of **33** (600 mg, 1.65 mmol) in a mixture of 25 mL of isopropanol and 6 mL of THF was added powdered $CaCl_2$ (2.8 g, 25 mmol). $LiOH.H_2O$ (280 mg, 6.6 mmol) in 7 mL of water was added and the mixture was vigorously stirred until TLC (98:2 DCM:MeOH) showed disappearance of the starting material (*ca*. 5 hrs). The pH was adjusted to 2 with 1% HCl and organic solvents were removed. The aqueous layer was extracted with DCM and the organic layer was washed with water and brine, dried over Na_2SO_4 and concentrated *in vacuo*. The product was purified by flash chromatography (98:2 DCM:MeOH) to yield 550 mg of **26** (95% yield) as a white solid. ^{1}H NMR (2:1 $CDCl_3/CD_3OD$, 400 MHz): δ_{ppm} 7.71 (d, 2H, J = 7.6 Hz), 7.58 (dd, 2H, J = 7.1, 3.9 Hz), 7.35 (t, 2H, J = 7.6 Hz), 7.27 (t, 2H, J = 7.6 Hz), 4.35 (m, 3H), 4.18 (t, 1H, J = 6.8 Hz), 2.24 (m, 2H), 2.09 (m, 1H), 2.01 (t, 1H, J = 2.6 Hz), 1.86 (m, 1H). ^{13}C NMR ($CDCl_3/CD_3OD$ 2/1, 100 MHz): δ_{ppm} 173.9, 156.7, 143.8, 143.7, 141.2, 141.2, 127.7, 127.0, 125.0, 119.8, 82.6, 77.5, 69.3, 66.9, 53.0, 47.1, 30.9, 14.9. ESI-MS *m/z* calcd for $C_{21}H_{19}NO_4$ $[M + Na]^+$: 372.12. Found: 372.24.

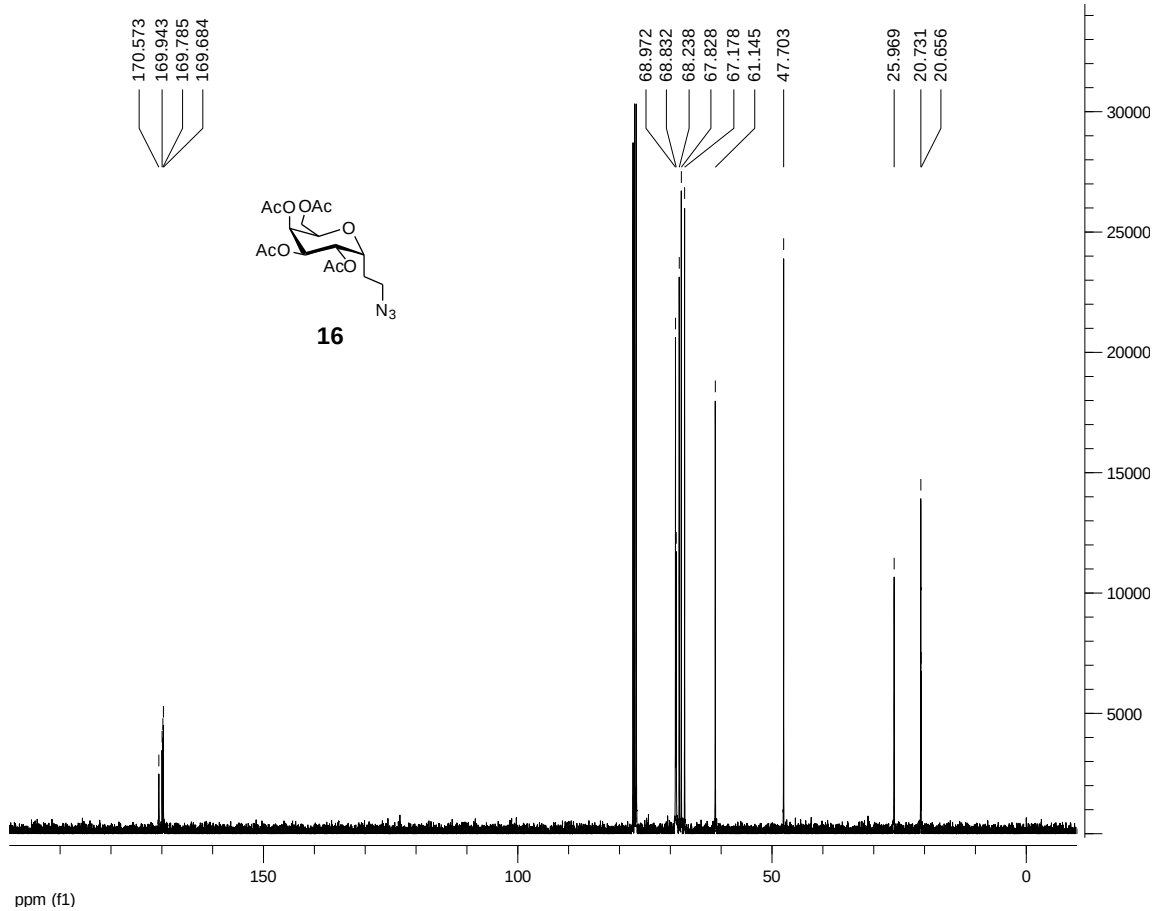

7.777
7.758
7.620
7.601
7.423
7.404
7.386
7.340
7.321
7.300
5.974
5.960
5.946
5.933
5.917
5.904
5.891
5.876
5.673
5.653
5.384
5.344
5.341
5.292
5.289
5.265
5.263
4.706
4.703
4.699
4.599
4.588
4.577
4.567
4.555
4.411
4.393
4.267
4.249
4.231
2.817
2.813
2.078
FmocHN
O
O
13
2.00
1.84
2.04
2.08
0.96
0.85
1.00
1.09
1.00
1.14
1.04
1.00
1.77
0.95
20000
15000
10000
5000
0
10.0
5.0
0.0
ppm (t1)

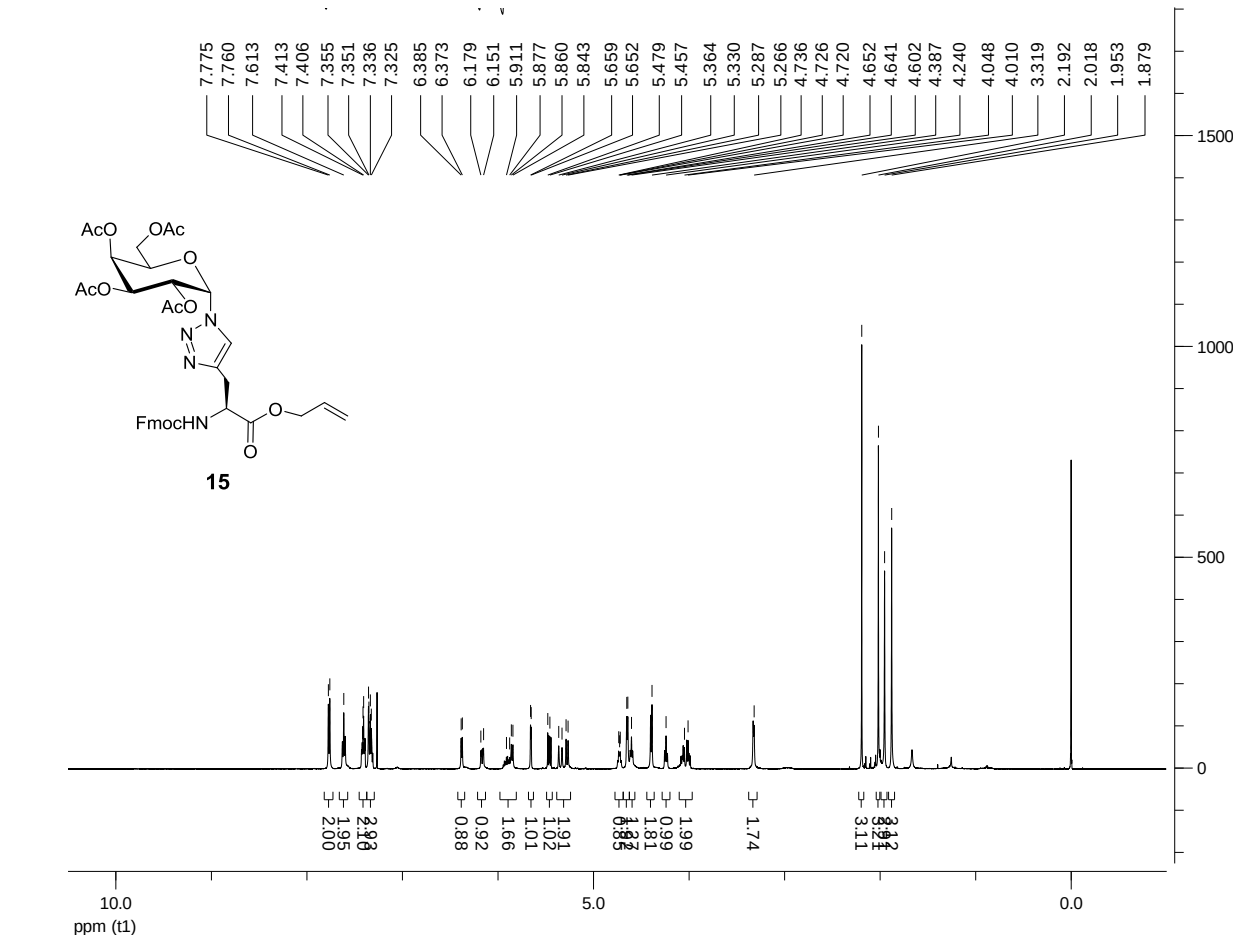

169.996
155.608
143.802
143.699
141.295
131.325
127.739
127.081
125.121
120.003
119.039
71.958
67.286
66.446
52.370
47.109
22.811
FmocHN
O
O
13
70000
60000
50000
40000
30000
20000
10000
200
150
100
50
0
ppm (f1)

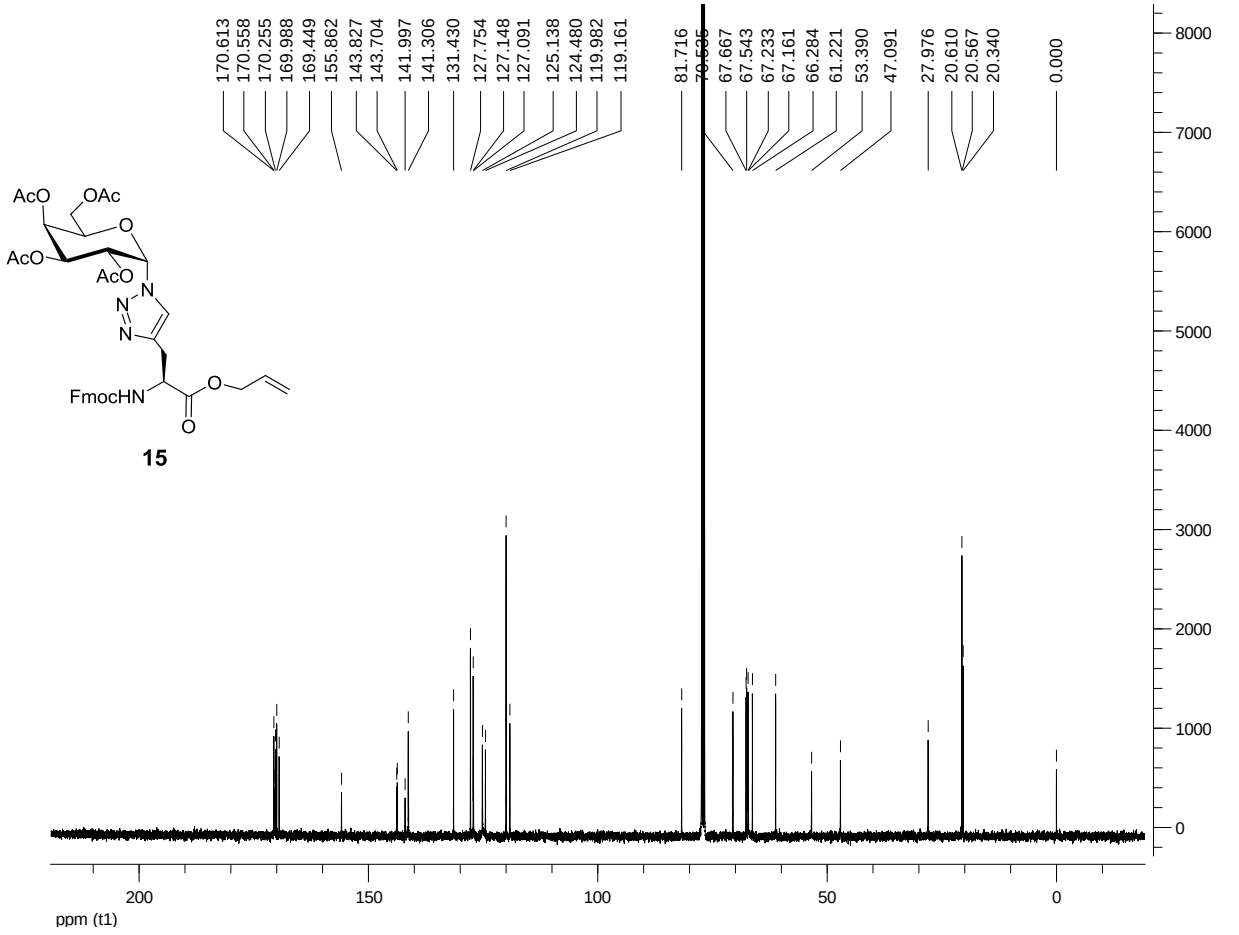

5.675
5.666
5.465
5.462
5.458
5.455
5.268
5.260
5.241
5.233
5.218
5.208
5.191
5.181
4.384
4.382
4.367
4.352
4.350
4.137
4.127
4.122
4.110
2.149
2.114
2.065
1.995
AcO
OAc
O
AcO
AcO
N3
14
0.99
1.00
2.04
1.01
2.13
3.12
ppm (t1)

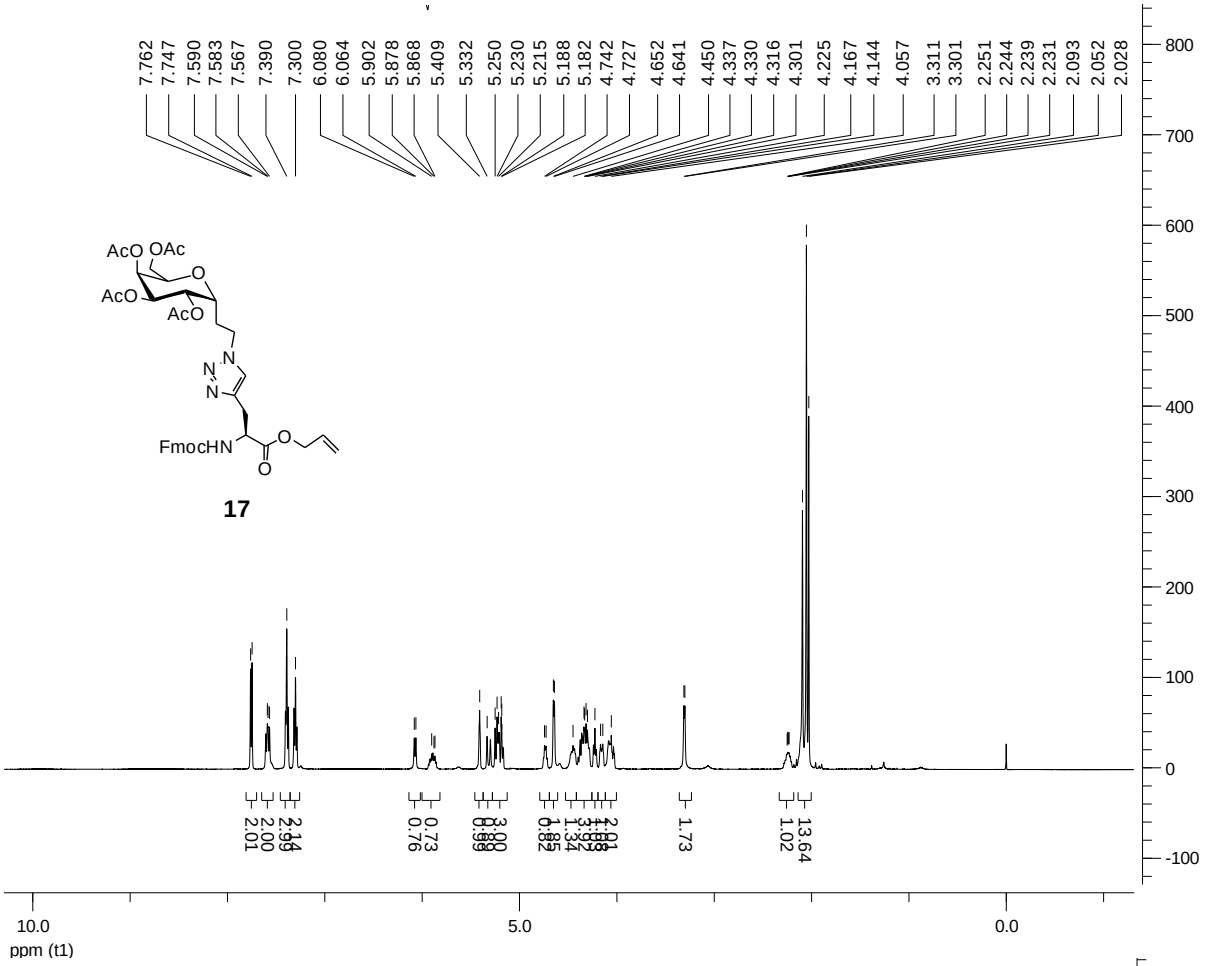

170.381
170.149
170.017
169.799
86.740
68.571
67.627
67.361
67.215
61.493
20.668
20.643
20.591
20.530
AcO
OAc
O
AcO
AcO
N3
14
ppm (t1)


5.416
5.247
5.235
5.195
5.187
4.330
4.321
4.097
4.084
4.082
4.077
3.429
3.413
2.124
2.097
2.071
2.050
1.924
1.911
1.725
1.720
1.717
1.709
1.707
1.698
AcO OAc
O
AcO
AcO
N3
16
10000
5000
0
1.02
0.99
0.99
1.96
2.03
2.03
12.08
1.07
1.00
10.0
5.0
0.0
ppm (t1)

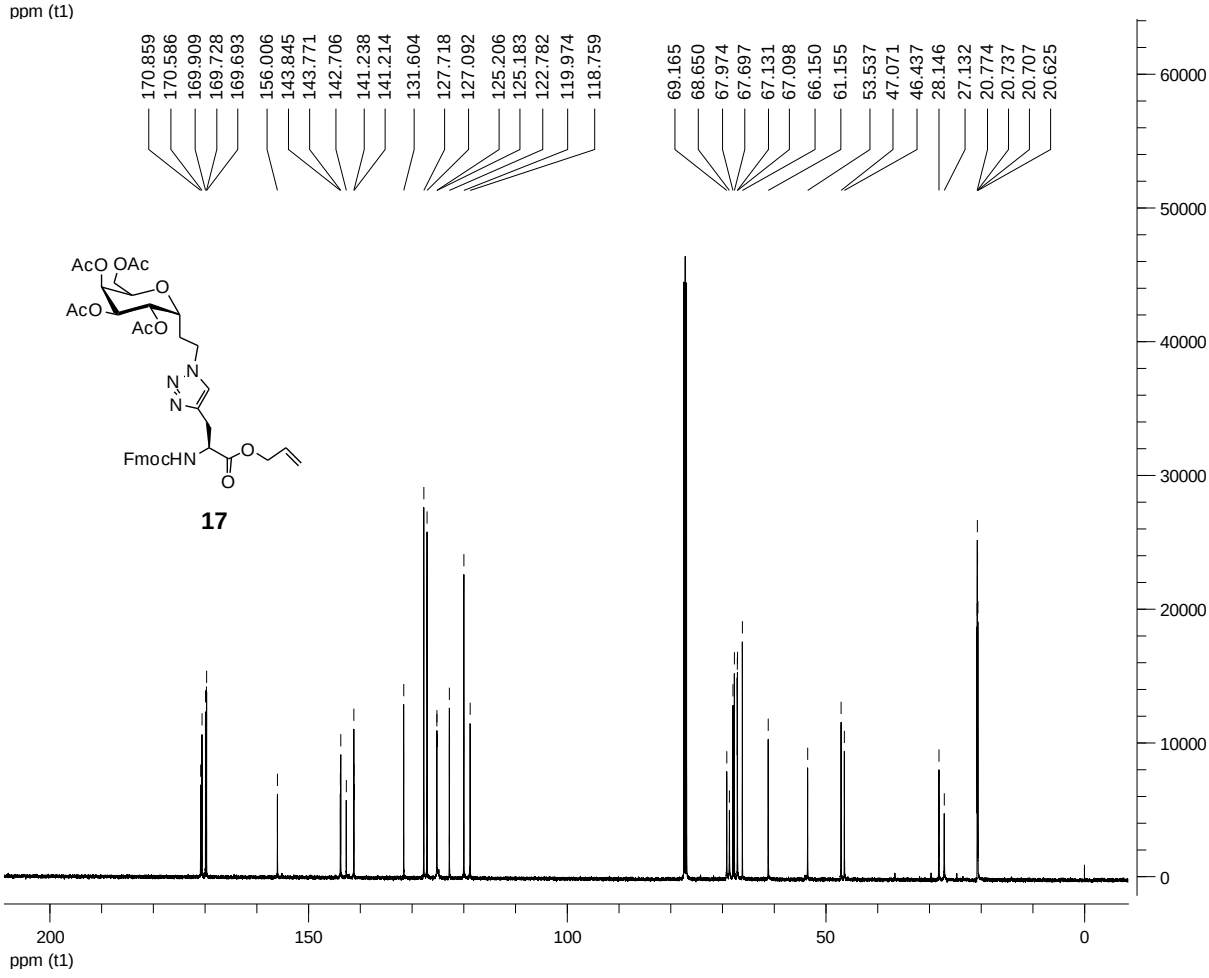

170.573
169.943
169.785
169.684
68.972
68.832
68.238
67.828
67.178
61.145
47.703
25.969
20.731
20.656
AcO OAc
O
AcO
AcO
N3
16
30000
25000
20000
15000
10000
5000
150
100
50
0
ppm (f1)


7.775
7.760
7.613
7.413
7.406
7.355
7.351
7.336
7.325
6.385
6.373
6.179
6.151
5.911
5.877
5.860
5.843
5.659
5.652
5.479
5.457
5.364
5.330
5.287
5.266
4.736
4.726
4.720
4.652
4.641
4.602
4.387
4.240
4.048
4.010
3.319
2.192
2.018
1.953
1.879
AcO
OAc
AcO
AcO
FmocHN
15
10.0
5.0
0.0
ppm (t1)

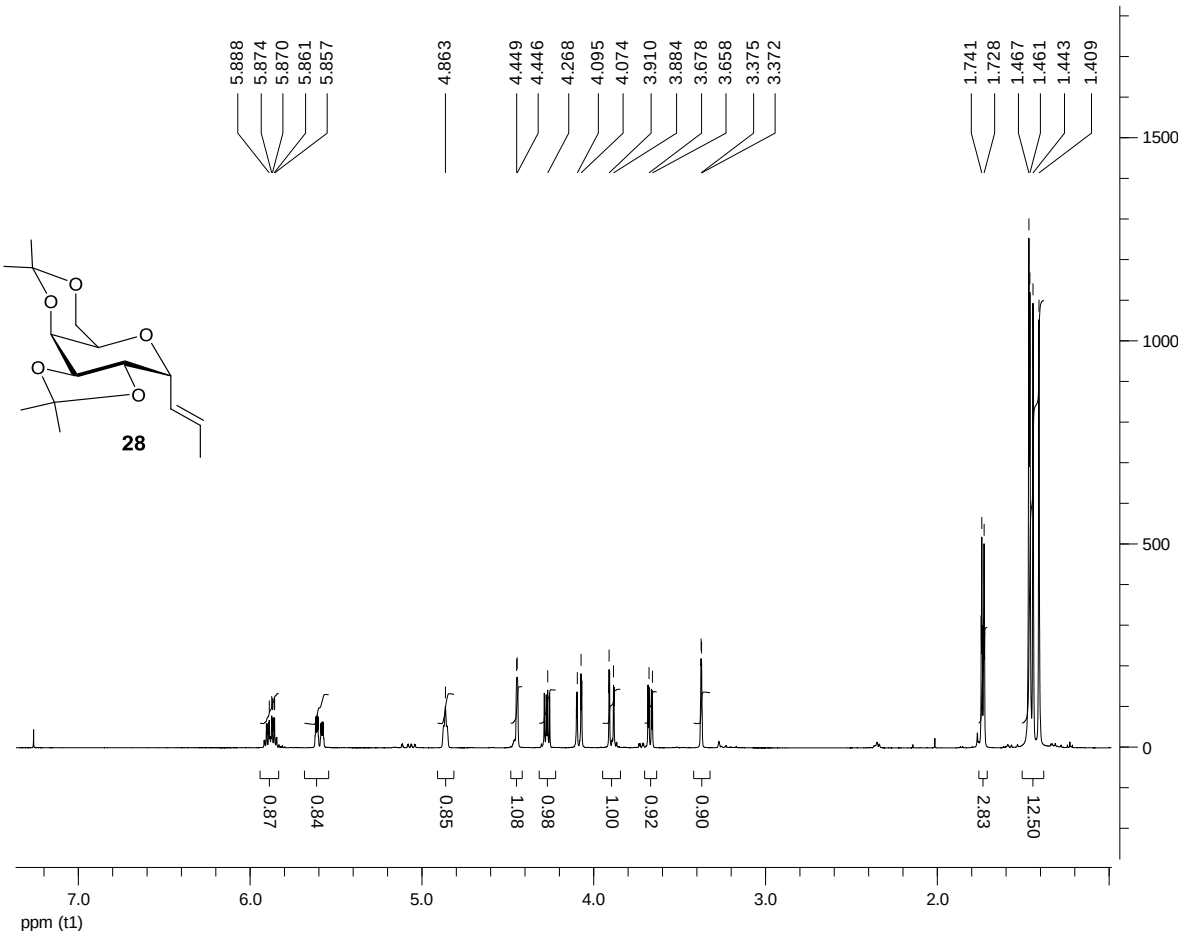

170.613
170.558
170.255
169.988
169.449
155.862
143.827
143.704
141.997
141.306
131.430
127.754
127.148
127.091
125.138
124.480
119.982
119.161
81.716
67.667
67.543
67.233
67.161
66.284
61.221
53.390
47.091
27.976
20.610
20.567
20.340
0.000
AcO
OAc
AcO
AcO
FmocHN
15
200
150
100
50
0
ppm (t1)

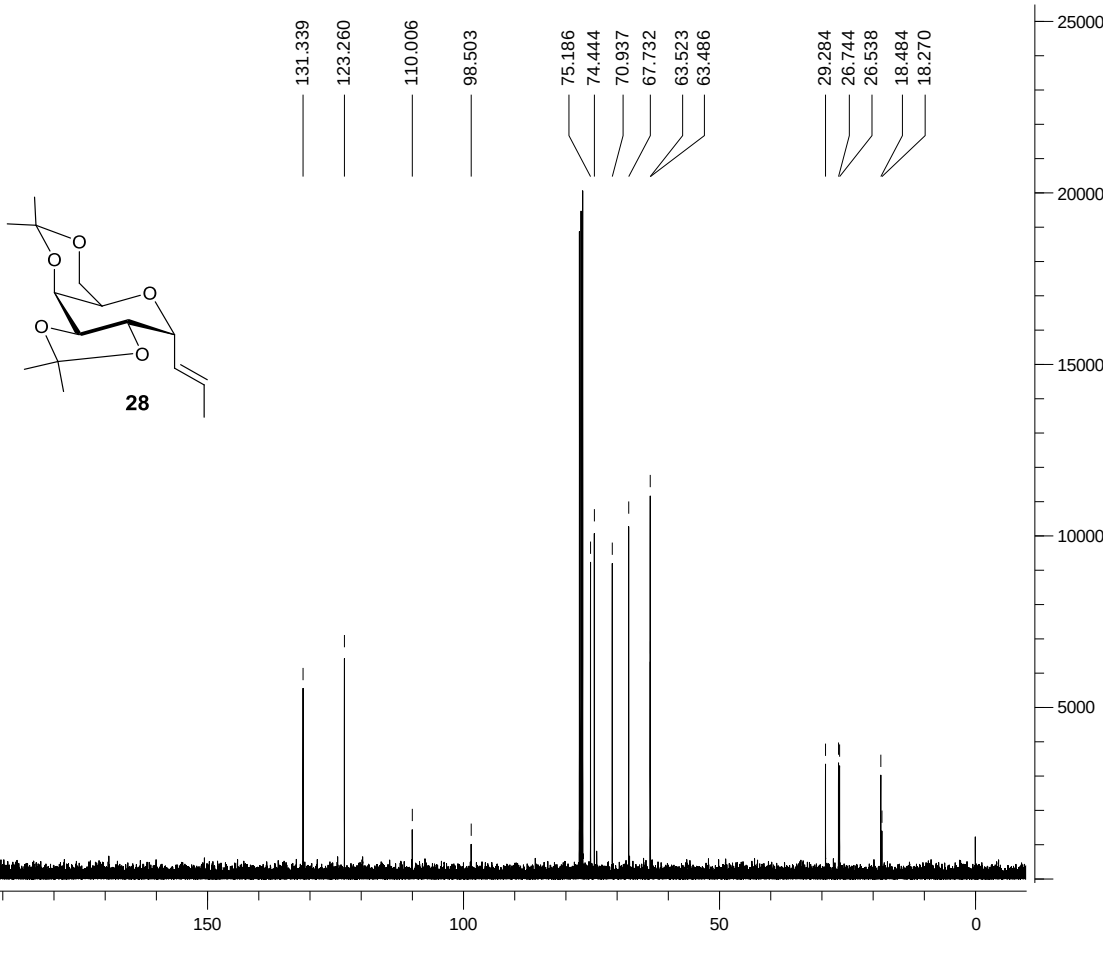

7.762
7.747
7.590
7.583
7.567
7.390
7.300
6.080
6.064
5.902
5.878
5.868
5.409
5.332
5.250
5.230
5.215
5.188
5.182
4.742
4.727
4.652
4.641
4.450
4.337
4.330
4.316
4.301
4.225
4.167
4.144
4.057
3.311
3.301
2.251
2.244
2.239
2.231
2.093
2.052
2.028
AcO OAc
AcO
AcO
FmocHN
2.01
2.00
2.14
2.69
0.76
0.73
1.73
1.02
13.64
10.0
5.0
0.0
ppm (t1)

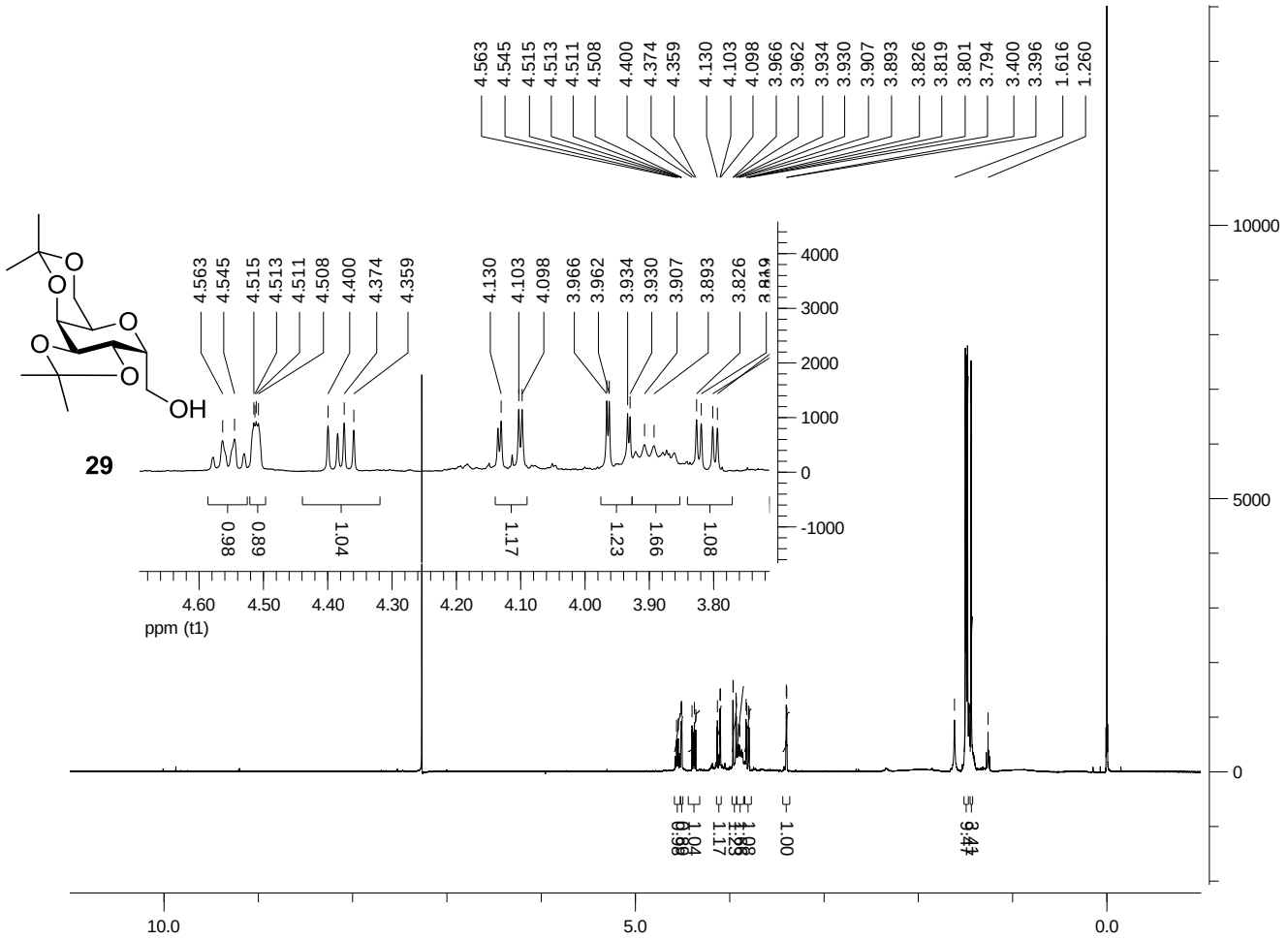
17

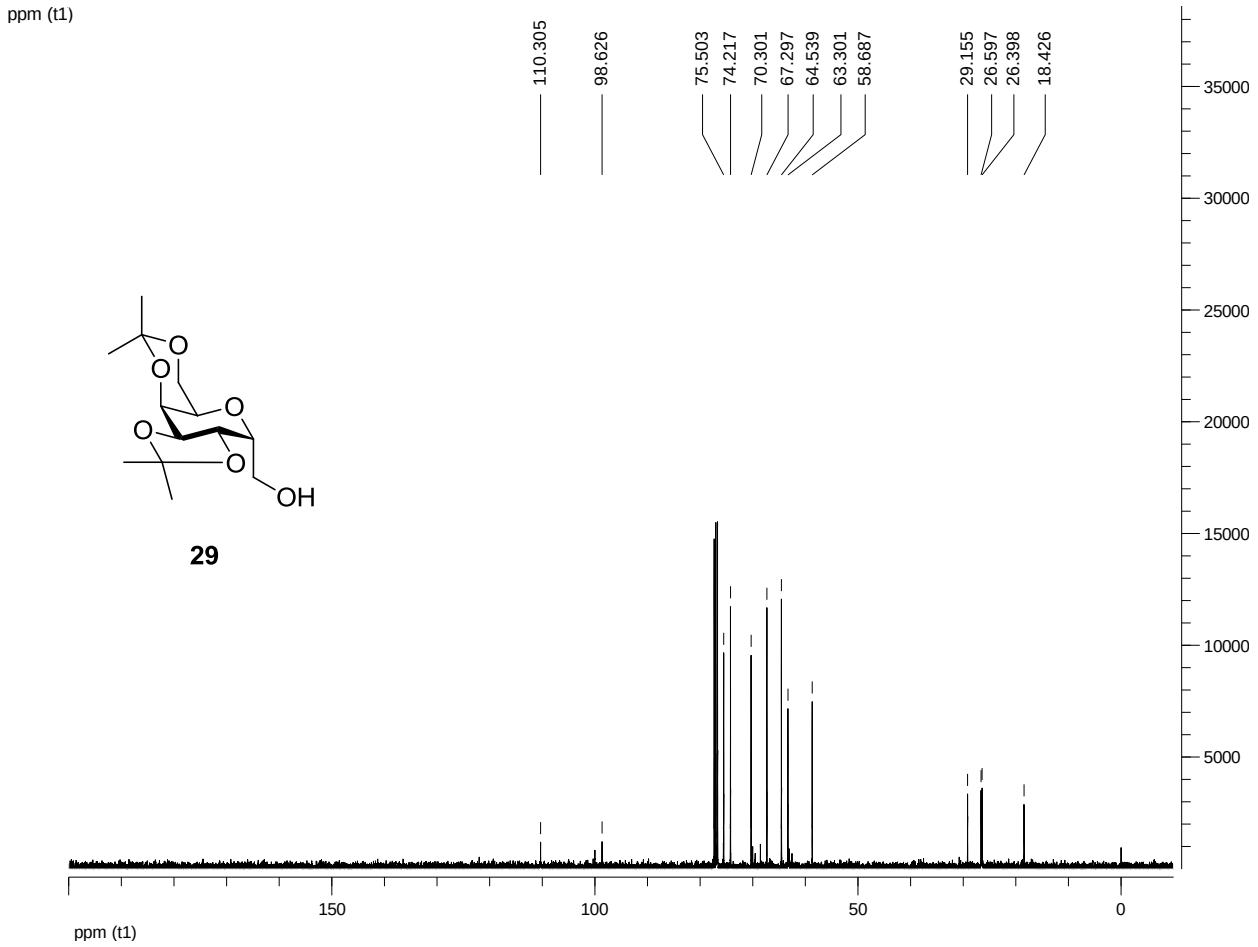

170.859
170.586
169.909
169.728
169.693
156.006
143.845
143.771
142.706
141.238
141.214
131.604
127.718
127.092
125.206
125.183
122.782
119.974
118.759
69.165
68.650
67.974
67.697
67.131
67.098
66.150
61.155
53.537
47.071
46.437
28.146
27.132
20.774
20.737
20.707
20.625
AcO OAc
AcO
AcO
FmocHN
200
150
100
50
0
ppm (t1)

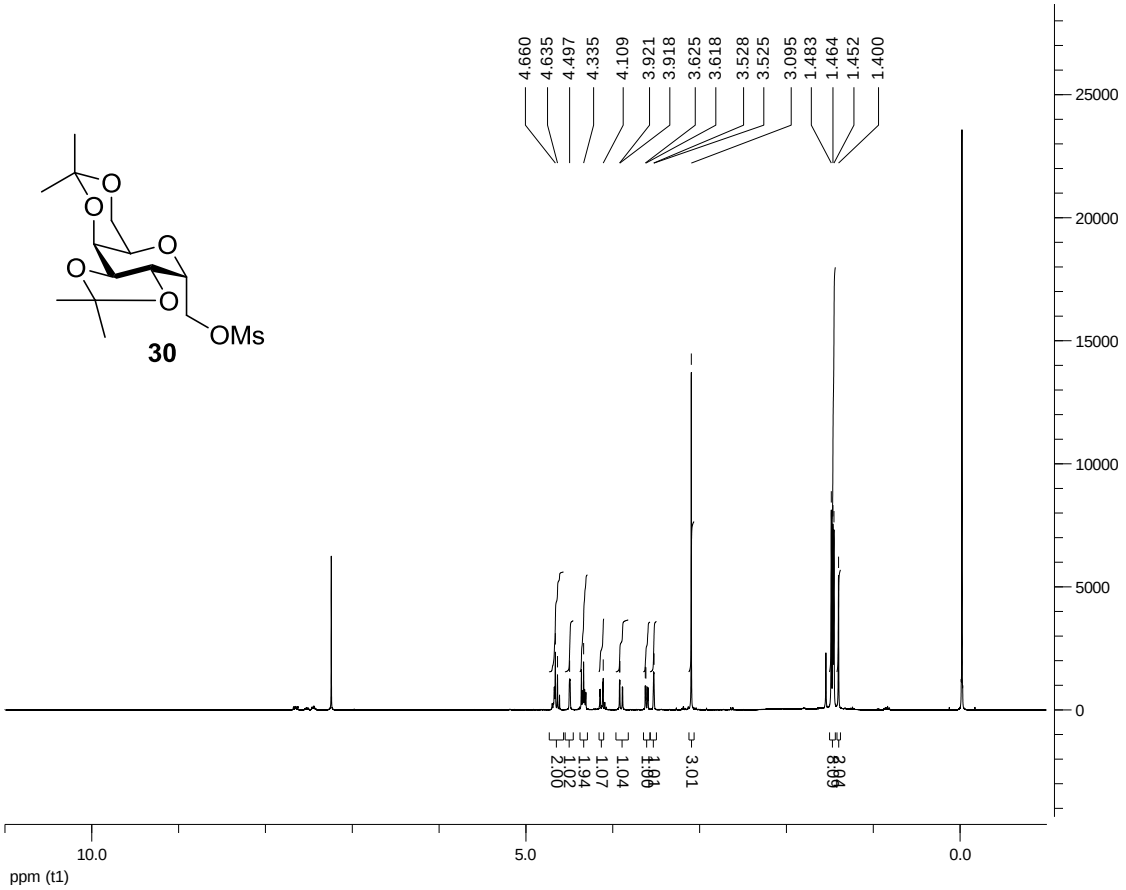
17

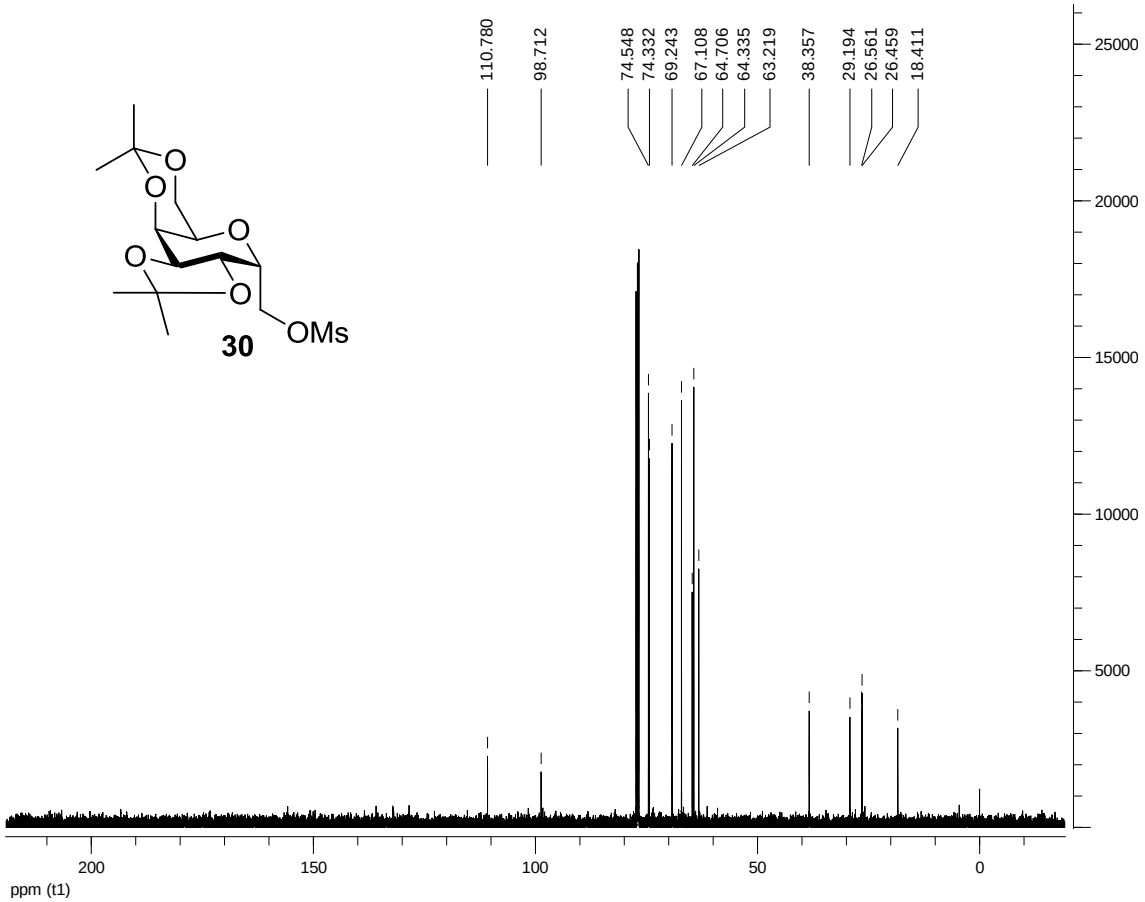

5.888
5.874
5.870
5.861
5.857
4.863
4.449
4.446
4.268
4.095
4.074
3.910
3.884
3.678
3.658
3.375
3.372
1.741
1.728
1.467
1.461
1.443
1.409
28
0.87
0.84
0.85
1.08
0.98
1.00
0.92
0.90
2.83
12.50
ppm (t1)

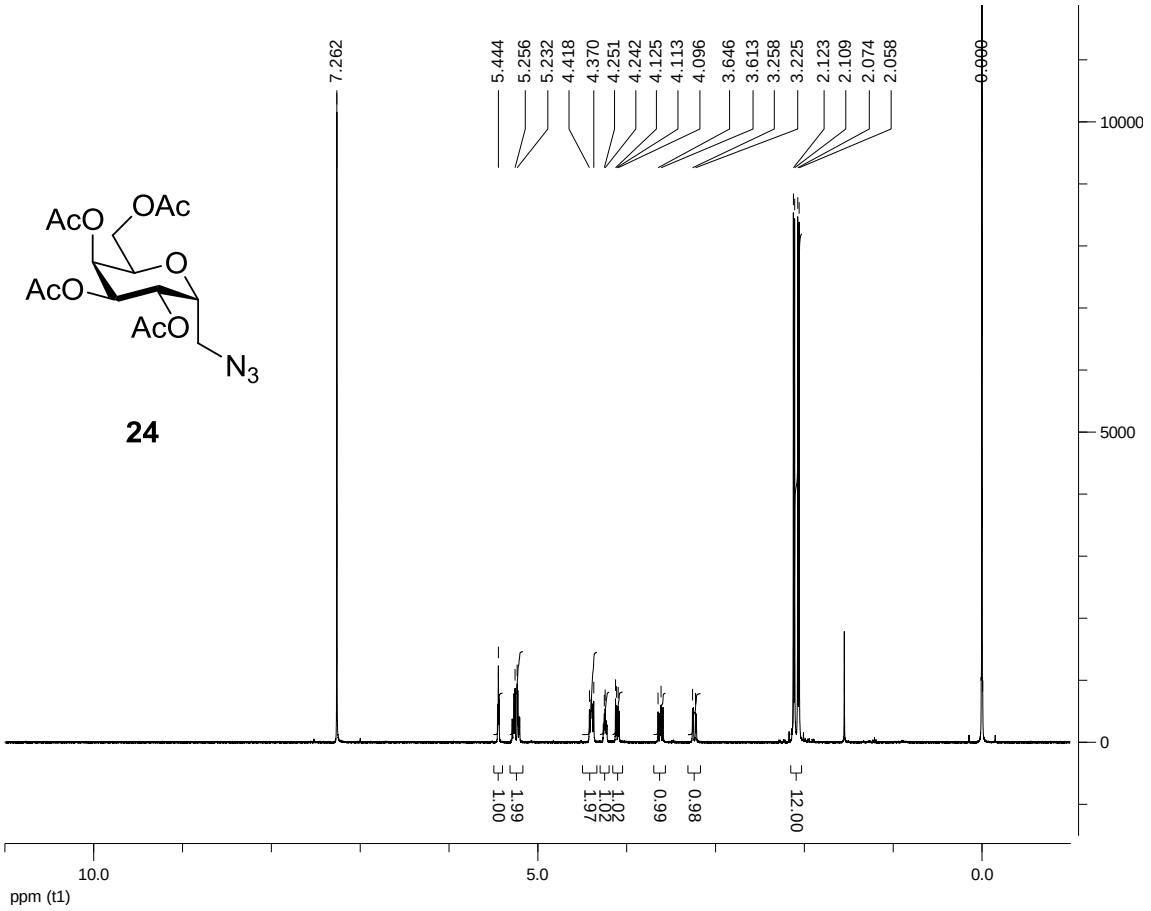

131.339
123.260
110.006
98.503
75.186
74.444
70.937
67.732
63.523
63.486
29.284
26.744
26.538
18.484
18.270
28
ppm (t1)

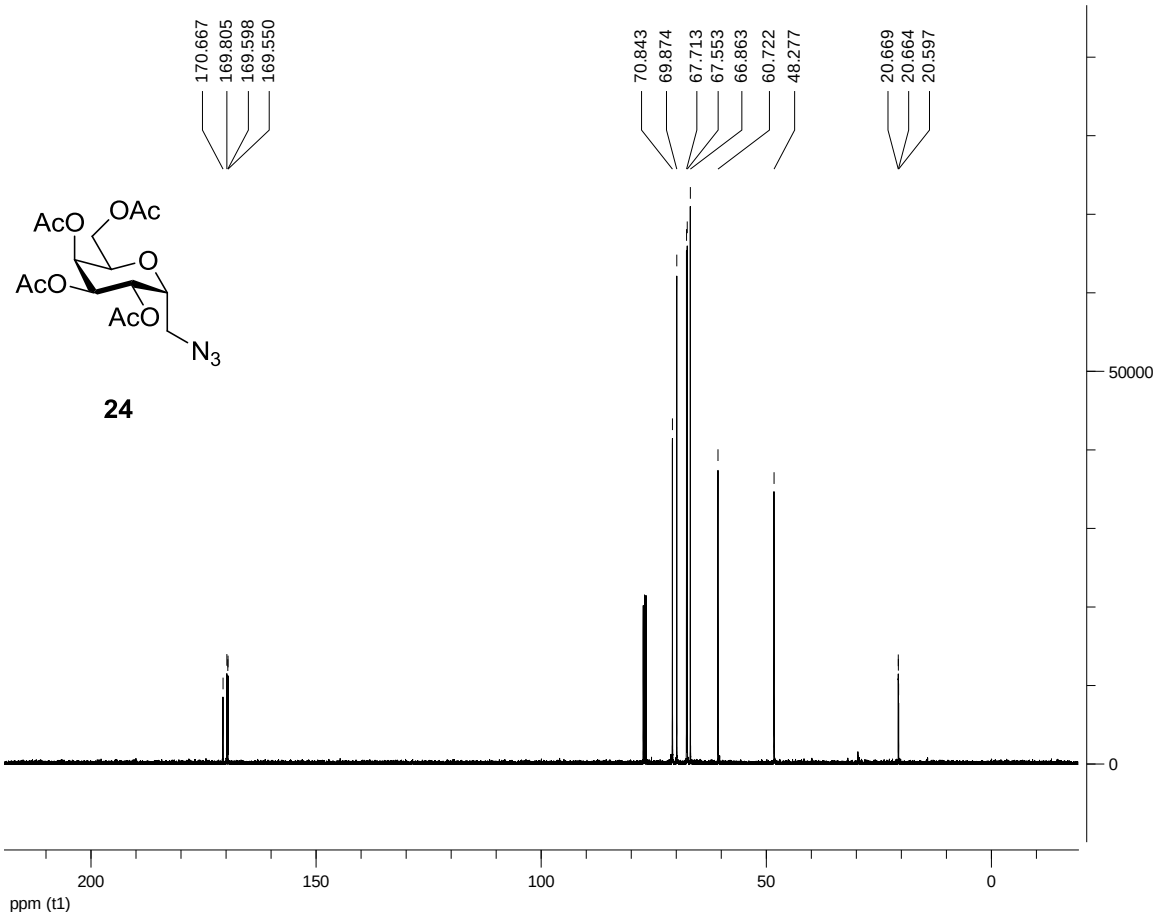

4.563
4.545
4.515
4.513
4.511
4.508
4.400
4.374
4.359
4.130
4.103
4.098
3.966
3.962
3.934
3.930
3.907
3.893
3.826
3.819
3.801
3.794
3.400
3.396
1.616
1.260
OH
29
0.98
0.89
1.04
1.17
1.23
1.66
1.08
1.00
8.47
ppm (t1)

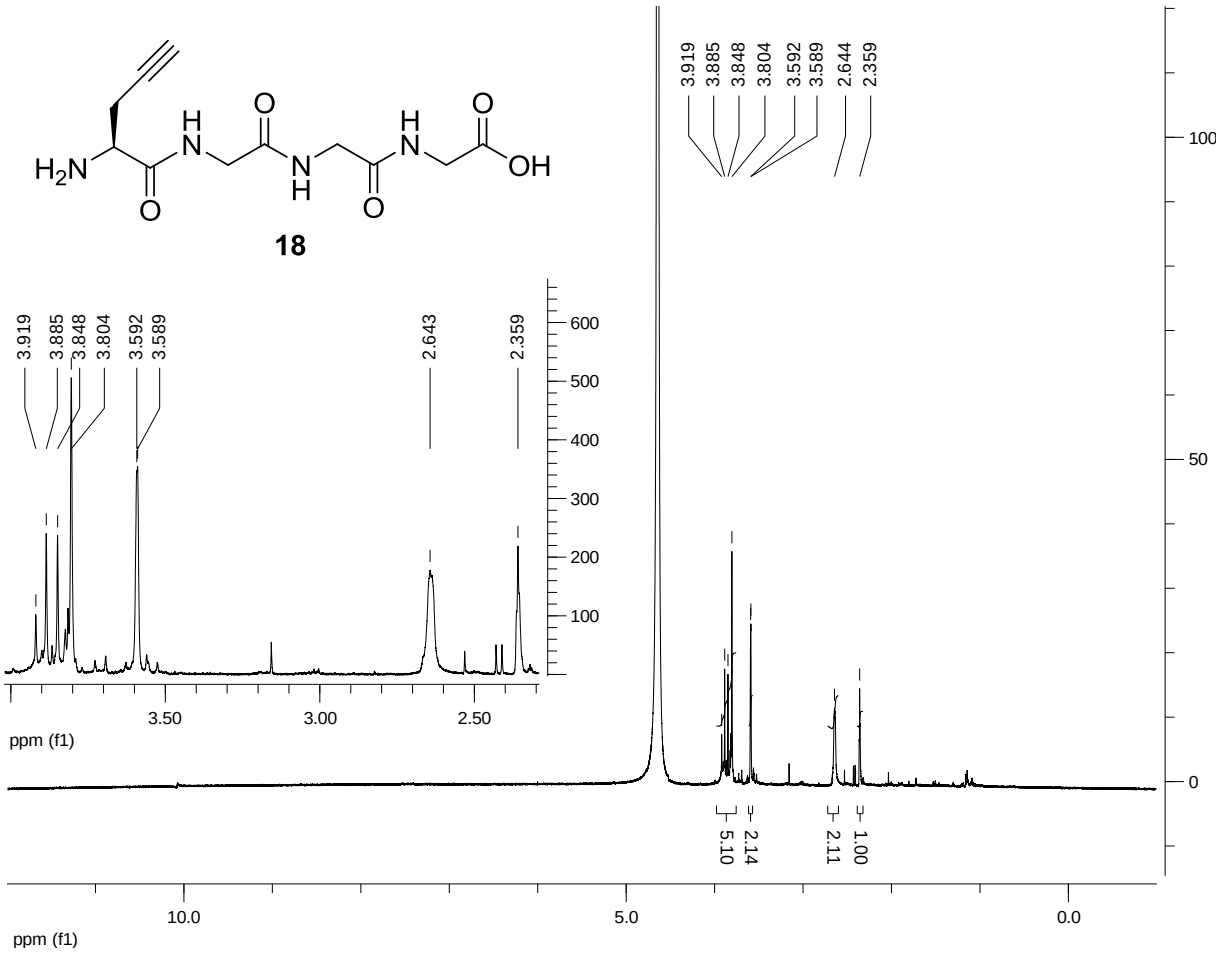

110.305
98.626
75.503
74.217
70.301
67.297
64.539
63.301
58.687
29.155
26.597
26.398
18.426
OH
29
ppm (t1)

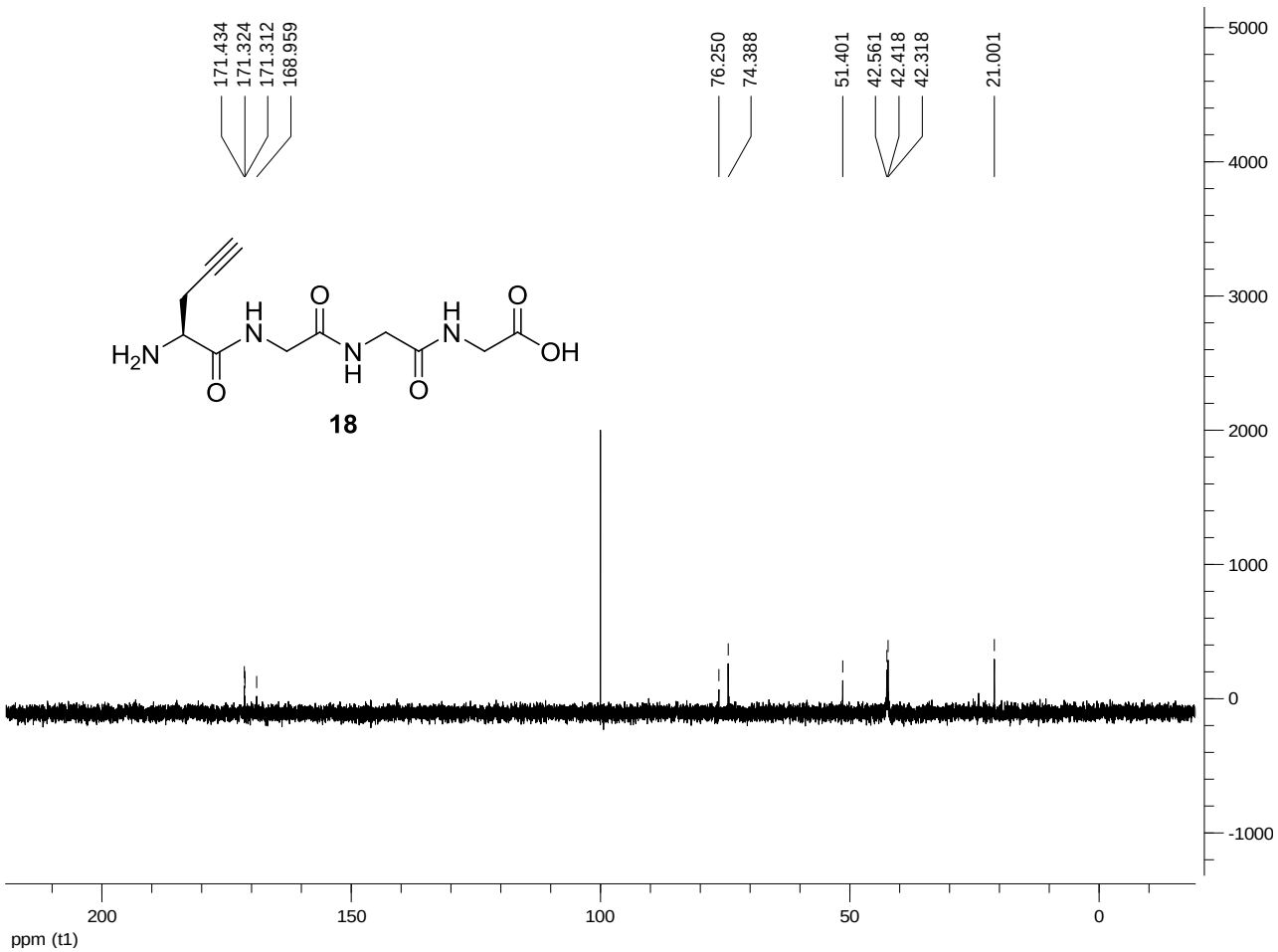

4.660
4.635
4.497
4.335
4.109
3.921
3.918
3.625
3.618
3.528
3.525
3.095
1.483
1.464
1.452
1.400
OMs
30
25000
20000
15000
10000
5000
0
2.00
2.02
1.94
1.07
1.04
1.00
1.01
3.01
8.09
8.04
10.0
5.0
0.0
ppm (t1)

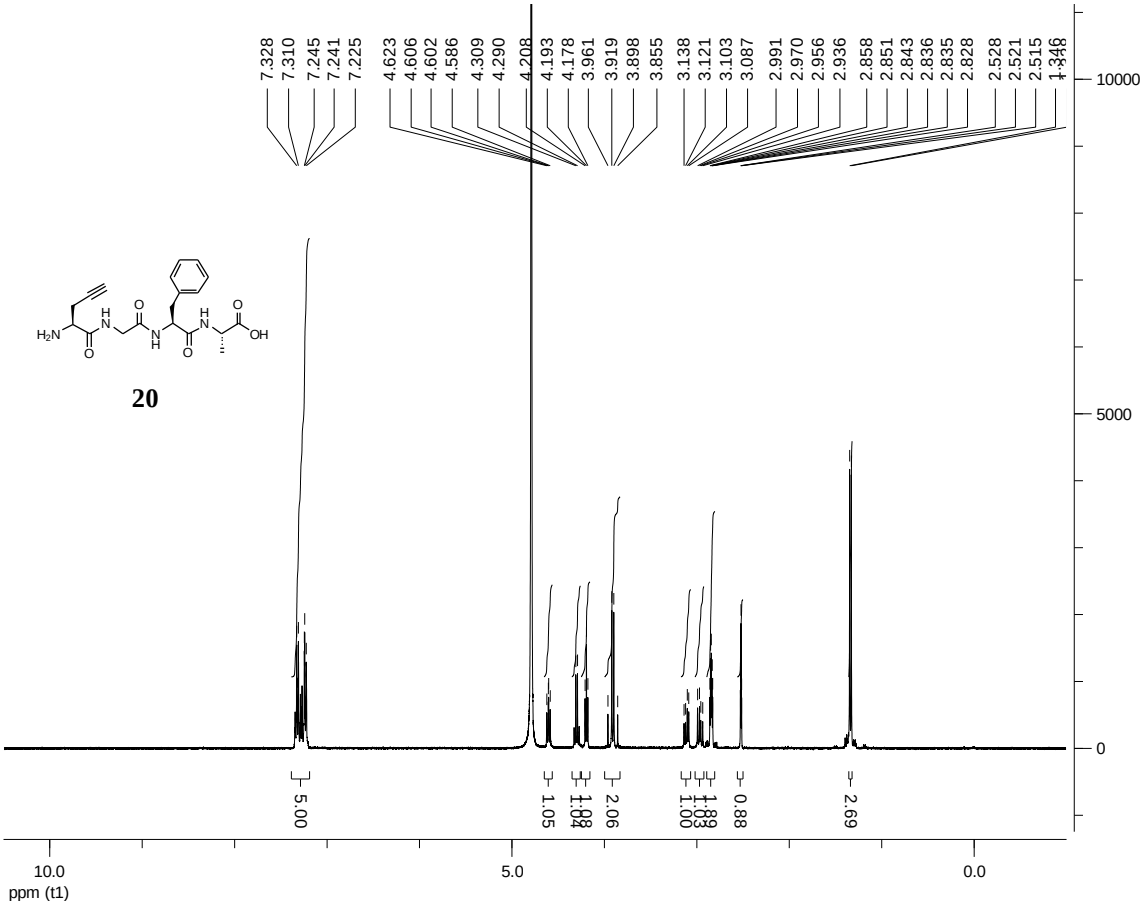

110.780
98.712
74.548
74.332
69.243
67.108
64.706
64.335
63.219
38.357
29.194
26.561
26.459
18.411
OMs
30
25000
20000
15000
10000
5000
200
150
100
50
0
ppm (t1)


7.262
5.444
5.256
5.232
4.418
4.370
4.251
4.242
4.125
4.113
4.096
3.646
3.613
3.258
3.225
2.123
2.109
2.074
2.058
0.000
AcO
OAc
AcO
O
AcO
N3
24
10000
5000
0
1.00
1.99
1.97
1.02
1.02
1.02
0.99
0.98
12.00
10.0
5.0
0.0
ppm (t1)

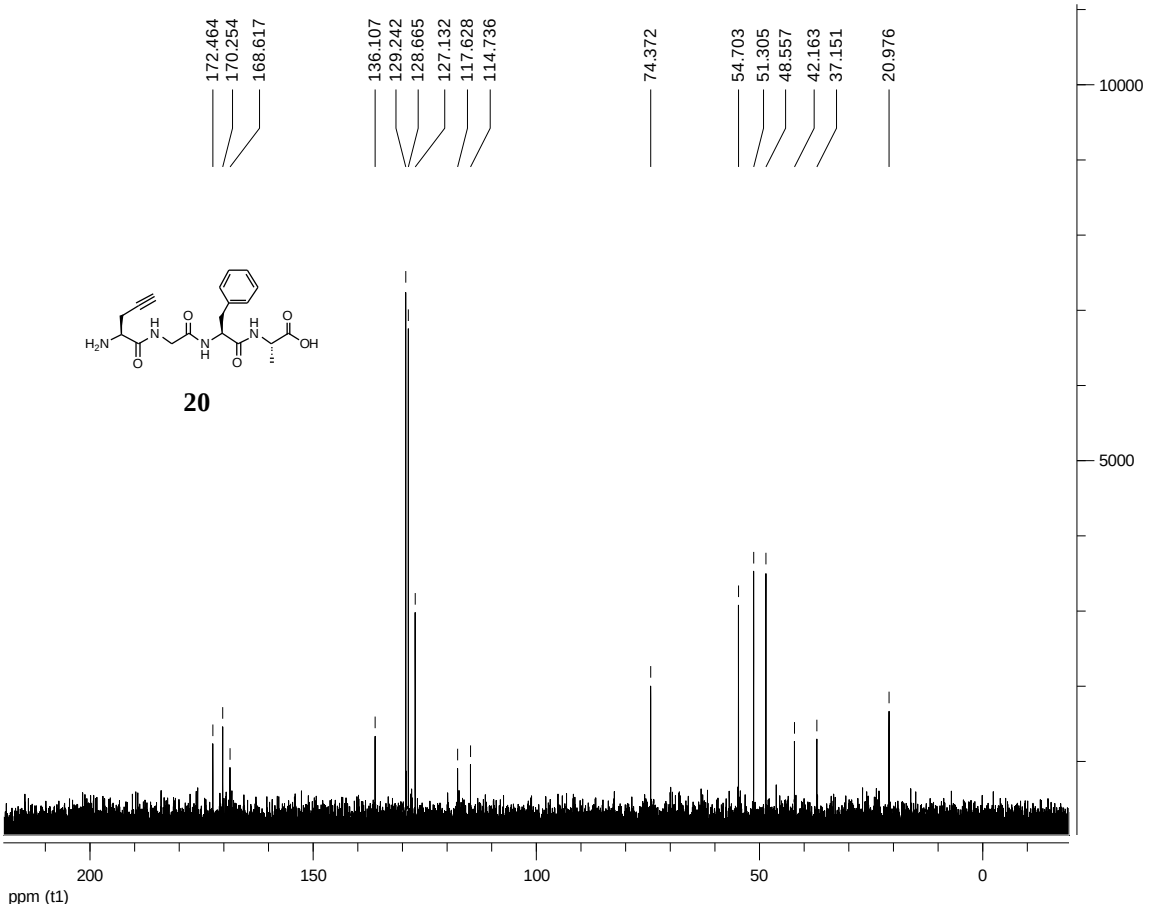

170.667
169.805
169.598
169.550
70.843
69.874
67.713
67.553
66.863
60.722
48.277
20.669
20.664
20.597
AcO
OAc
AcO
O
AcO
N3
24
50000
0
200
150
100
50
0
ppm (t1)


18
3.919
3.885
3.848
3.804
3.592
3.589
2.644
2.359
2.643
5.10
2.14
2.11
1.00
ppm (f1)
ppm (f1)

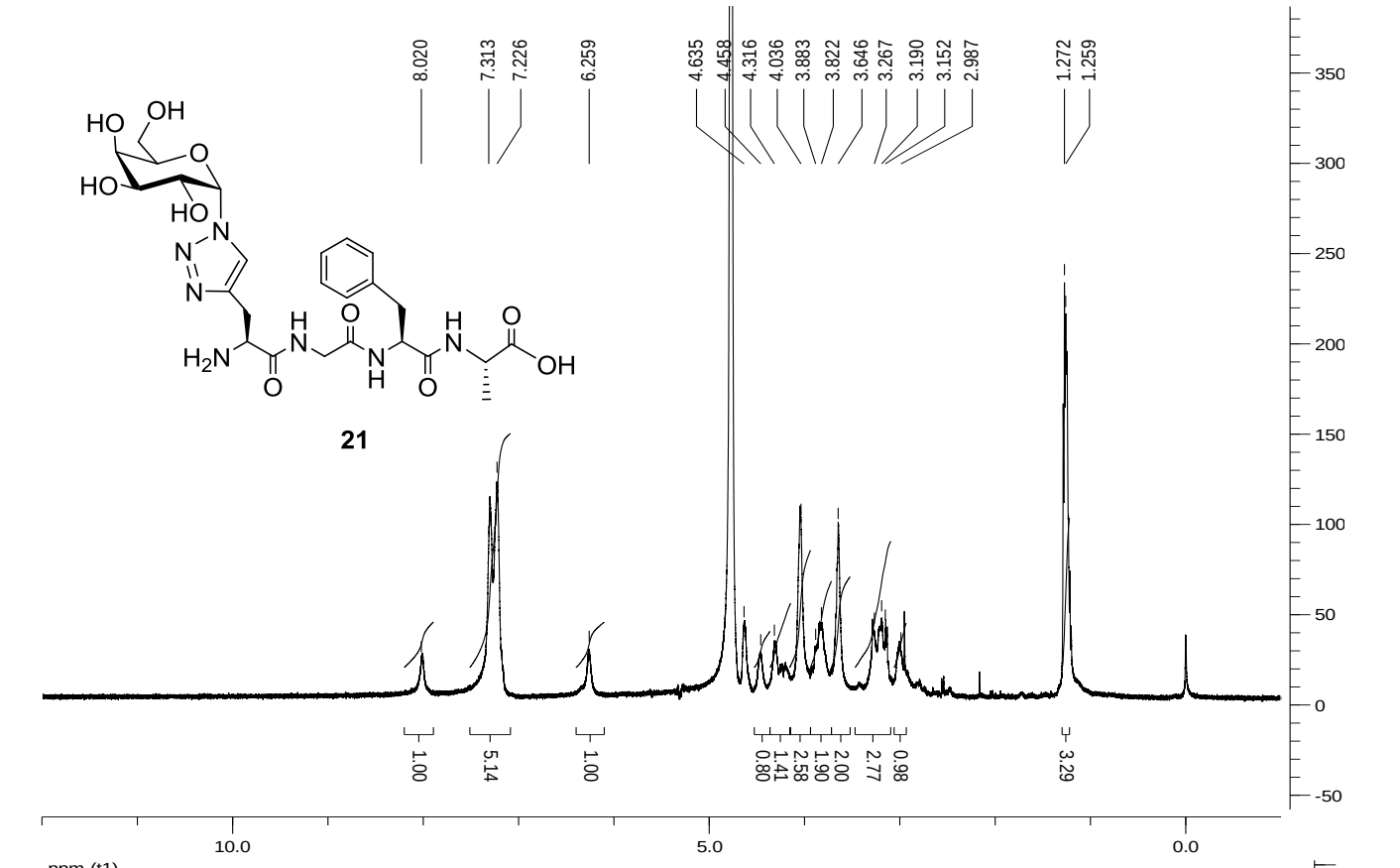

18
171.434
171.324
171.312
168.959
76.250
74.388
51.401
42.561
42.418
42.318
21.001
ppm (t1)


7.328
7.310
7.245
7.241
7.225
4.623
4.606
4.602
4.586
4.309
4.290
4.208
4.193
4.178
3.961
3.919
3.898
3.855
3.138
3.121
3.103
3.087
2.991
2.970
2.956
2.936
2.858
2.851
2.843
2.836
2.835
2.828
2.528
2.521
2.515
1.346
10000
5000
0
5.00
1.05
1.08
1.04
2.06
1.00
1.03
1.03
0.88
2.69
10.0
5.0
0.0
ppm (t1)

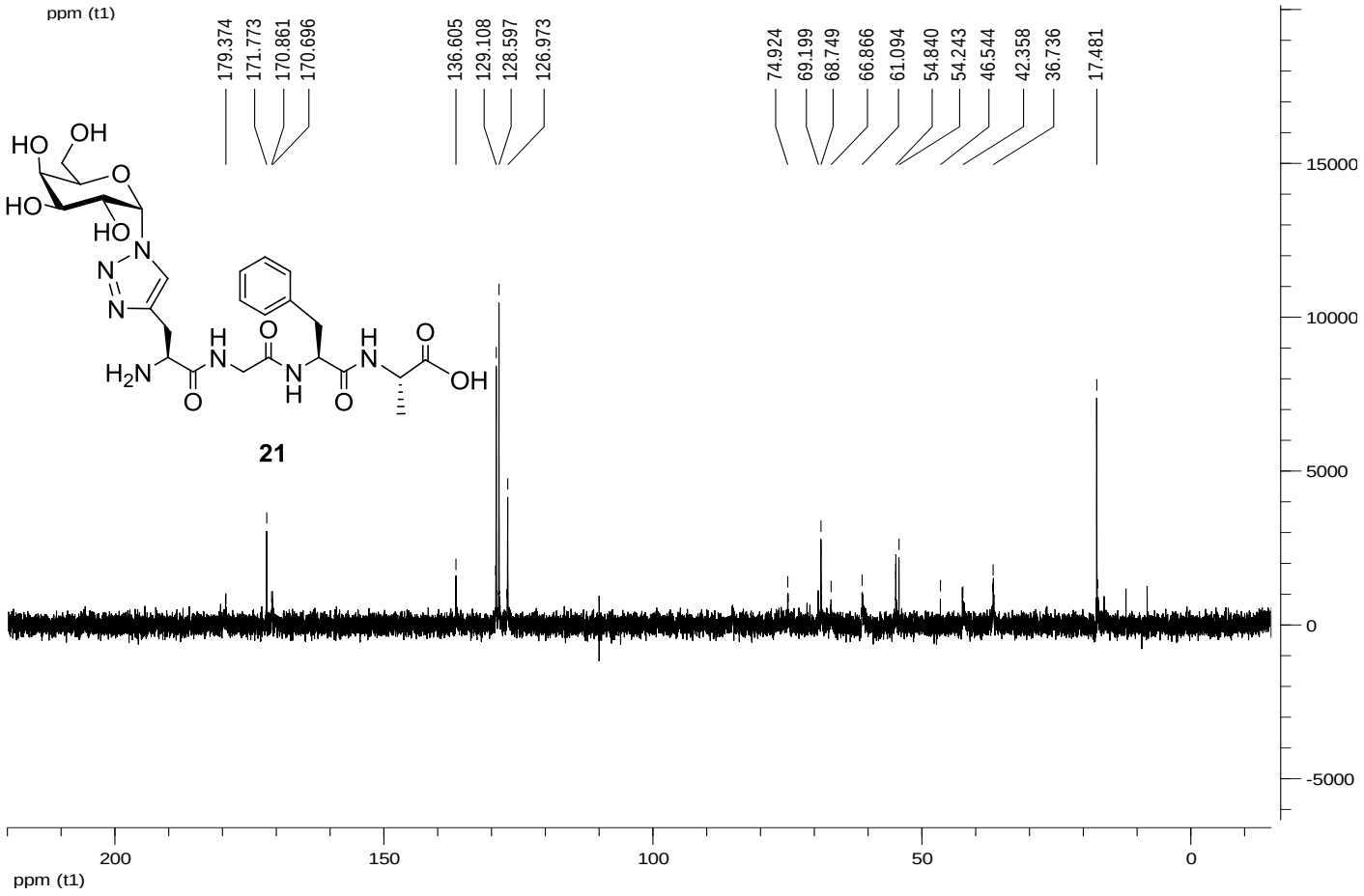
20


172.464
170.254
168.617
136.107
129.242
128.665
127.132
117.628
114.736
74.372
54.703
51.305
48.557
42.163
37.151
20.976
10000
5000
200
150
100
50
0
ppm (t1)

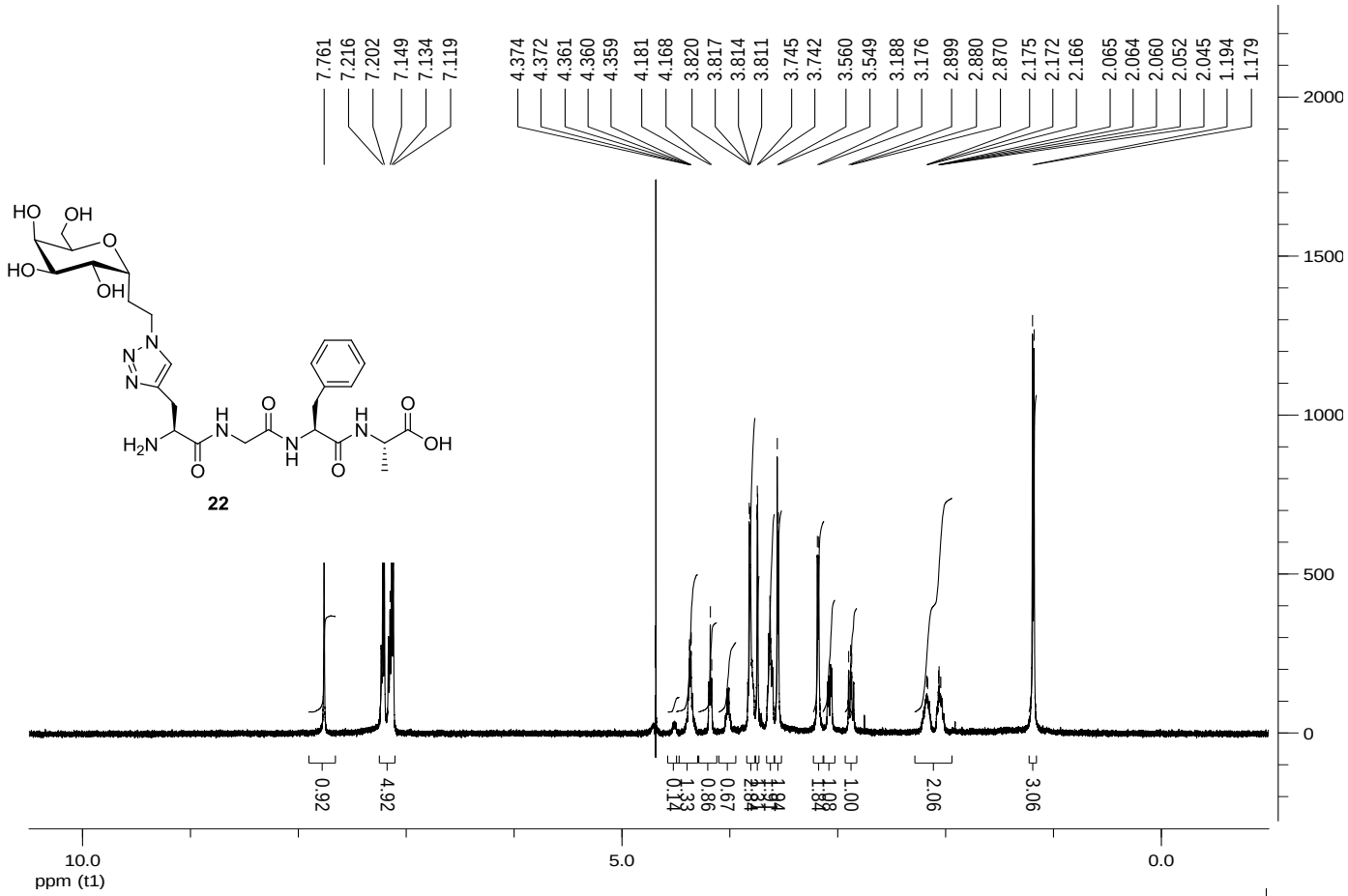
20

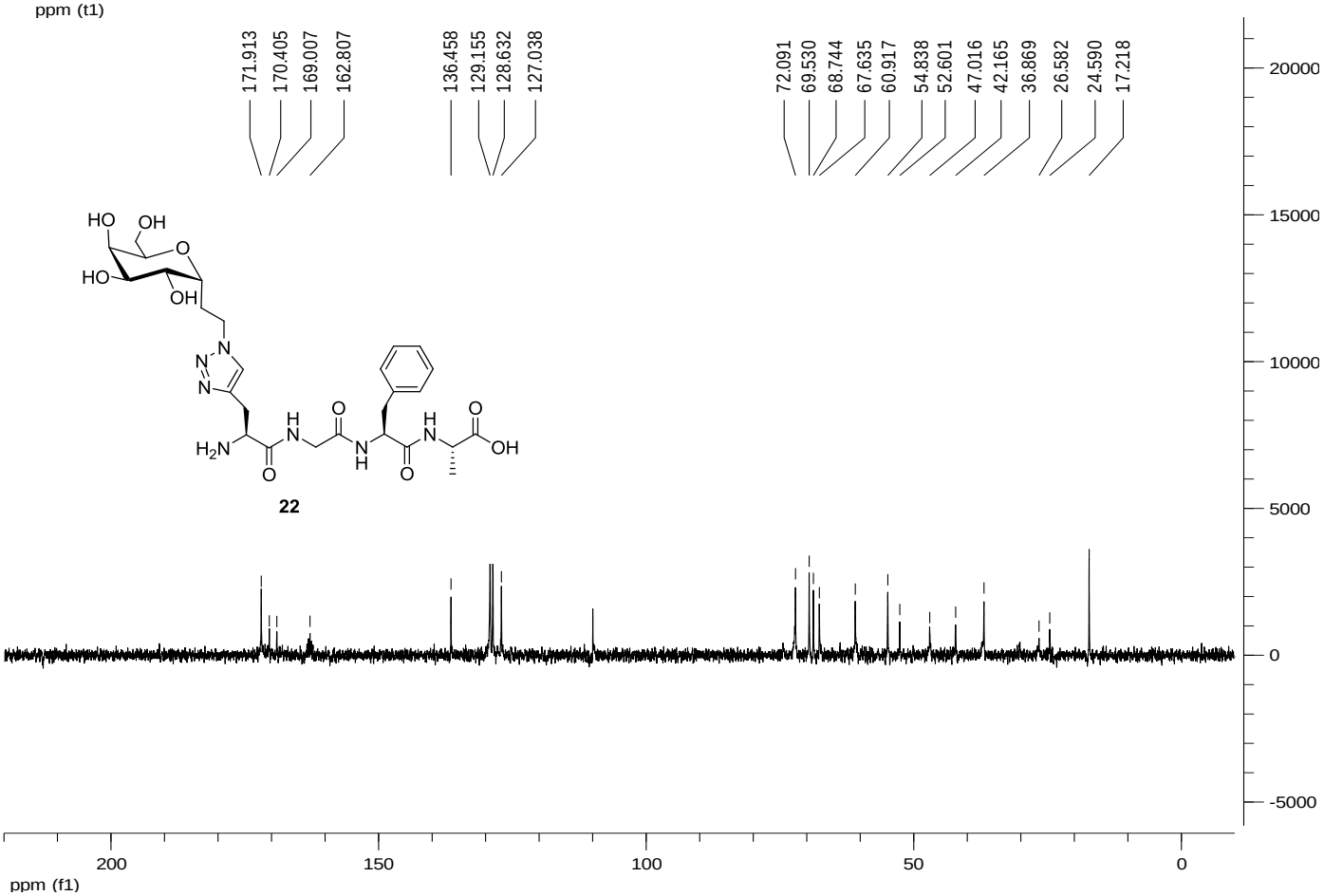

8.020
7.313
7.226
6.259
4.635
4.458
4.316
4.036
3.883
3.822
3.646
3.267
3.190
3.152
2.987
1.272
1.259
1.00
5.14
1.00
0.80
1.41
2.58
1.90
2.00
2.77
0.98
3.29
ppm (t1)

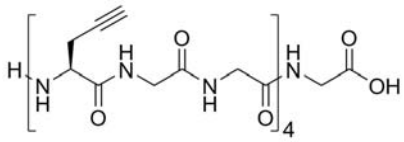
21


179.374
171.773
170.861
170.696
136.605
129.108
128.597
126.973
74.924
69.199
68.749
66.866
61.094
54.840
54.243
46.544
42.358
36.736
17.481
ppm (t1)

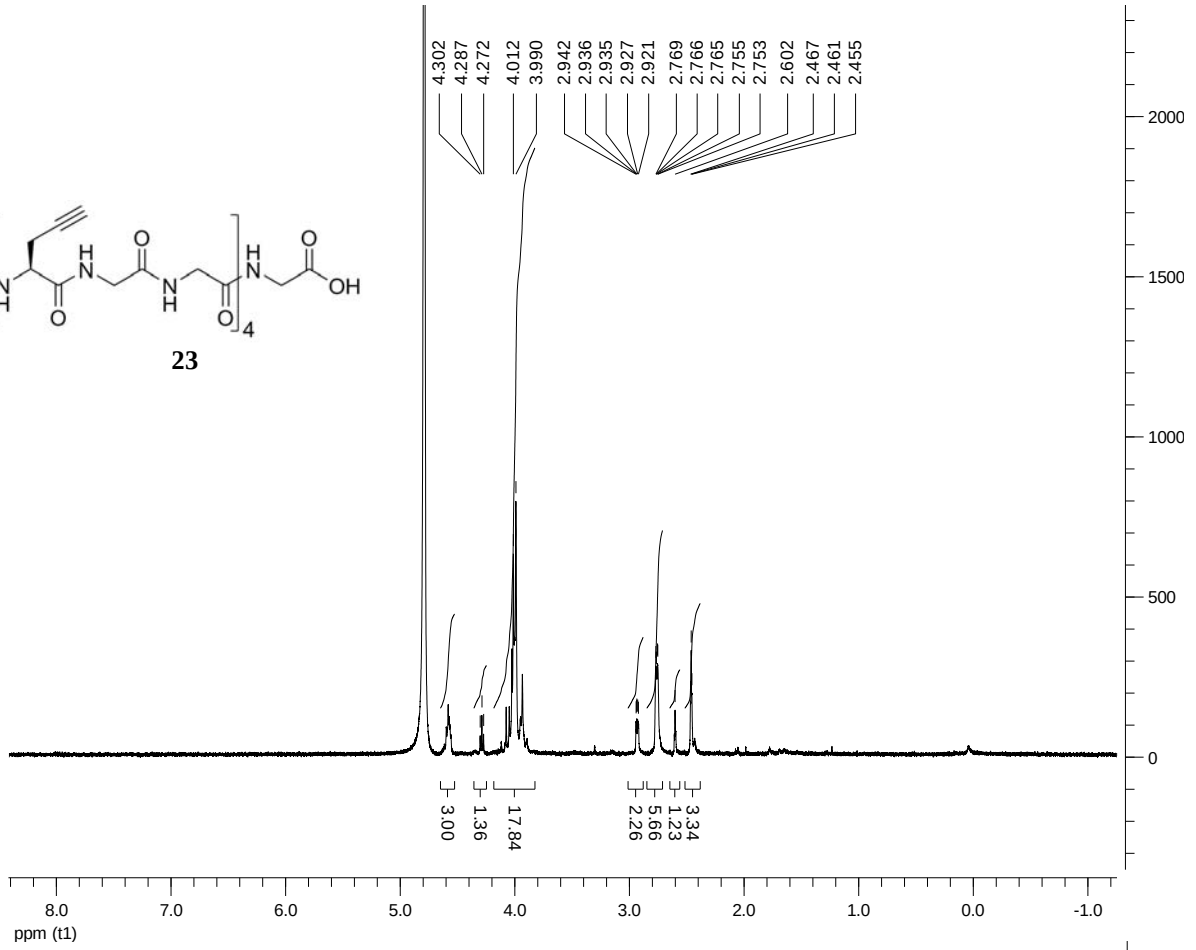
21


7.761
7.216
7.202
7.149
7.134
7.119
4.374
4.372
4.361
4.360
4.359
4.181
4.168
3.820
3.817
3.814
3.811
3.745
3.742
3.560
3.549
3.188
3.176
2.899
2.880
2.870
2.175
2.172
2.166
2.065
2.064
2.060
2.052
2.045
1.194
1.179
0.92
4.92
0.14
0.23
0.86
0.67
2.84
2.81
1.94
1.80
1.00
2.06
3.06
10.0
5.0
0.0
ppm (t1)
22

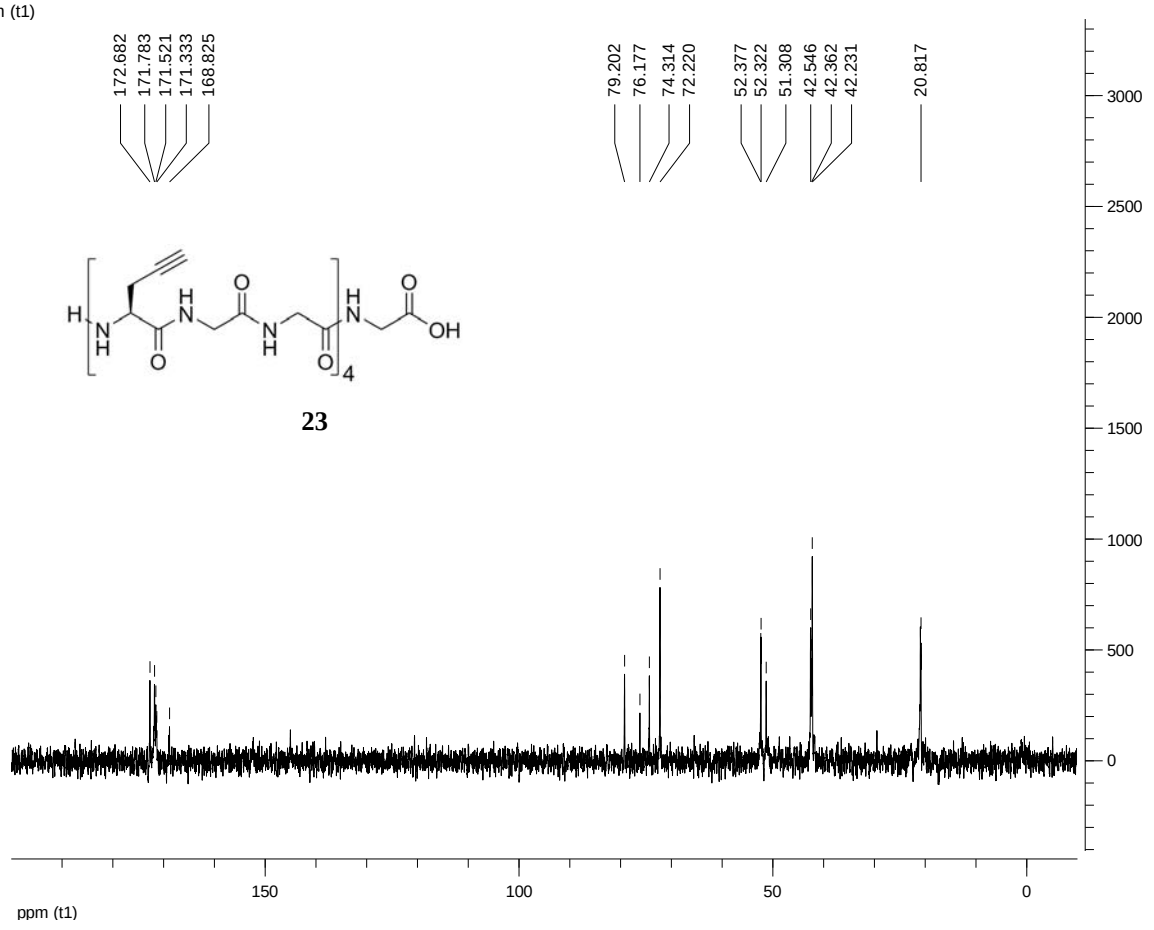

171.913
170.405
169.007
162.807
136.458
129.155
128.632
127.038
72.091
69.530
68.744
67.635
60.917
54.838
52.601
47.016
42.165
36.869
26.582
24.590
17.218
200
150
100
50
0
ppm (f1)
22

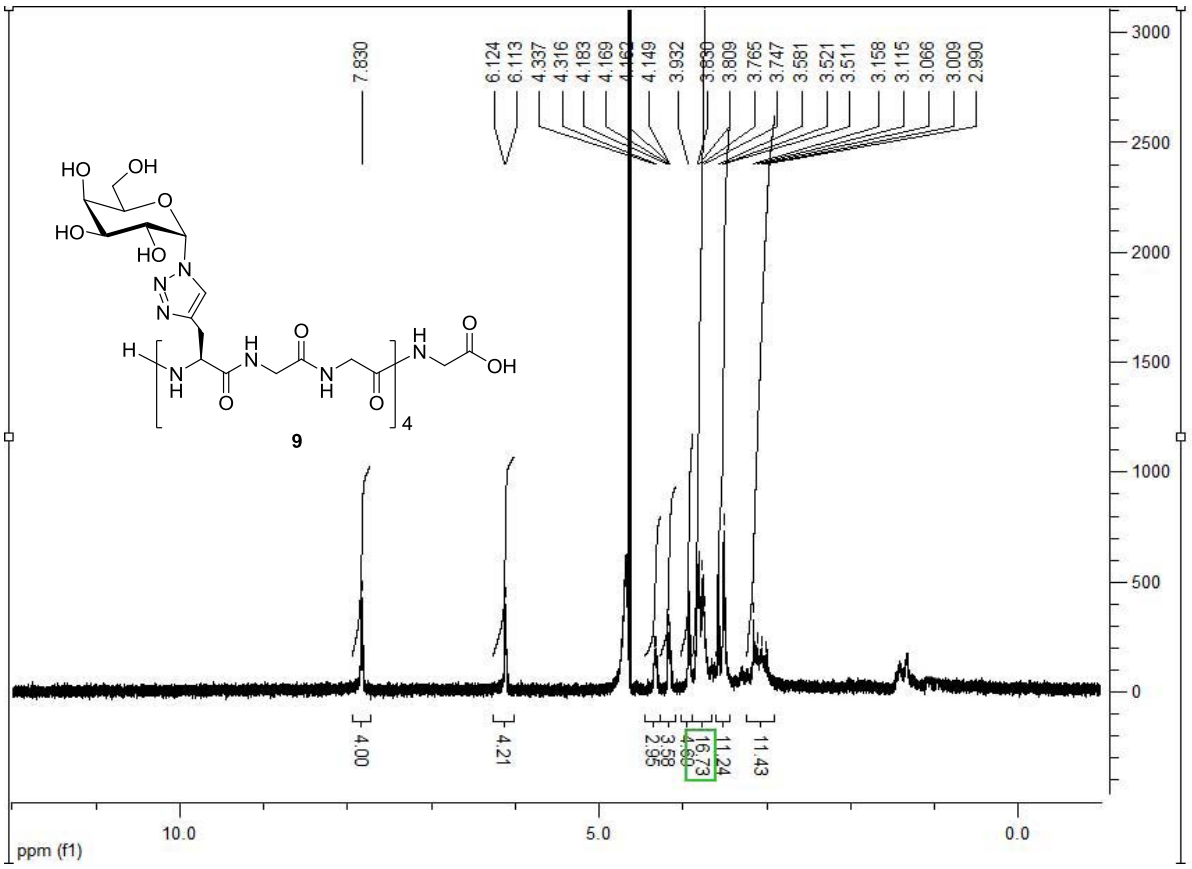


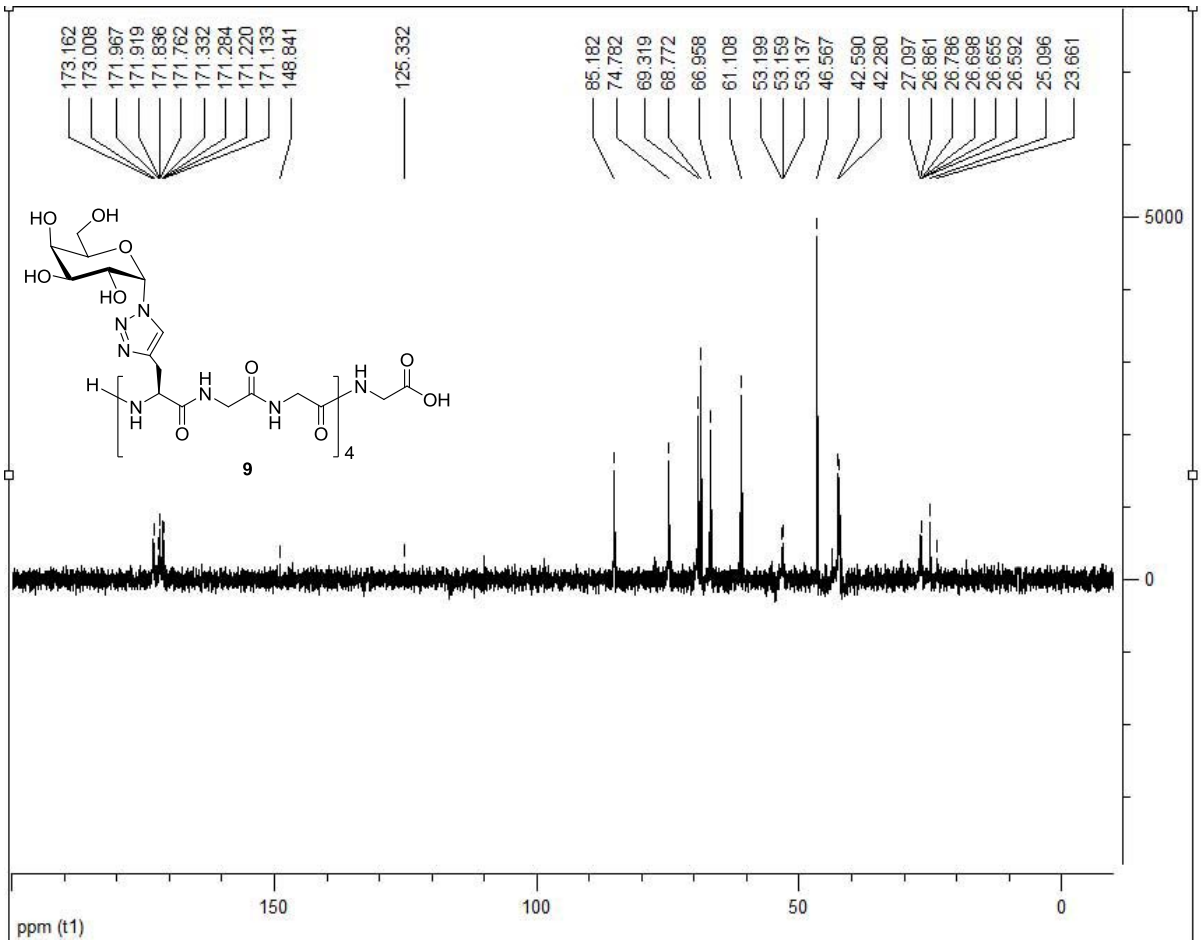
23

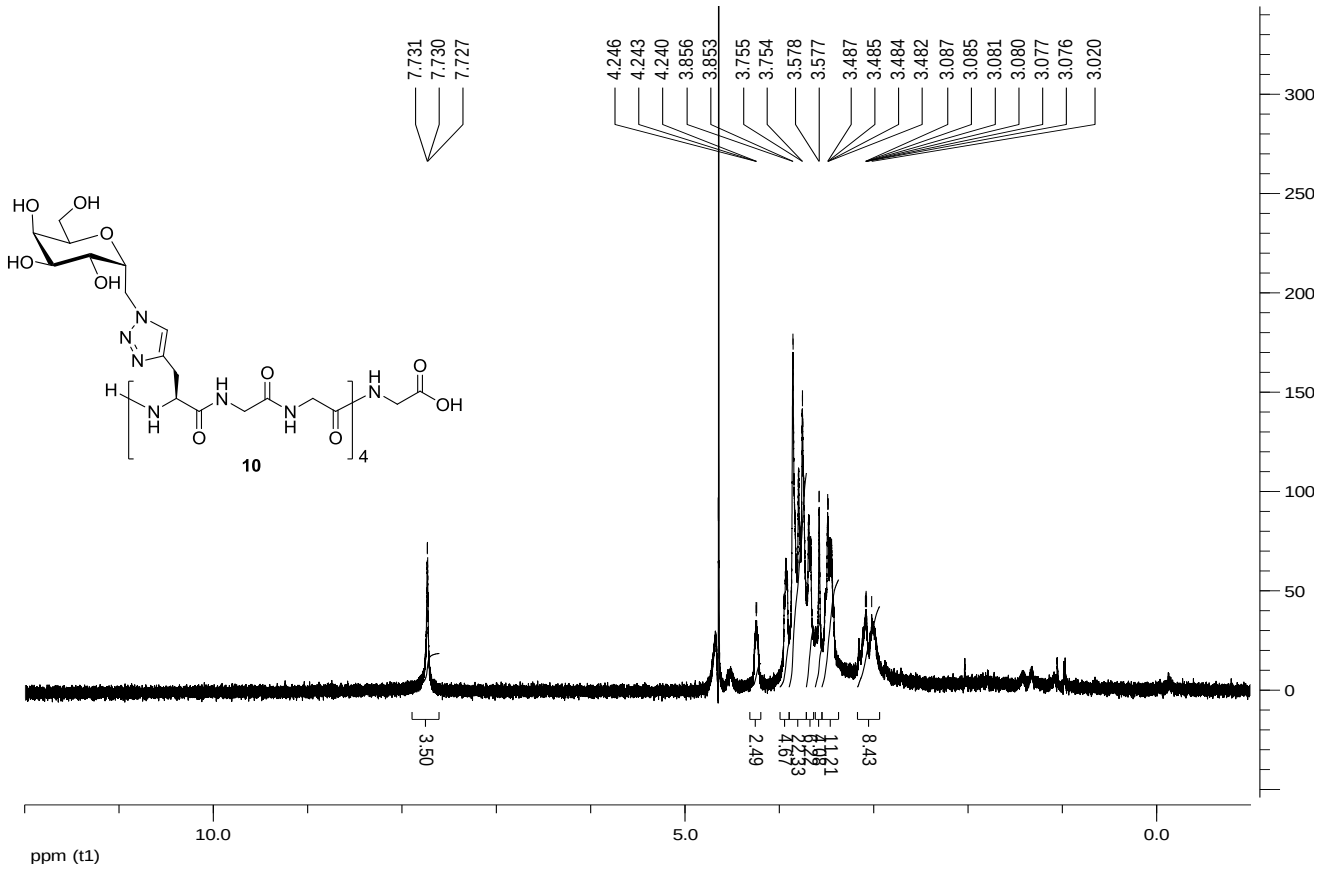

4.302
4.287
4.272
4.012
3.990
2.942
2.936
2.935
2.927
2.921
2.769
2.766
2.765
2.755
2.753
2.602
2.467
2.461
2.455
3.00
1.36
17.84
2.26
5.66
1.23
3.34
8.0
7.0
6.0
5.0
4.0
3.0
2.0
1.0
0.0
-1.0
ppm (t1)

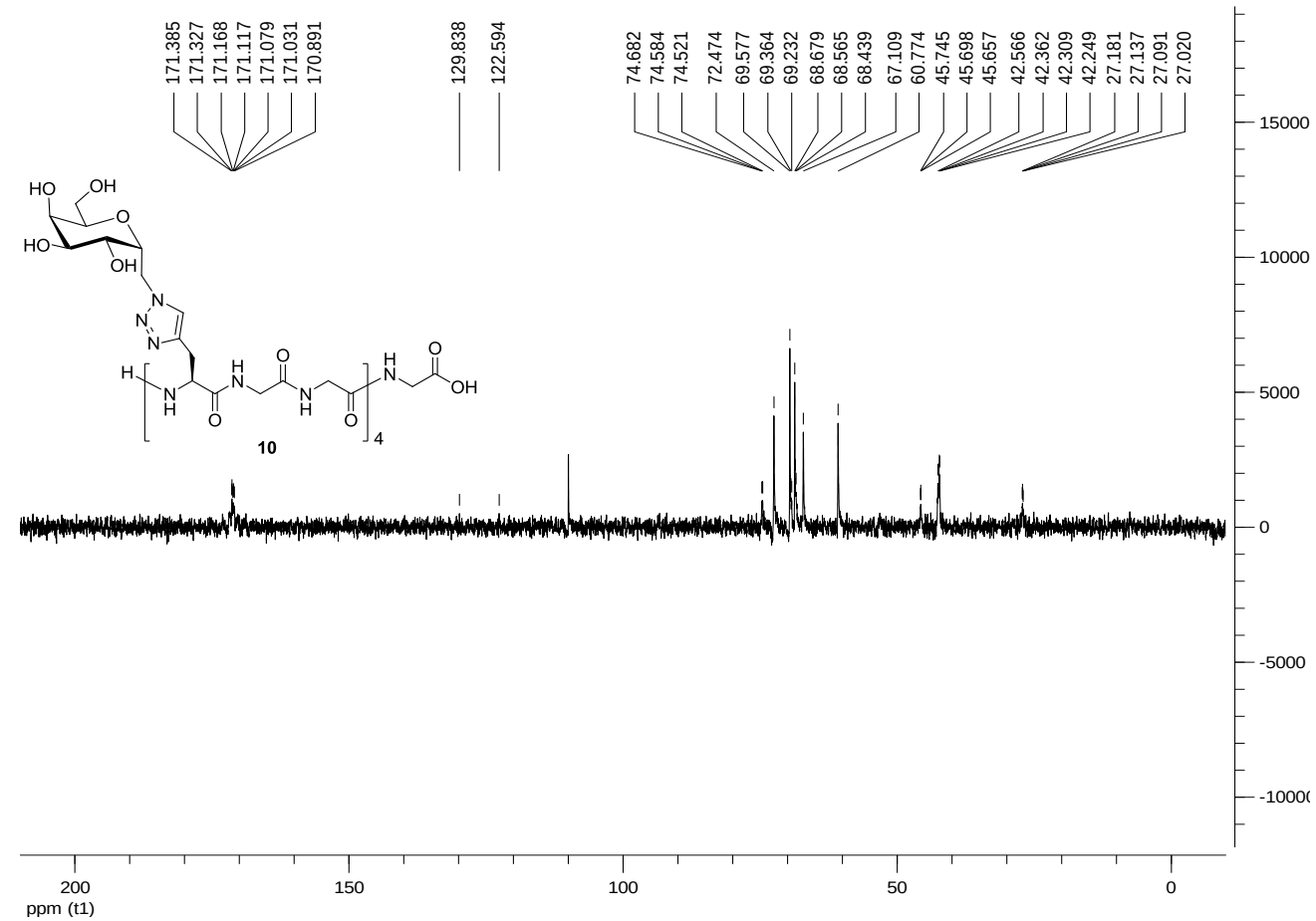
23

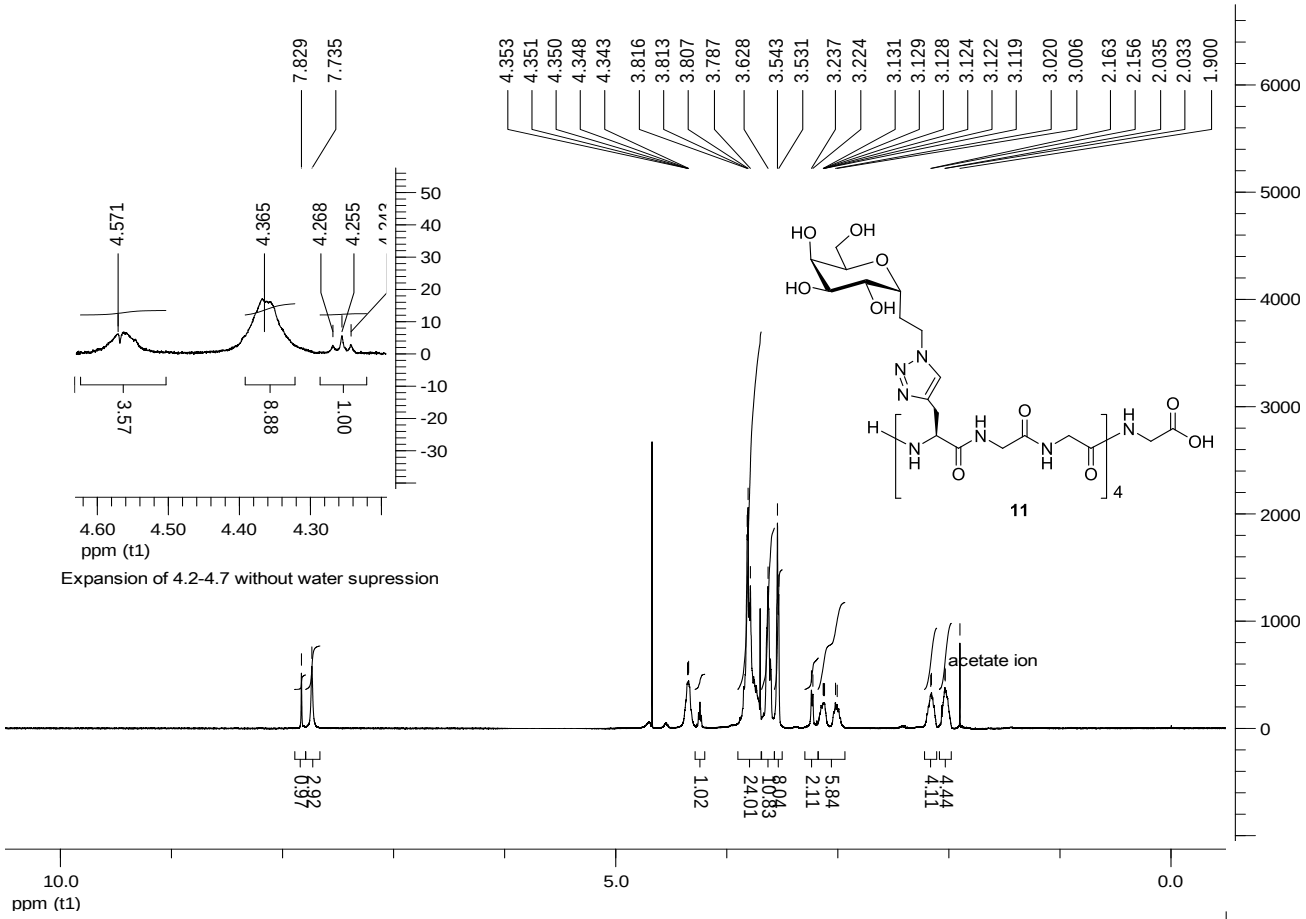

172.682
171.783
171.521
171.333
168.825
79.202
76.177
74.314
72.220
52.377
52.322
51.308
42.546
42.362
42.231
20.817
150
100
50
0
ppm (t1)

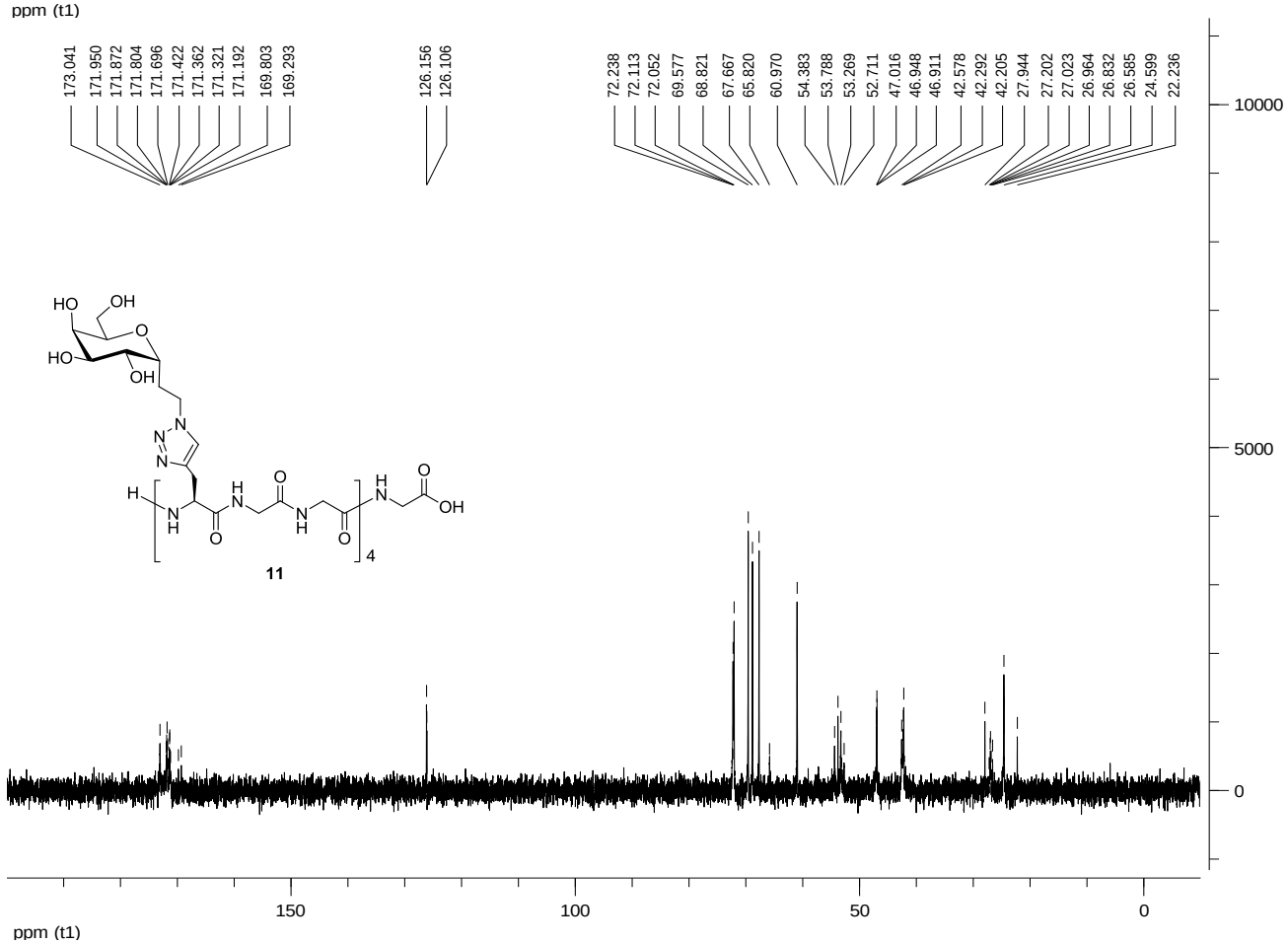

7.830
6.124
6.113
4.337
4.316
4.183
4.169
4.162
4.149
3.932
3.830
3.809
3.765
3.747
3.581
3.521
3.511
3.158
3.115
3.066
3.009
2.990
4.00
4.21
2.99
2.88
16.73
11.24
11.43
10.0
5.0
0.0
ppm (f1)
9

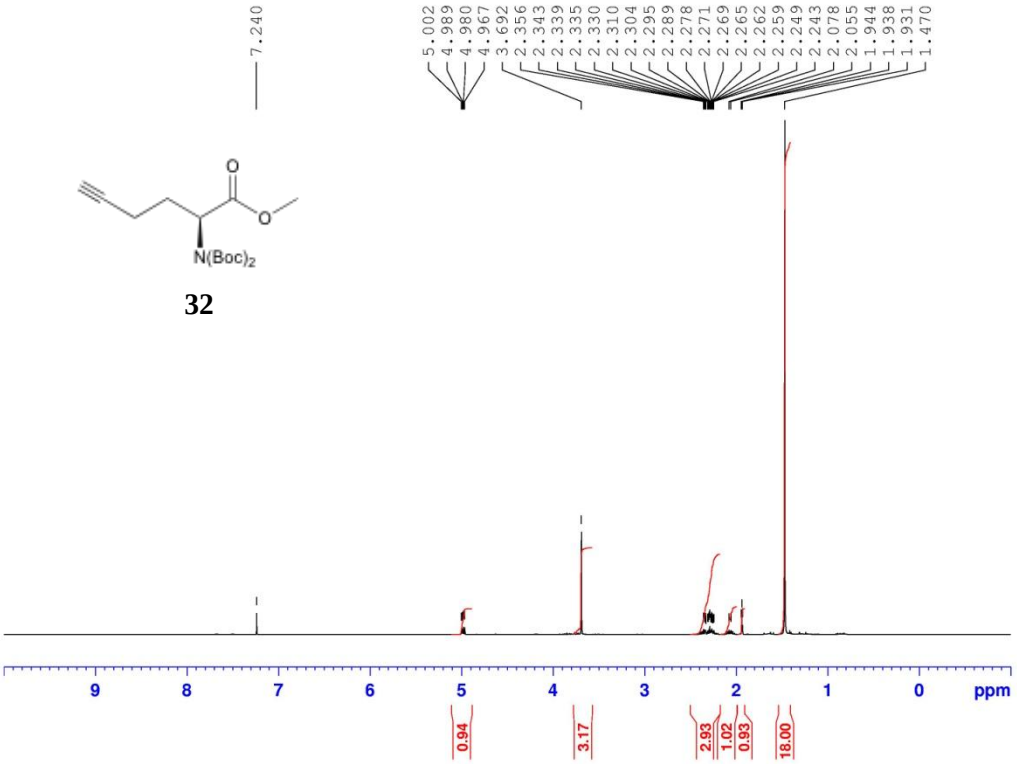

173.162
173.008
171.967
171.919
171.836
171.762
171.332
171.284
171.220
171.133
148.841
125.332
85.182
74.782
69.319
68.772
66.958
61.108
53.199
53.159
53.137
46.567
42.590
42.280
27.097
26.861
26.786
26.698
26.655
26.592
25.096
23.661
150
100
50
0
ppm (t1)
9


7.731
7.730
7.727
4.246
4.243
4.240
3.856
3.853
3.755
3.754
3.578
3.577
3.487
3.485
3.484
3.482
3.087
3.085
3.081
3.080
3.077
3.076
3.020
HO
OH
O
HO
OH
N
N
N
H
N
H
O
H
N
O
N
H
O
H
N
O
OH
4
10
3.50
2.49
8.43
10.0
5.0
0.0
ppm (t1)

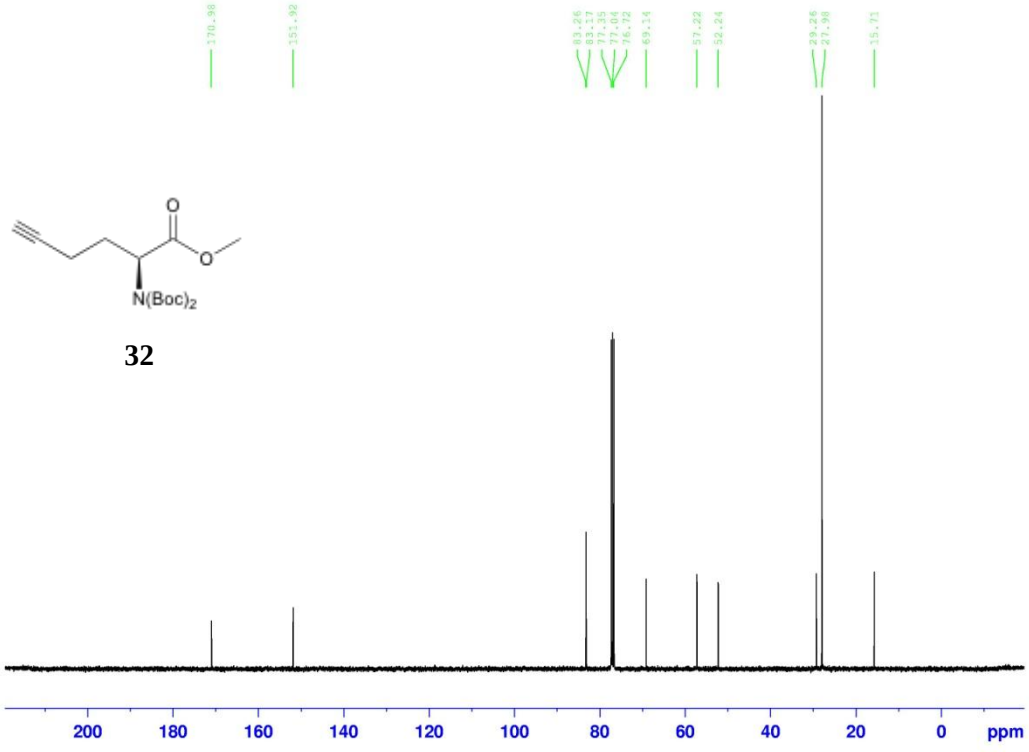

171.385
171.327
171.168
171.117
171.079
171.031
170.891
129.838
122.594
74.682
74.584
74.521
72.474
69.577
69.364
69.232
68.679
68.565
68.439
67.109
60.774
45.745
45.698
45.657
42.566
42.362
42.309
42.249
27.181
27.137
27.091
27.020
HO
OH
O
HO
OH
N
N
N
H
N
H
O
H
N
O
N
H
O
H
N
O
OH
4
10
200
150
100
50
0
ppm (t1)


7.829
7.735
4.353
4.351
4.350
4.348
4.343
3.816
3.813
3.807
3.787
3.628
3.543
3.531
3.237
3.224
3.131
3.129
3.128
3.124
3.122
3.119
3.020
3.006
2.163
2.156
2.035
2.033
1.900
4.571
4.365
4.268
4.255
3.57
8.88
1.00
4.60
4.50
4.40
4.30
ppm (t1)
Expansion of 4.2-4.7 without water supression
11
acetate ion
2.92
0.97
1.02
24.01
8.04
1.03
5.84
2.11
4.44
4.11
10.0
5.0
0.0
ppm (t1)

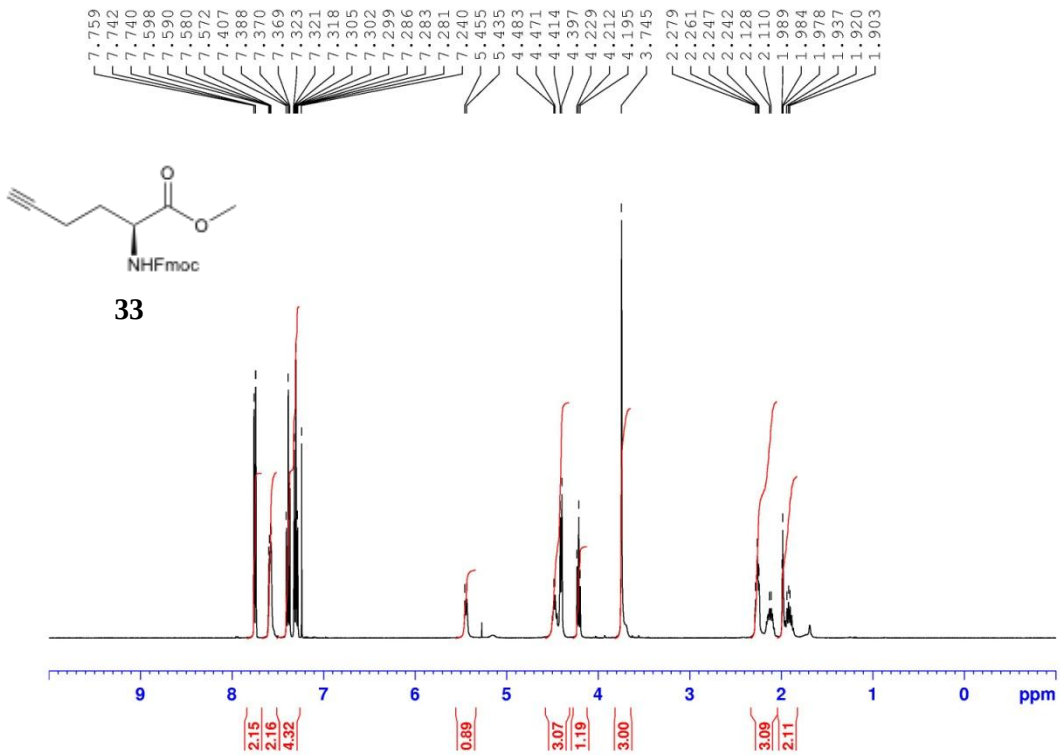

173.041
171.950
171.872
171.804
171.696
171.422
171.362
171.321
171.192
169.803
169.293
126.156
126.106
72.238
72.113
72.052
69.577
68.821
67.667
65.820
60.970
54.383
53.788
53.269
52.711
47.016
46.948
46.911
42.578
42.292
42.205
27.944
27.202
27.023
26.964
26.832
26.585
24.599
22.236
11
150
100
50
0
ppm (t1)


7.240
5.002
4.989
4.980
4.967
3.692
2.356
2.343
2.339
2.335
2.330
2.310
2.304
2.295
2.289
2.278
2.271
2.269
2.265
2.262
2.259
2.249
2.243
2.078
2.055
1.944
1.938
1.931
1.470
O
O
N(Boc)2
9
8
7
6
5
4
3
2
1
0
ppm
0.94
3.17
2.93
1.02
0.93
18.00

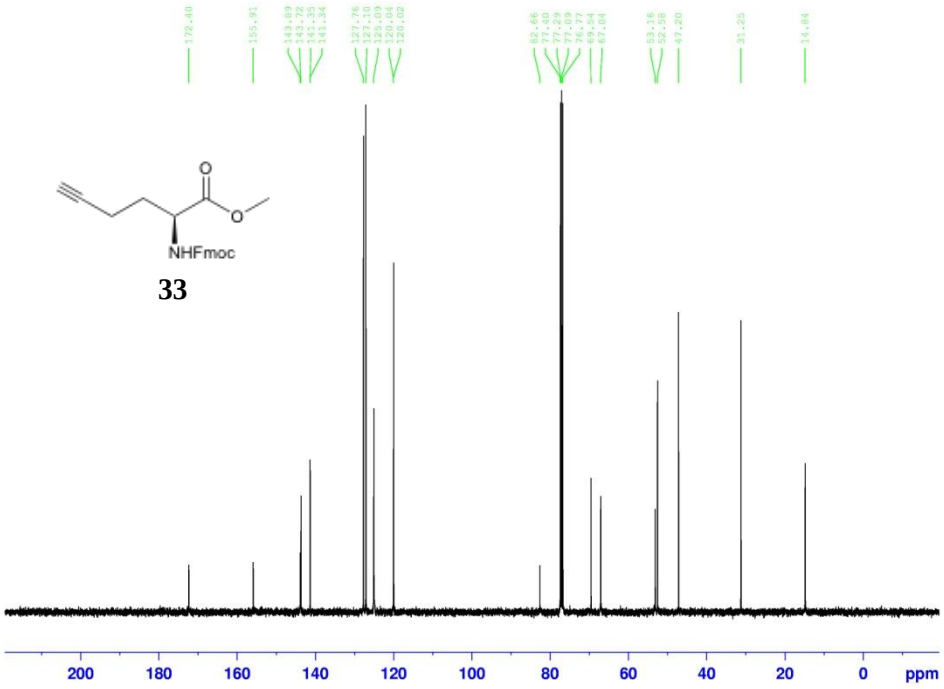
32


170.98
151.92
83.26
83.17
77.35
77.04
76.72
69.14
57.22
52.24
29.26
27.90
15.71
O
O
N(Boc)2
200
180
160
140
120
100
80
60
40
20
0
ppm

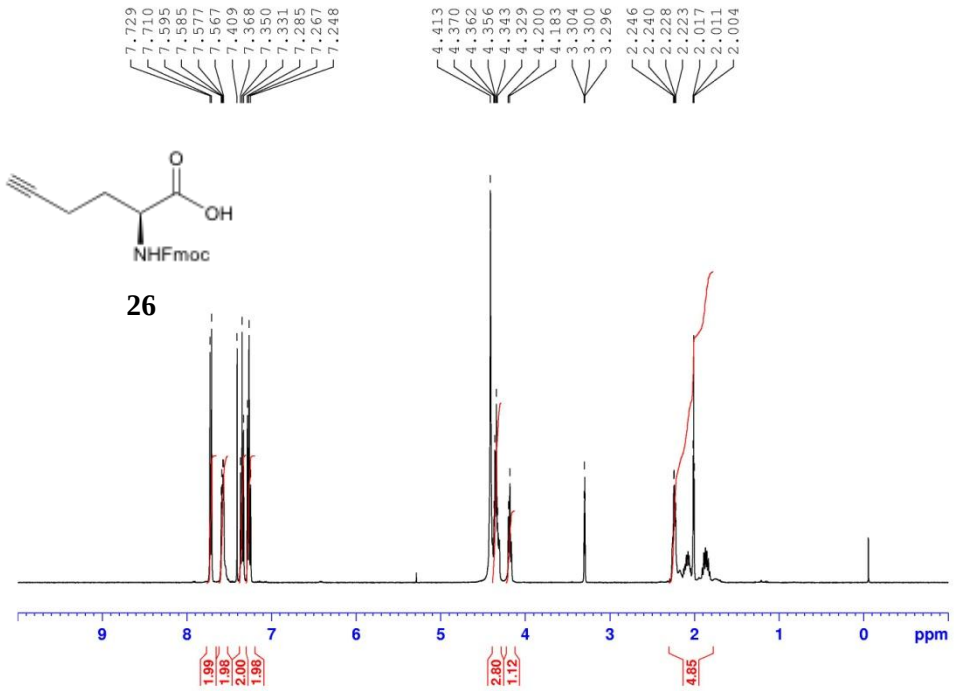
32


7.759
7.742
7.740
7.598
7.590
7.580
7.572
7.407
7.388
7.370
7.369
7.323
7.321
7.318
7.305
7.302
7.299
7.286
7.283
7.281
7.240
5.455
5.435
4.483
4.471
4.414
4.397
4.229
4.212
4.195
3.745
2.279
2.261
2.247
2.242
2.128
2.110
1.989
1.984
1.978
1.937
1.920
1.903
O
O
NHFmoc
9
8
7
6
5
4
3
2
1
0
ppm
2.15
2.16
4.32
0.89
3.07
1.19
3.00
3.09
2.11

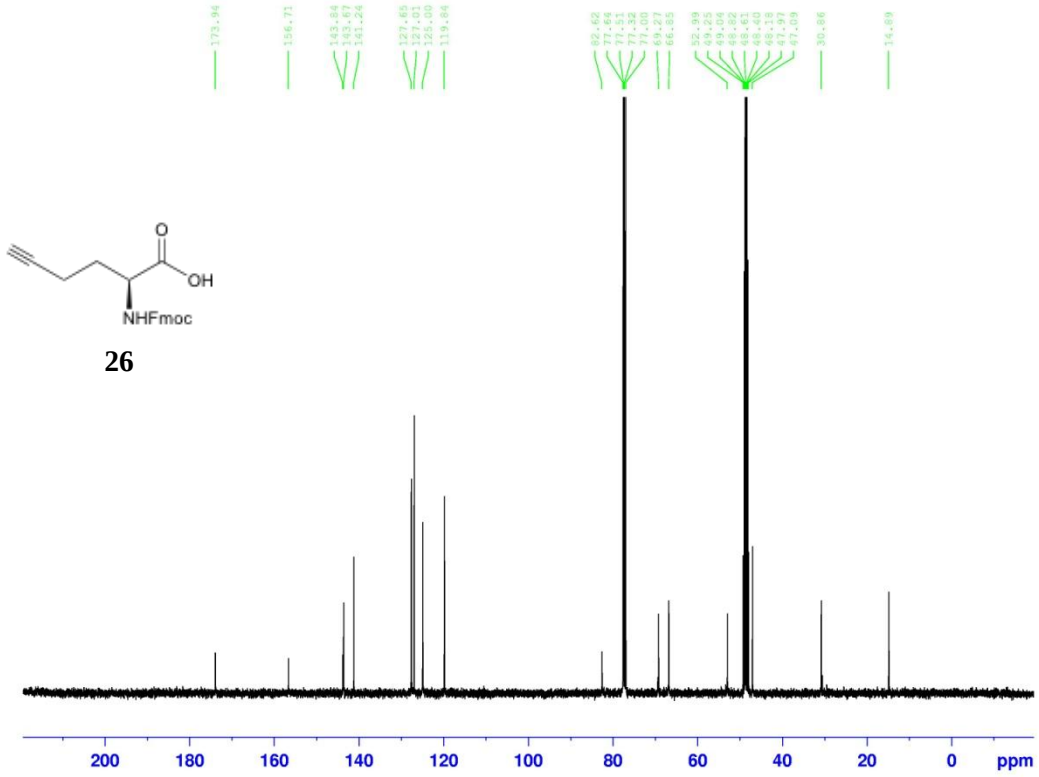
33


172.40
155.91
143.89
143.72
141.36
141.34
127.76
127.10
125.09
120.04
120.02
82.66
77.40
77.29
77.09
76.77
68.54
67.04
53.15
52.58
47.20
31.25
14.84
O
O
NHFmoc
200
180
160
140
120
100
80
60
40
20
0
ppm

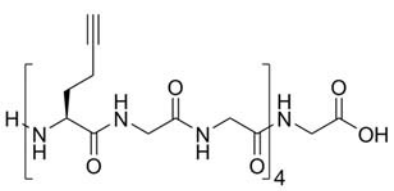
33


7.729
7.710
7.595
7.585
7.577
7.567
7.409
7.368
7.350
7.331
7.285
7.267
7.248
4.413
4.370
4.362
4.356
4.343
4.329
4.200
4.183
3.304
3.300
3.296
2.246
2.240
2.228
2.223
2.017
2.011
2.004
O
OH
NHFmoc
9
8
7
6
5
4
3
2
1
0
ppm
1.99
1.98
2.00
1.98
2.80
1.12
4.85

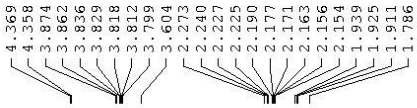
26

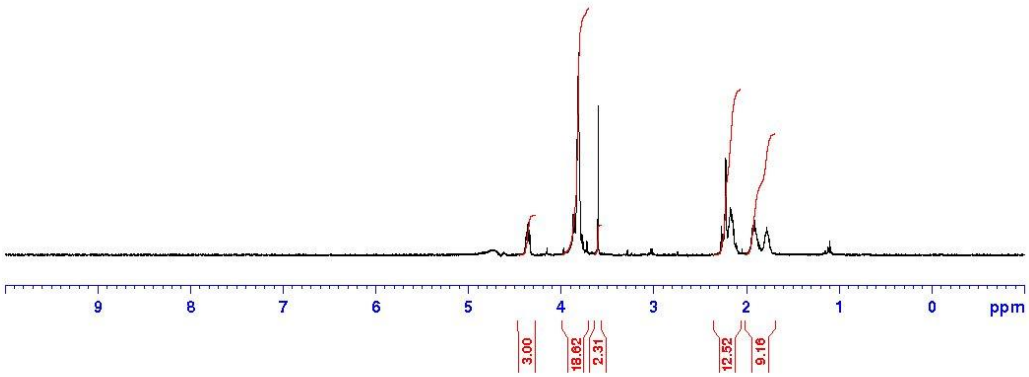

173.94
156.71
143.84
143.67
141.24
127.65
127.01
125.00
119.84
82.62
77.64
77.31
77.32
77.00
69.27
66.85
52.99
49.25
49.04
48.82
48.61
48.40
48.18
47.97
47.09
30.86
14.89
O
OH
NHFmoc
200
180
160
140
120
100
80
60
40
20
0
ppm

26

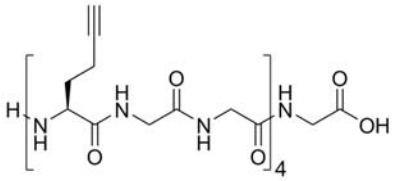


25

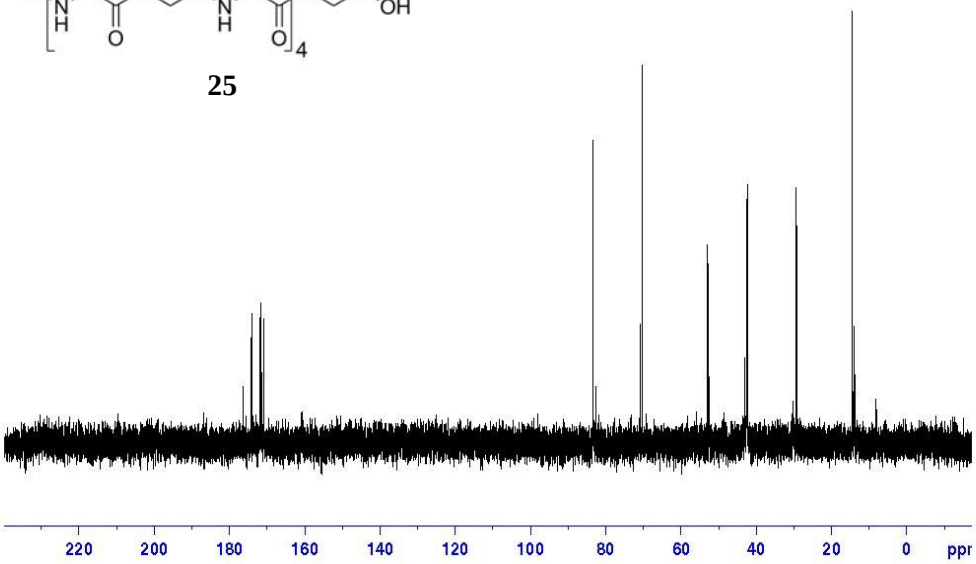

4.369
4.358
3.874
3.862
3.836
3.829
3.818
3.812
3.799
3.604
2.273
2.240
2.227
2.225
2.190
2.177
2.171
2.163
2.156
2.154
1.939
1.925
1.911
1.786

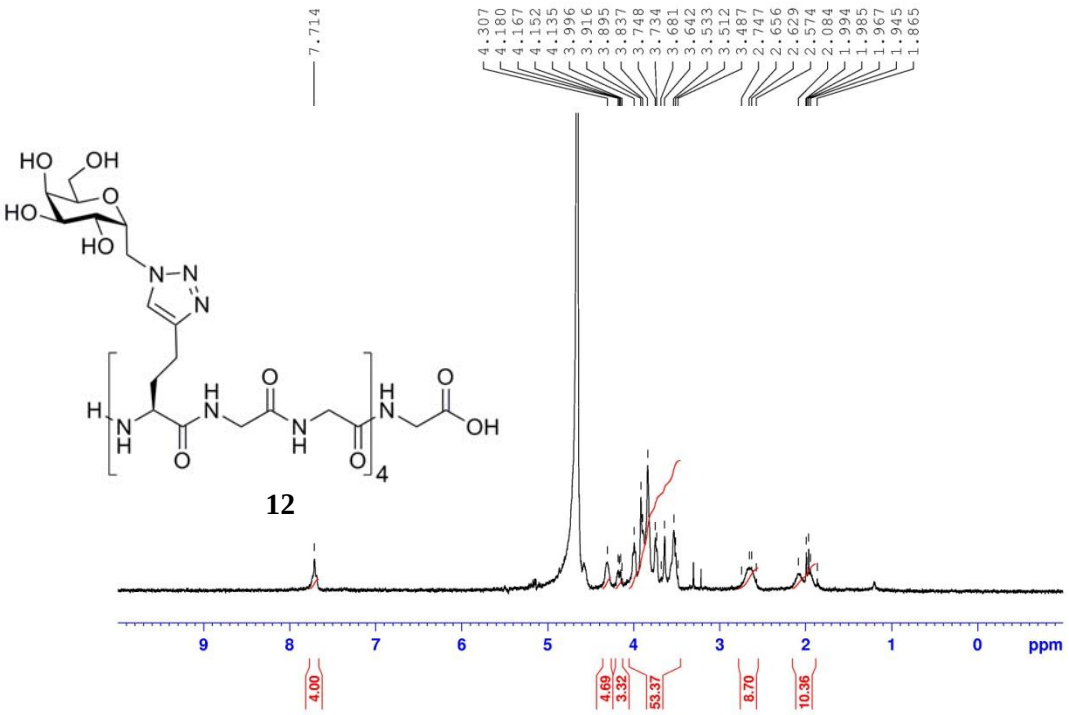

9
8
7
6
5
4
3
2
1
0
ppm
3.00
18.62
2.31
12.52
9.16


176.37
174.33
174.20
174.12
171.91
171.76
171.73
171.67
171.64
171.50
170.92
83.35
82.59
70.78
70.26
52.89
52.85
52.79
52.59
52.08
43.52
42.53
42.29
29.30
29.23
14.42
13.89

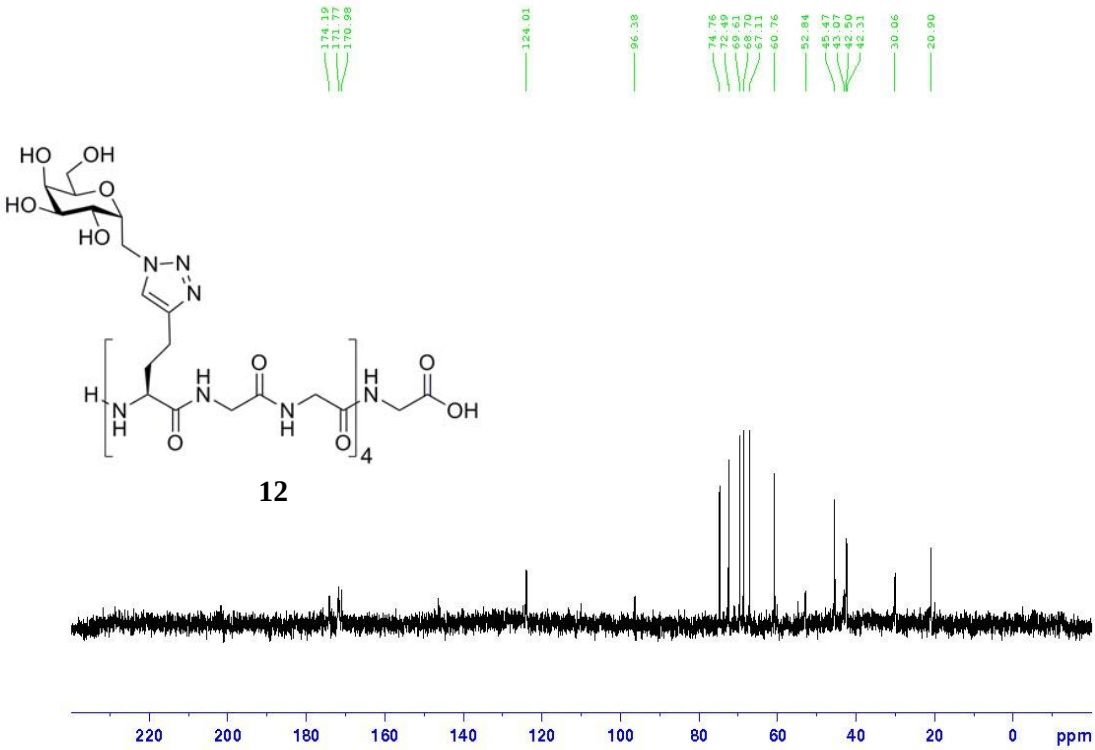


25


220
200
180
160
140
120
100
80
60
40
20
0
ppm


7.714
4.307
4.180
4.167
4.152
4.135
3.996
3.916
3.895
3.837
3.748
3.734
3.681
3.642
3.533
3.512
3.487
2.747
2.656
2.629
2.574
2.084
1.994
1.985
1.967
1.945
1.865
HO
OH
HO
HO
N–N
N
H
N
H
O
N
H
O
N
H
O
O
OH
4
9
8
7
6
5
4
3
2
1
0
ppm
4.00
4.69
3.32
53.37
8.70
10.36

12


174.19
171.77
170.98
124.01
96.38
74.76
72.49
69.61
68.70
67.11
60.76
52.84
45.47
45.07
42.50
42.31
30.06
20.90
HO
OH
HO
HO
N–N
N
H
N
H
O
N
H
O
N
H
O
O
OH
4
220
200
180
160
140
120
100
80
60
40
20
0
ppm

12

Bioconjugate Chemistry

ARTICLE

pubs.acs.org/bc

Synthesis and Properties of Star-Comb Polymers and Their Doxorubicin Conjugates

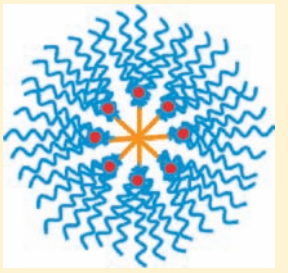
Bo Chen,[†,‡] Derek G. van der Poll,[‡] Katherine Jerger,[†] William C. Floyd,[‡] Jean M. J. Fréchet, and Francis C. Szoka*[,†]

[†]Department of Bioengineering, Therapeutic Sciences and Pharmaceutical Chemistry, University of California, San Francisco, California 94143-0912, United States

[‡]Department of Chemistry, University of California, Berkeley, California 94720-1460, United States

Supporting Information

ABSTRACT: We describe a six-step synthesis to water-soluble doxorubicin (DOX)-loaded biodegradable PEGylated star-comb polymers with favorable pharmaceutical properties by atom transfer radical polymerization (ATRP) starting with a commercially available tripentaerythritol carrying eight reactive sites. The low polydispersity polymers degrade in a stepwise manner into lower molecular weight (MW) fragments by 15 days at 37 °C at either pH 5.0 or pH 7.4. The half-life of the star-comb polymers in blood is dependent upon the molecular weight; the 44 kDa star-comb has a $t_{1/2,\beta}$ of 30.5 ± 2.1 h, which is not significantly changed (28.6 ± 2.7 h) when 6.6 wt % of DOX is attached to it via a pH-sensitive hydrazone linker. The star-comb polymers have low accumulation in organs but a high accumulation in C26 flank tumors implanted in Balb/C mice. The hydrodynamic diameter of polymer−DOX conjugates measured by dynamic light scattering increases from 8 to 35 to 41 nm as the loading is increased from 6.6 to 8.4 to 10.2 wt %. Although there is no significant difference in the $t_{1/2,\beta}$ or in the accumulation of polymer−DOX in C-26 tumors, the uptake of polymer in the spleen is significantly higher for polymers with DOX loadings greater than 6.6 wt %. Polymer accumulation in other vital organs is independent of the DOX loading. The facile synthesis, biodegradability, long circulation time, and high tumor accumulation of the attached drug suggests that the water-soluble star-comb polymers have promise in therapeutic applications.



INTRODUCTION

In the past three decades, there has been extensive exploration of a variety of polymers as drug carriers, a concept introduced by Kopecek, Ringsdorf, and Duncan.[1] In a recent exploration, PEGylated star polymers have been demonstrated to be well-suited for drug delivery applications due to their high solubility, biocompatibility, low toxicity, low organ accumulation, and high accumulation in tumor sites.[2−5] In contrast to traditional linear polymers, star polymers possess a very narrow polydispersity index and a defined number of functional groups; this enables a consistent drug loading and promotes reproducible pharmacokinetic behavior.[2,6] Polyester linkages provide the additional advantage of biodegradability,[7] and PEGylated polyester star polymers of high molecular weight show excellent promise as drug carriers.[2,6,8] The doxorubicin (DOX) conjugated "bow-tie" structure with a fourth generation of 2,2-bis(hydroxymethyl)propionic acid (bis HMPA) and eight 5 kDa PEG chains showed antitumor activity comparable to the FDA approved liposome DOX (DOXIL).[2]

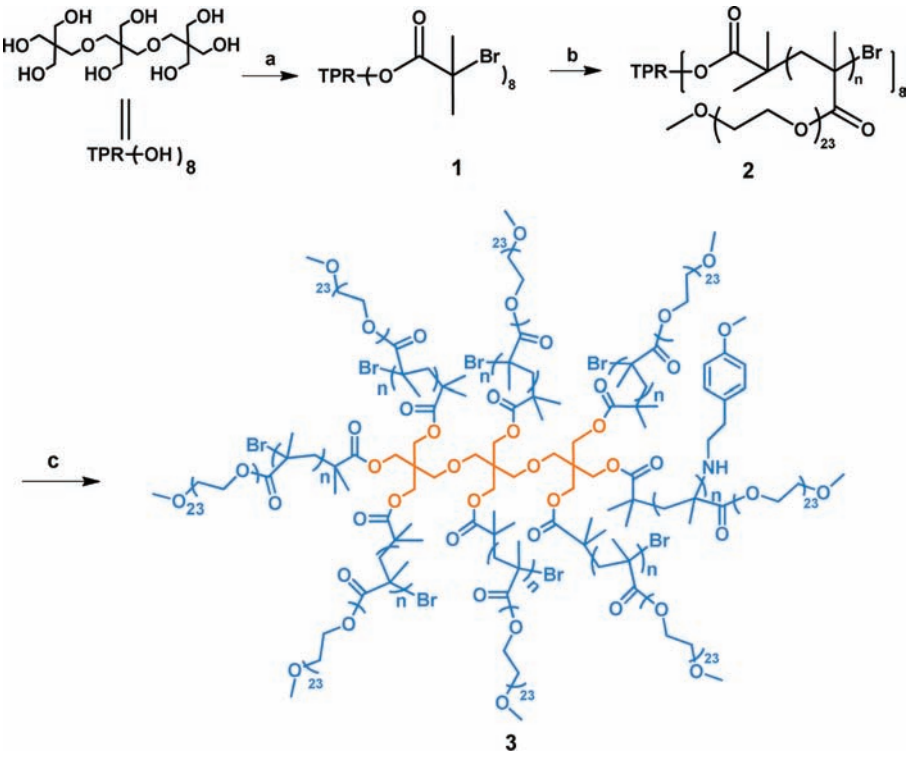
PEGylated star polymers are commonly prepared by coupling activated PEG chains to dendrimer cores, which are prepared by a multistep synthetic procedure.[2,4,9−12] Specialized PEG reagents with reactive functionalities and long reaction times are required to transform the dendritic cores into high molecular weight, branched polymers. PEGylated star polymers have also been prepared by living polymerization, such as atom transfer radical polymerization (ATRP) of poly(ethylene glycol) methylether methacrylate (PEGMA) using dendritic cores as initiators, which allows for the rapid buildup of polymers while also providing for control over molecular weight and polydispersity.[10,13,14] However, the core initiators of these polymers either have a core that is difficult to synthesize[13] or are not biodegradable.[10] In addition, these PEGylated star polymers prepared by living polymerization have neither been characterized *in vivo* nor used as drug carriers.[14]

Herein, we describe a facile approach to biodegradable PEGylated star-comb polymers (Scheme 1) by using a commercially available "tripentaerythritol" with eight reactive sites. Due to the large amount of PEGMA incorporated into the carrier by grafting from the tripentaerythritol core, this structure should be inherently water-soluble and exist as a unimolecular species,[15,16] as opposed to noncovalent aggregate structures such as the micelles prepared from amphiphilic block copolymers[17−19] or other systems such as shell cross-linked knedel-like (SCK) nanoparticles.[20,21] We evaluated the pharmacokinetics of the star-comb polymers with various molecular weights in mice.

Received: September 7, 2010
Revised: January 19, 2011
Published: March 04, 2011

ACS Publications © 2011 American Chemical Society

Scheme 1. Synthesis of Star-Comb Polymer with One Methoxyphenol Group[a]



[a] a. DCM, pyridine, 2-bromoisobutyryl bromide; b. PEGMA, CuBr, PMDETA, anisole; c. TEA, MPEA, DMF.

Following these initial studies, the polymer with a molecular weight of 45 kDa was selected to attach DOX via a pH-sensitive acyl hydrazone bond (Scheme 2).[2,22] We studied the biodistribution of this polymer−DOX conjugate to explore the potential of this star-comb polymer as an antitumor-modality.

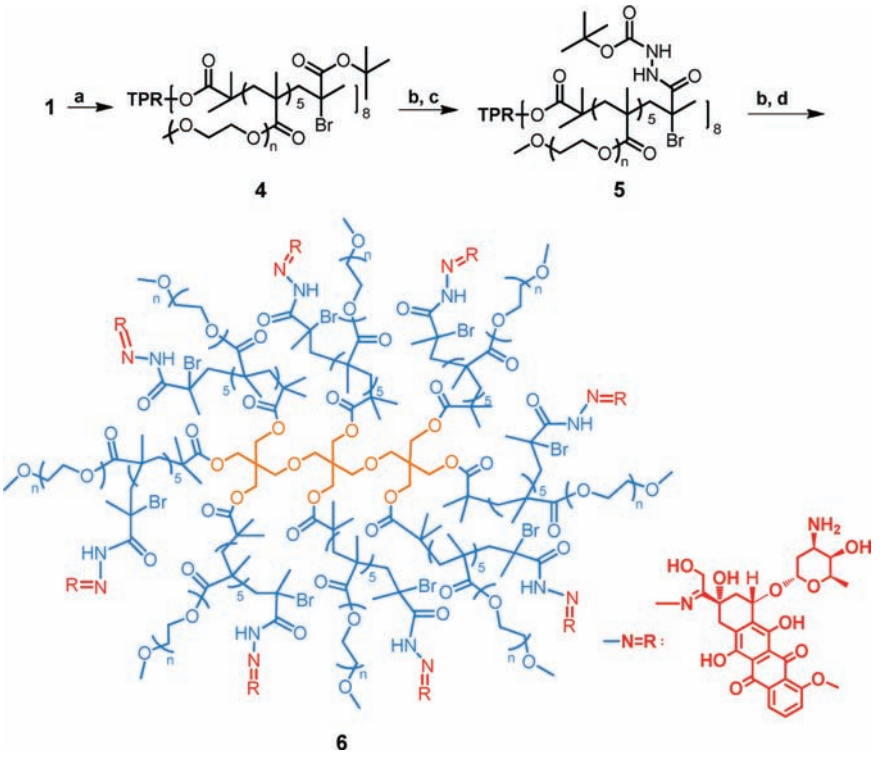
MATERIALS AND METHODS

General Procedures and Materials. 2-(4-Methoxyphenyl) ethylamine (MPEA) was purchased from ARCO Chemical Company. All other chemicals of the highest grade available, including solvents, were purchased from Sigma-Aldrich and used without further purification. Poly(ethylene glycol) methyl ether methacrylate (PEGMA) with molecular weights of 1100 and 2080 Da was purchased from Sigma-Aldrich. High performance flash chromatography (HPFC) was carried out on a Biotage (Charlottesville, VA) Horizon system with prepacked silica gel columns. ^{1}H NMR spectra were recorded on a Bruker Avance 300 MHz ultrashield NMR. NMR chemical shifts are reported in ppm and calibrated against solvent signals. MALDI-TOF MS data were collected on a PerSeptive Biosystems Voyager-DE instrument in positive ion mode using a 2,5-dihydroxybenzoic acid (DHB) matrix and calibration against bovine insulin standards. Gel permeation chromatography (GPC) consisted of a Viscotek 1122 pump, a Viscotek 270 dual detector, and a Viscotek 3500 differential refractive index (RI) detector. GPC was performed at 1.0 mL/min in two Resipore (3 μm) columns (Polymer Laboratories, 300 × 7.5 mm) thermostatted to 50 °C using THF as the mobile phase and poly(methyl methacrylate) as the calibration standards. Refractive index increment (dn/dc) values are determined by plotting the refractive index values of polymer solutions versus varying polymer concentrations (2.5, 5.0, 10.0, and 15.0 mg/mL). The number average diameters of the polymer−DOX conjugates were determined by using dynamic light scattering. Experiments were performed three times at 25 °C in distilled water using filtered 1.0 mg/mL samples with a Zetasizer Nano ZS (Malvern Instruments, Malvern, U.K.) equipped with a 4 mW He−Ne laser at 633 nm.

ATRP Initiator (1). Tripentaerythritol (1.0 g, 2.7 mmol) was suspended in dry dichloromethane (25.0 mL), followed by the addition of pyridine (10.0 mL). The solution was then cooled by ice and 2-bromoisobutyryl bromide (9.7 g, 42.0 mmol) dissolved in 20.0 mL of dichloromethane was added dropwise over a period of 30 min. The reaction continued 2 days at room temperature. The mixture was washed with 0.3 M $NaHCO_3$ (3 × 50.0 mL), 0.3 M $NaHSO_4$ (3 × 50.0 mL), and water (2 × 50.0 mL). The organic layer was dried over Na_2SO_4 and filtered. The solution was concentrated by rotary evaporator and purified by HPFC to provide initiator **1** as a white solid (2.5 g, 61%). ^{1}H NMR (300 MHz, $CDCl_3$): δ 1.94 (m, 48H), 3.60 (d, 8H), 4.29 (d, 16H). MALDI-TOF MS. $[M + H]^+$ Calcd: m/z = 1563.81. Found: m/z = 1565.15.

Synthesis of Polymer 2. In a typical experiment, initiator **1** (50.0 mg, 32.0 μmol) and PEGMA (1.1 kDa) (563.0 mg, 512.0 μmol) were added in anisole (0.5 mL) followed by the addition under argon of CuBr (55.5 mg, 384.0 μmol) and *N*,*N*,*N*′,*N*′,*N*″-pentamethyldiethylenetriamine (PMDETA) in a round-bottom flask equipped with a magnetic stir bar. The solution was deoxygenated by three freeze−pump−thaw cycles. The polymerization was carried out at 90 °C under argon and stopped after the appropriate time by being exposed to air and diluted with dichloromethane. The solution was passed through an alumina column to remove the copper catalyst. The excess solvent was removed on a rotary evaporator under reduced pressure. The

Scheme 2. Synthesis of Star-Comb Polymer (45 kDa)−DOX Conjugate[a]



[a] *a.* PEGMA, CuBr, PMDETA, *t*-butyl methacrylate, anisole; b. TFA, DCM; c. HBTU, HOBt, DiPEA, *t*-butyl carbazate, DMF; d. DOX, acetic acid, pyridine, methanol.

Table 1. Synthesis Conditions and Characterization of Star-Comb Polymers

[M]/[I]	time (min)	conversion %[a]	M_n (kDa) [a]	M_n (kDa) [b]	PDI [b]
10	30	95	12	12	1.10
20	30	95	23	19	1.09
30	35	95	33	32	1.08
50	60	80	46	44	1.13
70	60	80	63	64	1.06
150	90	60	101	97	1.07

[a] Determined by ^{1}H NMR. [b] Determined by GPC.

Table 2. Pharmacokinetic Data for the Evaluated Polymers

polymer M_w (kDa)	avg no of MPEA per polymer	$t_{1/2,\alpha}$ (h)[a]	$t_{1/2,\beta}$ (h)[a]	$AUC_{0\rightarrow\infty}$ (% dose. h/g)[a]
12	3.5	0.10 ± 0.04	6.7 ± 0.8	30 ± 10
19	3.5	0.24 ± 0.06	8.7 ± 1.8	110 ± 40
32	3	0.61 ± 0.12	24.5 ± 4.6	1110 ± 140
44	2	0.89 ± 0.24	30.5 ± 2.1	1310 ± 130
64	2.5	0.95 ± 0.45	33.2 ± 3.4	1540 ± 170
97	1	0.96 ± 0.31	36.9 ± 6.3	1800 ± 290

[a] Values are the mean ± S.D., n = 3.

unreacted PEG monomers were removed by precipitation of the polymer into diethyl ether. The molecular weight of polymers was determined by ^{1}H NMR and GPC (Table 1).

Synthesis of Polymer 3. Polymer **2** (0.1 g) was dissolved in 2.0 mL of anhydrous DMF, and 10 μL (12.0 equiv) of triethylamine was added, followed by MPEA (12.0 mg, 6.0 equiv per polymer hydroxyl). The reaction mixture was stirred at room temperature for 2 days and dialyzed against methanol to remove the unreacted MPEA. The degree of substitution on the polymer was quantified by ^{1}H NMR spectroscopy and ranged from 1.0 to 3.5/polymer (Table 2).

General Deprotection by Trifluoroacetic Acid. Polymer **4** or **5** (0.1 g) was dissolved in a 1:1 mixture of trifluoroacetic acid (TFA) and CH_2Cl_2. After stirring overnight, the solvents were removed under reduced pressure, and the products were precipitated into diethyl ether twice. ^{1}H NMR spectroscopy was used to verify the absence of residual *t*-butyloxycarbonyl protecting groups.

Synthesis of Polymer 4. Initiator **1** (50.0 mg, 32.0 μmol) and PEGMA (1.1 kDa) (1.7 g, 1.6 mmol) were added in anisole (1.7 mL) followed by the addition under argon of CuBr (55.5 mg, 0.4 mmol) and PMDETA (155 μL) in a round-bottom flask equipped with a magnetic stir bar. The solution was deoxygenated by three freeze−pump−thaw cycles. The polymerization was carried out at 90 °C, and degassed *t*-butyl methacrylate (420 μL, 2.9 mmol) was added after 50 min. After 2.5 h, the reaction was exposed to air and diluted with dichloromethane. The solution was passed through an alumina column to remove the copper catalyst. The excess solvent was removed on a rotary evaporator under reduced pressure. The unreacted PEG monomers and *t*-butyl methacrylate were removed by precipitation of the polymer into diethyl ether. The molecular weight of polymers was determined by GPC (M_n = 45 kDa, PDI = 1.13). About five molecules of PEGMA and one molecule of *t*-butyl methacrylate (tBMA) were added to each initiator site by ^{1}H NMR.

Synthesis of Polymer 5. The deprotected polymer **4** (820.0 mg, ~150.0 μmol of acid) was dissolved in 5.0 mL of DMF, and then 2-(1*H*-benzotriazol-1-yl)-1,1,3,3- tetramethyluronium

dx.doi.org/10.1021/bc100400u |*Bioconjugate Chem.* 2011, 22, 617–624

Table 3. Characterization and Pharmacokinetic Data for the Evaluated Polymer-DOX Conjugates

polymer−DOX conjugate	PEG monomer M_w (kDa)	Dox loading (wt %)	hydrodynamic diameter (nm)	$t_{1/2,\beta}$ (h)[a]
1	1	6.6	8 ± 2.3	28.6 ± 2.7
2	1	8.4	35 ± 6.4	31.2 ± 3.4
3	1	10.2	41 ± 7.5	31.7 ± 4.2
4	2	8.4	56 ± 10.8	25.7 ± 5.3

[a] Values are the mean ± S.D., n = 3.

hexafluorophosphate (HBTU, 170.0 mg, 450.0 μmol) and hydroxybenzotriazole (HOBt, 61.0 mg, 450.0 μmol) were added. Next, *t*-butyl carbazate (59.0 mg, 450.0 μmol) and *N*,*N*-diisopropylethylamine (DiPEA, 270 μL) were added and the reaction mixture was stirred at room temperature for one day. The product was then precipitated into diethyl ether three times. The average number of *t*-butyl carbazate moieties attached to each polymer was about 8.2 by ^{1}HNMR. The average molecular weight (M_n) is about 46 kDa by GPC (PDI = 1.13).

Synthesis of the Acyl Hydrazone-Linked Polymer−DOX Conjugate (6). The deprotected polymer **5** (35.0 mg, 76.0 μmol) was dissolved in 0.4 mL methanol with 40 μL acetic acid and 40 μL pyridine. DOX HCl (3.3 mg, 5.7 mmol, 8.0 equiv) was added, and the reaction mixture was heated at 60 °C overnight in the dark. The reaction mixture was then purified by preparative SEC (Sephadex LH20, GE Healthcare, Piscataway, NJ) in methanol to separate polymer-bound DOX from free DOX. The high molecular weight fractions were evaporated, dissolved in water, and purified further by preparative SEC (Sephadex G25, GE Healthcare) in water. The high molecular weight fraction was lyophilized to provide the product as a red powder. The amount of DOX conjugated to the polymer was determined by measuring the absorbance at 485 nm of the polymer solution in water (Table 3).

Polymer Degradation Study. Polymer **2** (40 kDa) was dissolved at a concentration of 1.0 mg/mL in a solution containing either 30.0 mM acetate buffer (pH 5.0) with 70.0 mM $NaNO_3$ or 30.0 mM phosphate buffer (pH 7.4) with 70.0 mM $NaNO_3$. The samples were incubated at 37 °C, and a 0.3 mL aliquot was removed at intervals, lyophilized, and redissolved in THF, then measured by GPC.

Radioiodination of Methoxyphenol Functionalized Polymers. 2-(4-Methoxyphenyl) ethylamine functionalized polymers were iodinated based upon the method described by Krummeich et al.[23] In brief, 3.0 mg of polymer **3** was dissolved in 250 μL of trifluoroacetic acid (TFA), and 10 μL of an aqueous solution of ^{125}I was added containing 1.0 mCi ^{125}I. Chloramine T (540.0 μg) dissolved in 50 μL of TFA was added to the mixture, and the reaction was heated at 60 °C for 5 min. The reaction was stopped by the addition of sodium metabisulfite (1.0 mg in 10 μL of water), and the TFA was evaporated under a stream of nitrogen that was vented through a trap containing activated carbon (Dupont-New England Nuclear, MA). The residue was dissolved in 10 μL of 100.0 mM HEPES buffer (pH 7.4) and chromatographed on a column containing 1.8 mL bed volume of Dowex 2 anion-exchange resin in the chloride form. The radiolabeled polymer was eluted in the first 4.0 mL using water as the mobile phase. Polymers were separated from low molecular weight radioactive contaminants by SEC on Bio-Rad 10DG desalting columns equilibrated with phosphate buffered saline (PBS). The initial, high molecular weight fractions were collected and pooled. A suitable quantity of radiolabeled polymer was mixed with cold polymer in sterile PBS to create a solution with 5.0 mg/mL polymer and specific activities ranging from 3.0 to 25.0 μCi/mL.

Animal Experiments. All animal experiments were performed in compliance with the National Institutes of Health guidelines for animal research under a protocol approved by the Committee on Animal Research at University of California (San Francisco, CA) (UCSF). C26 colon carcinoma cells obtained from the UCSF cell culture facility were cultured in RPMI medium 1640 containing 10% FBS. Female BALB/c mice were obtained from Simonsen Laboratories, Inc. (Gilroy, CA).

Biodistribution Studies. Polymer solutions (200 μL) were administered intravenously via the tail vein to 6- to 8-week-old BALB/c female mice. The mice were sacrificed at seven different time points (three mice per group) ranging from 5 min to 48 h postinjection for biodistribution analyses. The blood (collected by heart puncture), heart, lungs, liver, stomach, spleen, intestines, kidney, body, tail, and head were weighed, and the amount of radioactivity present in each organ was quantified. Periodically, blood was also collected from the retroorbital sinus at intermediate time points to determine the dose of polymer in the blood. For the 24 h time points, mice were housed in metabolic cages to allow for the collection of urine and feces. The % injected dose per gram (% ID/g) of blood versus time curve was analyzed using a two-compartment model.[24]

Biodistribution Studies of Radiolabeled Polymer in Tumored Mice. The 6- to 8-week-old female BALB/c mice were injected with 3.0×10^5 C26 cells colon carcinoma cells on the right rear flank by subcutaneous administration. The mice (three per group) were injected intravenously via the tail vein with 200 μL of radiolabeled polymer solution prepared as described previously. The mice were sacrificed at 24 and 48 h postinjection; their blood, liver, muscle and tumor were collected and weighed; and the radioactivity in each was quantified.

Biodistribution Studies of Polymer−DOX Conjugates in Tumored Mice. The 6- to 8-week-old female BALB/c mice were injected with 3.0×10^5 C26 colon carcinoma cells on the right rear flank by subcutaneous administration. The mice (three per group) with tumor size about 100.0−250.0 mg were injected intravenously via the tail vein with 200 μL of polymer−DOX solution (8.0 mg Dox equiv/kg) in PBS. Two control mice were also injected with 200 μL of PBS. The mice were sacrificed 48 h postinjection. The blood (collected by heart puncture), heart, liver, spleen, kidney, muscle, and tumor were collected for analyses by following the procedure described before.[9] Briefly, each organ was weighed and 200−300 mg of the collected organs were homogenized with zirconium beads and 1.0 mL acidified isopropyl alcohol (75.0 mM HCl, 90% IPA). The samples then incubated at 4 °C for 24 h. Serum was collected using Microtainer serum separator vials and processed in the same manner as the organs. The samples were frozen in a −80 °C freezer until measurements could be made. At measurement time, samples were thawed, briefly vortexed, and centrifuged for 5 min at 14 000 rpm. Then, 80 μL of supernatant was combined with 920 μL of acidified IPA for fluorescence measurements. Dox fluorescence (excitation 485 nm; emission 595 nm) was measured on a Spex Fluorolog fluorimeter. Calibration curves were made from organ samples collected from an untreated mouse.

RESULTS AND DISCUSSION

A straightforward two-step synthesis was used to create the desired eight-arm star-comb architecture (Scheme 1). The

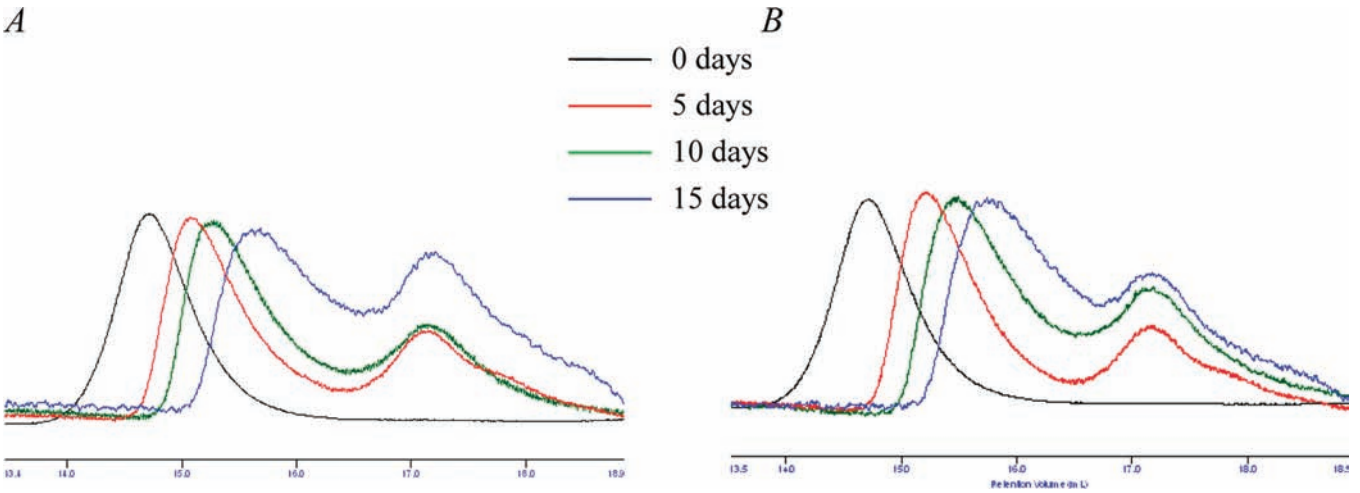


Figure 1. Time-dependent GPC profiles of the polymer (40 kDa) upon incubation in (A) pH 5.0 and (B) pH 7.4 buffer at 37 °C.

polymerization of PEGMA (1100 Da) was initiated by α-bromoisobutyryl functionalized tripentaerythritol. This novel dendritic core has eight sites that may be used to initiate polymerization. The molecular weights of the star-combs were adjusted by controlling the feed ratio and using appropriate reaction times (Table 1). The star-combs are soluble in a variety of common organic solvents and water. Precipitation in diethyl ether or dialysis using 50 000 molecular weight cutoff regenerated cellulose membranes against methanol was used to remove unreacted monomers, generally producing isolated yields of polymer greater than 60%. In the synthesis of polymers with molecular weight less than 32 kDa, the monomers react completely so that no further purification is required. The polydispersity index of all the eight-arm star-combs was less than 1.15, and their molecular weights were in good agreement with the theoretical molecular weight values. Furthermore, the eight reactive bromide functionalities that remain on each star-comb can easily be used to generate sites for drug attachment.[25,26] A drug such as DOX can be attached to the star-comb in six rapid and easily scalable synthetic steps, which is fewer than that typically used in the preparation of drug-loaded star polymers.[2] The starting materials, including tripentaerythritol and PEGMA, are inexpensive and commercially available.

PEG is attached to the backbone of the branches by ester bonds while the eight branches are themselves attached via ester bonds to the dendritic scaffold, and both ester linkages are susceptible to hydrolysis.[2] Complete ester hydrolysis should release PEG chains (1 kDa) as well as the dendritic core. To confirm that the polymeric carriers degrade under physiological conditions, a representative polymer (40 kDa) was incubated in pH 5.0 and pH 7.4 buffers at 37 °C, and the molecular weight distribution was monitored over time by SEC. At pH 5.0 and over a period of 5 days, there is an increase in the retention time of the peak corresponding to the PEG−dendrimer hybrid (Figure 1A), indicating a decrease in molecular weight due to polymer degradation. In addition, a new peak corresponding to the molecular weight of the 1 kDa PEG monomer appears in the chromatographic trace. Almost complete degradation was evidenced by the presence of a high proportion of low molecular weight material after 15 days. At pH 7.4 (Figure 1B), a similar decrease in the polymer molecular weight was observed with the appearance of a new peak with a retention time corresponding to a molecular weight of 1 kDa.

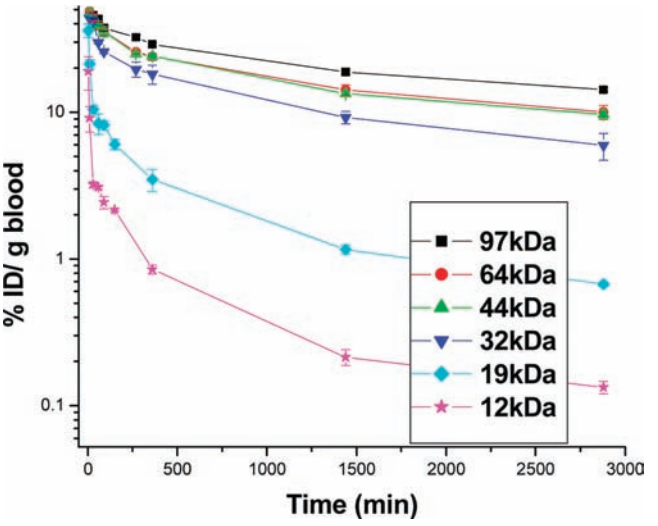


Figure 2. Polymer concentration in the blood over time as a function of time after intravenous administration (mean ± S.D., $n = 3$).

We also determined the time-dependent biodistribution profiles to examine the effect of molecular weight on bioaccumulation. In order to track the polymers *in vivo*, a number of terminal bromide groups of each star-comb polymer were substituted by 2-(4-methoxyphenyl) ethylamine (MPEA) as shown in Scheme 1. The number of MPEA molecules on the polymers were subsequently quantified by ^{1}H NMR spectroscopy (Table 2), and the polymers were then radiolabeled with ^{125}I using the electrophilic chloramine T method as previously described[23] before being administered to mice. Elimination half-lives ($t_{1/2}$) and areas under the % dose/g versus time curve from 0 to infinity ($AUC_{0\rightarrow\infty}$) were calculated using the two-compartment model[24] and are shown in Table 2. As expected, increasing the molecular weight of these star-comb polymers from 12 to 97 kDa leads to the expected increases in both the $t_{1/2,\,\beta}$ and $AUC_{0\rightarrow\infty}$ values (Figure 2). Interestingly, there is a sharp decrease of $t_{1/2,\,\beta}$ when the molecular weight was decreased from 32 to 19 kDa, which indicates that the threshold molecular weight for renal filtration is within this range. This value is lower than the molecular weight cutoff for renal filtration of 30 to 40 kDa previously described for linear PEG.[27] Indeed, these star-comb polymers showed much

dx.doi.org/10.1021/bc100400u |*Bioconjugate Chem.* 2011, 22, 617–624

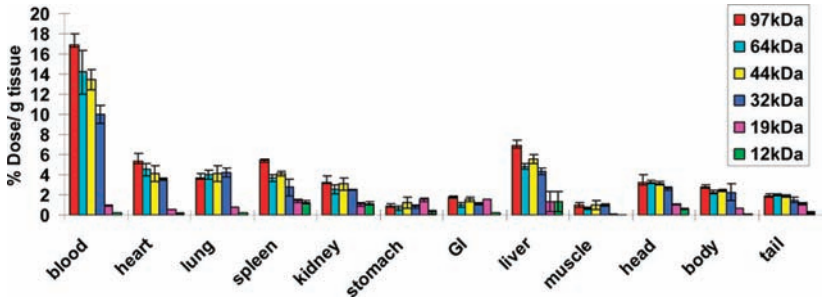


Figure 3. Biodistribution of drug-free polymers in nontumored mice at 48 h as a function of molecular weight reported as % dose/g tissue (mean ± S.D., $n = 3$).

longer circulation time than linear PEG. The $t_{1/2,\ \beta}$ value reported for linear 50 kDa PEG is 16.5 h and the corresponding $AUC_{0\rightarrow\infty}$ value is 600% dose h/g. In this study, the star-combs with molecular weights above 32 kDa had long blood circulation times. As molecular weight increases from 32 to 44, to 64, and to 97 kDa, $t_{1/2,\ \beta}$ increased from 24.5 to 30.5, 33.2, and 36.9 h, while the corresponding $AUC_{0\rightarrow\infty}$ values increased from 1110%, 1310%, 1540%, to 1800% dose h/g, respectively. We observed that the 44 kDa star-comb had similar $t_{1/2,\ \beta}$ and $AUC_{0\rightarrow\infty}$ values to a "bow-tie" dendritic polymer[2] with a molecular weight of 45 kDa and greater values than those of a PEGylated 42 kDa dendrimer with an aspartic acid modified bis-2,2-hydroxymethyl propanoic acid (bisHMPA) based core.[9] In contrast to polymers with higher molecular weights, the 19 and 12 kDa polymers are cleared rapidly from circulation. Significant amounts of polymer were found in urine (36% for 12 kDa and 29% for 19 kDa) and feces (15% for 12 kDa and 26% for 19 kDa), while only small amounts of polymers with molecular weights above 32 kDa were eliminated in urine (around 10%) and feces (<5%) at 24 h. No specific organ accumulation was observed for these macromolecules (Figure 3). The results indicate that the hydrolysis of the star-comb polymers larger than 32 kDa can lead to fast elimination, thus preventing their long-term accumulation.

A biodistribution study in BALB/c mice tumored with the C26 colon carcinoma in the flank was performed to evaluate the tumor accumulation of star-comb polymers with different molecular weights. Polymers with molecular weights of 97, 44, and 19 kDa were selected in order to span a range of circulation lifetimes. The concentration of polymer found in tumor tissue was directly related to molecular weight. Polymers having molecular weights of 19, 44, and 97 kDa had drug tumor levels of 2.8 ± 0.17%, 12.1 ± 3.3%, and 15.2 ± 3.1% dose/g, respectively, after 24 h and 2.2 ± 0.36%, 14.2 ± 1.9%, and 18.9 ± 0.62% dose/g, respectively, after 48 h (Figure 4). The 19 kDa star-comb had a maximum tumor accumulation at 24 h. The tumor concentration of star-combs with molecular weights of 44 and 97 kDa increased from 24 to 48 h. This can be ascribed to the EPR effect.[2,28,29] These values compare favorably with the tumor accumulations reported for other polymers such as PEGylated "bow-tie" dendrimer, HPMA, and PEO.[2,30,31] The tumor/muscles accumulation ratios for the 44 kDa polymer are 16 at 24 h and 11 at 48 h, and the ratios of the 97 kDa polymer are 11 at 24 h and 7 at 48 h on a % dose/g basis. The tumor/muscle ratios decrease from 24 to 48 h due to the increased accumulation in muscles for both polymers at 48 h. Such high levels of tumor accumulation should provide star-combs with the capability to effectively deliver drugs to tumor sites.

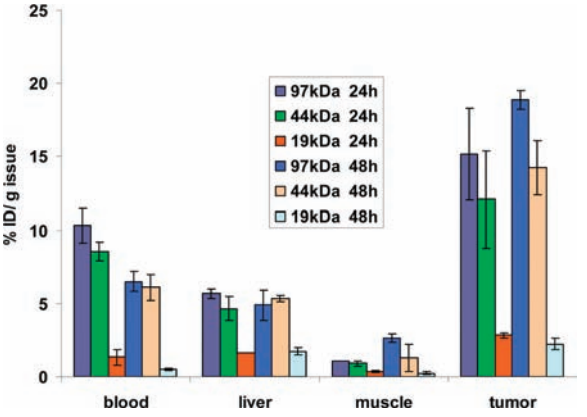


Figure 4. Biodistribution of drug-free polymers in mice bearing subcutaneous C26 tumors at 24 and 48 h based on % dose/g tissue (mean ± S.D., $n = 3$).

To further evaluate the potential of this polymer to be a drug carrier, DOX was conjugated to the 45 kDa star-comb through a hydrazone bond[2,22] to form a stealth PEG corona-drug core structure (Scheme 2). The molecular weight of 45 kDa was chosen because it provides a good balance between the theoretical drug loading and the circulation half-life based on the previous studies.[2,8,9] It is also easy to compare this polymer with other the DOX loaded polymers, such as PEGylated ester-amide dendrimer and polylysine dendrimer.[8,9] The hydrazone linkage can release DOX in its biologically active form after endocytosis but is stable at the physiological pH of 7.4. About one *t*-butyl methacrylate was introduced to each of the eight branches for attachment of *t*-butylcarbazate. Deprotection of the hydrazide Boc group followed by hydrazone formation with DOX in methanol afforded polymer containing DOX (Scheme 2). The loading of DOX is controlled by the molar ratio of DOX and hydrazide (Table 3). Interestingly, the size of the particles is dependent on the loading of DOX. As the loading increased from 6.6 to 8.4 and 10.2 wt %, the polymer−DOX conjugates formed aggregates and the particle size increased from 8 to 35 nm to 41 nm (Table 3). Even when 2 kDa PEGMA was used instead of the corresponding 1 kDa as monomer and the molecular weight of the polymer was kept at 45 kDa, aggregates were still observed (56 nm) at a loading of 8.4 wt %. Tumored mice were injected with polymer−DOX conjugates (**1**−**4**) at a dose of 8.0 mg DOX/kg. All the polymer−DOX conjugates, similar to the radiolabeled 44 kDa polymer, have $t_{1/2,\ \beta}$ values of about 30 h (Table 3). Therefore, their blood circulation time was not significantly changed by the addition of the functional moieties,

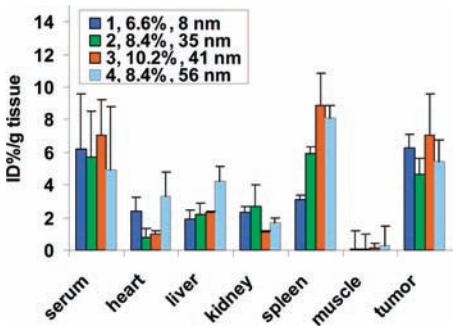


Figure 5. Biodistribution of polymer−DOX conjugates in mice bearing subcutaneous C26 tumors at 48 h based on % dose/g tissue (mean ± S.D., $n = 3$). **1**−**4** correspond to the samples in Table 3.

the attachment of a drug payload, or the diameter of the polymer−DOX conjugates.

Furthermore, the accumulation of DOX loaded polymers in the tumor (~6% ID/g tissue) is comparable to the levels of accumulation we have previously observed for related macromolecules.[2,8,9] The tumor accumulation of DOX for the polymer−DOX conjugates was also similar to what is observed for the PEGylated liposome formulation known as DOXIL (Figure 5).[9] Interestingly, the polymer−DOX conjugate with a diameter of 8 nm showed a lower accumulation in the spleen than the other three polymer−DOX conjugates with larger diameters or DOXIL with a diameter of 100 nm. All of the DOX-loaded polymers accumulated at less than 5% ID/g tissue in the other vital organs. Therefore, the polymer−DOX conjugate with a diameter of 8 nm has a more favorable tissue distribution compared to the other polymers, as it maintains a high drug concentration in the tumor while accumulating less in the organs. Because of this carrier's low toxicity and high tumor accumulation, it could provide an alternative solution to DOXIL for reducing the side effects caused by DOX.

In conclusion, a biodegradable polyester star-comb polymer-PEG hybrid was synthesized by ATRP using an inexpensive dendritic core that is accessible in a rapid, high yielding, and reproducible synthetic scheme. The polymer was also shown to deliver large dose percentages of DOX to C26 tumors when injected into mice.

■ ASSOCIATED CONTENT

Supporting Information. ^{1}H NMR spectra for target compounds. This material is available free of charge via the Internet at http://pubs.acs.org.

■ AUTHOR INFORMATION

Corresponding Author

*Corresponding author. E-mail Address: szoka@cgl.ucsf.edu.

Present Addresses

§153 2nd Ave, Genzyme Corporation, Drug Discovery and Biomaterials R&D, Waltham, MA 02451.

■ ACKNOWLEDGMENT

This work was supported by NIH grant R01-EB 002047.

■ REFERENCES

(1) Duncan, R. (2009) Development of HPMA copolymer-anticancer conjugates: Clinical experience and lessons learnt. *Adv. Drug Delivery Rev. 61*, 1131–1148.

(2) Lee, C. C., Gillies, E. R., Fox, M. E., Guillaudeu, S. J., Frechet, J. M., Dy, E. E., and Szoka, F. C. (2006) A single dose of doxorubicin-functionalized bow-tie dendrimer cures mice bearing C-26 colon carcinomas. *Proc. Natl. Acad. Sci. U.S.A. 103*, 16649–16654.

(3) Grayson, S. M., and Godbey, W. T. (2008) The role of macromolecular architecture in passively targeted polymeric carriers for drug and gene delivery. *J. Drug Targeting 16*, 329–356.

(4) Lim, J., Chouai, A., Lo, S. T., Liu, W., Sun, X., and Simanek, E. E. (2009) Design, synthesis, characterization, and biological evaluation of triazine dendrimers bearing paclitaxel using ester and ester/disulfide linkages. *Bioconjugate Chem. 20*, 2154–2161.

(5) Lo, S. T., Stern, S., Clogston, J. D., Zheng, J., Adiseshaiah, P. P., Dobrovolskaia, M., Lim, J., Patri, A. K., Sun, X., and Simanek, E. E. (2010) Biological assessment of triazine dendrimer: toxicological profiles, solution behavior, biodistribution, drug release and efficacy in a PEGylated, paclitaxel construct. *Mol. Pharm. 7*, 993–1006.

(6) Fox, M. E., Szoka, F. C., and Frechet, J. M. (2009) Soluble polymer carriers for the treatment of cancer: the importance of molecular architecture. *Acc. Chem. Res. 42*, 1141–1151.

(7) Dailey, L. A., Wittmar, M., and Kissel, T. (2005) The role of branched polyesters and their modifications in the development of modern drug delivery vehicles. *J. Controlled Release 101*, 137–149.

(8) van der Poll, D. G., Kieler-Ferguson, H. M., Floyd, W. C., Guillaudeu, S. J., Jerger, K., Szoka, F. C., and Frechet, J. M. (2010) Design, synthesis, and biological evaluation of a robust, biodegradable dendrimer. *Bioconjugate Chem. 21*, 764–773.

(9) Guillaudeu, S. J., Fox, M. E., Haidar, Y. M., Dy, E. E., Szoka, F. C., and Frechet, J. M. (2008) PEGylated dendrimers with core functionality for biological applications. *Bioconjugate Chem. 19*, 461–469.

(10) Chen, H. T., Neerman, M. F., Parrish, A. R., and Simanek, E. E. (2004) Cytotoxicity, hemolysis, and acute in vivo toxicity of dendrimers based on melamine, candidate vehicles for drug delivery. *J. Am. Chem. Soc. 126*, 10044–10048.

(11) Kaminskas, L. M., Boyd, B. J., Karellas, P., Krippner, G. Y., Lessene, R., Kelly, B., and Porter, C. J. (2008) The impact of molecular weight and PEG chain length on the systemic pharmacokinetics of PEGylated poly l-lysine dendrimers. *Mol. Pharm. 5*, 449–463.

(12) Kim, Y., Hechler, B., Gao, Z. G., Gachet, C., and Jacobson, K. A. (2009) PEGylated dendritic unimolecular micelles as versatile carriers for ligands of g protein-coupled receptors. *Bioconjugate Chem. 20*, 1988–1998.

(13) Hedrick, J. L., Trollsas, M., Hawker, C. J., Atthoff, B., Claesson, H., Heise, A., Miller, R. D., Mecerreyes, D., Jerome, R., and Dubois, P. (1998) Dendrimer-like star block and amphiphilic copolymers by combination of ring opening and atom transfer radical polymerization. *Macromolecules 31*, 8691–8705.

(14) Schramm, O. G., Pavlov, G. M., van Erp, H. P., Meier, M. A. R., Hoogenboom, R., and Schubert, U. S. (2009) A versatile approach to unimolecular water-soluble carriers: ATRP of PEGMA with hydrophobic star-shaped polymeric core molecules as an alternative for PEGylation. *Macromolecules 42*, 1808–1816.

(15) Jones, M. C., Ranger, M., and Leroux, J. C. (2003) pH-sensitive unimolecular polymeric micelles: synthesis of a novel drug carrier. *Bioconjugate Chem. 14*, 774–781.

(16) Wang, F., Bronich, T. K., Kabanov, A. V., Rauh, R. D., and Roovers, J. (2008) Synthesis and characterization of star poly(epsilon-caprolactone)-b-poly(ethylene glycol) and poly(L-lactide)-b-poly(ethylene glycol) copolymers: evaluation as drug delivery carriers. *Bioconjugate Chem. 19*, 1423–1429.

(17) Nasongkla, N., Shuai, X., Ai, H., Weinberg, B. D., Pink, J., Boothman, D. A., and Gao, J. (2004) cRGD-functionalized polymer micelles for targeted doxorubicin delivery. *Angew. Chem., Int. Ed. Engl. 43*, 6323–6327.

(18) Torchilin, V. P. (2002) PEG-based micelles as carriers of contrast agents for different imaging modalities. *Adv. Drug Delivery Rev. 54*, 235–252.

(19) Kabanov, A. V., Slepnev, V. I., Kuznetsova, L. E., Batrakova, E. V., Alakhov, V., Melik-Nubarov, N. S., Sveshnikov, P. G., and Kabanov, V. A. (1992) Pluronic micelles as a tool for low-molecular compound vector delivery into a cell: effect of Staphylococcus aureus enterotoxin B on cell loading with micelle incorporated fluorescent dye. *Biochem. Int. 26*, 1035–1042.

(20) Sun, X., Rossin, R., Turner, J. L., Becker, M. L., Joralemon, M. J., Welch, M. J., and Wooley, K. L. (2005) An assessment of the effects of shell cross-linked nanoparticle size, core composition, and surface PEGylation on in vivo biodistribution. *Biomacromolecules 6*, 2541–2554.

(21) Fukukawa, K., Rossin, R., Hagooly, A., Pressly, E. D., Hunt, J. N., Messmore, B. W., Wooley, K. L., Welch, M. J., and Hawker, C. J. (2008) Synthesis and characterization of core-shell star copolymers for in vivo PET imaging applications. *Biomacromolecules 9*, 1329–1339.

(22) Lee, C. C., Cramer, A. T., Szoka, F. C., and Frechet, J. M. J. (2006) An intramolecular cyclization reaction is responsible for the in vivo inefficacy and apparent pH insensitive hydrolysis kinetics of hydrazone carboxylate derivatives of doxorubicin. *Bioconjugate Chem. 17*, 1364–1368.

(23) Krummeich, C., Holschbach, M., and Stocklin, G. (1994) Direct n.c.a. electrophilic radioiodination of tyrosine analogues; their in vivo stability and brain-uptake in mice. *Appl. Radiat. Isot. 45*, 929–935.

(24) Welling, P. G. (1986) *Pharmacokinetics*; Americal Chemical Society: Washington, DC.

(25) Van Renterghem, L. M., Lammens, M., Dervaux, B., Viville, P., Lazzaroni, R., and Du Prez, F. E. (2008) Design and use of organic nanoparticles prepared from star-shaped polymers with reactive end groups. *J. Am. Chem. Soc. 130*, 10802–10811.

(26) Coessens, V., Pintauer, T., and Matyjaszewski, K. (2001) Functional polymers by atom transfer radical polymerization. *Prog. Polym. Sci. 26*, 337–377.

(27) Yamaoka, T., Tabata, Y., and Ikada, Y. (1994) Distribution and tissue uptake of poly(ethylene glycol) with different molecular weights after intravenous administration to mice. *J. Pharm. Sci. 83*, 601–606.

(28) Turk, H., Shukla, A., Alves Rodrigues, P. C., Rehage, H., and Haag, R. (2007) Water-soluble dendritic core-shell-type architectures based on polyglycerol for solubilization of hydrophobic drugs. *Chemistry 13*, 4187–4196.

(29) Gillies, E. R., and Frechet, J. M. (2005) Dendrimers and dendritic polymers in drug delivery. *Drug Discovery Today 10*, 35–43.

(30) Seymour, L. W., Miyamoto, Y., Maeda, H., Brereton, M., Strohalm, J., Ulbrich, K., and Duncan, R. (1995) Influence of molecular weight on passive tumour accumulation of a soluble macromolecular drug carrier. *Eur. J. Cancer 31A*, 766–770.

(31) Tabata, Y., Murakami, Y., and Ikada, Y. (1997) Photodynamic effect of polyethylene glycol-modified fullerene on tumor. *Jpn. J. Cancer Res. 88*, 1108–1116.

Supporting information

[a]Star-Comb Polymers and Their Doxorubicin Conjugates

*Bo Chen[†#], Derek G.van der Poll[‡], Katherine Jerger[†], William C. Floyd[‡], Jean M. J. Fréchet[‡] and Francis C. Szoka[†]**

[†] Department of Bioengineering, Therapeutic Sciences and Pharmaceutical Chemistry, University of California, San Francisco, California 94143-0912; and

[‡] Department of Chemistry, University of California, Berkeley, California 94720-1460

[a] Based on the classification, nomenclature, and structure representation described in L. Schultz and E. S. Wilks J. Chem. Inf. Comput. Sci. 1998, 38, 85-99, star-comb polymers comprises a dendritic core from which a number of comb arms emanate.

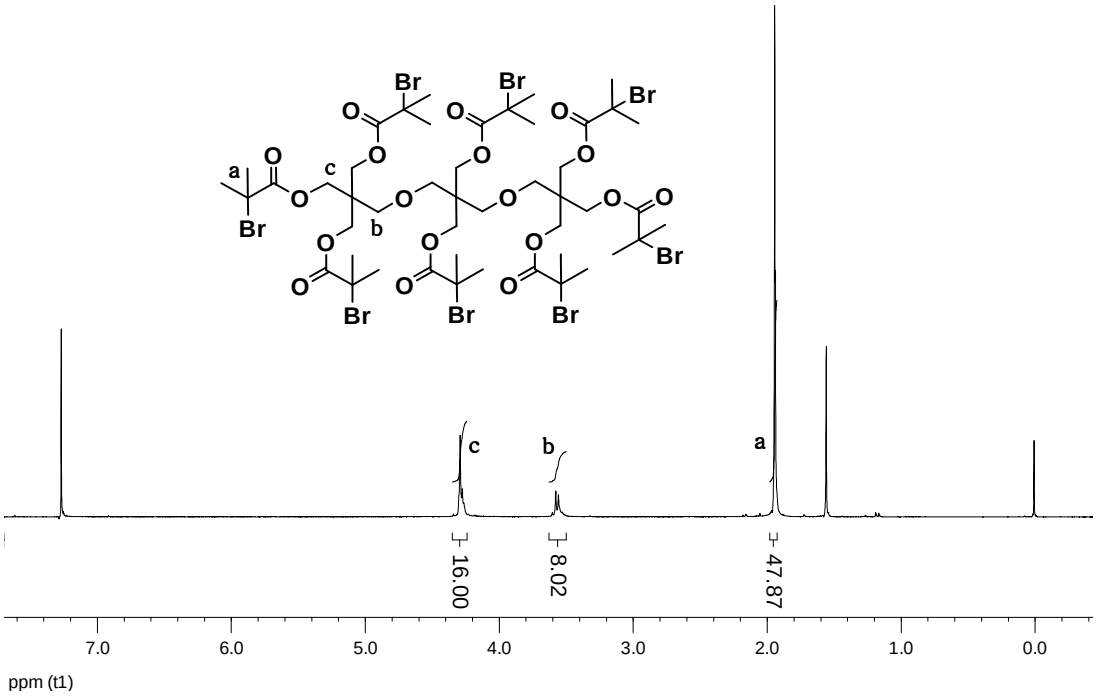


Figure S1. ^{1}H NMR spectrum of initiator 1 in *d*-chloroform.

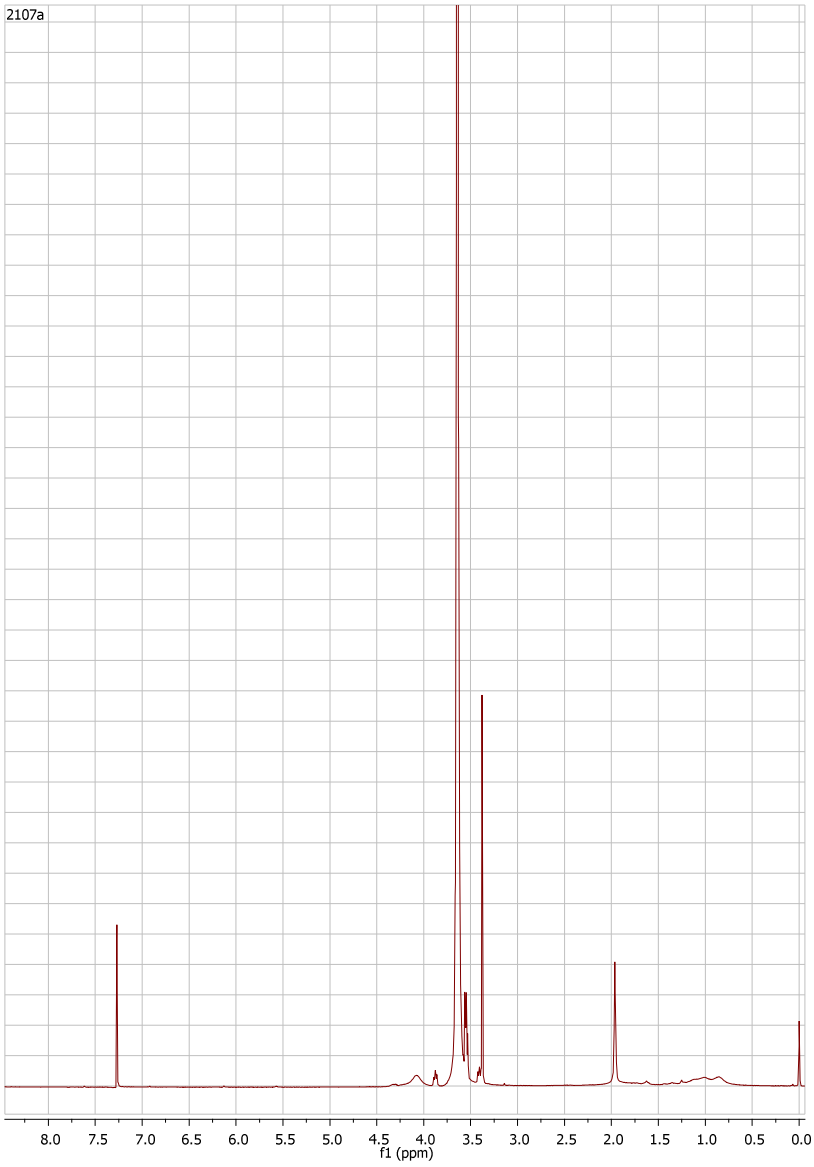


Figure S2. Representative ^{1}H NMR spectrum of polymer 2 in $CDCl_3$

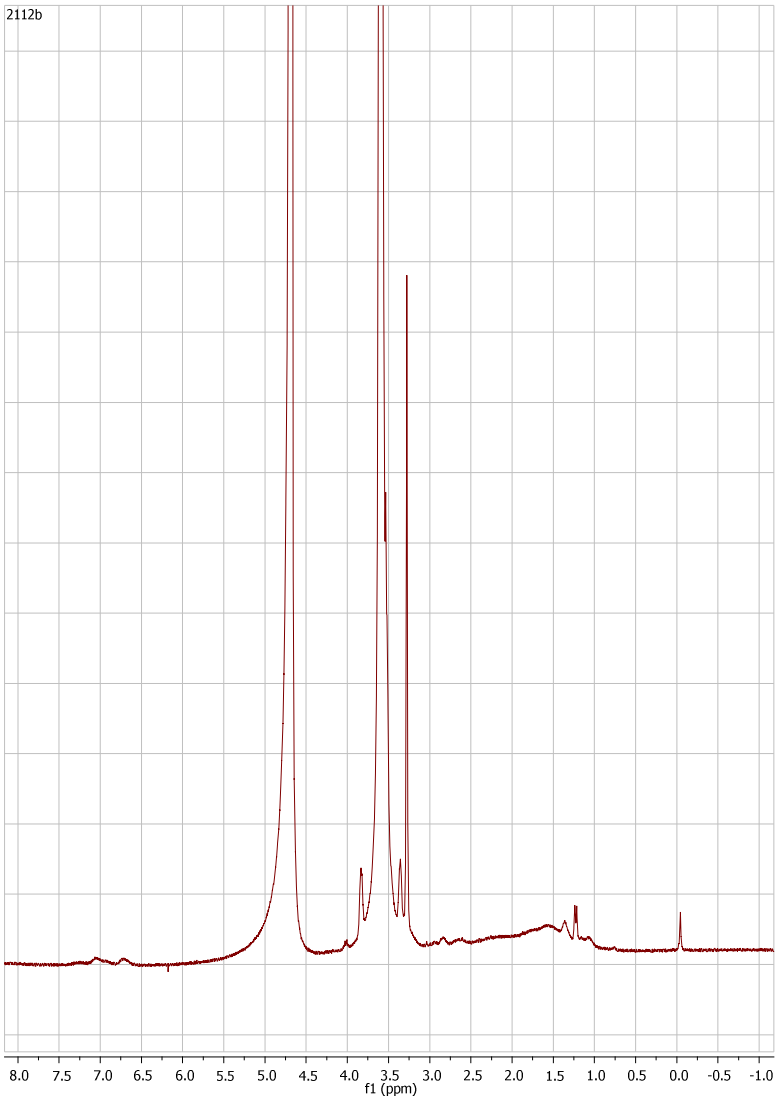


Figure S3. Representative ^{1}H NMR spectrum of polymer 3 in D_2O.

Bioconjugate Chemistry

ARTICLE

pubs.acs.org/bc

Mono-PEGylated Dimeric Exendin-4 as High Receptor Binding and Long-Acting Conjugates for Type 2 Anti-Diabetes Therapeutics

Tae Hyung Kim,[†] Hai Hua Jiang,[†] Seulki Lee,[‡] Yu Seok Youn,[∥] Chan Woong Park,[†] Youngro Byun,[§] Xiaoyuan Chen,[‡] and Kang Choon Lee*[,†]

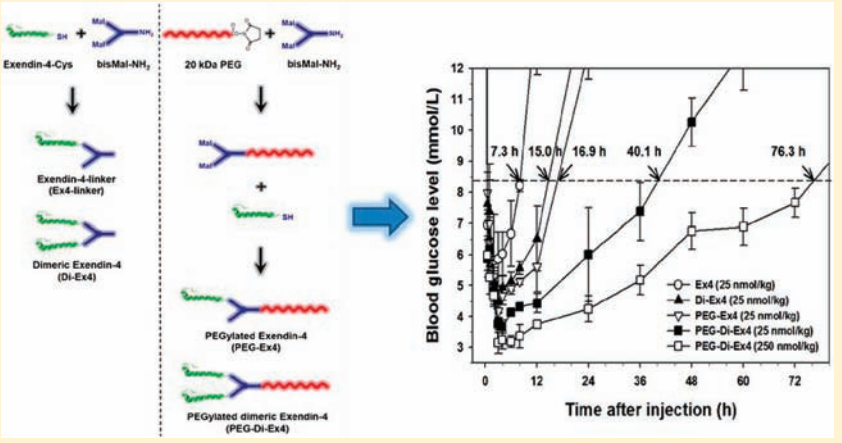
[†]College of Pharmacy, SungKyunKwan University, 300 Chonchon-dong, Jangan-ku, Suwon City 440-746, Korea

[‡]Laboratory of Molecular Imaging and Nanomedicine, NIBIB, NIH, Bethesda, Maryland 20892, United States

[∥]College of Pharmacy, Pusan National University, Busan 609-735, Korea

[§]College of Pharmacy, Seoul National University, Seoul 151-742, Korea

ABSTRACT: Dimerization is viewed as the most effective means of increasing receptor binding affinity, and both dimerization and PEGylation effectively prolong the life spans of short-lived peptides and proteins in vivo by delaying excretion via the renal route. Here, we describe the high binding affinities of two long-acting exendin-4 (Ex4) conjugates, dimerized Ex4 (Di-Ex4) and PEGylated Di-Ex-4 (PEG-Di-Ex4). Di-Ex4 and PEG-Di-Ex4 were prepared using cysteine and amine residue specific coupling reactions using Ex4-Cys, bisMal-NH_2, and activated PEG. The Ex4 conjugates produced were of high purity (>98.5%), as determined by size-exclusion chromatography and MALDI-TOF mass spectrometry. The receptor binding affinity of Di-Ex4 on RIN-m5F cells was 3.5-fold higher than that of Ex4, and the in vivo antihyperglycemic efficacy of Di-Ex4 was also greater than that of native Ex4 in type 2 diabetic db/db mice. Furthermore, Di-Ex4 and PEG-Di-Ex4 were found to have greater blood circulating $t_{1/2}$ and AUC_{inf} values than native Ex4 by 2.7- and 13.7-fold, and by 4.0- and 17.3-fold, respectively. Accordingly, hypoglycemic durations were greatly increased to 15.0 and 40.1 h, respectively, at a dose of 25 nmol/kg (native Ex4 7.3 h). The results of this study show that combined dimerization and PEGylation are effective when applied to Ex4, and suggest that PEG-Di-Ex4 has considerable potential as a type 2 anti-diabetic agent.



INTRODUCTION

Exendin-4 (Ex4), a naturally occurring dipeptidyl peptidase-IV (DPP IV) resistant GLP-1 analogue and GLP-1 receptor agonist, was first isolated from the saliva of the Gila monster and shares 53% homology with glucagon-like peptide-1 (GLP-1).[1−3] Ex4 has several beneficial anti-diabetic effects in type 2 diabetes. It increases the glucose-dependent enhancement of insulin secretion, suppresses inappropriately high glucagon secretion, reduces gastric mobility and food intake, and increases β-cell mass.[4−6] Overall, Ex4 is viewed as a potent therapeutic agent for type 2 diabetic patients, but its short circulating life (4−6 h) means that high doses must be administered frequently. A previous detailed examination revealed that the short biological half-life of Ex4 is mainly due to its rapid glomerular filtration, which can be attributed to its low molecular weight (~4.2 kDa).[7,8]

To overcome this problem, numerous approaches, such as the use of long-acting incretin mimetics and/or sustained release mimetics, have been devised to improve the therapeutic level of Ex4.[9−12] In particular, our group has previously investigated the use of Ex4 bioconjugated with vitamins, fatty acids, and bile acids for oral or long-acting delivery.[13−16] More specifically, the strategies used included modifying GLP-1 receptor agonists by conjugating them with poly(ethylene glycol). The resulting PEGylated GLP-1 receptor agonists showed typical long-acting characteristics and enhanced circulation half-lives.[9,10]

Dimeric interactions are frequently used in nature to increase the affinity of ligand−receptor interactions,[17,18] and thus, this strategy has attracted the interest of researchers. As a result, several research groups have already produced compounds that enhance interactions between ligands and target cells.[19] Goel et al. radiolabeled divalent and tetravalent scFv's of mAb CC49 with ^{99m}Tc and analyzed the imaging potentials of these

Received: September 9, 2010
Revised: January 19, 2011
Published: March 14, 2011

ACS Publications © 2011 American Chemical Society

radio-immunoconjugates.[20] Similarly, dimerized interferon-α2b[21] and dimerized adducts of therapeutic antibodies[22] have also been examined.

The covalent attachment of poly(ethylene glycol) (PEG) to peptides and proteins (PEGylation) provides a means of enhancing their therapeutic values. This technique increases molecular size, shields metabolic sites, and masks immunogenic sites and, thus, increases plasma half-lives and in vivo stabilities and diminishes immunogenicity. Moreover, PEGylated peptides/proteins are much more resistant to renal clearance because the linear hydrophilic nature of PEG molecule effectively increases Stokes' radius,[23−25] and furthermore, PEGylation has been shown to prolong the pharmacokinetic and pharmacodynamic properties of these entities.[26−28]

On the basis of the above, we undertook to synthesize PEG-conjugated dimeric Ex4. We hypothesized that PEG-conjugated dimeric Ex4 would retain the advantages of PEGylation and have higher affinity for pancreatic β-cells. In the present study, we prepared dimerized Ex4 and PEG conjugated dimerized Ex4 constructs and then explored their physicochemical and biological characteristics. In addition, the pharmacokinetic and anti-diabetic characteristics were investigated using a diabetic mouse model to determine which has much better anti-diabetic properties.

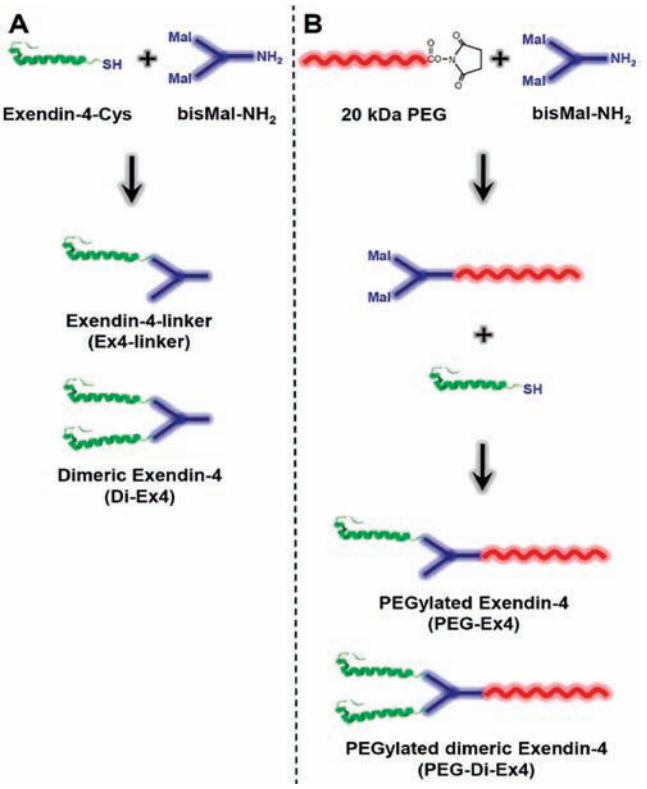
EXPERIMENTAL PROCEDURES

Materials. Exendin-4-Cys (M_w: 4290.7) with the sequence HGEGTFTSDLSKQMEEEAVRLFIEWLKNGGPSSGAPPPSC was purchased from AnyGen Co. (Gwangju, Republic of Korea (ROK)). Bis-Maleimide amine (bisMal-NH_2, M_w: 660.64) and succinimidyl activated monomethoxy PEG (M_w: 20 kDa) were purchased from Quanta Biodesign (Powell, Ohio) and Nektar Therapeutics (Huntsville, AL), respectively. All other reagents, unless otherwise indicated, were purchased from Sigma-Aldrich (Saint Louis, MO) and were used as received.

Experimental Animals. Type 2 diabetic C57BL/6 db/db mice (male, 4−5 weeks old) were purchased from the Korean Research Institute of Bioscience and Biotechnology (Daejon, ROK). ICR mice (male, 4−5 weeks old), weighing 16−18 g, were purchased from the Hanlim Experimental Animal Laboratory (Seoul). Animals were cared for in accordance with the National Institute of Health (NIH) guidelines for the care and use of laboratory animals (NIH publication 80−23, revised in 1996). Animals were housed in groups of 6−8 under a 12 h light/dark cycle (lights on at 6 a.m.), allowed food and water ad libitum, and were acclimatized for 2 weeks. This study was approved by the Ethical Committee on Animal Experimentation at SungKyunKwan University.

Preparation of Dimerized Exendin-4 (Di-Ex4). As shown in Scheme 1A, Di-Ex4 was synthesized by utilizing a coupling reaction between bis-maleimide amine (bisMal-NH_2, M_w: 660.64) and the cysteine residues of Ex4 in organic solvent using a modification of a previously described procedure.[13,14] Briefly, 100 μL of bisMal-NH_2 (1.5 mg/mL in dimethylsulfoxide (DMSO) containing 0.3% triethylamine (TEA)) was reacted with 100 μL of Ex4 (10 mg/mL in DMSO with 0.3% TEA) (an Ex4/bisMal-NH_2 molar ratio of 2) at room temperature with gentle mixing for 1 h. The reaction was then stopped by adding 100 μL of stop solution (deionized water containing 1% trifluoroacetic acid (TFA)). Di-Ex4 was purified from reaction mixtures using semipreparative reversed-phase HPLC (RP-HPLC) and a Capcell-pak RP-18 column (250 × 10 mm, 5 μm, Shiseido, Japan) operated at

Scheme 1. Syntheses of Di-Exendin-4 and PEG-Di-Exendin-4



room temperature and a constant flow rate of 5.0 mL/min. Eluate was monitored using a 215 nm UV detector. The mobile phase consisted of 0.1% TFA in deionized water (eluent A) and acetonitrile containing 0.1% TFA (eluent B) using a linear gradient (36−42% B over 30 min). Eluting peaks were collected separately, acetonitrile was then removed with nitrogen, and the solutions so obtained were concentrated using a Centricon-10 (M_w cutoff 3000, Millipore Corp., Billerica, MA). Products obtained were characterized by analytical size-exclusion chromatography and MALDI-TOF mass spectroscopy, and stored at 4 °C until required.

Preparation of PEGylated Di-Exendin-4 (PEG-Di-Ex4). As shown in Scheme 1B, bisMal-NH_2 conjugated Ex4 and PEG (PEG-Ex4 and PEG-Di-Ex4) were prepared using a modification of a previously described procedure.[14,28] Briefly, 10 mg of activated PEG (M_w: 20 kDa) was mixed with 0.3 mg of bisMal-NH_2 in 5 mL of a mixture of dimethylsulfoxide and dimethylformamide (70:30) containing 0.3% dimethylaminopyridine at room temperature for 1 h. To this mixture was added 2 mg of Ex4, and the reaction was then allowed to continue for another 1 h. The reaction was then quenched by adding 5 mL of 1% TFA/DW and shaking thoroughly. The resulting mixture was quickly transferred to a Sephadex G-25 desalting column (GE Healthcare Life Sciences, Piscataway, NJ, USA) previously equilibrated with 10 mM PBS. The first fraction was collected and centrifuged using a Centricon-10 concentrator (Millipore Amicon, Beverly, MA, USA), and a portion (0.2 mL) of the supernatant (containing PEG-Ex4 and PEG-Di-Ex4) was purified by size-exclusion chromatography using a Biosep SEC-S2000 column (300 × 7.8 mm, 5 μm, Phenomenex, Torrance, CA) and eluted with 10 mM PBS (pH 7.4) at a flow rate of 0.75 mL/min. Eluates were monitored at

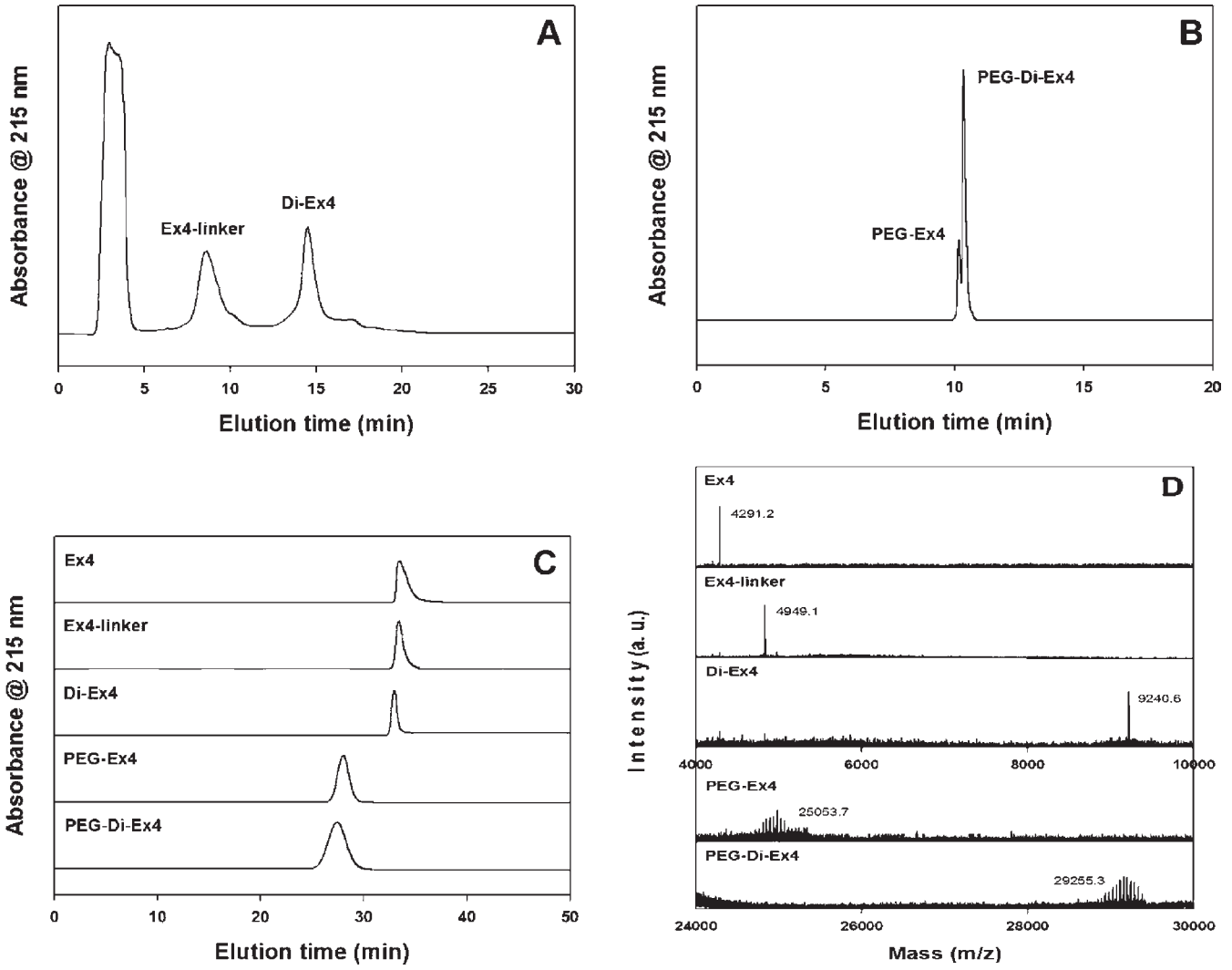


Figure 1. Purification and characterization of Di-Exendin-4 and PEG-Di-Exendin-4. (A) Reverse-phase HPLC chromatograms of Ex4 dimerization reaction mixtures. (B) Size-exclusion chromatography of Ex4 PEGylation reaction mixtures. (C) Size-exclusion chromatography of purified Ex4 analogues. (D) Total mass spectra of Ex4 analogues, obtained by MALDI-TOF MS.

215 nm. The products so obtained were characterized by analytical size-exclusion chromatography and MALDI-TOF mass spectroscopy, and stored at 4 °C until required.

Characterizations of Di-Ex4 and PEG-Di-Ex4. Ex4 analogues were characterized by size-exclusion chromatography using a Superdex 200 HR 10/30 column (300 × 10 mm, GE Healthcare Life Sciences, Piscataway, NJ, USA) and eluted with 10 mM PBS (pH 7.4) at a flow rate of 0.6 mL/min. Chromatograms were recorded at 215 nm. MALDI-TOF MS and a Voyager-RP Biospectrometry Workstation (PerSeptive Biosystems, Cambridge, MA) were used to confirm molecular weights. Briefly, sample−matrix solutions were prepared by mixing a 1 μL aliquot with 2 μL of matrix solution (a saturated solution of α-cyanohydroxycinnamic acid (α-CHCA) in 50% of water/ACN containing 0.1% (v/v) TFA). One microliter of this sample−matrix solution was then deposited onto a well of a sample plate and dried rapidly under vacuum. Data generated by 2 ns pulses of a 337 nm nitrogen laser were averaged for each spectrum in reflective mode using positive ion TOF detection and an accelerating voltage of 25 kV.

Receptor-Binding Affinities of Di-Ex4 and PEG-Di-Ex4 to RIN-m5F Cells. The receptor-binding affinities of Ex4 analogues were determined using a modification of a previously described method.[13,14] Briefly, RIN-m5F cells (ATCC, Manassas, VA) were seeded in 12 well plates at 3×10^5 cells per well, grown for 48 h, washed twice with binding buffer (120 mM NaCl, 1.2 mM $MgSO_4$, 13 mM sodium acetate, 5 mM KCl, 1.2 g/L Tris, 2 g/L bovine serum albumin, and 1.8 g/L glucose, pH 7.6), co-treated with the unlabeled Ex4 analogues (final concentrations range: 0.001−1000 nM) with 30 pM of ^{125}I-exendin-4 (9−39, PerkinElmer, Boston, MA), incubated for 2 h at room temperature, and washed three times with chilled PBS containing 1 mg/mL of bovine serum albumin. Cells were then lysed with cell lysis buffer (0.5 N NaOH with 1% SDS) for 15 min, and ^{125}I radioactivity levels were measured using a γ counter (GMI, Inc., Ramsey, MN).

Proteolytic Stability Tests. The proteolytic stabilities of the Ex4 analogues against rat kidney homogenate and plasma were evaluated as previously described,[13] by incubating samples at 37 °C in rat kidney homogenate and plasma and measuring their degradation profiles by reverse-phase HPLC.

Radioiodination. Radioiodinated samples were prepared using a modification of the IODO-GEN method.[29,30] In brief,

dx.doi.org/10.1021/bc100404x |*Bioconjugate Chem.* 2011, 22, 625–632

100 μL of water-soluble Bolton-Hunter reagent (*N*-sulfosuccinimidyl-3,4-hydroxyphenyl propionate; 0.13 mg/mL, 36 nmol) in 10 mM PBS (pH 7.0) was mixed with 150 μL of the Ex4 analogues (0.5 mg/mL, 18 nmol) at room temperature for 90 min and briefly dialyzed to remove the reagent. Separately, a 100 μL aliquot of an IODO-GEN (Pierce, Rockford, IL) solution in methylene chloride (0.5 mg/mL) was dispensed into a fresh tube and evaporated under a nitrogen stream. To these tubes were added 50 μL aliquots of each sample (approximately 50 μg/mL) and 50 μCi of $Na^{125}I$ (Perkin-Elmer, Boston, MA) diluted with 10 mM PBS (pH 7.4). Reactions were allowed to proceed for 5 min, and then supernatants were loaded onto a Sephadex G-25 desalting column (GE Healthcare Life Sciences, Piscataway, NJ) previously equilibrated with 10 mM of PBS. ^{125}I-labeled fractions were collected and stored in 10 mM PBS (pH 7.4), and their radioactivities were measured by γ counting (CobraTM Series Auto-Gamma Counting System, Packard Instruments Co., Groningen, The Netherlands). The specific radioactivities of radioiodinated samples were in the range $(4.8-5.9) \times 10^5$ cpm/μg.

Pharmacokinetics Tests. The pharmacokinetics of the Ex4 analogues were evaluated using a modification of a previously described method.[26,28] Radioiodinated samples were administered to ICR mice (~2 μg, ~25 nmol/kg body wt., i.p.). Mice were sacrificed at predetermined times by heart puncture for blood collection, and the radioactivities of 0.2 mL blood samples were determined by γ counting and used to calculate blood concentrations. Pharmacokinetic parameters were calculated by two-compartmental analysis using *WinNolin* v 1.1 (Scientific Consulting, Inc., Cary, NC). In particular, AUC_{inf} values were obtained by computing areas under the curve from zero to infinity using the trapezoidal rule. Circulating half-lives ($t_{1/2}$) were calculated using the same method.

Antihyperglycemic Efficacies in Fasted Type 2 Diabetic *db/db* Mice. Oral glucose tolerance testing (OGTT) was performed to evaluate the antihyperglycemic efficacies of the Ex4 analogues after an overnight fast (18 h), as previously described.[26,28] One hour prior to first oral glucose challenge (0.2 mL, 1.0 g/kg body wt.) (0 h), male *db/db* mice (n = 4/group, 8−9 weeks old) were administered saline, Ex4, or Di-Ex4 (i.p., 25 nmol/kg body wt.). Injection dose was prepared based on the peptide portion of the conjugate. A drop of blood was drawn from a tail vein of each animal at 0, 0.25, 0.5, 0.75, 1, 1.5, 2, and 3 h, and blood glucose levels were determined using a one-touch blood glucose meter (ACCU-CHEK Sensor, Roche Diagnostics Corp., USA). Antihyperglycemic efficacies were evaluated by calculating the total hypoglycemic degrees (HD_{total}; using $HD_{total} = AUC_{saline,\ 0-3\ h} - AUC_{test,\ 0-3\ h}$).

Hypoglycemic Efficacies Tests in Nonfasted *db/db* Mice. Hypoglycemic efficacies of Ex4 analogues were evaluated using a modification of a previously described method[13−15] using male *db/db* mice (6−7 weeks old). Under nonfasting conditions with free access to food and water, animals received a single i.p. injection of saline, Ex4, Di-Ex4, PEG-Ex4, or PEG-Di-Ex4 (5, 25, 250 nmol/kg body wt.). Blood glucose levels were monitored using the procedure mentioned above. In addition, a drop of blood was drawn from a tail vein of each animal at different times (0, 0.5, 1, 2, 3, 4, 6, 8, 12, 24, 36, 48, 60, 72, 96, 108 h) and blood glucose levels were determined using a one-touch blood glucose meter (ACCU-CHEK Sensor, Roche Diagnostics Corp., USA). Hypoglycemic efficacies are expressed as HD_{total}, as mentioned above, but measurement times differed in the saline, Ex4, Di-Ex4, PEG-Ex4, and PEG-Di-Ex4 groups (Figures 4B and 5). In addition, hypoglycemic durations to a blood glucose level of <8.35 nmol/L (150 mg/dL) were also checked.

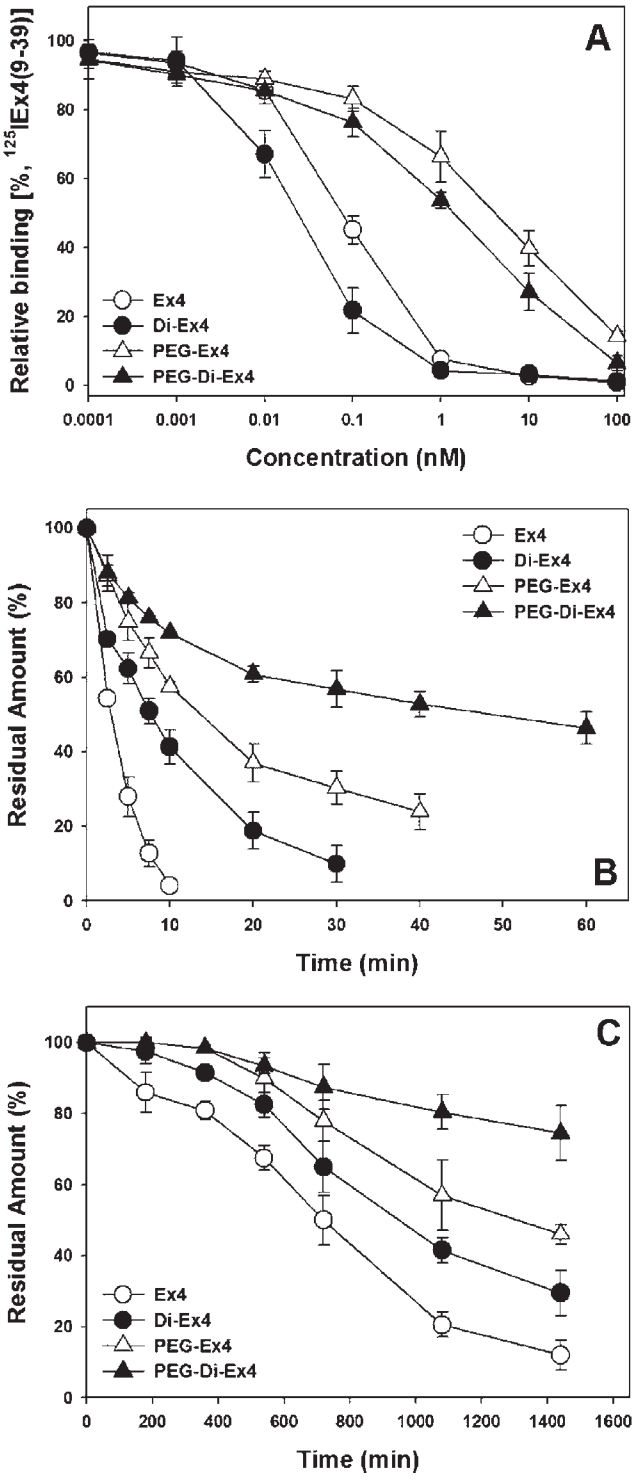


Figure 2. In vitro biological activity and proteolytic stability testing of Di-Exendin-4 and PEG-Di-Exendin-4. (A) Receptor-binding affinities of Exendin-4 analogues in RIN-m5F cells. (B) Stability testing of Ex4 analogues in rat kidney homogenate. (C) Stability testing of Ex4 analogues in rat plasma. Data represent the means ± SDs of five results.

Data Analysis. Data are presented as means ± SDs. Statistical significances were determined using one-way ANOVA, and P values of <0.05 were considered statistically significant.

dx.doi.org/10.1021/bc100404x |*Bioconjugate Chem.* 2011, 22, 625–632

Table 1. Pharmacokinetic Parameters of Ex4, Di-Ex4, PEG-Ex4, and PEG-Di-Ex4 in ICR Mice[a]

PK parameters	Ex4	Di-Ex4	PEG-Ex4	PEG-Di-Ex4
AUC_{inf} (ng/mL × h)	109.8 ± 28.4	433.7 ± 36.2	779.1 ± 42.7	1893.7 ± 152.4
Cl/F (mL/h)	9.1 ± 1.7	2.3 ± 0.4	1.2 ± 0.2	0.4 ± 0.1
$t_{1/2}$ (h, β)	2.1 ± 0.3	5.6 ± 1.3	11.8 ± 2.7	28.7 ± 2.4

[a] Data are means ± SDs. AUC_{inf} = area under the curve from zero to infinity; Cl/F = systemic clearance from zero time to last time; $t_{1/2}$ = half-life during the elimination phase (β).

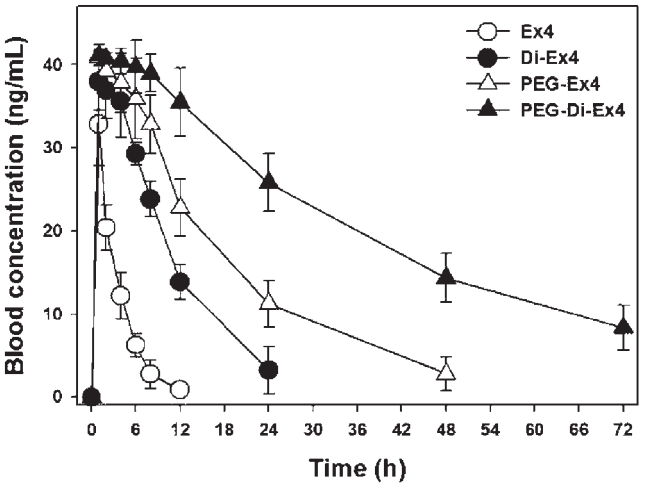


Figure 3. Pharmacokinetic profiles of Di-Exendin-4 and PEG-Di-Exendin-4 in ICR mice administered ~2 μg (approximately 25 nmol/kg) i.p. Data represent four mice and are presented as means ± SD.

Pharmacokinetic parameters were calculated by two-compartmental analysis (WinNolin, Scientific Consulting, Inc., Cary, NC).

RESULTS

Preparation and Characterization of Di-Ex4 and PEG-Di-Ex4. Di-Ex4 and PEG-Di-Ex4 were synthesized as described above, and finally, we obtained four different products containing control molecules (Scheme 1, Figure 1A,B). The four peaks in the size exclusion chromatogram corresponded to unreacted; Ex4 (elution time 33.4 min), Ex4-linker (elution time 33.3 min), Di-Ex4 (elution time 32.9 min), PEG-Ex4 (elution time 28.0 min), and PEG-Di-Ex4 (elution time 27.4 min). The size-exclusion chromatograms of the three purified Ex4 analogues showed that separations resulted in high-purity products (Figure 1C). The apparent molecular weights (M_w) of the three analogues were determined by MALDI-TOF MS. As shown in Figure 1D, their experimental mass-to-charge (m/z) ratios closely matched calculated values.

Receptor-Binding Affinities and Proteolytic Stabilities of Di-Ex4 and PEG-Di-Ex4. The receptor-binding affinities of Ex4 analogues were examined in RIN-m5F cells, which express high levels of GLP-1 receptor (GLP-1R). Di-Ex4 was found to have 3.5-fold higher affinity for GLP-1R (IC_{50} = 0.02 ± 0.12 nM) than native Ex4 (IC_{50} = 0.07 ± 0.05 nM), as shown in Figure 2A. Furthermore, PEG-Di-Ex4 was found to have 3.1-fold higher affinity for GLP-1R (IC_{50} = 1.34 ± 0.19 nM) than PEG-Ex4 (IC_{50} = 4.15 ± 0.14 nM) (Figure 2A). Ex4 was rapidly degraded by rat kidney homogenate (Figure 2B), with a $t_{1/2}$ of 1.88 ± 0.04 min, and Di-Ex4 was 4.99-fold more stable ($t_{1/2}$ = 9.38 ± 2.31 min).

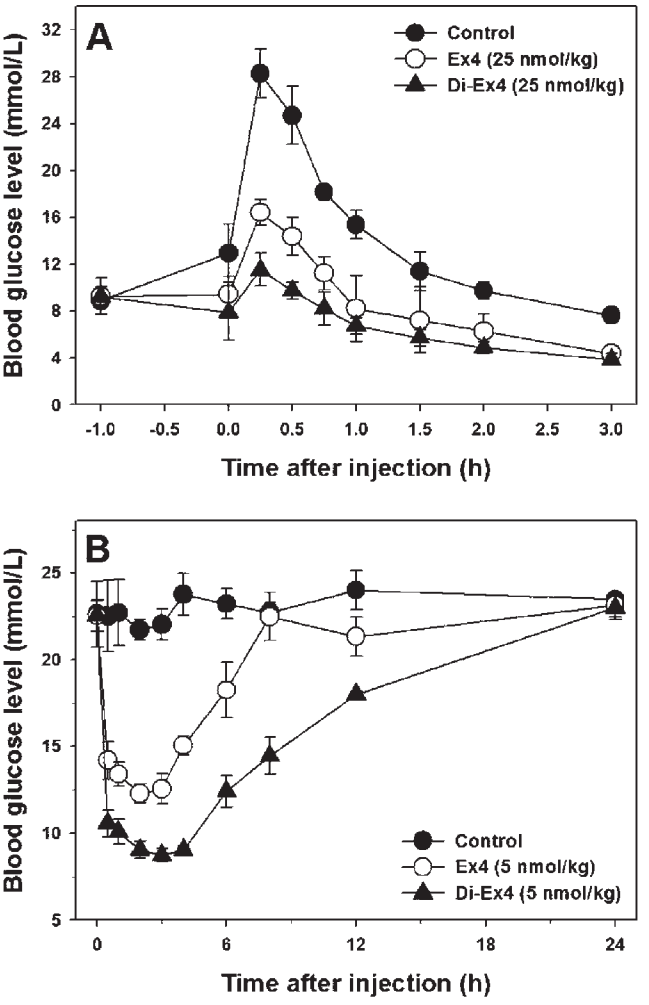


Figure 4. Antihyperglycemic activities of Exendin-4 and Di-Exendin-4 as determine by oral glucose tolerance testing in type 2 diabetic *db/db* mice fasted for 18 h and pretreated with each agent (25 nmol/kg, i.p.) (A). Hypoglycemic efficacies of low dose (5 nmol/kg) Exendin-4 and Di-Exendin-4 in nonfasted *db/db* mice (B). Data represent five mice and are presented as means ± SDs.

Furthermore, PEG-Di-Ex4 was 57.06-fold more stable than native Ex4 ($t_{1/2}$ = 107.29 ± 11.99 min) (Figure 2B). And plasma degradation of Ex4 analogues (Figure 2C) showed similar profile to kidney homogenate.

Pharmacokinetics Tests. The blood concentration vs time curves of Ex4 analogues were i.p. administered. As shown in Table 1 and Figure 3, Ex4 was rapidly removed from the circulation with a circulating $t_{1/2}$ of 2.1 ± 0.3 h, whereas Di-Ex4 was found to have a 2.66-fold longer presence ($t_{1/2}$ = 5.6 ± 1.3 h). Specifically, the $t_{1/2}$ of PEG-Di-Ex4 was 28.7 ± 2.4 h, which was

dx.doi.org/10.1021/bc100404x |*Bioconjugate Chem.* 2011, 22, 625–632

13.67 times greater than that of native Ex4, and its AUC_{inf} value (1893.7 ± 152.4 ng/mL × h) was 17.25 times greater than that of native Ex4 (109.8 ± 28.4 ng/mL × h). In addition, the systemic clearances (Cl/F) of Di-Ex4 and Di-PEG-Ex4 (2.3 ± 0.4 and 0.4 ± 0.1 mL/h) were 3.96- and 22.75-fold lower than those of native Ex4 (9.1 ± 1.7 mL/h).

Antihyperglycemic Efficacies in Fasted Type 2 Diabetic *db/db* Mice. The in vivo biological activities of Ex4 and of Di-Ex4 were examined in fasted type 2 diabetic *db/db* mice by performing oral glucose tolerance testing (OGTT) at 60 min after the i.p. administration of 25 nmol/kg. Blood glucose levels in the control group rapidly increased to 28.2 ± 1.9 mmol/L at 0.25 h after glucose administration and then decreased slowly. In accordance with their observed in vitro biological activities, maximum plasma glucose levels at 0.25 h after the administration of Di-Ex4 (11.5 ± 0.5 mmol/L; $P > 0.3$) were lower than that of Ex4 (16.3 ± 0.7 mmol/L) (Figure 4A). These results suggest that Di-Ex4 has higher in vivo biological activity than Ex4.

Hypoglycemic Duration Tests in Nonfasted *db/db* Mice. The hypoglycemic effects of the Ex4 analogues were examined at two doses (5 and 25 nmol/kg, i.p.) in *db/db* mice. At a dose of 5 nmol/kg, as shown in Figure 4B, the lowest glucose level (8.7 ± 0.5 mmol/L; $P > 0.2$) in Di-Ex4-treated mice was lower than in Ex4 treated mice (12.6 ± 0.4 mmol/L). At a dose of 25 nmol/kg, the HD_{total} values of Di-Ex4 and PEG-Di-Ex4 (504.1 ± 108.9 and 1427.6 ± 187.4 mmol × h/L, $P < 0.005$, respectively) were 1.65 and 4.66 times greater than that of native Ex4 (306.3 ± 86.3 mmol × h/L) (Figure 5A). Furthermore, hypoglycemic durations in Di-Ex4 or PEG-Di-Ex4 mice were much greater than Ex4, and the times required to rebound to a glucose level of 8.35 mmol/L were ~15.0 h and ~40.1 h in Di-Ex4 and PEG-Di-Ex4 mice as compared with ~7.3 h in Ex4 treated mice (Figure 5B). In particular, at the highest dose administered (250 nmol/kg), the $t_{\sim 8.35\ mmol/L}$ value of PEG-Di-Ex4 was 76.3 h, which means that a single PEG-Di-Ex4 administration stabilized blood glucose levels for nearly 3 days in *db/db* mice.

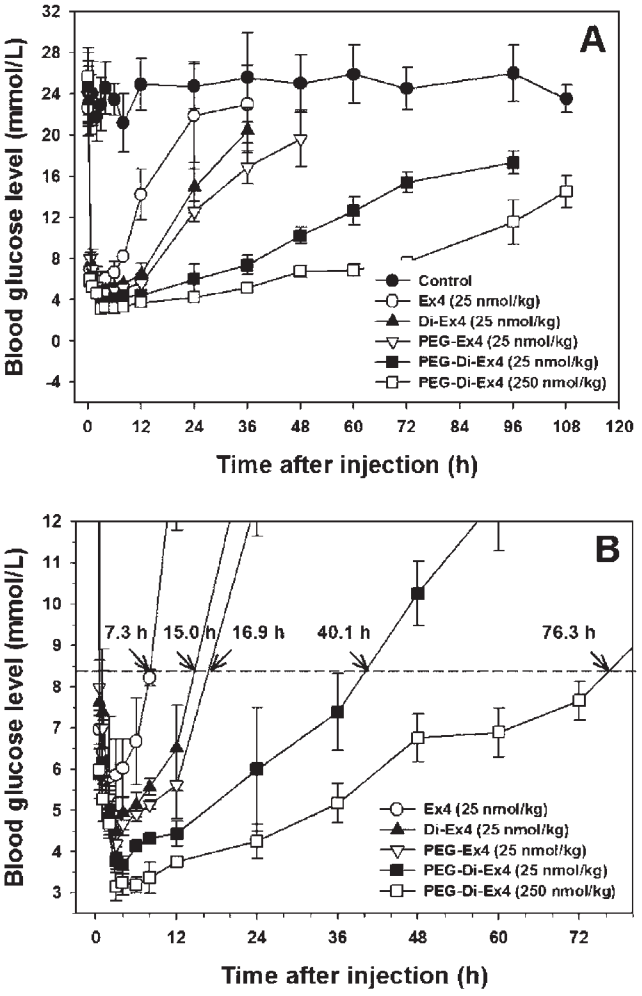


Figure 5. Hypoglycemic efficacies of high dose (25/250 nmol/kg) Exendin-4 analogues in nonfasted *db/db* mice (A). The focused profile of A (0−80 h, 3−12 mmol/L). Times depict hypoglycemic duration rebound to 8.35 mmol/L (B). Data represent five mice and are presented as means ± SDs.

DISCUSSION

Type 2 diabetes is a chronic, deteriorative metabolic disease, characterized by progressive hyperglycemia followed by dysfunctional insulin secretion and/or its impaired utilization. Progressive β-cell deficiencies associated with apoptosis and a malfunctional GLP-1 response after ingestion have encouraged researchers to consider incretin-based diabetic therapies.[1,7] Intensive research and developmental efforts have resulted in the clinical application of a DPP IV resistant GLP-1 receptor Ex4 agonist, which was first isolated from lizard saliva.[2,31]

Although the coadministrations of Ex4 and traditional hypoglycemic agents achieve better glycemic control and lower levels of glycated hemoglobins (HbA_{1C}) in serum and lower body weights,[31] the demand for more efficient incretin-based anti-diabetics has not been satisfied by Ex4 because of its short biological half-life and its rapid renal clearance.[8] In addition, recent research on long-acting incretin mimetics or sustained-release formula Ex4 systems has achieved more efficient glycemic control than twice-daily Ex4 injections.[32]

To develop efficient incretin-based anti-diabetics with protracted hypoglycemic efficacy in type 2 diabetes, we produced high binding affinity, long-acting Ex4 analogues, that is, Di-Ex4 (dimerized Ex4) and PEG-Di-Ex4 (PEGylated Di-Ex4), by PEGylating dimerized Ex-4. Di-Ex4 and PEG-Di-Ex4 were successfully prepared using cysteine and amine residue-specific coupling reactions using Ex4-Cys, bisMal-NH_2, and activated PEG (Scheme 1, Figure 1A,B). Interestingly, cysteine-specific (C-terminal domain) conjugations prevented the serious activity reduction caused by N-terminal conjugation (the N-terminal domain is known to play a crucial role during cellular response to GLP-1 signaling[9,33,34]). The Ex4 analogues were obtained in high purity (>98.5%), as determined by size-exclusion chromatography and MALDI-TOF (Figure 1C,D).

After dimerization, peptide and protein drugs often have higher binding affinities and therapeutic potencies than native drugs.[17−22] In the present study, we found that Di-Ex4 had 3.5-fold higher in vitro receptor-binding affinity than Ex4 (Figure 2A). Furthermore, in vivo OGTT results showed that the antihypoglycemic efficacy of Di-Ex4 was greater than that of native Ex4 (Figure 4A). However, the receptor binding affinity of PEG-Di-Ex4 was reduced by the presence of PEG (M_w: 20 kDa), which inhibits PEG-Di-Ex4 binding to GLP-1 receptor. Conversely, PEG-Di-Ex4 was found to have much greater resistance to rat kidney homogenate than Di-Ex4 (Figure 2B).

The improvements achieved to date provide reasons to extend the functional lifespan of Ex4 in vivo (Figure 3). In the present

Table 2. Pharmacological Scores of Ex4, Di-Ex4, PEG-Ex4, and PEG-Di-Ex4 in *db/db* Mice[a]

PK parameters	Ex4	Di-Ex4	PEG-Ex4	PEG-Di-Ex4
HD_{total} (5 nmol/kg) (mmol × h/L)	77.3 ± 18.2	161.2 ± 27.7	-	-
HD_{total} (25 nmol/kg) (mmol × h/L)	306.3 ± 86.3	504.1 ± 108.9	640.2 ± 124.2	1427.6 ± 187.4
HD_{total} (250 nmol/kg) (mmol × h/L)	-	-	-	1894.9 ± 193.3
hypoglycemic duration (h) (25 nmol/kg)	7.3	15.0	16.9	40.1
hypoglycemic duration (h) (250 nmol/kg)	-	-	-	76.3

[a] Data are means ± SDs.

study, dimerization and PEGylation greatly improved the pharmacokinetic profile of Ex4 (Table 2 and Figure 3), as the pharmacokinetic profiles of Di-Ex4 and PEG-Di-Ex4 were markedly better than that of Ex4 (their AUCs were 3.95- and 17.25-fold higher and their circulating $t_{1/2}$ values were 2.66- and 13.67-fold greater, respectively, than that of Ex4). Furthermore, the $t_{1/2}$ of Di-PEG-Ex4 in the circulation was 5.13-fold greater than that of Di-Ex4, probably due to the hydrodynamic size increase caused by the attached PEG. It should also be mentioned that Ex4 is a foreign material to mice, because of its reptile origins. So, it has the possibility for immunological side effects and responses. However, PEGylation diminishes immunogenicity, and thus, we suppose that the incorporation of PEG protects PEG-Di-Ex4 from mouse antibodies. The hypoglycemic durations of Di-Ex4 and of PEG-Di-Ex4 in *db/db* mice were also much greater than that of Ex4, regardless of the dose administered. In the present study, a blood glucose level of <8.35 mmol/L (150 mg/dL) was regarded as normal, and euglycemic durations under this value are considered a practical indication of potential for anti-diabetic treatment. The administration of Di-Ex4 or PEG-Di-Ex4 sustained normal glycemia for 2.05 or 5.49 times longer than Ex4. In addition, drug clearance in man is known to be much slower than in rodents, and thus, the anti-diabetic duration of PEG-Di-Ex4 may be substantially greater in man than the ~76 h observed in *db/db* mice in the present study.

Summarizing, both Di-Ex4 and PEG-Di-Ex4 were found to confer therapeutic benefits over Ex4. This study also shows that Di-Ex4 and PEG-Di-Ex4 have high GLP-1 receptor-binding affinity, better pharmacokinetics, and a markedly greater hypoglycemic duration than Ex4. Accordingly, we believe that PEG-Di-Ex4 should be viewed as a potential long-acting treatment for type 2 diabetes.

AUTHOR INFORMATION

Corresponding Author

*To whom correspondence should be addressed. (K. C. Lee) Tel.: +82-31-290-7704; Fax: +82-31-290-7724; E-mail: kclee@skku.edu.

REFERENCES

(1) Meier, J. J., and Nauck, M. A. (2005) Glucagon-like peptide 1(GLP-1) in biology and pathology. *Diabetes Metab. Res. Rev. 21*, 91–117.

(2) Eng, J., Kleinman, W. A., Singh, L., Singh, G., and Raufman, J. P. (1992) Isolation and characterization of exendin-4, an exendin-3 analogue, from Heloderma suspectum venom. *J. Biol. Chem. 267*, 7402–7405.

(3) Davidson, M. B., Bat, G., and Kirkpatrick, P. (2005) Exenatide. *Nat. Rev. Drug Discovery 4*, 713–714.

(4) Kolterman, O. G., Buse, J. B., Fineman, M. S., Gaines, E., Heintz, S., Bicsak, T. A., Taylor, K., Kim, D., Aisporna, M., Wang, Y., and Baron, A. D. (2003) Synthetic exendin-4 (exenatide) significantly reduces postprandial and fasting plasma glucose in subjects with type 2 diabetes. *J. Clin. Endocrinol. Metab. 88*, 3082–3089.

(5) Szayna, M., Doyle, M. E., Betkey, J. A., Holloway, H. W., Spencer, R. G., Greig, N. H., and Egan, J. M. (2000) Exendin-4 decelerates food intake, weight gain, and fat deposition in Zucker rats. *Endocrinology 141*, 1936–1941.

(6) Nielsen, L. L., Young, A. A., and Parkes, D. G. (2004) Pharmacology of exenatide (synthetic exendin-4): a potential therapeutic for improved glycemic control of type 2 diabetes. *Regul. Pept. 117*, 77–88.

(7) Drucker, D. J., and Nauck, M. A. (2006) The incretin system: glucagon-like peptide-1 receptor agonists and dipeptidyl peptidase-4 inhibitors in type 2 diabetes. *Lancet 368*, 1696–1705.

(8) Simonsen, L., Holst, J. J., and Deacon, C. F. (2006) Exendin-4, but not glucagon-like peptide-1, is cleared exclusively by glomerular filtration in anaesthetised pigs. *Diabetologia 49*, 706–712.

(9) Lee, S., Youn, Y. S., Lee, S. H., Byun, Y., and Lee, K. C. (2006) PEGylated glucagon-like peptide-1 displays preserved effects on insulin release in isolated pancreatic islets and improved biological activity in db/db mice. *Diabetologia 49*, 1608–1611.

(10) Tsubery, H., Mironchik, M., Fridkin, M., and Shechter, Y. (2004) Prolonging the action of protein and peptide drugs by a novel approach of reversible polyethylene glycol modification. *J. Biol. Chem. 279*, 38118–38124.

(11) Kim, D., MacConell, L., Zhuang, D., Kothare, P. A., Trautmann, M., Fineman, M., and Taylor, K. (2007) Effects of once-weekly dosing of a long-acting release formulation of exenatide on glucose control and body weight in subjects with type 2 diabetes. *Diabetes Care 30*, 1487–1493.

(12) Kim, J. G., Baggio, L. L., Bridon, D. P., Castaigne, J. P., Robitaille, M. F., Jetté, L., Benquet, C., and Drucker, D. J. (2003) Development and characterization of a glucagon-like peptide 1-albumin conjugate: the ability to activate the glucagon-like peptide 1 receptor in vivo. *Diabetes 52*, 751–759.

(13) Jin, C. H., Chae, S. Y., Son, S., Kim, T. H., Um, K. A., Youn, Y. S., Lee, S., and Lee, K. C. (2009) A new orally available glucagon-like peptide-1 receptor agonist, biotinylated exendin-4, displays improved hypoglycemic effects in db/db mice. *J. Controlled Release 133*, 172–177.

(14) Chae, S. Y., Jin, C. H., Shin, J. H., Son, S., Kim, T. H., Lee, S., Youn, Y. S., Byun, Y., Lee, M. S, and Lee, K. C. (2010) Biochemical, pharmaceutical and therapeutic properties of long-acting lithocholic acid derivatized exendin-4 analogs. *J. Controlled Release 142*, 206–213.

(15) Son, S., Chae, S. Y., Kim, C. W., Choi, Y. G., Jung, S. Y., Lee, S., and Lee, K. C. (2009) Preparation and structural, biochemical, and pharmaceutical characterizations of bile acid-modified long-acting exendin-4 derivatives. *J. Med. Chem. 52*, 6889–6896.

(16) Chae, S. Y., Choi, Y. G., Son, S., Jung, S. Y., Lee, D. S., and Lee, K. C. (2010) The fatty acid conjugated exendin-4 analogs for type 2 antidiabetic therapeutics. *J. Controlled Release 144*, 10–16.

(17) Johansson, S. M., Arnberg, N., Elofsson, M., Wadell, G., and Kihlberg, J. (2005) Multivalent HSA conjugates of 3′-sialyllactose are potent inhibitors of adenoviral cell attachment and infection. *ChemBioChem 6*, 358–364.

(18) Mammen, M., Choi, S. K., and Whitesides, G. M. (1998) Polyvalent interactions in biological systems: implications for design and use of multivalent ligands and inhibitors. *Angew. Chem. Int. Ed. 37*, 2754–2794.

(19) Joosten, J. A., Loimaranta, V., Appeldoorn, C. C., Haataja, S., El Maate, F. A., Liskamp, R. M., Finne, J., and Pieters, R. J. (2004) Inhibition of Streptococcus suis adhesion by dendritic galabiose compounds at low nanomolar concentration. *J. Med. Chem. 47*, 6499–6508.

(20) Goel, A., Baranowska-Kortylewicz, J., Hinrichs, S. H., Wisecarver, J., Pavlinkova, G., Augustine, S., Colcher, D., Booth, B. J., and Batra, S. K. (2001) 99mTc-labeled divalent and tetravalent CC49 single-chain Fv's: novel imaging agents for rapid in vivo localization of human colon carcinoma. *J. Nucl. Med. 42*, 1519–1527.

(21) Chang, C. H., Rossi, E. A., Cardillo, T. M., Nordstrom, D. L., McBride, W. J., and Goldenberg, D. M. (2009) A new method to produce monoPEGylated dimeric cytokines shown with human interferon-alpha2b. *Bioconjugate Chem. 20*, 1899–1907.

(22) Kubetzko, S., Balic, E., Waibel, R., Zangemeister-Wittke, U., and Plückthun, A. (2006) PEGylation and multimerization of the anti-p185HER-2 single chain Fv fragment 4D5: effects on tumor targeting. *J. Biol. Chem. 281*, 35186–35201.

(23) Harris, J. M., and Chess, R. B. (2003) Effect of pegylation on pharmaceuticals. *Nat. Rev. Drug Discovery 2*, 214–221.

(24) Veronese, F. M., and Pasut, G. (2005) PEGylation, successful approach to drug delivery. *Drug Discovery Today 10*, 1451–1458.

(25) Kang, J. S., Deluca, P. P., and Lee, K. C. (2009) Emerging PEGylated drugs. *Expert Opin. Emerg. Drugs 14*, 363–380.

(26) Chae, S. Y., Chun, Y. G., Lee, S., Jin, C. H., Lee, E. S., Lee, K. C., and Youn, Y. S. (2009) Pharmacokinetic and pharmacodynamic evaluation of site-specific PEGylated glucagon-like peptide-1 analogs as flexible postprandial-glucose controllers. *J. Pharm. Sci. 98*, 1556–1567.

(27) Uchio, T., Baudys, M., Liu, F., Song, S. C., and Kim, S. W. (1999) Site-specific insulin conjugates with enhanced stability and extended action profile. *Adv. Drug Delivery Rev. 35*, 289–306.

(28) Lee, S. H., Lee, S., Youn, Y. S., Na, D. H., Chae, S. Y., Byun, Y., and Lee, K. C. (2005) Synthesis, characterization, and pharmacokinetic studies of PEGylated glucagon-like peptide-1. *Bioconjugate Chem. 16*, 377–382.

(29) Shin, B. S., Kim, C. H., Lee, M. N., Hur, M. W., Lee, K. C., Youn, Y. S., and Yoo, S. D. (2006) Pharmacokinetics of 125I-GST-TatdMt, a recombinant fusion protein possessing potent anti-obesity activity, after intravenous, nasal, oral, and subcutaneous administration. *Regul. Pept. 140*, 74–80.

(30) Youn, Y. S., Na, D. H., Yoo, S. D., Song, S. C., and Lee, K. C. (2005) Carbohydrate-specifically polyethylene glycol-modified ricin A-chain with improved therapeutic potential. *Int. J. Biochem. Cell Biol. 37*, 1525–1533.

(31) Kendall, D. M., Riddle, M. C., Rosenstock, J., Zhuang, D., Kim, D. D., Fineman, M. S., and Baron, A. D. (2005) Effects of exenatide (exendin-4) on glycemic control over 30 weeks in patients with type 2 diabetes treated with metformin and a sulfonylurea. *Diabetes Care 28*, 1083–1091.

(32) Drucker, D. J., Buse, J. B., Taylor, K., Kendall, D. M., Trautmann, M., Zhuang, D., and Porter L for the DURATION-1 Study Group. (2008) Exenatide once weekly versus twice daily for the treatment of type 2 diabetes: a randomised, open-label, non-inferiority study. *Lancet 372*, 1240−1250.

(33) Göke, R., Fehmann, H. C., Linn, T., Schmidt, H., Krause, M., Eng, J., and Göke, B. (1993) Exendin-4 is a high potency agonist and truncated exendin-(9−39)-amide an antagonist at the glucagon-like peptide 1-(7−36)-amide receptor of insulin-secreting beta-cells. *J. Biol. Chem. 268*, 19650–19655.

(34) Al-Sabah, S., and Donnelly, D. (2003) A model for receptor-peptide binding at the glucagon-like peptide-1 (GLP-1) receptor through the analysis of truncated ligands and receptors. *Br. J. Pharmacol. 140*, 339–346.

Bioconjugate Chemistry

ARTICLE

pubs.acs.org/bc

Activation of Circularly Permutated β-Lactamase Tethered to Antibody Domains by Specific Small Molecules

Miki Kojima,[†] Hiroto Iwai,[†] Jinhua Dong,[†] Shean-Lee Lim,[†] Shigekazu Ito,[§] Koichi Okumura,[§] Masaki Ihara,[‡] and Hiroshi Ueda*[,†,‡,∥]

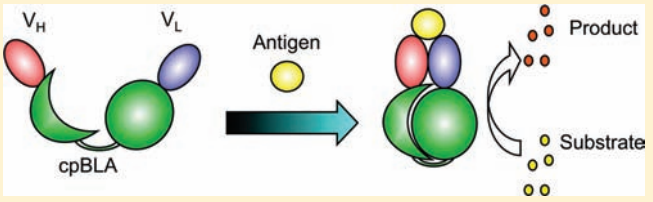
[†]Department of Chemistry and Biotechnology, and [‡]Department of Bioengineering, Graduate School of Engineering, The University of Tokyo, 7-3-1 Hongo Bunkyo-ku, Tokyo 113-8656, Japan

[§]Horiba Ltd., 2 Miyanohigashi, Kisshoin, Minami-ku Kyoto 601-8510, Japan

[∥]PRESTO, JST, Chiyoda-ku, Tokyo 102-0075, Japan

Supporting Information

ABSTRACT: Regulation of enzyme activity either by its substrates or by effectors is generally known as allostery. However, it has been considered hard to alter its effector specificity, despite its potential utility as a sensitive molecular sensor. To this end, we made fusion proteins consisting of an antibody variable region Fv and a circularly permutated TEM-1 β-lactamase cpBLA. Two expression vectors encoding Fv-cpBLA with different antigen specificities were made, in which cpBLA was inserted into the linker region of the single chain Fv that specifically binds either bone-related disease marker osteocalcin (BGP) C-terminal peptide or neonicotinoid insecticide imidacloprid (ICP). The cpBLA having new termini near the active site was activated upon binding with its cognate antigen, owing to the stabilization of tethered Fv by bound antigen. As a result, both Fv-cpBLA showed specific antigen binding as well as antigen-induced enhancement in catalytic activity. Moreover, *E. coli* cells expressing Fv-cpBLA for ICP showed ICP concentration dependent growth in the medium containing ampicillin. The system was also applied to select for Fv-cpBLA linker mutants that confer faster growth. This will be the first of an antibody-based small molecule indicator enzyme.



INTRODUCTION

Regulation of enzyme activity by specific small molecules would be a useful means for point-of-care diagnostics,[1] protein therapies,[2] and synthetic biology.[3−5] The activities of many natural proteins are regulated by posttranslational modifications or noncovalent interactions with an effector molecule. Such regulated enzymes will hereinafter be called protein biosensors. The most popular example of allostery is hemoglobin, a tetrameric protein that binds oxygen in a cooperative manner. The binding of O_2 to one subunit leads to conformational changes that increase the O_2 affinity of other subunits within the holoenzyme. Hemoglobin is thus a sensor and a carrier of oxygen. Allosteric proteins are fairly common in nature,[6] but are relatively difficult to design.[7,8]

Among protein biosensors, those utilizing antibody and enzyme are considered highly useful because of their potential in the range of recognition specificity as well as the affinity of the antibody, which will be enhanced by the signal amplification by biocatalysis. Until now, there have been a number of reports on such sensor proteins using an antibody and enzyme, in which the binding signal is detected as a change in catalytic activity. For example, epitope-inserted β-galactosidase,[9] alkaline phosphatase,[10] and β-lactamase[11] have been successfully controlled for their enzyme activity by the bound antibody to their inserted peptide. Also reported are fusion proteins consisting of a pair of antibody variable domain and β-galactosidase fragment,[12,13] a peptide tag, and a split TEM-1 β-lactamase,[14] and a peptide tag and β-glucuronidase[15] as the protein biosensors based on the protein-fragment complementation assay (PCA) principle. While these attempts are potentially useful for homogeneous immunoassays, they also have room for improvements. For example, epitope-inserted enzymes need the exogenous antipeptide antibody to perform the competitive assay, where one needs careful tuning of the assay conditions to attain acceptable sensitivity. Also, the detection of small chemicals is elusive, unless one can endeavor to obtain specific peptide aptamers. In the cases of PCA-based systems, noncompetitive detection of antigens including small haptens is possible without the need of additional antibodies. However, due to the nature of two-component systems, the system needs careful optimization of the protein concentrations since the error of each dispensed protein amount affects the signal. As a way to address these issues, here we attempt to create a single molecule antibody-based sensor protein utilizing a circularly permutated enzyme.

Received: September 16, 2010
Revised: February 28, 2011
Published: March 29, 2011

ACS Publications © 2011 American Chemical Society

dx.doi.org/10.1021/bc1004125 | *Bioconjugate Chem.* 2011, 22, 633–641

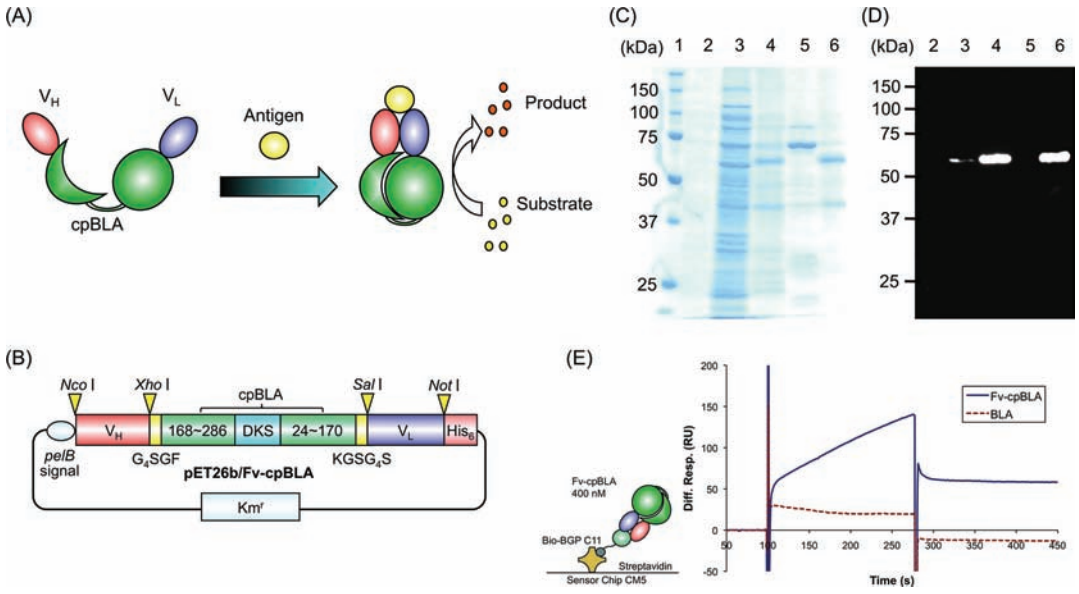


Figure 1. (A) Scheme of Fv-cpBLA and its activation. (B) Schematic structure of the pET26b/Fv-cpBLA expression plasmid. DKS denotes the three residue linker sequence. (C) Expression and purification of FvcpBLA. CBB-stained SDS−PAGE is shown. (1) MW marker, (2) concentrated culture supernatant, (3) soluble fraction from the cell lysate, (4) insoluble fraction from the same, (5) culture supernatant after purification, and (6) purified, refolded protein from the cell lysate. (D) Western blot to detect the His tag. Lanes are the same as in C. (E) Interaction analysis of Fv-cpBLA(BGP) and BGP-C peptide using BIAcore 2000. Sensorgrams for Fv-cpBLA(BGP) and BLA (400 nM each) are shown. *Y*-axis shows the signal difference between bioBGP-C11-immobilized and nonimmobilized streptavidin (440 RU)-immobilized flowcells.

Circular permutation is a method to create mutant proteins that have a set of new N- and C-termini, with the original termini connected by a generally short peptide linker.[16−19] Using this method, while retaining the activity of original protein, functional linkage of large exogenous protein domains can be achieved by choosing appropriate new termini of the protein, which enables the fabrication of various functional fusion proteins.[20−22] For example, Guntas et al. created a maltose/glucose sensor with large switching dynamics, by fusing each circularly permutated maltose binding protein and TEM-1 β-lactamase (cpBLA).[23] As an extension of this approach, here we tried to make a sensor protein Fv-cpBLA in which cpBLA, as a signaling domain of the sensor protein, was inserted to the interdomain linker region of a single-chain antibody (scFv), as a ligand recognition moiety. cpBLA, having new termini near the active site, was expected to be stabilized and activated by the bound antigen, owing to the stabilization of tethered Fv by the bound antigen (Figure 1A). Through this approach, we observed antigen-dependent activation of β-lactamase (BLA) activity *in vitro* for two specific antibody−antigen pairs and also resultant antigen-dependent growth promotion of *E. coli* expressing the fusion protein, in the medium containing ampicillin. The system was also applied to select functional mutant Fv-cpBLAs that confer improved cell growth, from a small library of constructs with randomized linker residues.

MATERIALS AND METHODS

Materials. Oligonucleotides were obtained from Texas Genomics Japan (Tokyo). The BGP C-terminal peptides were obtained from Genscript (Piscataway, NJ). Polymerase chain reaction (PCR) was performed in a T3000 thermocycler (Biometra, Goettingen, Germany). DNA sequences were determined using a CEQ 8000 Genetic Analysis System (Beckman Coulter, Fullerton, CA). Beta-lactamase (BLA) activity was either measured with fluorocillin (Invitrogen, Tokyo, Japan) using a fluorescence plate reader GENios Pro (Tecan, San Jose, CA), or with nitrocefin (Calbiochem) as substrate using a microplate reader Model 680 (Bio-Rad, Heracules, CA). The chemicals and other reagents, unless otherwise indicated, were obtained from Sigma (St. Lois, MO), Nacalai Tesque (Kyoto, Japan), or Wako Pure Chemical Industries (Osaka, Japan).

Construction of the cpBLA Gene. The DNA fragment encoding 24th−70th residues with a short peptide linker (DKS) at the N-terminus was obtained by PCR using the primers BLA24rev (5′-CATTGGGACAAGAGCCACCCAGAAACGCTGGTGAAA-3′) and BLA170for (5′-GGCGATATCGGCTTCATTCAGCT CCGGTTC-3′), encoding the linker and *Eco*RV site (underlined) at their 5′-termini, respectively, pET20b(+) (Merck, Tokyo, Japan) as a template, and *Ex-Taq* DNA polymerase (Takara-Bio). Similarly, the fragment encoding the 168th to 286th residues with the linker at the C-terminus was obtained with BLA168rev (5′-GGCGATAT-CAATGAAGCCATACCAAAC-3′) and BLA286for (5′- TGGGT GGCTCTTGTCCCAATGCTTAATCAGTGA-3′), encoding the *Eco*RV site and the linker at their 5′-termini, respectively, as primers. With the gel-purified PCR products (100 ng each), overlap-extension PCR was performed with *Ex-Taq* DNA polymerase for 10 cycles without primers and 25 cycles with BLA168rev and BLA170-for primers. After purification, the fragment was cloned into pCR4-TOPO (Invitrogen) according to the manufacturer. Plasmid DNA was purified with Wiazrd plus SV Minipreps (Promega) and the sequence of cpBLA confirmed.

Construction of Fv-cpBLA Fusion Protein Expression Vectors. The expression vector for scFv recognizing BGP C-terminal peptide pET/scFv(BGP) was made from a phagemid encoding the scFv (pIT2/scFv(BGP)), which was made from the plasmid encoding V_H and V_L cloned from KTM-219 hybridoma.[24] pIT2/scFv(BGP) was digested with *Nco*I and *Not*I, and was inserted into pET26b(+) (Novagen) digested with the same, resulting in

pET/scFv(BGP). To insert the cpBLA gene into the linker region of scFv, a *Dra*I site was made in the middle by the QuikChange mutagenesis kit (Stratagene) with primers Link-Drarev (5′-GGTGGAGGCGGTTCAGGCTTTAAAGGCAGT GGCGGTGGCGGG-3′) and LinkDrafor (5′-CCCGCCACCG CCACTGCCTTTAAAGCCTGAACCGCCTCCACC-3′) containing the underlined *Dra*I sites. Then, the *Eco*RV-digested cpBLA gene with blunt ends was inserted into *Dra*I-digested pET/scFv(BGP). The clones with objective orientation were selected and designated pET/Fv-cpBLA(BGP) (Figure 1B). Also, pET/Fv-cpBLA(ICP) was constructed similarly from a phagemid vector encoding anti-imidacloprid scFv pIT2/scFv(ICP).

Expression and Purification of Fv-cpBLA(BGP). BL21(DE3, pLysS) cells were transformed with pET/Fv-cpBLA, and the transformed cells were cultured at 37 °C overnight in LB medium containing antibiotics (34 μg/mL chloramphenicol and 50 μg/mL kanamycin) (LBCK) and 1.5% agar. To recover soluble proteins, a single colony was picked and grown overnight at 37 °C in 4 mL of LBCK medium, from which 1 mL was used to inoculate 250 mL of LBCK medium. The cells were cultured at 27 °C until OD_{600} reached 0.6, when final 0.4 mM IPTG was added and incubated for a further 16 h at 27 °C. After centrifugation (6,000*g*, 10 min, 4 °C), 107.5 g of $(NH_4)_2SO_4$ was added to the supernatant and incubated for 16 h at 4 °C. The solution was centrifuged at 10,000*g* for 20 min at 4 °C, and the pellet resuspended in Talon buffer (50 mM sodium phosphate and 300 mM NaCl, pH 7.0). The solution was purified with 0.2 mL of Talon metal affinity resin according to the manufacturer (Clontech, Takara-Bio). The bound proteins were eluted in 0.5 mL fractions with elution buffer (125 mM imidazole in Talon buffer).

To recover Fv-cpBLA from the insoluble fraction, 1 mL of the 4 mL overnight culture was used to inoculate 160 mL of LBCK medium, and cultured and induced with IPTG similarly but at 37 °C. The pellet after centrifugation was homogenized in 25 mL of Talon buffer and sonicated on ice with a supersonic homogenizer VP-15S (Taitec, Saitama, Japan). The pellet after centrifugation at 10,000*g* for 60 min at 4 °C was washed 3 times with 25 mL of 1% Triton X-100 and 1 mM EDTA, pH 8.0, and subsequently centrifuged at 6,000*g* for 15 min at 4 °C. The resultant pellet was dissolved in 10 mL of Talon buffer containing 6 M GdnHCl and purified with Talon resin according to the manufacturer. Refolding of the fusion protein from the insoluble fraction was performed as described.[25]

Western Blotting. Proteins were transferred to a nitrocellulose membrane and detected with anti-BLA polyclonal antibody (Chemicon, Millipore, Tokyo, Japan) and HRP-goat antirabbit Ig (Biosource, Camarillo, CA), or directly with HRP-Penta-His (Qiagen, Tokyo). The washed membrane was developed with a West-Pico detection kit (Pierce Biochemicals) and a LAS-4000 luminoimager (Fujifilm, Tokyo, Japan). The band intensities were quantified using ImageJ software (http://rsb.info.nih.gov/ij/).

ELISA. After ICP-BSA or BSA (10 μg/mL in PBS: 10 mM phosphate, 137 mM NaCl, and 3.7 mM KCl, pH 7.2) was immobilized in Falcon 3912 microplate (BD Bioscience, Tokyo) wells at 4 °C for 16 h, blocked with 25% immunoblock (DS Pharma, Osaka, Japan) at 25 °C, 2 h, and washed 3 times with 0.1% Tween 20 in PBS (PBST), samples in 100 μL 5% immunoblock in PBS were applied and incubated at 25 °C for 1.5 h. After 3 washes with PBST, bound Fv-cpBLA was probed with 1/2000 diluted HRP-Penta-His at 25 °C for 1 h, washed 3 times with PBST, and developed with 100 μL/well substrate solution (100 μg/mL 3,3′,5,5′-tetramethylbenzidine (Sigma) and 0.04 μL/mL H_2O_2, in 100 mM NaOAc, pH 6.0). After incubation for 5 min, the reaction was stopped with 50 μL per well of 1 M sulfuric acid and the absorbance read at 450 nm with a reading at 655 nm as a control.

BLA Activity Assay. The BLA activity was either assayed with the chromogenic substrate nitrocefin or fluorogenic substrate fluorocillin.[26] For nitrocefin, the mixture of protein (5 μL), antigen solution (5 μL), and 90 μL of 1 mM nitrocefin in PBS was incubated at 25 °C for 40 h, and the absorbance was read at 490 nm. In the fluorometric assay, unless otherwise indicated, the sample (10 μL) was added with 90 μL of 0 to 50 μM fluorocillin in PBS, incubated at 25 °C for 30 min, and read for its fluorescence intensity in a white microplate (Corning Costar 3693) at 535 nm with 485 nm excitation. The initial velocity values were fit to the Michaelis−Menten and Hill equations as follows:

$$v_i = \frac{V_{max}[S]^n}{K_m^n + [S]^n}$$

where n is the Hill coefficient, a measure of cooperativity by the nonlinear least-squares algorithm of Kaleidagraph 4.1 (Synergy Software, Reading, PA, USA).

Growth Assay and Selection of the Fv-cpBLA Expressing Strain. BL21(DE3, pLysS) cells were transformed with pET/Fv-cpBLA(ICP) and were cultured at 27 °C overnight in LB medium containing antibiotics (34 μg/mL chloramphenicol and 50 μg/mL kanamycin) (LBCK) and 1.5% agar. A single colony was picked and grown overnight at 27 °C in 4 mL of LBCK medium, from which 4 μL was inoculated to 4 mL of fresh LBCK medium supplemented with 1 mM isopropyl β-D-thiogalactoside (IPTG), 0 or 100 μg/mL ampicillin, and 0 to 10 ng/mL ICP or thiacloprid (TCP). Cells were shaken at 27 °C for 40 h, with periodical monitoring of the optical density with Mini Photo 518R (Taitec, Saitama, Japan).

In the growth assay using a microplate, confluent BL21(DE3, pLysS, pET/Fv-cpBLA) cells from a single colony derived of libraries were 1/1000-diluted into LB medium containing 34 μg/mL chloramphenicol, 30 μg/mL kanamycin, and 0.4 mM IPTG, and cultured at 27 °C until OD_{660} reached 0.4. The cells were divided into the wells at 100 μL each, supplemented with 100 μg/mL ampicillin and ICP as indicated. A flat-bottom transparent microplate (Costar 3799) was shaken at 270 rpm at 27 °C and measured for the absorbance at 612 nm at 15 min intervals using a GENios Pro microplate reader.

RESULTS AND DISCUSSION

Construction of Expression Vectors. The schematic structure of our sensor protein is depicted in Figure 1A. Since many antibody variable regions specific for small haptens are known to be stabilized by the bound antigen,[27] we reasoned that through the appropriate design it is possible to create such a fusion protein that can be stabilized and also activated by the bound antigen. However, selection of a suitable enzyme that responds to the antigen bound to the tethered Fv portion could be a challenge. As a possible candidate enzyme, we chose a circularly permutated β-lactamase (cpBLA).

Previously, the fusion proteins of cpBLA and circularly permutated *E. coli* maltose binding protein (MBP) were reported to show significant maltose-dependent modulation of its catalytic activity.[23] On the basis of this observation, a circularly permutated TEM-1 β-lactamase (cpBLA) gene with its 168th and

170th residues as new N/C-termini, respectively, was prepared and used to join with antibody fragments. In the wild-type enzyme, the 168−170th residues and the substrate-binding residue Glu166 are in a part of the Ω-loop associated with catalytic activity.[28,29] To make a fusion protein with possible antigen-dependent catalytic activity, the cpBLA gene was inserted into the $(G_4S)_3$ linker region of a single-chain Fv (scFv) expression vector, designated pET/Fv-cpBLA (Figure 1B). Our primary attempt was based on the scFv for human osteocalcin (BGP), a bone-related disease marker, which specifically binds its C-terminal epitope. This Fv is known to be significantly stabilized by the addition of an antigen peptide such as the 7 aa C-terminal peptide BGP-C7 (FW: 894), which was previously confirmed by phage ELISA using immobilized MBP-V_L fusion protein and V_H fragment labeled with bacterial alkaline phosphatase (open sandwich ELISA).[24]

Expression and Purification of Fv-cpBLA(BGP) Protein. To investigate the properties of Fv-cpBLA(BGP) protein, BL21-(DE3, pLysS) cells were transformed with the expression vector, and the expression of the fusion protein with its His_6-tag was investigated for the culture supernatant, the intracellular soluble fraction, and the insoluble fraction. According to the SDS−PAGE and Western blot using the HRP-anti-His_5 (PentaHis) antibody, a minute protein band of expected size (58 kD) was observed for the intracellular soluble fraction, and a clearer band of the protein was detected in the insoluble fraction (Figure 1C and D). Taking the amount of the expressed protein into account, we decided to recover and purify the protein from the insoluble fraction. The purified denatured protein was subjected to refolding by a stepwise dialysis and oxidation, and this refolded sample was used for further analyses.

As a measure of the integrity of refolded protein, the antigen-binding activity of Fv-cpBLA was evaluated by a kinetic analysis using a surface plasmon resonance biosensor Biacore 2000. As a target ligand, the biotinylated C-terminal 11-mer BGP peptide was immobilized on the sensor chip with immobilized streptavidin, to see the BGP-binding activity of Fv-cpBLA and commercially available BLA as a control. As shown in Figure 1E, a significant binding signal was observed for Fv-cpBLA, and subsequently, its equilibrium dissociation constant K_d was calculated as 77.6 nM (Table 1). Since this value was comparable to that of the Fv (137 nM),[30] the refolded Fv-cpBLA was considered to retain sufficient antigen-binding activity. The somewhat superior binding activity was probably because of the covalent linkage of V_H/V_L like scFv, which favored their association. However, BLA at the same concentration gave no specific binding signal to the immobilized BGP-C11 peptide, which clearly showed the binding specificity of refolded Fv-cpBLA.

BGP-Dependent Activation of Fv-cpBLA(BGP) Protein *in Vitro*. Next, the catalytic activity as well as its antigen dose-dependency of Fv-cpBLA was investigated using a fluorogenic BLA substrate fluorocillin. Compared with the wild-type BLA, the enzyme without BGP-C7 peptide showed 0.87% of the specific activity, which was a value comparable to that of other BLA mutants (Table 2).[11,14] Because of its relatively low catalytic activity, the dose-dependency was evaluated taking the fluorocillin fluorescence without Fv-cpBLA but in the presence of the same amounts of antigen as controls. Under this condition, we could observe a clear dose-dependent enhancement in BLA activity of Fv-cpBLA (Figure 2A). According to the dose-dependency curve, the EC50 calculated from the curve-fitting was 1.47 nM, also indicating that as low as 1 ng/mL (1.1 nM) of BGP-C7 was effective in enhancing the observed BLA activity. Surprisingly, this concentration was lower than the detection limit previously obtained in open sandwich ELISA.[24] Also, the specificity of the response was investigated using other peptides as well as unrelated organic compounds ICP and TCP as an antigen (see later). As shown in Figure 2B, the activation was only observed for the cognate antigens, suggesting the specificity of observed enhancement. As a comparison, the effect of BGP-C7 on the catalytic activity of BLA was investigated (Figure 2C). The result clearly showed a negligible effect of BGP-C7 on BLA activity itself.

Then the specific activity k_{cat} and Michaelis constant K_m were calculated from the kinetic assays for both Fv-cpBLA and the wild-type BLA by nonlinear least-squares curve fittings

Table 1. Binding Constants for Biotinylated BGP-C11 Obtained with Biacore 2000

	k_a ($M^{-1}s^{-1}$)	k_d ($\times 10^{-6}$ s^{-1})	K_D ($\times 10^{-9}$ M)
FvcpBLA(BGP)	193 ± 9.3	15.0 ± 1.8	77.6 ± 3.9
Fv[a]	778 ± 61	107 ± 58	137 ± 75

[a] Reported in ref 30.

Table 2. Catalytic Parameters Obtained for BLA and Fv-cpBLA(BGP) Regarding Fluorocillin Decomposition at 25°C

(A) Parameters Based on the Michaelis−Menten Equation

	BGP C7 (μM)	[E] (nM)	V_{max}[a] (min^{-1})	k_{cat} ($\times 10^9$ min^{-1} M^{-1})	k_{cat} relative value		K_m (μM)	k_{cat}/K_m ($\times 10^{15}$ min^{-1} M^{-2})	χ^2
BLA	0	0.512	187 ± 31	366 ± 60	1		25.3 ± 8.2	14.4 ± 5.2	502.83
FvcpBLA	0	70.3	222 ± 40	3.16 ± 0.57	0.0086	1	30.9 ± 8.8	0.102 ± 0.034	97.24
FvcpBLA	1.1	70.3	280 ± 29	3.98 ± 0.41	0.0109	1.26	33.0 ± 5.1	0.121 ± 0.023	40.61

(B) Parameters Obtained Based on the Hill Equation

	BGP C7 (μM)	[E] (nM)	V_{max}[a] (min^{-1})	k_{cat} ($\times 10^9$ min^{-1} M^{-1})	k_{cat} relative value		K_m (μM)	k_{cat}/K_m ($\times 10^{15}$ min^{-1} M^{-2})	n	χ^2
BLA	0	0.512	123 ± 3	241 ± 5	1		11.5 ± 0.4	20.8 ± 0.8	2.02 ± 0.10	12.3
FvcpBLA	0	70.3	119 ± 5	1.69 ± 0.07	0.0070	1	10.4 ± 0.7	0.163 ± 0.013	1.65 ± 0.10	7.8
FvcpBLA	1.1	70.3	249 ± 59	3.56 ± 0.85	0.0148	2.10	20.2 ± 11.2	0.176 ± 0.106	1.07 ± 0.12	27.5

[a] $V = d\mathrm{RFU} / dt$ (min^{-1})

dx.doi.org/10.1021/bc1004125 |*Bioconjugate Chem.* 2011, 22, 633–641

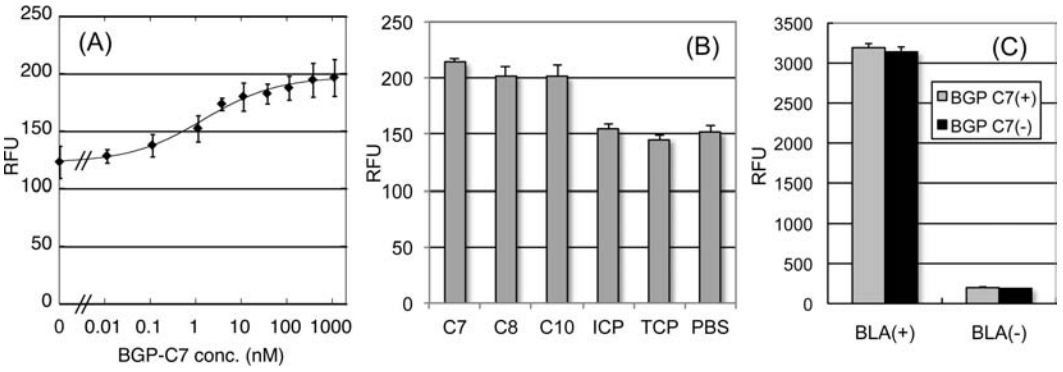


Figure 2. Antigen-dependent activation of Fv-cpBLA(BGP) catalytic activity. (A) Dose−response curve for BGP-C7 peptide. The mixture of 70 nM Fv-cpBLA, 1 μM fluorocillin, and 0−1100 nM BGP-C7 peptide in 100 μL of PBS was incubated at 27 °C for 1 h and read for fluorescence. Background fluorescence of the samples without Fv-cpBLA was subtracted for each BGP-C7 concentration. Averages of 3 samples with an error bar for 1 SD are shown. (B) Antigen specificity. Measurement was done as in A except that 1 μg/mL each of BGP-C8, BGP-C10 (peptides having additional one and three N-terminal residues to BGP-C7, respectively), ICP, and TCP were added instead of BGP-C7. (C) The effect of BGP-C7 on BLA activity. Measurement was done as in (B) except that BLA (37.5 nM) was used instead of Fv-cpBLA. Background fluorescence is also shown.

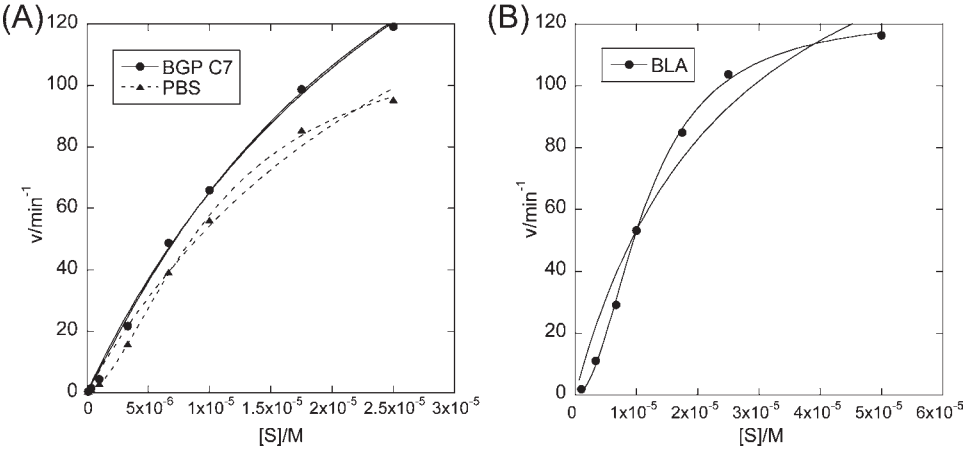


Figure 3. S−V plots for (A) FvcpBLA and (B) BLA. Fv-cpBLA (70.1 nM) was added with substrate fluorocillin as indicated in the presence or absence of antigen BGP-C7 (1.1 μM). Initial velocities are plotted against the substrate concentration. BLA (0.512 nM) was used as a comparison. Fitting curves based on Michaelis−Menten and Hill equations are shown for each condition.

(Figure 3). When we assumed Michaelis−Menten-type kinetics, the observed enhancement in k_{cat} was modest (26%) in the presence of 1.1 μM BGP-C7. However, when the Hill equation was employed for the fittings considering the sigmoid-like substrate dose-dependent activity, better fittings and calculated enhancement in specific activity as large as 110% was obtained (Table 2). To the best of our knowledge, this is the first report of allosteric behavior of the BLA enzyme. Though the reason for the sigmoidal kinetics observed especially for unliganded Fv-cpBLA and the wild-type BLA is unclear, and might be a substrate (fluorocillin)-specific phenomenon, the antigen-dependent catalytic behavior of Fv-cpBLA was clearly suggested.

Fv-cpBLA for Pesticide Also Showed Antigen Dependence. To show the generality of our attempt, another Fv-cpBLA recognizing different antigens was made and investigated for its catalytic properties. With an intention to make a sensor protein for environmental monitoring, the gene encoding antibody fragments of pET/Fv-cpBLA was swapped with those for the Fv that specifically binds a neonicotinoid insecticide imidacloprid (ICP, FW: 255.66) (Figure 4A). According to the Biacore measurement, the Fv and scFv showed dissociation constants K_d for the ICP-BSA conjugate of 67 and 12.7 nM, respectively. The Fv was also known to be stabilized by the addition of ICP, as well as by its analogue thiacloprid (TCP), to a lesser extent, which was confirmed by a phage ELISA using immobilized maltose binding protein−V_L fusion protein and the V_H fragment displayed on M13 phage (open sandwich ELISA, Figure S1 (Supporting Information)). The lower response to TCP was considered to reflect the cross-reactivity of this antibody to TCP (1.3%) obtained by a competitive assay.

When we prepared Fv-cpBLA for ICP in the same manner as that for BGP and used it to evaluate dose−response behavior, a similar ICP dose-dependent fluorescence was obtained (Figure 4B). The result again suggested the antigen-dependent catalytic activation of Fv-cpBLA protein *in vitro*. The calculated EC50 value was 20.3 nM (5.2 ng/mL), which was close to the K_d value of scFv. Moreover, when we tried to express Fv-cpBLA (ICP) at a lower temperature (27 °C), a limited amount of soluble protein was recovered from the culture supernatant (Figure S2A, Supporting Information). Hence, we used a concentrated, partially purified protein from the culture supernatant for further study. To confirm its antigen binding activity, ELISA

dx.doi.org/10.1021/bc1004125 |*Bioconjugate Chem.* 2011, 22, 633–641

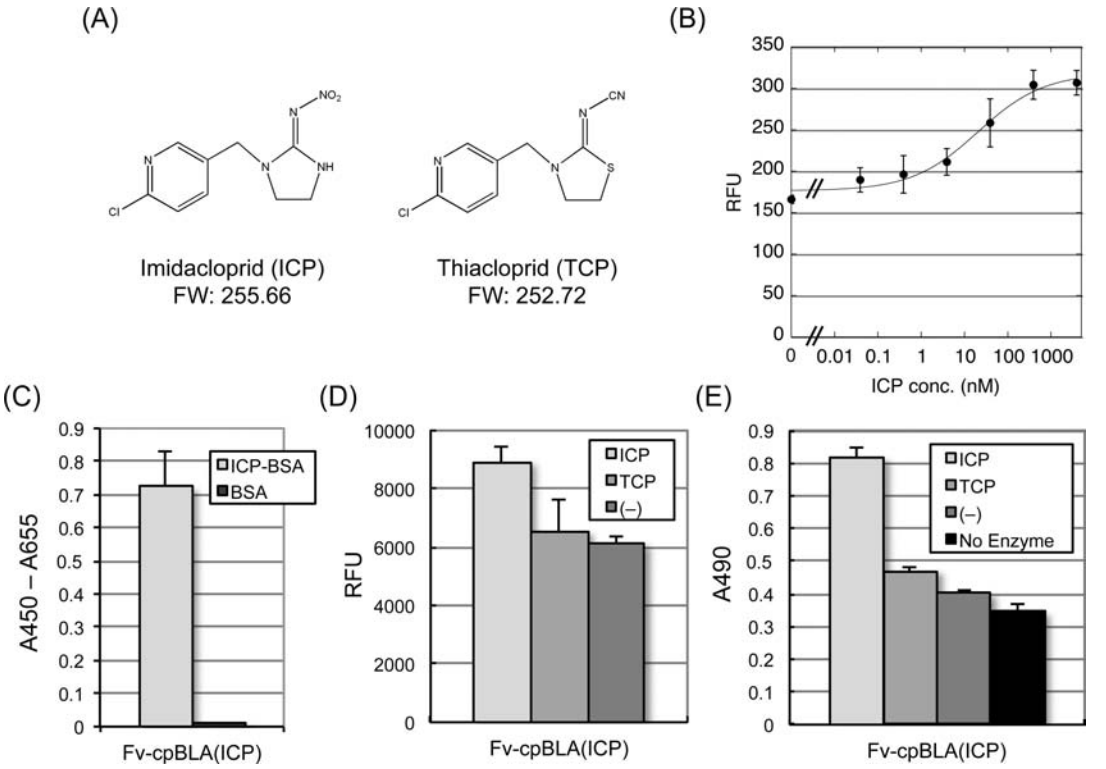


Figure 4. (A) Structures of ICP and TCP. (B) Dose−response curve for ICP pesticide with Fv-cpBLA recovered from the insoluble fraction. Other conditions are the same as in Figure 2A. (C) Specific binding of Fv-cpBLA(ICP) recovered from culture supernatant to immobilized ICP-BSA probed by ELISA. The names of immobilized protein are shown. Averages of 3 samples with an error bar showing 1 SD are shown. (D) BLA activity of Fv-cpBLA(ICP) measured with 9 μM fluorocillin. The names of antigen added are shown, and background fluorescence without Fv-cpBLA was subtracted. (E) BLA activity of the protein detected with nitrocefin. The names of antigen added are shown, while the background signal without the protein is shown as No Enzyme.

for the immobilized antigen was performed. The sample clearly showed a specific binding signal to ICP-BSA, while showing its negligible binding to carrier BSA (Figure 4C). We then evaluated its catalytic activity by using both fluorocillin and a more popular chromogenic substrate nitrocefin. When the catalytic activity was measured in the presence of ICP or its analogue TCP, the samples containing 500 ng/mL (~2 μM) of the antigen showed significantly higher activity than the control without ICP, irrespective of the substrate used (Figure 4D and E). These data suggest that Fv-cpBLA(ICP) recovered from the soluble fraction is also catalytically activated by its cognate antigen.

Control of Bacterial Growth. To investigate the possibility to utilize this antigen-dependent BLA activity as a means to control bacterial growth in the presence of a BLA substrate ampicillin, the effect of these insecticides on the growth of *E. coli* BL21(DE3, pLysS) cells was tested. When BL21(DE3, pLysS) cells without pET/Fv-cpBLA plasmid were cultivated with or without 100 ng/mL ICP, no significant difference in their growth was observed between the cultures, suggesting that ICP up to this concentration does not affect nor promote cell growth (data not shown). Next, to investigate the effect of ICP or TCP on BL21(DE3, pLysS) cells expressing Fv-cpBLA(ICP), the plasmid-bearing cells were cultured in LBCK medium supplemented with 1 mM IPTG at 27 °C. After dilution to the fresh LBCK medium containing 1 mM IPTG but without ampicillin, all the cells showed similar logarithmic growth curves irrespective of added ICP or TCP, which again suggests negligible toxicity of these pesticides to the bacteria (Figure 5A). The expression of Fv-cpBLA in the cell was confirmed by Western blotting using the anti-BLA polyclonal antibody, which clearly showed a 58 kD band corresponding to the expected size of the fusion protein. Also, the amount of protein was almost the same irrespective of added ICP or TCP in the culture media (Figure S2B, Supporting Information).

On the contrary, when the induced cells were diluted and cultivated in LBCK medium containing 100 μg/mL ampicillin (LBCKA) for more than 24 h at 27 °C, we could observe antigen-concentration dependent cell growth (Figure 5B). When TCP was added instead of ICP, the growth was slower but significantly faster than the culture without antigens, which was in accordance with the specificity of this antibody.

To further confirm ICP dose-dependent growth of the cells, the cells harboring pET/Fv-cpBLA were induced for protein expression for 3 h at 27 °C and diluted in microplate wells containing various concentrations (0−1000 ng/mL) of ICP to monitor their growth. As a result, in LBCKA media, the cells show a clear ICP dose-dependent growth (Figure S3, Supporting Information).

Selection of Fv-cpBLAs That Confer Superior Bacterial Growth. By taking advantage of the antigen-dependent growth behavior of the *E. coli*, we attempted to select functional Fv-cpBLA proteins from a library of constructs. To this end, two small libraries of variant Fv-cpBLA(ICP) were made, where the two flexible linkers between V_H and cpBLA, and cpBLA and V_L were substituted with two sets of α-helix-forming linkers (either EAAAK and $(EAAAK)_2$, or $(EAAAK)_2$ and $(EAAAK)_2$), and two junctional residues at the two termini of cpBLA were randomized

dx.doi.org/10.1021/bc1004125 |*Bioconjugate Chem.* 2011, 22, 633–641

(Figure 6A). The colonies (95 in total) from the two libraries were picked and screened on the microplate wells containing LBCKA medium with IPTG and ICP, and several clones that showed better growth than the original Fv-cpBLA-bearing cells were selected (Figure 6B and C, Table 3, and Figure S4, Supporting Information). One of the faster-growing clones that encoded an expected sequence of the second library V_H-$(EAAAK)_2$-N-cpBLA-K-$(EAAAK)_2$-V_L (AF6) was further analyzed for its catalytic property. When the purified protein refolded from the insoluble fraction was measured for its catalytic activity, the protein showed ICP-dependent BLA activity comparable to, or more than, the original Fv-cpBLA (G4S) in fluorocillin assay (Figure 6D). Because the increase in BLA activity of purified AF6 protein over G4S protein was minimal, the superior growth of the cells harboring AF6 would be mainly due to the improved stability/expression of soluble Fv-cpBLA in bacteria. To prove this possibility, Western blot analysis to quantify the amounts of soluble/insoluble Fv-cpBLA from the bacteria expressing either G4S or AF6 protein was performed (Figure 6E). The result clearly showed almost twice the soluble/insoluble ratio of AF6 (14.3%) compared with

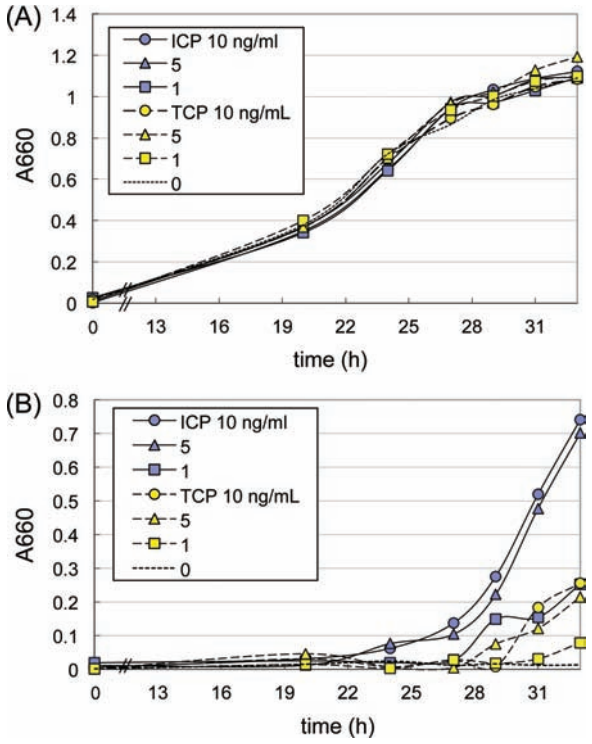


Figure 5. Growth curves of BL21(DE3, pLysS, pET26/Fv-cpBLA-(ICP)) in 4 mL of LBCK medium supplemented with (A) 0 or (B) 100 μg/mL ampicillin, at 27 °C.

Table 3. Amino Acid Sequences of the Linker Region for Selected Fv-cpBLA Clones

clone	V_H	linker		cpBLA		linker	V_L
WT		GGGGSG	F		K	GSGGGGS	
AC2		(EAAAK)	V		D	$(EAAAK)_2$	
AE2		(EAAAK)	Y		A	$(EAAAK)_2$	
AF2		(EAAAK)	S		T	$(EAAAK)_2$	
AC3	V_H	(EAAAK)	V	cpBLA	W	$(EAAAK)_2$	V_L
AF6		$(EAAAK)_2$	N		K	$(EAAAK)_2$	
AG6		$(EAAAK)_2$	R		K	GSGGGGS	
AA11		$(EAAAK)_2$	F		K	GSGGGGS	
AA12		$(EAAAK)_2$	S		V	$(EAAAK)_2$	

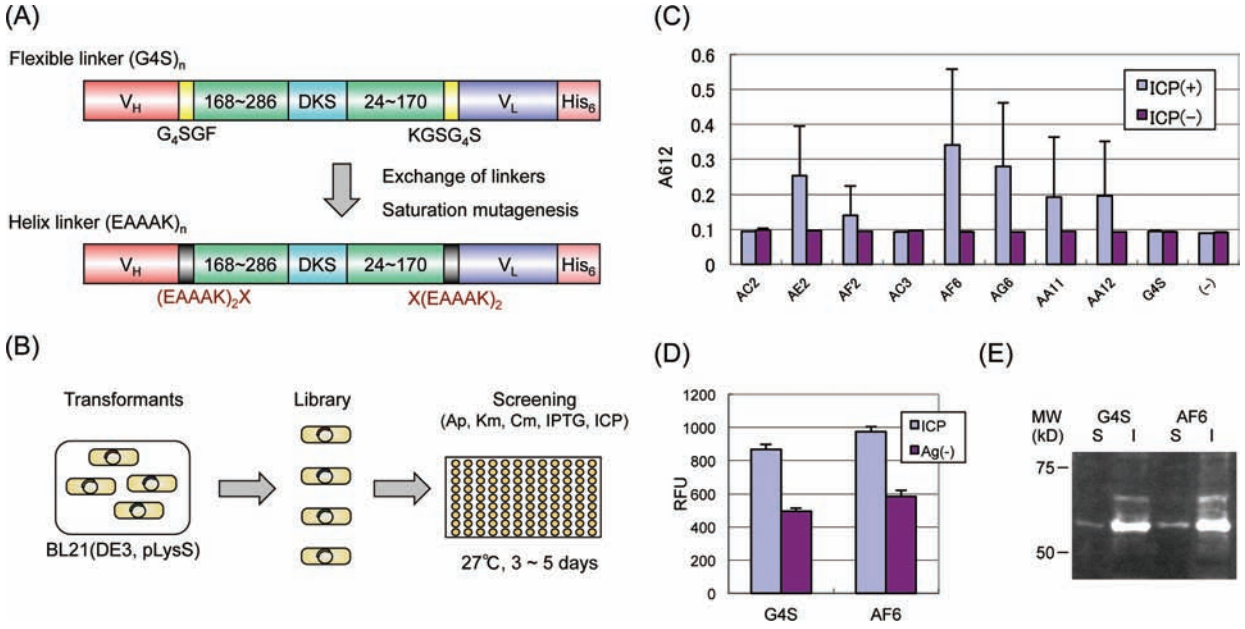


Figure 6. (A) Scheme of the linker engineering and (B) screening based on the bacterial growth in the presence of ampicillin and ICP. (C) The result of the growth screening of selected mutants with 100 mg/L ampicillin (n = 3). (D) Comparison of the BLA activity of refolded Fv-cpBLA (300 nM each) with the original linker (G4S) and one of selected linkers (AF6) with and without ICP (n = 3). (E) Western blot of Fv-cpBLA proteins recovered from the soluble (S) or insoluble (I) fractions after sonication detected using the anti-His5 antibody. The same amounts of cells were used for both G4S and AF6 samples.

dx.doi.org/10.1021/bc1004125 |*Bioconjugate Chem.* 2011, 22, 633–641

that of G4S (5.9%), suggesting that this was indeed the case. Also, since all the clones with faster growth showed functional Fv-cpBLA sequence without frame-shift or deletion, successful selection of antigen-responsive Fv-cpBLA proteins is strongly suggested.

Here, we constructed fusion proteins consisting of an antibody variable region and a circularly permutated β-lactamase Fv-cpBLA for two antibody−antigen systems. Unlike epitope-inserted enzymes,[9−11] Fv-cpBLA does not need additional antibodies and have the ability to noncompetitively detect small haptens. In addition, as a single molecule probe, optimization of probe concentration is not necessary and higher sensitivity can be expected than the corresponding bimolecular probe, which suffers from the entropic loss of the free energy upon complex formation of the probes and the target. This was actually proven true for both the BGP peptide and ICP pesticide detections by the respective Fv-cpBLA protein, where apparent EC50s of several ng/mL were attained. Though the obtained EC50 value for BGP was considerably lower than the K_d value obtained by Biacore, we think this might reflect the true affinity of the fully refolded Fv-cpBLA protein. Because of their sensitivity, the obtained Fv-cpBLA protein will be particularly useful as a biosensor protein, which can be directly utilized as an assay reagent of fluorescence-based homogeneous immunoassay.

The plausible working mechanism of the ICP sensor with *E. coli* growth as a signal was that the small difference in cellular and extracellular lactamase activity was reflected in the difference in lag periods of cell growth, which was required for the ampicillin concentration to be reduced to the threshold in which the surviving cells could grow. The system is potentially useful as an economical environmental monitor because our cells with Fv-cpBLA for ICP are sensitive enough to detect, for example, the Japanese criteria concentrations of ICP in agricultural crops (20 to 5,000 ng/mL). The current incubation period required for cell growth was rather long, probably due to the limited amount of soluble active Fv-cpBLA protein produced in bacteria. However, this problem was partially solved by the selection of faster-growth variant Fv-cpBLAs including AF6. The somewhat modest activity improvement of purified AF6 protein over the original Fv-cpBLA might be due to the suboptimal length of the encoded helical linkers in the library, or the intrinsic property of Fv-cpBLA. Possibly, circular permutation of Fv as well as BLA, connection of the domains with shorter linkers, and the selection based on the activity will enable us to create sensor proteins with more robust activity change.

Here, we showed that through the combination of rational design and molecular selection of antibody−enzyme fusion proteins, functional sensor enzymes whose BLA activity responds to a molecule of choice could be obtained. Considering similar dose−response curves obtained for the two different targets, the proposed strategy will be valid for many antibodies that recognize different types of antigens including haptens, peptides, and proteins. Since BLA can be utilized as a prodrug activator in antibody-directed enzyme prodrug therapy (ADEPT),[31] the use of antibody−enzyme conjugates with a sensor function might improve the specificity of anticancer ADEPT if we employ antibodies recognizing a suitable cell-surface cancer epitope. In the long term, our challenges will include a positive selection of novel Fv-cpBLAs with altered specificity from a library of randomized antibody domains. Hopefully, by selecting such libraries, many sensitive sensor enzymes with a specific antibody variable region will be created for a wide range of antigens.

■ ASSOCIATED CONTENT

Supporting Information. Open-sandwich ELISA for imidacloprid and thiacloprid haptens; Western blot of soluble Fv-cpBLA(ICP) protein recovered from the culture supernatant; growth of BL21(DE3, pLysS, pET26/Fv-cpBLA(ICP)) in 100 μL of LBCKA medium at 27°C in the presence of ICP; and results of the primary growth screening of the library in the presence of 50 mg/L ampicillin. This material is available free of charge via the Internet at http://pubs.acs.org.

■ AUTHOR INFORMATION

Corresponding Author
*E-mail: hueda@chembio.t.u-tokyo.ac.jp.

■ ACKNOWLEDGMENT

M.K. and H.I. contributed equally on this work. We thank Tatsuya Shinoda for kindly allowing the use of the anti-BGP antibody gene. This project was partly supported by the PRESTO program, JST, Japan, by a Grant-in-Aid for Scientific Research (B20360368) from JSPS, Japan, and by the Global COE Program for Chemistry Innovation, MEXT, Japan. J.D. was supported by the Postdoctral Fellowship for Foreign Researchers from JSPS, Japan. We also thank Fujifilm Co. for financial support.

■ ABBREVIATIONS

ADEPT, antibody-directed enzyme prodrug therapy; BLA, TEM-1 β-lactamase; cpBLA, circularly permutated BLA; DKS, aspartic acid-lysine-serine; dNTPs, deoxyribonucleotide triphosphate; ELISA, enzyme-linked immunosorbent assay; Fv, antibody variable region fragments; ICP, imidacloprid; IPTG, isopropyl-β-D-galactoside; PCR, polymerase chain reaction; RBS, ribosome binding site; RFU, relative fluorescence unit; scFv, single chain Fv; TCP, thiacloprid.

■ REFERENCES

(1) von Lode, P. (2005) Point-of-care immunotesting: approaching the analytical performance of central laboratory methods. *Clin. Biochem. 38*, 591–606.

(2) Bagshawe, K. D. (2006) Antibody-directed enzyme prodrug therapy (ADEPT) for cancer. *Expert Rev. Anticancer Ther. 6*, 1421–1431.

(3) Koide, S. (2009) Generation of new protein functions by nonhomologous combinations and rearrangements of domains and modules. *Curr. Opin. Biotechnol. 20*, 398–404.

(4) Channon, K., Bromley, E. H., and Woolfson, D. N. (2008) Synthetic biology through biomolecular design and engineering. *Curr. Opin. Struct. Biol. 18*, 491–498.

(5) Lim, W. A. (2002) The modular logic of signaling proteins: Building allosteric switches from simple binding domains. *Curr. Opin. Struct. Biol. 12*, 61–68.

(6) Swain, J. F., and Gierasch, L. M. (2006) The changing landscape of protein allostery. *Curr. Opin. Struct. Biol. 16*, 102–108.

(7) Huang, J., and Koide, S. (2010) Rational conversion of affinity reagents into label-free sensors for peptide motifs by designed allostery. *ACS Chem. Biol. 5*, 273–277.

(8) Edwards, W. R., Williams, A. J., Morris, J. L., Baldwin, A. J., Allemann, R. K., and Jones, D. D. (2010) Regulation of β-lactamase activity by remote binding of heme: functional coupling of unrelated proteins through domain insertion. *Biochemistry 49*, 6541–6549.

(9) Feliu, J. X., Ramirez, E., and Villaverde, A. (2000) Distinct mechanisms of antibody-mediated enzymatic reactivation in beta-galactosidase molecular sensors. *FEBS Lett. 478*, 267–271.

(10) Brennan, C. A., Christianson, K., La Fleur, M. A., and Mandecki, W. (1995) A molecular sensor system based on genetically engineered alkaline phosphatase. *Proc. Natl. Acad. Sci. U.S.A. 92*, 5783–5787.

(11) Legendre, D., Soumillion, P., and Fastrez, J. (1999) Engineering a regulatable enzyme for homogeneous immunoassays. *Nat. Biotechnol. 17*, 67–72.

(12) Yokozeki, T., Ueda, H., Arai, R., Mahoney, W., and Nagamune, T. (2002) A homogeneous noncompetitive immunoassay for the detection of small haptens. *Anal. Chem. 74*, 2500–2504.

(13) Ueda, H., Yokozeki, T., Arai, R., Tsumoto, K., Kumagai, I., and Nagamune, T. (2003) An optimized homogeneous noncompetitive immunoassay based on the antigen-driven enzymatic complementation. *J. Immunol. Methods 279*, 209–218.

(14) de las Heras, R., Fry, S. R., Li, J., Arel, E., Kachab, E. H., Hazell, S. L., and Huang, C.-Y. (2008) Development of homogeneous immunoassays based on protein fragment complementation. *Biochem. Biophys. Res. Commun. 370*, 164–168.

(15) Geddie, M. L., and Matsumura, I. (2007) Antibody-induced oligomerization and activation of an engineered reporter enzyme. *J. Mol. Biol. 369*, 1052–1059.

(16) Goldenberg, D. P., and Creighton, T. E. (1983) Circular and circularly permuted forms of bovine pancreatic trypsin inhibitor. *J. Mol. Biol. 165*, 407–413.

(17) Zhang, T., Bertelsen, E., Benvegnu, D., and Alber, T. (1993) Circular permutation of T4 lysozyme. *Biochemistry 32*, 12311–12318.

(18) Luger, K., Hommel, U., Herold, M., Hofsteenge, J., and Kirschner, K. (1989) Correct folding of circularly permuted variants of a beta alpha barrel enzyme in vivo. *Science 243*, 206–210.

(19) Pieper, U., Hayakawa, K., Li, Z., and Herzberg, O. (1997) Circularly permuted beta lactamase from *Staphylococcus aureus* PC1. *Biochemistry 36*, 8767.

(20) Baird, G. S., Zacharias, D. A., and Tsien, R. Y. (1999) Circular permutation and receptor insertion within green fluorescent proteins. *Proc. Natl. Acad. Sci. U.S.A. 96*, 11241–11246.

(21) Nagai, T., Yamada, S., Tominaga, T., Ichikawa, M., and Miyawaki, A. (2004) Expanded dynamic range of fluorescent indicators for Ca2+. *Proc. Natl. Acad. Sci. U.S.A. 101*, 10554–10559.

(22) Nakai, J., Ohkura, M., and Imoto, K. (2001) A high signal-to-noise Ca2+ probe composed of a single green fluorescent protein. *Nat. Biotechnol. 19*, 137–141.

(23) Guntas, G., Mansell, T. J., Kim, J. R., and Ostermeier, M. (2005) Directed evolution of protein switches and their application to the creation of ligand-binding proteins. *Proc. Natl. Acad. Sci. U.S.A. 102*, 11224–11229.

(24) Lim, S. L., Ichinose, H., Shinoda, T., and Ueda, H. (2007) Noncompetitive detection of low molecular weight peptides by open sandwich immunoassay. *Anal. Chem. 79*, 6193–6200.

(25) Tsumoto, K., Shinoki, K., Kondo, H., Uchikawa, M., Juji, T., and Kumagai, I. (1998) Highly efficient recovery of functional single-chain Fv fragments from inclusion bodies overexpressed in *Escherichia coli* by controlled introduction of oxidizing reagent—application to a human single-chain Fv fragment. *J. Immunol. Methods 219*, 119–129.

(26) Sigal, I. S., DeGrado, W. F., Thomas, B. J., and Petteway, S. R. J. (1984) Purification and properties of thiol beta-lactamase. A mutant of pBR322 beta-lactamase in which the active site serine has been replaced with cysteine. *J. Biol. Chem. 259*, 5327–5332.

(27) Suzuki, C., Ueda, H., Mahoney, W., and Nagamune, T. (2000) Open sandwich enzyme-linked immunosorbent assay for the quantitation of small haptens. *Anal. Biochem. 286*, 238–246.

(28) Chen, C. C., Rahil, J., Pratt, R. F., and Herzberg, O. (1993) Structure of a phosphonate-inhibited beta-lactamase. An analog of the tetrahedral transition state/intermediate of beta-lactam hydrolysis. *J. Mol. Biol. 234*, 165–178.

(29) Jelsch, C., Mourey, L., Masson, J. M., and Samama, J. P. (1993) Crystal structure of *Escherichia coli* TEM1 β-lactamase at 1.8 Å resolution. *Proteins 16*, 364–383.

(30) Iwai, H., Oztürk, B., Ihara, M., and Ueda, H. (2010) Antibody affinity maturation *in vitro* using unconjugated peptide antigen. *Protein Eng. Des. Sel. 23*, 185–193.

(31) Alderson, R., Toki, B., Roberge, M., Geng, W., Basler, J., Chin, R., Liu, A., Ueda, R., Hodges, D., Escandon, E., Chen, T., Kanavarioti, T., Babé, L., Senter, P., Fox, J., and Schellenberger, V. (2006) Characterization of a CC49-based single-chain fragment-beta-lactamase fusion protein for antibody-directed enzyme prodrug therapy (ADEPT). *Bioconjugate Chem. 17*, 410–418.

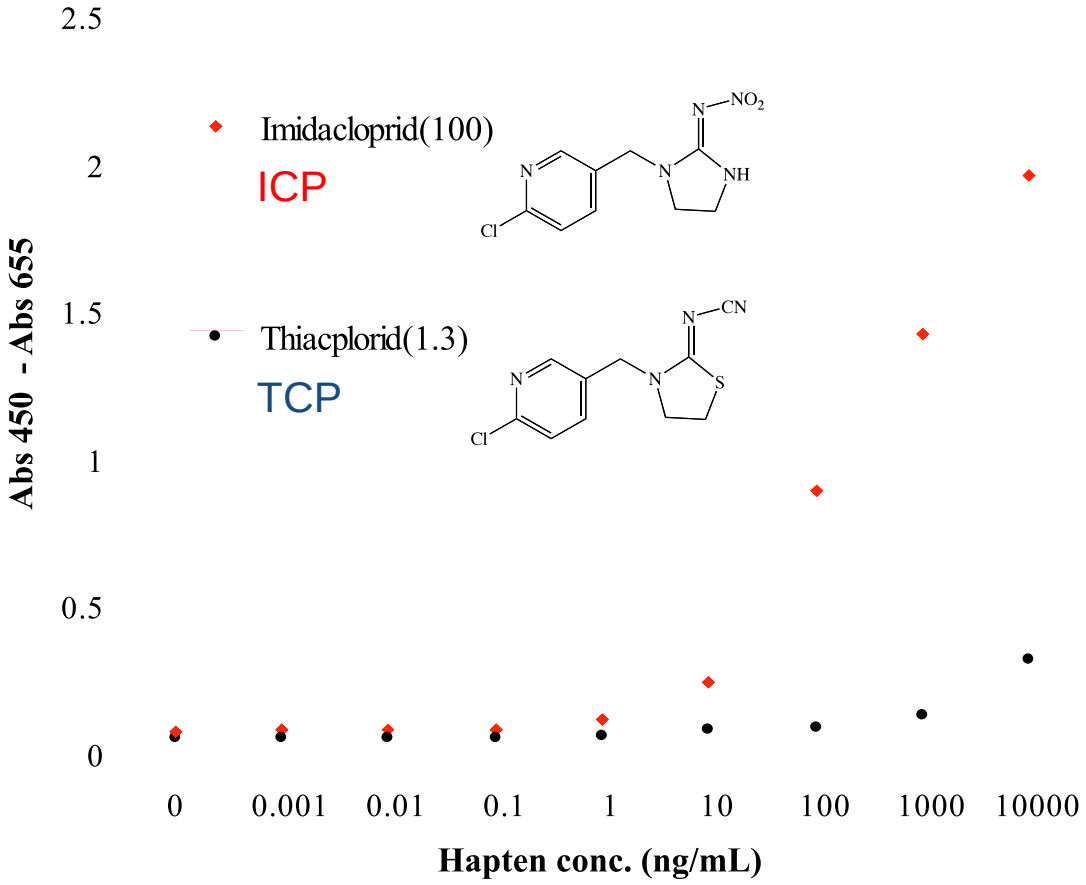


Fig. S1 Open-sandwich ELISA for imidacloprid and thiacloprid haptens. Mixture of V_H-displaying M13 phage and hapten was added to each microplate well that has been pre-coated with 5 μg/mL of MBP-V_L protein overnight at 4°C, before blocking with 2% skimmilk in PBS. After 2 h at 25°C, phages bound to the well was detected with HRP-conjugated anti-M13 antibody (GE Healthcare) as suggested by the manufacturer. Average ±1SD is shown (n=2).

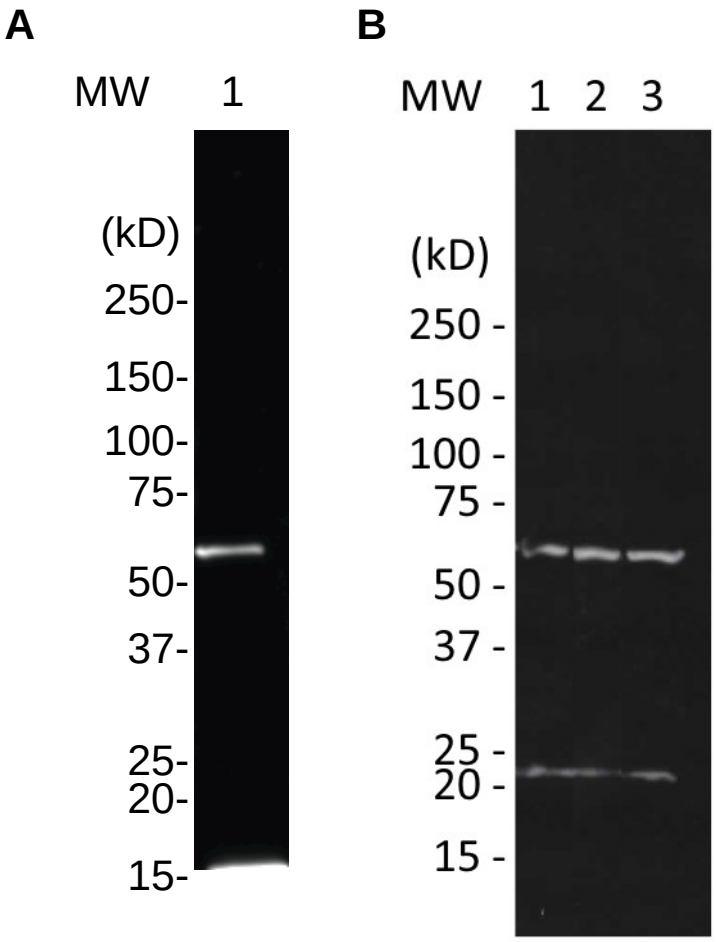


Fig. S2 A) Western blot of soluble Fv-cpBLA(ICP) protein recovered from the culture supernatant. Sample was subjected to 10% SDS-PAGE and Western blot was detected with HRP-anti His tag antibody. **B)** Western blot of BL21(DE3, pLysS, pET26/Fv-cpBLA(ICP)) cells detected with rabbit polyclonal anti-BLA antibody. The cells were grown in (Lane 1) LBCK medium, (Lane 2) supplemented with 10 ng/mL ICP, or (Lane 3) with 10 ng/mL TCP.

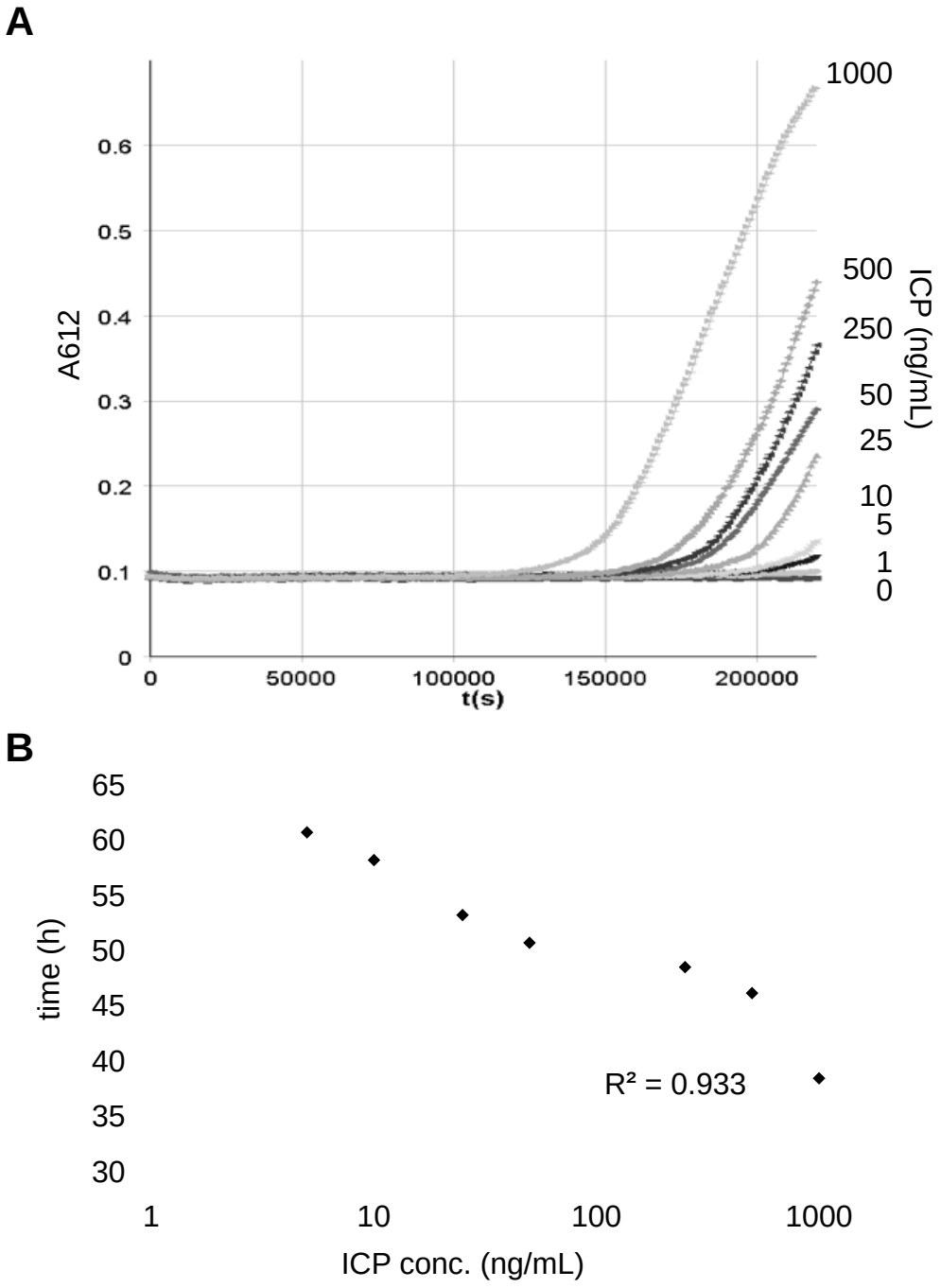


Fig. S3 A) Growth of BL21(DE3, pLysS, pET26/Fv-cpBLA(ICP)) in 100 µL LBCKA medium at 27°C in the presence of ICP as indicated. **B)** The relationship between ICP concentration and the time until OD_{612} of the cells increased by 0.02 in **A)**.

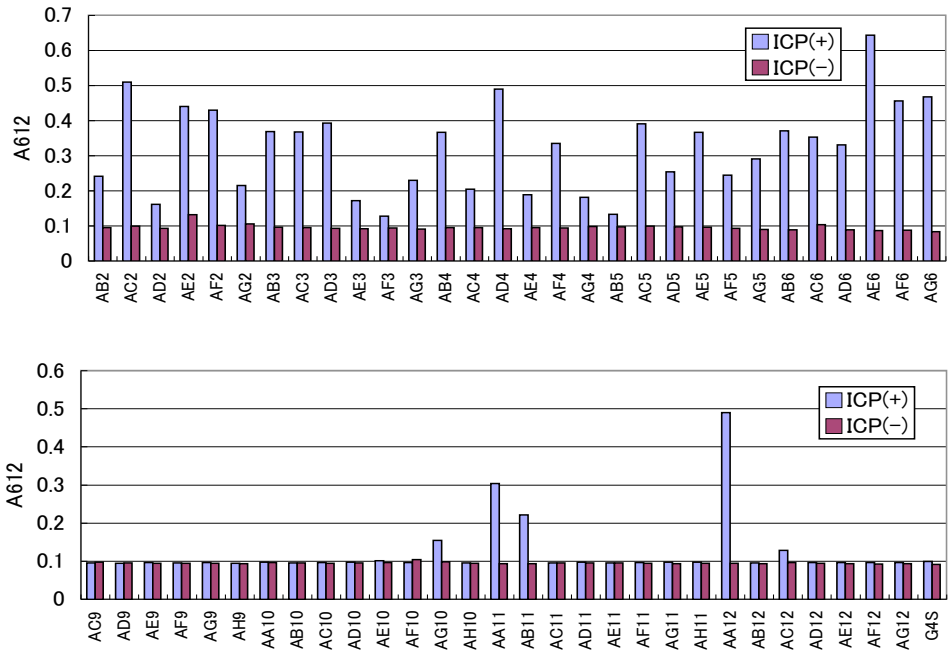


Fig. S4 The results of the primary growth screening of the library in the presence of 50 mg/L ampicillin.

Bioconjugate Chemistry

ARTICLE

pubs.acs.org/bc

New F-18 Prosthetic Group via Oxime Coupling

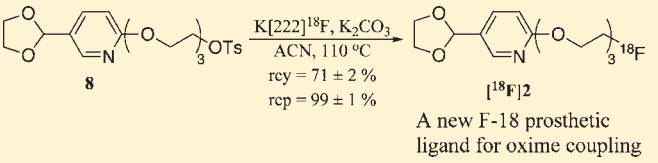
Patrick Carberry,[†] Brian P. Lieberman,[†] Karl Ploessl,[†] Seok R. Choi,[§] Danniebelle N. Haase,[†] and Hank F. Kung*[,†,‡]

[†]Departments of Radiology and [‡]Pharmacology, University of Pennsylvania, 3700 Market Street, Room 305, Philadelphia, Pennsylvania 19104, United States

[§]Avid Radiopharmaceuticals, Inc., Philadelphia, Pennsylvania 19104, United States

Supporting Information

ABSTRACT: A novel fluorine-18 prosthetic ligand, 5-(1,3-dioxolan-2-yl)-2-(2-(2-(2-fluoroethoxy)ethoxy)ethoxy)pyridine [^{18}F]**2**, has been synthesized. The prosthetic ligand is formed in high radiochemical yield (rcy = 71 ± 2%, n = 3) with excellent radiochemical purity (rcp = 99 ± 1%, n = 3) in a short reaction time (10 min). [^{18}F]**2** is a small, neutral, organic complex, easily synthesized in four steps from a readily available starting material. It can be anchored onto a target molecule containing an aminooxy functional group under acidic conditions by way of an oxime bond. We report herein two examples [^{18}F]**23** and [^{18}F]**24**, potential imaging agents for β-amyloid plaques, which were labeled with this prosthetic group. This approach could be used for labeling proteins and peptides containing an aminooxy group. Biodistribution in male ICR mice for both oxime labeled complexes [^{18}F]**23** and [^{18}F]**24** were compared to that of the known β-amyloid plaque indicator, [^{18}F]-AV-45, florbetapir **1**. Oximes [^{18}F]**23** and [^{18}F]**24** are larger in size and therefore should reduce the blood-brain barrier (BBB) penetration. The brain uptake for oxime [^{18}F]**23** appeared to be reduced, but still retained some capability to cross the BBB. Oxime [^{18}F]**24** showed promising results after 2 min post injection (0.48% dose/gram); however, the uptake increased after 30 min post injection (0.92% dose/gram) suggesting an in vivo decomposition/metabolism of compound [^{18}F]**24**. We have demonstrated a general protocol for the fluoride-18 labeling with a new prosthetic ligand [^{18}F]**2** that is tolerant toward several functional groups and is formed via chemoselective oxime coupling.



8 [^{18}F]**2**

A new F-18 prosthetic ligand for oxime coupling

INTRODUCTION

The use of molecular imaging agents plays a significant role in the advancement of medical procedures and is an important part of ongoing research.[1] In the forefront of molecular imaging is the use of positron emission tomography (PET), which relies on a biomarker that is labeled with short-lived positron emitting radionuclides. These PET imaging agents produce "hot" spots, where a large abundance of radioactivity congregates, due to the radioactive molecular probes. Fluorine-18 is one isotope that is widely used for PET imaging due to its unique physical and nuclear characteristics (ease of formation, half-life of 109.7 min, high resolution, and relative minor radiation dose to patients).[2]

Two methods are commonly used to incorporate fluorine-18 into a molecule, either by an electrophilic substitution or through nucleophilic displacement.[1−5] Electrophilic fluorination reactions are typically used in the carrier added (ca) form of [^{18}F]F^+ or [^{18}F]F_2, but have the drawbacks of low specific activity (theoretical achievable maximum radiochemical yield is limited to 50%)[6] and difficulty in controlled labeling.[1] An alternative option is the use of [^{18}F]F^- for nucleophilic substitution. High specific activity (theoretically 1.71 × 10^3 Ci/μmol)[3,4] is one advantage nucleophilic displacement possess over electrophilic substitution, which is achieved when [^{18}F]F^- is produced by the proton irradiation of enriched [^{18}O] water via the reaction ^{18}O(p, n)^{18}F. Typical S_N2 reactions dominate this avenue of chemistry. Due to the fact that the fluoride anion is highly electronegative and it is produced in an aqueous media, it is strongly hydrated and hence is not sufficiently reactive for nucleophilic substitution reactions. The fluoride anion therefore needs to be activated in the form of a "naked" anion for nucleophilic substitution, usually with "crown" ether such as K[222]. The K[222] contains two highly basic tertiary nitrogen atoms. The strong basic conditions are not suitable for compounds containing acidic protons, and thus may lead to their decomposition. To circumvent this problem, pre-existing fluorine-18 labeled molecules, known as prosthetic ligands, or biofunctional-labeling agents, are used to indirectly attach the fluorine-18 radionuclide onto a desired ligand, providing the fluorine-18 radiolabeled molecule.[1,5]

Several prosthetic ligands have been used with compounds that otherwise could not be labeled via a direct fluoride-18 nucleophilic substitution. The incorporation of these groups onto a target molecule can be achieved by methods that include the formation of an acyl,[7−12] sulfide,[13−16] alkyl,[17−20] hydrozone,[21] or oxime[9,22−31] bond formation, or with the use of photochemistry[32] and click chemistry.[33−36] Most of these prosthetic ligands are not ideal for routine applications because they require time-consuming and labor-intensive procedures with tedious purification processes. In general, prosthetic ligands may also be restricted to the type of

Received: September 24, 2010
Revised: February 3, 2011
Published: March 31, 2011

ACS Publications © 2011 American Chemical Society

dx.doi.org/10.1021/bc1004262 | *Bioconjugate Chem.* 2011, 22, 642–653

substrate used when coupled with the target ligand due to interfering nucleophilic groups. This may lead to cross-linked labeled products.[37] Therefore, site-specific linkage of a prosthetic ligand is necessary when attaching it to a target molecule.

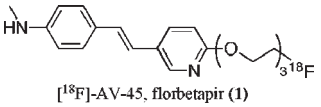
The oxime bond formation is highly chemoselective[38,39] and takes place under acidic conditions between aminooxy groups and aldehydes or ketones. Since the reaction is chemoselective, the use of protecting groups is unnecessary and the oxime coupling reaction is functional group tolerant.

The approach in designing a new prosthetic ligand for labeling compounds that pose a problem to direct fluoride-18 nucleophilic substitution, such as biologically active peptides, will need to follow four criteria. First, the prosthetic group is labeled with a [^{18}F]fluoride anion via S_N2 displacement, forming a stable C−F bond on an sp^3 hybridized carbon atom. The prosthetic ligand containing an end-capped pegylated fluorine atom is similar to [^{18}F]-AV-45 (**1**),[40,41] which has been well tested and prepared at multicurie levels; therefore, we expect the fluorination reaction will proceed smoothly.

[^{18}F]-AV-45, (*E*)-4-(2-(6-(2-(2-(2-^{18}F-fluoroethoxy)ethoxy) ethoxy)pyridin-3-yl)vinyl)-*N*-methyl benzenamine, florbetapir (**1**) (Figure 1), is a new imaging agent targeting β-amyloid plaques in the brain.[40,41] This agent is currently under a phase III clinical study. It is a small, neutral, and moderately lipophilic agent (measured log D = 1.70, calculated log P = 2.85). We reasoned that compounds with similar structural features to **1** were good candidates to test the coupling reaction of the prosthetic group, validating the chemistry prior to its application to more complicated compounds, such as peptides and proteins.

A second criterion for the prosthetic ligand is that the compound be a neutral molecule, soluble in organic media, to aid in the purification process (solid-phase extraction). Third, the site at which the prosthetic group attaches to the target molecule (i.e., via an aldehyde) would need to form chemoselectively an oxime bond with an aminooxy functional group. Finally, it would be ideal for the coupling between both the prosthetic ligand and the aminooxy compound to occur quickly, in an environment suitable to tolerate many different functional groups. The use of an oxime coupling reaction with aldehydes, for the attachment of prosthetic groups, has been successfully reported.[22−27,29−31,42]

Herein, we report the synthesis and characterization of a novel radiolabeled ligand, [^{18}F]**2**, which meet all four criteria listed above as a suitable prosthetic group (Figure 2). To test and optimize the oxime coupling reaction, we synthesized two aminooxy compounds, **21** and **22**, and used them as model complexes for the labeling with our prosthetic ligand, [^{18}F]**2**. Biodistribution studies were performed for these two radiolabeled new oximes.



[^{18}F]-AV-45, florbetapir (**1**)

Figure 1. Structure of [^{18}F]-AV-45, florbetapir (**1**).

EXPERIMENTAL PROCEDURES

General Information. All reagents used were commercial products purchased from Sigma-Aldrich and were used without further purification unless otherwise indicated. Fluoride-18 (nca) was purchased from IBA Molecular North America, Inc. All anhydrous reactions were run under positive pressure of argon, ultrahigh-purity. All syringes and reaction flasks required for anhydrous reactions were flame-dried and then cooled under argon atmosphere. All anhydrous solvents were dried by passage through an alumina column using an Innovation Technology, Inc., system. Flash chromatography was carried out with silica gel 60 (230−400 mesh, Sigma-Aldrich). Analytical thin-layer chromatography (TLC) was performed on precoated aluminum-backed plates (silica gel 60 F_{254}). ^{1}H and ^{13}C NMR spectra were recorded on 200 MHz/50 MHz (Bruker DPX spectrometer), in deuterated chloroform ($CDCl_3$) with residual chloroform protons (δ 7.26 ppm for ^{1}H NMR and δ 77.23 ppm for ^{13}C NMR) as the internal reference. Chemical shifts are reported in parts per million (ppm). Coupling constants are reported in hertz (Hz). The multiplicity is defined by s (singlet), d (doublet), t (triplet), dd (doublet of doublets), ddd (doublet of doublets of doublets), br (broad), and m (multiplet). High-resolution mass spectrometry experiments were performed at University of Pennsylvania, Department of Radiology, Radiopharmaceutical Chemistry Section, using an Agilent Technologies LC/MSD TOF mass spectrometer.

*2-Bromo-5-(1,3-dioxolan-2-yl)pyridine (**6**).* Ethylene glycol (0.54 mL, 601 mg, 9.7 mmol) was added to a suspension of 6-bromo-3-pyridine carbaldehyde (**5**) (1.0 g, 5.4 mmol) and *p*-toluene sulfonic acid, monohydride (102 mg, 0.54 mmol), in 27 mL of benzene. The flask was then fitted with a reflux condenser and placed in an oil bath set to 92 °C. The reaction mixture was refluxed for 19 h, upon which time it was removed from the oil bath and allowed to cool to room temperature. The reaction was quenched with dilute K_2CO_3 (aq) solution to adjust the pH to ∼11. The reaction media were then partitioned between ethyl acetate and H_2O. The organic phase was separated from the aqueous phase with the use of ethyl acetate (3 × 50 mL). The combined organic layers were washed with brine (50 mL), dried over $MgSO_4$, filtered, and concentrated to afford 1.21 g (98%) of acetal **6**, a yellow oil. ^{1}H NMR was consistent with the reported literature.[43]

*2-(2-(2-(5-(1,3-Dioxolan-2-yl)pyridin-2-yloxy)ethoxy)ethoxy) ethanol (**7**).* Acetal **6** (302 mg, 1.31 mmol) was dissolved in 13 mL of anhydrous *N*,*N*-dimethyl formamide and added to a microwave reaction vessel containing Cs_2CO_3 (1.28 g, 3.93 mmol) and triethylene glycol (0.43 mL, 475 mg, 3.16 mmol). The reaction vessel was sealed and placed in a microwave reactor (Biotage Initiator) set at 150 °C for 50 min. The reaction was allowed to cool to room temperature and then vented with a needle prior to breaking the seal. The reaction mixture was partitioned between dichloromethane and H_2O. The organic phase was extracted from the aqueous phase with the use of dichloromethane (3 × 20 mL). The combined organic layers

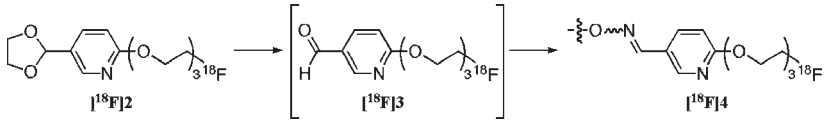


Figure 2. Structure of the prosthetic group [^{18}F]**2** and its transformation to fluorine-18 labeled oxime.

dx.doi.org/10.1021/bc1004262 |*Bioconjugate Chem.* 2011, 22, 642–653

were washed with brine (25 mL), dried over $MgSO_4$, filtered, and concentrated. Purification by flash chromatography (100% ethyl acetate) afforded 240 mg (61%) of alcohol **7**, a viscous pale yellow oil. R_f = 0.16 (100% ethyl acetate). ^{1}H NMR (200 MHz, $CDCl_3$): δ 8.20 (d, J = 2.3 Hz, 1H), 7.68 (dd, J = 8.6, 2.4 Hz, 1H), 6.80 (d, J = 8.6 Hz, 1H), 5.60 (s, 1H), 4.52−4.47 (m, 2H), 4.16−3.97 (m, 4H), 3.87−3.82 (m, 2H), 3.71−3.58 (m, 8H), 2.49 (br, s, 1H, OH). ^{13}C NMR (50 MHz, $CDCl_3$): δ 164.7, 146.0, 137.5, 126.9, 111.6, 102.5, 72.7, 70.9, 70.6, 69.9, 65.5, 65.4, 62.0. HRMS (ESI) m/z calcd for $C_{14}H_{22}NO_6$ $[M+H]^+$ 300.1447, found 300.1440.

*2-(2-(2-(5-(1,3-Dioxolan-2-yl)pyridin-2-yloxy)ethoxy)ethoxy) ethyl 4-methylbenzenesulfonate (**8**).* Alcohol **7** (50 mg, 0.17 mmol) was added to a flame-dried round-bottom flask and dissolved in 1 mL anhydrous dichloromethane. Triethyl amine (30 μL, 25 mg, 0.25 mmol) was added and the reaction mixture was cooled to 0 °C. *p*-Toluenesulfonyl chloride (35 mg, 0.18 mmol) followed by *N*,*N*-4-dimethylaminopyridine (4.0 mg, 0.03 mmol) was quickly added and the reaction was placed in an ice/water bath at 0 °C. The reaction was allowed to warm to room temperature over the course of 5 h at which point it was partitioned between ethyl acetate and H_2O. The organic layer was then extracted from the aqueous layer with the use of ethyl acetate (3 × 10 mL). The combined organic layers were washed with brine (15 mL), dried over $MgSO_4$, filtered, and concentrated. Purification by flash chromatography (45−70% ethyl acetate/hexanes) provided 62 mg (82%) of tosylate **8**, a viscous cloudy oil. R_f = 0.27 (60% ethyl acetate/hexanes). ^{1}H NMR (200 MHz, $CDCl_3$): δ 8.20 (d, J = 2.4 Hz, 1H). 7.80 (d, J = 8.2 Hz, 2H), 7.68 (dd, J = 8.6, 2.4 Hz, 1H), 7.33 (dd, J = 8.6, 0.6 Hz, 2H), 6.78 (d, J = 8.6 Hz, 1H), 5.77 (s, 1H), 4.49−4.44 (m, 2H), 4.18−4.09 (m, 4H), 4.06−3.98 (m, 2H), 3.82−3.78 (m, 2H), 3.71−3.60 (m, 6H), 2.43 (s, 3H). ^{13}C NMR (50 MHz, $CDCl_3$): δ 168.5, 164.6, 146.0, 137.4, 133.4, 130.1, 128.2, 126.8, 111.5, 102.4, 73.1, 71.0, 70.8, 69.9, 69.4, 68.9, 65.5, 65.4, 21.8. HRMS (ESI) m/z calcd for $C_{21}H_{28}NO_8S$ $[M+H]^+$ 454.1536, found 454.1524.

*5-(1,3-Dioxolan-2-yl)-2-(2-(2-(2-fluoroethoxy)ethoxy)ethoxy) pyridine (**2**).* Tosylate **8** (53 mg, 0.117 mmol) was dissolved in 2 mL of tetrahydrofuran and added to a 10 mL round-bottomed flask containing tetra-*n*-butylammonium fluoride hydrate (80 mg, 0.30 mmol). The color of the solution changes instantly upon addition from clear solution to a black solution. The 10 mL round-bottomed flask was then fitted with a reflux condenser and set in an oil bath at 76 °C. After 15 h, the reaction was removed from the heat, allowed to cool to room temperature, diluted with 15 mL ethyl acetate, and concentrated. Purification by flash chromatography (45−60% ethyl acetate/hexanes) provided 20 mg (57%) of a clear oil, compound **2**. R_f = 0.38 (60% ethyl acetate/hexanes). ^{1}H NMR (200 MHz, $CDCl_3$): δ 8.20 (d, J = 2.3 Hz, 1H), 7.68 (dd, J = 8.6, 2.4 Hz, 1H), 6.79 (d, J = 8.9 Hz, 1H), 5.77 (s, 1H), 4.70−4.65 (m, 1H), 4.52−4.42 (m, 3H), 4.17−3.98 (m, 4H), 3.88−3.80 (m, 3H), 3.74−3.65 (m, 5H). ^{13}C NMR (50 MHz, $CDCl_3$): δ 164.7, 145.9, 137.3, 126.9, 111.5, 102.4, 85.1, 81.8, 71.1, 71.0, 70.9, 70.5, 70.0, 65.5. HRMS (ESI) m/z calcd for $C_{14}H_{11}FNO_5$ $[M+H]^+$ 302.1404, found 302.1398; HPLC conditions: Gemini 5 μ C18 110A column, 250 × 4.60 mm, 5 μm; r_t = 4.79 min (280 nm) in acetonitrile/10 mM ammonium formate buffer 60/40 with a flow rate of 1.0 mL/min.

*6-(2-(2-(2-Hydroxyethoxy)ethoxy)ethoxy)nicotinaldehyde (**9**).* Pyridinium *p*-toluenesulfonate (38.0 mg, 0.150 mmol) was added to a solution of acetal **7** (150 mg, 0.50 mmol) in 5 mL acetone and 9 μL H_2O. The flask was then fitted with a reflux condenser and placed in an oil bath set to 70 °C. After 3 h, the reaction was removed from the oil bath, allowed to cool to room temperature, and concentrated. The reaction mixture was then partitioned between dichloromethane and $NaHCO_3$ (aq, sat). The organic layer was separated from the aqueous layer with the use of 5% methanol/dichloromethane (5 × 10 mL). The combined organic layers were then washed with brine (20 mL), dried over $MgSO_4$, filtered, and concentrated to provide 114 mg (89%) of a thick pale yellow oil, aldehyde **9**. R_f = 0.08 (100% ethyl acetate). ^{1}H NMR (200 MHz, $CDCl_3$): δ 9.96 (d, J = 0.6 Hz, 1H), 8.62−8.61 (m, 1H), 8.08 (dd, J = 8.7, 2.4 Hz, 1H), 6.91 (ddd, J = 8.6, 0.7, 0.6 Hz, 1H), 4.63−4.58 (m, 2H), 3.92−3.87 (m, 2H), 3.76−3.68 (m, 6H), 3.65−3.60 (m, 2H), 2.34 (br, s, 1H, OH). ^{13}C NMR (50 MHz, $CDCl_3$): δ 189.6, 167.3, 152.7, 137.7, 126.9, 112.5, 72.6, 70.8, 70.5, 69.5, 66.2, 61.8. HRMS (ESI) m/z calcd for $C_{12}H_{17}NO_5Na$ $[M+Na]^+$ 278.1004, found 278.1005.

*2-(2-(2-(5-Formylpyridin-2-yloxy)ethoxy)ethoxy)ethyl 4-Methyl benzenesulfonate (**10**).* Alcohol **9** (52 mg, 0.20 mmol) was added to a flame-dried round-bottom flask, dissolved in 1 mL of anhydrous dichloromethane, and cooled to 0 °C. Anhydrous pyridine (50 μL, 48 mg, 0.61 mmol) was added to the reaction mixture at 0 °C. After allowing the reaction mixture to stir at 0 °C for 5 min, *p*-toluenesulfonyl chloride (58 mg, 0.31 mmol) was quickly added to the solution. After 10 min, the reaction mixture was removed from the ice/water bath and allowed to warm to room temperature overnight. After 19 h, the reaction mixture was diluted with ethyl acetate and partitioned between H_2O. The organic phase was extracted from the aqueous phase with the use of ethyl acetate (3 × 10 mL). The combined organic layers were washed with brine (10 mL), dried over Na_2SO_4, filtered, and concentrated. Purification by flash chromatography (50−60% ethyl acetate/hexanes) provided 70 mg (84%) of tosylate **10**, a thick, milky oil. R_f = 0.32 (60% ethyl acetate/hexanes). ^{1}H NMR (200 MHz, $CDCl_3$): δ 9.95 (d, J = 0.5 Hz, 1H), 8.60 (dd, J = 2.3, 0.5 Hz, 1H), 8.06 (dd, J = 8.7, 2.4 Hz, 1H), 7.82−7.76 (m, 2H), 7.35−7.31 (m, 2H), 6.87 (ddd, J = 8.7, 0.6, 0.6 Hz, 1H), 4.58−4.54 (m, 2H), 4.18−4.13 (m, 2H), 3.86−3.81 (m, 2H), 3.71−3.60 (m, 6H), 2.43 (s, 3H). ^{13}C NMR (50 MHz, $CDCl_3$): δ 189.7, 167.5, 152.8, 145.0, 137.9, 130.1, 128.4, 127.1, 112.6, 71.0, 70.9, 69.7, 69.4, 69.0, 66.3, 21.8. HRMS (ESI) m/z calcd for $C_{19}H_{24}NO_7S$ $[M+H]^+$ 410.1273, found 410.1277.

*6-(2-(2-(2-Fluoroethoxy)ethoxy)ethoxy)nicotinaldehyde (**3**).* Tosylate **10** (40 mg, 0.10 mmol) was dissolved in tetrahydrofuran (1 mL) and added to a round-bottom flask containing tetra-*n*-butylammonium fluoride hydrate (61 mg, 0.23 mmol). The flask was fitted with a reflux condenser and heated to 76 °C under an inert atmosphere of argon. After 18 h, the reaction was removed from the oil bath and allowed to cool to room temperature (note: most of the solvent had evaporated over the course of the reaction; the reflux condensers had a leak). The reaction media were then condensed and purified by flash chromatography (50% ethyl acetate/hexanes) to afford 10 mg (40%) of fluoride **3**, a thin clear oil. R_f = 0.35 (60% ethyl acetate/hexanes). ^{1}H NMR (200 MHz, $CDCl_3$): δ 9.95 (s, 1H), 8.60 (d, J = 2.3 Hz, 1H), 8.06 (dd, J = 8.9, 2.3 Hz, 1H), 6.88 (dd, J = 8.7, 0.5 Hz, 1H), 4.69−4.65 (m, 1H), 4.61−4.57 (m, 2H), 4.45−4.41 (m, 1H), 3.90−3.80 (m, 3H), 3.72−3.65 (m, 5H). ^{13}C NMR (50 MHz, $CDCl_3$): δ 189.7, 167.5, 152.9, 137.8, 127.1, 112.6, 85.1, 81.7, 71.1, 71.0, 70.9, 70.5, 69.8, 66.4. HRMS (ESI) m/z calcd for $C_{12}H_{17}FNO_4$ $[M+H]^+$ 258.1142, found 258.1142.

*(E)-17-(5-(4-(tert-Butoxycarbonyl(methyl)amino)styryl) pyridin-2-yloxy)-3,6,9,12,15-pentaoxaheptadecyl 4-Methyl-benzenesulfonate (**12**).* Sodium hydride (60%, 22 mg, 0.54 mmol) was added to a flame-dried round-bottom flask.

Anhydrous *N,N*-dimethyl formamide (0.5 mL) was added, and the suspension was cooled to 0 °C. A solution of alcohol **11** (69 mg, 0.13 mmol), dissolved in 0.5 mL of anhydrous *N,N*-dimethyl formamide, was added to the reaction mixture at 0 °C. Diethylene glycol bis(*p*-toluenesulfonate) was then added to the reaction mixture at 0 °C, which was allowed to warm up to room temperature over the course of the night. After 24 h, the reaction was quenched with $NaHCO_3$ (sat. aq.) (10 mL). The organic phase was separated from the aqueous phase with the use of ethyl acetate (4 × 10 mL). The combined organic layers were then washed with brine (1 × 20 mL), dried over $MgSO_4$, filtered, and concentrated. Purification by flash chromatography (2−4% methanol/dichloromethane) afforded 73 mg (73%) of a yellow oil, tosylate **12**. R_f = 0.19 (5% methanol/dichloromethane). ^{1}H NMR (200 MHz, $CDCl_3$): δ 8.16 (d, J = 2.2 Hz, 1H), 7.78 (d, J = 8.4, 2H), 7.77 (d, J = 8.8 Hz, 1H), 7.43 (d, J = 8.6 Hz, 2H), 7.34−7.30 (m, 2H), 7.21 (d, J = 8.6 Hz, 2H), 6.95 (s, 2H), 6.77 (d, J = 8.8 Hz, 1H), 4.50−4.45 (m, 2H), 4.17−4.12 (m, 2H), 3.87−3.82 (m, 2H), 3.72−3.53 (m, 18 H), 3.26 (s, 3H), 2.42 (s, 3H), 1.45 (s, 9H). ^{13}C NMR (50 MHz, $CDCl_3$): δ 163.3, 154.8, 145.8, 144.9, 143.4, 135.5, 134.3, 129.9, 128.1, 127.5, 126.9, 126.6, 125.7, 124.7, 111.6, 80.6, 70.9, 70.8, 70.7, 70.7, 69.9, 69.4, 68.8, 65.5, 37.3, 28.5, 21.8. HRMS (ESI) m/z calcd for $C_{38}H_{53}N_2O_{11}S$ $[M+H]^+$ 745.3370, found 745.3384.

*(E)-tert-Butyl-4-(2-(6-(2-(2-(2-azidoethoxy)ethoxy)ethoxy) pyridin-3-yl)vinyl)phenyl(methyl)carbamate (**14**).* Tosylate **12** (380 mg, 0.62 mmol) and sodium azide (121 mg, 1.86 mmol) were added to a flame-dried round-bottom flask. Anhydrous *N,N*-dimethyl formamide (6 mL) was added to the reaction mixture and placed in an oil bath set to 60 °C. After 4 h, the reaction mixture was removed from the heat, allowed to cool to room temperature, and then partitioned between ethyl acetate and H_2O. The organic phase was separated from the aqueous phase with the use of ethyl acetate (3 × 20 mL). The combined organic layers were then washed with brine (2 × 20 mL), dried over $MgSO_4$, filtered, and concentrated. Purification by flash chromatography (35−50% ethyl acetate/hexanes) afforded 300 mg (quantitative) of a clear oil, azide **14**. R_f = 0.48 (50% ethyl acetate/hexanes). ^{1}H NMR (200 MHz, $CDCl_3$): δ 8.19 (d, J = 2.4 Hz, 1H), 7.79 (dd, J = 8.8, 2.6 Hz, 1H), 7.45 (d, J = 8.6 Hz, 2H), 7.23 (d, J = 8.6 Hz, 2H), 6.97 (s, 2H), 6.80 (d, J = 8.6 Hz, 1H), 4.53−4.48 (m, 2H), 3.90−3.85 (m, 2H), 3.77−3.66 (m, 6H), 3.39 (t, J = 5.2 Hz, 2H), 3.27 (s, 3H), 1.46 (s, 9H). ^{13}C NMR (50 MHz, $CDCl_3$): δ 163.4, 154.9, 145.9, 143.5, 135.6, 134.4, 127.5, 127.0, 126.7, 125.8, 124.8, 111.7, 80.6, 71.0, 70.3, 65.5, 50.9, 37.3, 28.6. HRMS (ESI) m/z calcd for $C_{25}H_{34}N_5O_5$ $[M+H]^+$ 484.2650, found 484.2546.

*(E)-tert-Butyl-4-(2-(6-(2-(2-(2-aminoethoxy)ethoxy)ethoxy) pyridin-3-yl)vinyl)phenyl(methyl)carbamate (**16**).* Triphenyl phosphine (271 mg, 1.03 mmol) was added to a solution of azide **14** (200 mg, 0.41 mmol) in 12.5 mL of tetrahydrofuran. After 1 h, water (1.5 mL) was added to the reaction mixture. The reaction mixture was heated to 60 °C for 18 h. The reaction was then removed from the heat and allowed to cool to room temperature and concentrated. Purification by flash chromatography (96:4:1−85:15:1 dichloromethane/methanol/ammonium hydroxide) provided 133 mg (70%) amine **16**, a white waxy material. R_f = 0.19 (8.5:1.5:0.1 dichloromethane/methanol/ammonium hydroxide). ^{1}H NMR (200 MHz, $CDCl_3$): δ 8.14 (d, J = 2.3 Hz, 1H), 7.74 (dd, J = 8.6, 2.4 Hz, 1H), 7.40 (d, J = 8.6 Hz, 2H), 7.18 (d, J = 8.5 Hz, 2H), 6.92 (s, 2H), 6.76 (d, J = 8.7 Hz, 1H), 4.48−4.43 (m, 2H), 3.85−3.80 (m, 2H), 3.71−3.58 (m, 4H), 3.49 (t, J = 5.2 Hz, 2H), 3.22 (s, 3H), 2.84 (t, J = 5.2 Hz, 2H), 2.30 (br, s, 2H, NH_2), 1.42 (s, 9H). ^{13}C NMR (50 MHz, $CDCl_3$): δ 163.2, 154.7, 145.7, 143.3, 135.5, 134.2, 127.4, 126.9, 126.5, 125.6, 124.6, 111.5, 80.5, 73.0, 70.7, 70.4, 69.8, 65.3, 41.7, 37.3, 28.4. HRMS (ESI) m/z calcd for $C_{25}H_{36}N_3O_5$ $[M+H]^+$ 458.2655, found 458.2642.

*Dicarbamate (**19**).* Amine **16** (132 mg, 0.29 mmol) and succinimide **18** (108 mg, 0.38 mmol) were dissolved in 6 mL of anhydrous *N,N*-dimethyl formamide, and to this solution was added *N,N*-diisopropylethylamine (1.0 mL, 744 mg, 5.76 mmol). The reaction was allowed to stir at room temperature. After 1 h, the reaction was concentrated (23 mbar at 60 °C, to facilitate the removal of *N,N*-dimethyl formamide) and purified by flash chromatography (2−6% methanol/dichloromethane) to provide 81 mg (45%) of dicarbamate **19**, a clear gummy material. R_f = 0.29 (5% methanol/dichloromethane). ^{1}H NMR (200 MHz, $CDCl_3$): δ 8.18 (d, J = 2.2 Hz, 1H), 7.98 (br s, 1H, NH), 7.80 (dd, J = 8.7, 2.3 Hz, 2H), 7.44 (d, J = 8.6 Hz, 2H), 7.22 (d, J = 8.6 Hz, 2H), 6.96 (s, 2H), 6.80 (d, J = 8.7 Hz, 1H), 4.52−4.47 (m, 2H), 4.34 (s, 2H), 3.90−3.85 (m, 2H), 3.76−3.47 (m, 8H), 3.27 (s, 3H), 1.46 (s, 9H), 1.46 (s, 9H). ^{13}C NMR (50 MHz, $CDCl_3$): δ 169.1, 163.2, 157.6, 154.8, 145.7, 143.3, 135.6, 134.3, 127.5, 126.9, 126.6, 125.6, 124.6, 111.6, 82.6, 80.6, 76.0, 70.7, 70.5, 69.8, 69.7, 65.4, 39.0, 37.3, 28.5, 28.3. HRMS (ESI) m/z calcd for $C_{32}H_{47}N_4O_9$ $[M+H]^+$ 631.3343, found 631.3345.

*(E)-2-(Aminooxy)-N-(2-(2-(2-(5-(4-(methylamino)styryl) pyridin-2-yloxy)ethoxy)ethoxy)ethyl)acetamide (**21**).* Trifluoroacetic acid (3 mL) was added to a solution of carbamate **19** (394 mg, 0.63 mmol) in dichloromethane (3 mL). The reaction was allowed to stir at room temperature for 3 h after which time the reaction mixture was concentrated down from 1 N HCl (2 × 3 mL) and placed under high vacuum for 30 min. Purification by flash chromatography (97:3:1−90:10:1 dichloromethane/methanol/ammonium hydroxide) provided 158 mg (59%) of aminooxy **21** a yellow, waxy solid. Due to its instability, full characterization was achieved from the subsequent step of the formation of oxime **23**; aminooxy **21** was determined by HRMS. R_f = 0.49 (9.0:1.0:0.1 dichloromethane/methanol/ammonium hydroxide). HRMS (ESI) m/z calcd for $C_{22}H_{31}N_4O_5$ $[M+H]^+$ 431.2294, found 431.2300.

*2-((E)-(6-(2-(2-(2-Fluoroethoxy)ethoxy)ethoxy)pyridin-3-yl) methyleneaminooxy)-N-(2-(2-(2-(5-((E)-4-(methylamino)styryl) pyridin-2-yloxy)ethoxy)ethoxy)ethyl)acetamide (**23**).* A solution of aldehyde **3** (7 mg, 0.03 mmol) dissolved in 1.4 mL of ethanol, 0.1 mL of H_2O, and 20 μL of trifluoroacetic acid was added to hydroxylamine **21** (12 mg, 0.03 mmol). The reaction mixture was placed in an oil bath set to 70 °C. After 2 h, the reaction mixture was removed from the heat and allowed to cool to room temperature. The reaction was then quenched with Na_2CO_3 (aq) and partitioned between 10% methanol/dichloromethane. The organic layer was separated from the aqueous layer with the use of 10% methanol/dichloromethane (4 × 10 mL). The combined organic layers were washed with brine (15 mL), dried over $MgSO_4$, filtered, and concentrated. Purification by flash chromatography (97:3:0.5−93:7:0.5 dichloromethane/methanol/ammonium hydroxide) provided 9 mg (50%) of oxime **23**, a viscous yellow oil. R_f = 0.33 (9.5:0.5:0.1 dichloromethane/methanol/ammonium hydroxide). ^{1}H NMR (200 MHz, $CDCl_3$): δ 8.28 (s, 1H), 8.28−8.14 (m, 2H), 7.95 (ddd, J = 8.9, 8.7, 2.2 Hz, 2H), 7.37 (d, J = 8.7 Hz, 2H), 6.96−6.78 (m, 4H), 6.64 (d, J = 8.6 Hz,

2H), 4.67−4.62 (m, 3H), 4.49−4.39 (m, 6H), 3.87−3.79 (m, 5H), 3.69−3.58 (m, 12H), 3.50−3.46 (m, 2H), 2.83 (s, 3H). ^{13}C NMR (50 MHz, $CDCl_3$): δ 172.5, 166.6, 164.0, 151.5, 149.6, 148.5, 146.3, 146.0, 137.7, 137.0, 130.3, 129.8, 128.8, 127.5, 123.2, 120.6, 113.6, 112.8, 112.2, 85.9, 82.6, 74.1, 72.0, 71.9, 71.5, 70.9, 70.7, 67.0, 66.7, 40.3, 30.8. HRMS (ESI) m/z calcd for $C_{34}H_{45}FN_5O_8$ $[M+H]^+$ 670.3252, found 670.3236. HPLC conditions: Gemini 5 μ C18 110A column, 250 × 4.60 mm, 5 μm; r_t = 6.83 min (280 nm) in acetonitrile/10 mM ammonium formate buffer 60/40 at a flow rate of 1.0 mL/min.

*(E)-17-(5-(4-(tert-Butoxycarbonyl(methyl)amino)styryl)pyridin-2-yloxy)-3,6,9,12,15-pentaoxaheptadecyl 4-Methylbenzenesulfonate (**13**).* Sodium hydride (60%, 22 mg, 0.54 mmol) was dissolved in 0.5 mL of *N,N*-dimethyl formamide in a flame-dried round-bottom flask. This solution was cooled to 0 °C. Alcohol **11** (69 mg, 0.13 mmol), dissolved in 0.5 mL of *N,N*-dimethyl formamide, was added to the reaction mixture at 0 °C. After 3 min of stirring at 0 °C, diethylene glycol bis(*p*-toluenesulfonate) (337 mg, 0.80 mmol) was added to the reaction. The ice/water bath was removed, and the reaction was allowed to warm to room temperature. After 24 h, the reaction media were buffered with $NaHCO_3$ (aq, sat) and partitioned between ethyl acetate. The organic layer was extracted from the aqueous layer with the use of ethyl acetate (4 × 20 mL). The combined organic layers were washed with brine (30 mL), dried over $MgSO_4$, filtered, and concentrated. Purification by flash chromatography (2−3% methanol/dichloromethane) provided 73 mg (73%) of tosylate **13**, a yellow oil. R_f = 0.19 (5% methanol/dichloromethane). ^{1}H NMR (200 MHz, $CDCl_3$): δ 8.16 (d, J = 2.2 Hz, 1H), 7.78 (d, J = 8.4 Hz, 2H), 7.77 (d, J = 8.8 Hz, 1H), 7.43 (d, J = 8.6 Hz, 2H), 7.34−7.30 (m, 2H), 7.21 (d, J = 8.6 Hz, 2H), 6.95 (s, 2H), 6.77 (d, J = 8.8 Hz, 1H), 4.50−4.45 (m, 2H), 4.17−4.12 (m, 2H), 3.87−3.82 (m, 2H), 3.72−3.53 (m, 18H), 3.26 (s, 3H), 2.42 (s, 3H), 1.45 (s, 9H). ^{13}C NMR (50 MHz, $CDCl_3$): δ 163.3, 154.8, 145.8, 144.9, 143.4, 135.5, 134.3, 129.9, 128.1, 127.5, 126.9, 125.7, 126.9, 126.6, 125.7, 124.7, 111.6, 80.6, 70.9, 70.8, 70.7, 70.7, 69.9, 69.4, 68.8, 65.5, 37.3, 28.5, 21.8. HRMS (ESI) m/z calcd for $C_{38}H_{53}N_2O_{11}S$ $[M+H]^+$ 745.3370, found 745.3384.

*(E)-tert-Butyl 4-(2-(6-(17-azido-3,6,9,12,15-pentaoxaheptadecyloxy)pyridin-3-yl)vinyl)phenyl(methyl)carbamate (**15**).* Tosylate **13** (300 mg, 0.40 mmol) was added to a flame-dried flask containing a solution of sodium azide (79 mg, 1.21 mmol) in 4 mL of anhydrous *N,N*-dimethyl formamide. The reaction mixture was heated to 60 °C. After 3 h, the reaction mixture was removed from the heat and allowed to cool to room temperature. It was then partitioned between ethyl acetate and H_2O. The organic phase was separated from the aqueous phase with the use of ethyl acetate (3 × 40 mL). The combined organic layers were washed with brine (2 × 20 mL), dried over $MgSO_4$, filtered, and concentrated. Purification by flash chromatography (80−85% ethyl acetate/hexanes) gave 150 mg (60%) of a viscous yellow oil, azide **15**. R_f = 0.24 (85% ethyl acetate/hexanes). ^{1}H NMR (200 MHz, $CDCl_3$): δ 8.18 (d, J = 2.2 Hz, 1H), 7.79 (dd, J = 9.0, 2.6 Hz, 1H), 7.45 (d, J = 8.9 Hz, 2H), 7.23 (d, J = 8.6 Hz, 2H), 6.97 (s, 1H), 6.79 (d, J = 8.6 Hz, 1H), 4.52−4.47 (m, 2H), 3.89−3.84 (m, 2H), 3.71−3.65 (m, 18H), 3.41−3.36 (m, 2H), 3.27 (s, 3H), 1.46 (s, 9H). ^{13}C NMR (50 MHz, $CDCl_3$): δ 163.3, 154.8, 145.8, 143.3, 135.3, 134.3, 127.5, 126.9, 126.6, 125.7, 124.8, 111.6, 80.6, 70.8, 70.8, 70.2, 69.9, 65.5, 50.8, 37.3, 28.5. HRMS (ESI) m/z calcd for $C_{31}H_{45}N_5O_8Na$ $[M+Na]^+$ 638.3166, found 638.3157.

*(E)-tert-Butyl 4-(2-(6-(17-amino-3,6,9,12,15-pentaoxaheptadecyloxy)pyridin-3-yl)vinyl)phenyl(methyl)carbamate (**17**).* Triphenyl phosphine (51 mg, 0.20 mmol) was added to a solution of azide **15** (48 mg, 0.08 mmol) in 2.7 mL of tetrahydrofuran. After 1 h, water (0.3 mL) was added to the reaction and heated to 60 °C for 17 h. The reaction was then removed from the heat and allowed to cool to room temperature and concentrated. Purification by flash chromatography (95:5:1−85:15:1 dichloromethane/methanol/ammonium hydroxide) provided 37 mg (80%) of amine **17**, a white wax. R_f = 0.28 (8.5:1.5:0.1 dichloromethane/methanol/ammonium hydroxide). ^{1}H NMR (200 MHz, $CDCl_3$): δ 8.23 (d, J = 2.3 Hz, 1H), 7.99 (dd, J = 8.8, 2.5 Hz, 1H), 7.55 (d, J = 8.6 Hz, 2H), 7.25 (d, J = 8.6 Hz, 2H), 7.12 (s, 2H), 6.85 (d, J = 8.7 Hz, 1H), 4.46−4.44 (m, 2H), 3.89−3.84 (m, 2H), 3.71−3.53 (m, 20H), 3.26 (s, 3H), 2.86 (t, J = 5.4 Hz, 2H), 1.47 (s, 9H). ^{13}C NMR (50 MHz, $CDCl_3$): δ 164.6, 156.6, 146.9, 144.4, 137.2, 136.5, 128.8, 128.8, 127.9, 127.2, 125.8, 112.3, 82.0, 72.3, 71.7, 71.6, 71.4, 71.3, 70.8, 66.8, 41.9, 38.0, 28.7. HRMS (ESI) m/z calcd for $C_{31}H_{48}N_3O_8$ $[M+H]^+$ 590.3441, found 590.3442.

*Dicarbamate (**20**).* Amine **17** (37 mg, 0.06 mmol) dissolved in 2 mL of anhydrous *N,N*-dimethyl formamide was added to succinimide **18** (24 mg, 0.08 mmol) in a flame-dried 10 mL round-bottom flask. *N,N*-Diethyl *iso*-propyl amine (0.22 mL, 163 mg, 1.26 mmol) was then added to the reaction mixture and allowed to stir at room temperature. After 1 h, the reaction was concentrated (23 mbar at 60 °C, to facilitate the removal of *N,N*-dimethyl formamide) and purified by flash chromatography (2−4% methanol/dichloromethane) to provide 29 mg (60%) of dicarbamate (**20**), a clear, gummy compound. R_f = 0.31 (5% methanol/dichloromethane). ^{1}H NMR (200 MHz, $CDCl_3$): δ 8.18−8.17 (m, 2H), 7.87 (br, s, 1H, NH), 7.79 (dd, J = 8.6, 2.5 Hz, 1H), 7.44 (d, J = 8.6 Hz, 2H), 7.22 (d, J = 8.5 Hz, 2H), 6.96 (s, 2H), 6.78 (d, J = 8.6 Hz, 1H), 4.50−4.45 (m, 2H), 4.33 (s, 2H), 3.87−3.82 (m, 2H), 3.78−3.45 (m, 20H), 3.26 (s, 3H), 1.46 (s, 9H), 1.45 (s, 9H). ^{13}C NMR (50 MHz, $CDCl_3$): δ 169.3, 163.3, 157.7, 155.0, 145.8, 143.5, 135.6, 134.4, 127.5, 127.0, 126.7, 125.8, 124.7, 111.6, 82.7, 80.7, 76.1, 70.8, 70.7, 70.5, 69.9, 69.8, 65.6, 53.3, 39.2, 37.5, 28.5, 28.4. HRMS (ESI) m/z calcd for $C_{38}H_{59}N_4O_{12}$ $[M+H]^+$ 763.4129, found 763.4130.

*(E)-2-(Aminooxy)-N-(17-(5-(4-(methylamino)styryl)pyridine-2-yloxy)-3,6,9,12,15-pentaoxaheptadecyl)acetamide (**22**).* Carbamate **20** (29 mg, 0.04 mmol) was dissolved in 1 mL dichloromethane and to it was added 1 mL of trifluoroacetic acid. The reaction was allowed to stir at room temperature for 5 h after which time the reaction mixture was concentrated down from 1 N HCl (2 × 3 mL) and placed under high vacuum to obtain 137 mg of a pale, yellow viscous oil of the aminooxy·*x*HCl salt **22**. Due to its instability, full characterization was achieved from the subsequent step of formation of oxime **24**.

*2-((E)-(6-(2-(2-(2-fluoroethoxy)ethoxy)ethoxy)pyridin-3-yl) methyleneaminooxy)-N-(17-(5-((E)-4-(methylamino)styryl) pyridin-2-yloxy)-3,6,9,12,15-pentaoxaheptadecyl)acetamide (**24**).* Trifluoroacetic acid (10 μL) was added to a solution of acetal **2** (10 mg, 0.03 mmol) dissolved in 1.0 mL ethanol and 0.5 mL H_2O to lower the pH to ~0. This was then placed in an oil bath and heated to 60 °C. After 5 min, a solution of diamine **22** (21 mg, 0.04 mmol) in 0.7 mL ethanol and 0.1 mL H_2O was added to the reaction mixture at 60 °C. After 10 min, the reaction mixture was removed from the heat, allowed to cool to room temperature, and concentrated down from 1 N HCl (2 × 1 mL). The crude reaction mixture was then partitioned

between 50% $NaHCO_3$ (aq, sat)/ice and 5% methanol/ethyl acetate. The organic layer was separated form the aqueous layer with the use of 5% methanol/ethyl acetate (3 × 5 mL). The combined organic layers were washed with brine (10 mL), dried over $MgSO_4$, filtered, and concentrated. Purification by flash chromatography (5−10% methanol/dichloromethane) provided 18 mg (67%) of oxime **24**, a pale yellow material. R_f = 0.28 (5% methanol/dichloromethane). ^{1}H NMR (200 MHz, $CDCl_3$): δ 8.26−8.24 (m, 2H), 8.11 (d, J = 2.5 Hz, 1H), 7.93 (ddd, J = 16.6, 8.9, 2.3 Hz, 2H), 7.33 (d, J = 8.5 Hz, 2H), 7.02−6.75 (m, 4H), 6.60 (d, J = 8.6 Hz, 2H), 4.64−4.57 (m, 3H), 4.47−4.36 (m, 6H), 3.85−3.78 (m, 6H), 3.67−3.40 (m, 24H), 2.79 (s, 3H). ^{13}C NMR (50 MHz, $CDCl_3$): δ 172.5, 166.5, 164.1, 151.5, 149.6, 148.5, 145.9, 137.8, 136.8, 130.3, 129.7, 128.8, 127.5, 123.3, 120.6, 113.6, 112.9, 112.3, 85.9, 82.6, 74.1, 71.9, 71.8, 71.7, 71.7, 71.6, 71.5, 70.9, 70.7, 70.6, 67.0, 66.7, 40.2, 30.7. HRMS (ESI) m/z calcd for $C_{40}H_{57}N_5O_{11}$ $[M+H]^+$ 802.4039, found 802.4016. HPLC conditions: Gemini 5 μ C18 110A column, 250 × 4.60 mm, 5 μm; r_t = 6.40 min (280 nm) in acetonitrile/10 mM ammonium formate buffer 60/40 with a flow rate of 1.0 mL/min.

Radiochemistry. A typical procedure for the formation of radioactive intermediate [^{18}F]**2** is as follows: A Sep-Pak light Accell Plus QMA (Waters Corporation) cartridge was activated with 1 N $NaHCO_3$ (10 mL), H_2O (10 mL), and dried with argon. [^{18}O]-Enriched aqueous solution of fluoride-18 (∼2 mCi) was taken up in 1 mL of H_2O (diluted) and passed through the activated QMA (light) cartridge. A solution of 1 mL (0.93 mL acetonitrile, 0.07 mL H_2O) containing Kryptofix[K222] (11 mg 4,7,13,16,21,24-hexaoxa-1,10-diazabicyclo[8.8.8]hexacosane) and 2 mg K_2CO_3, was then passed through the QMA cartridge into a reaction vessel to collect the K[222]^{18}F complex. This complex was dried at 110 °C with a flow of argon until most of the solvent was evaporated. The solution was further azeotroped with the use of acetonitrile (2 × 1 mL) at 110 °C with a stream of argon gas. A solution of tosylate **8** (1 mg) in 1 mL of anhydrous acetonitrile was added to the "dry" K[222]^{18}F complex at 110 °C. After 10 min, the reaction vessel was removed from the oil bath, cooled in an ice/water bath, and quenched with 8 mL of H_2O. The reaction medium was then passed through an OASIS HLB 3 cm^3 cartridge (activated by flushing with 3 mL ethanol followed by 10 mL H_2O). The OASIS cartridge was subsequently washed with H_2O (2 × 3 mL), and the desired radioactive ligand was eluted with ethanol (0.75 mL). The activity was measured from each washing to obtain the decay corrected radio chemical yield (rcy). The eluted ligand was used without any further purification. Radiochemical purity (rcp) of the prosthetic ligand [^{18}F]**2** was determined by HPLC. HPLC conditions: Gemini 5 μ C18 110A column, 250 × 4.60 mm, 5 μm; acetonitrile/10 mM ammonium formate buffer solution 60/40 with a flow rate of 1.0 mL/min; r_t = 4.79 min.

A typical procedure of the formation of oxime [^{18}F]**23** and [^{18}F]**24** is as follows: Water (0.2 mL) followed by trifluoroacetic acid (∼15 μL) was added to compound [^{18}F]**2**. The reaction vessel was then placed in an oil bath set to 70 °C. After 2 min at 70 °C, a solution of aminooxy **21** or **22** (∼4 mg, >1.1 equiv of tosylate **8**) in 0.3 mL of ethanol and 0.1 mL of H_2O was added to the reaction mixture. After an additional 25 min, the reaction vessel was removed from the oil bath, cooled in an ice/water bath, and quenched with 0.2 mL of 1 N $NaHCO_3$. This crude solution was then purified by HPLC (Gemini 5 μ C18 110A column, 250 × 10.00 mm, 5 μm; acetonitrile/10 mM ammonium formate buffer solution 60/40 as mobile phase with a flow rate of 2.0 mL/min; fractions were collected from 14.56 to 16.17 min). The fractions were then pooled together and diluted with 3 mL H_2O. The reaction media were then passed through an OASIS HLB 3 cm^3 cartridge (activated by flushing with 3 mL ethanol followed by 10 mL H_2O). The OASIS cartridge was washed with an organic solvent (ethanol or acetonitrile) (0.75 mL) to elute the desired radioactive oxime. The radiochemical purity and the specific activity for compounds [^{18}F]**23** and [^{18}F]**24** were determined by HPLC (Gemini 5 μ C18 110A column, 250 × 4.60 mm, 5 μm; acetonitrile/10 mM ammonium formate buffer 60/40 with a flow rate of 1.0 mL/min; retention time for [^{18}F]**23** r_t = 6.83 min; retention time for [^{18}F]**24** r_t = 7.37 min).

Biodistribution. *In Vivo Biodistribution Study in Mice.* Biodistribution studies were performed on ligands [^{18}F]**23** and [^{18}F]**24**, to evaluate their biological properties. Each of these radiotracers were tested in normal male ICR mice weighing 20−25 g. Each of the biodistribution studies used 6 mice per group with two time points taken at 2 and 30 min postinjection. The mice were put under isoflurane anesthesia (1−2%, 1 L oxygen/minute). A saline solution (0.15 mL) containing 25 μCi of each isomer, [^{18}F]**23** or [^{18}F]**24**, was injected via the lateral tail vein. The mice were sacrificed at 2 and 30 min postinjection by cardiac excision while under isoflurane anesthesia. The organs of interest were removed, weighed, and the radioactivity counted with a gamma counter (Packard Cobra). The percent dose per gram was calculated by a comparison of the tissue activity counts to counts of 1.0% of the initial dose. The initial dose consisted of 100× diluted aliquots of the injected material measured at the same rate.

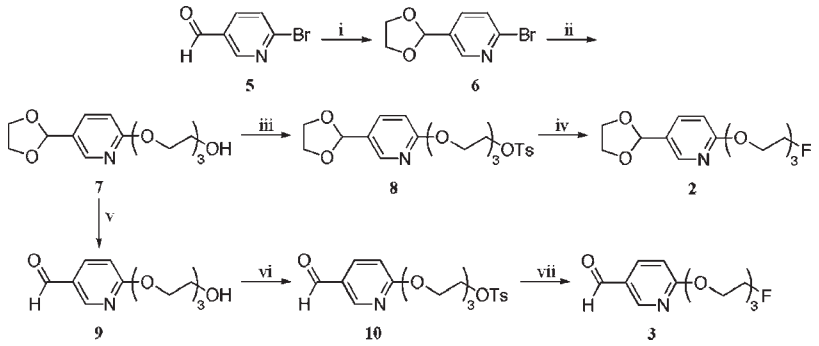
RESULTS AND DISCUSSION

Chemical Synthesis. The formation of the "cold" prosthetic ligand **2** is depicted in Scheme 1. The synthesis began with the formation of acetal **6**[43] through an acid-catalyzed protection of 6-bromo-3-pyridine carbaldehyde **5**. The triethylene glycol chain was tethered onto the molecule under basic conditions (cesium carbonate) with the aid of a microwave reactor. Alcohol **7** was converted into tosylate **8**, which was subsequently refluxed in the presence of tetra-*n*-butylammonium fluoride hydrate to provide the desired acetal, compound **2**.

The formation of compound **3** is depicted in Scheme 1. The acetal functional group of intermediate **7** was removed under acidic conditions to provide aldehyde **9**. It should be noted that direct addition of triethylene glycol to 6-bromo-3-pyridine carbaldehyde **5**, the same conditions used to form intermediate **7**, proved to be incompatible, providing only 2% of the desired aldehyde **9**. Therefore, two steps were necessary to synthesize aldehyde **9**: nucleophilic substitution of triethylene glycol followed by the removal of the acetal protecting group. The alcohol functional group of compound **9** was converted into the tosylate to provide intermediate **10**. Compound **10** was transformed into aldehyde **3** with the use of tetra-*n*-butylammonium fluoride hydrate in refluxing tetrahydrofuran.

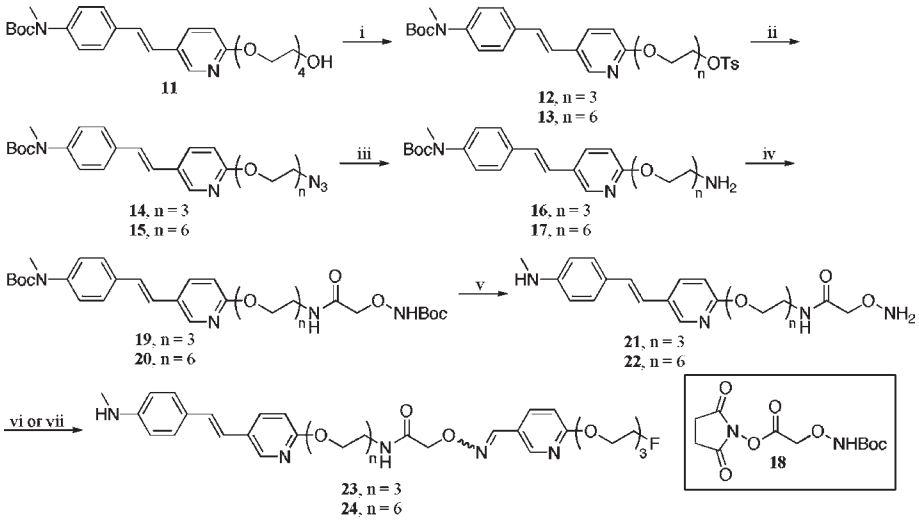
The syntheses of "cold" oximes **23** and **24** are illustrated in Scheme 2. Compound **13** was prepared from alcohol **11** (n = 4) with the use of sodium hydride and diethylene glycol bis(*p*-toluenesulfonate). Each of the tosylate groups in species **12** and **13**[44] were displaced with sodium azide at elevated temperatures. The azide functionality was then reduced to an amine, which led to the formation of compounds **14** and **15**, by way of a Staudinger

Scheme 1. Synthetic Pathway for the Preparation of Fluorides 2 and 3[a]



[a] Reagents and conditions: (i) ethylene glycol, *p*-TsOH, benzene, reflux (98%); (ii) triethylene glycol, Cs_2CO_3, DMF, microwave, 150 °C, 50 min (61%); (iii) *p*-TsCl, Et_3N, DMAP, CH_2Cl_2 (82%); (iv) TBAF·H_2O, THF, reflux (57%); (v) PPTS, acetone, H_2O, 70 °C (89%); (vi) *p*-TsCl, pyridine, CH_2Cl_2, 0 °C to rt (84%); (vii) TBAF·H_2O, THF, reflux (40%).

Scheme 2. Synthetic Pathway for the Formation of Oximes 23 (n = 3) and 24 (n = 6)[a]



[a] Reagents and conditions: (i) diethylene glycol bis(*p*-toluenesulfonate), NaH, DMF, 0 °C to rt (73%); (ii) NaN_3, DMF, 60 °C, 3 h (n = 3: 100%; n = 6: 60%); (iii) PPh_3, THF/H_2O (9:1), 60 °C (n = 3: 70%; n = 6: 80%); (iv) **18**, *i*-Pr_2NEt, DMF (n = 3: 45%; n = 6: 60%); (v) TFA/CH_2Cl_2, (1:1) (n = 3: 73%; n = 6: 100%); (vi) **3**, TFA, EtOH/H_2O, 70 °C (n = 3: 50%); (vii) **2**, TFA, EtOH/H_2O, 70 °C (n = 6: 67%).

reaction.[45,46] It was crucial that the correct reaction conditions be used to reduce only the azide functionality without saturating the carbon−carbon double bond. Succinimide **18**[47] was attached with **14** and **15** with excess Hünig's base to provide the dicarbamates **19** and **20**, respectively. Removal of both *t*-butoxycarbonyl (Boc) protecting groups was achieved using a 1:1 mixture of dichloromethane/trifluoroacetic acid. Subsequent addition of the free aminooxy compound into aldehyde **3** lead to the formation of the desired oxime **23** (n = 3). Likewise, aminooxy **22** was added to acetal **2** under acidic conditions to provide the desired oxime **24** (n = 6). The acetal group was removed in situ to form the aldehyde, which under an acidic environment has a high affinity to react with aminooxy groups.[38,39] The one pot deprotection/addition sequence to form the desired oxime proved to be essential for the radiosynthesis of compounds [^{18}**F**]**23** and [^{18}**F**]**24**. Although two isomers (*cis* and *trans*) are potentially formed, it appears that only one isomer was observed in the formation of both oximes **23** and **24** (confirmed by HPLC). It is hypothesized that this isomer is the more stable *trans*-complex. Work is currently underway to elucidate their structures by attempts to obtain crystal structures with the use of forming the salts with several different counterions. Oximes **23** and **24** are the "cold" standards for our labeling studies.

Radiolabeling. Our initial goal was to synthesize and evaluate a new prosthetic ligand with a future goal of radiolabel biologically active peptides and proteins by way of an oxime coupling reaction. Preliminary studies were done on two model aminooxy species, compounds **23** and **24**. We first fully characterized the "cold" oximes, and then radiolabeled each aminooxy compound with our prosthetic ligand. These small molecules were used as models, instead of the protein or peptide oxime adducts, due to their compatibility with more practical and manageable reagents and characterization methods (i.e., cost effectiveness and characterization without the use of MALDI). The radiolabeling of complexes **21** and **22** was used to demonstrate the capability of this methodology while attempting to optimize the reaction conditions to form the oxime bond.

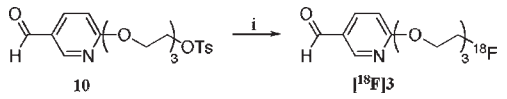
The first attempt at the formation of a prosthetic ligand was through the direct fluoride-18 (nca) labeling of aldehyde **10**

dx.doi.org/10.1021/bc1004262 |*Bioconjugate Chem.* 2011, 22, 642–653

(Scheme 3). The formation of an oxime with the use of an aminooxy group and an aldehyde under acidic conditions can be achieved. The fluoride-18 labeling of aldehyde **10** afforded compound [^{18}F]**3**. The formation of compound [^{18}F]**3** provided a reasonable radiochemical yield, however, with low radiochemical purity (42%). Several unidentified peaks were observed in the HPLC radioactive trace.

To circumvent the low radiochemical purity, the aldehyde group was protected prior to the fluoride-18 radiolabeling. Therefore, acetal **8** was used in place of aldehyde **10**. The formation of compound [^{18}F]**2** was achieved through a direct S_N2 displacement of a tosylate group (see Figure 3 for HPLC traces for cold and hot complexes). The acetal functionality protected the compound from the harsh environment present for the nucleophilic attack of a fluoride anion. The acetal, [^{18}F]**2**, is a stable, neutral molecule soluble in organic media. After successful fluoride-18 labeling, the acetal group was deprotected under an aqueous acidic media and converted to the aldehyde; aldehydes will chemoselectively react with aminooxy functional groups under these same conditions to provide an irreversible oxime bond.[38,39] This allows for both the deblocking of the acetal functionality and the formation of the oxime bond, to bestow the radiolabeled tracer.

Scheme 3. Direct Fluoride-18 (nca) Labeling of Aldehyde 10[a]



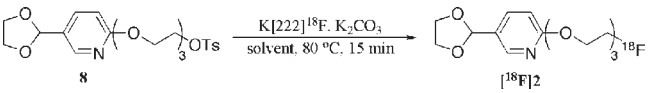
10 [^{18}F]**3**

[a] Reagents and conditions: (i) K[222]^{18}F, K_2CO_3, DMSO, 100 °C, 10 min (45% rcy; 42% rcp).

Several variables were studied (i.e., solvent, temperature, and time) to determine the most efficient and suitable conditions for radiosynthesis of acetal [^{18}F]**2**. A solvent screening was performed at a constant temperature (80 °C) and time (15 min) with the use of 4,7,13,16,21,24-hexaoxa-1,10-diazabicyclo-[8.8.8]-hexacosane (K[222]) and potassium carbonate as the catalysts for the preparation of "naked" fluoride (see Table 1). The radiochemical yields (rcy) were determined from the isolation of the product after solid-phase extraction (OASIS HLB 3 cm^3 cartridge), and the radiochemical purities (rcp) were determined by HPLC (for conditions, see Experimental Procedures section). These results suggested that dimethyl sulfoxide and acetonitrile are the solvents of choice. Due to the higher observed radiochemical purity (rcp) achieved with acetonitrile as the solvent (91 ± 4%, n = 3; see Table 1), all further experiments were performed with the use of acetonitrile.

A time study was performed for the radiolabeling of acetal [^{18}F]**2** in the presence of "dry" K[222]^{18}F catalyst (Table 2).

Table 1. Use of Varying Solvent for the Radiolabeling of Tosylate 8 (n = 3)



8 [^{18}F]**2**

entry	solvent	% rcy (isolated)	% rcp (HPLC)
1	DMSO	32 (±2)	84 (±15)
2	DMF	14 (±6)	78 (±11)
3	*t*-BuOH	7 (±2)	53 (±12)
4	ACN	35 (±2)	91 (±4)

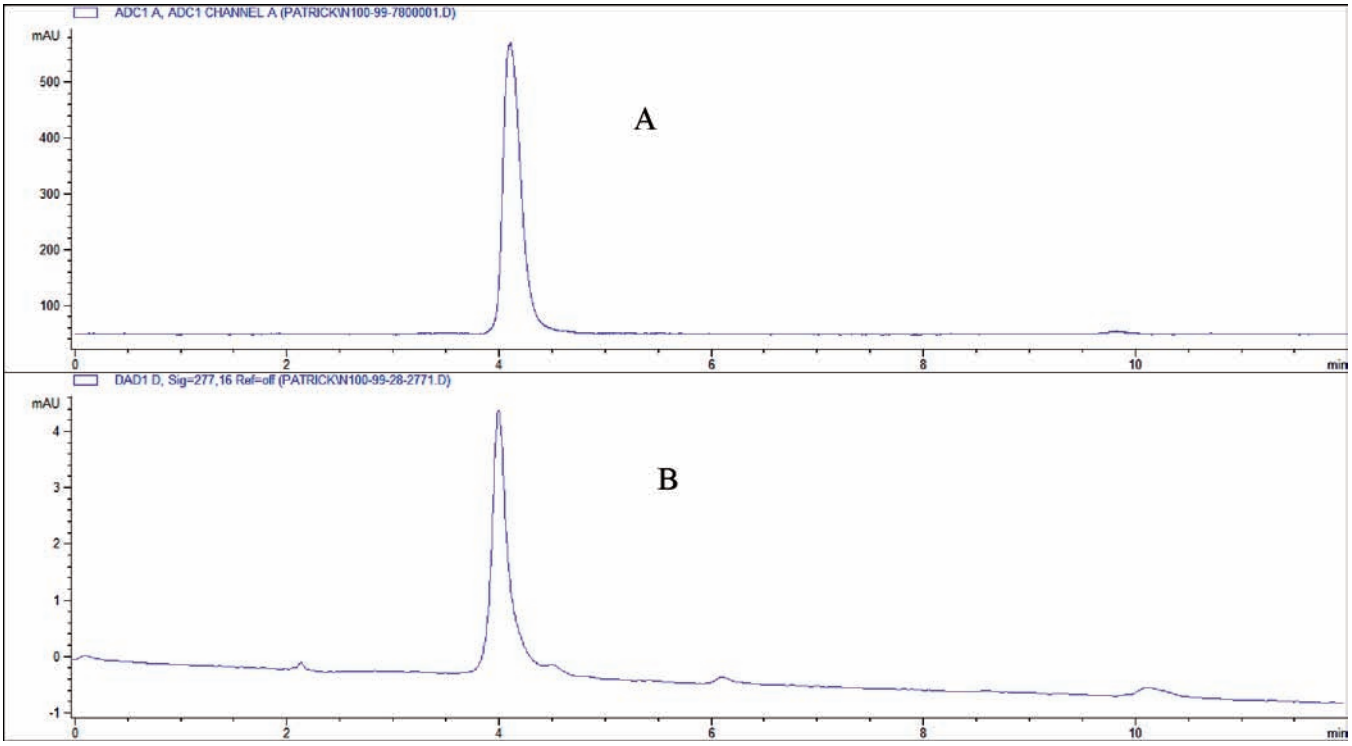
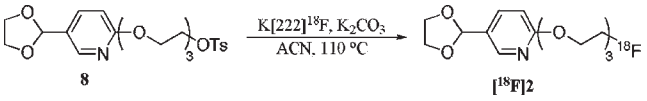


Figure 3. (A) HPLC profile of radiotrace [^{18}F]**2**. (B) HPLC profile of UV-spectra for compound **2** at 277 nm. Both samples were run on Gemini 5 μ C18 110A 250 × 4.60 mm column; ACN/10 mM AFB 60/40 with a flow rate of 1.0 mL/min; r_t = 4.10 min.

dx.doi.org/10.1021/bc1004262 |*Bioconjugate Chem.* 2011, 22, 642–653

Table 2. Time Study Results on the Radiochemical Synthesis of Compound [^{18}F]2



8 [^{18}F]2

entry	time (min)	% rcy (isolated)	% rcp (HPLC)
1	5	51	93
2[a]	10	71 (±2)	99 (±1)
3	15	65	96
4[b]	15	49	94
5	20	61	>99

[a] n = 3. [b] Reaction was run in a sealed tube.

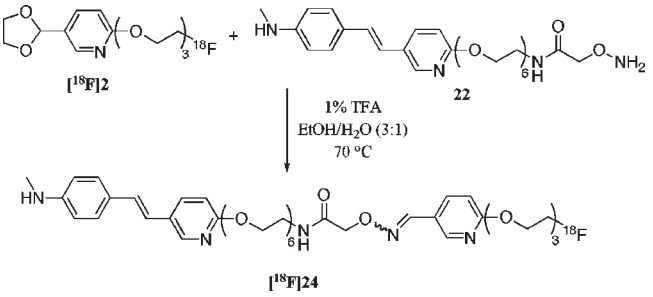
Reproducibility and greatest radiochemical yields were obtained when compound **8** was heated in an open test tube at 110 °C for 10 min (rcy = 71 ± 2%; rcp > 99 ± 1%, n = 3, Table 2, entry 2). The radiochemical yield was lower for shorter time spans (5 min). Noticeably lower radiochemical yields were routinely observed when the reaction was allowed to proceed for more than 15 min. This suggests decomposition of the desired product at elevated temperatures over extended time periods (i.e., greater than 15 min). When the reaction was run in a sealed tube for 15 min at 110 °C, lower radiochemical yields and lower radiochemical purities were observed (Table 2, entry 4). The lower radiochemical yields observed in the sealed tube experiments may be caused by concentration: when the reaction was performed in an open test tube, solvent was able to evaporate (acetonitrile's bp = 82 °C). It is unclear yet as to why the radiochemical purities would decrease in a sealed environment.

As mentioned earlier, aminooxy groups readily form oximes with aldehydes under acid conditions. An acetal can be converted to an aldehyde, in situ, under aqueous acidic conditions. If the in situ formed aldehyde was then subjected to the aminooxy under these same conditions, labeling via the oxime bond would be accomplished in one pot. To test our theory, aminooxy **22** was added to an HCl acidic aqueous/ethanol solution with acetal [^{18}F]**2** at 70 °C (Table 3). The pH of the solution was estimated at 0. At 5 min time intervals, an aliquot (5 μL) was removed from the reaction vessel, neutralized with 1 N $NaHCO_3$ (10 μL, pH ~9), and diluted with 100 μL of acetonitrile. The relative rates of the formation of product, which were equal to the disappearance of the starting material, were analyzed by HPLC. The reaction appeared to be complete after 35 min, with no starting material observed by HPLC analysis.

Species [^{18}F]**24** could be purified and isolated by semipreparative HPLC with a reversed phase column ($r_t \approx$ 15 min) in 41% decay corrected radiochemical yield end of synthesis (eos) with a radiochemical purity of >99%. The total preparation time for [^{18}F]**24** was 100 min (over two steps). The specific activity at eos was ~100 Ci/mmol. The radiolabeling of oxime [^{18}F]**23** provided similar results to a decay corrected radiochemical yield (eos) of 38% (over two steps) and a radiochemical purity of 94%. The specific activity was not determined for oxime [^{18}F]**23**.

In Vitro Binding Assays. Human brain sections containing Alzheimer disease (AD) plaque were obtained. The gray matter was separated from the white matter. The gray matter containing the AD plaques was dissected and processed. The brain tissue homogenates were prepared in phosphate buffered solution

Table 3. Formation of F-18 Labeled Oxime [^{18}F]24 over 5 min Increments



[^{18}F]2 22 [^{18}F]24

entry	time (min)	% rcy (= %rcp)
1	5	30
2	10	65
3	15	80
4	20	89
5	25	93
6	30	94
7	35	98

(PBS), pH = 7.2. The specific binding of [^{18}F]-AV-45 **1** was carried out in 12 × 75 mm borosilicate glass tubes. The reaction mixture contained 50 μL of brain homogenates (20−50 μg), 50 μL of ligand diluted in PBS, and 50 μL of inhibitors (10^{-5}−10^{-10} M diluted serially in PBS containing 0.1% bovine serum albumin in a final volume of 1 mL. Nonspecific binding was determined in the presence of IMPY (600 nM) within the same assay tubes. In competition experiments, compounds at concentrations up to 10^{-5} M were examined for their abilities to compete for the binding of [^{18}F]-AV-45 **1**. Incubations were carried out routinely at 37 °C for 120 min, and the bound and free radioactivity were separated by vacuum filtration. The samples were then filtered through glass fiber filters soaked in PBS (GF/B Whatman) using a Brandel M-24R cell harvester followed by 2 × 3-mL washes of PBS at room temperature. The filters containing bound [^{18}F] ligand were immediately counted with a gamma counter (Cobra II, Perkin-Elmer) with 70% counting efficiency. The results of the inhibition experiments were subjected to nonlinear regression analysis using equilibrium binding data analysis by which K_i values were calculated as [^{18}F]-AV-45 **1** K_i = 3.80 ± 1.82 nM (n = 5), [^{18}F]**23** K_i = 11.78 ± 3.06 nM (n = 5), [^{18}F]**24** K_i = 25.2 ± 0.9 nM (n = 6).

Biodistribution. Biodistribution studies of [^{18}F]**23** and [^{18}F]**24** were conducted in male ICR mice. The % dose/gram was compared to that of [^{18}F]-AV-45 (**1**) (Table 4). [^{18}F]-AV-45 (**1**)[40,41] is used as a PET imaging agent targeting β-amyloid plaques within the brain. Both oximes contain the core backbone structure found in [^{18}F]-AV-45 (**1**). The use of the neutral (calculated log P = 1.00) and hydrophilic spacer (triethylene glycol) on the prosthetic group was thought to increase the overall hydrophilicity and therefore deter the compound from passing the blood-brain barrier (BBB). Compounds [^{18}F]**23** and [^{18}F]**24** may be useful to image β-amyloid plaques located on the cerebral blood vessels outside the brain.

Table 4 depicts a comparison of the biodistribution for [^{18}F]-AV-45 (**1**), [^{18}F]**23**, and [^{18}F]**24** in normal mice. We were particularly interested in comparing the brain uptakes of [^{18}F]-AV-45

dx.doi.org/10.1021/bc1004262 |*Bioconjugate Chem.* 2011, 22, 642–653

Table 4. Biodistribution Study % Dose/Gram of [^{18}F]-AV-45 (1), [^{18}F]23, and [^{18}F]24 in Male ICR Mice

	[^{18}F]-AV-45 (1)[a]		[^{18}F]23		[^{18}F]24	
organ	2 min n = 3	30 min n = 3	2 min n = 3	30 min n = 3	2 min n = 3	30 min n = 3
blood	3.14 ± 0.69	2.80 ± 0.44	9.34 ± 1.37	4.94 ± 0.91	4.19 ± 1.04	2.81 ± 0.22
heart	6.25 ± 1.79	2.18 ± 0.32	13.1 ± 3.08	3.72 ± 0.84	12.3 ± 1.79	4.17 ± 0.61
muscle	1.06 ± 0.39	1.78 ± 0.34	1.32 ± 0.50	1.56 ± 0.27	1.42 ± 0.46	2.01 ± 0.21
lung	6.87 ± 1.36	3.20 ± 0.54	7.09 ± 1.37	3.53 ± 0.38	3.70 ± 1.06	2.43 ± 0.33
kidney	10.9 ± 2.63	6.31 ± 0.58	14.1 ± 2.85	6.83 ± 1.93	15.4 ± 3.54	7.78 ± 0.85
pancreas	--	-	5.13 ± 1.08	2.28 ± 0.48	3.32 ± 0.58	2.22 ± 0.23
spleen	4.57 ± 1.07	1.81 ± 0.24	4.81 ± 1.18	3.57 ± 0.68	3.11 ± 0.45	1.63 ± 0.19
liver	21.5 ± 1.07	12.9 ± 0.72	22.2 ± 3.99	19.1 ± 3.65	29.4 ± 5.09	10.9 ± 1.17
skin	1.18 ± 0.23	2.36 ± 0.29	0.79 ± 0.20	1.50 ± 0.25	1.14 ± 0.44	1.78 ± 0.13
brain	7.77 ± 1.70	1.59 ± 0.22	1.69 ± 0.44	0.96 ± 0.16	0.48 ± 0.12	0.92 ± 0.11
bone	1.43 ± 0.09	1.22 ± 0.17	2.00 ± 0.33	2.27 ± 0.41	1.76 ± 0.31	1.62 ± 0.10

[a] Data taken from Zhang, W., et al. (2005) F-18 Polyethyleneglycol stilbenes as PET imaging agents targeting Aβ aggregates in the brain. *Nucl. Med. Biol. 32*, 799−809.

(**1**) and the two new derivatives, [^{18}F]**23** and [^{18}F]**24**. The addition of the prosthetic group led to AV-45 derivatives with a much higher molecular weight, exceeding the limit for penetrating the intact BBB.[48,49] As expected, [^{18}F]-AV-45 (**1**) (molecular weight = 359.43 g/mol) has a high initial brain uptake after 2 min post injection (7.77% dose/gram). The tracer then proceeds to gradually wash out after 30 min post injection. Initial brain uptake of oxime [^{18}F]**23** (molecular weight = 668.74 g/mol) was rather respectable (1.69% dose/gram). On the other hand, [^{18}F]**24** (molecular weight = 799.91 g/mol) showed significantly lower uptake (0.48% dose/gram) at the 2 min post injection mark, indicating a far less efficient passage of the tracer through the intact BBB. To our surprise, an increase of uptake in the brain at 30 min post injection (0.92% dose/gram) was observed. We are suggesting that in vivo metabolites of [^{18}F]**24** may have contributed to the increase in brain uptake.

Compounds [^{18}F]**23** and [^{18}F]**24** display high initial uptake and slow retention, remaining rather consistent throughout the 30 min, in most of the organs tested. Heart uptake and retention drop fairly rapidly with time, showing low heart activity at 30 min post injection. There was no significant uptake within the lung, along with no significant retention within the first arteriovenous capillary bed. Rapid uptake is observed within the kidneys but is soon excreted to the urinary bladder. It should be noted that each labeled oxime showed the washing out of activity through the liver. During the time frame of the studies performed, there is very little defluorination occurring as depicted from the values in the bone (femur).

CONCLUSIONS

A new prosthetic radiolabeled ligand, [^{18}F]**2**, was successfully synthesized in a total of four steps, starting with readily available 6-bromo-3-pyridine carbaldehyde **5**. The fluoride-18 labeling of this compound was achieved in high radiochemical yields (71 ± 2%, n = 3) with excellent radiochemical purity (>99%, based on HPLC analyses) in short reaction time (10 min). The species could be easily purified through a solid phase extraction (OASIS HLB 3 cm^3 cartridge), eluted with a small volume of ethanol, and used directly in the next step of the synthetic sequence without any further purification. The coupling with species [^{18}F]**2** was demonstrated in two model complexes, oximes [^{18}F]**23** and [^{18}F]**24**.

Biodistribution studies were performed on each of the labeled oximes [^{18}F]**23** and [^{18}F]**24**, and compared to that of [^{18}F]-AV-45 (**1**). The major differences among [^{18}F]-AV-45 (**1**), [^{18}F]**23**, and [^{18}F]**24** are their size (molecular weight) and the hydrophilic spacer (triethylene glycol) from the prosthetic ligand. [^{18}F]-AV-45 (**1**) is a small and neutral molecule designed to serve as a brain-imaging agent to target Aβ-plaques inside the brain. Compounds [^{18}F]**23** and [^{18}F]**24** are larger in size (PEG, n = 3 and n = 6, respectively); therefore, they should reduce the BBB penetration. The use of the hydrophilic spacer (triethylene glycol) on the prosthetic group was thought to increase the overall hydrophilicity of the molecule. The brain uptake for oxime [^{18}F]**23** appeared to be reduced, but it retained some capability to cross the BBB. Oxime [^{18}F]**24** showed promising results after 2 min post injection (0.48% dose/gram); however, the uptake increased after 30 min post injection (0.92% dose/gram) suggesting an in vivo decomposition/metabolism of compound [^{18}F]**24**.

The prosthetic ligand, [^{18}F]**2**, has several advantages over other known prosthetic ligands in the literature: high radiochemical yield, ease of formation, the ability to label base sensitive compounds, and the chemoselective formation of the oxime bond. Future work will focus on using this prosthetic ligand to label larger molecules that are incompatible with direct labeling with fluoride-18 (nca) anion. We intend to use this methodology to label biologically active peptides and proteins modified with an aminooxy functional group.

ASSOCIATED CONTENT

Supporting Information. Spectroscopic data of key compounds **8**, **2**, **23**, and **24** are provided. This material is available free of charge via the Internet at http://pubs.acs.org.

AUTHOR INFORMATION

Corresponding Author

*Correspondence to Hank F. Kung, Department of Radiology, University of Pennsylvania, 3700 Market St., Room 305, Philadelphia, PA 19104. Telephone: (215) 662-3096; FAX: (215) 349-5035; E-mail: kunghf@sunmac.spect.upenn.edu.

ACKNOWLEDGMENT

This work was supported by the grants from NIH (AG-022559) and a grant from Avid Radiopharmaceuticals.

REFERENCES

(1) Tolmachev, V., and Stone-Elander, S. (2010) Radiolabelled proteins for positron emission tomography: Pros and cons of labelling methods. *Biochim. Biophys. Acta, Gen. Subj. 1800*, 487–510.

(2) Cherry, S. R. (2001) Fundamentals of positron emission tomography and applications in preclinical drug development. *J. Clin. Pharmacol. 41*, 482–491.

(3) Ametamey, S. M., Honer, M., and Schubiger, P. A. (2008) Molecular imaging with PET. *Chem. Rev. 108*, 1501–1516.

(4) Mach, R. H., and Schwarz, S. W. (2010) Challenges for developing PET tracers: isotopes, chemistry, and regulatory aspects. *PET Clinics 5*, 131–153.

(5) Kuhnast, B., and Dolle, F. (2010) The challenge of labeling macromolecules with fluorine-18: three decades of research. *Curr. Radiopharm. 3*, 174–201.

(6) Schubiger, P. A., Lehmann, L., and Friebe, M. (2006) *PET Chemistry*, Vol. 62, Springer, New York.

(7) Hultsch, C., Berndt, M., Bergmann, R., and Wuest, F. (2007) Radiolabeling of multimeric neurotensin(8−13) analogs with short-lived positron emitter fluorine-18. *Appl. Radiat. Isot. 65*, 818–826.

(8) Fredriksson, A., Johnstrom, P., Stone-Elander, S., Jonasson, P., Nygren, P.-A., Ekberg, K., Johansson, B.-L., and Wahren, J. (2001) Labeling of human C-peptide by conjugation with N-succinimidyl-4-[18F]fluorobenzoate. *J. Labelled Compd. Radiopharm. 44*, 509–519.

(9) Schottelius, M., Poethko, T., Herz, M., Reubi, J.-C., Kessler, H., Schwaiger, M., and Wester, H.-J. (2004) First 18F-labeled tracer suitable for routine clinical imaging of sst receptor-expressing tumors using positron emission tomography. *Clin. Cancer Res. 10*, 3593–3606.

(10) Guhlke, S., Wester, H.-J., Bruns, C., and Stoecklin, G. (1994) (2-[18F]fluoropropionyl-(D)phe1)-octreotide, a potential radiopharmaceutical for quantitative somatostatin receptor imaging with PET: Synthesis, radiolabeling, in vitro validation and biodistribution in mice. *Nucl. Med. Biol. 21*, 819–25.

(11) Olberg, D. E., Arukwe, J. M., Grace, D., Hjelstuen, O. K., Solbakken, M., Kindberg, G. M., and Cuthbertson, A. (2010) One step radiosynthesis of 6-[18F]fluoronicotinic acid 2,3,5,6-tetrafluorophenyl ester ([18F]F-Py-TFP): a new prosthetic group for efficient labeling of biomolecules with fluorine-18. *J. Med. Chem. 53*, 1732–1740.

(12) Wust, F., Hultsch, C., Bergmann, R., Johannsen, B., and Henle, T. (2003) Radiolabeling of isopeptide Ne-(gamma -glutamyl)-L-lysine by conjugation with N-succinimidyl 4-[18F]fluorobenzoate. *Appl. Radiat. Isot. 59*, 43–48.

(13) De Bruin, B., Kuhnast, B., Hinnen, F., Yaouancq, L., Amessou, M., Johannes, L., Samson, A., Boisgard, R., Tavitian, B., and Dolle, F. (2005) 1-[3-(2-[18F]Fluoropyridin-3-yloxy)propyl]pyrrole-2,5-dione: Design, synthesis, and radiosynthesis of a new [18F]fluoropyridine-based maleimide reagent for the labeling of peptides and proteins. *Bioconjugate Chem. 16*, 406–420.

(14) Prante, O., Einsiedel, J., Haubner, R., Gmeiner, P., Wester, H.-J., Kuwert, T., and Maschauer, S. (2007) 3,4,6-Tri-O-acetyl-2-deoxy-2-[18F]fluoroglucopyranosyl phenylthiosulfonate: a thiol-reactive agent for the chemoselective 18F-glycosylation of peptides. *Bioconjugate Chem. 18*, 254–262.

(15) Wangler, B., Quandt, G., Iovkova, L., Schirrmacher, E., Wangler, C., Boening, G., Hacker, M., Schmoeckel, M., Jurkschat, K., Bartenstein, P., and Schirrmacher, R. (2009) Kit-like 18F-labeling of proteins: synthesis of 4-(di-tert-butyl[18F]fluorosilyl)benzenethiol (Si[18F]FA-SH) labeled rat serum albumin for blood pool imaging with PET. *Bioconjugate Chem. 20*, 317–321.

(16) Glaser, M., Karlsen, H., Solbakken, M., Arukwe, J., Brady, F., Luthra, S. K., and Cuthbertson, A. (2004) 18F-Fluorothiols: a new approach to label peptides chemoselectively as potential tracers for positron emission tomography. *Bioconjugate Chem. 15*, 1447–1453.

(17) Mach, R. H., Leudtke, R. R., Unsworth, C. D., Boundy, V. A., Nowak, P. A., Scripko, J. G., Elder, S. T., Jackson, J. R., and Hoffman, P. L. (1993) et al. Fluorine-18 labeled benzamides for studying the dopamine D2 receptor with positron emission tomography. *J. Med. Chem. 36*, 3707–20.

(18) Garg, S., Thopate, S. R., Minton, R. C., Black, K. W., Lynch, A. J. H., and Garg, P. K. (2007) 3-Amino-4-(2-((4-[18F]fluorobenzyl) methylamino)methylphenylsulfanyl)benzonitrile, an F-18 fluorobenzyl analogue of DASB: synthesis, in vitro binding, and in vivo biodistribution studies. *Bioconjugate Chem. 18*, 1612–1618.

(19) Olberg, D. E., Hjelstuen, O. K., Solbakken, M., Arukwe, J., Karlsen, H., and Cuthbertson, A. (2008) A novel prosthetic group for site-selective labeling of peptides for positron emission tomography. *Bioconjugate Chem. 19*, 1301–1308.

(20) Olberg, D. E., Hjelstuen, O. K., Solbakken, M., Arukwe, J. M., Dyrstad, K., and Cuthbertson, A. (2009) Site-specific addition of an 18F-N-methylaminooxy-containing prosthetic group to a vinylsulfone modified peptide. *J. Labelled Compd. Radiopharm. 52*, 571–575.

(21) Bruus-Jensen, K., Poethko, T., Schottelius, M., Hauser, A., Schwaiger, M., and Wester, H.-J. (2006) Chemoselective hydrazone formation between HYNIC-functionalized peptides and 18F-fluorinated aldehydes. *Nucl. Med. Biol. 33*, 173–183.

(22) Toyokuni, T., Walsh, J. C., Dominguez, A., Phelps, M. E., Barrio, J. R., Gambhir, S. S., and Satyamurthy, N. (2003) Synthesis of a new heterobifunctional linker, N-[4-(aminooxy)butyl]maleimide, for facile access to a thiol-reactive 18F-labeling agent. *Bioconjugate Chem. 14*, 1253–1259.

(23) Berndt, M., Pietzsch, J., and Wuest, F. (2007) Labeling of low-density lipoproteins using the 18F-labeled thiol-reactive reagent N-[6-(4-[18F]fluorobenzylidene)aminooxyhexyl]maleimide. *Nucl. Med. Biol. 34*, 5–15.

(24) Namavari, M., Padilla De Jesus, O., Cheng, Z., De, A., Kovacs, E., Levi, J., Zhang, R., Hoerner Joshua, K., Grade, H., Syud Faisal, A., and Gambhir Sanjiv, S. (2008) Direct site-specific radiolabeling of an affibody protein with 4-[18F]fluorobenzaldehyde via oxime chemistry. *Mol. Imaging Biol. 10*, 177–81.

(25) Poethko, T., Schottelius, M., Thumshirn, G., Hersel, U., Herz, M., Henriksen, G., Kessler, H., Schwaiger, M., and Wester, H.-J. (2004) Two-step methodology for high-yield routine radiohalogenation of peptides: 18F-labeled RGD and ocreotide analogs. *J. Nucl. Med. 45*, 892–902.

(26) Namavari, M., Cheng, Z., Zhang, R., De, A., Levi, J., Hoerner, J. K., Yaghoubi, S. S., Syud, F. A., and Gambhir, S. S. (2009) A novel method for direct site-specific radiolabeling of peptides using [18F]FDG. *Bioconjugate Chem. 20*, 432–436.

(27) Li, X., Link, J. M., Stekhova, S., Yagle, K. J., Smith, C., Krohn, K. A., and Tait, J. F. (2008) Site-specific labeling of annexin V with F-18 for apoptosis imaging. *Bioconjugate Chem. 19*, 1684–1688.

(28) Hultsch, C., Schottelius, M., Auernheimer, J., Alke, A., and Wester, H.-J. (2009) 18F-Fluoroglucosylation of peptides, exemplified on cyclo(RGDfK). *Eur. J. Nucl. Med. Mol. 36*, 1469–1474.

(29) Wuest, F., Hultsch, C., Berndt, M., and Bergmann, R. (2009) Direct labelling of peptides with 2-[18F]fluoro-2-deoxy-D-glucose ([18F]FDG). *Bioorg. Med. Chem. Lett. 19*, 5426–5428.

(30) Abdel-Jalil, R. J., Aqarbeh, M., Loeffler, D., Shen, B., Orabi, S. A., Voelter, W., and Machulla, H.-J. (2010) Synthesis and radiolabeling of new N-[(4-[18F]fluorobenzylidene) aminooxy) alkyl]-2-nitroimidazoles as possible hypoxia imaging pharmaceuticals. *J. Radioanal. Nucl. Chem. 283*, 239–243.

(31) Glaser, M., Morrison, M., Solbakken, M., Arukwe, J., Karlsen, H., Wiggen, U., Champion, S., Kindberg, G. M., and Cuthbertson, A. (2008) Radiosynthesis and biodistribution of cyclic RGD peptides conjugated with novel [18F]fluorinated aldehyde-containing prosthetic groups. *Bioconjugate Chem. 19*, 951–957.

(32) Wester, H.-J., Hamacher, K., and Stoecklin, G. (1996) A comparative study of n.c.a. fluorine-18 labeling of proteins via acylation and photochemical conjugation. *Nucl. Med. Biol. 23*, 365–372.

(33) Thonon, D., Kech, C., Paris, J., Lemaire, C., and Luxen, A. (2009) New strategy for the preparation of clickable peptides and labeling with 1-(azidomethyl)-4-[18F]-fluorobenzene for PET. *Bioconjugate Chem. 20*, 817–823.

(34) Marik, J., and Sutcliffe, J. L. (2006) Click for PET: rapid preparation of [18F]fluoropeptides using CuI catalyzed 1,3-dipolar cycloaddition. *Tetrahedron Lett. 47*, 6681–6684.

(35) Inkster, J. A. H., Adam, M. J., Storr, T., and Ruth, T. J. (2009) Labeling of an antisense oligonucleotide with [18F]FPy5yne. *Nucleosides, Nucleotides Nucleic Acids 28*, 1131–1143.

(36) Inkster, J. A. H., Guerin, B., Ruth, T. J., and Adam, M. J. (2008) Radiosynthesis and bioconjugation of [18F]FPy5yne, a prosthetic group for the 18F labeling of bioactive peptides. *J. Labelled Compd. Radiopharm. 51*, 444–452.

(37) Okarvi, S. M. (2001) Recent progress in fluorine-18 labelled peptide radiopharmaceuticals. *Eur. J. Nucl. Med. 28*, 929–938.

(38) Adams, J. P. (2000) Imines, enamines and oximes. *Perkin 1*, 125–139.

(39) Singh, Y., Edupuganti, O. P., Villien, M., Defrancq, E., and Dumy, P. (2005) The oxime bond formation as a useful tool for the preparation of oligonucleotide conjugates. *C. R. Chim. 8*, 789–796.

(40) Choi, S. R., Golding, G., Zhuang, Z., Zhang, W., Lim, N., Hefti, F., Benedum, T. E., Kilbourn, M. R., Skovronsky, D., and Kung, H. F. (2009) Preclinical properties of 18F-AV-45: a PET agent for Aβ plaques in the brain. *J. Nucl. Med. 50*, 1887–1894.

(41) Lin, K.-J., Hsu, W.-C., Hsiao, I.-T., Wey, S.-P., Jin, L.-W., Skovronsky, D., Wai, Y.-Y., Chang, H.-P., Lo, C.-W., Yao, C. H., Yen, T.-C., and Kung, M.-P. (2010) Whole-body biodistribution and brain PET imaging with [18F]AV-45, a novel amyloid imaging agent - a pilot study. *Nucl. Med. Biol. 37*, 497–508.

(42) Poethko, T., Schottelius, M., Thumshirn, G., Herz, M., Haubner, R., Henriksen, G., Kessler, H., Schwaiger, M., and Wester, H.-J. (2004) Chemoselective pre-conjugate radiohalogenation of unprotected mono- and multimeric peptides via oxime formation. *Radiochim. Acta 92*, 317–327.

(43) Zoppellaro, G., Ivanova, A., Enkelmann, V., Geies, A., and Baumgarten, M. (2003) Synthesis, magnetic properties and theoretical calculations of novel nitronyl nitroxide and imino nitroxide diradicals grafted on terpyridine moiety. *Polyhedron 22*, 2099–2110.

(44) Zhang, W., Oya, S., Kung, M.-P., Hou, C., Maier, D. L., and Kung, H. F. (2005) F-18 Polyethyleneglycol stilbenes as PET imaging agents targeting Aβ aggregates in the brain. *Nucl. Med. Biol. 32*, 799–809.

(45) Mormeneo, D., Casas, J., Llebaria, A., and Delgado, A. (2007) Synthesis and preliminary antifungal evaluation of a library of phytosphingolipid analogues. *Org. Biomol. Chem. 5*, 3769–3777.

(46) Wascholowski, V., and Giannis, A. (2006) Sphingolactones: selective and irreversible inhibitors of neutral sphingomyelinase. *Angew. Chem., Int. Ed. Engl. 45*, 827–30.

(47) Deroo, S., Defrancq, E., Moucheron, C., Kirsch-De Mesmaeker, A., and Dumy, P. (2003) Synthesis of an oxyamino-containing phenanthroline derivative for the efficient preparation of phenanthroline oligonucleotide oxime conjugates. *Tetrahedron Lett. 44*, 8379–8382.

(48) Kung, H. F., Choi, S. R., Qu, W., Zhang, W., and Skovronsky, D. (2010) 18F stilbenes and styrylpyridines for PET imaging of Aβ plaques in alzheimer's disease: a miniperspective. *J. Med. Chem. 53*, 933–941.

(49) Dischino, D. D., Welch, M. J., Kilbourn, M. R., and Raichle, M. E. (1983) Relationship between lipophilicity and brain extraction of carbon-11-labeled radiopharmaceuticals. *J. Nucl. Med. 24*, 1030–1038.

Supplementary Information

A New F-18 Prosthetic Group via an Oxime Coupling

Patrick Carberry,[†] Brian P. Lieberman,[†] Karl Ploessl,[†] Seok R. Choi,[§] Danniebelle N. Haase,[†] and Hank F. Kung,[†,@]

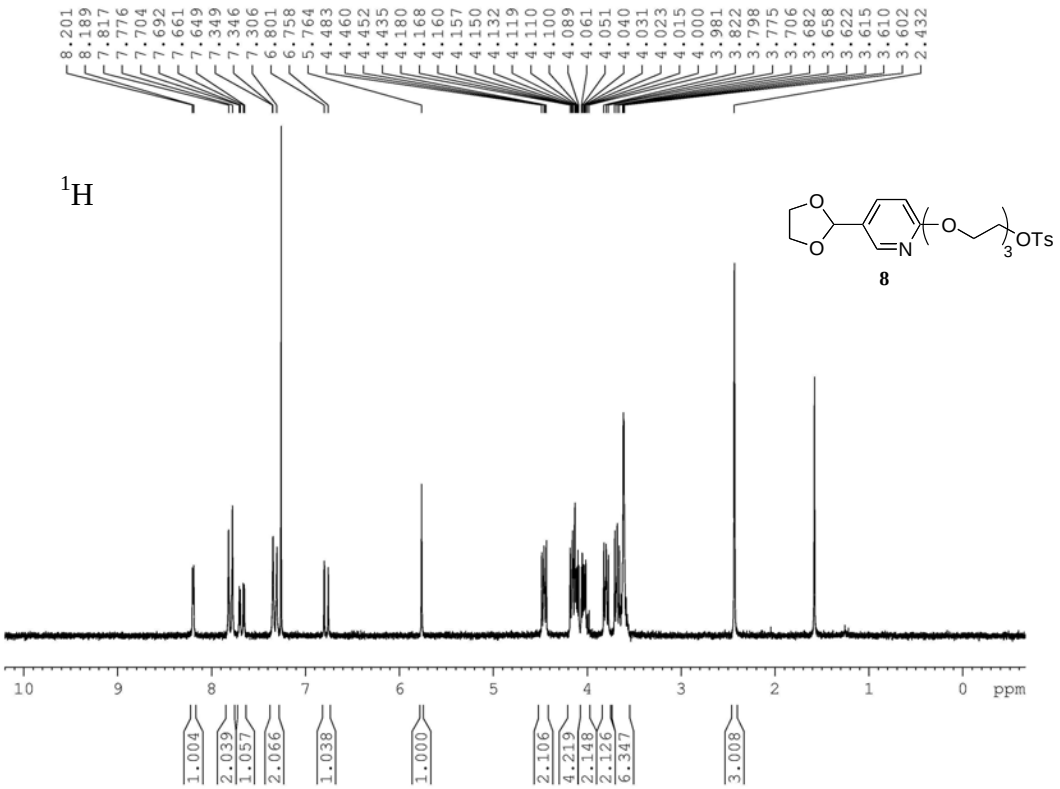
†Department of Radiology, University of Pennsylvania, University of Pennsylvania, 3700 Market Street, Room 305, Philadelphia, PA 19104
@Department of Pharmacology, University of Pennsylvania, University of Pennsylvania, 3700 Market Street, Room 305, Philadelphia, PA 19104
§ Avid Radiopharmaceuticals, Inc., 3624 Market Street, 5th Floor, Philadelphia, PA 19104

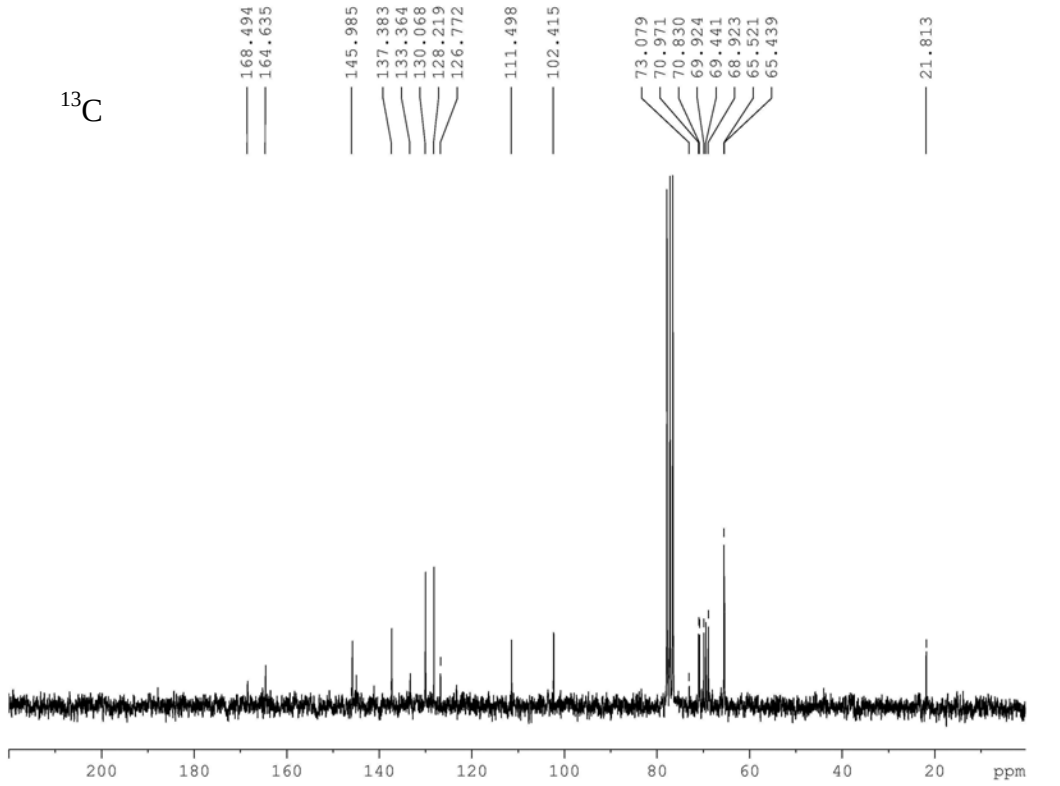
Correspondence should be addressed to Hank F. Kung (kunghf@sunmac.spect.upenn.edu)

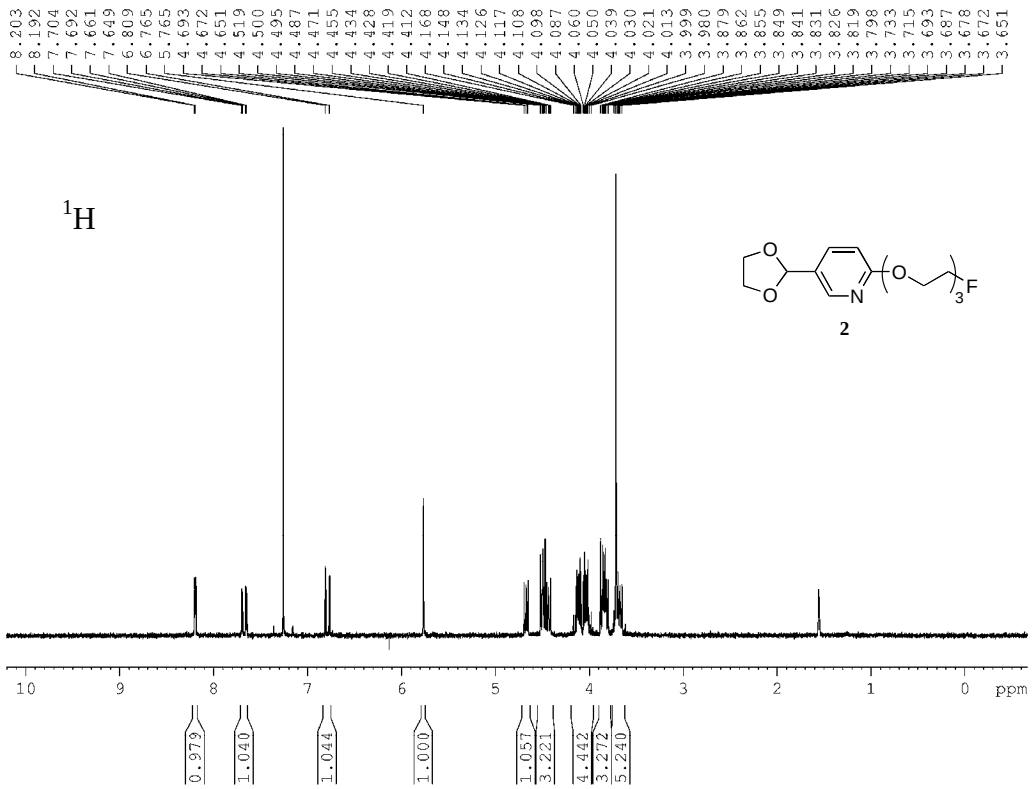
Table of Contents

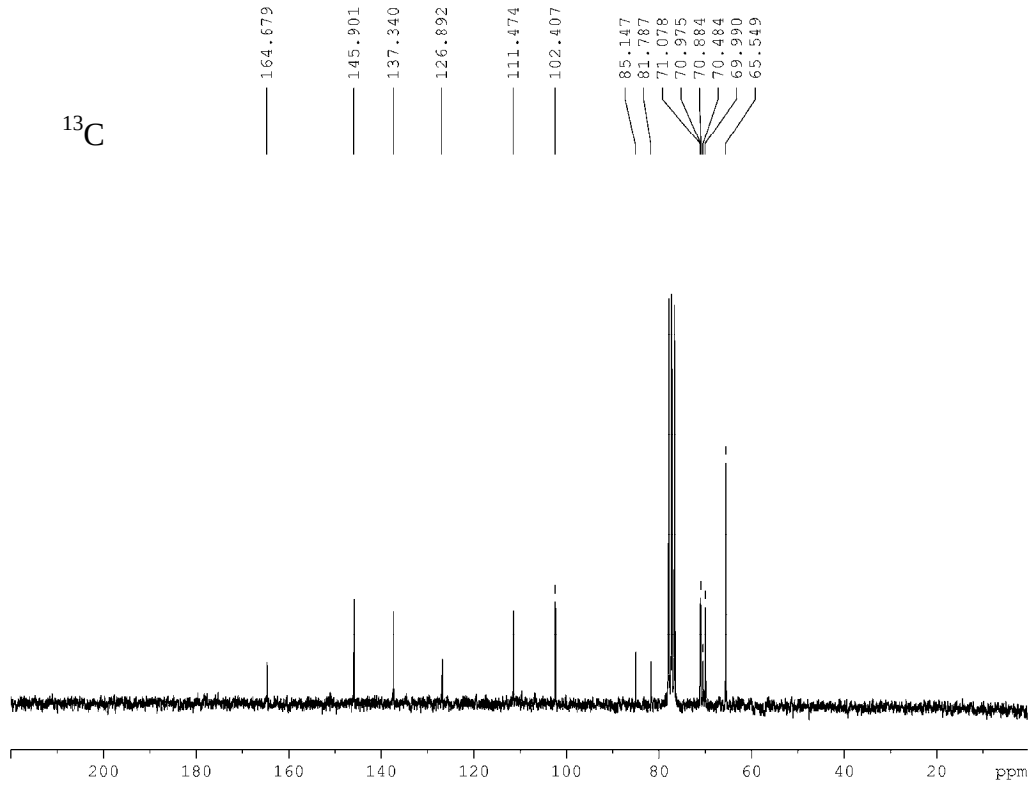
Spectroscopic data of compounds

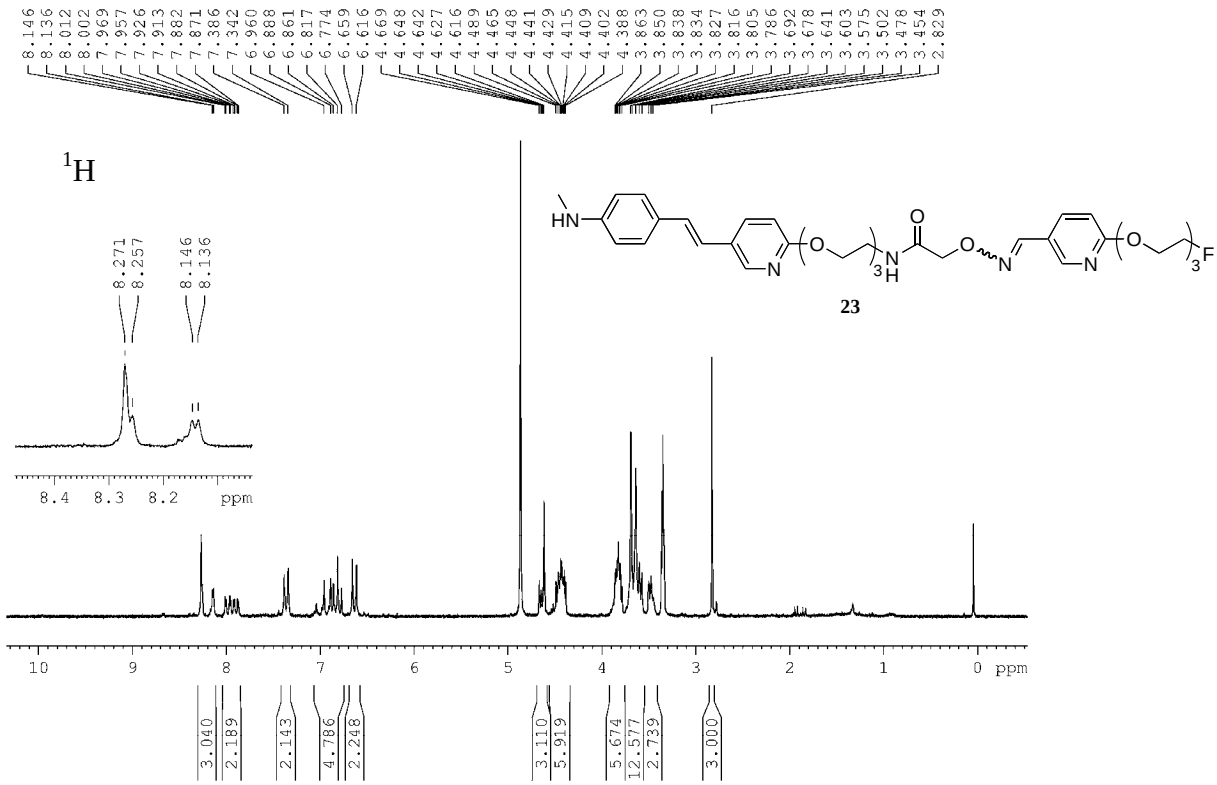
Tosylate (**8**) S3
Fluorine (**2**) S4
Oxime (**23**) S5
Oxime (**24**) S6

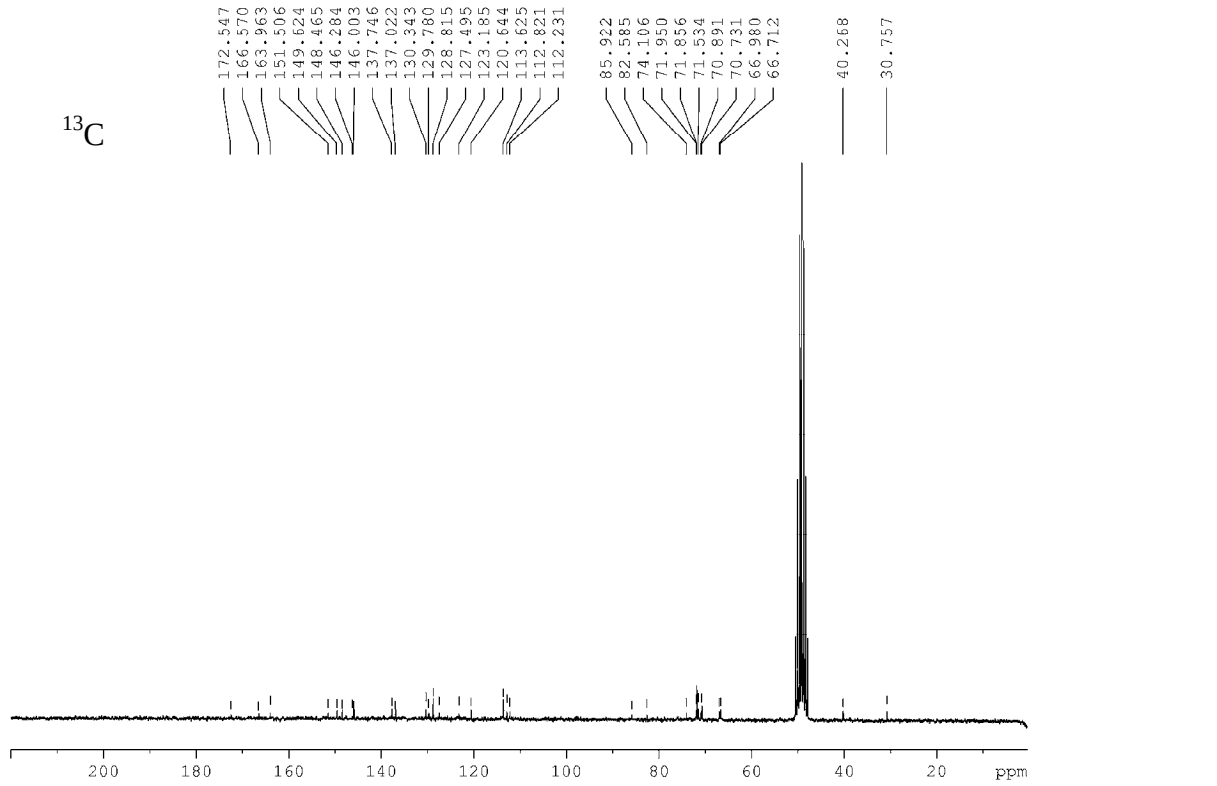

8.201
8.189
7.817
7.776
7.704
7.692
7.661
7.649
7.349
7.346
7.306
6.801
6.758
5.764
4.483
4.460
4.452
4.435
4.180
4.168
4.160
4.157
4.150
4.132
4.119
4.110
4.100
4.089
4.061
4.051
4.040
4.031
4.023
4.015
4.000
3.981
3.822
3.798
3.775
3.706
3.682
3.658
3.622
3.615
3.610
3.602
2.432
1H
O
O
O
N
O
3
OTs
8
10
9
8
7
6
5
4
3
2
1
0
ppm
1.004
2.039
1.057
2.066
1.038
1.000
2.106
4.219
2.148
2.126
6.347
3.008

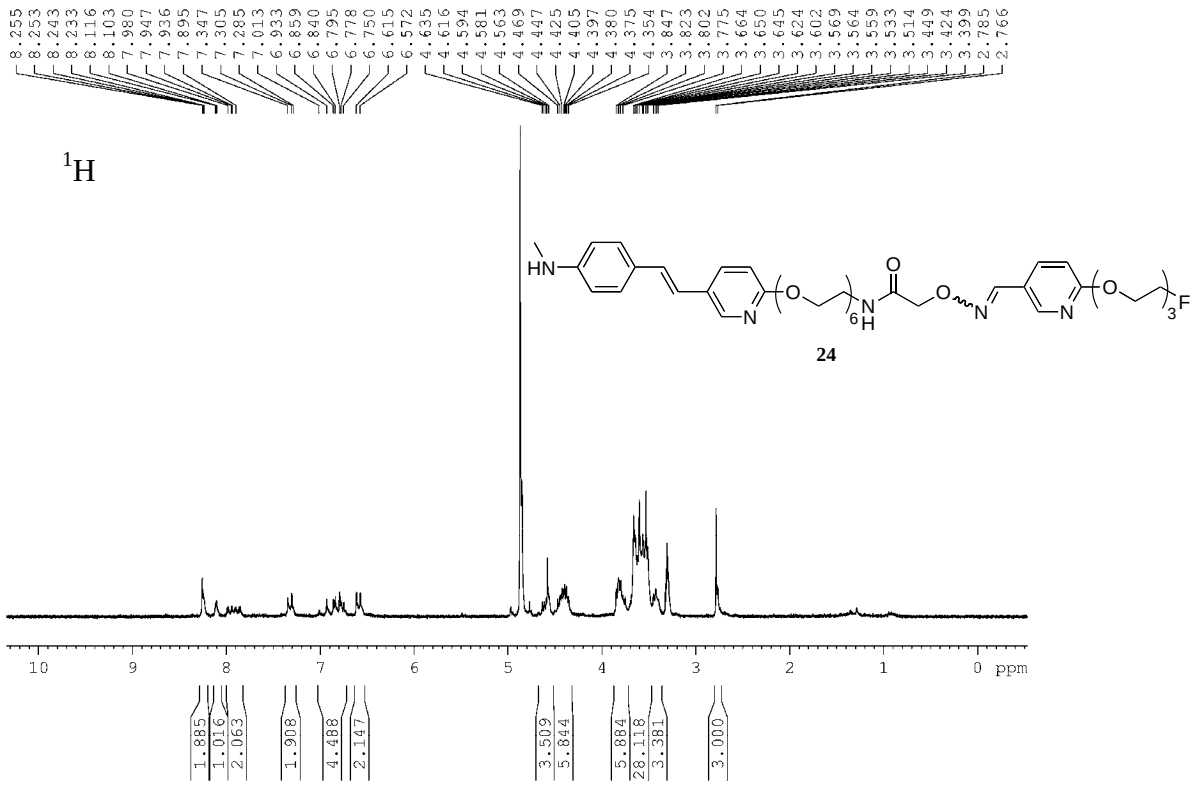

13C
168.494
164.635
145.985
137.383
133.364
130.068
128.219
126.772
111.498
102.415
73.079
70.971
70.830
69.924
69.441
68.923
65.521
65.439
21.813
200
180
160
140
120
100
80
60
40
20
ppm

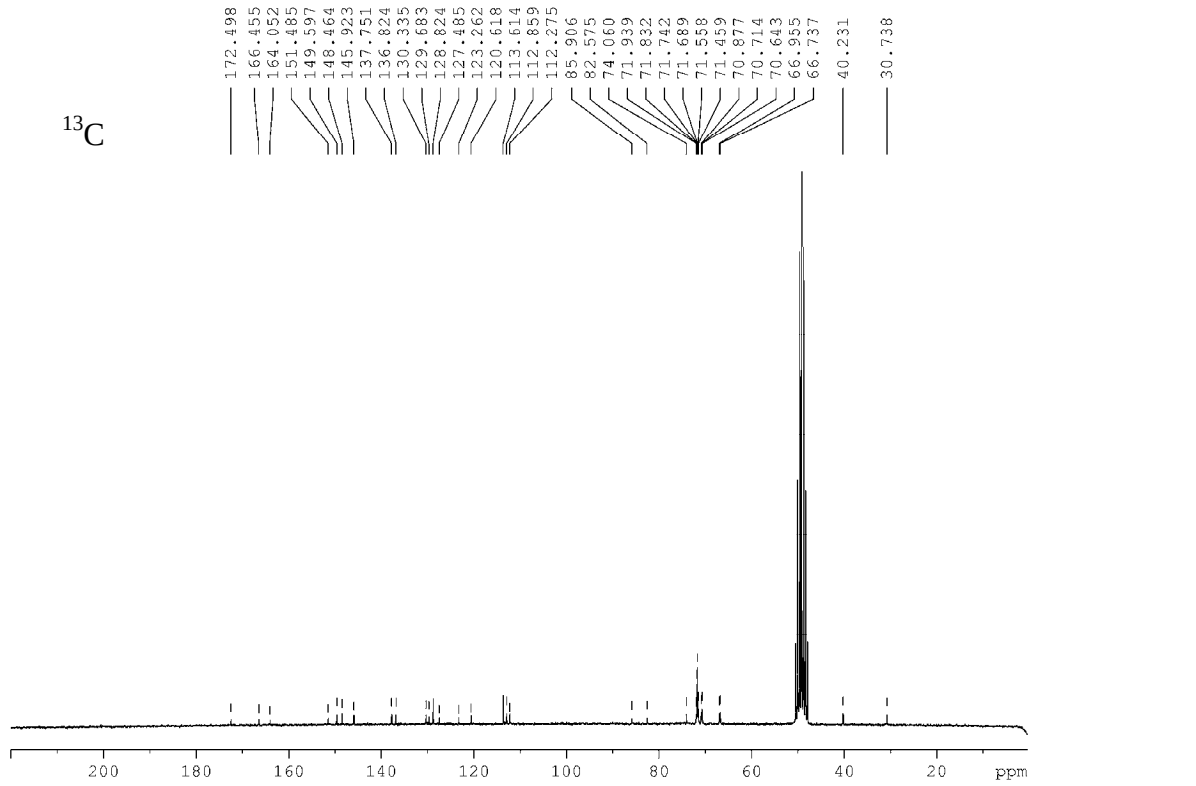

8.203
8.192
7.704
7.692
7.661
7.649
6.809
6.765
5.765
4.693
4.672
4.651
4.519
4.500
4.495
4.487
4.471
4.455
4.434
4.428
4.419
4.412
4.168
4.148
4.134
4.126
4.117
4.108
4.098
4.087
4.060
4.050
4.039
4.030
4.021
4.013
3.999
3.980
3.879
3.862
3.855
3.849
3.841
3.831
3.826
3.819
3.798
3.733
3.715
3.693
3.687
3.678
3.672
3.651
1H
O
O
O
N
O
3
F
2
10
9
8
7
6
5
4
3
2
1
0
ppm
0.979
1.040
1.044
1.000
1.057
3.221
4.442
3.272
5.240


13C
164.679
145.901
137.340
126.892
111.474
102.407
85.147
81.787
71.078
70.975
70.884
70.484
69.990
65.549
200
180
160
140
120
100
80
60
40
20
ppm


8.146
8.136
8.012
8.002
7.969
7.957
7.926
7.913
7.882
7.871
7.386
7.342
6.960
6.888
6.861
6.817
6.774
6.659
6.616
4.669
4.648
4.642
4.627
4.616
4.489
4.465
4.448
4.441
4.429
4.415
4.409
4.402
4.388
3.863
3.850
3.838
3.834
3.827
3.816
3.805
3.786
3.692
3.678
3.641
3.603
3.575
3.502
3.478
3.454
2.829
1H
8.271
8.257
8.146
8.136
8.4 8.3 8.2 ppm
HN
O
N
3
H
F
23
10 9 8 7 6 5 4 3 2 1 0 ppm
3.040
2.189
2.143
4.786
2.248
3.110
5.919
5.674
12.577
2.739
3.000


13C
172.547
166.570
163.963
151.506
149.624
148.465
146.284
146.003
137.746
137.022
130.343
129.780
128.815
127.495
123.185
120.644
113.625
112.821
112.231
85.922
82.585
74.106
71.950
71.856
71.534
70.891
70.731
66.980
66.712
40.268
30.757
200 180 160 140 120 100 80 60 40 20 ppm


8.255
8.253
8.243
8.233
8.116
8.103
7.980
7.947
7.936
7.895
7.347
7.305
7.285
7.013
6.933
6.859
6.840
6.795
6.778
6.750
6.615
6.572
4.635
4.616
4.594
4.581
4.563
4.469
4.447
4.425
4.405
4.397
4.380
4.375
4.354
3.847
3.823
3.802
3.775
3.664
3.650
3.645
3.624
3.602
3.569
3.564
3.559
3.533
3.514
3.449
3.424
3.399
2.785
2.766
1H
HN
O
N
6
H
O
N
O
N
3
F
24
10
9
8
7
6
5
4
3
2
1
0 ppm
1.885
1.016
2.063
1.908
4.488
2.147
3.509
5.844
5.884
28.118
3.381
3.000


172.498
166.455
164.052
151.485
149.597
148.464
145.923
137.751
136.824
130.335
129.683
128.824
127.485
123.262
120.618
113.614
112.859
112.275
85.906
82.575
74.060
71.939
71.832
71.742
71.689
71.558
71.459
70.877
70.714
70.643
66.955
66.737
40.231
30.738
13C
200
180
160
140
120
100
80
60
40
20
ppm

Bioconjugate Chemistry

ARTICLE

pubs.acs.org/bc

Targeting G-Quadruplex Structure in the Human c-Kit Promoter with Short PNA Sequences

Jussara Amato,[#,†] Bruno Pagano,[#,‡] Nicola Borbone,[†] Giorgia Oliviero,[*,†] Valérie Gabelica,[§] Edwin De Pauw,[§] Stefano D'Errico,[†] Vincenzo Piccialli,[∥] Michela Varra,[†] Concetta Giancola,[⊥] Gennaro Piccialli,[†] and Luciano Mayol[†]

[†]Dipartimento di Chimica delle Sostanze Naturali, Università degli Studi di Napoli Federico II, via D. Montesano 49, 80131, Napoli, Italy

[‡]Dipartimento di Scienze Farmaceutiche, Università di Salerno, via Ponte don Melillo, 84084, Fisciano (SA), Italy

[§]Physical Chemistry and Mass Spectrometry Laboratory, Department of Chemistry, University of Liège, 4000, Liège, Belgium

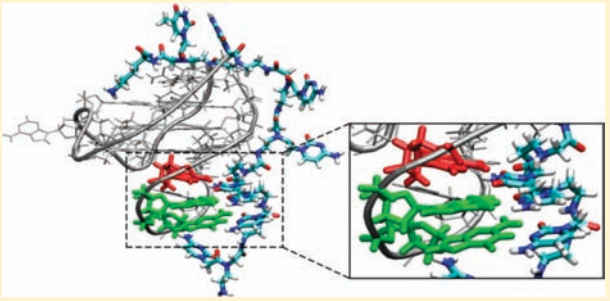
[∥]Dipartimento di Chimica Organica e Biochimica

[⊥]Dipartimento di Chimica "P. Corradini"

Università degli Studi di Napoli Federico II, via Cintia, 80126, Napoli, Italy

Supporting Information

ABSTRACT: The cKit87up sequence d($^{5'}$AGGGAGGGCGCTGGGAGGAGGG$^{3'}$) can form a unique G-quadruplex structure in the promoter region of the human c-kit protooncogene. It provides a peculiar platform for the design of selective quadruplex-binding agents, which could potentially repress the protooncogene transcription. In this study, we examined the binding of a small library of PNA probes (**P1**−**P5**) targeting cKit87up quadruplex in either K^+- or NH_4^+-containing solutions by using a combination of UV, CD, PAGE, ITC, and ESI-MS methodologies. Our results showed that (1) **P1**−**P4** interact with the cKit87up quadruplex, and (2) the binding mode depends on the quadruplex stability. In K^+ buffer, **P1**−**P4** bind the ckit87up quadruplex structure as "quadruplex-binding agents". The same holds for P1 in NH_4^+ solution. On the contrary, in NH_4^+ solution, **P2**−**P4** overcome the quadruplex structure by forming PNA/DNA hybrid complexes, thus acting as "quadruplex openers".



INTRODUCTION

Guanosine-rich nucleic acid sequences have a propensity to form DNA secondary structures, known as G-quadruplexes. These structures are made up of stacked G-tetrad subunits, wherein four coplanar guanines are linked together by Hoogsteen hydrogen bonds.[1] Recent studies have been reported about the high density of putative G-quadruplex-forming sequences in telomeres and in genomic regions adjacent to transcriptional start sites,[2−4] thus supporting the biological importance of these structures *in vivo*.[5−7] Evidence exists that GC-rich regions of gene promoters can transiently unwind and form single-stranded tracts, eventually folding into G-quadruplexes.[8] Hurley and coworkers have provided the direct evidence for a G-quadruplex structure formation in a promoter region of c-MYC and its stabilization with several small molecules, resulting in the repression of c-MYC transcription.[9,10] Two quadruplex-forming sequences have been identified in the promoter region of the c-kit gene. One sequence (c-Kit21) is located within −140 to −160 base pairs (bp) upstream of the transcription initiation site, and the other one (c-Kit87up) between −87 and −109 bp.[11,12] The alteration of c-kit expression has been implicated in a variety of human tumors.[13−16]

These findings suggest that G-quadruplex formation may be related to a general mechanism for gene regulation, and that the modulation of gene expression could be achieved by targeting these structures.[17] Therefore, molecules that selectively bind and stabilize G-quadruplex structures are emerging as attractive gene-related therapeutic agents.[18] A number of ligands able to bind telomeric G-quadruplexes have been investigated for their ability to disable the telomere maintenance in tumor cells,[19] but to date only a few molecules have been investigated for targeting G-quadruplex in gene promoter regions.[20,21]

Very interestingly, NMR analysis of the G-quadruplex structure formed by the 22-mer c-Kit87up sequence has revealed a highly unusual G-quadruplex folding topology.[22] It comprises three G-tetrads with all the guanines in an *anti*-glycosidic conformation and four characteristic loops, one of which comprises five

Received: October 7, 2010
Revised: January 6, 2011
Published: March 16, 2011

ACS Publications © 2011 American Chemical Society

residues (Figure 1). Moreover, a bioinformatic study has shown that the c-Kit87up sequence is unique within the human genome.[23]

Among molecules designed to target G-quadruplexes, peptide nucleic acids (PNAs) represent a promising class of synthetic DNA analogues in which the entire sugar−phosphate backbone is replaced by a pseudopeptide.[24] The lower electrostatic repulsion, resulting from the absence of phosphate groups, allows PNAs to form very stable duplexes and triplexes by displacing the cDNA strand in DNA duplexes.[25,26] Strategies usually used for targeting G-rich sequences with PNAs are the formation of PNA/DNA hybrid quadruplexes[27,28] or the induction of G-quadruplex formation by displacing the G-rich/C-rich double-stranded DNA by using short G-rich PNAs that bind to the C-rich strand of DNA.[29]

Herein, we report for the first time the c-Kit87up sequence targeting with PNA probes. Our strategy is based on the identification of PNAs that recognize and stabilize the quadruplex formed by the c-Kit87up sequence. The design and synthesis of short PNAs potentially able to bind to suitable complementary sequences of loops and/or stem regions of the G-quadruplex structure formed by the c-Kit87up sequence are reported. To investigate the physicochemical properties underlying the molecular recognition between the c-Kit87up quadruplex-forming sequence and PNA molecules, circular dichroism (CD) and UV spectroscopies,[30−32] polyacrylamide gel electrophoresis (PAGE), electrospray mass spectrometry (ESI-MS),[33] and calorimetric techniques (ITC)[34] were employed.

EXPERIMENTAL PROCEDURES

Preparation of c-Kit87up Quadruplex and Its Complexes with PNAs. DNA and PNA sequences (Table 1) have been assembled using standard procedures (see Supporting Information).[35−38] The c-Kit87up quadruplex structure (**Q**) was formed by dissolving ckit87up (40 μM) in potassium buffer (10 mM KH_2PO_4, 40 mM KCl, 0.2 mM EDTA, pH = 7.0) or in 150 mM NH_4OAc solution, pH = 7.0 (Sigma Aldrich), and annealed by heating to 90 °C for 5 min followed by slow cooling to room temperature. The quadruplex solutions were then equilibrated at 4 °C for 24 h before addition of the suitable PNA. Each DNA-PNA complex was prepared by mixing equimolar amounts of **Q** and PNA at 25 °C and incubating the resulting mixture for 24 h at the same temperature before data acquisition.

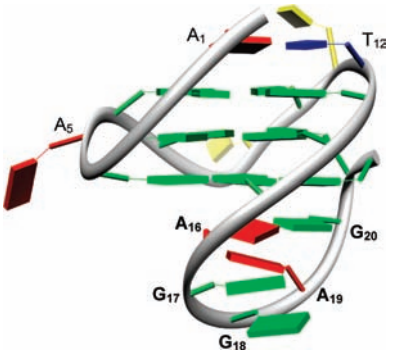


Figure 1. Schematic representation of ckit87up quadruplex structure annealed in K^+-containing solution. Guanine bases are in green, adenines are in red, cytosines are in yellow, and thymine is in blue. The residues belonging to loop-4 are in bold.

Circular Dichroism (CD). CD spectra of DNA, PNA, or mixed solutions (20 μM) were recorded by using a Jasco J-715 spectropolarimeter equipped with a Jasco JPT-423-S temperature controller in the 220−360 nm range, using 1 mm path-length cuvettes. Spectra were averaged over 5 scans, which were recorded at a scan rate of 100 nm/min with a response time of 1 s and a bandwidth of 1 nm. Buffer baseline was subtracted from each spectrum and the spectra were normalized to have zero ellipticity at 360 nm.

Thermal Difference Spectra (TDS) and UV-Melting Experiments. 20 μM solutions of DNA, PNA, and PNA/DNA mixture (0.5 mL) were placed in quartz cuvettes of 0.1 cm path length. Thermal difference spectra and UV-melting experiments were carried out using a Jasco V-530 UV−visible spectrophotometer equipped with a Jasco ETC-505-T temperature controller. TDS were obtained by recording the UV absorbance spectra in the range 220−320 nm at 5 and 90 °C and subsequently taking the difference between the two spectra.[32] UV-melting experiments were performed in the temperature range 5−90 °C by monitoring the absorbance at 295 nm,[31] at a 0.5 °C/min heating rate. The $T_{1/2}$ temperatures were calculated as previously reported by Mergny and Lacroix.[39]

Nondenaturing Polyacrylamide Gel Electrophoresis (PAGE). Nondenaturing gel electrophoreses were performed using 12% polyacrylamide gels, which were run in 1×TBE (Tris-Borate-EDTA) buffer supplemented with 50 mM KCl or 150 mM NH_4OAc, pH 7.0. Bands in the gels were visualized by SYBR Green staining (Sigma-Aldrich). A concentration of 10 μM was used for each sample.

ESI-Mass Spectrometry. ESI-MS studies were conducted using ammonium acetate at pH = 7.0.[33] The experiments were performed on a Q-TOF Ultima Global (Waters, Manchester, UK). The samples (DNA strand concentration = 10 μM) were infused at 4 μL/min in the electrospray source that operated in negative ion mode (capillary voltage = −2.2 kV). The source temperature was 80 °C and the nitrogen desolvation gas temperature was 100 °C. The pressure indicated on the source Pirani gauge was 3.0 mbar. For each sample, spectra were recorded using the following acceleration voltages: a cone voltage of 100 V, a RF Lens 1 voltage of 100 V, and a collision energy voltage (acceleration voltage before the collision hexapole) of 10 V. These voltage values represent a good compromise both to

Table 1. Mass Spectrometry Results of DNA and PNA Sequences Used in This Study[a]

		mass spectrometry results	
molecule	sequence	calculated (MW)	found (MW)
ckit87up	d($^{5'}$AGGGAGGGCGCTGGGAGGAGGG$^{3'}$)	7010.4	$(M+H)^+$ = 7011[b]
P1	H_2N -Lys- tcctc-H	1431.4	$(M+2H)^{2+}$ = 716.7[c]
P2	H_2N -Lys- tcctccc-H	1932.9	$(M+3H)^{3+}$ = 646.1[c]
P3	H_2N -Lys- tccctccc-H	2185.1	$(M+3H)^{3+}$ = 729.3[c]
P4	H_2N -Lys- tccctcccgcgac-H	3544.4	$(M+4H)^{4+}$ = 887.1[c]
P5	H_2N -Lys- ttttttt-H	2276.2	$(M+3H)^{3+}$ = 759.6[c]

[a] All PNA sequences are written from C to N terminus. [b] MALDI-TOF. [c] ESI-MS.

dx.doi.org/10.1021/bc100444v |*Bioconjugate Chem.* 2011, 22, 654–663

preserve the ammonium cations inside the G-quadruplexes and to observe the PNA/DNA complexes.[40] Complexes of higher m/z are not transmitted efficiently at low voltages through the mass spectrometer and, therefore, are not efficiently detected. The spectra were smoothed (2× mean, 10 channels), background-subtracted (polynomial order = 50, 1% below curve), and converted to centroid. The compounds were manually searched with the assistance of the *MassLynx 4.0* software. The average mass was calculated with its standard deviation.

Isothermal Titration Calorimetry (ITC). ITC experiments were performed using a CSC 5300 Nano-ITC microcalorimeter from Calorimetry Science Corporation (Lindon, Utah) with a cell volume of 1 mL. The buffer conditions used for ITC measurements were the same reported for the other experiments. Before each ITC experiment, the reference cell was filled with deionized water, and the DNA solutions were degassed for 5 min to eliminate air bubbles. The experiments were carried out at 25 °C. Care was taken to start the titration after achieving baseline stability. In each titration, volumes of 5−10 μL of a PNA containing solution (80−300 μM) were injected into a solution of quadruplex DNA (10−20 μM) in the same buffer, using a computer-controlled 250 μL microsyringe. The interval between PNA injections was 400 or 500 s. The heat produced by PNAs dilution was evaluated in control experiments by injecting each PNA solution into the buffer alone. The interaction heat for each injection was calculated after correction for the heat of PNA dilution. Measurement from the first injection was discarded from the analysis of the integrated data, in order to avoid artifacts due to the diffusion through the injection port occurring during the equilibration of the baseline. The corrected heat values were plotted as a function of the molar ratio. The integrated heat data were fitted using a nonlinear least-squares minimization algorithm to a theoretical binding isotherm, by means of the Bindwork program supplied with the instrument, to give the binding enthalpy ($\Delta_bH°$), equilibrium binding constant (K_b), and binding stoichiometry (n). The Gibbs energy and the entropic contribution were derived using the relationships $\Delta_bG° = -RT \ln K_b$ ($R = 8.314$ J mol^{-1} K^{-1}, $T =$ 298 K) and $-T\Delta_bS° = \Delta_bG° - \Delta_bH°$.

Molecular Modeling. To obtain a molecular model of the complex between **P3** and ckit87up quadruplex, the NMR solution structure of the quadruplex was used (Protein Data Bank entry number 2O3M), while the molecular model of **P3** was built using the Builder module of *Insight II* package (www.accelrys.com). **P3** was manually placed at a position so that the "$c_2c_3t_4$" bases of PNA form Watson−Crick base pairing with complementary "$A_{16}G_{17}G_{18}$" bases of the loop-4 of **Q**. **P3** backbone was then adapted to the structure of **Q**. The coordinates of the resulting **Q**-**P3** complex were energy minimized under vacuum with the *HyperChem 7.5* software,[41] using the steepest descent method, keeping the DNA residues fixed in position and allowing only the PNA to relax, until convergence to a rms gradient of 0.1 kcal/mol Å was reached.

RESULTS

Evaluation of G-Quadruplex Formation and Stability. The formation of the G-quadruplex structure by the 22-mer ckit87up sequence in potassium or ammonium solution was investigated by using CD, TDS, UV-melting, and PAGE techniques. ESI-MS experiments were also performed according to previous studies.[33,40] The structure formed by ckit87up sequence in the two different cation solutions was evaluated in comparison with that of the unstructured d($^{5'}$CCCTCCTCCCAGCGCCCTCCCT$^{3'}$) 22-mer oligonucleotide by examining the mobility in nondenaturing polyacrylamide gels. Figure 2A shows that **Q** possesses the same mobility in K^+ and NH_4^+ solutions and run faster than the unstructured 22-mer oligonucleotide, thus suggesting that the ckit-87up sequence adopts analogous folding in both the analyzed conditions.

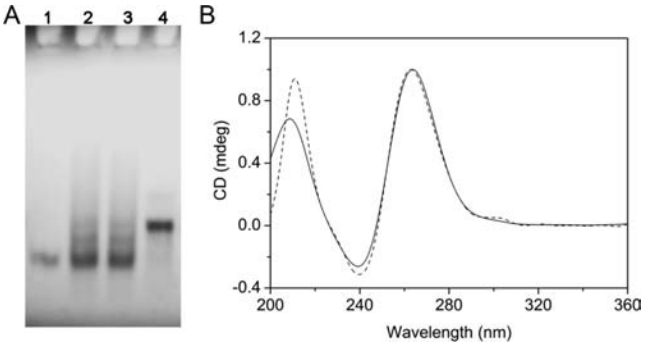


Figure 2. (A) PAGE of **Q** in K^+ and NH_4^+ containing solutions. Lane 1: [d(TGGGGT)]$_4$ in K^+ as quadruplex marker. Lane 2: **Q** annealed in K^+. Lane 3: **Q** annealed in NH_4^+. Lane 4: d($^{5'}$CCCTCCTCCCAGCGCCCTCCCT$^{3'}$) as unstructured 22-mer length marker. (B) Normalized CD spectra of ckit87up sequence annealed in K^+ (solid line) and NH_4^+ (dashed line) solutions.

To obtain a further structural insight into the above G-quadruplex structures,[42] CD spectra of **Q** were recorded either in potassium or in ammonium solution. Both spectra (Figure 2B) show two well-defined maxima around 210 and 263 nm and a minimum at 240 nm, suggesting that the oligonucleotide folds in a parallel-type quadruplex structure in both cases.[30] In addition, thermal difference spectra (TDS) were collected both in K^+ and NH_4^+ solutions. In agreement with CD experiments, the normalized differential absorbance signatures of **Q** show typical patterns of a G-quadruplex structure in both solution conditions (Figure 3, black traces), with two positive maxima at 243 and 273 nm and a negative minimum around 295 nm.[32] The temperature-dependent absorption of quadruplex-forming DNA was monitored at 295 nm (Supporting Information Figure S1). A hypochromic profile, characterized by a single transition, typical of the melting of a quadruplex structure,[31] is observed in both K^+ and NH_4^+ solutions. The thermal stability of **Q** was found to be higher in potassium ($T_{1/2}$ = 47.3 °C) than in ammonium solution ($T_{1/2}$ = 34.3 °C).

To gain information on the number of strands and cations involved in the quadruplex structure, electrospray mass spectrometry experiments were performed. The ckit87up ESI-MS spectrum (Supporting Information Figure S2) shows that the detected main species embeds two ammonium cations in the structure. In agreement with previous studies,[43] ammoniums are better preserved in ions of low charge states.

Evaluation of DNA-PNA Complex Formation. To probe the recognition phenomena between the ckit87up quadruplex-forming sequence and PNA molecules, the interaction of five different PNA sequences (Chart 1) was studied using CD, UV, ESI-MS, PAGE, and ITC techniques.

All the experiments were performed in K^+ and NH_4^+ solutions, except for the ESI-MS analyses that could only be performed in NH_4^+. **P1**−**P4** sequences can potentially target different tracts of the quadruplex structure (**Q**) formed by ckit87up. The 5-mer

P1 is fully complementary to the five bases $A_{16}-G_{20}$ (Figure 1), while **P2** and **P3** are complementary to the last seven and the first eight nucleosides of ckit87up sequence, respectively. The binding properties of these three shorter PNAs were compared to those of a 13-mer PNA strand, **P4**, which is fully complementary to the first thirteen nucleosides of ckit87up. **P2**−**P4** are also complementary to some residues belonging to loop-4 of **Q**. Finally, **P5**, an 8-mer poly-T PNA, noncomplementary to any portion of ckit87up, was used as a control sequence to show that the binding of PNA molecules is sequence specific.

The global structures of complexes formed by adding PNAs (**P1**−**P5**) to the prefolded quadruplex structure **Q**, either in NH_4^+ or in K^+ solutions, were compared by following their mobility on polyacrylamide gels. **Q**+**P1** and **Q**+**P5** mixtures (Figure 4, lanes 3 and 7) show almost the same mobility as **Q** (Figure 4, lane 2), in both potassium and ammonium solutions, while the remaining **Q**+(**P2**−**P4**) mixtures migrate with a lower mobility than **Q** (Figure 4, lanes 4, 5, and 6), thus suggesting the formation of different species.

Figure 5 shows circular dichroism spectra of 1:1 mixtures of **Q** with **P1**−**P4** (**Q**+**P1**, **Q**+**P2**, **Q**+**P3**, and **Q**+**P4**) recorded in potassium (panels A−D) and ammonium (panels E−H) solutions. The spectrum of each mixture is reported in comparison with the arithmetic sum of the individual components. The CD spectrum of **Q**+**P1** mixture recorded in potassium (Figure 5A) was almost identical to the sum of the spectra of the single components, displaying the CD signature characteristic of a parallel-stranded G-quadruplex. The CD spectra of mixtures obtained by adding **P2**, **P3**, or **P4** to **Q** in potassium buffer are all characterized by the maximum at 210 nm—ubiquitous for G-quadruplexes—and show the typical profile observed for parallel-type G-quadruplexes, although a small red-shift (2−5 nm) was observed for the minimum at 240 nm and the maximum at 263 nm (Figure 5, panels B, C, and D). The CD analysis of samples recorded in NH_4OAc solution revealed that the CD profile of the **Q**+**P1** mixture (Figure 5E) is almost superimposable to the sum of the single components, as observed in potassium buffer. Conversely, large changes in the CD spectra were observed upon addition of **P2**−**P4** PNAs to **Q**. Particularly, these mixtures showed significant shifts for the negative minimum (from 240 to 248 nm) and both positive maxima (from 210 to 223 nm and from 263 nm to 270−280 nm; Figure 5, panels F, G, and H). These values, namely, maxima at 223 and 280 nm and minimum at 248 nm, have been previously reported to be characteristic of hybrid PNA-DNA duplex tracts.[44,45] Finally, CD spectra of the **Q**+**P5** mixture recorded in both potassium and ammonium solutions are almost superimposable to the sum of the spectra of the single components, confirming, as expected, that no hybridization occurs in this case (Supporting Information Figure S3).

Figure 3 shows TDS signatures for the complexes formed by mixing equimolar quantities of **Q** and PNAs **P1**−**P4** in potassium buffer (A) and ammonium solution (B). The typical pattern of a G-quadruplex was observed for all the complexes in potassium

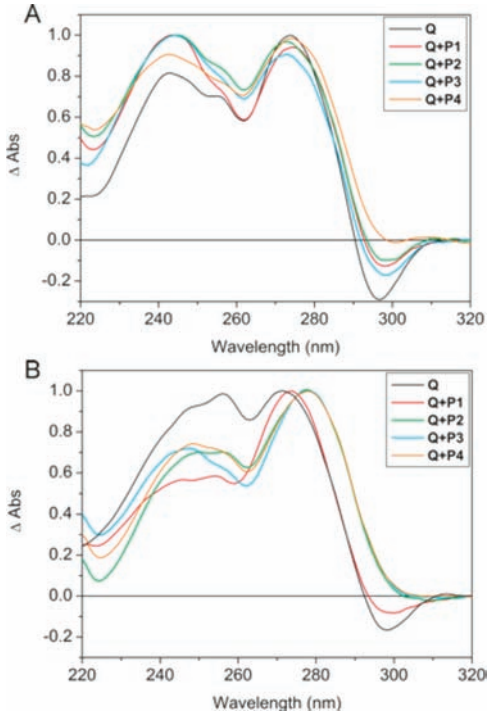


Figure 3. Normalized thermal difference spectra of 1:1 mixtures of **Q** and **Q**+(**P1**−**P4**) in K^+- (A) and in NH_4^+-containing solution (B).

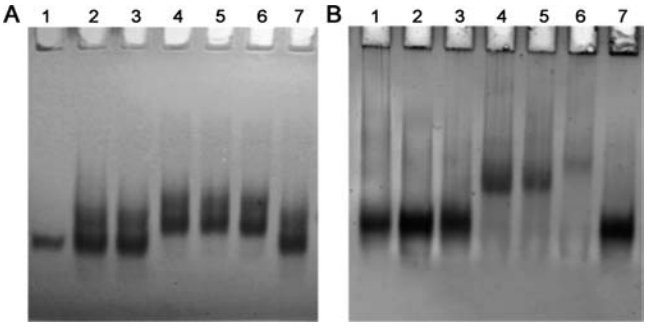


Figure 4. PAGE of 1:1 mixtures of **Q** and **Q**+(**P1**−**P5**), annealed in K^+- (A) and NH_4^+-containing solution (B). Lane 1: $[d(TGGGGT)]_4$ as quadruplex marker. Lane 2: **Q**. Lane 3: **Q**+**P1**. Lane 4: **Q**+**P2**. Lane 5: **Q**+**P3**. Lane 6: **Q**+**P4**. Lane 7: **Q**+**P5**.

Chart 1. Sequences of DNA and PNA Used in This Study[a]

ckit 87up	d($^{5'}$AGG-GAG-GGC-GCT-GGG-**AGG-AG**G-G$^{3'}$)
P1	H_2NLys-t-c-c-t-c-H
P2	H_2NLys-t-c-c-t-c-c-c-H
P3	H_2NLys-t-c-c-c-t-c-c-c-H
P4	H_2NLys-t-c-c-c-t-c-c-c-g-c-g-a-c-H
P5	H_2NLys-t-t-t-t-t-t-t-t-H

[a]Guanines in ckit87up sequences that participate in quadruplex formation are underlined. Residues in loop-4 of **Q** are in bold. DNA sequence is written 5′ to 3′, while the PNA sequences are written C to N terminus.

dx.doi.org/10.1021/bc100444v |*Bioconjugate Chem.* 2011, 22, 654–663

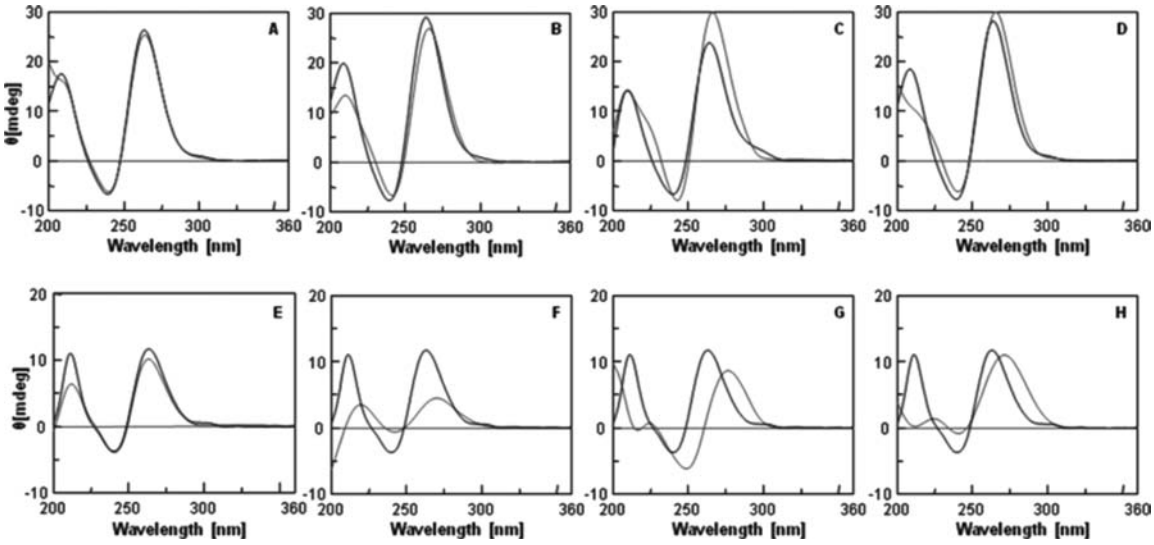


Figure 5. CD spectra of 20 μM **Q** + 20 μM PNAs mixtures (green line) and sum of the spectra of the single components (blue line) in potassium (A−D) and ammonium solution (E−H). **Q**+**P1** (A, E); **Q**+**P2** (B, F); **Q**+**P3** (C, G); **Q**+**P4** (D, H).

buffer. In particular, two positive maxima at 243 and 273 nm, a shoulder at 255 nm, and a negative minimum around 295 nm were observed in all the spectra. Conversely, TDS shapes of PNA-DNA complexes formed in ammonium solution showed the loss of the negative band at 295 nm, except for **Q**+**P1**. Moreover, the positive band at 273 nm was red-shifted to 277 nm, once again except for **Q**+**P1**. The loss of the negative band at 295 nm suggested the absence of Hoogsteen-bonded G-tetrads, while the presence of the peak at 277 nm is compatible with a Watson−Crick duplex-like structure[32] in all **Q**+(**P2**−**P4**) mixtures.

As previously described, a G-quadruplex structure melts with a characteristic hypochromic shift at 295 nm; thus, UV-melting experiments were performed for all the complexes, by recording the absorbance at 295 nm.[31] In potassium buffer, all the UV-melting profiles were consistent with the G-quadruplex foldings (Supporting Information Figure S1). The relative stabilities of PNA-complexed quadruplexes are reported in Table 2. In potassium, all complexes (Supporting Information Figure S1A) displayed $T_{1/2}$ values higher than that of **Q** (ΔT = 2−10 °C), with the exception of **Q**+**P4** for which a destabilizing effect is observed (ΔT = 5.5 °C). On the other hand, in ammonium solution, a hypochromic transition at 295 nm (Supporting Information Figure S1B) is observed only for **Q**+**P1**, once again suggesting the presence of the quadruplex structure. For all other samples, hyperchromic profiles are observed at this wavelength, suggesting the absence of the G-quadruplex scaffold in these complexes.

To better investigate the binding properties shown by the investigated PNA sequences (**P1**−**P4**), a calorimetric analysis of the interaction with **Q** was carried out both in K^+- and in NH_4^+-containing solutions (Figure 6). ITC experiments were also performed by using the poly-T PNA (**P5**, Table 1), as control sequence.

The results collected for titration of **Q** with the five PNAs in K^+ solution reveal that (a) **P1**, **P2**, and **P3** bind to the investigated quadruplex by forming a 1:1 complex; (b) **P4** interacts in a nonspecific manner with **Q**; (c) **P5** does not interact at all. The ITC data for the titrations of **Q** with **P1**, **P2**, and **P3** indicate that the interactions of the PNAs with the quadruplex are favored at 25 °C. However, the characterization of the binding reactions reveals that the interactions of the three PNAs are slightly different from a thermodynamic point of view (Table 4). In all three cases, the binding isotherms indicate exothermic interactions (Figure 6). Indeed, after each injection of PNA, less and less heat release was observed until constant values were obtained, hence reflecting a saturable process. The values of the binding constants clearly show that **P2** and **P3** bind to the investigated quadruplex with higher affinity (K_b = 1 and 3×10^6 M^{-1}, respectively) than **P1** ($K_b = 3 \times 10^5$ M^{-1}). In the cases of **P2** and **P3**, the values of $\Delta_bH°$ and $T\Delta_bS°$ show that the enthalpic contribution provides the driving force for the PNA−quadruplex interaction. However, the interaction of **P3** with **Q** is associated with a larger favorable enthalpy ($\Delta_bH°$ = −110 kJ mol^{-1}) as compared to **P2** ($\Delta_bH°$ = −90 kJ mol^{-1}). On the other hand, the interaction of **P1** is associated with a favorable enthalpic contribution ($\Delta_bH°$ = −12 kJ mol^{-1}) that acts together with the entropic one ($T\Delta_bS°$ = 19 kJ mol^{-1}). The favorable heat observed for the binding reaction is due to the net compensation of the exothermic heat from the formation of base pairs and the endothermic heats of possible H-bonds breaking. In the ITC titrations of **Q** with **P4**, a resolvable binding isotherm was never obtained using several combinations of reactant concentrations,

Table 2. Melting Temperatures for c-Kit87up Quadruplex-Forming Sequence and PNA-DNA Complexes Calculated from UV-Melting Curves Recorded at 295 nm

	$T_{1/2}$ (°C)	
sample	K^+ solution	NH_4^+ solution
Q	47.1 ± 0.1	34.3 ± 0.1
Q+**P1**	49.2 ± 0.2	37.6 ± 0.2
Q+**P2**	54.0 ± 0.2	n.d.
Q+**P3**	56.8 ± 0.2	n.d.
Q+**P4**	41.6 ± 0.2	n.d.

dx.doi.org/10.1021/bc100444v |*Bioconjugate Chem.* 2011, 22, 654–663

not allowing the determination of the thermodynamic parameters or the recognition of a defined stoichiometry. The raw ITC data for the titration of **Q** with **P5** (Supporting Information Figure S4) show constant heat release after each injection of PNA, only due to PNA dilution. A resolvable binding isotherm for the interaction with **Q** is not observed in this case as well, suggesting no affinity of **P5** for the investigated quadruplex.

When the same titrations were performed in the NH_4^+-containing solution, the binding behaviors turned out to be different, except for **P1**. As observed in K^+ solution, **P1** forms a 1:1 complex with **Q**. The thermodynamic parameters (Table 4) indicate that the interaction of **P1** is exothermic ($\Delta_bH^\circ = -13$ kJ mol^{-1}) and it is associated with a favorable entropic contribution ($T\Delta_bS^\circ = 18$ kJ mol^{-1}). On the other hand, the binding curves relative to **P2** and **P3** show less simple profiles compared to the analogous curves in K^+ solution (Figure 6). Indeed, at a molar ratio of 2:1 (PNA/DNA), fluctuating values of heat release were observed after injection of PNA, reflecting a nonsaturated process at that ratio. In NH_4^+ solution, **P4** shows behavior comparable to those of **P2** and **P3**, producing a similar binding profile. In particular, the **P2**−**P4** binding isotherms display a biphasic profile, revealing two consecutive binding events: (1) one PNA molecule interacts with the DNA; (2) a second PNA molecule binds to DNA, leading to the formation of a 2:1 PNA/DNA complex. The interpolation procedure of the experimental data has been carried out with a multiple-sites model. The thermodynamic results obtained from ITC data for **P2**, **P3**, and **P4** binding to DNA are given in Table 4. The thermodynamic characterization of the binding events revealed that the first binding event ($K_b = 2 \times 10^7$ and 3×10^7 M^{-1} for **P2** and **P3**, respectively; $K_b = 8 \times 10^7$ M^{-1} for **P4**) is stronger than the second one ($K_b = 8 \times 10^5$ M^{-1} for both **P2** and **P3**; $K_b = 1 \times 10^6$ M^{-1} for **P4**). Moreover, the analysis indicated that the two binding events are driven by a large enthalpic contribution, while there is an unfavorable entropic contribution.

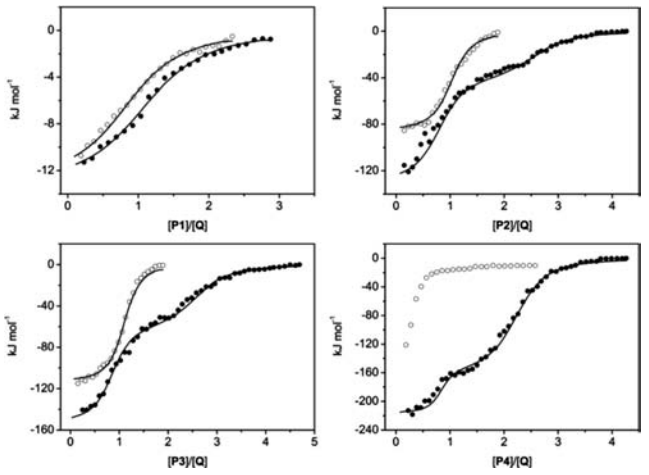


Figure 6. ITC profiles for the interaction between PNA sequences and ckit87up quadruplex in K^+ (open circles) and NH_4^+ (black circles) containing solution. The circles represent the experimental data obtained by integrating the raw data and subtracting the heat of PNA dilution. The lines represent the best-fit curve for the binding.

To establish the molecularity of the complexes in ammonium solution, MS spectra have been acquired by an ESI-Q-TOF instrument under conditions that preserve noncovalent interactions. ESI-MS was previously used to characterize intermolecular PNA/DNA complexes.[46] Here, ESI-MS was used to investigate the stoichiometry of the complexes formed when stoichiometric amounts of **P1**−**P5** are added to **Q** at room temperature (Supporting Information Figure S5). Table 3 summarizes the main species identified from the mass spectra of PNA/DNA complexes. The short **P1** probe interacts with **Q** without disrupting its scaffold, indeed the ESI-MS spectrum shows the presence of the $[\mathbf{Q}\text{-}(\mathbf{P1})_1]$ adduct with the inner ammoniums preserved (Figure 7). As expected for long PNA sequences, when **P2**−**P4** PNAs are mixed with **Q**, the main peaks observed correspond to 1:1 and 2:1 PNA/DNA hybrid complexes with $[\mathbf{ckit87up}\text{-}(\mathbf{P2}-\mathbf{P4})_1] > [\mathbf{ckit87up}\text{-}(\mathbf{P2}-\mathbf{P4})_2]$, in agreement with the ITC data. **Q** is less abundant, but always detected. Finally, the **Q**+**P5** spectrum shows no PNA/DNA complex formation, even by increasing PNA concentration (data not shown), thus suggesting that the PNA binding to DNA is sequence specific.

DISCUSSION

The present study reports the first example of PNA probes able to bind to a biologically relevant DNA quadruplex without disrupting its scaffold. While strand invasion of PNA into duplex and quadruplex DNA have been investigated in detail,[47,48] less attention has been paid to the ability of PNA to bind and stabilize the targeted quadruplex. We focused on some different PNA sequences and analyzed their interaction with the quadruplex formed by the ckit87up DNA sequence.

Table 3. Summary of the Peaks Observed in the Electrospray Mass Spectra of ckit87up Quadruplex (Q) + PNAs in 150 mM NH_4OAc at 1:1 DNA/PNA Ratio[a]

	DNA/PNA 1:1		
sample	$\mathbf{Q}^{z-} = [\text{ckit87up}\cdot(NH_4^+)_2]^{z-}$	$[\mathbf{Q}\text{-}(\mathbf{PNA})_n]^{z-}$ complex	$[\mathbf{ckit87up}\text{-}(\mathbf{PNA})_n]^{z-}$ hybrid
Q	$[\mathbf{Q}]^{4-\rightarrow5-}$	–	–
Q+**P1**	$[\mathbf{Q}]^{4-\rightarrow5-}$ m.p.	$[\mathbf{Q}\text{-}(\mathbf{P1})_1]^{5-}$	–
Q+**P2**	$[\mathbf{Q}]^{4-\rightarrow5-}$ m.p.	–	$[\mathbf{ckit87up}\text{-}(\mathbf{P2})_1]^{5-\rightarrow6-}$ $[\mathbf{ckit87up}\text{-}(\mathbf{P2})_2]^{6-\rightarrow7-}$
Q+**P3**	$[\mathbf{Q}]^{4-\rightarrow5-}$ l.p.	–	$[\mathbf{ckit87up}\text{-}(\mathbf{P3})_1]^{4-\rightarrow6-}$ $[\mathbf{ckit87up}\text{-}(\mathbf{P3})_2]^{5-\rightarrow7-}$
Q+**P4**	$[\mathbf{Q}]^{4-\rightarrow5-}$ l.p.	–	$[\mathbf{ckit87up}\text{-}(\mathbf{P4})_1]^{5-\rightarrow6-}$ $[\mathbf{ckit87up}\text{-}(\mathbf{P4})_2]^{5-\rightarrow6-}$
Q+**P5**	$[\mathbf{Q}]^{4-\rightarrow5-}$	–	–

[a] m.p. = "main product"; l.p. = "low product".

Table 4. Thermodynamic Parameters for the Interaction Between the c-Kit87up Quadruplex-Forming Sequence and PNAs Determined by ITC[a] at 298 K

	first event					second event				
PNA	n	K_b (M^{-1})	$\Delta_bH°$ (kJ mol^{-1})	$T\Delta_bS°$ (kJ mol^{-1})	$\Delta_bG°_{298K}$ (kJ mol^{-1})	n	K_b (M^{-1})	$\Delta_bH°$ (kJ mol^{-1})	$T\Delta_bS°$ (kJ mol^{-1})	$\Delta_bG°_{298K}$ (kJ mol^{-1})
				K^+ solution						
P1	1.0	3×10^5	−12	19	−31					
P2	1.0	1×10^6	−90	−56	−34					
P3	1.0	3×10^6	−110	−73	−37					
				NH_4^+ solution						
P1	1.2	3×10^5	−13	18	−31					
P2	0.9	2×10^7	−130	−88	−42	1.8	8×10^5	−50	−16	−34
P3	0.8	3×10^7	−150	−107	−43	1.8	8×10^5	−60	−26	−34
P4	0.8	8×10^7	−215	−170	−45	1.7	1×10^6	−160	−126	−34

[a] The experimental error for each thermodynamic property is <8%.

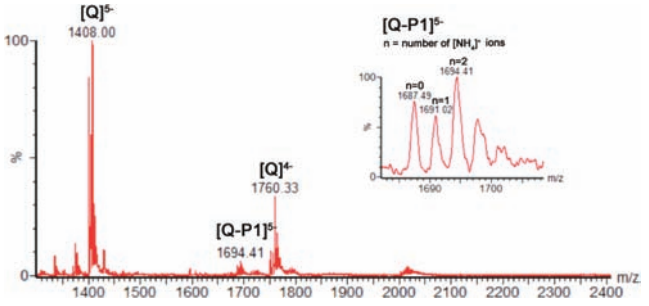


Figure 7. ESI-MS spectra of **Q**+**P1** in 150 mM NH_4OAc. The reported spectrum was acquired in the following soft source conditions: RF Lens1 = 100 V; cone = 100 V; collision energy = 10 V. The inset shows the distribution of the number of ammonium ions remaining in the G-quadruplex (from 0 to 2). [**Q**] = ckit87up quadruplex, namely, [M+2NH_4^+], where M is the single-stranded ckit87up ODN strand; [**Q-P1**] = **Q**+**P1** complex, namely [M+P1 + 2NH_4^+], in which the quadruplex is retained and coordinates two ammonium ions.

In general, the G-quadruplex structures are stabilized by monovalent cations, in particular, K^+ and to a lesser extent Na^+ and NH_4^+.[49] The ckit87up quadruplex predominantly exists in a parallel conformation *in vitro* in K^+ buffer, while in Na^+ solution, it forms aggregated species.[22] NH_4^+ stabilizes G-quadruplexes to an extent comparable with that observed for Na^+, but it displays a coordination geometry similar to that observed for K^+.[50] Therefore, to detect the differences in the molecular recognition process, the analysis was carried out in two different solutions, containing either potassium or ammonium ions.

The PAGE shows very similar behavior for **Q** annealed in K^+- or NH_4^+-containing solution, thus suggesting analogous folding in both ion conditions. Furthermore, ESI-MS data acquired in NH_4^+ solution (the ammonium is the only ion which can be used in the ESI-MS experiments) confirm the quadruplex structure adopted in ammonium showing that two NH_4^+ ions are retained in the quadruplex scaffold (see Supporting Information). In addition, CD and UV data also show the formation of a parallel quadruplex structure in both solutions and, as expected, UV-melting studies revealed that the thermal stability of **Q** in ammonium is lower than that observed in potassium solution.

Binding studies indicate that **P1**−**P4** PNAs are able to bind to ckit87up quadruplex-forming sequence. Interestingly, we observed that the different stability of the quadruplex arrangements affects the binding mode of three (**P2**, **P3**, and **P4**) out of four PNAs.

Our results show that the short **P1** probe binds to **Q** in both NH_4^+ and K^+ solutions without disrupting the target structure. The thermodynamic profiles determined by ITC for the **Q**−**P1** interaction, in the two different solutions, are qualitatively similar. In both cases, the 5-mer PNA binds to the quadruplex, even though with little affinity, and the stoichiometry observed is 1:1. Interestingly, the UV_{295}-melting experiments show that the **Q-P1** complex melts as a quadruplex structure at a temperature quite higher than **Q** alone in both NH_4^+ and K^+ solutions. CD, TDS, and PAGE studies suggested that the structure of the quadruplex is maintained upon **P1** addition in both investigated conditions. ESI-MS analysis confirms this result in ammonium solution. In fact, as for the quadruplex alone, the resulting **Q-P1** complex retains the two ammonium cations embedded in the structure (Figure 7). Since the 5-mer **P1** is complementary to the five bases A_{16}−G_{20} of the long loop-4 of **Q**, it is probably able to bind some of those bases, thus preserving the quadruplex scaffold. Since **Q** and **Q**+**P1** complexes run similarly on the gel, we suppose that the **Q**+**P1** complex retains the overall shape of free **Q**. On the other hand, the binding behavior of **P2**−**P4** PNAs was found to be completely different depending on the cation. Our data indicate that in ammonium solution **P2**−**P4** act as "openers" invading the quadruplex by forming PNA/DNA hybrid complexes. In that solution, the characteristic CD and TDS profiles of the quadruplex are lost upon addition of those PNAs and the typical UV_{295}-melting hypochromic transition of the quadruplex is not more observed. Nondenaturing gel electrophoresis show the formation of different species possessing lower mobility than **Q**, and the results of ESI-MS analysis are compatible with the formation of 1:1 and 2:1 PNA/DNA complexes without ammonium ions embedded, thus confirming that the G-quadruplex scaffold is not retained in these hybrid complexes. The thermodynamic characterization reveals some interesting features about the binding process in ammonium. In particular, ITC data clearly suggest that two consecutive binding events occur when a PNA solution is added in an incremental stepwise fashion to the DNA solution. The first, stronger, binding event has a binding stoichiometry of 1:1, then a weaker second process requiring a much higher PNA concentration for saturation occurs, suggesting that the resulting final complex is composed by two PNA and one DNA strands. The DNA/PNA

interaction yielded favorable, enthalpy-driven, free energy contributions, indicating that **P2**−**P4** are able to invade and disrupt the quadruplex structure by forming a stable product. The favorable heat for the first binding reaction is due to the net compensation of exothermic heat attributable to the formation of base-pair stacks and endothermic heat required for breaking the G-tetrad stacks of **Q**. The magnitude of the enthalpy values for the formation of 1:1 and 2:1 PNA/DNA hybrid complexes directly measured in ITC titrations increases by increasing the PNA length and clearly indicates the highest number of base-pair stacks formed in the case of **P4**. Therefore, all the above experiments demonstrate that in ammonium the **P2**, **P3**, and **P4** PNA probes can unfold the quadruplex structure, forming 1:1 and 2:1 PNA/DNA hybrid complexes with the target DNA. Since it is well-known that pyrimidine-rich PNA sequences are able to invade DNA strands by forming PNA-DNA-PNA triplexes, we believe that the 2:1 PNA:DNA complexes, observed in ammonium in the presence of an excess of **P2**, **P3**, and **P4**, can be PNA-DNA-PNA triplex-type complexes.[51]

Conversely, the results of the experiments performed in potassium-containing solution indicate that **P2**−**P4** PNAs are able to bind to **Q**, but none of them overcome the quadruplex structure. Indeed, CD, UV, and PAGE experiments reveal that the structure of the quadruplex is retained upon addition of **P2**, **P3**, or **P4**. Moreover, UV thermal denaturation data indicate that the binding of **P2** and **P3** to **Q** increases the $T_{1/2}$ values of the resulting quadruplex complexes. The energetic profiles, determined by ITC for the binding of **P2** and **P3** to **Q**, are qualitatively comparable, showing, in both cases, a single binding event with a stoichiometry of 1:1. The dissection of the Gibbs energy change into the enthalpy- and entropy-change contributions for the binding shows that the favorable Gibbs energy change is due to a favorable enthalpy change and an unfavorable entropy contribution. The entropy change values observed are the net compensation of (a) the unfavorable entropic contribution, due to the formation of a less relaxed complex with respect to unbounded components, and (b) the favorable entropic contribution, due to the release of coordinated water molecules to the bulk solvent. Moreover, the thermodynamic data revealed that **P3** has a higher affinity for **Q** (K_b for **P3** is three times larger than that for **P2**) and that its interaction is associated with a larger favorable enthalpy change. On the other hand, the ITC titration of **Q** with **P4** shows that the interaction between these molecules does not lead to the determination of thermodynamic parameters associated with a specific interaction.

The overall picture emerging from this study is that the investigated PNAs are able to interact with **Q** in both K^+ and NH_4^+ solutions, but with a different binding mode. As known, the nature of the cations in solution significantly influences the stability of G-quadruplexes. The different behavior of PNA molecules arises just from the relative stability of **Q** in the two ionic solutions. In NH_4^+ solution, the PNAs are able to overcome the less stable quadruplex structure of **Q** hybridizing the DNA sequence. Conversely, in K^+ solution, where the quadruplex structure stability is highest, the PNAs are still able to bind to the quadruplex without overcoming it. The melting experiments of the quadruplex structure in K^+ solution show that the binding of PNAs leads to a stabilization of **Q**, resulting in the following stability order: **Q-P3** > **Q-P2** > **Q-P1**. The ranking orders of binding constants and enthalpies found by ITC are in agreement with the order of thermal stability, and indicate that **P3** is the best quadruplex-binding agent among the investigated PNAs.

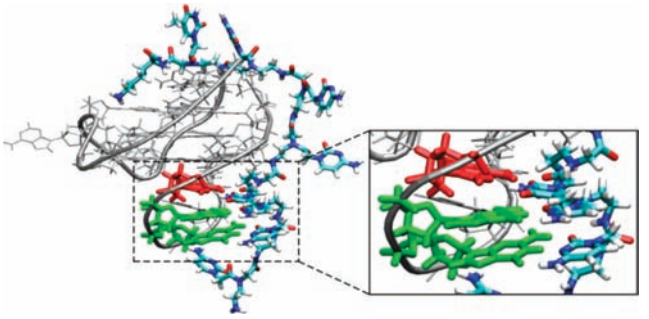


Figure 8. Molecular model of the complex between ckit87up quadruplex (**Q**) and **P3**. **Q** is in gray, and adenine (A_{16}) and guanine (G_{17} and G_{18}) bases involved in Watson−Crick base pairing with the complementary PNA residues are highlighted in red and green, respectively.

The NMR structure of **Q**[22] shows that the only residues potentially able to form Watson−Crick-type base pairs are the bases A_{16}, G_{17}, and G_{18} of the long loop-4; therefore, we speculate that the interaction with PNA involves one of its "c-c-t" stretch. Since **P2** and **P3** bind to **Q** with higher affinity than **P1**, we hypothesize that the best possible interaction occurs with the "c-c-t" motif at the N-terminus. Figure 8 shows a molecular model of **Q-P3** complex, built on the basis of these considerations. The model of the complex shows that the PNA molecule is able to form three Watson−Crick base pairing involving the "$c_2c_3t_4$" bases of **P3** and the complementary "$A_{16}G_{17}G_{18}$" bases. The model also shows that the PNA molecule can adapt its backbone to the structure of **Q**. The flexibility of PNA could allow the positively charged lysine residue to gain additional interactions with the backbone of the quadruplex. The origin of the nonspecific binding of **P4**, that match the C-terminus sequence of **P3**, could be due to the remaining bases at the N-terminus. These latter could also be responsible for the quadruplex destabilization observed in **Q-P4** complex in K^+.

In conclusion, in this paper we proposed a potential way to regulate the c-kit gene transcription by using short PNA sequences. The ckit87up sequence is unique within the human genome, and it folds into an unusual quadruplex structure embodying a peculiar long loop that may represent, as we have shown, the target of new quadruplex-binding agents. Our findings demonstrate that (i) PNAs can act as quadruplex-binding agents, that (ii) their affinity toward the quadruplex depends on PNA sequence and length, and that (iii) the binding mode could be related to the quadruplex stability. These studies open up new routes for the development of improved probes for the regulation of c-kit protooncogene transcription.

■ ASSOCIATED CONTENT

Supporting Information. Experimental procedures for the synthesis of DNA and PNA sequences; UV-melting curves for **Q** and **Q**+(**P1**−**P4**) complexes in potassium and ammonium solution; ESI-MS spectra of **Q** and **Q**+(**P1**−**P5**); CD spectra of **Q**+**P5** in potassium and ammonium solution; ITC data for titration of **Q** with **P5** in potassium solution. This material is available free of charge via the Internet at http://pubs.acs.org.

■ AUTHOR INFORMATION

Corresponding Author

*Tel: +39 081678540. Fax: +39 081678746. E-mail: golivier@unina.it.

Author Contributions

[#]These authors have contributed equally.

■ ACKNOWLEDGMENT

This work was supported by a PRIN grant 2007 from the Italian Ministero dell'Università e della Ricerca [2007EBYL8L_005], by the COST Action MP0802 [STSM5095 to J.A.], by the FRS-FNRS [CC 1.5.286.09 and research associate position to VG] and the University of Liège [FSR starting grant D08/10 to VG]. We would like to thank Dr. Frédéric Rosu and Dr. Luisa Cuorvo for their valuable technical assistance.

■ REFERENCES

(1) Neidle, S. (2009) The structures of quadruplex nucleic acids and their drug complexes. *Curr. Opin. Struct. Biol. 19*, 239–250.

(2) Huppert, J. L., and Balasubramanian, S. (2005) Prevalence of quadruplexes in the human genome. *Nucleic Acids Res. 33*, 2908–2916.

(3) Todd, A. K., Johnston, M., and Neidle, S. (2005) Highly prevalent putative quadruplex sequence motifs in human DNA. *Nucleic Acids Res. 33*, 2901–2907.

(4) Eddy, J., and Maizels, N. (2006) Gene function correlates with potential for G4 DNA formation in the human genome. *Nucleic Acids Res. 34*, 3887–3896.

(5) Shklover, J., Weisman-Shomer, P., Yafe, A., and Fry, M. (2010) Quadruplex structures of muscle gene promoter sequences enhance in vivo MyoD-dependent gene expression. *Nucleic Acids Res. 38*, 2369–2377.

(6) Cogoi, S., Paramasivam, M., Membrino, A., Yokoyama, K. K., and Xodo, L. E. (2010) The KRAS promoter responds to Myc-associated zinc finger and poly(ADP-ribose) polymerase 1 proteins, which recognize a critical quadruplex-forming GA-element. *J. Biol. Chem. 285*, 22003–22016.

(7) Palumbo, S. L., Memmott, R. M., Uribe, D. J., Krotova-Khan, Y., Hurley, L. H., and Ebbinghaus, S. W. (2008) A novel G-quadruplex-forming GGA repeat region in the c-myb promoter is a critical regulator of promoter activity. *Nucleic Acids Res. 36*, 1755–1769.

(8) Sun, D., Guo, K., Rusche, J. J., and Hurley, L. H. (2005) Facilitation of a structural transition in the polypurine/polypyrimidine tract within the proximal promoter region of the human VEGF gene by the presence of potassium and G-quadruplex-interactive agents. *Nucleic Acids Res. 33*, 6070–6080.

(9) Siddiqui-Jain, A., Grand, C. L., Bearss, D. J., and Hurley, L. H. (2002) Direct evidence for a G-quadruplex in a promoter region and its targeting with a small molecule to repress c-MYC transcription. *Proc. Natl. Acad. Sci. U.S.A. 99*, 11593–11598.

(10) Hurley, L. H., Von Hoff, D. D., Siddiqui-Jain, A., and Yang, D. (2006) Drug Targeting of the c-MYC promoter to repress gene expression via a G-quadruplex silencer element. *Semin. Oncol. 33*, 498–512.

(11) Rankin, S., Reszka, A. P., Huppert, J., Zloh, M., Parkinson, G. N., Todd, A. K., Ladame, S., Balasubramanian, S., and Neidle, S. (2005) Putative DNA quadruplex formation within the human c-kit oncogene. *J. Am. Chem. Soc. 127*, 10584–10589.

(12) Fernando, H., Reszka, A. P., Huppert, J., Ladame, S., Rankin, S., Venkitaraman, A. R., Neidle, S., and Balasubramanian, S. (2006) A conserved quadruplex motif located in a transcription activation site of the human c-kit oncogene. *Biochemistry 45*, 7854–7860.

(13) Sakurai, S., Fukasawa, T., Chong, J. M., Tanaka, A., and Fukayama, M. (1999) C-kit gene abnormalities in gastrointestinal stromal tumors (tumors of interstitial cells of Cajal). *Jpn J. Cancer Res. 90*, 1321–1328.

(14) Looijenga, L. H., de Leeuw, H., van Oorschot, M., van Gurp, R. J., Stop, H., Gillis, A., de Gouveia Brazao, C. A., Weber, R. E., Kirkels, W. J., van Dijk, T., and von Lindern, M. (2003) Stem cell factor receptor (c-KIT) codon 816 mutations predict development of bilateral testicular germ-cell tumors. *Cancer Res. 63*, 7674–7678.

(15) Wang, Y. Y., Zhou, G. B., Yin, T., Chen, B., Shi, J. Y., Liang, W. X., Jin, X. L., You, J. H., Yang, G., Shen, Z. X., Chen, J., Xiong, S. M., Chen, G. Q., Xu, F., Liu, Y. W., Chen, Z., and Chen, S. J. (2005) AML1-ETO and C-KIT mutation/overexpression in t(8;21) leukemia: implication in stepwise leukemogenesis and response to Gleevec. *Proc. Natl. Acad. Sci. U.S.A. 102*, 1104–1109.

(16) Fletcher, J. A., and Rubin, B. P. (2007) KIT Mutations in GIST. *Curr. Opin. Genet. Dev. 17*, 3–7.

(17) Kumar, N., Patowary, A., Sivasubbu, S., Petersen, M., and Maiti, S. (2008) Silencing c-MYC expression by targeting quadruplex in P1 promoter using locked nucleic acid trap. *Biochemistry 47*, 13179–13188.

(18) Ou, T. M., Lu, Y. J., Tan, J. H., Huang, Z. S., Wong, K. Y., and Gu, L. Q. (2008) G-quadruplexes: Targets in anticancer drug design. *ChemMedChem 3*, 690–713.

(19) Pagano, B., and Giancola, C. (2007) Energetics of quadruplex-drug recognition in anticancer therapy. *Curr. Cancer Drug Targets 7*, 520–540.

(20) Gunaratnam, M., Swank, S., Haider, S. M., Galesa, K., Reszka, A. P., Beltran, M., Cuenca, F., Fletcher, J. A., and Neidle, S. (2009) Targeting human gastrointestinal stromal tumor cells with a quadruplex-binding small molecule. *J. Med. Chem. 52*, 3774–3783.

(21) Bejugam, M., Sewitz, S., Shirude, P. S., Rodriguez, R., Shahid, R., and Balasubramanian, S. (2007) Trisubstituted isoalloxazines as a new class of G-quadruplex binding ligands: small molecule regulation of c-kit oncogene expression. *J. Am. Chem. Soc. 129*, 12926–12927.

(22) Phan, A. T., Kuryavyi, V., Burge, S., Neidle, S., and Patel, D. J. (2007) Structure of an unprecedented G-quadruplex scaffold in the human c-kit promoter. *J. Am. Chem. Soc. 129*, 4386–4392.

(23) Todd, A. K., Haider, S. M., Parkinson, G. N., and Neidle, S. (2007) Sequence occurrence and structural uniqueness of a G-quadruplex in the human c-kit promoter. *Nucleic Acids Res. 35*, 5799–5808.

(24) Nielsen, P. E., Egholm, M., Berg, R. H., and Buchardt, O. (1991) Sequence-selective recognition of DNA by strand displacement with a thymine-substituted polyamide. *Science 254*, 1497–1500.

(25) Nielsen, P. E., and Christensen, L. (1996) Strand displacement binding of a duplex-forming homopurine PNA to a homopyrimidine duplex DNA target. *J. Am. Chem. Soc. 118*, 2287–2288.

(26) Zhang, X., Ishihara, T., and Corey, D. R. (2000) Strand invasion by mixed base PNAs and a PNA-peptide chimera. *Nucleic Acids Res. 28*, 3332–3338.

(27) Roy, S., Tanious, F. A., Wilson, W. D., Ly, D. H., and Armitage, B. A. (2007) High-affinity homologous peptide nucleic acid probes for targeting a quadruplex-forming sequence from a MYC promoter element. *Biochemistry 46*, 10433–10443.

(28) Paul, A., Sengupta, P., Krishnan, Y., and Ladame, S. (2008) Combining G-quadruplex targeting motifs on a single peptide nucleic acid scaffold: a hybrid (3 + 1) PNA-DNA bimolecular quadruplex. *Chemistry 14*, 8682–8689.

(29) Onyshchenko, M. I., Gaynutdinov, T. I., Englund, E. A., Appella, D. H., Neumann, R. D., and Panyutin, I. G. (2009) Stabilization of G-quadruplex in the BCL2 promoter region in double-stranded DNA by invading short PNAs. *Nucleic Acids Res. 37*, 7570–7580.

(30) Kypr, J., Kejnovska, I., Renciuk, D., and Vorlickova, M. (2009) Circular dichroism and conformational polymorphism of DNA. *Nucleic Acids Res. 37*, 1713–1725.

(31) Mergny, J. L., Phan, A. T., and Lacroix, L. (1998) Following G-quartet formation by UV-spectroscopy. *FEBS Lett. 435*, 74–78.

(32) Mergny, J. L., Li, J., Lacroix, L., Amrane, S., and Chaires, J. B. (2005) Thermal difference spectra: a specific signature for nucleic acid structures. *Nucleic Acids Res. 33*, e138.

(33) Rosu, F., De Pauw, E., and Gabelica, V. (2008) Electrospray mass spectrometry to study drug-nucleic acids interactions. *Biochimie 90*, 1074–1087.

(34) Pagano, B., Mattia, C. A., and Giancola, C. (2009) Applications of isothermal titration calorimetry in biophysical studies of G-quadruplexes. *Int. J. Mol. Sci. 10*, 2935–2957.

(35) Matteucci, M. D., and Caruthers, M. H. (1981) Synthesis of deoxyoligonucleotides on a polymer support. *J. Am. Chem. Soc. 103*, 3185–3191.

(36) Beaucage, S. L., and Caruthers, M. H. (1981) Deoxynucleoside phosphoramidites--A new class of key intermediates for deoxypolynucleotide synthesis. *Tetrahedron Lett. 22*, 1859–1862.
(37) McBride, L. J., and Caruthers, M. H. (1983) An investigation of several deoxynucleoside phosphoramidites useful for synthesizing deoxyoligonucleotides. *Tetrahedron Lett. 24*, 245–248.
(38) Christensen, L., Fitzpatrick, R., Gildea, B., Petersen, K. H., Hansen, H. F., Koch, T., Egholm, M., Buchardt, O., Nielsen, P. E., Coull, J., and Berg, R. H. (1995) Solid-phase synthesis of peptide nucleic acids. *J. Pept. Sci. 3*, 175–183.
(39) Mergny, J. L., and Lacroix, L. (2003) Analysis of thermal melting curves. *Oligonucleotides 13*, 515–537.
(40) Smargiasso, N., Rosu, F., Hsia, W., Colson, P., Baker, E. S., Bowers, M. T., De Pauw, E., and Gabelica, V. (2008) G-quadruplex DNA assemblies: Loop length, cation identity, and multimer formation. *J. Am. Chem. Soc. 130*, 10208–10216.
(41) *HyperChem 7.5*; Hypercube, Inc.; Gainesville, FL, 2002.
(42) Paramasivan, S., Rujan, I., and Bolton, P. H. (2007) Circular dichroism of quadruplex DNAs: Applications to structure, cation effects and ligand binding. *Methods 43*, 324–331.
(43) Gabelica, V., Baker, E. S., Teulade-Fichou, M. P., De Pauw, E., and Bowers, M. T. (2007) Stabilization and structure of telomeric and c-myc region intramolecular G-quadruplexes: The role of central cations and small planar ligands. *J. Am. Chem. Soc. 129*, 895–904.
(44) Ganesh, K. N., and Nielsen, P. E. (2000) Peptide nucleic acids: Analogs and derivatives. *Curr. Org. Chem. 4*, 931–943.
(45) Kushon, S. A., Jordan, J. P., Seifert, J. L., Nielsen, H., and Armitage, B. A. (2001) Effect of secondary structure on the thermodynamics and kinetics of PNA hybridization to DNA hairpins. *J. Am. Chem. Soc. 123*, 10805–10813.
(46) Amato, J., Oliviero, G., De Pauw, E., and Gabelica, V. (2009) Hybridization of short complementary PNAs to G-quadruplex forming oligonucleotides: An electrospray mass spectrometry study. *Biopolymers 91*, 244–255.
(47) Kushon, S. A., Jordan, J. P., Seifert, J. L., Nielsen, H., Nielsen, P. E., and Armitage, B. A. (2001) Effect of secondary structure on the thermodynamics and kinetics of PNA hybridization to DNA hairpins. *J. Am. Chem. Soc. 123*, 10805–10813.
(48) Datta, B., and Armitage, B. A. (2001) Hybridization of PNA to structured DNA targets: quadruplex invasion and the overhang effect. *J. Am. Chem. Soc. 123*, 9612–9619.
(49) Hardin, C. C., Perry, A. G., and White, K. (2000) Thermodynamic and kinetic characterization of the dissociation and assembly of quadruplex nucleic acids. *Biopolymers 56*, 147–194.
(50) Schultze, P., Hud, N. V., Smith, F. W., and Feigon, J. (1999) The effect of sodium, potassium and ammonium ions on the conformation of the dimeric quadruplex formed by the Oxytricha nova telomere repeat oligonucleotide d(G(4)T(4)G(4)). *Nucleic Acids Res. 27*, 3018–3028.
(51) Ray, A., and Nordén, B. (2000) Peptide nucleic acid (PNA): its medical and biotechnical applications and promise for the future. *FASEB J. 14* (9), 1041–1060.

Supplementary Information

Targeting G-quadruplex structure in the human c-kit promoter with short PNA sequences

Jussara Amato[†,#], *Bruno Pagano*[‡,#], *Nicola Borbone*[†], *Giorgia Oliviero*[*,†], *Valérie Gabelica*[§], *Edwin De Pauw*[§], *Stefano D'Errico*[†], *Vincenzo Piccialli*[□], *Michela Varra*[†], *Concetta Giancola*[°], *Gennaro Piccialli*[†] and *Luciano Mayol*[†]

[†]Dipartimento di Chimica delle Sostanze Naturali, Università degli Studi di Napoli Federico II, via D. Montesano 49, 80131, Napoli, Italy.

[‡]Dipartimento di Scienze Farmaceutiche, Università di Salerno, via Ponte don Melillo, 84084, Fisciano (SA), Italy.

[§]Physical Chemistry and Mass Spectrometry Laboratory, Department of Chemistry, University of Liège, 4000, Liège, Belgium.

[□]Dipartimento di Chimica Organica e Biochimica, Università degli Studi di Napoli Federico II, via Cintia, 80126, Napoli, Italy.

[°]Dipartimento di Chimica "P. Corradini", Università degli Studi di Napoli Federico II, via Cintia, 80126, Napoli, Italy.

[#]These authors have contributed equally.

*Corresponding author. Tel: +39 081678540; Fax: +39 081678746; Email: golivier@unina.it

Running title: Targeting G-quadruplex of c-kit promoter with PNAs

List of Contents

- **General Experimental Methods**. p. 2
  Synthesis of DNA sequences
  Synthesis of PNA sequences
- **Figures S1-S5.** p. 3-6

General Experimental Methods.

Synthesis of DNA sequences

The purine-rich 22-mer ODN corresponding to the c-Kit87up sequence $^{5'}$AGGGAGGGCGCTGGGAGGAGGG$^{3'}$ has been synthesized using the standard phosphoramidite chemistry on controlled pore glass supports using an Expedite 8909 DNA synthesizer (Applied Biosystems) (15 μmol). After automated synthesis, the oligonucleotides were detached from the support, deprotected, and purified by HPLC on an anion exchange column (Macherey Nagel Nucleogel Sax 1000-8), followed by desalting on a molecular exclusion column (BIORAD Biogel P-2 fine). The oligonucleotide was then characterized by MALDI-TOF mass spectrometry (Bruker Autoflex I instrument) using a mixture of picolinic/3-hydroxypicolinic acids in presence of ammonium citrate as the matrix. DNA concentration for all the experiments was determined by UV absorbance using the ε_{260} = 226700 M^{-1} cm^{-1}.

Synthesis of PNA sequences

The syntheses of PNA sequences H-ctcct-Lys-NH_2 (**P1**), H-ccctcct-Lys-NH_2 (**P2**), H-ccctccct-Lys-NH_2 (**P3**), H-cagcgccctccct-Lys-NH_2 (**P4**) and H-tttttttt-Lys-NH_2 (**P5**) were performed on a Rink-amide resin using the FMOC chemistry (27). PNAs were purified by RP-HPLC (0.05% TFA in

water; 0.05% TFA in CH_3CN) and characterized by ESI-MS (Applied Biosystem API 2000 mass spectrometer). Stock solutions of **P1**-**P5** were prepared in double distilled water and their concentration were calculated by UV absorbance using the ε_{260} (M^{-1} cm^{-1}): $\varepsilon_{\mathbf{P1}}$ = 38700; $\varepsilon_{\mathbf{P2}}$ = 53100; $\varepsilon_{\mathbf{P3}}$ = 60300; $\varepsilon_{\mathbf{P4}}$ = 119100, $\varepsilon_{\mathbf{P5}}$ = 65400.

Figures S1-S5

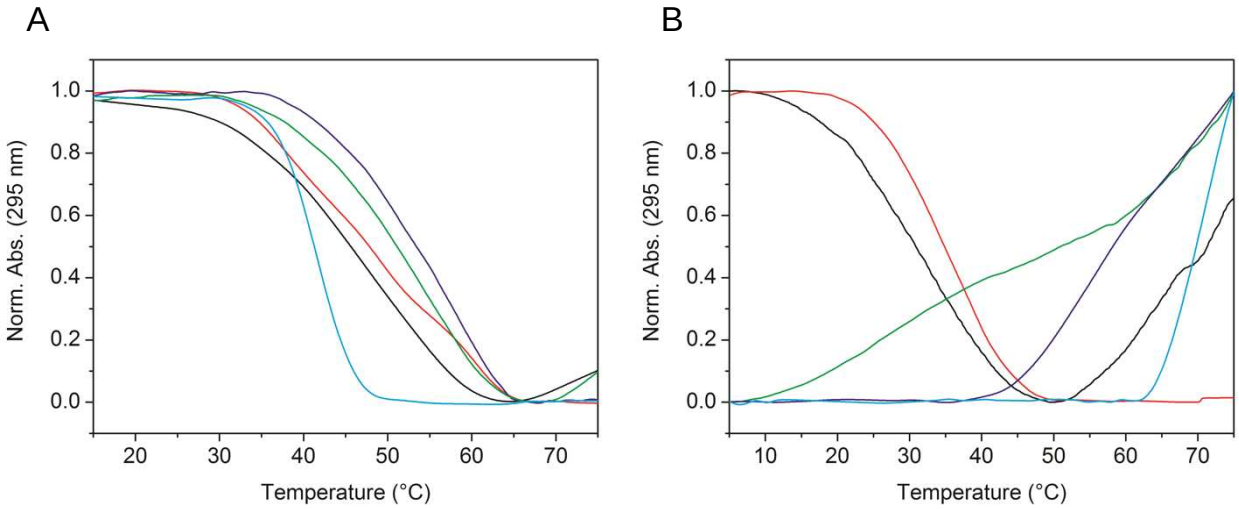


Figure S1. Normalized UV-melting curves for **Q** (black line), **Q**+**P1** (red line), **Q+P2** (green line), **Q+P3** (blue line) and **Q+P4** (cyan line), in potassium (A) and ammonium (B) solution, recorded at 295 nm at a heating rate of 0.5 °C/min.

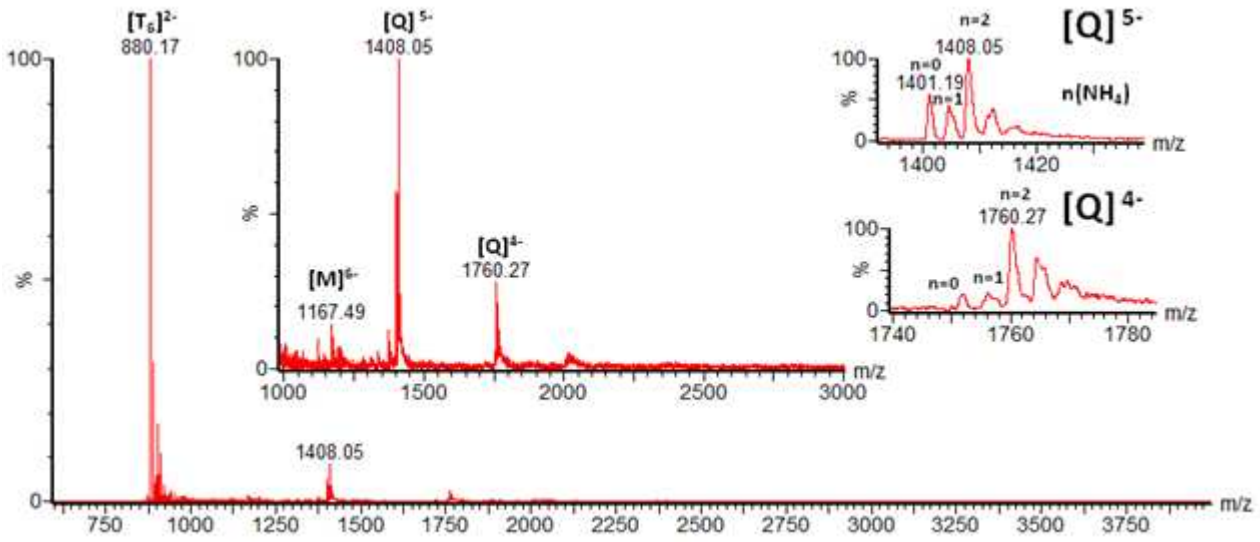


Figure S2. ESI-MS spectra of ckit87up in 150 mM NH_4OAc. The reported spectrum was acquired in the following soft source conditions: RF Lens1 = 100 V; cone = 100 V; collision energy = 10 V. Zooms on the right show the distribution of the number of ammonium ions remaining in the G-quadruplex (from 0 to 2). [**T6**] is the 6-mer homo-thymidine DNA sequence used as internal standard. [**M**] = single-stranded ckit87up. [**Q**] = ckit87up quadruplex, namely [$M+2NH_4^+$].

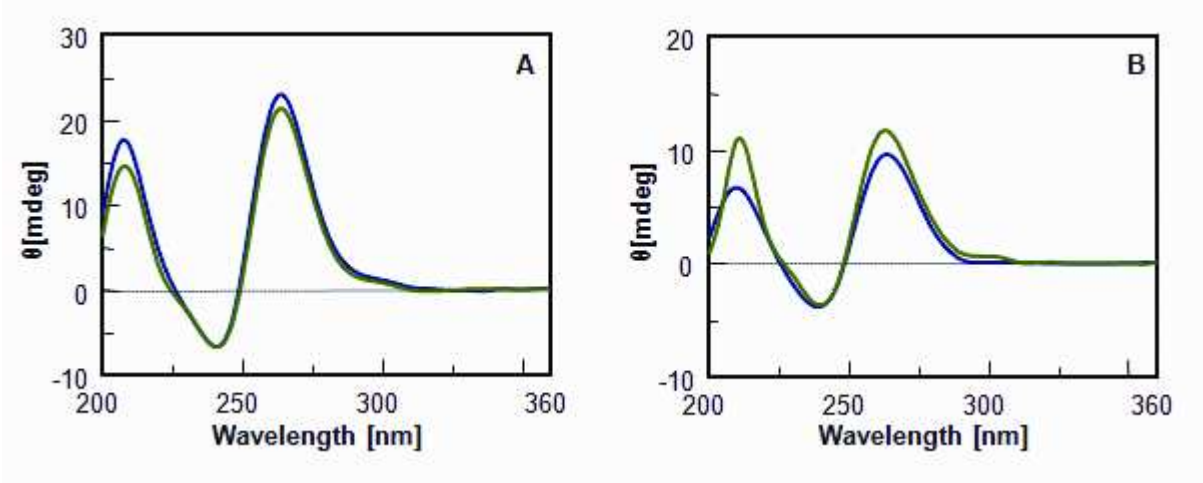


Figure S3. CD spectra of **Q**+**P5** in potassium (A) and ammonium solution (B). Spectrum of the mixture (green line); arithmetic sum of the spectra of the single components **Q** and **P5** (blue line).

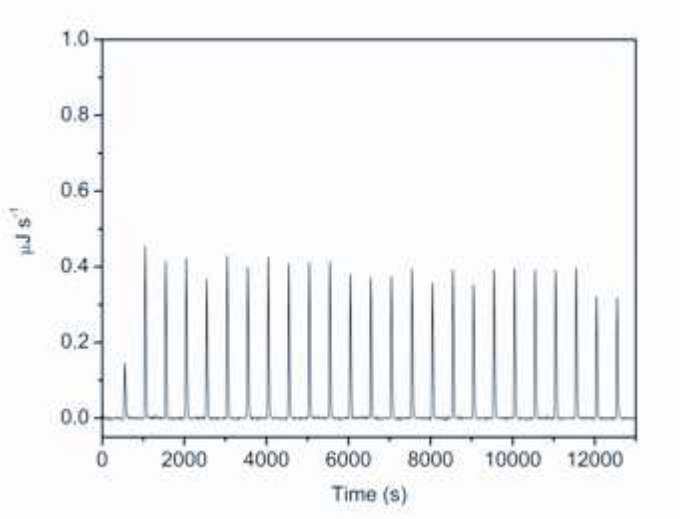


Figure S4. Raw ITC data for titration of ckit87up quadruplex with **P5** in K^+-containing solution. With each injection of PNA, constant heat release was observed due only to ligand dilution.

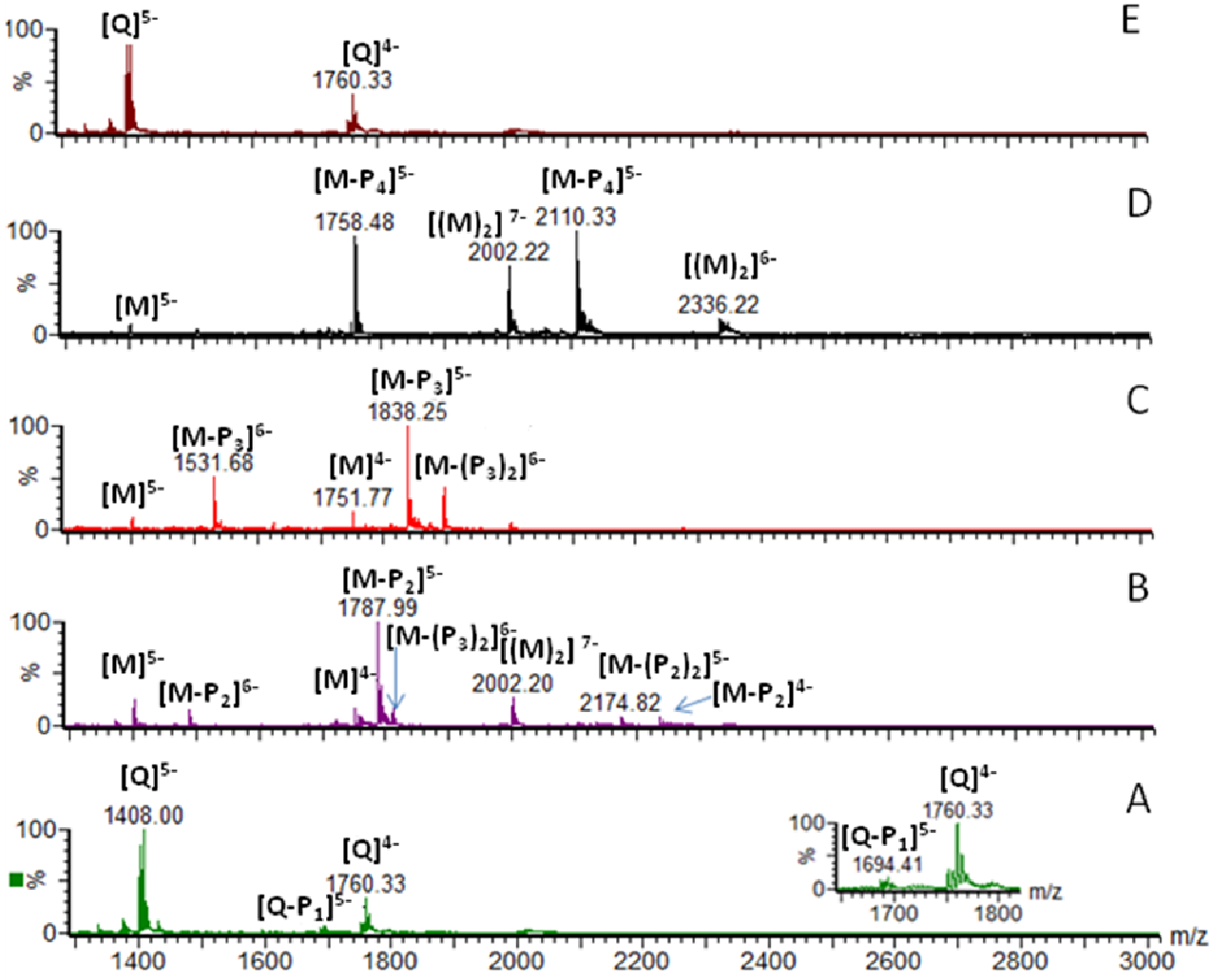


Figure S5. ESI-MS spectra of **Q**+(**P1**-**P5**) PNAs in 150 mM NH_4OAc. (A) **Q**+**P1**; (B) **Q**+**P2**; (C) **Q**+**P3**; (D) **Q**+**P4**; (E) **Q**+**P5**. The reported spectra were acquired in the following soft source conditions: RF Lens1 = 100 V; cone = 100 V; collision energy = 10 V. [**M**] = single-stranded ckit87up. [**Q**] = ckit87up quadruplex, namely $[M+2NH_4^+]$.

Bioconjugate Chemistry

ARTICLE

pubs.acs.org/bc

Cyclic RGD Functionalized Gold Nanoparticles for Tumor Targeting

Daniela Arosio,*[,†] Leonardo Manzoni,[†] Elena M. V. Araldi,[‡] and Carlo Scolastico[§]

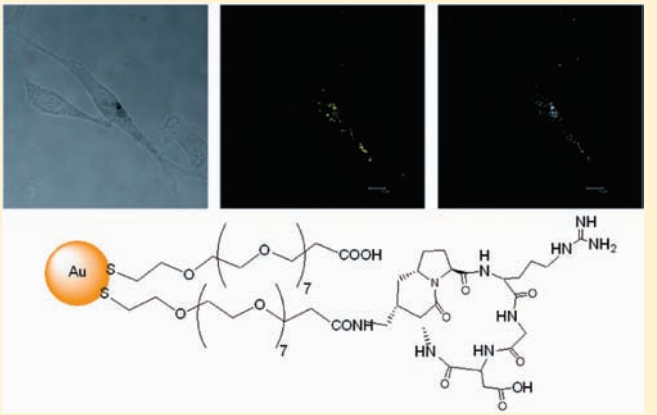
[†]CNR-Istituto di Scienze e Tecnologie Molecolari (ISTM), Via Fantoli 16/15, I-20138, Milan, Italy

[‡]Centro Interdipartimentale di Studi Biomolecolari e Applicazioni Industriali (CISI) of the University of Milan, Via Fantoli 16/15, I-20138, Milan, Italy

[§]CISI scrl, Via Fantoli 16/15, I-20138, Milan, Italy

Supporting Information

ABSTRACT: Integrin $\alpha_v\beta_3$ is an adhesion molecule involved in physiological and pathological angiogenesis as well as tumor invasion and metastasis. Therefore, it is considered an important target for molecular imaging and delivery of therapeutics for cancer, and there is a strong interest in developing novel agents interacting with this protein. Nevertheless, the interaction of individual ligands is often still weak for efficient tumor targeting, and many research groups have synthesized multivalent displays in order to overcome this problem. Gold nanoparticles can be considered a smart platform for polyvalent presentation on account of their globular shape, tunable size, facile surface chemistry, and biocompatibility. Moreover, their unique physical properties render gold nanoparticles ideal candidates for tumor diagnosis and therapy. Here, we report the synthesis and characterization of gold nanoparticles functionalized with cRGD integrin ligand and their employment for targeting human cancer cells expressing $\alpha_v\beta_3$ integrin.



INTRODUCTION

Integrins are heterodimeric transmembrane cell surface proteins expressed by most cell types.[1] $\alpha_v\beta_3$ integrin is the receptor for a variety of extracellular matrix proteins containing an RGD sequence[2,3] and serves as a marker of angiogenesis, tumor development, and metastasis, since it is barely detectable on quiescent vessels and highly expressed during the angiogenic switch.[4−6] It is also highly expressed by several solid tumors such as glioblastomas,[7] melanomas,[8] and ovarian, [9] breast, and prostate cancers,[10] where it is involved in processes governing metastatization. For these reasons, integrins are considered an important target for molecular imaging and drug delivery for cancer diagnosis and therapy, and many efforts have addressed the synthesis of integrin ligands. The most common integrin ligands are peptides, because they can be readily generated. Linear peptide sequences containing the RGD motif are known to bind integrins, and these have been employed as cell-targeting agents.[11] Nevertheless, on account of the low affinity and high biodegradability of such linear peptides, their utility for selective cell targeting is limited. Cyclic peptide derivatives, such as cyclo(RGDfV) or Cilengitide, have been used as tumor-homing agents due to their selectivity for $\alpha_v\beta_3$ integrin.[12−14]

In past years, our research group reported a library of 15-member cyclic RGD pentapeptide mimics based on 1-aza-oxobicyclo[X.3.0]alkane amino acids (Figure 1) containing specific high-affinity ligands for $\alpha_v\beta_3$ and $\alpha_v\beta_5$ integrins.[15,16] However, the need of moieties suitable for conjugation prompted us to synthesize new cyclic RGD pentapeptide mimics based on functionalized azabycycloalkane scaffolds.[17] This small collection was found to contain specific ligands for $\alpha_v\beta_3$ integrin. Furthermore the functionalization of the azabicycloalkane scaffolds with heteroalkyl substituents enabled us to conjugate RGD containing compounds with different diagnostic or therapeutic entities[18] without losing activity.

Nevertheless, the affinity of individual ligands is seldom enough for efficient tumor detection or selective drug homing. For this reason, many research groups have designed multivalent displays based on dendrimers,[19−26] polymers,[27,28] liposomes,[29] and others[30] in order to exploit multiple interactions with integrin clusters on cell membrane to increase the binding. Thus, by increasing the peptide multiplicity, they significantly enhance the avidity of the multiple ligand for the $\alpha_v\beta_3$ integrin with a trend that is frequently proportional to the number of RGD moieties. On the other hand, the synthesis and purification of such multivalent systems are often challenging requiring efficient and chemoselective conjugation techniques.

In recent years, metal nanoparticles have generated much interest in biology and medicine due to their unique physical and

Received: October 12, 2010
Revised: February 3, 2011
Published: March 24, 2011

ACS Publications © 2011 American Chemical Society

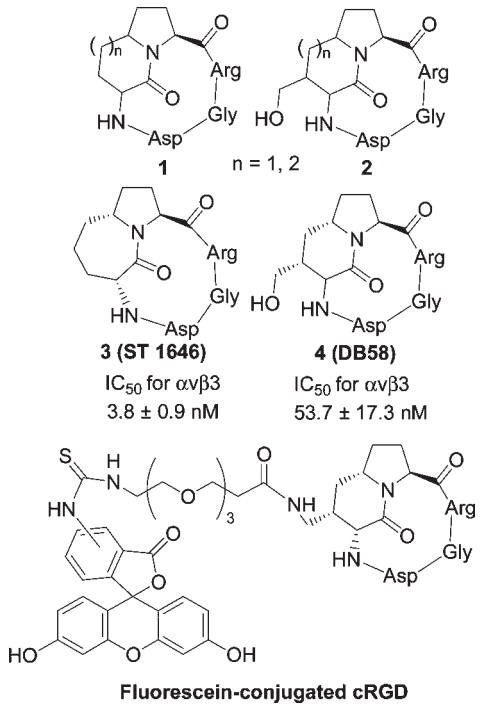


Figure 1. Most potent $\alpha_v\beta_3$ integrin inhibitors and Fluorescein conjugated cRGD synthesized by our research group.

chemical properties and have widely been employed in tumor targeting. Furthermore, they constitute a three-dimensional platform for multipresentation. Among them, gold nanoparticles (AuNPs) are particularly interesting for cancer diagnosis and therapy.[31,32] Their relatively easy preparation, tunable size, facile surface chemistry, and biocompatibility[32] render AuNPs very attractive as carriers for drug or gene delivery.[34−36] Moreover, their surface plasmon resonance (SPR) enhanced light scattering and absorption make colloidal AuNPs a potential candidate for optical imaging and hyperthermia therapy.

Gold nanoparticles with different characteristics can be obtained by varying size, shape, and stabilizing agent.[31] A large number of synthetic procedures are reported for preparing gold nanoparticles. The method reported by Turkevich[37] involves the citrate reduction of Au(III) to Au(0) in water. This method and further modifications[37,38] allow the synthesis of citrate coated nanoparticles within the 9−120 nm range. However, the replacement of the coating with another stabilizing agent and/or an appropriate ligand must be obtained in a further step of the preparation. The synthesis by the method of Brust[39] and the related method modified by Penades[40,41] involves the reduction of Au(III) to Au(0) by $NaBH_4$ in the presence of a thiol (or a mixture of thiols). It results in relatively small polydisperse thiolate monolayer protected AuNPs. These nanoparticles are characterized by a small core size (1−3 nm), and on this account, they partially lose the typical behavior of colloidal gold, making their application as diagnostic probes less efficacious. On the other hand, these synthetic procedures guarantee a chemically well-defined composition determined by the composition of the starting thiols mixture, thus making their employment as drug carriers less complex.

Here, we employed the method described by Penades for the synthesis of gold nanoparticles functionalized with cRGD peptidomimetic **4** (**DB58**, Figure 1) which showed the highest affinity for $\alpha_v\beta_3$ integrin in an *in vitro* binding assay.[17] The selected integrin ligand was functionalized with a short PEG linker armed with a thiol group and the so-synthesized molecule was employed in the preparation of the nanoparticles. In a similar way, nanoparticles functionalized with both cRGD and FITC were prepared.

The resulting cRGD functionalized nanoparticles were tested for their ability to bind $\alpha_v\beta_3$ integrin by means of a solid-phase receptor-binding assay, which is a simple and precise method to analyze protein−protein interactions.[13,16,17,42] The reported AuNPs showed a highly enhanced affinity in comparison with the unconjugated ligand. This positive result was also confirmed by *in vitro* studies on cell cultures showing how nanoparticles functionalized with cRGD were able to selectively interact with cells expressing $\alpha_v\beta_3$ integrin.

MATERIALS AND METHODS

General. All chemicals and solvents, purchased from Sigma-Aldrich, were of reagent grade and were used without further purification. Solvents were dried by standard procedures, and reactions requiring anhydrous conditions were performed under nitrogen or argon atmosphere. UPLC-MS analysis were obtained with an Aquity Waters apparatus. Mass spectra were obtained with an ESI apparatus Bruker Esquire 3000 plus. Semipreparative HPLC was carried out with a Atlantis Prep T3 OBD, 5 μm, 19 × 150 mm Waters column using gradient mixture of CH_3CN/H_2O + 0.1% TFA. ^1H and ^{13}C NMR spectra were recorded at 300 K on Bruker AVANCE 400 and 600 MHz. Chemical shifts δ are expressed in ppm relative to internal Me_4Si as standard. UV/vis spectra were measured with a Thermo Scientific, Evolution 600 UV−visible spectrophotometer. For transmission electron microscopy (TEM) characterization, a single drop (10 μL) of aqueous solution of gold NPs (ca. 0.1 mg/mL in Milli-Q water) was placed on a Formvar/carbon-coated copper grid (Electron Microscopy Science) and left to dry in air for several hours. The sample grids were examined by an EFTEM LEO 912AB microscope (Zeiss), operating at 80 kV. The average diameter of the AuNPs was obtained from evaluation of several TEM micrographs by means of an algorithm for automatic image analysis developed by our group.

Synthesis of Disulfide Linker ***8***. To a solution of commercially available linker **5** (50.0 mg, 0.11 mmol) in MeOH (2 mL), MeONa (25% in MeOH, 40 μL) was added. The reaction mixture was stirred for ca. 18 h at room temperature following the formation of the disulfide by UPLC-MS. After reaction completion, Amberlyst IRA 120 H+ was added until acid pH was reached. The solution was filtered and evaporated under reduced pressure yielding the disulfide linker **8** quantitatively. The product was used in the following reaction without any further purification.

Synthesis of cRGD Conjugated Compound ***9***. The disulfide linker **8** (30 mg, 0.033 mmol) and *N*-hydroxysulfosuccinimide sodium salt (18 mg, 0.0825 mmol) were solved in dry DMF (1.4 mL), and under argon and at room temperature, dicyclohexyl carbodiimide (15 μL, 0.099 mmol) was added. The reaction mixture was stirred for 24 h, and after this time, the solvent was removed under reduced pressure. The crude was dissolved in PBS/CH_3CN 3:1 (2 mL) and cRGD **6** in PBS (1.0 mL) was added. The pH was adjusted to pH 7.3 by adding NaOH 0.2 N, and the reaction mixture was stirred for ca. 24 h monitoring by UPLC-MS. After reaction completion, the solvent was evaporated under reduced pressure and the crude was

purified by HPLC. (Column: Waters Atlantis Prep 19 × 50 mm, 5 μm; 15 mL/min flow; gradient from 0% B to 50% B over 15 min, wash then 100% B for 3 min, A: H_2O + 0.1% TFA; B: CH_3CN + 0.1% TFA, collecting λ 216 nm). The desired product was collected in 52% yield. The monofunctionalized compound and the unreacted starting cRGD-NH_2 were also recovered (white solid). ^{1}H NMR (600 MHz, D_2O): δ 1.21 (m, 1H, *H*-5), 1.40−1.56 (m, 3H, 2 *Hγ* Arg, *Hβ* Arg), 1.60 (m, 1H, *H*-7), 1.82 (m, 1H, *H*-8), 2.01 (m, 1H, *Hβ* Arg), 2.34−2.45 (m, 5H, CH_2SH, *H*-5, *H*-7, *H*-8), 2.66 (dd, 1H, *J* = 16.9 Hz, *J* = 7.1 Hz, *Hβ* Asp), 2.72 (m, 1H, *H*-4), 2.87 (t, 2H, *J* = 6.5 Hz, CH_2NHCO), 3.03 (dd, 1H, *J* = 16.9 Hz, *J* = 7.5 Hz, *Hβ* Asp), 3.07 (m, 2H, C-4CH_2NH), 3.12 (m, 2H, 2 *Hδ* Arg), 3.45 (d, 1H, *J* = 14.6 Hz, *Hα* Gly), 3.55−3.65 (m, 28H, CH_2O), 3.67 (t, 2H, *J* = 6.0 Hz, OCH_2), 3.74 (t, 2H, *J* = 6.1 Hz, OCH_2), 3.95 (m, 1H, *H*-6), 4.20−4.27 (m, 2H, *Hα* Gly, *H*-9), 4.33 (d, 1H, *J* = 8.2 Hz, *H*-3), 4.46 (t, 1H, *J* = 7.3 Hz, *Hα* Asp), 4.53 (dd, 1H, *J* = 11.0 Hz, *J* = 3.7 Hz, *Hα* Arg,). ^{13}C NMR (150.9 MHz, D_2O): δ 174.9, 174.5, 174.3, 174.0, 173.0, 171.5, 170.2, 156.7, 69.6, 69.5, 69.4, 68.4, 66.7, 62.1, 56.0, 53.0, 51.6, 51.4. 42.4, 40.4, 38.7, 37.3, 36.0, 35.7, 33.4, 32.9, 32.6, 30.2, 26.9, 24.4. MS (ESI$^+$) *m*/*z*: 1955.3 $(M+H)^+$, 977.9 $(M+2H)^{2+}$.

Synthesis of Functionalized Fluorescein ***7***. To a solution of Boc monoprotected 4,7,10-trioxa-1,13-tridecane diamine (34 mg, 0.11 mmol), in dry DCM (3 mL), FITC (50 mg, 0.13 mmol) in dry DMF (1 mL) was added, and finally TEA (50 μL, 0.36 mmol) was added. The reaction mixture was stirred at room temperature, in the dark, for ca. 18 h. After reaction completion, the PS-NH_2 resin was added (70 mg) and the mixture was stirred for ca. 4 h to remove unreacted FITC. After this time, the solution was filtered and the solvent was evaporated under reduced pressure. The crude was dissolved in CH_2Cl_2 (1 mL), and TFA (1 mL) was added. The mixture was stirred at room temperature in the dark for ca. 1 h, then the solvent was evaporated under reduced pressure and the product was dried under vacuum overnight. 88% yield. (yellow oil). ^{1}H NMR (400 MHz, methanol-d_4): δ 1.90−2.00 (m, 4H, $CH_2CH_2CH_2$), 3.11 (m, 2H, CH_2NH_2), 3.57−3.70 (m, 12H, CH_2O), 3.76 (m, 2H, CH_2NHCS), 6.70 (m, 2H, *aromatic protons*), 6.83−6.98 (m, 4H, *aromatic protons*), 7.23 (m, 1H, *aromatic proton*), 7.84 (m, 1H, *aromatic proton*), 8.24 (s, 1H, *aromatic proton*). ^{13}C NMR (100.6 MHz, methanol-d_4): δ 141.3, 129.7, 128.3, 113.8, 111.5, 102.1, 70.1, 70.0, 69.8, 69.7, 69.6, 68.8, 68.7, 47.7, 38.6, 28.6, 26.8. MS (ESI$^+$) *m*/*z*: 610.4 $(M+H)^+$.

Synthesis of Fluorescein Conjugated Compound ***10***. The disulfide linker **8** (24 mg, 0.026 mmol) and *N*-hydroxysulfosuccinimide (14 mg, 0.065 mmol) were solved in dry DMF (1.0 mL), and under argon and at room temperature, dicyclohexyl carbodiimide (12 μL, 0.078 mmol) was added. The reaction mixture was stirred for 24 h. After this time, a solution of functionalized fluorescein **7** (59.0 mg, 0.097 mmol) and TEA (280 μL, 2.0 mmol) in dry DMF (1.5 mL) was added. The reaction mixture was stirred for ca. 3 h monitoring by HPLC-MS. After reaction completion, the solvent was evaporated under reduced pressure and the crude was purified by HPLC. (Column: Waters Atlantis Prep 19 × 50 mm, 5 μm; 15 mL/min flow; gradient from 20% B to 80% B over 15 min, wash then 100% B for 3 min, A: H_2O + 0.1% TFA; B: CH_3CN + 0.1% TFA, collecting λ 216 nm).

The desired product was collected in 36% yield. The monofunctionalized compound and the unreacted starting compound **7** were also recovered. (yellow oil). ^{1}H NMR (400 MHz, methanol-d_4): δ 1.76 (m, 2H, $CH_2CH_2CH_2$), 1.99 (m, 2H, $CH_2CH_2CH_2$), 2.44 (m, 2H, CH_2CONH), 2.90 (m, 2H, CH_2S), 3.27 (m, 2H, CH_2NH), 3.53 (m, 2H, CH_2O), 3.55−3.80 (m, 44H, 21 CH_2O, CH_2NH), 6.85 (m, 2H, *aromatic protons*), 6.98 (s, 2H, *aromatic protons*), 7.10 (m, 2H, *aromatic protons*), 7.28 (m, 1H, *aromatic proton*), 7.94 (m, 1H, *aromatic proton*), 8.33 (s, 1H, *aromatic proton*). ^{13}C NMR (100.6 MHz, methanol-d_4): δ 172.5, 141.7, 130.5, 102.1, 70.2, 70.1, 70.0, 69.9, 69.8, 69.7, 69.1, 68.8, 68.5, 66.9, 48.1, 47.9, 42.3, 38.2, 36.5, 36.4, 29.3, 29.0, 28.5. MS (ESI$^+$) *m*/*z*: 1049.5 $(M+2H)^{2+}$.

General Procedure for Nanoparticles Preparation. A 0.012 M (3 equiv) methanolic solution of the commercially available linker **5** and cRGD derivative **9** (or a mixture of cRGD disulfide derivative **9** and fluorescein disulfide derivative **10**) was added to a solution of tetrachloroauric acid (0.025 M, 1 equiv) in water. An aqueous solution of $NaBH_4$ (1 M, 22 equiv) was then added in four portions, with rapid shaking. The black suspension formed was shaken for an additional 2 h at room temperature. After this time, the obtained suspension was centrifuged (4000 rpm for 15 min), then the supernatant was removed and the residue was dissolved in the minimum volume of Milli-Q water (ca. 5 mL) and purified by dialysis (ca.10 cm segments of SnakeSkin pleated dialysis tubing Ø 32 mm, 2500 MWCO, SIGMA) or by centrifugal filtration (10 000 MWCO, Vivaspin filters). The solution was finally lyophilized to afford the desired AuNPs. ^{1}H NMR spectra of the obtained AuNPs were recorded. The particle size distribution of the gold nanoparticles was evaluated from TEM micrographs by means of an automatic image analyzer. The average molecular formula of the nanoparticles was calculated on the basis of the average diameter obtained by TEM.[43]

AuNPs ***11***. Linker **5** (100%): Reaction of **5** (87.0 mg, 0.189 mmol) in methanol (15 mL) with $HAuCl_4.3H_2O$ (25 mg, 0.067 mmol) in 2.5 mL H_2O and $NaBH_4$ (1.4 mL, 1 M) gave AuNPs **11** (6.3 mg) as a dark-brown powder. TEM (average diameter and calculated number of gold atoms): 1.7 ± 0.4 nm, 140; UV/vis (H_2O, 0.1 mg/mL): surface plasmon band not present.

AuNPs ***12***. cRGD-derivative **9** (20%), linker **5** (80%): Reaction of cRGD-derivative **9** (11.0 mg, 0.0055 mmol) and linker **5** (15.0 mg, 0.033 mmol) in methanol (4.6 mL) with $HAuCl_4.3H_2O$ (7.1 mg, 0.018 mmol) in 720 μL H_2O and $NaBH_4$ (400 mL, 1 M) gave AuNPs **12** (2.5 mg) as a dark-brown powder. TEM (average diameter and calculated number of gold atoms): 2.0 ± 0.7 nm, 314; UV/vis (H_2O, 0.1 mg/mL): λ = 500 nm (surface plasmon band).

AuNPs ***13***. cRGD-derivative **9** (20%), fluorescein-derivative **10** (5%), linker **5** (75%): Reaction of cRGD-derivative **9** (24.0 mg, 0.012 mmol), fluorescein-derivative **10** (6.3 mg, 0.003 mmol), and linker **5** (41.3 mg, 0.09 mmol) in methanol (10 mL) with $HAuCl_4.3H_2O$ (15.7 mg, 0.04 mmol) in 1.6 mL H_2O and $NaBH_4$ (880 mL, 1 M) gave AuNPs **13** (3.2 mg) as a dark-brown powder. TEM (average diameter and calculated number of gold atoms): 1.9 ± 0.8 nm, 225; UV/vis (H_2O, 0.1 mg/mL): λ = 482 nm (surface plasmon band).

AuNPs ***14***. Fluorescein-derivative **10** (5%), linker **5** (95%): Reaction of fluorescein-derivative **10** (6.0 mg, 0.0028 mmol) and linker **5** (50.0 mg, 0.11 mmol) in methanol (9.5 mL) with $HAuCl_4 \cdot 3H_2O$ (15.0 mg, 0.038 mmol) in 1.5 mL H_2O and $NaBH_4$ (840 mL, 1 M) gave AuNPs **14** (1.0 mg) as a dark-brown powder. TEM (average diameter and calculated number of gold atoms): 1.8_0.5 nm, 201; UV/vis (H_2O, 0.1 mg/mL): surface plasmon band not observed.

Solid-Phase Receptor-Binding Assay. Purified $\alpha_v\beta_3$ receptor (Chemicon International, Inc., Temecula, CA) was diluted to 0.5 μg/mL in coating buffer containing 20 mmol/L Tris-HCl

(pH 7.4), 150 mmol/L NaCl, 1 mmol/L $MnCl_2$, 2 mmol/L $CaCl_2$, and 1 mmol/L $MgCl_2$. An aliquot of diluted receptor (100 μL/well) was added to 96-well microtiter plates (NUNC MW 96F Medisorp Straight) and incubated overnight at 4 °C. The plates were then incubated with blocking solution (coating buffer plus 1% bovine serum albumin (Sigma) for additional 2 h at room temperature to block nonspecific binding followed by 3 h incubation at room temperature with various concentrations (10^{-12}−10^{-5} M or 10^{-15}−10^{-8} in the case of nanoparticles) of test compounds in the presence of 1 μg/mL vitronectin biotinylated using EZ-Link Sulfo-NHS-Biotinylation kit (Pierce, Rockford, IL). After washing, the plates were incubated for 1 h at room temperature with streptavidin−biotinylated peroxidase complex (Amersham Biosciences, Uppsala, Sweden) followed by 30 min incubation with 100 μL Substrate Reagent Solution (R&D Systems, Minneapolis, MN) before stopping the reaction by addition of 50 μL of 1 N H_2SO_4. Absorbance at 415 nm was read in a Synergy HT Multi-Detection Microplate Reader (BioTek Instruments, Inc.). Each data point is the result of the average of triplicate wells and was analyzed by nonlinear regression analysis with *GraphPad Prism* program.

Reagents for Cellular Experiments. All reagents were purchased from Sigma-Aldrich (unless otherwise indicated). For all our tests, phosphate buffer saline (PBS) supplemented with calcium and magnesium (Euroclone) was used.

Cell Lines and Culture. MDA-MB-231 human breast adenocarcinoma cells and PC3 human prostate cancer cells were purchased from Istituto Zooprofilattico Sperimentale della Lombardia e dell'Emilia (Brescia, Italy) and were grown on tissue flasks in medium RPMI supplemented with 10% fetal calf serum (FCS), 2 mM L-glutamine, penicillin (100 U/mL), and streptomycin (100 μg/mL). All cell lines were maintained at 37 °C in an atmosphere of 95% air and 5% CO_2.

Treatment of Cells with Compounds and Analysis. Cells (1.5×10^5/mL) were seeded and allowed to adhere overnight in complete medium on glass slides. Cells were treated 4 h at 37 °C with selected compounds diluted in fresh medium supplemented with 0.1% FCS. After the incubation, cells were extensively washed in PBS and fixed in 4% paraformaldehyde for 10 min at room temperature. Nuclei were then counterstained with 0.25 μg/mL 4′,6-diamidino-2-phenylindole (DAPI) diluted in PBS for 5 min at room temperature. Cells were finally mounted with Vectashield mounting medium and visualized with a Leica TCSNT confocal microscope (Leica Mikrisysteme Vertrieb GmbH, Germany). Experiments were repeated in triplicate.

RESULTS

Preparation of Thiol-Derivatizated Ligands. Among a small collection of functionalized cyclic RGD (**3**, Figure 1),[17] we chose compound **4** (**DB58**) that showed the highest affinity for $\alpha_v\beta_3$ integrin in an *in vitro* binding assay (IC_{50} of 53.7 ± 17.3 nM) as a good candidate for gold nanoparticle conjugation.

In order to conjugate cRGD to the AuNPs, we needed to introduce a spacer ending in a thiol group. The nature, the length, and the flexibility of this spacer can influence the way the ligands are presented on the surface of the gold cluster and their ability to bind the integrins. We chose the commercially available linker **5** (Scheme1) because its polyethylenic nature could favor nanoparticle stability in aqueous media and its flexibility could facilitate the interaction with integrin clusters on the cell surface. Furthermore, nanoparticles coated with poly(ethylene glycol)s are known to display stealth properties prolonging their circulation time and consequently the possibility of reaching the target organ.

To avoid the formation of complex mixtures during the synthesis, the linker was dimerized through the formation of a disulfide bridge. Divalent linker **8** was activated as *N*-hydroxysulfosuccinimide ester and then reacted with the amine derived cRGD **6** (prepared from **4** using the procedure reported in ref 17) in phospate buffer saline pH 7.3. Compound **9** was recovered after HPLC purification, together with the monoderivatized compound and the unreacted starting cRGD **6**.

Due to the small dimensions, the gold nanoparticles examined in this study partially lose the typical behavior of colloidal gold, thus not displaying the surface plasmon band. On this account, we were not sure that the usual techniques used to reveal gold nanoparticles inside the cells could be employed. On the other hand, other characteristics also, such as the fluorescence quenching of many fluorophores when they are in close proximity to gold surfaces, could be altered. For this reason, we prepared a fluorescein-derivatized linker in order to synthesize fluorescent gold nanoparticles.

Commercially available FITC was reacted with Boc (*N-tert*-butoxycarbonyl) monoprotected 4,7,10-trioxa-1,13-tridecane diamine, and after removal of the excess of FITC by PS-NH_2 resin, the protecting group was removed with TFA to yield **7**. Fluorescein derivative **7** was finally reacted with divalent linker **8** following the procedure reported above.

Nanoparticle Synthesis. The nanoparticles were synthesized using the procedure developed by Penades and co-workers.[37] This method involves the reduction of tetrachloroauric acid with an excess of sodium borohydride in the presence of a thiol or a mixture of thiols. The gold nanoparticles obtained by this procedure are characterized by a coating composition determined by the mixture of thiols used in their preparation. Thus, different AuNPs of controlled composition were prepared (Table 1). In particular, 20% cRGD density was chosen as a starting point. In fact, we supposed that, in nanoparticles with a high density of cRGD (>60%), the ligands would be too close to each other and this could not improve the binding. We prepared AuNPs **12** with 20% cRGD and AuNPs **13** with 20% cRGD and 5% fluorescein derivative (in order to visualize them inside the cells). AuNPs **11** without cRGD and nanoparticles **14** with 5% fluorescein derivative were also synthesized as negative controls.

All the synthesized AuNPs were water-soluble, although particles functionalized with 5% fluorescein partially precipitated after one night at 4 °C. Finally, all nanoparticles were characterized by transmission electron microscopy (TEM), ^{1}H NMR, and UV spectroscopy.

The TEM analysis showed AuNPs with a very small core (ca. 2 nm) and uniform dispersion. Moreover, nanoparticles did not appear to be aggregated. ^{1}H NMR spectrum of AuNPs **12**, although the broader feature of the peaks, confirmed the presence of the cRGD derivative on the surface of the nanoparticles (Figure 2). Furthermore, integrations of the proton signals were in agreement with a cRGD-PEG/HOOC-PEG ratio of 20:80 as expected. For FITC/cRGD fuctionalized NPs **13**, the ^{1}H NMR spectrum was similar (see Supporting Information, Figure 9). The peaks from fluorescein were barely detectable on account of low concentration.

The UV/vis spectra of AuNPs **12** and **13** showed a particularly weak surface plasmon band at around 500 nm. It is well known that in the case of nanoparticles smaller than 3 nm the surface

Scheme 1. Synthesis of Thiol Ending PEG Functionalized with cRGD or Fluoresceine and Their Employment in the Preparation of Gold Nanoparticles

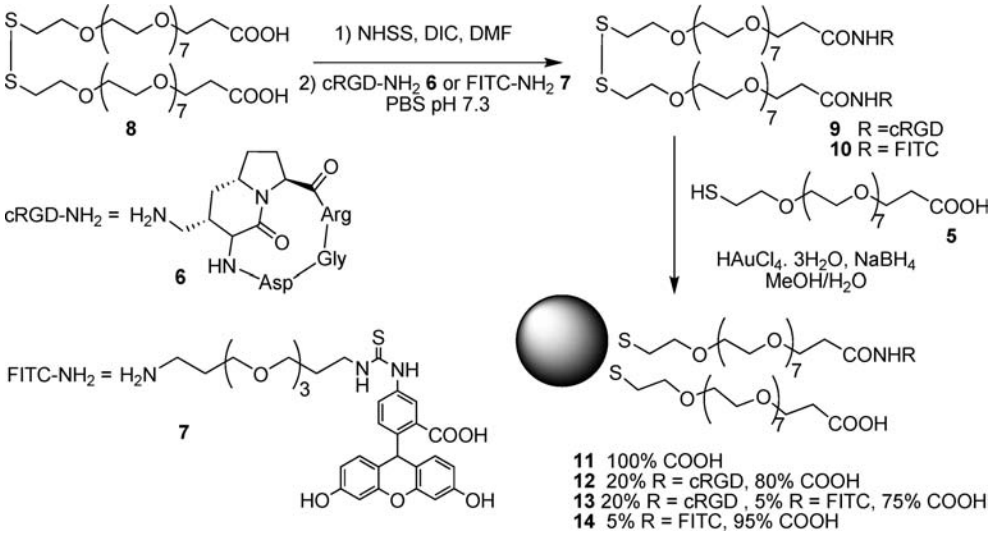


Table 1. Chemical Composition of Gold Nanoparticles

AuNPs	composition	average diameter of AuNPs (nm)	avg. no of gold atoms[a]	avg. molecular formula	avg. no of cRGD	avg. MW
11	100% linker **5**	1.66 ± 0.38	140	$(C_{19}H_{37}O_{10}S)_{53}Au_{140}$	-	51 825
12	20% cRGD 80% linker **5**	2.0 ± 0.69	314	$(C_{40}H_{70}N_9O_{16}S)_{18}(C_{19}H_{37}O_{10}S)_{73}Au_{140}$	18	112 837
13	5% FITC 20% cRGD 75% linker **5**	1.86 ± 0.81	225	$(C_{40}H_{70}N_9O_{16}S)_{14}(C_{50}H_{70}N_3O_{17}S_2)_3\ (C_{19}H_{37}O_{10}S)_{54}Au_{225}$	14	85 852
14	5% FITC 95% linker **5**	1.79 ± 0.49	201	$(C_{50}H_{70}N_3O_{17}S_2)_3(C_{19}H_{37}O_{10}S)_{68}Au_{225}$	-	73 851

[a] The average number of gold atoms and hence the molecular formulas and the molecular weights of the nanoparticles were calculated according to the literature on the basis of the average gold diameters obtained by TEM.

plasmon band is not observed;[44] however, this hardly detectable band was probably due to the very small fraction of nanoparticles with a diameter bigger than 3 nm (see size distribution B, Figure 2 and Figure S8 in Supporting Information). In the UV/vis spectra of AuNPs **13**, the band due to the presence of the fluorescein was also visible, supporting the thesis that the fluorescence quenching does not occur.

On the basis of the gold nanoparticle core size (determined by TEM), an average molecular formula was determined according to the literature[43] and a molecular weight was calculated (Table 1).

Solid-Phase Receptor Binding Assay. The AuNPs **12** and **13** together with the negative controls AuNPs **11** and **14** were examined *in vitro* for their ability to inhibit the binding of biotinylated vitronectin to the isolated, immobilized $\alpha_v\beta_3$ integrin (Table 2). Affinity of compound **4** (**DB58**) was determined as reference, in the same assays. The divalent derivative **9** was also tested.

As a general remark, we observed that multivalent ligands displayed an enhanced affinity (avidity) in comparison with the monovalent ligand **4** (53.7 ± 17.3 nM). In particular, an increase in affinity was already evident in the case of divalent ligand **9** that showed an IC_{50} value of 6.8 ± 2 nM (Table 2). The improvement was even greater for AuNPs **12** (0.4 ± 0.1 nM, Table 2) that bound integrin $\alpha_v\beta_3$ more than 100-fold in comparison with compound **4**.

In order to evaluate the previously mentioned results, we divided the avidity by the average number of cRGDs, obtaining an absolute value, namely, enhancement factor (β) (Table 2, col. 5).[45,46] In this way, it has been possible to compare the strength of multivalent effects when cRGD peptides are attached to nanoparticles at different densities.

Thus, the dimeric derivative **9** displayed an enhanced affinity of 8 and a β of 4 (Table 2). The functionalized AuNPs **12** displayed a relevant enhancement in binding affinity (more than 100-fold) toward $\alpha_v\beta_3$ integrin when compared to the nanomolar reference and a β of 7. This result suggested that multivalent interactions between gold nanoparticles and $\alpha_v\beta_3$ integrins enhanced the binding strength in a way that was greater than the sum of the affinity of the involved ligands.

In order to evaluate the influence of fluorescein on the AuNPs, nanoparticles **13** were also tested. They still showed a high affinity for $\alpha_v\beta_3$ integrin, although the value of IC_{50} (1.7 ± 0.6 nM, Table 2) was lower if compared with AuNPs **12**. This could probably be due to an interference of fluorescein on the surface of the nanoparticles in the binding process.

In summary, these data showed that the functionalization of gold nanoparticles with cRGD generated a great increase in the binding activity on account of polypresentation, suggesting that AuNPs could be employed as a suitable platform for tumor-targeted drug delivery.

Gold Nanoparticle Detection in Human Cell Lines. The above results demonstrated that gold nanoparticles **12** have a high affinity for the $\alpha_V\beta_3$ integrin; and the copresence of fluoresceine on nanoparticle surfaces in AuNPs **13** does not

dx.doi.org/10.1021/bc100448r |*Bioconjugate Chem.* 2011, 22, 664–672

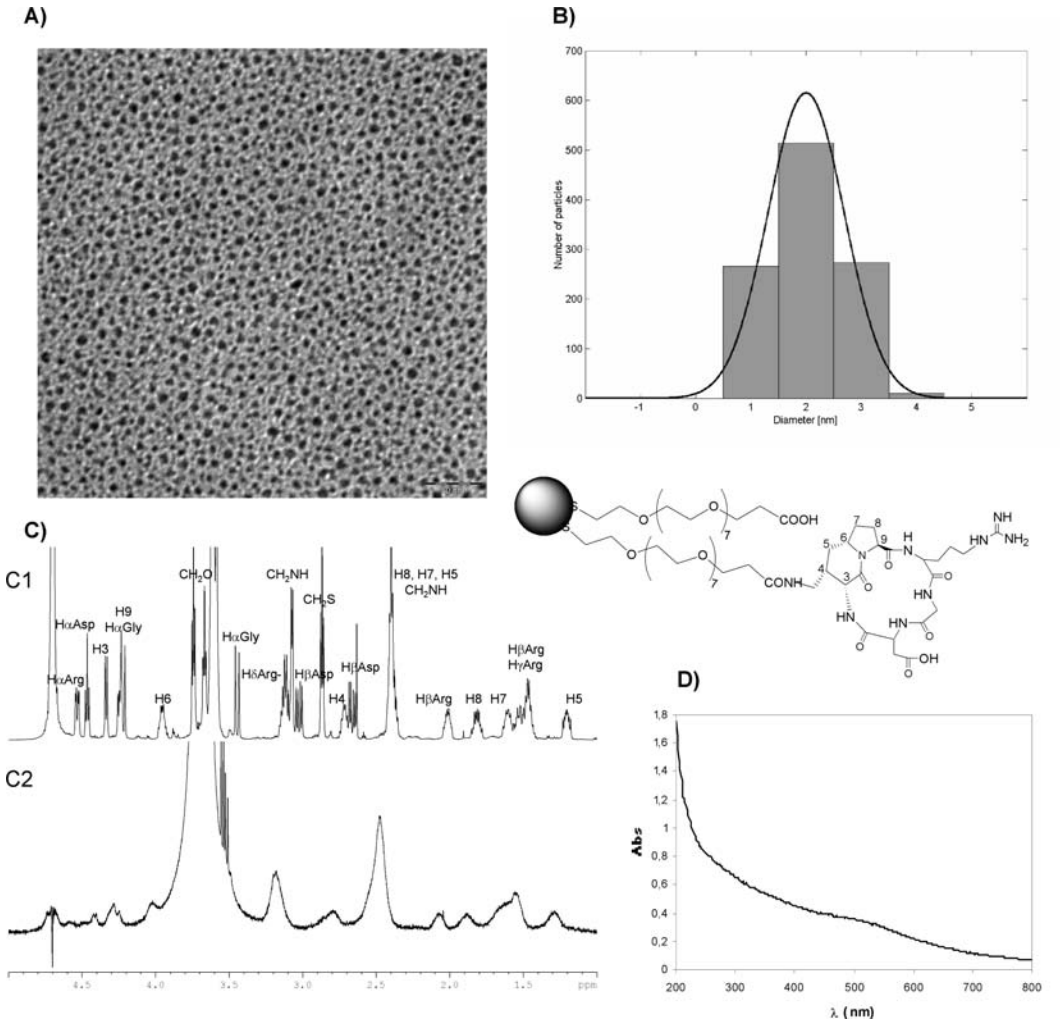


Figure 2. Characterization of AuNPs **12**. (A) TEM micrograph in H_2O; (B) size-distribution histogram; (C) ^1H NMR spectra of cRGD conjugated linker **9** (C1) and of gold nanoparticles **12** (C2); (D) UV/visible spectrum.

Table 2. Compound-Mediated Inhibition of Vitronectin Binding to $\alpha_V\beta_3$ Integrin[a]

compound	IC_{50} (nM) ± SD for $\alpha_V\beta_3$	increase in affinity	enhancement factor (β)[b]
Compound **4** (**DB58**)	53.7 ± 17.3	1	1
Compound **9**	6.8 ± 2	8	4
AuNPs **11**	inactive	-	-
AuNPs **12**	0.4 ± 0.1	134	7
AuNPs **13**	1.7 ± 0.6	31	2
AuNPs **14**	inactive	-	-

[a] IC_{50} values were calculated as the concentration of compound required for 50% inhibition of biotinylated vitronectin binding as estimated by the *GraphPad Prism* program. All values are the mean (±standard deviation) of triplicate determinations. [b] Enhancement Factor (β) = Increase in Affinity/Number of cRGD.

substantially alter their affinity. These data prompted us to test their possible use as vectors for cells highly expressing $\alpha_V\beta_3$ integrin.

Experiments were performed on PC-3 prostate cancer cells on account of their good responsiveness to fluorescein-conjugated cRGD compounds showed in previous experiments,[18] while MDA-MB-231 breast adenocarcinoma cells were used as a negative control due to the very faint levels of $\alpha_V\beta_3$ integrin expressed by this cell line.[47] All cell lines were exposed to scalar concentrations of gold nanoparticles. It was found that incubation with 1 μM AuNPs determined a good detection threshold in the tumor-derived cells expressing $\alpha_V\beta_3$ integrin.

PC-3 and MDA-MB-231 cells were exposed to a 4 h treatment with 1 μM AuNPs **13** and AuNPs **14** as a negative control. AuNPs **13** were demonstrated to positively stain prostate cancer cells with a spot-like pattern. The confocal analysis of PC-3 cells stained with AuNPs **13** revealed that the signal given by fluorescein and the reflection spectrum given by gold nanoparticles were perfectly merged and localized near the cell adhesive contacts (Figure 3). Therefore, this ultimately suggested that the internalization took place in the membrane zones where integrin $\alpha_V\beta_3$ is mainly expressed, which are focal contacts. Notably, breast adenocarcinoma cells subjected to the treatment previously described did not shown any sign of fluorescence or reflection. In addition, the control nanoparticles **14** gave no signal at all on both the cell lines (see Supporting Information, Figure 10), suggesting that the effectiveness and the specificity of AuNPs **13** were due to the presence of the cyclic RGD peptidomimetic.

dx.doi.org/10.1021/bc100448r |*Bioconjugate Chem.* 2011, 22, 664–672

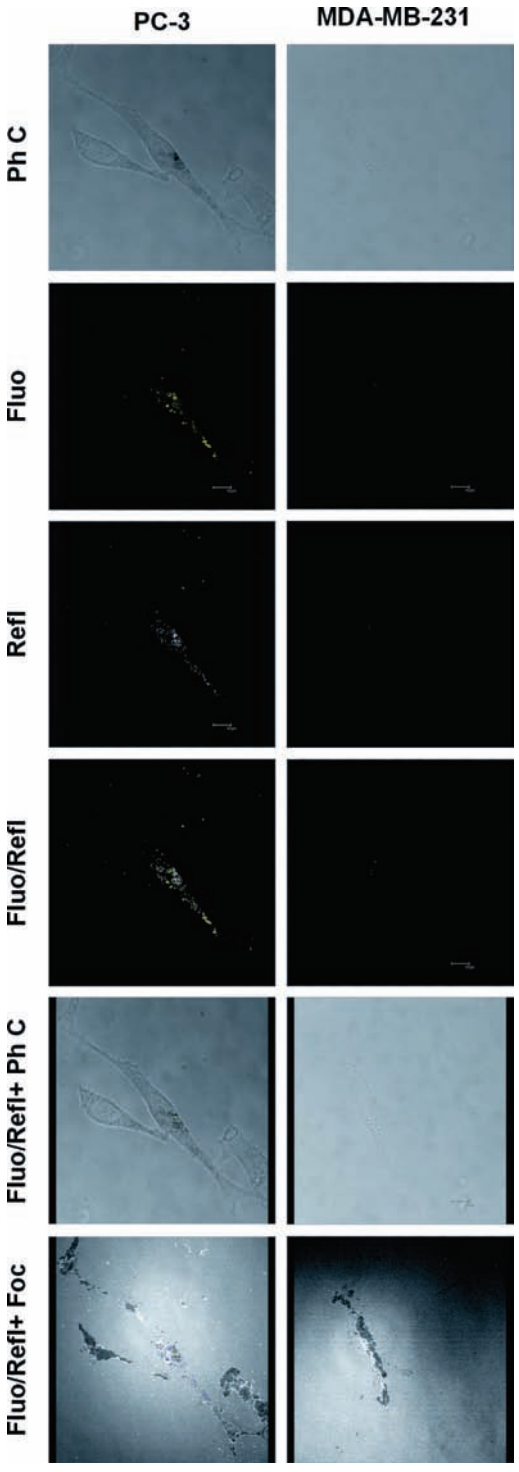


Figure 3. Biological activity of functionalized gold nanoparticles **13** on PC-3 and MDA-MB-231 cells. PC-3 and MDA-MB-231 cells were incubated 4 h with 1 μM AuNPs **13**. The signal provided by AuNPs **13** was detected in PC-3, but not in MDA-MB-231 cells. In particular, fluorescein signal and reflection spectrum of gold perfectly merged and were localized near the cell adhesive contacts. Ph C: phase contrast; Fluo: Fluorescence; Refl: Reflection; Foc: Focal adhesion. Gray: gold reflection; Green: fluorescein signal; Purple: merge. Original magnification 63×. Scale bar 10 μm.

AuNPs **12**, functionalized only with cRGD, were also tested on both PC-3 and MDA-MB-231 cell lines. As expected, the confocal analysis did not reveal any fluorescent signal, but only the reflection spectrum given by gold was detected in the case of PC-3 cells (see Supporting Information, Figure 11S). MDA-MB-231 cells showed only a slightly sign of reflection.

These data showed that gold nanoparticles fuctionalized with cRGD were able to interact specifically with cells expressing $\alpha_V\beta_3$ integrin; in fact, only a faint amount of gold nanoparticles were detected in the case of adenocarcinoma cells. It was interesting to note that the interaction occurred despite the negative charge present on the nanoparticle surfaces.

In order to evaluate the efficiency of gold nanoparticles in targeting $\alpha_V\beta_3$ expressing cells, we compared these results with data obtained with the most active fluorescein-conjugated compound (Figure 1) previously reported by our research group.[18] Surprisingly, we observed that the signal of PC-3 cells stained with 1 μM AuNPs **13** was stronger than the signal showed by the same cell line treated with a 10-fold higher concentration (10 μM) of fluorescein-conjugated cRGD (see Supporting Information, Figure 12). This result was in contrast with the expected quenching of the FITC signal by gold nanoparticles, but it was partially explained by the fact that very small gold nanoparticles are characterized by different properties in comparison with bigger AuNPs.

DISCUSSION

Gold nanoparticles are considered particularly interesting for cancer diagnosis and therapy on account of their unique physical properties. Moreover, the tunable size, the facile surface chemistry, and their reduced toxicity render Au nanoparticles even more attractive as polyvalent platform for targeted drug delivery.

In this paper, we describe the synthesis, characterization, and biological activity of gold nanoparticles conjugated on their surface with an RGD containing integrin ligand.

Gold nanoparticles **12** and **13** showed an enhanced ability to inhibit the binding of biotinylated vitronectin to immobilized $\alpha_V\beta_3$ integrin if compared with unconjugated compound **4** (**DB 58**), with affinity in the low or sub nanomolar range (0.4 nM and 1.7 nM, respectively). This result was obtained by the contemporary presentation of several cRGD ligands on the gold nanoparticles thus displaying a cooperative effect.

The cell studies showed that AuNPs **13** positively stained prostate cancer cells. In particular, the signal provided by fluorescein and that given by gold nanoparticles were perfectly merged and localized near the focal contacts. This evidence finally suggested that the internalization took place in the membrane zones where integrin $\alpha_V\beta_3$ is mainly expressed, that is, the cell adhesive contacts. The control nanoparticles **14** did not stain PC-3 cells at all. Moreover, MDA-MB-231 breast adenocarcinoma cells, expressing very low levels of $\alpha_V\beta_3$ integrin, did not show any sign of fluorescence either in the case of AuNPs **13** or AuNPs **14** treatment, thus demonstrating that AuNPs **13** interaction was specific for integrin $\alpha_V\beta_3$ overexpressing cells. AuNPs **12** revealed a similar behavior though they were detected only through the reflection signal given by gold.

In summary, the described cRGD conjugated gold nanoparticles display an enhanced affinity for $\alpha_V\beta_3$ integrin and *in vitro* positively and specifically target $\alpha_V\beta_3$ overexpressing cells, suggesting their potential future use as vectors for tumor targeted therapy.

ASSOCIATED CONTENT

Supporting Information. ^{1}H and ^{13}C NMR spectra of reported compounds; TEM micrograph, size-distribution

histogram, UV/visible spectrum of synthesized gold nanoparticles and images of *in vitro* assays. This material is available free of charge via the Internet at http://pubs.acs.org.

AUTHOR INFORMATION

Corresponding Author

*Corresponding author. Tel.: +39 02 50320907, Fax: +39 02 50320945, e-mail: daniela.arosio@istm.cnr.it.

ACKNOWLEDGMENT

The authors thank CNR and Comune di Milano (Convenzione 55/2008) for financial support and Comune di Milano (Convenzione 55/2008) for the PhD Fellowship to Elena Araldi (Doctorate School of Molecular Medicine, University of Milan). The authors thank Dr. Umberto Fascio and Dr. Nadia Santo of CIMA (Centro Interdipartimentale di Microscopia Avanzata) of the University of Milan for confocal analysis and for TEM analysis, respectively, and Claudio Arosio for the help in developing the algorithm for automatic TEM micrograph analysis.

REFERENCES

(1) Giancotti, F., and Ruoslahti, E. (1999) Integrin signaling. *Science 285*, 1028–1032.

(2) Horton, M. A. (1997) The alphaV beta3 integrin vitronectin receptor. *Int. J. Biochem. Cell Biol. 29*, 721–725.

(3) Arnaout, M. A., Goodman, S. L., and Xiong, J. P. (2002) Coming to grips with integrin binding to ligands. *Curr. Opin. Cell. Biol. 14*, 641–651.

(4) Brooks, P. C., Clark, R. A., and Cheresh, D. A. (1994) Requirement of vascular integrin alphav beta3 for angiogenesis. *Science 264*, 569–571.

(5) Costouros, N. G., Diehn, F. E., and Libutti, S. K. (2002) Molecular imaging of tumor angiogenesis. *J. Cell Biochem. Suppl. 39*, 72–78.

(6) Desgrosselier, J. S., and Cheresh, D. A. (2010) Integrins in cancer: biological implications and therapeutic opportunities. *Nat. Rev. Cancer 10*, 9–22.

(7) Ding, Q., Stewart, J., Olman, M. A., Klobe, M. R., and Gladson, C. L. (2003) The pattern of enhancement of Src kinase activity on platelet-derived growth factor stimulation of glioblastoma cells is affected by the integrin engaged. *J. Biol. Chem. 278*, 39882–39891.

(8) Kuphal, S., Bauer, R., and Bosserhoff, A.-K. (2005) Integrin signaling in malignant melanoma. *Cancer Metastasis Rev. 24*, 195–222.

(9) Beck, V., Herold, H., Benge, A., Luber, B., Hutzler, P., Tschesche, H., Kessler, H., Schmitt, M., Geppert, H. G., and Reuning, U. (2005) ADAM15 decreases integrin alphavbeta3/vitronectin-mediated ovarian cancer cell adhesion and motility in an RGD-dependent fashion. *Int. J. Biochem. Cell Biol. 37*, 590–603.

(10) Chen, X., Park, R., Tohme, M., Shahinian, A. H., Bading, J. R, and Conti, P. S. (2004) MicroPET and autoradiographic imaging of breast cancer alpha v-integrin expression using 18F- and 64Cu-labeled RGD peptide. *Bioconjugate Chem. 15*, 41–49.

(11) D'Andrea, L. D., Del Gatto, A., Pedone, C., and Benedetti, E. (2006) Peptide-based molecules in angiogenesis. *Chem. Biol. Drug Des. 67*, 115–126.

(12) Haubner, R., Gratias, R., Diefenbach, B., Goodman, S. L., Jonczyk, A., and Kessler, H. (1996) Structural and functional aspects of RGD-containing cyclic pentapeptides as highly potent and selective integrin alphavbeta3 antagonists. *J. Am. Chem. Soc. 118*, 7461–7472.

(13) Dechantsreiter, M. A., Planker, E., Matha, B., Lohof, E., Holzemann, G., Jonczyk, A., Goodmann, S. L., and Kessler, H. (1999) N-Methylated cyclic RGD peptides as highly active and selective $\alpha v\beta 3$ integrin antagonist. *J. Med. Chem. 42*, 3033–3040.

(14) Smith, J. W. (2003) Cilengitide Merck. *Curr. Opin. Invest. Drugs 4*, 741–745.

(15) Belvisi, L., Bernardi, A., Checchia, A., Manzoni, L., Potenza, D., Scolastico, C., Castorina, M., Cupelli, A., Giannini, G., Carminati, P., and Pisano, C. (2001) Potent integrin antagonist from a small library of RGD-including cyclic pseudopeptides. *Org. Lett.* 1001–1004.

(16) Belvisi, L., Riccioni, T., Marcellini, M., Chiarucci, I., Efrati, D., Vesci, L., Potenza, D., Scolastico, C., Manzoni, L., Lombardo, K., Stasi, M. A., Nico, B., Ribatti, D., Presta, M., Carminati, P., and Pisano, C. (2005) Biological and molecular properties of a new $\alpha v\beta 3/\alpha v\beta 5$ integrin antagonist. *Mol. Cancer Therapeut. 4*, 1670–1680.

(17) Manzoni, L., Belvisi, L., Arosio, D., Civera, M., Pilkington-Miksa, M., Potenza, D., Caprini, A., Araldi, E. M. V., Monferini, E., Mancino, M., Podestà, F., and Scolastico, C. (2009) Cyclic RGD-containing functionalized azabicycloalkane peptides as potent integrin antagonists for tumor targeting. *ChemMedChem 4*, 615–632.

(18) Arosio, D., Manzoni, L., Araldi, E. M. V., Caprini, A., Monferini, E., and Scolastico, C. (2009) Functionalized cyclic RGD peptidomimetics: conjugable ligands for $\alpha_V\beta_3$ receptor imaging. *Bioconjugate Chem. 20*, 1611–1617.

(19) Thumshirn, G., Hersel, U., Goodman, S., and Kessler, H. (2003) Multimeric cyclic RGD peptides as potentials tools for tumor targeting: solid-phase peptide synthesis and chemoselective oxime ligation. *Chem.—Eur. J. 9*, 2717–2725.

(20) Dijkgraar, I., Kruijtzer, J. A. W., Liu, S., Soede, A. C., Oyen, W. J. G., Corstens, F. H. M., Liskamp, R. M. J., and Boerman, O. C. (2007) Improved targeting of the $\alpha v\beta 3$ integrin by multimerisation of RGD peptides. *Eur. J. Nucl. Med. Mol. Imaging 34*, 267–273.

(21) Dijkgraar, I., Rijnders, A. Y., Soede, A., Dechesne, A. C., van Esse, G. W., Brouwer, A. J., Corstens, F. H. M., Boerman, O. C., Rijkers, D. T. S., and Liskamp, R. M. J. (2007) Synthesis of DOTA-conjugated multivalent cyclic-RGD peptide dendrimers *via* 1.3-dipolar cycloaddition and their biological evaluation: implications for tumor targeting and tumor imaging purposes. *Org. Biomol. Chem. 5*, 935–944.

(22) Dijkgraar, I., Liu, S., Kruijtzer, J. A. W., Soede, A. C., Oyen, W. J. G., Liskamp, R. M. J., Corstens, F. H. M., and Boerman, O. C. (2007) Effects of linker variation on the in vitro and in vivo characteristics of an ^{111}In-labeled RGD peptide. *Nucl. Med. Biol. 34*, 29–35.

(23) Cheng, Z., Wu, Y., Xiong, Z., Gambhir, S. S., and Chen, X. (2005) Near-infrared fluorescent RGD for optical imaging of integrin $\alpha v\beta_3$ expression in living mice. *Bioconjugate Chem. 16*, 1433–1441.

(24) Li, Z., Cai, W., Cao, Q., Chen, K., Wu, Z., He, L., and Chen, X. (2007) ^{64}Cu-labeled tetrameric and octameric RGD peptides for small-animal PET of tumor $\alpha v\beta_3$ integrin expression. *J. Nucl. Med. 48*, 1162–1171.

(25) Shukla, R., Thomas, T. P., Peters, J., Kotlyar, A., Myc, A., and Baker, J. R. J. Tumor angiogenic vasculature targeting with PAMAM dendrimer-RGD conjugates. *Chem. Commun.* 5739−5741.

(26) Liu, S. (2006) Radiolabeled multimeric cyclic RGD peptides as integrin $\alpha_v\beta_3$ targeted radiotracers for tumor imaging. *Mol. Pharmaceutics 3*, 472–487and reference therein.

(27) Hersel, U., Dahmen, C., and Kessler, H. (2003) RGD modified polymers: biomaterials for stimulated cell adhesion and beyond. *Biomaterials 24*, 4385–4415.

(28) Lieb, E., Hacker, M., Tessmar, J., Kunz-Schughart, L. A., Fiedler, J., Dahmen, C., Hersel, U., Kessler, H., Schulz, M. B., and Göpferich, A. (2005) Mediating specific cell adhesion to low-adhesive diblok copolymers by instant modification with cyclic RGD peptides. *Biomaterials 26*, 2333–2341.

(29) Zluza, E., van der Schaft, D. W. J., Hautvast, P. A. I., Mulder, W. J. M., Mayo, K. H., Griffioen, A. W., Strijkers, G. J., and Nicolay, K. (2010) Synergistic targeting of $\alpha v\beta_3$ integrin and galectin-1 with heteromultivalent paramagnetic liposomes for combined MR imaging and treatment of angiogenesis. *Nano lett. 10*, 52–58.

(30) Garanger, E., Boturyn, D., Renaudet, O., Defrancq, E., and Dumy, P. (2006) Chemoselectively addressable template: a valuable tool fort he engineering of molecular conjugates. *J. Org. Chem. 71*, 2402–2410.

(31) Boisselier, E., and Astruc, D. (2009) Gold nanoparticles: preparations, imaging, diagnostics, therapies and toxicity. *Chem. Soc. Rev. 38*, 1759–1782.

(32) Arvizio, R., Bhattacharya, R., and Mukherjee, P. (2010) Gold nanoparticles: opportunities and challenges in nanomedicine. *Expert Opin. Drug Delivery 7*, 753–763.

(33) Murphy, C. J., Gole, A. M., Stone, J. W., Sisco, P. N., Alkilany, A. M., Goldsmith, E. C., and Baxter, S. C. (2008) Gold nanoparticles in biology: beyond toxicity to cellular imaging. *Acc. Chem. Res. 41*, 1721–1730.

(34) Paciotti, G. F., Kingston, D. G. I., and Tamarkin, L. (2006) Colloidal gold nanoparticles: a novel nanoparticles platform for developing multifunctional tumor-targeted drug delivery vectors. *Drug Dev. Res. 67*, 47–54.

(35) Paciotti, G. F., Myer, L., Weinreich, D., Goia, D., Pavel, N., McLaughlin, R. E., and Tamarkin, L. (2004) Colloidal gold: a novel nanoparticle vector for tumor directed drug delivery. *Drug Delivery 11*, 169–183.

(36) Han, G., Ghosh, P., De, M., and Rotello, V. M. (2007) Drug and gene delivery using gold nanoparticles. *Nanobiotechnology 3*, 40–45.

(37) Turkevich, J., Stevenson, P. C., and Hillier, J. (1951) A study of the nucleation and growth processes in the synthesis of colloidal gold. *Discuss. Faraday Soc. 11*, 55–57.

(38) Kimling, J., Maier, M., Okenve, B., Kotaidis, V., Ballot, H., and Plech, A. (2006) Turkevich method for gold nanoparticles synthesis revisited. *J. Phys. Chem. B 110*, 15700–15707.

(39) Brust, M., Walker, M., Bethell, D., Schiffrin, D. J., and Whyman, R. (1994) Synthesis of thiol-derivatised gold nanoparticles in a two-phase liquid-liquid system. *J. Chem. Soc.: Chem. Commun.* 801–802.

(40) Barrientos, A. G., de la Fuente, J. M., Rojas, T. C., Fernandez, A., and Penades, S. (2003) Gold glyconanoparticles: synthetic polyvalent ligands mimicking glycocalyx-like surface as tools for glycobiological studies. *Chem.—Eur. J. 9*, 1909–1921.

(41) Martinez-Avila, O., Hijazi, K., Marradi, M., Clavel, C., Campion, C., Kelly, C., and Penades, S. (2009) Gold *manno*-glyconanoparticles: multivalent systems to block HIV-1 gp120 binding to the lectin DC-SIGN. *Chem.—Eur. J. 15*, 9874–9888.

(42) Mould, P. A. (2009) Solid phase assays for studing ECM protein-protein interactions. *Methods Mol. Biol. 222*, 124–138.

(43) Hostetler, M. J., Wingate, J. E., Zhong, C.-J., Harris, J. E., Vachet, R. W., Clark, M. R., Londono, J. D., Green, S. J., Stokes, J. J., Wignall, G. D., Glish, G. L., Porter, M. D., Evans, N. D., and Murray, R. W. (1998) Alkinothiolate gold cluster molecules with core diameters form 1.5 to 5.2: core and monolayer properties as a function of core size. *Langmuir 14*, 17–30.

(44) Varnavski, O., Ramakrishna, G., Kim, J., Lee, D., and Goodson, T. (2010) Critical size for the observation of quantum confinement in optically excited gold clusters. *J. Am. Chem. Soc. 132*, 16–17.

(45) Mammen, M., Choi, S.-K., and Whitesides, G. M. (1998) Polyvalent interactions in biological systems: implication for design and use of multivalent ligands and inhibitors. *Angew. Chem., Int. Ed. 37*, 2754–2794.

(46) Montet, X., Funovic, M., Montet-About, K., Weissleder, R., and Josephson, L. (2006) Multivalent effects of RGD peptides obtained by nanoparticle display. *J. Med. Chem. 49*, 6087–6093.

(47) Ramos, O. H. P., Kauskot, A., Cominetti, M. R., Bechyne, I., Salla Potes, C. L., Chareyre, F., Manent, J., Vassy, R., Giovannini, M., Legrand, C., Selistre-de-Araujo, H., Crépin, M., and Bonnefoy, A. (2008) A novel alpha(v)beta (3)-blocking disintegrin containing the RGD motive, DisBa-01, inhibits bFGF-induced angiogenesis and melanoma metastasis. *Clin. Exp. Metastasis 25*, 53–64.

Supporting Information

Cyclic RGD Functionalized Gold Nanoparticles for Tumor Targeting.

Daniela Arosio,[†,*] Leonardo Manzoni,[†,] Elena Araldi,[‡] and Carlo Scolastico.[§]

CNR-Istituto di Scienze e Tecnologie Molecolari (ISTM), Via Fantoli 16/15, I-20138, Milan, Italy
Centro Interdipartimentale di Studi Biomolecolari e Applicazioni Industriali (CISI) of the University of Milan, Via Fantoli 16/15, I-20138, Milan, Italy
CISI scrl, Via Fantoli 16/15, I-20138, Milan, Italy

* Corresponding author: Tel.: +39 02 50320907, Fax: +39 02 50320945, e-mail: daniela.arosio@istm.cnr.it

[†] CNR-ISTM
[‡] CISI, University of Milan, Doctorate school of molecular Medicine
[§] CISI scrl

Table of Contents:

Figure S1. ^{1}H-NMR spectrum of compound **9**. S03

Figure S2. ^{13}C-NMR spectrum of compound **9**. S03

Figure S3. ^{1}H-NMR spectrum of compound **7**. S04

Figure S4. ^{13}C-NMR spectrum of compound **7**. S04

Figure S5. ^{1}H-NMR spectrum of compound **10**. S05

Figure S6. ^{13}C-NMR spectrum of compound **10**. S05

Figure S7**.** Characterization of AuNPs **11**. S06

Figure S8. Characterization of AuNPs **13**. S07

Figure S9. Characterization of AuNPs **14**. S08

Figure S10. Biological activity of functionalized gold nanoparticles **14** on PC-3 and MDA-MB-231 cells. S09

Figure S11. Biological activity of functionalized gold nanoparticles **12** on PC-3 and MDA-MB-231 cells. S10

Figure S12. Comparison between biological activity of functionalized gold nanoparticles **13** and fluorescein-conjugated cRGD **compound 13**. S11

Figure S1. ^{1}H NMR (600 MHz, D_2O) of compound **9**.

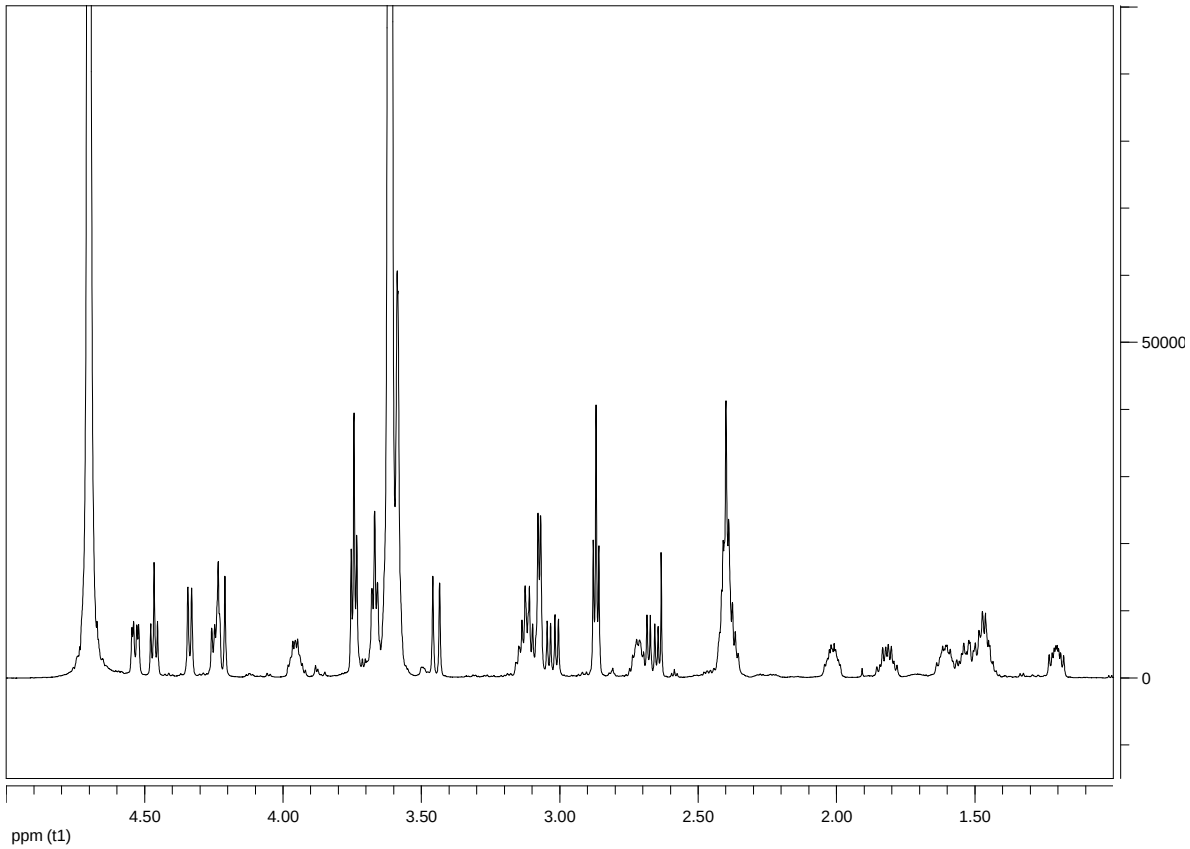


Figure S2. ^{13}C NMR (150.9 MHz, D_2O) of compound **9**.

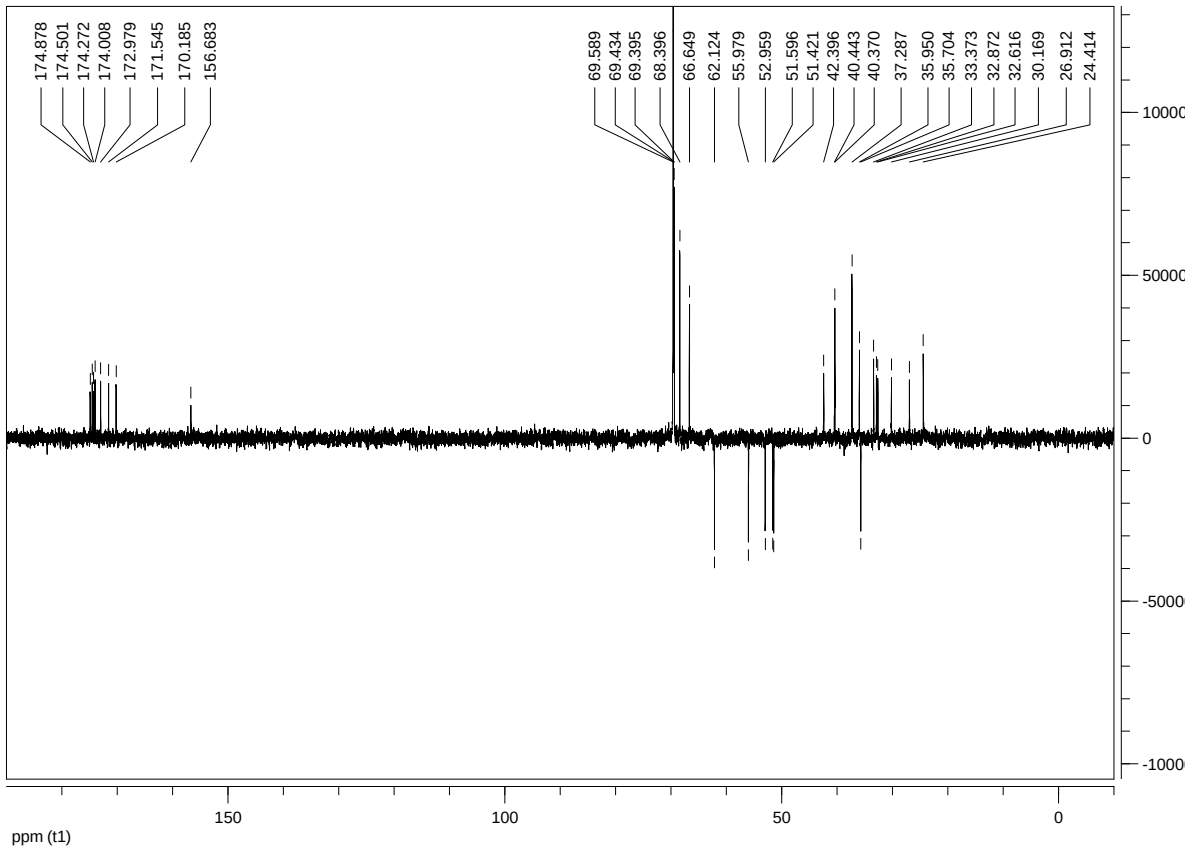


Figure S3. ^{1}H NMR (400 MHz, *Methanol-d4*) of compound **7**.

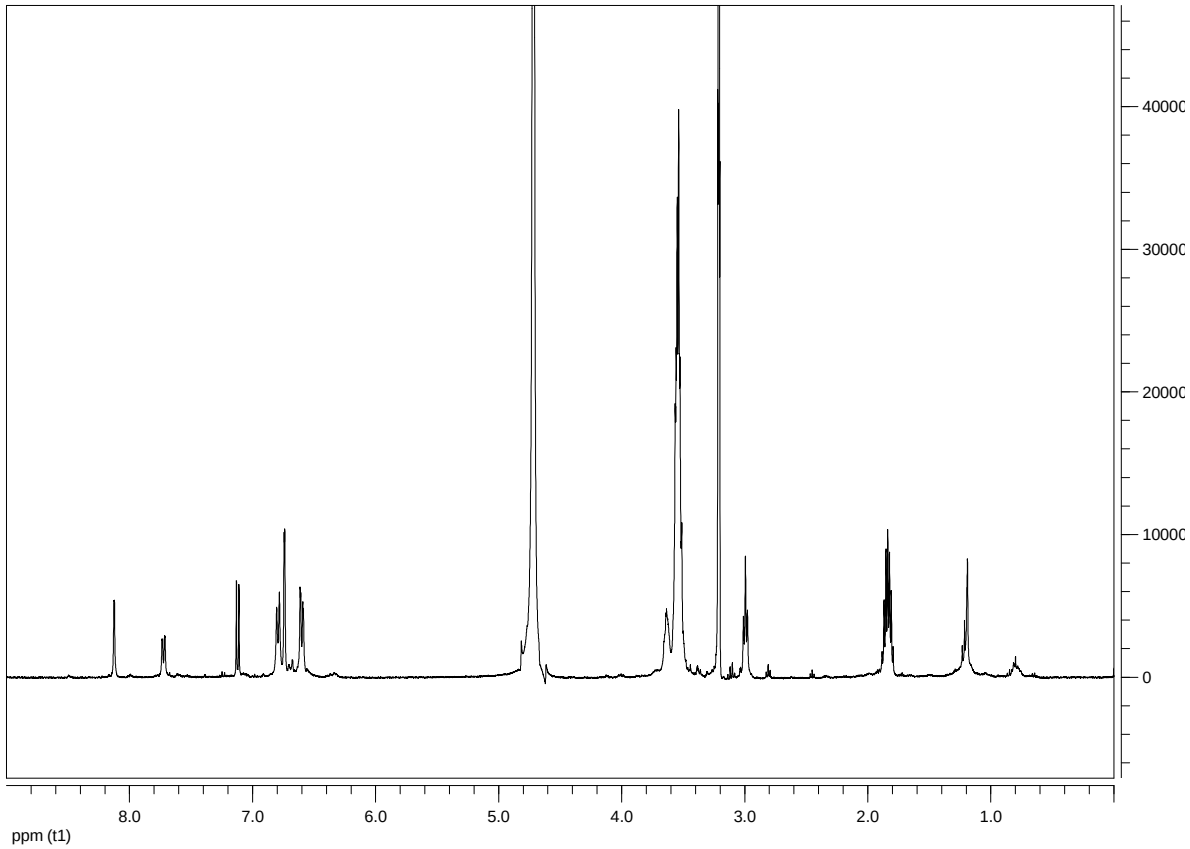


Figure S4. ^{13}C NMR (100.6 MHz, *Methanol-d4*) of compound **7**.

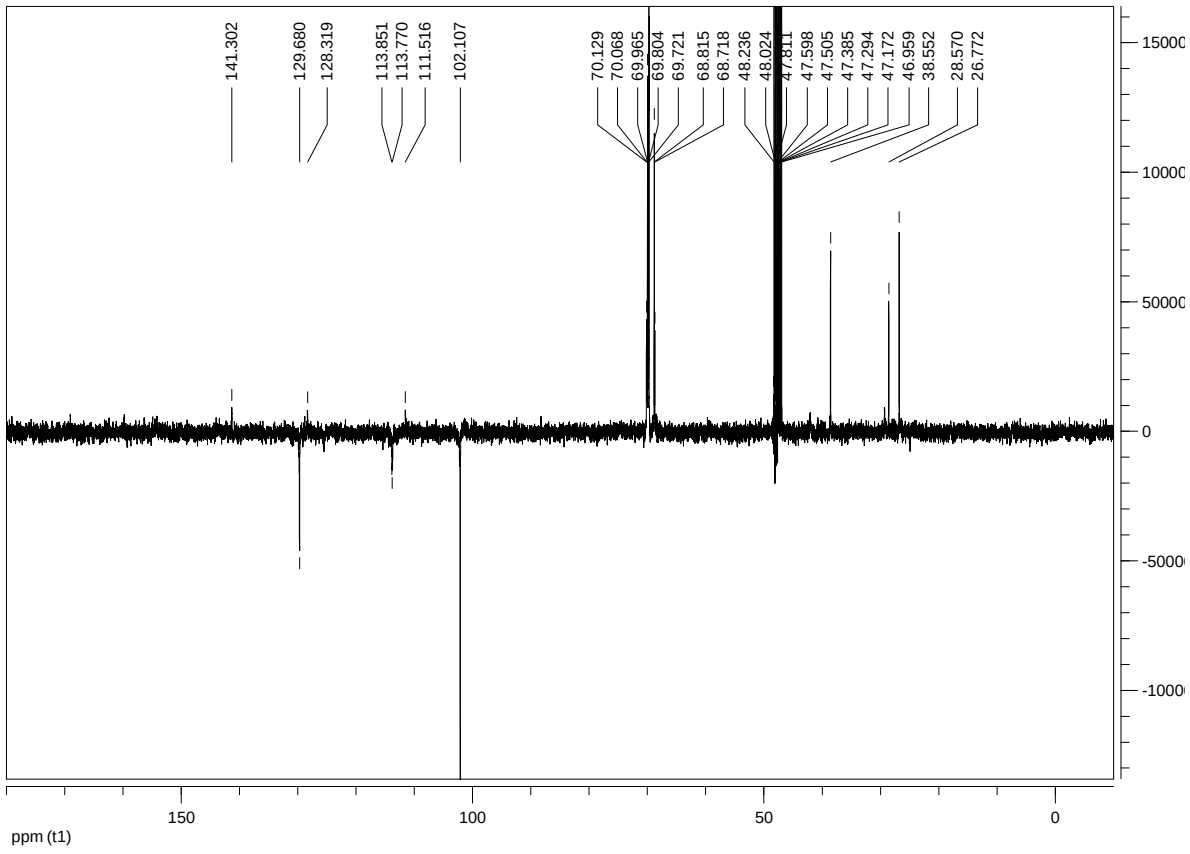


Figure S5. ^{1}H NMR (400 MHz, *Methanol-d4*) of compound **10**.

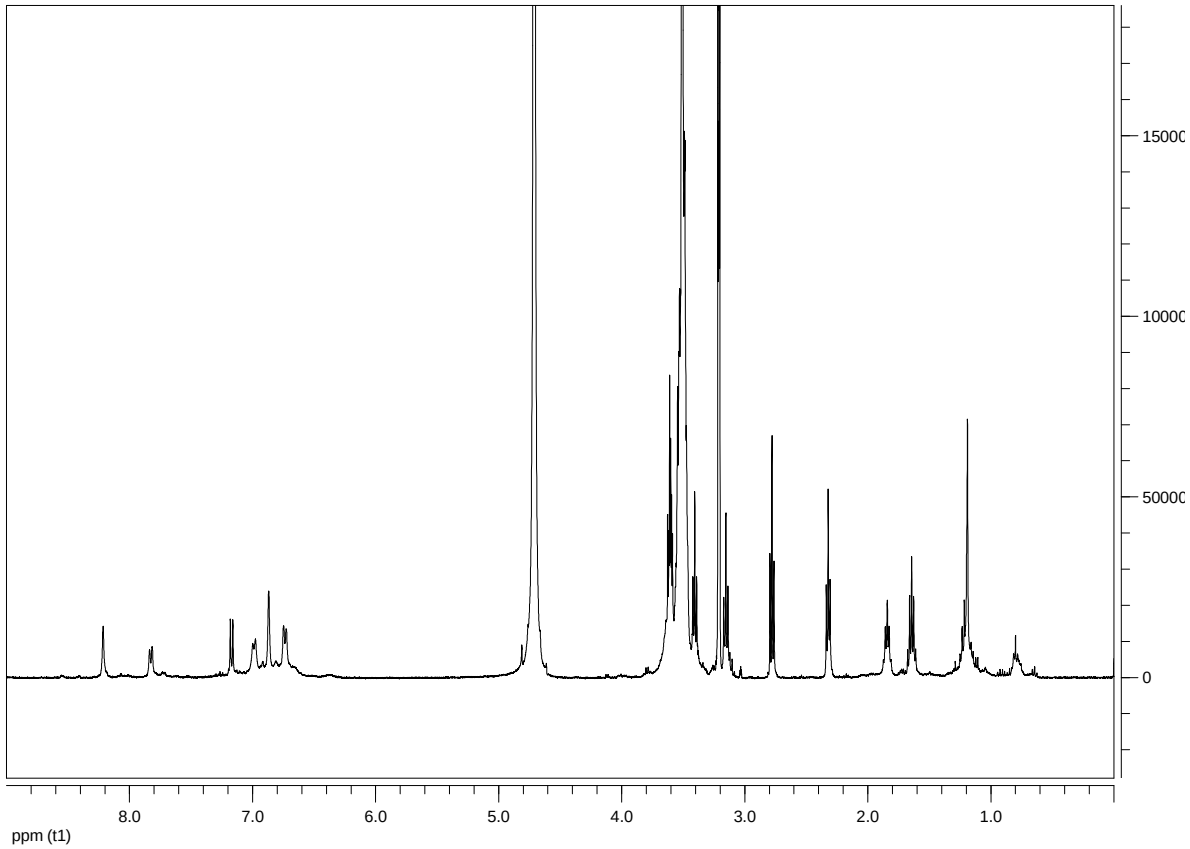
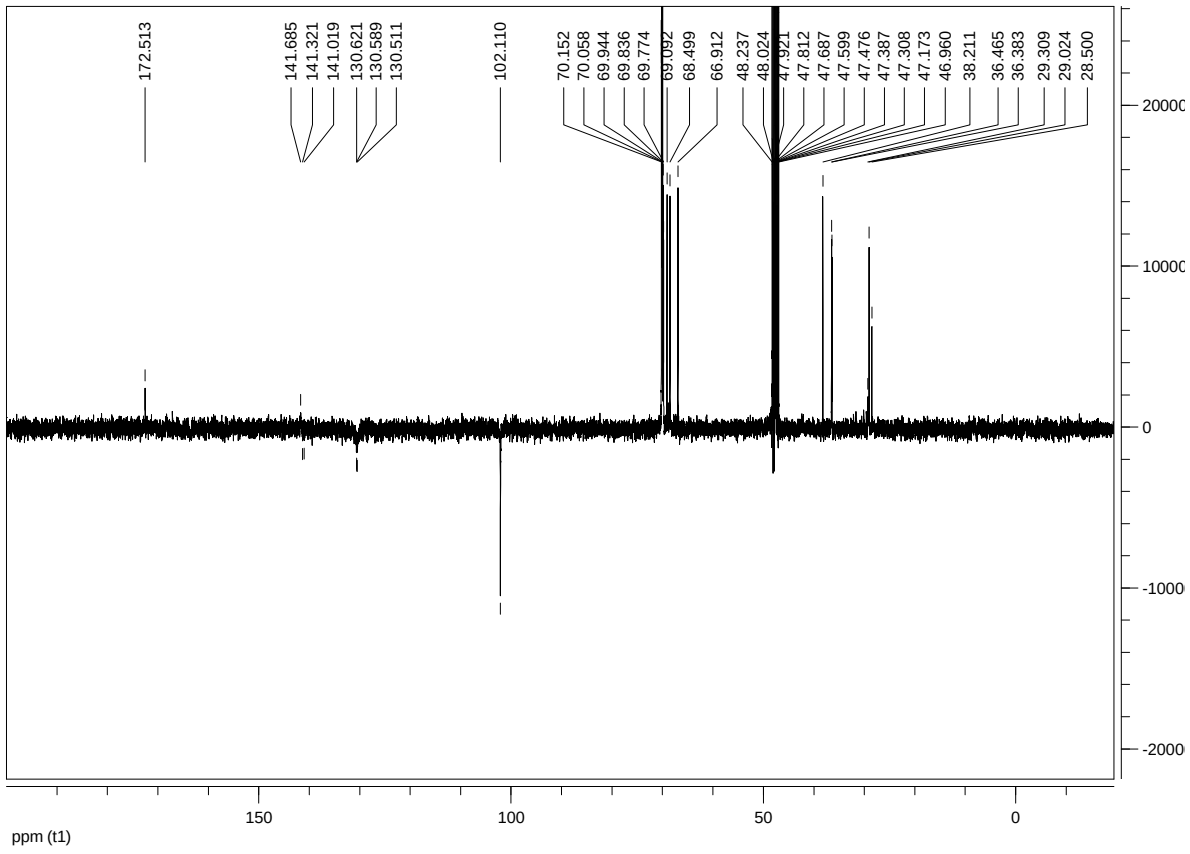


Figure S6. ^{13}C NMR (100.6 MHz, *Methanol-d4*) of compound **10**.



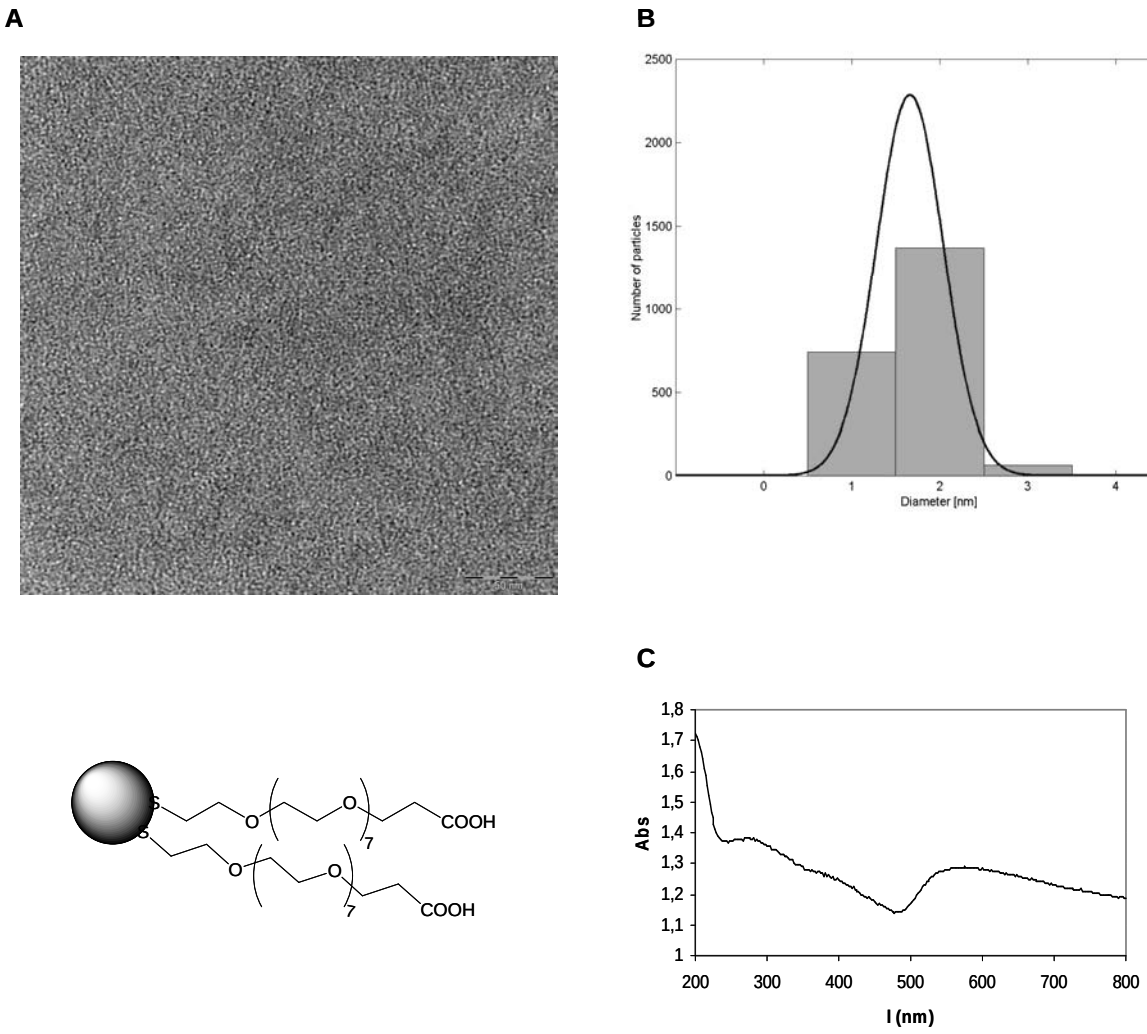


Figure S7. Characterization of AuNPs **11**. A) TEM micrograph in H_2O (Scale bar 50 nm); B) size-distribution histogram; C) Uv/Visible spectrum.

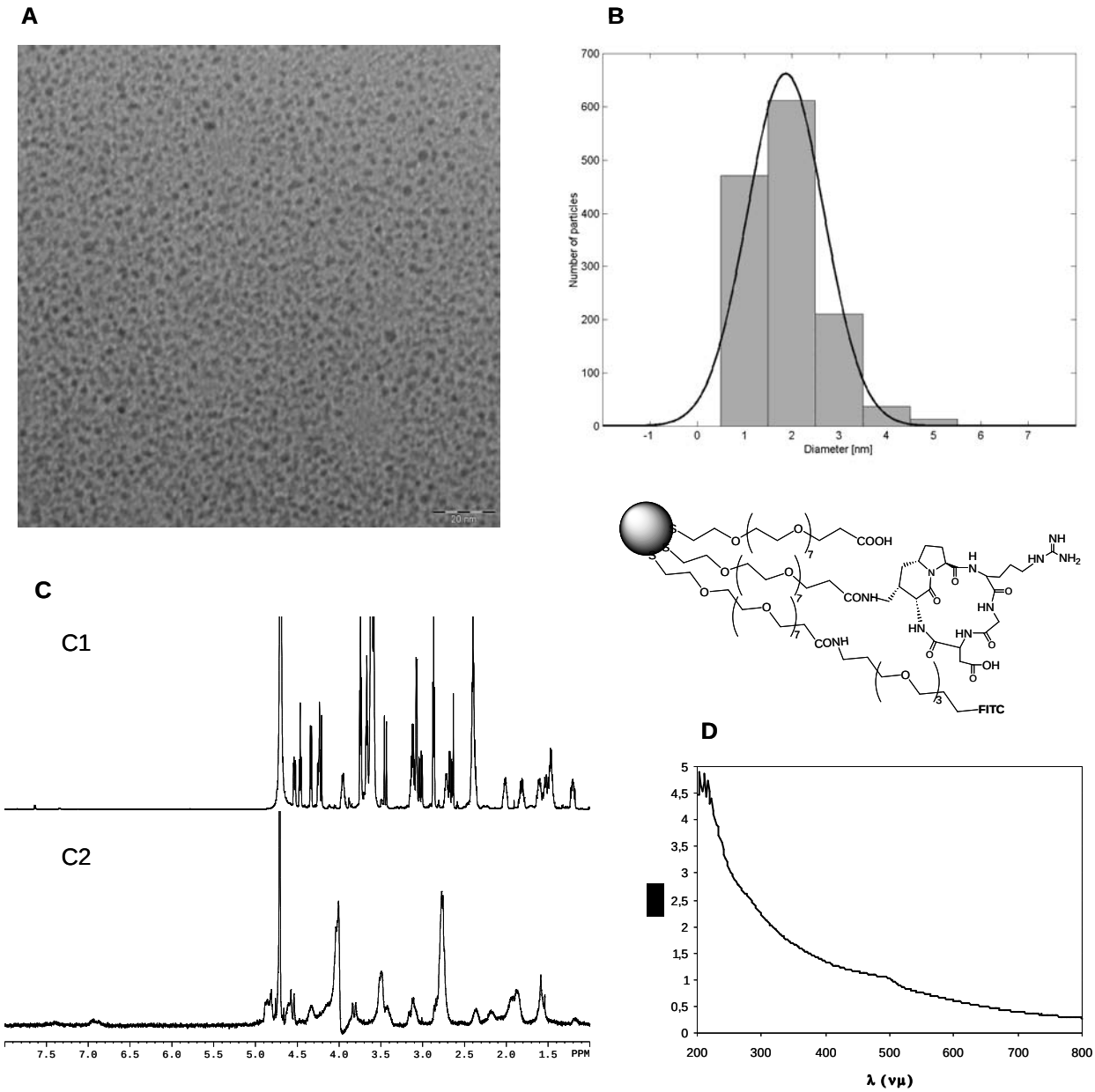


Figure S8. Characterization of AuNPs **13**. A) TEM micrograph in H_2O (Scale bar 20 nm); B) size-distribution histogram; C) ^{1}H-NMR spectra of cRGD conjugated linker **9** (C1) and of gold nanoparticles **13** (C2), D) Uv/Visible spectrum.

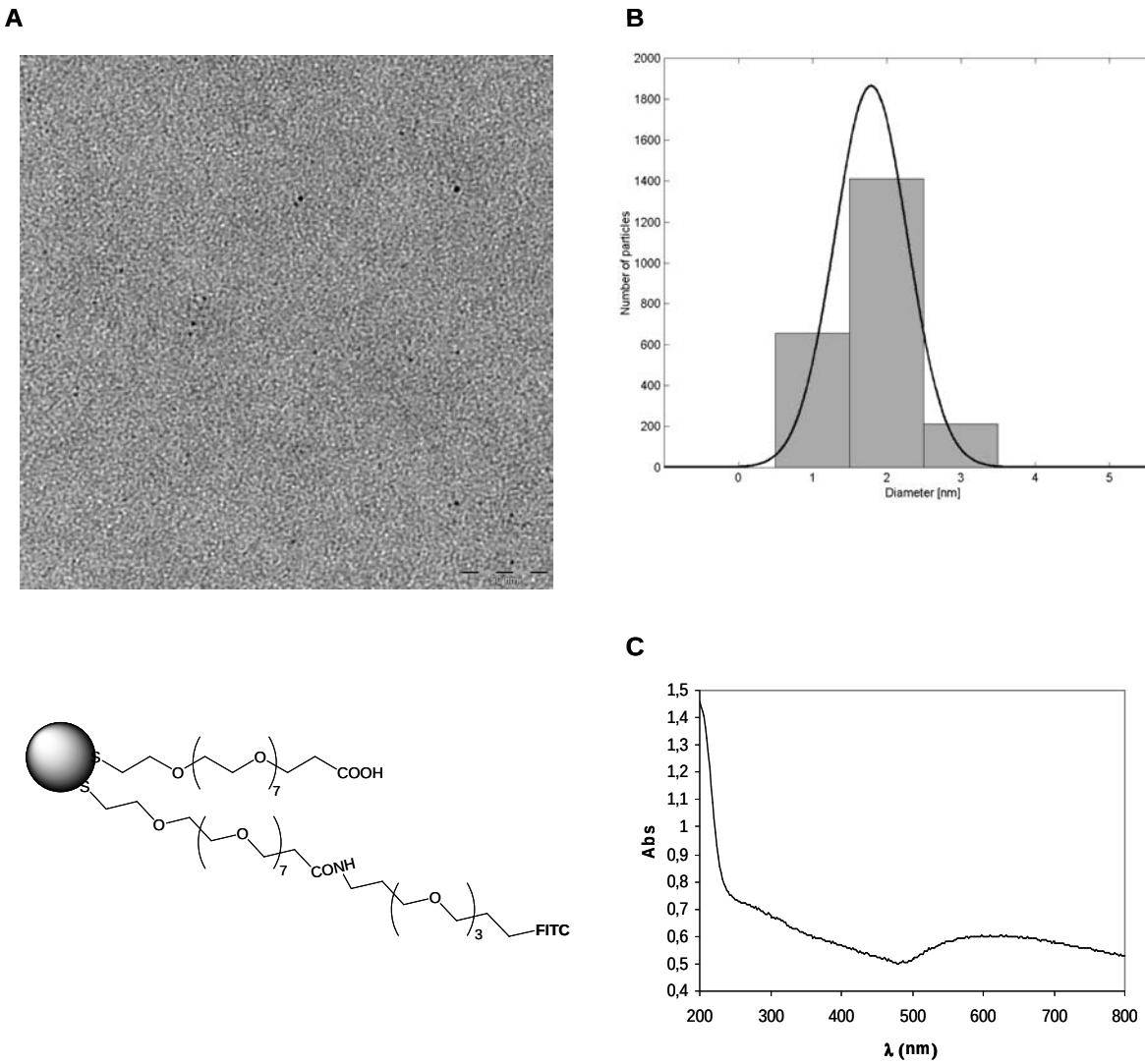


Figure S9. Characterization of AuNPs **14**. A) TEM micrograph in H_2O (Scale bar 50 nm); B) size-distribution histogram; C) Uv/Visible spectrum.

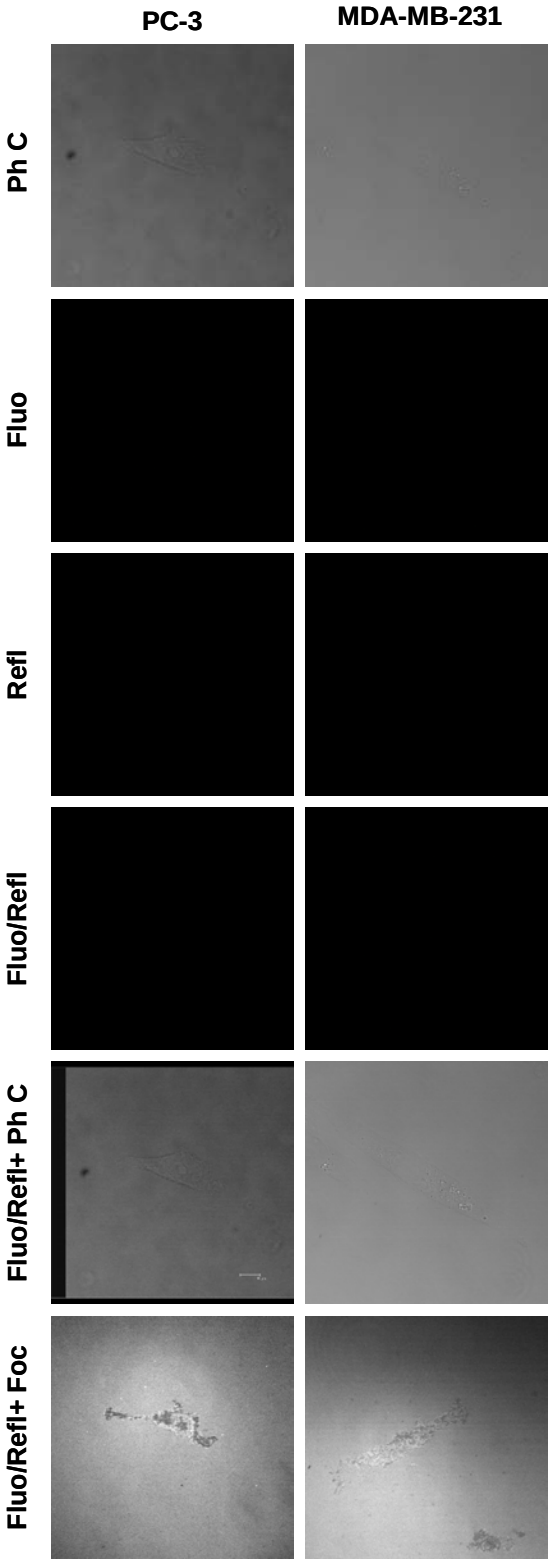


Figure S10. Biological activity of functionalized gold nanoparticles **14** on PC-3 and MDA-MB-231 cells. PC-3 and MDA-MB-231 cells were incubated 4 hours with 1 μM AuNPs **14**. AuNPs **14** gave non signal at all neither in PC-3 nor in MDA-MB-231 cells. Ph C: phase contrast; Fluo:

Fluorescence; Refl: Reflection; Foc: Focal adhesion. Grey: gold reflection; Green: fluorescein signal; Purple: merge. Original magnification 63x; scale bars: 10 μm.

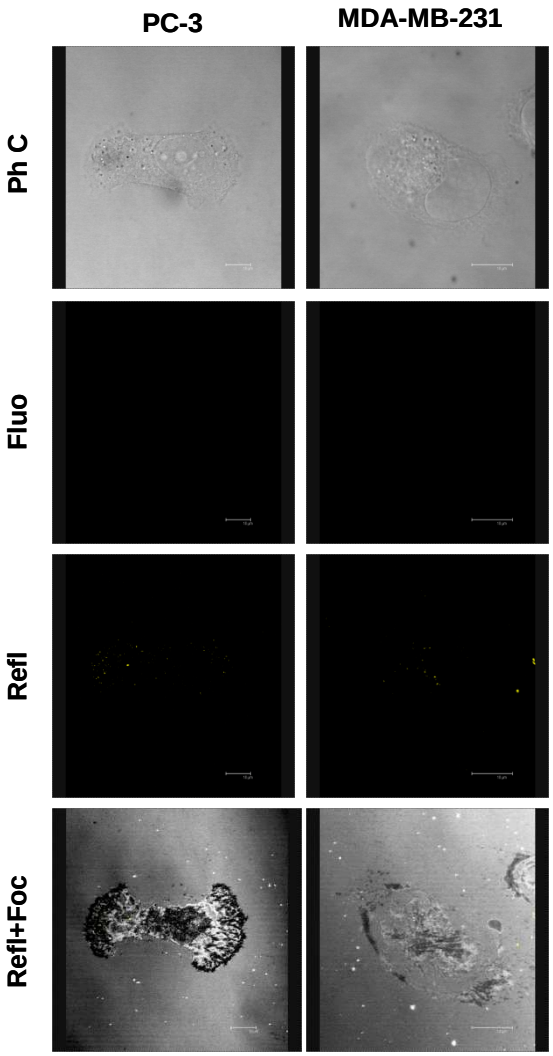


Figure S11. Biological activity of functionalized gold nanoparticles **12** on PC-3 and MDA-MB-231 cells. PC-3 and MDA-MB-231 cells were incubated 4 hours with 1 μM AuNPs **12**. AuNPs **12** gave only a reflection signal but not a fluorescence signal on PC-3 cells. In the case of MDA-MB-231 cells a slightly reflection signal was also detected. Ph C: phase contrast; Fluo: Fluorescence; Refl: Reflection; Foc: Focal adhesion. Yellow: gold reflection; Green: fluorescein signal. Original magnification 63x; scale bars: 10 μm.

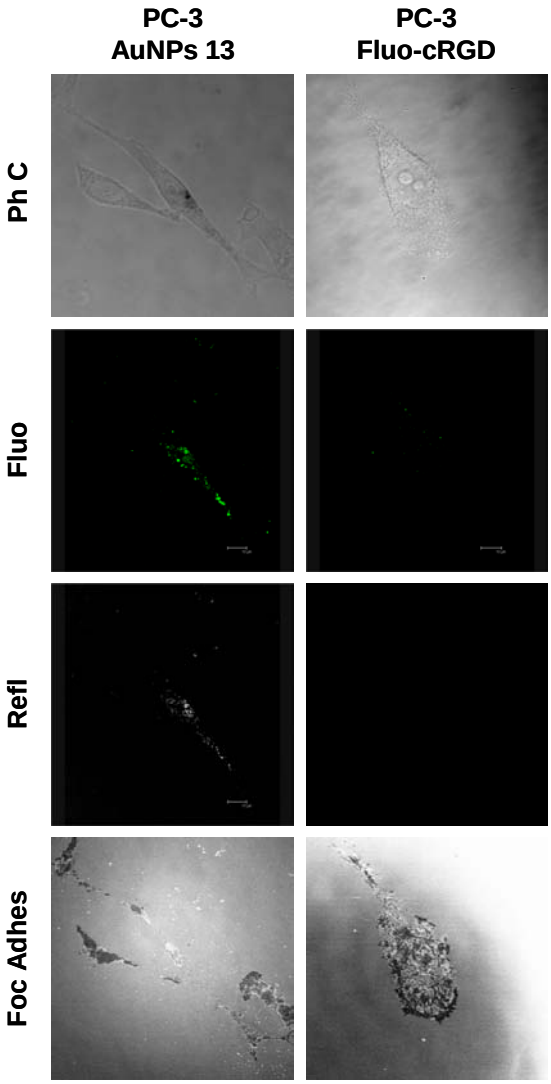


Figure S12. Comparison between biological activity of functionalized gold nanoparticles **13** and fluorescein-conjugated cRGD **compound 13** in ref. (*1*) on PC-3 cells. PC-3cells were incubated 4 hours with 1 μM AuNPs **13** or 10 μM **compound 13.** The signal displayed by cells treated with AuNPs **13** is significantly stronger in comparison with the signal given by cells treated with **compound 13** thought in a ten times lower concentration. Ph C: phase contrast; Fluo: Fluorescence; Refl: Reflection; Foc Adhes: Focal adhesion. Grey: gold reflection; Green: fluorescein signal. Original magnification 63x; scale bars: 10 μm.

References:

(1) Arosio, D., Manzoni, L., Araldi, E. M. V., Caprini, A., Monferini, E., and Scolastico, C. (2009) Functionalized cyclic RGD peptidomimetics: conjugable ligands for $\alpha_V\beta_3$ receptor imaging. *Bioconjugate Chem. 20*, 1611-1617.

Bioconjugate Chemistry

ARTICLE

pubs.acs.org/bc

Islet Surface Modification with Urokinase through DNA Hybridization

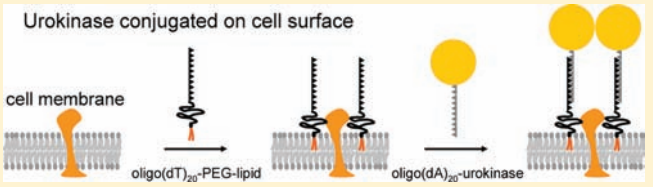
Naohiro Takemoto,[†] Yuji Teramura,[‡] and Hiroo Iwata*[,†]

[†]Department of Reparative Materials, Institute for Frontier Medical Sciences, Kyoto University, 53 Kawahara-Cho, Shogoin, Sakyo-Ku, Kyoto 606-8507, Japan

[‡]Radioisotope Research Center, Kyoto University, Yoshida-Konoe-Cho, Sakyo-ku, Kyoto 606-8501, Japan

Supporting Information

ABSTRACT: Transplantation of islets of Langerhans (islets) has been proposed as a safe, effective approach to treating patients with insulin-dependent diabetes mellitus (type I diabetes). It has been reported, however, that many islets are lost in the early phase after intraportal transplantation by instant blood coagulation-mediated inflammatory reactions. In this study, DNA hybridization was applied to conjugate the fibrinolytic enzyme urokinase on the islet surface. We synthesized amphiphilic polymers, PEG-lipids carrying oligo(dT)$_{20}$ (oligo(dT)$_{20}$−PEG-lipid; PEG MW = 5000) and urokinase (UK) carrying oligo(dA)$_{20}$. The oligo(dT)$_{20}$−PEG-lipid was spontaneously incorporated into the cell membrane through interactions between the hydrophobic parts of the PEG-lipids and the lipid bilayer, and UK was conjugated on the cell surface through DNA hybridization between oligo(dT)$_{20}$ on the cell and complementary oligo(dA)$_{20}$ on the UK. The activity of UK was maintained on the islet surface. The surface modification with UK did not influence islet morphology or islet ability to secrete insulin in response to changes in glucose concentration. No practical volume increase was observed with our method, indicating that islet graft loss could be suppressed at the early stage of intraportal islet transplantation.



INTRODUCTION

Transplantation of islets of Langerhans (islets) has been proposed as a safe and effective method for treating patients with insulin-dependent diabetes mellitus (type I diabetes).[1,2] Intraportal islet transplantation combined with the Edmonton protocol has had demonstrable clinical success. Multiple donors of pancreases, however, are still needed to achieve normalized blood glucose levels without insulin injection. This necessity is attributable to the loss of many islets in the early phase after intraportal transplantation by instant blood-mediated inflammatory reactions (IBMIR).[2−8] It has been reported that a lot of islets are known to be damaged by IBMIR within a few hours.[9] If blood coagulation induced by transplanted islets can be inhibited, most of the islets could be rescued.

Systemic administration of some anticoagulants has been tried to achieve this outcome,[6,7] but patients may then be at a high risk for bleeding. Recently, alternative ideas have been proposed for the suppression of IBMIR,[10−18] including islets coated with anticoagulants such as heparin,[10] thrombomodulin,[11] fibrinolytic urokinase (UK),[14,15] or living cells,[12,16,18] to localize their antithrombogenic effects. Various improvements are still needed, however, for clinical application of these approaches. In some studies, the biotin/streptavidin reaction has been used to conjugate antithrombogenic materials. Streptavidin, however, is an immunogenic protein derived from bacteria[19,20] and is likely not appropriate for use in surface modification of islets for clinical uses. In the other studies, chemical modification of membrane proteins has been employed, but this method is expected to deteriorate islet cell functions.

Our group has synthesized various amphiphilic polymers and applied them to surface modification of cells to conjugate antithrombogenic materials and modulate the immunogenicity of cells.[13−18,21−26] Poly(ethylene glycol)−phospholipid conjugates (PEG-lipids) have been successfully applied to cell surface modification. They are spontaneously incorporated into the cell membrane through interactions between the hydrophobic parts of the PEG-lipids and the lipid bilayer. We have further advanced our technology to easily modify the cell surface with various bioactive substances by conjugating single stranded DNA with PEG-lipids (ssDNA−PEG-lipids).[18,24] In this study, we employed DNA hybridization to modify the islet surface with the plasminogen activator UK using ssDNA−PEG-lipid.

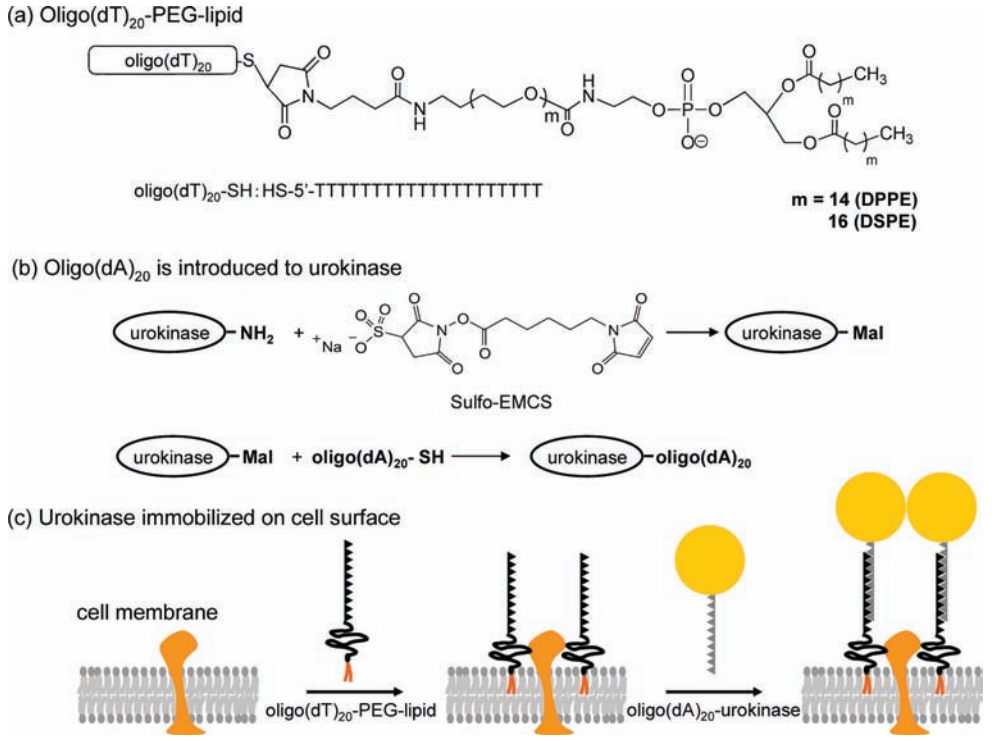
EXPERIMENTAL PROCEDURES

Materials. α-*N*-Hydroxysuccinimidyl-ω-maleimidyl poly(ethylene glycol) (NHS-PEG-Mal, MW 5000), 1,2-dipalmitoyl-*sn*-glycerol-3-phosphatidylethanolamine (DPPE), and 1,2-distearoyl-*sn*-glycerol-3-phosphatidylethanolamine (DSPE) were purchased from NOF Corporation (Tokyo, Japan). Dichloromethane, chloroform, diethyl ether, dimethyl sulfoxide (DMSO), triethylamine (TEA), penicillin−streptomycin mixed solution, and heparin sodium salt were bought from Nacalai Tesque (Kyoto, Japan). Fetal bovine serum (FBS) was purchased from BioWest (Miami, FL, USA) and

Received: October 13, 2010
Revised: March 9, 2011
Published: March 09, 2011

ACS Publications © 2011 American Chemical Society

Scheme 1. Method to Conjugate UK on the Cell Surface through DNA Hybridization[a]



[a] (a) Chemical structure of oligo(dT)$_{20}$-conjugated PEG-lipid (oligo(dT)$_{20}$−PEG-lipid). (b) UK is modified with Sulfo-EMCS to introduce maleimide groups, and then oligo(dA)$_{20}$-SH is conjugated on UK through the thiol/maleimide reaction. (c) Oligo(dT)$_{20}$−PEG-lipid is incorporated into the cell surface by the hydrophobic interaction between alkyl chains and the lipid bilayer of the cell membrane. Oligo(dA)$_{20}$-UK is applied to cells carrying oligo(dT)$_{20}$. UK is conjugated on the cell surface through oligo(dT)$_{20}$−oligo(dA)$_{20}$ hybridization.

phosphate-buffered saline (PBS) from Nissui Pharmaceutical, Co., Ltd. (Tokyo, Japan). Alexa 488-labeled rabbit antigoat IgG, HEPES buffer solution, Medium 199, and Hanks' balanced salt solution (HBSS) were purchased from Invitrogen, Co. (Carlsbad, CA, USA). Urokinase (UK) was purchased from American Research Products, Inc. (Belmont, MA, USA), polyclonal goat antihuman UK from Abcam plc. (Cambridge, UK), and *N*-[ε-maleimidocaproyloxy]sulfosuccinimide ester (Sulfo-EMCS) from Pierce Biotechnology, Inc. (Rockford, IL). Thrombin was obtained from Kayaku Co., Ltd. (Saitama, Japan). Fibrinogen type I, plasminogen (from human plasma), and oligo(dA)$_{20}$ and oligo(dT)$_{20}$ carrying a protected SH group at the 5′-end (oligo(dA)$_{20}$-SH, oligo(dT)$_{20}$-SH) were purchased from Sigma-Aldrich Chemical Co. (St. Louis, MO, USA). Oligo(dA)$_{20}$ and oligo(dT)$_{20}$ with a 5′-end SH group were prepared by reduction of the disulfide bond with dithiothreitol (DTT) according to the manufacturer's instructions.

Synthesis of Oligo(dT)$_{20}$−PEG-Lipids and Oligo(dA)$_{20}$-Conjugated UK. Oligo(dT)$_{20}$-conjugated PEG-lipids (oligo(dT)$_{20}$−PEG-DPPE, oligo(dT)$_{20}$−PEG-DSPE, Scheme 1(a)) were synthesized following the method reported previously.[18,24] UK (1 mg/mL in PBS, 100 μL) and sulfo-EMCS (0.38 mg/mL in PBS, 20 μL) were mixed together and left for 2 h at room temperature to prepare Mal-UK (Scheme 1(b)). Mal-UK was isolated with Sephadex G25 and freeze-dried. Mal-UK (1 mg/mL in PBS, 20 μL) was mixed with oligo(dA)$_{20}$-SH (150 μg/mL in PBS, 80 μL) for 2 h at room temperature to prepare oligo(dA)$_{20}$-UK.

Surface Modification of islets with UK through DNA Hybridization Using Oligo(dT)$_{20}$−PEG-Lipids. All animal experiments were approved and accepted by the animal care committee of Institute for Frontier Medical Sciences, Kyoto University. Pancreatic islets were isolated from the pancreas of Syrian hamsters (7 weeks old, female, Japan SLC, Inc., Shizuoka, Japan) by the collagenase digestion method.[27] As shown in Scheme 1(c), oligo(dT)$_{20}$−PEG-lipid was conjugated with islets as reported previously.[18,24] Briefly, oligo(dT)$_{20}$−PEG-lipid (500 μg/mL oligo(dT)$_{20}$−PEG-DPPE in PBS or 500 μg/mL oligo(dT)$_{20}$−PEG-DSPE in PBS containing 10% DMSO) was added to an islets suspension and left for 1 h at room temperature for oligo(dT)$_{20}$−PEG-DPPE or 30 min at 37 °C for oligo(dT)$_{20}$−PEG-DSPE. After the islets were washed with Medium 199 (serum free), oligo(dA)$_{20}$-UK (200 μg/mL) was added to the islets and left for 1 h at room temperature.

Immunostaining for UK was carried out as follows: UK-islets were incubated with 2% polyclonal goat antihuman UK antibody for 1 h at room temperature. After washing with medium, we incubated the UK-islets with fluorescence labeled secondary antibody and 0.2% Alexa 488-labeled rabbit antigoat IgG in medium for 1 h at room temperature, followed by washed with medium. Those islets were observed under a confocal laser scanning microscope (FV500; Olympus, Tokyo, Japan).

Measurement of UK Activity with the Fibrin Plate Assay. To examine the fibrinolytic activity of UK conjugated on islets, the fibrin plate assay was employed as previously reported with slight modifications.[28] Briefly, 8 mL of fibrinogen solution (10 mg/mL in saline supplemented with 0.2 mg plasminogen) was poured into a culture dish (ø =10 cm). A total of 30 μL of thrombin (60 IU/mL) was added to the solution and mixed well by rotating the plate. The plate was incubated for 3 h at room temperature to prepare a fibrin plate. The UK-islets (50 islets) cultured just after UK conjugation for 0 or 2 days and unmodified islets (50 islets) were applied to each spot on the fibrin plate. After incubation at 37 °C for 14 h, we

dx.doi.org/10.1021/bc100453r |*Bioconjugate Chem.* 2011, 22, 673–678

determined the size of the transparent area formed around the islet spots to measure fibrinolytic activity.

Glucose Stimulation Test of UK-Islets. Static insulin secretion tests were performed using 50 islets to examine their ability to change insulin secretion in response to changes in glucose concentration. Unmodified islets and UK-islets after 0 or 2 days in culture were used for the assay. Islets were exposed to 0.1 g/dL, then 0.3 g/dL, and finally 0.1 g/dL of glucose in Krebs-Ringer solution for 1 h each at 37 °C. The solutions were collected after the 1-h incubation in each glucose concentration, and insulin concentrations were determined in each solution by enzyme-linked immunosorbent assay (ELISA). The ELISA kit for the insulin assay was purchased from Shibayagi, Co., Ltd. (Gunma, Japan).

RESULTS

UK Conjugation on Islet Surfaces through DNA Hybridization. Scheme 1 shows the method for islet surface modification with UK through DNA hybridization using a ssDNA−PEG-lipid conjugate. When the oligo$(dT)_{20}$−PEG-lipid is mixed with islets, the hydrophobic lipid part is spontaneously incorporated into a lipid bilayer of the cell membrane through the hydrophobic interaction.[18,24] The oligo$(dT)_{20}$ segment of the oligo$(dT)_{20}$−PEG-lipid was presented on the cell surface. It can be used for the conjugation of bioactive substances on the cell surface through the hybridization of oligo$(dT)_{20}$−oligo$(dA)_{20}$.

Confocal Fluorescent Microscopic Observation of UK Conjugation on the Islet Surface. Islets were sequentially treated with oligo$(dT)_{20}$−PEG-DPPE or oligo$(dT)_{20}$−PEG-DSPE and oligo$(dA)_{20}$-UK as illustrated in Scheme 1(c). Oligo$(dA)_{20}$-modified UK was conjugated on a cell surface that had been modified with oligo$(dT)_{20}$−PEG-lipid. Figure 1 shows confocal laser-scanning fluorescence images of UK-islets, which were subjected to immunostaining for UK. Fluorescence was clearly observed on the UK-islets (Figure 1(a)). However, very weak fluorescence was observed on unmodified islets or islets treated with oligo$(dA)_{20}$-UK in the absence of oligo$(dT)_{20}$−PEG-lipids due to a nonspecific stain (Figure 1(b)). The conjugation of UK through DNA hybridization was also demonstrated on a gold surface carrying oligo$(dT)_{20}$ by surface plasmon resonance (SPR) measurement (see Figure S1 in Supporting Information). These results indicated that oligo$(dT)_{20}$ groups could be introduced onto the islet surface through the hydrophobic interaction between two long alkyl chains of the oligo$(dT)_{20}$−PEG-DPPE or oligo$(dT)_{20}$−PEG-DSPE and a lipid bilayer of the islet membrane, and oligo$(dA)_{20}$-UK could be conjugated through DNA hybridization onto the islet surface where oligo$(dT)_{20}$−PEG-lipids had been introduced.

The retention time of oligo$(dT)_{20}$−PEG-lipid on the cell membrane depends on the chain lengths of PEG-lipids.[26] Here, oligo$(dT)_{20}$−PEG-DPPE and oligo$(dT)_{20}$−PEG-DSPE with alkyl chains of 16 and 18 ($-CH_2-$) groups, respectively, were employed to determine the effect of chain lengths on the retention time of UK on islets. Oligo$(dA)_{20}$-UK could be conjugated onto the islet surface via oligo$(dT)_{20}$− oligo$(dA)_{20}$ hybridization without damaging islet morphology (Figure 1a). For 2 day cultures after conjugation, fluorescence was still observed for islets treated with oligo$(dT)_{20}$−PEG-DSPE, whereas fluorescence faded for those treated with oligo$(dT)_{20}$−PEG-DPPE. The retention of UK on the islet surface was prolonged with increasing alkyl chain length.

UK Conjugation onto the Islet Surface through DNA Hybridization. UK is a serine protease that activates plasminogen into plasmin, which dissolves fibrin blood clots. UK was

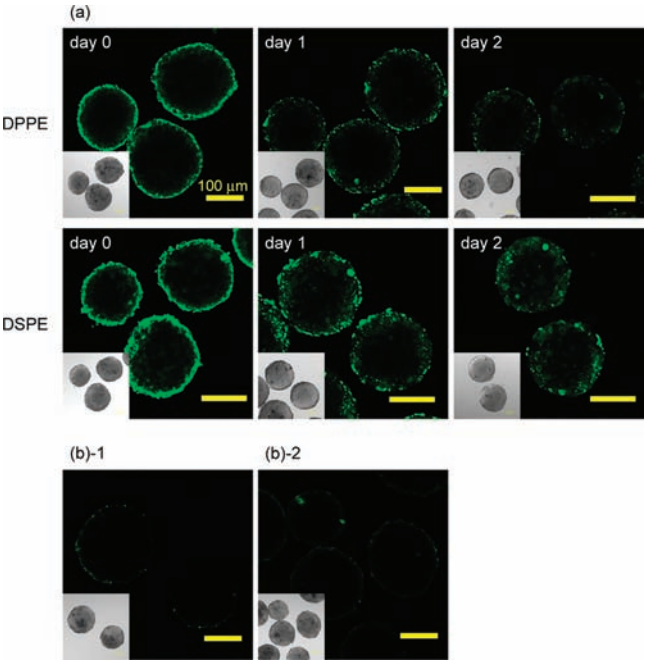


Figure 1. Confocal laser scanning microscopic images of UK-islets which were subjected to immunostaining for UK. (a) Islets were modified with oligo$(dT)_{20}$−PEG-DPPE or oligo$(dT)_{20}$−PEG-DSPE and then oligo$(dA)_{20}$-UK. The UK-islets just after treatment, after 1 and 2 days of culture. ((b)-1) Unmodified islets. ((b)-2) Islets without treatment with oligo$(dT)_{20}$−PEG-lipids. Insets: phase contrast microscopic image. Scale bar: 100 μm.

conjugated onto the surface of islets to dissolve blood clots surrounding islets in the liver for inhibition of the cascade reactions of IBMIR. Islets were treated with oligo$(dT)_{20}$−PEG-lipid (oligo$(dT)_{20}$−PEG-DPPE or oligo$(dT)_{20}$−PEG-DSPE) and then with oligo$(dA)_{20}$-UK as illustrated in Scheme 1(c). A fibrin plate−based assay was performed to assess the function of the UK conjugated on the islets. Fifty islets with/without UK were applied to each spot on a fibrin gel plate, and the area of dissolved fibrin formed around the spotted UK-islets was observed. Figure 2 shows the fibrin plate at 14 h after spotting of the UK-islets. Larger transparent areas were observed around the UK-islets than were seen surround the unmodified islets, as shown in Figure 2a 1, 2, and 4. These indicate that the UK retained its activity after conjugation on the islets. Islets that were cultured for 2 days after UK conjugation were also applied to the fibrin plate for the determination of the retention of UK activity. The transparent areas for the islets carrying UK through oligo$(dT)_{20}$−PEG-DSPE (Figure 2a 5) were slightly larger than that for the islets carrying UK through oligo$(dT)_{20}$−PEG-DPPE (Figure 2a 3). The morphology of all islets after modification with UK was maintained well after 7 days of culture in medium (Figure 2b). These results indicated that the conjugation of UK by DNA hybridization did not deteriorate the islets.

Glucose Stimulation Test of UK-Islets. Static glucose stimulation tests were performed to evaluate the effect of UK conjugation on the insulin-releasing ability of islets. The tests were performed just after UK conjugation or after an additional 2 days of culture. Figure 3 summarizes the results. When the glucose concentration was increased from 0.1 g/dL to 0.3 g/dL, amounts of released insulin increased from basal levels for all groups. Although the amounts of released insulin from UK-islets were less than those from the unmodified islets, the glucose

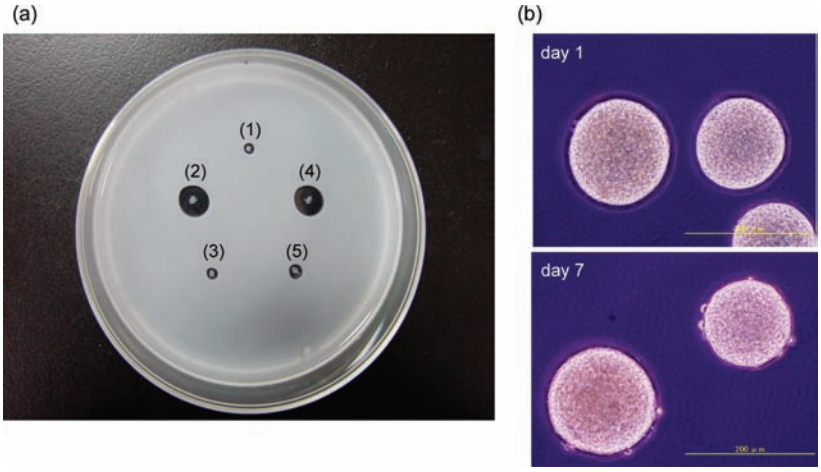


Figure 2. (a) Fibrin plate-based assay for UK-islets. (1) Unmodified islets; (2) UK conjugated on islets through oligo$(dT)_{20}$−PEG-DPPE just after preparation; (3) UK conjugated on islets through oligo$(dT)_{20}$−PEG-DPPE after 2 days of culture; (4) UK conjugated on islets through oligo$(dT)_{20}$−PEG-DSPE just after preparation; and (5) UK conjugated on islets through oligo$(dT)_{20}$−PEG-DSPE after 2 days of culture. Fifty islets were applied to each spot, and the plate was observed after incubation at 37 °C for 14 h. (b) Morphology of UK conjugated islets after 1 and 7 days of culture.

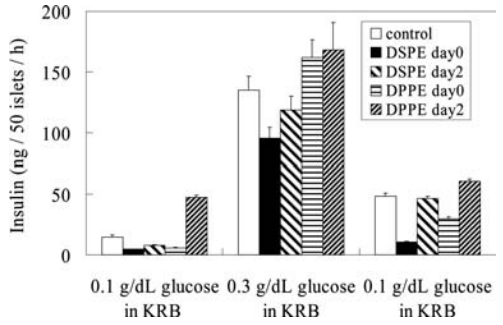


Figure 3. Glucose stimulation test. Bars from the left indicate amounts of insulin release for unmodified islets, UK-islets (oligo$(dT)_{20}$−PEG-DSPE) just after preparation, UK-islets (oligo$(dT)_{20}$−PEG-DSPE) after 2 days of culture, UK-islets (oligo$(dT)_{20}$−PEG-DPPE) just after preparation, and UK-islets (oligo$(dT)_{20}$−PEG-DPPE) after 2 days of culture.

stimulation indices for modified islets were greater than those of the unmodified islets. The amounts of released insulin decreased to basal levels when the islets were re-exposed to low glucose (0.1 g/dL). Although the surface modification with PEG-lipid and UK-conjugation slightly deteriorated the insulin secretion ability of islets, the modified islets controlled insulin release in response to glucose level changes.

DISCUSSION

Some obstacles remain for clinical islet transplantation, including the side effects of immune-suppressive drugs, low efficiency in islet isolation, difficulty of islet preservation, and early graft loss by IBMIR. With early graft loss induced by IBMIR, thrombotic reactions initiate when islets come into direct contact with blood in the portal vein. Blood coagulation triggers successive reactions, such as the inflammatory response, infiltration of leukocytes into islets, disruption of islet integrity, and resulting islet loss.[2−8] Therefore, it has been thought that suppression of blood coagulation would lead to better graft survival. To improve the blood compatibility of islets, the islet surface has been coated with anticoagulants such as heparin and thrombomodulin, or fibrinolytic UK, and the living cells examined.[10−18] Our group has reported some methods to conjugate bioactive substances onto the surface of islets using amphiphilic polymers such as PEG-lipid through hydrophobic interactions.[13−16] PEG-lipid is anchored to the lipid bilayer of the cell membrane through hydrophobic interactions, and the functional group at the other end of the PEG chain can be used for further conjugation of bioactive substances. In one study, we employed the biotin/streptavidin reaction;[14] although this reaction is strong and specific, it is difficult to apply in clinical islet transplantation because of the strong antigenecity of streptavidin, which is derived from bacteria. We also examined the thiol/maleimide reaction in another study[15] and found that the conjugation efficiency requires improvement because thiol groups easily form disulfide bonds under physiological conditions, resulting in low efficiency. We have sought improved methods to overcome these issues.

Further, our group has examined DNA hybridization to immobilize cells onto a surface. In a previous study,[24] oligo$(dT)_{20}$ carrying a thiol group was introduced onto a gold surface, and cells carrying oligo$(dA)_{20}$ were applied to the surface. The cells were locally immobilized on a specific site where oligo$(dT)_{20}$ was introduced. In the current study, we applied this method to conjugate UK on islets. We synthesized amphiphilic polymers, PEG-lipids carrying ssDNA. These were conjugated onto the cell membrane through interactions between the hydrophobic parts of the PEG-lipids and the lipid bilayer, and UK was conjugated on the cell surface through DNA hybridization between oligo$(dT)_{20}$ on the cell and complementary oligo$(dA)_{20}$ on the UK. As shown in Figures 1, 2, and 3, no adverse effect was observed in terms of islet morphology and function. This DNA hybridization is a versatile method for the conjugation of various bioactive substances on the cell surface. ssDNAs rapidly form a complex under physiological conditions, and the complex is biocompatible. Moreover, we expect that several different kinds of substances can be conjugated easily by using different DNA sequences.

The retention time of PEG-lipids on cell membranes depends on the alkyl chain length of lipids, and the retention time of PEG-DSPE on cell membranes is longer than that of PEG-DPPE.[26]

In this study, we expected UK to be retained longer on islets when oligo$(dT)_{20}$−PEG-DSPE was employed compared to when oligo$(dT)_{20}$−PEG-DPPE was employed; however, no clear prolongation was observed in UK activity, as shown in Figure 2a. UK activity disappeared during 4 days of culture in either case because the hydrophobicity of DSPE or DPPE was not great enough for the conjugation of a hydrophilic protein like UK with its high molecular weight (54 kDa).

Thrombosis formation initiates when islets come into direct contact with blood in the portal vein, resulting in early graft loss induced by IBMIR. On the basis of our findings, we expect that islets can be rescued by the conjugation of UK on the islet surface because UK controls thrombosis formation. The efficacy of our UK-islets in inhibiting IBMIR should be carefully examined using *in vivo* models.

CONCLUSIONS

Fibrinolytic UK can be conjugated on the surfaces of islets through DNA hybridization using ssDNA−PEG-lipid. The activity of UK was maintained on the islet surface, and the surface modifications did not influence islet morphology or islet ability to secrete insulin in response to changes in glucose concentration. We expect that UK on islets can inhibit instant blood coagulation-mediated inflammatory reactions, thus suppressing islet graft loss at the early stage of islet transplantation.

ASSOCIATED CONTENT

Supporting Information. SPR profiles for UK conjugation through DNA hybridization are shown in Figure S1. This material is available free of charge via the Internet at http://pubs.acs.org.

AUTHOR INFORMATION

Corresponding Author

*Phone/Fax: +81-75-751-4119. E-mail: iwata@frontier.kyoto-u.ac.jp.

ACKNOWLEDGMENT

This study was supported in part by a Grant-in-Aid for Scientific Research (A) (No. 21240051) and Challenging Exploratory Research (No.21650118) from the Ministry of Education, Culture, Sports, Science, and Technology (MEXT) of Japan and by the Ministry of Health, Labor, and Welfare of Japan (H20-007).

REFERENCES

(1) Shapiro, A. M., Lakey, J. R., Ryan, E. A., Korbutt, G. S., Toth, E., Warnock, G. L., Kneteman, N. M., and Rajotte, R. V. (2000) Islet transplantation in seven patients with type 1 diabetes mellitus using a glucocorticoid-free immunosuppressive regimen. *N. Engl. J. Med. 343*, 230–238.

(2) Ryan, E. A., Lakey, J. R., Rajotte, R. V., Korbutt, G. S., Kin, T., Imes, S., Rabinovitch, A., Elliott, J. F., Bigam, D., Kneteman, N. M., Warnock, G. L., Larsen, I., and Shapiro, A. M. (2001) Clinical outcomes and insulin secretion after islet transplantation with the Edmonton protocol. *Diabetes 50*, 710–719.

(3) Korsgren, O., Lundgren, T., Felldin, M., Foss, A., Isaksson, B., Permert, J., Persson, N. H., Rafael, E., Rydén, M., Salmela, K., Tibell, A., Tufveson, G., and Nilsson, B. (2008) Optimising islet engraftment is critical for successful clinical islet transplantation. *Diabetologia 51*, 227–232.

(4) Johansson, H., Lukinius, A., Moberg, L., Lundgren, T., Berne, C., Foss, A., Felldin, M., Kallen, R., Salmela, K., Tibell, A., Tufveson, G., Ekdahl, K. N., Elgue, G., Korsgren, O., and Nilsson, B. (2005) Tissue factor produced by the endocrine cells of the islets of Langerhans is associated with a negative outcome of clinical islet transplantation. *Diabetes 54*, 1755–1762.

(5) Moberg, L., Johansson, H., Lukinius, A., Berne, C., Foss, A., Kallen, R., Ostraat, O., Salmela, K., Tibell, A., Tufveson, G., Elgue, G., Ekdahl, K., Korsgren, O., and Nilsson, B. (2002) Production of tissue factor by pancreatic islet cells as a trigger of detrimental thrombotic reactions in clinical islet transplantation. *Lancet 360*, 2039–2045.

(6) Contreras, J. L., Eckstein, C., Smyth, C. A., Bilbao, G., Vilatoba, M., Ringland, S. E., Young, C., Thompson, J. A., Fernandez, J. A., Griffin, J. H., and Eckhoff, D. E. (2004) Activated protein C preserves functional islet mass after intraportal transplantation: a novel link between endothelial cell activation, thrombosis, inflammation, and islet cell death. *Diabetes 53*, 2804–2814.

(7) Bennet, W., Sundberg, B., Lundgren, T., Tibell, A., Groth, C. G., Richards, A., White, D. J., Elgue, G., Larsson, R., Nilsson, B., and Korsgren, O. (2000) Damage to porcine islets of Langerhans after exposure to human blood in vitro, or after intraportal transplantation to cynomologus monkeys: protective effects of sCR1 and heparin. *Transplantation 69*, 711–719.

(8) Bennet, W., Sundberg, B., Groth, C. G., Brendel, M. D., Brandhorst, D., Brandhorst, H., Bretzel, R. G., Elgue, G., Larsson, R., Nilsson, B., and Korsgren, O. (1999) Incompatibility between human blood and isolated islets of Langerhans: a finding with implications for clinical intraportal islet transplantation?. *Diabetes 48*, 1907–1914.

(9) Eich, T., Eriksson, O., Sundin, A., Estrada, S., Brandhorst, D., Brandhorst, H., Langstrom, B., Nilsson, B., Korsgren, O., and Lundgren, T. (2007) Positron emission tomography: a real-time tool to quantify early islet engraftment in a preclinical large animal model. *Transplantation 84*, 893–898.

(10) Cabric, S., Sanchez, J., Lundgren, T., Foss, A., Felldin, M., Kallen, R., Salmela, K., Tibell, A., Tufveson, G., Larsson, R., Korsgren, O., and Nilsson, B. (2007) Islet surface heparinization prevents the instant blood-mediated inflammatory reaction in islet transplantation. *Diabetes 56*, 2008–2015.

(11) Stabler, C. L., Sun, X. L., Cui, W., Wilson, J. T., Haller, C. A., and Chaikof, E. L. (2007) Surface Re-engineering of Pancreatic Islets with Recombinant azido-Thrombomodulin. *Bioconjugate Chem. 18*, 1713–1715.

(12) Johansson, U., Elgue, G., Nilsson, B., and Korsgren, O. (2005) Composite islet-endothelial cell grafts: a novel approach to counteract innate immunity in islet transplantation. *Am. J. Transplant. 5*, 2632–2639.

(13) Teramura, Y., and Iwata, H. (2010) Bioartificial pancreas microencapsulation and conformal coating of islet of Langerhans. *Adv. Drug Delivery Rev. 62*, 825–838.

(14) Teramura, Y., and Iwata, H. (2008) Islets surface modification prevents blood-mediated inflammatory responses. *Bioconjugate Chem. 19*, 1389–1395.

(15) Totani, T., Teramura, Y., and Iwata, H. (2008) Immobilization of urokinase to islet surface by amphiphilic poly (vinyl alcohol) carrying alkyl side chains. *Biomaterials 29*, 2878–2883.

(16) Teramura, Y., and Iwata, H. (2009) Islet encapsulation with living cells for improvement of biocompatibility. *Biomaterials 30*, 2270–2275.

(17) Teramura, Y., and Iwata, H. (2009) Surface modification of islets with PEG-lipid for improvement of graft survival in intraportal transplantation. *Transplantation 88*, 624–630.

(18) Teramura, Y., Minh, L. N., Kawamoto, T., and Iwata, H. (2010) Microencapsulation of islets with living cells using polyDNA-PEG-lipid conjugate. *Bioconjugate Chem. 21*, 792–796.

(19) Tausig, F., and Wolf, F. J. (1964) Streptavidin: A substance with avidin-like properties produced by microorganisms. *Biochem. Biophys. Res. Commun. 14*, 205–209.

(20) Meyer, D. L., Schultz, J., Lin, Y., Henry, A., Sanderson, J., Jackson, J. M., Goshorn, S., Rees, A. R., and Graves, S. S. (2001) Reduced antibody response to streptavidin through site-directed mutagenesis. *Protein Sci. 10*, 491–503.

(21) Miura, S., Teramura, Y., and Iwata, H. (2006) Encapsulation of islets with ultra-thin polyion complex membrane through poly(ethylene glycol)-phospholipids anchored to cell membrane. *Biomaterials 27*, 5828–5835.

(22) Teramura, Y., Kaneda, Y., and Iwata, H. (2007) Islet-encapsulation in ultra-thin layer-by-layer membranes of poly(vinyl alcohol) anchored to poly(ethylene glycol)-lipids in the cell membrane. *Biomaterials 28*, 4818–4825.

(23) Teramura, Y., Kaneda, Y., Totani, T., and Iwata, H. (2008) Behavior of Synthetic Polymers Immobilized on Cell Membrane. *Biomaterials 29*, 1345–1355.

(24) Teramura, Y., Chen, H., Kawamoto, T., and Iwata, H. (2010) Control of cell attachment through polyDNA hybridization. *Biomaterials 31*, 2229–2235.

(25) Teramura, Y., and Iwata, H. (2010) Cell surface modification with polymers for biomedical studies. *Soft Matter 6*, 1081–1091.

(26) Inui, O., Teramura, Y., and Iwata, H. (2010) Retention dynamics of amphiphilic polymers PEG-lipids and PVA-Alkyl on the cell surface. *ACS Appl. Mater. Interfaces 2*, 1514–1520.

(27) Iwata, H., Kobayashi, K., Takagi, T., Oka, T., Yang, H., Amemiya, H., Tsuji, T., and Ito, F. (1994) Feasibility of agarose microbeads with xenogeneic islets as a bioartificial pancreas. *J. Biomed. Mater. Res. 28*, 1003–1011.

(28) Gossage, J. A., Humphries, J., Modarai, B., Burnand, K. G., and Smith, A. (2006) Adenoviral urokinase-type plasminogen activator (uPA) gene transfer enhances venous thrombus resolution. *J. Vasc. Surg. 44*, 1085–1090.

SUPPORTING INFORMATION

Islet surface modification with urokinase through DNA hybridization

Naohiro Takemoto[a], Yuji Teramura[b], Hiroo Iwata[a]*

[a]Department of Reparative Materials, Institute for Frontier Medical Sciences, Kyoto University, 53 Kawara-Cho, Shogoin, Sakyo-Ku, Kyoto, 606-8507, Japan
[b]Radioisotope Research Center, Kyoto University, Yoshida-Konoe-Cho, Sakyo-ku, Kyoto, 606-8501, Japan
* Address correspondence and reprint requests to Hiroo Iwata, Ph.D.
E-mail: iwata@frontier.kyoto-u.ac.jp, PHONE/FAX: +81-75-751-4119

Surface plasmon resonance analyses of UK immobilization through DNA hybridization. To examine the conjugation of urokinase through DNA hybridization, an in-house–designed surface plasmon resonance (SPR) instrument (*1*) was used for monitoring the reaction. Gold-coated BK-7 glass plates (refractive index: 1.515, size: 25 × 25 × 1 mm, Arteglass Associates Co., Kyoto, Japan) were immersed in a solution of oligo$(dT)_{20}$-SH (50 μg/mL in PBS) for 24 h to conjugate oligo$(dT)_{20}$ onto the gold surface through Au/thiol bonding. The glass plates were washed thoroughly with pure water and 2-propanol sequentially. Each glass plate was set in the SPR flow cell, and a blocking solution of BSA (10 mg/mL in PBS) flowed onto the surface, followed by flowing of a solution of oligo$(dA)_{20}$-UK (5 μg/mL in PBS). In a control experiment, a solution of oligo$(dT)_{20}$-UK (5 μg/mL in PBS) was applied after flowing of blocking solution. The sample solutions and PBS were allowed to circulate through the flow cell at 4.0 mL/min, and all SPR measurements were performed at 37 °C.

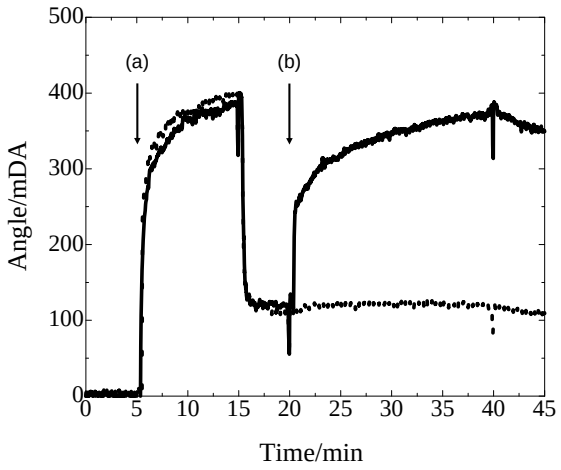


Figure S1. Surface plasmon resonance sensorigrams of interaction between oligo$(dA)_{20}$-UK and the oligo$(dT)_{20}$-incorporated surface. After a BSA solution was applied to block non-specific sites on the oligo$(dT)_{20}$-incorporated substrate (a), oligo$(dA)_{20}$-UK (solid line) or oligo$(dT)_{20}$-UK (dotted line) was allowed to flow (b).

The SPR method, which serves to monitor events on the gold surface, was employed to examine binding and stability of proteins through the DNA hybridization between oligo$(dA)_{20}$-modified proteins and oligo$(dT)_{20}$ on the gold thin layer in real time. Figure S1 shows the SPR profiles for interactions between oligo$(dA)_{20}$-UK or oligo$(dT)_{20}$-UK and oligo$(dT)_{20}$ on the substrate. The initial increases in the SPR profiles show conjugation of oligo$(dT)_{20}$-SH on the gold surface by the Au/thiol reaction. The surface was blocked by a BSA solution for 10 min before the addition of a oligo$(dA)_{20}$-UK or oligo$(dT)_{20}$-UK solution. The second increase in the solid line of Figure S1 shows the binding of oligo$(dA)_{20}$-UK onto the oligo$(dT)_{20}$ substrate, whereas no such increase was observed when oligo$(dT)_{20}$-UK was applied to the oligo$(dT)_{20}$ substrate, as shown by the dashed line in Figure S1. These results show that UK could be specifically conjugated on the surface through hybridization between oligo$(dA)_{20}$ on UK and oligo$(dT)_{20}$ on the surface. In addition, oligo$(dA)_{20}$-UK can be conjugated onto a cell surface modified with a oligo$(dT)_{20}$–PEG-lipid conjugate through DNA hybridization.

(1) Hirata, I., Morimoto, Y., Murakami, Y., Iwata, H., Kitano, E., and Kitamura, H. (2000) Study of complement activation on well-defined surfaces using surface plasmon resonance. *Colloids Surf B. 18*, 285–292.

Bioconjugate Chemistry

ARTICLE

pubs.acs.org/bc

Design, Synthesis, and Biological Functionality of a Dendrimer-Based Modular Drug Delivery Platform

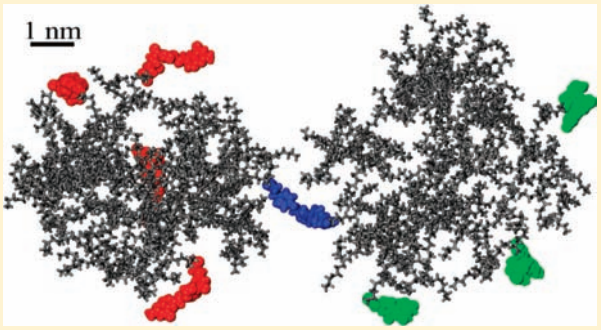
Douglas G. Mullen,[†,‡] Daniel Q. McNerny,[‡,⊥] Ankur Desai,[‡] Xue-min Cheng,[‡] Stassi C. DiMaggio,[§] Alina Kotlyar,[‡] Yueyang Zhong,[‡,#] Suyang Qin,[‡] Christopher V. Kelly,[‡,∥] Thommey P. Thomas,[‡] Istvan Majoros,[‡] Bradford G. Orr,[‡,∥] James R. Baker, Jr.,[‡] and Mark M. Banaszak Holl*[,†,‡,∥,#]

[†]Programs in Macromolecular Science and Engineering and [∥]Applied Physics, [#]Departments of Chemistry and [⊥]Chemical Engineering, [‡]Michigan Nanotechnology Institute for Medicine and Biological Sciences, University of Michigan, Ann Arbor, Michigan 48019, United States

[§]Department of Chemistry, Xavier University, New Orleans, Louisiana 70125, United States

Supporting Information

ABSTRACT: A modular dendrimer-based drug delivery platform was designed to improve upon existing limitations in single dendrimer systems. Using this modular strategy, a biologically active platform containing receptor mediated targeting and fluorescence imaging modules was synthesized by coupling a folic acid (FA) conjugated dendrimer with a fluorescein isothiocyanate (FITC) conjugated dendrimer. The two different dendrimer modules were coupled via the 1,3-dipolar cycloaddition reaction ("click" chemistry) between an alkyne moiety on the surface of the first dendrimer and an azide moiety on the second dendrimer. Two simplified model systems were also synthesized to develop appropriate "click" reaction conditions and aid in spectroscopic assignments. Conjugates were characterized by ^{1}H NMR spectroscopy and NOESY. The FA-FITC modular platform was evaluated *in vitro* with a human epithelial cancer cell line (KB) and found to specifically target the overexpressed folic acid receptor.



INTRODUCTION

The high toxicity of conventional cytotoxic anticancer drugs often forces these agents to be given at suboptimal dosages, and this can result in treatment failure.[1] To resolve this problem, delivery platforms that can discriminate between healthy and malignant cells have been developed.[1,2] Actively targeted therapeutic delivery platforms consist of three different components: a targeting component comprising targeting ligands with affinities for molecules expressed on cancer cells; a payload consisting of drug and/or imaging agents; and a nanoscale structure to which the targeting and payload moieties are attached. This platform targeting of anticancer drugs with cancer cell-specific ligands can dramatically improve a drug's therapeutic index. Conjugating multiple targeting ligands to a single platform molecule further increases the potential for specific targeting of cancer cells by allowing the possibility of multivalent interactions.[3,4]

The structural design of these types of delivery platforms is critical to the success of the delivery device. Numerous classes of targeted drug delivery platforms have been developed that potentially meet the requirements needed to combine targeting ligands, imaging agents, and drug molecules together to deliver the therapeutic payload to a desired location in the body. These include drug-target conjugates, linear polymers, lipid-based carriers (liposomes and micelles), carbon nanotubes, inorganic nanoparticles, and dendrimers. Several of these different delivery platforms are progressing toward or through clinical trials for cancer treatments with promising results.[2] Each approach, however, is not without limitations and the potential for widespread application of these platforms in their present design is unclear.

Dendrimer-based platforms have a unique branching structure which results in exceptionally high degrees of monodispersity and well-defined terminal groups that provide the ability to form soluble conjugates containing multiple copies of hydrophobic drug and/or targeting molecules. The compact, branched structures appear to enhance the ability of the targeting molecules to interact in a fashion conducive to multivalent binding to cell membrane receptors.[3] The dendrimer's small size enables efficient diffusion across the vascular endothelium to find tumors and also allows the rapid clearance of these molecules from the bloodstream. This clearance avoids potential long-term toxicities and reduces the necessity of a rapidly degradable platform. The most widely used dendrimer in biomedical applications, poly(amidoamine) (PAMAM), is nonimunogenetic and nontoxic once the surface primary amines have been modified.[5−10] There have been numerous, recent examples describing the development of dendrimer-based targeted

Received: October 15, 2010
Revised: February 3, 2011
Published: March 22, 2011

ACS Publications © 2011 American Chemical Society

delivery systems using a wide variety of targeting ligands including monoclonal antibodies,[11−15] peptides,[16] T-antigens,[17−19] and folic acid.[20−29]

Despite the success of these dendrimer-based platforms, this approach has several challenges associated with its implementation. First, the synthesis of dendrimers with different functional groups for targeted delivery (including targeting, drug, and imaging agents) requires a laborious chemical process that is unique for each different molecular combination. Second, the carrying capacity of a single dendrimer, although significantly better than other types of delivery platforms, is finite due to limits in surface molecule density and solubility. This becomes a problem when one attempts to conjugate multiple copies of the target, drug, and/or dye molecules to the same dendrimer. Third, significant increases in heterogeneity occur with the conjugation of each additional molecule to a single dendrimer platform due to the stochastic nature of these chemical reactions.[30] This has limited the flexibility of these systems.

To address the drawbacks of the single dendrimer platforms, several groups have sought to apply modular design concepts to dendrimer systems.[31−41] The common premise of this new approach is to use dendrimers or dendrons as modular units, each with multiple copies of a single functional molecule. Multifunctional platforms can be generated by combining different modules through a universal coupling mechanism. The main benefits of this design are twofold: First, segregating each functional group (drug/target/dye) to a different dendrimer module avoids the need to develop a new orthogonal coupling chemistry for each new combination of functional groups. This advantage should not be underestimated. Significant time is spent developing new orthogonal coupling strategies for desired functional combinations because many of the component drug molecules and targeting ligands (Taxol and RGD, for example) are susceptible to a loss of activity due to undesired cross reactions as well as degradation by hydrolysis. The second benefit of the modular strategy is a greater carrying capacity of the delivery platform, because the different functional molecules are localized on separate dendrimer units and the water solubilizing dendrimer backbone is effectively double the mass of the single dendrimer.

In the modular dendrimer systems synthesized to date, two coupling strategies have been used to combine different dendrimer-based modules together: oligonucleotide self-assembly and the 1,3-dipolar cycloaddition between an azide and an alkyne, commonly called "click" chemistry. Oligonucleotide self-assembly has been used to link both dendron and dendrimer modular units. Choi and co-workers demonstrated this strategy by using two complementary oligonucleotides to link two PAMAM dendrimers together.[31,32] DeMattie, Huang, and Tomalia used the same method to connect two unfunctionalized PAMAM dendrons together.[33] Characterization of these systems was accomplished by gel electrophoresis, AFM, MALDI, and UV/vis due to the small synthetic scales employed. For the dendrimer-based system, isolated dendrimer samples were not obtained; rather, the samples were generated in solution. Choi et al. did demonstrate biological functionality of the modular system in a cell culture assay[32] and an *in vivo* model.[34]

The use of "click" chemistry to create dendritic modular systems has mainly involved dendrons. "Click" chemistry is a particularly attractive coupling method because it can be performed with a wide variety of solvent conditions including aqueous environments. The stable triazole ring bridge, resulting from coupling alkyne with azide moieties, is frequently achieved at near quantitative yields and is considered to be biologically stable.[42−44] Furthermore, the "click" coupling chemistry is orthogonal to the coupling chemistries typically used to attach functional groups to the dendrimer. Lee and co-workers have detailed the synthesis of multimodule platforms using both unfunctionalized PAMAM dendrons[35−37] and unfunctionalized Frechet-type dendrons[38] for each of the modules. In all of these systems, the focal point of the dendron possessed either an azide or alkyne moiety. Wu and co-workers developed a 2,2-bis-(hydroxymethyl)propionic acid (bis-MPA) based asymmetric modular dendron with 16 mannose units and 2 coumarin chromophores, and demonstrated binding in a hemagglutination assay.[39] Goyal, Yoon, and Weck have also developed a poly(amine) dendrimer that possessed a single aldehyde or azide moiety on the dendrimer periphery capable of orthogonal functionalization by small molecule functional groups.[40,41] These approaches appear promising, but only the bis-MPA dendron system has been demonstrated to have function as a targeted drug delivery platform. In all cases, the dendrons used were G3 or smaller. This has significant limitations for widespread therapeutic use because of the limited carrying capacity of low generation dendrons. To date, click chemistry has not been applied to a modular dendrimer system.

In this paper, we report on a new modular approach based upon "clicking" together generation 5 (G5) PAMAM dendrimers containing either the targeting agent folic acid (FA) (**13**) or the dye fluorescein isothiocyanate (FITC) (**14**). The molecules were characterized by ^{1}H NMR spectroscopy and two-dimensional Nuclear Overhauser Effect Spectroscopy (NOESY). To the best of our knowledge, this is the first example of the successful "click" chemistry conjugation of dendrimers (as opposed to dendrons). Linking together two dendrimer-based modules was achieved by first conjugating one dendrimer module to an alkyne linker (**2b**) and conjugating a second dendrimer module to an azide linker (**3c**). The ability of this modular system to specifically target folic acid receptor (FAR) expressing cells has been verified by flow cytometric documentation of the uptake of the clicked FA-FITC modules into KB cells.

This dendrimer-based modular system has several potential benefits over predecessor systems. In using "click" chemistry rather than oligonucleotide linking, the modular system can be scaled up with far greater ease and at a substantially lower cost. Oligonucleotides are typically purchased in nanogram quantities, whereas the "click" linkers in this study were produced at the gram scale. Additionally, because the clicked dendrimers are covalently linked rather than joined via the hydrogen bond base-pairing oligonucleotide bridge, the platform is less likely to become unlinked. This characteristic proves beneficial when attempting to isolate and characterize multimodule platforms. In using generation 5 dendrimers with diameters of approximately 5 nm and over 630 hydrogen bonding sites, the carrying capacity is substantially greater than the previously used dendrons, which were approximately 2 nm in diameter and possess approximately 150 hydrogen bonding sites. In fact, efforts in our group to generate G2 and G3 PAMAM dendrons functionalized with folic acid, failed due to a loss of platform solubility.

EXPERIMENTAL PROCEDURES

Reagents and Materials. Biomedical grade, generation 5 PAMAM (poly(amidoamine)) dendrimer was purchased from Dendritech Inc. and purified by dialysis, as previously described,[30] to remove lower molecular weight impurities including trailing generation dendrimer defect structures.

MeOH (99.8%), acetic anhydride (99.5%), triethylamine (99.5%), dimethyl sulfoxide (99.9%), fluorescein isothiocyanate (98%), dimethylformamide (99.8%), 1-[3-(dimethylamino)-propyl-3-ethylcarbodiimide HCl (EDC) (98%), acetone (ACS reagent

grade ≥99.5%), methyl 3-(4-hydroxyphenyl)propanoate (97%), sodium azide (99.99%), 1-bromo-2-chloroethane (98%), ethyl acetate (EtOAc) (99.5%), copper sulfate pentahydrate (99%), sodium ascorbate, 18-crown-6, K_2CO_3, tetrahydrofuran (99.9%), *N*,*N*-diisopropylethylamine, benzotriazol-1-yl-oxytripyrrolidinophosphonium hexafluorophosphate (98%), D_2O, NaCl, 1 N HCl, 2 M KOH, and volumetric solutions (0.1 M HCl and 0.1 M NaOH) for potentiometric titration were purchased from Sigma Aldrich Co. and used as received. Hexanes (HPLC grade) and 10 000 molecular weight cutoff centrifugal filters (Amicon Ultra) were from Fisher Scientific. 1× phosphate buffer saline (PBS) (Ph = 7.4) without calcium or magnesium was purchased from Invitrogen. Sephadex G-25 and Sephadex LH-20 were purchased from GE Lifesciences.

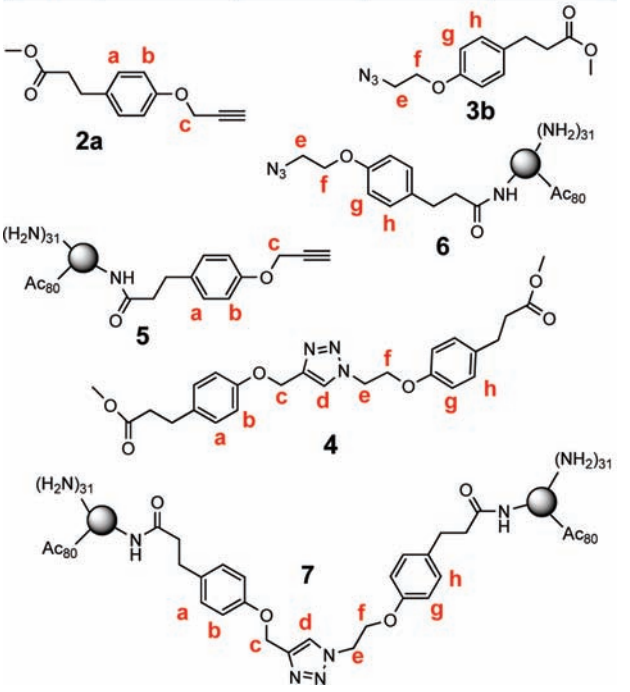
Nuclear Magnetic Resonance Spectroscopy. All ^{1}H NMR experiments were conducted using a Varian Inova 500 MHz instrument. For all dendrimer samples, the delay time was 10s. No delay time was used for small molecule samples. NOESY experiments on the dendrimer samples found in Figure 1 and utilized for Table 1 were also conducted using a Varian Inova 500 MHz instrument. For these experiments, the mixing time was 250 ms, the relaxation time was 1 s, and the number of increments was 128 with 32 scans per increment. Temperature was controlled at 25 °C. The NOESY experiments on the small molecule model system found in Figure 1 and utilized in Table 1 were conducted using a Varian MR400 (400 MHz) instrument. For the experiments on the small molecules, the mixing time was 800 ms, the relaxation time was 1.2 s, and the number of increments was 200 with 4 scans per increment. On the basis of work published by Hoffman, the internal solvent reference peak for all experiments in $CDCl_3$ was set to 7.26 ppm. For experiments conducted in D_2O, the internal reference peak was set to 4.72 ppm.[45]

Gel Permeation Chromatography. GPC experiments were performed on an Alliance Waters 2690 separation module equipped with a 2487 dual wavelength UV absorbance detector (Waters Corporation), a Wyatt Dawn DSP laser photometer, and an Optilab DSP interferometric refractometer (Wyatt Technology Corporation). Columns employed were TosoHaas TSK-Gel Guard PHW 06762 (75 mm × 7.5 mm, 12 μm), G 2000 PW 05761 (300 mm × 7.5 mm, 10 μm), G 3000 PW 05762 (300 mm × 7.5 mm, 10 μm), and G 4000 PW (300 mm × 7.5 mm, 17 μm). Column temperature was maintained at 25 ± 0.1 °C with a Waters temperature control module. The isocratic mobile phase was 0.1 M citric acid and 0.025 wt % sodium azide, pH 2.74, at a flow rate of 1 mL/min. The sample concentration was 10 mg/5 mL with an injection volume of 100 μL. The weight average molecular weight, M_w, was determined by GPC, and the number average molecular weight, M_n, was calculated with *Astra 4.7* software (Wyatt Technology Corporation) based on the molecular weight distribution.

Reverse Phase High Performance Liquid Chromatography. HPLC analysis was carried out on a Waters Delta 600 HPLC system equipped with a Waters 2996 photodiode array detector, a Waters 717 Plus auto sampler, and Waters Fraction collector III. The instrument was controlled by *Empower 2* software. For analysis of the conjugates, a C5 silica-based RP-HPLC column (250 × 4.6 mm, 300 Å) connected to a C5 guard column (4 × 3 mm) was used. The mobile phase for elution of the conjugates was a linear gradient beginning with 90:10 (v/v) water/acetonitrile and ending with 10:90 (v/v) water/acetonitrile over 25 min at a flow rate of 1 mL/min. Trifluoroacetic acid (TFA) at 0.14 wt % concentration in water as well as in acetonitrile was used as a counterion.

Table 1. Good Correlation is Found between the Small Molecule Model System (2a, 3b, and 4) and the Dendrimer Model System (5, 6, and 7) for the Chemical Shifts (ppm) of Triazole Related Protons (a−h) both before and after the "Click" Reaction[a]

	Compound			
	Before Reaction		After Reaction	
Proton	2a and 3b	5 and 6	4	7
a	7.14	7.13	7.11	7.09
b	6.91	6.90	6.91	6.90
c	4.67	4.69	5.19	5.15
d	n.a.	n.a.	7.80	--
e	3.58	3.61	4.75	4.76
f	4.13	4.13	4.33	4.35
g	6.85	6.90	6.78	6.74
h	7.13	7.13	7.11	7.06



[a] Chemical shifts for protons in the model dendrimer system were detected primarily via NOESY experiments.

Cell Culture and Treatment. The uptake of the synthesized conjugates was performed using FA-receptor-expressing KB cells (ATCC #CCL-17) as we have described previously.[23] Cells were maintained in FA-free Roswell Park Memorial Institute-1640 (RPMI 1640) medium supplemented with 10% fetal bovine serum (FBS), 2 μM L-glutamine, 100 U/mL penicillin, and 100 μg/mL streptomycin in 5% CO_2 at 37 °C. Cells were planted into 24 well plates at density of 250 000 per well and allowed to reach ~90% confluence on the day of the experiment. They were rinsed and incubated in serum free medium with conjugates for 1 h at 37 °C in 5% CO_2. In some wells, a 20-fold excess of free folic acid or the folic acid conjugated dendrimer was added 30 min prior to the addition of the dendrimer platform for the blocking of folate receptors.

Flow Cytometric Analysis. The cellular fluorescence was quantified on a Beckman-Coulter EPICS-XL MCL flow cytometer, and the data were analyzed using *Expo32* software (Beckman-Coulter,

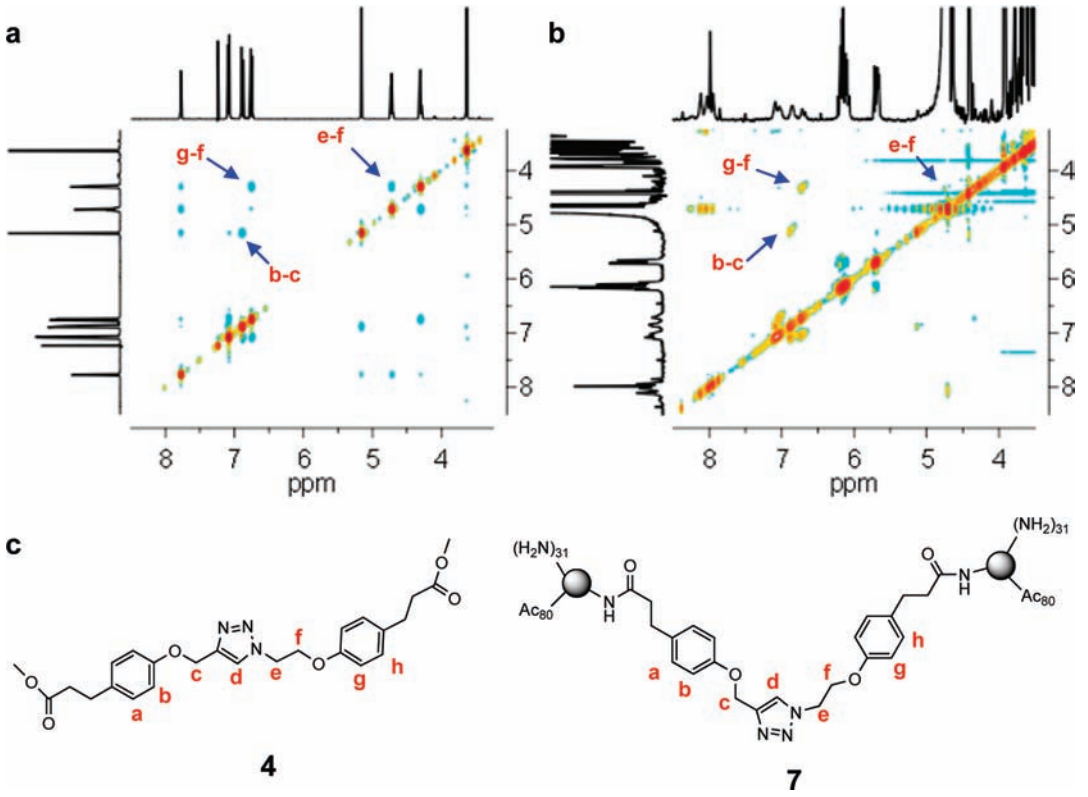


Figure 1. (a) NOESY of the small-molecule model system after the "click" reaction (**4**). NOE cross-peaks between triazole related protons (b, c, e, f, and g) are labeled. (b) NOESY of the model dendrimer system after the "click" reaction (**7**). NOE cross-peaks for the triazole related protons are similarly labeled. The cross-peaks in the 2D spectra reveal proton chemical shifts for the several of the triazole related protons that are otherwise obscured by overlapping dendrimer peaks. (c) Chemical structure and proton labels for the clicked small molecule model system (**4**) and the clicked dendrimer model system (**7**). The G5 PAMAM dendrimer is represented by a gray sphere.

Miami, FL). Cells were trypsinized, rinsed, and suspended in PBS containing 0.1% bovine serum albumin (PBSB). The viable cells were gated, and the mean FL1-fluorescence of 10 000 cells was quantified. Error bars are calculated using the half-peak coefficient of variation (HPCV).[46]

Synthesis. Dendrimers are identified by the core dendrimer (G5) and conjugated groups: Ac, Alkyne, Azide, FA, and FITC. In the cases where dendrimers are linked together via the triazole ring, alkyne and azide labels are replaced with "L." Ac refers to the acetamide termination, alkyne to linker **2b**, azide to linker **3c**, FA to folic acid, and FITC to fluorescein isothiocyanate.

Synthesis of Partially Acetylated Dendrimer ***1***. Partial acetylation of G5 PAMAM dendrimer was previously described.[5,30] The number average molecular weight (27 336 g/mol) and PDI (1.018) of the unacetylated dendrimer was determined by GPC. Potentiometric titration was conducted to determine the average number of primary amines per dendrimer (112 ± 5). Three batches of partially acetylated dendrimer were synthesized for further modification. **1′ G5Ac$_{72\%}$**: ^{1}H NMR integration determined the degree of acetylation to be 72%. Number average molecular weight (30 722 g/mol) was computed based on the addition of mass to the dendrimer from the acetyl groups as determined by NMR. PDI (1.019) of the purified acetylated dendrimer was determined by GPC. **1″ G5Ac$_{65\%}$**: ^{1}H NMR integration determined the degree of acetylation to be 65%. Number average molecular weight (30 394 g/mol) was computed based on the addition of mass to the dendrimer from the acetyl groups as determined by NMR. PDI (1.060) of the purified acetylated dendrimer was determined by GPC. **1‴ G5Ac$_{67\%}$**: ^{1}H NMR integration determined the degree of acetylation to be 67%. Number average molecular weight (30 473 g/mol) was computed based on the addition of mass to the dendrimer from the acetyl groups as determined by NMR. **1⁗ G5Ac$_{58\%}$**: ^{1}H NMR integration determined the degree of acetylation to be 58%. Number average molecular weight (30 064 g/mol) was computed based on the addition of mass to the dendrimer from the acetyl groups as determined by NMR. **1⁗′ G5Ac$_{68.8\%}$**: ^{1}H NMR integration determined the degree of acetylation to be 69%. Number average molecular weight (30 572 g/mol) was computed based on the addition of mass to the dendrimer from the acetyl groups as determined by NMR. **1⁗″ G5Ac$_{64\%}$**: ^{1}H NMR integration determined the degree of acetylation to be 64%. Number average molecular weight (30 347 g/mol) was computed based on the addition of mass to the dendrimer from the acetyl groups as determined by NMR.

Synthesis of Alkyne Linker (3-(4-(Prop-2-ynyloxy)phenyl)-propanoic Acid) ***2***. Synthesis of methyl 3-(4-(prop-2-ynyloxy)-phenyl)propanoate **2a** has been previously reported.[30] Synthesis of (3-(4-(prop-2-ynyloxy)phenyl)propanoic acid) **2b** has also been previously reported.[30]

Synthesis of Azide Linker (3-(4-(2-Azidoethoxy)phenyl)-propanoic Acid) ***3***. To a solution of methyl 3-(4-hydroxyphenyl)propanoate (1.699 g, 9.43 mmol) in dry acetone (47.5 mL) was added anhydrous K_2CO_3 (3.909 g, 0.0283 mol) followed by 1-bromo-2-chloroethane (1.56 mL, 0.0189 mol). The resulting suspension was refluxed for 43 h with vigorous stirring. The reaction mixture was cooled to room temperature and the salt was removed by filtration followed by washing with portions of

EtOAc (3 × 70 mL). The crude material was purified by silica chromatography (25:75 EtOAc/Hexane) and the solvent was removed under vacuum to give the desired product, methyl 3-(4-(2-chloroethoxy)phenyl)propanoate **3a**, as an oil (0.75 g, 33%). ^{1}H NMR (500 MHz, $CDCl_3$) δ 7.12 (d, J = 8.7, 2H), 6.84 (d, J = 8.7, 2H), 4.21 (t, J = 5.9, 2H), 3.80 (t, J = 5.9, 2H), 3.66 (s, 3H), 2.90 (t, J = 7.8, 2H), 2.60 (t, J = 7.8, 2H).

To a solution of methyl 3-(4-(2-chloroethoxy)phenyl)propanoate **3a** (0.75 g 3.1 mmol) in anhydrous DMF (6.1 mL) was added 18-crown-6 (3.4 mg, 0.013 mmol) and sodium azide (0.44 g, 6.8 mmol). The resulting solution was heated at 78 °C for 11 h. The reaction mixture was cooled to room temperature, diluted with ethyl acetate (50 mL), washed with a saturated $NaHCO_3$ solution (4 × 70 mL), and then dried over $MgSO_4$. The solvent was removed under vacuum to give methyl 3-(4-(2-azidoethoxy)-phenyl)propanoate **3b** as a yellow oil (0.58 g, 75%) ^{1}H NMR (500 MHz, $CDCl_3$) δ 7.12 (d, J = 8.6, 2H), 6.85 (d, J = 8.6, 2H), 4.13 (t, J = 5.0 2H), 3.67 (s, 3H), 3.58 (t, J = 5.0, 2H), 2.90 (t, J = 7.8, 2H), 2.60 (t, J = 7.8, 2H).

To a solution of methyl 3-(4-(2-azidoethoxy)phenyl)propanoate **3b** (3.88 g, 0.0156 mol) in methanol (102 mL) was added potassium hydroxide (2 M, 28.3 mL, 0.0566 mol). The resulting solution was refluxed at 70 °C for 3 h. The solution was cooled to room temperature and condensed under reduced pressure. The residue was dissolved in water (30 mL) and was acidified by addition of 1 N HCl to pH 1. The white cloudy solution was diluted with EtOAc. Layers were separated and the aqueous layer was extracted with EtOAc (2 × 70 mL). The combined organic extracts were washed with a saturated NaCl solution and dried over $MgSO_4$. Solvent was evaporated under vacuum to give the (3-(4-(2-azidoethoxy)phenyl)propanoic acid) **3c** as a white solid (3.44 g, 94%). ^{1}H NMR (500 MHz, $CDCl_3$) δ 7.14 (d, J = 8.5, 2H), 6.86 (d, J = 8.5, 2H), 4.13 (t, J = 5.0 2H), 3.58 (t, J = 5.0, 2H), 2.91 (t, J = 7.7, 2H), 2.65 (t, J = 7.7, 2H).

Synthesis of Small Molecule Model System ***4***. The methyl ester forms of the alkyne linker **2a** (448.0 mg, 1.80 mmol) and azide linker **3b** (371.5 mg, 1.70 mmol) were dissolved in a mixture of THF (1.6 mL) and water (0.4 mL). To this mixture was added copper sulfate pentahydrate (43.1 mg, 86.0 μmol) and sodium ascorbate (170.9 mg, 431 μmol). The resulting reaction mixture was stirred at room temperature for 24 h. The solution was then diluted in EtOAc (60 mL) and water (60 mL). Layers were separated, and the aqueous layer was extracted twice with EtOAc solution (2 × 70 mL). The combined organic extracts were washed with a saturated $NaHCO_3$ solution (3 × 70 mL) and then with saturated NaCl solution (2 × 70 mL). The organic extracts were finally dried over $MgSO_4$. Solvent was evaporated under reduced pressure to give the desired product **4** as a white solid (0.54 g, 95%). ^{1}H NMR (500 MHz, $CDCl_3$) δ 7.80 (s, 1H), 7.108 (overlapping d, J = 8.4, 4H), 6.91 (d, J = 8.6, 2H), 6.78 (d, J = 8.6, 2H), 5.18 (s, 2H), 4.75 (t, J = 5.0, 2H), 4.33 (t, J = 5.0, 2H), 3.66 (s, 3H), 3.657 (s, 3H), 2.890 (t, J = 7.8, 2H), 2.88 (t, J = 7.7, 2H), 2.59 (t, J = 7.8, 2H), 2.59 (t, J = 7.7, 2H).

Synthesis of G5-Ac$_{72\%}$-Alkyne$_{1.4}$ ***5***. A solution of partially acetylated dendrimer **1′** (54.6 mg, 1.78 μmol) was prepared with anhydrous DMSO (12.133 mL). The alkyne linker **2b** (0.9 mg, 4.4 μmol) was dissolved in DMSO (453 μL) and added to the dendrimer−DMSO solution. To this mixture was added *N*, *N*-diisopropylethylamine (4.6 μL, 26 μmol) and the resulting solution was stirred for 45 min. Benzotriazol-1-yl-oxytripyrrolidinophosphonium hexafluorophosphate (2.3 mg, 4.4 μmol) was dissolved in DMSO (462 μL) and added in a dropwise manner to the dendrimer/alkyne linker solution. The resulting solution was stirred for 24 h. All reaction steps were carried out in glass flasks at room temperature under nitrogen.

The reaction mixture was purified using 10 000 MWCO centrifugal filtration devices. Purification consisted of two cycles using 1× PBS and eight cycles using DI water. All cycles were 10 min at 5000 rpm. The resulting product **5** was lyophilized for three days to yield a white solid (41.5 mg, 75%). ^{1}H NMR integration determined an average of 1.4 alkyne linkers coupled to the dendrimer. The quantification of the number of linkers by NMR integration is described previously.[30] See Supporting Information for ^{1}H NMR spectrum of **5**.

Synthesis of G5-Ac$_{72\%}$-Azide$_{1.3}$ ***6***. A solution of partially acetylated dendrimer **1′** (60.5 mg, 1.97 μmol) was prepared with anhydrous DMSO (13.444 mL). The azide linker **3c** (1.2 mg, 4.9 μmol) was dissolved in DMSO (578 μL) and added to the dendrimer−DMSO solution. To this mixture was added *N*, *N*-diisopropylethylamine (5.1 μL, 30 μmol) and the resulting solution was stirred for 45 min. Benzotriazol-1-yl-oxytripyrrolidinophosphonium hexafluorophosphate (2.6 mg, 4.9 μmol) was dissolved in DMSO (511 μL) and added in a dropwise manner to the dendrimer/azide linker solution. The resulting solution was stirred for 24 h. All reaction steps were carried out in glass flasks at room temperature under nitrogen.

The reaction mixture was purified using 10 000 MWCO centrifugal filtration devices. Purification consisted of two cycles using 1× PBS and eight cycles using DI water. All cycles were 10 min at 5000 rpm. The resulting product **6** was lyophilized for three days to yield a white solid (50 mg, 91%). ^{1}H NMR integration determined an average of 1.3 alkyne linkers coupled to the dendrimer. See Supporting Information for ^{1}H NMR spectrum of **6**.

Synthesis of Model Dendrimer System G5-Ac$_{72\%}$-L-G5Ac$_{72\%}$ ***7***. Partially acetylated dendrimer with an average of 1.4 alkyne linkers **5** (15.30 mg, 0.493 μmol) and partially acetylated dendrimer with an average of 1.3 azide linkers **6** (15.4 mg, 0.496 μmol) was dissolved in deuterium oxide (0.820 mL) and placed in a glass microwave reactor vessel. Sodium ascorbate (6.9 mg, 35 μmol) and copper sulfate pentahydrate (5.9 mg, 24 μmol) was added to the dendrimer solution. The resulting solution was placed in a microwave reactor for 40 s at 100 W with a cutoff temperature of 100 °C. The microwave conditions were repeated for an additional 40 s. The cutoff temperature was then increased to 110 °C and the microwave was run at 100 W for 2 min. The resulting crude product was a turbid yellow. The crude product was transferred to an NMR tube and analyzed by NOESY and ^{1}H NMR. After two days, the crude product in solution turned to a red−brown solution with a precipitate at the bottom of the NMR tube. NOESY and ^{1}H NMR experiments were repeated at this time point. The supernatant was separated from the precipitate and lyophilized to yield 4.9 mg of a brown solid. See Supporting Information for ^{1}H NMR spectrum of **7**.

Synthesis of G5-Ac$_{65\%}$-Alkyne$_{1.6}$ ***8***. The alkyne linker was conjugated to the partially acetylated dendrimer in two consecutive reactions. First, a stock solution of the alkyne linker **2b** (9.5 mg, 0.047 mmol) was generated with a mixture of DMF (6.198 mL) and DMSO (3.099 mL). To this mixture was added EDC (124.9 mg, 0.651 mmol). The resulting solution was stirred for 2 h at room temperature to create the active ester form of the alkyne linker.

A solution of partially acetylated dendrimer **1″** (58.8 mg, 1.930 μmol) was prepared with DI water (13.099 mL). The active ester form of the alkyne linker (5.784 mL, 0.0289 mmol) in DMF/DMSO was added in a dropwise manner (0.13 mL/min) to the

dendrimer—water solution. The resulting reaction mixture was stirred for 2 days. All reaction steps were carried out in glass flasks at room temperature under nitrogen. The reaction mixture was purified using 10 000 MWCO centrifugal filtration devices. Purification consisted of five cycles using 1× PBS and five cycles using DI water. All cycles were 30 min at 5000 rpm. The resulting product **8** was lyophilized for three days to yield a white solid (55 mg, 92%). ^{1}H NMR integration determined an average of 1.6 alkyne linkers coupled to the dendrimer. See Supporting Information for ^{1}H NMR spectrum of **8**.

Synthesis of G5-Ac$_{65\%}$-Azide$_{2.5}$ ***9***. The azide linker was conjugated to the partially acetylated dendrimer in two consecutive reactions. First, a stock solution of the azide linker **3c** (7.6 mg, 0.032 mmol) was generated with a mixture of DMF (4.96 mL) and DMSO (2.48 mL). To this mixture was added EDC (86.7 mg, 0.452 mmol). The resulting solution was stirred for 1.75 h at room temperature to create the active ester form of the azide linker.

A solution of partially acetylated dendrimer **1**″ (58.8 mg, 1.930 μmol) was prepared with DI water (13.10 mL). The active ester form of the azide linker (6.66 mL, 0.0289 mmol) in DMF/DMSO was added in a dropwise manner (0.13 mL/min) to the first dendrimer—water aliquot. The resulting mixture was stirred for 2 days. All reaction steps were carried out in glass flasks at room temperature under nitrogen. The reaction mixture was purified using 10 000 MWCO centrifugal filtration devices. Purification consisted of five cycles using 1× PBS and five cycles using DI water. All cycles were 10 min at 5000 rpm. The resulting product **9** was lyophilized for three days to yield a white solid (55 mg, 89%). ^{1}H NMR integration determined an average of 2.5 azide linkers coupled to the dendrimer. See Supporting Information for ^{1}H NMR spectrum of **9**.

Synthesis of G5-Ac$_{65\%}$-Alkyne$_{1.6}$-FA$_{1.7}$ ***10***. Folic acid was conjugated to the alkyne linker-conjugated dendrimer **8** in two consecutive reactions. First, a solution of folic acid (1.9 mg, 4.26 μmol) was generated with a mixture of DMF (1.23 mL) and DMSO (0.62 mL). To this mixture was added EDC (11.4 mg, 59.7 μmol). The resulting solution was stirred for 1 h at room temperature to create the active ester form of folic acid.

A solution of partially acetylated dendrimer with an average number of 1.6 alkyne linkers **8** (20.8 mg, 0.752 μmol) was prepared with DI water (4.638 mL). The active ester form of folic acid (1.85 mL, 4.26 μmol) in DMF/DMSO was added in a dropwise manner to the dendrimer—water solution. The resulting reaction mixture was stirred for 3 days. All reaction steps were carried out in glass flasks at room temperature under nitrogen. The reaction mixture was purified using 10 000 MWCO centrifugal filtration devices. Purification consisted of five cycles using 1× PBS and four cycles using DI water. All cycles were 10 min at 5000 rpm. The resulting product **10** was lyophilized for three days to yield a yellow solid (15.6 mg, 73%). ^{1}H NMR integration determined an average of 1.7 folic acid molecules coupled to the dendrimer. See Supporting Information for ^{1}H NMR spectrum of **10**.

Synthesis of G5-Ac$_{65\%}$-Azide$_{2.5}$-FITC$_{3.2}$ ***11***. Partially acetylated dendrimer with an average number of 2.5 azide linkers **9** (21.5 mg, 0.694 μmol) was dissolved in DMSO (1.5 mL). Fluorescein isothiocyanate (1.4 mg, 3.5 μmol) was dissolved in DMSO (0.54 mL) and added in a dropwise fashion to the dendrimer solution. The resulting mixture was stirred for 24 h at room temperature. The reaction mixture was purified using 10 000 MWCO centrifugal filtration devices. Purification consisted of six cycles using 1× PBS and six cycles using DI water. All 1× PBS cycles were 15 min at 5 000 rpm and all DI water cycles were 15 min at 5000 rpm. HPLC analysis of the lyophilized product detected unconjugated FITC remaining in the sample. To remove the remaining unreacted FITC, the conjugate was purified by size exclusion chromatography using Sephadex G-25 beads in 1× PBS. The dendrimer fraction was collected and the elution buffer was exchanged with DI water using 10 000 MWCO centrifugal filtration devices (four cycles of 10 min at 5000 rpm). The purified product **11** was lyophilized to yield a yellow—orange solid (10.1 mg, 46%). ^{1}H NMR integration determined an average of 3.2 FITC coupled to the dendrimer. See Supporting Information for ^{1}H NMR spectrum of **11**.

Synthesis of G5-Ac$_{65\%}$-Alkyne$_{1.6}$-FA$_{3.5}$ ***12***. Additional folic acid was conjugated to the partially acetylated dendrimer with an average of 1.6 alkyne linkers and 1.7 folic acid molecules **10** in two consecutive reactions. First, a solution of folic acid (1.1 mg, 2.4 μmol) was generated with a mixture of DMF (0.69 mL) and DMSO (0.34 mL). To this mixture was added EDC (6.3 mg, 33 μmol). The resulting solution was stirred for 1 h at room temperature to create the active ester form of the folic acid.

A solution of partially acetylated dendrimer with an average number of 1.6 alkyne linkers and 1.7 folic acid molecules **10** (8.5 mg, 0.30 μmol) was prepared with DI water (1.90 mL). The active ester form of folic acid (1.03 mL, 2.4 μmol) in DMF/DMSO was added in a dropwise manner to the dendrimer—water solution. The resulting reaction mixture was stirred for 3 days. All reaction steps were carried out in glass flasks at room temperature under nitrogen. The reaction mixture was purified by size exclusion chromatography using Sephadex G-25 in 1× PBS. The dendrimer fraction was collected and the elution buffer was exchanged with DI water using 10 000 MWCO centrifugal filtration devices (four cycles of 10 min at 5000 rpm). The purified product **12** was lyophilized for three days to yield a yellow solid (7.0 mg, 80%). ^{1}H NMR integration determined an average of 3.5 folic acid molecules coupled to the dendrimer. See Supporting Information for ^{1}H NMR spectrum of **12**.

Synthesis of G5-Ac$_{107}$-Alkyne$_{1.6}$-FA$_{3.5}$ ***13***. Partially acetylated dendrimer with an average number of 1.6 alkyne linkers and 3.5 folic acid **12** (7.0 mg, 0.22 μmol) was dissolved in anhydrous methanol (1.124 mL). Triethylamine (1.7 μL, 0.012 mmol) was added to this mixture and stirred for 30 min. Acetic anhydride (0.9 μL, 9.6 μmol) was added in a dropwise manner to the dendrimer solution. The reaction was carried out in a glass flask, under nitrogen, at room temperature for 24 h. Methanol was evaporated from the resulting solution and the product was purified by size exclusion chromatography using Sephadex LH-20 in methanol. The purified dendrimer **13** was lyophilized for three days to yield a yellow solid (6.6 mg, 90%). ^{1}H NMR integration determined the degree of acetylation to be 100%. See Supporting Information for ^{1}H NMR spectrum of **13**.

Synthesis of G5-Ac$_{106}$-Azide$_{2.5}$-FITC$_{3.2}$ ***14***. Partially acetylated dendrimer with an average number of 2.5 azide linkers and 3.2 FITC **11** (7.5 mg, 0.23 μmol) was dissolved in anhydrous methanol (1.21 mL). Triethylamine (1.8 μL, 0.013 mmol) was added to this mixture and stirred for 30 min. Acetic anhydride (1.0 μL, 10.0 μmol) was added in a dropwise manner to the dendrimer solution. The reaction was carried out in a glass flask, under nitrogen, at room temperature for 24 h. Methanol was evaporated from the resulting solution, and the product was purified by size exclusion chromatography using Sephadex LH-20 in methanol. The purified dendrimer **14** was lyophilized for

three days to yield a yellow solid (7.1 mg, 91%). ^{1}H NMR integration determined the degree of acetylation to be 100%. See Supporting Information for ^{1}H NMR spectrum of **14**.

Synthesis of Folic Acid Targeted Dendrimer System FA$_{3.5}$-G5-Ac$_{107}$-L-G5-Ac$_{106}$-FITC$_{3.2}$ ***15***. Dendrimer with an average of 1.6 alkyne linkers and 3.5 folic acid molecules **13** (3.1 mg, 91 nmol) and dendrimer with an average of 2.5 azide linkers and 3.2 FITC molecules **14** (3.0 mg, 88 nmol) were dissolved in deuterium oxide (0.65 mL) and placed in a glass microwave reactor vessel. Sodium ascorbate (1.1 mg, 4.5 μmol) and copper sulfate pentahydrate (1.1 mg, 5.4 μmol) was added to the dendrimer solution. The resulting solution was placed in a microwave reactor for 6.5 min at 100 W with a cutoff temperature of 100 °C. The reaction mixture was transferred to an NMR tube and analyzed by NOESY and ^{1}H NMR spectroscopy. Lyophilization yielded 6.7 mg of a red solid. See Supporting Information for ^{1}H NMR spectrum of **15**.

Synthesis of G5-Ac$_{67\%}$-Alkyne$_{1.3}$ ***16***. A solution of partially acetylated dendrimer **1‴** (176.7 mg, 5.8 μmol) was prepared with anhydrous DMSO (39.27 mL). The alkyne linker **2b** (2.6 mg, 13 μmol) was dissolved in DMSO (1.31 mL) and added to the dendrimer−DMSO solution. To this mixture was added *N*, *N*-diisopropylethylamine (13.4 μL, 76.7 μmol) and the resulting solution was stirred for 45 min. Benzotriazol-1-yl-oxytripyrrolidinophosphonium hexafluorophosphate (6.7 mg, 13 μmol) was dissolved in DMSO (1.331 mL) and added in a dropwise manner to the dendrimer/alkyne linker solution. The resulting solution was stirred for 24 h. All reaction steps were carried out in glass flasks at room temperature under nitrogen.

The reaction mixture was purified using 10 000 MWCO centrifugal filtration devices. Purification consisted of two cycles using 1× PBS and eight cycles using DI water. All cycles were 10 min at 5000 rpm. The resulting product **5** was lyophilized for three days to yield a white solid (116.2 mg, 65.2%). ^{1}H NMR integration determined an average of 1.3 alkyne linkers coupled to the dendrimer. See Supporting Information for ^{1}H NMR spectrum of **16**.

Synthesis of G5-Ac$_{110.7}$-Alkyne$_{1.3}$ ***17***. Partially acetylated dendrimer with an average number of 1.3 alkyne linkers **16** (22.6 mg, 0.737 μmol) was dissolved in anhydrous methanol (3.0 mL). Triethylamine (5.8 μL, 0.042 mmol) was added to this mixture and stirred for 30 min. Acetic anhydride (3.2 μL, 34 μmol) was added in a dropwise manner to the dendrimer solution. The reaction was carried out in a glass flask, under nitrogen, at room temperature for 24 h. Methanol was evaporated from the resulting solution and the product was purified by size exclusion chromatography using Sephadex LH-20 in methanol. The purified dendrimer **17** was lyophilized for three days to yield a white solid (19.1 mg, 80.5%). ^{1}H NMR integration determined the degree of acetylation to be 100%. See Supporting Information for ^{1}H NMR spectrum of **17**.

Synthesis of Untargeted Dendrimer System G5-Ac$_{110.7}$-L-G5-Ac$_{106}$-FITC$_{3.2}$ ***18***. Dendrimer with an average of 1.3 alkyne linkers **17** (1.0 mg, 31 nmol) and dendrimer with an average of 2.5 azide linkers and 3.2 FITC molecules **14** (1.0 mg, 29 nmol) were dissolved in deuterium oxide (0.74 mL) and placed in a glass microwave reactor vessel. Sodium ascorbate (0.36 mg, 1.8 μmol) and copper sulfate pentahydrate (0.38 mg, 1.5 μmol) were added to the dendrimer solution. The resulting solution was placed in a microwave reactor for 6.5 min at 100 W with a cutoff temperature of 100 °C. The reaction mixture was transferred to an NMR tube and analyzed by NOESY and ^{1}H NMR spectroscopy.

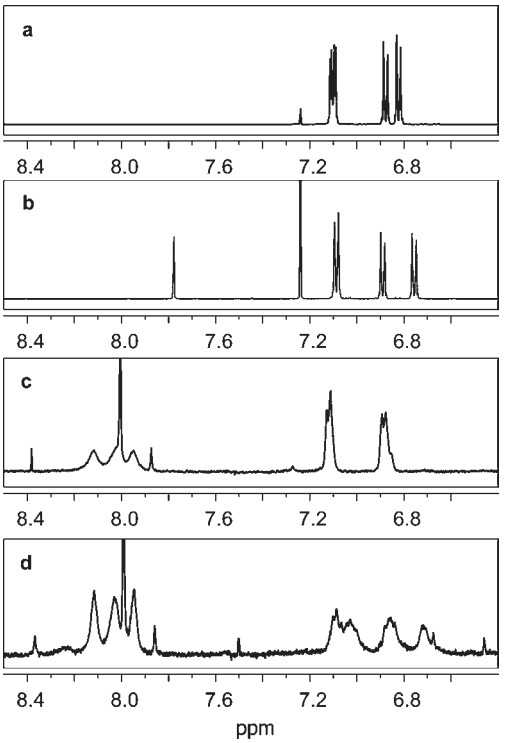


Figure 2. Proton NMR spectra of the small-molecule model system and model dendrimer system both pre- and post-"click" reaction. An upfield shift is observed for aromatic proton g as a result of the "click" reaction. (a) Spectrum of the small molecule model system before the "click" reaction (**2a** and **3b**), taken in $CDCl_3$. Proton g has a chemical shift of 6.85 ppm. (b) Spectrum of the small molecule model system after the "click" reaction (**4**), taken in $CDCl_3$. As a result of the "click" reaction, g has experienced an upfield change to 6.78 ppm. (c) Spectrum of the model dendrimer system before the "click" reaction (**5** and **6**), taken in D_2O. Proton g overlaps proton b at 6.90 ppm. (d) Spectrum of the model dendrimer system after the "click" reaction (**7**), taken in D_2O. Similar to the small molecule model system, proton g experiences an upfield change as a result of the "click" reaction. In the model dendrimer system, the new chemical shift is 6.74 ppm.

Lyophilization yielded 2.4 mg of a red solid. See Supporting Information for ^{1}H NMR spectrum of **18**.

RESULTS AND DISCUSSION

Synthesis and Characterization of the Small-Molecule Model System. A small molecule model system (**4**) was first synthesized to facilitate the spectroscopic assignment of triazole-related atoms resulting from successful "click" reactions between dendrimer modules with an azide linker (**3c**) and dendrimer modules possessing an alkyne linker (**2b**). This model system utilized the methyl ester forms of the two linkers (**2a** and **3b**). Proton assignments were based upon ^{1}H NMR and NOESY experiments in $CDCl_3$. Figure 1, panel a, displays the cross-peaks for the triazole related protons in the clicked product (**4**), and Table 1 contains the chemical shifts for these in both the pre- and post-"click" reaction states. Protons c, e, and f experience the greatest change in chemical shift as a result of the "click" reaction. Also of interest is the region between 6.4 and 8.5 ppm (Figure 2, panels a and b), which shows the upfield shift for peak g from 6.85 ppm to 6.78 ppm.

Synthesis and Characterization of the Model Dendrimer System. Dendrimers without target or dye functionalities, possessing

dx.doi.org/10.1021/bc100360v |*Bioconjugate Chem.* 2011, 22, 679–689

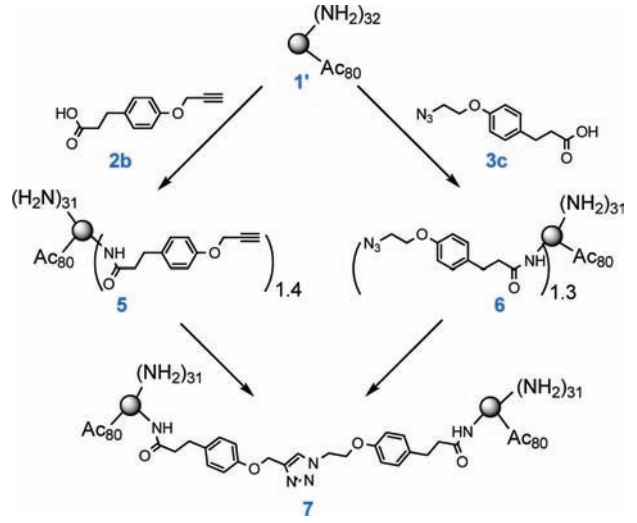


Figure 3. Synthetic scheme for the model dendrimer system (**7**). This simplified modular platform was developed to assist with the spectroscopic characterization of the folic acid targeted dendrimer system. The G5 dendrimer, used in this study, had an average of 112 end groups as determined by GPC and potentiometric titration.

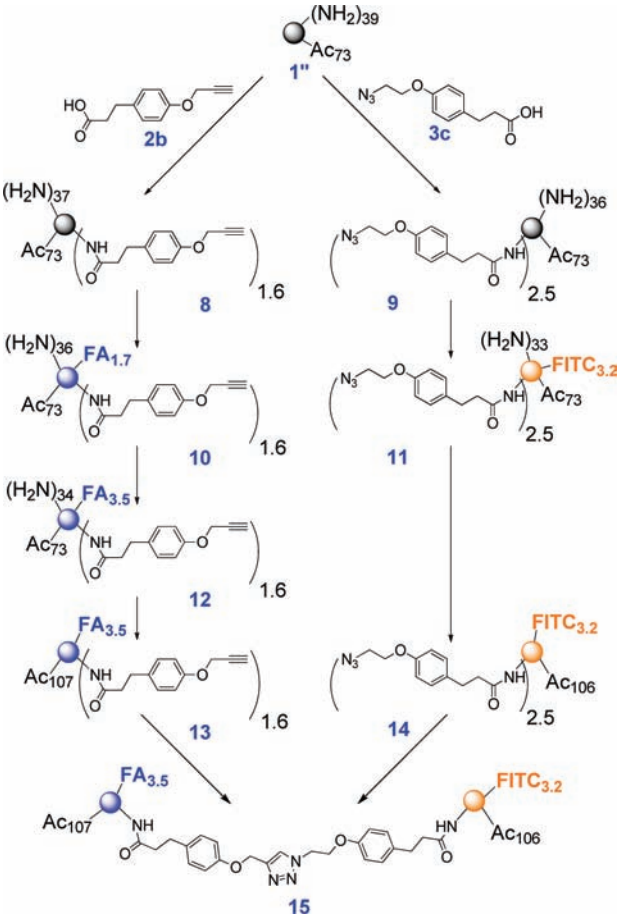


Figure 4. Synthetic scheme for the folic acid targeted modular dendrimer-based platform (**15**). A module possessing a terminal alkyne moiety and folic acid (**13**) is coupled to a second module possessing a terminal azide moiety and FITC (**14**) via the Cu-catalyzed 1,3-dipolar cycloaddition reaction. Both modules were fully acetylated to avoid nonspecific cellular interactions.

only the "click" reaction functional groups (**5** and **6**), were employed to develop "click" reaction conditions (Figure 3). Because many of the proton peaks associated with the dendrimer-conjugated alkyne and azide linkers (particularly those closest to the "click" reaction sites) overlap in the ^{1}H NMR spectra with other protons belonging to the PAMAM dendrimer, NOESY experiments were used to document proton chemical shifts via the resolution of cross peaks in the 2-D spectra (Figure 1, panel b). The chemical shifts for the triazole related protons in the dendrimer system both pre- and post-"click" reaction can be found in Table 1. The region between 6.4 and 8.5 ppm in the proton spectra for the pre- and post-"click"ed dendrimer samples can be found in Figure 2, panels c and d. In the spectra for the pre-"click" reaction mixture (panel c), both sets of aromatic protons overlap at 6.90 ppm (b and g) and 7.13 ppm (a and h). In the sample post-"click" reaction (panel d), the aromatic protons no longer overlap. Protons a and h partially overlap at 7.09 ppm and 7.06 ppm, and protons b and g are found at 6.90 ppm and 6.74 ppm, respectively.

A comparison of the chemical shifts in Table 1 for the small molecule system and the dendrimer system reveals good correlations for both the pre- and post-reaction states. This indicates that a successful "click" reaction has occurred between the azide and alkyne conjugated dendrimers. It is important to note that, whereas chemical shifts for the small molecule model system are determined in $CDCl_3$, the chemical shifts for the dendrimer sample were detected in D_2O. Although the different solvents could influence the proton chemical shifts, this does not appear to be an issue for these particular molecules.

A peak for the single proton in the triazole ring is absent from both the NOESY and 1D experiments. In the small molecule system, this peak is found at 7.80 ppm (Figure 2, panel b). Working with a similar system using PAMAM dendrons that contained the alkyne and azide moieties at the dendron focal point, Lee et al. found that the triazole proton peak gradually shifted downfield from 7.77 ppm to 7.93 ppm as the generation of the clicked dendrons increased from 1 to 3.[47] If this downfield change in chemical shift also holds for the generation 5 dendrimer case, the triazole proton would be overlapped by several peaks between 7.80 ppm and 8.20 ppm associated with the dendrimer (Figure 2, panel d). The NOESY spectra did not expose any cross peaks in this region with other protons in the linkers that are in close proximity to the triazole ring. The cross-peaks associated with the triazole proton appear to be below the intensity required for NMR detection.

Synthesis and Characterization of the Folic Acid Targeted Dendrimer System. Synthesis of the folic acid targeted modular dendrimer platform is outlined in Figure 4. Dendrimers with an average of 1.6 alkyne linkers (**8**) were functionalized with the targeting molecule folic acid. The formation of an amide linkage between one of the remaining primary amines on the dendrimer and one of the carboxylic acid groups in folic acid was achieved by EDC coupling chemistry as previously reported.[22] This reaction conjugated an average of 1.7 folic acid molecules per dendrimer as determined by NMR (**10**). Because this average was below the optimal range for multivalent binding,[3] the reaction was repeated using the dendrimer with an average of 1.6 alkyne linkers and 1.7 folic acid (**10**). The second reaction resulted in the addition of 1.8 folic acid molecules per dendrimer bringing the final average to 3.5 folic acid molecules per dendrimer (**12**). The remaining dendrimer primary amines were then fully acetylated to avoid positive charge-based cellular interactions (**13**).[6,9,10] Dendrimers

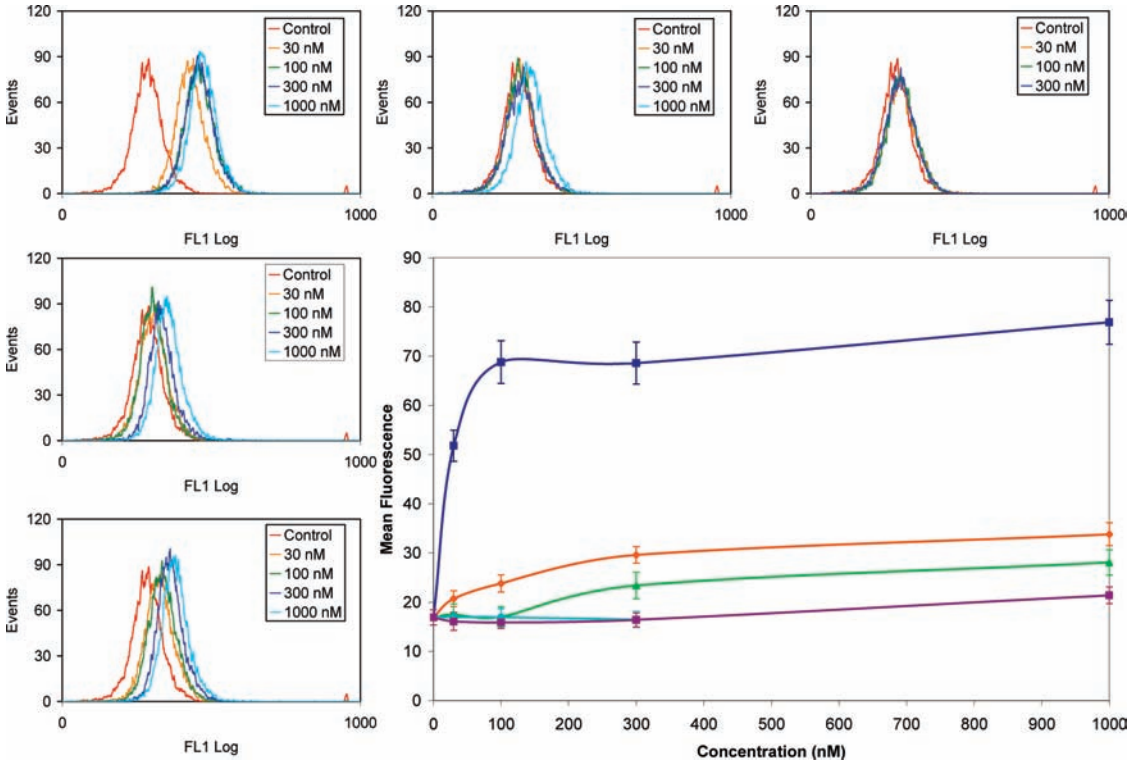


Figure 5. Binding and uptake of the fluorescent modular targeted dendrimer platform in KB cells as measured by flow cytometry. (a) Uptake of $FA_{3.5}$-G5-Ac_{107}-L-G5Ac_{106}-$FITC_{3.2}$ (**15**). (b) Uptake of G5-Ac_{106}-$Azide_{2.5}$-$FITC_{3.2}$ (**14**) is not observed for 30 nM, 100 nM, and 300 nM. Very minimal uptake of this untargeted module is observed at 1000 nM. (c) Similarly, no uptake is observed for an uncoupled mixture of G5-Ac_{106}-$Azide_{2.5}$-$FITC_{3.2}$ (**14**) and G5-Ac_{107}-$Alkyne_{1.6}$-$FA_{3.5}$ (**13**). (d) Uptake of $FA_{3.5}$-G5-Ac_{107}-L-G5Ac_{106}-$FITC_{3.2}$ (**15**) is successfully blocked using a 20-fold excess of free folic acid. (e) Uptake of $FA_{3.5}$-G5-Ac_{107}-L-G5Ac_{106}-$FITC_{3.2}$ (**15**) is also successfully blocked using a 20-fold excess (with respect to the folic acid content) of G5-Ac_{107}-$Alkyne_{1.6}$-$FA_{3.5}$ (**13**). (f) Summary of mean fluorescence values for **a**—**e**. Uptake of $FA_{3.5}$-G5-Ac_{107}-L-G5Ac_{106}-$FITC_{3.2}$ (**15**) is displayed in blue. Uptake of the targeted platform (**15**) blocked by a 20-fold excess of G5-Ac_{107}-$Alkyne_{1.6}$-$FA_{3.5}$ (**13**) is shown in orange. Uptake of the targeted platform (**15**) blocked by a 20-fold excess of free folic acid can be found in green. Uptake of a mixture of G5-Ac_{106}-$Azide_{2.5}$-$FITC_{3.2}$ (**14**) and G5-Ac_{106}-$Alkyne_{1.6}$-$FA_{3.5}$ (**13**) can be found in teal. Finally, uptake of G5-Ac_{106}-$Azide_{2.5}$-$FITC_{3.2}$ (**14**) can be found in purple. Error bars indicate standard deviation as computed from half-peak coefficient of variation (HPCV) values.

with 2.5 azide linkers (**9**) were functionalized with the dye molecule FITC. Using conditions similar to those in previously published work,[25] an average of 3.2 FITC molecules were coupled to the dendrimer via the formation of a thiourea bond between the primary amine on the dendrimer and the isothiocyanate group in FITC (**11**). This dendrimer conjugate also was fully acetylated (**14**). Reverse phase HPLC confirmed that any unreacted FITC or folic acid molecules had been removed by purification of dendrimer **13** and **14**.

The two dendrimer modules (**13** and **14**) were coupled together using the Cu-catalyzed 1,3-dipolar cycloaddition reaction under conditions similar to those used with the model dendrimer system. NOESY experiments provided direct spectroscopic proof that the functionalized dendrimers had been clicked together. Specifically, the AA′BB′ pattern was observed to shift in a fashion identical to that observed for the two model systems previously described (Table 1 and Figure 2).

***In Vitro* Testing of the Folic Acid Targeted Dendrimer System with KB Cells.** Cellular uptake of the folic acid targeted dendrimer system (**15**) at four different concentrations (30 nM, 100 nM, 300 nM, and 1000 nM of **15**) was measured in KB cells that express a high cellular membrane concentration of folic acid receptor (FAR). Fluorescence uptake was quantified by flow cytometry. As seen in Figure 5a and f-blue, a dose-dependent uptake was observed with saturation occurring at 100 nM. This binding affinity is consistent with previous studies on single dendrimer platforms possessing multiple FITC and multiple FA molecules.[23]

A series of control experiments were performed in order to ensure that uptake of the folic acid targeted dendrimer system (**15**) was occurring via receptor-mediated endocytosis and not nonspecific membrane interactions. The first set of controls measured uptake of single dendrimers possessing the azide linker and multiple FITC (**14**) at 30 nM, 100 nM, 300 nM, and 1000 nM (Figure 5b and f-purple). No uptake was observed for this sample above the background level. The second control sample contained a nonconjugated (unclicked) mixture of the two dendrimers functionalized with either FITC or folic acid (**13** and **14**). Uptake of this mixture was quantified at 30 nM, 100 nM, and 300 nM (Figure 5c and f-teal). At all three concentrations, no florescence uptake was observed. This control eliminates the possibility that the dendrimer modules could form a noncovalently linked complex that would be internalized. A third control sample (**18**) was composed of an untargeted dendrimer module (**17**) coupled to the FITC conjugated imaging module (**14**). The untargeted dual module platform (**18**) was assembled under the same conditions used to form the folic acid targeted platform (**15**). Mean fluorescence uptake of the untargeted platform can

be found in the Supporting Information. At concentrations up to 300 nM, no uptake was observed beyond the background level. This untargeted dendrimer platform is an essential control, because it matches the molecular weight and size of the folic acid targeted dendrimer system (**15**). This control will become even more important as evaluation of this system moves to an *in vivo* model.

The final set of controls investigated active blocking of the folic acid receptor by either free folic acid (Figure 5d and f-green) or a folic acid−dendrimer conjugate without a fluorescent dye (**13**) (Figure 5e and f-orange) to prevent the specific uptake of the folic acid targeted dendrimer system. A 20-fold excess of blocking agent was employed relative to the targeted platform. For the blocking experiment using the single dendrimer−folic acid conjugate (**13**), molar equivalence was based on the folic acid content of the sample rather than the dendrimer content. Both blocking agents were evaluated at 30 nM, 100 nM, 300 nM, and 1000 nM. Complete blocking is achieved using free folic acid concentrations up to 100 nM. While the dendrimer−folic acid conjugate is not as effective at blocking as the free folic acid, approximately 75% blocking is achieved. These binding data indicate that the cellular association of the folic acid targeted dendrimer system occurs through the folic acid receptor rather than via nonspecific interactions. On a more fundamental level, the biological results prove again that the folic acid conjugate dendrimer module is covalently linked by "click" chemistry to dendrimer module functionalized with FITC.

Design Analysis. One of the limitations of the modular platform design in its current iteration is that each module is composed of a heterogeneous distribution of dendrimer−ligand components.[30,48−50] To a first approximation, these distributions are consistent with Poissonian statistics. Not only are the modules composed of a distribution of dendrimer particles with different numbers of the biologically active ligand (folic acid, FITC), but the modules are also composed of a distribution of dendrimer with different numbers of the coupling ligands (azide and alkyne). The implication of these distributions is that the final "dual" module platform is most likely composed of a large number of different platforms with different numbers of modules linked together and different numbers of ligands per module. Future designs should incorporate characterization and control of these distributions in order to make a more controlled, reproducible material.

CONCLUSION

A delivery platform covalently linking two different PAMAM dendrimer modules through "click" chemistry was successfully designed and synthesized. Two model systems were also generated to assist in the NMR spectroscopy characterization of the modular platform. The folic acid targeted system was evaluated for functional activity *in vitro* with KB cells and found to selectively target the cancer cell line through the high-affinity folate receptor.

ASSOCIATED CONTENT

Supporting Information. ^{1}H NMR characterization of dendrimer conjugates and a plot of mean fluorescence for the untargeted modular platform (**18**) control. This material is available free of charge via the Internet at http://pubs.acs.org.

AUTHOR INFORMATION

Corresponding Author

*Corresponding author. Mark M. Banaszak Holl, mbanasza@umich.edu, 930 N. University Avenue, Ann Arbor, MI 48109-1055. TEL: 734-763-2283, FAX: 734-936-2307.

ACKNOWLEDGMENT

This project was supported with Federal funds from the National Cancer Institute, National Institutes of Health, under award 1 R01 CA119409.

REFERENCES

(1) Allen, T. M. (2002) Ligand-targeted therapeutics in anticancer therapy. *Nat. Rev. Cancer 2*, 750–763.

(2) Peer, D., Karp, J. M., Hong, S., FaroKhzad, O. C., Margalit, R., and Langer, R. (2007) Nanocarriers as an emerging platform for cancer therapy. *Nat. Nanotechnol. 2*, 751–760.

(3) Hong, S., Leroueil, P. R., Majoros, I. J., Orr, B. G., Baker, J. R., and Holl, M. M. B. (2007) The binding avidity of a nanoparticle-based multivalent targeted drug delivery platform. *Chem. Biol. 14*, 105–113.

(4) Mammen, M., Choi, S. K., and Whitesides, G. M. (1998) Polyvalent interactions in biological systems: Implications for design and use of multivalent ligands and inhibitors. *Angew. Chem., Int. Ed. 37*, 2755–2794.

(5) Majoros, I. J., Keszler, B., Woehler, S., Bull, T., and Baker, J. R. (2003) Acetylation of poly(amidoamine) dendrimers. *Macromolecules 36*, 5526–5529.

(6) Hong, S. P., Bielinska, A. U., Mecke, A., Keszler, B., Beals, J. L., Shi, X. Y., Balogh, L., Orr, B. G., Baker, J. R., and Holl, M. M. B. (2004) Interaction of poly(amidoamine) dendrimers with supported lipid bilayers and cells: Hole formation and the relation to transport. *Bioconjugate Chem. 15*, 774–782.

(7) Lee, C. C., MacKay, J. A., Frechet, J. M. J., and Szoka, F. C. (2005) Designing dendrimers for biological applications. *Nat. Biotechnol. 23*, 1517–1526.

(8) Svenson, S., and Tomalia, D. A. (2005) Commentary - Dendrimers in biomedical applications - reflections on the field. *Adv. Drug Delivery Rev. 57*, 2106–2129.

(9) Hong, S. P., Leroueil, P. R., Janus, E. K., Peters, J. L., Kober, M. M., Islam, M. T., Orr, B. G., Baker, J. R., and Holl, M. M. B. (2006) Interaction of polycationic polymers with supported lipid bilayers and cells: Nanoscale hole formation and enhanced membrane permeability. *Bioconjugate Chem. 17*, 728–734.

(10) Leroueil, P. R., Hong, S. Y., Mecke, A., Baker, J. R., Orr, B. G., and Holl, M. M. B. (2007) Nanoparticle interaction with biological membranes: Does nanotechnology present a janus face?. *Acc. Chem. Res. 40*, 335–342.

(11) Patri, A. K., Myc, A., Beals, J., Thomas, T. P., Bander, N. H., and Baker, J. R. (2004) Synthesis and in vitro testing of J591 antibody-dendrimer conjugates for targeted prostate cancer therapy. *Bioconjugate Chem. 15*, 1174–1181.

(12) Shukla, R., Thomas, T. P., Peters, J. L., Desai, A. M., Kukowska-Latallo, J., Patri, A. K., Kotlyar, A., and Baker, J. R. (2006) HER2 specific tumor targeting with dendrimer conjugated anti-HER2 mAb. *Bioconjugate Chem. 17*, 1109–1115.

(13) Wu, G., Barth, R. F., Yang, W. L., Kawabata, S., Zhang, L. W., and Green-Church, K. (2006) Targeted delivery of methotrexate to epidermal growth factor receptor-positive brain tumors by means of cetuximab (IMC-C225) dendrimer bioconjugates. *Mol. Cancer Ther. 5*, 52–59.

(14) Wu, G., Barth, R. F., Yang, W. L., Chatterjee, M., Tjarks, W., Ciesielski, M. J., and Fenstermaker, R. A. (2004) Site-specific conjugation of boron-containing dendrimers to anti-EGF receptor monoclonal antibody cetuximab (IMC-C225) and its evaluation as a potential delivery agent for neutron capture therapy. *Bioconjugate Chem. 15*, 185–194.

(15) Backer, M. V., Gaynutdinov, T. I., Patel, V., Bandyopadhyaya, A. K., Thirumamagal, B. T. S., Tjarks, W., Barth, R. F., Claffey, K., and Backer, J. M. (2005) Vascular endothelial growth factor selectively targets boronated dendrimers to tumor vasculature. *Mol. Cancer Ther. 4*, 1423–1429.

(16) Shukla, R., Thomas, T. P., Peters, J., Kotlyar, A., Myc, A., and Baker, J. R. (2005) Tumor angiogenic vasculature targeting with PAMAM dendrimer-RGD conjugates. *Chem. Commun.* 5739–5741.

(17) Sheng, K. C., Kalkanidis, M., Pouniotis, D. S., Esparon, S., Tang, C. K., Apostolopoulos, V., and Pietersz, G. A. (2008) Delivery of antigen using a novel mannosylated dendrimer potentiates immunogenicity in vitro and in vivo. *Eur. J. Immunol. 38*, 424–436.

(18) Baek, M. G., and Roy, R. (2002) Synthesis and protein binding properties of T-antigen containing GlycoPAMAM dendrimers. *Bioorg. Med. Chem. 10*, 11–17.

(19) Taite, L. J., and West, J. L. (2006) Poly(ethylene glycol)-lysine dendrimers for targeted delivery of nitric oxide. *J. Biomater. Sci., Polym. Ed. 17*, 1159–1172.

(20) Kono, K., Liu, M. J., and Frechet, J. M. J. (1999) Design of dendritic macromolecules containing folate or methotrexate residues. *Bioconjugate Chem. 10*, 1115–1121.

(21) Shukla, S., Wu, G., Chatterjee, M., Yang, W. L., Sekido, M., Diop, L. A., Muller, R., Sudimack, J. J., Lee, R. J., Barth, R. F., and Tjarks, W. (2003) Synthesis and biological evaluation of folate receptor-targeted boronated PAMAM dendrimers as potential agents for neutron capture therapy. *Bioconjugate Chem. 14*, 158–167.

(22) Majoros, I. J., Myc, A., Thomas, T., Mehta, C. B., and Baker, J. R. (2006) PAMAM dendrimer-based multifunctional conjugate for cancer therapy: Synthesis, characterization, and functionality. *Biomacromolecules 7*, 572–579.

(23) Thomas, T. P., Majoros, I. J., Kotlyar, A., Kukowska-Latallo, J. F., Bielinska, A., Myc, A., and Baker, J. R. (2005) Targeting and inhibition of cell growth by an engineered dendritic nanodevice. *J. Med. Chem. 48*, 3729–3735.

(24) Myc, A., Douce, T. B., Ahuja, N., Kotlyar, A., Kukowska-Latallo, J., Thomas, T. P., and Baker, J. R. (2008) Preclinical antitumor efficacy evaluation of dendrimer-based methotrexate conjugates. *Anti-Cancer Drugs 19*, 143–149.

(25) Majoros, I. J., Thomas, T. P., Mehta, C. B., and Baker, J. R. (2005) Poly(amidoamine) dendrimer-based multifunctional engineered nanodevice for cancer therapy. *J. Med. Chem. 48*, 5892–5899.

(26) Kukowska-Latallo, J. F., Candido, K. A., Cao, Z. Y., Nigavekar, S. S., Majoros, I. J., Thomas, T. P., Balogh, L. P., Khan, M. K., and Baker, J. R. (2005) Nanoparticle targeting of anticancer drug improves therapeutic response in animal model of human epithelial cancer. *Cancer Res. 65*, 5317–5324.

(27) Myc, A., Patri, A. K., and Baker, J. R. (2007) Dendrimer-based BH3 conjugate that targets human carcinoma cells. *Biomacromolecules 8*, 2986–2989.

(28) Myc, A., Majoros, I. J., Thomas, T. P., and Baker, J. R. (2007) Dendrimer-based targeted delivery of an apoptotic sensor in cancer cells. *Biomacromolecules 8*, 13–18.

(29) Landmark, K. J., DiMaggio, S., Ward, J., Kelly, C., Vogt, S., Hong, S., Kotlyar, A., Myc, A., Thomas, T. P., Penner-Hahn, J. E., Baker, J. R., Holl, M. M. B., and Orr, B. G. (2008) Synthesis, characterization, and in vitro testing of superparamagnetic iron oxide nanoparticles targeted using folic acid-conjugated dendrimers. *ACS Nano 2*, 773–783.

(30) Mullen, D. G., Desai, A. M., Waddell, J. N., Cheng, X.-M., Kelly, C. V., McNerny, D. Q., Majoros, I. J., Baker, J. R., Sander, L. M., Orr, B. G., and Banaszak Holl, M. M. (2008) The implications of stochastic synthesis for the conjugation of functional groups to nanoparticles. *Bioconjugate Chem. 19*, 1748–52.

(31) Choi, Y. S., Mecke, A., Orr, B. G., Holl, M. M. B., and Baker, J. R. (2004) DNA-directed synthesis of generation 7 and 5 PAMAM dendrimer nanoclusters. *Nano Lett. 4*, 391–397.

(32) Choi, Y., Thomas, T., Kotlyar, A., Islam, M. T., and Baker, J. R. (2005) Synthesis and functional evaluation of DNA-assembled polyamidoamine dendrimer clusters for cancer cell-specific targeting. *Chem. Biol. 12*, 35–43.

(33) DeMattei, C. R., Huang, B. H., and Tomalia, D. A. (2004) Designed dendrimer syntheses by self-assembly of single-site, ssDNA functionalized dendrons. *Nano Lett. 4*, 771–777.

(34) Choi, Y. (2005) in *Biomedical Engineering*, p 191, University of Michigan, Ann Arbor, MI.

(35) Lee, J. W., Kim, J. H., Kim, H. J., Han, S. C., Kim, J. H., Shin, W. S., and Jin, S. H. (2007) Synthesis of symmetrical and unsymmetrical PAMAM dendrimers by fusion between azide- and alkyne-functionalized PAMAM dendrons. *Bioconjugate Chem. 18*, 579–584.

(36) Lee, J. W., Kim, H. J., Han, S. C., Kim, J. H., and Jin, S. H. (2008) Designing poly(amido amine) dendrimers containing core diversities by click chemistry of the propargyl focal point poly(amido amine) dendrons. *J. Polym. Sci., Part A: Polym. Chem. 46*, 1083–1097.

(37) Lee, J. W., Kim, B. K., Kim, H. J., Han, S. C., Shin, W. S., and Jin, S. H. (2006) Convergent synthesis of symmetrical and unsymmetrical PAMAM dendrimers. *Macromolecules 39*, 2418–2422.

(38) Lee, J. W., Kim, J. H., Kim, B. K., Shin, W. S., and Jin, S. H. (2006) Synthesis of Frechet type dendritic benzyl propargyl ether and Frechet type triazole dendrimer. *Tetrahedron 62*, 894–900.

(39) Wu, P., Malkoch, M., Hunt, J. N., Vestberg, R., Kaltgrad, E., Finn, M. G., Fokin, V. V., Sharpless, K. B., and Hawker, C. J. (2005) Multivalent, bifunctional dendrimers prepared by click chemistry. *Chem. Commun.* 5775–5777.

(40) Goyal, P., Yoon, K., and Weck, M. (2007) Multifunctionalization of dendrimers through orthogonal transformations. *Chem.—Eur. J. 13*, 8801–8810.

(41) Yoon, K., Goyal, P., and Weck, M. (2007) Monofunctionalization of dendrimers with use of microwave-assisted 1,3-dipolar cycloadditions. *Org. Lett. 9*, 2051–2054.

(42) Rostovtsev, V. V., Green, L. G., Fokin, V. V., and Sharpless, K. B. (2002) A stepwise Huisgen cycloaddition process: Copper(I)-catalyzed regioselective "ligation" of azides and terminal alkynes. *Angew. Chem., Int. Ed. 41*, 2596–2599.

(43) Wu, P., Feldman, A. K., Nugent, A. K., Hawker, C. J., Scheel, A., Voit, B., Pyun, J., Frechet, J. M. J., Sharpless, K. B., and Fokin, V. V. (2004) Efficiency and fidelity in a click-chemistry route to triazole dendrimers by the copper(I)-catalyzed ligation of azides and alkynes. *Angew. Chem., Int. Ed. 43*, 3928–3932.

(44) Wu, P., and Fokin, V. V. (2007) Catalytic azide-alkyne cycloaddition: Reactivity and applications. *Aldrichim. Acta 40*, 7–17.

(45) Hoffman, R. E. (2006) Standardization of chemical shifts of TMS and solvent signals in NMR solvents. *Magn. Reson. Chem. 44*, 606–616.

(46) Marie, D., and Brown, S. C. (1993) A Cytometric exercise in plant DNA Hhistograms, with 2c-values for 70 species. *Biol. Cell 78*, 41–51.

(47) Lee, J. W., Kim, J. H., Kim, B. K., Kim, J. H., Shin, W. S., and Jin, S. H. (2006) Convergent synthesis of PAMAM dendrimers using click chemistry of azide-functionalized PAMAM dendrons. *Tetrahedron 62*, 9193–9200.

(48) Mullen, D. G., Fang, M., Desai, A., Baker, J. R., Orr, B. G., and Holl, M. M. B. (2010) A quantitative assessment of nanoparticle-ligand distributions: implications for targeted drug and imaging delivery in dendrimer conjugates. *ACS Nano 4*, 657–670.

(49) Mullen, D. G., Borgmeier, E. L., Fang, M., McNerny, D. Q., Desai, A., Baker, J. R., Orr, B. G., and Banaszak Holl, M. M. (2010) Effect of mass transport in the synthesis of partially acetylated dendrimer: Implications for functional ligand-nanoparticle distributions. *Macromolecules 43*, 6577−6587.

(50) Mullen, D. G., Borgemeier, E. L., Desai, A., van Dongen, M. A., Barash, M., Cheng, X., Baker, J. R., and Banaszak Holl, M. M. (2010) Isolation and characterization of dendrimer with precise numbers of functional groups, *Chem. Eur. J. 16*, 10675−10678.

Design, Synthesis, and Biological Functionality of a Dendrimer-based Modular Drug Delivery Platform

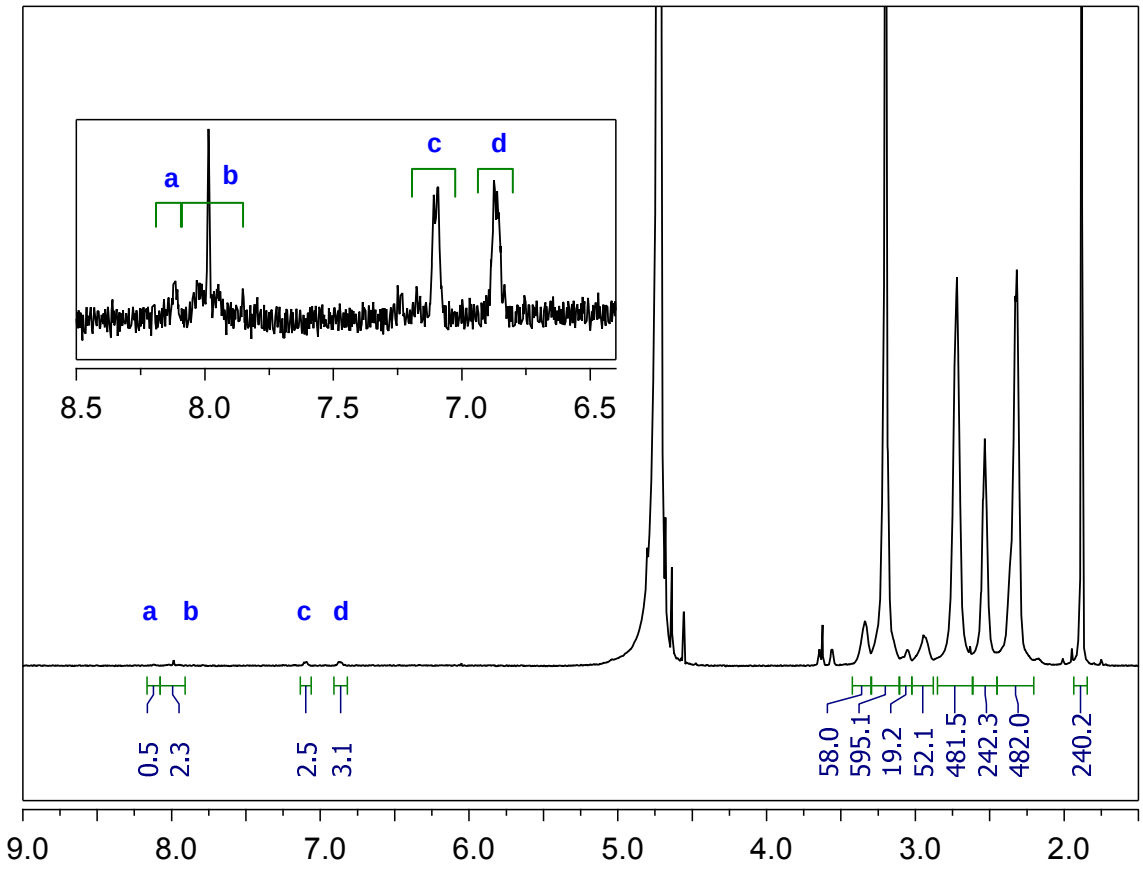
Supporting Information:

Douglas G. Mullen, Daniel Q. McNerny, Ankur Desai, Xue-min Cheng, Stassi C. DiMaggio, Alina Kotlyar, Yueyang Zhong, Suyang Qin, Christopher V. Kelly, Thommey P. Thomas, Joseph M. Wallace, Aniruddha Ray, Istvan Majoros, Bradford G. Orr, James R. Baker Jr., and Mark M. Banaszak Holl*

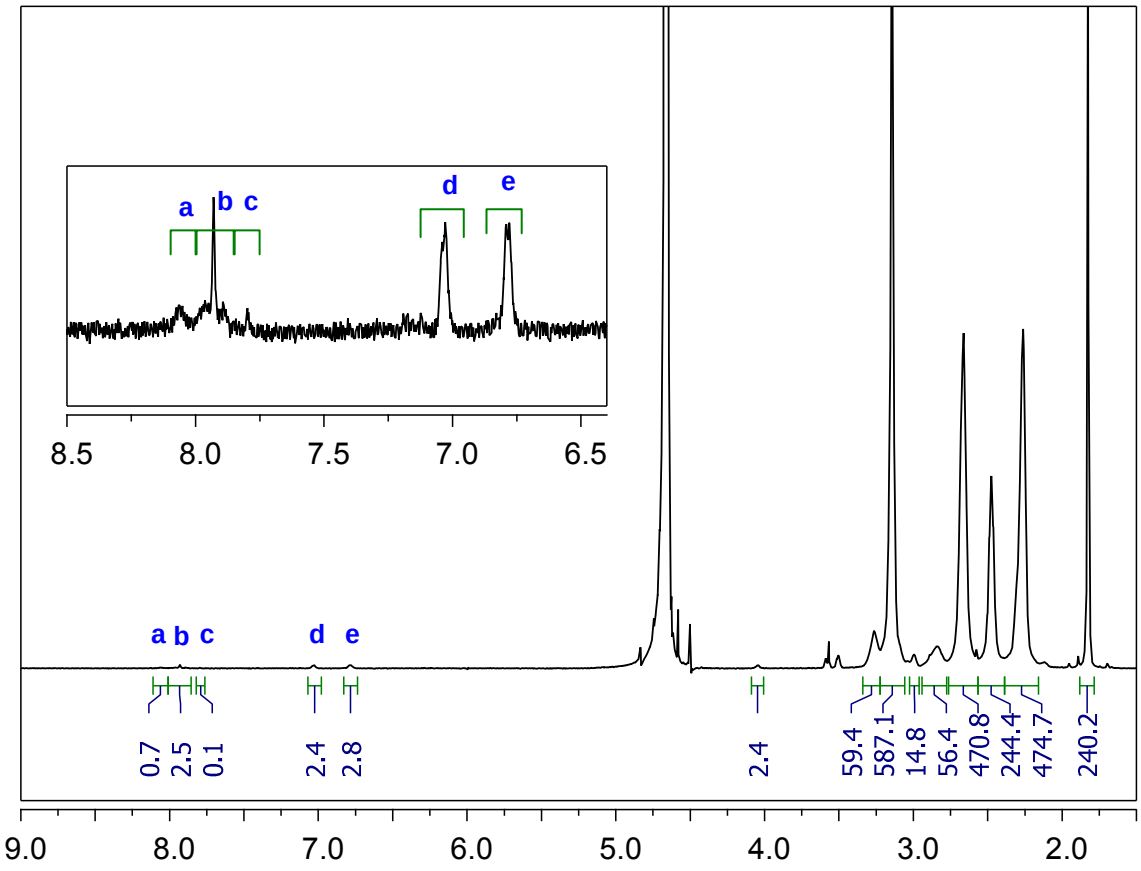
Programs in Macromolecular Science and Engineering and Applied Physics, Departments of Chemistry and Chemical Engineering, Michigan Nanotechnology Institute for Medicine and Biological Sciences, University of Michigan, Ann Arbor, MI 48019. Department of Chemistry, Xavier University, New Orleans, LA 70125.

S1: ^{1}H NMR Spectra for Dendrimer Conjugates

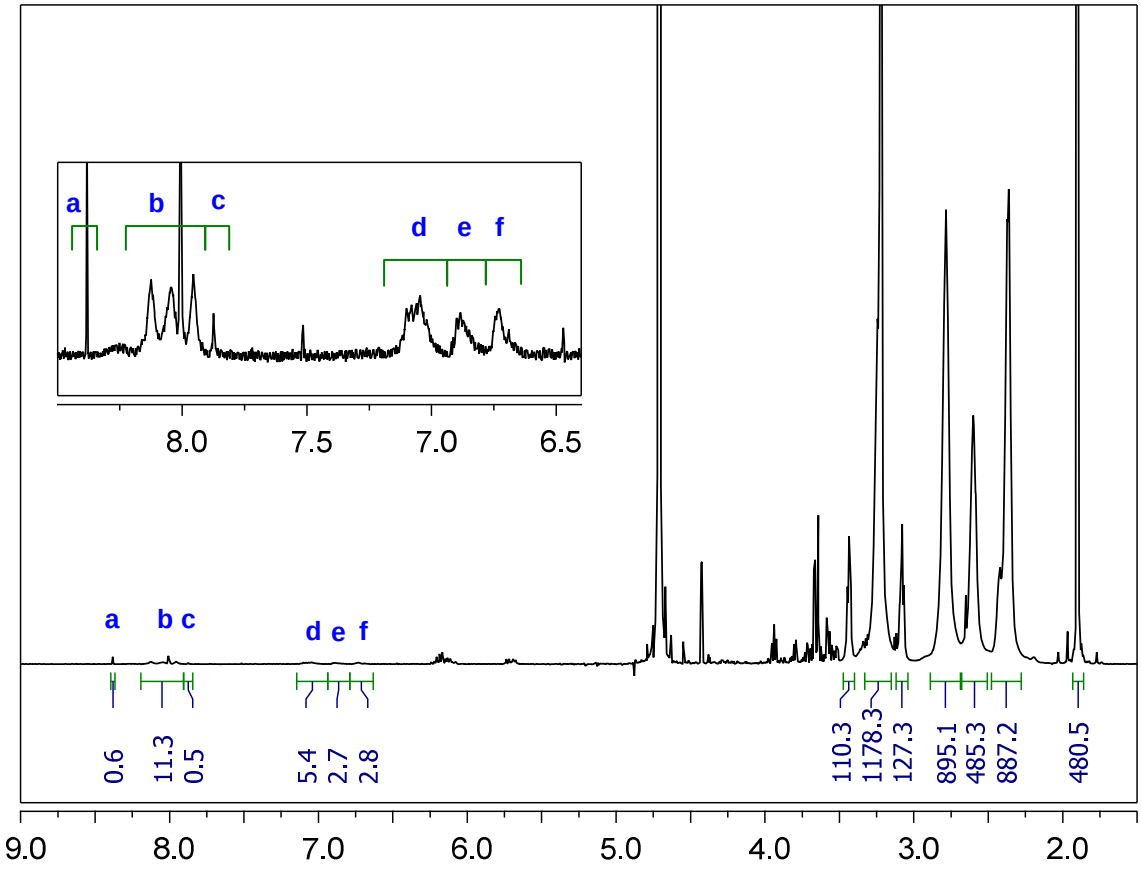
5. G5-Ac$_{72\%}$-Alkyne$_{1.4}$



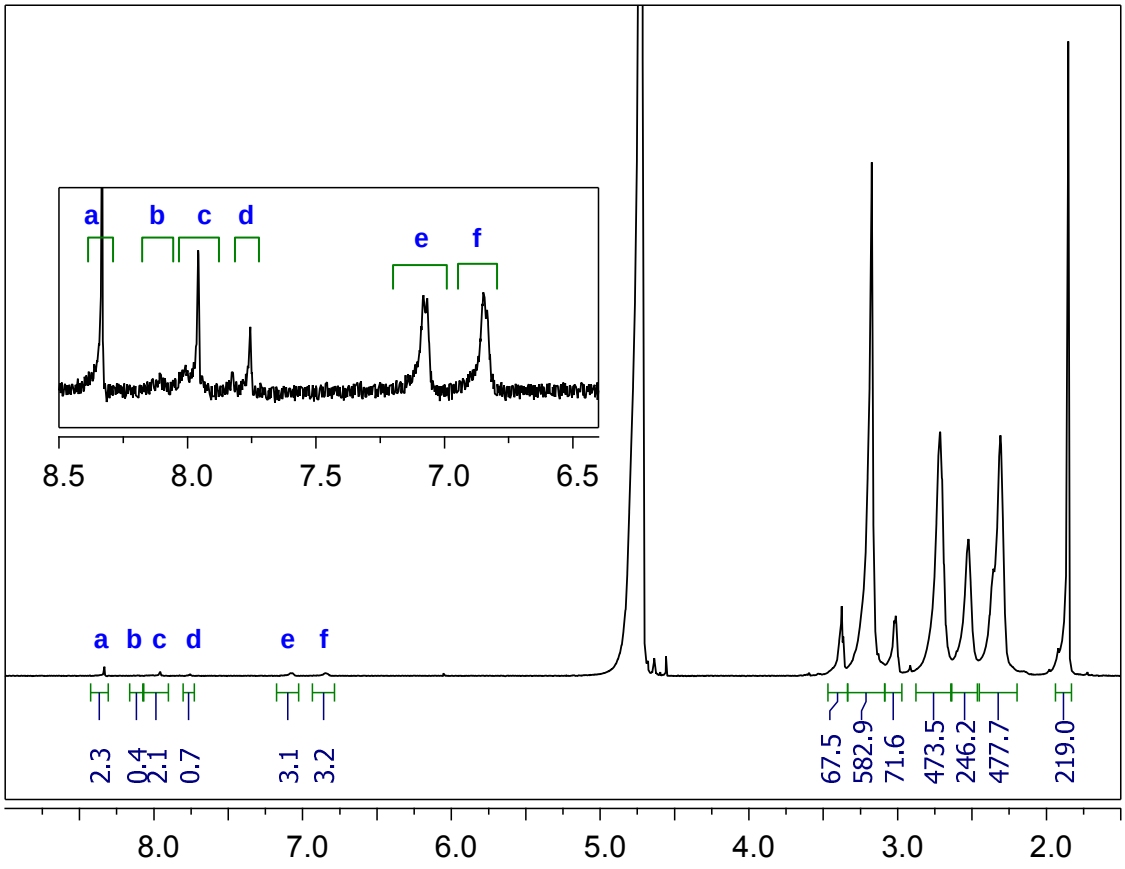
6. G5-Ac$_{72\%}$-Azide$_{1.3}$



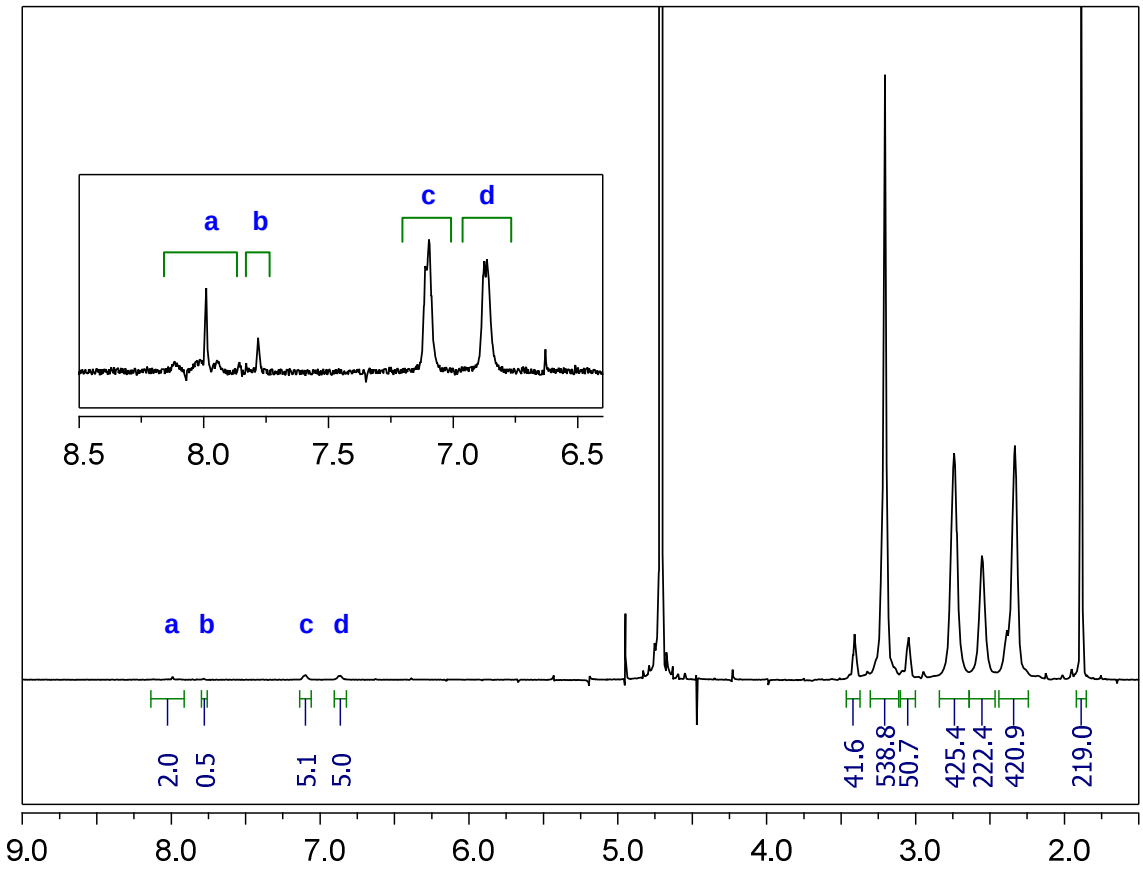
7. Model Dendrimer System G5-Ac$_{72\%}$-L-G5Ac$_{72\%}$



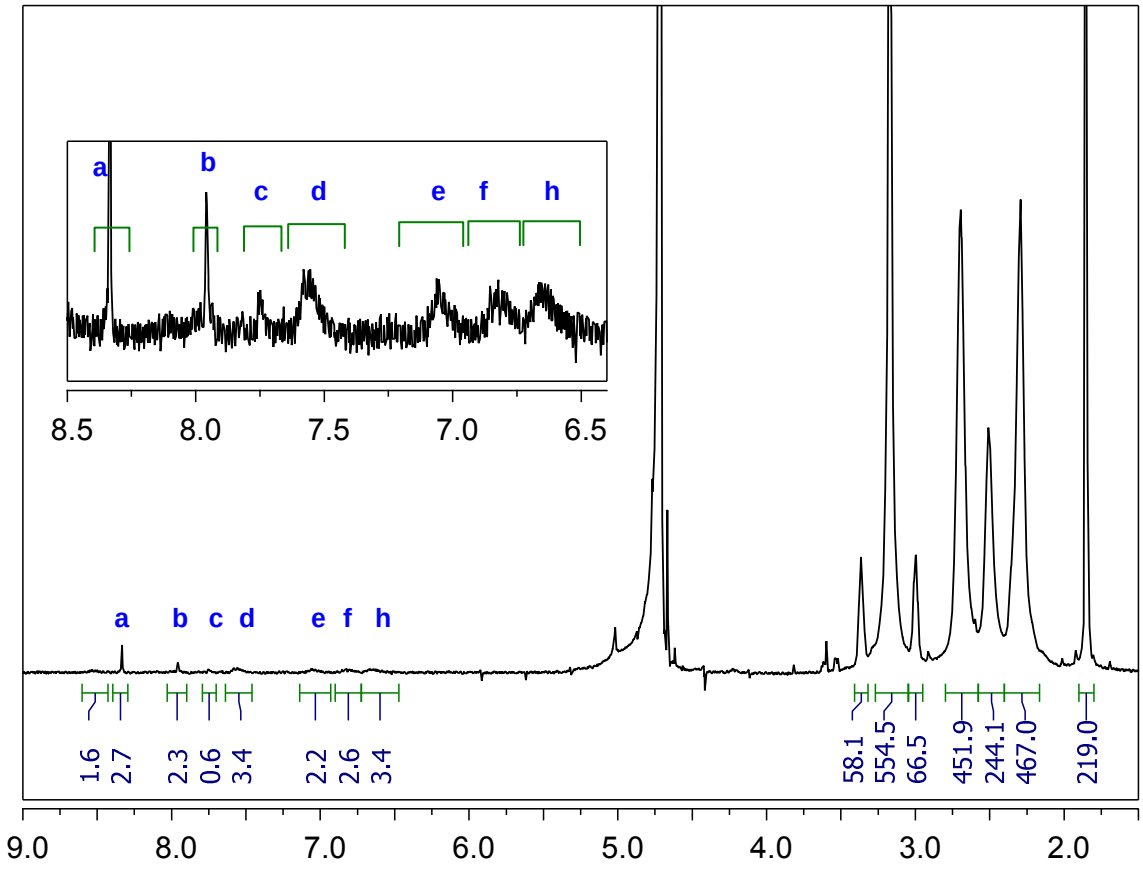
8. G5-Ac$_{65\%}$-Alkyne$_{1.6}$



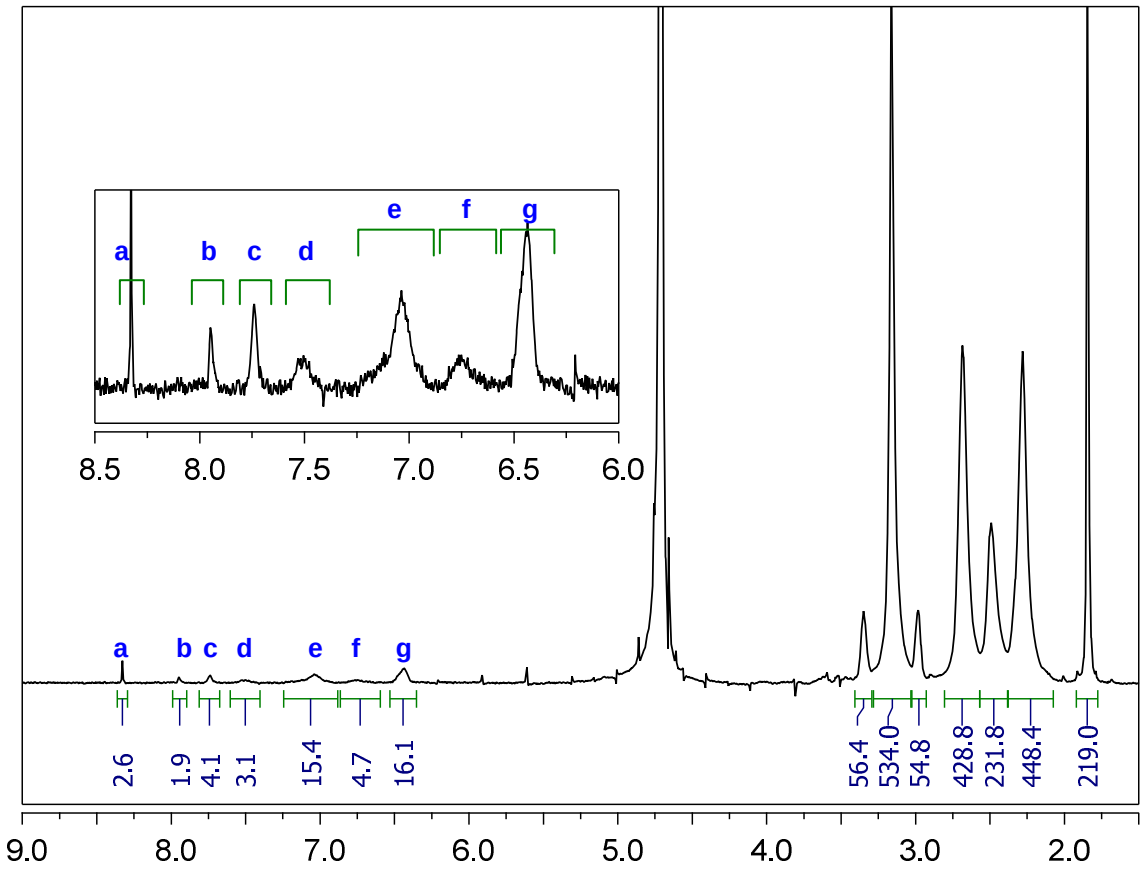
9. G5-Ac$_{65\%}$-Azide$_{2.5}$



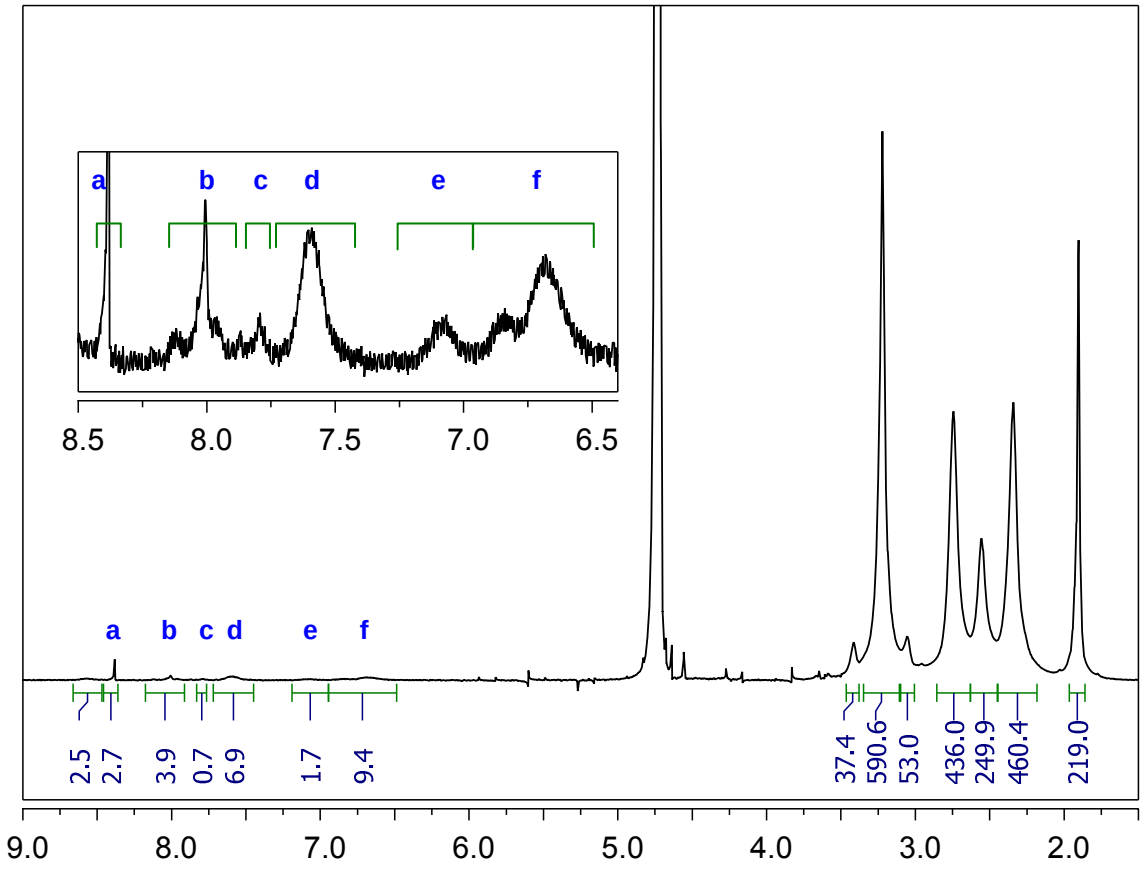
10. G5-Ac$_{65\%}$-Alkyne$_{1.6}$-FA$_{1.7}$



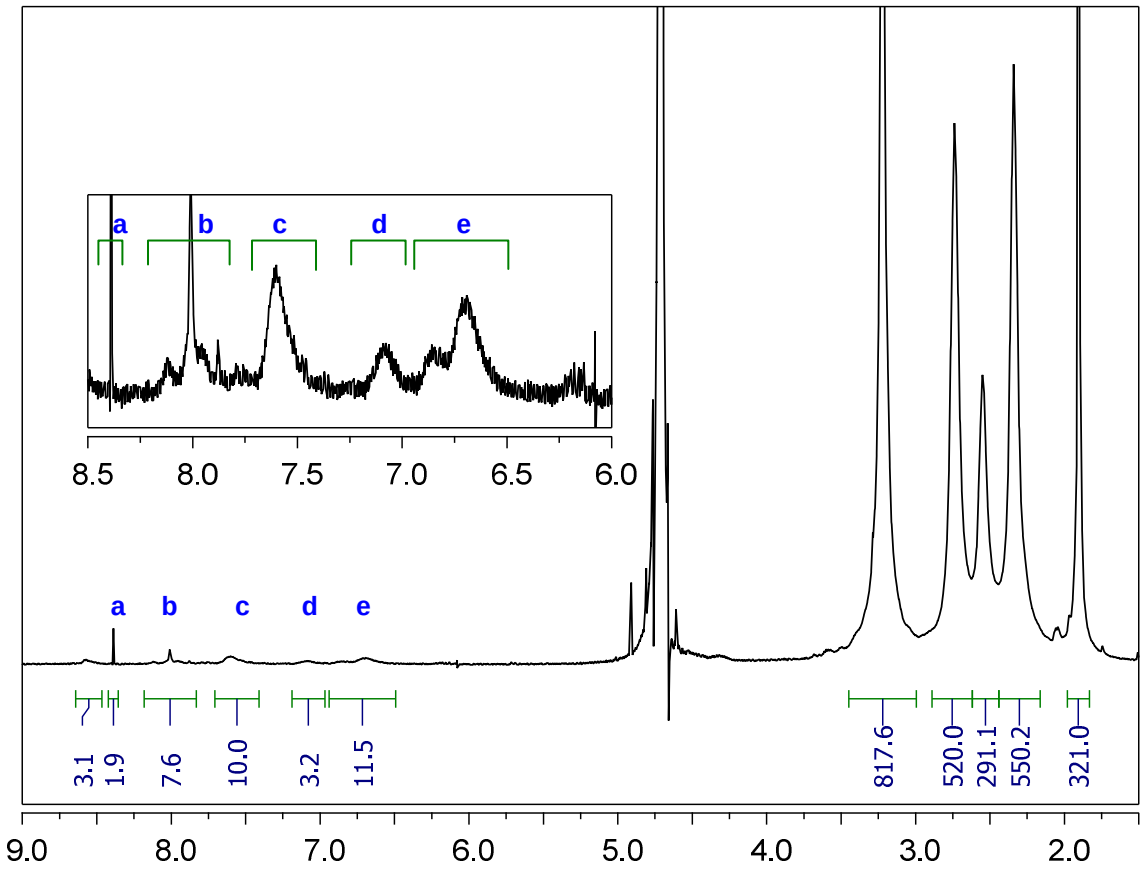
11. G5-Ac$_{65\%}$-Azide$_{2.5}$-FITC$_{3.2}$



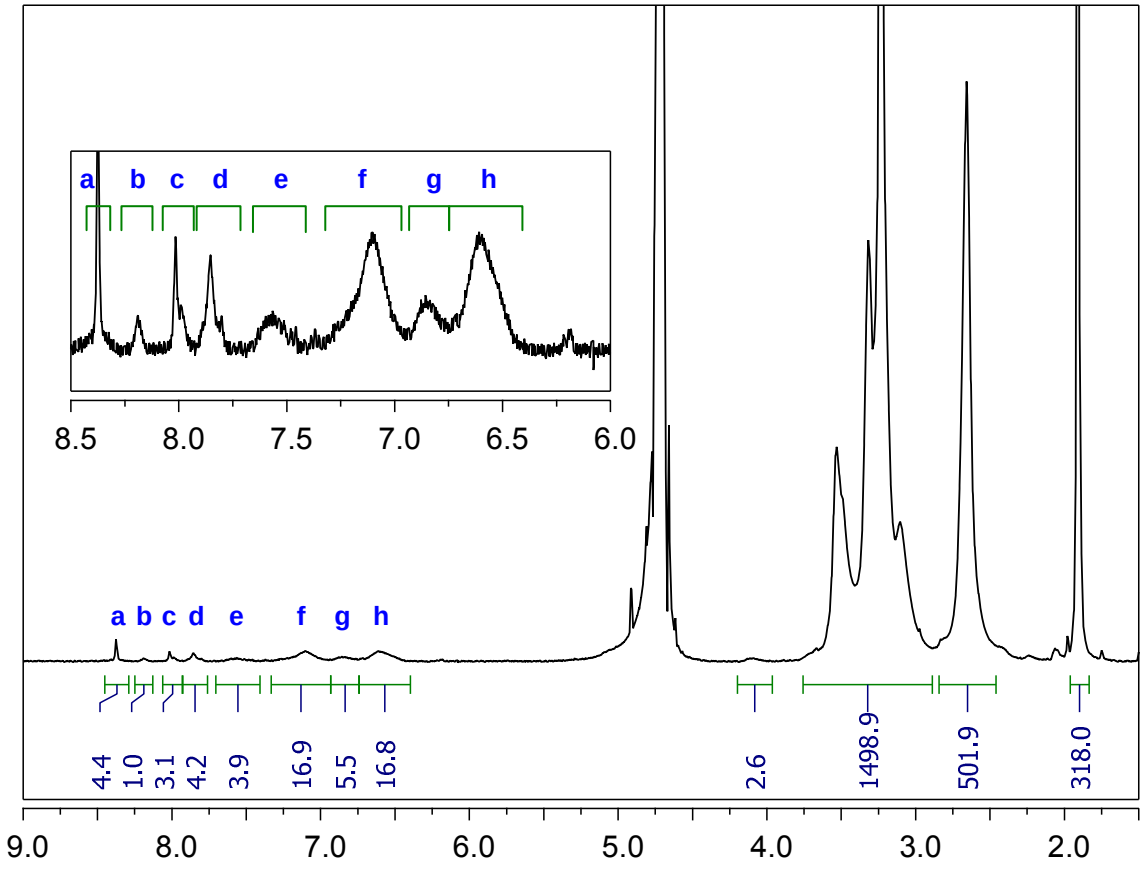
12. G5-Ac$_{65\%}$-Alkyne$_{1.6}$-FA$_{3.5}$



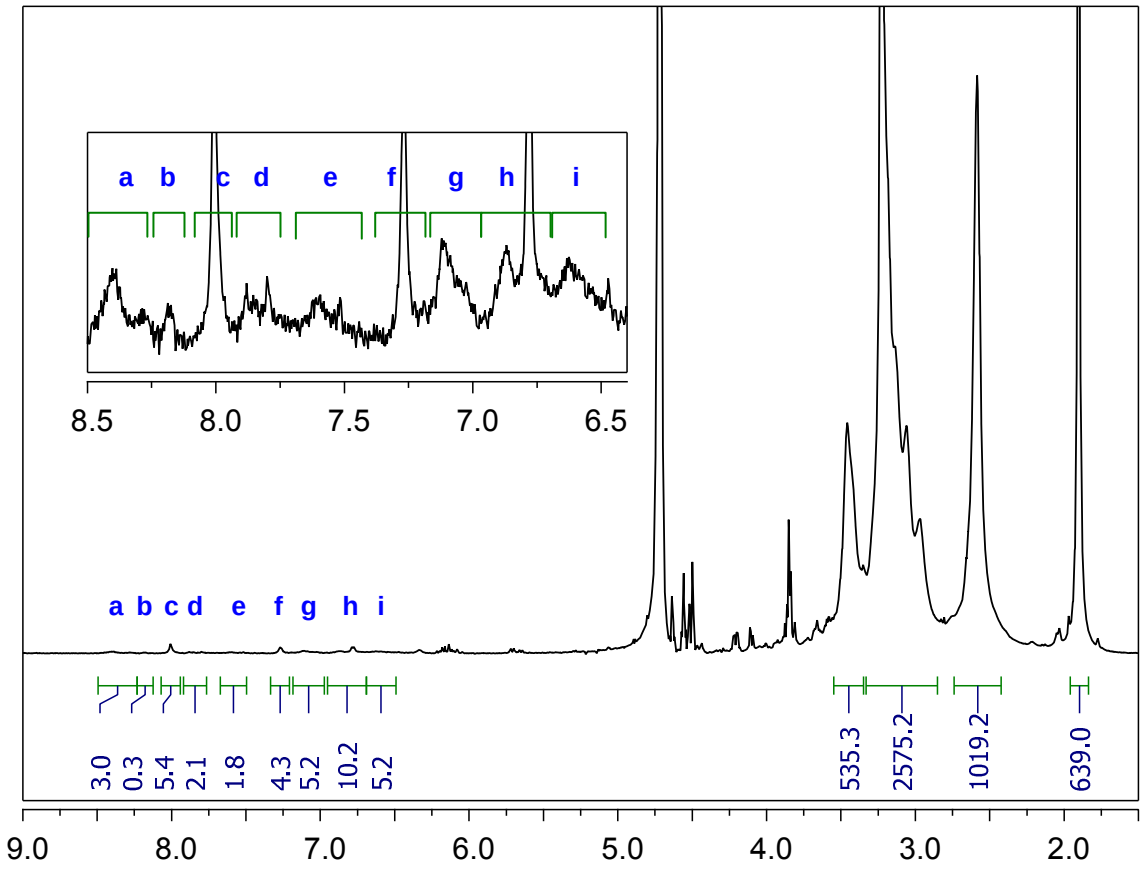
13. G5-Ac_{107}-$Alkyne_{1.6}$-$FA_{3.5}$



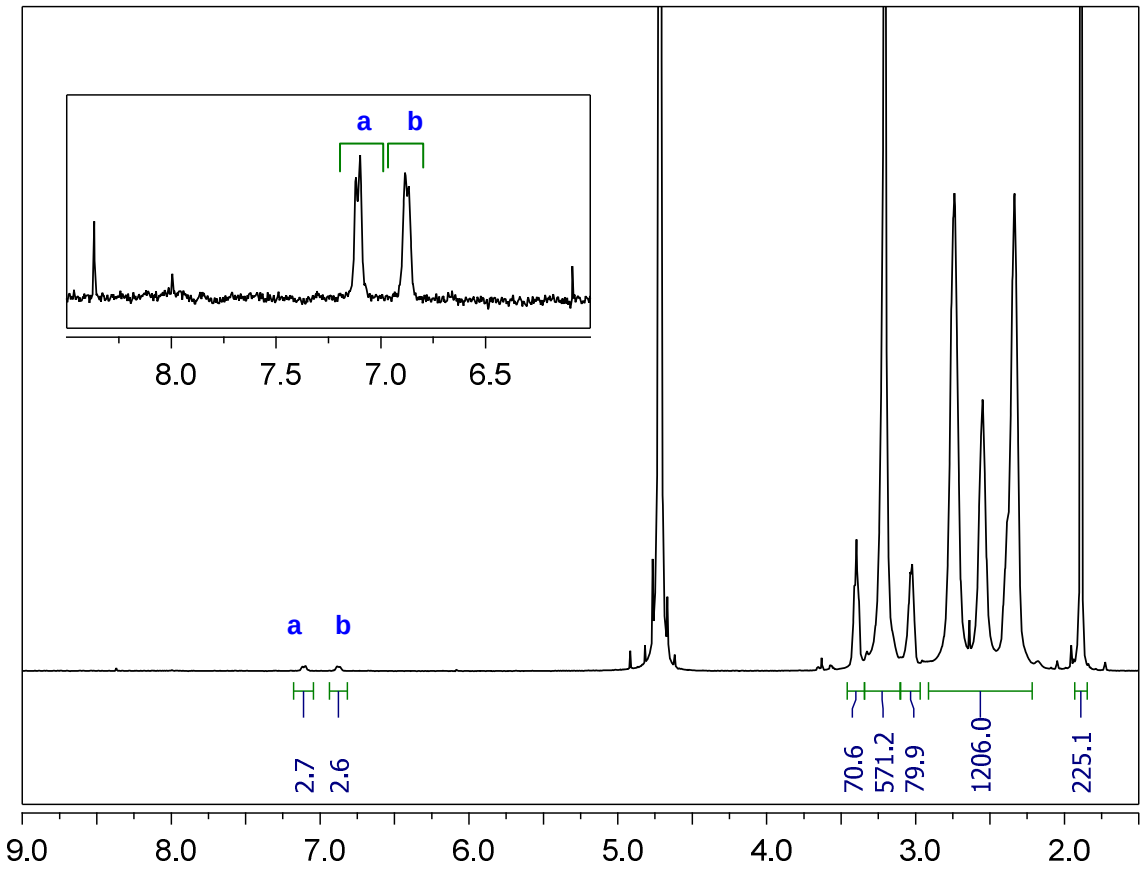
14. G5-Ac_{106}-$Azide_{2.5}$-$FITC_{3.2}$



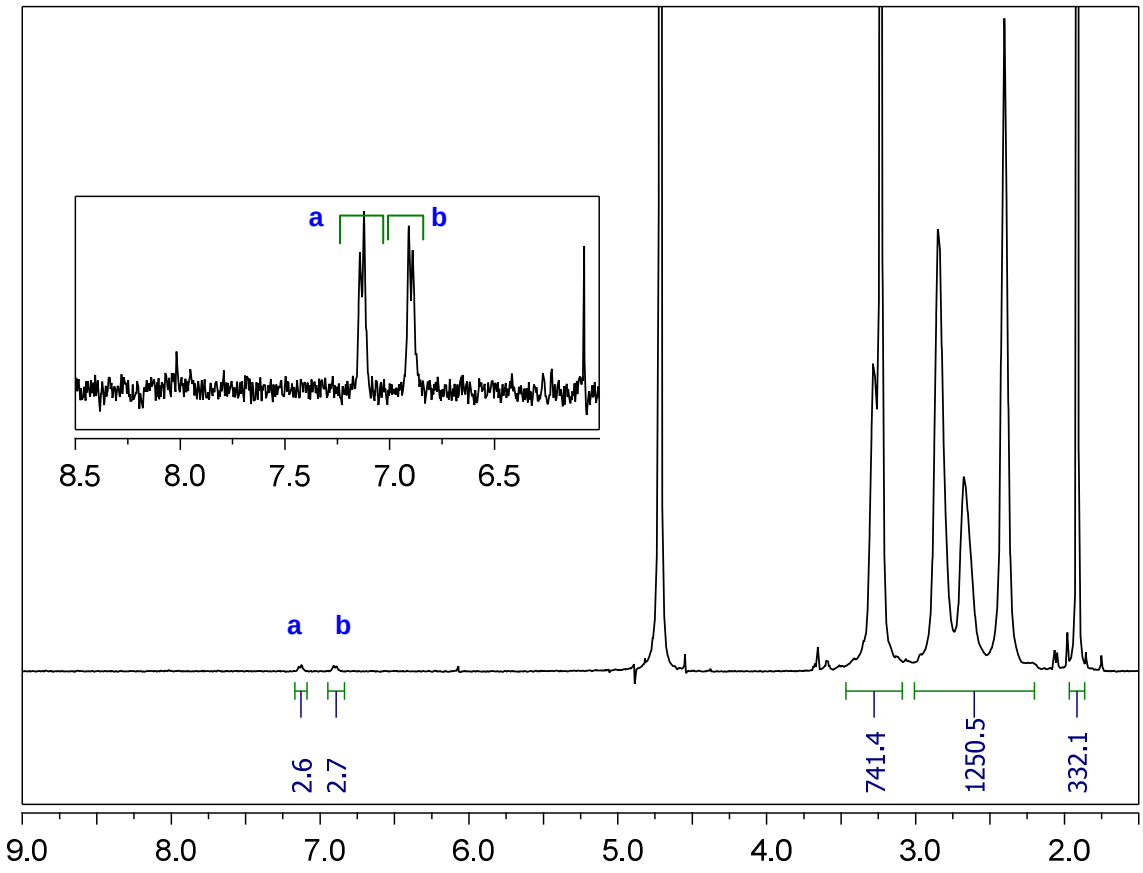
15. Folic Acid Targeted Dendrimer System $FA_{3.5}$-G5-Ac_{107}-L-G5Ac_{106}-$FITC_{3.2}$



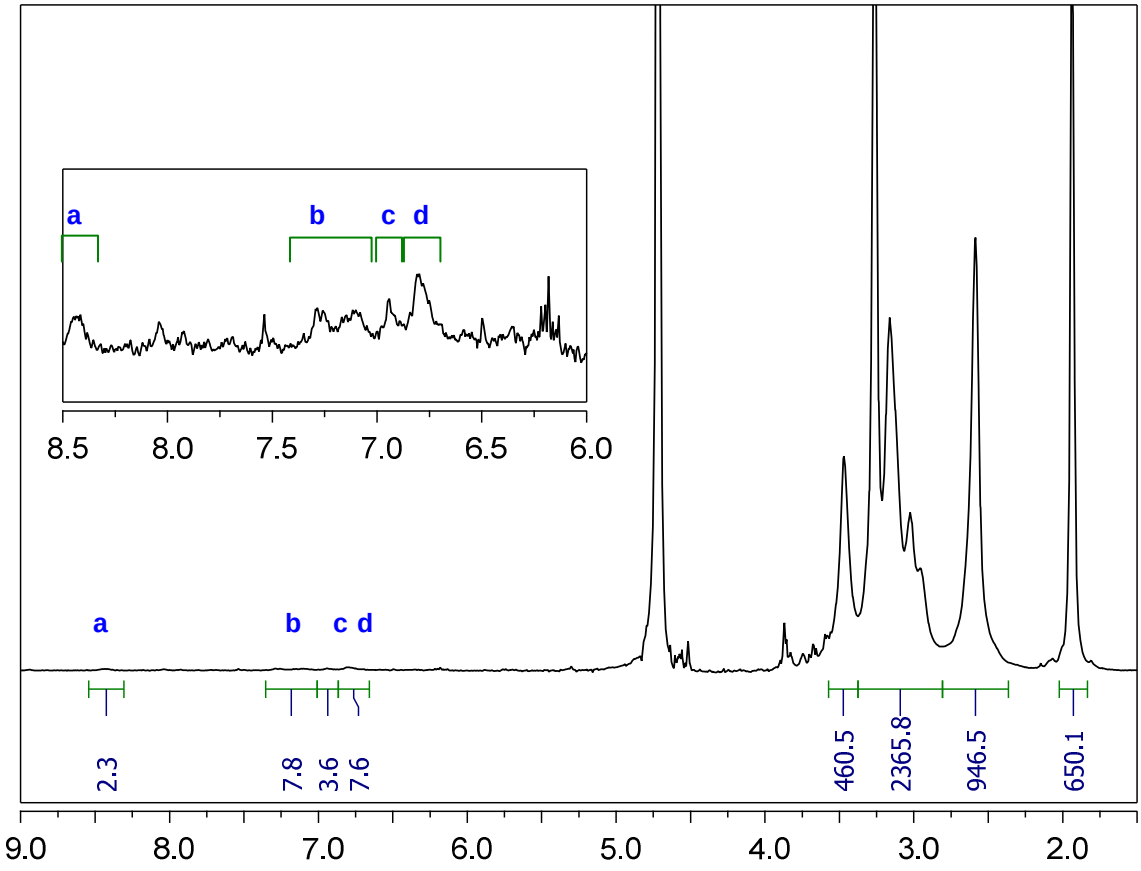
16. Synthesis of G5-Ac$_{67\%}$-Alkyne$_{1.3}$



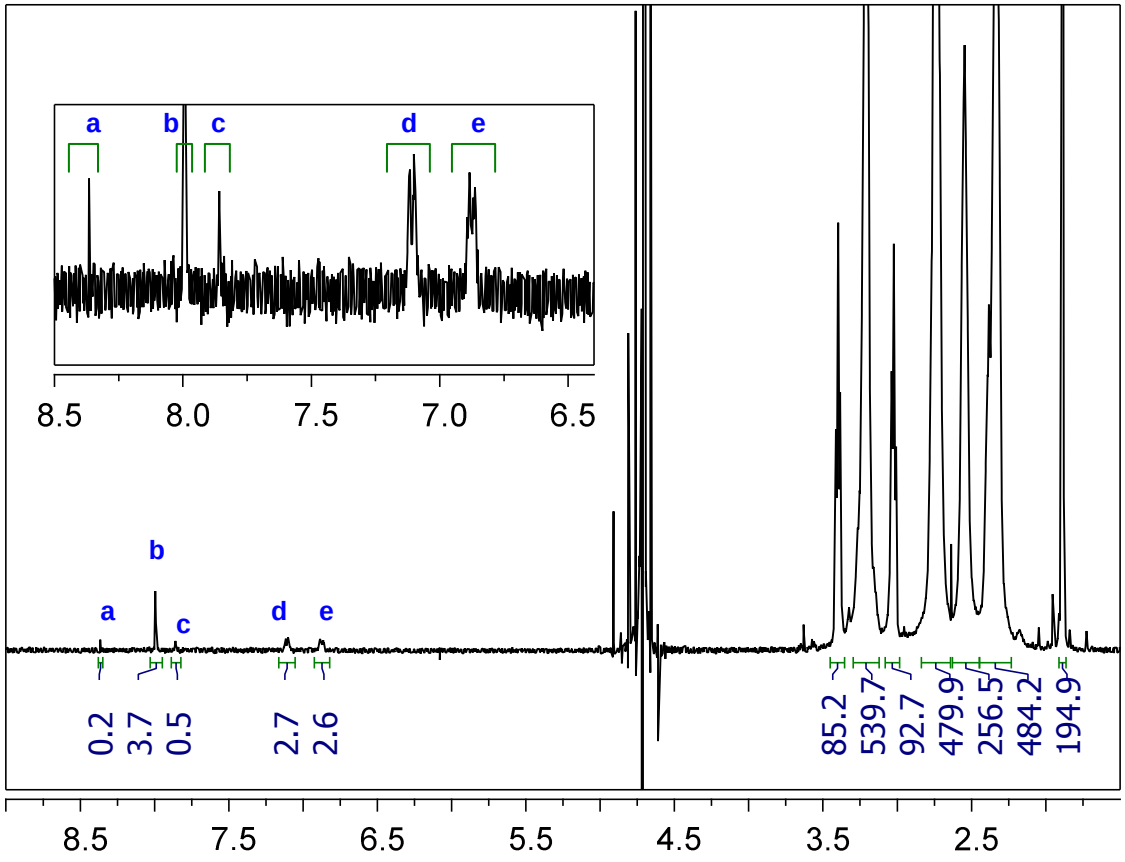
17. Synthesis of G5-Ac$_{110.7}$-Alkyne$_{1.3}$



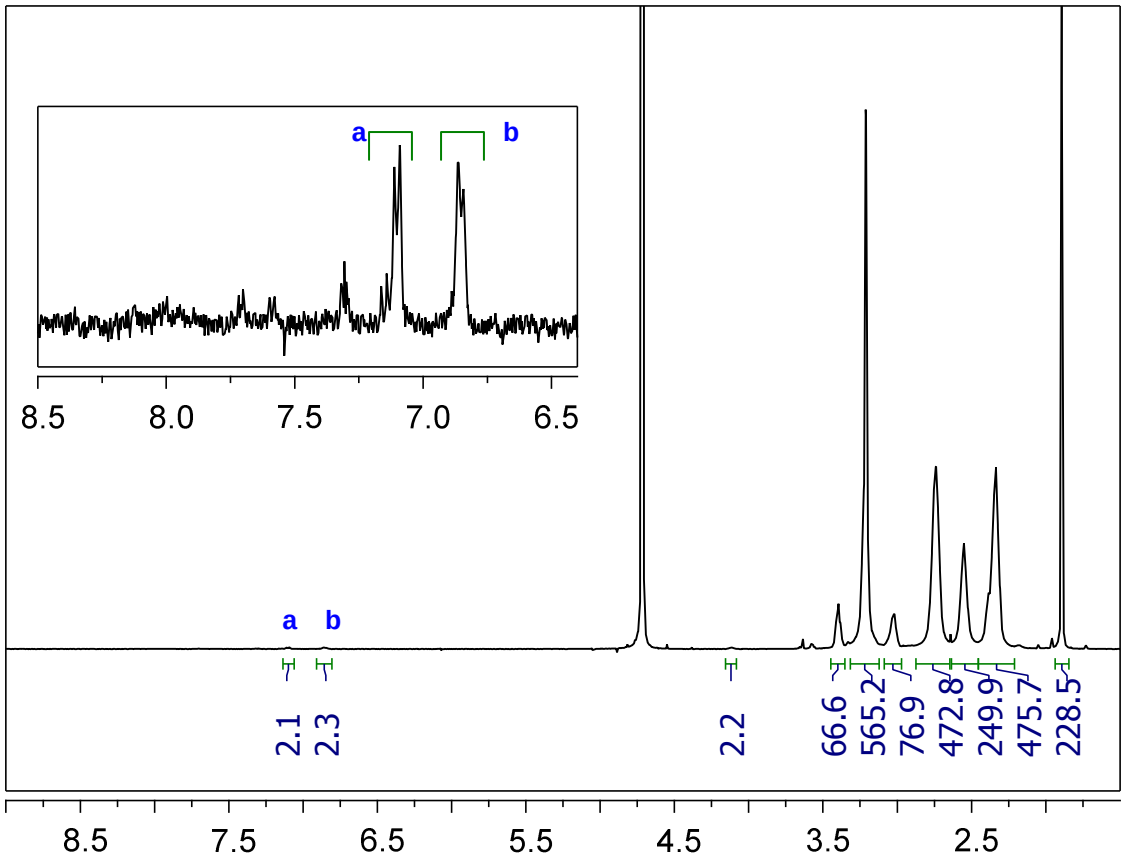
18. Synthesis of Un-targeted Dendrimer System G5-$Ac_{110.7}$-L-G5-Ac_{106}-$FITC_{3.2}$



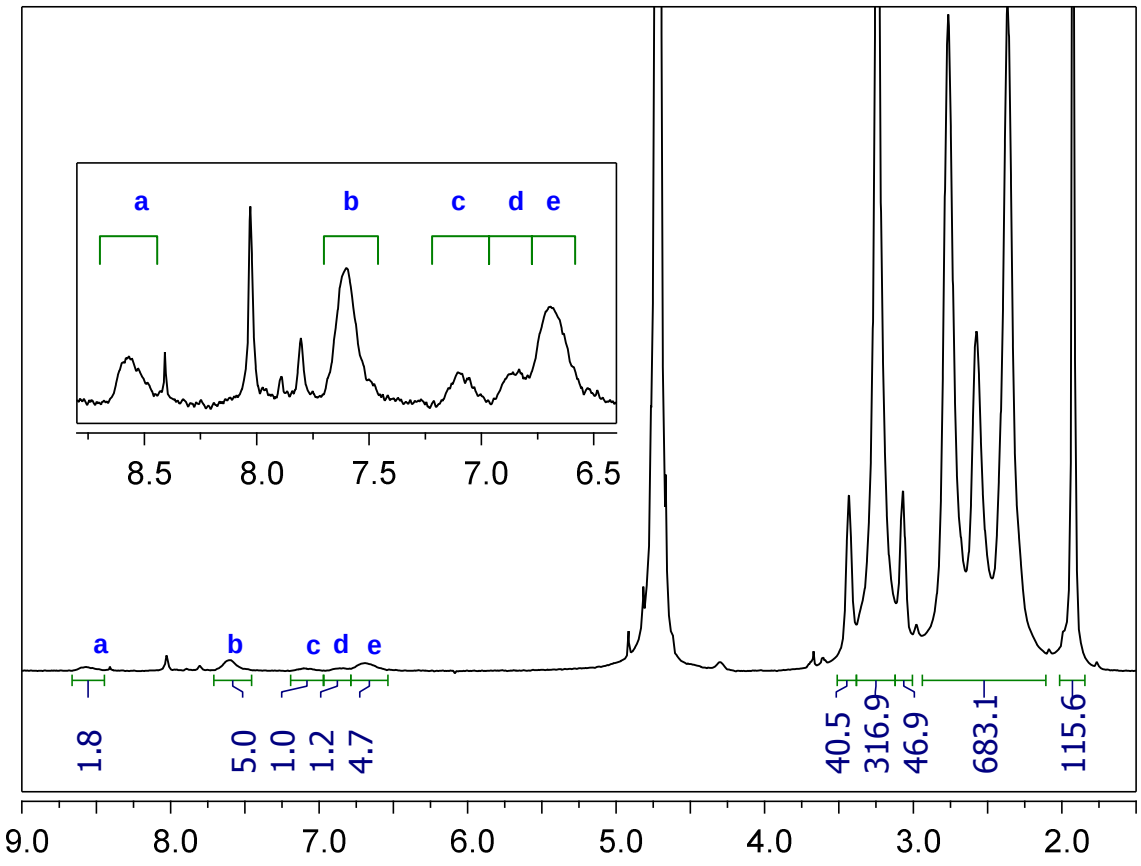
19. Synthesis of G5-Ac$_{58\%}$-Alkyne$_{1.2}$



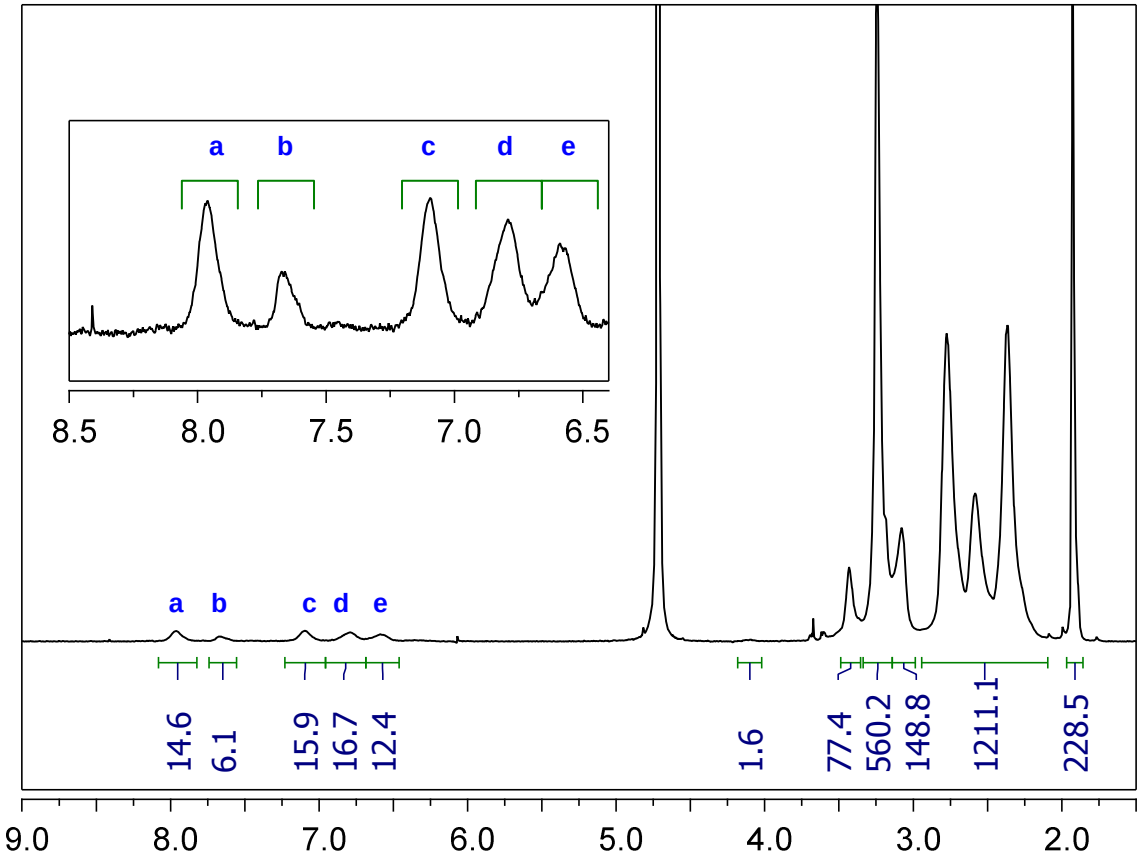
20. Synthesis of G5-Ac$_{68\%}$-Azide$_{1.1}$



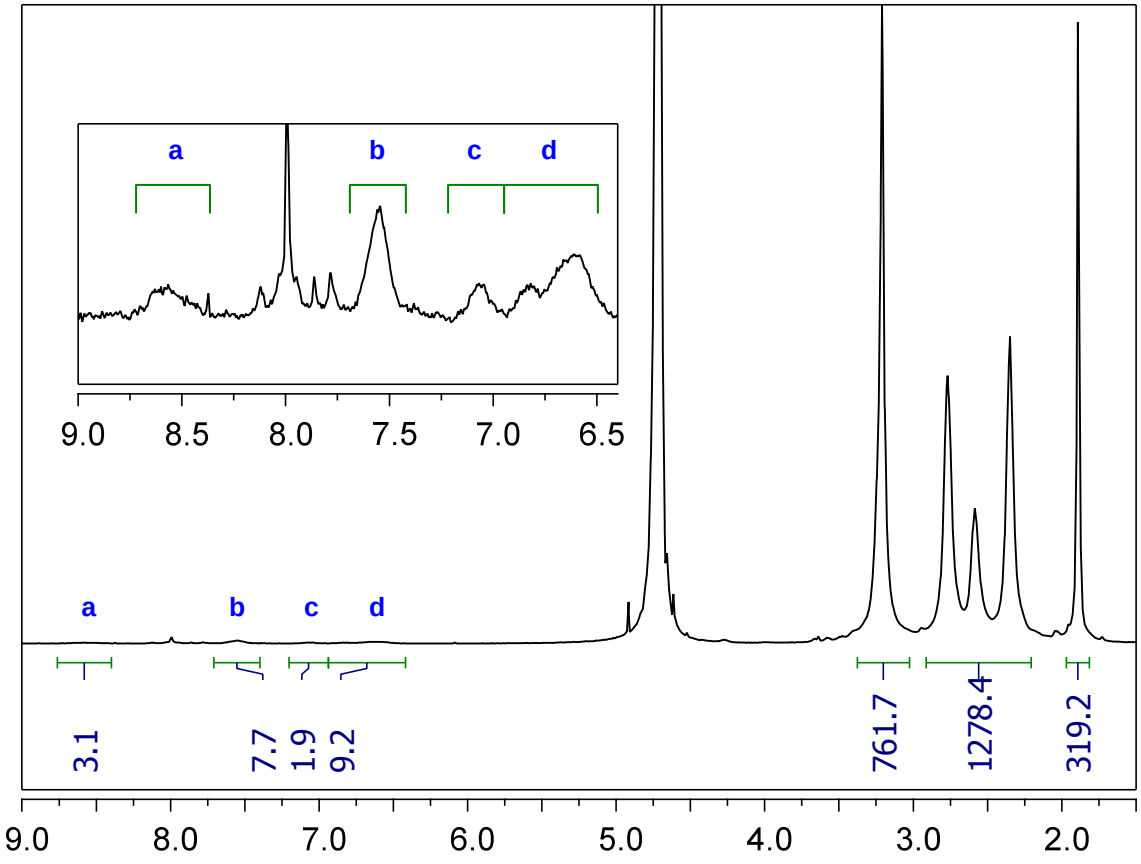
21. Synthesis of G5-Ac$_{58\%}$-Alkyne$_{1.2}$-FA$_{3.7}$



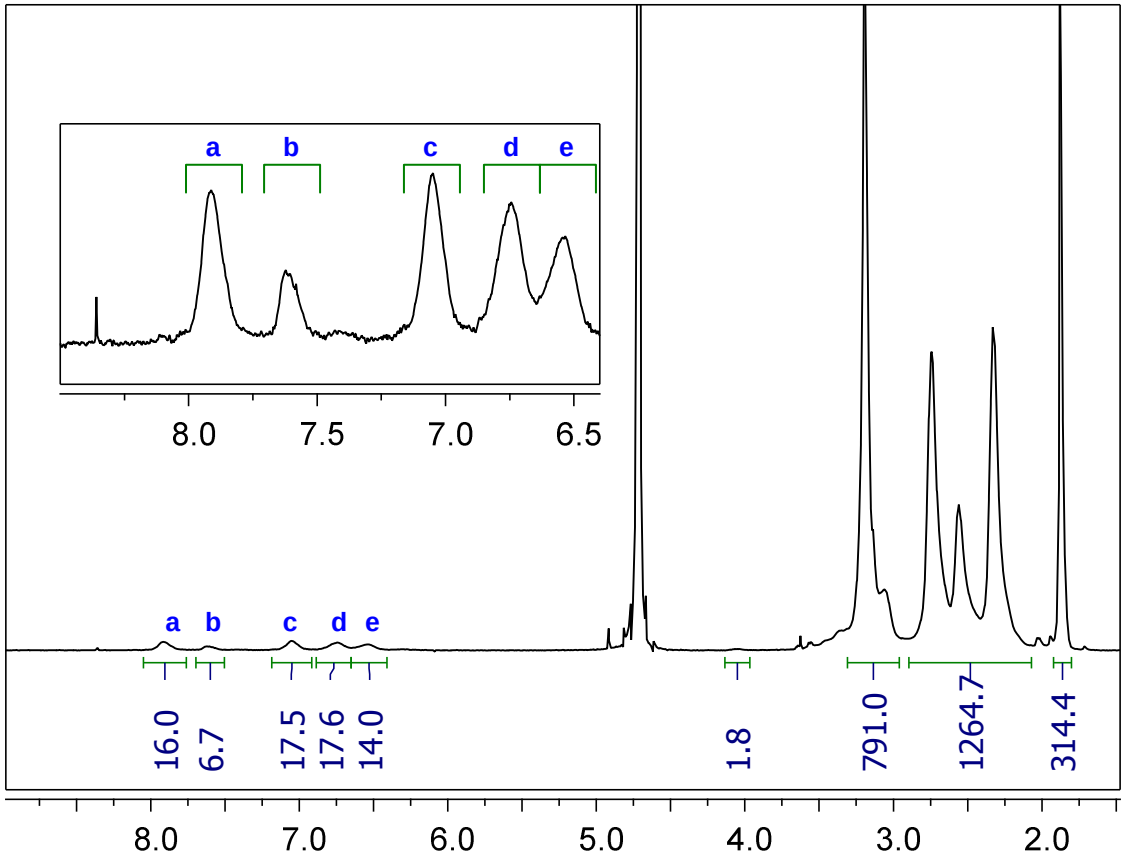
22. Synthesis of G5-Ac$_{65\%}$-Azide$_{1.1}$-6TAMRA$_{6.8}$



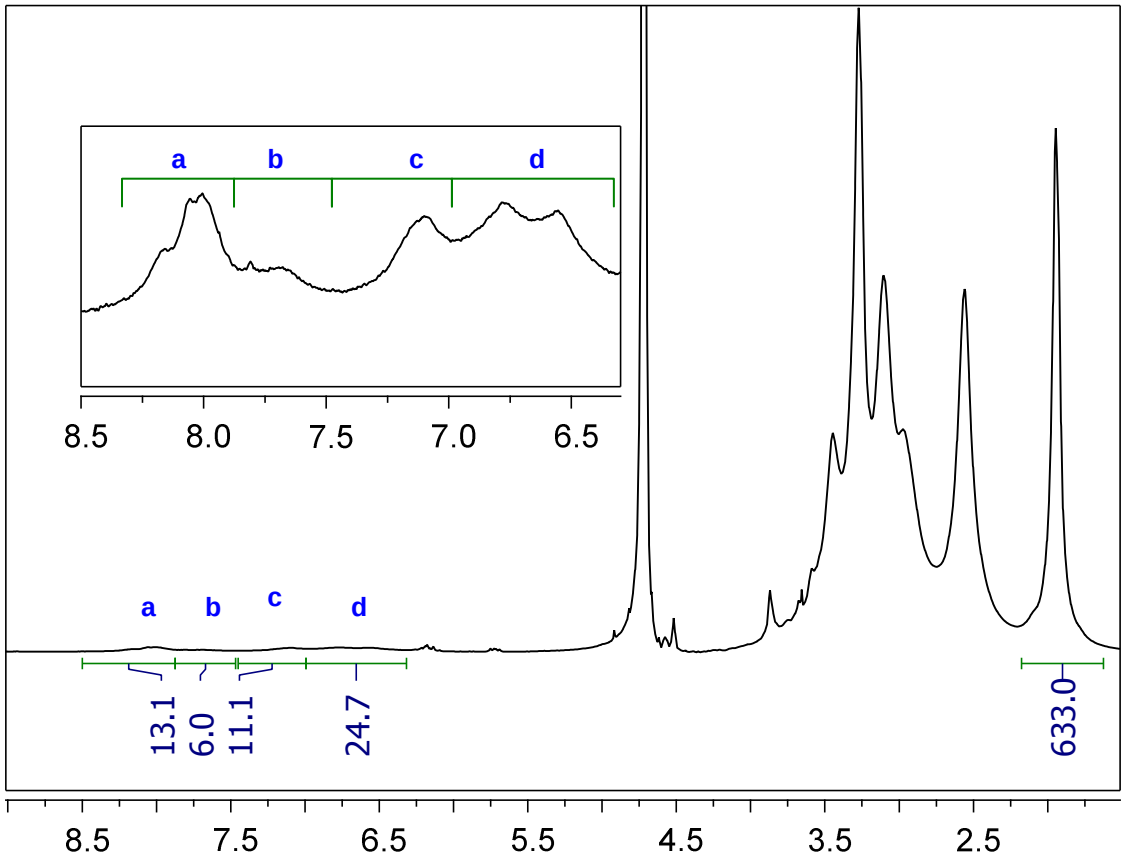
23. Synthesis of G5-Ac_{107}-$Alkyne_{1.2}$-$FA_{3.7}$



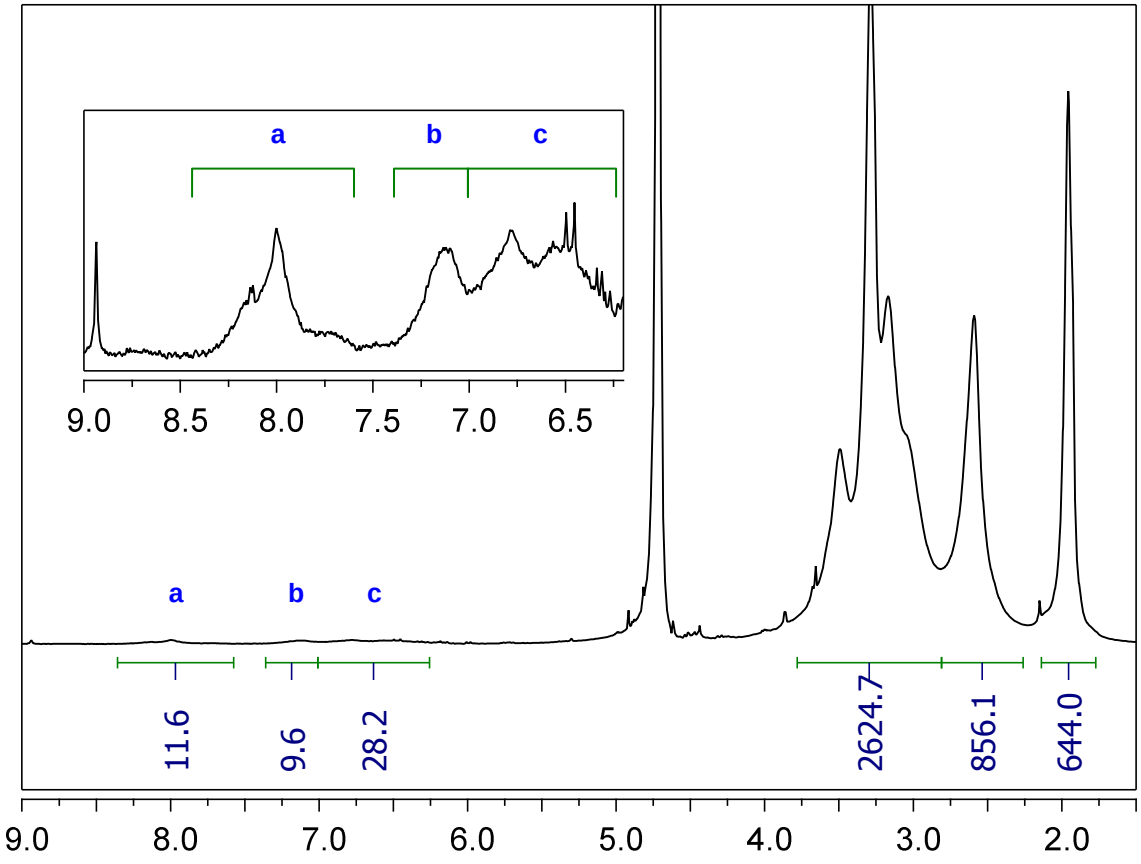
24. Synthesis of G5-Ac_{104}-$Azide_{1.1}$-$6TAMRA_{6.8}$



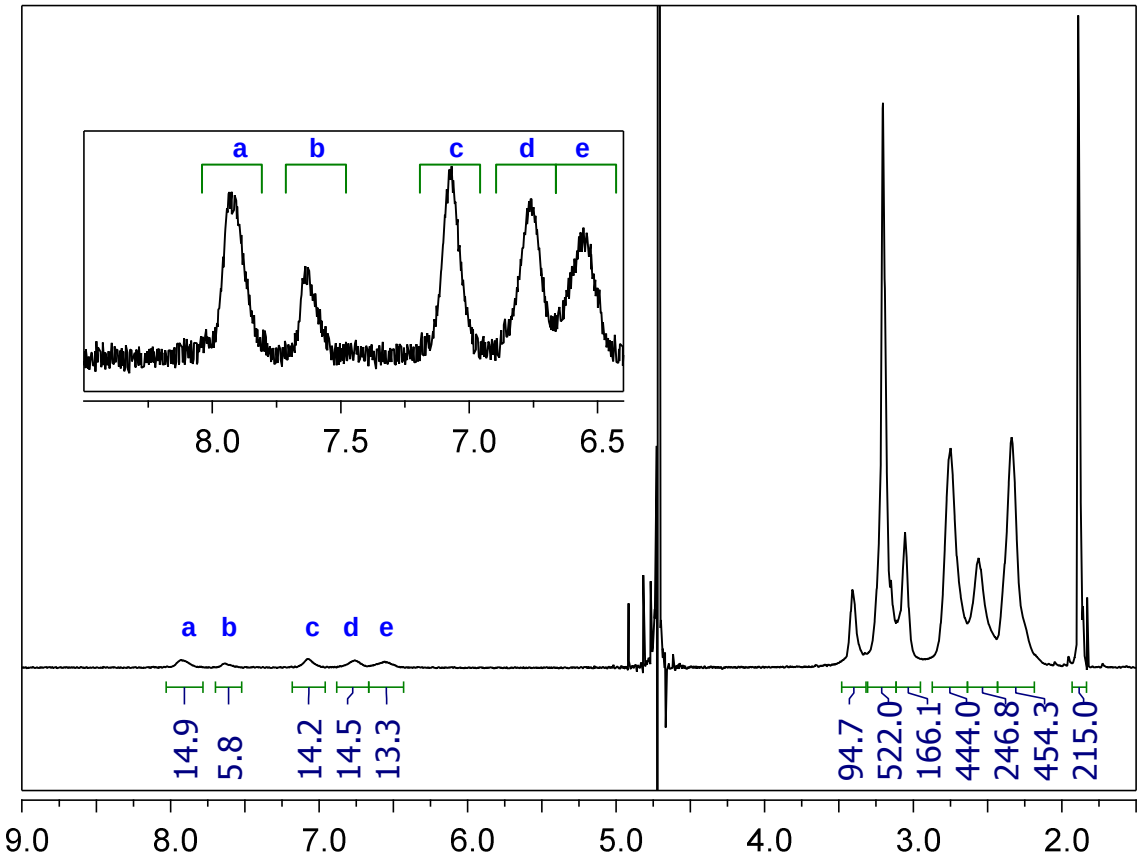
25. Synthesis of Folic Acid Targeted Dendrimer System with 6TAMRA $FA_{3.7}$-G5-Ac_{107}-L-G5-Ac_{104}-6TAMRA$_{6.8}$



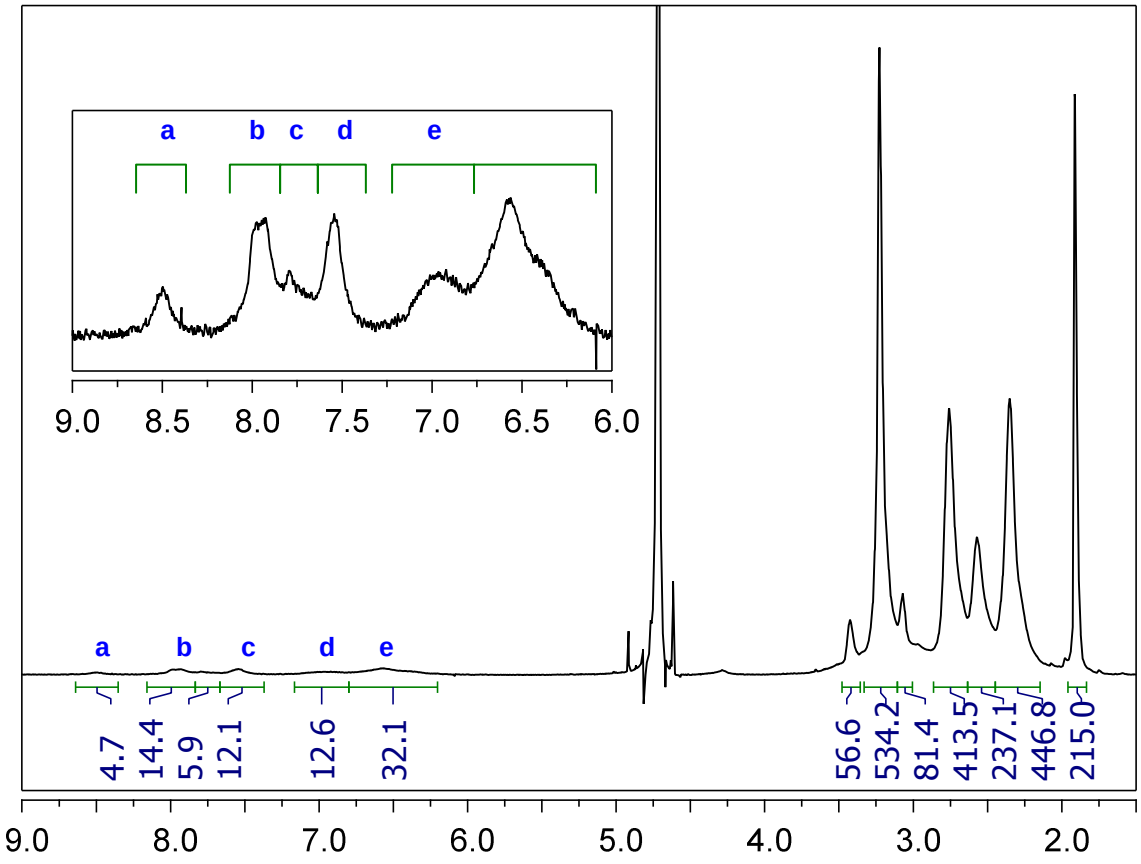
26. Synthesis of Un-targeted Dendrimer System G5-$Ac_{110.7}$-L-G5-Ac_{104}-$6TAMRA_{6.8}$



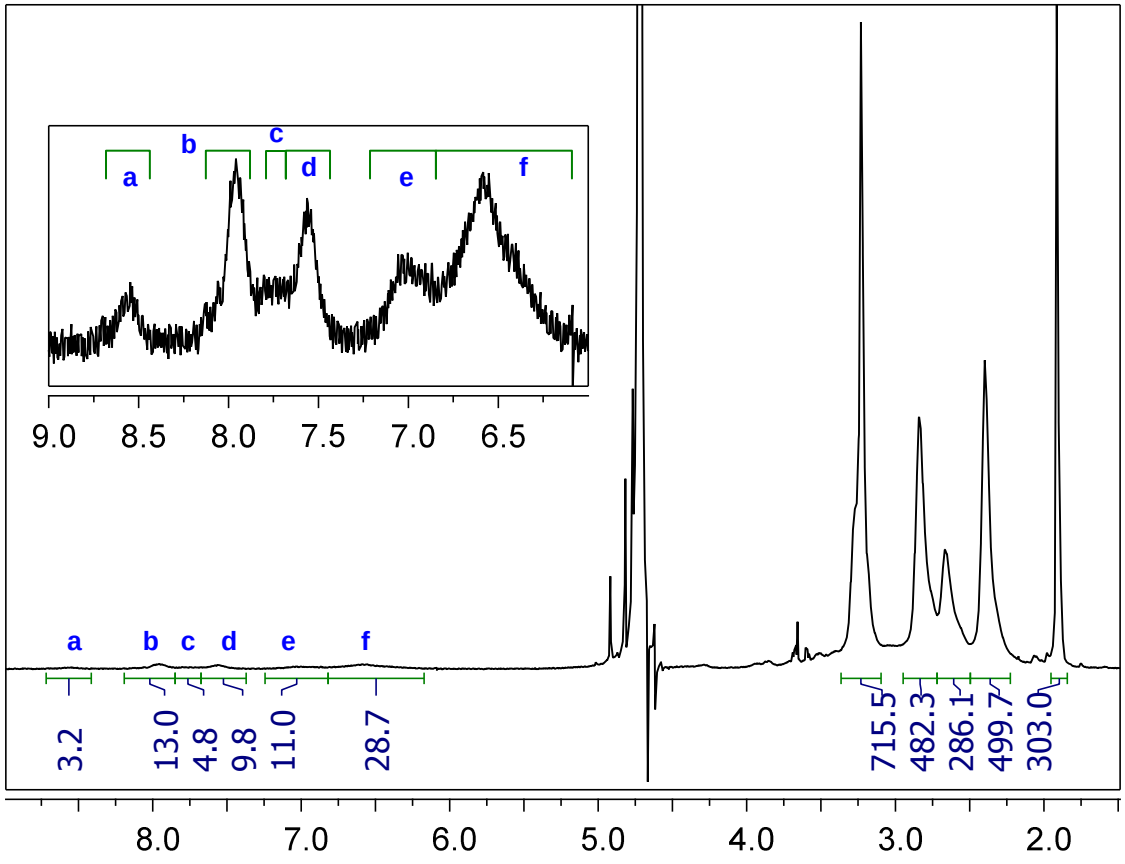
27. Synthesis of G5-$Ac_{64\%}$-$6TAMRA_{7.1}$



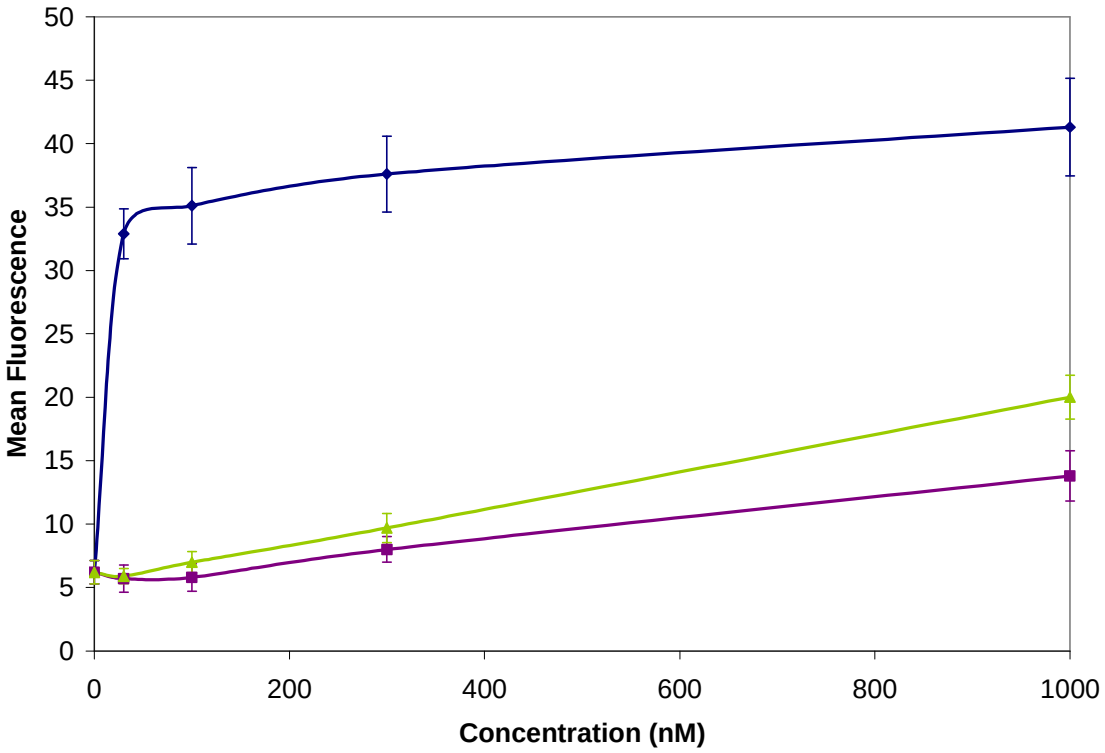
28. Synthesis of G5-Ac$_{64\%}$-6TAMRA$_{7.1}$-FA$_{4.0}$



29. Synthesis of G5-Ac_{101}-6TAMRA$_{7.1}$-$FA_{4.0}$



S2: Binding and uptake of the fluorescent modular targeted dendrimer platform and controls in KB cells as measured by Flow Cytometry. Uptake of $FA_{3.5}$-G5-Ac_{107}-L-G5Ac_{106}-$FITC_{3.2}$ (**15**) is displayed in blue. Mean fluorescence values for the un-targeted platform G5-$Ac_{110.7}$-L-G5-Ac_{106}-$FITC_{3.2}$ (**18**) is shown in green. Last, mean fluorescence values for the imaging module G5-Ac_{106}-$Azide_{2.5}$-$FITC_{3.2}$ (**14**) can be found in purple. Error bars indicate standard deviation as computed from half-peak coefficient of variation (HPCV) values.



Bioconjugate Chemistry

ARTICLE

pubs.acs.org/bc

Synthesis, Characterization, and *In Vitro* Transfection Activity of Charge-Reversal Amphiphiles for DNA Delivery

Xiao-Xiang Zhang,¶,‡ Carla A. H. Prata,¶,‡ Jason A. Berlin, Thomas J. McIntosh,§ Philippe Barthelemy,† and Mark W. Grinstaff*

Departments of Biomedical Engineering and Chemistry, Boston University, Boston, Massachusetts 02215, United States

†Inserm, U869, Bordeaux, F-33076 France

‡Université de Bordeaux, F-33076, Bordeaux, France

§Department of Cell Biology, Duke University Medical Center, Durham, North Carolina 27710, United States

Supporting Information

ABSTRACT: A series of charge-reversal lipids were synthesized that possess varying chain lengths and end functionalities. These lipids were designed to bind and then release DNA based on a change in electrostatic interaction with DNA. Specifically, a cleavable ester linkage is located at the ends of the hydrocarbon chains. The DNA release from the amphiphile was tuned by altering the length and position of the ester linkage in the hydrophobic chains of the lipids through the preparation of five new amphiphiles. The amphiphiles and corresponding lipoplexes were characterized by DSC, TEM, and X-ray, as well as evaluated for DNA binding and DNA transfection. For one specific charge-reversal lipid, stable lipoplexes of approximately 550 nm were formed, and with this amphiphile, effective *in vitro* DNA transfection activities was observed.



INTRODUCTION

Gene therapy offers the potential to treat a variety of diseases by delivering a functional copy of a missing or defective gene. Current research in this field focuses on two major classes of DNA carriers: viral[1−5] and nonviral.[6−16] Viral vectors transfect a significantly greater percentage of genetic material than nonviral systems, but suffer from a number of drawbacks, including toxicity and induced immunological response.[17] As a consequence, interest in synthesizing and evaluating nonviral delivery systems, including amphiphilic small molecule and polymeric compounds, has increased over the last 10 years. Cationic lipids are one type of amphiphile that can intracellularly transport DNA. Several liposome formulations are commercially available with a few in clinical trials.[16,18] Three examples of such lipids (DOTAP, DOTMA, and DMRIE) are shown in Figure 1.

Following the initial success of these lipids for DNA transfection, a number of different lipid forming complexes of varying structure and composition have been investigated. Within this context, a few representative examples are described below for DNA delivery. The acyl chain length and linker bonds connecting the cationic head to the acyl tail(s) have been varied to enhance transfection efficiency and decrease cytotoxic effects (e.g., DOTMA).[19] Lipospermines, with polycationic headgroups, have been investigated to increase the affinity for DNA.[20] Fluorinated analogues of cationic lipids such as DOTMA have been explored, and these amphiphilies exhibited higher transfection activities *in vitro*[21] and *in vivo*.[22] A hydrophilic spacer (such as PEG) has been placed between the cationic headgroup and the hydrophobic chains[23] to improve transfection efficiency. Researchers have explored the use of glycosidic cationic head groups in an attempt to lower toxicity through tighter interactions with DNA[24−26] or peptide head groups to mimic peptide−DNA binding interactions.[27−30] Recent reports from our laboratory have also described the use of cationic lipids possessing nucleic acid recognition components for nucleic acid delivery in an effort to use more than one type of molecular interaction for complexation.[31−39]

In addition to using these strategies to overcome the low transfection efficiencies of synthetic vectors (estimated to be 0.1% to 1%), functional or stimuli-responsive vectors have also been developed and evaluated. These cationic amphiphiles are able to respond to a stimulus that changes their chemical or physical properties, facilitating DNA delivery. Synthetic vectors have been prepared that are responsive to pH,[40−49] reducing conditions,[50−59] enzymes,[43,60−62] or temperature.[63,64] Many of these functional vectors that degrade or change conformation were designed based on the specific steps in the transfection pathway. This pathway starts with cellular entry of the DNA−amphiphile complex by endocytosis, followed by endosomal escape, and finally nuclear targeting and DNA expression.

Received: October 16, 2010
Revised: March 2, 2011
Published: April 01, 2011

ACS Publications © 2011 American Chemical Society

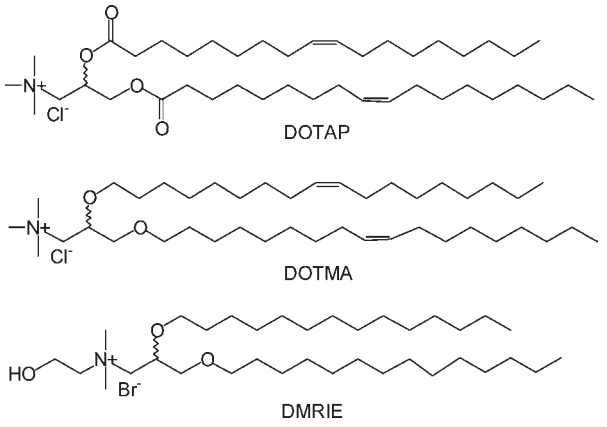


Figure 1. Chemical structures of several common cationic lipids.

Our research effort is centered on the release of DNA from the DNA−amphiphile supramolecular complex following cellular uptake, and as such, we have also focused on functional synthetic vectors. Given that a strong electrostatic assembly is formed between the cationic amphiphile and anionic DNA, and that this assembly is unlikely to disassemble spontaneously, we are interested in altering the electrostatic interaction to free the DNA.[54,65,66] To this end, we have synthesized and characterized new cationic amphiphiles that are capable of undergoing an intracellular electrostatic transition from cationic to anionic under the influence of esterases such as those found in cell lysosomes/endosomes.[67,68] This enables these amphiphiles to release DNA from the supramolecular assembly (Figure 2).

These charge-reversal or charge-switchable amphiphiles possess a positively charged ammonium headgroup that functions to complex DNA and lipophilic acyl chains to promote bilayer formation, similar to other cationic lipids like DOTAP (Figure 1). However, these new amphiphiles also contain ester functionalities near the terminal end of each acyl chain that, upon hydrolysis, switch the overall charge of the amphiphile from positive to negative. As an extension of our previous communication[54] in which we introduced the charge-reversal amphiphile, in this manuscript we have synthesized and investigated nine amphiphiles possessing C10, C12, or C16 acyl chain lengths terminally protected by benzyl, ethyl, butyl, or acetyl groups (Figure 3). The optimal chain length and terminal groups were determined based on amphiphile−DNA binding and DNA release. Standard ethidium bromide assays established the DNA binding capability of each of the vectors over a range of pH. The release of DNA from the DNA−amphiphile assembly was monitored also using an ethidium bromide assay. To determine the thermal and structural properties of the lipid and DNA−lipid complexes, differential scanning calorimetery (DSC), dynamic light scattering (DLS), transmission electronic microscopy (TEM), and X-ray diffraction were performed. Finally, the transfection of the amphiphile/DNA complexes was evaluated *in vitro* in several cell lines.

EXPERIMENTAL PROCEDURES

Please see the Supporting Information for complete experimental details.

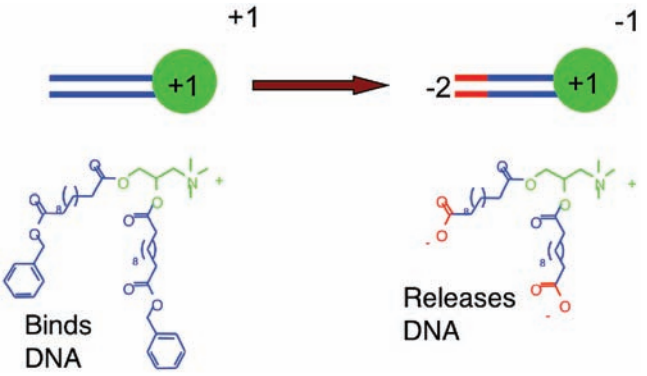


Figure 2. Charge-reversal or charge- switchable effect of the amphiphiles.

RESULTS AND DISCUSSION

To bind DNA, form lipoplexes, and then eventually release DNA, each amphiphile requires three distinct structural components: a cationic headgroup, hydrophobic chains, and terminal ester linkages. As shown in Figure 3, amphiphile **1** has a cationic headgroup to bind DNA, lipophilic acyl chains to form a bilayer, and ester linkages at the end of the acyl chains for enzymatic hydrolysis. We prepared the series of compounds **2**−**10**, shown in Figure 3, to systematically assess the role of each structural component and to evaluate the effects of amphiphile structure and reactivity (chain length, terminal end group, and ester or amide terminal group) on DNA binding/release, supramolecular assembly, and gene delivery efficacy. Specifically, amphiphile **1** possesses a cationic ammonium headgroup and two dodecanoic acid chains protected with benzyl esters. Hydrolysis of the benzyl esters of **1** affords compound **2**, which is negatively charged at neutral pH. Amphiphile **3** is an analogue of **1** that possesses noncleavable amide linkages, whereas compound **4** lacks the long acyl chains completely. Amphiphiles **6** and **7** are short and long acyl chain analogues of **1**, respectively, with the same terminal benzyl ester group. Amphiphiles **8** and **9** possess terminal alkyl ester linkages of two different chain lengths (ethyl and butyl ester, respectively). Finally, amphiphile **10** contains a similar terminal ester but upon hydrolysis affords two hydroxyl terminated acyl chains and thus remains cationic at neutral pH in aqueous solution.

The synthetic route to the amphiphiles is shown in Scheme 1. The preparation requires the use of functionalized fatty acids. The monoprotected benzyl ester fatty acids were prepared from the corresponding diacids (decanoic, dodecanoic, or hexanoic) with benzyl formate in the presence of Dowex 50W-X2 in octane at 80 °C. The butyl ester fatty acid was prepared in a similar manner using butyl formate. The ethyl ester fatty acids were obtained by the addition of ethanol to a solution of dodecanedioyl dichloride in tetrahydrofuran in the presence of triethylamine at 0 °C. The benzyl amide analogue was prepared in a similar manner using benzylamine. The acetylated fatty acid was prepared by acetylation of the hydroxydodecanoic acid using acetic anhydride in pyridine. Next, the monofunctionalized fatty acid derivatives were coupled to 3-dimethylaminopropanediol in the presence of DCC and DMAP in dichloromethane. The reaction yields ranged from 80% to 95% for all steps. Finally, the amphiphiles were reacted with methyl iodide in dichloromethane to quaternize the tertiary amine in quantitative yield. Complete details of the synthesis for each compound are found in the Supporting Information.

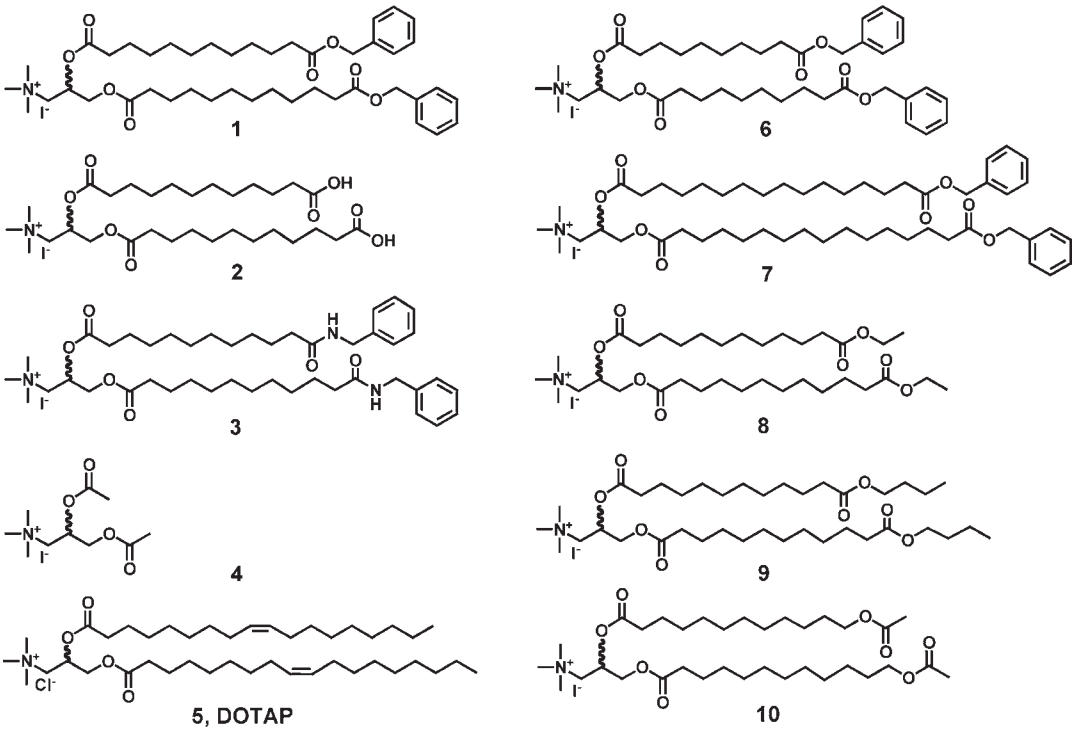
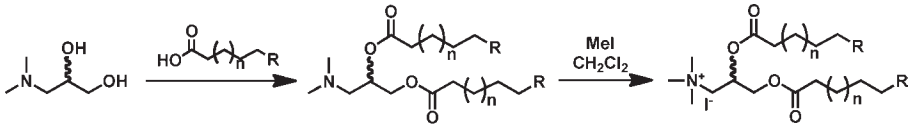


Figure 3. Structures of the charge-reversal amphiphiles under investigation for gene delivery.

Scheme 1. Synthesis of the Charge-Reversal Amphiphiles



1: n = 7; R = C(O)OBn
2: n = 7; R = C(O)OH
3: n = 7; R = C(O)NHBn
4: acetate derivative
6: n = 5; R = C(O)OBn
7: n = 11; R = C(O)OBn
8: n = 7; R = C(O)OEt
9: n = 7; R = C(O)OBu
10: n = 7; R = OC(O)CH3

As the first step toward evaluating these amphiphiles for the delivery of nucleic acids, we used an ethidium bromide displacement assay to determine whether the amphiphiles bind DNA.[69] This fluorescence quenching assay is an indirect method to measure DNA binding by monitoring the displacement of the ethidium bromide from DNA by the cationic amphiphile. This assay is widely used to assess small molecule/DNA binding, and it is assumed that the small molecule binder is responsible for displacing ethidium bromide and causing fluorescence decrease.

As shown in Figure 4, the fluorescence intensity decreases for amphiphiles **1**, **3**, **6**−**10**, and DOTAP upon addition to the ethidium bromide−DNA solution, but does not decrease for amphiphiles **2** and **4**. Amphiphile **2** possesses an overall negative charge and, consequently, does not bind DNA due to unfavorable electrostatic interactions. Compound **4** is a cationic amphiphile but does not bind DNA, indicating the importance of the hydrophobic acyl chains for the formation of a strong interaction with DNA.

The different terminal ester groups (ethyl, butyl, benzyl, acetyl) of the cationic amphiphiles do not appear to have a significant effect on DNA binding, as all of the amphiphiles bind DNA. The binding constants can be estimated and compared by measuring the loss of EtBr fluorescence as a function of the vector added. The concentration which produces 50% of the inhibition of fluorescence (IC_{50}) approximates the binding constant. The apparent binding constants were calculated as follows: $K_{app} = (1.26 \times 10^{-6}/\ IC_{50}) \times K_{EtBr}$ with $K_{EtBr} = 10^7\ M^{-1}$ as described elsewhere.[70] The binding constant for all the amphiphiles is on the order of $10^6\ M^{-1}$ and similar in magnitude to DOTAP ($K = 10^6\ M^{-1}$). These binding curves indicate that a ~1:1 charge complex is formed between DNA and most of these amphiphiles, except for **7**, which forms a ~ 2:1 charge complex with DNA.

We next determined the effect of pH on DNA binding for amphiphiles **1** and **2**. We chose two pH conditions near physiological pH (pH 7 and 8) and a lower pH of 5.5 that mimics the conditions of the early endosome. Figure 5 shows the fluorescence intensity as a function of amphiphile/DNA charge ratio for amphiphiles **1**, **2**, and **5** (DOTAP) at the three different pH conditions. The fluorescence intensity decreases as a function of charge ratio for both amphiphile **1** and DOTAP across all three

pHs. The binding curves look similar, with a 1:1 charge complex being formed between the amphiphile and DNA. The fluorescence intensity is constant and does not decrease for amphiphile **2**, indicating that **2** does not displace EtBr from DNA. This result is consistent with **2** being anionic over this pH range and as that the pK_a for the terminal carboxylic acids is below 5.5. Overall, these pH conditions do not play a significant role in DNA binding of the amphiphiles.

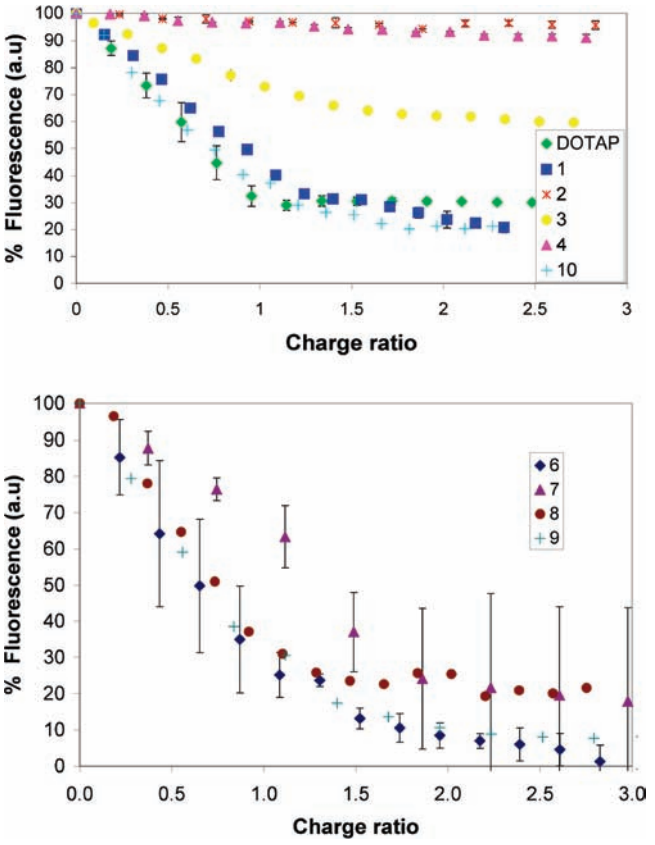


Figure 4. (top) Fluorescence intensity as a function of amphiphile/DNA charge ratio. (bottom) The fluorescence intensity as a function of amphiphile/DNA charge ratio for amphiphiles **1**, **6**−**10**, and DOTAP. N = 3 Avg ± SD.

To evaluate the release of the DNA from the amphiphile−DNA complex, the amphiphile/EtBr/DNA solution was incubated with a porcine liver esterase at pH 7.4 (1000 units/mL; 37 °C; 100 mM NaCl, 100 mM Tris buffer). For these release studies, the fluorescence intensities as a function of time for the various amphiphiles (including DOTAP) are shown in Figures 6 and 7. The increase in fluorescence from EtBr results from reintercalation of EtBr in the DNA; once the DNA is "free" from the amphiphile complex, ethidium bromide can bind with the DNA. As shown in Figure 6, amphiphile **1** no longer binds strongly to the DNA as a consequence of hydrolysis of its terminal benzyl esters. This result is consistent with the binding studies conducted with **2**, the hydrolyzed product of **1** prepared independently. However, in the presence of the enzyme, no increase in fluorescence over time is observed with amphiphile **3** or **5** (DOTAP), which possesses a terminal amide linkage or methyl group, respectively. A slightly slower increase in fluorescence is observed with compound **10**, which upon hydrolysis affords a neutral hydroxyl group.

To confirm that enzymatic hydrolysis cleaved the benzyl ester bond, liposomes formed from amphiphile **1** were incubated in PBS at 37 °C in the presence of porcine liver esterase, and the reaction products were examined by LC-MS. The results show that, within 30 min, ∼58% of **1** had converted to the hydrolyzed product **2**, and **1** was completely hydrolyzed by 2.5 h.

When the terminal ester is changed from a benzyl to an ethyl group as in compound **8**, similar EtBr−DNA binding curves to those of compound **1** are obtained (Figure 7). The increases in fluorescence indicate that both benzyl and ethyl terminal esters are readily hydrolyzed. Likewise, similar results are obtained when the acyl chain length is shortened from C12 to C10 (**1** vs **6**) while maintaining the terminal benzyl esters. However, upon extending the acyl chain length to C16 from C12 (**1** vs **7**), no increase in fluorescence is observed. Our interpretation of this

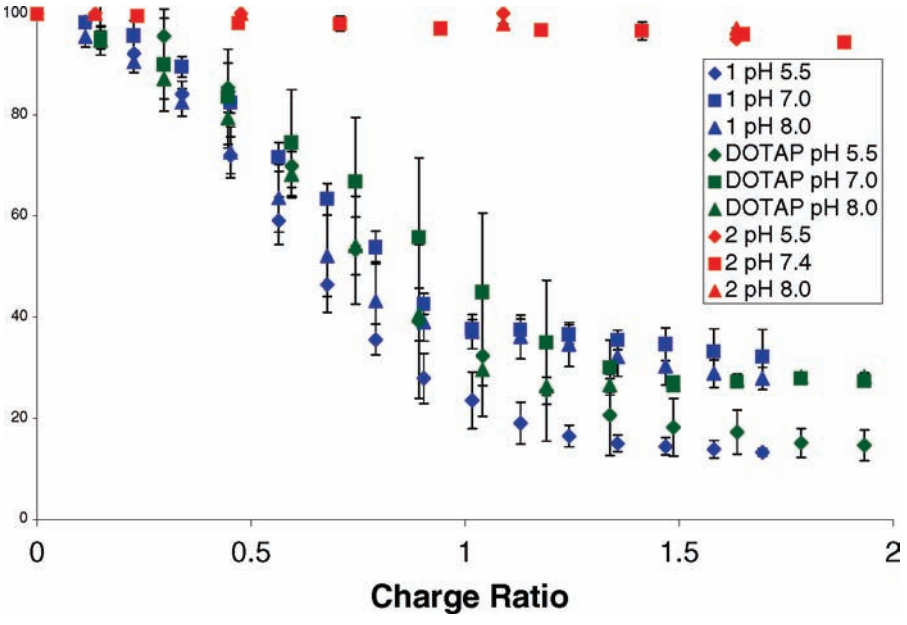


Figure 5. Fluorescence intensity as a function of amphiphile/DNA charge ratio in pH solutions of 5.5, 7.0 and 8.0. N = 3 Avg ± SD.

dx.doi.org/10.1021/bc1004526 |*Bioconjugate Chem.* 2011, 22, 690–699

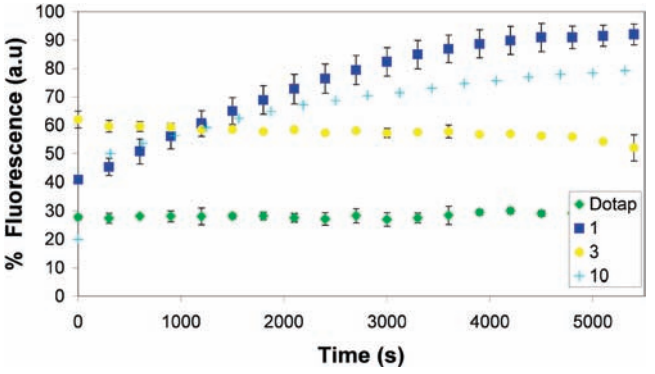


Figure 6. Ethidium bromide intercalation assay showing the fluorescence intensity as a function of time in the presence of a porcine liver esterase (1000 units/mL). $N = 3$ Avg ± SD.

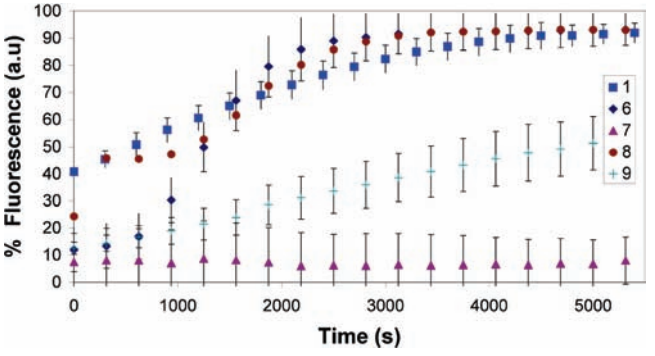


Figure 7. Ethidium bromide intercalation assay showing the fluorescence intensity as a function of time in the presence of a porcine liver esterase. $N = 3$ Avg ± SD.

result is that the long chain analogue forms a more stable bilayer structure, reducing accessibility of the ester bonds to the enzyme, and therefore inhibiting hydrolysis. The phase-transition temperature (T_m) for **7** is 23 °C higher than for **1**, as shown in Table 1, which is consistent with this interpretation. Upon changing the benzyl to an ethyl ester but maintaining the chain length of C12, we observe a similar rate of hydrolysis (**6** vs **8**). However, **9**, which possesses an *n*-butyl ester as opposed to an ethyl ester (**9** vs **1**), shows a slower rate of fluorescence increase during the assay. In this amphiphile, the hydrolyzable ester is buried further in the hydrophobic chain, leading to a slower rate of hydrolysis. The enzymatic mechanism is still unknown, although we suspect that, during the flip-flop of the lipids, the enzyme hydrolyzes the terminal ester bonds.

Overall, the fluorescence data indicate that release of DNA from the supramolecular assembly does not occur for amphiphiles lacking a terminal hydrolyzable ester linkage, and those linkages near the headgroup or buried deeper in the chain are less accessible to enzymatic hydrolysis. The data also show the difference in DNA release from an amphiphilic complex that generates a resulting anionic amphilphile product versus a neutral one (**1** vs **10**).

Next, transfection experiments using the reporter gene, β-galactosidase (β-gal, pVax-LacZ1, Invitrogen), were performed with Chinese hamster ovarian (CHO) cells. The reporter gene was first mixed with the cationic lipid, at a defined amphiphile/DNA ratio, in potassium phosphate buffer (PBS) at room temperature.

Table 1. DSC Results for the Amphiphile Assemblies

compound	T_m (°C)	ΔH (kcal/mol)
1	52.55	2.03
6	46.32	3.18
7	75.45	1.57
8	78.44	8.47
9	76.14	3.78
10	50.77	0.102

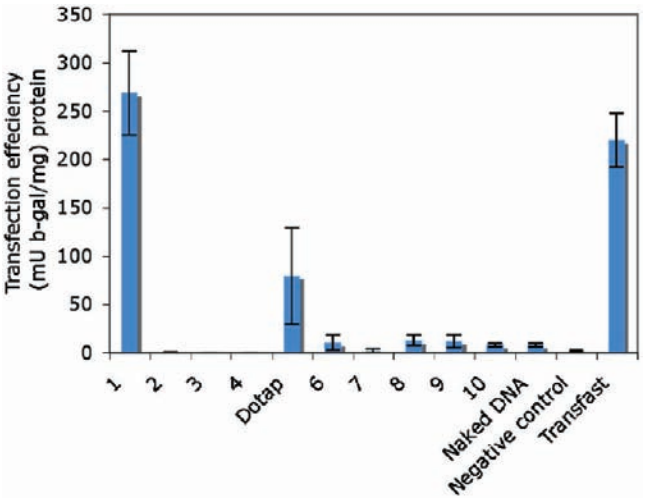


Figure 8. Transfection efficiency of the different amphiphiles in CHO cells. $N = 3$ Avg ± SD.

The complexes were added to CHO cells after 15 min. The amount of DNA used was the same as was used in the naked DNA control (no amphiphile) and positive control experiments (DOTAP and Transfast). The negative control was amphiphile **1** without DNA. After incubation at 37 °C and 5% CO_2 for 2 h, the solution containing the lipoplexes was removed and fresh growth medium with serum was added. Transfection efficiencies were assessed after 48 h using the β-galactosidase enzyme assay in conjunction with a standard curve. The efficacy of each transfection was calculated as β-gal activity normalized to total protein. We first performed a screen to identify the optimal amphiphile **1**/DNA ratio for greatest transfection examining ratios of 1:1, 2:1, 5:1, 10:1, 15:1, and 45:1. We also varied the time of incubation of the lipoplex with the cells from 30 min to 3 h, as well as performed analyses at the 24 and 48 h time points. On the basis of these experiments, the highest transfection efficiency was at a 5:1 ratio, an exposure time of 2 h, and analysis after 48 h. With these optimal conditions, we then performed a series of transfection experiments with the charge-reversal amphiphiles, as summarized in Figure 8. Amphiphile **1** was the most effective vector for transfection. The other compounds (**2**−**4** and **6**−**10**) showed minimal transfection activity, comparable to the negative control and naked DNA. The transfection efficacy of amphiphile **1** was significantly better than that of DOTAP ($p < 0.05$) and comparable to that of Transfast ($p > 0.05$). In the literature, it has also been shown that the addition of neutral lipids (i.e., helper lipids) such as dioleylphosphatidylethanolamine (DOPE) to a cationic lipid formulation can

dx.doi.org/10.1021/bc1004526 |*Bioconjugate Chem.* 2011, 22, 690–699

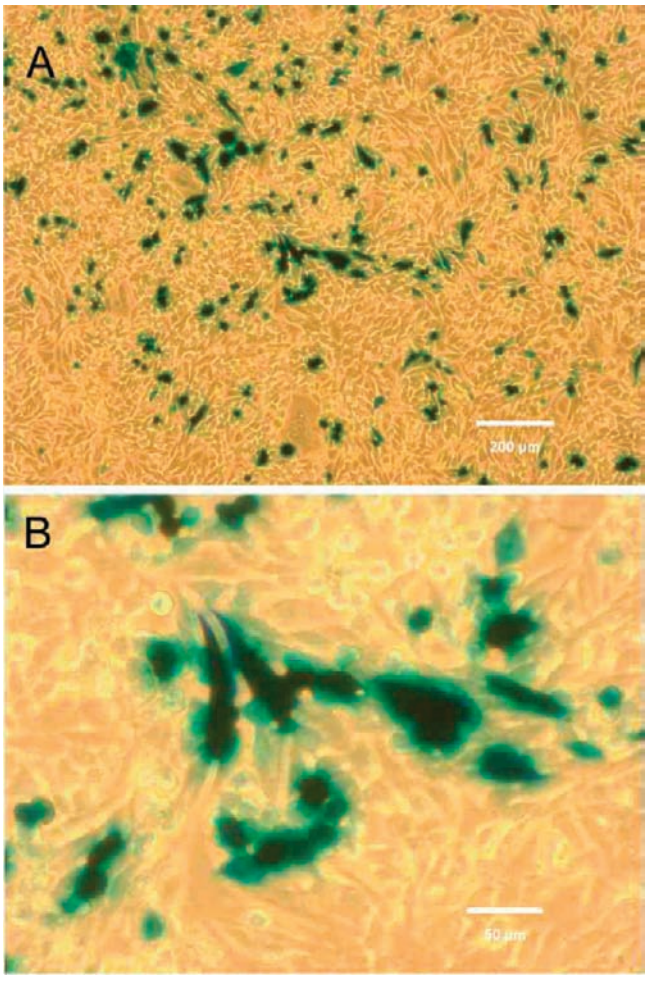


Figure 9. Photograph of β-galactosidase transfected cells using amphiphile **1** at low and high magnification. Dark blue stain represents B-gal expression.

improve DNA transfection efficiency.[19] Consequently, the above transfection experiments were repeated using the helper lipid, DOPE, and the charge-reversal amphiphiles at a 1:1 ratio. No increase in transfection efficiency was observed for these conditions (data not shown).

Micrographs of the β-galactosidase transfected CHO cells using amphiphile **1** are shown in Figure 9. This transfection experiment was conducted in a similar manner except it was done on a glass slide that had been previously modified with collagen to anchor the cells. The cells are expressing the protein β-gal (dark blue stain), and there appear to be few patches containing no cells, indicating minimal toxicity under these experimental conditions. This lack of cytotoxicity was quantitatively determined in our next set of experiments.

Cytotoxicity experiments were performed with CHO cells using both a formazan-based proliferation assay and a total protein assay. The cells were seeded onto a 96-multiwell microliter plate with an approximate density of 1×10^4 cells per well. The compounds were added to the cells 24 h later. After 24 h, cell proliferation was determined and expressed as a percentage of nontreated cells as shown in Figure 10. None of the amphiphiles showed a significant cytotoxicity, with values similar to the negative control (i.e., nontreated cells).

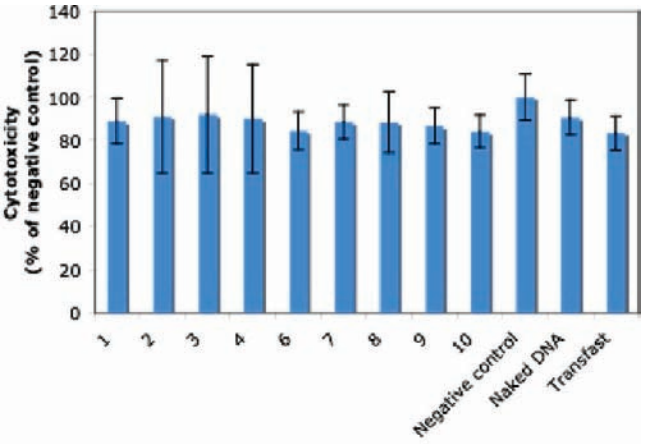


Figure 10. Cytotoxicity of the different lipids in CHO cells. $N = 3$ zAvg $\pm$ SD.

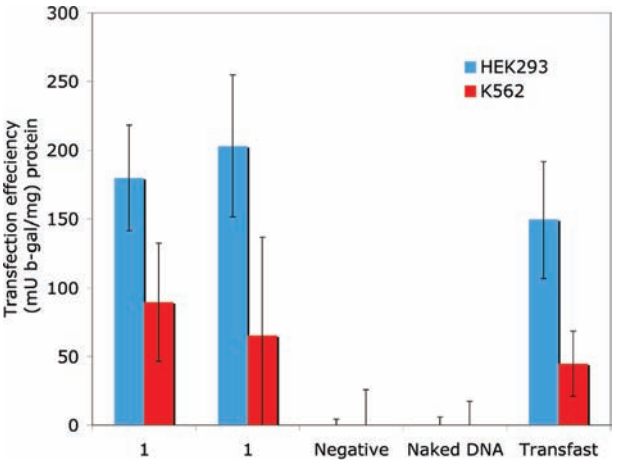


Figure 11. Transfection efficiency of amphiphile **1** with HEK293 and K562 cell lines. $N = 3$ Avg $\pm$ SD. First data set with **1** is at 15:1 and the second data set is at 45:1 charge ratio.

With these encouraging results, we then evaluated the transfection activity of amphiphile **1** in four other cell lines. Transfection experiments using human embryonic kidney (HEK293), erythroleukemic (K562), mouse fibroblast (NIH 3T3), and human liver carcinoma (HepG2) cell lines were performed with compound **1** (see Figure 11). Once again, we varied amphiphile **1**/DNA ratio, and only at high amphiphile/DNA ratio did we observe transfection (HEK 15:1; K562 45:1). Amphiphile **1** transfected DNA with similar efficiency to Transfast in the HEK293 and K562, but we did not observe significant transfection in the NIH 3T3 or HepG2 lines (data not shown).

With the above transfection activities recorded, we embarked on a series of physiochemical experiments to elucidate the key structural and physical properties of amphiphile **1** likely responsible for transfection activity. Given the polar headgroup and long hydrophobic acyl chains present in amphiphile **1**, it is likely to form bilayer structures in aqueous solution. To test this idea, differential scanning calorimeter (DSC), dynamic light scattering (DLS), transmission electron microscopy (TEM), and X-ray diffraction (XRD) experiments were performed. The samples were prepared for these studies by introducing a chloroformic

solution of amphiphiles into a pear-shaped flask. The solution was evaporated under vacuum, leaving a thin film deposited onto the flask wall. A total of 1 mL Tris buffer (100 mM Tris, 100 mM NaCl, pH 7.4) was then added, and the film was peeled off by vortexing. After 20 extrusions though a 50 nm polycarbonate membrane (Avanti Polar Lipids), the milky aqueous suspension turned into a homogeneous solution. The lipoplexes were prepared in an analogous manner by addition of the DNA to the previously prepared liposome solution.

DSC traces of the aqueous hydrated amphiphiles (**1**, **6**−**10**) show for each lipid a single phase-transition temperature (T_m). The T_m and transition enthalpy (ΔH) vary as the chain lengthens (C10, C12, and C16; **6** vs **1** vs **7**, respectively) when the end groups remain the same. For example, the T_m increases from 46 °C for **6** to 75 °C for **7**, indicating that amphiphile **7** forms a more stable structure than **1** or **6**. This trend with increasing chain length and higher T_m is true for T_m, but not for enthalpy. The enthalpy is smaller for **7** than for **6** or **1**. These results are consistent with reports on other lipid families (e.g., phosphatidylcholine and Avanti polar technical data). When the chain lengths are kept constant but the end group is changed from a benzyl to an alkyl ester on the amphiphile (e.g., **1** vs **8**), the T_m and enthalpy increase by about 25 °C. On the other hand, reversing the directionality of the ester linkage (**10** vs **8**) leads to a decrease in the T_m, possibly reflecting the greater ease that water molecules can hydrate and destabilize the terminal chain end group in **8** relative to **10**. In all, the DSC data showed that these charge-reversal lipids form organized structures with melting temperatures higher than 0 °C, the melting temperature of DOTAP, a common amphiphile used for gene transfection.

The mean diameter of the supramolecular structures formed by the different amphiphiles and by the amphiphile/DNA complexes was measured by dynamic light scattering (DLS). Compound **1** formed structures with a mean diameter of 110 nm, and the diameter increased to 562 nm in the presence of DNA. Amphiphile **6** formed structures with the same mean diameter (110 nm) and in presence of DNA formed structures with a mean diameter of 680 nm. Compounds **8** and **9** formed aggregates of 1 μm and larger in diameter as measured by DLS. Likewise, compounds **2**, **3**, **7**, and **10** afforded very large aggregates and precipitated products.

At 22 °C, X-ray diffraction patterns of amphiphile **1** in the absence of DNA gave three orders of a lamellar repeat period of 5.22 ± 0.03 nm with a sharp wide-angle spacing of 0.46 ± 0.01 nm. These data indicate that compound **1** formed gel-phase multibilayers at 22 °C, consistent with the DSC data (Table 1). In the presence of DNA, fully hydrated amphiphile **1** gave a lamellar repeat period of 5.31 ± 0.14 nm with a sharp wide-angle spacing of 0.46 ± 0.01 nm. Thus, the presence of the DNA did not significantly change d, indicating that the DNA was not intercalated between the lipid layers. Typically, an increase of 1 to 1.4 nm in d is observed with formation of a DNA−lipid sandwich structure.[71] These XRD data suggest a model where the DNA is entrapped at the surface or at the interface between the multilamellar vesicles (MLVs) in solution. This model is consistent with the increase in size observed by DLS, which could be caused by DNA bridging between these large MLVs. We were able to obtain a TEM image of amphiphile **1** in the presence, but not the absence, of DNA. The TEM micrograph showed multilamellar structures with an average vesicle diameter of 200 nm (Figure 12). Repeated attempts to obtain X-ray data on **6** in the presence and absence of DNA were unsuccessful.

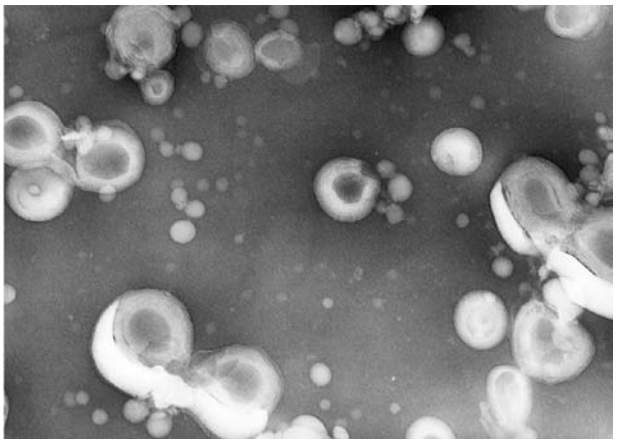


Figure 12. TEM micrographs of amphiphile **1** in aqueous solution, negative staining with ammonium molybdate 1% in water.

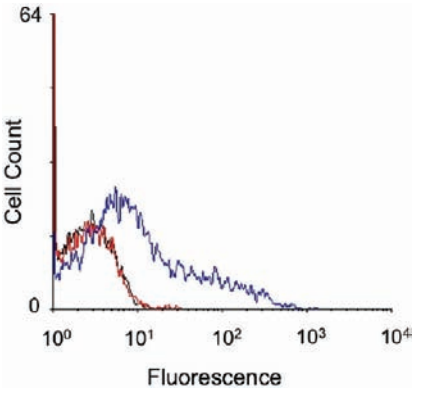


Figure 13. Flow cytometry histogram for CHO cells transfected with rhodamine-labeled DNA using either **1** (blue) or **6** (red). Negative control (black).

Of the amphiphiles, compound **6** has a melting temperature slightly lower than **1** and forms similarly sized structure by DLS as **1**, but does not give high transfection activity. We subsequently examined if the difference in activity between **1** and **6** was related to the amount of lipoplex taken up by the CHO cells. Cells were transfected with rhodamine-labeled DNA using either **1** or **6**, and the resulting cellular rhodamine fluorescence signal was recorded by flow cytometry. As shown in Figure 13, a significant amount of fluorescence was observed when DNA was delivered using **1**, while the fluorescence signal was almost the same as that of the negative control when delivered using **6**. Cell population analysis revealed that 27% of the cells were rhodamine-positive when transfected with **1**, compared to only 0.5% cells when transfected with **6**. These data suggest that the difference in cellular uptake may be responsible for the difference in the transfection activity between **1** and **6**. The underlying mechanism for the difference in cellular uptake is unknown and currently under investigation, but **6** does form a relatively weaker supramolecular structure than **1** as evident by the lower T_m.

Altogether, the results suggest a number of key findings responsible for the higher transfecton activity observed with amphiphile **1** compared to compounds **2**−**10**. First, compounds **2** and **4** do not bind DNA, while amphiphiles **1**, **3**, and **5**−**10** do bind DNA, at roughly the same magnitude. Amphiphiles **1**, **6**, **8**,

and **10** release DNA relatively rapidly in the presence of an esterase compared to the amphiphile **9**. Amphiphiles **3**, **5** (DOTAP), and **7** do not release DNA in the presence of an esterase. Amphiphiles **3**, **7**, **8**, **9**, and **10** formed aggregates of 1 μm or larger in diameter. Amphiphiles **1** and **6** both form similarly sized nanometer lipoplexes; however, more lipoplexes formed with amphiphile **1** are taken up by CHO than **6**.

In summary, *in vitro* gene delivery using charge reversal or charge switchable amphiphiles is a new approach and, like other functional delivery systems, provides a means to increase transfection activity, as well as potentially new reagents to study the transfection pathway. These amphiphiles were designed to transform from a cationic species that binds DNA to an anionic species that loses affinity to DNA after cleavage by an esterase. This charge-reversal effect would release DNA from the supramolecular complex. To evaluate the role of key amphiphile structural components, we synthesized in good yield a series of amphiphiles to determine the physicochemical properties and transfection efficiency of these amphiphiles. This series of amphiphiles included those that had C10 to C16 chains and a benzyl, *n*-butyl, or ethyl ester terminal group, as well as amphiphiles possessing very short alkyl chains and chains terminated with a carboxylate. All of these amphiphiles bind DNA and form amphiphile/DNA assemblies except for the compounds lacking long hydrophobic chains or those terminated with a carboxylate. The DNA release from the complexes and the dissociation rate of the complexes is controlled by the chemical structure of the lipid, which plays an important role in the stability and organization of the resulting supramolecular assembly. For example, the enzymatic hydrolysis rate of the ester linkage was dependent on hydrophobicity of the amphiphile, as the rate of hydrolysis was faster for the ethyl than the *n*-butyl analogue. The XRD data showed that amphiphile **1** forms bilayer organizations in the presence and absence of DNA, and DLS and TEM data showed that this amphiphile formed vesicles and lipoplexes with DNA on the order of 550 nm. The other amphiphiles organized themselves in larger aggregates. DSC data showed that the melting temperatures were between 45 and 80 °C, with those amphiphiles possessing the longer alkyl chains having higher melting temperatures.

The transfection experiments showed that the highest DNA transfection activity was observed for amphiphile **1**. This activity was observed in three different cell lines—Chinese hamster ovarian (CHO), human embryonic kidney (HEK293), and erythroleukemic (K562) cells. All other amphiphiles (except DOTAP and Transfast) showed minimal transfection activity, comparable to that of the negative control. Further studies will investigate the mechanism of cellular uptake and DNA delivery to the nucleus. This concept of charge reversal or charge switching has been successfully extended to additional cationic lipid structures,[66] zwitteronic lipids,[65] ferrocene-containing lipids,[55,56] and polymers[41,72] for DNA transfection, suggesting that this is an important, and potentially general, approach. Our data show that charge-reversal amphiphile **1** has all of the characteristics necessary for DNA delivery: it binds DNA, releases DNA upon charge reversal, forms well-ordered bilayers, forms lipoplexes of nanometer size, is taken up by cells, and efficiently transfects several cell types.

■ ASSOCIATED CONTENT

Ⓢ Supporting Information. Experimental procedures, fluorescence studies, DNA transfection, and cytotoxicity data. This material is available free of charge via the Internet at http://pubs.acs.org.

■ AUTHOR INFORMATION

Corresponding Author

*Corresponding author. E-mail: mgrin@bu.edu.

Author Contributions

¶Contributed equally to the work.

■ ACKNOWLEDGMENT

This work was supported by the Army Research Office (PB) and Grants GM27278 (TJM) and EB005658 (MWG) from the National Institutes of Health. We thank Dr. Dan Luo and Erin King for helpful discussions and technical advice at Cornell University. We thank Mr. Yuxing for help with the initial studies. We also thank Drs. Jun-lin Guan and Zara Melkoumian for providing the cell lines, and Dr. Stephen Lee (ARO) for support and discussions.

■ REFERENCES

(1) Deregowski, P., and Canalis, E. (2008) Gene delivery by retroviruses. *Methods Mol. Biol. 455*, 157–162.

(2) Flotte, T. R. (2004) Gene therapy progress and prospects: Recombinant adeno-associated virus (rAAV) vectors. *Gene Ther. 11*, 805–810.

(3) Lundstrom, K. (2004) Gene therapy applications of viral vectors. *Technol. Cancer Res. Treatment 3*, 467–477.

(4) Flotte, T. R. (2007) Gene therapy: The first two decades and the current state-of-the-art. *J. Cell. Physiol. 213*, 301–305.

(5) Ozawa, K. (2007) Gene therapy using AAV vectors. *Drug Delivery Syst. 22*, 643–650.

(6) Mintzer, M. A., and Simanek, E. E. (2009) Nonviral vectors for gene delivery. *Chem. Rev. 109*, 259–302.

(7) Ewert, K. K., Ahmad, A., Bouxsein, N. F., Evans, H. M., and Safinya, C. R. (2008) Non-viral gene delivery with cationic liposome-DNA complexes. *Methods Mol. Biol. 433*, 159–175.

(8) Wolff, J. A., and Rozema, D. B. (2007) Breaking the bonds: non-viral vectors become chemically dynamic. *Mol. Ther. 16*, 8–15.

(9) Wong, S. Y., Pelet, J. M., and Putnam, D. (2007) Polymer systems for gene delivery-past, present, and future. *Prog. Polym. Sci. 32*, 799–837.

(10) Dang, J. M., and Leong, K. W. (2006) Natural polymers for gene delivery and tissue engineering. *Adv. Drug Delivery Rev. 58*, 487–499.

(11) Christine, C. C., and Huang, L. (2005) Recent advances in non-viral gene delivery. *Adv. Genetics 53*, 3–18.

(12) Reineke, T. M., and Grinstaff, M. W. (2005) Designer materials for nucleic acid delivery. *Mat. Res. Soc. Bull. 30*, 635–639.

(13) Luo, D., and Saltzman, W. M. (2000) Synthetic DNA delivery systems. *Nat. Biotechnol. 18*, 33–37.

(14) Kabanov, A. V., Felgner, P. L., and Seymour, L. W. (1998) *Self-assembling complexes for gene delivery: From laboratory to clinical trial*, John Willey and Sons, New York.

(15) Behr, J. P. (1994) Gene transfer with synthetic cationic amphiphiles: prospects for gene therapy. *Bioconjugate Chem. 5*, 382–389.

(16) Miller, A. D. (1998) Cationic liposomes for gene therapy. *Angew. Chem. Int. 37*, 1768–1785.

(17) Marshall, E. (2000) Clinical research - FDA halts all gene therapy trials at Penn. *Science 287*, 565–567.

(18) Felgner, P. L., Gadek, T. R., Holm, M., Roman, R., Chan, H. W., Wenz, M., Northrop, J. P., Ringgold, G. M., and Danielsen, M. (1987) Lipofectin: A highly efficient, lipid mediated DNA-transfection procedure. *Proc. Natl. Acad. Sci. U.S.A. 84*, 7413–7417.

(19) Felgner, J. H., Kumar, R., Sridhar, C. N., Wheeler, C. J., Tsai, Y. J., Border, R., Ramsey, P., Martin, M., and Felgner, P. L. (1994) Enhanced gene delivery and mechanism studies with a novel series of cationic lipid formulations. *J. Biol. Chem. 269*, 2550–2561.

(20) Behr, J. P., Demeneix, B., Loeffler, J. P., and Perez-Mutul, J. (1989) Efficient gene transfer into mammalian primary endocrine cells with lipopolyamine coated DNA. *Proc. Natl. Acad. Sci. U.S.A. 86*, 6982–6986.

(21) Gaucheron, J., Santaella, C., and Vierling, P. (2002) Transfection with fluorinated lipoplexes based on fluorinated analogues of DOTMA, DMRIE and DPPES. *Biochim. Biophys. Acta — Biomembr. 1564*, 349–358.

(22) Boussif, O., Gaucheron, J., Boulanger, C., Santaella, C., Kolbe, H. V. J., and Vierling, P. (2001) Enhanced in vitro and in vivo cationic lipid-mediated gene delivery with a fluorinated glycerophosphoethanolamine helper lipid. *J.Gene Med. 3*, 109–114.

(23) Schulze, U., Schmidt, H., and Safinya, C. R. (1999) Synthesis of novel cationic poly(ethylene glycol) containing lipids. *Bioconjugate Chem. 10*, 548–552.

(24) Bessodes, M., Dubertret, C., Jaslin, G., and Scherman, D. (2000) Synthesis and biological properties of new glycosidic cationic lipids for DNA delivery. *Bioorg. Med. Chem. Lett. 10*, 1393–1395.

(25) Herscovici, J., Egron, M. J., Quenot, A., Leclercq, F., Leforestier, N., Mignet, N., Wetzer, B., and Scherman, D. (2001) Synthesis of new cationic lipids from unsaturated glycoside scaffold. *Org. Lett. 3* 1893–1896.

(26) Arigon, J., Prata, C. A. H., Grinstaff, M. W., and Barthélémy, P. (2005) Nucleic acid complexing glycosyl nucleoside-based amphiphile. *Bioconjugate Chem. 16*, 864–872.

(27) Prata, C. A. H., Zhang, X., Luo, D., McIntosh, T. J., Barthélémy, P., and Grinstaff, M. W. (2008) Lipophilic peptides for gene delivery. *Bioconjugate Chem. 19*, 418–420.

(28) Chan, E., Amon, M., Marano, R. J., Wimmer, N., Kearns, P. S., Manolios, N., Rakoczy, P. E., and Toth, I. (2007) Novel cationic lipophilic peptides for oligodeoxynucleotide delivery. *Bioorg. Med. Chem. 15*, 4091–4097.

(29) Montier, T., Benvegnu, T., Jaffres, P. A., Yaouanc, J. J., and Lehn, P. (2008) Progress in cationic lipid-mediated gene transfection: a series of bio-inspired lipids as an example. *Curr. Gene Ther. 8*, 296–312.

(30) Obata, Y., Suzuki, D., and Takeoka, S. (2008) Evaluation of cationic assemblies constructed with amino acid based lipids for plasmid DNA delivery. *Bioconjugate Chem. 19*, 1055–1063.

(31) Gissot, A., Camplo, M., Grinstaff, M. W., and Barthélémy, P. (2008) Nucleoside, nucleotide and oligonucleotide based amphiphiles: a successful marriage of nucleic acids with lipids. *Org. Biomol. Chem. 6*, 1324–1333.

(32) Moreau, L., Barthélémy, P., Maataoui, M. E., and Grinstaff, M. W. (2004) Supramolecular assemblies of nucleoside-based amphiphiles. *J. Am. Chem. Soc. 126*, 7533–7539.

(33) Moreau, L., Ziarelli, F., Grinstaff, M. W., and Barthélémy, P. (2006) Self-assembled microspheres from F-block elements and nucleoamphiphiles. *Chem. Commun. 15*, 1661–1663.

(34) Moreau, l., Campins, N., Grinstaff, M. W., and Barthélémy, P. (2006) A fluorocarbon nucleoamphiphile for the construction of actinide loaded microspheres. *Tetrahedron Lett. 47*, 7117–7120.

(35) Barthélémy, P., Prata, C. A. H., Filocamo, S. F., Immoos, C. E., Maynor, B. W., Hashmi, S. A. N., Lee, S. J., and Grinstaff, M. W. (2005) Supramolecular assemblies of DNA with neutral nucleoside amphiphiles. *Chem. Commun.* 1261–1263.

(36) Campins, N., Dieudonné, P., Grinstaff, M. W., and Barthélémy, P. (2007) Nanostructured assemblies from nucleotide based amphiphiles. *New. J. Chem. 31*, 1928–1934.

(37) Chabaud, P., Camplo, M., Payet, D., Serin, G., Moreau, L., Barthélémy, P., and Grinstaff, M. W. (2006) Cationic nucleoside lipids for gene delivery. *Bioconjugate Chem. 17*, 466–472.

(38) Moreau, L., Barthélémy, P., Li, Y., Luo, D., Prata, C. A. H., and Grinstaff, M. W. (2005) Nucleoside phosphocholine amphiphile for in vitro DNA transfection. *Mol. BioSystems 1*, 260–264.

(39) Camplo, M., Khiati, S., Ceballos, C., Prata, C. A. H., Giorgio, S., Marsal, P., Barthélémy, P., and Grinstaff, M. W. (2010) Cationic nucleoside lipids derived from universal bases: a rational approach for siRNA transfection. *Bioconjugate Chem. 21*, 1062–1069.

(40) Boomer, J. A., and Thompson, D. H. (1999) Synthesis of acid-labile diplasmenyl lipids for drug and gene delivery applications. *Chem. Phys. Lipids 99*, 145–153.

(41) Liu, X., Yang, J. W., and Lynn, D. M. (2008) Addition of 'charge-shifting' side chains to linear poly(ethyleneimine) enhances cell transfection efficiency. *Biomacromolecules 9*, 2063–2071.

(42) Bell, P. C., Bergsma, M., Dolbnya, I. P., Bras, W., Stuart, M. C., Rowan, A. E., Feiters, M. C., and Engberts, J. B. F. N. (2003) Transfection mediated by genimi Surfactants: Engineered escape from the endosomal compartment. *J. Am. Chem. Soc. 125*, 1551–1558.

(43) Lynn, D. M., and Langer, R. (2000) Degradable poly(beta-amino esters): Synthesis, characterization, and self-assembly with plasmid DNA. *J. Am. Chem. Soc. 122*, 10761–10768.

(44) Pack, D. W., Putnam, D., and Langer, R. (2000) Design of imidazole-containing endosomolytic biopolymers for gene delivery. *Biotechnol. Bioeng. 67*, 217–223.

(45) Jones, R. A., Cheung, C. Y., Black, F. E., Zia, J. K., Stayton, P. S., Hoffman, A. S., and Wilson, M. R. (2003) Poly(2-alkylacrylic acid) polymers deliver molecules to the cytosol by pH-sensitive disruption of endosomal vesicles. *Biochem. J. 372*, 65–75.

(46) Zhu, J., Munn, R. J., and Nantz, M. H. (2000) Self-cleaving ortho ester lipids: A new class of pH-vulnerable amphiphiles. *J. Am. Chem. Soc. 122*, 2645–2646.

(47) Jewell, C. M., Zhang, J., Fredin, N. J., Wolff, M. R., Hacker, T. A., and D.M., L. (2006) Release of plasmid DNA from intravascular stents coated with ultrathin multilayered polyelectrolyte films. *Biomacromolecules 7*, 2483–2491.

(48) Legendre, J. Y., and Szoka, F. C. J. (1992) Delivery of plasmid DNA into mammalian cell lines using pH sensitive liposomes: Comparison with cationic liposomes. *Pharm. Res. 10*, 1235–1242.

(49) Midoux, P., Pichon, C., Yaouanc, J. J., and Jaffrès, P. A. (2009) Chemical vectors for gene delivery: a current review on polymers, peptides and lipids containing histidine or imidazole as nucleic acids carriers. *Br. J. Pharmacol. 157*, 166–178.

(50) McGregor, C., Perrin, C., Monck, M., Camilleri, P., and Kirby, A. J. (2001) Rational apporaches to the design of cationic genimi surfactants for gene delivery. *J. Am. Chem. Soc. 123*, 6215–6220.

(51) Gosselin, M. A., Guo, W., and Lee, R. J. (2002) Incorporation of reversibly cross-linked polyplexes into LPDII vectors for gene delivery. *Bioconjugate Chem. 13*, 1044–1053.

(52) Tang, F., Wang, W., and Hughes, J. A. (1999) Cationic liposomes containing disuldide bonds in delivery of plasmid DNA. *J. Liposome Res. 9*, 331–347.

(53) Byk, G., Wetzer, B., Frederic, M., Dubertret, C., Pitard, B., Jaslin, G., and Scherman, D. (2000) Reduction-sensitive lipopolyamines as a novel nonviral gene delivery system for modulated release of DNA with improved transgene expression. *J. Med. Chem. 43*, 4377–4387.

(54) Prata, C. A. H., Zhao, Y., Barthélémy, B., Li, Y., Luo, D., McIntosh, T. J., Lee, S. J., and Grinstaff, M. W. (2004) Charge-reversal amphiphiles for gene delivery. *J. Am. Chem. Soc. 126*, 12744–12745.

(55) Abbott, N. L., Jewell, C. M., Hays, M. E., Kondo, Y., and Lynn, D. M. (2005) Ferrocene-containing cationic lipids: Influence of redox state on cell transfection. *J. Am. Chem. Soc. 127*, 11576–11577.

(56) Jewell, C. M., Hays, M. E., Kondo, Y., Abbott, N. L., and Lynn, D. M. (2008) Chemical activation of lipoplexes formed from DNA and a redox-active, ferrocene-containing cationic lipid. *Bioconjugate Chem. 19*, 2120–2128.

(57) Fuchs, S., Buethe, D., Khanna, A., Yadava, P., and Hughes, J. A. (2004) Sulfhydryl based cationic surfactants and the impact of polyanions on disulfide bond formation: Implications for gene transfer vectors. *J. Drug Targeting 12*, 347–353.

(58) Jewell, C. M., Hays, M. E., Kondo, Y., Abbott, N. L., and Lynn, D. M. (2006) Ferrocene-containing cationic lipids for the delivery of

DNA: Oxidation state determines transfection activity. *J. Controlled Release 112*, 129–138.

(59) Miyata, K., Kakizawa, Y., Nishiyama, N., Harada, A., Yamasaki, Y., Koyama, H., and Kataoka, K. (2004) Block catiomer polyplexes with regulated densities of charge and disulfide cross-linking directed to enhance gene expression. *J. Am. Chem. Soc. 126*, 2355–2361.

(60) Wang, J., Guo, X., Xu, Y., Barron, L., and Szoka, F. C. (1998) Synthesis and characterization of long chain alkyl acyl carnitine esters. Potentially biodegradable cationic lipids for use in gene delivery. *J. Med. Chem. 41*, 2207–2215.

(61) Pak, C. C., Ali, S., Janoff, A. S., and Meers, P. (1998) Triggerable liposomal fusion by enzyme cleavage of a novel peptide-lipid conjugate. *Biochem. Biophys. Acta 1372*, 13–27.

(62) Wang, J., Mao, H. Q., and Leong, K. W. (2001) A novel biodegradable gene carrier based on polyphosphoester. *J. Am. Chem. Soc. 123*, 9480–9481.

(63) Takeda, N., Nakamura, E., Yokoyama, M., and Teuro, O. (2004) Temperature-responsive polymeric carriers incorporating hydrophobic monomers for effective transfection in small doses. *J. Controlled Release 95*, 343–355.

(64) Kurisawa, M., Yokoyama, M., and Okano, T. (2000) Gene expression control by thermo-responsive polymeric gene carriers *J. Controlled Release 69*, 127–137.

(65) Prata, C. A. H., Li, Y., Luo, D., McIntosh, T. J., Barthélémy, P., and Grinstaff, M. W. (2008) A new helper phospholipids for gene delivery. *Chem. Commun.* 1566–1568.

(66) Zhang, X. X., Prata, C. A. H., McIntosh, T. J., Barthélémy, P., and Grinstaff, M. W. (2010) The effect of charge-reversal amphiphile spacer composition on DNA and siRNA delivery. *Bioconjugate Chem. 21*, 988–993.

(67) Mellman, I., Fuchs, R., and Helenius, A. (1986) Acidification of the endocytic and exocytic pathways. *Annu. Rev. Biochem. 55*, 663–700.

(68) Lavis, L. D., Chao, T. Y., and Raines, R. T. (2006) Fluorogenic label for biomolecular imaging. *ACS Chem. Biol. 1*, 252–260.

(69) Geall, A. J., and Blasgbrough, I. S. (2000) Rapid and sensitive ethidium bromide fluorescence quenching assay of polyamine conjugate-DNA interactions for the analysis of lipoplex formation in gene therapy. *J. Pharm. Biomed. Anal. 22*, 849–859.

(70) Cain, B. F., Baguley, B. C., and Demmy, M. W. (1978) Potential antitumor agents. 28. Deoxyribonucleic acid polyintercalating agents. *J. Med. Chem. 21*, 658–668.

(71) Koltover, I., Salditt, T., Radler, J. O., and Safinya, C. R. (1998) An inverted hexagonal phase of cationic liposome-DNA complexes related to DNA release and delivery. *Science 281*, 78–81.

(72) Liu, X. H., Yang, J. W., Miller, A. D., Nack, E. A., and Lynn, D. M. (2005) Charge-shifting cationic polymers that promote self-assembly and self-disassembly with DNA. *Macromolecules 38*, 7907–7914.

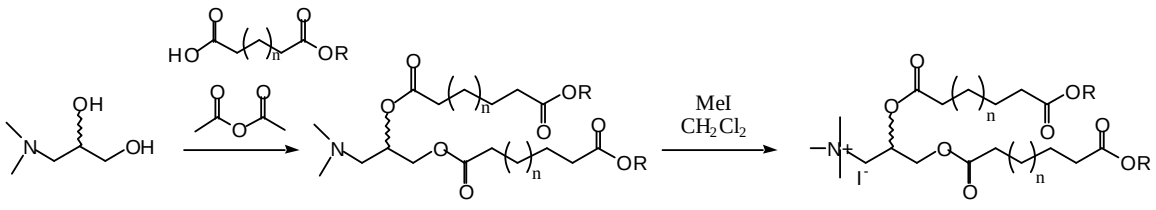
Synthesis, Characterization, and *IN VITRO* Transfection Activity of Charge-Reversal Amphiphiles for DNA Delivery

Xiao-Xiang Zhang,[¶] Carla A. H. Prata,[¶] Jason A. Berlin, Thomas J. McIntosh,[ψ] Philippe Barthelemy,[†] and Mark W. Grinstaff*

Departments of Biomedical Engineering and Chemistry, Boston University, Boston MA 02215. [†]Inserm, U869, Bordeaux, F-33076 France. [¶]Université de Bordeaux, F-33076, Bordeaux, France. [ψ]Department of Cell Biology, Duke University Medical Center, Durham, NC, 27710. [‡]Department of Biological and Environmental Engineering, Cornell University, Ithaca, NY, 14853. [Φ]Army Research Office, RTP, NC, 27709.

RECEIVED DATE (automatically inserted by publisher); Corresponding author E-mail: mgrin@bu.edu

All solvents were dried and freshly distilled prior to use. All chemicals were purchased from Aldrich or Acros and used without further purification. All reactions were performed under nitrogen atmosphere. NMR spectra were recorded on a Varian INOVA spectrometer operating at 400 MHz (for ^{1}H and ^{13}C). Elemental analysis was obtained from Atlantic Microlab, Inc. A TA Instruments DSC 2920 Modulated DSC was used to collect Tm data. Calf thymus DNA and EtBr were purchased from Sigma. Fluorescence studies were carried out with a Fluorolog 3, ISA Jobin Yvon-Spex, Horiba group.



1: n = 7; R = OBn
2: n = 7; R = OH
3: n = 7; R = NHBn
4: acetate derivative
6: n = 5; R = OBn
7: n = 11; R = OBn
8: n = 7; R = OEt
9: n = 7; R = OBu

Dodecanedioic acid monobenzyl ester[1] : Dodecanoic diacid (1 mmol) and Dowex 50W-X2 (50-100 mesh) (1.0 g) were stirred in benzyl formate/ octane (2:8, 10 mL) at 80 ºC. The reaction was continued for 12 h. The solution was then filtrated and the filtrate evaporated. The crude product was purified by column chromatography to afford the compound as a white powder (79 % yield). ^{1}H NMR ($CDCl_3$) δ ppm 1.34 (m, 10 H, $(CH_2)_n$), 1.61 (m, 4H, CH_2), 2.32 (m, 4H, CH_2), 5.08 (s, 2H, CH_2), 7.34 (m, 5H, Ph); ^{13}C NMR ($CDCl_3$) δ ppm 25.16 (CH_2), 25.25 (CH_2), 29.40 $(CH_2)_n$, 29.57 $(CH_2)_n$, 29.71 $(CH_2)_n$, 34.40 (CH_2), 34.62 (CH_2), 66.55 (CH_2), 127.22 (CH), 127.86 (CH), 128.38 (CH), 128.76 (CH), 136.29 (CH), 174.04 (CO_2), 179.73 (CO_2H). MH^+ (GC-CIMS) = 321. The data agreed with the literature values (Saitoh, M., Fujisaki, S., Ishii, Y., Nishiguchi, T.,Tetrahedron Letters, 1996, *37*, 6733-6736).

Dodecanedioic acid benzyl ester 2-(11-benzyloxycarbonyl-undecanoyloxy)-3-dimethylamino - propyl ester : To a solution of **7** (1.78 g, 5.5 mmol), 3-dimethylamino-propane-1,2-diol (0.3 mL, 2.5 mmol), DMAP (catalytic amount) in DCM (15 mL) and of DCC (1.1 g, 5.5 mmol) in DCM (5 mL) were added. The solution was subsequently stirred for 2 days. The reaction mixture was then filtered to remove the insoluble DCU. Concentration of the filtrate followed by chromatography (50% EtOAc/DCM to 100% EtOAc) afforded the product as colorless oil (80% yield). ^{1}H NMR ($CDCl_3$) δ ppm 1.23 (d, J = 4.8 Hz, 24H), 1.32 – 1.63 (m, 8H), 2.23 – 2.33 (m, 14H), 2.37 – 2.47 (m, 2H), 4.03 – 4.08 (m, 1H), 4.03 – 4.34 (m, 1H), 5.07 (s, 4H), 5.13 – 5.19 (m, 1H), 7.25 – 7.35 (m, 10H); ^{13}C NMR ($CDCl_3$) δ ppm 25.13 (CH_2), 29.30$(CH_2)_n$, 29.42$(CH_2)_n$, 29.58 $(CH_2)_n$, 34.17 (CH_2), 34.34 (CH_2), 34.51 (CH_2), 34.59 (CH_2), 46.22 $((CH_3)_3)N$), 59.55 (CH_2), 64.10 (CH_2), 66.10 (CH_2), 66.24 (CH_2), 69.36 (CH), 128.35 (CH), 128.73 (CH), 136.34 (CH), 173.38 (CO_2), 173.67 (CO_2), 173.84 (CO_2); HRMS calcd. for $[C_{43}H_{65}NO_8 + H]^+$ 724.4788, found 724.4785.

[2,3-Bis-(11-benzyloxycarbonyl-undecanoyloxy)-propyl]-trimethyl-ammonium; iodide (1): MeI (1 mL, 15 mmol) was added to a solution of **3** (0.9 g, 1.2 mmol) in DCM (5 mL). The solution was stirred for 4 hours and then concentrated. The residue was washed with ethyl ether to afford 0.9 g product (90 % yield) of a white powder. ^{1}H NMR ($CDCl_3$) δ ppm 1.22 (d, J = 3.6 Hz, 24H), 1.55 – 1.61 (m, 8H), 2.30 (t, J = 7.2 Hz, 8H), 3.49 (s, 9H), 3.82 – 3.87 (m, 1H), 4.08 – 4.13 (m, 1H), 4.45 – 4.49 (m, 2H), 5.07 (s, 4H), 5.57 (s, 1H), 7.27 – 7.34 (m, 10H); ^{13}C NMR ($CDCl_3$) δ ppm 24.78 (CH_2), 24.92 (CH_2), 25.11 (CH_2), 29.28 (CH_2), 29.38 (CH_2), 29.52 (CH_2), 29.56 (CH_2), 34.16 (CH_2), 34.38 (CH_2), 34.50 (CH_2), 54.95 (CH_2), 63.08 (CH_2), 65.89 (CH_2), 66.25 (CH_2), 66.38 (CH_2), 128.32 (CH), 128.35 (CH), 128.74 (CH), 136.32 (CH), 172.92 (CO_2), 173.37 (CO_2), 173.88 (CO_2); HRMS calcd. for $[C_{44}H_{68}NO_8I - I]^+$ 738.4945, found 738.4951. Elemental analysis: C, 61.28%; H, 8.10%; N, 2.33% (theory: C, 61.03%; H, 7.92%; N, 1.62%).

Dodecanedioic acid mono-tert-butyl ester:[2] To an ice-cold solution of dodecanedioic acid (15 g, 65 mmol), *tert*-butyl alcohol (64 mL, 650 mmol), DMAP (catalytic amount) in THF (80 mL) DCC (16 g, 78 mmol) in THF (20 mL) were added. The solution was subsequently warmed to room temperature and stirred for 24 hours. The reaction mixture was then filtered to remove the insoluble DCU. Concentration of the filtrate followed by chromatography (20% EtOAc / Hexane to 40% EtOAC / Hexane) afforded 9 g (50% yield) of the product. ^{1}H NMR ($CDCl_3$) δ ppm 1.23 (s, 12H), 1.40 (s, 9H), 1.51 – 1.60 (m, 4H), 2.16 (t, J = 7.2 Hz, 2H), 2.30 (t, J = 7.6 Hz, 2H); ^{13}C NMR ($CDCl_3$) δ ppm 24.85 (CH_2), 25.28 (CH_2), 28.30 $(CH_3)_3$, 29.24 $(CH_2)_n$, 29.37 $(CH_2)_n$, 29.43 $(CH_2)_n$, 29.55 $(CH_2)_n$, 34.23 (CH_2), 35.81 (CH_2), 80.13 (C), 173.62 (CO_2), 180.08 (CO_2H).

Dodecanedioic acid 2-(11-tert-butoxycarbonyl-undecanoyloxy)-3-dimethylamino-propyl ester tert-butyl ester: To a solution of dodecanedioic acid mono-tert-butyl ester (4.6 g, 16 mmol), 3-dimethylamino-propane-1,2-diol (0.9 mL, 7.6 mmol), DMAP

(catalytic amount) in DCM (40 mL), and DCC (4 g, 20 mmol) in DCM (10 mL) was slowly added. The solution was subsequently stirred for 2 days. The reaction mixture was then filtered to remove the insoluble DCU. Concentration of the filtrate followed by chromatography (50% EtOAc / DCM to 100% EtOAc) afforded 2.3 g (46% yield) product as colorless oil. ^{1}H NMR ($CDCl_3$) δ = 1.23 (d, 24H), 1.42 (s, 18H), 1.58 (m, 8H), 2.23 (m, 8H), 2.47 (m, 4H), 2.62 (m, 2H), 4.03 – 4.34 (m, 2H), 5.19 (m, 1H); ^{13}C NMR ($CDCl_3$) δ = 25.33 $(CH_2)_n$, 29.30 $(N(CH_3)_3)$, 29.40 $(CH_2)_n$, 29.52 $(CH_2)_n$, 30.0 $(CH_2)_n$, 30.3 $(CH_2)_n$, 34.27 (CH_2), 34.32 (CH_2), 46.22 $(CH_3)_2$, 64.10 (CH_2), 66.10 (CH_2), 69.36 (CH), 173.28 (CO_2), 173.47 (CO_2).

[2,3-Bis-(11-tert-butoxycarbonyl-undecanoyloxy)-propyl]-trimethyl-ammonium; iodide: MeI (1 mL, 15 mmol) was added to a solution of dodecanedioic acid 2-(11-tert-butoxycarbonyl-undecanoyloxy)-3-dimethylamino-propyl ester tert-butyl ester (1.1 g, 1.7 mmol) in DCM (5 mL). The solution was stirred for 4 hours and then concentrated. The residue was recrystallized in DCM/Ethyl ether to afford 1.0 g product (75 % yield) as a white powder. ^{1}H NMR ($CDCl_3$) δ ppm 1.23 (s, 24H), 1.39 (s, 9H), 1.52 – 1.56 (m, 8H), 2.15 (t, J = 7.6 Hz, 4H), 2.29 – 2.33 (m, 4H), 3.50 (s, 9H), 3.82 – 3.88 (m, 1H), 4.08 – 4.12 (m, 1H), 4.45 – 4.49 (m, 2H), 5.07 (s, 4H); ^{13}C NMR ($CDCl_3$) δ ppm 24.78 (CH_2), 24.93 (CH_2), 25.28 (CH_2), 28.31 $(CH_3)_3$, 29.26 $(CH_2)_n$, 29.37 $(CH_2)_n$, 29.45 $(CH_2)_n$, 29.55 $(CH_2)_n$, 29.60 $(CH_2)_n$, 34.16 (CH_2), 34.38 (CH_2), 35.79(CH_2), 54.95 $(N(CH_3)_3)$, 63.05 (CH_2), 65.88 (CH_2), 66.34 (CH), 80.09 (C), 172.91 (CO_2), 173.37(CO_2), 173.53 (CO_2); HRMS calcd for $[C_{38}H_{72}NO_8I - I]^+$ 670.5258, found 670.5268.

[2,3-Bis-(11-carboxy-undecanoyloxy)-propyl]-trimethyl-ammonium; iodide (2) : 0.70 g of [2,3-bis-(11-tert-butoxycarbonyl-undecanoyloxy)-propyl]-trimethyl-ammonium iodide and TFA (6 mL) in DCM (24 mL) were stirred at room temperature for 4 hours. The solution was then concentrated and the residue was recrystallized in

MeOH/ethyl ether to afford 0.54 g (90 % yield) of the product. ^{1}H NMR (DMSO – d_6) δ ppm 1.19 (s, 24H), 1.41 – 1.48 (m, 8H), 2.13 (t, J = 7.6 Hz, 4H), 2.24 – 2.34 (m, 4H), 3.05 (s, 9H), 3.64 – 3.74 (m, 2H), 4.00 – 4.04 (m, 1H), 4.31 – 4.34 (m, 1H), 5.44 (d, J = 3.2 Hz, 1H), 11.95 (s, 2H); ^{13}C NMR (DMSO – d_6) δ ppm 24.76 (CH_2), 24.93 (CH_2), 25.14 (CH_2), 29.04 $(CH_2)_n$, 29.21 $(CH_2)_n$, 29.35 $(CH_2)_n$, 29.40 $(CH_2)_n$, 29.52 $(CH_2)_n$, 33.89 (CH_2), 34.18 (CH_2), 34.31 (CH_2), 53.80 ($N(CH_2)_3$), 63.69 (CH_2), 65.47 (CH_2), 66.60 (CH), 172.75 (CO_2), 173.14 (CO_2), 175.11 (CO_2H); HRMS calcd for $[C_{30}H_{56}NO_8I - I]^+$ 558.4006, found 558.4001. Elemental analysis: C, 52.22%; H, 8.20%; N, 2.01% (theory: C, 52.55%; H, 8.23%; N, 2.04%).

11-Benzylcarbamoyl-undecanoic acid: To a solution of dodecanedioic acid (15 g, 65 mmol), benzylamine (64 mL, 650 mmol) in THF (80 mL), and a solution of DCC (16 g, 78 mmol) in THF (20 mL) were added. The reaction mixture was stirred for 24 hours and then filtered to remove the insoluble DCU. Concentration of the filtrate followed by chromatography (20% EtOAc/hexane) yielded 9 g (50% yield) of the product as colorless solid. ^{1}H NMR (DMSO) **δ** = 1.18 (m, 12H), 1.44 (m, 4H), 2.11 (m, 4H), 4.20 (s, 2H), 7.23 (m, 5H), 8.21 (m, 1H); ^{13}C NMR (DMSO) **δ** 24.86 (CH_2), 25.89 (CH_2), 29.09 $(CH_2)_n$, 29.35 $(CH_2)_n$, 29.48 $(CH_2)_n$, 29.67 $(CH_2)_n$, 29.86 $(CH_2)_n$, 33.91 (CH_2), 34.28 (CH_2), 35.78 (CH_2), 46.34 (CH_2), 127.99 (CH), 128.75 (CH), 140.07 (CH), 173.01 (CONH), 178.12 (CO_2H); HRMS calcd for $[C_{19}H_{29}NO_3H]^+$ 319.2147, found 320.2241.

11-Benzylcarbamoyl-undecanoic acid 2-(11-benzylcarbamoyl-undecanoyloxy)-3-dimethylamino-propyl ester: To a solution of 11-benzylcarbamoyl-undecanoic acid (0.5 g, 1.56 mmol), 3-dimethylamino-propane-1,2-diol (0.08 mL, 0.78 mmol), DMAP (catalytic amount) in DCM (20 mL) and DCC (0.4 g, 20 mmol) in DCM (5 mL) were added. The solution was stirred for an additional 2 days. The reaction mixture was then filtered to remove the insoluble DCU. Concentration of the filtrate followed by

chromatography (EtOAc) afforded 0.56 g (46% yield) of product as a colorless oil. ^{1}H NMR ($CDCl_3$) δ = 1.20 (m, 24H), 1.59 (m, 8H), 2.25 (m, 14H), 2.37 (m, 2H), 2.60 (m, 4H), 4.02-4.34 (m, 2H), 5.04 (s, 4H), 5.17 (m, 1H), 7.22 (m, 10H); ^{13}C NMR ($CDCl_3$) δ = 25.13 (CH_2), 28.79 $(CH_2)_n$, 29.31 $(CH_2)_n$, 29.43 $(CH_2)_n$, 29.58 $(CH_2)_n$, 34.33 (CH_2), 34.53 (CH_2), 46.24 (CH_2), 59.57 (CH_2), 64.10 (CH_2), 66.22 (CH_2), 69.38 (CH), 128.23, (CH) 128.59 (CH), 133.55 (CH), 144.52 (CH), 173.38 (CO_2), 173.66 (CONH), 173.89 (CONH); HRMS calcd for $[C_{43}H_{67}IN_3O_6H]^+$ 722.5108, found 722.5095.

[2,3-Bis-(11-benzylcarbamoyl-undecanoyloxy)-propyl]-trimethyl-ammonium; iodide (3) : MeI (1 mL, 15 mmol) was added to a solution of 11-benzylcarbamoyl-undecanoic acid 2-(11-benzylcarbamoyl-undecanoyloxy)-3-dimethylamino-propyl ester (0.5 g, 0.7 mmol) in DCM (5 mL). The solution was stirred for 4 hours and then concentrated. The residue was washed with ethyl ether to afford 0.57 g product (95 % yield) as a white powder. ^{1}H NMR (DMSO) δ ppm 1.18 (s, 24H), 1.45 (m, 8H), 2.30 (m, 8H), 3.27 (s, 9H), 3.36 (dd, 2H), 4.08 (m, 2H), 4.37 (m, 4H), 5.44 (s, 1H), 7.19 – 7.30 (m, 10H); ^{13}C NMR (DMSO) δ ppm 24.78 (CH_2), 24.98 (CH_2), 26.37 (CH_2), 29.05 $(CH_2)_n$, 29.40 $(CH_2)_n$, 29.56 $(CH_2)_n$, 29.64 $(CH_2)_n$, 29.86 $(CH_2)_n$, 33.91 (CH_2), 34.20 (CH_2), 53.85 (CH_3), 70.24 (CH_2), 72.42 (CH_2), 72.44 (CH), 127.98 (CH), 128.83 (CH), 139.38 (CH), 172.74 (CO_2), 173.12 (CONH); HRMS calcd for $[C_{44}H_{70}IN_3O_6^+ - I]^+$ 736.5265, found 736.5260. Elemental analysis: C, 61.22%; H, 8.17%; N, 4.86% (theory: C, 61.17%; H, 8.05%; N, 4.81%).

(2,3-Diacetoxy-propyl)-trimethyl-ammonium; iodide (4): A mixture of 3-dimethyl -amino-propane-1,2-diol (0.30 mL, 2.5 mmol), acetyl anhydride (2 mL, excess) and DCM (5mL) was stirred overnight at room temperature. MeI (2 mL, excess) was then added to the solution, and the reaction was stirred for an additional 4 hours. Next, the solution was concentrated and ethyl ether (20 mL) was added to precipitate the product (0.73 g, 85 %

yield). ^{1}H NMR (DMSO – d_6) δ ppm 2.02 (d, J = 10.8 Hz, 6H), 3.07 (s, 9H), 3.68 – 3.73 (m, 2H), 4.04 – 4.08 (m, 1H), 4.25 – 4.29 (m, 1H), 5.40 (d, J = 4 Hz, 1H); ^{13}C NMR (DMSO – d_6) δ ppm 21.22 (CH_3), 21.59 (CH_3), 53.89 $(CH_3)_3$, 63.76 (CH_2), 65.38 (CH_2), 66.72 (CH), 170.33 (CO_2), 170.70 (CO_2); HRMS calcd for $[C_{10}H_{20}NO_4I - I]^+$ 218.1392, found 218.1398. Elemental analysis: C, 34.76%; H, 5.77%; N, 4.03% (theory: C, 34.80%; H, 5.84%; N, 4.06%).

Decanedioic acid monobenzyl ester: We followed the same procedure used for the preparation of dodecanoic acid monobenzyl ester. ^{1}H NMR ($CDCl_3$) δ ppm 1.29 (m, 8 H, $(CH_2)_n$), 1.62 (m, 4H, CH_2), 2.34 (m, 4H, CH_2), 5.11 (s, 2H, CH_2), 7.34 (m, 5H, Ph); ^{13}C NMR ($CDCl_3$) δ ppm 24.61 (CH_2), 24.78 (CH_2), 28.88 $(CH_2)_n$, 28.91 $(CH_2)_n$, 33.96 (CH_2), 34.19 (CH_2), 66.14 (CH_2), 127.06 (CH), 127.51 (CH), 128.24 (CH), 128.48 (CH), 128.59 (CH), 136.09 (CH), 174.08 (CO_2), 178.86 (CO_2H). HRMS calcd. for $[C_{17}H_{24}O_4 + Na]^+$ 315.1572, found 315.1599.

Decanedioic acid benzyl ester 2-(11-benzyloxycarbonyl-nonanoyloxy)-3-dimethylamino - propyl ester: We used the same procedure as that described for decanedioic acid benzyl ester 2-(11-benzyloxycarbonyl-nonanoyloxy)-3-dimethylamino - propyl ester. ^{1}H NMR ($CDCl_3$) δ ppm 1.25 (d, 18 H, $(CH_2)_n$), 1.58 (m, 8H, CH_2), 2.23 – 2.33 (m, 14H, CH_2), 2.41 (m, 2H, CH_2), 3.66 (m, 2H, CH_2), 4.05 (m, 1H, CH_2), 4.34 (m, 2H, CH_2), 5.08 (s, 4H, CH_2), 5.16 (m, 1H, CH_2), 7.32 (m, 10H, CH_2); 13C NMR ($CDCl_3$) δ ppm 25.43 (CH_2), 25.54 (CH_2), 29.71 $(CH_2)_n$, 34.68 $(CH_2)_n$, 34.93$(CH_2)_n$, 45.82 ($(CH_3)_3$)N), 59.45 (CH_2), 64.40 (CH_2), 66.73 (CH_2), 68.94 (CH), 128.82 (CH), 129.19 (CH), 136.75 (CH), 173.82 (CO_2), 174.04 (CO_2), 174.32 (CO_2), 174.35 (CO_2); HRMS calcd. for $[C_{39}H_{58}NO_8 + H]^+$ 668.4162, found 668.4183.

2,3-Bis-(11-benzyloxycarbonyl-nonanoyloxy)-propyl]-trimethyl-ammonium; iodide (6): We followed the same procedure used for synthesizing compound **1**. ^{1}H NMR ($CDCl_3$) δ ppm 1.28 (m, 28 H, $(CH_2)_n$), 1.58 (m, 12H, CH_2), 2.55 (m, 8H, CH_2), 3.51 (m, 9H, CH_3), 3.84 (m, 1H, CH_2), 4.14 (dd, 1H, CH_2), 4.34 (m, 1H, CH_2), 4.54 (m, 2H, CH_2), 5.10 (s, 4H, CH_2), 5.54 (m, 1H, CH), 7.35 (m, 10H, Ph); ^{13}C NMR ($CDCl_3$) δ ppm 19.22 (CH_2), 24.82 (CH_2), 25.15 (CH_2), 29.27 $(CH_2)_n$, 34.22 (CH_2), 34.55 (CH_2), 55.00 (($CH_3)_2$N), 63.18 (CH_2), 66.00 (CH_2), 66.38 (CH_2), 128.43 (CH), 128.85 (CH), 136.35 (CH), 172.99 (CO_2), 173.48 (CO_2), 173.97 (CO_2). HRMS calcd. for $[C_{40}H_{68}NO_8I - I]^+$ 682.9063, found 682.9076 . Elemental analysis: C, 70.30%; H, 8.86%; N, 2.05% (theory: C, 70.03%; H, 8.92%; N, 2.82%).

Hexadecanedioic acid monobenzyl ester : We used the same procedure as that described for dodecanoic acid monobenzyl ester. ^{1}H NMR ($CDCl_3$) δ ppm 1.24 (m, 18 H, $(CH_2)_n$), 1.63 (m, 4H, CH_2), 2.35 (m, 4H, CH_2), 5.11 (s, 2H, CH_2), 7.35 (m, 5H, Ph); ^{13}C NMR ($CDCl_3$) δ ppm 24.88 (CH_2), 25.16 (CH_2), 29.26 $(CH_2)_n$, 29.34 $(CH_2)_n$, 29.45 $(CH_2)_n$, 29.64 $(CH_2)_n$, 29.77 $(CH_2)_n$, 29.80 $(CH_2)_n$, 34.21 (CH_2), 34.54 (CH_2), 66.27 (CH_2), 128.32 (CH), 128.70 (CH), 136.28 (CH), 173.91 (CO_2), 179.88 (CO_2H). HRMS calcd. for $[C_{23}H_{36}O_4+Na]^+$ 399.2511, found 399.2493.

Hexadecanedioic acid benzyl ester 2-(11-benzyloxycarbonyl-undecanoyloxy)-3-dimethylamino - propyl ester: We followed the same procedure used to prepare dodecanedioic acid benzyl ester 2-(11-benzyloxycarbonyl-undecanoyloxy)-3-dimethylamino - propyl ester. ^{1}H NMR ($CDCl_3$) δ ppm 1.25 (d, 40 H, $(CH_2)_n$), 1.61 (m, 8H, CH_2), 2.26 – 2.34 (m, 16H, CH_2), 2.42 (m, 2H, CH_2), 3.64 (m, 2H, CH_2), 4.07 (m, 1H, CH_2), 4.35 (m, 2H, CH_2), 5.09 (s, 4H, CH_2), 5.17 (m, 1H, CH_2), 7.31 (m, 10H, CH_2); ^{13}C NMR ($CDCl_3$) δ ppm 25.16 (CH_2), 25.73 (CH_2), 29.33 $(CH_2)_n$, 29.44 $(CH_2)_n$, 29.53 $(CH_2)_n$, 29.66 $(CH_2)_n$, 29.80 (CH_2), 34.12 (CH_2), 34.54 (CH_2), 45.02 (($CH_3)_3$)N), 61.67

(CH_2), 64.78 (CH_2), 65.34 (CH_2), 66.27 (CH_2), 128.37 (CH), 128.74 (CH), 136.11 (CH), 173.97 (CO_2); HRMS calcd. for $[C_{51}H_{82}NO_8 + H]^+$ 836.6040, found 836.5977.

2,3-Bis-(11-benzyloxycarbonyl-nonanoyloxy)-propyl]-trimethyl-ammonium; iodide (7): We used the same procedure as described for compound **1**. ^{1}H NMR ($CDCl_3$) δ ppm 1.27 (m, 52 H, $(CH_2)_n$), 1.61 (m, 16H, CH_2), 2.36 (m, 8H, CH_2), 3.52 (m, 9H, CH_3), 3.88 (m, 1H, CH_2), 4.14 (m, 2H, CH_2), 4.53 (m, 2H, CH_2), 5.11 (s, 2H, CH_2), 5.61 (m, 1H, CH), 7.34 (m, 10 H, Ph); ^{13}C NMR ($CDCl_3$) δ ppm 24.89 (CH_2), 25.10 (CH_2), 29.27 $(CH_2)_n$, 29.41 $(CH_2)_n$, 29.49 $(CH_2)_n$, 29.61 $(CH_2)_n$, 29.67 $(CH_2)_n$, 29.79 $(CH_2)_n$, 34.08 (CH_2), 34.47 (CH_2), 54.86 ($(CH_3)_2N$), 60.31 (CH_2), 62.99 (CH_2), 65.80 (CH_2), 66.20 (CH_2), 128.28 (CH), 128.68 (CH), 136.23 (CH), 172.89 ($\underline{C}O_2$), 173.36 ($\underline{C}O_2$), 173.89 ($\underline{C}O_2$). HRMS calcd. for $[C_{52}H_{85}NO_8I - I]^+$ 851.6275, found 851.6229. Elemental analysis: C, 63.66%; H, 8.99%; N, 2.00% (theory: C, 63.85%; H, 8.66%; N, 1.43%).

Dodecanedioic acid monoethyl ester: To an ice-cooled stirred solution of dodecanedioyl dichloride in THF, a solution of ethyl alcohol and TEA in THF was added dropwise over 2 h. After the addition was complete, the mixture was stirred overnight at room temperature. Water was added to the mixture and phases were then extracted with AcOEt. The organic layers were subsequently dried over Na_2SO_4 and concentrated. The residue was purified by silica gel chromatography with Hexane/AcOEt (8:2) to afford the compound with a yield of 55 %. ^{1}H NMR ($CDCl_3$) δ ppm 1.24 (m, 16 H, $(CH_2)_n$), 1.58 (m, 4H, CH_2), 2.29 (m, 4H, CH_2), 4.10 (m, 2H, CH_2); ^{13}C NMR ($CDCl_3$) δ ppm 14.45 (CH_3), 24.85 (CH_2), 25.16 (CH_2), 29.22 $(CH_2)_n$, 29.30 $(CH_2)_n$, 29.40 $(CH_2)_n$, 29.53 $(CH_2)_n$, 34.22 (CH_2), 34.58 (CH_2), 60.40 (CH_2), 174.22 (CO_2), 180.10 (CO_2H). HRMS calcd. for $[C_{14}H_{26}O_4+Na]^+$ 281.1729, found 281.1750.

Dodecanedioic acid ethyl ester 2-(11-benzyloxycarbonyl-undecanoyloxy)-3-dimethylamino - propyl ester: We followed the same procedure used as for the preparation of dodecanedioic acid benzyl ester 2-(11-benzyloxycarbonyl-undecanoyloxy)-3-dimethylamino - propyl ester. ^{1}H NMR ($CDCl_3$) δ ppm 1.21 (d, 30 H, $(CH_2)_n$), 1.56 (m, 8H, CH_2), 2.21 – 2.28 (m, 14H, CH_2), 2.41 (m, 2H, CH_2), 4.07 (m, 5H, CH_2), 4.35 (dd, 1H, CH_2), 5.14 (m, 1H, CH_2); ^{13}C NMR ($CDCl_3$) δ ppm 13.52 (CH_3), 24.22 (CH_2), 28.41 (CH_2), 28.57 (CH_2), 28.70 (CH_2), 33.31 (CH_2), 33.49 (CH_2), 45.30 ((CH_3)$_3$N), 58.71 (CH_2), 59.26 (CH_2), 63.17 (CH_2), 66.53 (CH), 172.30 (CO_2), 172.56 (CO_2), 172.88 (CO_2); HRMS calcd. for $[C_{33}H_{62}NO_8 + H]^+$ 600.4475, found 600.4485.

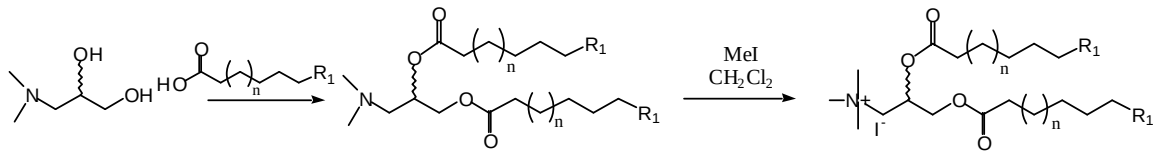
[2,3-Bis-(11-ethyloxycarbonyl-undecanoyloxy)-propyl]-trimethyl-ammonium; iodide (8): We followed the same procedure used as described for compound **1**. ^{1}H NMR ($CDCl_3$) δ ppm 1.25 (m, 25 H, $(CH_2)_n$), 1.61 (m, 12H, CH_2), 2.32 (m, 8H, CH_2), 3.54 (m, 9H, CH_3), 3.89 (m, 1H, CH_2), 4.14 (m, 5H, CH_2), 4.53 (m, 2H, CH_2), 5.61 (m, 1H, CH); ^{13}C NMR ($CDCl_3$) δ ppm 14.39 (CH_3), 24.71 (CH_2), 24.85 (CH_2), 25.08 (CH_2), 29.23 (CH_2)$_n$, 29.35 (CH_2)$_n$, 29.48 (CH_2)$_n$, 29.52 (CH_2)$_n$, 34.09 (CH_2), 34.49 (CH_2), 54.84 ((CH_3)$_2$N), 60.31 (CH_2), 62.99 (CH_2), 65.80 (CH_2), 66.16 (CH), 172.86 (CO_2), 173.33 (CO_2), 174.08 ($\underline{C}O_2$). HRMS calcd. for $[C_{34}H_{65}NO_8I - I]^+$ 615.4710, found 615.4708. Elemental analysis: C, 55.14%; H, 8.64%; N, 1.96% (theory: C, 55.05%; H, 8.70%; N, 1.89%).

Dodecanedioic acid monobutyl ester : Dodecanoic diacid (1 mmol) and Dowex 50W-X2 (50-100 mesh) (1.0 g) were stirred in butyl formate/ octane (2:8, 10 mL) at 80 ºC. The reaction was continued for 12 h. The solution was then filtrated and the filtrate evaporated. The crude was purified by column chromatography to afford the compound as a white powder (85 % yield). ^{1}H NMR ($CDCl_3$) δ ppm 0.86 (t, 3H, CH_3), 1.28 (m, 14 H, $(CH_2)_n$), 1.55 (m, 6H, CH_2), 2.25 (m, 4H, CH_2), 4.00 (t, 2H, CH_2); ^{13}C NMR ($CDCl_3$)

δ ppm 13.83 (CH_3), 19.33 (CH_2), 24.84 (CH_2), 25.18 (CH_2), 29.21 $(CH_2)_n$, 29.30 $(CH_2)_n$, 29.38 $(CH_2)_n$, 29.53 $(CH_2)_n$, 30.88 $(CH_2)_n$, 34.23 (CH_2), 34.58 (CH_2), 64.33 (CH_2), 174.30 (CO_2), 180.17 (CO_2H). HRMS calcd. for $[C_{16}H_{30}O_4+Na]^+$ 309.2042, found 309.2013.

Dodecanedioic acid butyl ester 2-(11-benzyloxycarbonyl-undecanoyloxy)-3-dimethylamino - propyl ester: We followed the same procedure as to synthesize dodecanedioic acid benzyl ester 2-(11-benzyloxycarbonyl-undecanoyloxy)-3-dimethylamino - propyl ester. ^{1}H NMR ($CDCl_3$) δ ppm 0.86 (t, 3H, CH_3), 1.28 (m, 28 H, $(CH_2)_n$), 1.55 (m, 12H, CH_2), 2.25 (m, 14H, CH_2), 2.50 (m, 2H, CH_2), 3.95 (m, 5H, CH_2), 4.23 (dd, 1H, CH_2), 5.24 (m, 1H, CH); ^{13}C NMR ($CDCl_3$) δ ppm 13.82 ($\underline{C}H_3$), 19.25 (CH_2), 24.95 (CH_2), 25.10 (CH_2), 29.23 $(CH_2)_n$, 29.34 $(CH_2)_n$, 29.49 $(CH_2)_n$, 30.82 $(CH_2)_n$, 34.17 (CH_2), 34.45 (CH_2), 45.50 ($(CH_3)_2N$), 59.02 (CH_2), 63.83 (CH_2), 64.33 (CH_2), 68.54 (CH), 173.23 (CO_2), 173.44 (CO_2), 174.00 (CO_2). HRMS calcd. for $[C_{37}H_{70}NO_8 + H]^+$ 656.5101, found 656.5167.

[2,3-Bis-(11-butyloxycarbonyl-undecanoyloxy)-propyl]-trimethyl-ammonium; iodide (9): We used the same procedure as that described for compound **1**. ^{1}H NMR ($CDCl_3$) δ ppm 0.86 (t, 6H, CH_3), 1.29 (m, 28 H, $(CH_2)_n$), 1.53 (m, 12H, CH_2), 2.25 (m, 8H, CH_2), 3.21 (m, 9H, CH_3), 3.00 (m, 8H, CH_2), 4.43 (dd, 1H, CH_2), 5.54 (m, 1H, CH); ^{13}C NMR ($CDCl_3$) δ ppm 13.70 (CH_3), 19.22 (CH_2), 24.81 (CH_2), 25.09 (CH_2), 29.21 $(CH_2)_n$, 29.33 $(CH_2)_n$, 29.50 $(CH_2)_n$, 30.75 $(CH_2)_n$, 34.25 (CH_2), 34.51 (CH_2), 54.55 ($(CH_3)_2N$), 59.02 (CH_2), 64.44 (CH_2), 64.53 (CH_2), 65.84 (CH_2), 173.50 (CO_2), 173.79 (CO_2), 174.70 ($\underline{C}O_2$). HRMS calcd. for $[C_{38}H_{73}NO_8I - I]^+$ 671.5336, found 671.5305. Elemental analysis: C, 58.63%; H, 9.36%; N, 1.67% (theory: C, 58.12%; H, 9.19%; N, 1.63%).



10: n = 7; R1 = OC(O)CH3

12-Acetoxy-dodecanoic acid : A mixture of 12-hydroxydodecanoic acid (0.30 mL, 2.5 mmol), acetyl anhydride (2 mL, excess), and pyridine (2 mL) was stirred overnight at room temperature. Next, the solution was concentrated and ethyl alcohol (20 mL) was added to precipitate the product (0.73 g, 95 % yield). ^{1}H NMR ($CDCl_3$) δ ppm 1.24 (m, 14 H, $(CH_2)_n$), 1.60 (m, 4H, CH_2), 2.01 (s, 3H, CH_3), 2.19 (d, 2H, CH_2), 2.42 (m, 2H, CH_2), 4.01 (m, 2H, CH_2); ^{13}C NMR ($CDCl_3$) δ ppm 21.25 (CH_3), 24.40 (CH_2), 24.88 (CH_2), 26.09 (CH_2), 28.79 $(CH_2)_n$, 29.06 $(CH_2)_n$, 29.23 $(CH_2)_n$, 29.39 $(CH_2)_n$, 29.43 $(CH_2)_n$, 29.56 $(CH_2)_n$, 29.65 $(CH_2)_n$, 34.07 (CH_2), 35.48 (CH_2), 64.88 (CH_2), 171.53 (CO_2), 179.09 (CO_2). HRMS calcd. for $[C_{14}H_{26}O_4+Na]^+$ 281.1729, found 281.1740.

12-Acetoxy-dodecanoic acid-1-(12-acetoxydodecanoyloxymethyl)-2-dimethylamino-ethyl ester: We followed the same procedure used for preparation of dodecanedioic acid benzyl ester 2-(11-benzyloxycarbonyl-undecanoyloxy)-3-dimethylamino - propyl ester. ^{1}H NMR ($CDCl_3$) δ ppm 1.24 (d, 15 H, $(CH_2)_n$), 1.58 (m, 4H, CH_2), 2.02 (m, 6H, CH_3), 2.26 (m, 8H, CH_3), 2.41 (m, 2H, CH_2), 4.03 (m, 5H, CH_2), 4.33 (dd, 1H, CH_2), 5.14 (m, 1H, CH_2); ^{13}C NMR ($CDCl_3$) δ ppm 21.52 (CH_3), 24.22 (CH_2), 28.41 (CH_2), 28.57 (CH_2), 28.70 (CH_2), 33.31 (CH_2), 33.49 (CH_2), 45.30 (CH_2), 58.71 (CH_2), 59.26 (CH_2), 63.17 (CH_2), 68.53 (CH), 172.30 (CO_2), 172.56 (CO_2), 172.88 (CO_2); HRMS calcd. for $[C_{33}H_{62}NO_8 + H]^+$ 600.4507, found 600.4485.

[2,3-Bis-(12-acetoxy-dodecanoyloxy)-propyl]-trimethyl-ammonium; iodide (10): Same procedure used then that described for compound **1**. ^{1}H NMR ($CDCl_3$) δ ppm 1.27

(d, 15 H, $(CH_2)_n$), 1.63 (m, 4H, CH_2), 2.05 (m, 4H, CH_3), 2.37 (m, 4H, CH_2), 3.54 (m, 9H, CH_3), 3.91 (m, 1H, CH), 4.03-5.15 (m, 5H, CH_2), 4.54 (dd, 1H, CH_2), 5.61 (m, 1H, CH_2); ^{13}C NMR ($CDCl_3$) δ ppm 21.23 (CH_3), 24.75 (CH_2), 24.88 (CH_2), 26.04 (CH_2), 26.51 (CH_2), 28.72 (CH_2), 29.22 (CH_2), 29.39 (CH_2), 29.63 (CH_2), 30.94 (CH_2), 34.12 (CH_2), 34.34 (CH_2), 54.88 ((CH_3)$_3$N), 63.00 (CH_2), 64.80 (CH_2), 65.82 (CH_2), 66.23 (CH), 171.47 (CO_2), 172.90 (CO_2), 173.37 (CO_2); HRMS calcd. for $[C_{34}H_{65}NO_8 + H]^+$ 615.4710, found 615.4688. Elemental analysis: C, 56.71%; H, 8.88%; N, 2.55% (theory: C, 55.05%; H, 8.70%; N, 1.892%).

Liposome preparation

Chloroform solutions of the amphiphiles were mixed and dried to a thin film by rotary evaporation. The residual solvent was removed under vacuum for 4h. The dried lipids were then dispersed with 100 mM Tris buffer, 100 mM NaCl, pH 7.4, and sonicated for 10 minutes.

Modulated differential scanning calorimetry.

0.5 mg of amphiphile in 5μL of water was hermetically sealed in an aluminum pan. The modulation was set to ±1.00 ºC every 40 s, and the pan was equilibrated at –15 ºC. The temperature was increased at 0.5 ºC/min to 70 ºC where it has held for 2 min. The temperature was then reduced to –10 ºC and held at this temperature for 2 min. This heating-cooling cycle was repeated two more times before the sample was held isothermal at –10 ºC for 20 min. The data colleted on the third cycle were analyzed.

DNA binding affinities [3]

DNA binding studies were carried out by competitive displacement fluorometric assay using ethidium bromide. This assay involves the addition of aliquots of the compound to

a 3 mL solution of EthBr (1.3 μM) and calfus thymus DNA (3 μM) in buffer (100 mM NaCl, 100 mM Tris, pH 7.4) with the decrease of fluorescence (λ_{exc}=546 nm, λ_{em}=600 nm; 1 cm path length glass cuvette, slit width 3 nm) recorded after 5 minutes of equilibrium time following each addition.

X-ray diffraction

The liposomes were centrifugated to give a hydrated pellet of multilamellar bilayers. The pellet was transferred then to a sealed quartz-glass X-ray capillary which was mounted in a temperature controllable chamber on a point-focus collimator. A stationary anode Jerrel-Ash generator (Jerrel-Ash Div., Fisher Scientific Co., Waltham, MA) was used to produce Cu Kα X-radiation.[4] Diffraction patterns were obtained using a flat plate film cassette loaded with Kodak DEF X-ray film. The specimen to film distance was 10 cm with exposure times of 2-6 hours. The low angle reflections were determined in accordance with Bragg's law $2d \sin\theta = h\lambda$, where λ is the wavelength (1.54Å), d is the repeat period, h is the number of the diffraction order, and θ is the Bragg angle.

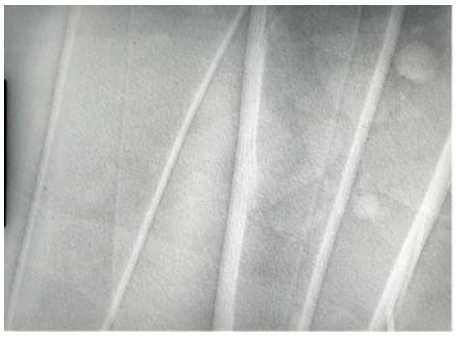


Figure S1. TEM micrographs of compound **7** in aqueous solution, negative staining with ammonium molybdate 1% in water.

TEM

TEM microscopy experiments were performed on a Philips CM 10 (negative staining with ammonium molybdate 1% in water, Cu/Pd carbon coated grids).

Besides, amphiphie **1**, all the the other amphilies gave large aggregarates except for amphiphile **7** that gave fiber-type structures upon extrusion as shown in Figure S1.

Cell culture and Transfection experiment

Chinese hamster ovarian cells (CHO, ATCC, Manassas, VA) were cultured in complete F12K media (ATCC) containing 10% fetal calf serum (Sigma) and 1% penicillin and streptomycin (500 IU/mL and 5000 μg/ml, respectively, Mediatech, Herndon, VA) at 37 ^{o}C in 5% CO_2 with humidity. When the CHO cells reached about 90% confluency, the cells were split into 24-well plates with a 1:6 ratio using a standard trypsin-based technique. Transfections were performed 24 hours later. Briefly stated, plasmid DNA coding for a reporter gene, β-galactosidase (β-gal, pVax-LacZ1, Invitrogen) was first mixed with lipids in potassium phosphate buffer (PBS) at room temperature. Depending on the experimental design, the ratio of DNA and amphiphile, the pH of the buffer used, or incubation time was varied. The mixture was incubated for 15 minutes at room temperature before adding to the cells. The amount of DNA used was the same as used in naked DNA control and positive control (commercially available transfection reagents). After incubation at 37 °C and 5% CO_2 for 2 hours, medium containing the mixtures was gently removed and fresh growth medium was added. Transfection efficiencies were assessed 48 h post transfection. Negative controls were constructed with 0.5 mL of serum-free F12 K medium and naked DNA controls were using 0.5 mL of serum-free F12 K medium with 1 μL (1 μg) of reporter gene. Positive controls were performed according to the manufacturer's protocol. Briefly stated, 2.0 μL of transfast® transfection reagent (1mg/mL) (Promega, Madison, WI) was mixed with 1 μL (1 μg) of reporter gene in 0.5 mL of serum free F12 K medium for 15 minutes at room temperature before transfecting cells.

Reporter gene transfection efficiency assay

Reporter gene (β-gal) assays were performed with a β-galactosidase enzyme assay system (Promega, Madison, WI) following the manufacturer protocol. Briefly cells were first lysed using M-PER buffer (Pierce, Rockford, Illinois) and enzyme activities were determined. A standard curve was constructed for each experiment using dilutions of purified β-gal protein. The β-gal activities from experimental samples were determined by comparison to the standard curve (enzyme activity vs. enzyme concentration). Efficiency of each transfection was calculated as β-gal activity normalized to total protein.

Cytotocixity

Cytotocixity was assessed using both a formazan-based proliferation assay (CellTiter 96 AQueous One Solution Cell Proliferation Assay kit, Promega) and a total protein-based assay (Pierce). Briefly stated, cells were seeded onto a 96-well plate with an appropriate density of 1×10^4 cells per well. A predetermined amount of test chemical was added onto the cells 24 hours later. After 24, 48, and 72 h MTS (substrates) were added to each well and the plate was incubated for 4 h at 37 ^{o}C in a humidified, 5% CO_2 incubator. The amount of soluble formazan produced by cellular reduction of the substrates MTS was recorded at 490 nm using a multi-well plate reader. For the total protein-based proliferation assay, cells were lysed at the same time when transfection efficiency was assayed. A 5 μL of lysates were transferred to a separate multi-well plate. Total protein contents were assessed using the Coomassie Blue protein kit (Pierce, Rockford, IL) following the manufacturer protocol. Negative and positive controls were non-treated cells and commercial lipids treated cells, respectively. The proliferation results were expressed as percentages of non-treated cells

1 Saitoh, M., Fujisaki, S., Ishii, Y., Nishiguchi, T., (1996) *Tetrahedron Letters*, *37*, 6733-6736.

2 Ogawa, Y., Kodaka, M. and Okuno, H. (2002) *Chemistry and Physics of Lipids*, *119*, 51 – 68

3 Geall, A.J.; Blasgbrough, I. S., (2000) *J. Pharm. Biomed.Anal*., *22*, 849-859.

4 McIntosh, T. J., (1980) *Biophys. J., 29*, 237-246

Bioconjugate Chemistry

ARTICLE

pubs.acs.org/bc

Evaluation of ^{64}Cu-Labeled Acridinium Cation: A PET Radiotracer Targeting Tumor Mitochondria

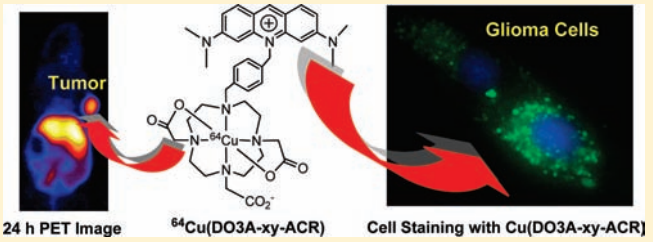
Yang Zhou,[†] Young-Seung Kim,[†] Jiyun Shi,[†] Orit Jacobson,[‡] Xiaoyuan Chen,[‡] and Shuang Liu*[,†]

[†]School of Health Sciences, Purdue University, West Lafayette, Indiana, United States

[‡]Laboratory of Molecular Imaging and Nanomedicine (LOMIN), National Institute of Biomedical Imaging and Bioengineering (NIBIB), the National Institutes of Health (NIH), Bethesda, Maryland, United States

Supporting Information

ABSTRACT: This report presents the synthesis and evaluation of ^{64}Cu(DO3A-xy-ACR) (DO3A-xy-ACR = 2,6-bis(dimethylamino)-10-(4-((4,7,10-tris(carboxymethyl)-1,4,7,10-tetraazacyclododecan-1-yl)methyl)benzyl)acridin-10-ium) as a radiotracer for imaging tumors in athymic nude mice bearing U87MG glioma xenografts by PET (positron emission tomography). The biodistribution data suggested that ^{64}Cu(DO3A-xy-ACR) was excreted mainly through the renal system with >65% of injected radioactivity being recovered from urine samples at 1 h post-injection (p.i.). The tumor uptake of ^{64}Cu(DO3A-xy-ACR) was 1.07 ± 0.23, 1.58 ± 0.55, 2.71 ± 0.66, 3.47 ± 1.19, and 3.52 ± 1.72%ID/g at 0.5, 1, 2, 4, and 24 h p.i., respectively. ^{64}Cu(DO3A-xy-ACR) had very high liver uptake (31.90 ± 3.98, 24.95 ± 5.64, 15.20 ± 4.29, 14.09 ± 6.82, and 8.18 ± 1.27%ID/g at 0.5, 1, 2, 4, and 24 h p.i., respectively) with low tumor/liver ratios. MicroPET studies showed that the tumors were clearly visualized as early as 30 min p.i. in the glioma-bearing mouse administered with ^{64}Cu(DO3A-xy-ACR). The high liver radioactivity accumulation was also seen. ^{64}Cu(DO3A-xy-ACR) had a relatively high metabolic stability during excretion via both renal and hepatobiliary routes, but it was completely decomposed in the liver homogenate. We explored the localization mechanism of Cu(DO3A-xy-ACR) using both U87MG human glioma and the cultured primary U87MG glioma cells. The results from the cellular staining assays showed that ^{64}Cu(DO3A-xy-ACR) is able to localize in the mitochondria of living U87MG glioma cells due to the enhanced negative mitochondrial potential as compared to normal cells. Although ^{64}Cu(DO3A-xy-ACR) is not an ideal PET radiotracer for tumor imaging due to its high liver uptake, the results from this study strongly suggest that ^{64}Cu-labeled acridinium cations are indeed able to localize in the energized mitochondria of tumor cells.



INTRODUCTION

Alteration in the mitochondrial potential ($\Delta\Psi_m$) is an important characteristic of cancer. It has been reported that the mitochondrial potential in carcinoma cells is significantly higher than that in normal epithelial cells.[1−5] Since the mitochondrial potentials are negative, the delocalized organic cations with appropriate structures tend to accumulate inside the energized mitochondria of carcinoma cells.[5] For example, rhodamine-123 and ^{3}H-tetraphenylphosphonium (^{3}H-TPP) have been used to measure mitochondrial potentials due to their preferential localization in tumor cells.[6−13] The observation that the enhanced mitochondrial potential is prevalent in tumor cell phenotype provides the conceptual basis to develop mitochondrion-targeting anticancer drugs and molecule imaging probes.[14−16]

We have been interested in ^{64}Cu-labeled phosphonium cations as PET (positron emission tomography) radiotracers for tumor imaging.[17−20] Biodistribution studies in the athymic nude mice bearing U87MG glioma xenografts showed that ^{64}Cu(DO3A-xy-TPEP) (Figure 1: DO3A-xy-TPEP = 2-(diphenylphosphoryl)ethyl)diphenyl(4-((4,7,10-tris(carboxymethyl)-1,4,7,10-tetraazacyclododecan-1-yl)methyl)benzyl)phosphonium) had a good tumor uptake with better tumor-to-background (T/B) ratios than those of ^{99m}Tc-Sestamibi.[19] Although *in vitro* assays indicated that ^{64}Cu radiotracers were able to localize in the tumor mitochondria, the evidence was not conclusive.[17] That has led us to explore other alternatives with the fluorescent emission so that their mitochondrial localization can be visualized.

Acridines are used as duplex DNA intercalators or "chemiluminescent agents" in many bioassays.[21] Recently, it was reported that the $Re(CO)_3$ complex [Re(3,6-bis-dimethylamino-10-(4-isocyanobutyl)acridinium)(2,4-pyridinedicarboxylato)$(CO)_3$]$^+$ ([Re(CN-C4-ACR)(2,4-pydic)$(CO)_3$]$^+$) was able to localize in the nuclei of tumor cells by binding to duplex and triplex DNAs.[22] Although the *in vivo* data were not reported, these promising results from *in vitro* assays have inspired us to prepare

Received: October 18, 2010
Revised: February 1, 2011
Published: March 17, 2011

ACS Publications © 2011 American Chemical Society

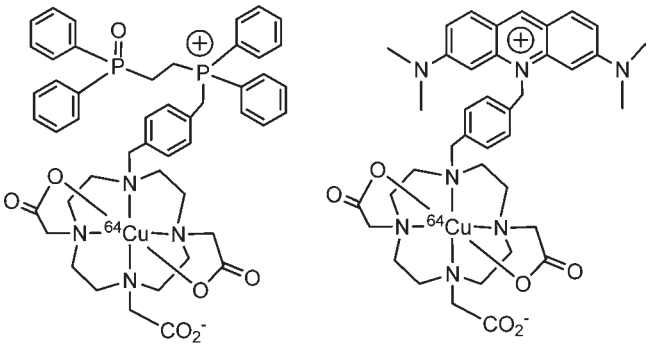


Figure 1. Proposed *Chemdraw* structures of ^{64}Cu(DO3A-xy-TPEP) and ^{64}Cu(DO3A-xy-ACR). Like 2-(diphenylphosphoryl)ethylphenyl-phosphonium (TPEP), the acridinium (ACR) cation is used as the mitochondrion-targeting molecule to carry ^{64}Cu into tumor cells, where the negative mitochondrial transmembrane potential is elevated.

the complex ^{64}Cu(DO3A-xy-ACR) (Figure 1: DO3A-xy-ACR = 2,6-bis(dimethylamino)-10-(4-((4,7,10-tris(carboxymethyl)-1,4,7,10-tetraazacyclododecan-1-yl)methyl)benzyl)acridin-10-ium). In this report, we present evaluation of ^{64}Cu(DO3A-xy-ACR) as a potential PET radiotracer for tumor imaging in athymic nude mice bearing U87MG glioma xenografts. We were interested in this tumor-bearing animal model because the xenografted U87MG glioma tissues have low expression of multidrug resistant P-glycoproteins (MDR Pgps) and multidrug resistance-associated proteins (MRPs).[20,23−26] Cu(DO3A-xy-ACR) was also prepared as a fluorescent probe for the cellular staining assay to demonstrate the intracellular location of ^{64}Cu-labeled ACR cations in tumor cells.

EXPERIMENTAL SECTION

Materials and Instruments. Acridine orange (ACR) and α,α′-dibromo-*p*-xylene were purchased from Sigma/Aldrich (St. Louis, MO). DO3A(OBu-t)$_3$ (1,4,7,10-tetraazacyclododecane-4,7,10-tris(*tert*-butyl acetate)) was obtained from Macrocyclics Inc. (Dallas, TX). NMR data were obtained using Bruker ARX 300 MHz FT NMR spectrometer. Chemical shifts are reported as δ in ppm relative to TMS. The ESI (electrospray ionization) mass spectral data were collected on a Finnigan LCQ classic mass spectrometer, School of Pharmacy, Purdue University. ^{64}Cu was produced using a CS-15 biomedical cyclotron at Washington University, School of Medicine, by the ^{64}Ni(p,n)^{64}Cu nuclear reaction.

HPLC Methods. The semiprep HPLC method (Method 1) used a LabAlliance system equipped with a UV/vis detector (λ = 254 nm) and Zorbax C_{18} semiprep column (9.4 × 250 mm, 100 Å pore size; Agilent Technologies, Santa Clara, CA). The flow rate was 2.5 mL/min and the mobile phase was isocratic with 60% A (0.1% TFA in water) and 40% B (0.1% TFA in methanol) at 0−5 min, followed by a gradient mobile phase going from 40% B at 5 min to 100% B at 20 min. The radio-HPLC method (Method 2) used the LabAlliance system equipped with a β-ram IN/US detector (Tampa, FL) and Vydac protein and peptide C_{18} column (4.6 × 250 mm, 300 Å pore size; Grace Davison Discovery Sciences, Hesperia, CA). The flow rate was 1 mL/min with the gradient mobile phase being isocratic with 90% solvent A (25 mM NH_4OAc, pH = 6.8) and 10% solvent B (acetonitrile) at 0−5 min, followed by a gradient mobile phase going from 10% B at 5 min to 90% B at 20 min. Method 3 used the LabAlliance HPLC system equipped with a UV/vis detector (λ = 254 nm), a β-ram IN-US detector and a Superose 12 10/300 GL size-exclusion column. The flow rate was 0.4 mL/min. The aqueous mobile phase was isocratic with 20 mM HEPES and 150 mM NaCl.

10-(4-(Bromomethyl)benzyl)-3,6-bis(dimethylamino)-acridin-10-ium Bromide (ACR-xy-Br). Acridine orange base (737 mg, 2.08 mmol) and α,α′-dibromo-*p*-xylene (500 mg, 1.89 mmol) were dissolved in 30 mL of toluene. The resulting mixture was refluxed for 20 h. After cooling to room temperature, the solid was filtered and washed with toluene (5 mL) and ether (5 mL) three times, respectively, and then dried under vacuum overnight. The yield was 580 mg (∼70%). ^{1}H NMR (in $CDCl_3$): 3.17 (s, 12H, NCH_3), 4.42 (s, 2H, CH_2Br), 6.25 (s, 2H, NCH_2), 6.66 (s, 2H, aromatic C_6H_3), 6.95 (d, 2H, aromatic C_6H_3), 7.27−7.40 (m, 4H, aromatic C_6H_4), 7.89 (d, 2H, aromatic C_6H_3), 8.27 (s, H, aromatic NC_5H_1).

2,6-Bis(dimethylamino)-10-(4-((4,7,10-tris(carboxymethyl)-1,4,7,10-tetraazacyclodo-decan-1-yl)methyl)benzyl)-acridin-10-ium (DO3A-xy-ACR). DO3A(OBu-t)$_3$ (22.8 mg, 44 μmol) and ACR-xy-Br (23.5 mg, 44 μmol) were dissolved in DMF (3 mL). To the mixture was added triethylamine (35 uL, 250 μmol). The reaction mixture was stirred at room temperature overnight. Upon removal of volatiles, the residue was dissolved in 3 mL of 12 N HCl. After being stirred at room temperature for 2 h, volatiles were completely removed. The residue was dissolved in 2 mL of 50% DMF/water mixture, and the solution was subjected to HPLC purification (Method 1). Fraction at 14.4 min was collected and lyophilized to give orange powder (19.7 mg, 63%). ESI-MS: m/z = 714.3 for $[M + H]^+$ (714.4 calcd. for $[C_{39}H_{52}N_7O_6]^+$).

Cu(DO3A-xy-ACR). To a clean vial containing DO3A-xy-ACR (16.9 mg, 22 μmol) and $Cu(OAc)_2 \cdot H_2O$ (9.2 mg, 45 μmol) was added 2.5 mL of NH_4OAc (0.5 M, pH = 5.5). The resulting solution was heated at 100 °C water bath for 30 min. After cooling it to room temperature, the product was isolated by HPLC (Method 1). Fraction 14 min was collected and lyophilized to give orange powder. The yield was 12.8 mg (75%). ESI-MS: m/z = 775.1 for $[M + H]^+$ (775.3 calcd. for $[C_{39}H_{49}CuN_7O_6]^+$). Anal. Calcd. for $C_{39}H_{49}CuN_7O_6 \cdot 2.5H_2O$: C, 57.09; H, 6.63; N, 11.95. Found: C, 56.94; H, 6.71; N, 11.70.

^{64}Cu-Labeling and Dose Preparation. To a clean Eppendorf tube was added 40 μg of DO3A-xy-ACR dissolved in 0.3 mL of 0.1 M NaOAc buffer (pH = 6.5) and 20 μL of $^{64}CuCl_2$ solution (∼500 μCi) in 0.05 N HCl. The reaction mixture was then heated at 100 °C for 20 min in a water bath. After heating, the vial was allowed to stand at room temperature for ∼5 min. The radiochemical purity was >95%. For biodistribution studies, ^{64}Cu(DO3A-xy-ACR) was prepared and purified by HPLC (Method 2). Volatiles in the HPLC mobile phase were removed on a rotary evaporator. Doses were prepared by dissolving the purified ^{64}Cu(DO3A-xy-ACR) in saline to ∼30 μCi/mL. The resulting solution was filtered with a 0.20 μm Millex-LG filter before being injected into animals. For the imaging study, ^{64}Cu(DO3A-xy-ACR) was prepared and the reaction mixture was then diluted to ∼5 mCi/mL with saline. The log *P* value of ^{64}Cu(DO3A-xy-ACR) was determined according to the literature procedure.[19]

Animal Model. Biodistribution studies were performed using athymic nude mice bearing U87MG human glioma xenografts in compliance with the NIH animal experiment guidelines

Table 1. Selected Biodistribution Data of ^{64}Cu(DO3A-xy-ACR) in the Athymic Nude Mice (n = 5) Bearing U87MG Human Glioma Xenografts

organ (% ID/gram)	0.5 h	1 h	2 h	4 h	24 h
Blood	0.90 ± 0.22	0.60 ± 0.17	0.70 ± 0.08	0.70 ± 0.19	0.53 ± 0.05
Brain	0.04 ± 0.02	0.05 ± 0.01	0.06 ± 0.02	0.10 ± 0.03	0.13 ± 0.07
Heart	0.66 ± 0.25	0.66 ± 0.08	0.70 ± 0.11	0.89 ± 0.13	1.14 ± 0.33
Intestine	10.81 ± 5.99	8.05 ± 6.61	3.46 ± 0.69	2.69 ± 1.02	1.93 ± 0.17
Kidney	2.89 ± 0.90	2.53 ± 0.37	2.63 ± 0.42	2.18 ± 0.39	2.38 ± 0.41
Liver	31.90 ± 3.98	24.95 ± 5.64	15.20 ± 4.29	14.09 ± 6.82	8.18 ± 1.27
Lungs	1.63 ± 0.28	1.61 ± 0.39	1.75 ± 0.35	2.00 ± 0.75	1.83 ± 0.17
Muscle	0.29 ± 0.18	0.24 ± 0.11	0.20 ± 0.13	0.33 ± 0.06	0.34 ± 0.17
Spleen	0.97 ± 0.53	0.97 ± 0.46	0.79 ± 0.05	0.73 ± 0.17	1.58 ± 0.37
U87MG	1.07 ± 0.23	1.58 ± 0.55	2.71 ± 0.66	3.47 ± 1.19	3.52 ± 1.72
U87MG/Blood	1.23 ± 0.29	2.82 ± 1.04	3.96 ± 1.29	5.40 ± 3.66	8.76 ± 2.03
U87MG/Heart	1.79 ± 0.60	2.46 ± 0.98	3.99 ± 1.28	3.94 ± 2.17	3.28 ± 1.85
U87MG/Kidney	0.41 ± 0.16	0.61 ± 0.16	1.05 ± 0.29	1.63 ± 0.92	1.53 ± 0.83
U87MG/Liver	0.03 ± 0.01	0.07 ± 0.02	0.20 ± 0.09	0.31 ± 0.25	0.44 ± 0.25
U87MG/Lung	0.66 ± 0.10	0.97 ± 0.23	1.55 ± 0.26	1.89 ± 0.70	1.92 ± 0.87
U87MG/Muscle	4.90 ± 2.56	7.52 ± 3.91	17.82 ± 8.66	11.54 ± 8.06	12.26 ± 8.60

(*Principles of Laboratory Animal Care*, NIH Publication No. 86−23, revised 1985). The animal protocol was approved by the Purdue University Animal Care and Use Committee (PACUC). U87MG cells were cultured in the Minimum Essential Medium, Eagle with Earle's Balanced Salt Solution (nonessential amino acids sodium pyruvate) (ATCC, Manassas, VA) in humidified atmosphere of 5% CO_2, and were supplemented with 10% fetal bovine serum and 1% penicillin and streptomycin solution (GIBCO, Grand Island, NY). Female athymic nu/nu mice (5−6 weeks) were purchased from Harlan (Indianapolis, IN). Each mouse was implanted with 5×10^6 tumor cells subcutaneously into the left and right upper shoulder flanks. Four weeks after inoculation, the tumor size was 0.1−0.4 g, and animals were used for biodistribution studies.

Biodistribution Protocol. Twenty-five tumor-bearing mice (20−25 g) were randomly divided into five groups. Each animal was administered with ∼3 μCi of ^{64}Cu(DO3A-xy-ACR) by tail vein injection. Five animals were sacrificed by sodium pentobarbital overdose (∼200 mg/kg) at 0.5, 1, 2, 4, and 24 h p.i. Blood samples were withdrawn from the heart of tumor-bearing mice. The tumor, brain, eyes, heart, spleen, lungs, liver, kidneys, muscle, and intestine were harvested, dried with absorbent tissue, weighed, and counted in a γ-counter (Perkin-Elmer Wizard −1480, Shelton, CT). The organ uptake was calculated as % ID/g and %ID/organ. Biodistribution data (%ID/g) and T/B ratios are reported as an average with the standard deviation based on results from 5 tumor-bearing mice (10 tumors) at each time point. Comparison between two radiotracers was made using the two-way ANOVA test (*GraphPad Prism 5.0*, San Diego, CA). The level of significance was set at $p < 0.05$.

MicroPET. MicroPET scans were performed using an Inveon DPET scanner (Siemens Medical Solutions). The tumor-bearing nude mice (n = 3) were imaged in the prone position in the microPET scanner. Each mouse was injected with ∼250 μCi of ^{64}Cu(DO3A-xy-ACR) via the tail vein, then anesthetized with 2% isoflurane and placed near the center of the FOV. Multiple static scans were obtained at 0.5, 1, 2, 4, and 24 h p.i. The images were reconstructed by a three-dimensional ordered subsets expectation maximum (3D-OSEM) algorithm, and no correction was applied for attenuation or scatter. Image analysis was done using *ASI Pro VM* software.

Metabolic Stability. Normal athymic nude mice were used to study the metabolic stability of ^{64}Cu(DO3A-xy-ACR). Each mouse was administered with ∼100 μCi ^{64}Cu(DO3A-xy-ACR) via tail vein. Urine samples were collected at 30 and 120 min p.i. by manual void, and were mixed with equal volume of 50% acetonitrile aqueous solution. The mixture was centrifuged at 8000 rpm. The supernatant was collected and passed through a 0.20 μm Millex-LG filter. The filtrate was analyzed by radio-HPLC (Method 2). Feces samples were collected at 120 min p.i. and suspended in 50% acetonitrile aqueous solution. The mixture was vortexed for 5−10 min. After centrifuging at 8000 rpm, the supernatant was collected and passed through a 0.20 μm Millex-LG filter unit. The filtrate was analyzed by radio-HPLC (Method 2). The percentage radioactivity recovery was >90% for both urine and feces samples. The liver tissue was harvested at 120 min p.i., counted in a γ-counter, cut into small pieces, and then homogenized. The homogenate was mixed with 2 mL of 50% acetonitrile aqueous solution. The mixture was vortexed for ∼5 min. After centrifuging at 8000 rpm for 5 min, the supernatant was collected and counted in a γ-counter. The radioactivity recovery was ∼35% from the liver homogenate. After filtration through a 0.20 μm Milex-LG filter unit to remove the precipitate and particles, the filtrate was then analyzed by radio-HPLC (Method 2).

Cellular Culture. All cell lines were purchased from American Type Culture Collection (ATCC, Manassas, VA). U87MG human glioma cells were cultured in the Minimum Essential Medium supplemented with 10% fetal bovine serum (FBS, ATCC) and 1% penicillin and streptomycin (GIBCO) solution. Human fibroblasts were cultured in fibroblast dermal media supplemented with low serum growth kit (ATCC, including 7.5 mM L-glutamine, 5 ng/mL rh FGF β, 5 μg/mL insulin, 1 μg/mL hydrocortisone, 50 μg/mL ascorbic acid, and 2% serum). The primary U87MG glioma cells were extracted from xenografted U87MG tumors. Briefly, tumor tissues were cut and immersed immediately in completed Minimum Essential Medium (ATCC) media. The tumor tissues were rinsed twice with the Hanks' solution and dissected into small pieces with razor blades. Small tumor pieces were digested with 0.25% Trypsin

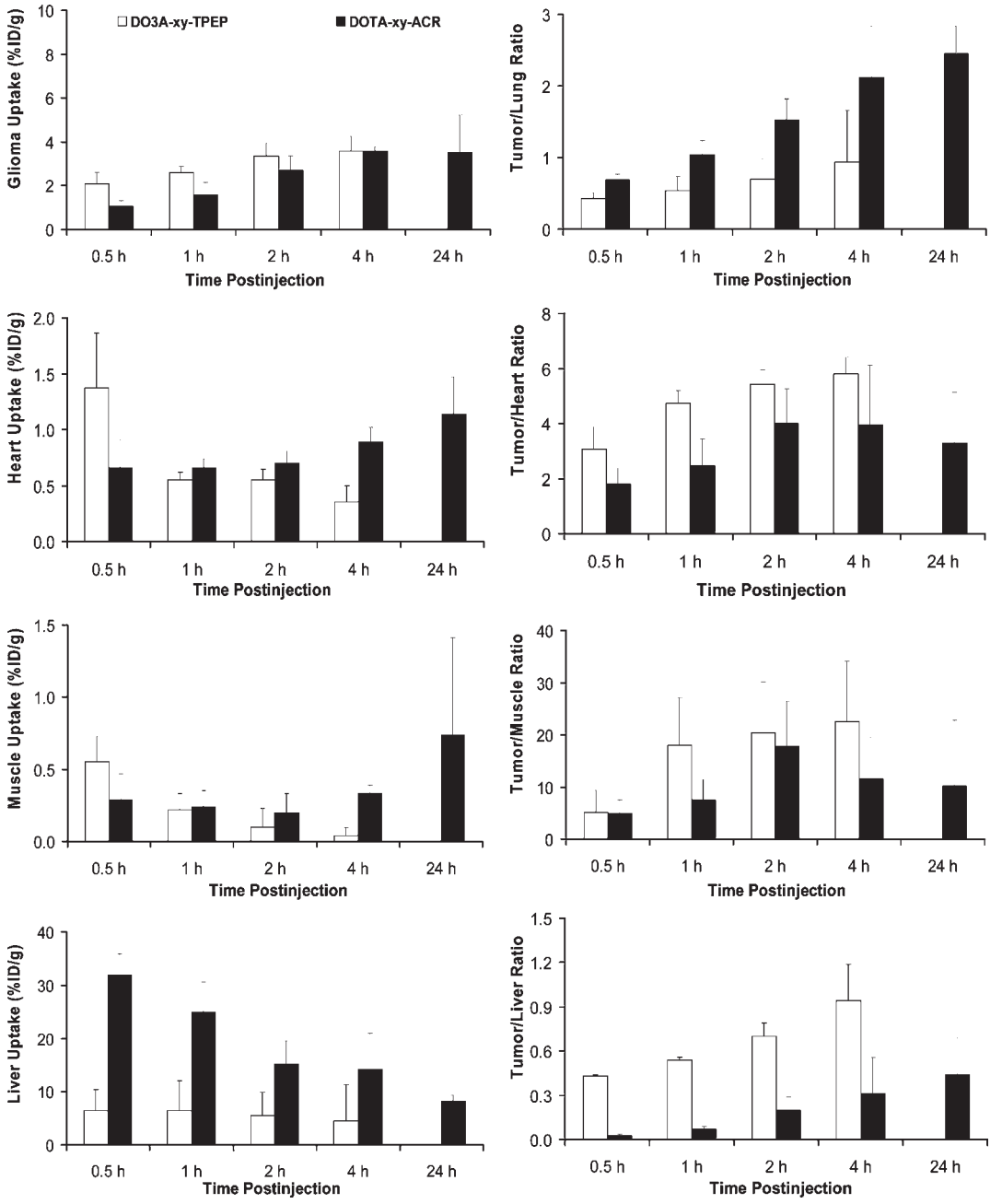


Figure 2. Comparison of the uptake (%ID/g) and T/B ratios for ^{64}Cu(DO3A-xy-ACR) and ^{64}Cu(DO3A-xy-TPEP) in selected organs of the athymic nude mice bearing U87MG human glioma xenografts.

(1 mM EDTA, without Ca^{2+} and Mg^{2+}) solution at 37 °C for 30 min, followed by vigorous pipetting and filtration through a 40 μm mesh nylon screen. After centrifugation at 1000 rpm for 5 min, the pellet was resuspended in the culture media. All cells were grown at 37 °C in a humidified atmosphere containing 5% CO_2.

Cellular Localization Study. Cells were allowed to culture in Lab-Tek 8-well glass chamber slides for at least 24 h before being used. Cu(DO3A-xy-ACR) was added into the culture media to achieve a concentration of 20 μM. Hoechst 33342 was added directly into the media to achieve 1 μM at 5 min before completion of incubation with Cu(DO3A-xy-ACR). After incubation for the indicated time, the cells were washed three times with phenol red-free Minimum Essential Medium. Lissamine (10 μM) was incubated along with Cu(DO3A-xy-ACR) to determine the mitochondrial localization. The fluorescence was visualized immediately with an Olympic BX51 fluorescence microscope (Olympus America Inc., Center Valley, PA) under 400× magnification. Images were acquired using a Hamamatsu digital CCD camera ORCA-R^2 (Hamamatsu Photonics K.K., Japan) with Olympus *MetaMorph* software.

RESULTS

DO3A-xy-ACR and Cu(DO3A-xy-ACR). DO3A-xy-ACR was prepared in two steps. First, ACR-xy-Br was allowed to react with DOTA(OBu-t)$_3$ in the presence of excess triehylamine in DMF. The intermediate DO3A(OBu-t)$_3$-xy-ACR was then hydrolyzed

dx.doi.org/10.1021/bc100458p |*Bioconjugate Chem.* 2011, 22, 700–708

to gave DO3A-xy-ACR in ~40% overall yield. Cu(DO3A-xy-ACR) was prepared by reacting DO3A-xy-ACR with one equivalent of Cu(II) acetate in 0.5 M NH_4OAc (pH = 5.5). Since phosphonium and acridinium cations share very similar structures, it is reasonable to believe that Cu(DO3A-xy-ACR) will exist in its zwitterion form, which has been established for ^{64}Cu-labeled phosphonium cations.[27] This statement is completely supported by the elemental analysis data.

Radiochemistry. ^{64}Cu(DO3A-xy-ACR) was prepared by reacting DO3A-xy-ACR with $^{64}CuCl_2$ in 100 mM NH_4OAc buffer (pH = 5.0) at 100 °C for 10 min. The radiochemical purity was >95% without HPLC purification with the specific activity of ~50 Ci/mmol. It had the log *P* value of -2.0 ± 0.2, which was more hydrophilic than ^{64}Cu(DO3A-xy-TPEP) (log $P = -1.7 \pm 0.1$).[19] ^{64}Cu(DO3A-xy-ACR) was stable for >24 h in the presence of excess EDTA (3 mg/mL in 25 mM phosphate buffer, pH = 7.4). Since Cu(DO3A-xy-ACR) and ^{64}Cu(DO3A-xy-ACR) share almost identical HPLC retention time in the concordance experiment (Supporting Information Figure SI1), it is reasonable to believe that they have the same chemical composition in solution.

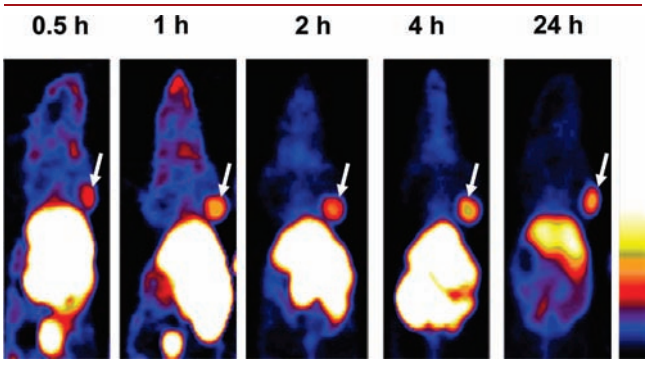


Figure 3. Decay-corrected whole-body coronal microPET images of the athymic nude mice bearing U87MG glioma xenografts administered with ~250 μCi of ^{64}Cu(DO3A-xy-ACR). Arrows indicate the presence of glioma tumors.

Biodistribution Characteristics. Selected biodistribution data for ^{64}Cu(DO3A-xy-ACR) are listed in Table 1. Figure 2 compares the organ uptake (%ID/g) and T/B ratios between ^{64}Cu(DO3A-xy-ACR) and ^{64}Cu(DO3A-xy-TPEP) in the same glioma-bearing animal model. ^{64}Cu(DO3A-xy-TPEP) was used only for comparison purposes since it has the best tumor uptake and T/B ratios among the ^{64}Cu-labeled phosphonium cations evaluated under the same conditions.[17−20] While its biodistribution data were obtained from our previous report,[19] the biodistribution data of ^{64}Cu(DO3A-xy-TPEP) at 4 h p.i. were added in this study. In general, ^{64}Cu(DO3A-xy-ACR) was excreted mainly through the renal route with >65% of injected radioactivity being recovered from urine samples at 1 h p.i. The tumor uptake of ^{64}Cu(DO3A-xy-ACR) was 1.07 ± 0.23, 1.58 ± 0.55, 2.71 ± 0.66, 3.47 ± 1.19, and 3.52 ± 1.72%ID/g at 0.5, 1, 2, 4, and 24 h p.i., respectively. The tumor uptake of ^{64}Cu(DO3A-xy-ACR) was significantly ($p < 0.05$) lower than that of ^{64}Cu(DO3A-xy-TPEP) at <1 h p.i., but this difference disappeared at 2−4 h p.i. The liver uptake of ^{64}Cu(DO3A-xy-ACR) was very high (31.90 ± 3.98, 24.95 ± 5.64, 15.20 ± 4.29, 14.09 ± 6.82, and 8.18 ± 1.27%ID/g at 0.5, 1, 2, 4, and 24 h p.i., respectively). As a result, it had very low tumor/liver ratios. The tumor/heart ratios (Figure 2) of ^{64}Cu(DO3A-xy-ACR) were comparable to those of ^{64}Cu(DO3A-xy-TPEP), but it had better tumor/lung ratios (Figure 2) than ^{64}Cu(DO3A-xy-TPEP).

MicroPET. Figure 3 shows microPET images of a glioma-bearing mouse administered with ~250 μCi of ^{64}Cu(DO3A-xy-ACR) at 0.5, 1, 2, 4, and 24 h p.i. The tumor was clearly visualized with excellent T/B contrast as early as 30 min p.i. High liver

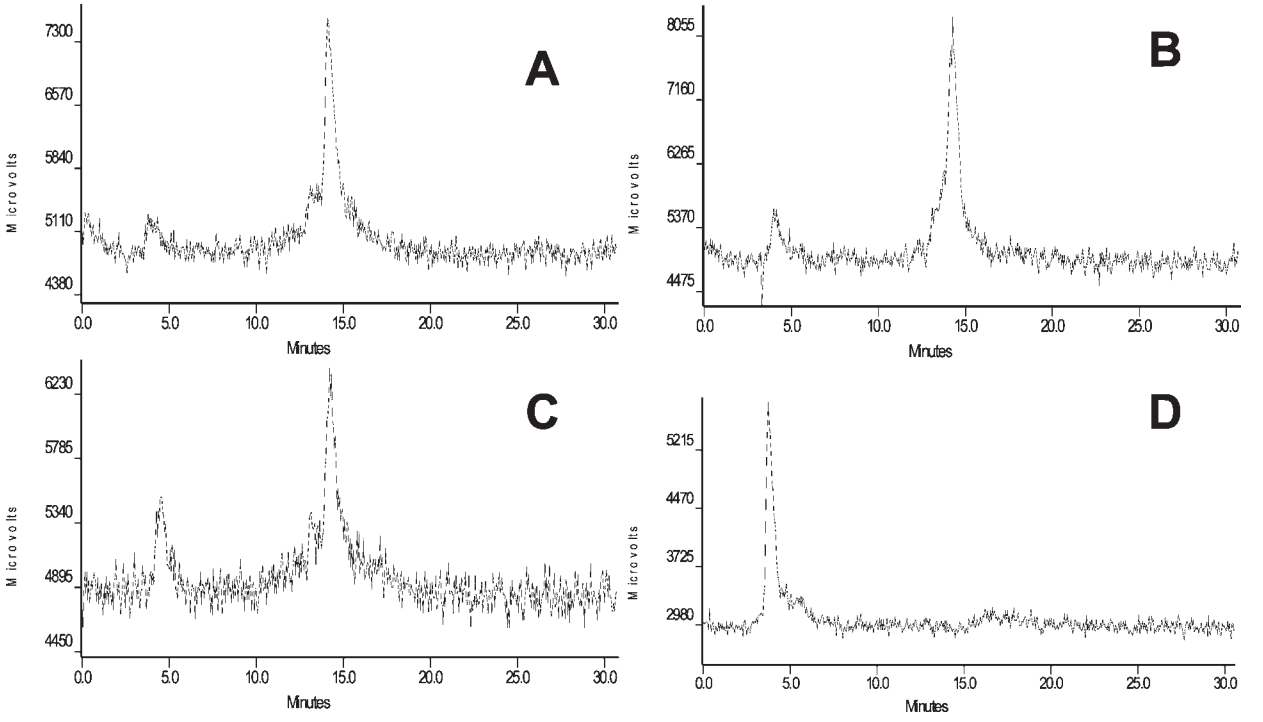


Figure 4. Representative radio-HPLC chromatograms of ^{64}Cu(DO3A-xy-ACR) in urine at 30 min (A) and 120 min p.i. (B), in feces at 120 min p.i. (C), and in the liver homogenate (D).

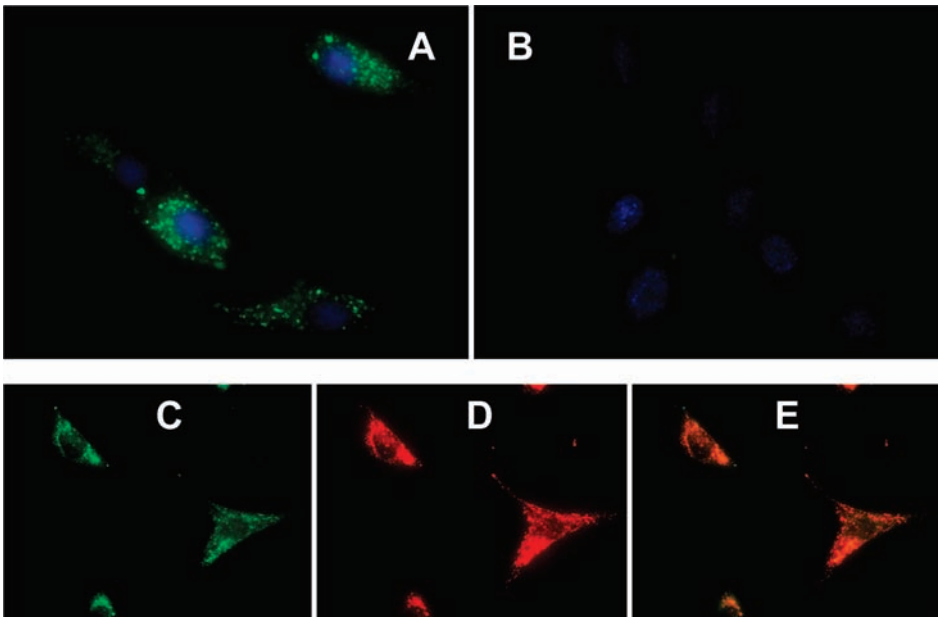


Figure 5. Representative microscopic images (magnification: 400×) of the cultured primary U87MG glioma cells (A) and normal human fibroblast cells (B) stained with 20 μM of Cu(DO3A-xy-ACR) (green color). The nuclei were stained with 1 μM of Hoechst 33342 (blue color). Normal fibroblast cell line was used as the "negative control" to demonstrate the tumor selectivity of ^{64}Cu(DO3A-xy-ACR). The colocalization experiment was performed using U87MG glioma cells stained with 40 μM of Cu(DO3A-xy-ACR) (C) and Lissamine Rhodamine B (D: red color), which was used as the "positive control" for mitochondrial staining of tumor cells. The orange color in the overlay image (E) indicates that Cu(DO3A-xy-ACR) is indeed able to selectively localize in the mitochondria of U87MG tumor cells.

uptake was seen at all time points. After normalization, the tumor uptake of ^{64}Cu(DO3A-xy-ACR) was calculated to be 0.8 ± 0.1, 1.0 ± 0.2, 1.4 ± 0.3, 2.27 ± 0.8, and 3.40 ± 0.25%ID/g at 0.5, 1, 2, 4, and 24 h p.i., respectively. These data were completely consistent with that observed in the biodistribution study (Figure 2).

Metabolic Stability. Figure 4 shows radio-HPLC chromatograms of ^{64}Cu(DO3A-xy-ACR). In general, ^{64}Cu(DO3A-xy-ACR) was stable in the urine sample over 2 h study period while ~80% of it remained intact in the feces sample. We also found that only ~35% of the liver radioactivity was recovered from the liver homogenate. The HPLC analysis showed only one radiometric peak at 4 min (Figure 4D) with no intact ^{64}Cu(DO3A-xy-ACR), and strongly suggested that ^{64}Cu(DO3A-xy-ACR) underwent complete transchelation in the liver during the 2 h study period.

Localization in Mitochondria. Figure 5 shows microscopic images of the cultured primary U87MG glioma and normal fibroblast cells stained with 20 μM of Cu(DO3A-xy-ACR). The human fibroblasts were used as the "negative control" to demonstrate the tumor selectivity of ^{64}Cu(DO3A-xy-ACR). Lissamine was used as the "positive control" since it is a well-known mitochondrion-targeting agent. Nuclear staining was achieved with Hoechst 33342 (1 μM). The orange color in the overlay image indicated that Cu(DO3A-xy-ACR) was able to colocalize with Lissamine in the tumor mitochondria. It was clear that Cu(DO3A-xy-ACR) (Figure 5A) localize mainly in the mitochondria of U87MG glioma cells. There was very little localization of Cu(DO3A-xy-ACR) in the nuclei of tumor cells. Similar results were also obtained with U87MG human glioma cells (Supporting Information Figure SI2). Although Cu(DO3A-xy-ACR) can localize in mitochondria of normal human fibroblasts, the fluorescent intensity was too low to be seen clearly using the same brightness and contrast as those for U87MG glioma cells. It is very interesting to note that the mitochondrial fluorescent intensity was dependent on the concentration (Supporting Information Figure SI3) and the incubation time (Supporting Information Figure SI4) of Cu(DO3A-xy-ACR). After 1 h incubation with 20 μM of Cu(DO3A-xy-ACR), the fluorescence was weak while the fluorescence in the U87MG glioma cells became much more intense after 24 h incubation (Supporting Information Figure SI4).

$[Re(CN\text{-}bn\text{-}ACR)(2,4\text{-}pydic)(CO)_3]^+$ was reported to localize in the tumor nuclei.[22] Since ^{64}Cu(DO3A-xy-ACR) and $[Re(CN\text{-}bn\text{-}ACR)(2,4\text{-}pydic)(CO)_3]^+$ share the same ACR cation, we decided to perform staining studies using both U87MG human glioma cells and the cultured primary U87MG glioma cells with ^{64}Cu(DO3A-xy-ACR) as a fluorescent probe. We found that, if U87MG glioma cells were not fixed with 4% formalin, the fluorescent signal was concentrated inside tumor mitochondria (Figure 6: left). If U87MG glioma cells were fixed with 4% formalin, the majority of fluorescence was inside the tumor cell nucleus while the remaining fluorescence was evenly distributed inside the cytoplasm of tumor cells (Figure 6: right). This distribution pattern was similar to that reported for $[Re(CN\text{-}C4\text{-}ACR)(2,4\text{-}pydic)(CO)_3]^+$ in B16-F1 and PC-3 cells fixed with 4% formalin;[22] but it was completely different from the "spotted" patterns in the tumor mitochondria without fixation (Figure 6: left). Obviously, the intracellular distribution patterns of ^{64}Cu(DO3A-xy-ACR) depend largely on formalin fixation.

DISCUSSION

In this study, we found that ^{64}Cu(DO3A-xy-ACR) and ^{64}Cu-(DO3A-xy-TPEP) shared similar tumor uptake (Figure 2) at 2−4 h p.i. Even though ^{64}Cu(DO3A-xy-ACR) (log P = −2.0 ± 0.2) is

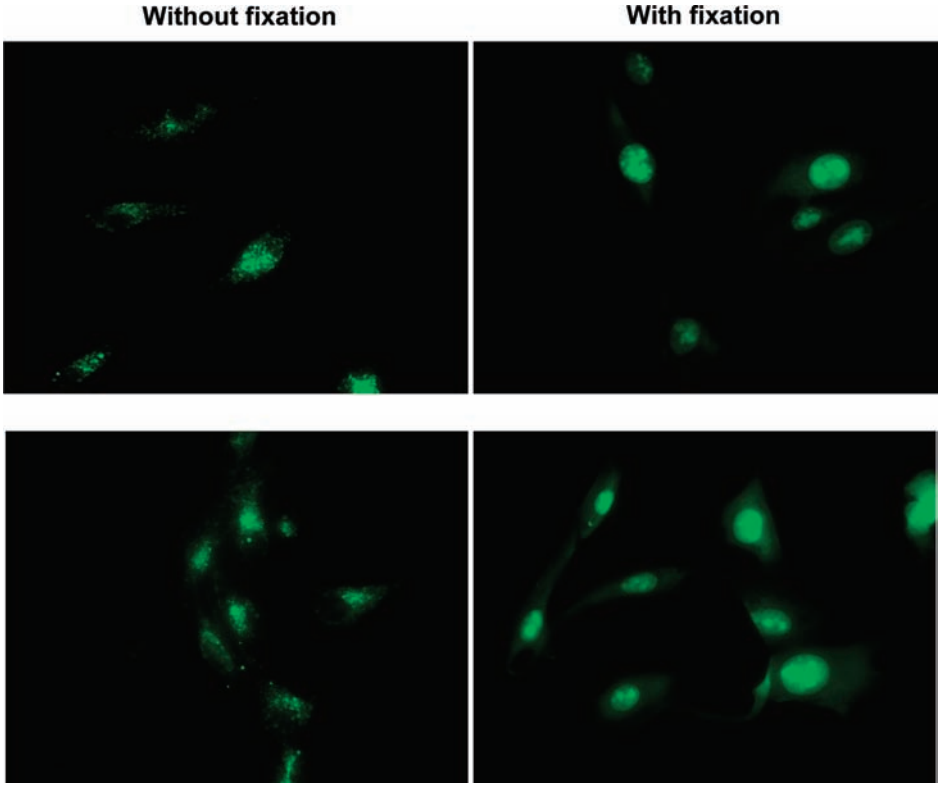


Figure 6. Microscopic images (magnification: 400×) of cultured primary U87MG (top) glioma cells and U87MG human cell line (bottom) stained with 40 μM of Cu(DO3A-xy-ACR) for 1 h with (right) and without (left) formalin fixation. All images were adjusted with the same brightness and contrast.

more hydrophilic than ^{64}Cu(DO3A-xy-TPEP) (log $P = -1.7 \pm 0.1$),[19] its liver uptake was very high with much lower tumor/liver ratios than those of ^{64}Cu(DO3A-xy-TPEP), suggesting that the radiotracer liver uptake is not completely due to its lipophilicity. Because of its lower liver uptake, ^{64}Cu(DO3A-xy-TPEP) is a better PET radiotracer than ^{64}Cu(DO3A-xy-ACR).

Another interesting finding of this study is that the targeting moiety has significant impact on metabolic stability of ^{64}Cu radiotracers. For example, ^{64}Cu(DO3A-xy-TPEP) has no metabolism during excretion from both renal and hepatobiliary routes.[19] However, ^{64}Cu-(DO3A-xy-ACR) has ~20% metabolism during hepatobiliary excretion (Figure 4C). We examined the liver stability of ^{64}Cu(DO3A-xy-ACR), and found that there was no intact ^{64}Cu(DO3A-xy-ACR) in liver homogenate (Figure 4D). Its HPLC profile is similar to that of ^{64}Cu(DO3A-xy-TPEP) in the liver homogenate.[19] Since Anderson's group has clearly demonstrated the in vivo instability of ^{64}Cu-labeled tetraazamacrocycles,[28−30] we believe that the observation of no intact ^{64}Cu(DO3A-xy-ACR) in the liver homogenate is most likely caused by transchelation of ^{64}Cu from ^{64}Cu(DO3A-xy-ACR) to the proteins in the liver.

The mitochondrial localization of ^{64}Cu(DO3A-xy-ACR) has been clearly demonstrated using Cu(DO3A-xy-ACR) as a fluorescent probe (Figure 5). Since Cu(DO3A-xy-ACR) can also localize in normal human fibroblasts with much less fluorescent intensity, the tumor selectivity of ^{64}Cu(DO3A-xy-ACR) is caused by the increased negative mitochondrial potential in U87MG glioma cells as compared with that in normal fibroblasts. The time-dependence (Supporting Information Figure SI4) of the mitochondrial fluorescent intensity for Cu(DO3A-xy-ACR) is consistent with the fact that ^{64}Cu(DO3A-xy-ACR) has a slow increase in the tumor uptake over the first 4 h p.i.

It must be noted that the cell fixation has a significant impact on the intracellular localization of fluorescent probes targeting mitochondria. For example, the fluorophor concentrates inside the tumor mitochondria with typical "spotted" patterns (Figure 6: left) if U87MG glioma cells are not fixed with 4% formalin. In the presence of formalin fixation, however, the intracellular distribution patterns (Figure 6: right) of ^{64}Cu-(DO3A-xy-ACR) are very similar to those of [Re(CN-bn-ACR)-(2,4-pydic)$(CO)_3$]$^+$ in of B16−F1 and PC-3 cells.[22] While there is no doubt that [Re(CN-bn-ACR)(2,4-pydic)$(CO)_3$]$^+$ is able to bind to duplex and triplex DNAs in the in vitro binding assays,[22] we believe that the nuclear localization (Figure 6: right) of ^{64}Cu(DO3A-xy-ACR) is most likely the artifacts caused by formalin fixation. Similar fixation artifacts were reported with the cell-penetrating peptides.[31−33] Cellular fixation with 3−4% formalin can cause significant damage in the mitochondrial membrane, which would result in the collapse of mitochondrial potential and lead to the localization of ^{64}Cu(DO3A-xy-ACR) inside cytoplasm and nuclei. Therefore, it is strongly recommended that living cells are used for studies related to the mitochondrial function.

CONCLUSION

In summary, we evaluated the potential of ^{64}Cu(DO3A-xy-ACR) as PET radiotracer for tumor imaging. Although tumors could be clearly visualized in the athymic nude mice bearing U87MG human glioma xenografts, ^{64}Cu(DO3A-xy-ACR) is not as good a PET radiotracer as ^{64}Cu(DO3A-xy-TPEP) because of

its much higher liver uptake. Even though it was reported that ($[Re(CN\text{-}C4\text{-}ACR)(2,4\text{-}pydic)(CO)_3]^+$) was able to localize in the nuclei of tumor cells by binding to the duplex and triplex DNAs,[22] our results from cellular staining assays show that Cu(DO3A-xy-ACR) is localized in the mitochondria of living U87MG glioma cells. Due to the similarity between ACR and TPEP cations with respect to their structure and overall molecular charge (Figure 1), ^{64}Cu(DO3A-xy-TPEP) also targets the tumor mitochondria, where negative mitochondrial transmembrane potential is significantly elevated as compared with normal cells of the surrounding tissues.

■ ASSOCIATED CONTENT

Supporting Information. The HPLC concordance (Figure SI1) for ^{64}Cu(DO3A-xy-ACR) and Cu(DO3A-xy-ACR), microscopic images (Figure SI2) of the U87MG human glioma cells stained with 20 μM of Cu(DO3A-xy-ACR), microscopic images (Figure SI3) of the cultured primary U87MG glioma cells stained with various concentration (1−100 μM) of Cu(DO3A-xy-ACR), and microscopic images (Figure SI4) of the cultured primary U87MG glioma cells stained with 20 μM of Cu(DO3A-xy-ACR) at different time points (1, 2, 4, and 24 h). This material is available free of charge via the Internet at http://pubs.acs.org.

■ AUTHOR INFORMATION

Corresponding Author

*Correspondence should be addressed to Dr. Shuang Liu, School of Health Sciences, Purdue University, 550 Stadium Mall Drive, West Lafayette, IN 47907. Phone: 765-494-0236. Fax 765-496-1377. Email: liu100@purdue.edu.

■ ACKNOWLEDGMENT

This work is supported, in part, by Purdue University and the research grant: R01 CA115883 from the National Cancer Institute (NCI).

■ REFERENCES

(1) Kroemer, G., Dallaporta, B., and Resche-Rigon, M. (1998) The mitochondrial death/life regulator in apoptosis and necrosis. *Annu. Rev. Physiol. 60*, 619–642.

(2) Modica-Napolitano, J. S., and Aprille, J. R. (2001) Delocalized lipophilic cations selectively target the mitochondria of carcinoma cells. *Adv. Drug Delivery Rev. 49*, 63–70.

(3) Duchen, M. R. (2004) Mitochondria in health and disease: perspectives on a new mitochondrial biology. *Mol. Aspects Med. 25*, 365–451.

(4) Modica-Napolitano, J. S., and Singh, K. K. (2002) Mitochondria as targets for detection and treatment of cancer. *Expert Rev. Mol. Med. 4*, 1–19.

(5) Mannella, C. A. (2006) The relevance of mitochondrial membrane topology to mitochondrial function. *Biochim. Biophys. Acta 1762*, 140–147.

(6) Johnson, L. V., Walsh, M. L., and Chen, L. B. (1980) Localization of mitochondria in liver cells with rhodamine 123. *Proc. Natl. Acad. Sci. U.S.A. 77*, 990–994.

(7) Summerhayes, I. C., Lampidis, T. J., Bernal, S. D., Nadakavukaren, J. J., Nadakavukaren, K. K., Shepard, E. L., and Chen, L. B. (1982) Unusual retention of rhodamine 123 by mitochondria in muscle and carcinoma cells. *Proc. Natl. Acad. Sci. U.S.A. 79*, 5292–5296.

(8) Modica-Napolitano, J. S., and Aprille, J. R. (1987) Basis for the selective cytotoxicity of rhodamine 123. *Cancer Res. 47*, 4361–4365.

(9) Davis, S., Weiss, M. J., Wong, J. R., Lampidis, T. J., and Chen, L. B. (1985) Mitochondrial and plasma membrane potentials cause unusual accumulation and retention of rhodamine 123 by human breast adenocarcinoma-derived MCF-7 cells. *J. Biol. Chem. 260*, 3844–3850.

(10) Dairkee, S. H., and Hackett, A. J. (1991) Differential retention of rhodamine 123 by breast carcinoma and normal human mammary tissue. *Breast Cancer Res. Treat. 18*, 57–61.

(11) Lightshtein, D., Kaback, H. R., and Blume, A. J. (1979) Use of a lipophilic cation for determination of membrane potential in neuroblastomas-glioma hybrid cell suspensions. *Proc. Natl. Acad. Sci. U.S.A. 76*, 650–654.

(12) Hockings, P. D., and Rogers, P. J. (1996) The measurement of transmembrane electric potential with lipophilic cations. *Biochem. Biophys. Acta 1282*, 101–106.

(13) Huang, S. G. (2002) Development of a high throughput screening assay for mitochondrial membrane potential in living cells. *J. Biomol. Screen. 7*, 383–389.

(14) Gottlieb, E., and Thompson, C. B. (2003) Targeting the mitochondria to enhance tumor suppression. *Methods Mol. Biol. 223*, 543–554.

(15) Ross, M. F., Kelso, G. F., Blaikie, F. H., James, A. M., Cocheme, H. M., Filipovska, A., Da Ros, T. D., Hurd, T. R., Smith, R. A. J., and Murphy, M. P. (2005) Lipophilic triphenylphosphonium cations as tools in mitochondrial bioenergetics and free radical biology. *Biochem. (Moscow) 70*, 222–230.

(16) Jakobs, S. (2006) High resolution imaging of living mitochondria. *Biochim. Biophys. Acta 1763*, 561–575.

(17) Wang, J., Yang, C., Kim, Y. S., Sreerama, S. G., Cao, Q., Li, Z., He, Z., Chen, X., and Liu, S. (2007) ^{64}Cu-Labeled triphenylphosphonium and triphenylarsonium cations as highly tumor-selective PET imaging agents. *J. Med. Chem. 50*, 5057–5069.

(18) Kim, Y. S., Yang, C., Wang, J., Sreerama, S. G., Cao, Q., Li, Z., He, Z., Chen, X., and Liu, S. (2008) Radiolabeled triphenylphosphonium cations as highly tumor-selective imaging agents: Effects of radiometals, bifunctional chelators and molecular charge. *J. Med. Chem. 51*, 2971–2984.

(19) Yang, C. T., Kim, Y. S., Wang, J., Wang, L., Shi, J., Li, Z., Chen, X., Fan, M., Li, J. J., and Liu, S. (2008) ^{64}Cu-labeled 2-(diphenylphosphoryl)ethyldiphenylphosphonium cations as highly selective tumor imaging agents: effects of linkers and chelates on biodistribution characteristics. *Bioconjugate Chem. 19*, 2008–2022.

(20) Liu, S., Kim, Y. S., Yang, C. T., Shi, J., Zhai, Z., and Hou, G. (2009) Evaluation of ^{64}Cu(DO3A-xy-TPEP) as a PET radiotracer for monitoring tumor multidrug resistance. *Bioconjugate Chem. 20*, 790–798.

(21) Agiamarnioti, K., Triantis, T., Papadopoulos, K., and Dimotikali, D. (2004) Synthesis and chemiluminescent properties of novel biotinylated acridinium esters. *Acta Chim. Slov. 51*, 67–76.

(22) Agorastos, N., Borsig, L., Renard, A., Antoni, P., Viola, G., Spingler, B., Kurz, P., and Alberto, R. (2007) Cell-specific and nuclear targeting with $[M(CO)_3]^+$ (M = ^{99m}Tc, Re)-based complexes conjugated to acridine orange and bombesin. *Chem.—Eur. J. 13*, 3842–3852.

(23) Bähr, O., Rieger, J., Duffner, F., Meyermann, R., Weller, M., and Wick, W. (2003) P-glycoprotein and multidrug resistance-associated protein mediate specific patterns of multidrug resistance in malignant glioma cell lines, but not in primary glioma cells. *Brain Pathol. 13*, 482–494.

(24) Le Jeune, N., Perek, N., Denoyer, D., and Dubois, F. (2004) Influence of glutathione depletion on plasma membrane cholesterol esterification and on Tc-99m-Sestamibi and Tc-99m-Tetrofosmin uptakes; a comparative study in sensitive U87MG and multidrug-resistant MRP1 human glioma cells. *Cancer Biother. Radiopharm. 19*, 411–421.

(25) Bähr, O., Wick, W., and Weller, M. (2001) Modulation of MDR/MRP by wild-type and mutant p53. *J. Clin. Invest. 107*, 643–645.

(26) Nakatsu, S., Kondo, S., Kondo, Y., Yin, D., Peterson, J. W., Kaakaji, R., Morimura, T., Kikuchi, H., Takeuchi, J., and Barnett, G. H.

(1997) Induction of apoptosis in multi-drug resistant (MDR) human glioblastoma cells by SN38, a metabolite of the camptothecin derivative CPT. *Cancer Chemother. Pharmacol. 39*, 417–423.

(27) Yang, C., Li, Y. X., and Liu, S. (2007) Synthesis and structural characterization of complexes of a DO3A-conjugated triphenylphosphonium cation with diagnostically important metal ions. *Inorg. Chem. 46*, 8988–8997.

(28) Bass, L. A., Wang, M., Welch, M. J., and Anderson, C. J. (2001) In vivo transchelation of copper-64 from TETA-Octreotide to superoxide dismutase in rat liver. *Bioconjugate Chem. 11*, 527–532.

(29) Boswell, C. A., Sun, X., Niu, W., Weisman, G. R., Wong, E. H., Rheingold, A. L., and Anderson, C. J. (2004) Comparative in vivo stability of copper-64-labeled cross-bridged and conventional tetraazamacrocyclic complexes. *J. Med. Chem. 47*, 1465–1474.

(30) Boswell, C. A., McQuade, P., Weisman, G. R., Wong, E. H., and Anderson, C. J. (2005) Optimization of labeling and metabolite analysis of copper-64-labeled azamacrocyclic chelators by radio-LC-MS. *Nucl. Med. Biol. 32*, 29–38.

(31) Horton, K. L., Stewart, K. M., Fonseca, S. B., Guo, Q., and Kelley, S. O. (2008) Mitochondria-penetrating peptides. *Chem. Biol. 15*, 375–382.

(32) Mahon, K. P., Potocky, T. B., Blair, D., Roy, M. D., Stewart, K. M., Chiles, T. C., and Kelley, S. O. (2007) Deconvolution of the cellular oxidative stress response with organelle-specific peptide conjugates. *Chem. Biol. 14*, 923–930.

(33) Li, L., Geisler, I., Chmielewski, J., and Cheng, J. X. (2010) Cationic amphiphilic polyproline helix P11LRR targets intracellular mitochondria. *J. Controlled Release 142*, 259–266.

Bioconjugate Chemistry

ARTICLE

pubs.acs.org/bc

Site-Specific Conjugation of Monodispersed DOTA-PEGn to a Thiolated Diabody Reveals the Effect of Increasing PEG Size on Kidney Clearance and Tumor Uptake with Improved 64-Copper PET Imaging

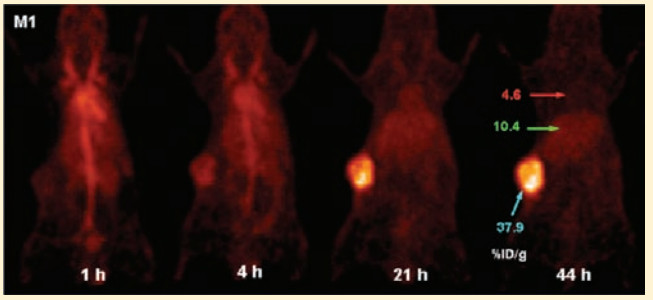
Lin Li,[†,∥] Desiree Crow,[§,∥] Fabio Turatti,[‡,∥] James R. Bading,[§] Anne-Line Anderson,[§] Erasmus Poku,[§] Paul J. Yazaki,[§] Jenny Carmichael,[‡] David Leong,[‡] Michael P. Wheatcroft,[‡] Andrew A. Raubitschek,[§] Peter J. Hudson,[‡,⊥] David Colcher,[§,⊥] and John E. Shively*[,†,⊥]

[†]Department of Immunology, Beckman Research Institute of City of Hope, Duarte, California 91010, United States

[‡]Avipep Pty Ltd., 343 Royal Parade, Parkville VIC 3008, Australia

[§]Department of Cancer Immunotherapeutics & Tumor Immunology, Beckman Research Institute of City of Hope, Duarte, California 91010, United States

ABSTRACT: Optimal PET imaging of tumors with radiolabeled engineered antibodies requires, among other parameters, matching blood clearance and tumor uptake with the half-life of the engineered antibody. Although diabodies have favorable molecular sizes (50 kDa) for rapid blood clearance ($t_{1/2}$ = 30−60 min) and are bivalent, thereby increasing tumor uptake, they exhibit substantial kidney uptake as their major route of clearance, which is especially evident when they are labeled with the PET isotope ^{64}Cu ($t_{1/2}$ = 12 h). To overcome this drawback, diabodies may be conjugated to PEG, a modification that increases the apparent molecular size of the diabody and reduces kidney uptake without adversely affecting tumor uptake or the tumor to blood ratio. We show here that site-specific attachment of monodispersed PEGn of increasing molecular size (n = 12, 24, and 48) can uniformly increase the apparent molecular size of the PEG-diabody conjugate, decrease kidney uptake, and increase tumor uptake, the latter due to the increased residence time of the conjugate in the blood. Since the monodispersed PEGs were preconjugated to the chelator DOTA, the conjugates were able to bind radiometals such as ^{111}In and ^{64}Cu that can be used for SPECT and PET imaging, respectively. To allow conjugation of the DOTA-PEG to the diabody, the DOTA-PEG incorporated a terminal cysteine conjugated to a vinyl sulfone moiety. In order to control the conjugation chemistry, we have engineered a surface thiolated diabody that incorporates two cysteines per monomer (four per diabody). The thiolated diabody was expressed and purified from bacterial fermentation and only needs to be reduced prior to conjugation to the DOTA-PEGn-Cys-VS. This novel imaging agent (a diabody with DOTA-PEG48-Cys-VS attached to introduced thiols) gave up to 80%ID/g of tumor uptake with a tumor to blood ratio (T/B) of 8 at 24 h when radiolabeled with ^{111}In and 37.9% ID/g of tumor uptake (T/B = 8) at 44 h when radiolabeled with ^{64}Cu in PET imaging in an animal model. Tumor uptake was significantly improved from the 50% ID/g at 24 h observed with diabodies that were pegylated on surface lysine residues. Importantly, there was no loss of immunoreactivity of the site-specific Cys-conjugated diabody to its antigen (TAG-72) compared to the parent, unconjugated diabody. We propose that thiolated diabodies conjugated to DOTAylated monodisperse PEGs have the potential for superior SPECT and PET imaging in a clinical setting.



INTRODUCTION

Optimal PET imaging of tumors with radiolabeled engineered antibodies requires, among other parameters, matching blood clearance and tumor uptake with the half-life of the engineered antibody.[1,2] Although diabodies have favorable molecular sizes (50 kDa) for rapid blood clearance ($t_{1/2}$ = 30−60 min) and are bivalent increasing tumor uptake, they exhibit substantial kidney uptake as their major route of clearance, which is especially evident when they are labeled with the PET isotope ^{64}Cu ($t_{1/2}$ = 12 h). To overcome this drawback, diabodies may be conjugated to PEG, a modification that increases the apparent molecular size of the diabody and reduces kidney uptake without adversely affecting tumor uptake or the tumor to blood ratio.[3] Recently, we have shown that monodispersed PEGs, as opposed to polymeric PEGs, not only can achieve this goal but also can incorporate bifunctional chelators such as DOTA to allow the preparation of a conjugate ready for radiolabeling with a variety of radiometals.[4] In that study, we synthesized a number of monodispersed PEGs of different sizes starting from FMOC-NH-PEGn-COOH (where n = 12, 24, 24, and 48) that had DOTA at the "amino-" terminus and cysteine at the

Received: October 21, 2010
Revised: March 5, 2011
Published: March 12, 2011

ACS Publications © 2011 American Chemical Society

"carboxy-" terminus using a standard solid phase peptide synthesis approach. The product DOTA-NH-PEGn-Cys, which had a free thiol was derivatized with vinyl sulfone, yielding a product that could be conjugated to proteins by Michael addition to either the thiol or amino groups by control of the pH.[5] Since the starting diabody had no surface thiol groups, all of the conjugations were made to surface amino groups. Although, we were successful in demonstrating the principle that addition of monodispersed PEG could favorably modify the diabody improving biodistributions and subsequent imaging, this approach does not allow a precise control of the addition of the PEG conjugates and may not be generally applicable to diabodies where overconjugation with PEG to amino groups may lead to decreased immunoreactivity.

A potential solution to this problem has been proposed by a number of groups through the incorporation of site-specific amino acid replacements to add surface thiol residues into intact antibodies. This included the recent study by Tinianow et al.[6] who generated a thiolated mAb that was site-specifically conjugated to a maleimido-desferrioxamine and radiolabeled with ^{89}Zr for PET imaging. In that study, the half-life of the radiolabel ($t_{1/2}$ = 4d) was well-matched with the blood clearance of an intact mAb ($t_{1/2}$ = 2−3d). However, as noted by Janutula et al.,[7] most single-site cysteine additions result in intermolecular aggregation, variable conjugation, and result in poor expression yield for large scale processing. Furthermore, intact antibodies that were conjugated onto cysteine residues by partial reduction of interchain-disulfide bonds had variable stoichiometry (zero to eight drugs per antibody) and potentially yielded >100 species.[7] For diabodies, both additional C-terminal cysteine residues[8] and intrachain disulfides[9] have been designed, although production yields were low.

In this article, we designed a stable intradomain disulfide bond in a surface-exposed region of FR1 in the VL domain of an anti-TAG-72 diabody. Molecular modeling ensured the two cysteine residues were about 6−7 Å apart and positioned so that their side chain thiol groups were exposed to solvent and could form a disulfide bond. This resulted in a stable, well-folded diabody, produced by bacterial expression and which could be reduced and conjugated to our previously described DOTA-NH-PEGn-Cys-VS where n = 12, 24, and 48 at pH 7, a pH where the Michael addition reaction is specific for thiols. The resulting conjugates exhibited an average substitution of 3 PEGs per dimeric diabody out of a theoretical maximum of 4 PEGs per diabody. When studied in a mouse xenograft model, the three conjugates exhibited a monotonic decrease in kidney uptake in the order of n = 0, 12, 24, and 48, with n = 48 giving the least kidney uptake (15% ID/g at 4−72 h) and the highest tumor uptake (80% ID/g at 24−72 h). The series also gave a monotonic increase in blood clearance in the order of n = 0, 12, 24, and 48, with n = 0 giving a blood clearance of $t_{1/2}$ = 0.5 h, and n = 48 a blood clearance of $t_{1/2}$ = 6.0 h. Thus, it appears possible to fine-tune the biodistribution properties of a thiolated diabody with site-specific conjugation of monodispersed PEGs. Since the n = 48 conjugate had the lowest kidney uptake, the highest tumor uptake, and an acceptable tumor to blood ratio (T/B = 8), this conjugate was radiolabeled with ^{64}Cu (half-life well matched to blood clearance) and subjected to PET imaging in the mouse xenograft model. The resulting PET image was excellent in terms of tumor to blood contrast (T/heart = 8) with minimal imaging of other organs including the kidney and liver.

EXPERIMENTAL PROCEDURES

Materials, Radiolabels, and Mass Spectrometry. LS-174T cells were obtained from ATCC and maintained as previously described.[10] 1,4,7,10-Tetraazacyclododecane-1,4,7-tris(*t*-butyl acetate)-10-acetic acid was obtained from Macrocyclics, Inc., Dallas, TX. *N*-FMOC-amido-dPEG-12 (and -24) acid was purchased from Quanta Biodesign Ltd. (Powell, OH). ^{111}In chloride was from Amersham, ^{64}Cu chloride from Washington University School of Medicine, St. Louis, MO. Mass spectra were recorded on an Agilent 6520 Q-TOF LC/MS.

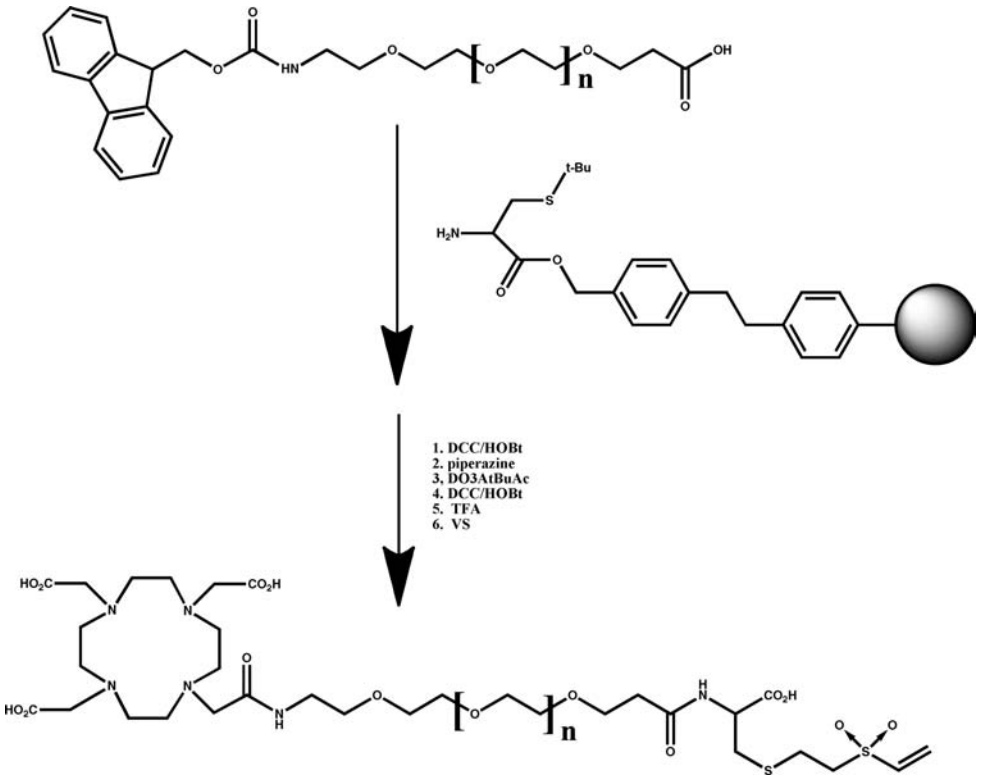
Construction, Cloning, Expression, and Purification of the Anti-TAG-72 diabody AVP04-50 from AVP04-07. The parent anti-TAG-72 diabody (AVP04-07)[4] was based on V-domains from the parent CC49 murine monoclonal antibody and derivative scFv fragments. The expression gene cassette had codons optimized for *E. coli* expression with the orientation V_H-V_L joined by a G_4S linker and included a C-terminal His_6 tail. Two cysteines were introduced by replacement of Pro at FR1−8 and Leu at FR1−11 in FR1 of the VL domain (Kabat numbering). This construct AVP04-50 was otherwise identical to the parent AVP04-07 except that it contained two additional cysteine residues per scFv monomer (4 cysteines per diabody). Molecular modeling had shown that these two cysteine residues were about 6−7 Å apart and positioned such that their side chain thiol groups could form a disulfide bond and, since exposed to solvent, could be reduced and labeled. Methods for determining solvent exposure or solvent accessible surface area included the Shrake-Rupley algorithm and LCPO method.[11] AVP04-50 was subcloned into *E. coli* BL21 (DE3)(F^- *ompT* $hsdS_B$(r_B^- m_B^-) *gal dcm* (DE3)) (Novagen) and produced in an 18 L fermentor. Bacterial lysate cleared by centrifugation (16,000*g*, 30 min) and filtration at 0.45 μm was purified using a three-step procedure (HisTrap, HiTrap SP HP, and Superdex 75 prep chromatography) on an AKTA Purifier 10 (GE Healthcare, Uppsala, Sweden). In this respect, the introduction of surface thiols into FR1 of the VL domain resulted in a well-folded diabody that could be expressed and purified from bacterial cell culture with equivalent yields to those reported earlier for the parent, nonthiolated, AVP04-07 diabody.[4]

Immunoreactivity. Binding of AVP04-50 to the TAG-72 antigen was determined using bovine submaxillary mucin (BSM, Aldrich-Sigma (St. Louis, MO) in a column shift assay (Superdex 200).

Synthesis of DOTA-PEGn-Cys-VS and Conjugation to AVP04-50. *N*-FMOC-amido-PEGn-acid (where n = 12 or 24) was coupled to Cys-polystyrene Wang resin, the FMOC removed, coupled to DO3AtBu-Acid, cleaved, and purified by RP-HPLC, reacted with a 10 molar excess of vinyl sulfone, and repurified by RP-HPLC. DOTA-PEGn-Cys-VS was reacted with reduced (10 molar excess of TCEP) AVP04-50 diabody in pH 7 PBS at a molar ratio of 50. PEG 48 was generated by coupling PEG24 twice followed by coupling DO3AtBu-Acid with the remaining steps identical to those described above. All conjugates were analyzed by mass spectrometry to determine their degree of substitution.

Radiolabeling of AVP04-50 and Its Conjugates. Radiometal labeling of DOTA-AVP04-50 was performed using $^{111}InCl_3$ (0.15 mBq/μg) or $^{64}CuCl_2$ (0.37 mBq/μg) as previously described.[12] Radiolabeling yields were typically 70−90%. The radiolabeled material was purified on Superdex-75 or 200 columns.

Scheme 1. Synthesis of DOTA-PEG-Cys-VS[a]



[a] FMOC-amido-PEG-acid was conjugated to *S*-*t*-butyl cysteine on Wang resin using standard activation chemistry (DCC/HOBt). The FMOC was removed with piperazine and conjugated to DO3AtBuAc using standard activation chemistry (DCC/HOBt). The product was removed from the resin with TFA, purified by reverse phase HPLC, reacted with excess vinyl sulfone in DMF, and repurified by reverse phase HPLC. $N = 12$ and 24. For $N = 48$, PEG24 was coupled twice prior to the addition of D03AtBu-Ac.

LS-174T Xenograft Model. Female, athymic *nu/nu* mice (Charles River Laboratories), 6−8 weeks old, were injected with LS-174T cells (10^6) s.c. in the flank. After 10 days, mice were injected i.v. with 150 kBq of ^{111}In-labeled AVP04-50 (2−6 μg of total protein) for biodistribution studies. Mice were euthanized at various time points: tumor, blood, and major organs were collected, weighed, and counted. Time−activity curves were corrected for radioactive decay and presented as percentage of injected dose/g tissue.

PET Imaging. Tumor-bearing mice were injected i.v. with ^{64}Cu-labeled DOTA-diabody or DOTA-PEGn-diabody conjugate and imaged at 1, 4, 21−22, and 45−46 h with a small-animal PET scanner (microPET Model R4; Siemens/CTIMI, Knoxville, TN). Mice anesthetized with isoflurane were scanned for 20 min for the 1 and 4 h time points, 45 min at 21−22 h, and 60 min at 44−45 h. Data were sorted into two-dimensional sinograms using the Fourier rebinning method and corrected for intrascan radiodecay, detector nonuniformity, and random coincidence noise. Images were reconstructed by the iterative three-dimensional ordered subsets expectation maximization (OSEM) method (2 iterations, 12 subsets), followed by a maximum a posteriori (MAP) algorithm (18 iterations).[13]

RESULTS

Generation and Characterization of AVP04-50 Diabody. The parent anti-TAG-72 diabody (AVP04-07)[4] was based on V-domains from the parent CC49 murine monoclonal antibody and derivative scFv fragments. The expression gene cassette had codons optimized for *E. coli* expression with the orientation V_H-V_L joined by a G_4S linker and included a C-terminal His_6 tail. Two cysteines were introduced by replacement of Pro at FR1−8 and Leu at FR1−11 in FR1 of the VL domain (Kabat numbering). This construct AVP04-50 was otherwise identical to the parent AVP04-07 except that it contained two additional cysteine residues per scFv monomer (4 cysteines per diabody). The AVP04-50 diabody expressed in *E. coli* and purified by a three-step method eluted as a single species on gel filtration as a monodispersed dimer with an apparent molecular mass of 52.5 kDa. The overall yield was 50−75% with immunoreactivity >99% as judged by a column shift assay (data not shown).

Synthesis and Biodistributions of DOTA-PEGn AVP04-50 Conjugates. Commercially available monodispersed PEG building blocks were converted into heterobifunctional reagents using a solid phase peptide synthesis methodology. First, we synthesized DOTA-PEGn-Cys-VS derivatives where $n = 12$, 24, and 48 as summarized in Scheme 1. Second, we conjugated DOTA-PEGn-Cys-VS to the surface thiols of the reduced diabody at pH 7.0 at a molar ratio of 50:1.[5] The unconjugated and conjugated versions of AVP04-50 were characterized by mass spectrometry (Figure 1). The unconjugated AVP04-50 had one major and two minor peaks, the major one ($m/z = 26822$) corresponding to the expected mass including the His6 C-terminal tag and a minor peak at $m/z = 25{,}999$ corresponding to the expected mass minus the His6 tag (a second minor peak corresponding to the loss of the His6 tag and two additional amino acids). The mass spectra of the conjugates reveals the presence of

dx.doi.org/10.1021/bc100464e |*Bioconjugate Chem.* 2011, 22, 709–716

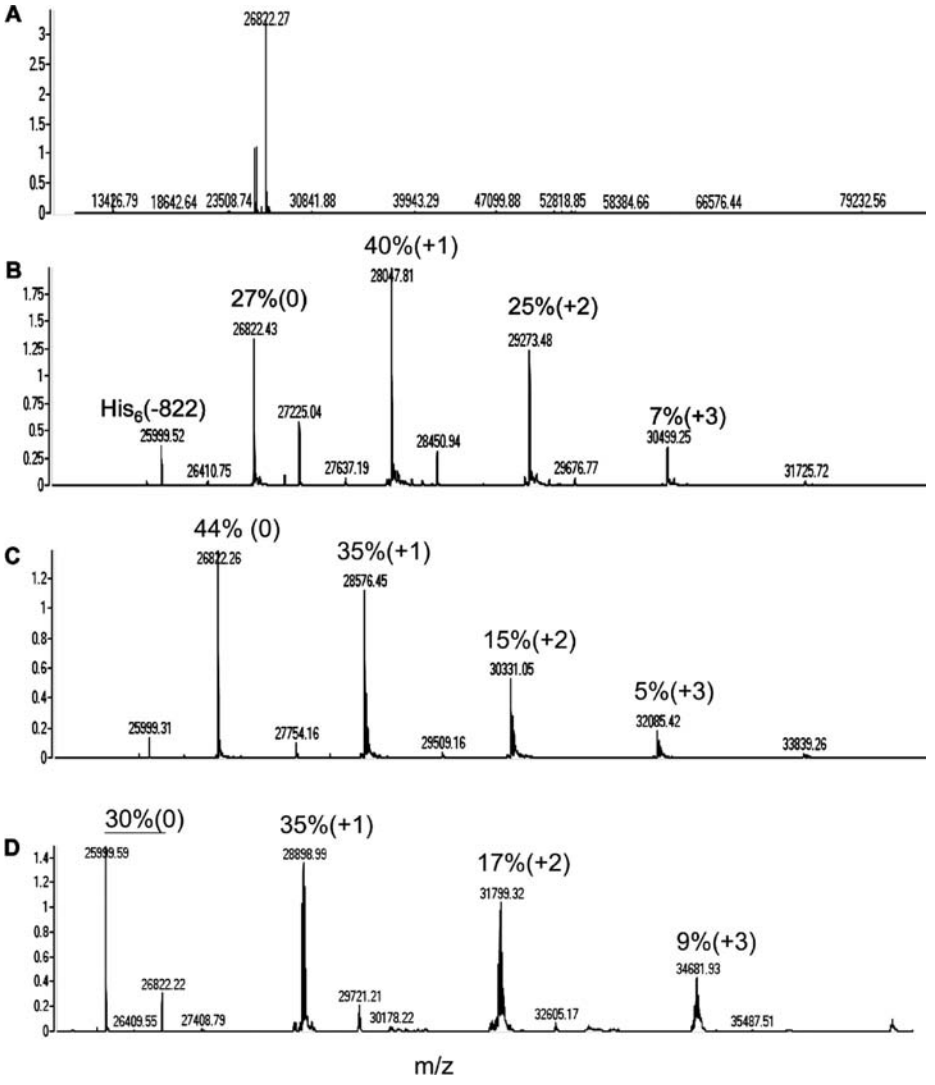


Figure 1. High resolution nanospray mass spectrometry analysis of PEGn AVP04-50 conjugates. (A) Deconvoluted mass spectrum for the non-PEGylated diabody (n = 0). (B) Deconvoluted mass spectrum for the PEG12 conjugate (n = 12). (C) Deconvoluted mass spectrum for the PEG24 conjugate (n = 24). (D) Deconvoluted mass spectrum for the PEG48 conjugate (n = 48). The percent peak height for unmodified (0), monoderivative (+1), and diderivatives (+2) are shown above the peaks. In the case of the PEG48 conjugate, the unmodified percent was summed for the parent mass (26,822) and the parent mass minus the His-6 tag (25,999).

both conjugated and unconjugated species demonstrating that the two cysteines per monomer are not fully substituted. However, since there are two monomers per diabody, the percent unsubstituted is reduced accordingly. Attempts to increase the degree of substitution by the use of higher reagent to diabody ratios revealed that no further substituion could be achieved. This result may indicate that the unconjugated species may have reformed their disulfide bonds and that the monoconjugated species may inhibit the addition of a second conjugate. The results may also indicate that the Michael addition reaction is incomplete under these reaction conditions. Nonetheless, a comparison of the spectra indicates a relatively uniform degree of substitution among the three conjugates with substantial levels for the 0, 1, and 2 levels of substitution. There is also evidence for a small amount of 3 substituents, perhaps due to a low level of reaction at surface amino groups.

The three conjugates and the unconjugated diabody (conjugated to DOTA) were radiolabeled with ^{111}In, purified by size exclusion chromatography, and subjected to biodistribution studies in athymic mice bearing LS-174T xenografts. The size exclusion chromatography profiles reveal an apparent shift to higher molecular size in the order of n = 0, 12, 24, and 48 for the PEG size corresponding to apparent molecular weights of 50 kDa, 60 kDa, 70 kDa, and 80 kDa, respectively (Figure 2). We conclude that increase in size of the monodispersed PEG is responsible for the uniform increase in the apparent size of the conjugates. In all cases, immunoreactivity of the conjugates was >95% (data not shown). Three major observations can be made from the biodistribution results shown in Figure 3A−D. First, the kidney uptake is uniformly reduced in the order n = 0, 12, 24, and 48 according to PEG size. For n = 0, kidney uptake is highest at 24 h with a value of 120% ID/g and lowest for n = 48 at 24 h with a value of 15% ID/g. This corresponds to an 8-fold reduction in kidney uptake. Higher n values for PEG were not tested due to their commercial unavailability and the fact that increasing blood clearance would eventually lead to diminishing returns. Our results are in agreement with the kidney threshold for protein clearance and are about 70−80 kDa. Second, tumor uptake

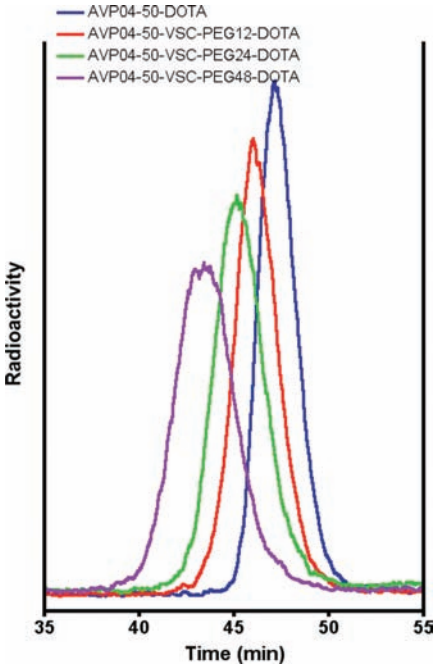


Figure 2. Size exclusion chromatography of radiolabeled uncojugated and PEGylated AVP04-50 diabody. All samples were radiolabeled with ^{111}In and run on a Superdex 75 size exclusion column as described in Experimental Procedures (radioactivity in arbitrary units). Blue: DOTA-non-PEGylated diabody conjugate. Red: DOTA-PEG12-diabody conjugate. Green: DOTA-PEG24-diabody conjugate. Purple: DOTA-PEG48-diabody conjugate.

is uniformly increased in the order n = 0, 12, 24, and 48 according to PEG size. Thus, tumor uptake for n = 0 at 24 h is 30% ID/g but rises to 80% ID/g for n = 48 at 24 h. Third, blood clearance uniformly decreased in the order n = 0, 12, 24, and 48 according to PEG size. For n = 0, the $t_{1/2}$ was about 0.5 h and for n = 48 about 6 h. The increase in blood clearance with n is expected to result in better absolute tumor uptake but can decrease the utility of the imaging agent if the T/B ratio starts to approach 1. A clinical consequence is the need to wait longer times for optimal T/B ratios, along with the need to match the radioisotope half-life with the blood clearance time. In this respect, the T/B for n = 0 is about 30 at 24 h and decreases to about 8 at 24 h for n = 48. In spite of these differences, it should be possible to image as early as 8 h for both conjugates, e.g., with the n = 0 conjugate, T/B = 6 at 8 h, compared to the n = 48 conjugate where T/B = 4 at 8 h. However, the high kidney uptake for the n = 0 conjugate and its reduced absolute tumor uptake compared to the n = 48 conjugate clearly make the n =48 conjugate the best choice of imaging agent for both the 8 h and 24 h times.

^{64}Cu PET Imaging of DOTA-PEG48 Conjugate of AVP04-50. On the basis of the ^{111}In-biodistribution results above, we concluded that the best candidate for ^{64}Cu PET imaging would be the n = 48 conjugate. This conjugate was expected to produce good tumor images as early as 8 h, reach a maximum of tumor uptake at 24−48 h, and have a very low kidney and blood background. Given the 12 h half-life of ^{64}Cu, imaging longer than 48 h is not feasible, especially in a clinical setting where large amounts of isotope would be required to extend imaging to longer time periods. When comparing the images of AVP04-50 with no PEG, PEG-12, PEG-24, and PEG-48, PEG-48 is the clear winner in terms of absolute tumor uptake and lowest kidney

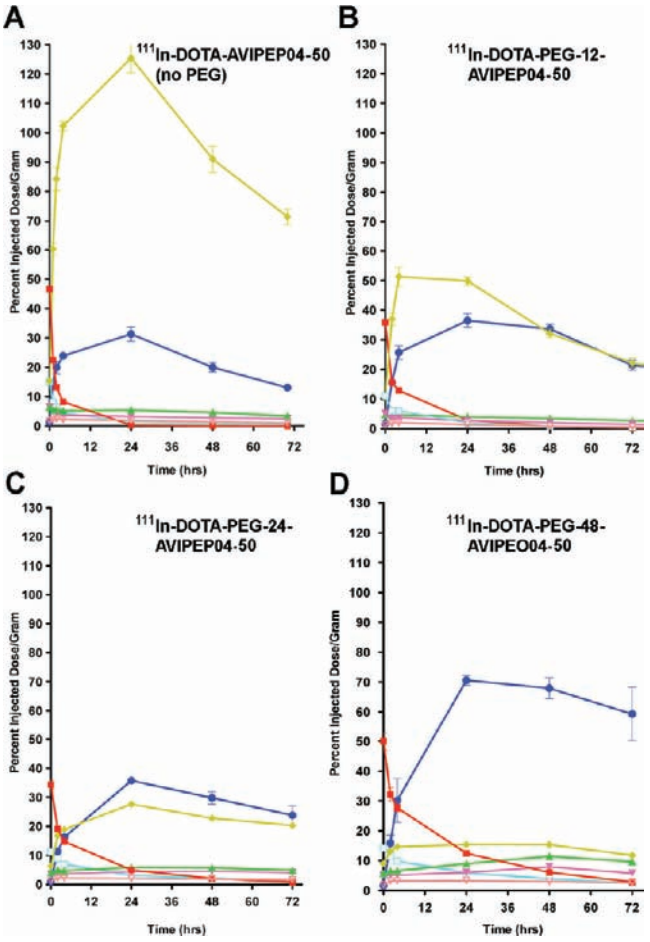


Figure 3. Biodistribution of DOTA-PEGn-AVP04-50 conjugates in athymic mice bearing LS-174T xenografts. The biodistribution of the constructs was determined in athymic mice bearing LS-174T xenografts as described in Experimental Procedures. (A) ^{111}In-DOTA-AVP04-50 (PEGn = 0). (B) ^{111}In-DOTA-PEG12-AVP04-50 (PEGn = 12). (C) ^{111}In-DOTA-PEG24-AVP04-50 (PEGn = 24). (D) ^{111}In-DOTA-PEG48-AVP04-50 (PEGn = 48). Key: yellow = kidney, dark blue = tumor, red = blood, green = liver, light blue = lungs, magenta = spleen, and orange = carcass.

uptake across the time points measured (Figure 4) or interms of time-activity curves (Figure 5). As expected, PET imaging of ^{64}Cu-labeled DOTA-PEG48-AVP04-50 (Figure 4D) demonstrated modest tumor uptake by 4 h and very high tumor uptake at 21 h and 44 h with very low backgrounds at the later time. The measured tumor uptake for the PEG48 conjugate was 37.9% ID/g at 44 h with a tumor to blood ratio of 8 and a tumor to liver ratio of 4. Under these conditions of PET imaging, there was no interference from kidneys. The ^{64}Cu-PET results are similar to those for the ^{111}In-labeled PEGn = 48 conjugate biodistribution study and suggest that choice of radiometal has little effect on the biodistribution, an observation we made previously for an anti-CEA diabody.[10]

DISCUSSION

Although antibodies have become an important source of targeted therapies, their routine use as imaging agents has not been fully realized. Obstacles to achieving this goal include matching the blood clearance half-life of the antibody with the radioisotope, maximizing both the absolute tumor uptake and

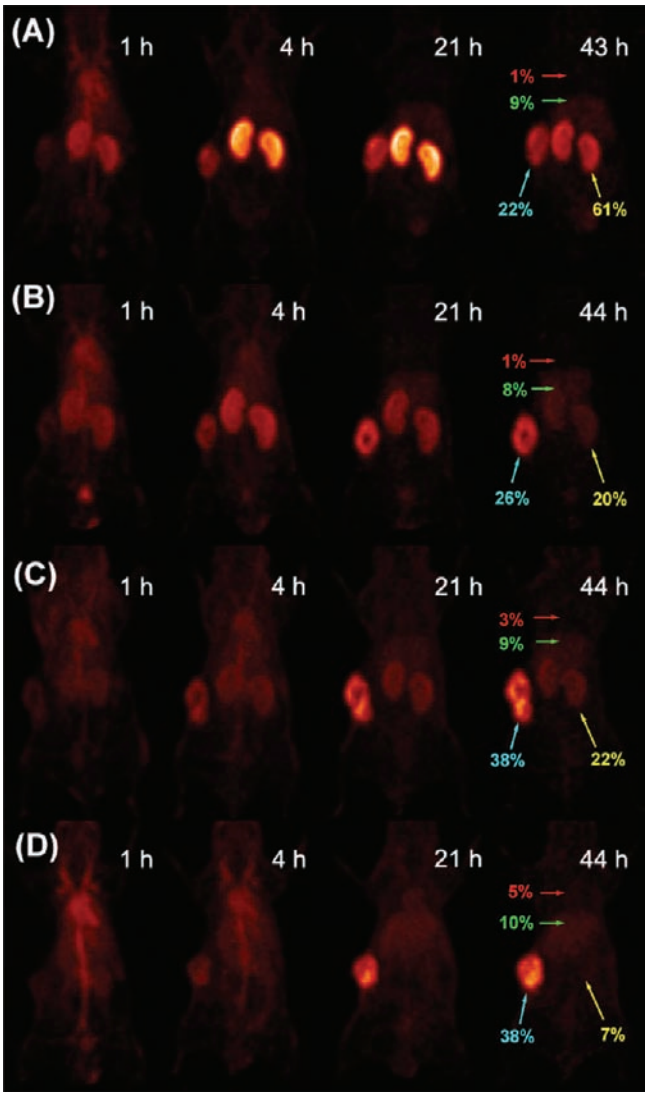


Figure 4. Serial PET imaging of ^{64}Cu-DOTA-PEGn-AVP04-50 in athymic mice bearing LS-174T xenografts. (A) PEG0, (B) PEG12, (C) PEG24, and (D) PEG48. Images are anterior-view maximum intensity projections (MIPs) normalized to reflect radiodecay-corrected relative image intensity per unit injected activity. Labels in red, green, yellow, and turquoise, respectively, show % ID/g in blood (heart), liver, kidney, and tumor as measured by direct assay following the final scan. Tumor weights at time of sacrifice were 314, 316, 382, and 341 mg in (A–D), respectively.

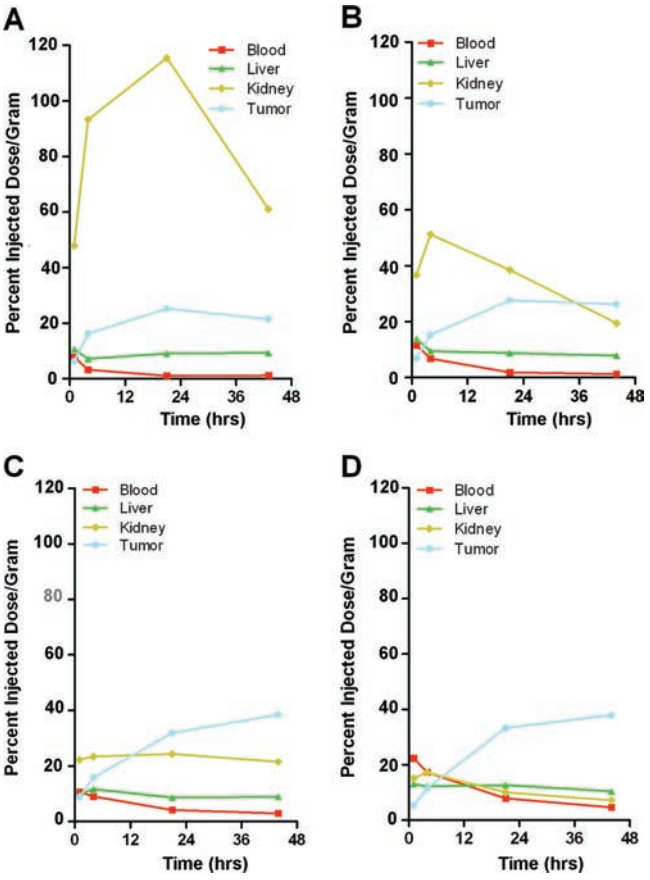


Figure 5. Time-activity curves derived from serial microPET studies depicted in Figure 4. (A) PEG0. (B) PEG12. (C) PEG24. (D) PEG48; 1 animal each.

tumor to blood ratio, and minimizing uptake into nontarget organs such as the liver and kidney. Although several obstacles have been addressed by engineering antibody fragments of different molecular sizes, many of these approaches have led to compromises such as increased T/B at the expense of decreased absolute tumor uptake for scFvs.[14] In this respect, diabodies that maintain the bivalency of intact antibodies but have faster blood clearance, appear to be a good choice in terms of maintaining good T/B ratios and absolute tumor uptake.[15−18] With the selection of the diabody as the best candidate for imaging, one is left with selecting the best radioisotope and imaging modality. In terms of the latter, PET imaging emerges as the best choice in terms of its inherent quantitative nature and its ability to render good images at tumor to tissue ratios as low as 2:1.[19] In terms of the former, the choice of best PET isotope depends strongly on matching the half-life with the blood clearance and consideration of nontarget uptake. Two radiometals, namely, ^{64}Cu and ^{89}Zr, stand out as good candidates for PET imaging because of their ease of preparation, uncomplicated decays, and adequate yield of positron emissions.[19] In terms of matching half-lives with blood clearance, ^{64}Cu ($t_{1/2}$ = 12 h) is most appropriate for fast clearing diabodies and ^{89}Zr ($t_{1/2}$ = 4d) for slower clearing whole antibodies. However, their use is often offset by the tendency of their antibody conjugates to have high uptake in nontarget organs. Alternatively, ^{124}I ($t_{1/2}$ = 4d) has the attraction that it is rapidly metabolized in the liver and kidney, reducing the uptake in nontarget organs.[20] The chief drawback to the use of this isotope is reduced uptake in tumor due to uptake and metabolism in the tumor itself if the antibody is internalized.

Given these considerations, we chose to optimize imaging using ^{64}Cu labeled diabodies realizing that nontarget organ uptake, especially the kidney, required more work. The problem with kidney uptake is well-understood. The kidney is the major excretion route for proteins with a molecular size less than 70 kDa. Although such proteins are filtered by the kidney, they are reabsorbed in the tubules and subjected to rapid degradation and recycling of their constituent components, some returned to blood and some excreted into urine. In the case of radiometal conjugates, the chelate−metal complex is only slowly excreted and therefore accumulates in the kidney. There are at least two potential solutions to this problem, either

dx.doi.org/10.1021/bc100464e |*Bioconjugate Chem.* 2011, 22, 709–716

blocking the initial uptake or raising the apparent molecular size of the protein above the kidney threshold. Unfortunately, blocking kidney uptake requires administering high doses of amino acids such as lysine[21] and is never complete. Raising the apparent molecular size of the protein has become the most attractive approach in spite of the fact that this will also increase blood retention and reduce the T/B. Thus, to effectively optimize this approach, one must carefully analyze a series of proteins that uniformly assess the key parameters of blood clearance, absolute tumor uptake, and T/B.

In terms of the choice of diabody, we chose anti-TAG-72. The anti-TAG-72 antibody CC49 and a diabody derivative of CC49 have been previously described,[22−25] and CC49 intact IgG has been used in many clinical studies,[26−28] making CC49 a good choice for a comparative study. In order to uniformly increase the apparent molecular size of the diabody, we engineered two cysteines per monomer into FR1 of the VL domain. Using a hexahistidine-tagged, *E. coli*-produced version of the CC49 diabody, namely, AVP04-50, we found an absolute tumor uptake in the LS-174T mouse model at 24 h of 30% ID/g, superior to that previously reported for a $(scFv)_2$ version of CC49 (4% ID/g).[29]

PEG was chosen as the best approach for modifying the apparent molecular size of the diabody because of the extensive literature demonstrating its beneficial effects on preventing rapid blood clearance of other proteins.[30] We chose monodispersed rather than polydispersed PEG because it was necessary to increase its size in discrete increments, modify its structure to allow attachment of DOTA for radiolabeling purposes, and attach a linker moiety for conjugation to the diabody. We chose vinyl sulfone as the linker because of its ability to undergo site-specific Michael addition to cysteines engineered into the diabody. In addition, we had previously shown that conjugation of DOTA-PEG-Cys-VS to amino groups in the anti-TAG-72 diabody dramatically improved tumor uptake and reduced kidney clearance.[4] We now proceeded to improve our optimization of this imaging agent by systematically examining the effect of different PEG sizes when conjugated to a thiolated diabody in a site-specific manner.

The results were satisfying in that we observed a uniform decrease in kidney uptake with increasing PEG size and a uniform increase in tumor uptake with increasing PEG size without a substantial compromise in T/B. On the basis of the comparisons, we selected the PEG of $n = 48$ for the optimal imaging agent and demonstrated excellent PET images at 24−48 h when the DOTA-PEG48-diabody was radiolabeled with ^{64}Cu. Taken together, the stable production platform offered by antibody fragments,[4] coupled to the advantages of site-specific (thiol-targeted) conjugation for radiolabels (this article) and new data on thiol-targeted antibody−drug conjugations,[31] now extends the clinical opportunities of diabodies from SPECT and PET tumor imaging to drug-loaded delivery vehicles for tumor therapy.

AUTHOR INFORMATION

Corresponding Author

*Tel: 626-359-8111 ext. 62601. E-mail: jshively@ coh.org.

Author Contributions

‖These authors contributed equally to this research.

Author Contributions

⊥These senior authors contributed equally to this research.

ACKNOWLEDGMENT

This research was supported by a research grant from Avipep Pty Ltd., 343 Royal Parade, Parkville VIC 3008, Australia. Avibody proteins were prepared and shipped by Harjit Khangura of Avipep. $^{64}CuCl_2$ was obtained from Washington University, St. Louis, MO under NIH grant R24CA86307.

REFERENCES

(1) Wu, A. M., and Olafsen, T. (2008) Antibodies for molecular imaging of cancer. *Cancer J. 14*, 191–197.

(2) Williams, L. E., Wu, A. M., Yazaki, P. J., Liu, A., Raubitschek, A. A., Shively, J. E., and Wong, J. Y. (2001) Numerical selection of optimal tumor imaging agents with application to engineered antibodies. *Cancer Biother. Radiopharm. 16*, 25–35.

(3) Yang, K., Basu, A., Wang, M., Chintala, R., Hsieh, M. C., Liu, S., Hua, J., Zhang, Z., Zhou, J., Li, M., Phyu, H., Petti, G., Mendez, M., Janjua, H., Peng, P., Longley, C., Borowski, V., Mehlig, M., and Filpula, D. (2003) Tailoring structure-function and pharmacokinetic properties of single-chain Fv proteins by site-specific PEGylation. *Protein Eng. 16*, 761–770.

(4) Li, L., Turatti, F., Crow, D., Bading, J. R., Anderson, A. L., Poku, E., Yazaki, P. J., Williams, L. E., Tamvakis, D., Sanders, P., Leong, D., Raubitschek, A., Hudson, P. J., Colcher, D., and Shively, J. E. (2010) Monodispersed DOTA-PEG-conjugated anti-TAG-72 diabody has low kidney uptake and high tumor-to-blood ratios resulting in improved 64Cu PET. *J. Nucl. Med. 51*, 1139–1346.

(5) Li, L., Tsai, S. W., Anderson, A. L., Keire, D. A., Raubitschek, A. A., and Shively, J. E. (2002) Vinyl sulfone bifunctional derivatives of DOTA allow sulfhydryl- or amino-directed coupling to antibodies. Conjugates retain immunoreactivity and have similar biodistributions. *Bioconjugate Chem. 13*, 110–115.

(6) Tinianow, J. N., Gill, H. S., Ogasawara, A., Flores, J. E., Vanderbilt, A. N., Luis, E., Vandlen, R., Darwish, M., Junutula, J. R., Williams, S. P., and Marik, J. (2010) Site-specifically 89Zr-labeled monoclonal antibodies for ImmunoPET. *Nucl. Med. Biol. 37*, 289–97.

(7) Junutula, J. R., Raab, H., Clark, S., Bhakta, S., Leipold, D. D., Weir, S., Chen, Y., Simpson, M., Tsai, S. P., Dennis, M. S., Lu, Y., Meng, Y. G., Ng, C., Yang, J., Lee, C. C., Duenas, E., Gorrell, J., Katta, V., Kim, A., McDorman, K., Flagella, K., Venook, R., Ross, S., Spencer, S. D., Lee Wong, W., Lowman, H. B., Vandlen, R., Sliwkowski, M. X., Scheller, R. H., Polakis, P., and Mallet, W. (2008) Site-specific conjugation of a cytotoxic drug to an antibody improves the therapeutic index. *Nat. Biotechnol. 26*, 925–32.

(8) Sirk, S. J., Olafsen, T., Barat, B., Bauer, K. B., and Wu, A. M. (2008) Site-specific, thiol-mediated conjugation of fluorescent probes to cysteine-modified diabodies targeting CD20 or HER2. *Bioconjugate Chem. 19*, 2527–34.

(9) Kim, K. M., McDonagh, C. F., Westendorf, L., Brown, L. L., Sussman, D., Feist, T., Lyon, R., Alley, S. C., Okeley, N. M., Zhang, X., Thompson, M. C., Stone, I., Gerber, H. P., and Carter, P. J. (2008) Anti-CD30 diabody-drug conjugates with potent antitumor activity. *Mol. Cancer Ther. 7*, 2486–97.

(10) Li, L., Yazaki, P. J., Anderson, A. L., Crow, D., Colcher, D., Wu, A. M., Williams, L. E., Wong, J. Y., Raubitschek, A., and Shively, J. E. (2006) Improved biodistribution and radioimmunoimaging with poly-(ethylene glycol)-DOTA-conjugated anti-CEA diabody. *Bioconjugate Chem. 17*, 68–76.

(11) Carmichael, J. A., Power, B. E., Garrett, T. P., Yazaki, P. J., Shively, J. E., Raubischek, A. A., Wu, A. M., and Hudson, P. J. (2003) The crystal structure of an anti-CEA scFv diabody assembled from T84.66 scFvs in V(L)-to-V(H) orientation: implications for diabody flexibility. *J. Mol. Biol. 326*, 341–351.

(12) Li, L., Bading, J., Yazaki, P. J., Ahuja, A. H., Crow, D., Colcher, D., Williams, L. E., Wong, J. Y., Raubitschek, A., and Shively, J. E. (2008) A versatile bifunctional chelate for radiolabeling humanized anti-CEA antibody with In-111 and Cu-64 at either thiol or amino groups: PET

imaging of CEA-positive tumors with whole antibodies. *Bioconjugate Chem. 19*, 89–96.

(13) Ruangma, A., Laforest, R., Bing, B., and Leahy, R. M. (2004) Characterization of USC-MAP image reconstruction on microPET-R4. *Nucl. Sci. Symp. Conf. Record 6*, 3449.

(14) Holliger, P., and Hudson, P. J. (2005) Engineered antibody fragments and the rise of single domains. *Nat. Biotechnol. 23*, 1126–1136.

(15) Robinson, M. K., Shaller, C., Garmestani, K., Plascjak, P. S., Hodge, K. M., Yuan, Q. A., Marks, J. D., Waldmann, T. A., Brechbiel, M. W., and Adams, G. P. (2008) Effective treatment of established human breast tumor xenografts in immunodeficient mice with a single dose of the alpha-emitting radioisotope astatine-211 conjugated to anti-HER2/neu diabodies. *Clin. Cancer Res. 14*, 875–882.

(16) Schneider, D. W., Heitner, T., Alicke, B., Light, D. R., McLean, K., Satozawa, N., Parry, G., Yoo, J., Lewis, J. S., and Parry, R. (2009) In vivo biodistribution, PET imaging, and tumor accumulation of 86Y- and 111In-antimindin/RG-1, engineered antibody fragments in LNCaP tumor-bearing nude mice. *J. Nucl. Med. 50*, 435–443.

(17) Leyton, J., V., Olafsen, T., Sherman, M. A., Bauer, K. B., Aghanjanian, P., Reiter, R. E., and Wu, A. M. (2009) Engineered humanized diabodies for microPET imaging of prostate stem cell antigen-expressing tumors. *Protein Eng. Des. Sel. 22*, 209–216.

(18) Cai, X., and Garen, A. (1997) Comparison of fusion phage libraries displaying VH or single-chain Fv antibody fragments derived from the antibody repertoire of a vaccinated melanoma patient as a source of melanoma-specific targeting molecules. *Proc. Natl. Acad. Sci. U. S.A. 94*, 9261–9266.

(19) McCabe, K. E., and Wu, A. M. (2010) Positive progress in ImmunoPET: not just a coincidence. *Cancer Biother. Radiopharm. 25*, 253–261.

(20) Sundaresan, G., Yazaki, P. J., Shively, J. E., Finn, R. D., Larson, S. M., Raubitschek, A. A., Williams, L. E., Chatziioannou, A. F., Gambhir, S. S., and Wu, A. M. (2003) 124I-labeled engineered anti-CEA minibodies and diabodies allow high-contrast, antigen-specific small-animal PET imaging of xenografts in athymic mice. *J. Nucl. Med. 44*, 1962–1969.

(21) Behr, T. M., Becker, W. S., Sharkey, R. M., Juweid, M. E., Dunn, R. M., Bair, H. J., Wolf, F. G., and Goldenberg, D. M. (1996) Reduction of renal uptake of monoclonal antibody fragments by amino acid infusion. *J. Nucl. Med. 37*, 829–833.

(22) Santos, A. D., Kashmiri, S. V., Hand, P. H., Schlom, J., and Padlan, E. A. (1999) Generation and characterization of a single gene-encoded single-chain-tetravalent antitumor antibody. *Clin. Cancer Res. 5*, 3118s–3123s.

(23) Chauhan, S. C., Jain, M., Moore, E. D., Wittel, U. A., Li, J., Gwilt, P. R., Colcher, D., and Batra, S. K. (2005) Pharmacokinetics and biodistribution of 177Lu-labeled multivalent single-chain Fv construct of the pancarcinoma monoclonal antibody CC49. *Eur. J. Nucl. Med. Mol. Imaging 32*, 264–273.

(24) Wittel, U. A., Jain, M., Goel, A., Chauhan, S. C., Colcher, D., and Batra, S. K. (2005) The in vivo characteristics of genetically engineered divalent and tetravalent single-chain antibody constructs. *Nucl. Med. Biol. 32*, 157–164.

(25) Goel, A., Baranowska-Kortylewicz, J., Hinrichs, S. H., Wisecarver, J., Pavlinkova, G., Augustine, S., Colcher, D., Booth, B. J., and Batra, S. K. (2001) 99mTc-labeled divalent and tetravalent CC49 single-chain Fv's: novel imaging agents for rapid in vivo localization of human colon carcinoma. *J. Nucl. Med. 42*, 1519–1527.

(26) Tempero, M., Leichner, P., Baranowska-Kortylewicz, J., Harrison, K., Augustine, S., Schlom, J., Anderson, J., Wisecarver, J., and Colcher, D. (2000) High-dose therapy with 90Yttrium-labeled monoclonal antibody CC49: a phase I trial. *Clin. Cancer Res. 6*, 3095–3102.

(27) Alvarez, R. D., Huh, W. K., Khazaeli, M. B., Meredith, R. F., Partridge, E. E., Kilgore, L. C., Grizzle, W. E., Shen, S., Austin, J. M., Barnes, M. N., Carey, D., Schlom, J., and LoBuglio, A. F. (2002) A Phase I study of combined modality (90)Yttrium-CC49 intraperitoneal radioimmunotherapy for ovarian cancer. *Clin. Cancer Res. 8*, 2806–2811.

(28) Meredith, R. F., Bueschen, A. J., Khazaeli, M. B., Plott, W. E., Grizzle, W. E., Wheeler, R. H., Schlom, J., Russell, C. D., Liu, T., and LoBuglio, A. F. (1994) Treatment of metastatic prostate carcinoma with radiolabeled antibody CC49. *J. Nucl. Med. 35*, 1017–1022.

(29) Beresford, G. W., Pavlinkova, G., Booth, B. J., Batra, S. K., and Colcher, D. (1999) Binding characteristics and tumor targeting of a covalently linked divalent CC49 single-chain antibody. *Int. J. Cancer 81*, 911–917.

(30) Pasut, G., and Veronese, F. M. (2009) PEGylation for improving the effectiveness of therapeutic biomolecules. *Drugs Today (Barc) 45*, 687–695.

(31) Junutula, J. R., Flagella, K. M., Graham, R. A., Parsons, K. L., Ha, E., Raab, H., Bhakta, S., Nguyen, T., Dugger, D. L., Li, G., Mai, E., Lewis Phillips, G. D., Hiraragi, H., Fuji, R. N., Tibbitts, J., Vandlen, R., Spencer, S. D., Scheller, R. H., Polakis, P., and Sliwkowski, M. X. (2010) Engineered Thio-TrastuzuMAb-DM1 conjugate with an improved therapeutic index to target human epidermal growth factor receptor 2-positive breast cancer. *Clin. Cancer Res. 16*, 4769–4778.

Bioconjugate Chemistry

ARTICLE

pubs.acs.org/bc

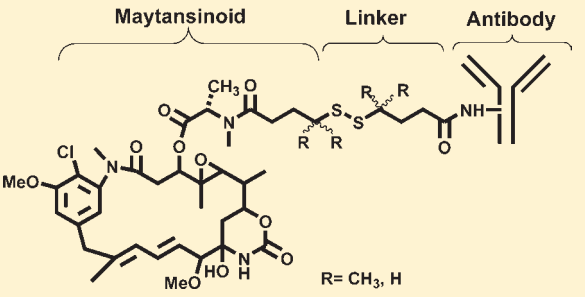
Disulfide-Linked Antibody−Maytansinoid Conjugates: Optimization of In Vivo Activity by Varying the Steric Hindrance at Carbon Atoms Adjacent to the Disulfide Linkage

Brenda A. Kellogg, Lisa Garrett,† Yelena Kovtun, Katharine C. Lai, Barbara Leece, Michael Miller, Gillian Payne, Rita Steeves,‡ Kathleen R. Whiteman, Wayne Widdison, Hongsheng Xie,ζ Rajeeva Singh,* Ravi V. J. Chari, John M. Lambert, and Robert J. Lutz

ImmunoGen, Inc., 830 Winter Street, Waltham, Massachusetts 02451, United States

Supporting Information

ABSTRACT: In this report, we describe the synthesis of a panel of disulfide-linked huC242 (anti-CanAg) antibody maytansinoid conjugates (AMCs), which have varying levels of steric hindrance around the disulfide bond, in order to investigate the relationship between stability to reduction of the disulfide linker and antitumor activity of the conjugate *in vivo*. The conjugates were first tested for stability to reduction by dithiothreitol *in vitro* and for plasma stability in CD1 mice. It was found that the conjugates having the more sterically hindered disulfide linkages were more stable to reductive cleavage of the maytansinoid in both settings. When the panel of conjugates was tested for *in vivo* efficacy in two human colon cancer xenograft models in SCID mice, it was found that the conjugate with intermediate disulfide bond stability having two methyl groups on the maytansinoid side of the disulfide bond and no methyl groups on the linker side of the disulfide bond (huC242-SPDB-DM4) displayed the best efficacy. The ranking of *in vivo* efficacies of the conjugates was not predicted by their *in vitro* potencies, since all conjugates were highly active *in vitro*, including a huC242-SMCC-DM1 conjugate with a noncleavable linkage which showed only marginal activity *in vivo*. These data suggest that factors in addition to intrinsic conjugate potency and conjugate half-life in plasma influence the magnitude of antitumor activity observed for an AMC *in vivo*. We provide evidence that bystander killing of neighboring nontargeted tumor cells by diffusible cytotoxic metabolites produced from target cell processing of disulfide-linked antibody−maytansinoid conjugates may be one additional factor contributing to the activity of these conjugates *in vivo*.



INTRODUCTION

Several antibody−maytansinoid conjugates (AMCs) are currently undergoing clinical evaluation for treatment of different cancers.[1,2] Each AMC consists of an antibody linked at lysine residues via a cleavable disulfide linker or a noncleavable thioether linker to ∼3−4 cytotoxic maytansinoid molecules. Upon binding of the antibody component of the AMC to antigen on the surface of cancer cells, the AMC is internalized and cleaved proteolytically, releasing maytansinoids that bind tubulin and interfere with microtubule dynamics, leading to cell cycle arrest and ultimately to cell death.[3] The linker type—noncleavable or disulfide—for each AMC in the clinic is based upon selection of the optimal linker from preclinical evaluation of different linkers in xenograft models. The HER2-targeting AMC, trastuzumab-DM1, is in advanced clinical evaluation for metastatic breast cancer, and consists of a noncleavable thioether linker.[4,5] However, most AMCs that have entered the clinic have cleavable, disulfide linkers, for example, cantuzumab mertansine, IMGN901 (lorvotuzumab mertansine), IMGN388, and SAR3419.[6−9]

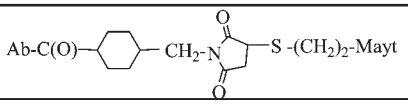
In an effort to understand the relationship of the lability of the disulfide linker to the activity of a conjugate, a study was initiated with a panel of huC242 conjugates containing linkers designed with different degrees of steric hindrance around the disulfide bond in order to vary the sensitivity of the disulfide linkage to cleavage via thiol−disulfide exchange reactions. HuC242 is a humanized IgG_1 antibody which recognizes CanAg, a tumor-specific antigen found on the surface of human colorectal carcinomas as well as a number of other human tumors.[10,11] The goal of the study was to select the disulfide linker with optimal *in vivo* efficacy and tolerability so as to maximize the therapeutic window for huC242 antibody−maytansinoid conjugates. The effect of altering disulfide bond reactivity toward thiol−disulfide exchange on the efficacy and tolerability of immunoconjugates is not easily predicted since the rate of cleavage of the disulfide bond is expected to influence both conjugate half-life in the plasma and rate of intracellular release of the cytotoxic agent.[12−16]

Here, we evaluate a panel of disulfide-linked huC242 AMCs, having varying degrees of steric hindrance around the disulfide

Received: November 2, 2010
Revised: January 25, 2011
Published: March 22, 2011

ACS Publications © 2011 American Chemical Society

Table 1. Structures, Nomenclature, and *in Vitro* Cytotoxic Potency on COLO205 Cells of a Panel of AMCs Made with huC242 Antibody

Conjugate Structure	Conjugate name (linker-drug)	Disulfide Notation	EC_{50} on COLO 205 (pM)[a]
Ab-C(O)-$(CH_2)_2$-SS-$(CH_2)_2$-Mayt	SPDP-DM1	0:0	15
Ab-C(O)-$(CH_2)_3$-SS-$(CH_2)_2$-Mayt	SPDB-DM1	0':0	ND
Ab-C(O)-$(CH_2)_2$-SS-CH(CH_3)-$(CH_2)_2$-Mayt	SPDP-DM3	0:1	5.0
Ab-C(O)-$(CH_2)_3$-SS-CH(CH_3)-$(CH_2)_2$-Mayt	SPDB-DM3	0':1	ND
Ab-C(O)-$(CH_2)_2$-CH(CH_3)-SS-$(CH_2)_2$-Mayt	SPP-DM1	1:0	15
Ab-C(O)-$(CH_2)_2$-SS-C$(CH_3)_2$-$(CH_2)_2$-Mayt	SPDP-DM4	0:2	5
Ab-C(O)-$(CH_2)_3$-SS-C$(CH_3)_2$-$(CH_2)_2$-Mayt	SPDB-DM4	0':2	ND
Ab-C(O)-$(CH_2)_2$-C$(CH_3)_2$-SS-$(CH_2)_2$-Mayt	SMPP-DM1	2:0	10
Ab-C(O)-$(CH_2)_2$-CH(CH_3)-SS-CH(CH_3)-$(CH_2)_2$-Mayt	SPP-DM3	1:1	5.5
Ab-C(O)-$(CH_2)_2$-CH(CH_3)-SS-C$(CH_3)_2$-$(CH_2)_2$-Mayt	SPP-DM4	1:2	10
Ab-C(O)-$(CH_2)_2$-C$(CH_3)_2$-SS-C$(CH_3)_2$-$(CH_2)_2$-Mayt	SMPP-DM4	2:2	10
	SMCC-DM1	NA	3.5

[a] *in vitro* cytotoxic potency of conjugate on COLO205 cells measured using a clonogenic assay with continuous exposure. EC_{50} is expressed as concentration of antibody; the AMCs contained, on average, 3.3 ± 1.0 conjugated DMx molecules per antibody molecule.

bond, for sensitivity to cleavage *in vitro* and *in vivo* and for efficacy in mouse xenograft models of human colon cancer expressing the CanAg antigen. We show that a huC242 conjugate with intermediate disulfide bond reactivity to thiol−disulfide exchange, having two methyl groups on the drug side of the disulfide bond and no methyl groups on the linker side, demonstrates the best activity *in vivo* in both homogeneous and heterogeneous CanAg expressing xenograft models. Comparisons of *in vitro* potency and bystander activity provide insights into the factors contributing to the superior activity observed for this conjugate.

EXPERIMENTAL PROCEDURES

General. Chemicals were from Sigma Aldrich. Human tumor cell lines were from ATCC. COLO205 (human colon cancer) and Namalwa (Burkitts lymphoma) cells were grown in RPMI containing 10% heat-inactivated FBS and 2 mM glutamine. HT29 (human colon cancer) cells were grown in DMEM containing 10% heat-inactivated FBS. The humanized anti-CanAg monoclonal antibody, huC242, and isotype matched nonbinding huIgG1 antibody (hu control mAb) were isolated at ImmunoGen. Maytansinoids and maytansinoid conjugates of the humanized C242 antibody (collectively referred to as huC242-DMx), with the exception of the 2:0 and 2:2 conjugates (see Table 1 for description of notation), were synthesized at ImmunoGen according to published procedures.[17,18] For the highly hindered 2:0 and 2:2 disulfide-linked conjugates with two methyl groups on the carbon atom adjacent to the sulfur of the linker, *N*-hydroxy succinimide (NHS) ester-bearing linker-maytansinoid reagents (sulfo-NHS-SMPP-DM1 and sulfo-NHS-SMPP-DM4 respectively, Figure 1B) were chemically synthesized and used for direct coupling to the antibody. The synthesis of these reagents are described in the Supporting Information. The conjugation reactions for the 2:0 and 2:2 conjugates were performed by adding 6−10-fold molar excess of purified NHS-ester-linker-maytansinoid reagent to antibody at a final concentration of 2.5 mg/mL in pH 7.5 phosphate buffer, 20% DMA (v/v). The reaction was left for 3 h at room temperature and then purified from excess reagent using G25 chromatography. The maytansinoid load on the final conjugate was characterized as previously described.[17]

Kinetic Studies to Measure Rates of Reduction of Disulfide Linkage in huC242−Maytansinoid Conjugates by Dithiothreitol (DTT). Reactions were initiated by addition of DTT to huC242−maytansinoid conjugates (1 mg/mL) equilibrated at 37 °C in 95% aqueous phosphate buffer, pH 6.5, (67 mM potassium phosphate, 67 mM NaCl, 2 mM EDTA) and 5% DMA (v/v). Maytansine (20 μM) was included as an internal standard. All reactions were carried out under pseudo first-order conditions with thiol (DTT) concentrations in excess to total accessible conjugate disulfide bonds. At several time points, aliquots of the reaction mixture were removed and quenched by addition to equal volumes of ice-cold ethanol (this does not cause protein precipitation) to promote dissociation of free drug from conjugate and then stored on dry ice prior to HPLC

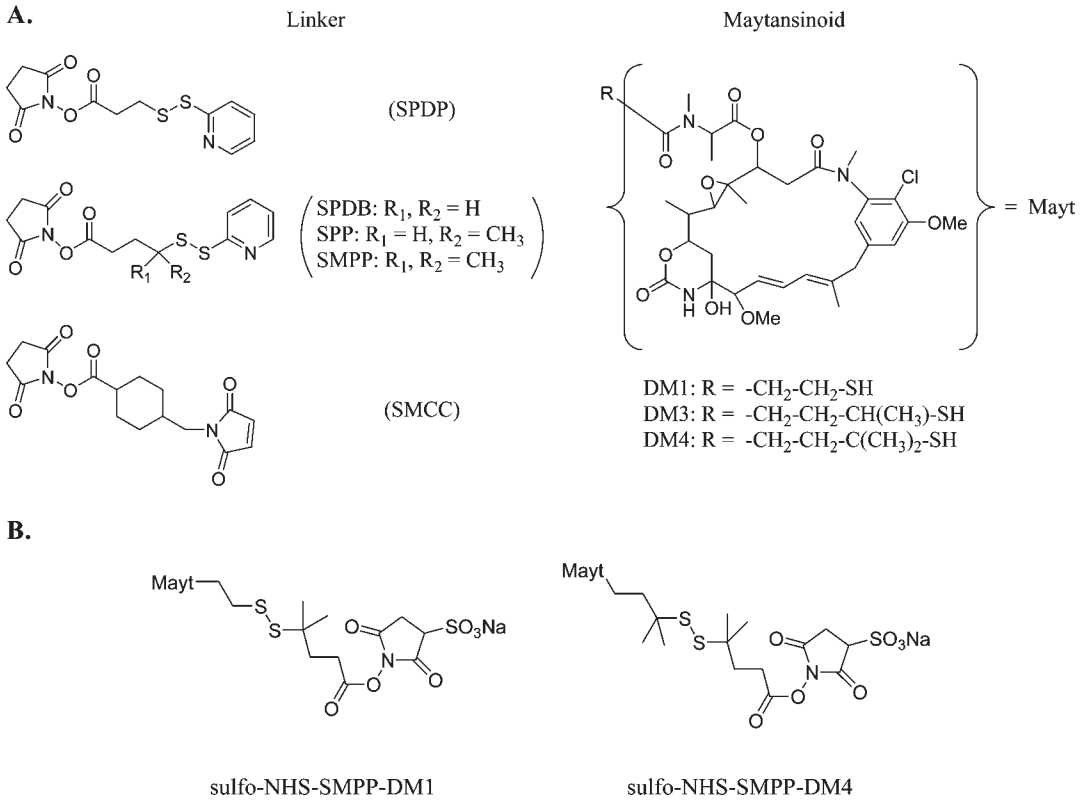


Figure 1. (A) Structures of linkers and maytansinoids utilized in antibody−maytansinoid conjugates (AMCs). In an AMC, a lysine residue on the antibody is connected via an amide bond to the linker moiety, and the maytansinoid thiol (DMx) is attached to the linker through a disulfide or thioether bond. Typically, AMCs contain about 3−4 maytansinoid molecules (average) per antibody molecule. (B) Structures of *N*-hydroxy succinimide (NHS) ester-bearing linker-maytansinoid reagents used for one step synthesis of the 2:0 and 2:2 conjugates.

Table 2. Rates of Reduction of Disulfide Bonds in AMCs by Dithiothreitol (DTT)[a]

disulfide conjugate	rate of reduction by thiol k (M^{-1} min^{-1})[b]	relative stability to thiol−disulfide exchange[c]
0′:0	14	1
1:0	2.0	7
0:2	0.98	14
2:0	0.83	17
0′:2	0.62	22
1:1	0.082	170
1:2	0.014	980
2:2	<6.4(10^{-4})	>22000

[a] Rates of reduction of disulfide-linked conjugates by dithiothreitol (DTT) were measured under pseudo first-order conditions (DTT in excess to total accessible disulfide bonds in the conjugate) at 37 °C in 95% aqueous phosphate buffer, pH 6.5, 2 mM EDTA/5% DMA (v/v). [b] k is the second-order rate constant obtained by dividing k_{obs} (pseudo first-order rate constant for release of maytansinoid from conjugate) by the concentration of DTT thiol. [c] Relative stability toward thiol−disulfide exchange normalized to the 0':0 conjugate (huC242-SPDB-DM1).

analysis. The quenched aliquots were brought to 4 °C and centrifuged at 14 000 rpm and then injected onto a Hisep HPLC column (Supelco) to separate the released maytansinoid thiol and the maytansine internal standard from the antibody species. A gradient of 25% CH_3CN (v/v) in 60 mM NH_4OAc aqueous buffer, pH 7.0, to 100% CH_3CN over 30 min was used for separation. Pseudo first-order rate constants were calculated by nonlinear regression fitting of the ratio of peak area of released maytansinoid (PA^{DMx}) to peak area of maytansine internal standard ($PA^{Internal\ std}$) vs time to a single exponential eq 1. Second-order rate constants (k) for the reaction of DTT thiol with the disulfide were calculated by dividing k_{obs} by the concentration of DTT thiol as determined by Ellman's assay.[19]

$$(PA^{DMx}/PA^{Internal\ std})_t = (PA^{DMx}/PA^{Internal\ std})_\infty [1 - \exp(-k_{obs}t)] \quad (1)$$

where PA^{DMx} = peak area at 252 nm due to the released DMx species; $PA^{Internal\ std}$ = peak area at 252 nm of the maytansine internal standard; t = time; k_{obs} = pseudo first-order rate constant for reduction of disulfide bond by DTT.

***In Vitro* Cytotoxicity.** Cytotoxicities of conjugates on COLO-205 cells were measured by a continuous exposure clonogenic assay. COLO205 cells were plated in round-bottom 96-well plates at 3, 10, 30, 100, 300, 1000, or 3000 cells per well with various concentrations of the huC242-DMx conjugates in 200 μL of the culture medium. The plates were incubated in a humidified incubator at 37 °C, 5% CO_2 for 14 days, and then scored under a microscope by counting the number of empty wells (wells with no viable cells or colonies). The plating efficiencies (PE) of the control (untreated) and conjugate-treated plates were calculated from eq 2 using the Poisson distribution:[20]

$$PE = \left[\frac{-\ln\left(\frac{\text{number of empty wells}}{\text{number of total wells}}\right)}{\text{number of cells plated per well}}\right] \quad (2)$$

dx.doi.org/10.1021/bc100480a |*Bioconjugate Chem.* 2011, 22, 717–727

To calculate the surviving fraction, the plating efficiency of the conjugate-treated plate was divided by the plating efficiency of the untreated (control) plates.

Cytotoxicities of unconjugated maytansinoids were measured using a continuous exposure cell viability assay. COLO205 and HT29 cells were initially plated at 1000 and 2000 cells/well, respectively, in flat-bottom plates. After 5 day incubation with the maytansinoids, WST-8 reagent (Dojindo Technologies) was added and absorbance at 450 nm was measured after 2 h at 37 °C.

Bystander Killing Assay. To test the bystander potency of the conjugates, antigen-negative Namalwa cells and antigen-positive COLO205 cells were mixed together at different ratios (5000 Namalwa cells/well plus 0, 125, 500, 1250, or 5000 COLO205 cells/well), and plated in 96-well round-bottomed plates. Then, 1 nM of huC242-DMx was added to the cell mixtures. This concentration of conjugate had previously been shown to kill all of the COLO205 cells but none of the Namalwa cells when each cell line was plated alone. Plates were incubated for 4 days at 37 °C, and viability of Namalwa cells in each well was determined using WST-8 reagent.

Pharmacokinetic Studies on huC242-DMx Conjugates in CD-1 Mice. CD-1 mice (9 mice/test substance) received 10 mg/kg of conjugate (antibody dose) as a single intravenous injection into a lateral tail vein. At 2 min, 30 min, and at 2, 4, and 8 h, and at 1, 2, 3, 5, 7, 10, 14, 21, and 28 days after administration of each test substance, approximately 70 μL of blood was collected from three mice per time point and centrifuged to separate the plasma. No mice were bled more than twice within 24 h. Plasma samples (~30 μL) were stored at −80 °C and assayed by ELISA for conjugate and antibody concentrations.

ELISA of Conjugate and Antibody. The huC242-DMx conjugate in mouse plasma was measured using a sandwich ELISA method, captured with murine monoclonal antimaytansinoid antibody (ImmunoGen, Inc.), and detected with horseradish peroxidase (HRP)-conjugated donkey antihuman IgG (H and L) antibody (Jackson Immunoresearch, cat no. 709−035−149). This format of the conjugate ELISA measures the concentration in plasma of conjugate with one or more conjugated maytansinoids per antibody. The antibody component of conjugate in plasma samples was measured by capturing with goat antihuman IgG antibody and detection with HRP-conjugated donkey antihuman IgG antibody.

Pharmacokinetic Analyses. Pharmacokinetic analyses were performed using the standard algorithm of the noncompartmental pharmacokinetic analysis program *WinNonlin* (Pharsight). First-order rate constants for the terminal elimination phase ($t_{1/2,\beta}$) were evaluated using the concentration data from 8 to 672 h postadministration. Where concentrations in plasma are expressed as percentage of injected dose, the plasma volume was assumed to be 4% of the body weight of mice.[21]

***In Vivo* Efficacy Studies with Human Tumor Xenograft Models in SCID Mice.** For the HT29 and COLO205 xenograft model of human colon adenocarcinoma, 2×10^6 and 3×10^6 cells, respectively, were injected subcutaneously into an area under the right shoulder. Dosing with 75 μg conjugated maytansinoid/kg/inj, qdx5, was initiated when the tumors had reached a size of approximately 100−200 mm^3. Volumes of administration were calculated based on antibody concentration and maytansinoid to Ab ratio (D/A) for each conjugate. Tumor size was measured twice weekly in three dimensions using a caliper. The tumor volume was expressed in mm^3 using the formula V = Length × Width × Height × 1/2.

Tolerability Studies in CD-1 Mice. CD-1 mice were randomly grouped according to their body weight with 12 mice per test substance. One to two intravenous injections of each conjugate were given through a tail vein. Animals were monitored daily for signs of toxicity including body weight loss, dehydration, hunched posture, ruffled fur, and loss of appetite or lethargy. If body weight loss exceeded 15% within the first 24 h after treatment or 20% at any other point in the study or if the animals were unable to reach food or water, they were sacrificed.

RESULTS

Synthesis and Nomenclature Used for Antibody−Maytansinoid Conjugates. In order to evaluate the impact of linker stability on the *in vivo* activity of disulfide linked AMCs, conjugates were synthesized using (1) a variety of linkers with different steric hindrance, 0, 1, or 2 methyl groups on the carbon atom next to the sulfur, and (2) three different maytansinoid thiols, DM1, DM3, and DM4 (collectively referred to as DM*x*), which differ in having 0, 1, or 2 methyl group substituents on the carbon next to the sulfur (Figure 1A). (Note: In these experiments, monosubstituted linker (SPP) and monosubstituted maytansinoid (DM3) were used, each being a mixture of stereoisomers at the monosubstituted carbon adjacent to the sulfur atom. As a result, conjugates made from these reagents are a mixture of diastereomers. The rates of reduction by a thiol such as cysteine or glutathione *in vivo* must then be considered to be a weighted average of the rates of reduction of each diastereomer in the mixture. It is possible that a diastereomerically pure conjugate might be reduced at a rate slightly different from that of the conjugate mixture used in these studies; however, we believe that the activities measured here, *in vitro* and *in vivo*, are likely reasonable estimates for the diastereomerically pure materials since it has been shown previously that for DM3 thiol the stereochemistry at the carbon adjacent to the thiol is not important for the activity of the free drug[18].) In the AMCs described here, the antibody is connected via lysine residues to one end of the bifunctional linker through an amide bond while the maytansinoid agent is connected to the other end of the linker through either a disulfide or a thioether bond. The steric hindrance around the disulfide bond of an antibody−maytansinoid conjugate will be specified using the notation *x*:*y*, where *x* = the number of methyl groups on the carbon adjacent to the sulfur on the linker side of the disulfide bond, and *y* = the number of methyl groups on the carbon adjacent to the sulfur on the maytansinoid side of the disulfide bond (see Table 1). In addition, two different carbon chain lengths were evaluated for unhindered disulfide linkers (derived from SPDP and SPDB) and are referred to as 0 or 0′, respectively, in the disulfide notation (Table 1). A nonreducible thioether-linked conjugate, huC242-SMCC-DM1, was also included in the analyses. All conjugates were characterized in terms of DMx/Ab ratio (3.3 ± 1.0), percent monomer (>95%), percent free drug associated with conjugate (<5%), and binding to CanAg positive tumor cell lines by FACS ($K_d^{conj}/K_d^{Ab} \leq 2.0$).

Rates of Reduction of Disulfide Linkage in AMCs *in Vitro*. In order to confirm that the level of steric hindrance around the disulfide bond altered the chemical stability of the linkage, the rate of reduction of disulfide-linked AMCs by DTT was measured at 37 °C, pH 6.5, using an HPLC assay to follow the release of maytansinoid. The measured second-order rate constants (k) for reduction are shown in Table 2. For cases where there is an

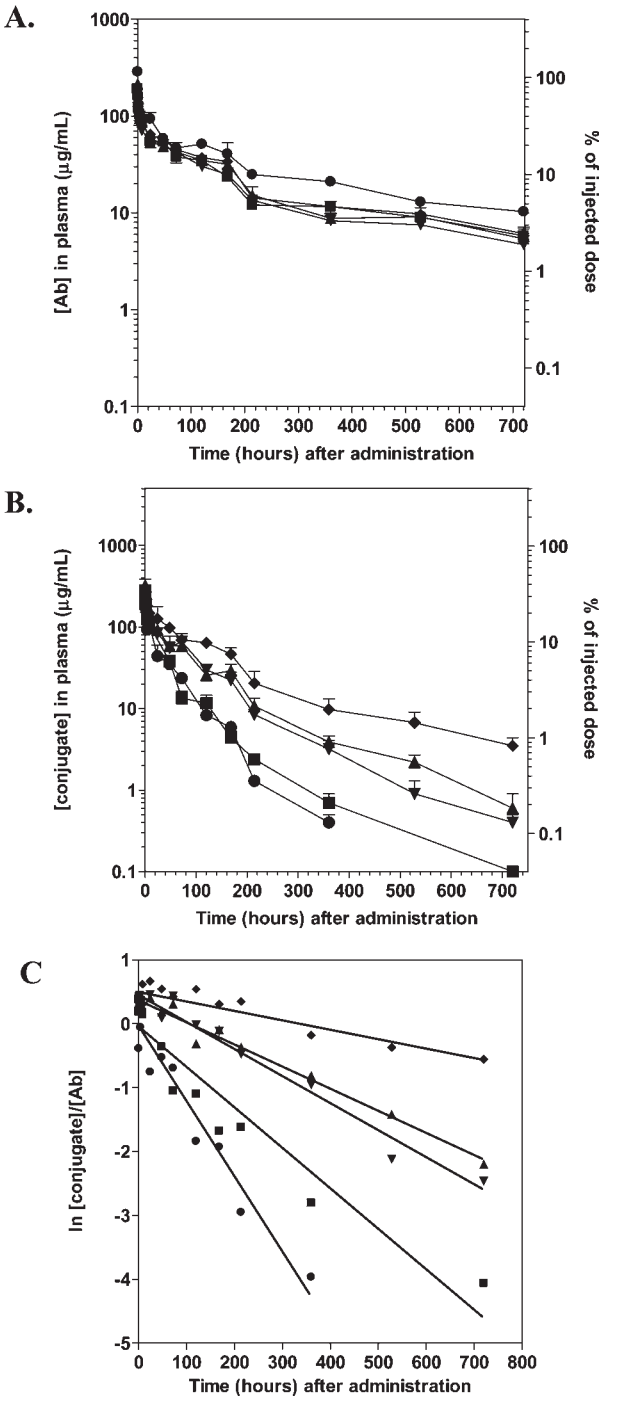


Figure 2. Representative pharmacokinetic study; CD-1 mice dosed with a single bolus IV injection of 10 mg/kg conjugate (Ab dose). (A) Concentration of the antibody moiety of AMCs in plasma; (B) concentration of AMC (conjugate) in plasma; (C) plot of ln-[conjugate]/[Ab] vs time for calculation of rate of maytansinoid cleavage from conjugate (k_{cl}) from the slope. Figure symbols: huC242-SMCC-DM1 (♦), huC242-SPDB-DM4 (0′:2; ▲), huC242-SPDP-DM4 (0:2; ▼), huC242-SPDB-DM3 (0′:1; ■), huC242-SPP-DM1 (1:0; ●).

equivalent degree of steric hindrance on both sides of the disulfide bond—0′:0, 1:1, and 2:2 conjugates—the rate constant represents the average of the rate of attack of DTT at each side of the disulfide bond. In cases where the disulfide is more sterically hindered on one side than the other, the rate constant is weighted toward attack of DTT at the less hindered side of the disulfide bond.

Introduction of steric hindrance at one side of the disulfide linkage (1:0, 0:2, 2:0, and 0′:2) results in a significant decrease in the rate of reduction compared to the unhindered (0′:0) conjugate. After normalizing the relative stability to reduction to the unhindered 0′:0 disulfide, the conjugates with steric hindrance at one side of the disulfide linkage (1:0, 0:2, 2:0, or 0′:2) are relatively more stable by 7-, 14-, 17-, and 22-fold, respectively. The 0′:2 conjugate appears to be slightly more stable to reduction than the 0:2 conjugate due to the longer carbon chain, which has been observed previously.[22] The similar rates of reduction of the 0:2 and 2:0 conjugates suggest that the location of steric hindrance on the disulfide bond (linker side vs DM*x* side) has little impact on stability to reduction *in vitro*.

Conjugates with hindrance on both sides of the disulfide linkage (1:1, 1:2, and 2:2) are much more stable to reduction compared to the unhindered 0′:0 conjugate and to conjugates with hindrance at only one side of the disulfide linkage (0:2, 2:0, 0′:2). The 1:1 conjugate is 170-fold more stable to reduction than the unhindered 0′:0 conjugate, while the most hindered 2:2 conjugate—with two methyl group substituents on carbon atoms on each side of the disulfide bond—is more than 22 000-fold more stable to reduction than the unhindered 0′:0 conjugate. Overall, the *in vitro* stability to reduction of various AMCs follows the order of increasing steric hindrance around the disulfide bond: 0′:0 < 1:0 < 0:2 ≈ 2:0 ≤ 0′:2 < 1:1 < 1:2 < 2:2.

Plasma Pharmacokinetic Studies of AMCs. To determine whether different disulfide bond stabilities translate to different pharmacokinetic properties for the AMCs, the plasma concentrations of several AMCs were measured over a four week period after a single intravenous administration of 10 mg/kg conjugate (antibody dose) in CD-1 mice. The concentrations of both total antibody and intact conjugate were measured using ELISA methods. The antibody and conjugate clearance curves for one representative PK study are shown in Figure 2A and B, respectively. For each conjugate, the slope of the linear plot of ln[conjugate]/[Ab] vs time was used to calculate the rate of maytansinoid cleavage from conjugate in plasma (k_{cl}) (Figure 2C). The complete set of PK parameters measured for conjugate clearance for the total set of AMCs tested in three independent PK studies are assembled in Table 3.

All of the AMCs tested in these studies have similar rates of clearance for the antibody moiety of the AMC (mean CL_{Ab} = 0.58 ± 0.15 mL/h/kg; mean $t_{1/2,\beta}^{Ab}$ = 226 ± 23 h). The volume of distribution (V_{ss}), C_{max}, and AUC parameters for the antibody component of the conjugates described in Table 3 also seem to be relatively unaffected by the nature of the linker and DM*x* moieties attached to the antibody (mean V_{ss} = 177 ± 34 mL/kg, mean C_{max} = 210 ± 50 µg/mL; mean AUC = 18593 ± 5706 µg·h/mL). Thus, the pharmacokinetic parameters describing antibody clearance and biodistribution appear to be relatively unaffected by the nature of the linker or maytansinoid moiety on the conjugate.

In contrast, the rate of conjugate clearance from plasma is significantly affected by the nature of the linker and maytansinoid moieties on the conjugate. As shown in Table 3, the conjugate half-life in plasma ($t_{1/2,\beta}^{conj}$) increases as the stability to reduction of the disulfide linker increases. The hindered conjugates with two methyl groups at the carbon adjacent to the disulfide linkage (0:2 or 0′:2) are significantly more stable in plasma ($t_{1/2,\beta}^{conj}$ of 87 and 102 h, respectively) compared to the less

dx.doi.org/10.1021/bc100480a |*Bioconjugate Chem.* 2011, 22, 717–727

Table 3. Summary of Pharmacokinetic Parameters for Conjugate (conj) Measured in Several Independent PK Studies

AMC	C_{max} (μg/mL)	CL_{conj} (mL/h/kg)	$t_{1/2,\beta}^{conj}$ (h)	$AUC_{0-\infty}$ (h·μg/mL)	k_{cl} (h^{-1})[a]	relative stability to DM*x* release[b]
0:0	206	6.0	15	1667	0.045	1
1:0	212	1.9	47	5186	0.012	4
0′:1	288	1.7	57	5817	0.0063	7
0:2	213	0.92	87	10929	0.0042	11
0′:2	331	0.84	102	11960	0.0035	13
1:2	208	0.44	218	22712	0.0012	37
SMCC-DM1	253	0.49	134	20453	NA	NA

[a] k_{cl} = rate of loss of maytansinoid from conjugate during circulation in the plasma due to a reductive cleavage event; measured from the slope of the plot of ln([conjugate]/[Ab]) vs time. [b] Relative stability to maytansinoid cleavage from conjugate *in vivo*, normalized to the rate of cleavage of the 0:0 conjugate (i.e., relative stability = $k_{cl}^{0:0}/k_{cl}^{x:y}$).

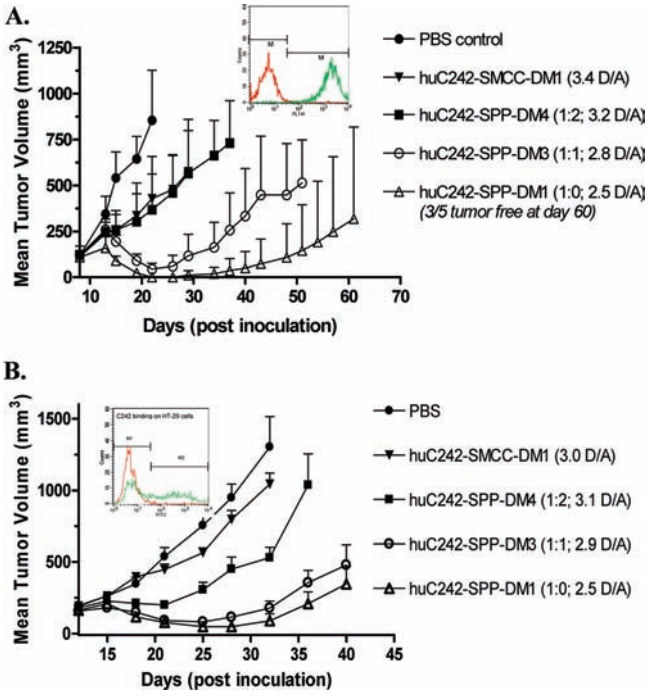


Figure 3. Comparison of antitumor activities of huC242 AMCs on human colon cancer xenograft models in SCID mice. Mice (5 per group) were dosed with 75 μg conjugated maytansinoid/kg/injection, daily for 5 days. AMCs with increasing steric hindrance on the maytansinoid side of the disulfide bond (1:0, 1:1, 1:2) were compared with the noncleavable SMCC-DM1 conjugate in COLO205 model (A) and HT29 model (B). The insets show CanAg expression levels determined by FACS on the two cell lines after staining with saturating huC242 antibody followed by FITC labeled goat antihuman IgG secondary reagent (M2 population) or secondary reagent only (M1 population). In cases where mice remained tumor free (TF) at the end of study, it is indicated in the figure.

hindered 1:0 or 0:0 conjugates ($t_{1/2,\beta}^{conj}$ of 47 and 15 h, respectively). The 1:2 conjugate with hindrance on both sides of the disulfide linkage is even more stable with $t_{1/2,\beta}^{conj}$ of 218 h. Conjugate clearance (CL_{conj}) represents the total clearance of conjugated maytansinoid from plasma due to a combination of antibody clearance (CL_{Ab}) and loss of maytansinoid from antibody due to a bond cleavage event. The rate constant k_{cl} for maytansinoid cleavage from antibody was calculated as described above for each conjugate and is given in Table 3. The relative stabilities of the conjugates to maytansinoid cleavage, normalized to the 0:0 conjugate ($k_{cl}^{0:0}/k_{cl}^{conj}$), are also shown in Table 3 and correlate with the level of steric hindrance around the disulfide bond, suggesting that the release of maytansinoid from conjugate during circulation in the blood is likely occurring through reductive cleavage.

***In Vivo* Efficacy of AMCs in Human Tumor Xenografts in SCID Mice.** Having determined that the level of steric hindrance around the disulfide bond impacts the chemical stability of the conjugate linkage, as well as the rate of clearance of conjugated maytansinoid during circulation in the blood, we evaluated the *in vivo* antitumor activity of a variety of the huC242-DM*x* conjugates in two human colon carcinoma xenograft models: COLO205 that expresses high levels of CanAg antigen homogeneously, and HT29 that expresses CanAg heterogeneously with a wide range of expression (see FACS histograms in Figure 3A and B).

In the first set of efficacy studies, we compared the activity of three different huC242-SPP-DMx conjugates having one methyl group on the linker side and increasing levels of steric hindrance on the maytansinoid side of the disulfide bond (1:0, 1:1, and 1:2; Figure 3A and B). The noncleavable huC242-SMCC-DM1 conjugate was also included. The level of efficacy varied greatly among the conjugates, with some showing partial and complete regressions and others having only minimal activity. In both the HT29 and COLO205 models, the order of efficacy observed was 1:0 > 1:1 > 1:2 = SMCC-DM1. Therefore, for conjugates with one methyl group on the linker side of the disulfide bond, increasing steric hindrance on the maytansinoid side leads to decreasing efficacy. These results suggest that, in this series of conjugates, the cleavability of the disulfide linkage is a more important determinant of antitumor activity than the increase in exposure (AUC) with increasing steric hindrance around the disulfide bond. The relative lack of activity for the noncleavable SMCC linked conjugate in these models supports this notion.

In a second set of efficacy studies (Figure 4), we compared the activity of conjugates having the same degree of steric hindrance on the maytansinoid side while having different steric hindrance on the linker side (1:0 and 2:0). In this case, there was little difference in the efficacy of these conjugates in either model. This again may suggest that there is an important balance between improved exposure vs ease of cleavability for *in vivo* activity. A nonbinding humanized IgG_1-SPP-DM1 conjugate had no activity in these models demonstrating that the activity observed for the huC242 conjugates is dependent on specific binding of conjugate to CanAg on the cell surface. In the same study, we also compared conjugates having the same degree of steric hindrance on the linker side vs the maytansinoid side of the disulfide bond

dx.doi.org/10.1021/bc100480a |*Bioconjugate Chem.* 2011, 22, 717–727

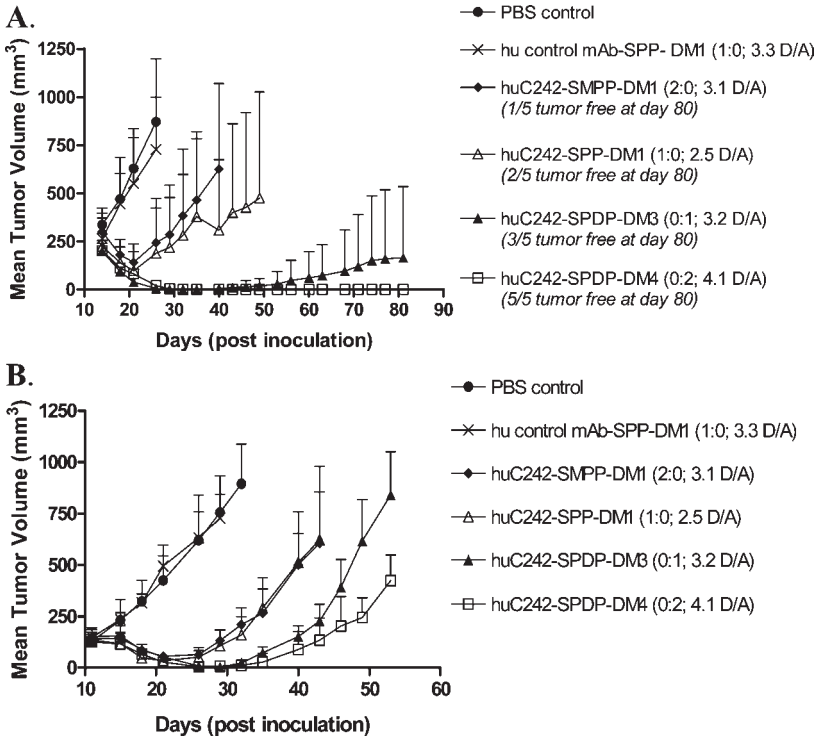


Figure 4. Panels (A) and (B) show results from a second set of efficacy studies in SCID mice comparing conjugates having the same level of steric hindrance, either on the linker side or on the maytansinoid side, of the disulfide bond (1:0 vs 0:1, 2:0 vs 0:2) on COLO205 and HT29, respectively. All other conditions are identical to those described in Figure 3.

(0:1 vs 1:0; 0:2 vs 2:0) to determine if the location of the steric hindrance impacted the efficacy of the conjugate. *In vivo* pharmacokinetic studies had demonstrated that the location of the hindrance did not appreciably change conjugate half-life or exposure (Table 3). In both the HT29 and the COLO205 efficacy studies, however, it was observed that the conjugate with the steric hindrance on the maytansinoid side of the disulfide bond was significantly more active than the corresponding conjugate with the same level of steric hindrance on the linker side. The order of activity of conjugates in both models was 0:2 > 0:1 > 2:0 ≈ 1:0. These results suggest that additional factors beyond PK exposure and cleavability of the disulfide linkage may be involved in determining *in vivo* efficacy.

In a further series of efficacy studies, we compared the activity of the 0:2 conjugate (SPDP-DM4) to the 0′:2 conjugate (SPDB-DM4) that has a longer linker carbon chain. The two conjugates had similar efficacy in the models tested (data not shown).

***In Vitro* Cytotoxicity of Unconjugated Maytansinoid Derivatives and AMCs.** In an effort to understand what additional factors may be involved in determining the *in vivo* efficacy of an AMC, we evaluated the intrinsic cytotoxic potency of the unlinked maytansinoids and various conjugates in *in vitro* cytotoxicity assays.

The *in vitro* cytotoxicity of unconjugated DM1 and DM4 maytansinoids were tested in COLO205 and HT29 cells as the stable *S*-methyl thioether species, since the potency of DM1 and DM4 measured in cell culture media can be variable due to formation of mixed disulfides by thiol/disulfide exchange with the cystine present in the media. In COLO205 cells, the IC_{50} values of the *S*-Me derivatives of DM1 and DM4 were 52 and 26 pM, while in HT29 cells, the IC_{50} values were 36 and 22 pM, respectively. These data suggest that introducing methyl groups on carbon adjacent to the thiol group (as in DM3 and DM4) may slightly increase the potency of these unconjugated maytansinoids relative to DM1, likely due to increased hydrophobicity resulting in greater membrane permeability and/or tighter binding to microtubules.

The cytotoxicity of huC242-DM*x* conjugates were tested in COLO205 cells *in vitro* using a clonogenic assay. All disulfide-linked conjugates were highly potent, with EC_{50} values ranging from 3.5 to 15 pM (antibody concentration; Table 1). There is no apparent correlation between the disulfide bond stability and the observed *in vitro* potency of the conjugates. Furthermore, the noncleavable thioether linked SMCC-DM1 conjugate showed similar *in vitro* cytotoxic potency to the disulfide-linked conjugates, suggesting that disulfide bond cleavage is not a critical factor for the *in vitro* cytotoxic potency of these conjugates, consistent with the demonstration of efficient lysosomal cleavage of AMCs in COLO205 cells.[3]

***In Vitro* Bystander Activity of Conjugates.** Previously, we have shown that, under conditions where cells are grown at very high densities, as in a solid tumor grown *in vivo*, disulfide-linked conjugates can kill neighboring nontargeted bystander cells after being internalized and processed by the target cell to generate diffusible cytotoxic metabolites.[23] This prompted us to investigate whether bystander killing potency of an AMC may vary with the stability of the disulfide linkage between antibody and maytansinoid and therefore be a factor that may contribute to *in vivo* efficacy. In Figure 5, we show the results of an experiment designed to measure the *in vitro* bystander killing activity of four maytansinoid conjugates: 1:0, 0:1, 0:2, and SMCC-DM1. In this experiment, COLO205 (antigen-positive) and Namalwa (antigen-negative) cells were mixed together in different ratios, and the huC242-DM*x* conjugates were added at a concentration

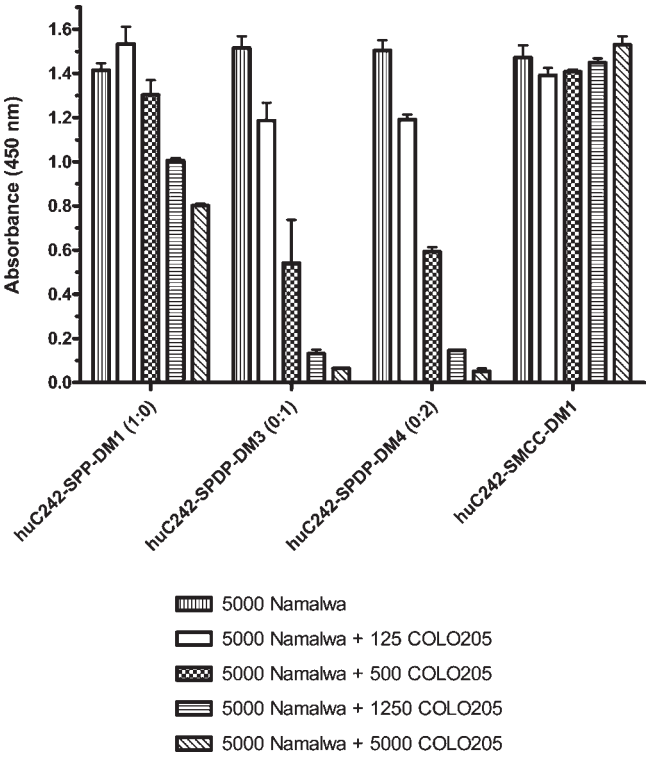


Figure 5. *In vitro* bystander killing of antigen-negative Namalwa cells by CanAg antigen-positive COLO 205 cells treated with huC242 AMCs. Namalwa and COLO205 cells were mixed in the ratios indicated and treated with one of C242-SPP-DM1 (1:0), C242-SPDP-DM3 (0:1), C242-SPDP-DM4 (0:2), or C242-SMCC-DM1 at 1 nM conjugate concentration. All conjugates had ~4 DM*x*/Ab. The absorbance at 450 nm is a measure of the viability of the Namalwa cells after a 4 day incubation with conjugate.

of 1 nM, sufficient to kill all the COLO205 cells but none of the Namalwa cells. In the absence of COLO205 cells, the Namalwa cells were not killed by any of the conjugates, as expected. In contrast, when COLO205 cells were present in the cell mixture, all of the disulfide-linked conjugates were able to kill surrounding antigen-negative Namalwa cells to some extent. However, the noncleavable SMCC-DM1 conjugate showed no bystander killing even at the highest ratio of COLO205:Namalwa cells used (1:1). These results are consistent with previously reported results showing that the cytotoxic metabolites produced upon target cell internalization of disulfide-linked conjugates include the membrane-permeable DM*x* thiol and *S*-methyl DMx species, while the sole metabolite produced from internalization of the SMCC-DM1 conjugate is the poorly membrane-permeable lysine-SMCC-DM1 species.[3,24] Overall, the trends in bystander killing potency *in vitro* agree well with the trends in antitumor activity of these conjugates *in vivo*, with 0:2 ≈ 0:1 > 1:0 > SMCC-DM1, suggesting that bystander killing may play a role in antitumor activity *in vivo*.

Tolerability of huC242-SPP-DM1 (1:0) and huC242-SPDB-DM4 (0′:2) Conjugates in CD-1 Mice. Interestingly, while the *in vivo* efficacy of the huC242-SPDB-DM4 (0′:2) conjugate is significantly greater than the huC242-SPP-DM1 (1:0) conjugate in the models tested, the acute toxicity of the two conjugates in mice is similar. CD-1 mice (12 mice/group) were dosed intravenously with either huC242-SPP-DM1 (1:0) or huC242-SPDB-DM4 (0′:2) conjugate. Measurements of toxicity based on body weight loss were similar for the two conjugates and the dose resulting in severe toxicity in 10% of the animals (STD_{10}) was found to be similar for the two conjugates (approximately 1.2 mg DM*x*/kg). These results suggest that the balance of factors determining efficacy and tolerability are different.

DISCUSSION

Cantuzumab mertansine (huC242-SPP-DM1), a disulfide-linked maytansinoid conjugate with sterically hindered (1:0) disulfide linkage, has been studied in several phase I human clinical trials, predominantly in subjects with colon cancer.[25−27] Because of its specificity and potency toward CanAg antigen-expressing tumors, the huC242-maytansinoid conjugate is able to selectively target malignant tumor cells for destruction while sparing healthy normal tissue. However, in humans[25] and in preclinical models,[6] the half-life of the conjugate in plasma was found to be significantly shorter than the half-life of the antibody component, likely due to reductive cleavage of DM1 from antibody as the conjugate circulates in the plasma compartment ($t_{1/2,\beta}$ conjugate = 41 h vs $t_{1/2,\beta}$ antibody = 230 h in humans). This observation prompted us to investigate whether huC242−maytansinoid conjugate activity might be improved by increasing the stability of the disulfide linker connecting the maytansinoid to the antibody toward thiol−disulfide exchange reactions, thereby increasing conjugate half-life and exposure of tumor to conjugated maytansinoid.

Toward this end, a panel of disulfide-linked huC242-DM*x* conjugates was generated with different degrees of steric hindrance around the disulfide bond, by introducing methyl groups on carbon atoms adjacent to the disulfide linkage (Table 1). The SMCC-DM1 conjugate with DM1 linked via a thioether bond was also included in this investigation to represent a conjugate with a nonreducible linker. Evaluation of this set of conjugates for their sensitivity to reductive cleavage *in vitro* demonstrated that as the degree of steric hindrance around the disulfide bond increased the rate of cleavage of maytansinoid from antibody decreased. *In vivo*, these conjugates showed an identical trend, with increasing steric hindrance around the disulfide bond leading to increased conjugate half-life in plasma, suggesting that maytansinoid is being lost from disulfide linked conjugates in plasma by a reductive cleavage event. The location of the steric hindrance (maytansinoid vs linker side) in the disulfide bond did not significantly influence the rate of cleavage of maytansinoid from conjugate, which is consistent with a chemical reduction occurring *in vivo* via a small molecule reductant like cysteine.[28] The rate of loss of maytansinoid from the AMCs *in vivo,* inferred from the pharmacokinetic measurements, is consistent with that predicted from the second-order rate constants for reduction measured *in vitro* (the second-order rate constant measured *in vitro* at pH 6.5 has to be adjusted upward by a factor of ~8 to correct for the higher pH found in plasma (7.4), which will lead to an 8-fold increase in the concentration of reactive thiolate nucleophile and a corresponding increase in rate of reduction) and the known concentrations of free thiol in plasma (~5 μM) in the form of cysteine.[28]

While the greater stability of the more sterically hindered disulfide-linked conjugates might be predicted to lead to increased tumor exposure and potentially greater efficacy for the more hindered conjugates, evaluation of the *in vivo* efficacy resulted in an unexpected ranking, with conjugates of intermediate disulfide bond stability having the greatest antitumor activity.

Overall, the order of efficacy observed was as follows: 0′:2 ≥ 0:2 > 0:1 > 1:0 ≈ 2:0 > 1:1 > 1:2 ≈ SMCC-DM1. The huC242−maytansinoid conjugates with a highly hindered disulfide linkage (1:2) or noncleavable thioether linkage (SMCC-DM1) were much less active suggesting that the reductive release of a maytansinoid thiol is required for maximal antitumor activity in these xenograft models.

We also observed that the configuration of steric hindrance at the disulfide bond for the conjugates with intermediate disulfide bond stability (the "sidedness") is important in determining the magnitude of antitumor activity. We found that having one or two methyl groups on the maytansinoid side of the disulfide bond confers an advantage relative to having the same degree of steric hindrance on the linker side, despite the fact that these conjugates have approximately equivalent *in vivo* plasma stability (Figure 4). This observation suggests that perhaps the nature of the maytansinoid metabolite released by reductive cleavage of the conjugate at the tumor cell is also important in determining conjugate activity (i.e., DM4 released from the 0:2 conjugate is more effective at inhibiting tumor growth than DM1 released from the 2:0 conjugate). Although the 0:2 and 0:1 conjugates do have slightly higher *in vitro* potencies than the corresponding 2:0 and 1:0 conjugates *in vitro* (Table 1), which is consistent with their greater activities *in vivo*, the order of intrinsic *in vitro* potency of the panel of conjugates taken as a whole does not adequately predict the trend in *in vivo* activities observed, suggesting additional factors contribute to activity *in vivo*. This is most clearly demonstrated by the fact that although the 0:2 and SMCC-DM1 conjugates have very similar potencies *in vitro*, the 0:2 conjugate is strikingly more active *in vivo*, despite having a shorter conjugate half-life in plasma and about half the plasma exposure ($AUC_{0-\infty}$).

One property differentiating tumor xenografts growing *in vivo* from tumor cells growing on a cell culture plate may be the presence of inaccessible (i.e., nontargeted) tumor cells in the tightly packed three-dimensional tumor spheroid *in vivo*. Such nontargeted cells may be tumor cells that lack expression of the target antigen (see, for example, the heterogeneous expression of the CanAg antigen in the HT29 xenograft model) or cells that are inaccessible to conjugate due to barriers to macromolecule delivery.[29,30] There is evidence in the literature from our group and others to support bystander killing of nontargeted tumor cells by immunoconjugates *in vivo*.[23,31] Bystander killing requires processing of the conjugate by target cells followed by release of a membrane-permeable cytotoxic metabolite which then diffuses into neighboring tumor cells. Disulfide-linked AMCs have been shown to be effective at bystander killing because target cell processing of these conjugates yields membrane-permeable DM*x* metabolites including the thiol and the *S*-methylated derivative of the thiol.[3,24] For bystander killing by disulfide-linked AMCs, release of the more hindered DM3 or DM4 thiols from a 0:1 or 0:2 conjugate might be expected to be more effective than release of the less hindered DM1 thiol from a 1:0 or 2:0 conjugate, since DM1, having a more reactive thiol, would likely be inactivated more quickly in the extracellular space by disulfide interchange with, for example, cystine. Additionally, it has been shown that the DM4 metabolite is efficiently *S*-methylated by the target cell *in vivo* (DM3 has also been shown to be efficiently S-methylated by COLO205 cells in vitro; unpublished data), while the DM1 metabolite is not.[3] This *S*-methylation prevents any possibility of thiol−disulfide exchange reactions of the DM4 metabolite, which may contribute to greater bystander activity. Finally, the increased hydrophobicity of the more substituted DM3 and DM4 thiols relative to DM1 may also promote more efficient passage across cell membranes and tighter binding to microtubules leading to better bystander killing. The data presented in this report showing that the 0:2 and 0:1 huC242 conjugates have superior *in vitro* bystander activity as well as superior *in vivo* efficacy supports a role for bystander killing in the *in vivo* activities of these conjugates.

The superior *in vivo* antitumor activity and improved therapeutic window of the 0′:2 disulfide-linked conjugate reported here for the huC242 maytansinoid conjugates has also been observed for other AMCs in development including antibody maytansinoid conjugates targeting αv integrin, CD19, CD33, and CD138.[8,9,32,33] However, the relationships reported here may not be true for all AMC targets. For example, one notable exception is trastuzumab-SMCC-DM1 targeting HER2, where the noncleavable thioether-linked conjugate has comparable activity to the disulfide-linked conjugates in xenograft models.[4] The accumulated preclinical data therefore suggests that the optimal linker for each AMC may depend on multiple factors and needs to be explored for each target and antibody.

For the CanAg-targeting huC242 antibody discussed in this report, the disulfide-linked huC242-SPDB-DM4 (0′:2) maytansinoid conjugate showed the best antitumor activity in the preclinical models. On the basis of the combined efficacy and tolerability results reported here, we conclude that this conjugate has an improved therapeutic window relative to the 1:0 conjugate, cantuzumab mertansine, which had previously been studied in clinical trials[25−27] and provides a rationale for its clinical development.

■ ASSOCIATED CONTENT

Supporting Information. Synthesis of sulfo-NHS-SMPP-DM1 and sulfo-NHS-SMPP-DM4 reagents is described. This material is available free of charge via the Internet at http://pubs.acs.org.

■ AUTHOR INFORMATION

Corresponding Author

*Corresponding author. Phone: 781-895-0600. Fax: 781-895-0611. E-mail: rajeeva.singh@immunogen.com.

Present Addresses

†Norfolk Agricultural School, 400 Main Street, Walpole, MA 02081−3709.

‡Acceleron Pharma, 128 Sidney St., Cambridge MA 02139.

§Shire HGT, 125 Spring Street, Lexington, MA 02421.

■ ABBREVIATIONS:

AMC, antibody−maytansinoid conjugate; AUC, area under the curve (plasma exposure); CL, plasma clearance; C_{max}, maximal plasma concentration; DM1, $N^{2'}$-deacetyl-$N^{2'}$(3-mercapto-1-oxopropyl)-maytansine; DM3, $N^{2'}$-deacetyl-$N^{2'}$-(4-mercapto-1-oxopentyl)-maytansine; DM4, $N^{2'}$-deacetyl-$N^{2'}$-(4-methyl-4-mercapto-1-oxopentyl)-maytansine; DM*x*, any of DM1, DM3, or DM4; DTT, dithiothreitol; mAb, monoclonal antibody; SMCC, *N*-succinimidyl 4-(*N*-maleimidomethyl)cyclohexane-1-carboxylate; SMPP, *N*-succinimidyl 4-methyl-4-(2-pyridyldithio)pentanoate; SPDB, *N*-succinimidyl 4-(2-pyridyldithio)butanoate; SPDP,

N-succinimidyl 3-(2-pyridyldithio)propanoate; SPP, *N*-succinimidyl 4-(2-pyridyldithio)pentanoate; sulfo-NHS-SMPP-DM1, *N*-sulfosuccinimidyl ester of $N^{2'}$-deacetyl-$N^{2'}$-[3-(3-carboxy-1, 1-dimethyl-propyl-dithio)-1-oxopropyl]-maytansine; sulfo-NHS-SMPP-DM4, *N*-sulfosuccinimidyl ester of $N^{2'}$-deacetyl-$N^{2'}$-(4-methyl-4-(2-methyl-5-carboxy)pentan-2-yl)disulfanyl)pentanoyl)-maytansine; $t_{1/2,\beta}$, β phase half-life for elimination; V_{ss}, volume of distribution.

REFERENCES

(1) Lambert, J. M. (2010) Antibody-maytansinoid conjugates: A new strategy for the treatment of cancer. *Drugs Future 35*, 471–480.

(2) Chari, R. V. (2008) Targeted cancer therapy: Conferring specificity to cytotoxic drugs. *Acc. Chem. Res. 41*, 98–107.

(3) Erickson, H. E., Park, P. U., Widdison, W. C., Kovtun, Y. V., Garrett, L. M., Hoffman, K., Lutz, R. J., Goldmacher, V. S., and Blättler, W. A. (2006) Antibody-maytansinoid conjugates are activated in targeted cancer cells by lysosomal degradation and linker dependent intracellular processing. *Cancer Res. 66*, 4426–4433.

(4) Lewis Phillips, G. D., Li, G., Dugger, D. L., Crocker, L. M., Parsons, K. L., Mai, E., Blättler, W. A., Lambert, J. M., Chari, R. V., Lutz, R. J., Wong, W. L., Jacobson, F. S., Koeppen, H., Schwall, R. H., Kenkare-Mitra, S. R., Spencer, S. D., and Sliwkowski, M. X. (2008) Targeting HER2-positive breast cancer with Trastuzumab-DM1, an antibody-cytotoxic drug conjugate. *Cancer Res. 68*, 9280–9290.

(5) Krop, I. E., Beeram, M., Modi, S., Jones, S. F., Holden, S. N., Yu, W., Girish, S., Tibbitts, J., Yi, J. H., Sliwkowski, M. X., Jacobson, F., Lutzker, S. G., and Burris, H. A. (2010) Phase I study of trastuzumab-DM1, an HER2 antibody-drug conjugate, given every 3 weeks to patients with HER2-positive metastatic breast cancer. *J. Clin. Oncol. 28*, 2698–2704.

(6) Xie, H., Audette, C., Hoffee, M., Lambert, J., and Blättler, W. (2004) Pharmacokinetics and biodistribution of the antitumor immunoconjugate, cantuzumab mertansine (huC242-DM1), and its two components in mice. *J. Pharmacol. Exp. Ther. 308*, 1073–1082.

(7) Tassone, P., Gozzini, A., Goldmacher, V., Shammas, M. A., Whiteman, K. R., Carrasco, D. R., Li, C., Allam, C. K., Venuta, S., Anderson, K. C., and Munshi, N. C. (2004) In vitro and in vivo activity of the maytansinoid immunoconjugate huN901-$N^{2'}$-deacetyl-$N^{2'}$-(3-mercapto-1-oxopropyl)-maytansine against CD56+ multiple myeloma cells. *Cancer Res. 64*, 4629–4636.

(8) Chen, Q., Millar, H. J., McCabe, F. L., Manning, C. D., Steeves, R., Lai, K., Kellogg, B., Lutz, R. J., Trikha, M., Nakada, M. T., and Anderson, G. M. (2007) α_v Integrin-targeted immunoconjugates regress established human tumors in xenograft models. *Clin. Cancer Res. 13*, 3689–3695.

(9) Al-Katib, A. M., Aboukameel, A., Mohammad, R., Bissery, M. C., and Zuany-Amorim, C. (2009) Superior antitumor activity of SAR3419 to Rituximab in xenograft models for non-hodgkin's lymphoma. *Clin. Cancer Res. 15*, 4038–4045.

(10) Johansson, C., Nilsson, O., Baeckström, D., Jansson, E. L., and Lindholm, L. (1991) Novel epitopes on the CA50-carrying antigen: chemical and immunochemical studies. *Tumour Biol. 12*, 159–170.

(11) Baeckström, D., Hansson, G. C., Nilsson, O., Johansson, C., Gendler, S. J., and Lindholm, L. (1991) Purification and characterization of a membrane-bound and secreted mucin-type glycoprotein carrying the carcinoma-associated sialyl-Le^a epitope on distinct core proteins. *J. Biol. Chem. 266*, 21537–21547.

(12) Thorpe, P. E., Wallace, P. M., Knowles, P. P., Relf, M. G., Brown, A. N., Watson, G. J., Knyba, R. E., Wawrzynczak, E. J., and Blakey, D. C. (1987) New coupling agents for the synthesis of immunotoxins containing a hindered disulfide bond with improved stability in vivo. *Cancer Res. 47*, 5924–5931.

(13) Thorpe, P. E., Wallace, P. M., Knowles, P. P., Relf, M. G., Brown, A. N., Watson, G. J., Blakey, D. C., and Newell, D. R. (1988) Improved antitumor effects of immunotoxins prepared with deglycosylated Ricin A-chain and hindered disulfide linkages. *Cancer Res. 48*, 6396–6403.

(14) Flavell, D. J., Boehm, D. A., Okayama, K., Kohler, J. A., and Flavell, S. U. (1994) Therapy of human T-cell acute lymphoblastic leukemia in severe combined immunodeficient mice with two different anti-CD7-saporin immunotoxins containing hindered or non-hindered disulphide cross linkers. *Int. J. Cancer 58*, 407–414.

(15) Arpicco, S., Dosio, F., Brusa, P., Crosasso, P., and Cattel, L. (1997) New coupling reagents for the preparation of disulfide cross-linked conjugates with increased stability. *Bioconjugate Chem. 8*, 327–337.

(16) Dosio, F., Arpicco, S., Adobati, E., Canevari, S., Brusa, P., De Santis, R., Parente, D., Pignanelli, P., Negri, D. R., Colnaghi, M. I., and Cattel, L. (1998) Role of cross-linking agents in determining the biochemical and pharmacokinetic properties of Mgr6-Clavin immunotoxins. *Bioconjugate Chem. 9*, 372–381.

(17) Chari, R. V., Martell, B. A., Gross, J. L., Cook, S. B., Shah, S. A., Blättler, W. A., McKenzie, S. J., and Goldmacher, V. S. (1992) Immunoconjugates containing novel maytansinoids: promising anti-cancer drugs. *Cancer Res. 52*, 127–131.

(18) Widdison, W. C., Wilhelm, S. D., Cavanagh, E. E., Whiteman, K. R., Leece, B. A., Kovtun, Y., Goldmacher, V. S., Xie, H., Steeves, R. M., Lutz, R. J., Zhao, R., Wang, L., Blättler, W. A., and Chari, R. V. (2006) Semisynthetic maytansine analogues for the targeted treatment of cancer. *J. Med. Chem. 49*, 4392–4408.

(19) Hermanson, G. T. (1996) *Bioconjugate Techniques, Part I*, Academic Press, San Diego.

(20) Furth, E. E., Thilly, W. G., Pennan, B. W., Liber, H. L., and Rand, W. M. (1981) Quantitative assay for mutation in diploid human lymphoblasts using microtiter plates. *Anal. Biochem. 110*, 1–8.

(21) Morton, D. B., Abbot, D., and Barclay, R. (1993) Removal of blood from laboratory mammals and birds. *Lab. Anim. 27*, 1–22.

(22) Worrell, N. R., Cumber, A. J., Parnell, G. D., Mirza, A., Forrester, J. A., and Ross, W. C. (1986) Effect of linkage variation on pharmacokinetics of ricin A chain-antibody conjugates in normal rats. *Anti-Cancer Drug Des. 1*, 179–188.

(23) Kovtun, Y. V., Audette, C. A., Ye, Y., Xie, H., Ruberti, M. F., Phinney, S. J., Leece, B. A., Chittenden, T., Blättler, W. A., and Goldmacher, V. S. (2006) Antibody-drug conjugates designed to eradicate tumors with homogeneous and heterogeneous expression of the target antigen. *Cancer Res. 66*, 3214–3221.

(24) Erickson, H. K., Widdison, W. C., Mayo, M. F., Whiteman, K., Audette, C., Wilhelm, S. D., and Singh, R. (2010) Tumor delivery and in vivo processing of disulfide linked antibody-maytansinoid conjugates. *Bioconjugate Chem. 21*, 84–92.

(25) Tolcher, A. W., Ochoa, L., Hammond, L. A., Patnaik, A., Edwards, T., Takimoto, C., Smith, L., de Bono, J., Schwartz, G., Mays, T., Jonak, Z. L., Johnson, R., DeWitte, M., Martino, H., Audette, C., Maes, K., Chari, R. V., Lambert, J. M., and Rowinsky, E. K. (2003) Cantuzumab Mertansine, a maytansinoid immunoconjugate directed to the CanAg antigen: A phase I, pharmacokinetic and biologic correlative study. *J. Clin. Oncol. 21*, 211–222.

(26) Helft, P. R., Schilsky, R. L., Hoke, F. J., Williams, D., Kindler, H. L., Sprague, E., DeWitte, M., Martino, H. K., Erickson, J., Pandite, L., Russo, M., Lambert, J. M., Howard, M., and Ratain, M. J. (2004) A phase I study of Cantuzumab Mertansine administered as a single intravenous infusion once weekly in patients with advanced solid tumors. *Clin. Cancer Res. 10*, 4363–4368.

(27) Rodon, J., Garrison, M., Hammond, L. A., de Bono, J., Smith, L., Forero, L., Hao, D., Takimoto, C., Lambert, J. M., Pandite, L., Howard, M., Xie, H., and Tolcher, A. W. (2008) Cantuzumab mertansine in a three-times a week schedule: a phase I and pharmacokinetic study. *Cancer Chemother. Pharmacol. 62*, 911–919.

(28) Mills, B. J., and Lang, C. A. (1996) Differential distribution of free and bound glutathione and cysteine in human blood. *Biochem. Pharmacol. 52*, 401–406.

(29) Jain, R. K. (1994) Barriers to drug delivery in solid tumours. *Sci. Am. 271*, 59–65.

(30) Minchinton, A. I., and Tannock, I. F. (2006) Drug penetration in solid tumours. *Nat. Rev. Cancer 6*, 583–592.

(31) Okeley, N. M., Miyamoto, J. B., Zhang, X., Sanderson, R. J., Benjamin, D. R., Sievers, E. L., Senter, P. D., and Alley, S. C. (2010) Intracellular activation of SGN-35, a potent anti-CD30 antibody-drug conjugate. *Clin. Cancer Res. 16*, 888–897.

(32) Giles, F., Morariu-Zamfir, R., Lambert, J.,Verstovsek, S., Thomas, D., Ravandi, F., and Deangelo, D. (2006) Phase I study of AVE9633, an antiCD33 maytansinoid immunoconjugate, administered as an intravenous infusion in patients with refractory/relapsed CD33 positive acute myeloid leukemia (AML). *Blood (ASH Annual Meeting Abstracts) 106*, Abstract 4548.

(33) Ikeda, H., Hideshima, T., Fulciniti, M., Lutz, R. J., Yasui, H., Okawa, Y., Kiziltepe, T., Vallet, S., Pozzi, S., Santo, L., Perrone, G., Tai, Y. T., Cirstea, D., Raje, N. S., Uherek, C., Dälken, B., Aigner, S., Osterroth, F., Munshi, N., Richardson, P., and Anderson, K. C. (2009) The monoclonal antibody nBT062 conjugated to cytotoxic maytansinoids has selective cytotoxicity against CD138-positive multiple myeloma cells in vitro and in vivo. *Clin. Cancer Res. 15*, 4028–4037.

Supporting Information

Disulfide-Linked Antibody-Maytansinoid Conjugates: Optimization of *IN VIVO* Activity by Varying the Steric Hindrance at Carbon Atoms Adjacent to the Disulfide Linkage

Brenda A. Kellogg,* Lisa Garrett, Yelena Kovtun, Kate Lai, Barbara Leece, Michael Miller, Gillian Payne, Rita Steeves, Kathy Whiteman, Wayne Widdison, Hongsheng Xie, Rajeeva Singh, Ravi V.J. Chari, John M. Lambert, Robert J. Lutz

ImmunoGen, Inc., 830 Winter Street, Waltham, Massachusetts 02451

List of Contents:

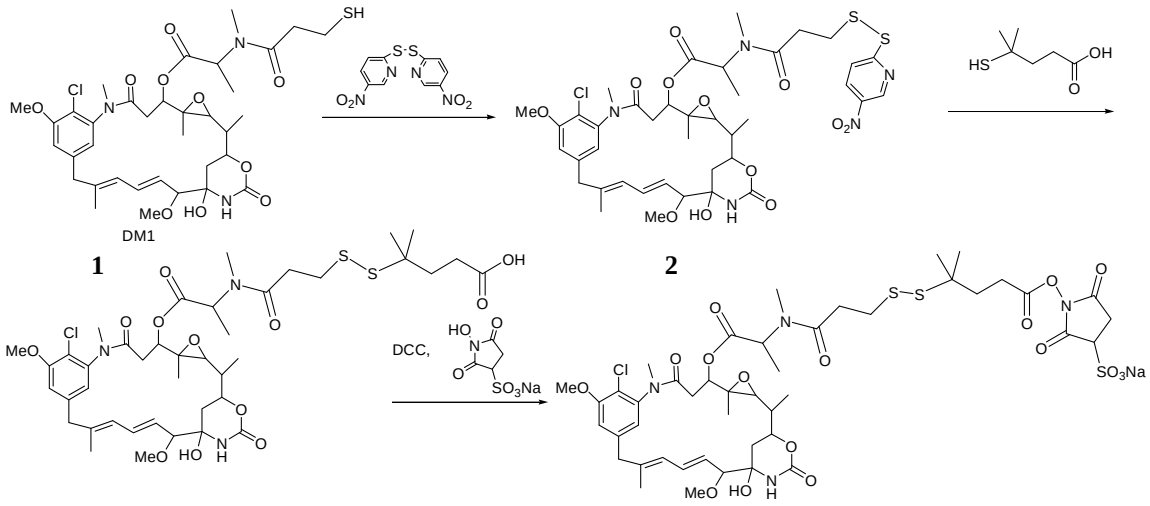
***SYNTHESIS OF SUIFO-NHS-SMPP-DM1*……..P 3**

***SYNTHESIS OF SUIFO-NHS-SMPP-DM4*……..P 5**

***REFERENCES*……....P 10**

SYNTHESIS OF SULFO-NHS-SMPP-DM1.

Scheme 1. Preparation of *N*-sulfosuccinimidyl ester of $N^{2'}$-Deacetyl-$N^{2'}$-[3-(3-carboxy-1,1-dimethyl-propyl-dithio)-1-oxopropyl]-maytansine (sulfo-NHS-SMPP-DM1).



***$N^{2'}$*-deacetyl-*$N^{2'}$*-[3-(5-nitropyridine-2-dithio)-1-oxopropyl]-maytansine (2).** To a 25 mL flask containing a solution of 2,2'-Dithiobis(5-nitropyridine) (100 mg, 0.323 mmol) in tetrahydrofuran (10 mL) and 4-methylmorpholine was added dropwise to a solution of DM1 **(1)** (106 mg, 0.145 mmol) in *N,N*-dimethylformamide (5 mL). After 90 min most of the solvent was removed by rotary evaporation and the residue was taken up in a minimum volume of *N,N*-dimethylformamide. The mixture was purified by preparative reverse phase HPLC on a Waters C8 symmetry shield 5 μm column (100 x 19 mm) at ambient temperature using a 19 mL/min flow rate, eluting with a linear gradient of acetonitrile (5% to 95% over 25 min) in deionized water containing 0.2% formic acid. Desired product **(2)** eluted at 23 min. Product containing fractions were combined and solvent was removed under vacuum to give 93 mg (72% yield) of product. ^{1}H NMR(400 MHz, $CDCl_3$) δ 9.13 (1H, s). 8.24 (1H, d, *J* = Hz), 7.75 (1H, d, *J* = Hz), 6.86 (1H, d, *J* = 1.5 Hz), 6.75 (1H, d, *J* = 11 Hz), 6.70 (1H, d, *J* = 1.5 Hz), 6.47 (1H, dd, *J* = 11,15 Hz), 6.25 (1H, s), 5.67 (1H, dd, *J* = 9, 15 Hz), 5.45 (1H, q, *J* = 7 Hz), 4.81 (1H, dd, *J* = 3, 12 Hz), 4.32 (1H, t, *J* = 10 Hz), 4.02 (3H, s), 3.71 (1H, d, *J* = 12 Hz), 3.55 (1H, d, *J* = 9 Hz), 3.39 (3H, s), 3.25 (3H, s), 3.08-3.20 (2H, m), 2.88 (3H, s), 2.60-2.82 (2H, m), 2.22 (1H,

dd, *J* = 3, 14 Hz), 1.68 (3H, s), 1.60 (3H, s), 1.35 (3H, d, *J* = 5 Hz), 1.33 (3H, d, *J* = 5 Hz), 0.84 (3H, s).

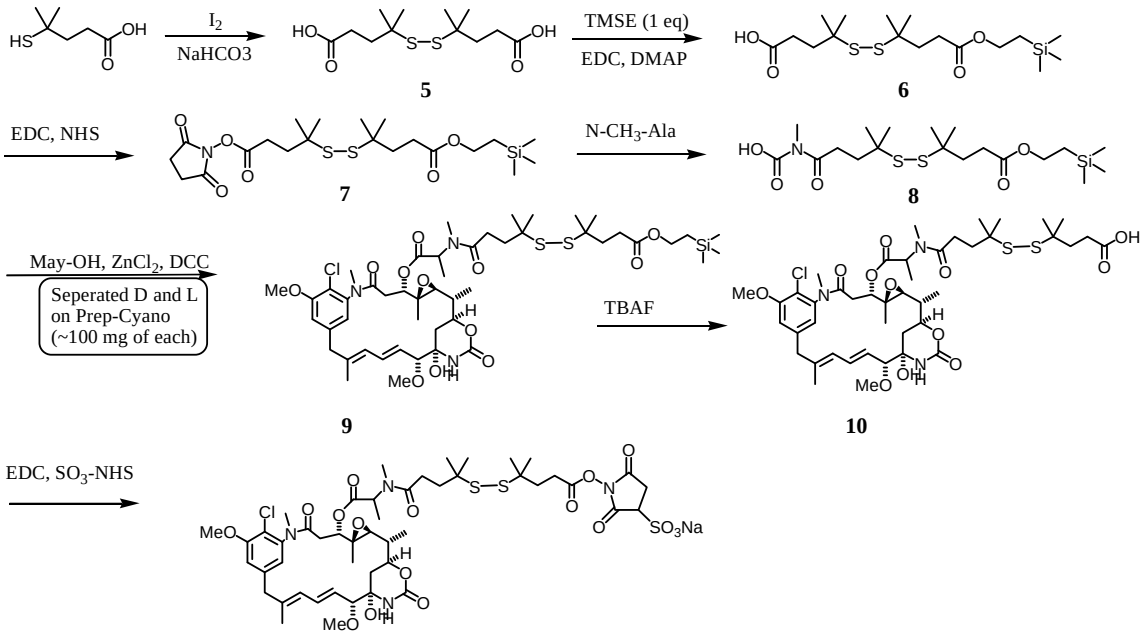
$N^{2'}$-Deacetyl-$N^{2'}$-[3-(3-carboxy-1,1-dimethyl-propyl-dithio)-1-oxopropyl]-maytansine (3). $N^{2'}$-deacetyl-$N^{2'}$-[3-(5-nitropyridine-2-dithio)-1-oxopropyl]-maytansine (60 mg, 0.067 mmol) was dissolved in *N,N*-dimethylformamide (1.0 mL) and 50 mM potassium phosphate buffer pH 7.5 (0.80 mL) to which a solution of 4-mercapto-4-methyl pentanoic acid (*1*) (22 mg, 0.149 mmol) in tetrahydrofuran (0.22 mL) was added dropwise. After 1 h the solution was purified by preparative reverse phase HPLC on a waters C8 symmetry shield 5 μm column (19 x 100 mm) at ambient temperature using a 19 mL/min flow rate, eluting with a linear gradient of acetonitrile (5% to 95% over 30 min) in deionized water containing 0.2% formic acid; the desired product eluted at 22 min. Product containing fractions were combined and solvent was removed under vacuum to give 50 mg (84% yield) of product. ^{1}H NMR(400 MHz, $CDCl_3$) δ 6.81-6.83 (1H, m), 6.64-6.68 (1H, m), 6.55-6.62 (2H, m), 6.47 (1H, dd, *J* = 11,15 Hz), 5.60-5.69 (1H, m), 5.17-5.25 (1H, m), 4.81 (1H, dd, *J* = 3, 12 Hz), 4.32 (1H, t, *J* = 10 Hz), 3.98 (3H, s), 3.63 (1H, d, *J* = 12 Hz), 3.48 (1H, d, *J* = 9 Hz), 3.36 (3H, s), 3.23 (3H, s), 3.08-3.14 (1H, m), 2.91-3.0 (2H, m), 2.90 (3H, s), 2.71-2.88 (1H, m), 2.57-2.70 (2H, m), 2.30-2.40 (2H, m), 2.22 (1H, m), 1.80-1.92 (1H, m), 1.64 (3H, s), 1.49-1.61 (1H, m), 1.20-1.40 (18H, m), 0.80 (3H, s).

***N*-sulfosuccinimidyl ester of $N^{2'}$-Deacetyl-$N^{2'}$-[3-(3-carboxy-1,1-dimethyl-propyl-dithio)-1-oxopropyl]-maytansine (4).** To a 2.0 mL vial was added $N^{2'}$-Deacetyl-$N^{2'}$-[3-(3-carboxy-1,1-dimethyl-propyl-dithio)-1-oxopropyl]-maytansine (10 mg, 0.011 mmol) and *N*-hydroxysulfosuccinimide sodium salt (4 mg, 0.018 mmol) suspended in anhydrous dimethyl formamide (140 μL) to which was added a solution of dicyclohexylcarbodiimide (5 mg, 0.027 mmol) in anhydrous *N,N*-dimethylformamide (60 μL). After 16 h the mixture was passed through a glass wool plug into a 500 μL capacity test tube and 2-propanol (250 μL) was added with mixing. The resulting precipitate was centrifuged to give a pellet and supernatant was removed by aspiration. The pellet was re-suspended in 2-propanol (200 μL) then centrifuged and supernatant was removed by

aspiration. The pellet was dried by vacuum centrifugation to give 10.8 mg (91% yield) which was used without further treatment. MS $(M - Na)^-$ for $C_{45}H_{60}ClN_4NaO_{17}S_3$ calculated 1059.3, found 1059.3.

SYNTHESIS OF SULFO-NHS-SMPP-DM4.

Scheme 2. Preparation of sulfo-NHS ester of $N^{2'}$-Deacetyl-$N^{2'}$-(4-methyl-4-(2-methyl-5-carboxy)pentan-2-yl)disulfanyl)pentanoyl)-maytansine (sulfo-NHS-SMPP-DM4).



4,4'-disulfanediylbis(4-methylpentanoic acid) (5). In a 250 ml round bottom flask was added 4-Mercapto-4-methylpentanoic acid[1] (2 g, 13.5 mmol) dissolved in ethyl acetate (25 mL) and to this stirring solution was added a 10% aqueous solution of sodium bicarbonate (25 mL). A solution of concentrated iodine in ethyl acetate was added dropwise until the color persisted (change from yellow to a burnt amber, ~35 mL). The solution was allowed to stir an additional 30 minutes to ensure that the color persists. The aqueous layer was then removed and a fresh aqueous solution containing 10 ml of 10% sodium bicarbonate and 15 ml of water was added to the ethyl acetate layer and stirred an additional 30 minutes. The aqueous layer was removed and the combined

aqueous layers were extracted with ethyl acetate (2 x 50 mL) and separated. The aqueous layer was then acidified with concentrated hydrochloric acid (~10 mL) and extracted with ethyl acetate (2 x 50 mL). The combined organic layers were then washed with brine (2 x 50 mL), dried over anhydrous sodium sulfate, filtered, and concentrated to give 4,4'-disulfanediylbis(4-methylpentanoic acid) (1.8 g, 90%) as a yellow solid. ^{1}H NMR (400 MHz, $CDCl_3$): δ 11.30 (br. S, 2H), 2.46 (t, 4H, *J* = 8.0 Hz), 1.88 (t, 4H, *J* = 8.0 Hz), 1.26 (s, 12H).

4-methyl-4-((2-methyl-5-oxo-5-(2-(trimethylsilyl)ethoxy)pentan-2yl disulfanyl) pentanoic acid (6). 4,4'-disulfanediylbis(4-methylpentanoic acid) (1.0 g, 3.4 mmol) was dissolved in methylene chloride (18 mL) and pyridine (2 mL) with stirring. To this solution was added 2-(trimethylsilyl)ethanol (0.14 mL, 1.0 mmol), dimethyl-aminopyridine (0.065 g, 0.5 mmol), and *N*-(3-Dimethylaminopropyl)-*N′*-ethylcarbodiimide (0.340 g, 2 mmol) and the resulting mixture was allowed to stir at room temperature for 2.5 hours. The reaction was then quenched with hydrochloric acid (1.0 N, 15 mL) to a pH of 3-4 and then extracted with methylene chloride (2 x 30 mL). The combined organic layers were washed with brine (2 x 50 mL), dried over anhydrous sodium sulfate, filtered, and concentrated. The residue was purified on silica gel eluting with 35% ethyl acetate in hexane which contained 1% acetic acid to give 4-methyl-4-((2-methyl-5-oxo-5-(2-(trimethylsilyl)ethoxy)pentan-2-yl)disulfanyl)pentanoic acid (0.25 g, 42% based on recovered starting material (0.550 g)). ^{1}H NMR (400 MHz, $CDCl_3$): δ 9.5 (br s, 1H), 4.11 (t, 2H, *J* = 6.8 Hz), 2.45 (t, 2H, *J* = 8.0 Hz), 2.35 (t, 2H, *J* = 8.0 Hz), 1.88 (m, 4H), 1.23 (s, 12H), 0.94 (t, 2H, *J* = 6.8 Hz), 0.00 (s, 9H).

NHS ester of 4-methyl-4-((2-methyl-5-oxo-5-(2-(trimethylsilyl)ethoxy)pentan-2-yl)disulfanyl)pentanoate (7). 4-methyl-4-((2-methyl-5-oxo-5-(2 (trimethylsilyl)ethoxy)-pentan-2-yl)disulfanyl)pentanoic acid (0.260 g, 0.66 mmol) was dissolved in methylene chloride (4 mL) and to this solution was added *N*-Hydroxysuccinimide (0.095 g, 0.825 mmol), and *N*-(3-Dimethylaminopropyl)-*N′*-ethylcarbodiimide (0.157 g, 0.825 mmol) and the reaction was allowed to stir at room temperature with monitoring. After 2 hours an additional portion of *N*-Hydroxysuccinimide and *N*-(3-Dimethylaminopropyl)-*N′*-

ethylcarbodiimide (0.15 eq of each) was added and the reaction stirred an additional hour. The reaction was then concentrated, dissolved in ethyl acetate (25 mL) and extracted with 50 mM potassium phosphate buffer (pH 6.0, 25 mL) and brine (25 mL), dried over anhydrous sodium sulfate, filtered, and concentrated. The residue was loaded onto a silica gel column eluting with 50% ethyl acetate in hexane and fractions containing the desired product were pooled and concentrated to give the NHS ester of 4-methyl-4-((2-methyl-5-oxo-5-(2-(trimethylsilyl)ethoxy)pentan-2-yl)disulfanyl)pentanoate (0.285 g, 88%). ^{1}H NMR ($CDCl_3$): δ 4.11 (t, 2H, *J* = 8.4 Hz), 2.79 (s, 4H), 2.69 (t, 2H, *J* = 8.4 Hz), 2.35 (t, 2H, *J* = 8.0 Hz), 1.94 (t, 2H, *J* = 8.0 Hz), 1.84 (t, 2H, *J* = 8.4 Hz), 1.26 (s, 6H), 1.23 (s, 6H), 0.94 (t, 2H, *J* = 8.4 Hz), 0.00 (s, 9H).

methyl(4-methyl-4-((2-methyl-5-oxo-5-(2-(trimethylsilyl)ethoxy)pentan-2-yl)disulfanyl)pentanoyl)carbamic acid (8). *N*-methyl-alanine (0.087 g, 0.84 mmol) was dissolved in a 1:1 mixture of *N*,*N*-Dimethylformamide and water (7 mL) and next triethylamine was added (0.156 mL, 1.12 mmol). To this mixture was added dropwise a solution of the NHS ester of 4-methyl-4-((2-methyl-5-oxo-5-(2-(trimethylsilyl) ethoxy)pentan-2-yl)disulfanyl)pentanoate (0.275 g, 0.56 mmol) in *N*,*N*-Dimethyl-formamide (4 mL) and the reaction mixture was allowed to stir for 3 hours at room temperature. The reaction was quenched by adding 3M hydrochloric acid until the pH reached ~2 and the reaction was then diluted with ethyl acetate (25 mL) and washed with hydrochloric acid (1M, 25 mL), then brine (25 mL). The combined organic layers were washed with ethyl acetate (2 x 25 mL) and the combined organic layers were dried over anhydrous sodium sulfate, filtered, and concentrated in vacuo. The residue was purified on silica gel using 75% ethyl acetate in hexane containing 1% acetic acid and fractions containing the desired product were pooled and concentrated to give methyl(4-methyl-4-((2-methyl-5-oxo-5-(2-(trimethylsilyl)ethoxy)pentan-2-yl)disulfanyl)pentanoyl)carbamic acid (0.240 g, 90%). ^{1}H NMR (400 MHz, $CDCl_3$): δ 10.57 (br s, 1H), 4.12 (t, 2H, *J* = 8.4 Hz), 2.96 (s, 4H), 2.45 (m, 2H), 2.36 (t, 2H, *J* = 8.4 Hz), 1.84 (m, 4H), 1.26 (s, 6H), 1.22 (s, 6H), 0.94 (t, 2H, *J* = 8.4 Hz), 0.00 (s, 9H).

$N^{2'}$-Deacetyl-$N^{2'}$-(4-methyl-4-((2-methyl-5-oxo-5-(2-(trimethylsilyl)ethoxy)pentan-2-yl)disulfanyl)pentanoyl)-maytansine (9). Maytansinol (0.150g, 0.27 mmol) was dissolved in methylene chloride (4 mL) and cooled to 0^{o} in an ice bath. A solution of methyl(4-methyl-4-((2-methyl-5-oxo-5-(2-(trimethylsilyl)ethoxy)pentan-2-yl)disulfanyl)pentanoyl)carbamic acid (0.325 g, 0.69 mmol) dissolved in methylene chloride (3 mL) was added dropwise to the cold maytansinol solution followed by a solution of *N,N'*-Dicyclohexylcarbodiimide (0.341 g, 6.6 mmol) dissolved in methylene chloride (4 mL). After one minute a 1.0 M solution of zinc chloride in diethyl ether (0.195 mL) was added and the ice bath was removed and the reaction allowed to stir for an additional two hours. The reaction was then diluted with ethyl acetate (25 mL) and passed through a glass wool plug to remove any residual solids. Concentrated aqueous sodium bicarbonate (25 mL) was added and the mixture was extracted with ethyl acetate (3 x 25 mL) and the combined organic layers were washed with brine, dried over anhydrous sodium sulfate, filtered, and concentrated in vacuo. The residue was purified by reverse phase HPLC using a preparative Cyano column (250 x 50 mm) at 118 mL/min with an isocratic elution of 68% hexane, 24% ethyl acetate, and 8% isopropanol to give both the purified L- (0.110 g) and D- (0.115 g) isomers of *$N^{2'}$*-Deacetyl-*$N^{2'}$*-(4-methyl-4-((2-methyl-5-oxo-5-(2-(trimethylsilyl)ethoxy)pentan-2-yl)disulfanyl)pentanoyl)-maytansine. ^{1}H NMR (400 MHz, $CDCl_3$): δ 6.81 (s, 1H), 6.76 (d, 1H, *J* = 11.2 Hz), 6.62 (s, 1H), 6.42 (dd, 1H, *J* = 11.2, 15.2 Hz), 6.22 (s, 1H), 5.68 (dd, 1H, *J* = 9.2, 15.2 Hz), 5.42 (q, 1H, *J* = 6.9 Hz), 4.77 (dd, 1H, *J* = 2.8, 12.0 Hz), 4.26 (t, 1H, *J* = 10.4 Hz), 4.14 (t, 2H, *J* = 8.4 Hz), 3.97 (s, 3H), 3.66 (d, 1H, *J* = 12.4 Hz), 3.49 (d, 1H, *J* = 9.2 Hz), 3.45 (s, 3H), 3.25 (s, 3H), 3.10 (d, 1H, *J* = 12.8 Hz), 3.04 (d, 1H, *J* = 9.2 Hz), 2.84 (s, 3H), 2.27-2.64 (m, 3H), 2.16 (dd, 1H, *J* = 2.8, 14.4 Hz), 1.75-1.88 (m, 4H), 1.63 (s, 3H), 1.56 (d, 1H, *J* = 13.2 Hz), 1.42-1.47 (m, 1H), 1.15-1.29 (m, 21H), 0.96 (t, 2H, *J* = 8.8 Hz), 0.79 (s, 3H), 0.04 (s, 9H). MS $(M + Na)^{+}$ for $C_{49}H_{76}ClN_3O_{12}S_2Si$: calculated 1025.4, found 1048.5.

L-$N^{2'}$-Deacetyl-$N^{2'}$-(4-methyl-4-(2-methyl-5-carboxy)pentan-2-yl)disulfanyl) pentanoyl)-maytansine (10). In a small vial dissolved *L-$N^{2'}$*-Deacetyl-*$N^{2'}$*-(4-methyl-4-((2-methyl-5-oxo-5-(2-(trimethylsilyl)ethoxy)pentan-2-yl)disulfanyl)pentanoyl)

maytansine (0.028 g, 0.0276 mmol) in anhydrous tetrahydrofuran (1.0 mL) and to this solution was added a 1.0M solution of Tetrabutylammonium fluoride in tetrahydrofuran (0.055 mL, 0.055 mmol) and the raction monitored by TLC. After 30 minutes the reaction was quenched with concentrated aqueous ammonium chloride (5 mL) and extracted into ethyl acetate (10 mL). The organic layer was separated and washed with brine, dried over anhydrous sodium sulfate, filtered and concentrated in vacuo. The residue was purified on silica preparative TLC by developing using 5% methanol, 2% acetic acid, and 93% methylene chloride. The band containing the desired product was scraped and filtered using the same ratio of solvents used to develop the plate to give *N*$^{2'}$-Deacetyl-*N*$^{2'}$-(4-methyl-4-(2-methyl-5-carboxy)pentan-2-yl)disulfanyl)pentanoyl)-maytansine (0.013 g, 82% based on recovered starting material (0.010 g)). MS (M + Na)$^+$ for $C_{44}H_{64}ClN_3O_{12}S_2$: calculated 925.4, found 948.3.

***N*-sulfosuccinimidyl ester of N$^{2'}$-Deacetyl-N$^{2'}$-(4-methyl-4-(2-methyl-5-carboxy)pentan-2-yl)disulfanyl)pentanoyl)-maytansine (11).** In a small vial *N*$^{2'}$-Deacetyl-*N*$^{2'}$-(4-methyl-4-(2-methyl-5-carboxy)pentan-2-yl)disulfanyl)pentanoyl)-maytansine (0.016 g, 0.0173 mmol) and a stir bar were added followed by the addition of *N*-Hydroxysulfosuccinimide sodium salt (0.094 g, 0.043 mmol) dissolved in *N*,*N*-Dimethylformamide (1 mL). After allowing this solution to stir for 5 minutes a solution of *N*,*N'*-Dicyclohexylcarbodiimide (0.009 g, 0.043 mmol) in *N*,*N*-Dimethylformamide (0.5 mL) was added and the reaction was wrapped in aluminum foil and allowed to stir at room temperature overnight. The mixture was concentrated in vacuo to a volume of ~0.3 mL and the mixture passed through a short plug of wool to remove the precipitate that had formed. The mixture was next diluted with isopropanol (1.5 mL) giving a cloudy mixture which was shaken, cooled in a dry ice acetone bath for 30 seconds, and centrifuged. The isopropanol was pipetted off and diethyl ether (1.0 mL) was next added to the residue and the mixture shaken, cooled, and centrifuged again. The diethyl ether was then pipetted off and the remaining residue placed under vacuum. The Sulfo-NHS ester of *N*$^{2'}$-Deacetyl-*N*$^{2'}$-(4-methyl-4-(2-methyl-5-carboxy)pentan-2-yl)disulfanyl)pentanoyl)-maytansine (9.2 mg) thus obtained was monitored by HPLC and

found to be 95% pure and was used as such without any further purification. MS (M – Na)$^-$ for $C_{48}H_{66}ClN_4NaO_{17}S_3$: calculated 1124.3, found 1101.4.

REFERENCES

(1) Widdison W.C., Wilhelm S.D., Cavanagh E.E., Whiteman K.R., Leece B.A., Kovtun Y., Goldmacher V.S., Xie H., Steeves R.M., Lutz R.J., Zhao R., Wang L., Blättler W.A., and Chari R.V. (2006) Semisynthetic maytansine analogues for the targeted treatment of cancer. *J. Med. Chem. 49,* 4392-4408.

Bioconjugate Chemistry

ARTICLE

pubs.acs.org/bc

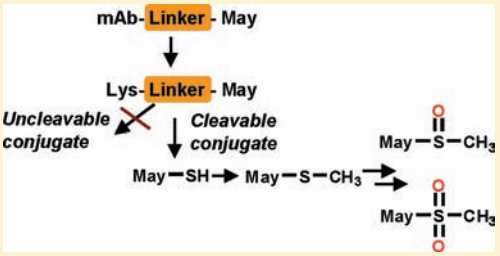
Design of Antibody−Maytansinoid Conjugates Allows for Efficient Detoxification via Liver Metabolism

Xiuxia Sun, Wayne Widdison, Michele Mayo, Sharon Wilhelm, Barbara Leece, Ravi Chari, Rajeeva Singh, and Hans Erickson*

ImmunoGen, Inc., 830 Winter Street, Waltham, Massachusetts 02451, United States

Supporting Information

ABSTRACT: Antibody−maytansinoid conjugates (AMCs) are targeted chemotherapeutic agents consisting of a potent microtubule-depolymerizing maytansinoid (DM1 or DM4) attached to lysine residues of a monoclonal antibody (mAb) using an uncleavable thioether linker or a stable disulfide linker. Most of the administered dose of an antibody-based therapeutic is slowly catabolized by the liver and other tissues of the reticuloendothelial system. Maytansinoids released from an AMC during this catabolic process could potentially be a source of toxicity. To investigate this, we isolated and identified liver metabolites in mice for three different [^{3}H]AMCs with structures similar to those currently undergoing evaluation in the clinic. We then synthesized each metabolite to confirm the identification and assessed their cytotoxic potencies when added extracellularly. We found that the uncleavable mAb-SMCC-[^{3}H]DM1 conjugate was degraded to a single major maytansinoid metabolite, lysine-SMCC-[^{3}H]DM1, that was nearly 50-fold less cytotoxic than maytansine. The two disulfide-linked conjugates, mAb-SPP-[^{3}H]DM1 and mAb-SPDB-[^{3}H]DM4, were also found to be catabolized to the analogous lysine-linked maytansinoid metabolites. However, subsequent reduction, *S*-methylation, and NADPH-dependent oxidation steps in the liver yielded the corresponding *S*-methyl sulfoxide and *S*-methyl sulfone derivatives. The cytotoxic potencies of the oxidized maytansinoids toward several human carcinoma cell lines were found to be 5- to 50-fold less potent than maytansine. Our results suggest that liver plays an important role in the detoxification of both cleavable and uncleavable AMCs.



INTRODUCTION

Antibody−drug conjugates (ADCs) are targeted chemotherapeutic agents that utilize the specificity of monoclonal antibodies (mAb) to deliver potent cell killing agents to cancer cells that express the target antigen.[1−3] Several antibody maytansinoid conjugates (AMCs) that utilize the tubulin-targeting maytansinoid thiols, $N^{2'}$-Deacetyl-$N^{2'}$-(3-mercapto-1-oxopropyl)-maytansine (DM1) and $N^{2'}$-Deacetyl-$N^{2'}$-(4-mercapto-4-methyl-1-oxopentyl)-maytansine (DM4), are currently being evaluated in clinical trials. The most advanced of these conjugates, trastuzumab-SMCC-DM1 (T-DM1), is in multiple advanced clinical trials for the treatment of HER-2 positive metastatic breast cancer.[4] Two other AMCs, SAR3419 (huB4-SPDB-DM4) and lorvotuzumab mertansine (huN901-SPP-DM1), have both shown promising results in early clinical trials for the treatment of B-cell malignancies and for treating solid and liquid tumors that express CD19 and CD56, respectively.[5,6] Three additional AMCs are in phase I testing.[7−9]

The AMCs currently in the clinic utilize three different linkers to attach the maytansinoid (DM1 or DM4) to a tumor-specific humanized antibody (Figure 1). T-DM1 utilizes an uncleavable thioether linker while the other candidates utilize disulfide linkers (Figure 1). During the preclinical evaluation of each AMC, conjugates with the different linkers were prepared and evaluated. The AMC that was found to yield the widest therapeutic window—as defined by the difference between the minimally effective dose (MED) in mouse xenografts models and the maximum tolerated dose (MTD)—was selected. In the majority of cases, preclinical evaluation of the disulfide-linked AMCs were found to yield the widest therapeutic window,[6−8,10] despite their having an MTD that was about 2-fold lower than that of the uncleavable versions.[11] An exception to these findings was the uncleavable T-DM1 conjugate that was found to be slightly more active in mouse xenograft models than several disulfide-linked versions.[11]

Several studies point to enhanced bystander killing of the disulfide-linked conjugates as a possible explanation for their typically greater activity when compared with uncleavable conjugates in mouse xenograft models.[10,12,13] Internalization and lysosomal processing of the uncleavable conjugate in targeted cancer cells yields the lysine-SMCC-DM1 metabolite. While this metabolite is highly cytotoxic to the targeted cell in which it is formed, it is unable to penetrate and kill neighboring "bystander" tumor cells. Internalization and lysosomal processing of the disulfide-linked conjugates yields the analogous lysine-linker-maytansinoid derivatives. However, additional intracellular

Received: November 15, 2010
Revised: January 26, 2011
Published: March 10, 2011

ACS Publications © 2011 American Chemical Society

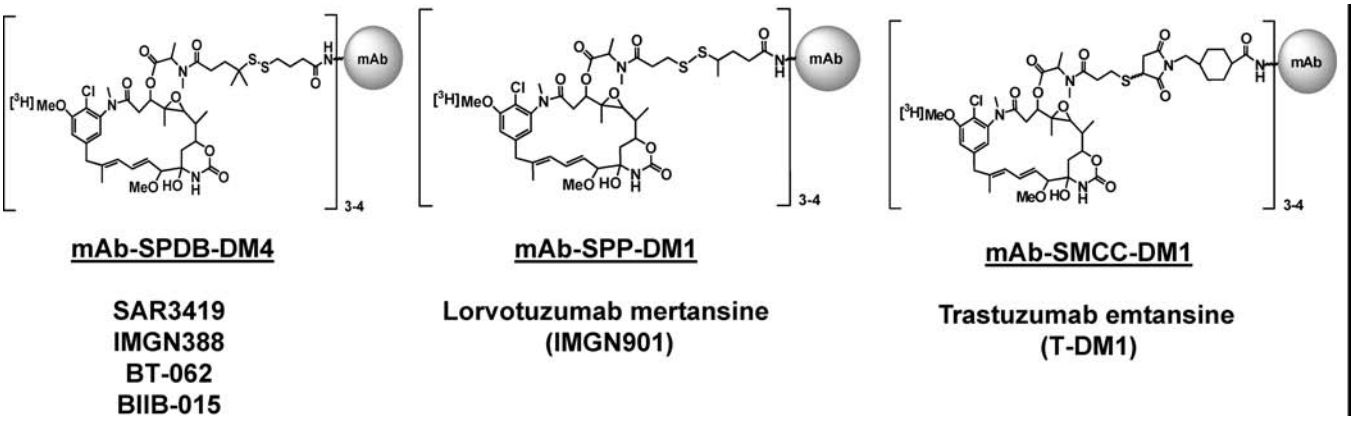


Figure 1. Structures of antibody−maytansinoid conjugates prepared for the current study. Tritium was incorporated into the C-20 methoxy group to allow for the detection of maytansinoid metabolites. Antibody-maytansinoid conjugates currently under clinical evaluation with similar structures that lack this tritium label are listed.

reduction and *S*-methylation steps yield hydrophobic maytansinoid derivatives that are potentially able to diffuse throughout the tumor, reaching tumor cells that would otherwise not accumulate sufficient maytansinoid to kill them due to low expression of the target antigen or inaccessibility to the conjugate. These diffusible metabolites may also increase the toxicity of the disulfide-linked conjugates by exposing healthy tissues to free maytansinoids. Significant levels of the catabolites would be expected to form in the liver which is known to be the primary site of antibody catabolism.[14,15] Other tissues of the reticuloendothelial system (RES) constitute additional potential catabolic sites for AMCs. Maytansinoid catabolites formed in these other tissues would ultimately be cleared through the liver since excretion studies have found liver to be the major route of AMC clearance (unpublished data). Given this central role of liver in antibody catabolism and clearance of AMCs, we set out to characterize the major maytansinoid catabolites and metabolites of the uncleavable mAb-SMCC-DM1 conjugate and the cleavable mAb-SPP-DM1 and mAb-SPDB-DM4 conjugates. Our findings suggest that catabolism and liver metabolism plays an essential role in limiting the potential toxicity of AMCs.

EXPERIMENTAL PROCEDURES

Reagents. RPMI 1640 and glutamine were from Cambrex Bioscience. Ultima Flo M scintillation fluid and Solvable were from PerkinElmer Life and Analytical Sciences. All cells were obtained from the American Type Culture Collection. All chemicals were obtained from Sigma Aldrich. The Gemini 5 μm C-18 column (0.46 × 25 cm) was obtained from Phenomenex and the 5 μm C8 column (150 × 2.1 mm) from Kromasil. The ULTRA-TURRAX T8 dispersing instrument with a S8N dispersing tool was obtained from IKA Works Inc. All antibody−maytansinoid conjugates were prepared at ImmunoGen from humanized anti-CD56 mAb, huN901[16] using methods described elsewhere by Widdison et al.[17] The linkers *N*-succinimidyl 4-(*N*-maleimidomethyl) cyclohexane-1 carboxylate (SMCC), *N*-succinimidyl 4-(2-pyridyldithio)butyrate (SPDB), and *N*-succinimidyl 4-(2-pyridyldithio) pentanoate (SPP), are all *N*-hydroxysuccinimide esters that react with amino groups of the protein. The ratio of linked maytansinoid molecules per antibody molecule (D/A) and the specific radioactivities for each conjugate was as follows: huN901-SPP-[^{3}H]DM1 (3.5 D/A, 852 mCi/mmol DM1), huN901-SMCC-[^{3}H]DM1 (3.6 D/A, 284 mCi/mmol DM1), and huN901-SPDB-[^{3}H]DM4 (2.9 D/A, 300 mCi/mmol DM4). The maytansinoid metabolites—lysine-N^{ϵ}-SPP-DM1, lysine-N^{ϵ}-SMCC-DM1, DM1-SMCC, lysine-N^{ϵ}-SPDB-DM4, *S*-methyl-DM1, *S*-methyl-DM4-sulfoxide, *S*-methyl-DM1 sulfoxide, and *S*-methyl-DM4 sulfone were synthesized at ImmunoGen (manuscript in preparation). The DM1, DM4, and *S*-methyl-DM4 were prepared as previously described.[17]

In Vitro Cell Proliferation Assays. The cytotoxic potencies of the maytansinoids toward human carcinoma cell lines were assessed using a WST-based cell viability assay. Cells were seeded in 96-well flat-bottom plates at a density of 1000 cells/well for A375, BJAB, COLO 205, and KB, and 5000 cells/well for MOLT-4. Dilutions of the AMC or free maytansinoid solutions were added to cells and incubated for 5 days at 37 °C with 6% CO_2. The WST-8 agent was added and developed for 1 h for A375, COLO 205, and KB, and 2 h for BJAB and MOLT-4. Surviving fractions of cells were plotted versus conjugate or maytansinoid concentrations for determining IC_{50} values.

Mouse Studies. Female CD-1 mice were obtained from Charles River Laboratory (Raleigh, North Carolina). Mice were intravenously injected with a bolus of 300 μg/kg (based on DM1 or DM4) of the conjugates or 1 mg/kg of free [^{3}H]DM4 or [^{3}H]DM1. Two mice were sacrificed at each of the designated time points following treatment. The gall bladder containing the bile was collected from the mice treated with [^{3}H]DM4 and [^{3}H]DM1 and frozen at −80 °C. After bile collection, the systemic circulation was flushed by injecting 5 mL PBS into the left ventricle and draining through an incision in the inferior vena cava. The whole liver tissues were collected in 50 mL preweighed polypropylene tubes and frozen at −80 °C.

Extraction of [^{3}H]Maytansinoid Metabolites from Liver Tissue. The liver tissues were thawed on ice, cut into small pieces, and homogenized with five volumes (v/w) 10 mM Tris-HCl buffer, pH 7.5 containing 5 mM *N*-ethylmaleimide (NEM). The NEM was added to prevent thiol/disulfide exchange reactions during the workup by capping the thiol groups. The homogenates were placed on ice for 2 h to ensure complete alkylation, and then a portion of each homogenate (0.4 mL) was added to a 20 mL glass scintillation vial. The radioactivity associated with each homogenate was determined after solubilization with Solvable as described for tumor homogenates

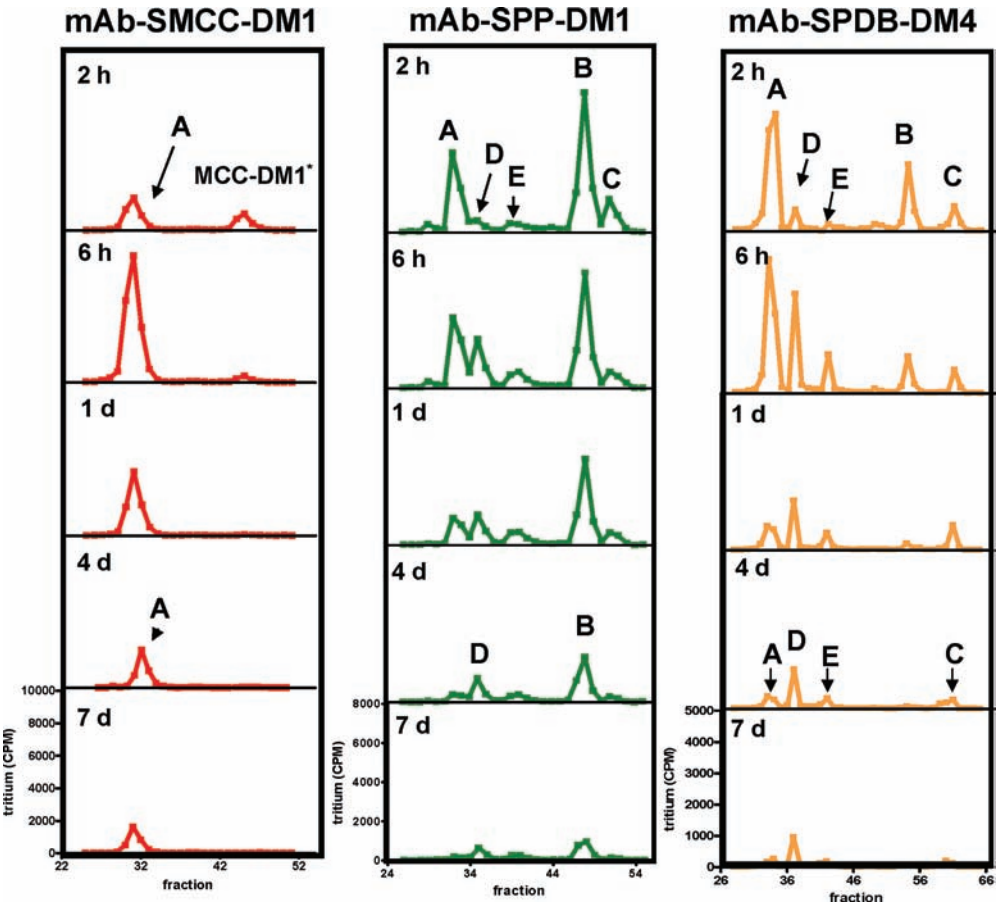


Figure 2. Maytansinoid metabolites of cleavable and uncleavable [^{3}H]AMCs formed in liver over time. Mice (n = 10) were treated with a single 300 μg/kg dose (based on DM1 or DM4) of mAb-SMCC-[^{3}H]DM1, mAb-SPP-[^{3}H]DM1, or mAb-SPDB-[^{3}H]DM4, and two mice from each group were sacrificed after 2 h, 6 h, 1 d, 4 d, and 7 d and liver tissues samples were collected. Liver tissues were homogenized and portions of the homogenates were extracted and analyzed for ^{3}H-maytansinoid metabolites by HPLC. The effluent from the samples was collected in 0.5 mL fractions, and the radioactivity corresponding to each fraction was determined by LSC. Alternatively, fractions in duplicate runs corresponding to the tritium peaks were analyzed by LC/MS for metabolite identification. The chromatograms show the fraction number on the abscissa and the counts per minute of tritium (CPM) on the ordinate. The sole metabolite (A) of the uncleavable conjugate is lysine-SMCC-DM1. The five metabolites for mAb-SPP-DM1 are lysine-SPP-DM1(A), DM1 (B), *S*-methyl-DM1 (C), *S*-methyl-DM1 sulfoxide (D), and *S*-methyl-DM1 sulfone (E). The corresponding five metabolites of mAb-SPDB-DM4 (lysine-SPDB-DM4, DM4, *S*-methyl-DM4, *S*-methyl-DM4 sulfoxide, and *S*-methyl-DM4 sulfone) are also denoted A−E.

previously.[18] [^{3}H]Maytansinoid metabolites were extracted by the procedure described previously with slight modifications.[18] Aliquots of the homogenates (0.4 mL) were extracted three times with 3.4 volumes of ethyl acetate/methanol (7.5:1, v/v), and the pooled extracts were evaporated to dryness in an evacuated centrifuge. The dried extracts were dissolved in 0.12 mL of 20% aqueous acetonitrile containing 0.025% trifluoroacetic acid (TFA) and 25 mM catechol (to prevent oxidation), and the metabolites were separated by reversed-phase HPLC. In separate experiments, we found that 83% of the synthetic standard, *S*-methyl-[^{3}H]DM1, could be recovered from the liver homogenate using this method. In addition, extracts from fresh liver homogenates mixed with mAb-SPDB-[^{3}H]DM4 were found to contain none of the metabolites, indicating that the ex vivo workup released no artifacts (data not shown). The radioactivity associated with the metabolites in Figure 2 was converted to pmol/g of metabolite using the specific radioactivity of the DM1 and DM4 and the measured liver weights. The values were multiplied by 1.2 to account for the extraction efficiency (83%) of the synthetic *S*-methyl-[^{3}H]DM1.

Extraction of [^{3}H]Maytansinoid Metabolites from Bile. The gall bladder containing the bile was mixed with 20% aqueous acetonitrile containing 5 mM NEM (0.12 mL), vortexed, and allowed to sit for 30 min to ensure complete alkylation of thiol groups. The debris was removed from the samples by sedimentation (13 000*g*, 5 min) and the supernatants were analyzed for metabolites by HPLC and liquid scintillation counting.

Analytical Methods. All maytansinoids were separated on a Gemini 5 μm C-18 column (0.46 × 25 cm) equilibrated with 20% aqueous CH_3CN containing 0.025% TFA. The chromatogram was developed with a 1 min hold at 20% aqueous CH_3CN containing 0.025% TFA, followed by a linear gradient of 2% CH_3CN/min for 15 min, and then 1% CH_3CN/min for 20 min with a flow rate of 1 mL/min. The effluent was collected in 0.5 mL fractions. Tritium (cpm) associated with each fraction was determined by mixing each vial (0.5 mL) with 4 mL Ultima Gold liquid scintillation cocktail and counting for 5 min in a Tri-Carb 2900T liquid scintillation counter. Alternatively, fractions in duplicate runs corresponding to the peaks of tritium were evaporated to dryness, dissolved in 0.02 mL 50% aqueous CH_3CN, and

dx.doi.org/10.1021/bc100498q |*Bioconjugate Chem.* 2011, 22, 728–735

analyzed for maytansinoids by liquid chromatography mass spectrometry (LC/MS). The [^{3}H]-maytansinoid metabolites were separated on a 5 μm C-8 column (150 × 2.1 mm) equilibrated with 15% aqueous CH_3CN containing 0.1% TFA. The chromatogram was developed with four linear gradients: 1.1% CH_3CN/min for the first 15 min, 1.6% CH_3CN/min for 10 min, 1% CH_3CN/min for 10 min, and 1.6% CH_3CN/min for 20 min with a flow rate of 0.22 mL/min.

RESULTS

Administration of Antibody−[^{3}H]Maytansinoid Conjugates to Mice. Three different antibody maytansinoid conjugates (AMCs) with structures similar to those currently undergoing clinical evaluation were prepared for in vivo evaluation (Figure 1). The three conjugates were prepared from a humanized anti-CD56 antibody that does not cross-react with any antigen in mice, using either tritium-labeled DM1 or DM4 to enable the detection of maytansinoid metabolites.[18] Mice were administered a single intravenous dose of 300 μg/kg (based on DM1 or DM4) of each ^{3}H-conjugate, and after 2 h, 6 h, 1 d, 4 d, or 7 d, mice were sacrificed and liver tissues were collected. The liver tissues were homogenized and alkylated with NEM to prevent thiol−disufide exchange reactions, and then analyzed for metabolites following extraction as described in Experimental Procedures.

[^{3}H]Maytansinoid Metabolites. Figure 2 shows the metabolites isolated from the livers of mice treated with the three ^{3}H-conjugates. The metabolites were identified by comparing their HPLC retention times and mass spectral fragmentation patterns to synthetic standards as described previously[18] (data not shown). The major metabolite of the uncleavable mAb-SMCC-[^{3}H]DM1 in all of the samples was lysine-N^{ϵ}-SMCC-DM1, suggesting complete proteolysis of the polypeptide backbone of the antibody component to its constituent amino acids. We also recently found this lysine-linker-maytansinoid to be the major metabolite in tumor tissue following administration of the anti-CanAg targeting huC242-SMCC-[^{3}H]DM1 to SCID mice bearing CanAg positive COLO 205 tumors.[18] We did not detect any additional liver metabolites, suggesting little if any metabolism of the maytansinoid macrocycle or the thioether linker. The additional minor peak in the 2 h sample was identified as *N*2′-[3-[[1-[[4-(carboxy)cyclohexyl]methyl]-2,5-dioxo-3-pyrrolidinyl]thio]-1-oxopropyl]-*N*2′-deacetyl-maytansine (MCC-DM1, 22.5 min, M + Na = 997.4)—an unconjugated maytansinoid species present at low levels in the preadministration conjugate preparation (less than 5% of the total maytansinoid in the conjugate sample).

As was observed for the uncleavable conjugate, significant levels of the lysine-linker-maytansinoid metabolites were detected in the liver extracts from the mice treated with the disulfide-linked conjugates (peak A, Figure 2) suggesting that the initial steps for AMC metabolism are linker independent. In addition to the lysine-linker-maytansinoids, DM1, DM4 (isolated as the stable NEM-trapped adducts DM1-NEM and DM4-NEM, formed during homogenization, Figure 2, peak B), and *S*-methyl DM4 (peak C) were also found to be significant metabolites of mAb-SPP-DM1 and mAb-SPDB-DM4, respectively. All of these metabolites had been identified in extracts from cancer cells exposed to the conjugates in previous studies.[10,18] Presumably, these liver metabolites are formed by lysosomal degradation, disulfide reduction, and *S*-methylation of DM4 thiol—steps similar to those described previously for targeted cancer cells.[10]

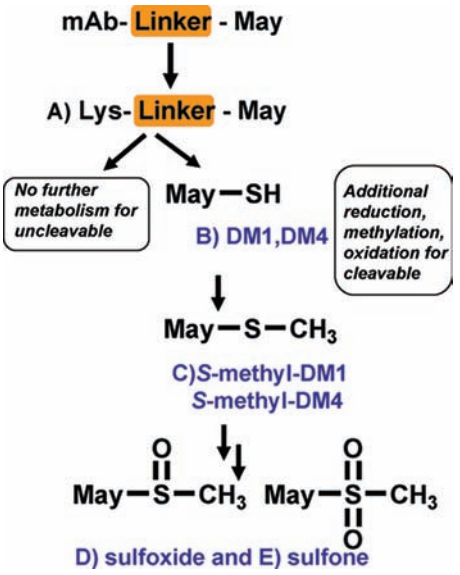


Figure 3. Scheme for the in vivo metabolism of cleavable and uncleavable AMCs. Initial catabolism of both cleavable and uncleavable conjugates yields the corresponding lysine-linker-maytansinoid (May) metabolites. For the uncleavable mAb-SMCC-DM1, the lysine-SMCC-DM1 is the only observed metabolite. For the cleavable disulfide-linked conjugates mAb-SPDB-DM4 and mAb-SPP-DM1, additional reduction yields DM4 and DM1, respectively. These free maytansinoid thiols are then methylated by an endogenous *S*-methyl transferase to form *S*-methyl-DM1 and *S*-methyl-DM4. Subsequent oxidation steps yield the corresponding sulfoxide and sulfone derivatives.

Importantly, several additional liver metabolites of the disulfide-linked conjugates were identified that were not observed in cancer cells from our prior studies. We observed *S*-methyl-DM1 from the livers of the mice treated with mAb-SPP-DM1 (peak C), which was unexpected because it was not identified as a tumor metabolite of mAb-SPP-DM1 in our previous study.[18] These observations suggest that, while the efficiency of DM1 *S*-methylation by several carcinoma cells was found to be very poor, and much lower than for DM4,[18] the liver has the capacity to more readily *S*-methylate both maytansinoid thiol compounds relative to tumor cells. The oxidized sulfoxide and sulfone derivatives of the *S*-methyl-DM1 or *S*-methyl-DM4 metabolites were also observed in the liver extracts of mice treated with the two disulfide-linked AMCs (peaks D and E in Figure 2). Ex vivo oxidation of both *S*-methyl-DM1 and *S*-methyl-DM4 to the corresponding sulfoxide and sulfone derivatives by human liver microsomes required NADPH, indicating that the oxidation was enzyme mediated (data not shown).

The metabolites of the three conjugates isolated from the liver tissues suggest the scheme for the metabolism of AMCs displayed in Figure 3 where the initial step for the catabolism of both cleavable and uncleavable AMCs is degradation of the intact conjugate to the corresponding lysine-linker-maytansinoid. For the uncleavable mAb-SMCC-DM1, no further metabolism is observed. For the cleavable conjugates, additional reduction yields the maytansinoid thiols allowing for the additional *S*-methylation and oxidation steps that ultimately yield the *S*-methyl sulfoxide and *S*-methyl-sulfone metabolites.

Exposure of Liver Tissue to Maytansinoid Metabolites. The concentration of the total metabolites of the conjugates in the liver tissue at each time (pmol/g) was determined from the

radioactivity associated with the metabolites (Figure 2) and plotted in Figure 4A. The AUCs for the metabolites of the three conjugates over 7 d were very similar, suggesting that the exposure of the liver tissue to the maytansinoid metabolites was linker independent. The fraction of the metabolite levels in Figure 4 as a percentage of total maytansinoids in the liver (intact conjugate + metabolites) was over 50% indicating that the observed metabolites represent the majority of the maytansinoids in the liver (Supporting Information Figure S1). While the exposure levels were similar for the three conjugates, the chemical structures of the metabolites of the three conjugates were notably different with the charged lysine-SMCC-DM1 as the predominant metabolite of the uncleavable conjugate and mixture of the lysine-linker-metabolite and the additional four metabolites described in Figure 3 comprising the metabolites of the disulfide linked conjugates. Differences in the distribution of the metabolites of the two disulfide-linked conjugates are evident in the radiograms shown in Figure 2. To more easily compare the metabolite distributions of the two disulfide-linked conjugates, the percentages of the total recovered metabolites of each of the five observed metabolites (calculated from Figure 2) were plotted at each time point in Figure 4B. Clear differences in the percentages for the five metabolites of the two conjugates were evident at each time point. The metabolite representing the largest fraction of the mAb-SPP-DM1 conjugate at 2 h was DM1 (34%) followed by lysine-SPP-DM1 (33%), *S*-methyl-DM1 (12%), *S*-methyl-DM1 sulfoxide (12%), and *S*-methyl-DM1 sulfone (9%). In contrast, lysine-SPDB-DM4 constituted the largest fraction of the metabolites of the mAb-SPDB-DM4 conjugate at 2 h (56%) followed by DM4 (24%), *S*-methyl-DM4 (10%), *S*-methyl-DM4 sulfoxide (7%), and *S*-methyl-DM4 sulfone (3%). The percentages for these five metabolites all change markedly over the first 24 h with decreases of the lysine-SPDB-DM4, DM4, and lysine-SPP-DM1 metabolites and increases for the sulfoxide and sulfone derivatives. From 24 h to 7 d, the metabolite percentages for all metabolites remain relatively constant even though the total metabolite levels are decreasing. The relative levels of lysine-SPP-DM1 and lysine-SPDB-DM4 versus DM1 and DM4, respectively, at the early time points (2−24 h) likely reflect the relative reactivity of the respective disulfide links to intracellular thiol−disulfide exchange reactions. Furthermore, DM1 levels may remain higher relative to DM4 levels throughout the time course (Figure 4B) if the rate of *S*-methylation of DM1 by liver cells is slower than for DM4, as described previously in human carcinoma cells.[18]

In Vitro Cytotoxic Potencies Associated with the Liver Metabolites. The metabolites reported here were all synthesized and the purified compounds were assayed for their cytotoxic potencies on a panel of tumor cell lines (Table 1). The *S*-methyl-DM1 and *S*-methyl-DM4 maytansinoids had similar potency to maytansine, and were about 1000-fold more cytotoxic than the lysine-linker-maytansinoids. Values for DM1 and DM4 are not presented because their IC_{50} values were highly variable when measured in vitro, likely due to the rapid formation of mixed disulfides via thiol/disulfide exchange reactions with cystine present at 0.2 mM in the culture medium (disulfides in serum proteins may also contribute to such reactions). The IC_{50} values for the *S*-methyl-DM1 sulfoxide were found to range from 7.1 nM to 23 nM—200- to 500-fold less potent than the *S*-methyl DM1 metabolite, whereas the *S*-methyl-DM4 sulfoxide was found to be 12- to 20-fold less cytotoxic than the *S*-methyl-DM4. The IC_{50} values for the *S*-methyl-DM1 sulfone and *S*-methyl-DM4 sulfone metabolites were 2- to 7-fold more potent than their sulfoxide precursors. That the *S*-methyl-DM4 sulfoxide is more cytotoxic than the *S*-methyl-DM1 sulfoxide toward the carcinoma cell lines is perhaps a consequence of the three extra carbons of DM4 (compared to DM1) that increase its hydrophobicity and may thus increase cell permeability. Nonetheless, the oxidation of the maytansinoid metabolites in the liver clearly serves to reduce the cytotoxic potencies of the metabolites of both disulfide-linked conjugates.

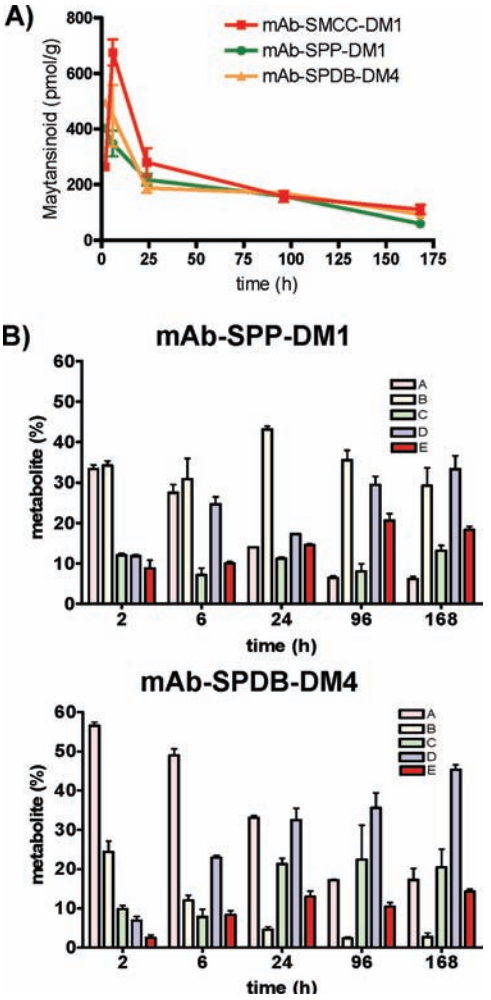


Figure 4. Exposure of liver tissue to maytansinoid metabolites in mice. (A) The levels for the total maytansinoid metabolites in liver tissue at 2 h, 6 h, 1 d, 4 d, and 7 d following a single intravenous administration of 300 μg/kg (DM1 or DM4 dose) of mAb-SMCC-[^{3}H]DM1 (■), mAb-SPP-[^{3}H]DM1 (●), and mAb-SPDB-[^{3}H]DM4 (▲). The radioactivities associated with the metabolites in Figure 2 were converted to pmol/g of metabolite using the specific radioactivities of the DM1 and DM4 and the measured liver weights as described in Experimental Procedures. (B) Amounts of the five observed metabolites of the disulfide-linked conjugates at each time as percentages of total metabolite levels. The percentages for each of the five metabolites of the two disulfide-linked conjugates were calculated by dividing the amount of each metabolite (pmol/g) by the sum of the five metabolites (shown in A). The five metabolites for mAb-SPP-DM1 are lysine-SPP-DM1(A), DM1 (B), *S*-methyl-DM1 (C), *S*-methyl-DM1 sulfoxide (D), and *S*-methyl-DM1 sulfone (E). The corresponding five metabolites of mAb-SPDB-DM4 (lysine-SPDB-DM4, DM4, *S*-methyl-DM4, *S*-methyl-DM4 sulfoxide, and *S*-methyl-DM4 sulfone) are also denoted A−E.

Table 1. Cytotoxic Potencies of Maytansinoids Towards Human Carcinoma Cell Lines in Vitro[a]

	in vitro IC_{50} (nM)				
metabolites	A375 (melanoma)	BJAB (B-cell)	COLO205 (colon)	KB (cervix)	MOLT-4 (T-cell)
Maytansine[b]	0.045	0.033	0.081	0.047	0.09
lysine-N^{ϵ}-SPP-DM1[b]	9.7	50	61	10	>100
lysine-N^{ϵ}-SPDB-DM4[b]	1.8	6.6	17	3.3	16
lysine-N^{ϵ}-SMCC-DM1[b]	8.1	7.5	17	9.7	16
S-methyl-DM1[b]	0.020	0.012	0.033	0.022	0.030
S-methyl-DM4[b]	0.017	0.014	0.031	0.026	0.027
S-methyl-DM1 Sulfoxide	9.7	7.1	17	23	19
S-methyl-DM1 Sulfone	-	1.7	5.9	3.5	-
S-methyl-DM4 Sulfoxide	0.55	0.55	1.3	0.12	1.9
S-methyl-DM4 Sulfone	0.075	0.17	0.63	0.80	1.1
DM1-MCC	22	21	50	29	50

[a] All metabolites were chemically synthesized. Cell-killing activities of the metabolites were measured after 5 days using a WST-based cell viability assay. [b] IC_{50} values were established previously[18] and shown here for comparison to liver-generated maytansinoid metabolites.

Metabolism of Intravenously Administered [^{3}H]DM4 and [^{3}H]DM1. Significant amounts of DM1, *S*-methyl-DM1, DM4, and *S*-methyl-DM4 metabolites were observed in the liver tissues up to 7 d after administration of the conjugates. If cleared from the liver without first being oxidized, these highly potent metabolites would likely be toxic to healthy tissue exposed to the metabolites during elimination. To test the efficiency of the liver oxidation, CD-1 mice were given a single dose of 1 mg/kg of unconjugated [^{3}H]DM1 or [^{3}H]DM4 (near the maximum tolerated dose), and after 1 h, mice were sacrificed and analyzed for maytansinoid metabolites in the liver tissue, bile, and plasma (Figure 5). Analysis of plasma indicated that the administered DM4 was rapidly *S*-methylated, possibly by the same *S*-methyltransferases in red blood cells shown to methylate the thiols of exogenous molecules such as penicillamine.[19] Conversely, little *S*-methyl DM1 was observed in the plasma of the mice treated with DM1—consistent with its slow rate of *S*-methylation in cancer cells. For the mice treated with DM4, nearly equivalent amounts of *S*-methyl DM4, *S*-methyl-DM4 sulfoxide, and *S*-methyl-DM4 sulfone were observed in the liver tissue after 1 h. The corresponding *S*-methyl DM1, *S*-methyl-DM1 sulfoxide, and *S*-methyl-DM1 sulfone metabolites were observed in the liver tissues of mice treated with DM1. In addition, significant levels of DM1 were observed in the liver tissues and bile—again suggesting a lower rate for the *S*-methylation of DM1 as compared to DM4. Although significant levels of the highly cytotoxic *S*-methyl DM1 and *S*-methyl-DM4 metaboiltes were observed in the liver tissues of the mice, little of the *S*-methyl maytansinoids were observed in the bile samples with nearly all of the metabolites being the *S*-methyl sulfoxide and *S*-methyl-sulfone metabolites, suggesting efficient oxidation steps prior to billiary elimination.

DISCUSSION

Our results suggest that liver plays an important role in the detoxification of both cleavable and uncleavable antibody−maytansinoid conjugates (AMCs). The lysine-SMCC-DM1 was the only metabolite observed for the noncleavable mAb-SMCC-DM1 conjugate. Significant levels were observed in the liver just 2 h following administration of the conjugates, consistent with other in vivo mouse studies that have reported efficient liver catabolism of radiolabeled antibodies[20,21] and antibody-auristatin conjugates.[22−24] The lysine-SMCC-DM1 metabolite of the uncleavable mAb-SMCC-DM1 was previously shown to have low cytotoxic potency toward human carcinoma cells in cell-based viability assays;[18] the low potency is most likely due to its inability to penetrate the cell due to the charged groups of the lysine residue. The lysine-SMCC-DM1 was found to be highly cytotoxic to the cancer cells in which it was formed following internalization and lysosomal degradation of the mAb-SMCC-DM1.[10] The lysine-SMCC-DM1 metabolite released by intracellular processing in the liver tissue could also be potentially cytotoxic. However, preclinical studies have shown the uncleavable T-DM1 conjugate to be well-tolerated at high doses (50 mg/kg) in rats,[11] and the uncleavable anti-CD79b conjugate, 10D10-SMCC-DM1, was found to be well-tolerated when administered to cynomologus monkeys at ∼30 mg/kg for two doses three weeks apart, although mild and reversible elevation of liver enzymes and minimal degeneration of hepatocytes in the monkeys was noted.[25] Furthermore, the dose-limiting toxicity observed in patients treated with T-DM1 was thrombocytopenia—no adverse liver toxicity was observed.[4] These observations suggest that the exposure of liver tissue to the lysine-SMCC-DM1 metabolite of the mAb-SMCC-DM1 conjugate reported here does not induce clinically significant liver toxicity at doses expected to be efficacious.[4,11] One factor that may contribute to the ability of liver tissue to generate and eliminate lysine-SMCC-DM1 from mAb-SMCC-DM1 conjugates without undue toxicity is that maytansinoids, as tubulin-binding agents,[26] are antimitotic and mature, fully differentiated, nondividing cells of organs such as liver may be able to tolerate significant exposure.

Analysis of the metabolites in liver tissues from mice treated with the cleavable disulfide-linked conjugates suggested the pathway for their degradation and metabolism shown in Figure 3. As was observed for the uncleavable conjugate, the two disulfide-linked conjugates were first degraded to yield the lysine-linker-maytansinoid metabolites. The amounts of these lysine-linker-maytansinoid metabolites were highest at the earliest 2 h time points. Unlike the lysine-SMCC-DM1 metabolite of the uncleavable conjugate, the lysine-SPDB-DM4 and lysine-SPP-DM1 metabolites of the disulfide-linked conjugates were found to undergo further intracellular transformations. The initial steps are similar to those described for the activation of the two conjugates in cancer cells.[18] First, the lysine-SPDB-DM4 and lysine-SPP-DM1 metabolites are reduced to DM4 and DM1, respectively, likely due to thiol−disulfide exchange reactions. Next, *S*-methylation of the released maytansinoid thiols yields *S*-methyl-DM1 and *S*-methyl-

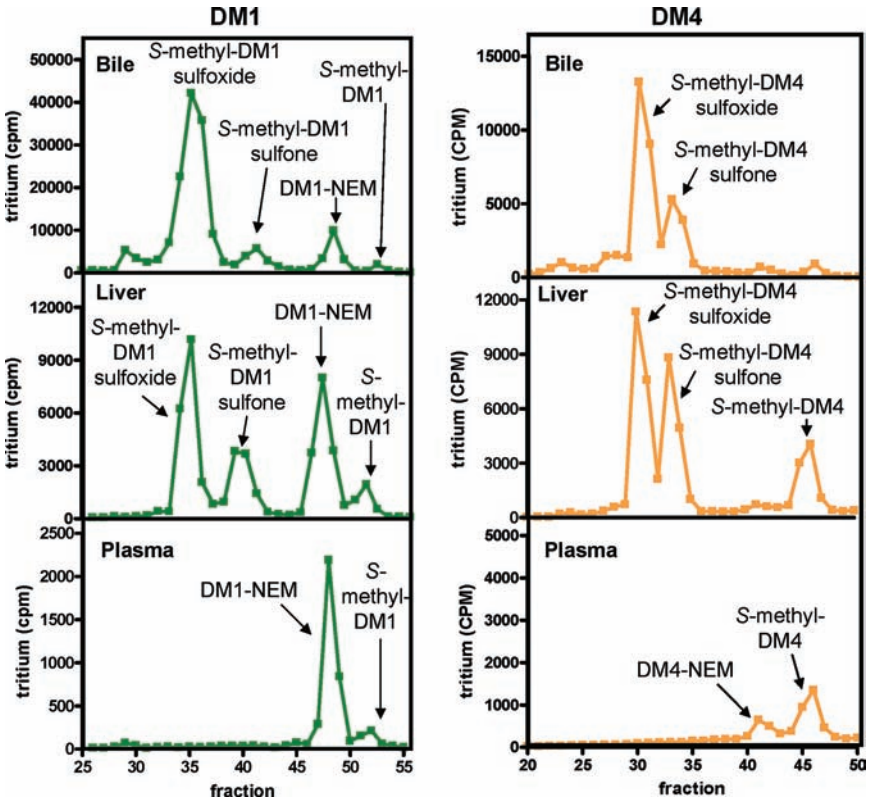


Figure 5. Maytansinoid metabolites in plasma, liver, and bile 1 h following a single bolus intravenous administration of [^{3}H]DM4 and [^{3}H]DM1. Mice ($n = 2$) were given a single bolus intravenous administration of 1 mg/kg [^{3}H]DM4 or [^{3}H]DM4, and after 1 h, mice were sacrificed and the plasma, bile, and liver tissues were extracted for metabolites. Extracts were analyzed by HPLC as described in Figure 2 for the disulfide-linked conjugates. The chromatograms show the fraction number on the abscissa and the counts per minute of tritium (CPM) on the ordinate.

DM4. These diffusible and highly cytotoxic maytansinoids are then efficiently oxidized in the liver to polar *S*-methyl-maytansinoid sulfoxide and sulfone derivatives that have reduced cytotoxic potencies most likely due to low cell permeability.

Interestingly, we observed no metabolism of the macrocyclic core of the maytansinoid molecule in any of the liver extracts. In a separate in vitro study, incubation of maytansine with purified human liver microsomes was reported to yield minor amounts of *O*-demethylation on the macrocyclic portion of maytansine.[27] However, the authors noted that the observed *O*-demethylation may have arisen from the low purity of the maytansine used in the experiment. We repeated the in vitro experiments using purified maytansine and human liver microsomes and could detect no metabolism on the macrocycle of maytansine (unpublished data), suggesting that the observed demethylation in the prior study[27] was presumably due to impurities in the maytansine. The resistance of maytansine to metabolism would explain why the most common and dose-limiting toxicity in patients treated with maytansine was gastrointestinal toxicity.[28] In contrast, gastrointestinal toxicity has not been found to be dose-limiting in patients treated with AMCs. While the reason for this difference may stem from the slower clearance rate for the antibody-drug conjugates as compared to the small molecule maytansine, the detoxification of the conjugates via the metabolism described here may also reduce their gastrointestinal toxicities.

■ ASSOCIATED CONTENT

Supporting Information. An assessment of the radioactivity associated with liver tissues (mass balance) is provided. This material is available free of charge via the Internet at http://pubs.acs.org.

■ AUTHOR INFORMATION

Corresponding Author

*Correspondence to Hans Erickson, ImmunoGen, Inc., 830 Winter Street, Waltham, MA 02451. Tel: 781-895-0734. Fax: 781-895-0611. E-mail: hans.erickson@immunogen.com.

■ ACKNOWLEDGMENT

We thank John Lambert for his many helpful suggestions and careful reading of the manuscript.

■ REFERENCES

(1) Senter, P. D. (2009) Potent antibody drug conjugates for cancer therapy. *Curr. Opin. Chem. Biol. 13*, 235–44.

(2) Polakis, P. (2005) Arming antibodies for cancer therapy. *Curr. Opin. Pharmacol. 5*, 382–7.

(3) Lambert, J. M. (2005) Drug-conjugated monoclonal antibodies for the treatment of cancer. *Curr. Opin. Pharmacol. 5*, 543–9.

(4) Krop, I. E., Beeram, M., Modi, S., Jones, S. F., Holden, S. N., Yu, W., Girish, S., Tibbitts, J., Yi, J. H., Sliwkowski, M. X., Jacobson, F., Lutzker, S. G., and Burris, H. A. (2010) Phase I study of trastuzumab-DM1, an HER2 antibody-drug conjugate, given every 3 weeks to patients with HER2-positive metastatic breast cancer. *J. Clin. Oncol. 28*, 2698−2704.

(5) Smith, S. V. (2005) Technology evaluation: huN901-DM1, ImmunoGen. *Curr. Opin. Mol. Ther. 7*, 394–401.

(6) Al-Katib, A. M., Aboukameel, A., Mohammad, R., Bissery, M. C., and Zuany-Amorim, C. (2009) Superior antitumor activity of SAR3419 to rituximab in xenograft models for non-Hodgkin's lymphoma. *Clin. Cancer Res. 15*, 4038–45.

(7) Chen, Q., Millar, H. J., McCabe, F. L., Manning, C. D., Steeves, R., Lai, K., Kellogg, B., Lutz, R. J., Trikha, M., Nakada, M. T., and Anderson, G. M. (2007) Alphav integrin-targeted immunoconjugates regress established human tumors in xenograft models. *Clin. Cancer Res. 13*, 3689–95.

(8) Ikeda, H., Hideshima, T., Fulciniti, M., Lutz, R. J., Yasui, H., Okawa, Y., Kiziltepe, T., Vallet, S., Pozzi, S., Santo, L., Perrone, G., Tai, Y. T., Cirstea, D., Raje, N. S., Uherek, C., Dalken, B., Aigner, S., Osterroth, F., Munshi, N., Richardson, P., and Anderson, K. C. (2009) The monoclonal antibody nBT062 conjugated to cytotoxic Maytansinoids has selective cytotoxicity against CD138-positive multiple myeloma cells in vitro and in vivo. *Clin. Cancer Res. 15*, 4028–37.

(9) Lambert, J. M. (2010) Antibody-maytansinoid conjugates; a new strategy for the treatment of cancer. *Drugs Future*.

(10) Erickson, H. K., Park, P. U., Widdison, W. C., Kovtun, Y. V., Garrett, L. M., Hoffman, K., Lutz, R. J., Goldmacher, V. S., and Blattler, W. A. (2006) Antibody-maytansinoid conjugates are activated in targeted cancer cells by lysosomal degradation and linker-dependent intracellular processing. *Cancer Res. 66*, 4426–33.

(11) Lewis Phillips, G. D., Li, G., Dugger, D. L., Crocker, L. M., Parsons, K. L., Mai, E., Blattler, W. A., Lambert, J. M., Chari, R. V., Lutz, R. J., Wong, W. L., Jacobson, F. S., Koeppen, H., Schwall, R. H., Kenkare-Mitra, S. R., Spencer, S. D., and Sliwkowski, M. X. (2008) Targeting HER2-positive breast cancer with trastuzumab-DM1, an antibody-cytotoxic drug conjugate. *Cancer Res. 68*, 9280–90.

(12) Kovtun, Y. V., Audette, C. A., Ye, Y., Xie, H., Ruberti, M. F., Phinney, S. J., Leece, B. A., Chittenden, T., Blattler, W. A., and Goldmacher, V. S. (2006) Antibody-drug conjugates designed to eradicate tumors with homogeneous and heterogeneous expression of the target antigen. *Cancer Res 66*, 3214–21.

(13) Kovtun, Y. V., and Goldmacher, V. S. (2007) Cell killing by antibody-drug conjugates. *Cancer Lett 255*, 232–40.

(14) Henderson, L. A., Baynes, J. W., and Thorpe, S. R. (1982) Identification of the sites of IgG catabolism in the rat. . *Arch Biochem Biophys 215*, 1–11.

(15) Wright, A., Sato, Y., Okada, T., Chang, K., Endo, T., and Morrison, S. (2000) In vivo trafficking and catabolism of IgG1 antibodies with Fc associated carbohydrates of differing structure. *Glycobiology 10*, 1347–55.

(16) Roguska, M. A., Pedersen, J. T., Henry, A. H., Searle, S. M., Roja, C. M., Avery, B., Hoffee, M., Cook, S., Lambert, J. M., Blattler, W. A., Rees, A. R., and Guild, B. C. (1996) A comparison of two murine monoclonal antibodies humanized by CDR-grafting and variable domain resurfacing. *Protein Eng. 9*, 895–904.

(17) Widdison, W. C., Wilhelm, S. D., Cavanagh, E. E., Whiteman, K. R., Leece, B. A., Kovtun, Y., Goldmacher, V. S., Xie, H., Steeves, R. M., Lutz, R. J., Zhao, R., Wang, L., Blattler, W. A., and Chari, R. V. (2006) Semisynthetic maytansine analogues for the targeted treatment of cancer. *J. Med. Chem. 49*, 4392–408.

(18) Erickson, H. K., Widdison, W. C., Mayo, M. F., Whiteman, K., Audette, C., Wilhelm, S. D., and Singh, R. (2010) Tumor delivery and in vivo processing of disulfide-linked and thioether-linked antibody-maytansinoid conjugates. *Bioconjugate Chem. 21*, 84−92.

(19) Keith, R. A., Otterness, D. M., Kerremans, A. L., and Weinshilboum, R. M. (1985) S-Methylation of D- and L-penicillamine by human erythrocyte membrane thiol methyltransferase. *Drug Metab. Dispos. 13*, 669–76.

(20) Franano, F. N., Edwards, W. B., Welch, M. J., and Duncan, J. R. (1994) Metabolism of receptor targeted 111In-DTPA-glycoproteins: identification of 111In-DTPA-epsilon-lysine as the primary metabolic and excretory product. *Nucl. Med. Biol. 21*, 1023–34.

(21) Novak-Hofer, I., Zimmermann, K., Maecke, H. R., Amstutz, H. P., Carrel, F., and Schubiger, P. A. (1997) Tumor uptake and metabolism of copper-67-labeled monoclonal antibody chCE7 in nude mice bearing neuroblastoma xenografts. *J. Nucl. Med. 38*, 536–44.

(22) Alley, S. C., Benjamin, D. R., Jeffrey, S. C., Okeley, N. M., Meyer, D. L., Sanderson, R. J., and Senter, P. D. (2008) Contribution of linker stability to the activities of anticancer immunoconjugates. *Bioconjugate Chem. 19*, 759–65.

(23) Alley, S. C., Zhang, X., Okeley, N. M., Anderson, M., Law, C. L., Senter, P. D., and Benjamin, D. R. (2009) The pharmacologic basis for antibody-auristatin conjugate activity. *J. Pharmacol. Exp. Ther. 330*, 932–8.

(24) Kim, K. M., McDonagh, C. F., Westendorf, L., Brown, L. L., Sussman, D., Feist, T., Lyon, R., Alley, S. C., Okeley, N. M., Zhang, X., Thompson, M. C., Stone, I., Gerber, H. P., and Carter, P. J. (2008) Anti-CD30 diabody-drug conjugates with potent antitumor activity. *Mol. Cancer Ther. 7*, 2486–97.

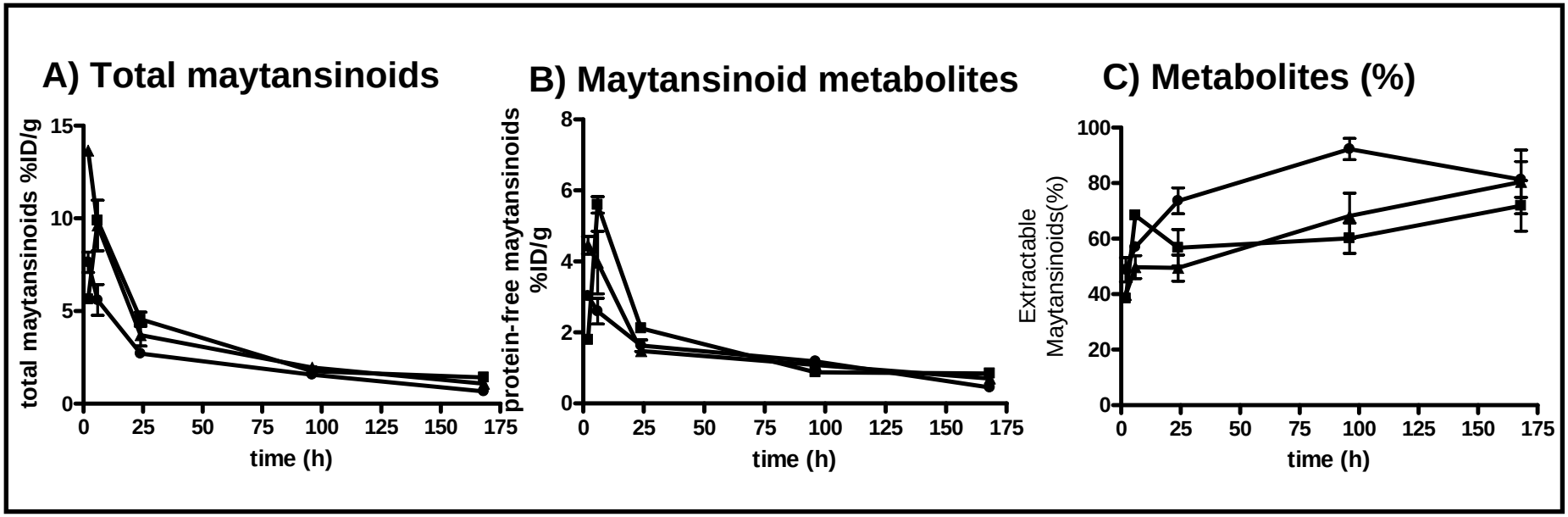
(25) Zheng, B., Fuji, R. N., Elkins, K., Yu, S. F., Fuh, F. K., Chuh, J., Tan, C., Hongo, J. A., Raab, H., Kozak, K. R., Williams, M., McDorman, E., Eaton, D., Ebens, A., and Polson, A. G. (2009) In vivo effects of targeting CD79b with antibodies and antibody-drug conjugates. *Mol. Cancer Ther. 8*, 2937–46.

(26) Gupta, S., and Bhattacharyya, B. (2003) Antimicrotubular drugs binding to vinca domain of tubulin. *Mol. Cell. Biochem. 253*, 41–7.

(27) Liu, Z., Floss, H. G., Cassady, J. M., and Chan, K. K. (2005) Metabolism studies of the anti-tumor agent maytansine and its analog ansamitocin P-3 using liquid chromatography/tandem mass spectrometry. *J. Mass Spectrom. 40*, 389–99.

(28) Issell, B. F., and Crooke, S. T. (1978) Maytansine. *Cancer Treat. Rev. 5*, 199–207.

Supplemental figure S1



Supplemental Figure 1. Exposure of liver tissue to total maytansinoids and protein-free maytansinoids. Liver tissues were analyzed at 2 h, 6 h, 1 d, 4 d, and 7 d following a single intravenous administration of 300 μg/kg (DM1 or DM4 dose) of mAb-SMCC-[^{3}H]DM1 (■), mAb-SPDB-[^{3}H]DM4 (▲) mAb-SPP-[^{3}H]DM1 (●) as described in Fig. 2. A) The total radioactivity associated with the liver homogenates determined by liquid scintillation counting of solubilized tissues were converted to the percentage of the total injected dose (based on DM1 or DM4) accumulated per gram of liver tissue (%ID/g). B) The radioactivity of extractable metabolites as a percentage of the total injected dose (based on DM1 or DM4) accumulated per gram of liver tissue (%ID/g). To determine the %ID/g, the radioactivity associated with HPLC-purified metabolites was divided by the total amount of radioactivity injected to the mice and by the weights associated with the liver samples. The data was then multiplied by 1.2 to account for the recovery (82%) of the synthetic *S*-methyl-[^{3}H]DM1 that had been added to liver homogenates during extraction in separate experiments. C) The amount of protein-free maytansinoid metabolites as a percentage of the total maytansinoids in the liver tissues. The percentages were calculated from the values in A and B.

Bioconjugate Chemistry

ARTICLE

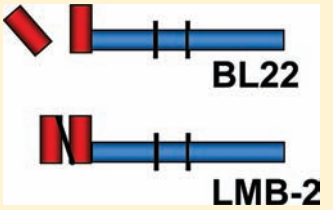
pubs.acs.org/bc

Renal Excretion of Recombinant Immunotoxins Containing *Pseudomonas* Exotoxin

Roberta Traini and Robert J Kreitman*

Laboratory of Molecular Biology, Center for Cancer Research, National Cancer Institute, National Institutes of Health, Bethesda, Maryland 20892, United States

ABSTRACT: Recombinant immunotoxins BL22 (CAT-3888) and LMB-2, composed of Fv fragments of anti-CD22 and CD25 MAbs, respectively, have produced major responses in patients with hematologic malignancies, and are also associated with renal toxicity, particularly with BL22. Characterization of the renal excretion of recombinant immunotoxins, which have 2−4 h half-lives in plasma, has not been reported in humans. To study the renal excretion of recombinant immunotoxins, urine from patients treated with BL22 was collected and the recombinant protein visualized after trichloroacetic acid (TCA) precipitation or anion exchange chromatography. BL22 viewed by immunoblot was found in the urine of patients within 8 h after dosing as an intact protein, and progressively degraded to fragments of <20 kDa within 1 day. We studied the stability of BL22 and LMB-2 added to urine at different time points and pH. When exposed to urine *ex vivo*, BL22 time-dependent proteolysis was similar to that observed in treated patients. By N-terminal sequencing, proteolysis was documented at positions 348−349 and 350−351 of BL22, and 339−340 and 341−342 of LMB-2, and other proteolytic sites were observed as well. Our data suggest that BL22 is excreted into the urine in a potentially cytotoxic form, even after its plasma level declines, and may remain intact long enough to cause renal toxicity.



BL22 (CAT-3888) and LMB-2 are recombinant immunotoxins that have been tested in patients with leukemia and lymphoma.[1−4] BL22 contains an anti-CD22 Fv fragment fused to truncated *Pseudomonas* exotoxin A (PE).[5] LMB-2 is composed of the Fv fragment of the anti-Tac mAb, recognizing the α-subunit of the IL-2 receptor (CD25), fused to the same truncated toxin as BL22.[6] The truncated toxin in both BL22 and LMB-2 is called PE38 and contains PE amino acids 253−364 and 381−613. Domain III, containing amino acids 395−613, contains the ADP ribosylation activity which catalytically inactivates elongation factor-2 (EF-2). Residues in domain II, amino acids 253−364 and 381−394, contain a proteolytic cleavage site and residues which translocate domain III to the cytosol.[7] PE38 is missing domain Ia, the binding domain of PE, which binds to normal cells.

LMB-2 induced major responses in a variety of B-and T-cell CD25+ hematologic malignancies, including hairy cell leukemia (HCL), chronic lymphocytic leukemia (CLL), cutaneous T-cell lymphoma (CTCL), Hodgkin's disease (HD), and adult T-cell leukemia (ATL).[1,2] BL22 had a complete remission rate of 47−61% in purine analogue-resistant HCL and has also shown some activity in CLL.[3,4,8] The dose-limiting toxicity of BL22 was due to a reversible hemolytic uremic syndrome (HUS) with kidney damage observed in 11% of the phase I patients. LMB-2 did not cause HUS, but did result in mild renal toxicity in some patients.

There is little known about the renal excretion of recombinant immunotoxins. In mice, at 45 and 90 min after an injected dose of LMB-2, 42.1% and 22.3%, respectively, of the injected dose per gram, was found in the kidney, a higher concentration than any other tissue.[9] However, anti-Tac(Fv)-PE38KDEL, a more toxic version of LMB-2, showed no histologic evidence of renal toxicity even at a dose which caused hepatic toxicity.[10] In humans, the half-lives of LMB-2 and BL22 are 2−4 h in the blood.[2,4,8] Characterization of urinary excretion of recombinant immunotoxin in humans has not yet been reported. As a first step to better understanding the mechanism of HUS with BL22, we decided to first characterize BL22 and LMB-2 after renal excretion. To determine stability of recombinant immunotoxins in urine, we examined urine from patients treated with BL22 and LMB-2, and also exposed the immunotoxins *ex vivo* to normal urine.

MATERIAL AND METHODS

TCA Precipitation. Aliquots of 1520 μL urine were treated with 380 μL of 60% TCA (final 12% TCA). After a brief vortex, the samples were centrifuged at 17 000 *g* for 5 min at 4 °C. The supernatant was aspirated and the pellet washed with 1 mL of 6% TCA. The samples were centrifuged, as above, for 2 min and the pellets washed with 1 mL of 93% acetone. The samples were centrifuged again for 2 min and the pellets resuspended in 10 μL of reducing SDS loading buffer and heated to 100 °C. Before loading the samples on SDS-PAGE, they were centrifuged at 17 000 *g* for 4 min at room temperature (RT).

Q-Sepharose Purification. Urine (100 mL) with or without exogenous BL22 1 μg/mL was diluted 5× with Buffer A (20 mM Tris pH 7.4 + 1 mM EDTA) at 4 °C, centrifuged in a 1 L bottle at 6000 *g* for 10 min at 4 °C, and then filtered over a cellulose acetate 0.2 μm filter.

Received: November 21, 2010
Revised: February 21, 2011
Published: March 16, 2011

ACS Publications This article not subject to U.S. Copyright. Published 2011 by the American Chemical Society

The filtrate was then applied to 5 mL of Q-Sepharose Fast-Flow anion exchange resin (GE Healthcare, Piscataway, NJ), washed in buffer A, and the protein eluted with buffer A containing 30% (v/v) buffer B (buffer A with NaCl 1 M) in 4 mL fractions. The fractions with peak protein concentration, as assessed by Pierce BCA assay (Thermo Scientific, Rockford, IL), were then assessed by immunoblot.

Immunotoxin Stability in Urine. To observe the stability of the immunotoxins in the urine, BL22 or LMB-2 was added to patient or healthy donor urine at a final concentration of 1 μg/mL, and incubated at 37 °C for 1, 8, and 24 h. The stability was tested at pH 5, 7, and 8. Urine samples were taken before adding immunotoxin, immediately after adding BL22 or LMB-2, and after 1, 8, and 24 h of incubation at 37 °C. The samples were TCA precipitated following the above protocol, loaded on SDS-PAGE 8−16% gradient gels (InVitrogen, Carlsbad, CA), and then detected by Western blot. For the Western blot, the primary antibody was affinity-purified rabbit anti-PE, the secondary antibody was horseradish peroxidase (HRP)-conjugated affinity-purified goat antirabbit immunoglobulin (JacksonImmuno Research, West Grove, PA), and the kit for detection of HRP was the SuperSignal West Pico Chemiluminescent assay (Thermo Scientific).

ADP-Ribosylation Assay. Wheat germ extract (10 μL) was incubated in 250 μL aliquots containing 50 mM Tris pH 8.0 and EDTA 1 mM, and {^{14}C}-nicotinamide adenine dinucleotide (NAD), with sample added last, as described.[10] BL22 or LMB-2 was incubated in urine (pH 7.0) at 100 μg/mL for 24 h at 37 °C, and complete cleavage verified by SDS-PAGE. 10 μL (1 μg) samples were added to the 240 μL wheat germ and {^{14}C}-NAD mixtures, and incubated for 15 min at 25 °C. The 250 μL aliquots were treated with 1 mL of 12% cold TCA, centrifuged, and the pellets washed twice with 1 mL 6% TCA. The pellets were each dissolved in 0.1 mL of 0.1 N NaOH, transferred to vials, neutralized with 0.5 mL of 0.4 M acetic acid, and finally mixed with scintillation fluid and counted.

RESULTS

The relatively small size (63 kDa) and short half-life (2−4 h) of recombinant immunotoxins suggest their rapid excretion into the urine. If so, their renal toxicity could in part be due to intoxication of the cells lining the collecting system, which could increase the concentration and exposure time of immunotoxin to glomerular endothelium. To characterize the urinary excretion of recombinant immunotoxins, urine from patients receiving immunotoxin was analyzed for the presence of toxin as well as their breakdown products, and stability of BL22 and LMB-2 was tested after exposure to urine.

Immunoblot Analysis of Urine from Patients Treated with BL22. To determine whether BL22 is excreted into the urine of patients, urine was analyzed before and at different time points after i.v. injection of 30−40 ug/kg of BL22. Figure 1A shows an immunoblot where TCA-precipitated protein, reduced in 2-mercaptoethanol, was analyzed by SDS-PAGE and exposed to polyclonal rabbit anti-PE. The major band 1−4 h after the end of the 30 min infusion corresponded to VH-PE38 (51 kDa), the reduced form of BL22 missing VL. As expected, the 13 kDa VL fragment was not visualized with the anti-PE polyclonal antibody. A contaminant present in pretreatment urine was visualized at >100 kDa. At 4−7 h after BL22 infusion, a ~17 kDa fragment first appeared and became the dominant band by 7−12 h after infusion. At 20−28 h after infusion, the VH-PE38 band decreased and bands at 17 and 6−8 kDa increased. However, even after 20 h after infusion, a significant percentage of full-length VH-PE38 remained. At 12−20 h, an unidentified band was also observed slightly higher than 51 kDa. Another representative

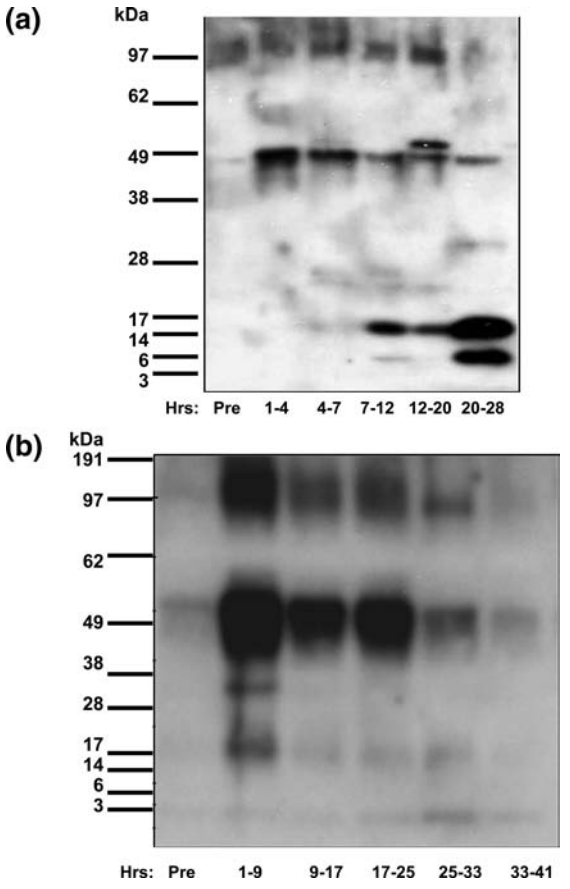


Figure 1. BL22 in urine of patients BH31 (A) and BH36 (B). 1.6 mL aliquots of urine from the indicated hours after end of 30 min infusion of BL22 (30 μg/kg) were subjected to TCA precipitation, and 15 μg of total protein/lane was added (except 3.75 μg at 1−4 h in A).

patient is included in Figure 1B, showing the major band at 51 kDa initially at 1−9 h, and then by 9−33 h a decrease in the 51 kDa band combined with an increase in the 17 kDa and smaller fragments. Interestingly, after 33 h, the 17 kDa and smaller kDa fragments were less visible for this patient, indicating further degradation and/or excretion.

Effect of Urine on the Integrity of Recombinant Immunotoxin. Since degradation of BL22 could occur prior to entering the collecting system, or upon exposure to urine, or both, the composition of BL22 was analyzed after *ex vivo* exposure of BL22 to urine. The calculated isoelectric point (pI) of BL22 is 5.08, based on the full sequence missing the carboxyl terminal lysine residue, which is rapidly removed upon exposure to plasma.[11] To determine whether the degradation of BL22 in the presence of urine is related to pH, possibly by inducing conformational changes close to the isoelectric point, the urine tested was adjusted to pH 5, 7, and 8. BL22 was incubated with urine at a final concentration of 1 μg/mL for 1 h at 37 °C, and the TCA-precipitated protein analyzed by Western blot. As shown in Figure 2A, normal urine at all 3 different pH conditions did not degrade the BL22 to lower molecular weight bands. Urine from the CLL patients produced slight degradation of BL22, producing 2 lower bands of molecular weights which were similar between patients BC01 and CL10. However, as shown by Coomassie-stained gels (Figure 2D−F), even normal urine is able to degrade BL22 after 24 h incubation, particularly at pH 7 and 8. On the Coomassie gel, the reduced VL

dx.doi.org/10.1021/bc1005152 |*Bioconjugate Chem.* 2011, 22, 736–740

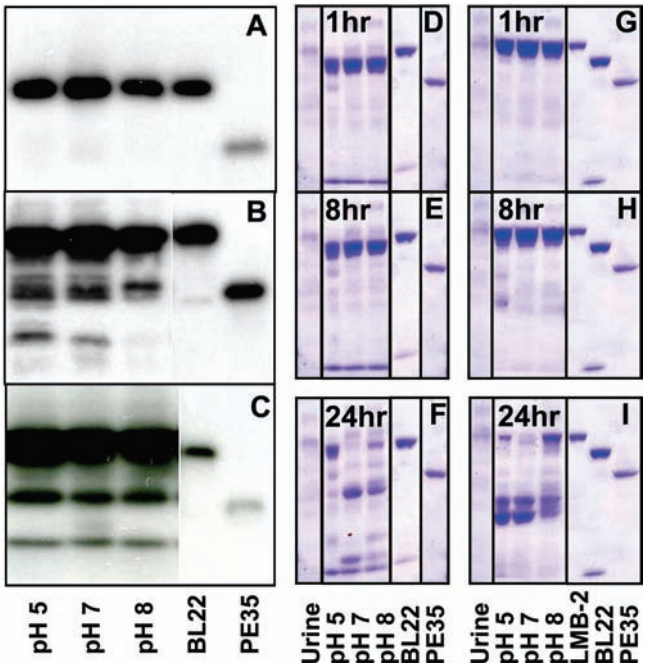


Figure 2. Degradation of BL22 and LMB-2 by normal urine. Immunoblots show BL22 incubated at a final concentration of 1 μg/mL for 1 h with urine at the indicated pH from a normal donor (A), and CLL patients BC01 (B) and CL10 (C). Controls include 2 ng of BL22 and PE35. Coomassie-stained gels in D-F include urine alone at pH 7 (first lane) followed by 2 μg BL22 added to normal urine incubated at 37 °C for the indicated time periods at the indicated pH. LMB-2 was incubated similarly in G−I and the indicated control lanes included LMB-2, BL22, and PE35.

fragment at 13 kDa is visible as shown in the BL22 control band. Figure 2G−I shows significant degradation of LMB-2 by urine at 24 h, which appeared less at pH 8. Since LMB-2 contains a linker rather than a disulfide bond connecting the VH to VL, no lower band representing a variable domain was expected.

Characterization of Degradation Products of Recombinant Immunotoxins. To determine which regions of the PE sequence are susceptible to urinary proteases, LMB-2 and BL22 were incubated with urine for 16 h at 37 °C and the products analyzed. As shown in Figure 3, BL22 was cleaved into 3 visible bands on reducing SDS-PAGE. The lowest band (C) co-migrated with the 12 kDa VL band. The upper band (A) was lower in molecular weight than the 35 kDa PE35 protein, indicating that, if the Arg279-Gly280 Furin protease site in BL22 was cleaved outside the cell, producing PE35, at least one additional site within this sequence was also cleaved. Cleavage of the Arg279-Gly280 Furin protease in PE is known to occur with proteases other than furin.[12] As shown in Figure 3, the size of the upper band (A) in cleaved BL22 was similar to upper band (E) in cleaved LMB-2. The size of the lower band (F) in LMB-2 is similar to the size of the 12 kDa VL band C in BL22 plus the slightly larger band B in BL22. Thus, the degradation products in Figure 3 are compatible with BL22 and LMB-2 each being cleaved once on the C-terminal side of the Arg279-Gly280 Furin cleavage site, with the difference between BL22 and LMB-2 being reduction in BL22 of the engineered disulfide bond linking Cys44 of VH with Cys100 of VL.

Identification of Urinary Protease Sites in Recombinant Immunotoxins. To determine the exact locations of cleavage in

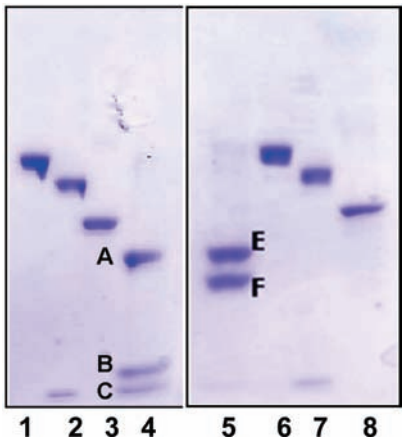


Figure 3. Characterization of proteolytic products of BL22 and LMB-2 in urine. BL22 or LMB-2 at 200 μg/mL was incubated with normal urine for 16 h at 37 °C at pH 7, and 2 μg was added to lane 4 or 5, respectively. Control molecules included 1 μg of LMB- 2 (63 kDa, lanes 1 and 6), BL22 (51 kDa + 12 kDa, lanes 2 and 7), and PE35 (35 kDa, lanes 3 and 8).

LMB-2 and BL22 by urinary proteases, the bands in BL22 and LMB-2 from Figure 3 were subjected to amino terminal sequencing. The N-terminal sequences are listed in Table 1. Bands B and F contained sequences corresponding to the N-terminus of the VH fragment of reduced BL22 and the N-terminus of LMB-2, respectively. The amino terminal end of the upper band (A) in BL22 indicates that the toxin is cleaved at 2 locations only 2 amino acids apart, Glu348-Arg349 and Phe350-Val351. Surprisingly, in LMB-2 the toxin was also cleaved in 2 locations 2 amino acids apart, but the cleavage sites, Ala339-Leu340 and Thr341-Leu342, were slightly different than those of BL22. Thus, even though the urine sample and toxin sequences were identical, BL22 and LMB-2 were cleaved within the toxin slightly differently.

ADP-Ribosylation Activity of Cleaved Recombinant Immunotoxins. To determine if the cleaved LMB-2 and BL22 fragments would retain ADP-ribosylation activity, they were incubated as in Figure 2F and I, in urine at pH 7.0 at 100 μg/mL for 24 h at 37 °C, when SDS-PAGE as in Figure 2F,I verified essentially complete cleavage. No cleavage was observed in urine at time 0. As shown in Figure 4, incubation of LMB-2 or BL22 with urine for either 0 or 24 h did not significantly decrease enzymatic activity. Figure 4 shows that 100 ng of LMB-2 alone had 21% less activity than 1 ug of LMB-2 alone and 19% less than completely cleaved LMB-2 after 1 h incubation with urine. Thus, in this semiquantitative assay, cleaved fragments of LMB-2 and BL22 retain 20−100% of their original ADP-ribosylation activity.

DISCUSSION

To study the renal toxicity of recombinant immunotoxins containing truncated PE, anti-CD25 and anti-CD22 recombinant immunotoxins LMB-2 and BL22 were detected and characterized in urine, either after i.v. injection of BL22 in patients or after incubation of LMB-2 or BL22 with urine. We found evidence of proteolysis of both LMB-2 and BL22, which varied with both time and pH. N-terminal analysis showed that incubation with urine resulted in cleavage of LMB-2 at Ala339-Leu340 and Thr341-Leu342, and cleavage of BL22 at Glu348-Arg349 and Phe350-Val351. Incubation with urine did not destroy enzymatic activity of the immunotoxins.

Table 1. Amino Terminal Sequencing of Degradation Products of BL22 and LMB-2 in Urine

protein	fragment	sequence	location of N-terminus of fragment
BL22	Band A	R F V R Q G T G N D or V R Q G T G N D E A	Amino acid 349 of PE Amino acid 351 of PE
BL22	Band B	M E V Q L V E S G G G	Amino terminus of BL22 VH
LMB-2	Band E	L T L A A A E S E R or L A A A E S E R F V	Amino acid 340 of PE Amino acid 342 of PE
LMB-2	Band F	M Q V H L Q QS G A E	Amino terminus of LMB-2 VH

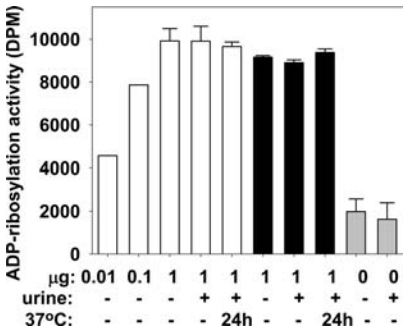


Figure 4. ADP-Ribosylation activity of urine-cleaved BL22 and LMB-2. LMB-2 (white) or BL22 (black) was tested for ADP-ribosylation activity using the indicated amounts in μg. As indicated, LMB-2 and BL22 were each mixed with urine for either 0 or 24 h at 37 °C, and the final 2 lanes (gray) show PBS and urine alone, respectively.

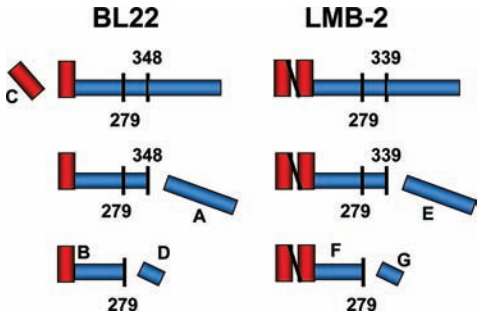


Figure 5. Model for urine protease fragments of BL22 and LMB-2. Fv and toxin fragments are shown in red and blue, respectively. Fragments labeled A−G represent bands on SDS-PAGE (Figure 3) except for bands D and G, which are too small.

Cleavage Locations within BL22 and LMB-2 for Urine Proteases. Based on SDS-PAGE (Figure 3) and N-terminal sequencing (Table 1), a model of proteolysis of recombinant immunotoxins by urine is shown in Figure 5, where BL22 and LMB-2 are cleaved prior to Arg349 and Leu340, respectively. Reduction of BL22 is expected to produce a free VL (Figure 5, fragment C), consistent with the ~13 kDa band C in Figure 3. Fragment A if containing amino acids 349−364 and 381−613 would be consistent with band A at 29 kDa. The remainder of VH-PE38 would include VH followed by the C3 connector (ASGGPE)[6] followed by amino acids 253−348 of PE, with estimated molecular weight of ~24 kDa. Since band B in Figure 3 is much smaller than 24 kDa, it is possible that BL22 is also cleaved between 253 and 348 such that the carboxyl terminal fragment (Figure 5, fragment D) would be too small to be visible. If the second proteolysis site were the Furin cleavage site between Arg279 and Gly280, fragment B would be ~16 kDa, most consistent with band B in Figure 3. Because of the covalent $(G_4S)_3$ linker between VH and VL of LMB-2, reduction alone would not result in fragmentation of LMB-2. Proteolytic cleavage of LMB-2 by urine before Leu340 would result in a carboxyl terminal fragment of ~30 kDa, represented by fragment E in Figure 5 and possibly corresponding to the upper band E in Figure 3 lane 5. If LMB-2 were also cleaved at the Arg279-Gly280 Furin site, the amino-terminal fragment F in Figure 5 would contain VH and VL connected by the linker, followed by the C3 connector, and finally followed by PE amino acids 253−279 (~28.5 kDa). In that case, the ~7 kDa fragment G in Figure 5 would be too small to see on the gel. Based on their size, fragments A and E, each with known amino-terminal sequence, should contain the ADP-ribosylating activity present in amino acids 395−602.[13] However, gel analysis could not exclude additional proteolysis just before amino acid 602, which could destroy ADP ribosylation activity. Therefore, urine-cleaved LMB-2 and BL22 were tested directly for ADP ribosylation activity, which was found to be retained (Figure 4). Thus, for either BL22 or LMB-2, the cleavage products in urine leave open the possibility that a fragment with cytotoxic activity may be nonspecifically internalized into renal endothelial cells or cells lining the collecting system, resulting in renal toxicity.

Renal Toxicity with Recombinant Toxins. Determining the mechanism of renal toxicity from recombinant immunotoxins can be difficult, since vascular leak syndrome can result in hypotension which can cause renal toxicity secondarily by pre-renal azotemia. However, denileukin diftitox was reported to result in proteinuria and microscopic hematuria in 6% of patients and this appeared dose-related,[14] suggesting that for at least some of the 10% of patients reported with an increase in creatinine, renal toxicity was related to direct intoxication of glomerular endothelium or renal tubules by the toxin. In the phase I trial of LMB-2, increased creatinine and proteinuria were observed in 9% of patients, and no cases of HUS were observed.[2] In the phase II trial of BL22, one cycle resulted in proteinuria in 33% of patients, microscopic hematuria in 19%, and creatinine elevation in 6%.[8] Including retreatment cycles, 3 (9%) of 36 phase II and 5 (11%) of 46 phase I patients receiving BL22 had HUS.[4,8] While the mechanism is unknown, functional plasma ADAMTS-13 was detected in all cases, and HUS during phase II resolved completely without plasmapheresis, suggesting that the syndrome may be due to endothelial damage localized to the kidney without a circulating inhibitor requiring removal. Thus, renal toxicity due to nonspecific internalization of ADP-ribosylation activity into the glomerular endothelium or tubular epithelium could possibly predispose or precipitate HUS. It should be noted that internalization of Shiga-like toxin into renal endothelium can cause HUS, and the toxin itself kills cells by ricin-like inhibition of protein synthesis, much like PE.[15] Based on our data, it may be advisible to maintain adequate hydration of patients for at least 24−48 h after a dose of BL22, and alkalinization of urine would not be recommend. We believe that additional knowledge of the behavior of recombinant immunotoxins during renal excretion

dx.doi.org/10.1021/bc1005152 |*Bioconjugate Chem.* 2011, 22, 736–740

may be important to ensure optimal safety of these potentially useful agents.

AUTHOR INFORMATION

Corresponding Author

*Address correspondence to Robert J. Kreitman, M.D., National Institutes of Health, Building 37, Room 5124b, 9000 Rockville Pike, Bethesda, MD 20854-4255, 301-496-6947 (phone), kreitmar@mail.nih.gov (email).

ACKNOWLEDGMENT

The authors wish to recognize Hong Zhou and Inger Margulies for technical assistance, Barbara Debrah for data management, and our clinical staff Rita Mincemoyer, Linda Ellison, Elizabeth Maestri, and Sonya Duke for assisting with patient samples.

We also thank Drs. David FitzGerald and Ira Pastan for helpful suggestions and for reviewing the manuscript. This work was supported in part by the NCI, intramural program, and MedImmune, LLC.

ABBREVIATIONS

ADAMTS-13,a disintegrin and metalloproteinase with a thrombospondin type 1 motif, member 13′; ADP,adenosine triphosphate; ATL,adult T-cell leukemia; CLL,chronic lymphocytic leukemia; CTCL,cutaneous T-cell lymphoma; Fv,variable fragment; HD, Hodgkin's disease; HRP,horseradish peroxidase; HUS,hemolytic uremic syndrome; kDa,kilodaltons; mAb,monoclonal antibody; PE, *Pseudomonas* exotoxin A; RT,room temperature; SDS,sodium dodecyl sulfate; PAGE,polyacrylamide gel electrophoresis; TCA, trichloroacetic acid; VH,variable heavy; VL,variable light

REFERENCES

(1) Kreitman, R. J., Wilson, W. H., Robbins, D., Margulies, I., Stetler-Stevenson, M., Waldmann, T. A., and Pastan, I. (1999) Responses in refractory hairy cell leukemia to a recombinant immunotoxin. *Blood 94*, 3340–3348.

(2) Kreitman, R. J., Wilson, W. H., White, J. D., Stetler-Stevenson, M., Jaffe, E. S., Waldmann, T. A., and Pastan, I. (2000) Phase I trial of recombinant immunotoxin Anti-Tac(Fv)-PE38 (LMB-2) in patients with hematologic malignancies. *J. Clin. Oncol. 18*, 1614–1636.

(3) Kreitman, R. J., Wilson, W. H., Bergeron, K., Raggio, M., Stetler-Stevenson, M., FitzGerald, D. J., and Pastan, I. (2001) Efficacy of the Anti-CD22 recombinant immunotoxin BL22 in chemotherapy-resistant hairy-cell leukemia. *New Engl. J. Med. 345*, 241–247.

(4) Kreitman, R. J., Squires, D. R., Stetler-Stevenson, M., Noel, P., Fitzgerald, D. J., Wilson, W. H., and Pastan, I. (2005) Phase I trial of recombinant immunotoxin RFB4(dsFv)-PE38 (BL22) in patients with B-cell malignancies. *J. Clin. Oncol. 23*, 6719–29.

(5) Kreitman, R. J., and Pastan, I. (2006) Immunotoxins in the treatment of refractory hairy cell leukemia. *Hematol. Oncol. Clin. North Am. 20*, 1137–51.

(6) Kreitman, R. J., Batra, J. K., Seetharam, S., Chaudhary, V. K., FitzGerald, D. J., and Pastan, I. (1993) Single-chain immunotoxin fusions between anti-Tac and *Pseudomonas* exotoxin: relative importance of the two toxin disulfide bonds. *Bioconjugate Chem. 4*, 112–120.

(7) Pastan, I., Hassan, R., FitzGerald, D. J. P., and Kreitman, R. J. (2006) Immunotoxin therapy of cancer. *Nat. Rev. Cancer 6*, 559–65.

(8) Kreitman, R. J., Stetler-Stevenson, M., Margulies, I., Noel, P., FitzGerald, D. J. P., Wilson, W. H., and Pastan, I. (2009) Phase II trial of recombinant immunotoxin RFB4(dsFv)-PE38 (BL22) in patients with hairy cell leukemia. *J. Clin. Oncol. 27*, 2983–90.

(9) Kreitman, R. J., and Pastan, I. (1998) Accumulation of a recombinant immunotoxin in a tumor in vivo: fewer than 1000 molecules per cell are sufficient for complete responses. *Cancer Res. 58*, 968–975.

(10) Kreitman, R. J., Bailon, P., Chaudhary, V. K., FitzGerald, D. J. P., and Pastan, I. (1994) Recombinant immunotoxins containing anti-Tac(Fv) and derivatives of *Pseudomonas* exotoxin produce complete regression in mice of an interleukin-2 receptor-expressing human carcinoma. *Blood 83*, 426–434.

(11) Hessler, J. L., and Kreitman, R. J. (1997) An early step in Pseudomonas exotoxin action is removal of the terminal lysine residue, which allows binding to the KDEL receptor. *Biochemistry 36*, 14577–14582.

(12) Chiron, M. F., Ogata, M., and FitzGerald, D. J. (1996) Pseudomonas exotoxin exhibits increased sensitivity to furin when sequences at the cleavage site are mutated to resemble the arginine-rich loop of diphtheria toxin. *Mol. Microbiol. 22*, 769–78.

(13) Chaudhary, V. K., Jinno, Y., FitzGerald, D., and Pastan, I. (1990) *Pseudomonas* exotoxin contains a specific sequence at the carboxyl terminus that is required for cytotoxicity. *Proc. Natl. Acad. Sci. U.S.A. 87*, 308–312.

(14) Olsen, E., Duvic, M., Frankel, A., Kim, Y., Martin, A., Vonderheid, E., Jegasothy, B., Wood, G., Gordon, M., Heald, P., Oseroff, A., Pinter-Brown, L., Bowen, G., Kuzel, T., Fivenson, D., Foss, F., Glode, M., Molina, A., Knobler, E., Stewart, S., Cooper, K., Stevens, S., Craig, F., Reuben, J., Bacha, P., and Nichols, J. (2001) Pivotal phase III trial of two dose levels of denileukin diftitox for the treatment of cutaneous T-cell lymphoma. *J. Clin. Oncol. 19*, 376–388.

(15) Moake, J. L. (2002) Thrombotic thrombocytopenic purpura and the hemolytic uremic syndrome. *Arch. Pathol. Lab. Med. 126*, 1430–3.

Bioconjugate Chemistry

ARTICLE

pubs.acs.org/bc

Strategies for Neoglycan Conjugation to Human Acid α-Glucosidase

Qun Zhou,* James E. Stefano, John Harrahy, Patrick Finn, Luis Avila, Josephine Kyazike, Ronnie Wei, Scott M. Van Patten, Russell Gotschall, Xiaoyang Zheng, Yunxiang Zhu, Tim Edmunds, and Clark Q. Pan

Genzyme Corporation, Framingham, Massachusetts 01701, United States

Supporting Information

ABSTRACT: Engineering proteins for selective tissue targeting can improve therapeutic efficacy and reduce undesired side effects. The relatively high dose of recombinant human acid α-glucosidase (rhGAA) required for enzyme replacement therapy of Pompe disease may be attributed to less than optimal muscle uptake via the cation-independent mannose 6-phosphate receptor (CI-MPR). To improve muscle targeting, Zhu et al.[1] conjugated periodate oxidized rhGAA with bis mannose 6-phosphate bearing synthetic glycans and achieved 5-fold greater potency in a murine Pompe efficacy model. In the current study, we systematically evaluated multiple strategies for conjugation based on a structural homology model of GAA. Glycan derivatives containing succinimide, hydrazide, and aminooxy linkers targeting free cysteine, lysines, and *N*-linked glycosylation sites on rhGAA were prepared and evaluated *in vitro* and *in vivo*. A novel conjugation method using enzymatic oxidation was developed to eliminate side oxidation of methionine. Conjugates derived from periodate oxidized rhGAA still displayed the greatest potency in the murine Pompe model. The efficiency of conjugation and its effect on catalytic activity were consistent with predictions based on the structural model and supported its use in guiding selection of appropriate chemistries.



INTRODUCTION

Pompe disease, or glycogen storage disease type II, is an autosomal recessive disorder whose underlying pathology is an accumulation of glycogen in lysosomes in many tissues, principally cardiac and skeletal muscle.[2] The accumulation of glycogen results from a deficiency in the glycogen-degrading lysosomal enzyme, acid α-glucosidase or GAA, leading to cardiac, skeletal, and respiratory muscle tissue damage and organ failure. The disease has a heterogeneous clinical presentation, from infants who have a rapidly progressive form of the disease resulting in early death, to older children and adults whose disease progresses at a slower rate but usually results in wheelchair use and the need for a ventilator as a consequence of the severe muscle weakness. Like most lysosomal enzymes, GAA contains mannose 6-phosphate (Man-6-P) in its oligomannose-type *N*-glycans, which directs its transport inside the cell from the Golgi to the lysosome via Man-6-P receptors.[3] GAA is initially synthesized as a 110 kDa protein in ER and Golgi of the cells, followed by proteolytically processing in the lysosome to mature forms.[4,5]

The enzyme replacement therapy with alglucosidase alfa (recombinant human α-glucosidase, rhGAA, Myozyme, Genzyme Corp) is used successfully for treating Pompe patients resulting in reduced cardiac hypertrophy, reduced the need for ventilation support, improved motor function, and increased life expectancy in infants.[6−11] However, even at doses which were high relative to other enzyme replacement therapeutics, the extent of glycogen clearance in skeletal muscle cells was found to vary among the infants treated with the enzyme.[12] The need for high dose has also been observed in clearing skeletal muscle glycogen of GAA knockout mouse, a murine Pompe model.[12,13] These findings could be caused by inefficient targeting of the recombinant enzyme to lysosomes through cation-independent Man-6-P receptor (CI-MPR) expressed on the surface of muscle cells, as rhGAA contains on average only a single Man-6-P and even lower amounts of bis Man-6-P, the preferred ligand for the receptor.[14] This hypothesis is supported by the finding that conjugation of bis Man-6-P bearing glycans to the terminal sialic acids of rhGAA (neoGAA) resulted in a ∼5-fold greater potency for clearing lysosomal glycogen in muscle of GAA knockout mice than the unmodified enzyme.[1,15,16]

Although the sialic acid-mediated conjugation strategy targeting the 6−7 copies of sialic acids in rhGAA[13] yielded a conjugate with greatly improved functional outcome in the murine Pompe model,[1] there are multiple approaches to produce such neoglycoproteins.[17] At one extreme, a single glycan can be conjugated to the single free cysteine on rhGAA via thiol-based chemistry to generate a defined product profile. At the other extreme, 10−20 copies of neoglycans can be conjugated to the 15 lysines, N-terminal amine, and possibly histidines on rhGAA through amine-based chemistry. Finally, the carbohydrate on rhGAA can be oxidized with an enzyme specific to galactose instead of periodate, resulting in galactose-mediated conjugation.

Received: December 1, 2010
Revised: February 14, 2011
Published: March 18, 2011

ACS Publications © 2011 American Chemical Society

dx.doi.org/10.1021/bc1005416 | *Bioconjugate Chem.* 2011, 22, 741–751

In the current study, we explored these three alternative conjugation strategies and compared the resulting conjugates with sialic acid-mediated conjugates both *in vitro* and *in vivo*.

EXPERIMENTAL PROCEDURES

Materials. rhGAA and neuraminidase from *Clostridium perfringens* were produced by Genzyme Corp. Bis Man-6-P neoglycans were synthesized as described previously.[1,16] SFB (or S-4FB, succinimidyl 4-formylbenzoate) and pentafluorobenzamide poly(ethylene glycol) 4 (PEG4/PFB) were purchased from Solulink Corp (San Diego, CA). Galactose oxidase (GAO) was obtained from Worthington Biochemicals (NJ). 1,4-Di-(3′-[2-pyridyldithiol]-propionamido) butane (DPDPB) was obtained from Pierce (Rockford, IL). Other reagents, including catalase and sodium periodate, were obtained from Sigma (St. Louis, MO).

Sialic Acid-Mediated (SAM) Conjugation. Glycan conjugation to sialic acids was performed according to a method described by Zhu et al.[1] except that buffer exchanges were performed by diafiltration on Pellicon XL 50 or Amicon ultra-4 (Millipore, MA).

Thiol-Based Conjugation. A thiol-reactive form of bis Man-6-P neoglycan was prepared by a condensation of the acid form with a previously described thiol-reactive linker (3-nitro-2-pyridinesulfenylethylamine, nipsylethylamine, NEA).[18] A crude fraction of the free-acid form of bis Man-6-P neoglycan was converted to the triethylammonium (TEA) salt by neutralization with TEA followed by chromatography on a Superdex Peptide column (GE Healthcare, NJ) using 30% acetonitrile and 0.1% TEA bicarbonate as a mobile phase. Pooled fractions were lyophilized and conjugated with NEA in a reaction containing glycan:NEA:EDAC:NHS:HOBt:TEA (1:1:1.5:1:1:1 mol:mol) incubated overnight at 25 °C with gentle shaking. The product was purified on a Superdex Peptide column as described above and lyophilized. The NEA-glycan was reconstituted in water and incubated with rhGAA at 15-fold molar excess over protein in 50 mM sodium phosphate and 50 mM hydroxylamine (pH 7.2) for 2 h at 25 °C. The pH was adjusted to 6.2 with 50 mM sodium phosphate (pH 4.1) and the incubation continued overnight. The product was buffer-exchanged into 25 mM sodium phosphate (pH 6.2) using Amicon (Millipore, MA). rhGAA (~3.5 mg/mL) was also modified with a thiol-reactive cross-linker by reaction with 60- to 108-fold molar excess of DPDPB in 25 mM sodium phosphate (pH 6.2) with 10−20% organic solvent overnight at 25 °C. The extent of the reaction was determined by monitoring the absorbance at 343 nm of released 2-thiopyridone observed in an ultrafiltrate (Microcon YM-30, Millipore, MA) on a Beckman DU640 spectrophotometer or the spectrum of unfiltered material corrected for light scattering using the spectral data above 400 nm and instrument software.[19]

Lysine-Mediated Conjugation. Lysine residues in rhGAA were modified with SFB to introduce aldehydes, followed by reaction with modified neoglycans to form either hydrazone or oxime linked conjugates. rhGAA was reacted with a 20-fold molar excess of SFB in 150 mM sodium chloride and 50 mM sodium phosphate (pH 7.2) for 30 min, followed by buffer exchange into 100 mM sodium acetate (pH 5.5). The SFB modified protein was then coupled with bis Man-6-P neoglycan (hydrazide) for 2 h at room temperature. Alternatively, it was reacted with bis Man-6-P neoglycan (aminooxy) in 100 mM sodium acetate (pH 5.6) for 6 h at 37 °C. The final products were buffer-exchanged into 25 mM sodium phosphate, 2% mannitol, and 0.005% Tween-80 (pH 6.25).

Galactose Aldehyde-Mediated (GAM) Conjugation. rhGAA was desialylated with 20 mU/mg *Clostridium perfringens* neuraminidase for 6 h at 37 °C in 25 mM sodium phosphate, 2% mannitol, and 0.005% Tween-80 (pH 6.25) and then treated with GAO (2−10 μg/mg) in the presence of catalase (2 U/mg) overnight at 37 °C. rhGAA was purified away from neuraminidase and GAO by anion-exchange chromatography. The reaction mixture was diluted with an equal volume of water and applied to a Poros 50D column equilibrated with 10 mM sodium phosphate (pH 6.9). Following a wash with 10 mM sodium acetate (pH 5.0), the protein was step eluted with 150 mM sodium acetate (pH 5.0). A 16.6-fold molar excess of bis Man-6-P neoglycan (aminooxy) was added directly to the eluate and the mixture incubated for 6 h at 37 °C. The product was then buffer-exchanged into 25 mM sodium phosphate, 2% mannitol, and 0.005% Tween-80 (pH 6.25) either by diafiltration with Pellicon XL 50 or by centrifugal ultrafiltration over Amicon filters (Millipore, MA) to yield GAM6.

Quantitation of Monosaccharides Including Man-6-P and Galacturonic Acid (GalA). The Man-6-P content was determined as described previously.[20] Hydrolysates were filtered through S Mini H cartridges (Sartorius, NY) and ribose-5-phosphate used as an internal standard. The number of glycans conjugated and conjugation efficiencies were calculated assuming 2 mol Man-6-P per mole neoglycan and correcting for the Man-6-P content of the starting rhGAA. Galactose and GalA were also quantified using HPAEC-PAD on a Dionex HPLC.[21,22] The GalA was identified using LC/MS/MS of glycans released with PNGase F and resolved by normal-phase HPLC (TSK gel amide-80 column) in an acetonitrile−water gradient with 10 mM ammonium formate (pH 4.0). Mass spectrometry detection of glycans was performed in-line, in negative ion mode, using QStar or LCT time-of-flight mass spectrometers.

HPLC-Based Cation-Independent Man-6-P Receptor (CI-MPR) Binding. Binding of rhGAA or neoGAA conjugates to CI-MPR was determined by HPLC affinity chromatography with soluble bovine CI-MPR (purified from fetal bovine serum) immobilized on Poros EP resin using step elution with Man-6-P. Protein was detected by intrinsic protein fluorescence (290 nm excitation/340 nm emission), and the relative amount of protein eluting at each step was determined by integration of the peak areas.

GAA Activity Assay. Enzymatic activity was determined using *p*-nitrophenyl-α-D-glucopyranoside as substrate as described.[13] One unit of activity is defined as the hydrolysis of 1 μmol of substrate per min at 37 °C.

Protein Structure Modeling. Two secondary structure prediction algorithms PSIPRED[23] and SSPRO[24] were used to align the GAA sequence with the structure of human intestinal maltase-glycoamylase (MGAM, PDB code 2QMJ),[25] followed by manual adjustment and model building in *Prime 2.1* (Schrödinger, OR). Loops of the resulting GAA model were refined using the default sampling for loops of 5 residues or shorter and the extended protocol for loops longer than 5 residues. Side chains were unfrozen within 7.5 Å of the corresponding loop and the energy cutoff was set to 10 kcal.

Animal Studies. For the determination of serum clearance, 3 groups of 5 male and 5 female GAA knockout mice at 3−6 months of age (Charles River Laboratories, Wilmington, MA) received a single intravenous administration of rhGAA, GAM, and SAM conjugates (GAM6 and SAM6) at 20 mg/kg. Blood samples for analysis were collected via the retro-

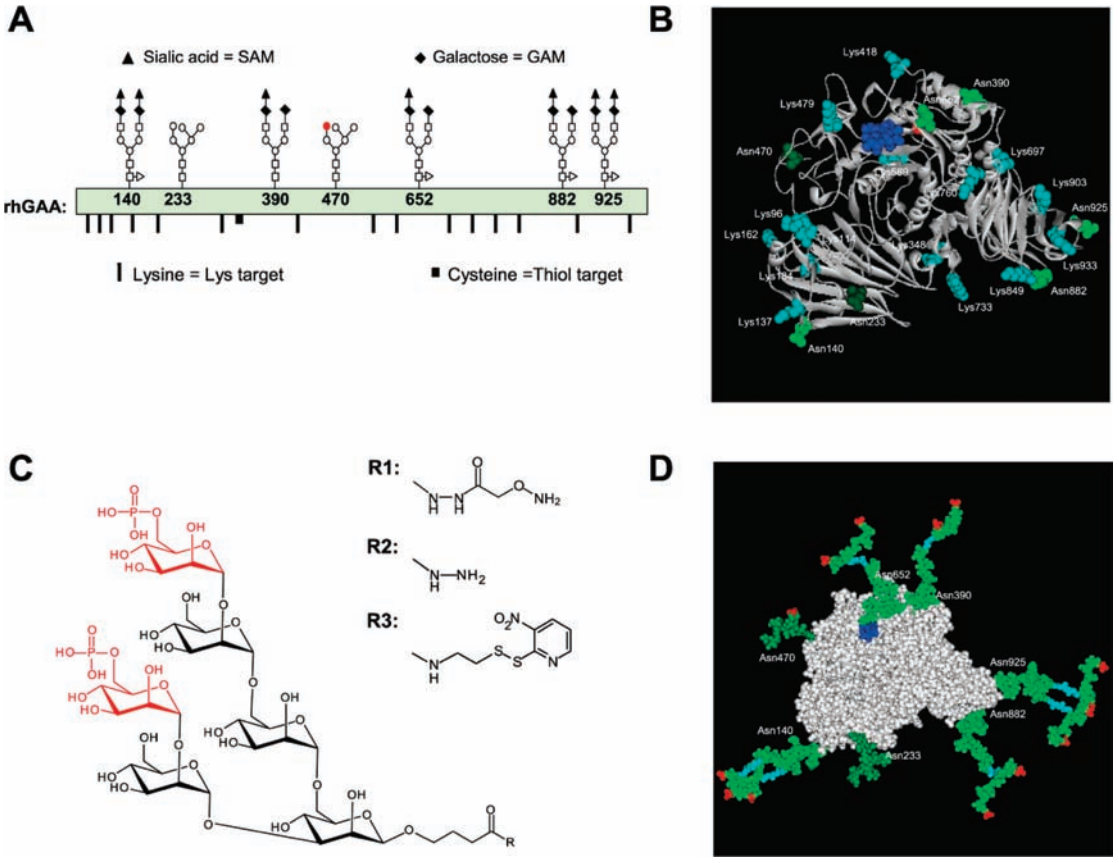


Figure 1. Structures for rhGAA, its conjugate, and bis Man-6-P neoglycan. (A) Linear structure of rhGAA. The positions of the lysine, cysteine, sialic acid, and galactose sites for neoglycan conjugation are shown. (B) A GAA structural model based on a crystal structure of human intestinal MGAM (see text). The *N*-linked glycosylation sites are shown in green (sites occupied by complex-type glycans as light green and those occupied by oligomannose-type glycans as dark green). Lysines are shown in light blue. Red ball: sulfur atom in the single free cysteine. Dark blue: acarbose substrate present in the MGAM structure. (C) Structure of the bis Man-6-P hexasaccharide glycan with different linkers (R groups): R1, aminooxy; R2, hydrazide; R3, thiol-reactive NEA group. (D) Potential structure for neoGAA SAM conjugate. Models for the predominant *N*-glycans identified at each glycosylation site in rhGAA were added to the protein structure shown in B, followed by linkage of a hypothetical model for the synthetic neoglycan with aminooxy linker (R1) as shown in C. Light green: complex-type *N*-glycans and bis Man-6-P neoglycans. Light blue: aminooxy linker. Red: terminal glycan phosphate. Other labels are similar to those in B.

orbital plexus in conscious mice. The concentrations of rhGAA, GAM6, and SAM6 in serum were determined by GAA activity assay.[13]

For the determination of efficacy in glycogen clearance from mouse, GAA knockout mice (3−6 months) were divided into 10 dose groups of 3 males and 3 females. Each group received vehicle; 20, 60, or 100 mg/kg rhGAA; and 4, 12, or 20 mg/kg of the GAM6 or SAM6 once a week for a total of 4 weeks. In order to prevent hypersensitivity induced by test articles, all groups received 5 mg/kg diphenhydramine (Baxter Deerfield, IL) intraperitoneally prior to each dose after the first administration. In the event that animals displayed clinical signs of hypersensitivity, an additional dose of 5 mg/kg diphenhydramine was administered intraperitoneally. Animals were euthanized 7 days after the last dose by CO_2 asphyxiation. Heart, quadriceps, triceps, diaphragm, and psoas were harvested and analyzed for glycogen content as described previously.[1,13,15,16] Statistical analysis was performed using one-way analysis of variance (ANOVA) followed by a Newman-Keuls test. A probability value of $p < 0.05$ was considered statistically significant. Animal experiments were conducted in accordance with the National Institutes of Health *Guide for the Care and Use of Laboratory Animals* (U.S. Department of Health and Human Services, NIH Publication No. 86−23) and were approved by Genzyme's Animal Care and Use Committee.

Other Methods. MALDI-TOF MS analysis was performed using a Voyager DE-PRO mass spectrometer as described in the previous report.[5] Protein aggregation was determined by HPLC size exclusion chromatography.[26] Identification of oxidized methionine residues was performed as described previously.[27] Uptake of proteins into rat L6 myoblasts was performed as described.[1,15,16]

RESULTS

neoGAA Conjugation Strategies. The rhGAA sequence contains a single free cysteine residue, 15 lysines, and 7 *N*-linked glycosylation sites (Figure 1A). In order to better design alternative conjugation strategies, the GAA structure was investigated. A homology model of GAA based on the structure of an α-glucosidase (maltase, MalA) from *S. solfataricus* has been published previously.[28] However, only half of the GAA could be modeled based on the 30% sequence identity with MalA over the 452 amino acid residues. To obtain structural information for

dx.doi.org/10.1021/bc1005416 |*Bioconjugate Chem.* 2011, 22, 741–751

the remainder to identify other potential sites of conjugation, we developed a model (Figure 1B) based on human intestinal maltase-glycoamylase (MGAM). Both GAA and MGAM belong to the glycosyl hydrolases family 31,[25] and the same enzyme class 3.2.1.20. GAA and the N-terminal catalytic subunit of MGAM (PDB codes 2QLY and 2QMJ) also share 44% sequence identities over 860 residues. The result shows the same overall fold of the glycosyl hydrolase family 31 enzymes with 5 structural domains: a trefoil type-P domain, a β-sandwich domain, N-terminal to the catalytic $(\beta/\alpha)_8$ TIM barrel domain, followed by two additional C-terminal β-sandwich domains. As expected from the strong homology to MGAM, the position of residues within the active site, including Trp-516 and Asp-518 within the WIDMNE element, which were previously identified in GAA by cross-linking of a substrate analogue and site-directed mutagenesis,[29] were preserved in the model and near the acarbose binding site. On the basis of this structural model, the lysines and *N*-linked glycosylation sites are found in solvent-exposed positions distributed relatively evenly over the entire structure without any notable clustering, suggesting those sites as potential alternative conjugation sites.

Conjugation of a synthetic bis Man-6-P neoglycan (Figure 1C) to sialic acids on rhGAA *N*-glycans provides a substantial increase in the efficacy in GAA knockout mice.[1,16] A structural model of such a conjugate was generated by linking in silico models of the dominant glycan forms at each site[13] extended in solution consistent with their hydrophilicity and addition of a model of the synthetic glycan assuming charge repulsion of the bis-phosphates (Figure 1D). This model suggested potentially rather large extensions of the existing GAA structure were possible. This observation suggested that conjugation of bis Man-6-P neoglycans to alternative sites might provide advantages in preserving the activity of the protein against its natural substrate glycogen, a complex polysaccharide which may be sterically hindered from interacting at the active site by large glycans nearby. A number of different conjugation chemistries targeting different functional groups were then explored. Bis Man-6-P hexasaccharide neoglycans were synthesized with different appended functionalities (Figure 1C), including terminal aminooxy (R1), hydrazide (R2), and thiol-reactive NEA groups (R3), for conjugating to either aldehydes or thiols.

A particularly interesting target was the single free thiol group (Cys-374) in rhGAA, since exclusive coupling to this site would provide a homogeneous conjugate. The structural model however suggested relatively limited access to this residue, which was confirmed by negligible conjugation of thiol-reactive NEA-neoglycan (data not shown). Quantitative modification of the thiol group was successful using a hydrophobic homobifunctional cross-linking reagent with spacer arm of 19.9 Å, 1,4-di-(3′-[2-pyridyldithiol]propionamido) butane (DPDPB, Pierce) but only in the presence of organic cosolvents, which resulted in very strong light scattering and formation of a precipitate (data not shown). These results suggest that modification of Cys-374 may be achieved, but only under harsh conditions unlikely to preserve the structural integrity of the protein and creating undesirable aggregation.

Conjugation to lysines was attractive because of the higher lysine content of rhGAA than sialic acids employed in previous conjugates[1,15,16] could allow a higher degree of modification. Conjugates containing neoglycans hydrazone-linked to lysines modified with an aromatic aldehyde (SFB) were obtained with Man-6-P contents consistent with up to ~4 mol neoglycan per mole rhGAA, in agreement with the conjugate molecular weights obtained by MALDI-TOF MS (Figure 2A and B). However, an accelerated stability study performed in pH 6.2 buffer at 40 °C resulted in more than 50% loss of neoglycan over 14 days (Figure 2A and B). These results indicate that the hydrazone bond between neoglycan hydrazide and the benzaldehyde linker was not stable for extended periods.

To increase the stability, the hydrazone linkage was replaced with a more stable oxime by use of an aminooxy form of the bis Man-6-P neoglycan (Figure 1C). Oxime linkages are known for their high stability over a broad range of pH including the mildly acidic conditions for storage buffer used here.[30] As shown in Figure 2C, a 16.6-fold molar excess of glycan was saturating for the Man-6-P content with the introduction of 5 mol neoglycan per mole rhGAA (10 mol Man-6-P per mole protein). Higher molar ratios of neoglycan failed to further increase the Man-6-P content. The number of neoglycans coupled was also significantly lower than the incorporated SFB benzaldehyde content determined by absorbance (~8−9 mol/mol). A high level of aggregation was also frequently observed (Figure 2D). In an attempt to overcome this problem, conjugation was also performed using a PEGylated version of SFB (PEG4/PFB, Solulink), in which the lysine-reactive pentafluoroester group is separated from the aromatic formylbenzoate by a hydrophilic PEG4 spacer. This failed to produce significant decrease in aggregation (data not shown), suggesting a very limited tolerance of the protein for hydrophobic substitutions.

The susceptibility of the protein to aggregation in response to hydrophobic modifications suggests the importance of maintaining a hydrophilic surface environment. Carbohydrate-mediated conjugation chemistries were therefore evaluated since the aldehydes required for conjugation could be generated directly by an oxidation step without the need for linkers containing hydrophobic functional groups. Aldehydes on terminal carbohydrate residues would be expected to be well-separated from the protein surface. Seven *N*-linked glycosylation sites are present on rhGAA including oligomannose, phosphorylated oligomannose, and complex-type glycans (Figure 1A and B).[13] Among these sites, Asn-390, Asn-652, Asn-882, and Asn-925 are occupied mainly by sialylated complex-type glycans, while a significant amount of oligomannose-type glycans are present on Asn-140, Asn-233, and Asn-470, with a higher abundance on Asn-233 and Asn-470. A fraction of the oligomannose-type glycans bear either a single (mono Man-6-P) or two phosphates (bis Man-6-P), resulting in an average Man-6-P content of 1 mol per mole in rhGAA. The complex-type glycans contain approximately 6−7 sialic acid and 10 galactose residues as potential sites of conjugation. Two methods for coupling these glycans were compared: a chemical oxidation process directed at sialic acids and an enzymatic approach targeting galactose.

Conjugation using sialic acid-mediated (SAM) chemistry was performed using a method described previously.[1] As expected, after periodate treatment, sialic acid was undetectable by HPAEC-PAD analysis, consistent with the complete oxidation to the aldehyde form (data not shown). Conjugation of the neoglycan with this intermediate was found to be highly reproducible, with yields of 13−17 mol Man-6-P per mole GAA consistent with an overall process efficiency approaching 100%. Strikingly different than the amino acid directed chemistries, the level of protein aggregation was consistently less than 3%. However, treatment by periodate also resulted in the nearly

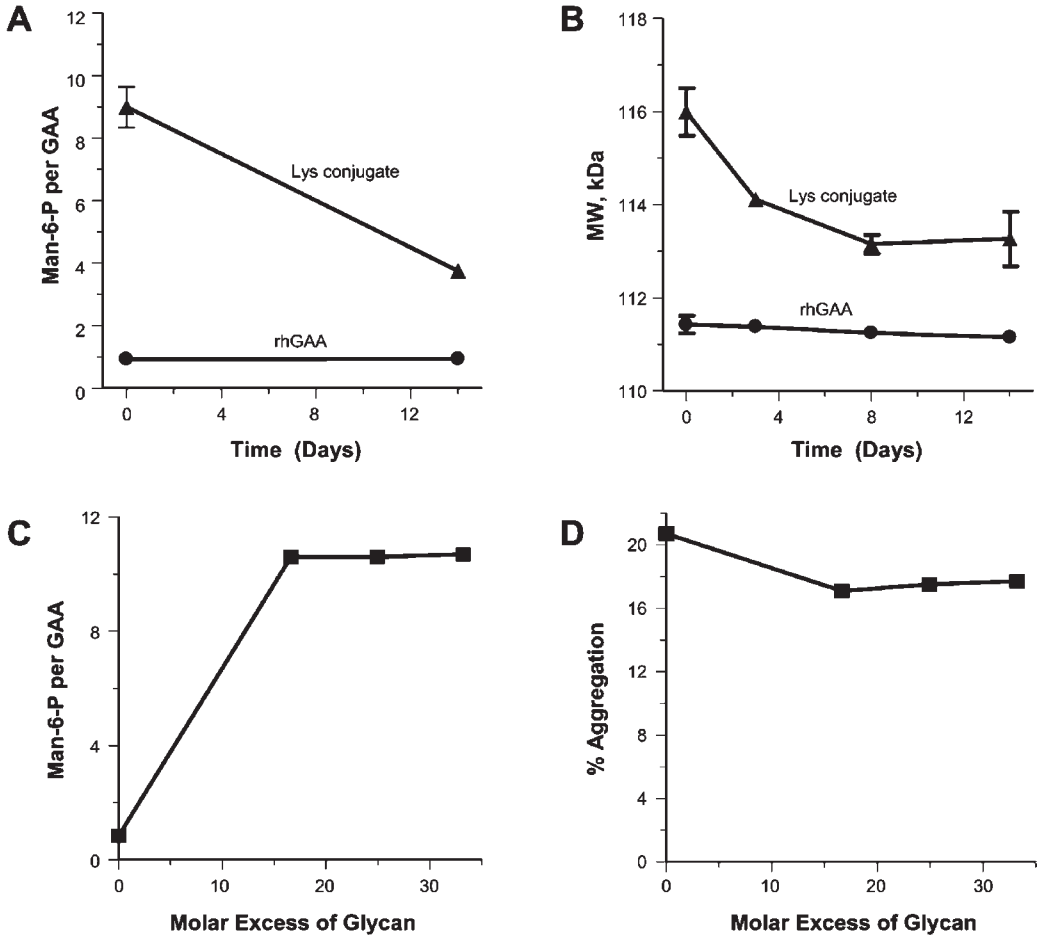


Figure 2. Properties of neoGAA conjugates prepared by introducing aldehyde groups at lysines. Man-6-P content (A) and MALDI-TOF MS analysis of the molecular weight (B) of rhGAA or SFB-hydrazone conjugate incubated at pH 6.2 at 40 °C. (C) Conjugation of SFB modified rhGAA with increasing amounts of aminooxy neoglycan. (D) Aggregation of the same conjugates in C as determined using size exclusion chromatography.

complete oxidation (>95%) of two methionine residues, Met-172 and Met-173, in the final conjugate (Figure 3A).

The generation of aldehyde groups on the glycans by enzymatic oxidation of galactose residues (GAM) with galactose oxidase (GAO) was explored as a means to avoid undesirable side products of chemical oxidation. However, since rhGAA is highly sialylated and GAO reacts only with galactose at the terminal position on glycans,[13,31] the protein was first treated with neuraminidase to remove the terminal sialic acids and expose the galactose residues. Following oxidation with GAO, the aldehydes were then coupled with the bis Man-6-P neoglycan (aminooxy) to yield a conjugate (GAM6) with an oxime-linked glycan. Initial evaluation showed that desialylation of rhGAA was complete after treatment with neuraminidase for 6 h at 20 mU/mg rhGAA. Following GAO treatment (10 μg/mg), conjugation was saturated with a 16.6-fold molar excess of the neoglycan over rhGAA, yielding active conjugates with high neoglycan contents (11−12 mol Man-6-P per mole protein) and low aggregation (<3%). The Man-6-P content of these conjugates suggested that 50−60% of the galactose residues had been coupled to neoglycan. Unexpectedly, ~26% of Met-172 and Met-173 were again found in oxidized form, as in the SAM process (Figure 3A). This oxidation may have occurred as a result of the presence of hydrogen peroxide, a byproduct of the GAO reaction. Consistent with this, inclusion of small amount of catalase (2 U/mg rhGAA) was found to be effective in eliminating this oxidation side product (Figure 3A).

SDS-PAGE of the SAM and GAM products showed a shift in the mobility of the predominant 110 kDa form of the protein, as expected from an increase in overall molecular weight as a result of neoglycan conjugation (Figure 3B). A smaller shift in mobility was obtained by GAM modification than SAM, most likely due to the removal of sialic acids during the GAM process, and relatively larger effect of the sialic acids on mobility than polypeptide mass. However, the GAM method also appeared to be more selective, in that the shifts in mobility were only apparent with the 110 kDa form, whereas the processed forms of rhGAA (76 kDa and 70 kDa)[4,5] were also modified by the SAM process. Trace amounts of high molecular weight products showing parallel molecular weight shifts were also visible in the SAM and GAM conjugation products after silver staining of overloaded SDS-PAGE gels (Figure 3B), likely reflecting a small amount of aggregated proteins possibly also conjugated with neoglycan.

The lower yield of noeglycan in the conjugates obtained with the GAM process was somewhat surprising, given the higher galactose than sialic acid content in rhGAA. The efficiency of each step in the process was thus followed by carbohydrate composition analysis of the intermediates and final product. As expected, neuraminidase treatment resulted in complete removal of sialic acids, and galactose was nearly undetectable following

dx.doi.org/10.1021/bc1005416 |*Bioconjugate Chem.* 2011, 22, 741–751

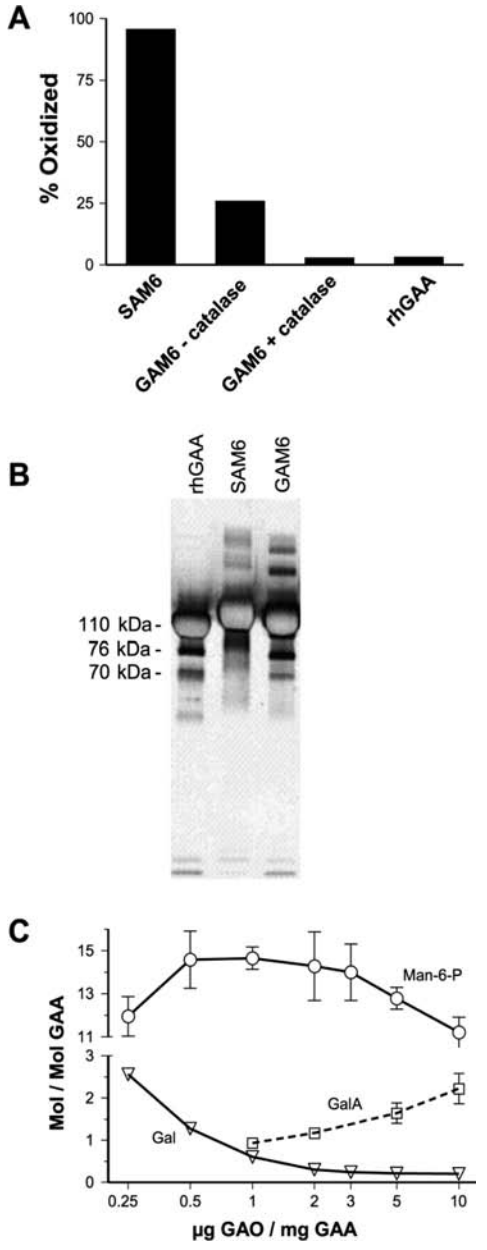


Figure 3. Characterization of SAM and GAM conjugates. (A) Oxidation of Met-172 and Met-173 determined by LC/MS. GAM6 was prepared with or without catalase. (B) SDS-PAGE of the SAM and GAM conjugates, followed by silver stain. The 110 kDa is precursor form, while 76 kDa and 70 kDa are processed forms of rhGAA. (C) Effect of GAO:rhGAA ratio on Man-6-P, GalA, and residual galactose levels in GAM conjugate.

GAO treatment at 10 μg/mg (data not shown). However, following GAO treatment, galacturonic acid (GalA), in which the C6 position of galactose is fully oxidized to the carboxylic acid form, was also identified by LC/MS/MS of protein glycans released by PNGase F. This product likely arose by further oxidation of the desired galactose aldehyde to the carboxylic acid form by the action of GAO during the reaction,[32,33] suggesting that the lower efficiency observed with GAM conjugation under these conditions may have resulted from the conversion of the aldehyde to the unconjugatable acid form. To improve on the Man-6-P content, the GAO:rhGAA ratio was varied to limit the extent of the reaction. The Man-6-P, GalA, and remaining galactose contents of the final conjugates were then determined by quantitative HPAEC-PAD. As shown in Figure 3C, the final Man-6-P content of the conjugates varied significantly with the amount of GAO used during the oxidation step. The highest level of Man-6-P was observed at ~1 μg GAO per mg GAA, with ~7 neoglycans coupled per rhGAA (15 mol/mol Man-6-P per rhGAA). Below this optimum GAO:GAA ratio, significant amounts of unmodified galactoses were observed (>1 mol/mol), which increased with further decreases in GAO. Above the optimum, a reduction in the amount of residual galactose was accompanied by a higher GalA content and a decrease in the final Man-6-P content, consistent with the loss of aldehyde groups available for conjugation. Even at the optimum ratio, a significant amount of both GalA and residual galactose were present.

***In Vitro* Comparison of SAM and GAM Conjugates.** The enzyme activity of a panel of SAM and GAM conjugates containing a wide distribution of neoglycan content was determined. All of the conjugates showed some reduction in specific activity relative to the rhGAA control (Figure 4A), and the loss in activity inversely correlated with the Man-6-P content of the conjugate (r^2 = 0.87, p < 0.0001). There was no significant difference between the activity of conjugates with comparable Man-6-P contents prepared by either the SAM or GAM process.

Binding of rhGAA and neoGAA to the cation-independent Man-6-P receptor (CI-MPR) was followed by HPLC-based affinity chromatography using immobilized bovine CI-MPR (Figure 4B). To assess receptor affinity, protein was applied to the column and the bound fraction eluted with steps of increasing Man-6-P concentration. Representative profiles from rhGAA, SAM, and GAM conjugates are shown in Figure 4B. The majority of unmodified rhGAA either failed to bind or eluted with a low concentration of Man-6-P (0.25 mM) in the mobile phase. In contrast, more than 95% of both GAM and SAM conjugates were bound and could be eluted only with 5 mM Man-6-P or above. SAM and GAM conjugates showed a similar profile by this method.

The uptake of rhGAA and neoGAA by rat L6 myoblast cells *in vitro* was followed to determine if differences in the conjugation method had an effect on the efficiency of internalization through CI-MPR. As shown in Figure 4C, more than 10-fold higher GAA activity was observed in cells incubated with neoGAA conjugates than with rhGAA lacking neoglycan over a wide range of protein concentrations. GAM and SAM conjugates showed a comparable saturable uptake with EC_{50} of ~5 nM (0.5 μg/mL) protein. The EC_{50} for rhGAA could not be determined in this experiment due to its low level of uptake.

Serum Half-Life and Glycogen Clearance in the GAA Knockout Mouse. The serum clearance of rhGAA and neoGAA was determined following tail vein injection at single dose (20 mg protein/kg) to GAA knockout mice. All proteins including rhGAA and neoGAA conjugates were rapidly cleared from circulation with serum half-lives ($T_{1/2}$) between 0.5 and 2.3 h (Figure 5). Both GAM and SAM conjugates demonstrated faster clearance than rhGAA ($T_{1/2}$ of 24% and 37% of rhGAA, respectively). The GAM conjugate was cleared most rapidly with a serum half-life of 33 min, and its serum concentration was below the limit of quantitation at both 240 and 480 min. The SAM conjugate was cleared at a relatively slower rate than GAM conjugate and it was below the limit of quantitation at 480 min with a serum half-life of 51 min.

The impact of bis Man-6-P neoglycan conjugation on glycogen clearance by rhGAA and both neoGAA conjugates (GAM6

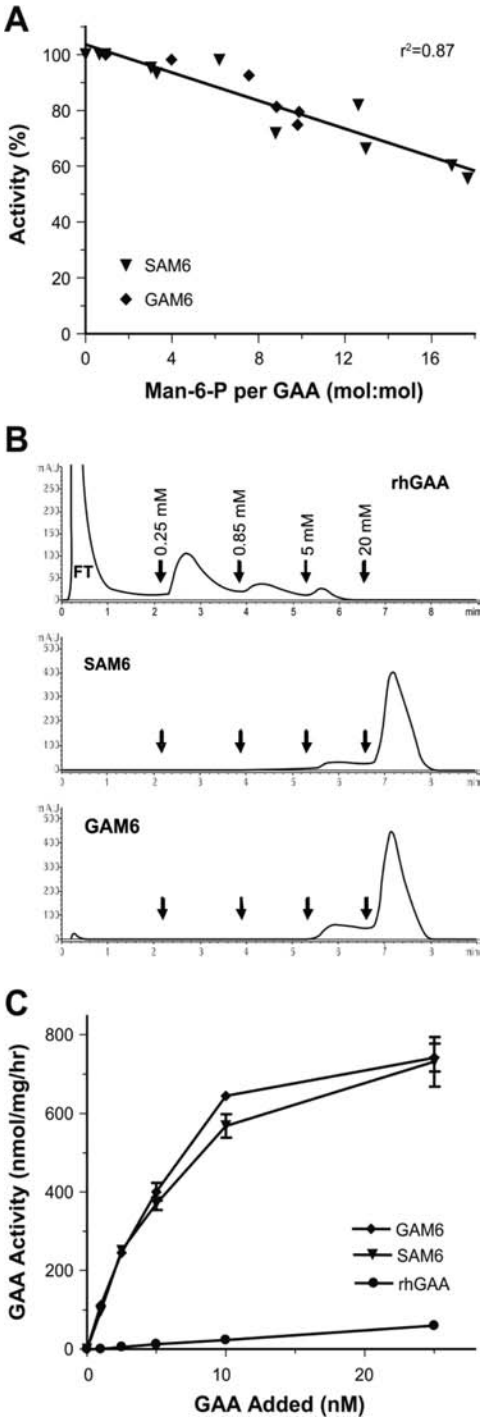


Figure 4. *In vitro* activity of neoGAA SAM and GAM conjugates. (A) Effect of Man-6-P content on GAA enzyme activity, which is presented as % activity from rhGAA. SAM6 (triangles) and GAM6 (diamonds) were prepared with different molar excess of bis Man-6-P neoglycan over GAA. (B) Binding of rhGAA, SAM6, and GAM6 to Man-6-P receptor (CI-MPR) affinity columns, which were eluted with increasing concentrations of Man-6-P as indicated by arrows. (C) Uptake of rhGAA or neoGAA by L6 myoblast cells *in vitro*.

and SAM6) was followed in GAA knockout mice. In this study, rhGAA and neoGAA conjugates were administered in four weekly doses via tail vein injection. The amount of glycogen in heart and skeletal muscles was measured one week after the final

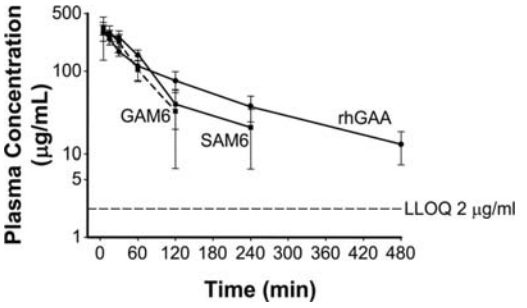


Figure 5. Serum clearance of neoGAA SAM and GAM conjugates in the GAA knockout mice. Animals were administered with rhGAA or neoGAA conjugates via the tail vein as a single bolus injection. The amount of proteins was determined using the GAA activity assay of blood collected at 5, 15, 30, 60, 120, 240, and 480 min post injection. The Man-6-P contents were 0.9, 13.3, and 11.3 mol per mole for rhGAA, SAM6, and GAM6, respectively.

administration. The dose ranges tested were 5-fold higher for rhGAA than for the neoGAA conjugates in order to obtain comparable glycogen clearance. At the lowest dose level, rhGAA (20 mg/kg) reduced glycogen in the heart by only 17% (Figure 6A). By comparison, the SAM conjugate produced a greater reduction (61%) in glycogen at a 5-fold lower dose (4 mg/kg), while the GAM conjugate at 4 mg/kg was less effective, showing a modest clearance comparable to rhGAA administered at 20 mg/kg (Figure 6A). At the intermediate dose level (60 mg/kg rhGAA and 12 mg/kg for neoGAAs), rhGAA or the SAM conjugate achieved 90% and 94% glycogen clearance, respectively, while the GAM conjugate reduced glycogen by 51%. Finally, at the highest dose level (100 mg/kg rhGAA and 20 mg/kg for neoGAAs), essentially complete clearance of glycogen was obtained with rhGAA or a 5-fold lower dose of the SAM conjugate but not the GAM conjugate, which showed a somewhat lower efficacy (79%). The dose required to achieve 50% reduction in glycogen in the heart was estimated as ~40, 12, and <4 mg/kg for rhGAA, GAM, and SAM conjugates, respectively.

In skeletal muscle, both rhGAA and SAM conjugate at the highest dose (100 mg/kg and 20 mg/kg, respectively) showed significant efficacy, reducing glycogen by 77% and 80% in the quadriceps, respectively (Figure 6B). In contrast, the GAM conjugate at 20 mg/kg achieved a lesser (59%) reduction. Triceps and diaphragm showed similar responses to treatment (data not shown). At an intermediate dose, the SAM conjugate (12 mg/kg) also cleared more glycogen (81%) than the GAM conjugate at the same dose or rhGAA at a 5-fold higher dose (45% or 56% reduction, respectively) in the quadriceps. Neither rhGAA nor the neoGAA conjugates were able to significantly clear glycogen from any skeletal muscle at the lowest dose. We conclude that the conjugates prepared using SAM chemistry are somewhat more potent than neoGAA generated using the GAM method.

We considered the possibility that the terminal GalA found in the GAM conjugate might contribute to its faster clearance and lower efficacy in glycogen clearance in muscle by the undesirable delivery to nontarget tissue by mechanisms such as uptake by the asialoglycoprotein receptor. To test this, GAM6 was prepared with either 2 μg/mg or 10 μg/mg GAO, yielding conjugates with a 2-fold difference in GalA content, which were administered at 20 mg/kg for 4 weekly doses to GAA knockout mice. However, no significant difference was observed in the clearance of glycogen in either heart or skeletal muscle between these two

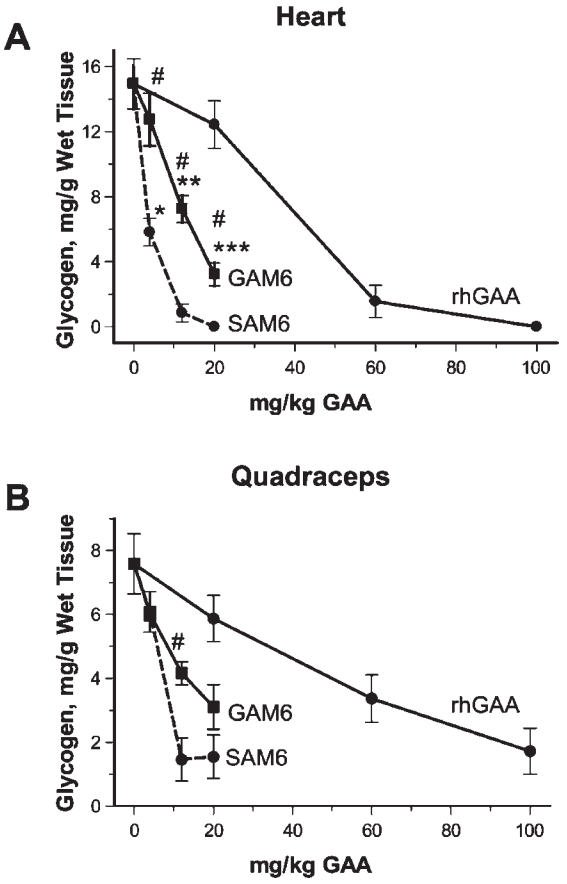


Figure 6. Glycogen clearance in the GAA knockout mice after treated with neoGAA SAM and GAM conjugates. Glycogen levels in heart (A) and quadriceps (B) determined following 4 weekly doses of rhGAA and neoGAA conjugates. rhGAA and neoGAA conjugates were the same as described in Figure 5. $^{*}p < 0.05$ as compared to rhGAA at 20 mg/kg dose; $^{**}p < 0.05$ as compared to rhGAA at 60 mg/kg dose; $^{***}p < 0.05$ as compared to rhGAA at 100 mg/kg dose; $\#p < 0.05$ as compared to equivalent doses of SAM6.

preparations (data not shown). Both conjugates showed similar serum clearance after a single dose injection at 20 mg/kg.

■ DISCUSSION

We have compared a number of strategies to conjugate synthetic bis Man-6-P neoglycans to rhGAA targeting either amino acids or protein carbohydrates. The simplest approach of conjugation to the unique free thiol group from Cys-374, although highly attractive from a development standpoint, was achieved only under partially denaturing conditions, and was consistent with the structural model in which the sulfur is only partially visible from protein surface, suggesting that its availability for modification may be quite limited. In contrast, lysine residues which are largely solvent-exposed in the structural model were modified at a higher efficiency by an amine-reactive aromatic bifunctional linker, SFB, which supported glycan conjugation through oxime chemistry. However, the extent of modification was ultimately limited by protein aggregation, suggesting that the higher efficiency obtained with SFB is a consequence of its aromaticity, with the expected reactivity toward lysines in partially buried positions. A number of lysines in the structural model are available to participate in interdomain salt bridges or hydrogen bonds. In addition, others occur between structural domains with relatively lower solvent accessibility and whose modification could destabilize the structure.

In contrast, both the GAM and SAM carbohydrate-directed chemistries for neoglycan conjugation were each more successful in achieving high Man-6-P levels and yielded stable conjugates with little aggregation in a consistent fashion. Both chemistries produced conjugates with very high affinities for the Man-6-P receptor (Figure 4B) which were internalized with high efficiency by rat myoblasts. On the basis of our GAA structural model with added model structures for the neoglycans coupled to complex-type glycans at the 5 known complex-type *N*-glycosylation sites,[13] a wide spatial distribution of bis Man-6-P appears to be achievable by both methods (Figure 1D). Such a distribution could provide for simultaneous interaction of Man-6-P residues with CI-MPR, which has been reported to have at least 3 Man-6-P binding domains.[34] Coupling of the bis Man-6-P neoglycans to the terminal sugars of *N*-glycans as suggested by the model may also produce an array of charged glycan structures, creating a charge shell and increasing the overall protein hydrophilicity and solubility and thereby suppressing any tendency toward aggregation.

Our parallel evaluation of these chemistries demonstrated a higher overall efficiency of conjugation with SAM than GAM in spite of the higher number of galactose than sialic acid conjugation sites. Even by use of the optimal amount of GAO in the GAM process, the observed yield of Man-6-P (15 mol per mol) in GAM6 was significantly less than the expected 20 mol per mol based on the protein galactose content, part of which is accounted for by overoxidation to the nonconjugatable form GalA. However, even accounting for the loss through GalA formation, the efficiency of the neoglycan coupling step appears to be lower than SAM (~75−85% vs ~100% for SAM). It is possible that the first neoglycan coupled to one of the two terminal sugars on biantennary *N*-glycans sterically interferes with coupling of a second glycan to the other terminus. Such an effect might be expected to be more pronounced for the galactose residues closer to the structurally crowded environment of the branch point than for the more distal sialic acid coupling sites in SAM.

Oxidation of galactose aldehyde to the acid GalA form by GAO has been described previously.[32] This reaction is relatively inefficient compared with the generation of the aldehyde, although catalase has also been shown to drive the reaction, likely due to oxygen regeneration.[32] However, a structural model of galactose docked with GAO[35−37] suggests that the additional hydroxyl group in the aldol form of the aldehyde can be easily accommodated in the active site, making discrimination of the two substrates difficult. The relative efficiency of the two oxidation events on rhGAA *N*-glycans appears to be sufficiently similar to render the exclusive preparation of an aldehyde form difficult and a challenge to defining a rational strategy to engineer GAO to limit its choice of substrates. Other strategies, such as controlling the available oxygen, may be possible but have not been explored because of the technical difficulty in both properly modeling and translating the process to production scale.

Although both GAM and SAM conjugates show a comparable high-affinity binding to CI-MPR and similar uptake into myoblast cells, SAM6 consistently showed higher efficacy *in vivo*. The high doses of either rhGAA or neoGAA which are required to achieve efficacy in these animal models compared to other enzyme replacement therapeutics suggest that muscle uptake is

inefficient and that delivery is critically dependent upon the circulating half-life to achieve a high systemic exposure. Thus, the lower efficiency of glycogen clearance obtained with GAM conjugate may result from its lower bioavailability due to faster clearance from circulation. It should be noted that the circulating level remaining even after clearance of 90% of both conjugates is still well above the EC_{50} for cell uptake via CI-MPR (5 nM or ~0.5 μg/mL, Figure 4C). Nonetheless, the window during which the protein concentration exceeds this level is longer for the SAM conjugate (Figure 5). It is also possible that a higher enzyme concentration in circulation is required to drive an inefficient transport process across the continuous endothelial layer into the interstitial space prior to the CI-MPR dependent uptake by myocytes. In this view, at a low enzyme concentration in the interstitial space well below the EC_{50} for uptake, a much greater effect of the degree of phosphorylation on the net uptake would be expected. In this situation, the higher Man-6-P content of the SAM conjugate would confer a modest advantage in addition to its longer circulating half-life.

The current study unexpectedly also identified a significant inverse correlation between the neoglycan content and GAA enzyme activity against a low molecular weight synthetic substrate (Figure 4A). On the basis of the GAA structural model, the *N*-linked glycosylation site at Asn-652, which is occupied mainly by sialylated complex-type glycans,[13] is in close proximity to the active site of rhGAA previously identified by site-directed mutagenesis [29] and the substrate site identified by acarbose binding in the MGAM structure which is preserved in the GAA model (Figure 1B). It is possible that an extended structure with bis Man-6-P neoglycan conjugated at this site interferes with substrate binding at the active site. With glycogen as the substrate, conjugation produced a significant increase in K_m and without a significant effect on V_{max}, consistent with steric hindrance of substrate binding (data not shown). However, any reduction in specific activity could be easily offset by a larger increase in uptake of conjugates achieved by neoglycan conjugation (Figure 4C). It is also possible that the neoglycans are either released by a low pH or removed by the action of glycosidases once in the lysosome, leading to a processed form of the enzyme similar to that obtained with rhGAA and with comparable activity.[30,38] Even without processing, however, the concentration of the glycogen substrate accumulated in Pompe myocytes is likely to minimize any effect on K_m. The intracellular fate of the neoGAA is currently under investigation.

CONCLUSION

A number of alternative strategies to conjugate synthetic bis Man-6-P neoglycans to rhGAA were investigated. Of these, oxime chemistry directed at the aldehydes generated chemically or enzymatically on carbohydrates was found to be most practical, consistently demonstrating high conjugation efficiency, low aggregation, and a high linkage stability. To eliminate the side oxidation of methionines by periodate during the SAM process, a novel three enzyme remodeling system (GAM) was devised to selectively generate a large number of aldehydes for conjugation. Although both SAM and GAM conjugates bound the Man-6-P receptor with comparable affinity which exceeded that for rhGAA, conjugate prepared by SAM chemistry displayed higher *in vivo* potency than GAM conjugate, likely as a result primarily of slower serum clearance. These results provide the support for the SAM conjugation process for further development as a next generation therapeutic for Pompe disease. Nonetheless, the GAM method produced a highly defined product profile typical of a more selective enzyme-mediated process, including fewer oxidative side products. This approach still achieved a significant increase of *in vivo* potency over unmodified rhGAA, suggesting that it represents an approach for improving targeting of proteins which show a higher sensitivity to periodate oxidation.

ASSOCIATED CONTENT

Supporting Information. Structure diagram. This material is available free of charge via the Internet at http://pubs.acs.org.

AUTHOR INFORMATION

Corresponding Author

*To whom correspondence should be addressed. Genzyme Corp., One Mountain Road, Framingham, Massachusetts 01701-9322, USA. E-mail: qun.zhou@genzyme.com.

ACKNOWLEDGMENT

The authors would like to thank John McPherson, Edward Cole, Robert Mattaliano, Seng Cheng, William Canfield, Mike Hayes, and Alison McVie-Wylie for advice or helpful discussion. We also want to thank Karen Lee, Joe Kutzko, Xuezhen Kang, Kerry Culm-Merdek, Cindy Rogers, Michael Huff, Eliza Yeung, Matthew DeFronzo, Robert Killeen, Jennifer Millian, Charles Lemire, Lihui Hou, Jennifer Kim, Denise Honey, Anna Park, Susan Boucher, Peng Pan, Cathleen Thurber, Karen Albee, Heather Hughes, Elizabeth Brunyak, Xiaoying Jin, Lee Sherman, Alison Schroeer, and Lauren Young for helpful suggestions and technical support.

ABBREVIATIONS

rhGAA, recombinant human acid α-glucosidase; Man-6-P, mannose 6-phosphate; neoGAA, rhGAA conjugated with bis Man-6-P neoglycans; CI-MPR, cation-independent Man-6-P receptor; SAM, sialic acid-mediated conjugation; SAM6, conjugate prepared using SAM conjugation; GAM, galactose aldehyde-mediated conjugation; GAM6, conjugate prepared using GAM conjugation; GAO, galactose oxidase; GalA, galacturonic acid; SFB, amine-reactive succinimidyl 4-formylbenzoate; PEG4/PFB, penta fluorobenzamide polyetheyleneglycol 4; NEA, nipsylethylamine; TEA, triethylamine; DPDPB, 1,4-di-(3′-[2-pyridyldithiol]-propionamido) butane; EDAC, 1-ethyl-3-(3-dimethylaminopropyl) carbodiimide; HOBt, hydroxybenzotriazole; NHS, N-hydroxysuccinimide; HPAEC-PAD, high pH anion exchange chromatography with pulsed amperometric detection; MGAM, maltase-glycoamylase.

REFERENCES

(1) Zhu, Y., Jiang, J. L., Gumlaw, N. K., Zhang, J., Bercury, S. D., Ziegler, R. J., Lee, K., Kudo, M., Canfield, W. M., Edmunds, T., Jiang, C., Mattaliano, R. J., and Cheng, S. H. (2009) Glycoengineered acid alpha-glucosidase with improved efficacy at correcting the metabolic aberrations and motor function deficits in a mouse model of Pompe disease. *Mol. Ther. 17*, 954–63.

(2) Fukuda, T., Roberts, A., Plotz, P. H., and Raben, N. (2007) Acid alpha-glucosidase deficiency (pompe disease). *Curr. Neurol. Neurosci. Rep. 7*, 71–7.

(3) Varki, A., and Kornfeld, S. (2009) P-type lectins. *Essentials of Glycobiology* (Varki, A., Cummings, R. D., Esko, J. D., Freeze, H. H., Stanley, P., Bertozzi, C. R., Hart, G. W., and Etzler, M. E., Eds) pp 425−7, Cold Spring Harbor Laboratory Press, New York.

(4) Wisselaar, H. A., Kroos, M. A., Hermans, M. M., van Beeumen, J., and Reuser, A. J. (1993) Structural and functional changes of lysosomal acid alpha-glucosidase during intracellular transport and maturation. *J. Biol. Chem. 268*, 2223–31.

(5) Moreland, R. J., Jin, X., Zhang, X. K., Decker, R. W., Albee, K. L., Lee, K. L., Cauthron, R. D., Brewer, K., Edmunds, T., and Canfield, W. M. (2005) Lysosomal acid alpha-glucosidase consists of four different peptides processed from a single chain precursor. *J. Biol. Chem. 280*, 6780–91.

(6) Nicolino, M., Byrne, B., Wraith, J. E., Leslie, N., Mandel, H., Freyer, D. R., Arnold, G. L., Pivnick, E. K., Ottinger, C. J., Robinson, P. H., Loo, J. C., Smitka, M., Jardine, P., Tato, L., Chabrol, B., McCandless, S., Kimura, S., Mehta, L., Bali, D., Skrinar, A., Morgan, C., Rangachari, L., Corzo, D., and Kishnani, P. S. (2009) Clinical outcomes after long-term treatment with alglucosidase alfa in infants and children with advanced Pompe disease. *Genet. Med. 11*, 210–9.

(7) Chen, L. R., Chen, C. A., Chiu, S. N., Chien, Y. H., Lee, N. C., Lin, M. T., Hwu, W. L., Wang, J. K., and Wu, M. H. (2009) Reversal of cardiac dysfunction after enzyme replacement in patients with infantile-onset Pompe disease. *J. Pediatr. 155*, 271–5 e2.

(8) Kishnani, P. S., Corzo, D., Leslie, N. D., Gruskin, D., Van der Ploeg, A., Clancy, J. P., Parini, R., Morin, G., Beck, M., Bauer, M. S., Jokic, M., Tsai, C. E., Tsai, B. W., Morgan, C., O'Meara, T., Richards, S., Tsao, E. C., and Mandel, H. (2009) Early treatment with alglucosidase alpha prolongs long-term survival of infants with Pompe disease. *Pediatr. Res. 66*, 329–35.

(9) Merk, T., Wibmer, T., Schumann, C., and Kruger, S. (2009) Glycogen storage disease type II (Pompe disease)--influence of enzyme replacement therapy in adults. *Eur. J. Neurol. 16*, 274–7.

(10) Strothotte, S., Strigl-Pill, N., Grunert, B., Kornblum, C., Eger, K., Wessig, C., Deschauer, M., Breunig, F., Glocker, F. X., Vielhaber, S., Brejova, A., Hilz, M., Reiners, K., Muller-Felber, W., Mengel, E., Spranger, M., and Schoser, B. (2009) Enzyme replacement therapy with alglucosidase alfa in 44 patients with late-onset glycogen storage disease type 2: 12-month results of an observational clinical trial. *J. Neurol. 257*, 91–7.

(11) van der Ploeg, A. T., Clemens, P. R., Corzo, D., Escolar, D. M., Florence, J., Groeneveld, G. J., Herson, S., Kishnani, P. S., Laforet, P., Lake, S. L., Lange, D. J., Leshner, R. T., Mayhew, J. E., Morgan, C., Nozaki, K., Park, D. J., Pestronk, A., Rosenbloom, B., Skrinar, A., van Capelle, C. I., van der Beek, N. A., Wasserstein, M., and Zivkovic, S. A. (2010) A randomized study of alglucosidase alfa in late-onset Pompe's disease. *N. Engl. J. Med. 362*, 1396–406.

(12) Thurberg, B. L., Lynch Maloney, C., Vaccaro, C., Afonso, K., Tsai, A. C., Bossen, E., Kishnani, P. S., and O'Callaghan, M. (2006) Characterization of pre- and post-treatment pathology after enzyme replacement therapy for Pompe disease. *Lab. Invest. 86*, 1208–20.

(13) McVie-Wylie, A. J., Lee, K. L., Qiu, H., Jin, X., Do, H., Gotschall, R., Thurberg, B. L., Rogers, C., Raben, N., O'Callaghan, M., Canfield, W., Andrews, L., McPherson, J. M., and Mattaliano, R. J. (2008) Biochemical and pharmacological characterization of different recombinant acid alpha-glucosidase preparations evaluated for the treatment of Pompe disease. *Mol. Genet. Metab. 94*, 448–55.

(14) Song, X., Lasanajak, Y., Olson, L. J., Boonen, M., Dahms, N. M., Kornfeld, S., Cummings, R. D., and Smith, D. F. (2009) Glycan microarray analysis of P-type lectins reveals distinct phosphomannose glycan recognition. *J. Biol. Chem. 284*, 35201–14.

(15) Zhu, Y., Li, X., Kyazike, J., Zhou, Q., Thurberg, B. L., Raben, N., Mattaliano, R. J., and Cheng, S. H. (2004) Conjugation of mannose 6-phosphate-containing oligosaccharides to acid alpha-glucosidase improves the clearance of glycogen in pompe mice. *J. Biol. Chem. 279*, 50336–41.

(16) Zhu, Y., Li, X., McVie-Wylie, A., Jiang, C., Thurberg, B. L., Raben, N., Mattaliano, R. J., and Cheng, S. H. (2005) Carbohydrate-remodeled acid alpha-glucosidase with higher affinity for the cation-independent mannose 6-phosphate receptor demonstrates improved delivery to muscles of Pompe mice. *Biochem. J. 389*, 619–628.

(17) Prescher, J. A., and Bertozzi, C. R. (2006) Chemical technologies for probing glycans. *Cell 126*, 851–4.

(18) Gianolio, D. A., Philbrook, M., Avila, L. Z., MacGregor, H., Duan, S. X., Bernasconi, R., Slavsky, M., Dethlefsen, S., Jarrett, P. K., and Miller, R. J. (2005) Synthesis and evaluation of hydrolyzable hyaluronan-tethered bupivacaine delivery systems. *Bioconjugate Chem. 16*, 1512–8.

(19) Winder, A. F., and Gent, W. L. (1971) Correction of light-scattering errors in spectrophotometric protein determinations. *Biopolymers 10*, 1243–51.

(20) Zhou, Q., Kyazike, J., Edmunds, T., and Higgins, E. (2002) Mannose 6-phosphate quantitation in glycoproteins using high-pH anion-exchange chromatography with pulsed amperometric detection. *Anal. Biochem. 306*, 163–70.

(21) Hardy, M. R., Townsend, R. R., and Lee, Y. C. (1988) Monosaccharide analysis of glycoconjugates by anion exchange chromatography with pulsed amperometric detection. *Anal. Biochem. 170*, 54–62.

(22) De Ruiter, G. A., Schols, H. A., Voragen, A. G., and Rombouts, F. M. (1992) Carbohydrate analysis of water-soluble uronic acid-containing polysaccharides with high-performance anion-exchange chromatography using methanolysis combined with TFA hydrolysis is superior to four other methods. *Anal. Biochem. 207*, 176–85.

(23) Jones, D. T. (1999) Protein secondary structure prediction based on position-specific scoring matrices. *J. Mol. Biol. 292*, 195–202.

(24) Pollastri, G., Przybylski, D., Rost, B., and Baldi, P. (2002) Improving the prediction of protein secondary structure in three and eight classes using recurrent neural networks and profiles. *Proteins 47*, 228–35.

(25) Sim, L., Quezada-Calvillo, R., Sterchi, E. E., Nichols, B. L., and Rose, D. R. (2008) Human intestinal maltase-glucoamylase: crystal structure of the N-terminal catalytic subunit and basis of inhibition and substrate specificity. *J. Mol. Biol. 375*, 782–92.

(26) Van Patten, S. M., Hughes, H., Huff, M. R., Piepenhagen, P. A., Waire, J., Qiu, H., Ganesa, C., Reczek, D., Ward, P. V., Kutzko, J. P., and Edmunds, T. (2007) Effect of mannose chain length on targeting of glucocerebrosidase for enzyme replacement therapy of Gaucher disease. *Glycobiology 17*, 467–78.

(27) Sendak, R. A., Ganesa, C., Lee, K. L., Harrahy, J. J., Theberge, R., Morgan, C. J., Cole, E. S., Kohn, L. D., and Mattaliano, R. J. (2003) The effect of posttranslational modifications on the in vitro activity of recombinant human thyroid-stimulating hormone. *Thyroid 13*, 1091–101.

(28) Tajima, Y., Matsuzawa, F., Aikawa, S., Okumiya, T., Yoshimizu, M., Tsukimura, T., Ikekita, M., Tsujino, S., Tsuji, A., Edmunds, T., and Sakuraba, H. (2007) Structural and biochemical studies on Pompe disease and a "pseudodeficiency of acid alpha-glucosidase. *J. Hum. Genet. 52*, 898–906.

(29) Hermans, M. M., Kroos, M. A., van Beeumen, J., Oostra, B. A., and Reuser, A. J. (1991) Human lysosomal alpha-glucosidase. Characterization of the catalytic site. *J. Biol. Chem. 266*, 13507–12.

(30) Kalia, J., and Raines, R. T. (2008) Hydrolytic stability of hydrazones and oximes. *Angew. Chem., Int. Ed. Engl. 47*, 7523–6.

(31) Avigad, G., Amaral, D., Asensio, C., and Horecker, B. L. (1962) The D-galactose oxidase of Polyporus circinatus. *J. Biol. Chem. 237*, 2736–43.

(32) Kelleher, F. M., and Bhavanandan, V. P. (1986) Re-examination of the products of the action of galactose oxidase. Evidence for the conversion of raffinose to 6′′-carboxyraffinose. *J. Biol. Chem. 261*, 11045–8.

(33) Basu, S. S., Dotson, G. D., and Raetz, C. R. (2000) A facile enzymatic synthesis of uridine diphospho-[14C]galacturonic acid. *Anal. Biochem. 280*, 173–7.

(34) Bohnsack, R. N., Song, X., Olson, L. J., Kudo, M., Gotschall, R. R., Canfield, W. M., Cummings, R. D., Smith, D. F., and Dahms, N. M. (2009) Cation-independent mannose 6-phosphate receptor: a composite of distinct phosphomannosyl binding sites. *J. Biol. Chem. 284*, 35215–26.

(35) Baron, A. J., Stevens, C., Wilmot, C., Seneviratne, K. D., Blakeley, V., Dooley, D. M., Phillips, S. E., Knowles, P. F., and McPherson, M. J. (1994) Structure and mechanism of galactose oxidase. The free radical site. *J. Biol. Chem. 269*, 25095–105.

(36) Ito, N., Phillips, S. E., Yadav, K. D., and Knowles, P. F. (1994) Crystal structure of a free radical enzyme, galactose oxidase. *J. Mol. Biol. 238*, 794–814.

(37) Ito, N., Phillips, S. E., Stevens, C., Ogel, Z. B., McPherson, M. J., Keen, J. N., Yadav, K. D., and Knowles, P. F. (1991) Novel thioether bond revealed by a 1.7 A crystal structure of galactose oxidase. *Nature 350*, 87–90.

(38) Asokan, A., and Cho, M. J. (2002) Exploitation of intracellular pH gradients in the cellular delivery of macromolecules. *J. Pharm. Sci. 91*, 903–13.

Supporting information

Strategies for Neoglycan Conjugation to Human Acid α-Glucosidase

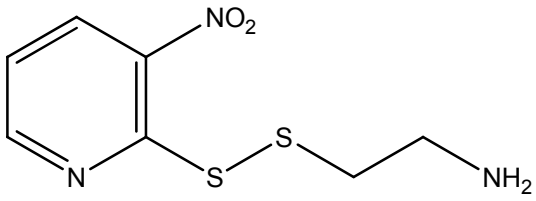
Qun Zhou*, James E. Stefano, John Harrahy, Patrick Finn, Luis Avila, Josephine Kyazike, Ronnie Wei, Scott M. Van Patten, Russell Gotschall, Xiaoyang Zheng, Yunxiang Zhu, Tim Edmunds, and Clark Q. Pan

Genzyme Corporation,
Framingham, MA 01701, USA

*Corresponding author. Genzyme Corp., One Mountain Road, Framingham, Massachusetts 01701-9322 USA. Email: qun.zhou@genzyme.com

Content

The structure of 3-Nitro-2-pyridinesulfenylethylamine, nipsyl ethylamine, NEA:



Bioconjugate Chemistry

ARTICLE

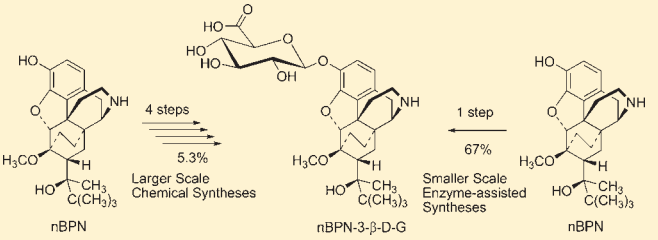
pubs.acs.org/bc

Chemical and Enzyme-Assisted Syntheses of Norbuprenorphine-3-β-D-glucuronide

Jinda Fan,[†,∥] Sarah M. Brown,[‡,∥] Zhude Tu,[†] and Evan D. Kharasch*[,‡,§]

[†]Department of Radiology, [‡]Department of Anesthesiology, and [§]Department of Biochemistry and Molecular Biophysics, Washington University in St. Louis, 660 S. Euclid Avenue, St. Louis, Missouri 63110, United States

ABSTRACT: Norbuprenorphine-3-β-D-glucuronide (nBPN-3-β-D-G, **1**) is a major phase II metabolite of buprenorphine, a pharmaceutical used for the treatment of opioid addiction. The pharmacological activity of compound **1** is not clear because investigations have been limited by the lack of chemically pure, well characterized **1** in sufficient quantities for *in vitro* and *in vivo* experiments. This work describes two concise, new methods of synthesis of **1**, a chemical and an enzyme-assisted synthesis. The chemical synthesis used a strategy based on a combination of Koenig-Knorr coupling and amino-silyl protection. The enzyme-assisted synthesis used dog liver to convert the substrate norbuprenorphine (nBPN, **2**) to **1**. Both methods provided **1**, characterized by ^{1}H NMR and tandem mass spectrometry, with purity >96%. The fractional yield of the enzyme-assisted synthesis was greater than that of the chemical synthesis (67% vs 5.3%), but due to larger reaction volumes, the chemical synthesis afforded greater amounts of total **1**.



INTRODUCTION

Drugs are metabolized in a two-phase biotransformation process that renders the drug more readily excreted in urine or bile. The first phase often produces a dealkylated or a hydroxylated metabolite that may then also undergo conjugation to a polar group such as glucuronic or sulfonic acid in the second phase. Phase I and phase II metabolites can circulate in concentrations equal to or greater than the parent drug, and in many instances have pharmacological activity that contributes significantly to the overall effects of the parent drug.[1,2] Thus, drug metabolites have the potential to be clinically important, and indeed, this is true in numerous instances. Many active phase I metabolites have been developed as new drugs. Some well-known examples are acetaminophen, a metabolite of phenacetin, fexofenadine, a metabolite of terfinadine, and nortryptyline, a metabolite of amitriptyline.[1] The opioid drug class has over 10 clinically important metabolites, including the phase 1 metabolites hydrocodone and hydromorphone.[2,3] This drug class also has important active phase II metabolites, the best described being morphine-6-glucuronide (M6G), which has greater pharmacological activity than the parent drug.[3,4] M6G has undergone phase III clinical trials as a drug for the treatment of postoperative pain,[5,6] showing benefit over the parent drug for producing analgesia with significantly fewer negative side effects (nausea, etc.), and less risk of respiratory depression.[7] The high potential for the contribution of drug metabolites to the overall effect of the parent drug has led to a recent guidance from the FDA wherein any major metabolite, defined as one comprising >10% of parent drug systemic exposure at steady-state, be considered for safety assessment (Guidance for Industry: Safety Testing of Drug Metabolites, Food and Drug Administration, Center for Drug Evaluation and Research, http://www.fda.gov/downloads/Drugs/GuidanceComplianceRegulatoryInformation/Guidances/ucm079266.pdf).

Buprenorphine (BPN) is a phenanthrene opioid used in the treatment of opioid addiction, and to a lesser extent, pain.[8] It is extensively metabolized to 3 main metabolites: an N-dealkylated product, norbuprenorphine (nBPN), and two *O*-glucuronides, buprenorphine-3-β-D-glucuronide (BPN-3-β-D-G) and norbuprenorphine-3-β-D-glucuronide (nBPN-3-β-D-G).[9] These metabolites are present in the circulation at concentrations greater than or equal to that of BPN. Plasma concentrations of nBPN and nBPN-3-β-D-G, specifically, are typically greater than that of BPN following an oral dose, and the area under the plasma concentration versus time curve for nBPN and nBPN-3-β-D-G is approximately 2 and 10 times greater, respectively, than that of the parent drug.[10−13] While there are some data regarding the pharmacological activity of nBPN,[12,14] the biological properties of the glucuronides and their contribution to the pharmacology of the parent drug remain unknown. The high concentration of nBPN-3-β-D-G and the precedent for active glucuronides warrant the investigation of the biological activity of this metabolite. However, such an investigation has been inhibited by the limited availability of the metabolites in quantities necessary for *in vitro* and *in vivo* studies. Thus, the development of an efficient means of nBPN-3-β-D-G synthesis is of considerable importance.

Glucuronides can be synthesized chemically, usually by the Koenigs−Knorr method.[15] However, glucuronides are notoriously more difficult to prepare than the corresponding glucopyranoside.

Received: December 4, 2010
Revised: February 27, 2011
Published: March 24, 2011

ACS Publications © 2011 American Chemical Society

Schmidt and co-workers have shown a difficulty scale: 3-deoxy-2-glyculosonates < ketoses < deoxy sugars < aldoses < glycuronates.[16] Of all common sugars, glucuronides require the highest activation for a given aglycone. Alternatively, glucuronide conjugates can be prepared through enzyme-assisted synthesis using liver microsomal enzymes.[17−20] The purpose of this investigation was to evaluate the synthesis of nBPN-3-D-G by two routes: enzyme-assisted synthesis using dog liver and chemical synthesis involving the development of silyl as a protective group.

EXPERIMENTAL SECTION

Chemicals and General Methods. All reagents were from Sigma-Aldrich (St. Louis, MO), unless otherwise noted. Norbuprenorphine glucuronide was purchased from Cerillant (Round Rock, TX) for use as an analytical standard. Norbuprenorphine was a generous gift from the National Institute on Drug Abuse. All organic solvents were distilled before use. After drying over Na_2SO_4, organic solvents were concentrated under diminished pressure at <40 °C (bath temperature), and NMR spectra were recorded at 300 MHz (^{1}H), in $CDCl_3$ or DMSO. Tetramethylsilane (TMS) was used as the internal standard (δ 0) for ^{1}H spectra. Chemical shifts are expressed in ppm. Preparative chromatography was performed using Merck 60 PF_{254} silica gel. Analytical thin layer chromatography (TLC) was performed on glass TLC plates coated with silica gel (Analtech) and visualized with UV light.

Formation of 1-[2-(Trimethylsilyl)ethoxycarbonyloxy]benzotriazole (TeocOBt) (3). Synthesis of Teoc-OBt was modified from published methods.[21] Briefly, to a solution of 2-trimethylsilyletanol (1.0 g, 8.5 mmol) in toluene (5 mL) at −10 to −5 °C was added powdered anhydrous potassium carbonate (1 g). To this vigorously stirred suspension, a 20% solution of phosgene in toluene (6.25 mL) was added dropwise over 14−30 min. On completion of the addition, the mixture was stirred over an ice bath for 30 min, followed by 1 h at room temperature. After stirring, nitrogen was bubbled through the mixture with the hood closed to remove the majority of the excess phosgene. The last traces of phosgene were removed from the mixture by rotary evaporation at a temperature <40 °C. The solids were then filtered off through a pad of anhydrous magnesium sulfate and washed with dry ether. The combined filtrate and washings were evaporated at a temperature not higher than 50 °C. The resultant oily carbonochloridate was used without further purification.

2-Trimethylsilylethyl carbonochloridate (1.54 g, 8.5 mmol) was taken up in acetonitrile (25 mL). The solution was cooled to 0 °C and solid 1-hydroxy-benzotriazole monohydrate (1.5 g, 11 mmol) was added with vigorous stirring followed by a solution of triethylamine (1.0 g, 10 mmol) in acetonitrile (2.5 mL). The mixture was stirred at low temperature for 15 min, then at room temperature overnight. The mixture was poured into water (100 mL) and extracted with ether (3 × 40 mL). The organic extracts were combined, washed with water (2 × 40 mL), 1 N hydrochloric acid (40 mL), and again water (2 × 40 mL), dried with sodium sulfate, and evaporated to dryness. The residue was taken up in boiling hexane (150−200 mL) and the solution allowed to cool. Crystallization, completed by storage at −15 °C, yielded a white solid (1.31 g, 58.7% for the two-step synthesis). ^{1}H NMR ($CDCl_3$): δ 0.12 (s, 9H, Si(CH_3)$_3$), 1.29 (t, 2H, *J* 9.0 Hz, SiCH_2), 4.65 (t, 2H, *J* 9.0 Hz, OCH_2), 7.54 (t, 1H, *J* 7.5 Hz, Ph*H*), 7.77 (t, 1H, *J* 7.5 Hz, Ph*H*), 8.02 (d, 1H, *J* 7.5 Hz, Ph*H*), 8.22 (d, 1H, *J* 7.5 Hz, Ph*H*). MS (ESI)$^+$ [M+H]$^+$ calcd 264.1; found 264.2.

Formation of *N*-(Trimethylsilyl)ethoxycarbonyl-norbuprenorphine (Teoc-nBPN) (4). To a 1,4-dioxane (2 mL) solution of nBPN (109 mg, 0.26 mMol) (**2**) and TeocOBt (69.6 mg, 0.26 mmol) (**3**), diisopropylethylamine (55 μL, 0.32 mMol) was added. The mixture was stirred at ambient temperature overnight. Solvent was removed under vacuum, and the residues were dissolved in ethyl acetate (10 mL), then washed with water (2 × 10 mL) and saline (10 mL), and finally dried over Na_2CO_3. The crude product was purified by flash-chromatography (25:75 ethyl acetate/hexanes) to produce Teoc-nBPN (**4**) as a white solid (118.3 mg, 80.4%). ^{1}H NMR ($CDCl_3$): δ 0.05 (s, 9H, Si(CH_3)$_3$), 0.99 (s, 9H, C(CH_3)$_3$), 1.26 (m, 2H, SiCH_2), 1.28 (m, 2H, CHCH_2C), 1.34 (s, 3H, CCH_3), 1.57 (m, 2H, CH_2CH_2C), 1.84, (m, 2H, CH_2CH_2C), 1.90 (m, 1H, C*H*), 2.05 (m, 2H, CCH_2CH_2), 2.84 (m, 2H, PhCH_2CH), 2.97 (m, 1H, NC*H*C), 3.53 (s, 3H, OCH_3), 4.14 (m, 2H, NCH_2C), 4.21 (m, 2H, OCH_2CH_2), 4.46 (s, 1H, OC*H*C2), 5.76 (s, 1H, O*H*), 6.54 (D, 1H, *J* 5.1 Hz, Ph*H*), 6.73 (D, 1H, *J* 5.1 Hz, Ph*H*). MS (ESI)$^+$ [M+H]$^+$ calcd 558.3; found 558.4.

Formation of *N*-(Trimethylsilyl)ethoxycarbonyl-norbuprenorphine-3-β-D-acetoglucuronide (Teoc-nBPN-3-β-D-AcG) (6). Teoc-nBPN (**4**) (116.3 mg, 0.21 mmol), Ag_2CO_3 (58 mg, 0.21 mmol), and 4 Å molecular sieves (200 mg) were dispersed in freshly distilled quinoline (2 mL, 17 mmol). Acetobromo-α-D-glucuronic acid methyl ester (167 mg, 0.42 mmol) was added to this mixture with stirring at 0 °C under argon. The mixture was allowed to warm to ambient temperature over an hour and was kept at ambient temperature overnight. Molecular sieves were removed by filtration. The precipitate was thoroughly washed with ethyl acetate (3 × 5 mL). The organic phase was combined, washed with brine (10 mL), dried over Na2SO4, and concentrated. The crude product was purified by flash chromatography with gradient eluents (from 25:75 to 50:50 ethyl acetate/hexanes) to produce Teoc-nBPN-3-β-D-G (**5**) as a white solid (33.1 mg, 18.0%). ^{1}H NMR ($CDCl_3$): δ 0.05 (s, 9H, Si(CH_3)$_3$), 0.99 (s, 9H, C(CH_3)$_3$), 1.26 (m, 2H, SiCH_2), 1.28 (m, 2H, CHCH_2C), 1.34 (s, 3H, CCH_3), 1.56 (m, 2H, CH_2CH_2C), 1.72, (m, 2H, CH_2CH_2C), 1.84 (m, 1H, C*H*), 2.04 (s, 9H, CH_3COO), 2.10 (m, 2H, CCH_2CH_2), 2.85 (m, 2H, PhCH_2CH), 2.97 (m, 1H, NC*H*C), 3.50 (s, 3H, OCH_3), 3.71 (s, 3H, COOCH_3), 4.14 (m, 2H, NCH_2C), 4.21 (m, 2H, OCH_2CH_2), 4.42 (s, 1H, OC*H*C2), 5.29 (m, 4H, C*H* on glucuronide), 5.71 (s, 1H, OC*H*), 6.54 (D, 1H, *J* 7.8 Hz, Ph*H*), 6.73 (D, 1H, *J* 7.8 Hz, Ph*H*). MS (ESI)$^+$ [M+Na]$^+$ calcd 896.4; found 896.5.

Chemical Synthesis of nBPN-3-β-D-G (1). *N*-(Trimethylsilyl) ethoxycarbonyl-norbuprenorphine-3-β-D-acetoglucuronide (**5**) (65.6 mg, 0.075 mmol) was dissolved in THF/H_2O (v/v 4:1 6.5 mL). Two molar KOH solution (225 μL, 0.45 mmol) was added with stirring at 0 °C. The mixture was then allowed to warm to ambient temperature and then kept at ambient temperature for two hours. After 2 h, acetic acid (8.6 μL, 0.17 mL) was added, and the mixture was extracted with dichloromethane (3× 15 mL). The combined organic phase was washed with saline (5 mL), dried over Na_2SO_4, and concentrated. This produced Teoc-nBPN-3-β-D-G (**7**) as a light yellow solid (54.7 mg 98%) which was used for the next step reaction without purification. To a solution of *N*-(Trimethylsilyl)ethoxycarbonyl-norbuprenorphine-3-β-D-glucuronide (Teoc-nBPN-3-β-D-G) (**7**) (55 mg, 0.075 mmol) in THF (4 mL), TBAF (71 mg, 0.225 mmol) was added and stirred at ambient temperature overnight. The crude product was partially purified by flash-chromatography (20:80 methanol: dichloromethane), followed by purification with a preparative

dx.doi.org/10.1021/bc100550u |*Bioconjugate Chem.* 2011, 22, 752–758

HPLC system to nBPN-3-β-D-G (**1**) as a white solid (16.1 mg, 36.4% for two steps).

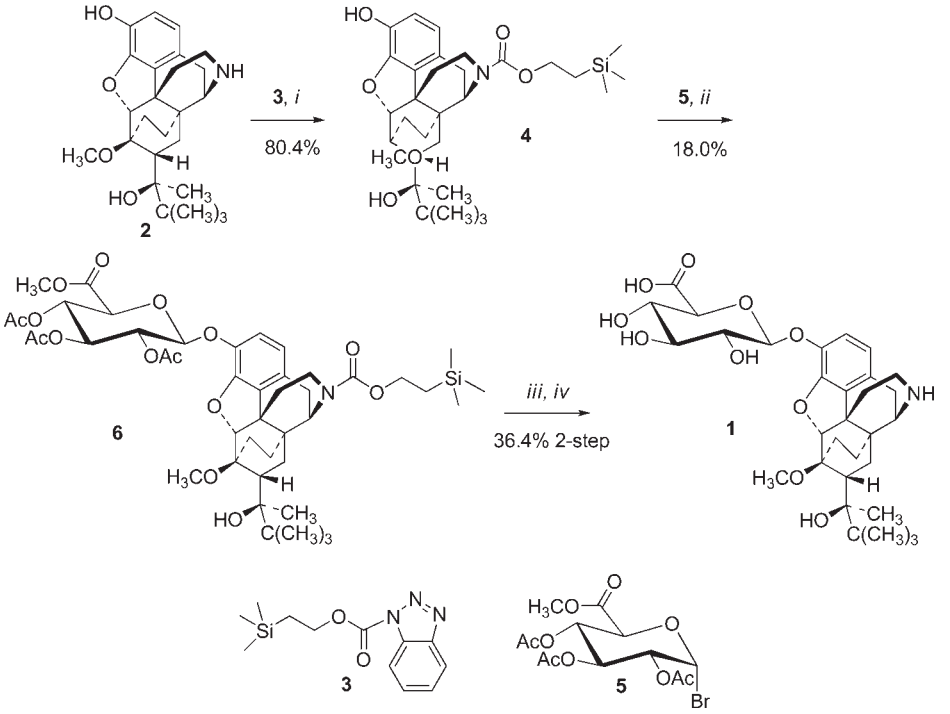
Preparation of S9. Fresh liver was obtained from a beagle dog that had been euthanized under a Washington University Animal Studies Committee approved protocol. The tissue was cut in to approximately 30 g pieces, with the removal of as much connective tissue as possible. The tissue was washed with ice-cold phosphate buffered saline (PBS) with stirring, with 6 changes of PBS. The washed tissue pieces were reduced in 3 volumes (by weight) of buffer (10 mM potassium phosphate, pH 7.4, with 0.25 M sucrose) in a chilled Waring blender and then homogenized on ice using a motorized glass-Teflon homogenizer. The homogenate was transferred to polystyrene tubes, centrifuged at 9,000*g* for 20 min, and the supernatant collected as the "S9 fraction", containing both cytosolic proteins and microsomes. Protein content of S9 was quantified by the Bradford assay.

Enzyme-Assisted Synthesis. In a typical 1 mL incubation, 640 μL of reaction buffer (100 mM potassium phosphate, pH 7.1, 1 mM MgCl, and 5 mM saccharic acid lactone) was added to 200 μL of S9 (10 μg/μL protein) in a glass test tube and the mixture sonicated for 1 min. After sonication, 10 mM nBPN (4 mg/mL), 10, 20, 30, or 50 mM UDPGA, and 150 mL of an NADPH-generating system (1.7 mg/mL β-$NADP^+$, 7.8 mg/mL glucose-6-phosphate, and 6 units/mL glucose-6-phosphate dehydrogenase, prewarmed to 37 °C) were added. The mixture was vortexed and then incubated overnight in a 37 °C water bath with gentle shaking. Larger reaction volumes (up to 5 mL without a decrease in yield) were also occasionally used. Ten millimolar aminobenzotriazole was added prior to the addition of nBPN to three of the 1 mL reaction tubes.

Partial Purification of nBPN-3-β-D-G from the Biocatalyzed Reaction. The reaction was terminated by protein precipitation with three volumes of ice-cold acetonitrile. The supernatant was evaporated under nitrogen to approximately 1 mL and then loaded onto a C18 solid phase extraction column (Sep-Pak C18 Plus 10 g, Waters Co. Massachusetts USA), preconditioned by washing with 3 column volumes of methanol followed by 3 column volumes of water. After loading the sample, the column was washed with 10 mL of water. The sample was eluted with 3 column volumes of methanol and then concentrated by centrifugation under vacuum.

HPLC Purification of nBPN-3-β-D-G. nBPN-3-β-D-G synthesized using either method was purified by preparative HPLC. The compound of interest was separated from impurities over a Sunfire Prep C18 OBD 19 mm × 150 mm x 5 μm column (Waters) using an 85% A (H_2O with 0.1% formic acid)/15% B (acetonitrile with 0.1% formic acid) isocratic method, with a 10 min run time on an Agilent 1100 series LC system. Fractions were collected every minute and analyzed by selected ion monitoring on an Agilent 1100 MSD instrument for the presence of nBPN-3-β-D-G (m/z 590). Fractions containing nBPN-3-β-D-G were pooled and dried by lyophilization. Purity of the synthesized compound was determined by a calibration curve. A 1 mg/mL solution of the synthesized compound was prepared in 0.1% formic acid. A 6-point calibration curve of the purchased standard, ranging from 0.1 mg/mL to 2 mg/mL was prepared. The synthesized compound, at 1 mg/mL, 0.5 mg/mL, and 0.25 mg/mL was analyzed with the calibration curve by selected ion monitoring on the Agilent 1100 LC-MS. The purity was determined as >95% based on comparison to the equation of the calibration curve.

Scheme 1. Synthesis of Norbuprenorphine-3-β-D-glucuronide (nBPN-3-β-D-G)[a]



[a] Reagents and conditions: (i) Et_3N, 1,4-dioxane; (ii) Ag_2CO_3, quinoline; (iii) KOH, H_2O/THF; (iv) TBAF, THF protection of the amine on nBPN with Teoc was followed by coupling Teoc-nBPN to a glucuronic acid by the donor acetobromo-α-D-glucuronic acid methyl ester (**5**) to give Teoc-nBPN-3-D-G (**6**). This step was followed by the hydrolysis of acetyl groups with a base and then the removal of the Teoc protecting group with fluoride, to yield nBPN-3-β-D-G (**1**).

dx.doi.org/10.1021/bc100550u |*Bioconjugate Chem.* 2011, 22, 752–758

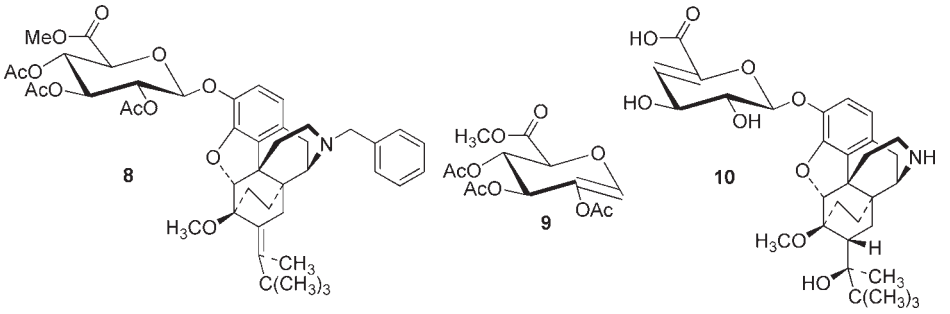


Figure 1. Structure of some of the byproducts of chemical synthesis. Dehydration product **8** formed during the coupling step when silver triflate was used; HBr elimination of **5** formed **9**; $\Delta_{4,5}$-glucuronides formed during the coupling and hydrolysis steps.

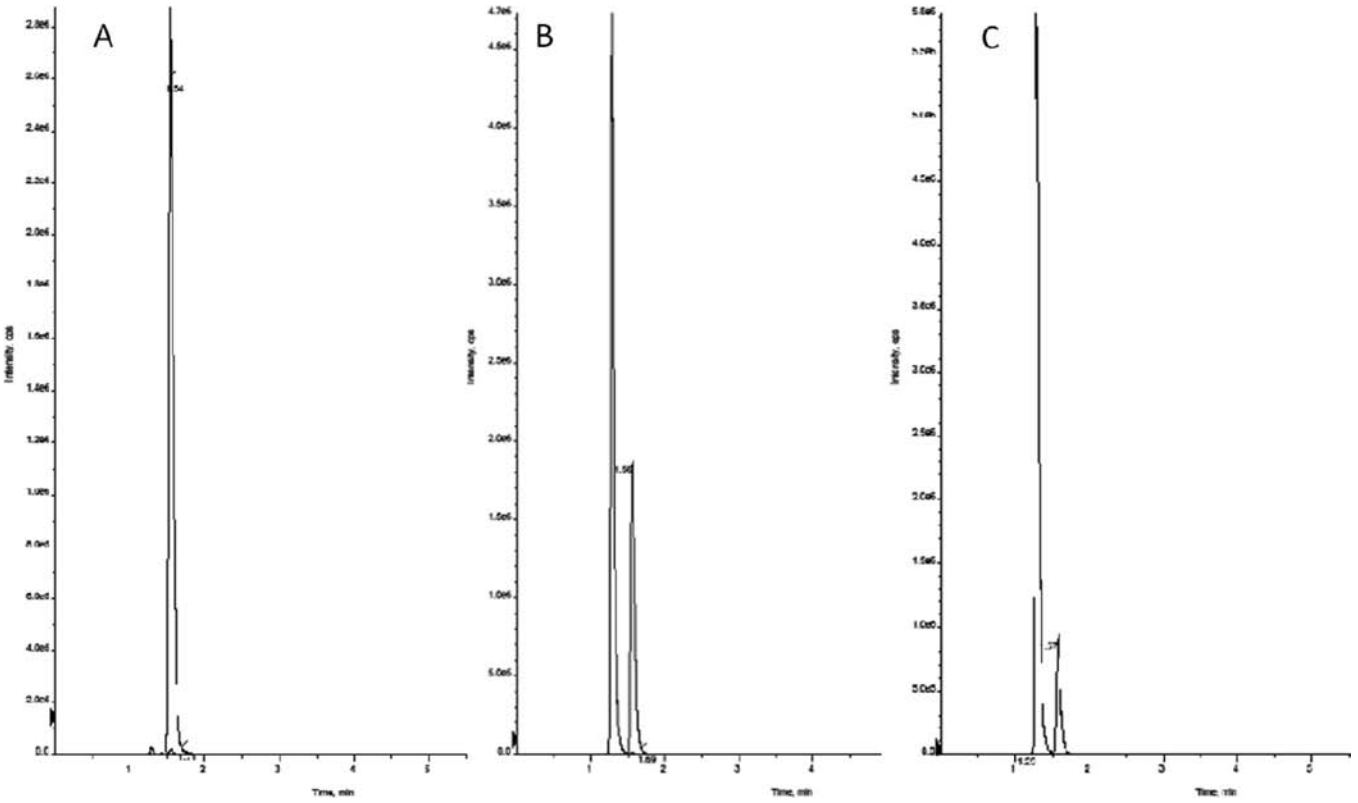


Figure 2. Addition of ABT to the enzyme-assisted reaction increased the conversion of nBPN to nBPN-3-β-D-G. HPLC analysis of the reaction mixture immediately preceeding incubation showed one peak (RT = 1.56 min) corresponding to nBPN (panel A). After overnight incubation, a second peak (RT = 1.28 min) corresponding to nBPN-3-β-D-G was observed (panel B). Addition of 10 mM ABT to the reaction resulted in a greater conversion of nBPN to nBPN-3-β-D-G (panel C).

Mass Spectral Characterization. Fragmentation was characterized by a product ion scan in positive electrospray mode on an 4000 QTRAP MS/MS (Applied Biosystems). The compound in solution (H_2O with 0.1% formic acid) was introduced to the source by direct infusion at a rate of 20 μL/min. MSD parameters: collision energy, 52 eV; declustering potential, 92 eV; exit cell potential, 10 eV; curtain gas, 15 eV; ion spray voltage, 5200 eV; collision gas, medium; ion source gas 1, 40; and ion source gas 2, 50.0. Fragmentation of the reference material was compared to that of the chemically and biologically synthesized compound.

NMR of nBPN-3-β-D-G. ^{1}H NMR ($CDCl_3$): δ 0.97 (s, 9H, $C(CH_3)_3$), 1.28 (m, 2H, $CHCH_2C$), 1.34 (s, 3H, CCH_3), 1.56 (m, 2H, CH_2CH_2C), 1.72, (m, 2H, CH_2CH_2C), 1.84 (m, 1H, CH), 2.05 (m, 2H, CCH_2CH_2), 2.78 (m, 2H, $PhCH_2CH$), 2.84 (m, 1H, $NCHC$), 3.42 (s, 3H, OCH_3), 3.48 (m, 1H, $CHOH$), 4.43 (s, 1H, OCH), 4.94 (m, 4H, $CHOH$), 5.06 (m, 1H, $CHOH$), 5.18 (m, 1H, $CHOH$), 5.46 (s, 1H, OCH), 6.55 (D, 1H, J 8.4 Hz, PhH), 6.87 (D, 1H, J 8.4 Hz, PhH). MS $(ESI)^+$ $[M+H]^+$ calcd 590.3; found 590.2.

RESULTS AND DISCUSSION

Chemical glucuronidation of nBPN with **5** under nonaqueous conditions was performed using the synthetic scheme shown (Scheme 1). While glycosylation of nBPN with protected, simple aldopyranosyl bromide to give its glucuronide directly has been reported, the reactions were performed in aqueous conditions

dx.doi.org/10.1021/bc100550u |*Bioconjugate Chem.* 2011, 22, 752–758

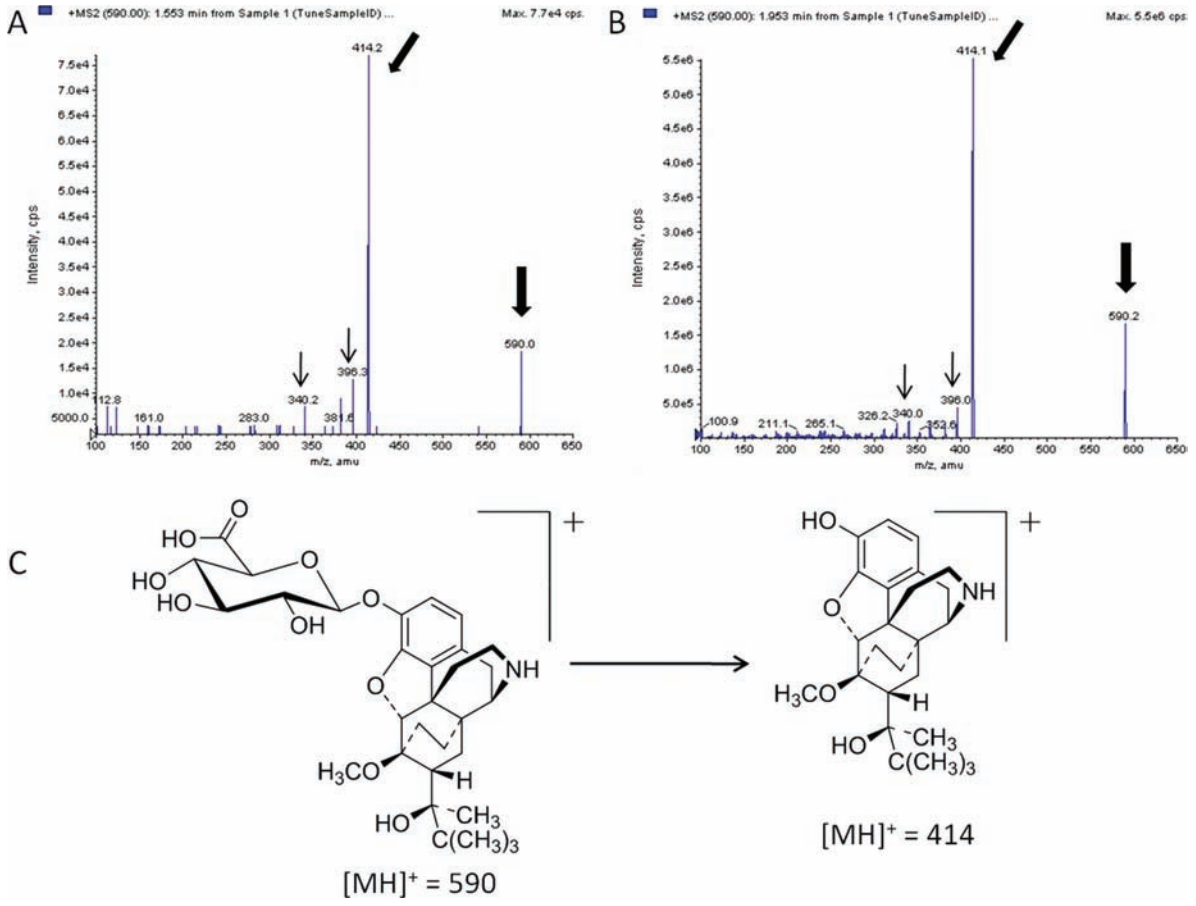


Figure 3. Purchased nBPN-3-β-D-G standard and the synthesized nBPN-3-β-D-G have the same fragmentation pattern. nBPN-3-β-D-G precursor (m/z 590) fragments at the 3-ether linkage to give the product ion m/z 414 (bold arrows). Two less abundant product ions are m/z 396 and m/z 340 (small arrows). The purchased standard (A) and the synthesized product (B) had the same fragmentation pattern.

with hydroxide catalysis,[22] and work from other groups suggests that C-ring cleavage is in fact the predominant reaction under these conditions.[23] The presence of two competitive glucuronic acid acceptors on nBPN, the phenol and secondary amine functional groups, necessitated protection of the amine group before the addition of glucuronic acid to prevent the formation of *N*-glucuronide. The amine group was protected with trimethylsilylethoxycarbonyll (Teoc), as it is stable to mild acid and base, and can be removed with the fluoride ion.[24,25] The use of a benzyl group as the amine protecting group was also tested, and although the benzyl groups were cleanly removed from *N*-benzyl protected nBPN (**2**) under relatively mild conditions such as palladium−carbon catalyzed hydrogenolysis, under the same conditions the deprotection of *N*-Bn-nBPN-3-β-D-G (**8**) was not successful because the glucuronic bond could not withstand even these mild hydrogenolysis conditions. A variety of other hydrogenolysis conditions were tried without success, including Pd/C catalyzed hydrogenolysis with H_2 in tetrahydrofuran (THF) or methanol/ethyl acetate at room temperature and Pd/C catalyzed hydrogenolysis with ammonium formate in THF, refluxed at 70 °C. TeocOBt, synthesized by modifying a reported procedure,[21] was used to protect nBPN, giving Teoc-nBPN in good yield. The coupling of Teoc-nBPN (**4**) with **5** to generate Teoc-nBPN-3-β-D-AcG (**6**) under the Koenigs−Knorr reaction conditions was the most challenging step of the synthesis. The commercially available glucuronidation intermediate,[26,27] 1α-bromo sugar **5**, was selected as the sugar source for this synthesis. The most common solvents used for the coupling reaction have been benzene, toluene, and quinoline; quinoline was used as both a base and solvent. Removal of any water produced is critical for the coupling reaction; 4 Å molecular sieves were used for the removal of water. A persistent byproduct from such coupling reactions is the glycosene or 2-acetoxyglycal **9**, formed by HBr elimination (Figure 1). A variety of salts can provide silver ions for the coupling reaction, and although silver trifluoromethanesulfonate (triflate) was used for the synthesis of retinyl glucuronide[28] to give a markedly better yield than Ag_2CO_3, we found that using silver triflate produced the dehydrated product **8** as the major product. Hence, Ag_2CO_3 was used. Following the success of the coupling reaction, the acetyl protecting groups and the Teoc protecting group were removed sequentially with KOH in H_2O/THF and TBAF in THF, respectively. During our synthesis, the formation of $\Delta_{4,5}$-glucuronides (dehydroglucuronides, **10**) was observed (Figure 1). Dehydroglucuronides are a particularly relevant byproduct of this step, as they may be formed in trace or even significant amounts during any basic hydrolysis. Similar results were obtained by Tajima,[29] who showed that the elimination was also facilitated by a 1β-substituent.

Enzyme-assisted synthesis was accomplished via incubation of nBPN, UDP-glucuronic acid, and an NADPH generating system with a fraction of liver homogenate. *In vivo*, norbuprenorphine is glucuronidated by hepatic uridine-5′-diphosphoglucuronosyltransferases (UGT).[30] These enzymes are located

dx.doi.org/10.1021/bc100550u |*Bioconjugate Chem.* 2011, 22, 752–758

in the endoplasmic reticulum, which are obtained as microsomes by differential ultracentrifugation of liver homogenate. An alternative is to use S9, a fraction of liver homogenate containing both microsomes and cytosol. The benefit to using S9 is the ease of preparation; instead of multiple ultracentrifugation steps, it is obtained by collecting the supernatant following one 9,000*g* spin of total homogenate. Dog liver was used as it is more readily available than human liver, and despite reports of low circulating concentrations of all BPN metabolites in dogs administered intravenous BPN,[31] dog liver was as efficient as the human liver for the conversion of BPN to BPN-3-β-D-G.[17] An NADPH-generating system rather than NADPH was used to supply a reductive cofactor, and while NADPH is not necessary for UGT enzymatic activity, it has been shown to enhance the activity of these enzymes.[32−35] UDP-glucuronic acid was added in equimolar (or greater) amount to nBPN. The S9 fraction was sonicated immediately prior to the addition of the reaction components in order to create pores in the microsomal membranes.[18] The progress of the reaction was monitored by LC/MS. An aliquot was removed from the total incubation, and the reaction stopped by adding three volumes of ice-cold acetonitrile. The supernatant was analyzed by selected ion monitoring on an 1100 MSD (Agilent) following the m/z 590 for the glucuronide and m/z 414 for the parent compound after LC separation. The conversion of nBPN to nBPN-3-β-D-G was not complete, even after an overnight incubation. In an effort to increase the yield of the glucuronide, we repeated the reaction with UDP-glucuronic acid in 2-, 3-, and 5-fold molar excess and found that the latter resulted in the greatest conversion (36%). In every reaction, we observed a peak with a mass to charge ratio (m/z) of 576 at a signal intensity equal to that of the nBPN-3-β-D-G (m/z 590) and nBPN (m/z 414). Since this is a 14 amu difference from the glucuronide (m/z 590), we hypothesized that this might correspond to a demethylated form of the glucuronide. Dealkylation by cytochrome P450 enzymes is a common step in drug metabolism. To test the hypothesis that this compound was a demethylated metabolite of nBPN-3-β-D-G, aminobenzotriazole (ABT), a nonspecific cytochrome P450 inhibitor,[36] was added to the reaction. While the addition of ABT to the reaction did not affect the presence or relative amount of m/z 576, it did increase the conversion of nBPN to nBPN-3-β-D-G, from 36 to 68% (Figure 2). Having thus optimized the reaction conditions, a set of 30 1-mL reactions was initiated. Following incubation, extraction, and purification, approximately 10 mg of nBPN-3-β-D-G was obtained.

Both the biologically and chemically synthesized compounds were characterized by HPLC and tandem mass spectrometry. Comparison to that of a purchased certified reference material showed that both the synthesized and reference compounds had the same retention time (1.28 min), and a mix of the two clearly showed only one peak. Additionally, the fragmentation pattern of the synthesized compound was compared to the fragmentation pattern of the certified reference standard; both fragmented to give one major product ion with m/z of 414, corresponding to the mass of nBPN after the loss of glucuronic acid (Figure 3).

In conclusion, nBPN-3-β-D-G was successfully prepared by two routes: a 4-step chemical synthesis using a silyl protecting group and an enzyme-assisted synthesis using a metabolically active fraction of dog liver. While the enzyme-assisted synthesis had a greater yield per batch, the batch volume was limited, and multiple reactions were required for significant yield. The chemical synthesis resulted in more product per batch, albeit with a lesser overall yield. Preparative HPLC was required for the final purification of nBPN-3-β-D-G prepared by either the chemical or biological synthetic route. Structure of the final product was confirmed by ^{1}H NMR, and purity was determined to be >95%.

AUTHOR INFORMATION

Corresponding Author

*Department of Anesthesiology, Washington University in St. Louis, 660 S. Euclid Ave., St. Louis, MO 63110. E-mail: kharasch@wustl.edu.

Author Contributions

‖Both authors contributed equally to this work.

ACKNOWLEDGMENT

We thank Rolly (Ed) Johnson of Reckitt Benckiser Pharmaceuticals and Dr. Moo Park of the National Institutes on Drug Abuse for their assistance in obtaining norbuprenorphine. This research was supported by National Institutes of Health grants R01 DA02931 and K24 DA00417 to E.D.K.

REFERENCES

(1) Kang, M. J., Song, W. H., Shim, B. H., Oh, S. Y., Lee, H. Y., Chung, E. Y., Sohn, Y., and Lee, J. (2010) Pharmacologically active metabolites of currently marketed drugs: Potential resources for new drug discovery and development. *Yakugaku Zasshi 130*, 1325–1337.

(2) Coller, J., Christrup, L., and Somogyi, A. (2009) Role of active metabolites in the use of opioids. *Eur. J. Clin. Pharmacol. 65*, 121–139.

(3) Paul, D., Standifer, K. M., Inturrisi, C. E., and Pasternak, G. W. (1989) Pharmacological characterization of morphine-6-ss-glucuronide, a very potent morphine metabolite. *J. Pharmacol. Exp. Ther. 251*, 477–483.

(4) Osborne, R., Thompson, P., Joel, S., Trew, D., Patel, N., and Slevin, M. (1992) The analgesic activity of morphine-6-glucuronide. *Br. J. Clin. Pharmacol. 34*, 130–138.

(5) Dahan, A., van Dorp, E., Smith, T., and Yassen, A. (2008) Morphine-6-glucuronide (M6G) for postoperative pain relief. *Eur. J. Pain 12*, 403–411.

(6) Smith, T. W., Binning, A. R., and Dahan, A. (2009) Efficacy and safety of morphine-6-glucuronide (M6G) for postoperative pain relief: A randomized, double-blind study. *Eur. J. Pain 13*, 293–299.

(7) van Dorp, E. L. A., Morariu, A., and Dahan, A. (2008) Morphine-6-glucuronide: Potency and safety compared with morphine. *Expert Opin. Pharmacother. 9*, 1955–1961.

(8) Collins, G. B., and McAllister, M. S. (2007) Buprenorphine maintenance: A new treatment for opioid dependence. *Cleve. Clin. J. Med. 74*, 514–520.

(9) Cone, E. J., Gorodetzky, C. W., Yousefnejad, D., Buchwald, W. F., and Johnson, R. E. (1984) The metabolism and excretion of buprenorphine in humans. *Drug Metab. Dispos. 12*, 577–581.

(10) Moody, D. E., Slawson, M. H., Strain, E. C., Laycock, J. D., Spanbauer, A. C., and Foltz, R. L. (2002) A liquid chromatographic-electrospray ionization-tandem mass spectrometric method for determination of buprenorphine, its metabolite, norbuprenorphine, and a coformulant, naloxone, that is suitable for in vivo and in vitro metabolism studies. *Anal. Biochem. 306*, 31–39.

(11) McCance-Katz, E. F., Moody, D. E., Morse, G. D., Friedland, G., Pade, P., Baker, J., Alvanzo, A., Smith, P., Ogundele, A., Jatlow, P., and Rainey, P. M. (2006) Interactions between buprenorphine and antiretrovirals. I. The nonnucleoside reverse-transcriptase inhibitors efavirenz and delavirdine. *Clin. Infect. Dis. 43*, S224–S234.

(12) Huang, W., Moody, D. E., and McCance-Katz, E. F. (2006) The in vivo glucuronidation of buprenorphine and norbuprenorphine

determined by liquid chromatography-electrospray ionization-tandem mass spectrometry. *Ther. Drug Monit. 28*, 245–251.

(13) McCance-Katz, E. F., Moody, D. E., Morse, G. D., Ma, Q., DiFrancesco, R., Friedland, G., Pade, P., and Rainey, P. M. (2007) Interaction between buprenorphine and atazanavir or atazanavir/ritonavir. *Drug Alcohol Depend. 91*, 269–278.

(14) Jensen, M. L., Foster, D., Upton, R., Grant, C., Martinez, A., and Somogyi, A. (2007) Comparison of cerebral pharmacokinetics of buprenorphine and norbuprenorphine in an in vivo sheep model. *Xenobiotica 37*, 441–457.

(15) Koenigs, W., and Knorr, E. (1901) Ueber einige derivate des traubenzuckers und der galactose. *Ber. Dtsch. Chem. Ges. 34*, 957–981.

(16) Muller, T., Schneider, R., and Schmidt, R. R. (1994) Utility of glycosyl phosphites as glycosyl donors: Fructofuranosyl and 2-deoxyhexopyranosyl phosphites in glycoside bond formation. *Tetrahedron Lett. 35*, 4763–4766.

(17) Soars, M. G., Mattiuz, E. L., Jackson, D. A., Kulanthaivel, P., Ehlhardt, W. J., and Wrighton, S. A. (2002) Biosynthesis of drug glucuronides for use as authentic standards. *J. Pharmacol. Toxicol. Methods 47*, 161–168.

(18) Soars, M. G., Ring, B. J., and Wrighton, S. A. (2003) The effect of incubation conditions on the enzyme kinetics of UDP-glucuronosyltransferases. *Drug Metab. Dispos. 31*, 762–767.

(19) Luukkanen, L., Kilpelainen, I., Kangas, H., Ottoila, P., Elovaara, E., and Taskinen, J. (1999) Enzyme-assisted synthesis and structural characterization of nitrocatechol glucuronides. *Bioconjugate Chem. 10*, 150–154.

(20) Kuuranne, T., Aitio, O., Vahermo, M., Elovaara, E., and Kostiainen, R. (2002) Enzyme-assisted synthesis and structure characterization of glucuronide conjugates of methyltestosterone 17 alpha-methylandrost-4-en-17 beta-ol-3-one) and nandrolone (estr-4-en-17 beta-ol-3-one) metabolites. *Bioconjugate Chem. 13*, 194–199.

(21) Shute, R. E., and Rich, D. H. (1987) Synthesis and evaluation of novel activated mixed carbonate reagents for the introduction of the 2-(trimethylsilyl)ethoxycarbonyl(teoc)-protecting group. *Synthesis* 346–349.

(22) ElSohly, M. A., Gul, W., Feng, S., and Murphy, T. P. (2005) Hydrolysis of conjugated metabolites of buprenorphine ii. The quantitative enzymatic hydrolysis of norbuprenorphine-3-β-D-glucuronide in human urine. *J. Anal. Toxicol. 29*, 570–573.

(23) Lewis, P., Kaltia, S., and Wahala, K. (1998) The phase transfer catalysed synthesis of isoflavone-O-glucosides. *J. Chem. Soc., Perkin Trans. 1* 2481–2484.

(24) Carpino, L. A., Tsao, J. H., Ringsdorf, H., Fell, E., and Hettrich, G. (1978) The β-(trimethylsilyl)ethoxycarbonyl amino-protecting group. *J. Chem. Soc., Chem. Commun.* 358–359.

(25) Trost, B. M., and Romero, A. G. (1986) Synthesis of optically-active isoquinuclidines utilizing a diastereoselectivity control element. *J. Org. Chem. 51*, 2332–2342.

(26) Bollenback, G. N., Long, J. W., Benjamin, D. G., and Lindquist, J. A. (1955) The synthesis of aryl-D-glucopyranosiduronic acids[1]. *J. Am. Chem. Soc. 77*, 3310–3315.

(27) Bowering, W. D. S., and Timell, T. E. (1960) Synthesis and characterization of 2-*O*-(β-D-glucopyranosyluronic acid)-D-xylopyranose. *J. Am. Chem. Soc. 82*, 2827–2830.

(28) Biesalski, H. K., Doepner, G., Kunz, H., Paust, J., and John, M. (1995) Convenient synthesis of biologically important retinoids. *Liebigs Ann.* 717–720.

(29) Tajima, K. (1986) Anomer-specificity in the degradation reaction of d-glucopyranuronic acid tetraacetate leading to comanic acid in the acetic anhydride-base system. *Tetrahedron Lett. 27*, 6095–6098.

(30) Chang, Y., and Moody, D. E. (2009) Glucuronidation of buprenorphine and norbuprenorphine by human liver microsomes and UDP-glucuronosyltransferases. *Drug. Metab. Lett. 3*, 101–107.

(31) Abbo, L. A., Ko, J. C., Maxwell, L. K., Galinsky, R. E., Moody, D. E., Johnson, B. M., and Fang, W. B. (2008) Pharmacokinetics of buprenorphine following intravenous and oral transmucosal administration in dogs. *Vet. Ther. 9*, 83–93.

(32) Hanninen, O., and Puukka, R. (1971) Activation of microsomal UDP glucuronyltransferase by phospholipases. *Chem.-Biol. Interact 3*, 282–284.

(33) Temple, A. R., George, D. J., and Done, A. K. (1971) Reduced nicotinamide-adenine dinucleotide phosphate (NADPH) enhancement of p-nitrophenol glucuronidation. *Biochem. Pharmacol. 20*, 1718–1720.

(34) Zakim, D., and Dannenberg, A. J. (1992) How does the microsomal membrane regulate UDP-glucuronosyltransferases? *Biochem. Pharmacol. 43*, 1385–1393.

(35) Kilford, P. J., Stringer, R., Sohal, B., Houston, J. B., and Galetin, A. (2009) Prediction of drug clearance by glucuronidation from in vitro data: Use of combined cytochrome P450 and UDP-glucuronosyltransferase cofactors in alamethicin-activated human liver microsomes. *Drug Metab. Dispos. 37*, 82–89.

(36) Linder, C. D., Renaud, N. A., and Hutzler, J. M. (2009) Is 1-aminobenzotriazole an appropriate in vitro tool as a nonspecific cytochrome P450 inactivator? *Drug Metab. Dispos. 37*, 10–13.

Bioconjugate Chemistry

ARTICLE

pubs.acs.org/bc

Hairpin-Like Fluorescent Probe for Imaging of NF-κB Transcription Factor Activity

Valeri Metelev,[†,§,∥] Surong Zhang,[†] David Tabatadze,[∥] and Alexei Bogdanov, Jr.*[,†,‡]

[†]Laboratory of Molecular Imaging Probes, Department of Radiology

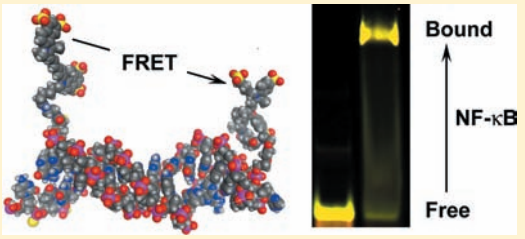
[‡]Department of Cell Biology, University of Massachusetts Medical School, Worcester, Massachusetts, United States

[§]Department of Chemistry, Moscow State University, Moscow, Russian Federation

[∥]ZATA Pharmaceuticals Inc., Worcester, Massachusetts, United States

Supporting Information

ABSTRACT: Three oligodeoxyribonucleotides (ODN) covalently labeled with near-infrared (NIR) fluorochromes were synthesized and characterized with a goal of comparing *in vitro* a hairpin-based and a duplex-based FRET probe designed for the detection of human recombinant NF-κB p50/p65 heterodimer binding to DNA. Using deoxyguanosine phosphoramidite with a phosphorus-linked aminoethylene (diethylene glycol) hydrophilic linker, we synthesized ODNs with internucleoside reactive sites. The hairpin loop amino linker was modified with IRDye 800CW (FRET acceptor), and the 3′-end was modified with Cy5.5 (FRET donor) using a dithio-linker. To obtain a duplex probe, we conjugated Cy5.5 and 800CW to complementary strands at the distance of ten base pairs in the resultant duplex. No quenching of dyes was observed in either probe. The FRET efficiency was higher in the duplex (71%) than in the hairpin (56%) due to a more favorable distance between the donor and the acceptor. However, the hairpin design allowed more precise ratiometric measurement of fluorescence intensity changes as a result of NF-κB p50/p65 binding to the probe. We determined that as a result of binding there was a statistically significant increase of fluorescence intensity of Cy5.5 (donor) due to a decrease of FRET if normalized by 800CW intensity measured independently of FRET. We conclude that the hairpin based probe design allows for the synthesis of a dual fluorescence imaging probe that renders signal changes that are simple to interpret and stoichiometrically correct for detecting transcription factor−DNA interactions.



INTRODUCTION

NF-κB is a fast-acting transcription factor with an established role in carcinogenesis and cancer progression due to NF-κB-mediated control of expression of the genes involved in the antiapoptotic response to tumor surveillance, regulation of tumor angiogenesis, and cell motility.[1] Several studies utilizing fluorescence energy transfer demonstrated that the interaction of NF-kB proteins with fluorescent labeled ODNs can be measured directly.[2,3] We previously reported ODN duplex probes carrying two covalently linked fluorescent dyes for detecting interactions with transcription factors that specifically recognize the DNA sequence encoded by the duplex.[4,5] These probes encoding NF-κB binding sequence were used for determining p50/p65 protein-mediated interference with the fluorescence resonance energy transfer from the donor near-infrared dye (Cy5.5) to a near-infrared acceptor.[5] Near-infrared fluorochromes potentially allow FRET measurements in live tissues due to a lower absorption and scattering of light in the near-infrared range of light.[6,7] The detection of such protein-mediated interference with FRET was accomplished by using either a migration shift assay or plate-capture based assay.[5,8] However, a disadvantage of the probes based on ODN duplexes as opposed to a hairpin, i.e., single self-complementary ODN, is in the effort required for purification of components that constitute the probe. Moreover, since such a hairpin is capable of carrying an equal number of donor and acceptor dyes, variations occurring in the formulations of duplexes during their preparation would also be eliminated.

However, linking of two different fluorescent dyes to a single hairpin would require introducing 3′- and 5′-terminal linkers with differential reactivity toward dye derivatives, i.e., for example, 3′-thio and 5′- amino linkers.[9] After the modified ODN folds with the formation of a hairpin, the dyes linked to the ends of the ODN are in a close proximity resulting in partial or complete quenching.[9] Alternatively, the aminohexyl linkers bridging the dye to dC, dA, or dG bases can also be used for the same purpose. In the latter case, the linked dyes can potentially interact with nucleoside bases and/or get partially buried in the DNA duplex. As an alternative, we used previously developed novel phosphoramidite synthons that by design allow the amino-linkers to be positioned between any adjacent nucleosides, i.e., between any bases in the sequence.[10] This synthon was

Received: December 10, 2010
Revised: February 18, 2011
Published: March 21, 2011

ACS Publications © 2011 American Chemical Society

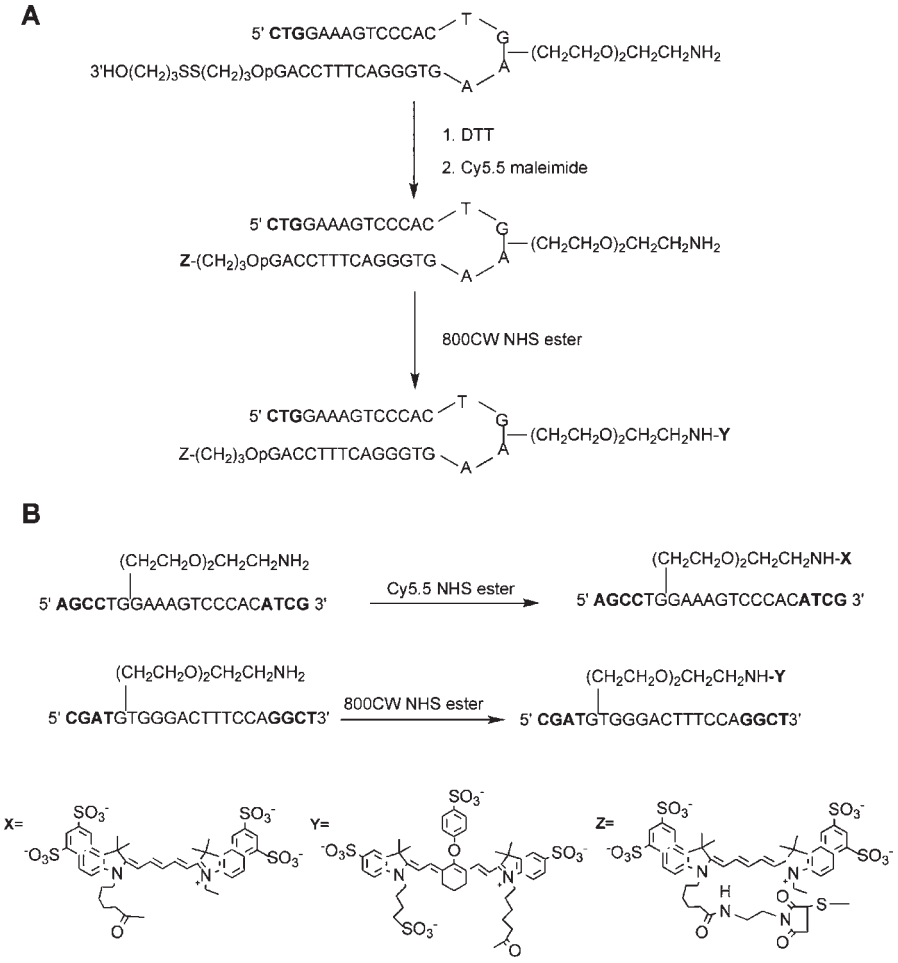


Figure 1. Synthesis of the probes: (A) synthetic steps leading to dual near-infrared fluorescent-labeled hairpin H-ODN probe; (B) synthesis of fluorescent ODN1 and ODN2. Phosphorothioates are shown in bold. X, Cy5.5 carboxylate; Y, IRDye 800CW carboxylate; Z, Cy5.5 thiopyrrolidine dione residues.

incorporated into a loop region of a hairpin probe. The 3′-end of the hairpin carried a reducible dithio bond enabling modifications with maleimides of cyanine dyes. We chose Cy5.5 maleimide to be used as the donor and IRDye 800CW as the acceptor components of FRET pair for the following reasons: (1) the excitation maximum of the donor lies in the near-infrared range of light that corresponds to the maximum depth of penetration in tissue; (2) there is a large spectral emission/excitation spectral overlap suggesting high theoretical energy transfer efficiency; (3) both dyes are hydrophilic and 800CW dye is very stable. Here, we report fluorescent and transcription factor binding properties of this newly designed hairpin probe.

MATERIALS AND METHODS

Materials. The reagents for ODN synthesis and purification were obtained from Glen Research (Sterling VA). A nucleoside phosphoramidite synthon ATG-dG-P developed for introducing internucleoside linkers was synthesized using an approach described in ref 10. The chemical structure of ATG-dG-P is shown in the Supporting Information. Cyanine fluorochrome Cy5.5 maleimide and Cy5.5 NHS ester were purchased from GE Healthcare (Piscataway NJ); IRDye 800CW NHS ester was obtained from Li-COR (Lincoln NE). All other chemicals were obtained from Sigma-Aldrich (St. Louis MO).

Oligodeoxyribonucleotide Synthesis and Chemical Modification. The semiautomated ODN synthesis of three oligonucleotides (ODN1, ODN2, and H-ODN, the sequences are shown below and in Figure 2), ODN purification, and characterization were performed as in ref 10. The capped 3′-dithiolinker was introduced by using a commercially available CPG derivative (Glen Research). The conjugation of Cy5.5 (donor) or IRDye 800CW (acceptor) fluorochromes to the internucleoside amino linkers was initially performed using ODN1, ODN2, and H-ODN (Figure 1). The conjugation of the donor fluorochrome (Cy5.5 mono maleimide) to H-ODN was performed after reducing hydroxypropyl dithiopropyl linker at the 3′-end of the hairpin with 1 M DTT and precipitation of the obtained reduced intermediate from ethanol/sodium acetate. The obtained ODNs were isolated on a C18-HPLC column using a gradient of acetonitrile in 0.1 M TEAA, pH 7.0, precipitated from ethanol/sodium acetate and characterized by using electrospray mass spectrometry: ODN1-Cy5.5 5′-**AGCC**TG*(Cy5.5) GAAAGTCCCAC**ATCG**-3′ *m/z* calc 7525.3, found 7527; ODN2-CW800 5′-**CGAT**G*(800CW)TGGGACTTTCCA**GGCT**-3′ *m/z* calc 7633.2, found 7634; H-ODN: 5′-**CTG**GAAAGTCCCACTG*-AAGTGGGACTTTCCAGpO$(CH_2)_3SS(CH_2)_3$OH-3′ *m/z* calc.

dx.doi.org/10.1021/bc100553e |*Bioconjugate Chem.* 2011, 22, 759–765

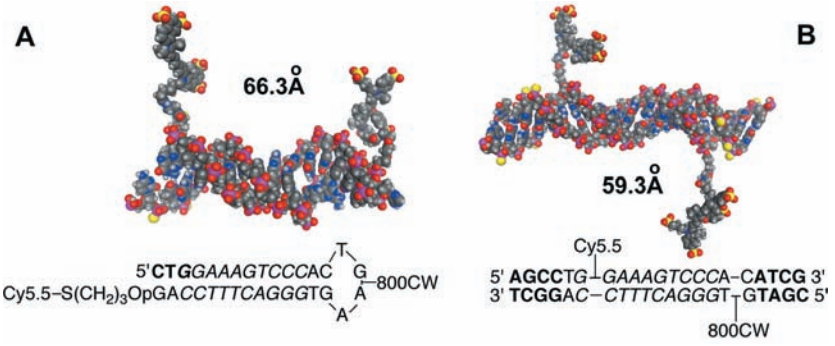


Figure 2. Interfluorochrome distances based on molecular modeling. Ball-and-stick model of H-ODN (A) and the duplex probe ODN1/ODN2 (B) with the sequences shown below. Phosphorothioates are shown in bold. The calculated effective distances between the donor and acceptor NIR dyes is shown next to the models. The models were built in MOE; energy minimization was accomplished by applying AMBER-94 force field parameter sets.

10257.4, found 10257 (* denotes the amino linker; phosphorothioates shown in boldface).

Spectral Measurements. All UV spectral measurements were performed at room temperature with a Cary 50 spectrophotometer (Varian). All fluorescence spectral measurements were carried out at room temperature in quartz microcuvettes using a Cary Eclipse fluorescence spectrophotometer (Varian).

Preparation of Hairpin and ODN Duplexes. Hairpin and ODN duplexes were prepared by adding a prespecified amount of hairpin or mixing equimolar amounts of the corresponding ODNs dissolved in 25 mM Hepes, 1 mM $MgCl_2$, 50 mM NaCl, pH 7.4. The solutions were heated to 95 °C for 5 min to dissociate any intrastrand secondary structures, and allowed to cool at room temperature to attain equilibrium. Hairpin and duplex formation were confirmed by measuring UV and fluorescence spectra.

Electrophoretic Mobility Shift Assays (EMSAs). EMSAs were performed using a mixture containing hairpin or ODN duplexes 20 nM incubated 30 min at RT in a volume of 0.01 mL NF-κB p50/p65 solution in PPB. Samples were loaded and run on 15% TBE Ready Gels (Bio-Rad Laboratories, Hercules CA) using 0.5× TBE buffer. The gels were imaged and digitized using an Odyssey Infrared Imaging system (LI-COR Biosciences, Lincoln NE).

Fluorescence Measurements Using Odyssey Infrared Imaging System. (Li-COR Biosciences, Lincoln NE.) The instrument utilizes simultaneous solid diode excitation of fluorescence at 685 and 785 nm and measures emitted light by using a dichroic mirror which transmits light above 810 nm ("800 channel" fluorescence band) and reflects light below 750 nm ("700 channel" fluorescence band). Fluorescence signals were processed to filter out scattered and stray light. The obtained images (16 bit TIFF) were analyzed, colorized, and fused using *ImageJ* 1.38 (NIH).

Calculation of Experimental Distance Values (*r*). The efficacy of energy transfer depends on the distance between the donor and acceptor dyes.[11] The Förster distance R_0,[12] where 50% of the donor excitation energy is transferred to the acceptor, is defined as $R_0 = 9.78 \times 10^3 (\kappa^2 \eta^{-4} \phi_D J(\lambda))^{1/6}$ where ϕ_D is the fluorescent quantum yield of the donor, i.e., 0.28; κ^2 is a factor accounting for the relative orientation of transition dipole moments of donor and acceptor. Isotropic orientation of donor and acceptor in space was assumed so that $\kappa^2 = 2/3$;[13] η is the refraction index of the solvent (for water, $\eta = 1.33$); $J(\lambda)$ is an overlap integral of the donor absorption spectrum and the acceptor emission spectrum and is given by

$$J(\lambda) = \frac{\int_0^\infty F_D(\lambda)\varepsilon_A(\lambda)\lambda^4 \, d\lambda}{\int_0^\infty F_D(\lambda) \, d\lambda}$$

where $F_D(\lambda)$ is the fluorescence spectrum of the donor at wavelength λ, and $\varepsilon_A(\lambda)$ is the absorption spectrum of the acceptor at wavelength λ. The total electronic coupling was assumed as Coulombic coupling,

The donor and acceptor distance r was calculated as

$$E = \frac{R_0^6}{R_0^6 + r^6}$$

$$E = 1 - \frac{F_{DA}}{F_D}$$

where E is the efficiency of energy transfer, R_0 the Förster distance, and F_D and F_{DA} the relative fluorescence intensity of the donor in the absence and in the presence of the acceptor, respectively.

The efficiency of energy transfer (E) was calculated from donor quenching using the equation $E = 1 - F/F_0$, where the steady-state relative fluorescence intensity is measured in the presence (F) and absence (F_0) of the acceptor.[14,15]

Molecular Modeling. Modeling was performed with *Molecular Operating Environment v 2.0* software (MOE, Chemical Computing Group Inc., Montreal, CA) using *AMBER-94* force field parameter sets. The transition dipole moment directions of cyanine dyes were used as given in ref 16.

Statistical Analysis. All experiments were performed in triplicate. Values were expressed as the mean ± the standard deviation (SD) and compared using double-tailed unpaired *t* test with Welch's correction (*Prism 4.0*, GraphPad).

RESULTS

Using a two-stage synthesis that took advantage of differential conjugation chemistries, we synthesized a 32 bp ODN bearing thio- and amino- group terminated linkers that self-assembles into a hairpin structure (Figure 1, Figure 2A). Consequently, an NF-κB duplex binding site, (i.e., GGAAAGTCCC Ig-box derived p50/p65-binding sequence) is formed in the resultant

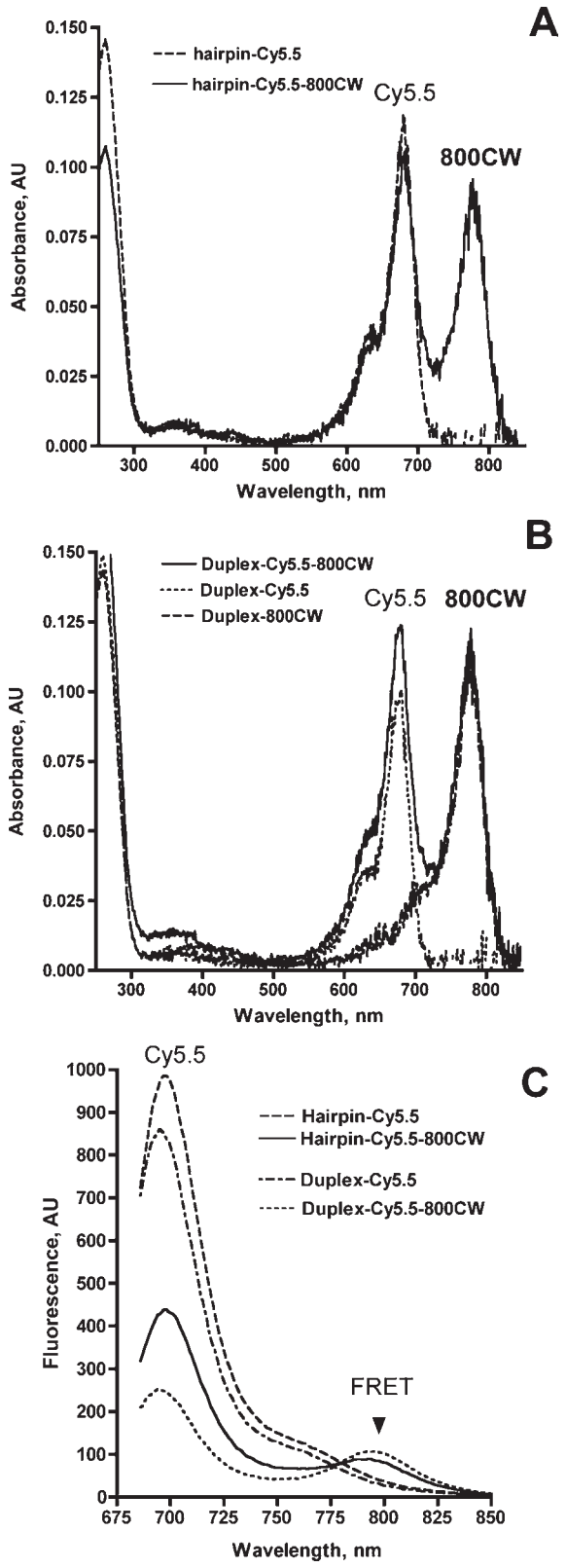


Figure 3. Spectral analysis of ODN probes: (A) absorbance spectra of Cy5.5- and dual Cy5.5/800CW labeled H-ODN probe; (B) absorbance spectra of Cy5.5-ODN1, 800CW-ODN2, and the resultant dual fluorescent duplex probe; (C) fluorescence spectra of Cy5.5-labeled hairpin and duplex probe showing Cy5.5 fluorescence spectra in the absence of FRET and the spectra of dual labeled probes with resultant FRET (shown by an arrowhead). Cy5.5 fluorescence was excited at 675 nm.

oligonucleotide duplex as a result of self-complementarity of the ODNs (Figure 2B).

Furthermore, the synthesized oligonucleotide was covalently modified with a pair of near-infrared fluorochromes capable of forming a FRET pair, i.e., one of the fluorochromes was conjugated to the internucleoside phosphate linker in the hairpin's loop (800CW, acceptor) and the other fluorochrome (Cy5.5, donor) was linked to the terminus. During the synthesis, 5′-terminal phosphorothioates were introduced to achieve higher stability against endonucleases.[4] The hairpin structure and the sites of fluorochrome dye conjugation are shown in Figure 2A. The linkers in the hairpin can theoretically exist in multiple conformations including limiting stretched or coiled states with the distance between nitrogen atoms of the linkers ranging from 23 to 70 Å. According to our calculations, the Förster distance between the NIR donor and acceptor pair (Cy5.5/800CW) corresponded to 68.8 Å. Actual FRET efficiency measurements obtained using the hairpin and duplex probes showed that FRET in the duplex probe was more efficient, i.e., 71% vs 56% FRET in the hairpin. On the basis of these results, we estimated that the distance between Cy5.5 and 800CW in the hairpin was close to the Förster distance, i.e., 66.3 Å, whereas in the duplex, the distance was 59.3 Å. The latter difference in distances between the donor and acceptor fluorochromes was confirmed by applying AMBER-94 force field parameter sets in Molecular Operating Environment (MOE, Figure 2A,B). The close quenching of the dyes was not anticipated due to the relative rigidity of the DNA duplex combined with the distance separating the donor and the acceptor that allows simplified assumption of Coulombic interaction as a dominant dipole coupling mechanism.[16] Spectral measurements demonstrated that the Cy5.5 absorbance spectrum in a hairpin linked to the 3′-Cy5.5 fluorochrome (Figure 3A, broken line) was similar to that of the hairpin with two linked dyes, i.e., Cy.5 and 800CW (Figure 3A, solid line). This result suggests that both fluorochromes do not engage in close interactions, i.e., there is no intramolecular π-bond overlap resulting in static quenching of fluorescence.

The same was true for a duplex probe consisting of two separate complementary ODNs that were used as a control in our studies. The spectrum of the duplex also resembled the superimposed spectra of individual dyes linked to individual ODNs (Figure 3B). The FRET effect in both hairpin and duplex was confirmed by measuring fluorescence spectra (Figure 3C). After exciting fluorescence at 675 nm (i.e., at the Cy5.5 excitation maximum in water), we observed a decrease of Cy5.5 fluorescence in a two-fluorochrome conjugate (hairpin-Cy5.5 −800CW) when compared to a single dye hairpin-Cy5.5 (Figure 3C). We also measured a concomitant 120% increase of fluorescence intensity in the range corresponding to the 800CW fluorescence peak (i.e., 790−810 nm). Therefore, our observations confirmed the role of Cy5.5 as a donor in FRET. Even higher loss of Cy5.5 fluorescence due to FRET was observed in the case of a duplex probe after hybridizing with 800CW-linked oligonucleotide. These spectra were used to calculate the Förster distances (see above).

Since the dual-fluorochrome labeled hairpin duplex has a fixed donor and acceptor stoichiometry (1:1 mol/mol), we decided to investigate whether the fluorescence intensity ratio of the donor/acceptor changes after the binding of a heterodimer of p50 and p65 NF-κB proteins, i.e., whether the hairpin probe responds to the binding. We used an electrophoretic separation technique to

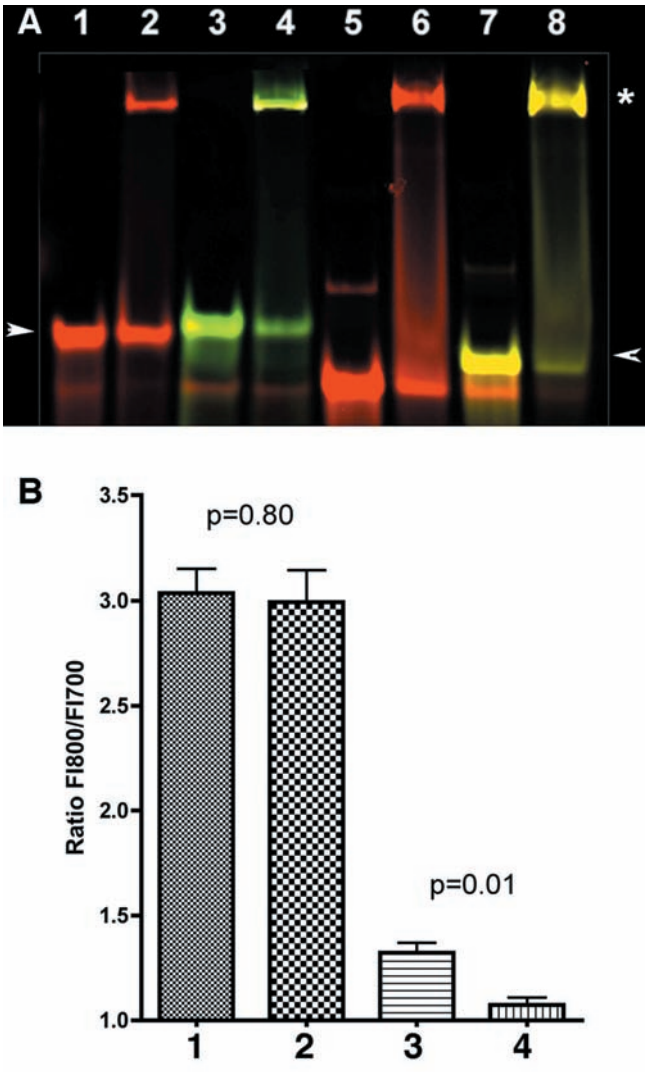


Figure 4. Electrophoretic mobility shift assay of NF-κB complex with ODN probes. (A) Dual wavelength imaging of PAGE gels in pseudo colors. Fluorescence intensities are as follows: red, Cy5.5; green, 800CW. Lanes: 1, Cy5.5ODN1/ODN2 duplex; 2, NF-κB p50/p65 complex with Cy5.5ODN1/ODN2 duplex; 3, dual labeled Cy5.5-ODN1/800CW-ODN2 duplex probe; 4, p50/p65 NF-κB complex with Cy5.5ODN1/800CW-ODN2; 5, Cy5.5-H-ODN (a minor band represents a duplex form of H-ODN); 6, p50/p65 NF-κB complex with Cy5.5-H-ODN; 7, dual labeled hairpin Cy5.5/80CW-H-ODN; 8, p50/p65 NF-κB complex with dual labeled hairpin Cy5.5/800CW-H-ODN. The p50/p65 NF-κB complex migration is marked by an asterisk. The free duplex probe shown with an arrow (left); migration of the free hairpin probe is shown with an arrowhead (right). (B) Ratio of fluorescence intensities of 800CW to Cy5.5 (Fl800/Fl700) measured using the EMSA gels (shown in A) showing a lack of difference between free (bar 1) and NF-κB p50/p65 bound (bar 2) Cy5.5-ODN1/800CW-ODN2 duplex probe (p = 0.8) and significant differences between free Cy5.5/800-H-ODN hairpin probe (bar 3) and NF-κB p50/p65 bound hairpin probe (p = 0.01), n = 4.

separate hairpin ODN complexed with transcription factor from free hairpin (Figure 4A lanes 5−8). We also compared the obtained results with the data acquired using the control NF-κB binding duplex composed of two complementary ODNs (Figure 4A, lanes 1−4). To determine the efficacy of probe binding, we initially used a 6-fold molar excess of NF-κB proteins over ODN probes during the incubation and tested ODNs labeled with a single Cy5.5 dye only (Figure 4A lanes 1,2; 5,6). By measuring reference fluorescence intensity at 800 nm (excitation at 780 nm), which is not appreciably affected by p50/p65 binding in dual-labeled probes (Figure 4A, lanes 3,4 and 7,8), or by using a single dye labeled probe, we determined that overall the hairpin was binding NF-κB proteins more efficiently, whether single dye labeled (69 ± 20% vs 38 ± 11%) or dual labeled (76 ± 2% vs 69 ± 16%), where the first number corresponds to the bound fraction of the hairpin, and the second corresponds to the bound duplex fraction. Moreover, the binding of dual-labeled probes on average appeared to be more efficient than binding of single-labeled ones although the differences were statistically insignificant. In the absence of p50/p65, only about 0.5% of total fluorescence was detectable in the upper part of the plate in both cases.

Furthermore, we determined the ratio of normalized fluorescence intensities of Cy5.5 donor at 700 nm and 800CW acceptor dye at 800 nm in ODN bands after separating the complex from the free ODN probes using electrophoresis. We compared the relative changes of Cy5.5 dye fluorescence intensity after the probes were incubated in the presence of p50/p65 NF-κB proteins. A lack of change in Cy5.5 intensity would indicate that after the protein heterodimer binds to either probe (i.e., duplex or hairpin) there is no change in FRET efficacy. An increase of Cy5.5 fluorescence intensity would indicate that the FRET efficacy decreased, i.e., that the protein binding interferes with FRET. First, we determined the ratios of fluorescence intensities (FI_{800}/FI_{700}) in free ODN probes.

The FI_{800}/FI_{700} ratio was higher in the case of the duplex than the hairpin (Figure 4B). The reason for this is that, during duplex preparation for EMSA analysis, the addition of a small excess of ODN carrying 800CW acceptor fluorochrome is required to ensure that the thermodynamic equilibrium is shifted toward the formation of a duplex from the individual single ODNs. In contrast, thermodynamic stability of hairpins is high at intermediate temperatures, relatively low ionic strength (<0.2 M), and the low ODN concentrations used in our study. Therefore, only a minor fraction of hairpins went through a hairpin-to-duplex transition as observed during the electrophoresis (Figure 4A lanes 5, 7). In both single Cy5.5-dye labeled free duplex and free hairpin, the intensity of fluorescence in the 700 nm channel was 2 times higher than in the case of double-labeled ODNs, indicating the presence of FRET effect in double-labeled probes. The majority of the double-labeled hairpin ODN appeared as a yellow color band as an overlay of green (800 nm) and red (700 nm) pseudocolor fluorescence signals. The above was reflected in the ratios of measured band intensities (Figure 4B) where in the case of a double-labeled duplex probe the ratio of fluorescence intensities (FI_{800}/FI_{700}) is closer to 1:1 than in the case of duplex probe. The intensity ratio itself reflects the relative concentrations of the two fluorochromes and is affected by quantum yields of fluorescence for each fluorochrome and the sensitivity of the light detector. The binding of NF-κB proteins caused not only a shift in migration of the fluorescence band, but also a change in the measured FI_{800}/FI_{700} ratio. There was a statistically significant decrease of this ratio measured in the band corresponding to the complex of a double-labeled hairpin probe with p50/p65 (P < 0.05; Figure 4A, asterisk). There was a much smaller decrease of the FI_{800}/FI_{700} ratio in the case of the duplex probe (Figure 4B)

and the measured differences were insignificant. This result can be interpreted as a consequence of a high signal in 800 nm fluorescence channel created by trailing of the excess of 800CW labeled ODN.

DISCUSSION

The detection of functional protein and nucleic acid complexes capable of regulating gene expression in live cells and whole organisms is one of the major goals of molecular imaging. The imaging of transcriptional activation in cells has been previously accomplished by using genetic constructs, e.g., knocked-in reporter expression cassettes.[17,18] However, the genetic approach is limited in that the imaging signal by design is produced by the protein product of gene expression, which introduces a number of uncertainty factors, which include mRNA and protein stability. These issues potentially complicate the interpretation of results.

We have investigated an alternative method that may allow the direct comparative analysis of transcription factor activity or transcription factor concentration in cells or animals. Several rapid-acting primary transcription factors, including the important ubiquitous NF-κB, undergo maturation in the cytoplasm as a result of the processing of precursor proteins in response to extracellular signaling. We previously investigated the potential of NF-κB detecting probes, which were designed to take advantage of the NF-κB protein-mediated interference with FRET within double-labeled ODN duplexes which encode the transcription binding sequences.[4,5,8] In the current report, we compared a single hairpin-forming ODN and a duplex-forming ODN probe, both of which carried two NIR dyes separated by a similar number of nucleotide base pairs. By using an electrophoretic assay for separating transcription-factor bound and free probes, we could monitor changes in FRET efficacy by directly measuring a change in fluorescence intensity of the donor fluorochrome (Cy5.5) normalized by fluorescence of the acceptor (800CW) dye. The latter measurement did not depend on FRET efficacy, since the fluorescence of the acceptor fluorochrome 800CW was excited at its characteristic maximum. The obtained results showed that the hairpin design had both advantages and disadvantages. The main advantage is in that the dye ratio per probe was much easier to control in the case of the hairpin, which resulted in more reliable measurements of the effects of NF-κB proteins on donor fluorescence. The disadvantage was in the need to implement two different chemistries of dye conjugation in order to link one of the dyes to the ODN terminus in order to achieve a donor/acceptor 1:1 molar ratio.

In conclusion, we showed that dual-labeled fluorescent hairpin probes can be designed with two NIR dyes that form a FRET pair. With this design, an equimolar ratio of donor and acceptor dyes enables the detection of transcription factor protein binding to the probe. The relatively modest effect observed during the in vitro tests suggests that the probe design would benefit from further optimization in order to be useful for reliable intracellular imaging.

ASSOCIATED CONTENT

Supporting Information. The structure of ATG-dG-P nucleoside phosphoramidite synthon. This material is available free of charge via the Internet at http://pubs.acs.org.

AUTHOR INFORMATION

Corresponding Author

*Author to whom correspondence should be addressed. E-mail: Alexei.Bogdanov@umassmed.edu, S6-434, Department of Radiology, University of Massachusetts Medical School, 55 Lake Ave North, Worcester MA 01655. Tel. 508-856-5571. FAX 508-856-1860.

ACKNOWLEDGMENT

This work was supported in part by NCI IMAT grant R33CA134385 to A.B.

ABBREVIATIONS

FRET, fluorescence resonance energy transfer; NIR, near-infrared; ODN, oligodeoxyribonucleotide.

REFERENCES

(1) Karin, M. (2006) Nuclear factor-kappaB in cancer development and progression. *Nature 441*, 431–436.

(2) Schmid, J. A., Birbach, A., Hofer-Warbinek, R., Pengg, M., Burner, U., Furtmuller, P. G., Binder, B. R., and de Martin, R. (2000) Dynamics of NF kappa B and Ikappa Balpha studied with green fluorescent protein (GFP) fusion proteins. Investigation of GFP-p65 binding to DNa by fluorescence resonance energy transfer. *J. Biol. Chem. 275*, 17035–17042.

(3) Altevogt, D., Hrenn, A., Kern, C., Clima, L., Bannwarth, W., and Merfort, I. (2009) A new assay format for NF-kappaB based on a DNA triple helix and a fluorescence resonance energy transfer. *Org. Biomol. Chem. 7*, 3934–3939.

(4) Zhang, S., Metelev, V., Tabatadze, D., Zamecnik, P., and Bogdanov, A., Jr. (2008) Near-infrared fluorescent oligodeoxyribonucleotide reporters for sensing NF-kappaB DNA interactions in vitro. *Oligonucleotides 18*, 235–243.

(5) Zhang, S., Metelev, V., Tabatadze, D., Zamecnik, P. C., and Bogdanov, A., Jr. (2008) Fluorescence resonance energy transfer in near-infrared fluorescent oligonucleotide probes for detecting protein-DNA interactions. *Proc. Natl. Acad. Sci. U.S.A. 105*, 4156–4161.

(6) Ntziachristos, V., Ripoll, J., Wang, L. V., and Weissleder, R. (2005) Looking and listening to light: the evolution of whole-body photonic imaging. *Nat. Biotechnol. 23*, 313–320.

(7) Frangioni, J. V. (2003) vivo near-infrared fluorescence imaging. *Curr. Opin. Chem. Biol. 7*, 626–634.

(8) Zhang, S., and Bogdanov, A. (2009) Plate capture assay of fluorescent oligonucleotide duplex reporter-transcription factor complexes. *Bioconjugate Chem. 20*, 1444–1448.

(9) Metelev, V., Weissleder, R., and Bogdanov, A., Jr. (2004) Synthesis and properties of fluorescent NF-kappa B-recognizing hairpin oligodeoxyribonucleotide decoys. *Bioconjugate Chem. 15*, 1481–1487.

(10) Tabatadze, D., Zamecnik, P., Yanachkov, I., Wright, G., Pierson, K., Zhang, S., Bogdanov, A., Jr., and Metelev, V. (2008) A novel thymidine phosphoramidite synthon for incorporation of internucleoside phosphate linkers during automated oligodeoxynucleotide synthesis. *Nucleosides Nucleotides Nucleic Acids 27*, 157–172.

(11) Stryer, L., and Haugland, R. P. (1967) Energy transfer: a spectroscopic ruler. *Proc. Natl. Acad. Sci. U.S.A. 58*, 719–726.

(12) Forster, T. (1948) Zwischenmoleculare Energiewanderung und Fluoreszenz. *Ann. Physik. 2*, 55–75.

(13) Lakowicz, J. (1999) *Principles of fluorescence spectroscopy*, 2nd ed.; Plenum, New York.

(14) Johnson, D. A., Voet, J. G., and Taylor, P. (1984) Fluorescence energy transfer between cobra alpha-toxin molecules bound to the acetylcholine receptor. *J. Biol. Chem. 259*, 5717–5725.

(15) Fung, B. K., and Stryer, L. (1978) Surface density determination in membranes by fluorescence energy transfer. *Biochemistry 17*, 5241–5248.

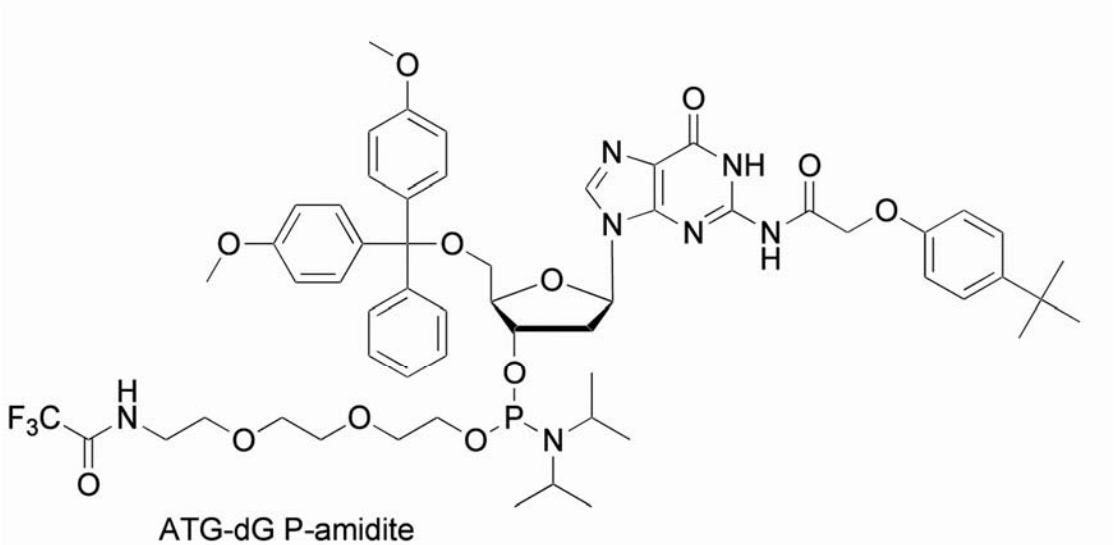
(16) Munoz-Losa, A., Curutchet, C., Krueger, B. P., Hartsell, L. R., and Mennucci, B. (2009) Fretting about FRET: failure of the ideal dipole approximation. *Biophys. J. 96*, 4779–4788.

(17) Carlsen, H., Moskaug, J. O., Fromm, S. H., and Blomhoff, R. (2002) In vivo imaging of NF-kappa B activity. *J. Immunol. 168*, 1441–1446.

(18) Ray, P., Pimenta, H., Paulmurugan, R., Berger, F., Phelps, M. E., Iye r, M., and Gambhir, S. S. (2002) Noninvasive quantitative imaging of protein-protein interactions in living subjects. *Proc. Natl. Acad. Sci. U.S.A. 99*, 3105–3110.

Metelev, V. et al. A hairpin-like fluorescent probe for imaging of NF-κB transcription factor activity. Supporting information.

Chemical formula of ATG-dG-P



5'-dimethoxytrityl-N^2-(4-(t-butyl)phenoxy)acetyl-2'-deoxyguanosine 3'-(2-(2-(2-(trifluoroacetamido)ethoxy)ethoxy)ethyl-N,N-diisopropyl)phosphoramidite

Bioconjugate Chemistry

ARTICLE

pubs.acs.org/bc

$LaPO_4$ Nanoparticles Doped with Actinium-225 that Partially Sequester Daughter Radionuclides

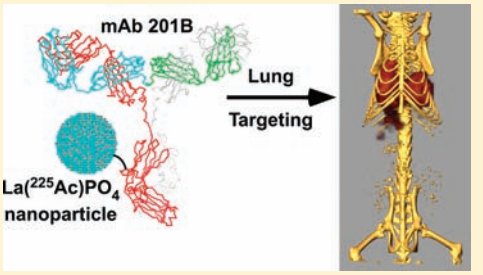
Jonathan Woodward,[†] Stephen J. Kennel,[‡] Alan Stuckey,[‡] Dustin Osborne,[‡] Jonathan Wall,[‡] Adam J. Rondinone,[†] Robert F. Standaert,[†] and Saed Mirzadeh*[,†]

[†]Oak Ridge National Laboratory, Oak Ridge, Tennessee 37831, United States

[‡]Graduate School of Medicine, University of Tennessee, Knoxville, Tennessee 37920, United States

Supporting Information

ABSTRACT: Nanoscale materials have been envisioned as carriers for various therapeutic drugs, including radioisotopes. Inorganic nanoparticles (NPs) are particularly appealing vehicles for targeted radiotherapy because they can package several radioactive atoms into a single carrier and can potentially retain daughter radioisotopes produced by *in vivo* generators such as actinium-225 (^{225}Ac, $t_{1/2}$ = 10 d). Decay of this radioisotope to stable bismuth-209 proceeds through a chain of short-lived daughters accompanied by the emission of four α-particles that release >27 MeV of energy. The challenge in realizing the enhanced cytotoxic potential of *in vivo* generators lies in retaining the daughter nuclei at the therapy site. When ^{225}Ac is attached to targeting agents via standard chelate conjugation methods, all of the daughter radionuclides are released after the initial α-decay occurs. In this work, ^{225}Ac was incorporated into lanthanum phosphate NPs to determine whether the radioisotope and its daughters would be retained within the dense mineral lattice. Further, the ^{225}Ac-doped NPs were conjugated to the monoclonal antibody mAb 201B, which targets mouse lung endothelium through the vasculature, to ascertain the targeting efficacy and *in vivo* retention of radioisotopes. Standard biodistribution techniques and microSPECT/CT imaging of ^{225}Ac as well as the daughter radioisotopes showed that the NPs accumulated rapidly in mouse lung after intravenous injection. By showing that excess, competing, uncoupled antibodies or NPs coupled to control mAbs are deposited primarily in the liver and spleen, specific targeting of NP-mAb 201B conjugates was demonstrated. Biodistribution analysis showed that ~30% of the total injected dose of La(^{225}Ac)PO_4 NPs accumulated in mouse lungs 1 h postinjection, yielding a value of % ID/g >200. Furthermore, after 24 h, 80% of the ^{213}Bi daughter produced from ^{225}Ac decay was retained within the target organ and ^{213}Bi retention increased to ~87% at 120 h. *In vitro* analyses, conducted over a 1 month interval, demonstrated that ~50% of the daughters were retained within the La(^{225}Ac)PO_4 NPs at any point over that time frame. Although most of the γ-rays from radionuclides in the ^{225}Ac decay chain are too energetic to be captured efficiently by SPECT detectors, appropriate energy windows were found that provided dramatic microSPECT images of the NP distribution *in vivo*. We conclude that La(^{225}Ac)PO_4–mAb 201B conjugates can be targeted efficiently to mouse lung while partially retaining daughter products and that targeting can be monitored by biodistribution techniques and microSPECT imaging.



INTRODUCTION

Recently, there has been widespread interest in biomedical applications of nanomaterials for diagnostic and therapeutic purposes. Various inorganic nanoparticles (NPs) have been coupled to antibodies, and the resulting conjugates have been shown to act as targeted drug delivery systems or imaging agents.[1−8] Although monitoring the biodistribution of these NPs has been dominated by fluorescence imaging,[9−17] a few quantitative studies using radioactive NPs have been published.[9,18−21] Radionuclides with specific emission properties can be incorporated into NPs and used for radioimmunotherapy and radioimaging. Nanoparticles are particularly well-suited for the delivery of α- or β^--emitters for radioimmunotherapy. One advantage is the potential for containment of several radioactive atoms within a single carrier. This feature is useful when a target tissue has only a few receptors per cell, limiting the dose that can be delivered.[22] A second potential advantage is the sequestration of daughter radioisotopes from *in vivo* generators such as ^{225}Ac.[22−28] *In vivo* generators utilize parent radioisotopes that decay to radioactive daughters which themselves decay quickly, potentially amplifying the dose at a target site. One such generator is ^{225}Ac, which has four short-lived α-emitting daughters (^{221}Fr, $t_{1/2}$ = 4.9 min; ^{217}At, $t_{1/2}$ = 32.3 ms; ^{213}Bi, $t_{1/2}$ = 46.8 min; ^{209}Pb, $t_{1/2}$ =3.25 h) in two decay chains leading to stable ^{209}Bi (Figure 1).[23,24] Decay through these chains releases >27 MeV of energy, ~90% of which is associated with four sequentially emitted α-particles with individual energies ranging from 5.7 to 8.4 MeV.[23,29,30] Retaining the decay daughters of *in vivo* radioisotope generator systems at the site of targeting would

Received: December 14, 2010
Revised: February 28, 2011
Published: March 24, 2011

ACS Publications © 2011 American Chemical Society

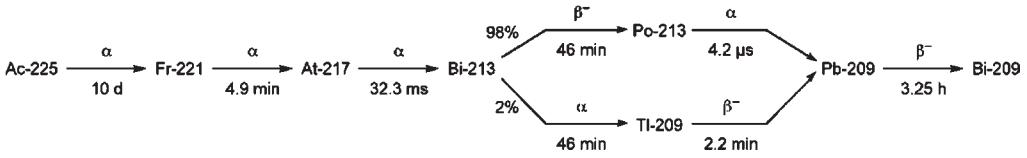


Figure 1. ^{225}Ac decay scheme. Decay of ^{225}Ac to stable ^{209}Bi releases >27 MeV of energy, ~90% of which is associated with four sequentially emitted α-particles with individual energies ranging from 5.7 to 8.4 MeV. Adapted from refs 23 and 24.

improve the specificity of the delivered absorbed dose by limiting nontarget toxicity.[29−34]

In this paper, we detail the synthesis and biofunctionalization of $LaPO_4$ (monazite) NP doped with ^{225}Ac [La(^{225}Ac)PO_4] to study the ability of metal phosphate nanomaterials to target biological epitopes and sequester radionuclides and daughter products, minimizing their release in biological systems. A model system of vascular targeting was used to evaluate NPs performance *in vivo*. This system has numerous advantages for testing the stability of radioconjugates and the retention of daughter radioisotopes from *in vivo* generators.[35,36] First, the radiolabeled monoclonal antibody 201B to murine thrombomodulin (TM) efficiently targets and delivers >30% of the total dose to lung endothelium, the major site of TM expression.[37,38] Targets on the surface of vasculature or circulating cells are necessary for efficient delivery of large constructs such as NPs [18,19] or liposomes,[39] since they do not effectively exit the vascular space.[21,40−42] Second, targeting with this antibody occurs within minutes of injection and depends on antibody specificity, not trapping of aggregated particles.[18,19] Third, radio-iodinated (^{125}I) mAb 201B is retained in lung with a half-life of 2−4 days,[38,39,43] allowing long-term studies. These properties permitted the first demonstration of specific targeting of the ^{225}Ac-doped NPs and determination of the fate of daughter radioisotopes (primarily ^{213}Bi) at various times after delivery. Through both standard biodistribution studies and microSPECT/CT (single photon emission computed tomography/X-ray computed tomography) imaging, we found that La(^{225}Ac)PO_4 NPs attached to a specific antibody can be targeted rapidly and efficiently to lung endothelium and that a significant fraction (~80%) of the daughter radionuclides are retained at the targeting site within 24 h. We conclude that $LaPO_4$ NPs have the potential to improve radioimmunotherapeutic efficacy of ^{225}Ac by effectively targeting the appropriate site while partially retaining daughter nuclides and that the distribution of ^{225}Ac and daughter radionuclides can be monitored by biodistribution techniques and microSPECT imaging.

EXPERIMENTAL SECTION

Reagents and Materials. The following chemicals were used as received: $LaCl_3 \cdot 7H_2O$ (99.9%, Aldrich), H_3PO_4 crystals (≥98%, Aldrich), tri-*n*-butyl phosphate (99%, EM Science), phenyl ether (99%, Acros), tri-*n*-octylamine (>90%, TCI), *n*-hexyl ether (>98%, TCI), hexadecane (≥99%, Aldrich), hexane (HPLC grade, 99.9%, Fisher), anhydrous tetrahydrofuran (≥99.9%, Aldrich), 6-aminohexanoic acid (≥99%, Aldrich), NaOH (99.99%, Aldrich), $Na_2HPO_4 \cdot 2H_2O$ (≥99%, Fluka), $NaH_2PO_4 \cdot H_2O$ (≥99.5%, Fluka), and tris(hydroxymethyl)aminomethane hydrochloride (tris-HCl, ≥99%, Fluka). All other chemical reagents used (HNO_3, HCl, and H_2O_2) were of analytical grade or better.

Nanoparticle purification was performed by dialysis using Spectra/Por regenerated cellulose membranes with a molecular weight cutoff of 10 (or 25) kDa. The dialysis tubing was washed thoroughly of all preservatives before use. Centrifugation was performed using an Eppendorf MiniSpin Plus (radius = 6 cm) in 1.5 mL polypropylene microcentrifuge tubes. Sonication was performed with a Branson microprobe sonicator at power setting 1. BALB/c female mice were obtained from Taconic, Germantown, NY. The monoclonal antibodies mAb 201B and mAb 33 were prepared and purified as previously described.[38,39] Clodronate-containing liposomes were obtained from the Department of Molecular Cell Biology VUmc, FdG, PO Box 7057, 1007 MB Amsterdam, The Netherlands.

Radioactivity Measurements. Gamma-spectrometry for *in vitro* measurements was performed using a calibrated intrinsic Ge detector (crystal active volume ~100 cm^3) and PC-based Multichannel Analyzer (MCA, Canberra). The detector has a resolution of 0.8 at 5.9 keV, 1.0 at 123 keV, and 1.9 at 1332 keV. Energy and efficiency calibrations were determined with γ-ray sources traceable to the National Institute of Standards and Technology. The γ-ray energies and their absolute intensities in parentheses used for determination of ^{225}Ac were 218.0 keV (11.58%) and 440.4 keV (26.1%) from the decay of ^{221}Fr ($t_{1/2}$ = 4.9 min) and ^{213}Bi ($t_{1/2}$ = 46.8 min), respectively.

An automated γ-ray scintillation counter consisting of a well-type NaI (Tl) detector (Perkin-Elmer Wizard model 1480) was used for the biodistribution studies detailed below. The two-channel discriminator windows were set to bracket the 218 keV (from ^{221}Fr) in the lower and 440 keV (from ^{213}Bi) in the upper energy windows. Organs (lungs, liver, spleen, and kidneys) harvested for the *in vivo* release of ^{213}Bi experiment were counted ~20 min after collection to ensure 99% equilibrium between ^{221}Fr and ^{225}Ac. The count rates in the lower window (^{221}Fr) and upper window (^{213}Bi) were indicative of ^{225}Ac and ^{213}Bi activities in the samples, respectively. Accordingly, the ^{213}Bi activities were corrected for decay during the 20 min waiting period. Alternatively, to ensure equilibrium between ^{213}Bi and ^{225}Ac, the same samples were recounted after 3 h and the count rates in the upper window were used for the equilibrium value of ^{213}Bi activity. The two approaches yielded similar results.

Preparation of $^{225}AcCl_3$. Actinium-225 was separated from a mixture of ^{225}Ra and ^{229}Th as described earlier.[44,45] The purified ^{225}Ac was evaporated to near-dryness on a hot-plate under an IR heat lamp, followed by addition of 0.5 mL of conc. HNO_3 and 3 drops of 30% H_2O_2 to the residue, and gentle evaporation of the solution to dryness. The unobservable residue was dissolved in 0.2 mL of 0.1 M HCl to afford $^{225}AcCl_3$ (with a negligible content of nitrate). Assay of a 5 μL aliquot of the purified ^{225}Ac sample (5 mCi) indicated the presence of <1% of ^{225}Ra and $<(1 \times 10^{-4})$% ^{229}Th.

Synthesis of La(^{225}Ac)PO_4 NPs. All reactions were performed in a radiochemical laboratory using a microscale apparatus consisting of a reflux condenser and inert gas adapter connected to a 5 mL Pyrex V-vial set within an aluminum heating block. For a typical preparation, 5.0 mg (14 μmol) of $LaCl_3 \cdot 7H_2O$ was

dx.doi.org/10.1021/bc100574f |*Bioconjugate Chem.* 2011, 22, 766–776

dissolved in 200 μL of 0.1 M HCl containing 5.4 mCi (0.41 nmol) of $^{225}AcCl_3$, and the solution was evaporated to dryness. An additional 200 μL aliquot of 0.1 M HCl was added to redissolve the $La^{3+}/^{225}Ac^{3+}$ mixture, and again the solution was evaporated to dryness. The solid was subsequently dissolved in a mixture of 75 μL of tri-*n*-butyl phosphate and 75 μL of phenyl ether and heated to 100 °C under vacuum with stirring. Residual water was removed by three cycles of evacuating for 30 min followed by backfilling with argon gas at this temperature. Concurrently, a solution was prepared containing 17.0 mg (0.17 mmol) of crystalline H_3PO_4 and 75 μL (0.17 mmol) of tri-*n*-octylamine dissolved in a mixture of 230 μL of tri-*n*-butylphosphate and 460 μL of *n*-hexyl ether by stirring at room temperature. Again, residual water was removed by three cycles of evacuation for 30 min followed by backfilling with argon gas at room temperature. A 60 μL aliquot of the H_3PO_4 solution (containing 14 μmol of H_3PO_4) was then added to the $La^{3+}/^{225}Ac^{3+}$ solution at 100 °C and the resulting reaction mixture was heated to 200 °C under an argon atmosphere and held at this temperature with stirring for 2 h. The initially colorless reaction mixture turned slightly brown during this time. After cooling to room temperature, the product was precipitated from the colloid by adding a mixture of 0.5 mL of hexane and 1.0 mL of hexadecane and then separated by centrifuging at 14 000 × *g* for 20 min. The product was washed with two cycles of redispersion in a mixture of 0.5 mL of hexane and 1.0 mL of hexadecane followed by centrifugation at 14 000 × *g* for 2 min. The activity of the product was 3.3 mCi, and the radiochemical yield for this step was 61%. The supernatant from each step was saved for radioactivity assay.

Surface Modification and Purification of La(^{225}Ac)PO_4 NPs. Freshly synthesized La(^{225}Ac)PO_4 NPs (containing 3.3 mCi of ^{225}Ac) were dispersed in 0.5 mL of tetrahydrofuran, added to a solution containing 200 mg of 6-aminohexanoic acid (AHA, 1.5 mmol) dissolved in 400 μL of 0.1 M NaOH, and stirred for 10 min at 90 °C. A 0.6 mL aliquot of 0.1 M tris-HCl buffer (pH = 9) was added to the mixture and stirred for an additional 5 min, whereby the solution clarified slightly. The surface-modified NPs were dialyzed (total sample volume ~1.5 mL) three times for 2 h each against 500 mL of 0.02 M phosphate buffer (pH = 6.5). Eventually, the NPs settled to the bottom of the membrane and a slightly discolored residue partitioned to the top of the dialysis solution. A 5 mL portion of each dialysate solution was saved for radioactivity assay. The activity of the final purified product was 2.4 mCi with an overall radiochemical yield of 44%. A portion of the surface-modified NPs (containing ~600 μCi of ^{225}Ac) was tested for *in vitro* leaching of radionuclides (detailed below), while the remainder (~1.7 mCi) was used for *in vivo* biodistribution and SPECT/CT experiments.

***In Vitro* Release of ^{225}Ac, ^{221}Fr, and ^{213}Bi from La(^{225}Ac)PO_4 NPs.** A sample of La(^{225}Ac)PO_4 NPs (~600 μCi) in 450 μL of phosphate buffer solution was dialyzed (total sample volume ~0.5 mL) against 500 mL of 0.02 M phosphate buffer for a period of 1 month. Periodically, a 5 mL aliquot of the dialysate was withdrawn and assayed for radioactivity. Samples were counted at 1 cm distance from the surface of a calibrated high-purity Ge detector (see Radioactivity Measurements section above). To determine ^{221}Fr activity, the time duration between withdrawal of the sample from the dialysis bag and start of the measurement was about 1 min, and the sample was counted for 2 min. This same measurement also provided quantitative measurements of ^{213}Bi activity. The quantity of ^{225}Ac was determined by recounting the same sample for 1 h using the same geometry on the following day.

Antibody Conjugation. The AHA surface-modified La(^{225}Ac)PO_4 NPs, containing ~1.6 mCi of activity and dispersed in ~1.5 mL of 0.02 M phosphate buffer (pH = 6.5), were sonicated at lowest power for 30 s. The NPs were then coupled to 300 μg of either mAb 201B or control antibody mAb 33 per 1 mg of NPs using conventional carbodiimide chemistry.[18] For this reaction, 2 μL each of 0.1 M 3-sulfo-*N*-hydroxysuccinimide (as sodium salt, sulfo-NHS) and 0.4 M 1-ethyl-3-(3-dimethylaminopropyl)-carbodiimide (EDC) aqueous solutions were added to the NP suspension and incubated for 10 min before addition of the mAbs. After overnight reaction at room temperature on a rotating disk to promote mixing, the solution was quenched by addition of glycine to a final concentration of 0.1 M. The suspension was sonicated as described above, and the mixture was separated on a 5 mL Aca34 Ultragel filtration column (Sigma) equilibrated in 0.01 M phosphate buffer, pH = 7.6, and 0.15 M NaCl (PBS) containing 5 mg/mL bovine serum albumin (BSA). The majority of the radioactivity (>90%) eluted in the void volume. The mAb-conjugated NPs were injected into mice tail veins within 1 h of preparation (see below).

***In Vivo* Mouse Biodistribution Experiments.** All experiments involving mice were performed according to the Institutional Animal Care and Use Committee of the University of Tennessee approved protocol 1502. Five-week-old female BALB/c mice (body mass ~15 g, 2 weeks postdelivery) were used for all biodistribution and imaging experiments. Three groups, consisting of five mice per group, were each injected intravenously (tail vein) with 0.2 mL of NP-mAb conjugates containing 5 μCi of ^{225}Ac. Groups 1 and 2 were injected with La(^{225}Ac)PO_4-mAb 201B conjugates, while group 3 was treated with La(^{225}Ac)PO_4-mAb 33, the control antibodies. Additionally, group 2 mice were injected with 0.1 mL of clodronate-containing liposome suspension 24 h prior to injection with radioactive NP-mAb conjugates. This procedure has been shown to enhance targeting of ZnS/Cd^{125m}Te NPs to endothelial tissue in the vascular model system by temporary depletion of phagocytic cells in the liver and spleen.[19,46,47] An additional separate group of three mice were also injected with 0.2 mL of La(^{225}Ac)PO_4-mAb 201B conjugates containing 5 μCi of ^{225}Ac for *in vivo* retention studies. Mice were housed with food and water *ad libitum* in a light/dark cycle environment before sacrificing at 1, 4, and 24 h postinjection for imaging and biodistribution experiments and 1, 4, 24, 48, and 120 h postinjection for *in vivo* retention studies.[18,48] Biodistribution studies were performed on lungs, liver, spleen, and kidneys to evaluate the amount of both ^{225}Ac and ^{213}Bi in target organs by measuring weighed tissue samples in a γ-ray scintillation counter at a specific time postsacrifice and again after the radioisotopes had achieved isotopic equilibrium (>3 h). Quantities of ^{225}Ac and ^{213}Bi present at the time of animal sacrifice were determined by appropriate crossover and decay corrections described above.

microSPECT/CT Imaging. Small animal imaging[48] was performed using a microCAT II+ SPECT dual modality platform (Siemens Preclinical Imaging, Knoxville, TN). Mice, treated 24 h prior with 100 μL of clodronate-containing liposomes, were injected intravenously with 0.2 mL containing 45 μCi of La(^{225}Ac)PO_4-mAb 201B conjugates (group 1, 2 mice per group); 45 μCi of La(^{225}Ac)PO_4-mAb 201B conjugates mixed with 300 μg of cold, uncoupled mAb 201B (competitor group 2, 1 mouse

per group); or 45 μCi of La(^{225}Ac)PO_4 mAb 33 conjugates (control group 3, 2 mice per group). Animals were sacrificed by overdose of isoflurane at 1 h postinjection and imaged via microSPECT/CT 3 h later when the ^{225}Ac and its daughters had reached equilibrium. SPECT data for the final images were acquired within energy windows of 12−268 keV at a detector operating bias of 760 V. Energy windows of 230−344 keV on detector 1 and 206−308 keV on detector 2, both operating at 700 V, were also examined. Data were collected using 2 mm pinhole collimators positioned ~60 mm from the center of rotation. Forty-five projections were acquired at 8° azimuths, each for a period of 60 s. Each projection was normalized using a corrected flood image to improve overall image quality and accuracy. The flood image was obtained by removing the collimator and detector housings. An ^{225}Ac source at equilibrium with daughter radioisotopes (^{221}Fr and ^{213}Bi) was used to uniformly flood both detectors over a 12 h time frame. The resulting data were normalized to unity and used to correct the individual SPECT projection data for nonlinear detector response. The data were reconstructed postacquisition using an 84 × 84 × 114 matrix, with isotropic voxels, and an ordered subset expectation maximization algorithm with eight subsets. Computed tomography (CT) data were collected following SPECT data acquisition[49] with 360° of rotation and one projection per degree. Data were acquired using an exposure time of 210 ms per projection and X-ray settings of 80 kVp and 500 μA. CT images were reconstructed in real time from a 512 × 512 × 768 matrix with 77 μm isotropic voxels using an implementation of the Feldkamp filtered back-projection algorithm (Cobra; Exxim Computing, Pleasanton, CA). CT and SPECT images were manually coregistered and visualized using the *Amira* image analysis software package (v 4.0; TGS, San Diego, CA). The CT data were rendered as a volume to aid in showing the location of the ^{225}Ac uptake. The SPECT data were also volume rendered in this fashion and registered to the CT data to better demonstrate the uptake of the different NP-mAb conjugates (or uncoupled mAbs). These volume renderings may not result in a linear scale that could reliably show relative uptake of the radioisotope.

RESULTS

Nanoparticle Synthesis and Surface Modification. The La(^{225}Ac)PO_4 NPs were synthesized by the reaction of $LaCl_3$ (14 μmol) with H_3PO_4 (14 μmol) in high-boiling organic solvents.[50] Solubility of the reagents in the solvents (*n*-hexyl and phenyl ether) is achieved by coordination of La^{3+}/$^{225}Ac^{3+}$ and H_3PO_4 by tri-*n*-butylphosphate and tri-*n*-octylamine surfactants, respectively. Addition of 5.4 mCi (0.41 nmol) of ^{225}Ac as the chloride salt to the reaction mixture ensured sufficient radioactivity for biodistribution and SPECT/CT imaging experiments while leaving the bulk chemical composition of the NPs unchanged. The synthesis is reproducible, and repeat experiments provided an average decay-corrected radiochemical yield of 66 ± 4% (n = 3). The NP surfaces were subsequently derivatized with 6-aminohexanoic acid (aminocaproic acid) using an adaptation of a reported procedure[51] and dialyzed against pH = 6.5 phosphate buffer solution for purification. Surface modification improved the aqueous dispersibility, although the product settles out of solution within 24 h, and the discolored residue at the top of the dialysis solution was likely displaced hydrophobic surfactants and solvents. The entire process, including synthesis, surface modification, and purification, took 24 h, with an overall average

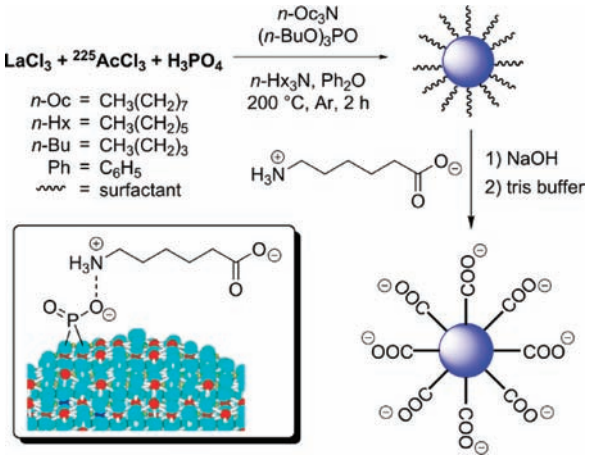


Figure 2. Schematic depiction of synthesis and surface modification of La(^{225}Ac)PO_4 NPs. Equimolar quantities of $LaCl_3$ (14 μmol) and H_3PO_4 (14 μmol), along with 5.4 mCi of $^{225}AcCl_3$ and tri-*n*-butylphosphate and tri-*n*-octylamine surfactants, react at 200 °C for 2 h within a phenyl ether/*n*-hexyl ether solvent mixture to form La(^{225}Ac)PO_4 NPs. The surfaces of the NPs were subsequently modified with 6-aminohexanoic acid. The amine moieties electrostatically bond to the phosphate groups on NP, leaving carboxylate functionalities at the surface.

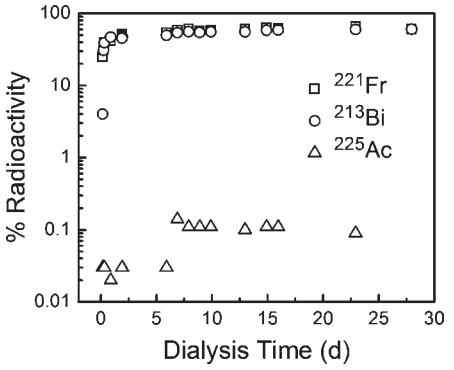


Figure 3. *In vitro* release of ^{225}Ac, ^{221}Fr, and ^{213}Bi from La(^{225}Ac)PO_4 NPs. While ^{225}Ac is nearly quantitatively retained, ~50% of ^{221}Fr and ^{213}Bi are released from the $LaPO_4$ NPs over a period of 30 days. Activity of ^{225}Ac = 600 μCi, pH = 6.5 phosphate buffer. For further details and determination of ^{221}Fr and ^{213}Bi activity, see Experimental Section.

decay-corrected yield of 47 ± 5% (n = 3). During this time, 7% of the initial radioactivity was lost to decay ($t_{1/2}$ = 10 d), and the remaining radioactivity was distributed among the residual organic supernatants and solvents in addition to the reaction vessel, stir bar, pipet tips, aqueous washes, and dialysis membranes. The NP synthesis and surface modification steps are depicted in Figure 2. Transmission electron microscopy of cold $LaPO_4$ NPs synthesized in an analogous protocol (no $^{225}AcCl_3$ added to the $LaCl_3$-tri-*n*-butylphosphate solution) confirmed the presence of unaggregated, 3−5-nm-diameter NPs.[52]

***In-Vitro* Release of ^{225}Ac, ^{221}Fr, and ^{213}Bi from $LaPO_4$ NPs.** To probe the release of ^{225}Ac as well as ^{221}Fr and ^{213}Bi daughters from the monazite host *in vitro*, a small portion of the surface-modified and purified La(^{225}Ac)PO_4 NPs was further dialyzed against pH = 6.5 phosphate buffer solution over a period of 1 month. Aliquots of the dialysate were assayed periodically to determine the amount of each radioisotope present in solution

dx.doi.org/10.1021/bc100574f |*Bioconjugate Chem.* 2011, 22, 766–776

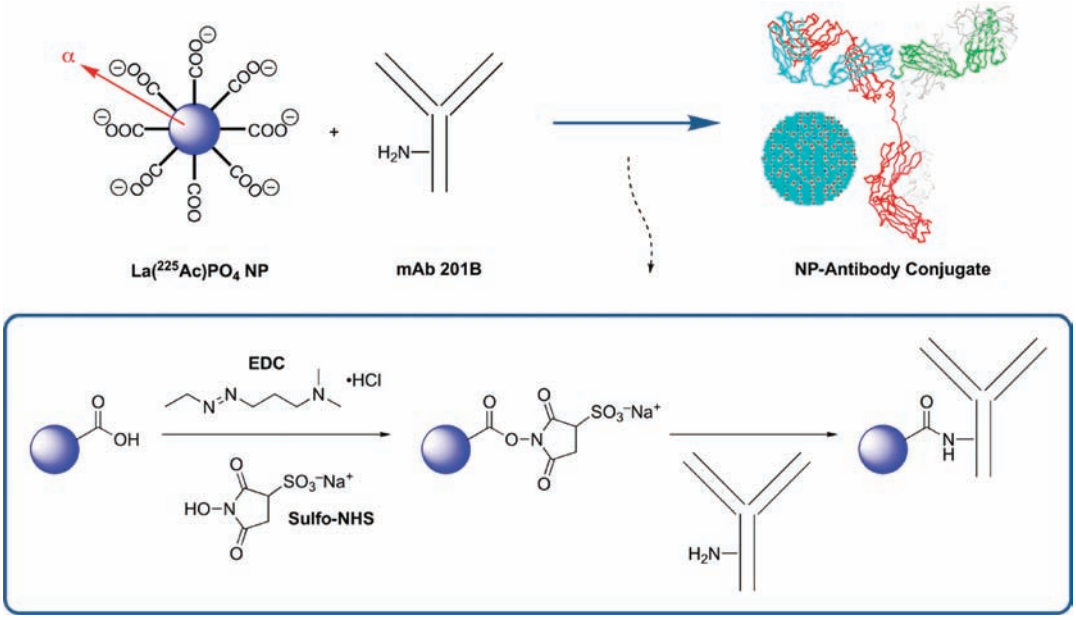


Figure 4. Schematic depiction of La(^{225}Ac)PO_4 NPs−mAb conjugation process. The 6-aminohexanoic acid modified La(^{225}Ac)PO_4 NPs with carboxylate moieties on the surfaces connect to free amine groups on the antibody via carbodiimide coupling to form the NP−mAb conjugate.

(Figure 3 and Supporting Information Table S1). The fraction of ^{225}Ac which was found in the dialysate increased from 0.03% of the initial quantity to 0.1% over the first 5−7 d and then remained constant over the next 25 d. Within the first 4 h, 24% of the initial quantity of ^{221}Fr was detected in the dialysate, which increased rapidly to ∼50% within 6 d and then remained relatively constant at ∼60% over the following 25 d. The fraction of ^{213}Bi in the dialysate was similar to that of ^{221}Fr, except for the first time point (3.8 h), at which time only 4% of ^{213}Bi was found in the dialysate. Note that, in Figure 3, the *y*-axis data are plotted on a logarithmic scale since the measured activity of ^{225}Ac in solution was vastly smaller compared to the activity of ^{221}Fr and ^{213}Bi. The higher initial fraction of ^{221}Fr measured in the dialysate is an indication that transport of ^{213}Bi through the NP lattice, the phosphate buffer, and/or the dialysis membrane is much slower than that of ^{221}Fr. Note that the majority of the ^{213}Bi detected in the dialysate originates from the decay of ^{221}Fr and is not directly released from the NPs. Eventually, an equilibrium was reached between ^{221}Fr and ^{213}Bi in the dialysate, since ^{221}Fr decays with a half-life ∼1/10 that of ^{213}Bi (see Discussion). These results indicate that, while the ^{221}Fr and ^{213}Bi daughters were only partially sequestered, the ^{225}Ac parent was nearly quantitatively retained in the $LaPO_4$ NPs.

Nanoparticle−Antibody Conjugation. The La(^{225}Ac)PO_4 NPs were coupled to mAb 201B and the control antibody, mAb 33, by linking the carboxylate moieties on the NP surfaces to amine groups on the antibodies through carbodiimide chemistry (Figure 4) as previously reported.[18,19] The molecular weight of a 5 nm diameter $LaPO_4$ NP with an estimated density of 5.12 g/mL[53] is 200 kDa. Using this estimate, the molecular ratio of mAb to NP in the reaction mix was ∼1:2.5. After coupling, the NP−mAb conjugates were briefly probe-sonicated at low power to break up any large aggregates and size-selected by gel filtration. The fraction of NP-mAb 201B or NP-mAb 33 that fractionated in the column void volume, corresponding to 1−5 MDa in size, comprised 95% of the initial radioactivity loaded on the column. Yields in excess of 50% were obtained, with 59 ± 9% (n = 2) and 92 ± 10% (n = 3) of the NP−mAb 201B conjugates eluting from the column in two separate experiments. Since the $LaPO_4$ NPs have molecular weights of ∼200 kDa, the 1−5 MDa gel fraction likely contains multiple NPs conjugated to multiple antibodies, and not aggregates of NPs.[18,19] A small portion of the remaining radioactivity consisting of large aggregated material filtered out on top of the resin. The specific activities of the NP preparations were ∼1.7 mCi of ^{225}Ac/mg of unconjugated $LaPO_4$ NPs, ∼1.2 mCi/mg of La(^{225}Ac)PO_4-mAb 201B conjugates, and ∼1.1 mCi/mg of La(^{225}Ac)PO_4-mAb 33-conjugates. (Values were corrected for 42 h of decay.) Once the NP−antibody conjugates were size-selected, they were diluted in BSA-containing buffer, where no significant aggregation over time was observed. Test samples were analyzed on SDS polyacrylamide gel electrophoresis. Greater than 95% of the radioactivity moved through the stacker gel (4% acrylamide) but did not enter the separation gel (10% acrylamide) confirming the gel filtration results that the NP-mAb conjugates were about 1−5 MDa in size.

Biodistribution of Targeted and Control NP−mAb conjugates in Normal and Clodronate-Treated Mice. La(^{225}Ac)PO_4 NP−antibody conjugates were injected intravenously into normal and clodronate-treated BALB/c mice within 1 h after column elution to avoid any aggregation or radiolysis that might occur, as well as minimize the loss of specific activity. Clodronate liposomes were injected 24 h prior to injection of NP−mAb conjugates. Groups of five mice were sacrificed at various periods (1, 24, and 48 h) postinjection and the organs collected for biodistribution analysis of radioisotopes in tissue by examining the γ-ray emissions of ^{213}Bi once in equilibrium with ^{225}Ac.

Within 1 h postinjection, the NPs coupled to mAb 201B (group 1 mice) primarily targeted the lungs (235% ID/g and ∼30% ID/lung), and while uptake measured in the liver (23.8% ID/g) and spleen (29.1% ID/g) was significant, the concentrations were approximately 10- and 8-fold less, respectively, compared to the concentration in the lungs (Table 1 and Supporting Information Figure S1). In contrast, the NPs coupled to the control mAb 33 (group 3 mice) did not accumulate

dx.doi.org/10.1021/bc100574f |*Bioconjugate Chem.* 2011, 22, 766–776

Table 1. Biodistribution of Targeted La(^{225}Ac)PO_4-mAb Conjugates in BALB/c Mice[a]

	injected dose per gram of tissue (ID/g) (%) ($\chi \pm \sigma$, n = 5)		
	time postinjection (h)		
tissue	1	24	48
	Targeted with mAb 201B (Group 1)		
Liver	24 ± 6	42 ± 12	48 ± 9
Spleen	29 ± 8	162 ± 33	297 ± 71
Kidney	2.9 ± 0.9	2.7 ± 0.3	2.7 ± 0.6
Lung	235 ± 29	184 ± 25	212 ± 28
	Clodronate-treated mice targeted with mAb 201B (Group 2)		
Liver	16 ± 7	20 ± 2	23 ± 3
Spleen	7.2 ± 2.1	18 ± 3	40 ± 3
Kidney	2.8 ± 1.6	1.6 ± 0.4	2.1 ± 0.4
Lung	279 ± 40	261 ± 20	276 ± 16
	Targeted with mAb 33 (Group 3)		
Liver	66 ± 3	74 ± 7	78 ± 4
Spleen	38 ± 8	66 ± 14	95 ± 19
Kidney	0.44 ± 0.03	0.38 ± 0.05	0.49 ± 0.04
Lung	2.0 ± 1.0	0.68 ±0.34	1.1 ± 0.2

[a] Number of mice per group = 5; Activity injected (i.v.) in each mouse = 5 μCi. Groups 1 and 2: La(^{225}Ac)PO_4 NPs-mAb 201B. Group 3 (control): La(^{225}Ac)PO_4 NPs-mAb 33. Group 2 mice were injected 24 h prior with 100 μL of clodronate-containing liposomes. Organs were analyzed in a γ-ray scintillation counter after ^{225}Ac and its daughters had reached equilibrium (~3 h).

significantly in the lungs (1.99% ID/g) but were predominately deposited in the liver (65.9% ID/g) and spleen (38.0% ID/g) (Table 1 and Supporting Information Figure S1). These results clearly indicate that the NPs bound to mAb 201B exclusively target the lungs and NP-mAb 33 conjugates do not. Over the course of 24 h, approximately 30% of the radioactivity in the NP-mAb 201B conjugates was lost from the lungs. By 5 d, the activity in the liver almost doubled from 23.8% to 42.1% ID/g. The concentration in the spleen increased dramatically from 29.1% to 161.8% ID/g, which is likely due to the atrophy of the spleen due to radiotoxicity, resulting in a much smaller organ weight (data not shown). After 24 h, activity in the liver for NP-mAb 33 conjugates increased by only 10% while the radioactivity in the spleen almost doubled. These trends continued in a similar fashion over the subsequent 24 h period for both NP-mAb 201B and NP-mAb 33 conjugates. Note that a small but measurable quantity of radioactivity was present in the kidneys and remained relatively constant over time due to the excretion of the ^{213}Bi daughter.

For clodronate-treated mice (group 2 mice), the NP-mAb 201B activity in the lung (279% ID/g) was higher compared to that in untreated mice (235% ID/g) at 1 h postinjection, while accumulation in the liver (15.9% versus 23.8% ID/g, respectively) and spleen (7.15% versus 29.1% ID/g, respectively) was lower (Table 1 and Supporting Information Figure S1). After 24 h, the activity of NP-mAb 201B conjugates in the lungs was reduced by only 10% in clodronate-treated mice and remained relatively constant thereafter compared to a 30% loss of radioactivity from the lungs of untreated mice. Accumulation of NP-mAb 201B

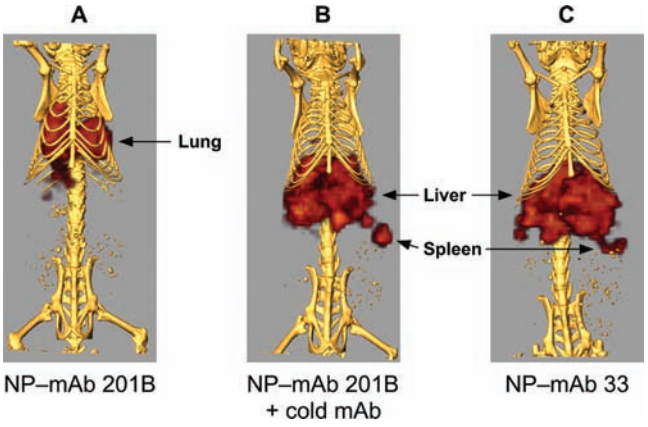


Figure 5. Whole body microSPECT/CT images of La(^{225}Ac)PO_4 targeted NPs of mice. NPs conjugated with mAb 201B target the lungs (A) but redistribute to the liver and spleen while in the presence of additional competing, unconjugated mAb 201B (B) as do NPs coupled to the control, mAb 33 (C). BALB/c mice treated 24 h prior with 100 μL of clodronate-containing liposomes were injected i.v. with 45 μCi of La(^{225}Ac)PO_4-mAb 201B (groups 1), 45 μCi of La(^{225}Ac)PO_4-mAb 201B mixed with 300 μg cold mAb 201B (competitor-group 2) or with 45 μCi of La(^{225}Ac)PO_4 mAb 33 (control-group 3). Animals were sacrificed by overdose of isoflurane at 1 h postinjection and imaged via microSPECT/CT 3 h later when the ^{225}Ac and daughters had reached equilibrium. Only the higher quality images per group of mice are shown. For further details, see Experimental Section.

conjugates in the liver and spleen of clodronate-treated mice increased slowly, but steadily, with time. Thus, temporary depletion of phagocytic cells enhanced both the accumulation and retention times in the lungs similarly to a previously reported study.[19]

microSPECT/CT Imaging. To confirm and illustrate the biodistribution data presented earlier, three-dimensional, whole-body microSPECT/CT images of mice treated with the following conjugates were collected: (A) La(^{225}Ac)PO_4-mAb 201B conjugates (NP-mAb 201B), (B) ~100-fold molar excess of uncoupled, cold, competing mAb 201B added prior to injection of NP-mAb 201B, and (C) control NP-mAb 33 conjugates. Mice were sacrificed 1 h postinjection and imaged 3 h postsacrifice when ^{225}Ac was in equilibrium with ^{213}Bi. The SPECT data, obtained by measuring the primary γ-ray emission of ^{221}Fr at 218 keV (the primary γ-ray of ^{213}Bi at 440 keV is too energetic to be collected efficiently by the thin microSPECT detectors), were superimposed onto the images of mouse skeletons from subsequent CT scans. The images clearly indicate that the radioactivity from NP-mAb 201B conjugates was present in the lungs while only slight levels of radioactivity were detected in the spleen and liver (Figure 5A). In contrast, when the NP-mAb 201B conjugates were mixed with an excess of competing mAb 201B, the majority of the radioactivity was found in the spleen and liver (Figure 5B). NPs conjugated with control mAb 33 likewise localized in the spleen and liver (Figure 5C). These results together show that the observed localization of NP-mAb 201B conjugates to the lung represents specific, antibody-mediated interaction with a saturable receptor.[38] Note that only the highest quality SPECT/CT images per group of mice are depicted in Figure 5.

***In Vivo* Release of ^{213}Bi following La(^{225}Ac)PO_4 NP Targeting to Mouse Lungs.** Data in Table 2 show the activity of ^{213}Bi daughter in the lungs and kidneys as a function of time

Table 2. *In Vivo* Release of ^{213}Bi following Targeting of La(^{225}Ac)PO_4-mAb 201B Conjugates to Lung of Mice[a]

time postinjection (h)	release of ^{213}Bi from lung (average % ± σ)	ratio of ^{213}Bi to ^{225}Ac activity in kidney (average ± σ)
1	39.8 ± 2.5 (n = 3)	12.1 ± 3.6 (n = 3)
4	34.9 ± 2.7 (n = 3)	10.4 ± 2.2 (n = 3)
24	20.1 ± 0.9 (n = 3)	8.5 ± 0.2 (n = 3)
48	24.5 ± 1.2 (n = 3)	8.3 ± 2.1 (n = 3)
120	13.1 (n = 1)	4.4 (n = 1)

[a] Activity injected (i.v.) in each mouse = 5 μCi of La(^{225}Ac)PO_4 NPs-mAb 201B. For determination of ^{213}Bi and ^{225}Ac activities, organs were assayed immediately after harvesting and then reassayed in 3−4 h, respectively. See Experimental Section for details regarding data treatment.

postinjection. Mice were injected with La(^{225}Ac)PO_4-mAb 201B conjugates and sacrificed at various time periods (1, 4, 24, 48, and 120 h) postinjection. The lungs, liver, spleen, and kidneys were collected for biodistribution analysis by examining the γ-ray emissions immediately after sacrifice and 3 h thereafter once ^{213}Bi and ^{225}Ac equilibrium was reestablished. The analysis showed a deficiency of ^{213}Bi activity (relative to the equilibrium ^{213}Bi/^{225}Ac ratio) in the lungs, liver, and spleen, and an elevated level of ^{213}Bi activity in the kidneys. Excess ^{213}Bi present in the kidneys is due to relocation of ^{213}Bi from elsewhere in the mouse. The data in Table 2 indicate that, at 1 h postinjection, ∼40% of ^{213}Bi produced from ^{225}Ac decay was released from the lungs. This result is consistent with the loss of ^{213}Bi from NPs *in vitro* (∼50%) detailed above. However, the release of ^{213}Bi from the lungs was reduced with time: after 24 h, only ∼20% of the ^{213}Bi was released from the lungs and just over ∼10% was released 5 d post-targeting. Although the data in Table 2 suggest an apparent increase for 48 h, considering the 5−10% errors associated with calculated values, it is believed that the general trend of decreasing release of ^{213}Bi holds. The data in Table 2 also indicate that, for the 1 h time point, the activity ratio of ^{213}Bi to ^{225}Ac in the kidneys was 12:1, which decreased over time, reaching a value of ∼4 after 120 h. This trend is also consistent with the decrease in ^{213}Bi release from the lungs over time.

DISCUSSION

Recent interest has focused on incorporating radionuclides with specific emission properties within nanoscale materials for site-specific radioimmunotherapy and diagnostic imaging. It is well-known that α-emitters can be very effective therapeutics against small, localized tumors.[34,35,37] In particular, 8 MeV α-particles (such those produced in the decay chain of ^{225}Ac) deliver their absorbed dose within a distance of ∼100 μm or approximately 10 cell diameters, thus limiting damage to non-target cells.[31] This potential has been realized in recent clinical trials of ^{213}Bi coupled to anti-CD33 mAb for treatment of acute myeloid leukemia.[34] Actinium-225 has been proposed as an attractive alternative to the ^{213}Bi treatment[25,54] since the former nuclide has a much longer half-life ($t_{1/2}$ = 10 d) and a single atom can produce 4 α-particle emissions with a total energy release of > 27 MeV per decay,[23,29,44] making it a potent radioisotope if all the energy is deposited at the tumor site. Two major issues limit this approach. The first problem is the overall low labeling yield of coupling antibodies to ^{225}Ac. In the best conventional method, ^{225}Ac is coordinated to DOTA (1,4,7,10-tetraazacyclododecane-1,4,7,10-tetraacetic acid), purified, and coupled to antibodies. The efficiency of the first (coordination) step is fairly high and the reaction can be forced to completion by increasing temperature and pH. However, the efficiency of the second (coupling) step at best is ∼10%.[25] The second problem is the potential loss of daughter radioisotopes (^{221}Fr and ^{213}Bi) from the chelator after decay of ^{225}Ac, which adds significantly to the *in vivo* global toxicity of ^{225}Ac.[55] The major advantage of incorporating ^{225}Ac within the NPs is to sequester the daughter radionuclides ^{221}Fr, ^{217}At, and ^{213}Bi at the site of targeting to mitigate the unintentional, nonspecific radiotoxicity.[54]

Monodisperse $LaPO_4$ NPs have been synthesized in both organic and aqueous media and investigated for their fluorescent and scintillation properties.[50,56−59] Rare earth phosphates with the monazite structure, such as bulk $LaPO_4$, have been studied extensively in the context of nuclear waste treatment for long-term sequestration of radioactive lanthanides and actinides. In the monazite crystal lattice, the lanthanide ion is bound to nine surrounding oxygen atoms[53] with sufficient energy to reduce leaching from energetic nuclear decay processes. Numerous studies have demonstrated that monazite is resistant to radiation damage, even under heavy metal ion bombardment.[60−62] The radiation-tolerant crystal structure of monazite, combined with its low aqueous solubility, makes it an ideal NP system for sequestering radionuclides and daughter products. Additionally, the small size of the NPs (∼5 nm) is much less than the average range (60−100 μm) of the 5−8 MeV α-particles in water, allowing facile escape of α-particles from the NP lattice.[23,44]

We have successfully and reproducibly synthesized 3−5-nm-diameter $LaPO_4$ NPs doped with ^{225}Ac with an overall radiochemical yield of 47 ± 5% (n = 3) following surface modification and purification. For *in vitro* and *in vivo* studies, the specific activity was ∼1.7 mCi of ^{225}Ac per mg of $LaPO_4$ (La/Ac ≈ 30 000). A 5-nm-diameter $LaPO_4$ NP contains on the order of 1000 La^{3+} ions, and thus, at La/Ac ≈ 30 000, there is approximately 1 Ac^{3+} ion per 30 NPs, leaving ample capacity for increased specific activity for therapy applications. Due to similar chemical properties and comparable ionic radii, the La^{3+} and $^{225}Ac^{3+}$ were expected to form isomorphous mixed crystals; i.e., $^{225}Ac^{3+}$ ions may replace La^{3+} ions in the crystal lattice and thus be "carried". Moreover, competition of common impurities in lanthanum (Fe^{3+}, Ca^{2+}, and Zn^{2+}) with $^{225}Ac^{3+}$ for cation sites within the monazite lattice is expected to be minimal. These hypotheses were confirmed in two ways. First, ∼66% of the initial $^{225}Ac^{3+}$ was captured in La(^{225}Ac)PO_4 NPs before surface modification and dialysis. Second, the observed loss of <0.1% of ^{225}Ac *in vitro* from La(^{225}Ac)PO_4 NPs indicates that Ac^{3+} is tightly bound within the NPs as expected. Data in Figure 3 (and Supporting Information Table S1) also show that ∼50% of the ^{221}Fr and ^{213}Bi (from the decay of ^{221}Fr) daughters were released from the NP lattice. The rate of release of these daughter radioisotopes remained constant *in vitro* over the 30 d observation period. While specific activities on the order of 1.7 mCi/mg of NP are sufficient for *in vivo* biodistribution and imaging studies, more ^{225}Ac can be incorporated within the NPs as required for therapeutic purposes.

Release of a daughter may result either from direct ejection during nuclear recoil or from leaching as a consequence of lattice damage. The recoiling ^{221}Fr nucleus has a kinetic energy of 107 keV and an expected range of about 20 nm in bulk monazite.[63,64] On this basis, one would expect essentially all of the ^{221}Fr would be ejected from a ∼5-nm-diameter particle. The observed 50%

retention of the daughters in the NP suggests that a fraction of the recoil energy may partition into translation of the whole NP rather than being dissipated entirely through atomic displacements, as occurs in the bulk, resulting in a shorter recoil range. Because momentum (p) is conserved in nuclear recoil ($p_\alpha = p_{recoil}$), the corresponding recoil energy depends on the mass of the recoiling particles. The minimum energy (E_r^{min}) available for bond breaking within the NP can be calculated as $E_r^{min} = E_r^{max} \cdot M_1/(M_1 + M_2)$, where E_r^{max} is the maximum recoil energy, M_1 is the atomic weight of the recoiling ^{221}Fr nucleus (221 amu), and M_2 is the molecular weight of the NP ($\sim 2 \times 10^5$ amu). At this limit, the result is $\sim 10^3$-fold reduction in the recoil energy and hence much shorter recoil range in the NPs versus bulk.[30] The actual recoil energy imparted to the ^{221}Fr nuclei most likely has a value between the two extremes. We are currently preparing ^{225}Ac-doped $LaPO_4$ NPs capped with a shell of cold $LaPO_4$ in an effort to reduce daughter escape through both direct ejection and leaching.

The dialysis experiments show a higher fraction of ^{221}Fr than ^{213}Bi in the dialysate after 4 h but essentially equal fractions at later time points over the span of 1 month. This observation suggests that transport of ^{213}Bi through the NP lattice, phosphate buffer, and/or dialysis membrane may be slower than that of ^{221}Fr. Because it is a singly charged alkali metal ion, and its phosphates exhibit considerable aqueous solubility, Fr^+ should not be strongly bound in the monazite lattice, nor should it be strongly adsorbed to monazite surfaces. Therefore, it is reasonable to assume that the ^{221}Fr concentration in the dialysate is representative of that inside the membrane. In contrast, Bi^{3+} is multiply charged, its phosphates exhibit poor aqueous solubility, and it may either be retained within or adsorbed to monazite surfaces. In solution, Bi^{3+} may further form colloidal hydroxides or phosphates that impede transport of Bi^{3+} ions through solution and the dialysis membrane. Very little activity (<1% of initial activity) remains associated with the dialysis membrane itself.

After synthesis, the NP surfaces were reacted with AHA, which improves dispersibility in water and phosphate buffer solution and provides functionality to connect the NPs to targeting antibodies. Although the product settles out of aqueous solution within 24 h, the NPs could be easily redispersed by sonication at low power. Meiser et al. first described surface modification of $LaPO_4$ NPs with AHA whereby the amine ends bind electrostatically to phosphate moieties on the NP surfaces, displacing existing surfactants, and forming $PO^-—^+H_3N$ ionic bonds that appear to be stable *in vitro*.[51] Consequently, free carboxylate functional groups are present on the NP surfaces. In this work, the *in vivo* results provided indirect evidence for the aqueous stability of the ionic linkages since retention of ^{213}Bi (and hence NP-mAb 201B conjugates) at the target site for 5 d suggests that the AHA remains bound to the NP surfaces over this time span as well. This stability is consistent with the findings of Xiong et al. in which AHA was used as a linker for up-converting nanophosphors.[65]

Once the NPs were synthesized, surface functionalized, and purified, they were coupled to either targeting or control antibodies. The carboxylate groups present on the NP surfaces react with exposed amine functionalities on mAb side chains, via conventional carbodiimide chemistry, to form amide bonds. Monoclonal antibody 201B has been shown to accumulate rapidly and efficiently in mouse lung and has been used in targeted imaging and therapy experiments.[18,19,37−39] The NP−mAb binding is to a lumenal epitope on the protein thrombomodulin (TM), which mediates targeting inside the vascular space. Since NPs, antibodies, and other large molecules do not exit the blood vessels readily, a vascular epitope is necessary for efficient targeting of NPs.[21,40−42] The targeting efficacy and biodistribution of the NP−antibody conjugates in female BALB/c mice was determined after sacrifice by measuring the radioactivity in major organs and confirmed through micro-SPECT/CT imaging of the entire animal. The biodistribution data as well as the SPECT/CT images clearly show that La-(^{225}Ac)PO_4 NPs conjugated to mAb 201B accumulated rapidly in the lungs. When excess uncoupled mAb 201B was added to the NP antibody preparation, the NPs accumulated in the liver and spleen, a result also observed in the NPs targeted with the control antibody (mAb 33). The biodistribution and imaging results are consistent with previous experiments involving ZnS/Cd^{125m}Te NPs where the NP-mAb 201B conjugates primarily targeted mouse lungs.[18,19]

The fact that the targeting process is dependent on the binding specificity of the mAb clearly differentiates it from the trapping of microaggregates such as microaggregated albumin (MAA) in small lung capillaries. In addition, targeted NPs are retained in the lungs for several days, whereas MAA is cleared from the lungs within hours. Furthermore, the NP−mAb conjugates are <100 μm in effective diameter, which leads to accumulation in the reticuloendothelial (RE) cells of the liver and spleen as opposed to trapping in lung capillaries.[19] All studies to date have shown that, once injected into the mice, NPs are recognized by the RE system chiefly of the liver and spleen.[41,66−68] Indeed, the biodistribution experiments detailed above show that the La-(^{225}Ac)PO_4-mAb conjugates are eventually redistributed to the liver and spleen. The efficient homing of mAb 201B targeted NPs to lung blood vessels partially circumvents the liver and spleen uptake by phagocytes, but does not eliminate it. [The NP-mAb 33 conjugates are quickly cleared from circulation postinjection (Table 1 and Supporting Information Figure S1)]. Thus, targeting can be further improved by injecting mice with clodronate liposomes, which temporarily inhibits the RE system by poisoning phagocytes.[19,46,47] Nanoparticle accumulation and retention in the lungs increased in clodronate-treated mice versus normal mice (Table 1 and Supporting Information Figure S1), which is consistent with, although not as dramatic as, the results in previous experiments involving ZnS/Cd^{125m}Te NPs.[19]

The goal of demonstrating at least partial retention of ^{225}Ac daughter radioisotopes within the NPs was achieved. As discussed earlier, at any time during the 1 month observation period, ~50% of the daughter radioisotopes remained within the NPs during *in vitro* leaching experiments. When the same tests were performed on NPs targeted to the lungs, at 1 h postinjection, ~50% of the daughter radioisotopes were retained at the target site. In contrast, while the ^{213}Bi loss from the NPs *in vitro* remained constant (~50%) for many days, the ^{213}Bi loss from the mouse lung decreased markedly (to ~10%) within 5 d after the initial targeting. We speculate that the NP-mAb 201B conjugates may have been taken into the endothelial cells lining the lung capillaries (endocytosed), such that ^{213}Bi released from the NPs was trapped within the cells, retarding its diffusion through the tissue and accounting for the decreased release over time. This hypothesis is supported by work of McDevitt et al., who showed that when ^{225}Ac was taken into prostate cancer cells, the daughter radioisotopes were trapped therein.[25]

This work with La(^{225}Ac)PO_4-mAb 201B conjugates demonstrates the potential for radioimmunotherapy and diagnostic imaging in the same NP−antibody constructs. Additionally,

the retention of ^{225}Ac as well as the partial *in vitro* and *in vivo* retention of the daughters, ^{221}Fr and ^{213}Bi, demonstrates the potential of NPs for trapping radionuclides after high-energy emissions. When ^{225}Ac is attached to antibodies with conventional molecular chelators such as DOTA, all the daughter radionuclides are released after the initial α-decay occurs.[25,30,33,55] Similarly, when ^{225}Ac is encapsulated in fullerenes, the daughter radioisotopes are released, likely due to breaking of the fullerene cage by the energy of nuclear decay recoil.[69,70] However, by employing $LaPO_4$ NPs to contain the radioisotopes rather than chelators, we show that nearly all of the ^{225}Ac and ∼50% of the ^{221}Fr and ^{213}Bi daughters are retained within the NPs *in vitro*, a dramatic improvement over conventional approaches. Although these NPs represent an improvement over other approaches, the extreme toxicity of α-particles from the escaped daughters ^{221}Fr and ^{213}Bi still presents a risk.[29,32,33] The toxicity could be reduced via the core−shell approach described above,[56] where a few nanometers thick shell of cold $LaPO_4$ can be epitaxially deposited onto the La(^{225}Ac)PO_4 core. The additional material at the surfaces should help with sequestering the decay daughters of ^{225}Ac doped within the NP cores.

CONCLUSIONS

In this paper, we incorporate ^{225}Ac within $LaPO_4$ NPs as a means of trapping radioisotopes and associated daughter products within an inorganic matrix to mitigate their unintentional release *in vivo*. We show via microSPECT/CT imaging and standard biodistribution techniques that La(^{225}Ac)PO_4 NPs coupled to the monoclonal antibody mAb 201B to murine thrombomodulin accumulates rapidly in mouse lung after intravenous injection. Furthermore, >80% of the ^{213}Bi daughter radioisotope is retained within the NP at the target site after 120 h *in vivo*. These results demonstrate the potential applicability of nanoscale materials for sequestering toxic daughter radionuclides. Improvements in the current NP technology will be necessary to achieve sufficiently complete daughter retention for clinical applications.

ASSOCIATED CONTENT

Supporting Information. Raw data are provided for the *in vitro* release of ^{225}Ac, ^{221}Fr, and ^{213}Bi from La(^{225}Ac)PO_4 NPs as a function of dialysis time (Table S1) as is a graphical depiction of the biodistribution of targeted La(^{225}Ac)PO_4-mAb conjugates in BALB/c mice (Figure S1). This material is available free of charge via the Internet at http://pubs.acs.org.

AUTHOR INFORMATION

Corresponding Author

*Author to whom correspondence should be addressed (mirzadeh@ornl.gov).

ACKNOWLEDGMENT

Research supported in part by the Office of Biologic and Environmental Research of the U.S. Department of Energy under contract ERKP 735 and in part by the Laboratory Directed Research and Development Program, managed by UT-Battelle, LLC, for the U.S. Department of Energy under contract DE-AC05-00OR22725. The work was also supported by the University of Tennessee, Graduate School of Medicine, through funding of the cancer imaging and tracer development program. The authors gratefully acknowledge Drs. Russ Knapp, Rose A. Boll, and Timothy McKnight (ORNL) for critical reviews of the manuscript and Jane Howe (ORNL High Temperature Materials Laboratory) for assistance during transmission electron microscopy measurements.

REFERENCES

(1) Mazumder, S., Dey, R., Mitra, M. K., Mukherjee, S., and Das, G. C. (2009) Review: biofunctionalized quantum dots in biology and medicine. *J. Nanomater. 2009*, 1–17.

(2) Arruebo, M., Valladares, M., and Gonzalez-Fernandez, A. (2009) Antibody-Conjugated nanoparticles for biomedical applications. *J. Nanomater. 2009*, 1–24.

(3) Chan, W. C. W., Maxwell, D. J., Gao, X. H., Bailey, R. E., Han, M. Y., and Nie, S. M. (2002) Luminescent quantum dots for multiplexed biological detection and imaging. *Curr. Opin. Biotechnol. 13*, 40–46.

(4) Huang, X. H., Jain, P. K., El-Sayed, I. H., and El-Sayed, M. A. (2007) Gold nanoparticles: interesting optical properties and recent applications in cancer diagnostic and therapy. *Nanomedicine 2*, 681–693.

(5) Jain, P. K., El-Sayed, I. H., and El-Sayed, M. A. (2007) Au nanopartices target cancer. *Nano Today 2*, 18–29.

(6) Loo, C., Lowery, A., Halas, N., West, J., and Drezek, R. (2005) Immunotargeted nanoshells for integrated cancer imaging and therapy. *Nano Lett. 5*, 709–711.

(7) Ito, A., Shinkai, M., Honda, H., and Kobayashi, T. (2005) Medical application of functionalized magnetic nanoparticles. *J. Biosci. Bioeng. 100*, 1–11.

(8) Lu, C. W., Hung, Y., Hsiao, J. K., Yao, M., Chung, T. H., Lin, Y. S., Wu, S. H., Hsu, S. C., Liu, H. M., Mou, C. Y., Yang, C. S., Huang, D. M., and Chen, Y. C. (2007) Bifunctional magnetic silica nanoparticles for highly efficient human stem cell labeling. *Nano Lett. 7*, 149–154.

(9) Cai, W. B., Chen, K., Li, Z. B., Gambhir, S. S., and Chen, X. Y. (2007) Dual-function probe for PET and near-infrared fluorescence imaging of tumor vasculature. *J. Nucl. Med. 48*, 1862–1870.

(10) Bruchez, M., Moronne, M., Gin, P., Weiss, S., and Alivisatos, A. P. (1998) Semiconductor nanocrystals as fluorescent biological labels. *Science 281*, 2013–2016.

(11) Wang, S. P., Mamedova, N., Kotov, N. A., Chen, W., and Studer, J. (2002) Antigen/antibody immunocomplex from CdTe nanoparticle bioconjugates. *Nano Lett. 2*, 817–822.

(12) Gao, X. H., Cui, Y. Y., Levenson, R. M., Chung, L. W. K., and Nie, S. M. (2004) In vivo cancer targeting and imaging with semiconductor quantum dots. *Nat. Biotechnol. 22*, 969–976.

(13) Chan, W. C. W., and Nie, S. M. (1998) Quantum dot bioconjugates for ultrasensitive nonisotopic detection. *Science 281*, 2016–2018.

(14) Bertolini, G., Paleari, L., Catassi, A., Roz, L., Cesario, A., Sozzi, G., and Russo, P. (2008) In vivo cancer imaging with semiconductor quantum dots. *Curr. Pharm. Anal. 4*, 197–205.

(15) Sun, L. L., Liu, D. J., and Wang, Z. X. (2008) Functional gold nanoparticle-peptide complexes as cell-targeting agents. *Langmuir 24*, 10293–10297.

(16) Smith, A. M., Duan, H. W., Mohs, A. M., and Nie, S. M. (2008) Bioconjugated quantum dots for *in vivo* molecular and cellular imaging. *Adv. Drug Delivery Rev. 60*, 1226–1240.

(17) Liong, M., Lu, J., Kovochich, M., Xia, T., Ruehm, S. G., Nel, A. E., Tamanoi, F., and Zink, J. I. (2008) Multifunctional inorganic nanoparticles for imaging, targeting, and drug delivery. *ACS Nano 2*, 889–896.

(18) Woodward, J. D., Kennel, S. J., Mirzadeh, S., Dai, S., Wall, J. S., Richey, T., Avenell, J., and Rondinone, A. J. (2007) *In vivo* SPECT/CT imaging and biodistribution using radioactive $Cd^{125m}Te$/ZnS nanoparticles. *Nanotechnology 18*, 1–5.

(19) Kennel, S. J., Woodward, J. D., Rondinone, A. J., Wall, J., Huang, Y., and Mirzadeh, S. (2008) The fate of MAb-targeted $Cd^{125m}Te$/ZnS nanoparticles *in vivo*. *Nucl. Med. Biol. 35*, 501–514.

(20) Schipper, M. L., Cheng, Z., Lee, S. W., Bentolila, L. A., Iyer, G., Rao, J. H., Chen, X. Y., Wul, A. M., Weiss, S., and Gambhirl, S. S. (2007) MicroPET-based biodistribution of quantum dots in living mice. *J. Nucl. Med. 48*, 1511–1518.

(21) Rossin, R., Pan, D. P. J., Qi, K., Turner, J. L., Sun, X. K., Wooley, K. L., and Welch, M. J. (2005) ^{64}Cu-labeled folate-conjugated shell cross-linked nanoparticles for tumor imaging and radiotherapy: Synthesis, radiolabeling, and biologic evaluation. *J. Nucl. Med. 46*, 1210–1218.

(22) McDevitt, M. R., Sgouros, G., Finn, R. D., Humm, J. L., Jurcic, J. G., Larson, S. M., and Scheinberg, D. A. (1998) Radioimmunotherapy with alpha-emitting nuclides. *Eur. J. Nucl. Med. 25*, 1341–1351.

(23) Mirzadeh, S. (1998) Generator-produced alpha-emitters. *Appl. Radiat. Isot. 49*, 345–349.

(24) Miederer, M., Scheinberg, D. A., and McDevitt, M. R. (2008) Realizing the potential of the Actinium-225 radionuclide generator in targeted alpha particle therapy applications. *Adv. Drug Delivery Rev. 60*, 1371–1382.

(25) McDevitt, M. R., Ma, D. S., Lai, L. T., Simon, J., Borchardt, P., Frank, R. K., Wu, K., Pellegrini, V., Curcio, M. J., Miederer, M., Bander, N. H., and Scheinberg, D. A. (2001) Tumor therapy with targeted atomic nanogenerators. *Science 294*, 1537–1540.

(26) Sofou, S., Kappel, B. J., Jaggi, J. S., McDevitt, M. R., Scheinberg, D. A., and Sgouros, G. (2007) Enhanced retention of the alpha-particle-emitting daughters of actinium-225 by liposome carriers. *Bioconjugate Chem. 18*, 2061–2067.

(27) Smith, S. V., Dibartolo, N., Mirzadeh, S., Lambrecht, R. M., Knapp, F. F. R., and Hetherington, E. L. (1995) [^{166}Dy]Dysporium/[^{166}Ho]Holmiun *in vivo* generator. *Appl. Radiat. Isot. 46*, 759–764.

(28) Ferro-Flores, G., Hernandez-Oviedo, O., de Murphy, C. A., Tendilla, J. I., Monroy-Guzman, F., Pedraza-Lopez, M., and Aldama-Alvarado, K. (2004) [^{166}Dy]Dy/^{166}Ho hydroxide macro aggregates: an *in vivo* generator system for radiation synovectomy. *Appl. Radiat. Isot. 61*, 1227–1233.

(29) Kennel, S. J., Lankford, T., Garland, M., Sundberg, J. P., and Mirzadeh, S. (2005) Biodistribution of ^{225}Ra citrate in mice: retention of daughter radioisotopes in bone. *Nucl. Med. Biol. 32*, 859–867.

(30) Mirzadeh, S., Kumar, K., and Gansow, O. A. (1993) The chemical fate of ^{212}Bi-DOTA formed by beta-decay of ^{212}Pb(DOTA)$_2$. *Radiochim. Acta 60*, 1–10.

(31) Humm, J. L., and Chin, L. M. (1993) A model of cell inactivation by alpha-particle internal emitters. *Radiat. Res. 134*, 143–150.

(32) Davis, I. A., Glowienka, K. A., Boll, R. A., Deal, K. A., Brechbiel, M. W., Stabin, M., Bochsler, P. N., Mirzadeh, S., and Kennel, S. J. (1999) Comparison of ^{225}Actinium chelates: Tissue distribution and radiotoxicity. *Nucl. Med. Biol. 26*, 581–589.

(33) Kennel, S. J., Chappell, L. L., Dadachova, K., Brechbiel, M. W., Lankford, T. K., Davis, I. A., Stabin, M., and Mirzadeh, S. (2000) Evaluation of ^{225}Ac for vascular targeted radioimmunotherapy of lung tumors. *Cancer Biother. Radiopharm. 15*, 235–244.

(34) Jurcic, J. G., Larson, S. M., Sgouros, G., McDevitt, M. R., Finn, R. D., Divgi, C. R., Ballangrud, A. M., Hamacher, K. A., Ma, D. S., Humm, J. L., Brechbiel, M. W., Molinet, R., and Scheinberg, D. A. (2002) Targeted alpha particle immunotherapy for myeloid leukemia. *Blood 100*, 1233–1239.

(35) Sofou, S. (2008) Radionuclide carriers for targeting of cancer. *Int. J. Nanomed. 3*, 181–199.

(36) Mausner, L. F., Straub, R. G., and Srivastava, S. C. (1989) The *in vivo* generator for radioimmunotherapy. *J. Labelled Compd. Radiopharm. 16*, 498–500.

(37) Kennel, S. J., Boll, R., Stabin, M., Schuller, H. M., and Mirzadeh, S. (1999) Radioimmunotherapy of micrometastases in lung with vascular targeted ^{213}Bi. *Brit. J. Cancer 80*, 175–184.

(38) Kennel, S. J., Lee, R., Bultman, S., and Kabalka, G. (1990) Rat monoclonal-antibody distribution in mice—an epitope inside the lung vascular space mediates very efficient localization. *Nucl. Med. Biol. 17*, 193–200.

(39) Hughes, B. J., Kennel, S., Lee, R., and Huang, L. (1989) Monoclonal-antibody targeting of liposomes to mouse lung *in vivo*. *Cancer Res. 49*, 6214–6220.

(40) Kirpotin, D. B., Drummond, D. C., Shao, Y., Shalaby, M. R., Hong, K. L., Nielsen, U. B., Marks, J. D., Benz, C. C., and Park, J. W. (2006) Antibody targeting of long-circulating lipidic nanoparticles does not increase tumor localization but does increase internalization in animal models. *Cancer Res. 66*, 6732–6740.

(41) Fang, C., Shi, B., Pei, Y. Y., Hong, M. H., Wu, J., and Chen, H. Z. (2006) In vivo tumor targeting of tumor necrosis factor-alpha-loaded stealth nanoparticles: Effect of MePEG molecular weight and particle size. *Eur. J. Pharm. Sci. 27*, 27–36.

(42) Medarova, Z., Pham, W., Farrar, C., Petkova, V., and Moore, A. (2007) *In vivo* imaging of siRNA delivery and silencing in tumors. *Nat. Med. 13*, 372–377.

(43) Kennel, S. J., Lankford, T., Hughes, B., and Hotchkiss, J. A. (1988) Quantitation of a murine lung endothelial-cell protein, P112, with a double monoclonal-antibody assay. *Lab. Invest. 59*, 692–701.

(44) Boll, R. A., Mirzadeh, S., and Kennel, S. J. (1997) Optimizations of radiolabeling of immunoproteins with ^{213}Bi. *Radiochim. Acta 79*, 145–149.

(45) Boll, R. A., Malkemus, D., and Mirzadeh, S. (2005) Production of actinium-225 for alpha particle mediated radioimmunotherapy. *Appl. Radiat. Isot. 62*, 667–679.

(46) Vanrooijen, N. (1989) The liposome-mediated macrophage suicide technique. *J. Immunol. Methods 124*, 1–6.

(47) Lasbury, M. E., Durant, P. J., Ray, C. A., Tschang, D., Schwendener, R., and Lee, C. H. (2006) Suppression of alveolar macrophage apoptosis prolongs survival of rats and mice with Pneumocystis pneumonia. *J. Immunol. 176*, 6443–6453.

(48) Wall, J. S., Kennel, S. J., Paulus, M., Gregor, J., Richey, T., Avenell, J., Yap, J., Townsend, D., Weiss, D. T., and Solomon, A. (2006) Radioimaging of light chain amyloid with a fibril-reactive monoclonal antibody. *J. Nucl. Med. 47*, 2016–2024.

(49) Wall, J. S., Paulus, M. J., Gleason, S., Gregor, J., Solomon, A., and Kennel, S. J. (2006) Micro-imaging of amyloid in mice, in *Amyloid, Prions, and Other Protein Aggregates, Pt B* pp 161−182, Elsevier Academic Press Inc., San Diego.

(50) Lehmann, O., Meyssamy, H., Kompe, K., Schnablegger, H., and Haase, M. (2003) Synthesis, growth, and Er^{3+} luminescence of lanthanide phosphate nanoparticles. *J. Phys. Chem. B 107*, 7449–7453.

(51) Meiser, F., Cortez, C., and Caruso, F. (2004) Biofunctionalization of fluorescent rare-earth-doped lanthanum phosphate colloidal nanoparticles. *Angew. Chem.-Int. Edit. 43*, 5954–5957.

(52) Unpublished results of Rondinone, A. J. (2007), Oak Ridge National Laboratory, Oak Ridge, TN. NP size and morphology were examined using a Hitachi HF-2000 transmission electron microscope (TEM) operating at 200 keV. Samples for TEM were prepared by dispersing a small quantity of nanoparticles into hexane. A drop of the dispersed sample was then placed on a carbon-coated copper TEM grid (300 mesh) and allowed to dry before measurement.

(53) Mullica, D. F., Milligan, W. O., Grossie, D. A., Beall, G. W., and Boatner, L. A. (1984) Ninefold coordination in $LaPO_4$ - Pentagonal interpenetrating tetrahedral polyhedron. *Inorg. Chim. Acta 95*, 231–236.

(54) Miederer, M., McDevitt, M. R., Sgouros, G., Kramer, K., Cheung, N. K. V., and Scheinberg, D. A. (2004) Pharmacokinetics, dosimetry, and toxicity of the targetable atomic generator, ^{225}Ac-HuM195, in nonhuman primates. *J. Nucl. Med. 45*, 129–137.

(55) Hamacher, K. A., and Sgouros, G. (2001) Theoretical estimation of absorbed dose to organs in radioimmunotherapy using radionuclides with multiple unstable daughters. *Med. Phys. 28*, 1857–1874.

(56) Buissette, V., Moreau, M., Gacoin, T., Boilot, J. P., Chane-Ching, J. Y., and Le Mercier, T. (2004) Colloidal synthesis of luminescent rhabdophane $LaPO_4$: $Ln^{3+}\cdot xH_2O$ (Ln = Ce, Tb, Eu; $x\approx0.7$) nanocrystals. *Chem. Mater. 16*, 3767–3773.

(57) Riwotzki, K., Meyssamy, H., Kornowski, A., and Haase, M. (2000) Liquid-phase synthesis of doped nanoparticles: Colloids of

luminescing $LaPO_4$:Eu and $CePO_4$:Tb particles with a narrow particle size distribution. *J. Phys. Chem. B 104*, 2824–2828.

(58) Meyssamy, H., Riwotzki, K., Kornowski, A., Naused, S., and Haase, M. (1999) Wet-chemical synthesis of doped colloidal nanomaterials: Particles and fibers of $LaPO_4$:Eu, $LaPO_4$:Ce, and $LaPO_4$:Ce,Tb. *Adv. Mater. 11*, 840–844.

(59) Riwotzki, K., Meyssamy, H., Schnablegger, H., Kornowski, A., and Haase, M. (2001) Liquid-phase synthesis of colloids and redispersible powders of strongly luminescing $LaPO_4$:Ce,Tb nanocrystals. *Angew. Chem.-Int. Edit. 40*, 573–576.

(60) Tabuteau, A., Pages, M., Livet, J., and Musikas, C. (1988) Monazite-like phases containing trans-uranium elements (neptunium and plutonium). *J. Mater. Sci. Lett. 7*, 1315–1317.

(61) Ewing, R. C. (1975) Crystal-chemistry of complex niobium and tantalum oxides. 4. Metamict state - discussion. *Am. Mineral. 60*, 728–733.

(62) Karioris, F. G., Gowda, K. A., and Cartz, L. (1981) Heavy-ion bombardment of monoclinic $ThSiO_4$, ThO_2, and monazite. *Radiat. Eff. Lett. 58*, 1–3.

(63) Eyal, Y., and Olander, D. R. (1990) Impact of alpha-decay on incongruent actinide isotope leaching from monazite. *J. Nucl. Mater. 170*, 117–120.

(64) Ziegler, J. F., Biersack, J. P., and Littmark, U. (1985) in *The Stopping and Range of Ions in Solids* (Ziegler, J. F., Ed.) Pergamon, New York.

(65) Xiong, L. Q., Chen, Z. G., Yu, M. X., Li, F. Y., Liu, C., and Huang, C. H. (2009) Synthesis, characterization, and *in vivo* targeted imaging of amine-functionalized rare-earth up-converting nanophosphors. *Biomaterials 30*, 5592–5600.

(66) Cheng, J., Teply, B. A., Sherifi, I., Sung, J., Luther, G., Gu, F. X., Levy-Nissenbaum, E., Radovic-Moreno, A. F., Langer, R., and Farokhzad, O. C. (2007) Formulation of functionalized PLGA-PEG nanoparticles for *in vivo* targeted drug delivery. *Biomaterials 28*, 869–876.

(67) Date, A. A., Joshi, M. D., and Patravale, V. B. (2007) Parasitic diseases: Liposomes and polymeric nanoparticles versus lipid nanoparticles. *Adv. Drug Delivery Rev. 59*, 505–521.

(68) Chen, J., Wu, H., Han, D. Y., and Xie, C. S. (2006) Using anti-VEGF McAb and magnetic nanoparticles as double-targeting vector for the radioimmunotherapy of liver cancer. *Cancer Lett. 231*, 169–175.

(69) Akiyama, K., Haba, H., Sueki, K., Tsukada, K., Asai, M., Toyoshima, A., Nagame, Y., and Katada, M. (2009) ^{225}Ac metallofullerene: toward ^{225}Ac nanogenerator in fullerene. *Chem. Lett. 38*, 978–979.

(70) McDevitt, M. R., Chattopadhyay, D., Kappel, B. J., Jaggi, J. S., Schiffman, S. R., Antczak, C., Njardarson, J. T., Brentjens, R., and Scheinberg, D. A. (2007) Tumor targeting with antibody-functionalized, radiolabeled carbon nanotubes. *J. Nucl. Med. 48*, 1180–1189.

$LaPO_4$ Nanoparticles Doped with Actinium-225 that Partially Sequester Daughter Radionuclides,

Mirzadeh, *et al.*

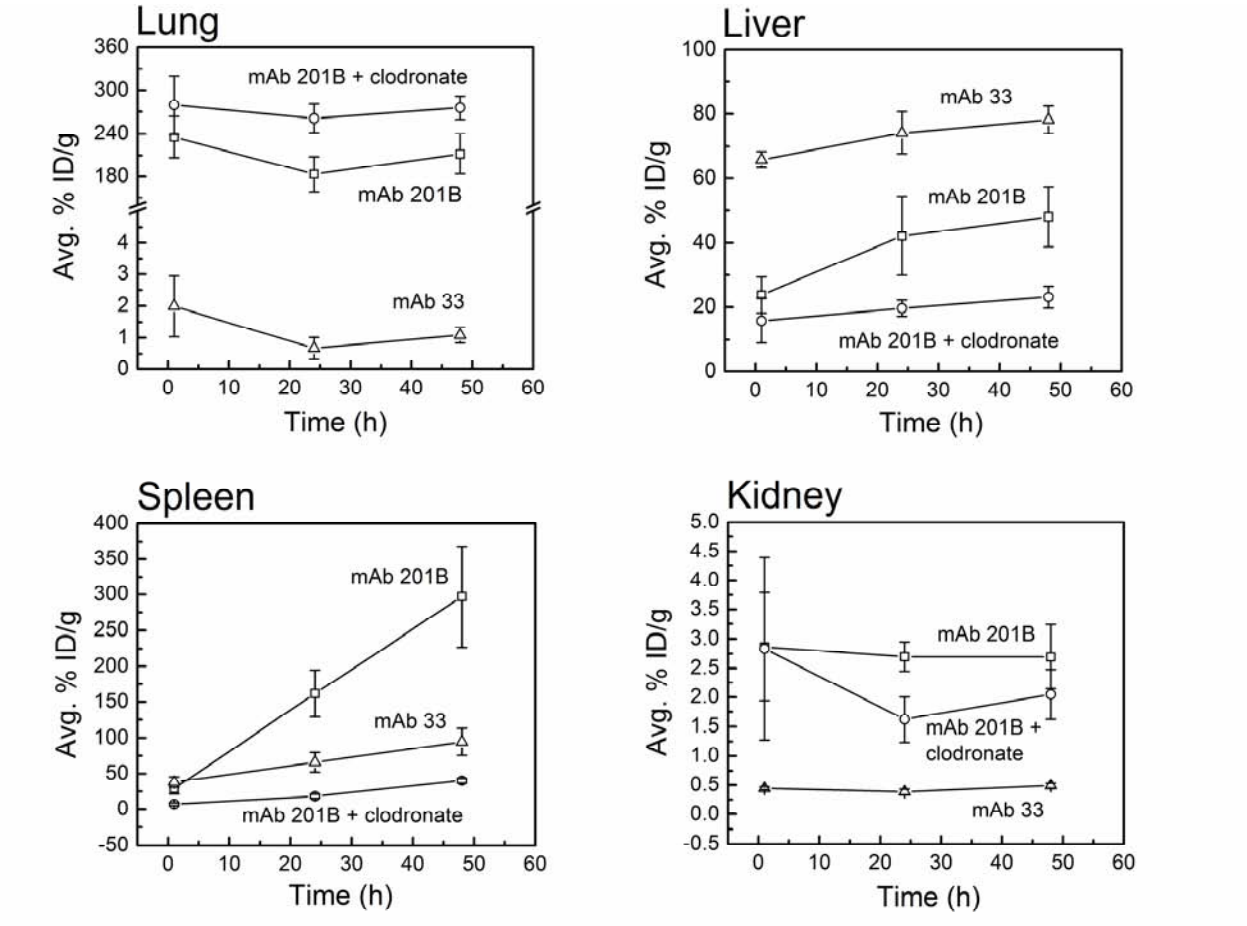
Supporting Information

Table S1. *In Vitro* release of ^{225}Ac, ^{221}Fr, and ^{213}Bi from La(^{225}Ac)PO_4 NPs as a function of dialysis time.[a]

Sample No.	Dialysis Time (d)	Radioactivity Lost (%)		
		^{221}Fr	^{213}Bi	^{225}Ac
1	0.16	24.78	4.01	0.03
2	0.24	30.78	30.75	0.03
3	0.31	39.77	39.23	0.03
4	0.89	41.28	46.87	0.02
5	1.92	51.98	47.82	0.03
6	2.90	52.91	48.68	0.03
7	5.90	53.97	49.80	0.03
8	6.89	58.98	54.19	0.14
9	7.90	61.08	56.13	0.11
10	8.89	57.59	54.54	0.11
11	9.90	58.25	55.31	0.11
12	12.97	60.22	55.64	0.10
13	14.90	63.50	58.46	0.11
14	15.96	61.98	58.71	0.11
15	22.91	65.75	59.71	0.09
16	27.97	60.38	60.35	0.10

[a] Activity of ^{225}Ac = 600 μCi, pH = 6.5 phosphate buffer. For further details and determination of ^{221}Fr and ^{213}Bi activity, see Experimental section.

Figure S1



Biodistribution of targeted La(^{225}Ac)PO_4-mAb conjugates in BALB/c mice. NP-mAb 201B conjugates target the lung while the NP-mAb 33 control conjugates redistribute to the liver and spleen. Temporary inhibition of RE system of liver and spleen improves both targeting and retention of NP-mAb 201B conjugates in the lung. Number of mice per group = 5; Activity injected (*iv*) in each mouse = 5 μCi; Groups 1 and 2: La(^{225}Ac)PO_4 NPs-mAb 201B; Group 3 (control): La(^{225}Ac)PO_4 NPs-mAb 33. Group 2 were injected 24 h prior with 100 μL of clodronate containing liposomes. Organs were analyzed in a γ-ray scintillation counter after ^{225}Ac and its daughters had reached equilibrium (~3 h).

Bioconjugate Chemistry

ARTICLE

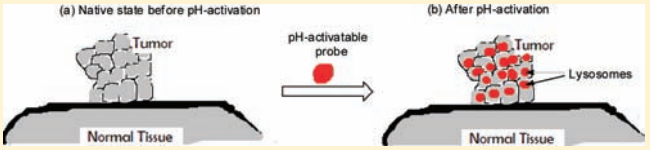
pubs.acs.org/bc

Near-Infrared pH-Activatable Fluorescent Probes for Imaging Primary and Metastatic Breast Tumors

Hyeran Lee, Walter Akers, Kumar Bhushan, Sharon Bloch, Gail Sudlow, Rui Tang, and Samuel Achilefu*

Department of Radiology, Washington University, St. Louis, Missouri 63110, United States

ABSTRACT: Highly tumor selective near-infrared (NIR) pH-activatable probe was developed by conjugating pH-sensitive cyanine dye to a cyclic arginine-glycine-aspartic acid (cRGD) peptide targeting $\alpha_v\beta_3$ integrin (ABIR), a protein that is highly overexpressed in endothelial cells during tumor angiogenesis. The NIR pH-sensitive dye used to construct the probe exhibits high spectral sensitivity with pH changes. It has negligible fluorescence above pH 6 but becomes highly fluorescent below pH 5, with a pK_a of 4.7. This probe is ideal for imaging acidic cell organelles such as tumor lysosomes or late endosomes. Cell microscopy data demonstrate that binding of the cRGD probe to ABIR facilitated the endocytosis-mediated lysosomal accumulation and subsequent fluorescence enhancement of the NIR pH-activatable dye in tumor cells (MDA-MB-435 and 4T1/*luc*). A similar fluorescence enhancement mechanism was observed in vivo, where the tumors were evident within 4 h post injection. Moreover, lung metastases were also visualized in an orthotopic tumor mouse model using this probe, which was further confirmed by histologic analysis. These results demonstrate the potential of using the new integrin-targeted pH-sensitive probe for the detection of primary and metastatic cancer.



INTRODUCTION

Optical molecular imaging often utilizes activatable probes where the fluorescence signal can be amplified by selective molecular events. These include the use of enzyme activity,[1−8] pH,[9−12] or the presence of reactive oxygen/nitrogen species [13] to visualize specific biological processes associated with the disease state. In particular, tumor-related enzyme activatable probes are widely used to visualize tumor biomarkers in vivo.[14−21] However, most tumor biomarkers are also a part of normal physiological processes, and thus, imaging sensitivity and specificity are hampered by high background signal from the nontarget tissues. Other tumor hallmarks such as acidosis and hypoxia have been explored as alternative approaches to enzyme-mediated imaging strategy to improve signal-to-background ratio. Acidosis has been an attractive target for tumor imaging,[22] and this strategy is based on the underlying principle that the tumor's extracellular metabolic microenvironment is relatively acidic because of the activated Na^+/H^+ exchanger (NHE1) and the H^+/lactate co-transporter systems in cancer cells.[23] However, there remains a challenge to design a probe targeting acidic tumor features. First, tumor cells have acidic interstitial extracellular pH (pHe, 6.2−6.9) rather than acidic intracellular pH (pHi) with a small pH difference from normal cells (7.3−6.4).[23] Second, the pK_a of the fluorescent probe has to match the acidic extracellular tumor pH. To overcome these challenges, Urano et al. recently developed pH-activatable BODIPY dyes that target the human epidermal growth factor receptor type 2 (HER2) for tumor imaging ex vivo.[11] The report demonstrated the potential of using pH-activatable dyes for tumor imaging with improved specificity by targeting acidic tumor organelles while minimizing signals from nontarget tissue. However, BODIPY dyes exhibit absorption maxima in the visible region where tissue penetration of light is shallow and thus less optimal for noninvasive in vivo imaging. Therefore, near-infrared (NIR) imaging probes are essential for deep tissue light penetration and low autofluorescence. In particular, NIR fluorescent probes that respond to pH changes within a physiologically relevant range would enhance tumor imaging while minimizing the background fluorescence.

With this goal in mind, we employed two complementary strategies to improve tumor targeting sensitivity and specificity of a NIR pH activatable probe: (1) conjugation of a pH-sensitive NIR dye to $\alpha_v\beta_3$ integrin receptor (ABIR)-avid peptide, cRGD, to promote selective accumulation of the probe in tumor cells and tissue; and (2) fluorescence amplification in the highly acidic lysosomes of tumor cells while minimizing fluorescence from nontarget tissues. RGD peptides have been shown to exhibit high binding affinity for ABIR that are up-regulated in tumor cells.[24−27] In addition, the new fluorescent probe is silent in the NIR window at pH > 5 but highly fluorescent in the acidic environment (pH < 5), with a pK_a value of 4.7 that closely matches lysosomal pH (Figure 1). We explored the probe's versatility as an imaging probe to detect primary and metastatic breast tumors in both subcutaneous and orthotopic mouse models.

MATERIALS AND METHODS

General. All chemicals were purchased from commercial sources and were used without further purification. The starting

Received: December 20, 2010
Revised: February 5, 2011
Published: March 09, 2011

ACS Publications © 2011 American Chemical Society

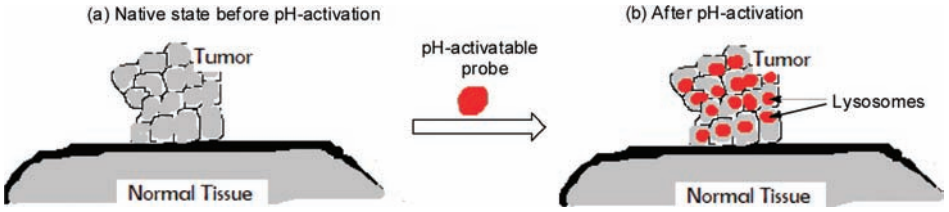


Figure 1. Selective pH activation of tumor in acidic lysosomal compartments. (a) Tumor in native state before pH activation and (b) selective activation of pH probe in lysosomal compartment of tumor cells with minimal fluorescence in nonlysosomal compartments of tumor cells and normal (non-target) tissue.

indole, sodium (2,3,3-trimethyl-3*H*-indole-5-yl)sulfonate (**2**) and Vilsmeier−Haack reagents **3** and **5** were prepared according to published procedures.[28,29] ^{1}H NMR data were recorded on a 300 MHz spectrometer at ambient temperature in DMSO-d_6 and referenced to tetramethylsilane (TMS) as an internal standard. High resolution mass spectra (HR-MS) were recorded on a hybrid linear ion trap-Fourier transform mass spectrometer.

Synthesis of pH-Activatable Dye 1. A mixture of the indole intermediate **2** (100 mg, mmol) and Vilsmeier−Haack reagent **3** (90 mg, mmol) were heated under reflux in the presence of sodium acetate (55 mg, 0.67 mmol) in 10 mL mixed solutions of CH_3CN/H_2O (95%/5%, v/v) for 20 h. After cooling, 5% of HCl in H_2O was added to the resultant mixture. MeOH was then added after the removal of H_2O, and the crude material was subjected to reverse-phase C-18 column chromatography eluting CH_3CN/H_2O to afford 46 mg of the desired dye. Yield 76%. ^{1}H NMR (300 MHz, DMSO-d_6) δ 1.47 (s, 12 H), 1.80 (m, 2H), 2.62 (m, 4H), 6.14 (br d, J = 14 Hz, 2H), 7.17 (d, J = 8 Hz, 2H), 7.61 (d, J = 8 Hz, 2H), 7.72 (s, 2H), 8.25 (br d, J = 14 Hz, 2H). NIR/vis: λ_{abs} = 778 nm, λ_{em} = 791 nm, $\varepsilon = 1.4 \times 10^5$ M^{-1} cm^{-1} (pH < 5), λ_{abs} = 516 nm (pH > 5), pK_a = 4.7. Φ_F (MeOH): 0.036. ESI-MS, m/z: 615 ($M^+ - Na + H$, 100%).

Meso-Carboxy Functionalized Dye 4. To a solution of sodium [1-(4′-sulfonatobutyl)-2,3,3-trimethyl-3*H*-indolium]-5-sulfonate (**2**, 45 mg, 0.17 mmol) was added Vilsmeier−Haack reagent **5** (35 mg, 0.086 mmol) in 10 mL mixed solutions of EtOH/acetic anhydride (1:1, v/v) in the presence of sodium acetate (14 mg, 0.17 mmol). This solution was then heated under reflux for 24 h. The reaction progress was monitored by UV/vis and LC-MS until starting materials **2** and **3** were almost consumed and the dye **4** was formed as the major product. After cooling, the crude material was subjected to reverse-phase C-18 column chromatography eluting with CH_3CN/H_2O to afford 11 mg of green dye powder. Yield 18%. ^{1}H NMR (300 MHz, DMSO-d_6) δ 1.26 (s, 12 H), 1.90 (m, 2H), 2.60 (m, 4H), 6.09 (br d, J = 14 Hz, 2H), 6.96 (br d, J = 14 Hz, 2H), 7.04 (d, J = 8 Hz, 2H), 7.34 (d, J = 8 Hz, 2H), 7.52 (d, J = 8 Hz, 2H), 7.61 (s, 2H), 8.15 (d, J = 8 Hz, 2H). NIR/vis: λ_{abs} = 755 nm, λ_{em} = 773 nm, $\varepsilon = 1.2 \times 10^5$ M^{-1} cm^{-1} (pH < 5), λ_{abs}= 513 nm (pH > 5). Φ_F (MeOH): 0.084. ESI-MS, m/z: 701 ($M^+ - Na + H$, 100%).

Peptide Synthesis and Conjugation with pH-Activatable Dye 4 (6, 7). Cyclic RGD **6** was prepared as previously described.[24] Conjugation of the peptide with dye was performed on solid supports. cRGD (**6**, 3.64 mg, 4 μmol), 2-(6-chloro-1*H*-benzotriazole-1-yl)-1,1,3,3-tetramethylaminium hexafluorophosphate (HCTU, 1.7 mg, 4.1 μmol), and *N*-methylmorpholine (0.45 μL, 4.1 μmol) were added at room temperature to **4** (2.8 mg, 4 μmol) in 0.2 mL anhydrous DMSO. The vortexing continued for 1 h at RT in the dark, and the reaction mixture was poured over 2 mL ice-cold water and purified by HPLC equipped with a C18 (22 × 250 mm, 10 μm) HPLC column. HPLC mobile phase was a mixture of solvent A = H_2O + 0.1% formic acid, and solvent B = CH_3CN + 0.1% formic acid at a flow rate of 12 mL/min. After lyophilization, compound **7** was obtained as a green powder (2.88 mg, 45%).

Deprotection of 7. Compound **7** was dissolved in a 1 mL mixture of 95% trifluoroacetic acid (TFA), 2.5% triisopropylsilane, and 2.5% water. The solution was vortexed at RT for 2.5 h, the residues were dissolved in 2 mL ice-cold water, and the product was purified by reverse phase HPLC as described above (retention time 23 min). After lyophilization, the dye−cRGD conjugate **8** (cyclo(Arg-Gly-Asp-D-Phe-Lys)-NH_2; 1.84 mg, 85%) was obtained as green powder. Yield 85%. MALDI-TOF MS m/z 1285 ($[M - Na + H]^+$, calcd 1285).

Spectral Properties and pK_a Measurements. The absorption and emission spectra were determined using a spectrophotometer and fluorometer, respectively. The molar extinction coefficient was determined by Beer's law at low concentrations of 0.1−0.6 μM. The relative fluorescence quantum yield was determined by using the equation[30]

$$\Phi_{F(x)} = (A_s/A_x)(F_x/F_s)(n_x/n_s)^2\Phi_{F(s)}$$

where $\Phi_{F(X)}$ is the fluorescence quantum yield, A is the absorbance, F is the area under the emission curve, n is the refractive index of the solvents used in the measurement, and the subscripts s and x represent the standard and unknown, respectively. Indocyanine green (ICG) was used as a reference standard, which has the value of 0.078 in MeOH.[31]

The spectral properties of NIR pH dye were determined in water, using a spectrophotometer for absorption and a fluorometer for fluorescence measurement. For pH titrations, dye **1** in water was acidified with dilute aq. HCl until the desired pH was obtained by titrating the solution with dilute aqueous NaOH with constant ionic strengths of 0.1 M. The pH of the solution was continuously measured with a pH meter. At each pH point, the absorption and fluorescence measurements were determined. The pK_a value was calculated from the sigmoidal dose−response curve fit using GraphPad *Prism 5.0* software.

Cell Culture. 4T1/*luc* breast cancer cells were purchased from Sibtech, and MDA-MB-435 breast cancer cells were purchased from ATCC. Cells were maintained in humidified atmosphere containing 5% CO_2 at 37 °C in DMEM culture medium supplemented with 10% fetal calf serum, 100 units/mL penicillin, and 100 units/mL streptomycin.

Tissue Homogenate Assays. Liver was dissected from rats after euthanasia and snap-frozen. Frozen tissue was homogenized

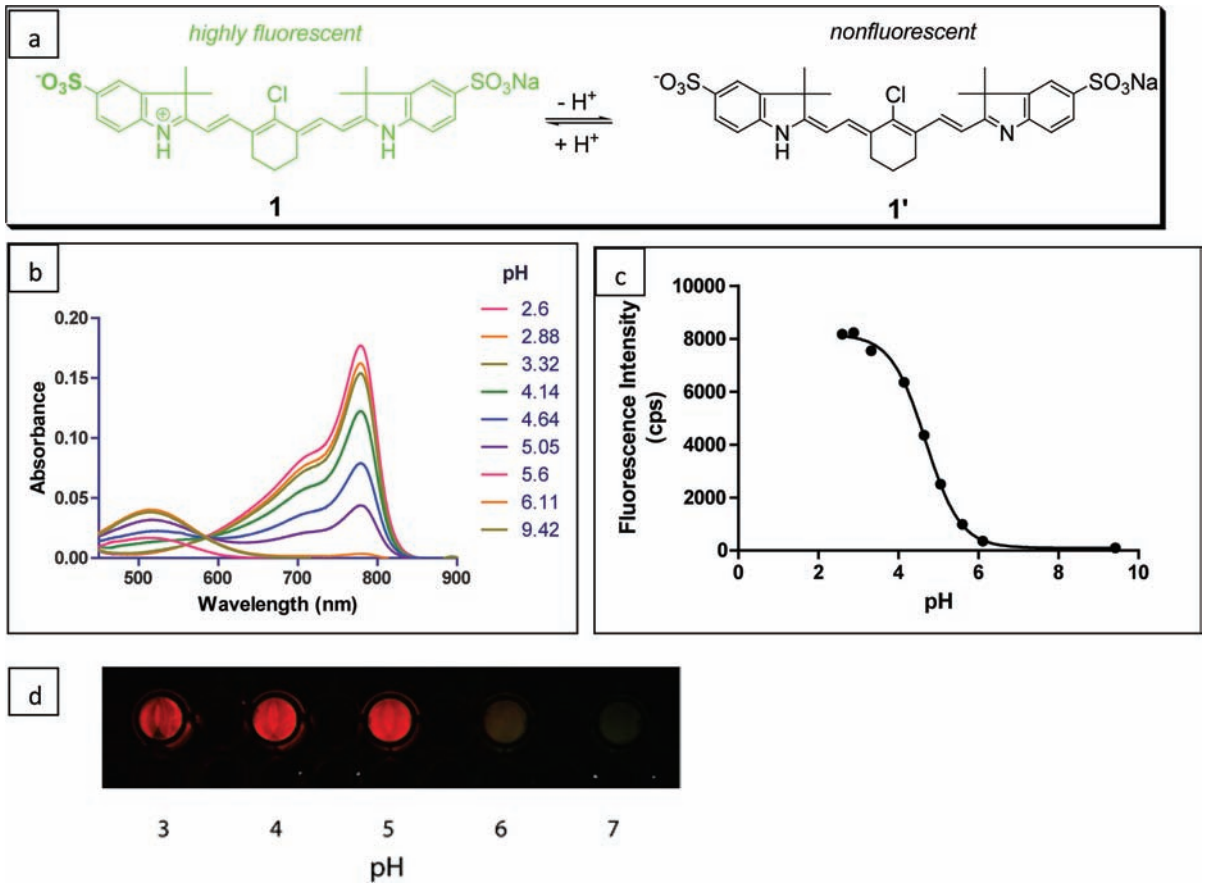


Figure 2. (a) Structure of pH-sensitive dye **1** in acidic and basic media. The reversible pH-sensitivity of dye **1** arises from the protonation−deprotonation of indolium nitrogen atom. (b) pH-dependent absorption spectral changes in the pH range 2.6−9.4. (c) pH response of dye **1** using fluorescence intensity at 795 nm to give pK_a of 4.7. (d) Fluorescence intensity change of dye **1** in liver tissue homogenate in the pH range 3−7.

using a Bessman tissue pulverizer followed by addition of sterile saline. The pH values of tissue homogenates were adjusted by addition of HCl to give pH in the range 3−7. Tissue homogenate solutions were pipetted into 96-well microtiter plates. NIR pH-activatable dye **1** was dissolved in DMSO and added to homogenate wells and mixed for a total volume of 0.25 mL per well and dye concentration of 10 μM. Fluorescence imaging was performed using the Pearl NIR fluorescence imaging system (LICOR Biosciences, Lincoln, NE) and eXplore Optix time-domain diffuse optical imaging system (Advanced Research Technologies, Montreal, Canada). The Pearl imaging system acquires images in brightfield as well as excitation and emission at 685/710 nm and 785/810 nm, respectively. The eXplore Optix utilizes a 780 nm pulsed laser for excitation with emission detected at 830 nm using time-correlated single photon counting (TCSPC) for fluorescence intensity measurements.

Confocal Microscopy of Internalization of Dye 8 into MDA-MB-435 and 4T1/*luc* Cells. Cells were grown on LabTek microscope slides. Cells were treated for 1, 4, or 6 h with dye **8**. For lysosomal staining, 100 nM Lysotracker Green was added for the last 2 h of incubation. After treatment, cells were rinsed with PBS containing 1 mM $CaCl_2$, mounted with ProLongGold mounting medium (Invitrogen), and covered with a coverslip. The slides were imaged the next day using a 60×/1.20 M, 0.13−0.21 NA water immersion objective, as well as 488 and 633 nm lasers for excitation.

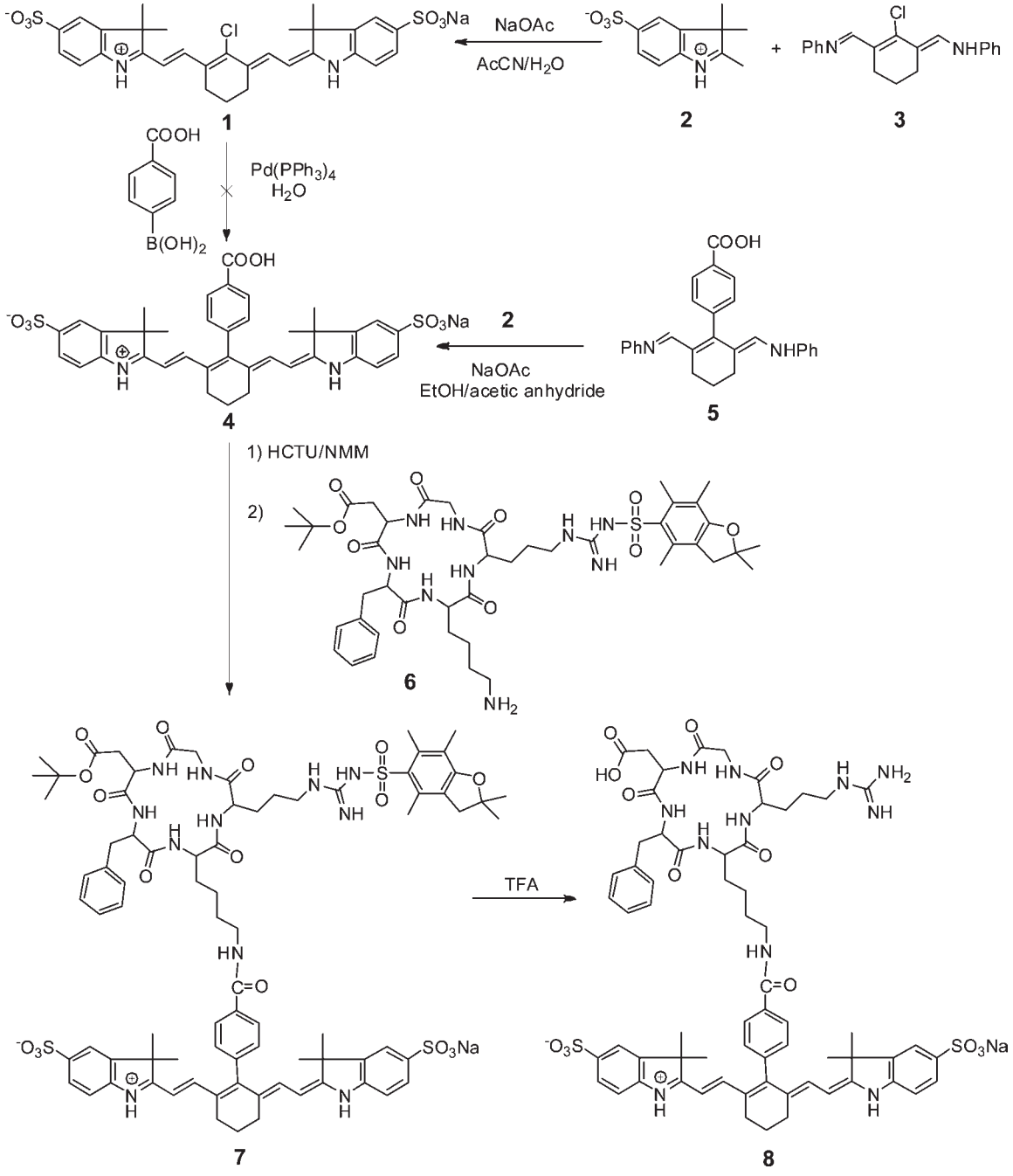
In Vivo and ex Vivo Tumor Imaging of Breast Cancer. All animal studies were performed in accordance with protocols approved by the Washington University School of Medicine Animal Studies Committee. Breast tumors were initiated in mice by injecting luciferase transfected mouse mammary carcinoma (4T1*luc*) cells either subcutaneously in 6-week-old female NCR nude mice or orthotopically into the mammary fat pad in 6-week-old female balb/c mice. After tumors had grown to 5−7 mm diameter, imaging studies were performed. The probe **8** was dissolved in DMSO then diluted with water for final concentration of 20 μM in 20% DMSO and 80% water. Probe **8** solution was injected intravenously via lateral tail vein (2 nmol/mouse, n =3). Fluorescence imaging was performed using the eXplore Optix TD-DOI system and the Pearl NIR imaging system at 1, 4, 6, and 24 h post injection. After the 24 h in vivo imaging time point, the mice were euthanized and organ tissues removed, placed on disposable Petri dish, and imaged as described above. Region of interest (ROI) analysis was performed using *ImageJ* image analysis software or Pearl imaging software. Mean fluorescence intensities were measured for each tissue to assess biodistribution of probe **8**.

RESULTS AND DISCUSSION

Synthesis and Spectral Properties of pH-Activatable NIR Fluorophore. For efficient tumor imaging, the pH-sensitive dye

dx.doi.org/10.1021/bc100584d |*Bioconjugate Chem.* 2011, 22, 777–784

Scheme 1. Synthetic Route to $\alpha_v\beta_3$-Targeting pH-Sensitive Dye 8



should possess the following features: (1) minimal or no fluorescence in neutral to basic media but highly fluorescent in acidic media (pH < 7); (2) maximum excitation wavelength in the NIR region (λ_{max} > 700 nm); (3) good water solubility; and (4) functionalizable group for conjugation to biomolecules. Among many pH-sensitive fluorophores, NIR-absorbing norcyanines satisfy most of these criteria. The typical molecular framework of norcyanines has a pH-sensitive site on the heterocyclic ring due to the presence of one or more nonsubstituted nitrogen atoms. Previously, our group and others reported the syntheses and spectral properties of NIR pH-sensitive dyes.[10,32] The limited water-solubility and lack of functionalizable groups for subsequent conjugation with biomolecules make these dyes less optimal for in vivo imaging. To overcome these drawbacks, we first developed a symmetrically substituted water-soluble norcyanine dye **1**. Dye **1** (Figure 2a) exhibited characteristic pH-dependent spectral changes, with absorption maxima in the NIR window in acidic media. A hypsochromic shift to the visible region was observed in basic media to give **1′** with calculated pK_a of 4.7 (Figure 2b,c).

This reversible, pH-dependent spectral shift arises from the protonation and deprotonation of the indolium ring nitrogen. The distinct characteristic alternation of π electronic charges that define a "polymethine state"[33] is lost during the deprotonation process, which results in the hypsochromic shift of the absorption maxima of these dyes from NIR to visible wavelength. To further

dx.doi.org/10.1021/bc100584d |*Bioconjugate Chem.* 2011, 22, 777–784

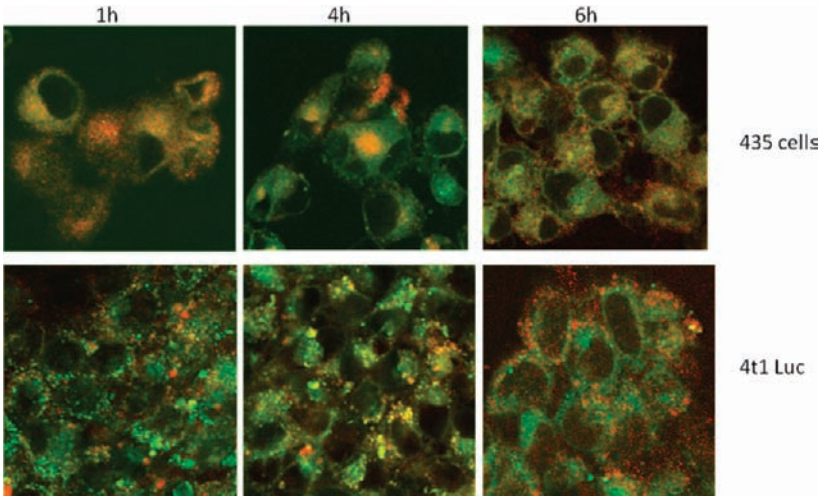


Figure 3. Lysosomal accumulation with MDA-MB-435 cells or 4T1 *luc* cells after incubation with **8** at 1, 4, and 6 h. When Dye8 (red) overlaps with the lysosomal stain (green) the resulting image is orange. The punctuate distribution of fluorescence is consistent with fluorescence activation occurring in the lysosomes.

explore the behavior of probe in tissue homogenates, fluorescence imaging was performed using homogenized liver tissues. The pH of tissue homogenates was adjusted by adjusting tissue pH with HCl to give the range 3−7. Expectedly, the fluorescence intensity of pH-activatable dye **1** at 800 nm was not detected at pH > 6, suggesting that the dye will have low background fluorescence in extracellular tissue (Figure 2d). In contrast, at pH < 6, bright fluorescence was observed. These data are in good agreement with the pK_a value determined in aqueous solution. The results indicate that fluorescence will be detected in acidic tissue compartments such as lysosomes.

Conjugation of pH-Sensitive Dye with a Tumor-Targeting cRGD for Selective Tumor Imaging. For efficient tumor targeting and selective activation of pH probes in the lysosomes, dye **1** was conjugated to ABIR targeting RGD peptides. The RGD sequence has high affinity for ABIR, which is overexpressed by many tumor cells. In addition, binding of this peptide to ABIR results in receptor-medicated endocytosis and lysosomal accumulation of the molecular probe in cancer cells. Synthesis of the molecular probe was achieved by introducing carboxylic acid functionality to the NIR pH-sensitive dye **1**. Previously, we reported the synthesis of *meso*-phenylcarboxylic acid functionalized dye using a modified Suzuki-Miyaura method.[34] However, attempts to incorporate free carboxy functionality using dye **1** failed to produce the desired dye **4**. The presence of unsubstituted heterocyclic nitrogen may promote a complex formation with palladium catalyst to give a dimeric isomer with absorption maxima in the visible range. Such compounds do not have apparent pH-dependent spectral properties. To overcome these drawbacks, Vilsmeier reagent **3** was first reacted with 4-carboxyphenyboronic acid under Suzuki-coupling conditions to give the intermediate **5**. Further heating of **5** with indolium moiety **2** in basic medium finally gave the desired dye **4** as a green solid.

Among many RGD peptides available to label the carboxy-functionalized fluorophore **4**, we chose cyclo(Arg-Gly-Asp-D-Phe-Lys)-NH_2 peptide. This peptide sequence includes an ABIR-targeting peptide motif as well as a free $-NH_2$ functionalizable group for conjugation to pH-sensitive dye **4**. Briefly, activation of carboxy-functionality of dye **4** with HCTU in *N*-methylmorpholine (NMM) followed by the reaction with the lysine residue of the cyclic peptide **6** provides the dye−peptide conjugate **7**. Removal of protecting groups with TFA affords the desired targeting probe **8**.

Internalization Studies. On the basis of the pK_a of the dye, selective accumulation of the probe in the late endosome or lysosome of tumor cells is necessary for fluorescence activation of the probe. Lysosomal uptake of pH probe **8** in 4T1/*luc* and MDA-MB-435 cells was evaluated by co-staining with Lysotracker green, a lysosome selective stain at 1, 4, and 6 h. Co-localization of pH-activatable probe **8** with Lysotracker and subsequent fluorescence amplification is evident in both cell lines, although higher accumulation of the probe was observed in MDA-MB-435. The cellular distribution of fluorescence was punctuate, as opposed to diffuse, which is consistent with fluorescence activation occurring in intracellular compartments such as the lysosomes and not in the cytosol. These data demonstrate the feasibility of using pH probe **8** for selective fluorescence activation in the target tumor lysosomes.

In Vivo Tumor Imaging of Breast Cancer 4T1/*luc*. To evaluate the feasibility of imaging tumor with pH-activatable probe, we developed subcutaneous 4T1/*luc* tumor in mice. The tumors were developed on the flanks of rodents, a model frequently used in our lab with minimal metastasis. The localized tumor allows direct assessment of the new probe in this confined in vivo environment. Selective uptake of the ABIR-targeted pH-activatable probe **8** for in vivo tumor imaging is shown in Figure 4A. The accumulation in tumor and subsequent fluorescence activation of pH probe **8** is evident as early as 1 h postinjection (Figure 4B) and reached maximum contrast by 4 h postinjection (Figure 4C).

In Vivo and ex Vivo Tumor Imaging of Orthotopic Breast Cancer 4T1/*luc*. Orthotopic tumor models closely resemble the biological environment of human tumors compared to subcutaneous xenografts models. To demonstrate the versatility of the pH probe **8** in imaging orthotopic tumor models and validate the selective amplification fluorescence in acidic compartment of tumor cells, we administered **8** to mice with orthotopic syngeneic breast tumors. In vivo fluorescence imaging results are shown in Figure 5. Immediately after injection, the fluorescence signal was equivalent to preinjection signal but increased with time. Fluorescence intensity increased in the tumor and liver regions,

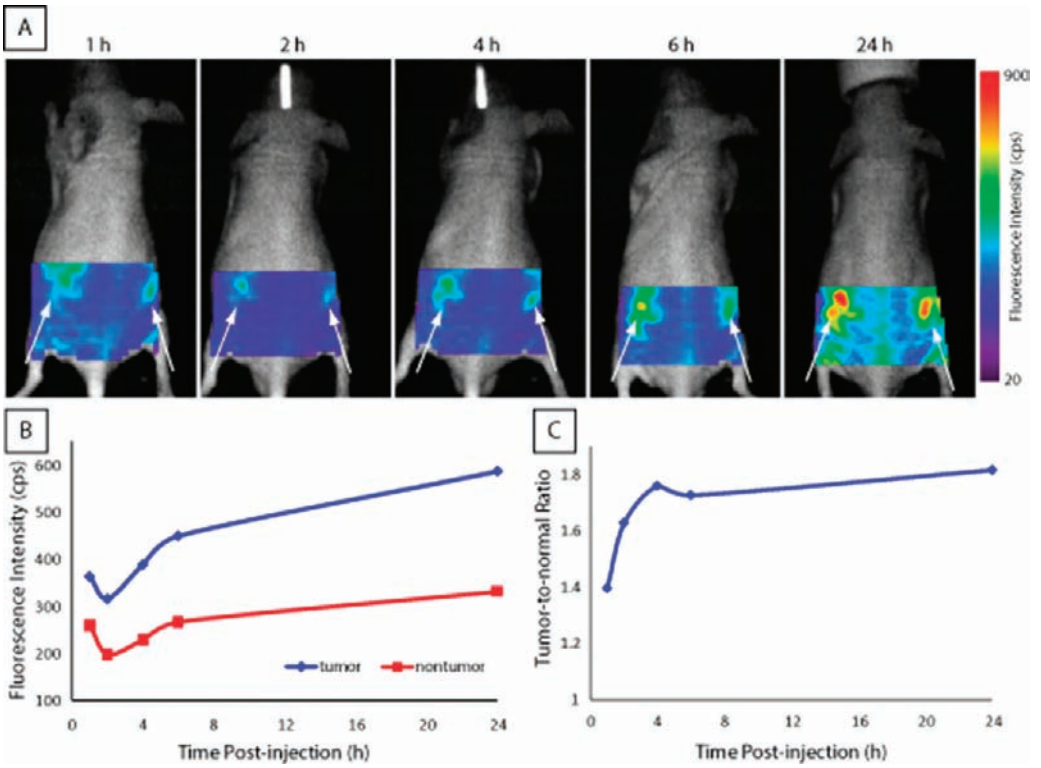


Figure 4. (A) Fluorescence image of NIR pH-activatable probe **8** in 4T1/*luc* tumor-bearing mouse at indicated times after intravenous administration. Arrows indicate bilateral subcutaneous tumor locations. (B) Plot of average fluorescence intensity values for tumor regions compared with nontumor control region selected in vivo imaging data. (C) Plot of in vivo tumor contrast at each time point showing that high contrast was achieved by 4 h and was maintained for at least 24 h postinjection.

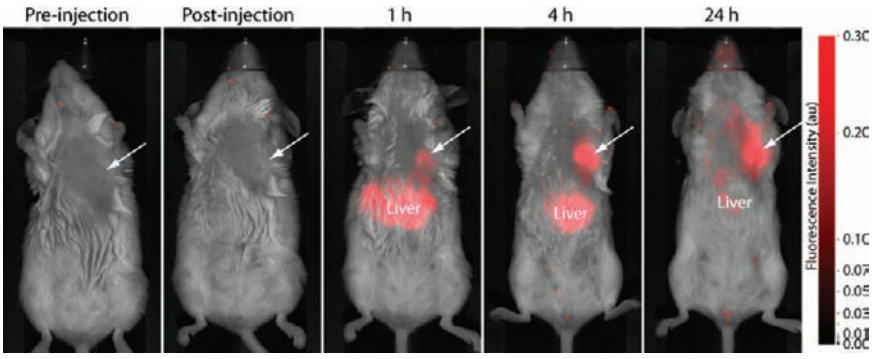


Figure 5. Fluorescence images of NIR pH-activatable probe **8** in orthotopic 4T1/*luc* tumor-bearing mice at various time points. Fluorescence intensity in the tumor region (arrow) increased with time relative to nontumor areas, reaching a plateau by 24 h.

indicating uptake of **8** in tumor cells and hepatocytes, respectively. The fluorescence intensity in the tumor region was high at 4 h after injection and remained high for up to 24 h postinjection. On the basis of previous studies with NIR dye-labeled cRGD peptides, uptake of the probe in the tumor cells is mediated by ABIR-endocytosis. As shown by the cell microscopy study, the observed fluorescence amplification is attributed to delivery of the probe to the lysosomes, which are more acidic than other cellular organelles. The increase in fluorescence is time-dependent and correlates with the trafficking of the probe from the early endosomes, through late endosomes, to the lysosomes. This pathway corresponds to an increase in intracellular acidity of the organelles. The liver is the primary excretion organ for this molecular probe, which is probably acidified in the process of the hepatobiliary excretion pathway. Fluorescence intensity increased to a lesser extent in other organs, reflecting the expression of ABIR in other tissues than the tumor.

The high tumor-specific contrast was confirmed by ex vivo tissue imaging (Figure 6A). Region of interest (ROI) analysis of ex vivo tissue fluorescence confirmed the tumor fluorescence signal enhancement observed in vivo (Figure 6B). Ex vivo fluorescence images of organ tissues show an excellent tumor-to-muscle ratio with an average value of 11:1 (tumor/muscle). High fluorescence was also detected in the kidneys and liver, indicating a mixed route of elimination from the body. Interestingly, tumor metastases (~1 mm) were detected in the lungs of

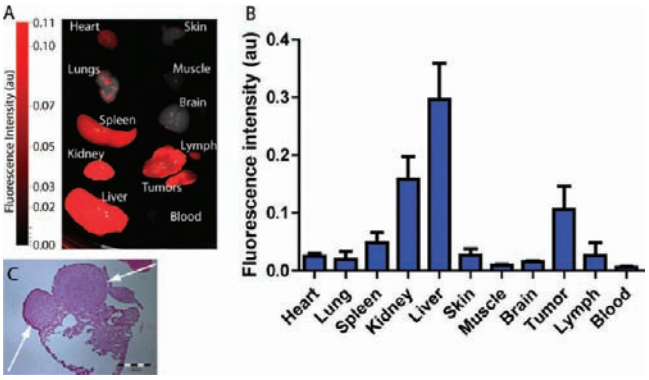


Figure 6. (A) Ex vivo fluorescence biodistribution image of **8** in organ tissues from 4T1/*luc* orthotopic tumor bearing mice at 24 h postinjection. (B) Fluorescence intensity data from ROI analysis of organ tissues. (C) Histologic confirmation of ~1 mm tumor metastases (arrow) in the lungs. Metastases to the lymph nodes were not confirmed.

one mouse by fluorescence imaging (Figure 6A), which was further confirmed by histological analysis (Figure 6C). It is well established that 4T1/*luc* tumors exhibit high metastastatic spread to the lungs.[35] The high fluorescence detected in these small tumor nodules further demonstrates the capability of detecting tumors in their natural environments due to the pH enhanced contrast mechanism.

CONCLUSION

We have developed ABIR-targeting NIR pH-activatable probe for in vivo imaging applications with high tumor selectivity. This pH-activatable probe offer several advantages over other NIR probes. First, NIR pH-sensitive probes are ideal for in vivo applications due to low background signal. Second, selective accumulation and subsequent fluorescence activation of pH-activatable probe in tumor lysosomes offer improved specificity with the high fluorescence signal from tumor compared to nontarget tissues. The results of in vitro and in vivo studies demonstrate the potential imaging applications of NIR pH-activatable probes for primary and metastatic tumor detection with high sensitivity and specificity.

AUTHOR INFORMATION

Corresponding Author

*Corresponding author. Samuel Achilefu, Ph.D., Department of Radiology, Washington University School of Medicine, 4525 Scott Avenue, St. Louis, MO 63110. Tel: 314-362-8599. E-mail: achilefus@mir.wustl.edu.

ACKNOWLEDGMENT

This study was supported in part by the U.S. National Institutes of Health NIBIB grants R01 EB007276, EB008111, EB 008458, and NCI R33 CA123537.

REFERENCES

(1) Kaijzel, E. L., van Heijningen, P. M., Wielopolski, P. A., Vermeij, M., Koning, G. A., van Cappellen, W. A., Que, I., Chan, A., Dijkstra, J., Ramnath, N. W., Hawinkels, L. J., Bernsen, M. R., Lowik, C. W., and Essers, J. Multimodality imaging reveals a gradual increase in matrix metalloproteinase activity at aneurysmal lesions in live fibulin-4 mice. *Circ. Cardiovasc. Imaging 3*, 567−77.

(2) Kim, D. E., Kim, J. Y., Schellingerhout, D., Shon, S. M., Jeong, S. W., Kim, E. J., and Kim, W. K. (2009) Molecular imaging of cathepsin B proteolytic enzyme activity reflects the inflammatory component of atherosclerotic pathology and can quantitatively demonstrate the antiatherosclerotic therapeutic effects of atorvastatin and glucosamine. *Mol. Imaging 8*, 291–301.

(3) Sheth, R. A., Upadhyay, R., Stangenberg, L., Sheth, R., Weissleder, R., and Mahmood, U. (2009) Improved detection of ovarian cancer metastases by intraoperative quantitative fluorescence protease imaging in a pre-clinical model. *Gynecol. Oncol. 112*, 616–22.

(4) Jaffer, F. A., Vinegoni, C., John, M. C., Aikawa, E., Gold, H. K., Finn, A. V., Ntziachristos, V., Libby, P., and Weissleder, R. (2008) Real-time catheter molecular sensing of inflammation in proteolytically active atherosclerosis. *Circulation 118*, 1802–9.

(5) Jaffer, F. A., Kim, D. E., Quinti, L., Tung, C. H., Aikawa, E., Pande, A. N., Kohler, R. H., Shi, G. P., Libby, P., and Weissleder, R. (2007) Optical visualization of cathepsin K activity in atherosclerosis with a novel, protease-activatable fluorescence sensor. *Circulation 115*, 2292–8.

(6) Barnett, E. M., Zhang, X., Maxwell, D., Chang, Q., and Piwnica-Worms, D. (2009) Single-cell imaging of retinal ganglion cell apoptosis with a cell-penetrating, activatable peptide probe in an in vivo glaucoma model. *Proc. Natl. Acad. Sci. U.S.A. 106*, 9391–6.

(7) Klohs, J., Baeva, N., Steinbrink, J., Bourayou, R., Boettcher, C., Royl, G., Megow, D., Dirnagl, U., Priller, J., and Wunder, A. (2009) In vivo near-infrared fluorescence imaging of matrix metalloproteinase activity after cerebral ischemia. *J. Cereb. Blood Flow Metab. 29*, 1284–92.

(8) Maxwell, D., Chang, Q., Zhang, X., Barnett, E. M., and Piwnica-Worms, D. (2009) An improved cell-penetrating, caspase-activatable, near-infrared fluorescent peptide for apoptosis imaging. *Bioconjugate Chem. 20*, 702–9.

(9) Hilderbrand, S. A., Kelly, K. A., Niedre, M., and Weissleder, R. (2008) Near infrared fluorescence-based bacteriophage particles for ratiometric pH imaging. *Bioconjugate Chem. 19*, 1635–9.

(10) Hilderbrand, S. A., and Weissleder, R. (2007) Optimized pH-responsive cyanine fluorochromes for detection of acidic environments. *Chem. Commun. (Camb.)* 2747–9.

(11) Urano, Y., Asanuma, D., Hama, Y., Koyama, Y., Barrett, T., Kamiya, M., Nagano, T., Watanabe, T., Hasegawa, A., Choyke, P. L., and Kobayashi, H. (2009) Selective molecular imaging of viable cancer cells with pH-activatable fluorescence probes. *Nat. Med. 15*, 104–9.

(12) Ogawa, M., Kosaka, N., Regino, C. A., Mitsunaga, M., Choyke, P. L., and Kobayashi, H. High sensitivity detection of cancer in vivo using a dual-controlled activation fluorescent imaging probe based on H-dimer formation and pH activation. *Mol. Biosyst. 6*, 888−93.

(13) Panizzi, P., Nahrendorf, M., Wildgruber, M., Waterman, P., Figueiredo, J. L., Aikawa, E., McCarthy, J., Weissleder, R., and Hilderbrand, S. A. (2009) Oxazine conjugated nanoparticle detects in vivo hypochlorous acid and peroxynitrite generation. *J. Am. Chem. Soc. 131*, 15739–44.

(14) Hilderbrand, S. A., and Weissleder, R. Near-infrared fluorescence: application to in vivo molecular imaging. *Curr. Opin. Chem. Biol. 14*, 71−9.

(15) Lee, H., Akers, W. J., Cheney, P. P., Edwards, W. B., Liang, K., Culver, J. P., and Achilefu, S. (2009) Complementary optical and nuclear imaging of caspase-3 activity using combined activatable and radiolabeled multimodality molecular probe. *J. Biomed. Opt. 14*, 040507.

(16) Levi, J., Kothapalli, S. R., Ma, T. J., Hartman, K., Khuri-Yakub, B. T., Gambhir, S. S. Design, synthesis, and imaging of an activatable photoacoustic probe. *J. Am. Chem. Soc. 132*, 11264-9.

(17) Mieog, J. S., Hutteman, M., van der Vorst, J. R., Kuppen, P. J., Que, I., Dijkstra, J., Kaijzel, E. L., Prins, F., Lowik, C. W., Smit, V. T., van de Velde, C. J., and Vahrmeijer, A. L. Image-guided tumor resection using real-time near-infrared fluorescence in a syngeneic rat model of primary breast cancer. *Breast Cancer Res. Treat*, DOI:10.1007/s10549-010-1130-6.

(18) Salthouse, C. D., Reynolds, F., Tam, J. M., Josephson, L., and Mahmood, U. (2009) Quantitative measurement of protease-activity

with correction of probe delivery and tissue absorption effects. *Sens. Actuators, B 138*, 591–597.

(19) Mu, C. J., Lavan, D. A., Langer, R. S., and Zetter, B. R. Self-assembled gold nanoparticle molecular probes for detecting proteolytic activity in vivo. *ACS Nano 4*, 1511−20.

(20) Elias, D. R., Thorek, D. L., Chen, A. K., Czupryna, J., and Tsourkas, A. (2008) In vivo imaging of cancer biomarkers using activatable molecular probes. *Cancer Biomark. 4*, 287–305.

(21) Kamiya, M., Kobayashi, H., Hama, Y., Koyama, Y., Bernardo, M., Nagano, T., Choyke, P. L., and Urano, Y. (2007) An enzymatically activated fluorescence probe for targeted tumor imaging. *J. Am. Chem. Soc. 129*, 3918–29.

(22) Zhang, X., Lin, Y., and Gillies, R. J. Tumor pH and its measurement. *J. Nucl. Med. 51*, 1167−70.

(23) Cardone, R. A., Casavola, V., and Reshkin, S. J. (2005) The role of disturbed pH dynamics and the Na+/H+ exchanger in metastasis. *Nat. Rev. Cancer 5*, 786–95.

(24) Ye, Y., Bloch, S., Xu, B., and Achilefu, S. (2008) Novel near-infrared fluorescent integrin-targeted DFO analogue. *Bioconjugate Chem. 19*, 225–34.

(25) Eliceiri, B. P., and Cheresh, D. A. (2000) Role of alpha v integrins during angiogenesis. *Cancer J. 6* (Suppl 3), S245–9.

(26) Ria, R., Vacca, A., Ribatti, D., Di Raimondo, F., Merchionne, F., and Dammacco, F. (2002) Alpha(v)beta(3) integrin engagement enhances cell invasiveness in human multiple myeloma. *Haematologica 87*, 836–45.

(27) Meyer, A., Auernheimer, J., Modlinger, A., and Kessler, H. (2006) Targeting RGD recognizing integrins: drug development, biomaterial research, tumor imaging and targeting. *Curr. Pharm. Des. 12*, 2723–47.

(28) Mason, J. C. (2001) in *Chemistry*, pp 1−202, Georgia State University, Atlanta.

(29) Lee, H., Mason, J. C., and Achilefu, S. (2008) Synthesis and spectral properties of near-infrared aminophenyl-, hydroxyphenyl-, and phenyl-substituted heptamethine cyanines. *J. Org. Chem. 73*, 723–5.

(30) Demas, J. N., and Crosby, G. A. (1971) Measurement of photoluminescence quantum yields.. *J. Phys. Chem. 75*, 991–1023.

(31) Benson, R. C., and Kues, H. A. (1978) Fluorescence properties of indocyanine green as related to angiography. *Phys. Med. Biol. 23*, 159–63.

(32) Zhang, Z., and Achilefu, S. (2005) Design, synthesis and evaluation of near-infrared fluorescent pH indicators in a physiologically relevant range. *Chem. Commun. (Camb.)* 5887–9.

(33) Tyutyulkov, N. F., J.; Mehlhorn, A.; Dietz, F.; Tadjer, A. (1991) *Polymethine Dyes: Structure and Properties*, St. Kliment Ohridski University Press, Sofia, Bulgaria.

(34) Lee, H., Mason, J. C., and Achilefu, S. (2006) Heptamethine cyanine dyes with a robust C-C bond at the central position of the chromophore. *J. Org. Chem. 71*, 7862–5.

(35) Hiraga, T., Hata, K., Ikeda, F., Kitagaki, J., Fujimoto-Ouchi, K., Tanaka, Y., and Yoneda, T. (2005) Preferential inhibition of bone metastases by 5′-deoxy-5-fluorouridine and capecitabine in the 4T1/luc mouse breast cancer model. *Oncol. Rep. 14*, 695–9.

Bioconjugate Chemistry

ARTICLE

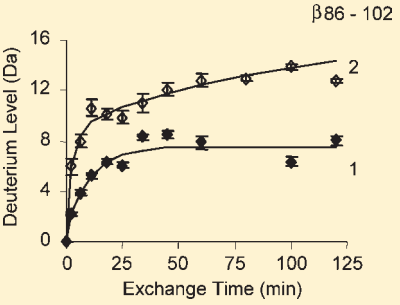
pubs.acs.org/bc

Structural Perturbation of Human Hemoglobin on Glutathionylation Probed by Hydrogen−Deuterium Exchange and MALDI Mass Spectrometry

Gopa Mitra,[†] Monita Muralidharan,[†] Jennifer Pinto, Krishnamachari Srinivasan, and Amit Kumar Mandal*

Molecular Medicine & Clinical Proteomics, St. John's Research Institute, St. John's National Academy of Health Sciences, Bangalore, India

ABSTRACT: Glutathionyl hemoglobin, an example of post-translationally modified hemoglobin, has been studied as a marker of oxidative stress in various diseased conditions. Compared to normal hemoglobin, glutathionyl hemoglobin has been found to have increased oxygen affinity and reduced cooperativity. However, detailed information concerning the structural perturbation of hemoglobin associated with glutathionylation is lacking. In the present study, we report structural changes associated with glutathionylation of deoxyhemoglobin by hydrogen/deuterium (H/D) exchange coupled to matrix assisted laser desorption ionization (MALDI) mass spectrometry. We analyzed isotope exchange kinetics of backbone amide hydrogen of eleven peptic peptides in the deoxy state of both hemoglobin and glutathionyl hemoglobin molecules. Analysis of the deuterium incorporation kinetics for both molecules showed structural changes associated with the following peptides: α34−46, α1−29, β32−41, β86−102, β115−129, and β130−146. H/D exchange experiments suggest that glutathionylation of hemoglobin results in a change in conformation located at the above-mentioned regions of the hemoglobin molecule. MALDI mass spectrometry based H/D exchange experiment might be a simple way of monitoring structural changes associated with post-translational modification of protein.



INTRODUCTION

Glutathione (γ-L-glutamyl−L-cysteinyl−glycine), a tripeptide, is the most abundant antioxidant in erythrocytes. It plays a crucial role in detoxifying ROS (reactive oxygen species) like hydroxyl, peroxo, and superoxo radicals by shifting the redox equilibrium from reduced glutathione (GSH) to oxidized glutathione (GSSG). In normal adult erythrocytes, the concentration of reduced and oxidized glutathione is 2.3 mM and 0.004 mM, respectively.[1] The enzyme glutathione reductase reduces GSSG to GSH, thus maintaining the redox balance in the cell. Under conditions of oxidative stress, GSSG accumulates inside the cell and subsequently undergoes thiol exchange with accessible free cysteine residues in protein resulting in protein glutathionylation. Recent studies have demonstrated protein glutathionylation in various medical conditions.[2−6]

Hemoglobin, the key molecule in oxygen transport, is a tetrameric protein consisting of α and β globin chains in duplicate. The interactions between amino acid residues within inter and intra subunits of Hb govern the dynamic equilibrium between its oxy and deoxy states, which eventually drives its function. Glutathionylation of protein is an example of nonenzymatic post-translational modification. In glutathionyl hemoglobin (GSHb), glutathione binds to Cys93 of the β globin chain through disulfide bond. Glutathionyl hemoglobin has also been reported to have 6-fold higher oxygen affinity compared to normal hemoglobin (HbA). The Hill coefficient at half saturation (n_{50}) is 1.5 for GSHb compared to 2.9 in HbA. The above-mentioned functional abnormality is presumed to be due to structural modification in hemoglobin associated with glutathionylation. Several studies have reported glutathionyl hemoglobin as a possible biomarker of oxidative stress in various medical conditions such as hyperlipidemia,[7] diabetes mellitus,[7] Friedreich's ataxia,[8] atherosclerosis,[2] and chronic renal failure.[9] In addition, Garel et al. reported that glutathionylation of sickle hemoglobin (HbS) results in inhibition of HbS polymerization that manifests in reduction of sickling of erythrocytes.[10]

Using nuclear magnetic resonance spectroscopy, Craescu et al. reported structural perturbations in GSHb compared to HbA. These include perturbation of β-heme pocket particularly in F helix, destabilization in the salt bridge between βAsp94 and βHis146, and the hydrogen bond between βAsp99 and αTyr42 at the $\alpha_1\beta_2$ interface.[11] However, details concerning perturbation in the hemoglobin structure on glutathionylation have not yet been reported.

Hydrogen/deuterium (H/D) exchange coupled to mass spectrometry has evolved into a useful tool for understanding solution-phase dynamics of protein molecules. In this method, protein is exposed to a solvent having a different isotope of hydrogen, viz, deuterium. The exchange of hydrogen atoms takes place depending on the local environment, as well as the inductive and charge effect of neighboring atoms. Thus, hydrogens attached to oxygen, nitrogen, and sulfur atoms exchange rapidly, whereas those attached to carbon atoms exchange very slowly. The exchange of peptide backbone amide hydrogens is

Received: December 29, 2010
Revised: February 11, 2011
Published: March 08, 2011

ACS Publications © 2011 American Chemical Society

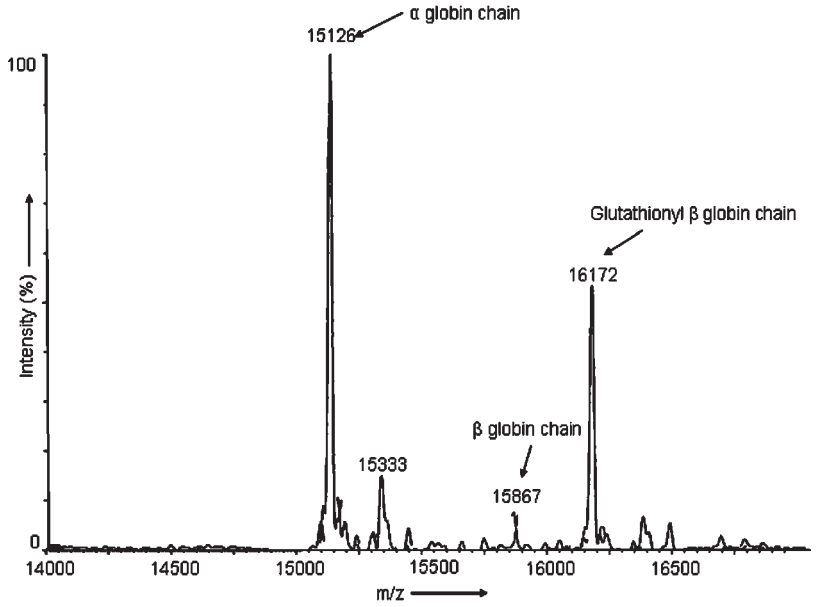


Figure 1. MALDI mass spectra of glutathionyl hemoglobin synthesized in vitro. Masses of different polypeptide chains are marked. The peak with m/z 16 172 represents the glutathionyl β globin chain, while peaks with m/z 15 867 and 15 126 represent the normal β and α globin chain, respectively.

mostly studied in the H/D exchange reaction with deuterium present in the surroundings, as they exchange on a convenient and measurable time scale. Depending on solvent accessibility and hydrogen bonding strength, the different peptide amide hydrogens undergo isotopic exchange at different rates. The side chain hydrogens exchange very rapidly, which are beyond the experimental measurement limit. Subsequent proteolytic cleavage of deuterated polypeptide followed by mass spectrometric measurement of proteolytic peptides provides the kinetics of deuterium incorporation. This in turn helps in understanding the conformational dynamics of the protein in those selective regions.

In the present study, we have investigated the structural and dynamic features of the deoxy state of normal hemoglobin and glutathionyl hemoglobin, through H/D exchange of peptide amide hydrogens probed by MALDI mass spectrometry.

EXPERIMENTAL PROCEDURE

Materials. Pepsin crystalline, deuterium oxide (99.9%), 2,2′-dithiodipyridine (2-PDS), Sephadex G-50, sodium hydrosulfite, reduced glutathione (GSH), and sinapinic acid were purchased from Sigma (St. Louis, MO). Synthesis-grade trifluoroacetic acid (TFA) was from Merck, Germany, whereas poly(ethylene glycol) (PEG) mix, the external calibrant for mass spectrometer, was purchased from Waters, Milford, MA. α-Cyano-4-hydroxy cinnamic acid (CHCA) was obtained from Fluka, Germany. The nitrogen controller unit for the mass spectrometer was supplied by Peak Scientific. All other chemicals used were of analytical grade.

Extraction of Hemoglobin. Whole blood was collected from healthy volunteers. Venous blood anticoagulated with EDTA was used for the study. Plasma was aspirated off after centrifugation of whole blood at 3000 rpm for 10 min at 25 °C. The erythrocytes, obtained as precipitate, were washed with 0.9% NaCl (aqueous) thrice and then lysed with eight volumes of ice cold distilled water. The hemolysate was centrifuged at 12 000 rpm for 10 min at 4 °C to remove the erythrocyte membranes. The clear supernatant was used to measure hemoglobin concentration using UV−vis (Shimadzu spectrophotometer) at 548 nm and concentration was calculated using ε = 12.51 mM^{-1} cm^{-1}.

Chemical Modification of Hemoglobin. Chemical modification of HbA with 2-PDS was performed using modified protocol as reported by Garel et al.[10] In short, 7.0 mM 2-PDS was incubated with 0.7 mM hemoglobin in 50 mM aqueous ammonium bicarbonate solution (pH 7.4) for 1 h at 0 °C. The excess PDS was removed by allowing the reaction mixture to pass through a Sephadex G-50 spin column. The thiopyridinyl hemoglobin was then allowed to react with reduced glutathione (GSH) in a molar ratio of HbA/GSH = 1/40 at 0 °C for 1 h. This reaction mixture was passed through a Sephadex G-50 spin column to remove excess GSH. To monitor the extent of glutathionylation of hemoglobin, 1 μL of the reaction mixture was mixed with 1 μL of sinnapinic acid (10 mg/mL in ACN/H_2O: 40/60, containing 0.1% TFA) and spotted on a MALDI plate. The ratio of ion counts obtained in the mass spectrum indicated more than 85% conversion of hemoglobin into glutathionyl hemoglobin (Figure 1).

Preparation of Deoxyhemoglobin. Hemoglobin (20 μM) was added to 50 mM ammonium bicarbonate/D_2O buffer (pD 7.4) containing 66 mM sodium hydrosulfite. The dissolved oxygen in solution was removed by sodium hydrosulfite to ensure that hemoglobin was in the deoxy state. Pure nitrogen gas was continuously bubbled through the solution at a rate of 40 mL/min to maintain the deoxy state of hemoglobin throughout the exchange experiment. The resulting solution was used for isotope exchange kinetics experiments. A similar procedure was followed for glutathionyl hemoglobin.

Hydrogen−Deuterium (H/D) Exchange Experiment. H/D exchange was initiated in hemoglobin by the addition of 15-fold excess of 50 mM ammonium bicarbonate/D_2O buffer (pD 7.4) at 25 °C with the concentration of hemoglobin at 20 μM. Isotope exchange kinetics was followed for 2 h. At different time intervals, 10 μL of reaction mixture was taken out and diluted with 90 μL of

dx.doi.org/10.1021/bc100602f |*Bioconjugate Chem.* 2011, 22, 785–793

ice cold aqueous 0.1% TFA (pH 2.5) to facilitate the quenching of the H/D exchange. Immediately, 2 μL of aqueous pepsin solution was added to the acidic protein solution (enzyme/substrate ratio 1:10, mol/mol). Digestion was carried out for 5 min at 0 °C. 1 μL of digested sample and 1 μL matrix (5 mg/mL of α-cyano-4-hydroxy cinnamic acid in 2:8:1 acetonitrile/ethanol/0.1% aqueous TFA, pH 2.5) were mixed together, and 0.5 μL of this mixture was spotted on the MALDI plate. The spot was dried rapidly using moderate vacuum in a desiccator, and following drying, the MALDI plate was then immediately loaded into a mass spectrometer for mass analysis. The above experimental procedure was followed to ensure that there was minimal loss of incorporated deuterium (back exchange of D to H) in the exchange experiment.[12]

Completely deuterated hemoglobin (100% control) was used to calculate the number of deuterium lost during the analysis, whereas unlabeled hemoglobin (0% control) was used to calculate the number of deuterium gained during analysis. For 0% control experiment, hemoglobin was dissolved directly into a solution equivalent to postquench conditions containing pepsin. For 100% control experiment, the isotope exchange reaction was continued for 6 h followed by digestion and analysis. The 100% control data and 0% control data were used to calculate the molecular mass of peptides in conditions where hemoglobin was fully deuterated and not deuterated, respectively.

In H/D exchange experiments, the exchangeable hydrogen present in the side chain group of amino acid residues and that in terminal groups undergo exchange and back exchange at a rapid rate. Therefore, in the present study the exchange kinetics of backbone amide hydrogens were monitored. The occurrence of back exchange of amide hydrogens during analysis was addressed using the procedure described by Nazabal et al.[12] In brief, the exchange reaction was quenched by rapid cooling and acidification, which increased the half-life of back exchange by several orders of magnitude.[13,14] For example, one unit decrease in pH leads to a 10-fold decrease in exchange rate of peptide amide hydrogen, which attains minima at pH 3. Similarly the above exchange rate decreases by 3-fold per 10 °C decrease in temperature.[15] MALDI MS spectra were collected on all samples.

Mass Spectrometry. All MS analyses were performed on a Waters Synapt HDMS mass spectrometer equipped with a MALDI source. Analyses were conducted in the positive ion mode. MALDI MS spectra for proteolytic peptides were recorded in the 900 to 3500 m/z range in positive ion V mode using 200 Hz solid-state laser (λ = 355 nm). The mass spectrometer was calibrated using an external calibrant, PEG mix. Mass spectra were acquired by integrating an average of 50 shots/spot and analyzed using *MassLynx* software version 4.1.

Sequencing of Peptic Peptides. Tandem mass spectrometry was used to obtain sequence information of peptide molecular ions. Peptide digest solution (1 μL) was mixed with 1 μL of α-cyano-4-hydroxy cinnamic acid matrix solution and 1 μL of the mixture was spotted on the MALDI plate. Mass spectra were recorded for the digest, and subsequently, tandem mass spectra of selected precursor ions were acquired using 200 Hz laser (λ = 355 nm) and by increasing trap collision energy. The generated tandem mass spectra were analyzed by manual assignment of product ions to obtain sequence information of precursor ion.

Data Analysis. The spectra were baseline corrected and the isotope averaged centroid mass of each molecular ion (M_t) was measured using the software *HX Express* Version Beta (http://www.hxms.com/HXExpress). The number of deuterium incorporated in a peptide at a given time t was calculated as per the following eq 1:[16]

$$D(t) = \frac{(M_t - M_0)}{(M_\infty - M_0)} \times N \quad (1)$$

where M_t is the observed centroid mass of the peptide at time t, M_0 is the observed mass at zero time control experiment, M_∞ is the observed mass for a fully deuterated experiment (100% control experiment), and N is the total number of backbone amide hydrogens in the peptide. Four data sets obtained for each peptide ion were averaged. At a fixed pH and temperature and in the presence of large excess of D_2O, the isotope exchange of each peptide amide hydrogen follows pseudo first order kinetics. In principle, for a peptide fragment consisting of N amide hydrogens, the deuterium content can be described by summation of N exponential terms[17]

$$D = N - \sum_{i=1}^{N} \exp^{-k_i t} \quad (2)$$

where D is the deuterium content of the peptide at time t, k_i is the rate constants for ith amide hydrogen, and N is the total number of peptide amide hydrogens present in the fragment.

In practice, peptide backbone amide hydrogens can be categorized on the basis of their corresponding H/D exchange rate constants into fast, intermediate, and slow exchanging group according to the following equation:

$$D = N - Ae^{-k_1 t} - Be^{-k_2 t} - Ce^{-k_3 t} \quad (3)$$

where A, B, and C are the number of fast, intermediate, and slow exchanging amide hydrogens with rate constants k_1, k_2, and k_3, respectively. The isotope exchange rates were quantitatively assessed by fitting the data obtained from eq 1 into eq 3.[16] The exchange rate constants and the population of amide hydrogens in different groups were varied to minimize the sum of squared residuals (SSR). MS *Excel* solver was used to obtain the best fitted curve. The SSR for each data set was calculated using the following equation:

$$\mathrm{SSR} = \sum_i ((y_{i\mathrm{obs}} - y_{i\mathrm{calc}})/y_{i\mathrm{obs}})^2$$

$y_{i\ \mathrm{obs}}$, $y_{i\ \mathrm{calc}}$ were calculated from eq 1 and eq 3, respectively.[18]

RESULTS AND DISCUSSION

Human hemoglobin has one cysteine residue in each α globin subunit (αCys104) and two cysteine residues in each β globin subunit (βCys93, βCys112). Among the three cysteine residues, βCys93 is the preferred site for glutathione binding, which is 5-fold more accessible than βCys112, whereas αCys104 is completely buried and thus inaccessible to glutathione.[9] In spite of the large excess of GSH compared to GSSG in a normal erythrocyte, glutathionylation of hemoglobin occurs to a small extent (~3% of total Hb).[9] In this study, we have synthesized glutathionyl hemoglobin in vitro. Figure 1 shows the MALDI mass spectra of glutathionyl hemoglobin synthesized in vitro, where glutathionyl β globin chain appeared with m/z 16 172 along with a normal β-globin chain (m/z 15 867) and normal α-globin chain (m/z 15 126). The synthesized GSHb molecule with at least 85% abundance was chosen for further experiments.

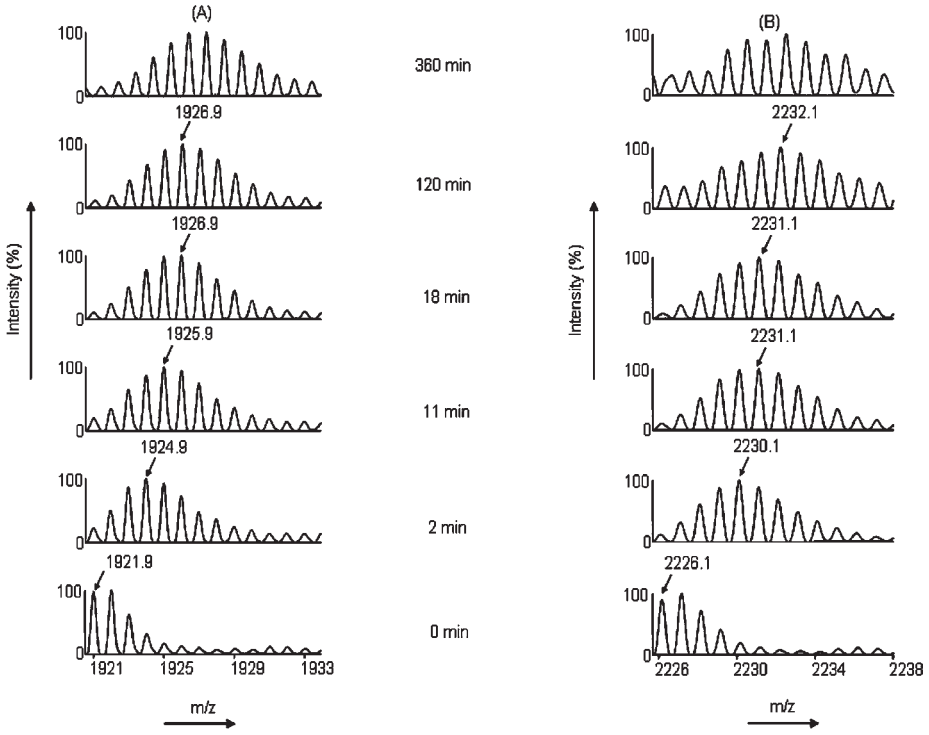
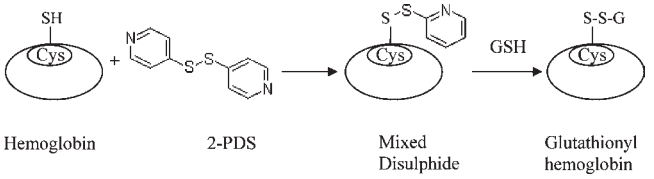


Figure 2. MALDI mass spectra for the peptide 1921.9 m/z obtained on hydrogen/deuterium exchange kinetics. Panels A and B represent the isotope exchange kinetics for the peptide fragment in HbA and GSHb, respectively. Glutathionylation leads to an increase in the mass of the peptide from 1921.9 to 2226.1. The spectra labeled as 0 and 360 min represent the data for 0% control and 100% control experiments, respectively.

A schematic representation of hemoglobin glutathionylation has been provided below.



An illustration of the actual mass spectra obtained for H/D exchange kinetics of peptic peptides is shown in Figure 2, Figure 3, and Figure 4. In the H/D exchange process, on replacement of one hydrogen atom by one deuterium, the envelope corresponding to a peptide molecular ion shows an increase in mass by one unit. As more hydrogens are replaced by deuterium with time, the envelope shows a progressive mass shift, which eventually represents kinetic behavior of H/D exchange process for that peptide. Figure 2 represents mass spectra of a β globin fragment with m/z 1921.9, consisting of residues 86 to 102. Panel A shows the mass spectra obtained from 1921.9 m/z for normal hemoglobin, while panel B represents the data for glutathionyl peptide. Upon glutathionylation, the mass of the peptide fragment shifted to 2226.1 m/z. On H/D exchange, the mass of the peptide fragment increased with time. The spectra labeled as 0 and 360 min represent the 0% control data and the 100% control data, respectively. Figure 3 represents mass spectra obtained for the α globin fragment (α34−46) with m/z 1585.8. Panels A and B represent the isotope exchange kinetics for the peptide in HbA and GSHb molecules, respectively. Similarly, Figure 4 represents mass spectra of a β globin fragment with m/z 1494.8 consisting of residues 1 to 14, and panels A and B show kinetic behavior of the peptide fragment with time for HbA and GSHb, respectively.

After quenching the H/D exchange kinetics followed by pepsin digestion, we analyzed a total of eleven peptides by MALDI-MS. The sequence coverage obtained from the identified peptides was 29.7% for α globin and 67.8% for β globin chains, respectively. A few peptides in the close m/z range had overlapping envelopes after mass shift due to H/D exchange, which made the analysis improbable for those peptides and was hence excluded in sequence coverage for globin chain analysis.

Figure 5, Figure 6, and Figure 7 represent plots of kinetic data for deuterium incorporation in eleven different peptic peptides obtained from both HbA and GSHb molecules. The peptide amide hydrogens have been grouped into fast (A), intermediate (B), and slow (C) exchanging for each peptide fragment, and the corresponding rate constants have been assigned as k_1, k_2, and k_3, respectively. The number of differently grouped peptide amide hydrogens and corresponding rate constants for all eleven peptic peptides are listed in Table-1.

The analysis of tandem mass spectra followed by sequence assignments confirmed that the peptic fragment of HbA with m/z 1921.9 originated from the β globin chain spanning residues 86−102, consisting of βCys93 residue. The same fragment in the GSHb digest appeared at m/z 2226.1, showing a shift in mass by 305 Da consistent with a glutathione moiety attached to βCys93 by disulfide linkage. Figure 5A represents the best fit curve according to eq 3, obtained from deuterium incorporation kinetics data for HbA (trace 1) and GSHb (trace 2). Sequence analysis of peptide fragments showed that the numbers of exchangeable amide hydrogens are 15 and 17 for HbA and

dx.doi.org/10.1021/bc100602f |*Bioconjugate Chem.* 2011, 22, 785–793

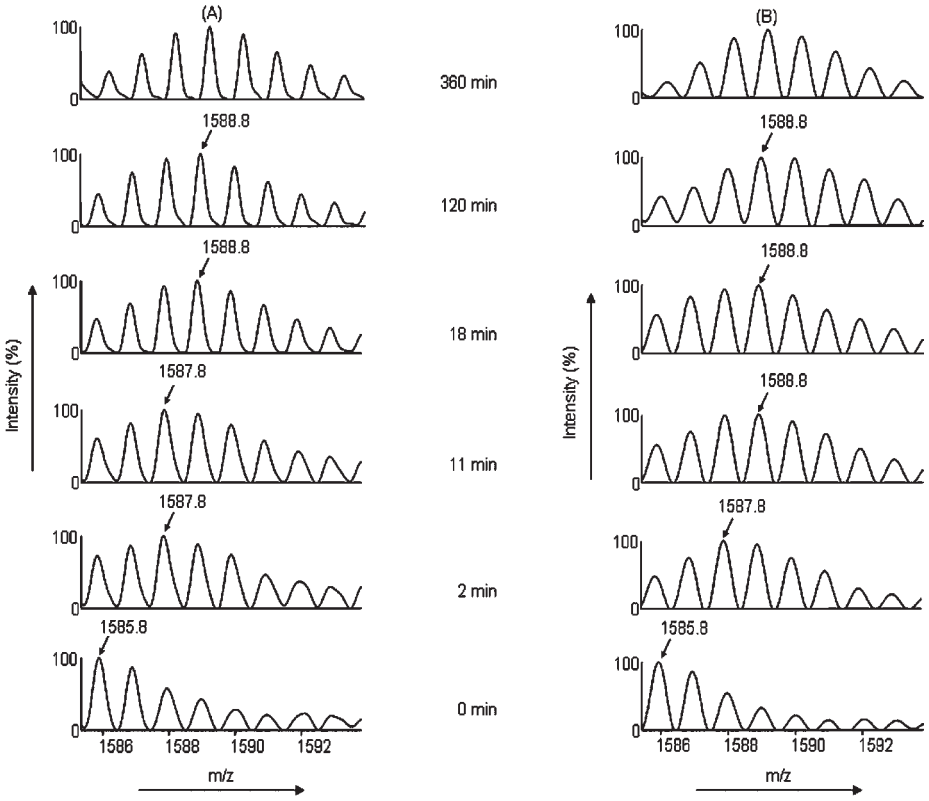


Figure 3. MALDI mass spectra for the peptide 1585.8 *m/z* obtained on hydrogen/deuterium exchange kinetics. Panels A and B represent the isotope exchange kinetics for the peptide fragment in HbA and GSHb, respectively. The spectra labeled as 0 and 360 min represent the data for 0% control and 100% control experiments, respectively.

GSHb, respectively. The numbers of fast exchanging amide hydrogens are 1.23 and 8.0 for peptides 1921.9 *m/z* and 2226.1 *m/z*, respectively (Table 1). Being a tripeptide, the glutathione moiety has two exchangeable peptide amide hydrogens. We assumed that these two amide hydrogens in GSHb were exposed to solvent molecules. Therefore, among the eight fast exchanging hydrogens in peptide 2226.1 *m/z*, two are contributed by the glutathione moiety. Hence, the number of fast exchanging peptide amide hydrogens for the peptide 1921.9 *m/z* changed from 1.2 to 6.0 upon glutathionylation. The increase in the number of fast exchanging hydrogens was compensated by a simultaneous decrease in the number of slow and intermediate exchanging hydrogens in peptide 2226.1 *m/z*. The average rate constants for all H/D exchange steps increased. The covalent binding of glutathione to HbA is expected to perturb the conformation of amino acid residues in the vicinity of βCys93. The large change in the fast exchanging peptide amide hydrogen number indicated that glutathionylation resulted in a significant change in solvent accessibility of those hydrogens in the β86−102 segment of hemoglobin. Craescu et al. reported that in GSHb the hydrogen bond between βAsp99 and αTyr42, which is a characteristic feature of deoxyhemoglobin in its $\alpha_1\beta_2$ interface, is destabilized and the salt bridge between βHis146 and βAsp94 is also perturbed.[11] Due to limitations in assigning HDX to a single amide linkage, it may be concluded that glutathionylation drives an increase in the solvent accessibility in the β86−102 region, which in turn suggests that the region became highly dynamic due to loss of localized tertiary and quaternary interactions.[19,20]

The peptic peptide fragment with *m/z* 1635.8 was found to be a β globin chain segment containing residues 115 to 129 with 12 exchangeable backbone amide hydrogens. Figure 5B shows the fitted curve of H/D exchange kinetics data for the peptic fragment 1635.8 *m/z*. The values of kinetic parameters as well as the number of differentially populated exchangeable amide hydrogens showed that glutathionylation caused an increase in rate constants for all exchange processes with a simultaneous increase in the number of exchangeable hydrogens for fast and intermediate exchanging groups (Table 1). The observed data clearly show that as a result of glutathionylation there is a substantial change in the solvent accessibility in this region of hemoglobin. Adachi et al. reported that βHis116 plays a crucial role in stabilizing $\alpha_1\beta_1$ interactions and inhibits hemoglobin oxidation.[21] Though structural change in this region of glutathionyl hemoglobin has not yet been reported, our H/D exchange data suggest that glutathionylation led to a significant structural change in this segment of the hemoglobin molecule resulting in the region being highly dynamic.

The sequence assignment of a peptide fragment with *m/z* 1585.8 indicated that it is an α globin chain fragment containing amino acid residues 34 to 46. This fragment has 10 exchangeable peptide amide hydrogens. Figure 5C shows fitted curves of isotope exchange kinetics data of 1585.8 for both HbA and GSHb. The fitted parameters indicated that the rate constant for slow exchanging amide hydrogens increased while that of intermediate exchange pattern decreased. The rate of fast exchange kinetics remained almost unaltered on glutathionylation. The number of fast exchanging hydrogens increased considerably,

dx.doi.org/10.1021/bc100602f |*Bioconjugate Chem.* 2011, 22, 785–793

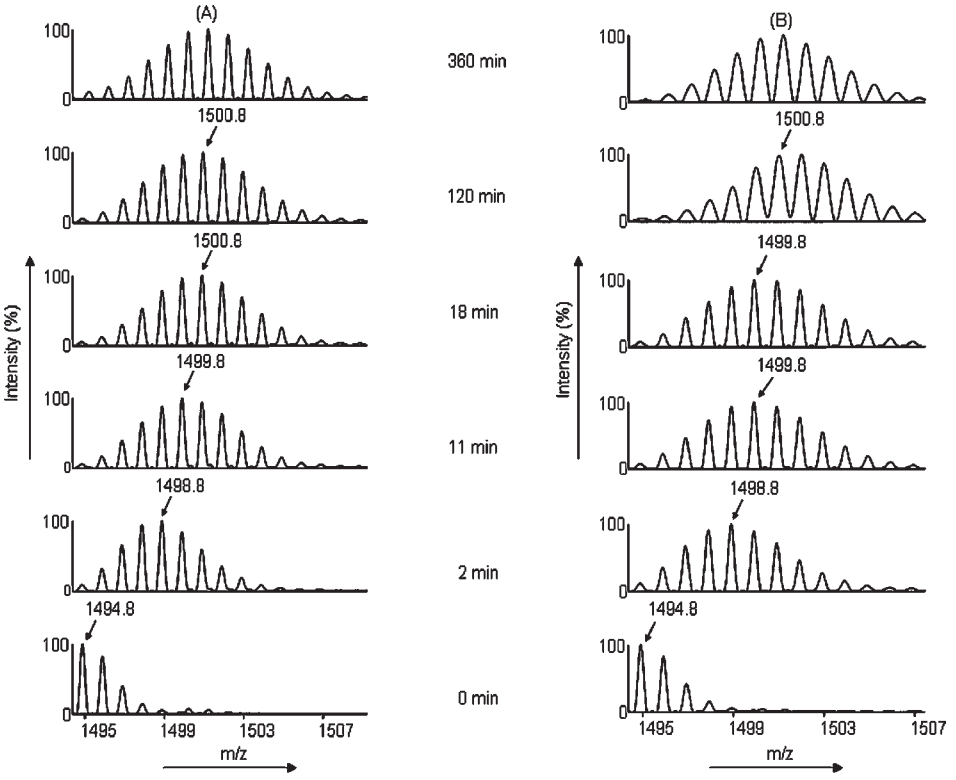


Figure 4. MALDI mass spectra for the peptide 1494.8 *m*/*z* obtained on hydrogen/deuterium exchange kinetics. Panels A and B represent the isotope exchange kinetics for the peptide fragment in HbA and GSHb, respectively. The spectra labeled as 0 and 360 min represent the data for 0% control and 100% control experiments, respectively.

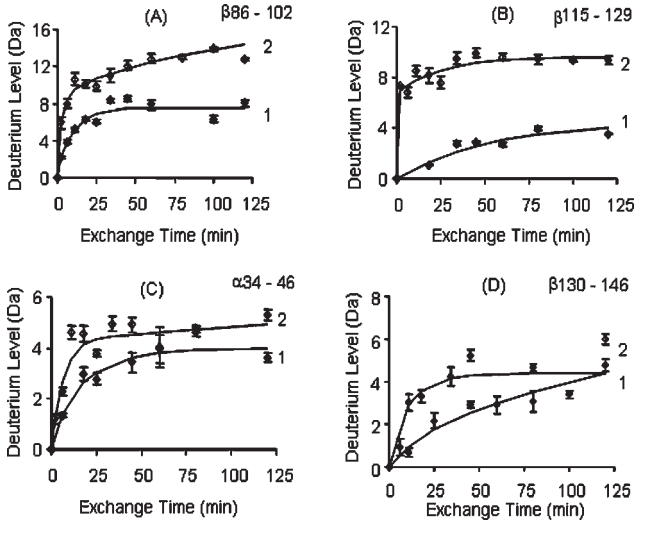


Figure 5. Representation of hydrogen/deuterium exchange kinetics of peptic peptides. The *Y*-axis is labeled with number of deuterium incorporated and *X*-axis with the corresponding exchange time. Trace 1 in each panel (filled diamond) represents the best fit curve of the exchange kinetics for the corresponding peptide obtained from native hemoglobin digestion, and trace 2 in each panel (hollow diamond) represents the same for the peptide obtained from glutathionyl hemoglobin digestion. Panel A represents peptide fragment 1921.9 *m*/*z* (*β*86−102). Panel B represents peptide fragment 1635.8 *m*/*z* (*β*115−129). Panel C represents peptide fragment 1585.8 *m*/*z* (α34−46). Panel D represents peptide fragment 1868.9 *m*/*z* (*β*130−146).

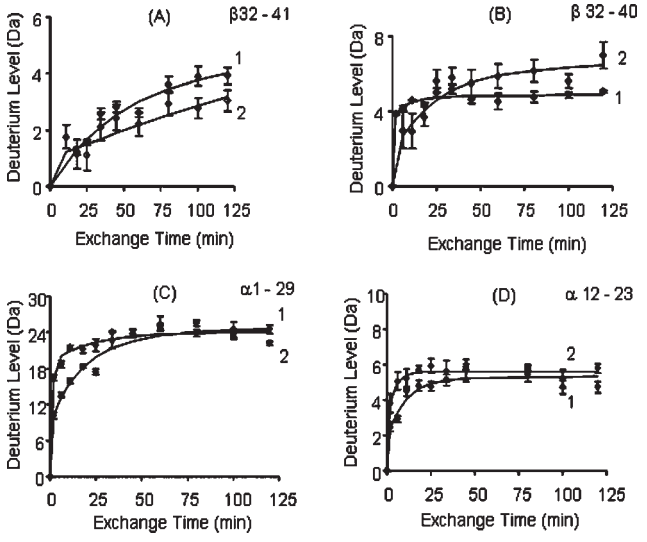


Figure 6. Representation of hydrogen/deuterium exchange kinetics of peptic peptides. The *Y*-axis is labeled with the number of deuterium incorporated and the *X*-axis with the corresponding exchange time. Trace 1 in each panel (filled diamond) represents the best fit curve of the exchange kinetics for the corresponding peptide obtained from native hemoglobin digestion, and trace 2 in each panel (hollow diamond) represents the same for the peptide obtained from glutathionyl hemoglobin digestion. Panel A represents peptide fragment 1308.6 *m*/*z* (*β*32−41). Panel B represents peptide fragment 1161.6 *m*/*z* (*β*32−40). Panel C represents peptide fragment 2910.4 *m*/*z* (α1−29). Panel D represents peptide fragment 1153.6 *m*/*z* (α12−23).

dx.doi.org/10.1021/bc100602f |*Bioconjugate Chem.* 2011, 22, 785–793

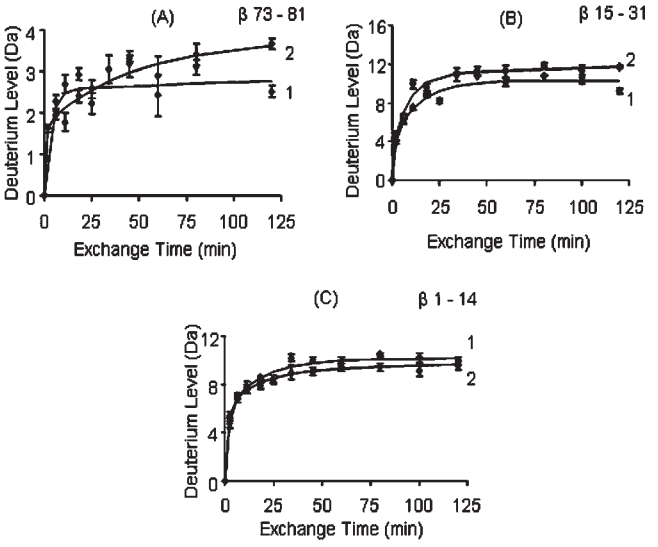


Figure 7. Representation of hydrogen/deuterium exchange kinetics of peptic peptides. The *Y*-axis is labeled with the number of deuterium incorporated and the *X*-axis with the corresponding exchange time. Trace 1 in each panel (filled diamond) represents the best fit curve of the exchange kinetics for the corresponding peptide obtained from native hemoglobin digestion, and trace 2 in each panel (hollow diamond) represents the same for the peptide obtained from glutathionyl hemoglobin digestion. Panel A represents peptide fragment 967.5 m/z (β73−81). Panel B represents peptide fragment 1798.9 m/z (β15−31). Panel 7C represents peptide fragment 1494.8 m/z (β1−14).

whereas the numbers for intermediate and slow exchanging hydrogens decreased. Though the change in the incorporation pattern of deuterium is not unidirectional, it suggests some conformational rearrangement in the vicinity of this peptide. The crystallographic data of deoxyhemoglobin showed that βHis97 was linked to αPro44 and αThr41.[22,23] Using nuclear magnetic resonance spectroscopy, it was reported that the three T-like inter subunit contacts are perturbed upon glutathionylation of hemoglobin. These are the carboxyl group of βHis146 and ε amino groups of αLys40, βHis97 and αPro44, βAsp99 and αTyr42.[11] Garel et al. concluded that glutathionylation leads to perturbation in conformation of four α globin residues αLys40, αThr41, αTyr42, and αPro44.[10] Thus, inter subunit contacts of many amino acid residues belonging to this peptide fragment undergo changes on glutathionylation of hemoglobin.

Sequence assignment of the peptide fragment with m/z 1868.9 confirmed that it was a β chain fragment spanning residues 130 to 146 with 16 exchangeable amide hydrogens. Figure 5D illustrates the best fit curve of H/D exchange kinetics of 1868.9 for both HbA and GSHb molecules. From the values of fitted parameters (Table 1), it is clear that glutathionylation caused an increase in the rate constant of amide hydrogens for fast and intermediate exchange kinetics, while that of slow exchanging hydrogens decreased. The number of fast and slow exchanging hydrogens increased, whereas that of intermediate exchange kinetics decreased on glutathionylation for this peptide fragment. One of the key features in localized structural perturbation of GSHb is the destabilization of the salt bridge between βHis146 and βAsp94.[11] βHis146 which contributes 40% to the alkaline Bohr effect in hemoglobin is the C-terminal most amino

Table 1. Total Numbers of Exchangeable Amide Hydrogens for Each Peptide Is Given by *N*, While *A*, *B*, and *C* Represent the Number of Fast, Intermediate, and Slow Exchangeable Hydrogens, Respectively[a]

peptide mass (m/z)	residues	N	molecule	k_1	k_2	k_3	A	B	C
1921.9[b]	β86−102	15	Hb A	1.5419	0.0893	0.000016	1.23	6.29	7.48
2226.1		17	GSHb	2.0260	0.2708	0.0093	8.00	5.49	3.51
1635.8	β115−129	12	HbA	0.0199	0.0013	4.15×10^{-6}	4.25	1.43	6.32
			GSHb	2.5822	0.0412	0.000014	6.72	2.83	2.45
1585.8	α34−46	10	HbA	0.1553	0.0456	0.00002	1.11	2.87	6.02
			GSHb	0.1561	0.0012	0.0010	4.27	2.39	3.34
1868.9	β130−146	16	HbA	0.0427	0.0018	0.0017	8.85	5.44	1.72
			GSHb	1.0977	0.0791	0.000028	11.63	0.95	3.41
1308.6	β 32−41	8	HbA	0.0235	0.0077	0.000014	2.99	2.01	3.00
			GSHb	1.2143	0.0035	0.0023	0.93	4.92	2.09
1161.6	β32−40	7	HbA	1.5538	0.1015	0.0004	3.83	0.97	2.20
			GSHb	1.1450	0.0449	0.0070	1.70	4.03	1.28
1153.6	α12−23	11	HbA	7.6775	0.0988	0.0002	1.77	3.44	5.79
			GSHb	1.0860	0.2015	0.000001	3.58	2.04	5.38
2910.4	α1−29	27	HbA	1.3112	0.0495	0.0019	9.44	14.53	3.02
			GSHb	0.8840	0.0448	0.0001	18.92	5.10	2.98
967.5	β73−81	8	HbA	0.2964	0.0011	0.0002	2.56	1.22	4.22
			GSHb	1.3012	0.0239	0.0004	1.67	1.87	4.46
1798.9	β15−31	16	HbA	0.7153	0.0723	0.0001	3.97	6.30	5.73
			GSHb	8.0783	0.1191	0.0014	2.85	8.09	5.07
1494.8	β1−14	12	HbA	0.6677	0.0552	0.0001	5.86	4.24	1.91
			GSHb	0.9349	0.0653	0.0022	5.83	3.11	3.05

[a] The corresponding rate constants are given by k_1, k_2, and k_3, respectively. [b] For the peptide 1921.9, after glutathionylation, the mass is 2226.1 and the number of exchangeable hydrogen is 17, taking into account two hydrogens from the glutathione moiety.

dx.doi.org/10.1021/bc100602f |*Bioconjugate Chem.* 2011, 22, 785–793

acid residue in the 1868.9 fragment.[24] Therefore, glutathione-mediated destabilization of deoxyhemoglobin might have made this region more dynamic such that the fast exchanging amide hydrogen displayed several-fold increase in its isotope exchange rate with a concomitant increase in its number.

One of the most intense peaks in the MS profile of pepsin digest was obtained at 1308.6 m/z. Sequence analysis identified it as a β chain fragment consisting of residues β32 to β41. The number of exchangeable backbone amide hydrogens is eight in this fragment. Figure 6A shows the best fitted curve of isotope exchange data for the fragment 1308.6 in both HbA and GSHb molecules. The analysis of H/D exchange data of this peptide indicates that on glutathionylation the fast and slow exchanging rate constants increased while that of the intermediate exchange process decreased. The number of differentially populated amide hydrogens got rearranged among the groups. In an earlier study, crystal structure data of deoxyhemoglobin showed that the αY42A mutation in hemoglobin caused destabilization of hydrogen bonds between αAsp94 and βTrp37.[25] NMR data also reported that glutathionylation leads to perturbation in interchain contact between αTyr42 and βAsp99.[11] Therefore, it is possible that glutathionylation causes weakening of the βTrp37-αAsp94 hydrogen bond that might have resulted in a small change in the solvent exposure of this segment of peptide. The peptide of m/z 1161.6 has the overlapping sequence with 1308.6, spanning residues β32 to β40. Figure 6B shows the best fitted curve of isotope exchange data for the fragment 1161.6 in both HbA and GSHb molecules. Analysis of H/D exchange data for the rate constants as well as the number of exchangeable hydrogens showed that the peptide followed the same trend as 1308.6, with the exception of fast exchange rates, which showed a slight decrease in the case of the 1161.6 peptic fragment.

Pepsin digestion of both hemoglobin and glutathionyl hemoglobin generated two overlapping peptide fragments from α subunit of the molecule, one with m/z 1153.6 which corresponds to residue spanning α12 to α23 and the other with m/z 2910.4 spanning residues α1 to α29. The numbers of exchangeable backbone peptide amide hydrogens are 11 and 27 for fragments 1153.6 and 2910.4, respectively. The deuterium exchange kinetics of peptide fragments 2910.4 and 1153.6 in both HbA and GSHb is shown in Figure 6C and D, respectively. From the values of best fitted parameters, it is clear that on glutathionylation the peptides 2910.4 exhibited a considerable increase in the number of fast exchanging amide hydrogens with a concomitant decrease in the intermediate and slow exchanging amide hydrogens. For the peptide fragment 1153.6 m/z, the same trend was observed. Information related to glutathionylation mediated structural change in this segment of hemoglobin is not yet reported. Our observed results for 2910.4 m/z indicate that this segment of hemoglobin has become more dynamic upon glutathionylation. The fragment 2910.4 m/z belongs to the N terminus of α globin chain, a region important for hemoglobin allostery.[26] The change in rate constants for both the peptides, 2910.4 and 1153.6, did not behave exactly in the same manner on modification. This is quite possible, as the peptide 2910.4 is extended in both N and C terminal ends compared to the peptide 1153.6. The difference in peptide length may also lead to significantly different subtotal solvent interaction.

Sequence assignment of the peptide fragment with m/z 967.5 confirmed that it was a β chain fragment spanning residues 73 to 81 with 8 exchangeable amide hydrogens in it. Figure 7A illustrates the best fit curve of H/D exchange kinetics data of the peptide 967.5 m/z for both HbA and GSHb molecules. The fitted parameters (Table-1) show that the rate constants increased for all kinetics step, while the number of intermediate and slow amide hydrogens increased and that of fast exchanging hydrogens decreased. There is no substantial structural perturbation in this peptide segment of the molecule. It is possible that while primary structural information shows this peptide is located in close proximity to the glutathione-binding site but the actual spatial orientation of this peptide segment may not be close enough to the modified site to get perturbed significantly. Unavailability of crystal structure of GSHb molecule makes the interpretation difficult. Moreover, backbone amides without any solvent accessibility in X-ray structures sometime show isotope exchange in solution. This might be due to the presence of small openings or mobile defects in the protein structure allowing diffusion of D_2O into the protein,[27,28] or local unfolding of protein structure or global unfolding mechanisms.[29−33]

The two other peptide fragments with m/z 1798.9 (β15−31) and 1494.8 (β1−14) showed small changes in both isotopic exchange rates and in the number of exchangeable amide hydrogens accompanying glutathionylation of hemoglobin (Figure 7B and C, respectively). Therefore, these regions of hemoglobin may be highly solvent shielded and/or have strong secondary and tertiary structures.

CONCLUSION

The primary goal of the study was to analyze the structural changes of hemoglobin on glutathionylation. The isotope exchange kinetics of peptide backbone amide hydrogen with deuterium, recorded in MALDI-MS, has been used to provide insights into the conformational rearrangements occurring in tetrameric hemoglobin. The novelty of the hydrogen−deuterium exchange method coupled with MALDI mass spectrometry lies in its simplicity and requirement of very small amount of protein, compared to other conventional techniques like NMR spectroscopy and X-ray crystallography. The technique could be immensely useful in extracting information in structural change on protein−ligand interaction, post-translational modification of protein, and protein folding−unfolding pathway. Our results clearly indicate structural rearrangement of hemoglobin molecule upon nonenzymatic post-translational modification of βCys93. The perturbation has been found to be delocalized on residues in the following segments of both the globin chains: α34−46, α1−29, β32−41, β86−102, β115−129, and β130−146. GSHb, a biomarker of oxidative stress under various diseased conditions, is a good model system to study structural perturbation associated with glutathionylation. Further study is required to correlate the structural changes and increased oxygen affinity of GSHb following H/D exchange in dynamic equilibrium between its oxy and deoxy forms and comparing it with that of normal hemoglobin.

AUTHOR INFORMATION

Corresponding Author

*Corresponding author address: Dr. Amit Kumar Mandal, Molecular Medicine & Clinical Proteomics, St. John's Research Institute, St. John's National Academy of Health Sciences, 100ft Road, Koramangala, Bangalore − 560034, India. Phone: +91-80-25532037. Fax: +91-80-25501088. E mail: amit@sjri.res.in.

Author Contributions

[†]The authors share equal contribution.

■ ACKNOWLEDGMENT

We acknowledge Nano Science Mission DST, Govt. of India, for providing mass spectrometry facility in St. John's Research Institute. We acknowledge all volunteers who provided samples in the study. We also acknowledge Dr. Anura V. Kurpad, Dean, St. John's Research Institute, for helping us in data analysis. This study was funded by Research Society of St. John's Medical College.

■ REFERENCES

(1) Birchmeier, W., Tuchshmid, P. E., and Winterhalter, K. H. (1973) Comparison of human hemoglobin A carrying glutathione as a mixed disulfide with the naturally occurring human hemoglobin A. *Biochemistry 12*, 3667–3672.

(2) Nonaka, K., Kume, N., Urata, Y., Seto, S., Kohno, T., Honda, S., Ikeda, S., Muroya, T., Ikeda, Y., Ihara, Y., Kita, T., and Kondo, T. (2007) Serum levels of S-glutathionylated proteins as a risk-marker for arteriosclerosis obliterans. *Circ. J. 71*, 100–105.

(3) Linetsky, M., and LeGrand, R. D. (2005) Glutathionylation of lens proteins through the formation of thioether bond. *Mol. Cell. Biochem. 272*, 133–144.

(4) Lou, M. F. (2003) Redox regulation in the lens. *Prog. Retin. Eye Res. 22*, 657–682.

(5) Lou, M. F. (2000) Thiol regulation in the lens. *J. Ocul. Pharmacol. Ther. 16*, 137–148.

(6) Newman, S. F., Sultana, R., Perluigi, M., Coccia, R., Cai, J., Pierce, W. M., Klein, J. B., Turner, D. M., and Butterfield, D. A. (2007) An increase in S-glutathionylated proteins in the Alzheimer's disease inferior parietal lobule, a proteomics approach. *J. Neurosci. Res. 85*, 1506–1514.

(7) Niwa, T., Naito, C., Mawjood, A. H. M., and Imai, K. (2000) Increased glutathionyl hemoglobin in diabetes mellitus and hyperlipidemia demonstrated by liquid chromatography/electrospray mass spectrometry. *Clin. Chem. 46*, 82–88.

(8) Piemonte, F., Pastore, A., Tozzi, G., Tagliacozzi, D., Santorelli, F. M., Carrozzo, R., Casali, C., Damiano, M., Federici, G., and Bertini, E. (2001) Glutathione in blood of patients with Friedreich's ataxia. *Eur. J. Clin. Invest. 31*, 1007–1011.

(9) Mandal, A. K., Woodi, M., Sood, V., Krishnaswamy, P. R., Rao, A., Ballal, S., and Balaram, P. (2007) Quantitation and characterization of glutathionyl haemoglobin as an oxidative stress marker in chronic renal failure by mass spectrometry. *Clin. Biochem. 40*, 986–994.

(10) Garel, M. C., Domenget, C., Caburi-Martin, J., Prehu, C., Galacteros, F., and Beuzard, Y. (1986) Covalent binding of glutathione to hemoglobin. I. Inhibition of hemoglobin S polymerization. *J. Biol. Chem. 261*, 14704–14709.

(11) Craescu, C. T., Poyart, C., Schaeffer, C., Garel, M. C., Kister, J., and Beuzard, Y. (1986) Covalent binding of glutathione to hemoglobin. II. Functional consequences and structural changes reflected in NMR spectra. *J. Biol. Chem. 261*, 14710–14716.

(12) Nazabal, A., and Schmitter, J. M. (2006) Hydrogen-deuterium exchange analyzed by matrix-assisted laser desorption-ionization mass spectrometry and the HET-s prion model. *Methods Enzymol. 413*, 167–181.

(13) Bai, Y., Milne, J. S., Mayne, L., and Englander, S. W. (1993) Primary structure effects on peptide group hydrogen exchange. *Proteins 17*, 75–86.

(14) Molday, R. S., Englander, S. W., and Kallen, R. G. (1972) Primary structure effects on peptide group hydrogen exchange. *Biochemistry 11*, 150–158.

(15) Proteins: Structures and Molecular Properties, in *Proteins in Solution and in Membranes*, 2nd ed. (Creighton, T. E., Ed.) p 282, Chapter 7, W. H. Freeman and Company, New York.

(16) Zhang, Z., and Smith, D. L. (1993) Determination of amide hydrogen exchange by mass spectrometry: A new tool for protein structure elucidation. *Protein Sci. 2*, 522–531.

(17) Hoofnagle, A. N., Resing, K. A., and Ahn, N. G. (2003) Protein analysis by hydrogen exchange mass spectrometry. *Annu. Rev. Biophys. Biomol. Struct. 32*, 1–25.

(18) Kemmer, G., and Keller, S. (2010) Nonlinear least-squares data fitting in Excel spreadsheets. *Nat. Protoc. 5*, 267–281.

(19) Wales, T. E., and Engen, J. R. (2006) Hydrogen exchange mass spectrometry for the analysis of protein dynamics. *Mass Spectrom. Rev. 25*, 158–170.

(20) Morgan, C. R., and Engen, J. R. (2009) Investigating solution-phase protein structure and dynamics by hydrogen exchange mass spectrometry. *Curr. Protoc. Protein Sci. 17*, 1–17.

(21) Adachi, K., Yang, Y., Lakka, V., Wehrli, S., Reddy, K. S., and Surrey, S. (2003) Significance of beta116 His (G18) at alpha1beta1 contact sites for alphabeta assembly and autoxidation of hemoglobin. *Biochemistry 42*, 10252–10259.

(22) Fermi, G. (1975) Three-dimensional fourier synthesis of human deoxyhaemoglobin at 2−5 A resolution: refinement of the atomic model. *J. Mol. Biol. 97*, 237–256.

(23) Bolton, W., and Perutz, M. F. (1970) Three dimensional fourier synthesis of horse deoxyhaemoglobin at 2.8 Angstrom units resolution. *Nature 228*, 551–552.

(24) Kilmartin, J. V., Breen, J. J., Roberts, G. C., and Ho, C. (1973) Direct measurement of the pK values of an alkaline Bohr group in human hemoglobin. *Proc. Natl. Acad. Sci. U.S.A. 70*, 1246–1249.

(25) Kavanaugh, J. S., Rogers, P. H., Arnone, A., Hui, H. L., Wierzba, A., DeYoung, A., Kwiatkowski, L. D., Noble, R. W., Juszczak, L. J., Peterson, E. S., and Friedman, J. M. (2005) Intersubunit interactions associated with Tyr42 alpha stabilize the quaternary-T tetramer but are not major quaternary constraints in Deoxyhemoglobin. *Biochemistry 44*, 3806–3820.

(26) Bai, Y., Englander, J. J., Mayne, L., Milne, J. S., and Englander, S. W. (1995) Thermodynamic parameters from hydrogen exchange measurements. *Methods Enzymol. 259*, 344–356.

(27) Lumry., R., and Rosenberg, A. (1975) The mobile defect hypothesis of protein function. *Col. Int. CNRS L'Eau. Syst. Biol. 246*, 55–63.

(28) Richards, F. M. (1979) Packing defects, cavities, volume fluctuations, and access to the interior of proteins. *Carlsberg Res. Comm. 44*, 47–63.

(29) Neira, J. L., Itzhaki, L. S., Otzen, D. E., Davis, B., and Fersht, A. R. (1997) Hydrogen exchange in chymotrypsin inhibitor 2 probed by mutagenesis. *J. Mol. Biol. 270*, 99–110.

(30) Bai, Y., Sosnick, T. R., Mayne, L., and Englander, S. W. (1995) Protein folding intermediates: native-state hydrogen exchange. *Science 269*, 192–197.

(31) Kragelund, B. B., Knudsen, J., and Poulsen, F. M. (1995) Local perturbations by ligand binding of hydrogen deuterium exchange kinetics in a four-helix bundle protein, acyl coenzyme A binding protein (ACBP). *J. Mol. Biol. 250*, 695–706.

(32) Arrington, C. B., and Robertson, A. D. (1997) Microsecond protein folding kinetics from native-state hydrogen exchange. *Biochemistry 36*, 8686–8691.

(33) Yi, Q., and Baker, D. (1996) Direct evidence for a two-state protein unfolding transition from hydrogen-deuterium exchange, mass spectrometry, and NMR. *Protein Sci. 5*, 1060–1066.

Bioconjugate Chemistry

ARTICLE

pubs.acs.org/bc

DNA Gold Nanoparticle Conjugates Incorporating Thiooxonucleosides: 7-Deaza-6-thio-2′-deoxyguanosine as Gold Surface Anchor

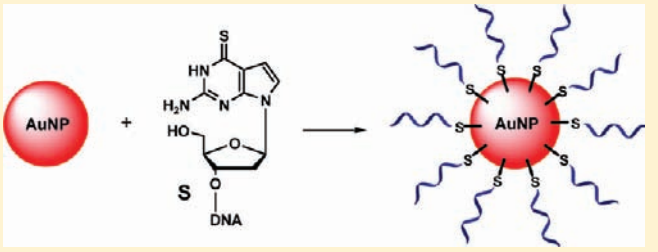
Frank Seela,*[,†,‡] Ping Ding,[†,‡] and Simone Budow[†]

[†]Laboratory of Bioorganic Chemistry and Chemical Biology, Center for Nanotechnology, Heisenbergstrasse 11, 48149 Münster, Germany

[‡]Laboratorium für Organische und Bioorganische Chemie, Institut für Chemie, Universität Osnabrück, Barbarastrasse 7, 49069 Osnabrück, Germany

Supporting Information

ABSTRACT: A new protocol for the covalent attachment of oligonucleotides to gold nanoparticles was developed. Base-modified nucleosides with thiooxo groups were acting as molecular surface anchor. Compared to already existing conjugation protocols, the new linker strategy simplifies the synthesis of DNA gold nanoparticle conjugates. The phosphoramidite of 7-deaza-6-thio-2′-deoxyguanosine (**6**) was used in solid-phase synthesis. Incorporation of the sulfur-containing nucleosides can be performed at any position of an oligonucleotide; even multiple incorporations are feasible, which will increase the binding stability of the corresponding oligonucleotides to the gold nanoparticles. Oligonucleotide strands immobilized at the end of a chain were easily accessible during hybridization leading to DNA gold nanoparticle network formation. On the contrary, oligonucleotides immobilized *via* a central position could not form a DNA-AuNP network. Melting studies of the DNA gold nanoparticle assemblies revealed sharp melting profiles with a very narrow melting transition.



INTRODUCTION

DNA guided assemblies of metal nanoparticles have great potential for advanced material applications, in biomedical sciences, and as diagnostics tools.[1,2] DNA nanoparticle conjugates have been employed in nucleic acid detection and labeling and were utilized as barcodes, biosensors, or carriers for the delivery of DNA.[1−6] Additionally, they can be used for the bottom-up assembly of nanoarchitectures.[7,8] Among the accessible metal nanoparticles, gold nanoparticles (AuNPs) gained particular attention due to their chemical inertness and the ease of surface modification.[1,9,10] DNA gold nanoparticle (DNA-AuNP) conjugates combine the favorable properties of gold colloids with those of DNA. A number of key advantages for using the DNA molecule as a "construction material" are (i) its unique molecular recognition properties, (ii) its easy access by automated DNA synthesis or enzymatic polymerization, and (iii) its self-assembly capacities to form multistranded aggregates allowing the construction of DNA-based nanoscaled devices.[7,11]

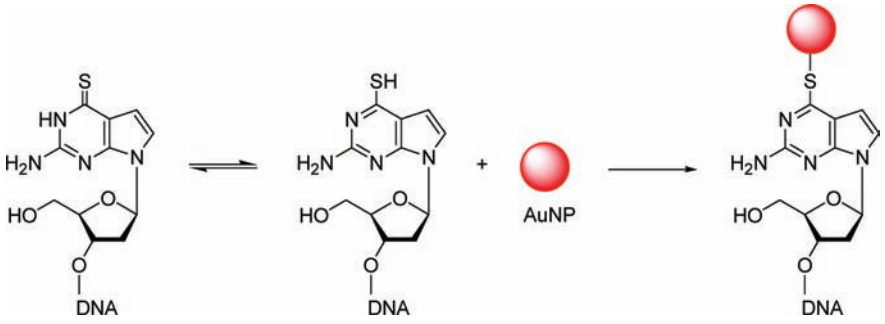
To meet the above-mentioned applications, the conjugates must be stable in aqueous buffer systems, even at elevated temperature. For this, several strategies were developed for preparing DNA-AuNP conjugates.[12−15] The common protocol employs oligonucleotides with 3′ or 5′-terminal thiol groups introduced by linker units. The covalent attachment to AuNPs proceeds *via* the thiol functionality thereby making use of its strong affinity to the noble metal gold. There is still a controversial discussion on the mechanism of immobilization. However, an X-ray structure of a thiol monolayer protected gold nanoparticle has been reported recently.[16] Further developments in the field of DNA-AuNPs include the incorporation of sulfur functionalities into the oligonucleotide chain as an alternative to the conventional alkylthiol linker.[17,18] Phosphorothioate-modified DNA was utilized for gold nanoparticle conjugation either by directly coupling the DNA backbone to AuNPs[19] or by using a short linker molecule connecting the DNA backbone and the AuNPs.[20]

It is worth mentioning that tRNAs contain a large diversity of modified nucleosides;[21] a few of them bear thio functions at the nucleobase. Examples are 2-thiouridine, 4-thiouridine, or 2-thiocytidine including derivatives with various substituents in the 5-position. Nucleosides with thiooxo groups have already been incorporated into artificial DNA, either chemically or by polymerases.[22−25] Consequently, we initiated a study to use these naturally occurring modification sites for oligonucleotide immobilization on gold nanoparticles.

Received: February 3, 2011
Revised: March 8, 2011
Published: March 28, 2011

ACS Publications © 2011 American Chemical Society

Scheme 1. Reaction Route for the Formation of Oligonucleotide AuNP Conjugates with Thionucleoside 1 as Anchor Molecule and Proposed Conjugate Structure



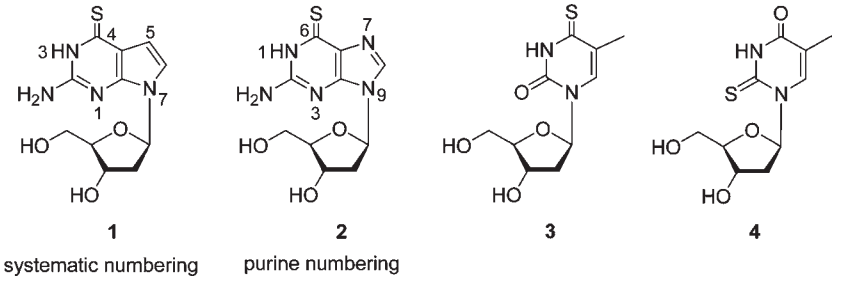


Figure 1. Thionucleosides **1**−**4** employed in this study.

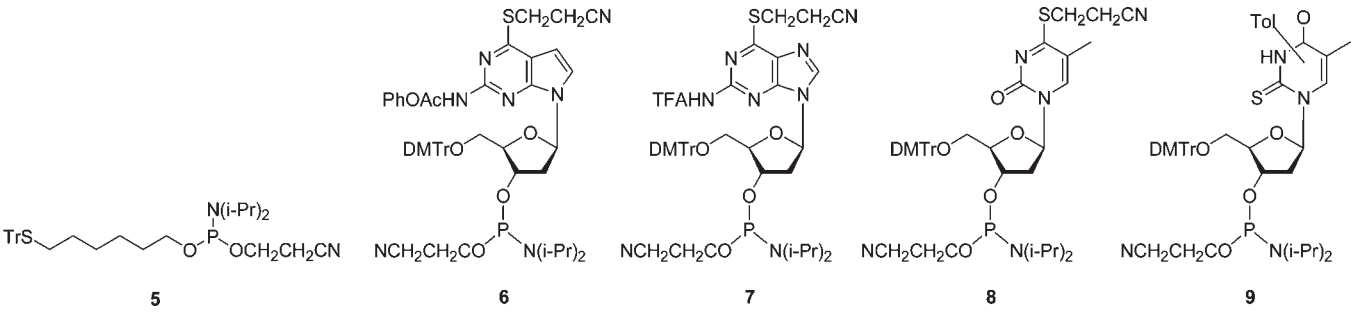


Figure 2. Phosphoramidite building blocks of the hexylthiol linker and the thionucleosides employed for oligonucleotide synthesis.

Herein, we report on a new strategy for conjugation of DNA with gold nanoparticles. In a first step, oligonucleotides are synthesized bearing a thiooxo function ("thio" anchor) at the nucleobase; in a second step, these oligonucleotides are directly attached to the gold surface without prior sulfur protection (Scheme 1). From that background, we selected the four nucleosides 7-deaza-6-thio-2′-deoxyguanosine (**1**), 6-thio-2′-deoxyguanosine (**2**), 4-thio-2′-deoxythymidine (**3**), and 2-thio-2′-deoxythymidine (**4**) for our study as shown in Figure 1. They were introduced into oligonucleotides *via* phosphoramidite chemistry to become an integer part of single-stranded oligonucleotides.

The thiooxo group was utilized as a molecular anchor to gold nanoparticles. First, the stability of the different thiooxonucleosides toward the conditions of solid-phase oligonucleotide synthesis was investigated, and conjugation to the gold surface was tested. Hybridization experiments employing DNA gold nanoparticle conjugates proved the formation of stable DNA-AuNP hybrids with thionucleosides, similar to those linked by conventional protocols.

EXPERIMENTAL PROCEDURES

General Methods and Materials. All chemicals were purchased from Acros, Aldrich, Sigma, or Fluka. The 5′-alkylthiol modifier 6-(triphenylmethyl)-S-$(CH_2)_6$-*O*-2-cyanoethyl diisopropylphosphoramidite (**5**) and phosphoramidites **7**−**9** were obtained from Glen Research (Virginia, USA) (Figure 2). 4-*tert*-Butylphenoxyacetyl protected canonical phosphoramidites were purchased from Millipore (Massachusetts, USA). Solvents were of laboratory grade. Thin-layer chromatography (TLC) was performed on TLC aluminum sheets covered with silica gel 60 F254 (0.2 mm, VWR International, Germany). Flash column chromatography (FC): silica gel 60 (VWR International, Darmstadt, Germany) at 0.4 bar; UV-spectra were recorded on a U-3000 spectrophotometer (Hitachi, Japan); λ_{max} (ε) in nm,

dx.doi.org/10.1021/bc200069j |*Bioconjugate Chem.* 2011, 22, 794–807

ε in $dm^3\ mol^{-1}\ cm^{-1}$. NMR spectra: DPX 300 spectrometer (Bruker, Germany) at 300 MHz for ^1H, 75 MHz for ^{13}C and 121.5 MHz for ^{31}P. The J values are given in Hz; δ values in ppm relative to Me_4Si as internal standard, or 85% H_3PO_4 for ^{31}P. For NMR spectra recorded in DMSO, the chemical shift of the solvent peak was set to 2.50 ppm for ^1H NMR and 39.50 ppm for ^{13}C NMR. Elemental analyses were performed by the Mikroanalytisches Laboratorium Beller, Göttingen, Germany. MALDI-TOF mass spectra were recorded in the linear negative mode with an Applied Biosystems Voyager DE PRO spectrometer with 3-hydroxypicolinic acid (3-HPA) as a matrix. Reversed-phase HPLC was carried out on a 4 × 250 mm RP-18 (10 mm) LiChrospher 100 column (VWR International) with a Merck-Hitachi HPLC pump (model L-6250) connected with a variable wavelength monitor (model 655-A), a controller (model L-500), and an integrator (model D-2500). Melting curves were measured with a Cary-100 Bio UV−vis spectrophotometer (Varian, Australia) equipped with a Cary thermoelectrical controller with a heating rate of 1 °C/min. The T_m values were calculated by *Meltwin 3.0* program. Nanopure water (resistance <0.055 μS/cm) from MembraPure water system (Astacus) was used for all experiments.

*7-(2-Deoxy-β-D-erythro-pentofuranosyl)-2-phenoxyacetamino-7H-pyrrolo[2,3-d]pyrimidin-4(3H)-thione (**10**).* Compound **1**[26] (1.6 g, 5.50 mmol) was dried by repeated coevaporation with anhydrous pyridine (3 × 5 mL), then suspended in pyridine (5 mL). To this solution, trimethylsilyl chloride (3.6 mL, 28.17 mmol) was added at room temperature. After 1 h, phenoxyacetyl chloride (1.1 mL, 7.96 mmol) was introduced, and the solution was stirred at room temperature for another 4 h. The mixture was cooled to 0 °C, diluted with H_2O (5 mL), and stirred for 10 min. Then, aq. ammonia (5 mL) was added, and the solution was stirred for an additional 15 min. The solvent was evaporated to dryness. Purification by FC (silica gel, column 8 × 15 cm, CH_2Cl_2/MeOH, 50:1→25:1) gave **10** as a colorless foam (1.9 g, 81%); mp 205 °C. TLC (CH_2Cl_2/MeOH, 9:1): R_f 0.53. UV λ_{max} (MeOH)/nm 333 (ε/$dm^3\ mol^{-1}\ cm^{-1}$ 47 600). Anal. ($C_{19}H_{20}N_4O_5S$) C, H, N. ^1H NMR (300 MHz, DMSO-d_6): δ = 2.15−2.23 (m, 1H, H_α-2′), 2.38−2.47 (m, 1H, H_β-2′), 3.51−3.54 (m, 2H, H-5′), 3.81−3.84 (m, 1H, H-4′), 4.33−4.36 (m, 1H, H-3′), 4.88 (s, 2H, Pac-CH_2), 4.95 (t, J = 5.3 Hz, 1H, HO-5′), 5.30 (d, J = 3.6 Hz, 1H, HO-3′), 6.41 (m, 1H, H-1′), 6.64 (d, J = 3.7 Hz, 1H, H-5), 6.96−7.01 (m, 3H, phenoxy), 7.29−7.34 (m, 2H, phenoxy), 7.49 (d, J = 3.7 Hz, 1H, H-6), 11.99 (br s, 1H, N−H), 12.89 (br s, 1H, CO-NH).

*4-[(2-Cyanoethyl)thio]-7-(2-deoxy-β-D-erythro-pentofuranosyl)-2-phenoxyacetamino-7H-pyrrolo[2,3-d]pyrimidine (**11**).* 3-Bromopropionitrile (4.0 mL, 48.07 mmol) and anhydrous K_2CO_3 (3.0 g, 21.71 mmol) were added to 25 mL dry DMF and the mixture was stirred vigorously. Compound **10** (1.9 g, 4.45 mmol) was dissolved in 5 mL dry DMF and added dropwise to the stirred solution within 30 min. The reaction mixture was stirred overnight until completion of the reaction (monitored by TLC). The solvent was removed by coevaporation with xylene and the residue was applied to FC (silica gel, column 8 × 15 cm, CH_2Cl_2/MeOH, 500:1→100:1). The main zone yielded **11** as a colorless solid (1.2 g, 55%). TLC (CH_2Cl_2/MeOH, 95:5): R_f 0.22. UV λ_{max} (MeOH)/nm 301 (ε/$dm^3\ mol^{-1}\ cm^{-1}$ 26 700), 244 (73 300). Anal. ($C_{22}H_{23}N_5O_5S$) C, H, N. ^1H NMR (300 MHz, DMSO-d_6): δ = 2.18−2.25 (m, 1H, H_α-2′), 2.50 (m, 1H, H_β-2′), 3.16 (t, 2H, CH_2−CN), 3.51−3.56 (m, 4H, H-5′, H-5″, CH_2−S), 3.84−3.85 (m, 1H, H-4′), 4.36−4.37 (m, 1H, H-3′), 4.94 (t, J = 5.4 Hz, 1H, HO-5′), 5.00 (s, 2H, Pac-CH_2), 5.32 (d, J = 5.3 Hz, 1H, HO-3′), 6.54−6.59 (m, 2H, H-5, H-1′), 6.93−6.98 (m, 3H, phenoxy), 7.28−7.33 (m, 2H, phenoxy), 7.65 (d, J = 3.9 Hz, 1H, H-6), 10.69 (s, 1H, CO-NH).

*4-[(2-Cyanoethyl)thio]-7-[2-deoxy-5-O-(4,4′-dimethoxytrityl)-β-D-erythro-pentofuranosyl]-2-phenoxyacetamino-7H-pyrrolo[2,3-d]pyrimidine (**12**).* Compound **11** (469.5 mg, 1.00 mmol) was coevaporated with anhydrous pyridine (3 × 5.0 mL) and then dissolved in pyridine (5.0 mL). To this solution, 4,4′-dimethoxytriphenylmethyl chloride (440.5 mg, 1.30 mmol) was added and the mixture was stirred at r.t. for 3 h. The reaction was quenched by the addition of MeOH and the mixture was evaporated to dryness. The mixture was subjected to FC (column 4 × 10 cm, elution with CH_2Cl_2/acetone, 20:1) to give **12** as a colorless foam (555.8 mg, 72%). TLC (CH_2Cl_2/MeOH, 95:5): R_f 0.61. UV λ_{max} (MeOH)/nm 302 (ε/$dm^3\ mol^{-1}\ cm^{-1}$ 14 400), 240 (53 500). Anal. ($C_{43}H_{41}N_5O_7S$) C, H, N. ^1H NMR (300 MHz, DMSO-d_6): δ = 2.27−2.31 (m, 1H, H_α-2′), 2.55−2.64 (m, 1H, H_β-2′), 3.13−3.17 (m, 4H, CH_2−CN, H-5′, H-5″), 3.52−3.56 (m, 2H, CH_2−S), 3.71 (s, 6H, OCH_3), 3.95 (m, 1H, H-4′), 4.37 (m, 1H, H-3′), 5.00 (s, 2H, Pac-CH_2), 5.37 (d, J = 4.2 Hz, 1H, HO-3′), 6.52−6.56 (m, 2H, H-5, H-1′), 6.78−7.35 (m, 18H, phenoxy), 7.46 (d, J = 3.6 Hz, 1H, H-6), 10.69 (s, 1H, CO-NH).

*4-[(2-Cyanoethyl)thio]-7-[2-deoxy-5-O-(4,4′-dimethoxytrityl)-β-D-erythro-pentofuranosyl]-2-phenoxyacetamino-7H-pyrrolo-[2,3-d]pyrimidine 3′-[(2-cyanoethyl)-N,N-diisopropylphosphoramidite] (**6**).* Compound **12** (555.8 mg, 0.72 mmol) was dissolved in anhydrous CH_2Cl_2 (3.0 mL) under argon and was reacted with (2-cyanoethyl)diisopropylphosphoramido chloridite (225 μL, 0.95 mmol) in the presence of $^iPr_2EtN$ (220 μL, 1.27 mmol) at room temperature. After 20 min, the reaction mixture was diluted with CH_2Cl_2 and the solution was washed with a 5% aqueous $NaHCO_3$ solution, followed by brine. The organic solution was dried over anhydrous Na_2SO_4, filtered, and concentrated. The residue was subjected to FC (column 4 × 10 cm, CH_2Cl_2/acetone, 25:1) yielding **6** as a colorless foam (429.1 mg, 61%). TLC (CH_2Cl_2/acetone, 95:5): R_f 0.64. ^{31}P NMR (121.5 MHz, $CDCl_3$): δ = 148.56; 148.69.

Hydrolytic Stability of Thiooxonucleosides. The hydrolytic stability of thiooxonucleosides **1**−**4** and **11** under standard deprotection conditions (25% aqueous NH_3, 14−16 h, 60 °C) was monitored by reversed-phase HPLC (RP-18, 250 × 4 mm). Nucleosides **1**−**4** and **11** (about 1 mg) were dissolved in 1 mL of 25% aq. ammonia in a sealed vessel and incubated at 60 °C. After 16 h incubation, aq. ammonia was removed by evaporation and the residue was redissolved in 1 mL HPLC buffer A. 50 μL aliquots of each sample were injected into the HPLC, and the spectra were recorded at 260 nm (for spectra see Supporting Information).

Synthesis, Purification, and Characterization of Oligonucleotides. The syntheses of oligonucleotides were performed on a DNA synthesizer, model 392−08 (Applied Biosystems, Weiterstadt, Germany) at 1 μmol scale. For oligonucleotides containing 7-deaza-6-thio-2′-deoxyguanosine (**1**), 2-thio-2′-deoxythymidine (**4**), or the hexylthiol linker, the corresponding phosphoramidites **5**, **6**, and **9** were used, and the standard synthesis protocol for 3′-(2-cyanoethyl phosphoramidites) was followed.[27] The average coupling yield was always higher than 95%. Oligonucleotides containing the hexylthiol linker, **1** or **4**, were cleaved from solid support with 25% aq. NH_3 and

deprotected for 14−16 h at 60 °C (standard deprotection conditions). Oligonucleotides containing 6-thio-2′-deoxyguanosine (**2**) and 4-thio-2′-deoxythmidine (**3**) were prepared using the corresponding phosphoramidites **7** and **8**, and reagents required for the fast deprotection procedure.[28] For that, 4-*tert*-butylphenoxyacetyl protected canonical phosphoramidites and the capping reagent 4-*tert*-butylphenoxyacetic anhydride instead of acetic anhydride were used. The coupling efficiency was always higher than 95%. Oligonucleotides incorporating **2** or **3** were cleaved from solid support and deprotected in 25% aq. NH_3 solution containing 50 mM NaSH at room temperature overnight (recommended conditions of the supplier). The DMT-containing oligonucleotides were purified on reversed-phase HPLC in the DMT-on modus (Merck-Hitachi-HPLC; RP-18 column) with the following gradient system [A: 0.1 M $(Et_3NH)OAc$ (pH 7.0)/MeCN 95:5; B: MeCN]: 3 min, 20% B in A, 12 min, 20−50% B in A and 25 min, 20% B in A, flow rate 1.0 mL/min. The solvent was evaporated, and the residue was treated with 2.5% $CHCl_2COOH/CH_2Cl_2$ (400 μL) for 5 min at 0 °C to remove the 4,4′-dimethoxytrityl residue. The detritylated oligomers were purified again by reversed-phase HPLC [gradient: 0−20 min 0−20% B in A; flow rate 1 mL/min]. The oligomers were desalted on a short column (RP-18, silica gel) using H_2O for elution of the salt, while the oligomers were eluted with MeOH/H_2O (3:2). The oligonucleotides were lyophilized on a Speed-Vac evaporator to yield colorless solids which were frozen at −24 °C. The 5′-alkylthiol-modified oligonucleotides 5′-d(trityl-S-$(CH_2)_6$-T_{10}-TAG GTC AAT ACT) (**40**) and 5′-d(trityl-S-$(CH_2)_6$-T_{10}-AGT ATT GAC CTA) (**41**) were only purified in the DMT-on modus by reversed-phase HPLC (RP-18) as described above.

The enzymatic hydrolysis of the oligonucleotides was performed as described[29] with snake venom phosphodiesterase (EC 3.1.15.1, *Crotallus adamanteus*) and alkaline phosphatase (EC 3.1.3.1, *Escherichia coli* from Roche Diagnostics GmbH, Germany) in 0.1 M Tris-HCl buffer (pH 8.3) at 37 °C. The hydrolysis product was analyzed by reversed-phase HPLC (RP-18). Quantification of the constituents was made on the basis of the peak areas, which were divided by the extinction coefficients ε_{260} of the nucleosides: dA 15400, dC 7300, dG 11700, dT 8800, 7-deaza-6-thio-2′-deoxyguanosine (**1**) 10100, 6-thio-2′-deoxyguanosine (**2**) 7300, 4-thio-2′-deoxythymidine (**3**) 1500. MALDI-TOF mass spectra were recorded in the linear negative mode with an Applied Biosystems Voyager DE PRO spectrometer with 3-hydroxypicolinic acid (3-HPA) as a matrix. The detected masses were identical with the calculated values (see Supporting Information).

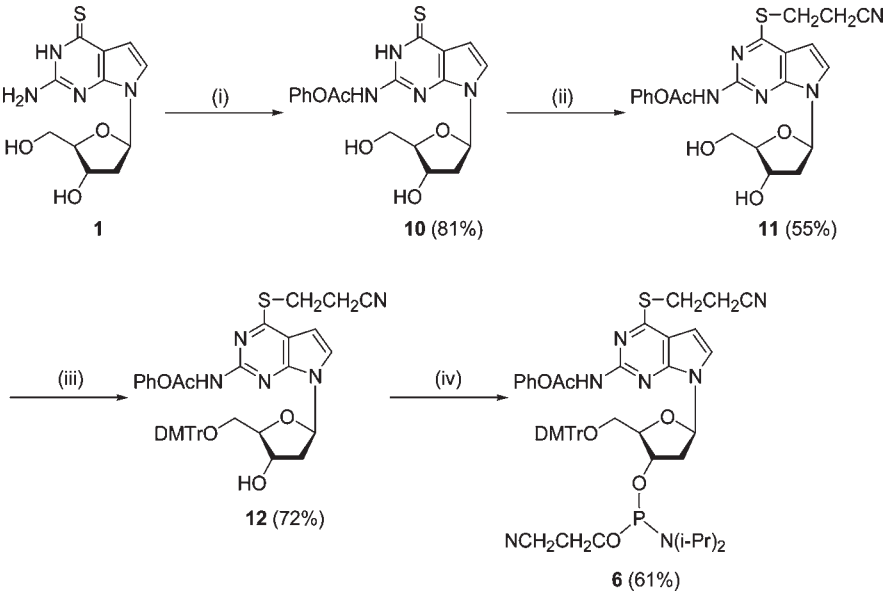
General Procedure for the Preparation of Oligonucleotide Gold Nanoparticle Conjugates Employing Thiooxonucleosides as Molecular Anchor. The gold nanoparticle solution (15 nm particle diameter) was prepared from a $HAuCl_4$ solution by citrate reduction according to the protocol originally reported by Turkevitch[30] and later described by Letsinger and Mirkin.[13] The nanoparticle concentration was determined by UV/vis using $\varepsilon_{520} = 4.2 \times 10^8\ M^{-1}\ cm^{-1}$ (UV/vis_{max}: 520 nm).[31] The gold nanoparticles (~3 nM) were functionalized with oligonucleotides **18**−**29** and **36**−**39** containing thiooxonucleosides **1**−**4** at different positions within their sequences. The DNA-AuNP conjugates **Au18**-**Au29** and **Au36**-**Au39** were prepared by mixing 1 mL of the respective AuNP solution with the aq. solution of the purified oligonucleotide (1−5 μL) to yield a final oligonucleotide concentration of 3 μM. The coupling reaction was performed at slightly elevated temperature (40 °C). After standing for 20 h, 5 μL of a 2 M NaCl, 0.2 mM phosphate buffer solution (pH 7.0) was added under constant stirring to bring the colloidal solutions to a 0.01 M NaCl concentration. The solution was allowed to stand for 6−8 h. The NaCl concentration was increased stepwise using 2 M NaCl and 0.2 mM phosphate buffer solution (pH 7.0). First, the colloids were salted to 0.02 M NaCl and allowed to age for another 6−8 h, then salted to 0.05 M NaCl with 6−8 h of incubation, and were finally salted to 0.1 M NaCl. Subsequently, the DNA gold nanoparticle solutions were centrifuged (8000 rpm, 45 min) and the clear supernatant was taken off to remove unbound oligonucleotides. The precipitate was redispersed in 1 mL of a 0.1 M NaCl, 10 mM phosphate buffer solution (pH 7.0). After incubation (24 h, 40 °C), the conjugate solutions were centrifuged and washed again with the same buffer, finally yielding 1 mL of the DNA-AuNP conjugates **Au18**-**Au29** and **Au36**-**Au39** (Table 1). The DNA-AuNP conjugates were characterized by UV/vis spectroscopy and stored at 4 °C.

Table 1. Gold Nanoparticle Conjugates Immobilizing an Arbitrary Number of Oligonucleotides and the Maximum of VIS Absorption[a]

Oligonucleotide Gold Nanoparticle Conjugates	Max. VIS Absorption [nm]
5′-d(1 T_{10} TAG GTC AAT ACT) (**Au18**)	524
5′-d(1 T_{10} AGT ATT GAC CTA) (**Au19**)	524
5′-d(2 T_{10} TAG GTC AAT ACT) (**Au20**)	524
5′-d(2 T_{10} AGT ATT GAC CTA) (**Au21**)	524
5′-d(3 T_{10} TAG GTC AAT ACT) (**Au22**)	524
5′-d(3 T_{10} AGT ATT GAC CTA) (**Au23**)	524
5′-d(4 T_{10} TAG GTC AAT ACT) (**Au24**)	524
5′-d(4 T_{10} AGT ATT GAC CTA) (**Au25**)	524
5′-d(11 T_{10} AGT ATT GAC CTA) (**Au26**)	526
5′-d(11 T_{10} AGT ATT GAC CTA) (**Au27**)	526
5′-d(111 T_{10} TAG GTC AAT ACT) (**Au28**)	526
5′-d(111 T_{10} AGT ATT GAC CTA) (**Au29**)	525
5′-d(TA1 GTC AAT ACT TAG GTC AAT ACT) (**Au36**)	526
5′-d(A1T ATT GAC CTA AGT ATT GAC CTA) (**Au37**)	525
5′-d(TAG GTC AAT ACT TA1 GTC AAT ACT) (**Au38**)	524
5′-d(AGT ATT GAC CTA A1T ATT GAC CTA) (**Au39**)	525
5′-d(S-$(CH_2)_6$-T_{10} TAG GTC AAT ACT) (**Au40**)	523
5′-d(S-$(CH_2)_6$-T_{10} AGT ATT GAC CTA) (**Au41**)	523

[a] Spacer T_{10} = 5′-d(TTT TTT TTT T).

Scheme 2. Synthesis of Phosphoramidite Building Block 6[a]



[a] Reagents and conditions: (i) Me_3SiCl, phenoxyacetyl chloride, pyridine, aq. NH_3, 4 h, r.t.; (ii) 3-bromopropionitrile, anh. K_2CO_3, DMF, overnight, r.t.; (iii) DMTr-Cl, pyridine, 3 h, r.t.; (iv) (2-cyanoethyl)diisopropylphosphoramido chloridite, *N,N*-diisopropylethylamine, anh. CH_2Cl_2, 20 min, r.t.

All conjugates show plasmon resonance at around 524 nm indicating a nonaggregated state (Table 1 and Supporting Information).

Preparation of DNA-AuNP Conjugates Employing the Hexylthiol Linker As Anchoring Site. DNA-AuNPs employing oligonucleotides with terminal alkylthiol linkers were prepared by a protocol reported previously.[13,32] The DNA-AuNP conjugates **Au40** and **Au41** were characterized by UV/vis spectroscopy showing plasmon resonance at 523 nm which is correlated to a nonaggregated state (for spectra, see Figure S2, Supporting Information).

Scanning Electron Microscopy (SEM). A typical sample was prepared by dropping a DNA-AuNP conjugate into a silicon wafer which was then subsequently dried and imaged.

RESULTS AND DISCUSSION

The conventional protocol for the attachment of oligonucleotides onto gold nanoparticle surfaces makes use of oligonucleotides modified at their 5′- or 3′-termini by an alkylthiol linker.[5,12−14,32−34] However, this protocol is laborious and accompanied by drawbacks to form SH-modified oligonucleotides ready for immobilization. This includes (i) the detritylation of the protected thiol-group with silver nitrate, (ii) removal of excess silver nitrate and (iii) desalting of the free thiol-modified oligonucleotides. Furthermore, the immobilization of the reactive oligonucleotides to the gold nanoparticles has to be performed shortly after preparation to reduce unwanted side reactions (e.g., disulfide formation). Moreover, silver ions or metallic silver which can bind to both oligonucleotides and gold nanoparticles are difficult to remove quantitatively.

In this study, we made use of the sulfur atom of thiooxonucleosides to conjugate oligonucleotides to gold nanoparticles. The sulfur atom of these nucleosides is expected to bind to the gold surface *via* the thiooxo group or the corresponding mercapto group. Recently, the triphosphate of 4-thio-2′-deoxythymidine was incorporated enzymatically into DNA, and the sulfur functionality was used to attach the DNA oligonucleotides to gold electrodes.[35,36] For our study, we selected the thiooxonucleosides **1**−**4** for incorporation into oligonucleotides *via* phosphoramidite chemistry. In this respect, the stability of **1**−**4** against nucleophilic sulfur displacement under alkaline deprotection conditions was investigated. Thiooxonucleosides **1**−**4** were used as a molecular anchor to the gold nanoparticle surface and their capability to form DNA-AuNPs was evaluated.

Building Block Synthesis. The phosphoramidites **5**−**9** were selected for oligonucleotide syntheses (Figure 2). Compounds **5** and **7**−**9** are commercially available, while phosphoramidite **6** has to be synthesized using nucleoside **1** as starting material.[26]

For the protection of the amino group, the phenoxyacetyl residue[37] was chosen, and the protocol of transient protection (→ **10**, 81% yield) was used (Scheme 2). The thiooxo function was protected with the cyanoethyl group (→ **11**, 55% yield) as described for the parent purine compound **2**.[38] The protected intermediate **11** was converted into the 5′-*O*-DMT derivative **12** under standard conditions. Phosphitylation with 2-cyanoethyl-*N,N* diisopropyl-phosphoramidochloridite furnished the phosphoramidite **6** (61% yield, Scheme 2).

All compounds were characterized by UV-spectra and ^{1}H- and ^{13}C NMR spectra as well as by elemental analysis (Table 2 and Experimental Procedures section). The assignments of ^{13}C NMR chemical shifts of the sugar moiety and the protecting groups were made on the basis of ^{1}H−^{13}C gated-decoupled spectra (for more data, see Supporting Information) in combination with already published data.[38] For 7-deaza-6-thio-2′-deoxyguanosine (**1**), the chemical shifts for C2 and C6 were only assigned tentatively.[38] Therefore, now we used the deuterium isotope upfield shift approach to assign the carbon-2 signal,[39,40] which is directly connected with the amino group. In a DMSO solution, containing a H_2O/D_2O mixture, the carbon-2 signal is split into two singlets (Figure S6, Supporting Information): the original one and one which is shifted 0.04 ppm upfield. Consequently, C2 was assigned to the 152.2 ppm signal and C6 to the 175.7 ppm signal (Table 2).

dx.doi.org/10.1021/bc200069j |*Bioconjugate Chem.* 2011, 22, 794–807

Table 2. ^{13}C-NMR Chemical Shifts (δ) of 7-Deaza-6-thio-2′-deoxyguanosine Derivatives[a]

	C(2)[b]	C(4)[b]	C(4a)[b]	C(5)[b]	C(6)[b]	C(7a)[b]					
compd	C(2)[c]	C(6)[c]	C(5)[c]	C(7)[c]	C(8)[c]	C(4)[c]	C(1′)	C(2′)	C(3′)	C(4′)	C(5′)
c^7G_d[e]	152.5	158.5	100.1	102.1	116.7	150.5	82.2	39.5	70.8	86.9	61.9
1	152.2	175.7	113.1	104.4	120.2	147.1	82.2	-[d]	70.9	87.1	61.9
10	145.4	174.8	116.8	104.7	122.7	143.4	82.5	-[d]	70.6	87.1	61.5
11	151.0	167.3	119.5	99.5	125.0	149.2	82.6	-[d]	70.9	87.4	61.8
12	151.1	167.3	119.4	99.5	124.8	149.2	82.7	-[d]	70.7	85.5	64.2

[a] Measured in DMSO-d_6 at 298 K. [b] Systematic numbering. [c] Purine numbering. [d] Superimposed by the DMSO signal. [e] c^7G_d: 7-deaza-2′-deoxyguanosine; ^{13}C NMR chemical shifts taken from ref 41.

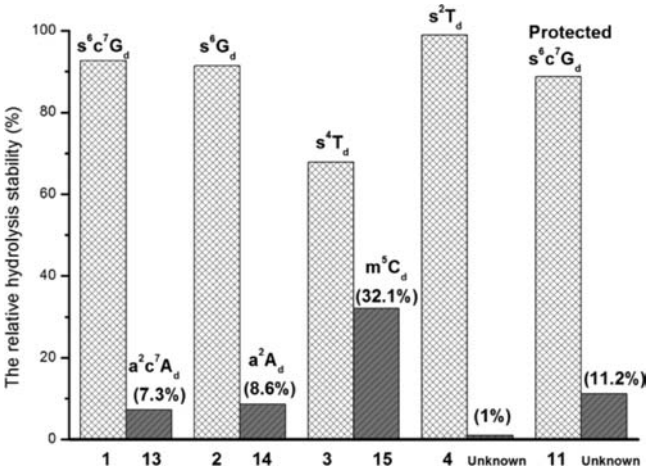


Figure 3. Graph showing the alkaline hydrolysis stability of thiooxonucleosides **1**−**4** and protected **11**. After incubation in a solution of 25% aq. NH_3 at 60 °C for 16 h, compounds **1**−**4** and **11** were analyzed by reversed-phase HPLC at 260 nm. Relative quantification was calculated on the basis of peak areas which were divided by the extinction coefficient (ε_{260}) of the respective nucleoside (for details see Supporting Information). $s^6c^7G_d$: 7-deaza-6-thio-2′-deoxyguanosine (**1**), $a^2c^7A_d$: 2-amino-7-deaza-2′-deoxyadenosine (**13**), s^6G_d: 6-thio-2′-deoxyguanosine (**2**), a^2A_d: 2-amino-2′-deoxyadenosine (**14**), s^4T_d: 4-thio-2′-deoxythymidine (**3**), m^5C_d: 5-methyl-2′-deoxycytidine (**15**), s^2T_d: 2-thio-2′-deoxythymidine (**4**), **11**: 6-[(2-cyanoethyl)thio]-2-phenoxyacetamino-7-deaza-2′-deoxyguanosine.

Moreover, compared to the parent nucleoside 7-deaza-2′-deoxyguanosine (c^7G_d; Table 2), the sulfur atom of thionucleoside **1** attached to carbon-6—instead of the oxygen atom of c^7G_d—induces a significant downfield shift of 17.2 ppm on C6.

Stability of Thiooxonucleosides 1−4 toward Alkaline Hydrolysis. Prior to oligonucleotide synthesis, the stability of the thiooxo group of nucleosides **1**−**4** toward the standard oligonucleotide deprotection conditions (25% aq. NH_3, 16 h, 60 °C) was investigated. This study was motivated by earlier reports on sulfur-amino group exchanges of 6-thio-2′-deoxyguanosine (**2**) (→ 2-amino-2′-deoxyadenosine, **14**)[24] and 4-thio-2′-deoxythymidine (**3**) (→ 5-methyl-2′-deoxycytidine, **15**)[42] under alkaline conditions. Moreover, the unknown compound **11** employing a cyanoethyl protecting group at the sulfur function and a 2-phenoxyacetamino group was also subject of this study. With this experiment, we intended to confirm the applicability of the cyanoethyl protecting group at sulfur-6 under standard oligonucleotide deprotection conditions and conversion to the desired 7-deaza-6-thio-2′-deoxyguanosine (**1**).

Thus, nucleosides **1**−**4** and **11** were incubated in 25% aq. NH_3, 16 h, 60 °C (standard oligonucleotide deprotection conditions) and analyzed by reversed-phase HPLC at 260 nm. Byproducts were identified by coelution with authentic nucleosides (for experimental procedure and HPLC profiles, see the Supporting Information).

The thiooxo group at position-6 of purine nucleosides or position-2 of pyrimidine nucleosides is considerably more stable compared to position-4 of pyrimidine nucleosides. Accordingly, among nucleosides **1**−**4**, the thiooxo group of 4-thio-2′-deoxythymidine (**3**) is the most labile one toward the standard oligonucleotide deprotection conditions (32% conversion to 5-methyl-2′-deoxycytidine, **15**). On the contrary, the thiooxo group of 2-thio-2′-deoxythymidine (**4**) was the most stable one, and less than 1% conversion into an unidentified product was detected (Figure 3 and Supporting Information). The thiooxo groups of the purine and 7-deazapurine nucleosides **1** and **2** showed similar stabilities (**1**: 7% conversion, **2**: 9% conversion, Figure 3). For the protected compound **11**, conversion into an unidentified side product amounts to 11% which is within the same range as for nucleosides **1** and **2**. However, it should be noted that, for **11**, the stability of the sulfur function is related to deprotection and conversion from 6-cyanoethyl(thio) into the desired 6-sulfur group (Figure 3 and Supporting Information). From the above-described experiments, the following order of stability of the thiooxo groups of nucleosides **1**−**4** and **11** toward alkaline hydrolysis (25% aq. NH_3, 16 h, 60 °C) was deduced: **4** > **1** > **2** > **11** > **3** (Figure 3).

Oligonucleotide Synthesis and Characterization. With the informations of the alkaline hydrolysis experiments in hand, a series of unmodified and modified oligonucleotides (**16**−**39**) containing thiooxonucleosides **1**−**4** at different positions were synthesized on solid phase at 1 μmol scale (Table 4), and the accessibility of pure oligomers was studied. Two different protocols of oligonucleotide syntheses were employed: (i) oligonucleotide synthesis using fast deprotectable building blocks and (ii) standard oligonucleotide synthesis employing standard building blocks. Oligonucleotides incorporating 4-thio-2′-deoxythymidine (**3**) or 6-thio-2′-deoxyguanosine (**2**) were synthesized under conditions already reported in the literature utilizing phosphoramidites **7** and **8** which are suitable for fast deprotection conditions.[38,43] Oligonucleotides were cleaved from solid support and deprotected in a 25% aq. NH_3 solution containing 50 mM NaSH at room temperature overnight. Sulfur exchange was avoided by employing the protocol of fast deprotection[28] and the presence of sodium hydrogensulfide. In contrast, oligonucleotides containing 2-thio-2′-deoxythmidine (**4**) or 7-deaza-6-thio-2′-deoxyguanosine (**1**) were synthesized and deprotected

dx.doi.org/10.1021/bc200069j |*Bioconjugate Chem.* 2011, 22, 794–807

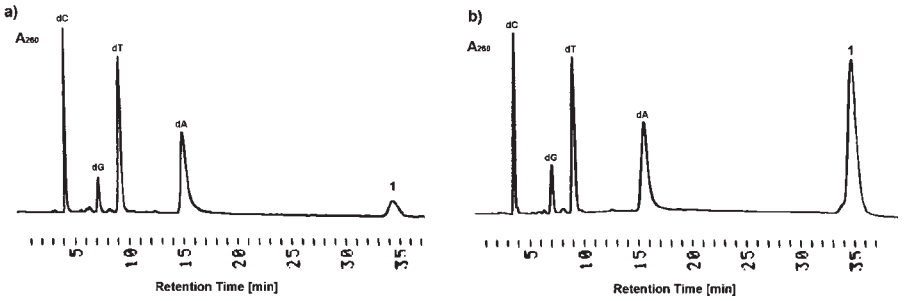


Figure 4. HPLC elution profiles of (a) the enzymatic hydrolysis products of oligonucleotide **30** obtained after hydrolysis with snake venom phosphodiesterase and alkaline phosphatase in 0.1 M Tris−HCl buffer (pH 8.5) at 37 °C and (b) the artifical mixture of the hydrolysis products of oligonucleotide **30** and thiooxonucleoside **1**. Column: RP-18 (200 × 10 mm); gradient [A: 0.1 M (Et_3NH)OAc (pH 7.0)/MeCN 95:5]: 100% A; flow rate: 0.7 mL/min.

under standard conditions (25% aq. NH_3, 14−16 h, 60 °C) in the absence of sodium hydrogensulfide. The oligonucleotides were isolated and purified by reversed-phase HPLC (for details see Experimental Procedures).

The nucleobase composition of the modified oligonucleotides was also confirmed by tandem enzymatic hydrolysis with snake-venom phosphodiesterase (EC 3.1.15.1, *Crotallus adamanteus*) followed by alkaline phosphatase (EC 3.1.3.1, *Escherichia coli*) in 0.1 M Tris-HCl buffer (pH 8.5) at 37 °C as described previously.[29] As an example, the HPLC profiles of the nucleoside composition of oligonucleotide **30** after enzymatic hydrolysis (Figure 4a) and the artificial mixture of the hydrolysis products of **30** and nucleoside **1** (Figure 4b) are shown depicting the correct nucleobase composition of the oligonucleotide.

Both MALDI-TOF mass spectrometry (Supporting Information, Table S1) and enzymatic hydrolysis confirm that deprotection of oligonucleotides containing **1** under standard conditions (25% aq. NH_3, 14−16 h, 60 °C) yields the desired 7-deaza-6-thio-2′-deoxyguanosine (**1**) as constituent of the respective oligonucleotides, as no significant side products pointing toward sulfur exchange were detected. These findings make **1** highly advantageous over its purine congener **2** from which severe side product formation was reported when treated under these conditions.[38]

A problem associated with oligonucleotides containing thionucleosides is disulfide formation leading to cross-linked oligonucleotides. Manuscripts reporting on interstrand cross-linking through thionucleosides describe template directed protocols and the application of mild oxidants to achieve disulfide formation.[44,45] In addition, according to Waters and Connolly,[24] disulfide formation is only observed when oligonucleotides are kept in aqueous solution at neutral pH values at room temperature. Therefore, to avoid disulfide formation, we always stored our oligonucleotides as dry material at −20 °C. Throughout synthesis, purification, and characterization of oligonucleotides incorporating thionucleosides **1**−**4**, we did not make any observations indicating cross-linking of oligonucleotides due to disulfide formation. As mentioned above, in all cases, the detected masses of oligonucleotides were identical with the calculated values (Supporting Information, Table S1). Moreover, it should be noted that covalent binding to AuNPs can be achieved *via* thiol groups as well as disulfides.[17,46]

Preparation of Oligonucleotide Gold Nanoparticle Conjugates. Next, the applicability of thionucleosides **1**−**4** as components of single-stranded oligonucleotides was evaluated for nanoparticle conjugation. Selected key properties of the corresponding DNA-AuNP conjugates, such as stability in the presence of NaCl, UV/vis absorption maximum, and the ability to hybridize with complementary conjugates, were compared to DNA-AuNP conjugates utilizing the 5′-hexylthiol linker as molecular anchor.

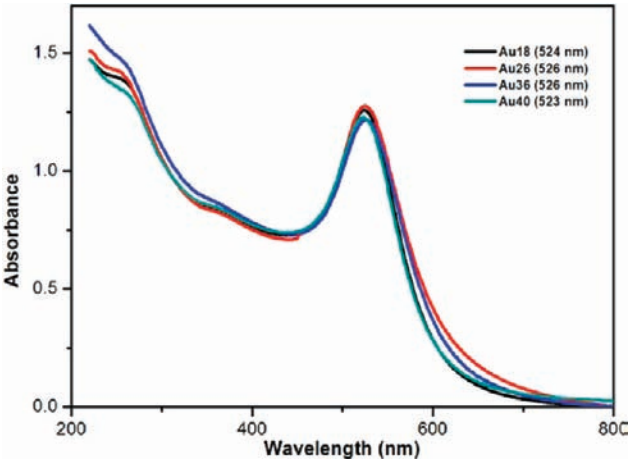


Figure 5. UV/vis profiles of selected DNA-AuNP conjugates in 0.1 M NaCl, 10 mM phosphate buffer, pH 7.0.

The unmodified AuNPs were functionalized with oligonucleotides **18**−**39** containing one or multiple thiooxonucleosides (**1**−**4**) at different positions. For that, 1 mL of the unmodified AuNP solution was mixed with the aqueous solution of the respective purified oligonucleotide (1−5 μL) to yield a final oligonucleotide concentration of 3 μM. The conjugation was performed at slightly elevated temperature (40 °C). The NaCl concentration of the DNA-AuNP solution was increased stepwise with phosphate buffer (2 M NaCl, 0.2 mM phosphate buffer, pH 7.0) to a final NaCl concentration of 0.1 M. Unbound oligonucleotides were removed from the DNA-AuNP solutions by a repeated washing and centrifugation protocol with 0.1 M NaCl, 10 mM phosphate buffer (pH 7.0) (for details see Experimental Procedures). During the whole procedure, the DNA gold nanoparticle solutions stayed deep red in color. However, we found that the preparation of DNA-AuNP conjugates with oligonucleotides **20**−**21** or **24**−**25** incorporating **2** and **4** were encountered with difficulties. Contrary to all other samples, conjugation of **20**−**21** and **24**−**25** to AuNPs failed several times (50% failure). Moreover, the centrifugation speed had to be reduced significantly from 8000 rpm (standard speed) to 5800 rpm; otherwise, it was not possible to redisperse the precipitate. Finally, all DNA-AuNP

Table 3. Applicability of Thiooxonucleosides 1−4 and 5′-Hexylthiol Linker for Gold Nanoparticle Conjugate Formation[e]

Entry	Nucleoside	Conjugate 5'-d(X T_{10} TAG GTC AAT ACT)	Conjugate 5'-d(X T_{10} AGT ATT GAC CTA)	Hybridization Capability
1	X = 1	**Au18**: yes[a,b]	**Au19**: yes[a,b]	yes
2	X = 2	**Au20**: yes[a,b]	**Au21**: yes[a,b]	yes[d]
3	X = 3	**Au22**: yes[a] / no[b]	**Au23**: yes[a] / no[b]	yes
4	X = 4	**Au24**: yes[a] / no[b]	**Au25**: yes[a] / no[b]	no
5	X = 5	**Au40**: yes[a,b]	**Au41**: yes[a,b]	yes

[a] Stable oligonucleotide gold nanoparticle conjugates were obtained in 0.1 M NaCl, 10 mM phosphate buffer, pH 7.0. [b] Stable oligonucleotide gold nanoparticle conjugates were obtained in 0.2 M NaCl, 10 mM phosphate buffer, pH 7.0. [c] The hybridization experiment was performed in 0.1 M NaCl, 10 mM phosphate buffer, pH 7.0 with overnight incubation time. [d] Formation of the DNA gold nanoparticle network occurred much more slowly and required several days. Spacer T_{10} = 5′-d(TTT TTT TTT T). [e] Red ball = 15-nm-diameter gold nanoparticle.

Table 4. T_m Values and Thermodynamic Data of Oligonucleotide Duplexes Containing Thiooxonucleosides 1−4 as Overhanging Ends or Opposite Canonical Nucleosides[a,b]

duplex		T_m [°C]	ΔT_m [°C][c]
5′-d(TAG GTC AAT ACT) 3′-d(ATC CAG TTA TGA)	(16) (17)	47	-
5′-d(**1** T_{10} TAG GTC AAT ACT) 3′-d(ATC CAG TTA TGA T_{10} **1**)	(18) (19)	48	+1
5′-d(**2** T_{10} TAG GTC AAT ACT) 3′-d(ATC CAG TTA TGA T_{10} **2**)	(20) (21)	47	0
5′-d(**3** T_{10} TAG GTC AAT ACT) 3′-d(ATC CAG TTA TGA T_{10} **3**)	(22) (23)	47	0
5′-d(**4** T_{10} TAG GTC AAT ACT) 3′-d(ATC CAG TTA TGA T_{10} **4**)	(24) (25)	47	0
5′-d(**11** T_{10} TAG GTC AAT ACT) 3′-d(ATC CAG TTA TGA T_{10} **11**)	(26) (27)	47	0
5′-d(**111** T_{10} TAG GTC AAT ACT) 3′-d(ATC CAG TTA TGA T_{10} **111**)	(28) (29)	47	0
5′-d(TAG GTC AAT ACT) 3′-d(ATC CAG TTA T**1**A)	(16) (30)	43	−4
5′-d(TAG GTC AAT ACT) 3′-d(ATC CA**1** TTA TGA)	(16) (31)	40	−7
5′-d(TA**11**TC AAT ACT) 3′-d(ATC CA**1** TTA T**1**A)	(32) (33)	17	−30
5′-d(TAG GTC AAT ACT TAG GTC AAT ACT) 3′-d(ATC CAG TTA TGA ATC CAG TTA TGA)	(34) (35)	65	-
5′-d(TA**1** GTC AAT ACT TAG GTC AAT ACT) 3′-d(ATC CAG TTA TGA ATC CAG TTA T**1**A)	(36) (37)	55	−10
5′-d(TAG GTC AAT ACT TA**1** GTC AAT ACT) 3′-d(ATC CAG TTA T**1**A ATC CAG TTA TGA)	(38) (39)	53	−12

[a] Measured at 260 nm in 0.1 M NaCl, 10 mM phosphate buffer (pH 7.0), with 5 μM single-strand concentration. [b] Spacer T_{10} = 5′-d(TTT TTT TTT T). [c] ΔT_m was calculated as $T_m^{\text{base mismatch}} - T_m^{\text{base match}}$.

conjugates **Au18**-**Au29** and **Au36**-**Au39** showed the expected plasmon resonance at around 524 nm indicating a nonaggregated state (Table 1, Figure 5, and Figure S2, Supporting Information). It is worthwhile to mention that the same absorption maximum (524 nm) is also observed for DNA-AuNP conjugates **Au36**-**Au39**, in which the attachment succeeds through thionucleoside **1** situated within an internal position of the respective oligonucleotide (Figure 5). Thus, it can be concluded that thionucleoside **1** can also function as a molecular anchor for AuNPs through an internal position of an oligonucleotide.

For comparison, oligonucleotides **40** and **41** incorporating a 5′-hexylthiol linker were conjugated to AuNPs (→ **Au40**, **Au41**; Table 1) employing the conventional protocol reported earlier by others.[47] The UV/vis spectra of DNA-AuNP conjugates **Au40** and **Au41** show a plasmon resonance at 523 nm (Table 1, Figure 5).

Next, the stability of DNA-AuNP conjugates **Au18**-**Au29** containing the different thiooxonucleosides **1**−**4** and **Au40**, **Au41** employing the hexylthiol linker was evaluated at higher salt concentration (0.2 M NaCl, 10 mM phosphate, pH 7.0 buffer solution). For that, UV/vis spectra of the DNA-AuNP conjugate solutions were recorded at different time intervals and compared (for UV/vis profiles at the different time intervals see the Supporting Information, Figure S3). This experiment was performed to provide more information on the applicability of **1**−**4** for AuNP conjugation and hence on the stability of the different conjugates (Table 3). The DNA-AuNP conjugates **Au22**-**Au25** using 4-thio-2′-deoxythymidine (**3**) or 2-thio-2′-deoxythymidine (**4**) as anchor molecules were unstable in the presence of higher NaCl concentration. This became immediately evident for DNA-AuNPs **Au24** and **Au25** containing 2-thio-2′-deoxythymidine (**4**), due to aggregation of the DNA-AuNPs (solutions turned black) followed by precipitation (Table 3, entry 4), whereas DNA-AuNPs **Au22** and **Au23** showed partial precipitation which was deduced from a significant decrease in the maximum of the UV/vis absorption profile (36%) after overnight incubation compared to the original profile (0 h incubation) (Figure S3, Supporting Information). However, the plasmon resonance of conjugates **Au22** and **Au23** was almost unchanged (524.5 nm), but the red color of the solutions was much fainter compared to the original solutions. According to these observations, we classified DNA-AuNP conjugates using 4-thio-2′-deoxythymidine (**3**) as anchor molecule (**Au22** and **Au23**) as not stable in the presence of higher NaCl concentration (see Table 3, entry 3).

dx.doi.org/10.1021/bc200069j |Bioconjugate Chem. 2011, 22, 794–807

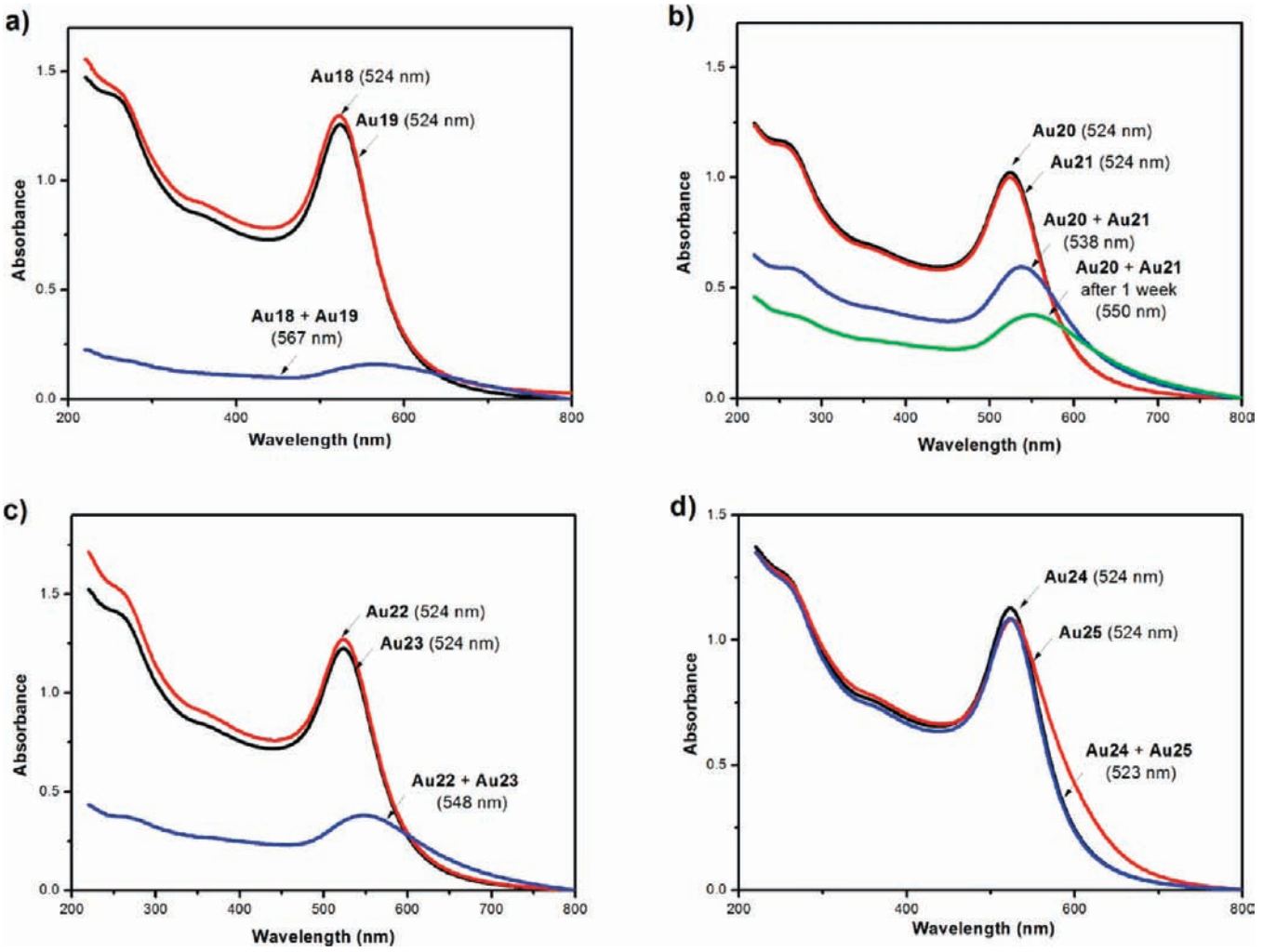


Figure 6. UV/vis spectra of (a) DNA-AuNP conjugates **Au18**, **Au19** using 7-deaza-6-thio-2′-deoxyguanosine (**1**) as anchor, and the DNA-AuNP network **Au18•Au19** formed after overnight incubation (blue curve). (b) DNA-AuNP conjugates **Au20** and **Au21** using 6-thio-2′-deoxyguanosine (**2**) as anchor (red and black curves), the DNA-AuNP network **Au20•Au21** formed after overnight incubation (blue curve) and after several days of incubation (green curve). (c) DNA-AuNP conjugates **Au22** and **Au23** using 4-thio-2′-deoxythymidine (**3**) as anchor and the DNA-AuNP network formed by **Au22•Au23** after overnight incubation (blue curve). (d) DNA-AuNP conjugates **Au24** and **Au25** using 2-thio-2′-deoxythymidine (**4**) as anchor (red and black curves) and after overnight incubation (blue curve).

On the contrary, the DNA-AuNPs **Au18**-**Au21** using 7-deaza-6-thio-2′-deoxyguanosine (**1**) or 6-thio-2′-deoxyguanosine (**2**) as conjugation site (Table 3, entry 1−2) and **Au40**, **Au41** making use of a hexylthiol linker (Table 3, entry 5) were of comparable stability, and all conjugates were significantly more stable than **Au22**-**Au25** under the higher salt concentration (see also Supporting Information, Figure S3).

Similar results were found for DNA-AuNP conjugates **Au26**-**Au29** having consecutive 7-deaza-6-thio-2′-deoxyguanosine (**1**) modifications at the 5′-end of oligonucleotides **26**−**29**, after overnight incubation in 0.2 M NaCl, 10 mM phosphate, pH 7.0 buffer solution (data not shown).

Duplex Stability of Oligonucleotides Containing Thiooxonucleosides 1−4 and Oligonucleotide Gold Nanoparticle Conjugates. It is well-known that in thiooxonucleosides the replacement of the oxygen atom by sulfur leads to a destabilization of duplex DNA since the thio group is a poorer hydrogen bond acceptor than the normal carbonyl, and bulkiness of the sulfur atom can interfere with hybridization.[48]

For clarification, hydridization studies were performed with non-immobilized oligonucleotide duplexes incorporating compounds **1**−**4** (Table 4). Single or multiple thiooxonucleosides (**1**−**4**) were incorporated as overhanging ends together with a 5′-d$(T)_{10}$ spacer. Table 4 shows that all duplexes have similar T_m values (47 °C) as the parent unmodified duplex 5′-d(TAG GTC AAT ACT) (**16**) • 3′-d(ATC CAG TTA TGA) (**17**).

As 7-deaza-6-thio-2′-deoxyguanosine (**1**) has not been incorporated into oligonucleotides before, its properties as a constituent of duplex DNA were investigated in more detail. Thus, consecutive and random positions have been selected for modification with **1**, and T_m values were determined.

A single replacement of nucleoside **1** in the center or at the periphery of the 12-mer duplex reduced the stability of the duplex. The effect was more pronounced when **1** was incorporated in the center of the oligonucleotide duplex (**16•31**: ΔT_m = −7 °C) than at the periphery (**16•30**: ΔT_m = −4 °C). Multiple modifications led to a significant further destabilization (ΔT_m = −30 °C for **32•33**) (Table 4). Consistently, two

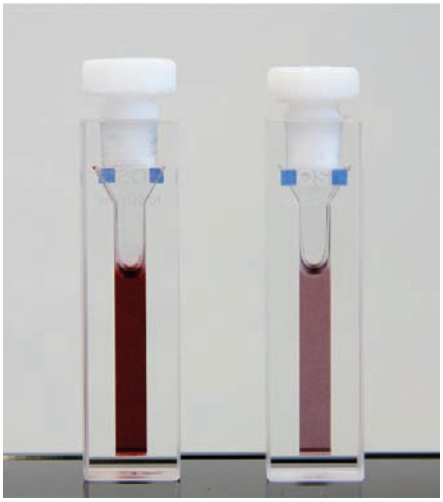


Figure 7. Left cuvette: unmodified deep red gold nanoparticle solution. Right cuvette: purple DNA-AuNP conjugate solution after assembly of **Au18•Au19** (12 h incubation, the sample is shown after intensive shaking).

incorporations of nucleoside **1** within the center or at the periphery of 24-mer duplexes (**36•37**, **38•39**) lead to a strong decrease of the duplex stability when compared to the parent unmodified duplex **34•35** ($\Delta T_m = -10$ °C for **36•37** and $\Delta T_m = -12$ °C for **38•39**). As can be seen from Table 4, 7-deaza-6-thio-2′-deoxyguanosine (**1**) has a strong destabilizing effect on duplex stability similar to that reported for the parent 6-thio-2′-deoxyguanosine (**2**).[48]

Next, hybridization experiments were performed with oligonucleotide gold nanoparticle conjugates. In a typical experiment, two DNA-AuNP conjugates carrying oligonucleotides with complementary sequences were mixed together (equal concentrations), e.g., DNA-AuNP conjugates **Au18** and **Au19** using 7-deaza-6-thio-2′-deoxyguanosine (**1**) as molecular anchor. After incubation overnight at 5 °C, the propensity of hybridization was evaluated by UV/vis measurements. Almost all complementary DNA-AuNP conjugates show hybridization evidenced by slow red shifting and broadening of the plasmon resonance band (Table 3 and Figures 6, 7) with the exception of the complementary conjugates **Au24** and **Au25** which utilize 2-thio-2′-deoxythymidine (**4**) as molecular anchor.

In the case of the complementary conjugates **Au18•Au19**, **Au22•Au23**, and **Au40•Au41**, hybridization led to the formation of a DNA gold nanoparticle network which precipitated from solution (→ dark red precipitate with a clear supernatant) within one night. After intensive shaking of the DNA-AuNP solution, the precipitate can be redispersed leading to a purple solution with UV/vis maxima of 567 nm for **Au18•Au19** (Figure 6a), 548 nm for **Au22•Au23** (Figure 6c), and 554 nm for **Au40•Au41** (spectra not shown).

On the contrary, the UV/vis spectrum of the DNA-AuNP solution containing the complementary conjugates **Au20** and **Au21**, which use 6-thio-2′-deoxyguanosine (**2**) as molecular anchor, shows only a moderate red shift (524 nm→538 nm) of the plasmon resonance band accompanied by a smaller decrease of the absorption and only a slight broadening of the plasmon resonance band (Figure 6b, blue curve). However, no precipitation of the DNA-AuNPs was observed after incubation overnight. Prolonged incubation of about 1 week finally led to the precipitation of the DNA gold nanoparticle network. After intensive shaking of the DNA-AuNP solution **Au20•Au21**, the

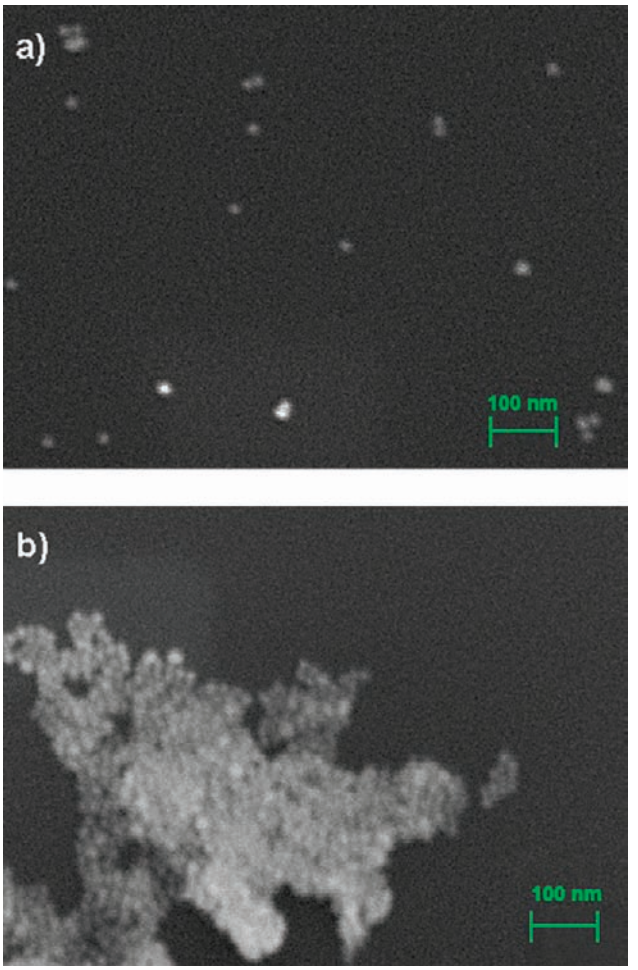


Figure 8. (a) SEM image of DNA-AuNP conjugate **Au18** employing 7-deaza-6-thio-2′-deoxyguanosine (**1**) as molecular anchor in 0.1 M NaCl, 10 mM phosphate buffer (pH 7.0); (b) SEM image of the DNA-AuNP network formed by complementary conjugates **Au18** and **Au19** in 0.1 M NaCl, 10 mM phosphate buffer (pH 7.0).

precipitate was redispersed leading to a purple solution with a UV/vis maximum of 550 nm (Figure 6b, green curve). Although the experiments was repeated several times, no network formation was observed for the complementary conjugates **Au24** and **Au25** containing 2-thio-2′-deoxythymidine (**4**), even after prolonged incubation of 1−2 weeks. The absorption maximum of the DNA-AuNP solution of **Au24** and **Au25** remained unchanged at around 524 nm (Figure 6d).

Taking together with the results summarized in Table 3, it can be concluded that, from all tested thionucleosides (**1**−**4**), the capability of 7-deaza-6-thio-2′-deoxyguanosine (**1**) as component of DNA oligonucleotides to form stable DNA gold nanoparticle conjugates is superior to that of thionucleosides **2**−**4**. DNA-AuNPs containing **1** are of comparable stability to those obtained from oligonucleotides containing the hexylthiol linker. On the contrary, thionucleosides **2**−**4** showed different drawbacks. For thionucleoside **2**, the time required for hybridization was much longer than for **1**. Up to now, we do not have an explanation regarding the prolonged incubation time required for the DNA-AuNP network formation of DNA-AuNPs with 6-thio-2′-deoxyguanosine (**2**) as molecular anchor. DNA-AuNPs with **3** and **4** were unstable in the presence of higher NaCl

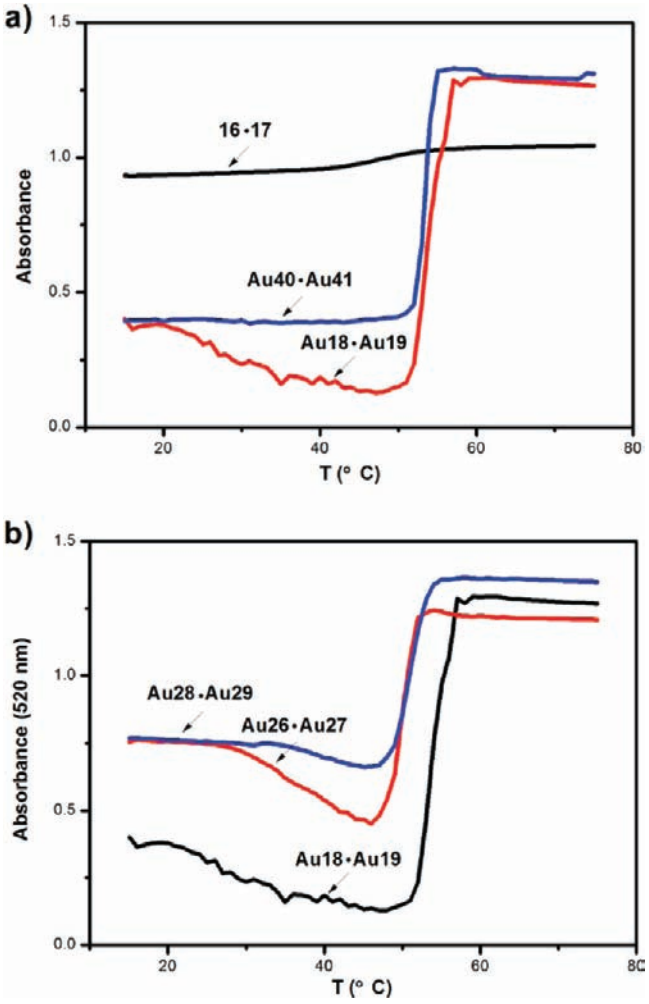


Figure 9. (a) Melting profile of the free duplex **16•17** determined at 260 nm (blue curve), and melting profiles of the DNA-AuNP assemblies of **Au18•Au19** (red curve) and **Au40•Au41** (blue curve) determined at 520 nm. (b) Melting profiles of the DNA-AuNP assemblies of **Au18•Au19** (black curve), **Au26•Au27** (red curve), and **Au28•Au29** (blue curve) determined at 520 nm.

concentration, and in addition, DNA-AuNPs with **4** are incapable of hybridization.

Thus, exemplarily, we selected DNA-AuNP solutions containing **1** to perform scanning electron microscopy (SEM) to visualize network formation. A representative section of an image showing the DNA-AuNP network formed by complementary conjugates **Au18** and **Au19** containing thionucleoside **1** is presented in Figure 8b. The SEM image shows the formation of large assembled networks of DNA-AuNP conjugates. Besides the assembled network, the neighboring area is remarkably "empty". For comparison, SEM images of nonassembled DNA-AuNP conjugates, such as **Au18** (Figure 8a), show small clusters of DNA-AuNPs which are fairly regularly distributed. The formation of large assembled networks as in Figure 8b was not observed in the case of **Au18**.

On the basis of the above-described results, melting studies were focused on DNA-AuNP conjugates employing thionucleoside **1** at different positions within the oligonucleotide chain. For comparison, T_m values were also determined for DNA-AuNP conjugates utilizing the hexylthiol linker. For this, the solutions

Table 5. T_m Values of DNA-AuNP Assemblies Incorporating Thionucleoside 1 and the Hexylthiol Linker.[a,b,c]

DNA-AuNP Assemblies	T_m [°C]
5′-d(**1** T_{10} TAG GTC AAT ACT) (**Au18**) 3′-d(ATC CAG TTA TGA T_{10} **1**) (**Au19**)	54
5′-d(**11** T_{10} TAG GTC AAT ACT) (**Au26**) 3′-d(ATC CAG TTA TGA T_{10} **11**) (**Au27**)	50
5′-d(**111** T_{10} TAG GTC AAT ACT) (**Au28**) 3′-d(ATC CAG TTA TGA T_{10} **111**) (**Au29**)	51
5′-d(TA**1** GTC AAT ACT TAG GTC AAT ACT) (**Au36**) 3′-d(ATC CAG TTA TGA ATC CAG TTA T**1**A) (**Au37**)	53
5′-d(TAG GTC AAT ACT TA**1** GTC AAT ACT) (**Au38**) 3′-d(ATC CAG TTA T**1**A ATC CAG TTA TGA) (**Au39**)	*n.m.*
5′-d(**S**-$(CH_2)_6$ T_{10} TAG GTC AAT ACT) (**Au40**) 3′-d(ATC CAG TTA TGA T_{10}-$(CH_2)_6$-**S**) (**Au41**)	53

[a] Measured at 520 nm in 0.1 M NaCl, 10 mM phosphate buffer (pH 7.0), with A_{520} = 2.1 for each DNA-AuNP conjugate solution. [b] Red ball = 15-nm-diameter gold nanoparticle. [c] Spacer T_{10} = 5′-d(TTT TTT TTT T). *n.m.* no melting observed.

containing the DNA-AuNP networks were heated (15 °C → 75 °C), and the vis absorption change at 520 nm was observed while stirring the DNA-AuNP solution. The T_m values were determined by taking the maximum of the first derivative of a melting transition and are enlisted in Table 5.

A typical sharp melting profile of **Au18•Au19** is shown in Figure 9a indicating a T_m value of 54 °C for the network of DNA-AuNPs assembled by duplex **18•19**. For comparison, the dissociation of the network formed by the conjugates **Au40** and **Au41** containing complementary oligonucleotides with hexylthiol linker was investigated under exactly the same conditions as described for the **Au18•Au19** assembly. For **Au40•Au41**, an almost identical T_m value of 53 °C was determined (Figure 9a and Table 5). It should be noted that both assemblies employ the same sequence consisting of a 12-mer oligonucleotide for base pairing and a 10-mer poly dT spacer, while the only difference is the molecular anchor being 7-deaza-6-thio-2′-deoxyguanosine (**1**) for **Au18•Au19** and the hexylthiol linker for **Au40•Au41**. Moreover, both assemblies exhibit melting profiles with a very narrow melting transition (about 4 °C) as demonstrated in Figure 9a, whereas for the parent free oligonucleotide duplex **16•17**, melting occurs over a much broader temperature range (about 20 °C) (Figure 9a). This finding is consistent with observations made earlier by others reporting that oligonucleotide duplexes covalently bound to gold nanoparticles show highly cooperative melting properties of the network forming duplexes, which is reflected by a sharp melting transition.[12,18,49]

Next, complementary DNA-AuNPs functionalized with multiple 5′-terminal thionucleosides **1** were allowed to hybridize (→ **Au26•Au27**, **Au28•Au29**). In both cases, the recognition sequence of **18•19** was used together with the 5′-d$(T)_{10}$ linker as described above. As shown in Table 5, these conjugate

assemblies exhibit very similar T_m values (**Au26•Au27**: T_m = 50 °C; **Au28•Au29**: T_m = 51 °C). The melting profiles of **Au26•Au27** and **Au28•Au29** also display a narrow melting transition range (around 4 °C) and are depicted in Figure 9b. However, compared to the T_m value found for the assembly **Au18•Au19** employing only one thionucleoside **1** per oligonucleotide strand, these values are 3−4 °C lower but still within the same range.

The melting behavior of complementary DNA-AuNP conjugates carrying 24-mer oligonucleotides which use thionucleoside **1** as anchor molecule at internal positions within their sequence was also investigated (**Au36-Au39**, Table 5). The oligonucleotides of **Au36-Au39** are composed of a twofold repeated recognition sequence allowing formation of 24 base pairs or partial hybridization (12 base pairs).

The DNA-AuNP conjugates **Au38** and **Au39** employing 24-mer complementary oligonucleotides with compound **1** located in the center of each oligonucleotide cannot form a DNA-AuNP interlinked network. Even prolonged incubation did not lead to a color change of the combined conjugate solution, and no shift of the vis maximum was observed. Thus, it can be concluded that no hybridization occurred, which is due to the negative effect of an internal thiooxo group on hybridization. Moreover, hybridization is probably additionally hindered by the short distance to the immobilization site of the gold nanoparticles.

On the contrary, a T_m value of 53 °C was detected for the closely related assembly **Au36•Au37** with thionucleoside **1** being located at the periphery of the 24-mer oligonucleotide sequences. This T_m value is consistent with that of **Au18•Au19** employing a complementary 12-mer duplex for assembly. In this regard, the observed T_m value points to a partial hybridization of the complementary oligonucleotides within the DNA-AuNP assembly. Two principle situations appear to be most conclusive, (i) a matched duplex with fraying ends and base pairing only in the center of the duplex and (ii) a shift of the complementary sequences with respect to each other leading to partial hybridization of the duplex and leaving the unpaired nucleosides as spacers between the recognition site and the gold nanoparticles. We think that a partial overlap of the recognition sites are responsible for the almost identical T_m values of **Au36•Au37** and **Au18•Au19**. Thus, the second recognition element is acting simply as spacer extending the distance to the gold nanoparticles not taking part in the hybridization process.

CONCLUSIONS

We have shown that thiooxo groups of base-modified nucleosides can be used as molecular anchors to conjugate oligonucleotides to gold nanoparticles. Compared to already existing gold nanoparticle conjugation protocols, the new linker strategy simplifies immobilization of oligonucleotides to gold nanoparticles. The method reduces additional steps such as (i) detritylation of the linker with silver nitrate which has to be performed immediately before the conjugation reaction and (ii) removal of excess silver nitrate, followed by (iii) desalting of the oligonucleotide.

Thionucleosides can be used in place of canonical DNA constituents. Incorporation of the sulfur containing nucleosides can be performed at any position of an oligonucleotide; even multiple incorporations are feasible, which will increase the binding stability of the corresponding oligonucleotides to the gold nanoparticles. 7-Deaza-6-thio-2′-deoxyguanosine (**1**) shows advantages over other thionucleosides, such as **2**−**4**, regarding stability during oligonucleotide synthesis, deprotection, and purification. Thus, solid-phase synthesis with phosphoramidites, e.g., with **6**, as well as enzymatic polymerization with corresponding triphosphates employing polymerases or terminal transferases can be performed. 7-Deaza-6-thio-2′-deoxyguanosine (**1**) can replace dG. The lower stability of nucleoside **1**•dC base pairs compared to those with dG or 7-deaza-2′-deoxyguanosine resulting from the bulkiness of the thiooxo group will not affect hybridization when the incorporation of **1** occurs outside of the recognition sequence. UV/vis spectra and hybridization properties of DNA-AuNP conjugates using thionucleoside **1** as molecular anchor reveal properties which are comparable to those containing the commercial hexanethiol linker.

ASSOCIATED CONTENT

Supporting Information. MALDI-TOF mass data of oligonucleotides, $^{1}H-^{13}C$ coupling constants, protocol of alkaline hydrolytic stability of thiooxonucleosides, HPLC profiles of the hydrolytic stability of thiooxonucleoside, UV/vis spectra of DNA-AuNP conjugates, UV/vis spectra of DNA-AuNP conjugates in high salt buffer, ^{1}H-, ^{13}C-, and ^{31}P NMR spectra of the synthesized compounds. This material is available free of charge via the Internet at http://pubs.acs.org.

AUTHOR INFORMATION

Corresponding Author

*Corresponding author. Prof. Dr. Frank Seela. Phone: +49(0)251 53406 500; Fax: +49(0)251 53406 857. E-mail: Frank.Seela@uni-osnabrueck.de. Homepage: www.seela.net.

ACKNOWLEDGMENT

We would like to thank Dr. Peter Leonard and Dr. Dieter Heindl for helpful discussions and support, and Mr. Suresh S. Pujari for critical reading of the manuscript. We also thank Dr. T. Koch from Roche Diagnostics GmbH, Penzberg, Germany, for the measurement of the MALDI spectra, Mr. Nhat Quang Tran for the oligonucleotide syntheses, and Dr. Chongwen Wang for SEM measurements. Financial support by the Roche Diagnostics GmbH and ChemBiotech, Muenster, Germany is highly appreciated.

REFERENCES

(1) Niemeyer, C. M., and Mirkin, C. A. (2004) *Nanobiotechnology*, Wiley-VCH, Weinheim.

(2) Mirkin, C. A., and Niemeyer, C. M. (2007) *Nanobiotechnology II*, Wiley-VCH, Weinheim.

(3) Niemeyer, C. M. (2001) Nanoparticles, proteins, and nucleic acids: biotechnology meets materials science. *Angew. Chem., Int. Ed. 40*, 4128–4158.

(4) Ghosh, P., Han, G., De, M., Kim, C. K., and Rotello, V. M. (2008) Gold nanoparticles in delivery applications. *Adv. Drug Delivery Rev. 60*, 1307–1315.

(5) Maxwell, D. J., Taylor, J. R., and Nie, S. (2002) Self-assembled nanoparticle probes for recognition and detection of biomolecules. *J. Am. Chem. Soc. 124*, 9606–9612.

(6) Zhao, H. Q., Lin, L., Li, J. R., Tang, J. A., Duan, M. X., and Jiang, L. (2001) DNA biosensor with high sensitivity amplified by gold nanoparticles. *J. Nanopart. Res. 3*, 321–323.

(7) Gothelf, K. V., and LaBean, T. H. (2005) DNA-programmed assembly of nanostructures. *Org. Biomol. Chem. 3*, 4023–4037.

(8) Baron, R., Willner, B., and Willner, I. (2007) Biomolecule-nanoparticle hybrids as functional units for nanobiotechnology. *Chem. Commun. (Cambridge, U. K.)* 323–332.

(9) Hutchings, G. J., Brust, M., and Schmidbaur, H. (2008) Gold-an introductory perspective. *Chem. Soc. Rev. 37*, 1759–1765.

(10) Daniel, M. C., and Astruc, D. (2004) Gold nanoparticles: assembly, supramolecular chemistry, quantum-size-related properties, and applications toward biology, catalysis, and nanotechnology. *Chem. Rev. 104*, 293–346.

(11) Seeman, N. C. (2003) DNA in a material world. *Nature 421*, 427–431.

(12) Mirkin, C. A., Letsinger, R. L., Mucic, R. C., and Storhoff, J. J. (1996) A DNA-based method for rationally assembling nanoparticles into macroscopic materials. *Nature 382*, 607–609.

(13) Storhoff, J. J., Elghanian, R., Mucic, R. C., Mirkin, C. A., and Letsinger, R. L. (1998) One-pot colorimetric differentiation of polynucleotides with single base imperfections using gold nanoparticle probes. *J. Am. Chem. Soc. 120*, 1959–1964.

(14) Alivisatos, A. P., Johnsson, K. P., Peng, X., Wilson, T. E., Loweth, C. J., Bruchez, M. P., Jr., and Schultz, P. G. (1996) Organization of 'nanocrystal molecules' using DNA. *Nature 382*, 609–611.

(15) Zhao, W., Lin, L., and Hsing, I. M. (2009) Rapid synthesis of DNA-functionalized gold nanoparticles in salt solution using mononucleotide-mediated conjugation. *Bioconjugate Chem. 20*, 1218–1222.

(16) Jadzinsky, P. D., Calero, G., Ackerson, C. J., Bushnell, D. A., and Kornberg, R. D. (2007) Structure of a thiol monolayer-protected gold nanoparticle at 1.1 Å resolution. *Science 318*, 430–433.

(17) Letsinger, R. L., Elghanian, R., Viswanadham, G., and Mirkin, C. A. (2000) Use of a steroid cyclic disulfide anchor in constructing gold nanoparticle-oligonucleotide conjugates. *Bioconjugate Chem. 11*, 289–291.

(18) Li, Z., Jin, R., Mirkin, C. A., and Letsinger, R. L. (2002) Multiple thiol-anchor capped DNA-gold nanoparticle conjugates. *Nucleic Acids Res. 30*, 1558–1562.

(19) Kumar, A., Phadtare, S., Pasricha, R., Guga, P., Ganesh, K. N., and Sastry, M. (2003) Assembling gold nanoparticles in solution using phosphorothioate DNA as structural interconnects. *Curr. Sci. 84*, 71–74.

(20) Lee, J. H., Wernette, D. P., Yigit, M. V., Liu, J., Wang, Z., and Lu, Y. (2007) Site-specific control of distances between gold nanoparticles using phosphorothioate anchors on DNA and a short bifunctional molecular fastener. *Angew. Chem. 119*, 9164–9168.

(21) Agris, P. F. (1996) The Importance of being modified: roles of modified nucleosides and Mg^{2+} in RNA structure and function, *Progress in Nucleic Acid Res and Molecular Biology* (Waldo, E. C., and Klvle, M., Eds.) pp 79−129, Vol. 53, Academic Press, New York.

(22) Rao, T. S., Durland, R. H., Seth, D. M., Myrick, M. A., Bodepudi, V., and Revankar, G. R. (1995) Incorporation of 2′-deoxy-6-thioguanosine into G-rich oligodeoxyribonucleotides inhibits G-tetrad formation and facilitates triplex formation. *Biochemistry 34*, 765–772.

(23) Nikiforov, T. T., and Connolly, B. A. (1991) The synthesis of oligodeoxynucleotides containing 4-thiothymidine residues. *Tetrahedron Lett. 32*, 3851–3854.

(24) Waters, T. R., and Connolly, B. A. (1992) Straightforward synthesis of 6-thiodeoxyguanosine and its incorporation into oligodeoxynucleotides. *Nucleosides Nucleotides Nucleic Acids 11*, 985–998.

(25) Yoshida, S., Yamada, M., Masaki, S., and Saneyoshi, M. (1979) Utilization of 2′-deoxy-6-thioguanosine 5′-triphosphate in DNA synthesis *in vitro* by DNA polymerase α from calf thymus. *Cancer Res. 39*, 3955–3958.

(26) Seela, F., Steker, H., Driller, H., and Bindig, U. (1987) 2-Amino-2′-desoxytubercidin und verwandte Pyrrolo[2,3-*d*]pyrimidinyl-2′-desoxyribofuranoside. *Liebigs Ann. Chem.* 15–19.

(27) User's manual of the DNA synthesizer, Applied Biosystems, Weiterstadt, Germany.

(28) Graham, D., Parkinson, J. A., and Brown, T. (1998) DNA duplexes stabilized by modified monomer residues: synthesis and stability. *J. Chem. Soc., Perkin Trans. 1* 1131–1138.

(29) Seela, F., and Driller, H. (1986) Palindromic oligonucleotides containing 7-deaza-2′-deoxyguanosine: solid-phase synthesis of d[(p)GG*AATTCC] octamers and recognition by the endodeoxyribonuclease *Eco*RI. *Nucleic Acids Res. 14*, 2319–2332.

(30) Turkevich, J., Stevenson, P. C., and Hillier, J. (1951) A study of the nucleation and growth processes in the synthesis of colloidal gold. *Discuss. Faraday Soc. 11*, 55–57.

(31) Demers, L. M., Mirkin, C. A., Mucic, R. C., Reynolds, R. A., Letsinger, R. L., Elghanian, R., and Viswanadham, G. (2000) A fluorescence-based method for determining the surface coverage and hybridization efficiency of thiol-capped oligonucleotides bound to gold thin films and nanoparticles. *Anal. Chem. 72*, 5535–5541.

(32) Seela, F., Budow, S., and Leonard, P. (2007) Oligonucleotides forming an i-motif: the pH-dependent assembly of individual strands and branched structures containing 2′-deoxy-5-propynylcytidine. *Org. Biomol. Chem. 5*, 1858–1872.

(33) Seela, F., and Budow, S. (2006) pH-Dependent assembly of DNA-gold nanoparticles based on the i-motif: a switchable device with the potential of a nanomachine. *Helv. Chim. Acta 89*, 1978–1985.

(34) Beermann, B., Carrillo-Nava, E., Scheffer, A., Buscher, W., Jawalekar, A. M., Seela, F., and Hinz, H.-J. (2007) Association temperature governs structure and apparent thermodynamics of DNA-gold nanoparticles. *Biophys. Chem. 126*, 124–131.

(35) Dinu, C. Z., Opitz, J., Pompe, W., Howard, J., Mertig, M., and Diez, S. (2006) Parallel manipulation of bifunctional DNA molecules on structured surfaces using kinesin-driven microtubules. *Small 2*, 1090–1098.

(36) Erler, C., and Mertig, M. (2009) Incorporation of DNA networks into microelectrode structures. *J. Vac. Sci. Technol. B 27*, 939–943.

(37) Schulhof, J. C., Molko, D., and Teoule, R. (1987) The final deprotection step in oligonucleotide synthesis is reduced to a mild and rapid ammonia treatment by using labile base-protecting groups. *Nucleic Acids Res. 15*, 397–416.

(38) Christopherson, M. S., and Broom, A. D. (1991) Synthesis of oligonucleotides containing 2′-deoxy-6-thioguanosine at a predetermined site. *Nucleic Acids Res. 19*, 5719–5724.

(39) Newmark, R. A., and Hill, J. R. (1976) Assignment of primary and secondary amide carbonyl resonances in carbon-13 NMR. *J. Magn. Reson. 21*, 1–7.

(40) Pfeffer, P. E., Valentine, K. M., and Parrish, F. W. (1979) Deuterium-induced differential isotope shift ^{13}C NMR. 1. Resonance reassignments of mono- and disaccharides. *J. Am. Chem. Soc. 101*, 1265–1274.

(41) Winkeler, H. D., and Seela, F. (1983) Synthesis of 2-amino-7-(2′-deoxy-β-D-erythro- pentofuranosyl)-3,7-dihydro-4*H*-pyrrolo[2,3-*d*]pyrimidin-4-one, a new isostere of 2′-deoxyguanosine. *J. Org. Chem. 48*, 3119–3122.

(42) Connolly, B. A., and Newman, P. C. (1989) Synthesis and properties of oligonucleotides containing 4-thiothymidine, 5-methyl-2-pyrimidinone-1-β-D-(2′-deoxyriboside) and 2-thiothymidine. *Nucleic Acids Res. 17*, 4957–4974.

(43) Coleman, R. S., and Kesicki, E. A. (1994) Synthesis and postsynthetic modification of oligodeoxynucleotides containing 4-thio-2′-deoxyuridine ($d^{s4}U$). *J. Am. Chem. Soc. 116*, 11636–11642.

(44) Coleman, R., S., McCary, J. L., and Perez, R., J. (1999) Thionucleoside disulfides as covalent constraints of DNA conformation. *Tetrahedron 55*, 12009–12022.

(45) Milton, J., Connolly, B. A., Nikiforov, T. T., and Cosstick, R. (1993) Site-specific disulfide bridges in oligodeoxyribonucleotide duplexes containing 6-mercaptopurine and 4-thiothymine bases. *J. Chem. Soc., Chem. Commun.* 779–780.

(46) Uznanski, P., Kurjata, J., and Bryszewska, E. (2009) Modification of gold nanoparticle surfaces with pyrenedisulfide in ligand-protected exchange reactions. *Mater. Sci.-Pol. 27*, 659–670.

(47) Hurst, S. J., Lytton-Jean, A. K. R., and Mirkin, C. A. (2006) Maximizing DNA loading on a range of gold nanoparticle sizes. *Anal. Chem. 78*, 8313–8318.

(48) Marathias, V. M., Sawicki, M. J., and Bolton, P. H. (1999) 6-Thioguanine alters the structure and stability of duplex DNA and inhibits quadruplex DNA formation. *Nucleic Acids Res. 27*, 2860–2867.

(49) Jin, R., Wu, G., Li, Z., Mirkin, C. A., and Schatz, G. C. (2003) What controls the melting properties of DNA-linked gold nanoparticle assemblies? *J. Am. Chem. Soc. 125*, 1643–1654.

Supporting Information

DNA Gold Nanoparticle Conjugates Incorporating Thiooxonucleosides: 7-Deaza-6-thio-2'-deoxyguanosine as Gold Surface Anchor

Frank Seela[1,2]*, Ping Ding[1,2] and Simone Budow[1]

[1]*Laboratory of Bioorganic Chemistry and Chemical Biology, Center for Nanotechnology, Heisenbergstraße 11, 48149 Münster, Germany and* [2]*Laboratorium für Organische und Bioorganische Chemie, Institut für Chemie, Universität Osnabrück, Barbarastraße 7, 49069 Osnabrück, Germany*

Phone: +49(0)251 53406 500; Fax: +49(0)251 53406 857

E-mail: Frank.Seela@uni-osnabrueck.de

Homepage: www.seela.net

Table of Contents

Table S1. Molecular masses $[M-1]^-$ of oligonucleotides measured by MALDI-TOF mass spectrometry ……..……..3

Table S2. ^{1}H-^{13}C-coupling constants of 7-deaza-6-thio-2'-deoxyguanosine derivatives…….....4

Hydrolytic stability of thiooxonucleosides in aq. ammonia…..…….……..……...5

Figure S1. The reversed-phase HPLC chromatograms of the hydrolytic stability of thiooxonucleosides……..…….6

Figure S2. UV-VIS spectra of DNA-AuNP conjugates…….……..……...8

Figure S3. UV-VIS spectra of DNA-AuNP conjugates in high salt buffer…….…..…10

Figure S4. ^{1}H-NMR spectrum of compound **1**……..11

Figure S5. ^{13}C-NMR spectrum of compound **1**……...……..12

Figure S6. Deuterium isotope effect on the ^{13}C-NMR spectrum of compound **1**…….13

Figure S7. ^{1}H-NMR spectrum of compound **10**……..……..…....14

Figure S8. ^{13}C-NMR spectrum of compound **10**……...……15

Figure S9. ^{1}H-NMR spectrum of compound **11**……..……..……....16

Figure S10. ^{13}C-NMR spectrum of compound **11**……...……..17

Figure S11. ^{1}H-NMR spectrum of compound **12**……..18

Figure S12. ^{13}C-NMR spectrum of compound **12**……...……..19

Figure S13. ^{31}P-NMR spectrum of compound **6**……..……..20

Table S1. Molecular masses $[M-1]^-$ of oligonucleotides measured by MALDI-TOF mass spectrometry.[a] [b]

Oligonucleotide	$[M-1]^-$ (Da)	
	Calc.	Found
5'-d(**1**-T_{10}-TAG GTC AAT ACT) (**18**)	7029.17	7029.81
5'-d(**1**-T_{10}-AGT ATT GAC CTA) (**19**)	7029.17	7030.08
5'-d(**2**-T_{10}-TAG GTC AAT ACT) (**20**)	7030.69	7031.49
5'-d(**2**-T_{10}-AGT ATT GAC CTA) (**21**)	7030.69	7031.96
5'-d(**3**-T_{10}-TAG GTC AAT ACT) (**22**)	7005.68	7006.16
5'-d(**3**-T_{10}-AGT ATT GAC CTA) (**23**)	7005.68	7005.38
5'-d(**4**-T_{10}-TAG GTC AAT ACT) (**24**)	7005.68	7005.71
5'-d(**4**-T_{10}-AGT ATT GAC CTA) (**25**)	7005.68	7006.20
5'-d(AGT ATT **1**AC CTA) (**31**)	3658.53	3658.68
5'-d(TA**1** GTC AAT ACT TAG GTC AAT ACT) (**36**)	7364.27	7364.64
5'-d(A**1**T ATT GAC CTA AGT ATT GAC CTA) (**37**)	7364.27	7364.21
5'-d(TAG GTC AAT ACT TA**1** GTC AAT ACT) (**38**)	7364.27	7364.43
5'-d(AGT ATT GAC CTA A**1**T ATT GAC CTA) (**39**)	7364.27	7364.85

[a] Determined as $[M-1]^-$ in the linear negative mode. [b] Spacer T_{10} = 5'-d(TTT TTT TTT T).

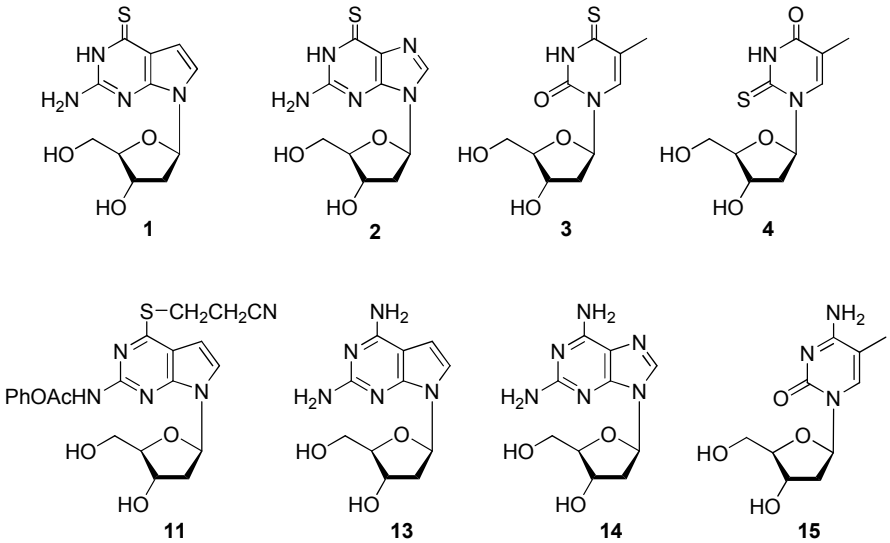
Table S2. ^{1}H-^{13}C-coupling constants of 7-deaza-6-thio-2'-deoxyguanosine derivatives.[a][b]

^{1}H-^{13}C-Coupling Constants	*J* (Hz)			
	1	**10**	**11**	**12**
^{1}J(C6, H-C6)	189.5	193.0	190.4	189.8
^{3}J(C4a, H-C6)	8.3	8.3	15.1	15.3
^{2}J(C4a, H-C5)	3.4	3.4	9.6	9.8
^{3}J(C7a, H-C6)	7.9	6.9	7.0	6.9
^{1}J(C5, H-C5)	177.2	178.7	178.5	178.6
^{2}J(C5, H-C6)	6.9	7.1	7.0	6.7
^{1}J(C1', H-C1')	161.9	163.2	162.7	165.4
^{1}J(C3', H-C3')	149.6	150.3	148.4	148.6
^{1}J(C4', H-C4')	146.7	147.6	147.6	74.3
^{1}J(C5', H-C5')	139.4	139.7	139.9	141.9
^{1}J(CH_2, H-C)phenoxyacetyl	--	147.3	147.8	146.2
^{2}J(C=O, H-C)phenoxyacetyl	--	3.7	5.1	5.2
^{1}J(CH_2, H-C)cyanoethyl	--	--	145.7	146.2
^{1}J(CH_2, H-C)cyanoethyl	--	--	138.5	138.4
^{1}J(OCH_3, H-C)DMT	--	--	--	144.2

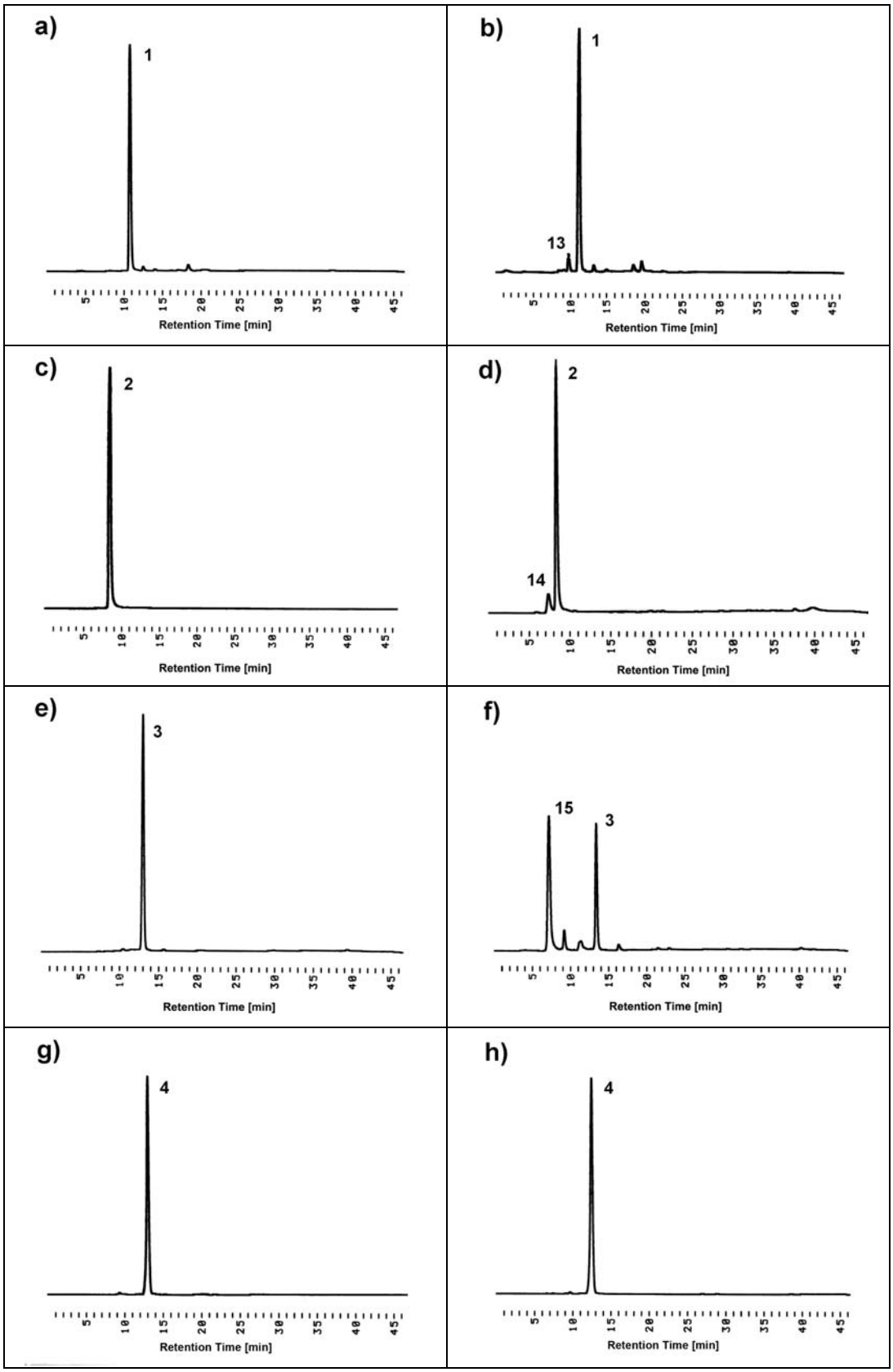
[a] Measured in DMSO-d_6 at 298 K. [b] Systematic numbering.

Hydrolytic stability of thiooxonucleosides in aq. ammonia

The hydrolysis stability of thiooxonucleosides **1**-**4** (Scheme S1) under standard deprotection conditions (25% aqueous NH_3, 14-16 h, 60°C) was monitored by reversed-phase HPLC (RP-18, 250 x 4 mm). Nucleosides **1**-**4** (about 1 mg) were dissolved in 1 mL 25% aq. ammonia in a sealed vessel and incubated at 60°C. After 16 h incubation, aq. NH_3 was removed by evaporation and the residue was redissolved in 1 mL HPLC buffer A. 50 µL of each sample were injected into the HPLC apparatus, and the HPLC profile was recorded at 260 nm (Figure S1). The following solvent gradient system was used: [A: 0.1 M (Et_3NH)OAc (pH 7.0)/MeCN 95:5; B: MeCN; gradient: 0–15 min 0–30% B in A, 30–40 min 30–40% B in A, 40–45 min 40–0% B in A, flow rate 0.7 mL/min]. The products were identified by coelution with standard nucleosides. Quantification of the constituents was made on the basis of the peak areas, which were divided by the extinction coefficients of nucleosides (ε_{260}). Extinction coefficients were determined in HPLC buffer A. 7-Deaza-6-thio-2'-deoxyguanosine (**1**) 10100, 2-amino-2'-deoxytubercidin (**13**) 9000, 6-thio-2'-deoxyguanosine (**2**) 7300, 2-amino-2'-deoxyadenosine (**14**) 8600, 4-thio-2'-deoxythymidine (**3**) 1500, 5-methyl-2'-deoxycytidine (**15**) 5900.



Scheme S1. Nucleosides employed in the hydrolysis studies.


a)
1
Retention Time [min]
b)
1
13
Retention Time [min]
c)
2
Retention Time [min]
d)
2
14
Retention Time [min]
e)
3
Retention Time [min]
f)
15
3
Retention Time [min]
g)
4
Retention Time [min]
h)
4
Retention Time [min]

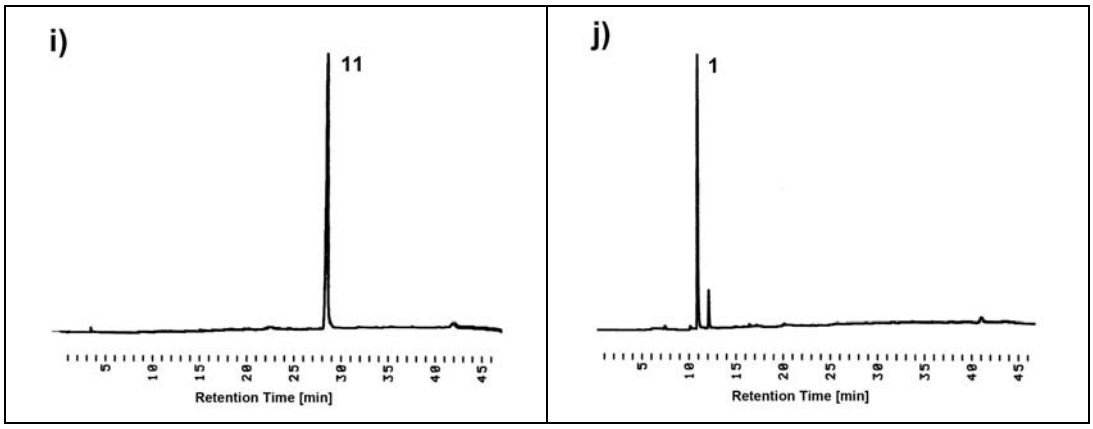
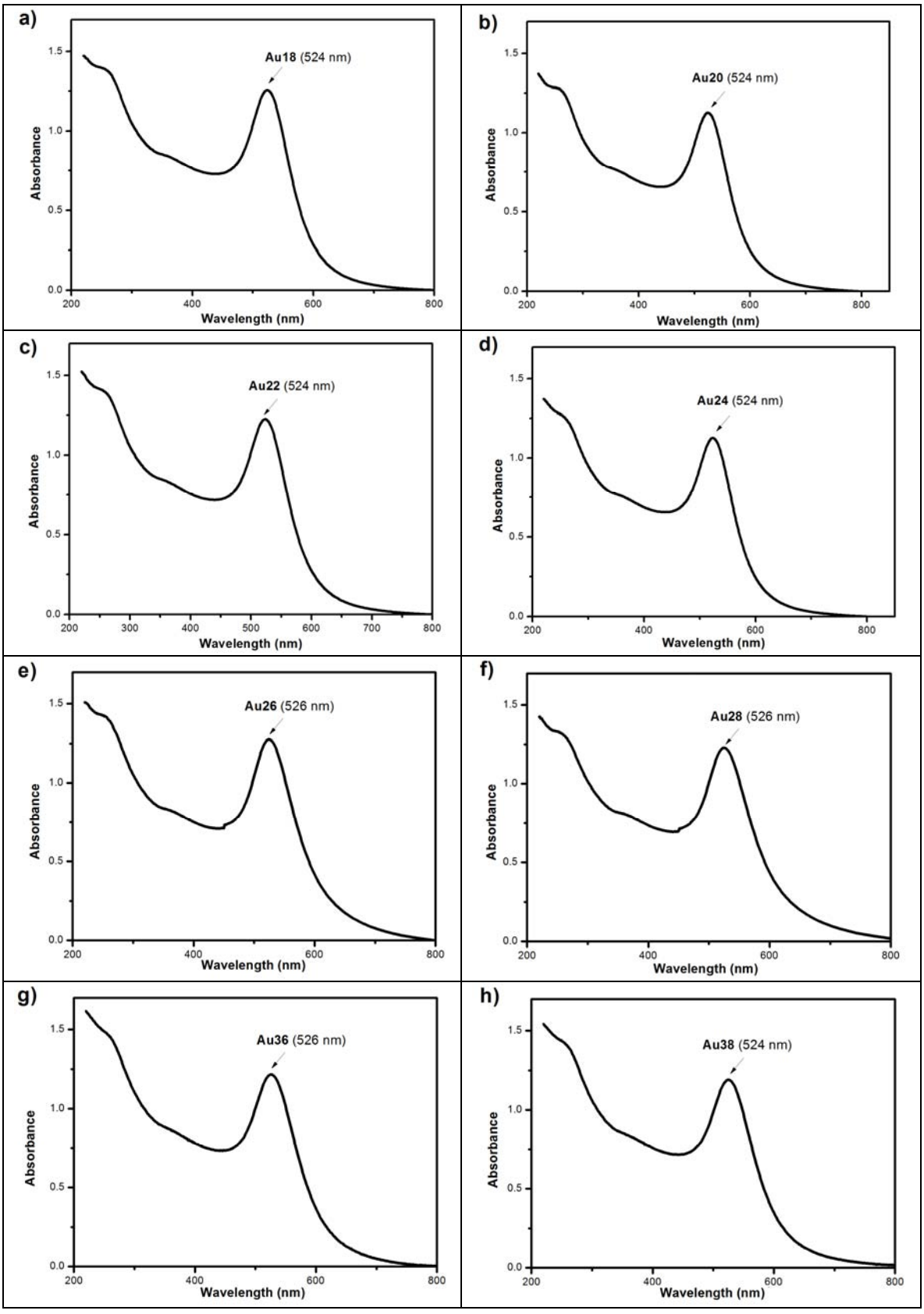


Figure S1. The reversed-phase HPLC chromatograms of thiooxonucleosides **1-4** before and after incubation in 25% aq. NH_3 at 60°C for 16 h. (a) HPLC profile of 7-deaza-6-thio-2'-deoxyguanosine (**1**). (b) HPLC profile obtained after incubation of **1**. The main side product was identified by coelution with 2-amino-2'-deoxytubercidin (**13**). (c) HPLC profile of 6-thio-2'-deoxyguanosine (**2**). (d) HPLC profile obtained after incubation of **2**. The main side product was identified by coelution with 2-amino-2'-deoxyadenosine (**14**). (e) HPLC profile of 4-thio-2'-deoxythymidine (**3**). (f) HPLC profile obtained after incubation of **3**. The main side product was identified by coelution with 5-methyl-2'-deoxycytidine (**15**). (g) HPLC profile of 2-thio-2'-deoxythymidine (**4**). (h) HPLC profile obtained after incubation of **4**. The side product was less than 1%. (i) HPLC profile of protected 7-deaza-6-thio-2'-deoxyguanosine (**11**). (j) HPLC profile obtained after incubation of **11**. The side product is unknown. The compounds were analyzed by reversed-phase HPLC at 260 nm on a RP-18 column (250 x 4 mm). Gradient: 0–15 min 0–30% B in A, 30–40 min 30–40% B in A, 40–45 min 40–0% B in A, flow rate 0.7 mL/min.

UV-VIS spectra of DNA-AuNP conjugates



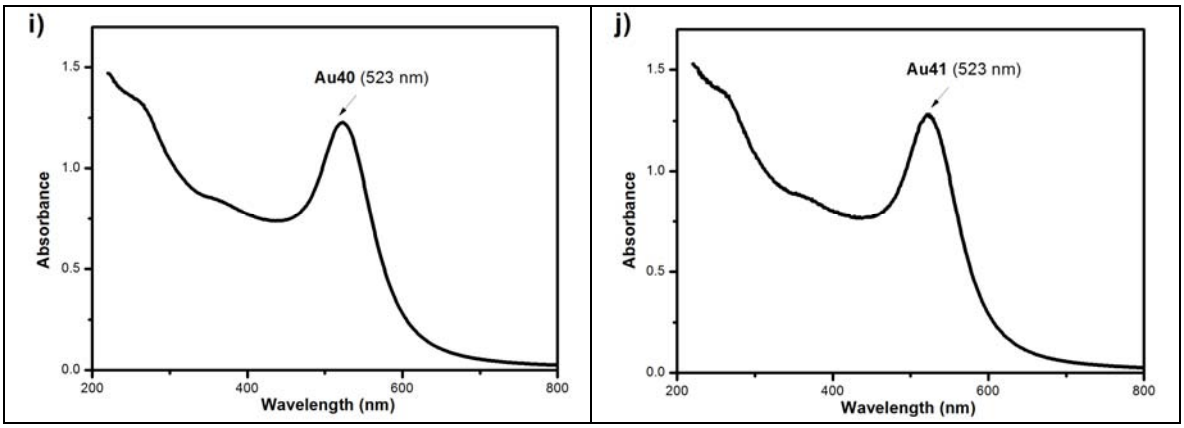


Figure S2. UV-VIS spectra of DNA-AuNP conjugates. (a) **Au18** using 7-deaza-6-thio-2'-deoxyguanosine (**1**) as molecular anchor at the 5'-terminal position; (b) **Au20** using 6-thio-2'-deoxyguanosine (**2**) as anchor at the 5'-terminal position; (c) **Au22** using 4-thio-2'-deoxythymidine (**3**) as anchor at the 5'-terminal position; (d) **Au24** using 2-thio-2'-deoxythymidine (**4**) as anchor at the 5'-terminal position; (e) **Au26** containing two 7-deaza-6-thio-2'-deoxyguanosine (**1**) modifications as multiple anchors at the 5'-terminal position; (f) **Au28** using three 7-deaza-6-thio-2'-deoxyguanosine (**1**) modifications as multiple anchors at the 5'-terminal position; (g) **Au36** using 7-deaza-6-thio-2'-deoxyguanosine (**1**) as molecular anchor within the periphery of the oligonucleotide chain; (h) **Au38** using 7-deaza-6-thio-2'-deoxyguanosine (**1**) as anchor at a central position of the oligonucleotide; (i) **Au40** using the commercial available hexylthiol linker as anchor at the 5'-terminal position and (j) **Au41** using the commercial available hexylthiol linker as anchor at the 5'-terminal position.

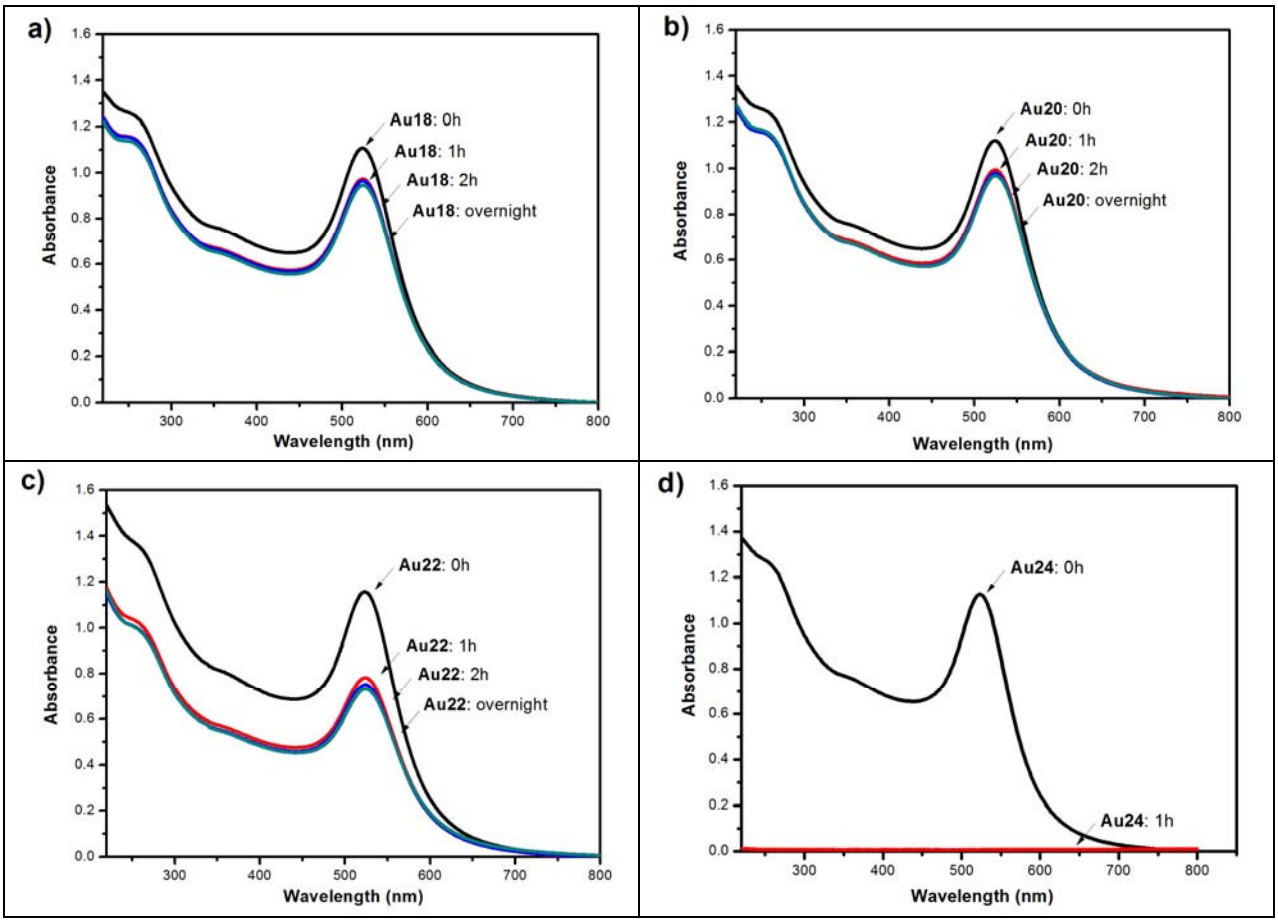


Figure S3. UV-VIS spectra of DNA-AuNP conjugates in a 0.2 M NaCl, 10 mM phosphate, pH 7.0 buffer solution recorded after different time intervals. (a) **Au18** using 7-deaza-6-thio-2'-deoxyguanosine (**1**) as molecular anchor. (b) **Au20** using 6-thio-2'-deoxyguanosine (**2**) as anchor. (c) **Au22** using 4-thio-2'-deoxythymidine (**3**) as anchor and (d) **Au24** using 2-thio-2'-deoxythymidine (**4**) as anchor.

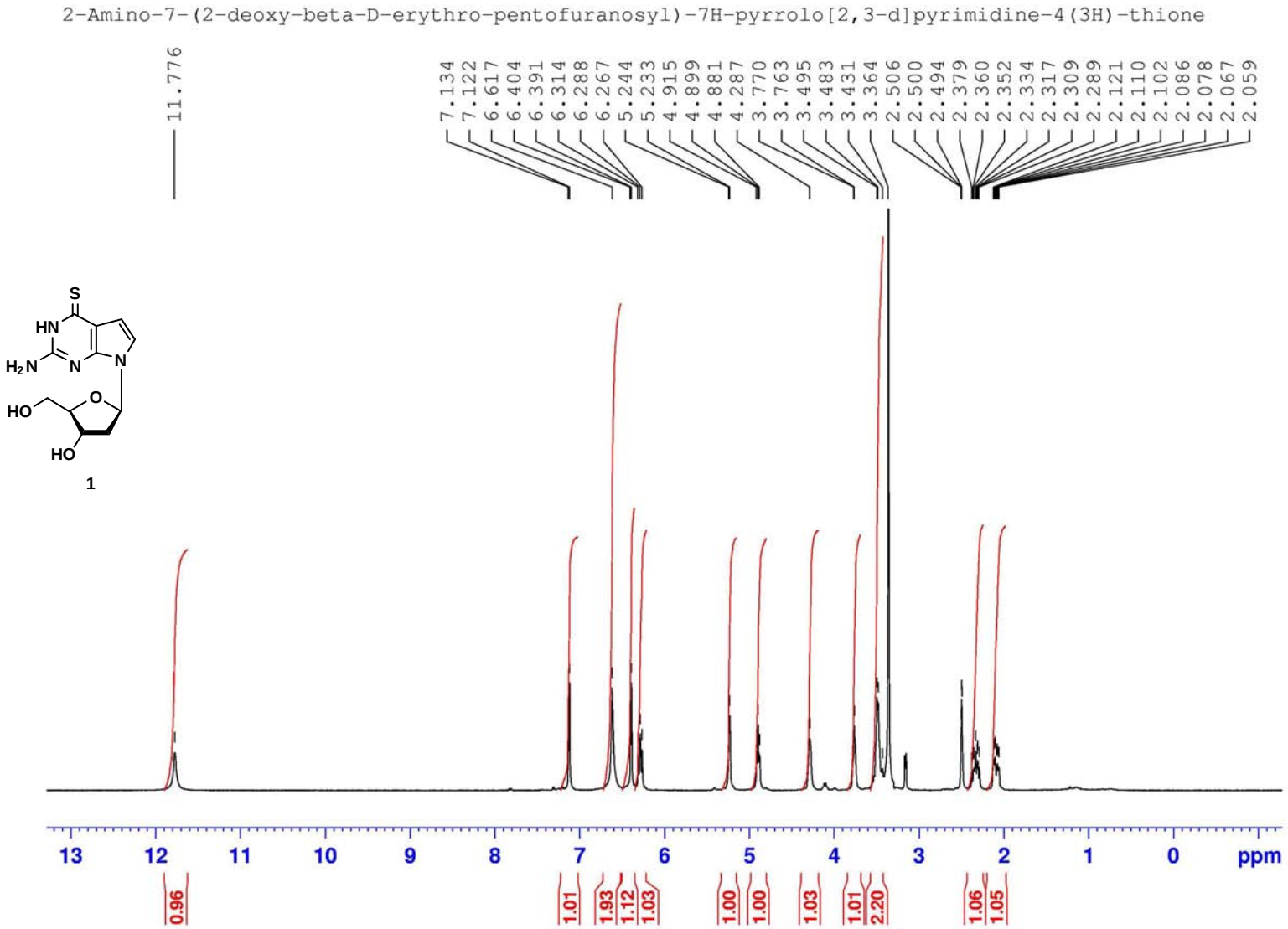


Figure S4. ^{1}H-NMR spectrum of compound 1.

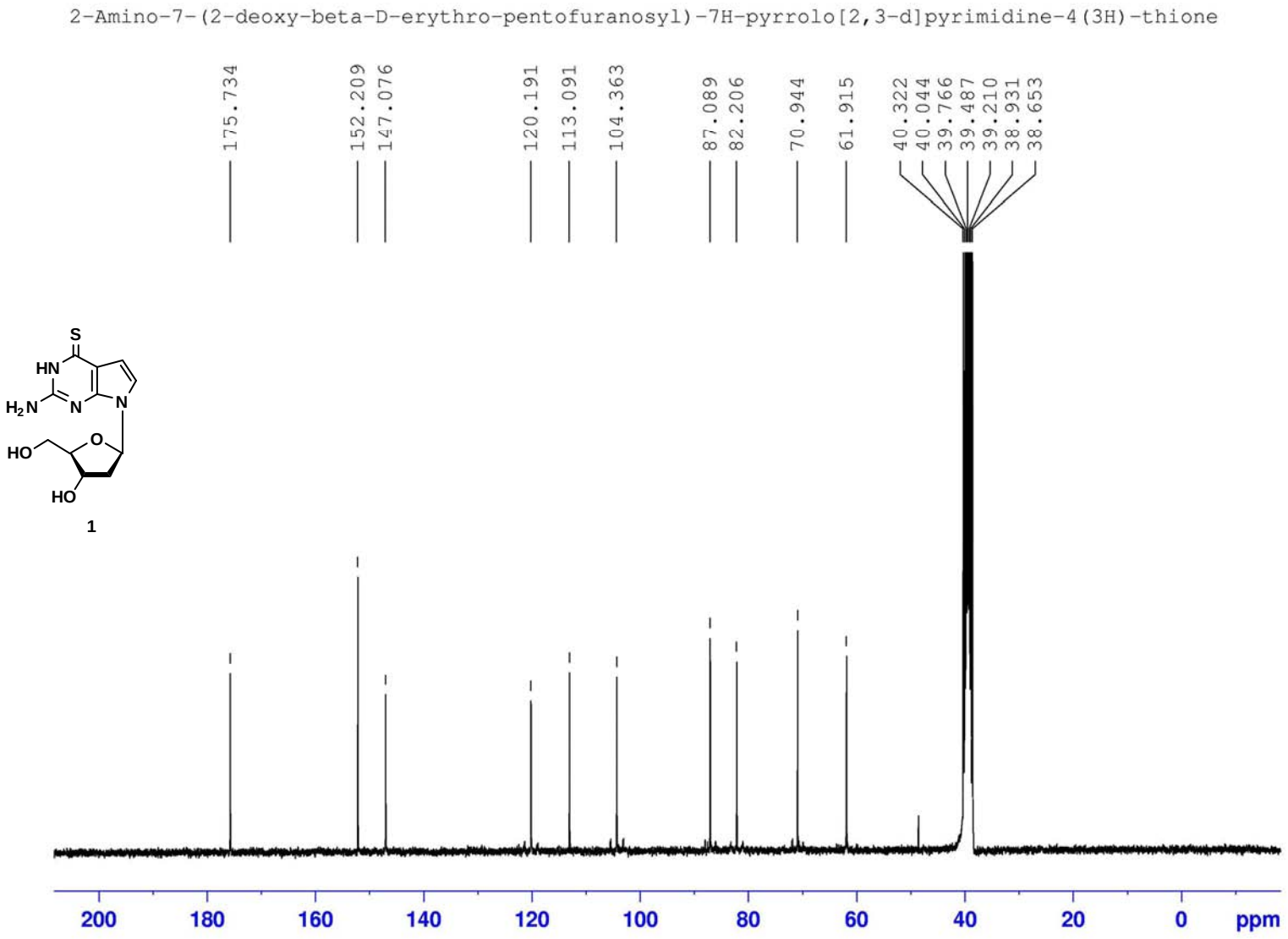


Figure S5. ^{13}C-NMR spectrum of compound 1.

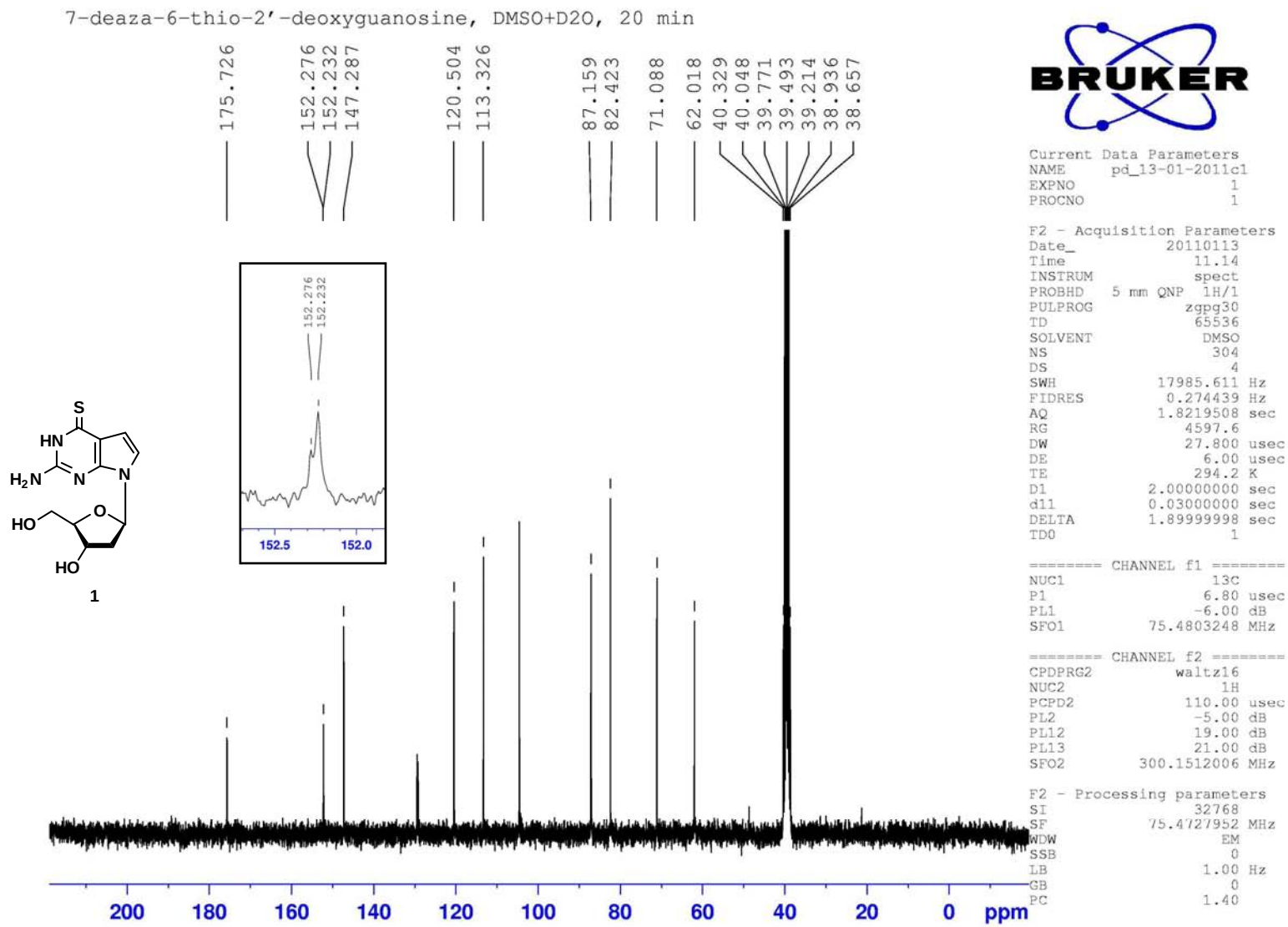


Figure S6. Deuterium isotope effect on the ^{13}C-NMR spectrum of compound 1.

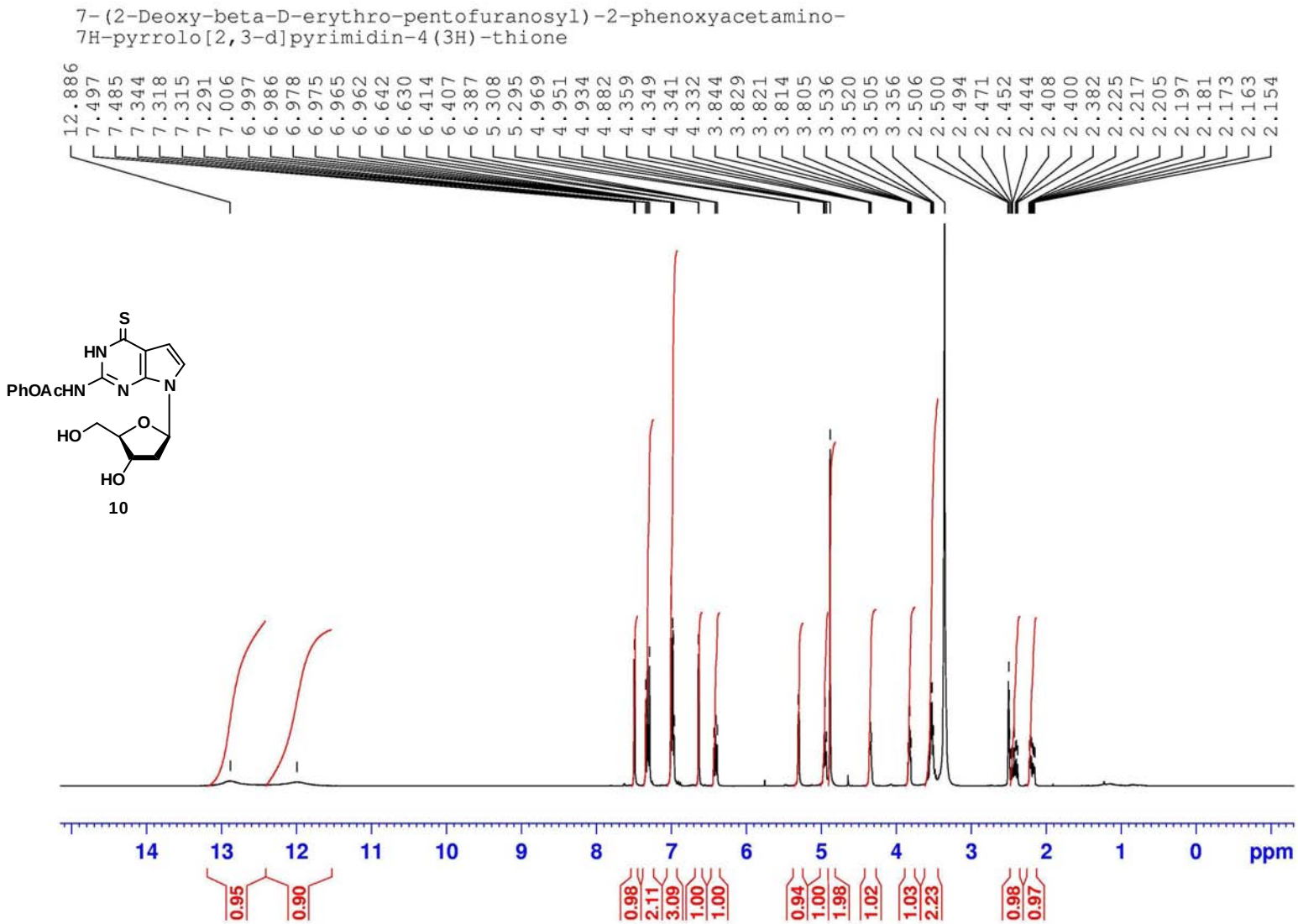


Figure S7. ^{1}H-NMR spectrum of compound 10.

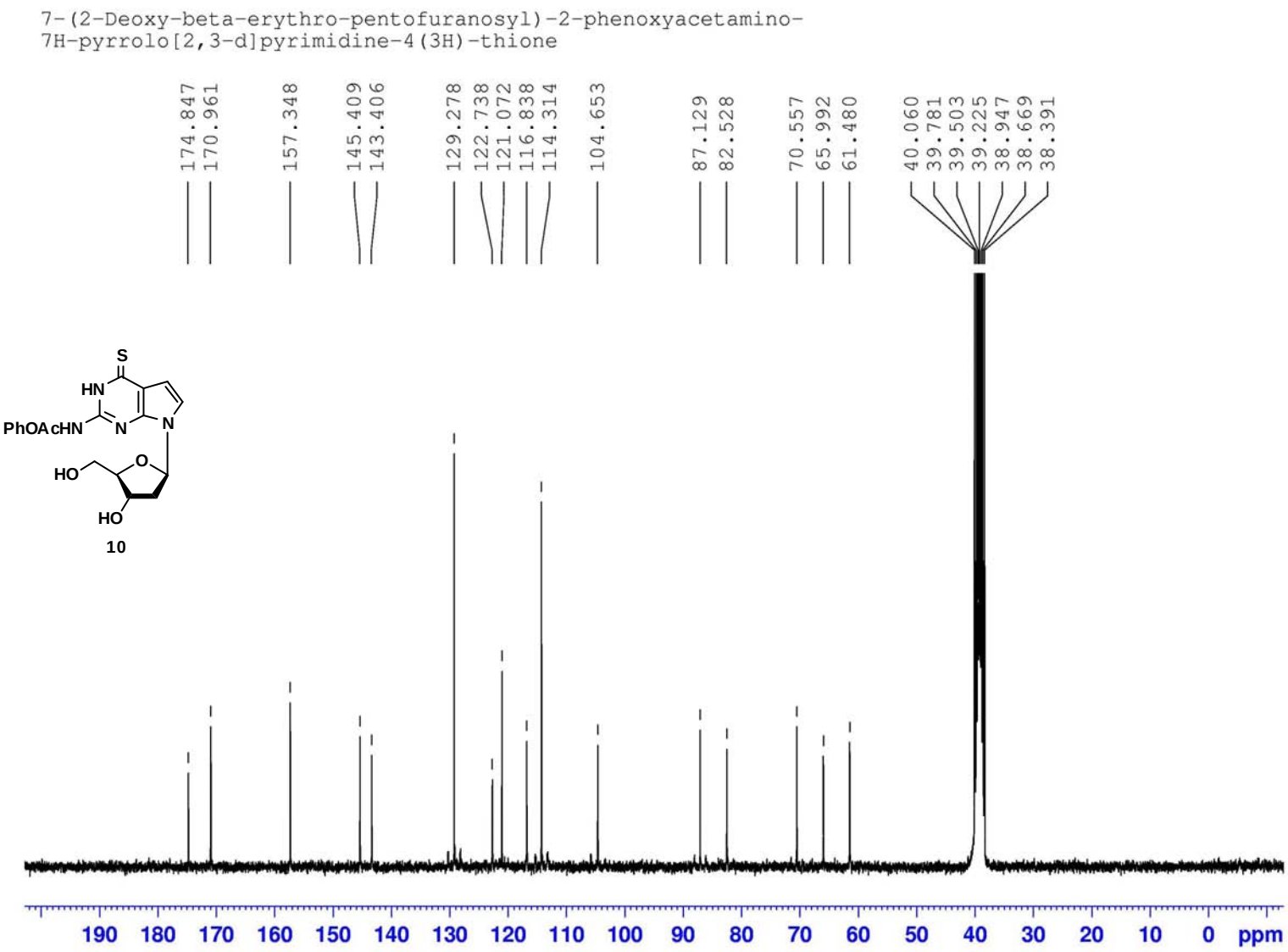


Figure S8. ^{13}C-NMR spectrum of compound 10.

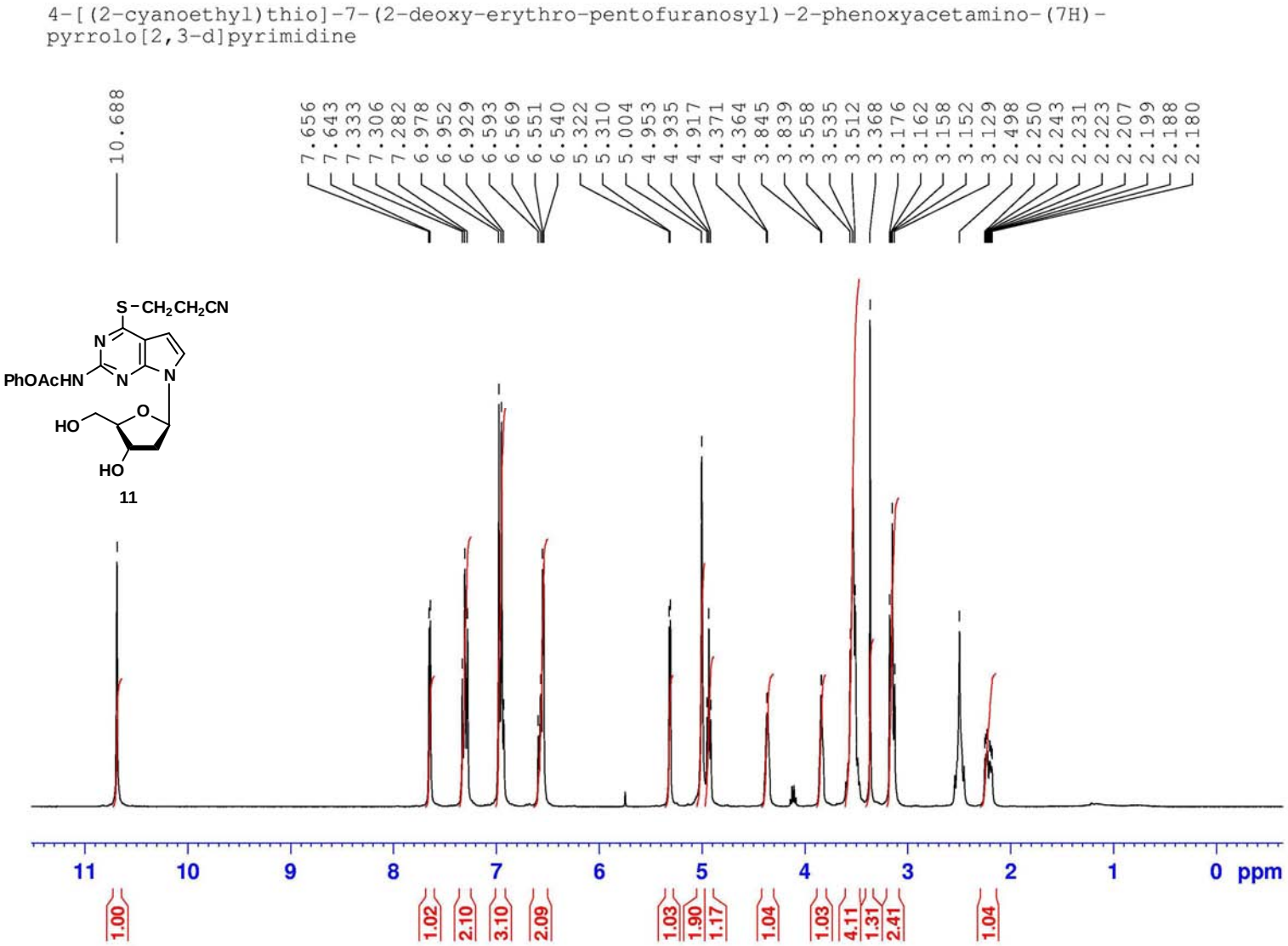


Figure S9. ^{1}H-NMR spectrum of compound 11.

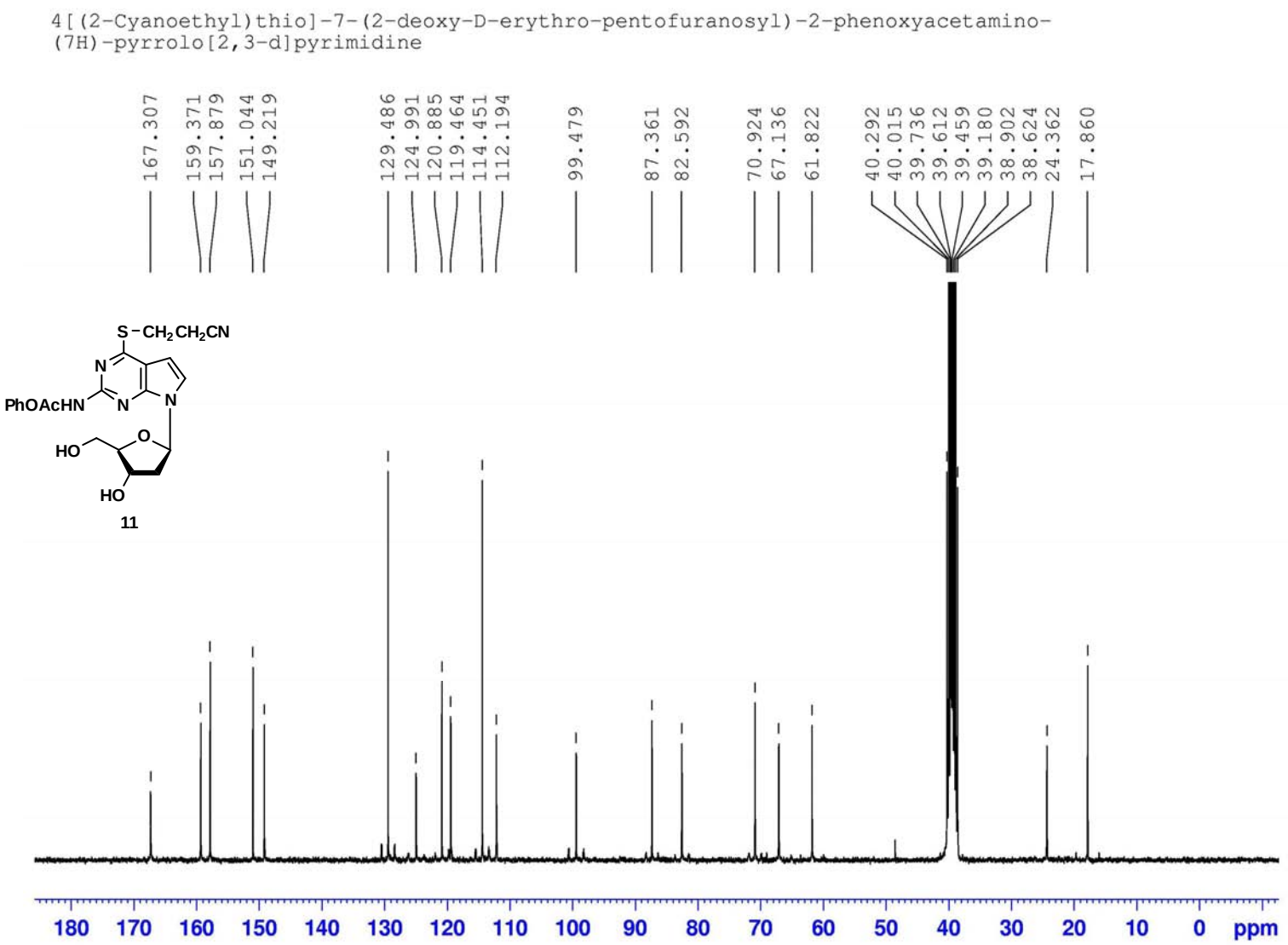


Figure S10. ^{13}C-NMR spectrum of compound 11.

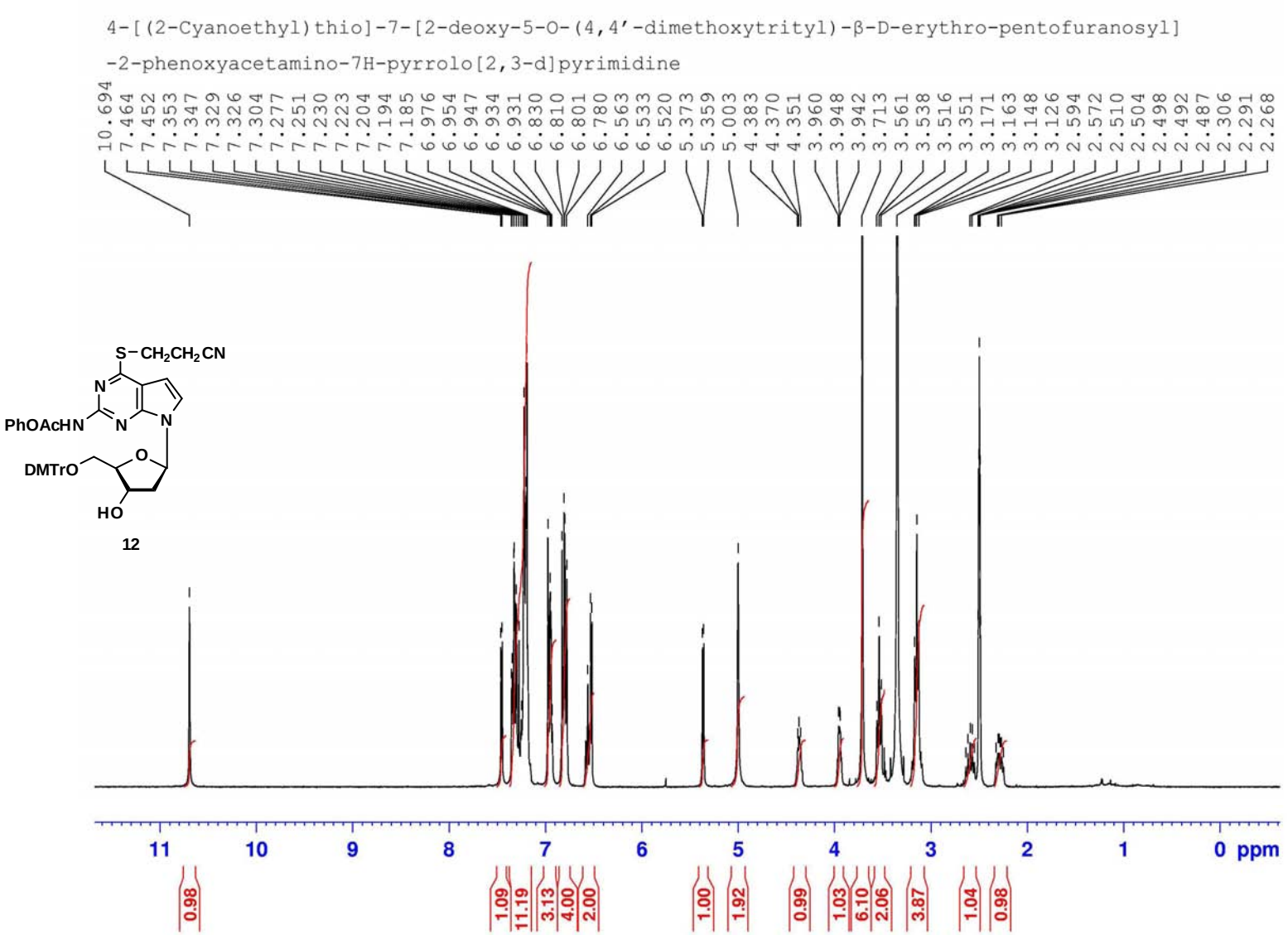


Figure S11. ^{1}H-NMR spectrum of compound 12.

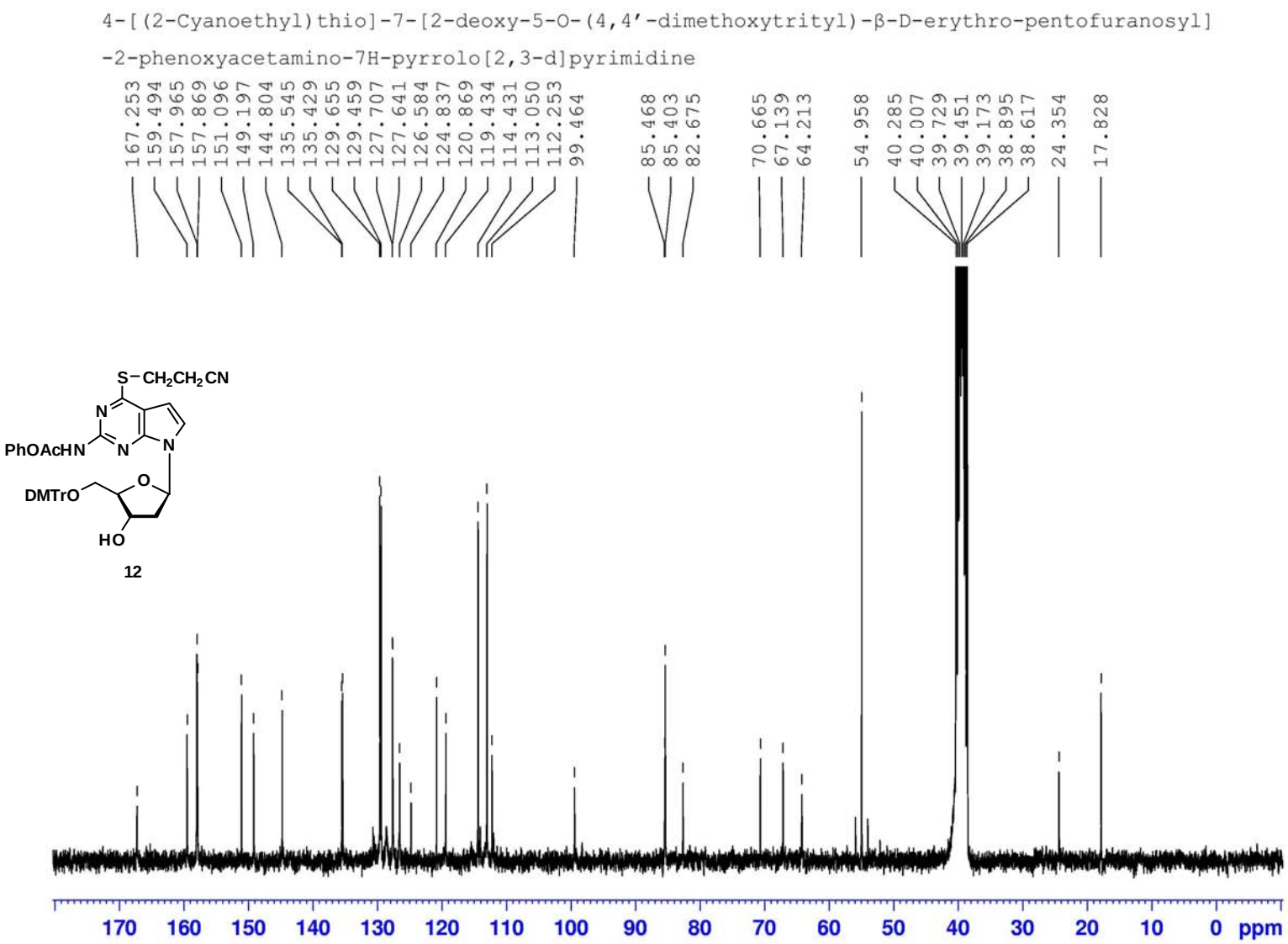


Figure S12. ^{13}C-NMR spectrum of compound 12.

4-[(2-Cyanoethyl)thio]-7-[2-deoxy-5-O-(4,4'-dimethoxytrityl)-β-D-erythro-pentofuranosyl]
-2-phenoxyacetamino-7H-pyrrolo[2,3-d]pyrimidine 3'-[(2-cyanoethyl)-N,N
-diisopropylphosphoramidite]

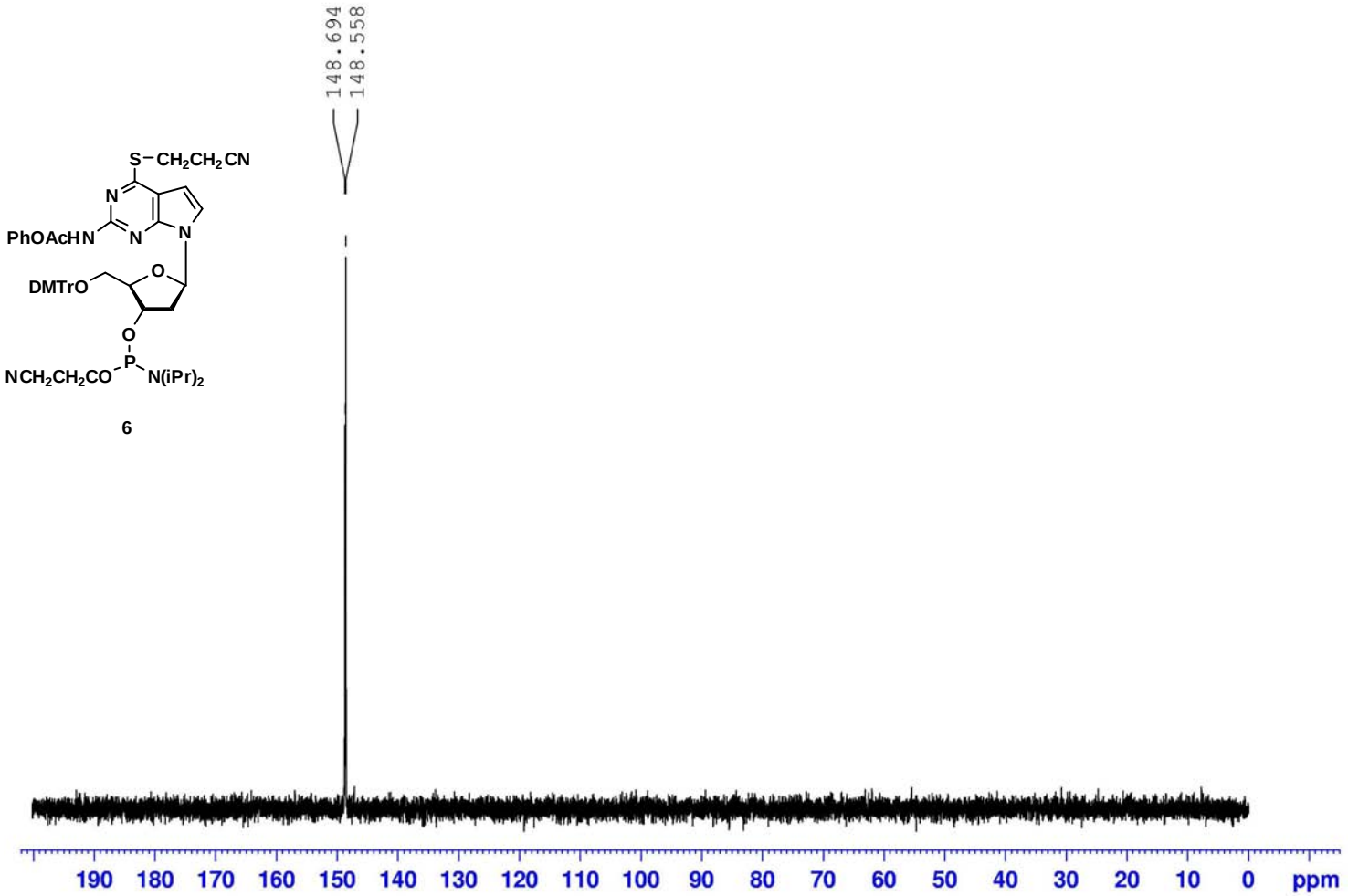


Figure S13. ^{31}P-NMR spectrum of compound 6.

Bioconjugate Chemistry

TECHNICAL NOTE

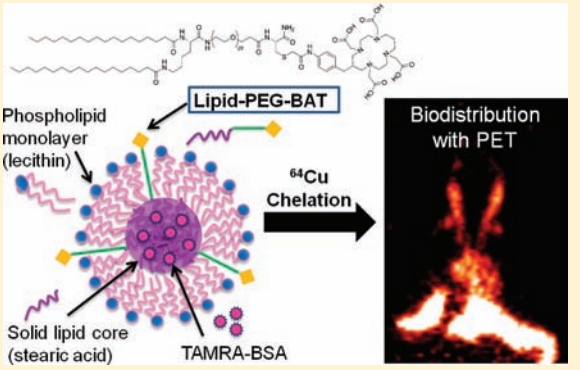
pubs.acs.org/bc

Novel Method to Label Solid Lipid Nanoparticles with ^{64}Cu for Positron Emission Tomography Imaging

Erica Andreozzi, Jai Woong Seo, Katherine Ferrara, and Angelique Louie*

Department of Biomedical Engineering, University of California, Davis, California, United States

ABSTRACT: Solid lipid nanoparticles (SLNs) are submicrometer (1−1000 nm) colloidal carriers developed in the past decade as an alternative system to traditional carriers (emulsions, liposomes, and polymeric nanoparticles) for intravenous applications. Because of their potential as drug carriers, there is much interest in understanding the *in vivo* biodistribution of SLNs following intravenous (i.v.) injection. Positron emission tomography (PET) is an attractive method for investigating biodistribution but requires a radiolabeled compound. In this work, we describe a method to radiolabel SLN for *in vivo* PET studies. A copper specific chelator, 6-[*p*-(bromoacetamido)-benzyl]-1,4,8,11-tetraazacyclotetradecane-*N*,*N*′,*N*″,*N*‴-tetraacetic acid (BAT), conjugated with a synthetic lipid, was incorporated into the SLN. Following incubation with $^{64}CuCl_2$ for 1 h at 25 °C in 0.1 M NH_4OAc buffer (pH 5.5), the SLNs (∼150 nm) were successfully radiolabeled with ^{64}Cu (66.5% radiolabeling yield), exhibiting >95% radiolabeled particles following purification. The ^{64}Cu-SLNs were delivered intravenously to mice and imaged with PET at 0.5, 3, 20, and 48 h post injection. Gamma counting was utilized post imaging to confirm organ distributions. Tissue radioactivity (% injected dose/gram, %ID/g), obtained by quantitative analysis of the images, suggests that the ^{64}Cu-SLNs are circulating in the bloodstream after 3 h (blood half-life ∼1.4 h), but are almost entirely cleared by 48 h. PET and gamma counting demonstrate that approximately 5−7%ID/g ^{64}Cu-SLNs remain in the liver at 48 h post injection. Stability assays confirm that copper remains associated with the SLN over the 48 h time period and that the biodistribution patterns observed are not from free, dissociated copper. Our results indicate that SLNs can be radiolabeled with ^{64}Cu, and their biodistribution can be quantitatively evaluated by *in vivo* PET imaging and *ex vivo* gamma counting.



INTRODUCTION

Solid lipid nanoparticles (SLNs) have emerged as an efficient, nontoxic, and versatile colloidal drug carrier system that avoids some of the disadvantages of liposomes and polymeric nanoparticles.[1] Because SLNs are composed of physiological lipids (i.e., fatty acids; mono, di, and triglycerides; phospholipids; etc.), they tend to show high compatibility and biodegradability and have a lower risk of the acute and chronic toxicity that is often associated with polymeric nanoparticles.[3,4] Furthermore, because SLNs comprise a solid lipid core instead of an aqueous core, they offer better protection against chemical degradation to their drug cargo than liposomes, and also facilitate sustained drug release due to the zero-order kinetic breakdown of the solid lipid matrix.[1,3,4] The solid lipid matrix of the SLN core can be modified to incorporate either hydrophobic or hydrophilic cargo.[4−6] The capability of SLNs to stably carry various types of cargo proteins[7,8] (cyclosporine,[9] insulin,[10] thymopentin,[11] etc.), antibiotics (tobramycin[12]), therapeutic agents[13] (camptothecin,[14] doxorubicin,[15] DNA,[16,17] siRNA,[18]), and diagnostic agents (gadolinium,[19,20] iron oxide nanoparticles,[21]) under various routes of administration (i.e., oral,[10] parenteral,[22] dermal,[23,24] ocular,[25,26] pulmonary,[27] and intravenous[28]) has generated increasing interest in their use as drug carriers.

To date, most of the studies evaluating SLNs as a drug carrier have focused on the delivery of the SLN cargo (i.e., encapsulated drug)[14,29] to the target site without investigating the fate of the SLN carrier itself. However, with the potential for release of cargo, it is crucial to understand the biodistribution of the carrier. This is especially important in guiding the appropriate SLN modifications necessary to control drug targeting behavior in a variety of applications. The aim of this work was to radiolabel SLNs with a positron emitting radionuclide (i.e., ^{64}Cu) in order to track their biodistribution *in vivo* using positron emission tomography (PET). PET is a noninvasive, nuclear imaging technique that is capable of visualizing deep tissues with a high sensitivity of 0.02−0.10 cps/Bq (2−10%)[30] and generating a three-dimensional image of living subjects. Using mathematical reconstruction methods and correction factors, quantitative information can be extracted from the images, and radioisotope concentration can be measured in a specific region of interest (ROI).[30,31] Herein, we describe a method to radiolabel SLNs with positron emitter ^{64}Cu (half-life = 12.7 h)[32] through the incorporation of a lipid-PEG-chelate (6-[*p*-(bromoacetamido)benzyl]-1,4,8,11-tetraazacyclotetradecane-*N*,*N*′,*N*″,*N*‴-tetraacetic acid (BAT) conjugated to a synthetic lipid)[2] into the phospholipid monolayer comprising the SLN surface (Figure 1). PET imaging was used to track the biodistribution of

Received: November 2, 2010
Revised: January 4, 2011
Published: March 09, 2011

ACS Publications © 2011 American Chemical Society

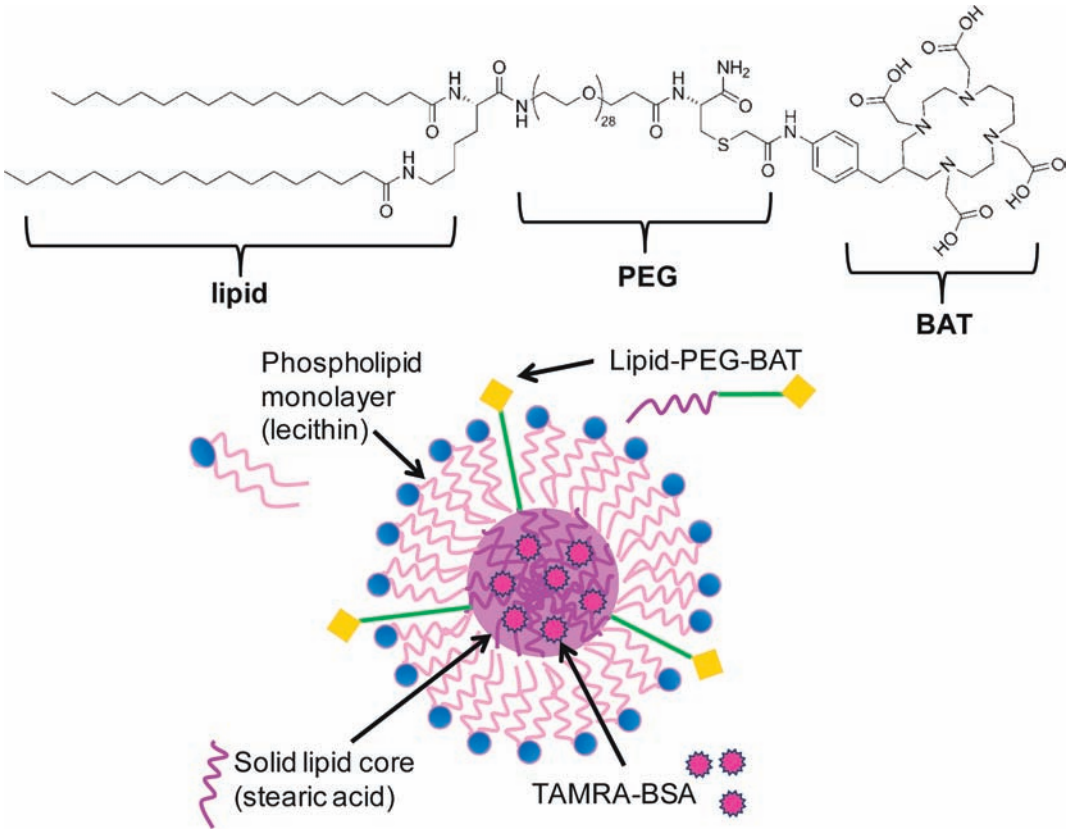


Figure 1. Schematic of SLN-BAT. The lipid-PEG-BAT (left) molecule is incorporated into the SLN such that the stearic acid lipid tail is embedded in the stearic acid lipid core, while the PEG is associated with the lecithin monolayer, and the BAT chelator remains accessible from outside the SLN (right). We anticipate that van der Waals forces would cause the lipid portion of the lipid-PEG-BAT molecule to associate with the lipid core of the SLN and therefore be incorporated inside. We also anticipate that van der Waals forces would cause the hydrophilic PEG portion of the lipid-PEG-BAT to be associated with the hydrophilic headgroups of the lecithin molecule, leaving the BAT accessible on the surface of the SLN. By testing the ability for the SLNs to radiolabel ^{64}Cu, we validate the incorporation of lipid-PEG-BAT into the SLN and the accessibility of the BAT groups on the surface.

the SLN and followed up to 48 h following intravenous (i.v.) administration.

EXPERIMENTAL PROCEDURES

Materials. Laboratory-grade vegetable lecithin, stearic acid, and 1-butanol were purchased from Fisher Chemical (Pittsburgh, PA). Sodium taurodeoxycholate hydrate, high-purity ammonium acetate (≥99.995%), and Sephadex (G-25, G-50) were purchased from Sigma-Aldrich (St. Louis, MO). Bovine serum albumin was from Acros Organics, Belgium, distributed by Fisher Scientific. 5-(and-6)-Carboxytetramethylrhodamine, succinimidyl ester (5(6)-TAMRA, SE) *mixed isomers* (TAMRA) (*Ex* = 555 nm, *Em* = 580 nm) was purchased from Invitrogen Corporation (Carlsbad, CA). Formvar coated copper grids (300 Mesh) were purchased from SPI Supplies (West Chester, PA). $^{64}CuCl_2$ was purchased from Washington University (St. Louis, MO). Nanopure water (18.0 MΩ·cm) was prepared from deionized water using a Barnstead nanopure filtration unit.

Encapsulation of Fluorescently Labeled Protein into SLN. *Fluorescent Labeling of BSA.* Bovine serum albumin (BSA) was labeled with the fluorophore, 5(6)-carboxytetramethyl-rhodamine *N*-hydroxy-succimide ester (TAMRA), following the standard Invitrogen protocol for labeling proteins with amine-reactive fluorophores. First, BSA was dissolved in 0.1 M sodium bicarbonate buffer (10 mg/mL). TAMRA (10 mg/mL in dimethyl sulfoxide) was slowly added to the BSA solution in a 2:1 molar ratio of TAMRA to BSA under continuous stirring for 1 h at room temperature. The unlabeled TAMRA was separated from the BSA-TAMRA conjugate through a Sephadex (G-25) packed bed column equilibrated with 0.1 M sodium bicarbonate buffer. After separation, the BSA-TAMRA conjugate was dialyzed (50,000 MWCO) for 3 days with 0.1 M sodium citrate (pH 7.2) to remove buffer salts.[33] BSA-TAMRA was encapsulated into solid lipid nanoparticles (SLNs) using a modification of a water/oil/water method.[11,34]

Incorporation of Labeled BSA into SLN: Water/Oil/Water Method. A warm W/O phase was first prepared by adding a warm aqueous solution of BSA-TAMRA (300 mg/mL) to a mixture of molten stearic acid, lecithin, and 1-butanol at 78 °C (Table 1). The W/O phase was then cooled to room temperature, and a portion of this warm solid phase was added to a warm mixture of nanopure water, lecithin, sodium taurodeoxycholate, and 1-butanol at 76 °C forming a W/O/W emulsion (amounts given in Table 1). The W/O/W (∼0.3 mL) was then dispersed in 10 mL of cold nanopure water (1/33, v/v) at 4 °C under rapid stirring, forming SLNs. The resulting SLN suspension was filtered through Millipore polyethersulfone syringe-filter units (0.22 μm pore size, Millipore) to select for particles of <220 nm. Then, the SLN-BSA-TAMRA suspension (10 mL) was washed

dx.doi.org/10.1021/bc100478k |*Bioconjugate Chem.* 2011, 22, 808–818

Table 1. Preparation of SLN with Optical Cargo: W/O and W/O/W Phase Composition

W/O phase		W/O/W phase	
material	amount	material	amount
Stearic acid	67.2 mg, 0.24 mol	Nanopure water	158.3 mg
Lecithin	40.2 mg, 0.05 mol	Lecithin	8.5 mg, 0.01 mol
1-Butanol	32.6 mg, 0.44 mol	Sodium taurodeoxycholate	10.4 mg, 0.02 mol
BSA-TAMRA (aq)	10.2 mg, 0.0002 mol	1-Butanol	2.8 mg, 0.04 mol
	N/A	W/O phase	18.00 mg

(3×) with nanopure water and concentrated (2 mL) using an Amicon ultrafiltration cell with 100 000 MWCO membrane filters (Millipore).

Characterization (Size, Morphology, Encapsulation Efficiency, Toxicity) of SLN. The average size and polydispersity index (PDI) of the protein-loaded SLNs were determined with dynamic light scattering (DLS) immediately following synthesis (Nanotrac 150 particle size analyzer, Microtrac). Particle size was also measured using transmission electron microscopy (TEM) (Phillips CM-120) operating at 80 keV. The SLN suspensions were diluted 10- and 20-fold and plated onto Formvar coated copper grids (300 Mesh) to dry overnight. Images were analyzed using *ImageJ* software (National Institutes of Health) and $n = 500$ particles were measured to yield average particle diameter. In addition to size analysis, the zeta potential of the SLNs was measured with a NICOMP 380 ZLS (Particle Sizing System, CA).

The amount (mg) of BSA-TAMRA found in the retentate (SLN-BSA-TAMRA) and the elutant (free BSA-TAMRA) after ultrafiltration was determined by measuring the fluorescence intensity (Fluoromax) at 580 nm and used to characterize the amount of fluorescently labeled protein encapsulated by the SLN. The % encapsulation efficiency (%EE) of the protein within the SLNs was calculated according to the following equation:

$$\%\mathrm{EE} = [\mathrm{BSA-TAMRA(mg)in\ retentate}]/[\mathrm{BSA-TAMRA\ (mg)in\ retentate + elutant}] \times 100\%$$

Cytotoxicity Measurements. Madin-Darby canine kidney cells (MDCK), a kind gift from the Reen Wu lab (University of California, Davis), were plated onto 96 well plates at a seeding density of $\sim 1 \times 10^3$ cells per well. The cells were maintained in phenol-red free Dulbecco's Eagle minimum essential medium (DMEM), supplemented with 2 mM L-glutamine, 10% fetal bovine serum (FBS), and streptomycin/penicillin (100 U/mL) at 5% CO_2 and 37 °C. The medium was changed every other day until the cells reached confluency, then the cells were washed three times with phosphate buffered saline (PBS)[35] and 100 μL of a 25 mM (lipid concentration) solid lipid nanoparticle (SLN) suspension was added above the cell monolayer in each well for the experimental group, while phenol-red free DMEM was added for the control. The SLNs in this suspension were reconstituted in DMEM free of phenol-red indicator in order to prevent any interference with the cell viability fluorescence assay measurements. The cells were incubated with the SLN for 24 h (5% CO_2, 37 °C) and then the medium was removed. Next, 100 μL of a LIVE/DEAD working solution (Invitrogen) containing 1 μM calcein AM and 2 μM EthD-1 was added to each well and allowed to incubate at room temperature for 30 min. Calcein (Ex/Em ~495 nm/~515 nm) is only retained in live cells, and cell viability was quantified by measuring the fluorescence (Ex/Em ~495 nm/~525 nm) of the cells using a microplate spectrophotometer (Safire II, Tecan Group Ltd.) The average fluorescence (Ex/Em ~495 nm/~515 nm) intensities of the cells incubated with and without SLNs (lipid concentration = 25 mM) were measured. A two-tailed *t*-test was performed to determine if there was a significant difference in viability between the cells that had been incubated with the SLNs and controls.

Radiolabeling, Purification, and Stability of Protein-Loaded SLNs. *Incorporation of BAT Chelator into the SLN (SLN-BAT).* Solid lipid nanoparticles (SLNs) were synthesized using the same W/O and W/O/W phase compositions as above, shown in Table 1, with the exception of adding 164.7 μg (0.062 μmol, 0.5% mol/mol ratio BAT to lipid) lipid-PEG-BAT (164.7 μL of 1 μg/μL solution) to the warm mixture of nanopure water, lecithin, sodium taurodeoxycholate, and 1-butanol before the addition of the W/O phase in the W/O/W formation. We used lipid-PEG-BAT conjugate previously synthesized by Fmoc solid-phase synthesis and purified by reverse-phase high-performance liquid chromatography (HPLC), with the mass confirmed by matrix-assisted laser desorption/ionization (MALDI) (measured, 2662).[2] The W/O/W (~0.3 mL) was then dispersed in 10 mL of cold nanopure water (1/33, v/v) at 4 °C under rapid stirring, forming SLNs. The SLNs were then filtered through Millipore polyethersulfone syringe-filter units (0.22 μm pore size, Millipore) to select for particles of <220 nm and particle size was determined using DLS. Immediately after sizing, the SLN suspension (10 mL) was washed (3×) and concentrated to 200 μL using an Amicon ultrafiltration cell with 300,000 MWCO membrane filters (Millipore).

^{64}Cu Radiolabeling of SLN-BAT (^{64}Cu-SLN). An aliquot of 0.1 M ammonium acetate (NH_4OAc solution, pH 5.6) was added to the concentrated SLN-BAT solution to adjust the pH to 5.5. Copper-64 chloride ($^{64}CuCl_2$) solution (4.1−5.1 mCi, 151.7−188.7 MBq in 10 mM HCl) was combined with the SLN-BAT solution, resulting in final concentration of ~10 mCi/mL and ~1.3 mCi/mg lipid. After vortexing, this solution was incubated for 1 h at room temperature. Then, EDTA solution (0.1 M, 30 μL, 1/10 v/v ratio) was added (final EDTA concentration 10 mM) to the mixture and incubated for 30 min at room temperature in order to chelate the unbound ^{64}Cu. Free ^{64}Cu-EDTA was removed from the ^{64}Cu-SLN suspension (0.3 mL) by chromatography through a G-50 Sephadex column (GE Healthcare, NJ) eluted with 0.9% saline, and the eluted fractions (~1.0 mL) were collected in 1.5 mL centrifuge tubes. Radioactivity of the ^{64}Cu-SLN suspension before and after column purification was measured with a Fluke Biomedical Dose calibrator (34−162 CAL/RAD MARK IV, Cleveland, OH). The radiolabeling yield (%) for the SLNs was determined by dividing the radioactivity of the largest fraction by the sum of all the fractions (total activity) and multiplying by 100. Thin-layer

dx.doi.org/10.1021/bc100478k |*Bioconjugate Chem.* 2011, 22, 808–818

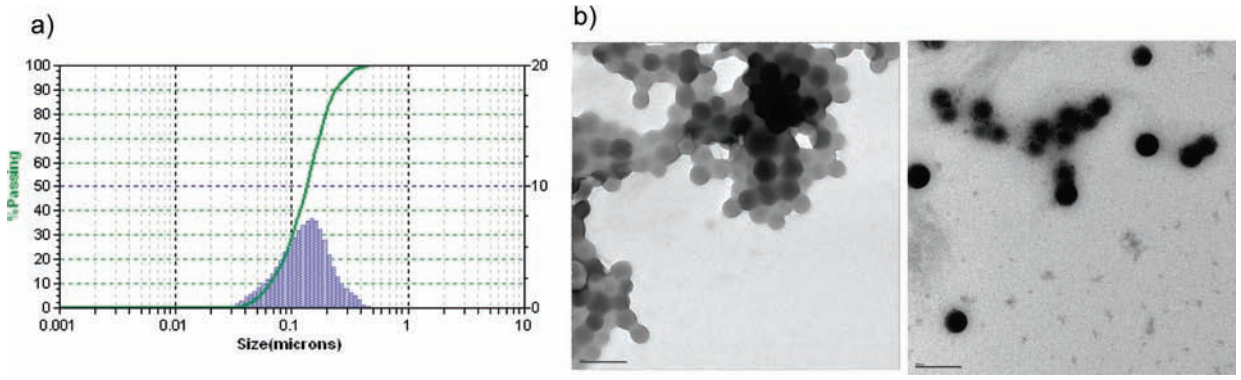


Figure 2. Size characterization of SLNs. (a) Average hydrodynamic diameter (145.2 ± 7.0 nm) of the optical SLNs, measured using dynamic light scattering (DLS). (b) Transmission electron microscopy (TEM) images of the 10-fold (left) and 20-fold (right) diluted SLN suspensions showing the mean dehydrated SLN diameter = 89 nm; scale bar = 100 nm.

chromatography (TLC) of the purified ^{64}Cu-SLNs was run on aluminum-backed silica gel sheets (silica gel 60 F_{254}, EMD, NJ), developed with methanol/ammonium acetate (10%) (50/50, v/v), and the radio TLC was recorded by a radio-TLC Imaging Scanner (Bioscan, NW).

Stability of ^{64}Cu-SLNs. ^{64}Cu-labeled SLNs were incubated in calf bovine serum (100%, pH 7.4) and saline solutions with varying pH (5.5, 4.0, and 2.0) for up to 48 h in order to assess the stability of the complexed copper before and after administration in mice. An aliquot (100 μL) was removed at each time point (0.5, 3, 20, and 48 h) and measured for initial activity (before purification) using a dose calibrator. The aliquots were incubated for 10 min with 10 μL (1/10, v/v) EDTA (0.1 M in water) and centrifuged through filter tubes (Millipore, molecular weight cutoff [MWCO] = 10,000, Billerica, MA) at 14,500 rpm for 30 min to separate dissociated ^{64}Cu-EDTA in solution from the labeled SLNs on the filter. The activity remaining on the filter post purification was measured and divided by the initial activity to calculate the percentage (%) of label remaining on the SLNs. Comparisons between values were determined using the least-squares means *t*-test, and differences observed were considered significant when $p < 0.01$. For further confirmation of stability, radio TLC was performed on aliquots of ^{64}Cu-SLNs incubated with serum for 24 and 48 h. EDTA was used to chelate unbound ^{64}Cu in both the centrifugation purification and radio TLC measurements.

***In Vivo* Studies: Biodistribution and Pharmacokinetics of ^{64}Cu-SLN Using PET Imaging and Gamma Counting.** All animal studies were conducted under a protocol approved by the University of California, Davis, Animal Use and Care Committee. A total of 3 mice (female, 39.71 ± 3.11 g, Charles River, MA) were examined over the course of this study. Mice were initially anesthetized with 3.0% isofluorane, then maintained at 2.0−2.5% isoflurane, and catheterized to ensure proper tail vein injection. Injections (280−320 μL) of ^{64}Cu-SLN (409.01 ± 43.11 μCi, 15.1 ± 1.6 MBq, 9.9 ± 1.6 mg) in 0.9% saline were administered via tail vein injection, yielding a lipid dose of 0.27 ± 0.04 mg/g animal and 38.36 ± 7.16 μCi/mg lipid (1.4 ± 0.3 MBq/mg lipid). Static PET scans (0.25, 1.0, 0.75, and 1.0 h duration scans) were acquired for each animal (anesthetized with 1.5% isoflurane maintenance dose) at 0.5, 3.0, 20, and 48 h post injection using the MicroPETII scanner.[36] The MicroPETII consists of 17,640 LSO crystals each measuring 0.975 × 0.975 × 12.5 mm^3, which are arranged in 42 contiguous rings, with 420 crystals per ring. The scanner has an axial field of view (FOV) of 4.9 cm and a transaxial FOV of 8.5 cm.[37] The limited transaxial FOV of ∼8.5 cm only enabled signal acquisition from the top of the head to the liver region. Therefore, signal from organs below the liver (i.e., kidney, bladder, etc.) was not included in the images. The reconstructed spatial resolution is ∼1 mm with an absolute system sensitivity of 2.26%.[36] Static scans yield a single image that represents the average intensities for a given acquisition time.

The static PET scans were reconstructed with a maximum a posteriori (MAP) algorithm and used to obtain quantitative activity levels in each organ of interest as a function of time. Tissue radioactivity was determined using the mean activity value given by the *ASIPro Virtual Machine* software (CTI Molecular Imaging) from defined regions of interest (ROI) within these MAP files. All values for ROI were decay corrected to the zero hour time point for comparison, and the percent injected dose (%ID) was determined by dividing the corrected ROI value for a given organ by the injected dose and multiplying by 100. A time activity curve (TAC) for blood was generated by drawing 0.03 cm^2 ROIs within the heart (∼5 slices) for all time points (0.5, 3, 20, 48 h) and expressing the mean measured activity as the percentage of injected dose per cubic centimeter (%ID/cc). A monoexponential curve was fit to the data series and used to estimate the blood half-life for the ^{64}Cu-SLNs.

After the 48 h PET scans, the mice were euthanized by administration of sodium pentobarbital (150 mg/kg) and perfused with 60 mL of 0.9% saline. Organs of interest were harvested and weighed and radioactivity was measured using a Wallac Wizard Automatic Gamma Counter model 1470 (Perkin-Elmer, Waltham, MA) at 52−55 h post i.v. injection. One-way analysis of variance (ANOVA) was conducted in *Prism* (GraphPad software Inc. San Diego, CA) and used to assess the significance of organ biodistribution.

RESULTS AND DISCUSSION

Preparation and Characterization (Size, Morphology, Charge, Toxicity) of Protein-Loaded SLNs. Because the size and the charge of nanoparticles are known to significantly influence their fate *in vivo*, it was important to measure these particle properties for SLNs. Using dynamic light scattering (DLS), the mean hydrodynamic diameter of the SLNs was

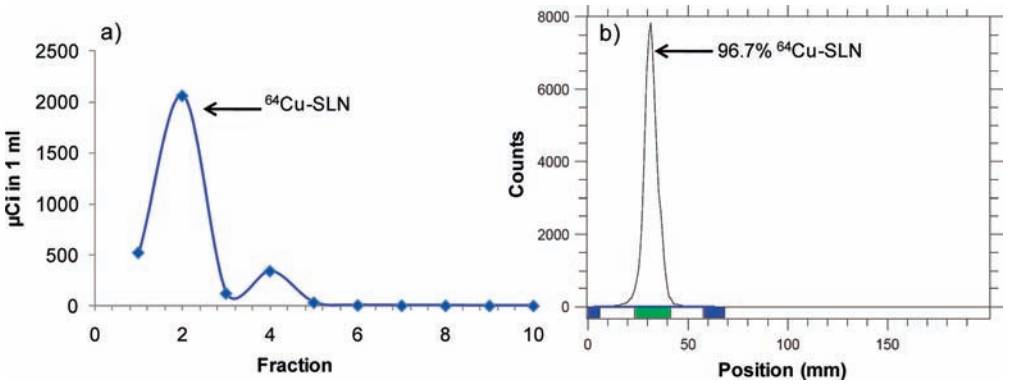


Figure 3. Radiolabeling yield (%) and purification of SLNs. (a) Elution profiles of ^{64}Cu-SLN after incubation with $^{64}CuCl_2$ (1 h) and EDTA (25 min) at 25 °C and separation through a size-exclusion column. (b) Following purification, radio TLC of ^{64}Cu-SLN on a silica plate was developed with methanol/ammonium acetate (10%) (50:50, v/v) and recorded by a radio-TLC imaging scanner. Results show >95% radiolabeled nanoparticles.

determined to be 145 ± 7.0 nm (Figure 2a). From the TEM images in Figure 2b, we observe that the SLNs exist as a uniform, monodisperse population of spherical particles with a diameter of 86 ± 0.6 nm (n = 500 particles, *ImageJ*). We believe that the difference in SLN diameter measured from DLS (∼150 nm) compared to TEM (∼90 nm) is due to the inability of TEM detect the hydration shell that surrounds the phospholipid monolayer of the SLN. By either measurement, the SLNs fall into the 20−200 nm size range reported for particles capable of avoiding rapid clearance through the kidneys,[6] thus making them attractive carriers for *in vivo* drug delivery.

To assess the stability of the SLN in suspension, we measured their zeta potential. A high zeta potential will confer stability (i.e., the solution or dispersion will resist aggregation) with the dividing line between stable and unstable suspensions generally considered to be at ±30 mV, and with maximum electrostatic stabilization reached at around ±60 mV.[38] The SLNs were measured to have a zeta potential of −36 mV, indicating an electrically stable, anionic particle solution. Previous studies show that negatively charged particles of ≥ −30 mV have good stability and could be optimal for drug delivery.[39,40] Aside from governing particle stability, zeta potential also influences particle recognition by the reticuloendothelial system (RES). In a previous study by Manjunath et al., highly negatively charged (−35.1 ± 0.5 mV) SLNs exhibited higher effective bioavailability (60.4%) of the encapsulated drug than less negatively charged particles (−18.2 ± 0.3 mV) SLNs (44.4%).[29] This is consistent with other studies showing that liposomes formed with negatively charged phospholipids maintained prolonged circulation time in mice.[41]

In order to provide an optical handle to track SLN during purification and characterization, we synthesized SLNs containing bovine serum albumin (BSA) labeled with the fluorophore, TAMRA. The encapsulation efficiency (EE, %) of BSA-TAMRA within SLNs was approximately 86.9 ± 5.3%, which is relatively high in comparison to other reported hydrophilic cargoes.[3−5,8,42] For example, the maximum EE for the hydrophilic drug Zidovudine (an antihuman immunodeficiency viral agent) in SLNs composed of stearic acid was 27%.[43] Because lipophilic agents have high solubility in the lipid microemulsion preceding SLN formation, SLNs are more efficiently loaded with lipophilic drugs. Entrapment of hydrophilic drugs inside the hydrophobic matrix of SLNs is a bit more challenging because the drug has a tendency to partition into the water phase during the fabrication process.[43] SLNs thus incorporate hydrophilic drugs at lower encapsulation efficiencies.[7,42,44−46] Zidovudine,[43] Atazanavir,[46] thymocratin,[47] insulin,[10] diminazene,[48] and thymopentin[11] are examples of hydrophilic drugs that have been successfully incorporated into SLNs. Interestingly, Singh et al. found that fatty acids (i.e., stearic acid) were superior to triglycerides to enhance entrapment efficiency.[49] This is consistent with our observations of high EE for BSA-TAMRA (hydrophilic protein) encapsulated in our SLNs, whose primary lipid was stearic acid. Furthermore, encapsulation of the hydrophilic HIV protease inhibitor, Atazanavir, into SLNs of similar size (∼167 nm) and composition (stearic acid) to our SLNs resulted in a similar EE (∼90%).[46] These results suggest that using stearic acid as the primary lipid component of our SLNs is favorable for achieving high EE of hydrophilic cargo.

Toxicity of the SLNs was assessed *in vitro*. Incubation (24 h) of SLNs at a lipid concentration of 25 mM with MDCK cells (data not shown) showed no statistical difference (p-value = 0.51) in viability compared to controls. The 25 mM lipid concentration that was tested *in vitro* was ∼2.5 times larger than the concentration of the injected dose to be used for *in vivo* studies. The lipid (molecular weight ∼500 g/mol) dose to each mouse was approximately 10 mg, yielding a circulating lipid dose of ∼10 mM, assuming total mouse blood volume of ∼2 mL. These results are consistent with previous investigations of stearic acid based SLNs that found them to be nontoxic to human promyelocytic leukemia (HL60) and human breast adenocarcinoma (MCF-7) cell lines.[42,50] In comparison to SLNs, FDA-approved polyester nanoparticles, i.e., poly(lactic-*co*-glycolic acid) (PLGA), polylactic acid (PLA), etc., were 10- to 20-fold more toxic to human granulocytes.[9,42] The low cytotoxicty of SLNs makes them very attractive for drug delivery, especially to highly sensitive organs like the brain.[42] Also, the ability to load drugs into SLNs with a high encapsulation efficiency (EE), such as 86.9 ± 5.3% observed with our system, further reduces the potential for cytotoxicity by reducing the dose of particles required to achieve a pharmacological effect. Overall, these *in vitro* cytotoxicity studies suggest that SLNs are nontoxic and that they can be used for *in vivo* animal imaging studies.

Preparation and Characterization (Radiolabeling, Purification, Stability) of ^{64}Cu-SLNs. Because the goal of this study was to track the biodistribution of the SLN carrier and not the cargo, we used a surface chelation method to radiolabel the SLNs

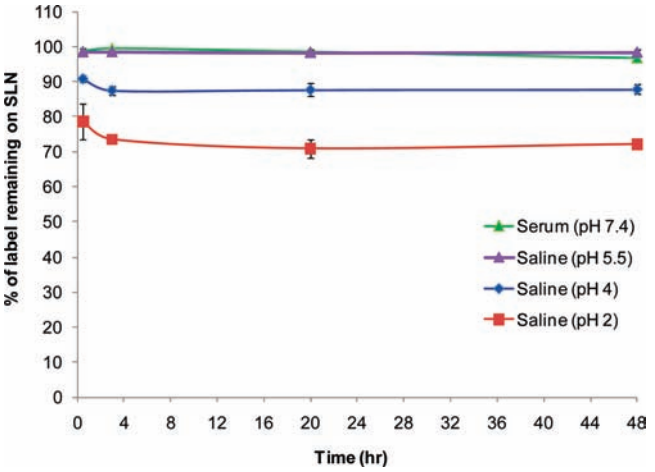


Figure 4. Stability of SLNs. Stability of radiolabeled solid lipid nanoparticles (SLNs) over 48 h in serum (pH 7.4), saline (pH 5.5), saline (pH 4), and saline (pH 2). Bars represent mean ± standard deviation (n = 3/group).

with ^{64}Cu. This chelation method required the incorporation of a lipid-PEG-chelate conjugate into the SLN so that the chelator remains accessible at the surface for ^{64}Cu chelation. We previously showed that liposomes could be radiolabeled after incorporation of this lipid-PEG-chelate conjugate into the liposome bilayer.[2]

High SLN Radiolabeling Yield (%). A ^{64}Cu-specific chelator, 6-[*p*-(bromoacetamido)benzyl]-1,4,8,11-tetraazacyclotetradecane-*N*,*N*′,*N*″,*N*‴-tetraacetic acid (BAT), conjugated to stearic acid (lipid-PEG-BAT) has been previously synthesized and used to radiolabel liposomes with ^{64}Cu,[2] and we hypothesized that this lipid-PEG-BAT molecule could function similarly to radiolabel our SLNs. We anticipated that the lipid portion of the lipid-PEG-BAT molecule would be incorporated into the solid lipid core, the PEG would be associated at the level of the lecithin headgroups, and the BAT would remain accessible on the surface. The elution profiles of radiolabeled SLNs following column purification are shown in Figure 3a, with fraction 2 representing the purified ^{64}Cu-SLN population. Fraction 2 was analyzed by radio-TLC as shown in Figure 3b. The TLC peak (green bar, 96.7%) represents ^{64}Cu-SLNs, which remain at the baseline. The negligible amount (2.94%) of free ^{64}Cu in the purified ^{64}Cu-SLN suspension confirms >95% radiolabeled particles. The radiolabeling yield (%) of SLNs was approximately 66.8%.

High Stability of Radiolabeled SLNs. A stability assay was performed in order to confirm that Cu-64 remains associated with the SLN over the 48 h time period and that the biodistribution patterns observed are not from free, dissociated Cu-64. Figure 4 shows that, over time (0.5, 3, 20, and 48 h), the SLNs in saline and serum do not lose radiolabel. The saline solution is a control to test the stability of the particles in solution before intravenous (i.v.) administration, while the serum solution mimics blood circulation. Because the molecular weight of the lipid-PEG-BAT is less than the 10,000 MWCO of the centrifugal filters used for purification, both dissociated free copper and dissociated lipid-PEG-BAT molecules are removed during centrifugation purification, while nanoparticles are retained in the filtrate. Radio TLC experiments (Figure 5) confirm that no peak corresponding to free ^{64}Cu (~85 mm, retention factor (R_f) = 0.66) was observed for filtrates after 24 and 48 h incubation in serum,

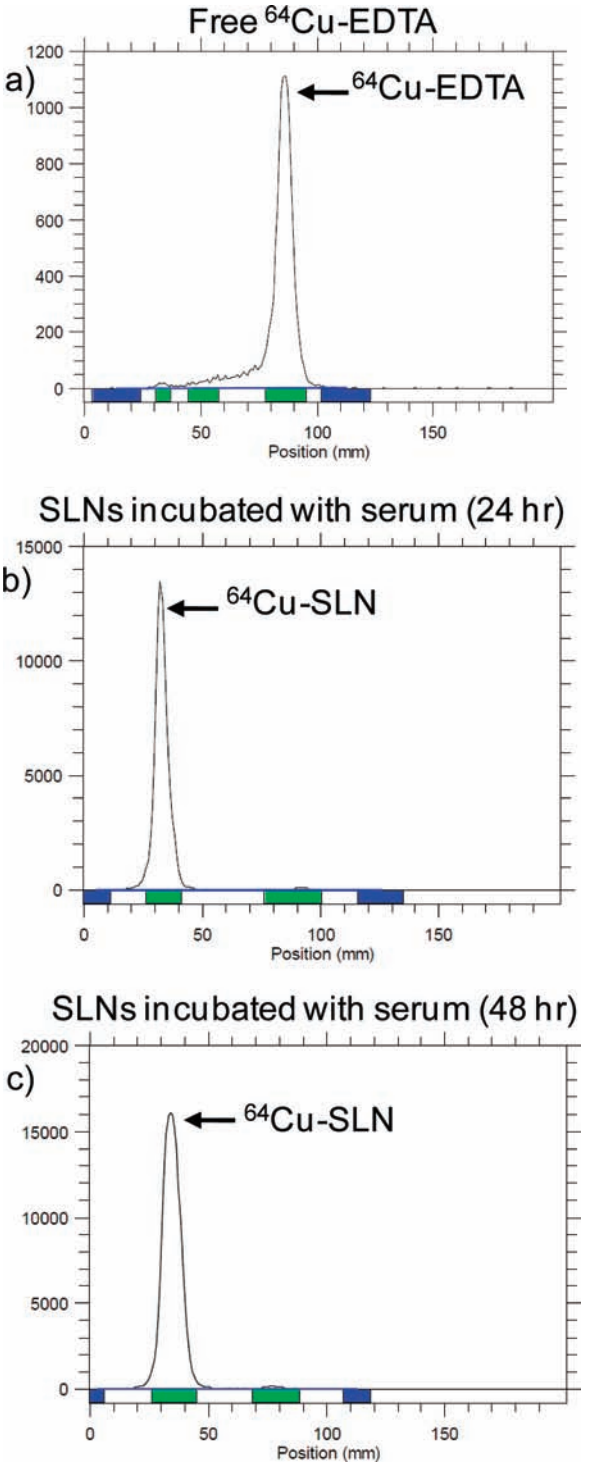


Figure 5. Radio TLC of SLNs incubated with serum. Cu-EDTA (a) and SLNs incubated with serum at 24 (b) and 48 h (c) were developed on a silica plate with methanol/ammonium acetate (10%) (50:50, v/v) and recorded by a radio-TLC imaging scanner. The absence of free ^{64}Cu-EDTA in (b) and (c) confirm that the ^{64}Cu-SLNs were stable in plasma after 24 and 48 h.

verifying the stability of these radiolabeled particles in the bloodstream up to 48 h. Overall, the results of this stability assay confirm that there is no significant loss ($p < 0.01$) of free copper or free lipid-PEG-BAT (chelated with Cu-64) from the SLNs in

dx.doi.org/10.1021/bc100478k |*Bioconjugate Chem.* 2011, 22, 808–818

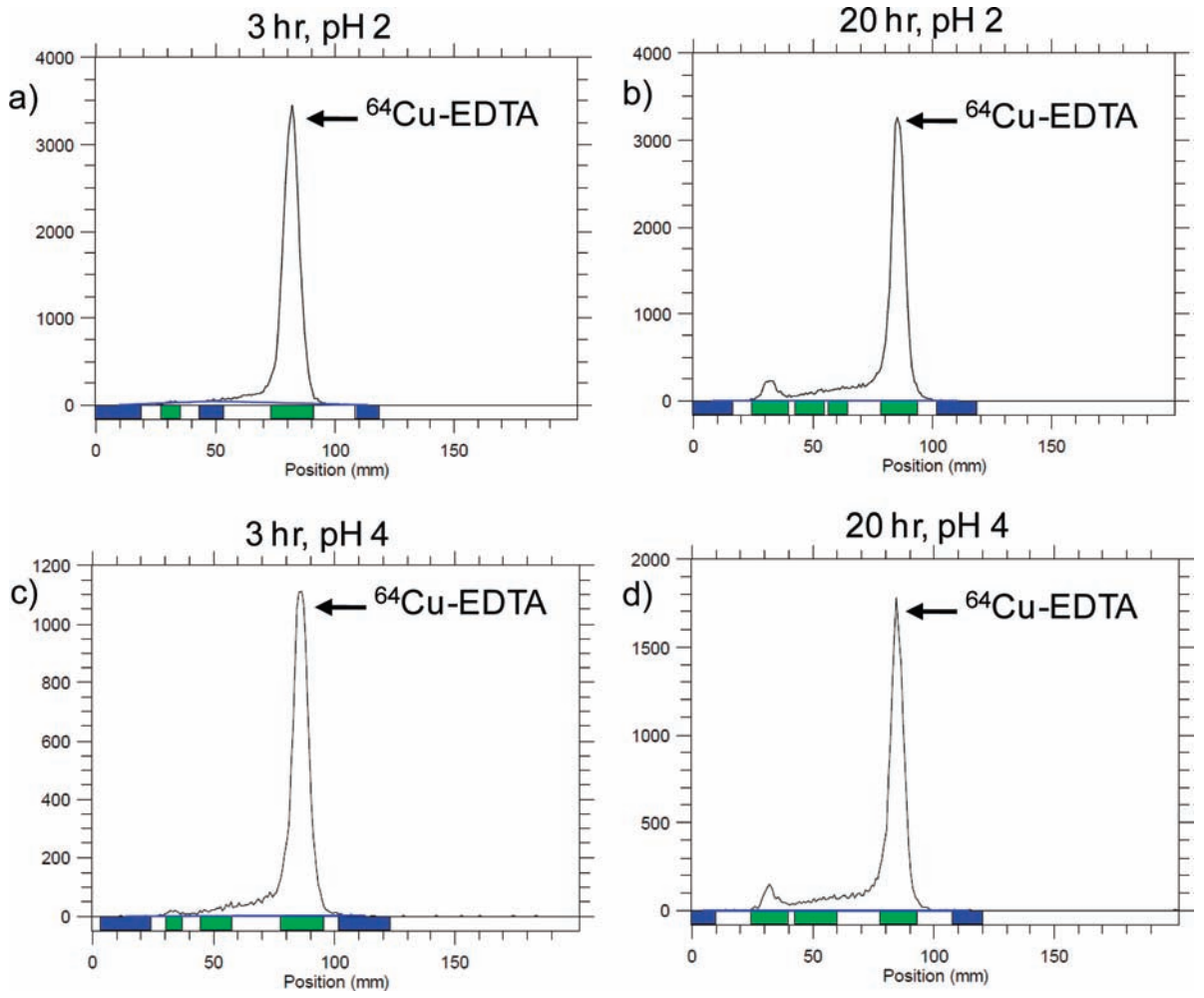


Figure 6. Radio TLC of supernatant resulting from centrifugation filtration of SLNs incubated with saline (pH 2) and saline (pH 4) at 3 and 20 h. Samples were developed on a silica plate was developed with methanol/ammonium acetate (10%) (50:50, v/v) and recorded by a radio-TLC imaging scanner. The TLC plots confirm that the loss of radiolabel observed (Figure 4) for ^{64}Cu-SLNs incubated with saline (pH 2) and saline (pH 4) were a result of ^{64}Cu-EDTA dissociating from the particle in these extreme conditions.

saline or plasma. Although the SLNs were quite stable in serum and in saline at pH 5.5, they showed a significant loss (p value > 0.01) of label over time when incubated in pH 2 and pH 4. Radio TLC was performed on the supernatants collected after centrifugation filtration of the SLNs incubated with saline (pH 2) and saline (pH 4) at 3 and 20 h. It is clear from these TLC plots (Figure 6) that saline (pH 2) and saline (pH 4) supernatant yield single peaks corresponding to ^{64}Cu (~85 mm, R_f = 0.66). This confirms that the loss of radiolabel for saline (pH 2) and saline (pH 4) observed in Figure 4 was due to free ^{64}Cu dissociating from the particle in these extreme conditions. Therefore, the observed ^{64}Cu dissociation at these conditions is not of significant concern.

Preliminary Biodistribution and Pharmacokinetics of ^{64}Cu-SLN *in Vivo* Using PET Imaging and Gamma Counting. Radiolabeling SLNs with ^{64}Cu facilitates the use of positron emission tomography (PET) for the investigation of SLN biodistribution *in vivo*. Imaging seldom has been used to describe the biodistribution of SLNs following i.v. administration. Instead, most researchers label SLNs with a gamma-emitting radioisotope and report biodistribution by gamma counting organs. For example, gamma counting methods have been used to describe full-body biodistribution of Technetium-99 m (^{99m}Tc)-labeled SLNs following endotracheal administration to mice[51] and Iodine-125 (^{125}I)-labeled SLNs following intravenous injection to rats.[28] Our results confirm a method to radiolabel solid lipid nanoparticles with ^{64}Cu through the incorporation of a lipid-PEG-BAT chelating molecule into SLNs carrying a cargo of fluorescently labeled hydrophilic protein (bovine serum albumin).

Preliminary biodistribution and blood clearance of the radiolabeled SLNs (^{64}Cu-SLNs) was assessed in the mouse model. From the biodistribution plot (Figure 7) obtained by gamma counting organs at 52−55 h post i.v. injection, we observe that the liver radioactivity (6.6 ± 0.7%ID/g) was significantly higher (p < 0.01) than all other organs, including heart (1.1 ± 0.4%ID/g), lung (1.2 ± 0.5%ID/g), gastrointestinal (GI) tract (1.7 ± 0.9%ID/g), right (2.2 ± 0.2%ID/g) and left (1.7 ± 1.1%ID/g) kidneys, spleen (2.9 ± 1.1%ID/g), and brain (0.03 ± 0.01%ID/g). This organ biodistribution obtained from gamma counting organs was compared with the *in vivo* biodistribution obtained from PET imaging. Figure 8a−d displays the biodistribution of ^{64}Cu-SLNs in mice from representative coronal PET images at 0.5, 3, 20, and 48 h post i.v. injection. There was obvious

dx.doi.org/10.1021/bc100478k |*Bioconjugate Chem.* 2011, 22, 808–818

radioactivity in the carotids (C) and the heart (H), at 0.5 and 3 h post injection (Figure 8a and b) indicating continuing circulation of the ^{64}Cu-SLNs; this signal disappeared by 20 h post injection (Figure 8c), indicating that the ^{64}Cu-SLNs had primarily cleared the bloodstream. Figure 8a,b also shows high liver (L) and spleen (S) activity, indicating that the ^{64}Cu-SLNs were cleared through the reticuloendothelial system (RES) by 0.5 and 3 h post injection. By 20 h post injection (Figure 5c), there was faint activity in the spleen, but more prominent was the activity in the intestines (I) and the liver (L). Verkade et al. showed that liposome-associated phosphatidylcholine is predominantly degraded by the liver, and that these degradation products are partially secreted into bile. Thus, the radioactivity we observe in the intestines is hypothesized to result from the liver slowly breaking down the SLNs and releasing radioactivity through the bile duct.[52] This is consistent with previous studies from Seo et al. showing radioactivity accumulation in the intestines following i.v. administration of radiolabeled liposomes in mice.[2] Only liver activity remains visible at 48 h post injection (Figure 8d), suggesting that ^{64}Cu-SLNs were primarily cleared through the RES by this time. Radioactivity in the liver (L) decreased over time as shown in Figure 6e (25.4 ± 0.9, 22.1 ± 4.0, 11.9 ± 0.9, and 5.6 ± 1.3%ID/g at 0.5, 3, 20, and 48 h, respectively), validating that SLNs do not remain in liver long-term.

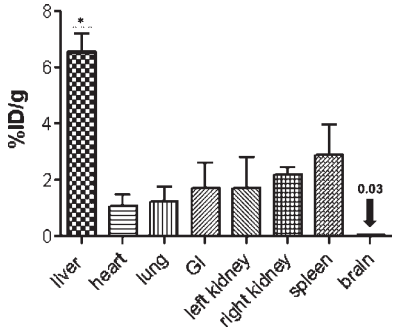


Figure 7. Biodistribution with gamma counting. Biodistribution of ^{64}Cu-SLNs in mice at 52−55 h post injection. Error bars represent mean ± standard deviation (n = 3). Liver activity (%ID/g) is significantly higher (p value <0.01) than that all other organs.

The liver activity at 52−55 h measured by gamma counting (6.6 ± 0.7%ID/g) was consistent with the liver activity measured by PET quantification (Figure 8e), which showed an average of 5.7 ± 1.1%ID/g at 48 h. The heart activity was also consistent between the two methodologies of quantization yielding values of 0.9 ± 0.1%ID/g with PET and 1.1 ± 0.4%ID/g with gamma counting. Nevertheless, the low activity of the other organs (lungs, GI, right kidney, left kidney, spleen, and brain) at 48 h results in the inability for the microPETII to appropriately detect their organ boundaries; at earlier time points, the activity is high enough to avoid this issue. Therefore, the use of a more sensitive (3×) PET scanner (absolute system sensitivity ~7%), such as the F120 produced by Siemens Medical Solutions, Inc. will enable one to appropriately define organ boundaries at the later time points (i.e., 48 h) in future studies.

Blood clearance was assessed by monitoring signal from the heart over time. The time activity curve (TAC) of blood in Figure 9 showed that ^{64}Cu-SLNs were still circulating in the bloodstream after 3 h, but were almost entirely cleared from

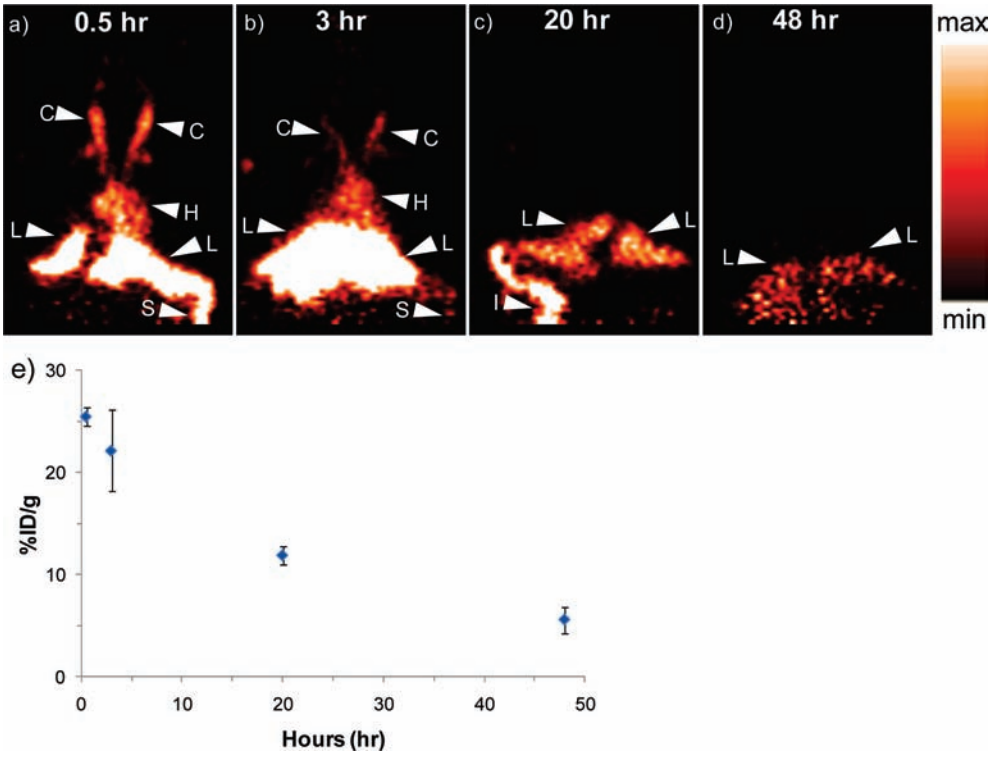


Figure 8. Preliminary biodistribution with PET. Coronal view of a microPET image acquired at (a) 0.5 h, (b) 3 h, (c) 20 h, and (d) 48 h post i.v. injection of ^{64}Cu-SLNs. Radioactive signal is present in C = carotid, H = heart, L = liver, S = spleen, and I = intestines. A relative scale (the brightest spot is maximum) was applied for the images. (e) Liver biodistribution obtained using ROI analysis on the microPET images. Error bars represent mean ± standard deviation (n = 3).

dx.doi.org/10.1021/bc100478k |*Bioconjugate Chem.* 2011, 22, 808–818

the bloodstream by 48 h. The monoexponential curve was fit to the data, yielding a correlation coefficient of 0.99. The blood half-life for the ^{64}Cu-SLNs was estimated to be approximately 1.4 h. This is very different behavior from free ^{64}Cu or free ^{64}Cu radiolabeled lipid-PEG-BAT that result in blood half-lives ~5−10 min and are known to clear almost entirely from the bloodstream at 15 min post i.v. injection.[2] The 1.38 ± 0.12 h blood half-life of our ^{64}Cu-SLNs was also much longer than that of most polymeric nanoparticles, which are reported to have blood lives of only a few minutes. For example, polysorbate 80 (P80) coated poly(α-butyl cyanoacrylate) (PBCA) nanoparticles loaded with ^{125}I radiolabeled quinoline derivatives and delivered to mice by intravenous (i.v.) injection were almost entirely cleared after 1 h, with a blood half-life of ~5 min.[53] Similarly, P80-coated poly(lactic-*co*-glycolic acid) (PLGA) nanoparticles labeled with ^{99m}Tc were cleared very rapidly from the blood after i.v. injection in mice, with 1.28 ± 0.07%ID/g remaining at 1 h post injection and a blood-half-life of only a few minutes.[54] Overall, the RES-mediated clearance of the SLNs from the bloodstream can be reduced further by coating the SLNs with a hydrophilic or flexible polymer and/or surfactant such as poly(ethylene glycol) (PEG) or polysorbate.[55] Coating with PEG has been shown to improve the pharmacokinetic profile of particles by reducing opsonization, phagocytosis, and clearance by the liver and RES.[55] We will investigate the influence of various hydrophilic coatings in order to reduce SLN clearance by the RES and prolong their circulation time in the bloodstream. This will facilitate the possibility of longer imaging studies to assess SLNs biodistribution *in vivo*.

Because of their lipophilic nature, most interest in SLNs involves their use as carriers for drug delivery to the brain.[3,6,42,55,56] The adsorption of a plasma protein, ApoE, onto the nanoparticles surface is thought to facilitate SLN uptake into the brain through the low density lipoprotein (LDL) receptors on the brain endothelial cells lining the blood brain barrier (BBB). From a close examination of the brain distribution (Figure 5), we observe approximately 0.03 ± 0.03%ID/g of activity at 52−55 h post injection. This small amount of SLNs delivered to the brain could be enhanced through surface modifications, such as coating with P80.[53] P80 remains to be the most successful "stealth" coating for delivering therapeutic agents into the brain,[39,42,57−60] reporting values as high 0.52%ID/g in the brain.[61] In a recent study, P80 coating of SLNs containing riluzole facilitated a significantly higher dose of riluzole to the brain in comparison to free riluzole alone.[62] Since P80 coating has also demonstrated the ability to enhance BBB transport,[63] we will coat radiolabeled SLNs with P80 and use PET to investigate the ability for SLNs to target the brain *in vivo*.

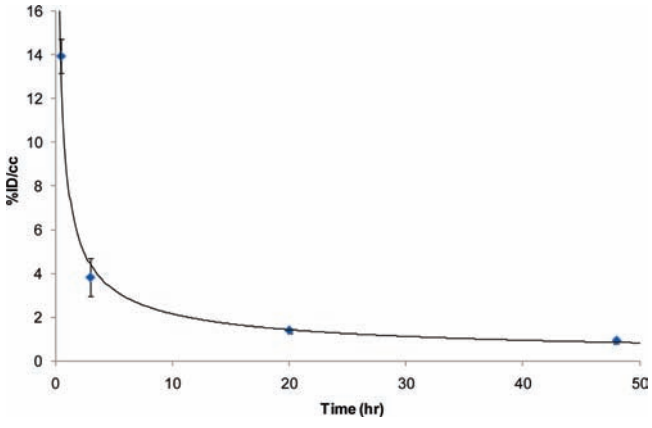


Figure 9. Time activity curve (TAC) of blood after bolus i.v. injection of ^{64}Cu-SLNs in mice. TACs were obtained with region-of-interest (ROI) analysis using *ASIPro* software and expressed as the percentage of injected dose per cubic centimeter (%ID/cc). Error bars represent mean ± standard deviation (n = 3). The monoexponential curve fit to the data was as follows: $y = 8.4363x^{-0.593}$.

CONCLUSION

Solid lipid nanoparticles (SLNs) are a versatile colloidal drug carrier system that combines the advantages of both liposomes and polymeric nanoparticles. Because of the potential for SLN to facilitate controlled drug delivery to a target tissue, there is much interest in understanding their *in vivo* biodistribution following intravenous (i.v.) injection. By incorporating a lipid-PEG-BAT chelator into the SLN monolayer, we have developed a method to radiolabel SLNs with ^{64}Cu for noninvasive mapping of biodistribution *in vivo* using PET. Preliminary *in vivo* biodistribution of these SLNs (^{64}Cu-SLNs) was evaluated in mice up to 48 h post i.v. injection using PET, and these values were then compared to *ex vivo* biodistribution from gamma counting of organs. The blood half-life for the ^{64}Cu-SLNs was ~1.4 h, which is longer than typical polymeric nanoparticles of similar size. Gamma counting confirmed significant activity in the liver at 48 h post i.v. injection. Coating SLNs with hydrophilic polymers such as PEG will be investigated in the future to reduce SLN clearance by the RES (kidneys, liver, and spleen) and increase the blood half-life. Longer blood circulation times will further enhance the appeal of SLNs as drug carriers, and the ability to radiolabel these SLNs for noninvasive assessment of biodistribution *in vivo* using PET will accelerate their development in the field of drug delivery, especially those drugs targeted to the brain.

AUTHOR INFORMATION

Corresponding Author

*To whom correspondence should be addressed. Prof. Angelique Y. Louie, Dept. of Biomedical Engineering, 451 East Health Sciences Drive, University of California, Davis, Davis, CA 95616. Phone: (530) 752-7134. E-mail: aylouie@ucdavis.edu.

ACKNOWLEDGMENT

Imaging was performed at the Center for Molecular and Genomic Imaging, University of California, Davis. We would like to acknowledge Jennifer Fung and Michelle Connell for their assistance with the animal imaging. We would also like to thank Dr. Reen Wu (University of California, Davis) for his donation of a Madin-Darby canine kidney (MDCK) cell line. The authors wish to acknowledge the support of the National Institutes of Health/NIBIB EB000993-06, NIH R01CA103828 and NIHT32 EB003827.

REFERENCES

(1) Rai, S., Paliwal, R., Gupta, P. N., Khatri, K., Goyal, A. K., Vaidya, B., and Vyas, S. P. (2008) Solid lipid nanoparticles (SLNs) as a rising tool in drug delivery science: One step up in nanotechnology. *Curr. Nanosci. 4*, 30–44.

(2) Seo, J. W., Zhang, H., Kukis, D. L., Meares, C. F., and Ferrara, K. W. (2008) A Novel method to label preformed liposomes with (CU)-C-64 for positron emission tomography (PET) imaging. *Bioconjugate Chem. 19*, 2577–2584.

(3) Mukherjee, S., Ray, S., and Thakur, R. S. (2009) Solid lipid nanoparticles: a modern formulation approach in drug delivery system. *Indian J. Pharm. Sci. 71*, 349–358.
(4) Martins, S., Sarmento, B., Ferreira, D. C., and Souto, E. B. (2007) Lipid-based colloidal carriers for peptide and protein delivery - liposomes versus lipid nanoparticles. *Int. J. Nanomed. 2*, 595–607.
(5) Gasco, M. R. (2007) Lipid nanoparticles: perspectives and challenges. *Adv. Drug Delivery Rev. 59*, 377–378.
(6) Mehnert, W., and Mäder, K. (2001) Solid lipid nanoparticles: Production, characterization and applications. *Adv. Drug Delivery Rev. 47*, 165–196.
(7) Souto, E. B., and Almeida, A. J. (2007) Solid lipid nanoparticles as a drug delivery system for peptides and proteins. *Adv. Drug Delivery Rev. 59*, 491–504.
(8) Lee, J. H., Il Ahn, S., Park, J. H., Kim, Y. T., Khang, G., Rhee, J. M., and Lee, H. B. (2008) Solid lipid nanoparticles as a drug delivery system for peptides and proteins. *Tissue Eng. Regen. Med. 5*, 215–228.
(9) Müller, R. H., Runge, S. A., Ravelli, V., Thünemann, A. F., Mehnert, W., and Souto, E. B. (2008) Cyclosporine-loaded solid lipid nanoparticles (SLN®): Drug-lipid physicochemical interactions and characterization of drug incorporation. *Eur. J. Pharm. Biopharm. 68*, 535–544.
(10) Sarmento, B., Martins, S., Ferreira, D., and Souto, E. B. (2007) Oral insulin delivery by means of solid lipid nanoparticles. *Int. J. Nanomed. 2*, 743–749.
(11) Morel, S., Ugazio, E., Cavalli, R., and Gasco, M. R. (1996) Thymopentin in solid lipid nanoparticles, international journal of pharmaceutics. *Int. J. Pharm. 132*, 259–261.
(12) Cavalli, R., Zara, G. P., Caputo, O., Bargoni, A., Fundarò, A., and Gasco, M. R. (2000) Transmucosal transport of tobramycin incorporated in SLN after duodenal administration to rats. Part I--A pharmacokinetic study. *Pharmacol. Res. 42*, 541–545.
(13) Wong, H. L., Bendayan, R., Rauth, A. M., Li, Y., and Wu, X. Y. (2007) Chemotherapy with anticancer drugs encapsulated in solid lipid nanoparticles. *Adv. Drug Delivery Rev. 59*, 491–504.
(14) Yang, S. C., Lu, L. F., Cai, Y., Zhu, J. B., Liang, B. W., and Yang, C. Z. (1999) Body distribution in mice of intravenously injected camptothecin solid lipid nanoparticles and targeting effect on brain. *J. Controlled Release 59*, 299–307.
(15) Fundaro, A., Cavalli, R., Bargoni, A., Vighetto, D., Zara, G. P., and Gasco, M. R. (2000) Non-stealth and stealth solid lipid nanoparticles (SLN) carrying doxorubicin: Pharmacokinetics and tissue distribution after i.v. administration to rats. *Pharmacol. Res. 42*, 337–343.
(16) Yu, W. Y., Liu, C. X., Liu, Y., Zhang, N., and Xu, W. F. (2010) Mannan-modified solid lipid nanoparticles for targeted gene delivery to alveolar macrophages. *Pharm. Res. 27*, 1584–1596.
(17) Pedersen, N., Hansen, S., Heydenreich, A. V., Kristensen, H. G., and Poulsen, H. S. (2006) Solid lipid nanoparticles can effectively bind DNA, streptavidin and biotinylated ligands. *Eur. J. Pharm. Biopharm. 62*, 155–162.
(18) Kim, H. R., Kim, I. K., Bae, K. H., Lee, S. H., Lee, Y., and Park, T. G. (2008) Cationic solid lipid nanoparticles reconstituted from low density lipoprotein components for delivery of siRNA. *Mol. Pharmaceutics 5*, 622–631.
(19) Oyewumi, M. O., and Mumper, R. J. (2002) Gadolinium-loaded nanoparticles engineered from microemulsion templates. *Drug Dev. Ind. Pharm. 28*, 317–328.
(20) Morel, S., Terreno, E., Ugazio, E., Aime, S., and Gasco, M. R. (1998) NMR relaxometric investigations of solid lipid nanoparticles (SLN) containing gadolinium (III) complexes. *Eur. J. Pharm. Biopharm. 45*, 157–163.
(21) Peira, E., Marzola, P., Podio, V., Aime, S., Sbarbati, A., and Gasco, M. R. (2003) In vitro and in vivo study of solid lipid nanoparticles loaded with superparamagnetic iron oxide. *J. Drug Targeting 11*.
(22) Joshi, M. D., and Müller, R. H. (2009) Lipid nanoparticles for parenteral delivery of actives. *Eur. J. Pharm. Biopharm. 71*, 161–172.
(23) Fang, J. Y., Fang, C. L., Liu, C. H., and Su, Y. H. (2008) Lipid nanoparticles as vehicles for topical psoralen delivery: Solid lipid nanoparticles (SLN) versus nanostructured lipid carriers (NLC). *Eur. J. Pharm. Biopharm. 70*, 633–640.
(24) Jain, S. K., Chourasia, M. K., Masuriha, R., Soni, V., Jain, A., Jain, N. K., and Gupta, Y. (2005) Solid lipid nanoparticles bearing flurbiprofen for transdermal delivery. *Drug Delivery 12*, 207–215.
(25) Kalam, M. A., Sultana, Y., Ali, A., Aqil, M., Mishra, A. K., and Chuttani, K. (2010) Preparation, characterization, and evaluation of gatifloxacin loaded solid lipid nanoparticles as colloidal ocular drug delivery system. *J. Drug Targeting 18*, 191–204.
(26) Basaran, E., Demirel, M., Sirmagul, B., and Yazan, Y. (2010) Cyclosporine-A incorporated cationic solid lipid nanoparticles for ocular delivery. *J. Microencapsul. 27*, 37–47.
(27) Nassimi, M., Schleh, C., Lauenstein, H. D., Hussein, R., Hoymann, H. G., Koch, W., Pohlmann, G., Krug, N., Sewald, K., Rittinghausen, S., Braun, A., and Muller-Goymann, C. (2010) A toxicological evaluation of inhaled solid lipid nanoparticles used as a potential drug delivery system for the lung. *Eur. J. Pharm. Biopharm. 75*, 107–116.
(28) Weyhers, H., Lobenberg, R., Mehnert, W., Souto, E. B., Kreuter, J., and Muller, R. H. (2006) In vivo distribution of I-125-radiolabelled solid lipid nanoparticles. *Pharm. Ind. 68*, 889–894.
(29) Manjunath, K., and Venkateswarlu, V. (2005) Pharmacokinetics, tissue distribution and bioavailability of clozapine solid lipid nanoparticles after intravenous and intraduodenal administration. *J. Controlled Release 107*, 215–228.
(30) Cherry, S. R. (2001) Fundamentals of positron emission tomography and applications in preclinical drug development. *J. Clin. Pharmacol. 41*, 482–491.
(31) Cherry, S. R., Sorenson., J. A., and Phelps, M. E. (2003) Counting systems and the gamma camera, In *Physics in Nuclear Medicine*, 3rd ed., Saunders, Philadelphia, PA.
(32) Liu, S. (2004) The role of coordination chemistry in the development of target-specific radiopharmaceuticals. *Chem. Soc. Rev. 33*, 445–461.
(33) Gustafsson, B., Youens, S., and Louie, A. Y. (2006) Development of contrast agents targeted to macrophage scavenger receptors for MRI of vascular inflammation. *Bioconjugate Chem. 17*, 538–547.
(34) Silvia, M., Gasco, M. R., and Cavalli, R. (1994) Incorporation in lipospheres of [D-Trp-6]LHRH. *Int. J. Pharm. 105*.
(35) Wang, Q., Rager, J. D., Weinstein, K., Kardos, P. S., Dobson, G. L., Li, J. B., and Hidalgo, I. J. (2005) Evaluation of the MDR-MDCK cell line as a permeability screen for the blood-brain barrier. *Int. J. Pharm. 288*, 349–359.
(36) Tai, Y. C., Chatziioannou, A. F., Yang, Y., Silverman, R. W., Meadors, K., Siegel, S., Newport, D. F., Stickel, J. R., and Cherry, S. R. (2003) MicroPET II: design, development and initial performance of an improved microPET scanner for small-animal imaging. *Phys. Med. Biol. 48*, 1519–37.
(37) Yang, Y. F., Tai, Y. C., Siegel, S., Newport, D. F., Bai, B., Li, Q. Z., Leahy, R. M., and Cherry, S. R. (2004) Optimization and performance evaluation of the microPET II scanner for in vivo small-animal imaging. *Phys. Med. Biol. 49*, 2527–2545.
(38) Heurtault, B., Saulnier, P., Pech, B., Venier-Julienne, M., Proust, J., Phan-Tan-Luu, R., and Benoît, J. (2003) The influence of lipid nanocapsule composition on their size distribution. *Eur. J. Pharm. Sci. 18*, 55–61.
(39) Ringe, K., and Waltz, C. (2004) Nanoparticulate drug delivery to the brain. *Encycl. Nanosci. Nanotechnol. 7*, 91–104.
(40) Chen, D. B., Yang, T. Z., Lu, W. L., and Zhang, Q. (2001) In vitro and in vivo study of two types of long-circulating solid lipid nanoparticles containing paclitaxel. *Chem. Pharm. Bull. 49*, 1444–1447.
(41) Park, Y. S., Maruyama, K., and Huang, L. (1992) Some negatively charged phospholipid derivatives prolong the liposome circulation in vivo. *Biochim. Biophys. Acta 1108*, 257–260.
(42) Blasi, P., Giovagnoli, S., Schoubben, A., Ricci, M., and Rossi, C. (2007) Solid lipid nanoparticles for targeted brain drug delivery. *Adv. Drug Delivery Rev. 59*, 454–477.
(43) Singh, S., Dobhal, A. K., Jain, A., Pandit, J. K., and Chakraborty, S. (2010) Formulation and evaluation of solid lipid nanoparticles of a water soluble drug: zidovudine. *Chem. Pharm. Bull. 58*, 650–655.

(44) Ugazio, E., Cavalli, R., and Gasco, M. R. (2002) Incorporation of cyclosporin A in solid lipid nanoparticles (SLN). *Int. J. Pharm. 241*, 341–344.
(45) García-Fuentes, M., Torres, D., and Alonso, M. J. (2003) Design of lipid nanoparticles for the oral delivery of hydrophilic macromolecules. *Colloids Surf., B 27*, 159–168.
(46) Chattopadhyay, N., Zastre, J., Wong, H. L., Wu, X. Y., and Bendayan, R. (2008) Solid lipid nanoparticles enhance the delivery of the HIV protease inhibitor atazanavir, by a human brain endothelial cell line. *Pharm. Res. 25*.
(47) Reithmeier, H., Herrmann, J., and Gopferich, A. (2001) Lipid microparticles as a parenteral controlled release device for peptides. *J. Controlled Release 73*, 339–350.
(48) Olbrich, C., Gessner, A., Schroder, W., Kayser, O., and Muller, R. H. (2004) Lipid-drug conjugate nanoparticles of the hydrophilic drug diminazene - cytotoxicity testing and mouse serum adsorption. *J. Controlled Release 96*, 425–435.
(49) Li, Z., Li, X. W., Zheng, L. Q., Lin, X. H., Geng, F., and Yu, L. (2010) Bovine serum albumin loaded solid lipid nanoparticles prepared by double emulsion method. *Chem. Res. Chin. Univ. 26*, 136–141.
(50) Miglietta, A., Cavalli, R., Bocca, C., Gabriel, L., and Gasco, M. R. (2000) Cellular uptake and cytotoxicity of solid lipid nanospheres (SLN) incorporating doxorubicin or paclitaxel. *Int. J. Pharm. 210*, 61–67.
(51) Videira, M. A., Gano, L., Santos, C., Neves, M., and Almeida, A. J. (2006) Lymphatic uptake of lipid nanoparticles following endotracheal administration. *J. Microencapsul. 23*, 855–862.
(52) Verkade, H. J., Derksen, J. T. P., Gerding, A., Scherphof, G. L., Vonk, R. J., and Kuipers, F. (1991) Differential hepatic processing and biliary-secretion of headgroup and acyl chains of liposomal phosphatidylcholines. *Biochem. J. 275*, 139–144.
(53) Roney, C., Kulkarni, P., Arora, V., Antich, P., Bonte, F., Wu, A. M., Mallikarjuana, N. N., Manohar, S., Liang, H. F., Kulkarni, A. R., Sung, H. W., Sairam, M., and Aminabhavi, T. M. (2005) Targeted nanoparticles for drug delivery through the blood-brain barrier for Alzheimer's disease. *J. Controlled Release 108*, 193–214.
(54) Halder, K. K., Mandal, B., Debnath, M. C., Bera, H., Ghosh, L. K., and Gupta, B. K. (2008) Chloramphenicol-incorporated poly lactide-co-glycolide (PLGA) nanoparticles: Formulation, characterization, technetium-99m labeling and biodistribution studies. *J. Drug Targeting 16*, 311–320.
(55) Kaur, I. P., Bhandarib, R., Bhandarib, S., and Kakkara, V. (2008) Potential of solid lipid nanoparticles in brain targeting. *J. Controlled Drug Release 127*.
(56) Kreuter, J., Shamenkov, D., Petrov, V., Ramge, P., Cychutek, K., Koch-Brandt, C., and Alyautdin, R. (2002) Apolipoprotein-mediated transport of nanoparticle-bound drugs across the blood-brain barrier. *J. Drug Targeting 10*, 317–325.
(57) Ramge, P., Unger, R. E., Oltrogge, J. B., Zenker, D., Begley, D., Von Briesen, H., and Kreuter, J. (2000) P80 coating enhances uptake of polybutylcyanoacrylate (PBCA)-nanoparticles by human and bovine primary brain capillary endothelial cells. *Eur. J. Neurosci. 12*, 1931–1940.
(58) Goppert, T. M, and Muller, R. H. (2005) Protein adsorption patterns on poloxamer- and poloxamine-stabilized solid lipid nanoparticles (SLN). *Eur. J. Pharm. Biopharm. 60*, 361–372.
(59) Reimold, I., Domke, D., Bender, J., Seyfried, C. A., Radunz, H. E., and Fricker, G. (2008) Delivery of nanoparticles to the brain detected by fluorescence microscopy. *Eur. J. Pharm. Biopharm. 70*, 627–632.
(60) You, J., Wan, F., Cui, F., Sun, Y., Du, Y., and Hu, F. (2007) Preparation and characteristic of vinorelbine bitartrate-loaded solid lipid nanoparticles. *Int. J. Pharm. 343*, 270–276.
(61) Soni, S., Babbar, A. K., Sharma, R. K., and Maitra, A. (2006) Delivery of hydrophobised 5-fluorouracil derivative to brain tissue through intravenous route using surface modified nanogels. *J. Drug Targeting 14*, 87–95.
(62) Bondi, M. L., Craparo, E. F., Giammona, G., and Drago, F. (2010) Brain-targeted solid lipid nanoparticles containing riluzole: preparation, characterization and biodistribution. *Nanomedicine 5*, 25–32.
(63) Wilson, B., Samanta, M. K., Santhi, K., Kumar, K. P., Paramakrishnan, N., and Suresh, B. (2008) Poly(n-butylcyanoacrylate) nanoparticles coated with polysorbate 80 for the targeted delivery of rivastigmine into the brain to treat Alzheimer's disease. *Brain Res. 1200*, 159–168.

Bioconjugate Chemistry

TECHNICAL NOTE

pubs.acs.org/bc

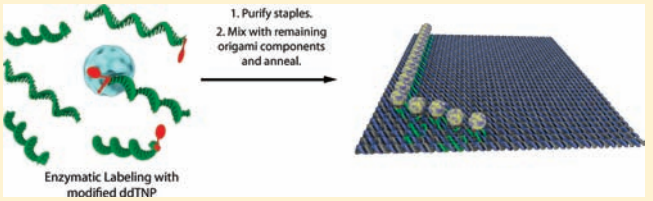
Functional Patterning of DNA Origami by Parallel Enzymatic Modification

Kasper Jahn,[†,‡] Thomas Tørring,[†,§] Niels Vinther Voigt,[†,§] Rasmus Schøler Sørensen,[†,‡] Anne Louise Bank Kodal,[†,§] Ebbe Sloth Andersen,[†,‡] Kurt Vesterager Gothelf,[†,§] and Jørgen Kjems[*,†,‡]

[†]Danish National Research Foundation: Center for DNA Nanotechnology at Interdisciplinary Nanoscience Center (iNANO), [‡]Department of Molecular Biology, [§]Department of Chemistry, Aarhus University, DK-8000 Aarhus, Denmark

Supporting Information

ABSTRACT: We demonstrate here a rapid and cost-effective technique for nanoscale patterning of functional molecules on the surface of a DNA origami. The pattern is created enzymatically by transferring a functionalized dideoxynucleotide to the 3′-end of an arbitrary selected set of synthetic DNA oligonucleotides positioned approximately 6 nm apart in a 70 × 100 nm^2 rectangular DNA origami. The modifications, which are performed in a single-tube reaction, provide an origami surface modified with a variety of functional groups including chemical handles, fluorescent dyes, or ligands for subsequent binding of proteins. Efficient labeling and patterning was demonstrated by gel electrophoresis shift assays, reverse-phase HPLC, mass spectrometry, atomic force microscopy (AFM) analysis, and fluorescence measurements. The results show a very high yield of oligonucleotide labeling and incorporation in the DNA origami. This method expands the toolbox for constructing several different modified DNA origami from the same set of staple strands.



INTRODUCTION

The field of designed artificial molecular self-assembly was revolutionized in 2006 by the invention of DNA origami,[1] a technique where a long, single-stranded DNA scaffold is folded into well-defined structures by a large number of smaller synthetic DNA oligonucleotides—so-called staple strands. Since then, the development and application of the DNA origami has evolved rapidly, resulting in a number of different two- and three-dimensional DNA structures with enormous potential.[2−7] In this process, it has also been demonstrated that DNA origami can function as a molecular pegboard, where the large number of uniquely positioned staple strands not only hold the origami together, but also function as handles for modifying the origami at specific positions. By chemically modifying specific staple strands, it is possible to functionalize the origami in well-defined positions with nanometer precision.[8−11] However, this process has so far required individual synthesis of the chemically modified staple strands for each of the selected positions on the origami.

We describe here an inexpensive enzymatic technique to label ensembles of unmodified stable strands that can direct the insertion of functional groups at selected locations of the DNA origami (Figure 1A). The technique relies on DNA nucleotidylexotransferase (terminal transferase) to attach modified dideoxynucleotide triphosphates to the 3′-end of an arbitrary subset of oligonucleotides to be incorporated at specific positions in the DNA origami. The use of dideoxynucleotides ensures that only a single modified nucleotide is attached. The method was applied to a rectangular origami comprising a 7-kilobase-long M13mp18 phage single-stranded DNA and 222 synthetic DNA oligonucleotides. The potential of the approach is demonstrated by attaching biotin-, amine-, digoxigenin-, and fluorescent groups to selected sites of the origami (Figure 1B). Hence, the technique provides a practical route for generating a large number of different modification patterns from just one set of staple-strands. Compared to the traditional method, where origami modifications are introduced by phosphoamidite chemistry in the individual staple strands, this method provides a rapid, efficient, and cost-effective protocol for functionalizing DNA origami.

EXPERIMENTAL PROCEDURES

Materials. Terminal transferase, antidigoxigenin monoclonal antibodies, biotin ddUTP, and DIG (digoxigenin)ddUTP were purchased from Roche Applied Science. The propargylamino ddUTP was purchased from Jena Bioscience. The Texas Red ddATP was purchased from Perkin-Elmer. THTA (tris-(1-[3-hydroxypropyl]triazolyl-4-methyl)amine) was synthesized according to the literature procedure.[8] All DNA oligonucleotides are purchased from DNA Technology A/S, Aarhus, Denmark. M13mp18 was purchased from New England Biolabs. Streptavidin was purchased from Sigma Aldrich. Water was purified using a Millipore Milli-Q purification system. SYBR Gold and SYBR Safe were both purchased from Invitrogen.

Terminal Transferase Reaction. Under standard conditions, 100 pmol oligonucleotide in total and 1 nmol of modified

Received: January 5, 2011
Revised: February 22, 2011
Published: March 17, 2011

ACS Publications © 2011 American Chemical Society

dx.doi.org/10.1021/bc2000098 | *Bioconjugate Chem.* 2011, 22, 819–823

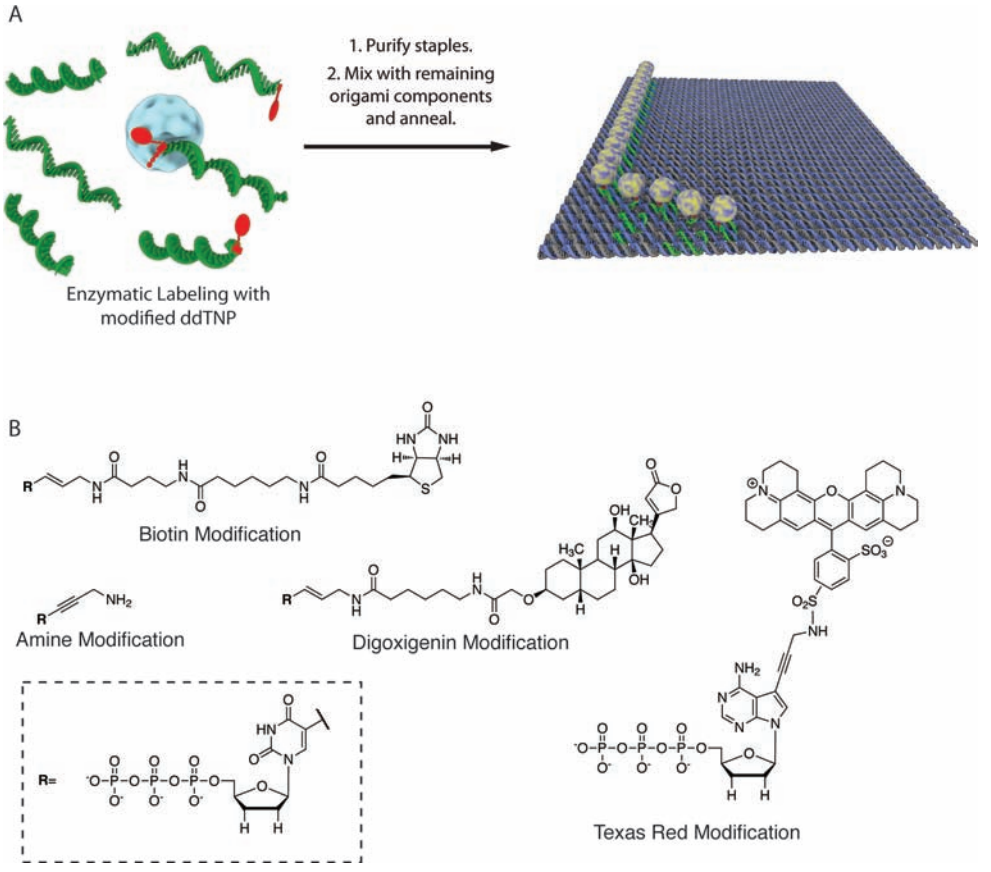


Figure 1. (A) Schematic representation of the DNA origami labeling process. The strands intended for modification are mixed and labeled by terminal transferase in a single reaction. After purification, the modified strands are annealed with the remaining origami components to create the patterned DNA origami. (B) Overview of the chemical structures of the modified dideoxynucleotide triphosphates applied in this study.

ddNTP were mixed in 20 μL with reaction buffer (1×), $CoCl_2$ (5 mM), and incubated with terminal transferase (20 U/μL) for 15 min at 37 °C. The reaction is stopped by adding EDTA (20 mM final concentration). Strands used for subsequent origami formation were precipitated with NaOAc (0.3 M, pH = 5.2) and 2.5 volumes of EtOH (−20 °C, 96%) for 15 min on dry ice, followed by centrifugation for 30 min at 20 000 *g*. The pellet was washed once with EtOH (−20 °C, 70%). Depending on the length of the oligonucleotides, up to 90% yield was obtained (see Supporting Information for details). Further purification considerations can also be seen in the Supporting Information.

RP-HPLC Analysis. The analysis was performed using a Hewlett-Packard Agilent 1100 Series and Phenomenex Clarity 3 μm Oligo-RP 4.6 × 50 mm columns. The standard gradient used was acetonitrile (MeCN)/TEAA (triethylammonium acetate, 0.1 M, pH = 7) with a 10−20% gradient over 15 min. Yields were determined by comparing integrals with a reference.

MALDI-TOF MS Analysis. Mass spectra were recorded using a Bruker Daltonics Autoflex MALDI−TOF MS spectrometer using AnchorChip as target plates using a mixture consisting of 90% 3-hydroxypicolinic acid (50 mg/mL) in H_2O/MeCN (1:1) and 10% diammonium citrate (50 mg/mL) in water as matrix.

Gel Shift Assay. A mixture of the selected staple strands for the DNA origami were labeled, precipitated, and purified as mentioned above. The 17 selected strands are given in Supporting Information, and the pattern is schematically indicated in Figure 1. The binding assay was performed with 5 pmol oligonucleotide and a 3× excess of ligand in buffer A (150 mM NaCl, 3 mM $MgCl_2$, 100 mM Tris-HCl, pH = 7.4). Glycerol loading buffer was added to 7% glycerol and the samples were analyzed in a 6% native PAGE gel, run at 4 °C. The DNA was stained with SYBR gold and scanned with a Typhoon Trio scanner from GE Healthcare at the following settings: laser, 488 nm; emission filter, 555 BP 20; photomultiplier, 450 V; sensitivity, normal.

To assay the modification efficiency, the reaction mixture was denatured by adding formamide/EDTA buffer (final concentration of 80% formamide, 8 mM EDTA) to the terminal transferase reaction and then heated to 95 °C. The samples were analyzed on a 16% denaturing polyacrylamide gel, with 5 pmol substrate in each lane. Following gel electrophoresis, the gel was stained with SYBR Gold for 15 min and scanned with a Typhoon scanner at the following settings: laser, 488 nm; emission filter, 555 BP 20; photomultiplier, 450 V; sensitivity, normal.

DNA Origami Assembly. For modified DNA origami, 17 of the staple strands were mixed, labeled, and purified prior to DNA assembly (Supporting Information). DNA origami assembly was performed by mixing 5 nM M13 ssDNA with 10× excess of staple strands in 50 μL TAE/Mg^{2+} buffer B (40 mM Tris−acetate, 1 mM EDTA, 12.5 mM Mg^{2+}, pH = 8.3). The assembly reaction was performed by incubating the samples at 95 °C for 5 min, followed by a temperature decrease of −0.1 °C/second until 60 °C, and afterward a decrease of −0.1 °C/minute until 20 °C. If "click" reactions were to be performed on the origami, the buffer was substituted with 50 μL HEPES/Mg^{2+}

dx.doi.org/10.1021/bc2000098 |*Bioconjugate Chem.* 2011, 22, 819–823

buffer C (20 mM HEPES, 12.5 mM Mg^{2+}, pH = 7.4) to avoid problems associated with TAE.[12] Furthermore, the annealing ramp was altered to 65 °C→4 °C overnight.

Fluorescence Measurements. The selected staple strands were labeled according to the general procedure (2, 4, or 8 staples per batch) with a 5-fold excess of ddUTP-Texas Red and a 2-fold reduction in terminal transferase concentration. The product was purified by RP-HPLC with a MeCN/TEAA gradient of 10% → 40%. The labeled and purified staple strands were combined with the rest of the origami components and annealed. The samples were analyzed in a 1% agarose gel run at 60 V at 5 °C for three hours in Buffer D (50 mM Tris, 45 mM boric acid, 0.5 mM EDTA, 5 mM $Mg(OAc)_2$, pH = 8.3). Texas Red fluorescence in the origami was quantified using a Typhoon Trio scanner with the following settings: laser, 532 nm; emission filter, 610 BP 30; photomultiplier, 600 V; sensitivity, normal. The gel was subsequently stained with SYBR Safe, and imaged again at following settings: laser, 488 nm; emission filter, 520 BP 20; photomultiplier, 600 V; sensitivity, normal. Controls were performed to ensure there was no "bleedthrough" of the fluorophores.

Alkyne Formation. The mixture of 17 staple strands (100 pmol of each) was labeled using a 20-fold reduced amount (2 U/μL final) of terminal transferase as compared to the recommendation by the company. The reaction mixture was lyophilized, redissolved, reacted with the NHS-ester of 4-pentynoic acid, precipitated, redissolved, and purified by preparative HPLC. The exact conditions and durations for each step are given in the Supporting Information.

"Click" Reaction. Origami containing alkyne-modified staple strands were purified using a Microcon centrifugal filter (100 000 Da, MWCO, 300 *g* speed, 15 min) followed by washing twice with HEPES/Mg^{2+} buffer C. Twenty microliters of the purified origami solution was mixed with a prepared coupling solution (20 μL) containing $CuSO_4$ (0.1 mM), THTA (0.5 mM), sodium ascorbate (2.5 mM), and azide functionalized biotin (2 mM).[8] After incubation for 30 min, the solution was filtered using a Microcon centrifugal filter (100 000 Da, MWCO, 300 *g* speed, 15 min) followed by washing twice with HEPES/Mg^{2+} buffer C.

AFM Imaging. The sample (3−5 μL) was deposited on freshly cleaved mica and left to adsorb for a few minutes. The liquid cell was washed twice with a TAE/Mg^{2+} buffer B to remove excess staple strands. When imaging the alkyne-modified origami, the buffer was exchanged to HEPES/Mg^{2+} buffer C. To image the streptavidin or antibody pattern, a 100-fold excess of the protein was added and left to absorb for 10 min. The sample was subsequently washed to remove excess protein. The AFM used was an Agilent AFM series 5500 (Agilent Technologies, USA) with 0.08 N/m force constant silicon nitride cantilevers with sharpened pyramidal tip (OMCL-TR400PSA, Olympus, Atomic Force F&E GmbH, Mannheim, Germany). After engagement, the tapping amplitude setpoint was typically 2.0 V and the scan rates ranged from 1 to 2 Hz. During the liquid AFM imaging, the highest resolution was usually obtained with minimal loading forces applied and optimized feedback parameters. Several 512 × 512 pixel AFM images were recorded from separate locations across the mica surfaces to ensure reproducibility of the results. All the images were analyzed using *Gwyddion 2.21* software.

■ RESULTS AND DISCUSSION

DNA origami is typically self-assembled by mixing the DNA staple strands and phage ssDNA before annealing. To create a specific functionalized pattern on the origami, the terminal transferase enzyme was used to add a single modified nucleotide to a subset of the staple strands prior to the self-assembly reaction. To analyze the efficiency of the reaction, we selected 17 staple strands that are arranged in a pattern resembling the letter "L" on a rectangular origami (Figure 1A) and labeled them with either biotin-modified ddUTP or digoxigenin (DIG)-modified ddUTP. Effective modification was demonstrated by electrophoretic mobility shift assay before and after adding the corresponding ligand (streptavidin for biotin and anti-DIG antibody for DIG; Figure 2). Multiple bands were observed for both for the untreated and dideoxynucleotide-modified strands, probably due to the sequence and length variation of the oligonucleotides. The dideoxynucleotide-modified strands migrate slightly more slowly owing to the extra nucleotide. Upon addition of the corresponding protein ligand, a large shift was seen for both the DIG-modified and the biotin-modified staple strands, indicating that the correct modification had been attached. No gel shift was observed if streptavidin is added to the DIG-modified DNA and *vice versa*, confirming the specificity of ligand binding.

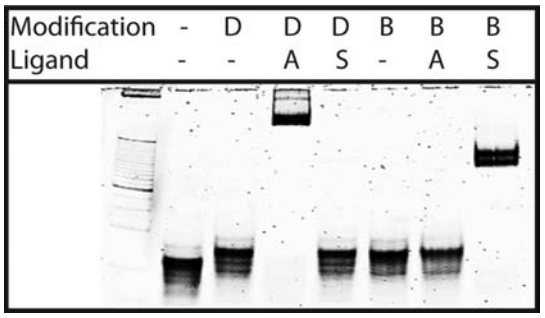


Figure 2. Gel mobility shift assay of the 17 non- (-), biotin- (B), or DIG-modified (D) staple strands bound to streptavidin (S) or DIG−antibody (A).

The integrity of the modifications after self-assembly of the origami was analyzed by AFM. However, in previous AFM studies it has been noted that rectangular DNA origami have a tendency to adsorb on the mica with the 3′ ends pointing toward the mica surface.[9] To ensure better accessibility, we altered the origami design to expose the 3′ ends at the opposite side of the origami (Supporting Information Figure S1). AFM analysis of the origami decorated with either streptavidin or antibody clearly resembled the designed pattern. Furthermore, nearly all origami displayed a right-turned L suggesting that the 3′ends are preferably facing upward as intended (Figure 3A,B; Supporting Information Figures S2 and S3). The short distance between the modifications and the multivalent binding nature of the protein used enables the proteins to bind more than one ligand; therefore, a 1:1 binding is not expected.

Although biotin and DIG labeling provides a variety of interesting possibilities, even more applications become achievable if a reactive chemical moiety, such as primary amines, are incorporated, demonstrated here by incorporating propargylamino-ddUTP. After the enzymatic incorporation by terminal transferase, the primary amine was reacted with activated esters of small organic molecules containing either alkynes or azides (see Supporting Information for more details) routinely used in the Huisgen-Meldal-Sharpless cycloaddition reaction (click reaction).[13,14] This reaction is widely used in bioconjugation because of is chemoselectivity and high yields. To test the efficiency of the combined enzymatic and chemical reactions,

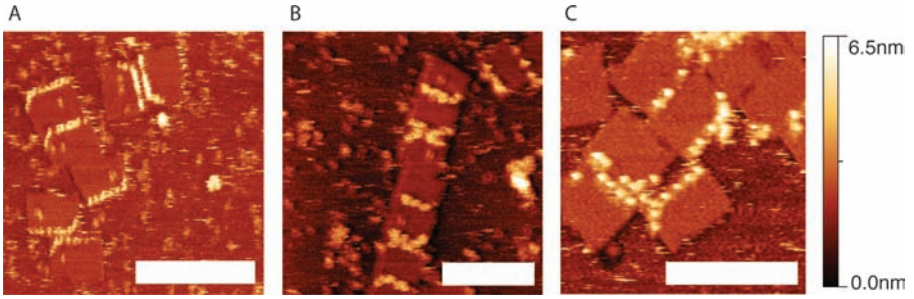


Figure 3. AFM image of a rectangular DNA origami modified with different modifications. (A) DNA origami with streptavidin attached to the patterned biotin modification. (B) DIG modification pattern imaged after DIG antibody addition. (C) Alkyne-modified DNA origami, which is subsequently reacted with azide-biotin compound and imaged after streptavidin addition. The expected letter "L" pattern is seen at all origami. The white scale bar is 200 nm.

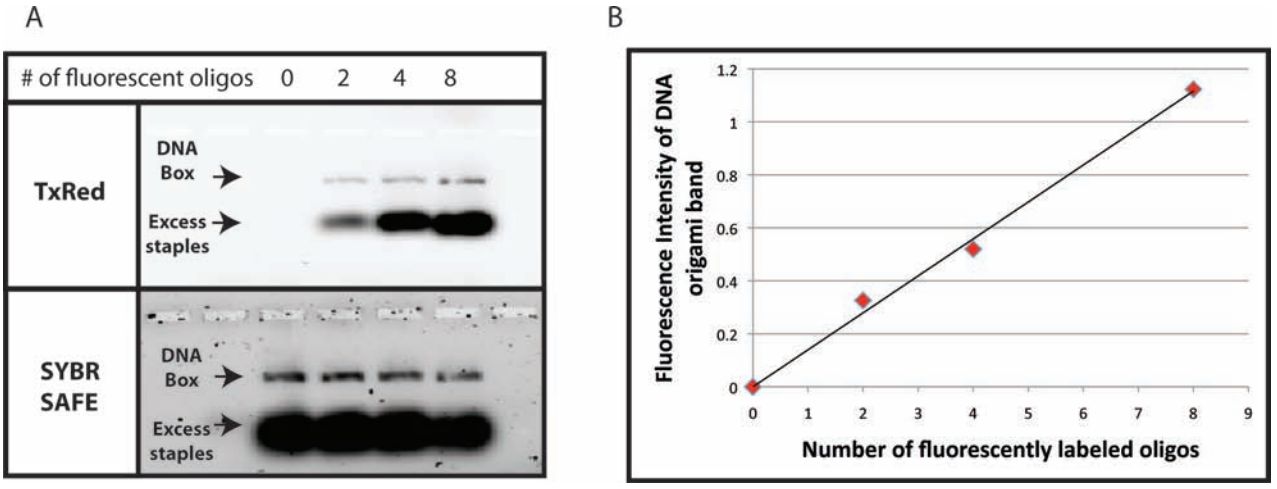


Figure 4. Fluorometric quantification of relative functionalization efficiency. (A) Fluorescent scan of an agarose gel containing DNA box origamis with a variable amount of fluorophore labeled staple strands. Scans shown in the upper and lower panels are performed with settings to detect exclusively TxRed fluorophore and SYBR safe stain, respectively. The positions of the DNA box origami and excess staple strands are marked. (B) A graph showing the TxRed fluorescence intensity of the origami bands, normalized to the intensity of the SYBR safe signal as a function of the number of labeled staple strands.

the origami was assembled from staple strands containing the same set of L-pattern-forming modified strands as above, but now labeled with propargylamino ddUTP followed by a treatment with the alkyne-tethered NHS-activated ester. After assembly of the DNA origami, the alkyne-modified staple strands were reacted with an azide-biotin followed by streptavidin addition (Supporting Information Figure S4). AFM images revealed L-patterns on the assembled origami structures. (Figure 3C; Supporting Information Figure S5).

Fluorescence Measurements. To quantify the relative degree of incorporation of modified oligoes into the DNA origami more accurately, we used the terminal transferase technique to attach a fluorescent (Texas Red) ddATP to different staple strands within a previously published three-dimensional DNA Box origami[3] (staple strands are listed in Supporting Information). A selected set of staple strands were fluorescently labeled, combined with the remaining origami components, and annealed. DNA boxes containing 0, 2, 4, or 8 fluorescently labeled staple strands were prepared and analyzed by agarose gel electrophoresis. The fluorescence in the band corresponding to the box was quantified by fluorescence scanning. The gel was subsequently stained with SYBR Safe and rescanned with different optical settings to quantify the amount of origami present (Figure 4A). The yield of Texas Red incorporation, normalized to the SYBR Safe signal, indicated a linear relationship between the fluorescence and number of labeled staple strands confirming that the efficiency of modified strand incorporation occurred independently of the other modifications in the DNA origami (Figure 4B).

Optimization. The cost of the modified nucleotide and the transferase enzyme are the limiting factors for scaleup of our method. To optimize the reaction conditions for larger quantities of modified DNA origami, we investigated the effect of lowering the concentration of the ddNTPs and the enzyme from the conditions suggested by the supplier. Denaturing PAGE was employed to assay the labeling efficiency at various conditions. In an experimental setup, where biotin-ddUTP was added in 0.5, 1, 2, 5, and 10 equiv to 5 μM DNA substrate, 5 equiv appears to be sufficient to obtain near complete incorporation (Figure 5A). Lowering the concentration to 2 equiv showed a decline in efficiency.

Next, we examined the possibility of lowering the enzyme concentration from the standard 20 U/μL in the presence of a 5× excess of the modified ddNTP (Figure 5B). The result indicated that the enzyme concentration can be reduced 27-fold

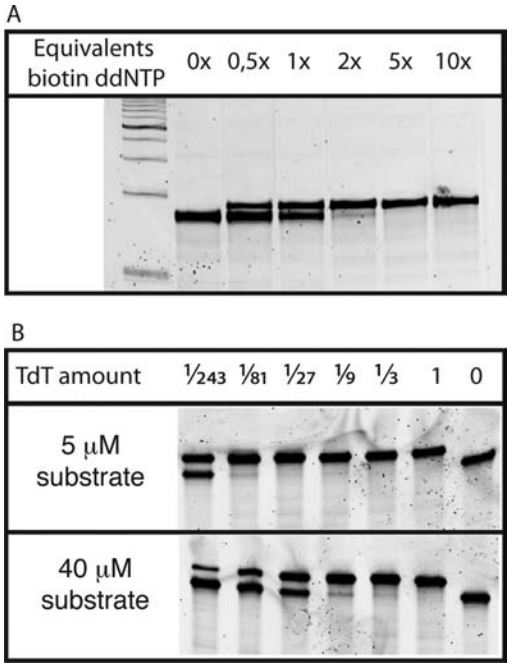


Figure 5. (A) Optimization of the terminal transferase reaction by biotin-ddNTP titration. Products were analyzed on 16% denaturing PAGE gel, with the upper band corresponding to the attachment of an extra nucleotide. (B) Titration of the enzyme (TdT) concentration. Top panel: standard reaction conditions using 5 μM substrate oligo (relative TdT concentrations are indicated above; 1 = 20 U/μL). Lower panel: high substrate concentration using 40 μM substrate oligo.

without compromising the efficiency to a detectable level. However, at higher substrate concentration (40 μM) the reaction is only completed with the standard amount of enzyme (20 U/μL). These results show that the standard protocol can be varied to limit the use of modified nucleotide and enzyme. However, it is possible that the labeling efficiency depends on the type of modified nucleotide used. We therefore recommend that similar labeling tests be performed when developing the method for a new ddNTP or enzyme batch, before scaling up the synthesis of modified DNA origami.

In summary, we have demonstrated a fast and robust method for modifying DNA origami in a desired pattern. It is a highly attractive alternative to the application of individually chemically labeled staple strands in terms of labor, cost, and processing time. The initial labeling reaction is quantitative as shown by gel mobility shift assays, and the AFM analysis revealed that the modifications are incorporated at the intended positions, creating the desired pattern on a DNA origami. In particular, the amine-modified staple strands hold great promise for a large variety of possible subsequent modifications. With all the applications of DNA origami yet to be unveiled, this method will clearly facilitate this process and make the field of modified DNA origami more accessible to the general user.

■ ASSOCIATED CONTENT

Supporting Information. Figures S1−S5 and protocol notes as described in the text along with DNA sequence lists. This material is available free of charge via the Internet at http://pubs.acs.org.

■ ACKNOWLEDGMENT

This work was funded by the Danish National Research Foundation, the iNANO Graduate School, and the OChem Graduate School.

■ REFERENCES

(1) Rothemund, P. (2006) Folding DNA to create nanoscale shapes and patterns. *Nature 440*, 297–302.

(2) Andersen, E. S., Dong, M., Nielsen, M. M., Jahn, K., Lind-Thomsen, A., Mamdouh, W., Gothelf, K. V., Besenbacher, F., and Kjems, J. (2008) DNA origami design of dolphin-shaped structures with flexible tails. *ACS Nano 2*, 1213–1218.

(3) Andersen, E. S., Dong, M., Nielsen, M. M., Jahn, K., Subramani, R., Mamdouh, W., Golas, M. M., Sander, B., Stark, H., Oliveira, C. L. P., Pedersen, J. S., Birkedal, V., Besenbacher, F., Gothelf, K. V., and Kjems, J. (2009) Self-assembly of a nanoscale DNA box with a controllable lid. *Nature 459*, 73–76.

(4) Douglas, S. M., Dietz, H., Liedl, T., Hogberg, B., Graf, F., and Shih, W. M. (2009) Self-assembly of DNA into nanoscale three-dimensional shapes. *Nature 459*, 414–8.

(5) Kuzuya, A., and Komiyama, M. DNA origami: fold, stick, and beyond. *Nanoscale 2*, 310−22.

(6) Nangreave, J., Han, D., Liu, Y., and Yan, H. DNA origami: a history and current perspective. *Curr. Opin. Chem. Biol. 14*, 608−15.

(7) Shih, W. M., and Lin, C. Knitting complex weaves with DNA origami. *Curr. Opin. Struct. Biol. 20*, 276−82.

(8) Voigt, N. V., Torring, T., Rotaru, A., Jacobsen, M. F., Ravnsbaek, J. B., Subramani, R., Mamdouh, W., Kjems, J., Mokhir, A., Besenbacher, F., and Gothelf, K. V. (2010) Single-molecule chemical reactions on DNA origami. *Nat. Nanotechnol. 5*, 200–3.

(9) Sacca, B., Meyer, R., Erkelenz, M., Kiko, K., Arndt, A., Schroeder, H., Rabe, K. S., and Niemeyer, C. M. (2010) Orthogonal protein decoration of DNA origami. *Angew. Chem., Int. Ed. Engl. 49*, 9378–9383.

(10) Shen, W., Zhong, H., Neff, D., and Norton, M. L. (2009) NTA directed protein nanopatterning on DNA Origami nanoconstructs. *J. Am. Chem. Soc. 131*, 6660–1.

(11) Sharma, J., Chhabra, R., Andersen, C. S., Gothelf, K. V., Yan, H., and Liu, Y. (2008) Toward reliable gold nanoparticle patterning on self-assembled DNA nanoscaffold. *J. Am. Chem. Soc. 130*, 7820–1.

(12) Hong, V., Presolski, S. I., Ma, C., and Finn, M. G. (2009) Analysis and optimization of copper-catalyzed azide-alkyne cycloaddition for bioconjugation. *Angew. Chem., Int. Ed. Engl. 48*, 9879–83.

(13) Tornoe, C. W., Christensen, C., and Meldal, M. (2002) Peptidotriazoles on solid phase: [1,2,3]-triazoles by regiospecific copper(i)-catalyzed 1,3-dipolar cycloadditions of terminal alkynes to azides. *J. Org. Chem. 67*, 3057–64.

(14) Rostovtsev, V. V., Green, L. G., Fokin, V. V., and Sharpless, K. B. (2002) A stepwise huisgen cycloaddition process: copper(I)-catalyzed regioselective "ligation" of azides and terminal alkynes. *Angew. Chem., Int. Ed. Engl. 41*, 2596–9.

Supporting Information

Functional patterning of DNA origami by parallel enzymatic modification

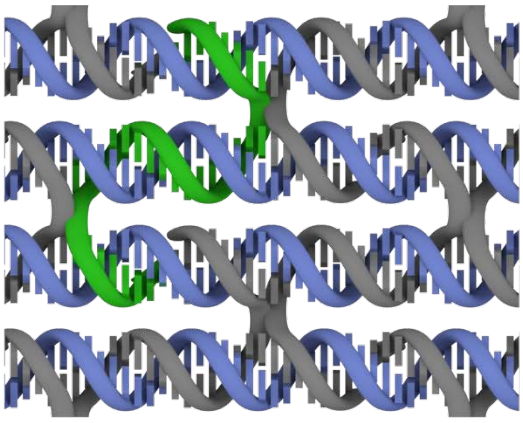
Kasper Jahn[1,2], Thomas Tørring[1,3], Niels Vinther Voigt[1,3], Rasmus Schøler Sørensen[1,2], Anne Louise Bank Kodal[1,3], Ebbe Sloth Andersen[1,2], Kurt Vesterager Gothelf[1,3] and Jørgen Kjems[1,2]

1. Danish National Research Foundation: Center for DNA Nanotechnology at Interdisciplinary Nanoscience Center (iNANO), 2. Department of Molecular Biology, 3. Department of Chemistry, Aarhus University, DK-8000 Aarhus, Denmark

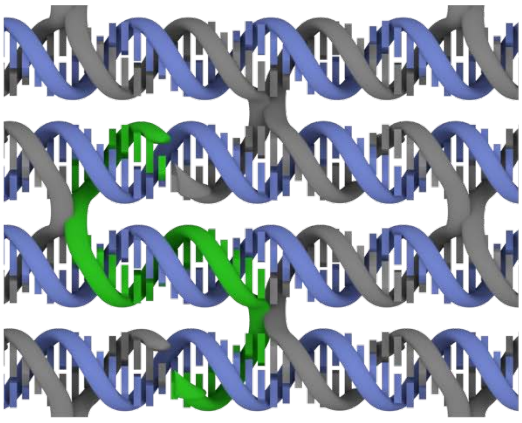
Contents

Figure S1 – Staple strand alteration in DNA origami design 3
Figure S2 – AFM image of streptavidin bound to biotin modified DNA origami 4
Figure S3 – AFM image for DIG antibody bound to DIG modified DNA origami 5
Figure S4 – Synthesis scheme for attachment of biotin to the amine-modified strands 6
Figure S5 – AFM image of streptavidin bound DNA origami, after biotin-azide is attached to the origami 7
Characterization and yields 8
Purification considerations 10
Batchwise alkyne modification 11
Fluorophore labelling procedure 12
Rectangular origami staple strand list 13
DNA Box Staple strand List 18

Figure S1 – Staple strand alteration in DNA origami design

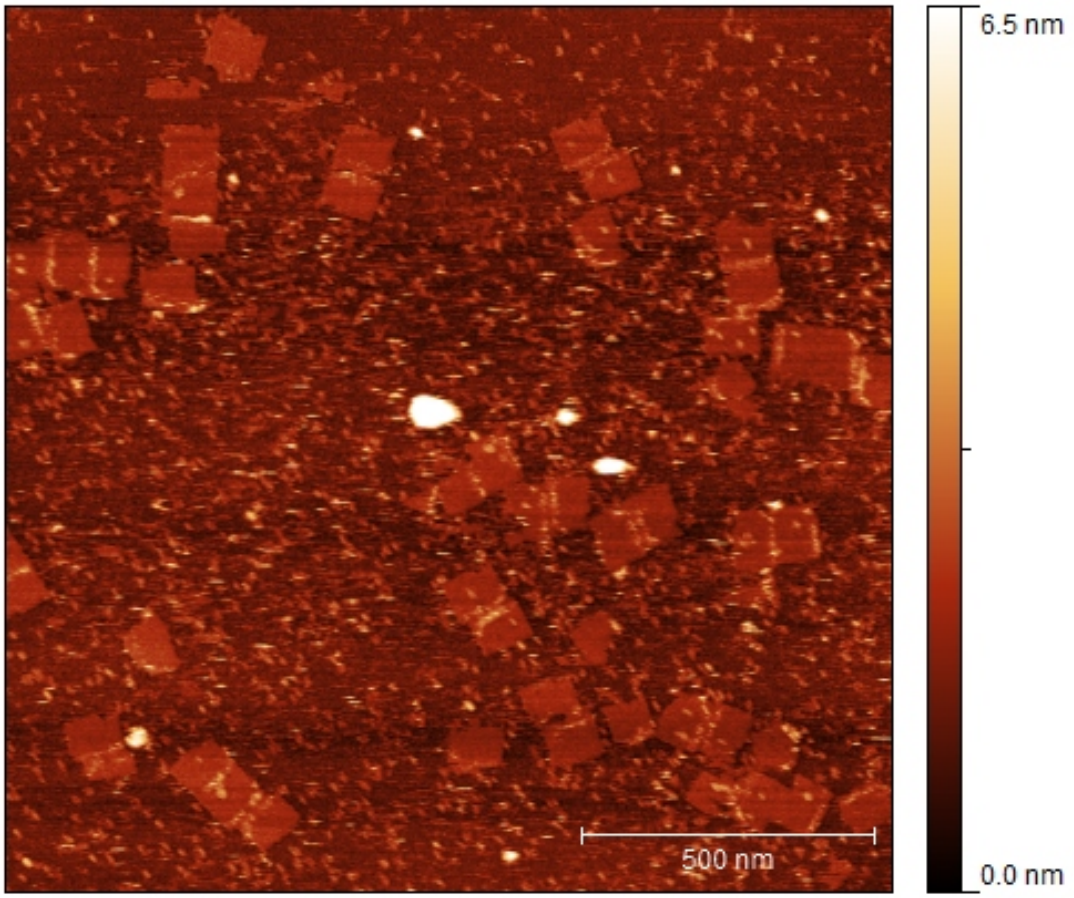


Regular staple pattern



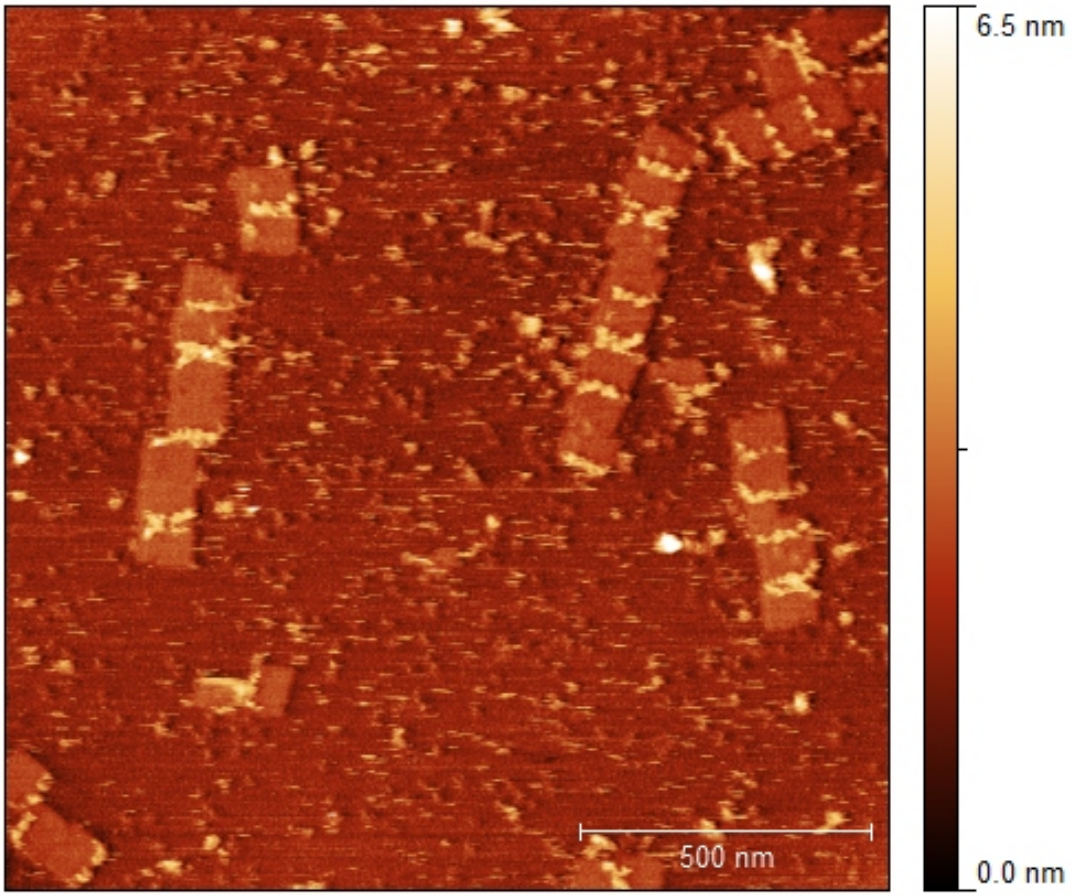
Staple pattern for the modified staples

Figure S2 – AFM image of streptavidin bound to biotin modified DNA origami



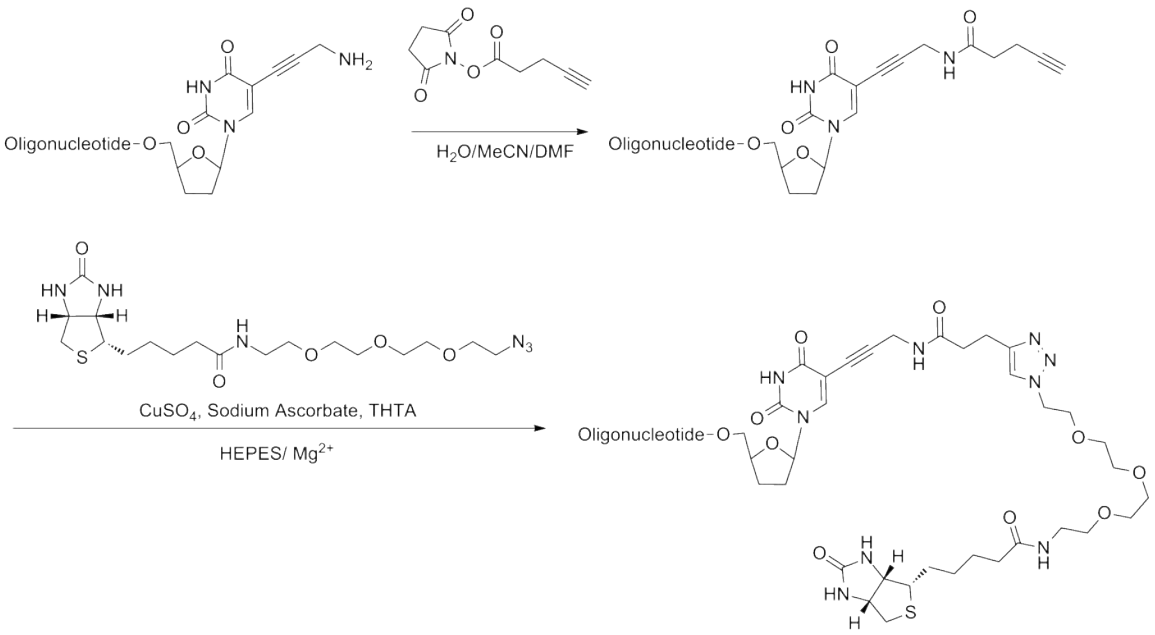
Representative AFM zoom out image of the biotin modified origami, with streptavidin attached. The intended "L" shape is seen on the origami.

Figure S3 – AFM image for DIG antibody bound to DIG modified DNA origami



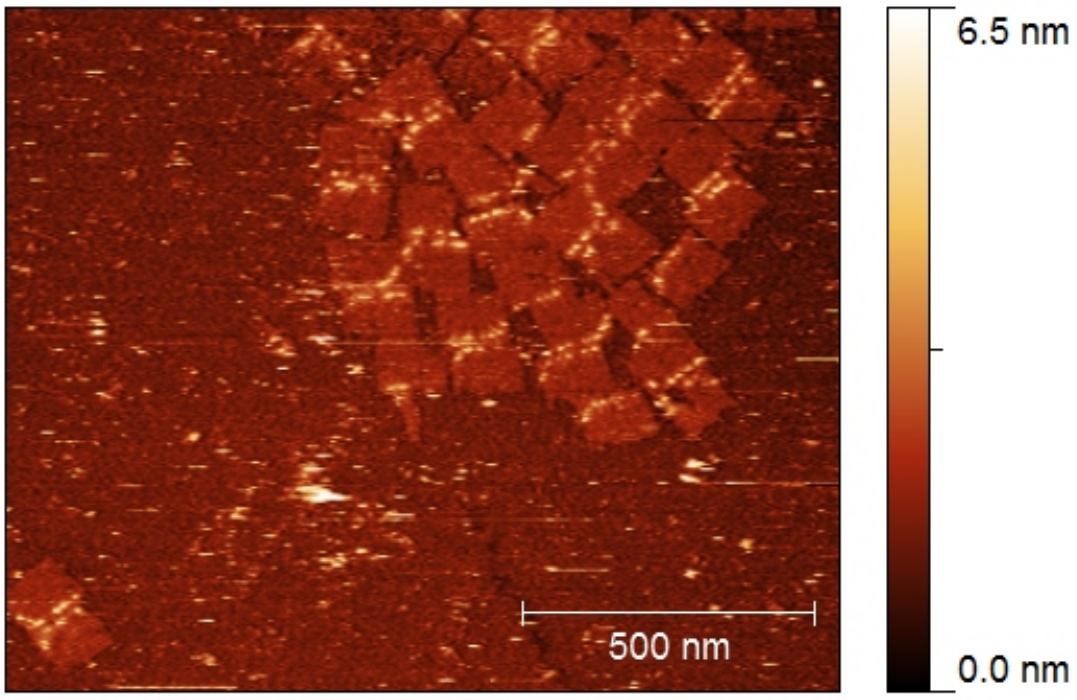
Representative AFM zoom out picture of the DIG modified origami, with Anti-DIG monoclonal antibody attached. The intended "L" shape is seen on the origami.

Figure S4 – Synthesis scheme for attachment of biotin to the amine-modified strands



Overview of the chemistry for attaching a biotin to the amine modified staple strands. The final step is performed after origami formation.

Figure S5 – AFM image of streptavidin bound DNA origami, after biotin-azide is attached to the origami

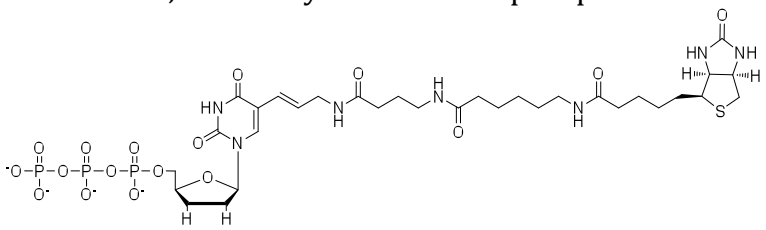


Representative AFM zoom out picture of the origami with biotins modifications originating from the amine modifications on the staple strand after addition of streptavidin. The intended "L" shape is seen on the origami.

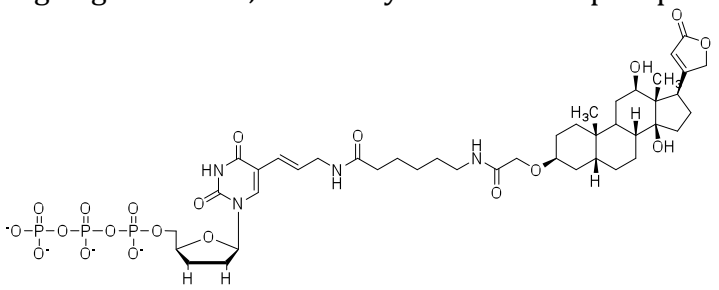
Characterization and yields

To test the purity and recovery yield for oligos labelled by terminal transferase a 42-nucleotide oligo was labelled with the following three ddNTPs;

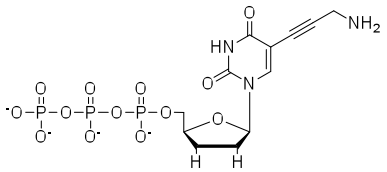
Biotin-16-2',3'-dideoxy-uridine-5'-triphosphate



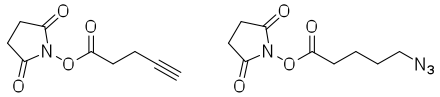
Digoxigenin-11-2',3'-dideoxy-uridine-5'-triphosphate



5-Propargylamino-2',3'-Dideoxy-uridine-5'-triphosphate



The amine modified ddNTP was further modified with an NHS-azide and an NHS-alkyne (below)



The oligonucleotide (200 pmol) was mixed with 10 equivalents of modified ddNTP (2 µL, 1 mM), Roche reaction buffer (4 µL, 5x) , $CoCl_2$(4 µL, 25 mM) and Roche recombinant terminal transferase (2 µL, 40 U/µL). This is 1/10 of the amount recommended by the supplier. The solution was incubated on a thermoshaker at 37°C for 30 min. EDTA (4 µL, 100 mM) was added and the solution was heated to 70°C to stop the reaction. Then the sample was diluted and NaOAc(pH=5.2) added (final volume 100 µL, $C_{(NaOAc)}$= 300 mM), this was followed by addition of cold ethanol (99%, 250 µL). The sample was incubated on dry ice for 15 min before centrifugating at 4°C for 30 min (20000 RCF). The supernatant was discarded and

the pellet redissolved in TEAA buffer (100 µL, 0.1 M, pH=7) and analyzed using RP-HPLC. The retention time and integral were compared to the starting oligo. As shown in the table below, the recovery yields after the reaction and precipitation were between 80-90% (calculated from HPLC integrals) and a single peak in all chromatograms indicated that HPLC purification was not necessary for most uses. The yields can vary depending on the purity of starting oligos, and as the procedure involves precipitation, shorter oligos might also provide lower yields. Mass spectrometric analysis of the HPLC purified samples clearly showed that the reaction was successful.

For the oligos modified with azides and alkynes, the starting oligo was enzymatically modified with the propargylamine as described above and precipitated. The pellet was redissolved in water (50 µL) and mixed with either an azide-NHS ester or an alkyne-NHS ester dissolved in DMF (50 mM, 50 µL). To this mixture MeCN (50 µL) and Et_3N (1 µL) was added. The mixture was left to react at rt for ½ h before precipitation and HPLC purification as described above.

Oligonucleotide	*Retention time (min)*	*Yield (%)*	*Calc. Mass*	*Found Mass*
Unmodified	7.2	-	12148	12149
Biotinylated	10.0	90	12902	12903
Digoxigenin modified	14.9	81	13021	13020
Amino modified	7.4	89	12475	12476
Alkyne modified	9.0	30	12555	12555
Azide modified	9.9	48	12600	12595

Purification considerations

The buffer used for the terminal transferase reaction is comprised of $CoCl_2$ and $K(CH_3)_2AsO_2$, which may influence origami assembly if transferred to the assembly reaction. Therefore, it is very important to purify the strands from the enzymatic reaction. Typically, precipitating in NaOAc and washing the pellet as described in Methods and Materials is sufficient.

We have however observed that if we for one origami label many strands individually instead of in a one-pot reaction the quality is worse. We hypothesize that this is due to a larger quantity of excess buffer derived from the individual labelling reactions. Therefore, we recommend HPLC/spin column purification, or several washing steps after pelleting the labelled oligos.

Batchwise alkyne modification

The mixture of 17 staple strands (100 pmol of each) were mixed with amino-modified ddNTP (17 µL, 1 mM, 10 equivalents), Roche reaction buffer (68 µL, 5x), $CoCl_2$ (68 µL, 25 mM), water (121.5 µL) and Roche recombinant terminal transferase (8.5 µL, 400U/µL). The solution was incubated on a thermoshaker at 37°C for 30 min. EDTA (34 µL, 0.2 M) was added and the mixture was freeze dried. The reaction mixture was redissolved in water (85 µL).
An aqueous solution of amino-modified staple strands (~ 0.85 nmol, 50 pmol of each, 42.5 µL) was mixed with the NHS ester of 4-pentynoic acid (4.25 µmol, 100 mM, 42.5 µL) in DMF, acetonitrile (42.5 µL), triethylamine (1.7 µL) and Milli-Q water (40.8 µL). The solution was incubated on a thermoshaker at 25°C overnight. The DNA was precipitated with glycogen (2 µL, 20mg/ml), NaOAc (3 M, 17 µL, pH 5) and cold ethanol (99%, 680 µL). The sample was incubated on dry ice for 15 min before centrifugating at 4°C for 30 min (20000 RCF). The supernatant was discarded and the pellet redissolved in TEAA buffer (150 µL, 0.1 M, pH=7) and purified by RP-HPLC. The yield (0.38 nmol, 45%) was determined by concentration measurement using a NanoDrop®.

Fluorophore labelling procedure

The selected staple strands (400 pmol mix pr. labelling reaction) were mixed with ddUTP-Texas Red® (2 μL, 1 mM, 5 equivalents), Roche reaction buffer (16 μL, 5x), $CoCl_2$ (16 μL, 25 mM) and Roche recombinant terminal transferase (2 μL, 400 U/μL). The solution was incubated on a thermoshaker at 37°C for 40 min. EDTA (16 μL, 100 mM) was added and the solution was heated to 70°C for 10 min to stop the reaction. Subsequently, the oligos were precipitated by adding NaOAc (15 μL, 5 M, pH = 5.2), cold EtOH (99%, 300 μL), incubating on dry ice for 30 min and centrifuging (40 min, 4°C, 20000g). The supernatant was decanted off, the pellet sonicated with washing solution (75% EtOH in water, 400 μL), centrifuged (40 min, 4°C, 20000g), the supernatant was removed and the last residue of solvent was removed by evaporation in a speed vac before the product was redissolved in water (100 μL). Three quarters (75 μL) of this was buffered (to 0.1M TEAA, pH = 7) and run through preparative RP-HPLC (10 → 40% MeCN over 15 min), product containing fractions (retention time: 9-12 min) were collected and freeze dried, redissolved and yields determined to 20-29% from UV-absorption measurements.

Rectangular origami staple strand list

Modified staple strands

TCATTTTCCGTAACACTGAGTTTCAAAGGAACTTT
AACTAAAGATCTCCAAAAAAAAGGCTTTTGCGTTT
GGATCGTCGGGTAGCAACGGCTACAAGTACAATTT
CGGAGATTCGCGACCTGCTCCATGACGTAACATTT
AAGCTGCTACACCAGAACGAGTAGATCAGTTGTTT
AGATTTAGCGCCAAAAGGAATTACCATTGAATTTT
CCCCCTCACCATAAATCAAAAATCATTGCTCCCCC
TTTTGATAATTGCTGAATATAATGGGGGCGCGTTT
AGCTGAAATTAACATCCAATAAATAAATGCAACCC
TGCCTGAGAAGGCCGGAGACAGTCTCATATGTTTT
ACCCCGGTTTGTATAAGCAAATATGATTCTCCTTT
GTGGGAACCGTTGGTGTAGATGGGGTGCGGGCTTT
CTCTTCGCGCAAGGCGATTAAGTTTTCCACACTTT
TATCAGGGCGAAAATCCTGTTTGACGGGCAACAGCTGATTACTCACATTTT
CACGACGTGTTTCCTGTGTGAAATTTGCGCTCACTGCCCGCTTTTCACTTT
CCCCGATTTAGAGCTTGACGGGGAAAAGAACGTGGACTCCGGCAAAATTTT
GCCAGCTGCGGTTTGCGTATTGGGAATCAAAAGAATAGCCACAAGAGTTTT

Non modified staple strands

AACATACGCCTAATGAGTGAGCTAGCCCTTCACCGCCTGGGGTTTGCC
TAATTGCGTGTTATCCGCTCACAAGGGTAACGCCAGGGTTTTGGGAAG
CAGTGAGATGGTGGTTCCGAAATCAACGTCAAAGGGCGAAAAGGGAGC
CCCTTATACGCCAGGGTGGTTTTTCTTTCCAGTCGGGAAAAATCATGG
CCACTATTAAGCCGGCGAACGTGGCGAGAAAGGAAGGGAATGCGCCGC
CTCAGAGCCACCACCC
ACGTTAGTTCTAAAGTTTTGTCGTGATACAGG
CGTAACGAAAATGAATTTTCTGTAGTGAATTT
AGTTTGGACGAGATAGGGTTGAGTGTAATAAC
GAACGTGGCGAGAAAGGAAGGGAATGCGCCGC
CAATGACAGCTTGATACCGATAGTCTCCCTCA
CTTAAACAACAACCATCGCCCACGCGGGTAAA
AAACGAAATGCCACTACGAAGGCAGCCAGCAA
ATACGTAAGAGGCAAAAGAATACACTGACCAA
CCAGGCGCGAGGACAGATGAACGGGTAGAAAA
CTTTGAAAATAGGCTGGCTGACCTACCTTATG
CCCTCAGAACCGCCACCCTCAGAAACAACGCC
ACGAACTATTAATCATTGTGAATTTCATCAAG
TTTCAACTACGGAACAACATTATTAACACTAT
ACTGGATATCGTTTACCAGACGACTTAATAAA
CATAACCCGCGTCCAATACTGCGGTATTATAG

GAAGCAAAAAAGCGGATTGCATCAATGTTTAG
TCAGAAGCCTCCAACAGGTCAGGATTTAAATA
TCGCAAATAAGTACGGTGTCTGGACCAGACCG
TGCAACTAGGTCAATAACCTGTTTAGAATTAG
CAACGCAAAGCAATAAAGCCTCAGGATACATT
CAAAATTAGGATAAAAATTTTTAGGATATTCA
AGAGAATCAGCTGATAAATTAATGCTTTATTT
ACCGTTCTGATGAACGGTAATCGTAATATTTT
CTTTCATCTCGCATTAAATTTTTGAGCAAACA
GTTAAAATAACATTAAATGTGAGCATCTGCCA
TTCGCCATGGACGACGACAGTATCGTAGCCAG
GTTTGAGGTCAGGCTGCGCAACTGTTCCCAGT
TCATAGCTTGTAAAACGACGGCCAAAGCGCCA
TGCTAAACTCCACAGACAGCCCTCTACCGCCA
TGTAGCATAACTTTCAACAGTTTCTAATTGTA
ATATATTCTCAGCTTGCTTTCGAGTGGGATTT
TCGGTTTAGGTCGCTGAGGCTTGCAAAGACTT
CTCATCTTGGAAGTTTCCATTAAACATAACCG
TTTCATGATGACCCCCAGCGATTAAGGCGCAG
AGTAATCTTCATAAGGGAACCGAACTAAAACA
ACGGTCAATGACAAGAACCGGATATGGTTTAA
AAAGATTCTAAATTGGGCTTGAGATTCATTAC
TAAATATTGAGGCATAGTAAGAGCACAGGTAG
TACCTTTAAGGTCTTTACCCTGACAATCGTCA
TTTCATTTCTGTAGCTCAACATGTTTAGAGAG
TATATTTTCATACAGGCAAGGCAAAGCTATAT
CATGTCAAAAATCACCATCAATATAACCCTCA
ACCCGTCGTTAAATTGTAAACGTTAAAACTAG
GGCGATCGCGCATCGTAACCGTGCGAGTAACA
GAGAATAGGTCACCAGTACAAACTCCGCCACC
CCAGCAGGCGATGGCCCACTACGTGAGGTGCC
GTAAAGCACTAAATCGGAACCCTAAAACCGTC
AAAGGCCGCTCCAAAAGGAGCCTTAGCGGAGT
GCGAAACAAGAGGCTTTGAGGACTAGGGAGTT
CCAAATCATTACTTAGCCGGAACGTACCAAGC
CATTCAACCTTGCCCTGACGAGAACATTCAGT
AAACAGTTTAATGCAGATACATAAGAATACCA
TTTTTGCGCAGAAAACGAGAATGAAATGCTTT
TCAATTCTGATGGCTTAGAGCTTAAGAGGTCA
AGGTAAAGACTAATAGTAGTAGCAAGGTGGCA
AGAAAAGCATTCAAAAGGGTGAGATAATGTGT
GATTGACCCCCAAAAACAGGAAGATGATAATC
CAGCTGGCGTAATGGGATAGGTCAAAACGGCG
GCATAAAGGAAAGGGGGATGTGCTTATTACGC
GAGTTGCATGTAAAGCCTGGGGTGAGCCGGAA
AATAATAAATAGGAACCCATGTACAGGGATAGCAAGCCCA

ACCCAAATGCAAGCGGTCCACGCTCCCTGAGA
CAAGTTTTTTGGGGTCGAACCATC
CAGCGAAATTTTTTCACGTTGAAAGAATTGCG
CGCCTGATGACAGCATCGGAACGAACCCTCAG
GAATAAGGAAATTGTGTCGAAATCTGTATCAT
GCGCTTAA
AGGGTTGATATAAGTATAGCCCGGAATAGGTG
TGAACAAAGATAACCCACAAGAATAAGACTCC
ATCAGAGAGTCAGAGGGTAATTGAACCAGTCA
TATTTTGCACGCTAACGAGCGTCTGAACACCC
TCTTACCAACCCAGCTACAATTTTAAAGAAGT
ATCGGCTGACCAAGTACCGCACTCTTAGTTGC
GGTATTAATCTTTCCTTATCATTCATATCGCG
CATATTTATTTCGAGCCAGTAATAAATCAATA
AGAGGCATACAACGCCAACATGTATCTGCGAA
ACAAAGAAAATTTCATCTTCTGACAGAATCGC
TTTTAGTTCGCGAGAAAACTTTTTTTATGACC
AAATCAATCGTCGCTATTAATTAAATCGCAAG
CTGTAAATATATGTGAGTGAATAAAAAGGCTA
TTTAACGTTCGGGAGAAACAATAACAGTACAT
CTTTTACACAGATGAATATACAGTGCCATCAA
TTATTAATGAACAAAGAAACCACCTTTTCAGG
ATTTTGCGTTTAAAAGTTTGAGTACCGGCACC
CTAAAGCAAATCAATATCTGGTCACCCGAACG
AAACCCTCTCACCTTGCTGAACCTAGAGGATC
GCCAACAGATACGTGGCACAGACATGAAAAAT
GCGTAAGAAGATAGAACCCTTCTGAACGCGCG
TAAGCGTCGGTAATAAGTTTTAACCCGTCGAG
AGTGTACTATACATGGCTTTTGATCTTTCCAG
GTTGTAGCCCTGAGTAGAAGAACTACATTCTG
ATCACTTGAATACTTCTTTGATTAGTTGTTCC
TACAGGGCGCGTACTATGGTTGCTAATTAACC
AACCAGAGACCCTCAGAACCGCCACGTTCCAG
GAGCCGCCCCACCACCGGAACCGCTGCGCCGA
GACTTGAGGTAGCACCATTACCATATCACCGG
AATCACCACCATTTGGGAATTAGACCAACCTA
TTATTACGTAAAGGTGGCAACATACCGTCACC
TACATACACAGTATGTTAGCAAACTGTACAGA
TGCTCAGTACCAGGCGGATAAGTGGGGGTCAG
GCGCATTAATAAGAGCAAGAAACAATAACGGA
GCCCAATAGACGGGAGAATTAACTTTCCAGAG
AGGTTTTGGCCAGTTACAAAATAAACAGGGAA
CCTAATTTAAGCCTTAAATCAAGAATCGAGAA
CTAATTTACCGTTTTTATTTTCATCTTGCGGG
CAAGCAAGCGAGCATGTAGAAACCAGAGAATA
ACGCTCAACGACAAAAGGTAAAGTATCCCATC

TAAAGTACCAGTAGGGCTTAATTGCTAAATTT
TATGTAAAGAAATACCGACCGTGTTAAAGCCA
AATGGTTTTGCTGATGCAAATCCATTTTCCCT
TTGAATTATTGAAAACATAGCGATTATAACTA
TAGAATCCCCTTTTTTAATGGAAACGGATTCG
ACAGAAATCTTTGAATACCAAGTTAATTTCAT
CCTGATTGAAAGAAATTGCGTAGAAGAAGGAG
CGACAACTTCATCATATTCCTGATCACGTAAA
CGGAATTACGTATTAAATCCTTTGGTTGGCAA
GCCACGCTTTGAAAGGAATTGAGGAAACAATT
ATCAACAGGAGAGCCAGCAGCAAAATATTTTT
GTCACACGATTAGTCTTTAATGCGGCAACAGT
GAATGGCTACCAGTAATAAAAGGGCAAACTAT
GGAAAGCGGTAACAGTGCCCGTATCGGGGTTT
TGCCTTGACAGTCTCTGAATTTACCCCTCAGA
GTAAAAGACTGGTAATATCCAGAAATTCACCA
CGGCCTTGGTCTGTCCATCACGCATTGACGAG
CACGTATAACGTGCTTTCCTCGTTGCCACCGA
GTTTGCCACCTCAGAGCCGCCACCGCCAGAAT
GCCACCACTCTTTTCATAATCAAATAGCAAGG
TTATTCATGTCACCAATGAAACCATTATTAGC
CCGGAAACTAAAGGTGAATTATCATAAAAGAA
ATACCCAAACACCACGGAATAAGTGACGGAAA
ACGCAAAGAAGAACTGGCATGATTTGAGTTAA
CCTCAAGAGAAGGATTAGGATTAGAAACAGTT
CTTTACAGTATCTTACCGAAGCCCAGTTACCA
GCAATAGCAGAGAATAACATAAAAACAGCCAT
GAGGCGTTTCCCAATCCAAATAAGATAGCAGC
ATTATTTATTAGCGAACCTCCCGACGTAGGAA
TAAGTCCTGCGCCCAATAGCAAGCAAGAACGC
TCATTACCGAACAAGAAAAATAATAATTCTGT
GCGTTATACGACAATAAACAACATACAATAGA
CCAGACGACAAATTCTTACCAGTAGATAAATA
TAACCTCCAATAAGAATAAACACCTATCATAT
AGGCGTTAGGCTTAGGTTGGGTTAAGCTTAGA
AAAACAAACTGAGAAGAGTCAATATACCTTTT
TTAAGACGATTAATTACATTTAACACAAAATC
AACCTACCGCGAATTATTCATTTCACATCAAG
GCGCAGAGATATCAAAATTATTTGTATCAGAT
GGATTTAGTTCATCAATATAATCCAGGGTTAG
GATGGCAAAAGTATTAGACTTTACAAGGTTAT
AGGCGGTCTCTTTAGGAGCACTAAACATTTGA
CTAAAATAAGTATTAACACCGCCTCGAACTGA
GAAATGGAAAACATCGCCATTAAACAGAGGTG
TAGCCCTATTATTTACATTGGCAGCAATATTA
ACAAACAACTGCCTATTTCGGAACCTGAGACT

AATGCCCCATAAATCCTCATTAAAAGAACCAC
AGAAGTGTCATTGCAACAGGAAAAAATCGTCT
CCGCCAGCTTTTATAATCAGTGAGAGAATCAG
AGCGGGAGCTAAACAGGAGGCCGAGAATCCTG
TCGGCATTCCGCCGCCAGCATTGATGATATTC
CACCAGAGTTCGGTCATAGCCCCCTCGATAGC
ATTGAGGGAATCAGTAGCGACAGACGTTTTCA
AGCACCGTAGGGAAGGTAAATATTTTATTTTG
GAAGGAAAAATAGAAAATTCATATTTCAACCG
TCACAATCCCGAGGAAACGCAATAATGAAATA
TGAAAGTATTAAGAGGCTATTATT
AAAAGTAAAACGTCAAAAATGAAAAAACGATT
TTTTGTTTGCTTATCCGGTATTCTAAATCAGA
TATAGAAGACGCGCCTGTTTATCAGTTCAGCT
AATGCAGAGAAAAAGCCTGTTTAGGGAATCAT
AATTACTACATAGGTCTGAGAGACGTGAATTT
ATCAAAATGAAGATGATGAAACAAAATTACCT
GAGCAAAAACTTCTGAATAATGGATGATTGTT
TGGATTATGCCGTCAATAGATAATCAACTAAT
AGATTAGACCAGCAGAAGATAAAAAATACCGA
ACGAACCACTACATTTTGACGCTCACGCTCAT
CTGAAACAGTCAGACGATTGGCCTCAGGAGGT
GGAAATACCAGGAACGGTACGCCATTAAAGGGATTTTAGA
TGAGGCAGGCGTCAGACTGTAGCGATCAAGTT
TGCCTTTAAGACAAAAGGGCGACAGGTTTACC
AGCGCCAAGCAGATAGCCGAACAATTTTTAAG
TATCACCGTACTCAGGAGGTTTAGATAGTTAG
GGACGTTGAGAACTGGCTCATTATGCGCTAAT
CGATTTTAGGAAGAAAAATCTACGGATAAAAA
TTTGCCAGGCGAGAGGCTTTTGCAATCCTGAA
CCAAAATAAGGGGGTAATAGTAAAAAAAGATT
TTTTAATTGCCCGAAAGACTTCAACAAGAACG
AAGAGGAACGAGCTTCAAAGCGAAAGTTTCAT
CGAGTAGAACAGTTGATTCCCAATATTTAGGC
TCCATATATTTAGTTTGACCATTAAGCATAAA
CTGTAATAGGTTGTACCAAAAACACAAATATA
GCTAAATCCTTTTGCGGGAGAAGCCCGGAGAG
TCAGGTCATTTTTGAGAGATCTACCCTTGCTT
GGTAGCTATTGCCTGAGAGTCTGGTTAAATCA
AAATAATTTTTAACCAATAGGAACAACAGTAC
GCTCATTTCGCGTCTGGCCTTCCTGGCCTCAG
GCTTCTGGCACTCCAGCCAGCTTTACATTATC
GAAGATCGTGCCGGAAACCAGGCAGTGCCAAG
CCCGGGTACCTGCAGGTCGACTCTCAAATATC
CTTGCATGCCGAGCTCGAATTCGTCCTGTCGT
GGGAGAGGCATTAATGAATCGGCCACCTGAAA

DNA Box Staple strand List

Eight fluorescently labelled staple strands

1. AACCCACATGATTAAGACTCCTTAATACATAA
2. CTCAGAACTTTACCGTTCCAGTAAGTACTGGT
3. TTTCATAAACCATTAGCAAGGCCGTTCATTAA
4. AGAGCAAGCAATAATAACGGAATACAAAGACA
5. CAGAGCCGTTAAAGCCAGAATGGACTTGAGTA
6. GGTCATAGAACCATCGATAGCAGCGAGGGAGG
7. CTTACCGAAACAAAGTTACCAGAACAATCAAT
8. CCGCCAGCGGCCTTGATATTCACAGCCCCCTG

When labelling two oligos we used 1-2, when labelling four we used 1-4, and when labelling eight we used 1-8.

Rest of Staples

AACAATTCGGAATTATCATCATATTTATTTGC
CCGAACGTTTTTGCGGAACAAAGAGCGTAGAT
ATTACCTGTTTTGGATTATACTTCTGAAATAATCCT
CAAAATCGACCTACCATATCAAAATCCTGATT
GGATTCGCCAGAAATAAAGAAATTAACCACCA
ATCAGATGGATTTAGAAGTATTAGATTGAGGA
GAAGGAGCGACAACTCGTATTAAACTGGTCAG
CATTTGAGATGGCAATTCATCAATTAATGGAA
AGGTTATCGGCGGTCAGTATTAACTAATGCGC
ATCGTCTGAGCCCTAAAACATCGCGATAAAAC
TTCACCAGAATGGCTATTAGTCTTACCGCCTG
TTGGCAAACCACGCTGAGAGCCAGACAGACAA
AGAGGTGATAAAATATCTTTAGGAAGATAATA
CAACAGTGTCAACAGTTGAAAGGAACTTTACA
GAAAAATCAACCCTCAATCAATATTCCTTTGC
GAACTGATAAATGGATTATTTACATCCAGAAC
TATTTTTGTCACACGACCAGTAATAAGAACTC
CATTCTGGCGTAAGAATACGTGGCCAGCAAAT
AATATTACGAAGTGTTTTTATAATCCTCGTTA
AAACTATCTAAAAGAGTCTGTCCAGGTTGCTT
TAATAACATTGTAGCAATACTTCTTTTTCGCTTAAT
AATCCTGACGCCAGCCATTGCAACGACGCTCA
CCACCGAGGGCCTTGCTGGTAATATTGGCAGA
ATTAACCGTCACTTGCCTGAGTAGAAAAGGGA
TCTATCAGCCCGAGATAGGGTTGAGACGGGCA
TTCCGAAAATCAAGTTTTTTGGGGTAAAGGGA
CCGTAAAGTTTTGGCGAAAATCCTGTTTCTGGTTTG
TCACCCAATCGGCAAAATCCCTTAGGCCCTGA
AAGAATAGGGCGATGGCCCACTACGAAAGCCG
AAGCATAAGTTGTAAAACGACGGCGCTATTAC

CCGCTCACTGCCTGCAGGTCGACTTGTTGGGA
CCAGTTTGCCAACGTCAAAGGGCGAAGAAAGC
GAGAGTTGCGCTTTCCAGTCGGGACGAGCCGG
ACAGCTGATGCATTAATGAATCGGATTGTTAT
TCACTGCCCAGCAAGCGGTCCACGGATGGTGG
GTGCCAGCTTGCCCTTCACCGCCTTAAATCAA
CGGGGAGATTCTTTTCACCAGTGAGTGTTGTT
AGGAAGATCGGTGCGGGCCTCTTCCAGTGCCA
CCGCTTCTATTCAGGCTGCGCAACCTAGAGGA
TTGTTAAACCGTAATGGGATAGGTGCATCTGC
GTCACGACAGTGTAAAGCCTGGGGCGTTGCGC
AGCTTGCAAATTCCACACAACATAAACCTGTC
TCCCCGGGCTGTTTCCTGTGTGAACCAACGCG
GCCAGCTGGGGGACGACGACAGTAACAAACGG
AGGGCGATCGCACTCCAGCCAGCTGCGAGTAA
CATTCGCCGGTGCCGGAAACCAGGTTTTCTGTAGCC
CAGTTTGAGCGAAAGGGGGATGTGTTTTCCCA
CAGCTCATCGGATTCTCCGTGGGATCGGCCTC
AAAAATAATCAACATTAAATGTGATTCCGGCA
ATCCAATATTTAAATGCAATGCCTAGAAAGGC
TAGCAAAACAAGGATAAAAATTTTTATGATAT
ATCAGAAATTTTAAGATTCAAAAGGGTGGAGTAATG
TAGCATGTGTCAAATCACCATCAATAGAACCC
ACAAGAGATCTAGCTGATAAATTAAGCCTTTA
TCATATATAATCATACAGGCAAGGTTTAGCTA
TTTCAACGTTAAGCAATAAAGCCTTTAGATAC
AAAGCTAAATACTTTTGCGGGAGAATGCCGGA
GAGTACCTATCAGGTCTTTACCCTCGGAATCG
CCGGAAGCAGCAAAGCGGATTGCAAAAATGTT
GCATCAATTTTTGCGGATGGCTTAGAGCATAAGAGG
TATTTTCAATGCTGTAGCTCAACAGGATTAGA
ATTTCGCACTAAAGTACGGTGTCTGAACCAGA
GAACGAGTATAACAGTTGATTCCCTTTTCAAATATC
TGAATATATTTGGGGCGCGAGCTGGCATTAAC
ATATGCAAAATGGTCAATAACCTGCAAAGAAT
CATTCCATAGATTTAGTTTGACCACAGAGCAT
AATCAAAATTAATTGCTCCTTTTGTTAATTGC
AAACCAAACAGAGGGGGTAATAGTTCAAAAAG
TAGTCAGAAAACTCCAACAGGTCATGTTTTAA
ATTAAGAGATTCGAGCTTCAAAGCGGAAGTTT
TTTAAACATTTTAACTAATGCAGATACATAGGAATACCACATTC
TCATAAATTACGAGGCATAGTAAGATTACAGG
TAGACTGGCCCTCGTTTACCAGACACGTTAAT
AGTTTTGCATAGCGAGAGGCTTTTTTTTTATACCAG
AAAGGAATATTCATTGAATCCCCCTGACCATA
TATCATAAATAGCGTCCAATACTGGACTATTA
TGTATCGGAACAGCTTGATACCGACACGCATA
TCATCGCCCATGTTACTTAGCCGGCGAACTGA
CCAAAAAAAACAAAGTACAACGGAATTATACC
ACTTTTTCCTACAGAGGCTTTGAG

TAAAATACGACAACAACCATCGCCTAGTTGCG
CCTAAAACTCTTTGACCCCCAGCGGATTTGTA
CCGACAATGTAATGCCACTACGAATAAACGGG
AACACTCAGAAAGAGGCAAAAGAATTTTGACTAAAG
AAGCGCGAAAGGCTCCAAAAGGAGGAAAATCT
TTAGCGTATAGTAAATGAATTTTCTTTCAGCG
TTACCCAAAAGGCTTGCCCTGACGGAGATGGT
CGCCTGTAATCTTGACAAGAACCGACCTTCAT
GCAGACGGAAACAACTTTCAACAGTGTATGGG
GAGTGAGAATAATTTTTTCACGTTCCTTTAAT
CCAACTTTGCGCATAGGCTGGCTGGATATTCA
ATTTTGCTTCAATCATAAGGGAACAACGAGGC
CAGACCAGGAAAGAGGACAGATGATTTTAATCCGCG
CAAGAGTAGCATTCCACAGACAGCAACTACAA
CAGAACGAGAGCCACCACCCTCATAGAACCGC
CACCCTCAGTAGTAAATTGGGCTTAGAAACAC
ACAAAAGGGTAATAAGAGAATATATT
ACAATAAAGTTTAGTATCATATGCTTACTAGA
TTGCTCAACAGTAGGGCTCCAGTATAAAGCCAACTTTTGCGTTAAA
GCGCCTGTAATAATATCCCATCCTCGGCTGTC
GTTTTTATGGGTTATATAACTATAACCTCCGG
CTGATGCACTTTTTCAAATATATTTGGTTTGA
AAAAGCCTCAACATGTTCAGCTAAAGACGACG
AGCATGTATCTGACCTAAATTTAATTAGTTAA
AATACCGAAACACCGGAATCATAAGTTATACA
TTTCCTTAGCACTCATCGAGAACAATTACCGC
TTTCATCTGAAACCAATCAATAATAATTTACG
GCCCAATATATTCTAAGAACGCGAGTTTTGAA
GCTAACGATGGAAACAGTACATAAGAATTACC
ATGTGAGTAATTAATTTTCCCTTAAAGACGCT
TTTTTTAAGCGTCTTTCCAGAGCCTTACCAAC
CTTAGGTTTTTCATCGTAGGAATCAGCAAGCC
AGCGAACCAGCGATAGCTTAGATTGAATCCTT
GAGAAGAGAGAGACTACCTTTTTATGTAAATG
GAAAACATTCCCGACTTGCGGGAGGGCGTTTT
TTTTGAGTAACATTATCATATTAATTTTTTTTTTAAGTTTTGTTTTGTACCGTA
TTTCGTCTTTCCAGACGTACGATCTATTTTTTTTTTTAAAAGTTTTTTGAACCTC
CAGTGAATATCAACGTAACAAAGCTTTGCAAAAGA
GCGTTTTAGAAGCCCGAAAGACTTTTTACGGTGTA
TTCCTTCTGACCTGAAAGCCAACAGATTTTTTTTCTTGCTTTTTTTAAAGGAAT
TTCGAGGTGAATTTCTTATTTATCAGTTTTTTTTTGATAGAACTTTTTTGATTAG
ATACAGTAACAGTACCTTAACGTCAGATGAATTT
TGCGAATAATAGAAAGGAACAACTTT
AAATATCATAAAGCATCACCTTGCTT
TTGCAGGGAGTTAAAGATTCGGTCGCTGAGGCTT
ACCTGCTCTGATAAATTGTGTCGATTTAATTCTGC
ACCCTGTAATCGGTTGTACCAAAATTTTACACTAA
AGCAACGGATGAGGAAGTTTCCATGGCACCAA
CGTGGACTGAACAAGAGTCCACTATTTGCGGGAT
ACCGATATGCCGCTTTTTGGCGCCAGGGTGGTTT

GGTCATAGTACCGAGCTCGAATTCTTTTACGAGGGT
CGTCACCCTCAGCAGCGAAAGACAGCATCGGATTTTCAAAGCGC
GGCGGTTTGCGTATTGTTTTGTAATCAT
TGTAGGTATTTTTCTACTAATTTTTTTTACAAGAAATTATCAACAATAGATATTTTAAGTACCG
CAAGTACCTCATTCCAAGAACGGGTTTTAGTCCTGATTTTTTTTTAGTAGTAAAAAGGTG
TCATTTTTTTTTGTTCAGAATTTTTTTTTTATCCGGGCAAGCAAATCAGATATTTTTATTAAAC
AATCCAATCGCAAGACTT
GAATAACCTTGCTTCTTTTTAACAAAAT
TCAATAGTGAATTTATTT
CCAGCTACTCAAGATTAGTTGCTATTTTTAGAAGGCTTTTTTTTAACGAGAATCAAATGC
GATTGTTTTTTGTAAATCGTCGCTATT
AACTAATATTTCAAAATCATAGGTCTG
ATACCGAATTTAAAGAACGCGAGAAAA
TTGATTAGAGCCGTCAATGCACTAAC
TTCGAACCACCAGCAGAACATTAAAA
TTGAAATACCTACATTTTAGGAAAAA
TAAGAATACCGTGTGATAAATAAGTT
CCCCAGCATTTTTTAACAACGCCAACATGTAATTT
AATTCTTATAATTGAGAATCGCCATATTTTTTAACTCAC
CGATTAAGTTTTGCATTTTCGAGCCA
AGGCAGAGTTTTGGCGCATCGTAACCGTCACGTTGG
ATTAATTGTGCCTAATGAGTGAGCTT
TTTTGGGTAACGCCAGGGCTGCAAGG
TAAAGTAATTCTGTCCTGCAGAAC
CTATCAGGCTATTTTTGAGAGATCTTTTACATTATG
TAAAGGGATTTCACTAAATCGGAACCCTCGAGGTG
CGGAGACACAATCATATGTACCCCTTTTTAATATT
CGGATTGAATTCGCATTAAATTTTTTTCGTAAAAC
TCAACCGTATCGATGAACGGTAATTTTTGTTAAAT
GCCCCCGATTTGCGGGAGCTAAACAGGTACGCCAG
GAATCAGATTTTTTAGAGCTTGACGGGGTGAACCA
GCGAACGTTTTACGTATAACGTGCTTTCAGTGAGG
TGACGAGCTTTGGCGAGAAAGGAAGGGAAAAACCG
GAAAGGAGTTTACAGGGCGCGTACTATTCACGCAA
GCGCCGCTTTTCGGGCGCTAGGGCGCTTTTTTTAAAGAA
CGCTCATGTTTTTTTAGACAGGAACGGAGGCCGAT
TGTAGATGTTTTATTTAAATTGTAAACGTTTGGTTGATA
CAACCCGTTTTTTAACCAATAGGATTTTGGAGCAA
GGGAGAATTAACTGAATTTAAAAATCTGACGATAA
GGGTTAGACGCAGAGGTTTAGACTCCTCAAGAGAA
CCTATTTCAGAGGCTGTTTCGAATTATTCATTTCA
GAGGGTAGTCATTGCCTGAGAGTCTTTACGCCATC
AGCTTTCATTCGCGTCTGGCCTTCTTTTACAAAGG
TAGAAAGATTCATCAGTTTGCAGCCTTATAGCTAT
GTCAAAAATGAAAATATTTTTGAGATTTAACGCCA
AAAACGAACTAACGGATTTGGGAAGCGCAATAATA
GAATAACATAAAAACATTTACAACATTAGCAACAC
TCAGGACGTTGGGAAGTTTCACCCTGAAGAGAGAT
ACGTAAAACTGATTGCTTTGGTTTTGCTCAGTACC
TTTCGTCACCAGTACACCTCATAG

TTTTAGTACCGCCACCCT
ACAGTGCCATTAGCGGTTTTTTGAATACCAAGTTA
TTTCAGGTTTTTACATTTTTCGAGAGGGTTGATAT
AATAAGTTAAGTGCCGTTTCGGGAGAAACAATAAC
TTAATTTCTTTTATTGAGCGCTAATATCACAAAGTCAGAGGGTA
TATGTTAGTTTTAACTTTAATCATTGTGTTTTTGCTCATT
CAGAACCGTTTTACCGCCTCCCTCAGAGCAGAGCCA
CATGGCTTTTTTCCACCCTCTTTCAGGGATAGCAAG
ACACTGAGCCCAATAGGAACCCATTT
AAATAAACAGCCATATTTTTTTTTGCAC
TTATTCTGTTTTTTTAACAATTTCATTTATCAATAT
TAATTACATTTTGGCAGGTCAGACGATTATTGACAGGAGGTTGATTTTCTTTAGCG
CAAAAGGGCATATGGTTTACCAGCTTTTCAGTTACA
GCCTTAAAAATTTTATCCTGAATCTAATTTGCTTTTAGTAAGCA
AAACATGAAAGTATTAGGAACCTA
CTATCAGGCTATTTTTGAGAGATCTTTACATTATG
CCACCGGATTTTTTAGAGCCAGCAAAATTTGAGCCA
AAGTATAGTTTTTTGATGATACAGGAGTGCGTCATA
AGGCGGATTTAACGGGGTCAGTGCAAGCGCAG
GGATTAGGCGTATAAACAGTTAATAACAAATA
TCTCTGAACGCCACCCTCAGAGCCTGCCATCT
AATCCTCACCACCAGAACCACCACGCATTTTC
AGGTGGCATATCACCGTCACCGACCACCAGTA
CCACGGAAATATTGACGGAAATTAGAAACGTC
AGAAAATTCGACATTCAACCGATTACCGTAAT
TCAGACTGACAGAATCAAGTTTGCTTTTGCCAAAGA
GCACCATTTCAAAATCACCGGAACCCGCCACC
ACCAATGACCCCCTTATTAGCGTTACCACCCT
CAGTAGCGTAGCGCGTTTTCATCGCAGAGCCG
TTTGGGAATTTTCAAACGTAGAAAATACTTACGCAG
AGGTGAATACATATAAAAGAAACGCCCAAAAG
GAAGGTAATAAGTTTATTTTGTCAGGAAACCG
AACTGGCAAGAATTGAGTTAAGCCCATTAGAC
AGGAAACGAAACAATGAAATAGCATACAGAGA
GATAGCCGAGCCCTTTTTAAGAAATTTTTGTTTAAC

Bioconjugate Chemistry

REVIEW

pubs.acs.org/bc

The Controlled Display of Biomolecules on Nanoparticles: A Challenge Suited to Bioorthogonal Chemistry

W. Russ Algar,[†,⊥] Duane E. Prasuhn,[†] Michael H. Stewart,[‡] Travis L. Jennings,[§] Juan B. Blanco-Canosa,[∥] Philip E. Dawson,[∥] and Igor L. Medintz*[,†]

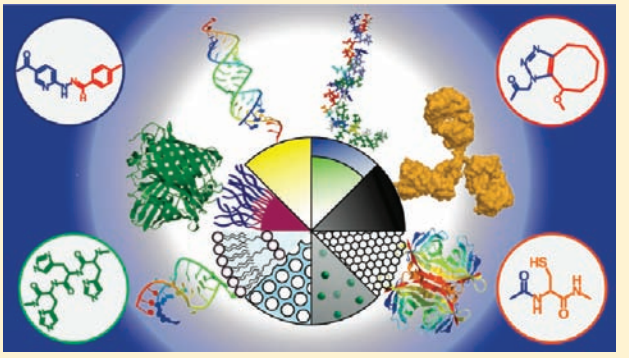
[†]Center for Bio/Molecular Science and Engineering, Code 6900, [‡]Optical Sciences Division, Code 5611, U.S. Naval Research Laboratory, 4555 Overlook Avenue, S.W., Washington, DC 20375, United States

[§]eBioscience, Inc., 10255 Science Center Drive, San Diego, California 92121, United States

[∥]Departments of Chemistry and Cell Biology, The Scripps Research Institute, La Jolla, California 92037, United States

[⊥]College of Science, George Mason University, 4400 University Drive, Fairfax, Virginia 22030, United States

ABSTRACT: Interest in developing diverse nanoparticle (NP)-biological composite materials continues to grow almost unabated. This is motivated primarily by the desire to simultaneously exploit the properties of both NP and biological components in new hybrid devices or materials that can be applied in areas ranging from energy harvesting and nanoscale electronics to biomedical diagnostics. The utility and effectiveness of these composites will be predicated on the ability to assemble these structures with control over NP/biomolecule ratio, biomolecular orientation, biomolecular activity, and the separation distance within the NP-bioconjugate architecture. This degree of control will be especially critical in creating theranostic NP-bioconjugates that, as a single vector, are capable of multiple functions in vivo, including targeting, image contrast, biosensing, and drug delivery. In this review, a perspective is given on current and developing chemistries that can provide improved control in the preparation of NP-bioconjugates. The nanoscale properties intrinsic to several prominent NP materials are briefly described to highlight the motivation behind their use. NP materials of interest include quantum dots, carbon nanotubes, viral capsids, liposomes, and NPs composed of gold, lanthanides, silica, polymers, or magnetic materials. This review includes a critical discussion on the design considerations for NP-bioconjugates and the unique challenges associated with chemistry at the biological−nanoscale interface—the liabilities of traditional bioconjugation chemistries being particularly prominent therein. Select bioorthogonal chemistries that can address these challenges are reviewed in detail, and include chemoselective ligations (e.g., hydrazone and Staudinger ligation), cycloaddition reactions in click chemistry (e.g., azide−alkyne cyclyoaddition, tetrazine ligation), metal-affinity coordination (e.g., polyhistidine), enzyme driven modifications (e.g., HaloTag, biotin ligase), and other site-specific chemistries. The benefits and liabilities of particular chemistries are discussed by highlighting relevant NP-bioconjugation examples from the literature. Potential chemistries that have not yet been applied to NPs are also discussed, and an outlook on future developments in this field is given.



INTRODUCTION

Nanoparticles (NPs) are materials with dimensions that are typically less than 100 nm. In many cases, NPs are synthetic colloids prepared from metals, alloys, semiconductors, carbon allotropes, or polymers. Other NP materials are biologically derived and include bacteriophages and other viral particles, liposomes, or biopolymers such as polysaccharides. The interest in NP materials is as diverse as the range of materials, with target applications in biology and medicine, catalysis, energy, electronics, and computing, to name only a few. In particular, the application of NPs in biological diagnostics, imaging, and therapeutics is an active area of research necessitating highly interdisciplinary efforts that combine materials science with expertise in biology and medicine. The ability to prepare NP-bioconjugates in a controlled manner is fundamental to these research efforts and is the focus of this review.

While NPs have their own intrinsic properties, it is generally necessary in biological applications to impart additional properties or functions through physical or chemical coupling between a NP and one or more molecules. For biologically derived NPs, a common example is labeling with a fluorescent dye or another type of reporter molecule to enable tracking and detection. The converse is often true in the case of many synthetic materials, where the NP enables detection but requires conjugation to a

Received: February 1, 2011
Revised: March 15, 2011
Published: May 18, 2011

ACS Publications © 2011 American Chemical Society

biological moiety for targeting or bioactivity. The association of one or more biologically relevant molecules at the interface of a NP defines a NP-bioconjugate, and combines the unique optoelectronic or physicochemical properties of NP materials with biological activity such as selective binding. Biomolecules of interest may include one or more of the following:

- Peptides, proteins, and antibodies
- Enzymes and ribozymes
- Oligonucleotides and aptamers
- Carbohydrates
- Lipids
- Drugs or other biologically active small molecules
- Reporter molecules or contrast agents (e.g., radiolabels, fluorescent dyes)

Analogous to traditional protein labeling chemistry, NP-bioconjugates can be prepared via the formation of new chemical bonds between functional groups associated with a NP and the biomolecule or small molecule of interest. NPs may also offer the potential for association through dative or coordinate bonding, electrostatic interactions, and van der Waals interactions. Moreover, it can often be necessary to account for a second conjugate preparation, where the biomolecule of interest is also conjugated with a reporter molecule. This is frequently the case in biosensing applications that use NPs. In general, the structure of a NP-bioconjugate affects its function, and the controlled display of biomolecules on NPs is paramount in obtaining conjugates with well-defined and reproducible properties.

To date, researchers have largely relied upon the traditional chemistries associated with protein labeling for the preparation of NP-bioconjugates. However, the range of bioconjugate chemistries used with NPs has lagged behind the multitude of biological applications proposed. Although traditional bioconjugate chemistries have been adequate for proof-of-concept studies, the optimization of NP-bioconjugates for real applications (e.g., clinical) will require much greater control than these chemistries can offer. "Shotgun" or heterogeneous approaches for the preparation of NP-bioconjugates are rarely suitable for maximizing the potential of NPs in biological applications. Rather, clean, efficient, and bioorthogonal conjugation reactions are required to eliminate undesirable side reactions, minimize nonspecific NP-bioconjugate activity, improve reproducibility in production, and maximize efficacy. This review highlights the emergence of novel approaches for the preparation of NP-bioconjugates that target these goals. The following sections highlight the properties of different NP materials and provide examples of their application as NP-bioconjugates. The ideals and challenges associated with NP-bioconjugates are discussed along with bioconjugation chemistry derived from chemoselective ligations, cycloaddition reactions, metal-affinity coordination, and enzymatic labeling in the context of their application to NPs. The reader should note that references to "standard bioconjugate chemistry" or "standard techniques" imply the family of currently used chemistries that were developed for modifying biomolecules with fluorophores and other labels. These are the techniques that are described extensively in Hermanson's *Bioconjugate Techniques* and Haugland's *The Handbook: A Guide to Fluorescent Probes and Labeling Technologies*.[1,2] Carbodiimide chemistry for coupling amines and carboxyls, succinimidyl (NHS) ester, or isothiocyanate targeting of primary amines, and maleimide reactions with thiols are typical examples.

NANOPARTICLE MATERIALS, PROPERTIES, AND APPLICATIONS

This section provides a brief overview of the NPs commonly used in biological applications: the different materials, their unique properties at the nanoscale, and the general features of their surface chemistry. The interested reader can find further details in the cited references, and should note that the list of materials and coatings described here is far from comprehensive. Figure 1 presents a summary of select NP materials and properties.

Gold and Silver. Gold NPs (Au NPs) typically range in size from 1 to 100 nm and are characterized by strong optical absorption and light scattering. These optical properties arise from the phenomenon of localized surface plasmon resonance (LSPR), wherein the conduction band electrons of an Au NP oscillate collectively and in resonance with certain wavelengths of incident light.[3−5] Solid spherical Au NPs exhibit a weakly size-dependent LSPR band in their extinction spectra that is located in the visible region of the spectrum. Rod-shaped Au NPs exhibit two LSPR bands that correspond to transverse and longitudinal oscillations of electrons. The longitudinal resonance mode is located in the near-infrared region of the spectrum, and is highly tunable by changing the aspect ratio of the nanorod. Hollow or dielectric-filled Au NPs are referred to as gold nanoshells and also exhibit a strong tunable LSPR mode that depends on the thickness of the shell. The wavelength-dependent intensity of the LSPR is very sensitive to changes in the dielectric environment surrounding the Au NP, as well as plasmonic coupling between NPs, and this has provided a mechanism for biological sensing based on colorimetric changes that result from selective binding interactions at the surface of Au NPs.[6] The ability of Au NPs to efficiently quench fluorescence has also been used to develop sensing methods.[7] Recent reviews have highlighted these applications.[3,4,8,9] The LSPR effect in Au NPs can also amplify Raman scattering due to local electric field enhancement at the NP during optical interrogation and provides another modality for sensing.[10,11] In imaging applications, Au NPs are potentially a very sensitive probe that can provide elastically scattered light intensities that are orders of magnitude larger than the fluorescence emission of dyes.[3,4,12] Furthermore, the absorption of light by Au NPs and the rapid thermalization of that energy are ideal for use in photothermal therapy.[3,4,13,14] Silver NPs (Ag NPs), Au−Ag alloyed NPs, and Au/Ag core/shell NPs are emerging as an alternative to Au NPs.[5] The LSPR effect with Ag NPs offers a narrower resonance, stronger elastic light scattering, and greater enhancement of Raman scattering potentially providing better sensitivity than Au NPs for some biological applications. Fluorescent Au and Ag NPs have been synthesized,[15] although their applications have not been widely characterized. Ag NPs also have strong antimicrobial properties that are being considered for use in medical applications.[16]

A wide array of synthetic methods for preparing Au and Ag NPs have been reported and are reviewed elsewhere.[17−22] The predominant chemistry for modifying Au NPs is the self-assembly of thiols via chemisorption.[3−5,12,23] Small molecules, polymers, and a variety of biomolecules can be anchored to Au NPs through thiol-terminated linkers. Bifunctional thiol ligands that display, for example, carboxyl or amine groups also enable further modifications using standard techniques to prepare Au NP-bioconjugates. The chemisorption of thiols on silver[24] can also be applied to the preparation of Ag NP-bioconjugates.[25]

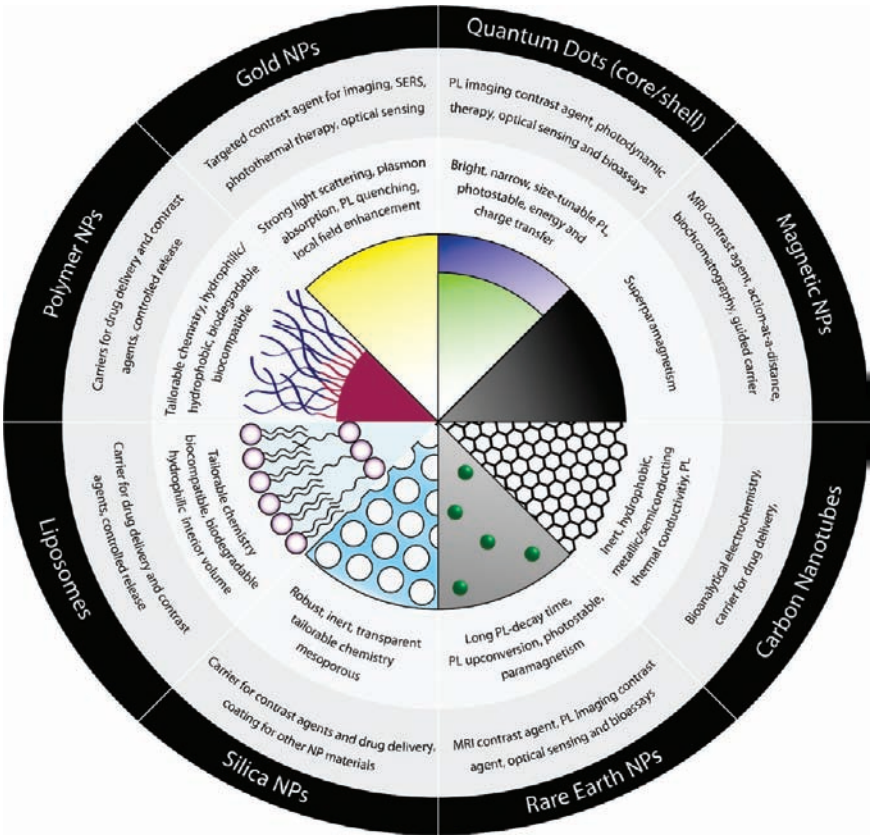


Figure 1. Select nanoparticle (NP) materials, their properties of interest, and prominent biological applications.

Semiconductors. Colloidal quantum dots (QDs) are luminescent crystalline NPs composed of semiconductor materials with radii that are typically between 2 and 10 nm.[26−28] Many different II−VI or III−V semiconductors,[29,30] alloys thereof,[31] and group IV semiconductors[32,33] have been used to synthesize colloidal QDs. In bioapplications, the interest has been in materials that offer visible or near-infrared photoluminescence (PL). The most widely used materials are CdX/ZnS QDs (X = Se, Te), where a CdX core is overcoated with a few atomic layers of wider bandgap ZnS or other binary semiconductor materials to improve its luminescence properties.[34,35] The optical properties of QDs are much different than their bulk analogues and arise from the quantum confinement of charge carriers within the dimensionality of the nanocrystal.[36−39] High-quality QDs exhibit a narrow PL band that can be tuned across a region of the visible or near-infrared spectrum by synthetically growing different nanocrystal sizes; the limits of the tunable emission range are determined by the choice of material.[26−28] Furthermore, the PL emission of QDs is more photostable than that of organic dye molecules, QDs offer stronger one- and two-photon absorption across a broader spectral range, and—similar to dye molecules—QDs can participate in energy transfer mechanisms that can modulate PL. The interest in QDs for biological applications is rooted in these more favorable optical properties. Several reviews have highlighted the use of QDs as probes for cellular, tissue, or in vivo imaging,[40] and in biological sensing.[41,42] Despite the success of CdX/ZnS QDs, there is a current trend toward developing QD materials that do not incorporate heavy metals and offer deep red or near-infrared PL at small nanocrystal dimensions. Examples include InP and CuInSe as core materials.[43,44] Quantum rods have also been developed and are essentially elongated QDs with a nonunity aspect ratio.[45,46] The optical properties of quantum rods are not dissimilar to those of QDs, but do exhibit some unique features such as polarized emission.

As synthesized with native alkyl coordinating ligands, II−VI QDs such as CdSe/ZnS are hydrophobic and insoluble in aqueous media. The two most common strategies for imparting aqueous solubility are the use of bifunctional ligand coatings and bifunctional polymer coatings.[26,28,47] The former coordinate to the QD surface through a chemical function (e.g., thiol, imidazole) and replace the native hydrophobic ligands; the latter have pendant alkyl chains that interdigitate with the native ligands via hydrophobic interactions. In both cases, a second and polar chemical function—such as a carboxylate, amine, or poly(ethylene glycol) (PEG) chain—mediates aqueous solubility. Mixtures of different ligands and the use of copolymers enable the modification of QDs with multiple functional groups. Ligand coatings are advantageous in that more compact QDs are obtained;[48] however, polymer coated QDs tend to have superior brightness and photostability. Standard bioconjugate techniques, such as carbodiimide coupling, are widely used with both ligand and polymer stabilized QDs. Ligand coatings have also frequently enabled the preparation of bioconjugates through self-assembly driven by coordination to the QD surface. Typical coating and bioconjugate methods for quantum rods are analogous to those for QDs.

Magnetic Materials. Magnetic NPs are typically less than 20 nm in diameter and have been prepared from different materials, including Co, Fe, Mn, Ni, γ-Fe_2O_3, Fe_3O_4, FePt, and other oxides or alloys.[49−56] Magnetic NPs are interesting due to

dx.doi.org/10.1021/bc200065z |*Bioconjugate Chem.* 2011, 22, 825–858

the combination of physical size and colloidal dispersion, the capacity for "action at distance" using magnetic fields, and their effectiveness as negative contrast agents in T2 weighted magnetic resonance imaging (MRI).[57,58] In addition to MRI imaging, magnetic NPs have potential as concurrent drug delivery vehicles or therapeutic agents in hyperthermia treatments with the added possibility of magnetic targeting. Magnetic NPs are also useful in bioaffinity chromatography methods (i.e., magnetic capture) for sample purification, analyte preconcentration, or toxin decorporation. These diverse applications are discussed in several reviews.[54,59−62] There has also been a recent trend toward the synthesis of "dumbbell" magnetic NPs that are inorganically linked dimers of a magnetic NP and a second class of NP. Most commonly, the latter is an optically active NP material such as gold or CdS[63,64] that allows the combination of optical tracking with the functionality of magnetic NPs. In addition to dumbbell NPs, analogous core/shell structures are also possible.[64]

Most synthetic methods yield hydrophobic magnetic NPs that are unsuitable for direct biological application. Similar to QD synthesis, the native ligands can be exchanged with bifunctional ligands or the NPs coated with polymer molecules. Functional groups that can bind to the surface of many magnetic NP materials include carboxylic acids, catechols, phosphates, sulfates, and amines. The groups that mediate aqueous solubility can often be used for subsequent bioconjugation using standard techniques. A second strategy commonly used with magnetic NPs is to coat them with an inorganic material such as silica, which can provide a hydrophilic protective layer against oxidation. The wide range of chemistry available to tailor the surface functionality of silica (*vide infra*) provides flexibility and the opportunity for bioconjugation in this approach.

Carbon Allotropes. Several different types of NP are derived from carbon allotropes. Carbon nanotubes (CNTs) are the most well-known of these materials, and are sheets of graphene rolled up into a seamless tube. If the nanotube is composed of a single graphene sheet, it is referred to as a single-walled carbon nanotube (SWCNT). In contrast, if it is composed of multiple sheets of graphene rolled concentrically, it is called a multiwalled carbon nanotube (MWCNT)—essentially a Russian doll of SWCNTs. Typical diameters of SWCNTs are 0.3−3.0 nm, whereas the diameter of MWCNTs can reach more than 100 nm. CNT lengths can vary from nanometers to micrometers. In bioapplications, it is the electronic and optical properties of CNTs combined with their large surface-to-volume ratios which are of interest.[65,66] A SWCNT can be metallic or semiconducting depending on its roll-up vector. The size of the band gap in chiral SWCNTs is dependent on the nanotube diameter, and photostable near-infrared PL can be associated with the band gap. Recent reviews have detailed the special properties and biological applications of CNTs,[67,68] including applications in electrochemical and electro-optical biosensing,[69−71] and as cellular delivery vectors and imaging probes.[72−74]

Similar to CNTs, fullerenes are composed of a graphene sheet, but are wrapped up into a closed, approximately spherical polyhedron rather than a tube. This geometry arises through the incorporation of five-membered rings into the otherwise six-membered ring structure of graphene. Buckminsterfullerene, C_{60}, is the most well-known example; however, C_{70} and other variants are also common. Fullerenes are interesting due to their photochemical activity (e.g., singlet oxygen production and DNA cleavage), their redox properties (e.g., radical scavenging), hydrophobicity, and electrophilicity (e.g., enzyme inhibition). The interested reader is referred to several reviews on the biological application of fullerenes.[75−77]

Both CNTs and fullerenes are extremely hydrophobic and poorly soluble in aqueous media; therefore, additional functionalization is required for most bioapplications. Two general strategies are utilized in this respect: the adsorption or complexation of macromolecules and surfactants, or alternatively, covalent modification of the carbon NP. For example, cyclodextrins or polyvinylpyrrolidone can be used to coat and solubilize C_{60}, while cycloaddition reactions are widely used to introduce new functional groups.[77] In the case of CNTs, a bifunctional pyrene molecule (e.g., 1-pyrenebutanoic acid succinimidyl ester) can irreversibly adsorb through π-stacking interactions and be used as a reactive linker for bioconjugation.[78,79] The method most commonly used for the covalent modification of CNTs is oxidation under acidic conditions, where carboxyl groups are introduced selectively at the highly curved tips of the CNT.[65,80] Modification of the sidewall is usually less efficient, and largely limited to defect sites. The introduction of carboxyl groups can enable many standard bioconjugate techniques including carbodiimide coupling. However, the drawback to this approach is a degradation of the electronic properties of the CNT due to the loss of π-conjugation at reaction sites. Further details on the chemistry of CNTs—including covalent modification schemes such as cycloaddition and reactivity with diazonium salts—can be found in reviews written by Tasis and co-workers.[81,82]

Other carbon allotropes have recently emerged as biologically useful nanomaterials, including two-dimensional graphene and graphene oxide sheets,[83,84] carbon quantum dots, as well as nanodiamonds.[85] In contrast to CNTs and fullerenes, nanodiamonds are not based on the sp^2-hybridized carbon centers of graphene. Rather, nanodiamonds are a lattice of tetrahedral sp^3-hybridized carbon centers, and exhibit visible and photostable PL due to the presence of defect sites.[86] The surface of nanodiamonds has intrinsic reactivity, and many synthetic preparations yield an interfacial layer of oxidized carbon groups. Carboxylated nanodiamonds are compatible with many standard bioconjugate techniques, are economical to synthesize, and are being explored as fluorescent cellular probes.[86]

Rare Earth Metals. The use of trivalent lanthanide ions in biology is well established. For example, Gd^{3+} is used as a contrast agent in MRI,[87] while Eu^{3+} and Tb^{3+} are used in time-resolved fluorescence immunoassays.[88] Historically, the properties of these ions have been harnessed in the form of chelates; however, incorporation of lanthanides into NPs provides many new opportunities and advantages.[89,90] Lanthanide ions have visible or near-infrared PL with narrow spectral bandwidth, excellent photostability, and decay times that are 10^3−10^6-fold longer than other luminophores.[89,90] The excitation of visible PL is possible using both ultraviolet and near-infrared light, where the latter is possible through the efficient luminescence upconversion exhibited by Er^{3+}, Tm^{3+}, and Ho^{3+} ions.[91−93] Although individual lanthanide ions tend to be weak absorbers, localizing multiple ions in a NP host can increase the effective absorption cross section. In the case of upconversion, more strongly absorbing lanthanide ions such as Yb^{3+} can be co-doped into the NP host as sensitizers that absorb NIR light and transfer the excitation energy to the emitter or activator ions (e.g., Er^{3+}).[91−93] In MRI, Gd^{3+} creates positive contrast in T1-weighted imaging through paramagnetic interactions with water. NPs provide the opportunity to concentrate multiple Gd^{3+} ions in small volume but retain a large surface area-to-volume ratio to promote

interactions between Gd^{3+} and water. Further optimization of MRI contrast is possible through the slower rotational diffusion of NPs compared to chelates and the ability to use NP surface chemistry to maximize the water exchange rate.[94]

Lanthanide NPs are typically composed of a lanthanide oxide (e.g., Y_2O_3), phosphate (e.g., $LaPO_4$), or (sodium) fluoride (e.g., LaF_3, $LaNaF_4$).[91,92,95] Most lanthanide ions easily substitute for another in a host lattice. In optical applications, luminescent dopant ions are typically incorporated at not more than a few percent. Sensitizer doping can be more substantial, on the order of 20%.[91,92] In the case of magnetic resonance applications, a Gd^{3+}-based NP material (e.g., GdF_3, Gd_2O_3) is generally used, and other lanthanide ion dopants can add luminescence functionality. Lanthanide NPs can be prepared by either aqueous or organic solvent routes,[92,96,97] where the latter require further surface modification for use in biological applications. In either case, aqueous lanthanide NPs are usually stabilized by surfactant ligands or polymers with carboxylate or phosphate groups that coordinate to the NP surface and also potentiate bioconjugation. A coating of hydrophilic silica can also be prepared around a lanthanide NP.[98] This provides a robust and hydrophilic coating, along with the opportunity for diverse surface modification and bioconjugation (*vide infra*).

Silica. Silica is a robust, hydrophilic, and biocompatible material that can be readily modified with diverse chemical functionality. As a consequence, silica is widely used as an inorganic coating for NPs of different composition (e.g., QDs,[99,100] magnetic NPs,[101−103] lanthanide NPs,[98] and Au NPs[104]), or as a NP-based carrier of functional molecules.[105] Using the diversity of silane chemistry,[106] a silica shell or coating can be tailored to have functional groups that can include, but are not limited to, amine, aldehyde, carboxyl, epoxy, and thiol groups. In addition to the use of silica as a structural shell on other NP materials, NPs composed of silica can be prepared with sizes that typically range between tens and hundreds of nanometers. The Stöber or reverse microemulsion methods are most commonly used for the synthesis of silica NPs.[107] In bioapplications, the ability to dope silica NPs with another material is of great utility. For example, up to 10^4 dye molecules can be incorporated into silica NPs (ca. 50−75 nm diameter) during synthesis.[108] The photostability of the dyes is greatly enhanced within the silica NP matrix, and the concentration of thousands of dye molecules into a single entity provides ultrabright labels for fluorescence imaging and assay applications. In addition, silica NPs can be used as carriers in drug delivery.[109,110] In this case, drug molecules must not be permanently incorporated within the NPs. The addition of surfactants and other manipulations of reaction conditions during silica NP synthesis can yield mesoporous silica NPs with pore sizes as small as 1 nm or as large as many tens of nanometers. These nanoscale mesopores allow both cargo transport and release and are therefore attractive for drug delivery applications. Typical values for pore surface area and volumes are close to 10^3 m^2 g^{-1} and 2 cm^3 g^{-1}, respectively, thereby offering small molecule (e.g., drug) cargo capacities on the order of $10^1−10^2$ mg g^{-1}.[110]

Polymer and Amphiphile Nanoparticles. Polymer and other amphiphile-based NPs are currently the most prominent materials being utilized as nanoscale drug carriers. These include: polymeric NPs, dendrimers, liposomes, polymersomes, and micelles.[111−114] The interest in these materials arises from the combination of nanoscale size with the nearly infinite diversity of physical properties and chemical functionality that can be obtained through organic chemistry. Polymer and amphiphile NPs can be designed to do the following:

- Carry molecular cargo externally or internally
- Carry hydrophilic or hydrophobic cargo
- Release cargo gradually
- Exhibit "smart" physicochemical responses to environmental stimuli (e.g., pH, thermal response) to selectively release cargo
- Evade the reticuloendothelial system and other immune responses
- Biodegrade
- Target different tissues or cell types

These different properties are tailored through the selection of the chemical composition of the polymer NPs. Bioconjugates of polymer and amphiphile NPs are typically prepared to assist targeting—antibody conjugates being particularly common. While there is no characteristic surface chemistry due to the diversity of materials, the introduction of carboxyl or amine groups into the polymer/amphiphile composition for purposes of bioconjugation is routine. Overall, the bioconjugation chemistry of these NPs is generally dictated by the functional groups associated with the material(s).

Polymer NPs are typically agglomerates of polymer chains with dimensionality that can range across the nanoscale. For example, poly(lactic acid) (PLA) and poly(lactic-*co*-glycolic acid) (PLGA) derivatives are commonly used to prepare NPs and are advantageous due to their biodegradability.[115] Dendrimers are fractal-like, hyperbranched polymers that can be size-controlled through their stepwise growth. A common example is polyamidoamine dendrimers, which form spherical NPs and display a high density of surface amine groups.[116,117] Liposomes and polymersomes are spherical NPs with unilamellar or multilamellar structures that separate and encapsulate an aqueous interior from bulk aqueous solvent. The lamellae of liposomes and polymersomes are composed of a bilayer of either lipids or synthetic block copolymer amphiphiles, respectively, with a hydrophobic midplane to separate the two aqueous volumes. Distearoylphosphatidylcholine is an example of a lipid material commonly used for assembling liposomes. In contrast to liposomes, micelles consist of amphiphiles or surfactants that assemble into spherical assemblies with a hydrophobic interior that excludes aqueous solvent and is thus able to carry hydrophobic molecular cargo. Micelles are typically prepared using the same types of amphiphiles as polymersomes—PEG-PLA is a common example.[113]

Viral Particles. Plant virus and bacteriophage capsids are natural examples of protein NPs. In nature, viruses are designed to carry genetic cargo, penetrate cells, and release their cargo—a natural parallel with the target application of many polymer and amphiphile-based NPs. Viral capsids are thus emerging as potential vehicles for drug delivery and contrast agents.[118−121] The unique advantage of such materials is that, in contrast to many synthetic NP materials, there is almost no polydispersity in their size and morphology. Being composed of many identical protein subunits, viral capsids offer a well-defined and regular array of amino acid residues for chemical modification or bioconjugation at both their interior and exterior surfaces. They are also amenable to recombinant modification allowing site-specific placement of unique groups such as cysteine-thiols where needed. The MS2 bacteriophage and cowpea mosaic virus (CPMV) capsids have dimensions of approximately 27 and 28 nm,[122,123] respectively, and are two prominent viral NP candidates being prototyped for drug delivery and other bioconjugate applications.[124]

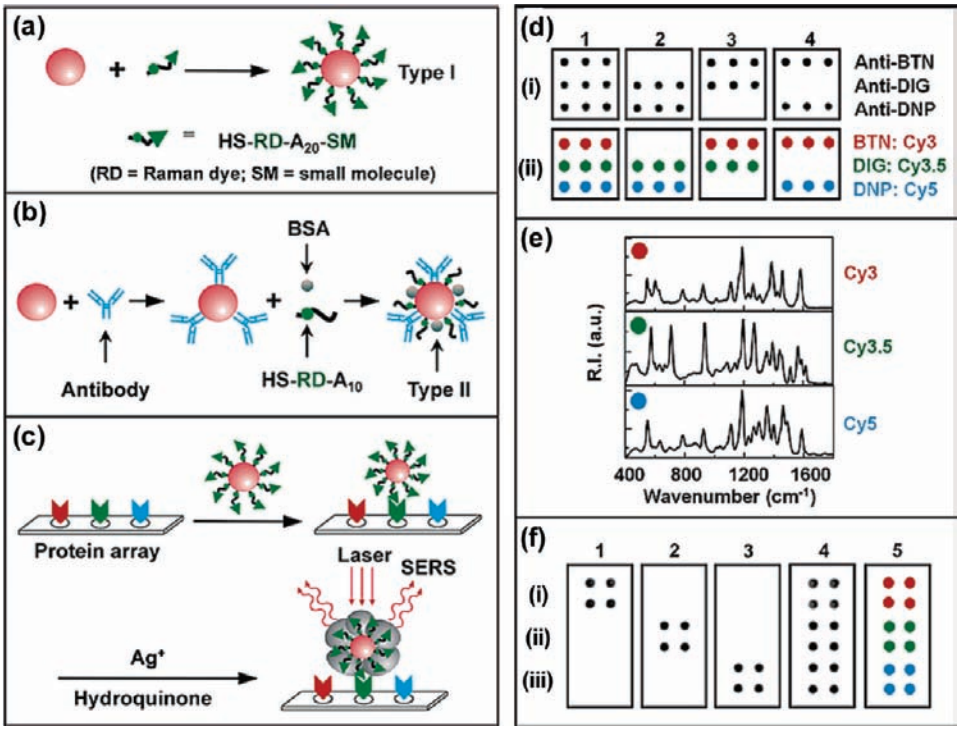


Figure 2. Protein microarray design using Au NPs. (a) Au NPs self-assembled with thiol-terminated oligonucleotides that are modified with a Raman active dye at the proximal terminus and small molecule probe at the distal terminus. (b) Au NPs modified with antibody probes and coated with Raman dye-modified oligonucleotides and bovine serum albumin (BSA). In panel and b, A_{20} and A_{10} refer to the number of adenine repeats. (c) Protein microarray experiments, showing the immobilization of proteins, selective labeling with Au NPs, and silver staining/enhancement. (d) Four different protein−small molecule binding experiments (1−4) with (i) flatbed scanner images and (ii) color codes for the Raman spectra associated with the probes in the corresponding spots (BTN = biotin; DIG = digoxigenin; DNP = dinitrophenyl). (e) Raman spectra for the color coded spots in (d). (f) Four different protein−protein binding experiments (1−4), and color codes for Raman identification (5), with flatbed scanner images for (i) Cy3-AuNP-antimouse IgG, (ii) Cy3.5-Au NP-antiubiquitin, and (iii) Cy5-Au NP-antihuman protein C. Figure adapted with permission from ref 125. Copyright 2003 American Chemical Society.

■ REPRESENTATIVE APPLICATIONS OF NANOPARTICLE BIOCONJUGATES

A comprehensive summary of NP-bioconjugate applications is beyond the scope of this review. Only a few select examples of their application are given herein to illustrate the utility of NP-bioconjugates.

Diagnostic Assay. The properties of optically active NPs can enable new possibilities in biological detection with high sensitivity. For example, Cao et al. developed a solid-phase hybridization assay[10] and protein microarray[125] (Figure 2) using Au/Ag NPs conjugated with dye-labeled oligonucleotides as reporters. The surface enhanced Raman scattering spectra of the dye on the NP provided both an analytical signal and analyte-specific fingerprint. In the case of the hybridization assay, detection was possible down to 20 fM. As described by Faulds et al., the narrow features of Raman spectra can enable multiplexed detection without the spatial registration of capture probes.[126,127] This is an example of a new method that exploits the special properties of a NP and relies on the preparation of a NP-bioconjugate to harness those properties.

Targeted Contrast Agent. Optically active NPs provide advantages in diagnostic imaging, particularly in terms of sensitivity and facilitating improved multicolor analyses. Liu et al. used QD-antibody conjugates that targeted four different protein biomarkers in histological tissue specimens from prostatectomy procedures (Figure 3).[128] Multispectral imaging of the heterogeneous fluorescence staining pattern enabled the observation of single malignant cells and progressive cancer development within the complex microenvironment of the histological specimens. These results are an example of how the uniquely advantageous properties of a NP can facilitate advances in an established technique such as immunohistochemical staining. Although not explored in this example, the large two-photon cross section of QDs could potentially be exploited—in addition to advantages in brightness and multiplexing—to suppress tissue autofluorescence for far more sensitive immunohistochemical detection.

Multimodal Contrast Agent. Different medical imaging techniques have different capabilities for spatial and temporal resolution, tissue penetration, and contrast generation. A single probe that could provide contrast in different imaging modalities would be highly advantageous in diagnostics. NPs provide the opportunity to incorporate multiple materials into a single probe to enable multiple imaging modalities and thus allow for better overall contrast or resolution. Cheung et al. explored the use of different formulations of soluble Gd^{3+}-rich and Tb^{3+} (or Eu^{3+}) doped lanthanide fluoride NP aggregates for multimodal imaging (Figure 4).[94] The NPs provided contrast enhancement in MRI imaging that was sufficient to enable animal perfusion imaging at NP doses that were 10-fold smaller than those associated with standard Gd^{3+} chelates. In addition, at the X-ray energies

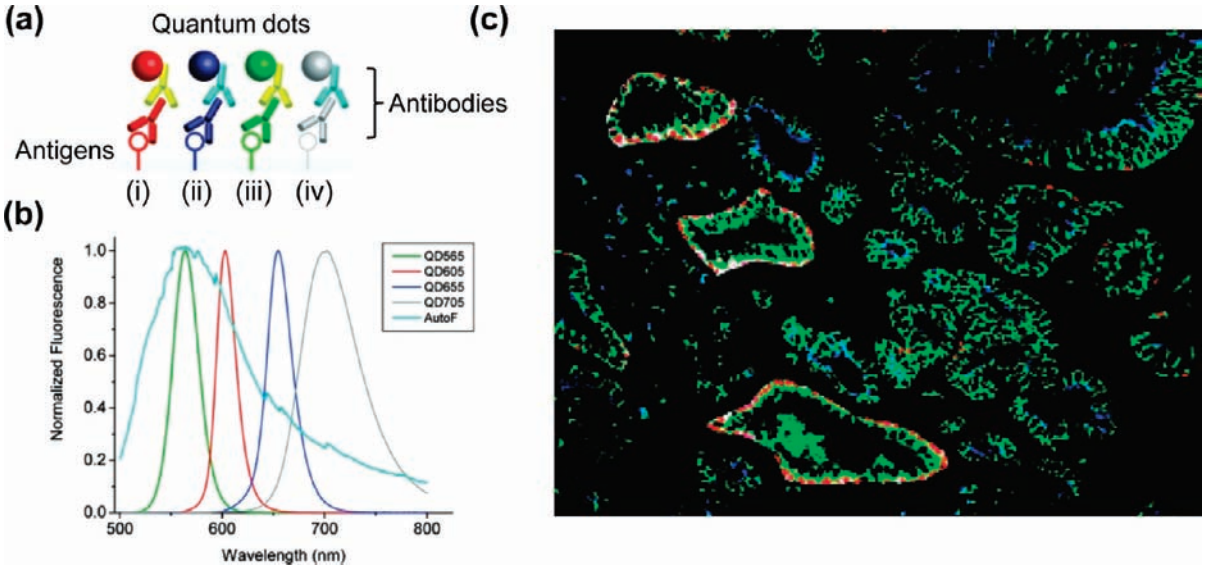


Figure 3. Multiplexed fluorescence immunostaining of prostate tissue specimens using QD-antibody conjugates. (a) Primary antibodies targeted tissue antigens and were labeled with secondary antibody-QD conjugates (i—iv). As shown in (b), the QD emission peaks were at (i) 605, (ii) 655, (iii) 565, and (iv) 705 nm. The tissue autofluorescence (AutoF) background is shown for reference. (c) Processed fluorescence images highlighting four different protein biomarkers using the four colors of QD, shown in blue, green, red, and white pseudocolors. The staining pattern can differentiate between healthy and cancerous tissue. Figure adapted with permission from ref 128. Copyright 2010 American Chemical Society.

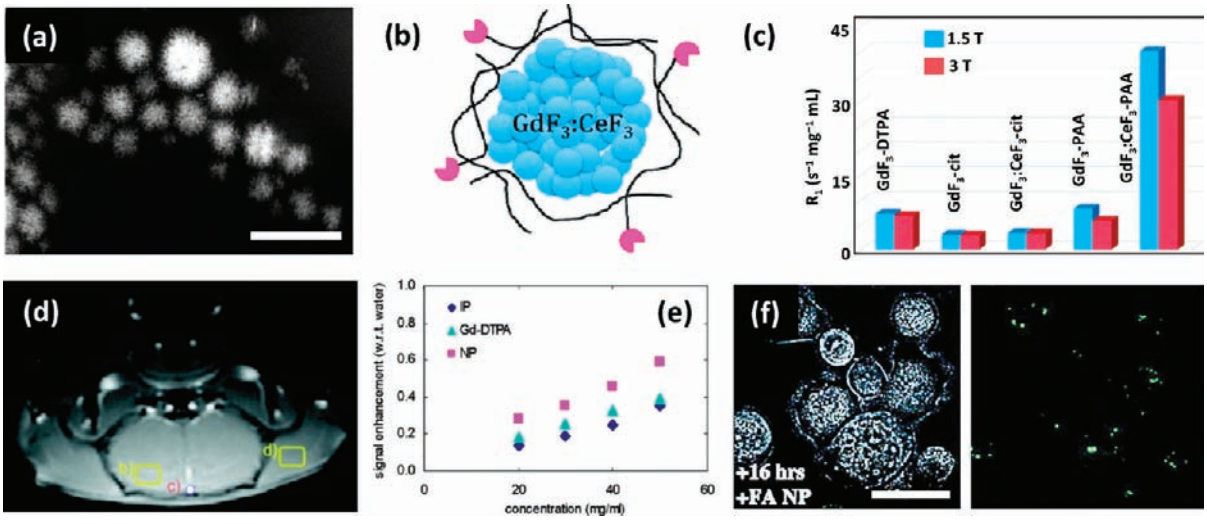


Figure 4. Potential for multimodal NPs. (a) STEM image of GdF_3:CeF_3 NP aggregates stabilized with poly(acrylic acid) (PAA). The scale bar is 150 nm. (b) Pictorial representation of $GdFe_3$:$CeFe_3$ NP aggregates stabilized with PAA. The mean aggregate size is ca. 70 nm, while the fundamental unit size is estimated to be 10—12 nm. (c) Mass relaxivities (R_1) for aqueous dispersions of different NP formulations. The GdF_3:CeF_3 NP aggregates have a much larger relaxivity than the commonly used Gd^{3+}-diethylenetriaminepentaacetic acid (DTPA) chelate. (d) Dynamic contrast enhancement MRI image of a rat brain using GdF_3:CeF_3 NP aggregates as a perfusion contrast agent. (e) Comparison of X-ray (25 kV) image signals as a function of mass concentration for aqueous PAA-stabilized $NaGdF_4$:Eu^{3+} NP aggregates and the commonly used contrast agents Gd^{3+}-DTPA and iopromide (IP). The NPA aggregates provide superior contrast. (f) Transmitted light (left) and confocal fluorescence (right) images of SK-BR-3 cells showing uptake of folate (FA)-modified $NaGdF_4$:Tb^{3+} NP aggregates. The scale bar is 20 μm. The punctate pattern of green emission in the fluorescence image is characteristic of endosomal uptake, and comparison with the transmitted light image indicates that the NPs are located within the cells. Figure adapted with permission from ref 94. Copyright 2010 American Chemical Society.

associated with mammography, the NPs were shown to have greater X-ray attenuation than the standard iopromide contrast agent used in computed tomography (CT). Luminescence from Tb^{3+} also provided the opportunity for fluorescence imaging of SK-BR-3 breast cancer cells using folate-conjugated NPs that promoted cellular uptake.[94] Although a single NP vector has not yet been fully developed to provide these three contrast mechanisms concurrently, this example makes clear the long-term potential for NP materials as multimodal contrast agents using a combination of fluorescence, MRI, and CT.

Drug Delivery Vehicle. NPs offer the potential to maximize the local efficacy of drugs while concurrently minimizing systemic

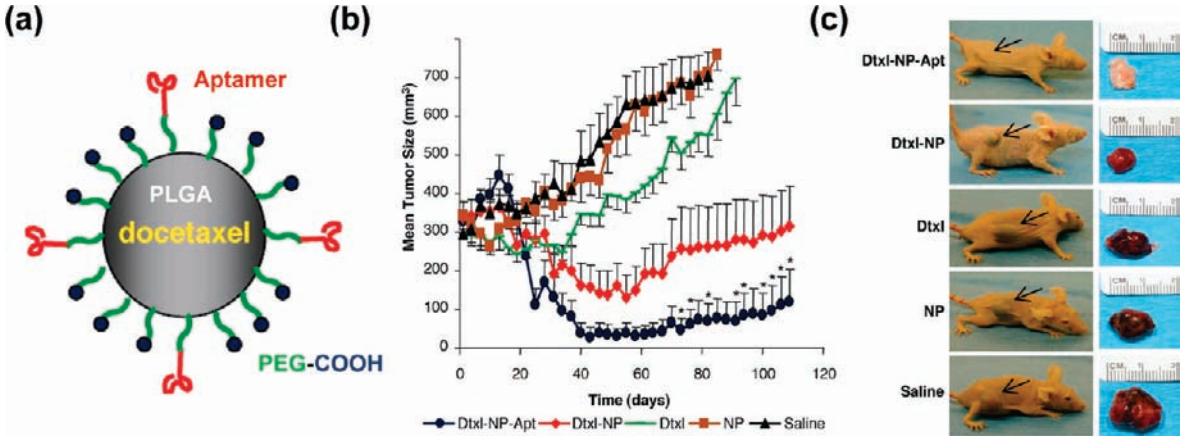


Figure 5. An example of drug delivery using polymeric NPs. (a) Poly(D,L-lactic-*co*-glycolic acid) or PLGA NPs were modified with prostate specific membrane antigen binding aptamer (Apt) and encapsulated the drug Docetaxel (Dtxl). (b) Quantitative and (c) qualitative changes in tumor size following administration of different formulations. The Dtxl-NP-Apt conjugate was the most efficacious, followed by the untargeted Dtxl-NP. The Dtxl alone was the least efficacious. Figure adapted with permission from ref 129. Copyright 2006 National Academy of Sciences, USA.

toxicity, thereby improving the quality of life and prognosis for patients undergoing chemotherapy. For example, Farokhzad et al. demonstrated that polymer NP-bioconjugates could increase the efficacy of chemotherapeutic treatment in mouse tumor models.[129] The drug Docetaxel was encapsulated within NPs composed of PEG-PLGA and conjugated with nucleic acid aptamers that targeted prostate specific membrane antigen. As shown in Figure 5, when compared to treatment with only Docetaxel, the NP(Docetaxel)-aptamer conjugates were found to cause concomitant and substantial reductions in both tumor size and treatment toxicity. Although treatment with NP(Docetaxel) was more efficacious than only Docetaxel, it was less than that with NP(Docetaxel)-aptamer conjugates, highlighting the importance of adding targeting to the NP-drug vector via the aptamer.

Theranostic Agent. "Theranostics" describes the combination of diagnostic and therapeutic utility in a single entity and has the potential to significantly enhance the treatment of disease. NPs have two important features that are highly favorable to theranostic application: (1) dimensionality that can allow cellular delivery and biodistribution and (2) nontrivial surface area or volume that can be derivatized with potentially many different molecules to impart a variety of functions (e.g., targeting, delivery). As shown in Figure 6, Cheng et al. recently reported the synthesis of trifunctional mesoporous silica NPs for theranostics.[130] The NP surface was decorated with cyclic Arg-Gly-Asp (cRGDyK) peptides to target the NPs to overexpressed integrins on cancer cells, and near-infrared fluorescent dye molecules were incorporated within the silica framework for visualization. In addition, a photosensitizer used in photodynamic therapy was loaded into the nanopores of the silica NP. Cellular studies indicated a high degree of targeting specificity and cytotoxicity. In some cases, NPs can also offer intrinsic features for theranostic purposes. For example, QDs allow the direct sensitization of conjugated photodynamic therapy drugs attached to them, while Au NPs can provide concomitant photothermal effects.[131,132]

The examples above highlight representative uses of several NP materials in different applications. For each material, many more applications have been reported, and similarly, for each application, many other NP materials have been used. Nonetheless, in nearly all cases, the controlled preparation of NP-conjugates is necessary to effectively combine and use the unique properties of both the NP material and the biomolecule for the intended application.

NANOPARTICLES AND BIOCONJUGATE CHEMISTRY

Challenge of Nanoparticles. It is difficult to generalize the many challenges associated with preparing NP bioconjugates. The diversity of NPs is such that dimensionality can vary by 2 orders of magnitude (1−100 nm) between materials, with each exhibiting different degrees of polydispersity. Nonetheless, several common features are important to recognize:

- NPs are large compared to most molecules.
- NPs are sufficiently small to be functionalized for colloidal solubility and are able to diffuse.
- NPs have nontrivial surface area and can occupy or contain nontrivial volumes that vary over a wide range of magnitudes based on NP size.
- NPs tend to exhibit heterogeneity across a population.

NPs thus have a character that is intermediate between molecules and bulk interfaces. Arguably, the closest molecular analogue for a NP is a protein. Proteins are large compared to most other molecules and are soluble, adopting a three-dimensional structure where the character of the amino acid residues exposed to solution largely determines protein solubility and the potential labeling methods. It is thus not surprising that much of the initial work in the preparation of NP-bioconjugates drew inspiration from standard protein labeling chemistries, such as those shown Figure 7. Despite the conceptual similarity between NPs and proteins, there are important differences between protein labeling and NP bioconjugation. Consider the labeling of proteins with fluorescent dyes: excesses of reactive dyes are frequently used to shotgun label proteins, and these approaches are often effective given the monoreactivity of the dyes and the availability of many reactive amino acid residues (e.g., lysine) at the surface of a folded protein. The degree of labeling is measured experimentally and the reaction optimized empirically. Since the size of the dye label is comparable to the size of the amino acid residues, the perturbation of the protein tends to be minimal. However, as outlined above, NPs are quite dissimilar to dye molecules by virtue of the nontrivial size and functionalization with polyreactive coatings.

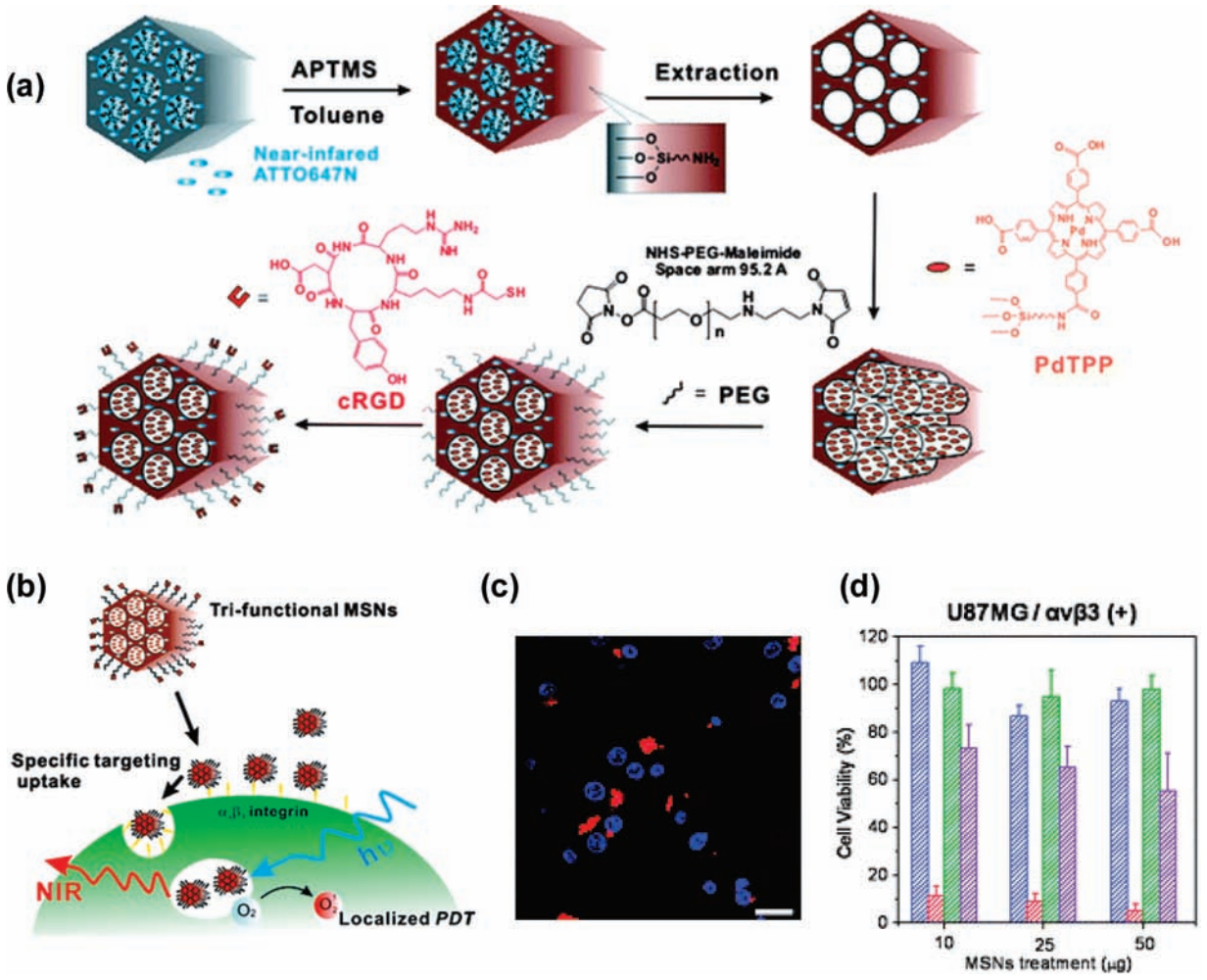


Figure 6. Trifunctional mesoporous silica NPs (MSNs) for theranostics. (a) Synthesis scheme showing incorporation of the Atto647N near-infrared fluorescent dye for tracking, surface modification with (3-aminopropyl)trimethoxysilane (APTMS), encapsulation of a Pd-porphyrin (PdTPP) photosensitizer for photodynamic therapy (PDT), and further surface modification with PEG and cyclic Arg-Gly-Asp (cRGD) for targeting $\alpha_v\beta_3$ integrin. (b) Theranostic scheme illustrating targeting, uptake, tracking, and localized PDT. (c) Two-color confocal fluorescence image of U87MG cells showing nuclei (blue: Hoechst dye) and MSN uptake (red: Atto647N). (d) U87MG toxicity data for targeted MSNs without (blue) and with (red) photoirradation, and for nontargeted MSNs without (green) and with (purple) photoirradiation. Figure adapted with permission from ref 130. Copyright 2010 Royal Society of Chemistry.

A good example of the potential liabilities of shotgun labeling methods is the popular cross-linking reaction between amines and carboxylic acids using carbodiimide activation (e.g., 1-ethyl-3-(3-dimethylaminopropyl)carbodiimide, or EDC), shown in Figure 7c. It is often the case that a NP displays a high density of carboxylic acid groups and a target biomolecule of interest has one or more primary amines. One of the disadvantages of carbodiimide chemistry is that the reactive *o*-acylisourea intermediate formed through the activation of carboxylic acids is prone to rapid hydrolysis.[1] As a consequence, a large excess of carbodiimide must be used to drive the desired cross-linking reaction to completion. Unfortunately, overactivation of the NP carboxyl groups—which often mediate aqueous solubility—can cause the loss of colloidal stability and aggregation due to the poor solubility of the *o*-acylisourea intermediate. This can be only partially ameliorated by converting the *o*-acylisourea to a more stable reactive intermediate using *N*-hydroxysuccinimide (NHS) or a sulfonated derivative thereof.[1] A sulfonated succinimidyl ester intermediate has greater solubility and helps maintain colloidal stability during the reaction. Although the succinimidyl ester intermediate is not resistant toward hydrolysis, it hydrolyzes more slowly than the *o*-acylisourea intermediate, and this tends to increase reaction efficiency. The conversion of the *o*-acylisourea intermediate to a (sulfo)fluorophenyl ester provides yet greater resistance toward hydrolysis[133] but, like NHS, is still limited by the dependence on EDC for *in situ* activation. Although EDC-driven coupling is a very powerful and popular chemistry that is often made to work with NPs, it is critical to realize that successful use of this shotgun cross-linking between a carboxylated NP and an aminated biomolecule (or *vice versa*) is not equivalent to controlling the display of that biomolecule on the NP.[134]

There are several criteria that define ideal chemistries for the controlled display of biomolecules on NPs, and these can often be difficult to realize in practice:

- The average number or ratio of biomolecules per NP (i.e., the conjugate valence) is both predictable and reproducible on the basis of reaction stoichiometry.

dx.doi.org/10.1021/bc200065z |*Bioconjugate Chem.* 2011, 22, 825–858

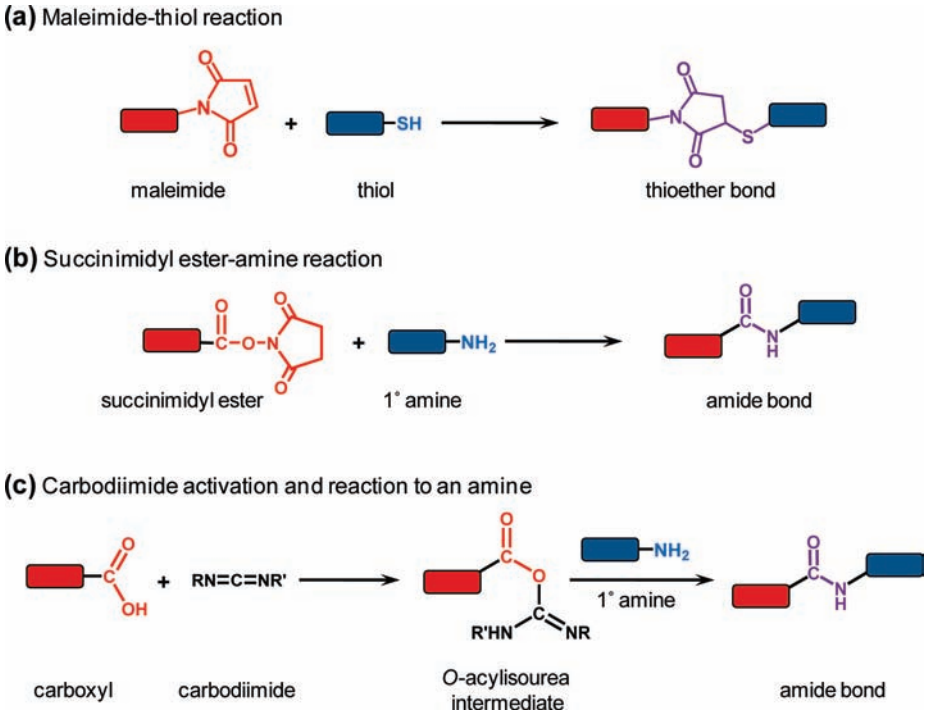


Figure 7. Standard bioconjugation reactions, including (a) maleimide−thiol, (b) succinimidyl ester-amine, and (c) carbodiimide-mediated coupling between carboxyls and amines.

- The NP-conjugates have minimal polydispersity in their valence across the ensemble.
- The attachment point of a biomolecule to the surface of the NP is both predictable and reproducible.
- The distance between the NP to a given moiety of a biomolecule is both predictable and reproducible.
- A corollary of the previous two points is that biomolecular orientation is controlled.
- The activity of a biomolecule or the efficacy of a small molecule is minimally compromised by its attachment to a NP. Similarly, NP functionality is not compromised.
- The linkage between the NP and the biomolecule is stable under most conditions, but is potentially labile under selected conditions (i.e., drug delivery). Stability or lability as a function of time, temperature, and pH may be important.
- The bioconjugate reaction proceeds to completion rapidly (<1 h) under mild aqueous conditions (i.e., does not require extremes of temperature or pH).
- The bioconjugate reaction is not prone to competing reactions (e.g., hydrolysis).
- The bioconjugate reaction is orthogonal to other bioconjugate chemistries (i.e., highly chemoselective).
- A corollary of the previous point is that the display of one type of biomolecule is compatible with the concurrent display of other biomolecules, as desired, using previous, parallel, or subsequent coupling reactions.

Given these considerations, it is clear that there are several challenges associated with the controlled display of biomolecules on NPs. Continuing with the example of carbodiimide coupling, polydispersity in NP size and surface area results in variability in the number of carboxylic acid groups available for activation per NP. This is exacerbated by the competition between overactivation and hydrolysis, which are very sensitive to reaction conditions such as pH and temperature. Therefore, reaction stoichiometry does not directly translate into conjugate valence. In the case of certain synthetic NPs, it is possible to address this challenge through the chemistry used to coat the NP. The display of multiple functional groups or a "mixed" surface, where one group mediates solubility and other groups mediate reactivity, offers a distinct advantage. Mei et al. prepared CdSe/ZnS quantum dots and Au NPs coated largely with unreactive methoxy-terminated PEG ligands, while also incorporating a small percentage of reactive carboxyl terminated PEG ligands.[135] The PEG provides aqueous solubility while allowing the carboxyl groups to be fully converted into reactive intermediates via EDC. Thus, some control can be exercised over the final conjugates by driving the cross-linking reaction to saturation. However, control over the conjugate valence and its polydispersity must be achieved in the preparation of the coated NPs—the conjugate reaction itself is still not well controlled. Moreover, the strategy is best suited for the preparation of small molecule-NP conjugates: it is generally impractical to use large excesses of biomolecules in conjugate reactions with NPs. In addition to biomolecules being a more limited resource, biomolecule solubility can be limited (often to micromolar concentrations) and it may not always be possible to efficiently purify NP-bioconjugates from excess biomolecules (e.g., low conjugate valence and similar size between NP and biomolecule).

Another challenge that can be associated with using carbodiimide coupling and NPs is control over biomolecular orientation in the conjugate. Proteins often have many lysine residues that can participate in carbodiimide coupling. The size of the NP is also nontrivial, and the point of attachment is important for bioconjugate function. If the binding site of an antibody or enzyme is oriented toward and in close proximity to the surface of the NP, then some loss of activity can be expected. Indeed, this effect of orientation has been observed with QD-antibody

conjugates.[136] A distribution of attachment points results in a distribution of orientation in NP-protein conjugates, and thus a distribution of protein activity or mixed avidity. Furthermore, the reactivity of many different amino acid residues can potentially result in undesirable side-reactions. It is generally the case that proteins have a comparable number of carboxyl (e.g., glutamic acid, aspartic acid) and lysine residues. Thus, protein−protein cross-linking efficiently competes with NP-protein coupling when using EDC chemistry. Multiple lysine residues can also drive protein-mediated NP-NP cross-linking. Such side reactions only increase the challenge of controlling bioconjugate valence and orientation, while introducing additional heterogeneity across an ensemble.

In contrast to proteins, it is often possible to design synthetic oligonucleotides and oligopeptides that are monoreactive. While this allows for control over the attachment, it does not necessarily guarantee orientation. Flexible linkages allow the biomolecules in NP-conjugates to adopt conformations that interact with the surface of the NP. For example, it has been shown that oligonucleotides can strongly adsorb to NPs such as CdSe/ZnS QDs,[137] gold NPs,[138] and carbon nanotubes.[139] It is critical to note that the interactions between a NP and a biomolecule in a conjugate are a function of the combination of the NP, its interfacial chemistry, and the biomolecule. Therefore, efforts to control the display of biomolecules on NPs must consider these factors in addition to the details of the coupling chemistry.

There are many applications in biosensing that require good control over conjugate valence and biomolecule orientation. As noted earlier, additional complexity is associated with these applications due to the frequent tendency toward "nested" conjugate preparation. That is, an optically active NP is conjugated with a biomolecule, and that biomolecule is also conjugated with a small molecule that acts as a reporter. Good examples are QD probes for protease activity. A peptide sequence cleaved by a target protease is connected to a QD at one terminus and a fluorescent dye at its other terminus. The peptide creates the proximity required for Förster resonance energy transfer (FRET), and this proximity is lost as a consequence of target protease activity, thereby generating an optical signal for transduction.[41,42,140] The important point is that FRET is sensitive to both the acceptor ratio and separation distance between the QD and dye in this configuration. Therefore, two-fold control over the preparation of the NP-bioconjugate is required for optimal function in this type of sensing.

There are also challenges associated with the preparation of NP-small molecule conjugates. Depending on the application, control over conjugate valence may not be critical. In the case of drug delivery, the intent is often to "load up" the NP to concentrate delivery. Providing that NP solubility is not compromised, shotgun-labeling strategies can thus be effective for preparing NP-drug conjugates. Many drugs and other small molecules can also be synthesized with a uniquely reactive group, used in excess in conjugate reactions, and are amenable to the efficient purification of NP-conjugates. These factors offer a degree of control that is often more difficult to achieve with large biomolecules. However, the relatively small size of drugs and other small molecules compared to NPs can also be a potential challenge. The mode of action of many drugs requires interaction with, for example, the binding site of a protein. NP-conjugated drug molecules can have availability for this interaction, but it must be mediated through long and flexible linkers, or triggered release of the drug from the NP under suitable conditions.

Overall, the controlled display of biomolecules on NPs is not a trivial feat. Although the optimization of most experiments will not necessarily require satisfying *all* of the ideal criteria discussed above, most would benefit tremendously by the development and use of bioconjugate chemistries that come close to satisfying a majority of these criteria.

Bioorthogonality. The example of EDC bioconjugate chemistry is a notorious one: it is both widely used and has several liabilities. However, there are many other standard bioconjugation chemistries that have, at least to some degree, similar liabilities. For example, isothiocyanate derivatives of biomolecules are amine reactive and stable in aqueous solution, potentially providing a greater degree of control. However, the resulting thiourea linkage can degrade,[141] and a major limitation is still the ubiquitous nature of lysine residues in proteins. In contrast, cysteine residues are scarce in proteins, and bioconjugate chemistries that target the reactive thiol of cysteine residues can potentially ameliorate many of the liabilities associated with EDC. For example, maleimides hydrolyze more slowly than *o*-acylisourea intermediates, and while the latter are reactive toward all good nucleophiles (e.g., amine, thiol, hydrazide), the reaction of maleimides with thiols is highly selective at near-neutral pH. This selectivity, combined with the ability to recombinantly engineer unique cysteine residues into proteins and synthetically insert them into peptides, can provide a well-defined point of attachment between a biomolecule and a maleimide-activated NP. This enables a degree of control over biomolecular orientation and largely avoids issues associated with undesirable cross-linking or other side reactions.

The idea of highly selective or specific bioconjugate chemistry reactions is captured in the concept of "bioorthogonality."[142−144] Bioconjugate chemistries that are bioorthogonal are those that do not have significant reactivity toward the functional groups that are intrinsic to biomolecules. This generally encompasses amine, carboxyl, hydroxyl, and thiol groups. However, to be strictly bioorthogonal, the chemistry must also be unreactive toward alkenes, amides, disulfides, esters, phosphodiesters, and a plethora of other functional groups that can be found within the biological milieu. The best candidates for strictly bioorthogonal reactions appear to be cycloaddition reactions from click chemistry. These reactions can enable clean and efficient labeling in biological matrices as complex as serum.[145] Other reactions, such as that between a hydrazide and an aldehyde/ketone (hydrazone ligation), are not strictly bioorthogonal, but can be *effectively* bioorthogonal if biological aldehydes/ketones are not native to a particular experimental matrix of interest. Several reactions with bioorthogonal character are discussed in detail later. An important caveat to bioorthogonal chemistries is that the functional groups providing the high reaction specificity are generally not naturally occurring. In the case of synthetic oligonucleotides and oligopeptides, incorporating a moiety with the necessary functional group(s) is readily accomplished during synthesis. However, in the case of proteins, the use of bioorthogonal chemistry may require a nested bioconjugate reaction using more traditional labeling chemistry. A common strategy is the use of heterobifunctional cross-linkers with a non-bioorthogonal reactive moiety (e.g., succinimidyl ester, maleimide) that introduces the desired bioorthogonal functional group(s) of interest through shotgun or site-directed labeling methods. An alternative to heterobifunctional cross-linkers is the incorporation of unnatural amino acids into proteins. These unnatural amino acids can have, for example, an azide or alkyne functionality on the side chain.[146]

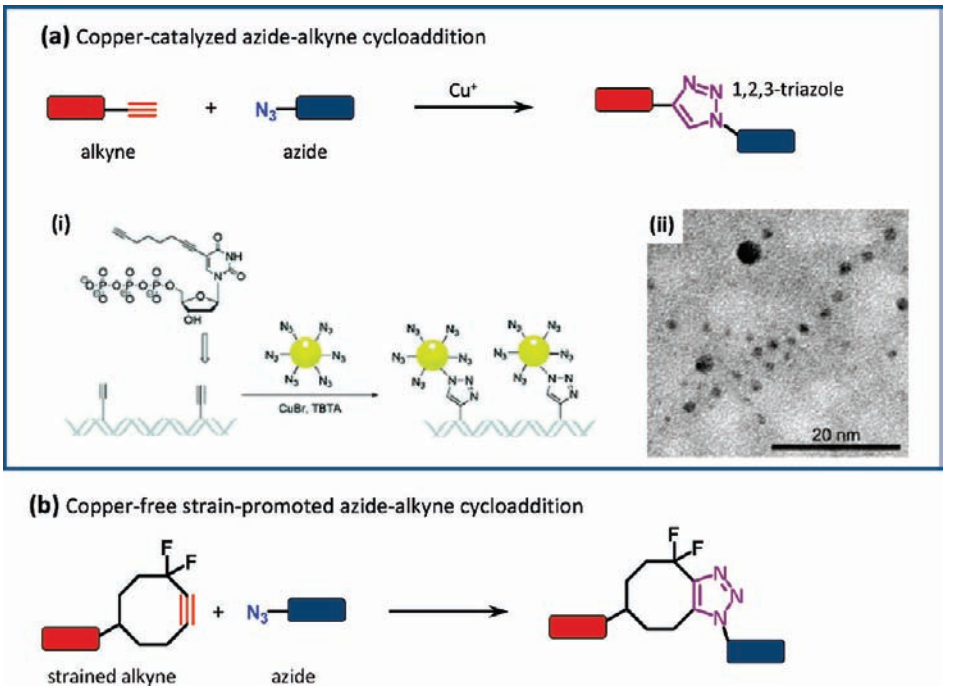


Figure 8. Azide−alkyne cycloaddition (AAC) reactions: (a) copper-catalyzed (CuAAC); (b) copper-free/strain-promoted. The example of the CuAAC shows (i) the use of alkyne-modified thymidine bases along double-stranded DNA to align azide-modified Au NPs. An electron microscope image of the aligned Au NPs is shown in (ii). Part of (a) is reproduced from ref 168. Copyright 2008 Royal Society of Chemistry.

Most NP-bioconjugates are prepared in clean matrices (e.g., buffers) and subsequently applied in a biological matrix. Bioorthogonal chemistry is therefore important because it potentially offers some control over NP bioconjugation by providing a well-defined point of attachment between the NP and the biomolecule, and does so without undesirable side reactions. Furthermore, bioorthogonal chemistries can facilitate nested conjugate reactions with control at each step. For example, a peptide can be coupled to a NP through a bioorthogonal reaction and concurrently labeled with a dye or other reporter through more traditional methods at lysine or cysteine residues. Similarly, the use of bioorthogonal chemistries also potentiates the controlled attachment of multiple biomolecules to a NP—for example, two different peptide sequences, a mixture of a peptide and an oligonucleotide, an antibody and a drug molecule, or other combinations of biomolecules that impart multifunctionality to a NP. This could take the form of two distinct bioorthogonal chemistries that are applied concurrently or in succession to conjugate a NP with two different biomolecules, and where the biomolecule orientations and conjugate valences are controlled and biological activities are not compromised. Such a level of control is extremely challenging to achieve using bioconjugate chemistries wherein two biomolecules compete for common reaction sites at a NP or have potential side-reactions with one another. The development of multifunctional NP-bioconjugates thus stands to benefit immensely from bioorthogonal reactions—particularly combinations that are also mutually orthogonal.

Bioorthogonality is just one important part of the toolkit that researchers are developing for the preparation of NP-bioconjugates. Another important part of the toolkit is reaction efficiency. Ideal conjugate chemistries use reactants that are stable in aqueous solution, proceed efficiently at 1:1 stoichiometries and at low concentrations, and have short reaction times at ambient or physiological temperature in aqueous media. Many of the chemistries that satisfy these criteria do not use an active cross-linker (e.g., EDC), but rather make use of a catalyst or strained bonds to drive the coupling reaction. Overall, the controlled display of biomolecules on NPs requires three ingredients: bioorthogonal reactivity, high reaction efficiency, and controlled NP properties.

■ ADVANCES IN NANOPARTICLE BIOCONJUGATION CHEMISTRY

Covalent Chemistries. *Cycloaddition Reactions.* A cycloaddition is a reaction where two unsaturated molecules combine to form a cyclic adduct in which the number of σ bonds increases.[147] Since biological macromolecues rarely contain moieties with nonaromatic double bonds, cycloaddition strategies have significant potential for bioorthogonality and have found increasing utility for the selective modification of NPs. The Huisgen 1,3-dipolar cycloaddition, illustrated in Figure 8a, is a reaction between an alkyne and an azide that produces a triazole linkage. In the presence of a copper(I) salt, the reaction is greatly accelerated, regioselective, and highly efficient. Referred to as the "copper-catalyzed azide−alkyne cycloaddition" (CuAAC), and well-known as the flagship reaction of the "click" chemistry family, this reaction has become a valuable ligation method for the preparation of bioconjugates. The CuAAC reaction is advantageous in that it is bioorthogonal and proceeds under relatively mild conditions in aqueous solution. In addition to being used in drug synthesis, controlled surface modification, protein labeling, and activity-based protein profiling,[148,149] the CuAAC has also been used to control the display of biomolecules on NPs.

Viral capsid bioconjugates were one of the first NP systems to which CuAAC chemistry was extensively applied. Bioconjugates

of this naturally occurring biological NP family have been prepared using CuAAC with fluorescent dyes,[150−155] MRI contrast agents,[154,156,157] biotin,[152,154] linear and branched polysaccharides,[150,155,158−160] peptides,[155,161] and proteins.[141,155] In most cases, the initial alkyne or azide functional group is introduced onto the virus capsid using a succinimidyl ester derivative that couples to available lysine residues. For example, CPMV was modified with an NHS-alkyne derivative and subsequently "clicked" with an azide-terminated PEG-folate conjugate for tumor cell targeting experiments.[162] Both CPMV and bacteriophage Qβ have been modified with lanthanide complexes to explore the biodistribution, toxicology, and pathology of viral particles in mice.[157,163] Here, the CPMV was modified with an NHS-azide derivative and clicked with an alkyne derivative of a Gd^{3+}-tetraazacyclododecanetetraacetic acid chelate. NP hybrids composed of C_{60} labeled Qβ bacteriophage particles have also been prepared using CuAAC chemistry.[164] It was estimated that 30−40 C_{60} molecules were attached per Qβ particle, with the final NP hybrids showing uptake in HeLa cells.

The CuAAC reaction has also been used to prepare controlled bioconjugates with a variety of inorganic NP materials. Examples include the enzymes trypsin, luciferase, and lipase being conjugated to Au NPs.[165−167] In the former, Au NPs were coated with a carboxyl-functionalized polymer, reacted with an amine-PEG-azide linker using EDC activation, and clicked with alkyne labeled trypsin. The trypsin was labeled via the reaction of its lysine residues with EDC activated 4-pentynoic acid. The activity of trypsin-Au NP conjugates prepared in this manner was 3-fold higher than analogous conjugates prepared using electrostatic adsorption or direct EDC coupling between the lysine residues and Au NPs.[165] As shown in Figure 8a (i) and (ii), alkyne modified nucleobases have also been used for the controlled alignment of azide functionalized Au NPs along a DNA strand at regular intervals.[168] Magnetic Fe_3O_4 NPs coated with silica/aminosilane have been functionalized with alkyne or azide groups and then clicked to display monosaccharides and disaccharides, the Tn antigen, the flag peptide, biotin, human serum albumin, and maltose binding protein (MBP).[169−171] Silica NPs have also been clicked to form conjugates with fluorescent dyes and bovine serum albumin.[172] In addition to the use of cross-linker chemistry to introduce azide or alkyne groups to the NPs with conventional functional groups (e.g., carboxyl, amine), azide and alkyne derivatives of silanes have been synthesized and used to coat NPs.[171,173] The CuAAC has been further applied to the preparation of fullerene[174] and carbon nanotube[175−177] bioconjugates with carbohydrates, porphyrins, and phthalocyanine derivatives. The alkyne functionality was introduced to CNTs through a diazonium salt, and introduced to C_{60} through a cyclopropanation reaction. Numerous reports detail the use of the CuAAC reaction for the synthesis of dendrimers, polymers, polymeric micelles, and polymersomes. These studies and the preparation of bioconjugates can be found in other reviews.[178−180]

The major limitation of the CuAAC reaction is the requirement of a Cu^+ catalyst. In cellular and protein-based applications, the cytotoxicity of Cu^+ and its ability to mediate protein modifications are potentially limiting. Although much of the undesired reactivity can be mitigated through the use of copper ligands and organic scavengers,[181] the use of a Cu^+ catalyst is nonetheless poorly suited to some experimental systems. To address this challenge, the Bertozzi group pioneered the use of strain-promoted AAC as an alternative ligation route that does not require a catalyst—"copper-free click chemistry". As illustrated in Figure 8b, the copper catalyst is avoided by using an alkyne in a strained geometry, such as by inclusion in a cyclooctyne-based ring system.[182,183] The copper-free AAC approach has already been utilized in several biological studies and applications.[184−187] However, it should be noted that the strained alkyne moiety is intrinsically more reactive toward other nucleophiles, and thus, chemoselectivity is potentially reduced in some systems. The application of the copper-free AAC reaction in the preparation of NP-bioconjugates has been limited, likely due to challenges associated with solubility and the multistep synthesis of the strained cyclooctyne structures. One of the few examples is the conjugation of QDs with mannosamine.[188] The use of the strain-promoted AAC was motivated by the irreversible PL quenching effect copper ions have on CdSe/ZnS QDs, and utilized an azido-derivative of mannosamine in combination with amine-modified QDs that were reacted with a carboxyl-derivative of cyclooctyne via EDC. In another example, chitosan-*g*-PEG NPs with available azide groups were conjugated to antibodies that had been labeled with a NHS-PEG-cyclooctyne derivative.[189] In this case, depolymerization initiated by the presence of Cu^+ motivated the use of the strain-promoted AAC.

In addition to reactions between an azide and an alkyne, cycloaddition reactions can occur between tetrazine and strained double bonds, such as those in *trans*-cyclooctene or norbornene, via a [4 + 2] cycloaddition. Tetrazine ligations are inverse-electron-demand Diels−Alder reactions that proceed rapidly (up to 2000 M^{-1} s^{-1}) without a catalyst, and with nearly 100% conversion at micromolar reactant concentrations and room temperature.[190] The reaction, illustrated in Figure 9a, is bioorthogonal and produces only nitrogen as a byproduct. Due to its relative novelty, application of tetrazine ligation to NPs has been more limited than CuAAC. Han et al. prepared QD-epidermal growth factor (EGF) conjugates using the tetrazine ligation,[191] where EGF was labeled with a succinimidyl ester derivative of 3-phenyl-1,2,4,5-tetrazine, and a QD coated with an amine-functionalized polymer was modified with a succinimidyl ester derivative of norbornene. The QD-EGF conjugates were prepared *in vitro* and subsequently used to label cells that expressed EGF receptor in vivo. The bioorthogonality of the chemistry enabled in situ conjugation, where cells were first incubated with tetrazine labeled EGF and subsequently exposed to norbornene-modified QDs for labeling. The tetrazine ligation has been used similarly by Haun et al. to prepare dye-labeled magnetic NP-antibody conjugates.[192] In this case, the strained alkene was a succinimidyl ester derivative of trans-cyclooctene that was used to label an anti-EGF receptor antibody rather than the NP. Amino-functionalized and dye-labeled magnetic NPs were modified with a succinimidyl ester derivative of 3-phenyl-1,2,4,5-tetrazine. The ligation reaction was then applied to cellular labeling, and could be done *in vitro* prior to cellular labeling, or *in situ* after labeling cells with antibody-cyclooctene conjugates.

Similar to the tetrazine ligation, Shi et al. have used a [4 + 2] cycloaddition reaction between a maleimide-labeled antibody and furan groups associated with the corona of poly(2-methyl-2-carboxytrimethylene-carbonate-*co*-D,L-lactide)-*graft*-poly(ethylene glycol)-furan biodegradable micellular NPs.[193] The chemistry is illustrated in Figure 9b. The maleimide was introduced site-specifically at the carbohydrate chains within the Fc region of the anti-HER2 antibodies (targeting breast cancer cells). This cycloaddition reaction was utilzed due to its selectivity and efficiency under mild conditions to help preserve antibody activity and avoid cross-linking reactions. The bioorthogonality

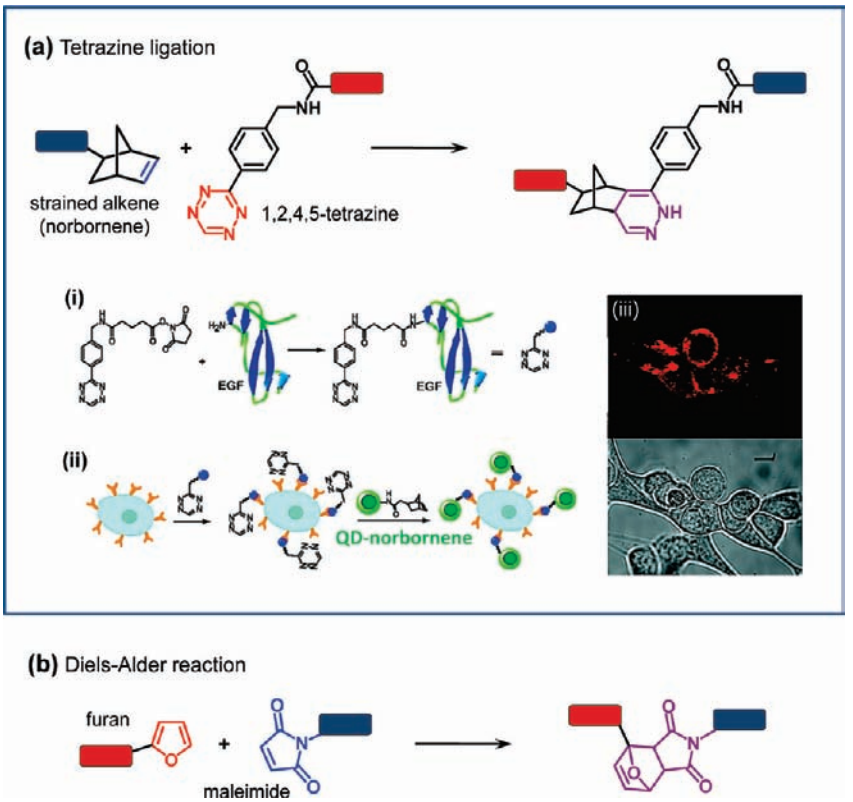


Figure 9. Cycloaddition reactions: (a) tetrazine ligation; (b) Diels–Alder reaction. The example of the tetrazine ligation shows (i) the labeling of epidermal growth factor (EGF) with a succinimidyl ester derivative of 1,2,4,5-tetrazine, and (ii) two-step labeling of cells with norbornene-modified QDs. Fluorescence and differential interference contrast (DIC) images of labeled cells are shown in (iii). Part of (a) is adapted with permission from ref 191. Copyright 2010 American Chemical Society.

of this chemistry requires the absence of other nontargeted thiol groups and control of pH to prevent the undesired reaction of amines with the maleimide.

Staudinger Ligation. Originally described in 1919, the Staudinger reduction is the reaction of a terminal azide with a phosphine to produce an aza-ylide intermediate that hydrolyzes under aqueous conditions to produce a primary amine.[194] In 2000, Saxon and Bertozzi developed a modified "Staudinger ligation," shown in Figure 10a, where the aza-ylide is trapped by an adjacent electrophilic carbonyl group to yield an amide bond after hydrolysis.[195] As a consequence of its bioorthogonality and chemoselectivity, the Staudinger ligation has been extensively used for joining or labeling biomolecules with applications that include the fluorescent labeling of proteins and DNA, protein immobilization to surfaces, and specific labeling of unnatural glycoproteins on cell-surfaces.[196] The shortcoming of this chemistry is the potential oxidation of phosphines under ambient conditions or by metabolic enzymes, which is commonly overcome through the use of excess reagents. It should also be noted that "traceless" Staudinger ligations have been developed, where the phosphine oxide is cleaved from the ligated intermediate during hydrolysis to form an amide.[197,198] Although the Staudinger ligation has been used with biomolecules in several studies, there have been only a few reports of the preparation of NP-bioconjugates. Zhang et al. used the Staudinger ligation to prepare liposome–lactose conjugates,[199] where the liposomes incorporated a phospholipid with a triphenylphosphine modification of its headgroup. The Staudinger ligation has also been used to attach RGD peptides to polyamidoamine-DNA NPs for improved cellular uptake of the NPs.[200]

Hydrazone and Oxime Ligations. The reaction between hydrazino groups (or hydrazido groups) and carbonyls (e.g., aldehydes or ketones) yields hydrazones as illustrated in Figure 10b. Although the reaction is reversible, the equilibrium favors the hydrazone under aqueous conditions ($K_{eq} = 10^4$–10^6 M^{-1}).[201] Forward and reverse reaction rates are slow at neutral pH but can be accelerated at acidic pH or with the use aniline as a catalyst.[201,202] The latter enables fast and efficient ligation (minutes to hours) at neutral pH and, since it is typically straightforward to remove aniline from the bioconjugates following the reaction, can yield relatively stable linkages due to the slow uncatalyzed rate of hydrolysis at neutral pH (10^{-6} s^{-1}).[201] In addition, hydrazone ligation is chemoselective and potentially bioorthogonal to the functional groups in proteins, oligonucleotides, and carbohydrates—the exception being reducing ends of the latter. As such, it is another attractive method for the preparing NP-bioconjugates.

Brunel et al. modified the lysine residues of CPMV NPs using sulfo-succinimidyl 4-formylbenzoate, and subsequently decorated the NP with two different hydrazido-terminated synthetic peptide sequences using hydrazone ligation.[203] The modified CPMV NP was then used as an imaging probe for cells and tumor xenografts, where one peptide was used for targeting and the other was modified with PEG for biocompatibility and fluorescently labeled for tracking. In a similar strategy, the use of arylhydrazino-terminated peptides has also been applied to the preparation of QD-bioconjugates.[204,205] As shown in Figure 10b, a "starter" peptide displaying a C-terminal hexahistidine sequence that enabled self-assembly onto CdSe/ZnS QDs (*vide infra*) and

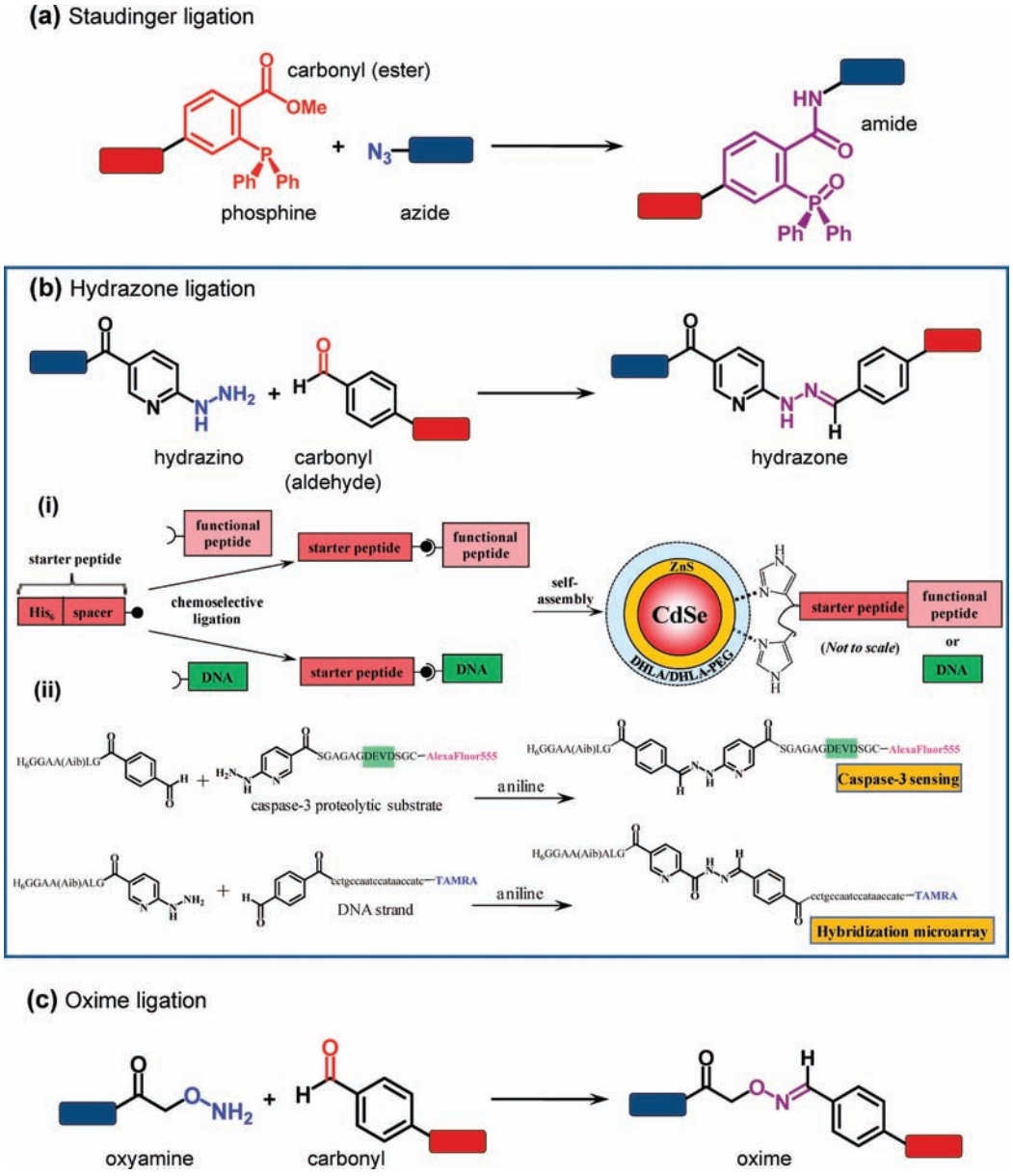


Figure 10. Chemoselective ligations: (a) the Staudinger ligation; (b) hydrazone ligation; (c) oxime ligation. The example for the hydrazone ligation (b) shows (i) a strategy for the modular assembly of functional peptides or DNA on QDs using a terminal polyhistidine "starter peptide" modified with a HYNIC or benzaldehyde group at the opposite terminus. The functional peptide or DNA is modified with the complementary functionality for hydrazone ligation (benzaldehyde or HYNIC, respectively). Two examples of modular assembly are shown in (ii), and include a peptide substrate for proteolytic monitoring and a DNA probe. Part of (b) is adapted with permission from ref 204. Copyright 2010 American Chemical Society.

an N-terminal 4-formylbenzoyl group was the basis for this strategy. Aniline-catalyzed hydrazone ligation between the starter peptide and another peptide or oligonucleotide modified with a terminal 2-hydrazinonicotinoyl group (HYNIC) yielded cell-penetrating peptides, protease substrates, or hybridization probes that were subsequently self-assembled to the QD to yield the final active bioconjugate. The nucleophilic aniline catalyst increased the conjugation rate and enabled the coupling reaction to proceed without an excess of hydrazine peptide (cf. Brunel et al.[203]). The hydrazone ligation could be done prior to or after *in situ* assembly of the starter peptide on the QD.[204,205]

Rather than being considered a potential liability, the pH-sensitivity of the hydrazone bond may actually be attractive for use in drug delivery. In the physiological pH range between 7.3 and 7.5, the hydrazone bond hydrolyzes very slowly and is thus stable over the time course of many experiments. However, the hydrolysis of the hydrazone bond becomes appreciable at the slightly acidic pH range (pH 5−6) associated with endosomes and lysosomes. As a consequence, doxorubicin has been conjugated to magnetic NPs[206,207] and Au NPs[208,209] through hydrazone linkages for targeted NP-drug conjugate delivery at physiological pH and subsequent drug release following endocytic cellular uptake. An analogous conjugation strategy has also been used with a *cis*-platin prodrug and polymer NPs.[210] In these studies, the hydrazido group was introduced to the NP through chemical modification of its stabilizing ligands or polymer coating. This included the hydrazinolysis of ester groups,[207−209] and the reaction of carboxyl groups with adipic acid dihydrazide via

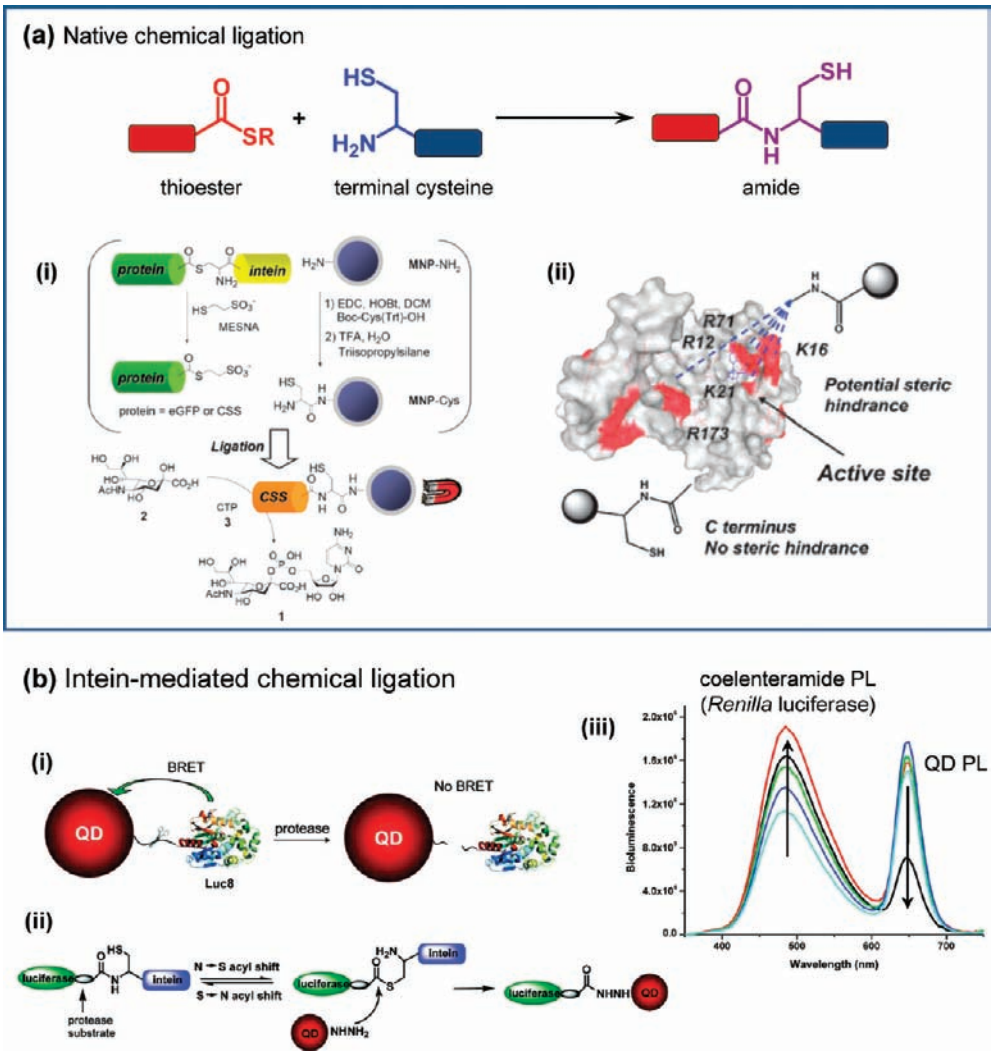


Figure 11. (a) Native chemical ligation between a thioester and a terminal cysteine. The example shows (i) enzyme (CSS) bioconjugate preparation using an intein to generate a thioester for native chemical ligation to a cysteine modified magnetic NP; and (ii) a comparison of the steric hindrance at the active site of CSS between labeling at the C-terminus via native chemical ligation and labeling at lysine (K) or arginine (R) residues. (b) Intein-mediated chemical ligation. The example shows (i) a proteolytic sensing strategy using QD-luciferase conjugates and BRET, (ii) the corresponding intein-mediated ligation chemistry, and (iii) loss of BRET between the excited state *Renilla* luciferase product (coelenteramide) and QDs. Increasing protease activity is in the direction of the arrows. Part of (a) is reproduced from ref 223. Copyright 2008 Royal Society of Chemistry. Figure in (b) are adapted with permission from ref 231. Copyright 2008 American Chemical Society.

carbodiimide coupling.[206] In particular, doxorubicin facilitates use of the hydrazone bond strategy since it has an intrinsic ketone group for site-specific ligation with hydrazido-modified NPs.

An oxime is the product of the ligation reaction between an oxyamine and an aldehyde or a ketone (Figure 10c). Although an oxime is more stable toward hydrolysis than a hydrazone ($K_{eq} \geq 10^8$ M^{-1}), it is similarly characterized by slow reaction rates at neutral pH and efficient ligation requires catalysis by aniline.[201,211] Oxime ligation has been used to prepare fluorescent dye and cell-penetrating peptide conjugates of polysaccharide NPs displaying a reducing chain end.[212] Both the dye and the peptide were aminooxy-modified for these purposes. Similarly, glycan conjugates of Au NPs coated with bifunctional aminooxy-alkyl-thiol ligands have been prepared via oxime ligation with the reducing ends of glycans.[213,214] This strategy was motivated by the observation of poor glycan-protein binding specificity when conjugates were prepared through reductive amination of the glycan.[215] In another example, the exterior lysine residues of capsids of bacteriophage MS2 were modified with succinimidyl 4-formylbenzoate and bound to a fluorescent dye synthetically modified with a PEG linker that terminated in an oxyamine group.[216]

Native Chemical Ligation. The reaction between a peptide with an N-terminal cysteine and a second peptide with a C-terminal thioester to yield an amide bond is illustrated in Figure 11a, and is referred to as native chemical ligation (NCL).[217−219] The reaction proceeds via transthioesterification, which links the peptides through an intermediate thioester that undergoes a spontaneous intramolecular S→N acyl shift rearrangement to form the amide and regenerate the cysteine side chain thiol. The reaction is highly chemoselective and does not require protection of any other amino acid side chains (including nonterminal cysteine residues, which do not form a stable amide). Furthermore, the C-terminal thioester may be associated

with any amino acid. These properties combine to make NCL an attractive chemistry for linking peptides to other peptides, proteins, or other substrates.

NCL has been used to chemoselectively modify lipid micelles and liposomes with single domain antibodies and a recombinant collagen binding protein, CNA35.[220−222] The phospholipids were modified at the headgroup with a cysteine terminated PEG chain, and a C-terminal thioester was introduced to the proteins using self-cleavable intein domains that were associated with the protein expression system. Similar expression techniques have been used with enhanced green fluorescent protein (eGFP) and CMP-sialic acid synthetase (CSS) to generate a C-terminal thioester that could be ligated with cysteine modified magnetic NPs (Figure 11a).[223] The magnetic NPs were synthesized with an amine coating, coupled with protected cysteine using carbodiimide/hydroxybenzotriazole activation, and deprotected for the NCL reaction. The conjugation of CSS to the magnetic NPs using NCL yielded a much smaller decrease in activity (33%) compared to nonchemoselective coupling via suberic acid bis-*N*-hydroxysuccinimide ester cross-linker (77%). This was attributed to the random enzyme orientation associated with reaction of the cross-linker with arbitrary CSS amine groups. Becker et al. have also used NCL to control the orientation of enzymes in NP-bioconjugates.[224] In this case, a guanosine triphosphate hydrolase (small GTPase) was expressed with an N-terminal peptide sequence that was cleaved at a cysteine residue by a protease. A bifunctional linker was synthesized with a terminal thioester and protected terminal thiol, where the former facilitated ligation to the GTPase and the latter was deprotected for subsequent assembly on Au NPs.

Expressed Protein Ligation. Biological expression of C-terminal thioester or N-terminal cysteine peptides enable the NCL strategy to be applied to large proteins and protein fragments with inteins.[225−227] Inteins are 100−800 residue polypeptide sequences found within proteins that are able to chemically excise themselves and rejoin the parent protein with a peptide bond in a reaction catalyzed by an active thioester intermediate.[225,228,229] This autocatalytic process is also referred to as intein-mediated protein splicing, and to date, more than 200 intein sequences have been identified in a wide range of protein families. Inteins are useful in applications such as protein synthesis, surface immobilization, and conjugation with fluorescent probes or affinity handles.[226,228,230] The chemistry of intein-mediated processes is complex and quite diverse, and the interested reader is referred to other reviews for further details.[225,226,228,229]

As shown in Figure 11b, Rao's group used intein chemistry to prepare QD-protein conjugates that functioned as bioluminescent protease sensors.[231] A *Renilla* luciferase fusion protein with two in-line C-terminal peptide sequences was genetically engineered. The peptide sequences were a VPLSLTMG sequence recognized and cleaved by matrix metalloproteinase-7 (MMP-7), and a 198-residue *GyrA* intein sequence. Carboxyl-coated QDs were modified with adipic acid dihydrazide using carbodiimide coupling, and the thioester group of the intein underwent nucleophilic attack by the distal hydrazide of the QDs. This ultimately cleaved out the intein sequence and resulted in a QD-luciferase conjugate linked through a protease substrate. In application, the addition of the luciferase substrate coelenterazine resulted in efficient bioluminescence resonance energy transfer (BRET) between the luciferase and the proximal QD. The addition of MMP-7 cleaved the bioconjugate linkage, disrupted BRET, and thus allowed monitoring of proteolytic activity.[231] Protein bioconjugates of liposomes and lipid bilayer-coated silica NPs have also been prepared using split intein ligation or trans-splicing.[232] In an elegant demonstration, two synthetic peptides—one modified with the C-terminal segment of a split DnaE intein, and the other modified with palmitoyl side chains for anchoring in a lipid bilayer—were joined by NCL and incorporated onto the lipid coated NPs. An eGFP fusion with the N-terminal segment of the split DnaE intein was then introduced and associated with the C-terminal segment resulting in excision of the intein to yield eGFP-NP conjugates.

Diazonium-Coupling to Tyrosine Side Chains. The reaction between a phenol and a diazonium salt to produce an azo compound is well-known in organic synthesis. In the case of proteins, diazonium salts can selectively react with the phenol and imidazole groups of tyrosine and histidine, respectively. The reaction to label the *ortho* position of tyrosine is illustrated in Figure 12a. Both tyrosine and histidine residues are typically low-abundance amino acids, found only sparingly in most proteins, and this may provide opportunities for site-specific labeling.

The Francis group has specifically modified tyrosine residues native to the interior surfaces of empty MS2 bacteriophage particles with nitro-phenyl diazonium salts.[233−236] The nitro-phenyl diazonium salts were linked to other functional groups that enabled the attachment of reporters such as organic dyes, MRI contrast agents, and radiolabels for positron emission tomography. As illustrated in Figure 12a, the diazonium reaction also allowed selective bioconjugation to the interior of the MS2 particles, while allowing lysine residues native to the exterior surface to be modified in orthogonal reactions. The latter included functionalization of the MS2 particles with succinimidyl esters of PEG and targeting ligands.[235] Although a nitro-phenyl diazonium salt derivative of a reporter may be prepared directly (e.g., fluorescein[2,81,82]), greater versatility has been achieved through the use of nitro-phenyl diazonium salts that can introduce a bioorthogonal functional group at tyrosine residues. For example, the Francis group labeled MS2 tyrosine residues with aldehyde functionalized nitro-phenyl diazonium salts for subsequent oxime ligations,[235] and developed a four-step hetero-Diels−Alder reaction that allowed further chemical modification.[122] Diazonium coupling to tyrosine was used to introduce ketones on the surface of tobacco mosaic virus (TMV) particles for coupling to PEG through secondary oxime ligation.[237] Similarly, Bruckman et al. have labeled TMV particles with alkyne-functionalized phenyl diazonium salts for subsequent CuAAC ligation with PEG, peptides, and dyes.[238]

Oxidative Coupling to Aniline-Containing Side Chains. The one-to-one oxidative coupling of aniline with *N*,*N*-diethyl-*N*′-acylphenylene diamine using sodium periodate was recently reported for the attachment of peptides to the surface of bacteriophage MS2.[239] The reaction is shown in Figure 12b, and is both chemoselective and efficient at low reactant concentrations. A single residue of the unnatural amino acid *p*-amino-L-phenylalanine was incorporated into MS2 through amber suppression methods to facilitate this coupling. A peptide with a phenylene diamine modified *N*-terminus was then oxidatively coupled to the virus particles. The peptides selected for coupling allowed the conjugate to achieve specific delivery to neuroblastoma, breast cancer cell lines, and kidneys, and target the matrix metalloproteinase 2 and 9 enzymes. Oxidative coupling to aniline was also used to decorate the exterior surface of MS2 particles with zinc porphyrins for photocatalysis[240] and a DNA aptamer for cellular delivery.[241]

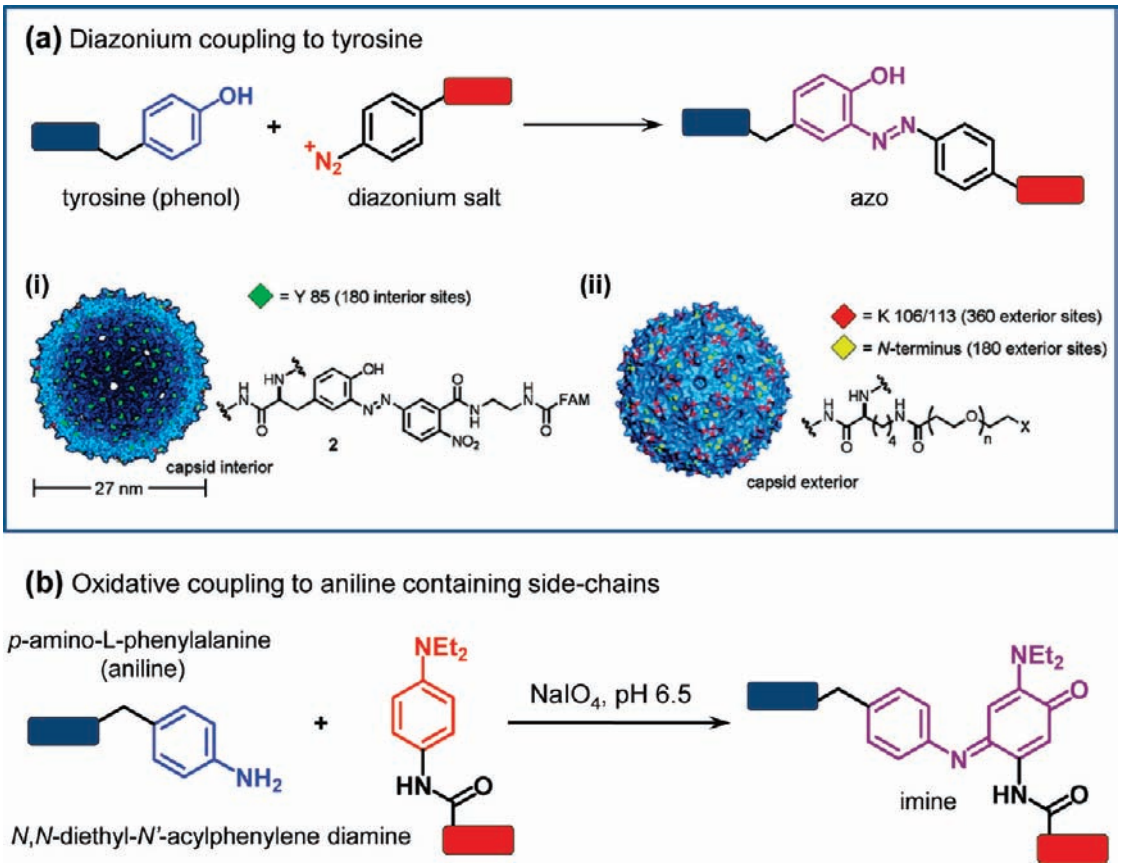


Figure 12. Coupling to protein/peptidyl side chains: (a) diazonium coupling to tyrosine residues; and (b) oxidative coupling to aniline containing side chains (e.g., *p*-amino-L-phenylalanine). The example for diazonium coupling to tyrosine shows (i) modification of tyrosine residues on the interior surface of an MS2 capsid with a fluorescent dye using a diazonium salt, and (ii) orthogonal coupling of PEG to exterior surface lysine residues using succinimidyl ester chemistry. Part of (a) adapted with permission from ref 216. Copyright 2007 American Chemical Society.

Self-Assembly. In contrast to the examples of the previous section, NP bioconjugate reactions based on self-assembly are not characterized by the formation of new covalent bonds. Rather, these reactions tend to be driven by comparatively weak coordination (or dative) bonding, wherein stability is dictated by equilibrium dissociation constants. Self-assembled NP bioconjugates are therefore sensitive to the concentrations of NP and biomolecule both during the preparation, and in subsequent application. However, through the use of moieties that self-assemble through multidentate coordination (e.g., polyhistidine vs monomeric histidine), the stability of self-assembled NP-bioconjugates can be greatly improved and allow use at the low concentrations ($\leq 10^{-6}$ M) typical of biological applications. Compared to covalent methods, self-assembly methods are advantageous in that they generally offer rapid and facile bioconjugation without the need for additional reagents, and can often provide better control as a result.

Polyhistidine Coordination. The polyhistidine motif is well-known for its role in the purification of proteins using immobilized metal ion affinity chromatography (IMAC) where it binds to Co^{2+}, Cu^{2+}, Ni^{2+}, Zn^{2+} and other divalent metal cations immobilized on solid supports through carboxylated chelates. These ions are also components of many different NP materials, including QDs and magnetic NPs. The imidazole ring of histidine, which coordinates divalent metal ions, can also interact with noble metals such as gold and silver. These properties suggest that polyhistidine can potentially be used to prepare bioconjugates from a variety of inorganic NPs. Indeed, this has been confirmed experimentally with several different materials, although there is certainly further untapped potential.

Our research group pioneered the use of polyhistidine tags for self-assembly with QDs. As shown in Figure 13a, we found that histidine could coordinate to the Zn^{2+} ions at the inorganic surface of CdSe/ZnS QDs and drive the self-assembly of QD-bioconjugates. The rapid and stable association of polyhistidine with the ZnS shell has proved highly advantageous for the preparation of QD-bioconjugates with polyhistidine-tagged recombinant proteins[242] and synthetic peptides.[140,204,243] Dissociation constants are typically in the range 10^{-1}–10^{2} nM and tend toward 1 nM in bulk solution, with equilibrium binding being reached within a few minutes at room temperature.[244] As a consequence, polyhistidine self-assembly enables control over QD-bioconjugate valence through an approximately one-to-one correlation with stoichiometry. This correlation applies to the average valency, where the actual distribution of QD-bioconjugate valences is known to follow a Poisson distribution—especially at lower ratios.[245] In addition, the polyhistidine motif offers several intrinsic advantages for assembly to CdSe/ZnS QDs:

- The polyhistidine motif is bioorthogonal, since it is not normally found in natural proteins.
- The polyhistidine motif is routinely introduced to recombinant proteins to facilitate purification.
- The small size of polyhistidine motif does not disrupt native protein function.

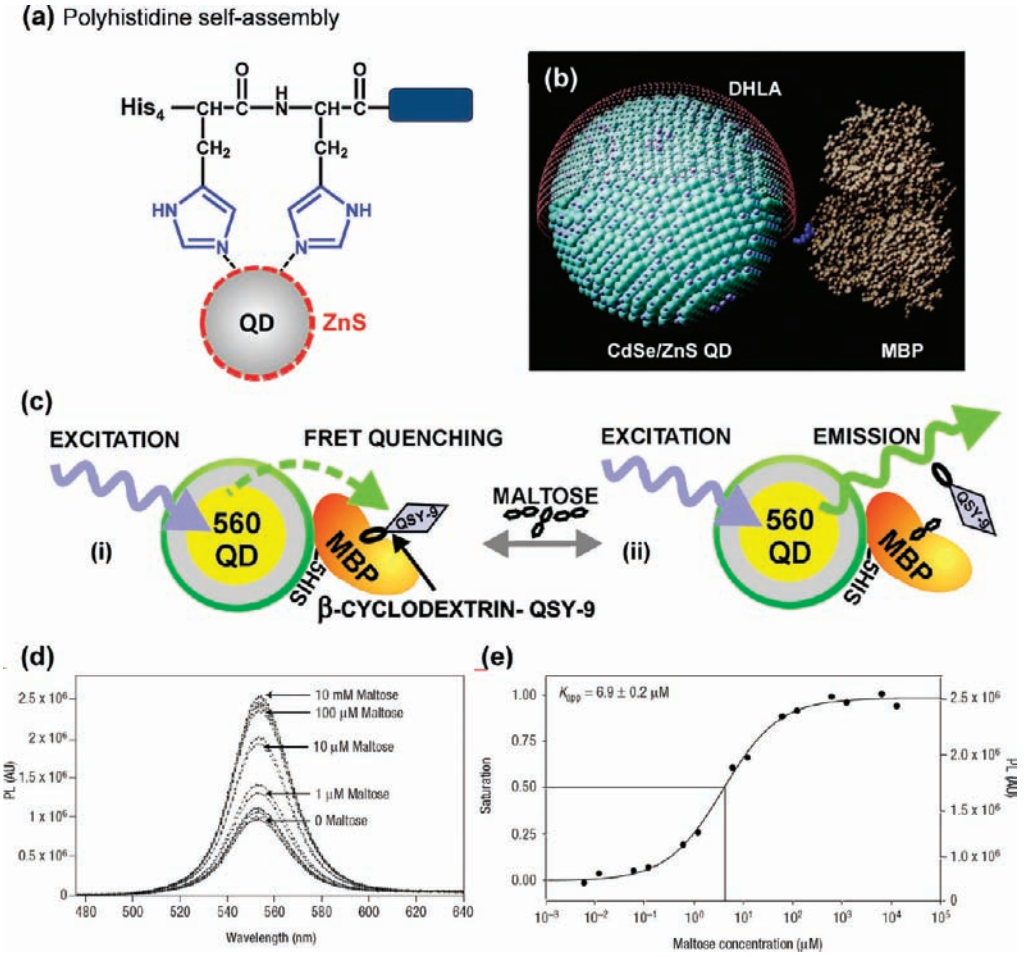


Figure 13. (a) Self-assembly of polyhistidine to the inorganic ZnS surface of a NP *via* direct coordination of the imidazole moieties. An example of the use of this bioconjugate chemistry is a FRET-based sensor for maltose using QD-His_5-maltose binding protein (MBP) conjugates. An experimentally validated model of MBP assembled to a CdSe/ZnS QD is shown in (b). The polyhistidine tag is highlighted in blue. The sensing scheme (c) is based on (i) binding of dark quencher (QSY-9)-labeled β-cyclodextrin by MBP, creating the proximity for quenching of the 560 nm emitting QD PL via FRET. The introduction of maltose (ii) displaces the quencher-labeled cyclodextrin and restores the QD PL in proportion to the maltose concentration. The QD PL recovery and a maltose binding isotherm are shown in (d) and (e), respectively. The image in (b) is reproduced from ref 246. The images in (c−e) are reproduced from ref 256.

- The single point of attachment offered by the polyhistidine motif eliminates undesirable cross-linking reactions and even enables control over biomolecular orientation.

Considering the latter point, a series of FRET experiments were used to determine the orientation of recombinant MBP assembled to a QD (Figure 13b). It was found that the polyhistidine tag interacted with the surface of the QD so as to orient the protein toward bulk solution.[246] To further enhance control over orientation and spacing, we have exploited structural peptide motifs in combination with polyhistidines. These peptide motifs have included a rigid variable-length peptide based on a repeating tyrosine-glutamic acid-histidine-lysine (YEHK) β-sheet,[247,248] and the inclusion of a rigid helical linker-spacer between an N-terminal polyhistidine tract and a C-terminal peptide suitable for use as proteolytic substrate.[140] The rigid helical linker was based on α-amino isobutyric acid and alanine, with glycine hinges to separate its structure from the polyhistidine and proteolytic substrate.

Polyhistidine self-assembly with QDs has been extended to the preparation of QD-oligonucleotide conjugates through use of modular "starter" peptide sequences with a hexahistidine tract at one terminus and a reactive group at the other. The latter have included pyridyl disulfide[249] and iodacetyl groups[250] that react with thiol-terminated oligonucleotides to form disulfide and thioether bonds, respectively. Thioether bonds are stable under most conditions; disulfides are labile under reducing conditions. Additional versatility is possible through polyhistidine starter peptides (Figure 10b) with a terminal benzaldehyde group that enables hydrazone ligation to a peptide or oligonucleotide modified with a terminal HYNIC group.[204,205] This bioorthogonal chemistry is compatible with two different strategies: ligation with the polyhistidine starter peptide prior to assembly with QDs,[204] or ligation after prior assembly of the polyhistidine starter peptide with QDs.[205]

The control provided by polyhistidine self-assembly has greatly facilitated the development of QD-based cellular probes,[243,251] and biosensors that use FRET (Figure 13c−e) or charge transfer for signal transduction.[252−258] The interactions associated with the latter arise from conjugation with reporter-labeled biomolecules and are very sensitive to both

dx.doi.org/10.1021/bc200065z |*Bioconjugate Chem.* 2011, 22, 825–858

the number of reporters per QD and the separation distance between reporter and QD, thus necessitating a high degree of control over the final bioconjugate architecture. In addition to CdSe/ZnS QDs, polyhistidine tagged recombinant enzymes have been assembled with CdS QDs.[259] Magnetic Ni/NiO NPs and Au NPs have also been found to assemble with polyhistidine tagged proteins or peptides.[260−262] A study of the assembly of polyhistidine tagged human acidic fibroblast growth factor with Au NPs found that the multichelate effect of the histidine imidazole groups was able to displace the strong thiol−Au NP interaction associated with a zwitterionic cysteine-containing peptide coating.[262] Dynamic measurements suggested that the fibroblast growth factor protein sampled a range of orientations at the Au NP surface before adopting a lowest energy state with attachment via the polyhistidine tag. While virus capsids have often been engineered with polyhistidine tags to facilitate purification, there is also the potential bioconjugation through polyhistidine. For example, heme groups have been conjugated to recombinant hepatitis B virus particles with N-terminal polyhistidine tags,[263] and also to Qβ particles with C-terminal polyhistidine tags.[264] Here, the assembly was driven by coordination to the iron center of heme.

Nickel(II) and Nitrilotriacetic Acid. Although direct polyhistidine coordination to the surface of NPs is a highly effective method for preparing controlled NP-bioconjugates, its application is limited to certain NP materials and thin coatings of solubilizing ligands that allow access to the inorganic surface of NPs. A more universal approach for the self-assembly of polyhistidine appended biomolecules to NPs is the use of nickel(II)-nitrilotriacetic acid (Ni^{2+}-NTA) modified NP coatings as shown in Figure 14a. This approach is borrowed from IMAC, where polyhistidine tags are known to bind to Ni^{2+}-NTA with dissociation constants on the order of $K_d = 10^{-13}$ M.[265] This affords many of the advantages and control associated with direct polyhistidine coordination while also being compatible with any NP material that displays a surface coating that can be chemically modified. The NTA-functionalization of a NP coating is facilitated by the availability of several NTA precursors and analogues. Many different NP materials have been modified with NTA for binding polyhistidine tagged proteins, including QDs,[265−268] Au NPs,[269] CNTs,[270] silica NPs,[271,272] and magnetic NPs.[273] The development of NTA-coated CNTs (Figure 14a) for controlled protein conjugation was motivated by the prior observation of protein denaturation on the hydrophobic surface of CNTs.[270] This was minimized by the use of NTA for conjugation. Importantly, Susumu et al. demonstrated that the polyhistidine-Ni^{2+}-NTA interaction in QD conjugates remained stable when delivered to the cellular cytosol.[268]

The most common approach for introducing NTA has been to activate NP coatings toward a nucleophilic derivative of NTA. For example, QDs and magnetic NPs displaying carboxyl groups have been activated with EDC/NHS toward N_α,N_α-bis(carboxymethyl)-L-lysine—an amine-terminated derivative of NTA.[266,267,273] Alternatively, succinic anhydride has been used to activate polyglycerol coated magnetic NPs toward the same lysine-NTA derivative,[274] and glutaraldehyde has been used for the same purpose with amine terminated silica NPs.[271] Silica NPs have also been directly modified with a silane derivative of NTA.[272] Thiolated derivatives of NTA have been shown to self-assemble on Au NPs[269] and QDs,[275] or react with amine functionalized polymer-coated QDs that had been activated with sulfosuccinimidyl-4-(*N*-maleimidomethyl)cyclohexane-1-carboxylate (SMCC).[265]

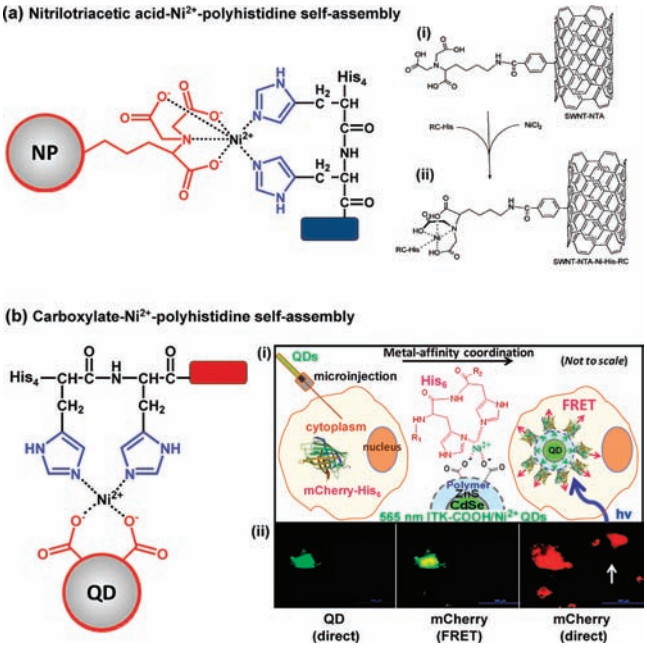


Figure 14. Self-assembly of polyhistidine through coordination to Ni^{2+} supplemented (a) nitrilotriacetic acid (NTA) coated NPs or (b) carboxylate coated NPs. The example for (a) shows (i) an NTA modified CNT and (ii) Ni^{2+} supplementation with the introduction of a polyhistidine tagged protein (RC-His). The example for (b) shows (i) the microinjection of carboxylate coated QDs into cells expressing polyhistidine tagged fluorescent protein (mCherry-His_6) and (ii) fluorescence images showing the intracellular QD-protein assembly through FRET between the QD and mCherry. The white arrow indicates a control cell expressing mCherry but not injected with QDs. Part of (a) is adapted with permission from ref 270. Part of (b) is adapted with permission from ref 278. Copyright 2008 American Chemical Society-Copyright 2010 American Chemical Society.

Using carbodiimide coupling, Au NPs coated with dihydrolipoic acid have been modified with Co^{2+}-NTA for self-assembly with polyhistidine tagged enzymes that largely retained their native activity.[276] Similarly, magnetic NPs with Cu^{2+}-NTA have also been prepared.[274]

Chelating agents such as NTA rely, at least in part, on the ability of carboxyl groups in close proximity to simultaneously coordinate a metal ion. It appears that the density of carboxyl groups associated with NP coatings may also be sufficient in this respect. Yao et al. demonstrated that carboxyl functionalized polymer-coated QDs were able to chelate Ni^{2+} directly, and thereby enable the controlled assembly of polyhistidine tagged *Renilla* luciferase enzyme for use in BRET-based sensing.[277] Boeneman et al. found that this interaction is surprisingly robust and efficient and could be extended to an intracellular environment.[278] Cells that expressed a polyhistidine tagged fluorescent protein (mCherry) were microinjected with Ni^{2+}-supplemented carboxyl polymer-coated QDs allowing the self-assembly process to occur *in vivo* (Figure 14b). This suggests suitability for similar *in vivo* bioconjugation of QDs with other target proteins.

Metallothionein Coordination. Metallothioneins (MTs) are low-molecular-weight proteins in which approximately one-third of the amino acid residues are cysteine. As a consequence, MTs have a high affinity for binding heavy metal ions. Similar to polyhistidine tags, MT tags that are appended to proteins can tightly bind the inorganic surface of QDs and Au NPs. The

Benson group demonstrated that a MT fusion of MBP was able to self-assemble on ligand coated CdSe QDs, CdSe/ZnS QDs, and Au NPs with dissociation constants on the order of 10^1-10^2 nM.[279] The interaction was strongest for Au NPs and weakest for CdSe/ZnS QDs. Furthermore, a direct comparison between MT-MBP and pentahistidine-MBP found that the former was bound more tightly to CdSe QDs.[279] In application, a C-terminal MT tag was used to assemble a lead-binding variant of phosphate binding protein onto to CdSe/ZnS QDs.[280] The protein was labeled with ruthenium phenanthroline to drive charge transfer quenching of QD PL in a manner dependent on the lead concentration present. MTs have also been used to assemble peptides and zinc finger proteins with Au_{11} nanoclusters,[281,282] and to drive the bacterial synthesis of a variety of different NP materials.[283] An interesting feature of the Benson group's MT strategy is that it was possible to site-specifically label a cysteine residue associated with a fusion protein of interest.[279] In the case of MT-MBP, the introduction of Cd^{2+} ion acted as a protecting group due to strong binding and folding by the MT domain. An activated maleimide label was thus able to attach specifically at the cysteine residue associated with the MBP. Removal of the Cd^{2+} using a chelating agent restored the availability of the MT domain for assembly with NPs. Thus, the use of MT tags enables the control over protein orientation in a NP-conjugate while retaining the ability to use mutant cysteine residues as unique labeling sites.

FlAsH/CrAsH System. In 1998, Roger Tsien's group reported a novel fluorescein-based dye that contained two As^{3+} atoms coordinated by 1,2-ethanedithiol at the 4′ and 5′ dye positions.[284] This compound—described as a fluorescein arsenical helix binder, FlAsH—could selectively interact with proteins that contained vicinal thiols in the amino acid sequence Cys-Cys-X_n-Cys-Cys. This motif displaced the ethanedithiol ligands and bound FlAsH, resulting in a 50 000-fold increase in dye fluorescence and provided sufficient affinity and selectivity to label proteins in vivo. A follow-up study demonstrated that the enhancement of dye fluorescence was maintained after protein denaturation.[285] More recently, the FlAsH dye was modified to contain an additional carboxyl group.[285,286] This so-called CrAsH dye exhibits a greater fluorescence enhancement than FlAsH upon binding to the tetracysteine motif under physiological conditions and offers improved signal-to-noise for in vivo experiments.[286] Typical dissociation constants for biarsenical ligands with tetracysteine motifs are approximately $10^{-11}-10^{-12}$ M.[285]

The combination of the affinity of the CrAsH dye for the tetracysteine motif and its available carboxyl group render it potentially useful as a cross-linker for NP bioconjugation. For example, Genin et al. used the CrAsH dye to prepare QD-integrase protein conjugates.[287] CdSe/ZnS QDs were coated with a mixture of PEG-modified phospholipids that displayed both terminal (unreactive) methoxy and (reactive) amine groups. The CrAsH molecule was ligated to the QD using EDC, and the integrase protein was recombinantly modified with a tetracysteine motif for subsequent assembly of the QD-bioconjugate. FlAsH and CrAsH are both organic dyes, and thus highly susceptible to photobleaching. The QD-CrAsH conjugate addresses this limitation via the superior photostability of QDs: the CrAsH PL photobleached within tens of seconds affording pure QD PL that was stable over an extended period of time. Ultimately, the utility of this approach may not be in the use of the CrAsH dye itself, but in exploiting similar, nonfluorescent arsenyl ligands for NPs that coordinate with tetracysteine motifs to accomplish controlled bioconjugation.

Enzyme Catalyzed Bioconjugation. *Biotin Ligase.* Biotin binding by avidin proteins is the strongest noncovalent interaction currently known with a dissociation constant of 10^{-15} M.[288] The specificity and stability of the interaction, combined with the ability to biotinylate a wide variety of biomolecules—as well as the ability to label avidin proteins with reporters—has resulted in the diverse use of biotin−avidin chemistry in bioconjugate preparation, immobilization, and labeling. The desire for site-specific biotinylation has driven the development of biotin ligase enzyme systems. For example, *E. coli* biotin ligase (BirA) transfers endogenous biotin to a specific lysine side chain found in a fifteen-residue acceptor peptide (AP) in an ATP-dependent manner.[289] Figure 15a illustrates the generic use of BirA in bioconjugation. Modifying different proteins with this AP sequence enables the enzymatic site-specific biotinylation of recombinant proteins that can, for example, be used in biological sensing[290] or cellular labeling.[291,292]

The Ting group adopted the use of BirA ligation to label cellular receptors with QDs.[293,294] The extracellular receptors in HeLa cells and neurons were modified with AP sequences and biotinylated by exogenous BirA present in the growth media. This allowed the rapid (2 min) and specific labeling of the live HeLa cells using streptavidin-conjugated QDs.[293] Similar labeling was also demonstrated using CHO cells.[295] Subsequent work used BirA in combination with yeast biotin ligase for multiplexed labeling (Figure 15a).[294] In this case, a yeast acceptor peptide was evolved to provide a second and orthogonal tag for two-color labeling of cell surface proteins, where the two different AP sequences defined the labeling specificity. In an alternative strategy, orthogonal two-color QD tracking of single interferon receptor units on live cells was achieved through the combination of BirA and polyhistidine-nickel(II)-NTA interactions.[296] The latter required the use of NTA-modified QDs as a chemistry that was orthogonal to streptavidin-coated QDs, and clearly demonstrated the great potential of orthogonal labeling chemistry—even at the single-molecule level. In addition to QDs, the Ting and Bartlett groups also used BirA to selectively label adeno-associated virus particles.[297] The virus capsid was engineered to display an available AP sequence that was then labeled by BirA with a chemically synthesized ketone isostere of biotin. The ketone group was chemoselectively labeled with a hydrazido-modified fluorescent dye for optical tracking and a hydrazido-terminated cyclic arginine-gylcine-aspartate (RGD) as a tumor-homing and cell-penetrating peptide. Magnetic NPs biosynthesized by *Magnetospirillum magneticum* have also been modified to display AP on their surface.[298]

Carrier Proteins. Peptidyl and acyl carrier proteins (PCP, ACP) can be specifically modified with a variety of fluorophores or affinity handles by phosphopantetheinyl (PPT) transferase. This enzyme catalyzes the transfer of the PPT unit from coenzyme A (CoA) to a conserved serine in the carrier protein.[292,299,300] Since both the carrier protein and PPT transferase tolerate a wide range of substitutions at the terminal end of the CoA, this system has been used to label ACP-fusion proteins with fluorophores, biotin, and digoxigenin.[299] George et al. utilized PPT to specifically biotinylate ACP fusion proteins displayed on yeast cells for labeling with streptavidin-coated QDs.[299] In addition, CoA-modified QDs have been used to label a PCP-tagged MBP that retained its binding function in subsequent assays, and also a PCP-tagged transferrin receptor at the membrane of CHO-TRVb cells.[295]

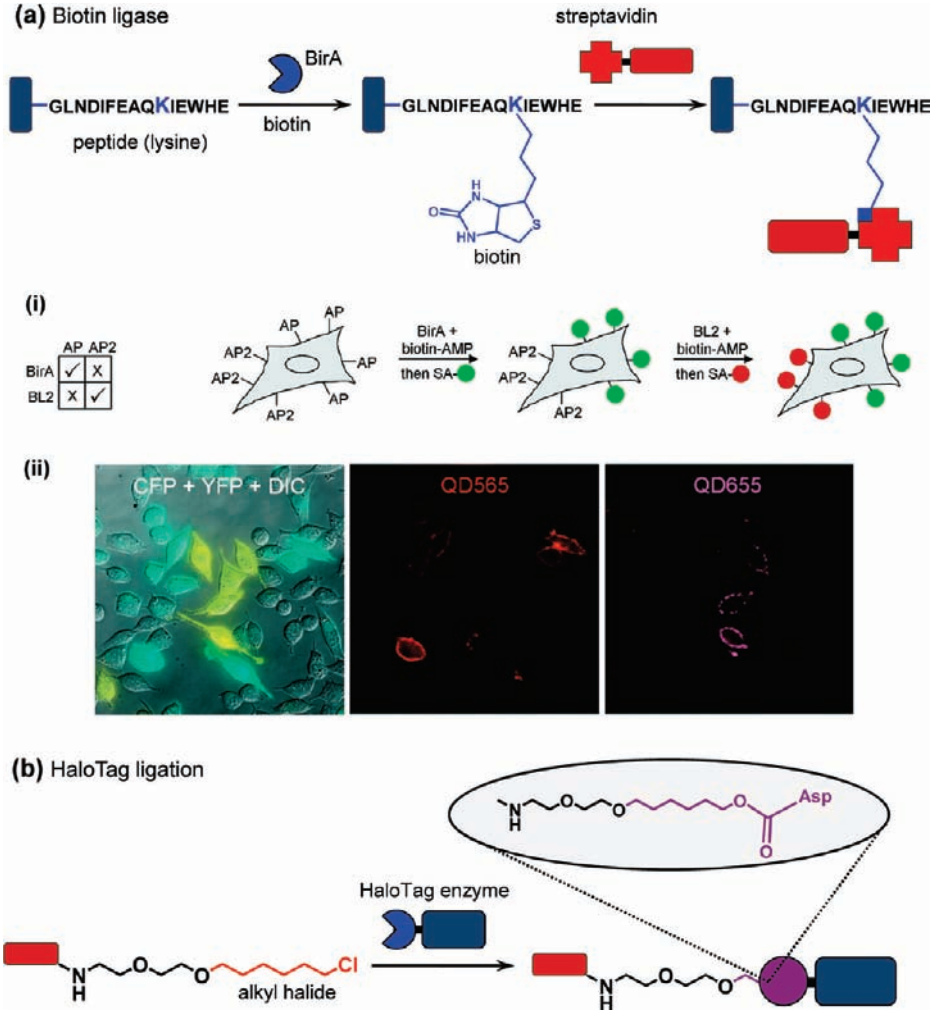


Figure 15. Enzymatic labeling systems: (a) biotin ligase and (b) HaloTag ligation. The example for biotin ligase shows (i) a two-step two-color cellular labeling scheme using two orthogonal biotin ligase enzymes (BirA and BL2) with two acceptor peptides (AP and AP2). Cellular labeling with streptavidin (SA)-coated green-emitting QDs (QD565) followed the ligation of biotin to AP. In turn, subsequent cellular labeling with SA-coated red-emitting QDs (QD655) followed the ligation of biotin to AP2. Differential interference contrast and fluorescence images of cells labeled with the two different colors of QD are shown in (ii). The two types of cells expressing AP and AP2 individually are distinguished by the expression of either cyan fluorescent protein (CFP) or yellow fluorescent protein (YFP), respectively. Part of (a) is adapted with permission from ref 294. Copyright 2007 American Chemical Society.

Enzyme—substrate/Inhibitor Binding. The ability of enzymes to selectively bind their target substrates and/or certain inhibitors is another potential route to the preparation of NP-bioconjugates. For example, the cutinase enzyme was inserted into the membrane protein integrin LFA-1 and used to bind QDs that were modified with its inhibitor *para*-nitrophenyl phosphonate (pNPP) in a cellular labeling reaction.[301] The pNPP-QDs were prepared from the activation of amine coated QDs with SMCC and a subsequent reaction with an alkyl thiol derivative of pNPP. Similarly, it has been shown that glutathione-*S*-transferase can bind to Au NPs coated with a mixed surface of thiol-terminated tri(ethylene glycol) and glutathione with high specificity.[302] Since glutathione-*S*-transferase-fusion proteins are routinely prepared,[303] this technique may also have potential for controlling the orientation of proteins attached to glutathione-modified NPs.

HaloTag. The HaloTag protein is a recombinantly modified haloalkane dehalogenase (www.Promega.com) that can be fused with other proteins of interest and used to covalently bind synthetic HaloTag ligands. The ligands are typically fluorescent dyes, affinity handles (e.g., biotin), or solid surfaces modified with a chloroalkane linker.[304] In the wild-type dehalogenase enzyme, the His272 residue acts as a base and catalyzes the hydrolysis and release of the substrate intermediate, thereby allowing enzyme regeneration. In contrast, the modified HaloTag enzyme expresses a mutated Phe272 that cannot act as a base and traps the reaction intermediate as a stable covalent adduct (Figure 15b). Both *in vitro* and *in vivo* labeling with fluorophores via the HaloTag system have been demonstrated.[304] The use of NPs modified with a HaloTag ligand offers the potential for control over the orientation of the HaloTag fusion protein partner in bioconjugation preparation. The Rao group demonstrated that carboxyl-coated QDs could be modified with a bifunctional amino-chloroalkane ligand that enabled subsequent ligation with a HaloTag-*Renilla* luciferase fusion protein.[305] BRET was used to track loading of the HaloTag-luciferase fusion protein, which depended on the number of chloroalkane ligands associated with the QD. The HaloTag system was also used for

in vivo labeling of cells with Streptavidin-coated QDs.[306] In this case, the HaloTag protein was expressed at a cell membrane anchoring domain and ligated with a biotin HaloTag ligand that was able to bind the Streptavidin-coated QDs.

■ PROMISING CHEMISTRIES FOR FUTURE DEVELOPMENT

This review has described several bioconjugate chemistries that are novel in their application to NPs, and offer greater control over NP-conjugate properties than traditional labeling chemistries. In many cases, the studies described represent more proof-of-concept than widespread applicability. Nonetheless, the advantages of the chemistries are evident—particularly the retention of native biomolecule structure and function through bioorthogonality. Despite this success, the toolkit for preparing NP-bioconjugates is far from complete. Fortunately, the continued development of new bioconjugation chemistries for biolabeling and modification will continue to drive new and improved NP-biological applications.

Several promising covalent chemistries are similar to some of the reactions previously described in this review, utilizing similar reactive moieties or analogous concepts in bioorthogonality. One such example relies on the aforementioned scarcity of free thiols in biological macromolecules, which makes the selective introduction of thiols (e.g., cysteine mutation) and their subsequent chemical modification an attractive approach for selective bioconjugation. To this end, several groups have developed alternative electrophiles to the ubiquitous *N*-alkylmaleimide moiety. For example, Bernardes et al. have used the site-selective introduction of dehydroalanine side chains into proteins and a subsequent Michael addition with thiol-modified labels.[307] While the dehydroalanine residues are not as reactive as N-alkyl maleimide groups, they have the advantage of site specific introduction through the elimination of cysteine residues using *O*-mesitylenesulfonylhydroxylamine,[307] or through genetic incorporation of either phenylselenocysteine[308,309] or selenalysine[310] followed by oxidative elimination with hydrogen peroxide. Another example is conceptually similar to the use of strained alkynes for CuAAC and utilizes the reaction between 1,3-nitrones (in place of the azide group) and alkynes. This strain-promoted alkyne-nitrone cycloaddition strategy has been used to N-terminally modify peptides[311] and proteins[312] with a biotin derivative of bicyclo[6.1.0]nonyne and a PEG-modified dibenzocyclooctyne, respectively, through the conversion of an N-terminal serine residue to a 1,3-nitrone. Nitrones will also undergo cycloadditions with maleimides.[313] Another novel cycloaddition strategy has addressed the challenge of chemical instability often associated with highly reactive moieties. Song et al. have taken advantage of photoactivation of 2,5-diaryl tetrazoles at 302 nm to generate a highly reactive nitrile imine that chemoselectively reacts with alkenes via a 1,3-dipolar cycloaddition to yield a stable pyrazoline cylcoadduct (Figure 16a).[314,315] One attractive aspect of this "photoclick chemistry" is that the resulting pyrazoline ligation product is fluorescent, facilitating direct observation of the reaction in complex systems. The compatibility of the reaction with physiological buffers and the wide utility of photoactivation in biological systems suggest the potential for broad application of this approach for *in vivo* labeling.

There are many other reactions that are well-known in organic synthesis and which hold great potential for the controlled display of biomolecules on NPs. Figure 16 highlights a few of these chemistries that, to our knowledge, have not yet been applied in the preparation of NP-bioconjugates. Several groups have focused on the unique reactivity of the tyrosine phenol ring, which is found on the surface of many proteins. For example, two-component[316] and three-component[317,318] Mannich condensations (Figure 16b) and ene-forming reactions with cyclic diazocarboxamides[319] have found utility. Some other reactions with significant promise for NP bioconjugation include *N*-terminal transamination with secondary oxime ligation,[320−322] olefin cross-metathesis (Figure 16c),[323−325] and palladium cross-coupling reactions (*vide infra*). Olefin cross-metathesis—awarded the 2005 Nobel Prize in Chemistry—is a highly efficient and reliable reaction in which carbon−carbon double bonds are broken and reformed catalytically.[326−328] In traditional formats, the limitation of olefin cross-metathesis has been poor compatibility with aqueous solvents and thus poor suitability for use in bioconjugate preparation. However, renewed interest in this type of transformation is leading to advances in catalyst design[329] and has allowed the expansion of this chemistry into low percentage mixtures of organic and aqueous solvent, thereby enabling limited utility with biomolecules.[324] In an early example of the application of olefin cross-metathesis to bioconjugation, Mortell et al. synthesized carbohydrate inhibitors of cell agglutination.[330] More recently, Lin et al. demonstrated olefin cross-metathesis in 30% *tert*-butanol/phosphate buffer between allyl alcohols and allyl sulfides that were chemoselectively conjugated to *subtilisin Bacillus lentus* protein.[323] With further developments, it is anticipated that olefin cross-metathesis will be a valuable addition to the toolkit for preparing NP-bioconjugates. Carbon−carbon bond formation via palladium catalysis (Figure 16d) has also been shown to have significant potential in the area of bioconjugation, and was recognized by the 2010 Nobel Prize in Chemistry for its larger contributions to the field. The Suzuki-Miyaura reaction consists of a cross-coupling reaction between an aryl halide (ArX, where X = I, Br) and a boronic acid (aryl or alkenyl) that is catalyzed by a palladium complex.[331] This chemistry has been used for the site-selective modification of peptides and proteins with small molecule boronic acids in aqueous solution, using *p*-boronophenylalanine,[332] *p*-iodophenylalanine,[333] or *p*-iodobenzyl modified cysteine side chains.[334] Similarly, the palladium catalyzed Mizoroki-Heck reaction[335] (unsaturated halides with alkenes) and Sonogashira coupling[336] (unsaturated halides with alkynes) have been applied to the covalent modification of peptides and proteins that incorporated *p*-iodophenylalanine[337−339] or were acylated with iodobenzoic acid.[340] The role of the palladium catalysts begs the question of whether composite NP materials—for example, dumbbells with a palladium NP component—might be able to catalyze their own bioconjugation.

Considering potential advances in self-assembly, the research of the Belcher group should be noted.[341−343] They have focused on the development of peptide sequences that coordinate specific metals through genetic engineering of bacteriophage M13. This work has led to many novel peptide sequences for assembly of metal-based materials. While the interest of the Belcher group has been in biomineralization and patterning applications, there may be potential for the development of metal NP-biological hybrid materials and bioconjugates. There may also be new opportunities in the synthesis of artificial amino acids designed to strongly bind NP materials and the subsequent incorporation of oligomeric tracts of these residues into synthetic

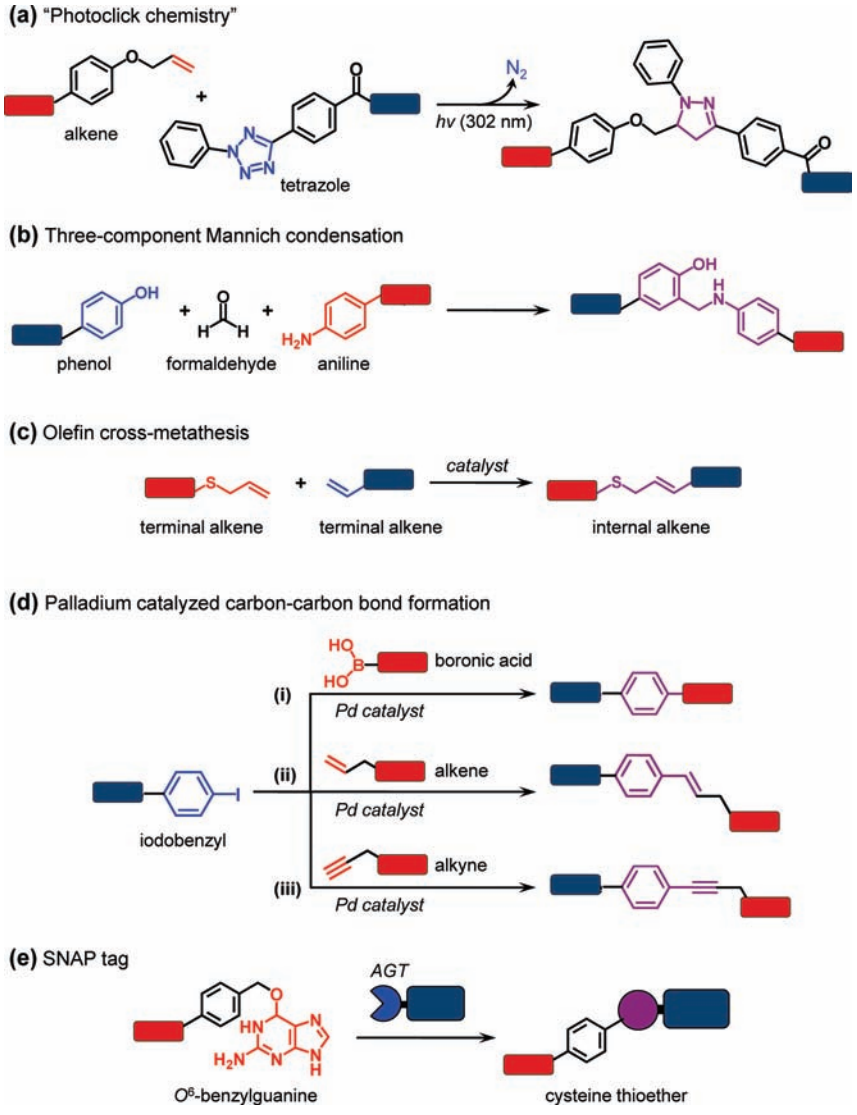


Figure 16. Promising chemistries for the future development of bioorthogonal NP bioconjugation chemistry: (a) "photoclick chemistry"; (b) three-component Manich condensations; (c) olefin cross-metathesis; (d) palladium catalyzed carbon−carbon bond formation; and (e) SNAP tag enzyme labeling. These and other promising chemistries are described in the text.

peptides or expressed proteins—analogous to the use of oligohistidine with semiconductor QDs.

The use of enzymatic labeling methods with NPs is still emerging, and many methods remain untapped. The most prominent of these is arguably the SNAP tag. The engineered human DNA repair enzyme alkylguanine-DNA alkyltransferase (AGT or SNAP-tag, www.neb.com) can be used as a tag for self-labeling, where a variety of modified O^6-benzylguanine derivatives can function as substrates for the AGT enzyme and are attached via the irreversible transfer of an alkyl group to a cysteine residue (Figure 16e).[344] Since its inception, the SNAP tag system has been significantly improved through the development of faster and more efficient enzymes. In addition, a wide range of benzylguanine substrates modified with fluorescent dyes or affinity handles are available, and have been demonstrated to be suitable for a multitude of *in vivo* cellular labeling applications.[292] Recent modifications of the SNAP-tag enzyme can also specifically target O^2-benzylcytosine derivatives, thereby enabling an orthogonal labeling approach using two enzymes.[345] Given the relative ease of modifying a variety of substrates with benzylguanine derivatives, it is only a matter of time until this system is used to label NPs in a manner akin to the HaloTag. Additional enzymatic labeling systems with good potential include dihydrofolate reductase, which can covalently bind trimethoprim;[346] transglutaminase, which can attach cadaverine-modified probes to small glutamine (Q) expressing peptide substrates, termed Q-tags;[347] and lipoic acid ligase, which can functionalize APs with various substituted substrates.[348]

SUMMARY AND CONCLUSIONS

This review has highlighted the recent application of non-traditional chemistries to the preparation of NP-bioconjugates, including chemical reactions to form new covalent bonds, self-assembly strategies, and enzymatic methods. These methods are novel in their application to NP materials and advance the degree of control over properties such as NP-bioconjugate valence, biomolecule orientation, reproducibility, and potential for

further bioconjugation. In turn, control over these properties is paramount in optimizing the function of NP-bioconjugates in applications such as diagnostic imaging, sensing, and drug delivery.

Efficient and bioorthogonal cycloaddition and ligation reactions enable greater levels of control in the display of one or more bio/molecules on NPs—particularly in terms of biomolecule orientation and conjugate valence. To date, many of these new developments in NP bioconjugation have followed the "rediscovery" of many classical synthetic organic chemistry reactions for protein labeling, and this trend is likely to continue. The potential limitation is the continued reliance on traditional labeling chemistries to introduce bioorthogonal groups to biomolecules. However, labeling NPs and biomolecules individually with bifunctional molecules (e.g., NHS-alkyne) using traditional methods, followed by an efficient bioorthogonal reaction (e.g., CuAAC), is more reliable and controllable than using traditional methods to couple the NP and biomolecule directly. This highlights the important point that bioorthogonal chemistries are not meant to completely replace standard bioconjugation approaches, but rather to supplement and augment them. Unnatural amino acid incorporation and other sophisticated methods of introducing bioorthogonal functional groups can provide an even greater degree of control than standard labeling techniques, but are much more time and resource intensive, while also more limited in their applicability.

The self-assembly of biomolecules to QDs using polyhistidine and metallothionein tags has been shown to provide excellent control over bioconjugate valence and orientation. Beyond synthetic peptides and recombinant proteins, the development of modular activated polyhistidine peptides extends the preparation of bioconjugates to include native proteins and synthetic oligonucleotides. Although limited in scope to date, it is anticipated that many of the chemical reactions described herein will be adaptable to modular polyhistidine tags and enable a highly versatile, chemoselective, and bioorthogonal toolkit for the controlled display of biomolecules on QDs and other metal-based NPs. Self-assembly methods are highly advantageous due to the overall simplicity and the determination of conjugate valence on the basis of stoichiometry and equilibrium constants. Self-assembly is also free of the irreproducibility that is often associated with chemical activation and cross-linkers. The disadvantage of self-assembly methods tends to be the scope of their applicability, which can be limited by NP composition and the properties of its coating. In some cases, self-assembly methods may also not be as robust as the formation of new covalent bonds.

Enzymatic labeling methods can be particularly advantageous in that they are highly specific, have little or no opportunity for cross-reactivity, do not require activated intermediates, and can provide a unique point of attachment. However, while enzyme reactions are efficient, they are not necessarily rapid, nor are they as readily scalable as chemical reactions. The scope of the applicability of different enzyme labeling methods is also limited, and variable between different methods. Enzymatic self-labeling (e.g., HaloTag) generally requires the preparation of a fusion protein. This significantly increases NP-bioconjugate size, can potentially affect the activity of the protein of interest, and is limited to NP-protein conjugates. Furthermore, both self-labeling enzymes and enzymes that modify a substrate generally require that molecular or peptidyl tags be introduced to the biomolecules of interest, thus creating the same potential challenges as the introduction of bioorthogonal groups for chemical labeling. In the case of slow reactions, the activity and long-term stability of the enzyme under different conditions of temperature or pH, and in various biological milieus, can be important to labeling efficiency. Moreover, the steric effect of a NP on enzyme labeling efficiency remains an open question.

The critical message is that traditional labeling chemistries (e.g., carbodiimide) are poorly suited to the controlled display of biomolecules on NPs. The novel application of reactions drawn from organic chemistry and biochemistry to NPs, as well as self-assembly, has provided new levels of control over the properties of NP-bioconjugates. This added control comes at a cost of increased complexity or a limited scope of applicability. Therefore, it is crucial that the toolkit of bioconjugate chemistries for different NP materials continue to be developed so that there are methods for the controlled preparation of NP-bioconjugates in every application. In turn, the function and efficacy of these NP materials in biological applications will be greatly advanced.

AUTHOR INFORMATION

Corresponding Author

*Ph: 202-404-6046. Fax: 202-767-9594. E-mail: Igor.medintz@nrl.navy.mil.

ACKNOWLEDGMENT

W.R.A. is grateful to the Natural Sciences and Engineering Research Council of Canada (NSERC) for support through a postdoctoral fellowship. D.E.P. acknowledges an ASEE fellowship through NRL. J.B.B.−C. acknowledges a Marie Curie IOF. The authors also acknowledge the CB Directorate/Physical S&T Division (DTRA), DARPA, ONR, NRL and the NRL-NSI for financial support.

ABBREVIATIONS:

ACP, acyl carrier protein; AP, acceptor peptide; BirA, biotin ligase; BRET, bioluminescence resonance energy transfer; CoA, coenzyme A; CPMV, cowpea mosaic virus; (SW/MW)CNT, (single walled/multiwalled)carbon nanotube; CSS, CMP-sialic acid synthetase; CuAAC, copper-catalyzed azide−alkyne cycloaddition; EDC, 1-ethyl-3-(3-dimethylaminopropyl)carbodiimide; EGF, epidermal growth factor; eGFP, enhanced green fluorescent protein; FRET, Förster resonance energy transfer; MBP, maltose binding protein; HYNIC, 2-hydrazinonicotinoyl; IMAC, immobilized metal affinity chromatography; LSPR, localized surface plasmon resonance; MBP, maltose binding protein; MRI, magnetic resonance imaging; MT, metallothionein; NCL, native chemical ligation; NHS, *N*-hydroxysuccinimide; NP, nanoparticle; NTA, nitrilotriacetic acid; PCP, peptidyl carrier protein; PEG, poly(ethylene glycol); PL, photoluminescence; PLA, poly(lactic acid); PLGA, poly(lactic-*co*-glycolic acid); pNPP, *para*-nitrophenyl phosphonate; PPT, phosphopantetheinyl; QD, quantum dot; SMCC, succinimidyl-4-(*N*-maleimidomethyl)-cyclohexane-1-carboxylate; TMV, tobacco mosaic virus

REFERENCES

(1) Haugland, R. P. (2005) *The Handbook A Guide to Fluorescent Probes and Labeling Technologies*, 10th ed., Invitrogen, San Diego.

(2) Hermanson, G. T. (2008) *Bioconjugate Techniques*, 2nd ed., Academic Press, San Diego.

(3) Jain, P. K., Huang, X., El-Sayed, I. H., and El-Sayed, M. A. (2007) Review of some interesting surface plasmon resonance-enhanced

properties of noble metal nanoparticles and their applications. *Plasmonics 2*, 107–118.

(4) Jain, P. K., Huang, X., El-Sayed, I. H., and El-Sayed, M. A. (2008) Noble metals on the nanoscale: Optical and photothermal properties and some applications in imaging, sensing, biology and medicine. *Acc. Chem. Res. 41*, 1578–1586.

(5) Moores, A., and Floch, P. L. (2009) The metal nanoparticle plasmon band as a powerful tool for chemo- and biosensing. *Biosensing Using Nanomaterials* (Merkoçi, A., Ed.) pp 137−176, Chapter 5, John Wiley & Sons, Inc., Hoboken, NJ.

(6) Elghanian, R., Storhoff, J. J., Mucic, R. C., Letsinger, R. L., and Mirkin, C. A. (1997) Selective colorimetric detection of polynucleotides based on the distance-dependent optical properties of gold nanoparticles. *Science 277*, 1078–1081.

(7) Dubertret, B., Calame, M., and Libchaber, A. J. (2001) Single-mismatch detection using gold-quenched fluorescent oligonucleotides. *Nat. Biotechnol. 19*, 365–370.

(8) Zhao, W., Brook, M. A., and Li, Y. F. (2008) Design of gold nanoparticle-based colorimetric biosensing assays. *ChemBioChem 9*, 2363–2371.

(9) Algar, W. R., Massey, M., and Krull, U. J. (2009) The application of quantum dots, gold nanoparticles, and molecular switches to optical nucleic-acid diagnostics. *Trends Anal. Chem. 28*, 292–306.

(10) Cao, Y. W. C., Jin, R. C., and Mirkin, C. A. (2002) Nanoparticles with Raman spectroscopic fingerprints for DNA and RNA detection. *Science 297*, 1536–1540.

(11) Stokes, R. J., Macaskill, A., Lundahl, P. J., Smith, W. E., Faulds, K., and Graham, D. (2007) Quantitative enhanced Raman scattering of labeled DNA from gold and silver nanoparticles. *Small 3*, 1593–1601.

(12) Murphy, C. J., Gole, A. M., Stone, J. W., Sisco, P. N., Alkilany, A. M., Goldsmith, E. C., and Baxter, S. C. (2008) Gold nanoparticles in biology: beyond toxicity to cellular imaging. *Acc. Chem. Res. 41*, 1721–1730.

(13) Hirsch, L. R., Stafford, R. J., Bankson, J. A., Sershen, S. R., Rivera, B., Price, R. E., Hazle, J. D., Halas, N. J., and West, J. L. (2003) Nanoshell-mediated near-infrared thermal therapy of tumors under magnetic resonance guidance. *Proc. Natl. Acad. Sci. U.S.A 100*, 13549–13554.

(14) Huang, X. H., El-Sayed, I. H., Qian, W., and El-Sayed, M. A. (2006) Cancer cell imaging and photothermal therapy in the near-infrared region by using gold nanorods. *J. Am. Chem. Soc. 128*, 2115–2120.

(15) Zheng, J., Nicovich, P. R., and Dickson, R. M. (2007) Highly fluorescent noble-metal quantum dots. *Annu. Rev. Phys. Chem. 58*, 409–431.

(16) Marambio-Jones, C., and Hoek, E. M. V. (2010) A review of the antibacterial effects of silver nanomaterials and potential implications for human health and the environment. *J. Nanopart. Res. 12*, 1531–1551.

(17) Pastoriza-Santos, I., Alvarez-Puebla, R. A., and Liz-Marzán, L. M. (2010) Synthetic routes and plasmonic properties of noble metal nanoplates. *Eur. J. Inorg. Chem.* 4288–4297.

(18) Xia, Y., Xiong, Y., Lim, B., and Skrabalak, S. E. (2008) Shape-controlled synthesis of metal nanocrystals: simple chemistry meets complex physics. *Angew. Chem., Int. Ed. 48*, 60–103.

(19) Biju, V., Itoh, T., Anas, A., Sujith, A., and Ishikawa, M. (2008) Semiconductor quantum dots and metal nanoparticles: syntheses, optical properties, and biological applications. *Anal. Bioanal. Chem. 391*, 2469–2495.

(20) Tao, A. R., Habas, S., and Yang, P. (2008) Shape control of colloidal metal nanocrystals. *Small 4*, 310–325.

(21) Wiley, B., Sun, Y., and Xia, Y. (2007) Synthesis of silver nanostrutures with controlled shapes and properties. *Acc. Chem. Res. 40*, 1067–1076.

(22) Park, J., Joo, J., Kwon, S. G., Jang, Y., and Hyeon, T. (2007) Synthesis of monodisperse spherical nanocrystals. *Angew. Chem., Int. Ed. 46*, 4630–4660.

(23) Love, J. C., Estroff, L. A., Kriebel, J. K., Nuzzo, R. G., and Whitesides, G. M. (2005) Self-assembled monolayers of thiolates on metals as a form of nanotechnology. *Chem. Rev. 105*, 1103–1169.

(24) Laibinis, P. E., and Whitesides, G. M. (1992) Omega-terminated alkanethiolate monolayers on surfaces of copper, silver, and gold have similar wettabilities. *J. Am. Chem. Soc. 114*, 1990–1995.

(25) Lee, J. S., Lytton-Jean, A. K. R., Hurst, S. J., and Mirkin, C. A. (2007) Silver nanoparticle-oligonucleotide conjugates based on DNA with triple cyclic disulfide moieties. *Nano Lett. 7*, 2112–2115.

(26) Medintz, I. L., Uyeda, H. T., Goldman, E. R., and Mattoussi, H. (2005) Quantum dot bioconjugates for imaging, labelling and sensing. *Nat. Mater. 4*, 435–446.

(27) Michalet, X., Pinaud, F. F., Bentolila, L. A., Tsay, J. M., Doose, S., Li, J. J., Sundaresan, G., Wu, A. M., Gambhir, S. S., and Weiss, S. (2005) Quantum dots for live cells, in vivo imaging, and diagnostics. *Science 307*, 538–544.

(28) Algar, W. R., and Krull, U. J. (2009) Quantum dots for the development of optical biosensors based on fluorescence. *Biosensing Using Nanomaterials* (Merkoçi, A., Ed.) pp 199−245, Chapter 7, John Wiley & Sons, Inc., Hoboken, NJ.

(29) Murray, C. B., Norris, D. J., and Bawendi, M. G. (1993) Synthesis and characterization of nearly monodisperse CdE (E = S, Se, Te) semiconductor nanocrystallites. *J. Am. Chem. Soc. 115*, 8706–8715.

(30) Guzelian, A. A., Banin, U., Kadavanich, A. V., Peng, X., and Alivisatos, A. P. (1996) Colloidal chemical synthesis and characterization of InAs nanocrystal quantum dots. *Appl. Phys. Lett. 69*, 1432–1434.

(31) Jiang, W., Singhal, A., Zheng, J. N., Wang, C., and Chan, W. C. W. (2006) Optimizing the synthesis of red- to near-IR-emitting CdS-capped CdTexSe1-x alloyed quantum dots for biomedical imaging. *Chem. Mater. 18*, 4845–4854.

(32) Pettigrew, K. A., Liu, Q., Power, P. P., and Kauzlarich, S. M. (2003) Solution snythesis of alkyl- and alkyl/alkoxy-capped silicon nanoparticles via oxidiation. *Chem. Mater. 15*, 4005–4011.

(33) Heath, J. R., Shiang, J. J., and Alivisatos, A. P. (1994) Germanium quantum dots - optical properties and synthesis. *J. Chem. Phys. 101*, 1607–1615.

(34) Dabbousi, B. O., Rodriguez-Viejo, J., Mikulec, F. V., Heine, J. R., Mattoussi, H., Ober, R., Jensen, K. F., and Bawendi, M. G. (1997) (CdSe)ZnS core-shell quantum dots. *J. Phys. Chem. B 101*, 9463–9475.

(35) Hines, M. A., and Guyot-Sionnest, P. (1996) Synthesis and characterization of strongly luminescing ZnS-capped CdSe nanocrystals. *J. Phys. Chem. 100*, 468–471.

(36) Alivisatos, A. P. (1996) Semiconductor clusters, nanocrystals, and quantum dots. *Science 271*, 933–937.

(37) Alivisatos, A. P. (1996) Perspectives on the physical chemistry of semiconductor nanocrystals. *J. Phys. Chem. 100*, 13226–13239.

(38) Wang, Y., and Herron, N. (1991) Nanometer-sized semiconductor clusters: materials synthesis, quantum size effects, and photophysical properties. *J. Phys. Chem. 95*, 525–532.

(39) Murphy, C. J., and Coffer, J. L. (2002) Quantum dots: a primer. *Appl. Spectrosc. 56*, 16A–27A.

(40) Smith, A. M., Duan, H. W., Mohs, A. M., and Nie, S. M. (2008) Bioconjugated quantum dots for in vivo molecular and cellular imaging. *Adv. Drug Delivery Rev. 60*, 1226–1240.

(41) Algar, W. R., Tavares, A. J., and Krull, U. J. (2010) Beyond labels: A review of the application of quantum dots as integrated components of assays, bioprobes, and biosensors utilizing optical transduction. *Anal. Chim. Acta 673*, 1–25.

(42) Medintz, I. L., and Mattoussi, H. (2009) Quantum dot-based resonance energy transfer and its growing application in biology. *Phys. Chem. Chem. Phys. 11*, 17–45.

(43) Guzelian, A. A., Katari, J. E. B., Kadavanich, A. V., Banin, U., Hamad, K., Juban, E., Alivisatos, A. P., Wolters, R. H., Arnold, C. C., and Heath, J. R. (1996) Synthesis of size-selected, surface-passivated InP nanocrystals. *J. Phys. Chem. 100*, 7212–7219.

(44) Allen, P. M., and Bawendi, M. G. (2008) Ternary I-III-VI quantum dots luminescent in the red to near-infrared. *J. Am. Chem. Soc. 130*, 9240–9241.

(45) Li, L. S., Hu, J. T., Yang, W. D., and Alivisatos, A. P. (2001) Band gap variation of size- and shape-controlled colloidal CdSe quantum rods. *Nano Lett. 1*, 349–351.

(46) Peng, X. G., Manna, L., Yang, W. D., Wickham, J., Scher, E., Kadavanich, A., and Alivisatos, A. P. (2000) Shape control of CdSe nanocrystals. *Nature 404*, 59–61.
(47) Hezinger, A. F. E., Teβmar, J., and Göpferich, A. (2008) Polymer coating of quantum dots. *Eur. J. Pharmaceut. Biopharmaceut. 68*, 138–152.
(48) Pons, T., Uyeda, H. T., Medintz, I. L., and Mattoussi, H. (2006) Hydrodynamic dimensions, electrophoretic mobility, and stability of hydrophilic quantum dots. *J. Phys. Chem. B 110*, 20308–20316.
(49) Kang, Y. S., Risbud, S., Rabolt, J. F., and Stroeve, P. (1996) Synthesis and characterization of nanometer-size Fe_3O_4 and gamma-Fe_2O_3 particles. *Chem. Mater. 8*, 2209–2211.
(50) Hyeon, T. (2003) Chemical synthesis of magnetic nanoparticles. *Chem. Commun.* 927–934.
(51) Sun, S. H., Zeng, H., Robinson, D. B., Raoux, S., Rice, P. M., Wang, S. X., and Li, G. X. (2004) Monodisperse MFe_2O_4 (M = Fe, Co, Mn) nanoparticles. *J. Am. Chem. Soc. 126*, 273–279.
(52) Jana, N. R., Chen, Y. F., and Peng, X. G. (2004) Size- and shape-controlled magnetic (Cr, Mn, Fe, Co, Ni) oxide nanocrystals via a simple and general approach. *Chem. Mater. 16*, 3931–3935.
(53) Lu, A. H., Salabas, E. L., and Schuth, F. (2007) Mangetic nanoparticles: synthesis, protection, functionalization, and application. *Angew. Chem., Int. Ed. 46*, 1222–1244.
(54) Gupta, A. K., and Gupta, M. (2005) Synthesis and surface engineering of iron oxide nanoparticles for biomedical applications. *Biomaterials 26*, 3995–4021.
(55) Sun, S. H. (2006) Recent advances in chemical synthesis, self-assembly, and applications of FePt nanoparticles. *Adv. Mater. 18*, 393–403.
(56) Laurent, S., Forge, D., Port, M., Roch, A., Robic, C., Elst, L. V., and Muller, R. N. (2008) Magnetic iron oxide nanoparticles: synthesis, stabilization, vectorization, physicochemial characterizations, and biological applications. *Chem. Rev. 108*, 2064–2110.
(57) Sosnovik, D. E., Nahrendorf, M., and Weissleder, R. (2008) Magnetic nanoparticles for MR imaging: agents, techniques and cardiovascular applications. *Basic Res. Cardiol. 103*, 122–130.
(58) Na, H. B., Song, I. C., and Hyeon, T. (2009) Inorganic nanoparticles for MRI contrast agents. *Adv. Mater. 21*, 2133–2148.
(59) Hao, R., Xing, R., Xu, Z., Hou, Y., Gao, S., and Sun, S. (2010) Synthesis, functionalization, and biomedical applications of multifunctional magnetic nanoparticles. *Adv. Mater. 22*, 2729–2742.
(60) Veiseh, O., Gunn, J. W., and Zhang, M. (2010) Design and fabrication of magnetic nanoparticles for targeted drug delivery and imaging. *Adv. Drug Delivery Rev. 62*, 284–304.
(61) Sandhu, A., Handa, H., and Abe, M. (2010) Synthesis and applications of magnetic nanoparticles for biorecognition and point of care medical diagnostics. *Nanotechnology 21*, 442001.
(62) Gao, J., Gu, H., and Xu, B. (2009) Multifunctional magnetic nanoparticles: design, synthesis, and biomedical applications. *Acc. Chem. Res. 42*, 1097–1107.
(63) Yu, H., Chen, M., Rice, P. M., Wang, S. X., White, R. L., and Sun, S. H. (2005) Dumbbell-like bifunctional Au-Fe_3O_4 nanoparticles. *Nano Lett. 5*, 379–382.
(64) Gu, H., Zheng, R., Zhang, X. X., and Xu, B. (2004) Facile one-pot synthesis of bifunctional heterodimers of nanoparticles: A conjugate of quantum dot and magnetic nanoparticles. *J. Am. Chem. Soc. 126*, 5664–5565.
(65) Compton, R. G., Wildgoose, G. G., and Wong, E. L. S. (2009) Carbon nanotube-based sensors and biosensors, *Biosensing Using Nanomaterials* (Merkoçi, A., Ed.) pp 3−37, Chapter 1, John Wiley & Sons, Inc., Hoboken, NJ.
(66) Ménard-Moyon, C., Kostarelos, K., Prato, M., and Bianco, A. (2010) Functionalized carbon nanotubes for probing and modulating molecular functions. *Chem. Biol. 17*, 107–115.
(67) Liu, Z., Tabakman, S., Welsher, K., and Dai, H. J. (2009) Carbon nanotubes in biology and medicine: in vitro and in vivo detection, imaging, and drug delivery. *Nano Res. 2*, 85–120.
(68) Yang, W. R., Thordarson, P., Gooding, J. J., Ringer, S. P., and Braet, F. (2007) Carbon nanotubes for biological and biomedical applications. *Nanotechnology 18*, 412001.
(69) Agui, L., Yanez-Sedeno, P., and Pingarron, J. M. (2008) Role of carbon nanotubes in electroanalytical chemistry. *Anal. Chim. Acta 622*, 11–47.
(70) Rivas, G. A., Rubianes, M. D., Rodriguez, M. C., Ferreyra, N. E., Luque, G. L., Pedano, M. L., Miscoria, S. A., and Parrado, C. (2007) Carbon nanotubes for electrochemical biosensing. *Talanta 74*, 291–307.
(71) Jacobs, C. B., Peairs, M. J., and Venton, B. J. (2010) Review: Carbon nanotube based electrochemical sensors for biomolecules. *Anal. Chim. Acta 662*, 105–127.
(72) Rosen, Y., and Elman, N. M. (2009) Carbon nanotubes in drug delivery. *Exp. Opin. Drug Delivery 6*, 517–530.
(73) Amiot, C. L., Xu, S. P., Liang, S., Pan, L. Y., and Zhao, J. X. J. (2008) Near-infrared fluorescent materials for sensing of biological targets. *Sensors 8*, 3082–3105.
(74) Liang, F., and Chen, B. (2010) A review on biomedical applications of single-walled carbon nanotubes. *Curr. Med. Chem. 17*, 10–24.
(75) Bosi, S., Ros, T. D., Spalluto, G., and Prato, M. (2003) Fullerene derivatives: an attractive tool for biological applications. *Eur. J. Med. Chem. 38*, 913–923.
(76) Jensen, A. W., Wilson, S. R., and Schuster, D. I. (1996) Biological applications of fullerenes. *Bioorg. Med. Chem. 4*, 767–779.
(77) Nakamura, E., and Isobe, H. (2003) Functionalized fulleres in water. The first 10 years of their chemistry, biology, and nanoscience. *Acc. Chem. Res. 36*, 807–815.
(78) Chen, R. J., Zhang, Y. G., Wang, D. w., and Dai, H. J. (2001) Noncovalent sidewall functionalization of single-walled carbon nanotubes for protein immobilization. *J. Am. Chem. Soc. 123*, 3838–3839.
(79) Zhao, Y. L., and Stoddart, J. F. (2009) Noncovalent functionalization of single-walled carbon nanotubes. *Acc. Chem. Res. 42*, 1161–1171.
(80) Contarino, M. R., and Withey, G., Chaiken, I. (2009) Isotropic display of biomolecules on CNT-arrayed nanostructures, *Biosensing Using Nanomaterials* (Merkoçi, A., Ed.) pp 39−65, Chapter 2, John Wiley & Sons, Inc., Hoboken, NJ.
(81) Tasis, D., Tagmatarchis, N., Bianco, A., and Prato, M. (2006) Chemistry of carbon nanotubes. *Chem. Rev. 106*, 1105–1136.
(82) Karousis, K., Tagmatarchis, N., and Tasis, D. (2010) Current progress on the chemical modification of carbon nanotubes. *Chem. Rev. 110*, 5366–5397.
(83) Zhu, Y. W., Murali, S., Cai, W. W., Li, X. S., Suk, W. J., Potts, J. R., and Ruoff, R. S. (2010) Graphene and graphene oxide: Synthesis, properties, and applications. *Adv. Mater. 22*, 3906–3924.
(84) Rao, C. N. R., Sood, A. K., Subrahmanyam, K. S., and Govindaraj, A. (2009) Graphene: the new two-dimensional nanomaterial. *Angew. Chem., Int. Ed. 48*, 7752–7777.
(85) Shenderova, O. A., Zhirnov, V. V., and Brenner, D. W. (2002) Carbon nanostructures. *Crit. Rev. Solid State Mater. Sci. 27*, 227–356.
(86) Barnard, A. S. (2009) Diamond standard in diagnostics: nanodiamond biolabels make their mark. *Analyst 134*, 1751–1764.
(87) Caravan, P., Ellison, J. J., McMurry, T. J., and Lauffer, R. B. (1999) Gadolinium(III) chelates as MRI contrast agents: structure, dynamics, and applications. *Chem. Rev. 99*, 2293–2352.
(88) Dickson, E. F. G., Pollak, A., and Diamandis, E. P. (1995) Time-resolved detection of lanthanide luminescence for ultrasensitive bioanalytical assays. *J. Photochem. Photobiol. B 27*, 3–19.
(89) Eliseeva, S. V., and Bünzli, J. C. G. (2010) Lanthanide luminescence for functional materials and bio-sciences. *Chem. Soc. Rev. 39*, 189–227.
(90) Bünzli, J. C. G. (2010) Lanthanide luminescence for biomedical analyses and imaging. *Chem. Rev. 110*, 2729–2755.
(91) Wang, F., Banerjee, D., Liu, Y., Chen, X., and Liu, X. (2010) Upconversion nanoparticles in biological labeling, imaging, and therapy. *Analyst 135*, 1839–1854.
(92) Wang, F., and Liu, X. (2009) Recent advances in the chemistry of lanthanide-doped upconversion nanocrystals. *Chem. Soc. Rev. 38*, 976–989.

(93) Ong, L. C., Gnanasammandhan, M. K., Nagarajan, S., and Zhang, Y. (2010) Upconversion: road to El Dorado of the fluorescence world. *Luminesc. 25*, 290–293.
(94) Cheung, E. N. M., Alvares, R. D. A., Oakden, W., Chaudhary, R., Hill, M. L., Pichaandi, J., Mo, G. C. H., Yip, C., Macdonald, P. M., Stanisz, G. J., Veggel, F. C. J. M. v., and Prosser, R. S. (2010) Polymer-stabilized lanthanide fluoride nanoparticle aggregates as contrast agents for magnetic resonance imaging and computer tomography. *Chem. Mater. 22*, 4728–4739.
(95) Shen, J., Sun, L. D., and Yan, C. H. (2008) Luminescent rare earth nanomaterials for bioprobe applications. *Dalton Trans.* 5687–5697.
(96) Yan, Z. G., and Yan, C. H. (2008) Controlled synthesis of rare earth nanostructures. *J. Mater. Chem. 18*, 5046–5059.
(97) Feng, W., Sun, L. D., Zhang, Y. W., and Yan, C. H. (2010) Synthesis and assembly of rare earth nanostructures directed by the principle of coordination chemistry in solution-based process. *Coord. Chem. Rev. 254*, 1038–1053.
(98) Sivakumar, S., Diamente, P. R., and Veggel, F. C. v. (2006) Silica coated Ln(3+)-doped LaF_3 nanoparticls as robust down- and upconverting biolabels. *Chem.—Eur. J. 12*, 5878–5884.
(99) Gerion, D., Pinaud, F., Williams, S. C., Parak, W. J., Zanchet, D., Weiss, S., and Alivisatos, A. P. (2001) Synthesis and properties of biocompatible water-soluble silica-coated CdSe/ZnS semiconductor quantum dots. *J. Phys. Chem. B 105*, 8861–8871.
(100) Wolcott, A., Gerion, D., Visconte, M., Sun, J., Schwartzberg, A., Chen, S. W., and Zhang, J. Z. (2006) Silica-coated CdTe quantum dots functionalized with thiols for bioconjugation to IgG proteins. *J. Phys. Chem. B 110*, 5779–5789.
(101) Santra, S., Tapec, R., Theodoropoulou, N., Dobson, J., Hebard, A., and Tan, W. H. (2001) Synthesis and characterization of silica-coated iron oxide nanoparticles in microemulsion: The effect of nonionic surfactants. *Langmuir 17*, 2900–2906.
(102) Kobayashi, Y., Horie, M., Konno, M., Rodriguez-Gonzalez, B., and Liz-Marzan, L. M. (2003) Preparation and properties of silica-coated cobalt nanoparticles. *J. Phys. Chem. B 107*, 7420–7425.
(103) Lee, D. C., Mikulec, F. V., Pelaez, J. M., Koo, B., and Korgel, B. A. (2006) Synthesis and magnetic properties of silica-coated FePt nanocrystals. *J. Phys. Chem. B 110*, 11160–11166.
(104) Liu, S., and Han, M. Y. (2010) Silica-Coated Metal Nanoparticles. *Chem. Asian J. 5*, 36–45.
(105) Burns, A., Ow, H., and Wiesner, U. (2006) Fluorescent core-shell silica nanoparticles: towards "Lab on a Particle" architectures for nanobiotechnology. *Chem. Soc. Rev. 35*, 1028–1042.
(106) Haensch, C., Hoeppener, S., and Schubert, U. S. (2010) Chemical modification of self-assembled silane based monolayers by surface reactions. *Chem. Soc. Rev. 39*, 2323–2334.
(107) Knopp, D., Tang, D., and Niessner, R. (2009) Review: Bioanalytical applications of biomolecule-functionalized nanometer-sized doped silica particles. *Anal. Chim. Acta 647*, 14–30.
(108) Yan, J., Estévez, M. C., Smith, J. E., Wang, K., He, X., Wang, L., and Tan, W. (2007) Dye-doped nanoparticles for bioanalysis. *Nano Today 2*, 44–50.
(109) Vivero-Escoto, J. L., Slowing, I. I., Trewyn, B. G., and Lin, V. S. Y. (2010) Mesoporous silica nanoparticles for intracellular controlled drug delivery. *Small 6*, 1952–1967.
(110) Vallet-Regí, M., Balas, F., and Arcos, D. (2007) Mesoporous materials for drug delivery. *Angew. Chem., Int. Ed. 46*, 7548–7558.
(111) Guo, X., and Szoka, F. C. (2003) Chemical approaches to triggerable lipid vesicles for drug and gene delivery. *Acc. Chem. Res. 36*, 335–341.
(112) Torchilin, V. P. (2006) Multifunctional nanocarriers. *Adv. Drug Delivery Rev. 58*, 1532–1555.
(113) Discher, D. E., and Ahmed, F. (2006) Polymersomes. *Ann. Rev. Biomed. Eng. 8*, 323–341.
(114) Peer, D., Karp, J. M., Hong, S., Farokhzad, O. C., Margalit, R., and Langer, R. (2007) Nanocarriers as an emerging platform for cancer therapy. *Nat. Nanotechnol. 2*, 751–760.
(115) Bala, I., Hariharan, S., and Kumar, M. N. V. R. (2004) PLGA nanoparticles in drug delivery: The state of the art. *Crit. Rev. Therapeut. Drug Carrier Sys. 21*, 387–422.
(116) Boas, U., and Heegaard, P. M. H. (2004) Dendrimers in drug research. *Chem. Soc. Rev. 33*, 43–63.
(117) Esfand, R., and Tomalia, D. A. (2001) PAMAM dendrimers: from biomimicry to drug delivery and biomedical applications. *Drug Discovery Today 6*, 427–436.
(118) Franzen, S., and Lommel, S. A. (2009) Targeting cancer with 'smart bombs': equiping plant virus nanoparicles for a 'seek and destroy' mission. *Nanomedicine 4*, 575–588.
(119) Portney, N. G., and Ozkan, M. (2006) Nano-oncology: drug delivery, imaging, and sensing. *Anal. Bioanal. Chem. 384*, 620–630.
(120) Steinmetz, N. F. (2010) Viral nanoparticles as platforms for next-generation therapeutics and imaging devices. *Nanomedicine 6*, 634–641.
(121) Manchester, M., and Singh, P. (2006) Virus-based nanoparticles: Platform technologies for diagnostic imaging. *Adv. Drug Delivery Rev. 58*, 1505–1522.
(122) Hooker, J. M., Kovacs, E. W., and Francis, M. B. (2004) Interior surface modification of bacteriophage MS2. *J. Am. Chem. Soc. 126*, 3718–3719.
(123) Steinmetz, N. F., Lomonossoff, G. P., and Evans, D. J. (2006) Decoration of cowpea mosaic virus with multiple, redox-active organometallic complexes. *Small 2*, 530–533.
(124) Soto, C. M., and Ratna, B. R. (2010) Virus hybrids as nanomaterials for biotechnology. *Curr. Opin. Biotechnol. 21*, 426–438.
(125) Cao, Y. C., Jin, R., Nam, J. M., Thaxton, C. S., and Mirkin, C. A. (2003) Raman dye-labeled nanoparticle probes for proteins. *J. Am. Chem. Soc. 125*, 14676–14677.
(126) Faulds, K., Jarvis, R., Smith, W. E., and Graham, D. (2008) Multiplexed detection of six labelled oligonucleotides using surface enhanced resonance Raman scattering (SERRS). *Analyst 133*, 1505–1512.
(127) Faulds, K., McKenzie, F., Smith, W. E., and Graham, D. (2007) Quantitative simultaneous multianalyte detection of DNA by dual-wavelength surface-enhanced resonance Raman scattering. *Angew. Chem., Int. Ed. 46*, 1829–1831.
(128) Liu, J., Lau, S. K., Varma, V. A., Moffitt, R. A., Caldwell, M., Liu, T., Young, A. N., Petros, J. A., Osunkoya, A. O., Krogstad, T., Jones-Leyland, B., Wang, M. D., and Nie, S. M. (2010) Molecular mapping of tumor heterogeneity on clinical tissue specimens with multiplexed quantum dots. *ACS Nano 4*, 2755–2765.
(129) Farokhzad, O. C., Cheng, J. J., Teply, B. A., Sherifi, I., Jon, S., Kantoff, P. W., Richie, J. P., and Langer, R. (2006) Targeted nanoparticle-aptamer bioconjugates for cancer chemotherapy in vivo. *Proc. Natl. Acad. Sci. U.S.A 103*, 6315–6320.
(130) Cheng, S. H., Lee, C. H., Chen, M. C., Souris, J. S., Tseng, F. G., Yang, C. S., Mou, C. Y., Chen, C. T., and Lo, L. W. (2010) Tri-functionalization of mesoporous silica nanoparticles for comprehensive cancer theranostics-the trio of imaging, targeting and therapy. *J. Mater. Chem. 20*, 6149–6157.
(131) Samia, A. C. S., Dayal, S., and Burda, C. (2006) Quantum dot-based energy transfer: Perspectives and potential for application in photodynamic therapy. *Photochem. Photobiol. 82*, 617–625.
(132) Huang, X. H., Jain, P. K., El-Sayed, I. H., and El-Sayed, M. A. (2008) Plasmonic photothermal therapy using gold nanoparticles. *Lasers Med. Sci. 23*, 217–228.
(133) Lockett, M. R., Phillips, M. F., Jarecki, J. L., Peelen, D., and Smith, L. M. (2008) A tetrafluorophenyl activated ester self-assembled monolayer for the immobilization of amine-modified oligonucleotides. *Langmuir 24*, 69–75.
(134) Medintz, I. (2006) Universal tools for biomolecular attachment to surfaces. *Nat. Mater. 5*, 842–842.
(135) Mei, B. C., Susumu, K., Medintz, I. L., Delehanty, J. B., Mountziaris, T. J., and Mattoussi, H. (2008) Modular poly(ehtylene glycol) ligands for biocompatible semiconductor and gold nanocrystals with extended pH and ionic stability. *J. Mater. Chem. 18*, 4949–4958.

(136) Pathak, S., Davidson, M. C., and Silva, G. A. (2007) Characterizaton of the functional binding properties of antibody conjugated quantum dots. *Nano Lett. 7*, 1839–1845.
(137) Algar, W. R., and Krull, U. J. (2006) Adsorption and hybridization of oligonucleotides on mercaptoacetic acid-capped CdSe/ZnS quantum dots and quantum dot-oligonucleotide conjugates. *Langmuir 22*, 11346–11352.
(138) Li, H. X., and Rothberg, L. (2004) Colorimetric detection of DNA sequences based on electrostatic interactions with unmodified gold nanoparticles. *Proc. Natl. Acad. Sci. U.S.A 101*, 14036–14039.
(139) Zheng, M., Jagota, A., Semke, E. D., Diner, B. A., Mclean, R. S., Lustig, S. R., Richardson, R. E., and Tassi, N. G. (2003) DNA-assisted dispersion and separation of carbon nanotubes. *Nat. Mater. 2*, 338–342.
(140) Medintz, I. L., Clapp, A. R., Brunel, F. M., Tiefenbrunn, T., Uyeda, H. T., Chang, E. L., Deschamps, J. R., Dawson, P. E., and Mattoussi, H. (2006) Proteolytic activity monitored by fluorescence resonance energy transfer through quantum-dot-peptide conjugates. *Nat. Mater. 5*, 581–589.
(141) Banks, P. R., and Paquette, D. M. (1995) Comparison of three common amine reactive fluorescent probes used for conjugation to biomolecules by capillary zone electrophoresis. *Bioconjugate Chem. 6*, 447–458.
(142) Best, M. D. (2009) Click chemistry and bioorthogonal reactions: Unprecedented selectivity in the labeling of biological molecules. *Biochemistry 48*, 6571–6584.
(143) Prescher, J. A., and Bertozzi, C. R. (2005) Chemistry in living systems. *Nat. Chem. Biol. 1*, 13–21.
(144) Sletten, E. M., and Bertozzi, C. R. (2009) Bioorthogonal chemistry: Fishing for selectivity in a sea of functionality. *Angew. Chem., Int. Ed. 48*, 6974–6998.
(145) Devaraj, N. K., Weissleder, R., and Hilderbrand, S. A. (2008) Tetrazine-based cylcoadditions: Application to pretargeted live cell imaging. *Bioconjugate Chem. 19*, 2297–2299.
(146) Bundy, B. C., and Swartz, J. R. (2010) Site-specific incorporation of p-propargyloxyphenylalanine in a cell free environment for direct protein-protein click conjugation. *Bioconjugate Chem. 21*, 255–263.
(147) Huisgen, R. (1968) Cycloadditions: definition classification and characterization. *Angew. Chem., Int. Ed. 7*, 321–328.
(148) Moses, J. E., and Moorhouse, A. D. (2007) The growing applications of click chemistry. *Chem. Soc. Rev. 36*, 1249–1262.
(149) Meldal, M., and Tornoe, C. W. (2008) Cu-catalyzed azide-alkyne cycloaddition. *Chem. Rev. 108*, 2952–3015.
(150) Gupta, S. S., Raja, K. S., Kaltgrad, E., Strable, E., and Finn, M. G. (2005) Virus-glycopolymer conjugates by copper(I) catalysis of atom transfer radical polymerization and azide-alkyne cycloaddition. *Chem. Commun.* 4315–4317.
(151) Hong, V., Presolski, S. I., Ma, C., and Finn, M. G. (2009) Analysis and optimization of copper-catalyzed azide-alkyne cycloaddition for bioconjugation. *Angew. Chem., Int. Ed. 48*, 9879–9883.
(152) Steinmetz, N. F., Mertens, M. E., Taurog, R. E., Johnson, J. E., Commandeur, U., Fischer, R., and Manchester, M. (2009) Potato virus X as a novel platform for potential biomedical applications. *Nano Lett. 10*, 305–312.
(153) Wang, Q., Chan, T. R., Hilgraf, R., Fokin, V. V., Sharpless, K. B., and Finn, M. G. (2003) Bioconjugation by copper(I)-catalyzed azide-alkyne [3 + 2] cycloaddition. *J. Am. Chem. Soc. 125*, 3192–3193.
(154) Strable, E., Prasuhn, D. E., Udit, A. K., Brown, S., Link, A. J., Ngo, J. T., Lander, G., Quispe, J., Potter, C. S., Carragher, B., Tirrell, D. A., and Finn, M. G. (2008) Unnatural amino acid incorporation into virus-like particles. *Bioconjugate Chem. 19*, 866–875.
(155) Gupta, S. S., Kuzelka, J., Singh, P., Lewis, W. G., Manchester, M., and Finn, M. G. (2005) Accelerated bioorthogonal conjugation: A practical method for the ligation of diverse functional molecules to a polyvalent virus scaffold. *Bioconj. Chem. 16*, 1572–1579.
(156) Prasuhn, D. E., Yeh, R. M., Obenaus, A., Manchester, M., and Finn, M. G. (2007) Viral MRI contrast agents: coordination of Gd by native virions and attachment of Gd complexes by azide-alkyne cycloaddition. *Chem. Commun.* 1269–1271.
(157) Singh, P., Prasuhn, D., Yeh, R. M., Destito, G., Rae, C. S., Osborn, K., Finn, M. G., and Manchester, M. (2007) Bio-distribution, toxicity and pathology of cowpea mosaic virus nanoparticles in vivo. *J. Controlled Release 120*, 41–50.
(158) Kussrow, A., Kaltgrad, E., Wolfenden, M. L., Cloninger, M. J., Finn, M. G., and Bornhop, D. J. (2009) Measurement of monovalent and polyvalent carbohydrate-lectin binding by back-scattering interferometry. *Anal. Chem. 81*, 4889–4897.
(159) Kaltgrad, E., O'Reilly, M. K., Liao, L., Han, S., Paulson, J. C., and Finn, M. G. (2008) On-virus construction of polyvalent glycan ligands for cell-surface receptors. *J. Am. Chem. Soc. 130*, 4578–4579.
(160) Kaltgrad, E., Gupta, S. S., Punna, S., Huang, C.-Y., Chang, A., Wong, C.-H., Finn, M. G., and Blixt, O. (2007) Anti-carbohydrate antibodies elicited by polyvalent display on a viral scaffold. *ChemBioChem 8*, 1455–1462.
(161) Udit, A. K., Everett, C., Gale, A. J., Kyle, J. R., Ozkan, M., and Finn, M. G. (2009) Heparin antagonism by polyvalent display of cationic motifs on virus-like particles. *ChemBioChem 10*, 503–510.
(162) Destito, G., Yeh, R., Rae, C. S., Finn, M. G., and Manchester, M. (2007) Folic acid-mediated targeting of cowpea mosaic virus particles to tumor cells. *Chem. Biol. 14*, 1152–1162.
(163) Prasuhn, D. E., Singh, P., Strable, E., Brown, S., Manchester, M., and Finn, M. G. (2008) Plasma clearance of bacteriophage Qβ particles as a function of surface charge. *J. Am. Chem. Soc. 130*, 1328–1334.
(164) Steinmetz, N. F., Hong, V., Spoerke, E. D., Lu, P., Breitenkamp, K., Finn, M. G., and Manchester, M. (2009) Buckyballs meet viral nanoparticles: Candidates for biomedicine. *J. Am. Chem. Soc. 131*, 17093–17095.
(165) Gole, A., and Murphy, C. J. (2008) Azide-derivatized gold nanorods: Functional materials for "click" chemistry. *Langmuir 24*, 266–272.
(166) Brennan, J. L., Hatzakis, N. S., Tshikhudo, T. R., Razumas, V., Patkar, S., Vind, J., Svendsen, A., Nolte, R. J. M., Rowan, A. E., and Brust, M. (2006) Bionanoconjugation via click chemistry: The creation of functional hybrids of lipases and gold nanoparticles. *Bioconjugate Chem. 17*, 1373–1375.
(167) Kim, Y.-P., Daniel, W. L., Xia, Z., Xie, H., Mirkin, C. A., and Rao, J. (2010) Bioluminescent nanosensors for protease detection based upon gold nanoparticle-luciferase conjugates. *Chem. Commun. 46*, 76–78.
(168) Fischler, M., Sologubenko, A., Mayer, J., Clever, G., Burley, G., Gierlich, J., Carell, T., and Simon, U. (2008) Chain-like assembly of gold nanoparticles on artificial DNA templates via 'click chemistry'. *Chem. Commun.* 169–171.
(169) Lin, P.-C., Ueng, S.-H., Yu, S.-C., Jan, M.-D., Adak, A. K., Yu, C.-C., and Lin, C.-C. (2007) Surface modification of magnetic nanoparticles via Cu(I)-catalyzed alkyne-azide [2 + 3] cycloaddition. *Org. Lett. 9*, 2131–2134.
(170) Polito, L., Monti, D., Caneva, E., Delnevo, E., Russo, G., and Prosperi, D. (2008) One-step bioengineering of magnetic nanoparticles via a surface diazo transfer/azide-alkyne click reaction sequence. *Chem. Commun.* 621–623.
(171) El-Boubbou, K., Gruden, C., and Huang, X. (2007) Magnetic glyco-nanoparticles: A unique tool for rapid pathogen detection, decontamination, and strain differentiation. *J. Am. Chem. Soc. 129*, 13392–13393.
(172) Achatz, D. E., Heiligtag, F. J., Li, X., Link, M., and Wolfbeis, O. S. (2010) Colloidal silica nanoparticles for use in click chemistry-based conjugations and fluorescent affinity assays. *Sens. Actuators, B 150*, 211–219.
(173) Mader, H. S., Link, M., Achatz, D. E., Uhlmann, K., Li, X., and Wolfbeis, O. S. (2010) Surface-modified upconverting microparticles and nanoparticles for use in click chemistries. *Chem.—Eur. J. 16*, 5416–5424.
(174) Pereira, G. R., Santos, L. J., Luduvico, I., Alves, R. B., and de Freitas, R. P. (2010) 'Click' chemistry as a tool for the facile synthesis of fullerene glycoconjugate derivatives. *Tetrahedron Lett. 51*, 1022–1025.

(175) Palacin, T., Khanh, H. L., Jousselme, B., Jegou, P., Filoramo, A., Ehli, C., Guldi, D. M., and Campidelli, S. (2009) Efficient functionalization of carbon nanotubes with porphyrin dendrons via click chemistry. *J. Am. Chem. Soc. 131*, 15394–15402.

(176) Campidelli, S., Ballesteros, B., Filoramo, A., Diaz, D. D., de la Torre, G., Torres, T., Rahman, G. M. A., Ehli, C., Kiessling, D., Werner, F., Sgobba, V., Guldi, D. M., Cioffi, C., Prato, M., and Bourgoin, J.-P. (2008) Facile decoration of functionalized single-wall carbon nanotubes with phthalocyanines via "click chemistry. *J. Am. Chem. Soc. 130*, 11503–11509.

(177) Guo, Z., Liang, L., Liang, J.-J., Ma, Y.-F., Yang, X.-Y., Ren, D.-M., Chen, Y.-S., and Zheng, J.-Y. (2008) Covalently β-cyclodextrin modified single-walled carbon nanotubes: a novel artificial receptor synthesized by 'click' chemistry. *J. Nanopart. Res. 10*, 1077–1083.

(178) van Dijk, M., Rijkers, D. T. S., Liskamp, R. M. J., van Nostrum, C. F., and Hennink, W. E. (2009) Synthesis and applications of biomedical and pharmaceutical polymers via click chemistry methodologies. *Bioconjugate Chem. 20*, 2001–2016.

(179) Dondoni, A. (2007) Triazole: The keystone in glycosylated molecular architectures constructed by a click reaction. *Chem. Asian J. 2*, 700–708.

(180) Iha, R. K., Wooley, K. L., Nystrom, A. M., Burke, D. J., Kade, M. J., and Hawker, C. J. (2009) Applications of orthogonal "click" chemistries in the synthesis of functional soft materials. *Chem. Rev. 109*, 5620–5686.

(181) Hong, V., Presolski, S. I., Ma, C., and Finn, M. G. (2009) Analysis and optimization of copper-catalyzed azide-alkyne cycloaddition for bioconjugation. *Angew. Chem., Int. Ed. 48*, 9879–9883.

(182) Agard, N. J., Prescher, J. A., and Bertozzi, C. R. (2004) A strain-promoted [3 + 2] azide-alkyne cycloaddition for covalent modification of biomolecules in living Systems. *J. Am. Chem. Soc. 126*, 15046–15047.

(183) Baskin, J. M., Prescher, J. A., Laughlin, S. T., Agard, N. J., Chang, P. V., Miller, I. A., Lo, A., Codelli, J. A., and Bertozzi, C. R. (2007) Copper-free click chemistry for dynamic in vivo imaging. *Proc. Natl. Acad. Sci. U.S.A. 104*, 16793–16797.

(184) Jewett, J. C., and Bertozzi, C. R. (2010) Cu-free click cycloaddition reactions in chemical biology. *Chem. Soc. Rev. 39*, 1272–1279.

(185) Zou, Y., and Yin, J. (2008) Cu-free cycloaddition for identifying catalytic active adenylation domains of nonribosomal peptide synthetases by phage display. *Bioorg. Med. Chem. Lett. 18*, 5664–5667.

(186) Xinghai, N., Jun, G., Margreet, A. W., and Geert-Jan, B. (2008) Visualizing metabolically labeled glycoconjugates of living cells by copper-free and fast Huisgen cycloadditions. *Angew. Chem., Int. Ed. 47*, 2253–2255.

(187) Laughlin, S. T., Baskin, J. M., Amacher, S. L., and Bertozzi, C. R. (2008) In vivo imaging of membrane-associated glycans in developing zebrafish. *Science 320*, 664–667.

(188) Bernardin, A., Cazet, A., Guyon, L., Delannoy, P., Vinet, F., Bonnaffe, D., and Texier, I. (2010) Copper-free click chemistry for highly luminescent quantum dot conjugates: Application to in vivo metabolic imaging. *Bioconjugate Chem. 21*, 583–588.

(189) Lallana, E., Fernandez-Megia, E., and Riguera, R. (2009) Surpassing the use of copper in the click functionalization of polymeric nanostructures: A strain-promoted approach. *J. Am. Chem. Soc. 131*, 5748–5750.

(190) Blackman, M. L., Royzen, M., and Fox, J. M. (2008) Tetrazine ligation: fast bioconjugation based on inverse-electron-demand diels-alder reactivity. *J. Am. Chem. Soc. 130*, 13518–13519.

(191) Han, H. S., Devaraj, N. K., Lee, J., Hilderbrand, S. A., Weissleder, R., and Bawendi, M. G. (2010) Development of bioorthogonal and highly efficiency conjugation method for quantum dots using tetrazine-norbornene cycloaddition. *J. Am. Chem. Soc. 132*, 7838–7839.

(192) Haun, J. B., Devaraj, N. K., Hilderbrand, S. A., Lee, H., and Weissleder, R. (2010) Bioorthogonal chemistry amplifies nanoparticle binding and enhances the sensitivity of cell detection. *Nat. Nanotechnol. 5*, 660–665.

(193) Shi, M., Wosnick, J. H., Ho, K., Keating, A., and Shoichet, M. S. (2007) Immuno-polymeric nanoparticles by Diels-Alder chemistry. *Angew. Chem., Int. Ed. 46*, 6126–6131.

(194) Staudinger, H., and Meyer, J. (1919) On new organic phosphorus binding III Phosphine methylene derivatives and phosphinimine. *Helv. Chim. Acta 2*, 635–646.

(195) Saxon, E., and Bertozzi, C. R. (2000) Cell surface engineering by a modified Staudinger reaction. *Science 287*, 2007–2010.

(196) Maja, K., and Rolf, B. (2004) The Staudinger ligation - A gift to chemical biology. *Angew. Chem., Int. Ed. 43*, 3106–3116.

(197) Saxon, E., Armstrong, J. I., and Bertozzi, C. R. (2000) A "traceless" staudinger ligation for the chemoselective synthesis of amide bonds. *Org. Lett. 2*, 2141–2143.

(198) Soellner, M. B., Nilsson, B. L., and Raines, R. T. (2002) Staudinger ligation of α-azido acids retains stereochemistry. *J. Org. Chem. 67*, 4993–4996.

(199) Zhang, H., Ma, Y., and Sun, X.-L. (2009) Chemically-selective surface glyco-functionalization of liposomes through Staudinger ligation. *Chem. Commun.* 3032–3034.

(200) Parkhouse, S. M., Garnett, M. C., and Chan, W. C. (2008) Targeting of polyamidoamine-DNA nanoparticles using the Staudinger ligation: Attachment of an RGD motif either before or after complexation. *Bioorg. Med. Chem. 16*, 6641–6650.

(201) Dirksen, A., and Dawson, P. E. (2008) Rapid oxime and hydrazone ligations with aromatic aldehydes for biomolecular labeling. *Bioconjugate Chem. 19*, 2543–2548.

(202) Dirksen, A., Dirksen, S., Hackeng, T. M., and Dawson, P. E. (2006) Nucleophilic catalysis of hydrazone formation and transimination: implications for dynamic covalent chemistry. *J. Am. Chem. Soc. 128*, 15602–15603.

(203) Brunel, F. M., Lewis, J. D., Destito, G., Steinmetz, N. F., Machester, M., Stuhlmann, H., and Dawson, P. E. (2010) Hydrazone ligation strategy to assemble multifunctional viral nanoparticles for cell imaging and tumor targeting. *Nano Lett. 10*, 1093–1097.

(204) Prasuhn, D. E., Blanco-Canosa, J. B., Vora, G. J., Delehanty, J. B., Susumu, K., Mei, B. C., Dawson, P. E., and Medintz, I. L. (2010) Combining chemoselective ligation with polyhistidine-driven self-assembly for the modular display of biomolecules on quantum dots. *ACS Nano 4*, 267–278.

(205) Blanco-Canosa, J. B., Medintz, I. L., Farrell, D., Mattoussi, H., and Dawson, P. E. (2010) Rapid covalent ligation of fluorescent peptides to water solubilized quantum dots. *J. Am. Chem. Soc. 132*, 10027–10033.

(206) Banerjee, S. S., and Chen, D. H. (2008) Multifunctional pH-sensitive magnetic nanoparticles for simultaneous imaging, sensing and targeted intracellular anticancer drug delivery. *Nanotechnology 19*, 505104.

(207) Yuan, Q., Venkatasubramanian, R., Hein, S., and Misra, R. D. K. (2008) A stimulus-responsive magnetic nanoparticle drug carrier: magnetite encapsulated by chitosan-grafted-copolymer. *Acta Biomater. 4*, 1024–1037.

(208) Aryal, S., Grailer, J. J., Pilla, S., Steeber, D. A., and Gong, S. (2009) Doxorubicin conjugated gold nanoparticles as water-soluble and pH-responsive anticancer drug nanocarriers. *J. Mater. Chem. 19*, 7879–7884.

(209) Prabaharan, M., Grailer, J. J., Pilla, S., Steeber, D. A., and Gong, S. (2009) Gold nanoparticles with a monolayer of doxorubicin-conjugated amphiphilic block copolymer for tumor-targeted drug delivery. *Biomaterials 30*, 6065–6075.

(210) Aryal, S., Hu, C. M. J., and Zhang, L. (2010) Polymer-cisplatin conjugate nanoparticles for acid-responsive drug delivery. *ACS Nano 4*, 251–258.

(211) Zeng, Y., Ramya, T. N. C., Dirksen, A., Dawson, P. E., and Paulson, J. C. (2009) High efficiency labeling of sialylated glycoproteins on living cells. *Nat. Methods 6*, 207–209.

(212) Beaudette, T. T., Cohen, J. A., Bachelder, E. M., Broaders, K. E., Cohen, J. L., Engleman, E. G., and Fréchet, J. M. J. (2009) Chemoselective ligation in the functionalization of polysaccharide-based particles. *J. Am. Chem. Soc. 131*, 10360–10361.

(213) Thygesen, M. B., Sorensen, K. K., Cló, E., and Jensen, K. J. (2009) Direct chemoselective synthesis of glyconanoparticles from unprotected reducing glycans and glycopeptide aldehydes. *Chem. Commun.* 6367–6369.

(214) Thygesen, M. B., Sauer, J., and Jensen, K. J. (2009) Chemoselective capture of glycans for analysis on gold nanoparticles: carbohydrate oxime tautomers provide functional recognition by proteins. *Chem.—Eur. J. 15*, 1649–1660.

(215) Liu, Y., Feizi, T., Carnpanero-Rhodes, M. A., Childs, R. A., Zhang, Y., Mulloy, B., Evans, P. G., Osborn, H. M. I., Otto, D., Crocker, P. R., and Chai, W. (2007) Neoglycolipid probes prepared via oxime ligation for microarray analysis of oligosaccharide-protein interactions. *Chem. Biol. 14*, 847–859.

(216) Kovacs, E. W., Hooker, J. M., Romanini, D. W., Holder, P. G., Berry, K. E., and Francis, M. B. (2007) Dual-surface-modified bacteriophage MS2 as an ideal scaffold for a viral capsid-based drug delivery system. *Bioconjugate Chem. 18*, 1140–1147.

(217) Dawson, P. E., and Kent, S. B. H. (2000) Synthesis of native proteins by chemical ligation. *Annu. Rev. Biochem. 69*, 923–960.

(218) Dawson, P. E., Muir, T. W., Clark-Lewis, I., and Kent, S. B. (1994) Synthesis of proteins by native chemical ligation. *Science 226*, 776–779.

(219) Dawson, P. E., Churchill, M. J., Ghadiri, M. R., and Kent, S. B. H. (1997) Modulation of reactivity in native chemical ligation through the use of thiol additives. *J. Am. Chem. Soc. 119*, 4325–4329.

(220) Reulen, S. W. A., Baal, I. v., Raats, J. M. H., and Merkx, M. (2009) Efficient, chemoselective synthesis of immunomicelles using single-domain antibodies with a C-terminal thioester. *BMC Biotechnol. 9*, 66.

(221) Reulen, S. W. A., Dankers, P. Y. W., Bomans, P. H. H., Meijer, E. W., and Merkx, M. (2009) Collagen targeting using protein-functionalized micelles: the strength of multiple weak interactions. *J. Am. Chem. Soc. 131*, 7304–7312.

(222) Reulen, S. W. A., Brusselaars, W. W. T., Langereis, S., Mulder, W. J. M., Breurken, M., and Merkx, M. (2007) Protein-Liposome conjugates using cysteine-lipids and native chemical ligation. *Bioconjugate Chem. 18*, 590–596.

(223) Yu, C. C., Lin, P. C., and Lin, C. C. (2008) Site-specific immobilization of CMP-sialic acid synthetase on magnetic nanoparticles and its use in the synthesis of CMP-sialic acid. *Chem. Commun.* 1308–1310.

(224) Becker, C. F. W., Marsac, Y., Hazarika, P., Moser, J., Goody, R. S., and Niemeyer, C. M. (2007) Functional immobilization of small GTPase Rab6A on DNA-gold nanoparticles by using a site-specifically attached poly(ethylene gylcol) linker and thiol place-exchange reaction. *ChemBioChem 8*, 32–36.

(225) Evans, T. C., and Xu, M. Q. (2002) Mechanistic and kinetic considerations of protein splicing. *Chem. Rev. 102*, 4869–4883.

(226) Muir, T. W. (2003) Semisynthesis of proteins by expressed protein ligation. *Annu. Rev. Biochem. 72*, 249–289.

(227) Perler, F. B., and Adam, E. (2000) Protein splicing and its applications. *Curr. Opin. Biotechnol. 11*, 377–383.

(228) Miller, L. W., and Cornish, V. W. (2005) Selective chemical labeling of proteins in living cells. *Curr. Opin. Chem. Biol. 9*, 56–61.

(229) Gogarten, J. P., Senejani, A. G., Zhaxybayeva, O., Olendzenski, L., and Hilario, E. (2002) Inteins: Structure, function, and evolution. *Annu. Rev. Microbiol. 56*, 263–287.

(230) Camarero, J. A. (2008) Recent developments in the site-specific immobilization of proteins onto solid supports. *Biopolymers 90*, 450–458.

(231) Xia, Z. Y., Xing, Y., So, M. K., Koh, A. L., Sinclair, R., and Rao, J. H. (2008) Multiplex detection of protease activity with quantum dot nanosensors prepared by intein-mediated specific bioconjugation. *Anal. Chem. 80*, 8649–8655.

(232) Chu, N. K., Olschewski, D., Seidel, R., Winklhofer, K. F., Tatzelt, J., Engelhard, M., and Becker, C. F. W. (2010) Protein immobilization on liposomes and lipid-coated nanoparticles by protein trans-splicing. *J. Pept. Sci. 16*, 582–588.

(233) Datta, A., Hooker, J. M., Botta, M., Francis, M. B., Aime, S., and Raymond, K. N. (2008) High relaxivity gadolinium hydroxypyridonate-viral capsid conjugates: Nanosized MRI contrast agents. *J. Am. Chem. Soc. 130*, 2546–2552.

(234) Hooker, J. M., O'Neil, J. P., Romanini, D. W., Taylor, S. E., and Francis, M. B. (2008) Genome-free viral capsids as carriers for positron emission tomography radiolabels. *Mol. Imaging Biol. 10*, 182–191.

(235) Kovacs, E. W., Hooker, J. M., Romanini, D. W., Holder, P. G., Berry, K. E., and Francis, M. B. (2007) Dual-surface-modified bacteriophage MS2 as an ideal scaffold for a viral capsid-based drug delivery system. *Bioconjugate Chem. 18*, 1140–1147.

(236) Hooker, J. M., Datta, A., Botta, M., Raymond, K. N., and Francis, M. B. (2007) Magnetic resonance contrast agents from viral capsid shells: A comparison of exterior and interior cargo strategies. *Nano Lett. 7*, 2207–2210.

(237) Schlick, T. L., Ding, Z., Kovacs, E. W., and Francis, M. B. (2005) Dual-surface modification of the tobacco mosaic virus. *J. Am. Chem. Soc. 127*, 3718–3723.

(238) Bruckman, M. A., Kaur, G., Lee, L. A., Xie, F., Sepulveda, J., Breitenkamp, R., Zhang, X., Joralemon, M., Russell, T. P., Emrick, T., and Wang, Q. (2008) Surface modification of tobacco mosaic virus with "click" chemistry. *ChemBioChem 9*, 519–523.

(239) Carrico, Z. M., Romanini, D. W., Mehl, R. A., and Francis, M. B. (2008) Oxidative coupling of peptides to a virus capsid containing unnatural amino acids. *Chem. Commun.* 1205–1207.

(240) Stephanopoulos, N., Carrico, Z. M., and Francis, M. B. (2009) Nanoscale integration of sensitizing chromophores and porphyrins with bacteriophage MS2. *Angew. Chem., Int. Ed. 48*, 9498–9502.

(241) Tong, G. J., Hsiao, S. C., Carrico, Z. M., and Francis, M. B. (2009) Viral capsid DNA aptamer conjugates as multivalent cell-targeting vehicles. *J. Am. Chem. Soc. 131*, 11174–11178.

(242) Irrgang, J., Ksienczyk, J., Lapiene, V., and Niemeyer, C. M. (2009) Analysis of non-covalent bioconjugation of colloidal nanoparticles by means of atomic force microscopy and data clustering. *ChemPhysChem 10*, 1483–1491.

(243) Delehanty, J. B., Medintz, I. L., Pons, T., Brunel, F. M., Dawson, P. E., and Mattoussi, H. (2006) Self-assembled quantum dot-peptide bioconjugates for selective intracellular delivery. *Bioconjugate Chem. 17*, 920–927.

(244) Sapsford, K. E., Pons, T., Medintz, I. L., Higashiya, S., Brunel, F. M., Dawson, P. E., and Mattoussi, H. (2007) Kinetics of metal-affinity driven self-assembly between proteins or peptides and CdSe-ZnS quantum dots. *J. Phys. Chem. C 111*, 11528–11538.

(245) Pons, T., Medintz, I. L., Wang, X., English, D. S., and Mattoussi, H. (2006) Solution-phase single quantum dot fluorescence resonance energy transfer. *J. Am. Chem. Soc. 128*, 15324–15331.

(246) Medintz, I. L., Konnert, J. H., Clapp, A. R., Stanish, I., Twigg, M. E., Mattoussi, H., Mauro, J. M., and Deschamps, J. R. (2004) A fluorescence resonance energy transfer-derived structure of a quantum dot-protein bioconjugate nanoassembly. *Proc. Natl. Acad. Sci. U.S.A. 101*, 9612–9617.

(247) Medintz, I. L., Sapsford, K. E., Clapp, A. R., Pons, T., Higashiya, S., Welch, J. T., and Mattoussi, H. (2006) Designer variable repeat length polypeptides as scaffolds for surface immobilization of quantum dots. *J. Phys. Chem. B 110*, 10683–10690.

(248) Pons, T., Medintz, I. L., Sapsford, K. E., Higashiya, S., Grimes, A. F., English, D. S., and Mattoussi, H. (2007) On the quenching of semiconductor quantum dot photoluminescence by proximal gold nanoparticles. *Nano Lett. 7*, 3157–3164.

(249) Medintz, I. L., Berti, L., Pons, T., Grimes, A. F., English, D. S., Alessandrini, A., Facci, P., and Mattoussi, H. (2007) A reactive peptidic linker for self-assembling hybrid quantum dot-DNA bioconjugates. *Nano Lett. 7*, 1741–1748.

(250) Berti, L., D'Agostino, P. S., Boeneman, K., and Medintz, I. L. (2009) Improved peptidyl linkers for self-assembly of semiconductor quantum dot bioconjugates. *Nano Res. 2*, 121–129.

(251) Medintz, I. L., Pons, T., Delehanty, J. B., Susumu, K., Brunel, F. M., Dawson, P. E., and Mattoussi, H. (2008) Intracellular delivery of

quantum dot-protein cargos mediated by cell penetrating peptides. *Bioconjugate Chem. 19*, 1785–1795.

(252) Clapp, A. R., Medintz, I. L., Mauro, J. M., Fisher, B. R., Bawendi, M. G., and Mattoussi, H. (2003) Fluorescence resonance energy transfer between quantum dot donors and dye-labeled protein acceptors. *J. Am. Chem. Soc. 126*, 301–310.

(253) Medintz, I. L., Clapp, A. R., Melinger, J. S., Deschamps, J. R., and Mattoussi, H. (2005) A reagentless biosensing assembly based on quantum dot-donor Förster resonance energy transfer. *Adv. Mater. 17*, 2450–2455.

(254) Goldman, E. R., Medintz, I. L., Whitley, J. L., Hayhurst, A., Clapp, A. R., Uyeda, H. T., Deschamps, J. R., Lassman, M. E., and Mattoussi, H. (2005) A hybrid quantum dot-antibody fragment fluorescence resonance energy transfer-based TNT sensor. *J. Am. Chem. Soc. 127*, 6744–6751.

(255) Boeneman, K., Mei, B. C., Dennis, A. M., Bao, G., Deschamps, J. R., Mattoussi, H., and Medintz, I. L. (2009) Sensing caspase 3 activity with quantum dot-fluorescent protein assemblies. *J. Am. Chem. Soc. 131*, 3828–3829.

(256) Medintz, I. L., Clapp, A. R., Mattoussi, H., Goldman, E. R., Fisher, B., and Mauro, J. M. (2003) Self-assembled nanoscale biosensors based on quantum dot FRET donors. *Nat. Mater. 2*, 630–638.

(257) Medintz, I. L., Sapsford, K. E., Clapp, A. R., Pons, T., Higashiya, S., Welch, J. T., and Mattoussi, H. (2006) Designer variable repeat length polypeptides as scaffolds for surface immobilization of quantum dots. *J. Phys. Chem. B 110*, 10683–10690.

(258) Sapsford, K. E., Medintz, I. L., Golden, J. P., Deschamps, J. R., Uyeda, H. T., and Mattoussi, H. (2004) Surface-immobilized self-assembled protein-based quantum dot nanoassemblies. *Langmuir 20*, 7720–7728.

(259) Ipe, B. I., and Niemeyer, C. M. (2006) Nanohybrids composed of quantum dots and cytochrome P450 as photocatalysts. *Angew. Chem., Int. Ed. 45*, 504–507.

(260) Lee, I. S., Lee, N., Park, J., Kim, B. H., Yi, Y. W., Kim, T., Kim, T. K., Lee, I. H., Paik, S. R., and Hyeon, T. (2006) Ni/NiO core/shell nanoparticles for selective binding and magnetic separation of histidine-tagged proteins. *J. Am. Chem. Soc. 128*, 10658–10659.

(261) Kogot, J. M., England, H. J., Strouse, G. F., and Logan, T. M. (2008) Single peptide assembly onto a 1.5 nm Au surface via a histidine tag. *J. Am. Chem. Soc. 130*, 16156–16157.

(262) Kogot, J. M., Parker, A. M., Lee, J., Blaber, M., and Strouse, G. F. (2009) Analysis of the dynamics of assembly and structural impact for a histidine tagged FGF1−1.5 nm gold nanoparticle bioconjugate. *Bioconjugate Chem. 20*, 2106–2113.

(263) Prasuhn, D. E., Kuzelka, J., Strable, E., Udit, A. K., Cho, S.-H., Lander, G. C., Quispe, J. D., Diers, J. R., Bocian, D. F., Potter, C., Carragher, B., and Finn, M. G. (2008) Polyvalent display of heme on hepatitis B virus capsid protein through coordination to hexahistidine tags. *Chem. Biol. 15*, 513–519.

(264) Udit, A. K., Hollingsworth, W., and Choi, K. (2010) Metal- and metallocycle-binding sites engineered into polyvalent virus-like scaffolds. *Bioconjugate Chem. 21*, 399–404.

(265) Kim, M. J., Park, H. Y., Kim, J., Ryu, J., Hong, S., Han, S. J., and Song, R. (2008) Western blot analysis using metal-nitrilotriacetate conjugated CdSe/ZnS quantum dots. *Anal. Biochem. 379*, 124–126.

(266) Gupta, M., Caniard, A., Touceda-Varela, A., Campopiano, D. J., and Mareque-Rivas, J. C. (2008) Nitrilotriacetic acid-derivatized quantum dots for simple purification and site-selective fluorescent labeling of active proteins in a single step. *Bioconjugate Chem. 19*, 1964–1967.

(267) Bae, P. K., Kim, K. N., Lee, S. J., Chang, H. J., Lee, C. K., and Park, J. K. (2009) The modification of quantum dot probes used for the targeted imaging of his-tagged fusion proteins. *Biomaterials 30*, 836–842.

(268) Susumu, K., Medintz, I. L., Delehanty, J. B., Boeneman, K., and Mattoussi, H. (2010) Modification of poly(ethylene glycol)-capped quantum dots with nickel nitrilioacetic acid and self-assembly with hisitidine-tagged proteins. *J. Phys. Chem. C 114*, 13526–13531.

(269) Lee, S. K., Maye, M. M., Zhang, Y. B., Gang, O., and van der Lelie, D. (2009) Controllable g5p-protein-directed aggregatin of ssDNA-gold nanoparticles. *Langmuir 25*, 657–660.

(270) Graff, R. A., Swanson, T. M., and Strano, M. S. (2008) Synthesis of Ni-NTA coupled single-walled carbon nanotubes for directed self-assembly with polyhistidine-tagged proteins. *Chem. Mater. 20*, 1824–1829.

(271) Kim, I., Park, Y. H., Rey, D. A., and Batt, C. A. (2008) Silica-deposited phospholipid nanotubes as a plausible drug targeting system. *J. Drug Targeting 16*, 716–722.

(272) Kim, S. H., Jeyakumar, M., and Katzenellenbogen, J. A. (2007) Dual-mode fluorophore-doped nickel nitrilotriacetic acid-modified silica nanoparticles combine histidine-tagged protein purification with site-specific fluorophore labeling. *J. Am. Chem. Soc. 129*, 13254–13264.

(273) Xie, H. Y., Zhen, R., Wang, B., Feng, Y. J., Chen, P., and Hao, J. (2010) Fe3O4/Au core/shell nanoparticles modified with Ni2+-nitrilotriacetic acid specific to histidine protein. *J. Phys. Chem. C 114*, 4825–4830.

(274) ShiXing, W., Sun, W., and Zhou, Y. (2010) Preparation of Cu^{2+}/NTA-derivatized branch polyglycerol magnetic nanoparticles for protein adsorption. *J. Nanopart. Res. 12*, 2467–2472.

(275) Park, H. Y., Kim, K., Hong, S., Kim, H., Choi, Y., Ryu, J., Kwon, D., Grailhe, R., and Song, R. (2009) Compact and versatile nickel-nitrilotriacetate-modified quantum dots for protein imaging and Förster resonance energy transfer based assay. *Langmuir 26*, 7327–7333.

(276) Abad, J. M., Mertens, S. F. L., Pita, M., Fernández, V. M., and Schiffrin, D. J. (2005) Functionalization of thioctic acid-capped gold nanoparticles for specific immobilization of histidine-tagged proteins. *J. Am. Chem. Soc. 127*, 5689–5694.

(277) Yao, H., Zhang, Y., Xiao, F., Xia, Z., and Rao, J. H. (2007) Quantum dot/bioluminescence resonance energy transfer for highly sensitive detection of proteases. *Angew. Chem., Int. Ed. 46*, 4346–4349.

(278) Boeneman, K., Delehanty, J. B., Susumu, K., Stewart, M. H., and Medintz, I. L. (2010) Intracellular bioconjugation to targeted proteins with semiconductor quantum dots. *J. Am. Chem. Soc. 132*, 5975–5977.

(279) Sandros, M. G., Gao, D., Gokdemir, C., and Benson, D. E. (2005) General high-affinity approach for the synthesis of fluorophore appended protein nanoparticle assemblies. *Chem. Commun.* 2832–2834.

(280) Shete, V., and Benson, D. E. (2009) Protein design provides lead(II) ion biosensors for imaging molecular fluxes around red blood cells. *Biochemistry 48*, 462–470.

(281) Ariyasu, S., Onoda, A., Sakamoto, R., and Yamamura, T. (2009) Alignment of gold clusters on DNA via a DNA-recognizing zinc finger-metallothionein fusion protein. *Bioconjugate Chem. 20*, 2278–2285.

(282) Ariyasu, S., Onoda, A., Sakamoto, R., and Yamamura, T. (2009) Conjugation of Au11 cluster with Cys-rich peptides containing the alpha-domain of metallothionein. *Dalton Trans.* 3742–3747.

(283) Park, T. J., Lee, S. Y., Heo, N. S., and Seo, T. S. (2010) In vivo synthesis of diverse metal nanoparticles by recombinant Escherichia coli. *Angew. Chem., Int. Ed. 49*, 7019–7024.

(284) Griffin, B. A., Adams, S. R., and Tsien, R. Y. (1998) Specific covalent labeling of recombinant protein molecules inside live cells. *Science 281*, 269–272.

(285) Adams, S. R., Campbell, R. E., Gross, L. A., Martin, B. R., Walkup, G. K., Yao, Y., Llopis, J., and Tsien, R. Y. (2002) New biarsenical ligands and tetracysteine motifs for protein labeling in vitro and in vivo: Synthesis and biological applications. *J. Am. Chem. Soc. 124*, 6063–6076.

(286) Cao, H., Chen, B., Squier, T. C., and Mayer, M. U. (2006) CrAsH: a biarsenical multi-use affinity probe with low non-specific fluorescence. *Chem. Commun.* 2601–2603.

(287) Genin, E., Carion, O., Mahler, B., Dubertret, B., Arhel, N., Charneau, P., Doris, E., and Mioskowski, C. (2008) CrAsH-quantum dot nanohybrids for smart targeting of proteins. *J. Am. Chem. Soc. 130*, 8596–8597.

(288) Green, N. M. (1963) Avidin. 1. Use of [14C]Biotin for kinetic studies and for assay. *Biochem. J. 89*, 585–591.

(289) Schatz, P. J. (1993) Use of peptide libraries to map the substrate-specficity of a peptide-modifying enzyme - A 13 residue consensus peptide specficies biotinylation in Escherichia-coli. *Bio-Technology 11*, 1138–1143.

(290) Medintz, I. L., Anderson, G. P., Lassman, M. E., Goldman, E. R., Bettencourt, L. A., and Mauro, J. M. (2004) General strategy for biosensor design and construction employing multifunctional surface-tethered components. *Anal. Chem. 76*, 5620–5629.

(291) Chen, I., Howarth, M., Lin, W. Y., and Ting, A. Y. (2005) Site-specific labeling of cell surface proteins with biophysical probes using biotin ligase. *Nat. Methods 2*, 99–104.

(292) O'Hare, H. M., Johnsson, K., and Gautier, A. (2007) Chemical probes shed light on protein function. *Curr. Opin. Struct. Biol. 17*, 488–494.

(293) Howarth, M., Takao, K., Hayashi, Y., and Ting, A. Y. (2005) Targeting quantum dots to surface proteins in living cells with biotin ligase. *Proc. Natl. Acad. Sci. U.S.A 102*, 7583–7588.

(294) Chen, I., Choi, Y. A., and Ting, A. Y. (2007) Phage display evolution of a peptide substrate for yeast biotin ligase and application to two-color quantum dot labeling of cell surface proteins. *J. Am. Chem. Soc. 129*, 6619–6625.

(295) Sunbul, M., Yen, M., Zou, Y. K., and Yin, J. (2008) Enzyme catalyzed site-specific protein labeling and cell imaging with quantum dots. *Chem. Commun.* 5927–5929.

(296) Roullier, V., Clarke, S., You, C., Pinaud, F., Gouzer, G., Schaible, D., Marchi-Artzner, V., Piehler, J., and Dahan, M. (2009) High-affinity labeling and tracking of individual histidine-tagged proteins in live cells using Ni^{2+}-nitrilotriacetic acid quantum dot conjugates. *Nano Lett. 9*, 1228–1234.

(297) Stachler, M. D., Chen, I., Ting, A. Y., and Bartlett, J. S. (2008) Site-specific modification of AAV vector particles with biophysical probes and targeting ligands using biotin ligase. *Mol. Ther. 16*, 1467–1473.

(298) Maeda, Y., Yoshino, T., Takahashi, M., Ginya, H., Asahina, J., Tajima, H., and Matsunaga, T. (2008) Noncovalent immobilization of streptavidin on in vitro- and in vivo-biotinylated bacterial magnetic particles. *Appl. Environ. Microbiol. 74*, 5139–5145.

(299) George, N., Pick, H., Vogel, H., Johnsson, N., and Johnsson, K. (2004) Specific labeling of cell surface proteins with chemically diverse compounds. *J. Am. Chem. Soc. 126*, 8896–8897.

(300) Gehring, A. M., Lambalot, R. H., Vogel, K. W., Drueckhammer, D. G., and Walsh, C. T. (1997) Ability of Streptomyces spp acyl carrier proteins and coenzyme A analogs to serve as substrates in vitro for E-coli holo-ACP synthase. *Chem. Biol. 4*, 17–24.

(301) Bonasio, R., Carman, C. V., Kim, E., Sage, P. T., Love, K. R., Mempel, T. R., Springer, T. A., and Andrian, U. H. v. (2007) Specific and covalent labeling of a membrane protein with organic fluorochromes and quantum dots. *Proc. Natl. Acad. Sci. U.S.A. 104*, 14753–14758.

(302) Zheng, M., and Huang, X. Y. (2004) Nanoparticles comprising a mixed monolayer for specific bindings with biomolecules. *J. Am. Chem. Soc. 126*, 12047–12054.

(303) Terpe, K. (2003) Overview of tag protein fusions: from molecular and biochemical fundamentals to commercial systems. *Appl. Microbiol. Biotechnol. 60*, 523–533.

(304) Los, G. V., Darzins, A., Karassina, N., Zimprich, C., Learish, R., McDougall, M. G., Encell, L. P., Friedman-Ohana, R., Wood, M., Vidugiris, G., Zimmerman, K., Otto, P., Klaubert, D. H., and Wood, K. V. (2005) HaloTag Interchangeable labeling technology for cell imaging and protein capture. *Cell Notes 11*, 2–6.

(305) Zhang, Y., So, M. K., Loening, A. M., Yao, H. Q., Gambhir, S. S., and Rao, J. H. (2006) HaloTag protein-mediated site-specific conjugation of bioluminescent proteins to quantum dots. *Angew. Chem., Int. Ed. 45*, 4936–4940.

(306) So, M. K., Yao, H. Q., and Rao, J. H. (2008) HaloTag protein-mediated specific labeling of living cells with quantum dots. *Biochem. Biophys. Res. Commun. 374*, 419–423.

(307) Bernardes, G. J. L., Chalker, J. M., Errey, J. C., and Davis, B. G. (2008) Facile conversion of cysteine and alkyl cysteines to dehydroalanine on protein surfaces: Versatile and switchable access to functionalized proteins. *J. Am. Chem. Soc. 130*, 5052–5053.

(308) Okeley, N. M., Zhu, Y. T., and Donk, W. A. v. d. (2000) Facile chemoselective synthesis of dehydroalanine-containing peptides. *Org. Lett. 2*, 3603–3606.

(309) Wang, J., Schiller, S. M., and Schultz, P. G. (2007) A Biosynthetic route to dehydroalanine-containing proteins. *Angew. Chem., Int. Ed. 46*, 6849–6851.

(310) Seebeck, F. P., and Szostak, J. W. (2006) Ribosomal synthesis of dehydroalanine-containing peptides. *J. Am. Chem. Soc. 128*, 7150–7151.

(311) Dommerholt, J., Schmidt, S., Temming, R., Hendriks, L. J. A., Rutjes, F. P. J. T., Hest, J. C. M. v., Lefeber, D. J., Friedl, P., and van Delft, F. L. (2010) Readily accessible bicyclononynes for bioorthogonal labeling and three-dimensional imaging of living cells. *Angew. Chem., Int. Ed. 49*, 9422–9425.

(312) Ning, X., Temming, R. P., Dommerholt, J., Guo, J., Ania, D. B., Debets, M. F., Wolfert, M. A., Boons, G. J., and Delft, F. L. v. (2010) Protein modification by strain-promoted alkyne-nitrone cycloaddition. *Angew. Chem., Int. Ed. 49*, 3065–3068.

(313) Allen, V. C., Philp, D., and Spencer, N. (2001) Transfer of stereochemical information in a minimal self-replicating system. *Org. Lett. 3*, 777–780.

(314) Song, W., Wang, J., Qu, J., Madden, M. M., and Lin, Q. (2008) A photoinducible 1,3-dipolar cycloaddition reaction for rapid, selective modification of tetrazole-containing proteins. *Angew. Chem., Int. Ed. 47*, 2832–2835.

(315) Song, W., Wang, Y., Qu, J., and Lin, Q. (2008) Selective functionalization of a genetically encoded alkene-containing protein via "Photoclick Chemistry" in bacterial cells. *J. Am. Chem. Soc. 130*, 9654–9655.

(316) Guo, H.-M., Minakawa, M., Ueno, L., and Tanaka, F. (2009) Synthesis and evaluation of a cyclic imine derivative conjugated to a fluorescent molecule for labeling of proteins. *Bioorg. Med. Chem. Lett. 19*, 1210–1213.

(317) Joshi, N. S., Whitaker, L. R., and Francis, M. B. (2004) A three-component Mannich-type reaction for selective tyrosine bioconjugation. *J. Am. Chem. Soc. 126*, 15942–15943.

(318) Romanini, D. W., and Francis, M. B. (2007) Attachment of peptide building blocks to proteins through tyrosine bioconjugation. *Bioconjugate Chem. 19*, 153–157.

(319) Ban, H., Gavrilyuk, J., and C., F. B., III (2010) Tyrosine bioconjugation through aqueous ene-type reactions: A click-like reaction for tyrosine. *J. Am. Chem. Soc. 132*, 1523–1525.

(320) Gilmore, J. M., Scheck, R. A., Esser-Kahn, A. P., Joshi, N. S., and Francis, M. B. (2006) N-Terminal protein modification through a biomimetic transamination reaction. *Angew. Chem., Int. Ed. 45*, 5307–5311.

(321) Scheck, R. A., Dedeo, M. T., Iavarone, A. T., and Francis, M. B. (2008) Optimization of a biomimetic transamination reaction. *J. Am. Chem. Soc. 130*, 11762–11770.

(322) Scheck, R. A., and Francis, M. B. (2007) Regioselective labeling of antibodies through N-terminal transamination. *ACS Chem. Biol. 2*, 247–251.

(323) Lin, Y. A., Chalker, J. M., Floyd, N., Bernardes, G. J. L., and Davis, B. G. (2008) Allyl sulfides are privileged substrates in aqueous cross-metathesis: Application to site-selective protein modification. *J. Am. Chem. Soc. 130*, 9642–9643.

(324) Binder, J. B., and Raines, R. T. (2008) Olefin metathesis for chemical biology. *Curr. Opin. Chem. Biol. 12*, 767–773.

(325) Lin, Y. A., Chalker, J. M., and Davis, B. G. (2009) Olefin metathesis for site-selective protein modification. *ChemBioChem 10*, 959–969.

(326) Grubbs, R. H. (2003) *Handbook of Metathesis*, Wiley-VCH, Weinheim.

(327) Hoveyda, A. H., and Zhugralin, A. R. (2007) The remarkable metal-catalysed olefin metathesis reaction. *Nature 450*, 243–251.

(328) Alois, F. (2000) Olefin metathesis and beyond. *Angew. Chem., Int. Ed. 39*, 3012–3043.

(329) Garber, S. B., Kingsbury, J. S., Gray, B. L., and Hoveyda, A. H. (2000) Efficient and recyclable monomeric and dendritic Ru-based metathesis catalysts. *J. Am. Chem. Soc. 122*, 8168–8179.

(330) Mortell, K. H., Gingras, M., and Kiessling, L. L. (1994) Synthesis of cell agglutination inhibitors by aqueous ring-opening metathesis polymerization. *J. Am. Chem. Soc. 116*, 12053–12054.
(331) Miyaura, N., and Suzuki, A. (1995) Palladium-catalyzed cross-coupling reactions of organoboron compounds. *Chem. Rev. 95*, 2457–2483.
(332) Brustad, E., Bushey, M. L., Lee, J. W., Groff, D., Liu, W., and Schultz, P. G. (2008) A genetically encoded boronate-containing amino acid. *Angew. Chem., Int. Ed. 47*, 8220–8223.
(333) Ojida, A., Tsutsumi, H., Kasagi, N., and Hamachi, I. (2005) Suzuki coupling for protein modification. *Tetrahedron Lett. 46*, 3301–3305.
(334) Chalker, J. M., Wood, C. S. C., and Davis, B. G. (2009) A convenient catalyst for aqueous and protein Suzuki-Miyaura cross-coupling. *J. Am. Chem. Soc. 131*, 16346–16347.
(335) Heck, R. F. (1979) Palladium-catalyzed reactions of organic halides with olefins. *Acc. Chem. Res. 12*, 146–151.
(336) Chinchilla, R., and Najera, C. (2007) The Sonogashira reaction: A booming methodology in synthetic organic chemistry. *Chem. Rev. 107*, 874–922.
(337) Kodama, K., Fukuzawa, S., Nakayama, H., Kigawa, T., Sakamoto, K., Yabuki, T., Matsuda, N., Shirouzu, M., Takio, K., Tachibana, K., and Yokoyama, S. (2006) Regioselective carbon-carbon bond formation in proteins with palladium catalysis: New protein chemistry by organometallic chemistry. *ChemBioChem 7*, 134–139.
(338) Kodama, K., Fukuzawa, S., Nakayama, H., Sakamoto, K., Kigawa, T., Yabuki, T., Matsuda, N., Shirouzu, M., Takio, K., Yokoyama, S., and Tachibana, K. (2007) Site-specific functionalization of proteins by organopalladium reactions. *ChemBioChem 8*, 232–238.
(339) Dibowski, H., and Schmidtchen, F. P. (1998) Bioconjugation of peptides by palladium-catalyzed C-C cross-coupling in water. *Angew. Chem., Int. Ed. 37*, 476–478.
(340) Bong, D. T., and Ghadiri, M. R. (2001) Chemoselective Pd(0)-catalyzed peptide coupling in water. *Org. Lett. 3*, 2509–2511.
(341) Lee, S.-W., Mao, C., Flynn, C. E., and Belcher, A. M. (2002) Ordering of quantum dots using genetically engineered viruses. *Science 296*, 892–895.
(342) Nam, Y. S., Magyar, A. P., Lee, D., Kim, J.-W., Yun, D. S., Park, H., Pollom, T. S., Weitz, D. A., and Belcher, A. M. (2010) Biologically templated photocatalytic nanostructures for sustained light-driven water oxidation. *Nat. Nanotechnol. 5*, 340–344.
(343) Nam, K. T., Wartena, R., Yoo, P. J., Liau, F. W., Lee, Y. J., Chiang, Y.-M., Hammond, P. T., and Belcher, A. M. (2008) Stamped microbattery electrodes based on self-assembled M13 viruses. *Proc. Natl. Acad. Sci. U.S.A 105*, 17227–17231.
(344) Keppler, A., Gendreizig, S., Gronemeyer, T., Pick, H., Vogel, H., and Johnsson, K. (2003) A general method for the covalent labeling of fusion proteins with small molecules in vivo. *Nat. Biotechnol. 21*, 86–89.
(345) Gautier, A., Juillerat, A., Heinis, C., Correa, I. R., Kindermann, M., Beaufils, F., and Johnsson, K. (2008) An engineered protein tag for multiprotein labeling in living cells. *Chem. Biol. 15*, 128–136.
(346) Miller, L. W., Cai, Y. F., Sheetz, M. P., and Cornish, V. W. (2005) In vivo protein labeling with trimethoprim conjugates: a flexible chemical tag. *Nat. Methods 2*, 255–257.
(347) Lin, C. W., and Ting, A. Y. (2006) Transglutaminase-catalyzed site-specific conjugation of small-molecule probes to proteins in vitro and on the surface of living cells. *J. Am. Chem. Soc. 128*, 4542–4543.
(348) Fernandez-Suarez, M., Baruah, H., Martinez-Hernandez, L., Xie, K. T., Baskin, J. M., Bertozzi, C. R., and Ting, A. Y. (2007) Redirecting lipoic acid ligase for cell surface protein labeling with small-molecule probes. *Nat. Biotechnol. 25*, 1483–1487.

Bioconjugate Chemistry

COMMUNICATION

pubs.acs.org/bc

Synthesis and Evaluation of a Bimodal CXCR4 Antagonistic Peptide

Joeri Kuil,[#,†] Tessa Buckle,[#,†] Hushan Yuan,[‡] Nynke S. van den Berg,[†] Shinya Oishi,[§] Nobutaka Fujii,[§] Lee Josephson,[‡] and Fijs W. B. van Leeuwen*[,†]

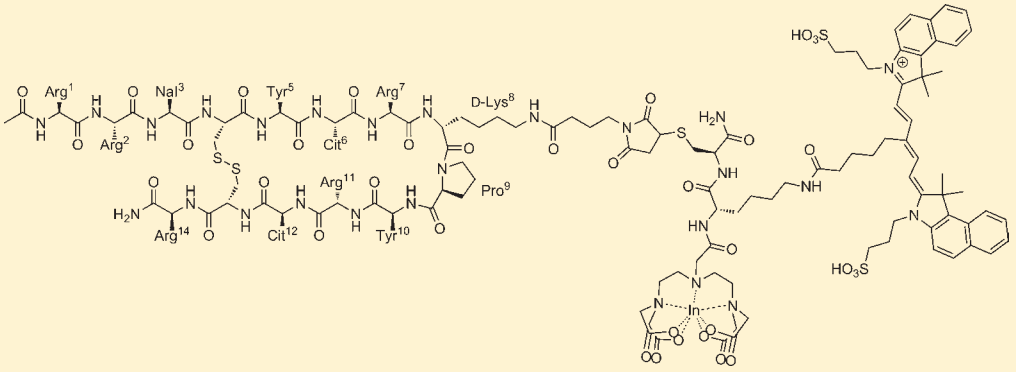
[†]Division of Diagnostic Oncology, The Netherlands Cancer Institute, Antoni van Leeuwenhoek Hospital, 1066 CX Amsterdam, The Netherlands

[‡]Center for Molecular Imaging Research, Massachusetts General Hospital and Harvard Medical School, Building 149, 13th Street, Charlestown, Massachusetts 02129, United States

[§]Department of Bioorganic Medicinal Chemistry, Graduate School of Pharmaceutical Sciences, Kyoto University, Kyoto, Japan

Supporting Information

ABSTRACT:



The antagonistic Ac-TZ14011 peptide, which binds to the chemokine receptor 4, has been labeled with a multifunctional single attachment point reagent that contains a DTPA chelate and a fluorescent dye with Cy5.5 spectral properties. Flow cytometry and confocal microscopy showed that the bimodal labeled peptide gave a specific receptor binding that is similar to monofunctionalized peptide derivatives. Therefore, the newly developed bimodal peptide derivative can be used in multimodal imaging applications.

The chemokine receptor 4 (CXCR4) is a G-protein-coupled membrane receptor which is present in various cell types.[1,2] Besides its expression in normal tissues, a 5.5-fold upregulation of CXCR4-expression was found in breast cancer tissue,[3] and CXCR4 upregulation is reported for at least 22 other types of cancer.[4,5] CXCR4 has also been shown to play a critical role in (breast) cancer progression and metastatic spread.[6,7] Because of its prominent role in oncology, overexpression of CXCR4 has been suggested to be of value in imaging applications.[8,9]

For molecular imaging of cancer-related biomarkers, several modalities are in use, including SPECT, PET, MRI, and fluorescence imaging.[10] Each modality has its own strengths and weaknesses, and therefore, often a combination of modalities is needed during the clinical trajectory.[11−14] Recently, we have shown the added value of multimodal imaging agents in surgical guidance.[15−17] In this application, combined pre- and intraoperative imaging is achieved, whereby surgical planning is based on the radioactive signal and optical surgical guidance is achieved via the fluorescent component. This application can be expanded to tumor targeting peptides.[13]

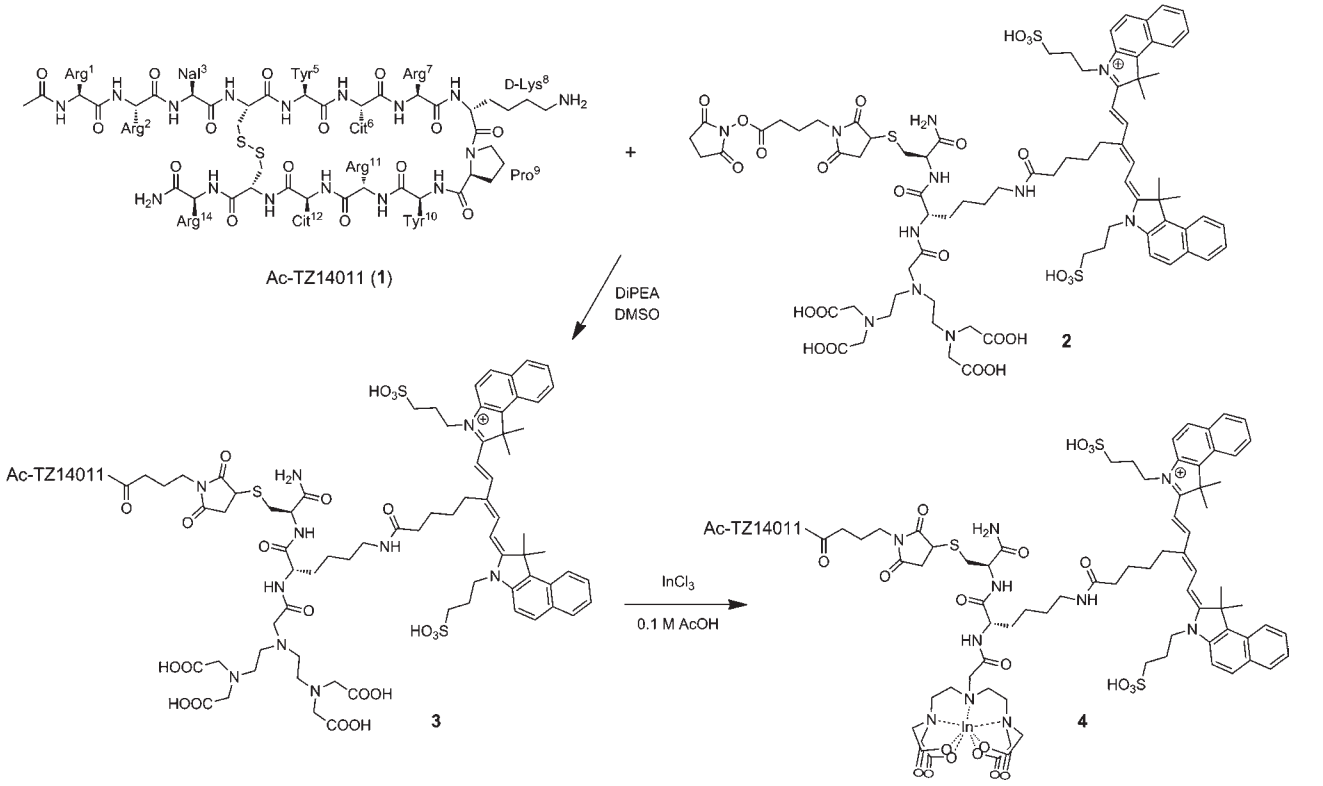
For an imaging agent to be detectable in multiple modalities, it needs to contain at least two different diagnostic labels. As we recently summarized, the combination of radiolabels for SPECT or PET, and fluorescent labels in particular, has potential in peptide-based molecular imaging.[13] This combination benefits from the high sensitivity of nuclear imaging and the high spatial resolution of fluorescence imaging[14] and allows the use of stoichiometric 1:1 labels.[13]

Several CXCR4 antagonistic peptides have been reported.[18,19] One of the most potent peptides, T140, is a 14 amino acid containing disulfide-bridged peptide with a rigid β-hairpin conformation.[20] Residues 2, 3, 5, and 14 of T140 are mainly responsible for CXCR4 binding, whereas the residues 7−10 in the type II′ β-turn do not have direct contacts with CXCR4 within 3.0 Å.[21] Recently, a crystal structure of CXCR4 with the horseshoe crab peptide polyphemusin analogue CVX15, which is similar to T140, confirmed that residues 2, 3, 5, and 14 form important interactions with the receptor.[22] T140 has been optimized to Ac-TZ14011 for better CXCR4 binding, higher *in vivo* stability, and easier functionalization, i.e., in Ac-TZ14011

Received: February 21, 2011
Revised: March 16, 2011
Published: April 12, 2011

ACS Publications © 2011 American Chemical Society

Scheme 1. Conjugation of the MSAP Label (2) to Ac-TZ14011 (1) and Subsequent Indium Labeling



only one amine group is present (D-Lys[8]).[23−25] The binding of dye- and chelate-labeled Ac-TZ14011 peptides to CXCR4 has already been validated *in vitro* and *in vivo*;[13,23−25] the specificity of Ac-TZ14011 for CXCR4 has been underlined by the fact that a scrambled peptide and a peptide with inversed stereocenters could not label CXCR4 expressing cells.[26] However, a multimodal derivative of this CXCR4-targeting peptide has not yet been reported.

Here, we report the conjugation of a multimodal imaging label (also referred to as multifunctional single-attachment-point, MSAP, reagent[27,28]) to Ac-TZ14011. We have performed *in vitro* validation studies to examine the influence of the MSAP label on the specificity and receptor affinity and we report initial *in vivo* experiments.

The bimodal peptide derivative was generated using the MSAP reagent (**2**), which bears a DTPA and a CyAL-5.5$_b$ fluorochrome reporter and a reactive NHS ester.[27−29] The synthesis of the MSAP reagent **2** is described in the Supporting Information. Via the active NHS ester, it was selectively coupled to the D-Lys[8] amine functionality on Ac-TZ14011 (**1**; see Scheme 1). The resulting peptide derivative Ac-TZ14011-MSAP (**3**) was purified with preparative HPLC and characterized using mass spectrometry. To study the possible influence of chelation of a metal ion in the DTPA moiety, a portion of Ac-TZ14011-MSAP (**3**) was coordinated to (nonradioactive) indium, yielding Ac-TZ14011-MSAP-In **4** (Scheme 1).

The absorption spectra of **3** and **4** were analogous and also the emission spectra were very similar (see Supporting Information Figure S1). In both cases, the absorption maximum was found at 680 nm and the emission maximum at 704 nm. Moreover, the fluorescent signal intensity was not reduced when indium was bound in the DTPA-chelate.

Table 1. Quantitative Analysis of Cellular Uptake of MDAMB231 and MDAMB231^{CXCR4+} Cells Using a CXCR4 Antibody and the Peptides 3 and 4[a]

compound	MFIR ± SD MDAMB231	MFIR ± SD MDAMB231^{CXCR4+}	ratio of MFIRs
12G5-PE antibody	1.116 ± 0.054	4.920 ± 1.46	4.4
3	10.94 ± 1.62	45.27 ± 2.19	4.1
4	18.24 ± 1.93	56.67 ± 2.84	3.1

[a] MFIR = mean fluorescence intensity ratio.

The ability of peptides **3** and **4** to discriminate between basal and CXCR4 overexpressing tumor cells was quantitatively examined with flow cytometry. As a reference "golden standard", the commercially available phycoerythrin (PE) labeled anti-CXCR4 antibody CD184, clone 12G5 (12G5-PE), was used. The 12G5-PE antibody showed that the higher CXCR4 expressing cells, MDAMB231^{CXCR4+}, had a 4.4× upregulation of CXCR4 compared to the basal cell line MDAMB231 (Table 1). This ratio of 4.4 is an intrinsic property of the two cell lines, and therefore, a peptide-based probe which can also obtain this ratio performs as well as the antibody. The ratio of the fluorescent signals found for peptide derivative **3** was 4.1, which nicely corresponds to the ratio obtained with the antibody (Figure 1 and Table 1). This indicates that this peptide is equally suited to detect CXCR4-expression levels.

The mean fluorescence intensity ratios (MFIRs) for Ac-TZ14011-MSAP (**3**) were approximately 10 times higher than

dx.doi.org/10.1021/bc2000947 |*Bioconjugate Chem.* 2011, 22, 859–864

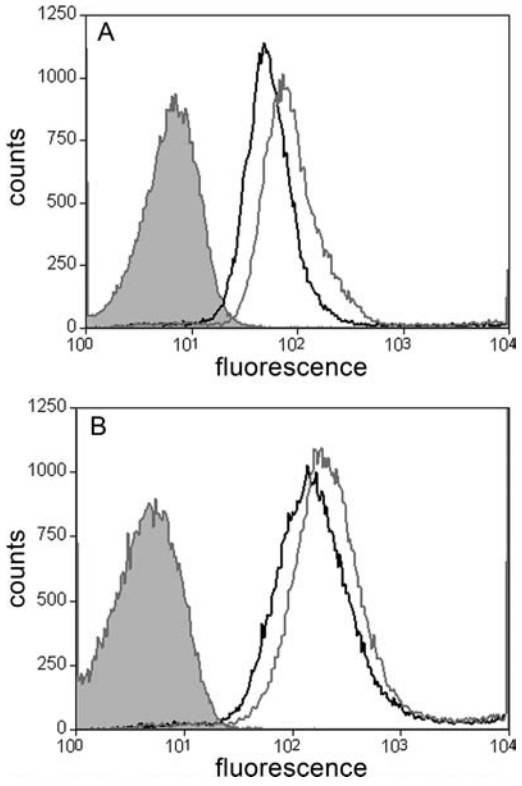


Figure 1. Flow cytometry analysis of the peptides **3** and **4** using (A) MDAMB231 cells or (B) MDAMB231^{CXCR4+} cells. Both graphs show untreated cells (trace filled with gray), 1 μM of **3** (black trace), and 1 μM of **4** (gray trace).

that of the antibody (Table 1). This difference is probably caused by the fact that the concentration used for the antibody was significantly lower than that of the peptides, 6.4 nM and 1 μM, respectively. Moreover, due to the lower autofluorescence with the flow cytometer settings used with the MSAP peptides, the voltage of the photomultiplier detector could be set higher when the MSAP peptides were measured, compared to the PE-labeled antibody.

For Ac-TZ14011-MSAP-In (**4**), the obtained uptake ratio for the MDAMB231^{CXCR4+} and MDAMB231 cells was somewhat lower, namely, 3.1 (Table 1). Since both cell types had a higher MFIR (Table 1), this is perhaps caused by an increase in nonspecific binding of **4** to the cells (Figure 1). The increased nonspecific binding most likely is a charge-related effect. The DPTA chelate in peptide **3** is mainly −2 charged (four carboxylates and two protonated nitrogen atoms), and indium-bound DTPA in **4** has a charge of −1 (four carboxylates, no protonated nitrogen atoms and In^{3+}),[30,31] increasing the hydrophobicity of the imaging label. In general, labels with increased hydrophobicity drive (nonspecific) cellular uptake.[13]

In general, conjugation of a bifunctional imaging label to a peptide reduces the receptor affinity.[13] Therefore, we have thoroughly studied the influence of our MSAP-label in peptides **3** and **4** on receptor binding and compared it to that of monofunctionalized derivatives and the parental peptide. Initially, we determined the dissociation constants (K_D) of **3** and **4** by a saturation binding assay (Figure 2A). The K_D value of **3** was used to determine the K_D values of Ac-TZ14011-DTPA (**5**), Ac-TZ14011-FITC (**6**), and Ac-TZ14011 (**1**) with competition experiments (Figure 2B,C).

Incubation of MDAMB231^{CXCR4+} cells with different concentrations of Ac-TZ14011-MSAP (**3**) yielded a binding curve that appears to exist out of two components (Figure 2A). The nonlinear component of the binding curve can be ascribed to specific receptor binding and the linear component to nonspecific cell binding. By using this binding model, it was not needed to determine the nonspecific binding directly. The K_D of Ac-TZ14011-MSAP (**3**) derived from this curve was 186.9 nM (Table 2). The indium labeled derivative Ac-TZ14011-MSAP-In (**4**) again gave somewhat higher fluorescent values (see Figure 1 and Figure 2A) and a K_D of 177.1 nM (Table 2). The similarity in the CXCR4-receptor affinities of **3** and **4** indicates that indium binding does not affect the interaction with CXCR4.

To compare the receptor affinities of **3** and **4** with the other peptide derivatives, different amounts of Ac-TZ14011 (**1**), Ac-TZ14011-DTPA (**5**), or Ac-TZ14011-FITC (**6**) were added in the presence of 250 nM of Ac-TZ14011-MSAP (**3**) (Figure 2B,C). All three peptide derivatives could compete with Ac-TZ14011-MSAP (**3**) for CXCR4 binding, confirming the specific CXCR4 binding of Ac-TZ14011-MSAP (**3**). The K_D values, obtained by fitting the inhibition curves with a competition model, of the monolabeled peptides Ac-TZ14011-DTPA (**5**) and Ac-TZ14011-FITC (**6**) were in the order of the K_D values of **3** and **4** (Table 2). These results illustrate that the bifunctional MSAP label does not hamper receptor binding more than the smaller FITC and DTPA labels. However, the unlabeled Ac-TZ14011 peptide **1** gave an approximately 20× higher receptor affinity than derivatives **3** and **4** (Table 2). Since the affinity of Ac-TZ14011-MSAP-In (**4**) remains in the nanomolar range, this decrease is not likely to be an obstruction for using **4** in molecular imaging applications.[32] The previously reported scrambled peptide TR14010 (**7**) showed no significant binding; K_D > 5000 nM (Table 2, see Supporting Information for the structure of TR14011).[26]

Molecular modeling studies showed that D-Lys^8 in T140 has no interactions with CXCR4.[21] Furthermore, the crystal structure of CVX15, which is similar to T140, with CXCR4 also showed no crucial interactions.[22] However, we found that D-Lys^8 functionalization in Ac-TZ14011 still influences binding affinity. This influence might be explained by looking at the different effects modifications of the peptide can have on (CXCR4) receptor binding. A modification on the peptide (i) can directly change a receptor interaction (e.g., a hydrogen bond), (ii) can change the 3D structure of the peptide, and/or (iii) can hinder the phamacophore to bind properly to the receptor via steric hindrance.[21] Here, the third effect is most likely to cause the drop in affinity.

A logical chemical modification to reduce the steric hindrance would be the incorporation of a larger spacer between the imaging label and the pharmacophore. Although it has been shown that incorporation of a 6-aminocaproic acid spacer does not yield a higher affinity,[24] it is possible that longer spacers will be more effective. However, this influence of the spacer still is under investigation.

Next to validating the receptor affinity of peptide **3**, also its cellular distribution needs to overlap with the locations where the G-protein-coupled receptor CXCR4 is most likely to be expressed, namely, the cell membranes.[1,2] Confocal microscopy imaging of MDAMB231^{CXCR4+} cells incubated with **3** indeed revealed clear cell membrane staining (Figure 3). The incubation

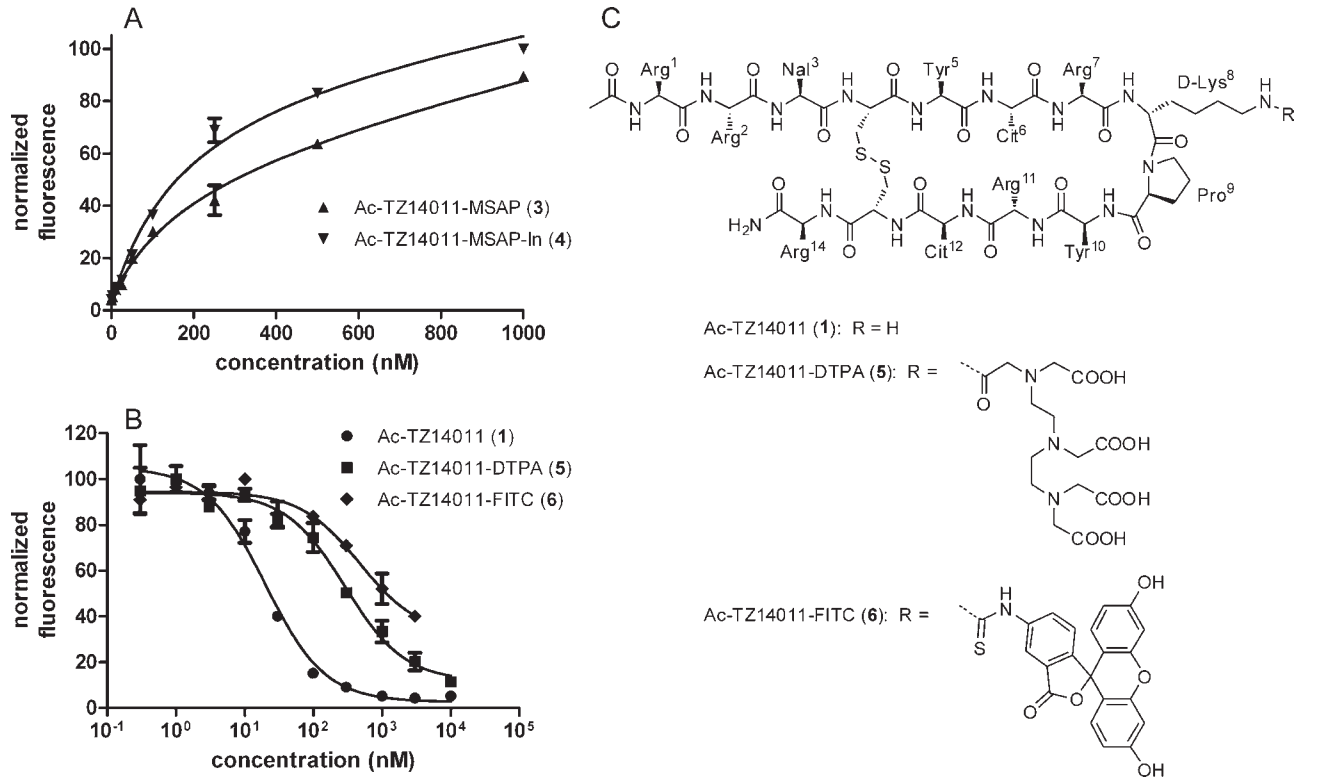


Figure 2. (A) Determination of affinity of constructs **3** and **4** with saturation binding experiments. (B) Competition experiments with three other Ac-TZ14011 peptides in the presence of 250 nM of **3**. (C) Structures of the peptides used for competition experiments.

Table 2. Dissociations Constants (K_D) of the Constructs

construct	K_D (nM)
Ac-TZ14011-unlabeled (**1**)	8.61 ± 1.42
Ac-TZ14011-MSAP (**3**)	186.9 ± 52.4
Ac-TZ14011-MSAP-In (**4**)	177.1 ± 37.2
Ac-TZ14011-DTPA (**5**)	124.4 ± 23.9
Ac-TZ14011-FITC (**6**)	203.5 ± 67.1
TR14010 (**7**)	>5000

was performed at 4 °C to minimize the initial metabolic activity. During imaging at 37 °C, minor staining in vesicular structures was detected. Vesicular internalization is common for liganded membrane receptors, and this form of signal accumulation in the cells proves the potential of using CXCR4 as a target in molecular imaging applications.

Initial *in vivo* studies were performed to evaluate the tumor targeting. Therefore, mice with CXCR4 positive "spontaneous" MIN-O tumors were used instead of the MDAMB231^{CXCR4+} cell line, because the CXCR4 expression in MDAMB231^{CXCR4+} cells decreases to basal levels *in vivo*. Mice were injected with ^{111}In-labeled Ac-TZ14011-MSAP, and after 24 h, the mice were imaged with SPECT/CT and fluorescence imaging (Figure 4). Both imaging modalities showed high tumor uptake.

For biodistribution studies, we again used mice with CXCR4 positive MIN-O tumors and mice with CXCR4 negative 4T1 tumors as negative control (both tumors had a murine background to prevent xenograph effects) (Table 3). The tumor-to-muscle ratio for the MIN-O tumor was 4.55 ± 0.68, and for the 4T1 tumor, it was 1.20 ± 0.12 ($p < 0.01$), indicating that

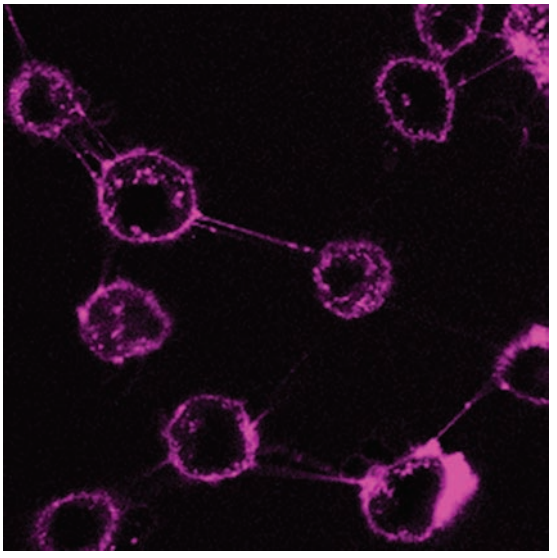


Figure 3. Confocal microscopy of Ac-TZ14011-MSAP (**3**) using MDAMB231^{CXCR4+} cells.

Ac-TZ14011-MSAP can be used to discriminate CXCR4 positive from CXCR4 negative tumors *in vivo*.

In conclusion, we report the first bifunctional CXCR4 antagonistic peptide, containing a Cy5.5-like dye and a DTPA chelate. Despite the functionalization with a relatively large MSAP label, *in vitro* the Ac-TZ14011 derivative retains its specificity and has a high CXCR4-affinity. Moreover, indium binding to the chelate does not affect the fluorescent properties. The initial *in vivo*

dx.doi.org/10.1021/bc2000947 |*Bioconjugate Chem.* 2011, 22, 859–864

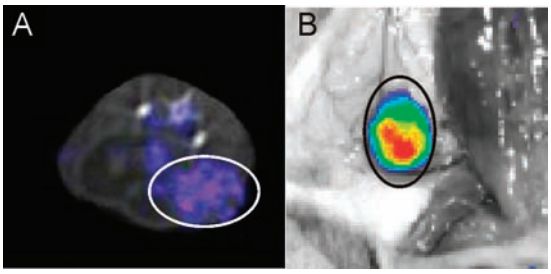


Figure 4. (A) SPECT/CT (axial) and (B) surgical fluorescence image of a MIN-O tumor bearing mouse.

Table 3. Biodistribution of Ac-TZ14011-MSAP in FVB Mice

tissue	uptake (%ID/g)
blood	0.13 ± 0.02
brain	0.02 ± 0.00
lungs	0.93 ± 0.12
heart	0.83 ± 0.20
liver	19.46 ± 4.84
kidneys	6.89 ± 1.29
spleen	4.38 ± 1.16
stomach	0.75 ± 0.14
intestines	1.70 ± 0.08
muscle	0.29 ± 0.01

studies showed the potential of Ac-TZ14011-MSAP for image guided surgery applications.

■ ASSOCIATED CONTENT

Supporting Information. Experimental procedures and spectra of **3** and **4**. This material is available free of charge via the Internet at http://pubs.acs.org.

■ AUTHOR INFORMATION

Corresponding Author

*E-mail: fw.v.leeuwen@nki.nl.

Author Contributions

#These authors contributed equally to this work.

■ ACKNOWLEDGMENT

This research is supported, in part, by a KWF-translational research award (Grant No. PGF 2009-4344; FvL), and within the framework of CTMM, the Centre for Translational Molecular Medicine (http://www.ctmm.nl), project Breast CARE (grant 030-104; JK).

■ REFERENCES

(1) Furusato, B., Mohamed, A., Uhlen, M., and Rhim, J. S. (2010) CXCR4 and cancer. *Pathol. Int. 60*, 497–505.

(2) Bhandari, D., Robia, S. L., and Marchese, A. (2009)The E3 ubiquitin ligase atrophin interacting protein 4 binds directly to the chemokine receptor CXCR4 via a novel WW domain-mediated interaction. *Mol. Biol. Cell 20*, 1324–1339.

(3) Kang, H., Watkins, G., Douglas-Jones, A., Mansel, R. E., and Jiang, W. G. (2005)The elevated level of CXCR4 is correlated with nodal metastasis of human breast cancer. *Breast 14*, 360–367.

(4) Kulbe, H., Levinson, N. R., Balkwill, F., and Wilson, J. L. (2004) The chemokine network in cancer—much more than directing cell movement. *Int. J. Dev. Biol. 48*, 489–496.

(5) Balkwill, F. (2004)The significance of cancer cell expression of the chemokine receptor CXCR4. *Semin. Cancer Biol. 14*, 171–179.

(6) Teicher, B. A., and Fricker, S. P. (2010)CXCL12 (SDF-1)/CXCR4 pathway in cancer. *Clin. Cancer Res. 16*, 2927–2931.

(7) Lazennec, G., and Richmond, A. (2010)Chemokines and chemokine receptors: new insights into cancer-related inflammation. *Trends Mol. Med. 16*, 133–144.

(8) Nimmagadda, S., Pullambhatla, M., Stone, K., Green, G., Bhujwalla, Z. M., and Pomper, M. G. (2010)Molecular imaging of CXCR4 receptor expression in human cancer xenografts with [^{64}Cu]-AMD3100 positron emission tomography. *Cancer Res. 70*, 3935–3944.

(9) Han, Y., Yin, D., Zheng, M., Zhou, W., Lee, Z., Zhan, L., Ma, Y., Wu, M., Shi, L., Wang, N., Lee, J., Wang, C., Lee, Z., and Wang, Y. (2010) Synthesis and preliminary evaluation of a novel ^{125}I-labeled T140 analog for quantitation of CXCR4 expression. *J. Radioanal. Nucl. Chem. 284*, 279–286.

(10) Mather, S. (2009)Molecular imaging with bioconjugates in mouse models of cancer. *Bioconjugate Chem. 20*, 631–643.

(11) Jennings, L. E., and Long, N. J. (2009)'Two is better than one'—probes for dual-modality molecular imaging. *Chem. Commun.* 3511–3524.

(12) Louie, A. (2010)Multimodality imaging probes: design and challenges. *Chem. Rev. 110*, 3146–3195.

(13) Kuil, J., Velders, A. H., and Van Leeuwen, F. W. B. (2010) Multimodal tumor-targeting peptides functionalized with both a radio- and a fluorescent-label. *Bioconjugate Chem. 21*, 1709–1719.

(14) Culver, J., Akers, W., and Achilefu, S. (2008)Multimodality molecular imaging with combined optical and SPECT/PET modalities. *J. Nucl. Med. 49*, 169–172.

(15) Buckle, T., Chin, P. T., van den Berg, N. S., Loo, C. E., Koops, W., Gilhuijs, K. G., and van Leeuwen, F. W. (2010)Tumor bracketing and safety margin estimation using multimodal marker seeds: a proof of concept. *J. Biomed. Opt. 15*, 056021.

(16) Buckle, T., van Leeuwen, A. C., Chin, P. T. K., Janssen, H., Muller, S. H., Jonkers, J., and van Leeuwen, F. W. B. (2010)A self-assembled multimodal complex for combined pre- and intraoperative imaging of the sentinel lymph node. *Nanotechnology 21*, 355101.

(17) Van der Poel, H. G., Buckle, T., Brouwer, O. R., Valdés Olmos, R. A., and Van Leeuwen, F. W. B. (2011)Intraoperative laparoscopic fluorescence guidance to the sentinel lymph node in prostate cancer patients; clinical proof of concept of an integrated functional imaging approach using a multimodal tracer. *Eur. Urol.*, doi:10.1016/j.eururo.2011.03.024.

(18) Tamamura, H., Omagari, A., Hiramatsu, K., Gotoh, K., Kanamoto, T., Xu, Y., Kodama, E., Matsuoka, M., Hattori, T., Yamamoto, N., Nakashima, H., Otaka, A., and Fujii, N. (2001)Development of specific CXCR4 inhibitors possessing high selectivity indexes as well as complete stability in serum based on an anti-HIV peptide T140. *Bioorg. Med. Chem. Lett. 11*, 1897–1902.

(19) Tamamura, H., Hiramatsu, K., Kusano, S., Terakubo, S., Yamamoto, N., Trent, J. O., Wang, Z., Peiper, S. C., Nakashima, H., Otaka, A., and Fujii, N. (2003)Synthesis of potent CXCR4 inhibitors possessing low cytotoxicity and improved biostability based on T140 derivatives. *Org. Biomol. Chem. 1*, 3656–3662.

(20) Tamamura, H., Sugioka, M., Odagaki, Y., Omagari, A., Kan, Y., Oishi, S., Nakashima, H., Yamamoto, N., Peiper, S. C., Hamanaka, N., Otaka, A., and Fujii, N. (2001)Conformational study of a highly specific CXCR4 inhibitor, T140, disclosing the close proximity of its intrinsic pharmacophores associated with strong anti-HIV activity. *Bioorg. Med. Chem. Lett. 11*, 359–362.

(21) Trent, J. O., Wang, Z. X., Murray, J. L., Shao, W., Tamamura, H., Fujii, N., and Peiper, S. C. (2003)Lipid bilayer simulations of CXCR4 with inverse agonists and weak partial agonists. *J. Biol. Chem. 278*, 47136–47144.

(22) Wu, B., Chien, E. Y. T., Mol, C. D., Fenalti, G., Liu, W., Katritch, V., Abagyan, R., Brooun, A., Wells, P., Bi, F. C., Hamel, D. J., Kuhn, P., Handel, T. M., Cherezov, V., and Stevens, R. C. (2010)Structures of the CXCR4 chemokine GPCR with small-molecule and cyclic peptide antagonists. *Science 330*, 1066–1071.

(23) Nomura, W., Tanabe, Y., Tsutsumi, H., Tanaka, T., Ohba, K., Yamamoto, N., and Tamamura, H. (2008)Fluorophore labeling enables imaging and evaluation of specific CXCR4-ligand interaction at the cell membrane for fluorescence-based screening. *Bioconjugate Chem. 19*, 1917–1920.

(24) Oishi, S., Masuda, R., Evans, B., Ueda, S., Goto, Y., Ohno, H., Hirasawa, A., Tsujimoto, G., Wang, Z., Peiper, S. C., Naito, T., Kodama, E., Matsuoka, M., and Fujii, N. (2008)Synthesis and application of fluorescein- and biotin-labeled molecular probes for the chemokine receptor CXCR4. *ChemBioChem 9*, 1154–1158.

(25) Hanaoka, H., Mukai, T., Tamamura, H., Mori, T., Ishino, S., Ogawa, K., Iida, Y., Doi, R., Fujii, N., and Saji, H. (2006)Development of a ^{111}In-labeled peptide derivative targeting a chemokine receptor, CXCR4, for imaging tumors. *Nucl. Med. Biol. 33*, 489–494.

(26) Nishizawa, K., Nishiyama, H., Oishi, S., Tanahara, N., Kotani, H., Mikami, Y., Toda, Y., Evans, B. J., Peiper, S. C., Saito, R., Watanabe, J., Fujii, N., and Ogawa, O. (2010)Fluorescent imaging of high-grade bladder cancer using a specific antagonist for chemokine receptor CXCR4. *Int. J. Cancer 127*, 1180–1187.

(27) Garanger, E., Aikawa, E., Reynolds, F., Weissleder, R., and Josephson, L. (2008)Simplified syntheses of complex multifunctional nanomaterials. *Chem. Commun.* 4792–4794.

(28) Garanger, E., Blois, J., Hilderbrand, S. A., Shao, F., and Josephson, L. (2010)Divergent oriented synthesis for the design of reagents for protein conjugation. *J. Comb. Chem. 12*, 57–64.

(29) Shao, F., Yuan, H., Josephson, L., Weissleder, R., and Hilderbrand, S. A. (2011)Facile synthesis of monofunctional pentamethine carbocyanine fluorophores. *Dyes Pigments 90*, 119–122.

(30) Moulin, C., Amekraz, B., Steiner, V., Plancque, G., and Ansoborlo, E. (2003)Speciation studies on DTPA using the complementary nature of electrospray ionization mass spectrometry and time-resolved laser-induced fluorescence. *Appl. Spectrosc. 57*, 1151–1161.

(31) Maecke, H. R., Riesen, A., and Ritter, W. (1989)The molecular structure of indium-DTPA. *J. Nucl. Med. 30*, 1235–1239.

(32) Schottelius, M., and Wester, H. J. (2009)Molecular imaging targeting peptide receptors. *Methods 48*, 161–177.

Supporting Information for:

Synthesis and evaluation of a bimodal CXCR4 antagonistic peptide

Joeri Kuil,[†,*] Tessa Buckle,[†,*] Hushan Yuan,[‡] Nynke S. van den Berg,[†] Shinya Oishi,[⊥] Nobutaka Fujii,[⊥] Lee Josephson[‡] and Fijs W.B. van Leeuwen[$,†]

[†] Division of Diagnostic Oncology, the Netherlands Cancer Institute Antoni van Leeuwenhoek Hospital, 1066 CX Amsterdam, The Netherlands.

[‡] Center for Molecular Imaging Research, Massachusetts General Hospital and Harvard Medical School, Building 149, 13th Street, Charlestown, MA 02129, USA

[⊥] Department of Bioorganic Medicinal Chemistry, Graduate School of Pharmaceutical Sciences, Kyoto University, Kyoto, Japan

* These authors contributed equally to this work.

Contents

Synthetic procedures	2
Spectroscopy	4
In vitro experiments	5
In vivo experiments	8
Literature cited	9

Synthetic procedures

General

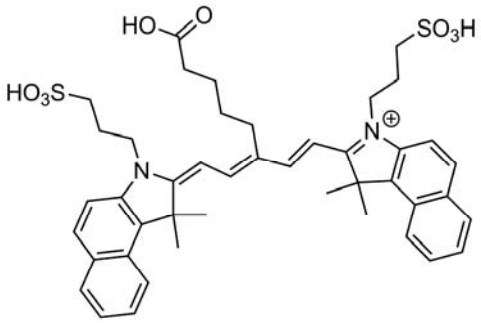
All chemicals were obtained from commercial sources and used without further purification. The reactions were monitored by thin layer chromatography (TLC).

Ac-TZ14011 (1)

Ac-TZ14011 was synthesized according to described procedures.[1]

CyAL-5.5$_b$

CyAL-5.5$_b$ was synthesized according to previously described procedures.[2]



MSAP reagent (2)

The multifunctional single attachment point (MSAP) reagent (**2**) was synthesized based on previously described procedures.[3,4] Briefly, the dipeptide (Fmoc-Lys(ivDde)-Cys(Trt)-Rink resin) was obtained with Fmoc synthesis on a Rink Amide MBHA resin. After Fmoc removal using a piperidine/DMF solution (1:4), DTPA-tetra-*t*-butyl ester (cat. # B-365, Microcyclics) was attached to the N-terminus of the peptide using 2 equiv of DTPA-tetra-*t*-butyl ester, 2 equiv of PyBop and 12 equiv of DiPEA (overnight, room temperature). The ivDde group was removed using 2% hydrazine in DMF (10 mL/g resin, 3 × 3 min) and the CyAL-5.5$_b$ fluorochrome was coupled using 1.5 equiv of CyAL-5.5$_b$, 2 equiv of PyBop and 8 equiv of DiPEA in DMF (overnight, room temperature). The dipeptide was cleaved from the resin and the trityl group was removed using

TFA/H_2O/TIS/EDT (88/2/5/5) for 2 × 4 h (3 mL each time). The resulting crude product was purified by a semi-preparative HPLC with a PLRP-S column. The product was identified by MS and is denoted as DTPA-Lys(CyAL-5.5$_b$)-Cys-NH_2. MS: $[M]^+$ calculated 1404.56, found 1404.15.

A solution of the bifunctional reagent 4-maleimidobutyric acid N-hydroxysuccinimide ester (Thermo Scientific, 11.7 mg, 41.8 μmol), DTPA-Lys(CyAL-5.5$_b$)-Cys-NH_2 (14.2 mg, 10.1 μmol) and DiPEA (5 μL, 28.7 μmol) in 800 μL of anhydrous DMF was stirred for 2 h at room temperature. Reversed phase-HPLC purification was employed on a semi-preparative HPLC with a Vydac C18 column. MSAP reagent **2** was obtained as a blue powder (8.2 mg, 48%) after pooling of the appropriate fractions and lyophilization. MS: $[M]^+$ calculated 1684.6, found 1684.4.

Ac-TZ14011-MSAP (3) (Scheme 1)

Ac-TZ14011 (**1**) (8.4 mg, 3.0 μmol) and the MSAP reagent (**2**) (3.4 mg, 2.0 μmol) were dissolved in 2 mL of DMSO. DiPEA (7.0 μL, 40 μmol) was added and the mixture was stirred overnight at room temperature, after which the mixture was purified by preparative HPLC using a Waters HPLC system with a UV detector operating at 230 nm and a Waters Atlantis C18 10 μm (250 × 19 mm) column. A gradient of 0.05% TFA in H_2O/CH_3CN 9:1 to 0.05% TFA in H_2O/CH_3CN 1:4 40 minutes was used. The product was obtained as a blue fluffy solid (3.9 mg, 45%) after pooling of the appropriate fractions and lyophilization. MS (MALDI-TOF): $[M+H]^+$ calculated 3676.677, found 3676.256.

Ac-TZ14011-MSAP-In (4) (Scheme 1)

A solution of **3** with a concentration of 160 μM in 0.1 M AcOH was prepared. Half of this solution was diluted (1:1 v/v) with 0.1 M of AcOH to yield a stock solution of 80 μM of **3**. The other half was added to the same amount of 160 μM of $InCl_3$ in AcOH, incubated for 30 minutes, yielding a stock solution of 80 μM of **4**.

Ac-TZ14011-DTPA (5)

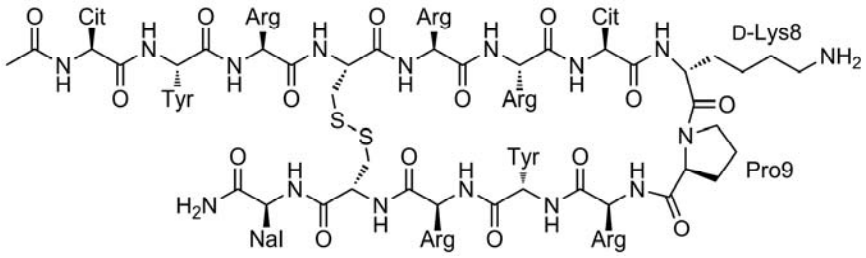
Ac-TZ14011-DTPA was synthesized according to previously described procedures.[1]

Ac-TZ14011-FITC (6)

Fluorescein isothiocyanate isomer I (FITC; 2.32 mg, 5.95 μmol) in 500 μL of DMSO was added to Ac-TZ14011 (11.1 mg, 3.96 μmol) in 1 ml of 0.1 M $NaHCO_3$ and 2 ml of CH_3CN. The mixture was stirred overnight at room temperature, the solution was concentrated and the product was purified by preparative HPLC using a Waters HPLC system with a UV detector operating at 230 nm and a Waters Atlantis C18 10 μm (250 × 19 mm) column using a gradient of 0.05% TFA in H_2O/CH_3CN 9:1 to 0.05% TFA in H_2O/CH_3CN 1:4 in 40 minutes. The product was obtained as a yellow fluffy solid (4.3 mg, 35%) after pooling of the appropriate fractions and lyophilization. MS (MALDI-TOF): $[M+H]^+$ calculated 2496.118, found 2495.168.

Scrambled peptide TR14010 (7)

TR14010 was synthesized according to previously described procedures.[5]



Spectroscopy

For the recording of absorption and emission spectra 0.25 mL of stock solution of **3** or **4** was added to 1 mL of EtOH and 2.25 mL of PBS. Absorption spectroscopy was performed on a Lambda Bio 20 spectrometer (Perkin Elmer). Emission spectra were recorded using a 627 nm LED lamp (Luxeon III Star, Lambt, red, Farnell) and a VS140-VISNIR-CCD spectrometer (Horiba Jobin Yvon). Absorption and emission spectra of **3** and **4** are shown in Figure S1.

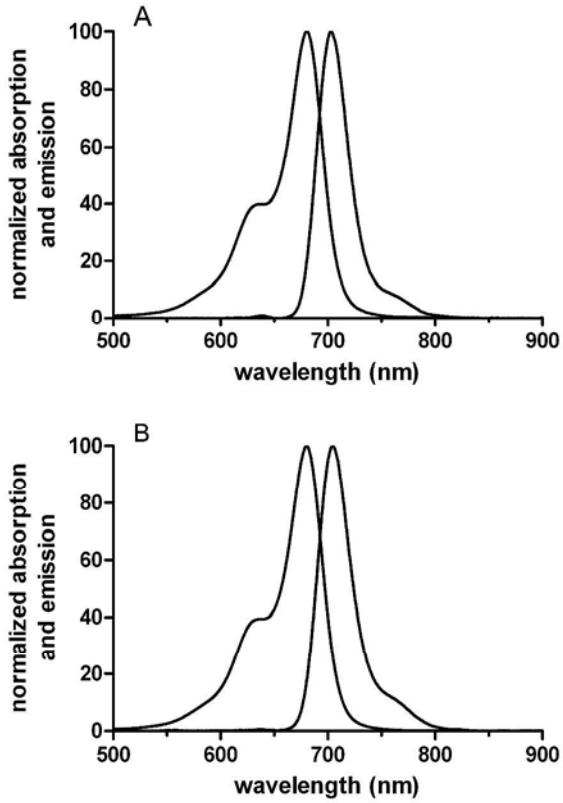


Figure S1. Absorption and emission spectra of compounds **3** (A) and **4** (B).

IN VITRO experiments

Cell culture

Human breast cancer cell lines MDAMB231 and MDAMB231^{CXCR4+} were kindly provided by Olaf van Tellingen and Ed Roos (both NKI-AvL, Amsterdam, The Netherlands), respectively. MDAMB231 cells were used as control based on their basal CXCR4 expression. MDAMB231^{CXCR4+} cells were selected by flow cytometry based on their high CXCR4-expression levels. Both cell lines were maintained in Gibco's minimum essential medium (MEM) enriched with 10% fetal bovine serum, Penicillin/Streptomycin, L-glutamine, non-essential amino acids, sodium pyruvate and MEM vitamins solution (all Life Technologies Inc.). Cells were kept under standard culture conditions.

Flow cytometry analysis of MDAMB231 and MDAMB231^{CXCR4+} cell binding (Figure 1 and Table 1)

Freshly cultured MDAMB231 or MDAMB231^{CXCR4+} cells were trypsinized, aliquoted in portions of 300 000 cells, centrifuged (1200 rpm, 5 min, 4 °C) and decanted. 6.4 nM of monoclonal phycoerythrin (PE) labeled anti-CXCR4 antibody (CD184 12G5-PE (12.5 μg/mL), BD Biosciences) or 1 μM of **3** or **4** in 50 μL of 0.1% bovine serum albumin (BSA) in phosphate buffered saline (PBS) was added to the cells. After 1 hour of incubation at 4 °C, the cells were washed (2 ×) with 300 μL of 0.1% BSA in PBS, resuspended in 300 μL of 0.1% BSA in PBS and fluorescence was measured using a CyAn ADP flow cytometer (DakoCytomation) with APC-Cy7 settings (635 nm laser and 750 nm long pass filter) for **3** and **4**. Live cells were gated on Forward Scatter, Side Scatter and Pulse Width and approximately 20 000 viable cells were analyzed. All experiments were performed in triplicate.

Determination of dissociation constants (Figure 2 and Table 2)

MDAMB231^{CXCR4+} cells were trypsinized and aliquoted in portions of 300 000 cells. For saturation binding experiments different concentrations of **3** or **4**, in a range of 0 – 1000 nM, were added. For competition experiments different concentrations (0 – 10000 nM) of Ac-TZ14011 (**1**), Ac-TZ14011-DTPA (**5**) or Ac-TZ14011-FITC (**6**) in the presence of 250 nM of **3** were added. Cells were incubated for 1 hour at 4 °C. The cells were washed (2 ×) with 300 μL of 0.1% BSA in PBS, resuspended in 300 μL of 0.1% BSA in PBS and fluorescence was measured using a CyAn ADP flow cytometer (DakoCytomation) with APC-Cy7 settings. Live cells were gated on Forward Scatter, Side Scatter and Pulse Width and approximately 20 000 viable cells were analyzed. All experiments were performed in duplicate.

The normalized geometric means were fitted with equations in the GraphPad Prism 5 software. The K_D values of **3** and **4** were calculated using the 'Binding – Saturation, One site – Total' nonlinear regression equation (Eq.1). The K_D values of Ac-TZ14011 (**1**), Ac-TZ14011-DTPA (**5**) and Ac-TZ14011-FITC (**6**) were calculated using the 'Binding – Competitive, One site – Fit K_i' nonlinear regression equation (Eq. 2 and 3).

$$y = \frac{B_{max} * x}{K_D + x} + NS * x + Background \qquad \text{(Eq. 1)}$$

y = normalized fluorescence

B_{max} = maximum specific binding in the units of the y axis

x = concentration of **3** or **4** in nM

K_D = equilibrium dissociation constant of **3** or **4** in nM

NS = slope of nonspecific binding

Background = amount of normalized fluorescence with no added compound

$$\log IC_{50} = \log(10^{\log K_D} * (1 + \frac{[\mathbf{3}]}{K_{D,\mathbf{3}}})) \qquad \text{(Eq. 2)}$$

$$y = Bottom + \frac{Top - Bottom}{1 + 10^{(x - \log IC_{50})}} \qquad \text{(Eq. 3)}$$

IC_{50} = concentration of competitor that results in binding half-way between Bottom and Top

K_D = equilibrium dissociation constant of the competitor in nM

[**3**] = concentration of **3** (250 nM)

$K_{D,\mathbf{3}}$ = dissociation constant of **3** (186.9 nM)

y = normalized fluorescence

Bottom and Top = plateaus in the units of the y axis

Confocal microscopy (Figure 3)

MDAMB231^{CXCR4+} cells were seeded onto coverslips (Ø 24mm; Karl Hecht GmbH & Co) and incubated overnight. The cells were washed with PBS and incubated with 1 μM of Ac-TZ14011-MSAP (**3**) for 1 h at 4 °C and washed again with ice cold PBS. Confocal microscopy images were taken at 37 °C on a Leica TCS-SP2-AOBS Live confocal microscope (Leica Microsystems Heidelberg GmbH).

IN VIVO experiments

IN VIVO model

For generation of the CXCR4-positive mouse tumor lesions, FVB mice (n = 3; 3-4 weeks of age) were used. Before transplantation (and imaging), mice were anaesthetized using a hypnorm (VetaPharma Ltd)/dormicum (Midazolam; Roche)/water solution (1:1:2; 5 µL/g i.p.). Via a small incision, the inguinal lymph node was excised where after a piece of preinvasive 8w-B MIN-O tissue was placed into the remaining tissue of the 4th mammary gland.[6-8] Approximately 3 weeks after transplantation, lesions were deemed suitable for further experiments. Control experiments were performed using orthotopic transplantation of 0.25×10^5 4T1 mouse tumor cells into the mammary tissue of Balb/c nude mice (n = 3; 6-8 weeks of age). Cells were cultured under standard conditions in MEM medium containing MEM vitamins, L-glutamine, non-essential amino acids, natrium pyruvate and penicillin/streptomycin solution (all BD Biosciences). Before transplantation, cells were trypsinized and washed with HBSS (BD Biosciences). Transplantation of cells was carried out under identical conditions as placement of the MIN-O segments. All animal experiments were performed in accordance with Dutch welfare regulations and approved by the local ethics committee.

Radiolabeling of Ac-TZ14011-MSAP (3)

Ac-TZ14011-MSAP (**3**) was dissolved in 0.1 M of acetic acid (50 µg / 100 µL) and $InCl_3$ (10 MBq / 50 ug of **3**; Covidien-Mallinkrodt) was added. After 30 minutes of incubation, labeling was validated with thin layer chromatography (TLC) using 74 mM of sodium citrate (pH 5) as an eluent and a VCS-201 TLC scanner (Veenstra Instruments). In all cases, labeling efficacy was >99%. Before injection, saline (1:1) was added.

Single photon emission computed tomography (SPECT)/computed tomography (CT) (Figure 4A)

24 Hours after intravenously injection of 50 µg of ^{111}In-labeled Ac-TZ14011-MSAP (10 MBq), the mice were placed in a temperature controlled (37 °C) animal holder (Equipment Veterinaire MINERVE) before performing a SPECT/CT scan on the

nanoSPECT/CT (Bioscan Inc.) The region of interest incorporating the whole body was selected, based on a (sagital) tomographic planning X-ray image followed by a helical 3D CT. After this, a sequential total body SPECT scan of the same field of view was performed. After acquisition, the data was reconstructed with HiSPECT software (Scivis GmbH). The SPECT and CT data sets were automatically co-registered. The images were analyzed using the InVivoScope post processing software (Bioscan, Inc.).

Fluorescence imaging (Figure 4B)

After SPECT/CT, the mice were sacrificed. In vivo fluorescence imaging was conducted on the IVIS 200 camera (Xenogen Corp.) using Living Imaging Acquisition and Analysis software (Xenogen Corp.). Images were acquired with standard Cy5.5 (excitation 615-665 nm and emission 695-770 nm) settings.

Biodistribution studies (Table 3)

After fluorescence imaging, tissues were excised. Tissues were weighed and the amount of radioactivity present in the tissues was counted using a Perkin Elmer 1480 Wizard 3'' automatic gamma counter (245 keV; 60 sec). Counts per minute were converted into MBq and corrected for decay. The percentage of the injected dose per gram of tissue (%ID/g) was calculated as followed: ((MBq measured in tissue/ injected dose) *100%) / weight of tissue.

Literature cited

(1) Hanaoka, H., Mukai, T., Tamamura, H., Mori, T., Ishino, S., Ogawa, K., Iida, Y., Doi, R., Fujii, N., and Saji, H. (2006) Development of a ^{111}In-labeled peptide derivative targeting a chemokine receptor, CXCR4, for imaging tumors. *Nucl. Med. Biol. 33*, 489-494.

(2) Shao, F., Yuan, H., Josephson, L., Weissleder, R., and Hilderbrand, S. A. (2011) Facile synthesis of monofunctional pentamethine carbocyanine fluorophores. *Dyes Pigments 90*, 119-122.

(3) Garanger, E., Aikawa, E., Reynolds, F., Weissleder, R., and Josephson, L. (2008) Simplified syntheses of complex multifunctional nanomaterials. *Chem. Commun.*, 4792-4794.

(4) Garanger, E., Blois, J., Hilderbrand, S. A., Shao, F., and Josephson, L. (2010) Divergent oriented synthesis for the design of reagents for protein conjugation. *J. Comb. Chem. 12*, 57-64.
(5) Nishizawa, K., Nishiyama, H., Oishi, S., Tanahara, N., Kotani, H., Mikami, Y., Toda, Y., Evans, B. J., Peiper, S. C., Saito, R., Watanabe, J., Fujii, N., and Ogawa, O. (2010) Fluorescent imaging of high-grade bladder cancer using a specific antagonist for chemokine receptor CXCR4. *Int. J. Cancer 127*, 1180-1187.
(6) Maglione, J. E., McGoldrick, E. T., Young, L. J., Namba, R., Gregg, J. P., Liu, L., Moghanaki, D., Ellies, L. G., Borowsky, A. D., Cardiff, R. D., and MacLeod, C. L. (2004) Polyomavirus middle T-induced mammary intraepithelial neoplasia outgrowths: single origin, divergent evolution, and multiple outcomes. *Mol. Cancer Ther. 3*, 941-953.
(7) Namba, R., Young, L. J., Maglione, J. E., McGoldrick, E. T., Liu, S., Wurz, G. T., DeGregorio, M. W., Borowsky, A. D., MacLeod, C. L., Cardiff, R. D., and Gregg, J. P. (2005) Selective estrogen receptor modulators inhibit growth and progression of premalignant lesions in a mouse model of ductal carcinoma in situ. *Breast Cancer Res. 7*, R881-889.
(8) Namba, R., Young, L. J., Abbey, C. K., Kim, L., Damonte, P., Borowsky, A. D., Qi, J., Tepper, C. G., MacLeod, C. L., Cardiff, R. D., and Gregg, J. P. (2006) Rapamycin inhibits growth of premalignant and malignant mammary lesions in a mouse model of ductal carcinoma in situ. *Clin. Cancer Res. 12*, 2613-2621.

Bioconjugate Chemistry

COMMUNICATION

pubs.acs.org/bc

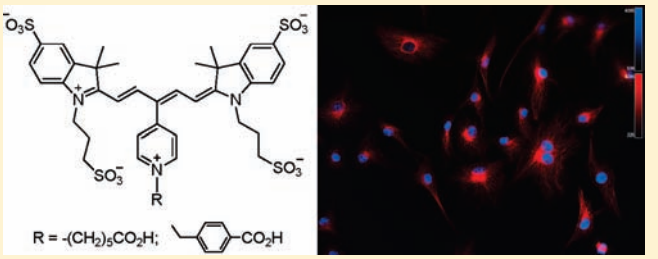
Facile Synthesis of Symmetric, Monofunctional Cyanine Dyes for Imaging Applications

Lai-Qiang Ying* and Bruce P. Branchaud

Life Technologies, 29851 Willow Creek Road, Eugene, Oregon 97402, United States

Supporting Information

ABSTRACT: Efficient syntheses of several members of a new class of symmetric, monocarboxylate-functionalized cyanine dyes have been developed. The synthesis is a simple two-step method, typically with greater than 60% yield and easy final product purification. The new monocarboxylate-functionalized cyanine dyes exhibit excellent water solubility and similar excitation and emission properties to those of Cy5 and Alexa Fluor 647. The application of the new dyes in cellular imaging has been demonstrated through direct conjugating of the dye with an antibody, then imaging of microtubules inside cells, visualized by near-infrared fluorescence microscopy.



Fluorescent dyes are generally well-known for fluorescence labeling and detection of biomolecules, in diverse applications to studies of cells, tissues, proteins, antibodies, and nucleic acids through fluorescence microscopy, fluorescence immunoassays, and flow cytometry.[1,2] The labeling of biomolecules with fluorescent dyes is generally achieved via amine-reactive functionalities such as isothiocyanate and *N*-hydroxysuccinimide esters[3−5] or thiol-reactive iodoacetamide and maleimide groups.[6−8] Near-infrared (NIR) fluorescent dyes with absorption and emission maxima over 600 nm are particular useful for *in vivo* imaging due to the minimal autofluorescence of biological samples in the NIR range.[9] Among the NIR probes, the cyanine dyes, with large extinction coefficients and high quantum yields, are the most widely used probes for optical imaging *in vivo* and in single molecule fluorescence microscopy.[10−17] The common, commercially available cyanine dyes such as Cy3, Cy5, and Cy7 are monofunctional and asymmetric, with a single activated carboxylic acid group attached to one of the indoleninium or benzindoleninium moieties.[3,18]

Cyanine dyes are usually prepared by condensing indoleninium or benzindoleninium moieties to a polymethine chain in a stepwise synthetic strategy. That synthetic approach can result in the formation of undesired symmetric difunctionalized or unfunctionalized dyes as byproducts, and the desired monofunctional products often must be purified by HPLC, resulting in lower overall yields (Scheme 1).[3] Alternative syntheses of monofunctional symmetric heptamethine cyanine dyes have been developed via the reaction of chloro-substituted cyanine dyes with either (1) nucleophiles or (2) in Suzuki-Miyaura cross-coupling reactions.[19−22]

Many cyanine dyes exhibit low quantum yields in H_2O, and many are also not very stable.[23] Recently, a synthetic method has been reported for the preparation of monofunctional (carboxyl, azido, and alkynyl groups) pentamethine carbocyanine dyes, based on modifications of the synthetic method using malonaldehyde dianil dye precursors.[24] The compounds prepared by that method have lower quantum yields than Cy5, and they have shown florescence quenching properties when the dye is conjugated to antibodies, similar to the florescence quenching seen with Cy5.[25]

Development of new NIR probes with increased fluorescence brightness, improved photostability, and lower nonspecific binding is needed for improved imaging applications. Also, better, facile, high-yield syntheses of NIR probes would also be a significant improvement over current methods. In this report, we present a simple two-step procedure for the synthesis of monocarboxylate-functionalized cyanine dyes based on the pyridine-containing malonaldehyde dianil dye precursor. The monocarboxylate-functionalized cyanine dyes can be prepared in high yield (>60%) with excellent water solubility and display similar excitation and emission properties as Cy5 and Alexa Fluor 647. To evaluate the utility of the monocarboxylate functionalized cyanine dyes, these probes were conjugated with goat antimouse IgG, and used for cell imaging. The results of microtubule imaging inside cells demonstrate the potential applications of the monocarboxylate functionalized cyanine dyes for use as NIR probes.

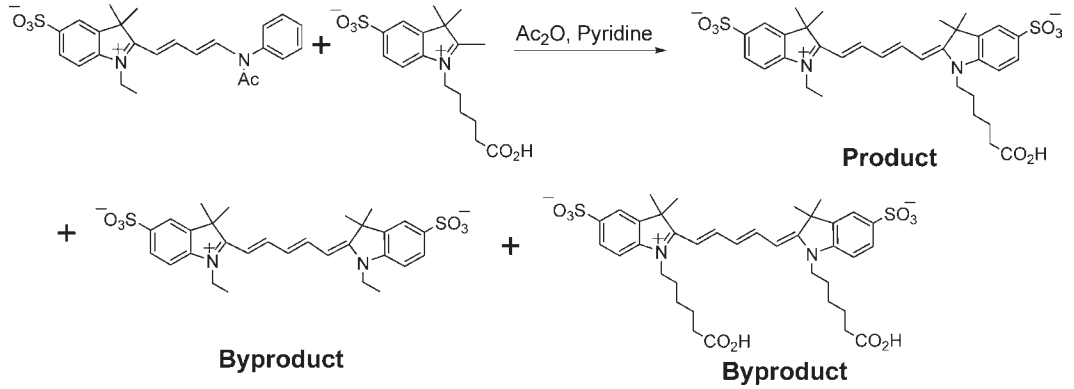
The synthesis of asymmetric cyanine dyes such as Cy5 by the stepwise condensation of indoleninium or benzindoleninium moieties to a polymethine chain always produces some of the undesired symmetric dyes as byproducts (Scheme 1). This methodology leads to low yields of the desired products and difficulty in purification.

Received: February 24, 2011
Revised: April 14, 2011
Published: April 26, 2011

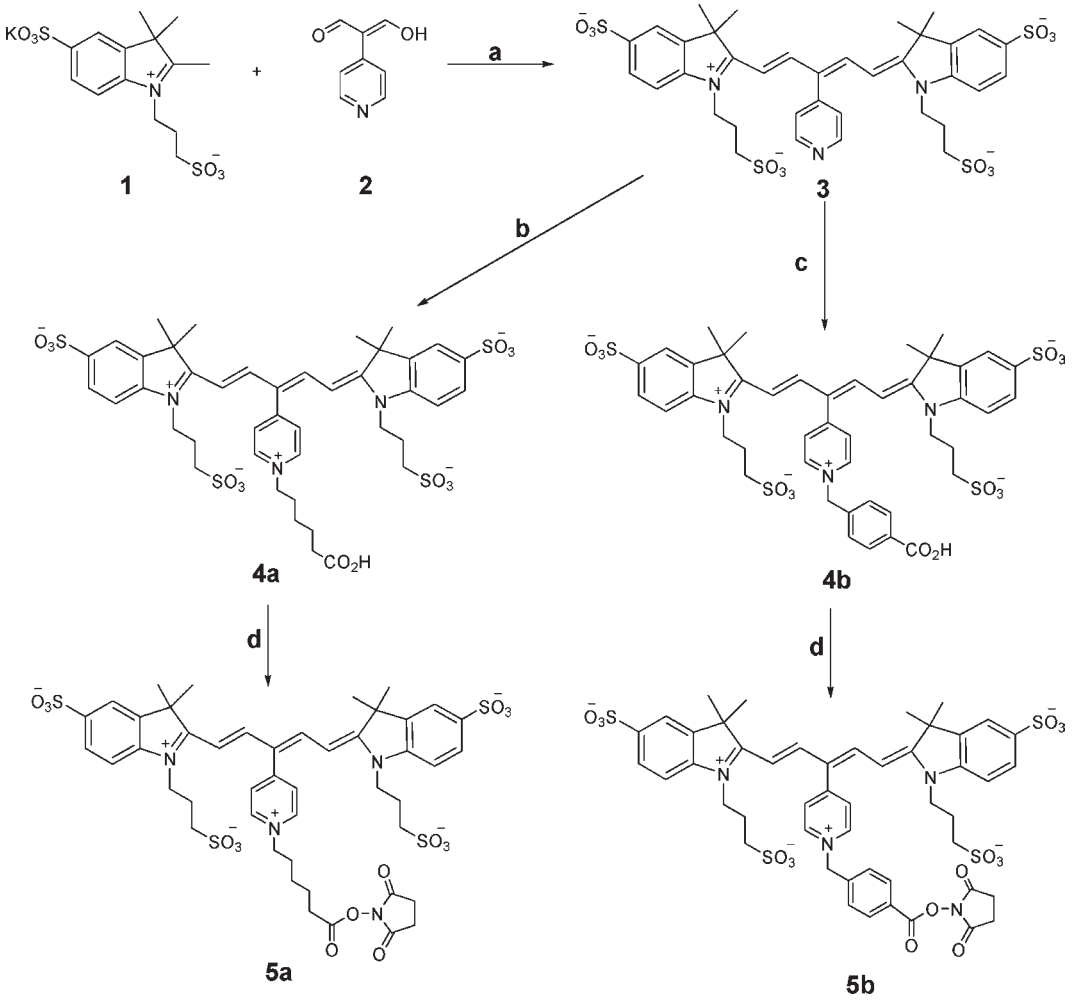
ACS Publications © 2011 American Chemical Society

dx.doi.org/10.1021/bc2001006 | *Bioconjugate Chem.* 2011, 22, 865–869

Scheme 1. Synthetic Route for Preparation of Cy5[3]



Scheme 2. Synthesis of Symmetric and Monofunctional Cyanine Dyes 5a and 5b[a]



[a] Reaction conditions: (a) NaOAc, Ac_2O, HOAc, 115 °C; (b) 6-bromohexanoic acid, KI, NMP, 115 °C; (c) 4-(bromomethyl)benzoic acid, KI, NMP, 115 °C; (d) TSTU, TEA, DMF.

In an effort to develop improved methods for the synthesis of NIR cyanine dyes suitable for bioconjugation, our synthesis of symmetric monocarboxylic acid derivatives has been developed, as shown in Scheme 2. These dyes have two identical monosulfonated indoleninium moieties **1** and are assembled from the aldol-like condensation of the indoleninium salt **1** and the iminium salt **2** in high yield (68%). The two sulfonate groups on the aromatic rings and two sulfopropyl groups on the nitrogen

dx.doi.org/10.1021/bc2001006 |*Bioconjugate Chem.* 2011, 22, 865–869

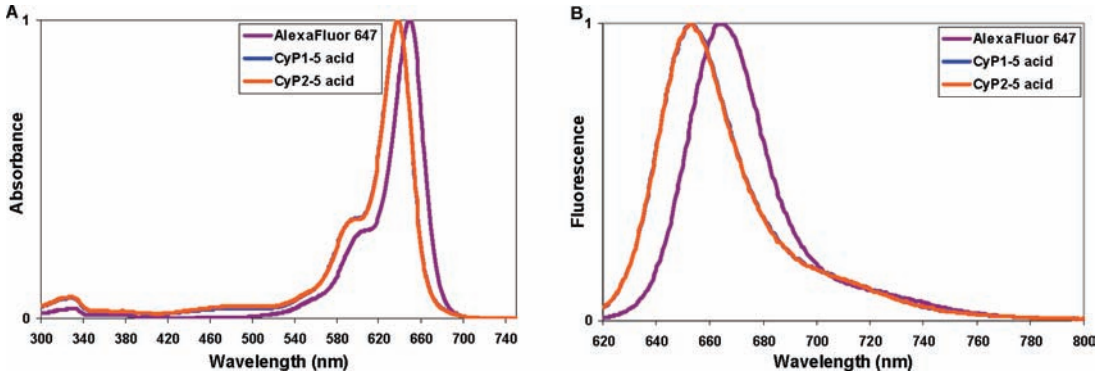


Figure 1. Normalized absorption (A) and emission spectra (B) of CyP1−5 acid, CyP2−5 acid, and Alexa Fluor 647 in PBS, pH 7.4.

Table 1. Optical Properties of Pentamethine Carbocyanine Dyes

fluorophore	λ_{abs} (nm)[a]	λ_{em} (nm)[a]	ε (M^{-1} cm^{-1})[b]	Φ[c]
CyP1−5 acid **4a**	638	653	220 000	0.19
CyP2−5 acid **4b**	638	653	223 000	0.18
Cy5	649	666	250 000	0.27
Alexa Fluor 647	649	664	240 000	0.28

[a] Spectra were obtained in PBS buffer, pH 7.4. [b] Extinction coefficients at 638 nm for dyes **4a** and **4b** are averaged over three sets of equivalent experiments. [c] Emission spectra were excited at 610 nm.

of the indolenine ring give all of the dyes (**3**, **4a**, **4b**, **5a**, and **5b**) excellent water solubility, which is particularly important, because the intrinsic hydrophobicity of the dye can lead to aggregation in an aqueous environment, which, in turn, can cause fluorescence quenching and a reduced quantum yield.[26] The carboxylic acid group is introduced onto the central carbon atom of the polymethine chain through alkylation of pyridine with 6-bromohexanoic acid or 4-(bromomethyl)benzoic acid. In the final step, the carboxylic acid group is converted to the succinimidyl ester using *O*-(*N*-succinimidyl)-1,1,3,3-tetramethyluronium tetrafluoroborate (TSTU). In combination with the simple isolation of the dyes by precipitation from ethyl acetate and HPLC purification, the overall yields for the dyes **5a** and **5b** are 55% and 53%, respectively.

Both CyP1−5 acid **4a** and CyP2−5 acid **4b** display nearly identical spectroscopic profiles. Absorption and emission spectra of both CyP1−5 acid **4a** and CyP2−5 acid **4b** are shown in Figure 1. The optical properties of CyP1−5 acid **4a**, CyP2−5 acid **4b**, Cy5, and Alexa Fluor 647 are summarized in Table 1. CyP1−5 acid **4a** and CyP2−5 acid **4b** have optical features of a typical pentamethine cyanine dye with absorption and emission maxima at 638 and 653 nm, respectively. The absorption and emission maxima of both dyes are blue-shifted by 11 nm in comparison to those of Alexa Fluor 647, whereas the Stokes shifts are nearly identical to that of Alexa Fluor 647, ~15 nm. Both CyP1−5 acid **4a** and CyP2−5 acid **4b** have a brightness of roughly 40−50K (brightness measured as quantum yield × extinction coefficient) with extinction coefficients greater than 220 000 M^{-1} cm^{-1} and quantum yields of 0.18 or higher in aqueous solution. Furthermore, both CyP1−5 acid **4a** and CyP2−5 acid **4b** show excellent photostability (Figure 2).

To evaluate the fluorescence properties of fluorophore labeled antibodies, CyP1−5 succinimidyl ester **5a** and CyP2−5 succinimidyl

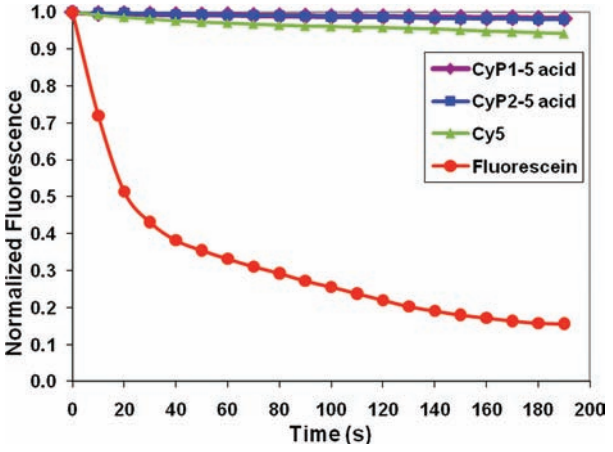


Figure 2. Photostability of CyP1−5 acid, CyP2−5 acid, Cy5, and fluorescein in PBS, pH 7.4.

ester **5b** were used to conjugate with antibody at three different molar ratios (MR = 6, 10, and 15; see Supporting Information for details). The higher fluorophore to antibody ratios are generally preferred to maximize the fluorescence signal from each antibody molecule. However, beyond some optimal fluorophore to antibody ratio, the fluorescence signal per antibody will decrease due to quenching by resonance energy transfer between fluorophores on the same protein molecule.[27] So, the parameters of optimal labeling for each dye must be developed. The fluorescence spectra of CyP1−5 succinimidyl ester **5a** and CyP2−5 succinimidyl ester **5b** labeled antibody are shown in Figure 3. As shown in Figure 3, antibodies labeled with either **5a** or **5b** fluoresce very well even at high fluorophore/protein ratios. The fluorescence properties of antibodies labeled with **5a** and **5b**, as well as Cy5, respectively, are summarized in Table 2. With increasing degree of labeling (DOL), the quantum yield of antibodies labeled with either **5a** or **5b** is consistently decreased due to fluorophore self-quenching. However, the mutual intramolecular quenching between **5a** (or **5b**) labels by the resonance energy transfer is much weaker than Cy5. For example, an antibody with ~5.5 Cy5 labels has a very low quantum yield of 0.02 due to quenching of the multiple dyes on the same antibody.[25] In contrast, fluorophores **5a** and **5b** can achieve brighter total fluorescence (TF) per antibody. The weaker quenching effect of antibodies labeled with either **5a** or **5b** is probably due to the repulsive electrostatic interactions of four sulfonate group negative charges inhibiting the

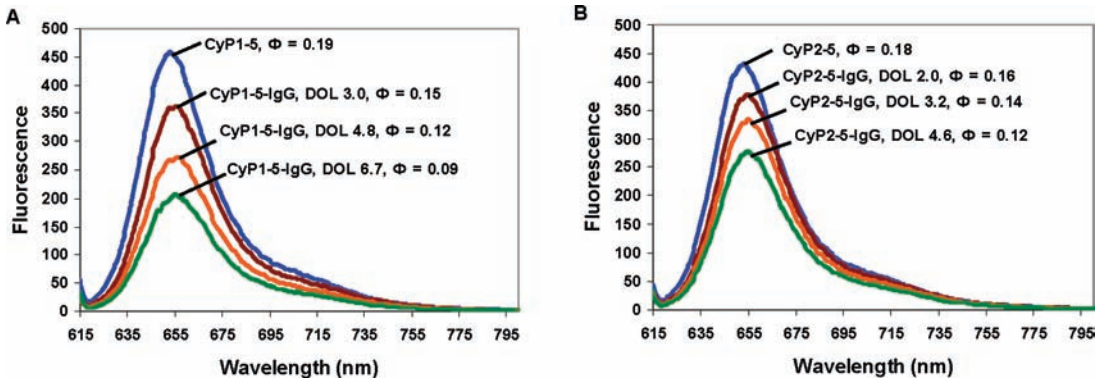


Figure 3. Emission spectra of CyP1−5 (A), and CyP2−5 (B) labeled antibody in PBS, pH 7.4.

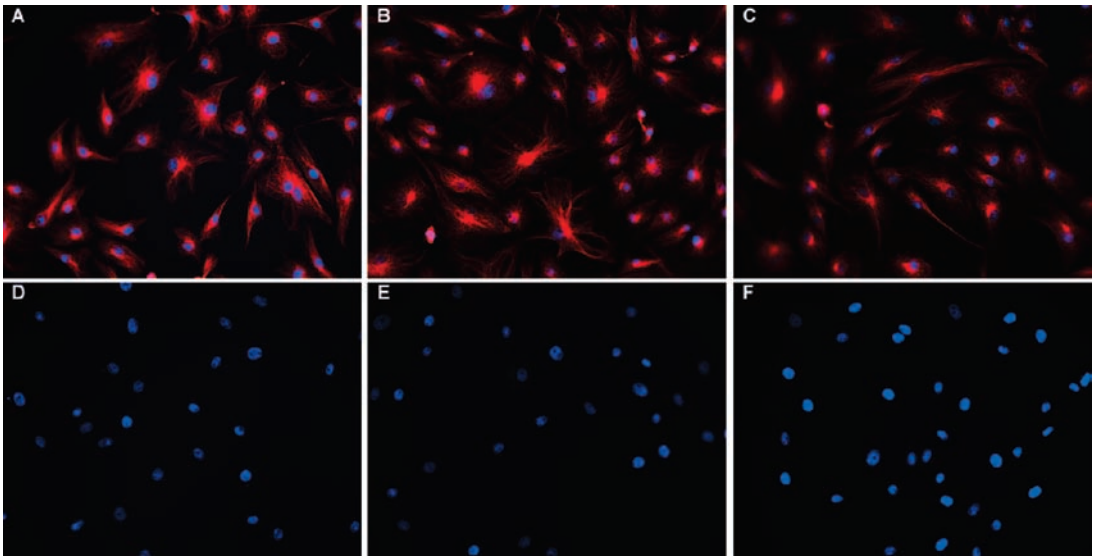


Figure 4. Fluorescene microscopy of BPAEC cells incubated fluorophore-labeled antibody. Cells incubated with **5a**-labeled antibody (A) and control (D), **5b**-labeled antibody (B) and control (E), and Alexa Fluor 647-labeled antibody (C) and control (F). Fluorescence signal from the nuclear stain, DAPI, colored in blue, NIR fluorophores colored in red.

Table 2. Fluorescence Properties of Fluorophore-Labeled Antibody

fluorophore	DOL	Φ[a]	TF (Φ × DOL)
CyP1−5 NHS **5a**	3.0	0.15	0.45
	4.8	0.12	0.58
	6.7	0.09	0.60
CyP2−5 NHS **5b**	2.0	0.16	0.32
	3.2	0.14	0.45
	4.6	0.12	0.55
Cy5	1.2	0.19	0.23
	3.0	0.09	0.27
	5.5	0.02	0.11

[a] Spectra were obtained in PBS buffer, pH 7.4.

close approach of the dyes to each other, thus minimizing the self-quenching.

To assess the performance of the fluorophore-labeled antibodies for cell imaging, the **5a**-labeled antibody (DOL 4.8) and **5b**-labeled antibody (DOL 4.6), as well as Alexa Fluor 647-labeled antibody (DOL 4.5), were chosen as secondary antibodies for imaging of tubulin on bovine pulmonary artery endothelial (BPAEC) cells. After BPAEC cells were fixed with 4% formaldehyde and permeabilized with 0.2% Triton-X, the cells were incubated with mouse antitubulin primary antibody, followed by incubating with dye-labeled (**5a**, **5b**, and Alexa Fluor 647) goat antimouse IgG secondary antibody, as well as the nuclear stain DAPI, respectively. As a control study, the cells were also directly incubated with dye-labeled (**5a**, **5b**, and Alexa Fluor 647) goat antimouse IgG secondary antibody without incubating mouse antitubulin primary antibody. The cells were monitored by fluorescence microscopy to visualize the distribution of microtubules inside cells (Figure 4). A good fluorophore should have bright fluorescence, good photostability, and low nonspecific binding. These new NIR dyes **5a** and **5b** certainly meet these criteria, showing bright fluorescence intensity similar to Alexa Fluor 647 and high specific staining for microtubules.

In conclusion, an efficient and facile methodology for synthesis of symmetric, monofunctional cyanine dyes has been developed. The obtained fluorophores exhibit bright fluorescence with extinction coefficients greater than 220 000 M^{-1} cm^{-1}

dx.doi.org/10.1021/bc2001006 |*Bioconjugate Chem.* 2011, 22, 865–869

and quantum yields of higher than 0.18, as well as good photostability. These dyes were also tested for antibody labeling and the obtained conjugates display excellent fluorescence properties. These new dyes are expected to have great potential in imaging applications.

■ ASSOCIATED CONTENT

Supporting Information. Experimental procedures, characterization, optical properties, general antibody labeling procedures, determination of the degree of labeling, fluorescence labeling and cell imaging procedures, HPLC profiles, ^{1}H NMR spectra, and additional cell imaging information and relative fluorescence intensity. This material is available free of charge via the Internet at http://pubs.acs.org.

■ AUTHOR INFORMATION

Corresponding Author

*E-mail: lai-qiang.ying@lifetech.com. Telephone: (541) 335-0158. FAX: (541) 335-0206.

■ ACKNOWLEDGMENT

We thank Judie Berlier for assistance with antibody conjugations.

■ REFERENCES

(1) Haugland, R. P. (2002) *Handbook of Fluorescent Probes and Research Products*, 9th ed., Molecular Probes, Eugene, OR.

(2) Goncalves, M. S. T. (2009) Fluorescent labeling of biomolecules with organic probes. *Chem. Rev. 109*, 190–212.

(3) Mujumdar, R. B., Ernst, L. A., Mujumdar, S. R., Lewis, C. J., and Waggoner, A. S. (1993) Cyanine dye labeling reagents: sulfoindocyanine succinimidyl esters. *Bioconjugate Chem. 4*, 105–111.

(4) Mank, A. J. G., van der Laan, H. T. C., Lingeman, H., Gooijer, C., Brinkmann, U. A. Th., and Velthorst, N. H. (1995) Visible diode laser-induced fluorescence detection in liquid chromatography after precolumn derivatization of amine. *Anal. Chem. 67*, 1742–1748.

(5) Flanagan, J. H., Jr., Khan, S. H., Menchen, S., Soper, S. A., and Hammer, R. P. (1997) Functionalized tricarbocyanine dyes as near-infrared fluorescent probes for biomolecules. *Bioconjugate Chem. 8*, 751–756.

(6) Ernst, L. A., Gupta, R. K., Mujumdar, R. B., and Waggoner, A. S. (1989) Cyanine dye labeling reagents for sulfhrdryl groups. *Cytometry 10*, 3–10.

(7) Gruber, H. J., Kada, G., Pragl, B., Riener, C., Hahn, C. D., Harms, G. S., Ahrer, W., Dax, T. G., Hohenthanner, K., and Knaus, H.-G. (2000) Preparation of thiol-reactive Cy5 derivatives from commercial Cy5 succinimidyl ester. *Bioconjugate Chem. 11*, 161–166.

(8) Toutchkine, A., Nalbant, P., and Hahn, K. M. (2002) Facile synthesis of thiol-reactive Cy3 and Cy5 derivatives with enhanced water solubility. *Bioconjugate Chem. 13*, 387–391.

(9) Weissleder, R., and Ntziachristos, V. (2003) Shedding light onto live molecular targets. *Nat. Med. 9*, 123–128.

(10) Pham, W., Medarova, Z., and Moore, A. (2005) Synthesis and application of a water-soluble near-infrared dye for cancer detection using optical imaging. *Bioconjugate Chem. 16*, 735–740.

(11) Tung, C. H., Lin, Y., Moon, W. K., and Weissleder, R. (2002) A receptor-targeted near-infrared fluorescence probe for in vivo tumor imaging. *ChemBioChem 3*, 784–786.

(12) Tung, C. H., Quinti, L., Jaffer, F. A., and Weissleder, R. (2005) A branched fluorescent peptide probe for imaging of activated platelets. *Mol. Pharmaceutics 2*, 92–95.

(13) Chen, X., Conti, P. S., and Moats, R. A. (2004) In vivo near-infrared fluorescence imaging of integrin alphavbeta3 in brain tumor xenografts. *Cancer. Res. 64*, 8009–8014.

(14) Zaheer, A., Lenkinski, R. E., Mahmood, A., Jones, A. G., Cantley, L. C., and Frangioni, J. V. (2001) In vivo near-infrared fluorescence imaging of osteoblastic activity. *Nat. Biotechnol. 19*, 1148–1154.

(15) Weissleder, R., Tung, C. H., Mahmood, U., and Bogdanov, A., Jr. (1999) In vivo imaging of tumors with protease-activated near-infrared fluorescent probes. *Nat. Biotechnol. 17*, 375–378.

(16) Ballou, B., Ernst, L. A., and Waggoner, A. S. (2005) Fluorescence imaging of tumors in vivo. *Curr. Med. Chem. 12*, 795–805.

(17) Bates, M., Huang, B., Dempsey, G. T., and Zhuang, X. (2007) Multicolor Super-Resolution Imaging with Photo-Switchable Fluorescent Probes. *Science 317*, 1749–1753.

(18) Mujumdar, S. R., Mujumdar, R. B., Grant, C. M., and Waggoner, A. S. (1996) Cyanine-labeling reagents:sulfobenzindocyanine succinimidyl esters. *Bioconjugate Chem. 7*, 356–362.

(19) Strekowski, L., Lipowska, M., and Patonay, G. (1992) Substitution reactions of a nucleofugal group in heptamethine cyanine dyes. Synthesis of an isothiocyanato derivative for labeling proteins with a near-infrared chromophore. *J. Org. Chem. 57*, 4578–4580.

(20) Flanagan, J. H., Jr., Khan, S. H., Menchen, S., Soper, S. A., and Hammer, R. P. (1997) Functionalized tricarbocyanine dyes as near-infrared fluorescent probes for biomolecules. *Bioconjugate Chem. 8*, 751–756.

(21) Hilderbrand, S. A., Kelly, K. A., Weissleder, R., and Tung, C. H. (2005) Monofunctional near-infrared fluorochromes for imaging applications. *Bioconjugate Chem. 16*, 1275–1281.

(22) Lee, H., CMason, J. C., and Achilefu, S. (2008) Synthesis and spectral properties of near-infrared aminophenyl-, hydroxyphenyl-, and phenyl-substituted heptamethine cyanines. *J. Org. Chem. 73*, 723–725.

(23) Zaheer, A., Wheat, T. E., and Frangioni, J. V. (2002) IRDye78 conjugates for near-infrared fluorescence imaging. *Mol. Imaging 1*, 354–364.

(24) Shao, F., Weissleder, R., and Hilderbrand, S. A. (2008) Monofunctional Carbocyanine Dyes for Bio- and Bioorthogonal Conjugation. *Bioconjugate Chem. 19*, 2487–2491.

(25) Gruber, H. J., Hahn, C. D., Kada, G., Riener, C. K., Harms, G. S., Ahrer, W., Dax, T. G., and Knaus, H.-G. (2000) Anomalous fluorescence enhancement of Cy3 and Cy3.5 versus anomalous fluorescence loss of Cy5 and Cy7 upon covalent linking to IgG and noncovalent binding to avidin. *Bioconjuate Chem. 11*, 696–704.

(26) West, W., and Pearce, S. (1965) The dimeric state of cyanine dyes. *J. Phys. Chem. 69*, 1894–1903.

(27) Steinberg, I. Z. (1971) Long-range nonradiative transfer of electronic excitation energy in proteins and polypeptides. *Annu. Rev. Biochem. 40*, 83–114.

Supporting Information

Facile Synthesis of Symmetric, Monofunctional Cyanine Dyes for Imaging Applications

Lai-Qiang Ying,* and Bruce P. Branchaud

Life Technologies

29851 Willow Creek Road, Eugene, OR 97402

*E-mail: lai-qiang.ying@lifetech.com

Table of Contents

General Materials and Methods	**S2**
Synthesis of 3, 4a, 4b, 5a, and 5b	**S2**
Optical Properties	**S6**
General Antibody Labeling Procedures	**S6**
Determination of the Degree of Labeling	**S7**
Fluorescence Labeling and Cell Imaging	**S7**
HPLC profiles and ^{1}H NMR Spectra	**S8**
Cell Imaging and Fluorescence Intensity	**S15**
References	**S16**

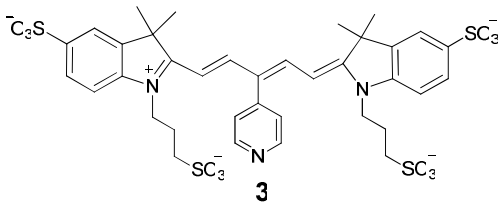
General Materials and Methods

All chemicals and solvents were purchased from Aldrich, Acros or TCI and were used without further purification. Thin layer chromatography (TLC) was performed on aluminum-backed plates with silica gel 60 with F_{254} indicator. All of the dyes for characterization were purified by high-performance liquid chromatography (HPLC) on a Waters prep LC instrument equipped with a Waters 2998 photodiode array detector. If not otherwise noted, HPLC solvent A is 25 mM triethylammonium acetate (TEAA) in water and solvent B is MeOH. All moisture- or air-sensitive reactions were carried out under a static argon atmosphere. ^{1}H NMR (400 MHz) spectra were recorded at room temperature on a Bruker ADVANCE-400 spectrometer with residual proton resonances in deuterated solvents (DMSO-d_6) as the internal standard. LC/MS spectra were obtained with a Waters micromass ZQ instrument. Absorption and emission spectra were determined using a PerkinElmer Lambda 35 UV−visible spectrophotometer and a PerkinElmer LS 55 fluorescence spectrophotometer, respectively. The molar extinction coefficient was obtained from HPLC-purified compounds using Beer's law at 0.1-1.0 μM concentration. The relative fluorescence quantum yield was determined using the model:

$\Phi_{F(X)} = (A_s/A_x)\,(F_x/F_s)\,(n_x/n_s)^2\,\Phi_{F(s)}$

where Φ_F is the fluorescence quantum yield, ***A*** is the absorbance, ***F*** is the area under the emission curve, and ***n*** is the refractive index of the solvents used in the measurement.[1] The subscripts ***s*** and ***x*** represent the standard and the unknown, respectively. Cy5 was used as a reference standard.[2]

Synthesis of intermediate (3).

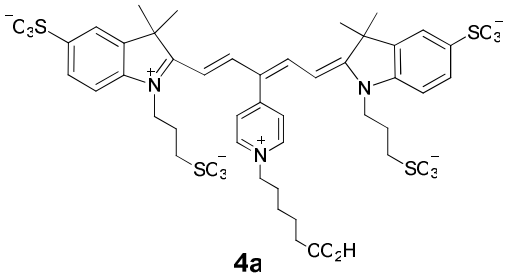


3

2,3,3-Trimethyl-1-(3-sulfonatopropyl)-3*H*-indoleninium-5-sulfonate (**1**) was prepared according to a literature procedures.[3] Indoleninium **1** (1.6 g, 4.2 mmol), 2-(4-pyridyl) malondialdehyde **2**

(283 mg, 1.9 mmol), and sodium acetate (1 g, 12 mmol) were dissolved in 15 mL acetic anhydride and 15 mL acetic acid. The reaction solution was heated at 115 °C for 4 h in a sealed pressure tube. The crude product was then precipitated by the addition of ethyl acetate (80 mL) and washed with additional ethyl acetate (50 mL × 2). Preparative HPLC (Phenomenex Luna C18 250 × 21.2 mm column, 20−40% buffer B over 40 min at a flow rate of 20 mL/min) was used to purify intermediate **3** (1.47 g, 68% yield) giving the blue dye as the triethylammonium salt. ^{1}H NMR (400 MHz, D_2O): δ 8.79 (d, 2H, *J* = 6.4 Hz), 8.19 (d, 2H, *J* = 14.4 Hz), 7.83 (s, 2H), 7.76 (m, 4H), 7.30 (d, 2H, *J* = 8.8 Hz), 5.70 (d, 2H, *J* = 14.0 Hz), 3.97 (t, 4H, *J* = 8.4 Hz), 3.11 (q, 18H, *J* = 7.2 Hz), 2.75 (t, 4H, *J* = 7.2 Hz), 1.98 (m, 4H), 1.69 (s, 12H), 1.19 (t, 27H, *J* = 7.2 Hz). ESI-MS $[M+H]^+$ *m*/*z* calcd. for 836.16, found 836.23.

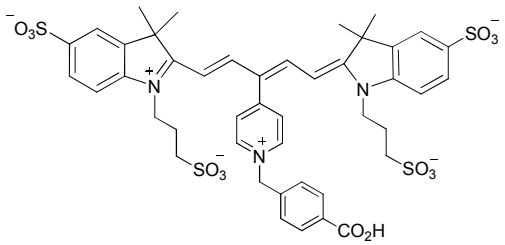
Synthesis of CyP1-5 acid (4a).



4a

Intermediate **3** (200 mg, 0.17 mmol), 6-bromohexanoic acid (663 mg, 3.4 mmol), and potassium iodide (56 mg, 0.34 mmol) were dissolved in 10 mL NMP. The reaction solution was heated at 115 °C for 5 days in a sealed pressure tube. The crude product was then precipitated by the addition of ethyl acetate (40 mL) and washed with additional ethyl acetate (20 mL × 2). Preparative HPLC (Phenomenex Luna C18 250 × 21.2 mm column, 10−40% buffer B over 40 min at a flow rate of 20 mL/min) was used to purify CyP1-5 acid **4a** (182 mg, 90% yield) giving the blue dye as the triethylammonium salt. ^{1}H NMR (400 MHz, D_2O): δ 8.85 (d, 2H, *J* = 6.8 Hz), 8.15 (d, 2H, *J* = 14.4 Hz), 7.93 (d, 2H, *J* = 6.8 Hz), 7.80 (s, 2H), 7.72 (d, 2H, *J* = 8.4 Hz), 7.24 (d, 2H, *J* = 8.4 Hz), 5.72 (d, 2H, *J* = 14.4 Hz), 4.59 (t, 2H, *J* = 7.2 Hz), 3.97 (t, 4H, *J* = 7.6 Hz), 3.09 (q, 24H, *J* = 7.2 Hz), 2.75 (t, 4H, *J* = 6.4 Hz), 2.15 (m, 4H), 1.92 (m, 4H), 1.66 (s, 12H), 1.63 (m, 2H), 1.44 (m, 2H), 1.16 (t, 36H, *J* = 7.2 Hz). ESI-MS $[M+H]^+$ *m*/*z* calcd. for 950.23, found 950.31.

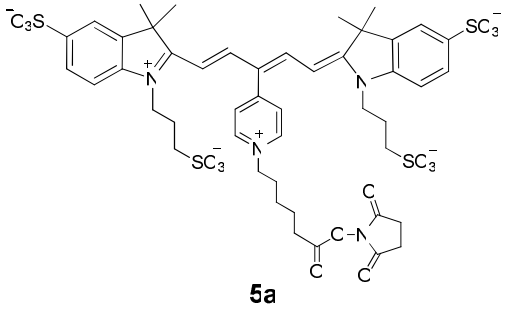
Synthesis of CyP2-5 acid (4b).



4b

Intermediate **3** (200 mg, 0.17 mmol), 4-(bromomethyl)benzoic acid (731 mg, 3.4 mmol), and potassium iodide (56 mg, 0.34 mmol) were dissolved in 10 mL NMP. The reaction solution was heated at 115 °C for 24 h in a sealed pressure tube. The crude product was then precipitated by the addition of ethyl acetate (40 mL) and washed with additional ethyl acetate (20 mL × 2). Preparative HPLC (Phenomenex Luna C18 250 × 21.2 mm column, 10−40% buffer B over 40 min at a flow rate of 20 mL/min) was used to purify CyP2-5 acid **4b** (187 mg, 91% yield) giving the blue dye as the triethylammonium salt. ^{1}H NMR (400 MHz, D_2O): δ 8.84 (m, 2H), 8.14 (dd, 2H, *J* = 4.4 Hz, 14.4 Hz), 7.95 (m, 4H), 7.81 (s, 2H), 7.74 (d, 2H, *J* = 8.8 Hz), 7.66 (d, 2H, *J* = 8.0 Hz), 7.27 (m, 2H), 5.86 (s, 2H), 5.73 (d, 2H, *J* = 14.4 Hz), 3.98 (t, 4H, *J* = 7.6 Hz), 3.10 (q, 24H, *J* = 7.2 Hz), 2.76 (t, 4H, *J* = 6.4 Hz), 1.94 (m, 4H), 1.66 (s, 12H), 1.16 (t, 36H, *J* = 7.2 Hz). ESI-MS $[M+H]^+$ *m*/*z* calcd. for 970.20, found 970.29.

Synthesis of CyP1-5 succinimidyl ester (5a).

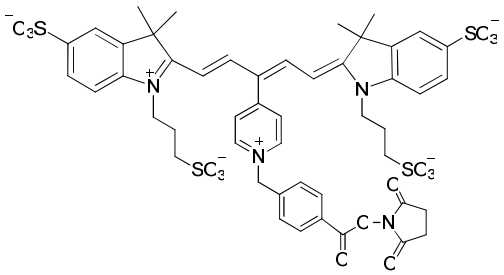


5a

CyP1-5 acid **4a** (25 mg, 0.02 mmol), O-(*N*-succinimidyl)-1,1,3,3-tetramethyluronium tetrafluoroborate (TSTU, 10 mg, 0.03 mmol), and Et_3N (10 μL, 0.07 mmol) were dissolved in 3 mL dry DMF. The reaction mixture was stirred at room temperature for 1 h under argon. The mixture was then precipitated by the addition of ethyl acetate (20 mL) and washed with ethyl

acetate (20 mL), acetone (20 mL), ether (20 mL), and dried under vacuum to afford CyP1-5 succinimidyl ester **5a** as a blue solid (24 mg, 90% yield). ^{1}H NMR (400 MHz, DMSO-d_6): δ 8.99 (d, 2H, *J* = 6.8 Hz), 8.50 (d, 2H, *J* = 14.4 Hz), 7.90 (d, 2H, *J* = 6.8 Hz), 7.85 (s, 2H), 7.62 (d, 2H, *J* = 8.4 Hz), 7.39 (d, 2H, *J* = 8.4 Hz), 5.89 (d, 2H, *J* = 14.4 Hz), 4.58 (t, 2H, *J* = 7.2 Hz), 4.13 (t, 4H, *J* = 7.6 Hz), 3.09 (q, 6H, *J* = 7.2 Hz), 2.89 (s, 4H), 2.81 (t, 4H, *J* = 6.4 Hz), 2.47 (m, 4H), 2.22 (m, 2H), 1.80 (m, 4H), 1.76 (s, 12H), 1.55 (m, 2H), 1.18 (t, 9H, *J* = 7.2 Hz). ESI-MS $[M+H]^+$ *m*/*z* calcd. for 1047.25, found 1047.44.

Synthesis of CyP2-5 succinimidyl ester (5b).



5b

CyP2-5 acid **4b** (20 mg, 0.017 mmol), O-(*N*-succinimidyl)-1,1,3,3-tetramethyluronium tetrafluoroborate (TSTU, 10 mg, 0.03 mmol), and Et_3N (10 μL, 0.07 mmol) were dissolved in 3 mL dry DMF. The reaction mixture was stirred at room temperature for 1 h under argon. The mixture was then precipitated by the addition of ethyl acetate (20 mL) and washed with ethyl acetate (20 mL), acetone (20 mL), ether (20 mL), and dried under vacuum to afford CyP2-5 succinimidyl ester **5b** as a blue solid (18 mg, 86% yield). ^{1}H NMR (400 MHz, DMSO-d_6): δ 8.94 (d, 2H, *J* = 6.8 Hz), 8.50 (d, 2H, *J* = 14.4 Hz), 8.21 (d, 2H, *J* = 8.0 Hz), 8.13 (d, 2H, *J* = 8.0 Hz), 7.95 (s, 2H), 7.85 (s, 2H), 7.63 (dd, 2H, *J* = 1.6 Hz, 8.4 Hz), 7.39 (d, 2H, *J* = 8.4 Hz), 6.06 (s, 2H), 5.93 (d, 2H, *J* = 14.4 Hz), 4.14 (t, 4H, *J* = 7.6 Hz), 3.10 (q, 12H, *J* = 7.2 Hz), 2.89 (s, 4H), 2.73 (t, 4H, *J* = 6.4 Hz), 1.82 (m, 4H), 1.76 (s, 12H), 1.17 (t, 18H, *J* = 7.2 Hz). ESI-MS $[M+H]^+$ *m*/*z* calcd. for 1067.22, found 1067.41.

Optical Properties

Absorption spectra and extinction coefficients of the fluorophores were obtained on a PerkinElmer Lambda 35 UV−visible spectrophotometer. Extinction coefficients were measured in phosphate-buffered saline (PBS, 137 mM NaCl, 2.7 mM KCl, 10 mM Na_2HPO_4, 2 mM KH_2PO_4, pH 7.4), and were averaged from three sets of parallel experiments. For each trial, 2~3 mg of the HPLC-purified dyes were weighed on a Mettler Toledo analytical balance with an error of ±0.01 mg and were dissolved in deionized water using a 10 mL volumetric flask to prepare the stock solutions. Emission spectra were collected on a PerkinElmer LS 55 fluorescence spectrophotometer. Quantum yields were measured for each dye derivative with the maximum absorption for each sample less than 0.1, using Cy5 as a standard (Φ = 0.27).[2] Photostability data were collected on a Nikon Eclipse E400 spectrofluorometer equipped with a Nikon mercury lamp. Dye photo-bleaching was observed by monitoring the fluorescence emission of absorbance-matched dye samples (absorbance ~0.03) at an excitation wavelength 630 nm for 3 min.

General Antibody Labeling Procedures

Stock solutions of the sulfoindocyanine succinimidyl esters were made in dry DMSO at 10 mg/mL concentration. Antibody was dissolved in 0.1 M $NaHCO_3$ buffer at 2 mg/mL concentration. The desired amount of dye was calculated as follows:

$$\text{mL of 10 mg/mL dye} = \frac{\text{mg protein}}{\text{Mw of protein}} \times \text{MR} \times \frac{\text{Mw of dye}}{10}$$

where MR is the molar ratio of dye to protein. For example, using 2 mg of Goat anti-mouse IgG (Mw 145,000) and a 10:1 molar ratio of dye **5a** (Mw 1,249) to protein gives:

$$\frac{2}{145{,}000} \times 10 \times \frac{1249}{10} = 0.017 \text{ mL of 10 mg/mL dye } \mathbf{5a}$$

The desired amount of dye was added to the above antibody solution and incubated at room temperature for 1 h with gentle stirring. Free dye was separated from the labeled antibody by gel permeation chromatography (Bio-Rad BioGel P-30 resin) using PBS buffer as eluent.

Determination of the Degree of Labeling

A simple method for estimating the degree of labeling (DOL) is determined by direct measuring the protein absorbance at 280 nm and dye absorbance at the absorption maximum. The protein concentration is calculated as follows:

$$\text{Protein concentration (M)} = \frac{A_{280} - XA_{dye}}{\varepsilon_{protein}}$$

where the molar extinction coefficient (ε) of a typical IgG at 280 nm is 203,000 $cm^{-1}M^{-1}$. The absorbance of dyes **5a** and **5b** is measured at 638 nm, and the correction factor (X) for the dyes **5a** and **5b** is about 0.04.

The degree of labeling (DOL) is calculated as follows:

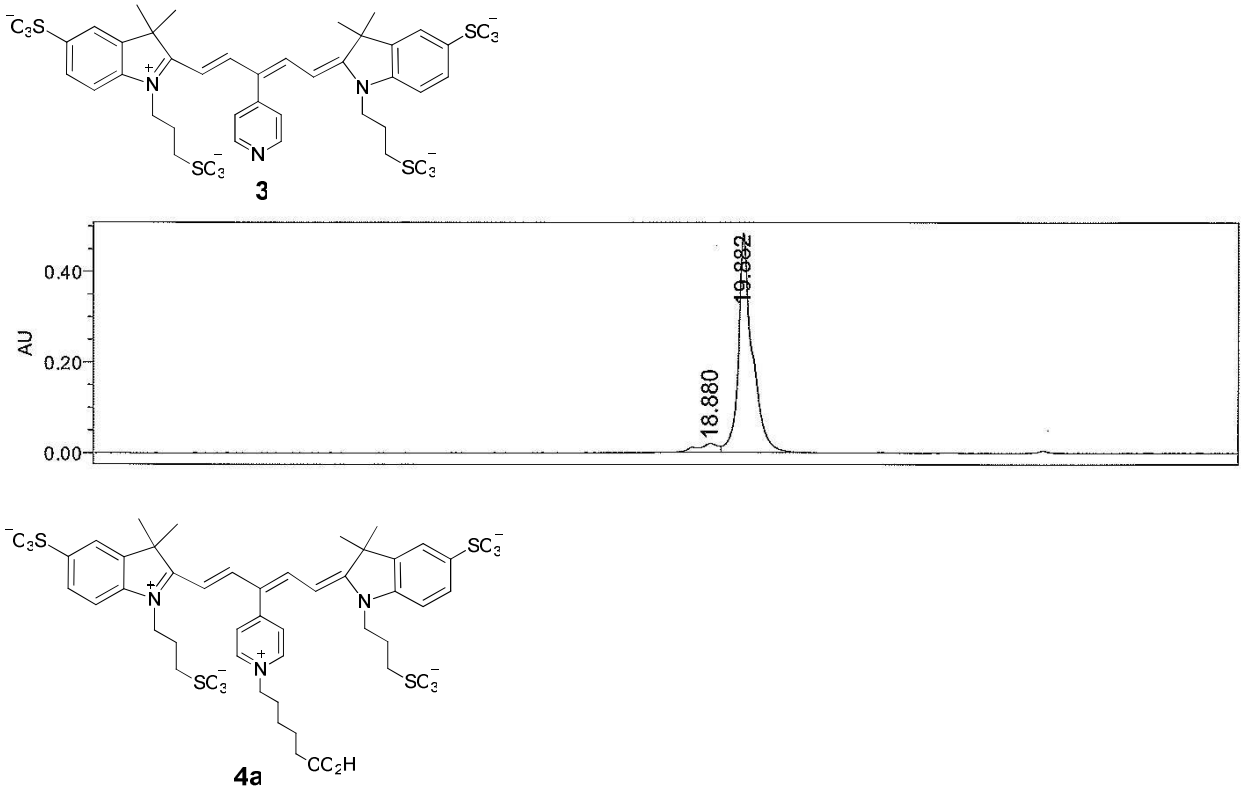
$$\text{DOL} = \frac{A_{dye}\,\varepsilon_{protein}}{(A_{280} - XA_{dye})\,\varepsilon_{dye}}$$

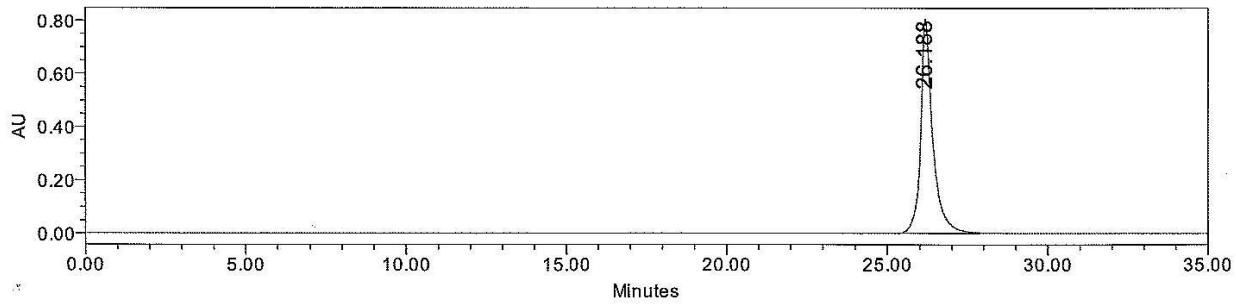
Fluorescence Labeling and Cell Imaging

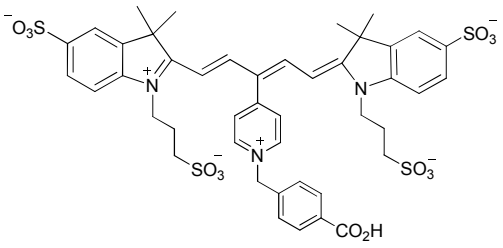
Bovine Pulmonary Artery Endothelial (BPAEC) cells in Dulbecco's modified eagle medium (DMEM) supplemented with 20% fetal bovine serum (FBS) were cultured on glass coverslips for 24 h to reach 50%-70% confluency. The cells were fixed with 4% formaldehyde in PBS for 15 min at 37 ºC, then washed with PBS (2X). The cells were permeabilized with 0.2% Triton-X in PBS for 5 min at room temperature, then washed with PBS (3×). The cells were blocked with blocking solution (5% normal goat serum (NGS)/0.2% BSA in PBS) for 30 min at room temperature. Then, the cells were incubated with mouse anti-tubulin primary antibody (2 μg/mL in blocking solution) at room temperature for 1 h. The cells were washed with PBS (3×), followed by incubating with dye-labeled goat anti-mouse secondary IgG antibody (10 μg/mL in blocking solution) at room temperature for 30 min. The cells were washed again with PBS (3×), and incubated with the nuclear stain 4',6-diamidino-2-phenylindole (0.2 μg/mL DAPI) in PBS for 2 min. The cells were washed with PBS (3×), eH_2O (1×), and 0.1% Tween-20 solution (1×). After the coverslips were air-dried, the coverslips were mounted in Cytoseal onto microscopy slides. Fluorescent images were captured on a Zeiss Axioskop 2 fluorescence microscope with 40× objective equipped with a Hamamatsu ORCA-ER CCD camera using excitation and

emission filters from Omega Optical. The nuclear stain DAPI was imaged using a 365 ± 5 nm band-pass filter for excitation and a 400 ± 5 nm cutoff filter for emission. The NIR fluorophore was imaged using a 610 ± 20 nm band-pass filter for excitation and a 650 ± 20 nm band-pass filter for emission. Exposure times of 100 and 200 ms, for the nuclear stain and carbocyanine dye channels, respectively, were used for image collection. All images from the carbocyanine dye channel were processed with identical leveling.

HPLC profiles and ^{1}H NMR Spectra

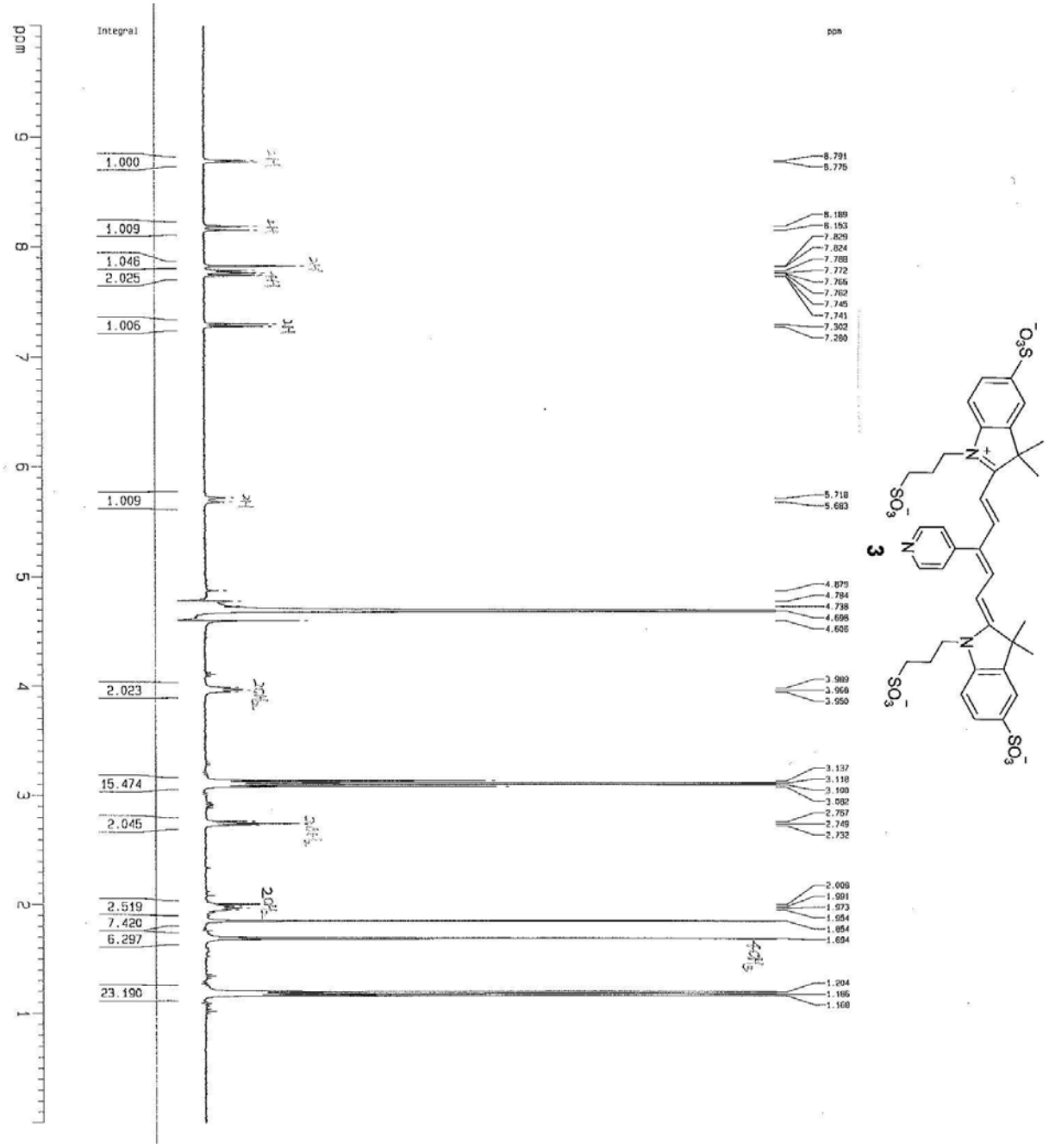


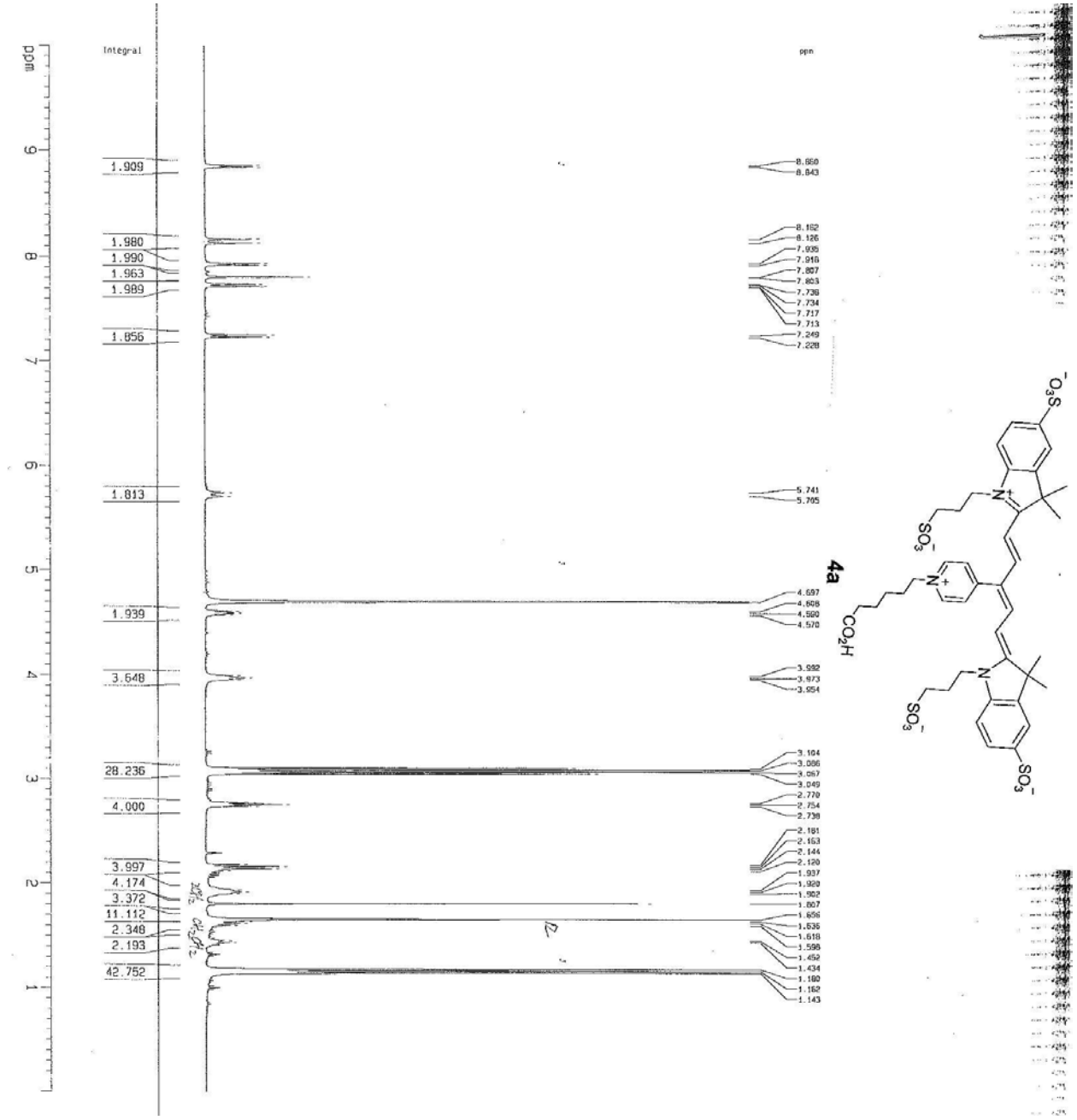

AU
0.80
0.60
0.40
0.20
0.00
26.188
0.00
5.00
10.00
15.00
20.00
25.00
30.00
35.00
Minutes

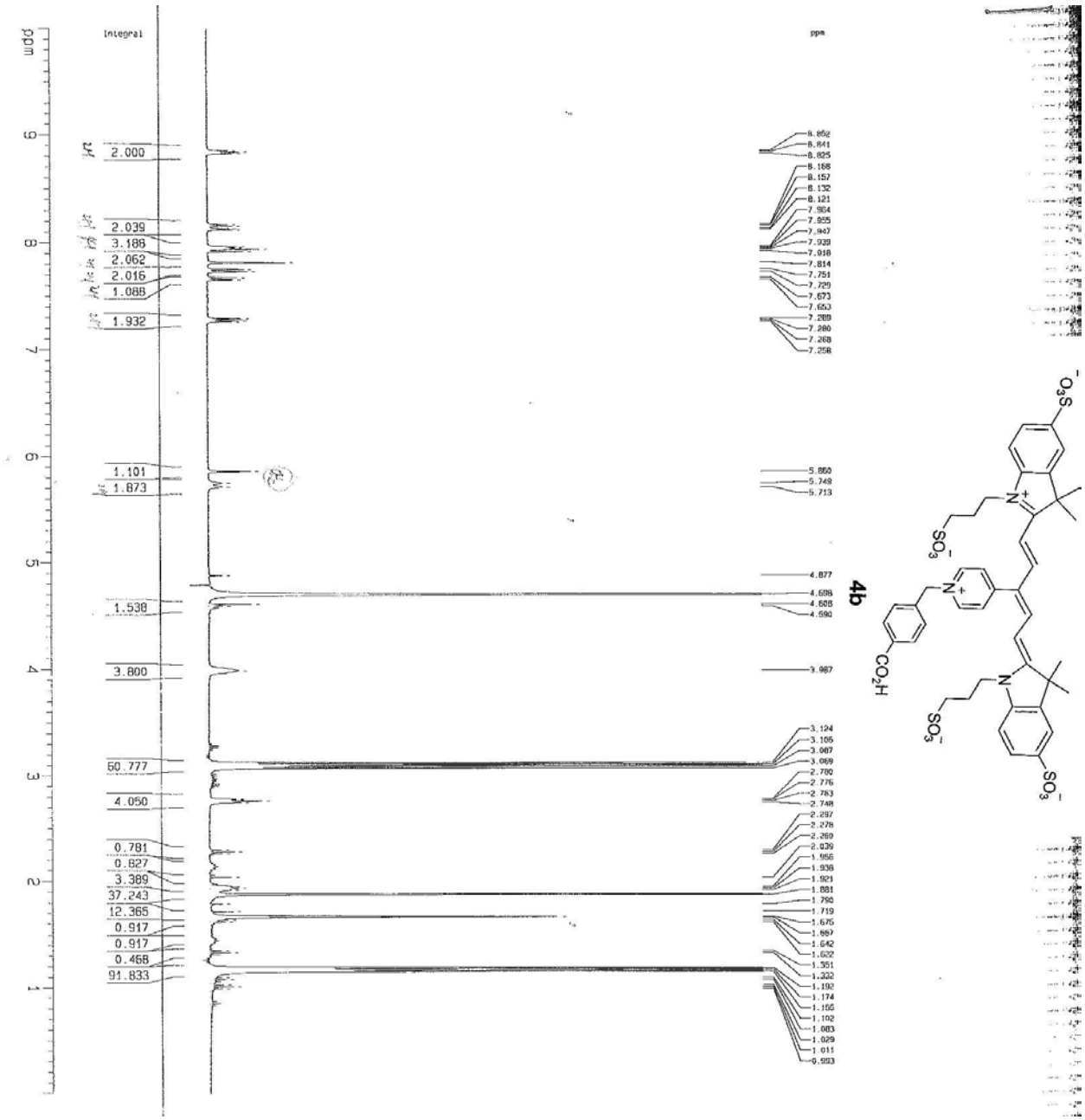

$^{-}O_3S$
SO_3^-
SO_3^-
SO_3^-
CO_2H

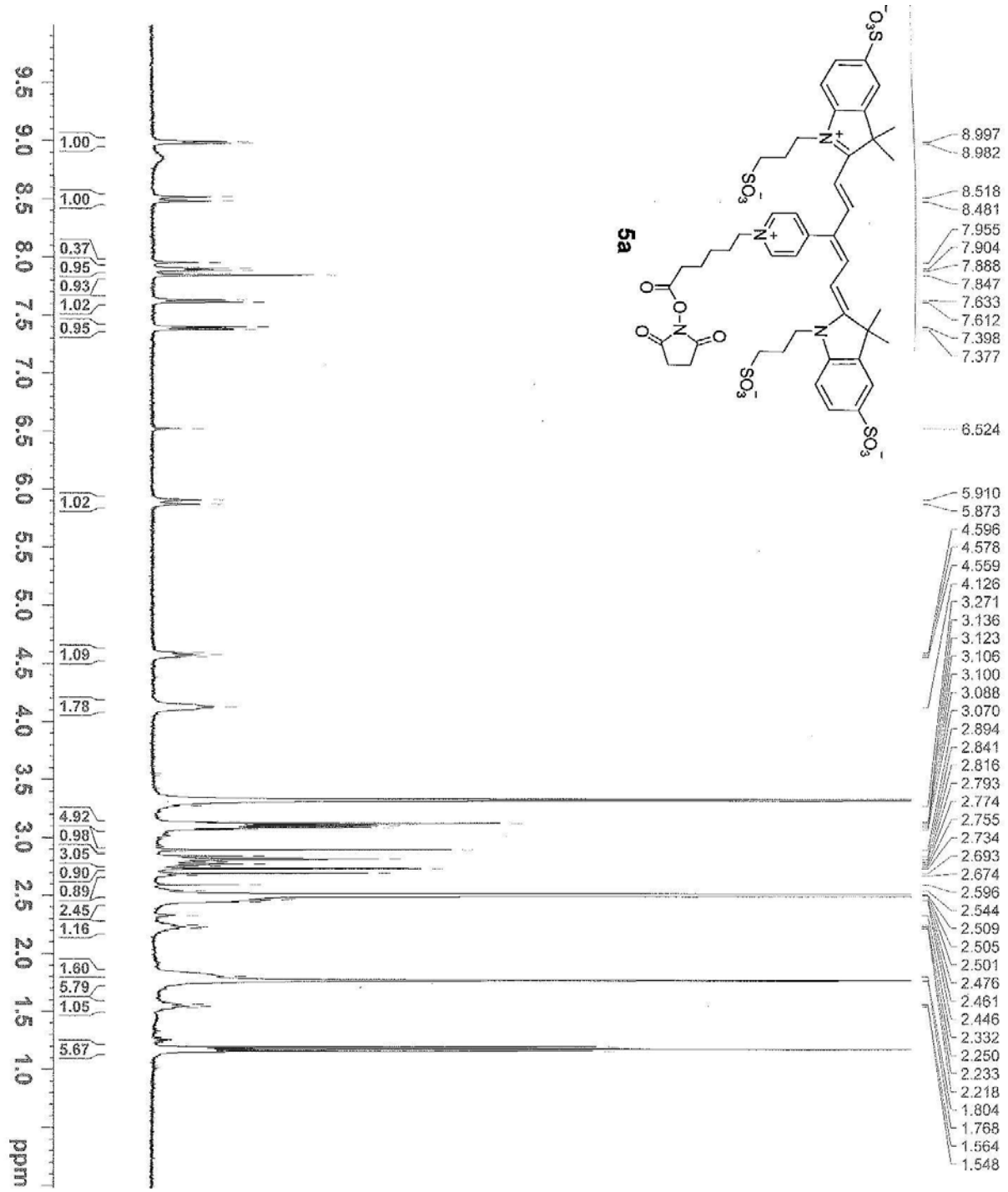
4b

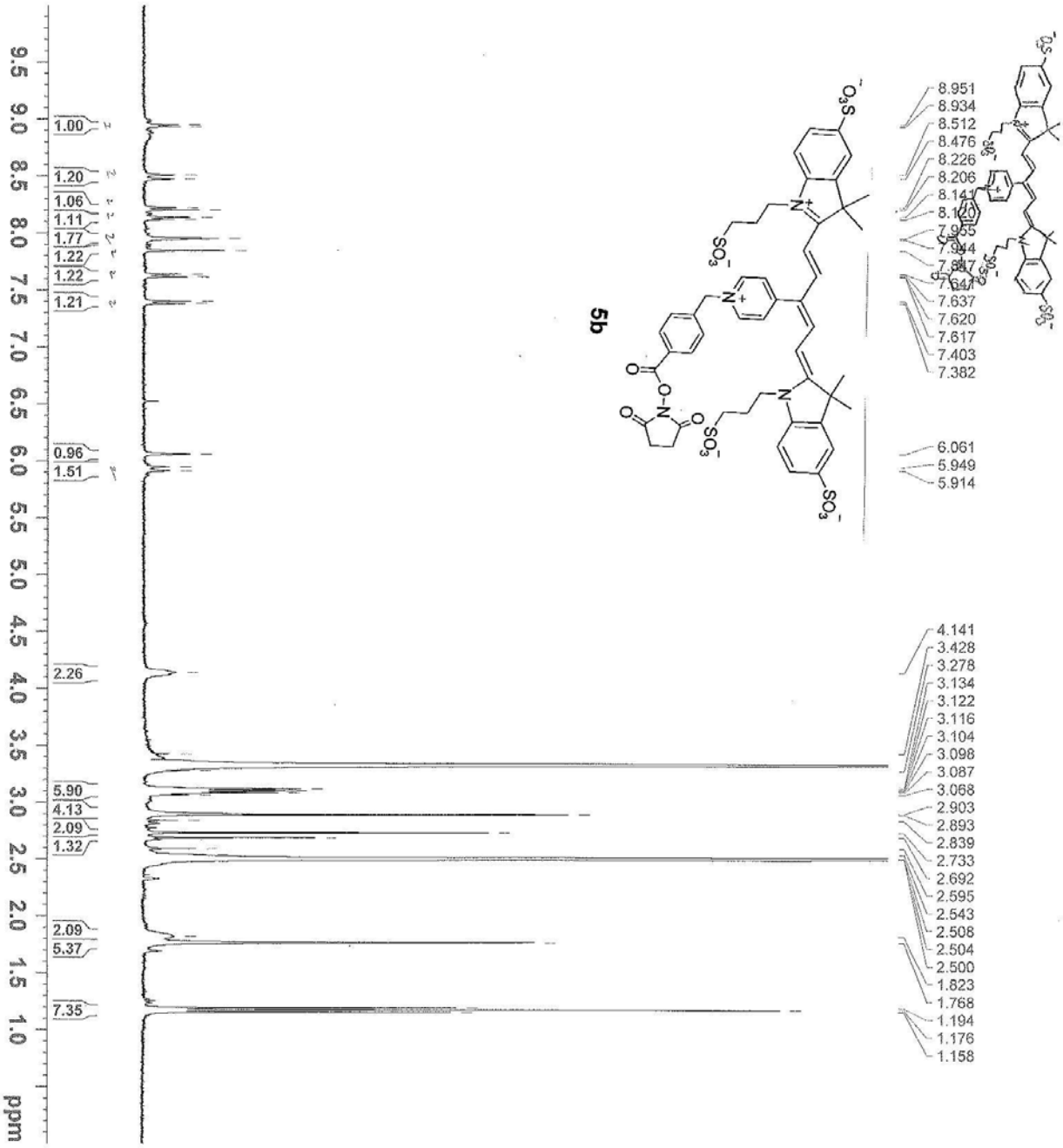

AU
0.30
0.20
0.10
0.00
23.016


Integral
ppm
1.000
1.009
1.046
2.025
1.006
1.009
2.023
15.474
2.045
2.519
7.420
6.297
23.190
8.791
8.775
8.189
8.153
7.829
7.824
7.788
7.772
7.765
7.762
7.745
7.741
7.302
7.280
5.718
5.683
4.879
4.784
4.738
4.698
4.606
3.989
3.968
3.950
3.137
3.118
3.100
3.082
2.757
2.749
2.732
2.009
1.991
1.973
1.954
1.954
1.694
1.204
1.186
1.168
3

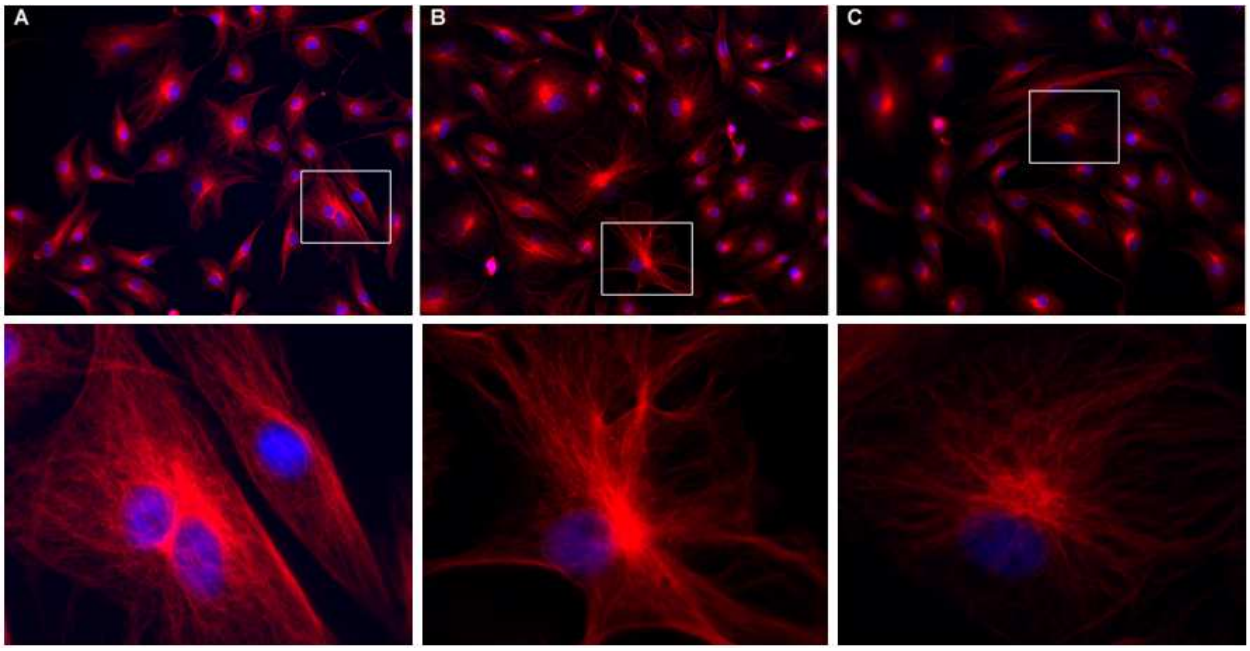

Integral
ppm
1.909
1.980
1.990
1.963
1.989
1.856
1.813
1.939
3.648
28.236
4.000
3.997
4.174
3.372
11.112
2.348
2.193
42.752
8.860
8.843
8.162
8.126
7.935
7.916
7.867
7.853
7.736
7.734
7.717
7.713
7.249
7.228
5.741
5.705
4.697
4.608
4.589
4.570
3.992
3.973
3.954
3.164
3.086
3.067
3.049
2.770
2.754
2.738
2.181
2.163
2.144
2.120
1.937
1.920
1.902
1.807
1.656
1.636
1.618
1.598
1.452
1.434
1.180
1.162
1.143
4a
O_3S
SO_3^-
CO_2H
SO_3^-
SO_3^-


Integral
ppm
2.000
2.039
3.188
2.062
2.016
1.088
1.932
1.101
1.873
1.538
3.800
60.777
4.050
0.781
0.827
3.389
37.243
12.365
0.917
0.917
0.468
91.833
4b

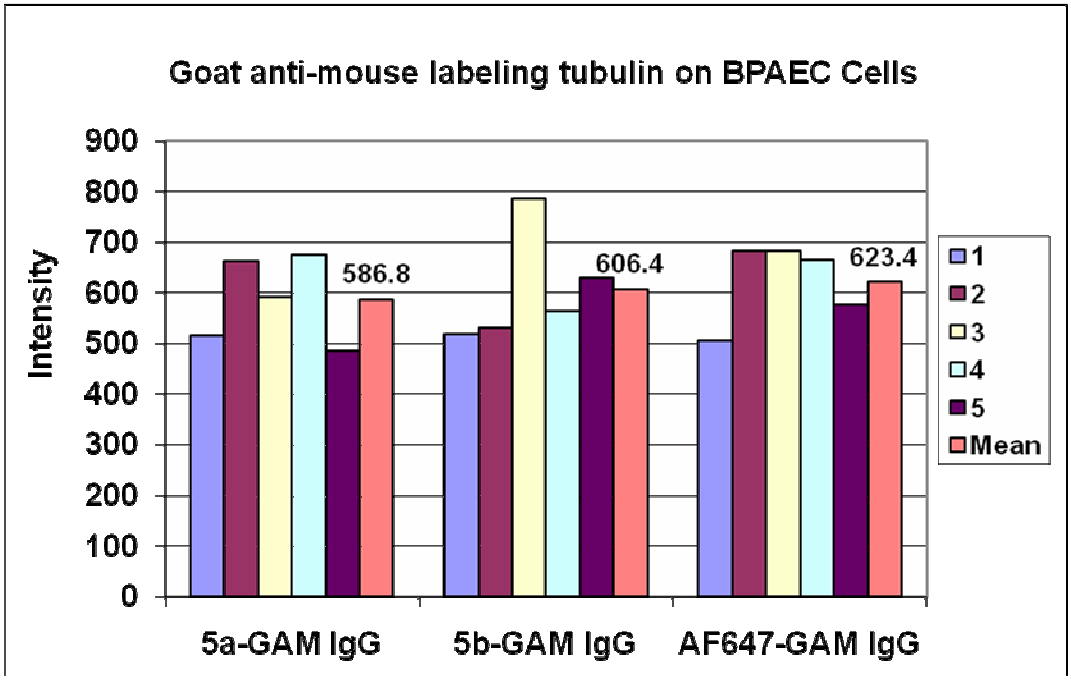

5a
8.997
8.982
8.518
8.481
7.955
7.904
7.888
7.847
7.633
7.612
7.398
7.377
6.524
5.910
5.873
4.596
4.578
4.559
4.126
3.271
3.136
3.123
3.106
3.100
3.088
3.070
2.894
2.841
2.816
2.793
2.774
2.755
2.734
2.693
2.674
2.596
2.544
2.509
2.505
2.501
2.476
2.461
2.446
2.332
2.250
2.233
2.218
1.804
1.768
1.564
1.548
1.00
1.00
0.37
0.95
0.93
1.02
0.95
1.02
1.09
1.78
4.92
0.98
3.05
0.90
0.89
2.45
1.16
1.60
5.79
1.05
5.67
ppm


5b
8.951
8.934
8.512
8.476
8.226
8.206
7.955
7.637
7.620
7.617
7.403
7.382
6.061
5.949
5.914
4.141
3.428
3.278
3.134
3.122
3.116
3.104
3.098
3.087
3.068
2.903
2.893
2.839
2.733
2.692
2.595
2.543
2.508
2.504
2.500
1.823
1.768
1.194
1.176
1.158
1.00
1.20
1.06
1.11
1.77
1.22
1.22
1.21
0.96
1.51
2.26
5.90
4.13
2.09
1.32
2.09
5.37
7.35
ppm

Cell Imaging and Fluorescence Intensity



Fluorescene microscopy of BPAEC cells incubated fluorophore-labeled antibody.
Cells incubated with **5a**-labeled antibody (A), **5b**-labeled antibody (B), and Alexa Fluor 647-labeled antibody (C). Imaging in the bottom is a close up view of representative cells. Fluorescence signal from the nuclear stain, DAPI, colored in blue, NIR fluorophores colored in red.



Fluorescence relative intensity of BPAEC cells labeled with **5a**-GAM IgG, **5b**-GAM IgG, and AF647-GAM IgG, respectively. The mean intensity was averaged based on five different images.

References

(1) Fery-Forgues, S., and Lavabre, D. (1999) Are fluorescence quantum yields so tricky to measure? A demonstration using familiar stationery products. *J. Chem. Educ. 76*, 1260−1264.

(2) Mujumdar, R. B., Ernst, L. A., Mujumdar, S. R., Lewis, C. J., and Waggoner, A. S. (1993) Cyanine dye labeling reagents: sulfoindocyanine succinimidyl esters. *Bioconjugate Chem. 4*, 105-111.

(3) Toutchkine, A., Nalbant, P., and Hahn, K. M. (2002) Facile synthesis of thiol-reactive Cy3 and Cy5 derivatives with enhanced water solubility. *Bioconjugate Chem. 13*, 387−391.

Bioconjugate Chemistry

ARTICLE

pubs.acs.org/bc

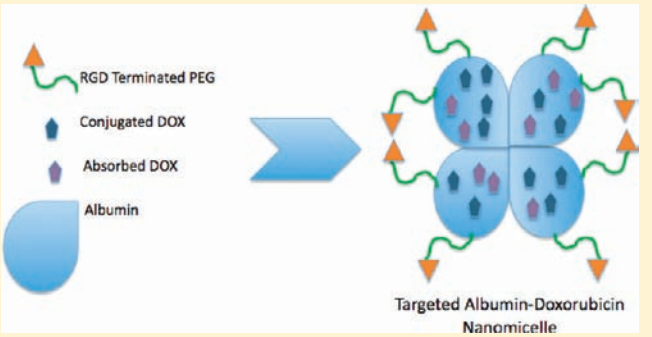
Targeted Albumin-Based Nanoparticles for Delivery of Amphipathic Drugs

Rongzuo Xu, Michael Fisher, and R. L. Juliano*

Division of Molecular Pharmaceutics, UNC Eshelman School of Pharmacy, University of North Carolina, Chapel Hill, North Carolina 27599, United States

Supporting Information

ABSTRACT: We report the preparation and physical and biological characterization of human serum albumin-based micelles of approximately 30 nm diameter for the delivery of amphipathic drugs, represented by doxorubicin. The micelles were surface conjugated with cyclic RGD peptides to guide selective delivery to cells expressing the $\alpha_v\beta_3$ integrin. Multiple poly(ethylene glycol)s (PEGs) with molecular weight of 3400 Da were used to form a hydrophilic outer layer, with the inner core formed by albumin conjugated with doxorubicin via disulfide bonds. Additional doxorubicin was physically adsorbed into this core to attain a high drug loading capacity, where each albumin was associated with about 50 doxorubicin molecules. The formed micelles were stable in serum but continuously released doxorubicin when incubated with free thiols at concentrations mimicking the intracellular environment. When incubated with human melanoma cells (M21+) that express the $\alpha_v\beta_3$ integrin, higher uptake and longer retention of doxorubicin was observed with the RGD-targeted micelles than in the case of untargeted control micelles or free doxorubicin. Consequently, the RGD-targeted micelles manifested cytotoxicity at lower doses of drug than control micelles or free drug.



INTRODUCTION

A major disadvantage of hydrophobic drugs is low water solubility and associated poor pharmacokinetic profiles, which in turn can contribute to adverse effects and low therapeutic efficacy. A variety of systems, including polymers, micelles, liposomes, nanoparticles, and microspheres, have been investigated to improve the parental delivery of hydrophobic agents. Albumin is a major blood protein, and due to its abundance, low immunogenicity, good biocompatibility, and ability to be transcytosed across vascular endothelia, it has been utilized in delivery systems for moieties such as anticancer drugs,[1,2] photosensitizers,[3] antifungal drugs, and diagnostic imaging agents.[4,5] In one approach, the albumin carrier is used as a single molecule, where the drugs are covalently conjugated to the free thiol in the cysteine-34 position[6] or to introduced free thiols.[7] This type of conjugation strategy maintains the physiochemical properties of albumin while significantly improving the tumor uptake of conjugated drugs. In this strategy, however, only one or a few therapeutic molecules are carried by each albumin molecule, leading to low delivery efficiency. Albumin can also be formulated into microspheres or nanoparticles through precipitation in organic solvent followed by cross-linking.[8−10] The formed particles can encapsulate tens to thousands of drug molecules per particle, achieving high drug-loading efficiency. However, with sizes in the range of several hundred nanometers to several micrometers, these particles are prone to uptake by reticuloendothelial system in liver and spleen. Another approach has been reported that can formulate hydrophobic drugs into albumin nanoparticles in the size range between 100 and 200 nm.[11,12] Thus, Abraxane, a paclitaxol−albumin nanoparticle with average size of 130 nm, has been extensively investigated in animal and clinical studies.[13]

Polymeric micelles with sizes of 20−100 nm provide effective carriers for delivery of hydrophobic or amphipathic compounds.[14,15] In aqueous media, amphiphilic block copolymers spontaneously assemble into micelles with a distinct core−shell structure. The hydrophilic portion of the copolymer, usually PEG with molecular weights ranging from 2 to 15 kD, forms a coronal layer; the hydrophobic portion, typically consisting of poly(propylene oxide), poly(D,L-lactic acid), poly(ε-caprolactone), poly(glutamic acid), or poly(L-aspartic acid), to name a few, forms a core that acts as a reservoir for drugs such as doxorubicin, paclitaxel, docetaxel, camptothecin, and others.[16−19] Polymeric micelles often have high drug payloads in the form of either chemically conjugated or physically entrapped drug. They typically have high stability in the circulation owing to low critical micelle concentration and long circulating lifetime due to a size above the renal filtration threshold and due to PEG's ability to evade recognition by the reticuloendothelial system (RES). These properties aid in the preferential

Received: May 17, 2010
Revised: March 25, 2011
Published: April 01, 2011

ACS Publications © 2011 American Chemical Society

accumulation of micelles in tumor tissue through the enhanced permeability and retention (EPR) effect,[20−22] resulting in reduced toxicity to healthy tissues and improved antitumor efficacy. However, there remain concerns about the possible toxicities of polymeric micelles, including general cytotoxicity, hematoxicity, immunogenicity, carcinogenicity, and other aspects,[23] making high biocompatibility a prerequisite for synthetic copolymer micelles.

With these considerations in mind, we report the first example of targeted albumin-based nanoscale micelles for delivery of amphipathic drugs. We hypothesize that increasing the hydrophobicity of PEGylated albumin by addition of drug, and diminishment of primary amine groups on the protein surface, can drive the aggregation and formation of polymeric micelles. In addition, functionalization of the distal ends of the PEG chains can be used to incorporate ligands into the micelle outer layer to guide active targeting. We use doxorubicin, an anthracycline agent widely used for the treatment of leukemia, lymphoma, and solid tumors, as a model compound.[24,25] Doxorubicin is conjugated to the amine group on albumin using a bifunctional linker that provides a disulfide bond between the protein and the drug, while additional doxorubicin molecules become physically entrapped in the micelle. A cyclic RGD peptide was conjugated to the micelle PEG chains, since it is a ligand with high binding affinity to $\alpha_v\beta_3$ integrin, a membrane protein highly expressed in angiogenic endothelia and in some cancer cells.[26,27] This targeted albumin micelle delivery system is described herein with focus on its synthesis, physiochemical characterization, and uptake and pharmacological efficacy in cultured cells.

MATERIALS AND METHODS

Materials. Human serum albumin, ethylene glycol-bis-(2-aminoethylether)-*N*,*N*,*N*′,*N*′-tetraacetic acid (EDTA), doxorubicin hydrochloride, 2-mercaptoethanol, ninhydrin, hydrindantin, and 2-methoxyethanol were purchased from Sigma-Aldrich (St. Louis, MO, USA). AlexaFluor 488 C5 maleimide was from Invitrogen (Carlsbad, CA, USA). Hydroxylamine hydrochloride, sulfosuccinimidyl 6-(3′-[2-pyridyldithio]-propionamido) hexanoate (Sulfo-LC-SPDP), and 2-iminothiolane were from Pierce (Rockford, IL, USA). Bifunctional poly(ethylene glycol) (PEG), Malhex-NH-PEG-O-C_3H_6-CONHS, was purchased from Rapp Polymere (Tubingen, German). Cyclo[RGDfK(Ac-SCH2CO)] peptide was from Peptide International (Louisville, KY, USA).

Preparation of Albumin Conjugates with Cyclic RGD PEG or 2-Mercaptoethanol PEG. Human serum albumin (30 mg, 4.44×10^{-7} mol) was reacted with AlexaFluor 488 C5 maleimide (1 mg, 1.39×10^{-6} mol) for 4 h at room temperature in phosphate saline buffer (PBS, pH 7.4) containing 1 mM EDTA. This was followed by dialysis in a MWCO 3500 cassette (Pierce, Rockford, IL) overnight at room temperature. Amine groups from lysine residues on the albumin surface were then reacted with Mal-hex-NH-PEG5000-C_3H_6-CONHS (60 mg, 1.2×10^{-5} mol) in PBS with 1 mM EDTA (pH 7.4) for 4 h. The unreacted PEG derivative was removed by dialysis in a MWCO 100 000 chamber (Havard Apparatus, Holliston, MA, USA). The PEGylated albumin (equivalent to 15 mg of albumin) was reacted with cyclo[RGDfK(Ac-SCH2CO)] (10 mg, 1.47×10^{-5} mol) in PBS with 1 mM EDTA and 50 mM hydroxylamine for 24 h at room temperature. The product, denoted as RPA, was purified by extensive dialysis in a MWCO 100 000 chamber for 24 h. MPA was prepared by conjugating PEGylated albumin (equivalent to 2 mg of albumin) with 100 μg of 2-mercaptoethanol in PBS with 1 mM EDTA for 24 h and dialysis in a MWCO 100 000 chamber overnight. The number of PEG molecules conjugated was estimated by determining the loss of surface amine groups using a ninhydrin test.

Preparation of RGD-PEG-Albumin-Doxorubicin Conjugates (RPA-DOX). RPA (equivalent to 2 mg albumin) was reacted with sulfo-LC-SPDP (0.5 mg, 9.5×10^{-7} mol) in PBS with 1 mM EDTA for 4 h at room temperature, followed by dialysis in a MWCO 100 000 chamber overnight. Doxorubicin hydrochloride (1.5 mg, 2.6×10^{-6} mol) was reacted with 2-iminothiolane (0.36 mg, 2.6×10^{-6} mol) for 2 h at PBS with 1 mM EDTA to create thiolated (-SH) doxorubicin (ESI-MS $[M+1]^+$: 647.47 (observed), 645.79 (calculated)). An excess of the resulting doxorubicin-thiol was then reacted with the product from the RPA and sulfo-LC-SPDP reaction; the final product RGD-PEG-albumin-doxorubicin conjugates (denoted as RPA-DOX) was thus prepared. RPA-DOX was further purified by dialysis in PBS with 1 mM EDTA for 24 h, and stored in a refrigerator at 4 °C. The number of doxorubicin molecules conjugated via the SPDP linker was estimated using the ninhydrin reaction. Please note that, for the sake of simplicity, here and in the sections that follow we refer to these materials as albumin−doxorubicin conjugates although it is actually a thiolated form of doxorubicin that is conjugated. Likewise, the drug that is released from the conjugate is termed doxorubicin although it is actually the thiolated form.

Preparation of 2-Mercaptoethanol-PEG-Albumin-Doxorubicin Conjugates (MPA-DOX). The preparation of MPA-DOX was exactly parallel to that of RPA-DOX except that MPA lacking RGD groups was utilized.

FPLC-QELS and Zeta Potential. Samples (100 μL) containing albumin conjugates at 0.1 to 0.5 mg protein per mL were loaded on a fast protein liquid chromatography (FPLC) system (GE Healthcare) equipped with a Superdex-200 size exclusion column and quasi-elastic light scattering (QELS) (Wyatt, Santa Barbara, CA, USA). The data were collected and analyzed using *Astra* software (Wyatt, Santa Barbara, CA, USA). The zeta potentials of the RPA-Dox and MPA-Dox were measured using a Zetasizer (Malvern Instruments, Westbury, MA).

TEM. The RPA-Dox and MPA-Dox were diluted and dropped on 200 mesh carbon-coated copper grids (Ted Pella, Redding CA) and allowed to attach for two minutes. Uranyl acetate aqueous solution (2−5%) was then added on the grid for 2 min to counterstain the nanoparticles. The TEM images were then acquired with magnification of 17 000 times using a JEOL 100CX II transmission electron microscope.

Conjugate Serum Stability. RPA-DOX and MPA-DOX containing 20 μM doxorubicin were incubated in PBS containing 10% serum, using PBS as a control. After incubation at 37 °C for 0.3, 2, 4, and 8 h, a fraction was collected and ultrafiltered at 3400 rpm for 3 min using a YM-50 filter (Millipore, Bedford, MA, USA). Both the eluted phase and the residual volume on top of the filter were collected. The volumes were measured (V_{up} denotes residual volume and V_{down} denotes volume of filtrate buffer) and the absorbance at 481 nm was determined (A_{up} denotes absorbance of residual and A_{down} denotes absorbance of filtered volume). The percentage of released doxorubicin was calculated by the equation: Percentage of released doxorubicin (%) = $[(A_{down} \times (V_{up} + V_{down})]/(A_{up} \times V_{up} + A_{down} \times V_{down}) - 6\%) \times 100$. The 6% is an estimate of the nonspecific leaking of RPA-DOX or MPA-DOX themselves. The serum stability curve was produced by plotting the percentage of released doxorubicin versus time.

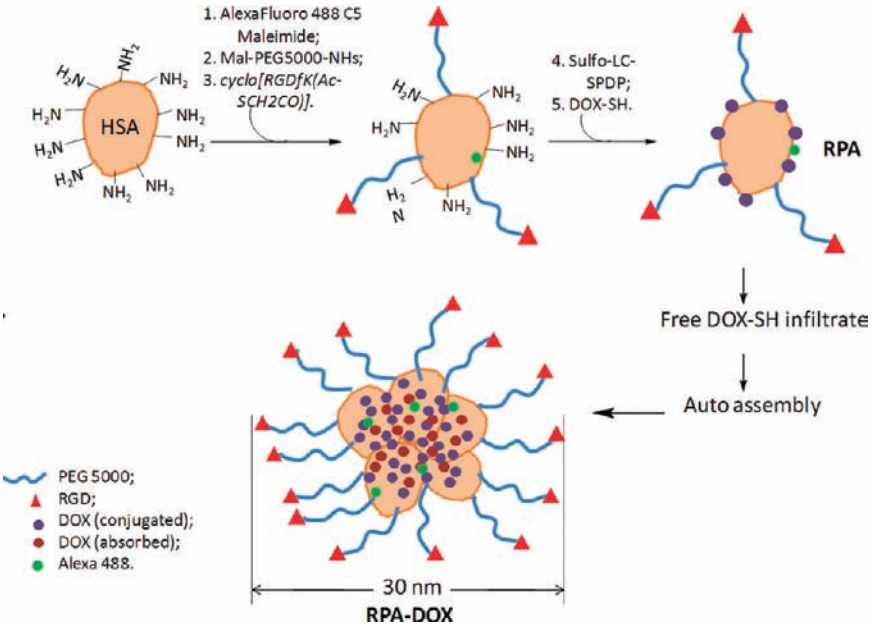


Figure 1. Preparation of RPA-Dox.

Release of Doxorubicin by Sulfhydryls. RPA-Dox and MPA-Dox containing 20 μM doxorubicin were incubated at 37 °C in PBS (pH 7.4) containing 10 mM glutathione and 100 μM cysteine, or in unmodified PBS as control. Samples were collected after 15, 120, and 240 min and 8, 24, and 48 h of incubation and ultrafiltered at 3400 rpm for 3 min using a YM-50 filter (Millipore, Bedford, MA, USA). The percentage of released doxorubicin was calculated, and the time course of doxorubicin release was then generated by plotting percent of released doxorubicin versus time.

Cell Uptake. M21+ human melanoma cells that express the $\alpha_v\beta_3$ integrin were seeded on 24 well plates at 4×10^4 cells per well and cultured overnight. The cells were either preincubated with 100 μM cyclic (RGDfV) for half an hour or directly incubated with doxorubicin, RPA-DOX, or MPA-DOX at concentrations ranging from 100 nM to 2 μM in Opti-MEM medium. After 4 h incubation, the cells were harvested by trypsinization. The fluorescence intensity at 488/575 nm of doxorubicin[28] per cell was determined using a Cyan flow cytometer (Beckman Coulter, Miami, FL).

Confocal Microscopy. M21+ cells were cultured in complete DMEM medium in a glass-bottom culture dish (MatTek, Ashland, MA) overnight. The medium was replaced with Opti-MEM medium containing 2 μM free doxorubicin, RPA-DOX, or MPA-DOX and incubated for 4 h at 37 °C. Additional samples were continued in culture in drug-free complete DMEM medium for 12 h. The doxorubicin distribution was imaged using a Zeiss confocal microscopy with a 63× objective lens and a 488 nm laser light source. The images were analyzed using Zeiss LSM software.

Cytotoxicity. M21+ cells were seeded into 96 well plates at a density of 5000 cells per well. After overnight incubation, the medium was aspirated and fresh DMEM medium containing different concentrations of free doxorubicin, RPA-Dox, or MPA-Dox was added; the concentrations of RPA-Dox and MPA-Dox are expressed in doxorubicin equivalents. The cells were continuously cultured at 37 °C and 5% CO_2 for 3 days. The cytotoxicity was then assessed by a modified MTT assay. Briefly, the medium was replaced by a mixture of 200 μL of fresh DMEM medium and 20 μL of MTT solution (5 mg/mL MTT in PBS), followed by 2 h incubation. The culture medium was then removed by aspiration. Then, 100 μL DMSO was added into each well, stirred, and absorbance at 540 nm of the cell suspension was determined using a FLUOstar Omega Microplate Reader (BMG Labtech, Offenburg, Germany). The cytotoxicity was evaluated through comparing absorbance of treated cells against the untreated controls. The results of cytotoxicity assay were used to construct dose−response curves and IC_{50} doses were determined.[29] The toxicities of RPA and MPA, without doxorubicin, were determined in a parallel assay. In a separate experiment, the toxicity of doxorubicin itself versus its thiolated derivative was also compared using the MTT assay.

RESULTS

Synthesis and Characterization. The preparation of albumin−doxorubicin micelles is outlined in Figure 1. First, human serum albumin (HSA) was labeled with the green fluorescent dye Alexa Fluor 488 at the free thiol group at Cys34. Subsequently, several Mal-PEG-NHS moieties with molecular weight of 3400 were conjugated to primary amines on the HSA surface to form PEGylated albumin. The unreacted PEG derivative was removed by dialysis in a MWCO 100 000 bag. Excess cyclo[RGDfK-($AcSCH_2CO$)] was then incubated with the PEGylated albumin in the presence of hydroxylamine to form RGD-PEG-HSA (RPA). Alternatively, 2-mercaptoethanol was used to react with PEGylated albumin to form 2-mercaptoethanol-PEG-HSA (MPA) as a control. The amount of PEG per albumin was determined using a ninhydrin test[30] to compare the primary amine density before and after the PEGylation reaction. RPA has an average of 17.5 PEGs per albumin molecule while MPA has 15.1 PEGs. Additional primary amine groups on the surface of RPA and MPA were reacted with sulfo-LC-SPDP followed by

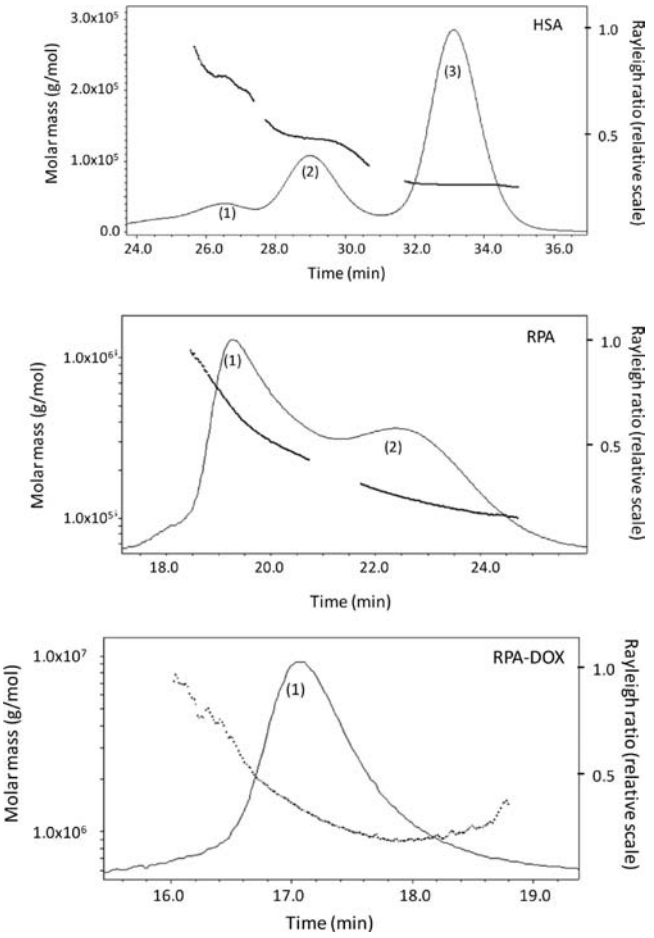


Figure 2. Reaction progress of RPA-DOX. The intermediates and final products were analyzed by FPLC-QELS. Dotted line: molar mass. Solid line: Rayleigh ratio.

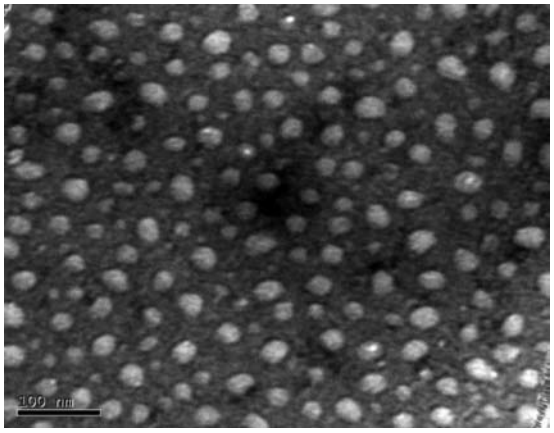


Figure 3. TEM image of RPA-DOX (170 000×). The sample is counterstained by uranyl acetate. The average particle size is around 30 nm.

conjugation with the thiolated doxorubicin derivative to form PEGylated albumin doxorubicin complexes termed RPA-DOX or MPA-DOX. The reaction between thiol and SPDP created a disulfide linker that can be potentially cleaved by endogenous thiols to liberate the thiolated doxorubicin.

Table 1. Physiochemical Properties of RPA-DOX, MPA-DOX, and Intermediates[a]

		Rh(z) (nm)	M_w	M_n	PDI
	Peak 1	3.2	2.16×10^5	2.15×10^5	1.01
HSA	Peak 2	3.8	1.30×10^5	1.29×10^5	1.01
	Peak 3	3.2	6.68×10^4	6.68×10^4	1.00
MPA	Peak 1	13.3	3.81×10^5	3.25×10^5	1.17
	Peak 2	6.9	1.21×10^5	1.18×10^5	1.03
RPA	Peak 1	14.1	3.77×10^5	3.36×10^5	1.12
	Peak 2	9.3	1.27×10^5	1.25×10^5	1.02
MPA-DOX	Peak 1	16.8	1.35×10^6	1.07×10^6	1.26
RPA-DOX	Peak 1	15.2	1.27×10^6	1.15×10^6	1.10

[a] Note: the peaks were numerated and displayed at Figure 2 and Supporting Information Figure S.1.

The physical aspects of the conjugates were monitored, as summarized in Figure 2, Supporting Information Figure S.1, Figure 3, and Tables 1 and 2. Significant size and apparent molecular weight increases were observed after the addition of the PEG derivative followed by cyclic RGD or 2-mercaptoethanol. Both RPA and MPA exist primarily as monomers and trimers with narrow molecular weight distributions, indicated by low polydispersity indices. However, FPLC-QELS analysis showed that the RPA-DOX has a hydrodynamic radius of about 15 nm and molecular weight of more than 1 million Da, with a single distribution and a low polydispersity index. The RPA-DOX was visualized by transmission electromicroscopy (TEM), revealing a diameter averaging about 30 nm, which is consistent with its hydrodynamic size (Figure 3). Compared with RPA, RPA-DOX has much larger particle size as well as apparent molecular weight. Thus, the RPA-DOX must contain several albumin molecules that have coaggregated. We postulate that RPA-DOX monomers oligomerize to form nanoscale micelles. This may be due to the amphiphilicity of PEGylated RPA-DOX, where the hydrophilicity can be attributed to PEG and the hydrophobicity is from albumin that has lost a significant fraction of its primary amines, with hydrophobicity further increased by the conjugation of doxorubicin molecules. The zetasizer revealed that the formed micelles had a slightly negative surface potential (Table 2).

As determined by a ninhydrin test, RPA-DOX had approximately 24.6 chemically conjugated doxorubicins per albumin. However, the total amount of doxorubicin associated with the albumin micelle was greater, as determined by measuring absorbance at 481 nm, where doxorubicin (as well as its thiolated derivative) has an extinction coefficient of 10 410 M^{-1} cm^{-1} at 25 °C.[31] This revealed that an average of 50.6 doxorubicin molecules were associated with each albumin molecule. This suggests that extra doxorubicin molecules were physically accommodated in the hydrophobic domain of the formed micelle, probably through hydrophobic interaction and van de Waals forces. This substantially increased the drug loading of the albumin micelles (Table 2).

The driving force of micelle formation was further evaluated by synthesizing a series of RPA derivatives, where each RPA was conjugated to sulfo-LC-SPDP and then to doxorubicin derivatives at ratios from 1:5:5 to 1:30:90. The FPLC analysis (Supporting Information Figure S.2) showed that higher molecular weight complexes started to form when each RPA was conjugated to doxorubicin derivatives at a molar ratio of 1:5. However, in this condition UV absorbance showed that only a

Table 2. Physiochemical Properties of RPA-DOX and MPA-DOX

	PEG per albumin[a]	total doxorubicn per albumin[b]	drug loadig ratio (%)	conjugated doxorubicin per albumin[a]	adsorbed doxorubicin per albumin	hydrodynamic size (Rh (z), nm)[c]	M_w[c]	poly dispersity[c]	zeta potential (mV)[d]
RPA-DOX	17.5	50.6	56.2	24.6	26	15.2	1.27×10^6	1.10	−2.6
MPA-DOX	15.1	56.5	62.3	20.7	35.8	16.8	1.35×10^6	1.26	−1.9

[a] Determined by ninhydrin test. [b] Determined by spectrum method. [c] Determined by FPLC-QELS. [d] Measured by zetasizer.

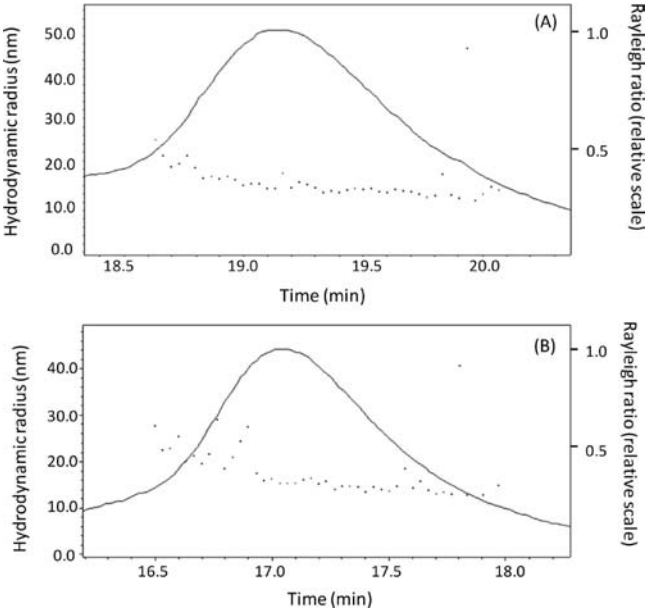


Figure 4. Stability of RPA-DOX. RPA-DOX sample were analyzed by FPLC-QELS in 3 days (A) and 5 weeks (B) postsynthesis.

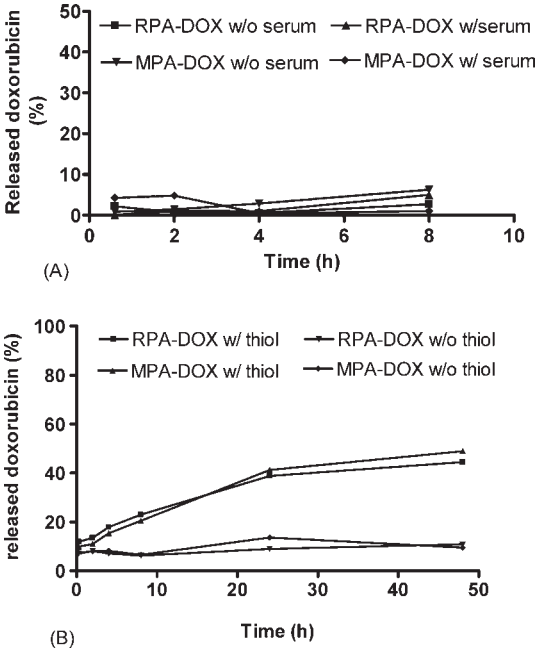


Figure 5. Doxorubicin release kinetics. (A) RPA-DOX and MPA-DOX were incubated with PBS only or PBS with 10% serum at 37 °C. (B) RPA-DOX and MPA-DOX were incubated at in PBS with thiols from 10 mM glutathione and 100 uM cysteine or PBS only at 37 °C.

part of RPA-DOX was formed into micelles with most of it staying in the same form and distribution as drug-free RPA. With the doxorubicin amount increased from 5 per RPA to 30 per RPA, additional RPA was incorporated into micelles. When doxorubicin was reacted to RPA at a molar ratio of 1:90, with excess doxorubicin derivatives, almost all RPA was formed into micelles with a single peak distribution. This result clearly shows that higher amounts of doxorubicin can function as a driving force for micelle formation. The doxorubicin conjugates on RPA were determined by observing the release of pyridine-2-thione (λ_{max} = 343 nm) from the reaction intermediate, and the final amount of doxorubicin associated with RPA was determined by the absorbance of doxorubicin at 481 nm (Supporting Information Table S.1). It shows that RPA5 and RPA30 lost significant amounts of loaded doxorubicin during dialysis while RPA90 retained approximately 44 doxorubicin molecules per RPA. This result shows that using extra amounts of doxorubicin in the formulation process can result in more doxorubicin loaded on RPA. Taken together, it suggests that formulating RPA with a high amount of doxorubicin will drive the formation of micelles that stably hold associated doxorubicin molecules.

The stability of the formed micelles was tested (Figure 4). After five weeks storage in PBS buffer with 1 mM EDTA at 4 °C, only trace amounts of doxorubicin were detected after ultrafiltration of the material. This result shows that the doxorubicin is stably held inside the micelle. The stored batch of RPA-DOX was also analyzed by FPLC-QELS. This showed that RPA-DOX kept its single peak distribution profile with a low polydispersity index and maintained its size close to freshly prepared material. This suggests that RPA-DOX does not aggregate into larger particles under this storage condition. The critical micelle concentration (CMC) was not determined. However, when diluted to concentrations lower than 0.2 μM albumin equivalent, the micelles maintained their structure when visualized by TEM. No doxorubicin leaked out into solution during ultracentrifugal filtration with a MWCO 50 kDa filter. This indicates that the albumin micelle has a similarly low CMC value to other polymeric micelles, typically on the order of 10^{-6}–10^{-7} M.

Doxorubicin Release. RPA-DOX was tested by incubation in PBS or PBS with 10% serum at 37 °C for up to 8 h (Figure 5A). Less than 5% of doxorubicin was released, suggesting that PBS or serum had little influence on the stability of RPA-DOX. RPA-DOX and MPA-DOX show similar doxorubicin release kinetics when incubated in PBS containing 10 mM L-glutathione and 100 μM cysteine, the typical free thiol concentrations of intracellular cytosol[32−34] (Figure 5B). The doxorubicin released from nanoparticles can pass through a MWCO 50 000 filter, while RPA-DOX and MPA-DOX show minimal filtration, thus allowing the liberated doxorubicin to be separated and quantified. Figure 5B shows that it took 8 h to release approximately 15% of doxorubicin from the micelle and 48 h to release 40%. Considering that the micelle would enter target cells through endocytosis, the breakdown of the albumin by

dx.doi.org/10.1021/bc1002295 |*Bioconjugate Chem.* 2011, 22, 870–878

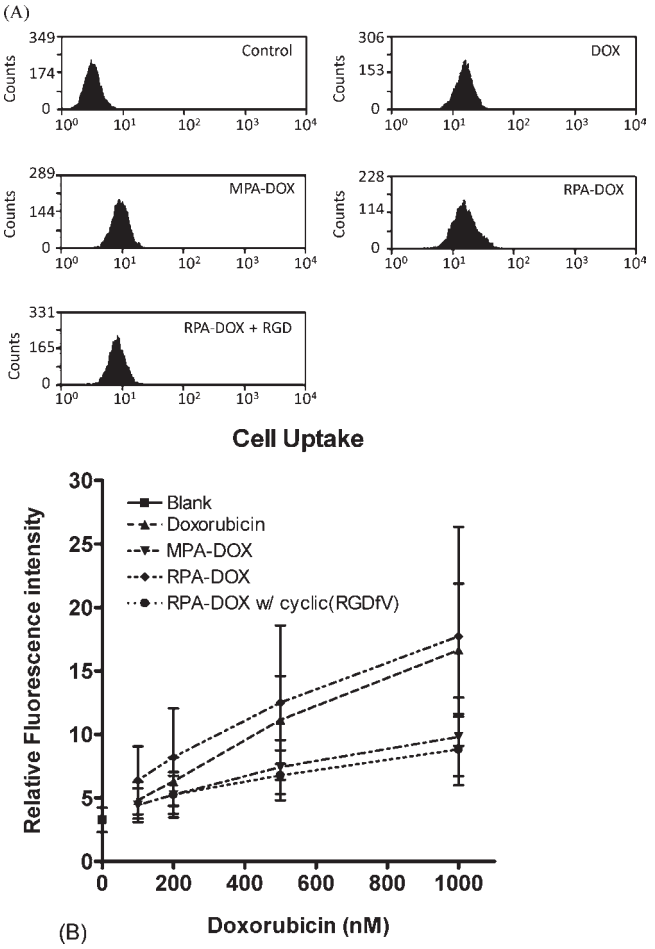


Figure 6. Cellular uptake of doxorubicin formulation. In (A), M21 cells were incubated 4 h in Opti-MEM medium containing medium only; 1 μM doxorubicin, RPA-DOX, and MPA-DOX with 1 μM doxorubicin; and RPA-DOX with 1 μM doxorubicin with preincubation of 100 μM of cyclic(RGDfV); FL2 channel of flow cytometry was set to collect doxorubicin fluorescence. (B) shows the dynamic cellular uptake of doxorubicin formulation. (mean ± SD, from about 5000 cells).

proteinases in endosomal and lysosomal compartments might be expected to accelerate the doxorubicin release. As a control, when incubated in PBS for 48 h, approximately 5% of doxorubicin was released.

Cell Uptake. The uptake of doxorubicin was examined by flow cytometry, as seen in Figure 6. The fluorescence intensity of doxorubicin was excited by 488 nm wavelength light and detected at 575 nm. The mean fluorescence intensity per cell was approximately linear with doxorubicin concentration in all cases. At concentrations ranging between 200 and 1000 nM, RPA-DOX displayed the highest doxorubicin uptake, followed by free doxorubicin and MPA-DOX. When the concentration of doxorubicin was 2 μM, free doxorubicin had the highest doxorubicin uptake, probably because it entered cells by passive diffusion, while RPA-DOX and MPA-DOX entered cells through endocytosis that could be saturated or rate limited. With cells preincubated half an hour with 100 μM cyclic(RGDfV), a ligand for $\alpha_v\beta_3$ integrin, the uptake of RPA-DOX was suppressed to a level close to MPA-DOX. This result shows that conjugation of cyclic RGD on the surface of the albumin micelles supports receptor mediated endocytosis.

The subcellular distribution of doxorubicin was imaged by confocal microscopy (Figure 7). With free doxorubicin, after 4 h incubation in Opti-MEM medium, the bulk of the fluorescence was located in the nucleus (Figure 7A). After a further 16 h culture in drug-free medium, only limited doxorubicin fluorescence was retained inside the nucleus, with the overall fluorescence significantly decreased. With RPA-DOX, after 4 h incubation most of the doxorubicin fluorescence was in cytoplasmic vesicles in the area surrounding the nucleus (Figure 7B), indicating that RPA-DOX enters the cell via a pathway different from free doxorubicin. After 16 h further culturing in drug-free medium, significant amounts of doxorubicin could be seen in the nucleus (Figure 7E), with overall fluorescence of doxorubicin remaining at a high level. This result indicates that doxorubicin delivered by RPA-DOX was retained in cells much longer than free doxorubicin and gradually infiltrated into the nucleus. The MPA-DOX showed similar subcellular distribution as RPA-DOX. However, the fluorescence intensity was much lower under the same imaging conditions, indicating that a lesser amount of doxorubicin was successfully delivered to cells by this nontargeted formulation.

Cytotoxicity. The cytotoxicity of the micelles to M21+ human melanoma cells was determined using an MTT assay and is shown in Figure 8. As shown, RPA-DOX has the highest potency, followed by free doxorubicin and then MPA-DOX. The IC_{50} doses for RPA-DOX, free doxorubicin, and MPA-DOX were calculated to be approximately 200 nM, 500 nM, and 1200 nM, respectively. The cytotoxicities of RPA and MPA were also evaluated by a similar method; after 72 h incubation with M21+ cells, neither of them caused significant toxicity. As a free drug, the thiolated form of doxorubicin that is associated with the nanoscale micelles is slightly less toxic than doxorubicin itself (see Supporting Information Figure S.3). Thus, the increased potency of RPA is not due to a greater effectiveness of the thiolated doxorubicin but rather to improved delivery. Since RPA-DOX contains both bound doxorubicin and conjugated doxorubicin, it is difficult to attribute the cytotoxic effect to one or the other of these components. Further, at present we do not know how quickly the conjugated drug is actually released within the cells. Although the data in Figure 5 suggest release over a period of hours in a reducing environment that mimics the cell interior, the actual release may be quicker due to contributions of endosomal proteases.

■ DISCUSSION

In this report, we describe targeted nanoscale micelles prepared from albumin and the amphipathic anticancer drug doxorubicin. There has been substantial interest in conjugates of antineoplastic agents with proteins, including albumin and monoclonal antibodies, and several moieties have reached clinical trials or entered the clinic.[35] However, in many cases only one or a few drug molecules are linked to the protein. In these cases, better effects are achieved with extraordinarily potent agents such as the calicheamicins rather than more conventional drugs.[36] Another approach has been to utilize micelles based on block copolymers to deliver antitumor agents.[15,37−39] This approach often has the advantage of allowing incorporation of a large number of drug molecules into micelles thus facilitating the utilization of well-known agents such as anthracyclines and taxanes. However, there are inevitably some concerns about possible toxicities of synthetic polymers.[40,41]

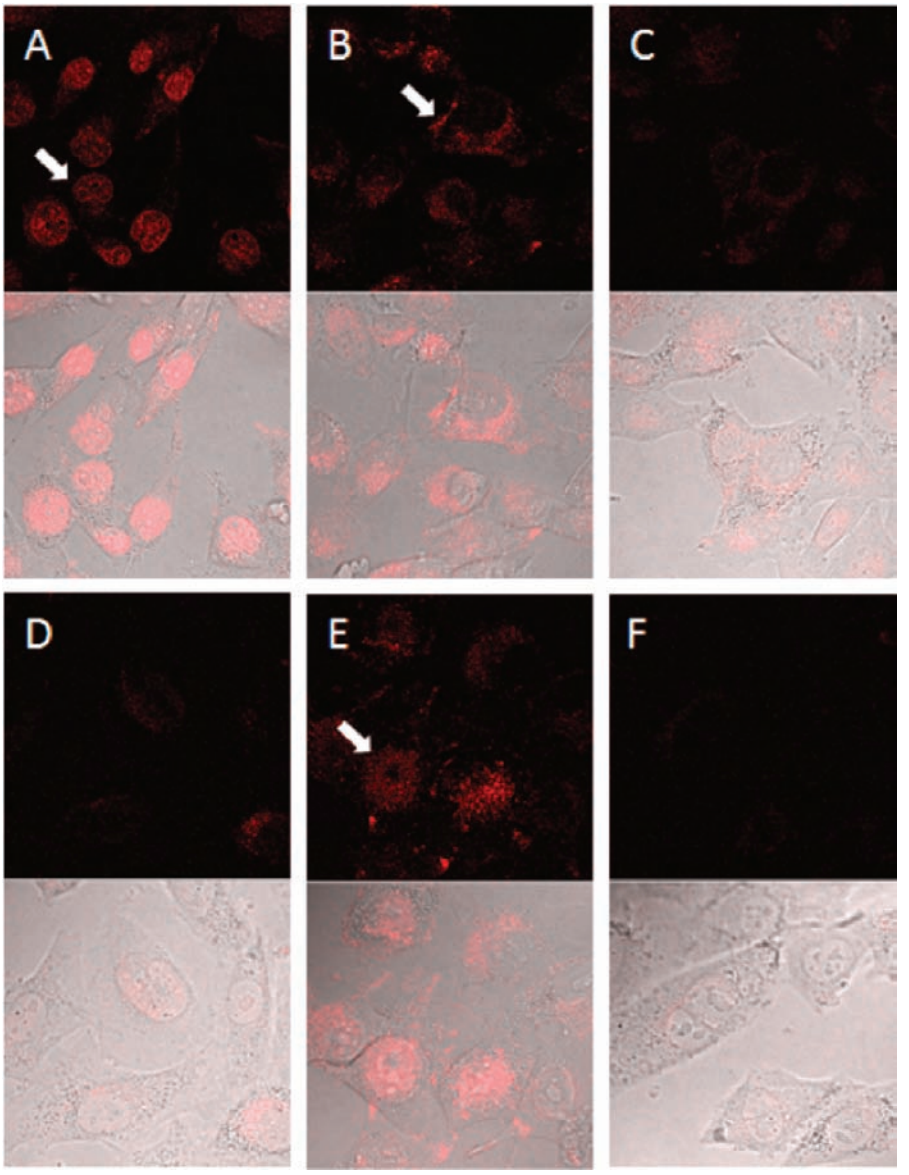


Figure 7. Confocal microscopy of doxorubicin uptake. Cells were incubated for 4 h with 2 μM doxorubicin in free form (A), RPA-DOX (B), or MPA-DOX (C), or further cultured in drug-free medium for 12 h; see (D), (E), and (F), respectively. Arrows point to the doxorubicin subcellular distributions.

The albumin-based nanoscale micelles described here may offer some advantages over other systems in that they provide a high degree of drug loading while being composed of nontoxic biocompatible materials. Our preparation process gives rise to multimeric aggregates of PEG-ylated albumin that contain about 50 doxorubicin molecules per albumin and that are relatively uniform in size with a mean diameter of about 30 nm. We describe this material as nanoscale micelles based on the fact that they are stable in aqueous suspension suggesting the presence of a hydrophilic outer region, but they noncovalently bind a substantial amount of doxorubicin suggesting a hydrophobic core. However, further work will be required to fully delineate the structure and assembly process for this material as well as the implications for pharmacological effects. Thus, at present we do not have detailed information on the structure of the RPA-DOX micelles or the placement of conjugated or bound doxorubicin moieties. Further, the relative contributions of the bound and conjugated drug to the overall pharmacological effect are not known.

The conjugation of RGD-terminated PEG to the albumin results in micelles capable of specifically targeting cells that express the $\alpha_v\beta_3$ integrin. Thus, the RGD-containing RPA-DOX is taken up more efficiently than MPA-DOX, the control conjugate. Further, the uptake of RPA-DOX by $\alpha_v\beta_3$-positive cells is almost completely blocked by the presence of excess RGD illustrating that uptake is ligand-specific. The RPA-DOX micelles displayed excellent potency versus $\alpha_v\beta_3$-positive melanoma cells with an IC_{50} 6-fold lower than that of the control conjugate. Once accumulated in cells, both the covalently linked and the noncovalently absorbed doxorubicin should be readily released from albumin carrier by a combination of reversal of disulfide bonds by intracellular thiols and by proteolytic processes in endosomes and lysosomes.

The strategy described here builds on our previous work using targeted albumin−PEG conjugates to deliver oligonucleotides.[42] However, in that case the conjugates remained as polydisperse but monomolecular entities. In the

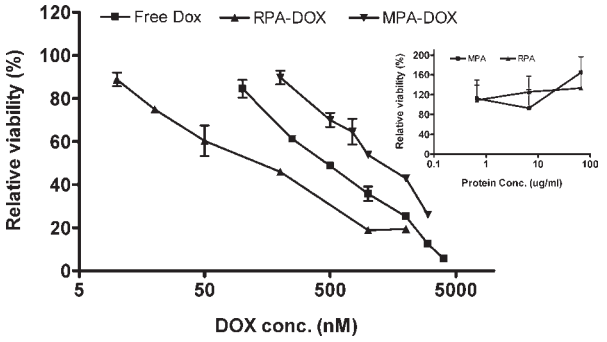


Figure 8. Cytotoxicity of RPA-DOX, MPA-DOX, and free doxorubicin on M21+ cells. The cytotoxicity of MPA and RPA equivalent to RPA-DOX and MPA-DOX containing 0.5 uM to 50 uM of doxorubicin was evaluated in a parallel assay; see inset.

present case, covalent linkage of doxorubicin to the PEG–albumin conjugates apparently drives their aggregation into nanoscale micelles. The ability of the micelles to accommodate additional noncovalently bound drug dramatically raises the drug-loading factor and may allow for very efficient delivery. However, the in vivo targeting and delivery capability of these constructs remains to be determined.

■ ASSOCIATED CONTENT

Supporting Information. Additional figures and tables as described in the text. This material is available free of charge via the Internet at http://pubs.acs.org.

■ AUTHOR INFORMATION

Corresponding Author

*Author e-mail: arjay@med.unc.edu.

■ ACKNOWLEDGMENT

This work was supported by NIH grant P01GM059299 to R.L.J. Authors also thank Dr. Ashutosh Tripathy of the UNC Macromolecular Interactions Core Facility for his helpful advice on FPLC-QELS experiments.

■ REFERENCES

(1) Kratz, F., and Beyer, U. (1998) Serum proteins as drug carriers of anticancer agents: a review. *Drug Delivery 4*, 281–299.

(2) Kratz, F. (2008) Albumin as a drug carrier: design of prodrugs, drug conjugates and nanoparticles. *J. Controlled Release 132* (3), 171–183.

(3) Chen, K., Preuss, A., Hackbarth, S., Wacker, M., Langer, K., and Roder, B. (2009) Novel photosensitizer-protein nanoparticles for photodynamic therapy: photophysical characterization and in vitro investigations. *J. Photochem. Photobiol. B 96* (1), 66–74.

(4) Bledin, A. G., Kim, E. E., Harle, T. S., Haynie, T. P., and Chuang, V. P. (1984) Technetium-99m-labeled macroaggregated albumin arteriography for detection of abnormally positioned arterial catheters during infusion chemotherapy. *Cancer 53* (4), 858–862.

(5) Chaumet-Riffaud, P., Martinez-Duncker, I., Marty, A. L., Richard, C., Prigent, A., Moati, F., Sarda-Mantel, L., Scherman, D., Bessodes, M., and Mignet, N. (2010) Synthesis and application of lactosylated, (99m)Tc chelating albumin for measurement of liver function. *Bioconjugate Chem. 21* (4), 589–596.

(6) Kratz, F., Muller-Driver, R., Hofmann, I., Drevs, J., and Unger, C. (2000) A novel macromolecular prodrug concept exploiting endogenous serum albumin as a drug carrier for cancer chemotherapy. *J. Med. Chem. 43* (7), 1253–1256.

(7) Di Stefano, G., Lanza, M., Kratz, F., Merina, L., and Fiume, L. (2004) A novel method for coupling doxorubicin to lactosaminated human albumin by an acid sensitive hydrazone bond: synthesis, characterization and preliminary biological properties of the conjugate. *Eur. J. Pharm. Sci. 23* (4–5), 393–397.

(8) Gupta, P. K., and Hung, C. T. (1989) Albumin microspheres. I: Physico-chemical characteristics. *J. Microencapsul. 6* (4), 427–462.

(9) Gupta, P. K., and Hung, C. T. (1989) Albumin microspheres. II: Applications in drug delivery. *J. Microencapsul. 6* (4), 463–472.

(10) Anhorn, M. G., Wagner, S., Kreuter, J., Langer, K., and von Briesen, H. (2000) Specific targeting of HER2 overexpressing breast cancer cells with doxorubicin-loaded trastuzumab-modified human serum albumin nanoparticles. *Bioconjugate Chem. 19* (12), 2321–2331.

(11) Stinchcombe, T. E. (2007) Nanoparticle albumin-bound paclitaxel: a novel Cremphor-EL-free formulation of paclitaxel. *Nanomedicine 2* (4), 415–423.

(12) Desai, N., Trieu, V., Yao, Z., Louie, L., Ci, S., Yang, A., Tao, C., De, T., Beals, B., Dykes, D., Noker, P., Yao, R., Labao, E., Hawkins, M., and Soon-Shiong, P. (2006) Increased antitumor activity, intratumor paclitaxel concentrations, and endothelial cell transport of cremophor-free, albumin-bound paclitaxel, ABI-007, compared with cremophor-based paclitaxel. *Clin. Cancer Res. 12* (4), 1317–1324.

(13) Gradishar, W. J., Tjulandin, S., Davidson, N., Shaw, H., Desai, N., Bhar, P., Hawkins, M., and O'Shaughnessy, J. (2005) Phase III trial of nanoparticle albumin-bound paclitaxel compared with polyethylated castor oil-based paclitaxel in women with breast cancer. *J. Clin. Oncol. 23* (31), 7794–7803.

(14) Torchilin, V. P. (2007) Micellar nanocarriers: pharmaceutical perspectives. *Pharm. Res. 24* (1), 1–16.

(15) Nishiyama, N., and Kataoka, K. (2006) Current state, achievements, and future prospects of polymeric micelles as nanocarriers for drug and gene delivery. *Pharmacol. Ther. 112* (3), 630–648.

(16) Farokhzad, O. C., Cheng, J., Teply, B. A., Sherifi, I., Jon, S., Kantoff, P. W., Richie, J. P, and Langer, R. (2006) Targeted nanoparticle-aptamer bioconjugates for cancer chemotherapy in vivo. *Proc. Natl. Acad. Sci. U.S.A. 103* (16), 6315–6320.

(17) Hamaguchi, T., Kato, K., Yasui, H., Morizane, C., Ikeda, M., Ueno, H., Muro, K., Yamada, Y., Okusaka, T., Shirao, K., Shimada, Y., Nakahama, H., and Matsumura, Y. (2007) A phase I and pharmacokinetic study of NK105, a paclitaxel-incorporating micellar nanoparticle formulation. *Br. J. Cancer 97* (2), 170–176.

(18) Uchino, H., Matsumura, Y., Negishi, T., Koizumi, F., Hayashi, T., Honda, T., Nishiyama, N., Kataoka, K., Naito, S., and Kakizoe, T. (2005) Cisplatin-incorporating polymeric micelles (NC-6004) can reduce nephrotoxicity and neurotoxicity of cisplatin in rats. *Br. J. Cancer 93* (6), 678–687.

(19) Koizumi, F., Kitagawa, M., Negishi, T., Onda, T., Matsumoto, S., Hamaguchi, T., and Matsumura, Y. (2006) Novel SN-38-incorporating polymeric micelles, NK012, eradicate vascular endothelial growth factor-secreting bulky tumors. *Cancer Res. 66* (20), 10048–10056.

(20) Hashizume, H., Baluk, P., Morikawa, S., McLean, J. W., Thurston, G., Roberge, S., Jain, R. K., and McDonald, D. M. (2000) Openings between defective endothelial cells explain tumor vessel leakiness. *Am. J. Pathol. 156* (4), 1363–1380.

(21) Maeda, H. (2001) The enhanced permeability and retention (EPR) effect in tumor vasculature: the key role of tumor-selective macromolecular drug targeting. *Adv. Enzyme Regul. 41*, 189–207.

(22) Matsumura, Y., Fau-Maeda, H., and Maeda, H. (1986) A new concept for macromolecular therapeutics in cancer chemotherapy: mechanism of tumoritropic accumulation of proteins and the antitumor agent smancs. *Cancer Res. 46*, 6387–6392.

(23) Ríhová, B. (1996) Biocompatibility of biomaterials: hemocompatibility, immunocompatiblity and biocompatibility of solid polymeric

materials and soluble targetable polymeric carriers. *Adv. Drug Delivery Rev. 21* (2), 157–176.

(24) Hortobagyi, G. N. (1997) Anthracyclines in the treatment of cancer. An overview. *Drugs 54* (Suppl 4), 1–7.

(25) Arcamone, F., Cassinelli, G., Fantini, G., Grein, A., Orezzi, P., Pol, C., and Spalla, C. (1969) Adriamycin, 14-hydroxydaunomycin, a new antitumor antibiotic from S. peucetius var. caesius. *Biotechnol. Bioeng. 11* (6), 1101–1110.

(26) Stupack, D. G., and Cheresh, D. A. (2004) Integrins and angiogenesis. *Curr. Top. Dev. Biol. 64*, 207–238.

(27) Desgrosellier, J. S., and Cheresh, D. A. (2010) Integrins in cancer: biological implications and therapeutic opportunities. *Nat. Rev. Cancer 10* (1), 9–22.

(28) Karukstis, K. K., Thompson, E. H., Whiles, J. A., and Rosenfeld, R. J. (1998) Deciphering the fluorescence signature of daunomycin and doxorubicin. *Biophys. Chem. 73* (3), 249–263.

(29) Malugin, A., Kopeckova, P., and Kopecek, J. (2007) Liberation of doxorubicin from HPMA copolymer conjugate is essential for the induction of cell cycle arrest and nuclear fragmentation in ovarian carcinoma cells. *J. Controlled Release 124* (1−2), 6–10.

(30) Kaiser, E., Colescott, R. L., Bossinger, C. D., and Cook, P. I. (1970) Color test for detection of free terminal amino groups in the solid-phase synthesis of peptides. *Anal. Biochem. 34* (2), 595–598.

(31) Tian, Y., Bromberg, L., Lin, S. N., Hatton, T. A., and Tam, K. C. (2007) Complexation and release of doxorubicin from its complexes with pluronic P85-b-poly(acrylic acid) block copolymers. *J. Controlled Release 121* (3), 137–145.

(32) de Graaf-Hess, A., Trijbels, F., and Blom, H. (1995) New method for determining cystine in leukocytes and fibroblasts. *Clin. Chem. 45* (12), 2224–2228.

(33) Andersson, A., Lindgren, A., and Hultberg, B. (1995) Effect of thiol oxidation and thiol export from erythrocytes on determination of redox status of homocysteine and other thiols in plasma from healthy subjects and patients with cerebral infarction. *Clin. Chem. 41* (3), 361–366.

(34) Deneke, S. M. (2000) Thiol-based antioxidants. *Curr. Top. Cell Regul. 36*, 151–180.

(35) Kratz, F., Abu Ajaj, K., and Warnecke, A. (2007) Anticancer carrier-linked prodrugs in clinical trials. *Expert Opin. Investig. Drugs 16* (7), 1037–1058.

(36) Ricart, A. D., and Tolcher, A. W. (2007) Technology insight: cytotoxic drug immunoconjugates for cancer therapy. *Nat. Clin. Pract. Oncol. 4* (4), 245–255.

(37) Vetvicka, D., Hruby, M., Hovorka, O., Etrych, T., Vetrik, M., Kovar, L., Kovar, M., Ulbrich, K., and Rihova, B. (2009) Biological evaluation of polymeric micelles with covalently bound doxorubicin. *Bioconjugate Chem. 20* (11), 2090–2097.

(38) Matsumura, Y. (2008) Polymeric micellar delivery systems in oncology. *Jpn. J. Clin. Oncol. 38* (12), 793–802.

(39) Upadhyay, K. K., Agrawal, H. G., Upadhyay, C., Schatz, C., Le Meins, J. F., Misra, A., and Lecommandoux, S. (2009) Role of block copolymer nanoconstructs in cancer therapy. *Crit. Rev. Ther. Drug Carrier Syst. 26* (2), 157–205.

(40) Rihova, B. (2000) Immunocompatibility and biocompatibility of cell delivery systems. *Adv. Drug Delivery Rev. 42* (1−2), 65–80.

(41) Kabanov, A. V. (2006) Polymer genomics: an insight into pharmacology and toxicology of nanomedicines. *Adv. Drug Delivery Rev. 58* (15), 1597–1621.

(42) Kang, H., Alam, M. R., Dixit, V., Fisher, M., and Juliano, R. L. (2008) Cellular delivery and biological activity of antisense oligonucleotides conjugated to a targeted protein carrier. *Bioconjugate Chem. 19* (11), 2182–2188.

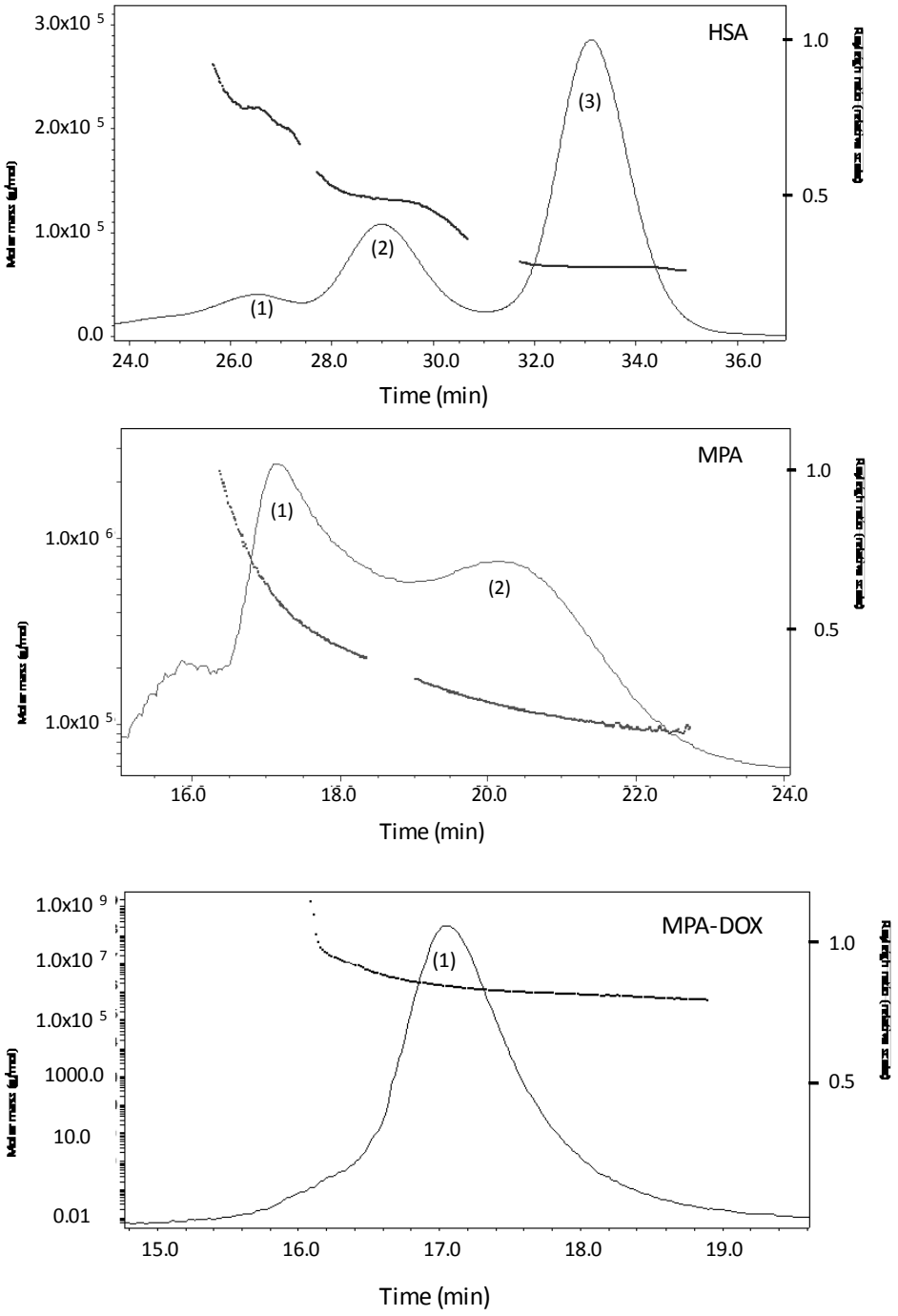


Figure S.1. The reaction progress of MPA-Dox. The intermediates and final products were analyzed by FPLC-QELS. Dotted line: molar mass. Solid line: Rayleigh ratio.

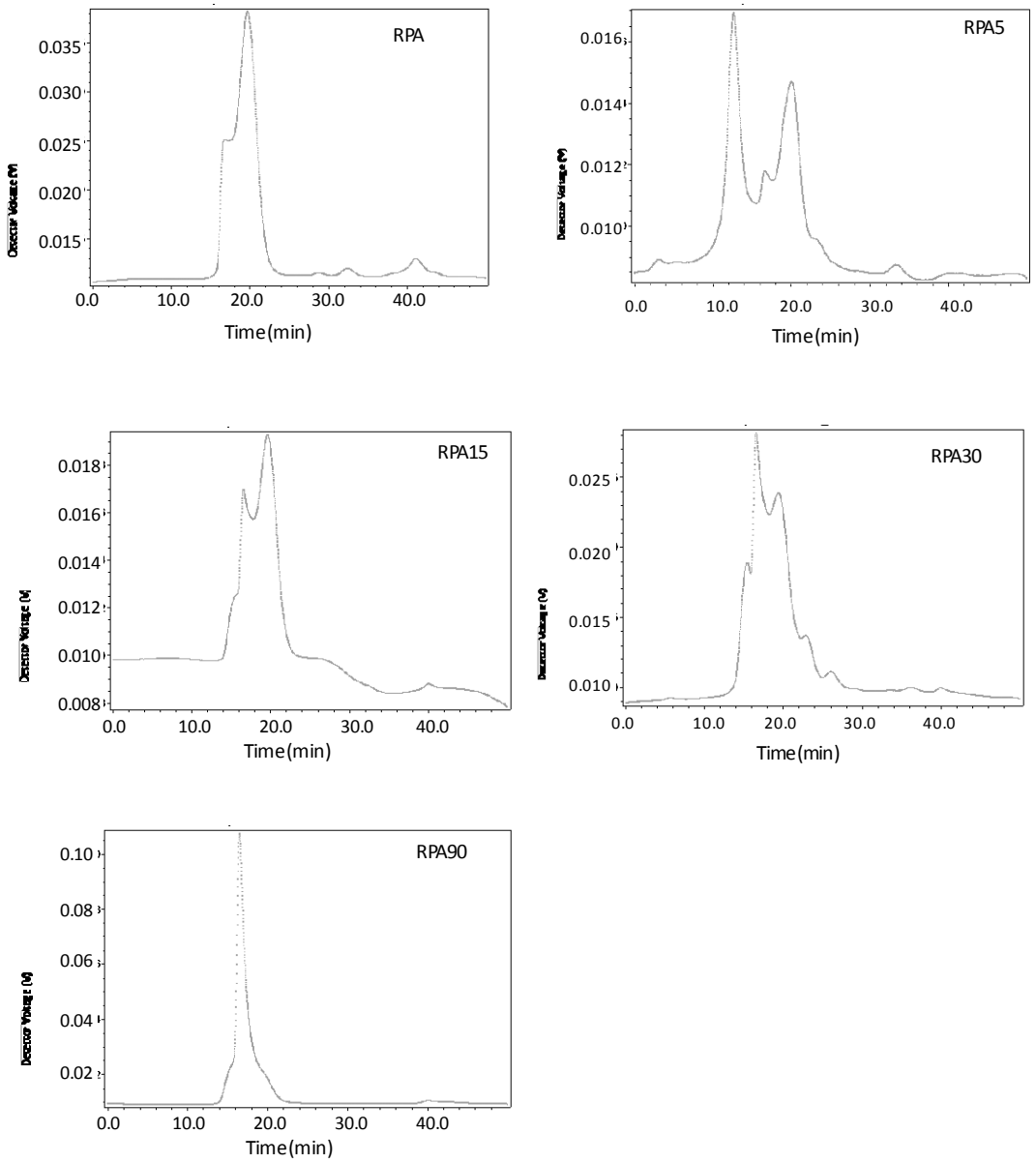


Figure S.2. FPLC_QELS analysis of RPA and its doxorubicin derivatives. UV absorbance versus column run time.

Table S.1. The formulation kinetics of RPA-DOX

	RPA5	RPA15	RPA30	RPA90
				
Input (RPA : SPDP : DOX)[a]	1 : 5 : 5	1 : 15 : 15	1 : 30 : 30	1:30:90
Conjugated DOX (before dialysis) (RPA : DOX)[b]	1 : 3.2	1 : 11.6	1 : 23.1	1 : 27.4
Final total DOX (After dialysis) (RPA : DOX)[c]	1 : 1.4	1 : 4.2	1: 13.1	1 : 44.0
Nanoparticle formation[d]	Partially	Partially	Partially	Completely

[a]: SPDP was in the form of sulfo-LC-SPDP, DOX was doxorubicin thiol derivative, the ratio among RPA and SPDP and DOX is a molar ratio;

[b]: the quantity of chemically conjugated doxorubicin was determined by monitoring the release of pyridine-2-thione from sulfo-LC-SPDP using UV spectrum[43];

[c]: the quantity of doxorubicin associated with RPA was determined by UV-Vis analysis method[31];

[d]: Nanoparticle formation was evaluated by FPLC-QELS, seen in Figure S.2.

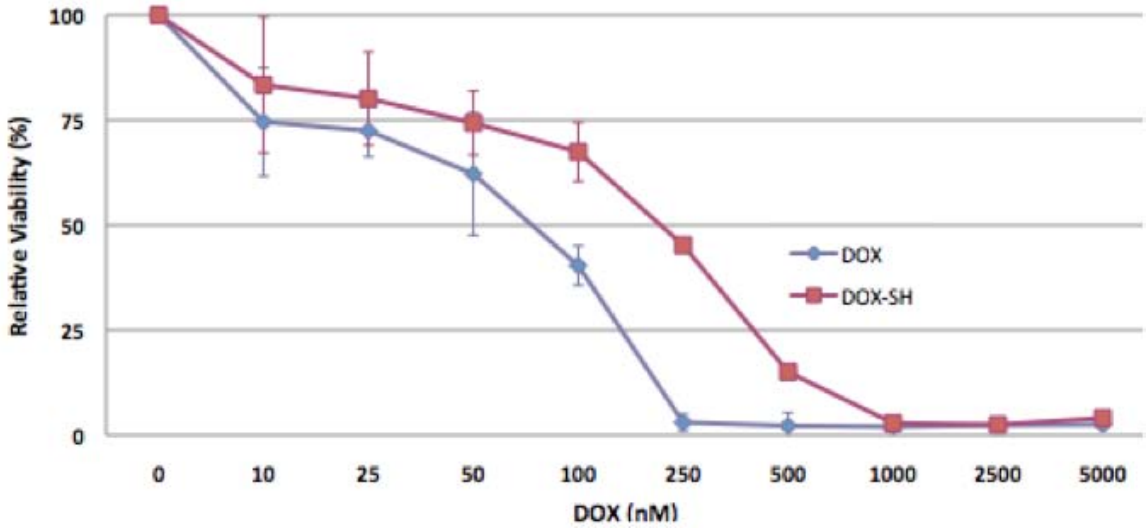


Figure S3. The relative cytotoxicity of unmodified doxorubicin versus the thiolated form used in this study was evaluated using an MTT assay. The data presented here derives from a separate experiment from that shown in Figure 8.

Bioconjugate Chemistry

ARTICLE

pubs.acs.org/bc

Synthesis and Characterization of a Theranostic Vascular Disrupting Agent for *In Vivo* MR Imaging

Tammy L. Kalber,[*,†] Nazila Kamaly,[†,‡] Stephanie A. Higham,[†] John A. Pugh,[§] Josephine Bunch,[§,∥] Cameron W. McLeod,[§] Andrew D. Miller,[‡] and Jimmy D. Bell[†]

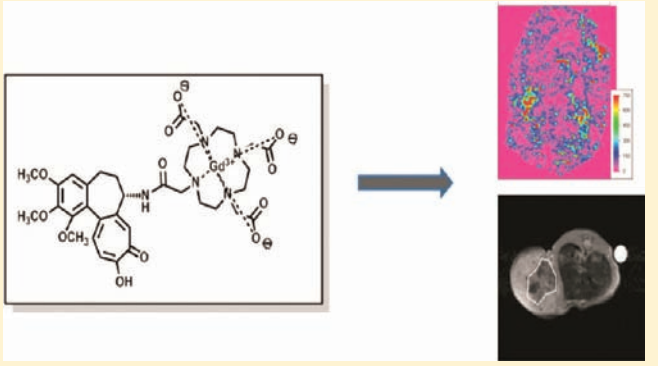
[†]Metabolic and Molecular Imaging Group, MRC Clinical Sciences Centre, Imperial College London, Hammersmith Hospital, London W12 0NN, U.K.

[‡]Imperial College Genetic Therapies Centre, Department of Chemistry, Flowers Building, Armstrong Road, Imperial College London, London SW7 2AZ, U.K.

[§]Centre for Analytical Sciences, Department of Chemistry, University of Sheffield, Brook Hill, Sheffield S3 7HF, U.K.

[∥]School of Chemistry, University of Birmingham, Edgbaston, Birmingham B15 2TT, U.K.

ABSTRACT: Colchicine, a known tubulin binding agent and vascular disrupting agent, causes rapid vascular shut down and central necrosis in tumors. The binding of tubulin results in tubulin destabilization, with characteristic cell shape changes and inhibition of cell division, and results in cell death. A gadolinium(III) labeled derivative of colchicine (Gd·DOTA·Colchicinic acid) was synthesized and characterized as a theranostic agent (enabling simultaneous diagnostic/real time MRI contrast imaging). *In vitro*, Gd·DOTA·Colchicinic acid was shown to initiate cell changes characteristic of tubulin-destabilization in both OVCAR-3 and IGROV-1 ovarian carcinoma cell lines *in vitro* over a period of 24 h, while maintaining the qualities of the MR imaging tracer. *In vivo*, Gd·DOTA·Colchicinic acid (200 mg/kg) was shown to induce the formation of central necrosis, which was confirmed *ex vivo* by histology, in OVCAR-3 subcutaneous tumor xenografts, while simultaneously acting as an imaging agent to promote a significant reduction in the MR relaxation time T_1 ($p < 0.05$) of tumors 24 h post-administration. Morphological changes within the tumor which corresponded with areas derived from the formation of central necrosis were also present on MR images that were not observed for the same colchicine derivate that was not complexed with gadolinium that also presented with central necrosis *ex vivo*. However, Gd·DOTA·Colchicinic acid accumulation in the liver, as shown by changes in liver T_1 ($p < 0.05$), takes place within 2 h. The implication is that Gd·DOTA·Colchicinic acid distributes to tissues, including tumors, within 2 h, but enters tumor cells to lower T_1 times and promotes cell death over a period of up to 24 h. As the biodistribution/pharmacokinetic and pharmacodynamics data provided here is similar to that of conventional colchicines derivatives, such combined data are a potentially powerful way to rapidly characterize the complete behavior of drug candidates *in vivo*.



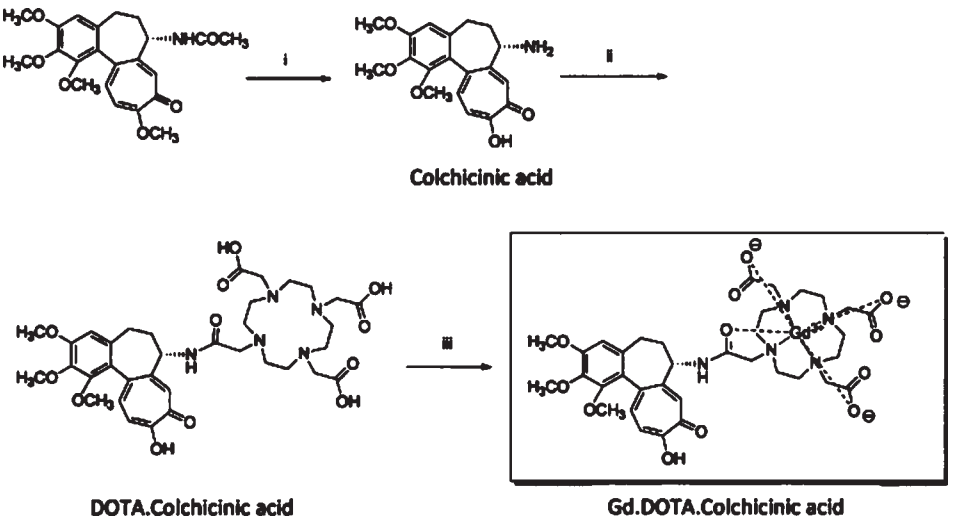
INTRODUCTION

It is well established that tumor growth is dependent upon the generation of a functional vascular supply and that tumor vasculature differs significantly from that of vessels in normal tissues.[1−4] Normal tissues have well-ordered vessels with quiescent endothelial cells, whereas tumor vasculature is a chaotic network of tortuous, thin-walled, leaky vessels, with a high proportion of immature, proliferating endothelial cells that rely on their tubulin cytoskeleton to maintain shape.[3,4] Consequently, tumor endothelium can be targeted in therapeutic approaches to cancer that leave normal blood vessels unaffected.[5] In particular, vascular disrupting agents (VDAs) invoke the selective collapse of tumor vasculature, leading to a loss in tumor blood flow, secondary cell death, and tumor necrosis due to ischemia.[6] VDAs have largely consisted of tubulin-depolymerizing agents such as colchicine and its derivatives, and more recently, the flavonids such as 5,6-dimethylxanthenone-4-acetic acid (DMXAA). Colchicine binds to β-tubulin, inhibiting tubulin polymerization, resulting in microtubule destabilization. Destabilization of the microtubule cytoskeleton induces cell shape changes, which in the endothelial cells of tumors, results in cell detachment, exposure of the basal lamina, and vessel occlusion.[7] However, colchicine is too toxic for clinical use as it is only effective close to its maximum tolerated dose (MTD). Derivatives of colchicine have therefore been developed, the best known being disodium combretastatin A-4 3-*O*-phosphate (CA-4-P) and ZD6126, both of which induce vascular occlusion and therefore antitumor effects in a wide range of tumor models at doses that are less than one-tenth of the MTD.[8−11]

Received: July 21, 2010
Revised: February 17, 2011
Published: March 16, 2011

ACS Publications © 2011 American Chemical Society

Scheme 1. Synthesis of Gd·DOTA·Colchicinic acid[a]



[a] (i) 30% H_2SO_4, 100 °C, 5 h, 20%; (ii) DOTA-NHS-ester, DCM, 40 °C, 3 eq. Et_3N, 12 h, 98%; (iii) $6H_2O \cdot GdCl_3$, H_2O, 90 °C, quantitative.

The impact of VDAs on tumor tissue has been demonstrated histologically in numerous tumor models, revealing central necrosis within 24 h of a single injection with a characteristic thin rim of viable tumor cells at the periphery.[9,12] The rim is thought to be a consequence of these cells receiving nutrients/oxygen from nontumor vessels in adjacent normal tissue allowing these tumor regions to regrow. Therefore, VDA treatment is not expected to cause tumor shrinkage or significant growth delay as a single therapy. Accordingly, in the absence of tumor shrinkage, there is a need for noninvasive methods that can provide an assessment of tumor vasculature and pathophysiology in response to VDA therapy *in vivo*. The hemodynamic tumor response to VDA therapy can be monitored by dynamic contrast enhanced magnetic resonance imaging (MRI) using gadolinium(III) (Gd) chelates,[13−17] as well as by intrinsic-susceptibility MRI, which is sensitive to changes in blood oxygenation.[18,19] Otherwise, pathological changes have been observed by MR methodologies such as diffusion-weighted MRI[20−22] or necrosis-avid contrast agents capable of detecting tumor necrosis,[23] as well as methods to investigate apoptosis and cell death, such as choline spectroscopy[24] or targeted contrast agents.[25] Since all these imaging methodologies are responding to secondary changes at selected time points after VDA administration, then this suggests that VDA imaging itself could provide the means not only to reach a better understanding of drug biodistribution/pharmacokinetics, routes of clearance, etc., but also to simultaneously monitor pharmacodynamic phenotypic effects in real time as well as tumor necrosis in particular.

Previously, colchicine has been conjugated with imaging agents[26−31] including Gd-chelates,[32] but mainly for applications *in vitro* or in terminal *in vivo* studies. The aim of the study reported here was to conjugate an MRI contrast agent to colchicine in order to produce a novel theranostic VDA capable of remaining as a functional VDA as well as acting as a competent contrast agent for similtaneous diagnostic/real time MRI contrast imaging *in vivo*. Here, we describe the synthesis and characterization of such a theranostic VDA followed by a range of *in vitro* and *in vivo* imaging studies over 24 h post-VDA administration, concluding with histology and laser ablation inductively coupled mass spectrometry (LA-ICP-MS) to correlate Gd (III) distribution with associated relaxation time (T_1) changes shown by *in vivo* MR.

EXPERIMENTAL SECTION

Gerneral procedures. All chemicals were of analytical/high grade and purchased from Sigma-Aldrich (Dorset, U.K.) or Macrocyclics (Dallas, USA). Mass spectrometry (MS) were performed using VG-070B, Joel SX-102, or Bruker Esquire 3000 electrospray mass spectrometry (ESI) instruments. ^{1}H NMR spectra were recorded on a 400 MHz Bruker Advance 400 spectrometer. All MRI experiments were conducted on a 4.7 T Varian Direct Drive MRI scanner (Varian Inc., Palo Alto, CA, USA). All procedures on animals were carried out in accordance with U.K. Home Office regulations and the Guidance for the Operation of Animals (Scientific Procedures) Act (1986).

Chemical Synthesis. Colchicinic acid (Scheme 1) was synthesized according to the previously reported method by Satpati et al.[26] Tetraazacyclododecanetetraacetic acid (DOTA) in the form of DOTA·NHS ester (100 mg, 0.121 mmol) and colchicinic acid (41.55 mg, 0.121 mmol) were added to an air-evacuated round-bottom flask, and to this, dry dichloromethane (30 mL) followed by triethylamine (3 eq 0.363 mmol) was added and stirred at 45 °C for 12 h. The solvent was removed and the crude mixture purified by flash column chromatography using Merck 0.040 to 0.063 mm, 230 to 400 mesh silica gel, and the product eluted with dichloromethane/methanol/acetic acid (6:3:1 v/v). The collected fractions were reduced to yield a solid (87 mg, 98%) DOTA·Colchicinic acid (Scheme 1). R_f [dichloromethane/methanol/acetic acid, 6:3:1 v/v] 0.11. ^{1}H NMR (400 MHz, MeOD) 8.28 (s, br, 1H, −OH, H_{10}), 7.76 (s, 1H, H_8), 7.46 (s, 1H, H_{11}), 7.11 (d, 1H, H_{12}), 6.92 (d, 1H, H_4), 6.48 (s, br, 1H, $-CNHCOCH_2-$), 4.34 (d, 2H, $-NCOCH_2N-$), 3.64 (m, 16H, 4× $-NCH_2CH_2N-$), 3.26 (m, 6H, 3× $-NCH_2COOH$), 3.12, (s, 3H, -OCH3, H_1), 3.08 (m, 4H, $-CH_2CH_2-$, $H_{5,6}$), 2.77 (s, 3H, −OCH3, H_2), 2.63 (s, 3H, $-OCH_3$, H_3). MS (ESI+) calculated for $C_{35}H_{47}N_5O_{12}$ m/z 729.7740; found, 730.10 $(M + H)^+$.

A stoichiometric amount of gadolinium chloride (20.90 mg, 0.056 mmol) was added to DOTA·Colchicinic acid (41.06 mg, 0.056 mmol) and stirred in doubly distilled water (20 mL) at 90 °C overnight. The water was freeze-dried to yield a powder (50 mg, quantitative yield): Gd·DOTA·Colchicinic acid (Figure 1). R_f [dichloromethane/methanol/acetic acid, 6:3:1

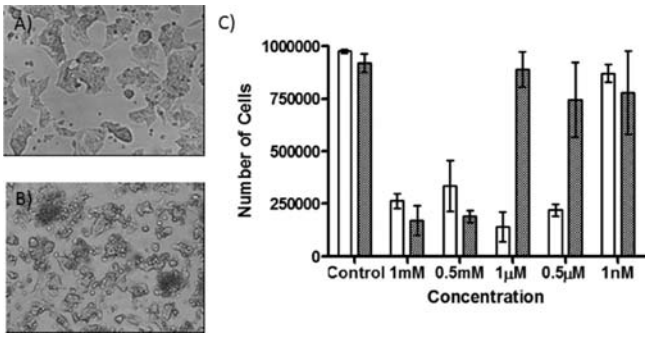


Figure 1. *In vitro* cell studies of DOTA·Colchicinic acid in OVCAR-3 cells. A histology picture of OVCAR-3 cells, (A) without and (B) with 1 mM 24 h after DOTA·Colchicinic acid; (C) cell counts for both colchicine (white) and DOTA·Colchicinic acid (gray) after 24 h at various concentrations. Magnification ×100.

v/v] 0.18. MS (ESI+) calculated for $C_{35}H_{44}GdN_5O_{12}$ m/z 884.00; found, 885.23 $(M + H)^+$. The gadolinium compound was characterized by ESI-MS, and the presence of free gadolinium ions was determined by the xylenol orange test previously described by Barge et al.[33]

In Vitro. *Phantom Studies.* 0.5 mM of Gd·DOTA·Colchicinic acid, DOTA·Colchicinic acid, Gd·DOTA (Dotarem, Guerbet, France), or water was used to assess signal enhancement. A range of 6 concentrations (0.03−0.5 mM) of Gd·DOTA·Colchicinic acid or Gd·DOTA was then used to calculate relaxivity for each contrast agent. Phantoms were placed in a quadrature ^1H volume coil and positioned into the MRI scanner. A spin−echo sequence with the following parameters was used to assess T_1: 10 TRs ranging from 50 to 7000 ms; TE = 10 ms; FOV = 45 × 45 mm; averages, 1; matrix size, 256 × 128 and a 2.0 mm thickness; and bore temperature, ∼ 20 °C.

Tissue Culture. Human ovarian carcinoma OVCAR-3 and IGROV-1 cell lines were grown in T175 flasks (Fisher Scientific, Loughborough, UK) in Dulbecco's modified Eagle's medium (DMEM) (Sigma), supplemented with 10% heat inactivated fetal calf serum (GIBCO, Grand Island NY, USA) in an incubator at 37 °C with 95% air and 5% CO_2. Cells were grown to 100% confluence before being trypsinized, counted, and then either plated for *in vitro* experiments or prepared for subcutaneous implantation.

Toxicity Studies. Cells were plated at 4×10^5 in 6 well plates 24 h prior to incubation with a range of concentrations (1 nM−1 mM) of either DOTA·Colchicinic acid or colchicine dissolved in serum free DMEM. Histological morphology of cells was recorded at 2 h intervals up to 8 h, and at 24 h using an Olympus IX71 microscope (Olympus, Middlesex, UK). The cells were harvested at the 24 h time point and the numbers counted using a hemocytometer.

Gd·DOTA·Colchicinic Acid Uptake. Cells were plated at 1.5×10^5 in T25 flasks 24 h prior to the incubation of 1 mL of 1 mM Gd·DOTA·Colchicinic acid (the most efficient incubation dose from toxicity studies). Cells were then washed, harvested, and pelleted and resuspended in 1% agarose (Sigma, UK) at 2 h intervals up to 8 h, and at 24 h after incubation and scanned as described for phantoms.

In Vivo. *MRI.* OVCAR-3 cells (5×10^6/0.1 mL) were inoculated into the flank of 6−8 weeks old Balb/c nude mice. Once palpable, tumors were measured in three orthogonal dimensions every 2 days up until treatment, then pre and 24 h post-treatment, using calipers. Tumor volumes were estimated assuming an ellipsoid shape using the formula volume = length × width × depth × $\pi/6$. When tumors reached approximately 7−10 mm^3, mice were anesthetized with an isoflurane/O_2 mix and scanned as described for phantoms using the parameters; 5 TRs ranging from 400−5000 ms; TE = 15 ms; FOV = 45 × 45 mm; averages, 1; matrix size, 256 × 128, 2.0 mm thickness; and 20 consecutive transverse slices covering the whole abdomen. Mice were removed from the magnet and a tail vein cannulated for the administration of 200 mg/kg (22.64 mmol) Gd·DOTA·Colchicinic acid (n = 4), 22.64 mmol DOTA·Colchicinic acid (n = 4), 22.64 mmol Gd·DOTA (n = 4), or 200 μL of saline (n = 4); 200 mg/kg was used as this is an optimal dose that has been used for both CA-4-P and ZD6126 in mice. Mice were then rescanned with the same parameters 2, 8, and 24 h post-injection. After the final scan mice were sacrificed, the tumor was excised and frozen for LA-ICP-MS and hematoxylin and eosin (H & E) staining. The liver and kidneys were also taken for H & E only.

MRI Data Analysis. A region of interest (ROI) was drawn around the whole tumor excluding the skin on MR images using Image J (National Institute of Health, USA).[34] Mean signal intensities of the ROIs at different TR values were measured and used to calculate the MR transverse relaxation time T_1 using Graphpad Prism (San Diego, California, USA). Mean T_1 values for each cohort were derived and a two-tailed unpaired t test assuming equal variances performed at each time point to determine significant difference, with a 5% level of statistical significance. Circular ROIs were then drawn in the liver and kidney to assess clearance and the signal intensities converted to T_1 as described above.

LA-ICP-MS. Frozen tissue was mounted onto a cryostat chuck using water/ice slush frozen to −20 °C and sections cut at 20 μm using a cryotome. The laser ablation system (LSX-200, Cetac, 266 nm Nd:YAG) was configured to perform multiple line rasters, generating 2D elemental distribution maps. A beam diameter of 50 μm was used for ablating tumor sections (with energy 0.6 mJ), a scanning speed of 50 μm/s and laser frequency of 10 Hz. For ICP-MS (Agilent, HP4500 Series 100), the elements Gd^{157} and Zn^{66} (an element widespread in biochemistry) were monitored in a time-resolved mode, isotopes were selected on the basis of high-percentage abundance, and minimal isobaric and polyatomic interferences. Tumor sample areas were in the range 130−190 mm^2. Elemental maps were produced using the Graphis software package (Kylebank Software Ltd., Ayr, UK). Adjacent sections where taken for H & E staining.

Histological Assessment. Sections were incubated with hematoxylin solution for 1 min, and then in freshly prepared eosin Y (both Sigma) for 30 s. The sections were then dehydrated with alcohol and passed through histoclear (Fisher Scientific), mounted with DPX (VWR), and imaged using the Olympus IX71 microscope as described in the toxicity studies.

RESULTS

Chemical Synthesis. The synthesis of Gd·DOTA·Colchicinic acid was carried out in three steps as shown in Scheme 1. The control compound DOTA·Colchicinic acid was obtained in good yield and was characterized by ^1H and MS spectroscopy. Complexation of Gd(III) within DOTA could not be confirmed by NMR due to the paramagnetic nature of Gd(III) and was therefore confirmed by ESI-MS and the xylenol orange assay. Isotopic peaks of Gd(III) were highly visible in the MS trace, and there were no significant free Gd(III) ions detectable after complexation according to the xylenol orange assay, thereby confirming the formation of Gd·DOTA·Colchicinic acid.

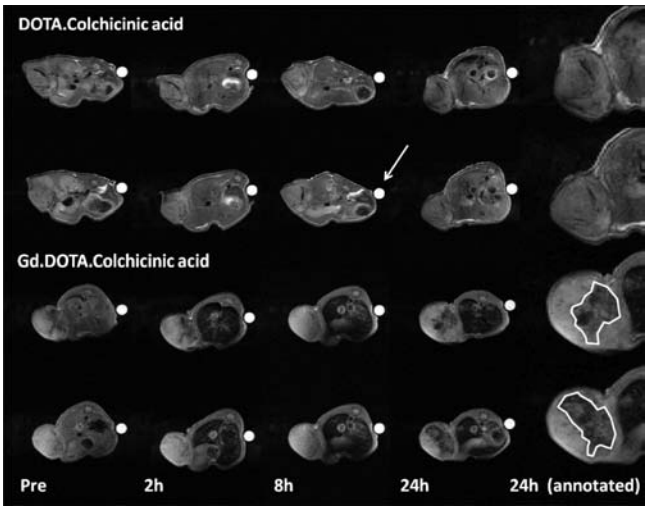


Figure 2. A set of two contiguous T_1 MRI images acquired from similar anatomic points from the same mouse bearing a subcutaneous OVCAR3 tumor pre, 2, 8, and 24 h after 200 mg/kg DOTA·Colchicinic acid or Gd·DOTA·Colchicinic acid administration. Column 24 h (annotated) shows the enlarged 24 h tumor image, which includes annotated areas of signal change in the Gd·DOTA·Colchicinic acid treated tumors. The white arrow denotes a phantom placed to correlate images.

In Vitro. Phantoms showed that Gd·DOTA·Colchicinic acid achieved a 96% reduction in T_1 compared to the same concentration of DOTA·Colchicinic acid or water, and its relaxivity was calculated at 3.83 $mM^{-1}s^{-1}$. This was equivalent to that of nonconjugated Gd·DOTA, which was calculated at 3.66 $mM^{-1}s^{-1}$. The efficiency of DOTA·Colchicinic acid for binding tubulin was assessed in two ovarian carcinoma cell lines. Normally, endothelial cell lines such as HUVEC's are used to assess the functionality of novel VDAs. However, the effects of tubulin-binding drugs are not specific to endothelial cells. Indeed, some tumor cell types are more sensitive to VDA tubulin depolymerization than endothelial cells.[35] The extent to which direct tumor cell death has contributed to VDA therapy is likely dependent on tumor type. Therefore, DOTA·Colchicinic acid was tested in tumor cells to assess tubulin binding and tubulin destabilization activities in order to obtain a better idea of the amount of cell death/antitumor effect that Gd·DOTA·Colchicinic acid may provide *in vivo*, in addition to VDA action.

Cell counts showed that colchicine was effective at significantly reducing cell numbers at all concentrations in both the OVCAR-3 and IGROV-1 cell lines, whereas DOTA·Colchicinic acid was only effective in the millimolar range, causing reductions in cell numbers in both cell lines (Fgure 1C). These high concentration effects were the same for the Gd(III) derivate (Gd·DOTA·Colchicinic acid) and correlated well with colchicine effects at the same high concentrations. Arguably, these data suggest that Gd·DOTA·Colchicinic acid may be much less cytotoxic than colchicine to cells in general but retains colchicine's drug-action mechanism in spite of the conjugated Gd·DOTA chelate (Figure 1C). Light microscopy demonstrated the emergence of initial cell shape changes as early as 2 h post-treatment with DOTA·Colchicinic acid, followed by rounding of the cells, and then detachment from the flask walls at 24 h (Figure 1A and B). MR images of cell pellets taken at specific time points after incubation with Gd·DOTA·Colchicinic acid (1 mM) showed a 54% reduction in T_1 at 2 h compared to that in control cells, which decreased further reaching a maximum of

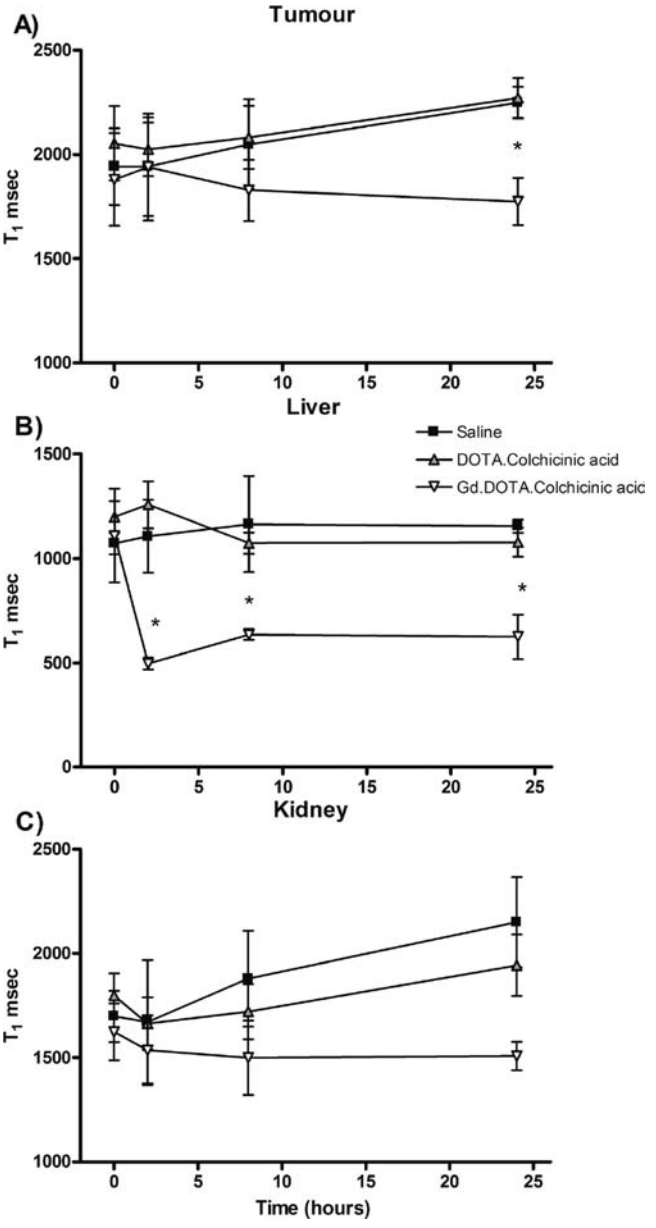


Figure 3. T_1 (ms) measured pre, 2, 8, and 24 h post-injection of 200 mg/kg (22.64 mmol) Gd·DOTA·Colchicinic acid, 22.64 mmol DOTA·Colchicinic acid, or 200 μL saline for (A) tumor, (B) liver, and (C) kidney. Data points ± standard error of the mean ($n = 4$ in each group). * = $P < 0.05$.

83% reduction at 6 h. After 6 h, T_1 recovered slightly, but at no point returned to baseline over the 24 h period (data not shown). These data are in accordance with the histology data and suggest that initial tubulin binding takes place *in vitro* within the first 2 h of incubation, followed by further cellular uptake and tubulin binding over 6 h.

In Vivo. Mice showed no adverse effects throughout the study. There was no significant difference in tumor size between cohorts, consistent with the fact that colchicine and its derivatives do not typically cause tumor shrinkage or growth delay. Images of pre-treated tumors appeared to be homogeneous in presentation. At 24 h, the tumor images showed evidence of morphological changes mainly evident in the central area of the tumor as areas of low signal intensity (dark areas) in 3 out of 4 of the Gd·DOTA·Colchicinic

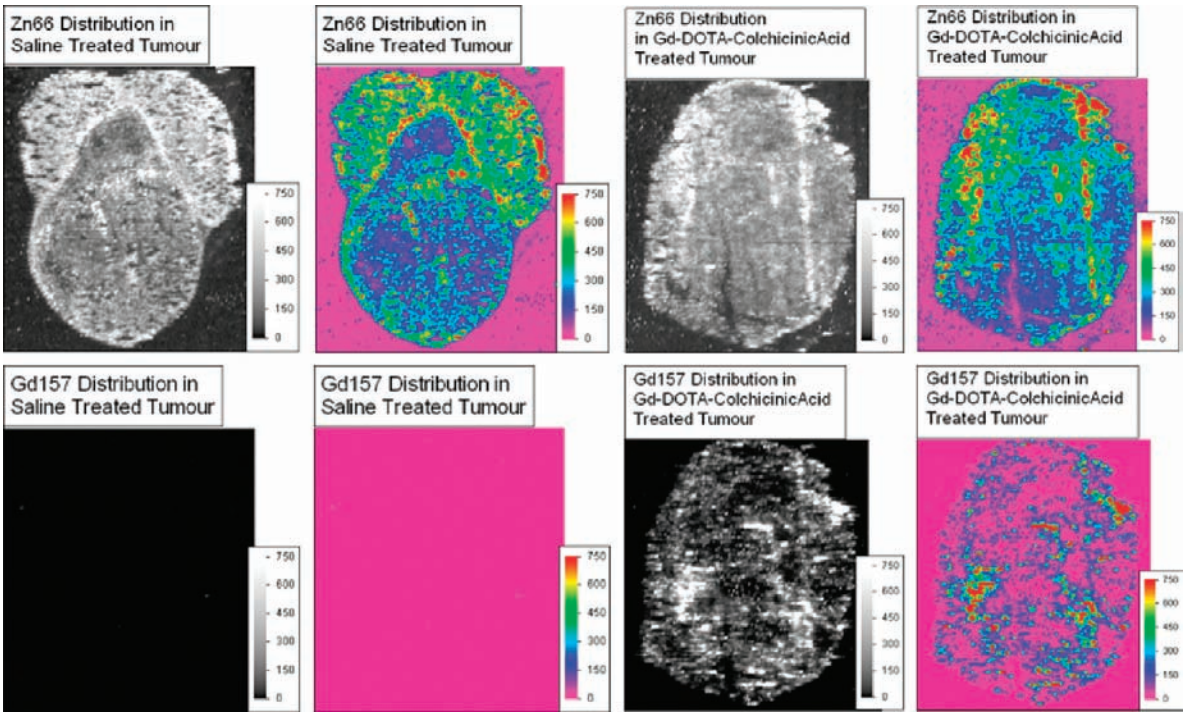


Figure 4. Laser ablation inductively coupled mass spectrometry data of Gd^{157} and Zn^{66} distribution in tumor sections of OVCAR3 tumors 24 h after 200 mg/kg Gd·DOTA·Colchicinic acid or 200 μL of saline administration.

acid treated mice (Figure 2). These changes in signal intensity were not observed at any time point, in any other cohort throughout the study.

Changes in mean T_1 are presented (Figure 3) for the tumor, liver, and kidney. Gd·DOTA exhibited similar values and trends as saline and DOTA·Colchicinic acid controls; therefore, these data have been omitted (from Figure 3). Tumor T_1 presented no change in mean T_1 from the baseline for any cohort at 2 h. A slight but nonsignificant reduction of 3% in mean T_1 was observed at 8 h post-Gd·DOTA·Colchicinic acid administration, which decreased further to become a significantly ($p < 0.05$) greater reduction of 6% in mean T_1 at 24 h post-administration in comparison with that in saline, Gd·DOTA, and DOTA·Colchicinic acid control cohorts (Figure 3A). A significant ($p < 0.05$) reduction of 55% in mean T_1 was also observed in the liver post-Gd·DOTA·Colchicinic acid administration at 2 h in comparison to that in saline, Gd·DOTA, or DOTA·Colchicinic acid control cohorts. This reduction in mean T_1 was sustained throughout, up until 24 h post-administration (Figure 3B). In the case of the kidney, no single significant change in T_1 was observed in any cohort (Figure 3C).

LA-ICP-MS. Elemental maps of Gd^{157} and Zn^{66} distribution in tumors against a saline control were generated 24 h post-Gd·DOTA·Colchicinic acid administration (Figure 4). LA-ICP-MS analysis indicated substantial amounts of Gd(III) present throughout the whole tumor. Using Zn^{66} as an indication of viable tissue, it can be clearly seen that the largest accumulation of Gd(III) takes place in complementary areas that may be necrotic. This suggests that Gd(III) has accumulated in tumor zones that were originally well perfused with blood vessels but became necrotic due to the occlusion of blood vessels post-VDA action. Our data indicate that the MRI-active VDA is still trapped within these apparently necrotic areas.

Histology. H & E staining showed that all tumors 24 h post-Gd·DOTA·Colchicinic acid or DOTA·Colchicinic acid administration possessed a large central core of necrosis with a rim of viable tumor tissue at the tumor periphery. Therefore, the degree of necrosis was not dependent on Gd(III) incorporation (Figure 5B). In contrast, tumors 24 h post-saline and Gd·DOTA administration possessed minimal necrosis and exhibited large areas of viable tumor tissue throughout the tumor (Figure 5A). Otherwise, the liver, which was also observed to accumulate substantial amounts of Gd(III) post-Gd·DOTA·Colchicinic acid as evidenced by substantial reductions in mean T_1 values (Figure 3B), showed no significant differences in liver morphology between animals treated with saline or any agent used in this work (Figure 5C and D). The kidney too was substantially unaffected by Gd·DOTA·Colchicinic acid administration or the administration of any other control compounds (data not shown).

DISCUSSION

In this study, we have synthesized and characterized a novel theranostic tubulin binding agent capable of working as a vascular disrupting agent that was capable of both reducing T_1 as well as keeping its efficacy to bind to tubulin *in vitro*, resulting in cell shape changes and central tumor necrosis *in vivo* characteristic of VDA treatment that could be followed with standard MR sequences longitudinally.

The conjugation of DOTA to colchicine resulted in DOTA·Colchicinic acid, which was complexed with gadolinium to produce the novel compound Gd·DOTA·Colchicinic acid. *In vitro* results showed that conjugation of Gd·DOTA to colchicine did not affect the relaxivity of the contrast agent as an MR probe. DOTA·Colchicinic acid was also found to be a functional therapeutic agent and was effective at causing characteristic VDA changes in both ovarian cell lines *in vitro* at concentrations of the millimolar range, suggesting that cells were less sensitive to the effects of cytotoxicity as afforded by unconjugated colchicine.

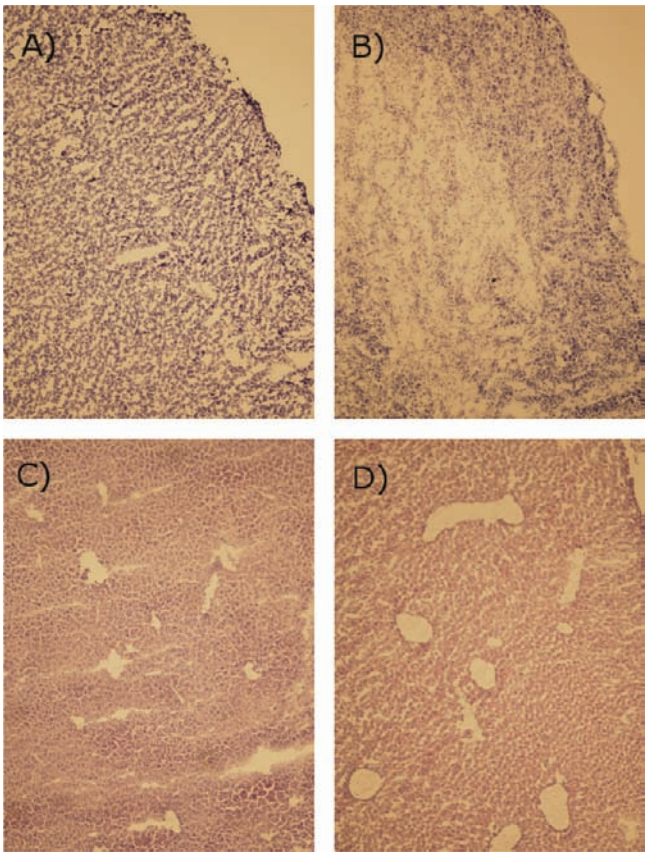


Figure 5. Hematoxylin and eosin stained sections of OVCAR-3 tumors (A,B) and normal liver parenchyma (C,D) 24 h after the administration of (A and C) saline and (B) 200 mg/kg Gd·DOTA·Colchicinic acid. Magnification is ×100.

Colchicine is too toxic for clinical use and is effective only at or close to its MTD, where direct cell cytotoxicity is the principal mechanism of action. A reduction in tumor cell cytotoxicity, therefore, suggests that DOTA·Colchicinic acid has a lower MTD and therefore a wider therapeutic window than colchicine, which would be well tolerated in animals.

DOTA·Colchicinic acid was tested in ovarian carcinoma cells initially *in vitro* instead of endothelial cells, as rapidly dividing tumor cells are also susceptible to VDA therapy and would give a better understanding about the secondary effects of VDA therapy on tumor cells that would be on top of the initial effect of vascular shut down.[35] Initial cell shape changes were observed at as early as 2 h after treatment with DOTA·Colchicinc acid, followed by cell rounding caused by the contraction of the tubulin cytoskeleton, decreasing intracellular adhesion, and subsequent cell loss due to detachment, similar to what has been shown in endothelial cells after doses of either ZD6126 or combretastatin derivatives *in vitro*.[9,36,37] Gd·DOTA·Colchicinic acid also caused T_1 reductions in cells *in vitro* at 2 h, which further decreased over 6 h. After 6 h, the T_1 recovery may be due to lower numbers of cells or changes in cell shape effecting water diffusion. However, as the T_1 does not recover completely, this implies that binding is irreversible as with colchicine itself,[38] resulting in long drug exposures that will therefore cause cell cytotoxicity, which would lead to increased tumor cell death.[39]

As expected for single dose VDA treatment, Gd·DOTA·Colchicinic acid did not cause tumor shrinkage or growth delay. Reductions in T_1 were apparent at 8 h and became significant at 24 h after treatment with Gd·DOTA.Colchcinic acid. As there was no change in T_1 for the saline or DOTA·Colchicinic acid cohorts, the decrease in T_1 relaxation is purely due to Gd·DOTA·Colchicinic acid acting as a contrast agent rather than effects caused by therapeutic effect, as these were not apparent in the nongadolinium derivative, which presented necrosis scores similar to that of Gd·DOTA.colchicinic acid by histology. Although Gd·DOTA also contains gadolinium, the nature of the molecule means that it has a short half-life and rapid clearance; therefore, the fact that there was no change in T_1 for this cohort suggests washout within the initial 2 h period. Morphological changes corresponding to necrosis were detected within the tumor at 24 h on MR images in the Gd·DOTA.Colchcicinic acid cohort only. Darkening of areas within the originally homogeneous tumor presentation were detected mainly within the center of the tumor and correlated well with the degree of necrosis by histology. LA-ICP-MS data revealed high concentrations of gadolinium throughout the tumor. Using Zn^{66} as a marker of viable tissue shows that areas assumed to be necrotic have high degrees of gadolinium present and therefore may represent previously well vascularised areas where Gd·DOTA·Colchicinic acid is still bound within the occluded vessels. The increased contrast between what is believed as the necrotic core and viable rim on images for the Gd·DOTA·Colchicinic acid cohort is most likely due to perfusion in the presence of bound Gd·DOTA·Colchicinic acid and is enough to enhance the signal intensity on T_1 images, whereas in areas of necrosis and increased paramagnetic substances due to therapy, such as increased permeability, platelet aggregation, coagulation, and hemorrhagic necrosis, it causes darkening on the image and therefore increases contrast between the two areas.[40] The liver also showed signal attenuation due to Gd·DOTA·Colchicinic acid accumulation, whereas no changes were observed in kidney T_1. As histology did not show any structural abnormalities and therefore no cyctoxicity to normal tissue in either organ, this may indicate the route of excretion as being via the liver and bile, which has also been shown for ZD6126 when tagged with carbon 14.[41,42]

The therapeutic effect of Gd·DOTA·Colchicinic acid is therefore comparable to changes induced by both CA-4-P and ZD6126 by MR where CA-4-P studies have shown early changes in signal with recovery to baseline at 24 h in both animal models and humans at clinically relevant doses,[17] whereas ZD6126 studies show no evidence of tumor recovery at 24 h[16,43] or up to 96 h after administration,[43] suggesting as with the *in vitro* data that the Gd·DOTA.Colchicine compound binds irreversibly in a similar manner to ZD6126.[38]

As well as carbon 14, colchicine has previously been conjugated to a wide range of imaging tracers, including Gd·DOTA, using the same demethylation of the methoxy group adjacent to the carbonyl.[26−32] These studies are mainly *in vitro* or if *in vivo* have required animal sacrifice at each end point, such as the radiolabeled studies,[26,30,31,41,42] and therefore do not provide longitudinal *in vivo* data. Studies that retained the toxicity of colchicine such as studies by Clark et al. evaluated the binding and subsequent cell changes *in vitro* but could not be used *in vivo*.[27] In other studies that reduced the toxicity of colchicines, although showing increased uptake and retention *in vitro*[32] and *in vivo*,[26] were unclear as to whether there was any significant therapeutic response.[26]

In conclusion, we have successfully synthesized and characterized a novel derivative of colchicine that is capable of functioning as a competent imaging tracer and as a therapeutic tubulin-binding agent *in vitro* and *in vivo*. The utilization of this has allowed for *in vivo* imaging of central necrosis as a therapeutic

response to VDA therapy in tumors in real time and has been validated by both histology and LA-ICP-MS. This has given a better understanding of the timing of necrosis and has strengthened the requirement for smart probes to be incorporated into the experimental design for *in vivo* applications.

AUTHOR INFORMATION

Corresponding Author

*Tel: +44 208 383 3497. Fax: +44 208 383 1511. E-mail: tammy.kalber@csc.mrc.ac.uk.

ACKNOWLEDGMENT

Funding for T.K. was provided by the MRC. The GTC is supported by EPSRC grant support and is also grateful for recent support from ImuThes Limited.

REFERENCES

(1) Vaupel, P., Kallinowski, F., and Okunieff, P. (1989) Blood flow, oxygen and nutrient supply, and metabolic microenvironment of human tumors: a review. *Cancer Res. 49*, 6449–6465.

(2) Denekamp, J. (1993) Review article: angiogenesis, neovascular proliferation and vascular pathophysiology as targets for cancer therapy. *Br. J. Radiol. 66*, 181–196.

(3) Carmeliet, P., and Jain, R. K. (2000) Angiogenesis in cancer and other diseases. *Nature 407*, 249–257.

(4) Bergers, G., and Benjamin, L. E. (2003) Tumorigenesis and the angiogenic switch. *Nat. Rev. Cancer 3*, 401–410.

(5) Siemann, D. W., Chaplin, D. J., and Horsman, M. R. (2004) Vascular-targeting therapies for treatment of malignant disease. *Cancer 100*, 2491–2499.

(6) Siemann, D. W., Bibby, M. C., Dark, G. G., Dicker, A. P., Eskens, F. A., Horsman, M. R., Marme, D., and Lorusso, P. M. (2005) Differentiation and definition of vascular-targeted therapies. *Clin. Cancer Res. 11*, 416–420.

(7) Micheletti, G., Poli, M., Borsotti, P., Martinelli, M., Imberti, B., Taraboletti, G., and Giavazzi, R. (2003) Vascular-targeting activity of ZD6126, a novel tubulin-binding agent. *Cancer Res. 63*, 1534–1537.

(8) Horsman, M. R., Ehrnrooth, E., Ladekarl, M., and Overgaard, J. (1998) The effect of combretastatin A-4 disodium phosphate in a C3H mouse mammary carcinoma and a variety of murine spontaneous tumors. *Int. J. Radiat. Oncol. Biol. Phys. 42*, 895–898.

(9) Blakey, D. C., Westwood, F. R., Walker, M., Hughes, G. D., Davis, P. D., Ashton, S. E., and Ryan, A. J. (2002) Antitumor activity of the novel vascular targeting agent ZD6126 in a panel of tumor models. *Clin. Cancer Res. 8*, 1974–1983.

(10) Tozer, G. M., Prise, V. E., Wilson, J., Locke, R. J., Vojnovic, B., Stratford, M. R., Dennis, M. F., and Chaplin, D. J. (1999) Combretastatin A-4 phosphate as a tumor vascular-targeting agent: early effects in tumors and normal tissues. *Cancer Res. 59*, 1626–1634.

(11) Siemann, D. W., and Horsman, M. R. (2002) Enhancement of radiation therapy by vascular targeting agents. *Curr. Opin. Invest. Drugs 3*, 1660–1665.

(12) Dark, G. G., Hill, S. A., Prise, V. E., Tozer, G. M., Pettit, G. R., and Chaplin, D. J. (1997) Combretastatin A-4, an agent that displays potent and selective toxicity toward tumor vasculature. *Cancer Res. 57*, 1829–1834.

(13) Dowlati, A., Robertson, K., Cooney, M., Petros, W. P., Stratford, M., Jesberger, J., Rafie, N., Overmoyer, B., Makkar, V., Stambler, B., Taylor, A., Waas, J., Lewin, J. S., McCrae, K. R., and Remick, S. C. (2002) A phase I pharmacokinetic and translational study of the novel vascular targeting agent combretastatin a-4 phosphate on a single-dose intravenous schedule in patients with advanced cancer. *Cancer Res. 62*, 3408–3416.

(14) Beauregard, D. A., Hill, S. A., Chaplin, D. J., and Brindle, K. M. (2001) The susceptibility of tumors to the antivascular drug combretastatin A4 phosphate correlates with vascular permeability. *Cancer Res. 61*, 6811–6815.

(15) Maxwell, R. J., Wilson, J., Prise, V. E., Vojnovic, B., Rustin, G. J., Lodge, M. A., and Tozer, G. M. (2002) Evaluation of the anti-vascular effects of combretastatin in rodent tumours by dynamic contrast enhanced MRI. *NMR Biomed. 15*, 89–98.

(16) Evelhoch, J. L., LoRusso, P. M., He, Z., DelProposto, Z., Polin, L., Corbett, T. H., Langmuir, P., Wheeler, C., Stone, A., Leadbetter, J., Ryan, A. J., Blakey, D. C., and Waterton, J. C. (2004) Magnetic resonance imaging measurements of the response of murine and human tumors to the vascular-targeting agent ZD6126. *Clin. Cancer Res. 10*, 3650–3657.

(17) Galbraith, S. M., Maxwell, R. J., Lodge, M. A., Tozer, G. M., Wilson, J., Taylor, N. J., Stirling, J. J., Sena, L., Padhani, A. R., and Rustin, G. J. (2003) Combretastatin A4 phosphate has tumor antivascular activity in rat and man as demonstrated by dynamic magnetic resonance imaging. *J. Clin. Oncol. 21*, 2831–2842.

(18) Robinson, S. P., McIntyre, D. J., Checkley, D., Tessier, J. J., Howe, F. A., Griffiths, J. R., Ashton, S. E., Ryan, A. J., Blakey, D. C., and Waterton, J. C. (2003) Tumour dose response to the antivascular agent ZD6126 assessed by magnetic resonance imaging. *Br. J. Cancer 88*, 1592–1597.

(19) Robinson, S. P., Kalber, T. L., Howe, F. A., McIntyre, D. J., Griffiths, J. R., Blakey, D. C., Whittaker, L., Ryan, A. J., and Waterton, J. C. (2005) Acute tumor response to ZD6126 assessed by intrinsic susceptibility magnetic resonance imaging. *Neoplasia 7*, 466–474.

(20) Thoeny, H. C., De Keyzer, F., Chen, F., Vandecaveye, V., Verbeken, E. K., Ahmed, B., Sun, X., Ni, Y., Bosmans, H., Hermans, R., van Oosterom, A., Marchal, G., and Landuyt, W. (2005) Diffusion-weighted magnetic resonance imaging allows noninvasive in vivo monitoring of the effects of combretastatin a-4 phosphate after repeated administration. *Neoplasia 7*, 779–787.

(21) Thoeny, H. C., De Keyzer, F., Chen, F., Ni, Y., Landuyt, W., Verbeken, E. K., Bosmans, H., Marchal, G., and Hermans, R. (2005) Diffusion-weighted MR imaging in monitoring the effect of a vascular targeting agent on rhabdomyosarcoma in rats. *Radiology 234*, 756–764.

(22) Wang, H., Sun, X., Chen, F., De Keyzer, F., Yu, J., Landuyt, W., Vandecaveye, V., Peeters, R., Bosmans, H., Hermans, R., Marchal, G., and Ni, Y. (2009) Treatment of rodent liver tumor with combretastatin a4 phosphate: noninvasive therapeutic evaluation using multiparametric magnetic resonance imaging in correlation with microangiography and histology. *Invest. Radiol. 44*, 44–53.

(23) Ni, Y., Bormans, G., Chen, F., Verbruggen, A., and Marchal, G. (2005) Necrosis avid contrast agents: functional similarity versus structural diversity. *Invest. Radiol. 40*, 526–535.

(24) Madhu, B., Waterton, J. C., Griffiths, J. R., Ryan, A. J., and Robinson, S. P. (2006) The response of RIF-1 fibrosarcomas to the vascular-disrupting agent ZD6126 assessed by in vivo and ex vivo 1H magnetic resonance spectroscopy. *Neoplasia 8*, 560–567.

(25) Zhao, M., Beauregard, D. A., Loizou, L., Davletov, B., and Brindle, K. M. (2001) Non-invasive detection of apoptosis using magnetic resonance imaging and a targeted contrast agent. *Nat. Med. 7*, 1241–1244.

(26) Satpati, D., Korde, A., Pandey, U., Dami, P., Banerjee, S., and Venkatesh, M. (2006) Synthesis and evaluation of 90Y-DOTA-Colchicine conjugate in murine fibrosarcoma model. *J. Labelled Compd. Radiopharm. 49*, 951–958.

(27) Clark, J. I., and Garland, D. (1978) Fluorescein colchicine. Synthesis, purification, and biological activity. *J. Cell Biol. 76*, 619–627.

(28) Bagnato, J. D., Eilers, A. L., Horton, R. A., and Grissom, C. B. (2004) Synthesis and characterization of a cobalamin-colchicine conjugate as a novel tumor-targeted cytotoxin. *J. Org. Chem. 69*, 8987–8996.

(29) van Rossenberg, S. M., Sliedregt-Bol, K. M., Koning, G., van den Elst, H., van Berkel, T. J., van Boom, J. H., van der Marel, G. A., and Biessen, E. A. (2003) Improvement of hepatocyte-specific gene expression by a targeted colchicine prodrug. *ChemBioChem 4*, 633–639.

(30) Zareneyrizi, F., Yang, D. J., Oh, C. S., Ilgan, S., Yu, D. F., Tansey, W., Liu, C. W., Kim, E. E., and Podoloff, D. A. (1999) Synthesis of [99mTc]ethylenedicysteine-colchicine for evaluation of antiangiogenic effect. *Anticancer Drugs 10*, 685–692.

(31) Korde, A., Satpati, D., Mathur, A., Mallia, M., Banerjee, S., Kothari, K., Sarma, H. D., Choudhari, P., and Venkatesh, M. (2006) 99mTc-labeling of colchicine using [99mTc(CO)3(H2O)3]+ and [99mTc triple bond N]2+ core for the preparation of potential tumor-targeting agents. *Bioorg. Med. Chem. 14*, 793–799.

(32) Efthimiadou, E. K., Katsarou, M. E., Fardis, M., Zikos, C., Pitsinos, E. N., Kazantzis, A., Leondiadis, L., Sagnou, M., and Vourloumis, D. (2008) Synthesis and characterization of novel natural product-Gd(III) MRI contrast agent conjugates. *Bioorg. Med. Chem. Lett. 18*, 6058–6061.

(33) Barge, A., Cravotto, G., Gianolio, E., and Fedeli, F. (2006) How to determine free Gd and free ligand in solution of Gd chelates. A technical note. *Contrast Media Mol. Imaging 1*, 184–188.

(34) Rasband, W. S. (1997−2008) *ImageJ*, U.S. National Institutes of Health, Bethesda, MD, http://rsb.info.nih.gov/ij/.

(35) Ahmed, B., Van Eijk, L. I., Bouma-Ter Steege, J. C., Van Der Schaft, D. W., Van Esch, A. M., Joosten-Achjanie, S. R., Lambin, P., Landuyt, W., and Griffioen, A. W. (2003) Vascular targeting effect of combretastatin A-4 phosphate dominates the inherent angiogenesis inhibitory activity. *Int. J. Cancer 105*, 20–25.

(36) Davis, P. D., Dougherty, G. J., Blakey, D. C., Galbraith, S. M., Tozer, G. M., Holder, A. L., Naylor, M. A., Nolan, J., Stratford, M. R., Chaplin, D. J., and Hill, S. A. (2002) ZD6126: a novel vascular-targeting agent that causes selective destruction of tumor vasculature. *Cancer Res. 62*, 7247–7253.

(37) Galbraith, S. M., Chaplin, D. J., Lee, F., Stratford, M. R., Locke, R. J., Vojnovic, B., and Tozer, G. M. (2001) Effects of combretastatin A4 phosphate on endothelial cell morphology in vitro and relationship to tumour vascular targeting activity in vivo. *Anticancer Res. 21*, 93–102.

(38) Lin, C. M., Ho, H. H., Pettit, G. R., and Hamel, E. (1989) Antimitotic natural products combretastatin A-4 and combretastatin A-2: studies on the mechanism of their inhibition of the binding of colchicine to tubulin. *Biochemistry 28*, 6984–6991.

(39) McGown, A. T., and Fox, B. W. (1989) Structural and biochemical comparison of the anti-mitotic agents colchicine, combretastatin A4 and amphethinile. *Anti-Cancer Drug Des. 3*, 249–254.

(40) Tozer, G. M., Kanthou, C., and Baguley, B. C. (2005) Disrupting tumour blood vessels. *Nat. Rev. Cancer 5*, 423–435.

(41) Partridge, E. A., D'Souza, R. A., Lenz, E. M., Smith, S. M., Clarkson-Jones, J., and Roberts, D. W. (2008) Disposition and metabolism of the colchicine derivative [14C]-ZD6126 in rat and dog. *Xenobiotica 38*, 399–421.

(42) D'Souza, R. A., Partridge, E. A., Roberts, D. W., Ashton, S., Ryan, A., Patterson, A. B., Wilson, Z., and Thurrell, C. C. (2007) Distribution of radioactivity and metabolite profiling in tumour and plasma following intravenous administration of a colchicine derivative (14C-ZD6126) to tumour-bearing mice. *Xenobiotica 37*, 328–340.

(43) McIntyre, D. J., Robinson, S. P., Howe, F. A., Griffiths, J. R., Ryan, A. J., Blakey, D. C., Peers, I. S., and Waterton, J. C. (2004) Single dose of the antivascular agent, ZD6126 (N-acetylcolchinol-O-phosphate), reduces perfusion for at least 96 h in the GH3 prolactinoma rat tumor model. *Neoplasia 6*, 150–157.

Bioconjugate Chemistry

ARTICLE

pubs.acs.org/bc

New Protein Purification System Using Gold-Magnetic Beads and a Novel Peptide Tag, "the Methionine Tag"

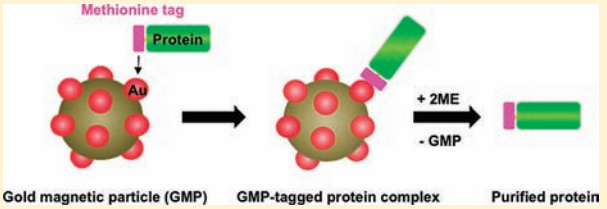
Yoshiaki Okada,[*,#,†] Tomoko Y. Takano,[#,†] Nozomi Kobayashi,[†] Arisa Hayashi,[†] Masaaki Yonekura,[†] Yuji Nishiyama,[†] Tomohiro Abe,[†] Takuya Yoshida,[†] Takao A. Yamamoto,[‡] Satoshi Seino,[‡] and Takefumi Doi[†]

[†]Graduate School of Pharmaceutical Sciences, Osaka University

[‡]Graduate School of Engineering, Osaka University

Supporting Information

ABSTRACT: Gold magnetic particles (GMP) are magnetic iron oxide particles modified with gold nanoparticles. The gold particles of GMP specifically bind to cysteine and methionine through Au−S binding. The aim of the present study was to establish a quick and easy protein purification system using novel peptide tags and GMP. Here, we created a variety of peptide tags containing methionine and cysteine and analyzed their affinity to GMP. Binding assays using enhanced green fluorescent protein (EGFP) as a model protein indicated that the tandem methionine tags comprising methionine residues had higher affinity to the GMP than tags comprising both methionine and cysteine residues. Tags comprising both methionine and glycine residues showed slightly higher affinity to GMP and higher elution efficiency than the all-methionine tags. A protein purification assay using phosphorylcholine-treated GMP demonstrated that both a tandem methionine-tagged EGFP and a methionine and glycine-tagged EGFP were specifically purified from a protein mixture with very high efficiency. The efficiency was comparable to that of a histidine-tagged protein purification system. Together, these novel peptide tags, "methionine tags", specifically bind to GMP and can be used for a highly efficient protein purification system.



INTRODUCTION

Protein purification using ion exchange, gel filtration, and affinity chromatography is commonly used to study protein function. Affinity chromatography is a powerful tool to purify a target protein by single column chromatography. Several protein and peptide tags are used for affinity chromatography such as glutathione S-transferase,[1] maltose-binding protein,[2,3] FLAG-tag,[4] hexahistidine tag,[5,6] calmodulin-binding peptide,[7] biotin acceptor peptide, [8] and strep-tag.[1,9] Each of these tags is fused to the target protein, and the tagged protein is purified using chemically modified beads with high affinity to the tag.

Magnet beads are used for protein purification. Because magnet beads in solution are easily collected with a magnet, these beads are used as biologic research tools for molecular interaction analysis, nucleic acid/protein purification in gene delivery,[10] cell separation,[11,12] tumor targeting,[13] magnetic resonance imaging,[14,15] and hyperthermic cancer therapy.[16,17] In most cases, chemically modified magnetic beads are used to immobilize a molecule (e.g., protein or DNA molecule) on the bead surface.[18]

The gold magnetic particle (GMP) is a novel magnetic bead on which nanoscale gold particles are immobilized.[19,20] Molecules including sulfur atoms (thiol sulfide and disulfide groups) bind to GMP through Au−S binding without the need for chemical linkers.[21,22] Only amino acids with sulfur atoms, such as cysteine and methionine residues, specifically bind to GMP.[23] In the present study, we developed novel peptide tags that strongly and specifically bind to GMP and successfully established a novel efficient protein purification system using these tags and GMP.

EXPERIMENTAL PROCEDURES

Preparation of Gold Magnetic Particle. Gold magnetic particles (GMP) were synthesized as previously described.[24] Briefly, 20 to 30 nm Fe_3O_4 nanoparticles (Nanostructured & Amorphous Materials, Inc., Houston, TX) were dispersed in water containing 0.5 mM $HAuCl_4$, 125 mM 2-propanol, and 1 mg/mL poly(vinyl pyrrolidone) (molecular weight 40 k) to prepare a 0.1 mg/mL Fe_3O_4 suspension. This suspension was irradiated with a 4.8 MeV high-energy electron beam at a dose rate of 3k Gy/s for 2 s in a glass vial. The resulting Au/Fe_3O_4 nanoparticles were collected with a magnet, washed with water three times, and resuspended in water. Production of Au/Fe_3O_4 particles containing 2 to 4 nm Au particles immobilized on the surface of Fe_3O_4 particles was confirmed by transmission electron microscopy. GMPs are now commercially available (Act Nonpareil, Osaka, Japan; URL: http://www.act-nonpareil.com/en/).

Received: September 29, 2010
Revised: February 17, 2011
Published: April 13, 2011

ACS Publications © 2011 American Chemical Society

To generate GMP-PC, gold magnetic particles were treated with phosphorylcholine.

Construction of Expression Vectors. Each tandem methionine tag was fused to enhanced green fluorescent proteins (EGFP) by a polypeptide linker that includes a protease recognition site, a helix linker, and a tag sequence (Supporting Information Figure S1). To generate pET-15b-EGFP-linker-MMM, a DNA fragment encoding the linker and the tandem methionine tag was generated by annealing several oligonucleotides. This fragment was cloned into *Eco*RI and *Bgl*II sites of pCruz-GFP (Santa Cruz Biotechnology, Santa Cruz, CA) (Supporting Information Figures S2 and S3). pCruz-EGFP-linker-MMM was then digested with *Nco*I and *Bgl*II, and the resulting fragment encoding EGFP-linker-MMM was inserted into the *Nco*I and *Bam*HI sites of pET-15b (Merck KGaA, Darmstadt, Germany) (Supporting Information Figure S3).

To generate the other tagged EGFP expression vectors, oligonucleotides encoding the tag sequences were cloned into *Not*I and *Sac*II sites of pCruz-EGFP-linker-MMM (Supporting Information Figure S2). The resulting plasmids were digested with *Nco*I and *Bgl*II, and the resulting fragments encoding the EGFP-linker-tag were inserted into the *Nco*I and *Bam*HI sites of pET-15b. The DNA sequences of each of the constructs were verified by automated DNA sequencing.

To generate pET-15b-CBFβ-linker-M3G4, a DNA fragment encoding CBFβ and a part of the polypeptide linker sequence was amplified by PCR. The resulting PCR product was digested with *Nco*I and *Sma*I, and cloned into the *Nco*I and *Sma*I sites of pET-15b-EGFP-linker-M3G4.

Preparation of the Tagged EGFPs. To prepare the tagged EGFPs, each of expression vectors for the tagged EGFP was transfected into *E. coli* strain BL21(DE3). The resulting *E. coli* were cultured in Luria−Bertani medium containing 50 μg/mL carbenicillin. When the OD_{600} reached 0.3, isopropyl β-D-thiogalactoside was added to a final concentration of 1 mM to induce the tagged EGFP. The cells were incubated for another 3 h at 30 °C and harvested. The cells were washed twice and resuspended with Buffer I (20 mM Tris-HCl [pH 8.0], 50 mM NaCl, 1 mM dithiothreitol (DTT), and protease inhibitor cocktail [Nacalai Tesque, Kyoto, Japan]). The resulting cell suspension was sonicated to extract and resolve the tagged EGFP. To purify the tagged proteins, the cell extract was applied to an Econo pack High Q cartridge (Bio-Rad, Hercules, CA). The column was then washed with Buffer II (20 mM Tris-HCl [pH 8.0], 80 mM NaCl, 1 mM DTT) and eluted with an 80−110 mM NaCl linear gradient. Fractions containing the tagged EGFP were collected and concentrated using Vivaspin 20 cartridges (Sartorius Stedim Biotech, Aubagne, France). The fluorescence intensity of the purified, tagged EGFP was measured using Gemini XPS (Molecular Devices, Sunnyvale, CA).

Protein Binding/Purification Assay and Sodium Dodecyl Sulfate-Polyacrylamide Gel Electrophoresis (SDS-PAGE) Analysis. For the protein binding assay, 15 000 fluorescence units of the tagged protein was mixed with GMP containing 10 mg iron in 300 μL of binding buffer (20 mM Tris-HCl [pH 8.0], 100 mM NaCl) and incubated for 30 min at 4 °C. The GMP in the resulting solution was collected with a magnet, and the fluorescence intensity of the supernatant was measured. The collected GMP was washed twice with binding buffer and incubated in 300 μL of binding buffer containing 24 mM 2-mercaptoethanol (2-ME) following for 30 min at 4 °C. The fluorescence intensity of the eluted proteins was measured. The same procedure was used for the protein purification assay with nonpurified *E. coli* extract containing 15 000 fluorescence units of the tagged EGFPs. For the protein purification assay using histidine tagged EGFP, Dynabeads TALON (Invitrogen, Carlsbad, CA) was used. Crude protein extract and eluted protein were subjected to SDS-PAGE following Coomassie Brilliant Blue staining.

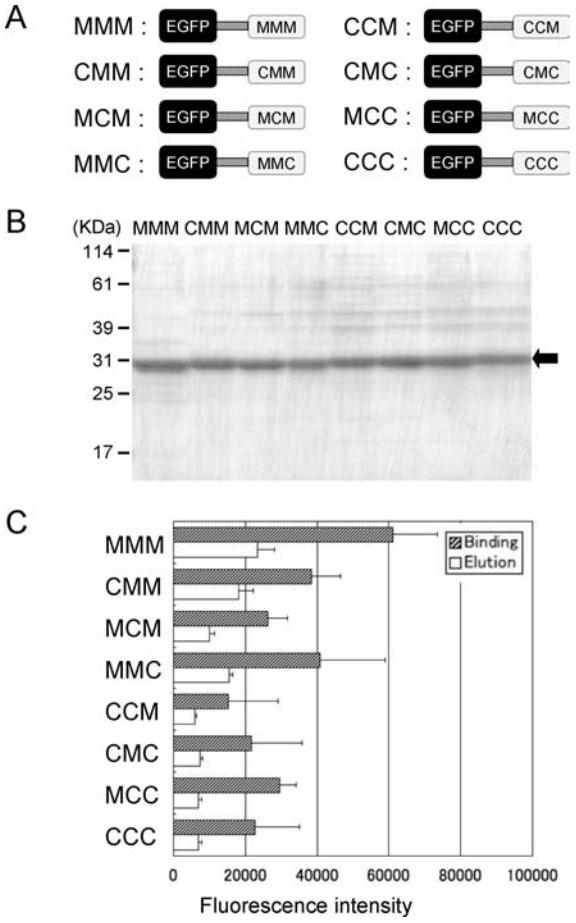


Figure 1. Binding affinity of tags comprising methionine and cysteine residues. (A) EGFPs tagged with peptides comprising three amino acids. The tags included methionine and/or cysteine and linked to the C-terminus of EGFP through a helix linker. (B) SDS-PAGE analysis of the tagged protein purified by ion exchange column chromatography. The gel was stained with Coomassie Brilliant Blue. The arrow indicates bands of tagged EGFPs. (C) Fluorescence intensities of the binding and eluted proteins obtained in the protein binding assay. The assay was performed three times. Each bar represents mean ± SD.

RESULTS

Three Amino Acid Tags Comprising Methionine and/or Cysteine. A goal of our research was to prepare a protein purification system using a novel peptide tag and GMP. To that end, we planned to develop novel peptide tags that specifically bind to GMP with high affinity. We first prepared eight peptide tags that included methionine and/or cysteine (MMM, CMM, MCM, MMC, CCM, CMC, MCC, and CCC), and each of them was fused to the C-terminus of EGFP with a polypeptide linker (Figure 1A and Supporting Information Figure S1). The tagged proteins were expressed in *E. coli* and purified with Q-Sepharose column chromatography (Figure 1B).

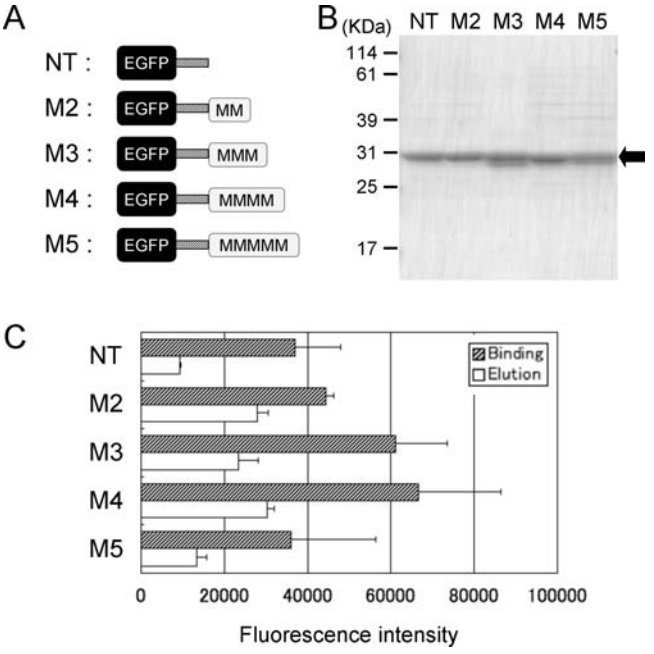


Figure 2. Binding affinity of tags comprising tandem methionine sequences. (A) EGFPs tagged with or without peptides comprising tandem methionine sequence. (B) SDS-PAGE analysis of the tagged protein purified by ion exchange column chromatography. The gel was stained with Coomassie Brilliant Blue. The arrow indicates bands of tagged EGFPs. (C) Fluorescence intensities of the binding and eluted proteins obtained in the protein binding assay. The assay was performed three times. Each bar represents mean ± SD.

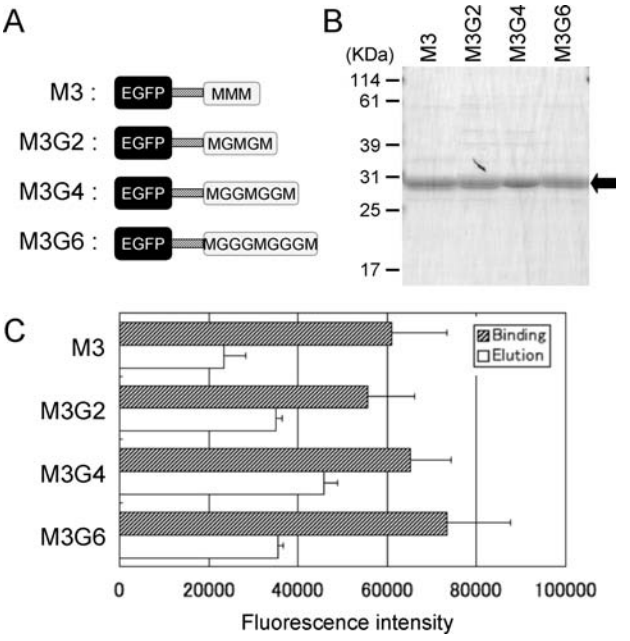


Figure 3. Binding affinity of the tags comprising methionine and glycine residues. (A) EGFPs tagged with the peptides comprising methionine and glycine residues. (B) SDS-PAGE analysis of the tagged protein purified by ion exchange column chromatography. The gel was stained with Coomassie Brilliant Blue. The arrow indicates bands of tagged EGFPs. (C) Fluorescence intensities of the binding and eluted proteins obtained in the protein binding assay. The assay was performed three times. Each bar represents mean ± SD.

A binding assay was performed to evaluate the affinity of the tagged proteins to GMP (Supporting Information Figure S4). Each of the tagged proteins was mixed with GMP for a binding reaction between GMP and the protein. The resulting GMP-protein complex was collected with a magnet and washed with the buffer to remove nonspecific binding proteins. The specific binding proteins were then eluted with the buffer containing 2-ME. Fluorescence intensities derived from binding and eluted protein were calculated by measuring the intensities of input, removed and eluted fractions (Figure 1D). MMM had the highest binding affinity for GMP. CMM and MMC had intermediate affinity for GMP (63% and 67% of the MMM intensity, respectively). MCM, CCM, CMC, MCC, CCC had low affinity for GMP (43%, 25%, 35%, 48%, and 37% of the MMM intensity, respectively). The fluorescence intensity of the eluted fraction showed the same pattern, that is, MMM had the highest intensity. CMM and MMC had intermediate affinity to GMP (78% and 66% of the MMM intensity, respectively). MCM, CCM, CMC, MCC, and CCC had low affinity to GMP (42%, 25%, 31%, 29%, and 29% of the MMM intensity, respectively). These results suggested that tags containing tandem methionine residues (e.g., MMM, CMM, and MMC) have high affinity to GMP.

Tandem Methionine Tags Containing Various Numbers of Methionine Residues. To further improve the binding affinity of the tandem methionine tag to GMP, we prepared tandem methionine tags comprising various numbers of methionine residues (M2, M4, and M5) and a control tag without methionine (NT) and coupled them to the C-terminus of EGFP (Figure 2A). These proteins were expressed in *E. coli* and purified with Q-Sepharose column chromatography (Figure 2B). Binding assays using these proteins showed that the fluorescence intensity of bound M3 and M4 was significantly higher than that of NT (1.7- and 1.8-fold compared to NT, respectively; Figure 2C). M2 had a moderately stronger intensity than NT (1.2-fold), while M5 and NT showed the similar intensities. A similar pattern was observed with the fluorescence intensities of the eluted proteins, with the exception of the strong intensity of M2 (the intensities of M2, M3, M4, and M5 were 3.0-, 2.6-, 3.3-, and 1.5-fold compared to NT). Together, these results indicate that the tags including three or four tandem methionine residues had the highest binding affinity to GMP and high elution efficiency from GMP.

Tags Comprising Three Methionine and Glycine Residues. To investigate whether the distance between methionine residues in the tag affects the binding affinity to GMP, 1 to 3 glycine residues (containing no sulfur atoms) were inserted between methionine residues of the M3 tag, and three new tags were prepared (Figure 3A). These tags were fused to the C-terminus of EGFP, and the tagged proteins (M3G2, M3G4, and M3G6) were expressed in *E. coli* and purified with Q-Sepharose column chromatography (Figure 3B). Binding assays using these proteins showed that the fluorescence intensity of binding proteins of M3G2, M3G4, and M3G6 were similar to that of M3 (0.9-, 1.1-, and 1.2-fold compared with M3, respectively; Figure 3C and Supporting Information Figure S5). In contrast, the fluorescence intensities of the eluted proteins containing M3G2, M3G4, and M3G6 were significantly higher than that of M3 (1.5-, 1.9-, and 1.5-fold compared to M3, respectively). This finding suggests that insertion of a glycine between methionine residues does not change the binding affinity of the tagged protein to GMP, and rather improved the elution efficiency.

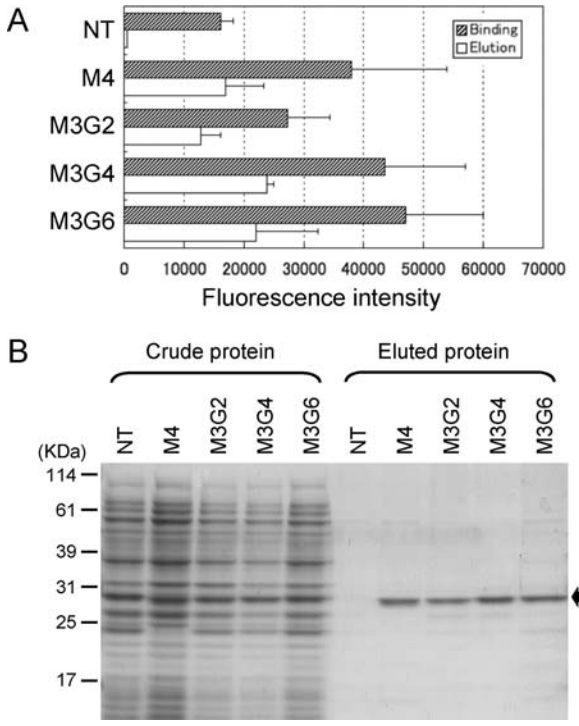


Figure 4. Purification of the tagged EGFPs from *E. coli* extract. (A) Fluorescence intensities of the binding and eluted proteins obtained in the protein purification assay. The assay was performed three times. Each bar represents mean ± SD. (B) SDS-PAGE analysis of the crude extract and purified protein. The arrow indicates bands of tagged EGFPs. The gel was stained with Coomassie Brilliant Blue.

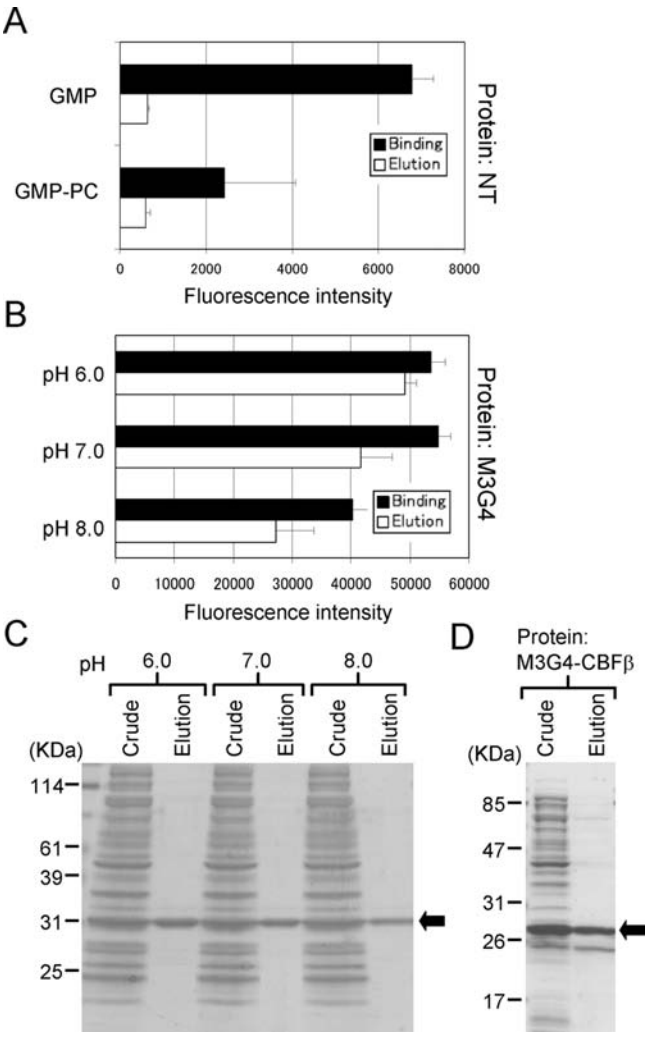


Figure 5. Treatment of GMP with phosphorylcholine improves the protein purification efficiency. (A) Fluorescence intensities of the binding and eluted proteins obtained in the protein purification assay using GMP or GMP-PC, and crude extract including NT. The assay was performed three times. Each bar represents mean ± SD. (B) Fluorescence intensities of the binding and eluted proteins obtained in the protein purification assay in pH 6−8 using GMP-PC and crude extract including M3G4. The assay was performed three times. Each bar represents mean ± SD. (C) SDS-PAGE analysis of the crude extract and purified protein. The arrow indicates bands of tagged EGFPs. The gel was stained with Coomassie Brilliant Blue. (D) Protein purification assay was performed using GMP-PC and *E. coli* extract containing M3G6 tagged CBFβ. The crude and eluted protein was analyzed by SDS-PAGE followed by Coomassie Brilliant Blue staining. The arrow indicates a band of tagged CBFβ.

Purification of the Tagged Protein from *E. coli* Extract. To investigate whether the tagged proteins can be purified from *E. coli* extract, each of five tagged or nontagged EGFPs (M4, M3G2, M3G4, M3G6, or NT) was expressed in *E. coli*. Crude protein extracts were prepared from *E. coli* and subjected to a protein purification assay. Fluorescence intensities of the binding proteins of M4, M3G2, M3G4, and M3G6 were significantly higher than that of NT (2.4-, 1.7-, 2.7-, and 2.9-fold, respectively; Figure 4A). Fluorescence intensities of the eluted proteins of M4, M3G2, M3G4, and M3G6 were also significantly higher than that of NT (51-, 38-, 72-, and 66-fold, respectively). These results indicate that tagged proteins were specifically purified by this purification step, though tag-independent nonspecific binding was observed with NT.

To further investigate the efficiency of the purification, the crude and eluted protein fractions were analyzed by SDS-PAGE following Coomassie Brilliant Blue staining (Figure 4B). The result indicated that the tagged EGFPs, but not the nontagged EGFP, were specifically purified from *E. coli* extract in very high purity. Together, these results indicated that the tagged proteins, including M4, M3G2, M3G4, and M3G6, can be purified from *E. coli* extract.

Improvement of the Purification Efficiency. A protein purification assay using tagged proteins indicated that there was tag-independent protein binding to GMP. To decrease this tag-independent protein binding to GMP, we treated GMP with phosphorylcholine (PC) and created GMP-PC. A binding assay using GMP or GMP-PC with NT showed that PC treatment resulted in a 65% decrease of the tag-independent protein binding to GMP, whereas the elution efficiency was not different between GMP and GMP-PC (Figure 5A). In addition, this PC treatment did not inhibit protein binding to GMP through gold nanoparticles (Supporting Information Figure S6). To determine the optimal pH for protein purification using GMP-PC, a protein purification assay was performed using M3G4 and buffers at pH 6, 7, and 8 (Figure 5B). The pH 6 and 7 buffers resulted in high fluorescence intensity of the binding proteins, while the pH 8 buffer resulted in 73% of intensity compared with the pH 6 and 7 buffers. In contrast, the fluorescence intensity of eluted protein was highest with the pH 6 buffer, while the pH 7

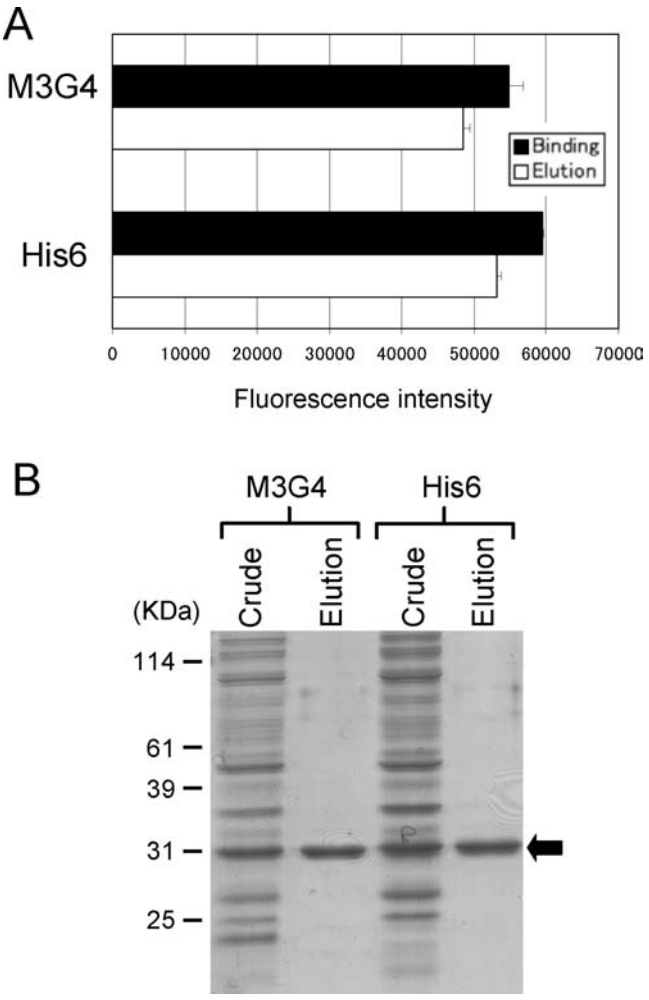


Figure 6. Comparison of the purification efficiency between system using a methionine tag or histidine tag. (A) Fluorescence intensities of the binding and eluted proteins obtained in the protein purification assay. The assay was performed three times. Each bar represents mean ± SD. (B) SDS-PAGE analysis of the crude extract and purified protein. The arrow indicates bands of tagged EGFPs. The gel was stained with Coomassie Brilliant Blue.

and 8 buffers showed reduced intensities (84% and 55% compared with pH 6, respectively). In this assay, 91%, 75%, and 67% of the binding proteins were eluted in pH 6, 7, and 8 buffers, respectively. To investigate the purity of the eluted protein, SDS-PAGE analysis was performed using crude and purified protein fractions (Figure 5C). The result showed that the tagged protein, M3G4, was specifically purified in all three buffers. In addition, another tagged protein, M3G4-CBFβ was also purified with GMP-PC in high purity (Figure 5D). Together, these results indicate that PC treatment of the GMP suppressed the tag-independent protein binding and significantly improved the efficiency of protein purification in buffer at a certain pH.

Comparison of Purification Efficiencies between Methionine Tag and Histidine Tag. To evaluate the efficiency of the established protein purification system in comparison with the common protein purification system, histidine-tagged EGFP (His6) was prepared. M3G4 or His6 was expressed in *E. coli*, and crude protein extracts were prepared. The same fluorescence intensity of the M3G4 and His6 was purified with the same amount (same iron weight) of GMP-PC or Co^{2+} chelated magnetic beads. Fluorescence intensities of both binding and eluted proteins of M3G4 were comparable to those of His6 (Figure 6A). SDS-PAGE analysis indicated that both M3G4 and His6 were specifically purified from the crude extract (Figure 6B). Together, these results indicate that the novel protein purification system using a methionine tag and GMP-PC has comparable efficiency to a common protein purification system.

DISCUSSION

We previously demonstrated that cystine (comprising 2 cysteine residues) and methionine specifically bind to GMP through Au−S binding and that cystine showed the significantly higher affinity to GMP than methionine.[23] On the basis of this finding, we hypothesized that peptide tags including methionine and/or cysteine residues would strongly bind to GMP. The aim of this study was to establish a novel protein purification system using novel peptide tags. To that end, we first generated the peptide tags comprising three amino acid peptide tags including methionine and/or cysteine residues. The tags with a tandem methionine sequence had high affinity to GMP and high elution efficiency from GMP. Unexpectedly, the tags with a number of cysteine residues had low affinity to GMP and also low elution efficiency, although cystine showed very strong affinity to GMP in our previous study.[23] We speculated that cysteine residues in the C-terminus of EGFP form intra- and/or intermolecular disulfide bonds, and that these might disturb the binding between the tags and GMP. In terms of the low elution efficiency of the tags with more than 2 cysteine residues, excessively strong binding between cysteine and GMP might inhibit the elution of the tagged EGFP.

The assay using three amino acid peptide tags indicated that tandem methionine residues improved the binding affinity of the tag. The binding assay using tandem methionine tags comprising different numbers of methionine residues indicated that increasing the number of methionine residues to four improved the binding affinity of the tag to GMP. However, the tag with five methionine residues has significantly decreased binding affinity to GMP. We speculated that the tag with five tandem methionine residues (M5) contributes to a hydrophobic interaction between tagged-EGFPs, which disturbs the Au−S binding between the tag and GMP. In addition, M5 expression level in *E. coli* was very low compared with that of M2, M3, or M4 (data not shown). A five tandem methionine sequence may disturb the protein expression in *E. coli*. This finding suggests that the tags with three or four methionine residues are preferable for protein purification.

We next hypothesized that the insertion of glycine residues between methionine residues would provide the peptide with a flexible conformation, thus making all the methionine residues contribute to Au−S binding, and we performed the assays using M3G2, M3G4, and M3G6. The insertion of glycine residues, however, did not change the binding affinity, but slightly improved the elution efficiency. Insertion of glycine residues might induce conformational changes of the tags and these tagged-EGFPs might then slightly increase the elution efficiency by improving the accessibility of 2-ME to the GMP.

The protein purification assays demonstrated that M4, M3G2, M3G4, and M3G6 can be purified from a protein mixture. However, not all the binding proteins were eluted from GMP, and this decreased the yield of the eluted protein. We speculated that this low purification efficiency derived from the nonspecific protein binding to GMP, which was observed in the binding assay

using NT. To decrease the nonspecific binding of protein to GMP, we treated GMP with PC that is known to have high free water fraction and decreased protein adsorption onto the polymer surface.[25−27] Treatment of GMP with PC and optimization of the buffer pH significantly reduced the nonspecific protein binding and increased the yield of the purified protein. Efficiency of the optimized protein purification system is comparable to that of the system using the histidine tag.

Thus, we successfully established a novel protein purification system using the novel peptide tags "methionine tags" and GMP. This purification system has several merits that are found in other protein purification systems. For example, the small tag sequence hardly interferes with protein expression in cells and does not affect protein structure and functions. Specialized binding buffers and substrates for protein elution are not necessary. All of the purification steps can be easily and quickly performed by using a magnet instead of a centrifuge. Thus, this protein purification system is convenient and useful. In addition, GMPs conjugated with methionine-tagged protein might be useful as tools for biological and clinical research.

■ ASSOCIATED CONTENT

Supporting Information. Information regarding the polypeptide linker sequence (Figure S1), construction of plasmids (Figure S2 and S3), protein purification procedure (Figure S4), protein binding assay using various amounts of proteins (Figure S5), and protein purification assay using magnetic particles (Figure S6). This material is available free of charge via the Internet at http://pubs.acs.org.

■ AUTHOR INFORMATION

Corresponding Author

*Yoshiaki Okada, Ph.D., Osaka University, Graduate School of Pharmaceutical Sciences, 1-6 Yamadaoka, Suita, Osaka, 565-0871, Japan. E-mail: okadabos@phs.osaka-u.ac.jp. Tel/Fax: +81-6-6879-8164.

Author Contributions

#Y.O. and T.Y.T. equally contributed to this work.

■ ACKNOWLEDGMENT

This work was supported by the Japan Science and TechnologyAgency (JST).

■ REFERENCES

(1) Schmidt, T. G., and Skerra, A. (1993)The random peptide library-assisted engineering of a C-terminal affinity peptide, useful for the detection and purification of a functional Ig Fv fragment. *Protein Eng. 6*, 109–22.

(2) di Guan, C., Li, P., Riggs, P. D., and Inouye, H. (1988)Vectors that facilitate the expression and purification of foreign peptides in Escherichia coli by fusion to maltose-binding protein. *Gene 67*, 21–30.

(3) Kapust, R. B., and Waugh, D. S. (1999)Escherichia coli maltose-binding protein is uncommonly effective at promoting the solubility of polypeptides to which it is fused. *Protein Sci. 8*, 1668–74.

(4) Einhauer, A., and Jungbauer, A. (2001)The FLAG peptide, a versatile fusion tag for the purification of recombinant proteins. *J. Biochem. Biophys. Methods 49*, 455–65.

(5) Gaberc-Porekar, V., and Menart, V. (2001)Perspectives of immobilized-metal affinity chromatography. *J. Biochem. Biophys. Methods 49*, 335–60.

(6) Marti, D., Schaller, J., Ochensberger, B., and Rickli, E. E. (1994) Expression, purification and characterization of the recombinant kringle 2 and kringle 3 domains of human plasminogen and analysis of their binding affinity for omega-aminocarboxylic acids. *Eur. J. Biochem. 219*, 455–62.

(7) Vaillancourt, P., Zheng, C. F., Hoang, D. Q., and Breister, L. (2000)Affinity purification of recombinant proteins fused to calmodulin or to calmodulin-binding peptides. *Methods Enzymol. 326*, 340–62.

(8) Schatz, P. J. (1993)Use of peptide libraries to map the substrate specificity of a peptide-modifying enzyme: a 13 residue consensus peptide specifies biotinylation in Escherichia coli. *Bio/Technology 11*, 1138–43.

(9) Voss, S., and Skerra, A. (1997)Mutagenesis of a flexible loop in streptavidin leads to higher affinity for the Strep-tag II peptide and improved performance in recombinant protein purification. *Protein Eng. 10*, 975–82.

(10) Kamei, K., Mukai, Y., Kojima, H., Yoshikawa, T., Yoshikawa, M., Kiyohara, G., Yamamoto, T. A., Yoshioka, Y., Okada, N., Seino, S., and Nakagawa, S. (2009)Direct cell entry of gold/iron-oxide magnetic nanoparticles in adenovirus mediated gene delivery. *Biomaterials 30*, 1809–14.

(11) Konishi, Y., Lindholm, K., Yang, L. B., Li, R., and Shen, Y. (2002) Isolation of living neurons from human elderly brains using the immunomagnetic sorting DNA-linker system. *Am. J. Pathol. 161*, 1567–76.

(12) Hoshino, A., Ohnishi, N., Yasuhara, M., Yamamoto, K., and Kondo, A. (2007)Separation of murine neutrophils and macrophages by thermoresponsive magnetic nanoparticles. *Biotechnol. Prog. 23*, 1513–6.

(13) Vonderheide, R. H., and June, C. H. (2003)A translational bridge to cancer immunotherapy: exploiting costimulation and target antigens for active and passive T cell immunotherapy. *Immunol. Res. 27*, 341–56.

(14) Lemke, A. J., Senfft von Pilsach, M. I., Lubbe, A., Bergemann, C., Riess, H., and Felix, R. (2004)MRI after magnetic drug targeting in patients with advanced solid malignant tumors. *Eur. Radiol. 14*, 1949–55.

(15) Fortin-Ripoche, J. P., Martina, M. S., Gazeau, F., Menager, C., Wilhelm, C., Bacri, J. C., Lesieur, S., and Clement, O. (2006)Magnetic targeting of magnetoliposomes to solid tumors with MR imaging monitoring in mice: feasibility. *Radiology 239*, 415–24.

(16) Ito, A., Shinkai, M., Honda, H., and Kobayashi, T. (2001)Heat-inducible TNF-alpha gene therapy combined with hyperthermia using magnetic nanoparticles as a novel tumor-targeted therapy. *Cancer Gene Ther. 8*, 649–54.

(17) Ito, A., Shinkai, M., Honda, H., and Kobayashi, T. (2005) Medical application of functionalized magnetic nanoparticles. *J. Biosci. Bioeng. 100*, 1–11.

(18) Gabrielsen, O. S., Hornes, E., Korsnes, L., Ruet, A., and Oyen, T. B. (1989)Magnetic DNA affinity purification of yeast transcription factor tau--a new purification principle for the ultrarapid isolation of near homogeneous factor. *Nucleic Acids Res. 17*, 6253–67.

(19) Seino, S., Kinoshita, T., Otome, Y., Okitsu, K., Nakagawa, T., and Yamamoto, T. A. (2003)Magnetic composite nanoparticles of Au/gamma-Fe_2O_3 synthesized by gammma-ray irradiation. *Chem. Lett. 32*, 690–691.

(20) Kinoshita, T., Seino, S., Okitsu, K., Nakayama, T., Nakagawa, T., and Yamamoto, T. A. (2003)Magnetic evaluation of nanostructure of gold-iron composite particles synthesized by a reverse micelle method. *J. Alloys Compd. 359*, 46–50.

(21) Nuzzo, R. G., and Allara, D. L. (1983)Adsorption of bifunctional organic disulfides on gold surfaces. *J. Am. Chem. Soc. 105*, 4481–4483.

(22) Karyakin, A. A., Presnova, G. V., Rubtsova, M. Y., and Egorov, A. M. (2000)Oriented immobilization of antibodies onto the gold surfaces via their native thiol groups. *Anal. Chem. 72*, 3805–3811.

(23) Kinoshita, T., Seino, S., Mizukoshi, Y., Otome, Y., Nakagawa, T., Okitsu, K., and Yamamoto, T. A. (2005)Magnetic separation of amino acids by gold/iron-oxide composite nanoparticles synthesized by gamma-ray irradiation. *J. Magn. Magn. Mater. 293*, 106–110.

(24) Seino, S., Kinoshita, T., Nakagawa, T., Kojima, T., Taniguci, R., Okuda, S., and Yamamoto, T. A. (2008)Radiation induced synthesis of gold/iron-oxide composite nanoparticles using high-energy electron beam. *J. Nanopart. Res. 10*, 1071–1076.

(25) Ishihara, K., Ishikawa, E., Iwasaki, Y., and Nakabayashi, N. (1999)Inhibition of fibroblast cell adhesion on substrate by coating with 2-methacryloxloxyethyl phosphorylcholine polymers. *J. Biomater. Sci., Polym. Ed. 10*, 1047–1061.

(26) Lu, D. R., Lee, S. J., and Park, K. (1991) Calculation of solvation interaction energies for protein adsorption on polymer surfaces. *Journal of biomaterials science. Polymer edition 3*, 127−147.

(27) Maeno, K., Hirayama, A., Sakuma, K., and Miyazawa, K. (2011) An activated medium with high durability and low nonspecific adsorption: Application to protein A chromatography. *Anal. Biochem. 409*, 123–129.

New protein purification system using gold-magnetic beads and a novel peptide tag, “the Methionine tag”

Yoshiaki Okada[1*#], Tomoko Y. Takano[1#], Nozomi Kobayashi[1], Arisa Hayashi[1], Masaaki Yonekura[1], Yuji Nishiyama[1], Tomohiro Abe[1], Takuya Yoshida[1], Takao A. Yamamoto[2], Satoshi Seino[2], Takefumi Doi[1]

[1]Graduate School of Pharmaceutical Science, Osaka University; [2]Graduate School of Engineering, Osaka University

Figure S1. Schematic representation of the tagged EGFP with the poly peptide linker... 2

Figure S2. DNA sequences encoding the polypeptide linker and methionine tags..... 2

Figure S3. Schematic representation of the construction of pET-15b-EGFP-linker-MMM..... 3

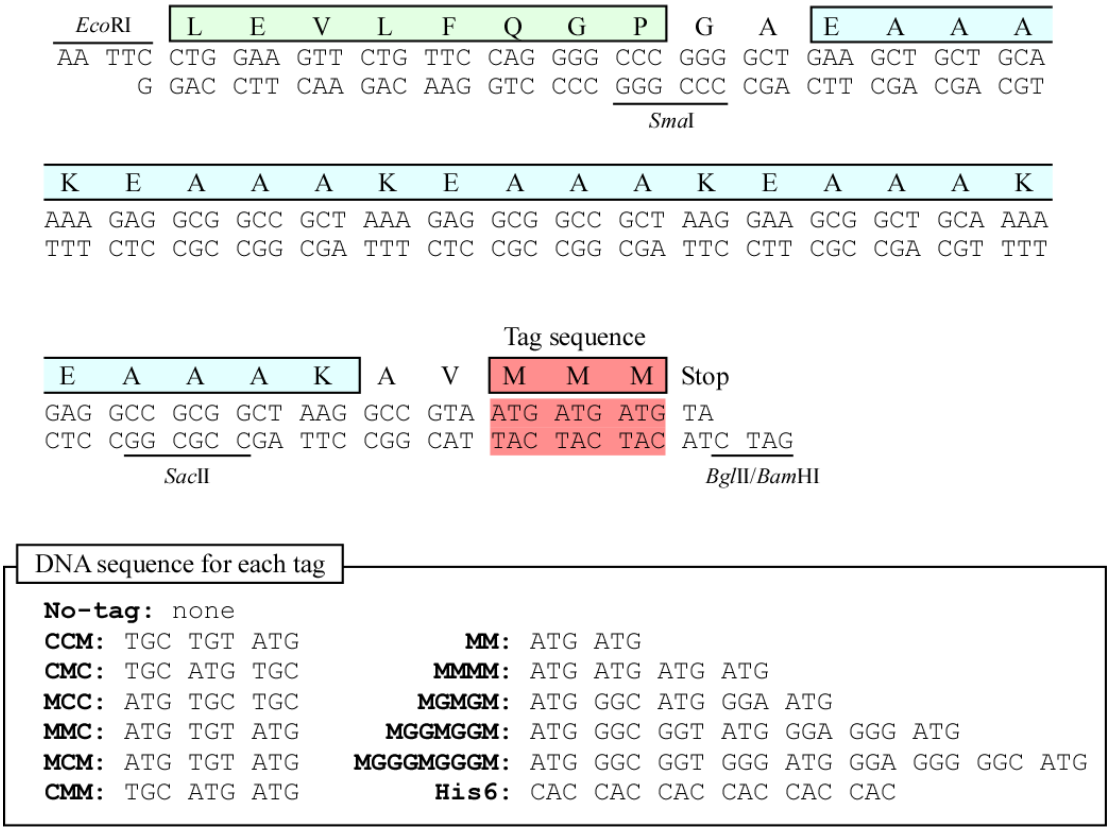
Figure S4. Schematic illustration of the protein binding/purification assay using the tagged EGFP and GMP..... 3

Figure S5. Protein binding assays using various amounts of tagged and non-tagged EGFP..... 4

Figure S6. Binding of The tagged protein to GMP through gold particles.....4



Figure S1 Schematic representation of the tagged EGFP with the polypeptide linker. The linker sequence includes a precision protease recognition site and a 5× EAAAK sequence which is known to form a helix structure (*1*). The protease recognition site is useful for removing the tag to obtain the intact protein. The function of the helix linker sequence is to retain the tag sequence outside of the EGFP structure.



DNA sequence for each tag

No-tag:	none		
CCM:	TGC TGT ATG	**MM:**	ATG ATG
CMC:	TGC ATG TGC	**MMMM:**	ATG ATG ATG ATG
MCC:	ATG TGC TGC	**MGMGM:**	ATG GGC ATG GGA ATG
MMC:	ATG TGT ATG	**MGGMGGM:**	ATG GGC GGT ATG GGA GGG ATG
MCM:	ATG TGT ATG	**MGGGMGGGM:**	ATG GGC GGT GGG ATG GGA GGG GGC ATG
CMM:	TGC ATG ATG	**His6:**	CAC CAC CAC CAC CAC CAC

Figure S2 DNA sequences encoding the polypeptide linker and methionine tags. Boxed amino acid sequences indicate the protease recognition site and 5× EAAAK sequence. Restriction sites in the sequence are used for plasmid construction.

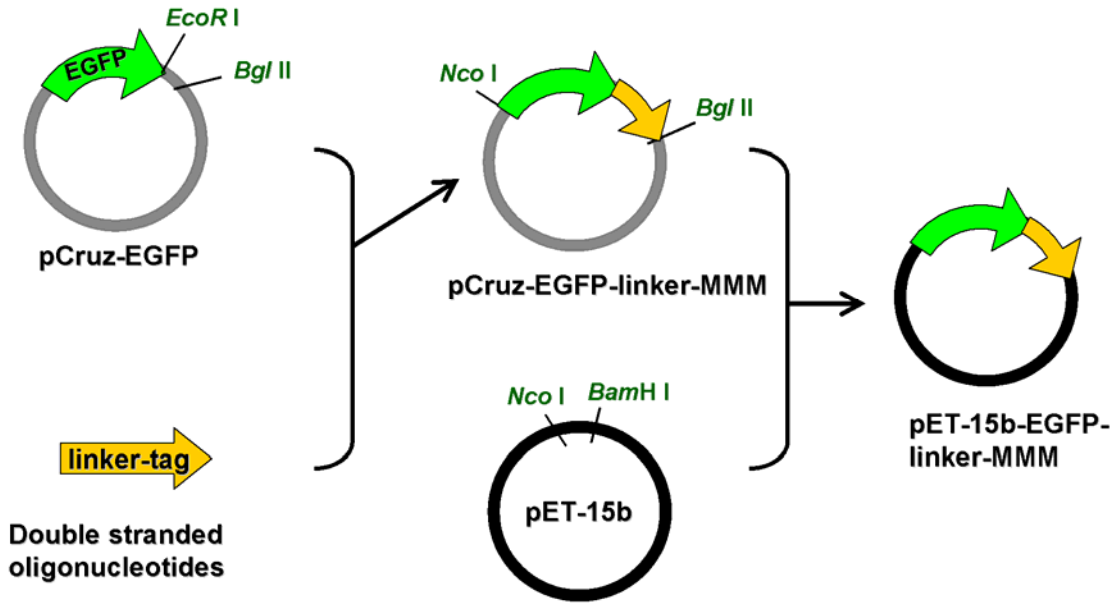


Figure S3 Schematic representation of the construction of pET-15b-EGFP-linker-MMM.

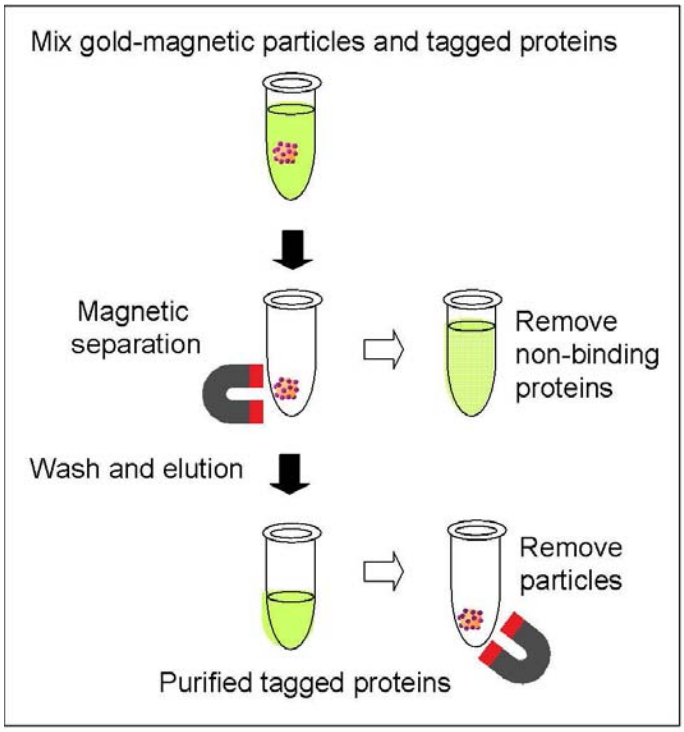


Figure S4 Schematic representation of the protein binding/purification assay using the tagged EGFP and GMP.

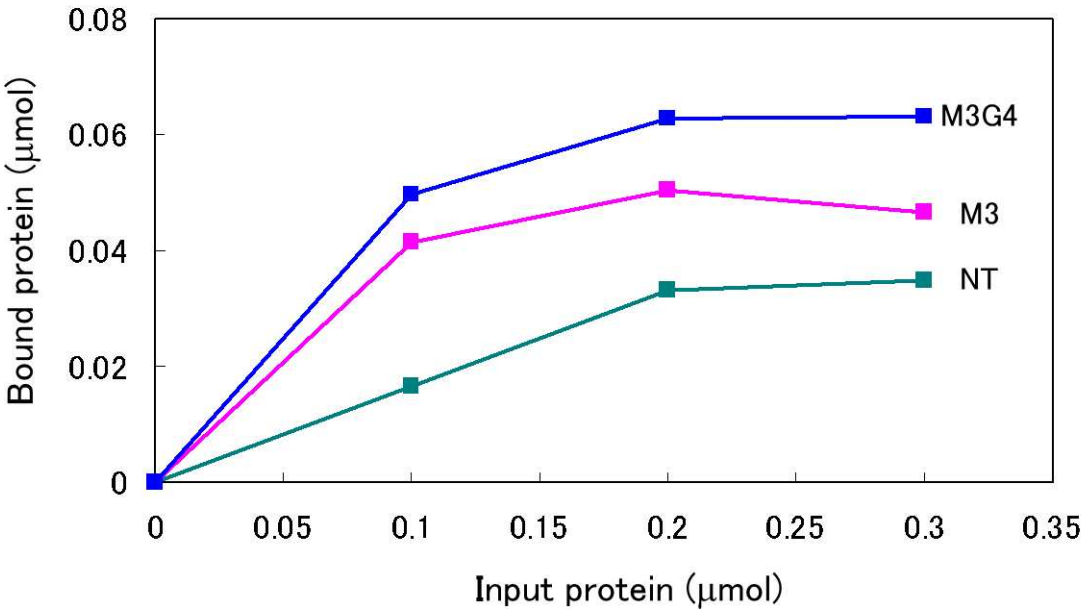


Figure S5 Protein binding assays using various amounts of tagged and non-tagged EGFP.

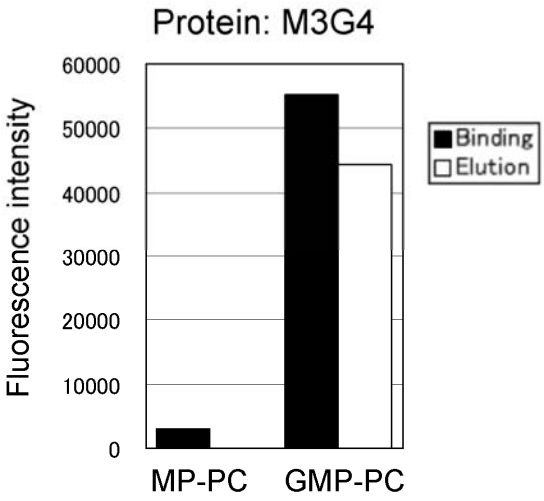


Figure S6 Binding of the tagged protein to GMP through gold particles.

A protein purification assay was performed using PC-treated GMPs and iron-oxide magnetic particles (MPs) that are not modified with gold particles. The assay was performed with a crude protein mixture including M3G4 in a pH6.5 buffer.

References

(1) Marqusee, S., and Baldwin, R. L. (1987) Helix stabilization by Glu-...Lys+ salt bridges in short peptides of de novo design. *Proc Natl Acad Sci U S A 84*, 8898-902.

Bioconjugate Chemistry

ARTICLE

pubs.acs.org/bc

Evaluation of a Maleimido Derivative of NOTA for Site-Specific Labeling of Affibody Molecules

Vladimir Tolmachev,*[,‡] Mohamed Altai,[‡] Mattias Sandström,[†] Anna Perols,[§] Amelie Eriksson Karlström,[§] Frederic Boschetti,[∥] and Anna Orlova[‡]

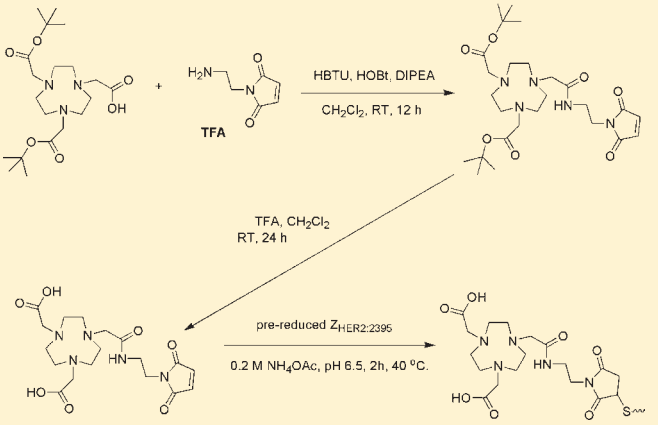
[‡]Unit of Biomedical Radiation Sciences, Rudbeck Laboratory, Uppsala University, Sweden

[†]Section of Medical Physics, Department of Oncology, Uppsala University Hospital, Uppsala, Sweden

[§]Division of Molecular Biotechnology, School of Biotechnology, KTH Royal Institute of Technology, Stockholm, Sweden

[∥]CheMatech, Djion, France

ABSTRACT: Radionuclide molecular imaging has the potential to improve cancer treatment by selection of patients for targeted therapy. Affibody molecules are a class of small (7 kDa) high-affinity targeting proteins with appreciable potential as molecular imaging probes. The NOTA chelator forms stable complexes with a number of radionuclides suitable for SPECT or PET imaging. A maleimidoethylmonoamide NOTA (MMA-NOTA) has been prepared for site-specific labeling of Affibody molecules having a unique C-terminal cysteine. Coupling of the MMA-NOTA to the anti-HER2 Affibody molecule $Z_{HER2:2395}$ resulted in a conjugate with an affinity (dissociation constant) to HER2 of 72 pM. Labeling of [MMA-NOTA-Cys^{61}]-$Z_{HER2:2395}$ with ^{111}In gave a yield of >95% after 20 min at 60 °C. In vitro cell tests demonstrated specific binding of [^{111}In-MMA-NOTA-Cys^{61}]-$Z_{HER2:2395}$ to HER2-expressing cell lines. In mice bearing prostate cancer DU-145 xenografts, the tumor uptake of [^{111}In-MMA-NOTA-Cys^{61}]-$Z_{HER2:2395}$ was 8.2 ± 0.9% IA/g and the tumor-to-blood ratio was 31 ± 1 (4 h postinjection). DU-145 xenografts were clearly visualized by a gamma camera. Direct in vivo comparison of [^{111}In-MMA-NOTA-Cys^{61}]-$Z_{HER2:2395}$ and [^{111}In-MMA-DOTA-Cys^{61}]-$Z_{HER2:2395}$ demonstrated that both conjugates provided equal radioactivity uptake in tumors, but the tumor-to-organ ratios were better for [^{111}In-MMA-NOTA-Cys^{61}]-$Z_{HER2:2395}$ due to more efficient clearance from normal tissues. In conclusion, coupling of MMA-NOTA to a cysteine-containing Affibody molecule resulted in a site-specifically labeled conjugate, which retains high affinity, can be efficiently labeled, and allows for high-contrast imaging.



INTRODUCTION

Increasing specificity of cancer treatment is currently based on molecular targeting of malignancy-associated molecular alterations in cancer cells. Both patient stratification for therapy and monitoring of therapy response require accurate detection of the expression level of a molecular target at the onset of therapy and during treatment.[1,2] Radionuclide imaging of molecular targets might be a valuable clinical tool, since it is less sensitive to heterogeneity of target expression and noninvasive permitting serial investigations, which is essential for pharmacodynamic studies.[1,2]

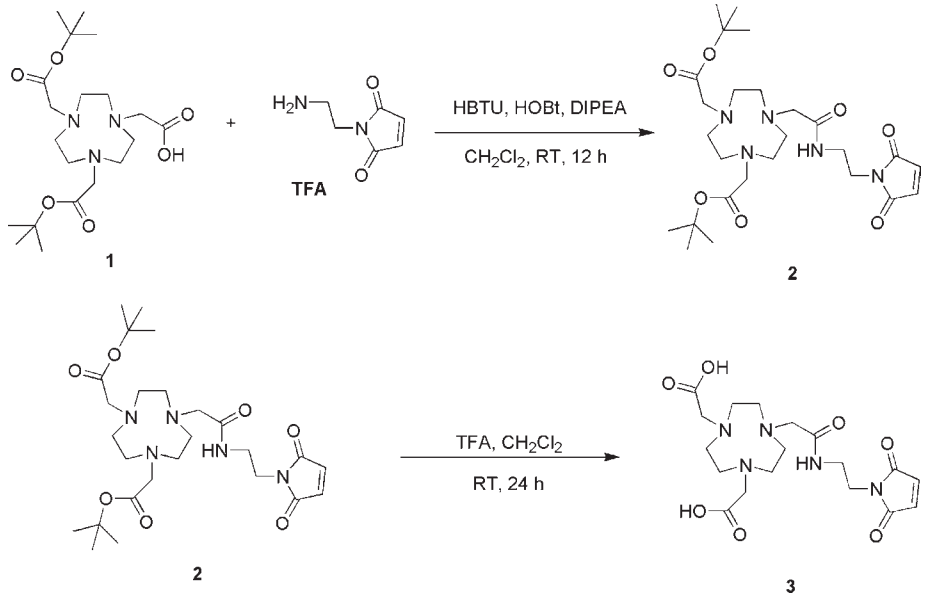
A new category of promising radionuclide imaging probes, scaffold-based proteins, has emerged during recent years.[3] The scaffold is a protein framework that can carry altered amino acids providing new binding specificities. Affibody molecules are a successful example of the application of the scaffold principle for the development of imaging agents.[4] The small size (ca. 7 kDa) and high affinity (low nanomolar to picomolar level) of Affibody molecules provide rapid extravasation and diffusion inside tumors, stable binding to molecular targets, and rapid clearance of nonbound probe, making high-contrast imaging possible. The robust disulfide-independent structure and rapid high-fidelity refolding of Affibody molecules in the physiological environment permit their labeling in harsh conditions.[5]

Site-specific labeling is important to provide chemically uniform radioconjugates with well-defined in vivo properties. For short peptides, such site-specificity is easy to achieve by incorporation of a chelator during peptide synthesis. This approach has been successfully applied to Affibody molecules as well.[5] It would be attractive, however, to be able also to label site-specifically recombinant proteins, since efficient peptide synthesis of, e.g. multimeric constructs or fusion proteins, is problematic. The feasibility of site-specific labeling of recombinant

Received: October 26, 2010
Revised: March 9, 2011
Published: March 29, 2011

ACS Publications © 2011 American Chemical Society

Scheme 1



Affibody molecules would provide high flexibility for production even of monomeric forms. The absence of cysteines in Affibody molecules enables us to solve this problem by the introduction of a unique cysteine residue in a desirable position and the use of thiol-directed chemistry for labeling or chelator coupling.[5] This approach has been used for labeling of Affibody molecules with radiobromine,[6] radioiodine,[7] ^{18}F,[8,9] ^{99m}Tc,[10] ^{111}In,[11−13] ^{57}Co,[14] and ^{64}Cu.[15,16]

A maleimido derivative of the macrocyclic chelator DOTA was used for labeling of Affibody molecules with ^{111}In, ^{57}Co, and ^{64}Cu. The use of DOTA provides stable coupling of many nuclides to targeting proteins.[17] However, DOTA is not always the chelator of choice. For example, DOTA is a suboptimal chelator for copper isotopes due to in vivo instability.[18] The use of NOTA[19] or cross-bridged chelators[20,21] for labeling with radiocopper provides more stable labeling than the use of DOTA, as well as lower liver uptake. Moreover, different chelators influence in different ways the affinity of an imaging peptide, the cellular processing and retention of a radionuclide, the biodistribution of a targeting peptide, and the excretion pathways of a nonbound tracer and radiocatabolites.[22] This influences the sensitivity and specificity of the imaging. Therefore, several chelators should be evaluated for each targeting protein to select the most suitable for each particular application.

NOTA (2,2′,2″-(1,4,7-triazacyclononane-1,4,7-triyl)triacetic acid) is a promising chelator for labeling of targeting agents with a number of radiometals. NOTA provides more stable complexes with gallium and indium than DOTA.[23,24] Several NOTA derivatives have been used for labeling of targeting peptides with Ga isotopes[25−27] and ^{111}In.[25] Biodistribution data indicate adequate in vivo stability of the conjugates. The feasibility of ^{68}Ga-labeling of NOTA-conjugated peptides at room temperature within a reasonable time (10 min) has been shown.[28] Recently, a very elegant method for labeling of peptides with ^{18}F using the formation of [^{18}F]aluminum fluoride and its complexation with NOTA has been proposed.[29] Taken together, derivatives of NOTA are very promising chelators for radiolabeling of targeting proteins and peptides.

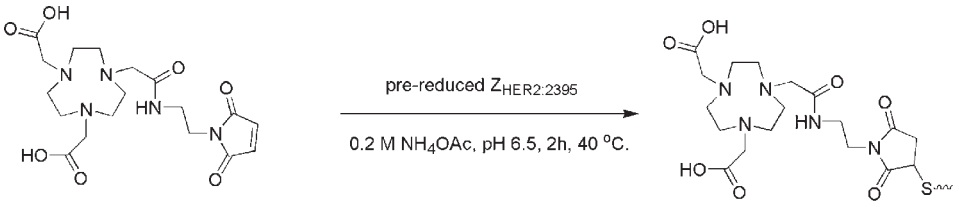
The goal of this study was to develop a maleimido derivative of NOTA (maleimide monoamide NOTA; MMA-NOTA), couple it to the HER2-binding Affibody molecule $Z_{HER2:2395}$ ([Ala^1, Glu^2,Thr^{23},Val^{59},Asp^{60},Cys^{61}]$Z_{HER2:342}$) having a C-terminal cysteine, and evaluate the ^{111}In-labeled conjugate in vitro and in vivo. ^{111}In is a widely used nuclide for single-photon emission tomography (SPECT). Indium forms stable hexacoordinate complexes with NOTA in aqueous solutions.[30] Although one carboxylic arm of NOTA participates in an amide bond in the case of MMA-NOTA, it was demonstrated earlier that the amide carbonyl oxygen can contribute to stable chelation of indium.[31]

MATERIALS AND METHODS

Material. $Z_{HER2:2395}$, a variant of $Z_{HER2:342}$ having a C-terminal cysteine, was produced according to Ahlgren and coworkers.[11] The commercially available (4,7-bis-*tert*-butoxycarbonylmethyl-[1,4,7]triazonan-1-yl)-acetic acid (NOTA(tBu)$_2$) was provided by CheMatech (Dijon, France). MMA-DOTA was purchased from Macrocyclics (Dallas, TX, USA). The purity and identity of all macromolecules and their conjugates was confirmed using high-performance liquid chromatography with on-line mass spectrometric detection, as described below. All purified proteins demonstrated a single peak with a mass coinciding with the theoretical molecular weight calculated with an accuracy of ±1.5 Da, which is within the accuracy of the instrument. Buffers, such as 0.1 M phosphate buffered saline (PBS), pH 7.5, and 0.2 M ammonium acetate, pH 6.5, were prepared using common methods from chemicals supplied by Merck (Darmstadt, Germany). High-quality Milli-Q water (resistance higher than 18 MΩ/cm) was used for preparing solutions. Buffers, which were used for conjugation and labeling, were purified from metal contamination using 2−3 g Chelex 100 resin per liter (Bio-Rad Laboratories, Richmond, CA, USA). NAP-5 size exclusion columns were from GE Healthcare Bio-Sciences (Uppsala, Sweden). [^{111}In]indium chloride was purchased from Covidien. The yield and radiochemical purity of the labeled Affibody constructs were analyzed using 150−771 dark

dx.doi.org/10.1021/bc100470x |*Bioconjugate Chem.* 2011, 22, 894–902

Scheme 2



3

green, Tec-Control chromatography strips from Biodex Medical Systems (New York, USA). The accuracy of radio-ITLC analysis was cross-validated by SDS-PAGE. Ketalar [ketamine] (50 mg/mL, Pfizer, NY, USA), Rompun [xylazin] (20 mg/mL, Bayer, Leverkusen, Germany), and Heparin (5000 IE/mL, Leo Pharma, Copenhagen, Denmark) were obtained commercially. The radioactivity was measured using an automated gamma counter with a 3-inch NaI(Tl) detector (1480 WIZARD, Wallac Oy, Turku, Finland). Distribution of radioactivity along the thin layer chromatography strips was measured on a Cyclone Storage Phosphor System and analyzed using the *OptiQuant* image analysis software. Cells were counted using an electronic cell counter (Beckman Coulter). Data on cellular uptake and biodistribution were analyzed by unpaired, two-tailed *t*-test using *GraphPad Prism* (version 4.00 for Windows GraphPad Software, San Diego, USA) in order to determine any significant differences ($P < 0.05$).

Synthesis and Characterization of ((4-Carboxymethyl-7-{[2-(2,5-dioxo-2,5-dihydro-pyrrol-1-yl)-ethylcarbamoyl]-methyl}-[1,4,7]triazonan-1-yl)-acetic acid) (MMA-NOTA, compound 3) (Scheme 1). Mass spectra were recorded on a Bruker Micro ToFQ Instrument in electrospray ionization (ESI) mode. NMR spectra were recorded on a 300 MHz BRUKER Avance spectrometer. Measurements were made using the "Plateforme d'Analyse Chimique et de Synthèse Moléculaire de l'Université de Bourgogne" (PACSMUB).

N,N-Diisopropylethylamine (DIPEA, 63 mg, 48 mmol, Acros, Geel, Belgium) was added to a solution of 100 mg (0.24 mmol) of NOTA(tBu)$_2$ (**1**), 97 mg (0.25 mmol) of 2-(1*H*-benzotriazole-1-yl)-1,1,3,3-tetramethyluronium hexafluorophosphate, (HBTU, Iris Biotech, Maktrewitz, Germany), 39 mg (0.29 mmol) of hydroxybenzotriazole (HOBt) (Sigma-Aldrich, Saint Quentin Fallavier, France), and 67 mg (0.25 mmol) of *N*-(2-aminoethyl)maleimide (Sigma-Aldrich, Saint Quentin Fallavier, France) in 12 mL of CH_2Cl_2 (Sigma-Aldrich, Saint Quentin Fallavier, France). The mixture was stirred at room temperature for 12 h. The solution was then diluted with 100 mL of CH_2Cl_2 and washed with 30 mL of 2.2 mM citric acid, 30 mL of an aqueous solution of $NaHCO_3$ (5%), and 50 mL of water. The organic phase was dried on $MgSO_4$ (Acros, Geel, Belgium), and the solvent was removed under vacuum. The residue, a yellow oil, was dissolved in 50 mL of diethyl ether (Sigma-Aldrich, Saint Quentin Fallavier, France). The white precipitate formed after filtration, and diethyl ether was removed under vacuum. The remaining oil was purified by chromatography (SiO_2, CH_2Cl_2, then EtOH/CH_2Cl_2 5/95 to 10/90). Compound **2** was obtained as a pale yellow oil (m = 80 mg, yield = 62%).

NMR ^{1}H ($CDCl_3$, 298 K, 300 MHz): δ 1.45 (s, 18H), 2.60 (br, 4H), 2.83 (br, 8H), 3.19 (s, 2H), 3.32 (S, 4H), 3.45 (m, 2H), 3.61 (m, 2H), 6.67 (s, 2H), 9.15 (s, 1H). ESI-MS m/z: calcd [MH]+, 537.32; found 537.33. Anal. ($C_{26}H_{43}N_5O_7$) C,H,N: calcd C, 58.08; H, 8.06; N, 13.03; found C, 57.83; H, 7.88, N, 12.77.

For deprotection, trifluoroacetic acid (TFA, 290 μL) was added to a solution of 38 mg of **2** in 192 μL of CH_2Cl_2. The mixture was stirred at room temperature for 24 h. The solvents were removed by heating under vacuum at maximum 35 °C. When the evaporation was almost complete, 10 mL of diethyl ether was added. A white precipitate was formed, filtered, and washed several times with diethyl ether. Compound **3** was obtained as a white hygroscopic powder (m = 10 mg).

NMR ^{1}H (D_2O, 298 K, 300 MHz): δ 3.07 (t, 4H, J = 5.6 Hz), 3.25 (t, 4H, J = 5.6 Hz), 3.32 (s, 4H), 3.42 (m, 2H), 3.59 (s, 2H), 3.64 (m, 2H), 3.92 (s, 4H). ESI-MS m/z: calcd [MH]+ 426.20; found 426.19. Anal. ($C_{18}H_{27}N_5O_7$, 1.5TFA) calcd C, 50.82; H, 6.40; N, 16.40; found C, 50.61; H, 6.21; N, 16.19.

Coupling of MMA-NOTA (3) to Affibody Molecules and Characterization of Conjugate (Scheme 2). Conjugation of MMA-NOTA (**3**) to $Z_{HER2:2395}$ was performed similarly to the coupling of MMA-DOTA described earlier.[11] Briefly, $Z_{HER2:2395}$ (stock solution, 5 mg/mL) was incubated during 2 h in 30 mM DTT at 40 °C to reduce any spontaneously formed disulfide bonds. After incubation, the reduced $Z_{HER2:2395}$ was purified using a NAP-5 column pre-equilibrated and eluted with degassed 0.2 M ammonium acetate, pH 6.5. The solution of freshly reduced Affibody molecules was mixed with a precalculated amount of a freshly prepared solution of MMA-NOTA in 0.2 M ammonium acetate, pH 6.5, (1 mg/mL) to obtain a chelator-to-protein ratio of 1:1 or 3:1. The vial was filled with argon gas, and the mixture was incubated at 40 °C for 2 h.

The coupling efficiency was determined using analytical RP-HPLC (Agilent 1200 series) with a Zorbax 300SB-C18 4.6 × 150 mm column with 3.5 μm particle size (Agilent, Santa Clara, CA, USA). A flow rate of 1 mL/min and a gradient of 25−45% B over 25 min (solvent A = 0.1%TFA-H_2O and solvent B = 0.1%TFA-CH_3CN) were used for analysis. The Affibody molecule conjugated with a chelator-to-protein ratio of 3:1 was purified for further experiments by semipreparative RP-HPLC, using a Reprosil Gold 300 C18 10 × 250 mm column with 5 μm particle size (Dr. Maisch, HPLC, GmbH, Ammerbuch, Germany). The flow rate was 2.5 mL/min and the gradient the same as above. The purified fraction was then analyzed by analytical RP-HPLC, as described above. The degree of conjugation as well as the final purity of the purified conjugate were determined by integrating the area of the peaks in the HPLC elution profiles. The molecular weights were determined by ESI-Q-TOF (Agilent).

The binding kinetics of the purified [MMA-NOTA-Cys^{61}]-$Z_{HER2:2395}$ Affibody molecule were investigated by real-time biospecific interaction analysis, using BIAcore 3000 (GE Healthcare, Uppsala, Sweden). The binding kinetics of [MMA-DOTA-Cys^{61}]-$Z_{HER2:2395}$ and parental $Z_{HER2:342}$ were investigated at

the same time, to avoid intra-assay variability. Human HER2-ECD (R&D systems, Minneapolis, MN, USA), recombinantly produced as an Fc-chimera, was diluted to 5 μg/mL in 10 mM NaOAc, pH 4.5, and immobilized by EDC/NHS-mediated coupling on a carboxymethylated dextran-coated CM5 chip. A flow cell activated with EDC/NHS and deactivated with ethanolamine was used as reference. All samples were diluted in HBS-EP buffer (10 mM HEPES, 150 mM NaCl, 3.4 mM EDTA, 0.05% Tween20, pH 7.2) and analyzed in duplicate in 6 concentrations ranging from 0.3 nM to 10 nM at a flow rate of 50 μL/min with a 5 min association phase and a 10 min dissociation phase. After each cycle. 15 mM HCl was injected to regenerate the surface. The final response was calculated by subtracting the reference surface, and the kinetic analysis was performed using *BIAevaluation 4.1* software using a 1:1 Langmuir model.

In order to measure the melting point of the [MMA-NOTA-Cys^{61}]-$Z_{HER2:2395}$ conjugate, variable temperature measurements were performed using a JASCO J-810 instrument (JASCO, Tokyo, Japan). The sample was diluted to 0.5 mg/mL in PBS (pH 7.2) and measured at 221 nm in a 1 mm optical cuvette. The temperature was increased by 5 °C/min ranging from 20 to 90 °C. The secondary structure was determined at 20 °C before and after melting point measurements using circular dichroism (CD) with wavelengths ranging from 195 to 250 nm.

Labeling [MMA-NOTA-Cys^{61}]-$Z_{HER2:2395}$ with ^{111}In. To establish the optimum labeling temperature, a solution of [MMA-NOTA-Cys^{61}]-$Z_{HER2:2395}$ (30 μg, 4 nmol) in 54 μL 0.2 M ammonium acetate, pH 5.5, was mixed with 40 μL ^{111}In chloride solution (15 MBq at calibration time). The mixture was incubated at room temperature, 40 or 60 °C. At 10, 20, and 30 min after the start of the incubation, a small aliquot (0.8 μL) of reaction mixture was taken and analyzed by radio-ITLC eluted with 0.2 M citric acid, pH 2.0. In this system, radiolabeled Affibody molecules remain at the application point while free ^{111}In or ^{111}In-chelates migrate with the solvent front. The analytical system was verified using a blank experiment, where no Affibody molecule was added to the reaction mixture. Blank experiments showed that less than 0.5% of radioactivity remained at the application point of ITLC. The experiments were performed at least in duplicate. For further experiments (stability tests, in vitro and in vivo studies), labeling at 60 °C during 30 min was selected.

An EDTA-challenge test was performed to evaluate the labeling stability of [^{111}In-MMA-NOTA-Cys^{61}]-$Z_{HER2:2395}$. Two samples were diluted with a 1000-fold molar excess of the disodium salt of EDTA solution in water, while two control samples were diluted with equal amount of PBS. After four-hour incubation at room temperature, all samples were analyzed using radio-ITLC.

Labeling of [MMA-DOTA-Cys^{61}]-$Z_{HER2:2395}$ with ^{111}In for comparative biodistribution experiments was performed as described by Ahlgren and co-workers.[11]

In Vitro Studies. For cell studies, the HER2-expressing ovarian carcinoma SKOV-3 (1.2×10^6 HER2 receptors per cell[32]) and prostate carcinoma DU-145 cell line ($\sim 5 \times 10^4$ HER2 receptors per cell, A. Orlova, unpublished results) (ATCC, purchased via LGC Promochem, Borås, Sweden) were used. The cell lines were cultured in RPMI medium (Flow Irvine, UK) supplemented with 10% fetal calf serum (Sigma, USA), 2 mM L-glutamine, and PEST (penicillin 100 IU/mL and 100 μg/mL streptomycin), all from Biokrom AG, Germany.

An in vitro specificity test was performed according to the methods described earlier.[33] Briefly, a solution of [^{111}In-MMA-NOTA-Cys^{61}]-$Z_{HER2:2395}$ (0.015 ng protein per dish, 2 nM) was added to six Petri dishes (ca. 10^6 cells in each). For blocking, an excess of nonlabeled recombinant $Z_{HER2:342}$ (2.5 μg) was added 10 min before [^{111}In-MMA-NOTA-Cys^{61}]-$Z_{HER2:2395}$ to saturate the receptors. The cells were incubated during one hour in a humidified incubator at 37 °C. Thereafter, the media was collected, the cells were detached by trypsin-EDTA solution, and the radioactivity in cells and media was measured to calculate a percentage of cell-bound radioactivity.

A comparison of [^{111}In-MMA-NOTA-Cys^{61}]-$Z_{HER2:2395}$ and [^{111}In-MMA-DOTA-Cys^{61}]-$Z_{HER2:2395}$ internalization by DU-145 cells was performed according to the method developed and validated by Wållberg and Orlova.[33] The cells (ca. 10^6 per dish) were incubated with the labeled compounds (0.015 ng protein per dish, 2 nM) at 37 °C, 5% CO_2. At predetermined time points (1, 2, 3, 4, and 8 h after incubation start), the media from a set of three dishes was removed and the cells were washed three times with ice-cold serum-free medium. The cells were then treated with 0.5 mL 0.2 M glycine buffer with 4 M urea, pH 2.5, for 5 min on ice. The acidic solution was collected and the cells were washed additionally with 0.5 mL glycine buffer, which was collected and pooled with the first fraction. The radioactivity in the acid wash fractions was considered as membrane-bound radioactivity. After addition of 0.5 mL 1 M NaOH, cells were incubated at 37 °C for 0.5 h before the alkali containing cell debris was collected. The cell dishes were washed with an additional 0.5 mL NaOH, and the alkaline fractions were pooled. The radioactivity in the alkaline fractions was considered internalized. A percent of internalized radioactivity was calculated for each time point.

Animal Studies. The animal experiments were planned and performed in accordance with the national regulation on laboratory animals' protection. The animal study plans have been approved by the local Ethics Committee for Animal Research in Uppsala. Nude male NMRI nu/nu mice bearing DU-145 prostate cancer xenografts were used. The mice were kept using standard sterile diet, bedding, and environment with free access to food and water. The mice were acclimatized for one week at the Rudbeck Laboratory animal facility before any experimental procedures. For tumor implantation, 5×10^6 DU-145 cells in Matrigel (BD Bioscience) were implanted on the right flank. Average tumor weight was 0.67 ± 0.26 g at the time of experiment. Average animal weight was 30 ± 2 g.

The mice were randomized into groups of four. Animals were injected intravenously (tail vein) with 0.3 μg conjugate (50 kBq) in 100 μL PBS. At four hours after injection, a mixture of Ketalar—Rompun (20 μL of solution per gram body weight; Ketalar, 10 mg/mL; Rompun, 1 mg/mL) was intraperitonealy injected and the mice were euthanized by a heart puncture using a 1 mL syringe, prewashed with diluted heparin (5000 IE/mL). Blood as well as lung, liver, spleen, kidneys, tumor, samples of muscle and bone, gastrointestinal tract (with its content), and remaining carcass were collected in preweighed plastic vials. Organs and tissue samples were weighed and measured for radioactivity using an automatic gamma counter. The tissue uptake values were calculated as percent injected activity per gram tissue (% ID/g), except for the gastrointestinal tract and the carcass, which were calculated as % ID per whole sample. The radioactivity in the gastrointestinal tract with its contents was used as a measure of hepatobiliary excretion.

To confirm that the xenograft accumulation of [^{111}In-MMA-NOTA-Cys^{61}]-$Z_{HER2:2395}$ was HER2-specific, the receptors in one

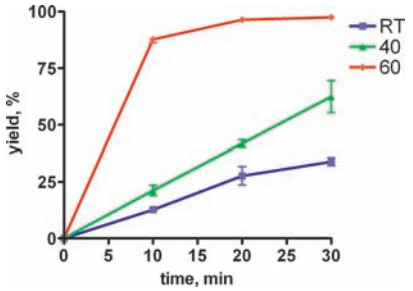


Figure 1. Labeling yield of [MMA-NOTA-Cys^{61}]-$Z_{HER2:2395}$ with ^{111}In in 0.2 M ammonium acetate buffer, pH 5.5, as a function of time at different temperatures. Data are presented as mean values of the results of two to eight experiments ± standard deviations.

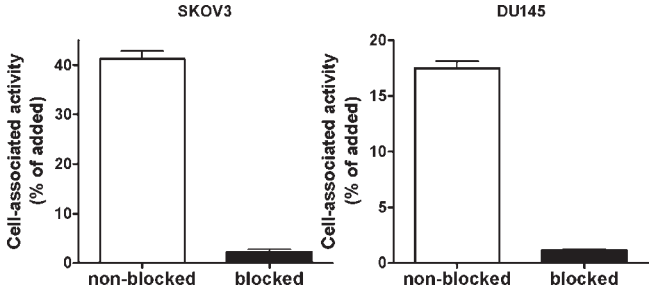


Figure 2. Cell-binding specificity of [^{111}In-MMA-NOTA-Cys^{61}]-$Z_{HER2:2395}$ labeled at 60 °C during 30 min. The test was performed with ovarian cancer cell line SKOV-3 and prostate cancer cell line DU145. In the blocking experiment, binding sites were saturated by adding to the cells an excess of nonlabeled $Z_{HER2:342}$. Data are presented as mean values for three samples ± maximum errors.

group of mice were presaturated by subcutaneous injection of 500 μg of unlabeled $Z_{HER2:342}$ 60 min prior to the injection of radiolabeled Affibody molecule, while another group was injected with [^{111}In-MMA-NOTA-Cys^{61}]-$Z_{HER2:2395}$ without preblocking. For comparison, the biodistribution of [^{111}In-MMA-DOTA-Cys^{61}]-$Z_{HER2:2395}$ was studied in DU-145 xenograft-bearing mice.

For gamma camera imaging, two DU-145 xenograft-bearing mice were injected with 2 MBq ^{111}In-[MMA-NOTA-Cys^{61}]-$Z_{HER2:2395}$ (amount of protein 1 μg). Four hours post-injection, the animals were sacrificed by overdosing Ketalar/Rompun followed by cervical dislocation. After euthanasia, the urine bladders were excised and cadavers were stored on ice until imaging. Imaging was performed at the department of Nuclear Medicine at Uppsala University Hospital using a GE Infinia gamma camera equipped with a medium energy general purpose (MEGP) collimator. Static images (40 min), obtained with a zoom factor of 2, were digitally stored in a 256 × 256 matrix. The evaluation of the images was performed using the *Osiris 4.19* software (University Hospital of Geneva, Switzerland). In each animal, a region of interest (ROI) was drawn around the tumor. The same region was copied to a contralateral thigh. Tumor-to-contralateral thigh ratios were calculated based on total counts in the ROIs.

RESULTS

Coupling of MMA-NOTA and Characterization of Conjugate. The degree of MMA-coupling to the Affibody molecules was determined by RP-HPLC analysis. Conjugation of MMA-NOTA to $Z_{HER2:2395}$-Cys using a chelator-to-protein ratio of 1:1 resulted in 49% conjugated protein, 3% nonconjugated disulfide-linked dimeric protein and the remaining found as nonconjugated monomeric protein. Increasing the chelator-to-protein molar ratio to 3:1 resulted in 80% of MMA-NOTA-conjugated $Z_{HER2:2395}$, while 17% was found as dimeric nonconjugated protein. The purification of [MMA-NOTA-Cys^{61}]-$Z_{HER2:2395}$ by RP-HPLC provided a product with 96% purity. This protein was used for further analysis.

Binding analyses of the conjugated molecules were performed using SPR-based biosensor interaction. The dissociation constant (K_D) for the interaction between the Affibody conjugate and the extracellular domain of the HER2 receptor (recombinantly produced as an Fc-chimera) was calculated to be 72 pM from the association rate constant (k_a) and the dissociation rate constant (k_d). In the same experiment, the dissociation constants for [MMA-DOTA-Cys^{61}]-$Z_{HER2:2395}$ and parental $Z_{HER2:342}$ were determined to be 74 pM and 78 pM, respectively.

The secondary structure determined by CD spectra showed α-helical content both before and after variable temperature measurements, indicating that the molecule refolds after heat treatment. The melting point of [MMA-DOTA-Cys^{61}]-$Z_{HER2:2395}$ was determined to be 68 °C.

Labeling [MMA-NOTA-Cys^{61}]-$Z_{HER2:2395}$ with ^{111}In. The kinetics of [^{111}In-MMA-NOTA-Cys^{61}]-$Z_{HER2:2395}$ formation at different temperatures is presented in Figure 1. The labeling at room temperature was inefficient. Increasing the reaction temperature to 40 °C improved the yield; however, the analytical radiochemical yield was only 62 ± 7% (n = 3) after 30 min incubation. Further temperature increase to 60 °C resulted in an increase of the radiochemical yield to 97.5 ± 0.5% (n = 12) within 30 min. For further experiments, the [MMA-NOTA-Cys^{61}]-$Z_{HER2:2395}$ was labeled at 60 °C and used without further purification. Conjugates with a specific radioactivity of 14.5 GBq/μmol (2 MBq/μg) were obtained with the yield of more than 95% (labeling at 60 °C), when indium-111 was used for labeling three days after production.

The stability of [^{111}In-MMA-NOTA-Cys^{61}]-$Z_{HER2:2395}$ was evaluated by challenge with a 1000-fold molar excess of EDTA over 4 h. The EDTA challenge demonstrated very high labeling stability. The radiochemical purity of the treated samples was 96.2 ± 0.6% (average ± SEM), while the purity of the untreated control was 98.7 ± 0.1%, i.e., the difference was within the accuracy of the analytical method.

In Vitro Studies. Binding specificity tests demonstrated that the binding of [^{111}In-MMA-NOTA-Cys^{61}]-$Z_{HER2:2395}$ to living HER2-expressing cells was receptor-mediated, because saturation of the receptors by preincubation with nonlabeled $Z_{HER2:342}$ significantly decreased the binding of the radiolabeled Affibody molecule (for all studied cell-lines, $p < 0.0001$) (Figure 2). The level of cell-associated radioactivity was appreciably lower for the nonblocked DU-145 cell line than for the SKOV-3 cell line, reflecting the lower expression level of HER2.

A comparison of the internalization of [^{111}In-MMA-NOTA-Cys^{61}]-$Z_{HER2:2395}$ and [^{111}In-MMA-DOTA-Cys^{61}]-$Z_{HER2:2395}$ by DU-145 prostate cancer cells is presented in Figure 3. The internalization of both compounds was relatively slow, although internalized fractions increased continuously throughout the experiment. The internalization rate of [^{111}In-MMA-NOTA-Cys^{61}]-$Z_{HER2:2395}$ was slightly higher than the rate of [^{111}In-MMA-DOTA-Cys^{61}]-$Z_{HER2:2395}$. After 8 h incubation, 27 ± 1% and 21.5 ± 0.6% of the cell-associated radioactivity was internalized for ^{111}In-MMA-NOTA-Cys^{61}]-$Z_{HER2:2395}$ and [^{111}In-MMA-DOTA-Cys^{61}]-$Z_{HER2:2395}$, respectively.

Animal Studies. In order to verify the specificity of [^{111}In-MMA-NOTA-Cys^{61}]-$Z_{HER2:2395}$ accumulation in HER2-expressing DU-145 xenografts, its biodistribution (4 h pi) was studied after saturating the binding epitope of HER2 by preinjection of a large excess of nonlabeled $Z_{HER2:342}$ (Figure 4). The tumor uptake was reduced from 8.3 ± 1.0% to 0.53 ± 0.5% IA/g ($p < 0.0001$), demonstrating specificity of HER2 targeting.

A comparison of [^{111}In-MMA-NOTA-Cys^{61}]-$Z_{HER2:2395}$ and [^{111}In-MMA-DOTA-Cys^{61}]-$Z_{HER2:2395}$ biodistribution is presented in Figure 5. Tumor targeting was equally efficient for both variants, and there was no significant difference in the tumor radioactivity accumulation. Both conjugates demonstrated rapid clearance from blood and the majority of normal organs and tissues. The renal excretion was dominating, which resulted in a low radioactivity accumulation in the gastrointestinal tract but high accumulation in kidneys due to reabsorption. There were, however, certain differences in biodistribution of [^{111}In-MMA-NOTA-Cys^{61}]-$Z_{HER2:2395}$ and [^{111}In-MMA-DOTA-Cys^{61}]-$Z_{HER2:2395}$. Radioactivity cleared more rapidly from blood in the case of [^{111}In-MMA-NOTA-Cys^{61}]-$Z_{HER2:2395}$. Significantly ($p < 0.005$) lower radioactivity concentration was also found in lung, liver, spleen, kidney, and bone (Figure 5a). Accordingly, [^{111}In-MMA-NOTA-Cys^{61}]-$Z_{HER2:2395}$ provides significantly higher tumor-to-blood, tumor-to-lung, tumor-to-spleen, tumor-to-muscle, and tumor-to-bone ratios (Figure 5b).

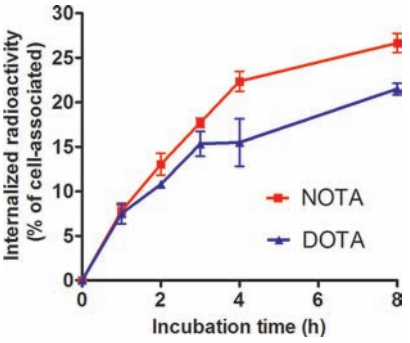


Figure 3. Internalization of [^{111}In-MMA-NOTA-Cys^{61}]-$Z_{HER2:2395}$ and [^{111}In-MMA-DOTA-Cys^{61}]-$Z_{HER2:2395}$ by HER2-expressing DU-145 cell line. Cells were incubated with radiolabeled Affibody molecules at 37 °C. Data presented as a percentage of internalized radioactivity (an average of three samples with standard deviations); error bars might be not seen because they are smaller than the symbols.

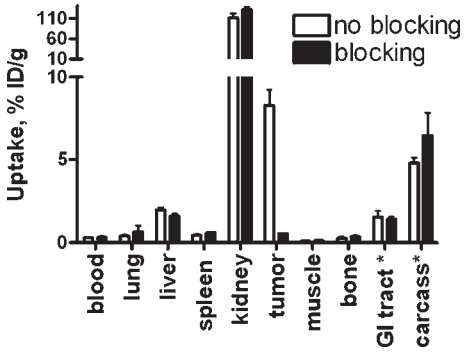


Figure 4. Specificity of [^{111}In-MMA-NOTA-Cys^{61}]-$Z_{HER2:2395}$ uptake in DU-145 xenografts 4 h after injection. To saturate HER2 in tumors, a group of animals in the blocking experiment was preinjected with 500 μg of nonlabeled $Z_{HER2:342}$ 60 min before injection of radiolabeled conjugate (designated as blocked). All animals were injected with 0.3 μg of labeled Affibody molecules. Data are expressed as %ID/g and are presented as mean ± SD for 4 animals. * Data for GI tract (with content) and carcass are presented as %ID per whole sample.

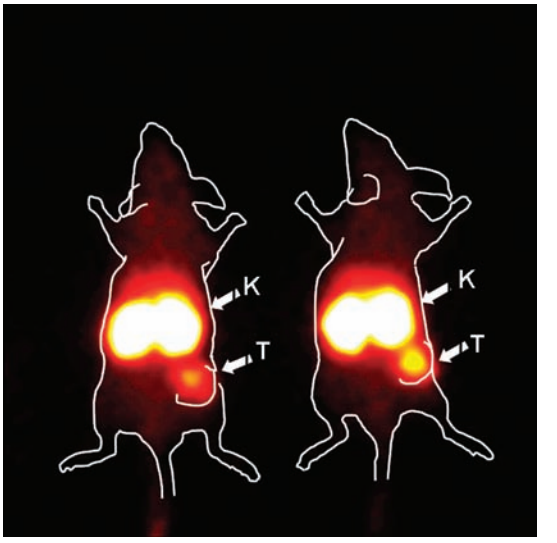


Figure 6. Anterior gamma camera images of nude mice bearing DU-145 xenografts 4 h after injection of [^{111}In-MMA-NOTA-Cys^{61}]-$Z_{HER2:2395}$. Contours derived from a digital photograph were superimposed over gamma camera images to facilitate interpretation. Arrows point at tumors (T) and kidneys (K).

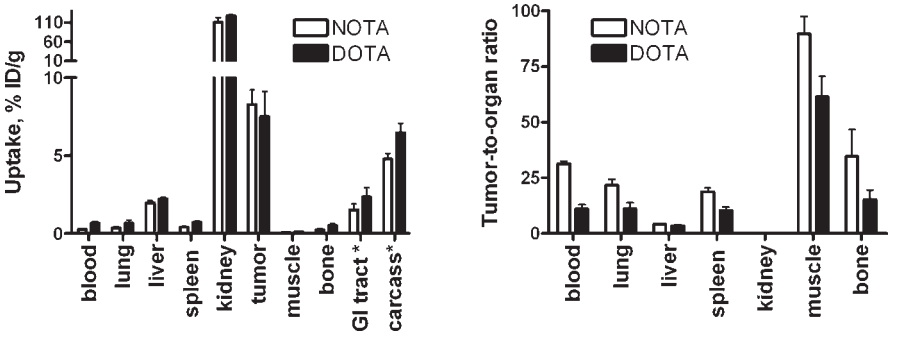


Figure 5. Comparison of targeting of DU-145 xenografts using [^{111}In-MMA-NOTA-Cys^{61}]-$Z_{HER2:2395}$ and [^{111}In-MMA-DOTA-Cys^{61}]-$Z_{HER2:2395}$. Data are presented as an average from four animals ± SD. Left panel: Biodistribution 4 h p.i. Data are expressed as % ID/g. *Data for the gastrointestinal tract (with its content) and for carcass are presented as % ID per whole sample. Right panel: Tumor-to-organ ratios 4 h p.i.

dx.doi.org/10.1021/bc100470x |*Bioconjugate Chem.* 2011, 22, 894–902

Images acquired four hours after the i.v. injection of the [^{111}In-MMA-NOTA-Cys^{61}]-$Z_{HER2:2395}$ into mice bearing DU-145 xenografts confirmed the capacity of this conjugate to visualize HER2-expression (Figure 6). In agreement with the biodistribution data, a prominent radioactivity uptake was observed in the kidneys. No radioactivity accumulation in other healthy organs and tissues was observed. Tumors were clearly visualized already at 4 h p.i. (tumor-to-contralateral side ratio 8.3 ± 0.8).

DISCUSSION

Currently, a major approach for the treatment of disseminated cancer is based on identification of molecular abnormalities causing malignant transformation of cells and molecular recognition of such abnormalities for selective treatment of cancer while sparing healthy tissues. One such abnormality is the overexpression of the transmembrane tyrosine kinase HER2, which is widely used as a target for different therapeutic strategies mainly in breast cancer.[34,35]

Expression of HER2 has also been suggested as one of the possible molecular pathways to androgen independence of prostate cancer.[36] Preclinical data suggest that HER2-targeting therapies can be efficient against androgen-independent prostate cancer.[37,38] However, treatment of prostate cancer with the HER2-targeting monoclonal antibody trastuzumab or the tyrosine kinase inhibitor lapatinib has failed to demonstrate efficacy in clinical trials.[39−41] The failure of these trials was attributed to the absence of patient stratification according to the HER2 expression level.[39] Since only a fraction of tumors express HER2, the patients should be stratified according to expression levels to select those who would most likely benefit from HER2-targeting therapy. This would make cancer treatment more personalized and, thus, more efficient. Radionuclide molecular imaging is a promising way to detect the HER2 expression level, since it is noninvasive and may overcome issues associated with heterogeneity of HER2 expression in primary tumors and metastases.[42] However, due to the relatively low level of HER2 expression in prostate cancer (Human Protein Atlas, http://www.proteinatlas.org/), further perfection of the radionuclide imaging probes is desirable.

Comparison of preclinical literature data suggests that small targeting agents provide higher tumor-to-organ ratios of radioactivity concentration and, for this reason, higher sensitivity of HER2 detection.[42] Particularly, Affibody molecules have demonstrated superior imaging properties in comparison with monoclonal antibodies and their fragments due to small size (7 kDa) and picomolar affinity. Direct head-to-head comparison of the ^{124}I-labeled anti-HER2 Affibody molecule $Z_{HER2:342}$ and the anti-HER2 antibody trastuzumab confirmed conclusions derived from literature data.[43] However, further improvement of imaging sensitivity is required, particularly for visualization of tumors with relatively low HER2 expression level, such as in castration-independent prostate cancer.

Besides selection of optimal targeting proteins, optimization of labeling chemistry might improve the sensitivity of radionuclide molecular imaging, as labeling chemistry can influence the targeting properties of an imaging agent.[22] NOTA and its derivatives seem to be attractive chelators for labeling of targeting proteins because of the versatility and high stability of the chelates with a number of nuclides suitable for imaging.

The use of site-specific labeling is essential, since this provides uniform biodistribution properties of the radiolabeled conjugates.[7] To provide site-specific chelator coupling, a cysteine was engineered at the C-terminus of anti-HER2 Affibody molecule $Z_{HER2:342}$, providing an Affibody molecule $Z_{HER2:2395}$ with a unique binding site for thiol-directed coupling of chelators.[11] To use this approach for NOTA coupling, a maleimido derivate of NOTA was developed in this study.

The synthesis of MMA-NOTA is based on a commercially available precursor NOTA(tBu)$_2$. It is straightforward and provides a reasonable overall yield of ∼20%. MMA-NOTA was efficiently coupled to prereduced $Z_{HER2:2395}$. Importantly, coupling of this chelator did not cause any measurable decrease of $Z_{HER2:2395}$ affinity to HER2 (the observed difference in K_D for [MMA-NOTA-Cys^{61}]-$Z_{HER2:2395}$, [MMA-DOTA-Cys^{61}]-$Z_{HER2:2395}$, and parental $Z_{HER2:342}$ was within the accuracy of the SPR method). This preservation of affinity is essential for targeting of cancer with low level of HER2 overexpression, such as prostate cancer. CD spectra have demonstrated that the coupling of MMA-NOTA does not prevent accurate refolding of [MMA-NOTA-Cys^{61}]-$Z_{HER2:2395}$ after heat treatment, permitting the use of elevated temperatures for the labeling reaction. This was essential, since efficient labeling with ^{111}In required some moderate (up to 60 °C) warming (Figure 1). Literature data suggest that warming (up to 70 °C) is required also for labeling of NOTA with copper radioisotopes.[19] In agreement with CD data, [^{111}In-MMA-NOTA-Cys^{61}]-$Z_{HER2:2395}$ was capable of specific binding to HER2-expressing cells after labeling at 60 °C (Figure 2).

It has been shown earlier that different chelators have different influence on the internalization rate of radiolabeled peptides, e.g., somatostatin analogues, by cancer cells.[44−46] Previous data indicated that internalization of $Z_{HER2:342}$ and its derivatives, including $Z_{HER2:2395}$, by HER2-expressing cancer cell lines is slow and that the influence of a chelator on the internalization rate is small.[10,11,33] However, our latest data suggested that internalization of [^{99m}Tc(CO)$_3$]$^+$-labeled $Z_{HER2:342}$ can depend on the nature of histidine-containing chelators.[47] The current study is another demonstration of the influence of the chelator on the internalization rate of Affibody molecules. Though the overall internalization rate of [^{111}In-MMA-NOTA-Cys^{61}]-$Z_{HER2:2395}$ was still slow (27 ± 1% of cell-bound radioactivity was internalized at 8 h), it was higher than the internalization of [^{111}In-MMA-DOTA-Cys^{61}]-$Z_{HER2:2395}$ (21.5 ± 0.6% internalized at 8 h) (Figure 3). The internalization of tracers labeled using residualizing radiometals is considered an important and useful factor for the accumulation of radiotracer in a cancer cell,[48] so the increased internalization rate is a positive influence of maleimido-NOTA on the targeting properties of $Z_{HER2:2395}$.

The excellent binding properties of [^{111}In-MMA-NOTA-Cys^{61}]-$Z_{HER2:2395}$ enables specific targeting of DU-145 prostate cancer xenografts, despite the relatively low HER2 expression of this cell line (Figure 5). Gamma camera experiments confirmed the results of the biodistribution studies demonstrating clear visualization of DU-145 xenografts 4 h p.i. (Figure 6). This was achieved despite location of the xenografts close to the kidneys, an organ with a high level of radioactivity accumulation.

The targeting properties of [^{111}In-MMA-NOTA-Cys^{61}]-$Z_{HER2:2395}$ and [^{111}In-MMA-DOTA-Cys^{61}]-$Z_{HER2:2395}$ were compared in nude mice bearing DU-145 prostate cancer xenografts (Figure 5). There was no significant difference between these conjugates in accumulation of radioactivity in tumors. However, [^{111}In-MMA-NOTA-Cys^{61}]-$Z_{HER2:2395}$ cleared more rapidly from blood, lung, liver, and spleen. Bone uptake of

radioactivity was also lower for this conjugate. This is important in the case of prostate cancer, where bones are the major metastatic site. This resulted in significantly higher tumor-to-organ ratios in the case of NOTA-conjugated Affibody molecules. This should provide better contrast on HER2 imaging and, hopefully, better sensitivity in clinical settings.

Apparently, the use of MMA-NOTA is not limited to site-specific labeling of Affibody molecules. Advantages of this chelator, such as high complex stability and thiol-directed site-specific labeling, can be used for development of a variety of targeting agents, such as scaffold-based affinity proteins and Fab′ antibody fragments.

In conclusion, MMA-NOTA is a very promising bifunctional chelator for thiol-directed site-specific labeling of Affibody molecules and other targeting proteins for in vivo radionuclide molecular imaging.

AUTHOR INFORMATION

Corresponding Author

*Vladimir Tolmachev, Biomedical Radiation Sciences, Rudbeck Laboratory, Uppsala University, S-751 81 Uppsala, Sweden. Phone: +46 18 471 3414. Fax: +46 18 471 3432. E-mail: Vladimir.tolmachev@bms.uu.se.

ACKNOWLEDGMENT

This work was supported by grants from Swedish Research Council (Vetenskapsrådet) and Swedish Cancer Society (Cancerfonden).

REFERENCES

(1) Mankoff, D. A. (2009) Molecular imaging to select cancer therapy and evaluate treatment response. *Q. J. Nucl. Med. Mol. Imaging 53*, 181–192.

(2) Tolmachev, V., Stone-Elander, S., and Orlova, A. (2010) Radiolabelled receptor-tyrosine-kinase targeting drugs for patient stratification and monitoring of therapy response: prospects and pitfalls. *Lancet Oncol. 11*, 992–1000.

(3) Grönwall, C., and Ståhl, S. (2009) Engineered affinity proteins - generation and applications. *J. Biotechnol. 140*, 254–269.

(4) Löfblom, J., Feldwisch, J., Tolmachev, V., Carlsson, J., Ståhl, S., and Frejd, F. Y. (2010) Affibody molecules: engineered proteins for therapeutic, diagnostic and biotechnological applications. *FEBS Lett. 584*, 2670–2680.

(5) Ahlgren, S., and Tolmachev, V. (2010) Radionuclide molecular imaging using Affibody molecules. *Curr. Pharm. Biotechnol. 11*, 581–589.

(6) Mume, E., Orlova, A., Larsson, B., Nilsson, A. S., Nilsson, F. Y., Sjöberg, S., and Tolmachev, V. (2005) Evaluation of ((4-hydroxyphenyl)ethyl)maleimide for site-specific radiobromination of anti-HER2 affibody. *Bioconjugate Chem. 16*, 1547–1555.

(7) Tolmachev, V., Mume, E., Sjöberg, S., Frejd, F. Y., and Orlova, A. (2009) Influence of valency and labelling chemistry on in vivo targeting using radioiodinated HER2-binding Affibody molecules. *Eur. J. Nucl. Med. Mol. Imaging 36*, 692–701.

(8) Kramer-Marek, G., Kiesewetter, D. O., Martiniova, L., Jagoda, E., Lee, S. B., and Capala, J. (2008) [^{18}F]FBEM-Z(HER2:342)-Affibody molecule-a new molecular tracer for in vivo monitoring of HER2 expression by positron emission tomography. *Eur. J. Nucl. Med. Mol. Imaging 35*, 1008–1018.

(9) Namavari, M., De Jesus, P. O., Cheng, Z., De, A., Kovacs, E., Levi, J., Zhang, R., Hoerner, J. K., Grade, H., Syud, F. A., and Gambhir, S. S. (2008) Direct site-specific radiolabeling of an Affibody protein with 4-[^{18}F]fluorobenzaldehyde via oxime chemistry. *Mol. Imaging Biol. 10*, 177–181.

(10) Ahlgren, S., Wållberg, H., Tran, T. A., Widström, C., Hjertman, M., Abrahmsén, L., Berndorff, D., Dinkelborg, L. M., Cyr, J. E., Feldwisch, J., Orlova, A., and Tolmachev, V. (2009) Targeting of HER2-expressing tumors with a site-specifically ^{99m}Tc-labeled recombinant affibody molecule, $Z_{HER2:2395}$, with C-terminally engineered cysteine. *J. Nucl. Med. 50*, 781–789.

(11) Ahlgren, S., Orlova, A., Rosik, D., Sandström, M., Sjöberg, A., Baastrup, B., Widmark, O., Fant, G., Feldwisch, J., and Tolmachev, V. (2008) Evaluation of maleimide derivative of DOTA for site-specific labeling of recombinant Affibody molecules. *Bioconjugate Chem. 19*, 235–243.

(12) Tolmachev, V., Xu, H., Wållberg, H., Ahlgren, S., Hjertman, M., Sjöberg, A., Sandström, M., Abrahmsén, L., Brechbiel, M. W., and Orlova, A. (2008) Evaluation of a maleimido derivative of CHX-A′′ DTPA for site-specific labeling of affibody molecules. *Bioconjugate Chem. 19*, 1579–1587.

(13) Tolmachev, V., Rosik, D., Wållberg, H., Sjöberg, A., Sandström, M., Hansson, M., Wennborg, A., and Orlova, A. (2010) Imaging of EGFR expression in murine xenografts using site-specifically labelled anti-EGFR ^{111}In-DOTA-$Z_{EGFR:2377}$ Affibody molecule: aspect of the injected tracer amount. *Eur. J. Nucl. Med. Mol. Imaging 37*, 613–622.

(14) Wållberg, H., Ahlgren, S., Widström, C., and Orlova, A. (2010) Evaluation of the radiocobalt-labeled [MMA-DOTA-Cys^{61}]-$Z_{HER2:2395}$(-Cys) affibody molecule for targeting of HER2-expressing tumors. *Mol. Imaging Biol. 12*, 54–62.

(15) Miao, Z., Ren, G., Liu, H., Jiang, L., and Cheng, Z. (2010) Small-animal PET imaging of human epidermal growth factor receptor positive tumor with a ^{64}Cu labeled affibody protein. *Bioconjugate Chem. 21*, 947–954.

(16) Cheng, Z., De Jesus, O. P., Kramer, D. J., De, A., Webster, J. M., Gheysens, O., Levi, J., Namavari, M., Wang, S., Park, J. M., Zhang, R., Liu, H., Lee, B., Syud, F. A., and Gambhir, S. S. (2010) ^{64}Cu-labeled affibody molecules for imaging of HER2 expressing tumors. *Mol. Imaging Biol. 12*, 316–324.

(17) De León-Rodríguez, L. M., and Kovacs, Z. (2008) The synthesis and chelation chemistry of DOTA-peptide conjugates. *Bioconjugate Chem. 19*, 391–402.

(18) Anderson, C. J., Wadas, T. J., Wong, E. H., and Weisman, G. R. (2008) Cross-bridged macrocyclic chelators for stable complexation of copper radionuclides for PET imaging. *Q. J. Nucl. Med. Mol. Imaging 52*, 185–192.

(19) Prasanphanich, A. F., Nanda, P. K., Rold, T. L., Ma, L., Lewis, M. R., Garrison, J. C., Hoffman, T. J., Sieckman, G. L., Figueroa, S. D., and Smith, C. J. (2007) [^{64}Cu-NOTA-8-Aoc-BBN(7−14)NH_2] targeting vector for positron-emission tomography imaging of gastrin-releasing peptide receptor-expressing tissues. *Proc. Natl. Acad. Sci. U.S.A. 104*, 12462–12467.

(20) Garrison, J. C., Rold, T. L., Sieckman, G. L., Figueroa, S. D., Volkert, W. A., Jurisson, S. S., and Hoffman, T. J. (2007) In vivo evaluation and small-animal PET/CT of a prostate cancer mouse model using ^{64}Cu bombesin analogs: side-by-side comparison of the CB-TE2A and DOTA chelation systems. *J. Nucl. Med. 48*, 1327–1337.

(21) Hausner, S. H., Kukis, D. L., Gagnon, M. K., Stanecki, C. E., Ferdani, R., Marshall, J. F., Anderson, C. J., and Sutcliffe, J. L. (2009) Evaluation of [(64)Cu]Cu-DOTA and [(64)Cu]Cu-CB-TE2A chelates for targeted positron emission tomography with an alpha(v)beta (6)-specific peptide. *Mol. Imaging 8*, 111–121.

(22) Tolmachev, V., and Orlova, A. (2010) Influence of labelling methods on biodistribution and imaging properties of radiolabelled peptides for visualisation of molecular therapeutic targets. *Curr. Med. Chem. 17*, 2636–2655.

(23) Clarke, E., and Martell, A, E. (1991) Stabilities of the Fe(III), Ga(III) and In(III) chelates of N,N′,N′′-triazacyclononanetriacetic acid. *Inorg. Chim. Acta 181*, 273–280.

(24) Clarke, E. T., and Martell, A. E. (1992) Stabilities of trivalent metal ion complexes of the tetraacetate derivatives of 12-, 13-, and 14-membered tetraazamacrocycles. *Inorg. Chim. Acta 190*, 37–46.

(25) Eisenwiener, K. P., Prata, M. I., Buschmann, I., Zhang, H. W., Santos, A. C., Wenger, S., Reubi, J. C., and Mäcke, H. R. (2002) NODAGATOC, a new chelator-coupled somatostatin analogue labeled with [$^{67/68}$Ga] and [^{111}In] for SPECT, PET, and targeted therapeutic applications of somatostatin receptor (hsst2) expressing tumors. *Bioconjugate Chem. 13*, 530–541.

(26) Jeong, J. M., Hong, M. K., Chang, Y. S., Lee, Y. S., Kim, Y. J., Cheon, G. J., Lee, D. S., Chung, J. K., and Lee, M. C. (2008) Preparation of a promising angiogenesis PET imaging agent: ^{68}Ga-labeled c(RGDyK)-isothiocyanatobenzyl-1,4,7-triazacyclononane-1,4,7-triacetic acid and feasibility studies in mice. *J. Nucl. Med. 49*, 830–836.

(27) Liu, Z., Niu, G., Shi, J., Liu, S., Wang, F., Liu, S., and Chen, X. (2009) ^{68}Ga-labeled cyclic RGD dimers with Gly3 and PEG4 linkers: promising agents for tumor integrin alphavbeta3 PET imaging. *Eur. J. Nucl. Med. Mol. Imaging 36*, 947–957.

(28) Velikyan, I., Maecke, H., and Langstrom, B. (2008) Convenient preparation of ^{68}Ga-based PET-radiopharmaceuticals at room temperature. *Bioconjugate Chem. 19*, 569–573.

(29) McBride, W. J., D'Souza, C. A., Sharkey, R. M., Karacay, H., Rossi, E. A., Chang, C. H., and Goldenberg, D. M. (2010) Improved ^{18}F labeling of peptides with a fluoride-aluminum-chelate complex. *Bioconjugate Chem. 21*, 1331–1340.

(30) Craig, A. S., Helps, I. M., Parker, D., Adams, H., Bailey, N. A., Williams, M. G., Smith, J. M. A., and Ferguson, M.. (1989) Crystal and molecular structure of a seven-coordinate chlorindium(III) complex of 1,4,7-triazacyclononanetetracetic acid. *Polyhedron 8*, 2481–2484.

(31) Maeke, H., Scherer, G., Heppeler, A., and Henig, M. (2001) Is In-111 an ideal surrogate for Y-90? If not, why?. *Eur. J. Nucl. Med. 28*, 967.

(32) Persson, M., Tolmachev, V., Andersson, K., Gedda, L., Sandstrom, M., and Carlsson, J. (2005) [^{177}Lu]pertuzumab: experimental studies on targeting of HER-2 positive tumour cells. *Eur. J. Nucl. Med. Mol. Imaging 32*, 1457–1462.

(33) Wållberg, H., and Orlova, A. (2008) Slow internalization of anti-HER2 synthetic affibody monomer ^{111}In-DOTA-$Z_{HER2:342-pep2}$: implications for development of labeled tracers. *Cancer Biother. Radiopharm. 23*, 435–442.

(34) Jones, K. L., and Buzdar, A. U. (2009) Evolving novel anti-HER2 strategies. *Lancet Oncol. 10*, 1179–1187.

(35) Murphy, C. G., and Fornier, M. (2010) HER2-positive breast cancer: beyond trastuzumab. *Oncology (Williston Park) 24*, 410–415.

(36) Pienta, K. J., and Smith, D. C. (2005) Advances in prostate cancer chemotherapy: a new era begins. *C.A. Cancer J. Clin. 55* 300–318.

(37) Agus, D. B., Scher, H. I., Higgins, B., Fox, W. D., Heller, G., Fazzari, M., Cordon-Cardo, C., and Golde, D. W. (1999) Response of prostate cancer to anti-Her-2/neu antibody in androgen-dependent and -independent human xenograft models. *Cancer Res. 59*, 4761–4764.

(38) Liu, Y., Majumder, S., McCall, W., Sartor, C. I., Mohler, J. L., Gregory, C. W., Earp, H. S., and Whang, Y. E. (2005) Inhibition of HER-2/neu kinase impairs androgen receptor recruitment to the androgen responsive enhancer. *Cancer Res. 65*, 3404–3409.

(39) Ziada, A., Barqawi, A., Glode, L. M., Varella-Garcia, M., Crighton, F., Majeski, S., Rosenblum, M., Kane, M., Chen, L., and Crawford, E. D. (2004) The use of trastuzumab in the treatment of hormone refractory prostate cancer; phase II trial. *Prostate 60*, 332–337.

(40) Lara, P. N., Jr., Chee, K. G., Longmate, J., Ruel, C., Meyers, F. J., Gray, C. R., Edwards, R. G., Gumerlock, P. H., Twardowski, P., Doroshow, J. H., and Gandara, D. R. (2004) Trastuzumab plus docetaxel in HER-2/neu-positive prostate carcinoma: final results from the California Cancer Consortium Screening and Phase II Trial. *Cancer 100*, 2125–2131.

(41) Sridhar, S. S., Hotte, S. J., Chin, J. L., Hudes, G. R., Gregg, R., Trachtenberg, J., Wang, L., Tran-Thanh, D., Pham, N. A., Tsao, M. S., Hedley, D., Dancey, J. E., and Moore, M. J. (2010) A multicenter phase II clinical trial of Lapatinib (GW572016) in hormonally untreated advanced prostate cancer. *Am. J. Clin. Oncol. 33*, 609−613

(42) Tolmachev, V. (2008) Imaging of HER-2 overexpression in tumors for guiding therapy. *Curr. Pharm. 14*, 2999–3019.

(43) Orlova, A., Wållberg, H., Stone-Elander, S., and Tolmachev, V. (2009) On the selection of a tracer for PET imaging of HER2-expressing tumors: direct comparison of a ^{124}I-labeled affibody molecule and trastuzumab in a murine xenograft model. *J. Nucl. Med. 50*, 417–425.

(44) de Jong, M., Breeman, W. A., Bakker, W. H., Kooij, P. P., Bernard, B. F., Hofland, L. J., Visser, T. J., Srinivasan, A., Schmidt, M. A., Erion, J. L., Bugaj, J. E., Mäcke, H. R., and Krenning, E. P. (1998) Comparison of (111)In-labeled somatostatin analogues for tumor scintigraphy and radionuclide therapy. *Cancer Res. 58*, 437–441.

(45) Decristoforo, C., Melendez-Alafort, L., Sosabowski, J. K., and Mather, S. J. (2000) ^{99m}Tc-HYNIC-[Tyr^3]-octreotide for imaging somatostatin-receptor-positive tumors: preclinical evaluation and comparison with ^{111}In-octreotide. *J. Nucl. Med. 41*, 1114–1119.

(46) Hofland, L. J., Breeman, W. A., Krenning, E. P., de Jong, M., Waaijers, M., van Koetsveld, P. M., Mäcke, H. R., and Lamberts, S. W. (1999) Internalization of [DOTA^0,^{125}I-Tyr^3]Octreotide by somatostatin receptor-positive cells in vitro and in vivo: implications for somatostatin receptor-targeted radio-guided surgery. *Proc. Assoc. Am. Physicians 111*, 63–69.

(47) Tolmachev, V., Hofström, C., Malmbeg, J., Ahlgren, S., Hosseinimehr, S. J., Sandström, M., Abrahmsén, L., Orlova, A., and Gräslund, T. (2010) HEHEHE-tagged Affibody molecules may be purified by IMAC, are conveniently labeled with $[^{99m}Tc(CO)_3]^+$, and show improved biodistribution. *Bioconjugate Chem. 21*, 2013–2022.

(48) Reubi, J. C. (2003) Peptide receptors as molecular targets for cancer diagnosis and therapy. *Endocr. Rev. 24*, 389–427.

Bioconjugate Chemistry

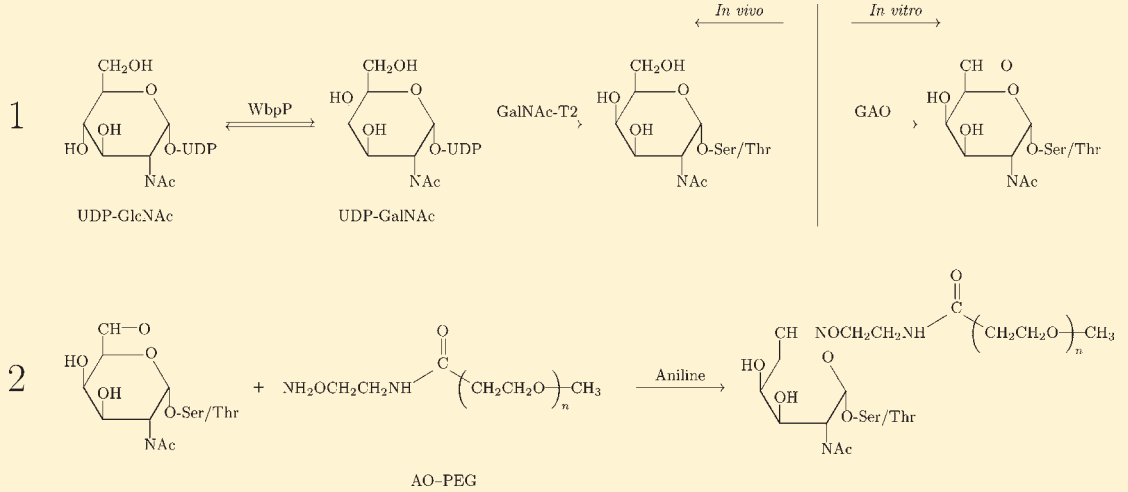
ARTICLE

pubs.acs.org/bc

Site-Specific Modification of Recombinant Proteins: A Novel Platform for Modifying Glycoproteins Expressed in *E. coli*

Grant E. Henderson Kevin D. Isett and Tillman U. Gerngross*

ABSTRACT:



The site-specific modification of proteins is expected to be an important capability for the synthesis of bioconjugates in the future. However, the traditional repertoire of reactions available for the direct modification of proteins suffers from lack of specificity, necessitating costly downstream processing to isolate the specific species of interest.[1] Here, we use a well-established, glycan-specific chemistry to PEGylate model glycoproteins, each containing a unique reactive GalNAc attached to a specifically engineered threonine residue. By engineering *E. coli* to execute the initial steps of human, mucin-type O-glycosylation, we were able to obtain homogeneous site-specifically modified glycoproteins with fully human glycan linkages. Two mucin-based reporters as well as several fusion proteins containing eight-amino-acid GalNAc-T recognition sequences were glycosylated in this engineered glycocompetent strain of *E. coli*. The use of one sequence in particular, PPPTSGPT, resulted in site-specific glycan occupancy of approximately 69% at the engineered threonine. The GalNAc present on the purified glycoprotein was oxidized by galactose oxidase and then coupled to hydroxylamine functionalized 20 kDa PEG in the presence of aniline. The glycoprotein could be converted to the PEGylated product at approximately 85% yield and >98% purity as determined by comparison to the products of control reactions.

INTRODUCTION

To date, modification of proteins at naturally occurring functional groups has been the predominant strategy for the synthesis of bioconjugates.[1] However, complications arise when proteins contain multiple reactive sites and/or have a reactive conjugation site near the active site. Traditionally, these problems have been solved by simply removing the reactive residues to convert the protein to a more suitable starting material or controlling the reaction to promote selectivity for the desired product. This process can be time-consuming and unreliable; therefore, new methods for protein modification are required. In order to improve upon traditional protocols, new methods should provide control over the conjugation reaction with minimal disruption of protein structure. This goal can be achieved through the selective targeting of bioorthogonal groups which have been engineered at desired locations within proteins of interest.[2−5] The targeting of glycans for chemical modification is not unprecedented. In particular, metabolic labeling of glycan structures through the use of chemically modified monosaccharides has found use in basic research involving the detection and characterization of glycosylation events *in vivo* [6−8] and likely could be employed for the synthesis of therapeutic bioconjugates in the future. However, this technique is limited to cell types with endogenous glycosylation capabilities, which due to heterogeneity in glycan structure and localization are not necessarily ideal hosts for the production of glycoprotein precursors for bioconjugation.

Since aldehyde groups are typically absent in proteins and biocompatible aldehyde-specific reactions have been reported, we developed a new, glycosylation-based method to introduce

Received: November 19, 2010
Revised: March 3, 2011
Published: March 12, 2011

ACS Publications © 2011 American Chemical Society

dx.doi.org/10.1021/bc100510g | *Bioconjugate Chem.* 2011, 22, 903–912

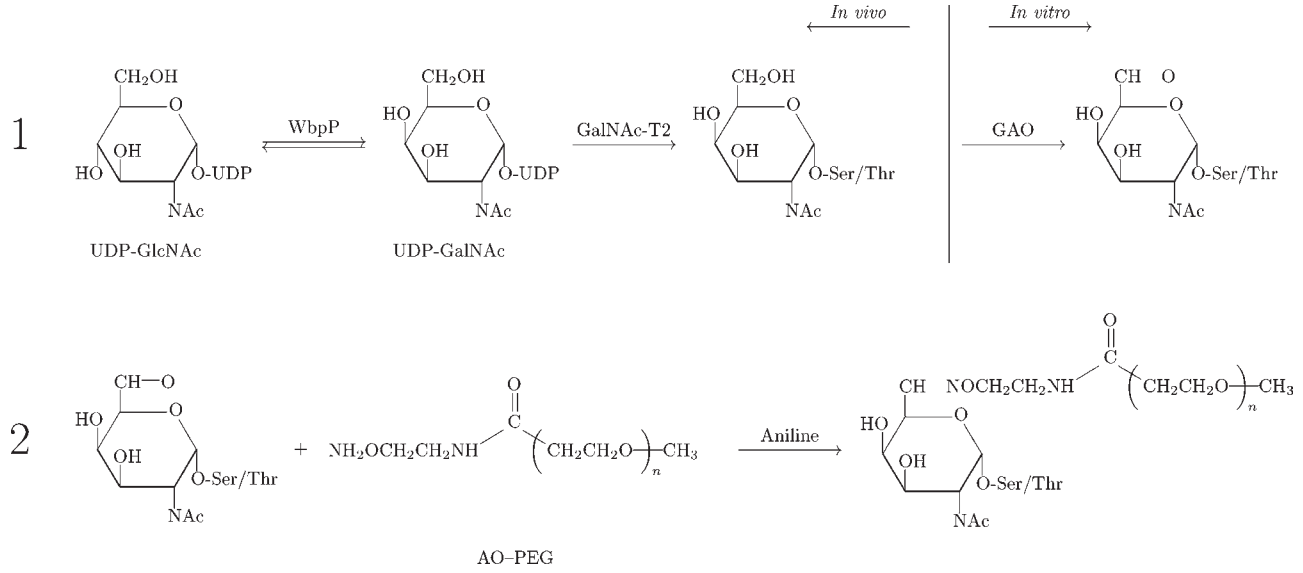


Figure 1. Reaction schematic: 1. The epimerization of UDP-GlcNAc to UDP-GalNAc by WbpP from *P. aerugosa* and transfer of GalNAc to Ser/Thr residues in *E. coli* followed by *in vitro* oxidiation by galactose oxidase resulting in aldehyde functionalized glycoproteins. 2. Subsequent nucleophilic addition of hydroxylamine-functionalized poly(ethylene glycol) in the presence of aniline.

aldehydes in a site-specific manner, resulting in the capability for site-specific protein modification. Although the functional groups typically found within proteins are not easily oxidized to carbonyls in a site-specific manner, the hydroxyls present on certain glycans *are* easily converted to aldehydes with high selectivity.[9−23] The use of galactose oxidase (GAO) in particular for the oxidation of glycoproteins is well-documented, but seems to have fallen out of use in favor of the alternative method of periodate oxidation of vicinal diols. Unfortunately, periodate can oxidize cysteine, methionine, tryptophan, tyrosine, and histidine residues regardless of their location within a protein, and serine and threonine are oxidized when located at the N-terminus. Furthermore, the subsequent labeling of periodate oxidized glycoproteins tends to result in heterogeneous product mixtures with higher than expected extents of conjugation.[19] In applications such as the modification of therapeutic proteins, where product homogeneity, structure, and function are extremely important, oxidation by GAO is preferred. Galactose oxidase is active toward several primary alcohols including but not limited to the C-6 hydroxyls of Gal and GalNAc.[24] While both the oxidation kinetics and equilibrium conversion have been reported to be affected by the microenvironment of the C-6 hydroxyl of the terminal sugar,[25] activity toward a diverse set of substituted Gal variants including both α- and β-linked GalNAc have been reported.[9,10]

The initiating step of mucin-type O-glycosylation in vertebrates involves the enzymatic transfer of GalNAc from UDP-GalNAc to certain serine and threonine residues of nascent glycoproteins resulting in proteins decorated with a single αGalNAc at the designated site. This basic process been studied extensively and the substrate requirements have been determined.[26,27] Nonpathogenic *E. coli* strains contain intracellular UDP-GlcNAc but not UDP-GalNAc; therefore, for cytoplasmic expression of GalNAc decorated glycoproteins, the initiating step of the mucin-type glycosylation pathway was reconstituted by coexpressing UDP-GlcNAc C-4 epimerase and UDP-GalNAc/polypeptide UDP-GalNAc transferase (GalNAc-T) along with a suitable target protein. The human GalNAc-T2 isoform was chosen for this study based on its relatively high *in vitro* activity and the abundance of information pertaining to potential O-glycosylation recognition sequence (OGRS).

In order to achieve mucin-type O-glycosylation in *E. coli*, we produced several reporter proteins, (i) a glutathione S-transfease/MUC1 fusion protein and (ii) a panel of OGRS peptides fused to human antibody fragments (Fabs) directed against TNF-α in a glycoengineered *E. coli* strain. In contrast to oligosaccharyltransferase-mediated transfer of N-glycans to asparagines within the recognition sequon Asn-X-Ser/Thr, which occurs *en bloc*, O-glycosyltransferases add sugars sequentially, requiring just the appropriate OGRS and UDP-GalNAc for the first addition. Gupta et al. have developed an OGRS database, O-GlycBase,[28] which has in the past been used to train computational neural networks for the prediction of O-glycosylation sites.[29,30] Although these programs can be used for generally predicting O-glycosylation sites, they cannot be used to model individual transferases due to the overlapping activities of the various GalNAc-T isoforms. To determine recognition sequence requirements for individual transferases, *in vitro* reactions involving purified enzymes and substrates are typically used[31−39] (a pH-based high-throughput assay for glycosyltransferase activity has been described, but it has not yet been used for the characterization of GalNAc-T isoforms[40]). Recently, the *in vitro* use of glycosyltransferases has been extended to engineering applications such as the generation of glycopeptide libraries[41] and use in bioconjugate chemistry.[42] To find a suitable OGRS for hGalNAc-T2, we evaluated a small subset of the OGRS present in *O-GlycBase* v 6.00 for use as glycosylation targets on recombinant proteins. Since GalNAc-T2 is an initiating transferase, only OGRS without trans-acting glycosylation sites were considered. The literature suggests that the eight amino acids from −3 to +4 relative to the glycosylated serine or threonine are involved in recognition by GalNAc-T. Ultimately, 17 eight-amino-acid sequences were selected. While this small library was by no means exhaustive, screening members for glycosylation resulted in the identification of an OGRS with relative high occupancy. In addition, this approach provides a simple

Table 1. Oligonucleotides Used in This Work

label	sequence (5′-3′)
oGH119	GAAGAAGGATCCAGGAAGGAGGACTGGAATG
oGH120	GAAGAAGCGGCCGCCTGCTGCAGGTTGAG
oGH174	TAATAAGAATTCAGGTGGCACTTTTCGGGG
oGH175	TAATAACCATGGTTCCATAGGCTCCGC
oGH176	GAGCGTGGCAGCCGCGGTATCATTGCAGCACTGGGGCC
oGH177	CCGCGGCTGCCACGCTCACCGGCTCCAGATTTA
oGH178	TAATAAGGCGCGCCCTACTACTGGGCTGCTTCC
oGH179	TAATAACCATGGCATTAATTGCGTTGCGC
oGH180	GCCCGTGAGCCTGGTGAAAAGAAAAACCACCCTGGCGCCC
oGH181	CCAGGCTCACGGGCAACAGCTGATTGCCCTTCACCGCC
oGH196	GAAGAAGCGGCCGCCAAAAATATGGGCGCAG
oGH199	TAATAAGAGCTCATGAGGAAGGAGGACTGGAATG
oGH200	TTATTAACCGGTTCAGTGGTGGTGGTGGTG
oGH286	TTAACCGGTTCATTTCAAAAACATGATG
oGH528	/5PHOS/GGAGCCACGCGGAACCAG
oGH529	TTTTGGGCTAGCAGGAGGAATTCACCATGTCCCCTATACTAGG
oGH530	CCTTCTAGACCAAAAAAACGGGTATG
oGH531	CGACCTGCAGGCATGCAAG
oGH589	/5PHOS/CACGGTGTTACTAGCGC
oGH590	TAATAAGAGCTCTTAACAAGATTTTGGTTCAGC
oGH601	/5PHOS/GCAAGTATGGGTTTTATCGC
oGH602	GCTGTTCCAACCACTGTAGTAGATGCTTGAGCATGCAAGCTTGGCTG
oGH603	GAAGCACAAACTGAACTGCCTCAAGCATGAGCATGCAAGCTTGGCTG
oGH604	ATCAACCCAACCACTCAGATGAAAGCTTGAGCATGCAAGCTTGGCTG
oGH605	CTGGCTGGTACTGAATCTCCTGTAGCATGAGCATGCAAGCTTGGCTG
oGH606	CTGGCTCCAACTGCACCACCTGAAGCTTGAGCATGCAAGCTTGGCTG
oGH607	CTGCAACCAACCCAAGGTGCAATGGCCTGAGCATGCAAGCTTGGCTG
oGH608	CTGACTCAAACCCCAGTTGTTGTTGCTTGAGCATGCAAGCTTGGCTG
oGH609	CCAGGTTCTACTGCTCCACCAGCTGCATGAGCATGCAAGCTTGGCTG
oGH610	CCTCCTCCAACTTCTGGTCCAACTGCATGAGCATGCAAGCTTGGCTG
oGH611	CCTGTTCCAACTCCTCCTGATAATGCATGAGCATGCAAGCTTGGCTG
oGH612	CAACCAGTAACTTCTCAACCACAAGCATGAGCATGCAAGCTTGGCTG
oGH613	CGTGCAGCAACTGTAGGTTCTCTGGCTTGAGCATGCAAGCTTGGCTG
oGH614	ACTCCACCAACTGTTCTGCCTGATGCATGAGCATGCAAGCTTGGCTG
oGH615	GTAGGCCTGACTCCGTCTGCAGCTGCTTGAGCATGCAAGCTTGGCTG
oGH616	GTACTGCCTACTCAATCTGCACATGCTTGAGCATGCAAGCTTGGCTG
oGH617	GTTCGTGCAACTCGTACCGTAGTAGCATGAGCATGCAAGCTTGGCTG
oGH618	GTTCGTCCTACTTCTGCTGTTGCTGCTTGAGCATGCAAGCTTGGCTG
L1	ATGAAAAAGACAGCTATCGCAATTGCAGTGGCCTTGGCTGGTT
L2	AAGGGCTTTGGGTCATTTGAATATCAGCTTGCGCTACGGTAGCGAAACCAGCCAAGGCC
L3	AATGACCCAAAGCCCTTCTTCTCTGAGCGCTTCTGTTGGTGATCGTGTGACCATCACCT
L4	TGATACCACGCAACGTTAGTACCGACGTTCTGGGACGCCTTACAGGTGATGGTCACACG
L5	AACGTTGCGTGGTATCAGCAGAAACCGGGCAAGGCACCTAAAGCCCTGATTTATTCTGC
L6	CGGAGAAGCGATACGGCACGCCAGAGTACAGGAAAGATGCAGAATAAATCAGGGCTTTA
L7	CCGTATCGCTTCTCCGGTTCTGGCTCTGGTACTGACTTCACTCTGACCATCTCCTCTCT
L8	TGTACTGCTGACAGTAGTAGGTAGCAAAATCTTCCGGTTGCAGAGAGGAGATGGTCAGA
L9	CTACTACTGTCAGCAGTACAACATCTACCCTCTGACGTTCGGCCAAGGCACCAAAGTTG
L10	GGAAGATGAACACAGACGGTGCCGCTACCGTACGTTTAATTTCAACTTTGGTGCCTTGG
L11	CGTCTGTGTTCATCTTCCCGCCGTCTGATGAACAACTGAAGTCTGGCACTGCGTCTGTA
L12	TGCACTTTAGCTTCACGCGGGTAAAAGTTATTCAGCAGACACACTACAGACGCAGTGCC
L13	CGTGAAGCTAAAGTGCAGTGGAAAGTCGATAACGCTCTGCAATCTGGTAATTCTCAGGA
L14	GAATAGGTGGAATCTTTGCTGTCCTGTTCAGTTACAGACTCCTGAGAATTACCAGATTG
L15	AGCAAAGATTCCACCTATTCTCTGTCTAGCACCCTGACCCTGTCCAAAGCGGATTACGA
L16	AGACCTTGGTGGGTTACTTCACACGCATATACTTTGTGTTTTTCGTAATCCGCTTTGGA

dx.doi.org/10.1021/bc100510g |*Bioconjugate Chem.* 2011, 22, 903–912

Table 1. Continued

label	sequence (5′-3′)
L17	GTAACCCACCAAGGTCTGTCCTCCCCGGTTACTAAATCCTTTAACCGTGGCGAATGTTG
L18	TCAACATTCGCCACGG
H1	ATGAAAAAGACAGCTATCG
H2	TGCGCTACGGTAGCGAAACCAGCCAAGGCCACTGCAATTGCGATAGCTGTCTTTTTCAT
H3	GCTACCGTAGCGCAAGCTGAAGTACAACTGGTAGAATCTGGTGGTGGTCTGGTTCAGCC
H4	AAACATAGCCGCTTGCGGCGCAAGACAGACGCAGAGAACCACCAGGCTGAACCAGACCA
H5	GCAAGCGGCTATGTTTTTACGGACTACGGCATGAACTGGGTTCGCCAGGCTCCGGGCAA
H6	TCGGTTCGCCGATGTAAGTGTTAATCCAGCCCATCCATTCCAGACCTTTGCCCGGAGCC
H7	ATCGGCGAACCGATCTATGCTGATTCTGTTAAGGGCCGTTTCACTTTCAGCCTGGACAC
H8	TGCGCGCAGGCTGTTCATTTGCAGGTAAGCGGTGGATTTGCTGGTGTCCAGGCTGAAAG
H9	GCCTGCGCGCAGAAGATACCGCTGTTTATTACTGCGCACGTGGCTACCGTAGCTACGCA
H10	GCAGAAGATACAGTCACCAGGGTGCCCTGACCCCAGTAATCCATTGCGTAGCTACGGTA
H11	GGTGACTGTATCTTCTGCTTCTACTAAAGGCCCGTCTGTATTCCCTCTGGCACCTTCTA
H12	ACCAGGCAACCCAGTGCCGCCGTACCACCGGAAGTGGATTTGCTAGAAGGTGCCAGAGG
H13	CTGGGTTGCCTGGTTAAAGATTATTTCCCGGAACCTGTAACTGTGAGCTGGAACTCCGG
H14	GATTGCAGAACCGCCGGGAAGGTATGCACGCCGGAAGTCAGCGCACCGGAGTTCCAGCT
H15	GGCGGTTCTGCAATCCAGCGGCCTGTACTCCCTGTCTAGCGTTGTTACCGTTCCGTCTA
H16	TATGGTTAACGTTGCAGATGTACGTCTGGGTGCCCAGAGAGCTAGACGGAACGGTAACA
H17	TCTGCAACGTTAACCATAAACCATCTAACACTAAAGTTGATAAGAAAGTCGAACCGAAA
H18	TCACGCCGCGCAAGTATGGGTTTTATCGCAAGATTTCGGTTCGACTTTCT
oKI158	/5PHOS/GAAAAAAAAATGAAAAAGACAGCTATCGCAATTG
oKI159	/5PHOS/CTCCTCAACACTCTCCTCTATTAAAGCTTTTTG
oKI160	TAGAGCTCATGAAAAAGACAGCTATCGCAATTG
oKI161	ATACCGGTTCACGCCGCGCAAGTATG
oKI162	ATACCGGTTCAACATTCGCCACGGTTAAAG
oKI464	TAGGAATTCACCATGGATATTCAAATGACCCAAAGCCCTTC
oKI465	ATGCATGCTCACGCCGCCGGCGCCGGGG
oKI481	/5PHOS/TCTACTGCGCCTCCTGCGGCGTGAGCATGCAAGC
oKI482	/5PHOS/ACCCGGTGCAGGTTTGTTATCGCAAGATTTCGGTTCGACTTTCTTATC

demonstration of the utility of O-glycocompetent *E. coli* for basic research on GalNAc-T substrate specificity.

Following the expression and purification of a glycosylated OGRS/Fab fusion protein selected from the library, we used a well-established glycan labeling technique to PEGylate the site-specifically placed *N*-acetylgalactosamine (GalNAc). In summary, this method entails enzymatic oxidation by GAO and reaction of the resultant aldehydes with hydroxylamine-functionalized molecules of interest in the presence of aniline to form stable oxime bonds (Figure 1). While this method has been used extensively for the labeling of glycoproteins, its use as a site-specific bioconjugation technique has been limited by the ability to produce homogeneously glycosylated proteins with unique oxidizable sugars. As previously discussed, we circumvented this problem by engineering *E. coli* with the ability to O-glycosylate proteins rather than using eukaryotic hosts, which typically contain an array of glycosylation modifications leading to numerous potentially reactive glycans. In contrast to previously reported techniques for glycoPEGylation,[42] the method reported here does not require an exogenous source of UDP-GalNAc and all enzymes and reagents are available from commercial sources.

EXPERIMENTAL PROCEDURES

Construction of the Glycosylation Helper Plasmid. An existing *BsaI* site was removed from the pUC19 origin and β-lactamase resistance marker by overlap PCR using oGH174 and oGH175 as flanking primers and oGH176 and oGH177 as internal overlapping primers (see Tables 1 and 2 for lists of primers and plasmids). The resulting DNA fragment contains *Eco*RI and *NcoI* sites at the 5′ and 3′ ends, respectively. The multiple cloning site from pGH11[43] was excised using *Eco*RI and *AscI*. A *BsmBI* site was removed from the lacI open reading frame by overlap PCR using oGH178 and oGH179 as flanking primers and oGH180 and oGH181 as internal overlapping primers. The resulting DNA fragment contains *AscI* and *NcoI* sites at the 5′ and 3′ ends, respectively. The three fragments were joined by triple ligation to make pMGV. The gene encoding polypeptide GalNAc transferase 2 was amplified from a human brain cDNA library using primers oGH119 and oGH120, which add *Bam*HI and *NotI* sites to the 5′ and 3′ ends, respectively. The PCR product was cloned between the *Bam*HI and *NotI* sites in pET21a(+) to make pET21GT2. The gene, along with the 6×His tag, was amplified from pET21GT2 using primers oGH199 and oGH200, which add *SacI* and *AgeI* sites to the 5′ and 3′ ends, respectively. The PCR product was cloned between the *SacI* and *AgeI* sites in pMGV to make pMGV(GT2). The gene encoding UDP-GlcNAc C-4 epimerase from *P. aeruginosa* was codon optimized for expression in *E. coli* and synthesized by DNA 2.0 (Menlo Park, CA) along with its endogenous promoter. The promoter and gene were amplified using primers oGH196 and oGH286, which add *NotI* and *AgeI* sites to the 5′

Table 2. Plasmids Used in This Work

identifier	description	reference
pMGV	*E. coli* multiple gene expression vector	This work
pMGV(GT2)	P_{T7}GalNAc-T2 in pMGV	This work
pMGV(wbpP)	P_{wbpP}wbpP in pMGV	This work
pMGV(GT2,wbpP)	P_{T7}GalNAc-T2 and P_{wbpP}wbpP in pMGV	This work
pMGV(OmpATNFαFab)	P_{T7}OmpATNFαFab in pMGV	This work
pMGV(TNFαFab)	P_{T7}TNFαFab in pMGV	This work
pBAD33(MC3)	p15a origin, Cm^R	Guzman et al.[45]
pBAD33(MC3)TNFαFab	P_{ara}TNFαFab in pBAD33(MC3)	This work
pBAD33(MC3)TNFαFab::OGRS##	Fab fusion to OGRS peptide	This work
00	DNKPAPGSTAPPAA	
01	AVPTTVVDA	
02	EAQTELPQA	
03	INPTTQMKA	
04	LAGTESPVA	
05	LAPTAPPEA	
06	LQPTQGAMA	
07	LTQTPVVVA	
08	PGSTAPPAA	
09	PPPTSGPTA	
10	PVPTPPDNA	
11	QPVTSQPQA	
12	RAATVGSLA	
13	TPPTVLPDA	
14	VGLTPSAAA	
15	VLPTQSAHA	
16	VRATRTVVA	
17	VRPTSAVAA	
pBAD33(MC3)GST::4xMuc1	GST fused four tandem repeats of Muc1	This work
pPB230	Mucin expression vector	gift from P. Bobrowicz, Glycofi, Inc.
pGal1-GST	Vector containing GST tag	gift from K. Griswold, Dartmouth College

and 3′ ends, respectively. The PCR product was cloned between the *NotI* and *AgeI* sites in pMGV to make pMGV(wbpP). The 1.5 kb *AscI*/*SphI* fragment of pMGV(wbpP) was cloned between the *BsmBI* and *SphI* sites in pMGV(GT2) to make pMGV(GT2, wbpP). This plasmid encodes the GalNAc-T and epimerase necessary for glycosylation of target proteins in the *E. coli* cytoplasm.

Cloning and Expression of the GST-Mucin Fusion Reporter Protein. The tandem repeat region of mucin was amplified from pPB230 using oGH589 and oGH590 to add a *SacI* site to the 3′ end. GST was amplified from pGal1-GST using oGH528 and oGH529 to add an *NheI* site to the 5′ end. pBAD33(MC3) was amplified using oGH530 and oGH531 to add *SacI* and *XbaI* sites to the 5′ and 3′ ends, respectively. The PCR products were digested with the enzymes listed above and ligated to form pBAD33(MC3)GST::4×Muc1. Shuffle T7 Express (NEB, Ipswich, MA) was transformed with pBAD33(MC3)GST::4×Muc1 either alone or in combination with pMGV(GT2, wbpP). Transformants were grown to approximately 1 g/L DCW in 5 mL LB containing 25 g/L chloramphenicol and 100 g/L ampicillin prior to induction by addition of 62.5 μL 40% arabinose. Cultures were induced overnight, and cell pellets were harvested by centrifugation at 5000 *g* for 5 min. The pellets were resuspended in 0.5 mL PBS containing 1× complete, EDTA free protease inhibitor (Roche). The cells were lysed by ultrasonication and insoluble lysate was removed by centrifugation at 16 000 *g*. Soluble lysates were analyzed for glycosylation by Western blot using HRP-conjugated *Vicia villosa* lectin (EY Laboratories, San Mateo, CA).

Cloning of anti-TNFα Fab and Creation of OGRS Fusions. The genes encoding heavy and light chain of anti-TNFα Fab secreted via OmpA leader peptides were synthesized by overlap extension PCR using oligonucleotides, L1-L18 for light chain and H1−H18 for heavy chain.[44] The PCR products were cloned between the *SacI* and *AgeI* sites in pMGV. The light chain was amplified using primers oKI160 and oKI62, and the heavy chain was amplified using primers oKI158 and oKI161. The PCR products were digested with *SacI* (light) or *AgeI* (heavy) and cloned between the *SacI* and *AgeI* sites of pMGV. The leaders were removed by quick-change PCR using primers oKI458−461. The leaderless construct was amplified using oKI464 and oKI465, which add *Eco*RI and *SphI* sites to the 5′ and 3′ end, respectively. The PCR product was cloned between the *Eco*RI and *SphI* sites in pBAD33(MC3)[45] to make pBAD33-(MC3)TNFαFab. The mucin-based OGRS was added by quick-change PCR using phosphorylated primers, oKI481 and oKI482 to make pBAD33(MC3)TNFαFab00. All other OGRS were added by quick change PCR using a phosphorylated reverse primer, oGH601, and a nonphosphorylated forward primer (oGH602−618) encoding an OGRS to make pBAD33(MC3)OgTNF01−17.

Table 3. Strains Used in This Work

identifier	description	strain
sGH683	pMGV(GT2) and pBAD33(MC3)GST::4xMuc1	Shuffle T7 Express
sGH684	pMGV(wbpP) and pBAD33(MC3)GST::4xMuc1	Shuffle T7 Express
sGH685	pMGV(GT2,wbpP) and pBAD33(MC3)GST::4xMuc1	Shuffle T7 Express
sKI396	pMGV(GT2,wbpP) and pBAD33(MC3)TNFαFab00	Shuffle T7 Express
sGH733	pMGV(GT2,wbpP) and pBAD33(MC3)TNFαFab01	Shuffle T7 Express
sGH734	pMGV(GT2,wbpP) and pBAD33(MC3)TNFαFab02	Shuffle T7 Express
sGH735	pMGV(GT2,wbpP) and pBAD33(MC3)TNFαFab03	Shuffle T7 Express
sGH736	pMGV(GT2,wbpP) and pBAD33(MC3)TNFαFab04	Shuffle T7 Express
sGH737	pMGV(GT2,wbpP) and pBAD33(MC3)TNFαFab05	Shuffle T7 Express
sGH738	pMGV(GT2,wbpP) and pBAD33(MC3)TNFαFab06	Shuffle T7 Express
sGH739	pMGV(GT2,wbpP) and pBAD33(MC3)TNFαFab07	Shuffle T7 Express
sGH740	pMGV(GT2,wbpP) and pBAD33(MC3)TNFαFab08	Shuffle T7 Express
sGH741	pMGV(GT2,wbpP) and pBAD33(MC3)TNFαFab09	Shuffle T7 Express
sGH742	pMGV(GT2,wbpP) and pBAD33(MC3)TNFαFab10	Shuffle T7 Express
sGH743	pMGV(GT2,wbpP) and pBAD33(MC3)TNFαFab11	Shuffle T7 Express
sGH744	pMGV(GT2,wbpP) and pBAD33(MC3)TNFαFab12	Shuffle T7 Express
sGH745	pMGV(GT2,wbpP) and pBAD33(MC3)TNFαFab13	Shuffle T7 Express
sGH746	pMGV(GT2,wbpP) and pBAD33(MC3)TNFαFab14	Shuffle T7 Express
sGH747	pMGV(GT2,wbpP) and pBAD33(MC3)TNFαFab15	Shuffle T7 Express
sGH748	pMGV(GT2,wbpP) and pBAD33(MC3)TNFαFab16	Shuffle T7 Express
sGH749	pMGV(GT2,wbpP) and pBAD33(MC3)TNFαFab17	Shuffle T7 Express

Screening of Glycosylation Activity against a Panel of Selected OGRS. Shuffle T7 Express (NEB, Ipswitch, MA) was transformed with pMGV(GT2,wbpP) and pBAD33-(MC3)OgTNF## (where ## corresponds to the OGRS peptide fusion; see Table 3). anti-TNFα Fab was expressed identically to the GST-Mucin reporter described above. Soluble lysates were analyzed for glycosylation by Western blot using HRP-conjugated *Vicia villosa* lectin.

Expression and Purification of Glycosylated Fabs. sGH741 was grown at 30 °C to approximately 1 g/L DCW in 800 mL LB media containing 25 g/L chloramphenicol and 100 g/L ampicillin. To induce Fab expression, arabinose was added at a final concentration of 0.5% and the cultures were incubated at 30 °C for an additional 20 h. The cultures were centrifuged at 5000 *g* for 5 min, and the cell pellets were resuspended in 800 mL LB containing 25 g/L chloramphenicol, 100 g/L ampicillin, and 0.2% dextrose. The cultures were incubated at 30 °C for an additional 3 h. After the second incubation, the cultures were centrifuged at 5000 *g* for 5 min and the cell pellets were resuspended in 50 mL lysis buffer (100 mM Tris HCl, pH 7.4; 10 mM EDTA). The cells were incubated overnight at 50 °C with shaking. The 50 °C incubation disrupts the cell membrane and precipitates poorly assembled Fab. After the 50 °C incubation, the lysate was centrifuged at 12 000 *g* for 30 min. The supernatant was passed through a 0.45 μm filter prior to Fab purification by FPLC. Protein-L resin was equilibrated using 10 colume volumes of PBS at 1 mL/min prior to loading the soluble lysate. After loading, the column was washed with 10 column volumes of PBS and Fab was eluted in 50 mM glycine HCl, pH 3.0. The pH was immediately adjusted to 6.5 by addition of 1 M Tris, pH 8.0. Fractions containing Fab were pooled, concentrated to 4 g/L, and aliquoted into 100 μL fractions.

PEGylation of Recombinant Glycoproteins. Glycoproteins (100 μM) and 20 kDa Aminooxy-PEG (AO-PEG) (1 mM) were reacted at room temperature in 100 mM anilinium acetate, pH 4.6, for two hours. The products were separated by SEC-HPLC on an agilent 1200 series HPLC equipped with a Bio Sil SEC 250 column from BioRad. The fractions containing unreacted protein were pooled and suspended in 50 mM sodium phosphate, pH 7.4, at a concentration of 100 μM. The glycoproteins were incubated for 20 h at room temperature in the presence of 5 μM galactose oxidase. Oxidized glycoproteins were passed over a zeba spin column pre-equilibrated with anilinium acetate, pH 4.6, and reacted with 1 mM 20 kDa Aminooxy-PEG for one hour.

Analysis of PEGylated Proteins. PEGylation reactions were analyzed by RP-HPLC, MALDI-TOF, and SDS-PAGE. For RP-HPLC, reactions were loaded directly onto the column. Fractions containing reacted and unreacted protein were collected and analyzed by MALDI-TOF. For SDS-PAGE analysis, unreacted AO-PEG was removed by protein-L immunoprecipitation prior to loading. In a 1.5 mL microcentrifuge tube, 15 μL Protein-L agarose (GenScript) was washed three times with PBS. Then, the PEGylation reactions were added and the tubes were incubated at room temperature for three hours with shaking. The supernatant containing unreacted Aminooxy-PEG was discarded, and the protein-L resin was washed once with PBS. Proteins were eluted by boiling in SDS-Loading buffer (Invitrogen) containing 100 mM DTT for 10 min.

RESULTS

***In Vivo* Glycosylation of Mucin-Based Reporter Proteins.** While activity has been observed for recombinant GalNAc-T expressed in eukaryotic cells, a literature search did not identify any studies involving soluble expression of active GalNAc-T in prokaryotes. In our hands, human GalNAc-T2 could be expressed under the control of the T7 promoter in *E. coli* only when cultures were not induced with IPTG. A Western blot using HRP conjugated *Vicia villosa* lectin showed that the GST::4×Muc1

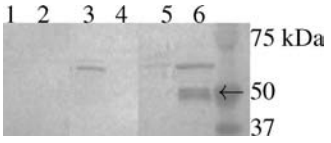


Figure 2. *Vicia villosa* lectin Western blot of the glycosylated mucin fusion protein: lane 1, UDP-GlcNAc C-4 epimerase only; lane 2, GST-Mucin coexpressed with UDP-GlcNAc C-4 epimerase; lane 3, GalNAc-T2 only; lane 4, GST-Mucin coexpressed with GalNAc-T2; lane 5, UDP-GlcNAc C-4 epimerase and GalNAc-T2; lane 6, GST-Mucin coexpressed with UDP-GlcNAc C-4 epimerase and GalNAc-T2. The arrow indicates the GST-Mucin fusion protein. Reactivity with vva lectin in lane 6 but not in lanes 1−5 shows that the reporter protein is only glycosylated in the presence of both epimerase and GalNAc-T2.

Table 4. Vertebrate OGRS Peptides Selected from OGlycBase and the Results of *in Vivo* Glycosylation by GalNAc-T2 in *E. coli*[a]

peptide	protein	glycosylated
AVPTTVVD	human α-2-HS-glycoprotein precursor	+
EAQTELPQ	human lithostathine precursor	−
INPTTQMK	human HMW I kininogen precursor	−
LAGTESPV	human transferrin receptor protein	++
LAPTAPPE	human plasminogen precursor	+++
LQPTQGAM	human G-CSF precursor	++
LTQTPVVV	bovine β-casein	+
PGSTAPPA	human muc1	+
PPPTSGPT	*Sus scrofa* plasminogen	+++
PVPTPPDN	α-1-microglobulin	++
QPVTSQPQ	human α-2-HS-glycoprotein precursor	−
RAATVGSL	human apolipoprotein E	−
TPPTVLPD	human IGF-2 precursor	+++
VGLTPSAA	human TNF-β	−
VLPTQSAH	sex hormone-binding globulin precursor	+++
VRATRTVV	platelet glycoprotein Ib-α chain	−
VRPTSAVA	human apolipoprotein C−III precursor	−

[a] − not glycosylated, + weak glycosylation, ++ moderate glycosylation, +++ strong glycosylation.

fusion protein was glycosylated in cells coexpressing GalNAc-T2 and epimerase, but not in the absence of either, indicating that the epimerase and transferase are required and sufficient to impart *E. coli* with the ability to O-glycosylate proteins *in vivo* (Figure 2). Detailed analysis of the GST::4×Muc1 was not done because the eight potential glycosylation sites present in this reporter likely would have complicated the analysis. However, fusion of a fifteen amino acid mucin-based peptide, CDNKPAPGSTAPPAA, to an anti-TNF-α antibody fragment also resulted in O-glycosylation as determined by Western blot. Analysis of this protein by LC/MS revealed an increase in molecular weight of 203 Da as is expected for addition of a single GalNAc (data not shown).

Screening OGRS Selected from O-GlycBase v 6.00. OGRS were selected from the OGlycBase database of mammalian O-glycoproteins. Several GalNAc-T isoforms are able to glycosylate nascent proteins, but others require prior glycosylation events. To enrich for OGRS that are recognized by initiating GalNAc-T isoforms, only sites that were separated from other

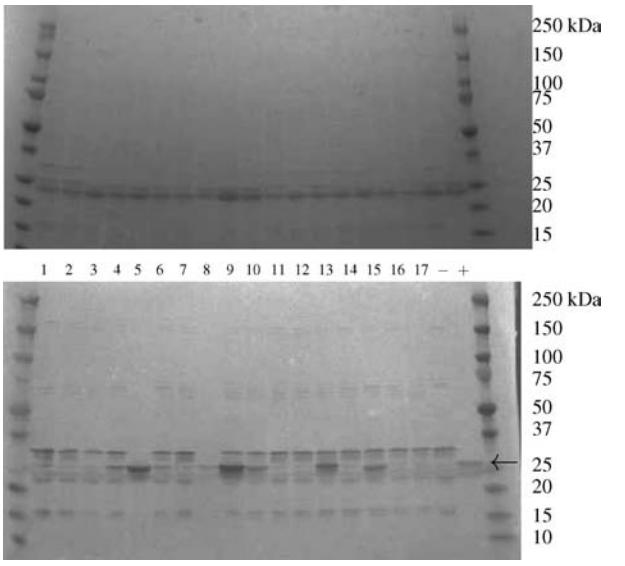


Figure 3. Coomasie stained SDS-PAGE (top) and *Vicia villosa* lectin Western blot (bottom) of Fab fused to OGRS #1−17: OGRS #1−17 were selected from O-GlycBase v 6.00 and fused to the C-terminus of Fab. The OGRS fusions were expressed in the glycocompetent *E. coli* strain and glycosylation was assessed by reactivity with vva lectin. The results of the screen are summarized in Table 4.

glycosylation sites by at least 30 amino acids were chosen. The selected OGRS were expressed as C-terminal fusions to the heavy chain of anti-TNF-α Fab separated by a single Gly-4-Ser linker. The fusion proteins were expressed in glycocompetent *E. coli* and reporters were screened for glycosylation by Western blot using VVA-lectin HRP conjugate, which is specific for terminal GalNAc. The results of the screen are shown in Table 4 and Figure 3. It is hypothesized that OGRS that did not interact with GalNAc-T2 were either structurally altered due to the presentation as C-terminal fusions or they are the targets for other GalNAc-T isoforms. The OGRS from *Sus scrofa* plasminogen, PPPTSGPT, showed the greatest degree of staining on *Vicia villosa* lectin Western blots, and subsequent LC-MS analysis confirmed a glycosidic linkage to HexNAc (Figure 4). This glycoprotein was purified by protein-L chromatography and further analysis showed up to 69% occupancy at Thr-4 (Figure 5).

PEGylation of O-Glycosylated anti-TNF-α Fab. The glycosylated PPPTSGPT peptide fused to anti-TNF-α Fab was PEGylated at the engineered GalNAc by reacting with a 10-fold molar excess 20 kDa AO-PEG in 100 mM anilinium acetate pH 4.6 following oxidation by GAO. Aniline catalyzed oxime bond formation is a generally accepted method for labeling glycans, and excess aniline can be easily removed by SEC following the reaction. The product was either precipitated on protein-L sepharose and checked by SDS-PAGE (Figure 6) or isolated by SEC-HPLC and analyzed by MALDI-TOF (Figures 7 and 8). On the basis of an estimated occupancy of 69%, the extent of conversion of the glycoprotein is 0.85 after one hour and the purity is >98% by comparison to control reactions containing nonoxidized glycoprotein.

Surprisingly, it was found that freshly purified glycoprotein reacts with AO-PEG to some extent even without prior oxidation (Figure 7). After direct reaction with AO-PEG, approximately 5−10% of the starting material is converted to a high molecular

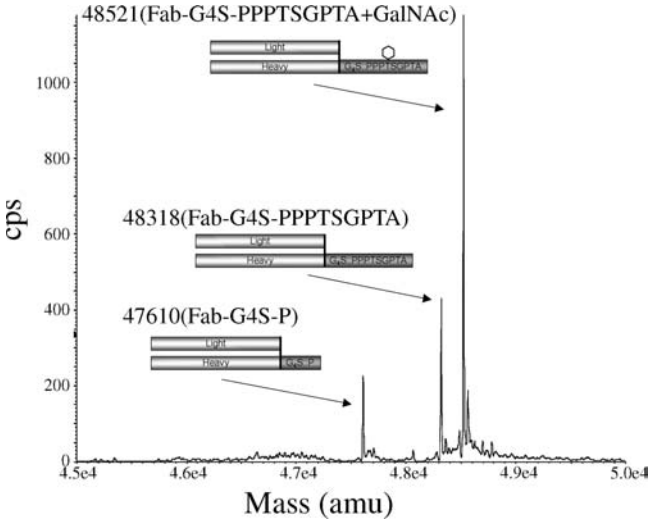


Figure 4. Analysis of glycosylated anti-TNFαFab09 by LC/MS: Glycoprotein was isolated as described and analyzed without further processing. The glycoprotein (MW 48524) comprises approximately 69% of the total. The unglycosylated full-length (MW 48318) and unglycosylated C-terminal degradation product (MW 47610) comprise the remaining 31%. The shift of 203 Da is expected upon glycosidic linkage to a single HexNAc. Lack of glycosylation of the proteolytically degraded product suggests that the glycosylation event was unique to the engineered peptide.

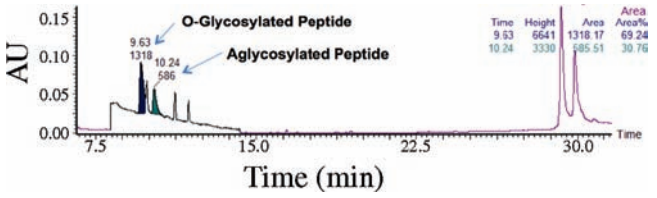


Figure 5. Quantification of glycan occupancy at OGRS peptide Thr-4 by RP-UPLC: The C-terminal glycopeptide elutes at 9.6 min and the aglycosylated C-terminal peptide elutes at 10.3 min. The glycopeptide and aglycopeptide are estimated at 69% and 31%, respectively.

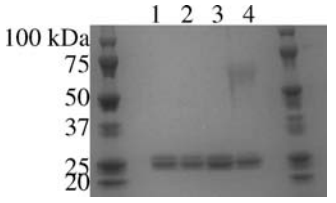


Figure 6. SDS-PAGE showing PEGylation of glycosylated Fab: After the reaction, excess 20 kDa AO-PEG was removed by immunoprecipitation using protein-L agarose. Lane 1, overnight incubation in oxidation reaction buffer followed by 1 h incubation in PEGylation buffer; lane 2, overnight incubation with GAO followed by 1 h incubation in PEGylation buffer; lane 3, overnight incubation in oxidation reaction buffer followed by 1 h incubation with 20 kDa AO-PEG; lane 4, overnight incubation with GAO followed by 1 h incubation with 20 kDa AO-PEG. The results indicate that sequential oxidation and incubation with AO-PEG are required for PEGylation. The light chain (bottom band) serves as a convenient internal control. Migration of the heavy chain to a single high molecular weight species in lane 4 indicates that the reaction is specific to a single location on that subunit.

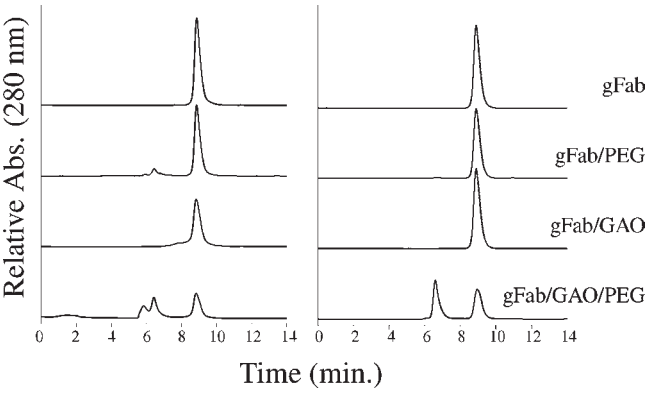


Figure 7. Analysis of PEGylation reactions by SEC-HPLC: Reactions were performed without removal (left) and with removal (right) of the contaminating reactive species. Without removal of the contaminant, approximately 6% of the nonoxidized starting material is converted to the high molecular weight species. Upon oxidation, the conversion increases to 70%. When the contaminant is removed, less than 2% of the nonoxidized starting material is converted, while 65% is converted after oxidation.

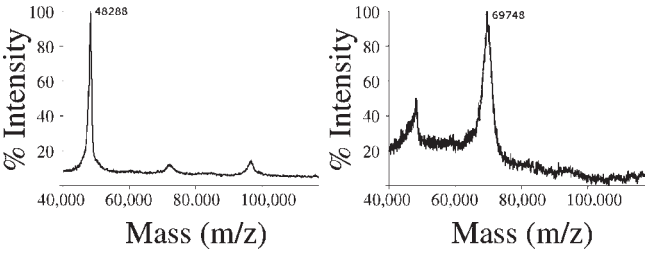


Figure 8. Analysis of PEGylation products by MALDI-TOF: The reaction products were separated by SEC-HPLC and fractions from each peak were pooled for MALDI-TOF analysis. Representative data from each peak is presented showing that the slow eluting peak is composed of unreacted Fab and the fast eluting peak is the PEGylated product as expected. The PEGylated product cannot be well-resolved due to the polydispersity of the 20 kDa AO-PEG.

weight product after four hours. The conversion does not increase appreciably when the reaction is allowed to proceed for an additional sixteen hours and the product is not hydrolyzed upon removal of the excess AO-PEG (data not shown) indicating a fast, irreversible reaction. This suggests that a reactive contaminant is present in the starting protein preparation, currently hypothesized to be due to carbonylation of a susceptible residue in the anti-TNF-α Fab. Indeed, UPLC analysis showed that approximately 5−10% of the purified Fab has a molecular weight 16 Da greater than the expected mass of the intact protein confirming the presence of an additional oxygen atom (data not shown). On the basis of the assumption of a reactive contaminant, the starting material was pretreated with AO-PEG and the high molecular weight product was removed by SEC-HPLC. The unmodified Fab was used as starting material for subsequent oxidation and PEGylation reactions. Nonoxidized control reactions run using this clean starting material resulted in <2% conversion to the side product indicating that the reactive contaminant had been removed by reaction with 20 kDa AO-PEG and SEC-HPLC (Figure 7).

DISCUSSION

We have developed a general method for the site-specific modification of proteins using a glycoengineered strain of *E. coli*. Once a sugar is placed on the recombinant protein, conventional techniques can be used to first oxidize and then conjugate any aminooxy-functionalized molecule of interest. Of central importance is the presence of a single reactive glycan moiety per glycoprotein molecule. The use of *E. coli* rather than a eukaryotic host offers the advantage that the glycans are uniform and placed at the desired location. Unlike previous studies utilizing aldehydes, we were able to achieve excellent conversion of the glycoprotein precursor with minimal contamination by non-site-specifically modifying side products through the removal of reactive contaminants. Carrico et al.[3] describe the reaction of aminooxy functionalized PEG with genetically encoded formylglycine residues, while the authors claim that this reaction scheme is site-specific (figure 2c of that publication shows multiple species). In each case, the spacing between the additional species corresponds to the size of an additional PEG molecule being added to the target protein. Thus, this reaction likely involves more than one PEG addition, implying that additional residues other than the engineered formylglycine are being modified. Furthermore, in another recent publication,[46] biological samples were shown to be susceptible to low levels of biotinylation by hydroxylamine functionalized reagents without the prior conversion to aldehydes. Taken together, it seems likely that the lack of specificity reported here is of general concern for aldehyde-based modification of biomolecules and that the removal of carbonylated species could be a valuable strategy for improving the purity of the PEGylated products when using these types of reactions. Considering the high level conversion of glycoprotein to the PEGylated product, further improvements to glycan occupancy would be expected to ultimately result in greater yield of PEGylated product. The PEGylated product is easily removed from the reactant pool by SEC-HPLC, but due to the physical properties of PEG, other chromatographic techniques such as ion exchange could be employed.

Repetition of the workflow described herein using the remaining initiating GalNAc transferases should allow for the creation of a small database linking GalNAc-T isoforms with their cognate OGRS. This database may prove useful for the introduction of OGRS at novel sites within proteins with minimal disruption of the native structure. In addition to providing precursors for bioconjugation, the ability to direct O-glycosylation in *E. coli* should provide tools for basic research on GalNAc-T as well as the ability to produce O-glycosylated mucin proteins.

AUTHOR INFORMATION

Corresponding Author

*E-mail: tillman.gerngross@Dartmouth.edu.

ACKNOWLEDGMENT

We thank Dr. Karl Griswold and Dr. Piotr Bobrowicz for supplying plasmids, Dr. Yingda Xu and Nicholas Gottlieb for technical assistance, and Mary Kay Brown for management of our laboratory. This research was supported by Eli Lilly and Company.

REFERENCES

(1) Fee, C. J., and Alstine, J. M. V. (2006) PEG-proteins: Reaction engineering and separation issues. *Chem. Eng. Sci. 61*, 924–939Biomolecular Engineering.

(2) Sletten, E. M., and Bertozzi, C. R. (2009) Bioorthogonal chemistry: fishing for selectivity in a sea of functionality. *Angew. Chem., Int. Ed. Engl. 48*, 6974–98.

(3) Carrico, I. S., Carlson, B. L., and Bertozzi, C. R. (2007) Introducing genetically encoded aldehydes into proteins. *Nat. Chem. Biol. 3*, 321–2.

(4) Laughlin, S. T., and Bertozzi, C. R. (2007) Metabolic labeling of glycans with azido sugars and subsequent glycan-profiling and visualization via Staudinger ligation. *Nat. Protoc. 2*, 2930–44.

(5) Hang, H. C., Yu, C., Kato, D. L., and Bertozzi, C. R. (2003) A metabolic labeling approach toward proteomic analysis of mucin-type O-linked glycosylation. *Proc. Natl. Acad. Sci. U.S.A. 100*, 14846–51.

(6) Dube, D. H., Champasa, K., and Wang, B. (2010) Chemical tools to discover and target bacterial glycoproteins. *Chem. Commun. (Camb.)* Online Early Access.

(7) Dube, D. H., Prescher, J. A., Quang, C. N., and Bertozzi, C. R. (2006) Probing mucin-type O-linked glycosylation in living animals. *Proc. Natl. Acad. Sci. U.S.A. 103*, 4819–24.

(8) Breidenbach, M. A., Gallagher, J. E. G., King, D. S., Smart, B. P., Wu, P., and Bertozzi, C. R. (2010) Targeted metabolic labeling of yeast N-glycans with unnatural sugars. *Proc. Natl. Acad. Sci. U.S.A. 107*, 3988–93.

(9) Osuga, D. T., Feather, M. S., Shah, M. J., and Feeney, R. E. (1989) Modification of galactose and N-acetylgalactosamine residues by oxidation of C-6 hydroxyls to the aldehydes followed by reductive amination: model systems and antifreeze glycoproteins. *J. Protein Chem. 8*, 519–28.

(10) Morell, A. G., Van den Hamer, C. J., Scheinberg, I. H., and Ashwell, G. (1966) Physical and chemical studies on ceruloplasmin. IV. Preparation of radioactive, sialic acid-free ceruloplasmin labeled with tritium on terminal D-galactose residues. *J. Biol. Chem. 241*, 3745–9.

(11) Poduslo, J. F., Quarles, R. H., and Brady, R. O. (1976) External labeling of galactose in surface membrane glycoproteins of the intact myelin sheath. *J. Biol. Chem. 251*, 153–8.

(12) Avigad, G. (1985) Oxidation rates of some desialylated glycoproteins by galactose oxidase. *Arch. Biochem. Biophys. 239*, 531–7.

(13) Solomon, B., Koppel, R., Schwartz, F., and Fleminger, G. (1990) Enzymic oxidation of monoclonal antibodies by soluble and immobilized bifunctional enzyme complexes. *J. Chromatogr. 510*, 321–9.

(14) O'Shannessy, D. J., Dobersen, M. J., and Quarles, R. H. (1984) A novel procedure for labeling immunoglobulins by conjugation to oligosaccharide moieties. *Immunol. Lett. 8*, 273–7.

(15) O'Shannessy, D. J., and Quarles, R. H. (1987) Labeling of the oligosaccharide moieties of immunoglobulins. *J. Immunol. Methods 99*, 153–61.

(16) O'Shannessy, D. J. (1990) Antibodies biotinylated via sugar moieties. *Methods Enzymol. 184*, 162–6.

(17) Bayer, E. A., Ben-Hur, H., and Wilchek, M. (1988) Biocytin hydrazide—a selective label for sialic acids, galactose, and other sugars in glycoconjugates using avidin-biotin technology. *Anal. Biochem. 170*, 271–81.

(18) Vandenheede, J. R., Ahmed, A. I., and Feeney, R. E. (1972) Structure and role of carbohydrate in freezing point-depressing glycoproteins from an antarctic fish. *J. Biol. Chem. 247*, 7885–9.

(19) Bílková, Z., Slováková, M., Lycka, A., Horák, D., Lenfeld, J., Turková, J., and Churácek, J. (2002) Oriented immobilization of galactose oxidase to bead and magnetic bead cellulose and poly(HEMA-co-EDMA) and magnetic poly(HEMA-co-EDMA) microspheres. *J. Chromatogr., B: Anal. Technol. Biomed. Life Sci. 770*, 25–34.

(20) Lee, J. A., and Fortes, P. A. (1985) Labeling of the glycoprotein subunit of (Na,K)ATPase with fluorescent probes. *Biochemistry 24*, 322–30.

(21) Hermanson, G. T. (1996) *Bioconjugate techniques*, Academic Press, San Diego.
(22) Wilchek, M., and Bayer, E. A. (1987) Labeling glycoconjugates with hydrazide reagents. *Methods Enzymol. 138*, 429–42.
(23) Zalipsky, S. (1995) Functionalized poly(ethylene glycol) for preparation of biologically relevant conjugates. *Bioconjugate Chem. 6*, 150–65.
(24) Schlegel, R. A., Gerbeck, C. M., and Montgome, R. (1968) Substrate specificity of Dgalactose oxidase. *Carbohydr. Res. 7*, 193–&.
(25) Kelleher, F. M., and Bhavanandan, V. P. (1986) Re-examination of the products of the action of galactose oxidase. Evidence for the conversion of raffinose to 6″-carboxyraffinose. *J. Biol. Chem. 261*, 11045–8.
(26) Van den Steen, P., Rudd, P. M., Dwek, R. A., and Opdenakker, G. (1998) Concepts and principles of O-linked glycosylation. *Crit. Rev. Biochem. Mol. Biol. 33*, 151–208.
(27) Hanisch, F. G. (2001) O-glycosylation of the mucin type. *Biol. Chem. 382*, 143–9.
(28) Gupta, R., Birch, H., Rapacki, K., Brunak, S., and Hansen, J. E. (1999) O-GLYCBASE version 4.0: a revised database of O-glycosylated proteins. *Nucleic Acids Res. 27*, 370–2.
(29) Caragea, C., Sinapov, J., Silvescu, A., Dobbs, D., and Honavar, V. (2007) Glycosylation site prediction using ensembles of Support Vector Machine classifiers. *BMC Bioinformatics 8*, 438.
(30) Julenius, K., Mølgaard, A., Gupta, R., and Brunak, S. (2005) Prediction, conservation analysis, and structural characterization of mammalian mucin-type O-glycosylation sites. *Glycobiology 15*, 153–64.
(31) Wandall, H. H., Hassan, H., Mirgorodskaya, E., Kristensen, A. K., Roepstorff, P., Bennett, E. P., Nielsen, P. A., Hollingsworth, M. A., Burchell, J., Taylor-Papadimitriou, J., and Clausen, H. (1997) Substrate specificities of three members of the human UDP-N-acetylalpha-D-galactosamine:Polypeptide N-acetylgalactosaminyltransferase family, GalNAc-T1, -T2, and -T3. *J. Biol. Chem. 272*, 23503–14.
(32) Tetaert, D., Richet, C., Gagnon, J., Boersma, A., and Degand, P. (2001) Studies of acceptor site specificities for three members of UDP-GalNAc:N-acetylgalactosaminyltransferases by using a synthetic peptide mimicking the tandem repeat of MUC5AC. *Carbohydr. Res. 333*, 165–71.
(33) Takeuchi, H., Kato, K., Hassan, H., Clausen, H., and Irimura, T. (2002) O-GalNAc incorporation into a cluster acceptor site of three consecutive threonines. Distinct specificity of GalNAc-transferase isoforms. *Eur. J. Biochem. 269*, 6173–83.
(34) Cheng, L., Tachibana, K., Zhang, Y., Guo, J. m., Kahori Tachibana, K., Kameyama, A., Wang, H., Hiruma, T., Iwasaki, H., Togayachi, A., Kudo, T., and Narimatsu, H. (2002) Characterization of a novel human UDP-GalNAc transferase, pp-GalNAc-T10. *FEBS Lett. 531*, 115–21.
(35) Brokx, R. D., Revers, L., Zhang, Q., Yang, S., Mal, T. K., Ikura, M., and Gariépy, J. (2003) Nuclear magnetic resonance-based dissection of a glycosyltransferase specificity for the mucin MUC1 tandem repeat. *Biochemistry 42*, 13817–25.
(36) Ten Hagen, K. G., Fritz, T. A., and Tabak, L. A. (2003) All in the family: the UDPGalNAc: polypeptide N-acetylgalactosaminyltransferases. *Glycobiology 13*, 1R–16R.
(37) Nakamura, N., Katano, K., Toba, S., and Kurosaka, A. (2004) Characterization of a novel polypeptide N-acetylgalactosaminyltransferase (dGalNAc-T3) from Drosophila. *Biol. Pharm. Bull. 27*, 1509–14.
(38) Pratt, M. R., Hang, H. C., Ten Hagen, K. G., Rarick, J., Gerken, T. A., Tabak, L. A., and Bertozzi, C. R. (2004) Deconvoluting the functions of polypeptide N-alphaacetylgalactosaminyltransferase family members by glycopeptide substrate profiling. *Chem. Biol. 11*, 1009–16.
(39) Pratt, M. R., and Bertozzi, C. R. (2005) Synthetic glycopeptides and glycoproteins as tools for biology. *Chem. Soc. Rev. 34*, 58–68.
(40) Persson, M., and Palcic, M. M. (2008) A high-throughput pH indicator assay for screening glycosyltransferase saturation mutagenesis libraries. *Anal. Biochem. 378*, 1–7.
(41) Blixt, O., Cló, E., Nudelman, A. S., Sørensen, K. K., Clausen, T., Wandall, H. H., Livingston, P. O., Clausen, H., and Jensen, K. J. (2010) A high-throughput O-glycopeptide discovery platform for seromic profiling. *J. Proteome Res. 9*, 5250–5261.
(42) DeFrees, S., Wang, Z.-G., Xing, R., Scott, A. E., Wang, J., Zopf, D., Gouty, D. L., Sjoberg, E. R., Panneerselvam, K., Brinkman-Van der Linden, E. C. M., Bayer, R. J., Tarp, M. A., and Clausen, H. (2006) GlycoPEGylation of recombinant therapeutic proteins produced in Escherichia coli. *Glycobiology 16*, 833–43.
(43) Barnard, G. C., Henderson, G. E., Srinivasan, S., and Gerngross, T. U. (2004) High level recombinant protein expression in Ralstonia eutropha using T7 RNA polymerase based amplification. *Protein Expr. Purif. 38*, 264–71.
(44) Hoover, D. M., and Lubkowski, J. (2002) DNAWorks: an automated method for designing oligonucleotides for PCR-based gene synthesis. *Nucleic Acids Res. 30*, e43.
(45) Guzman, L. M., Belin, D., Carson, M. J., and Beckwith, J. (1995) Tight regulation, modulation, and high-level expression by vectors containing the arabinose PBAD promoter. *J. Bacteriol. 177*, 4121–30.
(46) Zeng, Y., Ramya, T. N. C., Dirksen, A., Dawson, P. E., and Paulson, J. C. (2009) Highefficiency labeling of sialylated glycoproteins on living cells. *Nat. Methods 6*, 207–9.

Bioconjugate Chemistry

ARTICLE

pubs.acs.org/bc

Multimeric System of ^{99m}Tc-Labeled Gold Nanoparticles Conjugated to c[RGDfK(C)] for Molecular Imaging of Tumor α(v)β(3) Expression

Enrique Morales-Avila,[†,‡] Guillermina Ferro-Flores,[*,†] Blanca E. Ocampo-García,[†,‡] Luis M. De León-Rodríguez,[§] Clara L. Santos-Cuevas,[†] Rocío García-Becerra,[∥] Luis A. Medina,[⊥,#] and Leobardo Gómez-Oliván[‡]

[†]Departamento de Materiales Radiactivos, Instituto Nacional de Investigaciones Nucleares, Estado de México, Mexico

[‡]Universidad Autónoma del Estado de México, Estado de México, Mexico

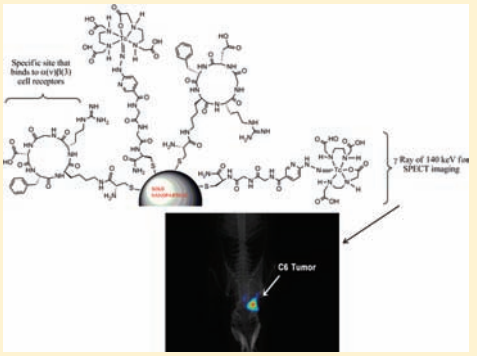
[§]Instituto de Investigaciones Científicas, Universidad de Guanajuato, Guanajuato, Mexico

[∥]Departamento de Biología de la Reproducción, Instituto Nacional de Ciencias Médicas y Nutrición Salvador Zubirán, Mexico City, Mexico

[⊥]Instituto de Física, Universidad Nacional Autónoma de México, Mexico City, Mexico

[#]Unidad de Investigación Biomédica en Cáncer INCAN-UNAM, Departamento de Medicina Nuclear, Instituto Nacional de Cancerología, Mexico City, Mexico

ABSTRACT: Integrin $\alpha_V\beta_3$ plays a critical role in tumor angiogenesis and metastasis. Suitably radiolabeled cyclic RGD peptides can be used for noninvasive imaging of $\alpha_V\beta_3$ expression. The aim of this research was to prepare a multimeric system of technetium-99m-labeled gold nanoparticles conjugated to c[RGDfK-(C)] and to evaluate its biological behavior as a potential radiopharmaceutical for molecular imaging of tumor angiogenesis. Hydrazinonicotinamide-GGC (HYNIC-GGC) and c[RGDfK(C)] peptides were synthesized and conjugated to gold nanoparticles (AuNP, 20 nm) by means of spontaneous reaction of the thiol groups of cysteine. The nanoconjugate was characterized by TEM, FT-IR, UV−vis, XPS, and Raman spectroscopy. To obtain ^{99m}Tc-HYNIC-GGC-AuNP-c[RGDfK(C)] (^{99m}Tc-AuNP-RGD), the ^{99m}Tc-HYNIC-GGC radiopeptide was first prepared and added to 1.5 mL of AuNP solution (1 nM) followed by c[RGDfK(C)] (10 μL, 50 μM) at 18 °C with stirring for 15 min. Radiochemical purity (RP) was determined by size-exclusion HPLC and ITLC-SG analyses. *In vitro* binding studies were carried out in $\alpha_V\beta_3$ receptor-positive C6 glioma cancer cells. Biodistribution studies were accomplished in athymic mice with C6-induced tumors with blocked and nonblocked receptors, and images were obtained using a micro-SPECT/CT. TEM and spectroscopy techniques demonstrated that AuNPs were functionalized with peptides. RP was 96 ± 2% without postlabeling purification. ^{99m}Tc-AuNP-RGD showed specific recognition for $\alpha_V\beta_3$ integrins expressed in C6 cells, and 3 h after i.p. administration in mice, the tumor uptake was 8.18 ± 0.57% ID/g. Micro-SPECT/CT images showed evident tumor uptake. ^{99m}Tc-AuNP-RGD demonstrates properties suitable for use as a target-specific agent for molecular imaging of tumor $\alpha_V\beta_3$ expression.



INTRODUCTION

Angiogenesis is a physiological process involving the growth of new blood vessels by the sprouting of existing vessels in avascular tissue. Angiogenesis is a requirement for tumor growth and metastasis. The angiogenic process is regulated by cell adhesion receptors, such as integrins. The $\alpha_v\beta_3$ integrin is expressed on the surface of normal endothelial cells at low levels, but is overexpressed in the tumor neovasculature and tumor cells of osteosarcoma, neuroblastoma, glioblastoma, melanoma, lung carcinoma, and breast cancer.[1,2]

Radiolabeled peptides based on the Arg-Gly-Asp (RGD) sequence have been reported as radiopharmaceuticals with high affinity and selectivity for the $\alpha_v\beta_3$ integrin and are therefore useful in the noninvasive monitoring of tumor angiogenesis by molecular imaging techniques.[3,4] Monomeric RGD radiopharmaceuticals tend to have fast blood clearance but relatively good tumor uptake and rapid tumor washout, whereas dimeric, tetrameric, and octameric cyclic-RGD peptides exhibit increased affinity and enhanced adhesion to target $\alpha_v\beta_3$ integrin due to an increase in multivalent sites.[1,2,5,6]

Nanoparticles can be defined as particles of any material having dimensions of 100 nm or less with novel properties that distinguish them from bulk materials due to size and surface effects, and they can be prepared as stable, homogeneous, and well-characterized systems in size and shape.[7,8] Nanoparticles produce multivalent effects due to multiple simultaneous interactions between the biomolecules

Received: December 7, 2010
Revised: April 12, 2011
Published: April 23, 2011

ACS Publications © 2011 American Chemical Society

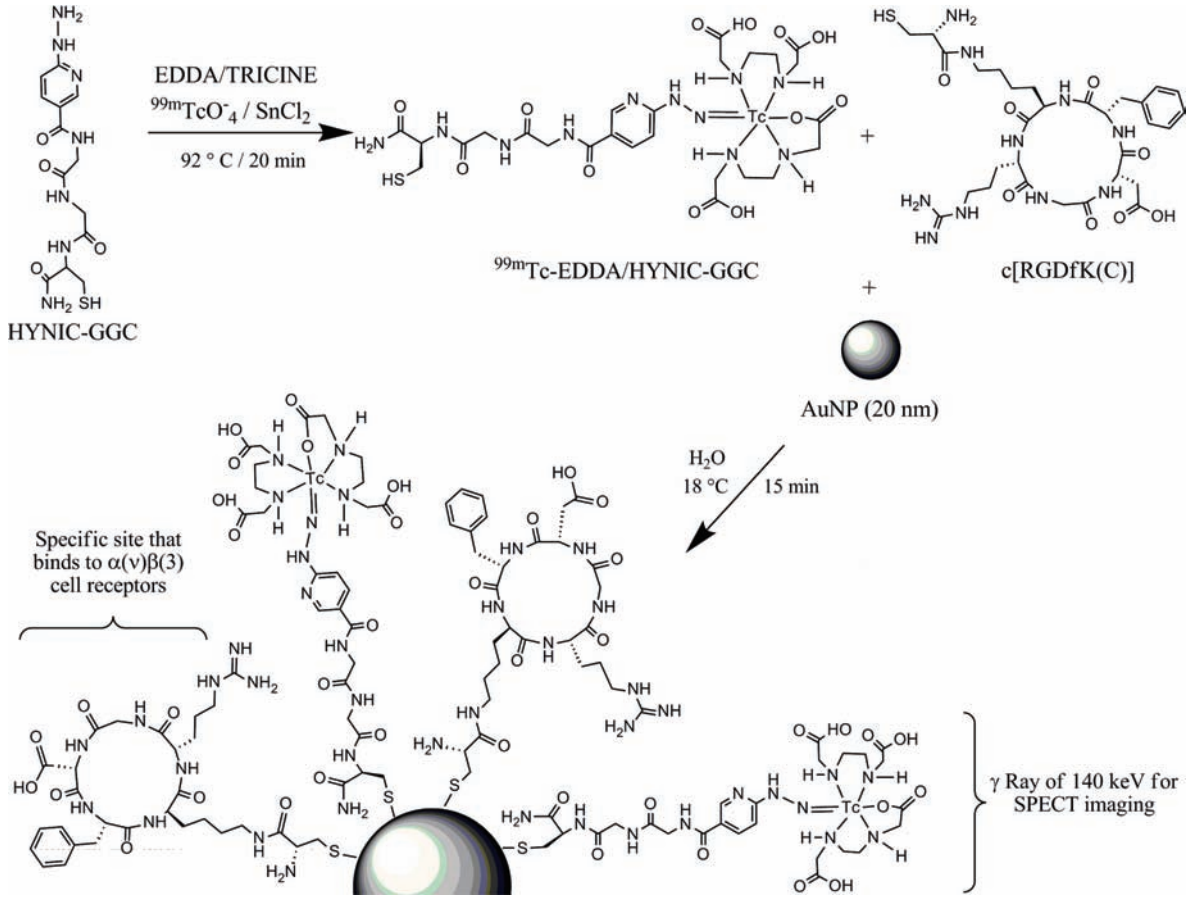


Figure 1. Overall scheme of ^{99m}Tc-EDDA/HYNIC-GGC-AuNP-c[RGDfK(C)] (^{99m}Tc-AuNP-RGD) preparation.

conjugated on the nanoparticle surface and the cell surface, with specific receptors for those biomolecules.[8] Recent studies have demonstrated that conjugating peptides to gold nanoparticles (AuNP) produces biocompatible and stable multifunctional systems with target-specific molecular recognition.[9−16] Peptides can be conjugated to one AuNP by spontaneous reaction of the AuNP surface with a thiol (cysteine) or an N-terminal primary amine.[9,11] The thiol group is considered to be the most important type of molecule to stabilize any size of AuNPs, by forming a "staple motif" chemical model of two thiol groups interacting with three gold atoms in a bridge conformation.[17]

Hydrazinonicotinamide (HYNIC) is a good chelator for technetium-99m and is suitable for radiolabeling peptides with high specific activity and favorable pharmacokinetics for imaging purposes.[18,19]

The aim of this research was to prepare a multimeric system of ^{99m}Tc-labeled gold nanoparticles (20 nm) conjugated to HYNIC-Gly-Gly-Cys-NH_2 (HYNIC-GGC) and cyclic[Arg-Gly-Asp-Phe-Lys(Cys)] (c[RGDfK(C)]) peptides and to evaluate its biological behavior as a potential specific radiopharmaceutical for tumor $\alpha_V\beta_3$ expression imaging.

EXPERIMENTAL PROCEDURES

Materials. *o*-Chlorotrityl chloride resin (Advanced Chem Tech), *N*,*N*-diisopropylethylamine (DIPEA), dichloromethane (DCM), dimethylformamide (DMF), 2-(1*H*-benzotriazole-1-yl)-1,1,3,3-tetramethyluronium hexafluorophosphate (HBTU), hydroxybenzotriazole (HOBt), piperidine, trifluoroacetic acid (TFA), 2,2,2-trifluoroethane (TFE), triisopropylsilane, 1-propanephosphonic acid cyclic anhydride (T3P), 4-dimethylaminopyridine (DMAP), Fmoc-Gly-OH, Fmoc-Arg(Pbf)-OH, Fmoc-D-Phe-OH, Fmoc-Asp(OtBu)-OH, Fmoc-Lys(Boc)-OH, Boc-Cys(Trt)-OH, and 20 nm gold colloid solution (AuNP-citrate, 6.99×10^{11} particles/mL, absorbance at 520 nm = 0.91) were purchased from Sigma-Aldrich Chemical Co. and used as received.

Synthesis of HYNIC-Gly-Gly-Cys-NH_2 (HYNIC-GGC). In the HYNIC-GGC molecule design, HYNIC was added as a ^{99m}Tc chelator group, -Gly-Gly- was used as a spacer, and -Cys- was used as the active group to interact with the gold nanoparticle surface (Figure 1). The HYNIC-GGC-NH_2 was synthesized following the method described by Ocampo-Garcia et al.[16]

Synthesis of cyclo[Arg-Gly-Asp-D-Phe-Lys-(Cys)] (c[RGDfK(C)]). In the c[RGDfK(C)] molecule design, the sequence -Arg-Gly-Asp- (-RGD-) acted as the active biological site, Phe (f) and Lys (K) residues completed the cyclic and pentapeptide structure, and Cys (C) was the spacer and active group to interact with the gold nanoparticle surface (Figure 1).

The synthesis of the linear peptide started with the incorporation of glycine onto an *o*-chlorotrityl chloride resin (with a 0.9 mmol/g load) at a 0.07 mmol scale by mixing the resin with a solution of Fmoc-Gly-OH (20.9 mg, 0.21 mmol) and DIPEA (33 μL, 0.20 mmol) in dry DCM in a peptide synthesis vessel. After shaking the reaction mixture for 2.5 h, it was removed and the resin was washed with DCM, followed by addition of 100 μL

dx.doi.org/10.1021/bc100551s |*Bioconjugate Chem.* 2011, 22, 913–922

of DIPEA in 2 mL of methanol to cap the unreacted sites on the resin. After 30 min, the resin was washed with DMF. The Fmoc-protecting group was then removed with a 20% solution of piperidine in DMF. Amino acids were then attached by using single-step couplings of 3 equiv of Fmoc-amino acid, 2.9 equiv HBTU and HOBt, and 6 equiv DIPEA in DMF in the order Fmoc-Arg(Pbf)-OH, Fmoc-Lys(Boc)-OH, Fmoc-D-Phe-OH, and Fmoc-Asp(OtBu)-OH, for 2 h each. The linear RGDfK peptide was cleaved from the resin without affecting other protecting groups by treating with 5 mL of a mixture of acetic acid, TFE, and DCM (1:1:3) for 1 h at room temperature. The resin was washed twice with 5 mL of the same mixture and then three times with DCM. The eluents were combined and concentrated. The excess acetic acid was removed by repeatedly adding hexanes to the residue and removing them by rotary evaporation. The head-to-tail cyclization was performed by slowly adding a solution of the linear peptide in 5 mL of DCM to a solution of 50% T3P in EtOAc (200 μL), DIPEA (200 μL), and DMAP (1 mg) in 5 mL of DCM. After stirring overnight, the reaction mixture was concentrated and purified by silica flash chromatography (methanol/ethyl acetate, 1:9) to afford 75 mg (MW = 1118.39, 96%) of the protected cyclic peptide as light-yellow solid. The previous intermediate was dissolved in 5 mL 2% hydrazine in DMF and stirred for 30 min at room temperature. The solvent was removed in vacuum, and the residue was triturated with water. The precipitated peptide was isolated by centrifugation. Coupling of Boc-Cys(Trt)-OH followed by reacting the cyclic peptide with 3 equiv of the amino acid, 2.9 equiv HBTU and HOBt, and 6 equiv DIPEA in DMF. The solvent was removed in vacuum, and the residue was triturated with water. The precipitated peptide was isolated by centrifugation. Coupling of Boc-Cys(Trt)-OH was followed by reacting the cyclic peptide with 3 equiv of the amino acid, 2.9 equiv HBTU, and HOBt, and 6 equiv DIPEA in DMF. The solvent was removed by rotary evaporation, and the residue was taken into DCM and washed with water. The collected organic phase was dried with anhydrous Na_2SO_4 and filtered, and the solvent was removed. The product was purified by silica flash chromatography (methanol/ethyl acetate, 1:9). The remaining protecting groups of the above cyclic peptide were removed by stirring the peptide for 2 h with 95% TFA, 2.5% triisopropylsilane, and 2.5% water mixture. The solvent was removed by rotary evaporation, and the residue was purified by HPLC with a gradient of water/acetonitrile containing 0.1% TFA from 90/10 to 10/90 in 35 min and lyophilized, giving 14 mg of c[RGDfK(C)] peptide (28% overall yield). R_t = 9.5 min (MALDI+) m/z = 707.36 $[M+H]^+$ (calcd. 707.81).

Synthesis of HYNIC-GGC-AuNP-c[RGDfK(C)]. The preparation was carried out by mixing 0.05 mL of HYNIC-GGC (0.025 mM in injectable-grade water) and 0.05 mL of c[RGDfK-(C)] (0.025 mM in injectable-grade water) with 1 mL of the AuNP solution (1 nM). The molar ratio for AuNP/HYNIC-GGC and AuNP/c[RGDfK(C)] was 1:1250. The mixture was stirred for 15 min to permit complete exchange of citrate with thiol on the particle surface. The AuNP−peptide conjugate (20 nm AuNP−peptide = 2.46×10^5 Au atoms, MW $\approx 4.8 \times 10^7$ g/mol, 0.034 mg Au/mL) was purified by size-exclusion chromatography (PD-10 column) using injectable water as eluent. The first eluted peak (3.0−4.0 mL) corresponded to the functionalized AuNP (AuNP−peptide); free peptides appeared at the 5.0−7.0 mL eluted fraction, and unfunctionalized AuNP remained trapped in the column matrix. Ten preparations of HYNIC-GGC-AuNP-c[RGDfK(C)] (10 mL) were mixed as a batch and stored for 9 months at 4 °C. During this time, the color of the solution did not change (no aggregation), no precipitate was observed, and the surface resonance plasmon (SRP = 522 nm) remained stable. AuNP-c[RGDfK(C)] without HYNIC-GGC was also prepared for comparative spectroscopic analyses.

Estimation of the Number of Peptide Molecules per AuNP. The number of peptides per nanoparticle was calculated by UV−vis titration of peptides (8 μM) using increasing gold nanoparticle concentration (from 0 to 1 nM). The peptide and AuNP−citrate solutions were incubated for 15 min at room temperature. AuNPs were removed by ultrafiltration (Ultrafree-PF filters 10 000 NWWL, Millipore), and the concentration of remaining free peptide in solution was measured from the absorbance at 280 nm. From a linear fit of data points, the number of HYNIC-GGC peptides per particle was calculated as 1.35 peptides/nm^2. As a 20 nm AuNP size was used (surface area = 1260 nm^2, 37 000 surface Au atoms), the maximum number of peptides bound to one AuNP was 1701. In the case of AuNP-c[RGDfK(C)], the free peptide concentration was quantified by UV-HPLC with a 1 mL injector loop and a μ-Bondapak C18 column (Waters, 3.9 × 300 mm), at a flow rate of 1 mL/min using a linear gradient of 0.1% TFA/water (solvent A)/0.1% TFA/CH_3CN (solvent B) from 0% to 50% of solvent B in 10 min, which was then maintained for 10 min (t_R = 8 min). From the linear fit of data points, the number of c[RGDfK(C)] was calculated as 520 peptides bound to one AuNP (0.41 peptides/nm^2). In the HYNIC-GGC-AuNP-c-[RGDfK(C)] preparation, approximately 850−900 HYNIC-GGC (free peptide determined by HPLC t_R = 5.1 min) and 260−280 c [RGDfK(C)] molecules were measured per AuNP molecule.

Chemical Characterization. *TEM.* The morphology and size distribution of AuNP and AuNP-peptides were analyzed by transmission electron microscopy (TEM) in a JEOL JEM 2010 HT microscope operating at 200 kV. Samples were prepared for analysis by evaporating a drop of aqueous product on a carbon-coated TEM copper grid.

Infrared Spectroscopy. The IR spectra of lyophilized samples were acquired on a PerkinElmer System 2000 spectrometer with an ATR platform (Pike Technologies) by applying the attenuated total reflection fourier transform infrared (ATR-FTIR) spectroscopy from 570 to 4400 cm^{-1}.

Raman Spectroscopy. Raman spectra of the samples were acquired on a MicroRaman (JOBIN-Yvon-Horiba, LABRAM HR800) spectrometer with optical microscope (OLYMPUS BX 41) and He−Ne Laser (632.817 nm) as excitation source, a D0.6 filter and a 100 micro Hole. Ten scans of 60 s were acquired.

On a pretreated cover glass (washed in three steps: 1HNO_3/3HCl (v/v) solution, bi-distilled water, and injectable water), 10 μL aliquots of the sample were deposited and dried under nitrogen atmosphere at room temperature in a laminar flow hood.

XPS. X-ray photoelectron spectra were acquired on a Jeol JPS 9200 spectrometer equipped with a MgK_α X-ray source (1253.6 eV). The source was operated at 10 kV/20 mA and calibrated using Au $4f_{7/2}$ (84.0 eV) and Ag $3d_{5/2}$ (368.2 eV) from foil samples. The samples were introduced into an ultrahigh-vacuum (UHV) chamber of the spectrometer (1.05×10^{-8} Torr) and measured at 24 °C (room temperature). The spot size in the beam was 100 μm. The pressure did not change during the analysis, and 10 scans for Au 4f were done with energy step size of 0.1 eV. The binding energies were referenced to the C 1s peak at 284.3 eV. From all spectra, a Shirley background was subtracted to perform the peak fitting with a symmetric Gauss-Lorentz sum function (*SpecSurf* software).

UV−vis Spectroscopy. Absorption spectra in the range 400−700 were obtained with a PerkinElmer Lambda-Bio spectrometer using 1 cm quartz cuvette. Nanoconjugates were measured by UV−vis analysis to monitor the AuNP surface plasmon resonance band (520 nm) shift.

Preparation of ^{99m}Tc-EDDA/HYNIC-GGC-AuNP-c[RGDfK(C)] (^{99m}Tc-AuNP-RGD) and ^{99m}Tc-EDDA/HYNIC-GGC-AuNP (^{99m}Tc-AuNP). *^{99m}Tc-EDDA/HYNIC-GGC.* To 5 μL of HYNIC-GGC (0.5 mg/mL, injectable-grade water) 0.5 mL of EDDA-tricine solution was added, which was prepared by mixing 30 mg of EDDA (*N*,*N*-ethylene diamine diacetic acid) in 1.5 mL of 0.1 M NaOH and 60 mg of tricine (*N*-tris[hydroxymethyl]methylglycine) in 1.5 mL of 0.2 M phosphate buffer, pH = 7. Finally, 10 μL of a freshly prepared anhydrous stannous chloride solution (1 mg/mL in 0.012 M HCl) was added, followed immediately by 1000−2400 MBq (0.5 mL) of ^{99m}Tc-pertechnetate, and then incubation at 92 °C for 20 min in a dry block heater. A radiochemical purity of ^{99m}Tc-EDDA/HYNIC-GGC higher than 95% was verified by ITLC-SG analyses using two different mobile phases: 2-butanone to determine the amount of free $^{99m}TcO_4^-$ (R_f =1), and methanol/1 M ammonium acetate (1:1 v/v) for ^{99m}Tc-colloid (R_f = 0). R_f values of the radiolabeled peptide in these three systems were 0.0 and 0.7−1.0, respectively.

^{99m}Tc-AuNP-RGD. To 1.5 mL of AuNP solution (1 nM, 1.05×10^{12} particles) 120 μL (120−288 MBq) of ^{99m}Tc-EDDA/HYNIC-GGC (0.3 μg of peptide; 4.9×10^{14} molecules of HYNIC-GGC; ∼465 HYNIC-GGC molecules per AuNP) was added. After 1 min of stirring, 10 μL of c[RGDfK(C)] (50 μM; 3×10^{14} molecules of peptide; peptide:AuNP ratio 285:1) was added with stirring for 15 min. No further purification was carried out. In order to determine the exact number of peptide molecules per AuNP, in some experiments AuNPs were removed from the ^{99m}Tc-AuNP-RGD solution (1 mL) by ultrafiltration (Ultrafree-PF filters 10 000 NWWL, Millipore), and the free peptide concentration was quantified by UV-HPLC with a 1 mL injector-loop following the procedure described above.

^{99m}Tc-AuNP. To 1.5 mL of AuNP solution (1 nM, 1.05×10^{12} particles), 120 μL (120−288 MBq) of ^{99m}Tc-EDDA/HYNIC-GGC (0.3 μg of peptide; 4.9×10^{14} molecules of HYNIC-GGC; ∼465 HYNIC-GGC molecules per AuNP) was added, and after 3 min under stirring, 25 μL of HYNIC-GGC (50 μM; 7.5×10^{14} molecules of peptide; peptide/AuNP ratio 715:1) was added. No further purification was carried out.

Radiochemical Purity of Radiolabeled AuNP. ITLC-SG/2-butanone (R_f value of the radiolabeled AuNP and ^{99m}Tc-EDDA = 0.0 and 1.0 for $^{99m}TcO_4^-$) and size-exclusion chromatography were used as radiochemical control methods for the final radiopharmaceutical solution. In a PD-10 column, using injectable water as eluent, the first and red radioactive eluted peak (3.0−4.0 mL) corresponds to the radiolabeled AuNP; the free radiolabeled peptide appears at the 5.0−7.0 mL eluted fraction, and $^{99m}TcO_4^-$ remains trapped in the column matrix. In the HPLC system (ProteinPak 300SW, Waters, 1 mL/min, injectable water), radiolabeled AuNP showed t_R = 4.5−5 min, t_R = 8 min for free ^{99m}Tc-peptide, and t_R = 11 min for $^{99m}TcO_4^-$. Ultrafiltration was also used as described above; radiolabeled AuNP remained in the filter, free ^{99m}Tc-peptide and $^{99m}TcO_4^-$ pass through the filter.

Preparation of ^{99m}Tc-EDDA/HYNIC-cRGDyK (^{99m}Tc-RGD). In order to compare the *in vivo* biodistribution between multimeric and monomeric RGD systems, a lyophilized formulation containing 20 μg of HYNIC-cRGDyK (Pichem Co., Austria), EDDA (10 mg), tricine (20 mg), mannitol (50 mg), and stannous chloride (0.02 mg) was prepared. The radiolabeling procedure was carried out by adding 1 mL of 0.2 M phosphate buffer pH 7.0 to the freeze−dried kit formulation and immediately adding 740−1110 MBq (1 mL) of ^{99m}Tc-pertechnetate followed by incubation in boiling water for 15 min. A radiochemical purity of ^{99m}Tc-RGD higher than 95% was verified by ITLC-SG analyses using three different mobile phases: 2-butanone to determine the amount of free $^{99m}TcO_4^-$ (R_f = 1), 0.1 M sodium citrate pH 5 to determine ^{99m}Tc-EDDA, and $^{99m}TcO_4^-$ (R_f = 1), and methanol/1 M ammonium acetate (1:1 v/v) for ^{99m}Tc-colloid (R_f = 0). R_f values of the radiolabeled peptide in these three systems were 0.0, 0.0, and 0.7−1.0, respectively.

***In Vitro* Stability Assay of ^{99m}Tc-AuNP-RGD in Human Serum.** To determine the stability of ^{99m}Tc-AuNP-RGD in serum, 200 μL of radiolabeled gold nanoparticles was diluted in the ratio 1:5 with fresh human serum and incubated at 37 °C. The chemical stability was determined by UV−vis analysis to monitor the AuNP surface plasmon resonance band (520 nm) at 1 and 24 h after dilution. Radiochemical stability was determined by taking samples of 0.01 mL at 1 and 24 h for ITLC-SG/2-butanone analysis and ultrafiltration as described above.

***In Vitro* Binding Assay.** Integrin $\alpha_v\beta_3$ receptor-positive C6 glioma cells (originally obtained from ATCC, USA) supplied in fresh medium were centrifuged at 2000 *g* for 20 min, and the pellet was diluted to 1×10^6 cells/tube with binding buffer (0.6 mL, pH 7.5; 1 M NaCl, 0.05 M $CaCl_2$, 0.05 M $MgCl_2$, 0.05 M Tris-HCl, 0.1% human serum albumin) and incubated with 0.05 mL (3.7 MBq) of ^{99m}Tc-AuNP-RGD or ^{99m}Tc-AuNP (n = 4) at 37 °C for 24 h. The test tubes were centrifuged at 2000 *g* for 20 min and washed with injectable water, and the activity of the cell pellet was determined in a crystal well-type scintillation detector. An aliquot with the initial activity was taken to represent 100%, and the percent of cell uptake activity was then calculated. Nonspecific binding (blocked $\alpha_v\beta_3$ integrin receptors) was determined in parallel, in the presence of 10 μM cRGDfK (Bachem, USA), with 1 h of preincubation.

***In Vivo Studies*.** Athymic female mice (20−25 g) were used. Tumors were induced by subcutaneous injection of C6 glioma cells (1×10^6 cells suspended in 200 μL of phosphate-buffered saline) in the dorsal surface of the scapula. The sites of injection were observed at regular intervals for the appearance of tumor formation and progression. The tumor type and tumor size play an important role in the radiopeptide uptake;[2] therefore, only mice with tumors between 0.1 and 0.3 g were selected in order to diminish the biological variability due to the physiologic nature of $\alpha_v\beta_3$ expression. All experiments were carried out in agreement with the Official Mexican Norm 062-ZOO-1999 for laboratory animal handling. Mice were kept in sterile cages with a sterile wood-shavings bed, constant temperature, humidity, noise, and 12:12 h light periods. Water and feed (standard PMI 5001 feed) were given *ad libitum*.

Biodistribution Studies. Ten groups (n = 3) of athymic nude mice bearing C6 human gliomas (20−25 g) were used. ^{99m}Tc-AuNP-RGD (3.7 MBq, 0.05 mL) was injected in the tail vein (four groups) or intraperitoneally (four groups). Complete dissection was carried out at 0.5, 1, 3, or 24 h. Whole heart, spleen, pancreas, and kidneys and samples of tumor, lung, liver, brain, blood, intestines, and muscle were saline-rinsed, paper-blotted, and placed into preweighed plastic test tubes. The activity was determined in a well-type scintillation detector (Canberra) along with 6 × 0.5 mL aliquots of the diluted standard representing

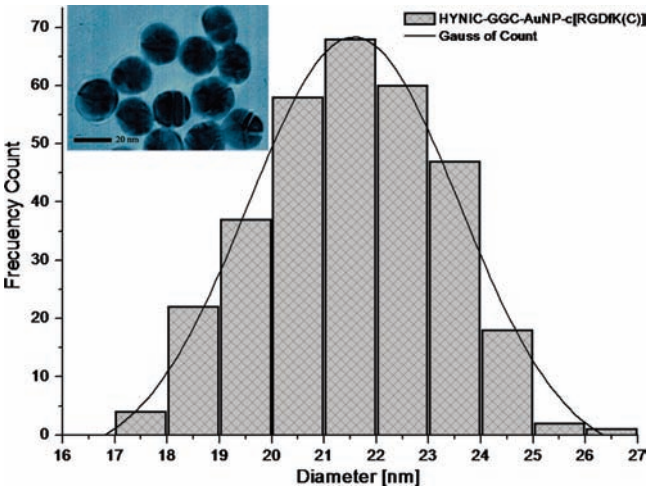


Figure 2. TEM image and size distribution of HYNIC-GGC-AuNP-c[RGDfK(C)].

100% of the injected dose. Mean activities were used to obtain the percentage of injected dose per gram of tissue (% ID/g).

A blocking study was performed in two groups of three athymic nude mice bearing C6 human gliomas. One hundred microliters (0.1 mM) of unlabeled cRGDfK (Bachem) was intraperitoneally administered one hour before intravenous ($n = 3$) or intraperitoneal ($n = 3$) injection of ^{99m}Tc-AuNP-RGD (3.7 MBq, 0.05 mL), and complete dissection was carried out 1 h after radiopharmaceutical administration, as described above.

^{99m}Tc-AuNP or ^{99m}Tc-RGD (monomer) were also administered in athymic mice with a C6-induced tumor and complete dissection carried out at 1 h after administration ($n = 3$).

Imaging Studies. Three mice with the implanted tumors were i.v. injected with 0.1 mL (7.4 MBq) of ^{99m}Tc-AuNP-RGD and anaesthetized with isoflurane 1 h later. Static images were obtained using a micro-SPECT/PET/CT system (ONCOVISION, Spain).

Statistical Analysis. Comparisons between groups in the binding assay and blocking assay were made using Student's t test (significance was defined as $P < 0.05$).

RESULTS

Chemical Characterization. *TEM.* Images of HYNIC-GGC-AuNP-c[RGDfK(C)] showed monodispersed solutions with an average particle diameter of 21.70 ± 0.07 nm. A higher diameter was observed with respect to AuNP stabilized with citrate (18.64 ± 0.13 nm) due to an increase of the hydrodynamic diameter. It was possible to observe a "corona" around the gold nanoparticle due to the poor interaction of the electron beam with the peptide molecules (low electron density), in contrast to the strong scattering of the electron beam when it interacted with the metallic nanoparticles (Figure 2).

IR Spectroscopy. In the c[RGDfK(C)] spectrum, the weak bands at 2574 cm^{-1} and at 722 cm^{-1} corresponding to the thiol (−SH) in AuNP-c[RGDfK(C)] disappeared, suggesting the formation of thiolate (−S−AuNP).[20] The strong band at 1636 cm^{-1} assigned to the guanidine group (C−N stretch vibration) in c[RGDfK(C)] was shifted to 1677 cm^{-1}, indicating some weak interaction on the AuNP surface.[21] In the HYNIC-GGC-AuNP-c[RGDfK(C)] spectrum, amide I (~1646 cm^{-1}, C═O stretching) and amide II (~1550 cm^{-1}, N−H bending) regions were shifted to higher energy by 20 cm^{-1} with respect to the free peptides, confirming the presence of peptides on the AuNP surface.

Raman Spectra. AuNP functionalized with c[RGDfK(C)] yielded a structured Raman spectrum in the 1800−600 cm^{-1} region (Figure 3). Several well-defined bands were observed with vibrational frequencies in the region of those associated with the main functional groups seen in the c[RGDfK(C)] spectrum, but they were characteristic of AuNP-c[RGDfK(C)] and HYNIC-GGC-AuNP-c[RGDfK(C)] because of shifts to lower or higher energies and increases in the band intensities (Figure 3). The 1605 cm^{-1} band observed in the c[RGDfK(C)] spectrum was assigned to the arginine guanidinium group (CN_3, stretch), and in the AuNP-c[RGDfK(C)] spectrum, the band shifted to 1611 cm^{-1} and increased in intensity, which indicates some interaction on the AuNP surface.[22] Gold nanoparticle interactions with amide groups AI (C═O, stretch), AII (N−H, bend), and AIII (C−N stretch) were also observed (1693 cm^{-1}, 1549 cm^{-1}, and 1231 cm^{-1}, respectively).

XP Spectroscopy. The AuNP spectrum (Figure 4) showed two main peaks corresponding to the binding energies (B.E., eV) of electrons in Au 4f orbitals at 87.0 eV (Au $4f_{5/2}$) and 83.4 eV (Au $4f_{7/2}$) with a characteristic difference of 3.6 eV and an intensity ratio of 3:4 between the two peaks.[23] The AuNP-c[RGDfK(C)] spectrum (Figure 4) showed two main peaks at 87.3 and 83.7 eV with a positive shift of 0.3 eV and a third peak at 89.1 eV due to atoms with different oxidative states.[17,23] The HYNIC-GGC-AuNP-c[RGDfK(C)] spectrum revealed a peak at 84.0 eV with a positive shift of 0.6 eV with respect to Au $4f_{7/2}$ of citrate-stabilized nanoparticles. The peak that correlated with the Au $4f_{5/2}$ orbital appeared at 87.4 eV, and the deconvoluted spectrum showed peaks at 87.4, 88.1, and 89.0 eV (Figure 4). The orbital energies of Au−Au or Au−citrate (Au^0) and Au−S- (Au^{1+}) bounds are related to changes in the oxidative states (Au^0 to Au^{1+}), so the shift of electron binding energies to higher values is an intrinsic property of the interaction between gold core electrons and peptides.[23]

UV−vis Spectroscopy. The AuNP spectrum showed a surface plasmon resonance at 520 nm. A red-shift to 522 nm was observed in the AuNP-c[RGDfK(C)] and HYNIC-GGC-AuNP-c[RGDfK(C)] spectra due to changes in the refraction index and the surrounding dielectric medium as a consequence of the interaction between the peptide and the AuNP surface.[24,25]

Preparation of ^{99m}Tc-AuNP-RGD and ^{99m}Tc-AuNP. After the labeling procedure, the radiochemical purity of ^{99m}Tc-AuNP-RGD and ^{99m}Tc-AuNP was 96 ± 2% ($n = 20$) without postlabeling purification. In both radiopharmaceuticals, the specific activity was 80−192 GBq/nmol. In the ^{99m}Tc-AuNP-RGD solution, the total number of HYNIC-GGC peptide molecules per AuNP was 460 (1.05×10^{12} gold particles and 1.05×10^{14} HYNIC-GGC molecules in 1.5 mL) and the total number of RGDfK(C) molecules per AuNP was at least 200 (1.05×10^{12} gold particles and 3×10^{14} HYNIC-GGC molecules in 1.5 mL), since no free peptide was detected by UV-HPLC (detection limit 0.1 μg at 260 nm = 5×10^{13} peptide molecules).

Human Serum Stability. ^{99m}Tc-AuNP-RGD diluted in human serum was stable over 24 h, because at this time, the radiochemical purity was 92.0 ± 1.1%. The SPR, characteristic of gold nanoparticles, remained stable and shifted slightly to higher energy (524 nm) because of protein interactions (Figure 5).

***In Vitro* Cell Binding Assay.** As shown in Table 1, ^{99m}Tc-AuNP-RGD had specific recognition, because the $\alpha_v\beta_3$ integrin receptor-positive cell uptake was 2.3 times higher with respect to that of ^{99m}Tc-AuNP ($p < 0.05$), and its specificity was confirmed

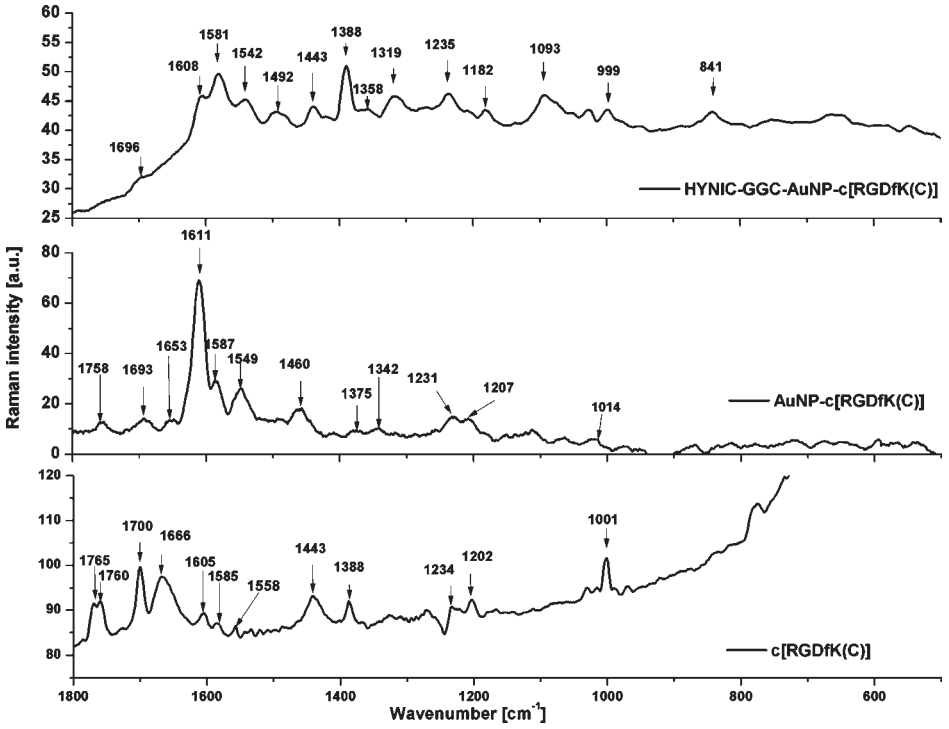


Figure 3. Raman spectra of c[RGDfK(C)], AuNP-c[RGDfK(C)], and HYNIC-GGC-AuNP-c[RGDfK(C)].

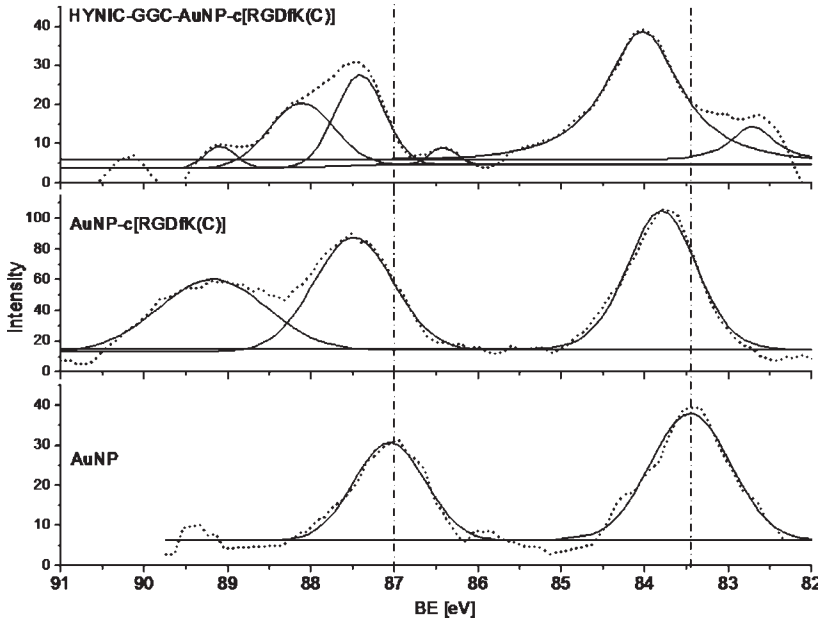


Figure 4. XPS spectra of c[RGDfK(C)], AuNP-c[RGDfK(C)], and HYNIC-GGC-AuNP-c[RGDfK(C)]. Experimental bands (dotted line) and deconvoluted experimental bands (solid line).

with the receptor blocking study (Table 1). The ^{99m}Tc-AuNP accumulation (14.97 ± 2.39%) in C6 cells could have been related to a passive uptake, because gold nanoparticles can be taken up by all mammalian cells due to their nanometric size (20 nm),[26] but with the conjugation of c[RGDfK(C)] to AuNPs, the tumor cell uptake was significantly increased (34.72 ± 1.42%). The significant difference in cell binding results (34.72% vs 14.97%) was due to active targeting, meaning specific $\alpha_v\beta_3$ integrin receptor recognition.

***In Vivo* Studies.** Biodistribution studies (Table 2, Table 3, and Figure 6) and *in vivo* micro-SPECT/CT images of mice (Figure 7) after ^{99m}Tc-AuNP-RGD administration showed evident tumor uptake via intravenous injection (3.65 ± 0.19% i.a. at 1 h) as well as intraperitoneal injection (8.18 ± 0.57% i.a. at 3 h). Liver and spleen uptake were significant due to their radiopharmaceutical colloidal nature. Tumor-to-blood, tumor-to-muscle, tumor-to-liver, and tumor-to-spleen ratios were 7.4, 10.0, 0.2, and 0.7, respectively, for the intravenous administration at 1 h; and for the intraperitoneal

dx.doi.org/10.1021/bc100551s |*Bioconjugate Chem.* 2011, 22, 913–922

administration, these ratios were 20.5 (tumor-to-blood), 27.3 (tumor-to-muscle), 2.1 (tumor-to-liver), and 3.4 (tumor-to-spleen). These results were expected because intravenous administration of nanoparticles results in opsonization followed by substantial uptake by macrophages present in the liver and spleen. The *in vivo* ^{99m}Tc-AuNP-RGD tumor uptake was significantly higher ($P < 0.05$) than that of ^{99m}Tc-AuNP or ^{99m}Tc-RGD (monomeric system) at 1 h after i.v. administration. Recently, Sadauskas et al.[27] demonstrated that the intraperitoneal mode of administration results in minimal uptake of AuNPs by Kupffer cells in the liver as compared to the intravenous route, and Chanda et al.[28] found that intraperitoneal injection of AuNP decreases uptake by organs of the reticuloendothelial system while maximizing receptor-mediated uptake in desired sites. Nevertheless, the maximum tumor uptake is faster (at 1 h) with the intravenous mode of administration and maybe more convenient for diagnostic imaging purposes than with the intraperitoneal mode (maximum tumor uptake at 3 h), in which there is a radiopharmaceutical absorption process and some remaining abdominal activity.

The specificity was confirmed by a receptor blocking study, in which the previous injection of cRGDfK diminished the activity in tumors. Reductions in tumor uptake percentages were 60% with intravenous administration (3.65% ID/g vs 1.46% ID/g, $P < 0.05$) and 64% with intraperitoneal administration (3.28% ID/g vs 1.18% ID/g, $P < 0.05$) (Tables 2 and 3). In general, the blood activity was slightly but significantly higher in the blocked groups with respect to unblocked. The uptake in nontargeted tissues was not significantly reduced by the blocking dose.

In spite of gold nanoparticles being taken up by all mammalian cells due to their nanometric size, ^{99m}Tc-AuNP-RGD was not taken up by all cells in the whole body of mice because nanoparticles cannot cross normal blood vessels (normal endothelium: gaps ~2−5 nm). As expected, the major accumulation occurred in the tumor (cancer endothelium: gaps ~400−800 nm) and reticuloendothelial system organs.

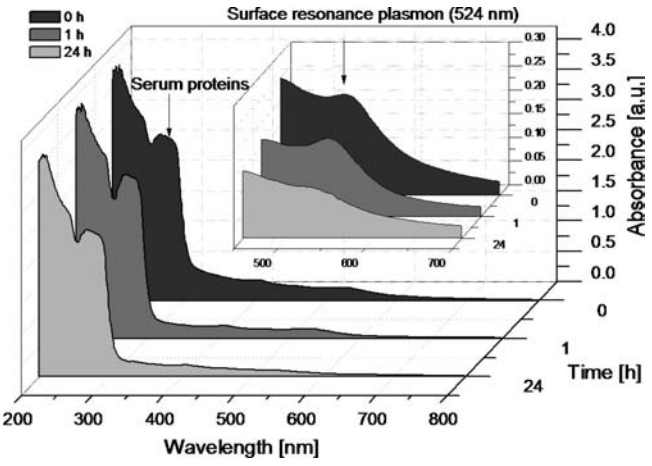


Figure 5. Stability in human serum of ^{99m}Tc-AuNP-RGD. Surface plasmon resonance (524 nm) remained stable for 24 h.

DISCUSSION

TEM and spectroscopy techniques demonstrated that AuNPs were functionalized with HYNIC-GGC and c[RGDfK(C)] through thiol groups and the presence of peptide molecules on the AuNP surface.

The aim of the development of cancer-receptor-specific AuNPs is to maximize the binding affinity via multimeric peptides based on the multivalency principle. For the multimeric RGD system reported in this study and intravenously administered, the C6 tumor-to-muscle ratio was 10 at 1 h, which is similar to that reported for tetrameric (U87MG tumor-to muscle ratio ≈ 10) and

Table 1. C6 Cell Uptake of ^{99m}Tc-AuNP-RGD and ^{99m}Tc-AuNP in Unblocked and Blocked RGD Receptors at 24 h (% of Total Activity ± SD, $n = 4$)

radiopharmaceutical	unblocked receptors (mean ± SD)	blocked receptors[a] (mean ± SD)
^{99m}Tc-AuNP-RGD	34.72 ± 1.42[b]	14.54 ± 1.93[b]
^{99m}Tc-AuNP	14.97 ± 2.39[b,c]	13.96 ± 0.95

[a] Blocked receptors were incubated with an additional RGDfK blocking dose to determine the nonspecific binding of radioactivity. [b] Significant difference ($P < 0.05$) between unblocked and blocked RGD-receptors. [c] Significant difference ($P < 0.05$) between ^{99m}Tc-AuNP-RGD and ^{99m}Tc-AuNP.

Table 2. Biodistribution in Mice with C6-Induced Tumors after Intravenous Administration of ^{99m}Tc-AuNP-RGD, Expressed as a Percentage of the Injected Dose per Gram of Tissue (% ID/g) (mean ± SD, $n = 3$)

	unblocked				blocked[a]
tissue	0.5	1	3	24	1
blood	1.41 ± 0.08	0.49 ± 0.04[b]	0.55 ± 0.06	0.22 ± 0.07	0.98 ± 0.20[b]
heart	1.34 ± 0.16	0.36 ± 0.09	0.44 ± 0.03	0.28 ± 0.11	0.33 ± 0.07
lung	2.31 ± 0.24	0.94 ± 0.13	1.21 ± 0.11	0.43 ± 0.10	0.73 ± 0.22
liver	21.76 ± 3.73	19.89 ± 2.42	5.57 ± 1.04	6.06 ± 0.73	18.48 ± 1.98
pancreas	0.51 ± 0.06	0.62 ± 0.08	0.33 ± 0.16	0.58 ± 0.09	0.55 ± 0.06
spleen	5.53 ± 0.16	5.54 ± 0.77	5.30 ± 0.82	1.47 ± 0.33	4.96 ± 0.82
kidneys	3.02 ± 0.29	2.42 ± 0.38	2.96 ± 0.16	1.46 ± 0.18	2.63 ± 0.17
intestine	1.88 ± 0.11	1.74 ± 0.15	1.71 ± 0.17	0.66 ± 0.10	1.97 ± 0.26
muscle	0.42 ± 0.02	0.36 ± 0.08	0.16 ± 0.01	0.12 ± 0.01	0. 69 ± 0.18
bone	0.93 ± 0.15	0.08 ± 0.07	0.11 ± 0.03	0.13 ± 0.05	0.12 ± 0.02
brain	0.22 ± 0.12	0.35 ± 0.10	0.03 ± 0.01	0.03 ± 0.02	0.41 ± 0.20
C6 Tumor	**3.48 ± 0.21**	**3.65 ± 0.19**[b]	**2.49 ± 0.13**	**1.94 ± 0.23**	**1.46 ± 0.23**[b]

[a] Blocked with an additional intraperitoneal cold cRGDfK blocking dose 1 h prior to administration of ^{99m}Tc-AuNP-RGD to determine the nonspecific binding of radioactivity. [b] Significant difference ($P < 0.05$) between unblocked and blocked c[RGDfK(C)]-receptors.

dx.doi.org/10.1021/bc100551s |*Bioconjugate Chem.* 2011, 22, 913–922

Table 3. Biodistribution in Mice with C6-Induced Tumors after Intraperitoneal Administration of ^{99m}Tc-AuNP-RGD, Expressed as a Percentage of the Injected Dose Per Gram of Tissue (% ID/g) (mean ± SD, n = 3)

	unblocked				blocked[a]
tissue	0.5	1	3	24	1
blood	0.06 ± 0.02	0.16 ± 0.02[b]	0.46 ± 0.07	0.03 ± 0.01	0.82 ± 0.18[b]
heart	0.07 ± 0.03	0.15 ± 0.06	0.40 ± 0.08	0.04 ± 0.02	0.18 ± 0.09
lung	0.33 ± 0.07	0.21 ± 0.09	0.23 ± 0.04	0.10 ± 0.01	0.31 ± 0.17
liver	0.53 ± 0.03	1.57 ± 0.18	2.28 ± 0.04	1.52 ± 0.05	1.33 ± 0.21
pancreas	0.96 ± 0.08	1.46 ± 0.21	1.18 ± 0.14	1.26 ± 0.20	0.99 ± 0.11
spleen	0.43 ± 0.05	0.98 ± 0.16	1.79 ± 0.14	1.06 ± 0.17	1.14 ± 0.22
kidneys	0.66 ± 0.03	1.35 ± 0.12	2.77 ± 0.10	1.60 ± 0.06	1.62 ± 0.13
intestine	0.34 ± 0.07	0.78 ± 0.09	0.92 ± 0.14	0.47 ± 0.08	0.83 ± 0.13
muscle	0.05 ± 0.02	0.12 ± 0.01	0.07 ± 0.02	0.07 ± 0.01	0.05 ± 0.01
bone	0.07 ± 0.01	0.16 ± 0.06	0.05 ± 0.03	0.06 ± 0.01	0.17 ± 0.09
brain	0.03 ± 0.01	0.10 ± 0.03	0.02 ± 0.01	0.01 ± 0.01	0.02 ± 0.01
C6 Tumor	**2.09 ± 0.35**	**3.28 ± 0.28**[b]	**8.18 ± 0.57**	**3.20 ± 0.19**	**1.18 ± 0.15**[b]

[a] Blocked with an additional intraperitoneal cold cRGDfK blocking dose 1 h prior to administration of ^{99m}Tc-AuNP-RGD to determine the nonspecific binding of radioactivity. [b] Significant difference (P < 0.05) between unblocked and blocked c[RGDfK(C)]-receptors.

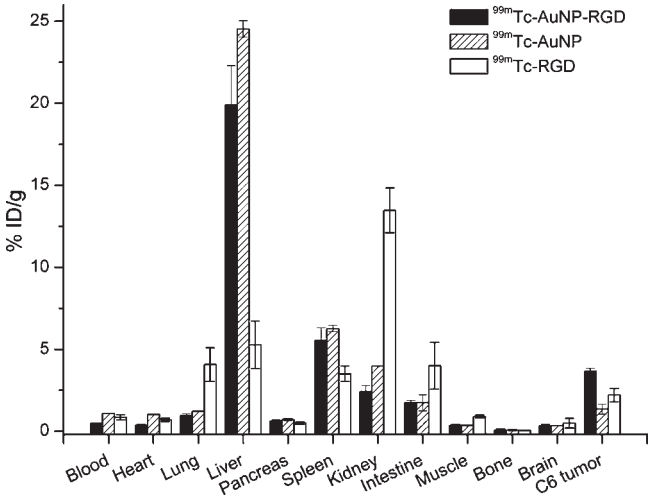


Figure 6. Biodistribution of ^{99m}Tc-AuNP-RGD, ^{99m}Tc-AuNP, and ^{99m}Tc-RGD (monomer) in athymic mice with a C6-induced tumor at 1 h after i.v. administration (n = 3). Tumor uptake was significantly higher (P < 0.05) for the ^{99m}Tc-AuNP-RGD multimeric system with respect to ^{99m}Tc-RGD or ^{99m}Tc-AuNP.

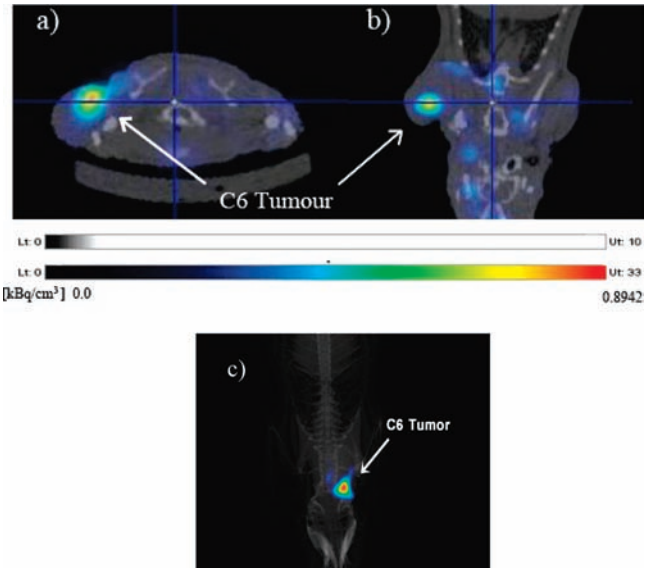


Figure 7. (a) Transaxial and (b) coronal micro-SPECT/CT images of an athymic mouse with a C6-induced tumor 1 h after ^{99m}Tc-AuNP-RGD intravenous administration. (c) Coronal micro-SPECT/CT image of an athymic mouse with a C6-induced tumor 3 h after ^{99m}Tc-AuNP-RGD intraperitoneal administration. SPECT image in the abdominal region was not included to highlight tumor uptake.

octameric (U87MG tumor-to muscle ratio ≈ 11) RGD peptides.[6] However, it is important to mention that the number of $\alpha_v\beta_3$ integrin receptors per cell in C6 gliomas is, on average, 1480, and in U87MG gliomas, the number is 2 orders of magnitude higher (128 000 receptors/cell).[29] Because the integrin $\alpha_v\beta_3$ level on tumor cells plays a significant role in radiopharmaceutical tumor uptake, it is expected that, in tumors with high $\alpha_v\beta_3$ density and therefore with short distances between integrin receptors, the multimeric ^{99m}Tc-AuNP-RGD radiopharmaceutical will achieve easier multivalency with a significant increase in the tumor uptake. For example, Liu et al.[30] investigated the biodistribution of ^{64}Cu-labeled single-walled carbon nanotubes (SWNTs) conjugated to PEG and RGD in mice with U87MG-induced tumors by positron emission tomography (PET) and ex vivo biodistribution, obtaining a high tumor conjugate accumulation (~7% at 1 h), which was attributed to the multivalent effect of the SWNTs.[30] Furthermore, ^{99m}Tc-AuNP-RGD does not have linkers with long chains as spacers between AuNP and RGD or RGD-RGD molecules, since it has been proven that the introduction of spacers and the increase of linker lengths significantly affecting the RGD multivalency effect may be related to the decrease of the effective RGD molarity.[31]

Detailed procedures for the preparation of RGD conjugated to other nanoparticles such as quantum dots or nanocrystals (semiconductor nanoparticles, 2−10 nm) have been reported with successful results to obtain *in vivo* imaging of human glioblastoma or melanoma tumors based on fluorescence imaging.[32,33] Recently, near-infrared gold nanoparticles (nanorods, 42 nm in

length, 10 nm in width) have proven useful as a new class of tracers for photothermal therapy, although they could also be used for near-infrared (NIR, 700−1000 nm wavelength) fluorescence-based imaging.[34] However, in human tissues these optical imaging methods have poor spatial resolution and limited optical signal penetration depth (<7 mm by fluorescence resonance imaging). ^{99m}Tc-AuNP-RGD could be used to detect tumor angiogenesis by binding to the specific $\alpha_v\beta_3$ receptor and producing images with high spatial resolution (e.g., 1.6 mm) and no depth limit in soft tissue, because nuclear imaging is an established clinical molecular imaging modality that offers good sensitivity deep in tissue.

Because of its colloidal nature, the intravenous administration of ^{99m}Tc-AuNP-RGD showed high spleen and liver uptake, which was significantly reduced when the intraperitoneal administration mode was used. However, this multimeric system (i.v. or i.p. administration) could be successfully used, for example, to acquire transaxial, coronal, and sagittal tomographic images using single-photon emission computed tomography (SPECT) or SPECT/CT systems for early detection of a primary breast tumor (by $\alpha_v\beta_3$ overexpression in both endothelial and breast cancer cells) and the involved axillary lymph nodes because the abdominal background-radiation interference would be minimal in breast cancer patients. Molecular imaging of $\alpha_v\beta_3$ integrin expression during tumor angiogenesis using ^{99m}Tc-AuNP-RGD could be useful in visualizing and quantifying $\alpha_v\beta_3$ expression level, in selecting patients more appropriately, and in monitoring treatment efficacy in $\alpha_v\beta_3$-positive patients.

CONCLUSIONS

TEM and spectroscopy techniques demonstrated that AuNPs can be successfully conjugated to HYNIC-GGC and c[RGDfK-(C)] through interactions with the thiol groups of cysteine. ^{99m}Tc-AuNP-RGD, with radiochemical purity ≥94%, is highly stable in human serum and shows high and specific $\alpha_v\beta_3$-positive tumor uptake in mice. Therefore, it is a potential target-specific radiopharmaceutical for molecular imaging of tumor $\alpha_V\beta_3$ expression.

AUTHOR INFORMATION

Corresponding Author

*Guillermina Ferro-Flores, Ph.D., Departamento de Materiales Radiactivos, Instituto Nacional de Investigaciones Nucleares, Carretera México-Toluca S/N, La Marquesa, Ocoyoacac, Estado de México, C.P. 52750, México. Tel + (52) (55)-53297200 ext. 3863. Fax + (52) (55)-53297306. e-mail: ferro_flores@yahoo.com.mx; guillermina.ferro@inin.gob.mx.

ACKNOWLEDGMENT

This study was supported by the Mexican National Council of Science and Technology (CONACYT-SEP-CB-2010-01-150942) and the International Atomic Energy Agency (Contract No. 14539/RO). The authors wish to thank Dr. Manuel Espinosa and M.C. Isidoro Martínez for their support during TEM analyses, Dr. Marco A. Camacho-López and Dr. F. de M. Ramírez for the vibrational spectroscopy analyses, and Dr. Pedraza and Dr. Murphy for the animal acquisition.

REFERENCES

(1) Liu, S. (2006) Radiolabeled multimeric cyclic RGD peptides as integrin alphavbeta3 targeted radiotracers for tumor imaging. *Mol. Pharmaceutics 3*, 472–487.

(2) Liu, S. (2009) Radiolabeled cyclic RGD peptides as integrin $\alpha v\beta 3$-targeted radiotracers: maximizing binding affinity via bivalency. *Bioconjugate Chem. 20*, 2199–2213.

(3) Haubner, R., and Decristoforo, C. (2009) Radiolabeled RGD peptides and peptidomimetics for tumor targeting. *Front. Biosci. 14*, 872–886.

(4) Mitrasinovic, P. M. (2009) Advances in $\alpha(v)\beta(3)$ integrin-targeting cancer therapy and imaging with radiolabeled RGD peptides. *Curr. Radiopharm. 2*, 214–219.

(5) Montet, X., Funovics, M., Montet-Abou, K., Weissleder, R., and Lee, J. (2006) Multivalent effects of RGD peptides obtained by nanoparticle display. *J. Med. Chem. 49*, 6087–6093.

(6) Li, Z., Cai, W., Cao, Q., Chen, K., Wu, Z., and Chen, X. (2007) ^{64}Cu-Labeled tetrameric and octameric RGD peptides for small-animal PET of tumor integrin $\alpha v\beta 3$ expression. *J. Nucl. Med. 48*, 1162–1171.

(7) Bhattacharya, R., and Mukherjee, P. (2008) Biological properties of "naked" metal nanoparticles. *Adv. Drug Delivery Rev. 60*, 1289–306.

(8) Kogan, M. J., Olmedo, I., Hosta, L., Guerrero, A. R., Cruz, L. J., and Albericio, F. (2007) Peptides and metallic nanoparticles for biomedical applications. *Nanomedicine 2*, 287–306.

(9) Levy, R., Thanh, N. T. K., Doty, R. C., Hussain, I., Nichols, R. J., and Schiffrin, D. J. (2004) Rational and combinatorial design of peptide capping ligands for gold nanoparticles. *J. Am. Chem. Soc. 126*, 10076–10084.

(10) De la Fuente, J. M., and Berry, C. C. (2005) Tat peptide as an efficient molecule to translocate gold nanoparticles into the cell nucleus. *Bioconjugate Chem. 16*, 1176–1180.

(11) Porta, F., Speranza, G., Krpetic, Z., Santo, V. D., Francescato, P., and Scari, G. (2007) Gold nanoparticles capped by peptides. *Mater. Sci. Eng., B 140*, 187–194.

(12) Olmedo, I., Araya, E., Sanz, F., Medina, E., Arbiol, J., and Toledo, P. (2008) How changes in the sequence of the peptide CLPFFD-NH2 can modify the conjugation and stability of gold nanoparticles and their affinity for beta-amyloid fibrils. *Bioconjugate Chem. 19*, 1154–1163.

(13) Surujpaul, P. P., Gutierrez-Wing, C., Ocampo-Garcia, B., Ramirez, F., de, M., Arteaga de Murphy, C., Pedraza-Lopez, M., Camacho-Lopez, M. A., and Ferro-Flores, G. (2008) Gold nanoparticles conjugated to [Tyr3]octreotide peptide. *Biophys. Chem. 138*, 83–90.

(14) Ferro-Flores, G., Ocampo-Garcia, B. E., Ramirez, F. de M., Gutierrez-Wing, C., Arteaga de Murphy, C., and Santos-Cuevas, C. L. Gold Nanoparticles Conjugated to Peptides, in *Colloids in Biothechnology* (Fanum, M., Ed.) pp 231−252, CRC Press/Taylor & Francis, Boca Raton, FL, 2010.

(15) Mendoza-Sanchez, A. N., Ferro-Flores, G., Ocampo-Garcia, B. E., Morales-Avila, E., Ramirez, F., de, M., Leon-Rodriguez, L. M., Santos-Cuevas, C. L., Medina, L. A., Rojas-Calderon, E. L., and Camacho-Lopez, M. A. (2010) Lys^3-bombesin conjugated to ^{99m}Tc-labeled gold nanoparticles for *in vivo* gastrin releasing peptide-receptor imaging. *J. Biomed. Nanotechnol. 6*, 375–384.

(16) Ocampo-Garcia, B. E., Ramirez, F., de, M., Ferro-Flores, G., Leon-Rodriguez, L. M., Santos-Cuevas, C. L., Morales-Avila, E., Arteaga de Murphy, C., Pedraza-Lopez, M., Medina, L. A., and Camacho-Lopez, M. A. (2011) ^{99m}Tc-labeled gold nanoparticles capped with HYNIC-peptide/mannose for sentinel lymph node detection. *Nucl. Med. Biol. 38*, 1–11.

(17) Jadzinsky, P. D., Calero, G., Ackerson, C. J., Bushnell, D. A., and Komberg, R. D. (2007) Structure of a thiol monolayer-protected gold nanoparticle at 1.1 A resolution. *Science 318*, 430–433.

(18) Decristoforo, C., Faintuch-Linkowski, B., Rey, A., von Guggenberg, E., Rupprich, M., and Hernandez, G. I. (2006) [^{99m}Tc]HYNIC-RGD for imaging integrin $\alpha_v\beta_3$ expression. *Nucl. Med. Biol. 33*, 945–952.

(19) Miranda-Olvera, A. D., Ferro-Flores, G., Pedraza-Lopez, M., Murphy, C. A., and Leon-Rodriguez, L. M. (2007) Synthesis of oxytocin HYNIC derivatives as potential diagnostic agents for breast cancer. *Bioconjugate Chem. 18*, 1560–1567.

(20) Krishnakumar, V., and Xavier, R. J. (2004) FT Raman and FT-IR spectral studies of 3-mercapto-1,2,4-triazole. *Spectrochim. Acta, Part A 60*, 709–714.

(21) Braiman, M. S., Briercheck, D. M., and Kriger, K. M. (1999) Modeling vibrational spectra of amino acid side chains in proteins: effects of protonation state, counterion, and solvent on Arginine C-N stretch frequencies. *J. Phys. Chem. B 103*, 4744–4750.

(22) Sension, R. J., Hudson, B., and Callis, P. R. (1990) Resonance Raman studies of guanidinium and substituted guanidinium ions. *J. Phys. Chem. 94*, 4015–4025.

(23) Joseph, Y., Besnard, I., Rosenberger, M., Guse, B., Nothofer, H.-G., Wessels, J. M., Wild, U., Knop-Gericke, A., Su, D., Schögl, R., Yasuda, A., and Vossmeyer, T. (2003) Self-assembled gold nanoparticle/alkanedithiol films: preparation, electron microscopy, XPS-analysis, charge transport, and vapor-sensing properties. *J. Phys. Chem. B. 107*, 7406–7413.

(24) Daniel, C., and Astruc, D. (2004) Gold nanoparticles: assembly, supramolecular chemistry, quantum-size-related properties, and applications toward biology, catalysis and nanotechnology. *Chem. Rev. 104*, 293–346.

(25) Aryal, S., Remant, B. K. C., Dharmaraj, N., Bhattarai, N., Kim, C. H., and Kim, H. Y. (2006) Spectroscopic identification of S-Au interaction in cysteine capped gold nanoparticles. *Spectrochim. Acta, Part A 63*, 160–163.

(26) Chithrani, B. D., Ghazani, A. A., and Chan, W. C. W. (2006) Determining the size and shape dependence of gold nanoparticle uptake into mammalian cells. *Nano Lett. 6*, 662–668.

(27) Sadauskas, E., Wallin, H., Stoltenberg, M., Vogel, U., Doering, P., Larsen, A., and Danscher, G. (2007) Kupffer cells are central in the removal of nanoparticles from the organism. *Part. Fibre. Toxicol. 4*, 1–7.

(28) Chanda, N., Kattumuri, V., Shukla, R., Zambre, A., Katti, K., and Upendran, A. (2010) Bombesin functionalized gold nanoparticles show *in vitro* and *in vivo* cancer receptor specificity. *Proc. Natl. Acad. Sci. U.S.A. 107*, 8760–8765.

(29) Zhang, X., Xiong, Z., Wu, Y., Cai, W., Tseng, J. R., Gambhir, S. S., and Chen, X. (2006) Quantitative PET imaging of tumor integrin $\alpha_v\beta_3$ expression with ^{18}F-FRGD2. *J. Nucl. Med. 47*, 113–121.

(30) Liu, Z., Cai, W., He, L., Nakayama, N., Chen, K., Sun, X., Chen, X., and Dai, H. (2007) In vivo biodistribution and highly efficient tumor targeting of carbon nanotubes in mice. *Nat. Nanotechnol. 2*, 47–52.

(31) Kubas, H., Schäfer, M., Bauder-Wüst, U., Eder, M., Oltmanns, D., Haberkorn, U., Mier, W., and Eisenhut, M. (2010) Multivalent cyclic RGD ligands: influence of linker lengths on receptor binding. *Nucl. Med. Biol. 37*, 885–891.

(32) Cai, W., and Chen, X. (2008) Preparation of peptide-conjugated quantum dots for tumor vasculature-targeted imaging. *Nat. Prot. 3*, 89–96.

(33) Shah, B. S., Clark, P. A., Moioli, E. K., Stroscio, M. A., and Mao, J. J. (2007) Labeling of mesenchymal stem cells by bioconjugated quantum dots. *Nano Lett. 7*, 3071–3079.

(34) Li, Z., Liu, B., Huang, P., Gao, F., Zhang, X., Xi, P., Ren, Q., Lin, J., Yang, S., and Cui, D. (2010) RGD-conjugated dendrimer-modified gold nanorods for in vivo tumor targeting and photothermal therapy. *Mol. Pharmaceutics 7*, 94–104.

Bioconjugate Chemistry

ARTICLE

pubs.acs.org/bc

Fluorescence-Quenching Screening of Protein Kinase C Ligands with an Environmentally Sensitive Fluorophore

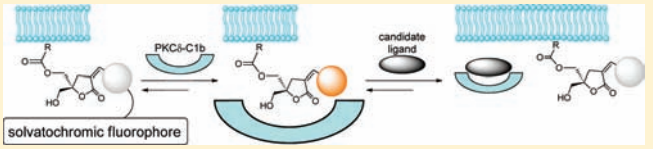
Wataru Nomura,[†] Nami Ohashi,[†] Yoshiaki Okuda,[†,‡] Tetsuo Narumi,[†] Teikichi Ikura,[‡] Nobutoshi Ito,[‡] and Hirokazu Tamamura*[,†,‡]

[†]Department of Medicinal Chemistry, Institute of Biomaterials and Bioengineering, Tokyo Medical and Dental University, 2-3-10 Kandasurugadai, Chiyoda-ku, Tokyo 101-0062, Japan

[‡]Graduate School of Biomedical Science, Tokyo Medical and Dental University, 1-5-45 Yushima, Bunkyo-ku, Tokyo 113-8510, Japan

Supporting Information

ABSTRACT: A novel fluorescence-quenching screening method for protein kinase C (PKC) ligands was developed utilizing solvatochromic fluorophores. Solvatochromic dyes, highly sensitive to the presence or the absence of competitive ligands in their binding to the C1b domain of PKCδ (δC1b), were combined with a known pharmacophoric moiety of 1,2-diacylglycerol (DAG) lactones, PKC ligands. Addition of δC1b to the fluorescent compounds caused a gradual increase in the fluorescent intensity in proportion to the increase of δC1b. As a competitive ligand was added to the complex of δC1b domain and fluorescent compounds, a gradual decrease in the fluorescent intensity was observed. The relative binding affinities of known ligands were successfully determined by this fluorescent method and corresponded well to the K_i values measured by a radioisotope method. These results indicate that washing, which is a laborious step in binding evaluations, is not required for this environmentally sensitive fluorophore based system. Screening with the system was performed for 2560 preselected library compounds with possible pharmacophores, and some lead compounds were found. This fluorescence-based method could be applied widely to known ligand−receptor combinations.



INTRODUCTION

Solvatochromic fluorophores are sensitive to immediate changes in their environment such as binding of ligands to proteins,[1] and significant biological issues have been examined by chemical probes with fluorescent dyes.[2,3] The major advantage of the fluorescence-based methods in the observation of physiological phenomena in cells is that detection and evaluation can be performed in real-time directly by microscopy. In these techniques, the signal/background ratio is critical to avoid the observation of artifacts or to obtain clearer images at high resolution. Screening methods of bioactive compounds have been developed as another application of fluorescence.[4] From the aspect of sensitivity, radioisotope (RI) based methods are more efficient but involve laborious experimental procedures. For the development of convenient screening procedures, a simple method for evaluation of binding is needed. By attachment of solvatochromic fluorophores to known ligands, the binding affinity of unknown ligands can be evaluated and related to RI methods.[5] Fluorescent intensity is highly dependent on the binding state to a target protein, and the signal/background ratio would be sufficient without washing steps, which are normally necessary in fluorescent analysis.[6,7]

In this study, we have developed reporter compounds containing solvatochromic dyes for the detection of ligand binding to a target protein and applied them to the screening of chemical libraries. Protein kinase Cδ (PKCδ) was chosen as a target protein because of its importance in physiological phenomena. The 11 isozymes that constitute PKC play pivotal roles in physiological responses to growth factors, oxidative stress, 1,2-diacylglycerol (DAG), and tumor promoters, such as phorbol esters. These responses regulate numerous cellular processes,[8,9] including proliferation,[10] differentiation,[11] migration,[12] and apoptosis.[13,14] Membrane translocation of PKC is caused by binding of ligands to the C1b domain and has been recognized as an important phenomenon in signal transduction because the localization of PKC is key in determining isozyme-specific functions by defining binding partners for downstream signaling.[15] Despite the complex regulatory mechanisms of PKC activation, considerable progress has been made in understanding isozyme-specific functions[16] and several ligands with high specificity for PKC isozymes have been developed as potential drugs.[17−23] Through the development of DAG-lactones, whose design is based on the endogenous ligand DAG, the importance of maintaining intact the pharmacophore triad of two carbonyl groups (*sn*-1 and *sn*-2) and the primary alcohol has been established as a requirement in high affinity ligands for PKC (Figure 1).[16] Various PKC ligands have been synthesized and found to be inhibitors of tumor promotion or of other diseases.

Received: December 13, 2010
Revised: March 13, 2011
Published: March 25, 2011

ACS Publications © 2011 American Chemical Society

However, there are limitations to the design of compound templates so far. Thus, in this study, we have attempted to develop the screening methods aimed at discovery of novel template structures for PKCδ ligands as drug leads.

EXPERIMENTAL PROCEDURES

General. ^{1}H NMR spectra were recorded using a Bruker AV500 spectrometer. Chemical shifts were reported in δ (ppm) relative to Me_4Si (in $CDCl_3$) as an internal standard. Low- and high-resolution mass spectra were recorded on a JMS-T1000LC AccuTOF and Bruker Daltonics microTOF-2focus in both positive and negative detection modes. Wakogel C-200 (Wako Pure Chemical Industries, Ltd.) and silica gel 60 N (Kanto Chemical Co., Inc.) were employed for flash chromatography. Fluorescent spectra were recorded on a JASCO FP-6600 spectrofluorometer and JASCO V-650 spectrophotometer using a quartz cell with 1.0 cm path length. Fluorescent intensities of samples in 96-well plates were recorded on Wallac ARVO MX.

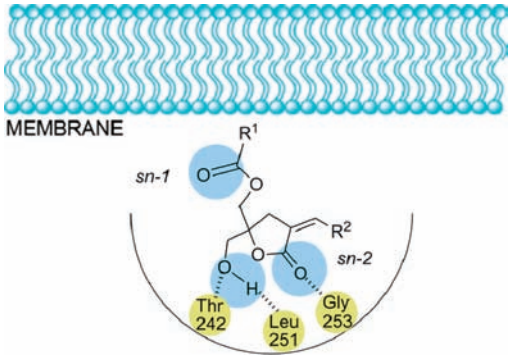


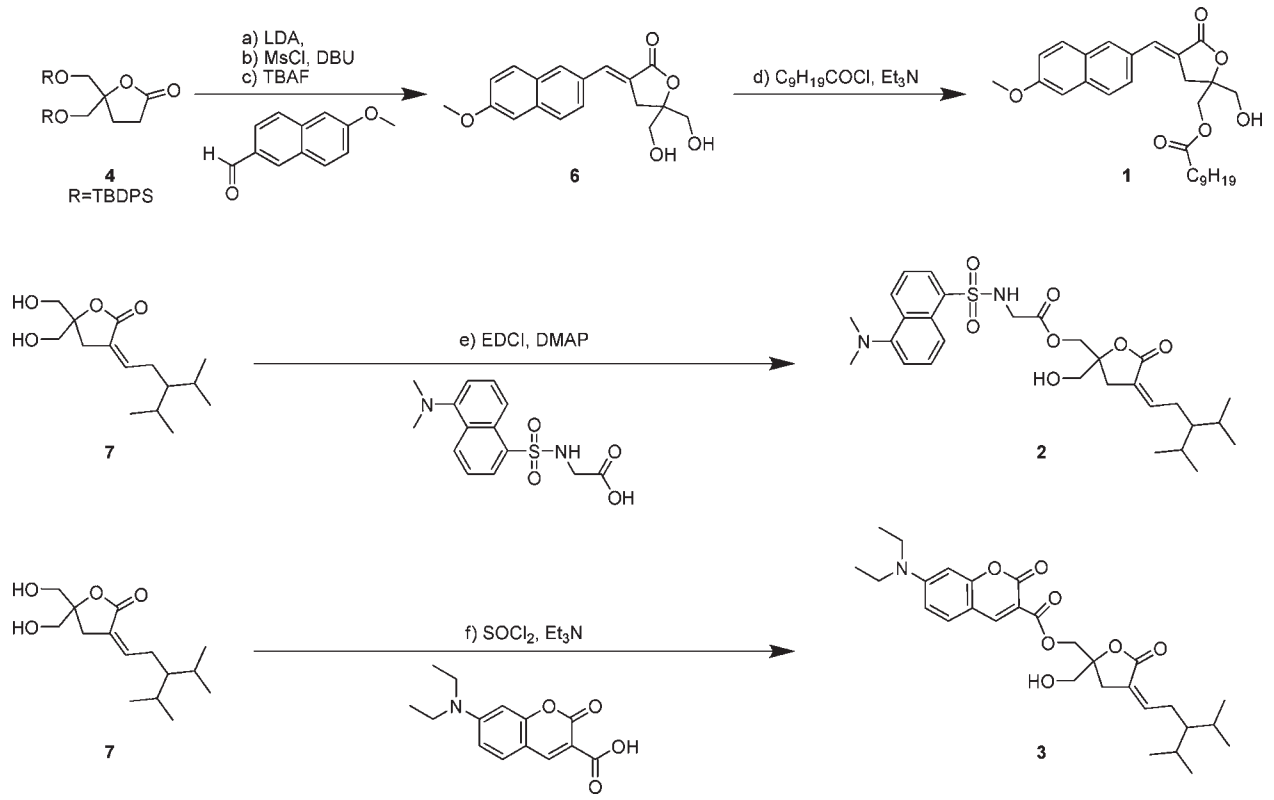
Figure 1. Binding mode of DAG-lactone derivatives to the δC1b domain. The *sn*-1 and *sn*-2 carbonyl groups are indicated. Three important pharmacophores are indicated by light blue spheres. Amino acid residues interacting with these pharmacophores (threonine at 242, leucine at 251, and glycine at 253) are indicated by red spheres.

Standard Monoacylation Procedure. Under argon, Et_3N (3 equiv) was added at 0 °C to a solution containing 5,5-bis(hydroxymethyl)oxalan-2-one in THF, and the mixture was stirred at 0 °C for 30 min. Then 0.2−1.1 equiv of a carboxylic acid derivative (an acyl chloride or carboxylic anhydride) was added. This mixture was stirred at 0 °C for a further 4 h. After evaporation of the solvent, the obtained residue was purified by flash column chromatography.

Preparation of Compounds 7, 10−13, 16, 17, and 19−21. Compounds **7**, **10**−**12**, and **16** were prepared as described in ref 17. Compounds **13** and **17** were prepared as described in refs 24 and 25. The synthesis of **19** is described elsewhere.[26] Compounds **20** and **21** are commercially available.

Expression and Purification of the δC1b Domain. DNA coding C1b domain of mouse PKCδ (231−280)[27] was subcloned into *Bam*H1 and *Eco*RI sites of pGEX-2tk (GE Healthcare) and expressed as gluthatione-*S*-transferase (GST) fusion protein in *Escherichia coli* C41 which contains extension sequences Gly-Ser-Arg-Arg-Ala-Ser-Val-Gly-Ser and Glu-Phe-Ile-Val-Thr-Asp at the N- and C-termini, respectively. The δC1b

Scheme 1. Synthesis of Fluorescent Compounds 1−3[a]



[a] (a) LDA, −78 °C; (b) MsCl, DBU, 0 °C to room temp; (c) TBAF, 0 °C to room temp; (d) $C_9H_{19}COCl$, Et_3N, 0 °C; (e) EDCI, DMAP, 0 °C; (f) $SOCl_2$, Et_3N, 0 °C.

dx.doi.org/10.1021/bc100567k |*Bioconjugate Chem.* 2011, 22, 923–930

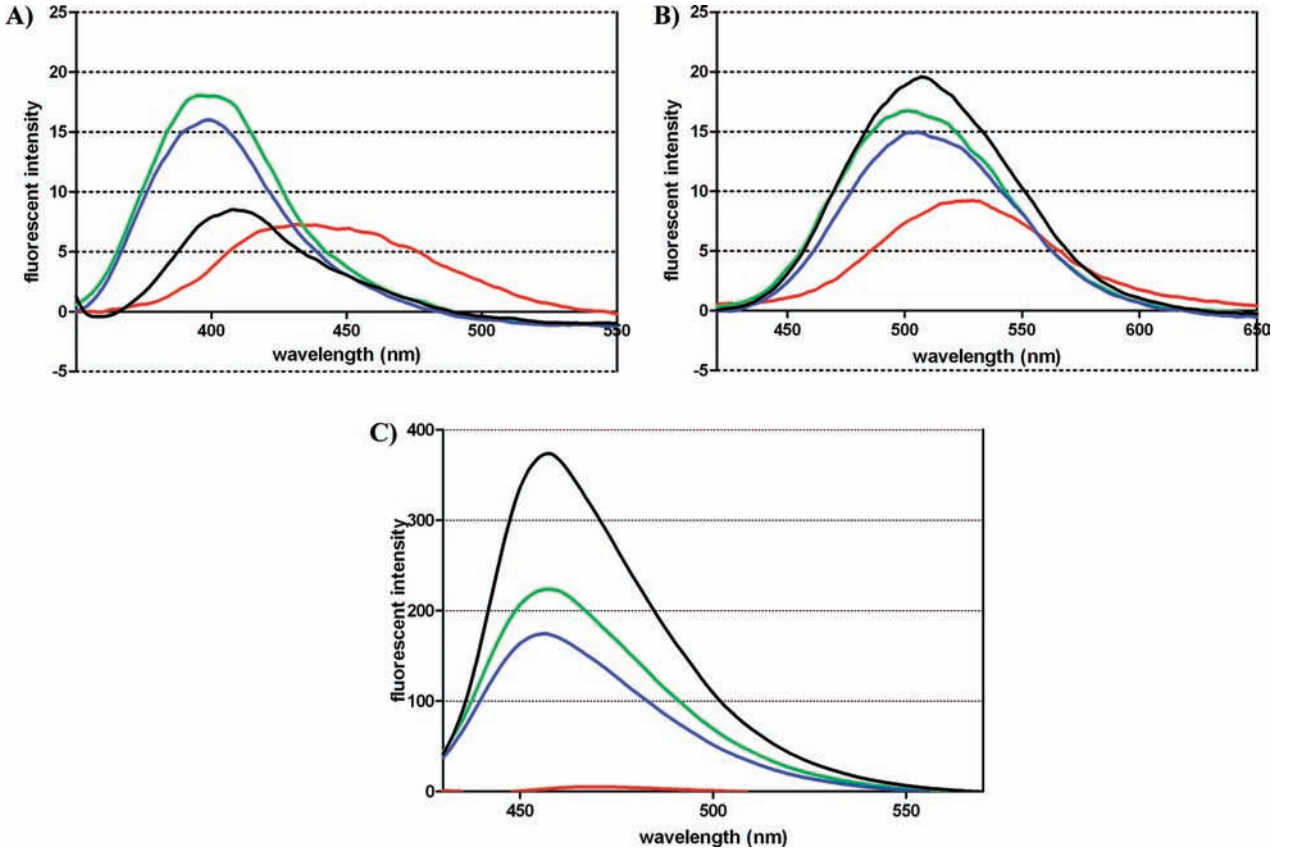


Figure 2. Fluorescent spectra of compounds **1** (A), **2** (B), and **3** (C) in different solvents. The spectra show fluorescence in the solvents color-coded as follows: red, MeOH; blue, THF; black, $CHCl_3$; green, EtOAc. Each ligand was prepared as 1 mM solution in DMSO. In UV measurement, 10 μL of ligand was added to 990 μL of solvents.

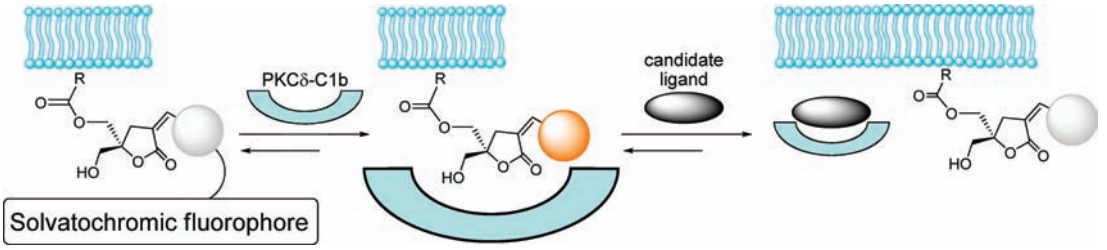


Figure 3. Schematic representation of a fluorescence-quenching screening system. In the presence of the δC1b domain, fluorescence of a solvatochromic fluorophore is enhanced. The replacement by candidate compounds results in fluorescence quenching.

Table 1. Changes of Fluorescent Intensity upon δC1b Binding and Inhibition Constants to δC1b Determined by Competition Assay against [^{3}H]PDBu

compd	ΔF [a]	K_i (nM) [b]
1	3.8	35.9
2	2.3	368
3	0.50	93.3

[a] Fluorescent change by binding of the δC1b domain. The values were determined by titration of the δC1b domain. The ΔF was determined by dividing F_1 by F_0 at the maximum of fluorescent emission in each spectrum. [b] Inhibitory constants determined by competition analysis against [^{3}H]PDBu.[28,36,37]

domain after cleavage contains 65 amino acid residues. Cells were grown at 37 °C in LB medium and induced with 0.3 mM IPTG at growth phase. Cells were cultured overnight at 20 °C after induction. Cells were collected and lysed in 50 mM Tris·HCl buffer (pH 8.0) containing 100 mM NaCl, 1 μg/mL leupeptine, 1 mM PMSF, and 1 mM DTT. Expressed protein was extracted by sonication, then purified by affinity chromatography utilizing glutathione-Sepharose 4B beads resin. GST moiety was cleaved by 300 units of thrombin at 4 °C overnight. The cleaved protein was eluted and further purified on a 2.6 cm × 60 cm Superdex S-75 gel filtration column. Purification was by FPLC system at a flow rate of 1 mL/min utilizing 0.1 M triethanolamine·HCl (pH 7.0) containing 0.5 M NaCl.

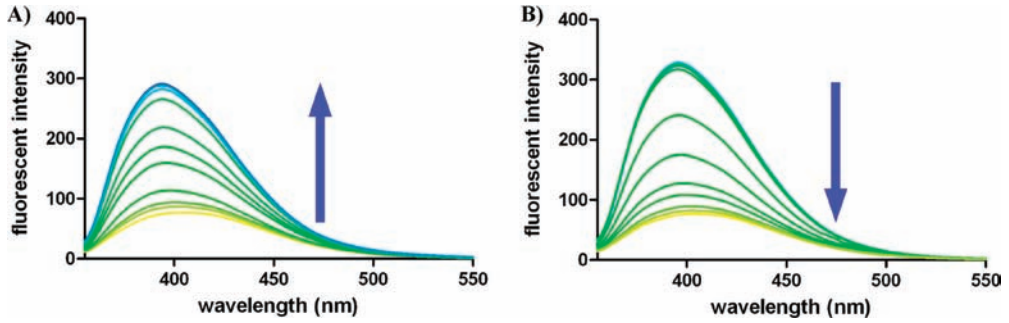


Figure 4. Changes of fluorescent spectra of compound **1** during titration of the δC1b domain (A) and during titration of PDBu (compound **8**) (B) after δC1b binding. The concentration of the δC1b domain was increased to 1.28 μM (6.4 equiv to compound **1**) by titration. The concentration of PDBu was increased to 10.2 μM (51.2 equiv to compound **1**) by titration.

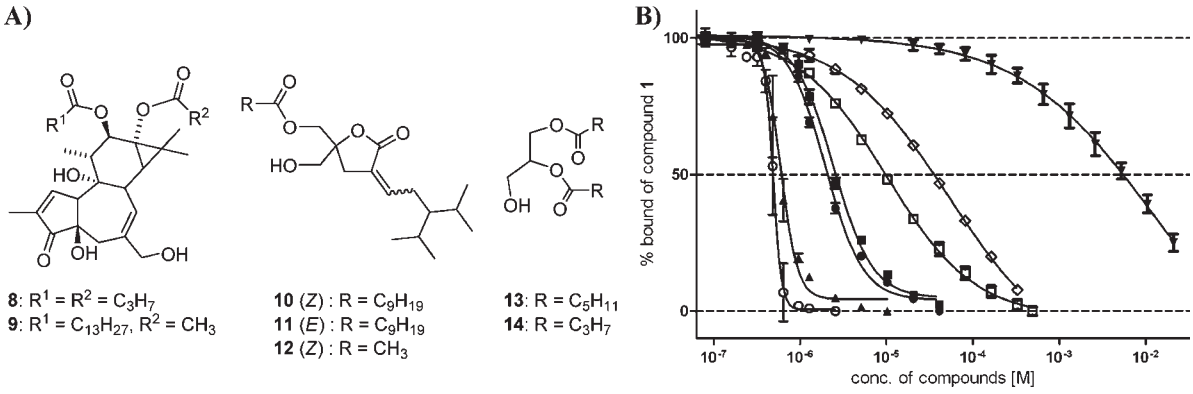


Figure 5. Competitive assay against compound **1** based on fluorescent intensity (spectrofluorometer). (A) Structures of test compounds. (B) Inhibition curves indicate results of compounds **8** (▲), **9** (○), **10** (●), **11** (■), **12** (□), **13** (◇), and **14** (▼).

Determination of K_i of Compounds for Full Length PKCδ. Enzyme−ligand interaction was assessed in vitro as the ability of the ligand to displace bound [20-^{3}H]phorbol 12,13-dibutyrate ([^{3}H]PDBu) from recombinant human PKCδ in the presence of phosphatidylserine (PS) in an experimental procedure that was described previously.[28] In constant concentration analysis, the concentrations of compounds were fixed at 100 nM for known compounds and at 10 μM for library compounds. The other procedures were the same as those of the standard evaluation.

Fluorescent Titration of the δC1b Domain. An amount of 25 μL of a solution of PS in chloroform (10 mg/mL) was evaporated to dryness under nitrogen. Then 50 mM Tris·HCl buffer (pH 7.4) was added and the PS was sonicated with a Microtip for a total of 15 s. A stock solution of compound **1** was diluted with 50 mM Tris·HCl buffer (pH 7.4) containing 100 μg/mL PS to prepare a 0.2 μM solution. The recombinant δC1b domain was added to the 0.2 μM solution of compound **1**, and fluorescent spectra (λ_{ex} = 340 nm) were measured at 25 °C. The concentration of the recombinant δC1b domain started at 0.01 μM and increased to 1.28 μM by titration. The final concentrations of compounds **2** and **3** were 0.2 and 0.05 μM, respectively. Change of fluorescent intensity (ΔF) was calculated at the following wavelengths, which showed λ_{max} in each evaluation; compound **1**, 406 (F_0) and 394 (F_1) nm; compound **2**, 520 (F_0) and 480 (F_1) nm; compound **3**, 463 (F_0) and 461 (F_1) nm. Wavelengths recorded before and after the addition of the δC1b domain.

Fluorescent Titration of Candidate Ligands. Compound **1** was diluted with 50 mM Tris·HCl (pH 7.4) containing 100 μg/mL PS to obtain a solution with a 0.2 μM final concentration. The δC1b domain was added to the above solution of compound **1** to be 0.96 μM. A candidate ligand was added to the solution, and fluorescent spectra were recorded with a spectrofluorometer at 25 °C. Fluorescent titration curves (λ_{em} = 407 nm) were analyzed by nonlinear regression, and IC_{50} values were estimated by a nonlinear least-squares curve-fitting method using GraphPad Prism 5 (GraphPad Software, Inc., La Jolla, CA, U.S.). In the constant concentration analysis, the concentrations of known compounds were fixed at 100 nM and of library compounds at 10 μM. The other procedures were the same as those in the standard evaluation.

Fluorescence-Quenching Analysis for Library Screening Recorded by Microplate Reader. Fluorescence intensity was recorded on Wallac ARVO MX (PerkinElmer) using a 96-well black plate. Compound **1** was diluted with 50 mM Tris·HCl (pH 7.4) containing 100 μg/mL PS to obtain a solution with a 0.2 μM final concentration. The δC1b domain was added to the above solution of compound **1** to be 0.96 μM. A candidate ligand (10 μM) was added to the compound **1**−δC1b domain complex solution, and fluorescent intensities (λ_{ex} = 355 nm, λ_{em} = 405 nm) were measured at 25 °C.

RESULTS AND DISCUSSION

Synthesis and Fluorescent Properties of Compounds 1−3. Three representative solvatochromic fluorophores, involving 6-methoxynaphthalene,[29] 5-(dimethylamino)naphthalene-1-sulfonyl (dansyl),[6,30,31] and diethylaminocoumarin,[32−35] have

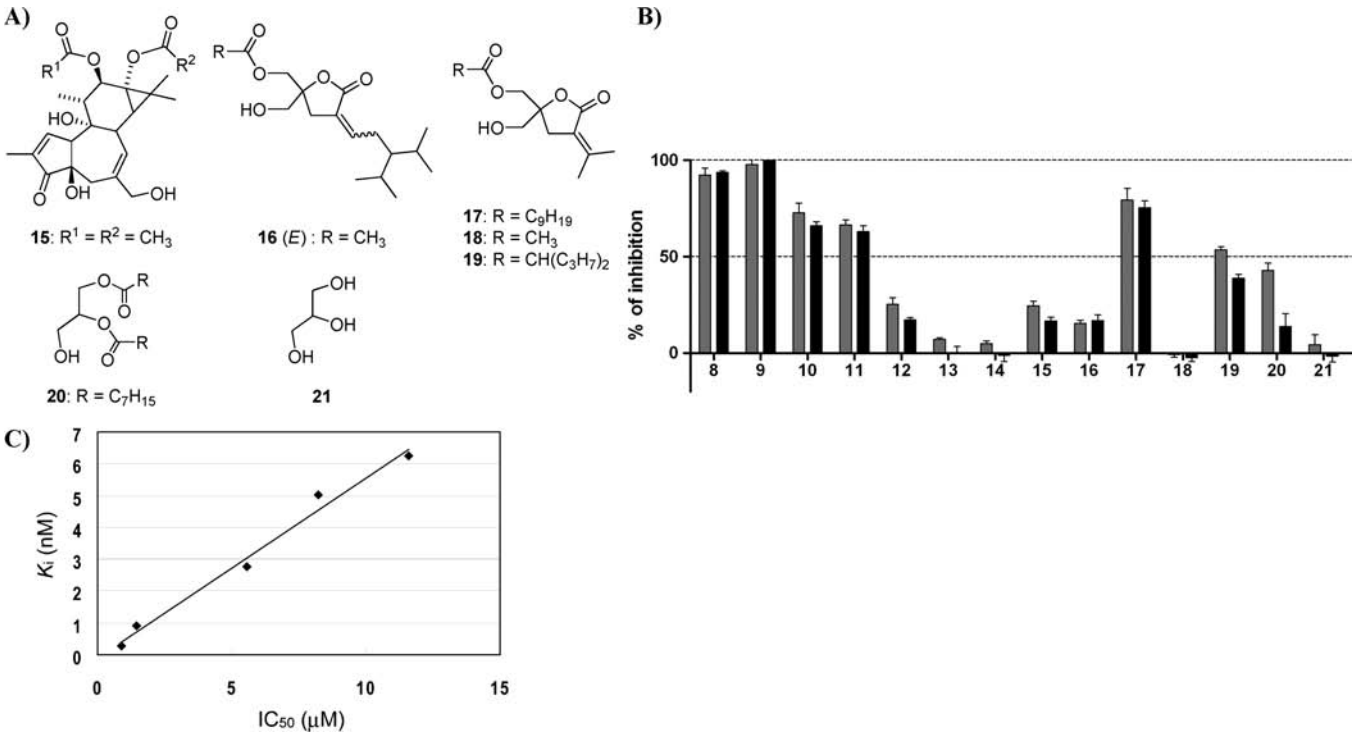


Figure 6. Comparison of inhibition percentages between the fluorescent assay (microplate reader) and the RI assay at a constant concentration of test compounds. (A) Structures of test compounds. (B) Inhibition of binding of compound **1** (fluorescent assay, left gray bars) or [^{3}H]PDBu (RI assay, right black bars) in the presence of test compounds (10 μM in the fluorescent assay and 100 nM in the RI assay). The final DMSO concentration is 4%. (C) Plots of IC_{50} values (μM) by the fluorescent assay versus K_i (nM) by the RI assay for compounds **8**, **9**, **10**, **11**, and **17**.

been utilized. The 6-methoxynaphthalene was incorporated at the α-carbon of the *sn*-1 carbonyl group of the DAG-lactone structure (Scheme 1). The dansyl and diethylaminocoumarin were incorporated into the *sn*-2 carbonyl group. In comparison with the fluorescent spectra of these compounds, obtained in various solvents, compound **1** showed the most variation with solvent polarity (Figure 2). It is known that solvatochromic fluorophores show higher fluorescent intensity in hydrophobic environments and that the fluorophores are sensitive to the environment of a binding pocket in target proteins. The fluorescent intensity of labeled DAG-lactones should reflect its binding to a target protein, PKCδ (Figure 3), and as expected, our reporter compounds **1** and **2** containing solvatochromic fluorophores exibited a remarkable increase of fluorescent intensity in the proximity of the C1b domain of PKCδ (δC1b), which is a specific target of DAG-lactone derivatives (Table 1 and Figure 4A). This indicates that in the binding of compounds **1** and **2** to the δC1b domain, the 6-methoxynaphthalene and dansyl moieties are located in the hydrophobic environment. However, for compound **3**, the fluorescent intensity was decreased as the concentration of δC1b increased. The spectra in various solvents showed dependence of the fluorescent intensity of the compound **3** on solvent polarity, and it was suggested that in the binding of compound **3** to the δC1b domain, the diethylaminocoumarin moiety could be located in the hydrophilic environment. The changes of fluorescent intensity of the synthetic compounds are summarized in Table 1. The binding constants of fluorescent compounds were evaluated by [^{3}H]PDBu competitive assay. Compound **1** showed the highest binding affinity for the δC1b domain. In the fluorescence-based analysis of binding, two factors are key to the sensitivity of the assay system: (i) the fluorescent change as a function of the ligand binding and (ii) the binding affinity of a reporter compound.

Evaluation of Binding to PKCδ by Fluorescent Change of Compound 1. The results obtained supported the selection of compound **1** as a reporter compound for further study. In competitive assays, when candidate ligands of PKCδ are present, they replace the fluorescent compounds, which are formerly bound to δC1b, and the fluorescent intensity should decrease. Practically, addition of PDBu to the complex of compound **1** and δC1b resulted in a remarkable decrease of fluorescent intensity (Figure 4B). By utilization of compound **1** as a reporter, binding analysis of known PKCδ ligands was performed to assess the reliability of the assay system. Compounds **8**−**14** were prepared as test compounds (Figure 5A), and their IC_{50} values, determined by the fluorescence-based competitive assay with a fluorospectrophotometer against compound **1**, were 0.60, 0.49, 1.95, 2.42, 10.0, 54.2, and 1.22 × 10^4 μM, respectively (Figure 5B). The order of the IC_{50} values of compounds **8**−**11** is identical to that of the K_i values (0.91, 0.26, 5.0, and 6.2 nM, respectively) determined by the [^{3}H]PDBu competitive assay.

The Binding Analysis by Competition with Compound 1 Showed Linearity with the Classical RI Assay. To further assess the collinearity of the fluorescent assay on microplates and the [^{3}H]PDBu assay, the inhibition percentages by compounds **8**−**21** in both assays (Figure 6A) at constant concentration were compared. The compound concentrations were set at 10 μM for the fluorescent assay and at 100 nM for the [^{3}H]PDBu assay. As shown in Figure 6B, the inhibition percentages of compounds **8**−**21** are similar in both assays. Comparison of the IC_{50} and K_i of compounds **8**, **9**, **10**, **11**, and **17**, possessing more than 60% inhibition percentages, showed acceptable linearity (Figure 6C).

dx.doi.org/10.1021/bc100567k |*Bioconjugate Chem.* 2011, 22, 923–930

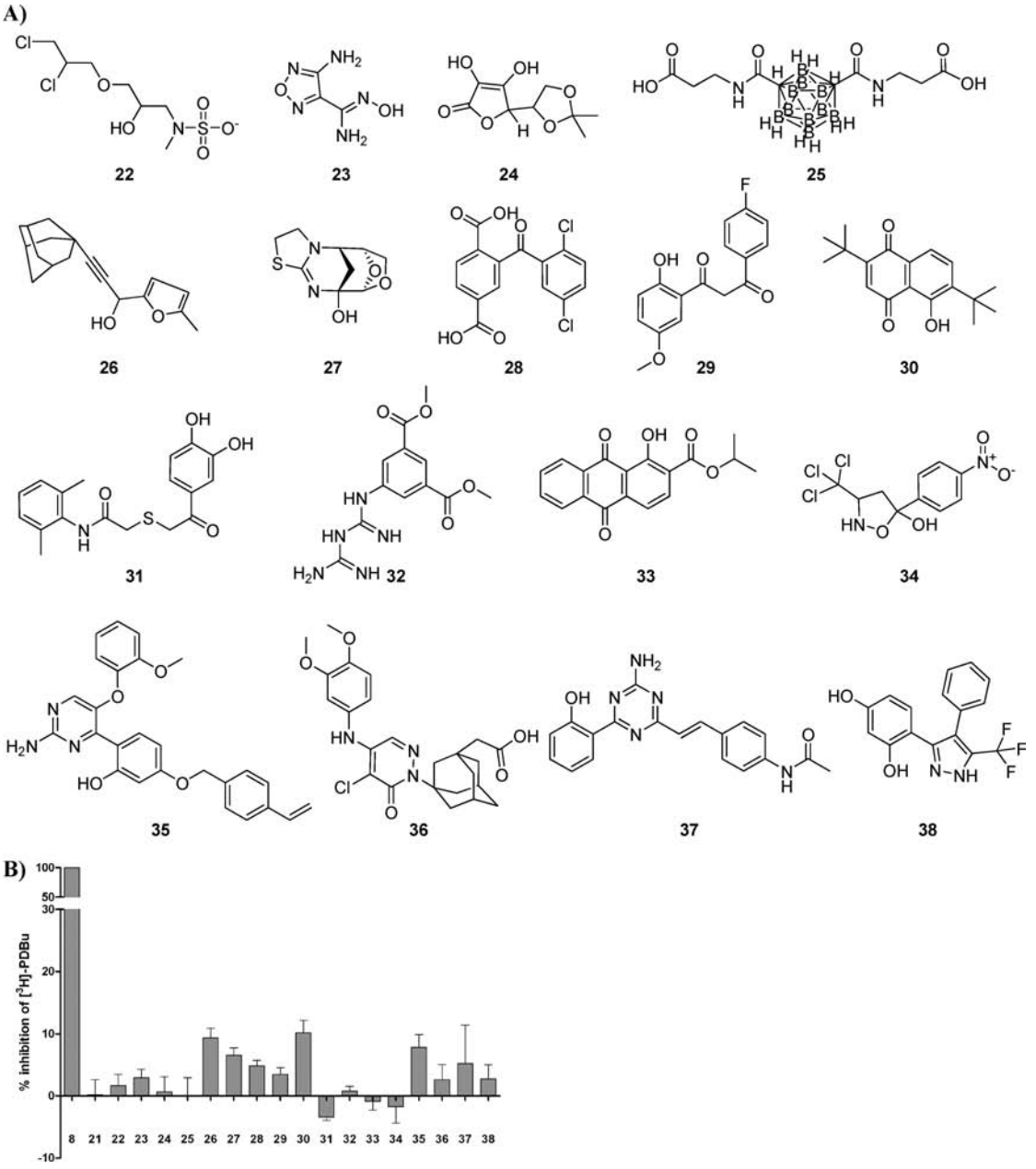


Figure 7. The RI competition assay of positive hit compounds found in fluorescent screening utilizing compound **1**. (A) Structures of test compounds obtained from screening. (B) Results of the inhibition assay based on RI methods. The concentration of compounds was fixed at 10 μM. The *X* axis indicates compound numbers. Columns show average inhibition obtained from triplicated experiments. Bars indicate standard errors.

In view of the above results, the present fluorescence-based evaluation of binding to the δC1b domain on microplates was deemed to be a promising alternative for the classical RI assay.

Expansion of the Fluorescence Evaluation to Screening of Library Compounds. As a proof-of-concept study, compound **1** was utilized in screening of a chemical library, supplied by the Screening Center at the Tokyo Medical and Dental University Screening Center. The structures of the library compounds were analyzed in advance of screening. For binding to the δC1b domain, pharmacophores including the carbonyl and hydroxy groups are necessary and only compounds including these functional groups were chosen. In the analysis of the library on microplates, compounds with more than 20% decrease of fluorescent intensity determined by triplicated assays were selected as candidates for further study. Compounds **22**−**38** were found from 2560 library compounds (Figure 7A) as candidate δC1b ligands. To further assess the binding affinity of these compounds, evaluation of binding by competition with the [^{3}H]PDBu was performed at a fixed concentration (10 μM) (Figure 7B). In this analysis, compounds **30** and **26**, with inhibition percentages at 10 μM of 10.2% and of 9.4%, respectively, showed the most and the second most potent binding affinities for the δC1b domain. The binding affinities of these compounds are still very low compared to that of DAG-lactones, but an SAR study of these compounds could lead to novel structure templates for synthetic PKC ligands. This analysis also revealed that compounds **24**, **25**, **31**, **32**, **33**, and **34** are false positive hits. The results obtained indicate that our screening system with a fluorescent

dx.doi.org/10.1021/bc100567k |*Bioconjugate Chem.* 2011, 22, 923–930

DAG-lactone derivative could be utilized for discovery of novel chemical leads for PKCδ.

CONCLUSION

A fluorescence-based method for chemical library screening has been developed. This method, which requires no washing steps, provides a linear response in relative binding affinity between compounds and is compatible with the classical RI assay for PKC ligands. By screening of more than 2500 library compounds, the method was proven to be a reliable means of discovery of compounds that bind to the C1b domain of PKCδ. The method would provide potent lead compounds that bind to the isozyme utilized in the assay. By utilization of the difference of the binding affinity of reporter compounds to different isozymes, it is possible that this screening system can provide an efficient selection of lead compounds highly specific to a target isozyme. This fluorescence-quenching method should be applicable to other known receptor−ligand combinations.

ASSOCIATED CONTENT

Supporting Information. Synthesis procedures and NMR, HRMS, and IR data. This material is available free of charge via the Internet at http://pubs.acs.org.

AUTHOR INFORMATION

Corresponding Author

*E-mail: tamamura.mr@tmd.ac.jp. Phone: +81-3-5280-8036. Fax: +81-3-5280-8039.

ACKNOWLEDGMENT

The authors thank Professor Masatoshi Hagiwara and Dr. Yukiko Okuno (Chemical Biology Screening Center, Tokyo Medical and Dental University) for their support in chemical library screening. This work was supported in part by Naito Foundation (W.N.) and Research Award of Graduate School of Biomedical Science, Tokyo Medical and Dental University (W.N. and T.I.)

REFERENCES

(1) Loving, G. S., Sainlos, M., and Imperiali, B. (2010) Monitoring protein interactions and dynamics with solvatochromic fluorophores. *Trends Biotechnol. 28*, 73–83.

(2) Rothman, D. M., Shults, M. D., and Imperiali, B. (2005) Chemical approaches for investigating phosphorylation in signal transduction networks. *Trends Cell Biol. 15*, 502–510.

(3) Terai, T., and Nagano, T. (2008) Fluorescent probes for bioimaging applications. *Curr. Opin. Chem. Biol. 12*, 515–521.

(4) Reymond, J. -L. (2008) Substrate arrays for fluorescence-based enzyme fingerprinting and high-throughput screening. *Ann. N.Y. Acad. Sci. 1130*, 12–20.

(5) Nomura, W., Tanabe, Y., Tsutsumi, H., Tanaka, T., Ohba, K., Yamamoto, N., and Tamamura, H. (2008) Fluorophore labeling enables imaging and evaluation of specific CXCR4−ligand interaction at the cell membrane for fluorescence-based screening. *Bioconjugate Chem. 19*, 1917–1920.

(6) Hayashida, O., Ogawa, N., and Uchiyama, M. (2007) Surface recognition and fluorescence sensing of histone by dansyl-appended cyclophane-based resorcinarene trimer. *J. Am. Chem. Soc. 129*, 13698–13705.

(7) Tsutsumi, H., Nomura, W., Abe, S., Mino, T., Masuda, A., Ohashi, N., Tanaka, T., Ohba, K., Yamamoto, N., Akiyoshi, K., and Tamamura, H. (2009) Fluorogenically active leucine zipper peptides as tag-probe pairs for protein imaging in living cells. *Angew. Chem., Int. Ed. 48*, 9164–9166.

(8) Nishizuka, Y. (1992) Intracellular signaling by hydrolysis of phospholipids and activation of protein kinase C. *Sceince 258*, 607–614.

(9) Newton, A. C. (1995) Protein kinase C: structure, function, and regulation. *J. Biol. Chem. 270*, 28495–28498.

(10) Watanabe, T., Ono, Y., Taniyama, Y., Hazama, K., Igarashi, K., Ogita, K., Kikkawa, U., and Nishizuka, Y. (1992) Cell division arrest induced by phorbol ester in CHO cells overexpressing protein kinase C-delta subspecies. *Proc. Natl. Acad. Sci. U.S.A. 89*, 10159–10163.

(11) Mischak, H., Pierce, J. H., Goodnight, J., Kazanietz, M. G., Blumberg, P. M., and Mushinski, J. F. (1993) Phorbol ester-induced myeloid differentiation is mediated by protein kinase C-alpha and -delta and not by protein kinase C-beta II, -epsilon, -zeta, and -eta. *J. Biol. Chem. 268*, 20110–20115.

(12) Li, C., Wernig, F., Leitges, M., Hu, Y., and Xu, Q. (2003) Mechanical stress-activated PKCdelta regulates smooth muscle cell migration. *FASEB J. 17*, 2106–2108.

(13) Ghayur, T., Hugunin, M., Talanian, R. V., Ratnofsky, S., Quinlan, C., Emoto, Y., Pandey, P., Datta, R., Huang, Y., Kharbanda, S., Allen, H., Kamen, R., Wong, W., and Kufe, D. (1996) Proteolytic activation of protein kinase C delta by an ICE/CED 3-like protease induces characteristics of apoptosis. *J. Exp. Med. 184*, 2399–2404.

(14) Alkon, D. L., Sun, M.-K., and Nelson, T. J. (2007) PKC signaling deficits: a mechanistic hypothesis for the origins of Alzheimer's disease. *Trends Pharmacol. Sci. 28*, 51–60.

(15) Wang, Q. J. (2006) PKD at the crossroads of DAG and PKC signaling. *Trends Pharmacol. Sci. 27*, 317–323.

(16) Marquez, V. E., and Blumberg, P. M. (2003) Synthetic diacylglycerols (DAG) and DAG-lactones as activators of protein kinase C (PK-C). *Acc. Chem. Res. 36*, 434–443.

(17) Nacro, K., Bienfait, B., Lee, J., Han, K.-C., Kang, J.-H., Benzaria, S., Lewin, N. E., Bhattacharyya, D. K., Blumberg, P. M., and Marquez, V. E. (2000) Conformationally constrained analogues of diacylglycerol (DAG). 16. How much structural complexity is necessary for recognition and high binding affinity to protein kinase C?. *J. Med. Chem. 43*, 921–944.

(18) Tamamura, H., Bienfait, B., Nacro, K., Lewin, N. E., Blumberg, P. M., and Marquez, V. E. (2000) Conformationally constrained analogues of diacylglycerol (DAG). 17. Contrast between *sn*-1 and *sn*-2 DAG lactones in binding to protein kinase C. *J. Med. Chem. 43*, 3209–3217.

(19) Tamamura, H., Sigano, D. M., Lewin, N. E., Blumberg, P. M., and Marquez, V. E. (2004) Conformationally constrained analogues of diacylglycerol. 20. The search for an elusive binding site on protein kinase C through relocation of the carbonyl pharmacophore along the *sn*-1 side chain of 1,2-diacylglycerol lactones. *J. Med. Chem. 47*, 644–655.

(20) Baba, Y., Ogoshi, Y., Hirai, G., Yanagisawa, T., Nagamatsu, K., Mayumi, S., Hashimoto, Y., and Sodeoka, M. (2004) Design, synthesis, and structure−activity relationship of new isobenzofuranone ligands of protein kinase C. *Bioorg. Med. Chem. Lett. 14*, 2963–2967.

(21) Baba, Y., Mayumi, S., Hirai, G., Kawasaki, H., Ogoshi, Y., Yanagisawa, T., Hashimoto, Y., and Sodeoka, M. (2004) Evaluation of series of isobenzofuranone dimers as PKCalpha ligands: implication for the distance between the two ligand binding sites. *Bioorg. Med. Chem. Lett. 14*, 2969–2972.

(22) Yanagita, R. C., Nakagawa, Y., Yamanaka, N., Kashiwagi, K., Saito, N., and Irie, K. (2008) Synthesis, conformational analysis, and biological evaluation of 1-hexylindolactam-V10 as a selective activator for novel protein kinase C isozymes. *J. Med. Chem. 51*, 46–56.

(23) Nakagawa, Y., Yanagita, R. C., Hamada, N., Murakami, A., Takahashi, H., Saito, N., Nagai, H., and Irie, K. (2009) A simple analogue of tumor-promoting aplysiatoxin is an antineoplastic agent rather than a tumor promoter: development of a synthetically accessible protein kinase C activator with bryostatin-like activity. *J. Am. Chem. Soc. 131*, 7573–7579.

(24) Martin, S. F., Josey, J. A., Wong, Y.-L., and Dean, D. W. (1994) General method for the synthesis of phospholipid derivatives of 1,2-*O*-diacyl-*sn*-glycerols. *J. Org. Chem. 59*, 4805–4820.

(25) Malolanarasimhan, K., Kedei, N., Sigano, D. M., Kelley, J. A., Lai, C. C., Lewin, N. E., Surawski, R. J., Pavlyukovets, V. A., Garfield, S. H., Wincovitch, S., Blumberg, P. M., and Marquez, V. E. (2007) Conformationally constrained analogues of diacylglycerol (DAG). 27. Modulation of membrane translocation of protein kinase C (PKC) isozymes alpha and delta by diacylglycerol lactones (DAG-lactones) containing rigid-rod acyl groups. *J. Med. Chem. 50*, 962–978.

(26) Nomura, W., Narumi, T., Ohashi, N., Serizawa, Y., Lewin, N. E., Blumberg, P. M., Furuta, T., and Tamamura, H. (2011) Synthetic caged DAG-lactones for photochemically-controlled activation of protein kinase C. *ChemBioChem 12*, 535–539.

(27) Mischak, H., Bodenteich, A., Kolch, W., Goodnight, J., Hofer, F., and Mushinski, J. F. (1991) Mouse protein kinase C-delta, the major isoform expressed in mouse hemopoietic cells: sequence of the cDNA, expression patterns, and characterization of the protein. *Biochemistry 30*, 7925–7931.

(28) Kazanietz, M. G., Krausz, K. W., and Blumberg, P. M. (1992) Differential irreversible insertion of protein kinase C into phospholipid vesicles by phorbol esters and related activators. *J. Biol. Chem. 267*, 20878–20886.

(29) List, B., Barbas, C. F., III, and Lerner, R. A. (1998) Aldol sensors for the rapid generation of tunable fluorescence by antibody catalysis. *Proc. Natl. Acad. Sci. U.S.A. 95*, 15351–15355.

(30) Davis, G. A. (1972) Dansylglycine as a fluorescent probe for aqueous solutions of cationic detergents. *J. Am. Chem. Soc. 94*, 5089–5090.

(31) Morii, T., Sugimoto, K., Makino, K., Otsuka, M., Imoto, K., and Mori, Y. (2002) A new fluorescent biosensor for inositol trisphosphate. *J. Am. Chem. Soc. 124*, 1138–1139.

(32) Matlock, D. L., and Heyduk, T. (1999) A real-time fluorescence method to monitor the melting of duplex DNA during transcription initiation by RNA polymerase. *Anal. Biochem. 270*, 140–147.

(33) Kakio, A., Nishimoto, S., Yanagisawa, K., Kozutsumi, Y., and Matsuzaki, K. (2001) Cholesterol-dependent formation of GM1 ganglioside-bound amyloid beta-protein, an endogenous seed for Alzheimer amyloid. *J. Biol. Chem. 276*, 24985–24990.

(34) Timofeevski, S. L., Prusakiewicz, J. J., Rouzer, C. A., and Marnett, L. J. (2002) Isoform-selective interaction of cyclooxygenase-2 with indomethacin amides studied by real-time fluorescence, inhibition kinetics, and site-directed mutagenesis. *Biochemistry 41*, 9654–9662.

(35) Sakamoto, S., and Kudo, K. (2008) Supramolecular control of split-GFP reassembly by conjugation of beta-cyclodextrin and coumarin units. *J. Am. Chem. Soc. 130*, 9574–9582.

(36) Sharkey, N. A., and Blumberg, P. M. (1985) Highly lipophilic phorbol esters as inhibitors of specific [^{3}H]phorbol 12,13-dibutyrate binding. *Cancer Res. 45*, 19–24.

(37) Ohashi, N., Nomura, W., Kato, M., Narumi, T., Lewin, N. E., Blumberg, P. M., and Tamamura, H. (2009) Synthesis of protein kinase Cdelta C1b domain by native chemical ligation methodology and characterization of its folding and ligand binding. *J. Pept. Sci. 15*, 642–646.

Supporting Information

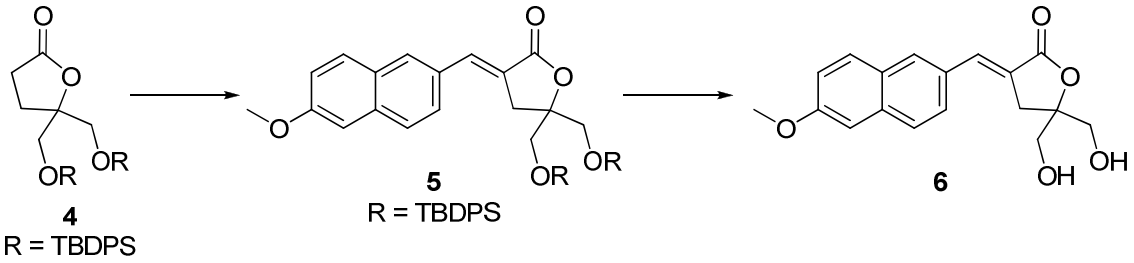
Fluorescence-Quenching Screening of Protein Kinase C Ligands with an Environmentally Sensitive Fluorophore

Wataru Nomura,[†] Nami Ohashi,[†] Yoshiaki Okuda,[†,‡] Tetsuo Narumi,[†] Teikichi Ikura,[‡] Nobutoshi Ito,[‡] and Hirokazu Tamamura*[†,‡]

[†]*Department of Medicinal Chemistry, Institute of Biomaterials and Bioengineering, Tokyo Medical and Dental University, 2-3-10 Kandasurugadai, Chiyoda-ku, Tokyo 101-0062, Japan,* [‡]*Graduate School of Biomedical Science, Tokyo Medical and Dental University, 1-5-45 Yushima, Bunkyo-ku, Tokyo 113-8510, Japan*

*correspondence to tamamura.mr@tmd.ac.jp

Synthesis of compound 1



(*E*)-5,5-Bis(hydroxymethyl)-3-((6-methoxynaphthalen-2-yl)methylene)dihydrofura n-2(*3H*)-one (6): Under argon, a -78 °C solution of **4** (1.24 g, 2.00 mmol) in THF (13 mL) was treated dropwise with LDA (2.00 mL, 2 M solution in heptane/THF/ethylbenzene) and stirred at -78 °C for 2 h. 6-Methoxy-2-naphtaldehyde (1.13 g, 4.00 mmol) was added slowly maintaining the same temperature, and the reaction was monitored by TLC. After 2 h's treatment, the reaction was quenched with saturated aqueous NH_4Cl and then warmed to room temperature. The aqueous layer was extracted 3 times with chloroform (50 mL x 3). The combined organic layer was wahed with water, dried over $MgSO_4$ and concentrated to give the alkylation crude product as an oil, which was used without further purification. A solution of the alkylation crude product in CH_2Cl_2 (40 mL) was treated with MsCl (330 μL, 4.00 mmol) and Et_3N (1.39 mL, 10.0 mmol) at 0 °C. This mixture was stirred at 0 °C for 30 min and then at room temperature at 2 h. The reaction mixture was then cooled to 0 °C, DBU (1.84 mL, 12.4 mmol) was added, and the resultant solution was stirred at room temperature overnight. The reaction mixture was diluted by chloroform, washed with saturated aqueous NH_4Cl, and dried over $MgSO_4$, and concentrated to give crude **5** as an oil, which was used in the next step without further purification. A stirred solution of crude **5** (1.58 g, 2.00 mmol) in THF (8.0 mL) was treated with a THF solution of tetrabutylammonium fluoride (1 M, 8.00 mL) at room temperature for 1 h. After the volatiles were removed under reduced pressure, the residue was partitioned between chloroform and water. The organic layer was separated and dried over Na_2SO_4. After evaporation of the solvent, the obtained residue was purified by flash column chromatography over silica gel using $CHCl_3$/MeOH (30:1) as eluant. The compound **6** (*E* isomer, 491 mg, 78% from **4**) was obtained as white crystals, mp 182-184 °C [from $CHCl_3$/MeOH (30:1)]. The *E* isomer was exclusibely obtained, which was based on tentative assignment.[1]

^{1}H-NMR (500 MHz; DMSO)

δ 8.17 (s, 1H), 7.97 (d, J = 9.0 Hz, 1H), 7.94 (d, J = 8.6 Hz, 1H), 7.75 (dd, J = 7.2, 1.4 Hz, 1H) 7.5 (t, J = 2.8 Hz, 1H) 7.42 (d, J = 2.4 Hz, 1H) 7.26 (dd, J = 6.4, 2.6 Hz, 1H),

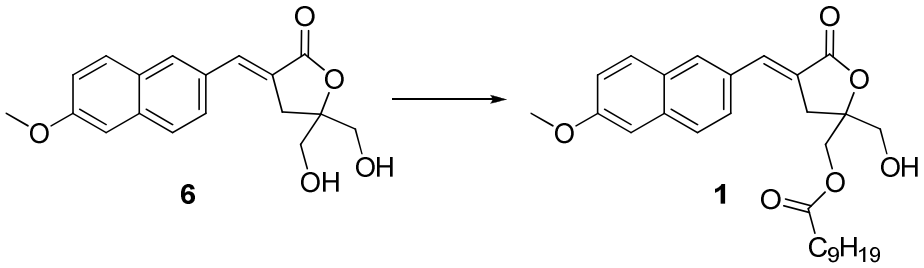
5.17 (t, *J* = 5.8 Hz, 2H), 3.94 (s, 3H), 3.54-3.62 (m, 4H), 3.21-3.21 (m, 2H).

^{13}C-NMR (125 MHz; DMSO)

δ 171.8, 158.9, 135.1, 134.3, 130.6, 130.5 (2), 128.7, 127.7 (2), 126.9, 119.8, 106.4, 86.7, 63.9 (2), 55.8, 31.7.

FAB-HRMS (*m*/*z*): Found [MH$^+$] 315.1228. $C_{18}H_{19}O_5$ requires *M*+H, 315.1232.

IR (neat): 3368 (OH), 2922-2852, 1714 (C=O), 1626 cm^{-1}.



(*E*)-(2-(Hydroxymethyl)-4-((6-methoxynaphthalen-2-yl)methylene)-5-oxotetrahydrofuran-2-yl)methyl decanoate (1): The standard monoacylation procedure starting from **6** (0.126 g, 0.400 mmol) was applied using decanoyl chloride (0.090 mL, 0.440 mmol). After flash column chromatography with hexane/EtOAc (15:1), the monodecanoate product **1** (89.2 mg, 48%) was isolated as white crystals, mp 178-179 °C [from hexane/EtOAc (15:1)].

^{1}H-NMR (500 MHz; $CDCl_3$)

δ 7.90 (s, 1H) 7.75-7.79 (m, 2H), 7.70 (t, *J* = 2.4 Hz, 1H), 7.55 (dd, *J* = 7.0, 2.4 Hz, 1H), 7.20 (dd, *J* = 6.5, 2.4 Hz, 1H) 7.14 (d, *J* = 2.4 Hz, 1H), 4.35 (d, *J* = 12.0 Hz, 1H), 4.28 (d, *J* = 12.0 Hz, 1H), 3.99 (s, 3H), 3.73-3.83 (m, 2H), 3.30-3.34 (m, 1H), 3.10-3.14 (m, 1H), 2.30-2.33 (m, 3H), 1.52-1.58 (m, 2H), 1.18-1.25 (m, 12H), 0.88 (t, *J* = 7.3 Hz, 3H).

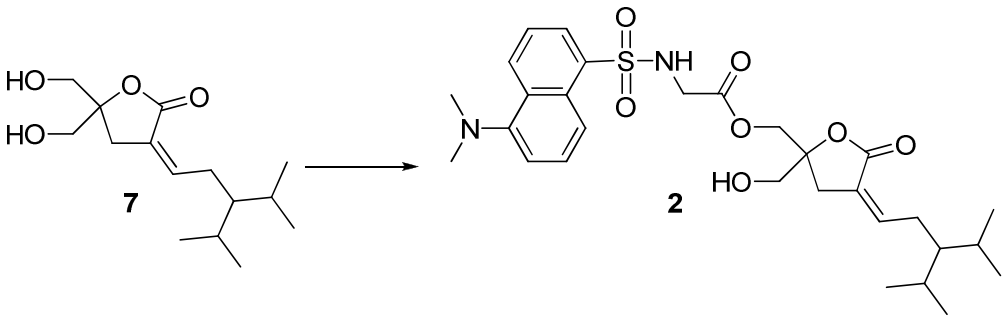
^{13}C-NMR (125 MHz; $CDCl_3$)

δ 173.7, 171.3, 159.2, 137.8, 135.3, 131.0, 130.2, 129.7, 128.6, 127.5, 126.9, 122.6, 119.8, 105.7, 83.2, 65.3, 64.8, 55.4, 34.0, 32.4, 31.8, 29.3, 29.2 (2), 29.1, 24.8 (2), 22.6, 14.1.

FAB-HRMS (*m*/*z*): Found [MH$^+$] 469.2601. $C_{28}H_{37}O_6$ requires *M*+H, 469.2590.

IR (neat): 3369 (OH), 2933, 1709 (C=O), 1626 cm^{-1}.

Synthesis of compound 2



(*Z*)-(2-(Hydroxymethyl)-4-(3-isopropyl-4-methylpentylidene)-5-oxotetrahydrofuran-2-yl)methyl 2-(5-(dimethylamino)naphthalene-1-sulfonamido)acetate (2): Under argon, a 0 °C solution of **7** (7.0 mg, 26 μmol) in CH_2Cl_2 (10 mL) was treated with DMAP (0.3 mg, 2.6 μmol) and EDCI (3.8 mg, 20 μmol) and stirred at 0 °C for 30 min. N^{α}-Dansyl-glycine (5.6 mg, 20 μmol) was added slowly maintaining the same temperature. This mixture was stirred at room temperature for 8 h. After evaporation of the solvent, the residue obtained was purified by flash column chromatography over silica gel using $CHCl_3$/MeOH (60:1) as eluant. The compound **2** (5.0 mg, 34%) was isolated as a yellow oil.

^{1}H-NMR (400 MHz; $CDCl_3$)

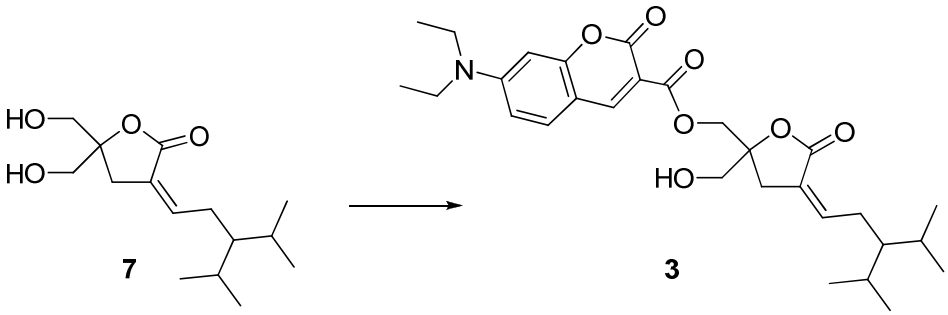
δ 8.57 (d, J = 8.5 Hz, 1H), 8.22-8.28 (m, 2H), 7.50-7.62 (m, 2H), 7.20 (d, J = 7.6 Hz, 1H), 6.24-6.28 (m, 1H), 5.27 (br s, 1H), 4.19-4.22 (m, 1H), 4.07-4.10 (m, 1H), 3.74 (d, J = 5.6 Hz, 2H), 3.57 (d, J = 6.0 Hz, 2H), 2.89 (s, 6H), 2.78-2.82 (m, 1H), 2.67-2.72 (m, 2H), 2.58-2.63 (m, 1H), 1.72-1.81 (m, 2H), 1.09-1.13 (m, 1H), 0.835-0.904 (m, 12H).

^{13}C-NMR (125 MHz; DMSO)

δ 168.8, 168.5, 151.2, 144.6, 136.0, 129.4, 129.0, 128.9, 127.8 (2), 123.9, 123.4, 119.1, 115.0, 82.4, 65.8, 63.2, 63.0, 50.0, 45.5, 45.0, 43.4, 32.1, 28.7, 28.6, 25.3, 21.3, 21.2, 19.2.

FAB-HRMS (*m*/*z*): Found [MH^+] 561.2632. $C_{29}H_{41}N_2O_7S$ requires *M*+H, 561.2634.

Synthesis of compound 3



(*Z*)-(2-(Hydroxymethyl)-4-(3-isopropyl-4-methylpentylidene)-5-oxotetrahydrofura n-2-yl)methyl 7-(diethylamino)-2-oxo-2*H*-chromene-3-carboxylate (3): To a stirred solution of 7-diethylamino coumarin 3-carboxylic acid (27.4 mg, 0.105 mmol) in THF (8 mL) were added dropwise thionyl chloride (8 μL, 0.116 mmol) and DMF (0.8 μL) at room temperature, and the mixture was refluxed at 70 °C for 2 h. The reaction mixture was concentrated to give 7-diethylamino coumarin 3-carbonyl chloride as a solid, which was used without further purification. The standard monoacylation procedure starting from **7** (40.0 mg, 0.150 mmol) was applied using 7-diethylamino coumarin 3-carbonyl chloride (29.4 mg, 0.105 mmol). After flash column chromatography with $CHCl_3$/MeOH (20:1), the compound **3** (27.9 mg, 36%) was isolated as orange-colored crystals, mp 97-98 °C [$CHCl_3$/MeOH (20:1)].

^{1}H-NMR (400 MHz; DMSO)

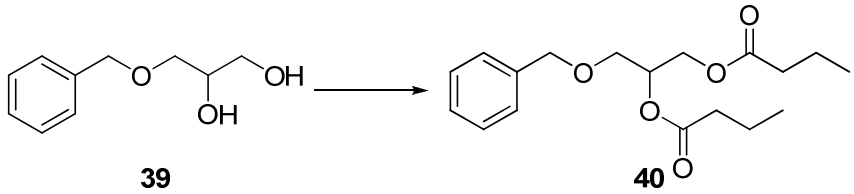
δ 8.45 (s, 1H), 7.58-7.61 (m, 1H), 6.77-6.80 (m, 1H), 6.54 (d, 1H, J = 2.3 Hz), 6.22-6.26 (m, 1H), 5.27 (t, 1H, J = 5.8), 4.28-4.36 (m, 2H), 3.58 (d, J = 6.0 Hz, 2H), 3.48 (q, J = 7.0 Hz, 4H), 2.78-2.89 (m, 2H), 2.61-2.68 (m, 1H), 2.50-2.51 (m, 1H), 1.64-1.74 (m, 2H), 1.10-1.16 (m, 6H), 1.06-1.09 (m, 1H), 0.742-0.853 (m, 12H).

^{13}C-NMR (100 MHz; DMSO)

δ 168.7, 162.8, 158.1, 156.7, 153.0, 149.4, 144.4, 131.7, 124.1, 109.8, 106.9, 106.4, 95.8, 82.9, 65.5, 63.1, 50.0, 44.3, 32.5, 28.9, 28.7, 28.6, 25.3, 21.3 (2), 19.2, 19.1, 12.2 (2)

FAB-HRMS (*m*/*z*): Found [MH^+] 514.2804. $C_{29}H_{40}NO_7$ requires *M*+H, 514.2805.

Synthesis of compound 14



39 **40**

3-(Benzyloxy)propane-1,2-diyl dibutyrate (40): Under argon, a solution of racemic 1-benzyl-glycerol **39** (0.74 g, 4.0 mmol)[2] in CH_2Cl_2 (5 mL) was treated with Et_3N (2.3 mL, 16 mmol) and stirred at room temperature for 15 min, and then treated with butanoic anhydride (2.0 mL, 12 mmol) and refluxed at 75 °C. After 3.5 h's reaction, the solvent was evaporated. The residue obtained was purified by flash column chromatography over silica gel using hexane/EtOAc (15:1) as eluant. The racemic compound **40** (1.18 g, 92%) was isolated as a light yellow oil.

^{1}H-NMR (500 MHz; $CDCl_3$)

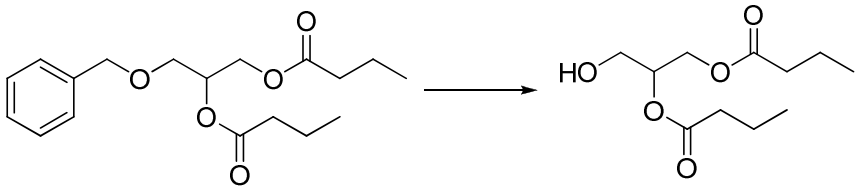
δ 7.26-7.35 (m, 5H), 5.23-5.27 (m, 1H), 4.51-4.57 (m, 2H), 4.34-4.37 (m, 1H), 4.18-4.21 (m, 1H), 3.58-3.60 (m, 2H), 2.25-2.32 (m, 4H), 1.58-1.73 (m, 4H), 0.916-0.961 (m, 6H).

^{13}C-NMR (125 MHz; $CDCl_3$)

δ 173.3, 172.9, 137.7, 128.4, 127.8, 127.7, 73.3, 70.0, 68.3, 62.7, 36.2, 36.0, 18.4 (2), 13.6 (2).

FAB-HRMS (*m*/*z*): Found [MH^+] 323.1853. $C_{18}H_{27}O_5$ requires *M*+H, 323.1858.

IR (neat): 2965-2876, 1740 (C=O) cm^{-1}.



40 **14**

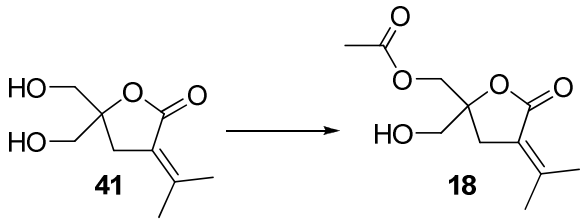
3-Hydroxypropane-1,2-diyl dibutyrate (14): A solution of **40** (1.12 g, 3.41 mmol) in EtOH (18 mL) was hydrogenated for 5 h under a balloon of hydrogen in the presence of 10% palladium on carbon (0.300 g). The reaction mixture was filtered, and the filtrate was concentrated in vacuo. The residue was purified by flash column chromatography over silica gel using hexane/EtOAc (2:1) as eluant. The compound **14** (0.580 g, 73%) was isolated as a light yellow oil.[3]

^{1}H-NMR (500 MHz; $CDCl_3$)

δ 5.08-5.12 (m, 1H), 4.32-4.36 (m, 1H), 4.20-4.24 (m, 1H), 3.73 (d, J = 5.0 Hz, 2H), 2.79

(br s, 1H), 2.30-2.35 (m, 4H), 1.61-1.70 (m, 4H), 0.935-0.973 (m, 6H).
^{13}C-NMR (125 MHz; $CDCl_3$)
δ 173.7, 173.4, 72.1, 62.3, 61.4, 36.2, 36.0, 18.4 (2), 13.6 (2).
FAB-HRMS (*m*/*z*): Found [MH^+] 233.1384. $C_{11}H_{21}O_5$ requires *M*+H, 233.1389.
IR (neat): 3473 (OH), 2966-2878, 1740 (C=O), 1667 cm^{-1}.

Synthesis of compound 18



(2-(Hydroxymethyl)-5-oxo-4-(propan-2-ylidene)tetrahydrofuran-2-yl)methyl acetate (18): The standard monoacylation procedure starting from 5,5-bis(hydromethyl)-3-(methylethylidene)-4,5-dihydrofuran-2-one **41** (140 mg, 0.750 mmol) was applied using acetic anhydride (15 μL, 0.150 mmol). After flash column chromatography with hexane/EtOAc (1:1), the monoacetate product **18** (11.4 mg, 7%) was isolated as a colorless oil.
^{1}H-NMR (500 MHz; $CDCl_3$)
δ 4.24 (d, *J* = 12.0 Hz, 1H), 4.17 (d, *J* = 12.0 Hz, 1H), 3.71 (d, *J* = 12.0 Hz, 1H), 3.63 (d, *J* = 12.0 Hz, 1H), 2.82-2.86 (m, 1H), 2.64-2.68 (m, 1H), 2.26-2.27 (m, 3H), 2.09 (s, 3H, $CH_2OOC\mathit{H_3}$), 1.89 (t, *J* = 1.5 Hz, 3H)
^{13}C-NMR (125 MHz; $CDCl_3$)
δ 170.9, 169.1, 151.9, 118.8, 81.1, 65.5, 64.8, 32.1, 24.6, 20.7, 20.0.
FAB-HRMS (*m*/*z*): Found [MH^+] 229.1077. $C_{11}H_{17}O_5$ requires *M*+H, 229.1076.
IR (neat): 3451 (OH), 2958-2873, 1749 (C=O), 1667 cm^{-1}.

Binding assay of compounds for full length PKCδ and recombinant δC1b domain.
Enzyme-lignd interactions were assessed *in vitro* in terms of the ability of the ligand to displace bound [20-^{3}H]phorbol-12,13-dibutyrate (PDBu) from recombinant human PKCδ and δC1b domain in the presence of phosphatydylserine.

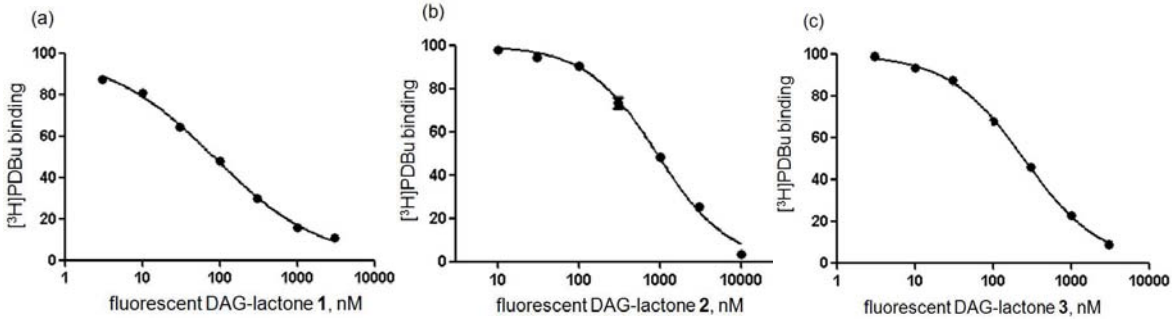
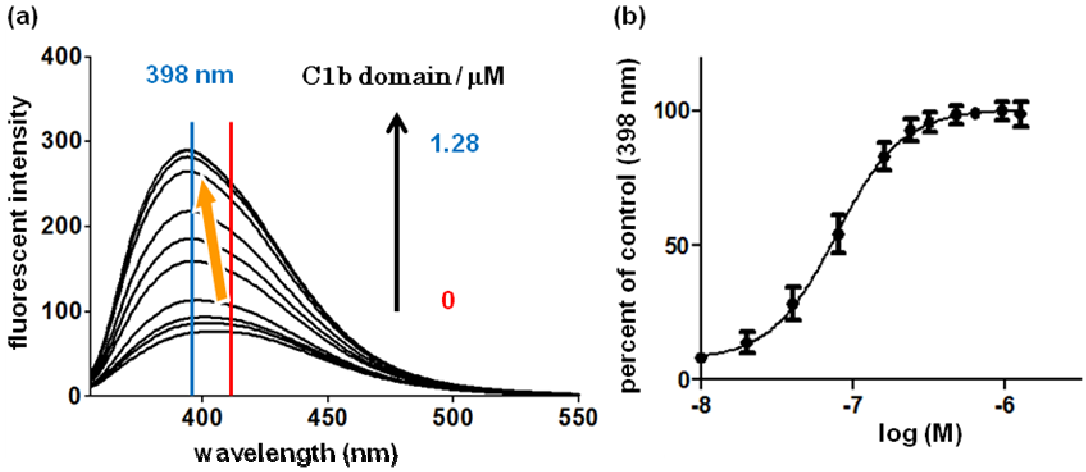


Figure S1. Inhibition of [^{3}H]PDBu binding by fluorescent DAG-lactones **1-3**.
(a) fluorescent DAG-lactone **1**, K_i: 35.9 ± 1.6 nM. (b) fluorescent DAG-lactone **2**, K_i: 368 ± 9.5 nM. (c) fluorescent DAG-lactone **3**, K_i: 93.3 ± 8.5 nM. (mean ± S.E.)



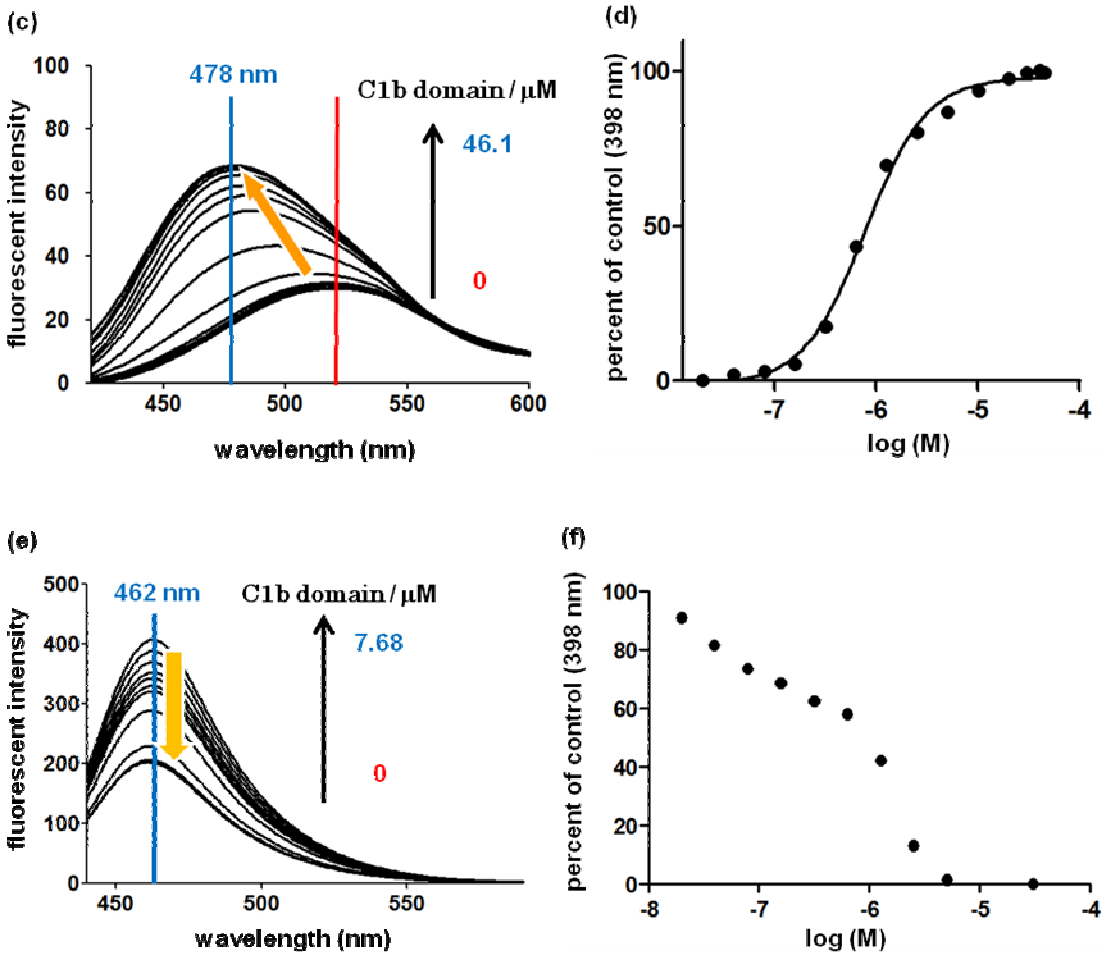


Figure S2. Fluorescent spectra with titration of δC1b domain and the relative intensity changes. (a) Fluorescent spectra of fluorescent DAG-lactone **1** during titration of δC1b domain. (b) Curve fitting of plots of relative intensity (%) (λ_{em} = 398 nm). (c) Fluorescent spectra of fluorescent DAG-lactone **2** with C1b domain titartion. (d) Curve fitting of plots of relative intensity (%) (λ_{em} = 478 nm). (e) Fluorescent spectra of fluorescent DAG-lactone **3** with C1b domain titartion. (f) Plots of relative intensity (%) (λ_{em} = 462 nm).

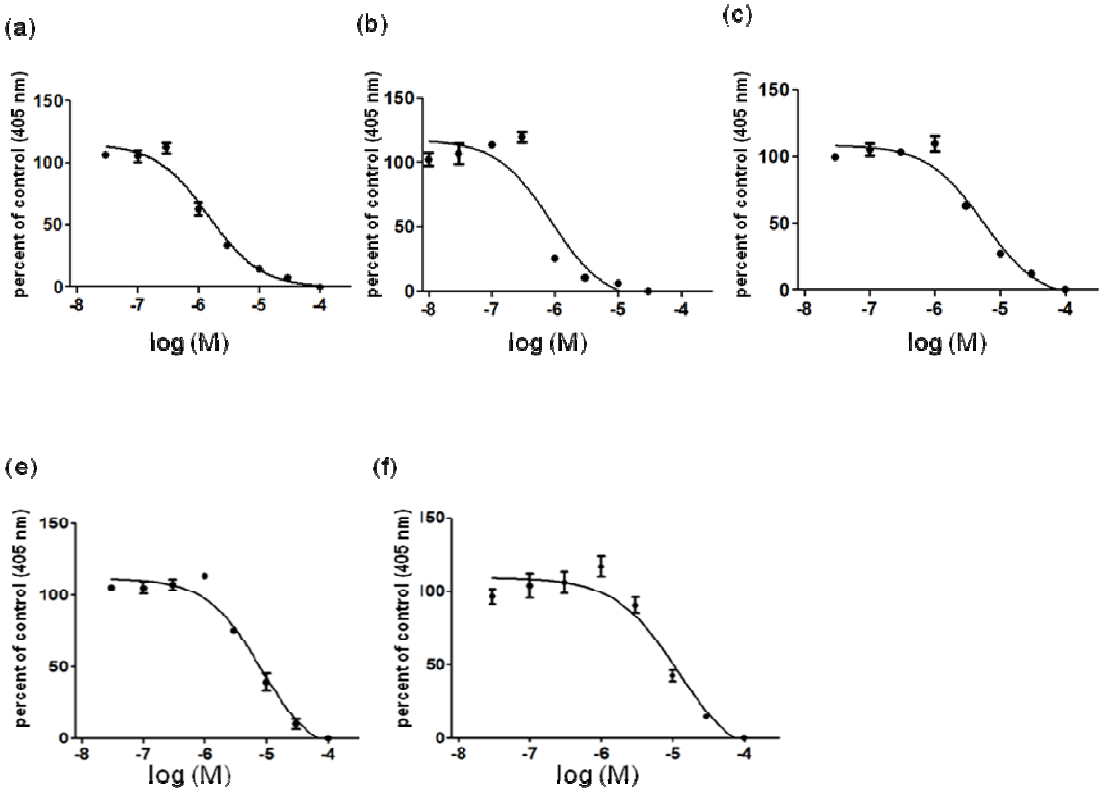


Figure S3. Inhibition of fluorescent DAG-lactone **1** by PKC ligands based on fluorescence-quenching analysis recorded by microplate reader.

(a) Compound **8**, IC_{50} = 1.47 μM, (b) compound **9**, IC_{50} = 0.87 μM, (c) compound **10**, IC_{50} = 7.91 μM, (d) compound **11**, IC_{50} = 11.6 μM, (e) compound **17**, IC_{50} = 5.54 μM.

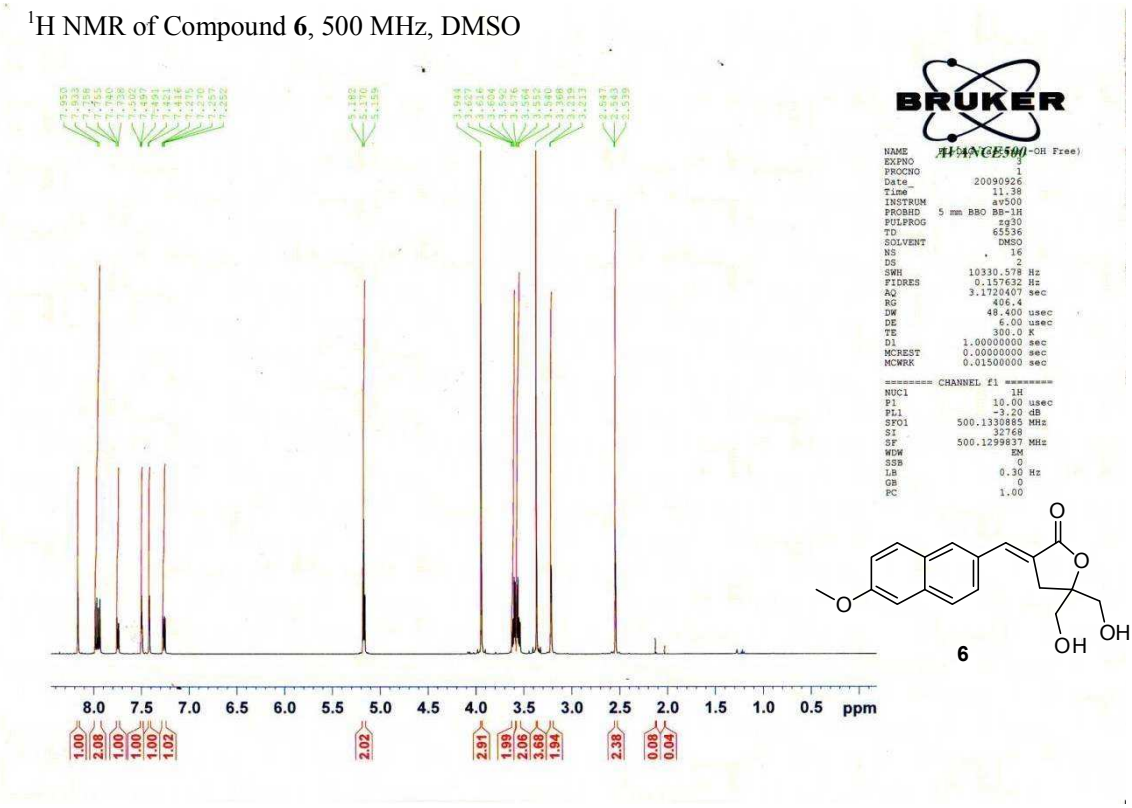
References

[1] S. E. Kazzouli, N. E. Lewin, P. M. Blumberg, V. E. Marquez, *J. Med. Chem.* **2008**, *51*, 5371-5386.

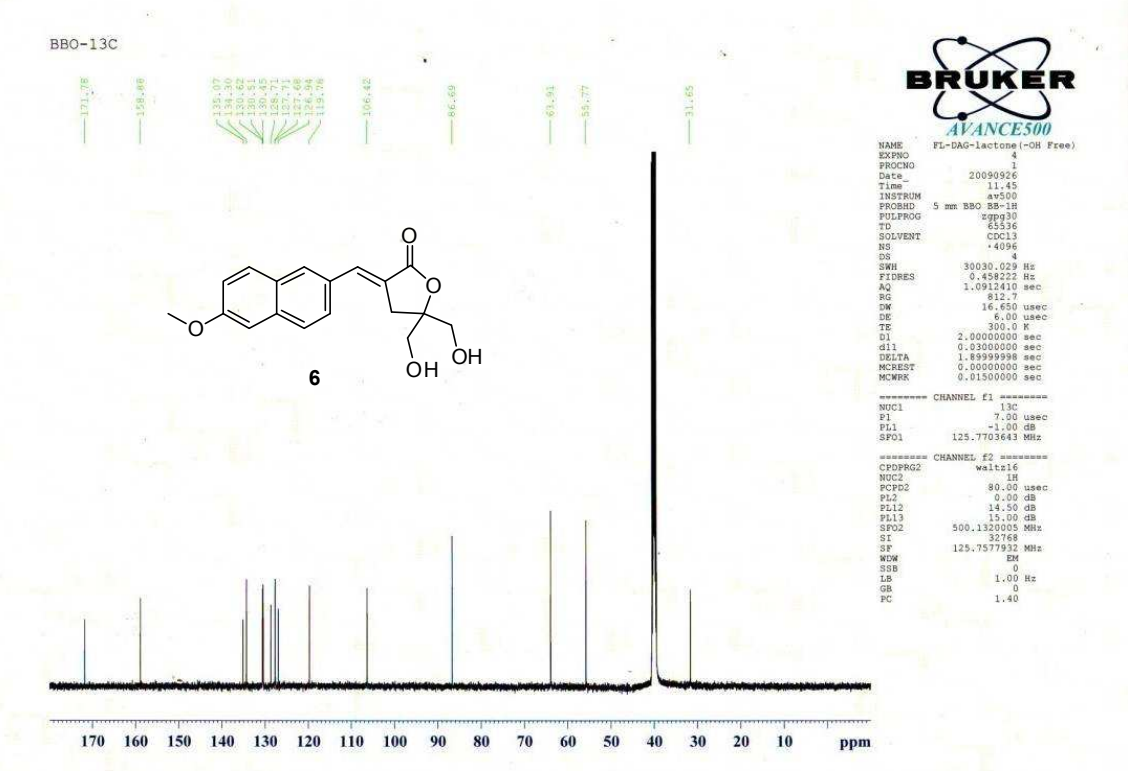
[2] K. Nacro, B. Bienfait, N. E. Lewin, P. M. Blumberg, V. E. Marquez, *Bioorg. Med. Chem. Lett.* **2000**, *10*, 653-655.

[3] A. Liljeblad, E. Vanttinen, L. Kanerva, *Chirality* **1999**, *11*, 432-439.

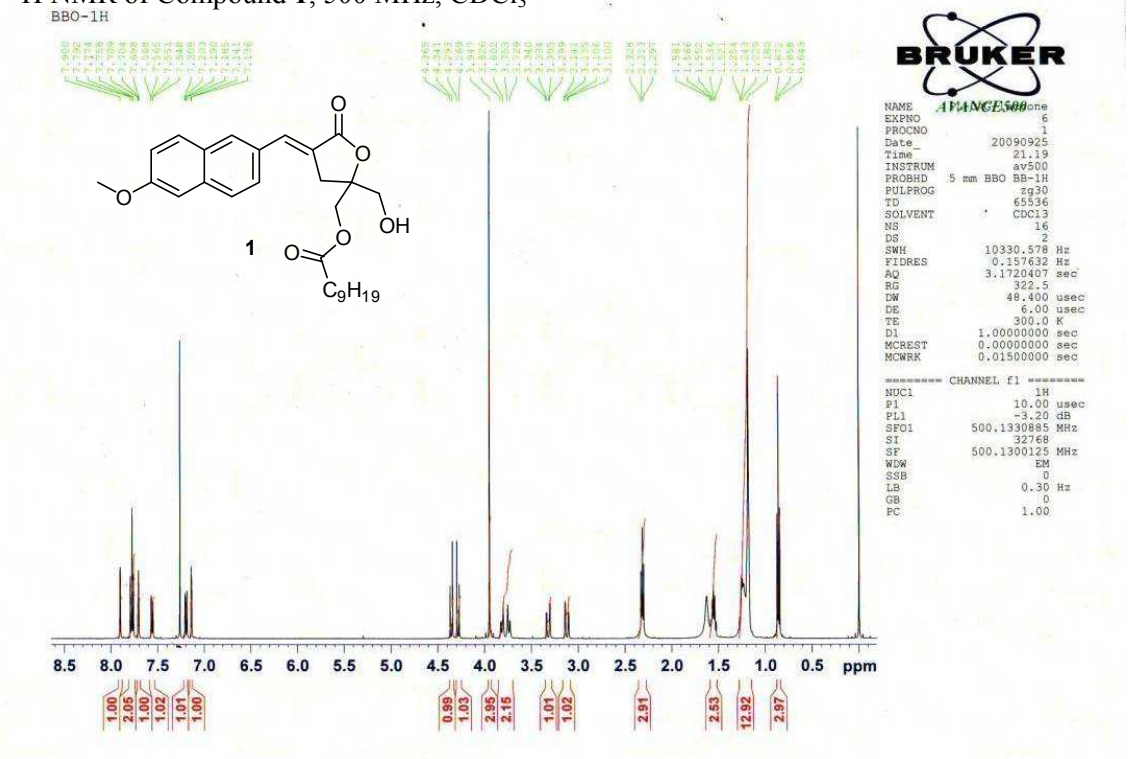
^{1}H NMR of Compound **6**, 500 MHz, DMSO



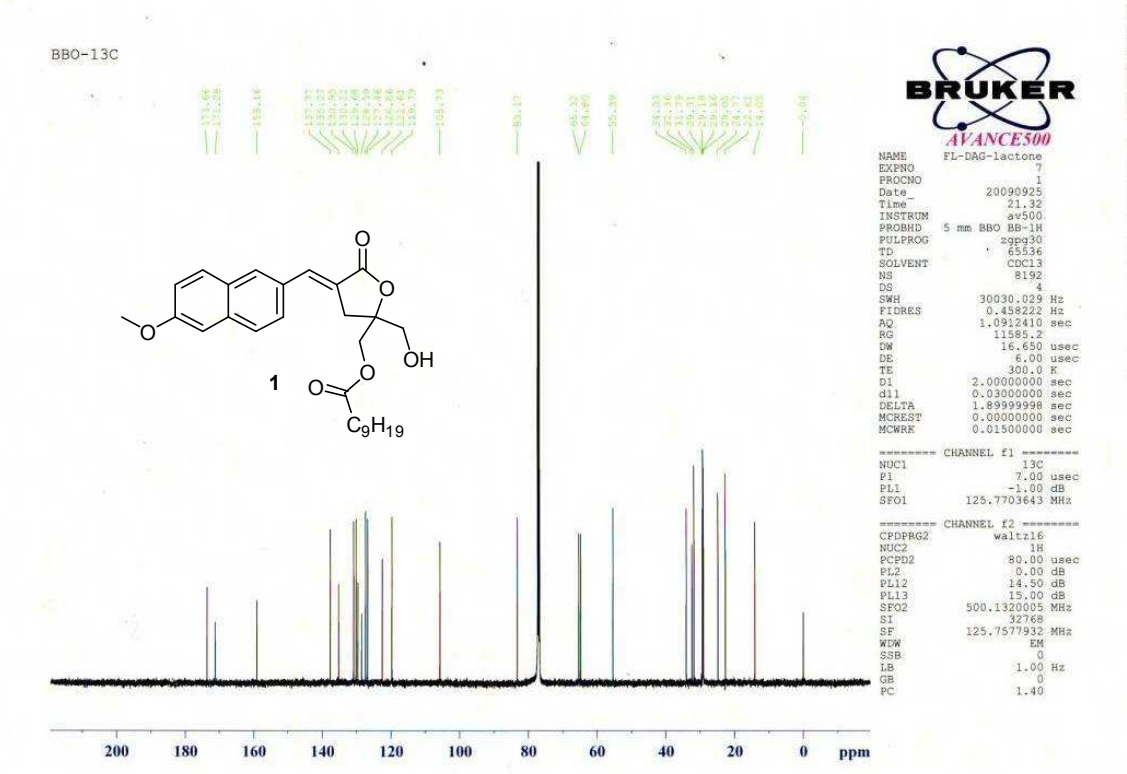
^{13}C NMR of Compound **6**, 125 MHz, DMSO



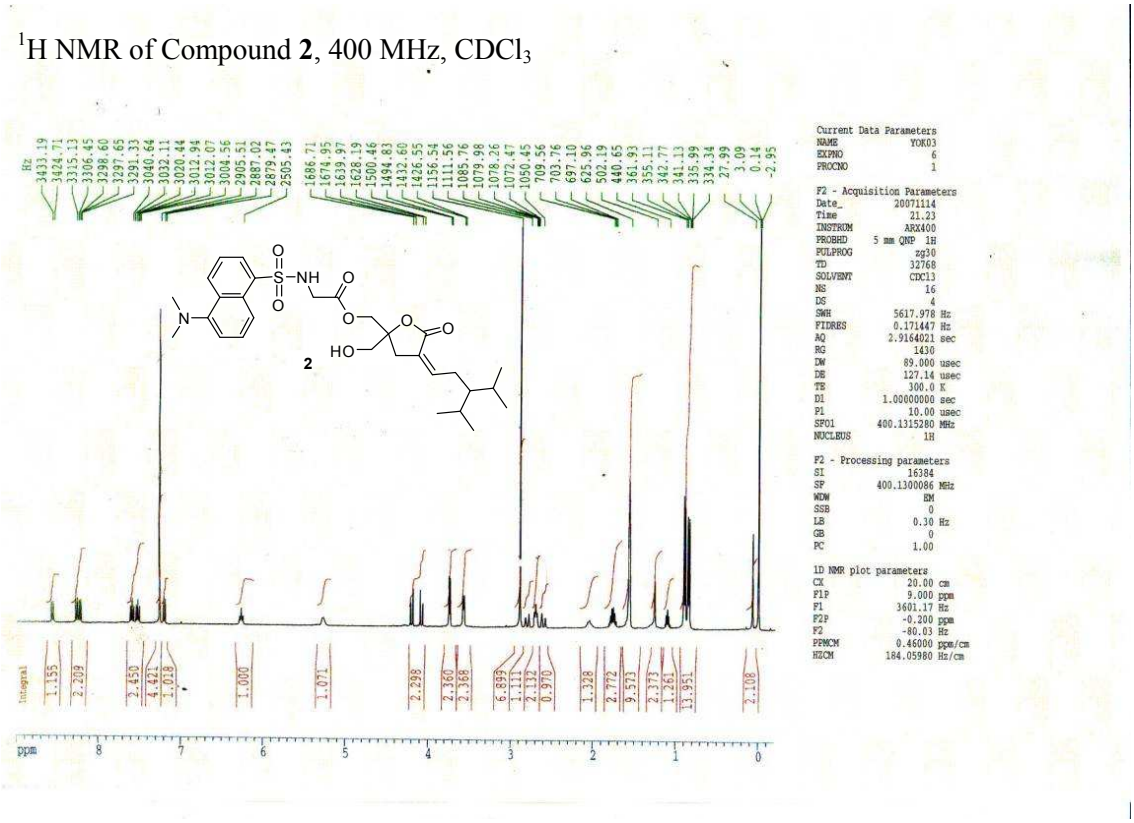
^{1}H NMR of Compound **1**, 500 MHz, $CDCl_3$



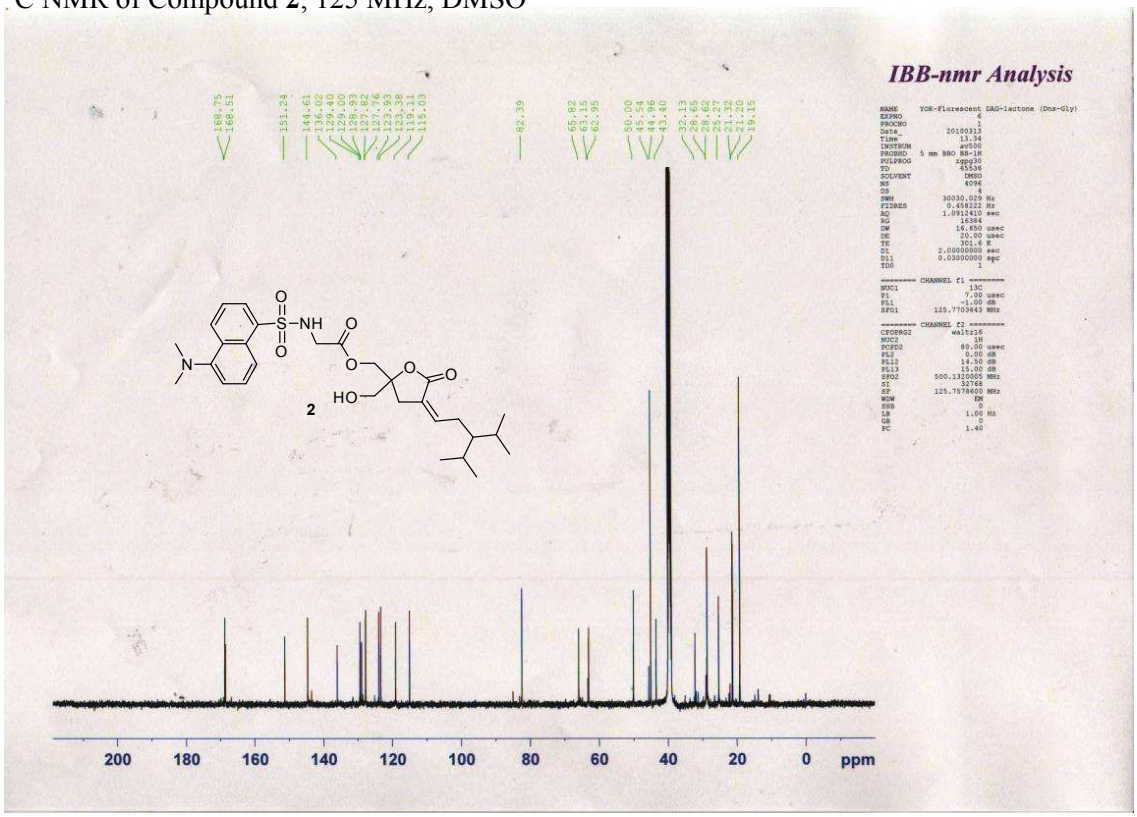
^{13}C NMR of Compound **1**, 125 MHz, $CDCl_3$



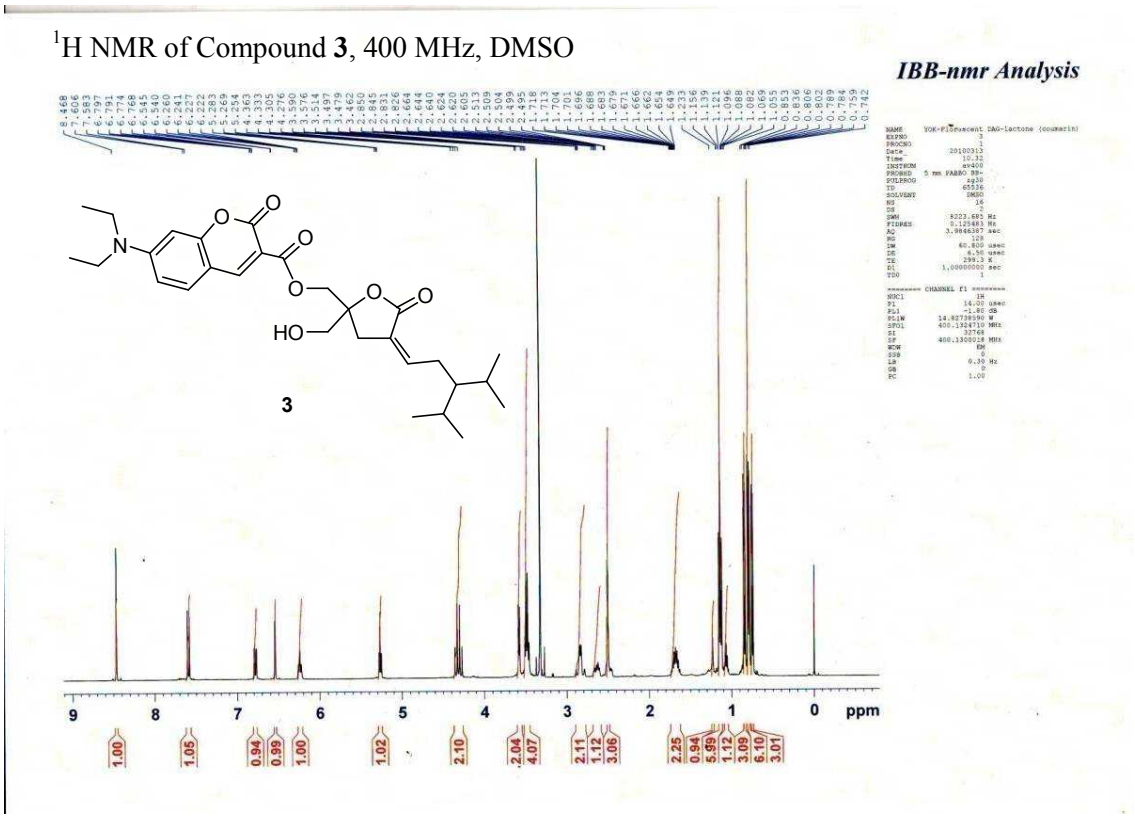
^{1}H NMR of Compound **2**, 400 MHz, $CDCl_3$



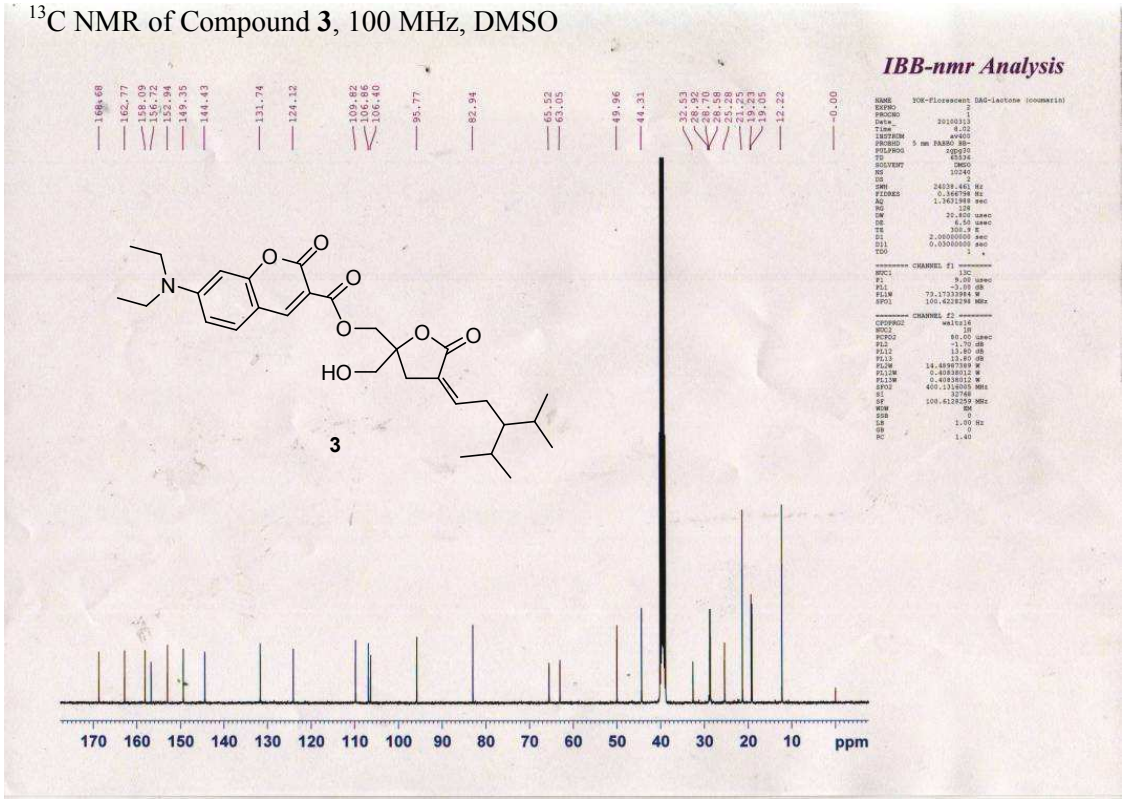
^{13}C NMR of Compound **2**, 125 MHz, DMSO



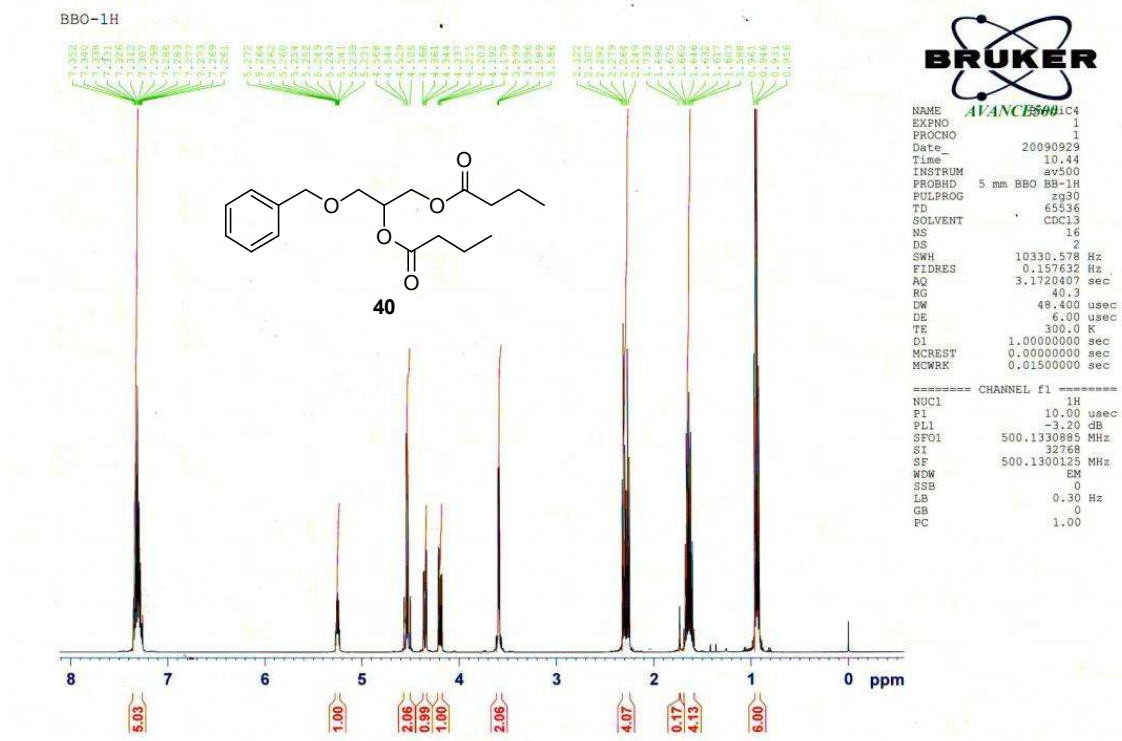
^{1}H NMR of Compound **3**, 400 MHz, DMSO



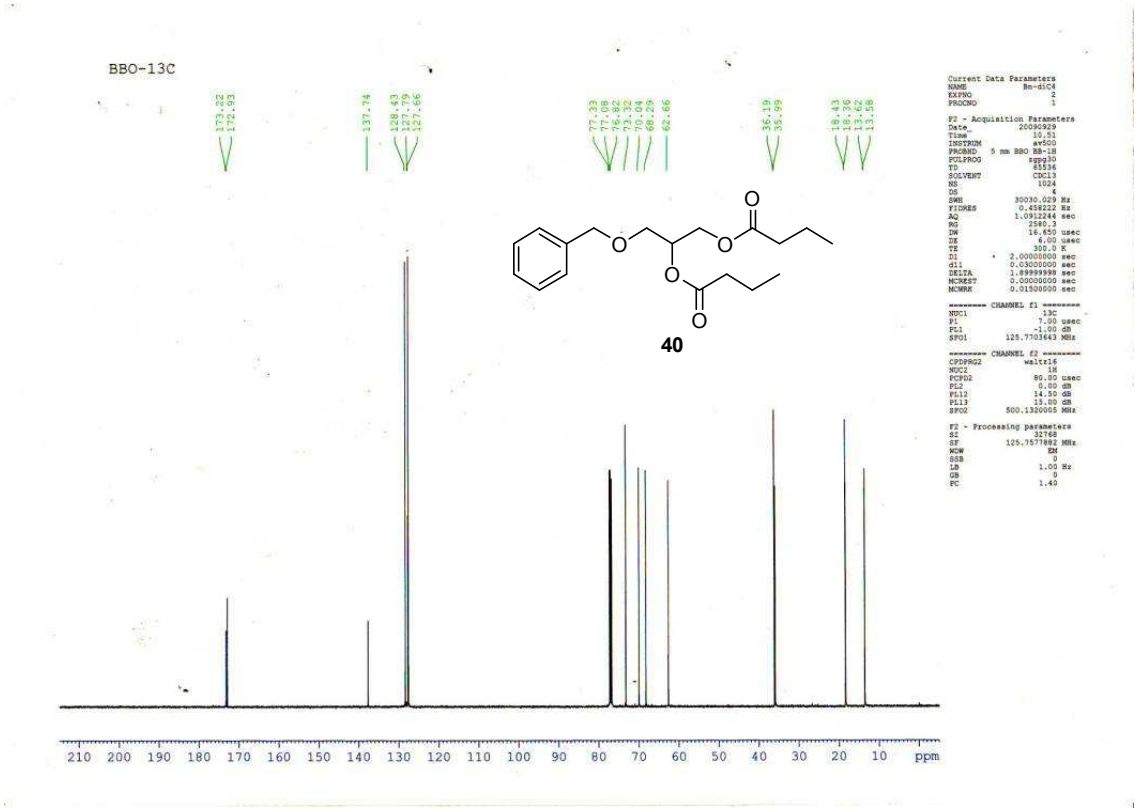
^{13}C NMR of Compound **3**, 100 MHz, DMSO



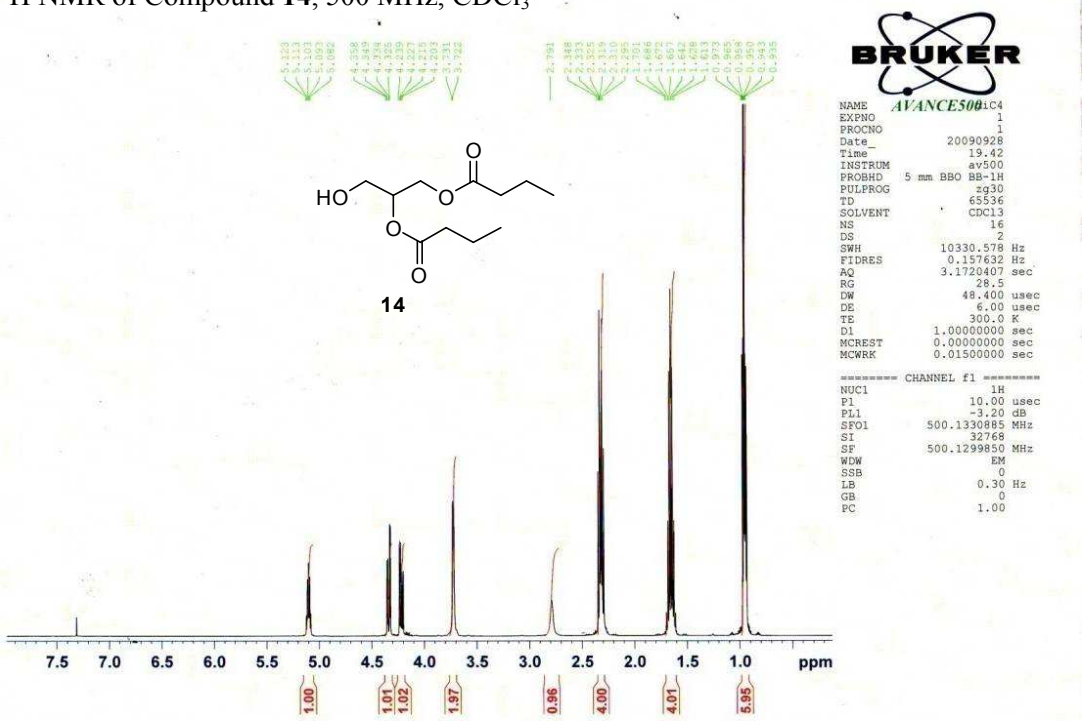
^{1}H NMR of Compound **40**, 500 MHz, $CDCl_3$



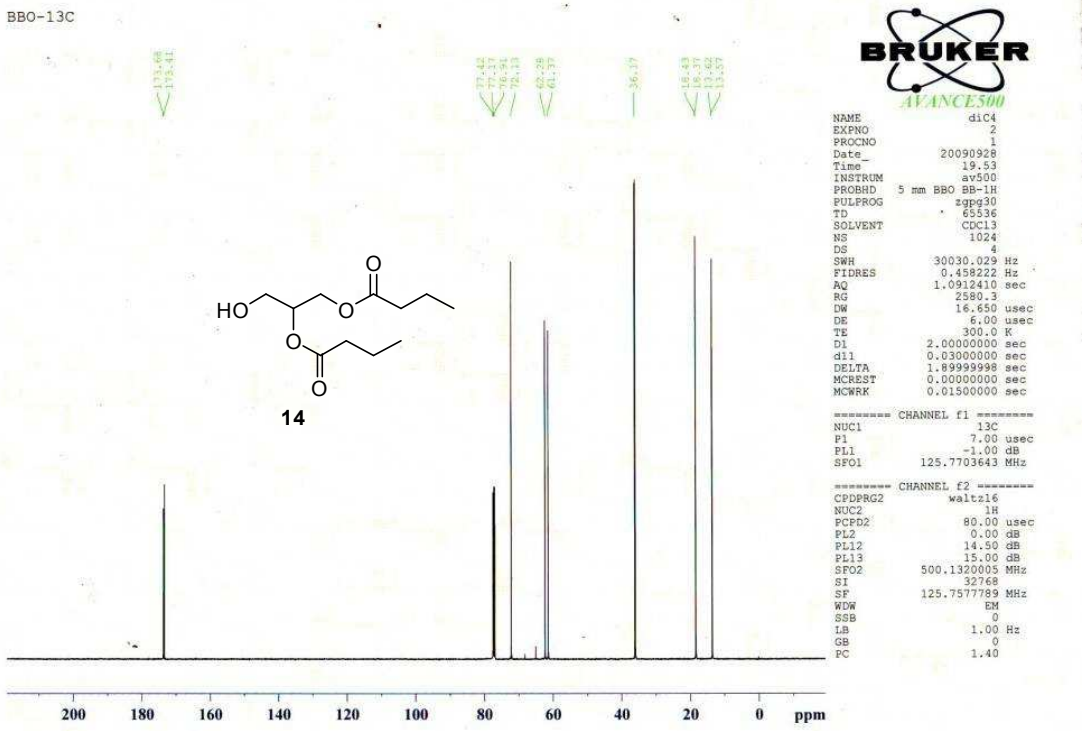
^{13}C NMR of Compound **40**, 125 MHz, $CDCl_3$



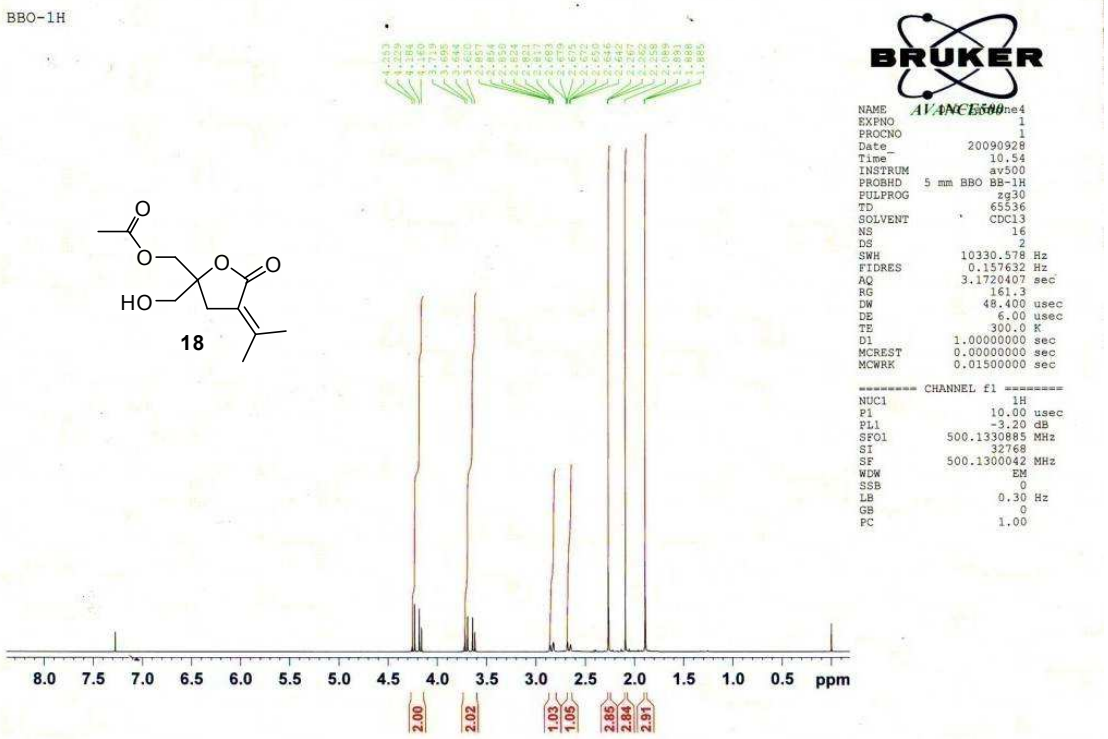
^{1}H NMR of Compound **14**, 500 MHz, $CDCl_3$



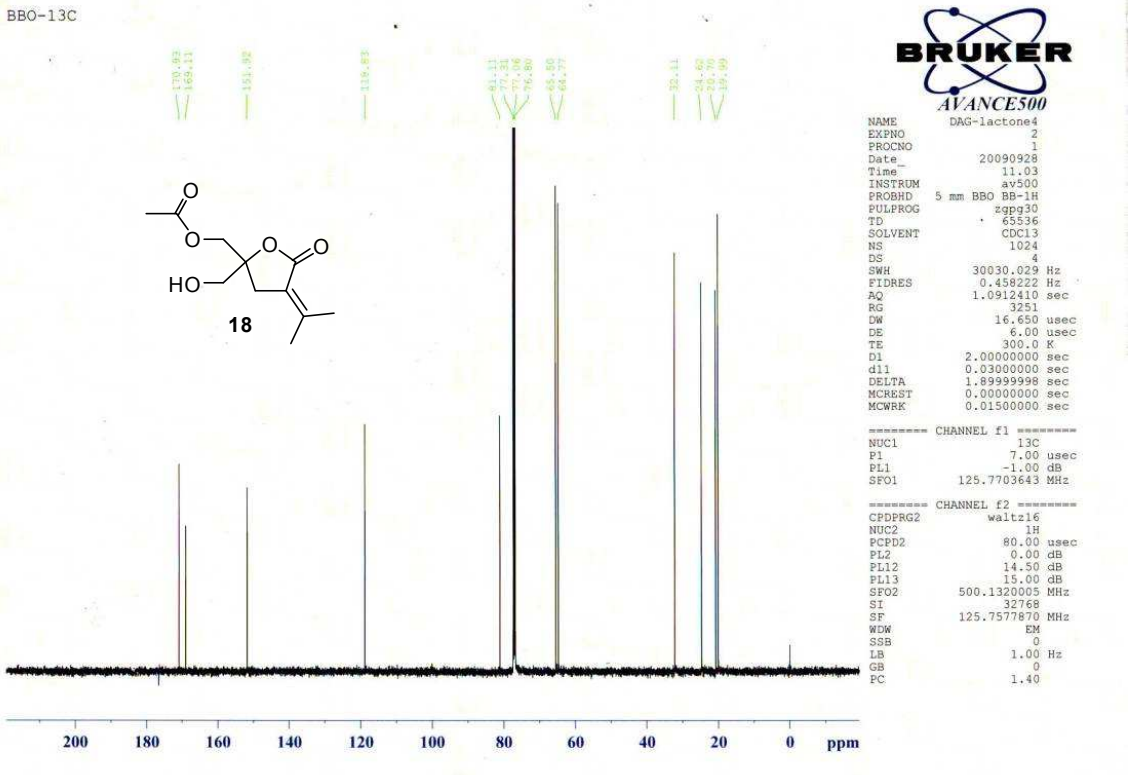
^{13}C NMR of Compound **14**, 125 MHz, $CDCl_3$



^{1}H NMR of Compound **18**, 500 MHz, $CDCl_3$



^{13}C NMR of Compound **18**, 125 MHz, $CDCl_3$



Bioconjugate Chemistry

ARTICLE

pubs.acs.org/bc

Synthesis and Evaluation of Nanoglobular Macrocyclic Mn(II) Chelate Conjugates as Non-Gadolinium(III) MRI Contrast Agents

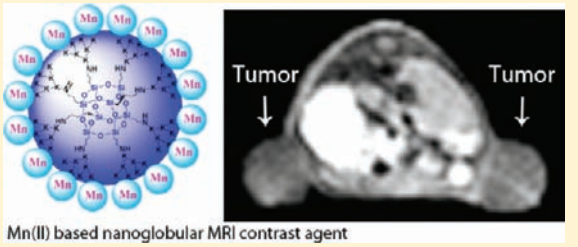
Mingqian Tan,[†,‡] Zhen Ye,[§] Eun-Kee Jeong,[§] Xueming Wu,[†] Dennis L. Parker,[§] and Zheng-Rong Lu*[,†]

[†]Department of Biomedical Engineering, Case Western Reserve University, Cleveland, Ohio 44106, United States

[‡]Laboratory of Biomedical Material Engineering, Dalian Institute of Chemical Physics, Chinese Academy of Sciences, Dalian 116023, China

[§]Department of Radiology, University of Utah, Salt Lake City, Utah 84108, United States

ABSTRACT: Because of the recent observation of the toxic side effects of Gd(III) based MRI contrast agents in patients with impaired renal function, there is strong interest on developing alternative contrast agents for MRI. In this study, macrocyclic Mn(II) chelates were conjugated to nanoglobular carriers, lysine dendrimers with a silsesquioxane core, to synthesize non-Gd(III) based MRI contrast agents. A generation 3 nanoglobular conjugate of Mn(II)-1,4,7-triaazacyclononane-1,4,7-triacetate-GA amide (G3-NOTA-Mn) was also synthesized and evaluated. The per ion T_1 and T_2 relaxivities of G2, G3, G4 nanoglobular Mn(II)-DOTA monoamide conjugates decreased with increasing generation of the carriers. The T_1 relaxivities of G2, G3, and G4 nanoglobular Mn(II)-DOTA conjugates were 3.3, 2.8, and 2.4 mM^{-1} s^{-1} per Mn(II) chelate at 3 T, respectively. The T_1 relaxivity of G3-NOTA-Mn was 3.80 mM^{-1} s^{-1} per Mn(II) chelate at 3 T. The nanoglobular macrocyclic Mn(II) chelate conjugates showed good in vivo stability and were readily excreted via renal filtration. The conjugates resulted in much less nonspecific liver enhancement than $MnCl_2$ and were effective for contrast-enhanced tumor imaging in nude mice bearing MDA-MB-231 breast tumor xenografts at a dose of 0.03 mmol Mn/kg. The nanoglobular macrocyclic Mn(II) chelate conjugates are promising nongadolinium based MRI contrast agents.



Mn(II) based nanoglobular MRI contrast agent

INTRODUCTION

Gadolinium-based chelates are the most commonly used contrast agents for clinical magnetic resonance imaging (MRI). However, the recently reported nephrogenic system fibrosis associated with Gd(III) based contrast agents causes serious safety concerns, especially for use in patients with abnormal kidney function.[1−3] There is continual interest in developing alternative MRI contrast agents with much less toxicity. Manganese(II) is an essential element for humans, and has relatively high electronic spins (5/2) and fast water exchange rate.[4] It is less toxic than other paramagnetic metal ions at low concentrations. Mn(II) chelates have been investigated as MRI contrast agents over the past decades. Two Mn(II) based contrast agents, hepatocyte-specific Mn(II) dipyridoxal diphosphate (Mn-DPDP) and an oral formulation containing $MnCl_2$, have been clinically used for liver imaging and gastro-intestinal imaging.[5] As compared to Gd(III) based agents, Mn(II) based MRI contrast agents have been investigated less.

The main challenges for Mn(II) based MRI contrast agents are the low chelation stability and low relaxivity of Mn(II) chelates. Low stability of Mn(II) chelates can result in the release of free Mn(II) ions in vivo. Overexposure to free Mn(II) ions could lead to neurodegenerative damage, such as Parkinson's disease.[6] The design of Mn(II) chelates with high stability is essential to minimize their potential toxicity as MRI contrast agents. Macrocyclic chelates of transition metal ions have shown higher kinetic stability than linear chelates. Mn(II) forms thermodynamically and kinetically stable chelates with macrocyclic ligands, such as DOTA (1,4,7,10-tetraazacyclododecane-1,4,7,10- tetraacetic acid), DO3A (1,4,7,10-tetraazacyclododecane-1,4,7-triacetic acid), and NOTA (1,4,7-triaazacyclononane-1,4,7-triacetic acid).[4,7,8] Stability constants (log K) of Mn(II)-DOTA, Mn(II)-DO3A7, and Mn(II)-NOTA8 are 19.89, 19.4, and 14.9, respectively. The macrocyclic Mn(II) chelates with high kinetic and thermodynamic stability can minimize in vivo release of free Mn(II) ions from the contrast agents.

Low relaxivity of Mn(II) based contrast agents could be overcome by conjugating multiple stable Mn(II) chelates to biocompatible polymers. Dendrimers are a class of highly functionalized macromolecules with precisely defined structures.[9] A large number of Mn(II) chelates can be conjugated to the surface of dendrimers, resulting in nanosized contrast agents with high overall relaxivity and improved contrast enhancement at reduced doses. Lysine dendrimers with a symmetric silsesquioxane cubic core were recently reported as a nanoglobular platform for the delivery of therapeutics and

Received: December 14, 2010
Revised: March 22, 2011
Published: April 07, 2011

ACS Publications © 2011 American Chemical Society

diagnostics.[10−12] Generations 1−3 nanoglobular Gd-DOTA monoamide conjugates have shown increased relaxivity and size-dependent contrast enhancement for magnetic resonance angiography and cancer imaging.[11] The conjugation of Mn(II)-DOTA into a CLT1 peptide targeted G3 nanoglobular lysine dendrimer resulted in a tumor specific contrast agent with high overall relaxivity and significant tumor enhancement at a low dose.[13]

In this study, we synthesized Mn(II)-DOTA monoamide conjugates of generations 2−4 nanoglobules to study size effect on the Mn(II) based nanoglobular MRI contrast agents. A generation 3 nanoglobular Mn(II)-NOTA-GA conjugate was also synthesized to study ligand effect on the relaxivity and in vivo contrast enhancement of the agents. The nanoglobular Mn(II)-based MRI contrast agents were characterized by mass spectrometry and inductively coupled plasma-optical emission spectroscopy (ICP-OES). The relaxivities of the nanoglobular Mn(II) agents were measured. The effectiveness of the Mn(II) based contrast agents in contrast enhanced MRI were evaluated in mice bearing breast cancer xenografts at a low dose.

MATERIALS AND METHODS

4-(4,7-Bis(2-*tert*-butoxy-2-oxoethyl)-1,4,7-triazonan-1-yl)-5-*tert*-butoxy-5-oxopentanoic acid [NODA-GA(tBu)$_3$] was purchased from CheMatech (Dijon, France). 1-Hydroxybenzotriazole (HOBt), 2-(1*H*-benzotriazole-1-yl)-1,1,3,3-tetramethyluronium hexafluorophosphate (HBTU), and N_α,N_ε-di-*t*-BOC-L-lysine dicyclohexylammonium salt [(di-*t*-BOC)$_2$-L-lys-OH•DCHA] were purchased from Nova Biochem (Darmstadt, Germany). 1,4,7,10-Tetraazacyclododecane-1,4,7-tris-*tert*-butyl acetate-10-acetic acid [DOTA-tris(t-Bu)] was purchased from Macrocyclics (Dallas, TX). *N*,*N*-Diisopropylethyl amine (DIPEA), trifluoroacetic acid (TFA), and *N*,*N*-dimethylformamide anhydrous (DMF) were purchased from Alfa Aesar (Ward Hill, MA). Kaiser test kit was purchased from Sigma-Aldrich, Inc. (Louis, MO). All reagents were used without further purification unless otherwise stated. Dendrimers and their conjugates were purified by ultrafiltration with Millipore's Amicon Ultra-15 centrifugal filter of 3 kDa molecular weight cutoff in deionized water. Matrix-assisted laser desorption/ionization time-of-flight (MALDI-TOF) mass spectra were acquired on a Voyager DE-STR spectrometer (PerSpeptive BioSystems) in linear mode with α-cyano-4-hydroxycinnamic acid as a matrix. The Mn(II) content was measured by inductively coupled plasma-optical emission spectroscopy (ICP-OES Optima 3100XL, Perkin-Elmer, Norwalk, CT).

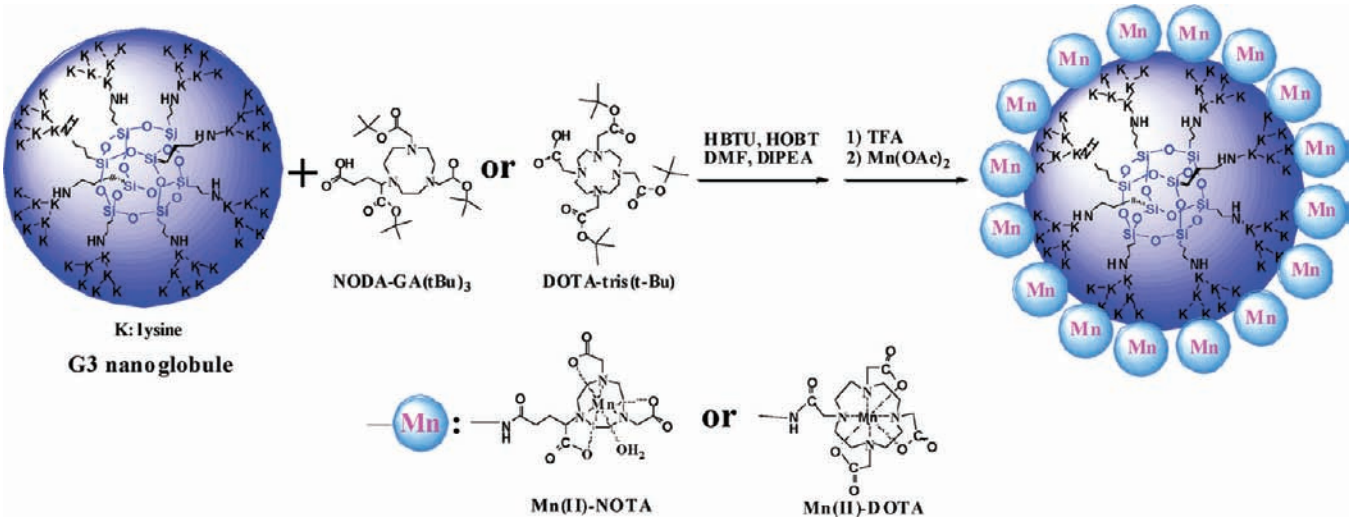
Synthesis of Nanoglobule-(Mn-DOTA) Monoamide Conjugates. Generations 2−4 (G2, G3, and G4) nanoglobules with an OAS core were synthesized using standard solution-phase peptide synthesis chemistry.[11,14] Octa(3-aminopropyl)-silsesquioxane hydrochloride (OctaAmmonium POSS-HCl) (0.70 g, 0.597 mmol), HOBt (2.70 g, 20.0 mmol), and (di-*t*-BOC)$_2$-L-lys-OH•DCHA (10.4 g, 20.0 mmol) were dissolved in 30 mL DMF. To the above solution was added 10 mL of DIPEA, and the mixture was stirred at room temperature for 48 h. The reaction mixture was added to 400 mL of 0.5 M citric acid aqueous solution giving a white, sticky precipitate. The precipitate was then treated with acetonitrile giving a colorless solid. The solid product was collected by filtration and dried under vacuum. Yield of [(t-BOC)$_2$-L-lysine]$_8$-OAS was 1.67 g, 80%. [(t-BOC)$_2$-L-lysine]$_8$-OAS (1.67 g) was dissolved in 7 mL ice-cold trifluoroacetic acid (TFA) and stirred at room temperature for one hour to remove t-BOC protection. The residue was treated with anhydrous diethyl ether giving a colorless solid product. The yield of (L-lysine)$_8$-OAS trifluoroacetate (G1) was 1.32 g (59.6%). The generations 2-4 nanoglobules were synthesized following the general procedure of G1.

The synthesis of G2 nanoglobular Mn(II)-DOTA monoamide was used as an example. G2 nanoglobule (50 mg, 6.57 μmol), DOTA-tris(*t*-Bu) (240 mg, 420 μmol), HBTU (159 mg, 420 μmol), HOBt (57 mg, 420 μmol), and DIPEA were dissolved in DMF (2.5 mL) and stirred at room temperature for 24 h. The product was precipitated by adding diethyl ether into the reaction mixture. The oily precipitate was washed several times with diethyl ether, and the *t*-butyl groups were removed by dissolving the precipitate in a mixture of trifluoroacetic acid and methylene chloride (6 mL, volume/volume = 1:1) for 4 h at room temperature. The residue was treated with ice-cold diethyl ether and purified with ultracentrifugation and then by dialysis to give a white solid after lyophilization. Yield of G2-DOTA monoamide conjugate was 65 mg, 70.6%, based on the G2 dendrimer. MALDI-TOF (m/z, $[M+H]^+$): 12 855 (calculated for G2 with 23 DOTA on average), 12 848 (observed). A mixture of G2 nanoglobule−DOTA conjugate (31 mg, 2.2 μmol) and Mn(OAc)$_2$ (70 mg, 282 μmol) in 1 mL 0.5 M ammonium acetate solution was refluxed for 50 min. The final product G2 nanoglobule-(Mn-DOTA) monoamide conjugate was further purified by dialysis with a membrane of 1000 Da molecule weight cutoff to remove the excess free Mn(II) ions. The yield of purified G2 nanoglobule-(Mn-DOTA) monoamide conjugate was 14 mg, 41%. The G3 and G4 nanoglobule-(Mn-DOTA) monoamide conjugates were similarly synthesized. Yield of G3-DOTA conjugate was 85 mg, 91%. MALDI-TOF (m/z, $[M+H]^+$): 28 560 (calculated for G3 with 53 DOTA on average), 28 785 (observed). Yield of G4-DOTA conjugate was 82 mg, 76.7%. MALDI-TOF (m/z, $[M+H]^+$): 54 465 (calculated for G4 with 99 DOTA on average), 54 399 (observed).

Synthesis of G3 Nanoglobule-(Mn-NOTA-GA) Conjugate. G3 nanoglobule (30 mg, 1.95 μmol), NODA-GA(tBu)$_3$ (100 mg, 184 μmol), HBTU (71 mg, 184 μmol), and HOBt (25 mg, 184 μmol) with DIPEA were reacted according to the above procedure to give G3 nanoglobular NOTA-GA conjugate. MALDI-TOF (m/z, $[M+H]^+$): 27 584 (calculated for G3 with 55 NOTA); 27 637 (observed). Yield of G3-NOTA conjugate was 55 mg, 92%. The complexation of G3 nanoglobule-(NOTA)$_{55}$ conjugate (40 mg, 1.45 μmol) with 4-fold excess Mn(OAc)$_2$ gave G3 nanoglobule-(Mn-NOTA)$_{55}$ as colorless solid (44 mg, 97%).

Measurement of Relaxivities of the Nanoglobular Contrast Agents. The T_1 and T_2 values of the aqueous solutions containing contrast agents were determined on a Siemens 3T MRI scanner at room temperature. The water proton T_1 relaxation times without and with the agents at different concentrations were measured using an inversion recovery prepared turbo spin echo imaging pulse sequence. The inversion times (TI) were 25, 35, 50, 75, 100, 200, 400, 800, 1600, and 3200 ms with repetition time (TR) = 5000 ms and echo time (TE) = 16.0 ms. The net magnetization of each sample was fit for multiparametric nonlinear regression analysis using a Marquardt−Levenberg algorithm and a *MATLAB* program to calculate T_1 and M_0. Relaxivity r_1 was determined from the slope of $1/T_1$ versus $[Mn^{2+}]$ plot. The T_2 relaxation times of the samples were measured using a

Scheme 1. Synthesis of G3 Nanoglobular Macrocyclic Mn(II) Chelate Conjugates



turbo spin echo sequence with turbo factor 3. The parameters were TE = 12, 24, 35, 47, 59, 71, 83, 94, and 106 ms, and TR = 3000 ms. T_2 values were calculated from $M_{TE} = M_0\, e^{(-TE/T_2)}$ after nonlinear regression with various TE values. The r_2 relaxivity was determined from the slope of $1/T_2$ versus $[Mn^{2+}]$ plot. The Mn(II) concentrations of the samples were measured by ICP-OES for r_1 and r_2 calculation.

Animal Tumor Model. Human breast cancer MDA-MB-231 cells were grown in L-15 medium supplemented with 10% fetal bovine serum and 1% penicillin at 37 °C in 5% CO_2. Female athymic nu/nu mice (6 weeks, 20−25 g) were purchased from the National Cancer Institute (Frederick, MD). Each mouse was subcutaneously implanted in both flanks with 2×10^6 MDA-MB-231 cells mixed with an equal volume of in a mixture of Matrigel (50 μL culture medium and 50 μL Matrigel). Three to four weeks after inoculation, tumors reached an average size of 0.5 cm in diameter. The mice were randomly divided into groups with three mice per group for MRI study. All animal experiments were performed in accordance with an animal protocol approved by the IACUC of the University of Utah.

Contrast Enhanced MRI. The mice were anesthetized by injecting a mixture of 12 mg/kg xylazine and 80 mg/kg ketamine. MRI contrast agents were administered via a tail vein at a dose of 0.03 mmol Mn/kg. The contrast agent $MnCl_2$ was injected at 0.05 mmol/kg. The mice were placed in a human wrist coil and scanned in a Siemens Trio 3 T MRI scanner before injection and at 2, 5, 10, 15, 20, and 25 min postinjection using a fat suppression 3D FLASH sequence (TR = 7.8 ms, TE = 2.74 ms, 25° flip angle, 0.4 mm slice thickness, 128 × 256 × 48 matrix size, 50 × 100 × 24 mm^3 field of view, 0.39 × 0.39 × 0.5 mm^3 spatial resolution, 4 averages, 47.3 s acquisition time for one image set, 25 min for full set of dynamic images). Axial tumor images were also acquired using a 2D spin−echo sequence (400 ms TR, 8.9 ms TE, 90° flip angle, 2.0 mm slice thickness, 0.125 × 0.5 mm^2 in-plane view, 384 × 192 matrix size, 48 × 96 mm^2 field of view, 76.8 s acquisition time for one image set, 2 averages, 25 min for full set of dynamic images) immediately after the acquisition of the 3D FLASH images. Signal intensity of the regions of interest (ROIs) was measured using *Osirix* software. Signal enhancement ratios (ER) in the liver, kidneys, and tumor at each time point were calculated using the equation $ER = S_{post}/S_{pre}$, where S_{post} (postinjection) and S_{pre} (preinjection) denote the signal within the ROIs, and averaged from three different mice ($N = 3$). Statistical analysis was performed using a two-way ANOVA with Bonferroni's, assuming statistical significance at $p < 0.05$.

RESULTS AND DISCUSSION

Chemistry and Characterization. The nanoglobular Mn(II)-DOTA monoamide and Mn(II)-NOTA conjugate were designed as the Mn(II) based macromolecular MRI contrast agents to improve their relaxivities. Macrocyclic ligands NOTA and DOTA monoamide were used to chelate paramagnetic Mn(II) ions. NOTA had a coordination number of 6 and DOTA monoamide had a coordination number of 8. The ligands with different coordination number were used to investigate the ligand effect on relaxivities of the agents. The synthetic procedure of nanoglobular Mn(II)-DOTA and Mn(II)-NOTA conjugates is depicted in Scheme 1. One-fold excess of DOTA-tris(*t*-Bu) and 50% excess of NODA-GA$(tBu)_3$ to the number of amines on the dendrimers were used for the conjugation of the ligands to the nanoglobules. The Boc protection was removed with TFA to yield nanoglobule-DOTA-monoamide or nanoglobule-(NOTA-GA) conjugates. Nanoglobular Mn(II) complexes were prepared by reacting the nanoglobular ligand conjugates with 4-fold excess $Mn(OAc)_2$ to each ligand molecule. High temperature (100 °C) was used to achieve complete complexation of Mn(II) with the ligands.[15] Both ultrafiltration and dialysis were effective to remove low molecular weight impurities before and after complexation with Mn(II) ions. Approximately 70−86% of the surface amino groups of the nanoglobules were conjugated with macrocyclic Mn(II) chelates (Table 1). Complete conjugation of the surface amino groups of nanoglobules was difficult to achieve due to steric hindrance. Higher conjugation degree might be achieved if a much larger excess of the protected ligands was used in the conjugation.

The physicochemical parameters of the nanoglobular Mn(II) complexes are summarized in Table 1. The manganese content of the agents was 1.45−1.89 mmol/g nanoglobules, as determined

dx.doi.org/10.1021/bc100573t |*Bioconjugate Chem.* 2011, 22, 931–937

Table 1. Physicochemical Properties of the Nanoglobular MRI Contrast Agents

contrast agents	Mn content (mmol Mn/g nanoglobule)	macrocyclic Mn chelates/ amino groups	molecular weight	r_1/r_2 [mM^{-1} (Mn)s^{-1}] at 3T	r_1/r_2 [mM^{-1} (nanoglobule) s^{-1}] at 3T
$MnCl_2$	-	-	125.8	2.4/103.5[a]	-
G2-DOTA-Mn	1.45	23/32 (72%)	14.1 kDa	3.3/14.7	76/340
G3-DOTA-Mn	1.71	54/64 (84%)	31.8 kDa	2.8/12.6	153/681
G4-DOTA-Mn	1.51	99/128 (77%)	59.8 kDa	2.4/8.7	233/863
G3-NOTA-Mn	1.89	55/64 (86%)	30.6 kDa	3.8/24.5	209/1345

[a] Note: The value is from ref 20.

by ICP-OES. Interestingly, the r_1 and r_2 relaxivities per Mn(II) chelate of the nanoglobular Mn(II)-DOTA conjugates decreased with increasing generation of the agents from G2 to G4, contrary to the observation of the nanoglobular Gd-DOTA monoamide conjugates.[11] The G2 nanoglobular conjugate, G2-DOTA-Mn, showed the highest relaxivities per Mn(II) chelate among the three nanoglobular Mn(II)-DOTA monoamide conjugates. The reverse size effect of nanoglobular Mn(II)-DOTA monoamide conjugates could be attributed to the saturated complexation of Mn(II) ions. Since Mn(II) has a maximum coordination of 7 with macrocyclic chelators,[7,16] the coordination of Mn(II) in Mn(II)-DOTA monoamide is saturated by the ligand without water molecules directly bound to it in the inner sphere. The water molecules immediately surrounding the Mn(II) macrocyclic chelates form a relatively ordered secondary solvation sphere due to hydrogen bonding between to the water molecules and the metal complexes. Water molecules beyond the secondary sphere are less organized and referred to as the outer solvation sphere where water diffuses freely.[17] For the paramagnetic metal chelates of saturated coordination, the contribution to their overall relaxivities could be mainly from the relaxivities of the secondary and outer solvation spheres, which were determined by the relaxation time (T'_{im}) and residency time (τ'_m) of secondary and outer sphere water molecules.[17] With the increased number of Mn(II) chelates on the surface and amino groups of larger nanoglobules, the residency time (τ'_m) of water molecules in the secondary sphere might increase due to the increased probability of hydrogen bonding of the water molecules. The increased residency time might outweigh the reduced relaxation times of water molecules in the secondary and outer sphere due to increased rotational correlation time (τ_R) of larger nanoglobular complexes. In addition, it may be possible that the DOTA chelates are buried in the G3 or G4 dendrimers and less accessible to solvation as compared to the G2 dendrimer. Consequently, the relaxivities per Mn(II) chelate of the nanoglobular Mn(II)-DOTA conjugates would decrease with the increased size and number of chelates of the agents.

The r_1 relaxivity of G2-DOTA-Mn was 3.32 mM^{-1} s^{-1} per Mn(II) chelate, about 9-fold higher than that (0.37 mM^{-1} s^{-1}) of MnO nanoparticle-based MRI contrast agent with a size of 7 nm.[18] The r_1 relaxivity of the nanoglobular Mn(II)-NOTA conjugate was 3.8 mM^{-1} s^{-1} per Mn(II) chelate, 35% higher than that of the corresponding G3-DOTA-Mn agent. NOTA is a hexadentate ligand with three oxygen and three nitrogen as donor atoms.[19] Mn(II)-NOTA chelate is not a saturated complex due to the ability of Mn(II) to form seven-coordinated complexes. A water molecule may complex to Mn(II) in the inner sphere of the Mn(II)-NOTA chelate to complete seven-coordination. Higher relaxivity G3-NOTA-Mn might be due to a bound water molecule in the inner solvation site. It was shown that the higher coordination number resulted in the lower relaxivity for the Mn(II) complexes of cyclen derivatives at 20 MHz.[4] The result in this study was consistent with what was previously observed. Most of the nanoglobular Mn(II) complexes had higher per-ion r_1 relaxivity than $MnCl_2$ except for G4-DOTA-Mn. The overall relaxivities of the nanoglobular Mn(II)-DOTA conjugates increased with size of the agents because of an increased number of chelates in higher generation nanoglobules. The overall r_1 relaxivity of G4-DOTA-Mn was as high as 233 mM^{-1} s^{-1} per molecule.

The ratio of the r_1 to r_2 relaxivities of the nanoglobular Mn(II) chelate conjugates was much lower than that of the corresponding nanoglobular Gd(III) chelates. High r_2 relaxivity could result in significant reduction signal intensity in T_1-weighted contrast enhancement. The ratio of the r_1 to r_2 relaxivities of the nanoglobular Mn(II) chelate conjugates was much higher than that of $MnCl_2$. As reported in the literature, $MnCl_2$ had r_2 relaxivity as high as 103.5 s^{-1} mM^{-1} at 3 T[20] and very high r_2 relaxivity at high magnetic field strength.[17] The complexation of Mn(II) resulted in significantly reduced r_2 relaxivity.

In Vivo MR Imaging. The effectiveness of the Mn(II) based nanoglobular MRI contrast agents, G2, G3, G4-DOTA-Mn, and G3-NOTA-Mn, were evaluated in female athymic nu/nu mice bearing MDA-MB-231 human breast carcinoma xenografts with $MnCl_2$ as a control. Figure 1 shows the dynamic 2D coronal images of mice before and at various time points after the injection of $MnCl_2$ at a dose of 0.05 mmol-Mn/kg and the nanoglobular agents at a dose of 0.03 mmol-Mn/kg. Little enhancement was observed in the blood pool for all agents, which could be attributed to rapid vascular clearance of the agents. Strong contrast enhancement was observed for all of the nanoglobular agents for the fluid in the urinary bladder 10−15 min after the injection, indicating rapid excretion of the nano-sized contrast agents via renal filtration. Little enhancement was observed inside the bladder for the mice injected with $MnCl_2$, indicating the uptake of Mn^{2+} ions in the body. $MnCl_2$ resulted in stronger liver enhancement than the chelated nanoglobular contrast agents. The nanoglobular Mn(II)-DOTA monoamide conjugates showed generation-dependent liver enhancement. G2-DOTA-Mn and G3-NOTA-Mn resulted in slightly stronger signal enhancement in the liver than the other nanoglobular agents, and G4-DOTA-Mn produced the least liver enhancement. $MnCl_2$ also resulted in stronger and more prolonged enhancement in the myocardium than the nanoglobular chelates. It is known that free Mn(II) ions can preferentially accumulate in the liver, myocardium, and other normal tissue through Ca^{2+} channels,[21,22] resulting in prolonged strong liver and myocardium enhancement. The relatively weak liver and myocardium enhancement of the nanoglobular agents suggested that these agents with macrocyclic Mn(II) chelates were stable in the

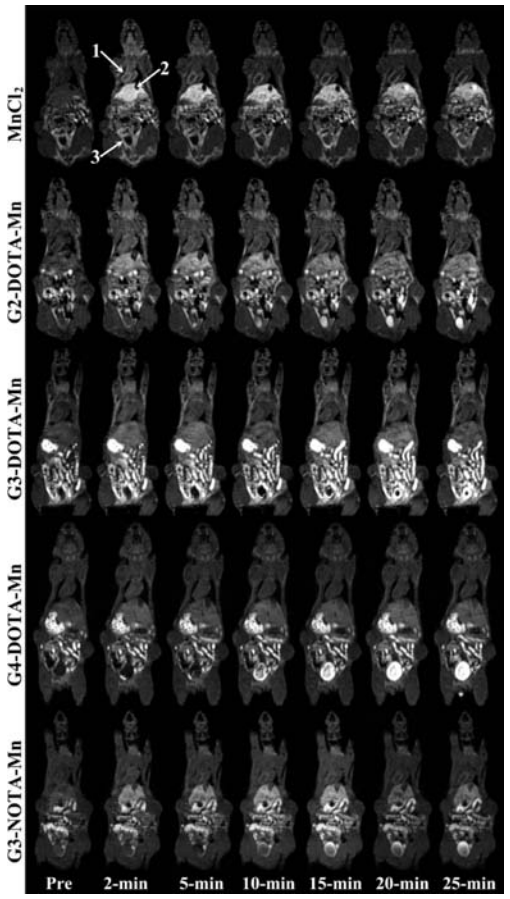


Figure 1. Representative 2D coronal T_1-weighted MR images of tumor bearing mice injected with Mn(II)-based nanoglobular MRI contrast agents G3-NOTA-Mn and G2, G3, G4-DOTA-Mn at 0.03 mmol-Mn/kg and $MnCl_2$ at 0.05 mmol/kg. Arrows 1, 2, and 3 point to the heart, liver, and bladder, respectively.

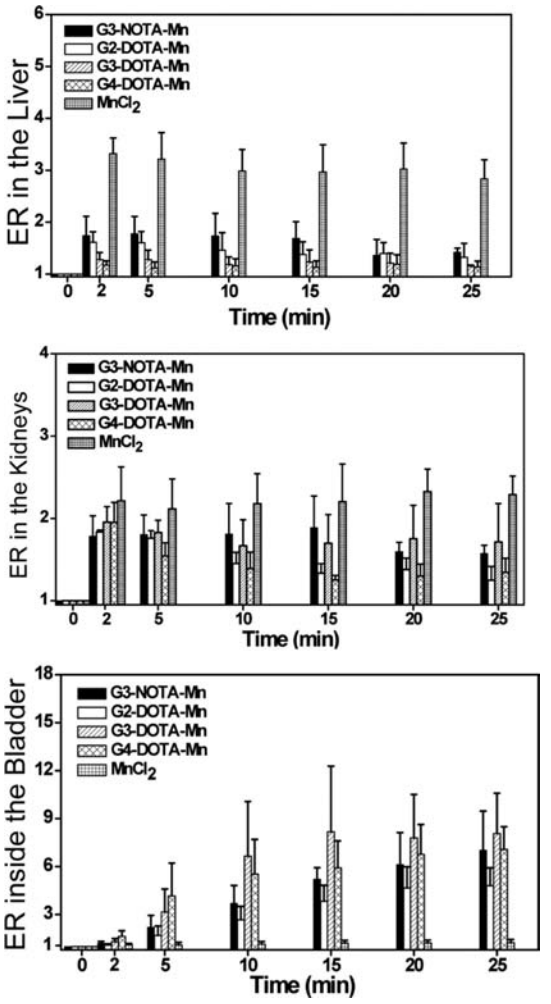


Figure 2. Enhancement ratio (ER) of the MR signal postinjection to that of preinjection in the liver and kidneys and inside the bladder of the nude mice with nanoglobular macrocyclic Mn(II) chelate conjugates G2, G3, G4-DOTA-Mn and G3-NOTA-Mn at 0.03 mmol-Mn/kg and $MnCl_2$ at 0.05 mmol/kg.

body within the time frame of the MRI study. Further detailed studies are required to demonstrate the in vivo stability of these agents.

The signal intensity of the liver, kidneys, and the fluid in the bladder was measured before and at various time points after injecting the contrast agents. Figure 2 shows the enhancement ratio, the ratio of the signal intensity postinjection to that before injection. $MnCl_2$ resulted in at least 2.8-fold signal increase in the liver due to high liver accumulation of free Mn^{2+}, which was much higher than the 1.2- to 1.8-fold signal increase generated by the nanoglobular complexes. The difference of the enhancement ratios in the liver among the nanoglobular agents was not significant. $MnCl_2$ also resulted in higher signal increase in the kidneys than the nanoglobular chelates, but the difference was not as significant as in the liver ($p > 0.05$), especially in the first 2 min postinjection. The enhancement ratio in the kidneys for the nanoglobular complexes decreased gradually during the period of 25 min post injection and the enhancement ratio inside the bladder correspondingly increased (Figure 2), indicating renal excretion of the agents. In comparison, the enhancement ratio in the kidneys for $MnCl_2$ did not change during the period and no enhancement was shown in the bladder, suggesting retention of Mn^{2+} ions in the tissue within the 25 min time frame of this study.

Figure 3 shows the axial 2D T_1-weighted spin−echo images of tumor tissue contrast enhanced by $MnCl_2$ and the nanoglobular MRI contrast agents. Substantial contrast enhancement was observed in the tumor after the injection of the nanoglobular contrast agents. It appears that G3-NOTA-Mn generated more tumor enhancement than the nanoglobular Mn(II)-DOTA monoamide conjugates. Quantitative analysis of the contrast enhancement ratio (ER) in the tumor tissue also suggested that G3-NOTA-Mn resulted in significantly higher enhancement ratio in tumor than the other tested agents after 2 min postinjection ($p < 0.05$) (Figure 4), possibly because of its larger r_1 relaxivity.

This study showed the conjugation of macrocyclic Mn(II) chelates on the highly functionalized nanoglobular dendrimers resulted in nongadolinium(III) based macromolecular MRI contrast agents with high overall relaxivities. The data of macrocyclic Mn(II) chelates suggested good in vivo stability against transmetalation with the endogenous metal ions, including Ca^{2+}, Cu^{2+}, and Zn^{2+}, which was similar to macrocyclic Gd chelates.[23] Consequently, the agents could readily clear from the major organs, particularly from the liver, and excrete via renal filtration.

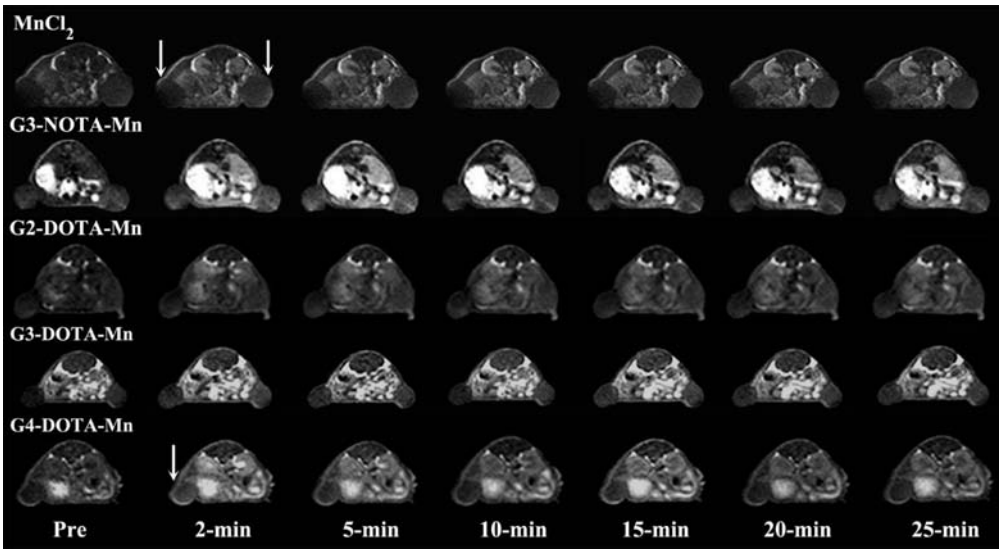


Figure 3. 2D axial T_1-weighted spin−echo MR images of MDA-MB-231 tumor xenografts in nu/nu female mice before and after the tail-vein injection of $MnCl_2$ at 0.05 mmol-Mn/kg and nanoglobular macrocyclic Mn(II) chelate conjugates G2, G3, G4-DOTA-Mn and G3-NOTA-Mn at 0.03 mmol-Mn/kg. Arrows point to the tumors.

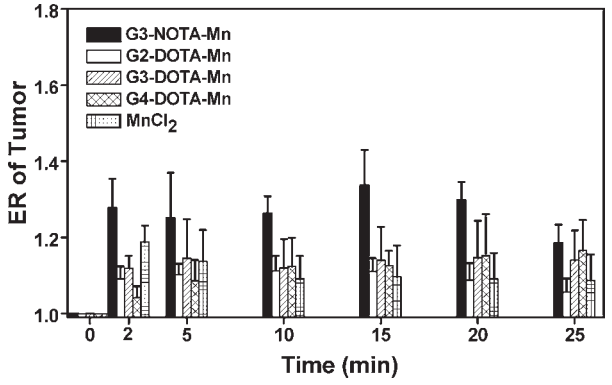


Figure 4. Enhancement ratio (ER) of the MR signal postinjection to that of preinjection in the tumor before and at various time points after injection of the nanoglobular MRI contrast agents G2, G3, G4-DOTA-Mn and G3-NOTA-Mn at 0.03 mmol Mn/kg and $MnCl_2$ at 0.05 mmol/kg in nu/nu female mice bearing MDA-MB-231 tumor xenografts.

As compared to the corresponding nanoglobular Gd(III)-DOTA monoamide conjugates,[11] G2-DOTA-Mn had similar in vivo enhancement as the G2-DOTA-Gd because both agents were rapidly excreted via renal filtration. G3-DOTA-Mn and G3-NOTA-Mn were less effective than the corresponding G3 Gd-DOTA monoamide conjugate for both blood pool and cancer imaging at the same dose, even though both Mn(II)-based agents had high overall T_1 relaxivity. It is plausible to assume that much higher T_2 relaxivity of nanoglobular Mn(II) complexes may reduce MR signal in the T_1-weighted contrast enhancement. The use of smaller macrocyclic ligand NOTA improved the relaxivity and in vivo contrast enhancement of the Mn(II)-based contrast agent. Nevertheless, we have shown in this study that it is possible to design macromolecular Mn(II) complexes to improve their relaxivity and for in vivo MR imaging. Future studies on the design and development effective Mn(II) based MRI contrast agents should focus on further improvement of the stability and T_1 relaxivity of Mn(II) chelates and reduction of the T_2 effect.

CONCLUSIONS

Nanoglobular Mn(II)-DOTA-monoamide and Mn-NOTA conjugates were synthesized as non-Gd(III) based macromolecular contrast agents for magnetic resonance imaging. The relaxivities per ion of the nanoglobular macrocyclic Mn(II) chelates decreased with the increasing generation of the dendrimers. The G3 nanoglobular Mn(II)-NOTA conjugate had higher relaxivities than the corresponding Mn(II)-DOTA conjugate. The nanoglobular macrocyclic Mn(II) chelates were readily excreted via renal filtration. They showed less nonspecific liver enhancement than $MnCl_2$. The Mn(II)-based nanoglobular agents were effective for contrast enhanced cancer imaging in the mouse tumor model at a low dose. The nanoglobular macrocyclic Mn(II) chelate conjugates are promising for MR cancer imaging as nongadolinium(III) based contrast agents.

AUTHOR INFORMATION

Corresponding Author

*Zheng-Rong Lu, Department of Biomedical Engineering, Wickenden Building, Room 427, Case Western Reserve University, 10900 Euclid Avenue, Cleveland, OH 44106-7207. E-mail: axl125@case.edu.

ACKNOWLEDGMENT

This work was supported in part by the NIH R01 CA097465. We greatly appreciate Dr. Yongen Sun and Dr. Xianfeng Shi for their technical assistance in animal handling and MRI data acquisition.

REFERENCES

(1) Marckmann, P., Skov, L., Rossen, K., Dupont, A., Damholt, M., Heaf, J., and Thomsen, H. (2006) Nephrogenic systemic fibrosis: Suspected causative role of gadodiamide used for contrast-enhanced magnetic resonance imaging. *J. Am. Soc. Nephrol. 17*, 2359–2362.

(2) Thakral, C., Alhariri, J., and Abraham, J. (2007) Long-term retention of gadolinium in tissues from nephrogenic systemic fibrosis

patient after multiple gadolinium-enhanced MRI scans: case report and implications. *Contr. Media Mol. Imaging 2*, 199–205.

(3) Sieber, M., Lengsfeld, P., Walter, J., Schirmer, H., Frenzel, T., Siegmund, F., Weinmann, H., and Pietsch, H. (2008) Gadolinium-based contrast agents and their potential role in the pathogenesis of nephrogenic systemic fibrosis: The role of excess ligand. *J. Magn. Reson. Imaging 27*, 955–962.

(4) Wang, S., and Westmoreland, T. (2009) Correlation of relaxivity with coordination number in six-, seven-, and eight-coordinate Mn(II) complexes of pendant-arm cyclen derivatives. *Inorg. Chem. 48*, 719–727.

(5) Bertin, A., Steibel, J., Michou-Gallani, A., Gallani, J., and Felder-Flesch, D. (2009) Development of a dendritic manganese-enhanced magnetic resonance imaging (MEMRI) contrast agent: synthesis, toxicity (in vitro) and relaxivity (in vitro, in vivo) studies. *Bioconjugate Chem. 20*, 760–767.

(6) Crossgrove, J., and Zheng, W. (2004) Manganese toxicity upon overexposure. *NMR Biomed. 17*, 544–553.

(7) Bianchi, A., Calabi, L., Giorgi, C., Losi, P., Mariani, P., Palano, D., Paoli, P., Rossi, P., and Valtancoli, B. (2001) Thermodynamic and structural aspects of manganese(II) complexes with polyaminopolycarboxylic ligands based upon 1,4,7,10-tetraazacyclododecane (cyclen). Crystal structure of dimeric [MnL](2)center dot 2CH(3)OH containing the new ligand 1,4,7,10-tetraazacyclododecane-1,4-diacetate. *J. Chem. Soc., Dalton Trans.* 917–922.

(8) Balogh, E., He, Z., Hsieh, W., Liu, S., and Toth, E. (2007) Dinuclear complexes formed with the triazacyclononane derivative ENOTA(4-): High-pressure O-17 NMR evidence of an associative water exchange on [Mn-2(II)(ENOTA)(H2O)(2)]. *Inorg. Chem. 46*, 238–250.

(9) Menjoge, A., Kannan, R., and Tomalia, D. (2010) Dendrimer-based drug and imaging conjugates: design considerations for nanomedical applications. *Drug Discovery Today 15*, 171–185.

(10) Henig, J., Toth, E., Engelmann, J., Gottschalk, S., and Mayer, H. A. (2010) Macrocyclic Gd^{3+} chelates attached to a silsesquioxane core as potential magnetic resonance imaging contrast agents: synthesis, physicochemical characterization, and stability studies. *Inorg. Chem. 49*, 6124–6138.

(11) Kaneshiro, T., Jeong, E., Morrell, G., Parker, D., and Lu, Z.-R. (2008) Synthesis and evaluation of globular Gd-DOTA-monoamide conjugates with precisely controlled nanosizes for magnetic resonance angiography. *Biomacromolecules 9*, 2742–2748.

(12) Tanaka, K., Kitamura, N., Naka, K., Morita, M., Inubushi, T., Chujo, M., Nagao, M., and Chujo, Y. (2009) Improving proton relaxivity of dendritic MRI contrast agents by rigid silsesquioxane core. *Polym. J. 41*, 287–292.

(13) Tan, M., Wu, X., Jeong, E., Chen, Q., Parker, D., and Lu, Z. (2010) An effective targeted nanoglobular manganese(II) chelate conjugate for magnetic resonance molecular imaging of tumor extracellular matrix. *Mol. Pharmaceut. 7*, 936–943.

(14) Kaneshiro, T. L., Wang, X., and Lu, Z. R. (2007) Synthesis, characterization, and gene delivery of poly-L-lysine octa(3-aminopropyl)-silsesquioxane dendrimers: nanoglobular drug carriers with precisely defined molecular architectures. *Mol. Pharmaceut. 4*, 759–68.

(15) Yang, C., Li, Y., and Liu, S. (2007) Synthesis and structural characterization of complexes of a DO3A-conjugated triphenylphosphonium cation with diagnostically important metal ions. *Inorg. Chem. 46*, 8988–8997.

(16) Aime, S., Anelli, P., Botta, M., Brocchetta, M., Canton, S., Fedeli, F., Gianolio, E., and Terreno, E. (2002) Relaxometric evaluation of novel manganese(II) complexes for application as contrast agents in magnetic resonance imaging. *J. Biol. Inorg. Chem. 7*, 58–67.

(17) Caravan, P., Farrar, C. T., Frullano, L., and Uppal, R. (2009) Influence of molecular parameters and increasing magnetic field strength on relaxivity of gadolinium- and manganese-based T1 contrast agents. *Contr. Media Mol. Imaging 4*, 89–100.

(18) Na, H., Lee, J., An, K., Park, Y., Park, M., Lee, I., Nam, D., Kim, S., Kim, S., Kim, S., Lim, K., Kim, K., Kim, S., and Hyeon, T. (2007) Development of a T-1 contrast agent for magnetic resonance imaging using MnO nanoparticles. *Angew. Chem., Int. Ed. 46*, 5397–5401.

(19) Cacheris, W. P., Nickle, S. K., and Sherry, A. D. (1987) Thermodynamic study of lanthanide complexes of 1,4,7-triazacyclononane-N,N′,N″-triacetic acid and 1,4,7,10-tetraazacyclododecane-N,N′,N″,N‴-tetraacetic acid. *Inorg. Chem. 26*, 958–960.

(20) Guo, H., Au, W. Y., Cheung, J. S., Kim, D., Jensen, J. H., Khong, P. L., Chan, Q., Chan, K. C., Tosti, C., H., T., Brown, T. R., Lam, W. W., Ha, S. Y., Brittenham, G. M., and Wu, E. X. (2009) Myocardial T2 quantitation in patients with iron overload at 3 T. *J. Magn. Reson. Imaging 30*, 394–400.

(21) Zhang, S., Zhou, Z., and Fu, J. (2003) Effect of manganese chloride exposure on liver and brain mitochondria function in rats. *Environ. Res. 93*, 149–157.

(22) Shukla, G. S., and Chandra, S. V. (1987) Concurrent exposure to lead, manganese, and cadmium and their distribution to various brain-regions, liver, kidney, and testis of growing-rats. *Arch. Environ. Contam. Toxicol. 16*, 303–310.

(23) Wu, X., Feng, Y., Jeong, E., Emerson, L., and Lu, Z. (2009) Tumor characterization with dynamic contrast enhanced magnetic resonance imaging and biodegradable macromolecular contrast agents in mice. *Pharm. Res. 26*, 2202–2208.

Bioconjugate Chemistry

ARTICLE

pubs.acs.org/bc

A Humanized Immunoenzyme with Enhanced Activity for Glucuronide Prodrug Activation in the Tumor Microenvironment

Kai-Chuan Chen,[†,‡] Shih-Yen Wu,[§] Yu-Lin Leu,[⊥] Zeljko M. Prijovich,[‡] Bing-Mae Chen,[‡] Hsin-Ell Wang,[§] Tian-Lu Cheng,[∥] and Steve R. Roffler*[,‡]

[†]Institute of Microbiology and Immunology, National Yang-Ming University, Taipei, Taiwan

[‡]Institute of Biomedical Sciences, Academia Sinica, Taipei, Taiwan

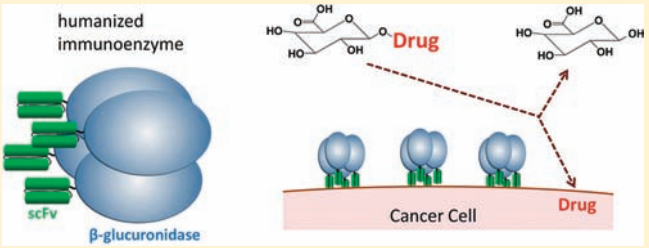
[§]Department of Biomedical Imaging and Radiological Sciences, National Yang-Ming University, Taipei, Taiwan

[⊥]Chia-Nan College of Pharmacy and Sciences, Tainan Hsien, Taiwan

[∥]School of Biomedical Science and Environmental Biology, Kaohsiung Medical University, Kaohsiung, Taiwan

Supporting Information

ABSTRACT: Antibody-directed enzyme prodrug therapy (ADEPT) utilizing β-glucuronidase is a promising method to enhance the therapeutic index of cancer chemotherapy. In this approach, an immunoenzyme (antibody-β-glucuronidase fusion protein) is employed to selectively activate anticancer glucuronide prodrugs in the tumor microenvironment. A major roadblock to the clinical translation of this therapeutic strategy, however, is the low enzymatic activity and strong immunogenicity of the current generation of immunoenzymes. To overcome this problem, we fused a humanized single-chain antibody (scFv) of mAb CC49 to S2, a human β-glucuronidase (hβG) variant that displays enhanced catalytic activity for prodrug hydrolysis. Here, we show that hcc49-S2 displayed 100-fold greater binding avidity than hcc49 scFv, possessed greater enzymatic activity than wild-type hβG, and more effectively killed antigen-positive cancer cells exposed to an anticancer glucuronide prodrug as compared to an analogous hβG immunoenzyme. Treatment of tumor-bearing mice with hcc49-S2 followed by prodrug significantly delayed tumor growth as compared to hcc49-hβG. Our study shows that hcc49-S2 is a promising targeted enzyme for cancer treatment and demonstrates that enhancement of human enzyme catalytic activity is a powerful approach to improve immunoenzyme efficacy.



INTRODUCTION

Conventional chemotherapy represents an important treatment option for advanced cancers, but the limited therapeutic index of most antineoplastic drugs can cause normal tissue toxicity and severe side effects. Antibody-directed enzyme prodrug therapy (ADEPT) seeks to increase tumor selectivity and reduce undesirable side effects of chemotherapy by targeting an antibody–enzyme conjugate (immunoenzyme) to cancer cells for preferential activation of nontoxic anticancer prodrugs in the tumor microenvironment.[1−3] We previously reported that immunoenzymes formed by chemical linkage of anticancer antibodies and *E. coli* β-glucuronidase could selectively activate glucuronide prodrugs at antigen-positive cancer cells, enhance antitumor immune responses, and produce long-term tumor regression in syngenic and xenograft cancer models.[4−9] However, a major impediment to clinical translation of immunoenzymes containing microbial enzymes is their high immunogenicity in patients, which dramatically hinders tumor targeting and prevents effective therapy.[10−12]

Immunoenzymes incorporating human enzymes should be nonimmunogenic but are limited by the relatively low activity of many human enzymes as compared to their bacterial counterparts and the possibility of systemic prodrug activation by endogenous enzymes present in patients.[13] Human β-glucuronidase (hβG) is a good target for creating human immunoenzymes[14−16] because hβG is largely sequestered in lysosomes, which limits hydrolysis of hydrophilic glucuronide prodrugs that do not readily diffuse across the plasma membrane of cells,[17,18] resulting in minimal in vivo prodrug toxicity.[19] hβG, however, displays relatively low enzymatic activity as compared to bacterial βG.[20,21] To preserve the advantages of human enzymes in ADEPT while overcoming the limitation of limited catalytic activity, we previously employed directed molecular evolution to create human enzyme variants with enhanced catalytic activity against anticancer prodrugs.[21] Here, we fused either wild-type hβG or a hβG variant (S2) with enhanced catalytic activity to a humanized single-chain antibody fragment (scFv) of CC49,[22] which binds the TAG-72 antigen expressed on many human tumor cells.[23,24] The humanized immunoenzymes retained enzymatic activity and bound antigen-positive cancer cells

Received: December 16, 2010
Revised: March 9, 2011
Published: March 28, 2011

ACS Publications © 2011 American Chemical Society

with high avidity. Importantly, hcc49-S2 in combination with an anticancer prodrug displayed significantly greater antitumor activity against human colorectal xenografts than an equivalent immunoenzyme containing wild-type hβG, demonstrating that enhancement of human enzyme activity can improve the therapeutic efficacy of ADEPT. Our results suggest that creation of highly active humanized immunoenzymes is feasible and may help overcome limitations of using microbial enzymes for ADEPT.

EXPERIMENTAL PROCEDURES

Cell Lines. BALB/3T3 fibroblasts (ATCC CCL-163) were grown in Dulbecco's Modified Eagle's Medium (high glucose) supplemented with 10% bovine serum, 2.98 g/L HEPES, 2 g/L $NaHCO_3$, 100 U/mL penicillin, and 100 μg/mL streptomycin. EJ human bladder carcinoma cells,[25] LS174T human colon adenocarcinoma (ATCC CCL-188), MCF-7 human breast adenocarcinoma (ATCC HTB 22), and HT-29 colorectal adenocarcinoma (ATCC HTB-38) cells were cultured in RPMI-1640 medium containing the same supplements. The cells were free of mycoplasma as determined by PCR.

Reagents and Antibodies. Fluorescein di-β-D-glucuronide (FDGlcU), ELF-97 alcohol and ELF-97 β-D-glucuronide (ELF = enzyme-labeled fluorescence) were from Molecular Probes (Eugene, OR, USA).[26] CPT-11, ovalbumin (A-2512), bovine serum albumin (A-7906), and catalase from bovine liver (C-3155) were from Sigma-Aldrich (St. Louis, MO, USA). Rabbit anti-6xHis was from LTK BioLaboratories (Bade, Taiwan). Biotinylated anti-HA antibody was from Vector Laboratories (Burlingame, CA, USA). Rhodamine-conjugated streptavidin was from Jackson ImmunoResearch Laboratories (Westgrove, PA, USA). Monoclonal antibody (7G8) against hβG has been described.[27] 7G8 was directly labeled with FITC as described.[28] HAMG was synthesized as described.[29]

Immunoenzymes. To construct a tumor targeting immunoenzyme, the variable regions of the heavy chain (V_H) and light chain (V_L) of a humanized single-chain antibody fragment of CC49 (hcc49 scFv)[22] were assembled with synthetic oligonucleotides P1 to P10 and P18 to P26 for V_H and P10 to P17 and P26 to P34 for V_L (Supporting Information Table 1) by a primerless PCR gene-assembly method.[30] PCR was carried out as follows: 95 °C for 5 min; 22 cycles at 95 °C for 30 s, 63 to 53 °C touchdown for 1 min (decrease 1 °C every 2 cycles), 72 °C for 1 min; 16 cycles at 95 °C for 30 s, 53 °C for 1 min, 72 °C for 1 min; 72 °C for 10 min. The V_H fragment was amplified with primers P1 and P36, and the V_L fragment was amplified with primers P34 and P35 by standard PCR. The V_H and V_L fragments were joined and amplified as hcc49 scFv using primers P1 and P34, which contain Sfi I and Xba I restriction sites, respectively. The PCR products were digested with Sfi I and Xba I and then subcloned into pLHCX-L6-hβG[31] to generate pLHCX-hcc49-hβG-myc-His. The hβG and S2 genes in pLNCX-hβGs-eB7 and pLNCX-S2-eB7[21] were ligated into the *Not*I and *Sal*I sites in pLHCX-hcc49-hβG-myc-His to remove the myc tag and generate pLHCX-hcc49-S2-His and pLHCX-hcc49-S2-His. pLHCX-αDNS-S2-His was generated by transferring the antidansyl scFv gene from pLNCX-DNS-eB7[19] in place of the hcc49 scFv gene present in pLHCX-hcc49-S2-His.

Production of Recombinant Proteins. To generate His-tagged immunoenzyme producer cells, plasmid DNA was co-transfected with pVSVG into GP293 cells (Clontech, Mountainview, CA) to produce recombinant retroviral particles. At 2 days after transfection, the culture medium was added to 3T3 cells in the presence of 8 μg/mL Polybrene. Stable cell lines were selected in medium containing 0.5 mg/mL G418 (Calbiochem, San Diego, CA). Recombinant his-tagged proteins were purified from the stable 3T3 fibroblast lines as described.[31]

Western Blot Analysis. His-tagged recombinant hcc49 scFv and immunoenzymes were boiled in reducing SDS buffer, electrophoresed on a 12.5% SDS-PAGE, and transferred to PVDF membranes. Membranes were sequentially stained with rabbit anti-His or rabbit anti-hβG antibody followed by HRP-conjugated secondary antibody. Bands were visualized by ECL detection (Pierce, Rockford, IL, USA).

HPLC Size Exclusion Analysis. Samples (10 μL, 1 mg/mL) were injected into an Aligent Bio SEC-5 column (300 × 7.8 mm, 300 Å) and separated at 1 mL/min in 150 mM sodium phosphate buffer, pH 7. Protein peaks were detected at 214 nm. Standard proteins included ovalbumin (44 kDa), bovine serum albumin (66 kDa), bovine liver catalase (250 kDa), and recombinant human β-glucuronidase (320 kDa).

Enzyme Assays. The enzyme activities of recombinant wild-type hβG, the hβG variant S2, hcc49-hβG, hcc49-S2, and αDNS-S2 were measured in triplicate with 0.1 mM ELF-97 β-D-glucuronide at 37 °C for 30 min at pH 7 in βG reaction buffer (50 mM bis-tris, 50 mM triethanol amine, 100 mM acetic acid, 100 ng/mL bovine serum albumin). The reaction was terminated by adding an equal volume of stop buffer (2 M tris-HCl, 0.8 M sodium bicarbonate, pH 8). The fluorescence of ELF-97 alcohol was measured at excitation/emission wavelengths of 355/555 nm in a Gemini EM microplate spectrofluorometer (Molecular Device, Sunnyvale, CA). To measure enzyme kinetic values, ELF-97 β-D-glucuronide (2 mM) in pH 4.5 or pH 7 βG reaction buffer was diluted 1:1 with defined concentrations of recombinant proteins. Fluorescence was immediately measured under thermal control at 37 °C for 8−10 min. The measurement was repeated using the same amount of enzyme for different concentrations of substrate over an optimal range. The acquired readings were converted to product concentration by pre-established standard curves. Double reciprocal plots were used to determine K_m and k_{cat}. Kinetic assays were performed at least 3 times and mean values were calculated.

Surface Plasmon Resonance. The binding kinetics of immunoenzymes and CC49 scFv were measured on a BIAcore (GE Lifesciences Uppsala, Sweden). Bovine submaxillary gland mucin was immobilized on the CM5 chips by amine coupling. BSA was immobilized as a negative control. Binding analysis was performed as described.[32]

Flow Cytometer Analysis. Cells were stained with immunoenzymes followed by FITC-conjugated mouse anti-hβG (7G8-FITC).[21] For competition assays, hcc49-S2 was mixed with various amounts of CC49 antibody[33] before staining MCF-7 cells. The surface immunofluorescence of 10^4 viable cells was measured with a FACScaliber flow cytometer (Becton Dickinson, Mountain View, CA, USA) and fluorescence intensities were analyzed with Flowjo (Tree Star Inc., San Carlos, CA, USA).

Immunofluorescence Staining. MCF-7 cells (5×10^5) were cultured overnight in 12-well plates. hcc49-S2 or αDNS-S2 (2 μg/well) was added to the cells at 37 °C for 1 h. After washing 3 times with PBS, the cells were incubated in complete medium at 37 °C. At defined times, the cells were washed with PBS and fixed with 2% paraformaldehyde in PBS for 15 min at room temperature. After washing, the cells were stained with 4 μg/mL 7G8-FITC for 45 min at 4 °C. The cells were viewed under a phase contrast microscope and a digital fluorescence microscope.

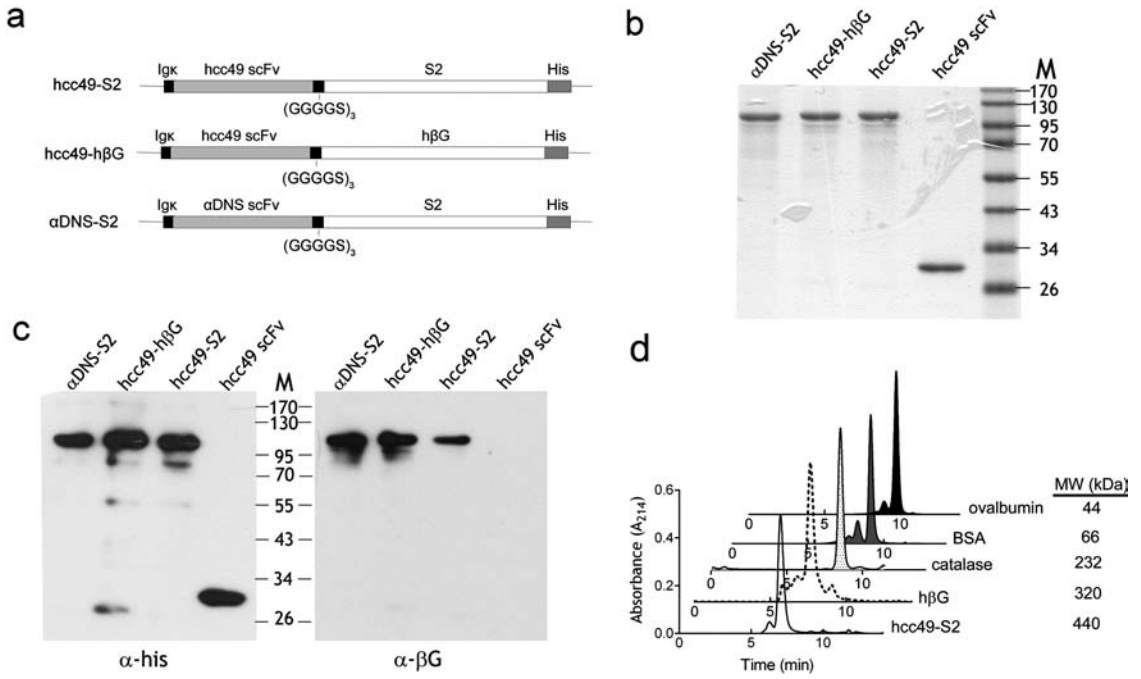


Figure 1. Analysis of purified scFv and immunoenzymes. (a) Schematic of immunoenzyme constructs. (b) Reducing SDS PAGE showing the Coomassie Blue staining of hcc49 scFv and immunoenzymes. (c) Western blots stained with anti-His (left) or anti-hβG (right) antibodies. (d) HPLC size exclusion chromatographs of ovalbumin, bovine serum albumin, catalase, hβG, and hcc49-S2.

^{3}H-Thymidine Incorporation Assay. hcc49-hβG, hcc49-S2, or αDNS-S2 (1 μg/well) were added to LS174T, MCF-7, or HT-29 cells at 37 °C for 1 h. After washing twice with PBS, graded concentrations of *p*-hydroxyaniline mustard (pHAM) or *p*-hydroxyaniline mustard glucuronide (HAMG) were added in triplicate at pH 6.8 for 48 h at 37 °C. The cells were then pulsed for 16 h with ^{3}H-thymidine (1 μCi/well). Results are expressed as percent inhibition of ^{3}H-thymidine incorporation into cellular DNA in comparison to untreated cells.

Radioiodination. Immunoenzymes were labeled with ^{131}I using a variation of the original iodogen method.[34] In brief, 120 μCi sodium [^{131}I]-iodide in 100 μL reaction buffer (0.1 M Na_2HPO_4, pH 6.5) was added to an iodogen precoated tube (Pierce Chemical Co.) followed by 50 μL hcc49-S2 or αDNS-S2 (2 mg/mL in PBS) and incubated for 10 min at room temperature. The reaction was terminated by transferring the reaction mixture to an Eppendorf tube and adding 50 μL reaction buffer. The radiochemical purity of ^{131}I-hcc49-S2 or ^{131}I-αDNS-S2 was 90−92% as measured by TLC using silica gel (Silica gel 60; Merck) and the specific activity was 57−66 Ci/mmol.

In Vivo Imaging and Biodistribution of Radiolabeled Immunoenzymes. BALB/c nu/nu mice bearing LS174T tumors (150−200 mm^3) in their right flank were i.v. injected with 100−115 μCi ^{131}I-hcc49-S2 or ^{131}I-αDNS-S2. The mice were killed after 24, 48, 72, and 96 h, and the radioactivity in the tissues was measured in a multichannel gamma counter. Whole-body scintigraphy of anesthetized mice was performed at 5 and 48 h with a gamma camera (Siemens ECAM+DHC) using a pinhole collimator.

In Vivo Pharmacokinetics. To determine the pharmacokinetics of immunoenzymes, Beige/SCID mice bearing LS174T tumors (150−200 mm^3) in their right flank were i.v. injected with 100 μg hcc49-hβG or hcc49-S2. Blood samples were collected from the tail vein of the mice or by retro-orbital punctuation. Plasma was prepared by centrifugation (5 min, 12 700 × *g*) and further diluted in pH 4.5 βG reaction buffer. The immunoenzyme levels in plasma were determined by measuring βG activity after capture of immunoenzymes on mucin-coated plates or by directly measuring βG activity. The initial and terminal half-lives of the immunoenzymes were estimated by fitting the data to a two-phase exponential decay model with *Prism 5* software (Graphpad Software, San Diego, CA, USA).

Imaging of Immunoenzyme Localization in Mice. BALB/c nu/nu mice (n = 3) bearing subcutaneous LS174T tumors (100−150 mm^3) in their right flank were i.v. injected with 200 μg immunoenzyme. After 2 or 48 h, mice were i.v. injected with 500 μg FDGlcU. After 30 min, mice were sacrificed and organs were excised. Images of tumors, liver, and muscles of mice were obtained on a Xenogen IVIS Spectrum imaging system.

In Vivo Antitumor Activity. Groups of BALB/c nu/nu mice (n = 8) bearing 50−100 mm^3 subcutaneous LS174T tumors in their right flank were intravenously injected with PBS or 500 μg immunoenzymes on days 0 and 8 and intravenously injected with three hourly doses of 70 mg/kg HAMG or PBS on days 1 and 10. Tumor sizes were measured every 2−3 days. Tumor volume was calculated according the formula: length × width × height × 0.5.

Haematological and Biochemical Evaluation. Groups of BALB/c nu/nu mice (n = 4−6) bearing ∼100 mm^3 subcutaneous LS174T tumors in their right flank were intravenously injected with PBS or 500 μg hcc49-S2 on day 0 and intravenously injected with three hourly doses of 70 mg/kg HAMG or PBS on day 1. Blood was collected in serum separation or blood collection tubes on day 8. Serum was obtained by leaving blood at room temperature for 30 min to clot and then centrifuged at 1000 × *g* at 4 °C for 10 min. Hepatic injury was assessed by measuring serum AST, ALT, and TBIL levels using a Fuji Dri-Chem 3500 biochemistry analyzer (Fujifilm, Japan). Hematological toxicity was determined by counting lymphocytes and red blood

dx.doi.org/10.1021/bc1005784 |*Bioconjugate Chem.* 2011, 22, 938–948

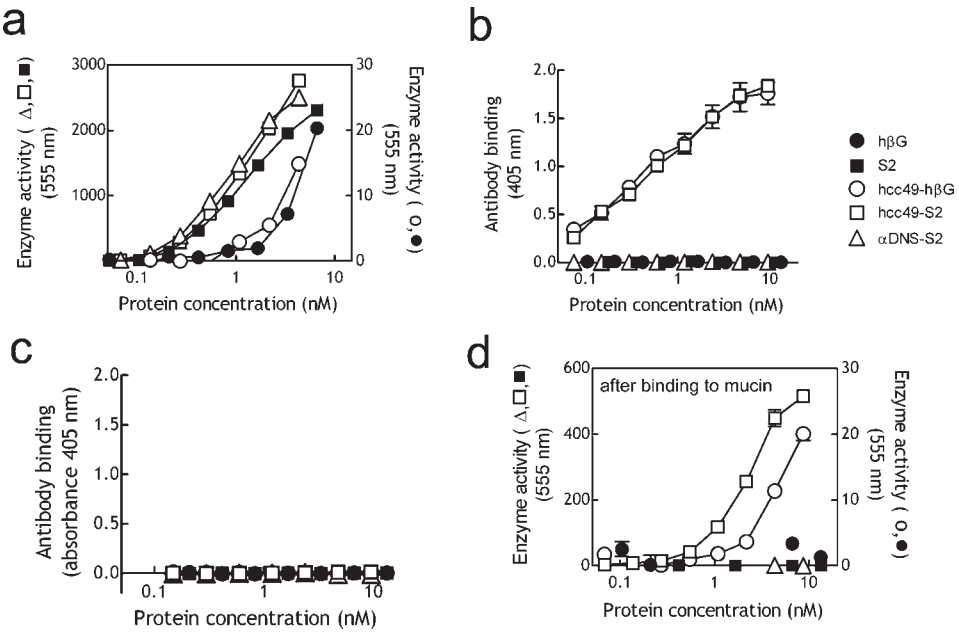


Figure 2. Enzyme and antibody-binding activity of immunoenzymes. (a) Enzyme activity of immunoenzymes and their parent enzymes was determined by measuring the fluorescence generated upon hydrolysis of ELF-97 β-D-glucuronide at pH 7. The left axis shows the activity of S2, hcc49-S2, and αDNS-S2, whereas the right axis displays the activity of hβG and hcc49-hβG. (b,c) Graded concentrations of the indicated recombinant proteins were incubated in mucin (b) or bovine-serum albumin-coated (c) microtiter plates. After washing, binding was determined by direct ELISA. (d) Graded concentrations of immunoenzymes and their parent enzymes were first incubated on mucin-coated plates. The plates were washed and bound βG enzyme activity was determined by measuring the fluorescence generated upon hydrolysis of ELF-97 β-D-glucuronide at pH 7. The left axis shows the activity of S2, hcc49-S2, and αDNS-S2, whereas the right axis displays the activity of hβG and hcc49-hβG. Error bars: SEM, $n = 3$.

cells with a Cell-Dyn hematology analyzer 3700 (Abbott Diagnostic Division, USA).

RESULTS

Expression and Purification of Humanized Immunoenzymes. A humanized cc49 scFv gene was fused to genes coding wild-type hβG or the enhanced activity hβG variant S2 to create hcc49-hβG and hcc49-S2, respectively (Figure 1a). The control immunoenzyme (αDNS-S2), with antigen-binding specificity for the chemical hapten dansyl, was also generated by fusing the antidansyl scFv and S2 genes. The immunoenzyme genes were inserted into a retroviral expression vector (pLHCX) to generate stable 3T3 fibroblast producer cell lines. Immunoenzyme proteins that were purified from the culture medium displayed the expected molecular sizes on a 12.5% SDS-PAGE (Figure 1b). Western blot analysis of purified hcc49 scFv and immunoenzymes with anti-His antibody (Figure 1c, left panel) or anti-hβG antibody (Figure 1c, right panel) showed that the immunoenzymes possessed both scFv and hβG moieties and displayed the expected molecular weights of approximately 110 kDa. Recombinant hcc49 scFv migrated with an apparent molecular weight of 30 kDa. HPLC size exclusion analysis of hcc49-S2 showed that it eluted before hβG and displayed an apparent molecular weight of ~440 kDa (Figure 1d), consistent with a tetrameric structure as found for wild-type hβG.[35]

Immunoenzymes Selectively Bind Antigen-Positive Cancer Cells with High Avidity. The immunoenzymes were characterized for antigen-binding activity and enzymatic activity. βG enzymatic activity was determined by incubating purified proteins with the βG substrate ELF-97 β-D-glucuronide. Hcc49-S2 displayed high enzymatic activity with kinetic properties that were similar to those of the S2 protein (Figure 2a, Table 1). Hcc49-hβG also possessed similar βG activity and kinetic properties to wild-type hβG. Both hcc49-hβG and hcc49-S2 immunoenzymes bound to bovine submaxillary gland mucin-coated 96-well microtiter plates,[36] whereas negligible mucin binding was observed for anti-DNS-S2 (Figure 2b). Binding appeared to be specific, because neither hcc49-hβG nor hcc49-S2 bound to BSA coated plates (Figure 2c). Surface plasmon resonance was used to quantify the binding kinetics of hcc49 scFv and hcc49 immunoenzymes. Hcc49 scFv displayed a K_D of $(4.4 \pm 1.2) \times 10^{-8}$ M (Table 2), which is similar to murine CC49 scFv.[32] The hcc49 immunoenzymes, on the other hand, displayed stronger binding avidity with K_D values of $\sim 4 \times 10^{-10}$ M, likely due to the attachment of four scFv molecules to each βG tetramer. βG activity was also examined after immunoenzymes were allowed to bind to mucin. βG activity of hcc49-S2 was about 20-fold higher than that of hcc49-hβG after binding to mucin-coated plate (Figure 2d). The enhanced enzymatic activity of hcc49-S2 reflects the greater βG activity of S2 (Figure 2a). Taken together, the data show that

Table 1. Kinetic Parameters of Proteins at pH 7.0[a]

enzyme	K_m (mM)	k_{cat} (s^{-1})	k_{cat}/K_m ($mM^{-1} \cdot s^{-1}$)
S2	0.050 ± 0.006	60 ± 3	1220 ± 160
αDNS-S2	0.055 ± 0.029	53 ± 9	1120 ± 410
Hcc49-S2	0.061 ± 0.032	57 ± 10	1050 ± 360
hβG	2.6 ± 0.57	49 ± 13	20 ± 10
Hcc49- hβG	4.3 ± 0.30	64 ± 13	14 ± 3

[a] Results represent mean values of triplicate determinations ± SD. The substrate was ELF-97 β-D-glucuronide.

Table 2. Kinetic Constants for Binding of Humanized Proteins to Immobilized Bovine Submaxillary Mucin[a]

	k_{on} (M^{-1} s^{-1})	k_{off} (s^{-1})	K_D (M)
Hcc49 scFv	$(6.01 \pm 1.62) \times 10^4$	$(2.54 \pm 0.48) \times 10^{-3}$	$(4.41 \pm 1.21) \times 10^{-8}$
Hcc49-S2	$(4.05 \pm 0.05) \times 10^5$	$(1.80 \pm 0.08) \times 10^{-4}$	$(4.45 \pm 0.20) \times 10^{-10}$
Hcc49-hβG	$(3.36 \pm 0.08) \times 10^5$	$(1.06 \pm 0.30) \times 10^{-4}$	$(3.19 \pm 0.95) \times 10^{-10}$

[a] Results represent mean values of triplicate determinations ± SD.

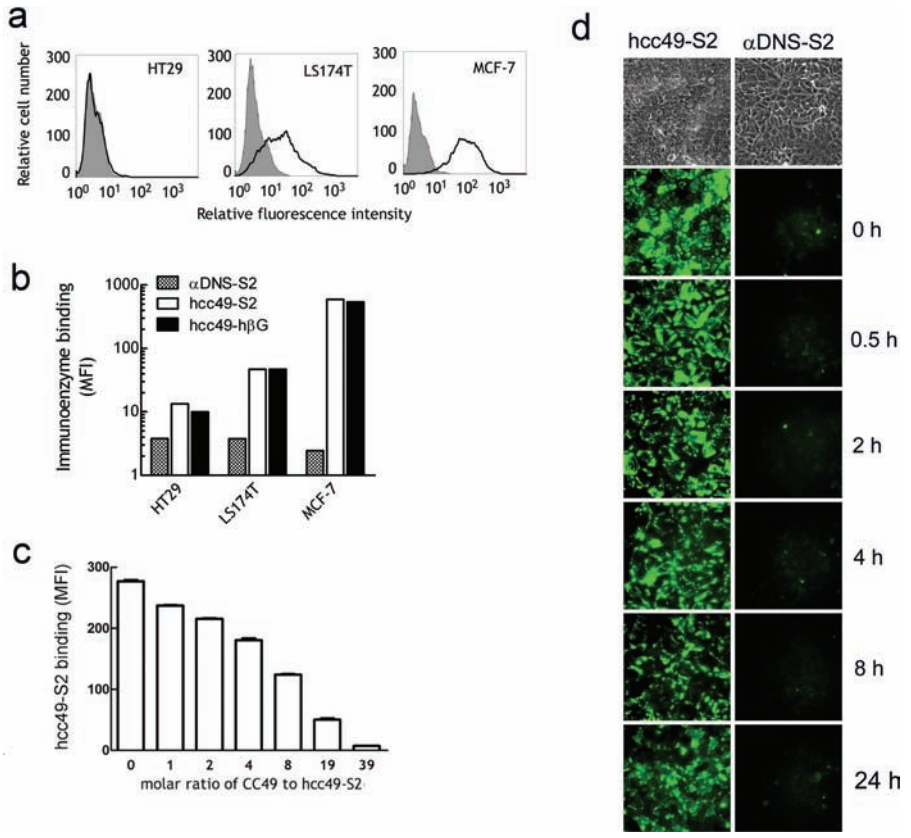


Figure 3. Binding of hcc49-S2 and hcc49-hβG to cancer cells. (a) mAb CC49 (solid line) or isotype control mAb 7G8 (gray filled) were incubated with HT29, LS174T, or MCF-7 cells followed by FITC-labeled goat antimouse second antibody. The results show the fluorescence of 10 000 live cells measured by flow cytometry. (b) HT29, LS174T, and MCF-7 cells were incubated with αDNS-S2 (shaded bars), hcc49-S2 (white bars), or hcc49-hβG (black bars) followed by FITC-labeled anti-hβG antibody before the fluorescence of 10 000 live cells was measured on a flow cytometer. (c) Increasing amounts of CC49 antibody were added with a fixed amount of hcc49-S2 to compete immunoenzyme binding. The binding of hcc49-S2 to MCF-7 cells was determined by flow cytometry. Bars, SEM ($n = 3$). (d) MCF-7 cells were incubated with hcc49-S2 (left panels) or αDNS-S2 (right panels), washed, and then incubated in complete medium at 37 °C. Cells were washed and fixed at the indicated times and then stained with anti-hβG-FITC conjugate to visualize immunoenzyme on the cells.

hcc49-S2 displayed antigen-binding activity with enhanced enzymatic activity as compared to hcc49-hβG.

To examine the binding ability of the immunoenzymes on tumor cell lines, we first utilized mAb CC49[37] to measure TAG-72 expression levels on HT29, LS174T, and MCF-7 cancer cell lines. Figure 3a shows that HT29 cells expressed undetectable levels of TAG-72, LS174T cells expressed moderate levels, and MCF-7 cancer cells expressed high levels of TAG-72, in agreement with previous reports.[38,39] The binding of immunoenzymes to these cancer cells was then examined by FACS analysis. hcc49 immunoenzymes bound HT29 cells at low background levels but selectively bound TAG-72 positive LS174T and MCF-7 cells (Figure 3b). In addition, soluble mAb CC49 competed with hcc49-S2 binding to MCF-7 cells in a dose-dependent fashion (Figure 3c), confirming that murine CC49 antibody and hcc49-S2 bind the identical epitope on TAG-72. To examine the persistence of hcc49-S2 binding to TAG-72 positive cells, MCF-7 cells were incubated with saturating concentrations of hcc49-S2 or αDNS-S2, washed, and then incubated at 37 °C for various times before surface immunoenzyme was detected by anti-hβG-FITC staining. Figure 3d shows that hcc49-S2 was clearly visible on MCF-7 cells even after 24 h, indicating prolonged retention of immunoenzyme on TAG-72 positive cells.

hcc49-S2 Can Effectively Activate a Prodrug at Antigen-Positive Cancer Cells. To examine if the immunoenzymes could preferentially activate glucuronide prodrugs at TAG-72 positive cells in vitro, MCF-7, LS174T, and HT-29 cells were incubated with hcc49 immunoenzymes or αDNS-S2, washed, and then exposed to the glucuronide prodrug HAMG (Figure 4a). None

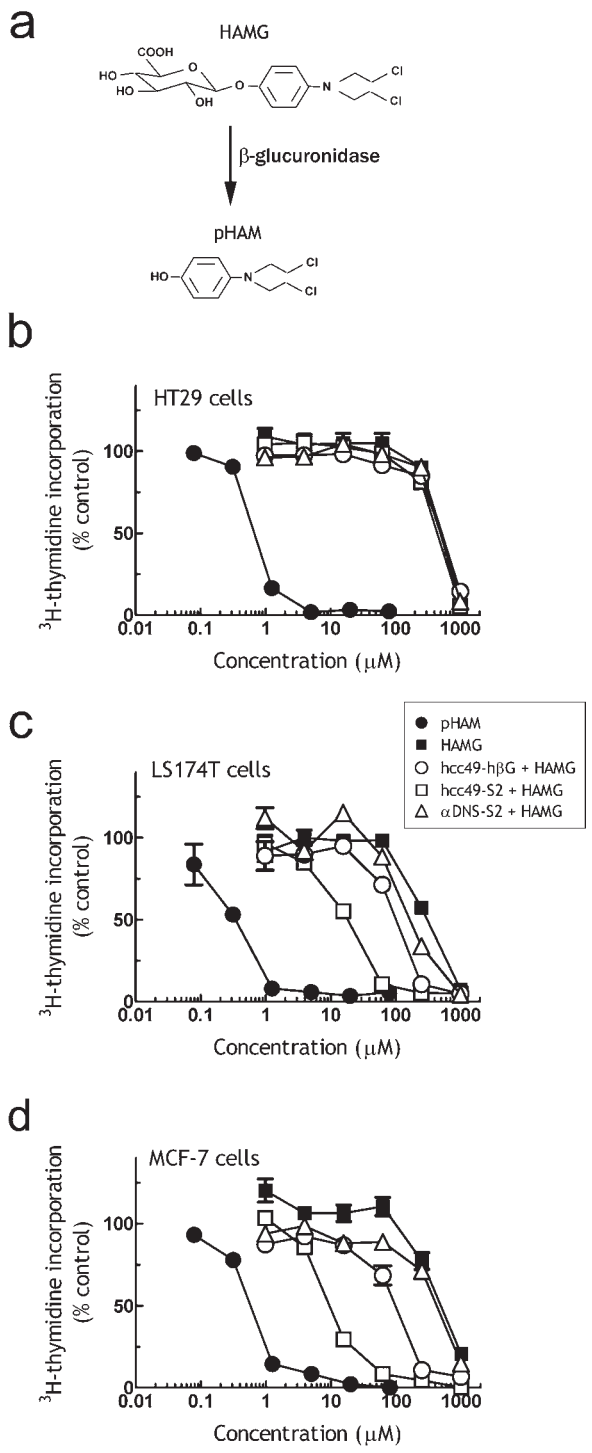


Figure 4. In vitro prodrug activation by immunoenzymes. (a) Hydrolysis of HAMG by βG releases the alkylating agent pHAM. HT-29 (b), LS174T (c), or MCF-7 (d) cells were incubated with PBS or 5 μg/mL immunoenzymes, washed, and then exposed to graded concentrations of pHAM or HAMG. The incorporation of ^{3}H-thymidine into cellular DNA was measured 48 h later. Bars, SEM (n = 3).

of the immunoenzymes increased the cytotoxicity of HAMG to TAG-72 negative HT29 cells (Figure 4b). On the other hand, LS174T (Figure 4c) and MCF-7 (Figure 4d) cells treated with hcc49-hβG and hcc49-S2 displayed augmented sensitivity to HAMG. There was a trend of increased cytotoxicity for cells treated with hcc49-S2 and for MCF-7 cells, indicating that both enhanced enzymatic activity and higher antigen levels promoted prodrug activation. Pretreatment of MCF-7 or LS174T cells with the control αDNS-S2 immunoenzyme produced similar IC_{50} values as prodrug alone, further demonstrating a requirement for antigen binding for effective prodrug activation by immunoenzymes.

Pharmacokinetics of Immunoenzymes in Tumor Bearing Mice. The plasma half-lives of the immunoenzymes were determined after i.v. injection of 100 μg hcc49-S2 or hcc49-hβG in Beige/SCID mice bearing 100−200 mm^3 LS174T tumors. Although MCF-7 cells expressed higher levels of TAG-72 antigen than did LS174T cells, we examined LS174T tumors in all in vivo experiments due to the more reproducible and uniform growth of these tumors. Immunoenzyme concentrations were determined by direct ELISA against mucin-coated microtiter plates (Figure 5a) or by directly measuring βG activity in blood samples (Figure 5b). The initial and terminal half-lives of the immunoenzymes were approximately 0.15 and 2.1 h, respectively, for hcc49-hβG, and 0.11 and 1.9 h for hcc49-S2. Direct measurement of enzymatic activity was more sensitive than ELISA, but both methods gave comparable results, indicating that the immunoenzymes retained both antigen-binding and enzymatic activity in vivo.

Imaging and Biodistribution of Immunoenzymes in Tumor-Bearing Mice. We first examined the tumor localization of the immunoenzymes by whole-body imaging in mice. Nude mice bearing 100−200 mm^3 LS174T xenografts were first imaged 5 and 48 h after i.v. injection of ^{131}I-hcc49-S2 (Figure 5c). After 48 h, ^{131}I-hcc49-S2 showed increased accumulation at the tumor site. ^{131}I-hcc49-S2 also clearly accumulated in the liver (Figure 5c). To further determine the amount of immunoenzymes in tumors, nude mice bearing 100−200 mm^3 LS174T xenografts were i.v. injected with 100 μg radiolabeled hcc49-S2 or αDNS-S2. The tumoral accumulation of ^{131}I-hcc49-S2 was stable after 24 h post injection (Table 3). By contrast, the accumulation of ^{131}I-αDNS-S2 decreased after 24 h post injection, indicating retention of hcc49-S2 but not αDNS-S2 in tumors. Liver uptake for both ^{131}I-hcc49-S2 and ^{131}I-αDNS-S2 was approximately 1% of the injected dose of radiolabeled fusion protein per gram of liver (% ID/g) after 48 and 72 h (Table 3). This might be due to the carbohydrate-mediated hepatic uptake of hβG.[40,41] Although the amount of ^{131}I-labeled hcc49-S2 was higher in the liver than in tumors, i.v. injection of FDGlcU resulted in significantly higher fluorescence signals in tumors as compared to the liver (Figure 5d). This result indicates that hcc49-S2 in the liver is likely sequestered inside cells and is not assessable for hydrolysis of glucuronide substrates. By contrast, the highly fluorescent signal in tumors shows that βG activity of hcc49-S2 is available for glucuronide hydrolysis in the tumor microenvironment.

ADEPT Therapy of Human Cancer Xenografts. To evaluate the therapeutic effect of tumor targeting immunoenzymes combined with prodrug treatment in vivo, BALB/c nu/nu mice bearing LS174T tumors were first i.v. injected with PBS or 500 μg/kg immunoenzyme on days 0 and 8. Mice were i.v. injected with PBS or three hourly doses of 70 mg/kg HAMG on days 1 and 10. Significant suppression of tumor growth with partial regression was observed in the mice injected with hcc49-S2 and HAMG (Figure 6a). By contrast, treatment of mice with hcc49-hβG and HAMG did not significantly suppress tumor growth as compared to treatment with αDNS-S2 and HAMG (p > 0.58). These data indicate that enhancing the enzymatic activity of hβG immunoenzymes resulted in greater therapeutic efficacy. Although previous data showed that liver accumulation of hcc49-S2 did not

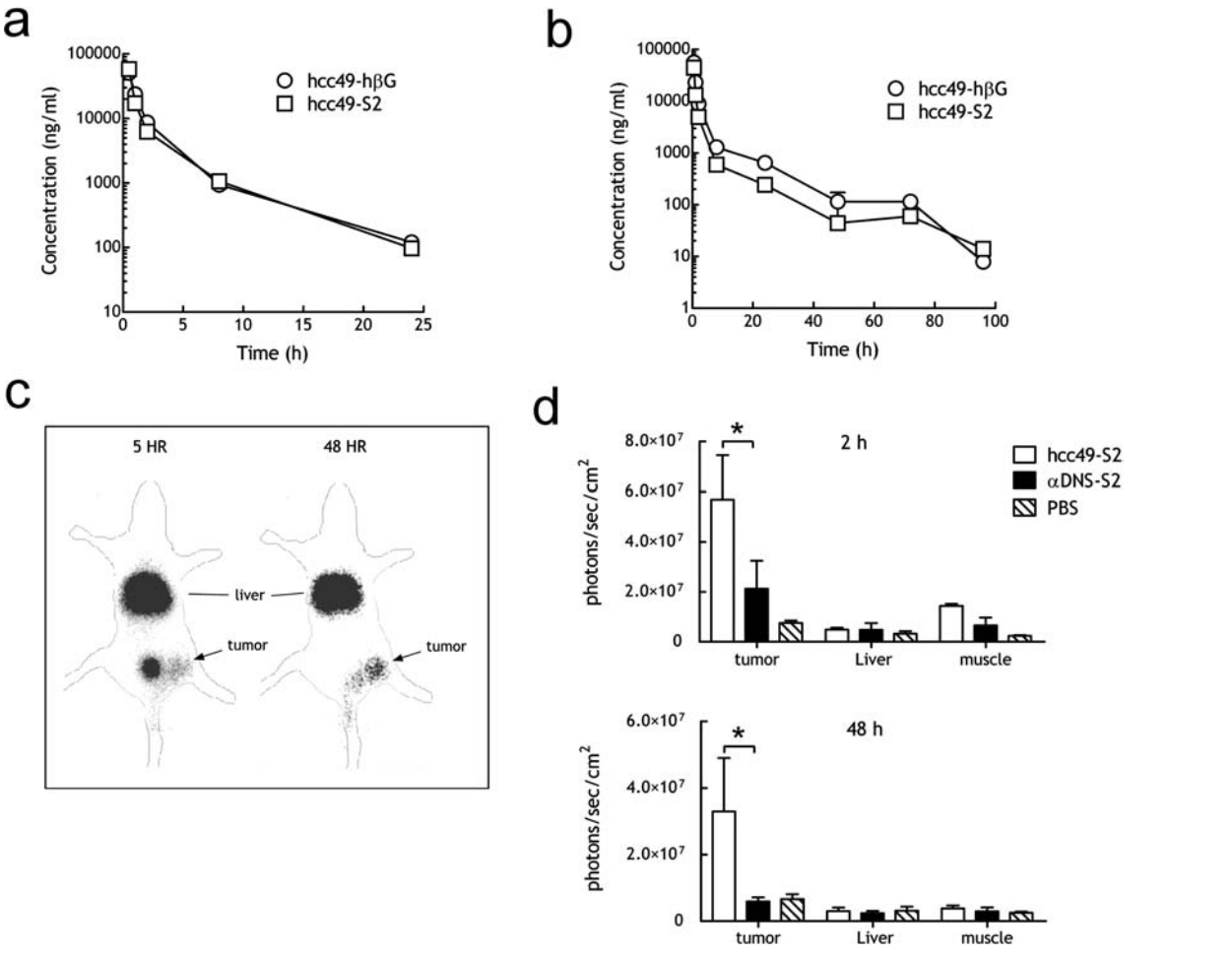


Figure 5. Pharmacokinetics of immunoenzymes in mice. Beige/SCID mice were i.v. injected with 100 μg hcc49-hβG or hcc49-S2. Mean plasma concentrations of the immunoenzymes were determined by measuring βG activity after capture of immunoenzymes on mucin-coated plates (a) or by directly measuring βG activity in serum (b). Bars, SEM (n = 3 mice). (c) Whole-body image of a representative nude mouse bearing a s.c. LS174T xenograft on the right flank at 5 and 48 h after i.v. injection of 100 μg of ^{131}I-hcc49-S2 (89 μCi). The images were obtained from the same mouse. (d) FDGlcU was administrated through the tail vein at 2 h (upper panel) or 48 h (lower panel) after i.v. injection of PBS, hcc49-S2, or αDNS-S2. The fluorescence intensity of tumor or liver was measured 30 min after injection of FDGlcU on an IVIS Imaging System (Xenogen, Alameda, CA, USA). The tumors and liver were analyzed with *Living Image* software. Significant differences between hcc49-S2 and αDNA-S2 fluorescence are indicated: *, $p < 0.05$.

hydrolyze a glucuronide substrate in the liver, we further investigated possible liver toxicity by measuring several hepatic enzyme markers 7 days after administration of immunoenzyme and HAMG. We also measured red blood cells (RBCs) and white blood cells (WBCs) because alkylating agents such as HAMG can cause dose-limiting leucopenia.[5] The mean numbers of RBCs in mice injected with hcc49-S2 and HAMG was slightly but not significantly lower (p = 0.19) than those of vehicle-treated mice (Figure 6b). Importantly, the number of WBCs in mice was not affected by immunoenzyme and prodrug treatment (p = 0.29). Likewise, the serum levels of hepatic enzyme markers were not significantly elevated in mice treated with immunoenzyme and HAMG (p = 0.09, 0.75, and 0.81 for AST, ALT, and TBIL, respectively) as compared to vehicle-treated mice (Figure 6c). Taken together, the hematological and hepatic enzyme measurements indicate that uptake of immunoenzymes in the liver did not cause excessive toxicity.

DISCUSSION

ADEPT is an attractive strategy to selectively treat cancer, but low catalytic activity and/or strong immunogenicity of currently investigated immunoenzymes has hampered clinical adoption. To help solve this problem, we created immunoconjugates linking the scFv fragment of a humanized CC49 antibody to S2, a hβG variant with enhanced enzymatic activity. We found that humanized immunoenzymes retained enzymatic activity and displayed exceptional antigen binding avidity ($K_D \approx 4 \times 10^{-10}$ M). The immunoenzymes could selectively bind and activate anticancer prodrug at TAG-72 positive cancer cells with more effective prodrug activation being achieved with hcc49-S2 as compared to hcc49-hβG. Importantly, the growth of human tumor xenografts in mice was significantly suppressed by treatment with hcc49-S2 and prodrug. Our results offer a promising approach to create highly active humanized immunoenzymes for ADEPT.

The use of hβG in immunoenzymes has been hampered by its relatively low enzymatic activity as compared to microbial sources of βG.[14−16] For example, the activity of *E. coli* βG is about 200-fold greater than hβG at pH 7,[27] and βG from *Staphylococcus* sp. displays about 2000-fold higher activity than hβG.[20] To help overcome this limitation, we recently developed a mammalian surface display system to facilitate the directed

dx.doi.org/10.1021/bc1005784 |*Bioconjugate Chem.* 2011, 22, 938–948

Table 3. Biodistribution of Humanized CC49 Fusion Proteins (% ID/g) in Nude Mice Bearing LS174T Colon Carcinoma Xenografts

	time (h)			
tissue	24	48	72	96
		hcc49-S2		
liver	4.74 ± 2.23	1.08 ± 0.15	1.16 ± 1.02	0.98 ± 0.25
muscle	0.04 ± 0.03	0.01 ± 0.00	0.01 ± 0.01	0.01 ± 0.01
blood	0.25 ± 0.16	0.05 ± 0.01	0.04 ± 0.01	0.02 ± 0.01
tumor	0.46 ± 0.27	0.37 ± 0.13	0.38 ± 0.20	0.43 ± 0.39
tumor/blood ratio	1.8	7.4	9.5	21.5
		αDNS-S2		
liver	4.30 ± 0.72	2.18 ± 1.02	1.18 ± 0.31	1.22 ± 0.3
muscle	0.10 ± 0.10	0.01 ± 0.00	0.004 ± 0.003	0.004 ± 0.001
blood	0.32 ± 0.08	0.08 ± 0.02	0.03 ± 0.00	0.03 ± 0.001
tumor	0.24 ± 0.10	0.07 ± 0.02	0.04 ± 0.01	0.05 ± 0.02
tumor/blood ratio	0.8	0.9	1.3	1.7

molecular evolution of human enzymes.[21] We successfully generated the hβG variant S2, which displays about 60-fold higher activity against ELF-97G and about 8-fold higher activity against several anticancer prodrugs.[21] Indeed, the immunoenzyme utilizing the S2 hβG variant more effectively activated a glucuronide prodrug at antigen-positive cancer cells (Figure 4) and produced significantly greater antitumor activity in vivo (Figure 6). Although it seems intuitive that more activity enzymes would improve prodrug activation in the tumor microenvironment, mathematical models have predicted that utilization of lower activity enzymes may be advantageous for ADEPT.[42,43] Our results, however, support the development of human enzymes with enhanced catalytic activity as an approach to improve the efficacy of ADEPT. We recently developed a more general screening approach for creating highly active human enzymes and successfully created hβG variants with 30-fold greater activity for anticancer glucuronide prodrugs (manuscript in preparation). Given the high activity of microbial sources of βG, we suspect that hβG variants with much higher catalytic activity can be generated. This approach should also be applicable to enhance the enzymatic activity of other human enzymes for ADEPT including β-galactosidase, β-glucosidase, carboxypeptidase A1, carboxylesterase, α-mannosidase, and purine nucleoside phosphorylase.[44−47]

In addition to enhanced enzymatic activity, hcc49-S2 displayed about 100-fold greater binding avidity for mucin as compared to hcc49 scFv (Table 2). The avidity of hcc49-S2 (K_D = 4.45 × 10^{-10} M) was also greater than that of the intact CC49 IgG molecule (K_D = 8.77 × 10^{-9} M[48]). The high avidity of hcc49-S2 is likely attributable to the tetrameric structure of hβG, which is required for enzymatic activity.[35] Thus, each immunoenzyme contains four scFv molecules (Figure 1d). The high affinity of hcc49-S2 should be beneficial for ADEPT because tumor retention correlates with antibody affinity.[49]

We observed that hcc49-hβG and hcc49-S2 were rapidly cleared from the circulation (Figure 5a,b). Imaging and radiolabeled immunoconjugate data demonstrated rapid liver uptake of the immunoenzyme, likely via mannose receptors (MR) and mannose 6-phosphate receptors (M6PR).[41,50] Fortunately, internalized immunoconjugates did not appear to be available for prodrug activation (Figure 5). On one hand, the rapid clearance of immunoenzyme from the circulation allows the tumor-to-plasma ratio to quickly reach suitable levels for prodrug administration. On the other hand, rapid clearance of immunoenzyme might hamper tumor localization. Chemical modification of hβG to hinder the uptake by MPR and M6PR on liver cells or pegylation of the immunoenzyme are approaches that may prolong immunoenzyme circulation to allow increased accumulation of immunoenzyme in tumor.[8,51,52] Future studies are required to determine the optimal half-life of the immunoconjugates for cancer therapy by ADEPT.

Strong immune response against antibody−enzyme conjugates adversely affects tumor localization and treatment efficacy in clinical trials of ADEPT, even with the administration of immunosuppressive drugs.[10,12] Murine antibodies such as CC49 also induce immune responses in patients that hamper antibody effectiveness.[53,54] Because humanized antibodies are less immunogenic as compared to murine and chimeric antibodies,[55] we utilized a humanized CC49 scFv to construct immunoenzymes.[22] However, reducing the immunogenicity of the enzyme portion of the immunoenzymes is more problematic. Besides using immunosuppressive drugs to blunt antienzyme immune responses,[56] foreign enzymes have been engineered to remove immunogenic epitopes[57,58] and catalytic antibodies have been employed to replace the enzyme portion of the immunoenzyme.[59] However, besides exhibiting limited effectiveness in suppressing strong immune responses against microbial enzymes, immunosuppressive drugs can cause undesirable side effects and may suppress desirable antitumor immune responses in cancer patients.[60] Removal of all immunogenic B cell and T cell epitopes of highly divergent foreign enzymes with retention of activity and stability remains a challenging problem[61,62] and creation of catalytic antibodies with enzymatic activities comparable to natural enzymes is not easily achieved.

Utilization of highly active human enzyme variants is an alternative approach that is expected to reduce immunoenzyme immunogenicity as compared to those incorporating microbial enzymes. For example, the amino acid sequence of *E. coli* βG differs from hβG at 322 positions and differs from mouse βG at 323 positions. Immunoenzymes utilizing *E. coli* βG are therefore highly immunogenic in mice.[7,63] By contrast, the S2 variant differs from hβG by only four amino acids, suggesting that immune responses against hcc49-S2 should be mild as compared to immunoenzymes created with microbial sources of βG. Studies showing that even partial replacement of mouse immunoglobulin sequences (57−72% identity to human immunoglobulin[64]) with the corresponding human immunoglobulin sequences can substantially reduce the immunogenicity of mouse antibodies also suggest that human enzymes with limited numbers of amino acid alterations should be less immunogenic than microbial enzymes.[55,65] However, further studies in appropriate transgenic mouse models or in human subjects will be required to define actual immunogenicity of human enzyme variants.

hcc49-S2 possesses potential advantages for cancer therapy. The high avidity of hcc49-S2 may promote better tumor delivery[66] and facilitate prolonged retention of the immunoenzyme at tumor cells in vivo (Table 3), resulting in high immunoconjugate tumor/blood ratios. The wide distribution of the TAG-72 antigen in colorectal, gastric, pancreatic, ovarian, endometrial, breast, nonsmall cell lung cancer, and prostate carcinomas suggests that hcc49-S2 may be useful for the treatment of many types of cancer.[67] The plethora of anticancer glucuronide prodrugs available also means that effective

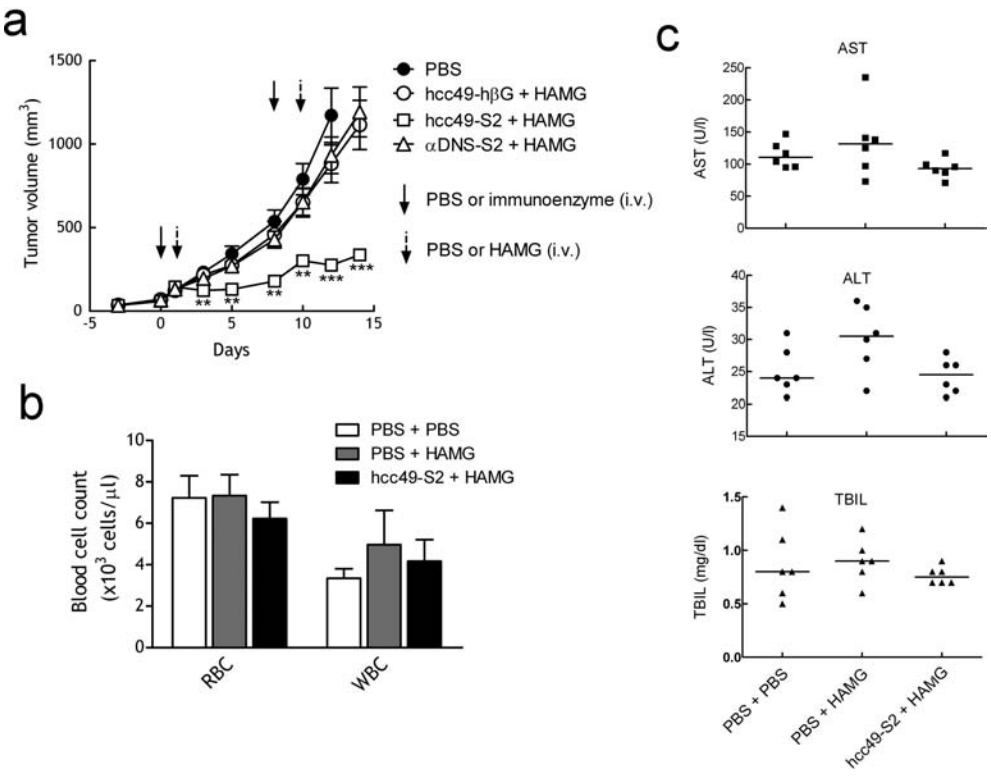


Figure 6. ADEPT with humanized immunoenzymes. (a) Nude mice bearing 50−100 mm^3 s.c. LS174T tumors were i.v. injected with PBS or 500 μg hcc49-hβG, hcc49-S2, or αDNS-S2 on days 0 and 8 and i.v. injected with three fractionated doses of 70 mg/kg HAMG or PBS on days 1 and 10. Bars, SEM (n = 8). Significant differences in mean tumor size in mice treated with hcc49-S2 or hcc49-hβG and HAMG are indicated: **, $p \leq 0.005$; ***, $p \leq 0.0005$. (b, c) Nude mice were i.v. injected with 500 μg hcc49-S2 or PBS, and after 24 h, mice were i.v. injected with three fractionated doses of 70 mg/kg HAMG or PBS. The numbers of the WBCs and RBCs (b) and the serum concentrations of aspartate aminotransferase (AST), alanine aminotransferase (ALT), and total bilirubin (TBIL) (c) were measured 7 days after HAMG administration. Bars, SD (n = 4−6).

combinations may be utilized depending on the tumor type under therapy. The enzymatic amplification of drug activity and the relatively fast diffusion of activated drug molecules within solid tumors may also help effectively treat antigen-negative and antigen-escape cancer cell variants.

In conclusion, our study demonstrates that hcc49-S2, a humanized immunoenzyme with enhanced enzymatic activity, displays promising therapeutic effects in combination with glucuronide prodrug in a human tumor xenograft model. Our study suggests that further improvement of treatment efficacy may be achieved by generation of more active enzyme variants and optimization of immunoenzyme pharmacokinetic properties, and possibly by utilization of more potent prodrugs or development of prodrugs with enhanced binding affinity to hβG variants. We hope that further development of highly active humanized immunoenzymes can accelerate the translation of ADEPT from the lab to the clinic.

■ ASSOCIATED CONTENT

Ⓢ Supporting Information. Table 1 shows the oligonucleotide sequences used for scFv assembly. This material is available free of charge via the Internet at http://pubs.acs.org.

■ AUTHOR INFORMATION

Corresponding Author

*Dr. Steve Roffler, Institute of Biomedical Sciences, Academia Sinica, Academia Road, Section 2, No. 128, Taipei 11529, Taiwan. Tel: 886-22-652-3079, Fax: 886-22-782-9142, E-mail: sroff@ibms.sinica.edu.tw.

■ ACKNOWLEDGMENT

This study was supported by a grant from Academia Sinica, Taipei, Taiwan (AS-98-TP-B09).

■ REFERENCES

(1) Houston, T. A. (2007)Painting the target around the arrow: two-step prodrug therapies from a carbohydrate chemist's perspective. *Curr. Drug Delivery 4*, 264–268.

(2) Bagshawe, K. D. (2006)Antibody-directed enzyme prodrug therapy (ADEPT) for cancer. *Expert Rev. Anticancer Ther. 6*, 1421–1431.

(3) Tietze, L. F., and Krewer, B. (2009) Antibody-directed enzyme prodrug therapy: a promising approach for a selective treatment of cancer based on prodrugs and monoclonal antibodies. *Chem. Biol. Drug Des. 74*, 205–211.

(4) Wang, S., Chern, J., Yeh, M., Ng, J., Tung, E., and Roffler, S. (1992) Specific activation of glucuronide prodrugs by antibody-targeted enzyme conjugates for cancer therapy. *Cancer Res. 52*, 4484–4491.

(5) Chen, B., Chan, L., Wang, S., Wu, M., Chern, J., and Roffler, S. (1997) Cure of malignant ascites and generation of protective immunity by monoclonal antibody-targeted activation of a glucuronide prodrug in rats. *Int. J. Cancer 73*, 392–402.

(6) Cheng, T., Wei, S., Chen, B., Chern, J., Wu, M., Liu, P., and Roffler, S. (1999) Bystander killing of tumour cells by antibody-targeted

enzymatic activation of a glucuronide prodrug. *Br. J. Cancer 79*, 1378–1385.

(7) Cheng, T., Wu, P., Wu, M., Chern, J., and Roffler, S. (1999) Accelerated clearance of polyethylene glycol-modified proteins by anti-polyethylene glycol IgM. *Bioconjugate Chem. 10*, 520–528.

(8) Cheng, T., Chen, B., Chern, J., Wu, M., and Roffler, S. (2000) Efficient clearance of poly (ethylene glycol)-modified immunoenzyme with anti-PEG monoclonal antibody for prodrug cancer therapy. *Bioconjugate Chem. 11*, 258–266.

(9) Chen, B., Cheng, T., Tzou, S., and Roffler, S. (2001) Potentiation of antitumor immunity by antibody directed enzyme prodrug therapy. *Int. J. Cancer 94*, 850–858.

(10) Francis, R. J., Sharma, S. K., Springer, C., Green, A. J., Hope-Stone, L. D., Sena, L., Martin, J., Adamson, K. L., Robbins, A., Gumbrell, L., O'Malley, D., Tsiompanou, E., Shahbakhti, H., Webley, S., Hochhauser, D., Hilson, A. J., Blakey, D., and Begent, R. H. (2002) A phase I trial of antibody directed enzyme prodrug therapy (ADEPT) in patients with advanced colorectal carcinoma or other CEA producing tumours. *Br. J. Cancer 87*, 600–607.

(11) Napier, M. P., Sharma, S. K., Springer, C. J., Bagshawe, K. D., Green, A. J., Martin, J., Stribbling, S. M., Cushen, N., O'Malley, D., and Begent, R. H. (2000) Antibody-directed enzyme prodrug therapy: efficacy and mechanism of action in colorectal carcinoma. *Clin. Cancer Res. 6*, 765–772.

(12) Mayer, A., Francis, R. J., Sharma, S. K., Tolner, B., Springer, C. J., Martin, J., Boxer, G. M., Bell, J., Green, A. J., Hartley, J. A., Cruickshank, C., Wren, J., Chester, K. A., and Begent, R. H. (2006) A phase I study of single administration of antibody-directed enzyme prodrug therapy with the recombinant anti-carcinoembryonic antigen antibody-enzyme fusion protein MFECP1 and a bis-iodo phenol mustard prodrug. *Clin. Cancer Res. 12*, 6509–6516.

(13) Oosterhoff, D., Pinedo, H. M., van der Meulen, I. H., de Graaf, M., Sone, T., Kruyt, F. A., van Beusechem, V. W., Haisma, H. J., and Gerritsen, W. R. (2002)Secreted and tumour targeted human carboxylesterase for activation of irinotecan. *Br. J. Cancer 87*, 659–664.

(14) de Graaf, M., Boven, E., Oosterhoff, D., van der Meulen-Muileman, I. H., Huls, G. A., Gerritsen, W. R., Haisma, H. J., and Pinedo, H. M. (2002) A fully human anti-Ep-CAM scFv-beta-glucuronidase fusion protein for selective chemotherapy with a glucuronide prodrug. *Br. J. Cancer 86*, 811–818.

(15) Haisma, H., Brakenhoff, R., vd Meulen-Muileman, I., Pinedo, H., and Boven, E. (1997) Construction and characterization of a fusion protein of single-chain anti-carcinoma antibody 323/A3 and human -glucuronidase. *Cancer Immunol. Immunother. 45*, 266–272.

(16) Haisma, H. J., Sernee, M. F., Hooijberg, E., Brakenhoff, R. H., Meulen-Muileman, I. H. v. d., Pinedo, H. M., and Boven, E. (1998) Construction and characterization of a fusion protein of single-chain anti-CD20 antibody and human beta -glucuronidase for antibody-directed enzyme prodrug therapy. *Blood 92*, 184–190.

(17) Houba, P. H., Leenders, R. G., Boven, E., Scheeren, J. W., Pinedo, H. M., and Haisma, H. J. (1996) Characterization of novel anthracycline prodrugs activated by human beta-glucuronidase for use in antibody-directed enzyme prodrug therapy. *Biochem. Pharmacol. 52*, 455–463.

(18) Cheng, T., Chou, W., Chen, B., Chern, J., and Roffler, S. (1999) Characterization of an antineoplastic glucuronide prodrug. *Biochem. Pharmacol. 58*, 325–328.

(19) Chuang, K., Cheng, C., Roffler, S., Lu, Y., Lin, S., Wang, J., Tzou, W., Su, Y., Chen, B., and Cheng, T. (2006) Combination cancer therapy by hapten-targeted prodrug-activating enzymes and cytokines. *Bioconjugate Chem. 17*, 707–714.

(20) Broothaerts, W., Mitchell, H. J., Weir, B., Kaines, S., Smith, L. M. A., Yang, W., Mayer, J. E., Roa-Rodriguez, C., and Jefferson, R. A. (2005) Gene transfer to plants by diverse species of bacteria. *Nature 433*, 629–633.

(21) Chen, K. C., Wu, C. H., Chang, C. Y., Lu, W. C., Tseng, Q., Prijovich, Z. M., Schechinger, W., Liaw, Y. C., Leu, Y. L., and Roffler, S. R. (2008) Directed evolution of a lysosomal enzyme with enhanced activity at neutral pH by mammalian cell-surface display. *Chem. Biol. 15*, 1277–1286.

(22) Yoon, S. O., Lee, T. S., Kim, S. J., Jang, M. H., Kang, Y. J., Park, J. H., Kim, K. S., Lee, H. S., Ryu, C. J., Gonzales, N. R., Kashmiri, S. V., Lim, S. M., Choi, C. W., and Hong, H. J. (2006) Construction, affinity maturation, and biological characterization of an anti-tumor-associated glycoprotein-72 humanized antibody. *J. Biol. Chem. 281*, 6985–6992.

(23) Schlom, J., Colcher, D., Siler, K., Thor, A., Bryant, G., Johnston, W. W., Szpak, C. A., Sugarbaker, P., Carrasquillo, J. A., and Reynolds, J. C. et al. (1990) Tumor targeting with monoclonal antibody B72.3: experimental and clinical results. *Cancer Treat. Res. 51*, 313–335.

(24) Colcher, D., Hand, P. H., Nuti, M., and Schlom, J. (1981) A spectrum of monoclonal antibodies reactive with human mammary tumor cells. *Proc. Natl. Acad. Sci. U.S.A. 78*, 3199–3203.

(25) Marshall, C. J., Franks, L. M., and Carbonell, A. W. (1977) Markers of neoplastic transformation in epithelial cell lines derived from human carcinomas. *J. Natl. Cancer Inst. 58*, 1743–1751.

(26) Zhou, M., Upson, R. H., Diwu, Z., and Haugland, R. P. (1996) A fluorogenic substrate for [beta]-glucuronidase: Applications in fluorometric, polyacrylamide gel and histochemical assays. *J. Biochem. Biophys. Methods 33*, 197–205.

(27) Chen, K. C., Cheng, T. L., Leu, Y. L., Prijovich, Z. M., Chuang, C. H., Chen, B. M., and Roffler, S. R. (2007) Membrane-localized activation of glucuronide prodrugs by beta-glucuronidase enzymes. *Cancer Gene Ther. 14*, 187–200.

(28) Goding, J. W. (1976) Conjugation of antibodies with fluorochromes: modifications to the standard methods. *J. Immunol. Methods 13*, 215–226.

(29) Roffler, S. R., Wang, S. M., Chern, J. W., Yeh, M. Y., and Tung, E. (1991) Anti-neoplastic glucuronide prodrug treatment of human tumor cells targeted with a monoclonal antibody-enzyme conjugate. *Biochem. Pharmacol. 42*, 2062–2065.

(30) Stemmer, W. P., Crameri, A., Ha, K. D., Brennan, T. M., and Heyneker, H. L. (1995) Single-step assembly of a gene and entire plasmid from large numbers of oligodeoxyribonucleotides. *Gene 164*, 49–53.

(31) Wu, C. H., Balasubramanian, W. R., Ko, Y. P., Hsu, G., Chang, S. E., Prijovich, Z. M., Chen, K. C., and Roffler, S. R. (2004) A simple method for the production of recombinant proteins from mammalian cells. *Biotechnol. Appl. Biochem. 40*, 167–172.

(32) Pavlinkova, G., Beresford, G. W., Booth, B. J., Batra, S. K., and Colcher, D. (1999) Pharmacokinetics and biodistribution of engineered single-chain antibody constructs of MAb CC49 in colon carcinoma xenografts. *J. Nucl. Med. 40*, 1536–1546.

(33) Muraro, R., Kuroki, M., Wunderlich, D., Poole, D. J., Colcher, D., Thor, A., Greiner, J. W., Simpson, J. F., Molinolo, A., Noguchi, P., and Schlom, J. (1988) Generation and characterization of B72.3 second generation monoclonal antibodies reactive with the tumor-associated glycoprotein 72 antigen. *Cancer Res. 48*, 4588–4596.

(34) Markwell, M. A., and Fox, C. F. (1978) Surface-specific iodination of membrane proteins of viruses and eucaryotic cells using 1,3,4,6-tetrachloro-3alpha,6alpha-diphenylglycoluril. *Biochemistry 17*, 4807–4817.

(35) Jain, S., Drendel, W. B., Chen, Z.-w., Mathews, F. S., Sly, W. S., and Grubb, J. H. (1996) Structure of human [beta]-glucuronidase reveals candidate lysosomal targeting and active-site motifs. *Nat. Struct. Mol. Biol. 3*, 375–381.

(36) King, D., Turner, A., Farnsworth, A., Adair, J., Owens, R., Pedley, R., Baldock, D., Proudfoot, K., Lawson, A., and Beeley, N. (1994) Improved tumor targeting with chemically cross-linked recombinant antibody fragments. *Cancer Res. 54*, 6176–6185.

(37) Kuroki, M., Fernsten, P., Wunderlich, D., Colcher, D., Simpson, J., Poole, D., and Schlom, J. (1990) Serological mapping of the TAG-72 tumor-associated antigen using 19 distinct monoclonal antibodies. *Cancer Res. 50*, 4872–4879.

(38) Greiner, J., Tobi, M., Fisher, P., Langer, J., and Pestka, S. (1985) Differential responsiveness of cloned mammary carcinoma cell populations to the human recombinant leukocyte interferon enhancement of tumor antigen expression. *Int. J. Cancer 36*, 159–166.

(39) Greiner, J., Ullmann, C., Nieroda, C., Qi, C., Eggensperger, D., Shimada, S., Steinberg, S., and Schlom, J. (1993) Improved radioimmunotherapeutic efficacy of an anticarcinoma monoclonal antibody (131I-CC49) when given in combination with gamma-interferon. *Cancer Res. 53*, 600–608.

(40) Schlesinger, P. H., Doebber, T. W., Mandell, B. F., White, R., DeSchryver, C., Rodman, J. S., Miller, M. J., and Stahl, P. (1978) Plasma clearance of glycoproteins with terminal mannose and N-acetylglucosamine by liver non-parenchymal cells. Studies with beta-glucuronidase, N-acetyl-beta-D-glucosaminidase, ribonuclease B and agalacto-orosomucoid. *Biochem. J. 176*, 103–109.

(41) Sly, W. S., Vogler, C., Grubb, J. H., Levy, B., Galvin, N., Tan, Y., Nishioka, T., and Tomatsu, S. (2006) Enzyme therapy in mannose receptor-null mucopolysaccharidosis VII mice defines roles for the mannose 6-phosphate and mannose receptors. *Proc. Natl. Acad. Sci. U.S.A. 103*, 15172–15177.

(42) Baxter, L., and Jain, R. (1996) Pharmacokinetic analysis of the microscopic distribution of enzyme-conjugated antibodies and prodrugs: comparison with experimental data. *Br. J. Cancer 73*, 447–456.

(43) Fang, L., and Sun, D. (2008) Predictive physiologically based pharmacokinetic model for antibody-directed enzyme prodrug therapy. *Drug Metab. Dispos. 36*, 1153–1165.

(44) Tietze, L. F., Schuster, H. J., Krewer, B., and Schuberth, I. (2008) Synthesis and biological studies of different duocarmycin based glycosidic prodrugs for their use in the antibody-directed enzyme prodrug therapy. *J. Med. Chem. 52*, 537–543.

(45) Afshar, S., Asai, T., and Morrison, S. (2009) Humanized ADEPT comprised of an engineered human purine nucleoside phosphorylase and a tumor targeting peptide for treatment of cancer. *Mol. Cancer Ther. 8*, 185–193.

(46) Smith, G., Banks, S., Blumenkopf, T., Cory, M., Humphreys, J., Laethem, R., Miller, J., Moxham, C., Mullin, R., and Ray, P. (1997) Toward antibody-directed enzyme prodrug therapy with the T268G mutant of human carboxypeptidase A1 and novel in vivo stable prodrugs of methotrexate. *J. Biol. Chem. 272*, 15804–15816.

(47) Uchino, J., Takayama, K., Harada, A., Sone, T., Harada, T., Curiel, D. T., Kuroki, M., and Nakanishi, Y. (2007) Tumor targeting carboxylesterase fused with anti-CEA scFv improve the anticancer effect with a less toxic dose of irinotecan. *Cancer Gene Ther. 15*, 94–100.

(48) Beresford, G. W., Pavlinkova, G., Booth, B. J. M., Batra, S. K., and Colcher, D. (1999) Binding characteristics and tumor targeting of a covalently linked divalent CC49 single-chain antibody. *Int. J. Cancer 81*, 911–917.

(49) Adams, G., Schier, R., Marshall, K., Wolf, E., McCall, A., Marks, J., and Weiner, L. (1998) Increased affinity leads to improved selective tumor delivery of single-chain Fv antibodies. *Cancer Res. 58*, 485.

(50) Schlesinger, P. H., Rodman, J. S., Doebber, T. W., Stahl, P. D., Lee, Y. C., Stowell, C. P., and Kuhlenschmidt, T. B. (1980) The role of extra-hepatic tissues in the receptor-mediated plasma clearance of glycoproteins terminated by mannose or N-acetylglucosamine. *Biochem. J. 192*, 597–606.

(51) Cheng, T., Chen, B., Chan, L., Wu, P., Chern, J., and Roffler, S. (1997) Poly (ethylene glycol) modification of -glucuronidase-antibody conjugates for solid-tumor therapy by targeted activation of glucuronide prodrugs. *Cancer Immunol. Immunother. 44*, 305–315.

(52) Grubb, J. H., Vogler, C., Levy, B., Galvin, N., Tan, Y., and Sly, W. S. (2008) Chemically modified beta-glucuronidase crosses blood-brain barrier and clears neuronal storage in murine mucopolysaccharidosis VII. *Proc. Natl. Acad. Sci. U.S.A. 105*, 2616–2621.

(53) Blanco, I., Kawatsu, R., Harrison, K., Leichner, P., Augustine, S., Baranowska-Kortylewicz, J., Tempero, M., and Colcher, D. (1997) Antiidiotypic response against murine monoclonal antibodies reactive with tumor-associated antigen TAG-72. *J Clin. Immunol. 17*, 96–106.

(54) Tempero, M., Leichner, P., Dalrymple, G., Harrison, K., Augustine, S., Schlam, J., Anderson, J., Wisecarver, J., and Colcher, D. (1997) High-dose therapy with iodine-131-labeled monoclonal antibody CC49 in patients with gastrointestinal cancers: a phase I trial. *J. Clin. Oncol. 15*, 1518–28.

(55) Hwang, W. Y., and Foote, J. (2005) Immunogenicity of engineered antibodies. *Methods 36*, 3–10.

(56) Ponder, K. (2008) Immune response hinders therapy for lysosomal storage diseases. *J. Clin. Invest. 118*, 2686–2689.

(57) Harding, F. A., Liu, A. D., Stickler, M., Razo, O. J., Chin, R., Faravashi, N., Viola, W., Graycar, T., Yeung, V. P., Aehle, W., Meijer, D., Wong, S., Rashid, M. H., Valdes, A. M., and Schellenberger, V. (2005) A β-lactamase with reduced immunogenicity for the targeted delivery of chemotherapeutics using antibody-directed enzyme prodrug therapy. *Mol. Cancer Ther. 4*, 1791–1800.

(58) Onda, M., Beers, R., Xiang, L., Nagata, S., Wang, Q.-c., and Pastan, I. (2008) An immunotoxin with greatly reduced immunogenicity by identification and removal of B cell epitopes. *Proc. Natl. Acad. Sci. U.S.A. 105*, 11311–11316.

(59) Abraham, S., Guo, F., Li, L.-S., Rader, C., Liu, C., Barbas, C. F., Lerner, R. A., and Sinha, S. C. (2007) Synthesis of the next-generation therapeutic antibodies that combine cell targeting and antibody-catalyzed prodrug activation. *Proc. Natl. Acad. Sci. U.S.A. 104*, 5584–5589.

(60) Sharma, S. K. (1996) Immune response in ADEPT. *Adv. Drug Delivery Rev. 22*, 369–376.

(61) Onda, M. (2009) Reducing the immunogenicity of protein therapeutics. *Curr. Drug Targets 10*, 131–139.

(62) Begent, R., Sharma, S., and Chester, K. (2010) Antibody-dependent enzyme prodrug therapy (ADEPT), *Antibody Engineering* (Kontermann, R., and Dübel, S., Eds.) pp 431−451, Springer, Berlin.

(63) Poláková, I., Pokorná, D., Dusková, M., and Smahel, M. (2010) DNA vaccine against human papillomavirus type 16: Modifications of the E6 oncogene. *Vaccine 28*, 1506–1513.

(64) Zhu, W., and Yu, G. L. (2009) Rabbit hybridoma, *Therapeutic Monoclonal Antibodies: From Bench to Clinic* (An, Z., Ed.) pp 152−168, Chapter 6, Wiley, New Jersey.

(65) Clark, M. (2000)Antibody humanization: a case of the'Emperor's new clothes'? *Immunol. Today 21*, 397.

(66) Adams, G. P., Schier, R., Marshall, K., Wolf, E. J., McCall, A. M., Marks, J. D., and Weiner, L. M. (1998) Increased affinity leads to improved selective tumor delivery of single-chain Fv antibodies. *Cancer Res. 58*, 485–490.

(67) Stigbrand, T., Eriksson, D., Riklund, K., and Johansson, L. (2008)Therapeutically used targeted antigens in radioimmunotherapy. *Targeted Radionuclide Tumor Therapy* 13–23.

Supplemental Table 1 Oligonucleotide sequences used for scFv assembly

Primer name	PRIMER SEQUENCE(5'-XXXXXXX-3')
P1	CCATGGAGACAGACACACTCCTGCTATGGGTACTGCTGCT
P2	CCAGGTTCCACTGGTGACGCGGCCCAGCCGGCCCAGGTGC
P3	GTCTGGGGCTGAGGTGAAGAAGCCTGGGGCCTCAGTGAAGG
P4	GGCTTCTGGATACACCTTCACTGACCATGCTATCCATTGGG
P5	CCCCCGGACAAAGGCTTGAGTGGATGGGATACTTCTCTCC
P6	CAAATATTCACAGAAGTTCCAGGGCAGAGTCACCATTACCGC
P7	GCGAGCACAGCCTACATGGAGCTGAGCAGCCTGAGATCTG
P8	GTGTATTACTGTGCAAGGTCATGGATCATGCAGTACTGGG
P9	CCCTGGTCACCGTGTCGAGCGGTGGTGGTGGATCAGGTGG
P10	GGTGGCGGCGGATCTGACATCGTGATGACCCAGTCTCCAGACTCC
P11	CTGGGCGAGAGGGCCACCATCAACTGCAAGTCCAGCCAGAG
P12	TTATACAGCTCCAACAATAAGAACTACTTAGCTTGGTACCAGC
P13	GGACAGCCTCCTAAGCTGCTCATTTACTGGGCATCTACCCGGG
P14	CCCTGACCGATTCAGTGGCAGCGGGTCTGGGACAGATTT
P15	CAGCAGCCTGCAGGCTGAAGATGTGGCAGTTTATTACTG
P16	CAATATTATAGTTACCCTCTCACGTTCGGTGGAGGGACCAAGG
P17	GGCTCCGGTGGTGGTGGATCAGGTGGAGG
P18	CACCAGTGGAACCTGGAACCCAGAGCAGCAGTACCCATAG
P19	CACCTCAGCCCCAGACTGCACCAGCTGCACCTGGGCCGGC
P20	GTGTATCCAGAAGCCTTGCAGGAAACCTTCACTGAGGCCCC
P21	GCCTTTGTCCGGGGGCCTGGCGCACCCAATGGATAGCATG
P22	CTTCTGTGAATATTTGAAGTCGTCATTGCCGGGAGAGAAGTATCCCA
P23	GTAGGCTGTGCTCGCGGATTTGTCAGCGGTAATGGTGACTC
P24	GCACAGTAATACACGGCCGTGTCTTCAGATCTCAGGCTGC
P25	ACACGGTGACCAGGGTACCTTGGCCCCAGTACTGCATGATC
P26	CGGAGCCGCCACCTCCACTTCCGCCTCCACCTGATCCACC
P27	GGCCCTCTCGCCCAGAGACACAGCCAGGGAGTCTGGAGACTG
P28	GTTGGAGCTGTATAAAACACTCTGGCTGGACTTGCAGTTG
P29	CTTAGGAGGCTGTCCTGGTTTCTGCTGGTACCAAGCTAAG
P30	ACTGAATCGGTCAGGGACCCCGGATTCCCGGGTAGATGCCCAG

P31	GCCTGCAGGCTGCTGATGGTGAGAGTGAAATCTGTCCCAG
P32	GAGGGTAACTATAATATTGCTGACAGTAATAAACTGCCAC
P33	ACCACCACCGGAGCCTTTGATCTCCACCTTGGTCCCTCCAC
P34	ATATCTAGAGCCACCTCCACTTCCGCCTCCACCTGATCC
P35	CCCTGGTCACCGTGTCGAGCGGTGGCGGTGGCTCGGGCGG
P36	CAGATCCGCCGCCACCCGACCCACCACCGCCCGAGCCACC

Bioconjugate Chemistry

ARTICLE

pubs.acs.org/bc

Mannosylated Dextran Nanoparticles: A pH-Sensitive System Engineered for Immunomodulation through Mannose Targeting

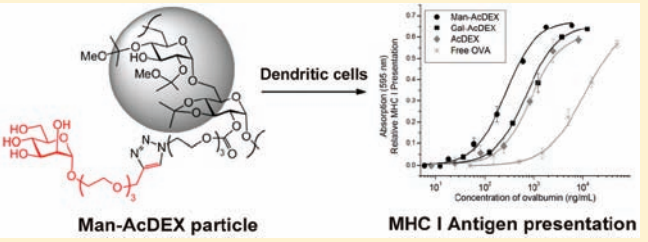
Lina Cui,[†] Joel A. Cohen,[†] Kyle E. Broaders,[†] Tristan T. Beaudette,[†] and Jean M. J. Fréchet*[,†,‡]

[†]College of Chemistry, University of California, Berkeley, California 94720-1460, United States and

[‡]King Abdullah University of Science and Technology, Thuwal, 23955-6900 Saudi Arabia

Supporting Information

ABSTRACT: Biotherapeutic delivery is a rapidly growing field in need of new materials that are easy to modify, are biocompatible, and provide for triggered release of their encapsulated cargo. Herein, we report on a particulate system made of a polysaccharide-based pH-sensitive material that can be efficiently modified to display mannose-based ligands of cell-surface receptors. These ligands are beneficial for antigen delivery, as they enhance internalization and activation of APCs, and are thus capable of modulating immune responses. When compared to unmodified particles or particles modified with a nonspecific sugar residue used in the delivery of antigens to dendritic cells (DCs), the mannosylated particles exhibited enhanced antigen presentation in the context of major histocompatibility complex (MHC) class I molecules. This represents the first demonstration of a mannosylated particulate system that enables enhanced MHC I antigen presentation by DCs *in vitro*. Our readily functionalized pH-sensitive material may also open new avenues in the development of optimally modulated vaccine delivery systems.



INTRODUCTION

Vaccination has been successful in preventing various diseases; however, the development of vaccines for illnesses such as cancer, AIDS, and malaria still suffers from ineffective or insufficient generation of protective immunity. One of the great challenges in the development of improved vaccines involves tailoring the type of immune response that a vaccine elicits to most effectively treat specific pathogens or cancers.[1] For example, cytotoxic T lymphocyte (CTL)-mediated immunity is believed to be critical for full protection from illnesses, such as HIV, malaria, and cancer.[2,3] Therefore, much effort has been put into guiding antigen into major histocompatibility complex (MHC) class I processing pathways of antigen presenting cells (APCs), which is critical for the generation of CTL responses.[4]

Dendritic cells (DCs)—the most potent APCs—endocytose, process, and load antigens onto MHC class I or II molecules for presentation to naïve $CD8^+$ or naïve $CD4^+$ T cells, respectively.[5] This MHC presentation, along with costimulatory signals, results in the activation of T cells, which then become effector T cells. DCs also express pathogen recognition receptors, such as Toll-like receptors (TLRs) and C-type lectins, with which DCs sense and/or capture microbes.[6,7] Targeting DCs with ligands specific for particular TLRs or C-type lectins can provide opportunities to alter the signaling pathways of DCs during activation, thus modulating the ultimate form of the cellular and/or humoral immune response that is generated.[8−10] Therefore, it is of great importance to develop a modular vaccine delivery system that can be used to address different activation mechanisms of the immune system.

Nanoparticles have received some attention for application as vaccine carriers because their size is in the range that can be taken up by phagocytic cells for the passive targeting of APCs. They can absorb, encapsulate, or be conjugated to antigens, and it is possible to incorporate ligands for the recognition and activation of APCs.[11−13] Besides targeting antigens to APCs, it is equally important to deliver those antigens into desired intracellular compartments.[14] Our group and others have reported acid-sensitive antigen delivery systems that allow antigens to be released under acidic conditions upon endocytosis by APCs and enter the MHC I presentation pathway.[15−21] Recently, we have developed a simple approach to modify dextran, a clinically approved biopolymer, into an acid-sensitive micro- or nanoparticulate delivery system, where dextran is rendered water-insoluble by modifying its hydroxyl groups with acid-labile acetal groups, forming acetalated dextran (AcDEX).[22] When tested *in vitro*, AcDEX particles encapsulating a model protein antigen led to significant enhancement of MHC class I presentation compared to the free protein or antigens delivered by commonly used materials such as poly(lactic-*co*-glycolic acid) (PLGA) or iron oxide particles, thus demonstrating the potential of AcDEX in vaccine development.[16]

We have now engineered the AcDEX system to display reactive groups on the particle surface, which can be readily functionalized with ligands capable of modulating immune

Received: December 26, 2010
Revised: April 6, 2011
Published: April 10, 2011

ACS Publications © 2011 American Chemical Society

responses. In this report, we demonstrate that introduction of mannose residues onto the surface of particles can enhance MHC I antigen presentation by DCs *in vitro*.

EXPERIMENTAL PROCEDURES

General Materials and Methods. All chemical reagents were purchased from Sigma-Aldrich (St. Louis, MO) and used as supplied, unless otherwise noted. Phosphate buffered saline (pH 7.4, PBS) was purchased from Invitrogen-Gibco (Carlsbad, CA). Water (dd-H_2O) was purified to a resistance of 18 MΩ using a NANOpure purification system (Barnstead, USA). All reactions were conducted under nitrogen. Organic solvents in reactions were purified by passing through two columns of neutral alumina on a commercial push still apparatus (Glass Contour, SG Water, NH). Analytical thin layer chromatography (TLC) was performed on silica gel 60-F_{254} (Merck). Plates were visualized by ultraviolet light or charring with basic potassium permanganate solution, triphenylphosphine/ninhydrin solution or ethanolic sulfuric acid-anisaldehyde solution. Column chromatography used silica gel (SiliCycle, F60, 40−63 μm, 60 Å) and solvents were of reagent grade, and used as supplied. ^{1}H NMR spectra were recorded at 400 or 500 MHz, and ^{13}C NMR spectra were recorded at 100 MHz. First-order chemical shifts are reported in δ (ppm) using residual solvent signals from deuterated solvents as references. For samples in D_2O, the chemical shifts are referenced to acetone (0.1% v/v) at δ 2.225. Signals in ^{1}H spectra were assigned with corresponding coupling constants or COSY spectra. NMR data reported are labeled according to IUPAC nomenclature for carbohydrate molecules. Mass spectrometry was performed under positive/negative-mode high-resolution electrospray ionization (ESI) on an Orbitrap instrument by the Chemistry Mass Spectrometry Facility of the University of California, Berkeley. Fourier transform infrared spectroscopy (FT-IR) was carried out on a Varian 3100 FT-IR spectrometer (Varian, USA). Particles used in the studies were suspended by alternately vortexing and sonicating in a VWR model 75 water bath. Fluorescence measurements for microplate-based assays were obtained on a Spectra Max Gemini XS (Molecular Devices, USA), usage courtesy of Professor Jonathan Ellman. UV−vis absorbances for microplate-based assays were measured using Spectra Max 190 (Molecular Devices, USA), and flow cytometry was performed using Becton-Dickinson Biosciences FACSCalibur flow cytometer, usage courtesy of Professor Carolyn Bertozzi.

Cell Lines and Culture. DC 2.4 cells were generously donated by Professor Kenneth Rock (University of Massachusetts Medical Center) and were cultured in RPMI 1640 (Invitrogen) supplemented with 10% fetal bovine serum (FBS, from Hyclone), 2 mM GlutaMAX (Invitrogen), 100 U/mL penicillin (Invitrogen), 100 μg/mL streptomycin (Invitrogen), 10 mM MEM Non-Essential Amino Acids (NEAA, from Invitrogen), 10 mM HEPES buffer (Invitrogen), and 0.055 mM 2-mercaptoethanol (Invitrogen). RAW 309 and RAW 264.7 macrophages were purchased from ATCC (Manassas, VA) and were cultured in Dulbecco's Modified Eagle Medium (DMEM, Invitrogen-Gibco 11960) supplemented with 10% FBS, 100 U/mL of penicillin, 100 μg/mL streptomycin, and 2 mM GlutaMAX. B3Z ($CD8^+$) cells were kindly provided by Professor Nilabh Shastri (University of California, Berkeley) and were cultured in RPMI 1640 supplemented with 10% FBS, 2 mM GlutaMAX, 100 U/mL penicillin, 100 μg/mL streptomycin, 1 mM sodium pyruvate (Invitrogen), and 0.055 mM 2-mercaptoethanol. Cells were incubated in a water-jacketed incubator at 37 °C with 5% CO_2.

Synthesis of Azido-Dextran. To a solution of dextran (MW = 10 500 g/mol, 1.57 g, 0.15 mmol) in anhydrous DMSO (30 mL) was added imidazole-1-carboxylic acid 2-[2-(2-azido-ethoxy)-ethoxy]-ethyl ester (2.61 g, 9.705 mmol) and 4-dimethylamino-pyridine (DMAP, 1.30 g, 10.676 mmol). The reaction mixture was stirred for 2 days under argon and dialyzed using regenerated cellulose-based dialysis bag (MWCO = 3 kDa) against 8 × 4 L distilled water over 3 days. Lyophilization gave the product as a white fluffy powder (1.88 g, 85.3%). IR (KBr, cm^{-1}): 3409, 2929, 2362, 2340, 2115, 1751, 1268, 1150, 1104, 1017. ^{1}H NMR (400 MHz, D_2O): δ 5.01−4.88 (m, 1.4H, H-1), 4.40−4.26 (br, 1H, $CH_2OC{=}O$), 4.02−3.42 (m, 12.9H, H-2, H-3, H-4, H-5, H-6, CH_2O, CH_2N_3). ^{13}C NMR (125 MHz, D_2O): δ 155.7, 155.0, 97.8, 80.3, 73.4, 71.4, 70.9, 70.2, 69.8, 69.7, 69.6, 69.4, 69.3, 68.4, 67.9, 67.5, 65.6. 50.2, 38.8.

Synthesis of Acetalated Azido-Dextran (Azido-AcDEX). Azido-dextran (MW = 14 700 g/mol, 1.47 g, 0.100 mmol) was dissolved in anhydrous DMSO (10 mL) in a 20 mL scintillation vial, followed by addition of 2-methoxypropene (3.4 mL, 37 mmol) and pyridinium *p*-toluenesulfonate (15.6 mg, 0.062 mmol). The reaction flask was sealed with parafilm, and the reaction was allowed to proceed for 2 h (fast-degrading azido-AcDEX) or 20 h (slow-degrading azido-AcDEX) at r.t.[16] Triethylamine (0.1 mL, 0.7 mmol) was added to quench the reaction, and the dextran derivative was precipitated in dd-H_2O (pH 8, 100 mL). The product was collected by centrifugation at 14 000 × *g* for 10 min, and washed with dd-H_2O (pH 8, 2 × 50 mL). The resulting pellet was then lyophilized to yield a white power (1.07 g). ^{1}H NMR (500 MHz, CD_2Cl_2): δ 5.18 (1H), 4.95 (2H), 4.28 (2H), 3.97−3.65 (19H), 3.49 (2H), 3.38 (2H), 3.24−3.21 (4H), 2.50 (1H), 1.42, 1.38−1.34 (20H) (all reported as broad peaks).

Preparation of Nanoparticles Encapsulating Proteins (Azido-AcDEX). Ovalbumin (OVA) or bovine serum albumin (BSA) labeled by fluorescein isothiocyanate (FITC) was encapsulated into nanoparticles using a double emulsion water/oil/water (w/o/w) evaporation method similar to that described previously.[16] Briefly, OVA or BSA-FITC (8 mg) was dissolved in phosphate buffered saline (PBS, 137 mM NaCl, 10 mM phosphate, 2.7 mM KCl, pH 7.4, 40 μL), and added to an azido-AcDEX (160 mg) solution in CH_2Cl_2 (1.6 mL). This mixture was then vortexed immediately and emulsified for 30 s on ice using a probe sonicator (Branson Sonifier 450, output setting at 5.5, duty cycle at 70%). An aqueous solution of poly(vinyl alcohol) (PVA, M_w = 13 000−23 000 g/mol, 87−89% hydrolyzed, 3.2 mL, 3% w/w in PBS) was added to the first emulsion, and sonicated for 30 s on ice using the same settings. The resulting double emulsion was immediately transferred into a second PVA solution (16 mL, 0.3% w/w in PBS) and stirred for 2 h to evaporate the CH_2Cl_2. The particles were isolated by centrifugation (14 000 × *g*, 15 min) and washed with dd-H_2O (pH 8, 3 × 15 mL). The particle pellets were sonicated to a nice suspension between each wash. The washed particles were suspended in dd-H_2O (pH 8, 2 mL) and lyophilized to give a white fluffy solid (105 mg).

Preparation of Empty Nanoparticles (Azido-AcDEX). Particles containing no protein were made in the same manner as above without the first emulsion with the OVA solution.

Preparation of Microparticles Using Emulsion Method. Micrometer-sized particles were prepared in a similar manner as that previously described.[23] Azido-AcDEX (50 mg) was dissolved

in ice-cold CH_2Cl_2 (1 mL) in a 15 mL round-bottom polypropylene tube. PBS buffer (50 μL) was added, and the first solution and the mixture were sonicated for 5−10 s to a milky emulsion using a Branson Sonifier 450 (Branson Ultrasonics, Danbury, CT) with a 1/8 in microtip, an output setting of 1, and a continuous duty cycle. This primary emulsion was transferred dropwise to an ice-cold solution of PVA (12.5 mL, 3% w/w in PBS) that was being homogenized at 9600 rpm using an IKA T-25 Ultra-Turrax digital homogenizer with an S25N-10G generator. The homogenization was allowed to proceed for 30 s, and the resulting double emulsion was poured into a second PVA solution (25 mL, 0.3% w/w in PBS) and stirred for 2 h to evaporate CH_2Cl_2. Particles were centrifuged (4000 × *g*, 4 min), washed with dd-H_2O (3 × 20 mL, pH 8), resuspended in dd-H_2O (1 mL, pH 8) and lyophilized to yield a white fluffy solid (46 mg, 92%).

Quantification of Encapsulated OVA. Particles containing OVA were suspended at 5 mg/mL in 30 mM acetate buffer (pH 5.0) and incubated at 37 °C under gentle agitation for 2 days using a Thermomixer R heating block (Eppendorf). After complete degradation, protein content was analyzed by a microplate assay using fluorescamine (1 mM in acetone) as described in the literature.[24] Empty Ac-DEX particles were degraded in a similar fashion and used to determine background fluorescence.

Quantification of Encapsulated BSA-FITC. Particles containing BSA-FITC were suspended at 5 mg/mL in dd-H_2O (pH 8) in a microplate, and fluorescence of FITC was measured in triplicate and analyzed against a standard fluorescence curve of BSA-FITC.

Size Measurements of Nanoparticles by Dynamic Light Scattering. Particles were suspended in dd-H_2O (pH 8) in a disposable sizing cuvette at a concentration of 1 mg/mL. Particle size distributions and average particle diameters were determined in three measurements by dynamic light scattering using a Zetasizer Nano ZS (Malvern Instruments, United Kingdom). Size distributions in the text are described as average particle diameters ± half width of the distribution at half maximal height.

Size Measurements of Microparticles by Light Scattering. The size distribution of the microparticles was determined using a Horiba Partica LA-950 laser scattering particle size distribution analyzer after suspending the particles at 2 mg/mL in PBS. The reported results represent the geometric mean ± standard deviation of the size distribution.

Scanning Electron Microscopy. Suspensions of nanoparticles or microparticles (1 mg/mL) in dd-H_2O (pH 8) were dripped onto silicon wafers and allowed to dry in the air. The particles were then sputtercoated with a 2 nm layer of a palladium/gold alloy and imaged using an S-5000 microscope (Hitachi, Japan) or TM-1000 microscope (Hitachi, Japan).

Preparation of Mannosylated or Galactosylated Particles (Man-AcDEX or Gal-AcDEX). Azido-AcDEX nanoparticles or microparticles (20 mg) were suspended in a 2 mL N_2 protected aqueous solution of copper sulfate (1 mM), potassium 5,5′,5″-(2,2′,2″-nitrilotris(methylene)tris(1*H*-benzimidazole-2,1-diyl))tripentanoate $(BimC_4A)_3$ (1.2 mM), ascorbic acid (10 mM), and HEPES buffer (0.1 mM, pH 8.5), and the reaction mixture was stirred for 1 h at r.t. The particles were then isolated by centrifuge (14 000 × *g*, 10 min), washed with EDTA solution (10 mM in dd-H_2O, 3 × 2 mL, pH 8) and dd-H_2O (3 × 2 mL, pH 8), and resuspended in dd-H_2O (pH 8, 1 mL). The suspension was lyophilized to give white fluffy powder (18 mg, 90%).

Quantification of Mannose or Galactose Incorporation. Man-AcDEX or Gal-AcDEX particles (2 mg) were suspended in D_2O (0.7 mL) in an NMR tube, and DCl (5 μL) was added to the inside rim of the tube. The NMR tube was then capped and sealed immediately, and the suspension inside was mixed well until clear. After 10 min, NaOD (6 μL, 40 wt % in D_2O) was added to adjust the pH to 12. The solution was kept at r.t for 10 min, and ^{1}H NMR spectrum was acquired to observe the disappearance of the peak corresponding to ethylene protons adjacent to carbonate group (4.2−4.3 ppm), indicating the cleavage of the side chains from the dextran backbone. Spin−lattice relaxation times (T1) of the triazole proton of the mannoside and H-1 of glucose residue of dextran were measured (2.29 and 1.53 s, repsectively), and the values were used in the acquisition of ^{1}H NMR spectrum of the mixture of dextran, mannoside, and azido-TEG. The ratio of the integration of triazole and glucose H-1 gave the ratio of mannoside residue and glucose residue of dextran.

Release of OVA from Particles. Particles containing OVA were suspended at 5 mg/mL in either a sodium acetate buffer (30 mM, pH 5.0) or PBS buffer (pH 7.4, GIBCO, 1×), and gently agitated at 37 °C using a Thermomixer R heating block (Eppendorf). At desired time points, aliquots (100 μL) were removed and centrifuged at 14 000 × *g* for 10 min. The supernatant was collected, stored at −20 °C, and analyzed for the presence of protein using a microplate fluorescamine assay as described before.

Confocal Microscopy. Azido-AcDEX, Man-AcDEX, Gal-AcDEX, and HO-AcDEX microparticles (100 μg) were incubated with ConA-FITC (1 mg/mL) in PBS buffer (pH 7.4, 100 μL) with BSA (3 wt %) in the dark for 10 min at r.t. The particle suspension was then centrifuged (10 000 *g*, 3 min), washed with PBS buffer (1 mL × 3), resuspended in PBS buffer (2 mL), and loaded in a 35 mm #1.5 glass-bottomed tissue culture dish (MatTek, MA). Imaging was performed using a Zeiss LSM 510 Meta confocal microscope with an Apo 63× water dipping objective (Carl Zeiss, Germany) using an excitation wavelength of 488 nm for FITC.

Particle Uptake. DC 2.4 cells were seed to a 24-well tissue culture plate (Corning-Costar, NY) at 3.0 × 10^5 cells/well (1 mL/well) in growth medium. After overnight incubation at 37 °C, the medium was aspirated, and suspensions of particles encapsulating BSA-FITC at 2 mg/mL (250 μL/well) were added. At the indicated time points, medium was removed, and cells were washed with PBS buffer (Ca^{2+}-, Mg^{2+}-, 3 × 300 μL), trypsinized (50 μL trypsin/well), collected in PBS (300 μL), centrifuged (3000 × *g*, 5 min), and fixed in PBS buffer (300 μL) containing 4% paraformaldehyde (Electron Microscopy Sciences, Hatfield, PA). Cells were analyzed for particle uptake by a Becton-Dickinson Biosciences FACSCalibur flow cytometer (San Jose, CA) with 488 nm excitation. The fluorescence of cells incubated with different particles was normalized by the amount of BSA-FITC encapsulated in each type of particles.

MHC Class I Presentation (B3Z) Assay. B3Z cells[21] were freshly thawed and cultured in growth medium over 5 days. Dendritic cells (DC2.4, 5 × 10^4/well) were cultured overnight in a 96-well plate and subsequently incubated with particles encapsulating OVA or free OVA. After 6 h, the cells were washed carefully with the medium for B3Z cells (3 × 100 μL/well), and B3Z cells (1 × 10^5/well) were added to the dendritic cells and co-cultured for 16 h. The medium was replaced with 100 μL of CPRG buffer (91 mg of chlorophenol red β-D-galactopyranoside (CPRG, Roche, USA), 1.25 mg of NP40 (EMD Sciences, USA),

and 900 mg $MgCl_2$ per 1 L of PBS). The plates were kept in the dark at r.t. for 72 h, and the absorbance at 595 nm was measured (microplate reader, SpectraMax 190, Molecular Devices).

Mannose Inhibition MHC Class I Presentation (B3Z) Assay. Dendritic cells DC 2.4 (5×10^4/well) were cultured overnight in a 96-well plate. The medium was then aspirated and OVA-containing particles suspended in medium containing various concentrations of free mannose were added to the cells. After 6 h, the cells were washed carefully and B3Z cells (1×10^5/well) were added to the dendritic cells/macrophages and co-cultured for 16 h. The medium was replaced with 100 μL of CPRG buffer, the plates were kept in the dark at r.t. for 72 h, and the absorbance at 595 nm was measured.

Cell Viability Assay. Viability of cells was assessed using a standard MTT assay. Briefly, dendritic cells were seeded onto 96-well microtiter plates (Corning-Costar, NY) at 5×10^4 cells/well, respectively, for 24 h. The growth medium was replaced with 100 μL suspensions of particles or solutions of their degraded compounds at various concentrations. After incubation for 24 h, a 3 mg/mL solution of MTT (3-(4,5-dimethyl-2-thiazolyl)-2,5-diphenyl-2*H*-tetrazolium bromide) in growth medium (40 μL) was added directly to each well and the plates were returned to incubator. After 30 min (for DC 2.4 cells), purple crystals were observed at the bottom of each well. The plates were centrifuged ($500 \times g$, 5 min), and the medium was replaced with DMSO (200 μL/well) to dissolve the crystals of formazan. Glycine buffer (25 μL/well, 0.1 M glycine, 0.1 M NaCl, pH 10.5) was added, and absorbances at 570 nm were measured (Spectra Max 190 plate reader, Molecular Devices). Cell viability was normalized in percentage as the ratio of the absorbances measured from treated and untreated cells.

RESULTS AND DISCUSSION

Preparation and Modification of "Clickable" pH-Sensitive Dextran Particles. We developed a general protocol to prepare pH-sensitive AcDEX particles that can be modified to introduce multiple copies of a ligand on their surface. In a first step, a fraction of the hydroxyl groups of dextran were modified with an amphiphilic linker bearing a reactive functional group. This was followed by a second step in which the majority of the remaining hydroxyl groups were protected by acetal moieties to render the modified dextran organic-soluble in order to enable particle fabrication via a double emulsion process. We hypothesized that these amphiphilic linkers would be oriented to the interface between water and organic solvent phase during particle formation, so that the reactive functional groups would largely be located on the surface of the particles, thus accessible for future modification (Figure 1).

We used azido groups as the reactive functionalities at the termini of the linkers due to their ease of conjugation in aqueous phase via a variety of bio-orthogonal approaches such as azide–alkyne cycloaddition, Staudinger ligation, and others.[25,26] In this instance, dextran was modified using carbonyldiimidazole-activated azido-triethylene glycol (azido-TEG) to afford azido-dextrans with various degrees of modification (Figure 1 and Supporting Information Figure S1).[27] These azido-dextran materials were then acetalated by reaction with 2-methoxypropene to obtain the acid-sensitive azido-AcDEX polymer. The resulting water-insoluble polymer containing 0.4 azido-TEG/glucose residue was then used to prepare particles using standard emulsion-based techniques,[22] to afford nanoparticles with low polydispersity

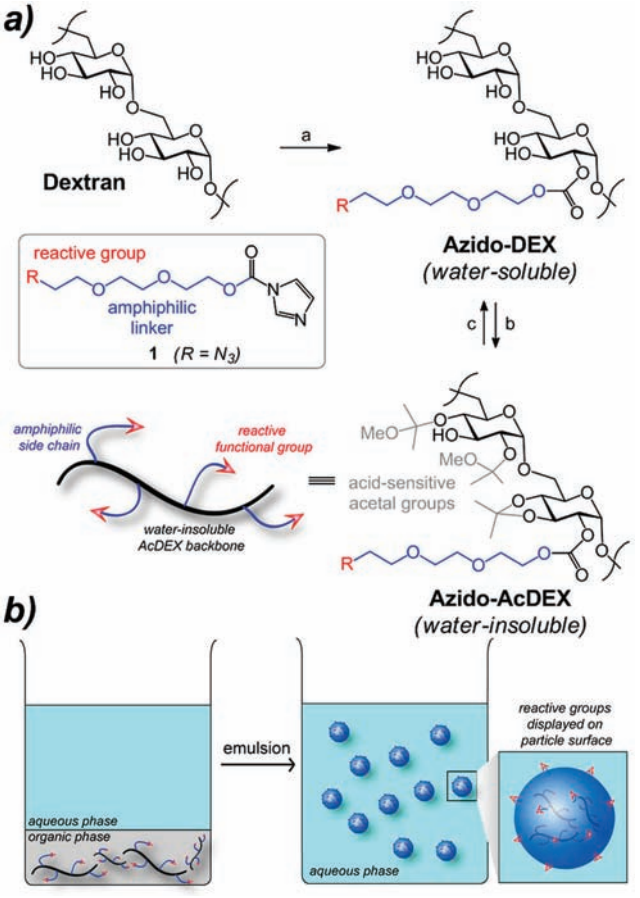


Figure 1. Preparation of "clickable" acid-sensitive dextran nanoparticles. (a) Synthesis of azido-AcDEX material. Reagents and conditions: a. **1**, DMSO, DMAP; b. DMSO, 2-methoxypropene, pyridinium *p*-toluenesulfonate; c. acidic conditions (e.g., in endosomes). (b) Display of reactive functional groups on particle surface using emulsion.

(0.070) as measured by dynamic light scattering (DLS) (Figure 2). It should be mentioned that aggregation of particles was observed when using azido-AcDEX materials with degree of modification higher than 0.4 azido-TEG per glucose residue.

We then explored the surface modification of the azido-AcDEX nanoparticles with an appropriately functionalized mannose derivative. As a proof of concept, the ligand-assisted copper-catalyzed azide–alkyne cycloaddition (CuAAC) was used because it is a very efficient reaction for which Cu-ligands capable of significantly increasing the coupling rate are available.[28] Briefly, azido-AcDEX particles were suspended in HEPES buffer (0.1 M, pH 8.0) and stirred with an alkynylated mannoside in the presence of Cu(I) and its ligand $(BimC_4A)_3$ (Figure 2).[29] To monitor the heterogeneous CuAAC reaction, aliquots of the particle suspension were removed at desired time points, washed to remove unbound molecules and salts, and lyophilized. The dry particles were then degraded in D_2O by addition of DCl to hydrolyze the acetal groups, followed by addition of NaOD solution to cleave the carbonate bonds linked to dextran (Supporting Information Figure S3. The solutions of degraded particles were then examined by ^1H NMR, and the signal corresponding to the triazole proton (the product of azide alkyne cycloaddition at 8.0 ppm was used to monitor the progress of the reaction (Figure S3). Using the integration of the triazole proton relative

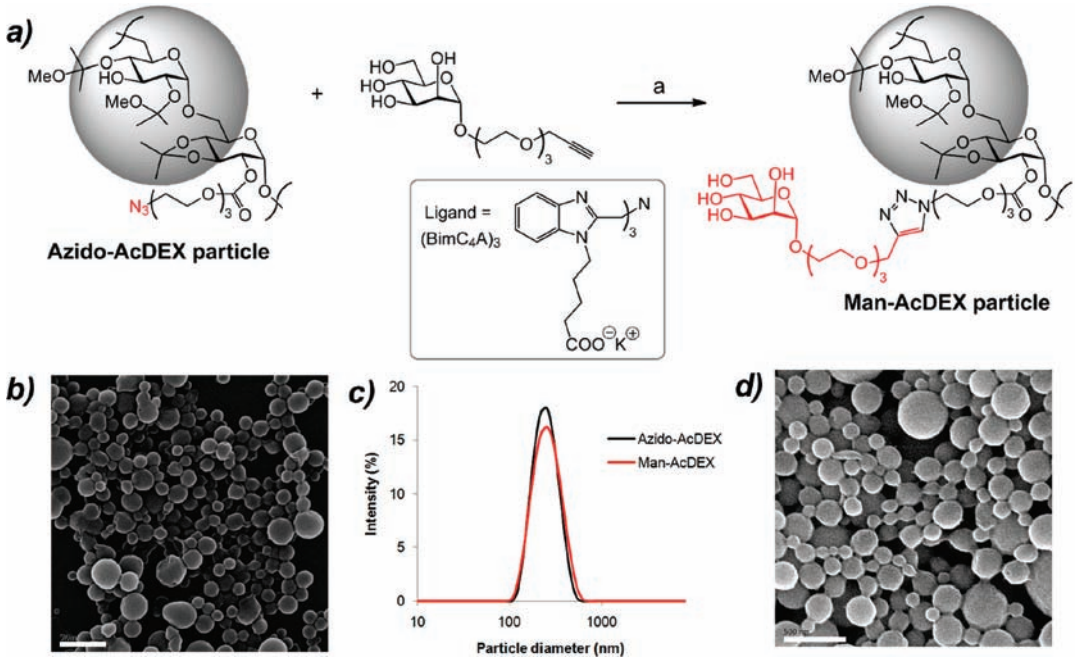


Figure 2. Synthesis of mannosylated AcDEX particles by CuAAC. (a) Synthetic scheme. Reagents and conditions: a. $CuSO_4$, ligand, ascorbic acid, HEPES buffer. (b) SEM image of Azido-AcDEX particles. (c) Size distribution of particles measured using DLS. (d) SEM image of Man-AcDEX particles (Scale bar = 500 nm).

to the anomeric proton, the number of mannose residues conjugated to particles were quantified by NMR and found to reach 2 mannose/100 glucose residues on dextran, leading to the estimate that a particle 200 nm in diameter would contain a few million mannose residues.

To verify that the reaction occurs at the surface of the particles, we prepared micrometer-sized particles large enough to visualize using confocal microscopy. These microparticles were subjected to the same reaction conditions as used for the nanoparticles and were surface-modified with mannoside, galactoside, or hydroxylated moieties, the latter two samples serving as negative controls. This was followed by incubation of the three types of modified microparticles with fluorescein isothiocyanate (FITC)-labeled concanavalin A (ConA), a reagent that specifically binds to α-mannose residues.[30] The particles were then washed to remove unbound reagents, and visualized using confocal microscopy (Figure 3). Only the mannosylated particles (Man-AcDEX) showed surface-associated fluorescence. In sharp contrast, galactosylated (Gal-AcDEX), hydroxylated, and unmodified azido-AcDEX particles showed no visible fluorescence, suggesting that the fluorescence halo around Man-AcDEX particles was due to specific binding between ConA and mannose residues on the particle surface.

Since all the above-mentioned particles could be used in the delivery of therapeutics, the cytotoxicity of the particles and that of the soluble materials obtained after their degradation were evaluated. All particles had a cytotoxicity comparable to that of PLGA and were fully degradable affording free dextran and nontoxic small molecules (Supporting Information Figure S4), supporting their potential use as biocompatible delivery vehicles.

Mannosylation of Particles Enhances MHC I Antigen Presentation by DCs. Recent reports have shown that soluble protein antigens taken up by DCs via mannose receptor[31]-mediated endocytosis bypass intracellular diversion and enter the MHC I antigen presentation pathway directly.[32] Therefore, targeting MRs of DC could constitute a useful route to enhance MHC class I antigen presentation. It is known that MRs contains 8 carbohydrate recognition domains (CRDs), 5 of which (CRDs 4−8) are involved in binding and endocytosis of mannose and related structures.[33,34] Therefore, using multivalently displayed ligands to target the CRDs of MR or multiple MRs can be a reasonable strategy to deliver antigens into MR-mediated endocytosis pathway. A terminal mannose monosaccharide is known to be a favorable ligand for MRs, but other C-type lectins, including DEC-205, Endo180, dendritic cell-specific intercellular adhesion molecule grabbing nonintegrin (DC-SIGN), Dectin-2 and langerin, can also interact with mannose-containing structures.[35] Hence, in practice, it is difficult to direct mannose-conjugates exclusively to MRs. However, differences in the spatial display of these mannose structures can produce a distinct set of carbohydrate recognition profile for each receptor. For example, DC-SIGN prefers to bind internal structures of high mannose oligosaccharides, therefore providing a certain degree of selectivity.[36−40]

Particulate systems provide a scaffold to incorporate multiple copies of targeting groups, which can help to increase the overall binding avidity to the cell surface receptors.[41] For example, mannose residues can be directed to the surface by self-assembly as seen in the preparation of liposomal or micellar carriers.[42−45] However, few reports exist on the development of mannosylated polymer-based particles.[46−51] Since it is not known if mannosylated particulate systems can improve the level of antigen presentation via the MHC class I pathway, we used our newly devised "clickable" particle system to study this effect. Mannosylation of our particles afforded a dense surface layer of mannose monosaccharide (up to 10^6/particle) while also preserving the integrity of the particles and their acid-degradability, thus supporting their use as a carrier for the delivery of protein antigen to DCs.

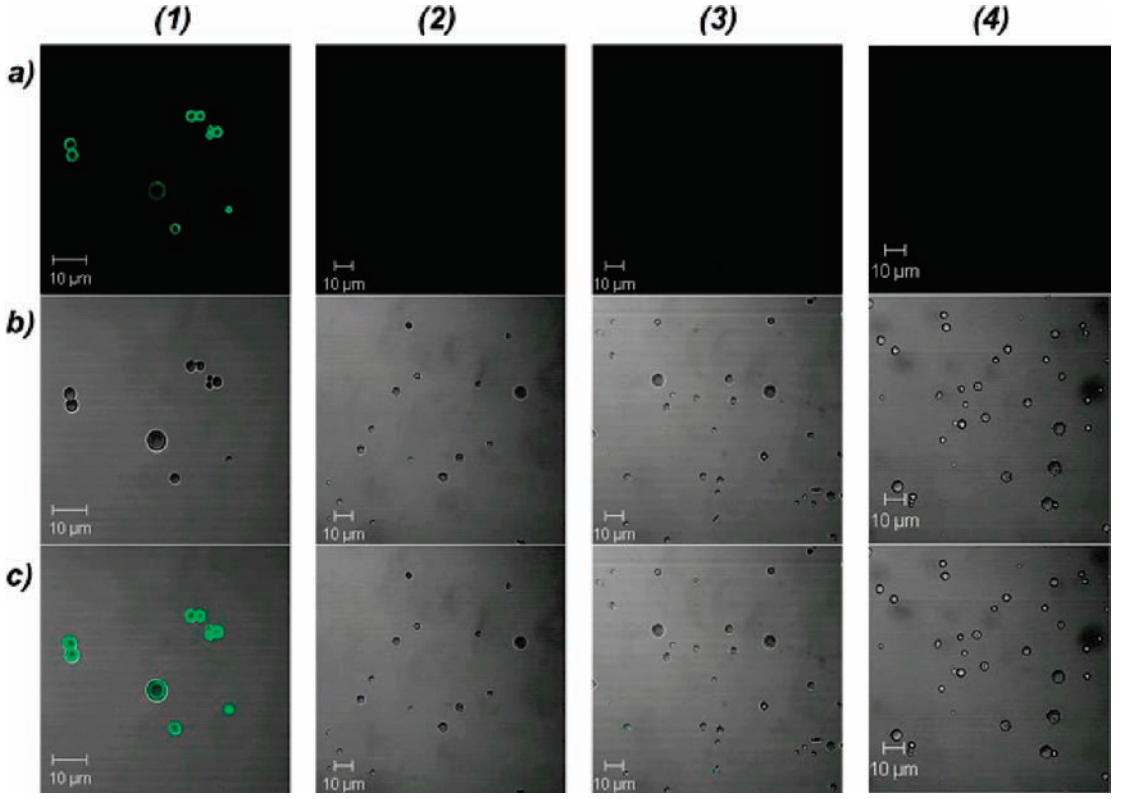


Figure 3. Confocal microscope images of microparticles ((1) Man-AcDEX particles, (2) azido-AcDEX particles, (3) Gal-AcDEX particles, (4) HO-AcDEX particles) after incubation with ConA-FITC. (a) Fluorescence image obtained using excitation wavelength of 488 nm; (b) differential interference contrast image; (c) merge of panels (a) and (b).

To test this hypothesis *in vitro*, we used a DC 2.4 cell line derived from murine bone marrow DCs[52] that is known to express MRs on its cell surface.[43] We first performed a cellular uptake experiment to see whether the mannose residues on the particle surface were available to MRs, and how that might contribute to particle internalization. FITC-labeled bovine serum albumin (FITC-BSA) was encapsulated into AcDEX or azido-AcDEX particles, and the latter were modified by the protocol described above to yield dye-containing Man-AcDEX and, as a negative control, Gal-AcDEX particles (Figure 2). These particles were then incubated with DC 2.4 cells for fixed lengths of time before they were washed and collected. Flow cytometry was then used to analyze the cellular uptake of particles (Figure 4). At all time points, Man-AcDEX particles showed a 1.5- to 2-fold increased uptake when compared to Gal-AcDEX particles and unmodified azido-AcDEX or AcDEX particles, respectively. Given that DCs also perform phagocytosis, macropinocytosis, and other receptor-mediated uptake, mannosylation was not expected to cause a drastic increase in cellular internalization. However, this finding suggests that mannose residues were accessible to MRs on DCs and that mannose targeting groups may indeed help enhance cellular uptake to an appreciable extent.

MHC I presentation of antigen-derived peptides from DC 2.4 was examined using the B3Z cell assay.[16,17,21,53,54] B3Z cells are $CD8^+$ T cell hybridomas engineered to express β-galactosidase when their T cell receptor recognizes the OVA-derived SIINFEKL epitope ($OVA_{257-264}$) in the context of MHC I molecules. We first prepared AcDEX or azido-AcDEX particles encapsulating

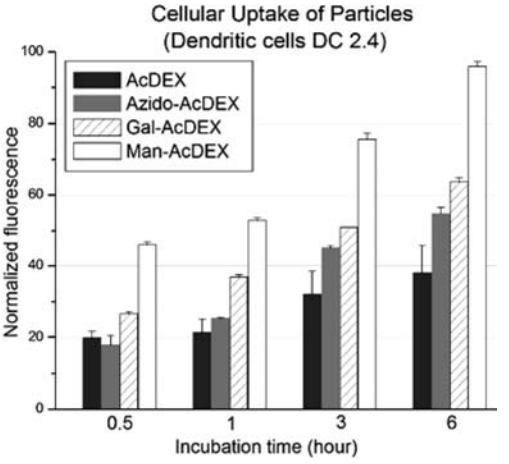


Figure 4. Cellular uptake of particles by DC 2.4 cells. Particles (2 mg/mL) were incubated with DC 2.4 at 37 °C. The fluorescence of cells was analyzed by a Becton-Dickinson Biosciences FACSCalibur flow cytometer with 488 nm excitation, and was normalized by the amount of BSA-FITC encapsulated in each type of particles.

OVA using a traditional double emulsion technique,[55] then surface-modified the latter with mannose or galactose, and incubated these particles with DC 2.4 cells (Figure 5). Antigen presentation was then determined using the B3Z assay. While all particulate formulations of OVA enhanced MHC I antigen presentation compared to free OVA, the performance of Man-AcDEX was about 5-fold better than that of Gal-AcDEX. This

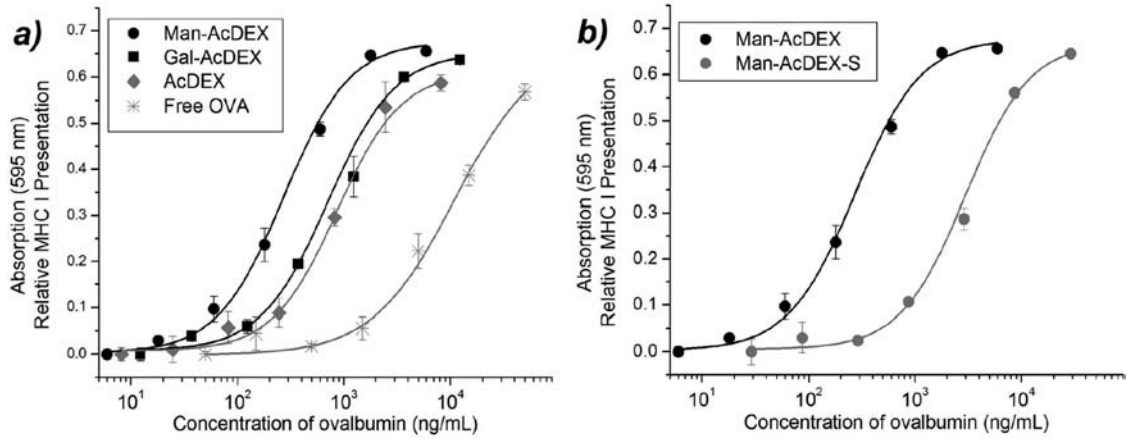


Figure 5. MHC I antigen presentation (B3Z assay) by DC 2.4. (a) Comparison of MHC I antigen presentation of OVA encapsulated in Man-AcDEX, Gal-AcDEX, and AcDEX particles, and free OVA. (b) Comparison of MHC I antigen presentation of OVA encapsulated in Man-AcDEX (fast-degrading) and Man-AcDEX-S (slow-degrading).

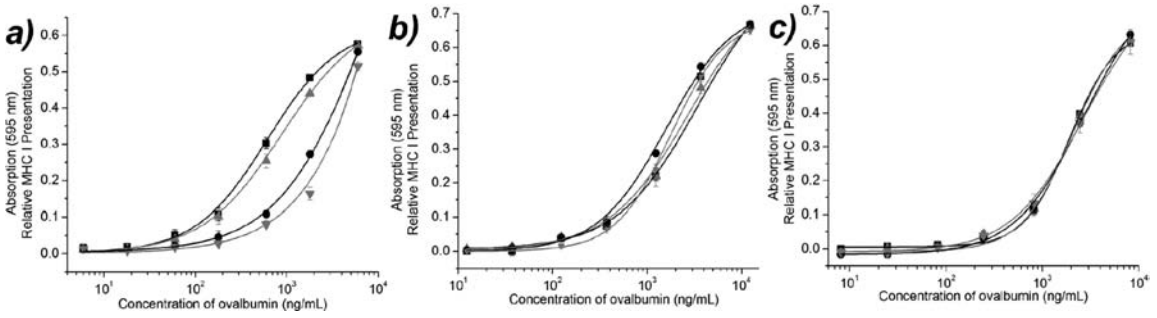


Figure 6. Mannose inhibition B3Z assay of DC 2.4. (a), (b), and (c) are Man-AcDEX, Gal-AcDEX, and AcDEX particles, respectively. Square, no addition of free mannose; triangle, with 10 mM free mannose; circle, with 50 mM free mannose; inverse triangle, with 100 mM free mannose.

finding could not be attributed to differences in antigen-release profiles, as both particles released antigen at similar rates at endosomal pH (Figure 5 and Supporting Information Figure S5). In addition, this may not be explained solely by the 1.5-fold difference in uptake of Man-AcDEX particles relative to Gal-AcDEX particles. One possible reason for this can be that these two types of particles go through different cellular uptake pathways, which causes differences in antigen presentation levels.

To verify that the enhanced MHC I antigen presentation from Man-AcDEX particles was indeed related to the surface-bound mannose groups, we incubated particles with DCs in the presence of free mannose, thus serving as a competitive ligand for the MRs (Figure 6). For Man-AcDEX particles, antigen presentation was suppressed upon addition of free mannose, and this inhibition was proportional to the concentration of free mannose. However, addition of free mannose did not inhibit antigen presentation from Gal-AcDEX or AcDEX particles. Collectively, these observations suggest that MRs and/or related C-type lectins were involved in the delivery and presentation of antigens in the case of Man-AcDEX particles, but not Gal-AcDEX or AcDEX particles.

In a previous report, we demonstrated that particle degradation and antigen release rates can influence the levels of antigen presentation observed—fast-degrading particles led to more efficient and enhanced class I presentation than slow-degrading particles.[16] However, besides the differences in particle degradation kinetics, particles made from the two types of materials may go through different internalization pathways due to their different surface chemistry. Hence, we prepared particles using a slower-degrading azido-AcDEX material (azido-AcDEX-S) and modified the particles with mannose to obtain slow-degrading Man-AcDEX particles (Man-AcDEX-S), to compare their antigen presentation efficiency to that of Man-AcDEX particles. Because both particles had the same surface modification, they should go through the same cellular uptake mechanism, so that the only difference would be their degradation rate. The use of the faster-degrading Man-AcDEX polymer led to a 10-fold increase in the levels of MHC I presentation compared to Man-AcDEX-S (Figure 5). AcDEX particles used in this study degraded faster than Man-AcDEX or Gal-AcDEX particles (Supporting Information Figure S5), and they showed similar antigen presentation abilities as Gal-AcDEX particles. Since receptors on DCs may also bind galactose, the difference in degrading speed between AcDEX particles and Gal-AcDEX particles might be partially offset.[56] On the other hand, possible uptake of Gal-AcDEX via receptors that recognize galactose may also compensate for the difference in antigen presentation compared to Man-AcDEX.[57]

■ CONCLUSION

We have reported a particulate system made of a dextran-based pH-sensitive material that can be engineered to display

immunomodulatory properties. The feasibility of the novel system was evaluated by conjugating mannose to the particles using a simple procedure that complements the chemoselective ligation method we introduced earlier for dextran particles.[58] We have found that mannose monosaccharide-targeted cellular uptake by DCs led to enhanced MHC I antigen presentation compared to nontargeted particles. To our knowledge, this is the only example of a mannosylated particulate system leading to enhanced MHC I antigen presentation by DCs.

Delivery systems that can be engineered for immunomodulation are beneficial in a multitude of areas.[59] For vaccine development, conjugation of cell-surface receptor ligands can deliver antigens to specific intracellular pathways, providing opportunities to better control the antigen presentation to T cells. The materials used for these systems can also be modified by ligands to produce specific "danger" signals to manipulate the cytokine production and activation of APCs. Besides offering benefits for medical advances, such materials can also perform as model systems, providing help to better understand basic immunobiology.

■ ASSOCIATED CONTENT

Supporting Information. Synthesis and characterization of small molecules. Quantification of mannose conjugated to particles. Cytotoxicity data of particles and their degraded products. Protein release curve from particles. Size of particles. This material is available free of charge via the Internet at http://pubs.acs.org.

■ AUTHOR INFORMATION

Corresponding Author

*Prof. Jean M. J. Fréchet, 718 Latimer Hall, College of Chemistry, University of California, Berkeley, Berkeley, CA 94720-1460. E-mail: frechet@berkeley.edu and jean.frechet@KAUST.edu.sa. Tel: (510) 643-3077 and (+966)28083055.

■ ACKNOWLEDGMENT

This research was funded through the Fréchet "various gifts" fund for the support of research in new materials. We also thank Ann Fischer in the U.C. Berkeley Cell Culture Facility for her help with cell culture preparation, Dr. Valentin Rodionov for providing ligand used in CuAAC reactions, and Dr. Chris Canlas and Dr. Eric M. Bachelder for helpful discussions.

■ REFERENCES

(1) Pulendran, B. (2004) Modulating vaccine responses with dendritic cells and Toll-like receptors. *Immunol. Rev. 199*, 227–250.

(2) Jager, E., Jager, D., and Knuth, A. (1999) CTL-defined cancer vaccines: Perspectives for active immunotherapeutic interventions in minimal residual disease. *Cancer Metastasis Rev. 18*, 143–150.

(3) Zinkernagel, R. M. (2002) Immunity, immunopathology and vaccines against HIV? *Vaccine 20*, 1913–1917.

(4) Durrant, L. G., and Ramage, J. M. (2005) Development of cancer vaccines to activate cytotoxic T lymphocytes. *Expert Opin. Biol. Ther. 5*, 555–563.

(5) Steinman, R. M., and Banchereau, J. (2007) Taking dendritic cells into medicine. *Nature 449*, 419–426.

(6) Pulendran, B. (2004) Modulating vaccine responses with dendritic cells and Toll-like receptors. *Immunol. Rev. 199*, 227–250.

(7) Proudfoot, O., Apostolopoulos, V., and Pietersz, G. A. (2007) Receptor-mediated delivery of antigens to dendritic cells: Anticancer applications. *Mol. Pharmaceutics 4*, 58–72.

(8) van Vliet, S. J., Garcia-Vallejo, J. J., and van Kooyk, Y. (2008) Dendritic cells and C-type lectin receptors: coupling innate to adaptive immune responses. *Immunol. Cell Biol. 86*, 580–587.

(9) Kanzler, H., Barrat, F. J., Hessel, E. M., and Coffman, R. L. (2007) Therapeutic targeting of innate immunity with Toll-like receptor agonists and antagonists. *Nat. Med. 13*, 552–559.

(10) Wilson-Welder, J. H., Torres, M. P., Kipper, M. J., Mallapragada, S. K., Wannemuehler, M. J., and Narasimhan, B. (2009) Vaccine adjuvants: current challenges and future approaches. *J. Pharm. Sci. 98*, 1278–1316.

(11) Reddy, S. T., Swartz, M. A., and Hubbell, J. A. (2006) Targeting dendritic cells with biomaterials: developing the next generation of vaccines. *Trends Immunol. 27*, 573–579.

(12) Singh, M., Chakrapani, A., and O'Hagon, D. (2007) Nanoparticles and microparticles as vaccine-delivery systems. *Expert Rev. Vaccines 6*, 797–808.

(13) Fahmy, T. M., Demento, S. L., Caplan, M. J., Mellman, I., and Saltzman, W. M. (2008) Design opportunities for actively targeted nanoparticle vaccines. *Nanomedicine 3*, 343–355.

(14) Hubbell, J. A., Thomas, S. N., and Swartz, M. A. (2009) Materials engineering for immunomodulation. *Nature 462*, 449–460.

(15) Bachelder, E. M., Beaudette, T. T., Broaders, K. E., Paramonov, S. E., Dashe, J., and Frechet, J. M. J. (2008) Acid-degradable polyurethane particles for protein-based vaccines: Biological evaluation and in vitro analysis of particle degradation products. *Mol. Pharmaceutics 5*, 876–884.

(16) Broaders, K. E., Cohen, J. A., Beaudette, T. T., Bachelder, E. M., and Frechet, J. M. J. (2009) Acetalated dextran is a chemically and biologically tunable material for particulate immunotherapy. *Proc. Natl. Acad. Sci. U.S.A.106*, 5497–5502.

(17) Kwon, Y. J., Standley, S. M., Goh, S. L., and Frechet, J. M. J. (2005) Enhanced antigen presentation and immunostimulation of dendritic cells using acid-degradable cationic nanoparticles. *J. Controlled Release 105*, 199–212.

(18) Standley, S. M., Kwon, Y. J., Murthy, N., Kunisawa, J., Shastri, N., Guillaudeu, S. J., Lau, L., and Frechet, J. M. J. (2004) Acid-degradable particles for protein-based vaccines: Enhanced survival rate for tumor-challenged mice using ovalbumin model. *Bioconjugate Chem. 15*, 1281–1288.

(19) Rock, K. L., and Shen, L. (2005) Cross-presentation: underlying mechanisms and role in immune surveillance. *Immunol. Rev. 207*, 166–183.

(20) Beaudette, T. T., Bachelder, E. M., Cohen, J. A., Obermeyer, A. C., Broaders, K. E., Fréchet, J. M. J., Kang, E.-S., Mende, I., Tseng, W. W., Davidson, M. G., and Engleman, E. G. (2009) In vivo studies on the effect of co-encapsulation of CpG DNA and antigen in acid-degradable microparticle vaccines. *Mol. Pharmaceutics 6*, 1160–1169.

(21) Murthy, N., Xu, M. C., Schuck, S., Kunisawa, J., Shastri, N., and Frechet, J. M. J. (2003) A macromolecular delivery vehicle for protein-based vaccines: Acid-degradable protein-loaded microgels. *Proc. Natl. Acad. Sci. U.S.A.100*, 4995–5000.

(22) Bachelder, E. M., Beaudette, T. T., Broaders, K. E., Dashe, J., and Frechet, J. M. J. (2008) Acetal-derivatized dextran: An acid-responsive biodegradable material for therapeutic applications. *J. Am. Chem. Soc. 130*, 10494–10495.

(23) Cohen, J. A., Beaudette, T. T., Cohen, J. L., Broaders, K. E., Bachelder, E. M., and Fréchet, J. M. J. (2010) Acetal-modified dextran microparticles with controlled degradation kinetics and surface functionality for gene delivery in phagocytic and non-phagocytic cells. *Adv. Mater.*

(24) Lorenzen, A., and Kennedy, S. W. (1993) A fluorescence-based protein assay for use with a microplate reader. *Anal. Biochem. 214*, 346–348.

(25) Saxon, E., and Bertozzi, C. R. (2000) Cell surface engineering by a modified Staudinger reaction. *Science 287*, 2007–2010.

(26) Becer, C. R., Hoogenboom, R., and Schubert, U. S. (2009) Click chemistry beyond metal-catalyzed cycloaddition. *Angew. Chem., Int. Ed. 48*, 4900–4908.

(27) vanDijkWolthuis, W. N. E., Tsang, S. K. Y., Kettenesvanden-Bosch, J. J., and Hennink, W. E. (1997) A new class of polymerizable

dextrans with hydrolyzable groups: hydroxyethyl methacrylated dextran with and without oligolactate spacer. *Polymer 38*, 6235–6242.

(28) Kolb, H. C., Finn, M. G., and Sharpless, K. B. (2001) Click chemistry: Diverse chemical function from a few good reactions. *Angew. Chem., Int. Ed. 40*, 2004–2021.

(29) Rodionov, V. O., Presolski, S. I., Gardinier, S., Lim, Y. H., and Finn, M. G. (2007) Benzimidazole and related Ligands for Cu-catalyzed azide-alkyne cycloaddition. *J. Am. Chem. Soc. 129*, 12696–12704.

(30) Barre, A., Bourne, Y., Van Damme, E. J. M., Peumans, W. J., and Rouge, P. (2001) Mannose-binding plant lectins: Different structural scaffolds for a common sugar-recognition process. *Biochimie 83*, 645–651.

(31) Ismaili, J., Rennesson, J., Aksoy, E., Vekemans, J., Vincart, B., Amraoui, Z., Van Laethem, F., Goldman, M., and Dubois, P. M. (2002) Monophosphoryl lipid A activates both human dendritic cells and T cells. *J. Immunol. 168*, 926–932.

(32) Burgdorf, S., Kautz, A., Bohnert, V., Knolle, P. A., and Kurts, C. (2007) Distinct pathways of antigen uptake and intracellular routing in CD4 and CD8 T cell activation. *Science 316*, 612–616.

(33) Taylor, P. R., Gordon, S., and Martinez-Pomares, L. (2005) The mannose receptor: linking homeostasis and immunity through sugar recognition. *Trends Immunol. 26*, 104–110.

(34) Taylor, M. E., Bezouska, K., and Drickamer, K. (1992) Contribution to ligand-binding by multiple carbohydrate-recognition domains in the macrophage mannsoe receptor. *J. Biol. Chem. 267*, 1719–1726.

(35) van Kooyk, Y. (2008) C-type lectins on dendritic cells: key modulators for the induction of immune responses. *Biochem. Soc. Trans. 36*, 1478–1481.

(36) Largent, B. L., Walton, K. M., Hoppe, C. A., Lee, Y. C., and Schnaar, R. L. (1984) Carbohydrate-specific adhesion of alveolar macrophages to mannose-derivatized surfaces. *J. Biol. Chem. 259*, 1764–1769.

(37) East, L., Rushton, S., Taylor, M. E., and Isacke, C. M. (2002) Characterization of sugar binding by the mannose receptor family member, Endo180. *J. Biol. Chem. 277*, 50469–50475.

(38) McGreal, E. P., Rosas, M., Brown, G. D., Zamze, S., Wong, S. Y. C., Gordon, S., Martinez-Pomares, L., and Taylor, P. R. (2006) The carbohydrate-recognition domain of Dectin-2 is a C-type lectin with specificity for high mannose. *Glycobiology 16*, 422–430.

(39) McGreal, E. P., Miller, J. L., and Gordon, S. (2005) Ligand recognition by antigen-presenting cell C-type lectin receptors. *Curr. Opin. Immunol. 17*, 18–24.

(40) Mitchell, D. A., Fadden, A. J., and Drickamer, K. (2001) A novel mechanism of carbohydrate recognition by the C-type lectins DC-SIGN and DC-SIGNR - Subunit organization and binding to multivalent ligands. *J. Biol. Chem. 276*, 28939–28945.

(41) Mammen, M., Choi, S. K., and Whitesides, G. M. (1998) Polyvalent interactions in biological systems: Implications for design and use of multivalent ligands and inhibitors. *Angew. Chem., Int. Ed. 37*, 2755–2794.

(42) White, K., Rades, T., Kearns, P., Toth, I., and Hook, S. (2006) Immunogenicity of liposomes containing lipid core peptides and the adjuvant Quil A. *Pharm. Res. 23*, 1473–1481.

(43) Hattori, Y., Kawakami, S., Lu, Y., Nakamura, K., Yamashita, F., and Hashida, M. (2006) Enhanced DNA vaccine potency by mannosytated lipoplex after intraperitoneal administration. *J. Gene Med. 8*, 824–834.

(44) Copland, M. J., Baird, M. A., Rades, T., McKenzie, J. L., Becker, B., Reck, F., Tyler, P. C., and Davies, N. M. (2003) Liposomal delivery of antigen to human dendritic cells. *Vaccine 21*, 883–890.

(45) Arigita, C., Bevaart, L., Everse, L. A., Koning, G. A., Hennink, W. E., Crommelin, D. J. A., van de Winkel, J. G. J., van Vugt, M. J., Kersten, G. F. A., and Jiskoot, W. (2003) Liposomal meningococcal B vaccination: Role of dendritic cell targeting in the development of a protective immune response. *Infect. Immun. 71*, 5210–5218.

(46) Kim, T. H., Jin, H., Kim, H. W., Cho, M. H., and Cho, C. S. (2006) Mannosylated chitosan nanoparticle-based cytokine gene therapy suppressed cancer growth in BALB/c mice bearing CT-26 carcinoma cells. *Mol. Cancer Therapeut. 5*, 1723–1732.

(47) Park, I. Y., Kim, I. Y., Yoo, M. K., Choi, Y. J., Cho, M. H., and Cho, C. S. (2008) Mannosylated polyethylenimine coupled mesoporous silica nanoparticles for receptor-mediated gene delivery. *Int. J. Pharm. 359*, 280–287.

(48) Wattendorf, U., Coullerez, G., Voros, J., Textor, M., and Merkle, H. P. (2008) Mannose-based molecular patterns on stealth microspheres for receptor-specific targeting of human antigen-presenting cells. *Langmuir 24*, 11790–11802.

(49) Rieger, J., Freichels, H., Imberty, A., Putaux, J. L., Delair, T., Jerome, C., and Auzely-Velty, R. (2009) Polyester nanoparticles presenting mannose residues: toward the development of new vaccine delivery systems combining biodegradability and targeting properties. *Biomacromolecules 10*, 651–657.

(50) Su, R. M., Li, L., Chen, X. P., Han, J. H., and Han, S. F. (2009) Multivalent mannose-displaying nanoparticles constructed from poly-{styrene-co-(maleic anhydride)-alt-styrene}. *Org. Biomol. Chem. 7*, 2040–2045.

(51) Irache, J. M., Salman, H. H., Gamazo, C., and Espuelas, S. (2008) Mannose-targeted systems for the delivery of therapeutics. *Expert Opin. Drug Delivery 5*, 703–724.

(52) Shen, Z. H., Reznikoff, G., Dranoff, G., and Rock, K. L. (1997) Cloned dendritic cells can present exogenous antigens on both MHC class I and class II molecules. *J. Immunol. 158*, 2723–2730.

(53) Karttunen, J., Sanderson, S., and Shastri, N. (1992) Detection of rare antigen-presenting cells by the LacZ T-cells activation assay suggests an expression cloning strategy for T-cell antigens. *Proc. Natl. Acad. Sci. U.S.A.89*, 6020–6024.

(54) Karttunen, J., and Shastri, N. (1991) Measurement of ligand-induced activation in single viable T-cells using the LacZ reporter gene. *Proc. Natl. Acad. Sci. U.S.A.88*, 3972–3976.

(55) Bilati, U., Allemann, E., and Doelker, E. (2003) Sonication parameters for the preparation of biodegradable nanocapsules of controlled size by the double emulsion method. *Pharmaceut. Dev. Technol. 8*, 1–9.

(56) Higashi, N., Fujioka, K., Denda-Nagai, K., Hashimoto, S., Nagai, S., Sato, T., Fujita, Y., Morikawa, A., Tsuiji, M., Miyata-Takeuchi, M., Sano, Y., Suzuki, N., Yamamoto, K., Matsushima, K., and Irimura, T. (2002) The macrophage C-type lectin specific for galactose/N-acetylgalactosamine is an endocytic receptor expressed on monocyte-derived immature dendritic cells. *J. Biol. Chem. 277*, 20686–20693.

(57) van Vliet, S. J., Saeland, E., and van Kooyk, Y. (2008) Sweet preferences of MGL: carbohydrate specificity and function. *Trends Immunol. 29*, 83–90.

(58) Beaudette, T. T., Cohen, J. A., Bachelder, E. M., Broaders, K. E., Cohen, J. L., Engleman, E. G., and Fréchet, J. M. J. (2009) Chemoselective ligation in the functionalization of polysaccharide-based particles. *J. Am. Chem. Soc. 131*, 10360–10361.

(59) Bachelder, E. M., Beaudette, T. T., Broaders, K. E., Fréchet, J. M. J., Albrecht, M. T., Mateczun, A. J., Ainslie, K. M., Pesce, J. T., and Keane-Myers, A. M. (2010) In vitro analysis of acetalated dextran microparticles as a potent delivery platform for vaccine adjuvants. *Mol. Pharmaceutics 7*, 826–835.

SUPPORTING INFORMATION FOR

Mannosylated Dextran Nanoparticles: a pH-Sensitive System Engineered for Immunomodulation through Mannose Targeting

Lina Cui[1], Joel A. Cohen[1], Kyle E. Broaders[1], Tristan T. Beaudette[1], Jean M. J. Fréchet[1,2]*

[1]College of Chemistry, University of California, Berkeley, California 94720-1460, USA
and
[2]King Abdullah University of Science and Technology, Thuwal, 23955-6900 Saudi Arabia

Synthesis of CDI-TEG-Azide (1). Azidotriethylene glycol (4.00 g, 22.88 mmol) (1) was stirred with molecular sieves (5.00 g, 4 Å) in THF (50 mL) for 30 min. under argon, and 1,1'-carbonyldiimidazole (CDI) (2.55 g, 25.06 mmol) was added to the reaction mixture. The reaction was complete in 1 h, then the molecular sieves were filtered, and THF was evaporated. The crude residue was then dissolved in ethyl acetate (200 mL) and washed with ammonium chloride (10%, 200 mL) then brine (100 mL) and then dried over magnesium sulfate. Evaporation of the solvents gave the product as a colorless clear oil (6.00 g, 98%). IR (KBr, cm^{-1}): 2913, 2870, 2109, 1748, 1443, 1265, 1124, 1063. ^{1}H NMR (500 MHz, $CDCl_3$): δ 7.97 (s, 1H, imidazole-H2), 7.71 (s, 1H, imidazole-H4), 7.08 (s, 1H, imidazole-H5), 4.27 (dd, 2H, J = 4.8, 4.0 Hz, CH_2OC=O), 3.72 (dd, 2H, J = 4.8, 3.7 Hz, CH_2O), 3.66-3.64 (m, 6H, CH_2O), 3.37 (t, 2H, J = 5.1 Hz, CH_2N_3). ^{13}C NMR (125 MHz, $CDCl_3$): δ 155.0, 135.1, 121.6, 70.6, 70.5, 70.0, 68.9, 67.0, 50.6.

Synthesis of Alkynyl Mannoside 2. Propargyl triethylene glycol (0.46 g, 2.44 mmol) and glycosyl donor 2,3,4,6-tetra-*O*-acetyl-D-mannopyranosyl trichloroacetamide (1.80 g, 3.66 mmol) were dissolved in dry dichloromethane (20 mL). Molecular sieves (2.0 g, 4 Å) were added and the mixture was stirred for 1 h at room temperature under argon. The reaction mixture was cooled to 0 °C, and boron trifluoride etherate (0.60 mL) was added slowly over 5 min. The reaction was allowed warm to r.t. and the reaction finished in 1 h. Triethylamine (0.05 mL) was added to neutralize the solution, and column chromatography (1:8 acetone:toluene, R_f = 0.2) gave compound **2** as a yellowish syrup (α only, 1.14 g, 85%). ^{1}H NMR (400 MHz, $CDCl_3$): δ 5.36–5.25 (m, 3H, H-2, H-3, H-4), 4.86 (s, 1H, H-1), 4.27 (dd, 1H, J = 12.5, 5.1 Hz, H-6a), 4.19 (s, 2H, OCH_2C≡CH), 4.09-4.04 (m, 2H, H-5, H-6b), 3.83-3.79 (m, 1H, CH_2O), 3.68-3.64 (m, 11H, CH_2O), 2.42 (s, 1H, $OCH_2C{\equiv}CH$), 2.14 (s, 3H, OAc), 2.09 (s, 3H, OAc), 2.03 (s, 3H, OAc), 1.97 (s, 3H, OAc). ^{13}C NMR (125 MHz, $CDCl_3$): δ 170.7, 170.1, 170.0, 169.7, 97.7, 79.7, 74.5, 70.7, 70.6, 70.4, 70.0, 69.6, 69.1, 68.4, 67.4, 66.2, 62.4, 58.4, 20.9, 20.8, 20.7, 20.6. ESI HRMS calcd for $C_{23}H_{34}O_{13}Na$ (M + Na): 541.1892, found: 541.1885.

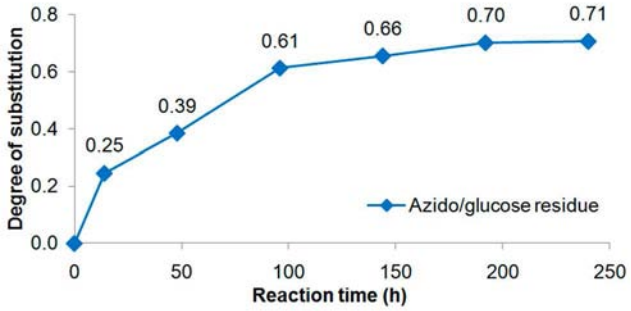
Synthesis of Alkynyl Mannoside 3. Compound **2** (702 mg, 1.35 mmol) was dissolved in dry methanol (5 mL) under argon. Sodium methoxide in methanol solution (25 wt%, 100 μL) was added, and the reaction mixture was stirred at r.t. for 15 min. Dowex 650C H^+ resin was added to

neutralize the solution, and the resin was removed by filtration. The filtrate was evaporated to dryness and the residue was purified by a C_{18} silica column (SepPak-10g, Waters) with a MeOH-H_2O gradient to afford compound **3** as a clear syrup (470 mg, 90%). IR (KBr, cm^{-1}): 3353, 2887, 2113, 1133, 1091, 1060, 1029. ^{1}H NMR (500 MHz, D_2O): δ 4.79 (d, 1H, *J* = 1.6 Hz, H-1), 4.16 (d, 2H, *J* = 2.4 Hz, OC*H*$_2$C≡CH), 3.87 (dd, 1H, *J* = 3.4, 1.7 Hz, H-2), 3.81-3.76 (m, 2H, H-6a, CH_2O), 3.72 (m, 1H, H-3), 3.69-3.53 (m, 14H, H-4, H-5, H-6b, CH_2O), 2.82 (t, 1H, *J* = 2.3 Hz, $OCH_2C{\equiv}CH$). ^{13}C NMR (125 MHz, D_2O): δ 100.0, 79.4, 76.1, 72.8, 70.5, 70.0, 69.7, 69.6, 69.5, 69.4, 68.7, 66.8, 66.4, 61.0, 57.9. ESI HRMS calcd for $C_{15}H_{26}O_9Li$ (M + Li): 357.1731, found: 357.1728.

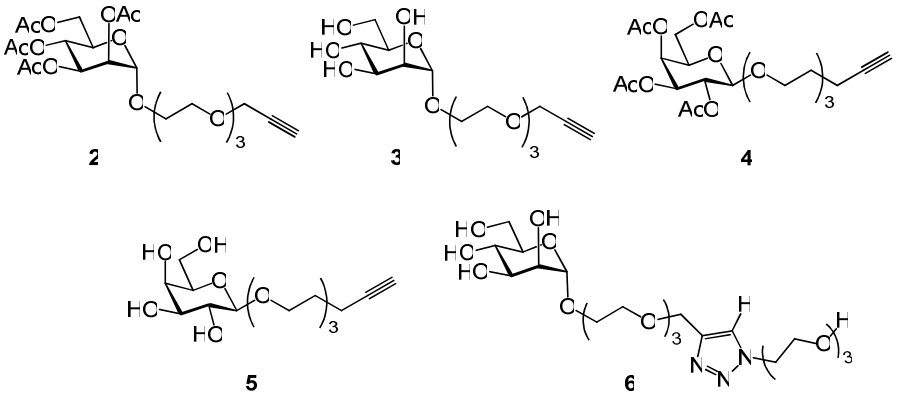
Synthesis of Alkynyl Galactoside 4. Compound **4** was synthesized and purified in a similar manner as compound **2** as a yellowish syrup (β only, 1.30 g, 77%). ^{1}H NMR (500 MHz, $CDCl_3$): δ 5.40 (d, 1H, *J* = 3.2 Hz, H-4), 5.22 (dd, 1H, *J* = 10.0, 8.1 Hz, H-2), 5.04 (dd, 1H, *J* = 10.5, 3.4 Hz, H-3), 4.60 (d, 1H, J = 8.1 Hz, H-1), 4.23 (d, 2H, J = 2.2 Hz, OC*H*$_2$C≡CH), 4.21-4.13 (m, 2H, H-6a, H-6b), 4.00-3.92 (m, 2H, H-5), 3.81-3.75 (m, 1H, CH_2O), 3.75-3.63 (m, 11H, CH_2O), 2.46 (t, 1H, *J* = 2.2 Hz, $OCH_2C{\equiv}CH$), 2.17 (s, 3H, OAc), 2.09 (s, 3H, OAc), 2.07 (s, 3H, OAc), 2.01 (s, 3H, OAc). ^{13}C NMR (125 MHz, $CDCl_3$): δ 170.4, 170.3, 170.2, 169.5, 101.4, 79.7, 74.5, 70.9, 70.7, 70.6, 70.4, 70.3, 69.1, 69.0, 68.9, 67.1, 61.3, 58.4, .8, 20.7, 20.6, 20.5. ESI HRMS calcd for $C_{23}H_{34}O_{13}Na$ (M + Na): 541.1892, found: 541.1891.

Synthesis of Alkynyl Galactoside 5. Compound **5** was synthesized and purified in a similar manner as compound **3** as a clear syrup (β only, 370 mg, 78%). IR (KBr, cm^{-1}): 3408, 2882, 2115, 1718, 1077. ^{1}H NMR (500 MHz, D_2O): δ 4.27 (d, 1H, *J* = 7.9 Hz, H-1), 4.09 (m, 2H, OC*H*$_2$C≡CH), 3.93 (ddd, 1H, *J* = 11.3, 4.0, 4.0 Hz, H-5), 3.76 (d, 1H, *J* = 3.76 Hz, H-4), 3.71-3.52 (m, 14H, H-6a, H-6b, CH_2O), 3.50 (dd, 1H, *J* = 10.1, 3.7 Hz, H-3), 3.38 (dd, 1H, *J* = 10.0, 7.9 Hz, H-2), 2.73 (t, 1H, *J* = 2.4 Hz, $OCH_2C{\equiv}CH$). ^{13}C NMR (125 MHz, D_2O): δ 102.9, 79.5, 76.1, 75.2, 72.8, 70.8, 69.8, 69.6, 69.5, 69.4, 68.7, 68.6, 61.0, 57.9. ESI HRMS calcd for $C_{15}H_{26}O_9Li$ (M + Li): 357.1731, found: 357.1731.

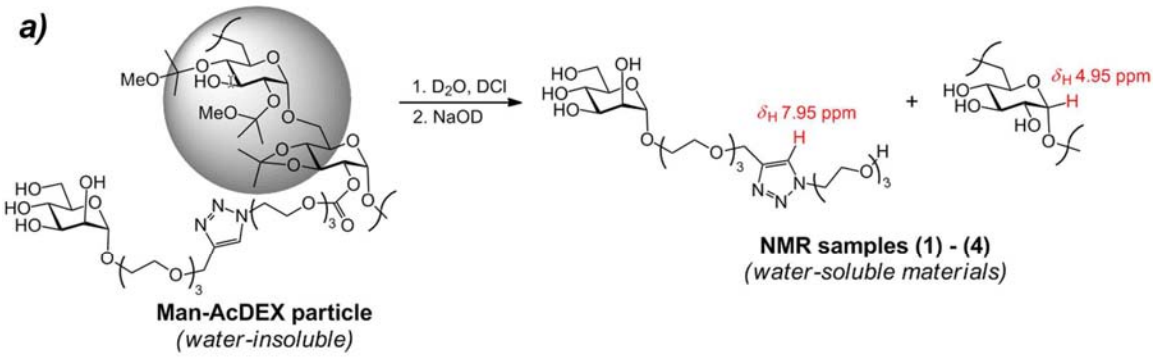
Synthesis of Compound 6. Compound **3** (26.3 mg, 0.100 mmol) and azidotriethylene glycol (17.5 mg, 0.100 mmol) were subjected to the same reaction condition as that to prepare Man-AcDEX or Gal-AcDEX particles, except that the reaction was stopped after 30 min at r.t. The compound was purified by a C_{18} silica column (SepPak-10g, Waters) with a MeOH-H_2O gradient to afford compound **6** as a clear syrup (41 mg, 94%): ^{1}H NMR (500 MHz, D_2O): δ 7.95 (s, 1H, triazole-H), 4.71 (d, 1H, *J* = 1.4 Hz, H-1), 4.63 (d, 2H, OC*H*$_2$-triazole), 4.50 (t, 2H, *J* = 5.0 Hz, NC*H*$_2$$CH_2O$), 3.83 (t, 2H, *J* = 5.2 Hz, NCH_2CH_2O), 3.77 (dd, 1H, *J* = 3.4, 1.7 Hz, H-2), 3.76-3.45 (m, 23H, H-3, H-4, H-5, H-6a, H-6b, CH_2O), 3.40 (dd, 2H, *J* = 5.0, 3.5 Hz, C*H*$_2$OH). ^{13}C NMR (100 MHz, $CDCl_3$): δ 126.7 (triazole), 125.5 (triazole), 99.9 (C-1), 72.7, 71.6, 70.8, 70.4, 69.9, 69.6, 69.3, 68.8, 68.7, 66.7, 66.3, 63.0, 60.8, 60.3, 50.0. ESI HRMS calcd for $C_{21}H_{40}N_3O_{12}$ (M + H): 526.2606, found: 526.2620.



S1. Formation of azido-DEX as a function of time at r.t. Degree of substitution was defined as azido group per glucose residue in dextran.



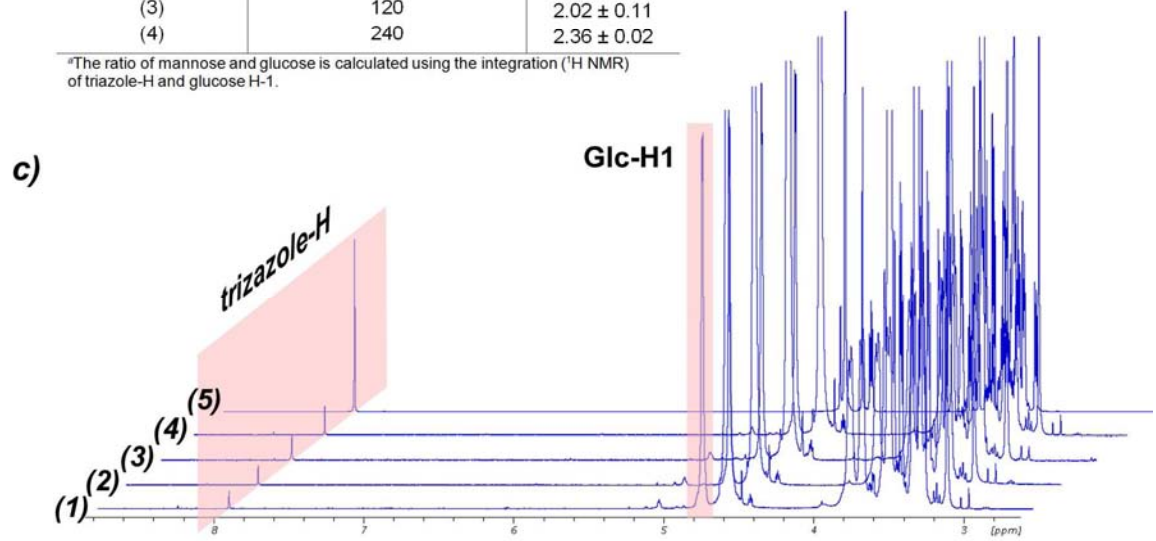
S2. Structures of compounds **2** to **6**.



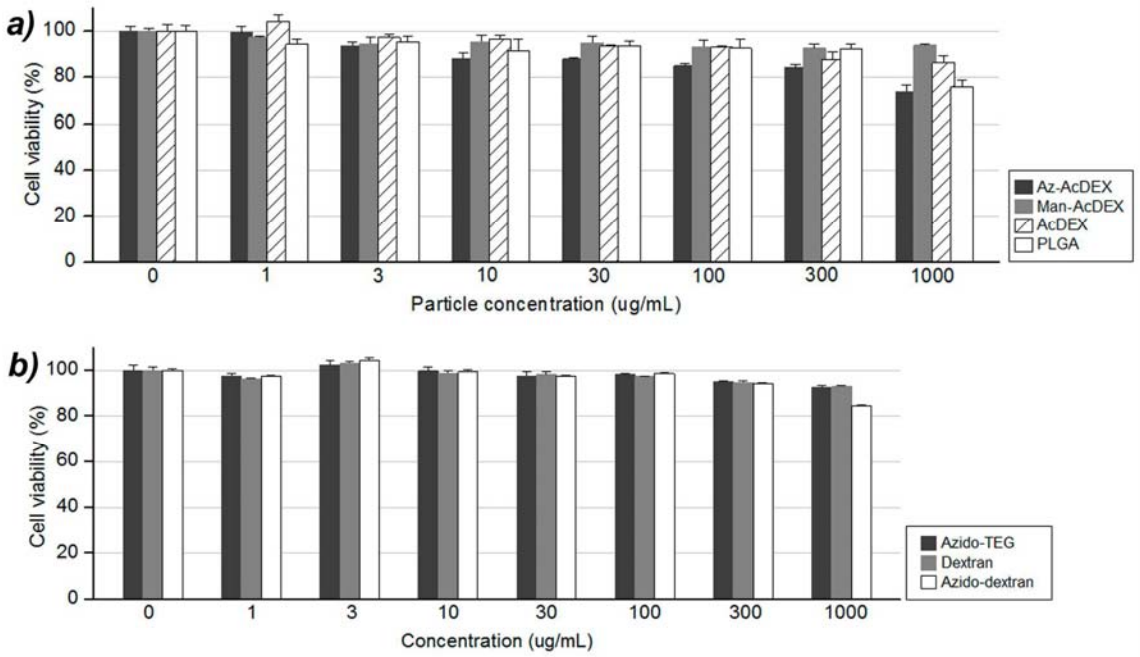
b)

Spectrum ID in c)	CuAAC reaction time (min)	Man/Glc[a]
(1)	30	1.25 ± 0.03
(2)	60	1.41 ± 0.04
(3)	120	2.02 ± 0.11
(4)	240	2.36 ± 0.02

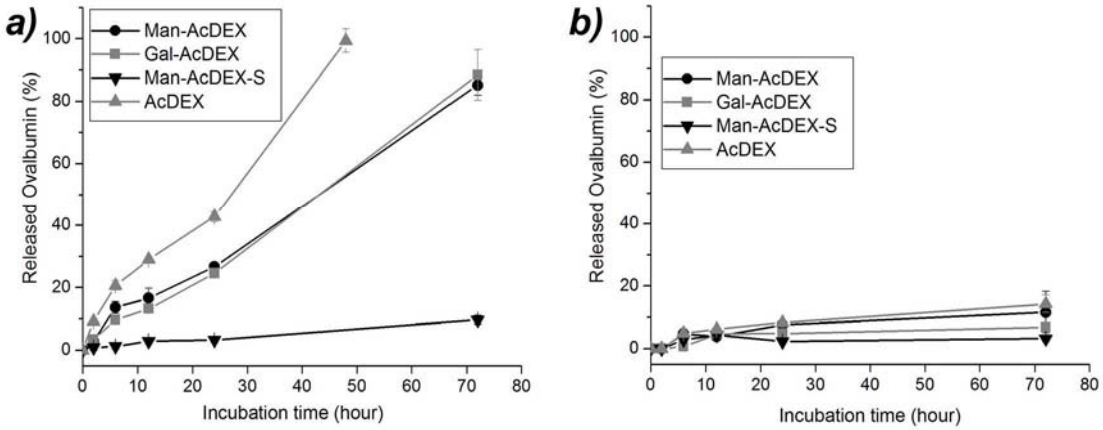
[a]The ratio of mannose and glucose is calculated using the integration (^{1}H NMR) of triazole-H and glucose H-1.



S3. Quantification of mannose on Man-AcDEX particles by NMR. a). Man-AcDEX particles were treated with DCl and then NaOD to obtain their degradation products, free dextran and mannoside, in D_2O; b). Quantification of mannose residues attached to particles after CuAAC. c). Comparison of ^{1}H-NMR spectra of degraded Man-AcDEX particles obtained after CuAAC [(1), (2), (3), (4) each represents products of 30, 60, 120, 240 min reaction], and small molecule **6** (5).



S4. Cytotoxicity of a) particles and b) their degradation products evaluated by MTT assay.



S5. Release of OVA from particles. a) pH 5.0; b) pH 7.4.

Experiment	**Particle ID**	**Average Diameter (nm)**
Cellular uptake	Azido-AcDEX	219 ± 51.5
	Man-AcDEX	190 ± 58.6
	Gal-AcDEX	191 ± 51.6
	AcDEX	221 ± 53.3
B3Z assay	Azido-AcDEX	235 ± 76.5
	Man-AcDEX	240 ± 83.4
	Man-AcDEX-S	228 ± 92.6
	Gal-AcDEX	237 ± 75.2
	AcDEX	232 ± 88.1

MTT assay	Azido-AcDEX	259 ± 106
	Man-AcDEX	234 ± 86.5
	Gal-AcDEX	248 ± 94.6
	AcDEX	230 ± 72.5
	PLGA	249 ± 76.1
Confocal microscopy	Azido-AcDEX	4578 ± 1898
	Man-AcDEX	4839 ± 2185
	Gal-AcDEX	4261 ± 1717
	HO-AcDEX	4629 ± 1935

S6. Size of particles used in different experiments.

References

1. Tahtaoui C*, et al.* (2004) Fluorescent pirenzepine derivatives as potential bitopic ligands of the human m1 muscarinic receptor. *J Med Chem* 47:4300-4315.

Bioconjugate Chemistry

ARTICLE

pubs.acs.org/bc

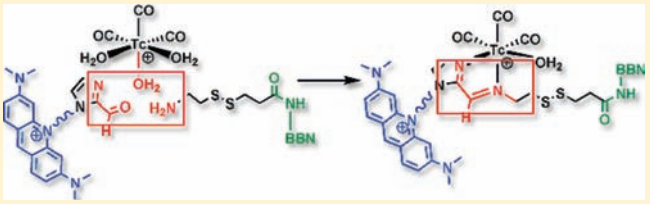
Metal Complex Mediated Conjugation of Peptides to Nucleus Targeting Acridine Orange: A Modular Concept for Dual-Modality Imaging Agents

Karel Zelenka,[†] Lubor Borsig,[‡] and Roger Alberto*[,†]

[†]Institute of Inorganic Chemistry and [‡]Institute of Physiology, University of Zürich, Winterthurerstrasse 190, 8057 Zürich, Switzerland

Supporting Information

ABSTRACT: To target the nucleus of specific cells, trifunctional radiopharmaceuticals are required. We have synthesized acridine orange derivatives which comprise an imidazole-2-carbaldehyde function for coordination to the $[Re(CO)_3]^+$ or $[^{99m}Tc(CO)_3]^+$ core. Upon coordination, this aldehyde is activated and rapidly forms imines with amines from biological molecules. This metal-mediated imine formation allows for the conjugation of a nuclear targeting portion with a specific cell receptor binding function directly on the metal. With this concept, we have conjugated the acridine orange part to a bombesin peptide directly on the ^{99m}Tc core and in one step. In addition, a linker containing an integrated disulfide has been coupled to bombesin. LC/MS study showed that the disulfide was reductively cleaved with a 60 min half-life time. This concept enables the combination of a nucleus targeting agent with a specific cell receptor molecule directly on the metal without the need of separate conjugation prior to labeling, thus, a modular approach. High uptake of the BBN conjugate into PC-3 cells was detected by fluorescence microscopy, whereas uptake into B16BL6 cells was negligible.



INTRODUCTION

Molecular imaging modalities such as single photon emission computed tomography (SPECT) and positron emission tomography (PET) are major methods for noninvasive diagnosis of organ malfunctions or diseases.[1] Over the past years, the combination of different imaging modalities has become a major focus in advanced imaging. By using different regions of the electromagnetic spectrum for imaging, complementary information about, e.g., physiology and metabolism of particular sites in cells or even in entire organisms may be received concertedly.[2,3] Combination of SPECT or PET and CT, for instance, is at the stage of clinical routine and allows for combining radionuclide distribution in tissue with anatomical information.[4,5] Although both SPECT and PET have achieved millimeter resolution, it would be desirable to combine either of these two methods with optical imaging techniques. Luminescence-based imaging allows at least on the *in vitro* level following in real time the compound in the intracellular space. Highly accurate sensing allows assessment of the particular intracellular compartment in which the compound accumulates. Numerous examples for fluorescence imaging appeared in the literature with organic or metal-based fluorescence markers.[6−11] Ideally, optical imaging would also be possible *in vivo*; however, many fluorescence markers are not suitable for deep-body penetration visualization of biological events. *In vitro* optical imaging does allow, however, localization of a compound on the subcellular level. This is particularly important if a diagnostic or therapeutic radionuclide-based agent is designed to target a particular cell compartment such as the cell nucleus. Confirmation of compound accumulation in the target is preferentially received from optical imaging since this modality allows nanometer resolution in cells. *In vitro* knowledge about site specificity of a compound can then be extended to the second modality, namely, *in vivo* radioimaging. For a successful combination of optical and radioimaging, chemical identification of the cold, luminescent, and radioactive compound is mandatory. An increasing number of publications are emphasizing the importance of single-compound-based dual-modality imaging based on a combination of subcellular luminescence and *in vivo* imaging from γ-emission.[12−14] One main strategy to target nuclei of living cells with radiolabeled compounds is based on conjugation of a suitable chelator to NLS (nucleus localizing signal) peptides.[15] Such cell and nucleus penetrating peptides can cargo various molecules such as simple metal complexes,[16] peptides, proteins, antisense PNA, or plasmid DNA[17] or are labeled with radioisotopes to quantify *in vitro* and *in vivo* biodistribution.[18−22]

In our own endeavors to target the nucleus of specific cells, we combined ^{99m}Tc as a favorable SPECT radionuclide with fluorescence markers such as acridine orange or pyrene.[21,23] The rationale behind these studies is to benefit from the Auger electrons of ^{99m}Tc to double-strand break DNA of, e.g., cancerous cells.[24−26] Along this strategy, a bioconjugate consists of a nuclear targeting agent (with luminescence properties) and a cell

Received: January 14, 2011
Revised: March 15, 2011
Published: April 12, 2011

ACS Publications © 2011 American Chemical Society

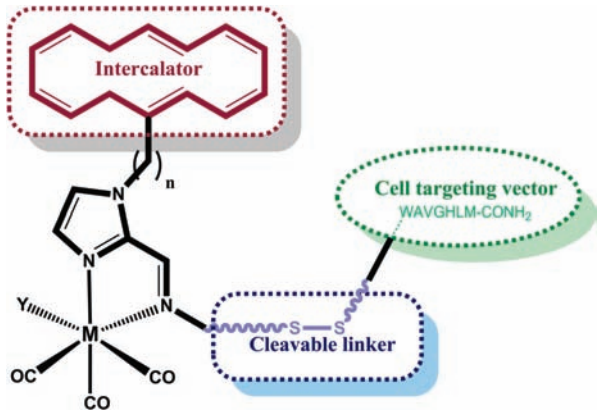
dx.doi.org/10.1021/bc2000269 | *Bioconjugate Chem.* 2011, 22, 958–967

receptor specific compound such as a peptide (Scheme 1). The peptide moiety (e.g., bombesin) targets cells with a specific, strongly (over)expressed receptor (GRP receptor for bombesin). Active, receptor-mediated uptake results in site-specific accumulation of the conjugate. Degradation of the peptide in lysosomes sets the intercalator (fluorescent marker) free, which often exhibits strong interaction with and uptake into the DNA. Such fluorescent carriers enhance the accumulation of complexes in the cell nucleus. Optionally, a cleavable linker ensures the cleavage of the receptor targeting agent from the nucleus targeting complex. This bifunctional bioconjugate is then radiolabeled for *in vivo* imaging (Scheme 1).

The synthesis of such constructs is demanding, and any new combination entails a new "total synthesis" of DNA targeting agent, cell receptor specific moiety, and chelator. Lengthy procedures are not very convenient for efficient drug finding or development. Conjugating these two principles directly on the SPECT imaging modality (^{99m}Tc) introduces an *in situ* building block concept. The metal complex fragment does mediate the conjugation of the nuclear targeting and the cell targeting molecules. Accordingly, each individual vector can be replaced without the need of new additional syntheses.

We present in this study the metal-mediated conjugation of a nuclear targeting agent (violet in Scheme 1) with cell receptor targeting peptides (green) and model molecules. In this approach, the aldehyde coordinates to the $[^{99m}Tc(CO)_3]^+$ moiety. The activated aldehyde is susceptible for imine formation with the H_2N-terminus of a peptide (Scheme 2). Fluorescence microscopy studies confirm highly selective uptake of this bioconjugate in the targeted cells.

Scheme 1. Concept of a Cell-Specific, Nuclear Targeting Trifunctional Bioconjugate

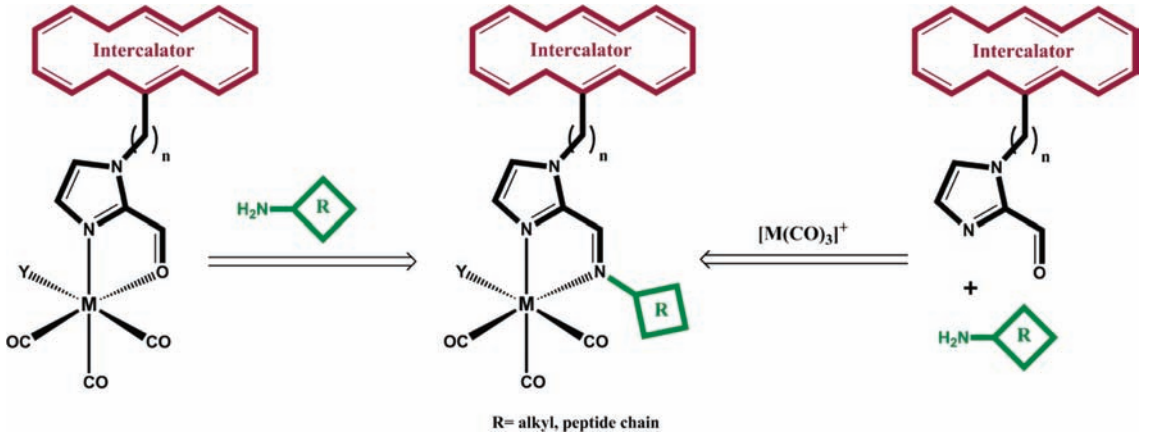


RESULTS AND DISCUSSION

Syntheses. In the building block approach, the combination of a nucleus targeting function and a cell targeting vector is bound to the $[^{99m}Tc(CO)_3]^+$ core via a bidentate imine or hydrazone chelator. The *in situ* formation of these bidentate ligands from an amine and aldehyde represents the base for the building block concept, since each part can be altered while maintaining an identical synthetic procedure. The resulting complex is cationic and of the general form $[Re(OH_2)(L^2)(CO)_3]^+$. An anion replaces the coordinated water ligand, yielding an overall neutral complex. Due to its strongly fluorescent properties, we have selected acridine orange (AO) as the intercalating nucleus targeting agent and imidazole-2-carboxyaldehyde (ima) as bidentate ligand. We and others have shown previously that heteroaromatic aldehydes are strong ligand groups for coordination to the $[^{99m}Tc(CO)_3]^+$ moiety.[27−31] Compound **1** was prepared according to a published procedure[32] followed by alkylation of the imidazole-2-carboxyaldehyde to yield **2** in reasonable yield. Coupling of a hydrazine model compound gave the corresponding hydrazone **4**, which now contains a strong bidentate chelator. Reaction with $[Re(OH_2)_3(CO)_3]^+$ in methanol/water gave the model complex **6**. Complex **7** which contains both the nucleus targeting agent and a receptor-specific bombesin peptide (BBN) was prepared similarly. The reaction of **2** with the bombesin peptide **3** afforded the hydrazone **5**. Subsequent addition of $[Re(OH_2)_3(CO)_3]^+$ gave the complex **7**. Complex **7** is now a model for trifunctional radiopharmaceuticals and comprises the nucleus targeting agent, the cell targeting vector, and the metal center (Scheme 3). Since the hydrazones **4** and **5** are water stable, they can directly be subjected to labeling studies.

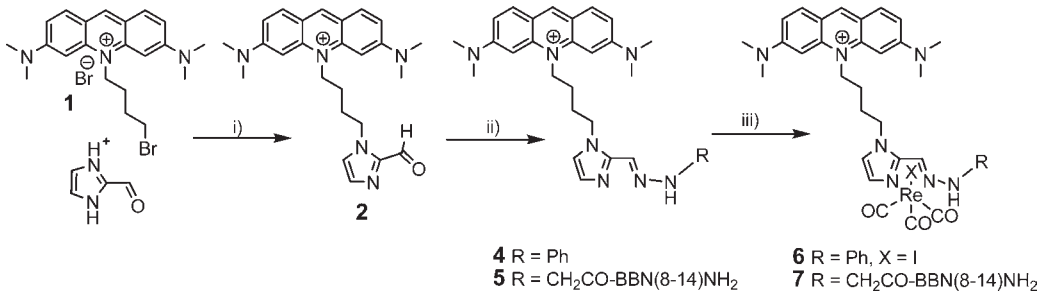
A further building block for a final conjugate is the cleavable linker. Disulfide bonds are known to be cleaved by thiols via thiol/disulfide exchange.[33] They are frequently used in prodrug designs for pharmaceuticals. In the intracellular space, they are cleaved by reduction with GSH which sets the active drug free.[34−36] For our purposes, the disulfide containing cleavable linker **10** was prepared

Scheme 2. Building Block Concept for the Metal-Mediated Formation of Cell-Specific, Nucleus Targeting Radiopharmaceuticals



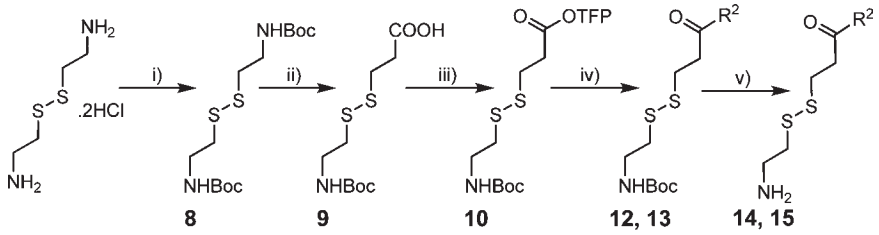
dx.doi.org/10.1021/bc2000269 |*Bioconjugate Chem.* 2011, 22, 958–967

Scheme 3[a]



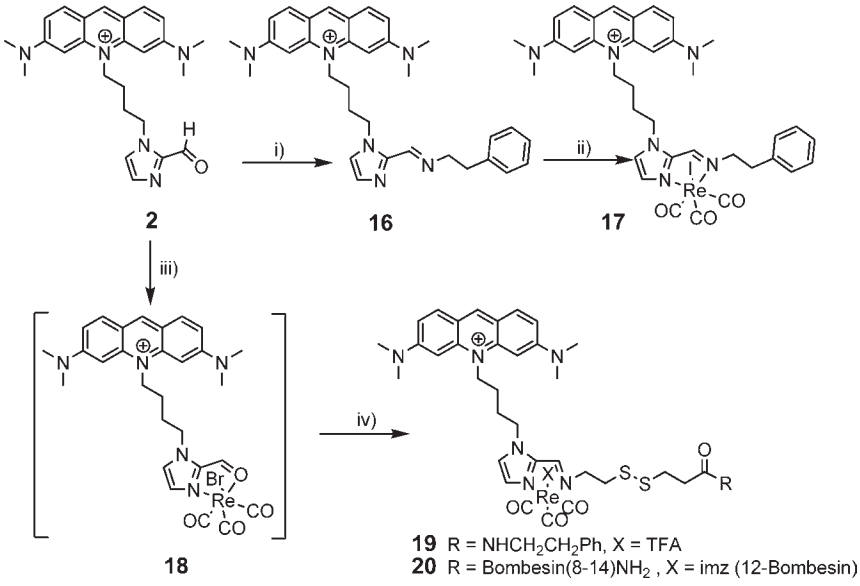
[a] (i) K_2CO_3, DMF; (ii) phenyl-hydrazine, EtOH or **3**, PBS; (iii) $[Re(OH_2)_3(CO)_3]^+$, KI, MeOH/H_2O or MeCN/PBS.

Scheme 4. Synthesis of the Orthogonal, Disulfide-Based Cleavable Linker 10 and Its Conjugate to a Peptide 15 [a]



[a] (i) Boc_2O, NaOH, dioxane/water; (ii) $HSCH_2CH_2COOH$, Et_3N, $CHCl_3$; (iii) DIPC, TFP, DMF; (iv) Et_3N, DMF; (v) TFA/CH_2Cl_2. **12**, **14**: R = $NH(CH_2)_2Ph$; **13**, **15**: R^2 = -BBN(8-14)NH_2.

Scheme 5[a]



[a] (i) $PhCH_2CH_2NH_2$, $MgSO_4$, $CHCl_3$; (ii) $[Re(OH_2)_3(CO)_3]^+$, KI, MeOH/PBS; (iii) $[Re(OH_2)_3(CO)_3]^+$, H_2O; (iv) **14** or **15** PBS, MeCN.

in a three-step synthesis. The amino groups of cysteamine were BOC-protected to give **8**. Thiolysis of the disulfide with mercaptopropionic acid afforded the acid **9**. The activated TFP ester **10** for coupling to terminal amines was prepared along standard procedures. The TFP ester **10** was then used for the preparation of compounds **12** and **13**. The free amines **14** and **15** were obtained after BOC deprotection (Scheme 4).

Hydrazones such as **4** or **5** are relatively stable toward hydrolysis, but imines are not. The model complex **17** was first prepared by the reaction of imine **16** with $[Re(OH_2)_3(CO)_3]^+$. Isolation of the free imines from the reaction of the aldehyde **2** with **14** or **15** was not possible due to their fast hydrolysis. To receive the true trifunctional compounds **19** and **20**, the aldehyde **2** was reacted in water with an excess of $[Re(OH_2)_3(CO)_3]^+$. The orange compound **18** precipitated from solution. In **18**, the aldehyde is coordinated to the rhenium center. ^1H NMR confirmed the presence of the coordinating aldehyde rather than a coordinated semiacetal.[27]

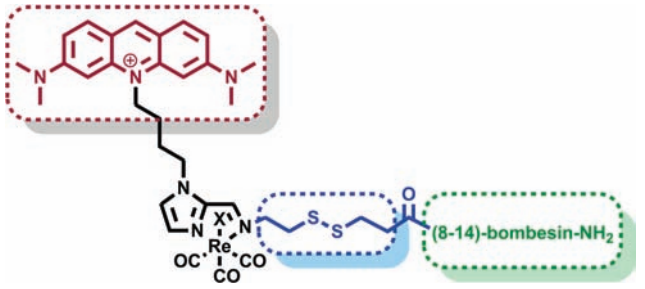
dx.doi.org/10.1021/bc2000269 |*Bioconjugate Chem.* 2011, 22, 958–967

Compound **18** is the key model compound for labeling reactions and therefore for the metal-mediated assembly of two different types of targeting agents. Compound **18** reacted with **14** or **15** under imine formation to give the trifunctional compounds **19** and **20**, respectively (Scheme 5). Important for the later labeling with ^{99m}Tc, the complexes **19** or **20** were also obtained from a "one-pot" reaction. Compound **2**, **14**, or **15** together with $[Re(OH_2)_3(CO)_3]^+$ was dissolved in a MeOH/PBS mixture (1:1). After 12 h at 50 °C, compound **19** or **20** could be purified by preparative HPLC chromatography. The yields after purification for both procedures were comparable.

Complex **20** now comprises the nucleus targeting agent, the cell targeting vector with a disulfide cleavable linker, and the metal center (Scheme 6).

Ideally, complete complex **20** is taken up by the cell through receptor-mediated endocytosis, thus ensuring cell specificity. Inside the cell, the disulfide linker is cleaved with the reduced form of GSH, cleaving the peptide vector from the metal-nucleus targeting moiety complex. Since the remaining complex is relatively small, it can permeate the nuclear membrane without necessity of active transport. Intercalation with DNA proved to be a key process for accumulation of such conjugates in the cell nucleus.[24] The cleavage of the disulfide bond also prevents the exclusion of the complex from the cell through a receptor. The trifunctional complexes **19** and **20** are rhenium-based and can be used for fluorescence imaging (see later). Fluorescence microscopy allows for following the biological pathways of these compounds on the subcellular level, whereas the ^{99m}Tc homologues can be used for *in vivo* imaging. The unprecedented advantage of this building block principle is the fact that not only **14** and **15** but principally any amines can be selected to complete the trifunctional conjugates. Coordination of the aldehyde in **2** to the $[Re(CO)_3]^+$ center activates the carbonyl carbon. Although nucleophilic attack of water competes for imine formation, once formed, the imine complex (e.g., **17**) is so strong that the reaction is irreversible and runs to completion. This is crucial for the ^{99m}Tc experiments, since quantitative formation of the radiopharmaceutical is mandatory.

Scheme 6. Complex 20 Comprising Nucleus Targeting Agent (Red), Cell Targeting Vector (Green) with a Disulfide Cleavable Linker (Blue), and Hexacoordinated Metal Center



Cleavage Studies. Compounds **19** and **20** comprise the disulfide-cleavable linker which is expected to be reduced in the intracellular space and to release the nucleus targeting function. *In vitro* studies should elucidate rate and mechanism of glutathione GSH-mediated cleavage of the disulfide bond. Compound **19** (in PBS) was added to a freshly prepared GSH solution (in PBS). The final concentrations of the GSH and complexes were 0.5 mM and 0.01 mM, respectively. This GSH concentration is normally found in cells.[37] The solution was incubated at 37 °C and samples were taken every 26 min and analyzed with HPLC-MS (see Supporting Information). Figure 1 shows the progress of the cleavage reaction. The integrated chromatograms of total ion counts (TIC) of one of the cleavage products (**21** m/z: 515.3$[M]^+$) is plotted versus the starting materials (sum of the intensities of **19** m/z 1066.4 $[M]^+$, **19a** m/z 988.4 $[M\text{-}TFA+Cl]^+$, and **19b** m/z 476.7 $[M\text{-}TFA]^{2+}$ are plotted). Compounds **19a** and **19b** are formed in solution via slow anion exchange and change over time.

The TIC of complex **22a** (m/z: 781.3 $[M]^+$, major product) exhibits the same growing trend as **21**. The different physicochemical properties of **22a** influenced the MS measurement (ion trapping, ejection, and detection). The maximum of the **22a** signal was about three times below the trace of **21**. The disulfide bridge in **19** can be cleaved by GSH on the peptide side, resulting in **21**, or on the complex side resulting in **24**. HPLC-MS evidenced that the formation of undesired **24** (or **24a** and **24b**

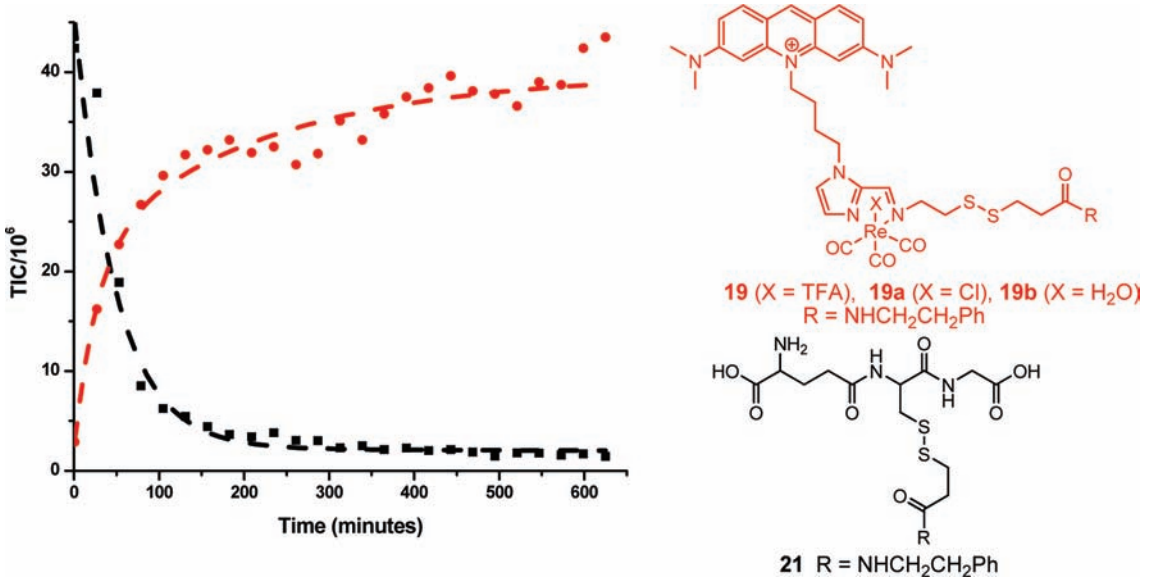
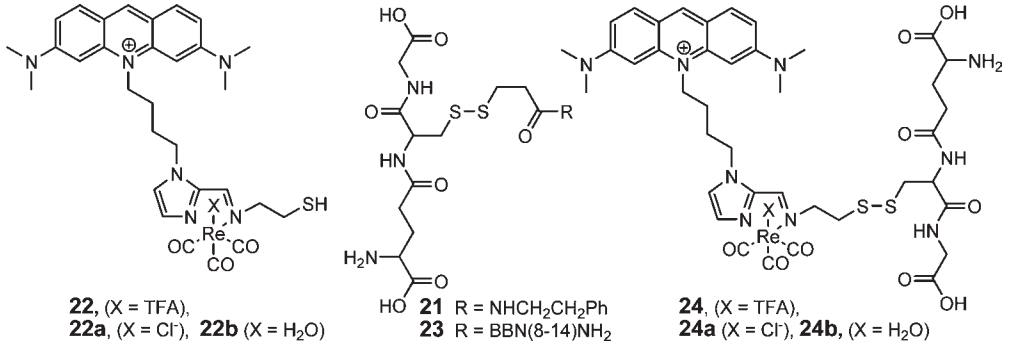
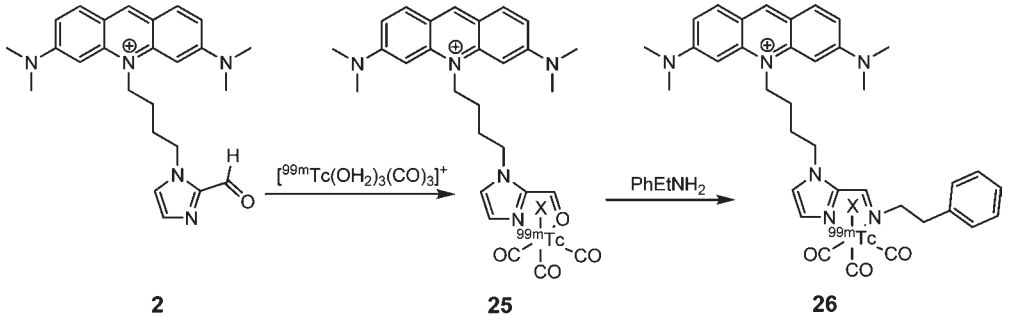


Figure 1. Plot of the time dependence of TIC intensities of **21** (red line) and **19** (sum of **19**, **19a**, and **19b**; black line).

dx.doi.org/10.1021/bc2000269 |*Bioconjugate Chem.* 2011, 22, 958–967

Scheme 7. Cleavage Products after Reaction of 18 or 19 with GSH





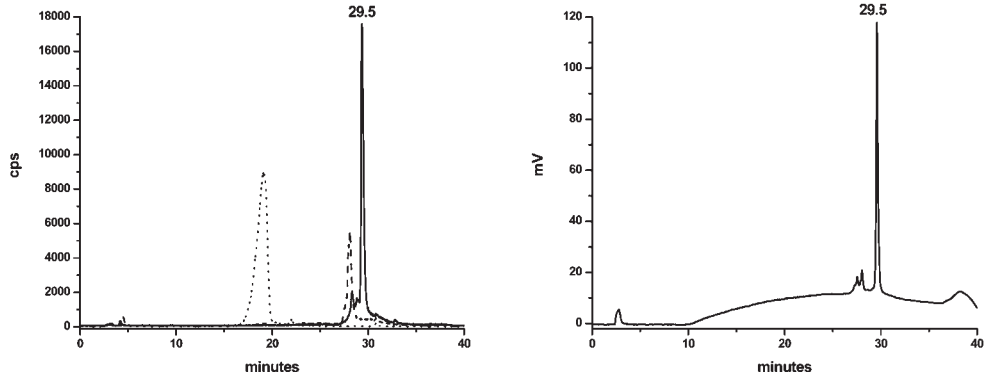


Figure 2. Left: radioactive HPLC traces of $[^{99m}Tc(OH_2)_3(CO)_3]^+$ (dotted line), **25** (dashed line), and **26** (solid line). Right: UV−vis trace of corresponding Re complex **17a** (X = Cl^-; see ESI); Gradient D.

after exchange of X) was negligible as compared to **22a** or **21**. The half-life of disulfide cleavage with the GSH was about 60 min. Due to "steady state" intracellular GSH concentration,[37,38] cleavage inside the cells could be even faster. A similar study was done with complex **20**. The formation of the cleavage products **22a** and **23** displayed similar trends as for **19** (Figure 1.). An overview for the cleavage products is given in the Scheme 7.

^{99m}Tc-Labeling Studies. The precursor $[^{99m}Tc(OH_2)_3(CO)_3]^+$ was prepared from $[^{99m}TcO_4]^-$ according to literature procedures or with the commercially available Isolink kit (Covidien, Tyco-Mallinckrodt Med. B.V. Petten, NL).[39,40] It should be emphasized that ^{99m}Tc concentrations are in the range of 10^{-6} to 10^{-9} M. After preparation, the solution was buffered with 0.1 M phosphate buffer to pH 7.4. Conversions to products were quantified by HPLC analyses with γ-detection. Reaction times, concentrations, and temperature varied.

Depending on the ligand, the synthesis of complexes of the general type $[^{99m}Tc(X)(L^2)(CO)_3]^+$ can be done in one or two steps. Solvent or an anion X is coordinated to the sixth available coordination site on the *fac*-$[^{99m}Tc(CO)_3]^+$. Labeling was first tested with a model amine and amino acids under various conditions to confirm the feasibility of the process with ^{99m}Tc. The preparation of complex **26** was done in two steps. The reaction of aldehyde **2** (0.1 mM, 30 min, 90 °C) with $[^{99m}Tc(OH_2)_3(CO)_3]^+$ (Figure 2, R_t = 19.2 min dotted line) gave the intermediate **25** (dashed line, R_t = 28 min). After addition of the phenylethylamine (0.2 mM), the mixture was heated to 90 °C for 45 min to yield the complex **26** (R_t = 29.5 min, solid line). The same result was also obtained from the "one-pot" preparation, mixing all components together and heating at 90 °C for 45 min. The formation of complex **26** was confirmed by comparing the retention time of with the Re analogue **17a** (Figure 2, also see ESI).

dx.doi.org/10.1021/bc2000269 |*Bioconjugate Chem.* 2011, 22, 958–967

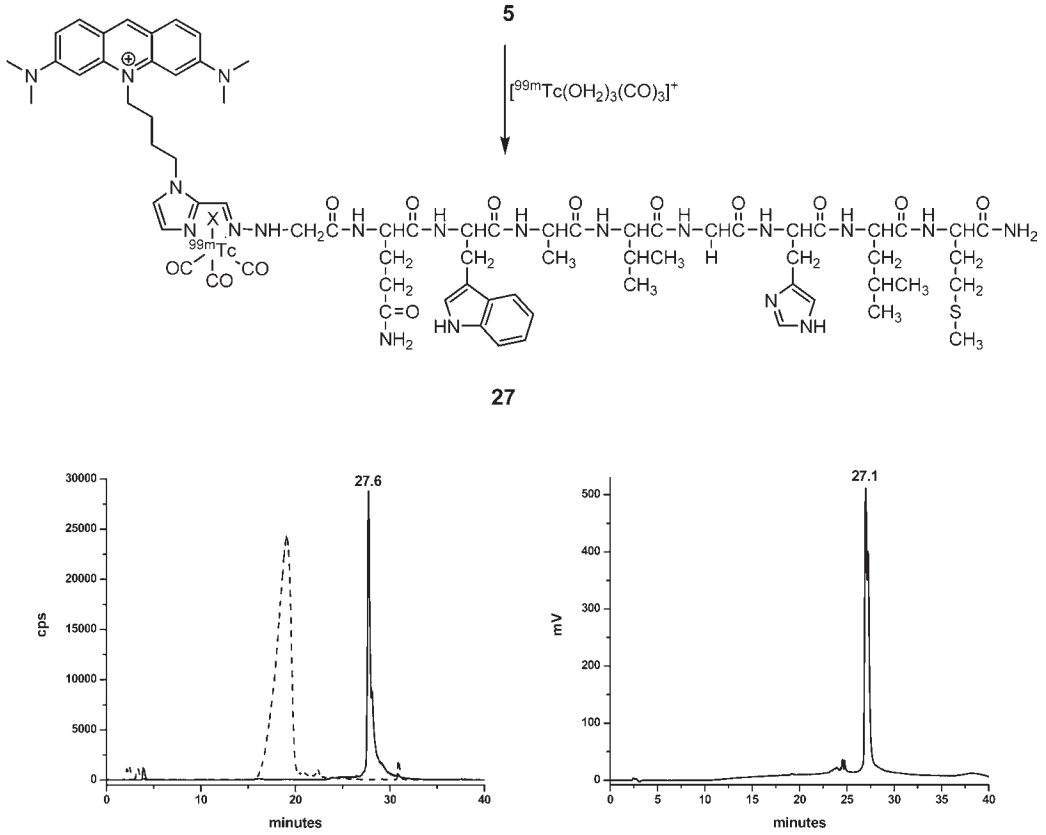


Figure 3. Left: radioactive HPLC traces of $[^{99m}Tc(OH_2)_3(CO)_3]^+$ (dashed line) and **27** (solid line). Right: UV trace of corresponding Re complex **7** (Gradient D).

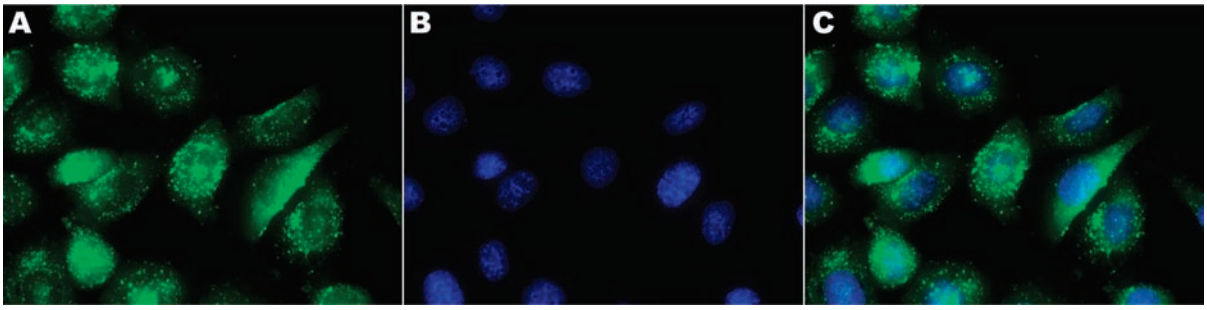


Figure 4. Uptake of the complex **20** into PC-3 cells by fluorescence microscopy. Cells were incubated with 20 μM complex **20** for 6 h, washed, then an additional 18 h in the fresh medium, followed by fixation of cells and nuclear staining by DAPI. (A) PC-3 cells, loaded with **20** in the cytoplasm (green), clear structured staining. (B) DAPI staining of nucleus (blue). (C) Merged image (overlay).

The same approach was used to prepare the ^{99m}Tc analogue of **20**. However, even by variation of gradients and solvents, the aldehyde complex **25** and resulting imine complex (**25** + **15**) were hardly distinguishable and displayed comparable retention times. For detailed labeling study and comparison with corresponding Re complex **20**, see ESI. The labeling of **5** (0.22 mM) with $[^{99m}Tc(OH_2)_3(CO)_3]^+$ at 90 °C after 60 min provided product **27** with a retention time of 27.6 min (Figure 3, solid line).

Cell Uptake Studies. We selected a human prostate adenocarcinoma cell line, PC-3, which does express the GRP receptor and B16-BL6 mouse melanoma cell line with little or no expression of the GRP receptor. The cell uptake of complex **20** was monitored in the green fluorescence filter as described in the Experimental Section. To localize the compound in the cell, we stained nuclei with DAPI (4′,6-diamidino-2-phenylindol), routinely used in cell biology. The PC-3 cells were exposed to **20** (20 μM) and the uptake was followed by fluorescence microscopy (Figure 4). Complex **20** clearly accumulated in the cell. Green fluorescence was mainly detected in the cytoplasm, exhibiting substructured distribution, probably in lysosomes. There is no enhanced accumulation of fluorescence in the nucleus. Complex **7** was studied in a similar manner to **20**. The accumulation in the cell was also observed with comparable intensities to those for **20**.

The trifunctional complex **20** contains the cell-specific vector (truncated 8−14 BBN peptide). Thus, only cells with the corresponding receptor should accumulate **20**. To confirm such a specific uptake, cell studies were performed on a B16-BL6

dx.doi.org/10.1021/bc2000269 |*Bioconjugate Chem.* 2011, 22, 958–967

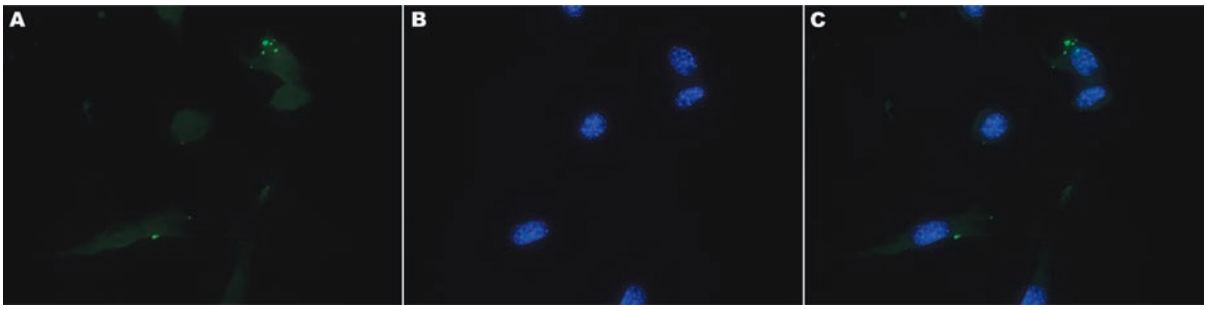


Figure 5. Uptake of complex **20** by B16BL6 cells, performed as described for PC-3. (A) Green channel image. (B) DAPI nucleus staining (blue). (C) Merged image (overlay).

mouse melanoma cell line which does not express the GRP receptor. The difference between the PC-3 (Figure 4) and B16-BL6 (Figure 5) is significant. While PC-3 cells were loaded with **20** in the cytoplasm, there was virtually no accumulation in the B16BL6 cell line. The uptake of complex **20** by PC-3 cells was consistent with the presence of the GRP receptor, indicating a receptor-mediated uptake.[32]

■ CONCLUSIONS

The efficient development of imaging probes containing a therapeutic modality demands a flexible building block concept. Herein, we presented an approach in which the conjugation of a nucleus targeting part with a cell-specific vector is metal-mediated, yielding a trifunctional diagnostic and potentially therapeutic radiopharmaceutical. A disulfide-based cleavable linker was introduced on the cell receptor targeting part. *In vitro*, the disulfide linker was cleaved with GSH at a reasonable rate. Fluorescence microscopy with rhenium analogues using GRP/non-GRP expressing cell lines confirmed the cell specificity concept. However, studies with complex **20** did not display increased uptake in the nucleus but stained mainly substructures of the cytoplasm for so far unknown reasons. Detailed cell studies with the trifunctional complex **20** and similar systems, prepared according to the presented building block concept, are currently under investigation. The approach represents a very general method for the *in situ* preparation of strong bidentate ligands and its use for further development of functional multimodality systems.

■ EXPERIMENTAL SECTION

General Information. The commercially available reagents were used as received without further purification. Analytical thin-layer chromatography (TLC) was carried out with aluminum-based plates (silica gel 60 F_{254}) from Merck. Plates were visualized under UV light (λ = 254 nm). Flash chromatography was carried out on Flashmaster Solo (Argonaut) by using Merck silica gel 60 (0.040−0.063 mm). Samples were applied as almost saturated solutions in the appropriate solvent. ^{1}H NMR and ^{13}C NMR spectra were performed on a Bruker 400 and 500 spectrometers at 400/500 and 100/125 MHz, respectively. The reported chemical shifts (in δ) are relative to the solvent protons and carbons as a reference. HPLC-MS (ESI) spectra were measured on a Bruker HCT spectrometer with Aquinity UPLC (Waters) with alternating polarity ion detection, using a Macherey-Nagel EC 250/3 Nucleodur C18 Gravity 5 μm. HPLC solvents were 0.1% formic acid (solvent A) and methanol (solvent B). The gradients used for analyses were as follows: Gradient A: 0−5 min 90% A, 5−17 min 90−0% A, 17−25 min 0% A, 25−27 min 0−90% A, 27−35 min 90% A, flow 0.3 mL.min^{-1}; Gradient B: 0−2 min 90% A, 2−12 min 90−0% A, 12−17 min 0% A, 17−18 min 0−90% A, 18−25 min 90% A, flow 0.25 mL.min^{-1}. HPLC analyses were performed on a Merck L7000 system using a Macherey-Nagel EC 250/3 Nucleodur C18 Gravity 5 μm for radioactive compounds. HPLC solvents were 0.1% trifluoroacetic acid (solvent A) and MeOH or MeCN HPLC grade (solvent B). Gradient C (MeOH): 0−5 min 90% A, 5−15 min 90−0% A, 15−20 min 0% A, 20−22 min 0−90% A, 22−30 min 90% A. Gradient D (MeCN): 0−5 min 90% A, 5−20 min 90−60% A, 20−23 min 60% A, 23−28 min 0% A, 28−33 min 0% A, 33−34 min 0−90% A, 34−40 min 90% A. Flow rates: 0.5 mL/min, detection with a γ-detector for the radiolabeled compounds. Preparative HPLC was performed on a Varian Pro Star system by using either a Macherey-Nagel VP 250/21 Nucleodur C18 Gravity 5 μm or a Macherey-Nagel VP 250/40 Nucleosil 100−7 C18 column with a flow rate of 12 mL.min^{-1} and 40 mL.min^{-1} respectively. The solvents were 0.1% trifluoroacetic acid (solvent A) and methanol or acetonitrile (solvent B).

Cell Culture and Complex Uptake. Human prostate cancer cells, PC-3 were incubated in F12K medium supplemented with 10% fetal calf serum. For microscopy, cells were cultured overnight on four-chamber slides (Nunc) in which ca. 50 000 cells were plated. Next day, cells were washed and fresh media containing complexes **20** or **7** (20 μm) were added. Cells were incubated with the complex for 6 h. After the loading with a complex, the fresh medium was added and the cells were incubated for additional 18 h, washed with phosphate buffer saline (PBS), and fixed in 4% paraformaldehyde for 10 min in at r.t. After three washings with PBS, cells were incubated in 1 mg.mL^{-1} 4′,6-diamidino-2-phenylindole (DAPI) for nuclear staining for 10 min at r.t. Cells were washed three times with phosphate-buffered saline (PBS), chambers from the slides were detached, and cells were covered with coverslips in Prolong Mounting medium (Invitrogen). Slides were evaluated on Zeiss Axiovert 200 m with the corresponding fluorescence filters for DAPI (λ_{ex} = 360 nm, λ_{em} = 420 nm) and acridine orange (λ_{ex} = 496 nm, λ_{em} = 525 nm).

General Remarks to the Re Complexes. Under common HPLC or HPLC-MS conditions, typically two peaks with a ratio of 1:10 (respectively 1:1 with TFA anion) were observed. The first peak represents the complex, where the anion is replaced with a solvent, while the second peak belongs to the original (whole) complex. During the MS acquisition, the coordinated solvent is usually lost. For complexes containing peptides, the sixth coordination position is probably occupied by imidazole from histidine. Both double- and single-charged species were

observed under HPLC-MS conditions. The elementary analyses were not performed due to the various content of TFA after purification with the preparative HPLC. Thus, to be consistent, the M.W. and concentrations of the compounds were calculated without counterions (e.g., as drawn in the schemes). If not specified in the scheme, the counterions are trifluoroacetates.

3,6-Bis(dimethylamino)-10-(4-(2-formyl-1*H*-imidazol-1-yl)-butyl)acridinium (2). A suspension of 1*H*-imidazole-2-carbaldehyde (11 mg, 0.11 mmol) and K_2CO_3 (100 mg, 0.72 mmol) in DMF (10 mL, dry) was stirred at r.t. under N_2. After 10 min, **1** (70 mg, 0.14 mmol) was added, and the mixture stirred and heated to 50 °C under N_2. After 16 h, the solvent was removed under HV. The residue was dissolved in 15 mL of CH_2Cl_2, filtered over Celite, and dried again. Purification by preparative HPLC afforded 36 mg **2** (75%) as an orange powder. ^{1}H NMR (CD_3CN, 400 MHz) δ 9.65 (d, ^4J = 0.8 Hz, 1H), 8.49 (s, 1H), 7.79 (d, ^3J = 9.3 Hz, 2H), 7.31 (bs, 1H), 7.18 (d, ^4J = 0.7 Hz, 1H), 7.14 (dd, ^3J = 9.3 Hz, ^4J = 2.2 Hz, 2H), 6.45 (d, ^4J = 1.8 Hz, 2H), 4.53 (bt, ^3J = 8 Hz, 2H), 4.43 (t, ^3J = 6.9 Hz, 2H), 3.20 (s, 12H), 2.07−1.97 (m, 2H), 1.93−1.83 (m, 2H). MS (ESI, Gradient B): t_R 9.3 min; positive mode *m/z* 448.2 (100) $[M + MeOH]^+$, 416.2 (33) $[M]^+$. MS (ESI) *m/z* (%) 416.2 (100) $[M]^+$, 448.2(17) $[M + MeOH]^+$; calcd for $C_{25}H_{30}N_5O^+$: 416.24 (100.0).

$NH_2NH_2CH_2CO$-Bombesin WAVGHLM (3). Truncated hydrazinoacetyl-bombesin **3** (sequence: WAVGHLM) was synthesized SPPS according to the procedure reported previously for hydrazino derivatives of peptides.[41] The product was then purified by reverse-phase HPLC on a preparative C18 column (Macherey-Nagel VP 250/40 Nucleosil 100−7 C18 column), fractions with the peptide were lyophilized, and pure peptide was kept under N_2 in the freezer at −25 °C. **3** was obtained as a white solid. HPLC-MS (ESI, Gradient A): t_R 13.4 min; positive mode *m/z* 884.5 (100) $[M+H]^+$; calcd for $C_{40}H_{61}N_{13}O_8S$: 883.45 (100.0); negative mode *m/z* 882.6 (60) $[M-H]^-$, 996.6 (100) $[M+TFA]^-$.

3,6-Bis(dimethylamino)-10-(4-(2-((2-phenylhydrazono)-methyl)-1*H*-imidazol-1-yl)butyl)acridinium (4). The aldehyde **2** (26 mg, 0.062 mmol) was dissolved in the EtOH (1 mL, dry), and phenyl hydrazine (7 mg, 6.3 μL, 0.062 mmol) was added to the mixture. Reaction was stirred and heated to 80 °C for 4 h; the solvent was then removed in vacuo. The crude product **4** (31 mg, 98%) was pure enough for use in the next step without further purification. ^{1}H NMR (CD_3CN, 400 MHz): δ 10.00 (bs, 1H), 8.42 (s, 1H), 7.94 (s, 1H), 7.70 (d, ^3J = 9.3 Hz, 2H), 7.12−6.93 (m, 8H), 6.75 (t, ^3J = 7.3 Hz, 1H), 6.40 (d, ^4J = 1.7 Hz, 2H), 4.55 (t, ^3J = 7.4 Hz, 2H), 4.35 (t, ^3J = 6.6 Hz, 2H), 3.08 (s, 12H), 2.10−2.01 (m, 2H), 2.01−1.92 (m, 2H). HPLC-MS (ESI, Gradient B): t_R 10.8 min; positive mode *m/z* 506.4 (100) $[M]^+$, $[M+H]^+$ 253.1 (40) $[M+H]^{2+}$; calcd for $C_{31}H_{36}N_7^+$: 506.3 (100).

3,6-Bis(dimethylamino)-10-(4-(2-((2-(2-(Bombesin 8−14)-2-oxoethyl)hydrazono)methyl)-1*H*-imidazol-1-yl)butyl)-acridinium (5). The aldehyde **2** (8 mg, 0.019 mmol) and hydrazino bombesin **3** (25 mg, 0.028 mmol) were dissolved in the PBS (15 mL, pH = 6.5). The mixture was stirred at r.t under N_2 for 3 days. The orange precipitate was filtered and washed with water and PBS. The crude product was purified by preparative HPLC to give **5** as orange powder in a yield of (12 mg, 48%). HPLC-MS (ESI, Gradient B): t_R 10.0 min; positive mode *m/z* 641.6 (100) $[M+H]^{2+}$, 1281.7 (75) $[M]^+$; calcd for $C_{65}H_{89}N_{18}O_8S^+$: 1281.7 (100.0).

$[Re(I)(4)(CO)_3]^+$ (6). The hydrazone **4** (8 mg, 0.016 mmol) and KI (50 mg, 0.3 mmol) were dissolved in the methanol/water mixture (6 mL, 2:1), then $[NEt_4]_2[ReBr_3(CO)_3]$ (15 mg, 0.019 mmol) was added. The mixture was stirred 3 h at 60 °C. The solvents were removed in vacuo, and the crude product was purified by preparative HPLC to give **6** as dark orange powder in a yield of (7 mg, 49%). ^{1}H NMR (DMSO-d_6, 400 MHz): δ 10.40 (s, 1H), 8.77 (s, 1H), 8.57 (s, 1H), 7.90 (d, ^3J = 9.4 Hz, 2H), 7.59 (d, J = 1.4 Hz, 1H), 7.45 (d, J = 1.4 Hz, 1H), 7.24 (dd, ^3J = 9.4 Hz, ^4J = 2.0 Hz, 2H), 7.18−7.12 (m, 2H), 7.05−7.00 (m, 3H),6.54 (bs, 2H), 4.78−4.63 (m, 2H), 4.32 (t, ^3J = 6.6 Hz, 2H), 3.20 (s, 12H), 2.03−1.93 (m, 2H), 1.77−1.67 (m, 2H). HPLC-MS (ESI, Gradient B): t_R 12.8 min; positive mode *m/z* 904.3 (100), 902.3 (58) $[M]^+$; calcd fro $C_{34}H_{36}IN_7O_3Re^+$: 904.15 (100.0), 902.15 (57.0).

$[Re(5)(CO)_3]^+$ (7). To a solution of **5** (10 mg, 0.007 mmol) dissolved in the acetonitrile/PBS mixture (4 mL, 1:1, pH = 7.4), $[NEt_4]_2[ReBr_3(CO)_3]$ (20 mg, 0.026 mmol) was added. The mixture was stirred under N_2 at 40 °C. After 2 d, the solvents were removed and the crude product purified by preparative HPLC to give **7** as orange powder in a yield of (4 mg, 33%). HPLC-MS (ESI, Gradient B): t_R 11.2 min; positive mode *m/z* 776.4 (100) $[M]^{2+}$, 1551.5 (10) $[M-H]^+$; calcd for $C_{68}H_{89}N_{18}O_{11}ReS^{2+}$: 1552.62 (100.0).

***N,N′*-Bis-*tert*-butoxycarbonylcystamine (8).** Compound **8** was prepared according to the published procedure and the analysis was similar to the literature.[42]

3-((2-(*tert*-Butoxycarbonylamino)ethyl)disulfanyl)propanoic acid (9). Compound **9** was prepared according to the published procedure[43] using the 3-mercaptopropanoic acid instead of 2-mercaptoacetic acid. 300 mg (yield 30%) of the acid **9** were obtained. TLC R_f = 0.26 ($CHCl_3$/MeOH, 9/1). ^{1}H NMR ($CDCl_3$, 400 MHz): δ 4.93 (bs, 1H), 3.46 (bs, 2H), 2.95 (bt, ^3J = 6.9 Hz, 2H), 2.84−2.77 (m, 4H), 1.46 (s, 9H). MS (ESI) *m/z* (%) 304.1 (100) $[M + Na]^+$; 316.1(100) $[M + Cl]^-$, 280.4 (90) $[M - H]^-$; calcd for $C_{10}H_{19}NO_4S_2$: 281.08 (100.0).

2,3,5,6-Tetrafluorophenyl 3-((2-(*tert*-butoxycarbonylamino)ethyl)disulfanyl)propanoate (10). A solution of **9** (170 mg, 0.6 mmol) in DMF (1 mL, dry) was cooled to 4 °C and diisopropylcarbondiimid (93 μL, 76 mg, 0.6 mmol) was added. The mixture was stirred 15 min under N_2, and then 2,3,5,6-tetrafluorophenol (100 mg, 0.6 mmol) in DMF(0.5 mL, dry) was slowly added and reaction was stirred at r.t. After 12 h, CH_2Cl_2 (3 mL) was added, precipitate was filtered, and filtrate was evaporated to dryness. Purification by flash chromatography (gradient, hexane to hexane:MTBE 6:1) afforded compound **10** (100 mg, 38%) as a white solid. ^{1}H NMR ($CDCl_3$, 500 MHz) δ 7.05−7.00 (m, 1H), 4.90 (bs, 1H), 3.46 (bd, ^3J = 6.0 Hz, 2H), 3.13 (t, ^3J = 6.9 Hz, 2H), 3.05 (t, ^3J = 6.9 Hz, 2H), 2.83 (t, ^3J = 6.7 Hz, 2H), 1.45 (s, 9H). MS (ESI) positive mode *m/z* (%) 452.0 (100) $[M + Na]^+$, 467.9 (80) $[M + K]^+$; negative mode 464.0 (100) $[M + Cl]^-$; calcd 429.07 (100.0). Elemental analysis (%) calcd for $C_{16}H_{19}F_4NO_4S_2$: C 44.75, H 4.46, N 3.26, S 14.93; found C 44.52, H 4.47, N 3.00.

Bombesin WAVGHLM (11). Truncated bombesin **11** (sequence: WAVGHLM) was synthesized SPPS and purified according to the procedure reported previously[24]).

***tert*-Butyl 2-((3-oxo-3-(phenethylamino)propyl)disulfanyl)-ethylcarbamate.TFA (14).** A solution containing **10** (10 mg, 0.023 mmol) and Et_3N (6.4 μL, 4.7 mg, 0.046 mmol) in 0.3 mL of DMF was stirred for 30 min at room temperature. After addition of 2-phenylethanamine (3.2 μL, 3.1 mg, 0.025 mmol), the solution

was further stirred for 12 h. The removal of the solvent in vacuo afforded crude product **12**. The residue was dissolved in 1.5 mL of the mixture of dichloromethane−TFA (1:0.5). The mixture was stirred for 3 h under N_2 at r.t. After removal of the solvent in vacuo, the crude product was purified by preparative HPLC to afford 3 mg (31%) of compound **14** as a white solid. ^{1}H NMR ($CDCl_3$, 400 MHz): δ 8.31 (bs, 2H), 7.29−7.12 (m, 5H), 6.20 (t, ^3J = 5.6 Hz, 1H), 3.46 (q, ^3J = 6.5 Hz, 2H), 3.28 (bt, ^3J = 5.5 Hz, 2H), 2.94 (bt, ^3J = 6.0 Hz, 2H), 2.90 (t,^3J = 6.6 Hz, 2H), 2.77 (t, ^3J = 7.0 Hz, 2H), 2.49 (t, ^3J = 6.7 Hz, 2H). HPLC-MS (ESI, Gradient B): t_R 10.2 min; positive mode m/z: 285.3 (100) $[M+H]^+$; calcd for $C_{13}H_{20}N_2OS_2$: 284.11 (100.0).

Bombesin (15). Truncated bombesin **11** (40 mg, 0.049 mmol, prepared according to the literature) was dissolved in the DMF (dry, 0.5 mL) with Et_3N (20 μL, 15 mg, 0.148 mmol). The mixture was stirred at r.t under N_2. After 15 min, the solution of **10** (24 mg, 0.056 mmol) in DMF (0.5 mL) was added and mixture was stirred at r.t under N_2 for 20 h. The solvent was removed in vacuo to afford crude product **13**. The residue was dissolved in 1 mL of the mixture of dichloromethane−TFA (1:1). The mixture was stirred for 12 h under N_2 at r.t. After removal of the solvent in vacuo, the crude product was purified by preparative HPLC to afford 30 mg (62%) of compound **15** as a white solid. HPLC-MS (ESI, Gradient A): t_R 13.8 min; positive mode m/z 975.4 (100) $[M+H]^+$, 488.2 (66) $[M+2H]^{2+}$; negative mode m/z 1087.5 (100) $[M+TFA]^-$, 973.4 (15) $[M-H]^-$; calcd for $C_{43}H_{66}N_{12}O_8S_3$: 974.43 (100.0).

3,6-Bis(dimethylamino)-10-(4-(2-((phenethylimino)methyl)-1*H*-imidazol-1-yl)butyl)acridinium (16). 2-Phenylethanamine (6.12 μL, 5.9 mg, 0.048 mmol) was added to the suspension of **2** (8 mg, 0.019 mmol) with dry $MgSO_4$ (50 mg) in $CHCl_3$ (1 mL, dry). Reaction mixture was stirred at 60 °C for 12 h, filtered over Celite, and evaporated to dryness to give imine **16** (9.8 mg, 99%). ^{1}H NMR ($CDCl_3$, 400 MHz): δ 8.41 (s, 1H), 8.18 (s, 1H), 7.76 (d, ^3J = 9.3 Hz, 2H), 7.15−7.08 (m, 3H), 7.08−7.00 (m, 6H), 6.49 (bs, 2H), 4.62 (bt, ^3J = 7.8 Hz, 2H), 4.55 (t,^3J = 6.8 Hz, 2H), 3.74 (t,^3J = 7.2 Hz, 2H), 3.22 (s, 12H), 2.76 (t,^3J = 7.2 Hz, 2H), 2.11−2.01 (m, 2H), 1.95−1.84 (m, 2H). MS (ESI) m/z (%) 519.5 (100) $[M]^+$; calcd for $C_{33}H_{39}N_6^+$: 519.32 (100.0).

[Re(I)(16)(CO)$_3$]$^+$ (17). Imine **16** (10 mg, 0.019 mmol), KI (50 mg, 0.3 mmol), and $[NEt_4]_2[ReBr_3(CO)_3]$ (20 mg, 0.026 mmol) were consecutively dissolved in 4 mL of the mixture of MeOH and PBS (1:1, pH = 6.4). Reaction was stirred for 4 h at 40 °C under N_2. HPLC-MS analysis showed complete product formation. The solvent was removed in vacuo and the product was dried at high vacuum. The crude product was purified by preparative HPLC to afford 8 mg (45%) of compound **17** as a bright orange powder. ^{1}H NMR (DMSO-d_6, 400 MHz): δ 8.94 (s, 1H), 8.78 (s, 1H), 7.90 (d, ^3J = 9.4 Hz, 2H), 7.70 (d, J = 1.3 Hz, 1H), 7.59 (d, J = 1.2 Hz, 1H), 7.24 (dd, ^3J = 9.4 Hz, ^4J = 2.0 Hz, 2H), 7.21−7.14 (m, 4H), 7.10−7.04 (m, 1H), 6.54 (bs, 2H), 4.78−4.73 (m, 2H), 4.36 (t, ^3J = 6.8 Hz, 2H), 4.19−4.09 (m, 2H), 3.20 (s, 12H), 3.17−3.07 (m, 1H), 3.06−2.96 (m, 1H), 2.04−1.94 (m, 2H), 1.75−1.64 (m, 2H). MS (ESI, Gradient B): t_R 13.5 min; positive mode m/z 917.2 (100) $[M]^+$, 915.2 (56) $[M]^+$; calcd for $C_{36}H_{39}IN_6O_3Re^+$: 917.17 (100.0), 915.17 (56.7).

[Re(TFA)(14)(CO)$_3$]$^+$ (19). The aldehyde **2** (2 mg, 0.005 mmol) and the $[NEt_4]_2[ReBr_3(CO)_3]$ (10 mg, 0.013 mmol) were dissolved in PBS (2 mL, pH = 6.5). The mixture was stirred and heated under N_2 at 50 °C for 30 min. The formed precipitate was spun down, and supernatant removed. The remaining precipitate was dissolved in the mixture of MeCN:PBS (14 mL, 9:5). The orange solution was added to the flask containing the amine **14** (3 mg, 0.007 mmol) and the mixture was stirred at r.t for 16 h; HPLC-MS showed the product formation. The product was purified by preparative HPLC to afford 1 mg (18%) of compound **18** as an orange powder. ^{1}H NMR (DMSO-d_6, 400 MHz): δ 9.09 (s, 1H), 8.77 (s, 1H), 7.94 (t, ^3J = 5.5 Hz, 1H), 7.90 (d, ^3J = 9.4 Hz, 2H), 7.78 (d, J = 1.3 Hz, 1H), 7.58 (d, J = 1.2 Hz, 1H), 7.27−7.07 (m, 7H), 6.54 (bs, 2H), 4.75−4.65 (m, 2H), 4.50−4.36 (m, 2H), 4.24−4.14 (m, 1H), 4.14−4.04 (m, 1H), 3.21−2.14 (m, 2H), 3.18 (s, 12H), 3.08−2.91 (m, 2H), 2.70 (t, ^3J = 7.0 Hz, 2H), 2.63−2.58 (m, 2H). 2.33−2.28 (m, 2H), 2.11−2.01 (m, 2H), 1.81−1.61 (m, 2H). HPLC-MS (ESI, Gradient B): t_R 12.5 min; positive mode m/z 1066.2 (100) $[M]^+$, 1064.3 (60) $[M]^+$; calcd for $C_{43}H_{48}F_3N_7O_6ReS_2^+$: 1066.26 (100.0), 1064.26 (58.6); t_R 11.0 min; positive mode m/z 476.6 (100) $[M\text{-}TFA]^{2+}$; calcd for $C_{41}H_{48}N_7O_4ReS_2^{2+}$: 953.28 (100).

[Re(15)(CO)$_3$] (20)$^+$. The aldehyde **2** (4.2 mg, 0.01 mmol) and the $[NEt_4]_2[ReBr_3(CO)_3]$ (22 mg, 0.028 mmol) were dissolved in PBS (5 mL, pH = 6.5). The mixture was stirred and heated under N_2 at 50 °C for 15 min. The formed precipitate was spun down, and supernatant removed. The remaining precipitate was dissolved in the mixture of MeCN:PBS (10 mL, 1:1, pH = 7.4). The orange solution was added to the flask containing the peptide **15** (30 mg, 0.03 mmol) and the mixture was stirred at 66 °C for 24 h. The crude product was purified by preparative HPLC to afford 4 mg (24%) of complex **19** as an orange powder. HPLC-MS (ESI, Gradient A): t_R 15.7 min; positive mode m/z 821.9 (100) $[M]^{2+}$, 1642.4 (50) $[M-H]^+$; calcd for $C_{71}H_{94}N_{17}O_{11}ReS_3^{2+}$: 1643.60 (100.0), 1644.61 (75.1).

■ ASSOCIATED CONTENT

Supporting Information. Detailed materials and methods. This material is available free of charge via the Internet at http://pubs.acs.org.

■ AUTHOR INFORMATION

Corresponding Author
*E-mail: ariel@aci.uzh.ch.

■ REFERENCES

(1) Bartholoma, M. D., Louie, A. S., Valliant, J. F., and Zubieta, J. (2010) Technetium and gallium derived radiopharmaceuticals: comparing and contrasting the chemistry of two important radiometals for the molecular imaging era. *Chem. Rev. 110*, 2903–20.

(2) Jennings, L. E., and Long, N. J. (2009) 'Two is better than one'-probes for dual-modality molecular imaging. *Chem. Commun.* 3511–24.

(3) Louie, A. (2010) Multimodality imaging probes: design and challenges. *Chem. Rev. 110*, 3146–95.

(4) Mariani, G., Bruselli, L., Kuwert, T., Kim, E. E., Flotats, A., Israel, O., Dondi, M., and Watanabe, N. (2010) A review on the clinical uses of SPECT/CT. *Eur. J. Nucl. Med. Mol. I 37*, 1959–85.

(5) Marti-Bonmati, L., Sopena, R., Bartumeus, P., and Sopena, P. (2010) Multimodality imaging techniques. *Contr. Media Mol. I 5*, 180–89.

(6) Puckett, C. A., Ernst, R. J., and Barton, J. K. (2010) Exploring the cellular accumulation of metal complexes. *Dalton Trans. 39*, 1159–70.

(7) Splith, K., Hu, W. N., Schatzschneider, U., Gust, R., Ott, I., Onambele, L. A., Prokop, A., and Neundorf, I. (2010) Protease-activatable organometal-peptide bioconjugates with enhanced cytotoxicity on cancer cells. *Bioconjugate Chem. 21*, 1288–96.

(8) Bartholoma, M., Valliant, J., Maresca, K. P., Babich, J., and Zubieta, J. (2009) Single amino acid chelates (SAAC): a strategy for

the design of technetium and rhenium radiopharmaceuticals. *Chem. Commun.* 493–512.

(9) Deshpande, M. S., Kumbhar, A. A., Kumbhar, A. S., Kumbhakar, M., Pal, H., Sonawane, U. B., and Joshi, R. R. (2009) Ruthenium(II) complexes of bipyridine-glycoluril and their interactions with DNA. *Bioconjugate Chem. 20*, 447–59.

(10) Puckett, C. A., and Barton, J. K. (2007) Methods to explore cellular uptake of ruthenium complexes. *J. Am. Chem. Soc. 129*, 46–47.

(11) Puckett, C. A., and Barton, J. K. (2008) Mechanism of cellular uptake of a ruthenium polypyridyl complex. *Biochemistry 47*, 11711–16.

(12) James, S., Maresca, K. P., Babich, J. W., Valliant, J. F., Doering, L., and Zubieta, J. (2006) Isostructural Re and Tc-99m complexes of biotin derivatives for fluorescence and radioimaging studies. *Bioconjugate Chem. 17*, 590–96.

(13) Schaffer, P. J. A. G., Lemon, J. A., Reid, L. C., Pacey, L. K. K., Farncombe, T. H., Boreham, D. R., Zubieta, J., Babich, J. W., Doering, L. C., and Valliant, J. F. (2008) Isostructural fluorescent and radioactive probes for monitoring neural stem and progenitor cell transplants. *Nucl. Med. Biol. 35*, 159–69.

(14) Stephenson, K. A., Banerjee, S. R., Besanger, T., Sogbein, O. O., Levadala, M. K., Mcfarlane, N., Lemon, J. A., Boreham, D. R., Maresca, K. P., Brennan, J. D., Babich, J. W., Zubieta, J., and Valliant, J. F. (2004) Bridging the gap between in vitro and in vivo imaging: isostructural Re and Tc-99m complexes for correlating fluorescence and radioimaging studies. *J. Am. Chem. Soc. 126*, 8598–99.

(15) Miller, A. M., and Dean, D. A. (2009) Tissue-specific and transcription factor-mediated nuclear entry of DNA. *Adv. Drug Delivery Rev. 61*, 603–13.

(16) Noor, F., Kinscherf, R., Bonaterra, G. A., Walczak, S., Wolfl, S., and Metzler-Nolte, N. (2009) Enhanced cellular uptake and cytotoxicity studies of organometallic bioconjugates of the NLS peptide in Hep G2 cells. *ChemBioChem 10*, 493–502.

(17) Bendifallah, N., Rasmussen, F. W., Zachar, V., Ebbesen, P., Nielsen, P. E., and Koppelhus, U. (2006) Evaluation of cell-penetrating peptides (CPPs) as vehicles for intracellular delivery of antisense peptide nucleic acid (PNA). *Bioconjugate Chem. 17*, 750–58.

(18) Sarko, D., Beijer, B., Boy, R. G., Nothelfer, E. M., Leotta, K., Eisenhut, M., Altmann, A., Haberkorn, U., and Mier, W. (2010) The pharmacokinetics of cell-penetrating peptides. *Mol. Pharmaceut. 7*, 2224–31.

(19) Zanta, M. A., Belguise-Valladier, P., and Behr, J. P. (1999) Gene delivery: a single nuclear localization signal peptide is sufficient to carry DNA to the cell nucleus. *Proc. Natl. Acad. Sci. U.S.A. 96*, 91–96.

(20) Adam, S. A., and Gerace, L. (1991) Cytosolic proteins that specifically bind nuclear location signals are receptors for nuclear import. *Cell 66*, 837–47.

(21) Häfliger, P., Agorastos, N., Renard, A., Giambonini-Brugnoli, G., Marty, C., and Alberto, R. (2005) Cell uptake and radiotoxicity studies of an nuclear localization signal peptide-intercalator conjugate labeled with [Tc-99m(CO)(3)](+). *Bioconjugate Chem. 16*, 582–87.

(22) Fischer, R., Fotin-Mleczek, M., Hufnagel, H., and Brock, R. (2005) Break on through to the other side - Biophysics and cell biology shed light on cell-penetrating peptides. *ChemBioChem 6*, 2126–42.

(23) Häfliger, P., Agorastos, N., Spingler, B., Georgiev, O., Viola, G., and Alberto, R. (2005) Induction of DNA-double-strand breaks by auger electrons from 99mTc complexes with DNA-binding ligands. *ChemBioChem 6*, 414–21.

(24) Agorastos, N., Borsig, L., Renard, A., Antoni, P., Viola, G., Spingler, B., Kurz, P., and Alberto, R. (2007) Cell-specific and nuclear targeting with [M(CO)(3)](+) (M=Tc-99m, Re)-based complexes conjugated to acridine orange and bombesin. *Chem.—Eur. J. 13*, 3842–52.

(25) Wendisch, M., Freudenberg, R., Drechsel, J., Runge, R., Wunderlich, G., and Kotzerke, J. (2010) Tc-99m reduces clonogenic survival after intracellular uptake in NIS-positive cells in vitro more than I-131. *Nuklearmedizin 49*, 154–60.

(26) Alexandre, A., Tavares, S., and Tavares, J. M. R. S. (2010) *Int. J. Radiat. Biol. 86*, 261–70.

(27) Wang, W. W., Spingler, B., and Alberto, R. (2003) Reactivity of 2-pyridine-aldehyde and 2-acetyl-pyridine coordinated to [Re(CO)(3)](+) with alcohols and amines: metal mediated schiff base formation and dimerization. *Inorg. Chim. Acta 355*, 386–93.

(28) Bourkoula, A., Paravatou-Petsotas, M., Papadopoulos, A., Santos, I., Pietzsch, H. J., Livaniou, E., Pelecanou, M., Papadopoulos, M., and Pirmettis, I. (2009) Synthesis and characterization of rhenium and technetium-99m tricarbonyl complexes bearing the 4-[3-bromophenyl]quinazoline moiety as a biomarker for EGFR-TK imaging. *Eur. J. Med. Chem. 44*, 4021–27.

(29) Benny, P. D., Fugate, G. A., Barden, A. O., Morley, J. E., Silva-Lopez, E., and Twamley, B. (2008) Metal-assisted in situ formation of a tridentate acetylacetone ligand for complexation of fac-Re(CO)-(3)(+) for radiopharmaceutical applications. *Inorg. Chem. 47*, 2240–42.

(30) Saw, M. M., Kurz, P., Agorastos, N., Hor, T. S. A., Sundram, F. X., Yan, Y. K., and Alberto, R. (2006) Complexes with the fac-{M-(CO)(3)}(+) (M=Tc-99m, Re) moiety and long alkyl chain ligands as Lipiodol surrogates. *Inorg. Chim. Acta 359*, 4087–94.

(31) Alvarez, C. M., Garcia-Rodriguez, R., and Miguel, D. (2007) Pyridine-2-carboxaldehyde as ligand: Synthesis and derivatization of carbonyl complexes. *Dalton Trans.* 3546–54.

(32) Zelenka, K., Borsig, L., Alberto, R. (2010). *Org. Biomol. Chem.* Online Early Access. DOI: 10.1039/C0OB00504E.

(33) Rabenstein, D. L., and Weaver, K. H. (1996) Kinetics and equilibria of the thiol/disulfide exchange reactions of somatostatin with glutathione. *J. Org. Chem. 61*, 7391–97.

(34) Endres, P. J., Macrenaris, K. W., Vogt, S., and Meade, T. J. (2008) Cell-permeable MR contrast agents with increased intracellular retention. *Bioconjugate Chem. 19*, 2049–59.

(35) Ojima, I. (2007) Guided molecular missiles for tumor-targeting chemotherapy a case studies using the second-generation taxoids as warheads. *Acc. Chem. Res. 41*, 108–19.

(36) Satyam, A. (2008) Design and synthesis of releasable folate-drug conjugates using a novel heterobifunctional disulfide-containing linker. *Bioorg. Med. Chem. Lett. 18*, 3196–99.

(37) Meister, A., and Anderson, M. E. (1983) Glutathione. *Annu. Rev. Biochem. 52*, 711–60.

(38) Gilbert, H. F., and Lester, P. (1995) In *Methods in Enzymology*, pp 8−28, Vol. 251, Academic Press, London.

(39) Alberto, R., Schibli, R., Schubiger, A. P., Abram, U., Pietzsch, H. J., and Johannsen, B. (1999) First application of fac-[Tc-99m(OH2)-(3)(CO)(3)](+) in bioorganometallic chemistry: design, structure, and in vitro affinity of a 5-HT1A receptor ligand labeled with Tc-99m. *J. Am. Chem. Soc. 121*, 6076–77.

(40) Alberto, R., Ortner, K., Wheatley, N., Schibli, R., and Schubiger, A. P. (2001) Synthesis and properties of boranocarbonate: a convenient in situ CO source for the aqueous preparation of [99mTc(OH2)3-(CO)3]+. *J. Am. Chem. Soc. 123*, 3135–36.

(41) Bonnet, D., Grandjean, C., Rousselot-Pailley, P., Joly, P., Bourel-Bonnet, L., Santraine, V., Gras-Masse, H., and Melnyk, O. (2003) Solid-phase functionalization of peptides by an hydrazinoacetyl group. *J. Org. Chem. 68*, 7033–40.

(42) Baugh, S. D. P., Yang, Z., Leung, D. K., Wilson, D. M., and Breslow, R. (2001) Cyclodextrin dimers as cleavable carriers of photodynamic sensitizers. *J. Am. Chem. Soc. 123*, 12488–94.

(43) Byk, G., Wetzer, B., Frederic, M., Dubertret, C., Pitard, B., Jaslin, G., and Scherman, D. (2000) Reduction-sensitive lipopolyamines as a novel nonviral gene delivery system for modulated release of DNA with improved transgene expression. *J. Med. Chem. 43*, 4377–87.

Supporting information for

Metal complex mediated conjugation of peptides to nucleus targeting acridine orange: A modular concept for dual-modality imaging agents

Karel Zelenka[a] , Lubor Borsig[b] and Roger Alberto[*a]

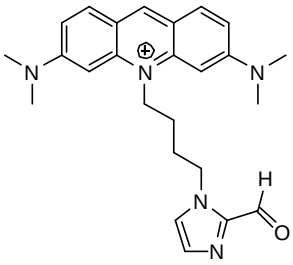
[a]*Institute of Inorganic Chemistry and* [b]*Institute of Physiology, University of Zürich, Winterthurerstr. 190, 8057 Zürich, Switzerland*

General information:

The HPLC-MS data acquisition and processing were performed as described in experimental section. For the cleavage studies of compounds **19** and **20** with GSH, HPLC-ESI-MS-MRM (Multiple Reaction Monitoring) method was used to trap and accumulate selected ions. This method allows trapping and accumulation/fragmentation up to 10 different masses. In the cleavage experiment, only accumulation and TIC (total ion counts) of given mass were monitored. Expert setting of MS was following: Ultra Scan 100-2000 M.W., Scan delay= 0, Capillary -4000V, End plate offset -500V, Nebulizer 35 psi, Dry gas 8l/min, Dry temp 350°C, Skimmer 40V, Cap Exit 147.3V, Oct 1 DC 12V, Oct 2 DC 2.12V, Trap drive 67.8, Oct RT 200 Vpp, Lens 1 -5V, Lens 2 -60V; Mode positive MRM isolation on (isolation width was 4), Rolling averaging on (2). The HPLC was performed as described in experimental section. Several optimization runs were performed prior to measurement to find optimal conditions for acquisition. Monitored masses for **19** were: 1066.4, 988.4, 476.7, 515.3, 859.2, 781.3, 745.3, 373.0, 1086.6, 525.5 and for **20** : 1066.4, 988.4, 476.7, 1205.4, 781.3, 745.3, 373.0, 1086.6, 525.5 representing different starting/cleavage products (also see Scheme **7** in manuscript). The analyses were repeated under identical conditions to assure reproducibility.

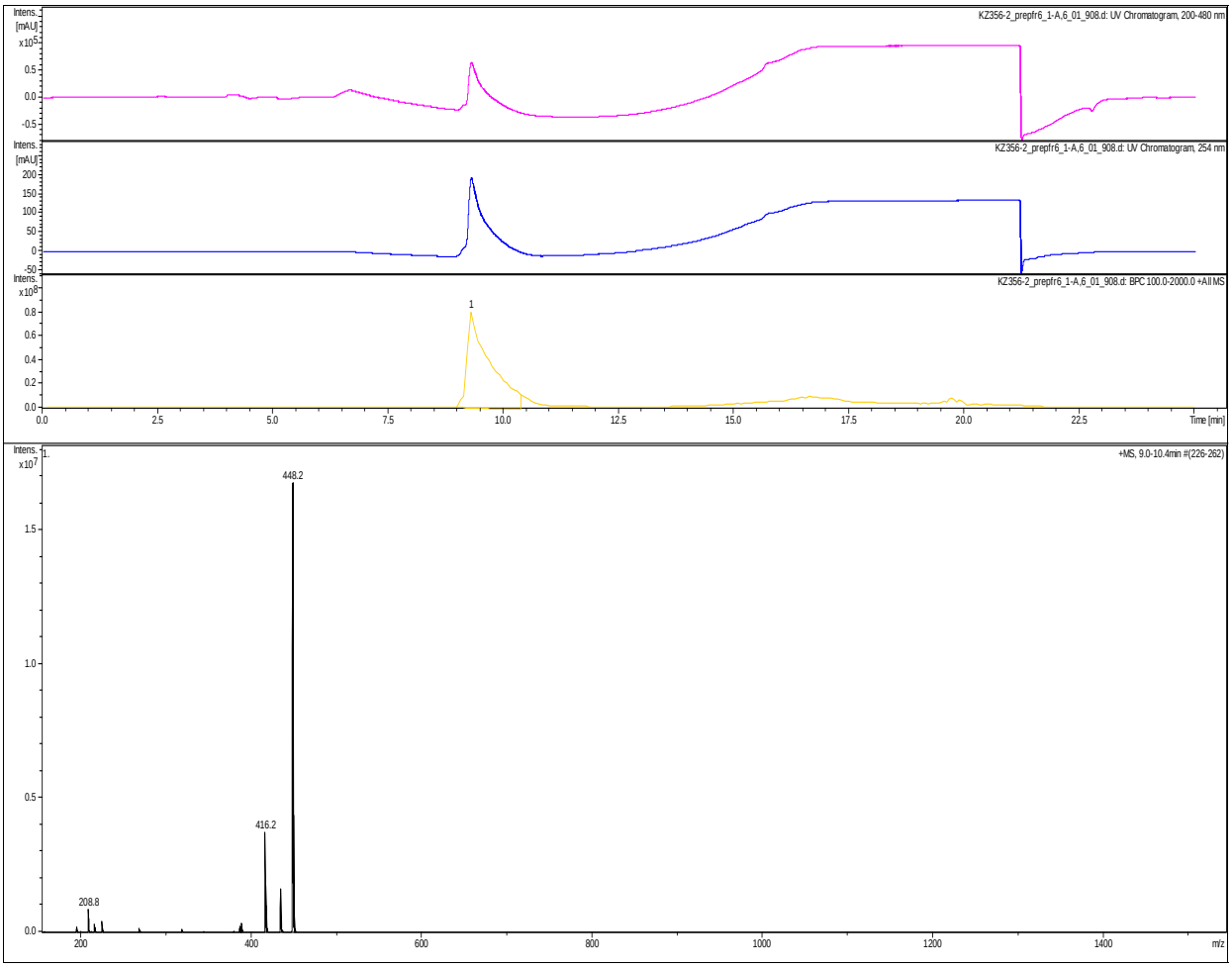
* Corresponding author, E-mail: ariel@aci.uzh.ch,

3,6-bis(dimethylamino)-10-(4-(2-formyl-1*H*-imidazol-1-yl)butyl)acridinium (2)

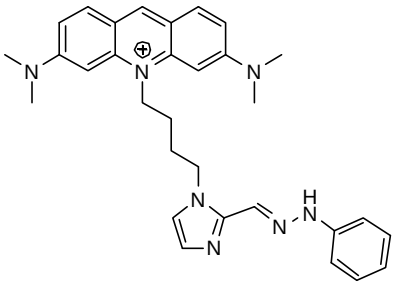


^{13}C NMR (CD_3CN, 100 MHz) δ 182.4, 156.4, 143.6, 143.35, 133.6, 131.6, 127.6, 117.5, 114.9, 92.8, 47.4, 47.3, 40.6, 28.5, 23.00. Calcd for $C_{25}H_{30}N_5O^+$: 416.24.

The HPLC-MS (UV) trace of compound **2** (Gradient B).

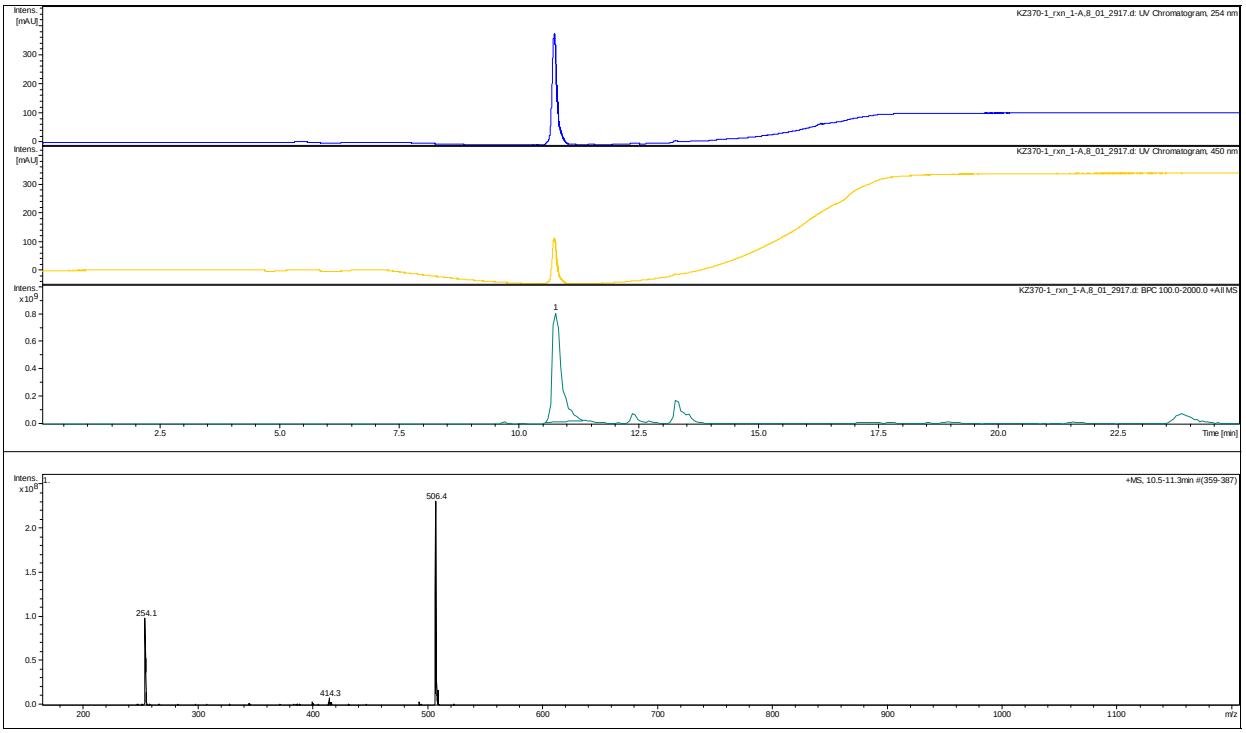


3,6-bis(dimethylamino)-10-(4-(2-((2-phenylhydrazono)methyl)-1*H*-imidazol-1-yl)butyl)acridinium (4)

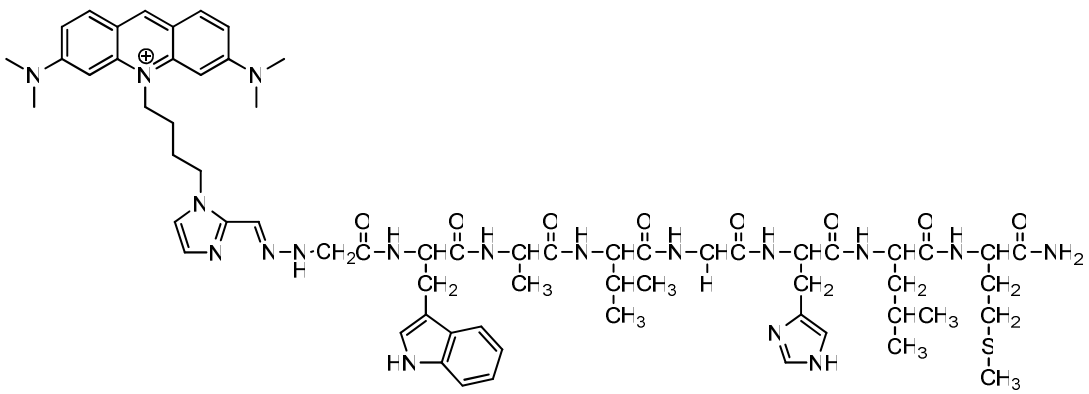


^{13}C NMR (CD_3CN, 100 MHz): δ 156.2, 144.6, 143.5, 143.3, 142.0, 133.5, 129.7, 123.7, 121.2, 117.4, 114.8, 113.2, 92.9, 48.2, 46.9, 40.5, 27.3, 23.2. Calcd for $C_{31}H_{36}N_7^+$: 506.3.

The HPLC-MS (UV) trace of compound **4** (Gradient B).

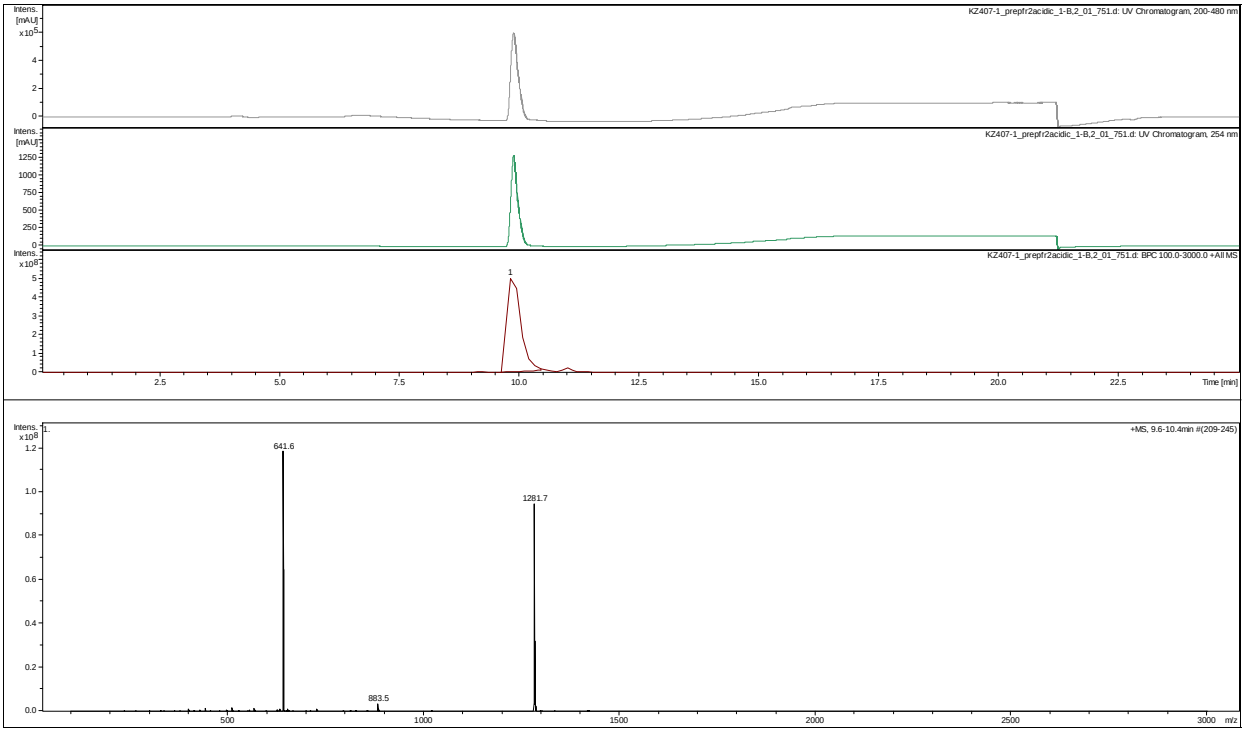


3,6-bis(dimethylamino)-10-(4-(2-((2-(2-(Bombesin 8-14)-2-oxoethyl)hydrazono)methyl)-1*H*-imidazol-1-yl)butyl)acridinium (5)

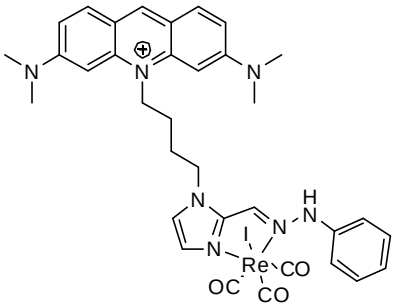


Calcd for $C_{65}H_{89}N_{18}O_8S^+$: 1281.7.

The HPLC-MS (UV) trace of compound **5** (Gradient B).

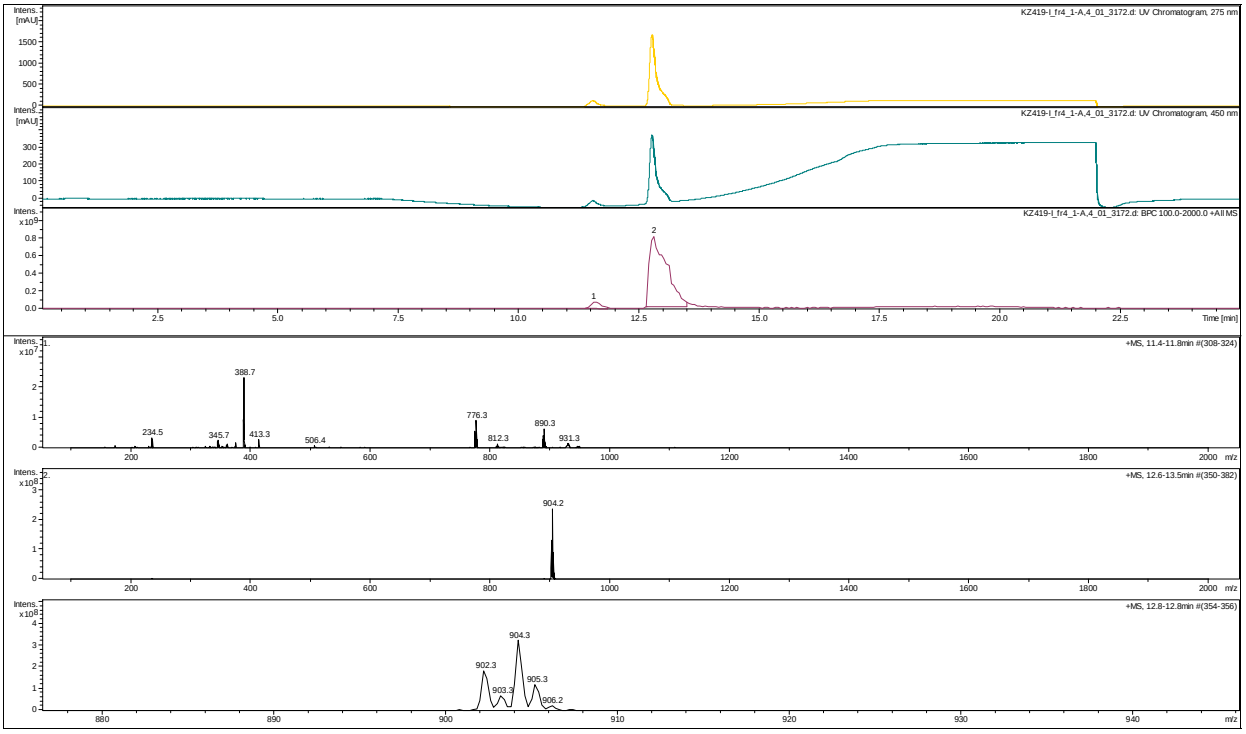


$[Re(I)(4)(CO)_3]^+$ (6)

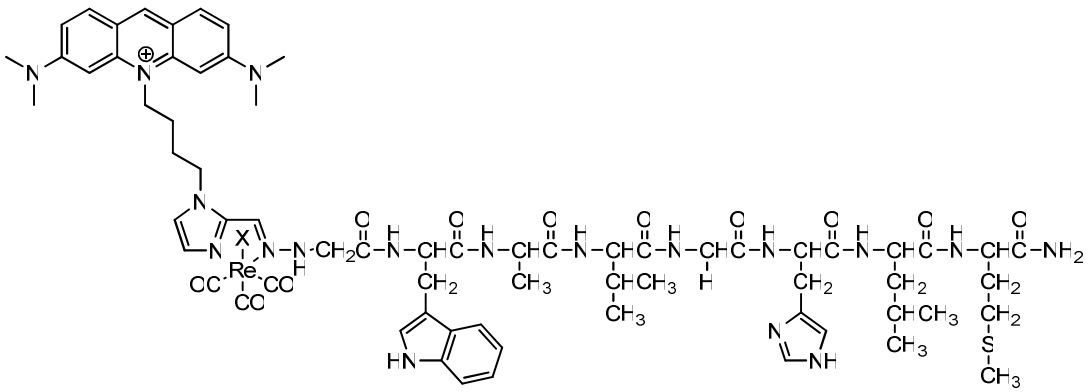


^{13}C NMR (DMSO-D_6, 100 MHz): 156.6, 148.7, 144.0, 143.2, 142.9, 138.0, 134.0, 132.0, 129.9, 125.4, 125.3, 122.3, 117.6, 115.5, 93.7, 47.9, 46.92, 41.4, 28.8, 23.58. Calcd for $C_{34}H_{36}IN_7O_3Re^+$: 904.15, 902.15.

The HPLC-MS (UV) trace of compound **6** (Gradient B).

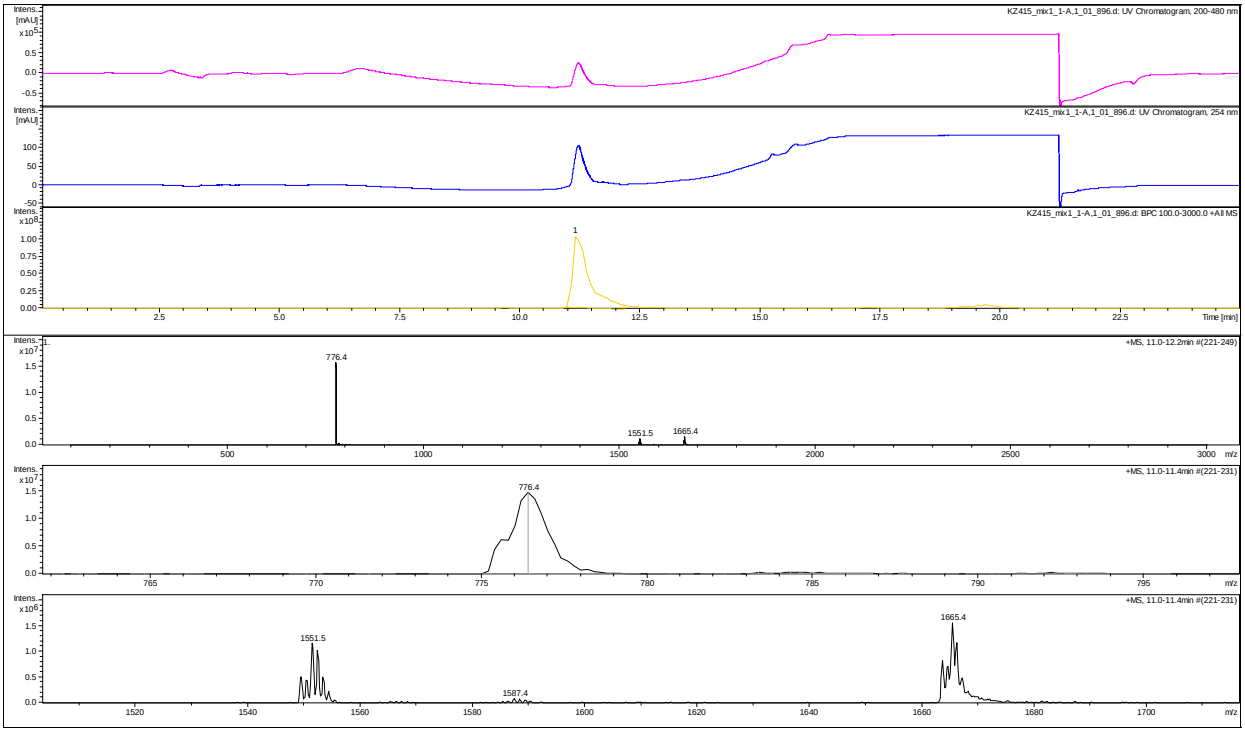


$[Re(5)(CO)_3]^+$ (7)

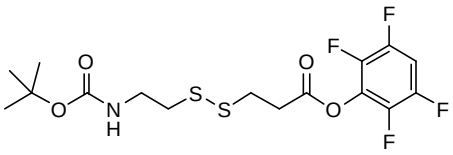


Calcd for $C_{68}H_{89}N_{18}O_{11}ReS^{2+}$: 1552.62.

The HPLC-MS (UV) trace of compound **7** (Gradient B)**.**

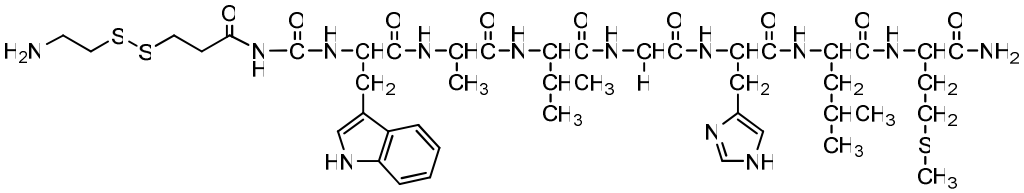


2,3,5,6-tetrafluorophenyl 3-((2-(*tert*-butoxycarbonylamino)ethyl)disulfanyl)propanoate (10)



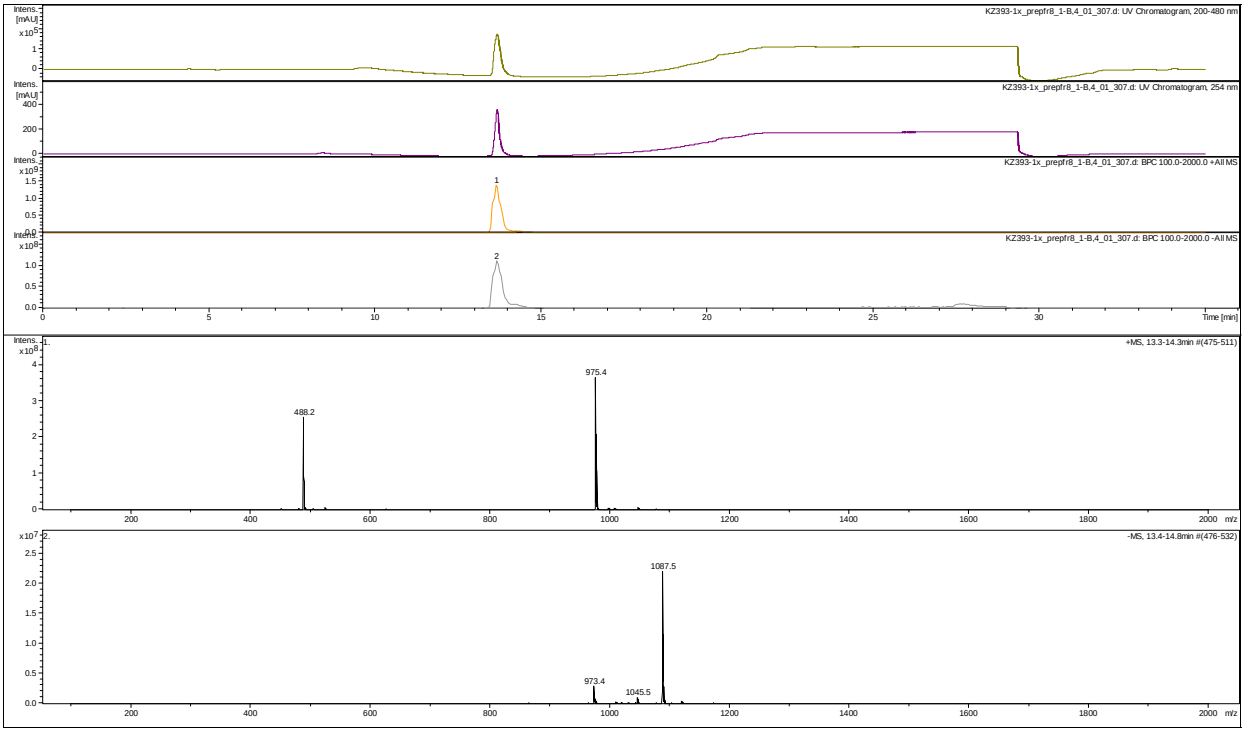
^{13}C NMR ($CDCl_3$, 125 MHz) δ 167.9, 155.9, 147.3, 145.3, 141.7, 139.8, 129.6, 103.6, 38.6, 33.6, 32.6, 28.6. ^{19}F NMR ($CDCl_3$, 188 MHz) δ -140.3 (m, 2F), 154.1 (m, 2F).

Bombesin (15)

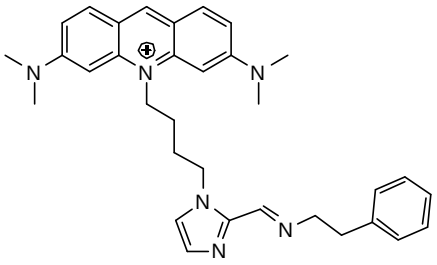


Calcd for $C_{43}H_{66}N_{12}O_8S_3$: 974.43.

The HPLC-MS (UV) trace of compound **15** (Gradient B).

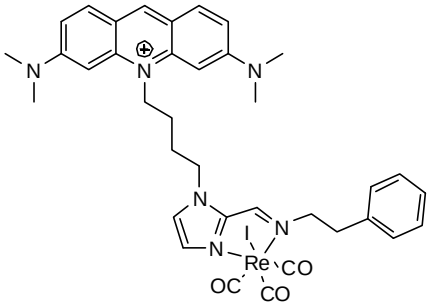


3,6-bis(dimethylamino)-10-(4-(2-((phenethylimino)methyl)-1H-imidazol-1-yl)butyl)acridinium (16)



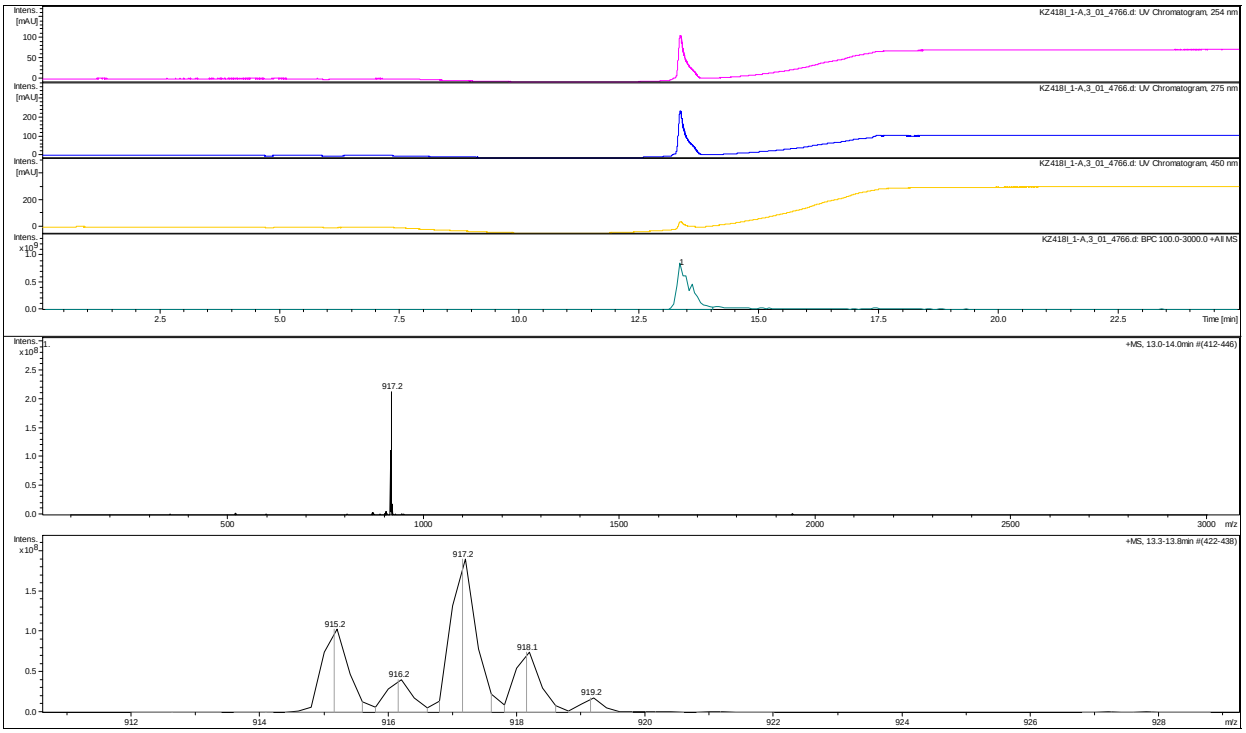
^{13}C NMR ($CDCl_3$, 100 MHz): δ 156.2, 153.9, 143.3, 143.0, 140.2, 138.8, 133.6, 130.0, 129.1, 128.8, 126.6, 124.7, 117.6, 114.8, 93.2, 63.5, 47.8, 47.0, 41.2, 37.9, 28.7, 23.3.

$[Re(I)(16)(CO)_3]^+$ (17)

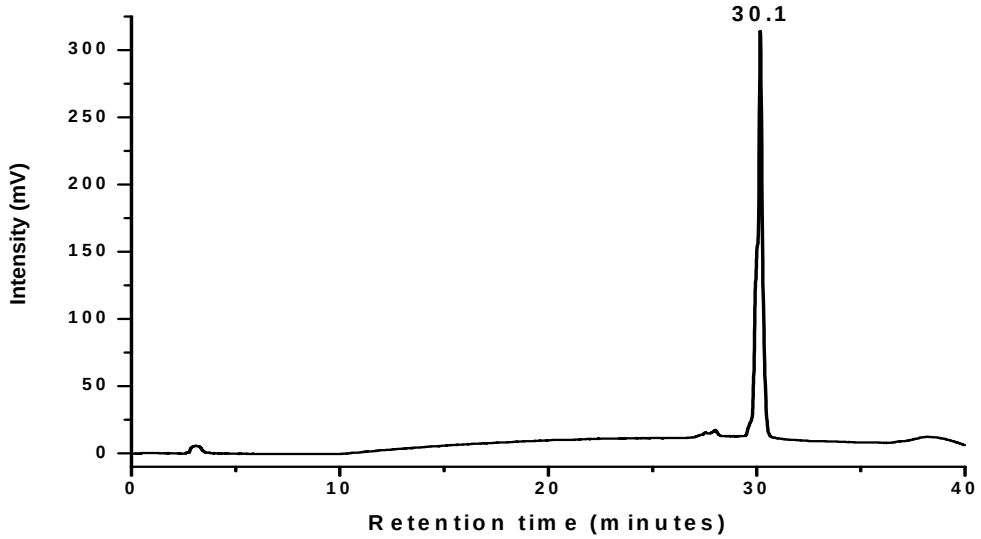


^{13}C NMR (DMSO-D_6, 100 MHz): δ 156.9, 156.5, 149.4, 144.0, 143.2, 138.6, 134.1, 133.2, 129.6, 127.6, 126.8, 117.6, 115.5, 93.6, 66.7, 48.4, 46.9, 41.4, 37.3, 29.0, 23.5. Calcd for $C_{36}H_{39}IN_6O_3Re^+$: 917.17, 915.17.

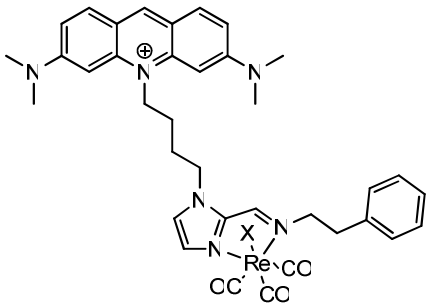
The HPLC-MS trace (UV) of complex **17** (Gradient B).



The HPLC trace (UV) of complex **17** (Gradient D).

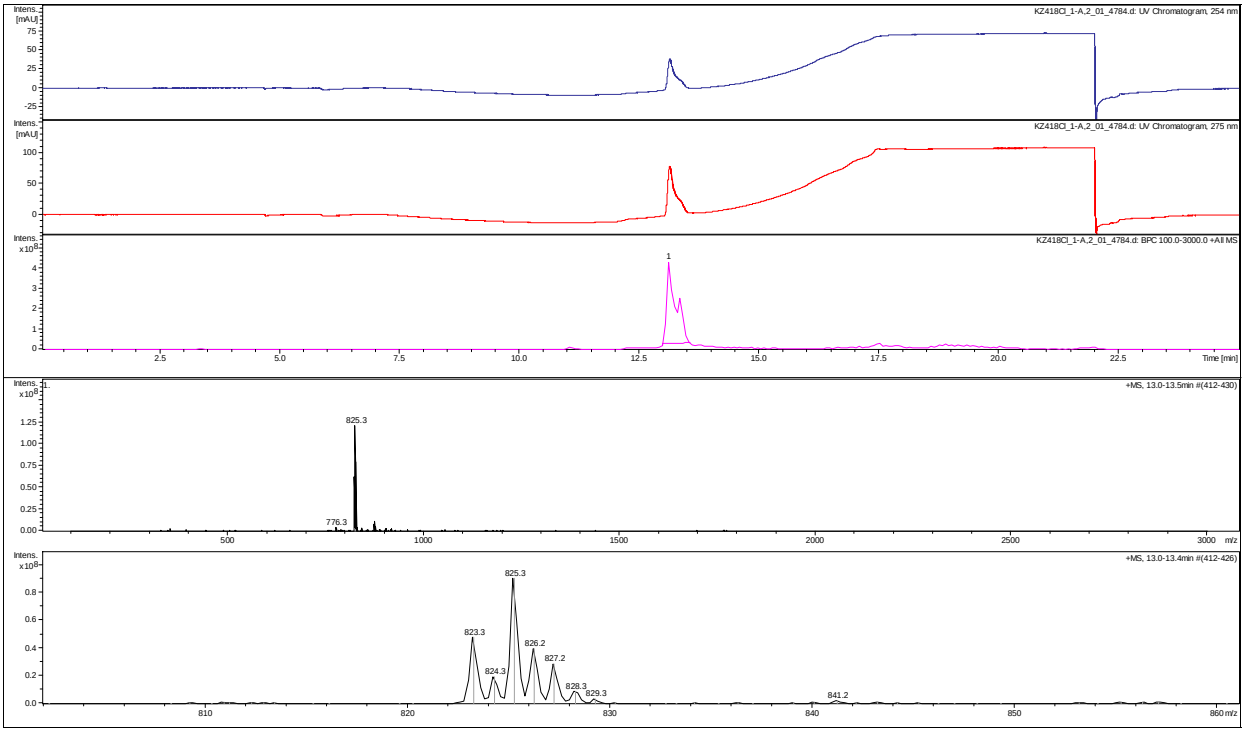


$[Re(X)(16)(CO)_3]^+$ (17a, X = Cl) and (17b, X = Br)



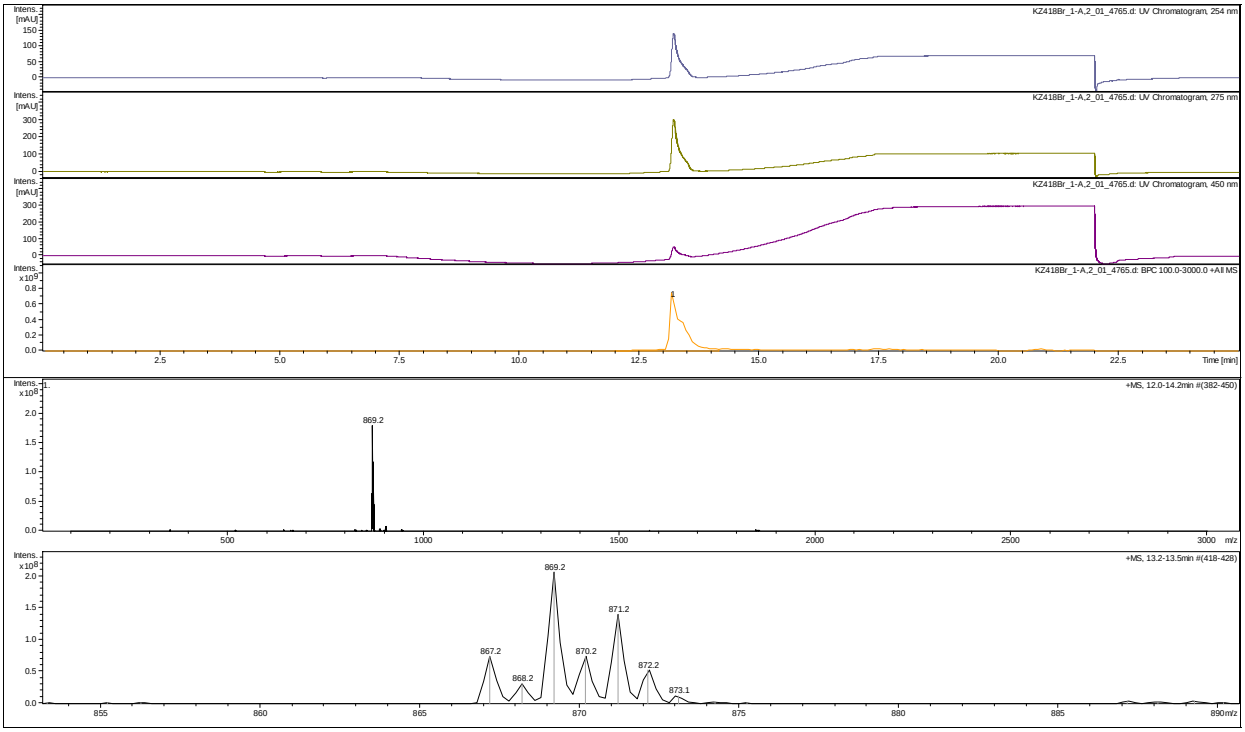
Calcd for $C_{36}H_{39}ClN_6O_3Re^+$: 825.23, 823.23.

The HPLC-MS trace (UV) of complex **17a** (Gradient B).

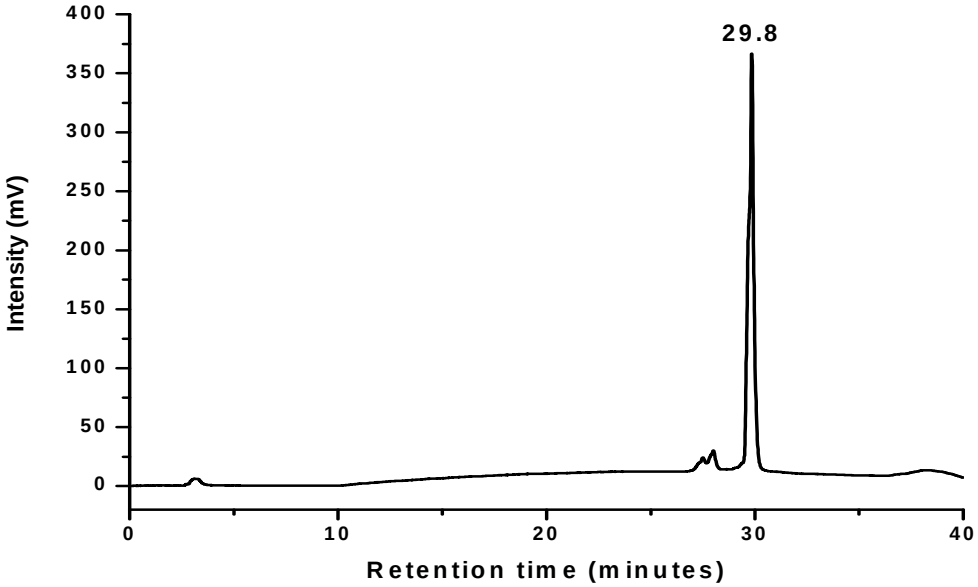


Calcd for $C_{36}H_{39}BrN_6O_3Re^+$: 869.18, 871.18, 867.1.

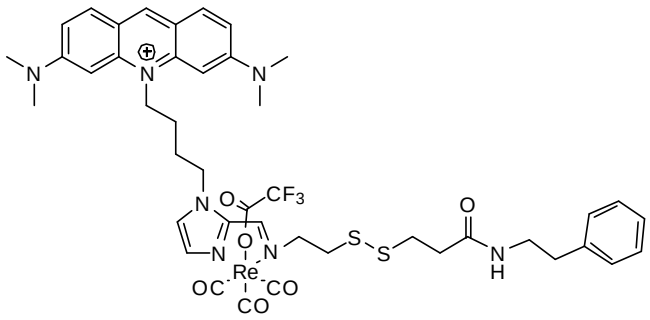
The HPLC-MS trace (UV) of complex **17b** (Gradient B).



The HPLC trace (UV) of complex **17b** (Gradient D).



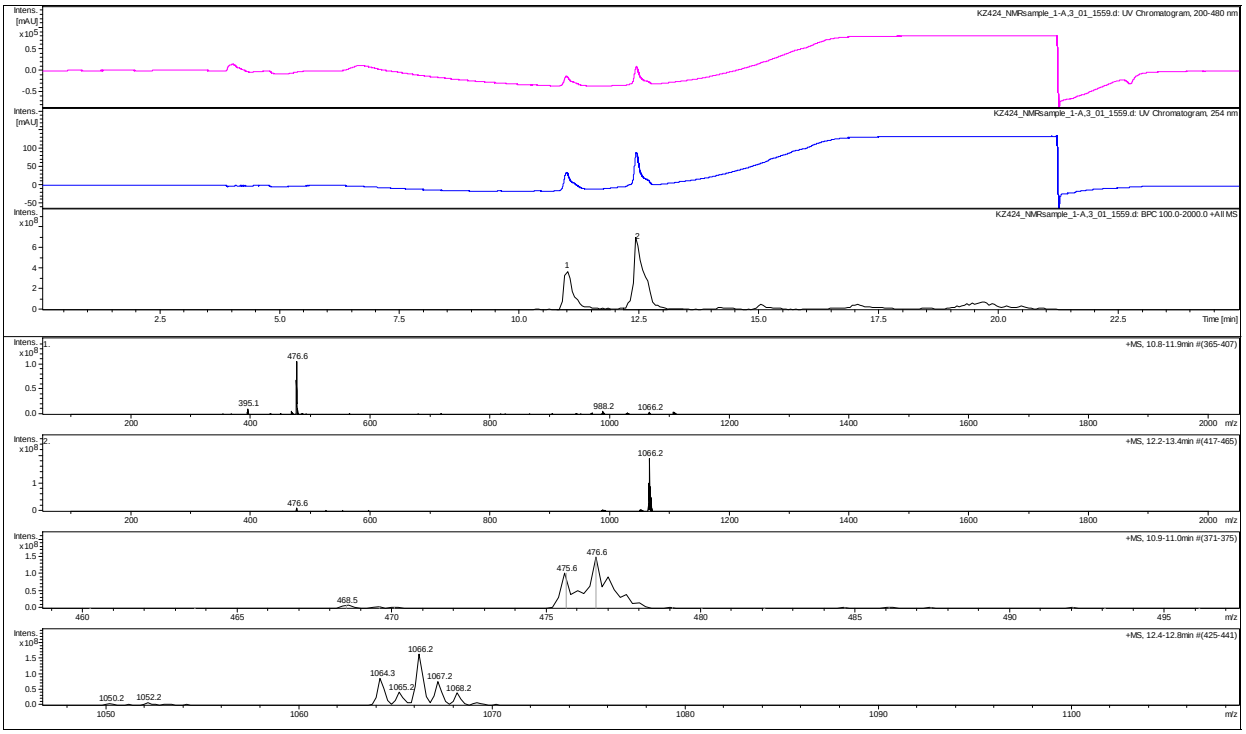
$Re(TFA)(14)(CO)_3]^+$ (19) and $Re(H_2O)(14)(CO)_3]^+$ (19a)



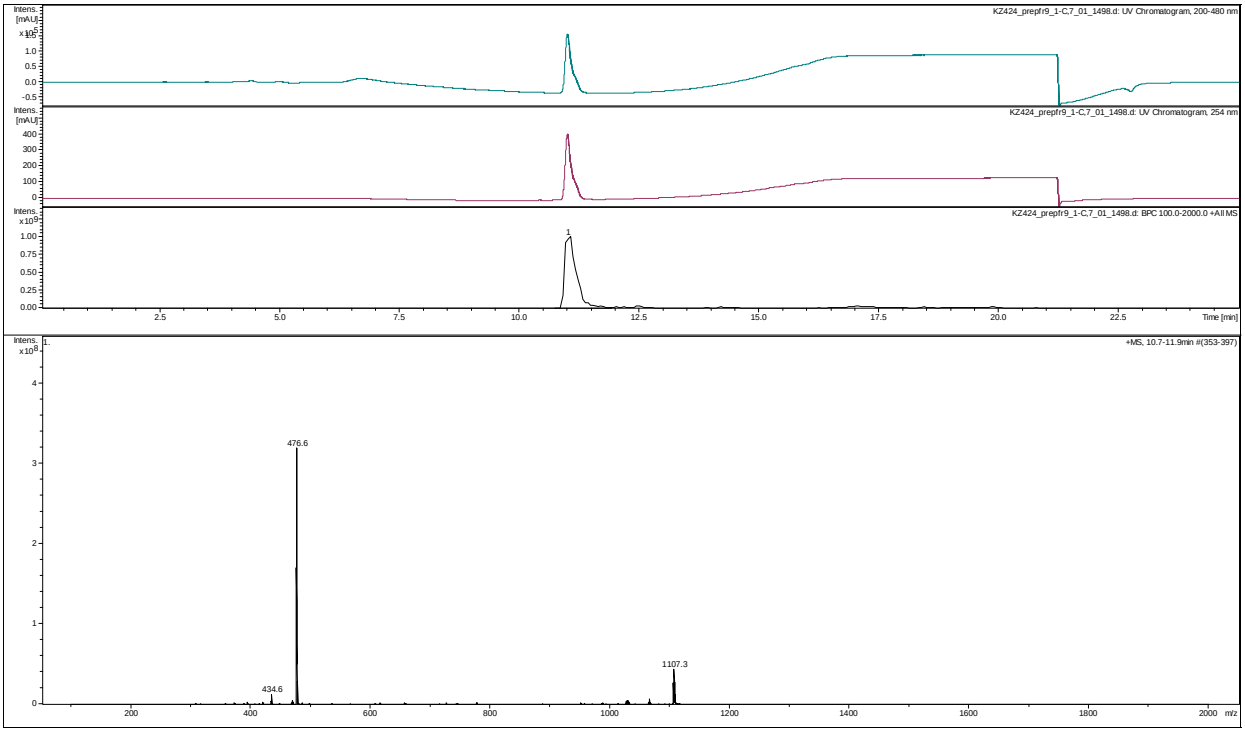
Calcd for $C_{43}H_{48}F_3N_7O_6ReS_2^+$: 1066.26, 1064.26.

Calcd for $C_{41}H_{48}N_7O_4ReS_2^{2+}$: 953.27.

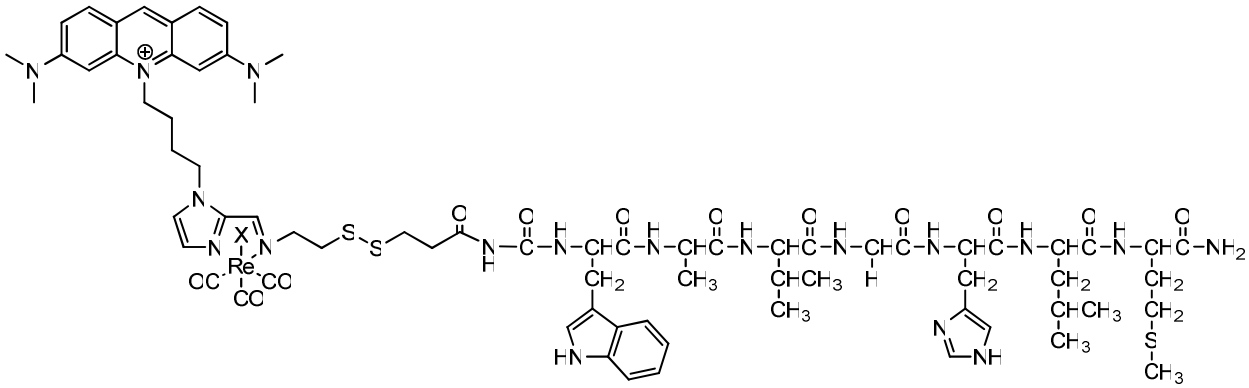
The HPLC-MS trace (UV) of complex **19** (Gradient B).



The HPLC-MS trace (UV) of complex **19a** (Gradient B).

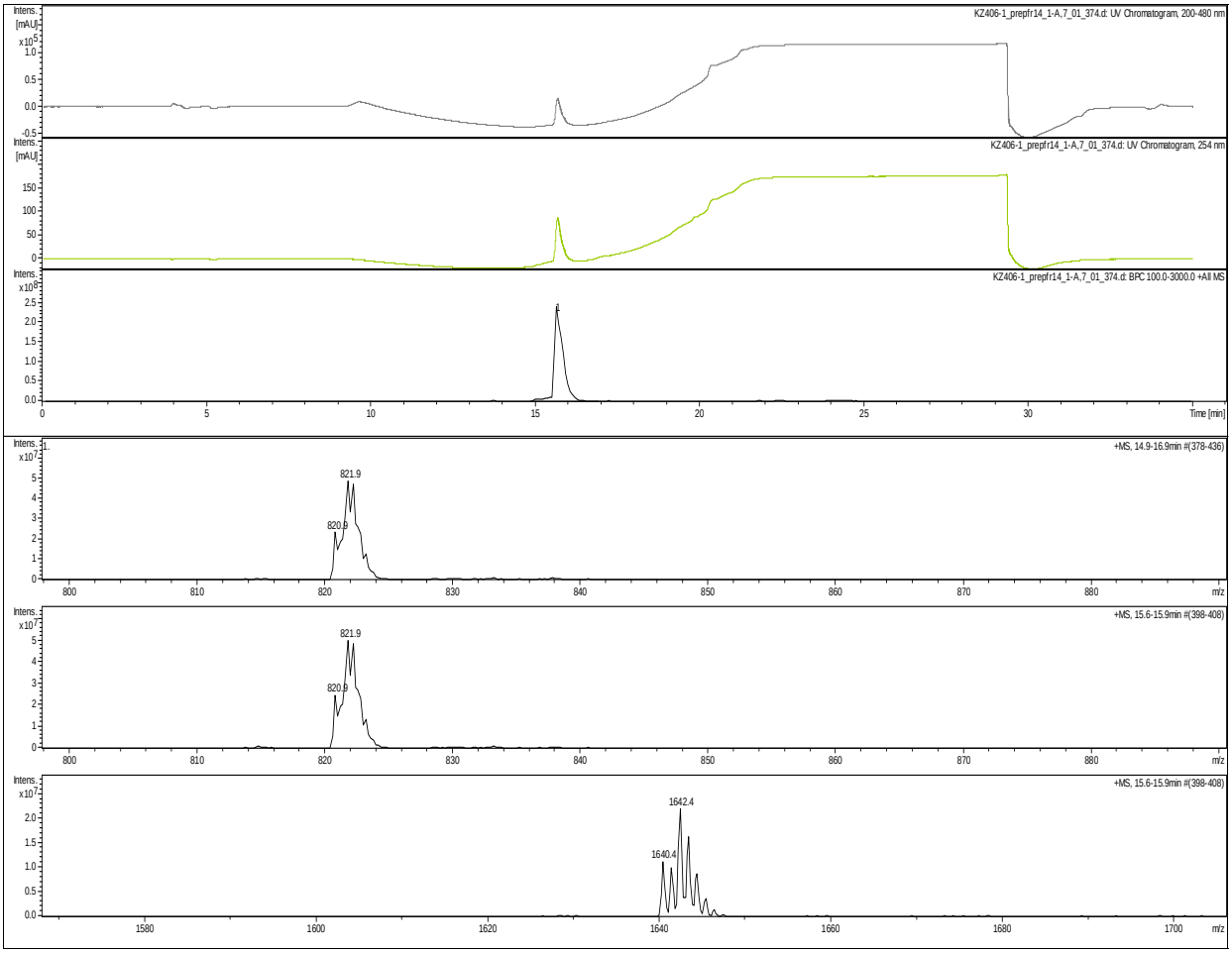


[Re(15)(CO)$_3$]$^+$ (20)

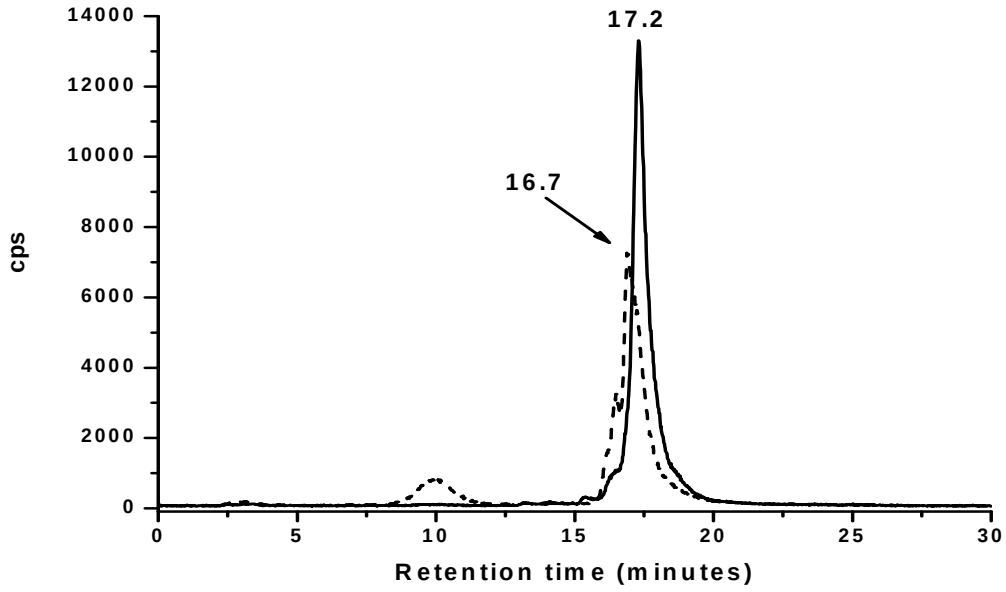


Calcd for $C_{71}H_{94}N_{17}O_{11}ReS_3^{2+}$: 1643.60, 1644.61.

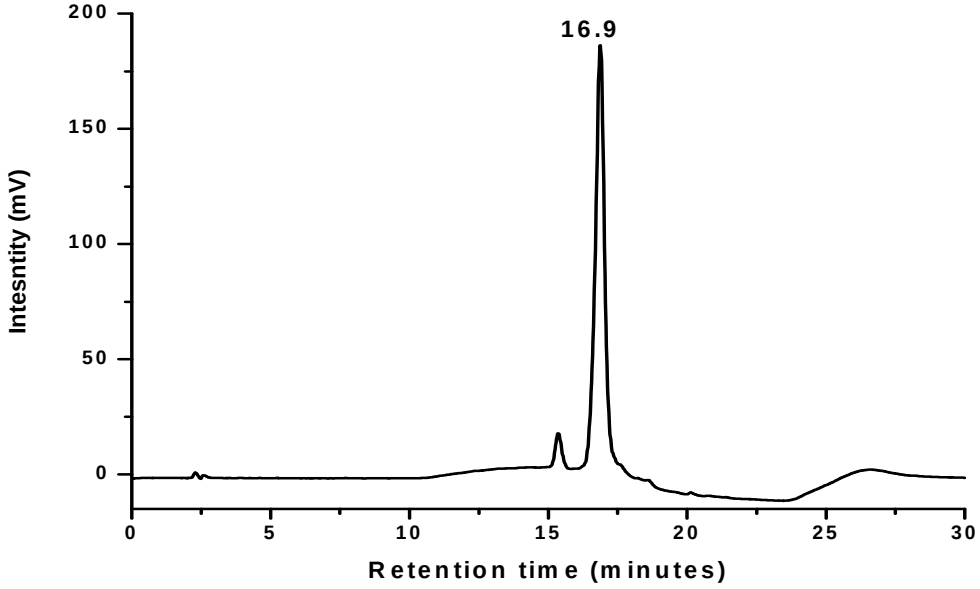
The HPLC-MS trace (UV) of complex **20** (Gradient B).



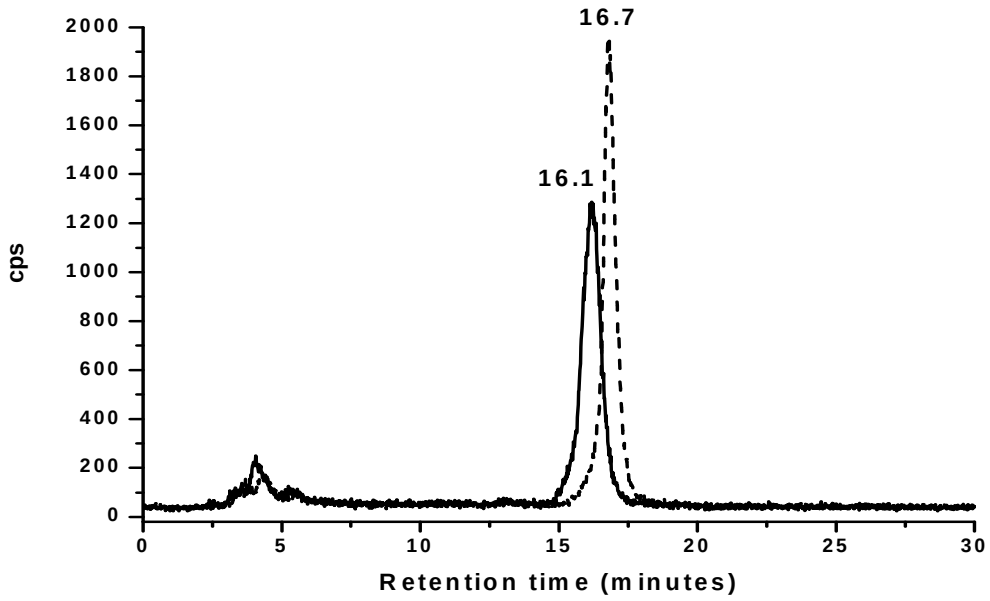
The radioHPLC trace of complex **25** (dashed line) and trace of complex **28** (^{99m}Tc analog of **20**, solid line) after labeling (Gradient 0-3 min 30%, 3-5 min 30-50%, 5-15 min 50-100%, 15-30 min 100% MeOH)



The HPLC trace (UV) of complex of **20** (Gradient 0-3 min 30%, 3-5 min 30-50%, 5-15 min 50-100%, 15-30 min 100% MeOH).



The radioHPLC trace of complex **25** (dashed line) and trace of complex **28** (^{99m}Tc analog of **20**, solid line) after labeling (Gradient 0-10 min 40%, 10-15 min 40-100%, 15-30 min 100% MeCN).



Bioconjugate Chemistry

ARTICLE

pubs.acs.org/bc

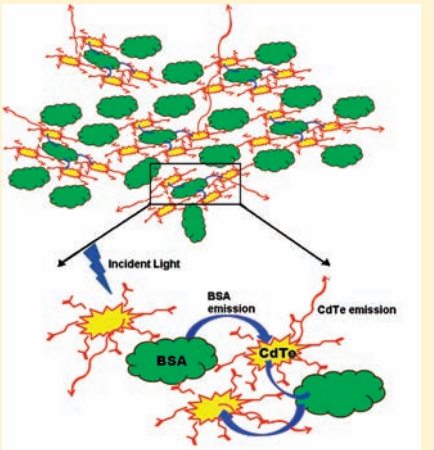
Photoabsorption and Resonance Energy Transfer Phenomenon in CdTe−Protein Bioconjugates: An Insight into QD−Biomolecular Interactions

Aaydha C. Vinayaka and Munna S. Thakur*

Fermentation Technology & Bioengineering Department, Central Food Technological Research Institute (A constituent laboratory of Council of Scientific and Industrial Research, New Delhi), Mysore-570020, India

Supporting Information

ABSTRACT: Luminescent quantum dots (QDs) possess unique photophysical properties, which are advantageous in the development of new generation robust fluorescent probes based on Forster resonance energy transfer (FRET) phenomena. Bioconjugation of these QDs with biomolecules create hybrid materials having unique photophysical properties along with biological activity. The present study is aimed at characterizing QD bioconjugates in terms of optical behavior. Colloidal CdTe QDs capped with 3-mercaptopropionic acid (MPA) were conjugated to different proteins by the carbodiimide protocol using *N*-(3-dimethylaminopropyl)-*N*-ethylcarbodiimide hydrochloride (EDC) and a coupling reagent like *N*-hydroxysuccinimide (NHS). The photoabsorption of these QD−protein bioconjugates demonstrated an effective coupling of electronic orbitals of constituents. A linear variation in absorbance of bioconjugates at 330 nm proportionate to conjugation suggests a covalent attachment as confirmed by gel electrophoresis. A red shift in the fluorescence of bovine serum albumin (BSA) due to conjugation inferred a decrease in Stokes shift and solvent polarization effects on protein. A proportionate quenching in BSA fluorescence followed by an enhancement of QD fluorescence point toward nonradiative dipolar interactions. Further, reduction in photobleaching of BSA suggests QD−biomolecular interactions. Bioconjugation has significantly influenced the photoabsorption spectrum of QD bioconjugates suggesting the formation of a possible protein shell on the surface of QD. The experimental result suggests that these bioconjugates can be considered nanoparticle (NP) superstructures for the development of a new generation of robust nanoprobes.



Schematic representation of photo-absorption and resonance energy transfer in protein bioconjugated CdTe quantum dots

INTRODUCTION

A quantum dot is a crystal of semiconductor material (periodic groups II−VI, III−V, or IV−VI elements) with a diameter on the order of the compound's exciton Bohr radius.[1] They display a characteristic size dependence of their electronic and optical properties due to a phenomenon known as quantum confinement effects. Properties such as high emission quantum yield, sharp emission spectra, broad absorption spectra, chemical and photostability, long lifetimes, and tunability of emission frequencies make them a superior tool as biomarkers for various applications.[2] The development of any QD-based biosensing modality would essentially require the generation of bioactive QD conjugates. The coupling of inorganic nanoparticles with biomolecules generates hybrid particles possessing unique photophysical properties along with biological activity.[3,4] Being novel constructs, such conjugates need to be characterized to understand the full range of their modified properties before they can be utilized for biosensor applications.

Forster resonance energy transfer (FRET) is a distance-dependent nonradiative energy transfer between the excited electronic states of fluorescent molecules. This phenomenon is a useful tool to study molecular dynamics such as biomolecular interactions and conformational changes.[5] The unique properties of QDs suggest that the replacement of organic fluorophores in FRET studies with QDs could lead to an experimental setup, which would be ultrasensitive, economical, and easy to configure, as well as provide the capability to make simultaneous measurements of different macromolecular systems.[6] Two-color organic/inorganic fluorophores are currently being used for coincidence detection based on FRET.[6,7] However, their functional limitations, such as the spectral cross-talk, nonuniform fluorophore photobleaching rates, and significant background fluorescence make subsequent quantification complicated. These limitations can be obviated by QDs, which have broad excitation and size-tunable photo luminescence spectra with narrow emission bandwidth, exceptional photochemical stability, and relatively high quantum yield. Further, the target signal can be amplified through enhanced energy-transfer efficiency by increasing the

Received: January 19, 2011
Revised: February 23, 2011
Published: April 01, 2011

ACS Publications © 2011 American Chemical Society

number of acceptors linked to a donor. These features should allow QD-FRET-based nanosensors to generate a very distinct target signal effectively. QDs offer several advantages when used as FRET donors in place of organic dyes.[8] Their size-tunable and narrow emission spectra can considerably reduce donor spectral leakage into the acceptor channel. At the same time, their broad absorption spectrum at wavelengths to the blue of their emission allows choice of excitation that corresponds to the acceptor absorption minimum, substantially reducing direct excitation. QDs are expected to significantly improve assay performances in a wide variety of sensing schemes.

Although the interactions between QDs and biological molecules are known, complete characterization of such bioconjugates to understand the full range of their modified properties for biosensing applications has not been explored properly. The correlation between photoabsorption and resonance energy transfer phenomena in CdTe protein complexes has not been explored completely. The present work is aimed at characterizing QD bioconjugates based on the photoabsorption and other optical properties for the development of novel FRET-based biosensing formats. Thus, coupling the superior optical properties of QDs with a separation-free and immobilization-free FRET-based format may revolutionize the generation of robust nanobiosensors in the future.

EXPERIMENTAL SECTION

Materials and Instruments. Cadmium acetate [$Cd(CH_3COO)_2$], MPA, propionic acid (PA), sodium borohydride ($NaBH_4$), tellurium, *N*-(3-dimethylaminopropyl)-*N*-ethylcarbodiimide hydrochloride (EDC), *N*-hydroxysuccinimide (NHS), BSA, streptavidin (SA), alkaline phosphatase (ALP), and horseradish peroxidase (HRP) were procured from Sigma Chemicals, St. Louis, USA. All reagents used were of analytical grade and acquired from standard suppliers. Dialysis membranes having 6−8 kDa molecular weight cutoff and 1 kDa molecular weight cutoff were procured from Spectra/Por, USA. The following instruments were used: UV−vis spectrophotometer (UV-1601, Shimadzu, Japan), spectrofluorimeter (RF-5301 PC, Shimadzu, Japan), transmission electron microscope (Jeol 2100, USA). Samples were analyzed using a 400-mesh carbon grid obtained from Pacific Grid Technology (101 California Street, San Francisco, CA 94111, USA).

Synthesis of CdTe Qds. CdTe QDs of different fluorescent emission spectra (CdTe 523, 557, 573, 601, and 640 nm) were synthesized as reported by Li et al. (2007) with modification.[9] In brief, 25 mL of aqueous solution containing 0.02 M Cd-$(CH_3COO)_2$ was mixed with 0.05 M of MPA, and the solution was degassed followed by adjusting the pH to 9.2. In a separate reaction, sodium hydrogen telluride (NaHTe) was synthesized by reacting 0.03 M of $NaBH_4$ and 0.01 M of Te in ice-cooled water and purged with argon gas for 30 min. The metal dissolved, leaving a faint pinkish-colored solution. A few drops of NaHTe were added dropwise to the above synthesized solution until the solution turned orange. The solution was refluxed for 120 min. Transmission electron microscopy (TEM) determined the size of thus-synthesized QDs. These QDs were bioconjugated to different biomolecules as explained below.

Bioconjugation of QDs. The following two-step protocol was used for the conjugation of QD to primary amine-containing biomolecules.[10] 0.05 M EDC and 5 mM NHS were mixed and the pH adjusted to 7.4, followed by incubating with QD solution in PBS at 32 °C for 15 min at 110 rpm. The protein solution in PBS was added to the reaction mixture and further incubated at 32 °C for 150 min at 110 rpm. The solution was then kept at 4 °C overnight to deactivate the remaining EDC-NHS. The conjugate solution was then dialyzed against PBS using Spectra/Por dialysis membranes of 6−8 kDa cutoffs with 4 changes of buffer.

A standard protein, BSA, was conjugated to four different QDs to observe the difference in their conjugation efficiency. 50 μL aliquots of QD_{523}, QD_{557}, QD_{573}, QD_{601}, and QD-GSH in PBS were conjugated separately with 1 mg of BSA in 1000 μL by the above-mentioned EDC/NHS conjugation protocol.

Further, conjugation was also performed between varying concentrations of BSA in the first set of experiments keeping the QD concentration constant. 50 μL aliquots of QD_{557} in PBS were conjugated separately with 50, 100, 250, 500, 1000, and 2000 μg of BSA in 1000 μL by the EDC/NHS protocol. In the second set, the conjugation was performed between varying concentrations of QD (5, 10, 20, 50, 100, and 150 μL of QD_{557} in 1000 μL PBS) keeping the BSA concentration constant (50 μg) by the EDC/NHS protocol. In the third set of experiments, QD_{557} was conjugated with other proteins to formalize the results obtained with BSA conjugates. 50 μL of QD_{557} in PBS was conjugated separately with 50, 100, 250, and 500 μg of SA, ALP, and HRP sequentially in 1000 μL of PBS by the EDC/NHS protocol.

Absorption Spectrometry. The conjugates were subjected to spectrophotometry to probe the changes in the spectral properties of the conjugates due to the interfacing of inorganic nanoparticles with biomolecules. The absorbance spectra of QD bioconjugates were acquired in two ways: by restricting the protein concentration to 50 μg/mL and by restricting the QD concentration to 5 μL/mL.

Fluorescence Spectrometry. The influence of bioconjugation on QD photoluminescence (PL) was studied through fluorimetry. Fluorescence spectra were taken for QD-BSA conjugates restricting the protein concentration at 5 μg/mL and restricting the QD concentration at 2 μL/mL. The emission spectra were generated at the excitation wavelengths of 280, 320, and 350 nm in separate experiments. The excitation at 280 nm leads to excitation of both protein and QD components, while the excitation of 320 and 350 nm excites only the QD component of the conjugate.

Time course fluorescence of standard BSA and BSA-QD_{557} conjugate samples were obtained by monitoring emission (λ_{em}) at 350 nm for BSA component and 557 nm for QD_{557} component with excitation at 280 nm. This method was used for the calculation of photobleaching time and FRET efficiency.

Native PAGE. Native-PAGE analyses of QD−protein conjugates was performed to confirm bioconjugation and to monitor the effects of CdTe QD on the mobility of proteins under electric field. The electrophoresis was run on 10% separating gel and 5% stacking gel by the protocol described by Laemmli. To observe the difference in mobility of the conjugates, the gel was stained with silver nitrate stain.

RESULTS AND DISCUSSION

Synthesis and Bioconjugation of CdTe QDs. Thiol-stabilized CdTe QDs were synthesized by aqueous method to attain biocompatibility, which was the primary criterion necessary for bioconjugation. In aqueous method, synthesis of colloidal nanoparticles generally depends on the molar concentrations of precursors and capping material at a particular temperature.

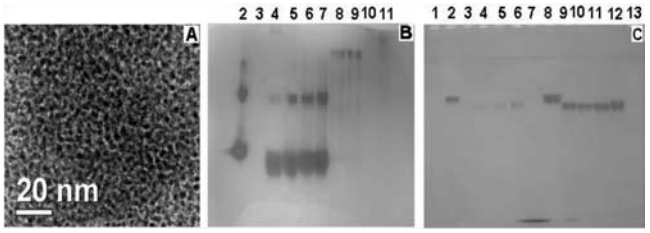


Figure 1. (A) Transmission electron micrograph of MPA capped CdTe QD (QD_{557}) taken on TEM Jeol 2100, USA, at 200 KV using 400 mesh carbon copper grid from pacific grid technology. (B) Native PAGE analysis of QD_{557} conjugates of BSA, ALP, and HRP. Standard BSA, ALP, and HRP were loaded on wells 2, 8, and 10, respectively. BSA-QD_{557} conjugates of conjugation ratios 3, 2, 1, and 0.5 were loaded in wells 4, 5, 6, and 7, respectively. ALP-QD_{557} and HRP-QD_{557} were loaded in wells 9 and 11. (C) Native PAGE analysis of QD_{557} conjugates of SA. Standard SA was loaded on well 2, while SA-QD_{557} conjugates of conjugation ratios 1, 0.5, 0.2, and 0.1 were loaded in wells 3, 4, 5, and 6, respectively, at 1 μg SA/well. A duplicate set was loaded onto wells 8 through 12 at higher protein loading of 5 μg SA/well. Standard QD_{557} was loaded on well 7.

Nanocrystal growth with the nucleation process is temperature dependent, wherein the precursors chemically transform into monomers to attain supersaturation and further atomic rearrangement.[11] CdTe QDs thus synthesized have shown convincing absorption and fluorescence properties (Figure 1S, Supporting Information). The presence of well-defined broad absorption spectra at shorter wavelength suggests the larger distances in the band gap of these particles. The shifts observed in the emission peak of thus-synthesized CdTe QDs were correlated to their size and in turn to the band gap energy of the particle. Thus, CdTe QDs having emission peaks at 523, 557, 576, and 601 nm with narrower full width at half-maximum (fwhm) in the range 45−70 nm and higher photoluminescence were synthesized at 100 °C in aqueous medium. Transmission electron microscopy (TEM) has determined the size of QD_{557} nanocrystal that is having a narrow size range of 3 ± 0.2 nm with good dispersion in aqueous medium without any aggregation (Figure 1A).

Since QDs are synthesized from organometallic precursors, they have no intrinsic aqueous solubility. The native coordinating organic ligands on the surface of QDs must either be exchanged or functionalized with a ligand that can impart both solubility and potential bioconjugation sites.[2] Ligands that form a capping layer on the surface of the QDs must be biocompatible as biomolecules, and most of biological reactions are highly hydrophilic in nature. Therefore, MPA was used to stabilize the QDs that impart biocompatibility and necessary functional carboxylic groups for bioconjugation in aqueous media. CdTe QDs having emission peaks at 523, 557, 576, and 601 nm were conjugated to BSA, and QD_{557} was further conjugated with ALP, HRP, and SA separately by two-step EDC/NHS protocol, as QD_{557} has shown very prominent absorption and higher photoluminescence compared to other QD particles. The protein-conjugated samples have shown strong fluorescence when exposed to UV light (366 nm) after 2 h of incubation at 32 °C followed by dialysis to remove unconjugated QDs inferring retention of conjugated QD_{557}, QD_{576}, and QD_{601}. However, conjugate samples with QD_{523} displayed no fluorescence under UV light.

Figure 1B,C represents native PAGE analysis of QD_{557} conjugated BSA, ALP, HRP, and SA. BSA-QD_{557} conjugates of varying conjugation ratio (3:1, 2:1, 1:1, and 0.5:1) were observed to have acquired greater mobility as compared to standard BSA. This can be ascribed to the increase in overall negative charge of the conjugates rendering them more mobility under electric field. Schroedter et al. (2002) has reported this property of nanoparticles to influence the charge density as a result of conjugation.[12] The increased molecular weight of conjugate was apparently overcome by the high negative charge and compactness of QD.[13] The observed drift in bands with an increase in conjugation ratio for BSA-QD_{557} conjugates has suggested a greater density of QD per protein molecule. ALP conjugate also showed an observable drift. However, HRP conjugate developed a diffuse band due to enhancement of overall negative charge. The SA conjugates of varying conjugation ratio also showed a pattern similar to that of BSA conjugates. The standard QD can be observed to have moved along with the electrophoretic front due to its high mobility caused by small size and a high negative charge.

Effect of Bioconjugation on Photoabsorption Properties. QD bioconjugates were subjected to photoabsorption studies to probe the changes in spectral behavior due to interactions of inorganic nanoparticles with biomolecules. Absorption spectra were taken for various protein conjugates of CdTe QDs. A remarkable change in the photoabsorption spectra was observed for all the protein bioconjugates of CdTe QDs. Protein bioconjugates of CdTe QDs such as QD_{523}, QD_{557}, QD_{576}, QD_{601} conjugated to BSA, and QD_{557} conjugated to different proteins such as ALP, HRP, and SA displayed a remarkable deviation from their individual components in terms of their absorption spectra (Figure 2A,B and Supporting Information Figure 2S).

A new peak was observed in the 320−330 nm range, which was absent in the spectra of both QD and protein standards. The peak was absent when QD_{557} and BSA were simply mixed in the same ratio, suggesting absorption at 320−330 nm could be due to covalent conjugation of QD_{557} and BSA but not some electrostatic interactions among them. However, there was an enhancement of absorption at 280 nm, characteristic of a protein molecule and a slight depression of absorption from 200 to 270 nm for BSA−QD_{557}, a region where QDs absorb strongly. Idowu et al. (2008) has reported the decrease of QD absorption due to conjugation with BSA.[14] Thus, the decrease in absorption of QD coupled to an increase in absorption of protein points toward coupling of the intrinsic energy states of two chromophores.

Absorption in the range 320−330 nm for QD−protein bioconjugates could be due to nonradiative dipole−dipole interaction among them. The intensity of absorption in the range 320−330 nm was found to correlate with percentage retention of QD from fluorescence data suggesting a link between absorption and the degree of conjugation. To probe this link, conjugations were performed varying the ratio between QD_{557} and in BSA concentration. It was observed that absorption in the range 320−330 nm was gradually decreased with increase in BSA concentration (50, 100, 250, 500, 1000, 1500, 2000 μg/mL) during bioconjugation (Figure 2C). A maximum absorption was observed for 50 μg/mL of BSA conjugated to QD_{557} (concentration of QD taken was 0.1 absorption unit at its excitation wavelength, 500 nm). Concomitantly, a gradual increase in absorption was observed when bioconjugation was done with increasing QD_{557} concentration at BSA concentration of 50 μg/mL (Figure 2D).

Absorption was found to decrease logarithmically with the increase in ratio between QD_{557} and different protein concentration, wherein absorption was correlated with percentage

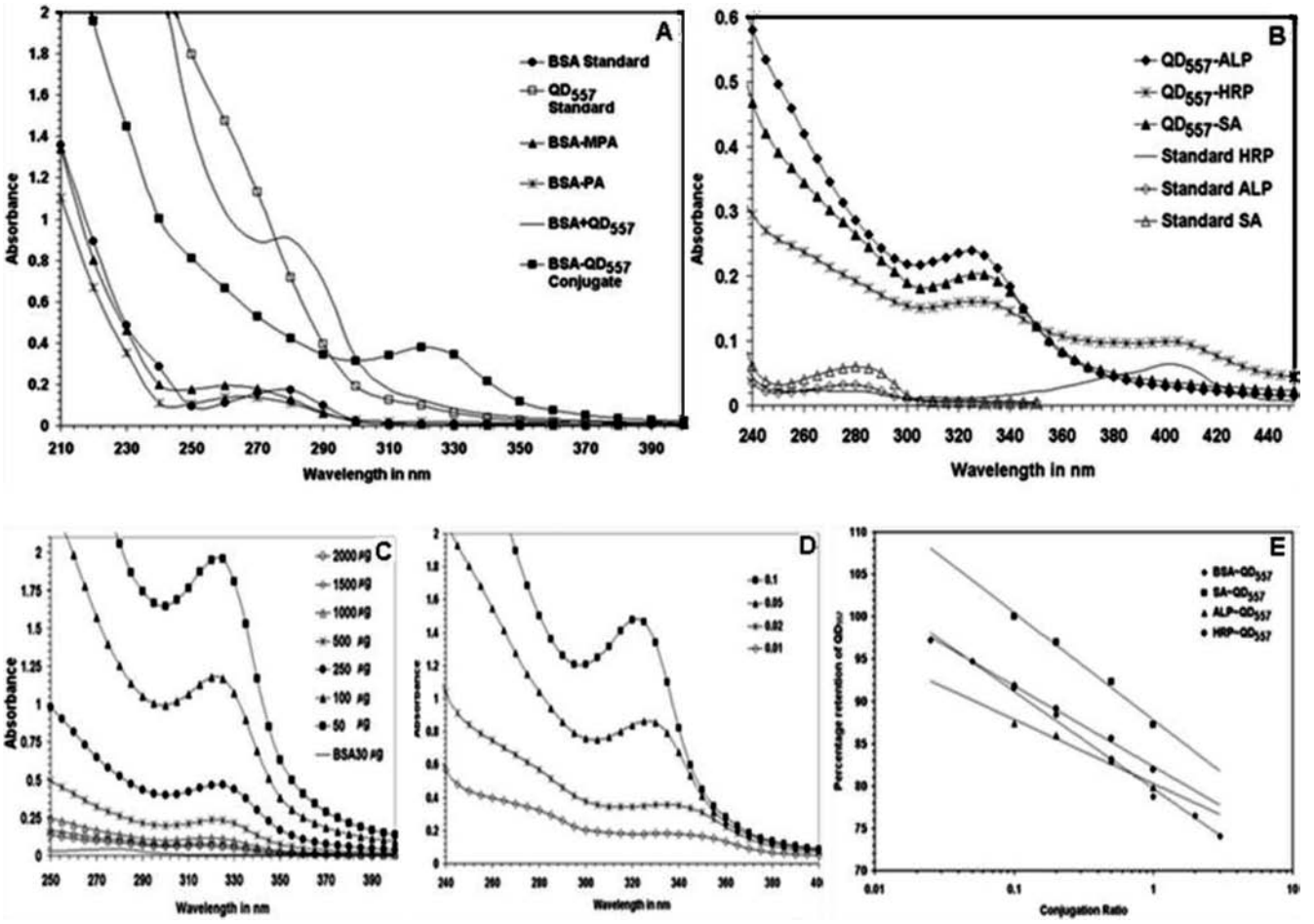


Figure 2. (A) Absorption spectra of BSA, CdTe QD_{557} standard, MPA, PA, BSA-QD_{557} conjugate, BSA-MPA conjugate, BSA-PA conjugate, and a mixture of BSA and QD_{557} in the amounts present in the conjugate sample. (B) Absorption spectra of QD_{557} conjugate with different proteins. (C) Variation of A_{330} for QD_{557} conjugates with different BSA concentration. (D) Variation of A_{330} with different QD_{557} concentration. (E) Variation of percentage retention of QD_{557} with the conjugation ratio in four different QD_{557}−protein bioconjugates from QD restricted absorbance spectrum. (QD_{557}:protein is 1:0.025, 0.05, 0.1, 0.2, 0.5, 1, 2, and 3).

retention of QD_{557} in the bioconjugates (Figure 2E). This suggests that absorption in the range 320−330 nm depends purely on the covalent attachment of protein to QD. Variation in slope can be attributed to the difference in percentage conjugation for different proteins. This further strengthens the above-mentioned hypothesis that absorption in the range 320−330 nm depends on covalent attachment of QD to protein alone. The occurrence of an absorption peak at 320−330 nm can thus be attributed to the effective coupling of the electronic orbitals of the conjugating entities. However, BSA-MPA and BSA-PA conjugates did not show any remarkable absorption in the range 320−330 nm that further confirms QD−biomolecular interactions (Figure 2A). Here, PA was used for conjugating BSA to ensure the absorption in the range 320−330 nm was not due to ligand binding which appeared in the presence of covalently conjugated CdTe QD. The deviation in optical behavior of protein-bioconjugated QD may be due to the formation of a possible protein shell on the surface of QD. Wang et al. (2006) have reported the use of denatured BSA to modify the surface of QDs to improve the chemical stability and photoluminescence. Further, Wang et al. (2006) have also reported a similar possibility when denatured BSA was used to modify the surface of CdTe QD.[15]

CdTe-QD Retention and Fluorescence Quenching in Bioconjugates. The fluorescence spectra were taken for QD-BSA conjugates (QD_{523}, QD_{557}, QD_{576}, and QD_{601}) restricting the protein concentration to 5 μg/mL for spectral analysis with excitation wavelength at 280, 320, and 350 nm separately. Fluorescence spectra gave a rough estimate of percentage retention of QD (Figure 3A). Additionally, blue shifts of 5 nm for QD_{557}, 8 nm for QD_{576}, and 13 nm for QD_{601} were observed in the fluorescence spectra of QD after conjugation with BSA inferring a net reduction in Stokes shift of the conjugate. In addition, varying levels of fluorescence quenching were observed for BSA in QD_{523}, QD_{557}, QD_{576}, and QD_{601} conjugates (Figure 3B).

Further, it was observed that the percentage retention of QD and the percentage quenching of BSA fluorescence were proportionate to each other (Table 1). BSA−QD_{557} conjugates have shown a red shift in the fluorescence peak of BSA with respect to conjugation ratio inferring solvent polarization effects on protein molecules due to the close proximity of QD (Figure 3S, Supporting Information). Generally, fluorescence spectra of proteins undergo a shift upon varying the polarity in the environment of aromatic amino acid residues as a result of binding of substrates, denaturation, and interactions with other

dx.doi.org/10.1021/bc200034a |*Bioconjugate Chem.* 2011, 22, 968–975

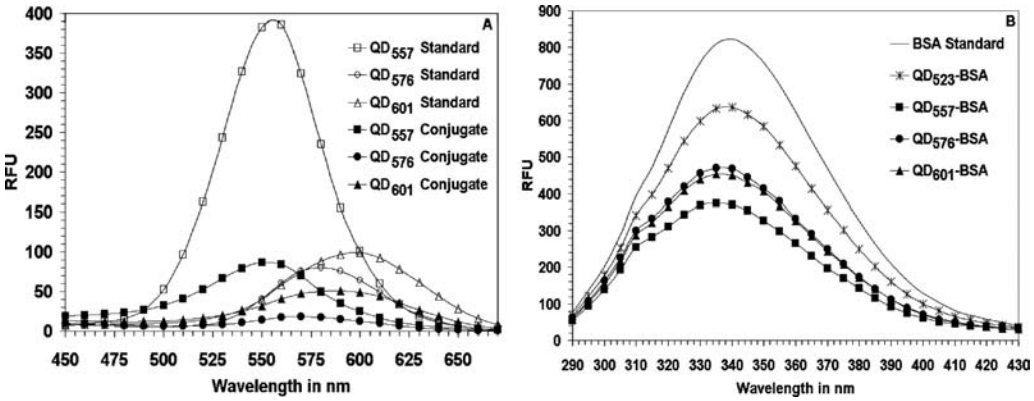


Figure 3. (A) Fluorescence spectra for standard QDs and their respective BSA conjugates. (B) Quenching of BSA fluorescence due to conjugation with various QDs.

Table 1. Percentage Retention and Percentage Quenching for BSA Conjugates with Different QDs

sample	percentage retention of QD (%)	percentage quenching of BSA fluorescence (%)
QD_{523}–BSA	56.89	25.7
QD_{557}–BSA	99.24	55.78
QD_{576}–BSA	73.67	42.1
QD_{601}–BSA	76.78	43.89

molecules.[16] A spectral blue shift of protein fluorescence may also occur due to the shielding of tryptophan residues from the hydrophilic environment.[16] Therefore, the red shift in protein fluorescence signifies the conformational changes induced by the interaction of QD and further exposure of tryptophan residues to the hydrophilic aqueous environment.[17] Generally, the tyrosine fluorescence (λ_{max} 303 nm) is not significantly influenced by the environmental conditions.[18] Furthermore, there was an enhancement of QD_{557} fluorescence at a higher ratio of QD_{557} to BSA in the range 400–650 nm as observed in Figure 4A. The degree of fluorescence enhancement was increased with an increase in the energy of excitation. While excitation at 350 nm caused an enhancement of 100%, excitation at 280 nm caused 200% enhancement.

The enhancement of QD fluorescence upon bioconjugation was ascribed to the passivation of the QD surface by proteins against solvent effects in the aqueous media. Different proteins displayed various enhancement profiles as evident from Figure 4B. Idowu et al. (2008) have reported enhancement of QD emission in the presence of BSA, which signifies inhibition of nonradiative recombination of the surface vacancies.[14] Thus, a decrease in fluorescence emission of BSA after bioconjugation with CdTe QD_{557} could be due to radiationless quenching and was found to be concentration-dependent. There was a linear decrease in BSA fluorescence with increasing concentration of CdTe QD after bioconjugation, suggesting an interaction between CdTe QD and BSA. Similar observations were made by Idowu et al. (2008), and it was reported that a progressive decrease in BSA fluorescence with increasing concentration of QD could be due to static and dynamic quenching together.[14] Fluorescence quenching as a result of the conjugation process may be due to energy transfer phenomena, excited-state reactions, or complex formation, which is referred to as static quenching.[19] The appearance of a new absorption peak in the range 320–330 nm further confirms such nanobiomolecular interactions and suggests CdTe QD-BSA complex formation, which could be due to the formation of a possible protein shell on the surface of QD. As CdTe QD was synthesized in aqueous environment, there is a possibility of having certain trap sites on the surface of QDs. During CdTe QD-BSA complex formation, the formation of a possible protein shell on the surface of QD may eliminate nonradiative transitions. Further, the protein shell may passivate the surface of QDs, thereby inhibiting the radiationless recombination at the surface vacancies (Figure 5).[19]

Photobleaching and Resonance Energy Transfer Phenomenon in CdTe QD Bioconjugates. Several studies have demonstrated the effective use of QDs as FRET donors. FRET is a distance-dependent dipole–dipole interaction phenomenon of nonradiative transfer of excited-state energy from an excited donor molecule to an acceptor molecule. Generally, FRET may lead to a decrease in the fluorescence of donor chromophores and subsequent increase in the fluorescence of an acceptor chromophores.[20] QDs have been used to detect small analytes by utilizing a common strategy that relies on conjugating QDs to target binding receptors.[7] The QD conjugates are then exposed to appropriate acceptor-labeled target analogues, which are brought in close proximity to the QD by binding to the receptors. In this initial state, the QD-donor PL is quenched by efficient FRET to the proximal acceptor-labeled analogues. The presence of the target then displaces bound analogues from the surrounding conjugated receptors that can be detected through a reduction in FRET efficiency and a concomitant increase in PL of QD. The main limiting factor for QDs as FRET donors lies in their size, as FRET efficiency depends on center-to-center separation between donor and acceptor chromophores. Three variables contribute to overall QD donor size: core shell radius, coating, and bioconjugation. Therefore, successful QD FRET designs most often include very thin solubilization layers and direct attachment of bioreceptors to the QD surface to overcome this limiting factor.[21] Covalent conjugations between protein moiety and nanoparticles may lead to dipolar resonance interactions resembling Forster resonance energy transfer phenomenon.[7,12,13] CdTe QD has a broad excitation spectrum by virtue of its nature, and thus, it may be possible for CdTe QD to influence the optical properties of proteins as a result of covalent conjugation. This tightly bound covalent attachment between protein and CdTe QD has resulted in spatial closeness of the

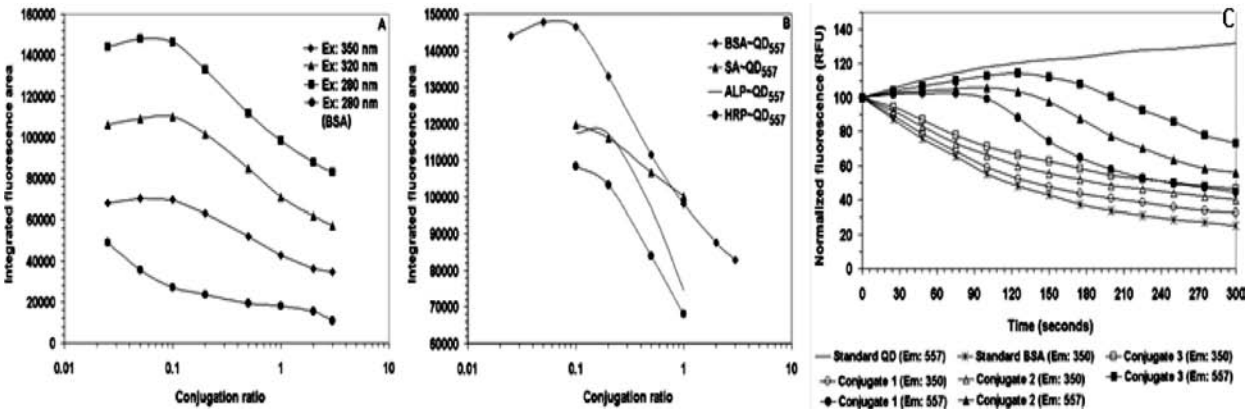


Figure 4. Variation in fluorescence emission spectra for protein−QD_{557} bioconjugates proportional to the conjugation ratio. (A) Variation of integrated fluorescence area for BSA−QD_{557} bioconjugates proportional to the conjugation ratios excited at three wavelengths: 280, 320, and 350 nm. The emission for QD component was collected from 450 to 650 nm, while that for the BSA component was collected in the 300−400 nm range. (B) Variation of integrated fluorescence area with conjugation ratio for QD_{557} conjugates of BSA, SA, ALP, and HRP excited 280 nm. Emission for the QD component was collected from 450 to 650 nm. (C) Variation of normalized fluorescence over time for standard QD_{557}, standard BSA, and BSA−QD_{557} conjugates of three different ratios (conjugate 1 is BSA−QD_{557} at 1:0.1, conjugate 2 is BSA−QD_{557} at 1:1, and conjugate 3 is BSA−QD_{557} at 1:3 ratio) from time course fluorescence spectra. The fluorescence of the BSA component was monitored at 350 nm, while that of the QD component was monitored at 530 nm.

molecules in the bioconjugate. Thus, covalent conjugation might have brought BSA and CdTe QD into such close proximity that has led to the appreciable spectral overlap between BSA and CdTe QD. This has resulted in the dipolar resonance interaction between BSA and CdTe QD as a donor−acceptor pair, respectively (Figure 5). This, in turn, might have allowed sufficient resonance energy transfer between BSA and CdTe QD in the BSA−QD_{557} complex. FRET efficiency for various BSA−QD_{557} conjugates were calculated by the following equation:[22,23]

$$E = 1 - F_{da}/F_{d} \quad (1)$$

where F_{da} is the integrated BSA fluorescence in the presence of QD_{557} and F_{d} is the integrated BSA fluorescence in the absence of QD_{557}.

FRET efficiencies can also be inferred from the photobleaching rates of the donor in the presence and absence of an acceptor.[24] Photobleaching is the irreversible photochemical destruction of a fluorophore and always occurs from its excited state.[22] Resonance energy transfer from an excited donor to an acceptor fluorophore prevents the photobleaching of that donor fluorophore, and thus, high FRET efficiency leads to a longer photobleaching decay time constant. The energy transfer efficiency for BSA−QD_{557} conjugate was determined by the following equation:[22]

$$E = 1 - \tau_{pb}/\tau'_{pb} \quad (2)$$

where τ'_{pb} and τ_{pb} are the photobleaching decay time constants of the donor in the presence and absence of the acceptor, respectively. The fact that time measurements are over seconds rather than nanoseconds makes measurement easier than fluorescence lifetime measurements, and because photobleaching decay rates do not generally depend on donor concentration, the careful control of concentrations needed for intensity measurements is not required. Time course fluorescence was obtained for standard QD_{557}, standard BSA, and BSA−QD_{557} conjugate samples excited at 280 nm. Fluorescence emission

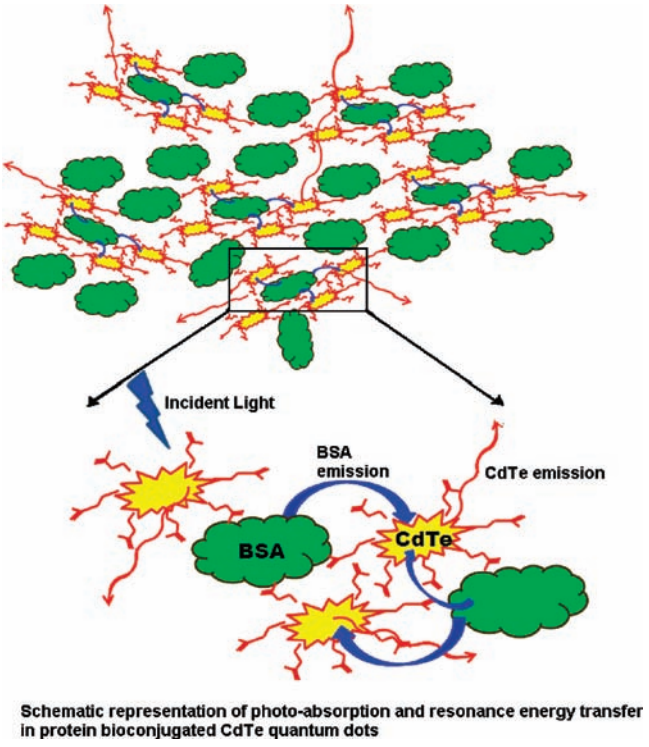


Figure 5. Schematic representation of possible QD-BSA complex formation and resonance photoenergy transfer phenomenon.

was monitored at 350 nm for the BSA component and 557 nm for the QD_{557} component (Figure 4C).

The energy transfer efficiency for BSA−QD_{557} conjugates was determined by making use of eq 1. Photobleaching lifetime was estimated for the BSA component by fitting the photobleaching curves to eq 2 (Table 2). Photobleaching-based calculation of FRET is based on the theory that the occurrence of resonance energy transfer reduces the fluorescence lifetime of the donor molecule, effectively protecting it against photobleaching.

Table 2. Photobleaching Time (τ_{pb}) and FRET Efficiency (E) Determined for BSA−QD_{557} Samples

sample	photobleaching time (s)	E (%)
BSA	68.5	-
BSA−QD_{557} (1:0.1)	82.6	17.11
BSA−QD_{557} (1:1)	92.6	26.02
BSA−QD_{557} (1:3)	106.4	35.61

Calculations of photobleaching FRET are based on the decreased rate of donor photobleaching relative to that measured for the donor in the absence of resonance energy transfer.

CONCLUSION

In summary, various optical and biological properties of CdTe-QD bioconjugates were characterized using absorption spectroscopy, fluorescence spectroscopy, and gel electrophoresis. Bioconjugation has significantly influenced the photoabsorption spectrum of QD−bioconjugates suggesting formation of a possible protein shell on the surface of QD. A proportionate quenching in BSA fluorescence with respect to conjugation ratio followed by an enhancement of QD fluorescence point toward possible nonradiative dipolar interactions between the two chromophores. Further, a reduction in photobleaching time for BSA as a result of bioconjugation with QD_{557} supports the possibility of dipolar interactions, which are attributed to the nanobiomolecular interactions between CdTe-QD and tyrosine/tryptophan moieties of protein molecule. Thus, the initial experimental results suggest these bioconjugates can be considered as nanoparticle (NP) superstructures for the development of new-generation robust nanoprobes.

ASSOCIATED CONTENT

Supporting Information. Absorption and emission spectra of QDs synthesized by aqueous method and spectrum showing quenching of BSA fluorescence for BSA−QD_{557} conjugates. This material is available free of charge via the Internet at http://pubs.acs.org.

AUTHOR INFORMATION

Corresponding Author

*M. S. Thakur, Ph.D. Senior scientist, Fermentation Technology & Bioengineering Department, Central Food Technological Research Institute, Mysore-570020, India. E-mail: msthakur@cftri.res.in, msthakur@yahoo.com.

ACKNOWLEDGMENT

The authors gratefully acknowledge the Director, CFTRI, and CSIR for providing necessary laboratory facilities. Mr. A. C. Vinayaka is thankful to CSIR for providing research fellowship. Dr. Sanjukta Patra, IIT, Gowhati is greatly acknowledged for kind help and support. Authors also thank Aeronautical Development Agency (ADA), Bangalore, for providing the required financial support for this project under National Programme on Micro and Smart Systems (NPMASS) scheme.

REFERENCES

(1) Bao, H., Gong, Y., Li, Z., and Gao, M. (2004)Enhancement effect of illumination on the photoluminescence of water soluble CdTe nanocrystals: Towards highly fluorescent CdTe/CDs core shell structure. *Chem. Mater. 16*, 3853–3859.

(2) Sapsford, K., Pons, T., Medintz, I. L., and Mattousi, H. (2006) Biosensing with luminescent semiconductor quantum dots. *Sensors 6*, 925–953.

(3) Vinayaka, A. C., Basheer, S., and Thakur, M. S. (2009)Bioconjugation of CdTe quantum dot for the detection of 2,4-D by competitive fluoroimmunoassay based biosensor. *Biosens. Bioelectron. 24*, 1615–1620.

(4) Chouhan, R. S., Vinayaka, A. C., and Thakur, M. S. (2010)Thiol-stabilized luminescent CdTe quantum dot as biological fluorescent probe for sensitive detection of methyl parathion by a fluoroimmunochromatographic technique. *Anal. Bioanal. Chem. 397*, 1467–1475.

(5) Chen, Q., Ma, Q., Wan, Y., Su, X., Lin, Z., and Jin, Q. (2005) Studies on fluorescence resonance energy transfer between dyes and water-soluble quantum dots. *Luminescence 20*, 251–255.

(6) Wang, J. H. (2007)Fluorescence resonance energy transfer between FITC and water-soluble CdSe/ZnS quantum dots. *Colloids Surf., A 30*, 168–173.

(7) Vinayaka, A. C., and Thakur, M. S. (2010)Focus on quantum dots as potential fluorescent probes for monitoring food toxicants and foodborne pathogens. *Anal. Bioanal. Chem. 397*, 1445–1455.

(8) Clapp, A. R., Medintz, I. L., Uyeda, H. T., Fisher, B. R., Goldman, E. R., Bawendi, M. G., and Mattoussi, H. (2005)Quantum dot-based multiplexed fluorescence resonance energy transfer. *J. Am. Chem. Soc. 127*, 18212–18221.

(9) Li, M., Ge, Y., Chen, Q., Xu, S., Wang, N., and Zhang, X. (2007) Hydrothermal synthesis of highly luminescent CdTe quantum dots by adjusting precursors' concentration and their conjunction with BSA as biological fluorescent probes. *Talanta 72*, 89–94.

(10) Hermanson, G. T., Mallia, A. K., Smith, P. K. (1992) *Immobilized Affinity Ligand Techniques*, pp 53−98, Academic Press, San Diego.

(11) Mahler, B., Spinicelli, P., Buil, S., Quelin, X., Hermier, J. P., and Dubertret, B. (2008) *Nat. Mater. 7*, 659–664.

(12) Schroedter, A., Weller, H., Eritija, R., Ford, W. E., and Wessels, J. M. (2002)Biofunctionalization of silica-coated CdTe and gold nanocrystals. *Nano Lett. 2*, 1363–1367.

(13) Mamedova, N. N., Kotov, N. A., Rogach, A. L., and Studer, J. (2001)Protein-CdTe nanoparticle conjugates: preparation, structure and interunit energy transfer. *Nano Lett. 1*, 281–286.

(14) Idowu, M., Lamprecht, E., and Nyokong, T. (2008)Interaction of water-soluble thiol capped CdTe quantum dots and bovine serum albumin. *J. Photochem. Photobiol. A: Chem. 198*, 7–12.

(15) Wang, Q., Kuo, Y., Wang, Y., Shin, G., Ruengruglikit, C., and Huang, Q. (2006)Luminescent properties of water-soluble denatured bovine serum albumin-coated CdTe quantum dots. *J. Phys. Chem. B 110*, 16860–16866.

(16) Güney, O., Saraç, A. S., and Mustafaev, M. (1997)Fluorescence and turbidimetry study of complexation of human serum albumin with polycations. *J. Bioact. Compat. Polym. 12*, 231–244.

(17) Tian, J., Liu, J., Hu, Z., and Chen, X. (2005)Binding of the scutellarin to albumin using tryptophan fluorescence quenching, CD and FT-IR spectra. *Am. J. Immunol. 1*, 21–23.

(18) Ruan, K., Li, J., Liang, R., Xu, C., Yu, Y., Lange, R., and Balny, C. (2002)A rare protein fluorescence behavior where the emission is dominated by tyrosine: case of the 33-kDa protein from spinach photosystem II. *Biochem. Biophys. Res. Commun. 293*, 593–597.

(19) Liu, P., Wang, Q., and Li, X. (2009)Studies on CdSe/L-cysteine quantum dots synthesized in aqueous solution for biological labeling. *J. Phys. Chem. C 113*, 7670–7676.

(20) Förster, T. (1948)Zwischenmolekulare energiewanderung und fluoreszenz. *Annalen. Physik. 6*, 55–75.

(21) Goldman, E. R., Anderson, G. P., Tran, P. T., Mattoussi, H., Charles, P. T., and Mauro, J. M. (2002)Conjugation of luminescent

quantum dots with antibodies using an engineered adaptor protein to provide new reagents for fluoroimmunoassays. *Anal. Chem. 74*, 841–847.

(22) Patel, R. C., Lange, D. C., and Patela, Y. C. (2002) Photobleaching fluorescence resonance energy transfer reveals ligand-induced oligomer formation of human somatostatin receptor subtypes. *Methods 27*, 340–348.

(23) Chong, E. Z., Matthews, D. R., Summers, H. D., Njoh, K. L., Errington, R. J., and Smith, P. J. (2007)Development of FRET-based assays in the far-red using CdTe quantum dots. *J. Biomed. Biotechnol. 2007*, 1–7.

(24) Wang, L., Chen, T., Qu, J., and Wei, X. (2010)Photobleaching-based quantitative analysis of fluorescence resonance energy transfer inside single living cell. *J. Fluoresc. 20*, 27–35.

Supporting information

Photo-absorption and Resonance Energy Transfer Phenomenon in CdTe-protein Bioconjugates: An Insight towards QD-biomolecular Interactions

Aaydha C. Vinayaka and Munna S. Thakur*

Fermentation Technology & Bioengineering Department

Central Food Technological Research Institute

(A constituent laboratory of Council of Scientific and Industrial Research, New Delhi),

Mysore-570020,

India

* Corresponding author

M.S. Thakur, Ph.D.

Senior scientist

Fermentation Technology & Bioengineering Department

Central Food Technological Research Institute, Mysore-570020, India

msthakur@cftri.res.in, msthakur@yahoo.com

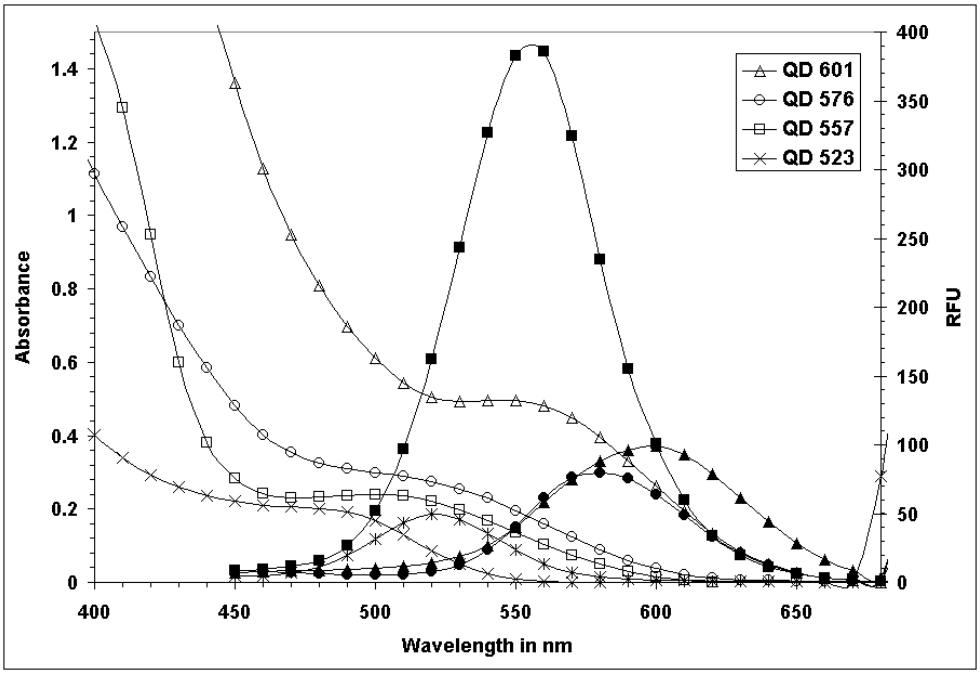


Figure 1S. Absorption and emission spectra of QDs synthesized by aqueous method.

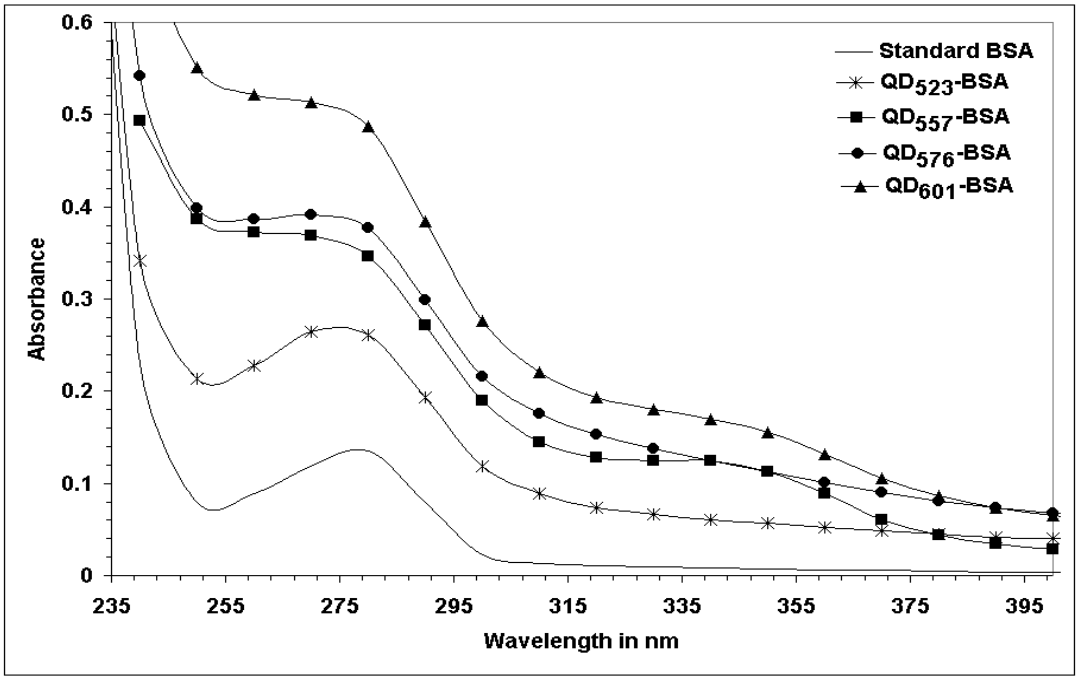


Figure 2S. The absorbance spectra of BSA conjugate with five different QD samples.

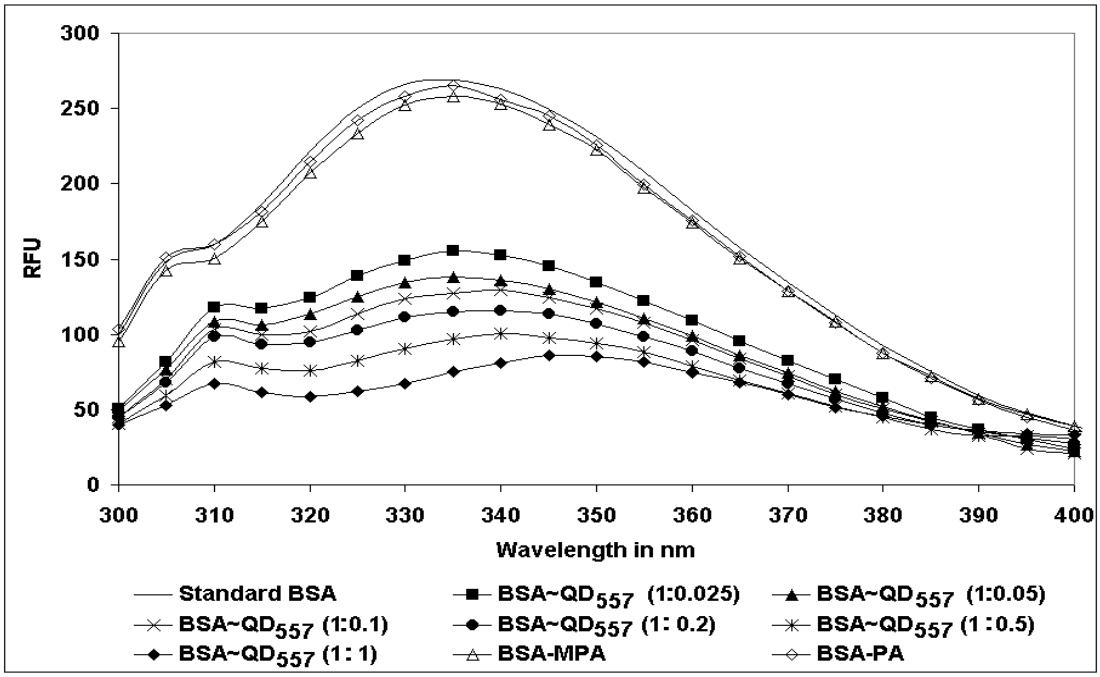


Figure 3S. Quenching of BSA fluorescence for BSA~QD_{557} conjugates.

Bioconjugate Chemistry

ARTICLE

pubs.acs.org/bc

Polyoxazoline: Chemistry, Properties, and Applications in Drug Delivery

Tacey X. Viegas,*[,†] Michael D. Bentley,[†] J. Milton Harris,[†] Zhihao Fang,[†] Kunsang Yoon,[†] Bekir Dizman,[†] Rebecca Weimer,[†] Anna Mero,[§] Gianfranco Pasut,[§] and Francesco M. Veronese[§]

[†]Serina Therapeutics, Inc., 601 Genome Way, Huntsville, Alabama 35806, United States

[§]Department of Pharmaceutical Sciences, University of Padua, Via F. Marzolo 5, 35131 Padua, Italy

ABSTRACT: Polyoxazoline polymers with methyl (PMOZ), ethyl (PEOZ), and propyl (PPOZ) side chains were prepared by the living cationic polymerization method and purified by ion-exchange chromatography. The following properties of polyoxazoline (POZ) were measured: apparent hydrodynamic radius by aqueous size-exclusion chromatography, relative lipophilicity by reverse-phase chromatography, and viscosity by cone−plate viscometry. The PEOZ polymers of different molecular weights were first functionalized and then conjugated to model biomolecules such as bovine serum albumin, catalase, ribonuclease, uricase, and insulin. The conjugates of catalase, uricase, and ribonuclease were tested for *in vitro* activity using substrate-specific reaction methods. The conjugates of insulin were tested for glucose lowering activity by injection to naïve Sprague−Dawley rats. The conjugates of BSA were injected into New Zealand white rabbits and serum samples were collected periodically and tested for antibodies to BSA. The safety of POZ was also determined by acute and chronic dosing to rats. The results showed that linear polymers of POZ with molecular weights of 1 to 40 kDa can easily be made with polydispersity values below 1.10. Chromatography results showed that PMOZ and PEOZ have a hydrodynamic volume slightly lower than PEG; PEOZ is more lipophilic than PMOZ and PEG; and PEOZ is significantly less viscous than PEG especially at the higher molecular weights. When PEOZ was attached to the enzymes catalase, ribonuclease, and uricase, the *in vitro* activity of the resultant bioconjugates depended on the extent of protein modification. POZ conjugates of insulin lowered blood glucose levels for a period of 8 h when compared to 2 h for insulin alone. PEOZ, like PEG, was also able to successfully attenuate the immunogenic properties of BSA. The POZ polymers (10 and 20 kDa) are safe when administered intravenously to rats, and the maximum tolerated dose (MTD) was greater than 2 g/kg. Blood counts, serum chemistry, organ weights, and the histopathology of key organs were normal. These results conclude that POZ has the desired drug delivery properties for a new biopolymer.

INTRODUCTION

Biocompatible polymers are used in drug delivery in a number of complex formats. They can be attached directly to pharmaceutical actives where they are part of the drug substance, conjugated to lipids where they become part of the liposomal delivery system, and linked with cationic molecules where they become part of a nucleic acid complexing polymer. Some examples of biostable and biodegradable polymers that have been tested in medicines are poly(ethylene glycol) (PEG), hyaluronic acid (HA), polysialic acid (PSA), hydroxyethyl starch (HES), polyglutamic acid (PGA), polylactic and polyglutaric acid (PLGA), *N*-(2-hydroxypropyl) methacrylamide (HPMA), polyvinylpyrrolidone (PVP), and polydextrans. From this list, PEG is the one polymer that has had wide success in delivering proteins, aptamers, and small molecule drugs. The conjugation of biopharmaceuticals to PEG by a process called "PEGylation" has led to the clinical and marketing success of a number of blockbuster macromolecule drugs for the treatment of hepatitis C, neutropenia, and anemia.[1] The polymer has the ability to negate several limitations of therapeutic proteins, such as rapid clearance, proteolysis, and immunogenicity. It provides a camouflaging shield around the protein and produces an apparent hydrodynamic size that reduces proteolysis and renal glomerular filtration. This shield also protects the drug from possible protein antigen−antibody-like reactions.

Although PEG has been clinically proven and more then ten conjugates are already on the market, this polymer is not completely devoid of technical and commercial challenges. Recent observations of specific antibodies against PEG were detected in the serum of patients treated with PEG-asparaginase[2] and PEG-uricase[3] that have resulted in a neutralizing effect with loss of therapeutic efficacy. These reports also suggest that pre-existing anti-PEG antibodies, of the IgM and IgG types, were identified in over 25% of patients, during screening, who never received prior treatment with PEG drugs.[4,5] This observation can be correlated to the large use of PEG in food, beauty, and body care products. Another controversy relates to possible kidney cell vacuolization observed in animals following repeated administration of PEG drug conjugates of hemoglobin,[6] TNF-α bp,[7] and leptin.[8] While marked vacuolation has been reported with the conjugates itself, these observations were not noted when PEG was administered alone. There are numerous patents on the

Received: January 24, 2011
Revised: March 7, 2011
Published: April 01, 2011

ACS Publications © 2011 American Chemical Society

dx.doi.org/10.1021/bc200049d | *Bioconjugate Chem.* 2011, 22, 976–986

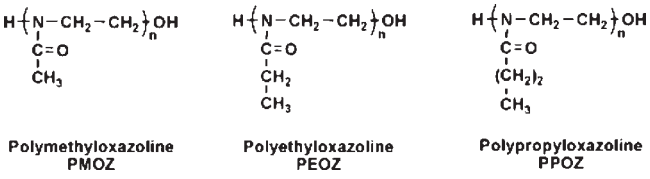


Figure 1. Chemical structures of three types of polyalkyloxazoline (POZ).

compositions and applications of PEG in drug delivery that hamper the ability to introduce new PEGylated therapies into the clinic. This hindrance in "freedom to operate" has forced drug companies to seek and test alternative polymers such as HPMA,[9] PSA,[10] and PVP.[11]

Another class of polymers called polyoxazolines (POZ) is described in this paper. These polymers can be made with high quality, of different architectures, and with different functional groups. They not only possess the key beneficial properties of PEG, but have characteristics that are novel and unique for different drug delivery applications. They are nonionic, stable, and highly soluble in water and organic solvent. The generic chemical structures of polymethyloxazoline (PMOZ), polyethyloxazoline (PEOZ), and polypropyloxazoline (PPOZ) are shown in Figure 1.

A review of the literature shows that the interest in POZ has existed for the past thirty years. It was first developed as a food additive in the early 1980s for which elaborate animal safety studies were completed and documented.[12] Studies reported by other scientists showed that POZ can be used in multiple pharmaceutical and medical applications.[13,14] It can be conjugated to protein and small molecule drugs,[15] grafted onto liposomal bilayers,[16,17] formulated into micelles,[18] and applied onto surfaces.[19] In all these applications, POZ has the same "stealth" properties as PEG without any adverse effects in animal models. Recent studies completed with radiolabeled POZ suggest that the polymer is rapidly excreted by the kidney with no significant accumulation in tissues.[20,21]

Polyoxazoline polymers are prepared by the living cationic polymerization method. A number of processes have been reported in the literature. One method discusses the stoichiometric addition of an electrophile initiator such as an alkyl tosylate or alky triflate to the oxazoline monomer that is dissolved in a dry organic solvent and in an inert atmosphere.[22−24] The propagation phase is conducted at 80 °C for approximately 1 to 3 days. In the second method, the polymerization is carried out with microwave energy to reduce the propagation time from days to hours.[25,26] In both cases, the living cation is terminated by the introduction of a nucleophile such as OH^-, NH^-, COO^-, or S^-. Termination is conducted with aqueous sodium carbonate to give a hydroxyl terminal group or by reacting with a secondary amine such as morpholine or piperidine to give a terminal tertiary amine. POZ can be monofunctionalized at one end of the chain during the initiation step[27] or at the termination step with the use of carboxylate ions.[28] POZ has also been synthesized with pendant functional aldehyde and amine groups and terminated with inert groups.[29,30] These chemistries allow for higher drug loading which is not possible with linear polymers like PEG.

The synthetic methods described in the above-mentioned references appear to be straightforward, but in reality, they do have a number of process difficulties in relation to scaling up and reproducibility. The various side reactions that occur have led to impurities that are difficult to remove, thereby creating products that are yellow in color and with polydispersity indices of >1.3. In addition, the termination with the weak nucleophile water does not always give the desired product of 5-position attack (the "thermodynamic" product), but rather gives an attack in the 2-position (the "kinetic" product). This kinetic product is not stable and can rearrange to give an ester product or undergo reversal to the cation.[31] These polymers have a high MW shoulder of approximately 5−10% and significant low MW tailing, when tested and detected by gel permeation chromatography.[32] It is generally stated in the literature that this broadening of the MW distribution is due to the chain transfer process through an elimination−dimerization mechanism, although structural details and experimental support for this process are scarce.[33] To the extent that chain transfer reactions do occur, such reactions then cannot be considered to be truly living polymerizations.

In this paper, the chemistry and properties of POZ are described and compared against PEG. In addition, the chemical and biological properties of POZ conjugates of some model proteins and peptides were determined and compared against similar PEG conjugates. Conjugates of ribonuclease (RNase), uricase, and catalase were prepared and their activity measured by *in vitro* assays. The activity of POZ insulin conjugates was determined *in vivo* by measuring the glucose lowering effect in normal rats. The ability of POZ to camouflage the immunogenicity of bovine serum albumin (BSA) was evaluated in a 72 day rabbit study. The acute toxicity of POZ was determined following single and repeated intravenous administration to rats.

MATERIALS AND METHODS

Materials. Bovine albumin, uricase, catalase, ribonuclease, cytidine 2′,3′-phosphate, uric acid, and hydrogen peroxide, *N*-hydroxysuccinimide (NHS), dicyclohexylcarbodiimide (DCC), 2,4,6-trinitrobenzene sulfonic acid (TNBS), trifluoroacetic acid (TFA), methyl trifluoromethylsulfonate (MeOTf), disuccinimidyl carbonate (DSC), *p*-nitrophenyl chlroformate (PNPC), potassium *t*-butoxide, and sodium hydride were purchased from Sigma-Aldrich, St. Louis, MO. The organic solvents acetonitrile, dichloromethane, dimethylacetamide, dichloromethane, dimethylformamide, chlorobenzene, chloroform, methanol, and diethyl ether were obtained from EMD Chemicals. The monomers of 2-methyl-2-oxazoline, 2-ethyl-2-oxazoline and 2-propyl-2-oxazoline were obtained from Sigma Chemicals and Acros Chemicals. Methyl 3-mercaptopropionate was obtained from Sigma Chemicals and Chevron-Philips, Belgium. Amberlite desalting resins IRA67 and IR120H were purchased from Dow Chemicals, Midland, MI, and ion-exchange media such as DEAE sepharose FF resin and SP Sepharose were purchased from GE Healthcare (Amersham Biosciences). Insulin and insulin glargine were obtained from Biocon Ltd., Bangalore, India. The bicinchoninic acid (BCA) assay kit is from Pierce. Poly(ethylene glycol) (PEGs) reagents of 5 and 10 kDa were purchased from LaysanBio, Huntsville, AL.

POZ Synthesis and Purification. The monomers and organic solvent were first dried by refluxing over calcium hydride and then distilled and collected in a dry flask containing molecular sieves. In a clean and dry flask and under an argon atmosphere, the organic solvent was first siphoned in. Different organic solvents were tested during the polymerization process. They were acetonitrile, chloroform, chlorobenzene, and dimethylacetamide. A measured amount of methyl or ethyl or propyl oxazoline M_0 was

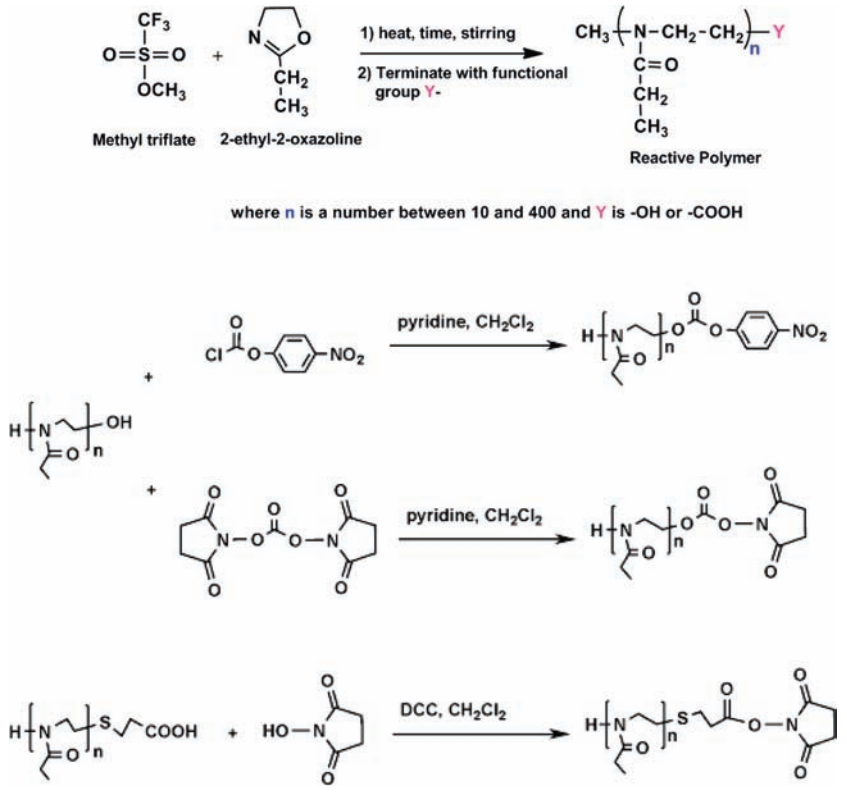


Figure 2. Synthetic schemes used to polymerize and functionalize POZ-OH and POZ-COOH.

next added, followed by an accurate measurement and transfer of the MeOTf initiator I_0. The molecular weight of the polymer being synthesized depends on the molar ratio of M_0/I_0. The contents in the flask were then heated at temperatures between 60 and 90 °C for extended periods of time, depending on the desired molecular weight of the polymer prepared and the boiling point of the solvent used. The flask was then cooled and the solution containing the living polymer was slowly transferred to a mixture of the terminating agent in dry organic solvent and mixed overnight with constant stirring. The terminating agent used depended on the end terminal group desired. When a hydroxy group was required, the terminating mixture was either a methanolic potassium hydroxide solution or a 5% sodium carbonate solution in water. When a carboxylic acid group was desired, the terminating mixture was methyl 3-mercaptopropionate and potassium *t*-butoxide. The solvent was then stripped from the polymer by rotary evaporation. The thiopropionate-terminated residue was dissolved in an aqueous solution containing 0.1 N sodium hydroxide and mixed for a couple of hours to hydrolyze the thiopropionate ester. Figure 2 outlines a general polymerization scheme.

The following example outlines the specific procedures used for the synthesis of a 5 kDa PEOZ polymer. Chlorobenzene (100 mL) and 2-ethyl-2-oxazoline (39.7 g, 400 mmol, 50 equiv) were mixed at room temperature under argon and in a 250 mL round-bottom flask. The initiator, methyl triflate (MeOTf, 880 μL, 8 mmol, 1 equiv), was carefully added into the flask with constant stirring. The mixture was then heated at 80 °C for 1.75 h and then rapidly cooled to room temperature by immersing the flask in an ice bath. When a 10 kDa PEOZ polymer was made, the amount of MeOTf used was less (440 μL, 4 mmol, 0.5 equiv) and the polymerization time was 3.5 h. When acetonitrile was used as the solvent, the polymerization was carried out at 80 °C for 28−30 h for the 5 kDa polymer and 40−42 h for the 10 kDa polymer. The termination of the polymerization was carried out as follows:

(a) When a hydroxy group terminus was required, 40 mL of a 5% sodium carbonate solution was added to the polymer solution (5 kDa or 10 kDa) and the mixture was stirred for 30 min. The aqueous layer was separated and the organic layer was extracted once more with an additional 40 mL of a 5% sodium carbonate solution. The aqueous layer was separated, combined and stirred overnight at room temperature. The cloudy mixture formed (~80 mL) was acidified with 40 mL of 0.5 M HCl acid in order to give a clear solution of pH < 6. The polymer was then extracted into methylene chloride (3 × 200 mL), and the combined organic layers were dried with anhydrous magnesium sulfate for one hour, concentrated to 25 mL, and precipitated by dropwise addition to 250 mL of diethyl ether. The resulting white solid was filtered and dried overnight in a vacuum oven.

(b) When a carboxylic acid group terminus was required, the polymer solution (5 kDa or 10 kDa) was transferred into a 500 mL round-bottom flask containing a mixture of chlorobenzene (100 mL), methyl 3-mercaptopropionate (1.3 g, 8 mmol, 2 equiv), and potassium *t*-butoxide (0.67 g, 6 mmol, 1.5 equiv), and stirred overnight at room temperature. The chlorobenzene in the mixture was evaporated out, and the residue of the thioester was hydrolyzed by dissolving in 100 mL of 0.1 M sodium hydroxide solution and stirring at room temperature for 4 h. The crude acid (POZ-COOH) was desalted in an Amberlite ion-exchange resin IRA67/IR120H bed and then purified by ion-exchange chromatography (IEC)

dx.doi.org/10.1021/bc200049d |*Bioconjugate Chem.* 2011, 22, 976–986

using a column packed with DEAE sepharose FF resin. The aqueous layer was extracted, precipitated, and dried as described above.

POZ Characterization. The purified POZ-OH and POZ-COOH of different molecular weights were analyzed by nuclear magnetic resonance (NMR), matrix-assisted laser desorption/ionization time-of-flight (MALDI-TOF), gel filtration chromatography (GFC), gel permeation chromatography (GPC), reverse-phase chromatography (RP), and viscometry. Proton NMR experiments were performed on a 500 MHz Varian NMR spectrometer. Samples (10−20 mg) were first dissolved in 0.75 mL of $CDCl_3$ or D_2O and then analyzed. Mass spectrometry measurements were performed on a Bruker Microflex MALDI time-of-flight instrument (Bruker-Daltonics, Billerica, MA, USA). A stock solution was prepared mixing equal volumes of 0.1% TFA in water and 0.1% TFA in acetonitrile. Separate solutions of the polymer, the matrix (α-cyano-4-hydroxycinnamic acid) and the salt (sodium iodide) solution were prepared in the stock solution. Equal and micromolar amounts of each solution were spotted on the target for mass and polydispersity measurements.

High-performance liquid chromatography (HPLC) was used for the both size exclusion methods. The GFC method was used to determine the relative hydrodynamic radius of each polymer type and size. A Bio-Sep-SEC-S-400 column (Phenomenex) was used and the mobile phase was 1 mM HEPES (pH 7.0) buffer. A GPC method was used to determine the size and polydispersity of each polymer. Two Phenogel columns (5 μ, 500A°, 300 × 7.8 mm, Phenomenex) were used in series and maintained at 60 °C, and the mobile phase was *N*,*N*-dimethylformamide (DMF). In the case of the lipophilicity method, a C-8 column was used and an isocratic mobile phase was used that comprised of a mixture of 70:30 methanol/water. In all these methods, an ultraviolet and refractive index detector were used in series.

The viscosity of PEOZ-OH of molecular weight 10−40 kDa was measured on a Brookfield LVDV-II cone and plate viscometer fitted with a temperature-controlled jacketed plate. The polymer sample (0.5 mL of a 10%, 20%, 30%, and 40% w/w solution in water) was placed on the center of the plate, which was attached to the main drive of the instrument. The cone (CPE-40) was rotated at different rates (rpm) and the viscosity (mPas) was recorded each time at 25 °C. The viscosities of similar concentrations of PEG-OH and branched $PEOZ_2$-OH were also measured for comparison.

Functionalizing POZ. POZ-OH and POZ-COOH were functionalized as follows. Figure 2 illustrates the different synthetic schemes for these reagents.

(a) Activation of POZ-OH with *p*-nitrophenylchloroformate: PEOZ-OH (5.3 kDa, 0.05 mmol, 1 equiv) was dissolved in toluene and dehydrated by azeotropic distillation to give a small amount of concentrated solution. It was cooled to room temperature before dichloromethane, *p*-nitrophenylchloroformate (pNPC, 0.95 mmol, 6 equiv), and pyridine were added. The mixture was stirred overnight at room temperature and then precipitated by dropwise addition to prechilled diethyl ether. The PEOZ-pNPC precipitate was collected and dried under vacuum to give a yield of 0.45 g or 95%. To determine the degree of pNPC substitution, an accurate amount of the reagent was dissolved in a known volume of 0.2 M NaOH solution. After 2 h at room temperature, the amount of *p*-nitrophenol released was measured by spectrophotometry at 410 nm ($\varepsilon = 1.7 \times 10^4\ M^{-1}\ cm^{-1}$). The degree of activation, evaluated on the basis of *p*-nitrophenol release, was 87%.

(b) Activation of POZ-OH with disuccinimidylcarbonate: PEOZ-OH (5.3 kDa, 0.05 mmol, 1 equiv) was dissolved in acetonitrile and dehydrated by azeotropic distillation to give a small amount of concentrated solution. After cooling to room temperature, disuccinimidyl carbonate (DSC, 0.2 mmol, 4 equiv) and pyridine were added and the mixture was stirred overnight. The solvent was removed using a rotary evaporator, and anhydrous dichloromethane was added to dissolve the residue. Any insoluble material was removed by filtration, and the filtrate was washed with a pH 4.5 sodium chloride saturated acetate buffer. The dichloromethane phase was separated, dried over anhydrous sodium sulfate, and then concentrated to a small volume before it was precipitated by slow addition to diethyl ether. The PEOZ-SC precipitate was collected and dried under vacuum to give a yield of 0.40 g or 80%. To determine the degree of SC substitution, an accurate amount of reagent was reacted with glycine−glycine (Gly-Gly) to evaluate the degree of amino group modification.[34] Briefly, a Gly-Gly solution of 0.285 mg/mL was prepared in borate buffer 0.2 M, pH 8. An equimolar amount of PEOZ-SC (10.8 mg) was added and the reaction mixture was stirred for 30 min. The assay was conducted by preparing two solutions: solution A: 950 μL of borate buffer (0.1 M, pH 9.3), 25 μL of the reaction mixture and 25 μL of 2,4,6-trinitrobenzene sulfonic acid solution (TNBS, 1% w/v in DMF); and solution B: 950 μL of borate buffer (0.1 M, pH 9.3), 25 μL of Gly-Gly, and 25 μL of TNBS solution. After 30 min, the absorbance of both solutions was measured by UV spectrophotometry at 420 nm, i.e., the amount of trinitrophenyl glycine−glycine complex formed from the coupling of unreacted Gly-glyamino group with TNBS was measured. The polymer activation was calculated by applying the following formula:

$$\text{polymer activation} = (\text{absorbance}_{\text{solution A}}/\text{absorbance}_{\text{solution B}}) \times 100$$

The percentage of activation of PEOZ-SC was 85%.

(c) Activation of POZ-COOH with *H*-hydroxysuccinimide: The purified PEOZ-COOH (5.3 kDa, 600 mg, 0.11 mmol) was dissolved in anhydrous dichloromethane, and *N*-hydroxysuccinimide (NHS, 104 mg, 0.9 mmol) and dicyclohexylcarbodiimide (DCC, 185 mg, 0.9 mmol) were added. The reaction mixture was allowed to react for 24 h, and the product (PEOZ-NHS) was precipitated in diethyl ether, collected, and dried. The degree of NHS activation was evaluated by the method described above and the percentage of activation was 90%.

(d) Hydrolysis and reactivity of PEOZ-NHS, PEOZ-p-NPC, and PEOZ-SC: In the hydrolysis experiments, the activated polymer was accurately weighed and dissolved in dioxane. 50 μL of this stock solution was withdrawn and added to 950 μL of borate buffer 0.1 M, pH 8.0, and at room temperature (5% of dioxane in the mixture). The rates of hydrolysis of the POZ reagents were evaluated by the release of *N*-hydroxysuccinimide and its absorbance measurement at 260 nm using a UV spectrophotometer

(Perkin-Elmer instruments, Northwolk, CT, USA). In the reactivity experiment, the stock solution was added to glycyl-glycine dissolved in borate buffer 0.1 M, pH 8.0, and at room temperature (ratio of polymer reagent/glycyl-glycine was 1:1). The rate at which the primary amine of glycyl-glycine reacted with the POZ reagents to release of *N*-hydroxysuccinimide, was measured at 260 nm. The spectrophotometer was programmed to take a reading every 5 s, in order to plot the rate of the reaction. From these plots, the half-lives of hydrolysis and reactivity were calculated and reported in minutes.

POZ and PEG Conjugation to Enzymes. Three different enzymes, RNase, uricase, and catalase, were reacted with PEOZ-NHS (5.3 kDa) and PEG-NHS (5.5 kDa) reagents. The RNase, uricase, and catalase concentrations in the test solutions were measured by UV spectrophotometry using molar extinction coefficients of 9.45×10^3, 13×10^3, and 1.67×10^5 M^{-1} cm^{-1} at 280 nm, respectively. RNase has a molecular weight of 13.7 kDa and 11 amino groups available for conjugation; uricase has a molecular weight of 130 kDa and 100 amino groups for conjugation; and catalase has a molecular weight of 240 kDa and 112 available amino groups for conjugation. The ratios of polymer to the number of amino groups on each enzyme were 2:1 and 1:1. The conjugation reactions were carried out for 30 min in a 0.2 M borate buffer (pH = 8.5). To remove the unreacted polymer, the free *N*-hydroxysuccinimide (NHS), and any remaining native protein, the crude polymer−enzyme mixtures were purified using a Sephadex G-75 column, eluting with phosphate buffer 0.1 M, pH 7.4, at the flow rate of 1.5 mL/min. The effluent from the column was monitored at 226 nm. The first eluting fractions containing only the conjugated proteins were collected, concentrated, and desalted by dialysis. The samples were then lyophilized to give a dry powder. The purity of the collected fractions was verified by the gel filtration column. The protein content in each sample was determined by bicinchoninic acid reaction (BCA assay) using a Pierce protein assay kit and the degree of protein modification was evaluated spectrophotometrically by the trinitrobenzensulfonic acid reaction method described by Habeeb.[34] The results are expressed as a percentage of modified amino groups relative to the total amount of amine groups present on the enzyme.

Enzymatic Assays. *RNase Assay.* The enzymatic activity of the native and conjugated RNase was evaluated as described by Crook et al.[35] Briefly, 100 μL aliquots of free and conjugated enzyme (0.2−0.4 mg/mL) were added to 1 mL of 1.5 mg/mL of cytidine 2′,3′-cyclic monophosphate dissolved in 0.1 M Tris/acetate buffer pH 7.0. The solution was immediately transferred in a 1 cm cuvette and the hydrolysis of the substrate was measured by UV for 20 min at 287 nm. The data were plotted with a first-order rate equation, and the rate of the reaction was calculated. This kinetic rate is directly proportional to the activity of the enzyme. The activity of the POZylated or PEGylated enzyme is reported as a percentage of the native enzyme.

Uricase Assay. The method described by Mahler[36] was followed for uricase. Briefly, 100 μL of free and conjugated enzyme (0.5−1 mg/mL) was added to 1 mL of 0.002 mg/mL of uric acid dissolved in 0.05 M borate buffer pH 9.0. The solution was immediately transferred into a 1 cm cuvette, and the hydrolysis of the substrate was measured by UV for 3 min at 292 nm. The residual activity of the conjugates was calculated as reported above.

Catalase Assay. The catalase activity was determined according to the method of Beers and Sizer.[37] Briefly, 100 μL aliquots of free and conjugated enzyme (0.05−1 mg/mL) were added to 0.05% (v/v) of hydrogen peroxide in 0.01 M phosphate buffer pH 7.0. The solution was immediately transferred into a 1 cm cuvette and the hydrolysis of the substrate was measured by UV for 2 min at 240 nm. The residual activity of the conjugates was calculated as reported above.

Conjugation of POZ-NHS to Insulin. A suspension of insulin (250 mg, MW 5807 Da) in 5.6 mL of boric acid (50 mM) was slowly acidified by the addition of 1 N HCl until a clear solution was obtained. The solution pH was then adjusted to 10.5 by the addition of 1 N NaOH solution. To this solution was slowly added 6.9 mL of a solution of PEOZ-NHS 10K in HCl solution (pH 2.5, 70 mg/mL, 4.1×10^{-5} mol). The solution pH was adjusted to 10.5 by adding 0.5 N NaOH solution. The clear solution was allowed to mix gently at room temperature for 5−7 min, before it was acidified to 2.4 by the addition of 1 N HCl acid. This reaction was monitored by reverse phase HPLC using a C-18 column. The chromatogram showed that there was 48.5% monoconjugated PEOZ-Insulin and 10.6% diconjugated PEOZ-Insulin and the rest native insulin. The monoconjugated PEOZ-Insulin was separated primarily as the lysine (B29) conjugated species using ion-exchange chromatography (IEC, Sepharose SP column) and the eluent was desalted by buffer exchange into deionized water.[38] The product was analyzed for purity by SDS-PAGE and reverse-phase chromatography and for mass by MALDI-TOF.

Conjugation of POZ-NHS to BSA. BSA (90 mg, 1.344 μmol, with 60 available amino groups) was dissolved in 0.1 M sodium borate buffer pH 8.5, and a 5× molar excess of activated polymer, PEOZ-NHS 5 kDa, PEG-NHS 5 kDa, PEOZ-NHS 10 kDa, or PEG-NHS 10 kDa, was added. Each was mixed for several seconds until a homogeneous solution was obtained, then allowed to sit at room temperature for 5 h. The reaction was terminated by the addition of a 5× molar excess of glycine. An ultrafiltration cell with a 30 kDa molecular weight cutoff membrane (Amicon XM-30) was used to remove unreacted polymer. Cationic exchange chromatography was next used to separate the conjugate from the protein and polymer. A SP-Sephadex C-25 column (3 × 18 cm) was equilibrated with 20 mM phosphate buffer pH 3.9 and eluted with a 0 to 0.5 M sodium chloride gradient at a flow rate of 1 mL/min. The fractions containing the conjugated protein were collected and concentrated and desalted by ultrafiltration. The samples were then lyophilized to give a dry powder. The protein content in each sample was determined by the BCA assay, and the degree of protein modification was evaluated by the trinitrobenzensulfonic acid reaction method.

Erythrocyte Compatibility Study. One milliliter of freshly collected heparinized mouse blood was centrifuged at 2000 rpm for 10 min, and the precipitated erythrocytes were washed three times with PBS buffer. The red blood cells (RBCs) were resuspended in the buffer and diluted to have an optical density between 0.6 and 0.7 at 650 nm. This stock solution dispersion was freshly prepared and used within 48 h after preparation. Erythrocyte suspension (300 μL) was added to 300 μL of phosphated buffered saline solutions (PBS buffer) containing either PEOZ or PEG (0.2−10 mg/mL) at different molecular weights (5, 10, and 20 kDa), and the samples were incubated at 37 °C for 60 min under constant shaking. After centrifugation at 2000 rpm for 10 min, the released hemoglobin was measured by optical density (OD) at 414 nm. Complete hemolysis, as a

positive control, was achieved by using a 1% v/v solution of Triton X-100 in water, a surfactant known to lyse RBCs. The RBC-PBS solution was used as the negative control. The percentage RBC lysis was calculated according the following formula:

$$\%\text{lysis} = [(A_{\text{polymers}} - A_{\text{blank}})/(A_{100\%\text{lysis}} - A_{\text{blank}})]100$$

where A_{polymer} is the absorbance value of the hemoglobin released from the RBCs treated with the polymer solution; A_{blank} is the absorbance value of the hemoglobin released from the RBCs treated with PBS buffer; and $A_{100\%\text{lysis}}$ is the absorbance value of the hemoglobin released from RBCs treated with 1% Triton X-100.

Efficacy of POZ-Insulin in Rat Model. The effect of POZ conjugated insulin on blood glucose lowering in naïve rats was the efficacy model used to study the activity of the conjugate. An in-house institutional animal care and use committee (IACUC) reviewed and approved the study protocol. Four groups of female Sprague−Dawley rats (8−9 weeks, 200 g) with four animals per group were subcutaneously dosed with normal saline (control), insulin, insulin glargine, or PEOZ 10K insulin. The insulin and insulin glargine samples were dissolved in acidified normal saline. The dose of each insulin formulation was 10 IU/kg. At time intervals of 0, 0.5, 1, 2, 4, 6, 8, and 24 h, blood drops of 5−10 μL volume were removed from the tail vein through a needle prick. Each drop was analyzed with the aid of a blood glucose meter (OneTouch) and measurements were recorded in mg/dL of glucose.

Immunogenicity of POZ-BSA in Rabbit Model. The 70 day standard rabbit protocol was used in this study. An IACUC at the contract research laboratory reviewed and approved the study protocol. New Zealand white rabbits were divided into 5 groups of 2 animals per group. The test formulation for each group contained BSA, PEOZ 5 kDa BSA, PEG 5 kDa BSA, PEOZ 10 kDa BSA, and PEG 10 kDa BSA dissolved in normal saline. On day 0, 10 mL of blood was bled from each animal and spun to collect a baseline serum sample. The animals then received their primary immunization dose of 500 μg of antigenic protein injected subcutaneously. At the same time, Freund's adjuvant was also injected subcutaneously through a different site on the skin. Booster doses of 250 μg antigen and Freund's adjuvant were administered on days 14, 28, and 42. At time points of 35, 58, and 72 days, a 5 mL sample of blood was collected from each animal for serum sample analysis.

Each serum sample was assayed by ELISA for antibodies to BSA. 96 well flat-bottom high binding polystyrene plates (Immulon 2HP, ThermoFisher) were coated with BSA dissolved in borate buffer and allowed to incubate overnight in a refrigerator. The next day, the excess buffer was discarded and each well was washed. A measured amount of rabbit serum was added to the first well, mixed, and then appropriately diluted to the adjacent well by a factor of 2 each time. The plate was then incubated overnight in a refrigerator. The secondary antibody, HRP-SA 2° (goat antirabbit) dissolved in blocking buffer, was added to each well and the plate allowed to stand at room temperature for 3 h. The developer solution consisted of 2,2′-azino-bis(3-ethylbenzthiazoline-6-sulfonic acid) in citrate buffer with 30% hydrogen peroxide. A measured volume of the developer solution was added to each well, and after 20 min, the color produced was measured at 405 nm in a plate reader.

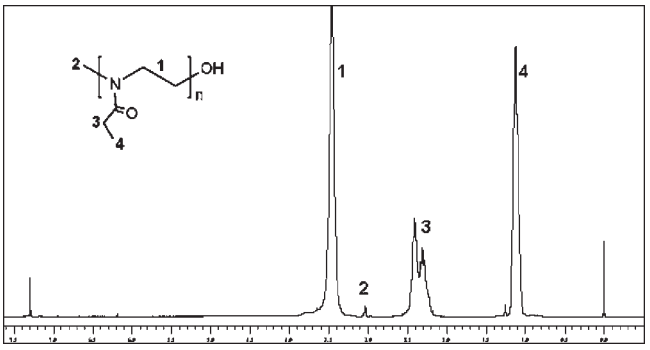


Figure 3. ^{1}H NMR spectrum of PEOZ ($CDCl_3$ as solvent).

Toxicity Studies. Two acute dose studies were performed in female Sprague−Dawley rats (8−9 weeks, ~200 g) to determine the maximum tolerated dose (MTD) of a PEOZ−OH 10 kDa polymer. The animals (3 per dose group) were intravenously administered the test article dissolved in 0.9% sodium chloride injection. A control group was administered 0.9% sodium chloride injection.

In the single acute dose tolerance study, the doses were 0.5, 1, and 2 g/kg. Blood was collected 1 and 7 days postdose for serum and complete blood count (CBC) analysis. Animals sacrificed on day 7 for gross examination of organs. In the repeat dose study, the animals received 4 weekly doses of 0.5, 1, and 2 g/kg. Blood was collected 1 and 7 days after the last day of dosing for serum and CBC analysis. Animals were sacrificed for gross examination of organs.

One multiple dose study was performed in female Sprague−Dawley rats (8−9 weeks, ~200 g) to determine the maximum tolerated dose (MTD) of a PEOZ-COOH 20 kDa polymer. Eight animals were dosed intravenously (tail vein) at a dose of 50 mg/kg on days 0, 2, 4, 7, 9, 11, and 14. The dose volume was between 0.3 and 0.5 mL. Blood was collected on days 15 and 21 for serum chemistry analysis and comprehensive CBC. Half the number of animals was sacrificed on day 15 and the rest on day 21. The kidneys (left and right), liver, and spleen were harvested from each animal and stored in 10% neutral buffered formalin. Each organ was imbedded in wax, sectioned, fixed on slides, and examined under a light microscope.

■ RESULTS AND DISCUSSION

Polymer Properties. Different solvents were tested as suitable polymerization media in the preparation of PEOZ, PMOZ, and PPOZ. Acetonitrile and chloroform were the desired solvents for PMOZ, PEOZ, and PPOZ, while chlorobenzene and dimethylacetamide worked well with PEOZ and PPOZ only. The polymerization times ranged from 1 to 40 h and this was dependent on the molecular weight being synthesized, the solvent selection, and the temperature of the reaction. Each batch of POZ-OH and POZ-COOH was characterized by ^{1}H NMR spectroscopy, MALDI-TOF mass spectrometry, and size exclusion chromatography (SEC). The ^{1}H NMR data of a typical PEOZ sample showed the pendent peaks at 1.12 ppm ($\boldsymbol{CH_3}CH_2CO-$); 2.41 ppm ($CH_3\boldsymbol{CH_2}CO-$), and the backbone peak of 3.47 ppm (-N$\boldsymbol{CH_2CH_2}$N-) as shown in Figure 3. When methyltriflate was used as the initiator, the initiating methyl peak appeared as two singlets at 2.9 ppm (small) and 3.05 ppm (large) ($\boldsymbol{CH_3}$-NCH_2CH_2-). When the polymer was terminated with a

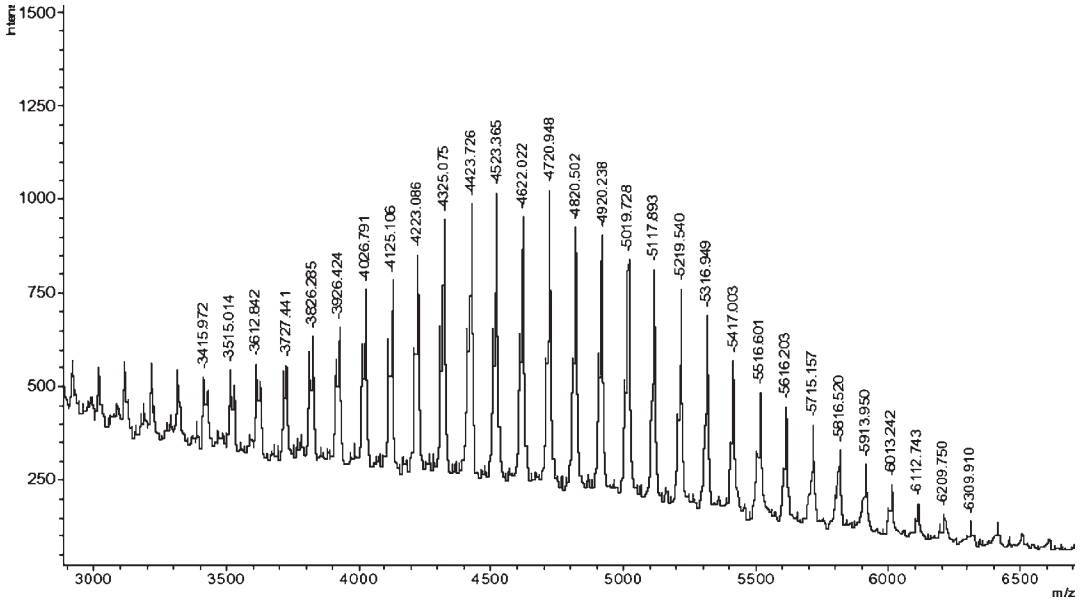


Figure 4. Example of a MALDI-TOF spectrum of PEOZ detected in reflection mode with a mass cutoff at 1000 m/z. M_{eox} = 99.1 g/mol.

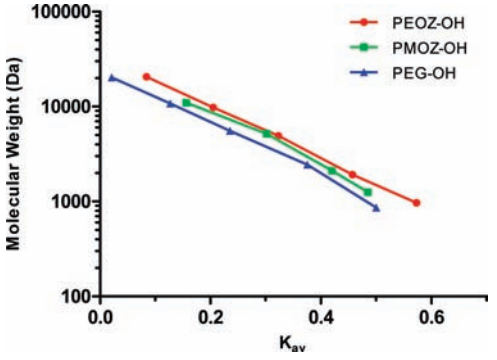


Figure 5. Correlation of hydrodynamic volume and molecular weight of PEG, PEOZ, and PMOZ determined by aqueous size-exclusion chromatography. The hydrodynamic volume is directly related to the distribution coefficient (K_{av}).

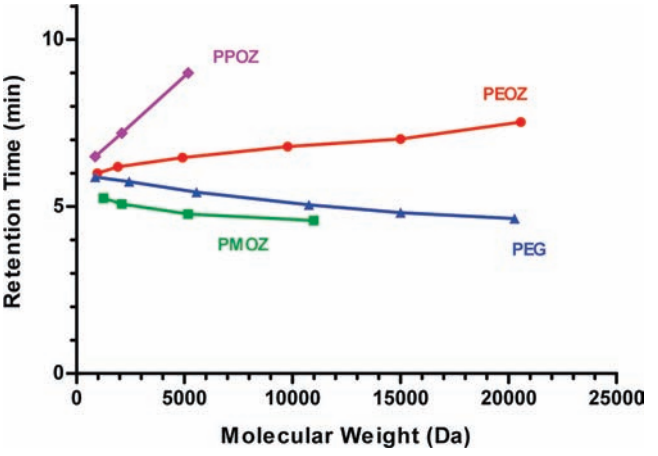


Figure 6. Correlation of the hydrophilicity−lipophilicty balance of PEG, PMOZ, PEOZ, and PPOZ as determined by reverse phase chromatography.

hydroxyl group, the terminal methylene group appeared at 3.8 ppm (-$\boldsymbol{CH_2}$-OH).

MALDI-TOF mass spectrometry was also performed to evaluate the polymer distribution. The polymers showed a monomodal polymer distribution with main mass signals spaced by $\Delta m/z$ = 99 in agreement with the monomer unit mass of ethyloxazoline = 99.13 g/mol. Figure 4 is an example of a 5 kDa PEOZ-OH polymer.

GPC chromatographic analyses were used to confirm that purified POZ reagents had a defined molecular weight (MW) with polydispersity indices 1.02−1.10. Their retention times were comparable to PEG reagents of similar molecular weights. However, GFC analyses showed that PEG has a hydrodynamic volume slightly larger than that of PMOZ and PEOZ. Figure 5 compares the molecular weight (log scale) against the distribution coefficient (K_{av}) for each polymer type and size. The value of K_{av} is calculated from the solute elution volume, the void volume, and the volume of the SEC media in the columns used.[39] The data also suggest that POZ is less hydrated than PEG, a property that can be verified by microcalorimetry. This observation suggests that POZ is less of a desiccant than PEG.

RP-HPLC chromatography of PMOZ, PEOZ and PPOZ showed differences in retention times relative to polymer type and size. Figure 6 shows that, as the molecular weights of PMOZ and PEG increase, their retention times decrease thereby suggesting increased hydrophilic behavior. On the other hand, the retention time of PEOZ and PPOZ increase with increasing molecular weights. This suggests that PEOZ is relatively more lipophilic than PMOZ and PEG. It is important to note that PMOZ and PEOZ are highly water-soluble, while PPOZ is sparingly water-soluble.

The viscosity of aqueous PEG and PEOZ solutions is illustrated in Figure 7. The plot compares the viscosity of a 40% w/v solution of PEG and PEOZ at molecular weights of 10, 20, 30, and 40 kDa. The results show that linear and branched PEOZ have a significantly lower viscosity than PEG especially at the higher molecular weights of 20, 30, and 40 kDa. This property is important, as it allows for ease of formulation, filterability, and syringeability of POZ conjugates at higher concentrations.

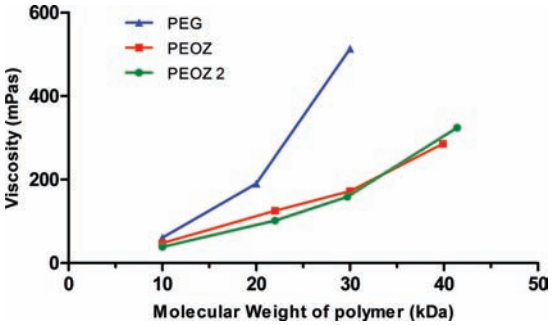


Figure 7. Viscosity of PEG and PEOZ of different molecular weights at 40% w/v solution and at 25 °C.

Table 1. Hydrolysis and Reactivity Rates of PEOZ and PEG Reagents

	half- life, $t_{1/2}$, at pH 8.0 (min)	
polymer	hydrolysis	reactivity with glycyl-glycine
PEOZ-SC (5 kDa)	5.40	3.28
PEG-SC (5 kDa)	5.90	3.02
PEOZ-p-NPC (5 kDa)	31.02	19.10
PEG-p-NPC (5 kDa)	40.03	25.14
PEOZ-NHS (10 kDa)	15.47	7.54
PEOZ-NHS (5 kDa)	14.08	5.75
PEG-NHS (5 kDa)	20.08	6.02

Functional POZ. In order to investigate the different strategies employed in POZ conjugation to proteins or peptides, several functional POZ reagents had to be made and characterized. The procedures previously described for other polymer activation were found to be suitable for the synthesis of electrophilic reagents such as PEOZ-NHS, PEOZ-p-NPC, and PEOZ-SC. Kinetic investigation of these POZ reagents showed that they had comparable reactivity towards amino groups on proteins and peptides, but slightly weaker stability in alkaline water, when compared to similar PEG reagents. The half-lives ($t_{1/2}$) for the hydrolysis of PEOZ-NHS, PEOZ-p-NPC, and PEOZ-SC in pH 8 borate buffer are 14.08, 31.02, and 5.4 min as shown in Table 1. The $t_{1/2}$ hydrolysis values were about 75% the value of their PEG counterparts. The $t_{1/2}$ reactivity values of PEOZ and PEG SC and NHS reagents were similar, but the PEOZ-p-NPC reagent was about 75% that of the corresponding PEG reagent. A comparison of $t_{1/2}$ values of each reagent showed that the reactivity rates with glycyl-glycine were twice as fast as their corresponding hydrolysis values. Even though one cannot rule out the effect of alkaline pH conditions on the premature release of *N*-hydroxysuccinimide, one must note that the fast amine-directed reactivity rate would be an important property when describing the functionality of these POZ reagents.

Enzyme Conjugation. To study the conjugation of PEG and POZ to enzymes, we selected three different candidates, namely, RNase, catalase, and uricase. They were chosen because their natural molecular conformation, i.e., a monomeric form for RNase, the dimeric form for catalase, and the tetrameric form for uricase. The molar ratios of polymer to available amino groups on each enzyme were 1:1 and 2:1. Each conjugation mixture was analyzed by gel filtration HPLC and then purified to remove free polymer or proteins. As an example, Figure 8 shows

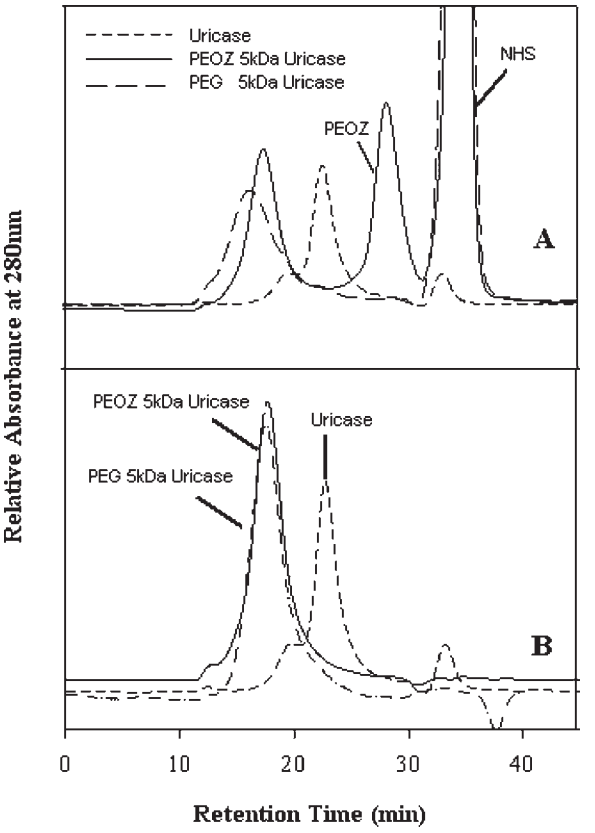


Figure 8. Panel A: HPLC-GFC profiles of uricase, PEOZ 5 kDa uricase, and PEG 5 kDa uricase in reaction mixtures after 30 min of mixing. Panel B: HPLC-GFC profiles of native uricase, PEOZ 5 kDa uricase, and PEG 5 kDa uricase after purification with Sephadex G-75.

the chromatographic elution of uricase conjugates before (panel A) and after purification (panel B). Uricase almost completely reacts with the functional polymers, and after purification, the excess of PEOZ and free *N*-hydroxysuccinimide (NHS) was removed. The degree of conjugation was determined by the Habeeb method,[34] and each enzyme had its own biological activity tested as mentioned in the Methods and Materials section. The results showed that the degree of modification and the *in vitro* bioactivity for each enzyme conjugate were similar for PEOZ and PEG of 5 kDa and 10 kDa molecular weights (Table 2). As expected, when the degree of enzyme modification was lower (as in the case of the 1:1 conjugates), the enzyme activity was higher.

Insulin Conjugation. The pure lyophilized PEOZ 10 kDa insulin product was analyzed by reverse phase chromatography and shown to have a purity of >97%. SDS-PAGE was used to verify a single monoconjugated species, and the mass was measured by MALDI-TOF as 16 496 Da. The IEC method was able to identify the desired B29 conjugated isomer from the A1 and B1 conjugated isomers.

BSA Conjugation. BSA was chosen as the model antigenic protein because of its known immunogenicity in different animal models. The method of conjugation employed uses a large excess of PEOZ-NHS or PEG-NHS at molecular weights of 5 and 10 kDa.[40] The titration of the free amino groups in the conjugated samples showed that both POZ and PEG provided similar degrees of modification. They were about 60% for the 5 kDa polymers and about 74% for the 10 kDa polymers

Table 2. Characteristics of Polymer−Enzyme Conjugates

compounds	polymer:NH_2 molar ratio	% of modified amino groups	% activity
RNase			100
PEOZ 5 kDa RNase	1:1	50	30
PEOZ 5 kDa RNase	2:1	70	25
PEG 5 kDa RNase	1:1	48	35
PEG 5 kDa RNase	2:1	72	27
uricase			100
PEOZ 5 kDa uricase	1:1	38	70
PEOZ 5 kDa uricase	2:1	50	45
PEG 5 kDa uricase	1:1	35	72
PEG 5 kDa uricase	2:1	53	48
catalase			100
PEOZ 5 kDa catalase	1:1	35	90
PEOZ 5 kDa catalase	2:1	37	88
PEG 5 kDa catalase	1:1	38	85
PEG 5 kDa catalase	2:1	40	79

Table 3. Characteristics of Polymer Conjugates for the Immunogenic Studies

compounds	protein content[a] (wt)%	% of modified amino groups	M_w[b] (kDa)
BSA			66
PEOZ 5 kDa BSA	0.18	60	151.8
PEG 5 kDa BSA	0.11	66	145.2
PEOZ 10 kDa BSA	0.034	74	158.4
PEG 10 kDa BSA	0.016	72	168.3

[a] Protein content evaluated in 1 mg of conjugates. [b] Estimated by SEC using protein standards.

(Table 3). Each PEOZ conjugate was analyzed by GPC for apparent molecular weights and for traces of free polymer or BSA. After purification, the amounts of free BSA and unreacted PEOZ were below quantifiable limits.

Erythrocyte Compatibility Study. The effect of POZ on the integrity of the erythrocyte membrane was investigated by the hemolysis study. The percent of cell lysis, as observed by absorbance measurements at 414 nm, showed that the $A_{polymers}$ value for POZ was negligible even at the polymer concentration of 10 mg/mL. The A_{blank} value, which corresponded to the solution of RBCs incubated with PBS, was slightly higher than that of the $A_{polymers}$ solution. This observation is consistent with reports on other polymers like PEG, where it is suggested that nonionic polymers might have a protective effect on cell membranes. It is important to note that the plasma was washed out in this study. This would make the RBCs more sensitive to cell-to-cell contact, external stress, and lytic agents. Therefore, POZ acts like a protective agent in the same way that plasma proteins behave in providing hemocompatibility against external stress and foreign bodies.[41]

Efficacy of POZ-Insulin in Rat Model. The blood glucose lowering in naïve rats is the quickest and most efficient way to determine the activity of polymer conjugated insulin. It provides two parameters, the initial onset of action in lowering of blood glucose levels (an indirect t_{max} parameter) and the sustainability of blood glucose lowering (a steady-state pharmacodynamic parameter). Figure 9 illustrates the glucose lowering effect of insulin, insulin-glargine, and PEOZ 10 kDa insulin after subcutaneous administration in naïve female Sprague−Dawley rats. The results showed that the test compounds were active and were able to lower the blood glucose levels from 120 to about 40 mg/dL. This effect was achieved within 1 h, 2 h, and 4 h for insulin, insulin-glargine, and PEOZ 10 kDa insulin, respectively. The effect was reversed after 2 and 4 h for insulin and insulin-glargine, respectively. However, the blood glucose lowering effect was sustained for about 8 h in the case of PEOZ 10 kDa insulin. This suggests that PEOZ was able to protect insulin from rapid clearance and proteolysis.

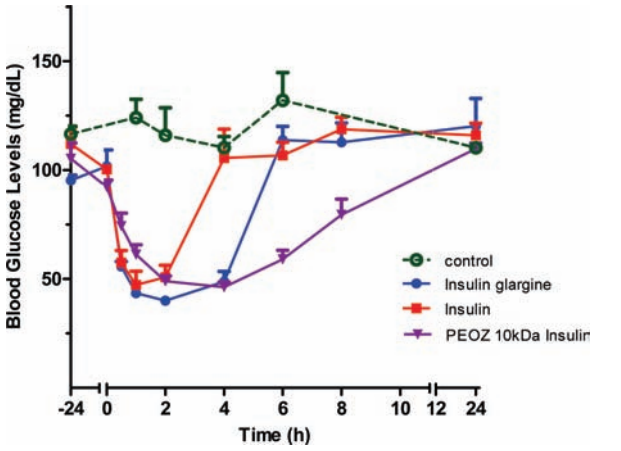


Figure 9. Effect of subcutaneous injection of insulin, insulin glargine, and PEOZ 10 kDa insulin on the blood glucose levels in male Sprague−Dawley rats (dose = 10 U/kg; n = 4; mean ± SEM).

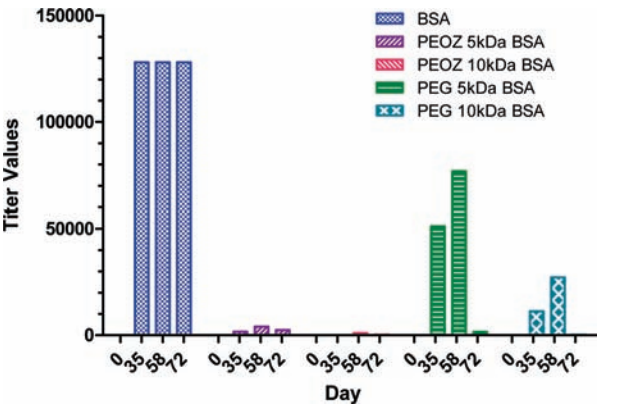


Figure 10. Relative immunogenicity of BSA, PEG BSA, and PEOZ BSA in rabbits treated as measured by anti-BSA antibody levels. Animals with treated with immune booster on days 1, 14, 28, and 42.

Immunogenicity Studies of BSA Conjugates. The ability of POZ to camouflage the immunogenicity of BSA was determined in a 72 day rabbit protocol study. The animals were dosed on days 1, 14, 28, and 42 and the serum samples collected on days 0, 35, 58, and 72. Figure 10 shows that antibody titer values for BSA were extremely high and the maximum limit of the ELISA assay. PEOZ BSA and PEG BSA dosed animals had significantly lower titer values and the 10 kDa conjugate was better than the 5 kDa conjugates because of the higher degree of amine modification and the larger hydrodynamic volume of the conjugate (Table 3). POZ had a slightly higher attenuation of BSA immunogenicity than PEG at each molecular weight tested.

dx.doi.org/10.1021/bc200049d |*Bioconjugate Chem.* 2011, 22, 976–986

Table 4. Differences in Properties between PEG and POZ

PEG	POZ
Difficult polymerization process and there are limited suppliers of quality raw PEG	POZ easily synthesized with standard glassware and with nonexplosive materials
Forms peroxides (need to add antioxidant)	Does not form peroxides
Stable only at temperatures < −20 °C	Stable at room temperature and in water
Diol content of 2−6%	No Diol
Highly viscous when in aqueous solutions	Low viscosity
Low drug loading	High drug loading
Difficult to actively target	Active targeting possible with pendent polymers
Can accumulate in some organs and form vacuoles because of desiccant nature of PEG	Readily cleared from body and is not hygroscopic

Toxicity Studies. In the acute dose studies, PEOZ 10 kDa was administered intravenously to Sprague−Dawley rats, in single and multiple injections at doses of 500, 1000, and 2000 mg/kg. No adverse events were observed. The body weights and food intake levels of each animal were normal. Blood counts and serum chemistry were normal when compared to the control group that received 0.9% (w/v) sodium chloride. The key organ (liver, kidney, lung, spleen, heart, and gastrointestinal tract) sizes, weights, morphology, and texture were also normal. In the multiple dose study, rats received seven intravenous doses of 50 mg/kg of PEOZ 20 kDa, over a period of 14 days. The blood counts and serum chemistry at days 15 and 21 were normal when compared to the control group. The key organ sizes, weights, morphology, and texture were also normal, and the histopathology of the kidney and spleen showed no microscopic differences when compared against the organs from the control animals. PEOZ was well-tolerated at the molecular weights of 10 and 20 kDa.

CONCLUSIONS

Three types of POZ polymers were prepared and characterized. Linear POZ with molecular weights of 1−40 kDa were synthesized, with high batch to batch reproducibility, low polydispersity values, and yields of ∼60−80%. The polymers prepared had no chain transfer biproducts and no high molecular weight species. Characterization studies show that both PMOZ and PEOZ are highly water-soluble; they have hydrodynamic volumes that are comparable and slightly lower than PEG; PEOZ is slightly more lipophilic than PMOZ and PEG, and is also significantly less viscous than PEG. The latter observation allows for the delivery of high dose proteins and peptides where viscosity is a hindrance in product formulation and administration. POZ can be easily functionalized from the terminal hydroxyl or carboxyl group to allow for conjugation to amine, thiol, aldehyde, ketone, and acetylene groups. POZylation of enzymes, proteins, and peptides produced conjugates with retained bioactivity that were comparable to similar conjugates modified with PEG. The attachment of POZ 10 kDa to lysine B29 of insulin produced a monoconjugate product that was able to lower blood glucose levels and also sustain its activity for a period of 8 h. In future papers, we will discuss other types of POZ attachments using click chemistry and enzyme catalyzed techniques. Toxicity studies in rats showed that PEOZ is safe when administered intravenously and the maximum tolerated dose (MTD) was greater than 2 g/kg. In addition, PEOZ can shield the immunogenic sites on an antigenic protein such as BSA.

POZ is a suitable alternative to PEG. Table 4 list the areas where POZ has many advantages over PEG. Another advantage not discussed in this paper is the ability to link several small drug molecules to a single polymer backbone, sometimes called "pendant drug attachment". The terminal end of the polymer remains free and can be functionalized for the attachment of targeting moieties. Hence, POZ not only has the ability to increase drug loading, but also the ability to carry this payload to specific molecular receptors.

AUTHOR INFORMATION

Corresponding Author

*E-mail: tviegas@serinatherapeutics.com.

REFERENCES

(1) Veronese, F. M., Mero, A., and Pasut, G. (2009) Protein PEGylation, basic science and biological applications. *PEGylated protein drugs: basic science and clinical applications, Milestones in drug therapy series* (Veronese, F. M., Ed.) pp 11−31, Birkhauser Verlag, Berlin.

(2) Armstrong, J. K., Hempel, G., Koling, S., Chan, L. S., Fisher, T., Meiselman, H. J., and Garratty, G. (2007) Antibody against poly(ethylene glycol) adversely affects PEG-asparaginase therapy in acute lymphoblastic leukemia patients. *Cancer 110*, 103–11.

(3) Sherman, M. R., Saifer, M. G., and Perez-Ruiz, F. (2008) PEG-uricase in the management of treatment-resistant gout and hyperuricemia. *Adv. Drug Delivery Rev. 6*, 59–68.

(4) Leger, R. M., Arndt, P., Garratty, G., Armstrong, J. K., Meiselman, H. J., and Fisher, T. C. (2001) Normal donor sera can contain antibodies to polyethylene glycol (PEG). *Transfusion 41*, 29S.

(5) Armstrong, J. K., Leger, R., Wenby, R. B., Meiselman, H. J, Garratty, G., and Fisher, T. C. (2003) Occurrence of an antibody to poly(ethylene glycol) in normal donors. *Blood 102*, 556A.

(6) Bendele, A., Seely, J., Richey, C., Sennello, G., and Shopp, G. (1998) Short communication: renal tubular vacuolation in animals treated with polyethylene-glycol-conjugated proteins. *Toxicol. Sci. 42*, 152–157.

(7) Conover, C., Lejeune, L., Linberg, R., Shum, K., and Shorr, R. G. L. (1996) Transitional vacuole formation following a bolus infusion of PEG-hemoglobin in the rat. *Artific. Cells, Blood Subst., Immob. Biotechnol. 24*, 599–611.

(8) Kinstler, O., and Gegg, C. (2002) Site directed dual pegylation of proteins for improved bioavailability and biocompatibility. U.S. Patent No. 6420339B1.

(9) Tao, L., Liu, J., and Davis, T. P. (2009) Branched polymer-protein conjugates made from mid-chain-functional P(HPMA). *Biomacromolecules 12*, 2847–2851.

(10) Jain, S., Hreczuk-Hirst, D. H., McCormack, B., Mital, M., Epenetos, A., Laing, P., and Gregoriadis, G. (2003) Polysialylated insulin:

synthesis, characterization and biological activity in vivo. *Biochim. Biophys. Acta 1622*, 42–49.

(11) Veronese, F. M., Sartore, L., Caliceti, P., Schiavon, O., Ranucci, E., and Ferruti, P. (1990) Low molecular weight end-functionalized poly(N-vinylpyrrolidinone) for the modification of polypeptide amino groups. *J. Bioact. Compat. Polym. 5*, 167–178.

(12) Food additive petition for Polyethyloxazoline, *The Dow Chemical Company*, May 8, 1985.

(13) Adams, N., and Schubert, U. S. (2007) Poly(2-oxazolines) in biological and biomedical application contexts. *Adv. Drug Delivery Rev. 59*, 1504–1520.

(14) Hoogenboom, R. (2009) Poly(2-oxazoline)s: A polymer class with numerous potential applications. *Angew. Chem., Int. Ed. 48*, 7978–7994.

(15) Mero, A., Pasut, G., Dalla, Via L., Fijten, M. W., Schubert, U. S., Hoogenboom, R., and Veronese, F. M. (2008) Synthesis and characterization of poly(2-ethyl 2-oxazoline)-conjugates with proteins and drugs: suitable alternatives to PEG-conjugates? *J. Controlled Release 2*, 87–95.

(16) Zalipsky, S., Hansen, C. B., Oaks, J. M., and Allen, T. M. (1996) Evaluation of blood clearance rates and biodistribution of poly (2-oxazoline)-grafted liposomes. *J. Pharm. Sci. 85*, 133–137.

(17) Woodle, M. C., Engbers, C. M., and Zalipsky, S. (1994) New amphipatic polymer-lipid conjugates forming long-circulating reticuloendothelial system-evading liposomes. *Bioconjugate Chem. 5*, 493–496.

(18) Wang, C. H., and Hsiue, G. H. (2005) Polymeric micelles with a pH-responsive structure as intracellular drug carriers. *J. Controlled Release 108*, 140–149.

(19) Konradi, R., Pidhatika, B., Hlebach, A. M., and Textor, M. (2008) Poly-2-methyl-2-oxazoline: a peptide-like polymer for protein-repellent surfaces. *Langmuir. 24*, 613–616.

(20) Goddard, P., Hutchinson, L. E., Brown, J., and Brookman, L. J. (1989) Soluble polymeric carriers for drug delivery. Part 2. Preparation and in vivo behaviour of N-acylethylenimine copolymers. *J. Controlled Release 10*, 5–16.

(21) Gaertner, F. C., Luxenhofer, R., Blechert, B., Jordan, R., and Essler, M. (2007) Synthesis, biodistribution and excretion of radiolabeled poly(2-oxazoline)s. *J. Controlled Release 119*, 291–300.

(22) Kobayashi, S., Mureo, K., Sawada, S., and Saegusa, T. (1985) Synthesis of poly(2-methyl-2-oxazoline) macromers. *Polym. Bull. 13*, 447–451.

(23) Kobayashi, S., Masuda, E., Shoda, S. I., and Shimano, Y. (1989) Synthesis of acryl- and methacryl-type macromonomers and telechelics by utilizing living polymerization of 2-oxazolines. *Macromolecules 22*, 2878–2884.

(24) Liu, Q., Konas, M., and Riffle, J. S. (1993) Investigations of 2-ethyl-2-oxazoline polymerizations in chlorobenzene. *Macromolecules 26*, 5572–5576.

(25) Hoogenboom, R., Leenen, M. A. M., Wiesbrock, F., and Schubert, U. S. (2005) Microwave accelerated polymerization of 2-phenyl-2-oxazoline: Microwave or temperature effects? *Macromol. Rapid Commun. 26*, 1773–1778.

(26) Wiesbrock, F., Hoogenboom, R., Leenen, M. A. M., Meier, M. A. R., and Schubert, U. S. (2005) Investigation of the living cationic ring-opening polymerization of 2-methyl, 2-ethyl, 2-nonyl, and 2-phenyl-2-oxazoline in a single-mode microwave reactor. *Macromolecules 38*, 5025–5034.

(27) Gross, A., Maier, G., and Nuyken, O. (1996) Synthesis and copolymerization of macromonomers based on 2-nonyl- and 2-phenyl-2-oxazoline. *Macromol. Chem. Phys. 197*, 2811–2826.

(28) Miyamoto, M., Naka, K., Tokumizu, M., and Saegusa, T. (1989) End capping of growing species of poly(2-oxazoline) with carboxylic acid: a novel and convenient route to prepare vinyl- and carboxy-terminated macromonomers. *Macromolecules 22*, 1604–1607.

(29) Taubmann, C., Luxenhofer, R., Cesana, S., and Jordan, R. (2005) First aldehyde-functionalized poly(2-oxazoline)s for chemoselective ligation. *Macromol. Biosci. 5*, 603–612.

(30) Cesana, S., Auernheimer, J., Jordan, R., Kessler, H., and Nyuken, O. (2006) First poly(2-oxazoline)s with pendant amino groups. *Macromol. Chem. Phys. 207*, 183–192.

(31) Nuyken, O., Maier, G., and Gross, A. (1996) Systematic investigations on the reactivity of oxazolinium salts. *Macromol. Chem. Phys. 197*, 83–85.

(32) Park, J. S., and Kataoka, K. (2006) Precise control of lower critical solution temperature of thermosensitive poly(2-isopropyl-2-oxazoline) via gradient copolymerization with 2-ethyl-2-oxazoline as a hydrophilic comonomer. *Macromolecules 39*, 6622–6630.

(33) Litt, M., Levy, A., and Herz, J. (1975) Polymerisation of cyclic imino ethers. X. Kinetics, chain transfer, and repolymerisation. *J. Macromol. Sci.-Chem. A9*, 703–727.

(34) Habeeb, A. F. (1966) Determination of free amino groups in protein by trinitrobenzensulphonic acid. *Anal. Biochem. 14*, 328–336.

(35) Crook, E., Mathias, A., and Rabin, B. (1960) Spectrophotometric assay of bovine pancreatic ribonuclease by the use of cytidine 2′,3′-phosphate. *Biochem. J. 74*, 234.

(36) Mahler, J. L. (1970) A new bacterial uricase for uric acid determination. *Anal. Biochem. 38*, 65–84.

(37) Beers, R. F., and Sizer, I. W. (1952) A spectrophotometric method for measuring the breakdown of hydrogen peroxide by catalase. *J. Biol. Chem. 195*, 133–140.

(38) Hinds, K. D., and Kim, S. W. (2002) Effects of PEG conjugation on insulin properties. *Adv. Drug Delivery Rev. 54*, 505–530.

(39) Fee, C. J., and Van Alstine, J. M. (2004) Prediction of viscosity radius and the size exclusion chromatography behavior of PEGylated proteins. *Bioconjugate Chem. 15*, 1304–1313.

(40) Abuchowski, A., Van Es, T., Palczuk, N. C., and Davis, F. (1977) Alteration of immunological properties of bovine serum albumin by covalent attachment of polyethylene glycol. *J. Biol. Chem. 252*, 3576–3581.

(41) Allison, B. C., Applegate, B. M., and Youngblood, J. P. (2007) Hemocompatibility of hydrophilic antimicrobial copolymers of alkylated 4-vinylpyridine. *Biomacromolecules 8*, 2995–2999.

Bioconjugate Chemistry

TECHNICAL NOTE

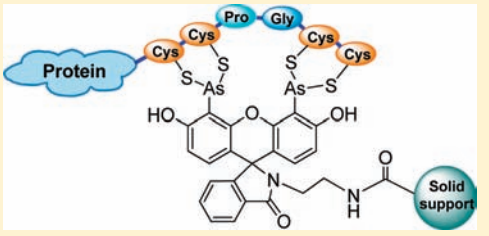
pubs.acs.org/bc

Purification of Tetracysteine-Tagged Proteins by Affinity Chromatography Using a Non-Fluorescent, Photochemically Stable Bisarsenical Affinity Ligand

Lai-Qiang Ying* and Bruce P. Branchaud

Life Technologies, 29851 Willow Creek Road, Eugene, Oregon 97402, United States

ABSTRACT: The use of genetically encoded small peptide tags such as polyhistidine and tetracysteine tags has become important for protein purification and enrichment. An improved affinity purification of tetracysteine (CCXXCC) tagged proteins has been achieved using a nonfluorescent, photochemically stable bisarsenical affinity ligand SplAsH. The photochemical stability of the SplAsH-biotin, shown in compound **5**, is superior to FlAsH-EDT$_2$ and ReAsH-EDT$_2$. An application of the SplAsH tag for affinity purification of tetracysteine-tagged proteins is reported.



INTRODUCTION

Protein modification with reporter tags has allowed the study of protein localization and protein−protein interactions inside living cells.[1−3] Traditionally, the protein of interest has to be isolated *in vitro*, labeled with a reporter tag, then reintroduced into cells by microinjection or electroporation. The use of genetically encoded fluorescent proteins such as green fluorescent protein (GFP) has provided a simple and powerful tool to study protein dynamics in cell biology.[4,5] However, GFP is a large protein (27 kDa), which could interfere with the physiological role of the protein of interest.[6,7] Small peptide tags, such as the hexahistidine (His$_6$) tag and tetracysteine (CCPGCC) tag, have greater advantage than GFP in protein labeling, because the small tags have minimal interference with the protein of interest.[6,8] The tetracysteine tag combined with either fluorescein arsenical hairpin binder (FlAsH-EDT$_2$, Figure 1) or Resorufin arsenical hairpin binder (ReAsH-EDT$_2$, Figure 1) provide useful tools for site-specific labeling of recombinant proteins inside live cells.[9−12] An especially important and useful feature of these molecules is their fluorogenicity; the small molecules FlAsH-EDT$_2$ and ReAsH-EDT$_2$ are membrane-permeant and almost nonfluorescent, so they can easily get into cells, then they bind with high affinity and specificity to the tetracysteine domain, causing the protein-bound dyes to become highly fluorescent.

On the basis of the high affinity and high specificity of the interaction of biarsenical dyes with the tetracysteine motif, methods using biarsenicals immobilized on a matrix as a stationary phase for affinity purification of tetracysteine-tagged proteins have been developed.[11,13,14] The interaction between biarsenical dyes and the tetracysteine motif can be easily reversed by incubation with dithiols such as 1,2-ethanedithiol (EDT) or dithiothreitol (DTT). This gives a gentle and mild elution condition with minimal disruption of protein structure and activity.

The most commonly used His$_6$-tag proteins are purified by binding to metal ions (Ni^{2+} or Co^{2+}) which are chelated to an affinity matrix followed by elution with high concentrations of imidazole or low pH.[15] This condition may disrupt some protein structure and activity.[16] In addition, the purified protein is often contaminated with intrinsic histidine-rich proteins and small amounts of metal ions, which may inhibit many enzyme activities.[11,13]

The major limitation to using the FlAsH affinity matrix for purification of tetracysteine-tagged proteins is a stability issue. The compounds FlAsH-EDT$_2$ and ReAsH-EDT$_2$ are photochemically unstable,[17] which limits their wide application in purification of tetracysteine-tagged proteins. We report herein on our successful efforts to apply a photochemically stable bisarsenical affinity ligand for affinity purification of tetracysteine-tagged proteins.

EXPERIMENTAL PROCEDURES

General Materials and Methods. All chemicals and solvents were purchased from Aldrich, Acros, or TCI and were used without further purification. Thin layer chromatography (TLC) was performed on aluminum-backed plates with silica gel 60 with F_{254} indicator. Flash column chromatography was carried out on silica gel (230−400 mesh). High-performance liquid chromatography (HPLC) analysis was performed on a Waters 600 instrument equipped with a Waters photodiode array detector. All moisture- or air-sensitive reactions were carried out under a static argon atmosphere. ^{1}H NMR (400 MHz) spectra were recorded at room temperature on a Bruker ADVANCE-400 spectrometer with residual proton resonances in deuterated solvents (DMSO-d_6, or MeOD-d_4) as the internal standard. LC/MS spectra were obtained with a Waters micromass ZQ instrument.

***tert*-Butyl 2-(3′,6′-dihydroxy-3-oxospiro[isoindoline-1,9′-xanthene]-2-yl) ethylcarbamate (1).** Fluorescein methyl ester was prepared according to a literature procedure from

Received: January 19, 2011
Revised: April 4, 2011
Published: April 11, 2011

ACS Publications © 2011 American Chemical Society

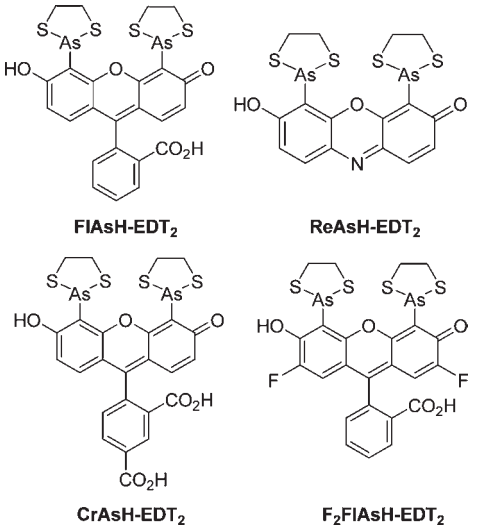


Figure 1. FlAsH-EDT$_2$, ReAsH-EDT$_2$, and related analogues.

fluorescein in 95% yield.[18] Fluorescein methyl ester (1.0 g, 2.9 mmol), and BocHNCH$_2$CH$_2$NH$_2$·HCl (1.14 g, 5.8 mmol) were dissolved in 10 mL DMF. Triethylamine (806 μL, 5.8 mmol) was added. The reaction mixture was heated at 100 °C overnight in a sealed pressure tube. After cooling to room temperature, the solvent was evaporated *in vacuo*. The residue was dissolved in ethyl acetate (80 mL); washed with H$_2$O (40 mL), 0.1 M HCl (40 mL), and brine (40 mL); dried over Na$_2$SO$_4$; and concentrated *in vacuo*. The crude mixture was purified by column chromatography on SiO$_2$ (EtOAc/Hexane = 1:1−2:1) to afford **1** (1.12 g, 2.4 mmol, 82% yield) as a white solid. The obtained compound matches with data that is in the literature.[17]

***tert*-Butyl 2-(4′,5′-bis(mercuric acetate)-3′,6′-dihydroxy-3-oxospiro[isoindoline-1,9′-xanthene]-2-yl) ethylcarbamate (2).** Compound **1** (1.1 g, 2.3 mmol) was dissolved in 60 mL ethanol, then the solution was added to a solution of mercuric acetate (1.53 g, 4.8 mmol) in 4 mL HOAc and 100 mL H$_2$O. The reaction mixture was stirred at 65 °C overnight in a sealed pressure tube. After cooling to room temperature, the resulting white precipitate was filtered through filter paper, washed with H$_2$O (3 × 20 mL), and then dried under high vacuum to afford **2** (2.05 g, 2.1 mmol, 90% yield) as a white solid. The obtained compound matches with data that is in the literature.[17]

***tert*-Butyl 2-(4′,5′-bis(1,3,2-dithiaarsolan-2-yl)-3′,6′-dihydroxy-3-oxospiro [isoindoline-1,9′-xanthene]-2-yl) ethylcarbamate (3).** Compound **2** (1.0 g, 1.0 mmol) was suspended in 20 mL THF. Di-isopropylethylamine (DIPEA, 1.4 mL, 8.0 mmol), AsCl$_3$ (1.6 mL, 20 mmol, caution: very toxic), and Pd(OAc)$_2$ (20 mg) were added. The reaction mixture was stirred at 50 °C for 2 h under argon, then at room temperature overnight under argon. The reaction mixture was poured into acetone/aqueous phosphate buffer (1:1, 0.5 M K$_2$HPO$_4$, pH 7, 100 mL) containing ethanedithiol (EDT, 3 mL). After stirring for 30 min, CHCl$_3$ (50 mL) was added, and the mixture was stirred for another 30 min. The organic layer was collected, and the aqueous layer was washed with CHCl$_3$ (3 × 30 mL). The combined organic layers were dried over Na$_2$SO$_4$ and concentrated *in vacuo*. The crude mixture was purified by column chromatography on SiO$_2$ (elute first with toluene to remove arsenic−EDT complex, then elute with EtOAc/Hexane = 2:3) to afford **3** (760 mg, 0.94 mmol, 94% yield) as a white solid. The obtained compound matches with data in the literature.[17]

2-(2-Aminoethyl)-4′,5′-di(1,3,2-dithiarsolan-2-yl)-3′,6′-dihydroxyspiro[isoindoline-1,9′-xanthen]-3-one (4). Compound **3** (300 mg, 0.37 mmol) was dissolved in 8 mL CH$_2$Cl$_2$ at 0 °C. TFA (4 mL) was added. The reaction mixture was stirred at 0 °C for 2 h. The reaction mixture was concentrated *in vacuo*. The residue was precipitated in diethyl ether and dried under reduced pressure via a vacuum pump to afford **4** (290 mg, 0.35 mmol, 95% yield) as a yellow solid. ^{1}H NMR (400 MHz, DMSO-d_6): δ 10.01 (s, 2H), 7.85 (dd, 1H, J = 2.0, 6.6 Hz), δ 7.60 (s, 2H), 7.56 (m, 2H), 7.05 (dd, 1H, J = 2.0, 6.6 Hz), 6.52 (m, 4H), 3.50 (m, 8H), 3.26 (t, 2H, J = 5.8 Hz), 2.39 (m, 2H). ESI-MS $[M+H]^+$ m/z calcd. for 706.91, found 706.87.

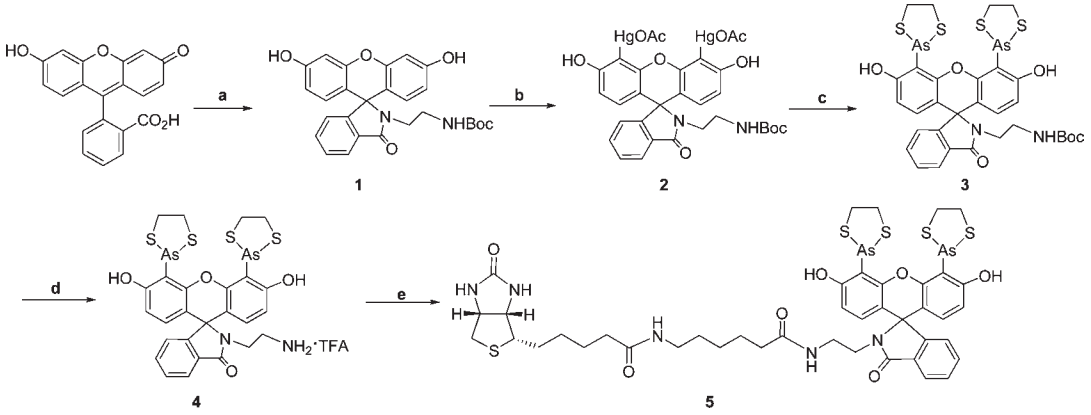
***N*-(2-(4′,5′-Di(1,3,2-dithiarsolan-2-yl)-3′,6′-dihydroxy-3-oxospiro[isoindoline-1,9′-xanthene]-2-yl)ethyl)-6-(5-((3a*S*,-4*S*,6a*R*)-2-oxohexahydro-1*H*-thieno[3,4-*d*]imidazol-4-yl)pentanamido)hexanamide (5).** Compound **4** (72 mg, 0.09 mmol) and 6-((biotinoyl)amino)hexanoic acid succinimidyl ester (40 mg, 0.09 mmol, Life Technologies) were dissolved in 3 mL dry DMF. TEA (37 μL, 0.26 mmol) was added. The reaction mixture was stirred at room temperature for 1 h. Diethyl ether (20 mL) was added to the reaction mixture. The precipitate was collected by centrifuge and purified by column chromatography on SiO$_2$ (CHCl$_3$/MeOH = 10:1) to afford **5** (80 mg, 0.08 mmol, 85% yield) as a white solid. ^{1}H NMR (400 MHz, DMSO-d_6): δ 7.95 (s, 2H), 7.90 (dd, 1H, J = 2.0, 6.6 Hz), 7.58 (m, 2H), 7.06 (dd, 1H, J = 2.0, 6.6 Hz), 6.50 (m, 4H), 4.50 (m, 1H), 4.30 (m, 1H), 3.60 (m, 8H), 3.18 (m, 5H), 2.99 (m, 3H), 2.71 (m, 1H), 2.19 (t, J = 7.2 Hz, 2H), 2.03 (t, J = 7.2 Hz, 2H), 1.66−1.30 (m, 12H). ESI-MS $[M+H]^+$ m/z calcd. for 1046.07, found 1046.34.

Synthesis of Affinity Matrix 6. CrAsH-EDT$_2$ succinimidyl ester was prepared according to a literature procedure.[11] To a 20 mL plastic, fritted column with a Teflon stopcock and a cap to seal the column, 10 mL of amino-agarose (Affi-Gel 102, Biorad) in PBS buffer containing 0.1 mM EDTA, 5 mM β-mercaptoethanol (BME), and 0.1 mM EDT, pH 7.4 was added, followed by addition of 1 mL of CrAsH-EDT$_2$ succinimidyl ester (10 mM solution in DMSO, 10 μmol) and 0.5 mL of 1 M NaHCO$_3$. The resin was mixed at RT for 4 h by end-to-end rotation, and washed extensively with the same buffer. Capping of free amines was achieved by treatment with a 10-fold excess of *N*-acetoxysuccinimide (prepared from acetic acid and *N*-hydroxysuccinimide with dicyclohexylcarbodiimide in CH$_2$Cl$_2$) over total amines (~12 μmol/mL) in the same phosphate buffer with slow rotation for additional 2 h. The immobilized affinity matrix **6** was washed and stored in 50% EtOH at 4 °C.

Synthesis of Affinity Matrix 7. To a 20 mL plastic, fritted column with a Teflon stopcock and a cap to seal the column, 10 mL of *N*-hydroxysuccinimidyl ester (NHS) activated agarose (Affi-Gel 10, Biorad) in 1/1 isopropanol/DMF was added, followed by addition of 1 mL of compound **4** (20 mM solution in DMSO, 20 μmol) and 0.2 mL of TEA. The resin was mixed at RT for 2 h by end-to-end rotation, and washed with isopropanol and DMF. Unreacted NHS groups were quenched by treatment with 0.5 M ethanolamine in isopropanol for an additional 1 h. The immobilized affinity matrix **7** was washed with PBS buffer containing 0.1 mM EDTA, 5 mM BME, and 0.1 mM EDT, pH 7.4, and stored in 50% EtOH at 4 °C.

Affinity Purification of Tetracysteine-Tagged Proteins Using Affinity Matrixes 6 and 7. The GFP with a *C*-terminal CCPGCC tag as well as a *N*-terminal his$_6$ tag was overexpressed

Scheme 1. Synthesis of Nonfluorescent SplAsH-Biotin 5[a]



[a] Reaction conditions: (a) H_2SO_4, MeOH; $BocHNCH_2CH_2NH_2HCl$, TEA, DMF; (b) $Hg(OAc)_2$, HOAc, EtOH/H_2O; (c) $AsCl_3$, DIPEA, $Pd(OAc)_2$, THF; ethandithiol, acetone/PBS; (d) TFA, DCM; (e) 6-((Biotinoyl)amino) hexanoic acid succinimidyl ester, TEA, DMF.

in *Escherichia coli* using standard methods.[5] The collected cell pellet was lysed in 250 mM KCl, 50 mM KPO_4, 1 mM EDTA, 10 mM 2-mercaptoethane-sulfonate (MES), and 1 mM tris-(carboxyethyl) phosphine (TCEP), pH 7.5, by sonication. The total protein concentration of the lysate was measured using EZQ protein quantitation kit (Life Technologies), and GFP concentration was quantified by GFP intrinsic fluorescence. The freshly prepared GFP lysate (1 mL, ~2.5 mg/mL) was added to 0.5 mL of affinity matrixes **6** and **7**, respectively. The resin was mixed at RT for 2 h by end-to-end rotation. The mixture was transferred to a short column, the unbound material was collected, and the resin was washed with buffer (250 mM KCl, 50 mM KPO_4, 1 mM EDTA, 10 mM MES, 1 mM TCEP, pH 7.5, 3 × 2 mL), and then eluted with buffer (250 mM KCl, 50 mM KPO_4, 1 mM EDTA, 10 mM 2,3-dimercapto-propanesulfonate (DMPS), 3 × 0.5 mL). Fractions were analyzed by SDS-PAGE (NuPAGE, 4−12% Bis-Tris Gel, Life Technologies).

Purification by the polyhistidine tag was done using the standard immobilized metal affinity chromatography method (Life Technologies), as follows. The freshly prepared GFP lysate (1 mL) in 50 mM NaH_2PO_4, 500 mM NaCl, pH 8.0, was incubated with 1 mL of Ni^{2+}-NTA resin at RT for 1 h by end-to-end rotation. The mixture was transferred to a short column, the unbound material was collected, and the resin was washed with buffer (50 mM NaH_2PO_4, 500 mM NaCl, 20 mM imidazole, pH 8.0, 3 × 5 mL) and then eluted with buffer (50 mM NaH_2PO_4, 500 mM NaCl, 250 mM imidazole, pH 8.0, 3 × 0.5 mL). Fractions were analyzed by SDS-PAGE (NuPAGE, 4−12% Bis-Tris Gel, Life Technologies).

Kinetic Measurement of Binding Affinity of SplAsH-biotin 5 and Tetracysteine-Tagged Protein (GFP). The kinetic measurement of binding affinity of SplAsH-biotin **5** and tetracysteine-tagged protein (GFP) was carried out using the ForteBio system, which is a label-free, real-time detection system.[19] The streptavidin biosensor tips from ForteBio were prewet for 30 min in water prior to use. All interaction analyses were conducted at 25 °C in PBS buffer (pH 7.2) containing 5 mM MES, 0.1% BSA, and 0.05% Tween-20. The streptavidin biosensor tips were first incubated with SplAsH-biotin **5** (50 μM) to immobilize the SplAsH ligand onto the tips. Then, the SplAsH ligand coated tips were incubated with purified tetracysteine-tagged GFP (50 nM) in duplicate to generate the association curve. As a reference control, the SplAsH ligand coated tip was also incubated with a buffer solution. The dissociation curve was generated by incubating these tips with the PBS buffer described above. The *ForteBio Data Analysis Octet* software was used to process the curve by subtracting a sample curve from the reference curve, and the kinetic data were calculated by curve fitting.

RESULTS AND DISCUSSION

To improve the utility of carboxy-FlAsH-EDT_2 (CrAsH-EDT_2, Figure 1) in affinity purification of tetracysteine-tagged proteins,[11,20,21] our focus is to apply a photochemically stable FlAsH−EDT_2 analogue. Recently, a fluoro-substituted FlAsH (F_2FlAsH, Figure 1) has been reported to dramatically improve photostability.[22] However, the synthesis of F_2FlAsH gives poor overall yield (<4%), which limits its practical usefulness in applications in affinity purification.

We decided to focus on the use of a readily available nonfluorescent SplAsH **4** (Spirolactam Arsenical Hairpin binder, Scheme 1). SplAsH **4** was prepared according to the published procedure.[17] Briefly, fluorescein was converted to fluorescein methyl ester in MeOH using H_2SO_4 as a catalyst,[18] then the ester was reacted with mono Boc-protected ethylenediamine to give fluorescein spirolactam **1**.[23] The fluorescein spirolactam **1** was then converted to the bis-mercuric acetate derivative **2**[13] and then to the bis-arsenical derivative **3** by transmetalation with palladium acetate as a catalyst.[9] After cleavage of the Boc protecting group with TFA, SplAsH **4** was obtained in 63% overall yield in six steps. This synthesis can be easily scaled up for the preparation of multigram amounts of **4**. Compared to the synthesis of CrAsH-EDT_2 (16% overall yield),[11] the synthesis of SplAsH **4** has great advantages in terms of easy preparation and easy purification. The SplAsH **4** can be easily converted to SplAsH-biotin **5**. The absorbance maximum of SplAsH-biotin **5** was shifted from 509 to 242 nm with ε_{242} = 26 000 compared to FlAsH-EDT_2 (Figure 2), thus providing no inherent fluorescence whether or not it is bound to the tetracysteine motif.

To test the photochemical stability, CrAsH-EDT_2 and SplAsH-biotin **5** were each prepared in 100 μM concentration in degassed PBS buffer with 1 mM EDT, and 1 mL of each sample in a sealed quartz curvette was irradiated with a xenon arc lamp at 250 mW/cm^2. Samples were checked by HPLC every 30 min,

dx.doi.org/10.1021/bc200038t |*Bioconjugate Chem.* 2011, 22, 987–992

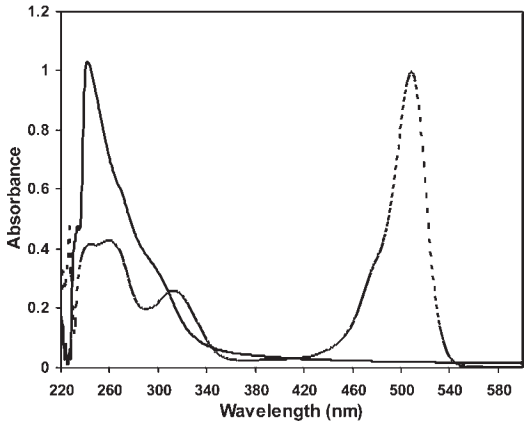


Figure 2. Absorbance spectra of FlAsH-EDT$_2$ (···) and SplAsH-biotin **5** (—) at PBS buffer.

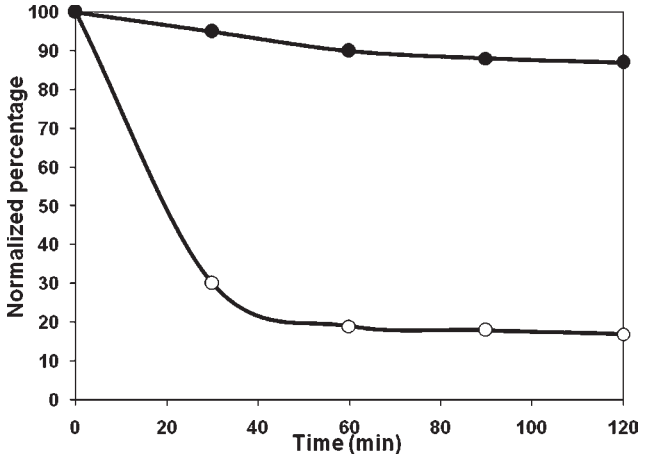


Figure 3. Photostability of CrAsH-EDT$_2$ (○) and SplAsH-biotin **5** (●) irradiated with a xenon arc lamp at 250 mW/cm^2.

and the results are shown in Figure 3. The results clearly show that the CrAsH-EDT$_2$ exhibits poor photochemical stability.[17] SplAsH-biotin **5** exhibits remarkably improved photochemical stability because blocking the quinoid tautomer formation by spirolactam formation eliminates the excited state that serves as an intermediate in the photobleaching process.[24]

In order to measure the binding affinity of SplAsH and tetracysteine-tagged protein, SplAsH-biotin **5** was first immobilized onto streptavidin sensor tips through biotin−streptavidin interaction. Then, the SplAsH coated sensor tips were incubated with tetracysteine-tagged GFP to generate the association curve, followed by incubating in buffer to get the dissociation curve (Figure 4). On the basis of the on-and-off rate, the dissociation constant K_D was calculated to be approximately 2.4 ± 1.2 nM. Compared to the dissociation constant K_D (~μM) for the interaction between His tag and Ni_2^+-NTA,[25] the SplAsH ligand has more than 1000-fold higher affinity (stronger, tighter binding) and thus should be much more useful for the capture and purification of low-abundance proteins.

To evaluate the application in affinity purification of tetracysteine-tagged proteins, the CrAsH-EDT$_2$ succinimidyl ester was coupled to Affigel-102 (Biorad), and the remaining free amines were capped with excess of *N*-acetoxysuccinimide.[11]

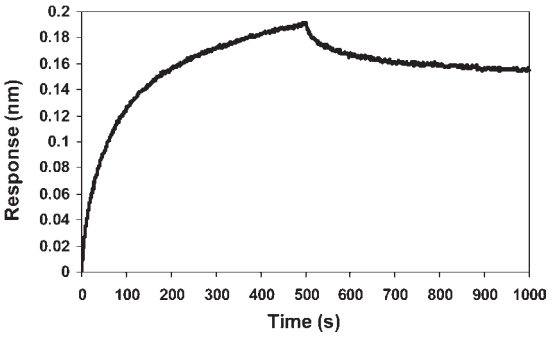


Figure 4. Kinetics of association and dissociation of SplAsH-biotin **5** and tetracysteine-tagged GFP.

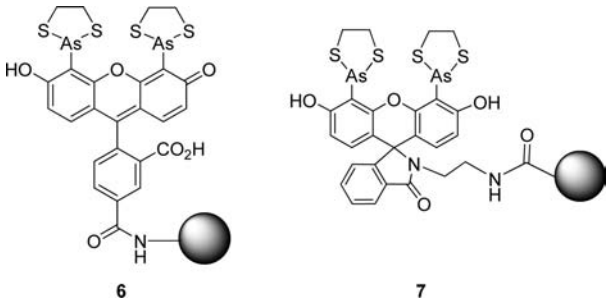


Figure 5. Affinity matrixes **6** and **7** used for purification of tetracysteine-tagged proteins.

SplAsH **4** was conjugated with Affigel-10 (Biorad), and unreacted NHS groups were quenched with ethanolamine. We chose the GFP with a *C*-terminal CCPGCC tag as well as a *N*-terminal his$_6$ tag as model test protein, because its recovery yield can be easily quantified by measuring the intrinsic fluorescence, and it can also be used to evaluate whether the two different purification methods will affect the GFP fluorescence property.[5,26] In separate, parallel experiments, the freshly prepared GFP lysate was mixed with CrAsH-EDT affinity matrix **6** and the new nonfluorescent affinity matrix **7** (Figure 5) in a buffer containing 250 mM KCl, 50 mM KPO_4, 1 mM EDTA, 10 mM MES, 1 mM TCEP, pH 7.5, for 2 h. The supernatant was collected from each, then each resin was washed with buffer, followed by eluting with buffer containing 10 mM DMPS. Fractions were analyzed by SDS-PAGE. For another comparsion, the same protein construct was purified by the conventional His$_6$:Ni^{2+}-NTA column.

It is well-known that the FlAsH ligand binds to the tetracysteine motif with high affinity and specificity, and the binding can be easily reversed by competing ligands, such as EDT, DTT, and DMPS.[11] These methods can be useful for the purification of native tetracysteine-tagged proteins. However, due to poor photochemical stability of CrAsH-EDT$_2$, the CrAsH-EDT affinity matrix **6** gave inconsistent results. Instead, SplAsH **4** displays superior photochemical stability. As shown in Figure 6, by using the new nonfluorescent affinity matrix **7** the desired protein was specifically captured and then eluted with DMPS to afford highly purified protein (90% purity) with reasonable yield (52% yield). Using the conventional His$_6$:Ni^{2+}-NTA method, the GFP was isolated in 92% purity and 70% recovery yield. The lower recovery yield is probably due to a stability issue of tetracysteine tag *in vitro*, by

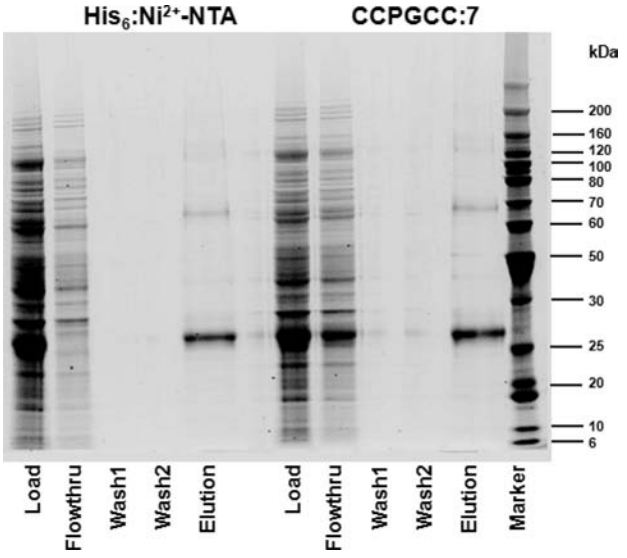


Figure 6. Affinity purification of a tetracysteine-tagged and his_6-tagged GFP using affinity matrix **7** and Ni^{2+}-NTA column. GFP lysate (load) was incubated with two supports, separated by pouring into columns (flowthrough), washed (wash), and eluted with either 10 mM DMPS or 250 mM imidazole (elution), respectively. The collected fractions were analyzed by a reducing 4−12% SDS-PAGE gel and stained with SYPRO-Ruby.

air oxidation and inactivation of the tetracysteine tag, and not due to instability of the new nonfluorescent affinity matrix **7**.

CONCLUSION

In summary, the superior photochemical stability of SplAsH **4** compared to CrAsH-EDT_2 can be applied for a new, improved method for protein affinity purification. SplAsH **4** can be easily prepared in large scale and high yield. SplAsH **4** retains high affinity and specificity for tetracysteine tags. This provides better affinity purification of tetracysteine-tagged proteins with SplAsH **4** than with CrAsH-EDT_2. In addition, SplAsH **4** is nonfluorescent whether or not it is bound to tetracysteine tags. This quenched property of SplAsH **4** provides an opportunity for potential surface-based applications by immobilizing SplAsH **4** onto beads or array surfaces to capture tetracysteine-tagged proteins, then performing protein detection, quantitation, and functional assays using dye-labeled detection antibody. Detailed studies of surface-based applications are currently underway.

AUTHOR INFORMATION

Corresponding Author

*E-mail: lai-qiang.ying@lifetech.com. Telephone: (541) 335-0158. FAX: (541) 335-0206.

ACKNOWLEDGMENT

We thank Michael O'Grady for assistance with GFP protein expression.

REFERENCES

(1) Giepmans, B. N., Adams, S. R., Ellisman, M. H., and Tsien, R. Y. (2006)The fluorescent toolbox for assessing protein location and function. *Science 312*, 217–224.

(2) Marks, K. M., and Nolan, G. P. (2006)Chemical labeling strategies for cell biology. *Nat. Methods 3*, 591–596.

(3) Morris, M. C. (2010)Fluorescent biosensors of intracellular targets from genetically encoded reporters to modular polypeptide probes. *Cell Biochem. Biophys. 56*, 19–37.

(4) Tsien, R. Y. (1998)The green fluorescent protein. *Annu. Rev. Biochem. 67*, 509–544.

(5) Chalfie, M., Tu, Y., Euskirchen, G., Ward, W. W., and Prasher, D. C. (1994)Green fluorescent protein as a marker for gene expression. *Science 263*, 802–805.

(6) Andresen, M., Schmitz-Salue, R., and Jakobs, S. (2004)Short tetracysteine tags to beta-tubulin demonstrate the significance of small labels for live cell imaging. *Mol. Biol. Cell 15*, 5616–5622.

(7) Hoffmann, C., Gaietta, G., Bunemann, M., Adams, S. R., Oberdorff-Maass, S., Behr, B., Vilardaga, J. P., Tsien, R. Y., Ellisman, M. H., and Lohse, M. J. (2005)A FlAsH-based FRET approach to determine G protein-coupled receptor activation in living cells. *Nat. Methods 2*, 171–176.

(8) Lata, S., Gavutis, M., Tampe, R., and Piehler, J. (2006)Specific and stable fluorescence labeling of histidine-tagged proteins for dissecting multi-protein complex formation. *J. Am. Chem. Soc. 128*, 2365–2372.

(9) Griffin, B. A., Adams, S. R., and Tsien, R. Y. (1998)Specific covalent labeling of recombinant protein molecules inside live cells. *Science 281*, 269–272.

(10) Griffin, B. A., Adams, S. R., Jones, J., and Tsien, R. Y. (2000) Fluorescent labeling of recombinant proteins in living cells with FlAsH. *Methods Enzymol. 327*, 565–578.

(11) Adams, S. R., Campbell, R. E., Gross, L. A., Martin, B. R., Walkup, G. K., Yao, Y., Llopis, J., and Tsien, R. Y. (2002)New biarsenical ligands and tetracysteine motifs for protein labeling in vitro and in vivo: synthesis and biological applications. *J. Am. Chem. Soc. 124*, 6063–6076.

(12) Hoffmann, C., Gaietta, G., Zurn, A., Adams, S. R., Terrillon, S., Ellisman, M. H., Tsien, R. Y., and Lohse, M. J. (2010)Fluorescent labeling of tetracysteine-tagged proteins in intact cells. *Nat. Protoc. 5*, 1666–1677.

(13) Thorn, K. S., Naber, N., Matuska, M., Vale, R. D., and Cooke, R. (2000)A novel method of affinity-purifying proteins using a bis-arsenical fluorescein. *Protein Sci. 9*, 213–217.

(14) Uljana Mayer, M., Shi, L., and Squier, T. C. (2005)One-step, non-denaturing isolation of an RNA polymerase enzyme complex using an improved multi-use affinity probe resin. *Mol. Biosyst. 1*, 53–56.

(15) Porath, J., Carlsson, J., Olsson, I., and Belfrage, G. (1975)Metal chelate affinity chromatography, a new approach to protein fractionation. *Nature 258*, 598–599.

(16) Soh, N. (2008)Selective chemical labeling of proteins with small fluorescent molecules based on metal-chelation methodology. *Sensors 8*, 1004–1024.

(17) Bhunia, A. K., and Miller, S. C. (2007)Labeling tetracysteine-tagged proteins with a SplAsH of color: a modular approach to bis-arsenical fluorophores. *ChemBioChem 8*, 1642–1645.

(18) Adamczyk, M., Grote, J., and Moore, J. A. (1999)Chemoenzymatic synthesis of 3′-O-(carboxyalkyl)fluorescein labels. *Bioconjugate Chem. 10*, 544–547.

(19) Abdiche, Y., Malashock, D., Pinkerton, A., and Pons, J. (2008) Determining kinetics and affinities of protein interactions using a parallel real-time label-free biosensor, the Octet. *Anal. Biochem. 377*, 209–217.

(20) Cao, H., Chen, B., Squier, T. C., and Mayer, M. U. (2006) CrAsH: a biarsenical multi-use affinity probe with low non-specific fluorescence. *Chem. Commun.* 2601–2603.

(21) Adams, S. R., and Tsien, R. Y. (2008)Preparation of the membrane-permeant biarsenicals FlAsH-EDT_2 and ReAsH-EDT_2 for fluorescent labeling of tetracysteine-tagged proteins. *Nat. Protoc. 3*, 1527–1534.

(22) Spagnuolo, C. C., Vermeij, R. J., and Jares-Erijman, E. A. (2006) Improved photostable FRET-competent biarsenical-tetracysteine probes based on fluorinated fluoresceins. *J. Am. Chem. Soc. 128*, 12040–12041.

(23) Adamczyk, M., and Grote, J. (2000)Synthesis of novel spirolactams by reaction of fluorescein methyl ester with amines. *Tetrahedron Lett. 41*, 807–809.

(24) Kasche, V., and Lindqvist, L. (1964)Reactions between the triplet state of fluorescein and oxygen. *J. Phys. Chem. 68*, 817–823.

(25) Nieba, L., Nieba-Axmann, S. E., Persson, A., Hamalainen, M., Edebratt, F., Hansson, A., Lidholm, J., Magnusson, K., Karlsson, A. F., and Pluckthun, A. (1997)BIACORE analysis of histidine-tagged proteins using a chelating NTA sensor chip. *Anal. Biochem. 252*, 217–228.

(26) Nakanishi, J., Nakajima, T., Sato, M., Ozawa, T., Tohda, K., and Umezawa, Y. (2001)Imaging of conformational changes of proteins with a new environment-sensitive fluorescent probe designed for site-specific labeling of recombinant proteins in live cells. *Anal. Chem. 73*, 2920–2928.

Bioconjugate Chemistry

REVIEW

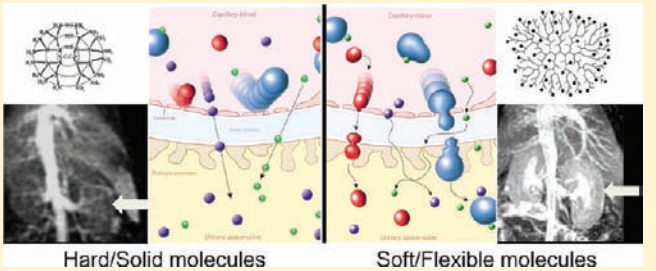
pubs.acs.org/bc

Biologically Optimized Nanosized Molecules and Particles: More than Just Size

Michelle R. Longmire, Mikako Ogawa, Peter L. Choyke, and Hisataka Kobayashi*

Molecular Imaging Program, National Cancer Institute, National Institutes of Health, 10 Center Drive, Bethesda, Maryland 20892-1088, United States

ABSTRACT: The expanded biological and medical applications of nanomaterials place a premium on better understanding of the chemical and physical determinants of in vivo particles. Nanotechnology allows us to design a vast array of molecules with distinct chemical and biological characteristics, each with a specific size, charge, hydrophilicity, shape, and flexibility. To date, much research has focused on the role of particle size as a determinant of biodistribution and clearance. Additionally, much of what we know about the relationship between nanoparticle traits and pharmacokinetics has involved research limited to the gross average hydrodynamic size. Yet, other features such as particle shape and flexibility affect in vivo behavior and become increasingly important for designing and synthesizing nanosized molecules. Herein, we discuss determinants of in vivo behavior of nanosized molecules used as imaging agents with a focus on dendrimer-based contrast agents. We aim to discuss often overlooked or, yet to be considered, factors that affect in vivo behavior of synthetic nanosized molecules, as well as aim to highlight important gaps in current understanding.



INTRODUCTION

To create the least toxic and most biocompatible imaging agents, we must understand the behavior of nanosized particles and molecules in the human system. Defining optimal size, shape, and flexibility; determining core and surface modifications that alter in vivo behavior; as well as using methods for characterizing particles during synthesis that are predictive of in vivo behavior, will be important measures for successful clinical translation. Among the various nanomaterials, dendrimers are a promising platform for biomedical imaging and targeted drug delivery. Their versatility, tunable size, and highly adaptable surface chemistry make these particles advantageous for numerous imaging applications. Herein, we discuss often overlooked factors influencing the pharmacokinetics of nanosized molecules and particles designed for imaging and drug delivery, with a focus on dendrimer-based imaging agents. In addition, we aim to address broader issues related to nanotoxicology as it applies to the translation of nanomaterial science into clinical nanomedicine.

IDEAL IN VIVO BEHAVIOR

Ideally, all nanosized imaging agents would demonstrate high target tissue accumulation, rapid clearance from the body, and no associated toxicity. Although such an agent does not currently exist, the rational design of probes optimized for the above end points will lead to the development of better nanosized molecule-based imaging probes. Regardless of the nanomaterial employed, reducing exposure by optimizing clearance is a central principle for minimizing unwanted effects of foreign materials within the human body. Of course, the material must exist within the system for sufficient time to produce desired effects such as tumor accumulation for imaging or drug delivery. Ideally, however, the agent would be cleared as soon as this was achieved. Nanosized molecules and particles are cleared from the vascular compartment through three primary mechanisms: renal clearance with excretion into the urine, hepatic clearance with biliary excretion, or uptake by macrophages into the reticuloendothelial system (RES) (liver, spleen, bone marrow).[1−13] Within the kidney, molecules may be cleared through glomerular filtration or tubular excretion. Generally, molecules approximately 6 nm or smaller in diameter may be excreted through glomerular filtration.[11,14−16] Glomerular filtration represents the ideal mechanism for nanoparticle clearance from the body, as molecules are excreted without requisite cellular internalization or metabolism as is required for renal tubular secretion, as well as the two other modes of clearance. Renal clearance is achieved rapidly with glomerular filtration, making this a desired route for excretion.[5,11,17] However, after the particle has undergone filtration, the surface should be designed to avoid tubular reabsorption.[11] We propose that the design of nanosized molecules or particles for human application should focus on optimization of particles for renal clearance.

Received: March 3, 2011
Revised: April 10, 2011
Published: April 23, 2011

ACS Publications This article not subject to U.S. Copyright. Published 2011 by the American Chemical Society

DEFINING IDEAL MATERIAL CHARACTERISTICS

Given the enormous diversity of nanomaterials and rapid growth in the field of nanoscience, efficient translation of nanomaterials into medicine will likely rely upon effective categorization of particles based on in vivo properties such as pharmacokinetics and toxicity. However, this is challenging as the huge variation among nanomaterials makes relevant categorization difficult. Currently, the US Food and Drug Administration (FDA) groups nanoparticles by chemical composition of the material. Yet, from a biological perspective, this division may not be the most relevant to human health. For example, when considering nanoparticles that undergo renal clearance, the short life of the particle in the human body markedly reduces exposure and the chance for "off target" effects. Other particle properties such as particle size are therefore equally, and possibly more, relevant than chemical composition when thinking about nanotoxicology. Tomalia recently proposed classifying nanomaterials as "hard" or "soft" based on compositional/architectural criteria for traditional organic and inorganic materials.[18] Within this classification system, the soft group includes the following: dendrimers, nanolatexes, polymeric micelles, proteins, viral capsids, and polynucleic acids. So-called "hard" categories include the following: metal nanoclusters, metal chalcogenic nanocrystals, metal oxide nanocrystals, silica nanoparticles, fullerenes, and carbon nanotubes.[18] The system is based on the premise of building blocks that are primarily defined by the nature of the core material and subsequently modified by the addition of other nanomaterials, to achieve further classification as soft−soft (e.g., dendrimer core with dendrimer shell) or soft−hard (e.g., dendrimer core with silica nanoparticle shell). Further work is needed to determine if these proposed divisions translate into biologically relevant or useful groups, but at a glance, the division of hard versus soft will likely have greater medical relevance in terms of toxicity and biological properties for agents that do not undergo renal clearance, as these agents will be retained by the body over sufficient time course to observe material-specific pathological or biological effects. The hard versus soft distinction may have special relevance for intermediate-sized particles that are capable of undergoing renal clearance with a given degree of particle flexibility. As of yet, the broad field of nanoscience as applied to medicine lacks clear direction in terms of classifying and defining agent behavior in vivo, an undoubtedly important aspect for clinical translation. Herein, we discuss what is known and what remains to be explored regarding the rational design of nanosized particles- or molecule-based agents for medical applications and address basic design strategies for minimizing toxicity and nonspecific probe uptake, while maximizing tumor accumulation. Therefore, the majority of nanosized agents, which are discussed in this review, avoid nonspecific RES uptake by appropriate surface modifications and are excreted through other physiologic mechanisms, i.e., renal excretion or biliary excretion.

SIZE

The impact of particle size on in vivo behavior is one of the most well studied aspects of nanoparticle pharmacokinetics and biodistribution. It is generally accepted that particles smaller than 5.5 nm primarily undergo renal clearance, whereas particles of intermediate size are more variable and those >12 nm primarily undergo hepatic clearance. Research demonstrates that spherical particles smaller than 5.5 nm reliably are excreted by the kidneys,[5,19] while larger particles demonstrate more variable behavior that is determined in part by shape, rigidity of the material, particle charge, and architectural flexibility. However, a factor limiting generalization of the role of size on nanosized particle/molecule behavior is that research has been limited primarily to spherical particles. We hypothesize, however, that regardless of shape, the majority of particles smaller than 5.5 nm will undergo renal clearance. Yet, more work needs to be done to determine if this is indeed the case. This size issue has been investigated in the case of a few nanomaterials including dendrimers[14,19] and metal nanocrystals. [5] A series of dendrimers with similar spherical shapes and identical core and surface chemistry but with differences in diameter were synthesized, and their pharmacokinetics, whole-body retention, and dynamic magnetic resonance imaging (MRI) were evaluated in mice. Polypropylenimine (PPI) dendrimer-based agents cleared more rapidly from the body than polyamidoamine (PAMAM) dendrimer-based agents with the same number of branches.[14] Smaller dendrimer conjugates were more rapidly excreted from the body than the larger dendrimer conjugates.[14,20]

The size measurements of macromolecules or nanoparticles have been obtained with mass spectroscopy for molecular mass, the electron microscope for crystallized size, and dynamic light scattering (DLS) and size-exclusion liquid chromatography (SE-LC) for functional hydrodynamic size in solution. The hydrodynamic size of a particle in solution is generally thought to be the most relevant measurement technique to predict in vivo behavior. SE-LC is theoretically the most relevant for predicting particle vascular permeability and renal filtration, as this measurement technique involves physical flow through pores. However, the functional size measured by DLS or SE-LC is an average regardless of particle shape and flexibility. Therefore, these measurements do not comprehensively reflect the in vivo functional behavior of macromolecules or nanoparticles. Developing and/or utilizing measurement techniques that gauge other particle traits, such as flexibility and shape, are necessary for designing more biocompatible nanosized agents.

SHAPE

Taking into consideration the vast array of naturally occurring biomolecules, it is rational to hypothesize that shape is an important determinant of biological function. However, our current understanding of in vivo behavior is derived from studies limited to average sizes of nanoparticles.[21] While this work is valuable, it also has important limitations: (1) most naturally occurring matter is nonsperical, as are many available and emerging nanomaterials, and (2) biological processes occur under dynamic conditions in which the motion of spherical and nonspherical objects will differ.[21] The construction possibilities of nanoparticles are nearly infinite, and many nonspherical particles have been created and have demonstrated preclinical promise. Additionally, given the role of shape in biological function of molecules, this same parameter is likely important in achieving optimal function from nanoparticles. In this section, we will review current insights into the influence of shape on in vivo nanoparticle behavior.

Although the effect of shape on in vivo behavior has not yet been extensively explored, several studies have evaluated this topic. A comparison of linear copolymers to branched spherical PAMAM hydroxylated dendrimers with regard to biodistribution found that the molecular weight, hydrodynamic size, and polymer architecture (or shape) affected biodistribution. [22] The

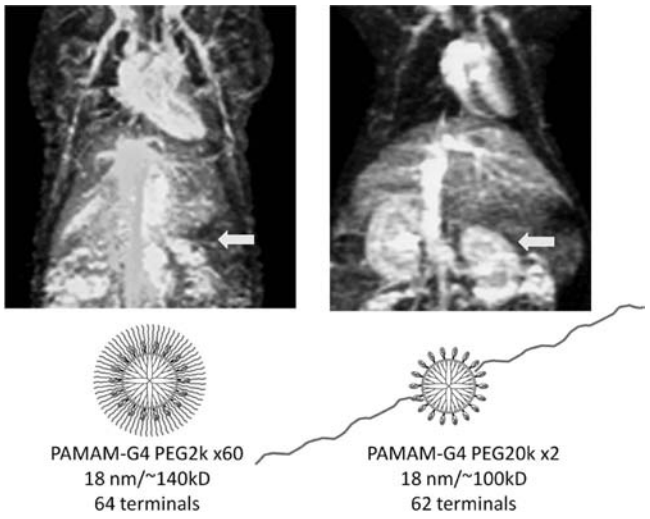


Figure 1. Two long, linear PEG (20 kD) conjugated PAMAM-G4-Gd shows renal excretion. However, short PEG (2 kD) conjugated PAMAM-G4-Gd of similar physical size shows no renal excretion.

dendrimers were retained in the kidney for over 1 week, while copolymers of approximately the same molecular weight were excreted into the urine and did not show persistent renal accumulation. [22] Another group compared the effect of nanoparticle shape on flow and drug delivery by comparing linear polymer micelles known as filomicelles to spheres of the same chemistry in rodents. Filomicelles remained in circulation ten times longer than their chemically similar spherical counterparts, suggesting that shape played a significant role in in vivo behavior. [23] Another group compared the biodistribution of PEGylated rod-shaped gold nanoparticles with PEGylated spherical counterparts and found that the gold nanorods were taken up to a lesser extent by the liver and had longer circulation time in the blood and higher accumulation in tumors, compared to their spherical counterparts. Additionally, the rods were taken up to a lesser extent than the spheres by macrophages. [24]

Traditionally, dendrimers were synthesized as spherical nanoparticles. However, recently surface modifications conjugating linear molecules to the surface produce nonspherical shapes with different pharmacokinetics. Despite a large particle size conferred by one or two linear, long PEGylated tails,[10] the particles may still undergo relatively rapid renal clearance. In contrast, the same generation of dendrimers with short PEG tails does not show renal clearance (Figure 1). [25]

SURFACE MODIFICATIONS TO ALTER BIODISTRIBUTION

To achieve target tissue accumulation, probes must avoid nonspecific uptake. Of the strategies to alter in vivo behavior, addition of poly(ethylene glycol) (PEG) is among the most widely utilized approaches. One consistent limitation to the use of polymeric nanoparticles in vivo is their premature elimination from the circulatory system by the mononuclear phagocyte system.[7,26] This process is initiated by serum opsonins attaching to the surface of nanoparticles in circulation. Following opsonization, macrophages recognize, phagocytose, and then sequester the particles in the liver, spleen, and/or bone marrow. PEGylation is one method to camouflage nanosize molecules and to prevent adhesion of opsonins so that the particles remain in

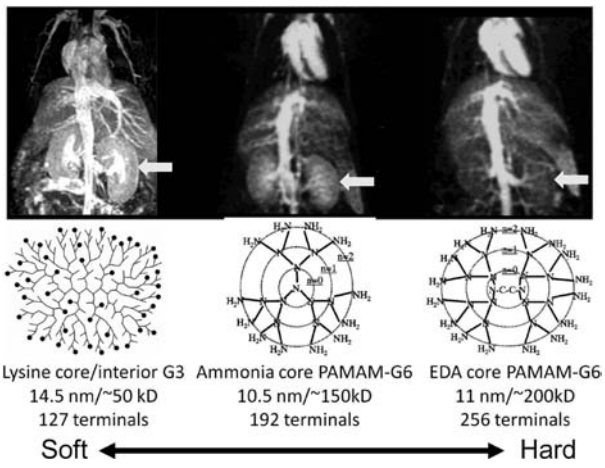


Figure 2. Despite the small size, hard interior (high density) EDA-core PAMAM-G6 does not show renal excretion. Two other "softer" interior dendrimers show renal excretion.

circulation and evade the reticuloendothelial system, a process referred to as the "stealth effect".[7] It is proposed that PEG reduces opsonization through steric and hydration effects.[7,27] Interestingly, although PEGylation increases size, which has been associated with faster uptake by the liver and RES, numerous reports indicate that PEGylation increases circulatory retention times and decreases liver uptake.[28]

FLEXIBILITY

At this time, particle flexibility is not widely considered an important determinant of in vivo nanosized molecule or particle behavior. However, given the dynamic nature of living systems and the time course over which particles interact with internal tissues, particle flexibility may have an important role in how nanosized molecules or particles interface with living tissues. Research suggests flexibility is an important determinant of in vivo behavior. Given the highly adaptable nature of these particles, it is possible to achieve high degrees of intramolecular flexibility. Dendrimers may represent an ideal particle to study the effects of particle flexibility in living systems as well as an ideal platform to then harness the insights for optimizing particle platforms. In one example, in a large particle conferred by one or two linear, long PEGylated tails[17] or the use of more flexible interiors including lysine dendrimers[29] or ammonia core PAMAM dendrimer,[30] the more flexibile particle demonstrated increased renal clearance (Figure 2). In contrast, less flexible ethylenediamine (EDA) core dendrimers[17] or dendrimers grafted with short PEG tails did not show renal clearance.[25] Interestingly, flexible dendrimer-based MR contrast agents exhibited improved renal clearance but retained similar relaxivity compared with "hard" dendrimers, which were not excreted by the kidneys.[19]

BIOLOGICAL APPLICATION OF PHYSICAL CHARACTERISTICS

The in vivo affinity of nanoparticles for specific anatomic locations and their behavior at specific biological interfaces plays an important role in probe characteristics and toxicity. Specific interfaces include the glomerular basement membrane, the blood-brain barrier, vascular and lymphatic endothelial linings, and hepatic sinusoids. The ability or inability of nanoparticles to

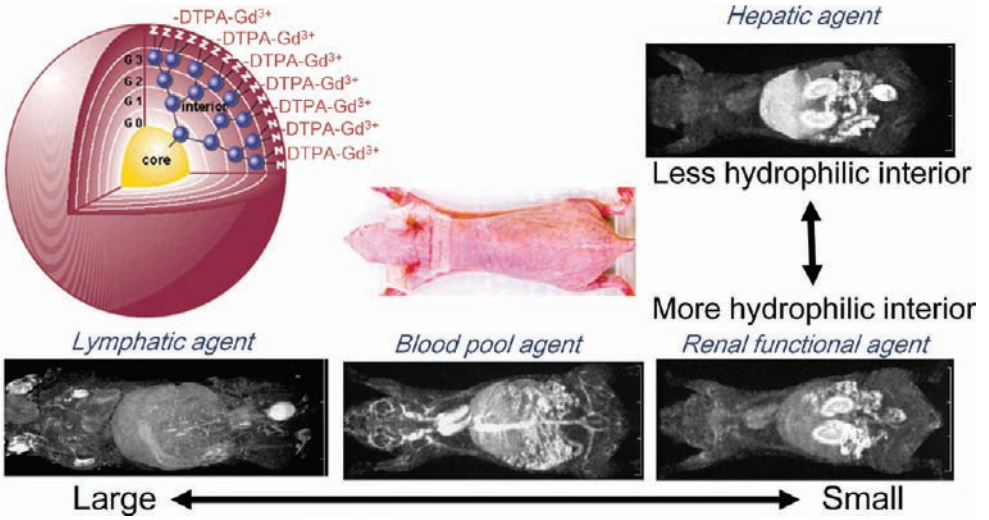


Figure 3. Strategic use of dendrimer size to achieve organ-specific imaging. This schema depits a generation 3 dendrimer,with core chemistry, shape, and surface modifications functionalized for use as an MRI contrast agent. Images of mice demonstrate that strategic selection of dendrimer size enables target organ-specific imaging. For example, PAMAM-G8 shows the lymphatic system; PAMAM-G6 shows the blood pool; PAMAM-G4 depicts renal function; and PPI/DAB-G4 depicts liver parenchyma.

cross these interfaces will in large part determine their biodistribution and hence their utility.

Dendrimers have been shown to be useful imaging agents of various anatomic and physiologic processes. Preclinical studies demonstrate PAMAM-based contrast agents are effective for MR liver imaging,[31,32] renal functional imaging,[33,34] and angiography[35−37] and lymphography[20,38] (Figure 3). Macromolecular MR contrast agents prepared from dendrimers have the advantage of uniform molecular weight distribution, relatively controlled structure, high relaxivities, and high loading of gadolinium chelates on the surface.[39,40] Dendrimers are particularly well suited for lymphatic imaging,[41−43] as this requires a modality with high spatial resolution and high sensitivity for contrast agents, since the lymphatics themselves are so small.[19,41−52] Dendrimers are retained within the lymphatics, especially when their surface charge is modified with an appropriate coating or when conjugated to specific fluorophores.[35,40,53−55] Smaller molecules (<6 nm) are taken up by the lymphatics, but do not remain in the lymphatic vessels, whereas large molecules (>20 nm) are taken up very slowly but are retained.[41] Dendrimer-based contrast agents between 6 and 10 nm are retained within the lymphatic system but are cleared from the sentinel lymph nodes within a day, which enables repeated injections. Additionally, these particles can be labeled with organic fluorophores (for optical imaging), radioisotopes (for scintigraphy), and paramagnetic lanthanide ions (for MRI).[40] Preclinical MR lymphangiography demonstrates that intradermally injected dendrimers are effective for imaging lymphatics in small and large animal models.[41,43] This may eventually play a vital role in identifying otherwise life-threatening thoracic duct injuries that occur during some pediatric cardiovascular surgeries.

Dendrimers are also useful nanoparticles for urinary tract imaging as well as for studying nanosized molecular pharmacokinetics. PAMAM-based Gd(III) complexes have shown size-dependent pharmacokinetics and renal filtration.[19] For instance, particles 2 nm in size are handled very similarly to low molecular weight contrast agents; yet, chemically similar but larger (6 nm) probes undergo comparatively slow renal clearance and particles that are 11 nm or larger do not undergo renal clearance at all.[56] Research suggests that the generation-4 (G4) dendrimer, which is approximately 6 nm in diameter, is ideal for renal imaging.[15,57] When administered in a normally functioning kidney, the G4 dendrimer accumulates in the proximal tubules, which is seen on imaging as enhancement of the outer stripe of the medulla.[56] This phenomenon enables the depiction of acute tubular injury (seen as loss of the medullary stripe), which correlates with the extent of renal impairment.[16] Advancements in dendrimer-based contrast agents include the advent of biodegradable agents, which typically rely on endogenous enzymes to cleave the probe, creating smaller, more easily cleared biproducts. Recently, a biodegradable macromolecular dendrimer-based agent, nanoglobule-G4-cystamin-(Gd-DO3A) conjugate, was created as an extracellular degradable nanosized contrast agent for dynamic contrast enhanced MRI. A disulfide spacer was introduced to accelerate the renal excretion of gadolinium chelates by reducing the spacer with free endogenous thiols and homocysteine in the plasma such that released chelates underwent rapid renal filtration with subsequent urinary tract accumulation sufficient for MR urography. The nanoglobular dendrimer demonstrated lower cytotoxicity, relatively rapid renal filtration, and low liver uptake[58] and in vivo studies demonstrated fast elimination kinetics that were ideal for evaluation of the kidneys.[59]

■ EFFECT OF TARGETING ON BIODISTRIBUTION

Conjugation of targeting ligands directly and indirectly alters biodistribution and clearance of nanoparticle-based imaging agents. Numerous strategies have been developed to manipulate in vivo behavior of nanoparticles by modifying the surface chemistry. Among the various nanoparticles, dendrimers present an ideal platform for conjugation of various targeting ligands, such as folic acid, avidin−biotin complex, RGD peptides, and carbohydrate molecules. Attachment of such ligands alters particle shape, flexibility, and size. Yang et al. conjugated anti-epidermal growth factor (EGF) antibody to boronated PAMAM-G4 dendrimers for targeting to EGF receptor expressing tumor cells and found that, at

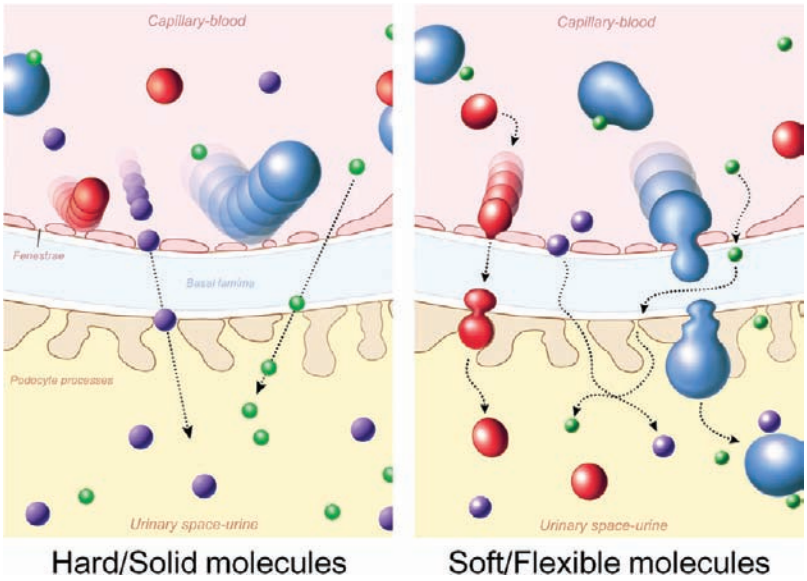


Figure 4. Schema for glomerular filtration of hard and soft nanosized molecules or particles.

24 h postinjection, the conjugates were highly localized in EGF-positive glioma with a tumor to blood ratio substantially higher than mice bearing tumors without EGF receptors or mice injected with nonconjugated PAMAM dendrimers.[60] Dendrimers have also been targeted with smaller molecules such as folate.[61−67] Folate-modified PAMAM dendrimers showed significantly high probe accumulation; however, hepatic and renal accumulation was also observed, likely due to the presence of folate receptors in hepatic macrophages and renal proximal tubules.[68]

Another targeting molecule is the avidin−biotin complex system, which selectively targets various types of tumors. Wilbur et al. showed that ^{125}I-labeled iodobenzoate-biotinylated PAMAM dendrimers (G0−4) were quickly cleared, giving low blood levels and high kidney and liver accumulation compared to unmodified counterparts.[68,69] G4 dendrimers complexed with olig-DNA and ^{111}In demonstrated lower hepatic uptake and higher kidney and spleen uptake than similar constructs without a dendrimer carrier. A similar construct containing oligo-DNA and avidin−biotin conjugated to a G4 dendrimer demonstrated very high uptake in the lung, which was thought to be due to trapping of large molecular weight complexes within the lung.[70] Avidin−biotin targeting has been extended for MRI, Gd-neutron capture therapy, and gene delivery.[71,72] After intraperitoneal administration, avidin-conjugated PAMAM-G6-Gd conjugates exhibited specific accumulation in intraperitoneally disseminated SHIN3 ovarian cancer tumors with 366- and 3.4-fold greater values than Gd-DTPA and unconjugated PAMAM-Gd, respectively.[71]

Baker et al. have used PAMAM dendrimers as a vehicle to achieve cancer-targeted drug delivery by functionalizing the particles with riboflavin, methotrexate, and other tumor-cell binding moieties.[73−75] By utilizing generation-5 PAMAM dendrimers, it is possible to deliver sizable chemotherapeutic payloads, and the particles can be synthesized as an appropriately monodispersed product that demonstrates optimal pharmacokinetics.

CONCLUSION

To effectively move nanosized molecules or particles from the bench to human applications requires gaining a better understanding of their in vivo behavior. At this time, our understanding is rather limited, as studies have primarily focused on the pharmacokinetics of relatively spherical molecules and size has been the primary parameter evaluated. To improve upon this, we need to consider other molecular parameters such as shape and flexibility, as well as expand biodistribution studies beyond hard and spherical particles (Figure 4). As more information becomes available regarding the effects of these other parameters and particle types, we may move toward categorization systems that reflect in vivo behavior. Such a step forward will facilitate efficient and effective design and chemical synthesis and may also expedite the approval process for use in humans.

AUTHOR INFORMATION

Corresponding Author

*Correspondence to Hisataka Kobayashi, M.D., Ph.D., Molecular Imaging Program, National Cancer Institute/NIH, Bldg. 10, Room B3B69, MSC 1088, 10 Center Dr., Bethesda, Maryland 20892-1088, United States. E-mail: Kobayash@mail.nih.gov.

ACKNOWLEDGMENT

This research was supported by the Intramural Research Program of the National Institutes of Health, National Cancer Institute, Center for Cancer Research.

REFERENCES

(1) Alexis, F., Pridgen, E., Molnar, L. K., and Farokhzad, O. C. (2008) Factors affecting the clearance and biodistribution of polymeric nanoparticles. *Mol. Pharm. 5*, 505–15.

(2) Bartneck, M., Keul, H. A., Zwadlo-Klarwasser, G., and Groll, J. (2010) Phagocytosis independent extracellular nanoparticle clearance by human immune cells. *Nano Lett. 10*, 59–63.

(3) Briley-Saebo, K. C., Johansson, L. O., Hustvedt, S. O., Haldorsen, A. G., Bjørnerud, A., Fayad, Z. A., and Ahlstrom, H. K. (2006) Clearance of iron oxide particles in rat liver: effect of hydrated particle size and coating material on liver metabolism. *Invest. Radiol. 41*, 560–71.

(4) Bulte, J. W., and Kraitchman, D. L. (2004) Iron oxide MR contrast agents for molecular and cellular imaging. *NMR Biomed. 17*, 484–99.

(5) Choi, H. S., Liu, W., Misra, P., Tanaka, E., Zimmer, J. P., Itty Ipe, B., Bawendi, M. G., and Frangioni, J. V. (2007) Renal clearance of quantum dots. *Nat. Biotechnol. 25*, 1165–70.

(6) Choi, H. S., Liu, W., Liu, F., Nasr, K., Misra, P., Bawendi, M. G., and Frangioni, J. V. (2010) Design considerations for tumour-targeted nanoparticles. *Nat. Nanotechnol. 5*, 42–7.

(7) Gonçalves, C., Torrado, E., Martins, T., Pereira, P., Pedrosa, J., and Gama, M. (2010) Dextrin nanoparticles: studies on the interaction with murine macrophages and blood clearance. *Colloids Surf., B: Biointerfaces 75*, 483–9.

(8) He, X., Nie, H., Wang, K., Tan, W., Wu, X., and Zhang, P. (2008) In vivo study of biodistribution and urinary excretion of surface-modified silica nanoparticles. *Anal. Chem. 80*, 9597–603.

(9) Jain, T. K., Reddy, M. K., Morales, M. A., Leslie-Pelecky, D. L., and Labhasetwar, V. (2008) Biodistribution, clearance, and biocompatibility of iron oxide magnetic nanoparticles in rats. *Mol. Pharm. 5*, 316–27.

(10) Kobayashi, H., Sato, N., Kawamoto, S., Saga, T., Hiraga, A., Ishimori, T., Konishi, J., Togashi, K., and Brechbiel, M. W. (2001) Novel intravascular macromolecular MRI contrast agent with generation-4 polyamidoamine dendrimer core: accelerated renal excretion with coinjection of lysine. *Magn. Reson. Med. 46*, 457–64.

(11) Longmire, M., Choyke, P. L., and Kobayashi, H. (2008) Clearance properties of nano-sized particles and molecules as imaging agents: considerations and caveats. *Nanomedicine (Lond.) 3*, 703–17.

(12) Schipper, M. L., Iyer, G., Koh, A. L., Cheng, Z., Ebenstein, Y., Aharoni, A., Keren, S., Bentolila, L. A., Li, J., Rao, J., Chen, X., Banin, U., Wu, A. M., Sinclair, R., Weiss, S., and Gambhir, S. S. (2009) Particle size, surface coating, and PEGylation influence the biodistribution of quantum dots in living mice. *Small 5*, 126–34.

(13) Sigovan, M., Boussel, L., Sulaiman, A., Sappey-Marinier, D., Alsaid, H., Desbleds-Mansard, C., Ibarrola, D., Gamondès, D., Corot, C., Lancelot, E., Raynaud, J. S., Vives, V., Laclédère, C., Violas, X., Douek, P. C., and Canet-Soulas, E. (2009) Rapid-clearance iron nanoparticles for inflammation imaging of atherosclerotic plaque: initial experience in animal model. *Radiology 252*, 401–9.

(14) Kobayashi, H., Kawamoto, S., Jo, S. K., Bryant, H. L., Brechbiel, M. W., and Star, R. A. (2003) Macromolecular MRI contrast agents with small dendrimers: pharmacokinetic differences between sizes and cores. *Bioconjugate Chem. 14*, 388–94.

(15) Kobayashi, H., and Brechbiel, M. W. (2004) Dendrimer-based nanosized MRI contrast agents. *Curr. Pharm. Biotechnol. 5*, 539–49.

(16) Kobayashi, H., Jo, S. K., Kawamoto, S., Yasuda, H., Hu, X., Knopp, M. V., Brechbiel, M. W., Choyke, P. L., and Star, R. A. (2004) Polyamine dendrimer-based MRI contrast agents for functional kidney imaging to diagnose acute renal failure. *J. Magn. Reson. Imaging 20*, 512–8.

(17) Kobayashi, H., Kawamoto, S., Saga, T., Sato, N., Hiraga, A., Ishimori, T., Konishi, J., Togashi, K., and Brechbiel, M. W. (2001) Positive effects of polyethylene glycol conjugation to generation-4 polyamidoamine dendrimers as macromolecular MR contrast agents. *Magn. Reson. Med. 46*, 781–8.

(18) Tomalia, D. A. (2009) In quest of a systematic framework for unifying and defining nanoscience. *J. Nanopart. Res. 11*, 1251–1310.

(19) Kobayashi, H., and Brechbiel, M. W. (2005) Nano-sized MRI contrast agents with dendrimer cores. *Adv. Drug Delivery Rev. 57*, 2271–86.

(20) Sato, N., Kobayashi, H., Hiraga, A., Saga, T., Togashi, K., Konishi, J., and Brechbiel, M. W. (2001) Pharmacokinetics and enhancement patterns of macromolecular MR contrast agents with various sizes of polyamidoamine dendrimer cores. *Magn. Reson. Med. 46*, 1169–73.

(21) Canelas, D. A., Herlihy, K. P., and DeSimone, J. M. (2009) Top-down particle fabrication: control of size and shape for diagnostic imaging and drug delivery. *Wiley Interdiscip. Rev. Nanomed. Nanobiotechnol. 1*, 391–404.

(22) Sadekar, S., Ray, A., Janàt-Amsbury, M., Peterson, C. M., and Ghandehari, H. (2011) Comparative biodistribution of PAMAM dendrimers and HPMA copolymers in ovarian-tumor-bearing mice. *Biomacromolecules 12*, 88–96.

(23) Geng, Y., Dalhaimer, P., Cai, S., Tsai, R., Tewari, M., Minko, T., and Discher, D. E. (2007) Shape effects of filaments versus spherical particles in flow and drug delivery. *Nat. Nanotechnol. 2*, 249–55.

(24) Arnida, Janát-Amsbury, M. M., Ray, A., Peterson, C. M., and Ghandehari, H. (2010) Geometry and surface characteristics of gold nanoparticles influence their biodistribution and uptake by macrophages. *Eur. J. Pharm. Biopharm.*

(25) Kojima, C., Regino, C., Umeda, Y., Kobayashi, H., and Kono, K. (2010) Influence of dendrimer generation and polyethylene glycol length on the biodistribution of PEGylated dendrimers. *Int. J. Pharm. 383*, 293–6.

(26) Owens, D. E., and Peppas, N. A. (2006) Opsonization, biodistribution, and pharmacokinetics of polymeric nanoparticles. *Int. J. Pharm. 307*, 93–102.

(27) Sheng, Y., Yuan, Y., Liu, C., Tao, X., Shan, X., and Xu, F. (2009) In vitro macrophage uptake and in vivo biodistribution of PLA-PEG nanoparticles loaded with hemoglobin as blood substitutes: effect of PEG content. *J. Mater. Sci. Mater. Med. 20*, 1881–91.

(28) Gaumet, M., Vargas, A., Gurny, R., and Delie, F. (2008) Nanoparticles for drug delivery: the need for precision in reporting particle size parameters. *Eur. J. Pharm. Biopharm. 69*, 1–9.

(29) Ogawa, M., Regino, C. A., Marcelino, B., Williams, M., Kosaka, N., Bryant, L. H., Jr., Choyke, P. L., and Kobayashi, H. (2010) New nanosized biocompatible MR contrast agents based on lysine-dendrigraft macromolecules. *Bioconjugate Chem. 21*, 955–60.

(30) Kobayashi, H., Sato, N., Kawamoto, S., Saga, T., Hiraga, A., Haque, T. L., Ishimori, T., Konishi, J., Togashi, K., and Brechbiel, M. W. (2001) Comparison of the macromolecular MR contrast agents with ethylenediamine-core versus ammonia-core generation-6 polyamidoamine dendrimer. *Bioconjugate Chem. 12*, 100–7.

(31) Kobayashi, H., Saga, T., Kawamoto, S., Sato, N., Hiraga, A., Ishimori, T., Konishi, J., Togashi, K., and Brechbiel, M. W. (2001) Dynamic micro-magnetic resonance imaging of liver micrometastasis in mice with a novel liver macromolecular magnetic resonance contrast agent DAB-Am64-(1B4M-Gd)(64). *Cancer Res. 61*, 4966–70.

(32) Kobayashi, H., Kawamoto, S., Saga, T., Sato, N., Hiraga, A., Ishimori, T., Akita, Y., Mamede, M. H., Konishi, J., Togashi, K., and Brechbiel, M. W. (2001) Novel liver macromolecular MR contrast agent with a polypropylenimine diaminobutyl dendrimer core: comparison to the vascular MR contrast agent with the polyamidoamine dendrimer core. *Magn. Reson. Med. 46*, 795–802.

(33) Dear, J. W., Kobayashi, H., Jo, S. K., Holly, M. K., Hu, X., Yuen, P. S., Brechbiel, M. W., and Star, R. A. (2005) Dendrimer-enhanced MRI as a diagnostic and prognostic biomarker of sepsis-induced acute renal failure in aged mice. *Kidney Int. 67*, 2159–67.

(34) Kobayashi, H., Kawamoto, S., Jo, S., Sato, N., Saga, T., Hiraga, A., Konishi, J., Hu, S., Togashi, K., Brechbiel, M. W., and Star, R. A. (2002) Renal tubular damage detected by dynamic micro-MRI with a dendrimer-based MR contrast agent. *Kidney Int. 61*, 1980–5.

(35) Kobayashi, H., Sato, N., Hiraga, A., Saga, T., Nakamoto, Y., Ueda, H., Konishi, J., Togashi, K., and Brechbiel, M. W. (2001) 3D-micro-MR angiography of mice using macromolecular MR contrast agents with polyamidoamine dendrimer core with reference to their pharmacokinetic properties. *Magn. Reson. Med. 45*, 454–60.

(36) Kobayashi, H., Kawamoto, S., Saga, T., Sato, N., Hiraga, A., Konishi, J., Togashi, K., and Brechbiel, M. W. (2001) Micro-MR angiography of normal and intratumoral vessels in mice using dedicated intravascular MR contrast agents with high generation of polyamidoamine dendrimer core: reference to pharmacokinetic properties of dendrimer-based MR contrast agents. *J. Magn. Reson. Imaging 14*, 705–13.

(37) Kobayashi, H., Sato, N., Kawamoto, S., Saga, T., Hiraga, A., Ishimori, T., Konishi, J., Togashi, K., and Brechbiel, M. W. (2001) 3D MR angiography of intratumoral vasculature using a novel macromolecular MR contrast agent. *Magn. Reson. Med. 46*, 579–85.

(38) Xu, R., Wang, Y., Wang, X., Jeong, E. K., Parker, D. L., and Lu, Z. R. (2007) In Vivo evaluation of a PAMAM-cystamine-(Gd-DO3A)

conjugate as a biodegradable macromolecular MRI contrast agent. *Exp. Biol. Med. (Maywood) 232*, 1081–9.

(39) Kobayashi, H., and Brechbiel, M. W. (2003) Dendrimer-based macromolecular MRI contrast agents: characteristics and application. *Mol. Imaging 2*, 1–10.

(40) Kobayashi, H., Ogawa, M., Kosaka, N., Choyke, P. L., and Urano, Y. (2009) Multicolor imaging of lymphatic function with two nanomaterials: quantum dot-labeled cancer cells and dendrimer-based optical agents. *Nanomedicine (Lond.) 4*, 411–9.

(41) Kobayashi, H., Kawamoto, S., Choyke, P. L., Sato, N., Knopp, M. V., Star, R. A., Waldmann, T. A., Tagaya, Y., and Brechbiel, M. W. (2003) Comparison of dendrimer-based macromolecular contrast agents for dynamic micro-magnetic resonance lymphangiography. *Magn. Reson. Med. 50*, 758–66.

(42) Koyama, Y., Talanov, V. S., Bernardo, M., Hama, Y., Regino, C. A., Brechbiel, M. W., Choyke, P. L., and Kobayashi, H. (2007) A dendrimer-based nanosized contrast agent dual-labeled for magnetic resonance and optical fluorescence imaging to localize the sentinel lymph node in mice. *J. Magn. Reson. Imaging 25*, 866–71.

(43) Sena, L. M., Fishman, S. J., Jenkins, K. J., Xu, H., Brechbiel, M. W., Regino, C. A., Kosaka, N., Bernardo, M., Choyke, P. L., and Kobayashi, H. (2010) Magnetic resonance lymphangiography with a nano-sized gadolinium-labeled dendrimer in small and large animal models. *Nanomedicine (Lond.) 5*, 1183–91.

(44) Hama, Y., Koyama, Y., Urano, Y., Choyke, P. L., and Kobayashi, H. (2007) Two-color lymphatic mapping using Ig-conjugated near infrared optical probes. *J. Invest. Dermatol. 127*, 2351–6.

(45) Kim, S., Lim, Y. T., Soltesz, E. G., De Grand, A. M., Lee, J., Nakayama, A., Parker, J. A., Mihaljevic, T., Laurence, R. G., Dor, D. M., Cohn, L. H., Bawendi, M. G., and Frangioni, J. V. (2004) Near-infrared fluorescent type II quantum dots for sentinel lymph node mapping. *Nat. Biotechnol. 22*, 93–7.

(46) Kobayashi, H., Kawamoto, S., Bernardo, M., Brechbiel, M. W., Knopp, M. V., and Choyke, P. L. (2006) Delivery of gadolinium-labeled nanoparticles to the sentinel lymph node: comparison of the sentinel node visualization and estimations of intra-nodal gadolinium concentration by the magnetic resonance imaging. *J. Controlled Release 111*, 343–51.

(47) Kobayashi, H., Kawamoto, S., Sakai, Y., Choyke, P. L., Star, R. A., Brechbiel, M. W., Sato, N., Tagaya, Y., Morris, J. C., and Waldmann, T. A. (2004) Lymphatic drainage imaging of breast cancer in mice by micro-magnetic resonance lymphangiography using a nano-size paramagnetic contrast agent. *J. Natl. Cancer Inst. 96*, 703–8.

(48) Kobayashi, H., Kawamoto, S., Star, R. A., Waldmann, T. A., Tagaya, Y., and Brechbiel, M. W. (2003) Micro-magnetic resonance lymphangiography in mice using a novel dendrimer-based magnetic resonance imaging contrast agent. *Cancer Res. 63*, 271–6.

(49) Kobayashi, H., Kawamoto, S., Brechbiel, M. W., Bernardo, M., Sato, N., Waldmann, T. A., Tagaya, Y., and Choyke, P. L. (2005) Detection of lymph node involvement in hematologic malignancies using micromagnetic resonance lymphangiography with a gadolinum-labeled dendrimer nanoparticle. *Neoplasia 7*, 984–91.

(50) Kobayashi, H., Hama, Y., Koyama, Y., Barrett, T., Regino, C. A., Urano, Y., and Choyke, P. L. (2007) Simultaneous multicolor imaging of five different lymphatic basins using quantum dots. *Nano Lett. 7*, 1711–6.

(51) Kobayashi, H., Koyama, Y., Barrett, T., Hama, Y., Regino, C. A., Shin, I. S., Jang, B. S., Le, N., Paik, C. H., Choyke, P. L., and Urano, Y. (2007) Multimodal nanoprobes for radionuclide and five-color near-infrared optical lymphatic imaging. *ACS Nano 1*, 258–64.

(52) Mounzer, R., Shkarin, P., Papademetris, X., Constable, T., Ruddle, N. H., and Fahmy, T. M. (2007) Dynamic imaging of lymphatic vessels and lymph nodes using a bimodal nanoparticulate contrast agent. *Lymphat. Res. Biol. 5*, 151–8.

(53) Kono, K., Kojima, C., Hayashi, N., Nishisaka, E., Kiura, K., Watarai, S., and Harada, A. (2008) Preparation and cytotoxic activity of poly(ethylene glycol)-modified poly(amidoamine) dendrimers bearing adriamycin. *Biomaterials 29*, 1664–75.

(54) Kojima, C., Kono, K., Maruyama, K., and Takagishi, T. (2000) Synthesis of polyamidoamine dendrimers having poly(ethylene glycol) grafts and their ability to encapsulate anticancer drugs. *Bioconjugate Chem. 11*, 910–7.

(55) Sato, N., Kobayashi, H., Saga, T., Nakamoto, Y., Ishimori, T., Togashi, K., Fujibayashi, Y., Konishi, J., and Brechbiel, M. W. (2001) Tumor targeting and imaging of intraperitoneal tumors by use of antisense oligo-DNA complexed with dendrimers and/or avidin in mice. *Clin. Cancer Res. 7*, 3606–12.

(56) Choyke, P. L., and Kobayashi, H. (2006) Functional magnetic resonance imaging of the kidney using macromolecular contrast agents. *Abdom. Imaging 31*, 224–31.

(57) Kobayashi, H., Reijnders, K., English, S., Yordanov, A. T., Milenic, D. E., Sowers, A. L., Citrin, D., Krishna, M. C., Waldmann, T. A., Mitchell, J. B., and Brechbiel, M. W. (2004) Application of a macromolecular contrast agent for detection of alterations of tumor vessel permeability induced by radiation. *Clin. Cancer Res. 10*, 7712–20.

(58) Kaneshiro, T. L., Jeong, E. K., Morrell, G., Parker, D. L., and Lu, Z. R. (2008) Synthesis and evaluation of globular Gd-DOTA-mono-amide conjugates with precisely controlled nanosizes for magnetic resonance angiography. *Biomacromolecules 9*, 2742–8.

(59) Xu, R., Kaneshiro, T. L., Jeong, E. K., Parker, D. L., and Lu, Z. R. (2010) Synthesis and evaluation of nanoglobule-cystamine-(Gd-DO3A), a biodegradable nanosized magnetic resonance contrast agent for dynamic contrast-enhanced magnetic resonance urography. *Int. J. Nanomed. 5*, 707–13.

(60) Yang, W., Barth, R. F., Adams, D. M., and Soloway, A. H. (1997) Intratumoral delivery of boronated epidermal growth factor for neutron capture therapy of brain tumors. *Cancer Res. 57*, 4333–9.

(61) Kono, K., Liu, M., and Frechet, J. M. (1999) Design of dendritic macromolecules containing folate or methotrexate residues. *Bioconjugate Chem. 10*, 1115–21.

(62) Sideratou, Z., Kontoyianni, C., Drossopoulou, G. I., and Paleos, C. M. (2010) Synthesis of a folate functionalized PEGylated poly(propylene imine) dendrimer as prospective targeted drug delivery system. *Bioorg. Med. Chem. Lett. 20*, 6513–7.

(63) Wiener, E. C., Konda, S., Shadron, A., Brechbiel, M., and Gansow, O. (1997) Targeting dendrimer-chelates to tumors and tumor cells expressing the high-affinity folate receptor. *Invest. Radiol. 32*, 748–54.

(64) Zhang, Y., Sun, Y., Xu, X., Zhang, X., Zhu, H., Huang, L., Qi, Y., and Shen, Y. M. (2010) Synthesis, biodistribution, and microsingle photon emission computed tomography (SPECT) imaging study of technetium-99m labeled PEGylated dendrimer poly(amidoamine) (PAMAM)-folic acid conjugates. *J. Med. Chem. 53*, 3262–72.

(65) Cao, W., Zhou, J., Wang, Y., and Zhu, L. (2010) Synthesis and in vitro cancer cell targeting of folate-functionalized biodegradable amphiphilic dendrimer-like star polymers. *Biomacromolecules 11*, 3680–7.

(66) Glickson, J. D., Lund-Katz, S., Zhou, R., Choi, H., Chen, I. W., Li, H., Corbin, I., Popov, A. V., Cao, W., Song, L., Qi, C., Marotta, D., Nelson, D. S., Chen, J., Chance, B., and Zheng, G. (2008) Lipoprotein nanoplatform for targeted delivery of diagnostic and therapeutic agents. *Mol. Imaging 7*, 101–10.

(67) Konda, S. D., Aref, M., Wang, S., Brechbiel, M., and Wiener, E. C. (2001) Specific targeting of folate-dendrimer MRI contrast agents to the high affinity folate receptor expressed in ovarian tumor xenografts. *MAGMA 12*, 104–13.

(68) Wijagkanalan, W., Kawakami, S., and Hashida, M. (2010) Designing dendrimers for drug delivery and imaging: pharmacokinetic considerations. *Pharm. Res.*

(69) Wilbur, D. S., Pathare, P. M., Hamlin, D. K., Buhler, K. R., and Vessella, R. L. (1998) Biotin reagents for antibody pretargeting. 3. Synthesis, radioiodination, and evaluation of biotinylated starburst dendrimers. *Bioconjugate Chem. 9*, 813–25.

(70) Mamede, M., Saga, T., Ishimori, T., Higashi, T., Sato, N., Kobayashi, H., Brechbiel, M. W., and Konishi, J. (2004) Hepatocyte targeting of 111In-labeled oligo-DNA with avidin or avidin-dendrimer complex. *J. Controlled Release 95*, 133–41.

(71) Kobayashi, H., Kawamoto, S., Saga, T., Sato, N., Ishimori, T., Konishi, J., Ono, K., Togashi, K., and Brechbiel, M. W. (2001) Avidin-dendrimer-(1B4M-Gd)(254): a tumor-targeting therapeutic agent for

gadolinium neutron capture therapy of intraperitoneal disseminated tumor which can be monitored by MRI. *Bioconjugate Chem. 12*, 587–93.

(72) Xu, H., Regino, C. A., Koyama, Y., Hama, Y., Gunn, A. J., Bernardo, M., Kobayashi, H., Choyke, P. L., and Brechbiel, M. W. (2007) Preparation and preliminary evaluation of a biotin-targeted, lectin-targeted dendrimer-based probe for dual-modality magnetic resonance and fluorescence imaging. *Bioconjugate Chem. 18*, 1474–82.

(73) Baker, J. R., Jr. (2009) Dendrimer-based nanoparticles for cancer therapy. *Hematol. Am. Soc. Hematol. Educ. Program* 708–19.

(74) Majoros, I. J., Williams, C. R., and Baker, J. R., Jr. (2008) Current dendrimer applications in cancer diagnosis and therapy. *Curr. Top. Med. Chem. 8*, 1165–79.

(75) Quintana, A., Raczka, E., Piehler, L., Lee, I., Myc, A., Majoros, I., Patri, A. K., Thomas, T., Mule, J., and Baker, J. R., Jr. (2002) Design and function of a dendrimer-based therapeutic nanodevice targeted to tumor cells through the folate receptor. *Pharm. Res. 19*, 1310–6.

Bioconjugate Chemistry

COMMUNICATION

pubs.acs.org/bc

Dual-Functional, Receptor-Targeted Fluorogenic Probe for In Vivo Imaging of Extracellular Protease Expressions

Lei Zhu,[†,‡] Jin Xie,[†] Magdalena Swierczewska,[†,§] Fan Zhang,[†] Xin Lin,[†] Xuexun Fang,[‡] Gang Niu,[†] Seulki Lee,[*,†] and Xiaoyuan Chen[*,†]

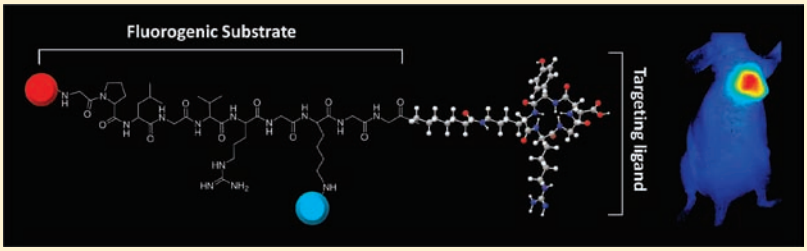
[†]National Institute of Biomedical Imaging and Bioengineering (NIBIB), National Institutes of Health (NIH), 31 Center Drive, Bethesda, Maryland 20892, United States

[‡]Key Laboratory for Molecular Enzymology and Enzyme Engineering, Jilin University, Changchun 130021, China

[§]Department of Biomedical Engineering, Stony Brook University, Stony Brook, New York 11794, United States

Supporting Information

ABSTRACT:



Herein, we report a new type of *in vivo* fluorogenic probe that enables simultaneous and active targeting of overexpressed receptors, $\alpha_V\beta_3$ integrins, and extracellular proteases, matrix metalloproteinases (MMPs), in the tumor regions. This c(RGDyK)-conjugated MMP fluorogenic probe efficiently targets the tumor regions with high retention time while maintaining receptor binding affinity and substrate activity. The probe minimizes nonspecific accumulation, thus demonstrating improved tumor-to-background signal ratio (T/N) in both $\alpha_V\beta_3$ integrin- and MMP-overexpressing U87MG tumor-bearing mouse model. This strategy can be easily tuned for a wide array of applications targeting various receptors and extracellular proteases *in vivo*.

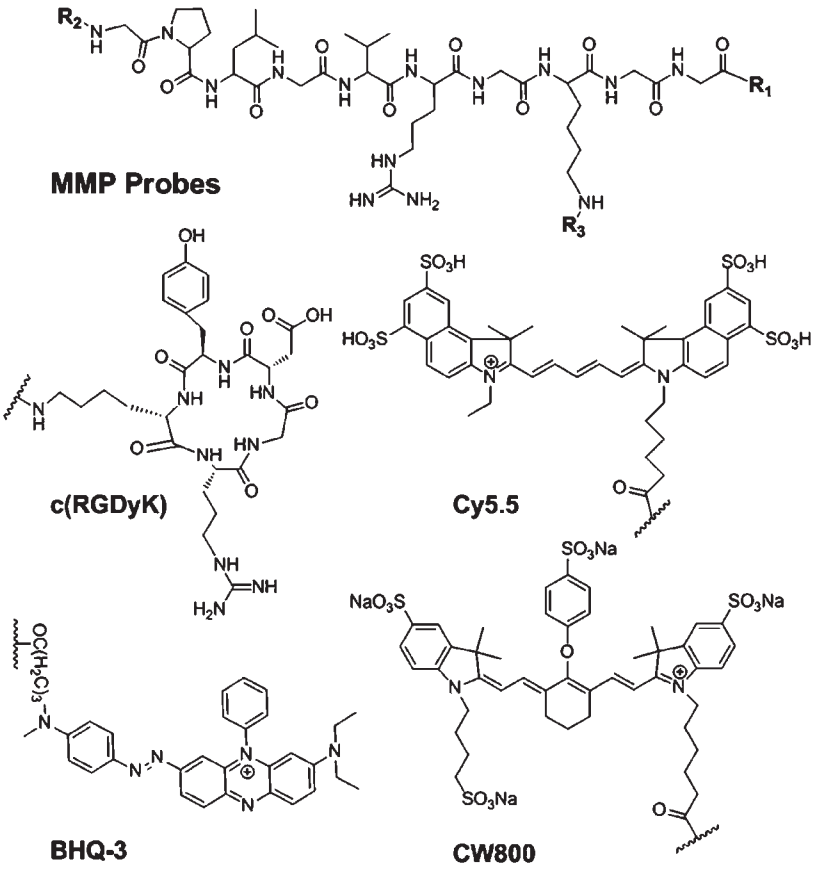
Fluorogenic substrates, consisting of protease substrates labeled with a fluorescent reporter and a quencher dye, are highly sensitive and sequence specific and have long been used in in vitro diagnostic assays. Recent advances in optical imaging instrumentation and development of various near-infrared (NIR) fluorescent dyes and NIR quenchers enabled the use of conventional fluorogenic substrates for in vivo imaging applications. Any reported fluorogenic substrate with known sequences can be easily modified to NIR fluorogenic probes, so-called peptide-based activatable probes,[1−6] for in vivo imaging by replacing conventional dye molecules to a NIR fluorescent dye/quencher pair. Although reported NIR fluorogenic probes showed potential in in vivo imaging, short half-life, poor pharmacokinetic profiles, instability, and high background induced by a nonspecific degradation of fluorogenic substrates still hamper its application.

Development of novel techniques for noninvasive imaging of specific protease activity is critical and urgently needed. Proteases are known as extremely important signaling molecules that are involved in numerous pathological processes including cancer, inflammatory, neurological, and cardiovascular diseases.[7−9] Successful protease imaging techniques can be used for studying the role of protease expressions in protease-associated disease animal models or monitoring therapeutic efficacy of a number of newly developed protease inhibitors in vivo. Various unique forms of protease-activatable probes have been designed in combination with fluorogenic substrates and materials including targeting ligands, polymers, and inorganic metals such as gold nanoparticles and quantum dots.[1−6,10−18] Although the use of activatable probes seems to be popular, surprisingly, very limited platforms of activatable probes are available which can clearly image proteases' activity in vivo after systemic administration. Unfortunately, the majority of reported systems demonstrate their proof-of-concept only in vitro or in ex vivo conditions such as after intratumoral injection in tumor models.

Ideal activatable probes can be designed by increasing in vivo stability and/or target (i.e., tumor) specificity of the fluorogenic probe while maintaining biological activity against specific proteases. Chemically, these improvements can be achieved by modifying fluorogenic peptides with water-soluble biomacromolecules such as PEGylated poly(L-lysine)[11,19] or tumor-homing polymeric nanoparticles,[10] since both polymers can increase the circulation half-life and efficiently deliver fluorogenic probes to

Received: January 3, 2011
Revised: May 13, 2011
Published: May 17, 2011

ACS Publications © 2011 American Chemical Society



Probes	Structures
4	R_1 = c(RGDyK), R_2 = Cy5.5, R_3 = BHQ-3
5	R_1 = c(RGDyK), R_2 = Cy5.5, R_3 = H
6	R_1 = H, R_2 = Cy5.5, R_3 = BHQ-3
7	CW800-c(RGDyK)

Figure 1. Chemical structures of relevant compounds.

the tumor mainly by the enhanced permeability retention (EPR) effect.[20] Indeed, these concepts showed promising results in many in vivo models; however, there are some drawbacks. For example, such probes take a long time for full activation due to the decreased substrate sensitivity from the conjugated high molecular weight polymer backbone, and more importantly, their EPR effect may cause nonspecific uptake causing false fluorescence signals in vivo.

In this study, we report a fluorogenic probe with an active targeting ligand that can be used as an efficient optical imaging probe to monitor extracellular protease expressions. We hypothesize that a targeting ligand will efficiently increase the retention time of the probe in the target region and maintain substrate activity, minimizing nonspecific accumulation and enhancing tumor-to-background signal ratio. To test the rationale of our strategy, we adopted a cyclic Arg-Gly-Asp peptide, c(RGDyK), a well-known $\alpha_v\beta_3$ integrin ligand that is overexpressed on the surface of angiogenic endothelial cells that mediates cell adhesion.[21−23] We synthesized c(RGDyK)-labeled matrix metalloproteinase (MMPs) specific fluorogenic probes, confirmed their enzyme and receptor activity in vitro, and demonstrated enhanced imaging of MMPs in both an $\alpha_v\beta_3$ integrin- and MMP-overexpressing tumor-bearing mouse model. MMPs are a large family of zinc-dependent proteases and play a crucial role in a variety of pathological disorders including cancer and inflammation diseases.[24] Accordingly, MMPs are important pharmaceutical and diagnostic targets for treatment of these diseases.

Our lead compound, MMP-P-RGD conjugate **4**, is composed of (i) Cy5.5 as a NIR dye (ex/em; 675/695 nm), (ii) the MMP-cleavable substrate G*PLGVR*GKGG as a recognition site indicated by italics with the cleavage site between Gly and Val, (iii) NIR dark quencher BHQ-3[25] (abs. 650 nm), and (iv) c(RGDyK) as a targeting ligand. Two Gly residues were incorporated as a spacer between the MMP-activatable fluorogenic peptide and the targeting ligand. Figure 1 shows the chemical structure of **4**. The multistep synthetic route involves three parts: (i) conjugation of c(RGDyK) to NHS ester activated C-terminal carboxyl group in

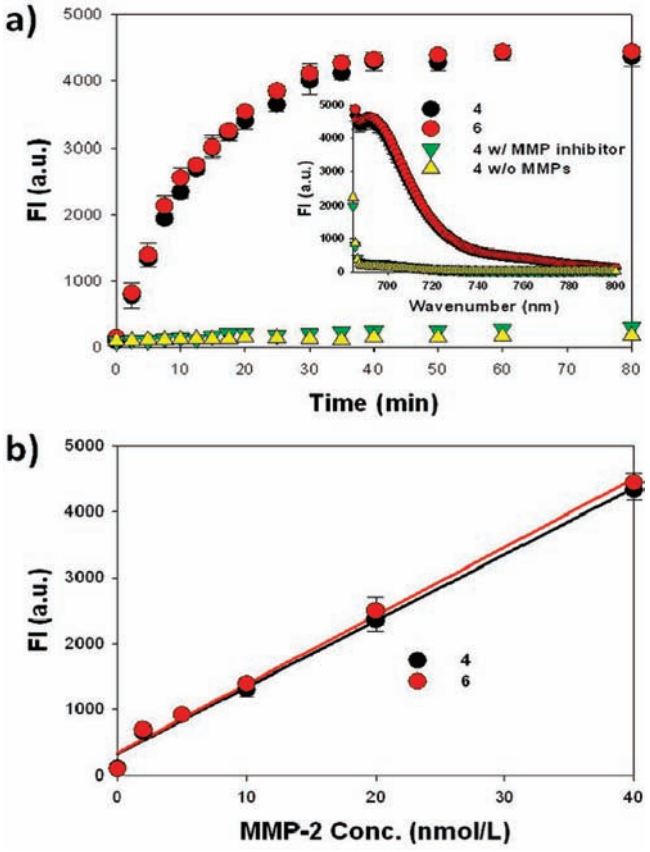


Figure 2. In vitro MMP specificy of MMP-P-RGD **4** and MMP-P **6**. (a) Fluorescence emission kinetic spectra of the probes in the presence of MMP-2 with and without a broad spectrum MMP inhibitor. Inset: Fluorescence emission spectra of the probes at 80 min. (b) Fluorescence intensities of the probes in the presence of various concentrations of activated MMP-2 (0, 2, 5, 10, 20, and 40 nM) following an 80 min incubation. Means ± SD (n = 3).

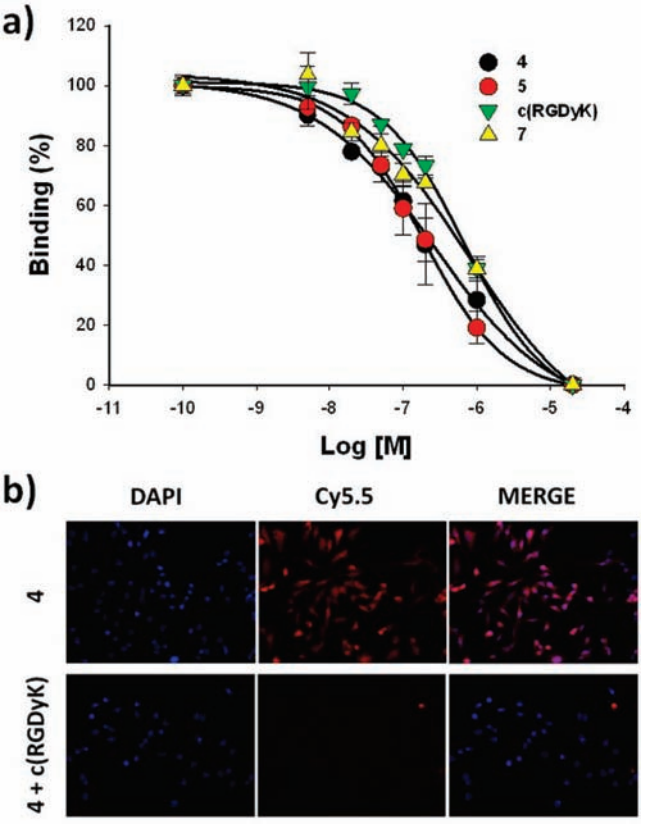


Figure 3. (a) Competitive $\alpha_v\beta_3$ integrin receptor assay of c(RGDyK), **4**, **5**, and **7** to U87MG human glioma cells. Means ± SD (n = 3). (b) Specific $\alpha_v\beta_3$ integrin receptor binding of **4**. NIR fluorescence images of U87MG cells were taken after 30 min incubation at 37 °C in the presence of **4** with and without a blocking dose of c(RGDyK) (10 μM).

fully protected MMP substrate **1**, Fmoc-GPLGVR(Pbf)GK-(tboc)GG; (ii) labeling NHS ester of NIR Cy5.5 dye to the Fmoc-deprotected N-terminal α-amino group of **2**, GPLGVR-(Pbf)GK(tboc)GG-c(RGDyK); (iii) conjugation of NHS ester of NIR dark quencher BHQ-3 to the ε-amino group of lysine followed by TFA cleavage of **3**, Cy5.5-GPLGVRGKGG-c-(RGDyK). The peptide sequence of **1** was synthesized by standard solid-phase Fmoc peptide chemistry. In addition, only Cy5.5-labeled analogue, Cy5.5-MMP-RGD **5**, was prepared for cellular imaging. As controls, an MMP fluorogenic peptide without c(RGDyK) ligand, MMP-P **6**, and CW800 dye (ex/em; 775/790 nm)-labeled c(RGDyK), CW800-RGD **7**, were also synthesized. Serial conjugation and deprotection of the peptide was performed in solution followed by preparative HPLC purifications. Purified products were confirmed by analytical HPLC and LC/MS (see Supporting Information for details).

First, the MMP specificity of **4** was compared to that of **6** to confirm whether conjugation of the targeting ligand affects its enzyme specificity. In vitro enzyme specificity was measured in the reaction buffer (100 mM Tris, 200 mM NaCl, 5 mM $CaCl_2$, 0.1% Brij, pH 7.5) containing activated MMP-2 with and without a homophenylalanine-hydroxamine acid based broad spectrum MMP inhibitor (EMD Bioscience) using a spectrofluorometer. The MMP-2 was activated by incubation of 2.5 mM of *p*-aminophenyl mercuric acid (APMA) in the reaction buffer for 2 h at 37 °C prior to use. As shown in Figure 2a, MMP-2 (40 nM) treatment of **4** and **6** (15 nM) resulted in an increased recovery of the NIR fluorescence signal and showed greater than 20-fold increase relative to the control sample without MMP-2. The fluorescence recovery of **4** was inhibited in the presence of the MMP inhibitor indicating probe selectivity. Similar experiments were performed by incubating **4** in the presence of different concentrations of MMP-2 (0, 2, 5, 10, 20, 40 nM) and the recovery of fluorescence was dependent on the MMP-2 concentration (Figure 2b). The overall MMP specificity of **4** against MMP-2 was similar to that of **6**. These results indicate that conjugation of the targeting ligand c(RGDyK) did not alter the MMP specificity of the probe.

Second, the effect of a bulky fluorogenic peptide on the $\alpha_v\beta_3$ binding affinity of c(RGDyK) was measured by a competitive cell-binding assay in U87MG cells. ^{125}I-eschistatin was used as a specific radioligand for competitive displacement. The U87MG cell is known to have high $\alpha_v\beta_3$ integrin density on the cell surface. All analogues containing c(RGDyK) ligand maintained reasonable binding affinities to its receptor. The IC_{50} values of c(RGDyK), **4**, **5**, and **7** were 592, 267, 184, and 456 nM, respectively (Figure 3a). Next, receptor specificity of the probes in cell culture was verified by fluorescent microscopic studies. The probes were incubated in fixed U87MG cells with and without a blocking dose of c(RGDyK) (10 μM). Since **5**, the nonquenched form of **4**, showed similar $\alpha_v\beta_3$ binding to **4** and **5**

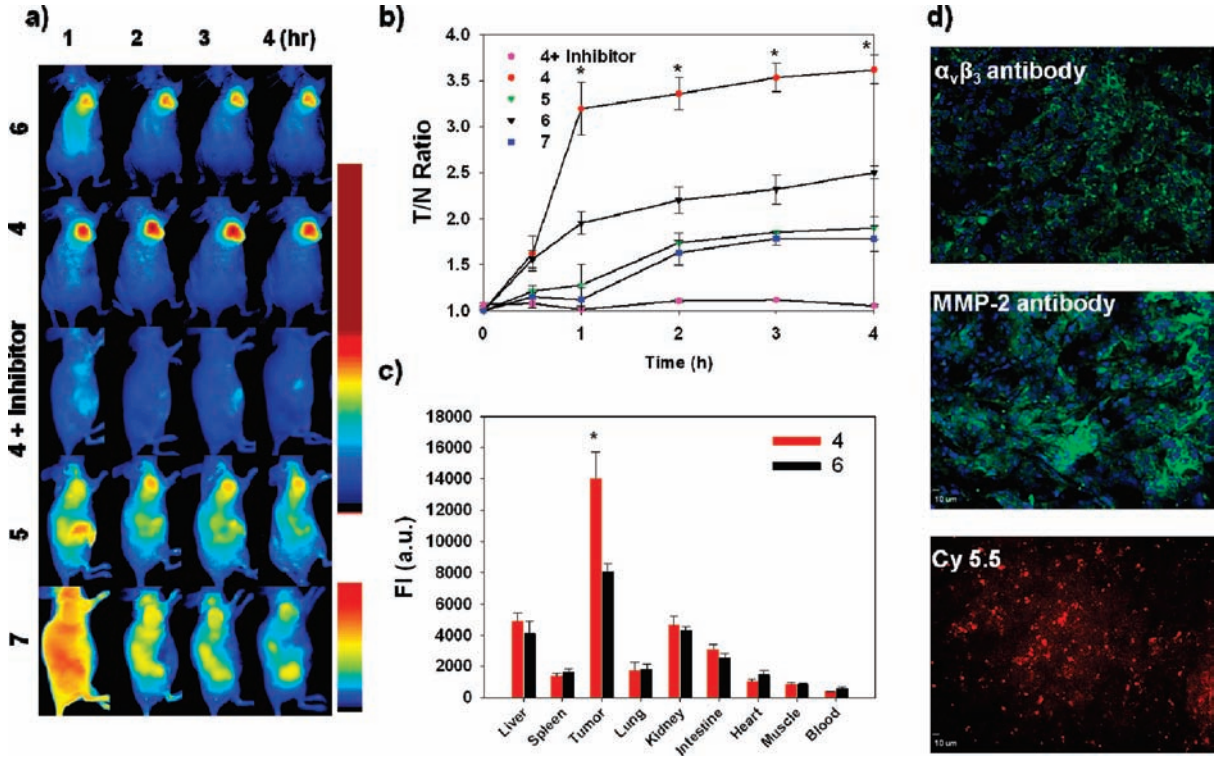


Figure 4. (a) Representative serial in vivo NIR fluorescence images of MMP- and $\alpha_V\beta_3$ integrin receptor-positive U87MG tumor-bearing mice injected intravenously with **4**, **5**, **6**, **4** with MMP inhibitor, and **7**. Images were acquired at the indicated time points and were normalized by the maximum average value. The color bar indicates radiant efficiency (upper bar; for Cy5.5, low 0, high 0.111, lower bar; for CW800, low 0, high 0.03 scaled counts/s). (b) T/N ratio analysis of NIR fluorescence intensity of U87MG tumor in vivo. (c) Biodistribution of **4** and **6**. Means ± SD ($n = 3$), * $P < 0.05$. (d) Tumor section counterstained with FITC-labeled antibody for $\alpha_V\beta_3$ integrin receptor (upper) and MMP-2 (middle). NIR fluorescence microscopy of tumor section injected with **4** (lower).

was used for in vitro cellular imaging studies. As shown in Figure 3b, **5** showed strong positive fluorescent signals on the cell membranes after 30 min of incubation at 37 °C. Since receptor blocking with an excess c(RGDyK) significantly decreased binding of **5**, the probe exhibits significant receptor specificity. Taken together, an NIR fluorogenic probe containing c-(RGDyK) ligand shows specific activities against both MMP-2 and $\alpha_v\beta_3$ signifying **4** could be used as an $\alpha_v\beta_3$ receptor-targeted MMP-specific molecular beacon.

To investigate whether the receptor-targeting ligand can enhance the visualization of extracellular protease expression in vivo, 3 nmol of **4** was intravenously injected into U87MG tumor-bearing mice treated with and without an MMP inhibitor. In order to inhibit the activity of MMPs in U87MG tumor, MMP inhibitor was intratumorally injected 30 min before the injection of **4**. To demonstrate the superiority of this new receptor-targeted fluorogenic probe over existing NIR dye-labeled receptor-targeted peptides in tumor imaging, **5** and **7** (0.5 nmol) were each also injected into an U87MG tumor model. It should be noted that only a limited dose of dye-labeled peptide probe like **5** and **7** can be injected for whole body imaging because of its high fluorescent background from the dye. In contrast, since fluorogenic probes are strongly quenched and a majority of the probe is activated at the target site, higher doses of the probe can be injected to enhance the ratio of region-of-interest (ROI) signal of tumor to normal tissue, muscle (T/N), at very early times. After injection, in vivo optical imaging was performed for 4 h using a small animal imaging system (Maestro 2) equipped with appropriate filters for Cy5.5 and CW800. Figure 4a shows representative serial images of mice at selected time points. Both **4** and **6** enabled visualization of MMP expression in an MMP-positive tumor, but **4** provided brighter NIR fluorescent images compared to **6** from 1 h postinjection. As expected, when MMP expression was inhibited by MMP inhibitors, the NIR fluorescence signal from the tumor was significantly reduced. In addition, tumor uptake was effectively blocked at 30 min postinjection with an excess amount of unlabeled c(RGDyK) (200 nmol) with **4** demonstrating the c(RGDyK)-mediated specific binding of **4** in vivo (see Supporting Information, Figure S3). Like other conventional types of NIR dye-labeled peptide probes, **5** and **7** showed gradually increased fluorescent signals in the tumor after the probe was slowly cleared from the blood and other organs. T/N ratios are illustrated in Figure 4b. **4** showed enhanced T/N and were up to 2.3, 1.5, 2.0, and 3.4-fold higher than **5**, **6**, **7**, and **4** treated with an inhibitor, respectively. After whole-mouse imaging at 4 h time point, tumors and organs were carefully removed and the biodistribution of **4** and **6** was evaluated (Figure 4c). Ex vivo biodistribution studies also indicated that **4** was predominantly activated in the tumors among other organs and compared to other groups. Selective tumor tissues were also analyzed by immunohistochemistry and NIR fluorescent microscopy to confirm the expression of biomarkers and accumulation of the probe. As shown in Figure 4d, $\alpha_v\beta_3$ integrin and MMP-2 antibody staining revealed strong expression of biomarkers in U87MG tumors and NIR fluorescence microscopy images showed a strong Cy5.5 signal, consistent with in vivo imaging.

Overall, our in vivo results markedly supported the role of c-(RGDyK) as a receptor-targeting ligand.

Tumor-targeting fluorogenic probes and dye-labeled peptide ligands have different targets; fluorogenic probes target overexpressed enzymes around the tumor site and peptide ligands target overexpressed receptors in the tumor. Yet, both probes can be used in combination to target the entire tumor area. Our results demonstrate the advantages of receptor-targeted fluorogenic probes for in vivo imaging applications. We anticipate that the combination of NIR fluorogenic probes and peptide ligands becomes applicable to a wide variety of target extracellular proteases and receptors, offering a series of receptor-targeted fluorogenic probes as novel imaging probes with improved efficacy in vivo.

■ ASSOCIATED CONTENT

Supporting Information. Details of synthesis and experimental methods. This material is available free of charge via the Internet at http://pubs.acs.org.

■ AUTHOR INFORMATION

Corresponding Author

*E-mail: Shawn.Chen@nih.gov; Seulki.Lee@nih.gov.

■ ACKNOWLEDGMENT

This work was supported by the Intramural Research Program (IRP) of the National Institute of Biomedical Imaging and Bioengineering (NIBIB), National Institutes of Health (NIH), and the International Cooperative Program of National Science Foundation of China (NSFC) (81028009).

■ REFERENCES

(1) Lee, S., Park, K., Kim, K., Choi, K., and Kwon, I. C. (2008) Activatable imaging probes with amplified fluorescent signals. *Chem. Commun. (Camb.)* 4250–4260.

(2) Kobayashi, H., and Choyke, P. L. (2011) Target-cancer-cell-specific activatable fluorescence imaging probes: rational design and in vivo applications. *Acc. Chem. Res. 44*, 83–90.

(3) Lee, S., Park, K., Lee, S. Y., Ryu, J. H., Park, J. W., Ahn, H. J., Kwon, I. C., Youn, I. C., Kim, K., and Choi, K. (2008) Dark quenched matrix metalloproteinase fluorogenic probe for imaging osteoarthritis development in vivo. *Bioconjugate Chem. 19*, 1743–1747.

(4) Zhu, L., Xie, J., Swierczewska, M., Zhang, F., Quan, Q., Ma, Y., Fang, X., Kim, K., Lee, S., and Chen, X. (2011) Real-time video imaging of protease expression in vivo. *Theranostics 1*, 18–27.

(5) Lee, S., Xie, J., and Chen, X. (2010) Activatable molecular probes for cancer imaging. *Curr. Top. Med. Chem. 10*, 1135–1144.

(6) Lee, S., Xie, J., and Chen, X. (2010) Peptides and peptide hormones for molecular imaging and disease diagnosis. *Chem. Rev. 110*, 3087–3111.

(7) Drag, M., and Salvesen, G. S. (2010) Emerging principles in protease-based drug discovery. *Nat. Rev. Drug Discovery 9*, 690–701.

(8) Turk, B. (2006) Targeting proteases: successes, failures and future prospects. *Nat. Rev. Drug Discovery 5*, 785–799.

(9) Cudic, M., and Fields, G. B. (2009) Extracellular proteases as targets for drug development. *Curr. Protein Pept. Sci. 10*, 297–307.

(10) Lee, S., Cha, E. J., Park, K., Lee, S. Y., Hong, J. K., Sun, I. C., Kim, S. Y., Choi, K., Kwon, I. C., Kim, K., and Ahn, C. H. (2008) A near-infrared-fluorescence-quenched gold-nanoparticle imaging probe for in vivo drug screening and protease activity determination. *Angew. Chem., Int. Ed. Engl. 47*, 2804–2807.

(11) Bremer, C., Tung, C. H., and Weissleder, R. (2001) In vivo molecular target assessment of matrix metalloproteinase inhibition. *Nat. Med. 7*, 743–748.

(12) Zheng, G., Chen, J., Stefflova, K., Jarvi, M., Li, H., and Wilson, B. C. (2007) Photodynamic molecular beacon as an activatable photosensitizer based on protease-controlled singlet oxygen quenching and activation. *Proc. Natl. Acad. Sci. U.S.A. 104*, 8989–8994.

(13) Lee, S., Ryu, J. H., Park, K., Lee, A., Lee, S. Y., Youn, I. C., Ahn, C. H., Yoon, S. M., Myung, S. J., Moon, D. H., Chen, X., Choi, K., Kwon, I. C., and Kim, K. (2009) Polymeric nanoparticle-based activatable near-infrared nanosensor for protease determination in vivo. *Nano Lett. 9*, 4412–4416.

(14) Barnett, E. M., Zhang, X., Maxwell, D., Chang, Q., and Piwnica-Worms, D. (2009) Single-cell imaging of retinal ganglion cell apoptosis with a cell-penetrating, activatable peptide probe in an in vivo glaucoma model. *Proc. Natl. Acad. Sci. U.S.A. 106*, 9391–9396.

(15) Medintz, I. L., Clapp, A. R., Brunel, F. M., Tiefenbrunn, T., Uyeda, H. T., Chang, E. L., Deschamps, J. R., Dawson, P. E., and Mattoussi, H. (2006) Proteolytic activity monitored by fluorescence resonance energy transfer through quantum-dot-peptide conjugates. *Nat. Mater. 5*, 581–589.

(16) Nguyen, Q. T., Olson, E. S., Aguilera, T. A., Jiang, T., Scadeng, M., Ellies, L. G., and Tsien, R. Y. (2010) Surgery with molecular fluorescence imaging using activatable cell-penetrating peptides decreases residual cancer and improves survival. *Proc. Natl. Acad. Sci. U.S.A. 107*, 4317–4322.

(17) Park, K., Kim, J. H., Nam, Y. S., Lee, S., Nam, H. Y., Kim, K., Park, J. H., Kim, I. S., Choi, K., Kim, S. Y., and Kwon, I. C. (2007) Effect of polymer molecular weight on the tumor targeting characteristics of self-assembled glycol chitosan nanoparticles. *J. Controlled Release 122*, 305–314.

(18) Stefflova, K., Li, H., Chen, J., and Zheng, G. (2007) Peptide-based pharmacomodulation of a cancer-targeted optical imaging and photodynamic therapy agent. *Bioconjugate Chem. 18*, 379–388.

(19) Nahrendorf, M., Waterman, P., Thurber, G., Groves, K., Rajopadhye, M., Panizzi, P., Marinelli, B., Aikawa, E., Pittet, M. J., Swirski, F. K., and Weissleder, R. (2009) Hybrid in vivo FMT-CT imaging of protease activity in atherosclerosis with customized nanosensors. *Arterioscler. Thromb. Vasc. Biol. 29*, 1444–1451.

(20) Fang, J., Nakamura, H., and Maeda, H. (2011) The EPR effect: Unique features of tumor blood vessels for drug delivery, factors involved, and limitations and augmentation of the effect. *Adv. Drug Delivery Rev.* DOI:10.1016/j.addr.2010.04.009

(21) Chen, X. (2006) Multimodality imaging of tumor integrin alphavbeta3 expression. *Mini. Rev. Med. Chem. 6*, 227–234.

(22) Niu, G., and Chen., X. (2011) Why integrin as a primary target for imaging and therapy. *Theranostics 1*, 30–47.

(23) Chen, X. (2011) Integrin targeted imaging and therapy. *Theranostics 1*, 28–29.

(24) Kessenbrock, K., Plaks, V., and Werb, Z. (2010) Matrix metalloproteinases: regulators of the tumor microenvironment. *Cell 141*, 52–67.

(25) Johansson, M. K., and Cook, R. M. (2003) Intramolecular dimers: a new design strategy for fluorescence-quenched probes. *Chemistry 9*, 3466–3471.

Supporting Information

Dual-Functional, Receptor-Targeted Fluorogenic Probe for In Vivo Imaging of Extracellular Protease Expressions

Lei Zhu,[†, ‡] Jin Xie,[†] Magdalena Swierczewska,[†, §] Fan Zhang,[†] Xin Lin,[†] Xuexun Fang,[‡] Gang Niu,[†] Seulki Lee[†, *] and Xiaoyuan Chen[†,*]

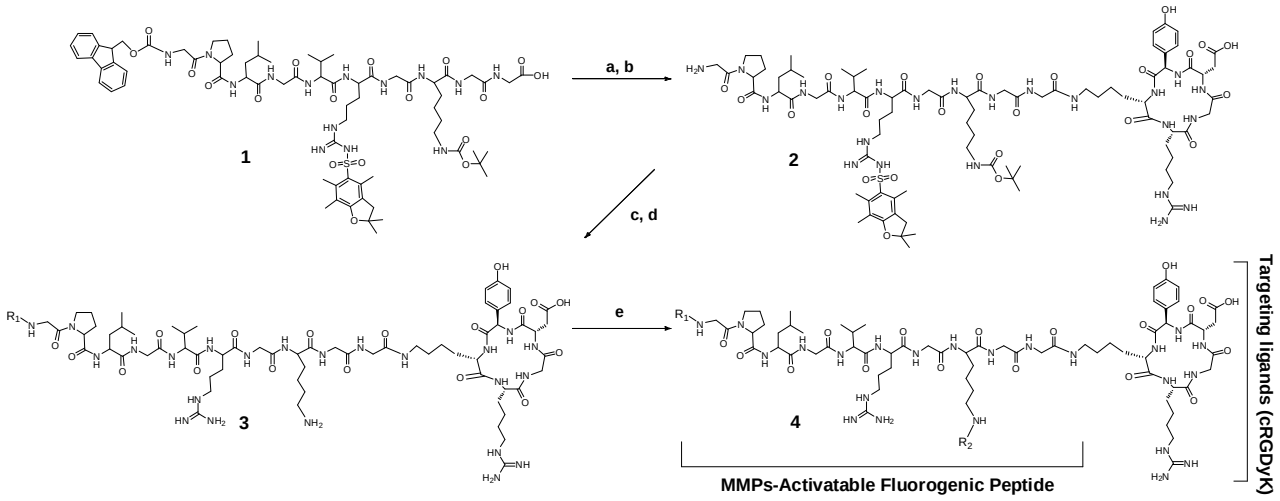
Cell culture. The U87MG human glioblastoma multiforme cell line was obtained from American Type Culture Collection (ATCC, Manassas, VA). U87MG cells were cultured in DMEM medium containing 10% (v/v) fetal bovine serum (GIBCO, Grand Island, NY) supplemented with penicillin (100 μg/mL), streptomycin (100 μg/mL), non-essential amino acids (100 μM) and sodium pyruvate (1 mM) at 37 ˚C with 5% CO_2.

Animal models. Female athymic nude mice were supplied from Harlan (Indianapolis, IN) at 4 to 5 wk of age. U87MG tumor model was generated by subcutaneous injection of 5×10^6 cells in Matrigel into the right front flank of female athymic nude mice at a volume of about 80 μL. The mice were used for optical studies when the tumor volume reached about 300 mm^3. All animal studies were conducted in accordance with the principles and procedures outlined in the

Guide for the Care and Use of Laboratory Animals and were approved by the Institutional Animal Care and Use Committee of Clinical Center, NIH.

Peptide probes. The peptide sequence of 1 was synthesized by standard solid-phase Fmoc peptide chemistry. To synthesize 4 (Scheme S1), 5 mg of 1 was dissolved in 500 µl N,N-dimethylformamide (DMF) solution containing 2% diisopropylethyalamine (DIPEA). 2 mg N,N,N',N'-Bis(tetramethylene)-O-(N-succinimidyl)uronium hexafluorophosphate (HSPyU) was added into the solution to activate the C-terminal carboxylic group and stirred for 30 min at room temperature. Next, 2.5 mg of c(RGDyK) was dissolved in 250 µl DMF solution containing 2% DIPEA and mixed with the activated 1. The reaction mixture was stirred at room temperature and monitored by analytical HPLC. To remove the Fmoc group, 10% piperidine was added into the solution and stirred for 30 min. The crude product was precipitated in cold ether and the pellet was lyophilized and purified by preparative HPLC. The collected fraction 2 was lyophilized and labelled with Cy5.5 NHS ester in DMF solution containing 2% DIPEA. The reaction solution was precipitated against cold ether, lyophilized, and subjected to TFA/H2O/TIS/EDT (85/5/5/5, v/v/v/v) cocktail to remove the protection groups. Crude product was purified by preparative HPLC. The desired fraction containing 3 was collected and lyophilized. In the last step, BHQ-3 NHS ester was conjugated and the final compound 4 was was purified by HPLC on a C18 semi-preparative column using a linear gradient of 10% to 55% acetonitrile/water (0.1% trifluoroacetic acid), for 30 min at a 10 mL/min flow rate. 5 and 6 were synthesized by serial conjugations and deprotections of the peptides as described followed by preparative HPLC purifications. 7 was synthesized by conjugation of CW800 NHS ester and c(RGDyK) in DMF solution containing 2% DIPEA. The reaction solution was precipitated

against cold ether, lyophilized, and purified by HPLC. All purified products were confirmed by analytical HPLC and LC/MS. Figure S1 shows the representative HPLC and LC/MS spectra of 4.



Scheme S1. Synthesis of 4. a) HSPyU in DMF containing 2% DIPEA, c(RGDyK); b) 10% piperidine; c) Cy5.5 NHS ester in DMF containing 2% DIPEA; d) TFA/H_2O/TIS/EDT (85/5/5/5, v/v/v/v); e) BHQ-3 NHS ester in DMF containing 2% DIPEA

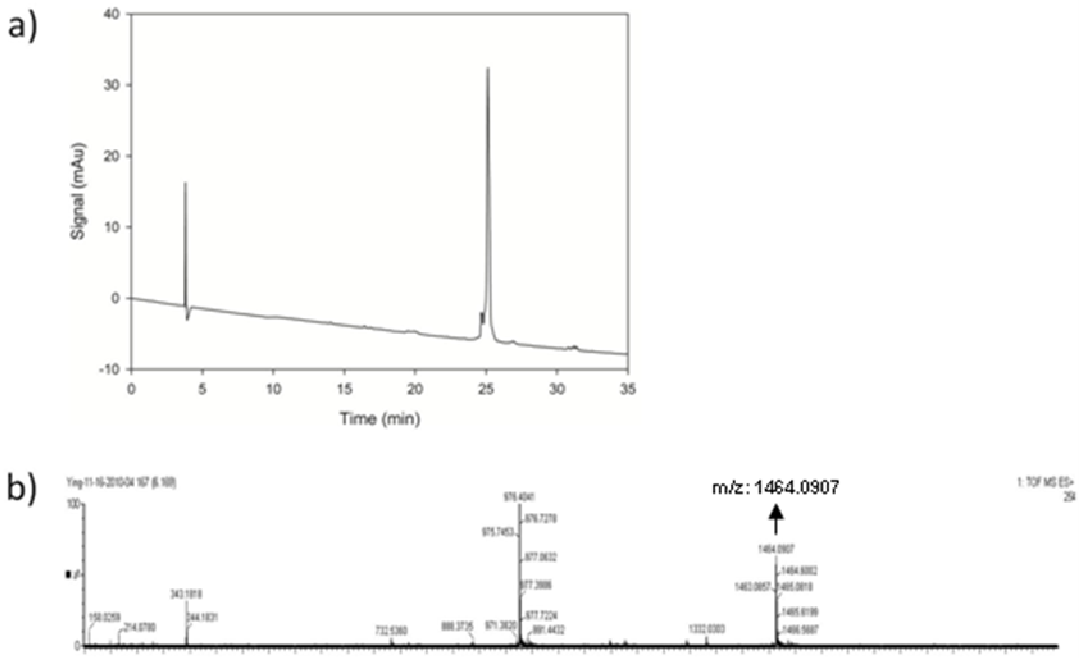


Figure S1. (a) HPLC and (b) LC/MS spectra of 4. MS calculated/found; 2926.20/2926.18

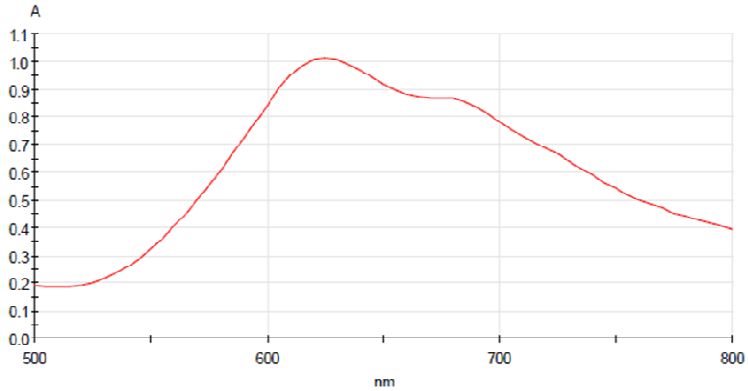


Figure S2. UV-Vis spectrum of 4 in PBS

.

In vitro enzyme test. The fluorogenic property of the peptide probes was examined by incubating the probes in the reaction buffer (100 mM Tris, 200 mM NaCl, 5 mM $CaCl_2$, 0.1% Brij, pH 7.5) containing 40 nM of APMA-activated recombinant human MMP-2. Fluorescence intensity was monitored using a spectrofluorometer (F-7000 Fluorescence Spectrophotometer, Hitach, Tokyo, Japan) every 10 min at 37 °C using quartzose cuvette. The excitation wavelength

was set at 675 nm and emission spectra recorded from 680 to 800 nm. The same experimental conditions were applied to various concentrations of MMP-2 in the presence of fixed concentrations of the probes.

Receptor binding assay. Briefly, U87MG cell line was cultured in DMEM medium containing 10% (v/v) fetal bovine serum supplemented with penicillin (100 μg/mL), streptomycin (100 μg/mL), non-essential amino acids (100 mM) and sodium pyruvate (1 mM) at 37˚C with 5% CO_2. After reaching 80% confluence, cells were scraped off and suspended with binding buffer (25 mM 2-amino-2-(hydroxymethyl)-1,3-propanediol, hydrochloride (Tris-HCl), pH 7.4, 150 mM NaCl, 1 mM $CaCl_2$, 0.5 mM $MgCl_2$ and 1 mM $MnCl_2$, 0.1% bovine serum albumin (BSA)) at a final concentration of 4×10^6 cells/mL. In a 96-well plate, 2×10^5 U87MG cells/well were incubated with ^{125}I-Echistatin (0.02 mCi/well, PerkinElmer Inc.) in binding buffer in the presence of different concentrations of c(RGDyK) and the peptide probes at room temperature for 2 hrs. After incubation, the plate was washed three times with PBS containing 0.1% BSA, and the radioactivity was measured by γ-counting. The IC_{50} values were calculated by nonlinear regression analysis.

***IN VIVO* optical imaging.** Optical imaging acquirement and analysis were done using Maestro 2.10 in vivo imaging system (Cambridge Research & Instrumentation, Woburn, MA, USA). U87MG tumor-bearing mice were injected via tail vein with **4**, 5, **6**, **7**, and **4** with MMP inhibitor or unlabeled c(RGDyK), respectively, under isoflurane anaesthesia (n = 3 per group).

The molar concentration of each samples were calculated by the sample weight. 1, 2, 3, 4 hrs post-injection, the mice were subjected to optical imaging using appropriate filters for Cy5.5 and CW800. For the inhibition experiment, MMP inhibitor was intratumorally injected into tumor-bearing mice 30 minutes before the probe injection. After image acquisition, spectral unmixing yielded the pseudocolor images of the pure spectrum of respective dyes. Images were normalized and analyzed using Maestro software. For quantitative comparison, regions of interest (ROI) were drawn over tumors and muscle, and the average signal (10^6 photons×cm^{-2}×s^{-1}) for each area was measured. Values were expressed as mean ± SD for a group of three animals.

***EX VIVO* biodistribution.** *Ex vivo* imaging of excised tumor and organs further confirm the targeting specificity and activation of the probes (Figure S4). At 4 hrs post-injection, the mice were sacrificed and major organ tissues and tumors were harvested, and placed on black paper for *ex vivo* imaging. For quantitative comparison, ROIs were drawn over tumors and the other organs, and the average signal for each area was measured. The results were presented as the average scaled signal from the organs and tumors. Values were expressed as mean ± SD for a group of three animals.

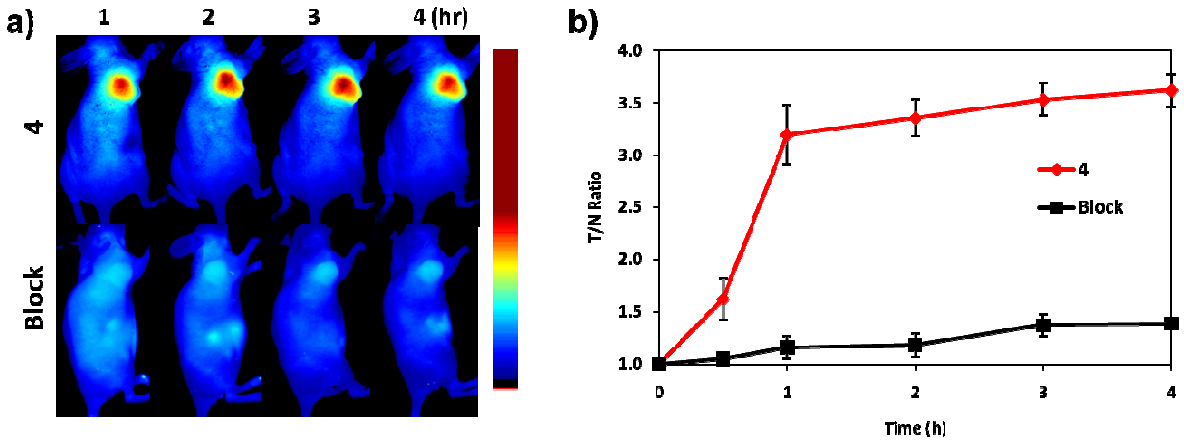


Figure S3. (a) Representative serial in vivo NIR fluorescence images of U87MG tumor-bearing mice injected intravenously with **4** and **4** with unlabeled c(RGDyK) (block). (b) T/N ratio analysis of NIR fluorescence intensity of U87MG tumor *in vivo*.

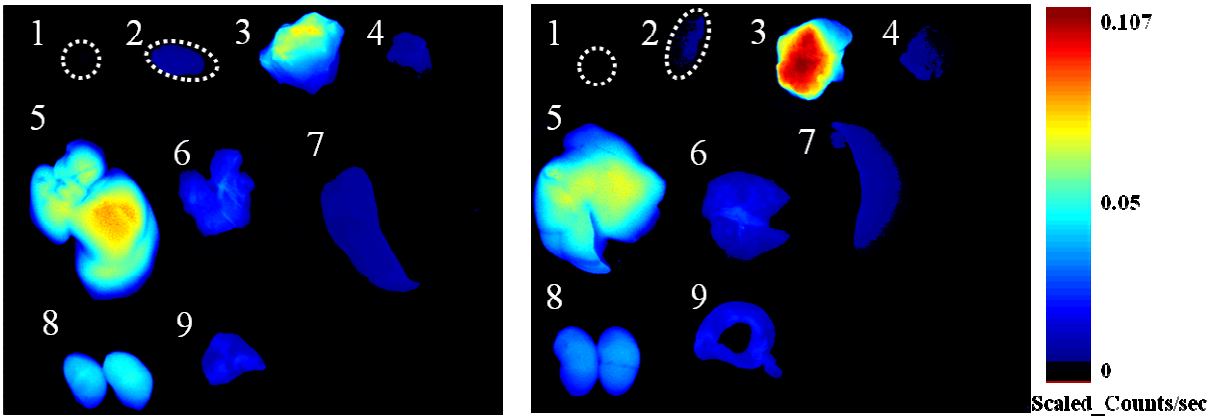


Figure S4. Biodistribution of **4** (left) and **6** (right).

Immunohitochemistry. Frozen U87MG tumor tissue slices (4 μm) from the tumor-bearing nude mice were fixed with cold acetone for 20 min and dried in air for 30 min at room temperature. After blocking with 10% BSA for 30 min, the sections were incubated with Rabbit anti-integrin αvβ3 and Rabbit anti-MMP-2 and antibodies (10 μg/mL) for 60 min at room temperature in the dark. Samples were then visualized with FITC-conjugated donkey anti-rabbit secondary antibody. Finally, the slices were mounted with DAPI-containing mounting medium under an epifluorescence microscope (Olympus, X81). The tumor slices were also observed directly after mounting with DAPI-containing mounting medium under an epifluorescence microscope and fluorescence images were taken using Cy5.5 filter settings.

Statistical analysis. Results were expressed as mean ± SD. Two-tailed paired and unpaired Student's t tests were used to test differences within groups and between groups, respectively. P values < 0.05 were considered statistically significant.

Bioconjugate Chemistry

COMMUNICATION

pubs.acs.org/bc

Aromatic Aldehyde and Hydrazine Activated Peptide Coated Quantum Dots for Easy Bioconjugation and Live Cell Imaging

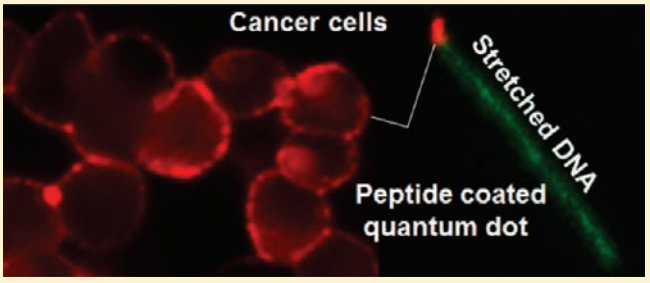
Gopal Iyer,[*,§,†] Fabien Pinaud,[*,‡,§] Jianmin Xu,[†] Yuval Ebenstein,[†] Jack Li,[†] Jessica Chang,[†] Maxime Dahan,[‡] and Shimon Weiss[*,†]

[†]Department of Chemistry and Biochemistry, California NanoSystems Institute, University of California at Los Angeles, 607 Charles E. Young Drive East, Los Angeles, California 90095, United States

[‡]Laboratoire Kastler Brossel, Ecole Normale Supérieure, Université Pierre et Marie Curie — Paris 6

Supporting Information

ABSTRACT: We present a robust scheme for preparation of semiconductor quantum dots (QDs) and cognate partners in a conjugation ready format. Our approach is based on bis-aryl hydrazone bond formation mediated by aromatic aldehyde and hydrazinonicotinate acetone hydrazone (HyNic) activated peptide coated quantum dots. We demonstrate controlled preparation of antibody—QD bioconjugates for specific targeting of endogenous epidermal growth factor receptors in breast cancer cells and for single QD tracking of transmembrane proteins via an extracellular epitope. The same approach was also used for optical mapping of RNA polymerases bound to combed genomic DNA in vitro.



Biofunctionalization of quantum dots (QDs) for both *in vitro* and *in vivo* applications is challenging, since many criteria, such as long-term stability, overall size, efficient and straightforward conjugation of functional biomolecules, and easy QDs targeting to cellular components all have to be simultaneously optimized. We have previously developed a compact surface coating chemistry that employs synthetic peptides for solubilization, biofunctionalization, and long-term stabilization of colloidal QD solutions (>6 month).[1,2] These peptide coated QDs (pcQDs) have been targeted in cells and animals using various small functional groups such as biotin,[2,3] FITC,[4] or DOTA.[5,6] The results have provided ample proof of pcQDs advantages for both live cell single molecule imaging[7] and whole animal imaging applications. However, as recently demonstrated by the monofunctional conjugation of avidin to pcQDs[7] conjugation of large molecules to QDs is still challenging because steric hindrance, geometry, stoichiometry of the conjugate, and its final functional activity have to be addressed. For that reason, we have focused our efforts here on developing "conjugation-ready" pcQDs that are stable at 4 °C for >4—6 months and provide a flexible approach for rapid bioconjugation to antibodies and other biomolecules in aqueous buffers and with precise and reproducible control over the conjugate stoichiometry. Previously, commercial linkers and activators have been used for various types of pcQD conjugation reactions with mixed success. For instance, cetuximab, a clinical anti-EGFR (epidermal growth factor receptor) antibody conjugated to QDs via EDC (1-ethyl-3-(3 dimethylaminopropyl) carbodiimide hydrochloride) was observed to have low reactivity and the QD conjugates were prone to aggregation.[8] Alternative QD—cetuximab conjugation strategies using succinimidyl-4-(*N*-maleimidomethyl)cyclohexane-1-carboxylate (SMCC) or *N*-succinimidyl-6-(3′-(2-pyridyldithio)-propionamido)-hexanoate LC-(SPDP)/SMCC linkers were more successful but required multiple preparative steps and reduction of the antibody which could compromise its activity.[8]

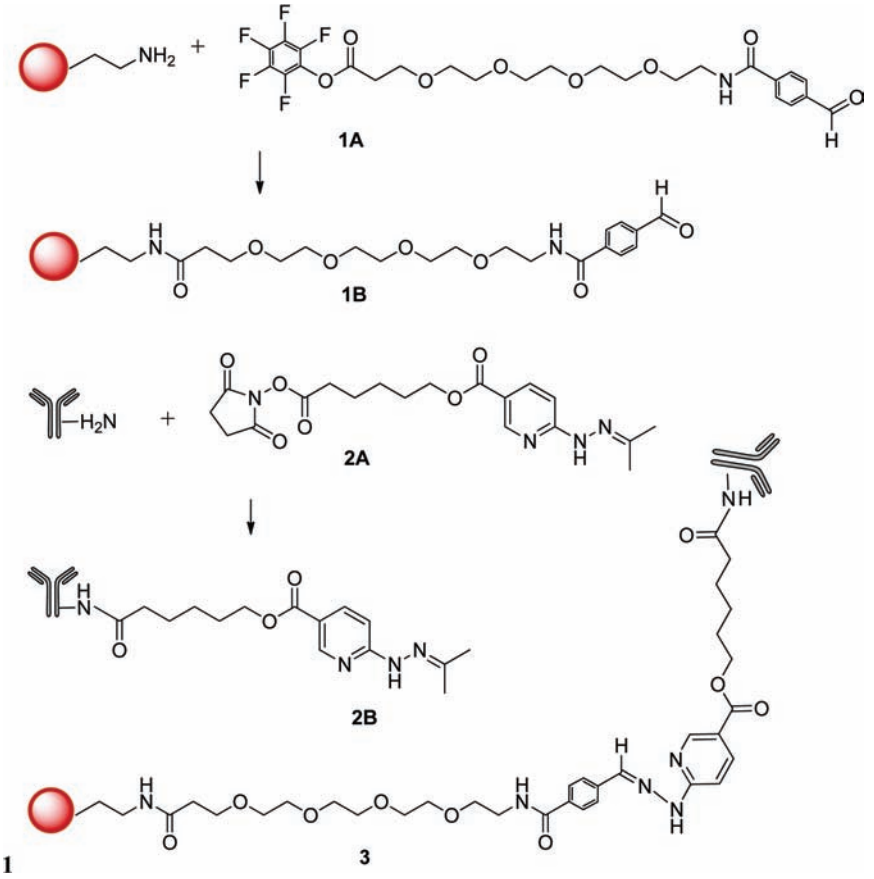
To overcome some of these limitations, we developed a bis-aryl hydrazone linkage strategy for the coupling of pcQDs to antibodies. We demonstrate the utility of this approach in live cells labeling and for in *vitro* applications. This reaction is based on the bio-orthogonal stable Schiff base mediated conjugation between aromatic aldehydes and aromatic hydrazines.[9−11]

In this scheme, UV traceable bifunctional linkers, succinimidyl-4-formylbenzamide (NHS-FB) or pentafluorophenyl-poly(ethylene glycol)-4-formylbenzamide (PF-PEG-FB) and succinimidyl-6-hydrazinonicotinate acetone hydrazone (NHS-HyNic) were conjugated to pcQD and antibodies, respectively, and further reacted together to yield stable QD conjugates via the formation of a covalent bis-aryl hydrazone bond with virtually no competing side reactions (Scheme 1). These linkers can be used interchangeably on pcQDs and antibodies or other biomolecules without a loss of generality, yield, or stability. Bis-aryl hydrazone bond formation can also be catalyzed and reaction kinetics improved 10—100-fold in the pH range 5—8 in the presence of aniline.[12−14] The reaction of

Received: January 18, 2011
Revised: May 6, 2011
Published: May 10, 2011

ACS Publications © 2011 American Chemical Society

Scheme 1. Preparation of Aromatic Benzaldehyde Capped CdSe/ZnS Peptide Coated QDs and Aromatic Hydrazine Functionalized Antibodies[a]



[a] Not to scale. Peptide coated quantum dots (pc-QDs) are modified with PEG-4FB, **1A**, via their primary amines to yield PEG-4FB-pcQDs, **1B**. Antibodies are modified with C6-SANH, **2A**, via surface exposed primary amines to yield C6-SANH-Abs, **2B** (nucleophilic aromatic hydrazine is protected as an acetone hydrazone); **1B** is conjugated to **2B** to form a pc-QD-Abs, **3**, bioconjugate via stable uv-traceable bis-aryl hydrazone linkage.

aromatic aldehyde with aromatic hydrazine is also completely bioorthogonal, as the functional linkers do not cross-react with other side groups present in the side chains of natural amino acids or oligonucleotides. To provide additional flexibility and control for conjugation, QDs were also coated with peptides directly synthesized with an N-terminal HyNic group. This approach saves an extra step for the preparation of reactive pcQDs and permits better control of the number of HyNic reactive groups available at the surface of QDs using mixture of peptides with different functionalities during the coating procedure.[1,2]

CdSe/CdS/ZnS QDs emitting at 630 nm (Supporting Information Figure S.1) were synthesized as described previously.[15] CdSe/ZnS QDs emitting at 605 nm were obtained in their hydrophobic form from commercial vendors. Both types of QDs were coated with glycine or lysine N-terminated synthetic peptides which resulted in available primary amines[1,2] for NHS-FB or PF-PEG-FB modifications of pcQD (see Supporting Information methods for peptide sequences). For the production of hydrazine functionalized QDs, QDs were directly coated with HyNic N-terminated synthetic peptides (HyNic-pcQD). The mean core/shell diameter of these 630 or 605 nm red-emitting QDs was ~7.5 nm and ~5.0 nm, respectively, based on TEM measurements[16] (Supporting Information Figure S.1) and their hydrodynamic diameter increased to ~12.0 nm and ~9.5 nm, respectively, once coated with peptides.[17]

Scheme 1 illustrates one approach for the conjugation of pcQDs to antibodies via bis-aryl hydrazone linkage. NHS-FB or PF-PEG-FB (**1A**) were mixed with amine terminated pcQDs either in DMSO or directly in aqueous buffer at pH 7.2 to obtain pcQDs activated with FB or with PEG-FB which further enhances the solubility pcQDs. The resulting FB-activated pcQDs (**1B**) were purified via gel filtration using water as mobile phase and rapidly exchanged into a 100 mM Na-phosphate, 150 mM NaCl, pH 6.0 conjugation buffer in which they were reactive and stable for more than 6 months when kept at 4 °C. To generate a cognate aromatic hydrazine reactive molecule, NHS-HyNic (**2A**) was similarly reacted with amine groups on anti-EGFR or anti-GFP antibodies to obtain HyNic-activated antibodies (**2B**). Once desalted into a buffer containing 100 mM Na phosphate, 150 mM NaCl, pH 6.0, HyNic-activated antibodies possessed surface exposed alkyl hydrazones that maintained a dynamic equilibrium between alkyl protecting groups and reactive hydrazine groups[18] primed to receive FB-activated pcQDs and to yield a stable QD-antibody conjugate (**3**). The QD-antibody conjugate was stored in 0.01% Tween-20 and 0.1% BSA at 4 °C. The functional stability of the conjugate was confirmed by labeling EGFR on the cell surface of live MCF-7 cells two months after 4 °C storage. It is important to note that QD-conjugates prepared using this method should be stored undiluted in micromolar concentrations.

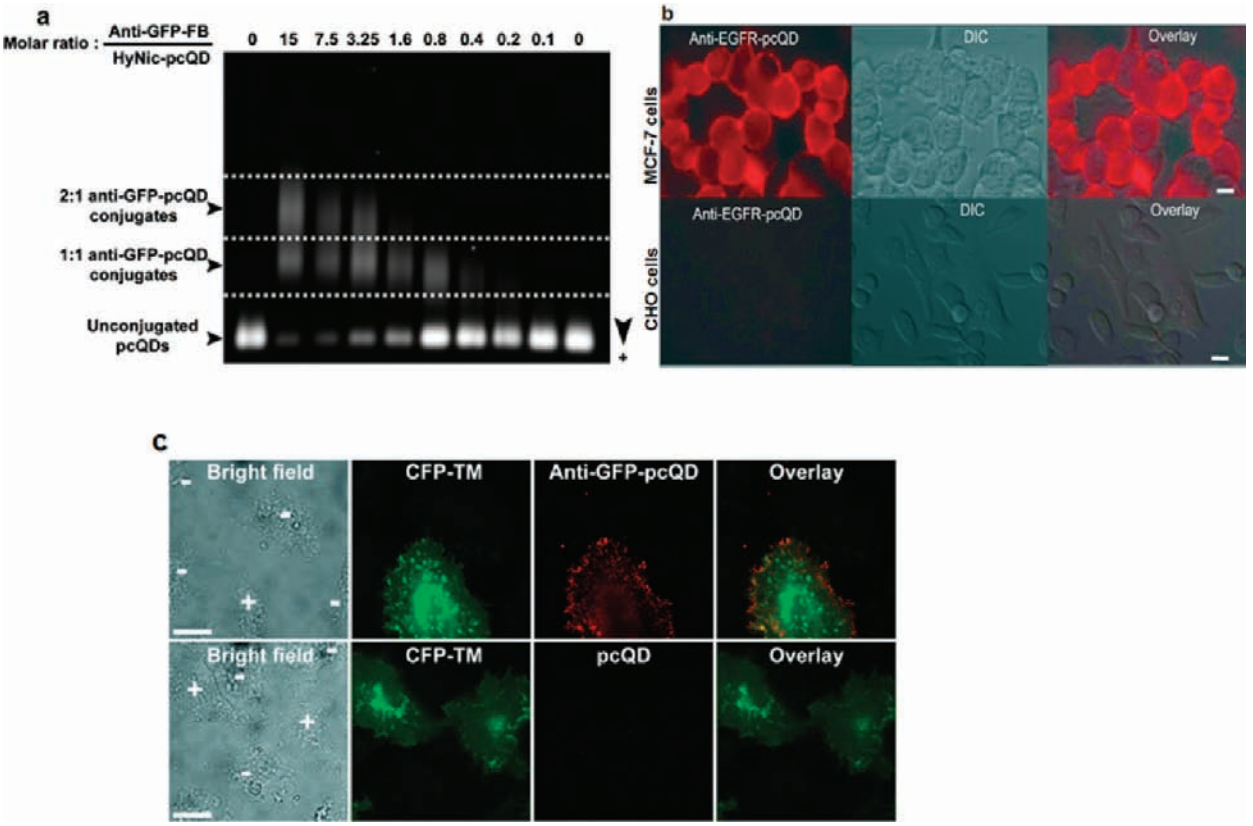


Figure 1. Cell labeling with antibody−peptide quantum dots conjugates formed by bis-aryl hydrazone linkage chemistry. (a) Gel electrophoresis of conjugation reactions between anti-GFP-FB and HyNic-pcQDs at different molar ratio. The faster migrating unconjugated HyNic-pcQD fluorescence band is depleted with increasing conjugation ratio, and discrete 1:1 and 2:1 stoichiometry anti-GFP-pcQD conjugate bands migrating more slowly in the gel appear. The side arrow indicates the direction of the electric field. (b) Labeling of live breast cancer cells MCF-7 overexpressing EGFR at the plasma membrane showing specificity with anti-EGFR-pcQD conjugate (top left); DIC image (top center) and overlay (top right). Corresponding labeling of nonexpressing EGFR live CHO cells shows no binding of anti-EGFR-pcQDs as seen in bottom right and overlay. Scale bar: 5 μm. (c) Labeling of live HeLa cells with anti-GFP-pcQD conjugates formed by the reaction of HyNic-activated anti-GFP IgG with FB-activated pcQDs (top) or with unconjugated FB-activated pc-QDs (bottom). Anti-GFP-pcQD conjugates specifically bind the plasma membrane of HeLa cell expressing a transmembrane CFP-TM receptor (+) with little nonspecific binding to nonexpressing cells (−). In the absence of antibody conjugation, no labeling to expressing cells was observed. Scale bars: 20 μm.

While generating the complementary and reactive QD (**1B**) and antibody (**2B**) species, it was important to validate the presence and to quantify the respective cross-linkers on the QDs and the antibodies. This was done using absorbance spectroscopy (Supporting Information Figure S.2) followed by a calculation of the molar substitution ratios (MSR) of each reaction. The presence and quantity of FB or HyNic groups on the surface of pcQDs and on secondary antimouse $F(ab)_2$ antibodies (used as substitutes to the more expensive anti-EGFR or anti-GFP antibodies) were measured by monitoring the increase in absorbance at 350 and 390 nm. No further increase in absorbance was observed after 100 min of reaction (Supporting Information Figure S2). The MSR of FB-activated pcQDs and HyNic-activated $F(ab)_2$ antibodies was calculated to be 10 and 1.15, respectively. In general, increasing the linker concentration beyond a maximum of 20 mol equiv for NHS-FB, PF-PEG-FB, or NHS-HyNic resulted in precipitation of the antibodies or pcQDs. For the conjugation of anti-EGFR antibodies to pcQDs, the reaction was optimized using PEG-FB-pcQDs and HyNic-modified anti-EGFR at a 1:4 molar ratio. For conjugation to anti-GFP, a 1:10 molar ratio of FB-pcQDs to HyNic-modified anti-GFP antibodies was used. When reactive groups were reversed, for instance, using HyNic-pcQD and FB-activated anti-GFP antibodies, the reaction ratio was optimized by gel electrophoresis. As shown in Figure 1a, the conjugation efficiency increased with increasing anti-GFP-FB:HyNic-pcQD ratios and was characterized by the depletion in unconjugated HyNic-pcQD fluorescent bands and the appearance of discrete and gel-shifted anti-GFP-pcQDs 1:1 and 2:1 conjugate bands. The distribution of stoichiometries (of anti-GFP-pcQDs and free pcQDs) was in good agreement with the expected Poisson distribution as previously observed for monofunctional bioconjugation of pcQD[17] (Supporting Information Figure S.3).

To demonstrate the activity of the different antibody-pcQD conjugates obtained by bis-aryl hydrazone chemistry, we tested their ability to specifically recognize membrane bound antigens in living cells. EGFR, which is often overexpressed on the cell surface in several cancers is a potential target for clinical therapy, was specifically recognized by anti-EGFR-pcQD conjugates in live MCF-7 breast cancer cells (Figure 1b) and in live U87 human glioblastoma cells (Supporting Information Figure S.4). No cell membrane staining was observed for CHO cells (Figure 1b) that do not express EGFR. An overlay of the fluorescent and DIC channel clearly confirmed the localization of the anti-EGFR-pcQD

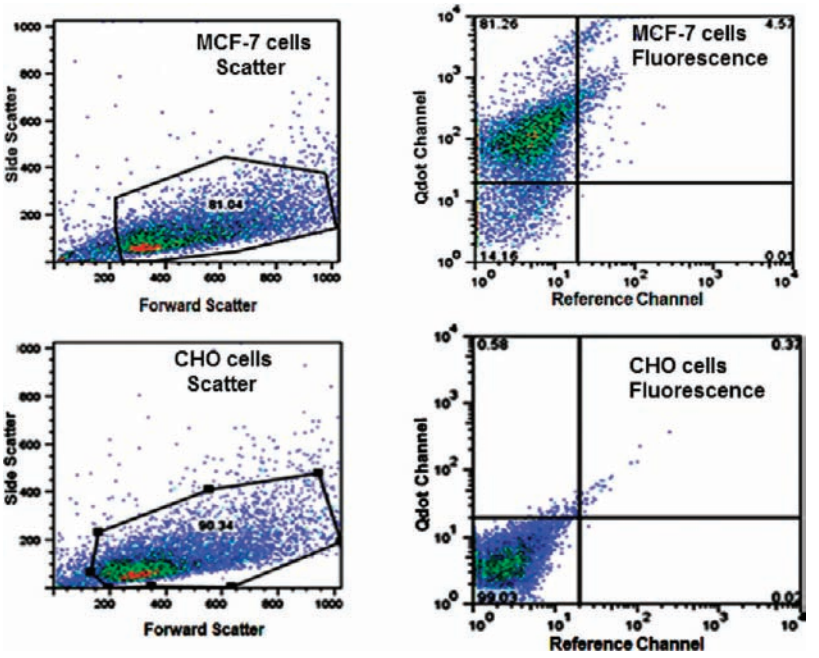


Figure 2. Flow cytometry analysis of live MCF-7 and CHO cells labeled with anti-EGFR-pcQDs. Top panel shows specific binding of 25 nM of anti-EGFR-pcQD conjugates to MCF-cells overexpressing EGFR while the bottom panel shows absence of binding to EGFR negative CHO cells at a similar concentration.

conjugates on the cell surface of cancer cells (Figure 1b), and the limited nonspecific binding observed was likely due to the presence of PEG in the linker. Similar results were obtained with anti-GFP-pcQD conjugates that specifically cross-reacted with cyan fluorescent protein (CFP) fused to the transmembrane domain of the platelet-derived growth factor receptor (CFP-TM) when expressed in the plasma membrane of HeLa cells (Figure 1c, Supporting Information Figure S.5). Again, minor nonspecific binding to nonexpressing cells was observed and cells were not labeled with unconjugated pc-QDs (Figure 1c, Supporting Information Figure S.5). Single QD tracking of CFP-TM receptors in the plasma membrane of live HeLa cells could be achieved using monofunctional anti-GFP-pcQD conjugates (Supporting Information video 1). When delivered within the cytoplasm of living cells, for instance, using INFLUX pinocytic loading[19] anti-GFP-pcQD conjugates also efficiently targeted intracellular GFP fusion proteins such as the integral membrane anchored caveolin-1-GFP (Supporting Information Figure S.6, video 2).

To extend the utility of anti-EGFR-pcQD conjugates, in particular, for immunophenotyping experiments,[20] titration and binding efficiencies were compared for EGFR overexpressing MCF-7 breast cancer cells versus nonexpressing CHO cells by flow cytometry measurements (Figure 2, Supporting Information Figure S.7). More than 80% of MCF-7 cells were fluorescent when stained with a 25 nM concentration of anti-EGFR-pcQD, while less than 1% CHO cells were labeled under the same conditions (Figure 2). Control experiments with pcQD reacted with a normal mouse IgG_{2a} isotypic antibody (25 nM IgG_{2a}-pcQDs) via the same bis-aryl hydrazone conjugation strategy showed an absence of cell surface staining for both MCF-7 and CHO cell lines (Supporting Information Figure S.8). The combined results from fluorescence microscopy and flow cytometry experiments clearly demonstrate the utility of this bis-aryl hydrazone conjugation chemistry for the production of relatively small size, active antibody-QD conjugates. In addition to pcQDs,

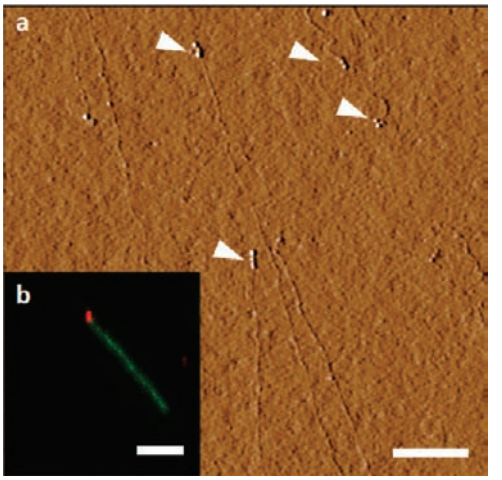


Figure 3. *In vitro* detection of DNA binding proteins using antiRNAP-pcQDs. (a) AFM height image of extended T7 bacteriophage DNA reacted with *E. coli* RNAPs. The protrusions at the end of the DNA fiber (arrows) confirm specific binding of RNAPs to their expected location on the T7 genome. Scale bar 1 μm. (b) Fluorescence image of the same sample after incubation with pcQDs conjugated to antibodies against *E. coli* RNAP allows specific QD recognition of RNAP on the T7 genome. Scale bar 5 μm.

commercial amine-PEG-545 nm and amine-coated 611 nm QDs (Life Technologies or eBioscience) conjugated to antibodies via the same bis-aryl hydrazone linkage showed similar conjugation kinetics and labeling efficiency in living cells, although their larger size compared to pcQDs prevented the isolation of antibody-QD conjugates with well-defined stoichiometry (unpublished results).

To further demonstrate the utility of bis-aryl hydrazone linked antibody-pcQD conjugates, we employ them for an *in vitro* optical imaging application. The detection of *E. coli* RNA polymerases

(RNAPs) interacting with T7 bacteriophage genomic DNA combed on glass surfaces was taken as a model system. *E. coli* RNAPs strongly interact with binding sites (promoters) in the first 750 base pairs of the T7 genome[21] as confirmed by atomic force microscopy (AFM) imaging[22] (Figure 3a). For optical detection of RNAPs along the T7 genome, hydrophobic QDs emitting at 605 nm were coated with peptides described above and conjugated to antibodies directed against the β subunit of *E. coli* RNAP. The anti-RNAP-pcQD conjugates were reacted with the T7-genome/RNAP complex and the sample was stretched on a polylysine modified glass coverslip after staining with YoYo-1, a DNA intercalating dye (Life Technologies). When the complexes were imaged by fluorescence microscopy, anti-RNAP-pcQDs (Figure 3b, red) were detected at the extremity of the T7-genomic DNA (Figure 3b, green), an indication of effective and specific RNAP targeting *in vitro*.

A substantial body of work related to hydrazone bonds have been implemented for a variety of pH-sensitive conjugates of anticancer drug doxorubicin with antibodies, polymers, micelles, and particles.[23,24] The stability of certain types of hydrazone linkers is well documented at 7.4, while at a lower pH 5.0 these linkers undergo hydrolysis.[23,25] Few examples of hydrazone linker technology incorporated in antibody drug conjugates are as follows: (i) Mylotarg,[26] (ii) the antibody−calicheamicin conjugate,[27] and (iii) CMC-544, a promising drug−antibody conjugate—N-acetyl γ calicheamicin dimethylhydrazide (CalichDMH) conjugated to humanized anti-CD22 monoclonal antibody.[28] While Mylotarg was recently withdrawn from the market by FDA due to fatalities reported in humans, CMC-544 is currently being evaluated in a phase III study for the treatment of B-lymphoid malignancies. Both drugs have incorporated the concept of acid hydrolyzable linker which is different from the aromatic bis-aryl hydrazone conjugate used in this study. The aromatic bis-aryl hydrazone is more stable in the pH range 5−8 relevant to *in vitro* and cell surface labeling experiments. It would therefore be interesting to test in the future the efficacy and stability of the bis-aryl hydrazone linker technology in preclinical settings in mice.

There are several advantages to the aromatic aldehyde-hydrazone QD conjugation strategy described here. First, FB-pcQDs, PEG-FB-pcQDs, or HyNic-pcQDs obtained after purification of the linkers or removal of excess coating peptides, can be stored for 4−6 months at 4 °C with minimal loss in activity. Second, proteins or other biomolecules conjugated with either of these linkers can themselves be conserved for extensive periods by freezing. Third, the internal UV traceable markers built in both types of linkers allows for easy monitoring and control of the MSR when modifying QDs or proteins. Fourth, bioconjugation only requires mixing the two active (QD and protein) components and the reaction efficiency of bis-aryl hydrazone formation can be further improved in the presence of aniline.[11,12,29,30] In this context, a method for controlled assembly of QD-biomolecule hybrids using aniline catalyzed hydrazone ligation has been successfully demonstrated.[31] Further utility of the aniline catalyzed hydrazone reaction has been shown for attaching protein capture reagents to model silicon dioxide surface suggesting that it can be used for biosensor applications in the biomedical field.[32] Fifth, the small size of pcQDs and that of the antibody-pcQD conjugates allows for an easy production and purification of monofunctional conjugates and antibody-pcQDs with well-defined stoichiometry. Sixth, the bioorthogonal reactivity of the bis-aryl hydrazone linkage should favor the control grafting of multiple proteins or reactive moieties on the surface of individual pcQD, and should facilitate the production of multifunctional QD probes. Finally, for bioorthogonal site-specific targeting and imaging in living cells, a formylglycine aldehyde tag[33,34] can be genetically engineered into proteins, which can be potentially targeted via hydrazone activated pc-QDs.

■ ASSOCIATED CONTENT

Supporting Information. Additional figures and methods as described in text. Experimental procedures, synthesis of quantum dots, UV−vis kinetics of conjugation and titration of bioconjugates using flow cytometry, stoichiometry of antibody binding to QDs using gel electrophoresis and fluorescence microscopy. This material is available free of charge via the Internet at http://pubs.acs.org.

■ AUTHOR INFORMATION

Corresponding Author

*E-mail: gopal@chem.ucla.edu; fabien.pinaud@lkb.ens.fr; sweiss@chem.ucla.edu.

Author Contributions

§These authors contributed equally.

■ ACKNOWLEDGMENT

We thank Jieun Choi for recording absorbance measurements using UV−vis spectroscopy and David Schwartz (SoluLink Biosciences, Inc.) for critical reading of the manuscript. Electron microscopy was performed at the Electron Imaging Center for Nanomachines (EICN) at the UCLA/California Nanosystems Institute (CNSI) core facility. We acknowledge UCLA Jonsson Comprehensive Cancer Center (JCCC) and Center for AIDS Research Flow Cytometry Core Facility that is supported by National Institutes of Health awards CA-16042 and AI-28697, and by the Johsson Cancer Center, the UCLA AIDS Institute, and the David Geffen School of Medicine at UCLA. Fluorescence imaging was performed at the UCLA/CNSI Advanced Light Microscopy Shared Facility. This work was supported by NIH/NIBIB BRP Grant R01-EB000312 and the NSF, The Center for Biophotonics, an NSF Science and Technology Center managed by the University of California, Davis, under Cooperative Agreement PHY0120999. F.P. acknowledges financial support from a Marie Curie-Intra-European Fellowship under contract number MEIF-CT-2006-040210, an EMBO long-term fellowship, and a fellowship from Centre de Nanoscience Ile de France. M.D. acknowledges support from Fondation pour la Recherche Médicale."

■ REFERENCES

(1) Iyer, G., Pinaud, F., Tsay, J., and Weiss, S. (2007) Solubilization of quantum dots with a recombinant peptide from Escherichia coli. *Small 3*, 793–798.

(2) Pinaud, F., King, D., Moore, H. P., and Weiss, S. (2004) Bioactivation and cell targeting of semiconductor CdSe/ZnS nanocrystals with phytochelatin-related peptides. *J. Am. Chem. Soc. 126*, 6115–23.

(3) Pinaud, F., Michalet, X., Iyer, G., Margeat, E., Moore, H.-P., and Shimon, W. (2009) Dynamic partitioning of a glycosyl-phosphatidylinositol-anchored protein in glycosphingolipid-rich microdomains imaged by single-quantum dot tracking. *Traffic 10*, 691–712.

(4) Iyer, G., Michalet, X., Chang, Y.-P., Pinaud, F. F., Matyas, S. E., Payne, G., and Weiss, S. (2008) High affinity scfvâ'hapten pair as a tool

for quantum dot labeling and tracking of single proteins in live cells. *Nano Lett. 8*, 4618–4623.

(5) Schipper, M. L., Iyer, G., Koh, A. L., Cheng, Z., Ebenstein, Y., Aharoni, A., Keren, S., Bentolila, L. A., Li, J., Rao, J., Chen, X., Banin, U., Wu, A. M., Sinclair, R., Weiss, S., and Gambhir, S. S. (2009) Particle size, surface coating, and pegylation influence the biodistribution of quantum dots in living mice. *Small 5*, 126–134.

(6) Schipper, M. L., Cheng, Z., Lee, S.-W., Bentolila, L. A., Iyer, G., Rao, J., Chen, X., Wu, A. M., Weiss, S., and Gambhir, S. S. (2007) microPET-based biodistribution of quantum dots in living mice. *J. Nucl. Med. 48*, 1511–1518.

(7) Pinaud, F., Clarke, S., Sittner, A., and Dahan, M. (2010) Probing cellular events, one quantum dot at a time. *Nat. Methods 7*, 275–285.

(8) Lee, J., Choi, Y., Kim, K., Hong, S., Park, H.-Y., Lee, T., Cheon, G. J., and Song, R. (2010) Characterization and cancer cell specific binding properties of Anti-EGFR antibody conjugated quantum dots. *Bioconjugate Chem. 21*, 940–946.

(9) Yuan, Q., Yeudall, W. A., and Yang, H. (2010) PEGylated polyamidoamine dendrimers with bis-aryl hydrazone linkages for enhanced gene delivery. *Biomacromolecules 11*, 1940–1947.

(10) Kozlov, I. A., Melnyk, P. C., Stromsborg, K. E., Chee, M. S., Barker, D. L., and Zhao, C. (2004) Efficient strategies for the conjugation of oligonucleotides to antibodies enabling highly sensitive protein detection. *Biopolymers 73*, 621–630.

(11) Prasuhn, D. E., Blanco-Canosa, J. B., Vora, G. J., Delehanty, J. B., Susumu, K., Mei, B. C., Dawson, P. E., and Medintz, I. L. (2010) Combining chemoselective ligation with polyhistidine-driven self-assembly for the modular display of biomolecules on quantum dots. *ACS Nano 4*, 267–278.

(12) Dirksen, A., and Dawson, P. E. (2008) Rapid oxime and hydrazone ligations with aromatic aldehydes for biomolecular labeling. *Bioconjugate Chem. 19*, 2543–2548.

(13) Grotzky, A., Manaka, Y., Kojima, T., and Walde, P. (2010) Preparation of catalytically active, covalent α-polylysine−enzyme conjugates via UV/vis-quantifiable bis-aryl hydrazone bond formation. *Biomacromolecules 12*, 134–144.

(14) Dirksen, A., Yegneswaran, S., and Dawson, P. E. (2010) Bisaryl hydrazones as exchangeable biocompatible linkers. *Angew. Chem., Int. Ed. 49*, 2023–2027.

(15) Li, J. J., Wang, Y. A., Guo, W., Keay, J. C., Mishima, T. D., Johnson, M. B., and Peng, X. (2003) Large-scale synthesis of nearly monodisperse CdSe/CdS core/shell nanocrystals using air-stable reagents via successive ion layer adsorption and reaction. *J. Am. Chem. Soc. 125*, 12567–12575.

(16) Clarke, S., Pinaud, F., Sittner, A., Gouzer, G., Beutel, O., Piehler, J., and Dahan, M. (2010) Monofunctional quantum dot probes for single-molecule imaging. *Biophys. J. 98*, 403a–403a.

(17) Clarke, S., Pinaud, F., Beutel, O., You, C., Piehler, J., and Dahan, M. (2010) Covalent monofunctionalization of peptide-coated quantum dots for single-molecule assays. *Nano Lett. 10*, 2147–2154.

(18) Schwartz, D. A., Abrams, M. J., Hauser, M. M., Gaul, F. E., Larsen, S. K., Rauh, D., and Zubieta, J. A. (1991) Preparation of hydrazino-modified proteins and their use for the synthesis of technetium-99m-protein conjugates. *Bioconjugate Chem. 2*, 333–336.

(19) Okada, C. Y., and Rechsteiner, M. (1982) Introduction of macromolecules into cultured mammalian cells by osmotic lysis of pinocytic vesicles. *Cell 29*, 33–41.

(20) Chattopadhyay, P. K., Price, D. A., Harper, T. F., Betts, M. R., Yu, J., Gostick, E., Perfetto, S. P., Goepfert, P., Koup, R. A., De Rosa, S. C., Bruchez, M. P., and Roederer, M. (2006) Quantum dot semiconductor nanocrystals for immunophenotyping by polychromatic flow cytometry. *Nat. Med. 12*, 972–977.

(21) Dunn, J. J., and Studier, F. W. (1983) Complete nucleotide sequence of bacteriophage T7 DNA and the locations of T7 genetic elements. *J. Mol. Biol. 166* (4), 477–535.

(22) Ebenstein, Y., Gassman, N., Kim, S., Antelman, J., Kim, Y., Ho, S., Samuel, R., Michalet, X., and Weiss, S. (2009) Lighting up individual DNA binding proteins with quantum dots. *Nano Lett. 9*, 1598–1603.

(23) Senter, P. D., and Meyer, D. L. (2007) Monoclonal antibody drug conjugates for cancer therapy, in *Prodrugs* (Stella, V. J., Borchardt, R. T., Hageman, M. J., Oliyai, R., Maag, H., and Tilley, J. W., Eds.) pp 507−524, Springer, New York.

(24) McCarron, P. A., Olwill, S. A., Marouf, W. M. Y., Buick, R. J., Walker, B., and Scott, C. J. (2005) Antibody conjugates and therapeutic strategies. *Mol. Interventions 5*, 368–380.

(25) Mahato, R., Tai, W., Cheng, K. Prodrugs for improving tumor targetability and efficiency. *Adv. Drug Delivery Rev.* In Press.

(26) Sievers, E. L. (2003) Antibody-targeted chemotherapy of acute myeloid leukemia using gemtuzumab ozogamicin (Mylotarg). *Blood Cells, Molecules, and Diseases 31*, 7–10.

(27) Alley, S. C., Okeley, N. M., and Senter, P. D. (2010) Antibody-drug conjugates: targeted drug delivery for cancer. *Curr. Opin. Chem. Biol. 14*, 529–537.

(28) Wong, B. Y., and Dang, N. H. (2010) Inotuzumab ozogamicin as novel therapy in lymphomas. *Expert Opin. Biol. Ther. 10*, 1251–1258.

(29) Dirksen, A., Dirksen, S., Hackeng, T. M., and Dawson, P. E. (2006) Nucleophilic catalysis of hydrazone formation and transimination: implications for dynamic covalent chemistry. *J. Am. Chem. Soc. 128*, 15602–15603.

(30) Dirksen, A., Hackeng, T. M., and Dawson, P. E. (2006) Nucleophilic catalysis of oxime ligation. *Angew. Chem., Int. Ed. 45*, 7581–7584.

(31) Blanco-Canosa, J. B., Medintz, I. L., Farrell, D., Mattoussi, H., and Dawson, P. E. (2010) Rapid covalent ligation of fluorescent peptides to water solubilized quantum dots. *J. Am. Chem. Soc. 132*, 10027–10033.

(32) Byeon, J.-Y., Limpoco, F. T., and Bailey, R. C. (2010) Efficient bioconjugation of protein capture agents to biosensor surfaces using aniline-catalyzed hydrazone ligation. *Langmuir 26*, 15430–15435.

(33) Rush, J. S., and Bertozzi, C. R. (2008) New aldehyde tag sequences identified by screening formylglycine generating enzymes in vitro and in vivo. *J. Am. Chem. Soc. 130*, 12240–12241.

(34) Frese, M. A., and Dierks, T. (2009) Formylglycine aldehyde tag—protein engineering through a novel post-translational modification. *ChemBioChem 10*, 425–427.

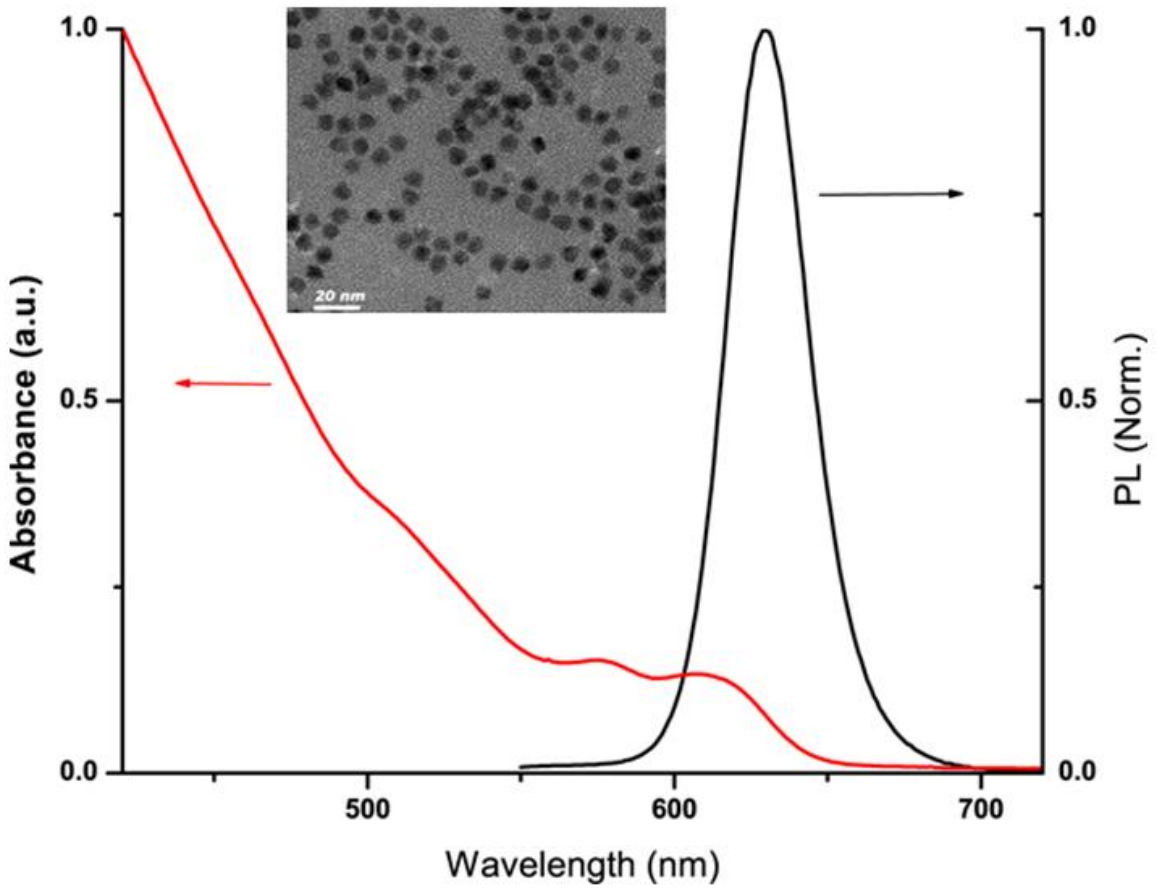


Figure S1. Absorbance (red) and emission spectra of peptide coated 630 nm CdSe/ZnS QDs. Transmission Electron micrography of QDs. (Scale bar – 20 nm)

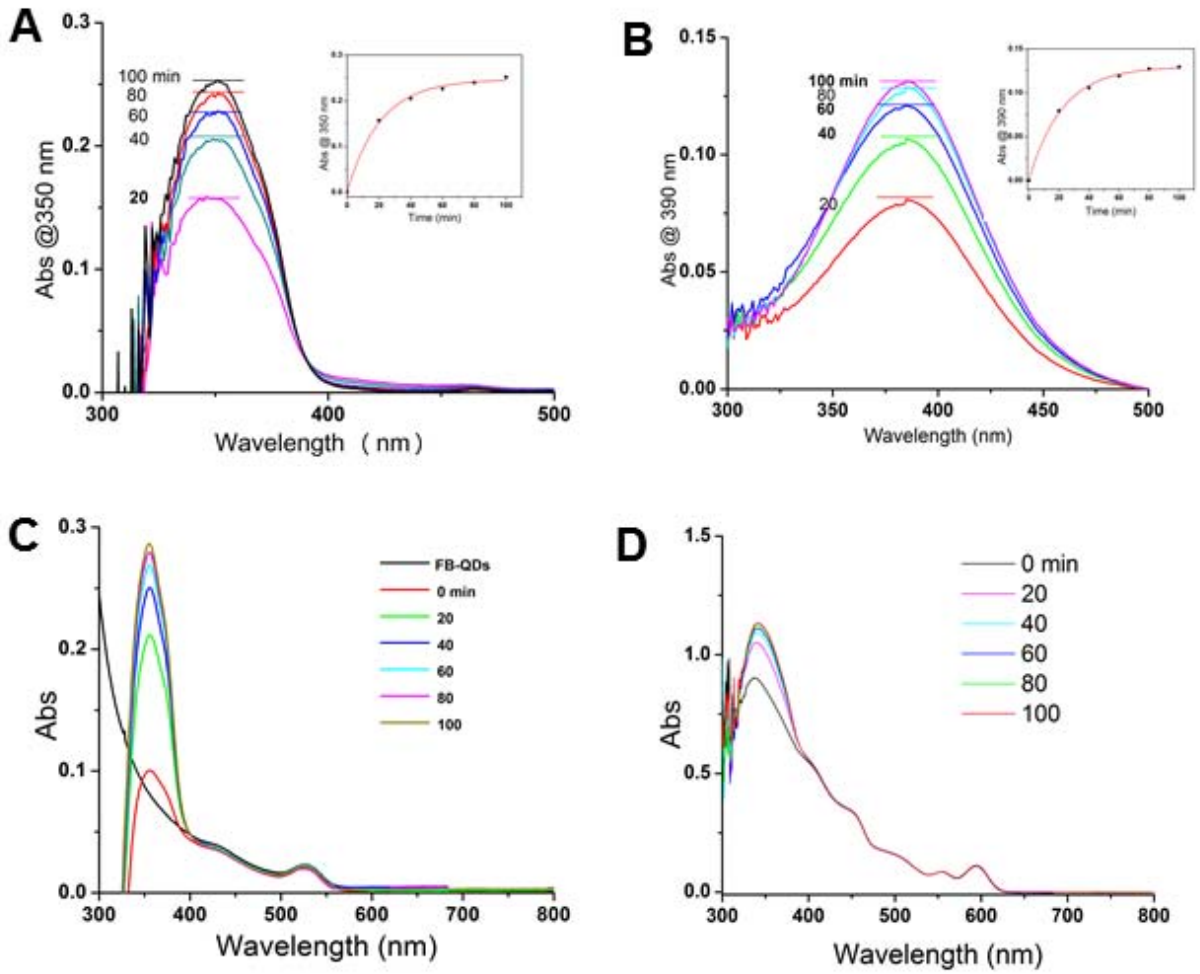
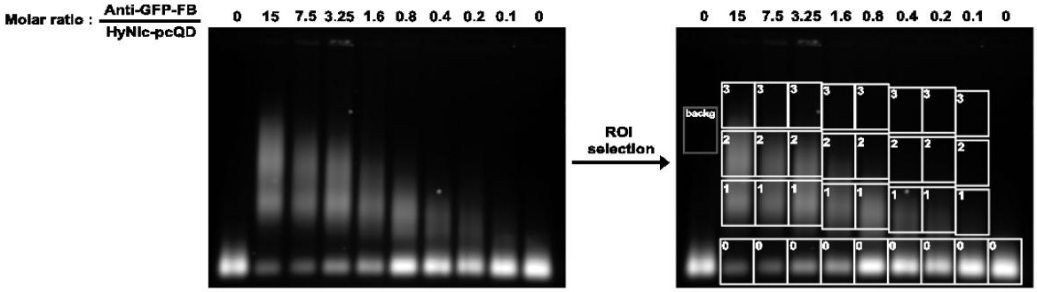


Figure S2. Absorbance studies to confirm the presence of the 4FB linkers on the surface of peptide coated QDs **(A)**, commercial Invitrogen PEG-amine coated QD-605 nm **(B)**.commercial eBioscience amine-coated QD-611nm **(C)**. Similar study was carried to confirm the presence of HyNic linkers on the $F(ab)_2$ antibodies **(D)**. Reaction kinetics of conjugation of 0.5 mM 2-hydrazinopyridine with 4FB activated QDs and 0.5 mM p-nitrobenzaldehyde with HyNic activated antibodies for 100 minutes in **(A)** and **(B).** Inset figures in A and B is plotted as absorbance vs time. 0.5 mM 2-hydrazinopyridine and 0.5 mM p-nitrobenzaldehyde prepared in 0.1 M MES buffer, pH5.0 was reacted with 4FB-QDs and HyNic-Abs respectively. Absorbance 350 and 390 nm was monitored by a uv-vis spectrophotometer using a blank containing 0.5 mM 2-hydrazinopyridine and 0.5 mM p-nitrobenzaldehyde solution mixed with 1X conjugation buffer (100 mM NaCl, 100 mM Na-phosphate, pH6.0).



Ratio	0		0.1		0.2		0.4		0.8		1.6		3.25		7.5		15	
Average	0		0.14		0.31		0.36		0.53		0.90		1.21		1.36		1.50	
Band #	M	P	M	P	M	P	M	P	M	P	M	P	M	P	M	P	M	P
N=0	1	1	0.87	0.87	0.72	0.73	0.67	0.70	0.55	0.59	0.36	0.41	0.22	0.30	0.19	0.26	0.13	0.22
N=1	0	0	0.12	0.12	0.25	0.23	0.31	0.25	0.38	0.31	0.41	0.37	0.41	0.36	0.37	0.35	0.34	0.33
N=2	0	0	0.01	0.01	0.03	0.04	0.03	0.04	0.07	0.08	0.19	0.17	0.31	0.22	0.38	0.24	0.42	0.25
N=3	0	0	0.00	0.00	0.00	0.00	0.00	0.01	0.01	0.01	0.04	0.05	0.06	0.09	0.08	0.11	0.11	0.13

Figure S3 Analysis of heterogeneities in the conjugation of anti-GFP-FB with HNA-pcQDs. Mean fluorescence intensity values were determined from region of interests corresponding to discrete bands in the agarose electrophoresis gel (ROI, white squares), and were corrected for background fluorescence (red square). For each conjugation molar ratios, the distribution intensity of each discrete bands (N=0, 1, 2 and 3) was reported and compared to the theoretical distribution in stoichiometry expected for a Poisson statistical process (Table). *Ratios* corresponds to the ratio of anti-GFP-FB:HNA-pcQD in the coupling solution. *Average* is the average number of conjugated anti-GFP-pcQDs for a given ratio. *M* is the measured fraction of HNA-pcQDs for a given ratio of anti-GFP-FB. *P* is the theoretical fraction $P(N) = a^N e^{-a}/N!$ computed for a Poisson distribution with average value a = *Average*. For all conjugation ratio tested, the distribution in stochiometry of anti-GFP-pcQDs and free pcQDs was in good agreements with that expected for a Poisson statistic.

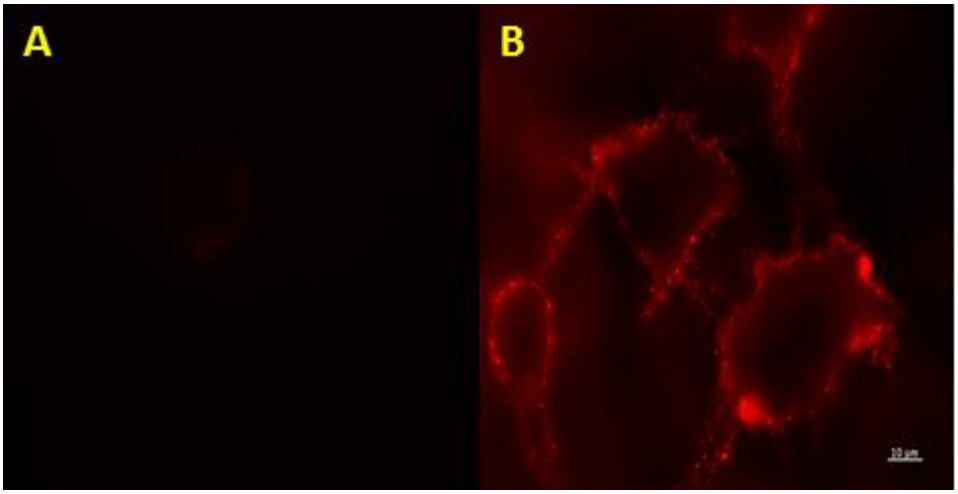


Figure S4. Fuoresence microscopy images of endogenous overexpressing EGFR receptors on plasma membrane of U87 Glioblastoma cells. (A) Cells were labeled with PEG4-4FB pcQDs showing absence of labeling of EGFR. (B) Same cells were labeled with anti-EGFR-PEG4-4FB pc-QDs showing distinct labeling of EGFR on the cell surface. Scale bar: 10 μm.

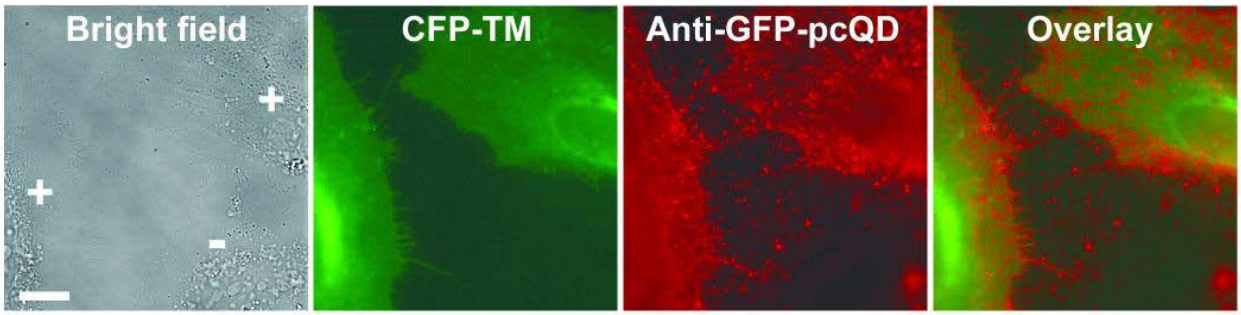


Figure S5. Labeling of live HeLa cells with 1:1 anti-GFP-pcQD conjugates formed by the reaction of anti-GFP-4FB with HyNic-pcQDs at 1.6 molar ratio. As observed for other conjugates, HeLa cells expressing the transmembrane CFP-TM receptors (+) are specifically labeled. Scale bar: 10 μm.

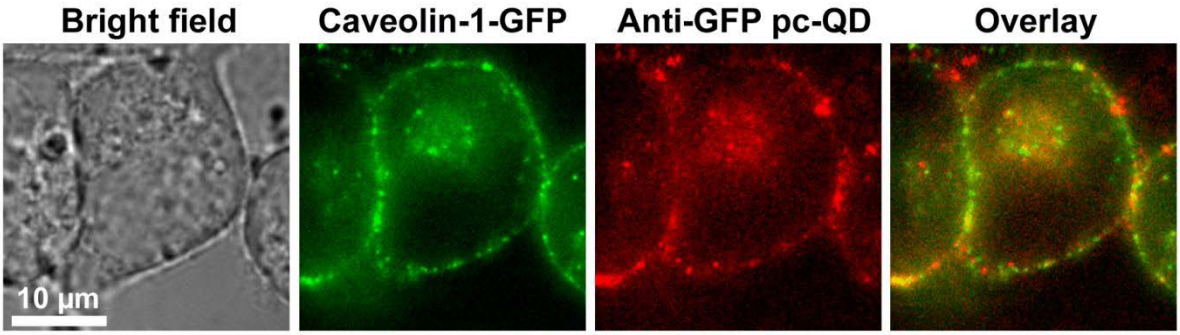


Figure S6. Live cells intracellular protein staining with peptide-coated QD-antibody conjugates

Living HeLa cells expressing the intracellular and integral plasma membrane protein caveolin-1-GFP are labeled with peptide-coated QDs conjugated to anti-GFP antibodies by the reaction of HyNic-activated anti-GFP IgG with FB-activated pc-QDs. QD-anti-GFP conjugates are translocated to the cells' cytoplasm by pinocytic loading using INFLUX reagent. When imaged by wide field fluorescence microscopy, the typical punctuated pattern of caveolae-associated cav-1-GFP at the plasma membrane of HeLa cells and a perinuclear pool of cav-1-GFP are visible in the GFP channel. When the cells are imaged in the QD channel, a similar staining pattern is observed indicating effective targeting of cav-1-GFP by the QD conjugate. Colocalization of caveolae and QD-anti-GFP is observed at the plasma membrane despite the presence of a few QDs still associated with pinosomes and not released during pinocytic loading.

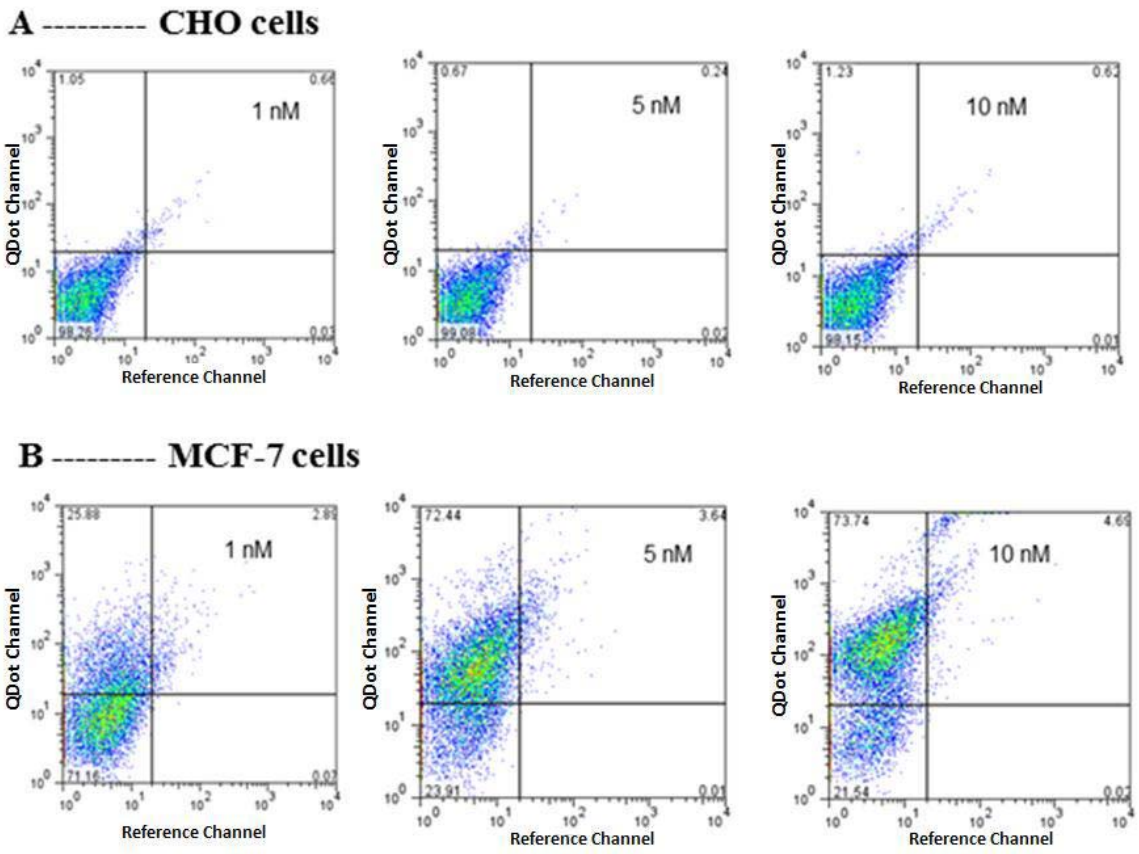


Figure S7. Flow cytometry of Chinese Hamster ovary non expressing EGFR and MCF-7 breast cancer cells overexpressing EGFR. Staining of CHO cells (A-top panel) and MCF-7 cells (B-bottom panel) was carried out by titrating anti-EGFR PEG4-4FB-pcQDs at 1, 5 and 10 nM concentration. A clear labeling of EGFR receptors on MCF-7 cells was observed with increasing concentration while it was absent in CHO cells at similar range of concentration of pc-QD bioconjugate.

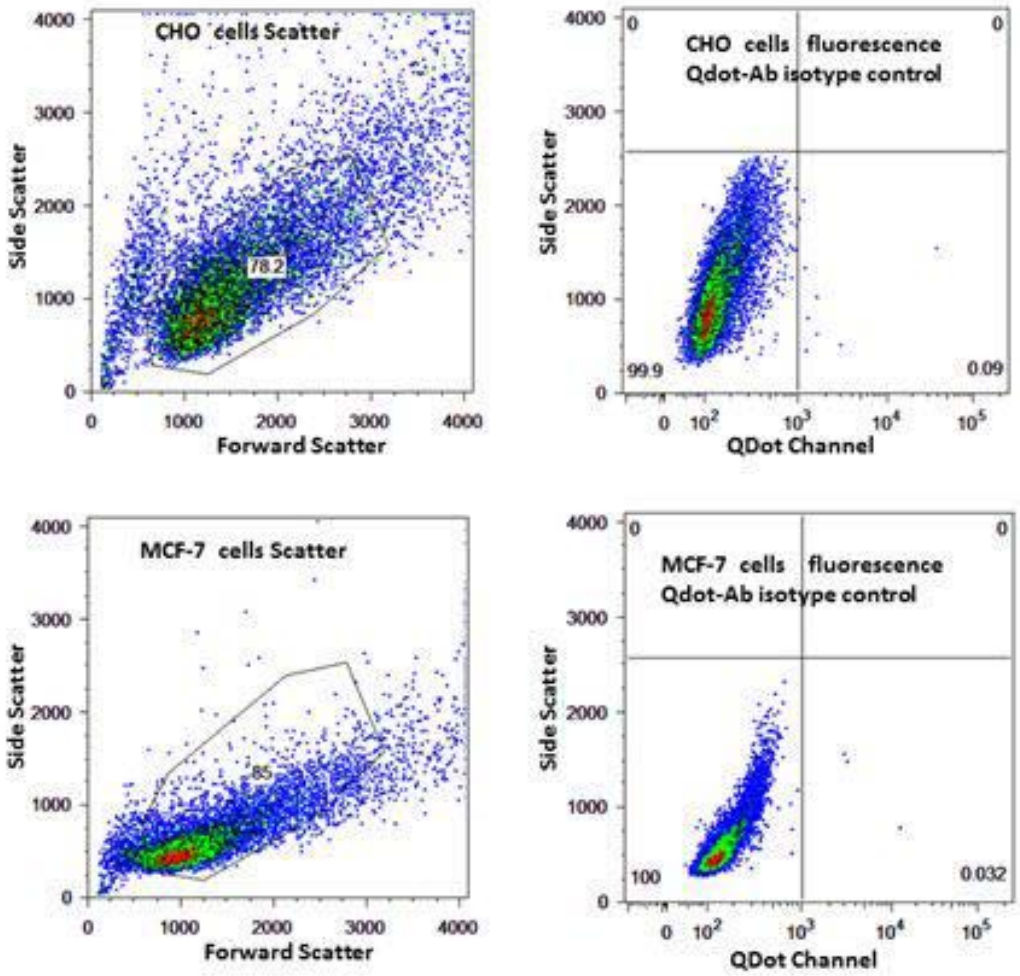


Figure S8.

Flow cytometry of and Chinese Hamster ovary non expressing EGFR (top) and MCF-7 breast cancer cells overexpressing EGFR (bottom) using normal mouse IgG_{2a} isotype control conjugated to pc-QDs. Staining of CHO cells (top panel) and MCF-7 cells (bottom panel) was carried out at 25 nM concentration. A clear absence of labeling of cell surface of either cell line using the isotype control suggested the specificity of the antibodies to EGFR-pcQDs using this conjugation strategy as shown in Figure S7.

Experiment Details

Preparation of Quantum dots: The synthesis of CdSe/CdS/ZnS core/shell QDs followed the description in reference (Li, JACS 2003). Post-synthesized CdSe was purified from the excess ligands and the unreacted precursors. Predegassed hexadecylamine and 1-octadecene were mixed with purified CdSe core for core/shell growth. SILAR approach was applied for multiple shells growth by dripping Cd, S and Zn precursor solutions (all at 0.04M) alternatively and sequentially into the reaction media at 235ºC. Shell growth was allowed for about 10 min following the finish of each precursor addition. With a 3.8 nm CdSe core, 3 layers of CdS and 2 layers of ZnS were grown intentionally. The final absorption was peaked at 608 nm, emission at 629 nm. Transmission Electron Microscopy (TEM) images were taken on Titan 80-300 kV S/TEM (FEI) on ultra-thin carbon coated copper grids.

Commercial Quantum dots: NH_2-PEG 545 nm (Invitrogen), Amine-605nm (Ebioscience) and inorganic 611 nm in toluene (Evident Technologies) CdSe/ZnS QDs was purchased for this study.

Modification of terminated peptide-coated quantum dot with 4-formylbenzoate and PEG4-4FB: Hydrophobic CdSe/ZnS QDs (Evident Technology, λ_{em} =605 nm) were coated with 100% of lysine and glycine terminated phytochelatin-related peptides using published procedures (Pinaud, King et al. 2004; Iyer, Pinaud et al. 2007). In brief, 45 µL of QD stock solution in toluene was heated fully to remove the toluene solvent and redispersed in 450 µL of pyridine, under gentle heating. 4 mg of an N-terminal acetylated $_{ac}$-FCCFCCFCCFGSESGGSESGK

peptide and Amide FCCFCCFCCFGSESGGSESG-NH_2 (New England Peptide) was dissolved in 50 µL dimethyl sulfoxide (DMSO), mixed with the QDs in pyridine, and peptide exchange was triggered by the addition of 10 µL of tetramethylammonium hydroxide (25% w/v in methanol). After centrifugation and redissolution in DMSO, pcQDs were eluted through a G25 Sephadex column equilibrated with H_2O and excess non-bound peptides were removed by two consecutive run on G-50 spin columns (Harvard Apparatus) equilibrated with 50 mM borate + 50 mM NaCl pH 7.4 buffer. Lysine terminated pcQDs at ~ 400 nM were kept at 4°C until further use. For activation of lysine terminated pcQDs with succinimidyl 4-formylbenzoate (SFB), a SureLINK™ bionconjugation kit (KPL) was used. A fresh solution of SFB and PEG4-4FB was prepared in DMSO at 6 mM and a 20-fold molar excess of SFB and PEG4-4FB was incubated with lysine and glycine terminated pcQdots for 2 hours at room temperature in 50 mM borate + 50 mM NaCl pH 7.4 buffer. After conjugation excess SFB was removed by two consecutive run on G-10 spin columns (Harvard Apparatus) equilibrated with 100 mM NaCl + 50 mM Na-phosphate pH 5.7. FB-activated pcQdots at ~400 nM were kept at 4°C until further use.

Quantum dot coating with hydrazine functionalized synthetic peptides. Hydrophobic CdSe/ZnS QDs (Evident Technology, λ_{em} =605 nm) were coated with 100% of phytochelatin-related peptides synthesized with HydraLinK™ 6-Fmoc-HNA reagent (Merck4Biosciences) to add the 6-hydrazinonicotate (HNA) at the N-terminus of the peptide as follow : HNA-GGSESGGSESGFCCFCCFCCF$_{\text{-amide}}$. Peptide coating was performed exactly as above, except that excess non-bound peptides were removed by two consecutive run on G-50 spin columns equilibrated with 100 mM NaCl + 50 mM Na-phosphate pH 5.7. HNA-pcQDs at ~400 nM were kept at 4°C until further use.

Modification of anti-GFP,anti-EGFR and secondary $F(ab)_2$ antibodies with 6-hydrazinonicotinate acetone hydrazone (HyNic), Succinidyml-C6-HyNic (C6-SANH) or 4-formylbenzoate. For 6-hydrazinonicotinate acetone hydrazone modification, anti-GFP rabbit IgG antibodies that cross reacted with CFP (Invitrogen) at 2 mg/ml in PBS buffer PH 7.2 were reacted with a 20 fold molar excess of succinimidyl 6-hydrazinonicotinate acetone hydrazone (SHNA) in DMSO from the SureLINK™ bionconjugation kit. Incubation was done for 2 hours at room temperature and excess SHNA was removed by two consecutive run on G-10 spin columns equilibrated with 100 mM NaCl + 50 mM Na-phosphate pH 5.7. HNA-activated anti-GFP IgG at ~2 mg/ml were kept at 4°C until further use. For C6-SANH modification, anti-EGFR monoclonal antibodies (sc-120, 200 μg/ml. special order, gelatin free, Santa Cruz Biotechnology) and goat anti-mouse $F(ab)_2$ at 2mg/ml (Pierce biotechnology) were reacted with a 15 fold molar excess of C6-SANH and incubated for 2 hours at room temperature. Excess linkers were removed and exchanged into 150 mM NaCl + 100 mM Na-phosphate pH 6.0 using pre-equilibrated 2 ml Pierce desalting column. C6-SANH antibodies obtained were quantified using a uv-vis spectrophotometer at 280 nm and stored at 1-2 mg/ml concentration. For 4-formylbenzoate modification, anti-GFP rabbit IgG antibodies at 2 mg/ml in PBS buffer PH 7.2 were reacted with a 20 fold molar excess of SFB from the SureLINK™ bionconjugation kit, and incubated for 2 hours at room temperature. Excess SFB was clean by two consecutive run on G-10 spin columns equilibrated with 100 mM NaCl + 50 mM Na-phosphate pH 5.7, and FB-activated anti-GFP IgG at ~2 mg/ml were kept at 4°C until further use.

Conjugation of anti-GFP and anti-EGFR antibodies to pcQD: A 10-fold molar excess of HNA-activated anti-GFP IgG was reacted with 300 nM of FB-activated pcQdots in 100 mM NaCl + 50 mM Na-phosphate pH 5.7 for 3 hours at 4°C, and use without further purification for

cell labeling assays. 0.5 nmole of PEG4-4FB-pcQDs was reacted with 3.6 nmole of C6-SANH-anti-EGFR antibodies and $F(ab)_2$antibody conjugation in 150 mM NaCl + 100 mM Na-phosphate pH 6.0 overnight at 4°C for 24 hours and used without further purification for cell labeling assays. The reaction of HNA-pcQDs with FB-activated anti-GFP IgG for gel assays was optimized by incubating of 1 µl of 400 nM HNA-pcQDs with 1 µl of FB-activated anti-GFP IgG at the indicated final molar ratio. The incubation was performed for 3 hours at room temperature before immediate loading on agarose gels. The reaction of HNA-pcQDs with FB-activated anti-GFP IgG for cell staining was done by incubating 20 µl of 400 nM HNA-pcQDs with 20 µl of FB-activated anti-GFP IgG at 750 nM (1.8 molar excess) for 150 min at room temperature. The reaction was then quenched by the sequential addition of 600 µM 4-nitrobenzaldehyde and 500 µM 2-hydrazinopyridine and further incubation for 2 hours. Half of the reaction volume was analyzed by agarose gel electrophoresis, while the other half was used for cell staining.

Gel electrophoresis. Conjugation reactions at different molar ratio between HNA-pcQDs and FB-activated anti-GFP IgG were loaded on 0.8% agarose gels in x1 TAE buffer (40 mM Tris, 40 mM acetate, 1 mM EDTA, pH 8.3). The 2 µl samples were diluted into 6 µl loading buffer and gel where run for 40 minutes at 110V, before being imaged using ultraviolet excitation and detection with a CCD camera (Kodak). For electrophoresis of large volumes of HNA-pcQDs / FB-activated anti-GFP conjugates at 1.8 molar ratio, half of the reaction was loaded into five different wells, and electrophoresed on a 0.8% agarose gels in x0.5 TAE buffer for 40 min at 35V. After electrophoresis, fluorescence bands corresponding to anti-GFP-pcQD conjugates or to non-conjugated pcQDs were cut and QDs were eluted from the gel as previously described(Pinaud, Clarke et al. 2010).

Estimation of 4FB groups on pc-QDs: 0.5 mM of 2-hydrazinopyridine-2HCl (2HP) solution was prepared in fresh 2-(N-morpholino) ethanesulfonic acid (MES) buffer, pH 5.0. 10µl of 0.5 nmole 4FB activated pc-QDs solution was mixed with 90 µl 2HP reagents at room temperature. Reaction kinetics of bis aryl-hydrazone bond formation between 2HP and FB-QDs was monitored for 100 min at 350 nm using a uv-vis spectrophotometer. After 100 min, the molar substitution ratio for FB-QDs was calculated to be 10 using the extinction coefficient at 18000 for the hydrazone chromophore (Solulink).

Estimation of HyNic groups on antibodies: 0.5 mM solution of p-nitrobenzaldehdye (pNB) solution in fresh 2-(N-morpholino) ethanesulfonic acid (MES) buffer, pH 5.0. 10 uL of the C6-SANH activated $F(ab)_2$ antibodies was reacted with 90 ul pNB solution at room temperature. The formed hydrazone bond was monitored by UV-Vis at 390 nm and the molar substitution ratio for protein was 4.15 using the extinction coefficient at 24,000 (Solulink).

Cells staining and imaging. HeLa and MCF-7 cells were maintained at 37 °C and 5% CO_2 in Dulbecco's modified Eagle's medium (DMEM) supplemented with 10% fetal bovine serum, 100 U/mL penicillin, 100 µg/mL streptomycin while CHO cells were maintained under identical conditions in F-12 media. One day before transfection, HeLa cells were plated on fibronectin-coated glass coverslips to achieve a confluency of 50-80% while MCF-7 and CHO cells were plated on 35 mm Mattek No 1.5 glass bottomed petridishes. Cells were transfected with a plasmid encoding the transmembrane domain of the platelet-derived growth factor receptor fused to CFP (AP-CFP-TM, a gift from Alice Ting) using Fugene 6 (Roche). 48 hours after transfection, cells were briefly washed with HBSS buffer + 1% BSA, and incubated in this buffer for 3 minutes at 37°C, before adding anti-GFP-pcQD and anti-EGFR-pcQD conjugates at 5 nM

and 10 nM final concentration and incubating for 10 min at 37°C. Cells were then washed with HBSS buffer before being imaged. Imaging of HeLa cells was done in HBSS buffer at 37°C on an inverted wide-field epifluorescent microscope (IX70, Olympus) equipped with a 100X oil objective (NA=1.45, Olympus) a broad-spectrum mercury lamp excitation source and appropriate emission filters for CFP and pcQD-605 while imaging of MCF-7 and CHO cells was done on with a Zeiss 200M epifluorescence microscope with a 63× water-immersion objective (NA)=1.2 (Carl Zeiss) equipped with a motorized platform for *z*-stack imaging and deconvolution, a 100 W mecury lamp as excitation source and appropriate emission cubes for pcQD-630 nm. Images were acquired with a QuantEM:512SC EMCDD camera (Photometrics).

Flow cytometry. Labeled mammalian MCF-7 and CHO cells were measured using the BD FACSAria (Becton Dickinson, Franklin Lakes, NJ) digital cell sorter equipped with BD FACSDiVa software. The cytometer has three lasers emitting at 488, 633, and 405 nm. The 405 laser nm laser was used to excite anti-EGFR pcQDs whose emission was detected using a 630/30 band pass filter. Cells were gated based on their forward versus side scatter profile and fluorescence was measured in a 2-dimensional plot of FITC versus QD. A negative control which were unlabeled cells was used to check the voltages for leak through and no compensation was necessary. Titration experiments with anti-EGFR emitting 630 QDs were carried out at 1, 5, 10 and 25 nm concentrations.

Supplementary video 1: Cell membrane diffusion of targeted anti-GFP-pcQD conjugates. anti-GFP-pcQD were incubated for 10 min with CFP-TM expressing (bottom) and non-expressing (top) HeLa cells. Anti-GFP-pcQD conjugates specifically recognize the CFP-TM receptors and diffuse in the plasma membrane. The video is a composite overlay of a fixed CFP-TM fluorescence image (green) and its corresponding anti-GFP-pcQDs video taken at a rate of 100

ms per frame (red). The last frames correspond to the maximum intensity projection image for all the frames of the anti-GFP-pcQDs video (red) overlaid with the CFP-TM fluorescence image (green). Playback: 30 fps.

Video 2. Sequential video imaging of cav-1-GFP (green, top) and QD-anti-GFP conjugates (red, bottom) of cav-1-GFP expressing or non-expressing HeLa cells after cytoplasmic delivery of QD-anti-GFP conjugates by pinocytic loading. Please note the similar staining patterns of GFP and QD for expressing cells and the absence of QD plasma membrane staining for the non-expressing cell. Acquisition: 100 ms/frame; Playback: 30 frames/s.

Bioconjugate Chemistry

COMMUNICATION

pubs.acs.org/bc

Assembly of Single-Walled Carbon Nanohorn Supported Liposome Particles

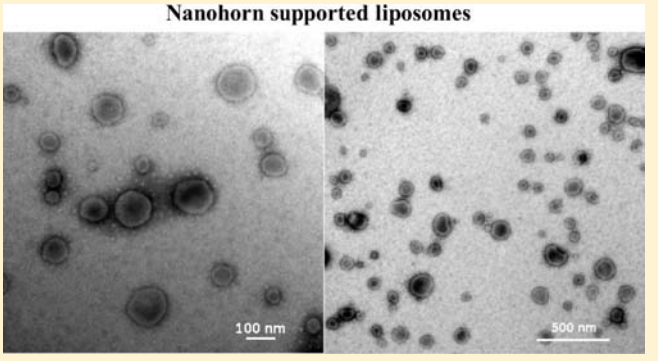
Wei Huang,[†] Jianfei Zhang,[‡] Harry C. Dorn,[‡] David Geohegan,[§] and Chenming Zhang*[,†]

[†]Department of Biological Systems Engineering

[‡]Department of Chemistry, Virginia Tech, Blacksburg, Virginia 24061, United States

[§]Center for Nanophase Materials Sciences and SHaRE Facilities, Oak Ridge National Laboratories, Oak Ridge, Tennessee 37831, United States

ABSTRACT: Nanoparticle-supported liposomes can be a promising platform for drug delivery, vaccine development, and biomedical imaging. Single-walled carbon nanohorns are a relatively new carbon nanomaterial, and they could be used as carriers of drug and imaging reagents. Assembling lipids around carbon nanohorns would confer this nanomaterial much broader applications such as vaccine development and targeted drug delivery by embedding a target protein or immunogenic protein into the lipid bilayer structure. Here, we show the assembly of functionalized single-walled carbon nanohorns ($-CH_2-CH_2-COOH)_x$, ~100 nm) with positively charged lipids through a freeze and thaw cycle. The assembled complex particles can be readily separated from individual nanohorns or liposomes under specific centrifugation conditions. The results from transmission electronic microscopy, flow cytometry through nitrobenzoxadiazole labeled lipids, and zeta potential analysis clearly show that the nanohorns are encapsulated by liposomes with a median size of ca. 120 nm.



Liposomes and many types of nanoparticles have been studied as potential drug delivery vehicles. Despite the similarities, i.e., they both can have a desirable loading capacity and release the contents at a controlled rate in a specific location when attached with targeting ligands, liposomes and nanoparticles are complementary delivery systems because (1) nanoparticles tend to have a longer half-life during the circulation in blood and the extravasations from plasma to the tumor cells;[1,2] (2) liposomes provide a better chance to deliver drugs across cell membrane at the targeting site; and (3) they have different drug preferences, loading, and releasing chemistry.[1,2] However, the combination of the two types of particles could possess unique advantages over any of the particles alone. Nanoparticle supported liposomes (NsLs) have recently been assembled and described.[3] Nanoparticles usually stabilize the liposomes through electrostatic interactions and may also increase the concentrations of poly(ethylene glycol) (PEG) that can be attached to the surface of liposomes, resulting in NsLs, when intravenously injected, with improved ability to evade clearance by the reticuloendothelial system (RES).[3] NsLs could have a large loading capacity and a desirable controlled release rate depending on the large adsorption area and special pore surface chemistry of the encapsulated nanoparticle.[4] Moreover, a targeting ligand attached liposome could transport nanoparticles into cells through receptor-mediated endocytosis. This is critical when large molecule drugs or therapeutic genes are to be released into the cytoplasm.[5]

In this report, functionalized (carboxylated) carbon single-walled nanohorns, SWNH $(-CH_2-CH_2-COOH)_x$, were prepared to provide SWNHs with hydrophilic surfaces for encapsulation into the liposomes. The SWNH$(-CH_2-CH_2-COOH)_x$ are nontoxic[6,7] nanoparticle aggregates of single graphene tubules and are spherical dahlia-like-shaped with a narrow diameter range reported as 80−100 nm.[8] The surface area of SWNHs range from 300 to 1000 m^2/g.[9] The functionalization process introduces mesoporous structures on the SWNHs, and consequently, drug molecules could bind not only to the surface, but also to the inner graphene wall. Research has also shown that molecules that have stacking aromatic rings once diffused into SWNHs will release in a slow and stable manner.[10]

Single-walled nanohorns were synthesized by Nd:YAG laser vaporization of graphite rods in an argon atmosphere at 1100 °C as described in detail elsewhere.[11,12] Functionalized SWNH-$(-CH_2-CH_2-COOH)_x$ with carboxyl groups was obtained by high-speed vibration milling as previously described.[13] Briefly, a mixture of nanohorns and succinic acid acyl peroxide (1:100 in mass) was vigorously shaken in a stainless steel capsule for 1.5 h. The ground ultrafine powder was washed three times with acetone and centrifuged to collect the sediment. Twenty minute

Received: February 25, 2011
Revised: April 11, 2011
Published: May 02, 2011

ACS Publications © 2011 American Chemical Society

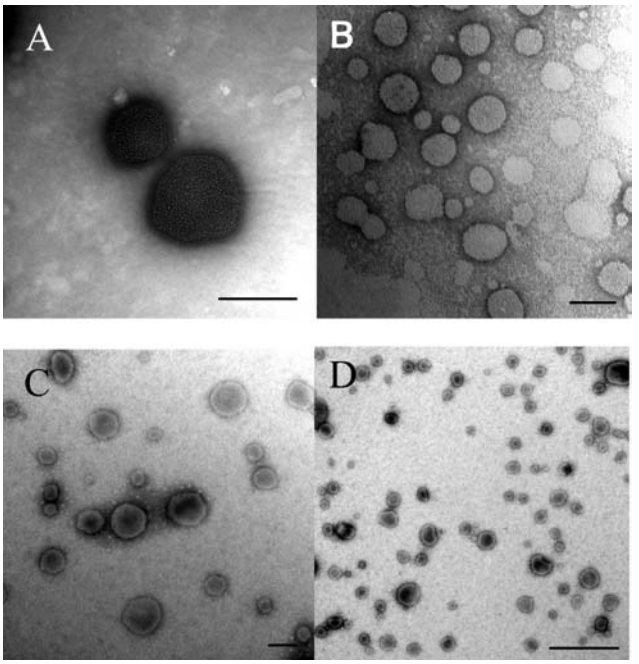


Figure 1. Representative TEM images of (A) SWNH($-CH_2-CH_2-COOH)_x$, (B) hollow DOTAP liposomes, and (C) and (D) SWNH($-CH_2-CH_2-COOH)_x$ supported liposomes. Scale bar in (A), (B), and (C) = 100 nm. Scale bar in (D) = 500 nm. Samples were deposited onto carbon coated copper grids. Negative staining was performed using 2% phosphotungstic acid.

sonication was performed to dissolve the sediment in ultrapure water yielding solutions of SWNH($-CH_2-CH_2-COOH)_x$. On the other hand, cationic liposomes were made by extruding 0.4 mg hydrated 1,2-dioleoyl-3-trimethylammonium-propane (DOTAP) lipid film through polycarbonate membranes with pore sizes of 100 nm. The hydration buffer contains 0.9 NaCl, 5% dextrose, and 10% sucrose in Tris-HCl buffer with a pH at 7.4. SWNH($-CH_2-CH_2-COOH)_x$ were briefly sonicated to break up aggregates and incubated with freshly made cationic liposomes. Particles of these functionalized SWNHs and liposome were quantified by flow cytometer (FCM), and the concentrations were both optimized to ~100 particles/μL. After gently homogenizing the optimized samples at a volume ratio of 1:10 SWNH($-CH_2-CH_2-COOH)_x$:liposomes, a ratio chosen to ensure there are excessive liposomes for functionalized SWNHs, three freeze and thaw cycles were applied using liquid nitrogen and a warm water bath. Samples were then centrifuged under 10 000 rcf for 10 min, and SWNH($-CH_2-CH_2-COOH)_x$ supported liposomes were collected in the top layer. It was also found that, in the presence of 10% sucrose, DOTAP liposomes could be collected in the top layer after 30 min of centrifugation under 16 000 rcf, and SWNH($-CH_2-CH_2-COOH)_x$ could be collected in the top liquid layer after 30 min of centrifugation under 10 000 rcf. Therefore, washing the SWNH($-CH_2-CH_2-COOH)_x$ supported liposomes with the hydration buffer and repeating the centrifugation (10 000 rcf, 10 min) can significantly increase the purity.

Transmission electronic microscopy (TEM) images for SWNH($-CH_2-CH_2-COOH)_x$, hollow liposomes, and SWNH-($-CH_2-CH_2-COOH)_x$ supported liposomes are shown in Figure 1. As can be seen, all particles are of spherical shape and

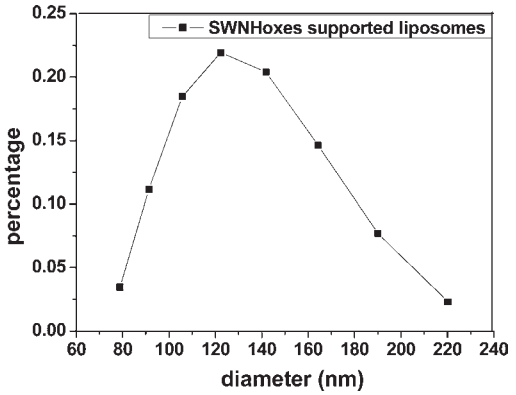


Figure 2. Size distribution of SWNH($-CH_2-CH_2-COOH)_x$ supported liposomes. Refractive index = 1.33. Viscosity = 0.8872 cP. Samples were measured at 25 °C.

have a narrow distribution centered at around 120 nm, which was confirmed by the dynamic light scattering test result shown in Figure 2. As shown in Figure 1C, a SWNH($-CH_2-CH_2-COOH)_x$ supported liposome is a combination of the particles shown in (A) and (B). A negatively charged SWNH($-CH_2-CH_2-COOH)_x$ is encapsulated in a cationic liposome and could stabilize and support the liposome from inside. The large-scale view of the particles shown in Figure 1D illustrates that a high purity of the assembled complex particles can be achieved by the centrifugation step described above. Centrifugation in the presence of 10% sucrose was performed only once in this case, but no hollow liposome or unencapsulated SWNH($-CH_2-CH_2-COOH)_x$ was observed in Figure 1D.

To further confirm the structure of the particles, nitrobenzoxadiazole (NBD) labeled 1,2-dioleoyl-*sn*-glycero-3-phosphoethanolamine was added to the lipid mixture (up to 15% mass ratio) to produce NBD-DOTAP liposomes and SWNH($-CH_2-CH_2-COOH)_x$ supported NBD-DOTAP liposome assembly. Results of the fluorescence of different particles detected by FCM are shown in Figure 3. The overlay histogram shows a similar fluorescence intensity shared by NBD-DOTAP liposomes and SWNH($-CH_2-CH_2-COOH)_x$ supported NBD-DOTAP liposomes, and SWNH($-CH_2-CH_2-COOH)_x$ particles without liposomes assembled around show no fluorescence signal. These results indicate that the surface structure of SWNH($-CH_2-CH_2-COOH)_x$-supported liposome samples is most likely the same as that of hollow NBD-DOTAP liposomes, since the granularity and fluorescence intensity are almost identical (see FCM scatter plots in Figure 3). Zeta potential and electrophoresis mobility of the three particles shown in Table 1 further confirm the similar surface characteristics of DOTAP liposomes and SWNH($-CH_2-CH_2-COOH)_x$-supported DOTAP liposomes (N^-sL^+, negatively charged nanohorn supported positively charged liposomes), since their zeta potentials significantly differ from that of SWNH($-CH_2-CH_2-COOH)_x$. As expected, those N^-sL^+ particles and SWNH($-CH_2-CH_2-COOH)_x$ particles travel in opposite directions in an applied electric field. These results confirm the encapsulation of SWNH-($-CH_2-CH_2-COOH)_x$ in liposomes and that the gray circle surrounding SWNH($-CH_2-CH_2-COOH)_x$ in Figure 1C and D represents DOTAP lipid bilayers. The FCM results shown in Figure 3 also serve as a strong indication that a high purity of the N^-sL^+ particles can be achieved using the purification method described above.

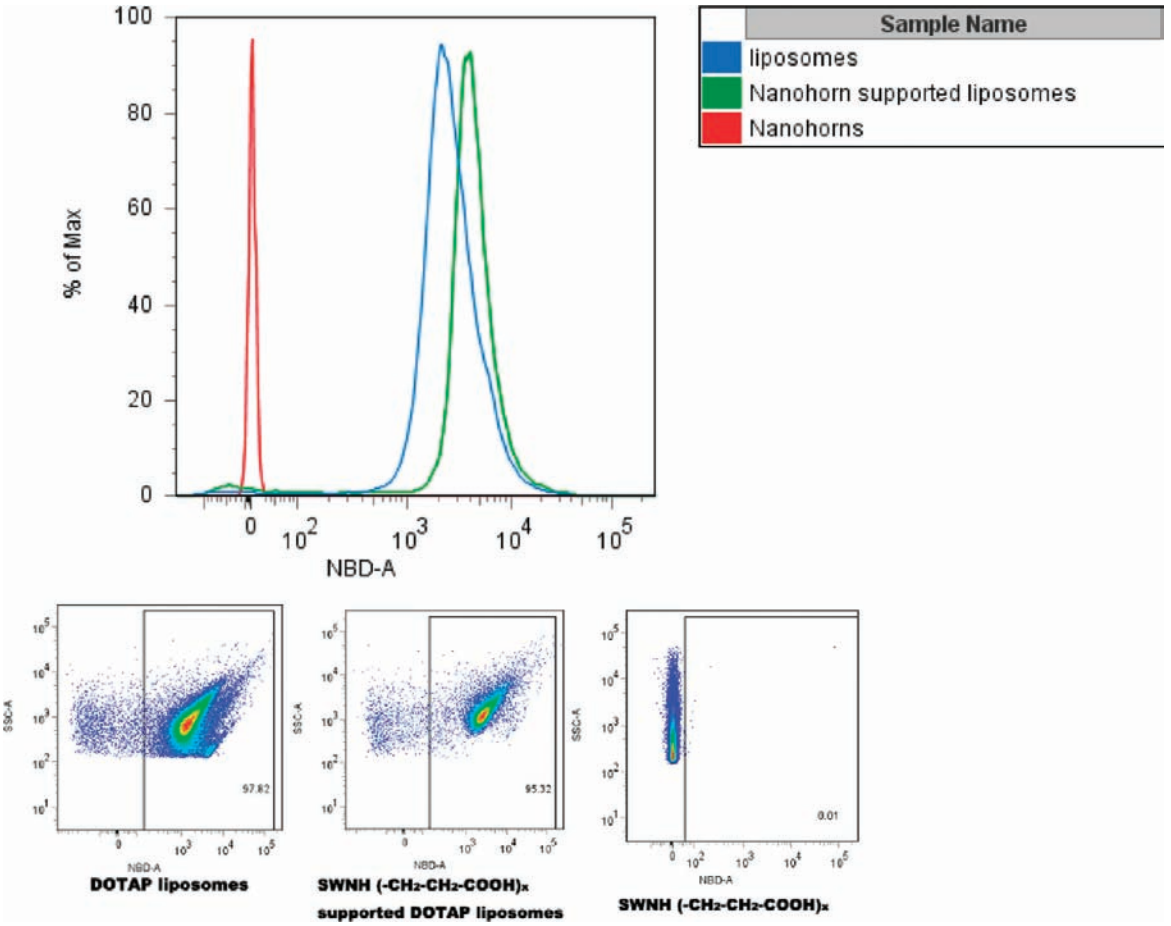


Figure 3. Fluorescent intensity of different particles. The histogram shows the fluorescent intensity distribution of NBD-DOTAP liposomes (blue), SWNH$(-CH_2-CH_2-COOH)_x$ (red), and SWNH$(-CH_2-CH_2-COOH)_x$ supported liposomes (green). The three corresponding FCM scatter plots show distribution of fluorescent intensity (horizontal axis, NBD-A) versus granularity (vertical axis, SSC-A).

Table 1. Zeta Potential and Electrophoresis Mobility of Particles[a]

sample	zeta potential (mv)	electrophoretic mobility (μm·cm/V·s)
hollow DOTAP liposome	24.6	1.928
nanohorn	34.4	−2.694
SWNH$(-CH_2-CH_2-COOH)_x$ supported liposome	22.1	1.732

[a] All samples are in the hydration buffer (pH = 7.4), 25 °C.

Conceivably, functionalized nanohorn supported liposomes will not be limited just to N^-sL^+ types of particles. Positively charged nanohorns can be synthesized by the aryl diazonium functionalization as reported,[14] and therefore, it is possible to assemble the complex particles using negatively charged lipids (N^+sL^-), which are more commonly found in various biological membranes, for biomimetic purposes. The combination of positively or negatively charged nanohorns with anionic or cationic liposomes will significantly broaden the types of drugs that can be loaded, depending specifically on their charge or hydrophobicity. So far, many successful cases have shown that SWNH$(-CH_2-CH_2-COOH)_x$ could be a very promising drug delivery vehicle in terms of the loading capacity and the controlled release. A good example is the anticancer drug cisplatin, which has recently become a commonly used molecule to test the two properties of certain functionalized nanohorns mentioned above.[15,16] However, the effects were mainly evaluated by directly providing cancer cell cultures with treatment of the drug carrying nanohorns. The targeting effect of nanohorns *in vivo* has not been well addressed. How many of the particles injected would nonspecifically bind to normal living cells and lead to their apoptosis is still unknown. On the other hand, liposomes conjugated with targeting ligands such as antibodies can navigate themselves to the cells that have corresponding receptors presented on the cell surface.[17] The particles assembled by the combination of ligand-attached liposomes and nanohorns could present a new and much improved drug delivery platform. For example, cisplatin could be loaded into SWNH$(-CH_2-CH_2-COOH)_x$ particles,[15,16] which could subsequently be assembled with liposomes that contain lipids sensitive to the change of pH (such as dioleoyl-phosphatidyl-ethanolamine, DOPE). Targeting antibodies, such as antihuman epidermal growth factor receptor-2 (HER2) antibody (Herceptin),[18] could be attached to the assembled particles via poly(ethylene glycol) (PEG) on PEGylated phospholipids.[3] The presence of the lipid

bilayer will deter the escape of cisplatin from the particles through diffusion during circulation in blood. However, once the particles enter the targeted cells (such as breast cancer cells via Herceptin-HER interaction[18]), defects will appear on the lipid bilayer structure due to the presence of pH-sensitive lipids,[19] and cisplatin will be released from the particles via the lipid bilayer defects. Research on this novel drug delivery system is currently under investigation in our laboratories.

Functionalized single-walled nanohorn supported liposomes can have more novel applications beyond drug delivery systems. Magnetic resonance imaging (MRI) contrast agents containing Gd^{3+} ions have been loaded into SWNH$(-CH_2-CH_2-COOH)_x$ in the form of $Gd_3N@C_{80}$, trimetallic nitride template endohedral metallofullerenes (TNT-EMFs)[10] to lower the toxicity to the host because (1) lower amount is required due to the high ^1H magnetic resonance (MR) relaxivities of these TNT-EMF contrast agents[20] and (2) the encapsulation of $(Gd_3N)^{+6}$ clusters into fullerene cages limits the exposure to free Gd^{3+} ions.[12] Gadolinium containing SWNH$(-CH_2-CH_2-COOH)_x$ supported liposomes reveal an opportunity to make the drug carrier itself an MRI biosensor. This allows the in situ monitoring of the in vivo biodistributions of drugs in a macro or real-time manner.[21] For example, clearance of liposomes from the bloodstream by the RES, which has greatly limited the development and applications of liposomal models, can be further studied and understood in detail. Locating the pathogenic cells also becomes a possibility when using $Gd_3N@C_{80}$ TNT-EMFs encapsulated targeting nanohorn supported liposomes. The SWNH$(-CH_2-CH_2-COOH)_x$ along with the contrast agent will most likely be found inside the cytoplasm and remain there allowing a slow release of the therapeutic drugs, as the $(Gd_3N)^{+6}$ clusters remain detectable for several days post infusion.[12]

Liposomal vaccines are a new type of vaccine that are assembled by associating antigens with liposomes, and they have attracted much attention because of their high immunogenicity[22] and gene-free nature.[23] Size, exposure of epitopes, and stability of the liposomal vaccine particles are parameters most critical for their immunogenicity.[24,25] A commonly accepted measure to increase the stability is to incorporate PEGylated phospholipids into the liposome, especially when the vaccines are to be injected intravenously. However, the grafting density and polymer length of PEG strongly influence the exposure of the epitopes that need to be presented.[26] SWNH$(-CH_2-CH_2-COOH)_x$ stabilizes liposomes from inside and enables the entire liposome surface to be solely used for epitope presenting, and the size of the assembled particle (80−220 nm, see Figure 2) falls within the range that can be efficiently taken up by dendritic cells.[24]

In summary, we have shown the assembly and structure of SWNH$(-CH_2-CH_2-COOH)_x$ supported DOTAP liposomes. The combination of functionalized single-walled nanohorns with liposomes reveals a variety of opportunities for the complex particle not only as drug delivery vehicles in terms of high loading capacity, broad drug selectivity, cell targeting, and controlled release, but also as many more potential promising applications such as drug biodistribution real-time MRI, MRI contrast agent targeting, and liposomal vaccine assembly. It can be a useful platform to load with different types of molecules or a promotion for developing other similar nanoparticle complexes for various applications.

AUTHOR INFORMATION

Corresponding Author

*Correspondence to Chenming (Mike) Zhang, 210 Seitz Hall, Dept. of Biological Systems Engineering, Virginia Tech, Blacksburg, VA 24061. (540) 231-7601; (540) 231-3199 (Fax); e-mail Chzhang2@vt.edu.

ACKNOWLEDGMENT

This work was supported primarily by the Institute for Critical Technology and Applied Science (ICTAS) at Virginia Tech, and partially funded by a grant from Jeffress Memorial Trust, grant no. J-994. Authors gratefully acknowledge Dr. Richey M. Davis for his support in particle size experiments, Kathy Lowe for her technical assistance with TEM imaging, and Melissa Makris for the assistance with FCM.

REFERENCES

(1) Sapra, P., and Allen, T. M. (2003) Ligand-targeted liposomal anticancer drugs. *Prog. Lipid Res. 42*, 439–462.

(2) Singh, R., and Lillard, J. W., Jr. (2009) Nanoparticle-based targeted drug delivery. *Exp. Mol. Pathol. 86*, 215–223.

(3) Li, S. D., and Huang, L. (2009) Nanoparticles evading the reticuloendothelial system: Role of the supported bilayer. *BBA Biomembranes 1788*, 2259–2266.

(4) Liu, J., Stace-Naughton, A., Jiang, X., and Brinker, C. J. (2009) Porous nanoparticle supported lipid bilayers (Protocells) as delivery vehicles. *J. Am. Chem. Soc. 131*, 1354–1355.

(5) Kunisawa, J., Masuda, T., Katayama, K., Yoshikawa, T., Tsutsumi, Y., Akashi, M., Mayumi, T., and Nakagawa, S. (2005) Fusogenic liposome delivers encapsulated nanoparticles for cytosolic controlled gene release. *J. Controlled Release 105*, 344–353.

(6) Miyawaki, J., Yudasaka, M., Azami, T., Kubo, Y., and Iijima, S. (2008) Toxicity of single-walled carbon nanohorns. *ACS Nano 2*, 213–226.

(7) Lynch, R. M., Voy, B. H., Glass, D. F., Mahurin, S. M., Zhao, B., Hu, H., Saxton, A. M., Donnell, R. L., and Cheng, M.-D. (2007) Assessing the pulmonary toxicity of single-walled carbon nanohorns. *Nanotoxicology 1*, 157–166.

(8) Iijima, S., Yudasaka, M., Yamada, R., Bandow, S., Suenaga, K., Kokai, F., and Takahashi, K. (1999) Nano-aggregates of single-walled graphitic carbon nano-horns. *Chem. Phys. Lett. 309*, 165–170.

(9) Iijima, S. (2002) Carbon nanotubes: past, present, and future. *Physica B 323*, 1–5.

(10) Xu, J., Yudasaka, M., Kouraba, S., Sekido, M., Yamamoto, Y., and Iijima, S. (2008) Single wall carbon nanohorn as a drug carrier for controlled release. *Chem. Phys. Lett. 461*, 189–192.

(11) Kasuya, D., Yudasaka, M., Takahashi, K., Kokai, F., and Iijima, S. (2002) Selective production of single-wall carbon nanohorn aggregates and their formation mechanism. *J. Phys. Chem. B 106*, 4947–4951.

(12) Zhang, J., Ge, J., Shultz, M. D., Chung, E., Singh, G., Shu, C., Fatouros, P. P., Henderson, S. C., Corwin, F. D., Geohegan, D. B., Puretzky, A. A., Rouleau, C. M., More, K., Rylander, C., Rylander, M. N., Gibson, H. W., and Dorn, H. C. (2010) In vitro and in vivo studies of single-walled carbon nanohorns with encapsulated metallofullerenes and exohedrally functionalized quantum dots. *Nano Lett. 10*, 2843–2848.

(13) Shu, C., Zhang, J., Ge, J., Sim, J. H., Burke, B. G., Williams, K. A., Rylander, N. M., Campbell, T., Puretzky, A., Rouleau, C., Geohean, D. B., More, K., Esker, A. R., Gibson, H. W., and Dorn, H. C. (2010) A facile high-speed vibration milling method to water-disperse single-walled carbon nanohorns. *Chem. Mater. 22*, 347–351.

(14) Pagona, G., Karousis, N., and Tagmatarchis, N. (2008) Aryl diazonium functionalization of carbon nanohorns. *Carbon 46*, 604–610.

(15) Ajima, K., Yudasaka, M., Murakami, T., Maigne, A., Shiba, K., and Iijima, S. (2005) Carbon nanohorns as anticancer drug carriers. *Mol. Pharmaceutics 2*, 475–480.

(16) Matsumura, S., Ajima, K., Yudasaka, M., Iijima, S., and Shiba, K. (2007) Dispersion of cisplatin-loaded carbon nanohorns with a conjugate comprised of an artificial peptide aptamer and polyethylene glycol. *Mol. Pharmaceutics 4*, 723–729.

(17) Wright, S., and Huang, L. (1989) Antibody-directed liposomes as drug-delivery vehicles. *Adv. Drug Delivery Rev. 3*, 343–389.

(18) Arehalli, S. M., Kiran, R. C., Makam, P. V., Prudhviraju, D., Biswarup, N., Chennakesavulu, S., Krutika, K. S., and Rayasa, S. R. M. (2010) Antibody derivatization and conjugation strategies: Application in preparation of stealth immunoliposome to target chemotherapeutics to tumor. *J. Controlled Release 10*, 1016.

(19) Sudimack, J. J., Guo, W., Tjarks, W., and Lee, R. J. (2002) A novel pH-sensitive liposome formulation containing oleyl alcohol. *Biochim. Biophys. Acta 1564*, 31–37.

(20) Shu, C., Corwin, F. D., Zhang, J., Chen, Z., Reid, J. E., Sun, M., Xu, W., Sim, J. H., Wang, C., Fatouros, P. P., Esker, A. R., Gibson, H. W., and Dorn, H. C. (2009) Facile preparation of a new gadofullerene-based magnetic resonance imaging contrast agent with high ^{1}H relaxivity. *Bioconjugate Chem. 20*, 1186–1193.

(21) Sato, K. T., Larson, A. C., Rhee, T. K., Salem, R. A., Nemcek, A. A., Mounajjed, T., Paunesku, T., Woloschak, G., Nikolaides, P., and Omary, R. A. (2005) Real-time MRI monitoring of transcatheter hepatic artery contrast agent delivery in rabbits. *Acad. Radiol. 12*, 1342–1350.

(22) Galdero, F., Carratelli, C. R., Nuzzo, I., Bentivoglio, C., De Martino, L., Folgore, A., and Galdiero, M. (1995) Enhanced cellular response in mice treated with a Brucella antigen-liposome mixture. *FEMS Immunol. Med. Microbiol. 10*, 235–243.

(23) Noad, R., and Roy, P. (2003) Virus-like particles as immunogens. *Trends Microbiol. 11*, 438–444.

(24) Xiang, S. D., Scholzen, A., Minigo, G., David, C., Apostolopoulos, V., Mottram, P. L., and Plebanski, M. (2006) Pathogen recognition and development of particulate vaccines: does size matter? *Methods 40*, 1–9.

(25) Pellequer, Y., Ollivon, M., and Barratt, G. (2004) Formulation of liposomes associated with recombinant interleukin-2: effect on interleukin-2 activity. *Biomed. Pharmacother. 58*, 162–167.

(26) Kaasgaard, T., Mouritsen, O. G., and Jorgensen, K. (2001) Screening effect of PEG on avidin binding to liposome surface receptors. *Int. J. Pharm. 214*, 63–65.

Bioconjugate Chemistry

COMMUNICATION

pubs.acs.org/bc

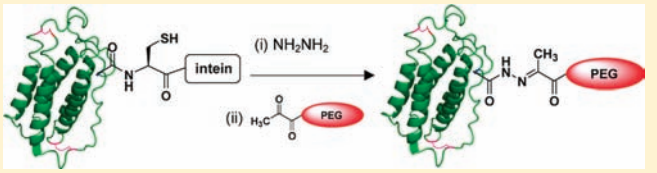
Recombinant Protein Hydrazides: Application to Site-Specific Protein PEGylation

Jennifer Thom,[†] David Anderson,[†] Joanne McGregor,[†,‡] and Graham Cotton*[,†]

[†]Almac Sciences, Elvingston Sciences Centre, Gladsmuir, East Lothian, EH33 1EH, United Kingdom

Supporting Information

ABSTRACT: Here, we describe a novel method for the site-specific C-terminal PEGylation of recombinant proteins. This general approach exploits chemical cleavage of precursor intein-fusion proteins with hydrazine to directly produce recombinant protein hydrazides. This unique functionality within the protein sequence then facilitates site-specific C-terminal modification by hydrazone-forming ligation reactions. This approach was used to generate folded, site-specifically C-terminal PEGylated IFNalpha2b and IFNbeta1b, which retained excellent antiviral activity, demonstrating the utility of this technology in the PEGylation of therapeutic proteins. As this methodology is straightforward to perform, is compatible with disulfide bonds, and is exclusively selective for the protein C-terminus, it shows great potential as general technology for the site-specific engineering and labeling of recombinant proteins.



Recombinant protein therapeutics have emerged as an effective treatment for a variety of conditions ranging from cancer to metabolic disorders and autoimmune diseases, but they are commonly limited by their poor pharmacokinetics and immunogenicity. Arguably, the most widely used and accepted method for improving the pharmacokinetics of proteins is through PEGylation.[1,2] The covalent attachment of poly(ethylene glycol) (PEG) increases the half-life of the protein *in vivo* by decreasing renal clearance, due to the large hydrodynamic radius of the polymer, as well as masking potentially immunogenic epitopes and protease cleavage sites. Furthermore, PEGylation of a target protein can substantially improve its solubility and stability. There are currently nine PEGylated protein therapeutics approved for clinical use;[1] however, established methods for PEGylation are generally non-site-selective, resulting in a mixture of protein PEG-positional isomers with significantly decreased biological activity. For example, ViraferonPEG/PegIntron (Schering Plough), approved for the treatment of Hepatitis C, is produced by conjugating recombinant interferon alpha2b (IFNalpha2b) to a single chain 12 kDa succinimidyl carbonate PEG. This results in 95% monoPEGylated protein comprising 14 positional isomers, and as a consequence, PegIntron retains only 28% antiviral activity in *in vitro* assays compared to non-PEGylated IFNalpha2b.[3]

There is therefore a pressing need for methods to site-specifically PEGylate proteins. By incorporating a single PEG moiety at a defined position within the protein sequence, the deleterious effects associated with nonselective PEGylation may be minimized. In addition, approaches that yield homogeneous PEGylated proteins are potentially attractive from a regulatory perspective. While a number of protein engineering approaches have been applied to this end,[4−6] one particularly versatile technology for site-specific protein modification is expressed protein ligation (EPL). The basis of EPL is the production of recombinant C-terminal thioester proteins through thiol-mediated cleavage of the corresponding intein fusion protein.[7,8] The protein thioester functionality enables peptides and labels to be chemoselectively attached to the protein using the well-established native chemical ligation reaction.[9] In addition, C-terminal cleavage of the protein thioester with nucleophiles has also been used to introduce reactive moieties into proteins to enable subsequent modification through alternative chemistries.[10−12] While the EPL approach has proven extremely powerful, the steps are performed in the presence of thiol additives, which may compromise its use with certain protein families (for example, disulfide bond containing proteins), and the protein thioesters themselves are often labile.

Here, we report the development of a versatile complementary protein ligation approach for site-specific protein PEGylation, which is compatible with folded disulfide bond-containing proteins. This process is based on chemical interception of intein-mediated protein splicing,[13] to create C-terminal hydrazide recombinant proteins. This facile production of recombinant hydrazide proteins then facilitates direct site-specific C-terminal PEGylation (or other modifications) of the target protein using hydrazone bond-forming reactions[14,15] (Figure 1). In principle, any PEG derivative (or alternative label) containing the appropriate functionality, namely, a ketone or aldehyde, can be chemoselectively attached to the C-terminus of the protein in this one-step process. For the approach described here, we have developed novel pyruvoyl PEG derivatives for attachment to the

Received: March 18, 2011
Revised: May 11, 2011
Published: May 14, 2011

ACS Publications © 2011 American Chemical Society

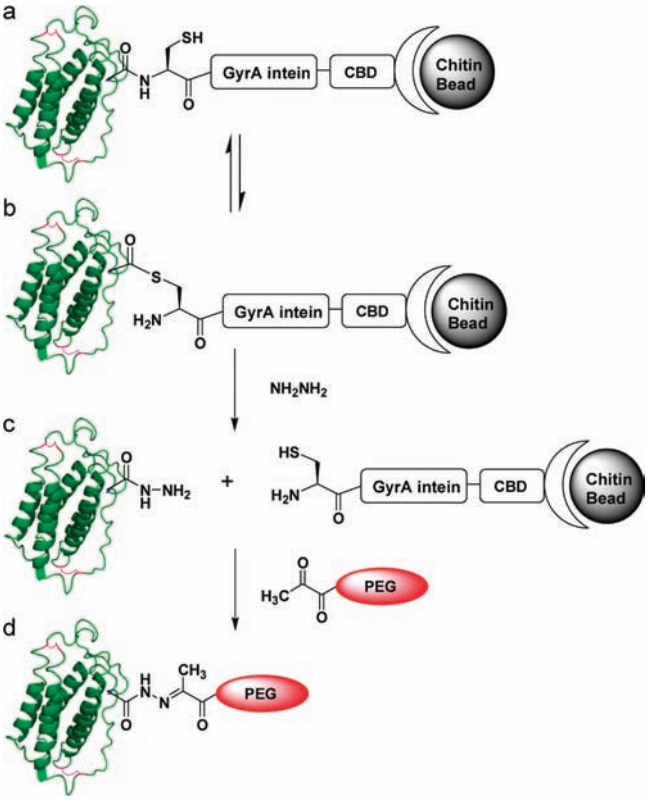
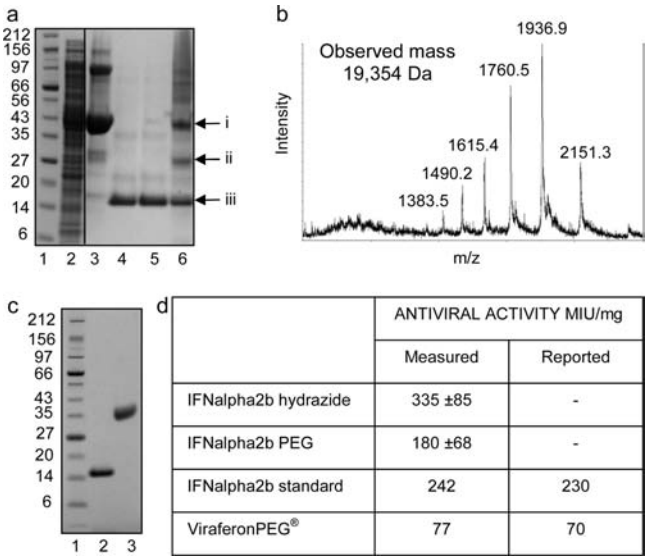


Figure 1. Use of intein technology to generate recombinant C-terminal hydrazide proteins for site-specific PEGylation. (a) The recombinant protein of interest (IFNalpha2b shown here) is genetically fused to the N-terminus of an engineered GyrA intein and chitin binding domain (CBD), expressed in *E. coli* and purified by immobilization onto chitin beads. (b) The first residue of this intein domain is a cysteine. The properties of the intein domain are such that it induces an N to S acyl shift at this protein-intein junction to form a branched thioester intermediate. (c) This thioester intermediate is chemically cleaved using hydrazine to liberate the corresponding C-terminal hydrazide derivative of the target protein. The intein-CBD remains bound to the chitin beads. (d) The protein C-terminal hydrazide chemoselectively reacts with ketone or aldehyde containing moieties. Here the reaction with a pyruvoyl functionalized PEG is shown, resulting in site-specific C-terminal PEGylation of the target protein via the resonance stabilized α-oxo hydrazone linkage.



d

	ANTIVIRAL ACTIVITY MIU/mg	
	Measured	Reported
IFNalpha2b hydrazide	335 ±85	-
IFNalpha2b PEG	180 ±68	-
IFNalpha2b standard	242	230
ViraferonPEG®	77	70

Figure 2. Generation and antiviral activity of site-specifically C-terminal PEGylated IFNalpha2b. (a) SDS PAGE analysis of IFNalpha2b-intein-CBD fusion protein expression in *E. coli*, purification using chitin beads and hydrazine cleavage. Protein standard (lane 1), cell lysate (lane 2), IFNalpha2b-intein-CBD purified by immobilization on chitin beads (lane 3), supernatant from hydrazine cleavage (lane 4), supernatant from washed beads (lane 5), cleaved and washed chitin beads (lane 6). Arrows indicate IFNalpha2b-intein-CBD fusion protein (i), intein-CBD (ii), and IFNalpha2b C-terminal hydrazide (iii). (b) Electrospray mass spectra of purified IFNalpha2b hydrazide, expected mass (without the N-terminal methionine) is 19 340 Da. The higher observed mass probably reflects methionine oxidation, previously reported for IFNalpha2b and shown not to significantly affect the activity of the protein.[24] (c) SDS PAGE analysis of IFNalpha2b hydrazide (lane 2) and purified C-terminal PEGylated IFNalpha2b (lane 3). (d) Antiviral activity of IFNalpha2b derivatives in a cytopathic effect inhibition assay using human A549 lung carcinoma cells and EMC virus. Measured activities are in million international units, MIU/mg IFNalpha2b protein ± SD where appropriate; IFNalpha2b hydrazide and C-terminal PEGylated IFNalpha2b ($n = 8$), IFNalpha2b standard ($n = 2$) and ViraferonPEG ($n = 2$). For reported values, see Supporting Information. IFNalpha2b standard and ViraferonPEG activities are in line with previous reports.[3].

protein C-terminus, as the resulting α-oxo hydrazone bonds are stabilized through resonance effects.[16,17]

IFNalpha2b was chosen as our initial target for this C-terminal PEGylation approach. As discussed above, this therapeutically important protein is currently administered as the PEG isomer mixture, and thus there is scope for improvement through site-specific PEGylation. IFNalpha2b was expressed in *E. coli* as a soluble N-terminal fusion to the *Mycobacterium xenopi* GyrA intein, and purified from the supernatant by immobilization on chitin beads using a chitin binding domain (CBD) fused to the C-terminus of the intein domain (Figure 2a lane 3 and Supporting Information). The immobilized IFNalpha2b-intein-CBD protein was cleaved with hydrazine to generate the corresponding IFNalpha2b C-terminal hydrazide (Figure 2a,b). The isolated protein (Figure 2c lane 2) contained two disulfide bonds (Supporting Information) and had potent antiviral activity (Figure 2d) indicating that folded IFNalpha2b C-terminal hydrazide was directly produced after expression and hydrazine cleavage of the corresponding intein fusion protein. This is in contrast to standard intein cleavage methods that use thiols such as dithiothreitol (DTT) and sodium mercaptoethylsulfonate (MESNa) that usually reduce disulfide bonds within the target protein.

For the PEGylation reactions, a pyruvoyl derivative of 10 kDa PEG was synthesized and incubated with IFNalpha2b hydrazide as described in the Supporting Information. This typically afforded 60−75% yield of the C-terminal PEGylated IFNalpha2b protein (Supporting Information, Figure S1). Importantly, no PEGylation product was observed when a C-terminal thioester derivative of IFNalpha2b was incubated with pyruvoyl PEG under the same conditions, consistent with site-specific PEGylation via the C-terminal hydrazide group only (data not shown). PEGylated IFNalpha2b was purified in 2 steps: ion exchange to remove unreacted pyruvoyl-PEG, followed by gel filtration to separate PEGylated IFNalpha2b from any unreacted IFNalpha2b hydrazide (Supporting Information, Figure S2) to yield pure C-terminal, mono PEGylated IFNalpha2b (Figure 2c, lane 3).

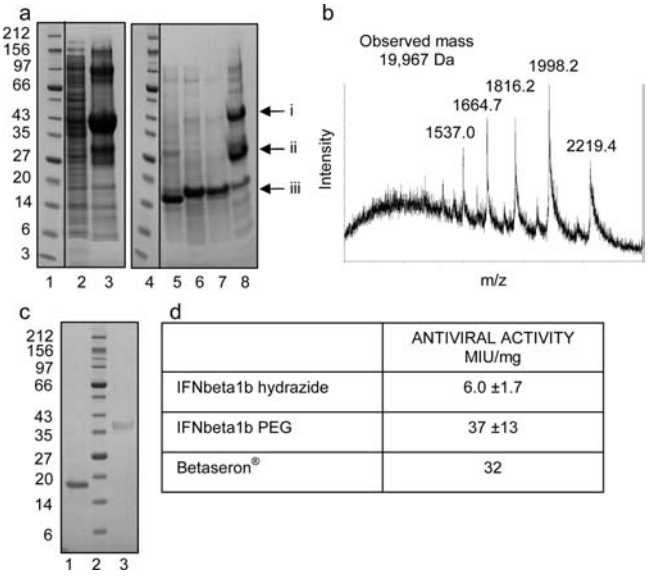
The antiviral activities of the C-terminally PEGylated IFNalpha2b and IFNalpha2b hydrazide control purified under the

same conditions were measured in a cytopathic effect inhibition assay with human A549 lung carcinoma cells and encephalomyocarditis (EMC) virus (Figure 2d). The site-specifically C-terminal PEGylated IFNalpha2b retained 74% of the activity of the standard IFNalpha2b protein, more than double that of the current heterogeneous PEGylated IFNalpha2b therapeutic ViraferonPEG, clearly demonstrating the advantage of this technology.

To further exemplify this site-specific C-terminal PEGylation technology, IFNbeta1b was deemed to be an attractive target. This protein is also an important therapeutic, but currently there are no PEGylated versions approved. Betaseron (Betaferon in the EU, Bayer Shering Pharma) and more recently Extavia (Novartis) are recombinant IFNbeta1b proteins used in the treatment of multiple sclerosis, and are under clinical evaluation for the treatment of other diseases including hepatitis and certain cancers.[18,19] IFNbeta1b is rapidly cleared from blood necessitating frequent administration regimes that can result in injection site necrosis and decreased patient compliance. Neutralizing antibodies are also problematic, with up to 35% of patients developing these in one reported study.[20] In addition, IFNbeta1b is a very unstable protein, prone to aggregation.[21] Work to address these issues includes random PEGylation of side-chain primary amines, which results in a mixture of 5 major positional isomers, and PEGylation of (predominantly) the N-terminal amine, resulting in products with 22−31% and 19−66% activity of the unmodified IFNbeta1b, respectively.[22] Attempts at site specific PEGylation using an engineered free cysteine residue at either position 79 (the natural glycosylation site) or the N- or C-termini were unsuccessful due to insufficient site specific attachment.[22] Another strategy used bicin (bis-*N*-2-hydroxyethylglycinamide) linkers to randomly attach 2−3 PEG molecules. Under physiological conditions, rapid hydrolysis of the bicin releases the PEG to leave the active IFNbeta1b. However, the activity of these releasable PEGylated forms was only between 7% and 27% that of the unmodified IFNbeta1b.[23]

We expressed soluble IFNbeta1b-intein-CBD fusion protein in *E. coli* and purified the target protein through immobilization onto chitin beads. Intein cleavage was induced by overnight treatment with hydrazine and the resulting IFNbeta1b-hydrazide was purified by gel filtration (Figure 3a,b; Supporting Information). As with IFNalpha2b, IFNbeta1b C-terminal hydrazide was generated with the natural disulfide bond intact indicating that the protein was correctly folded (Figure 3a and Supporting Information). To generate site-specifically C-terminal PEGylated IFNbeta1b, IFNbeta1b C-terminal hydrazide was mixed with the pyruvoyl PEG 10 kDa derivative and left overnight at room temperature. This typically gave ~55% yield of the C-terminal PEGylated protein (Supporting Information, Figure S3a). No PEGylation product was observed when IFNbeta1b C-terminal acid was incubated with pyruvoyl PEG under similar conditions, consistent with site-specific PEGylation via the C-terminal hydrazide group only (Supporting Information, Figure S3b).

The site-specifically C-terminal PEGylated IFNbeta1b was purified by ion exchange and gel filtration as described in the Supporting Information to generate pure C-terminal PEGylated IFNbeta1b (Figure 3c lane 3). The antiviral activity was measured in a cytopathic effect inhibition assay with human A549 lung carcinoma cells and EMC virus (Figure 3d). The activity of IFNbeta1b hydrazide was lower than that reported for Betaseron, potentially due to the inherent instability of the protein and the lack of stabilizing ingredients in our formulation. Site-specifically



	ANTIVIRAL ACTIVITY MIU/mg
IFNbeta1b hydrazide	6.0 ±1.7
IFNbeta1b PEG	37 ±13
Betaseron®	32

Figure 3. Generation and antiviral activity of site-specifically C-terminal PEGylated IFNbeta1b. (a) SDS PAGE analysis of IFNbeta1b-intein-CBD fusion protein expression in *E. coli* and the subsequent purification and hydrazine cleavage. Samples were reduced with DTT after heating in loading buffer unless stated otherwise: protein standard (lanes 1 and 4), cell lysate (lane 2), IFNbeta1b-intein-CBD purified by immobilization on chitin beads (lane 3), hydrazine cleavage supernatant without DTT (lane 5), hydrazine cleavage supernatant (lane 6), supernatant from washed beads (lane 7), cleaved and washed chitin beads (lane 8). Arrows indicate IFNbeta1b-intein-CBD fusion protein (i), intein-CBD (ii), and IFNbeta1b C-terminal hydrazide (iii). There is clearly a shift in the migration of cleaved IFNbeta1b hydrazide upon DTT treatment, consistent with the native disulfide bond being intact in the liberated protein. (b) Electrospray mass spectra of purified IFNbeta1b hydrazide, expected mass 19 950 Da. The higher observed mass probably again reflects methionine oxidation. (c) SDS PAGE analysis of purified IFNbeta1b hydrazide (lane 1) and C-terminal PEGylated IFNbeta1b (lane 3); protein standard (lane 2). (d) Antiviral activity of IFNbeta1b derivatives in a cytopathic effect inhibition assay using human A549 lung carcinoma cells and EMC virus. Activities are in million international units, MIU/mg IFNbeta protein ± SD; $n = 8$. The reported antiviral activity of Betaseron, the current IFNbeta1b therapeutic, is also shown (Betaseron prescribing information; http://berlex.bayerhealthcare.com/html/products/pi/Betaseron_PI.pdf). WHO calibrated IFNbeta protein was used as a standard in the assays.

C-terminal PEGylated IFNbeta1b showed greater activity than the hydrazide, probably reflecting the increased protein stability brought by the PEGylation, and this activity was in line with that reported for the current unPEGylated IFNbeta1b therapeutic, Betaseron. This, to the best of our knowledge, represents the most potent PEGylated IFNbeta1b derivative generated to date.

In summary, we have demonstrated the feasibility of generating active, site-specifically C-terminal PEGylated therapeutic proteins through cleavage of the corresponding soluble intein fusion proteins with hydrazine, followed by reaction of the resulting protein hydrazide with pyruvoyl functionalized PEG. Importantly, this approach is compatible with proteins containing disulfide bonds, enabling folded proteins to be directly produced as the C-terminal hydrazide derivatives in high yield, with the integrity of any disulfide bonds and tertiary structure maintained during the PEGylation reaction. While the potential of this technology has been highlighted through the generation of

highly active C-terminal PEGylated derivatives of IFNalpha2b and IFNbeta1b, we have now used this technology to C-terminally PEGylate proteins from a variety of classes, including antibody fragments, with PEGs of different molecular weights. In addition to PEGylation, this technology has broader applications in protein engineering and has been successfully used to attach an array of probes and labels, including fluorophores and synthetic peptides, onto a variety of recombinant proteins in a site-specific fashion (unpublished data). Given the ease of the process, the yields of the associated steps, and the compatibility with disulfide bond-containing proteins, this technology offers an attractive approach for the site-specific PEGylation and modification of therapeutically important proteins and is an attractive addition to the repertoire of methodologies available for protein engineering, opening up new opportunities in this field.

■ ASSOCIATED CONTENT

Supporting Information. Experimental procedures and supplementary data. This material is available free of charge via the Internet at http://pubs.acs.org.

■ AUTHOR INFORMATION

Corresponding Author

*Graham Cotton, Almac Sciences (Scotland) Ltd, Elvingston Science Centre, By Gladsmuir, East Lothian, EH33 1EH United Kingdom. Tel. +44 (0)28 3839 5879, Fax. +44 (0)18 7540 8151, E-mail graham.cotton@almacgroup.com.

Present Addresses

‡Current address: GSK, 315 Cambridge Science Park, Milton Road, Cambridge, CB4 0WG, UK.

■ ACKNOWLEDGMENT

We thank Moredun Research Institute (Edinburgh, UK) for MALDI mass-spectrometry analysis, Crystelle Bermand (Almac Sciences, UK) for technical advice on the synthesis of PEG derivatives, and the Scottish Executive for financial support.

■ REFERENCES

(1) Veronese, F. M., and Mero, A. (2008) The impact of PEGylation on biological therapies. *BioDrugs 22*, 315–329.

(2) Jevsevar, S., Kunstelj, M., and Porekar, V. G. (2010) PEGylation of therapeutic proteins. *Biotechnol. J. 5*, 113–128.

(3) Wang, Y. S., Youngster, S., Grace, M., Bausch, J., Bordens, R., and Wyss, D. F. (2002) Structural and biological characterization of pegylated recombinant interferon alpha-2b and its therapeutic implications. *Adv. Drug Delivery Rev. 54*, 547–570.

(4) Brocchini, S., Godwin, A., Balan, S., Choi, J. W., Zloh, M., and Shaunak, S. (2008) Disulfide bridge based PEGylation of proteins. *Adv. Drug Delivery Rev. 60*, 3–12.

(5) DeFrees, S., Wang, Z. G., Xing, R., Scott, A. E., Wang, J., Zopf, D., Gouty, D. L., Sjoberg, E. R., Panneerselvam, K., Brinkman-Van der Linden, E. C., Bayer, R. J., Tarp, M. A., and Clausen, H. (2006) GlycoPEGylation of recombinant therapeutic proteins produced in Escherichia coli. *Glycobiology 16*, 833–843.

(6) Xie, J., and Schultz, P. G. (2006) A chemical toolkit for proteins - an expanded genetic code. *Nat. Rev. Mol. Cell Biol. 7*, 775–782.

(7) Muir, T. W., Sondhi, D., and Cole, P. A. (1998) Expressed protein ligation: a general method for protein engineering. *Proc. Natl. Acad. Sci. U.S.A. 95*, 6705–6710.

(8) Muir, T. W. (2001) Development and application of expressed protein ligation. *Synlett. 6*, 733–740.

(9) Dawson, P. E., Muir, T. W., Clark-Lewis, I., and Kent, S. B. (1994) Synthesis of proteins by native chemical ligation. *Science 266*, 776–779.

(10) Weikart, N. D., and Mootz, H. D. (2010) Generation of site-specific and enzymatically stable conjugates of recombinant proteins with ubiquitin-like modifiers by the Cu(I)-catalyzed azide-alkyne cycloaddition. *ChemBioChem 11*, 774–777.

(11) Yi, L., Sun, H., Wu, Y. W., Triola, G., Waldmann, H., and Goody, R. S. (2010) A highly efficient strategy for modification of proteins at the C terminus. *Angew. Chem., Int. Ed. Engl. 49*, 9417–9421.

(12) Kalia, J., and Raines, R. T. (2006) Reactivity of intein thioesters: appending a functional group to a protein. *ChemBioChem 7*, 1375–1383.

(13) Cheriyan, M., and Perler, F. B. (2009) Protein splicing: A versatile tool for drug discovery. *Adv. Drug Delivery Rev. 61*, 899–907.

(14) Gaertner, H. F., Offord, R. E., Cotton, R., Timms, D., Camble, R., and Rose, K. (1994) Chemo-enzymic backbone engineering of proteins. Site-specific incorporation of synthetic peptides that mimic the 64−74 disulfide loop of granulocyte colony-stimulating factor. *J. Biol. Chem. 269*, 7224–7230.

(15) Gaertner, H. F., Rose, K., Cotton, R., Timms, D., Camble, R., and Offord, R. E. (1992) Construction of protein analogues by site-specific condensation of unprotected fragments. *Bioconjugate Chem. 3*, 262–268.

(16) Bourel-Bonnet, L., Pecheur, E. I., Grandjean, C., Blanpain, A., Baust, T., Melnyk, O., Hoflack, B., and Gras-Masse, H. (2005) Anchorage of synthetic peptides onto liposomes via hydrazone and alpha-oxo hydrazone bonds, preliminary functional investigations. *Bioconjugate Chem. 16*, 450–457.

(17) Kochendoerfer, G. G., Tack, J. M., and Cressman, S. (2002) Total chemical synthesis of a 27 kDa TASP protein derived from the MscL ion channel of M. tuberculosis by ketoxime-forming ligation. *Bioconjugate Chem. 13*, 474–480.

(18) Fine, H. A., Wen, P. Y., Robertson, M., O'Neill, A., Kowal, J., Loeffler, J. S., and Black, P. M. (1997) A phase I trial of a new recombinant human beta-interferon (BG9015) for the treatment of patients with recurrent gliomas. *Clin. Cancer Res. 3*, 381–387.

(19) Fukutomi, T., Nakamuta, M., Fukutomi, M., Iwao, M., Watanabe, H., Hiroshige, K., Tanabe, Y., and Nawata, H. (2001) Decline of hepatitis C virus load in serum during the first 24 h after administration of interferon-beta as a predictor of the efficacy of therapy. *J. Hepatol. 34*, 100–107.

(20) Malucchi, S., Sala, A., Gilli, F., Bottero, R., Di Sapio, A., Capobianco, M., and Bertolotto, A. (2004) Neutralizing antibodies reduce the efficacy of betaIFN during treatment of multiple sclerosis. *Neurology 62*, 2031–2037.

(21) Filpula, D., Yang, K., Basu, A., and Wang, M. (2005) WO2005/084303A2 Interferon beta polymer conjugates. PCT/US2005/006575.

(22) Basu, A., Yang, K., Wang, M., Liu, S., Chintala, R., Palm, T., Zhao, H., Peng, P., Wu, D., Zhang, Z., Hua, J., Hsieh, M. C., Zhou, J., Petti, G., Li, X., Janjua, A., Mendez, M., Liu, J., Longley, C., Zhang, Z., Mehlig, M., Borowski, V., Viswanathan, M., and Filpula, D. (2006) Structure-function engineering of interferon-beta-1b for improving stability, solubility, potency, immunogenicity, and pharmacokinetic properties by site-selective mono-PEGylation. *Bioconjugate Chem. 17*, 618–630.

(23) Zhao, H., Yang, K., Martinez, A., Basu, A., Chintala, R., Liu, H. C., Janjua, A., Wang, M., and Filpula, D. (2006) Linear and branched bicin linkers for releasable PEGylation of macromolecules: controlled release in vivo and in vitro from mono- and multi-PEGylated proteins. *Bioconjugate Chem. 17*, 341–351.

(24) Gitlin, G., Tsarbopoulos, A., Patel, S. T., Sydor, W., Pramanik, B. N., Jacobs, S., Westreich, L., Mittelman, S., and Bausch, J. N. (1996) Isolation and characterization of a monomethioninesulfoxide variant of interferon alpha-2b. *Pharm. Res. 13*, 762–769.

Recombinant protein hydrazides: Application to site-specific protein PEGylation.

Jennifer Thom[†], David Anderson[†], Joanne McGregor[†‡] and Graham Cotton*[†]

[†]Almac Sciences, Elvingston Sciences Centre, Gladsmuir, East Lothian, EH33 1EH, UK

[‡] Current address: GSK, 315 Cambridge Science Park, Milton Road, Cambridge, CB4 0WG, UK

Email: graham.cotton@almacgroup.com Tel. +44 (0)28 3839 5879 Fax. +44 (0)1875 408151

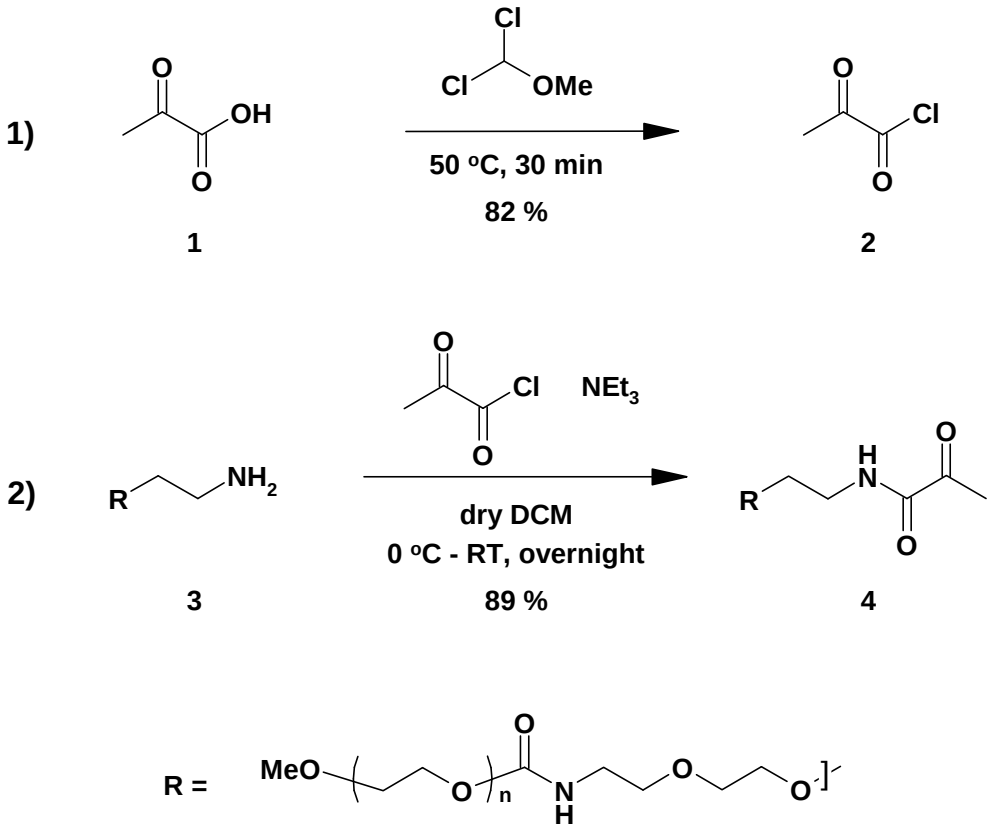
SUPPORTING INFORMATION

General methods

SDS PAGE analyses used NuPAGE 4-12% Bis-Tris gels run in MES buffer (Invitrogen) and coomassie staining, unless otherwise indicated. Analytical RP HPLC was carried out on an Agilent 1100 or 1200 series system with a Jupiter C5 column (Phenomenex). All runs used linear gradients of water/acetonitrile containing 0.1% TFA, with a flow rate of 1 ml/min. Electrospray mass spectroscopy was performed on either a Mariner Time of Flight or Brucker micrOTOF instrument. Protein concentrations were determined from the UV absorbance at 280 nm (Varian Cary 50 UV-Vis Spectrophotometer) using the protein's extinction coefficient generated by ProtParam (http://www.expasy.org/tools/protparam.html).

Generation of pyruvoyl PEG

A 10.4 kDa PEG target compound (4), containing an N-terminal pyruvoyl functionality, was prepared as shown in Scheme S1 below.



Scheme S1

This was achieved by overnight acylation of the commercially available PEG amine (3) with the preformed pyruvoyl chloride (2). The PEG amine was obtained from Nektar [MeO-PEG-NH2Nektar/2M2U0l01/PT03F24] and was, at the time and to the best of our knowledge, the closest in size commercially available PEG amine to that used by Schering Plough in their PEGylated IFNalpha2b (ViraferonPEG® / PegIntron®)[1].

The acid chloride (**2**) was formed by treatment of pyruvic acid (**1**) with α,α-dichloromethyl methyl ether. α,α-dichloromethyl methyl ether (5.16 ml, 57.0 mmol) was added dropwise under N_2 to pyruvic acid (5.00 g, 57.0 mmol) with stirring. The reaction mixture was heated at 50 °C for 30 min. Evaporation of the methyl formate byproduct (at 20 °C to avoid product degradation) afforded the crude acid chloride as a yellow oil (4.92 g, 82 % yield), in sufficient purity (as determined by ^{1}H NMR) to be used directly in the next step.

The target compound (**4**) was formed in 89 % yield by overnight coupling between acid chloride (**2**) and PEG amine (**3**). Briefly, MeO-PEG-NH_2 (500 mg, 50.0 mmol) in anhydrous DCM (5 ml) was treated with

pyruvoyl chloride (**2**, 10.0 mg, 100 mmol) under N_2 in the presence of triethylamine (11 µl, 100 mmol) at 0 ^{o}C. The reaction mixture was allowed to warm to room temperature and stirred overnight. Aqueous workup and trituration with Et_2O afforded the pure product as a white solid (425 mg, 82 % yield). ^{1}H NMR (500 MHz, $CDCl_3$): δ 3.64 (s, $(CH_2)_n$), 3.38 (s, 3H), 2.47 (s, 3H). ^{13}C NMR (125 MHz, $CDCl_3$): δ 197.0, 156.5, 90.5, 73.0-68.0$(CH_2)_n$, 58.5, 51.0, 41.5, 39.0, 23.5.

Generation of IFNalpha2b hydrazide

IFNalpha2b cDNA (IMAGE clone 30915269) was purchased from Gene Service Ltd, UK. The IFNalpha2b coding sequence was amplified by PCR using the following primers:

The forward primer was designed to include an *Nde*I site immediately prior to the 5' IFNalpha2b sequence:

5' – GGTGGTCATATGTGTGATCTGCCTCAAACCC – 3'

The reverse primer was designed to eliminate the STOP codon at the end of the IFNalpha2b coding sequence, replacing it with a glycine codon followed immediately with a *Sap*I site:

5' – GGTGGTTGCTCTTCCGCACCCTTCCTTACTTCTTAAACTTTCTTGC – 3'

The resulting PCR product was cloned into the *Nde*I *Sap*I sites of the pTXB1 vector (New England Biolabs). This pTXB1 IFNalpha2b GLY construct encodes a fusion protein whereby IFNalpha2b is linked via glycine to the N-terminus of *Mycobacterium xenopi* GyrA intein that is in turn fused to the N-terminus of a chitin binding domain (CBD). This was transformed into *E. coli* Rosetta gami B (DE3) pLysS cells (Novagen) and protein expression was induced with 0.2 mM IPTG overnight at 18 ºC. Cells were pelleted by centrifugation and lysed in lysis buffer (20 mM sodium phosphate pH 7.4, 0.5 M NaCl, 0.5 mM EDTA, 15 % glycerol, 0.1 % Sarkosyl NL) with 1 mM AEBSF by sonication. The soluble fraction was mixed with chitin beads pre-equilibrated in lysis buffer, 4 ºC for 1.5 hours. The beads were then washed extensively with lysis buffer followed by cleavage buffer (200 mM sodium phosphate pH 7.4, 200 mM NaCl, 0.05% Zwittergent 3-14) to yield purified IFNalpha2b GyrA intein CBD fusion protein immobilized on chitin beads. These beads were mixed with 1% hydrazine in cleavage buffer with 1 mM EDTA at room temperature overnight. The soluble supernatant contained the cleaved IFNalpha2b hydrazide, which was purified by RP HPLC on a Gilson preparative HLPC system with a Jupiter C5 column (Phenomenex) in water with 0.1 % TFA over a linear gradient of acetonitrile 0.1% TFA. Fractions were analyzed by electrospray mass spectrometry and analytical RP HPLC. Pure fractions were pooled and lyophilised. A typical yield is ~0.7 mg / L cell culture. The sequence of the IFNalpha2b hydrazide made here is:

CDLPQTHSLGSRRTLMLLAQMRRISLFSCLKDRHDFGFPQEEFGNQFQKAETIPVLHEMIQQIFNLFSTKDS
SAAWDETLLDKFYTELYQQLNDLEACVIQGVGVTETPLMKEDSILAVRKYFQRITLYLKEKKYSPCAWEVVR
AEIMRSFSLSTNLQESLRSKEG-$NHNH_2$

Reaction with N-ethyl maleimide (NEM) was used to confirm that the IFNalpha2b C-terminal hydrazide was correctly folded. A few µg of IFNalpha2b C-terminal hydrazide or positive control peptide CERGDKGYVPSVF (Almac Sciences, UK) were dissolved in 20 µl water. 10 µl was removed for the control (no NEM) and 5 µl 1 mg/ml NEM was added to the remaining and incubated at room temperature for at least 30 mins. Reactions were analyzed by electrospray mass spectrometry. NEM reacts with free cysteines resulting in an increase in mass of 125 Da. IFNalpha2b has 4 cysteines that form 2 disulfide bonds in the folded protein. The IFNalpha2b C-terminal hydrazide did not react with NEM in contrast to the positive control peptide that increased in mass by 125 Da under the same conditions (data not shown).

IFNalpha2b C-terminal thioester was prepared by cleaving the IFNalpha2b-intein-CBD beads with 100 mM MESNa in cleavage buffer and purified and analyzed as above.

PEGylation of IFNalpha2b

IFNalpha2b C-terminal hydrazide was dissolved in 100 µl 40 % acetonitrile with 0.1 % TFA to a final concentration of ~250 µM. A 20 fold molar excess of pyruvoyl-PEG 10K was added and reactions left at room temperature overnight (~16 hours).

The PEGylation reaction was diluted 10 fold in buffer A (20 mM Tris-HCl pH 7.3, 0.05 % Zwittergent 3-14) and loaded onto a 1 ml HiTrap Q FF anion exchange column via AKTA purifier system (GE Healthcare). The column was washed with 5-10 CV buffer A to remove the unbound, unreacted pyruvoyl-PEG and the bound protein was eluted over a 0-1 M NaCl gradient (20 CV). Unbound and eluted fractions were analyzed on duplicate SDS PAGE gels; one was stained with coomassie and the other was stained for PEG, based on the methods in the literature[2,3]. The fractions containing the desired PEGylated IFNalpha2b were concentrated using VivaSpin2 3K MWCO centrifugal concentrators (Sartorius) and run through a Superdex 200 10/300 GL column (GE Healthcare) in 10 mM sodium phosphate pH 7.4, 50 mM NaCl, 0.05 % Zwittergent 3-14. This yielded pure site-specifically C-terminal PEGylated IFNalpha2b.

Generation of IFNbeta1b hydrazide

DNA encoding the IFNbeta1b protein sequence with an additional C-terminal glycine:

SYNLLGFLQRSSNFQSQKLLWQLNGRLEYCLKDRMNFDIPEEIKQLQQFQKEDAALTIYEMLQNIFAIFRQDS
SSTGWNETIVENLLANVYHQINHLKTVLEEKLEKEDFTRGKLMSSLHLKRYYGRILHYLKAKEYSHCAWTIVR
VEILRNFYFINRLTGYLRNG

was optimized for expression in *E. coli* and synthesized by GeneArt with the following flanking DNA sequences containing a 5' *Nde*I site and a 3' *Sap*I site:

5’ - GGT GGT CAT . . . [IFNbeta1b sequence] . . . TGC GGA AGA GCA ACC ACC – 3’

Digestion of the supplied DNA with *Nde*I and *Sap*I resulted in an IFNbeta1b fragment that could be directly ligated into a similarly digested pTXB1 vector. This pTXB1 IFNbeta1b GLY construct encodes a fusion protein whereby IFNbeta1b is linked via glycine to the N-terminus of *Mycobacterium xenopi* GyrA intein that is in turn fused to the N-terminus of a chitin binding domain (CBD). This was transformed into *E. coli* Origami (DE3) cells (Novagen) and expression induced with 0.2 mM IPTG overnight at 18 ºC. Cells were pelleted by centrifugation and lysed by sonication in lysis buffer (20 mM sodium phosphate pH 7.4, 0.5 M NaCl, 0.5 mM EDTA, 15 % glycerol, 0.1 % Sarkosyl NL) containing 1 mM AEBSF. The soluble fraction was mixed with chitin beads pre-equilibrated in lysis buffer, 4 ºC for 1.5 hours. The beads were then washed extensively with lysis buffer followed by cleavage buffer (200 mM sodium phosphate pH 7.4, 200 mM NaCl, 0.05% Zwittergent 3-14) to yield purified IFNbeta1b GyrA intein CBD fusion protein immobilized on chitin beads. These beads were mixed with 1% hydrazine in cleavage buffer with 1 mM EDTA at room temperature overnight. The soluble supernatant containing the cleaved IFNbeta1b hydrazide was purified on a Superdex 75 column (GE Healthcare) in 5 mM acetic acid pH 3.5 with 0.05 % Zwittergent 3-14 and 1mM EDTA to give the pure protein hydrazide. Aliquots were lyophilized with 50 µg mannitol / µg IFNbeta1b hydrazide. These IFNbeta1b hydrazide control aliquots were redissolved immediately prior to use in 10 mM sodium phosphate pH 7.4 to give final buffer composition 10 mM sodium phosphate pH 7.4, 50 mM NaCl, 0.05% Zwittergent 3-14 and 50 µg mannitol / µg IFNbeta1b.

Reaction with N-ethyl maleimide (NEM) was used to indicate that the IFNbeta1b C-terminal hydrazide was correctly folded. A few µg of IFNbeta1b C-terminal hydrazide or positive control peptide CERGDKGYVPSVF (Almac Sciences, UK) were dissolved in 20 µl 40 % acetonitrile. 10 µl was removed for the control (no NEM) and 5 µl 1 mg/ml NEM was added to the remaining sample and incubated at room temperature for at least 30 mins. Reactions were analyzed by electrospray mass spectrometry. IFNbeta1b has 2 cysteines that form a disulfide bond in the folded protein. The IFNbeta1b C-terminal hydrazide did not react with NEM in contrast to the positive control peptide that increased in mass by 125 Da under the same conditions (data not shown).

A small amount of the IFNbeta1b C-terminal acid was generated by leaving the IFNbeta1b-intein-CBD beads in cleavage buffer with 1 M imidazole to catalyze hydrolysis of the intein. Protein was purified as described above and analyzed by SDS PAGE, RP HPLC and electrospray mass spectroscopy.

PEGylation of IFNbeta1b

The pooled IFNbeta1b C-terminal hydrazide containing Superdex 75 fractions (~4 µM) were immediately added to 1 mM pyruvoyl PEG 10K and left at room temperature overnight (~16 hours). The IFNbeta1b PEG reaction was diluted 5 fold in buffer A (25 mM sodium phosphate pH 7.4, 0.05 % Zwittergent 3-14, 1 mM EDTA) and loaded onto a 1 ml HiTrap SP XL cation exchange column via AKTA purifier system (GE Healthcare). The column was washed with 5 CV buffer A to remove unbound, unreacted pyruvoyl-PEG and the bound protein was eluted over a 0-0.5 M NaCl gradient (20 CV). Fractions were analyzed by Western blot using sheep polyclonal anti human IFNbeta primary antibody (PBL Interferon Source) and rabbit anti sheep HRP conjugated secondary antibody (Invitrogen). Fractions containing the C-terminal PEGylated IFNbeta1b were concentrated using VivaSpin2 3K MWCO centrifugal concentrators (Sartorius) and run through a Superdex 200 10/300 GL column (GE Healthcare) in PBS (Sigma tablets) with 0.05 % Zwittergent 3-14 and 1 mM EDTA to separate the PEGylated IFNbeta1b from the unreacted IFNbeta1b hydrazide. The fractions were analysed by Western blot as above and the pure fractions were concentrated, aliquotted and lyophilized with 50 µg mannitol / µg IFNbeta1b. Aliquots were redissolved in water to give the final buffer composition PBS with 0.05% Zwittergent 3-14, 1 mM EDTA and 50 µg mannitol / µg IFNbeta1b.

Antiviral activity assays

Cytopathic effect inhibition assays using human A549 lung carcinoma cells and Encephalomyocarditis virus (EMCV) were run by PBL Interferon Source, NJ, USA (#91199-1 and #91400-1 for IFNalpha2b and IFNbeta1b assays respectively). Cells were plated in a 96 well plate at 100,000 cells/ml. Serial two fold dilutions of IFN samples were incubated with the cells for 18-24 hours. A dilution of EMCV pre-determined to kill 100 % of the cells was added to each well and incubated for 42-56 hours. Cell controls (no IFN, no virus), virus controls (no IFN, virus added) and dilutions of PBL WHO calibrated IFN standards were run for every 2 samples. The media was removed, live cells fixed and stained with crystal violet and dried overnight. The $OD_{562\text{-}570}$ for each well was read on a plate reader and transformed to % protection by setting the cell control as 100% and the virus control as 0%. The data was graphed and the unit activity of samples (i.e. the quantity of IFN required to produce a cytopathic effect of 50 %) was adjusted to International units (IU) using the PBL WHO calibrated IFN standards.

ViraferonPEG® with a reported activity of ~70 x 10^6 IU / mg IFNalpha2b was purchased through Almac Clinical Services. Human IFNalpha2b standard with a reported activity of 230 x 10^6 IU / mg was purchased from PBL Interferon Source (#11105-1).

Supporting References

(1) Wang, Y. S., Youngster, S., Grace, M., Bausch, J., Bordens, R., and Wyss, D. F. (2002) *Adv. Drug Deliv. Rev. 54*, 547-570.

(2) Kurfurst, M. M. (1992) *Anal. Biochem. 200*, 244-248.

(3) Lee, D. L., Sharif, I., Kodihalli, S., Stewart, D. I., and Tsvetnitsky, V. (2008) *J. Interferon Cytokine Res. 28,* 101-112.

Supporting Figures

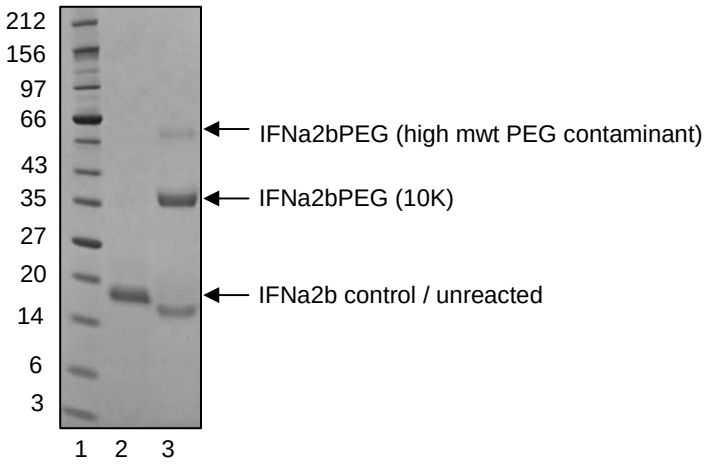


Figure S1

SDS PAGE analysis of the reaction of IFNalpha2b C-terminal hydrazide with pyruvoyl functionalized PEG 10K. Lanes 1 protein standard, 2 IFNalpha2b hydrazide control (no pyruvoyl PEG), 3 IFNalpha2b hydrazide reaction with pyruvoyl PEG.

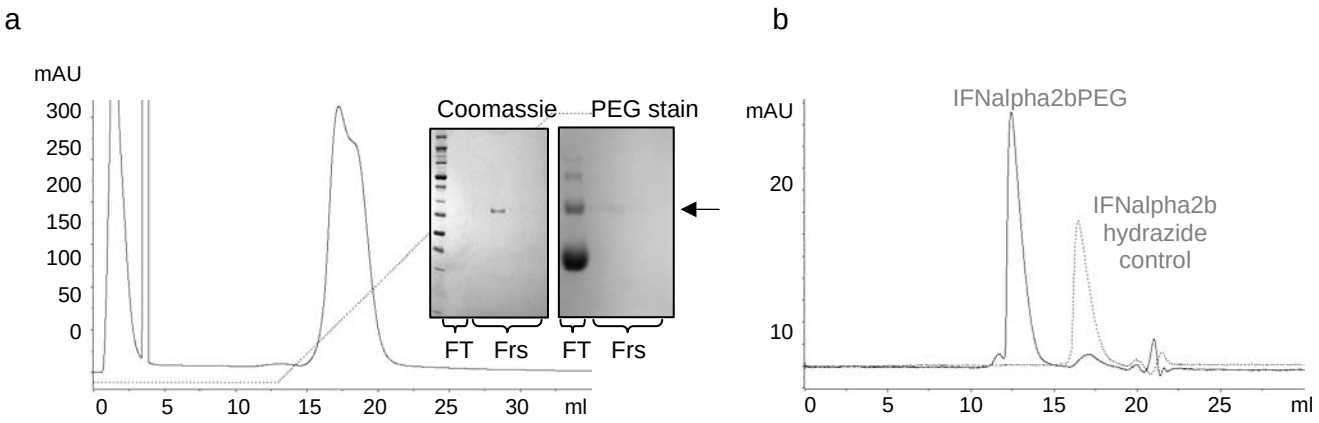


Figure S2

Two step purification of site-specifically C-terminal PEGylated IFNalpha2b. a) Ion exchange to remove unreacted pyruvoyl PEG 10K. The unbound flow through (FT) and eluted fractions (Frs) were analyzed on duplicate SDS PAGE gels. One gel was stained with coomassie and the other was stained for PEG. Arrow shows the position of the C-terminal PEGylated IFNalpha2b (NB PEG 10K dimer runs at the same position). b) Gel filtration to separate C-terminal PEGylated IFNalpha2b from the unreacted IFNalpha2b hydrazide.

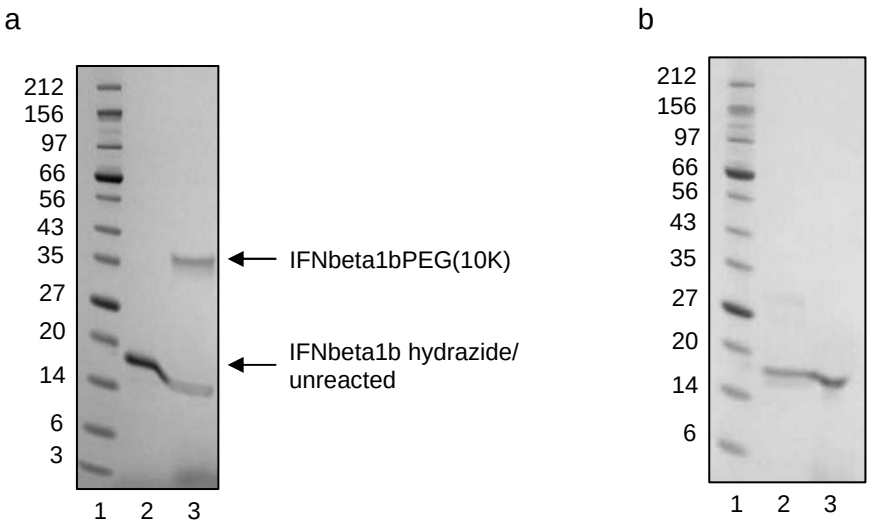


Figure S3

SDS PAGE analysis of a) IFNbeta1b hydrazide reaction with pyruvoyl functionalized PEG 10K and b) IFNbeta1b acid reaction with pyruvoyl functionalized PEG 10K. Lanes 1 protein standard, 2 IFNbeta1b controls (no pyruvoyl PEG), 3 IFNbeta1b reactions with pyruvoyl PEG. The shift in the unreacted IFNbeta1b in lanes 3 is probably due to distortion caused by the unreacted pyruvoyl PEG (not stained) that runs just above the unreacted IFbeta1b. A small amount of IFNbeta1b acid dimer is formed in the control after incubation (b lane 2).

Bioconjugate Chemistry

COMMUNICATION

pubs.acs.org/bc

Imaging of Specific Activation of Photodynamic Molecular Beacons in Breast Cancer Vertebral Metastases

Tracy W. Liu,[†,‡] Margarete K. Akens,[§] Juan Chen,[‡] Lisa Wise-Milestone,[§] Brian C. Wilson,[†,‡] and Gang Zheng*[,†,‡]

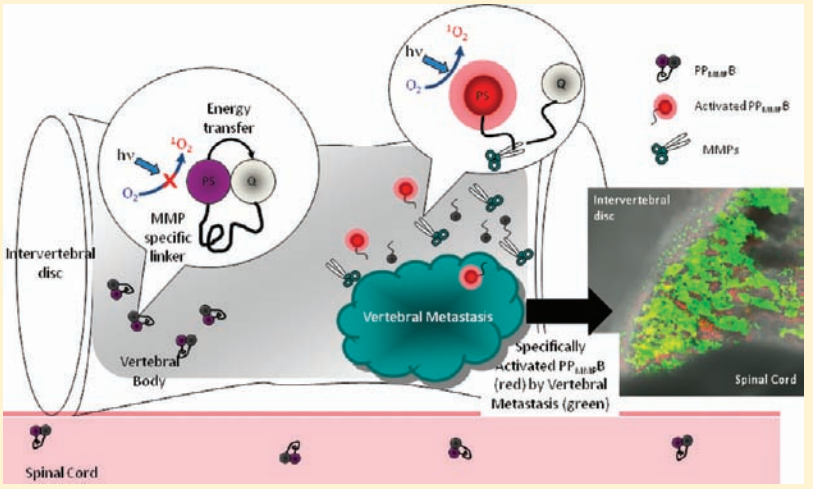
[†]Department of Medical Biophysics, University of Toronto, Canada

[‡]Ontario Cancer Institute, University Health Network, Canada

[§]Sunnybrook Health Science Centre, Canada

Supporting Information

ABSTRACT:



Breast cancer is the second leading cause of cancer-related death in women. Approximately 85% of patients with advanced cases will develop spinal metastases. The vertebral column is the most common site of breast cancer metastases, where overexpression of matrix metalloproteinases (MMPs) promotes the spread of cancer. Current therapies have significant limitations due to the high associated risk of damaging the spinal cord. An attractive alternative is photodynamic therapy providing noninvasive and site-selective treatment. However, current photosensitizers are limited by their nonspecific accumulation. Photodynamic molecular beacons (PP$_{MMP}$B), activated by MMPs, offer another level of PDT selectivity and image-guidance preserving criticial tissues, specifically the spinal cord. Metastatic human breast carcinoma cells, MT-1, were used to model the metastatic behavior of spinal lesions. *In vitro* and *in vivo* evidence demonstrates MMP specific activation of PP$_{MMP}$B in MT-1 cells. Using a clinically relevant metastatic model, fluorescent imaging establishes the specific activation of PP$_{MMP}$B by vertebral metastases versus normal tissue (i.e., spinal cord) demonstrating the specificity of these beacons. Here, we validate that the metastasis-selective mechanism of PP$_{MMP}$Bs can specifically image breast cancer vertebral metastases, thereby differentiating tumor and healthy tissue.

INTRODUCTION

Metastatic spread of tumor cells is the most devastating attribute of cancer and is often the cause of mortality. Due to the unique microenvironment of the bone, it is the most common site of distant metastases from cancers of the breast, lung, kidney, thyroid, and prostate.[1] The bone provides a fertile environment for the growth of cancer and promotes the aggressive behavior of tumor cells, since the mineralized bone matrix houses many growth factors, bone-destroying osteoclasts and bone-forming osteoblasts.[1] Approximately 85% of breast cancer patients with metastatic disease will develop bone metastases, in which the vertebral column is the most common site for metastatic formation.[2,3] Matrix metalloproteinases (MMPs) are a family of structurally related, zinc-dependent endopeptidases implicated in the invasion and metastasis of cancer through the degradation of the basement membrane and collagen-rich extracellular matrix.[4−7] Furthermore, MMPs are exquisite regulators of the tumor microenvironment by

Received: April 1, 2011
Revised: May 16, 2011
Published: May 18, 2011

ACS Publications © 2011 American Chemical Society

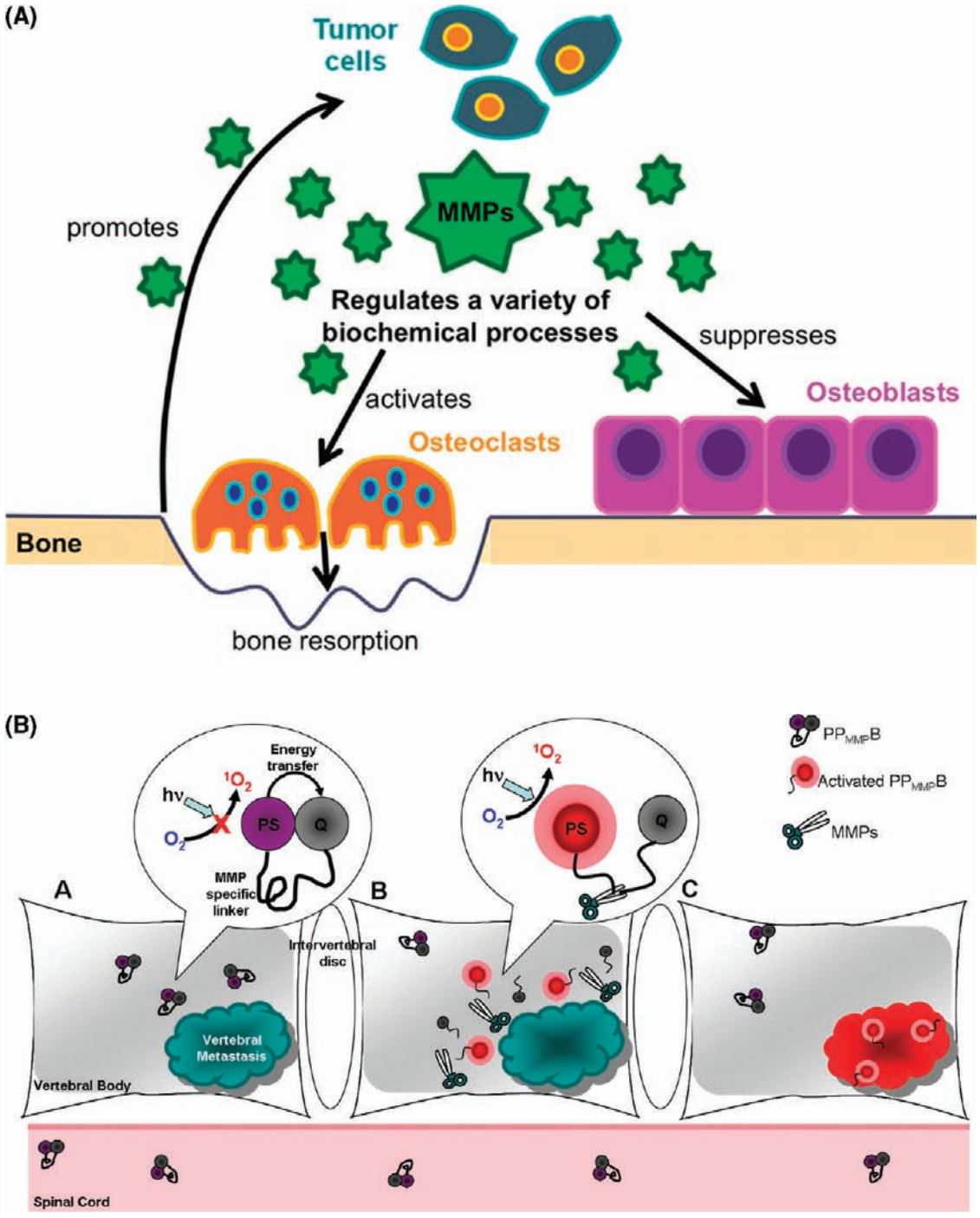


Figure 1. (A) MMP involvement in the tumor-bone vicious cycle. MMPs directly promote tumor progression but also indirectly promote tumor progression by activation of osteoclasts and suppressing osteoblasts. (B) Schematic of photodynamic molecular beacon ($PP_{MMP}B$) activation by vertebral metastases. The beacon accumulates in tissue but remains photodynamically and optically silent (A) until cleaved by MMPs at sites of vertebral metastases (B), which restores both its fluorescence for imaging and generation of singlet oxygen for treatment (C).

virtue of their ability to process many biological modulators, such as cytokines and growth factors within the bone matrix.[4−6]

Breast cancer spinal metastases are predominantly osteolytic (bone destructive), which is associated with an increase in osteoclast activity.[1] Metastasis disrupts the dynamic balance between bone resorption by osteoclasts and bone formation by osteoblasts, inducing a vicious cycle whereby tumor cells reprogram osteoclasts, leading to osteolysis and promotion of tumor growth.[1,2] MMPs play a vital role in signaling cascades involved in metastatic growth, and their upregulation leads to the processing of many growth factors, including TGF-β,[8] IGFs,[9] E-caderin,[10] and RANKL,[11] that are all essential for metastatic tumor progression within the vertebral body.[7,12,13] MMPs themselves also destroy healthy tissue, particularly in the bone, since the matrix is composed primarily of mineralized fibrillar type I collagen,[7] a main substrate of many MMPs. The upregulation of MMPs is thus critically involved in the

destruction of the delicate balance between bone formation and degradation, reducing bone integrity (Figure 1A).[1,2] Hence, MMPs not only aid the spread of tumor cells to distant sites, but are also involved in the local dissolution of the vertebral body and promote tumor progression within the vertebrae.

The resulting osteolysis causes bone pain, vertebral pathological fractures, progressive deformity, hypercalcemia, and spinal instability.[1,2] Patients with spinal metastases have a high risk of spinal cord compression, resulting in motor dysfunction, neurological compromise, and an overall poor prognosis.[1,2] The associated 5-year survival rate in patients with spinal metastases is below 20% compared to a 5-year survival rate over 85% in patients with early stage breast cancer.[14] Regardless of the symptoms, all patients suffering from spinal metastases experience a substantial decrease in their quality of life. Surgery and radiation therapy are the main treatment options for these patients. Surgical treatments, however, carry a high risk of morbidity due to the proximity of the spinal cord, while radiation therapy is limited to a level far below the optimal therapeutic dose because of the low tolerance of the spinal cord.[15] Clinical studies of radiotherapy have reported recurrence of symptoms, and pain relief is not experienced until at least 3 months after treatment.[16] Lastly, although pain relief and, in part, tumor regression are addressed by radiation treatment, spinal instability is not. Therein lies the need for improved therapies that specifically target metastatic tumor cells while preserving the spinal cord to address pain relief, tumor regression, and mechanical instability of the spine.

Protease activatable probes have been generating a great amount of promise for cancer imaging. They offer control of fluorescence emission in response to specific cancer targets and, thus, are useful tools for *in vivo* imaging. With our increasing knowledge about the human genome in health and disease, peptide-based "smart" probes are continually developed for *in vivo* optical imaging of specific molecular targets, biological pathways, and cancer progression. We introduced photodynamic molecular beacons which provide an additional therapeutic mechanism by exploiting the intrinsic fluorescence capabilities of photosensitizers.[17] Photosensitizers are light activated drugs used in photodynamic therapy (PDT). PDT is an approved cancer treatment modality that destroys target cells when light activates a nontoxic photosensitizer (PS) to generate cytotoxic excited-state (singlet) oxygen.[18−20] Photodynamic molecular beacons provide an additional mechanism of selectivity in PDT over and above the targeting afforded by current photosensitizers and specific light delivery.[17] This is illustrated in Figure 1B. The beacons comprise a photosensitizer and a quencher moiety, linked, in the present case, by a MMP-cleavable peptide ($PP_{MMP}B$). They remain "optically silent", i.e., photodynamically inactive, until transformed into an activated state through cleavage of the linker, upon which both the PDT activity and PS fluorescence are restored, the latter providing the potential for real-time image guidance.[17] Furthermore, as $PP_{MMP}Bs$ are only activated in the presence of these secreted tumor-specific proteases, normal tissues, including the spinal cord, should remain relatively protected.[17] One concern is that uptake of activated $PP_{MMP}Bs$ by the spinal cord may occur if activated beacons are allowed sufficient time to diffuse from the tumor to normal tissues. Here, as a first step in implementing $PP_{MMP}Bs$ as a therapeutic strategy for the management of vertebral metastases, we validate that the metastasis-selective mechanism of $PP_{MMP}Bs$ can specifically target breast cancer vertebral metastases, thereby differentiating tumor and healthy tissue.

MATERIALS AND METHODS

Study Design. $PP_{MMP}B$ activation was validated *in vitro* using the human MT-1 metastatic breast cancer cell line. Breast cancer tissue and cell lines have been shown to overexpress MMPs (Supporting Information Figure S1).[21,22] Preliminary *in vivo* activation was demonstrated in MT-1 xenografts grown subcutaneously on the flank of athymic mice. A scrambled beacon, $PP_{scrambled}B$, in which the peptide linker sequence is not cleavable by MMPs,[20] was used to validate the specific activation of $PP_{MMP}B$ by the MT-1 cells. As a relevant preclinical model of vertebral metastases, MT-1 cells were injected intracardially to establish metastases in athymic rats. The activation of $PP_{MMP}B$ within the spinal column was assessed at each of 2, 4, 12, and 24 h after intravenous injection of $PP_{MMP}B$. $PP_{MMP}B$ activation was further compared in tumor-bearing versus healthy animals, at 2 and 4 h post injection. The fixed dose of $PP_{MMP}B$ was 3 mg per kg bodyweight, equivalent to that using Visudyne in previous studies with this model.[23]

$PP_{MMP}B$ Synthesis. The $PP_{MMP}B$ consists of the photosensitizer Pyropheophorbide-α (PS) and black hole quencher 3 (Q), linked by the amino acid sequence GPL*G*LARK, which is an MMP-cleavable peptide: italics indicate the cleavage site. It was synthesized as described previously.[17] $PP_{scrambled}B$ comprises the same PS and Q but with a linker sequence, tsgpnqeqk, composed of D-amino acids that has been shown not to be cleaved by MMPs.[24]

Cells. MT-1 cells, a human metastatic breast cancer cell line, were kindly provided by Dr. O. Engebraaten, Norwegian Radium Hospital, Norway.[25,26] Cells were grown and maintained in Roswell Park Memorial Institute (RPMI) 1640 media supplemented with 10% fetal bovine serum at 37 °C in an atmosphere of 5% CO_2 in a humidified incubator. The MT-1 cells were stably transfected with a double-fusion plasmid (luciferase and green flurescent protein, GFP) kindly provided by Dr. Joseph Wu (Stanford University) and a lentivirus kindly provided by Dr Ren-Ke Li, (University of Toronto). The expression of GFP and luciferase provides a means to identify the cells and assess their viability.[23,27−31]

***In Vitro* Model.** *In vitro* activation of $PP_{MMP}B$ was evaluated by both confocal microscopy and flow cytometry. $PP_{MMP}B$ (2 nmol) or $PP_{scrambled}B$ (2 nmol) were first dissolved in 2% dimethyl sulfoxide, DMSO (Sigma Aldrich), and 0.025% Cremophore.[17] The solutions were then diluted with the culture medium to a final concentration of 10 μM (molecular weight of the $PP_{MMP}B$ is 1856 g/mol). 2×10^4 cells in 0.4 mL of culture medium per well were seeded in Nunc Laboratory-TekII-CC2 8-well chamber slides and incubated for 2 days at 37 °C under 5% CO_2 in a humidified incubator to grow to 80% confluency. $PP_{MMP}B$ activation after 6 h incubation of MT-1 cells was assessed using a laser scanning confocal microscope (Olympus FluoView 1000: 633 nm excitation, >650 nm detection). To quantify $PP_{MMP}B$ fluorescence activation and uptake in MT-1 cells, 2×10^5 cells in 2 mL of medium per well were inoculated in 6-well plates and incubated for 2 days at 37 °C under 5% CO_2 in a humidified incubator. The cells were then incubated with 1 mL of $PP_{MMP}B$ or $PP_{scrambled}B$ solution (10 μM) for 1 and 6 h, respectively (similar to previous studies[17]), at 37 °C under 5% CO_2. The beacon solution was then removed after the above incubation times and assessed by HPLC-MS to confirm the beacon cleavage. The cells were trypsinized from the well plates and transferred to a 15 mL centrifuging tube containing 2 mL PBS. The cells were centrifuged at 1000 rpm for 6 min and the

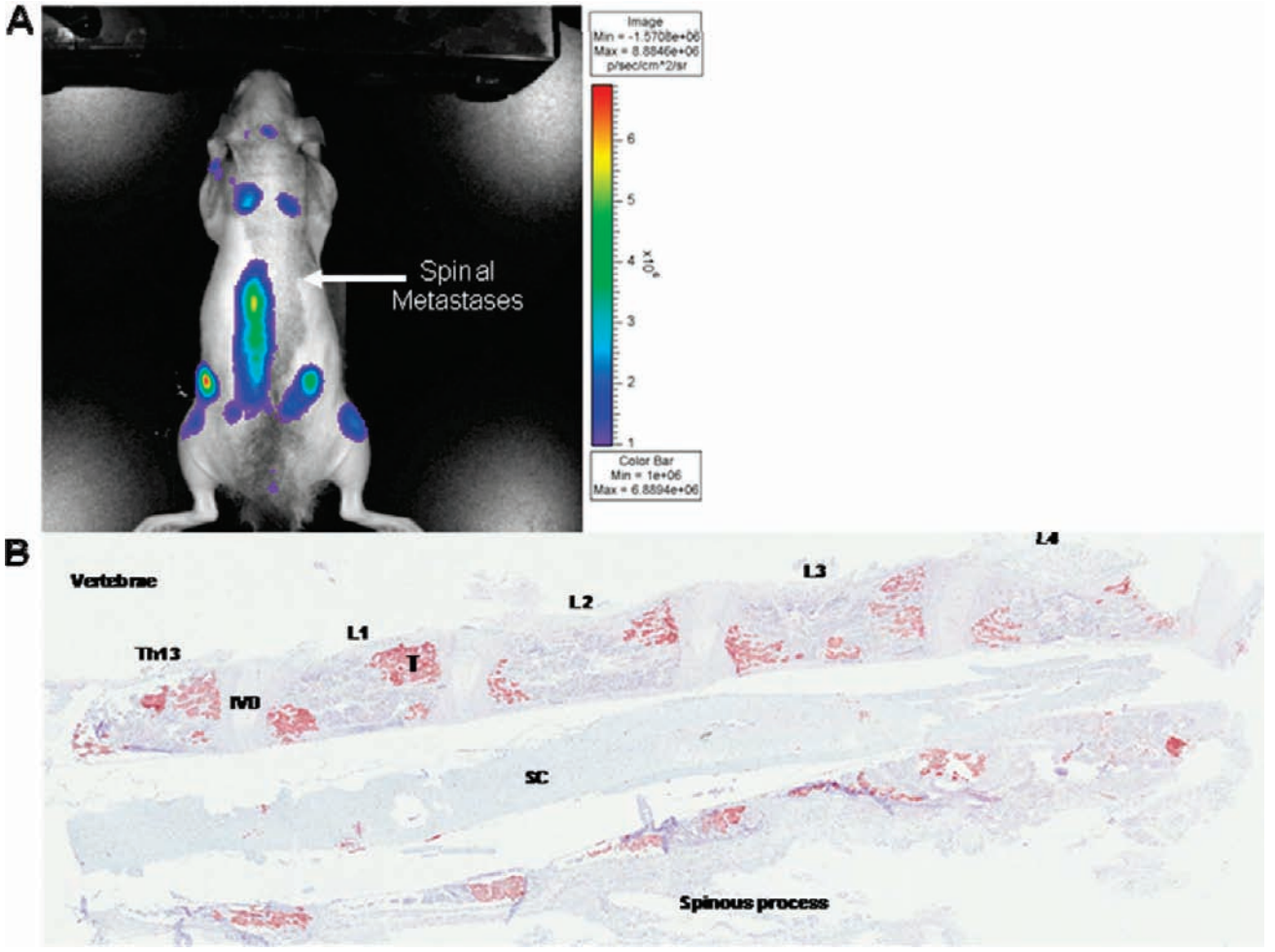


Figure 2. *In vivo* breast cancer vertebral metastases model. (A) Example of bioluminescent imaging of MT-1 vertebral metastases development at 14 days after intracardiac injection of 1×10^6cells, showing multiple sites of metastitic growth, including in the spine. (B) Example of immunohistology section of vertebral column where hEGFr immunhisto stains for viable tumor (red sections) (T - tumor, SC - spinal cord, IVD - intervertebral disk, L - lumbar, Th - thoracic).

PBS was removed. This rinsing procedure was repeated 3 times. The cells were fixed by a 2% paraformaldehyde solution for 10 min, after which they were centrifuged and rinsed twice with PBS. The fluorescence intensities of the cells were measured by flow cytometry (CytomicsFC 500, Beckman Coulter, CA, USA: 633 nm excitation, 660−690 nm detection). The maximum cell count was approximately 10 000 in each sample.

***In Vivo* Xenograft Model.** All animal studies were carried out under institutional approval (University Health Network, Toronto, Canada). Adult athymic female nude mice (Hsd:Athymic Nude-Foxn1^{nu}; Harlan, Indianapolis, IN, USA) were inoculated subcutaneously with 1×10^6 MT-1 cells in 200 μL of media in both the left and right flanks for intratumoral injection studies of $PP_{MMP}B$. To evaluate the activation of $PP_{MMP}B$ by a systemic injection, mice were inoculated similarly only on the right flank. Animals were maintained in pathogen-free conditions in autoclaved microisolator cages. After 2 weeks, by which time the tumors were 5−10 mm in diameter, the mice were fed a low-fluorescence diet (Harlan Tekland) for 4 days to reduce the autofluoresence background. A 2 mg/kg dose of $PP_{MMP}B$ or $PP_{scrambled}B$ (corresponding to the dose used in previous studies[17]) was formulated in 30 μL of aqueous solution with 2% DMSO and 0.5% Tween-80.[17] Under general anesthesia (isofluorane in oxygen), a 27G needle was used to inject this in multiple locations in the tumor to improve the distribution. A 2 mg/kg intravenous injection (tail vein) of $PP_{MMP}B$ was formulated in 150uL of aqueous solution with 2% DMSO and 0.5% Tween-80. Whole-body *in vivo* fluorescence imaging was performed before and at multiple time points after injection (Maestro, CRi: 650 nm excitation, ≥700 nm detection, auto-exposure integration time).

***Ex Vivo* Xenograft Studies.** MT-1 tumors harvested from mice 24 h following intratumor injections of beacon and were snap-frozen in liquid nitrogen and stored at −70 °C. Frozen sections (10 μm) were cut on a cryostat. After 5 min at room temperature, the slides were immersed in PBS for another 5 min, then dried, and 4 μL of mounting solution with DAPI, 4′,6-diamidino-2-phenylindole (Vector laboratories. Inc.), was added as a nuclear stain. The sections were covered by a coverslip and imaged by confocal microscopy similar to the *in vitro* studies above.

***In Vivo* Vertebral Metastases Model.** Female 5−6-week-old athymic rats (rnu/rnu; Harlan Sprague−Dawley, Indianapolis, IN, USA) were used as a model to mimick vertebral metastatic spread. The activation of $PP_{MMP}B$ was compared in the spinal column in tumor-bearing and healthy animals. Under general

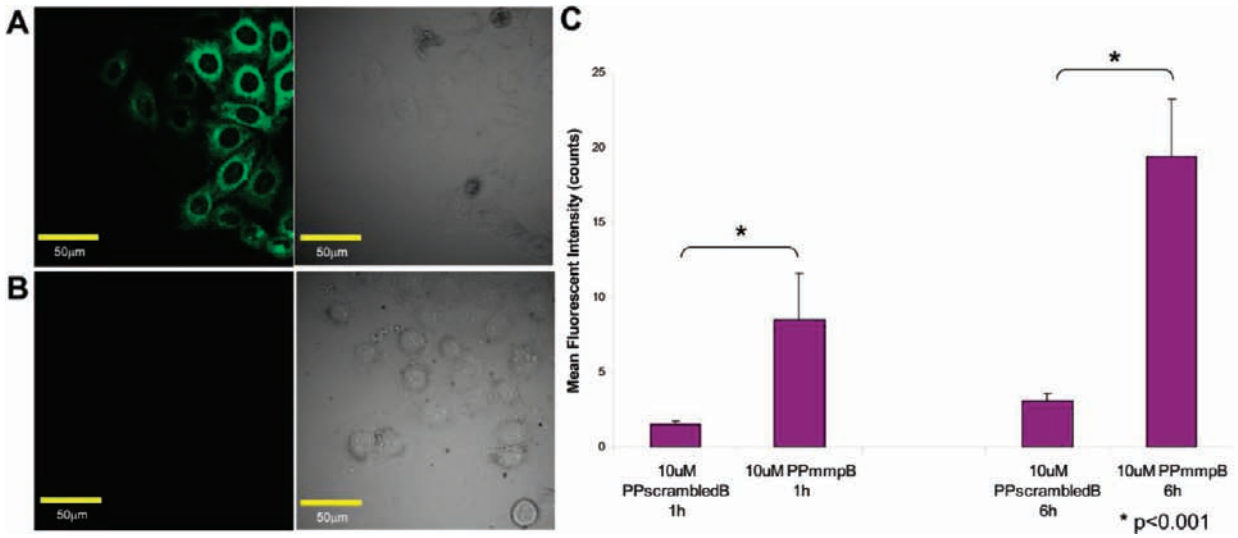


Figure 3. *In vitro* fluorescence and corresponding brightfield images of MT-1 cells after 6 h incubation in (A) 10 μM $PP_{MMP}B$, (B) 10 μM $PP_{scrambled}B$. (C) Comparison of the fluorescence intensity of MT-1 cells incubation with $PP_{MMP}B$ and $PP_{scrambled}B$ for 1 or 6 h monitored by flow cytometry ($n = 3$ samples, $p < 0.001$).

inhalation anesthesia (isofluorane in oxygen), MT-1 cells were injected intracardially at a concentration of 2×10^6 in 0.2 mL of RPMI 1640 media. Fourteen days later, *in vivo* bioluminescence imaging was performed as follows to confirm the establishment of metastases. Luciferin (Xenogen Corp., MA, USA) was dissolved in 0.9% NaCl at a concentration of 30 mg/mL and a single dose of 60 mg/kg was injected intraperitoneally into anaesthetized animals. Bioluminescent images were taken 15 min post luciferin injection where animals were placed ventrally in a whole-body bioluminescence imager (IVIS Spectrum: Caliper Life Sciences, CA, USA), integrating the counts over 30 s (Figure 2A). Following this, 3 mg/kg of $PP_{MMP}B$ (corresponding to equivalent Visudyne dose used in previous PDT studies[23,30,31]) in 2.5% DMSO, 0.5% Tween80 was injected through the tail vein and, at each time point above, cohorts were euthanized by pentobarbital overdose.

***Ex Vivo* Vertebral Metastases Studies.** At the time of necroscopy in these animals, the T13−L4 vertebrae were harvested intact, transferred to PBS, and immediately cut in the sagittal plane using a low-speed precision saw (IsoMet, Buehler, Illinois). $PP_{MMP}B$ activation by MT-1 vertebral tumors was assessed by confocal microscopy of the cut surface (633 nm excitation, >650 nm detection) at 10× magnification. These images were overlaid by corresponding GFP images from the MT-$1^{luc/GFP}$ cells (488 nm excitation, >520 nm detection), in order to evaluate the specific activation of $PP_{MMP}B$ *in vivo* by MT-1 metastases. Using commercial software (*Olympus Fluoview FV 1000*), the degree of colocalization of $PP_{MMP}B$ and MT-1 metastatic cells within the vertebral column was assessed by calculating the Pearson coefficient between the two fluorophores (activated $PP_{MMP}B$ and GFP), with −1 representing no overlap and +1 representing 100% concordance of localization. $PP_{MMP}B$ activation was quantified in these samples using the Maestro imaging system (650 nm excitation, ≥700 nm detection, autoexposure integration time), normalizing the total fluorescence signal within a defined region of interest (ROI) by the exposure time and the ROI area. The values used were based on the midsagittal images of the fluorescence within the vertebral body and the spinal cord, and the difference between these was compared using a Student *t* test. To confirm metastatic formation within the vertebral column, the spines were then fixed in 10% buffered formalin, decalcified, sectioned (10 μm), and stained either with H&E or immunhistochemically using a mouse-antihuman epidermal growth factor receptor (hEGFr) antibody (Zymed, Laboratories Inc., San Francisco, CA, USA). This antibody does not cross react with rat tissues, enabling specific visualization of the metastatic human breast cancer cells withzin the rat vertebral bone and bone marrow compartments (Figure 2B).

RESULTS

The *in vitro* specific activation of $PP_{MMP}B$ by MT-1 cells was compared with that of the scrambled beacon ($PP_{scrambled}B$) in which the linker is not MMP cleavable, as illustrated by confocal fluorescence microscopy: Figure 3A and B. HPLC-MS of the culture media following incubation with cells shows 2 peaks corresponding to the expected MMP cleaved fragments of $PP_{MMP}B$, Pyro-GPLG and LARK-BHQ3 (SI Figure S2). Examples of flow cytometry quantifying the fluorescence intensity of $PP_{MMP}B$ and $PP_{scrambled}B$ in cells incubated for different times are shown in Figure 3C. At all time points, the fluorescence intensity was 5- to 10-fold higher in cells incubated with $PP_{MMP}B$ than with the scrambled beacon ($p < 0.001$). The distributions and shape of the cells are largely homogeneous after incubation with the beacons, suggesting minimal toxicity (SI Figure S3).

The activation of $PP_{MMP}B$ *in vivo* was first examined in subcutaneous MT-1 xenografts, following i.v. administration of 2 mg/kg $PP_{MMP}B$, monitoring whole-body fluorescence following cleavage of $PP_{MMP}B$. A strong fluorescence signal localized within the tumor was seen in experimental animals (Figure 4A), demonstrating $PP_{MMP}B$ activation in the tumor. To further validate the *in vivo* MMP specificity, mice bearing tumors on both flanks were injected intratumorally with 2 mg/kg of either $PP_{MMP}B$ (left) or $PP_{scrambled}B$ (right) and followed over time. Initially, little fluorescence was observed in either tumor. However, at 6 h a 9-fold increase in tumor fluorescence was observed with $PP_{MMP}B$ (3.5 ± 0.02 average fluorescent counts/(s × area)) compared with $PP_{scrambled}B$ (0.4 ± 0.09

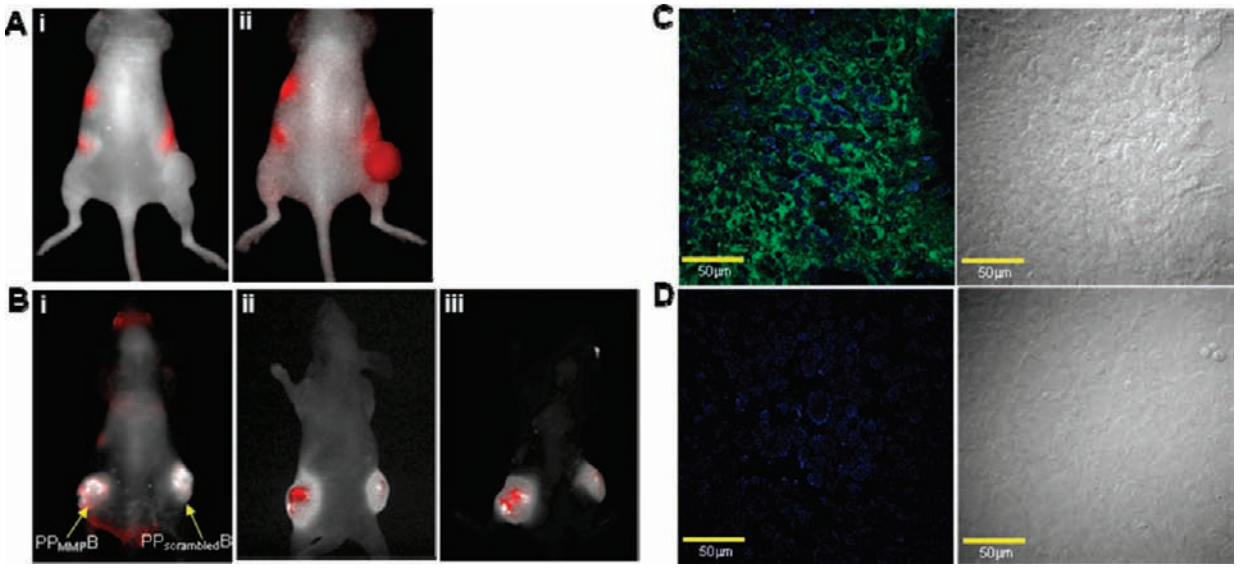


Figure 4. *In vivo* fluorescence images in the MT-1 subcutaneous xenograft tumor model: (A) before (i) and 17 h after (ii) i.v. injection of 2 mg/kg $PP_{MMP}B$ and (B) $PP_{MMP}B$ (left tumor) versus $PP_{scrambled}B$ (right tumor) images at (i) 10 min, (ii) 6 h, and (iii) 24 h post intratumor injection. Fluorescence micrographs and corresponding differential contrast images of MT-1 frozen tissue sections 24 h after administration of $PP_{MMP}B$ (C) or $PP_{scrambled}B$ (D) (n = 5, Green - activated $PP_{MMP}B$ fluorescence, DAPI - blue nucleus stain).

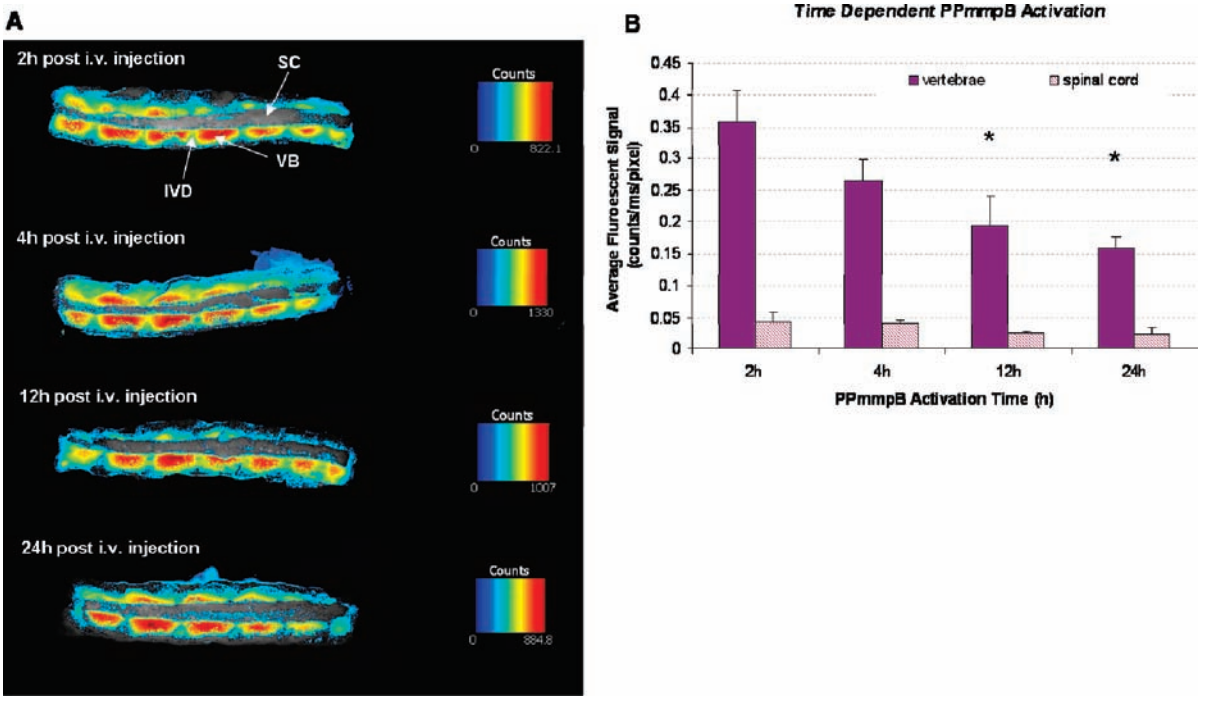


Figure 5. Time-dependent activation of $PP_{MMP}B$ by vertebral metastases imaged *ex vivo*. (A) Composite fluorescence images at 2, 4, 12, and 24 h after intravenous injection of 3 mg/kg $PP_{MMP}B$: SC – spinal cord, VB – vertebral body, IVD – intervertebral disk. (B) Average fluorescent signal comparing $PP_{MMP}B$ activation in the vertebrae and spinal cord: * indicates statistically significant difference ($p < 0.05$) in $PP_{MMP}B$ activation between vertebrae and spinal cord at all imaging time points (n = 4 for 2 and 4 h time points, n = 2 for 12 and 24 h).

average fluorescent counts/(s × area)), the latter showing minimal change in fluorescence (Figure 4B). Even after 24 h, confocal images of frozen sections of harvested tumors confirmed that fluorescence was only detectable in tumors injected with $PP_{MMP}B$ (Figure 4C).

Although these results are promising, evaluation of $PP_{MMP}B$ specific activation in veretebral metastases is necessary to validate the PDT beacon concept for this particular clinical application. Following intracardiac injection of MT-1 cells, metastatic spread to the spine was seen in all animals using bioluminescent imaging. *Ex vivo* fluorescence imaging of the sagitally cut spine over 24 h evaluated $PP_{MMP}B$ activation in vertebral metastases. As shown in Figure 5, the highest fluorescence signal was between 2 and 4 h and then significantly decreased ($p < 0.05$) at 12 and 24 h.

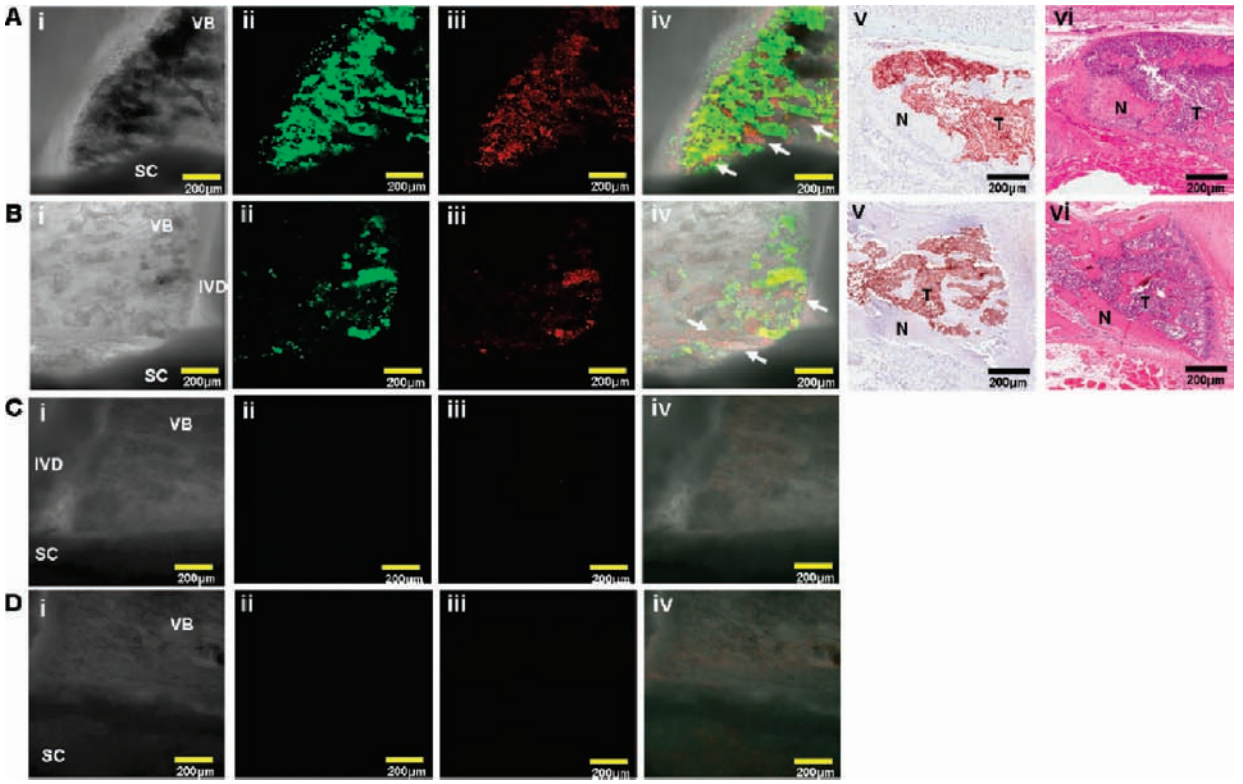


Figure 6. Micrographs of vertebrae at 2 h post i.v. injection of 3 mg/kg $PP_{MMP}B$ into (A,B) MT-1 tumor-bearing rats, (C,D) healthy rats. (i) brightfield image, (ii) GFP image showing the MT-1 cells, (iii) activated $PP_{MMP}B$, (iv) merged images of GFP and cleaved beacon (VB − vertebral body, IVD − intervertebral disk, SC − spinal cord) and corresponding (v) hEGFr and (vi) H&E stained histology sections (T −tumor, N − normal, 5× magnification). Note: in the merged images in panel iv $PP_{MMP}B$ activation extends beyond the GFP, indicating uptake/activation by surrounding tumor stroma (white arrows).

Importantly, no fluorescence signal from activated beacons was detected above background within the spinal cord at any time point (Figure 5B and SI Figure S4). Weak fluorescence was observed within the intervertebral discs (Figure 5A). The strongest fluorescence was within the vertebral body, where metastases most commonly form. At all imaging time points, the fluorescence intensity was 6- to 9-fold higher in the vertebral body versus the spinal cord ($p < 0.05$) (Figure 5B), demonstrating that $PP_{MMP}B$ activation is substantively confined to sites where vertebral metastases develop, with rapid onset of beacon activation after administration. Thus, either the beacon is not significantly taken up in or activated by the spinal cord or, at least over the time period of observation, there is no significant diffusion of cleaved $PP_{MMP}B$ activated by tumors (local or distant) into the spinal cord.

To ensure that $PP_{MMP}B$ activation was a result of the vertebral metastases expressing MMPs and not due to normal bone tissues, spines from tumor-bearing and healthy animals were imaged *ex vivo* at 2 and 4 h after i.v. administration of $PP_{MMP}B$. No fluorescence was observed in the spinal cord in either case. Under confocal microscopy, in which the unquenched beacon fluorescence was overlaid with the GFP signal of the cells, sites with positive GFP showed detectable activation (Figure 6A,B), whereas no activation was detected in the healthy animals (Figure 6C,D). Furthermore, no $PP_{MMP}B$ activation was seen within the spinal cord. The Pearson coefficients for the degree of overlap between $PP_{MMP}B$ activation and MT-1 vertebral tumors (Figure 6A,B and SI Figure S5) were 0.76 and 0.68 at 2 and 4 h post injection, respectively. This was not applicable in the healthy animal cohort, since no signal was detected in either imaging channel (tumor or cleaved beacon).

DISCUSSION

These data demonstrate that specific activation (enzymatic cleavage resulting in unquenching of the photosensitizer fluorescence) of $PP_{MMP}Bs$ is mediated by breast cancer vertebral metastases that express MMPs. Among the MMPs, other than MMP 7, $PP_{MMP}B$'s peptide linker sequence, GPLGLA, can also be specifically cleaved by MMP 10 and MMP 12, although at a lower rate than MMP 7 (data not shown). However, this additional cleavage would not be a disadvantage in this application, since both MMP 10 and 12 also play roles in bone development and bone matrix solubilization.[32−35] Since tumor cells have already hijacked the normal osteolytic cycle, MMP 10 and 12-mediated beacon activation may then aid in further disrupting the vicious tumor-bone cycle. The *in vitro* studies confirm this specific activation by the MT-1 breast cancer cells. The *in vivo* experiments in MT-1 xenografts demonstrate specific activation of $PP_{MMP}B$ by these tumors, using both systemic (i.v.) and intratumoral injection of the beacon. In the more clinically relevant metastatic model, fluorescent imaging also confirmed tumor-specific activation of $PP_{MMP}B$. There are, however, limitations with this model. The attenuation of the fluorescent signal by the overlying bone and soft tissue confounds quantitative *in vivo* imaging to determine the activation kinetics. Nevertheless, this could be determined by imaging the sectioned vertebrae *ex vivo*, albeit at only select time points, and showed that the beacon can reach and target

the intravertebral tumor tissue. In addition, it remained inactive (uncleaved) within the spinal cord, which is the critical dose-limiting tissue. It may be anticipated then that $PP_{MMP}Bs$ may serve as both a vertebral metastases-specific imaging agent and a directed PDT agent, and thus, there are a number of potential applications of $PP_{MMP}Bs$ in the treatment of patients with spinal metastases.

Surgical debulking is currently a main treatment option for spinal metastases, but recurrence is common due to incomplete resection. The strong fluorescence signal and specificity of $PP_{MMP}B$ could enable intraoperative image guidance to increase the completeness of resection and to aid in the intraoperative detection of small metastatic lesions that are otherwise not visible. Thereby, the risk of recurrence would be reduced. This is also analogous to fluorescence image-guided tumor resection in other organs.[18,36−41] Original protease activatable probes were developed to differentiate tumor versus healthy tissue, better defining surgical margins.[42−45] Thus, the initial *in vivo* and clinical application of beacons was intended for fluorescence image-guided tumor resection.[19,43,45−48] We have demonstrated tumor-specific activation for both systemic and local administration in tumor xenografts. Intratumoral injection was not technically feasible in the vertebral metastasis model due to the size limitation, but this will not be the case in patients. It is encouraging that activation occurs fairly rapidly, so that the beacon could be administered shortly before or during surgery, assuming comparable activation kinetics in humans after a local injection at the tumor site.

Furthermore, since pyropheophorbide-α is a potent PDT agent[17,24] in addition to being a fluorescence marker, PDT could be used as a means to "clean up" the surgical bed following resection, as has been used in gliomas with conventional photosensitizers.[36,49] The high degree of quenching in the intact beacon (>99%) and the tumor specificity of activation are then distinct advantages, by markedly reducing the risk of collateral damage to normal tissues that are within range of the photoactivating light. Thus, PDT treatment of the entire surgical bed post resection could result in the eradication of any residual tumor mass and microscopic vertebral metastatic deposits, while preserving normal tissues, specifically the spinal cord. Furthermore, based upon the confocal imaging of tumor cell GFP and beacon activation in vertebral metastases (Figure 6Aiv and Biv), there is evidence of beacon uptake by tumor stroma as well as by the tumor cells themselves. This is not too surprising, since it is known that MMPs are also secreted by tumor stroma.[4,5] This multicompartment targeting provides a further means to interrupt the signaling between the stroma and adjacent cancer cells by identifying cells hijacked by the tumor to promote osteolysis. Hence, eradication of the tumor microenvironment could result in further synergistic effects.

The metastases-specific activation of $PP_{MMP}B$ with its ability to remain inactive in critical normal tissues (i.e., spinal cord) combined with the potent PDT capability of Pyro in beacons makes $PP_{MMP}B$ highly attractive by providing an additional mechanism of selectivity in PDT. [17,24] PDT has been proposed as a promising therapeutic strategy for patients suffering from spinal metastases. It is an approved cancer treatment modality with several potential advantages over current cancer treatments due to its minimally invasive nature, selectivity, ability to treat patients with repeated doses without initiating resistance or exceeding total-dose limitations, fast healing that results in little or no scarring, the ability to administer in an outpatient setting, minimal associated side effects, and lack of contraindication with other modalities.[18−20] We have previously proposed and reported several preclinical studies on the concept of using PDT for destroying spinal metastases, particularly to debulk lesions as an adjuvant to vertebroplasty or kyphoplasty in order to mechanically stabilize weak or fractured vertebrae:[23,27,30,31,50,51] These surgical procedures involve injection of a plastic compound or placement of an inflatable balloon into the vertebral body, which is often limited by the space-occupying tumor mass. We have shown that not only can PDT (using the clinical photosensitizer Visudyne) ablate spinal metastatic tumors,[23] but unexpectedly it also enhances vertebral mechanical stability.[30,31] This has led to a phase I clinical trial with the clinically approved photosensitzer Visudyne (QLT Inc., Vancouver, BC, Canada), in which the objective is to debulk the intravertebral space-occupying tumor mass that often impedes these surgical approaches. However, current photosensitizers are limited by their nonspecific accumulation in normal tissues, e.g., Visudyne has nonspecific uptake in the spinal cord, limiting the therapeutic window which, in turn, reduces the aggressiveness of treatment in order to stay well within safe dose limits.[23,27] Clearly, preservation of spinal cord structure and function is critical in the management of vertebral metastases. $PP_{MMP}B$ potentially addresses this limitation and may be a key component in the use of PDT as a new, minimally invasive, safe, and effective therapy for the management of patients with spinal metastases. Although in this initial study we have not directly tested the photodynamic efficacy of the cleaved beacon against the tumor tissue, previous studies of a variety of PDT beacons in tumor xenograft models[17] have shown that this tracks with the fluorescence characteristics, as would be expected from the photophysics. Direct studies of the PDT effect are in progress, although a second limitation of the intracardiac-injection metastatic model is that the animals survive for only a few weeks[23] due to widespread disease, so that long-term treatment responses cannot be evaluated. Due to the small size of the animals, evaluation of the PDT effect due to an intratumoral injection of $PP_{MMP}B$ within the vertebrae is not possible.

In summary, we have demonstrated the specific activation of $PP_{MMP}B$ by MMP-expressing vertebral metastases in a relevant preclinical model illustrating defined kinetics and the ability to target intravertebral metastatic tumors with minimal uptake or activation in the spinal cord. This is a first step in the further development of such beacons and their potential translation into useful clinical tools for a range of applications.

■ ASSOCIATED CONTENT

Supporting Information. Additional figures as described in the text. This material is available free of charge via the Internet at http://pubs.acs.org.

■ AUTHOR INFORMATION

Corresponding Author

*Gang Zheng, 5-363 101 College St., Toronto, Canada M5G 1L7, 416-581-7666 (Primary); 416-581-7667 (Fax); gang.zheng@uhnres.utoronto.ca.

■ ACKNOWLEDGMENT

This work was supported by the Canadian Institutes of Health Research, DOD BCRP Predoc Award W81XWH-10-1-0115, and

Joey and Toby Tanenbaum/Brazilian Ball Chair in Prostate Cancer Research. Partial support was provided by the Princess Margaret Hospital Foundation and the Ontario Ministry of Health & Long Term care.

REFERENCES

(1) Mundy, G. R. (2002) Metastasis to bone: causes, consequences and therapeutic opportunities. *Nat. Rev. Cancer 2*, 584–93.

(2) Siclari, V. A., Guise, T. A., and Chirgwin, J. M. (2006) Molecular interactions between breast cancer cells and the bone microenvironment drive skeletal metastases. *Cancer Metastasis Rev. 25*, 621–33.

(3) Kingsley, L. A., Fournier, P. G., Chirgwin, J. M., and Guise, T. A. (2007) Molecular biology of bone metastasis. *Mol. Cancer Ther. 6*, 2609–17.

(4) Brinckerhoff, C. E., and Matrisian, L. M. (2002) Matrix metalloproteinases: a tail of a frog that became a prince. *Nat. Rev. Mol. Cell Biol. 3*, 207–14.

(5) Kessenbrock, K., Plaks, V., and Werb, Z. Matrix metalloproteinases: regulators of the tumor microenvironment. *Cell 141*, 52-67.

(6) Woodward, J. K., Holen, I., Coleman, R. E., and Buttle, D. J. (2007) The roles of proteolytic enzymes in the development of tumour-induced bone disease in breast and prostate cancer. *Bone 41*, 912–27.

(7) Guise, T. A. (2009) Breaking down bone: new insight into site-specific mechanisms of breast cancer osteolysis mediated by metalloproteinases. *Genes Dev. 23*, 2117–23.

(8) Yu, Q., and Stamenkovic, I. (2004) Transforming growth factor-beta facilitates breast carcinoma metastasis by promoting tumor cell survival. *Clin. Exp. Metastasis 21*, 235–42.

(9) Kasper, G., Reule, M., Tschirschmann, M., Dankert, N., Stout-Weider, K., Lauster, R., Schrock, E., Mennerich, D., Duda, G. N., and Lehmann, K. E. (2007) Stromelysin-3 over-expression enhances tumourigenesis in MCF-7 and MDA-MB-231 breast cancer cell lines: involvement of the IGF-1 signalling pathway. *BMC Cancer 7*, 12.

(10) Noe, V., Fingleton, B., Jacobs, K., Crawford, H. C., Vermeulen, S., Steelant, W., Bruyneel, E., Matrisian, L. M., and Mareel, M. (2001) Release of an invasion promoter E-cadherin fragment by matrilysin and stromelysin-1. *J Cell Sci 114*, 111–118.

(11) Lynch, C. C., Hikosaka, A., Acuff, H. B., Martin, M. D., Kawai, N., Singh, R. K., Vargo-Gogola, T. C., Begtrup, J. L., Peterson, T. E., Fingleton, B., Shirai, T., Matrisian, L. M., and Futakuchi, M. (2005) MMP-7 promotes prostate cancer-induced osteolysis via the solubilization of RANKL. *Cancer Cell 7*, 485–96.

(12) Egeblad, M., and Werb, Z. (2002) New functions for the matrix metalloproteinases in cancer progression. *Nat. Rev. Cancer 2*, 161–74.

(13) Page-McCaw, A., Ewald, A. J., and Werb, Z. (2007) Matrix metalloproteinases and the regulation of tissue remodelling. *Nat. Rev. Mol. Cell. Biol. 8*, 221–33.

(14) American Cancer Society. *Breast Cancer Facts & Figures* 2009−2010. Atlanta: American Cancer Society, I.

(15) Finn, M. A., Vrionis, F. D., and Schmidt, M. H. (2007) Spinal radiosurgery for metastatic disease of the spine. *Cancer Control 14*, 405–11.

(16) Bartels, R. H., van der Linden, Y. M., and van der Graaf, W. T. (2008) Spinal extradural metastasis: review of current treatment options. *CA Cancer J. Clin. 58*, 245–59.

(17) Zheng, G., Chen, J., Stefflova, K., Jarvi, M., Li, H., and Wilson, B. C. (2007) Photodynamic molecular beacon as an activatable photosensitizer based on protease-controlled singlet oxygen quenching and activation. *Proc. Natl. Acad. Sci. U.S.A. 104*, 8989–94.

(18) Wilson, B. C., and Patterson, M. S. (2008) The physics, biophysics and technology of photodynamic therapy. *Phys. Med. Biol. 53*, R61–109.

(19) Celli, J. P., Spring, B. Q., Rizvi, I., Evans, C. L., Samkoe, K. S., Verma, S., Pogue, B. W., and Hasan, T. (2010) Imaging and photodynamic therapy: mechanisms, monitoring, and optimization. *Chem. Rev. 110*, 2795–838.

(20) Pervaiz, S., and Olivo, M. (2006) Art and science of photodynamic therapy. *Clin. Exp. Pharmacol. Physiol. 33*, 551–6.

(21) Kohrmann, A., Kammerer, U., Kapp, M., Dietl, J., and Anacker, J. (2009) Expression of matrix metalloproteinases (MMPs) in primary human breast cancer and breast cancer cell lines: New findings and review of the literature. *BMC Cancer 9*, 188.

(22) Giambernardi, T. A., Grant, G. M., Taylor, G. P., Hay, R. J., Maher, V. M., McCormick, J. J., and Klebe, R. J. (1998) Overview of matrix metalloproteinase expression in cultured human cells. *Matrix Biol. 16*, 483–96.

(23) Akens, M. K., Hardisty, M. R., Wilson, B. C., Schwock, J., Whyne, C. M., Burch, S., and Yee, A. J. (2010) Defining the therapeutic window of vertebral photodynamic therapy in a murine pre-clinical model of breast cancer metastasis using the photosensitizer BPD-MA (Verteporfin). *Breast Cancer Res. Treat. 119*, 325–33.

(24) Lo, P. C., Chen, J., Stefflova, K., Warren, M. S., Navab, R., Bandarchi, B., Mullins, S., Tsao, M., Cheng, J. D., and Zheng, G. (2009) Photodynamic molecular beacon triggered by fibroblast activation protein on cancer-associated fibroblasts for diagnosis and treatment of epithelial cancers. *J. Med. Chem. 52*, 358–68.

(25) Engebraaten, O., and Fodstad, O. (1999) Site-specific experimental metastasis patterns of two human breast cancer cell lines in nude rats. *Int. J. Cancer 82*, 219–25.

(26) Engebraaten, O., Sivam, G., Juell, S., and Fodstad, O. (2000) Systemic immunotoxin treatment inhibits formation of human breast cancer metastasis and tumor growth in nude rats. *Int. J. Cancer 88*, 970–6.

(27) Akens, M. K., Yee, A. J., Wilson, B. C., Burch, S., Johnson, C. L., Lilge, L., and Bisland, S. K. (2007) Photodynamic therapy of vertebral metastases: evaluating tumor-to-neural tissue uptake of BPD-MA and ALA-PpIX in a murine model of metastatic human breast carcinoma. *Photochem. Photobiol. 83*, 1034–9.

(28) Klerk, C. P., Overmeer, R. M., Niers, T. M., Versteeg, H. H., Richel, D. J., Buckle, T., Van Noorden, C. J., and van Tellingen, O. (2007) Validity of bioluminescence measurements for noninvasive in vivo imaging of tumor load in small animals. *Biotechniques 43* (7−13), 30.

(29) Sato, A., Klaunberg, B., and Tolwani, R. (2004) In vivo bioluminescence imaging. *Comp. Med. 54*, 631–4.

(30) Won, E., Akens, M. K., Hardisty, M. R., Burch, S., Bisland, S. K., Yee, A. J., Wilson, B. C., and Whyne, C. M. (2010) Effects of photodynamic therapy on the structural integrity of vertebral bone. *Spine (Phila Pa 1976) 35*, 272–7.

(31) Won, E., Wise-Milestone, L., Akens, M. K., Burch, S., Yee, A. J., Wilson, B. C., and Whyne, C. M. (2010) Beyond bisphosphonates: photodynamic therapy structurally augments metastatically involved vertebrae and destroys tumor tissue. *Breast Cancer Res. Treat.*

(32) Nabha, S. M., dos Santos, E. B., Yamamoto, H. A., Belizi, A., Dong, Z., Meng, H., Saliganan, A., Sabbota, A., Bonfil, R. D., and Cher, M. L. (2008) Bone marrow stromal cells enhance prostate cancer cell invasion through type I collagen in an MMP-12 dependent manner. *Int. J. Cancer 122*, 2482–90.

(33) Hou, P., Troen, T., Ovejero, M. C., Kirkegaard, T., Andersen, T. L., Byrjalsen, I., Ferreras, M., Sato, T., Shapiro, S. D., Foged, N. T., and Delaisse, J. M. (2004) Matrix metalloproteinase-12 (MMP-12) in osteoclasts: new lesson on the involvement of MMPs in bone resorption. *Bone 34*, 37–47.

(34) Bord, S., Horner, A., Hembry, R. M., and Compston, J. E. (1998) Stromelysin-1 (MMP-3) and stromelysin-2 (MMP-10) expression in developing human bone: potential roles in skeletal development. *Bone 23*, 7–12.

(35) Andersen, T. L., del Carmen Ovejero, M., Kirkegaard, T., Lenhard, T., Foged, N. T., and Delaisse, J. M. (2004) A scrutiny of matrix metalloproteinases in osteoclasts: evidence for heterogeneity and for the presence of MMPs synthesized by other cells. *Bone 35*, 1107–19.

(36) Bogaards, A., Varma, A., Zhang, K., Zach, D., Bisland, S. K., Moriyama, E. H., Lilge, L., Muller, P. J., and Wilson, B. C. (2005) Fluorescence image-guided brain tumour resection with adjuvant metronomic photodynamic therapy: pre-clinical model and technology development. *Photochem. Photobiol. Sci. 4*, 438–42.

(37) Troyan, S. L., Kianzad, V., Gibbs-Strauss, S. L., Gioux, S., Matsui, A., Oketokoun, R., Ngo, L., Khamene, A., Azar, F., and Frangioni, J. V. (2009) The FLARE intraoperative near-infrared fluorescence imaging system: a first-in-human clinical trial in breast cancer sentinel lymph node mapping. *Ann. Surg. Oncol. 16*, 2943–52.

(38) Stenzl, A., Burger, M., Fradet, Y., Mynderse, L. A., Soloway, M. S., Witjes, J. A., Kriegmair, M., Karl, A., Shen, Y., and Grossman, H. B. (2010) Hexaminolevulinate guided fluorescence cystoscopy reduces recurrence in patients with nonmuscle invasive bladder cancer. *J. Urol. 184*, 1907–13.

(39) Upile, T., Jerjes, W., Sterenborg, H. J., El-Naggar, A. K., Sandison, A., Witjes, M. J., Biel, M. A., Bigio, I., Wong, B. J., Gillenwater, A., MacRobert, A. J., Robinson, D. J., Betz, C. S., Stepp, H., Bolotine, L., McKenzie, G., Mosse, C. A., Barr, H., Chen, Z., Berg, K., D'Cruz, A. K., Stone, N., Kendall, C., Fisher, S., Leunig, A., Olivo, M., Richards-Kortum, R., Soo, K. C., Bagnato, V., Choo-Smith, L. P., Svanberg, K., Tan, I. B., Wilson, B. C., Wolfsen, H., Yodh, A. G., and Hopper, C. (2009) Head & neck optical diagnostics: vision of the future of surgery. *Head Neck Oncol. 1*, 25.

(40) Wilson, B. C. (2007) Detection and treatment of dysplasia in Barrett's esophagus: a pivotal challenge in translating biophotonics from bench to bedside. *J. Biomed. Opt. 12*, 051401.

(41) Gibbs-Strauss, S. L., O'Hara, J. A., Hoopes, P. J., Hasan, T., and Pogue, B. W. (2009) Noninvasive measurement of aminolevulinic acid-induced protoporphyrin IX fluorescence allowing detection of murine glioma in vivo. *J. Biomed. Opt. 14*, 014007.

(42) Campo, M. A., Gabriel, D., Kucera, P., Gurny, R., and Lange, N. (2007) Polymeric photosensitizer prodrugs for photodynamic therapy. *Photochem. Photobiol. 83*, 958–65.

(43) Weissleder, R., Tung, C. H., Mahmood, U., and Bogdanov, A., Jr. (1999) In vivo imaging of tumors with protease-activated near-infrared fluorescent probes. *Nat. Biotechnol. 17*, 375–8.

(44) Bullok, K., and Piwnica-Worms, D. (2005) Synthesis and characterization of a small, membrane-permeant, caspase-activatable far-red fluorescent peptide for imaging apoptosis. *J. Med. Chem. 48*, 5404–7.

(45) McIntyre, J. O., Fingleton, B., Wells, K. S., Piston, D. W., Lynch, C. C., Gautam, S., and Matrisian, L. M. (2004) Development of a novel fluorogenic proteolytic beacon for in vivo detection and imaging of tumour-associated matrix metalloproteinase-7 activity. *Biochem. J. 377*, 617–28.

(46) Jiang, T., Olson, E. S., Nguyen, Q. T., Roy, M., Jennings, P. A., and Tsien, R. Y. (2004) Tumor imaging by means of proteolytic activation of cell-penetrating peptides. *Proc. Natl. Acad. Sci. U.S.A. 101*, 17867–72.

(47) Weissleder, R., and Ntziachristos, V. (2003) Shedding light onto live molecular targets. *Nat. Med. 9*, 123–8.

(48) Lee, S., Xie, J., and Chen, X. (2010) Activatable molecular probes for cancer imaging. *Curr. Top. Med. Chem. 10*, 1135–44.

(49) Muller, P. J., and Wilson, B. C. (2006) Photodynamic therapy of brain tumors--a work in progress. *Lasers Surg. Med. 38*, 384–9.

(50) Burch, S., Bisland, S. K., Bogaards, A., Yee, A. J., Whyne, C. M., Finkelstein, J. A., and Wilson, B. C. (2005) Photodynamic therapy for the treatment of vertebral metastases in a rat model of human breast carcinoma. *J. Orthop. Res. 23*, 995–1003.

(51) Burch, S., Bogaards, A., Siewerdsen, J., Moseley, D., Yee, A., Finkelstein, J., Weersink, R., Wilson, B. C., and Bisland, S. K. (2005) Photodynamic therapy for the treatment of metastatic lesions in bone: studies in rat and porcine models. *J. Biomed. Opt. 10*, 034011.

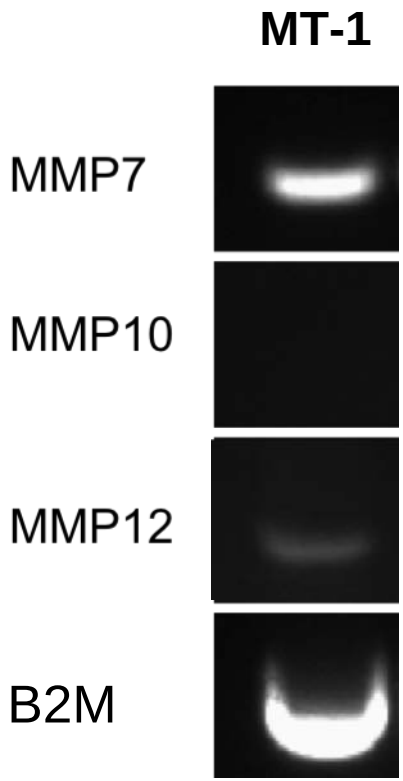


Figure S1. Preliminary reverse transcription polymerase chain reaction (RT-PCR) analysis of MMP gene expression in MT-1 cells. Beta-2-microglobulin (B2M) was used as a control. MMP primer sequences and RT-PCR protocol were previously described by Giambernardi *et al.,* 1998.

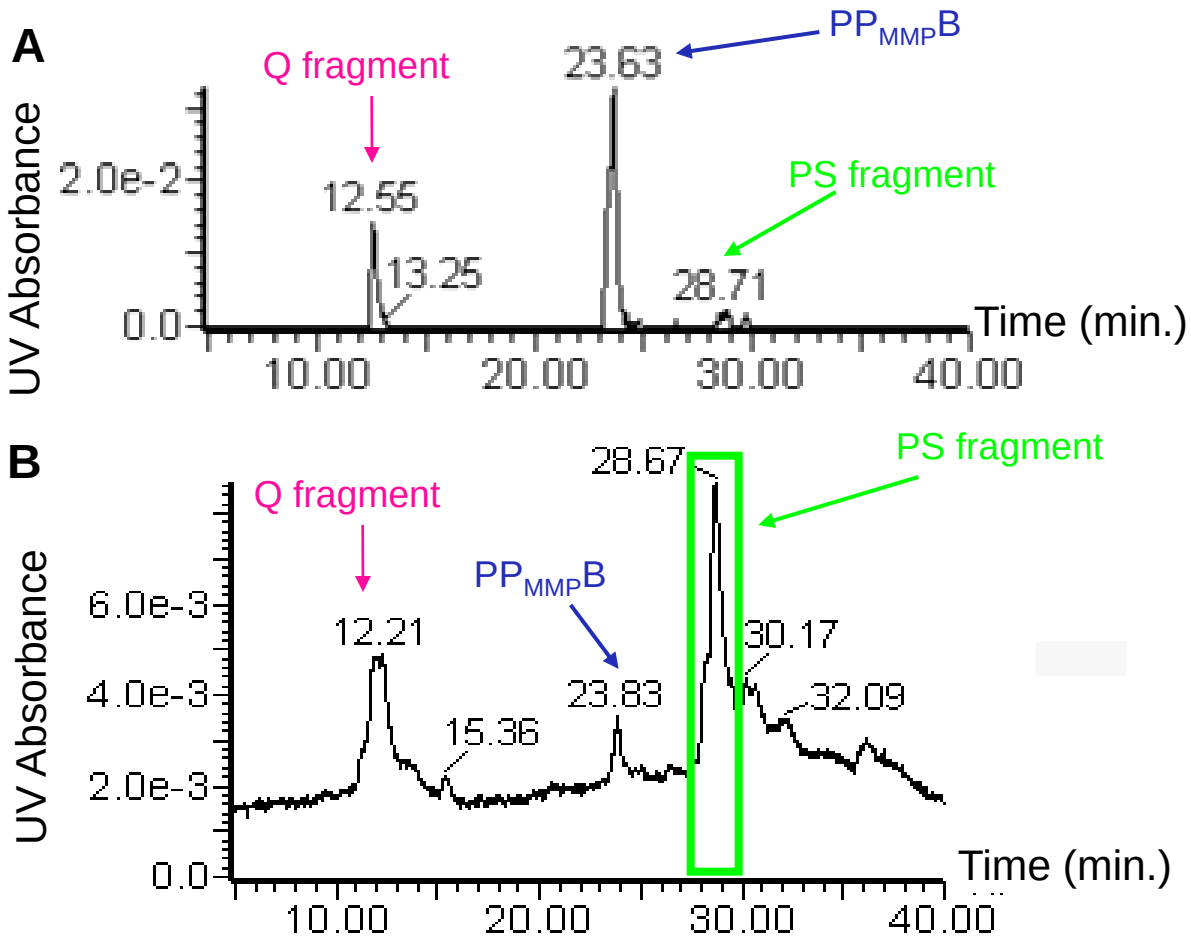


Figure S2. High Performance Liquid Chromatography (HPLC) analysis of $PP_{MMP}B$ cleavage in A) cell media and B) cell lysate evaluated at 665nm.

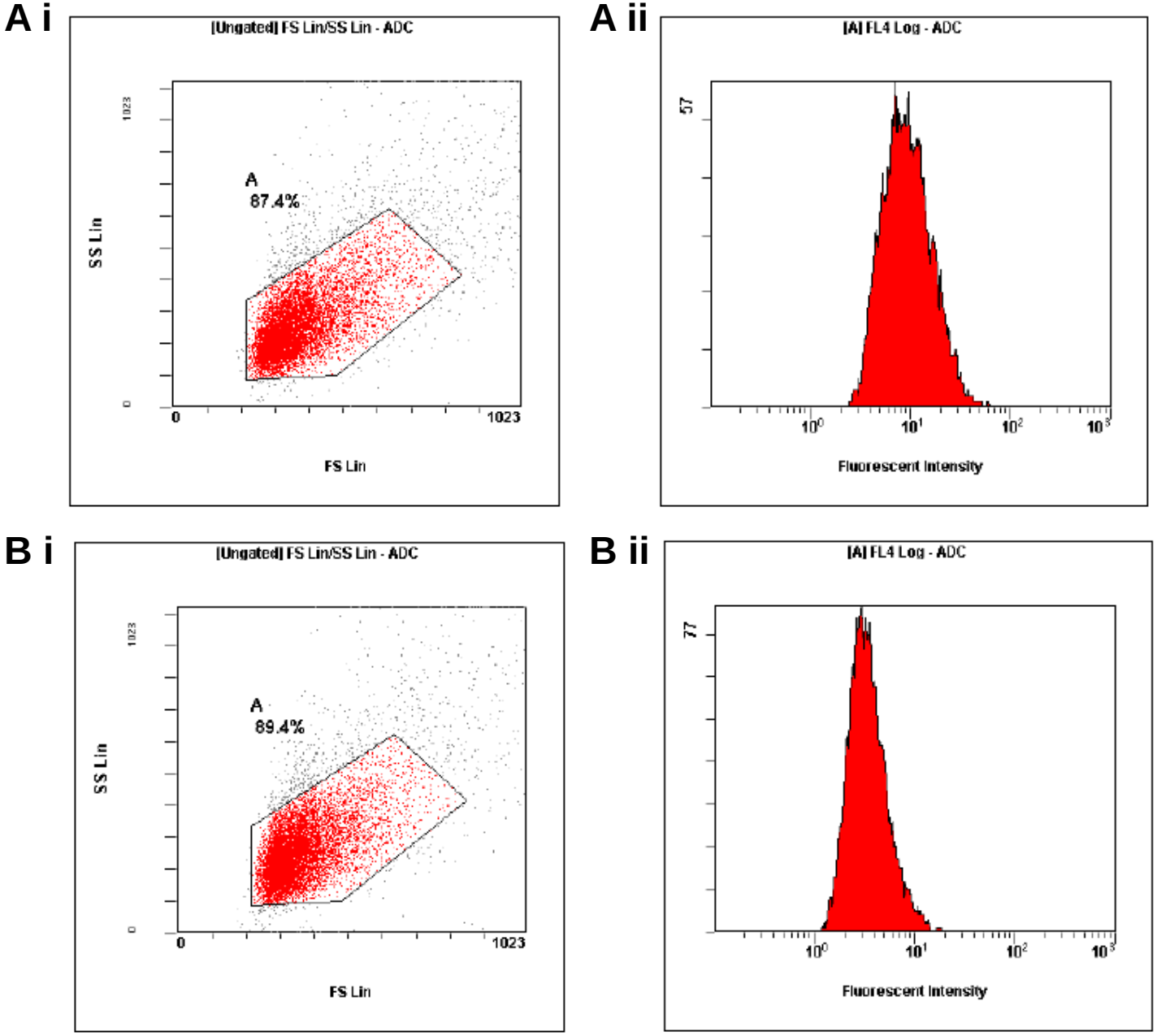


Figure S3. Flow cytometry of A) $PP_{MMP}B$ and B) $PP_{scrambled}B$ activation by MT-1 cells of i) scatterplot and ii) histogram

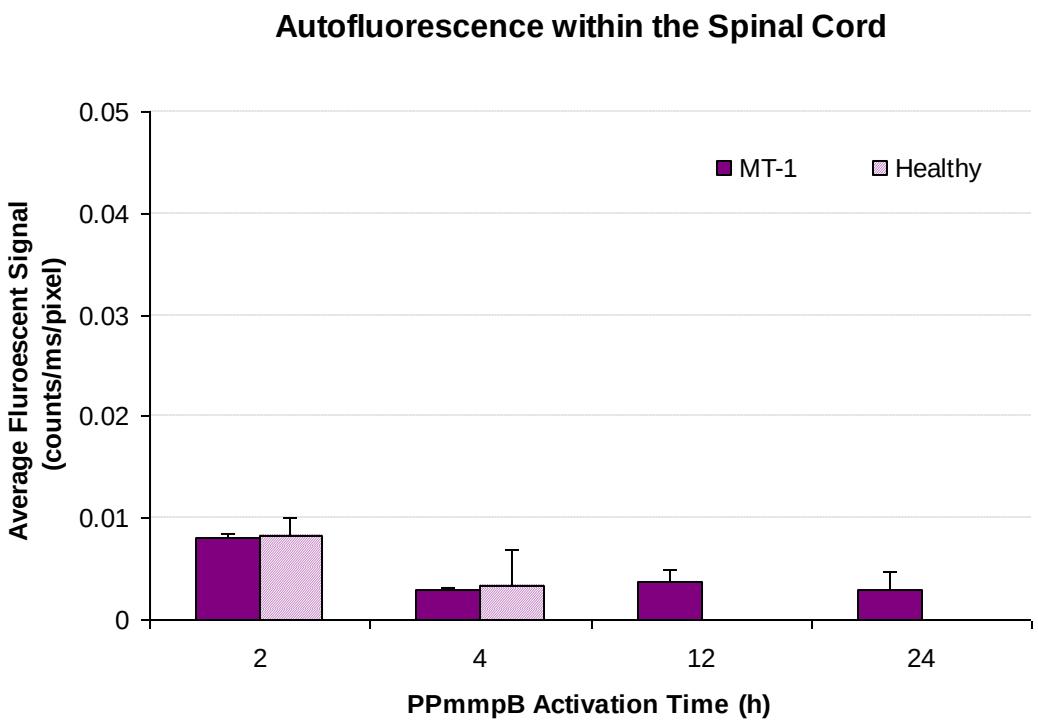


Figure S4. Autofluorescence within the spinal cord in tumor bearing versus healthy animals.

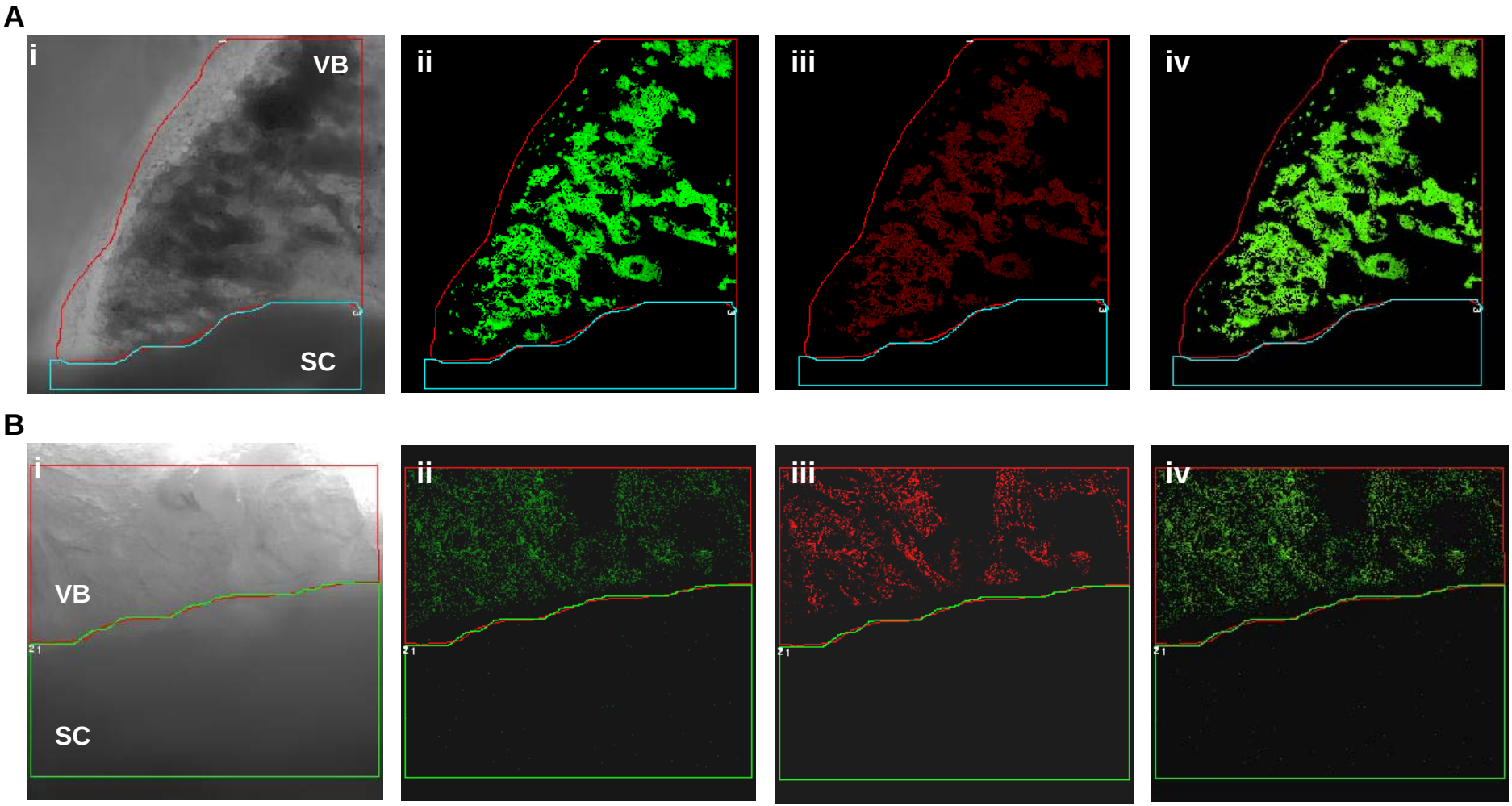


Figure S5. Colocalization Imaging analysis of A) 2h $PP_{MMP}B$ activation and B) 4h $PP_{MMP}B$ activation in vertebral metastases bearing animals. i) Brightfield image, ii) GFP (MT-1 cells) colocalization signal, iii) Activated $PP_{MMP}B$ colocalization signal, iv) colocalization images where VB – vertebral bodyand SC – spinal cord.

Bioconjugate Chemistry

ARTICLE

pubs.acs.org/bc

NONOates—Polyethylenimine Hydrogel for Controlled Nitric Oxide Release and Cell Proliferation Modulation

Jihoon Kim,[†] Yanggy Lee,[‡] Kaushik Singha,[†] Hyun Woo Kim,[†] Jae Ho Shin,[§] Seongbong Jo,[⊥] Dong-Keun Han,[‡] and Won Jong Kim*[,†]

[†]Department of Chemistry, Pohang University of Science and Technology, Pohang 790-784, Korea

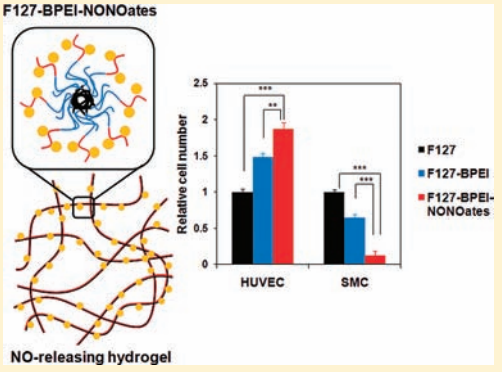
[‡]Biomaterials Research Center, Korea Institute of Science and Technology, P.O. Box 131, Seoul 130-650, Korea

[§]Department of Chemistry, Kwangwoon University, Seoul 139-701, Korea

[⊥]Department of Pharmaceutics, School of Pharmacy, The University of Mississippi, University, Mississippi 38677, United States

Supporting Information

ABSTRACT: In recent years, numerous research activities have been devoted to the controlled release of nitric oxide (NO) due to its potential as a restenosis inhibitor which inhibits the proliferation of vascular smooth muscle cells, the apoptosis of vascular endothelial cells, and aggregation of platelets. This work has demonstrated the development of a novel NO-conjugated gel system comprising of thermosensitive Pluronic F127, branched polyethylenimine (BPEI), and diazeniumdiolates (NONOates). Synthesis of conjugated Pluronic-BPEI-NONOates involved coupling of activated F127 to BPEI followed by the installation of NONOates at the secondary amine sites of branched PEI backbone under high pressure. NO-conjugated gel system, F127-BPEI-NONOates, reduced the initial burst of NO release and prolonged NO release. Furthermore, F127-BPEI-NONOates polymer coated on cell culture dish displayed much higher increase of endothelial cell proliferation and reduction of smooth muscle cell proliferation than that exhibited by non-NO releasing control. Such an NO-releasing device can operate locally and has a great potential in several biomedical applications due to high biocompatibility imparted by the conjugated F127.



INTRODUCTION

Nitric oxide (NO) is a small reactive molecule that plays a major role in proliferation and apoptosis of cells, neurotransmitters, and regulation of vasomotor tone.[1−3] Especially in vascular vessels, NO has been known to affect relaxation, inhibition of proliferation, and induction of apoptosis of vascular smooth muscle cells. In contrast to these effects on vascular smooth muscle cells, NO is also known to induce the growth of endothelial cells.[4,5] In addition, NO exerts an inhibitory effect on platelet aggregation, which can cause thrombogenicity.[6−8]

Despite the various and selective functions of NO, as well as in vivo generation of NO by three types of nitric oxide synthase, it is very difficult to apply NO to biomedical and therapeutic fields because NO could easily react with other components to produce a variety of nitrate/nitrite and could be released very rapidly from NO donors. Thus, there has been enormous interest in developing biomaterials which could facilitate the controlled and prolonged release of NO for modulating its concentration-dependent functions.[9] Several types of NO donors have been developed and evaluated in vitro and in vivo. Nitroglycerin,[10] sodium nitroprusside,[11] *S*-nitrosothiol,[12−15] NO aspirin,[16−18] and 1-substituted diazen-1-ium-1,2-diolates (NONOates)[19−28] and its derivatives[16,29] are typical examples of NO donors. Among these types of NO donors, NONOates, containing the $[N(O)NO]^-$ functional group, are considered as the most attractive candidates for practical application due to their spontaneous dissociation under physiological conditions to yield 2 mol of NO per mole of $[N(O)NO]^-$ functional group and structural flexibility of synthesis.[26]

Recently, NO donors were incorporated into stents covalently and noncovalently and thus used as restenosis inhibitors.[12,14,20−22,25,27] There are mainly two distinct structural systems which are utilized as NO donors in coating materials for drug-eluting stent (DES). The majority of the NO-releasing polymers incorporate NO through covalent conjugation as found in diaminoalkyltrimethoxylsilane silicone rubber-NONOates (DACA/NONO-SR),[27] polypropylenimine dendrimers-NONOates,[22] and polyethyleneimine-NONOates.[19] Using this system, it is possible to incorporate NO in abundance into polymers; however, a supporting material which could bind NO donors into the substrate is essential. Unless NONOates polymers remain bound to the supporting material, the detached

Received: September 9, 2010
Revised: March 10, 2011
Published: April 29, 2011

ACS Publications © 2011 American Chemical Society

polymer could be dispersed into the body through the bloodstream and may induce toxicity. Another type of NO donor includes a mixture of small NO donor noncovalently mixed with polymers, for example, the mixture of diethylamine-NONOates (DEA-NONO) with poly(ethylene glycol) (PEG),[28] diethylenetriamine-NONOates (DETA-NONO) with polycaprolactone,[28] *S*-nitrosoglutathione with poly(vinyl alcohol)/poly(vinyl pyrrolidone) film,[15] and *S*-nitrosoglutathione or *S*-nitroso-*N*-acetylcysteine with Pluronic F127 gel.[14] Especially, it has been reported that NO release from *S*-nitrosoglutathione or *S*-nitroso-*N*-acetylcysteine in thermosensitive Pluronic F127 hydrogel is slower than that in H_2O. However, these mixed systems may induce leaching out of small molecules, which can cause cytotoxicity.

In this study, we developed a conjugated gel system by integrating advantageous features of two distinct systems in a single system. We used Pluronic F127, a commercially available thermosensitive triblock copolymer which was approved by FDA, to prolong the NO release by a cage recombination mechanism.[14] In addition, we have conjugated BPEI which has a large amount of secondary amines, designed for conjugation of NONOates to Pluronic F127. We have also investigated the kinetics of NO release from F127-BPEI-NONOates hydrogel and their effects on endothelial as well as smooth muscle cell proliferation.

EXPERIMENTAL PROCEDURES

Materials. Branched PEIs (BPEI, MW 600 Da, 10 kDa,) were obtained from Polyscience, Inc., (Warrington, PA) and high molecular weight BPEI (MW 25 kDa), sodium methoxide (NaOMe), Pluronic F127, and *p*-nitrophenyl chloroformate (*p*-NPC) were purchased from Sigma Aldrich (St. Louis, MO). Tetrahydrofuran (THF) and diethyl ether were purchased from Dae Jung Chemical Co. (Seoul, Korea). Dichloromethane (DCM) was purchased from Samchun Chemical Co. (Korea). Methyl alcohol (MeOH) was purchased from Mallinckrodt (St. Louis, MO). A Griess assay system was purchased from Promega (Madison, WI). Nitric oxide (NO) and argon (Ar) gases were obtained from HANA gas (Gimhae, Korea). Human umbilical vein endothelial cells (HUVEC), coronary artery smooth muscle cells (SMC), endothelial basal medium-2 (EBM-2) with full supplements (EGM-2 siglequots), and smooth muscle basal medium (SmBM) with full supplements were obtained from Lonza (Walkersville, MD). Dulbecco's phosphate buffered saline (DPBS) was purchased from Invitrogen-Gibco (Carlsbad, CA). Cell viability was estimated by Cell Counting Kit-8 obtained from Dojindo Molecular Technologies, Inc. (Gaithersburg, MD).

Synthesis and Charaterization of BPEI-NONOates. BPEI-NONOates was prepared as previously reported.[19] Briefly, a solution of BPEI (0.5 g each for M_w: 600 Da, 10 kDa, and 25 kDa) in dry MeOH (10 mL) and dry THF (20 mL) was prepared in 100 mL beaker. After the solution was stirred, NaOMe (1 mol equiv with respect to the total amine sites) in MeOH (10 mL) was added to the BPEI solution and placed in an in-house high-pressure reactor. The high-pressure reactor was flushed with 20 psi Ar (g) twice and then subsequently charged with NO (g) at 80 psi. After 3 days, NO was vented and the reactor was flushed with 20 psi Ar (g) twice before each product was precipitated with cold dry ether. The solvent was quickly removed by filtration, and the product was washed with cold dry ether and then vacuum-dried to yield a light yellow product. The products were stored at −20 °C. The conjugation ratios of BPEI-NONOates were characterized by ^{1}H NMR in D_2O using 300 MHz NMR spectrometer (Bruker, Germany). The characteristic absorption bands for NONOates and *N*-nitrosoamine were 250−260 nm and 330−360 nm, respectively, as measured by UV/vis spectrophotometry (UV 2550, Shimadzu, Japan).

Measurement of NO Release from BPEI-NONOates by Griess Assay. NO release profile was monitored using the Griess assay (Promega), which quantifies the amount of nitrites, the primary degradation byproduct of NO. In brief, each 250 mg aliquot of BPEI-NONOates was incubated in DPBS (50 mL) at 37 °C. After sampling 60 μL in predetermined time intervals, fresh DPBS (60 μL) was added to the vial to maintain the overall volume. After mixing the acquired samples with DPBS, the samples (50 μL) were added to a sulfanilamide solution (50 μL) and incubated in the dark at room temperature for 5 min. Naphthylethylenediamine (50 μL) was added to the mixture to stimulate a colorimetric change; intensity was measured at 548 nm by microplate spectrofluorometer (VICTOR3 V Multilabel Counter, Perkin-Elmer, Wellesley, MA) and compared to known sodium nitrite standards.

Synthesis and Characterization of F127-BPEI. F127-BPEI was prepared using the modified method as reported previously.[30,31] To prepare the hydroxyl-activated Pluronic F127, Pluronic F127 (10 g, 0.79 mmol) was dissolved in anhydrous DCM (70 mL). The solution was added dropwise to a stirred solution of *p*-NPC (1.29 g, 6.35 mmol) in anhydrous DCM (70 mL). The reaction was carried out for 24 h at room temperature with gentle stirring under nitrogen atmosphere. The activated Pluronic F127 was precipitated by addition of ice-cold ether and dried under vacuum. To synthesize the F127-BPEI, a DCM solution (20 mL) containing activated Pluronic F127 (0.6 g) was added dropwise to a solution of BPEI600 (1.5, 3, and 10 mol equiv with respect to activated F127) and triethylamine (1 mL) in DCM (20 mL) at ice-cold conditions. The reaction was carried out for 24 h at room temperature with gentle stirring under nitrogen atmosphere. After evaporating the DCM and dissolving with water, each product was dialyzed by a Spectra/Por dialysis membrane M_w cutoff of 10 000 against water. The conjugation ratios of F127-BPEI were determined by ^{1}H NMR taken in D_2O using 300 MHz NMR spectrometer (Bruker, Germany). Temperature-responsive sol−gel transition behaviors were monitored using a modified vial tilting method.[32]

Synthesis and Characterization of F127-BPEI-NONOates. To a solution of F127-BPEI (0.5 g) in dry THF (2.3 mL) was added a solution of NaOMe in dry MeOH (0.5 M, 2.3 mL). The solution was stirred for 30 min and was then placed in a high-pressure reactor. The high-pressure reactor was flushed with 20 psi Ar (g) twice and subsequently charged with NO (g) at 80 psi. After 3 days, NO was vented and the reactor was flushed with 20 psi Ar (g) twice before each product was precipitated with cold dry ether. The solvent was quickly removed by filtration, and the product was washed with cold dry ether and then vacuum-dried. The products were stored at −20 °C. The conjugation ratios of BPEI-NONOates were determined by ^{1}H NMR in D_2O using 300 MHz NMR spectrometer (Bruker, Germany).

Measurement of NO Release from F127-BPEI-NONOates by Griess Assay. Each of F127-BPEI-NONOates (150 mg) was dissolved in deionized water at 4 °C to prepare 20 wt % solutions and incubated in 600 μL DPBS at 37 °C. Release of NO was monitored using the Griess assay (Promega). In brief, after sampling 600 μL at predetermined time intervals, fresh DPBS (600 μL) was added to the vial. A sample (50 μL) was added to a

sulfanilamide solution (50 μL) and incubated at room temperature for 5 min, protected from light. Then, naphthylethylenediamine (50 μL) was added to the mixture to stimulate a colorimetric change; intensity was measured at 548 nm by microplate spectrofluorometer (VICTOR3 V Multilabel Counter, Perkin-Elmer, Wellesley, MA) and compared to known sodium nitrite standards.

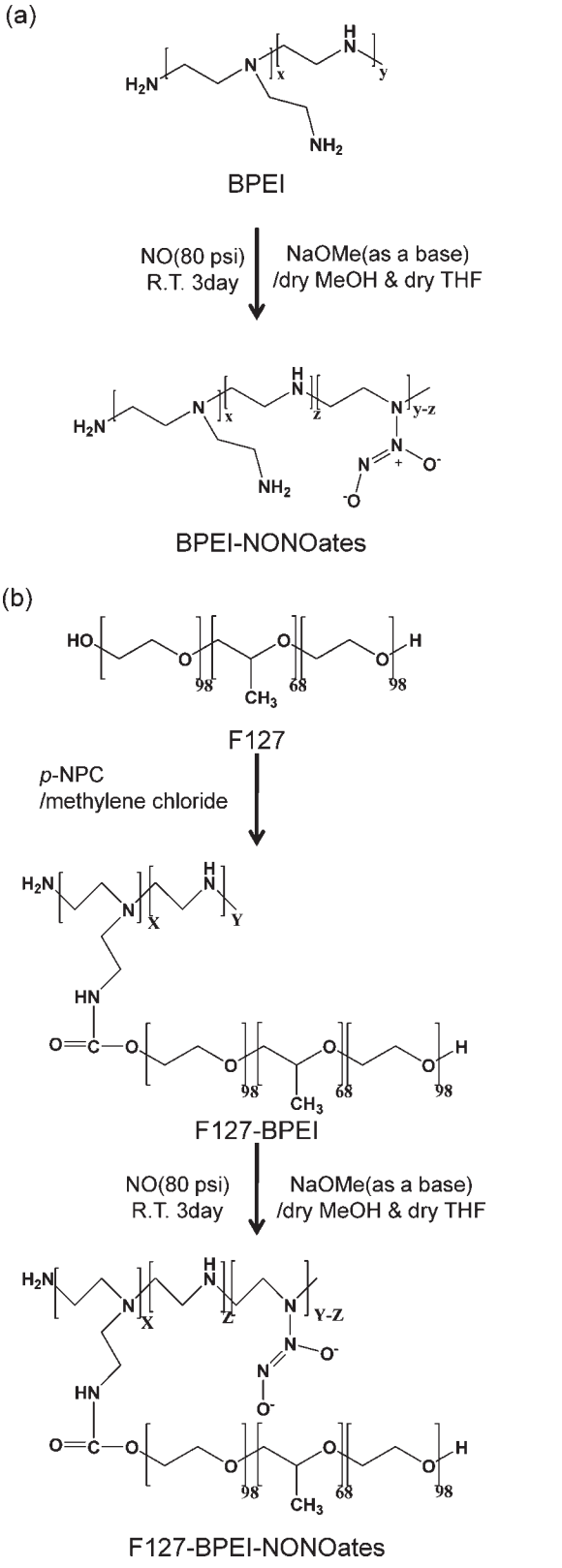
In Vitro Cell Proliferation Test. All materials such as F127, F127-BPEI, F127-BPEI-NONOates, deionized water, DPBS, and media were sterilized under UV for 30 min prior to carrying out the in vitro experiments. F127 (100 mg), a mixture of F127 (50 mg) and F127-BPEI (50 mg) or a mixture of F127 (50 mg) and F127-BPEI-NONOates (50 mg) were dissolved separately in deionized water at 4 °C to yield 25 wt % solutions and kept at 4 °C for 1 h, and then gelation was performed on the cell culture dish at 37 °C for 2 min. HUVEC and SMC were seeded on the coated cell culture plates (24 well) at a density of 1×10^4 cells/well and further incubated at 37 °C for 24 h. After 24 h incubation, cell proliferation was investigated by cell counting kit-8 (CCK-8) assay.[33] This CCK-8 uses the water-soluble tetrazolium salts (WST-8) (2-(2-methoxy-4-nitrophenyl)-3-(4-nitrophenyl)-5-(2,4-disulfophenyl)-2*H*-tetrazolium) which is a derivative of MTT (3-(4,5-Dimethylthiazol-2-yl)-2,5-diphenyl-tetrazolium bromide).

RESULTS AND DISCUSSION

Synthesis and Characterization of BPEI-NONOates. Three types of BPEI-NONOates having BPEI with different MW were synthesized by the method described above, and the structural characteristics of each type of BPEI-NONOates were confirmed by ^{1}H NMR and UV/vis spectroscopy (Scheme 1, and Figures 1 and 2). In ^{1}H NMR, the proton signals of methylene groups adjacent to amine sites of BPEI at 2.7 ppm were shifted downfield to about 3.1 ppm in BPEI-NONOates due to the electron-withdrawing effect of the NONOates group. The integration of the shifted proton signals compared to the total proton integration of each type of BPEI-NONOates revealed that the conjugation ratios of NONOates to BPEI600, BPEI10K, and BPEI25K were 15.3%, 13.8%, and 16.0%, respectively (Figure 1 and Table 1). The UV/vis absorption spectra also showed the characteristic absorption peaks for NONOates at about 250 nm[19] as measured in DPBS buffer (Figure 2).

NO Release Profile of BPEI-NONOates. NO release from three types of BPEI-NONOates was measured in DPBS solution at physiological temperature using a Griess assay (Figure 3) method for nitrite measurement based on the oxidation of highly reactive NO to nitrite. As shown in NO release profile in Figure 3, at initial stages NO was released rapidly from BPEI25K-NONOates and release was completed within 10 h. Likewise, BPEI10K-NONOates showed a similar initial NO release profile, but the NO release was completed within 22 h. However, BPEI600-NONOates having low MW of BPEI showed a different NO release profile. NO was released rapidly at the initial few hours, but showed a sustained NO release pattern. Moreover, NO was released from BPEI600-NONOates for an extended time over 50 h. Longevity can be defined as the duration of NO release, while sustainability can be defined as the degree of sustained release of NO at the initial state, and quantitative evaluation of longevity and sustainability of NO release was summarized in Table 1. These results could be rationalized by considering the protonation of the primary amine group. The protonated primary amine groups (pK_a = 9.73−11.02) are expected to confer stability to NONOates derivative through the hydrogen bonding formation between protonated primary

Scheme 1. Synthetic Route for (a) BPEI-NONOates and (b) F127-BPEI-NONOates



dx.doi.org/10.1021/bc100405c |*Bioconjugate Chem.* 2011, 22, 1031–1038

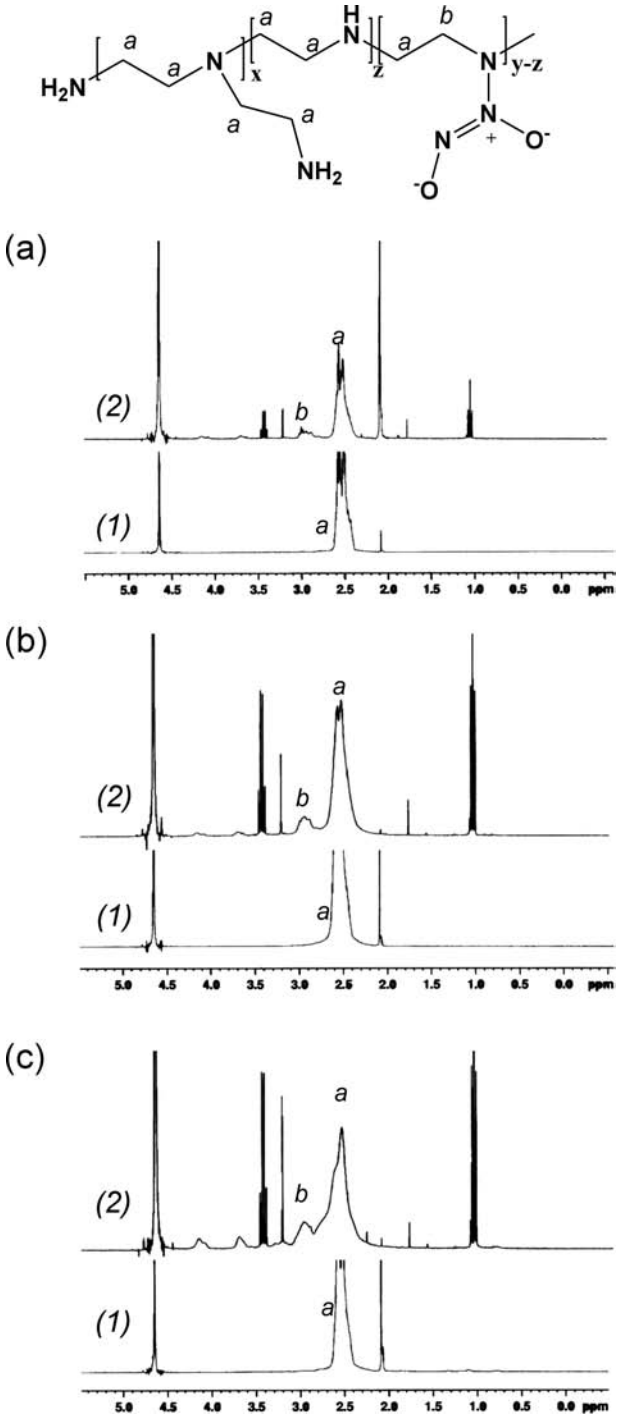


Figure 1. ^{1}H NMR spectra of (1) BPEI and (2) BPEI-NONOates. (a) BPEI600 Da, (b) BPEMOkDa, and (c) BPEI25 kDa.

amine group and NONOates anion.[34] Therefore, the presence of primary amine in close proximity of the NONOate moieties could be an important factor, which may regulate the extent of stabilization of NONOates. In other words, sustained release of NO through the dissociation of NONOates depends on the relative disposition of primary amine and NONOate groups within the polymeric framework. In BPEIs used in this study, the ratio of primary to secondary amine is almost constant, which implies that the dissociation kinetics is governed by some other

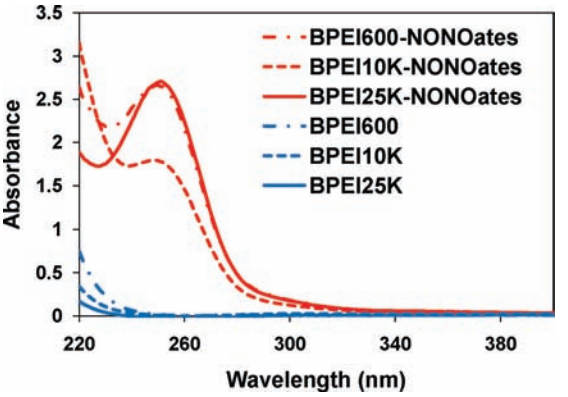


Figure 2. UV−vis spectra of BPEIs and the corresponding BPEI-NONOates at a concentration of 0.14 mg/mL.

Table 1. NO Release Properties of BPEI-NONOates and F127-BPEI-NONOates[a]

polymer	% conv[b]	$t_{1/2}$[c]	t[NO] (μmol/mg)[d]	longevity (h)
BPEI600-NONOates	15.3	<1 min	1.07	53.7
BPEI10K-NONOates	13.8	<1 min	1.29	23.5
BPEI25K-NONOates	16.0	<1 min	1.12	11.1
F127-BPEI0.8-NONOates	35.1	1.91 h	1.10	32.2
F127-BPEI1.0-NONOates	33.1	1.68 h	0.99	54.1
F127-BPEI1.3-NONOates	35.1	2.04 h	1.38	54.1

[a] Determined by Griess assay in DPBS at 37 °C. [b] NONOates conversion efficiency of total amine. [c] Half-life of NO released from each product. [d] Total NO concentration (t[NO]) released from the products.

factors presumably by the degree of stabilization of NONOates moieties conferred by primary amine groups. The assumption could be extended further to assign the crucial role of the three-dimentional structure in regulating the distance between primary amine and NONOates, which in turn could govern the extent of stabilization of NONOate moieties. The primary amines are believed to be populated primarily on the surface and thereby have less opportunity to stabilize the NONOates which are attached to secondary amines and reside at the interior core of the three-dimensional structures (Figure 3b). The increase in molecular weight or size of the polymers increases the distance between primary amine at the surface and secondary amines at the core, which leads to less stabilization and hence faster release of NO. This hypothesis can be substantiated firmly from the following correlations among the molecular weight, size, and NO release profile of the respective BPEI-NONOates. As the radius of BPEI600 is smaller than BPEI10K and BPEI25K, the primary amines in BPEI600-NONOates are located much closer to the NONOates compared to BPEI10K and BPEI25K. Consequently, primary amines of BPEI600-NONOates impart greater stabilization to the NONOate moieties leading to slower NO release. These results are in good agreement with previous reports,[34] and it is expected that F127-BPEI600-NONOates will show slow and sustained NO release compared to high MW BPEIs counterparts.

Synthesis and Characterization of F127-BPEI. The half-life of BPEI600-NONOates, which demonstrated slow and sustained NO release, is only 1 min, and this is considered unfavorable for the actual application of NO donor. In order to increase

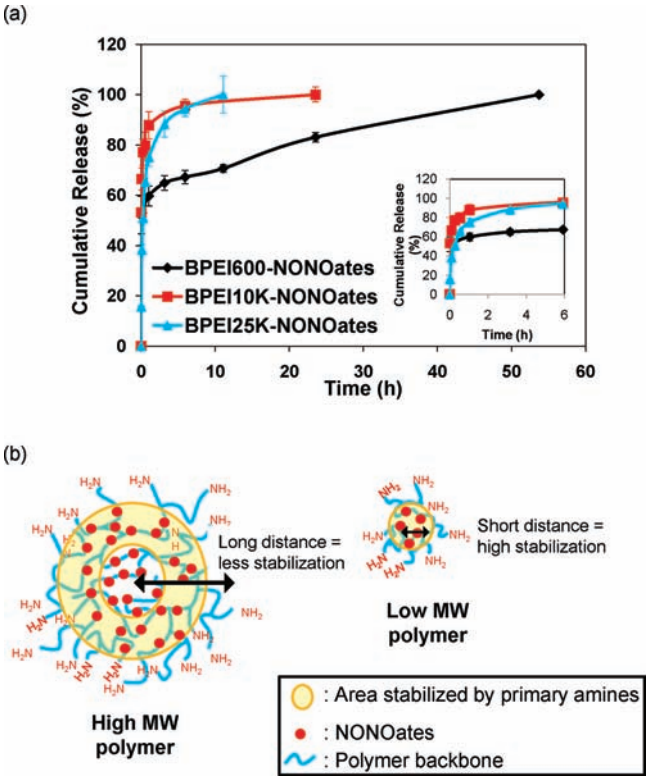


Figure 3. NO release profile and schematic diagram for BPEI-NONOates. (a) Cumulative NO release (%) from BPEI-NONOates in DPBS at 37 °C. Inset: NO release profiles of the compounds during initial 6 h. Data are represented as a mean ± SD ($n = 3$). (b) Schematic diagram for representing the stabilization of the NONOate moieties by primary amine as the molecular weight of polymer.

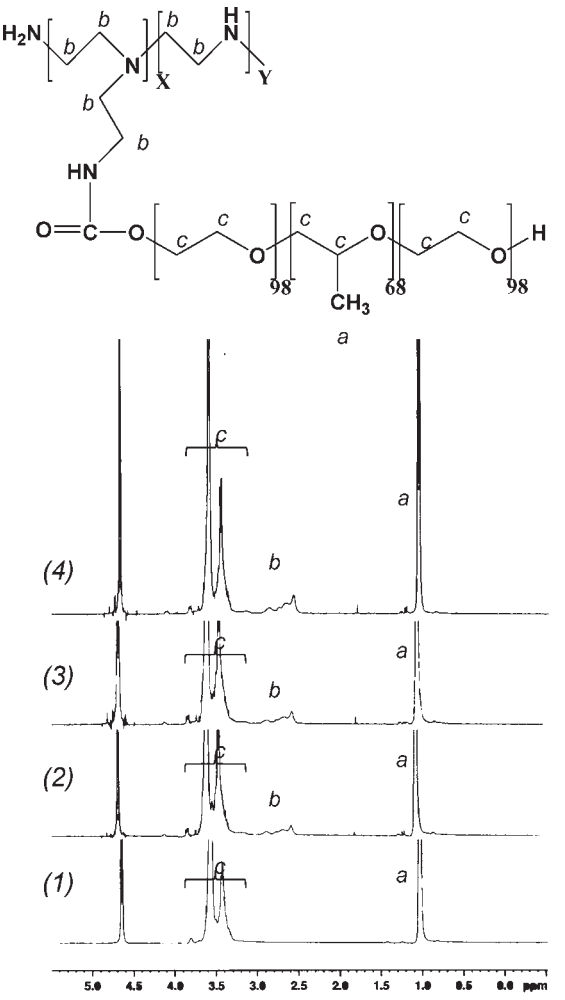


Figure 4. ^{1}H NMR spectra of (1) F127, (2) F127-BPEI0.8, (3) F127-BPEI1.0, and (4) F127-BPEI1.3.

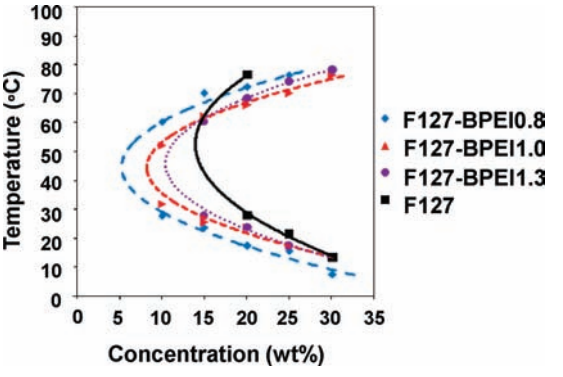


Figure 5. Thermosensitive sol−gel transition behavior of hydrogels formed by F127 and F127-BPEI.

the half-life of NO release, BPEI600 was conjugated to the thermosensitive Pluronic F127 polymer. It is assumed that in the gel state NONOates remains caged in the F127 gel. However, it could be dissociated, and NO release could be triggered by the initial inclusion of water and accelerated further by the disruption of gel.

Three types of F127-BPEI were synthesized by changing the feed ratio of the BPEI600 to the F127 (Scheme 1), and the structural characteristics of each type of F127-BPEI were confirmed by ^{1}H NMR. In the ^{1}H NMR spectrum, the proton signals of methylene groups in F127 were observed at 1.15 ppm and methylene proton signals of BPEI were detected at 2.7 ppm -(Figure 4). The relative integration of the proton signals of BPEI compared to the methylene groups in F127 revealed conjugation ratios. There were no large differences in conjugation ratios of F127 to the BPEI, although the feed ratios of the F127 to BPEI were 1:1.5, 1:3, and 1:10. F127-BPEI0.8, F127-BPEI1.0, and F127-BPEI1.3 represent F127-BPEI conjugates having F127 and BPEI residues in a molar ratio of 0.8, 1.0, and 1.3, respectively.

Generally, Pluronic F127 shows thermosensitive sol−gel transition properties as a function of concentration. Therefore, to study the effect of BPEI conjugation on the thermosensitive properties of F127-BPEI, the sol−gel transition profile was investigated under different concentrations by the tilting method.

As shown in Figure 5, F127-BPEI showed decreased critical gelation concentrations and narrower curve of gelation temperature compared to unmodified F127. This change in gelation profile could be attributed to the incorporation of the hydrophilic BPEI to the F127. The hydrophilic part is known to stabilize the micelle−micelle interaction through the bridge effect and thereby facilitates the formation of three-dimensional micelle networks leading to gelation at lower concentration. However, as shown in Figure 5, though incorporation of hydrophilic BPEI certainly lowers the critical gelation concentration in comparison

dx.doi.org/10.1021/bc100405c |*Bioconjugate Chem.* 2011, 22, 1031–1038

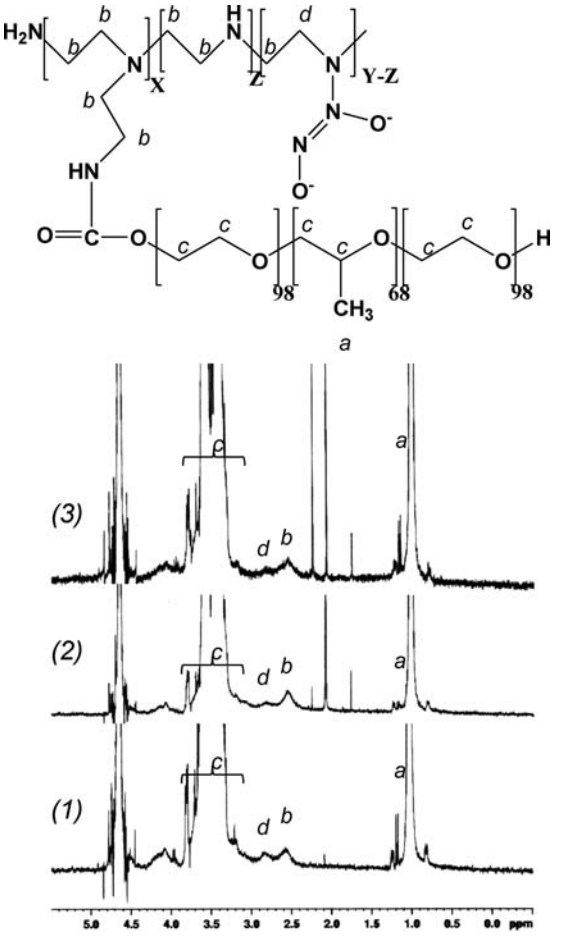


Figure 6. ^{1}H NMR spectra of (1) F127-BPEI0.8-NONOates, (2) F127-BPEM.O-NONOates, and (3) F127-BPEI1.3-NONOates.

to unmodified F127, the trends within F127-BPEI derivatives contradict the above logic. The F127-BPEI polymers with the increasing proportion of BPEI to F127-BPEI, as estimated in F127-BPEI0.8, F127-BPEI1.0, and F127-BPEI1.3, demonstrated gradual increase in critical gelation concentration. Such an increase in critical gelation concentration with increasing BPEI content in F127-BPEI derivatives is in agreement with the observed increase in the critical gelation temperature.[35−38] We assume that, though hydrophilic BPEI moiety favors stabilization of micelle−micelle interaction, the BPEI part might also impart some sort of destabilization to the micelle framework due to the electrostatic repulsion. The BPEI content may influence stabilization and destabilization differently under different concentration.

Synthesis and Characterization of F127-BPEI-NONOates. Three types of F127-BPEI which have secondary amines were modified with NONOates. F127-BPEI-NONOates were synthesized by the method described above (Scheme 1), and the synthesis was confirmed by ^{1}H NMR (Figure 6). In comparison to the proton signals in F127-BPEI, F127-BPEI-NONOates showed a downfield shift of proton signals of methylene groups adjacent to amine sites in BPEI to 3.1 ppm. Therefore, the conjugation ratio of the NONOates to the F127-BPEI could be determined by the same method described earlier. The amounts of NONOate groups that were incorporated in F127-BPEIs during NONOates reaction were found to be 35.1%, 33.1%, and 35.1% for F127-BPEI0.8-NONOates, F127-BPEI1.0-NONOates,

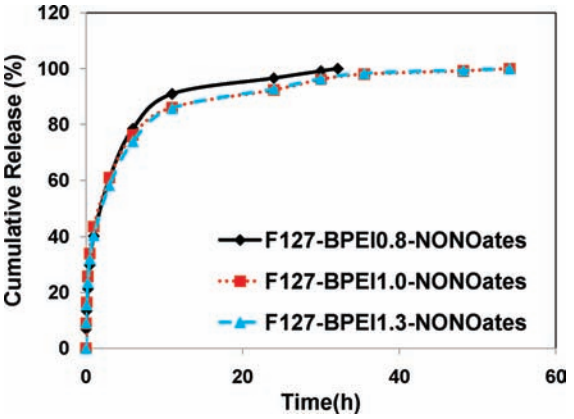


Figure 7. Cumulative NO release (%) from three types of F127-BPEI-NONOates in DPBS at 37 °C. Data are represented as mean ± SD (n = 3).

and F127-BPEI1.3-NONOates, respectively. The extent of conjugation through incorporation of NONOates to F127-BPEI was found to be much higher than that observed for BPEI600-NONOates formation using the same amount of BPEI. This observation could be rationalized by considering the structural features of the polymers. In the case of F127-BPEI, F127 having higher MW acts as a template for BPEI, and therefore, the reactive secondary amine functionalities of BPEI remain largely exposed toward the external agents such as NaOMe and NO gas. On the contrary, these secondary amines are somewhat concealed inside the molecular framework of BPEI, resulting in lower conjugation ratio for BPEI600-NONOates.

NO Release Profile of F127-BPEI-NONOates. We have investigated NO release profile of three types of F127-BPEI-NONOates. The half-life of NO release from F127-BPEI-NONOates was 1.68 to 2.0 h, which was considerably higher compared to unmodified BPEI only (Figure 3, Figure 7, and Table 1). It can be argued that F127-BPEI-NONOates polymer formed a hydrogel at critical concentration and NO was released slowly by the cage recombination effect,[14] which reduces the diffusion of NO in the gel. The NONOate moieties are believed to be encaged inside the gel and such physical shielding averts rapid mixing of NONOate functionalities with water which may otherwise trigger rapid uncontrolled NO release. The slow diffusion of water leads to slow and sustained release of NO. However, the sustainability among F127-BPEI-NONOates does not differ appreciably. On the other hand, as shown in Figure 7, there was a considerable difference in longevity among F127-BPEI-NONOates. In case of F127-BPEI0.8-NONOates, NO release was completed within 32.2 h, while F127-BPEI1.0-NONOates and F127-BPEI1.3-NONOates released NO over an extended period of time. This difference in longevity is considered to be related to the decay process of Pluronic gel. In the case of F127-BPEI0.8-NONOates, gel decayed rapidly after 28 h incubation time, and thus, NO was released rapidly after this point in time. On the other hand, in the case of F127-BPEI1.0-NONOates and F127-BPEI1.3-NONOates, the gel state was maintained up to 54 h incubation time, and after this point, gel started decaying and NO was released rapidly.

In terms of gelation properties as observed in Figure 5, F127-BPEI0.8 forms the most stable gel whereas F127-BPEI1.3 forms the most unstable gel; therefore, it is expected that F127-BPEI0.8-NONOates should release NO during a longer incubation time. However, the reverse trend was observed in the NO

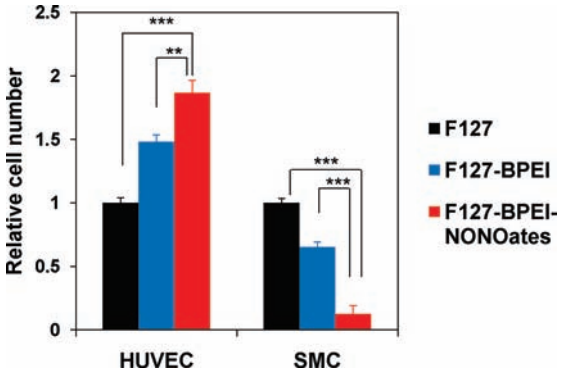


Figure 8. Cellular proliferation test for HUVEC and SMC on F127, F127-BPEI, or F127-BPEI-NONOates-coated plate. Data are represented as a mean ± SD (n = 3). Statistical analysis was done using the Student t test. The symbols **and *** indicate statistical significance at levels of $p < 0.01$ and $p < 0.001$, respectively.

release profile of F127-BPEI0.8-NONOates. These results could be explained by the salting-out effect as reported by Silvia Mike Shishido et al.[14] Generally, adding a salting-out salt such as NaCl to the thermosensitive gel reduces critical micelle concentration (cmc) and accelerates stable gelation at low temperature and concentration, while salting-in salt such as NaSCN increases cmc. Salting-out salts such as NONOates and its derivatives, NO^{2-} and NO^{3-}, which are generated from F127-BPEI-NONOates gel accelerate gelation and thus stabilize gels. Therefore, F127-BPEI1.0-NONOates and F127-BPEI1.3-NONOates gels in which larger amount of NONOates are conjugated in gels are more stable than F127-BPEI0.8-NONOates due to the salting-out effect. The salting-out effect of NONOates is different with a mixed system. In the report of Silvia et al., *S*-nitrosothiol was mixed with F127, and gelation temperature of F127 was increased by the salting-in effect of *S*-nitrosothiol and its salt. However, the gelation temperature of the NONOates-conjugated system in F127 was decreased, implying stabilization of the gel formation by the salting-out effect, although the precise mechanism was not explored yet. These results imply that conjugation to F127 is more useful to the cage effect-mediated gel system than a simple mixing system.

Considering the practical use of this NO-hydrogel system in vivo, the NO release profile in varied conditions needs to be investigated such as under hypoxic vs normoxic and different pH conditions. Accordingly, we investigated the NO release profile under hypoxic as well as normoxic conditions. For the hypoxic condition, we added DPBS to the F127-BPEI1.3-NONOates hydrogel under the N_2-purged condition and then monitored NO release. As shown in Supporting Information Figure S2, the NO release pattern under hypoxic conditions was similar to that observed under normoxic condition. We also evaluated pH-dependency of NO release from NONOates hydrogel. The NONOates hydrogel (F127-BPEI1.3-NONOates) was formed, and then DPBS at various pH conditions (pH 5.2, 7.0, and 9.0) was added to the hydrogel to initiate the NO release. The pH-dependency of the NO release was shown in Supporting Information Figure S3. The NO release pattern did not vary at different pH conditions of releasing buffer surrounding the hydrogel. These results conform to those reported by Masters et al.[39]

In Vitro Cell Proliferation Test. NO has been known to accelerate endothelial cell proliferation and inhibit smooth muscle cell proliferation[12,20] when administered in optimal amounts. To ascertain the effectiveness of NONOates-hydrogel in releasing NO in a controlled manner and at a prolonged time span, we have investigated the HUVEC and SMC proliferation study on the cell culture plates coated with F127, F127-BPEI, and NO-releasing F127-BPEI-NONOates. As shown in Figure 8, F127-BPEI-NONOates demonstrated 48.1% and 26.1% enhancement in the proliferation of HUVEC compared to those achieved by F127 and F127-BPEI mediated proliferation, respectively. Furthermore, the proliferation of SMC was significantly reduced by 35.0% and 80.8% on the F127-BPEI-NONOates-coated plates compared to F127 and F127-BPEI-coated plates, respectively. It was known that inhibition of smooth muscle cell proliferation had a pronounced effect on the blocking restenosis, as well as that exerted by acceleration of endothelial cells.[40,41] Therefore, this hydrogel-based NO-releasing system could provide an efficient strategy to inhibit restenosis. The observation clearly substantiates the effectiveness of F127-BPEI-NONOates in enhancing HUVEC proliferation and inhibiting SMC proliferation through sustained release of NO. Therefore, F127-BPEI-NONOates could be applied as stent coating materials to accomplish efficient restenosis inhibition.

CONCLUSION

In this study, we have successfully developed NO-releasing polymers which can release NO slowly over an extended period of time. The NO-release profile varies with the change in the MW of BPEI conjugated to the F127. This unique feature obviously enables us to modulate the NO-release profile easily by altering the MW of BPEI and thus provides us with the simple and facile strategy to manipulate the NO-release profile and design an optimal NO-release polymer. Apart from the manipulation in conjugation ratio, application of various NO donor polymers could also be exploited to develop an efficient stent coating material to inhibit restenosis.

ASSOCIATED CONTENT

Supporting Information. FT-IR and NO release data under hypoxic vs normoxic and different pH condition and elemental analysis are available. This material is available free of charge via the Internet at http://pubs.acs.org.

AUTHOR INFORMATION

Corresponding Author

*Won Jong Kim, Department of Chemistry, Pohang University of Science and Technology, Pohang 790-784, Korea. Phone: 82-54-279-2104. Fax: 82-54-279-3399. E-mail: wjkim@postech.ac.kr.

ACKNOWLEDGMENT

This work supported by the Pioneer Research Center Program (20100002175) and Bio R&D Program (20100019914) through the National Research Foundation of Korea (NRF) funded by the Ministry of Education, Science and Technology, and by a grant (K0006028) from the Fundamental R&D Program for Core Technology of Materials funded by the Ministry of Knowledge Economy, Republic of Korea.

REFERENCES

(1) Vural, K. M., and Bayazit, M. (2001) Nitric oxide: implications for vascular and endovascular surgery. *Eur. J. Vasc. Endovasc. Surg. 22*, 285–293.

(2) Chen, C., Shi, Y., Li, S., Qi, Q., Gu, L., Song, J., and Wang, P. G. (2006) A glycosylated nitric oxide donor, beta-Gal-NONOate, and its site-specific antitumor activity. *Arch. Pharm. Chem. Life Sci. 339*, 366–371.

(3) Feldman, P. L., Griffith, O. W., and Stuehr, D. J. (1993) The surprising life of nitric-oxide. *Chem. Eng. News 71*, 26–38.

(4) Loscalzo, J., and Welch, G. (1995) Nitric oxide and its role in the cardiovascular system. *Prog. Cardiovasc. Dis. 38*, 87–104.

(5) Loscalzo, J. (1996) Nitric oxide and restenosis. *Clin. Appl. Thromb/Hemostas. 2*, 7–10.

(6) Guo, J. P., Milhoan, K. A., Tuan, R. S., and Lefer, A. M. (1994) Beneficial effect of SPM-5185, a cysteine-containing nitric oxide donor, in rat carotid artery intimal injury. *Circ. Res. 75*, 77–84.

(7) von der Leyen, H. E., Gibbons, G. H., Morishita, R., Lewis, N. P., Zhang, L., Nakajima, M., Kaneda, Y., Cooke, J. P., and Dzau, V. J. (1995) Gene therapy inhibiting neointimal vascular lesion: in vivo transfer of endothelial cell nitric oxide synthase gene. *Proc. Natl. Acad. Sci. U.S.A. 92*, 1137–1141.

(8) Mowery, K. A., Schoenfisch, M. H., Saavedra, J. E., Keefer, L. K., and Meyerhoff, M. E. (2000) Preparation and characterization of hydrophobic polymeric films that are thromboresistant via nitric oxide release. *Biomaterials 21*, 9–21.

(9) Mocellin, S., Bronte, V., and Nitti, D. (2007) Nitric oxide, a double edged sword in cancer biology: searching for therapeutic opportunities. *Med. Res. Rev. 27*, 317–352.

(10) Chung, S. J., and Fung, H. L. (1990) Identification of the subcellular site for nitroglycerin metabolism to nitric oxide in bovine coronary smooth muscle cells. *J. Pharmacol. Exp. Ther. 253*, 614–619.

(11) Page, I. H., Corcoran, A. C., Dustan, H. P., and Koppanyi, T. (1955) Cardiovascular actions of sodium nitroprusside in animals and hypertensive patients. *Circulation 11*, 188–198.

(12) Bohl, K. S., and West, J. L. (2000) Nitric oxide-generating polymers reduce platelet adhesion and smooth muscle cell proliferation. *Biomaterials 21*, 2273–2278.

(13) Seabra, A. B., Pankotai, E., Feher, M., Somlai, A., Kiss, L., Biro, L., Szabo, C., Kollai, M., de Oliveira, M. G., and Lacza, Z. (2007) *S*-nitrosoglutathione-containing hydrogel increases dermal blood flow in streptozotocin-induced diabetic rats. *Br. J. Dermatol. 156*, 814–818.

(14) Shishido, S. M., Seabra, A. B., Loh, W., and de Oliveira, M. G. (2003) Thermal and photochemical nitric oxide release from *S*-nitrosothiols incorporated in Pluronic F127 gel: potential uses for local and controlled nitric oxide release. *Biomaterials 24*, 3543–3553.

(15) Seabra, A. B., and De Oliveira, M. G. (2004) Poly(vinyl alcohol) and poly(vinyl pyrrolidone) blended films for local nitric oxide release. *Biomaterials 25*, 3773–3782.

(16) Burgaud, J. L., Ongini, E., and Del Soldato, P. (2002) Nitric oxide-releasing drugs: a novel class of effective and safe therapeutic agents. *Ann. N.Y. Acad. Sci. 962*, 360–371.

(17) Gao, J., Liu, X., and Rigas, B. (2005) Nitric oxide-donating aspirin induces apoptosis in human colon cancer cells through induction of oxidative stress. *Proc. Natl. Acad. Sci. U.S.A. 102*, 17207–17212.

(18) Parinandi, N. L., Sharma, A., Eubank, T. D., Kaufman, B. F., Kutala, V. K., Marsh, C. B., Ignarro, L. J., and Kuppusamy, P. (2007) Nitroaspirin (NCX-4016), an NO donor, is antiangiogenic through induction of loss of redox-dependent viability and cytoskeletal reorganization in endothelial cells. *Antioxid. Redox. Signal. 9*, 1837–1849.

(19) Zhou, Z., Annich, G. M., Wu, Y., and Meyerhoff, M. E. (2006) Water-soluble poly(ethylenimine)-based nitric oxide donors: preparation, characterization, and potential application in hemodialysis. *Biomacromolecules 7*, 2565–2574.

(20) Taite, L. J., Yang, P., Jun, H. W., and West, J. L. (2008) Nitric oxide-releasing polyurethane-PEG copolymer containing the YIGSR peptide promotes endothelialization with decreased platelet adhesion. *J. Biomed. Mater. Res. B: Appl. Biomater. 84*, 108–116.

(21) Janero, D. R., and Ewing, J. F. (2000) Nitric oxide and postangioplasty restenosis: pathological correlates and therapeutic potential. *Free Radic. Biol. Med. 29*, 1199–1221.

(22) Stasko, N. A., and Schoenfisch, M. H. (2006) Dendrimers as a scaffold for nitric oxide release. *J. Am. Chem. Soc. 128*, 8265–8271.

(23) Shin, J. H., Metzger, S. K., and Schoenfisch, M. H. (2007) Synthesis of nitric oxide-releasing silica nanoparticles. *J. Am. Chem. Soc. 129*, 4612–4619.

(24) Rothrock, A. R., Donkers, R. L., and Schoenfisch, M. H. (2005) Synthesis of nitric oxide-releasing gold nanoparticles. *J. Am. Chem. Soc. 127*, 9362–9363.

(25) Jo, Y. S., van der Vlies, A. J., Gantz, J., Thacher, T. N., Antonijevic, S., Cavadini, S., Demurtas, D., Stergiopulos, N., and Hubbell, J. A. (2009) Micelles for delivery of nitric oxide. *J. Am. Chem. Soc. 131*, 14413–14418.

(26) Hrabie, J. A., and Keefer, L. K. (2002) Chemistry of the nitric oxide-releasing diazeniumdiolate ("nitrosohydroxylamine") functional group and its oxygen-substituted derivatives. *Chem. Rev. 102*, 1135–1154.

(27) Zhang, H., Annich, G. M., Miskulin, J., Osterholzer, K., Merz, S. I., Bartlett, R. H., and Meyerhoff, M. E. (2002) Nitric oxide releasing silicone rubbers with improved blood compatibility: preparation, characterization, and in vivo evaluation. *Biomaterials 23*, 1485–1494.

(28) Smith, D. J., Chakravarthy, D., Pulfer, S., Simmons, M. L., Hrabie, J. A., Citro, M. L., Saavedra, J. E., Davies, K. M., Hutsell, T. C., Mooradian, D. L., Hanson, S. R., and Keefer, L. K. (1996) Nitric oxide-releasing polymers containing the [N(O)NO]- group. *J. Med. Chem. 39*, 1148–1156.

(29) Yamamoto, T., and Bing, R. J. (2000) Nitric oxide donors. *Proc. Soc. Exp. Biol. Med. 225*, 200–206.

(30) Lee, J. I., and Yoo, H. S. (2008) Pluronic decorated-nanogels with temperature-responsive volume transitions, cytotoxicities, and transfection efficiencies. *Eur. J. Pharm. Biopharm. 70*, 506–513.

(31) Choi, S. H., Lee, S. H., and Park, T. G. (2006) Temperature-sensitive pluronic/poly(ethylenimine) nanocapsules for thermally triggered disruption of intracellular endosomal compartment. *Biomacromolecules 7*, 1864–1870.

(32) Chung, H. J., Lee, Y., and Park, T. G. (2008) Thermo-sensitive and biodegradable hydrogels based on stereocomplexed Pluronic multiblock copolymers for controlled protein delivery. *J. Controlled Release 127*, 22–30.

(33) Choi, B. G., Park, M. H., Cho, S. H., Joo, M. K., Oh, H. J., Kim, E. H., Park, K., Han, D. K., and Jeong, B. (2010) In situ thermal gelling polypeptide for chondrocytes 3D culture. *Biomaterials 31*, 9266–9272.

(34) Shin, J. H., and Schoenfisch, M. H. (2008) Inorganic/Organic hybrid silica nanoparticles as a nitric oxide delivery scaffold. *Chem. Mater. 20*, 239–249.

(35) Zhang, H., Yu, L., and Ding, J. (2008) Roles of hydrophilic homopolymers on the hydrophobic-association-induced physical gelling of amphiphilic block copolymers in water. *Macromolecules 41*, 6493–6499.

(36) Yu, L., Zhang, Z., Zhang, H., and Ding, J. (2009) Mixing a sol and a precipitate of block copolymers with different block ratios leads to an injectable hydrogel. *Biomacromolecules 10*, 1547–1553.

(37) Garripelli, V. K., Kim, J. K., Namgung, R., Kim, W. J., Repka, M. A., and Jo, S. (2010) A novel thermosensitive polymer with pH-dependent degradation for drug delivery. *Acta Biomater. 6*, 477–485.

(38) Jeong, B., Bae, Y. H., and Kim, S. W. (1999) Thermoreversible gelation of PEG-PLGA-PEG triblock copolymer aqueous solutions. *Macromolecules 32*, 7064–7069.

(39) Masters, K. S., Leibovich, S. J., Belem, P., West, J. L., and Poole-Warren, L. A. (2002) Effects of nitric oxide releasing poly(vinyl alcohol) hydrogel dressings on dermal wound healing in diabetic mice. *Wound Repair Regen. 10*, 286–294.

(40) Bauters, C., and Isner, J. M. (1997) The biology of restenosis. *Prog. Cardiovasc. Dis. 40*, 107–116.

(41) Sarkar, R., and Webb, R. C. (1998) Does nitric oxide regulate smooth muscle cell proliferation? A critical appraisal. *J. Vasc. Res. 35*, 135–142.

SUPPORTING INFORMATION

NONOATES-POLYETHYLENIMINE HYDROGEL FOR CONTROLLED NITRIC OXIDE RELEASE AND CELL PROLIFERATION MODULATION

Jihoon Kim, Yanggy Lee, Kaushik Singha, Hyun Woo Kim, Jae Ho Shin, Seongbong Jo, Dong-Keun Han, Won Jong Kim*

Figure S1. FT-IR spectra of F127-BPEI1.3 and F127-BPEI1.3-NONOates

Fourier transform infrared (FT-IR) spectra were recorded on a BRUKER VORTEX 70 spectrometer over the frequency range 2300−700 cm^{-1} system using KBr as media.

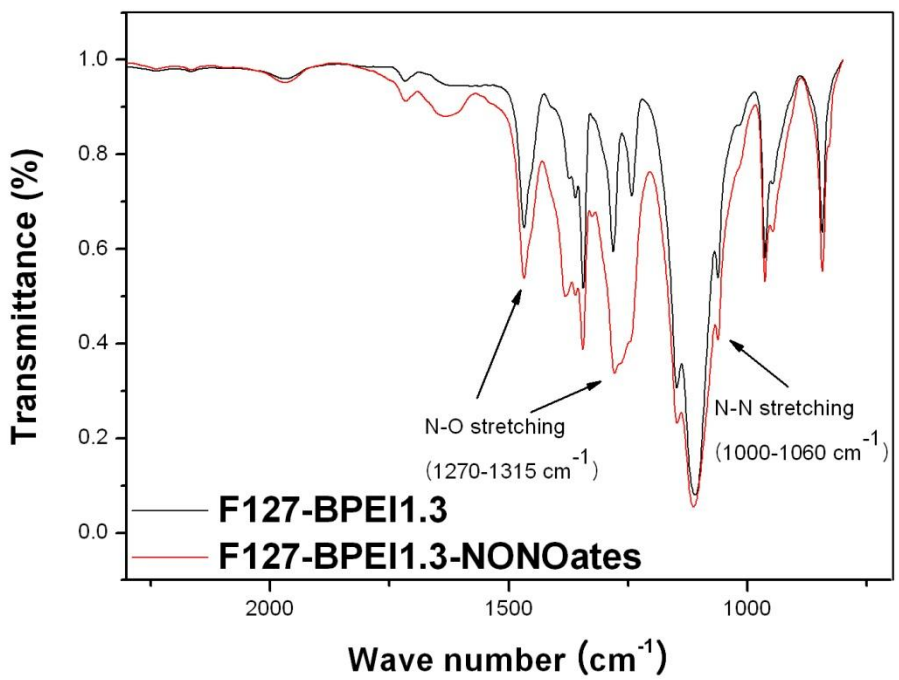


Figure S1. FT-IR spectra of F127-BPEI1.3 and F127-BPEI1.3-NONOates

Figure S2. Measurement of NO release in normoxic and hypoxic condition

F127-BPEI1.3-NONOates (75 mg) was dissolved in deionized water at 4 ˚C to prepare 20 wt% solutions and incubated in 300 mL N_2-purged DPBS at 37 ˚C. Release of NO was monitored using the Griess assay (Promega). In brief, after sampling 300 mL in predetermined time intervals, fresh N_2-purged DPBS (300 mL) was added to the vial. A sample (50 mL) was added to a sulfanilamide solution (50 mL) and incubated at room temperature for 5 min, protected from light. Then, naphthylethylenediamine (50 mL) was added to the mixture to stimulate a colorimetric change; intensity was measured at 548 nm by microplate spectrofluorometer (VICTOR3 V Multilabel Counter, Perkin-Elmer, Wellesley, MA) and compared to known sodium nitrite standards.

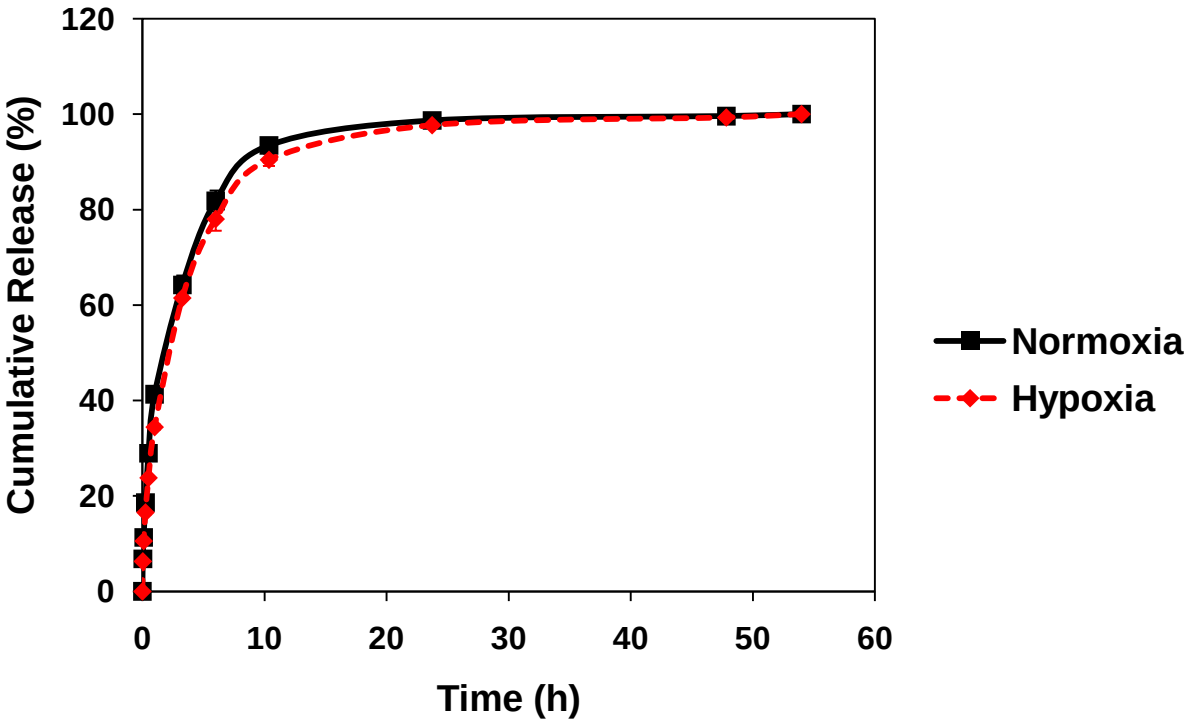


Figure S2. Cumulative NO release (%) from F127-BPEI1.3-NONOates in normoxic and hypoxic condition at 37 °C. Data are represented as a mean ±SD (n=3).

Figure S3. Measurement of NO release in different pH

F127-BPEI1.3-NONOates (75 mg) was dissolved in deionized water at 4 ˚C to prepare 20wt% solutions and incubated in 300 mL DPBS with different pH adjusted by NaOH and HCl at 37 ˚C. Release of NO was monitored using the Griess assay (Promega).

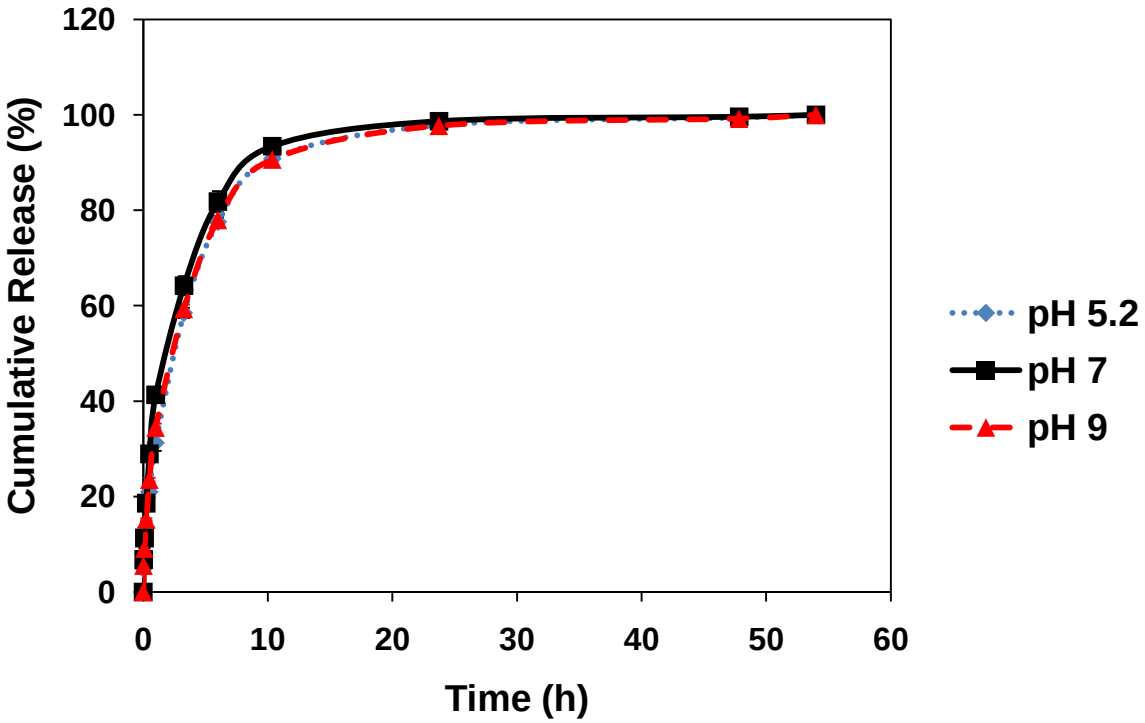


Figure S3. Cumulative NO release (%) from F127-BPEI1.3-NONOates in DPBS at 37 ˚C at different pH. Data are represented as a mean ±SD (n=3).

Table S1. Nitrogen Content (w%,N), Amine Concentration (C_{amine}), N-Diazeniumdiolate Concentration (C_{diaz}), and Amine to N-Diazeniumdiolate Conversion Efficiency (% Conv) of Various F127-BPEI-NONOates[a]

	N (w%)[b]	C_{amine} (μmol/mg)[c]	C_{diaz} (μmol/mg)[d]	% conv[e]
F127-BPEI0.8-NONOates	3.12	2.22	1.10	32.9
F127-BPEI1.0-NONOates	3.05	2.17	0.99	29.6
F127-BPEI1.3-NONOates	3.43	2.45	1.38	39.2

[a] Determined by Griess assay in DPBS at 37 °C and elemental analysis. [b] Weight percent of nitrogen in products using elemental analsysis. [c] Total amine concentration in products by calculating the elemental analysis [d] Total NO concentration released from the products determined by Griess assay. [e] NONOates conversion efficiency of total amine.

Bioconjugate Chemistry

ARTICLE

pubs.acs.org/bc

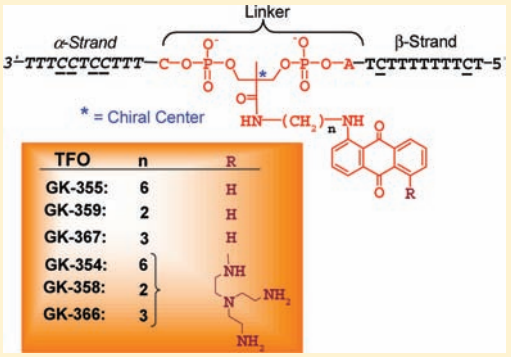
Stabilizing Effect of Propionic Acid Derivative of Anthraquinone−Polyamine Conjugate Incorporated into α−β Chimeric Oligonucleotides on the Alternate-Stranded Triple Helix

Tomohisa Moriguchi, A. T. M. Zafrul Azam,[†] and Kazuo Shinozuka*

Department of Chemistry and Chemical Biology, Graduate School of Engineering, Gunma University, 1-5-1 Tenjin-cho, Kiryu, Gunma 376-8515, Japan

Supporting Information

ABSTRACT: Two types of anthraquinone conjugates were synthesized as non-nucleosidic oligonucleotide components. These include an anthraquinone derivative conjugated with 2,2-bis(hydroxymethyl)propionic acid and an anthraquinone−polyamine derivative conjugated with 2,2-bis(hydroxymethyl)propionic acid. The conjugates were successfully incorporated into the "linking-region" of the α−β chimeric oligonucleotides via phosphoramidite method as non-nucleosidic backbone units. The resultant novel α−β chimeric oligonucleotides possessed two diastereomers that were generated by the introduction of the anthraquinone conjugate with a stereogenic carbon atom. The isomers were successfully separated by a reversed-phase HPLC. UV-melting experiments revealed that both stereoisomers formed a substantially stable alternate-strand triple helix, irrespective of the stereochemistry of the incorporated non-nucleosidic backbone unit. However, the enhancing effect on thermal stability depended on the length of the alkyl linker connecting anthraquinone moiety and the propionic acid moiety. The sequence discrimination ability of the chimeric oligonucleotides toward mismatch target duplex was also examined. The T_m values of the triplexes containing the mismatch target were substantially lower than the T_m values of those containing the full-match target. The thermodynamic parameters ($\Delta H°$, $\Delta S°$, and $\Delta G°$) required for the dissociation of the triplexes into the third strand and target duplex were also measured.



INTRODUCTION

Synthetic oligonucleotide-directed triple-helix formation presents a promising way to interfere with gene expression through direct interaction with genomic dsDNA and has become an area of intense investigation,[1−4] as demonstrated by many recent *in vitro* and *in vivo* experiments.[5−7] Indeed, the oligonucleotides forming a triplex with certain gene promoters can modulate the level of transcription of that gene (antigene strategy).[8−11] The limitation to the application of this approach in therapeutics and biotechnology is related to the relatively low stability of triple helical complexes under physiological conditions; sufficiently stable triplexes can be obtained only by targeting substantially long (at least 16−17 bases) tracts of homopurines, which are rarely found in biologically relevant DNA sequences. Considerable effort has been devoted to overcoming such limitations of the antigene strategy. A possible method to extend the range of targets is to utilize a specifically designed triplex forming oligonucleotide (TFO) capable of forming a triplex with adjacent and alternating homopurine strands because such a sequence would be more conceivable. On the basis this logic, Horne and Dervan reported a unique type of TFO consisting of 3′-3′ linked polythymidylate.[12] In the TFO, two short homopyrimidine strands were coupled by 1,2-dideoxy-D-ribose through a 3′-3′ phosphodiester linkage. Thus, the TFO formed a so-called "alternate-stranded triplex" with an adjacent and alternating homopurine strand in the manner of parallel orientation through Hoogsteen hydrogen bonds. In the TFO, the 1,2-dideoxy-D-ribose moiety served as the "linker" portion connecting two independent TFO molecules.

Many 3′-3′ or 5′-5′ linked TFOs capable of forming an alternate-strand triple helix by switching strand at the junction between the oligopurine and the oligopyrimidine domain via a Hoogsteen-hydrogen bonding pattern were reported.[13−22] However, these TFOs are constructed with a natural β-anomeric polypyrimidine strand in combination with a specifically designed "linker molecule". To create a new class of TFOs based on the strategy described above, we have developed a unique class of chimeric TFOs composed of a contiguous β-anomeric polypyrimidine strand and an α-anomeric polypyrimidine strand.[23] In the TFO, mononucleotide units are connected through natural 3′-5′ phosphodiester linkages, although the 3′-half of the linkage exclusively consists of α-anomeric polypyrimidylate, and the

Received: October 10, 2010
Revised: March 29, 2011
Published: May 02, 2011

ACS Publications © 2011 American Chemical Society

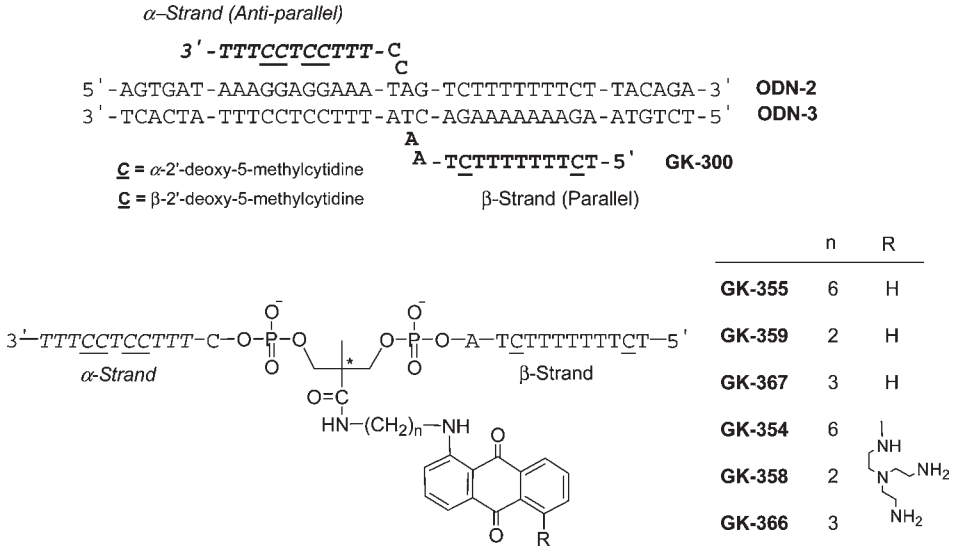


Figure 1. Sequence and structure of α–β chimeric TFO. In the sequence, italic letters represent the α-anomeric polypyrimidylate component and Roman letters represent the β-anomeric polypyrimidylate component, respectively. The linker portion of the chimera TFO consist of a β-anomeric 5′-AACC-3′ sequence in **GK-300**, whereas AC of the portion is replaced with a non-nucleotidic anthraquinone bearing unit in modified TFOs.

remaining portion consists of β-anomeric polypyrimidylate. In the TFO, the 3′-half binds to the purine tract of a target dsDNA in an antiparallel orientation, while the remaining β-DNA portion, except that which serves as a "linker" connecting the α- and β-DNA portions, binds to another purine tract in a parallel orientation.

Several approaches have been attempted to stabilize the triple helix, which is relatively less stable than the double helix. One approach is the conjugation of the intercalation moiety to TFO.[23−28] In this study, we found that the substitution of a normal nucleoside unit in the linker region of the original chimeric TFO[29] with a multiconjugate of the non-nucleosidic unit, 2,2-bis(hydroxymethyl)propionic acid, and an intercalator-polyamine complex substantially improves the thermal stability of the resulting alternate-strand triplex. This may be due to the intercalation of the complex to the target dsDNA.[30,31] In this paper, we will describe the results of our detailed study on the triplex-forming ability of the modified complex including the triplex-stabilizing effect of the polyamine moiety connected to the intercalator and the length of the alkyl chain linking the non-nucleosidic unit and the complex, as well as the sequence-discriminating ability of the modified chimeric TFO.

RESULTS AND DISCUSSION

Synthesis and Purification of Modified α–β Chimeric TFOs with an Anthraquinone Conjugate as a Non-Nucleosidic Oligonucleotide Component. Two types of anthraquinone conjugates were utilized as non-nucleosidic oligonucleotide components. These included an anthraquinone derivative conjugated with 2,2-bis(hydroxymethyl)propionic acid and an anthraquinone–polyamine derivative conjugated with 2,2-bis-(hydroxymethyl)propionic acid.[32] Synthesis of the modified chimeric chimeric triplex forming oligonucleotides (TFOs), **GK-354**, **GK-355**, **GK-358**, **GK-359**, **GK-366**, and **GK-367** along with the parental unmodified chimeric TFO (**GK-300**) (Figure 1) were carried out by an automated DNA synthesizer starting from CPG-bound α-thymidine, which was prepared

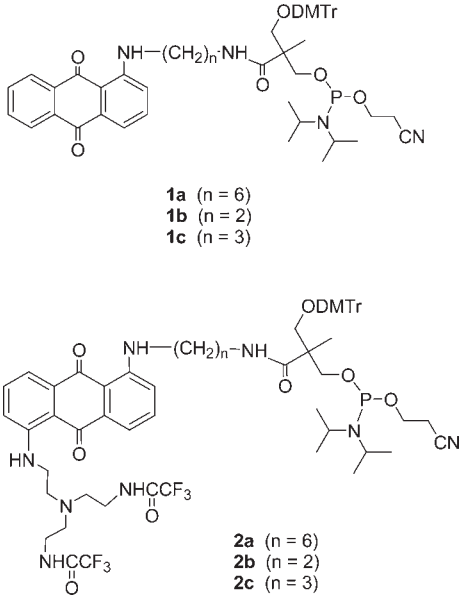


Figure 2. Structure of the phosphoramidite derivatives **1** and **2** bearing conjugated anthraquinone.

according to a previously described procedure.[32] The phosphoramidite derivatives bearing conjugated-anthraquinone (**1a**,**b**,**c** and **2a**,**b**,**c**, Figure 2) were incorporated into the middle of the "linker" region of the chimera TFOs instead of a normal nucleotide unit. It should be noted that, in the chimera TFOs, the central 5′-AC-3′ portion of the linker region of the parental **GK-300** was substituted with the conjugate as shown in Figure 1. The coupling reaction of the phosphoramidite reagents of anthraquinone conjugate was carried out for 360 s with a double coupling procedure using 0.3 M CH_3CN solution instead of normally used 0.1 M solution. Under the conditions, the coupling yields of **1a**,**b**,**c** and **2a**,**b**,**c** estimated from the conventional trityl assay were 93%, 86%, 88%, 93%, 96%, and 90%, respectively. The incorporation of other unnatural α-nucleoside

units into the chimera TFO was also accomplished within the extended coupling period (360 s). The obtained CPG-bound oligomers were treated with concentrated ammonia at 55 °C for 12 h.

The obtained oligomers were purified by reversed-phase HPLC. As stated previously, the DMTr-off form of the α−β chimeric oligonucleotides bearing the anthraquinone conjugates gave two peaks with almost equal intensity because of the existence of diastereomers. Thus, the faster elutes (**GK-354A**, **GK-355A**, **GK-358A**, **GK-359A**, **GK-366A**, and **GK-367A**) and the slower elutes (**GK-354B**, **GK-355B**, **GK-358B**, **GK-359B**, **GK-366B**, and **GK-367B**) were separately isolated. The oligomers were further purified by ethanol precipitation followed by Sephadex G-25 gel filtration. The modified TFO, **GK-368**, with a 3-nucleotide (nt) linker (5′-AAC-3′, Figure 3) was also synthesized as the reference oligomer according to standard solid-phase DNA synthesis. The yield and characterization data of the oligomers are listed in Supporting Information Table S1.

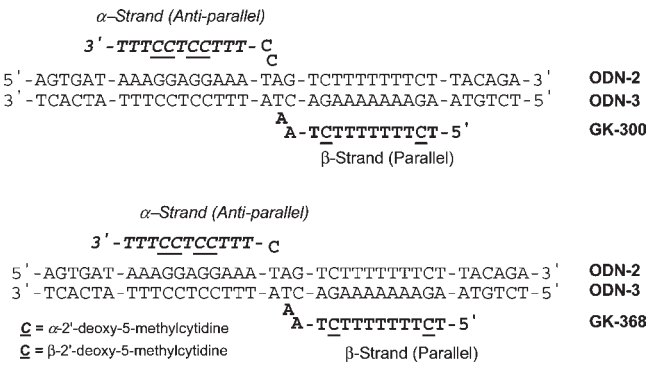


Figure 3. Sequence and structure of α−β chimeric TFO (**GK-300** and **GK-368**). In the sequence, italic letters represent the α-anomeric polypyrimidylate component and Roman letters represent the β-anomeric polypyrimidylate component, respectively. The linker portion of the chimera TFO consist of a β-anomeric 5′-AACC-3′ sequence in **GK-300** and β-anomeric 5′-AAC-3′ sequence in **GK-368**.

UV-Melting Experiment of Chimera TFOs. The formation and thermal stability of the triplex were examined by UV-melting experiments under slightly acidic and neutral conditions (pH 6.1, 6.5, and 7.0) in appropriate buffer systems. The melting temperature (T_m) was calculated from the first derivative of the melting curve obtained (Supporting Information Figures S1−S3) for all the system studied, and the results are summarized in Table 1. **GK-368** with the 3-nt linker stabilizes the triplex more efficiently than **GK-300** with the 4-nt linker (ΔT_m > 2.5 °C) at all pH values. Thus, the use of 3-nt linker instead of the original 4-nt linker in chimera TFOs is more feasible for the triplex formation. In addition, all modified TFOs with the anthraquinone moiety formed a much more stable triplex than the unmodified **GK-300** and **GK-368**. The magnitude of the stabilizing effect on modified TFOs for the triple helix, however, varied considerably. TFOs with a longer linker arm between the anthraquinone and 2,2-bis(hydroxymethyl)propionic acid moieties tend to form a more stable triplex than those with a shorter linker arm.

As shown in Table 1, the T_m values of the triplex consisting of modified TFO and full-matched target (**ODN-2**:**ODN-3**) are considerably higher (ΔT_m > 10−17 °C) than that of the triplex containing unmodified **GK-300**. The triplex-stabilizing effect, however, depends on the length of the alkyl linker connecting the anthraquinone and propionic acid moieties in the incorporated anthraquinone conjugate. Thus, the TFO bearing a longer alkyl linker (**GK-354** and **GK-355**) exhibited higher T_m values compared to the TFO bearing a shorter alkyl linker (**GK-358**, **-359**, **-366**, **-367**). On the other hand, no apparent difference in thermal stability was observed between the TFOs consisting of two carbon alkyl linkers (**GK-358** and **GK-359**) and three carbon alkyl linkers (**GK-366** and **GK-367**) at pH 6.1 (Table 1).

Table 1. Melting Temperature (T_m) of the Triplex and Full-Match Duplex (ODN-2:ODN-3) at Different pH Levels

		T_m[b] (full-match)								
		pH 6.1			pH 6.5			pH 7.0		
TFO	n[a]	triplex	ΔT_m[c]	ΔT_m[d]	triplex	ΔT_m[c]	ΔT_m[d]	triplex	ΔT_m[c]	ΔT_m[d]
GK-300	-	40.0	-		35.8	-		23.6	-	
GK-368	-	43.2	3.2		38.3	2.5		26.4	2.8	
GK-355A	6	55.7	15.7		49.6	13.8		38.5	14.9	
GK-355B	6	56.9	16.9	1.2	51.4	15.6	1.8	38.3	14.7	−0.2
GK-359A	2	51.2	11.2		45.6	9.8		32.9	9.3	
GK-359B	2	51.5	11.5	0.3	45.3	9.5	−0.3	33.4	9.8	0.5
GK-367A	3	51.5	11.5		-	-	-	-	-	-
GK-367B	3	51.6	11.6	0.1	-	-	-	-	-	-
GK-354A	6	56.2	16.2		50.3	14.5		40.4	16.8	
GK-354B	6	57.5	17.5	1.3	51.2	15.4	0.9	40.2	16.6	−0.2
GK-358A	2	53.0	13.0		46.4	10.6		35.5	11.9	
GK-358B	2	52.8	12.8	−0.2	46.6	10.8	0.2	36.4	12.8	0.9
GK-366A	3	53.1	13.1		-	-	-	-	-	-
GK-366B	3	53.2	13.2	0.1	-	-	-	-	-	-

[a] n indicates the amount of carbon in the alkyl linker that connects anthraquinone moiety with the propionic acid moiety. [b] T_m values (°C) were determined by computer fitting of the first derivative of the absorbance with respect to $1/T$. Each T_m value is the average of three separate experiments. [c] ΔT_m indicates the deviation from the T_m value of the corresponding triplex consisting of **GK-300** and the duplex. [d] ΔT_m indicates the T_m differences between diastereomeric counterparts.

dx.doi.org/10.1021/bc100446w |*Bioconjugate Chem.* 2011, 22, 1039–1045

The T_m values tend to depend on the pH of the media. The T_m values showed a greater decrease at high pH values than at low pH values. For example, the T_m of **GK-354A** decreased from 56.2 to 40.4 °C when the pH changes from 6.1 to 7.0. This may be due to inadequate protonation of cytidine residues in the TFOs. However, even at pH 7.0, the T_m values of **GK-354** and **GK-355** exceeded the physiological temperature.

Interestingly, the data in Table 1 also reveal that the difference in the T_m values between the two diastereomers **A** and **B** was very low in all TFOs at all pH values (<1.5 °C). This small difference in the T_m values between the diastereomers indicates that the environment around the linker region of the modified TFOs is very flexible. It also suggests that it is highly versatile, since the modification at the linker region of the chimera TFOs with this type of non-nucleosidic unit can functionalize it without taking into account the stereochemistry of the modification. Thus, both **GK-354A** and **GK-354B** stabilized an alternate-strand triplex at a temperature of >16 °C with a single modification of the parental chimera TFO.

Sequence Discrimination Ability of the Modified Chimera TFOs. Generally, the thermal stability of a triplex decreases substantially (>10 °C) in the case of a mismatch between the TFO and the target duplex.[33] To estimate the specificity of modified TFOs in triplex formation, a single mismatch target duplex **ODN-4:ODN-5** was prepared as shown in Figure 4. The T_m values of the triplex consisting of the modified chimera TFO and the mismatch target duplex were measured using the thermal denaturation study, as described in the previous section.

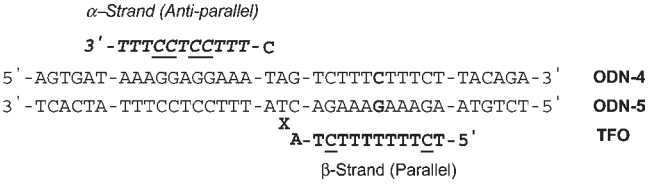


Figure 4. Alternate-stranded triplex consisting of modified chimera TFOs and single mismatch target duplex (**ODN-4:ODN-5**). X represents the non-nucleosidic anthraquinone conjugate.

The T_m values of the triplexes consisting of the modified TFOs and the mismatched target (**ODN-4:ODN-5**) decreased significantly as shown in Table 2. The magnitude of T_m decrement for the tested TFOs was nearly the same as that of the parental unmodified **GK-300** at all pH values (6.1, 6.5, and 7.0). The results clearly indicate that the modified TFO retains at least the same degree of sequence discrimination ability as the unmodified TFO. Thus, the introduction of the intercalator−propionic acid conjugate to the chimeric TFO will not abolish its ability to discriminate between sequences, despite apparent enhancement of the thermal stability with the full-matched target.

The magnitude of T_m decrement with respect to the corresponding diastereomer is also quite small, as shown in Table 2. Thus, the results clearly indicate that the sequence discrimination ability of the modified TFOs is not influenced by the existence of the stereogenic carbon in them.

Effect of Polyamine Moiety on the Thermal Stability of the Alternate-Strand Triplex. To check the effect of polyamine moiety on the thermal stability of the alternate-strand triplex, T_m differences among the sets of corresponding TFOs with or without the polyamine moiety on the anthraquinone moiety were analyzed. As shown in Table 3, T_m values increased in the presence of polyamine in the TFO, but only by a small margin (0.2−3.0 °C). Such smaller T_m increments might be due to the apparent distance of the polyamine moiety from the interacting target duplex. In the case of the short alkyl linker between anthraquinone and 2,2-bis(hydroxymethyl)propionic acid (**GK-359** and **GK-358**), the T_m increment was slightly higher (2.0−3.0 °C) than that in the case of the long alkyl linker (**GK-355** and **GK-354**), because of the presence of the polyamine moiety on the anthraquinone moiety. In this case, the polyamine moiety could interact with the target duplex more easily than in the above case. This notion can be supported by the observation of similar effects of the polyamine moiety on the thermal stability of the triplex consisting of modified TFOs and single mismatch target duplex (Table 3, mismatch).

Temperature-Dependent UV-Absorption Changes of the Anthraquinone Moiety. To confirm the interaction of the anthraquinone moiety in the modified TFOs with the

Table 2. Melting Temperature (T_m) of the Triplex and the Full-Match Duplex (ODN-2:ODN-3) and Mismatch Duplex (ODN-4:ODN-5) at Different pH Levels

		T_m[b] (mismatch)											
		pH 6.1				pH 6.5				pH 7.0			
TFO	n[a]	triplex	ΔT_m[c]	ΔT_m[d]	ΔT_m[e]	triplex	ΔT_m[c]	ΔT_m[d]	ΔT_m[e]	triplex	ΔT_m[c]	ΔT_m[d]	ΔT_m[e]
GK-300	-	29.2	-		−10.8	26.2	-		−9.6	16.3	-		−7.3
GK-355A	6	45.4	16.2		−10.3	40.4	14.2		−9.2	31.9	15.6		−6.6
GK-355B	6	45.7	16.5	0.3	−11.2	40.9	14.7	0.5	−10.5	31.6	15.3	−0.4	−6.7
GK-359A	2	41.4	12.2		−9.8	34.8	8.6		−10.8	26.2	9.9		−6.7
GK-359B	2	41.2	12.0	−0.2	−10.3	35.3	9.1	0.5	−10.0	26.4	10.1	0.2	−7.0
GK-354A	6	45.6	16.4		−10.6	42.4	16.2		−7.9	33.3	17.0		−7.1
GK-354B	6	46.4	17.2	0.8	−11.1	42.2	16.0	−0.2	−9.0	33.6	17.3	0.3	−6.6
GK-358A	2	43.3	14.1		−9.7	39.1	12.9		−7.3	28.8	12.5		−6.7
GK-358B	2	43.4	14.2	0.1	−9.4	39.4	13.2	0.3	−7.2	30.1	13.8	1.3	−6.3

[a] *n* indicates the amount of carbon in the alkyl linker that connects the anthraquinone moiety with the propionic acid moiety. [b] T_m values (°C) were determined by computer fitting of the first derivative of the absorbance with respect to $1/T$. Each T_m value is the average of three separate experiments. [c] ΔT_m indicates the deviation from the T_m value of the corresponding triplex consisting of **GK-300** and the duplex. [d] ΔT_m indicates the T_m differences between the diastereomeric counterparts. [e] ΔT_m indicates the deviation from the T_m value of the corresponding full-match triplex.

Table 3. Comparison of Triplex Melting Temperature (T_m) of the TFOs with or without Polyamine Moiety at Different pH Levels

			full-match						mismatch					
			pH 6.1		pH 6.5		pH 7.0		pH 6.1		pH 6.5		pH 7.0	
TFO	n[a]	R[b]	T_m	ΔT_m[c]	T_m	ΔT_m[c]	T_m	ΔT_m[c]	T_m	ΔT_m[c]	T_m	ΔT_m[c]	T_m	ΔT_m[c]
GK-355A	6	H	55.7		49.6		38.5		45.4		40.4		31.9	
GK-354A	6	polyamine	56.2	+0.5	50.3	+0.7	40.4	+1.9	45.6	+0.2	42.4	+2.0	33.3	+1.4
GK-355B	6	H	56.9		51.4		38.3		45.7		40.9		31.6	
GK-354B	6	polyamine	57.5	+0.6	51.2	−0.2	40.2	+1.9	46.4	+0.7	42.2	+1.3	33.6	+2.0
GK-359A	2	H	51.2		45.6		32.9		41.4		34.8		26.2	
GK-358A	2	polyamine	53.0	+1.8	46.4	+0.8	35.5	+2.6	43.3	+1.9	39.1	+4.3	28.8	+2.6
GK-359B	2	H	51.5		45.3		33.4		41.2		35.3		26.4	
GK-358B	2	polyamine	52.8	+1.3	46.6	+1.3	36.4	+3.0	43.4	+2.2	39.4	+4.1	30.1	+3.7

[a] n indicates the amount of carbon in the alkyl linker that connects the anthraquinone moiety with the propionic acid moiety. [b] R indicates the C-5 substituent of the anthraquinone moiety. [c] ΔT_m (°C) indicates the deviation from the T_m value of corresponding TFOs without polyamine in the C-5 position of the anthraquinone moiety.

Table 4. Thermodynamic Parameters for Dissociation of the Third Strand from the Target Duplex (ODN-2:ODN-3) at pH 6.5

TFO	$\Delta H°$ (kcal mol^{-1})	$\Delta\Delta H°$[a] (kcal mol^{-1})	$\Delta S°$ (cal mol^{-1} K^{-1})	$\Delta\Delta S°$[a](cal mol^{-1}K^{-1})	$\Delta G°_{37}$(kcal mol^{-1})	$\Delta\Delta G°_{37}$[a](kcal mol^{-1})
GK-300	−112.9	-	−340.3	-	−7.3	-
GK-354A	−159.0	−46.1	−462.8	−122.5	−15.4	−8.1
GK-354B	−164.2	−51.3	−478.7	−138.4	−15.7	−8.4
GK-358A	−148.3	−35.4	−436.6	−96.3	−12.9	−5.5
GK-358B	−151.7	−38.8	−446.4	−106.0	−13.2	−5.9

[a] $\Delta\Delta H°$, $\Delta\Delta S°$, and $\Delta\Delta G°_{37}$ values indicate the deviation from the corresponding value of the triplex consisting of the unmodified parental **GK-300** and the duplex.

double-stranded portion of the target dsDNA, experiments monitoring changes in the UV-absorption of the anthraquinone moiety with increasing temperature were carried out. The complex formed between **GK-354A** or **GK-355A** and the dsDNA (**ODN-2:ODN-3**) was heated at an elevated temperature from 20 to 80 °C, and the UV-absorbance was monitored in the range 400−700 nm. In this experiment, the same buffer system as that for the UV-melting experiment (pH 6.1) was used, although the concentration of oligomers was increased to 28.0 μM for clear monitoring of the anthraquinone-based absorbance changes. As shown in Supporting Information Figure S7(A), anthraquinone-based absorbance in **GK-354A** bearing the anthraquinone−polyamine multiconjugate exhibited a marked shift to the shorter wavelength (blue shift, 551.0−543.5 nm) according to the elevation of the temperature.[34−36] At the same time, the absorption maximum also increased (hyperchromicity, 12.4%). A combination of these characteristic behaviors in UV-spectroscopy strongly suggests that the anthraquinone moiety actually intercalates to the target dsDNA when the modified TFO binds to form the triplex. Similarly, **GK-355A** bearing the anthraquinone conjugate without the polyamine moiety showed a blue shift (536.0−525.5 nm) and hyperchromicity (12.4%) in UV spectroscopy (Supporting Information Figure S8(A)). Similar patterns of blue shift and hyperchromicity were observed in the case of other TFOs also (data not shown).

Subsequently, the UV-absorbances of **GK-354A** at 550 nm and **GK-355A** at 535 nm were plotted against temperature and the results are shown in Supporting Information Figures S7(B) and S8(B), respectively. The plots show a prominent increment in the absorbance between 50 and 60 °C. Essentially identical results were obtained from the corresponding experiment for the other modified TFOs. The obtained plots would reflect the association and dissociation of the anthraquinone conjugate from the target dsDNA. The results indicate that the anthraquinone conjugate in the modified TFO strongly intercalates with dsDNA.

Thermodynamic Analysis of the Triplex. The thermodynamic values of the triplex containing TFOs (**GK-300**, **GK-354A**, **GK-354B**, **GK-358A**, and **GK-358B**) and the full-match duplex **ODN-2:ODN-3** were measured at pH 6.5 by using the same buffer system as the UV-melting experiment at different oligomer concentrations (2.5 μM, 1.25 μM, 0.625 μM, and 0.313 μM). Supporting Information Figure S3 showed the van't Hoff plot of $1/T_m$ vs ln C_t for the transition of the triplex to the third strand and corresponding target duplex. The plots obtained for **GK-354A** and **GK-354B** were almost identical, confirming almost identical stability between the two diastereomers. A similar observation was made in the case of the diastereomers **GK-358A** and **GK-358B**.

The thermodynamic values, calculated from the slope and intercept of the van't Hoff plot by using the appropriate equations,[37−41] are summarized in Table 4. Inspection of these data revealed that the triplex consisting of the anthraquinone−polyamine conjugate was thermally more stable than the triplex consisting of the unmodified parent. In terms of enthalpy, **GK-354A** and **GK-354B** were more stable than those with a shorter alkyl linker (**GK-358A** and **GK-358B**). The significant difference in enthalpy data revealed that the modified triplex is more favorable than the unmodified parental TFO (**GK-300**). On the other hand, oligomers with longer alkyl linkers showed a

significant loss of entropy than the oligomers with shorter alkyl linkers ($\Delta\Delta S^\circ = -30$ cal mol^{-1} K^{-1}) and **GK-300**.

Comparing the ΔG°_{37} values of the triplex, **GK-354B** formed the most stable triplex (-15.7 kcal mol^{-1}). The ΔG°_{37} value of **GK-300** (-7.3 kcal mol^{-1}) was significantly smaller than those of the other triplex consisting of modified TFOs, indicating that it has relatively low stability. As a total effect, modified TFOs with longer alkyl linkers result in more stable triplex compared to those with shorter linkers. For instance, **GK-354A** ($\Delta G^\circ_{37} = -15.4$ kcal mol^{-1}) had greater stability than **GK-358A** ($\Delta G^\circ_{37} = -12.9$ kcal mol^{-1}). The thermodynamic values of the two diastereomers **A** and **B** in both **GK-354** and **GK-358** are essentially identical; as mentioned above, this indicates the structural flexibility of the two isomers.

CONCLUSION

Chimera TFO bearing non-nucleosidic anthraquinone conjugates with or without a polyamine moiety on anthraquinone moiety exhibited more significant thermal stability than the unmodified parental TFO **GK-300** because of the interaction of the anthraquinone moiety with the target dsDNA. The enhancing effect depended on the length of the alkyl linker between the anthraquinone and propionic acid moieties. However, no apparent differences were observed in the thermal stability of the two diastereomeric counterparts **A** and **B** in any case. This indicates that the extent of the intercalation of the anthraquinone moiety to the dsDNA is almost independent of the stereochemistry of the conjugate. It also indicates that the environment around the linker region of the modified TFOs is very flexible.

On the other hand, TFOs bearing the polyamine moiety on the anthraquinone ring showed higher stability than those without the polyamine moiety, but with a relatively small margin. The polyamine moiety was found to be more effective in stabilizing the triplex in the case of TFOs bearing shorter alkyl linkers. This may be because the polyamine moiety with a short alkyl linker would be located near the dsDNA, and therefore would interact more efficiently than its counterpart with a longer alkyl linker. Even in this case, however, the thermal stability of the two diastereomeric counterparts was observed to be almost the same. This result indicates that the polyamine moiety introduced into DNA did not distinguish both diastereoisomers.

The mismatch studies revealed that T_m values of triplexes consisting of modified TFOs and mismatch target duplex are significantly reduced (about -10 °C). The extent of T_m decrement is almost the same as that of the unmodified parental **GK-300** which indicates that the modified TFOs retain, at least, the same degree of sequence discrimination ability without abolishing the sequence specificity as the unmodified **GK-300**.

The thermodynamic values also revealed that the alternate-stranded triplex consisting of modified TFO and target dsDNA is thermodynamically more stable than the parental **GK-300**, whereas the TFOs having a longer alkyl linker result in a more stable triplex compared to that of short linker. The effect is brought about by the favorable enthalpic factor.

All the above-mentioned properties would make the modified TFOs a unique class of alternate-stranded triplex-forming oligonucleotide feasible for practical use as a gene-regulating agent.

ASSOCIATED CONTENT

Supporting Information. Experimental procedures and characterization data for phosphoramidite derivatives **1a**, **b**,**c**, and **2a**,**b**,**c**, and the UV melting curves of the triplexes. This material is available free of charge via the Internet at http://pubs.acs.org/.

AUTHOR INFORMATION

Corresponding Author

*E-mail: sinozuka@chem-bio.gunma-u.ac.jp; Fax: 81-277-30-1321; Tel: 81-277-30-1320.

Present Addresses

† Present address: Department of Pharmaceutical Chemistry, Faculty of Pharmacy, University of Dhaka, Dhaka-1000, Bangladesh.

ACKNOWLEDGMENT

The work was partially supported by a Grant-in-Aid for Scientific Research from the Ministry of Education, Culture, Sports, Science and Technology, Japan. K. S. also thanks the Ministry for supporting A. Z. A. as a scholar of the Monbukagakusho Scholarship for Foreign Graduate Students.

REFERENCES

(1) Thuong, N. T., and Hélène, C. (1993) Sequence-specific recognition and modification of double-helical DNA by oligonucleotides. *Angew. Chem., Int. Ed. Engl. 32*, 666–690.

(2) Doronina, S. O., and Behr, J. P. (1997) Towards a general triple helix mediated DNA recognition scheme. *Chem. Soc. Rev. 26*, 63–71.

(3) Giovannangeli, C., and Hélène, C. (1997) Progress in developments of triplex-based strategies. *Antisense Nucleic Acid Drug Dev. 7*, 413–421.

(4) Hélène, C. (1999) The antigene strategy: Progress and perspectives in selective gene silencing. *Triple Helix Forming Oligonucleotides* (Malvy, C., Harel-Bellam, A., and Pritchard, L. L., Eds.) pp 3−16, Chapter 1, Kluwer Academic Publishers, Norwell, MA, USA.

(5) Upegui-Gonzalez, L. C., Francois, J. C., Ly, A., and Trojan, J. (2000) The approach of triple helix formation in control of gene expression and the treatment of tumors expressing IGF-I. *Adv. Exp. Med. Biol. 465*, 319–332.

(6) Barre, F. X., Ait-Si-Ali, S., Giovannangeli, C., Luis, R., Robin, P., Pritchard, L. L., Hélène, C., and Harel-Bellen, A. (2000) Unambiguous demonstration of triple-helix-directed gene modification. *Proc. Natl. Acad. Sci. U.S.A. 97*, 3084–3088.

(7) Praseuth, D., Guieysse, L., and Hélène, C. (1999) Triple helix formation and the antigene strategy for sequence-specific control of gene expression. *Biochem. Biophys. Acta 1489*, 181–206.

(8) Hélène, C. (1991) The anti-gene strategy: Control of gene expression by triplex-forming-oligonucleotides. *Anti-Cancer Drug Des. 6*, 569–584.

(9) Luyten, I., and Herdewijn, P. (1998) Hybridization properties of base-modified oligonucleotides within the double and triple helix motif. *Eur. J. Med. Chem. 33*, 515–576.

(10) Gowers, D. M., and Fox, K. R. (1999) Towards mixed sequence recognition by triple helix formation. *Nucleic Acids Res. 27*, 1569–1577.

(11) Grigoriev, M., Praseuth, D., Guieysse, A. L., Robin, P., Thuong, N. T., Hélène, C., and Harel-Bellan, A. (1993) Inhibition of gene expression by triple helix-directed DNA cross-linking at specific sites. *Proc. Natl. Acad. Sci. U.S.A. 90*, 3501–3505.

(12) Horne, D. A., and Dervan, P. B. (1990) Recognition of mixed-sequence duplex DNA by alternate-strand triple-helix formation. *J. Am. Chem. Soc. 112*, 2435–2437.

(13) Griffin, L. C., and Dervan, P. B. (1989) Recognition of thymine adenine base pairs by guanine in a pyrimidine triple helix motif. *Science 245*, 967–971.

(14) Fossella, J. A., Kim, Y.-J., Shih, H., Richard, E. G., and Fresco, J. R. (1993) Relative specificities in binding of Watson - Crick base pairs

by third strand residues in a DNA pyrimidine triplex motif. *Nucleic Acids Res. 21*, 4511–4515.

(15) Mergny, J.-L., Sun, J.-S., Rougée, M., Garestier, T., Barcelo, F., Chomilier, J., and Hélène, C. (1991) Sequence specificity in triple helix formation: Experimental and theoretical studies of the effect of mismatches on triplex stability. *Biochemistry 30*, 9791–9798.

(16) Ono, A., Chen, C.-N., and Kan, L.-S. (1991) DNA triplex formation of oligonucleotide analogs consisting of linker groups and octamer segments that have opposite sugar-phosphate backbone polarities. *Biochemistry 30*, 9914–9921.

(17) Best, G. C., and Dervan, P. B. (1995) Energetics of formation of sixteen triple helical complexes which vary at a single position within a pyrimidine motif. *J. Am. Chem. Soc. 117*, 1187–1193.

(18) Greenberg, W. A., and Dervan, P. B. (1995) Energetics of formation of sixteen triple helical complexes which vary at a single position within a purine motif. *J. Am. Chem. Soc. 117*, 5016–5022.

(19) Gowers, D. M., and Fox, K. R. (1997) DNA triple helix formation at oligopurine sites containing multiple contiguous pyrimidines. *Nucleic Acids Res. 25*, 3787–3794.

(20) Ueno, Y., Mikawa, M., Hoshika, S., and Matsuda, A. (2001) Nucleosides and Nucleotides. 208. Alternate-strand triple-helix formation by the 3′-3′-linked oligodeoxynucleotides with the anthraquinonyl group at the junction point. *Bioconjugate Chem. 12*, 635–642.

(21) Hishika, S., Ueno, Y., and Matsuda, A. (2003) Nucleosides and nucleotides. 218. Alternate-strand triple-helix formation by the 3′-3′-linked oligodeoxynucleotides using a purine motif. *Bioconjugate Chem. 14*, 607–613.

(22) Hoshika, S., Ueno, Y., Kamiya, H., and Matsuda, A. (2004) Nucleosides and nucleotides. Part 226: Alternate-strand triple-helix formation by 3′-3′-linked oligodeoxynucleotides composed of asymmetrical sequences. *Bioorg. Med. Chem. Lett. 14*, 3333–3336.

(23) Silver, G. C., Sun, J.-S., Nguyen, C. H., Boutorine, A. S., Bisagni, E., and Hélène, C. (1997) Stable triple-helical DNA complexes formed by benzopyridoindole- and benzopyridoquinoxaline-oligonucleotide conjugates. *J. Am. Chem. Soc. 119*, 263–268.

(24) Silver, G. C., Nguyen, C. H., Boutorine, A. S., Bisagni, E., Garestier, T., and Hélène, C. (1997) Conjugates of oligonucleotides with triplex-specific intercalating agents. Stabilization of triple-helical DNA in the promoter region of the gene for the a-subunit of interleukin 2 (IL-2Ra). *Bioconjugate Chem. 8*, 15–22.

(25) Garbesi, A., Bonazzi, S., Zanella, S., Capobianco, M. L., Giannini, G., and Arcamone, F. (1997) Synthesis and binding properties of conjugates between oligodeoxynucleotides and daunorubicin derivatives. *Nucleic Acid Res. 25*, 2121–2128.

(26) Belousov, E. S., Afonina, I. A., Kutyavin, I. V., Gall, A. A., Reed, M. W., Gamperm, H. B., Wydro, R. M., and Meyer, R. B. (1998) Triplex targeting of a native gene in permeabilized intact cells: Covalent modification of the gene for the chemokine receptor CCR5. *Nucleic Acid Res. 26*, 1324–1328.

(27) Capobianco, M. L., De Champdoré, M., Francini, L., Lena, S., Garbesi, A., and Arcamone, F. (2001) New TFO conjugates containing a carminomycinone-derived chromophore. *Bioconjuagte Chem. 12*, 523–528.

(28) Carbone, G. M., McGuffie, E., Napoli, S., Flanagan, C. E., Dembech, C., Negri, U., Arcamone, F., Capobianco, M. L., and Catapano, C. V. (2004) DNA binding and antigene activity of a daunomycin-conjugated triplex-forming oligonucleotide targeting the P2 promoter of the human c-*myc* gene. *Nucleic Acid Res. 32*, 2396–2410.

(29) Shinozuka, K., Matsumoto, N., Suzuki, H., Moriguchi, T., and Sawai, H. (2002) Alternate stranded triplex formation of chimeric DNA composed of tandem α- and β-anomeric strands. *Chem. Commun.* 2712–2713.

(30) Azam, A. T. M. Z., Hasegawa, M., Moriguchi, T., and Shinozuka, K. (2004) α−β Chimeric oligo-DNA bearing intercalator-conjugated nucleobase inside the linker sequence remarkably improves thermal stability of an alternate-stranded triple helix. *Bioorg. Med. Chem. Lett. 14*, 5747–5750.

(31) Azam, A. T. M. Z., Moriguchi, T., and Shinozuka, K. (2006) Modified α−β chimeric oligoDNA bearing a multi-conjugate of 2,2-bis(hydroxymethyl)propionic acid−anthraquinone−polyamine exhibited improved and stereo-nonspecific triplex-forming ability. *Chem. Commun.* 335–337.

(32) Gough, G. R., Brunden, M. J., and Gilham, P. T. (1981) Recovery and recycling of synthetic units in the construction of oligodeoxyribonucleotides on solid supports. *Tetrahedron Lett. 22*, 4177–4180.

(33) Mergny, J. -L., Sun, J. -S., Rougée, M., Montenay-Garestier, T., Barcelo, F., Chomilier, J., and Hélène, C. (1991) Sequence specificity in triple helix formation: Experimental and theoretical studies of the effect of mismatches on triplex stability. *Biochemistry 30*, 9791–9798.

(34) Ly, D., Sanii, L., and Schuster, G. B. (1999) Mechanism of charge transport in DNA: Internally-linked anthraquinone conjugates support phonon-assisted polaron hopping. *J. Am. Chem. Soc. 121*, 9400–10.

(35) Yamana, K., Nishijima, Y., Ikeda, T., Gokota, T., Ozaki, H., Nakano, H., Sangen, O., and Shimidzu, T. (1990) Synthesis and interactive properties of an oligonucleotide with anthraquinone at the sugar fragment. *Bioconjugate Chem. 1*, 319–324.

(36) Deshmukh, H., Joglekar, S. P., and Broom, A. D. (1995) Self-complementary oligodeoxyribonucleotides containing 2′-*O*-(anthraquinone-2-methyl)adenosine. *Bioconjugate Chem. 6*, 578–586.

(37) Puglisi, J. D., and Tinoco, I., Jr. (1989) Absorbance melting curves of RNA. *Methods Enzymol. 180*, 304–325.

(38) Marky, L. A., and Breslauer, K. J. (1987) Calculating thermodynamic data for transitions of any molecularity from equilibrium melting curves. *Biopolymers 26*, 1601–1620.

(39) Fresco, J. R., and Lavelle, L. (1995) UV spectroscopic identification and thermodynamic analysis of protonated third strand deoxycytidine residues at neutrality in the triplex $d(C^{+}\text{-}T)_6$:[$d(A\text{-}G)_6d(C^{-}\text{-}T)_6$]; evidence for a proton switch. *Nucleic Acids Res. 23*, 2692–2705.

(40) Sugimoto, N., Nakano, S. −I., Katoh, M., Matsumura, A., Nakamuta, H., Ohmichi, T., Yoneyama, M., and Sasaki, M. (1995) Thermodynamic parameters to predict stability of RNA/DNA hybrid duplexes. *Biochemistry 34*, 11211–11216.

(41) Giancola, C., Petraccone, L., Pieri, M., and Barone, G. (2001) Thermodynamic and computational studies of DNA triple helices containing a nucleotide or a non-nucleotide linker in the third strand. *Biophys. Chem. 94*, 23–31.

Supporting Information

Title:

Stabilizing Effect of Propionic Acid Derivative of Anthraquinone-Polyamine Conjugate Incorporated into α-β Chimeric Oligonucleotides on the Alternate-Stranded Triple Helix.

Running Title:

Stabilization of triplex by modified chimeric TFO

Tomohisha MORIGUCHI, A.T.M. Zafrul AZAM, and Kazuo SHINOZUKA*

Department of Chemistry and Chemical Biology, Graduate School of Engineering, Gunma University, 1-5-1 Tenjin-cho, Kiryu, Gunma 376-8515, Japan
E-mail: sinozuka@chem-bio.gunma-u.ac.jp;
Fax: 81-277-30-1321;
Tel: 81-277-30-1320

Content

(1) General Procedures
(2) Preparation of phosphoramidite derivatives **1**
(3) Preparation of phosphoramidite derivatives **2**
(4) Figure S1
(5) Figure S2
(6) Figure S3
(7) Figure S4
(8) Figure S5
(9) Figure S6
(10) Figure S7
(11) Table S1

Experimental Procedures

General remarks

Thin layer column chromatography was carried out on Merck silica gel 60 F254-precoated plate. Column chromatography was performed with silica gel 60 N (neutral, spherical, 63-210 μm). ^{1}H NMR and ^{31}P NMR spectra were recorded on JOEL (JNM-AL300) FT NMR SYSTEM at 300 MHz, using tetramethylsilane as internal standard. ESI-Mass spectra were recorded on Perkin Elmer API-100 ESI-MS Spectrophotometer. Reversed-phase HPLC was carried out with quaternary gradient pump (PU-2089 plus, JASCO) attached with UV-vis detector (SPD-10A VP, SHIMADZU) and chromatopac (C-R8A, SHIMADZU) using Wakosil 5C18 Column (ø 4.6 mm X 250mm). Elemental analyses were performed by the Microanalytical Laboratory, Faculty of Engineering, Gunma University. Melting point was measured with the melting point apparatus (Sibata).

Oligonucleotides Synthesis.

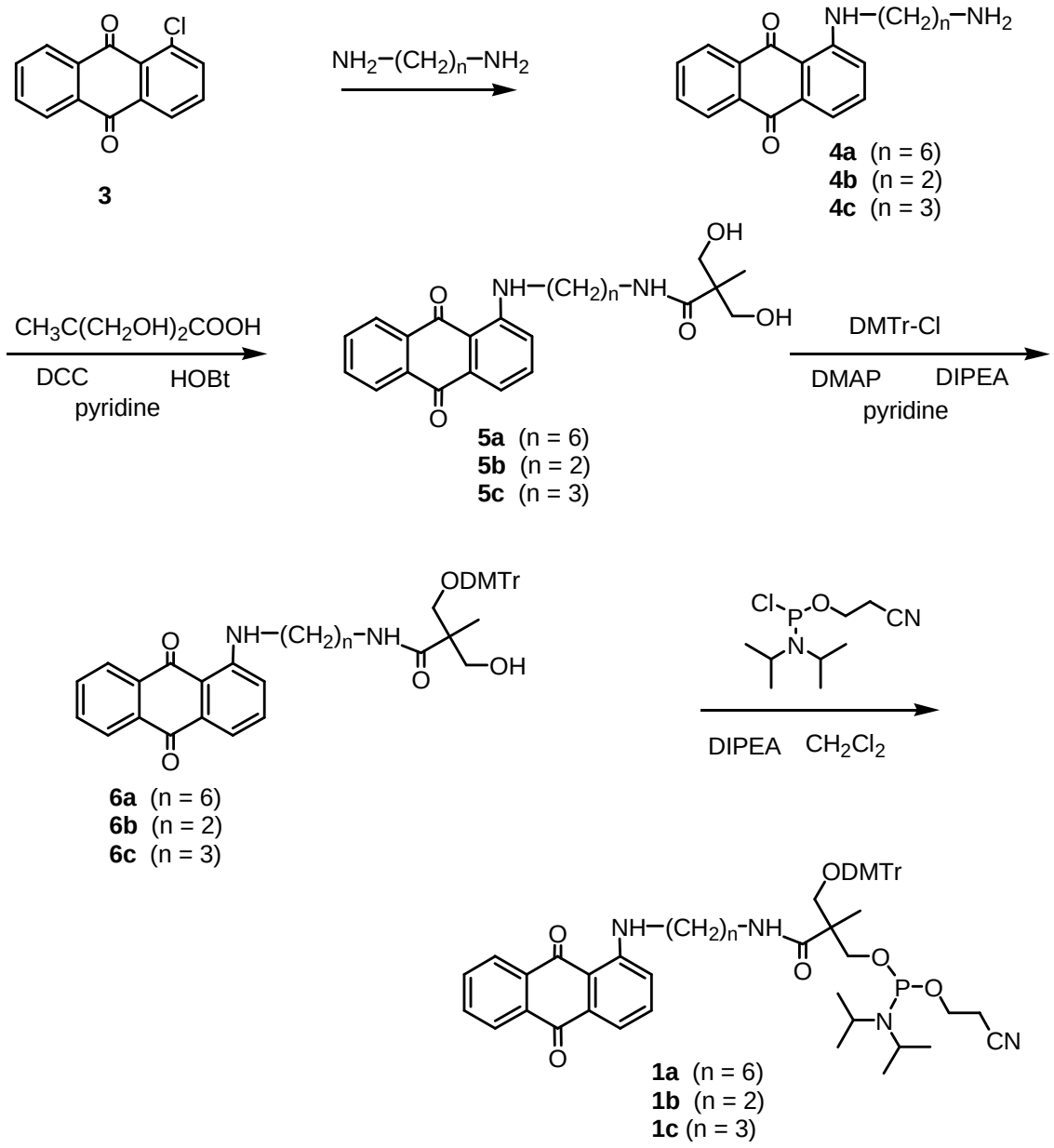
Oligonucleotides were synthesized on an Applied Biosystems 392 DNA/RNA synthesizer on 0.2 μmol scale, using standard phosphoramidites from Glen Research. The synthesized oligonucleotides were purified by a standard procedure.

Melting Temperature Analysis.

UV absorbance was measured with a Shimadzu UV-2450 spectrophotometer equipped with a Temperature Controller. The rate of heating or cooling was 0.1 °C/min. Tm values were obtained in 10 mM sodium phosphate buffer (pH 7.2) containing 100 mM NaCl and 1 mM EDTA. Absorbance and temperature data were analyzed by a TMSPC-8 Tm analysis system.

Thermodynamic Parameter.

Thermodynamic parameters for the triple helix formation were determined by plotting the reciprocal of the melting temperature (T_m^{-1}), versus ln C_t, where C_t is the total concentration of strands.



Scheme S1 Preparation of anthraquinone bearing phosphoramidite reagents for the automated solid-phase oligonucleotide synthesis.

1-(6-Aminohexylamino)anthraquinone (4a)

The mixture of 1,6-hexanediamine (10.4 g, 89.4 mmol) and 1-chloroanthraquinone (**3**) (2.17 g, 8.94 mmol) was stirred at 55 °C for 24 h. Then the reaction mixture was dissolved in CH_2Cl_2 (200 ml) and washed with 1.0 N KOH solution (2 × 200 ml) and sat. $NaHCO_3$ solution (200 ml). The organic layer was dried over Na_2SO_4, and evaporated under reduced pressure. The residue was chromatographed on a column of silica gel with CH_2Cl_2/MeOH/aq.NH_3 (4:1:0.2, v/v/v). Collection and evaporation of appropriate fractions afforded compound **4a** (2.0 g, 69.4%) as red foam. ^{1}H NMR ($CDCl_3$) δ 1.22 (br. 2H, NH_2), 1.36-1.73 (m, 6H, CH_2), 1.73-1.83 (m, 2H, CH_2), 2.69 (t, *J* = 6.9 Hz, 2H, CH_2), 3.30 (dd, *J* = 12.3, 6.9 Hz, 2H, CH_2), 7.03 (dd, *J* = 8.1, 1.2 Hz, 1H, H-Ar of Aq), 7.49-7.56 (m, 2H, H-Ar of Aq), 7.66-7.78 (m, 2H, H-Ar of Aq), 8.21-8.24 (m, 2H, H-Ar of Aq), 9.73 (br. 1H, NH).

1-(2-Aminoethylamino)anthraquinone (4b)

Compound **4b** was obtained by the reaction of ethylenediamine (12.4 ml, 185 mmol) and 1-chloroanthraquinone (**3**) (3.0 g, 12.4 mmol) by same manner as compound **4a**. The product was chromatographed on a column of silica gel with CH_2Cl_2/MeOH/aq.NH_3 (5:1:0.2, v/v/v). Collection and evaporation of appropriate fractions afforded compound **4b** (2.98 g, 90.5%) as red solid. m.p. 152-155 °C. ^{1}H NMR ($CDCl_3$) δ 3.08-3.11 (m, 2H, CH_2), 3.41-3.47 (m, 2H, CH_2), 7.08 (d, *J* = 8.1 Hz, 1H, H-Ar of Aq), 7.51-7.62 (m, 2H, H-Ar of Aq), 7.68-7.78 (m, 2H, H-Ar of Aq), 8.22-8.30 (m, 2H, H-Ar of Aq), 9.92 (br. 1H, NH).

1-(3-Aminopropylamino)anthraquinone (4c)

Compound **4c** was obtained by the reaction of 1,3-propanediamine (12.9 ml, 155 mmol) and 1-chloroanthraquinone (**3**) (2.5 g, 10.3 mmol) by same manner as compound **4a**. The product was chromatographed on a column of silica gel with CH_2Cl_2/MeOH/aq.NH_3 (4:1:0.2, v/v/v). Collection and evaporation of appropriate fractions afforded compound **2c** (2.47 g, 85.5%) as red solid. m.p. 130-32 °C. ^{1}H NMR ($CDCl_3$) δ 1.21 (br. 2H, NH_2), 1.87-1.96 (m, 2H, CH_2), 2.91-2.96 (m, 2H, CH_2), 3.40-3.46 (m, 2H, CH_2), 7.07 (d, *J* = 8.1 Hz, 1H, H-Ar of Aq), 7.51-7.78 (m, 4H, H-Ar of Aq), 8.22-8.28 (m, 2H, H-Ar of Aq), 9.76 (br. 1H, NH).

***N*-[6-(Anthraquinon-1-ylamino)hexyl]-2,2-bis(hydroxymethyl) propionamide (5a)**

2,2-Bis(hydroxymethyl)propionic acid (0.54 g, 3.99 mmol) was added to a solution of **3a** (0.99 g, 3.07 mmol) in dry pyridine (31 ml). Then *N,N'*-dicyclohexyl carbodiimide (1.27 g, 6.14 mmol) and 1-hydroxybenzotriazole monohydrate (0.70 g, 4.61 mmol) were added to the mixture under cooling with ice then stirred at room temperature for 4 h. After the removal of precipitated dicyclohexyl urea, the filtrate was evaporated in vacuo. The residue was dissolved in CH_2Cl_2 (150 ml) and washed with sat. $NaHCO_3$ solution (3 × 150 ml). The organic layer was dried over Na_2SO_4, and evaporated under reduced pressure. The residue was chromatographed on a column of silica gel with 10% MeOH in CH_2Cl_2. Collection and evaporation of appropriate fractions afforded compound **5a** (0.99 g, 73.5%) as red solid.

***N*-[2-(Anthraquinon-1-ylamino)ethyl]-2,2-bis(hydroxymethyl) propionamide (5b)**

Compound **5b** was obtained from compound **4b** (1.95 g, 7.32 mmol) by the reaction with 2,2-bis(hydroxymethyl)propionic acid (1.28 g, 9.52 mmol), *N,N'*-dicyclohexyl carbodiimide (3.78 g, 18.3 mmol) and 1-hydroxybenzotriazole monohydrate (1.68 g, 11.0 mmol) in dry pyridine (73 ml) by same manner as compound **5a**. The product was chromatographed on a column of silica gel with 15% MeOH in CH_2Cl_2. Collection and evaporation of appropriate fractions afforded compound **5b** (2.46 g, 87.8%) as red solid.

***N*-[3-(Anthraquinon-1-ylamino)propyl]-2,2-bis(hydroxymethyl) propionamide (5c)**

Compound **5c** was obtained from **4c** (1.25 g, 4.46 mmol) by the reaction of 2,2-bis(hydroxymethyl)propionic acid (0.78 g, 5.80 mmol), *N,N'*-dicyclohexyl carbodiimide (2.3 g, 11.1 mmol) and 1-hydroxybenzotriazole monohydrate (1.0 g, 6.69 mmol) in dry pyridine (45 ml) by same manner as compound **5a**. The product was chromatographed on a column of silica gel with 10% MeOH in CH_2Cl_2. Collection and evaporation of appropriate fractions afforded compound **5c** (1.51 g, 85.4%) as red solid. ^{1}H NMR ($CDCl_3$) δ 1.11 (s, 3H, CH_3), 1.96-2.04 (m, 2H, CH_2), 3.29-3.51 (m, 4H, CH_2OH), 3.29-3.51 (m, 2H, CH_2) 3.73-3.83 (m, 2H, CH_2), 7.01 (d, J = 8.4 Hz, 1H, H-Ar of Aq), 7.48-7.77 (m, 4H, H-Ar of Aq), 8.19-8.23 (m, 2H, H-Ar of Aq), 9.72 (br. 1H, NH).

2-(Dimethoxytrityloxymethyl)-2-methyl-*N*-[6-(anthraquinon-1-ylamino)hexyl] -3-hydroxypropionamide (6a)

4,4'-Dimethoxytrityl chloride (1.0 g, 2.94 mmol) and *N,N*-diisopropylethylamine (0.98 ml, 5.65 mmol) were added to a solution of **5a** (0.99 g, 2.26 mmol) in dry pyridine (45 ml) in the presence of 4-dimethylaminopyridine (14 mg, 0.113 mmol). The mixture was stirred at room temperature for 4 h. The reaction was quenched by adding of dry MeOH (2 ml). After the evaporation of the mixture in vacuo, resulted oil was dissolved in CH_2Cl_2 (100 ml) and washed with sat. $NaHCO_3$ solution (2 × 100 ml). The organic layer was collected and dried over Na_2SO_4, and then evaporated under reduced pressure. The residue was chromatographed on a column of silica gel with AcOEt/CH_2Cl_2 (1:1, v/v) containing 1% TEA. Collection and evaporation of appropriate fractions afforded compound **6a** (1.03 g, 61.6%) as red foam. Elem. anal. calcd. for $C_{46}H_{48}N_2O_7$.0.2 TEA: C, 74.48; H, 6.75; N, 4.05 %; Found: C, 74.60; H, 6.81; N, 4.28 %. ^{1}H NMR ($CDCl_3$) δ 1.20 (s, 3H, CH_3), 1.37-1.54 (m, 8H, CH_2), 3.21-3.37 (m, 4H, CH_2O), 3.21-3.37 (m, 2H, CH_2), 3.59-3.61 (m, 2H, CH_2), 3.77 (s, 6H, OCH_3 of DMTr), 6.82-6.85 (m, 4H, H-Ar of DMTr), 6.99 (m, 1H, H-Ar of Aq),7.02-7.41 (m, 9H, H-Ar of DMTr), 7.51-7.76 (m, 4H, H-Ar of Aq), 8.23-8.29 (m, 2H, H-Ar of Aq), 9.74 (br., 1H, NH).

2-(Dimethoxytrityloxymethyl)-2-methyl-N-[2-(anthraquinon-1-ylamino)ethyl] -3-hydroxypropionamide (6b)

Compound **6b** was obtained from compound **5b** (2.46 g, 6.43 mmol) by the reaction of 4,4'-dimethoxytrityl chloride (2.6 g, 7.72 mmol) and *N,N*-diisopropylethylamine (2.2 ml, 12.9 mmol) in dry pyridine (96 ml) in the presence of 4-dimethylaminopyridine (40 mg, 0.322 mmol) by same manner as compound **6a**. The product was chromatographed on a column of silica gel with AcOEt/CH_2Cl_2 (1:1, v/v) containing 1% TEA. Collection and evaporation of appropriate fractions afforded compound **6b** (2.76 g, 62.6%) as red foam. Elem. anal. calcd. for $C_{42}H_{40}N_2O_7$.0.25 AcOEt. 0.5 TEA: C, 72.95; H, 6.59; N, 4.62 %; Found: C, 72.89; H, 6.26; N, 4.78 %. ^{1}H NMR ($CDCl_3$) δ 1.24 (s, 3H, CH_3), 3.31-3.45 (m, 4H, CH_2), 3.31-3.45 (m, 4H, CH_2O), 3.69 (s, 6H, OCH_3 of DMTr), 6.74-6.76 (m, 4H, H-Ar of DMTr), 7.08-7.16 (m, 1H, H-Ar of Aq), 7.24-7.37 (m, 9H, H-Ar of DMTr), 7.52-7.70 (m, 4H, H-Ar of Aq), 8.15-8.20 (m, 2H, H-Ar of Aq), 9.74 (br., 1H, NH).

2-(Dimethoxytrityloxymethyl)-2-methyl-*N*-[3-(anthraquinon-1-ylamino)propyl] -3-hydroxypropionamide (6c)

Compound **6c** was obtained from compound **5c** (1.37 g, 3.46 mmol) by the reaction of 4,4'-dimethoxytrityl chloride (1.4 g, 4.15 mmol) and *N*,*N*-diisopropylethylamine (0.8 ml, 4.493 mmol) in dry pyridine (52 ml) in the presence of 4-dimethylaminopyridine (21 mg, 0.173 mmol) by the same manner as compound **6a**. The product was chromatographed on a column of silica gel with AcOEt/CH_2Cl_2 (1:1, v/v) containing 1% TEA. Collection and evaporation of appropriate fractions afforded compound **6c** (1.07 g, 44.3%) as red foam. Elem. anal. calcd. for $C_{43}H_{42}N_2O_7$.0.25 AcOEt. 0.25 TEA: C, 73.24; H, 6.45; N, 4.22 %; Found: C, 73.39; H, 6.17; N, 4.48 %. ^{1}H NMR ($CDCl_3$): δ 1.23 (s, 3H, CH_3), 1.91-1.96 (m, 2H, CH_2), 3.24-3.45 (m, 4H, CH_2OH), 3.24-3.45 (m, 2H, CH_2) 3.63-3.65 (m, 2H, CH_2), 7.74 (s, 6H, OCH_3 of DMTr), 6.78-6.94 (m, 4H, H-Ar of DMTr), 7.14-7.26 (m, 1H, H-Ar of Aq), 7.28-7.45 (m, 9H, H-Ar of DMTr), 7.47-7.79 (m, 4H, H-Ar of Aq), 8.23-8.28 (m, 2H, H-Ar of Aq), 9.73 (br. 1H, NH).

2-(Dimethoxytrityloxymethyl)-2-methyl-*N*-[6-(anthraquinon-1-ylamino)hexyl]prop ionamido-3-yl 2-cyanoethyl *N*,*N*-diisopropyl phosphoramidite (1a)

Compound **6a** (0.53 g, 0.715 mmol) was co-evaporated twice with dry pyridine then dissolved in dry CH_2Cl_2 (11 ml) and chilled in ice bath. DIPEA (0.50 ml, 2.86 mmol) followed by 2-cyanoethyldiisopropylchlorophosphoramidite (0.48 ml, 2.146 mmol) were added dropwise to the chilled mixture then the mixture was stirred at room temperature for 30 min. The excess phosphoramidite reagent was decomposed by addition of dry MeOH (2.5 ml). After the evaporation of the mixture under reduced pressure, resulted oil was dissolved in AcOEt (50 ml) and washed with sat. $NaHCO_3$ solution (2 × 50 ml), followed by sat. NaCl solution (50 ml). The organic phase was collected and dried over Na_2SO_4 then evaporated under reduced pressure. The residue was chromatographed on a column of silica gel with AcOEt/CH_2Cl_2/TEA (45:45:10, v/v/v). The pure compound **1a** was dissolved in small amount of CH_2Cl_2 and dropwised to rapidly stirring cold hexane (150 ml) to precipitate as red solid (0.44 g, 65.4%). ^{1}H NMR ($CDCl_3$) δ 1.08-1.23 (m, 14H, iPr), 1.16 (s, 3H, CH_3), 1.26-1.69 (m, 8H, CH_2), 2.52-2.54 (m, 2H, CH_2 of amidite), 3.20-3.30 (m, 4H, CH_2O), 3.20-3.30 (m, 2H, CH_2 of amidite), 3.53-3.74 (m, 4H, CH_2), 3.77 (s, 6H, OCH_3 of DMTr), 6.81-6.84 (m, 4H, H-Ar of DMTr), 6.98-7.01 (m, 1H, H-Ar

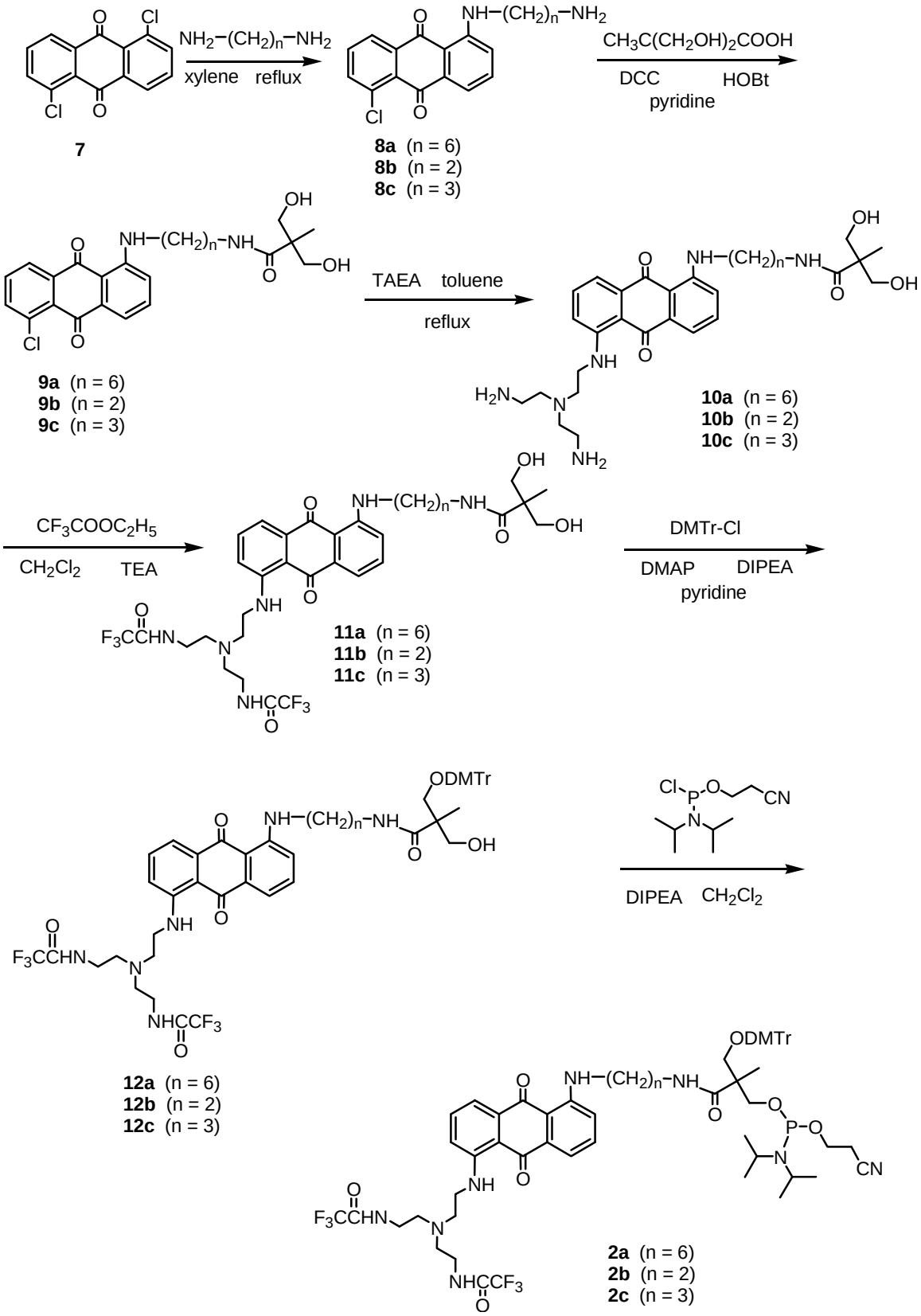
of Aq), 7.20-7.58 (m, 9H, H-Ar of DMTr), 7.68-7.74 (m, 4H, H-Ar of Aq), 8.20-8.27 (m, 2H, H-Ar of Aq), 9.73 (br., 1H, NH), ^{31}P NMR ($CDCl_3$) δ 148.43.

2-(Dimethoxytrityloxymethyl)-2-methyl-*N*-[2-(anthraquinon-1-ylamino)ethyl]propionamido-3-yl 2-cyanoethyl *N*,*N*-diisopropyl phosphoramidite (1b)

Compound **6b** (0.50 g, 0.730 mmol) was converted to the corresponding phosphoramidite derivative (**7b**) by same manner as compound **1a**. The product was chromatographed on a column of silica gel with AcOEt/CH_2Cl_2/TEA (45:45:10, v/v/v). The pure compound **7b** was isolated by precipitation in the same manner as compound **1a** as red solid (0.46 g, 71.2%). ^{1}H NMR ($CDCl_3$) δ 1.06-1.30 (m, 14H, iPr), 1.18 (s, 3H, CH_3), 2.50-2.54 (m, 4H, CH_2 of amidite), 3.40-3.56 (m, 4H, CH_2O), 3.40-3.56 (m, 4H, CH_2), 3.72 (s, 6H, OCH_3 of DMTr), 6.75-6.79 (m, 4H, H-Ar of DMTr), 7.13-7.18 (m, 1H, H-Ar of Aq), 7.21-7.42 (m, 9H, H-Ar of DMTr), 7.54-7.75 (m, 4H, H-Ar of Aq), 8.22-8.25 (m, 2H, H-Ar of Aq), 9.74 (br., 1H, NH), ^{31}P NMR ($CDCl_3$) δ 148.54, 148.59.

2-(Dimethoxytrityloxymethyl)-2-methyl-*N*-[3-(anthraquinon-1-ylamino)propyl]propionamido-3-yl 2-cyanoethyl *N*,*N*-diisopropyl phosphoramidite (1c)

Compound **6c** (0.51 g, 0.730 mmol) was converted to the corresponding phosphoramidite derivative (**1c**) by same manner as compound **1a**. The product was chromatographed on a column of silica gel with AcOEt/CH_2Cl_2/TEA (45:45:10, v/v/v). The pure compound **1c** was isolated by precipitation in the same manner as compound **1a** as red solid (0.35 g, 53.3%). ^{1}H NMR ($CDCl_3$) δ 1.07-1.29 (m, 14H, iPr), 1.13 (s, 3H, CH_3), 1.86-1.91 (m, 2H, CH_2), 2.50-2.56 (m, 2H, CH_2 of amidite), 3.26-3.37 (m, 4H, -CH_2O), 3.26-3.37 (m, 2H, CH_2 of amidite), 3.26-3.37 (m, 2H, CH_2), 3.51-3.54 (m, 2H, CH_2), 7.74 (s, 6H, OCH_3 of DMTr), 6.79-6.82 (m, 4H, H-Ar of DMTr), 6.91-6.94 (m, 1H, H-Ar of Aq), 7.19-7.50 (m, 9H, H-Ar of DMTr), 7.57-7.78 (m, 4H, H-Ar of Aq), 8.23-8.28 (m, 2H, H-Ar of Aq), 9.71 (br. 1H, NH), ^{31}P NMR ($CDCl_3$) δ 148.45.



Scheme S2 Preparation of 5-tris(aminoethyl)anthraquinone bearing phosphoramidite reagents for the automated solid-phase oligonucleotide synthesis.

1-(6-Aminohexylamino)-5-chloroanthraquinone (8a)

The mixture of 1,6-hexanediamine (5.5 g, 47.6 mmol) and 1,5-dichloroanthraquinone (**7**) (4.4 g, 15.9 mmol) in xylene (48 ml) was reacted under reflux at 150 °C for 30 min. After the evaporation of the mixture under reduced pressure, the residue was dissolved in CH_2Cl_2 (300 ml) and washed with 1.0 N KOH solution (2 × 300 ml) and sat. $NaHCO_3$ solution (2 × 300 ml). The organic layer was collected and dried over Na_2SO_4 then evaporated under reduced pressure. The residue was purified by a column of silica gel with CH_2Cl_2/MeOH/aq.NH_3 (4:1:0.2, v/v/v). Collection and evaporation of appropriate fractions afforded compound **8a** (3.19 g, 56.3%) as red solid. ^{1}H NMR ($CDCl_3$) δ 1.40-1.60 (m, 6H, CH_2), 1.73-1.80 (m, 2H, CH_2), 2.70-2.74 (m, 2H, CH_2), 2.30-3.37 (m, 2H, CH_2), 7.00-7.05 (m, 1H, H-Ar of Aq), 7.50-7.72 (m, 4H, H-Ar of Aq), 8.27 (dd, *J* = 7.5, 1.2 Hz, 1H, H-Ar of Aq), 9.61 (br. 1H, NH).

1-(2-Aminoethylamino)-5-chloroanthraquinone (8b)

Compound **8b** was obtained by the reaction of ethylendiamine (2.2 ml, 32.5 mmol) and 1,5-dichloroanthraquinone (**7**) (3.0 g, 10.8 mmol) in xylene (32.5 ml) by the same manner as compound **8a**. The product was chromatographed on a column of silica gel with CH_2Cl_2/MeOH/aq.NH_3 (4:1:0.2, v/v/v). Collection and evaporation of appropriate fractions afforded compound **8b** (1.84 g, 56.5%) as red solid. ^{1}H NMR ($CDCl_3$) δ 3.08-3.48 (m, 4H, CH_2), 7.00-7.05 (m, 1H, H-Ar of Aq), 7.51-7.70 (m, 4H, H-Ar of Aq), 8.25 (dd, *J* = 7.5, 1.2 Hz, 1H, H-Ar of Aq), 9.51 (br. 1H, NH).

1-(3-Aminopropylamino)-5-chloroanthraquinone (8c)

Compound **8c** was obtained by the reaction of 1,3-propanediamine (3.6 ml, 43.3 mmol) and 1,5-dichloroanthraquinone (**7**) (4.0 g, 14.4 mmol) in xylene (43 ml) by the same manner as compound **8a**. The product was chromatographed on a column of silica gel with CH_2Cl_2/MeOH/aq.NH_3 (4:1:0.2, v/v/v). Collection and evaporation of appropriate fractions afforded compound **7c** (2.54 g, 55.9%) as red powder. ^{1}H NMR ($CDCl_3$) δ 1.18 (br., 2H, NH_2), 1.86-1.95 (m, 2H, CH_2), 2.90-2.95 (m, 2H, CH_2), 3.39-3.48 (m, 2H, CH_2), 7.02-7.06 (m, 1H, H-Ar of Aq), 7.52-7.71 (m, 4H, H-Ar of Aq), 8.27 (dd, *J* = 7.8, 1.5 Hz, 1H, H-Ar of Aq), 9.61 (br. 1H, NH).

***N*-{3-(5-chloroanthraquinon-1-ylamino)hexyl}-2,2-bis(hydroxymethyl)propionamide (9a)**

The compound **8a** (1.54 g, 4.32 mmol) was converted to the compound **9a** (1.66 g, 81.3%) as red solid by same manner as compound **5a**. ^{1}H NMR ($CDCl_3$) δ 1.10 (s, 3H, CH_3), 1.37-1.79 (m, 8H, CH_2), 3.22-3.36 (m, 4H, CH_2), 3.72-3.76 (m, 4H, CH_2OH), 6.99-7.03 (m, 1H, H-Ar of Aq), 7.51-7.72 (m, 4H, H-Ar of Aq), 8.25-8.28 (m, 1H, H-Ar of Aq), 9.59 (br. 1H, -NH-).

***N*-{3-(5-chloroanthraquinon-1-ylamino)ethyl}-2,2-bis(hydroxymethyl)propionamide (9b)**

Compound **8b** (1.84 g, 6.12 mmol) was converted to compound **9b** (1.54 g, 60.4%) as red solid (sticky) by same manner as compound **5a**.

***N*-{3-(5-chloroanthraquinon-1-ylamino)propyl}-2,2-bis(hydroxymethyl)propionamide (9c)**

Compound **8c** (2.45 g, 7.78 mmol) was converted to compound **9c** (2.70 g, 80.5%) as red solid (sticky) by same manner as compound **5a**. ^{1}H NMR ($CDCl_3$): δ 1.10 (s, 3H, CH_3), 1.94-2.02 (m, 2H, CH_2), 3.37-3.3.41 (m, 4H, CH_2OH), 3.44-3.83 (m, 2H, CH_2), 6.96-6.99 (m, 1H, H-Ar of Aq), 7.49-7.70 (m, 4H, H-Ar of Aq), 8.19-8.58 (m, 1H, H-Ar of Aq), 9.56 (br. 1H, NH).

***N*-[3-[5-[2-{Bis(2-aminoethyl)amino}ethylamino]anthraquinon-1-ylamino]hexyl]-2,2-bis(hydroxymethyl)propionamide (10a)**

Tris(2-aminoethyl)amine (3.15 ml, 21.1 mmol) was refluxed with **9a** (1.66 g, 3.51 mmol) in dry toluene (28 ml) at 110-115 °C for 6 h. After cooling down and evaporation of the mixture, resulted oil was dissolved in CH_2Cl_2 (250 ml) and washed with water (2 × 250 ml). The organic layer was collected and dried over Na_2SO_4 then evaporated under reduced pressure. The residue was undergone silica gel column chromatography using CH_2Cl_2/MeOH/NH_3aq. (4:1:0.2, v/v/v). Collection and evaporation of appropriate fractions afforded compound **10a** (1.33 g, 65.0%) as red oil, ^{1}H NMR ($CDCl_3$) δ 1.03 (s, 3H, CH_3), 1.23-1.53 (m, 6H, CH_2), 1.64-1.71 (m, 2H, CH_2), 2.56-2.60 (m, 4H, CH_2), 2.77-2.84 (m, 6H, CH_2 of polyamine), 3.17-3.28 (m, 4H, CH_2 of polyamine), 3.32-3.37

(m, 2H, CH_2 of polyamine), 3.64-3.71 (m, 4H, CH_2OH), 6.85-6.91 (m, 2H, H-Ar of Aq), 7.41-7.50 (m, 4H, H-Ar of Aq), 9.60 (t, *J* = 5.4 Hz, 1H, NH), 9.86 (t, *J* = 4.5 Hz, 1H, NH).

***N*-[3-[5-[2-{Bis(2-aminoethyl)amino}ethylamino]anthraquinon-1-ylamino]ethyl]-2, 2-bis(hydroxymethyl)propionamide (10b)**

Tris(2-aminoethyl)amine (3.96 ml, 26.5 mmol) was refluxed with **9b** (1.84 g, 4.41 mmol) in dry toluene (35 ml) at 110-115 °C for 6 h. After cooling down and evaporation, resulted oil was undergone silica gel column chromatography using CH_2Cl_2/MeOH/aq.NH_3 (4:1:0.2, v/v/v). Collection and evaporation of appropriate fractions afforded compound **10b** (1.2 g, 51.6%) as red oil, ^{1}H NMR (D_2O) δ 0.93 (s, 3H, CH_3), 2.74-2.78 (m, 6H, CH_2 of polyamine), 2.97-3.01 (m,4H, -CH_2 of polyamine), 3.19-3.27 (m, 4H, CH_2 of polyamine), 3.32-3.40 (m, 4H, CH_2OH), 3.47-3.51 (m, 2H, CH_2O), 6.72-6.75 (m, 1H, H-Ar of Aq), 6.81-6.84 (m, 1H, H-Ar of Aq), 6.99-7.03 (m, 2H, H-Ar of Aq), 7.23-7.31 (m, 2H, H-Ar of Aq).

***N*-[3-[5-[2-{Bis(2-aminoethyl)amino}ethylamino]anthraquinon-1-ylamino]propyl]-2,2-bis(hydroxymethyl)propionamide (10c)**

Compound **9c** (2.54 g, 5.90 mmol) was converted to compound **10c** by the same manner as compound **10b**. The product was undergone silica gel column chromatography using CH_2Cl_2/MeOH/aq.NH_3 (3:2:0.2, v/v/v). Collection and evaporation of appropriate fractions afforded compound **10c** (1.95 g, 61.2%) as red oil, ^{1}H NMR (D_2O) δ 1.06 (s, 3H, CH_3), 1.73-1.75 (m, 2H, CH_2), 2.79-2.86 (m, 6H, CH_2 of polyamine), 2.04-3.06 (m, 6H, CH_2 of polyamine), 3.20-3.25 (m, 4H, CH_2OH), 3.47-3.51 (m, 2H, CH_2O), 3.60-3.64 (m, 2H, CH_2O), 6.64-6.71 (m, 2H, H-Ar of Aq), 6.89-6.91 (m, 2H, H-Ar of Aq), 7.16-7.27 (m, 2H, H-Ar of Aq).

***N*-[6-[5-[2-[Bis{2-(2,2,2-trifluoroacetamino)ethyl}amino]ethylamino]anthraquinon-1-ylamino]hexyl]-2,2-bis(hydroxymethyl)propionamide (11a)**

Ethyl trifluoroacetate (1.36 ml, 11.4 mmol) was added to the mixture of **10a** (1.33 g, 2.28 mmol) in dry CH_2Cl_2 (45 ml) and dry TEA (4.8 ml, 34.23 mmol) and the mixture was stirred at room temperature for 2 h. After the evaporation of the mixture, resulted oil was dissolved in CH_2Cl_2 (200 ml) and washed with water (2 × 200 ml). The organic layer was collected and dried over Na_2SO_4 then evaporated under reduced pressure. The

residue was undergone silica gel column chromatography using 10% MeOH in CH_2Cl_2. Collection and evaporation of appropriate fractions afforded compound **11a** (1.51 g, 85.4%) as red foam, ^{1}H NMR ($CDCl_3$) δ 1.10 (s, 3H, CH_3), 1.43-1.62 (m, 6H, CH_2), 1.75-1.80 (m, 2H, CH_2), 2.74-2.77 (m, 4H, CH_2 of polyamine), 2.87-2.90 (m, 2H, CH_2 of polyamine), 3.27-3.3.35 (m, 6H, CH_2 of polyamine), 3.45-3.46 (m, 4H, CH_2), 3.70-3.75 (m, 4H, CH_2OH), 6.91-6.99 (m, 1H, H-Ar of Aq), 7.00-7.03 (m, 1H, H-Ar of Aq), 7.50-7.62 (m, 3H, H-Ar of Aq), 7.93-7.95 (m, 1H, H-Ar of Aq), 9.77 (br., 1H, NH), 9.93 (br., 1H, NH).

***N*-[2-[5-[2-[Bis{2-(2,2,2-trifluoroacetamino)ethyl}amino]ethylamino]anthraquinon-1-ylamino]ethyl]-2,2-bis(hydroxymethyl)propionamide (11b)**

Compound **10b** (0.99 g, 1.88 mmol) was converted to compound **11b** by same manner as compound **10a**. The product was isolated by silica gel column chromatography in the same manner as compound **10a** to afford compound **11b** (0.82 g, 60.7%) as red foam, ^{1}H NMR ($CDCl_3$) δ 1.10 (s, 3H, CH_3), 2.73-2.76 (m, 4H, CH_2), 3.30-3.33 (m, 2H, CH_2 of polyamine), 3.42-3.54 (m, 6H, CH_2 of polyamine), 3.62-3.65 (m, 4H, CH_2 of polyamine), 3.74-3.85 (m, 4H, CH_2OH), 6.88-6.91 (m, 1H, H-Ar of Aq), 7.04-7.09 (m, 1H, H-Ar of Aq), 7.44-7.56 (m, 3H, H-Ar of Aq), 7.93-7.97 (m, 1H, H-Ar of Aq), 9.82 (br., 1H, NH), 9.89 (br., 1H, NH).

***N*-[3-[5-[2-[Bis{2-(2,2,2-trifluoroacetamino)ethyl}amino]ethylamino]anthraquinon-1-ylamino]propyl]-2,2-bis(hydroxymethyl)propionamide (11c)**

Compound **10c** (1.78 g, 3.29 mmol) was converted to compound **11c** by same procedure as compound **10a**. The product was isolated by silica gel column chromatography in the same manner as compound **10a** to obtain compound **11c** (1.41 g, 58.5%) as red foam, ^{1}H NMR ($CDCl_3$) δ 1.10 (s, 3H, CH_3), 1.96-2.03 (m, 2H, CH_2), 2.74-2.77 (m, 4H, CH_2 of polyamine), 2.86-2.90 (m, 2H, CH_2 of polyamine), 3.05-3.09 (m, 2H, CH_2 of polyamine), 3.34-3.51 (m, 4H, CH_2 of polyamine), 3.34-3.51 (m, 4H, CH_2), 3.71-3.82 (m, 4H, CH_2OH), 6.90-6.93 (m, 1H, H-Ar of Aq), 7.00-7.04 (m, 1H, H-Ar of Aq), 7.51-7.61 (m, 3H, H-Ar of Aq), 7.90-7.92 (m, 1H, H-Ar of Aq), 9.80 (br., 1H, NH), 9.92 (br., 1H, NH).

2-(Dimethoxytrityloxymethyl)-2-methyl-*N*-[6-[5-[2[bis{2-(2,2,2-trifluoroacetamido) ethylamino}]ethylamino]anthraquinon-1-ylamino]hexyl]-3-hydroxypropionamide (11a)

4,4'-Dimethoxytrityl chloride (DMTr-Cl) (1.31 g, 3.87 mmol) and *N,N*-diisopropylethylamine (DIPEA) (0.56 ml, 3.23 mmol) were added in a solution of **11a** (1.0 g, 1.29 mmol) in dry pyridine (39 ml) in the presence of 4-dimethylaminopyridine (DMAP) (8 mg, 0.06 mmol) and the mixture was stirred at room temperature for 3.5 h. The reaction was quenched by addition of dry MeOH (5 ml). After evaporation of the mixture in vacuo, resulted oil was dissolved in CH_2Cl_2 (100 ml) and washed with sat. $NaHCO_3$ solution (2 × 100 ml). The organic layer was collected and dried over Na_2SO_4 then evaporated under reduced pressure. The residue was chromatographed on a column of silica gel with AcOEt/CH_2Cl_2 (1:1, v/v) containing 1 % TEA. Collection and evaporation of appropriate fractions afforded compound **12a** (1.03 g, 74.0%) as red foam, Elem. anal. calcd. for $C_{56}H_{62}F_6N_6O_9$: C, 62.44; H, 5.80; N, 7.80 %; Found: C, 62.49; H, 5.94; N, 7.80 %, ^{1}H NMR ($CDCl_3$) δ 1.21 (s, 3H, CH_3), 1.33-1.50 (m, 6H, CH_2), 1.68-1.71 (m, 2H, CH_2), 2.75-2.78 (m, 4H, CH_2 of polyamine), 2.87-2.90 (m, 2H, CH_2 of polyamine), 3.20-3.37 (m, 6H, CH_2 of polyamine), 3.45-3.46 (m, 4H, CH_2), 3.60-3.63 (m, 4H, CH_2O), 3.77 (s, 6H, OCH_3 of DMTr), 6.82-6.85 (m, 4H, H-Ar of DMTr), 6.91-7.02 (m, 2H, H-Ar of Aq), 7.21-7.41 (m, 9H, H-Ar of DMTr), 7.49-7.63 (m, 3H, H-Ar of Aq), 7.93-9.96 (m, 1H, H-Ar of Aq), 9.77 (br., 1H, NH), 9.94 (br., 1H, NH).

2-(Dimethoxytrityloxymethyl)-2-methyl-*N*-[2-[5-[2[bis{2-(2,2,2-trifluoroacetamido) ethylamino}]ethylamino]anthraquinon-1-ylamino]ethyl]-3-hydroxypropionamide (11b)

Compound **11b** (0.82 g, 1.14 mmol) was converted to the corresponding monotritylated derivative (**12b**) by the procedure as compound **12a**. The product was isolated by silica gel column chromatography in the same manner as compound **12a** to obtain compound **12b** (0.77 g, 66.1%) as red foam, Elem. anal. calcd. for $C_{52}H_{54}F_6N_6O_9$: C, 61.17; H, 5.33; N, 8.23 %; Found: C, 61.41; H, 5.38; N, 8.35 %, ^{1}H NMR ($CDCl_3$) δ 1.24 (s, 3H, CH_3), 2.75-2.86 (m, 4H, CH_2), 3.33-3.55 (m, 12H, CH_2 of polyamine), 3.60-3.67 (m, 4H, CH_2O), 3.72 (s, 6H, OCH_3 of DMTr), 6.77 (m, 4H, H-Ar of DMTr), 6.89-7.06 (m, 2H, H-Ar of Aq), 7.15-7.39 (m, 9H, H-Ar of DMTr), 7.52-7.54 (m, 3H, H-Ar of Aq), 7.90-7.94 (m, 1H, H-Ar of Aq), 9.79 (br., 1H, NH), 9.89 (br, 1H, NH).

2-(Dimethoxytrityloxymethyl)-2-methyl-*N*-[2-[5-[2[bis{2-(2,2,2-trifluoroacetamido) ethylamino}]ethylamino]anthraquinon-1-ylamino]propyl]-3-hydroxypropionamide (12c)

Compound **11c** (1.30 g, 1.77 mmol) was converted to the corresponding monotritylated derivative (**12c**) by the procedure as compound **12a**. The product was isolated by silica gel column chromatography in the same manner as compound **12a** to obtain compound **12c** (1.10 g, 59.9%) as red foam, Elem. anal. calcd. for $C_{53}H_{56}F_6N_6O_9$: C, 61.50; H, 5.45; N, 8.12 %; Found: C, 61.19; H, 5.51; N, 8.34 %. ^{1}H NMR ($CDCl_3$) δ 1.23 (s, 3H, CH_3), 1.90-1.94 (m, 2H, CH_2), 2.74-2.77 (m, 4H, CH_2 of polyamine), 2.87-2.90 (m, 2H, CH_2 of polyamine), 3.24-3.38 (m, 6H, CH_2 of polyamine), 3.40-3.46 (m, 4H, CH_2), 3.63-3.65 (m, 4H, CH_2O), 3.74 (s, 6H, OCH_3 of DMTr), 6.81-6.86 (m, 4H, H-Ar of DMTr), 6.89-6.94 (m, 2H, H-Ar of Aq), 7.19-7.40 (m, 9H, H-Ar of DMTr), 7.43-7.62 (m, 3H, H-Ar of Aq), 7.90-7.94 (m, 1H, H-Ar of Aq), 9.77 (br., 1H, NH), 9.93 (br., 1H, NH).

2-(Dimethoxytrityloxymethyl)-2-methyl-*N*-[5-[2[bis{2-(2,2,2-trifluoroacetamido) ethylamino}]ethylamino]anthraquinon-1-ylaminohexyl]-propionamido-3-yl 2-cyanoethyl *N*,*N*-diisopropyl phosphoramidite (2a)

Compound **12a** (0.53 g, 0.49 mmol) was converted to the corresponding phosphoramidite derivative (**2a**) by same manner as **1a**. The product was chromatographed on a column of silica gel with AcOEt/CH_2Cl_2/TEA (45:45:10, v/v/v). The pure compound **2a** was isolated by precipitation in the same manner as compound **5a** as red solid (0.51 g, 81.0%), ^{1}H NMR ($CDCl_3$) δ 1.18 (s, 3H, CH_3), 1.01-1.23 (m, 14H, iPr), 1.38-1.60 (m, 8H, CH_2), 2.44-2.53 (m, 4H, CH_2 of amidite), 2.59-2.81 (m, 6H, CH_2 of polyamine), 3.12-3.27 (m, 6H, CH_2 of polyamine), 3.38-3.51 (m, 8H, CH_2O), 3.70 (s, 6H, OCH_3 of DMTr), 6.74-6.76 (m, 4H, H-Ar of DMTr), 6.83-6.92 (m, 2H, H-Ar of Aq), 7.19-7.36 (m, 9H, H-Ar of DMTr), 7.42-7.55 (m, 3H, H-Ar of Aq), 7.85-7.88 (m, 1H, H-Ar of Aq), 9.69 (br., 1H, NH), 9.86 (br., 1H, NH), ^{31}P NMR ($CDCl_3$) δ 148.4.

2-(Dimethoxytrityloxymethyl)-2-methyl-N-[5-[2-[bis{2-(2,2,2-trifluoroacetamido) ethylamino}]ethylamino]anthraquinon-1-ylaminoethyl]-propionamido-3-yl 2-cyanoethyl *N*,*N*-diisopropyl phosphoramidite (2b)

Compound **12b** (0.37 g, 0.362 mmol) was converted to the corresponding phosphoramidite derivative (**2b**) by same manner as **1a**. The product was chromatographed on a column of silica gel with AcOEt/CH_2Cl_2/TEA (45:45:10, v/v/v). The pure compound **2b** was isolated by precipitation in the same manner as compound **1a** as red solid (0.31 g, 70.1%), ^{1}H NMR ($CDCl_3$) δ 1.06-1.13 (m, 14H, iPr), 1.25 (s, 3H, CH_3), 2.49-2.51 (m, 4H, CH_2 of amidite), 2.74-2.78 (m, 4H, CH_2), 3.30-3.52 (m, 12H, CH_2 of polyamine), 3.67-3.73 (m, 4H, CH_2O), 3.75 (s, 6H, OCH_3 of DMTr), 6.78 (m, 4H, H-Ar of DMTr), 7.10-7.22 (m, 2H, H-Ar of Aq), 7.24-7.42 (m, 9H, H-Ar of DMTr), 7.51-7.58 (m, 3H, H-Ar of Aq), 7.92-7.94 (m, 1H, H-Ar of Aq), 9.82 (br., 1H, NH), 9.92 (br., 1H, NH), ^{31}P NMR ($CDCl_3$) δ 148.55.

2-(Dimethoxytrityloxymethyl)-2-methyl-N-[5-[2-[bis{2-(2,2,2-trifluoroacetamido) ethylamino}]ethylamino]anthraquinon-1-ylaminopropyl]-propionamido-3-yl 2-cyanoethyl *N*,*N*-diisopropyl phosphoramidite (2c)

Compound **12c** (0.52 g, 0.502 mmol) was converted to the corresponding phosphoramidite derivative (**2c**) by same manner as **1a**. The product was chromatographed on a column of silica gel with AcOEt/CH_2Cl_2/TEA (45:45:10, v/v/v). The pure compound **2c** was isolated by precipitation in the same manner as compound **1a** as red solid (0.445 g, 71.8%), ^{1}H NMR ($CDCl_3$) δ 1.07-1.15 (m, 14H, iPr), 1.28 (s, 3H, CH_3), 1.86-1.90 (m, 2H, CH_2 of propylene), 2.50-2.55 (m, 2H, CH_2 of amidite), 2.75-2.89 (m, 6H, CH_2 of polyamine), 3.27-3.35 (m, 8H, CH_2 of polyamine and amidite), 3.45-3.53 (m, 4H, CH_2), 3.70-3.84 (m, 4H, CH_2O), 3.74 (s, 6H, OCH_3, DMTr), 6.80-6.87 (m, 4H, H-Ar of DMTr), 6.90-6.93 (m, 1H, H-Ar of Aq), 7.21-7.32 (m, 9H, H-Ar of DMTr), 7.41-7.62 (m, 4H, H-Ar of Aq), 7.92-7.95 (m, 1H, H-Ar of Aq), 9.75 (br., 1H, NH), 9.92 (br., 1H, NH), ^{31}P NMR ($CDCl_3$) δ 148.44.

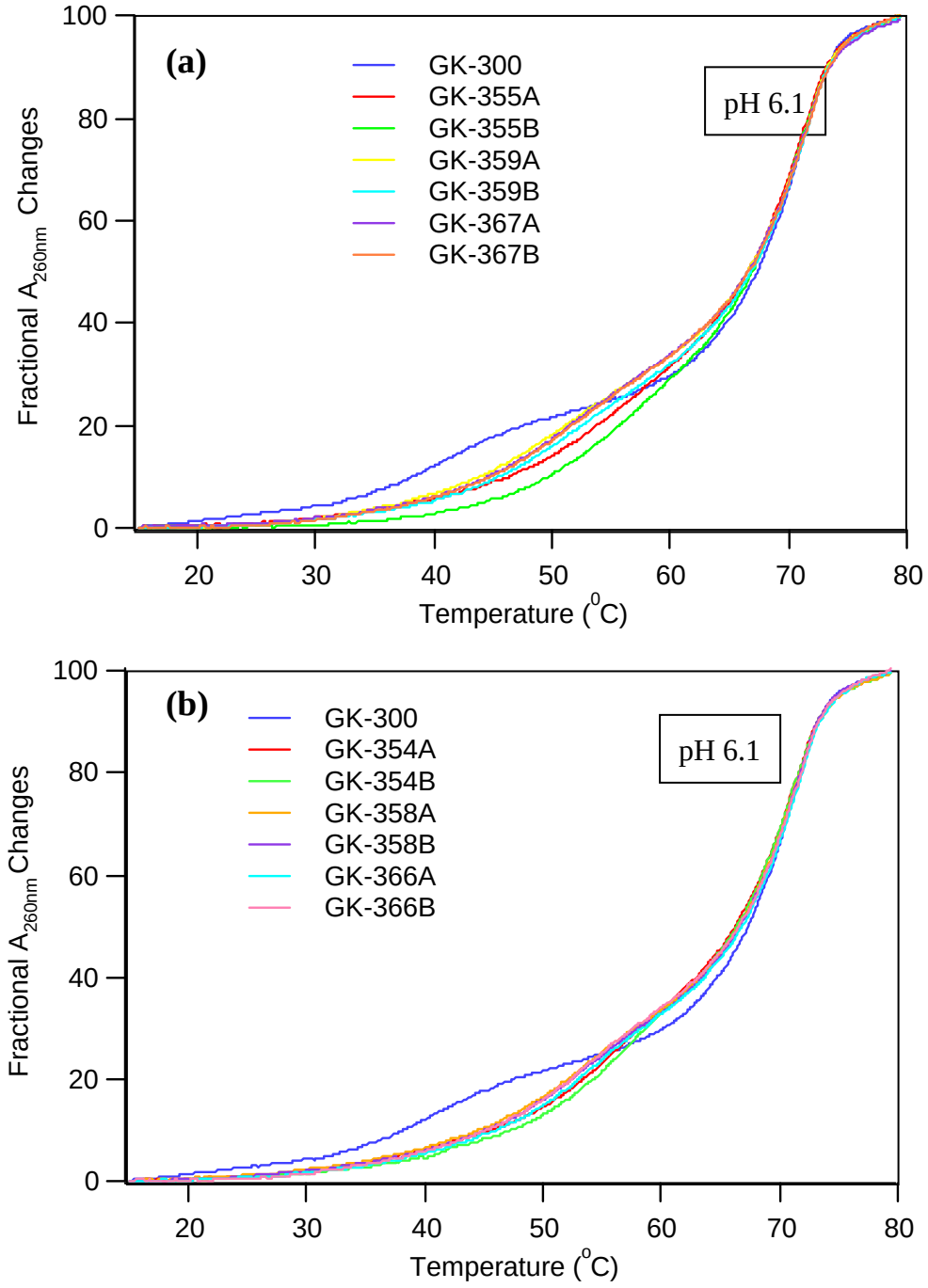


Figure S1. UV-melting profiles of the triple helicles at pH 6.1. The full-match duplex consisting of **ODN-2** and **ODN-3** (1.5 μM) was mixed with appropriate TFO (1.5 μM) in sodium cacodylate buffer (10 mM, pH 6.1) containing 100 mM NaCl, 1.0mM spermine, and 10 mM $MgCl_2$. The temperature was raised at 0.1 °C/min and thermally induced transition of each mixture was monitored at 260nm. a) TFOs without polyamine moiety, b) TFOs with polyamine moiety on the anthraquinone ring.

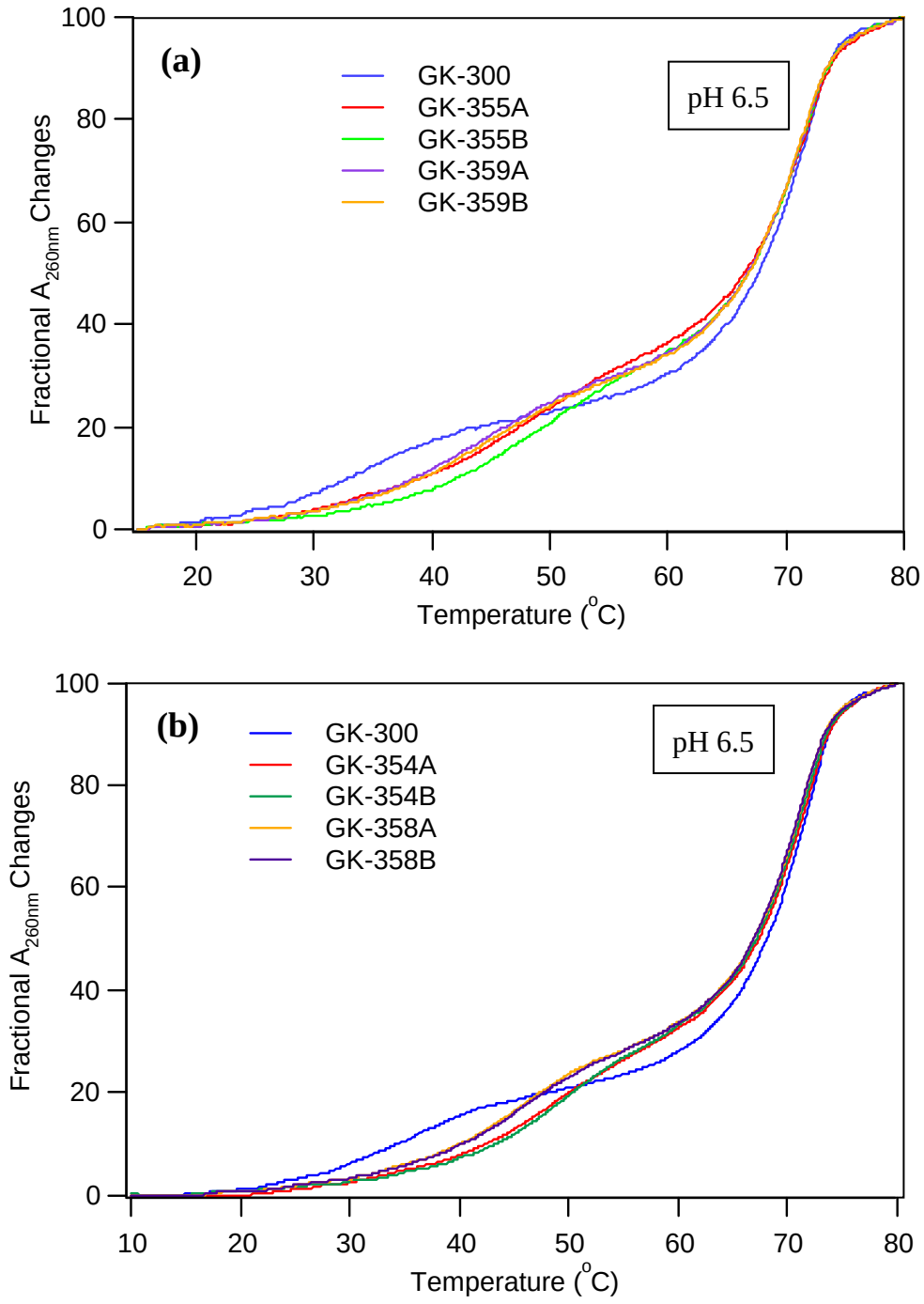


Figure S2. UV-melting profiles of the triple helicles at pH 6.5. The full-match duplex consisting of **ODN-2** and **ODN-3** (1.5 μM) was mixed with appropriate TFO (1.5 μM) in sodium cacodylate buffer (10 mM, pH 6.5) containing 100 mM NaCl, 1.0 mM spermine, and 10 mM $MgCl_2$. The temperature was raised at 0.1 °C/min and thermally induced transition of each mixture was monitored at 260nm. a) TFOs without polyamine moiety, b) TFOs with polyamine moiety on the anthraquinone ring.

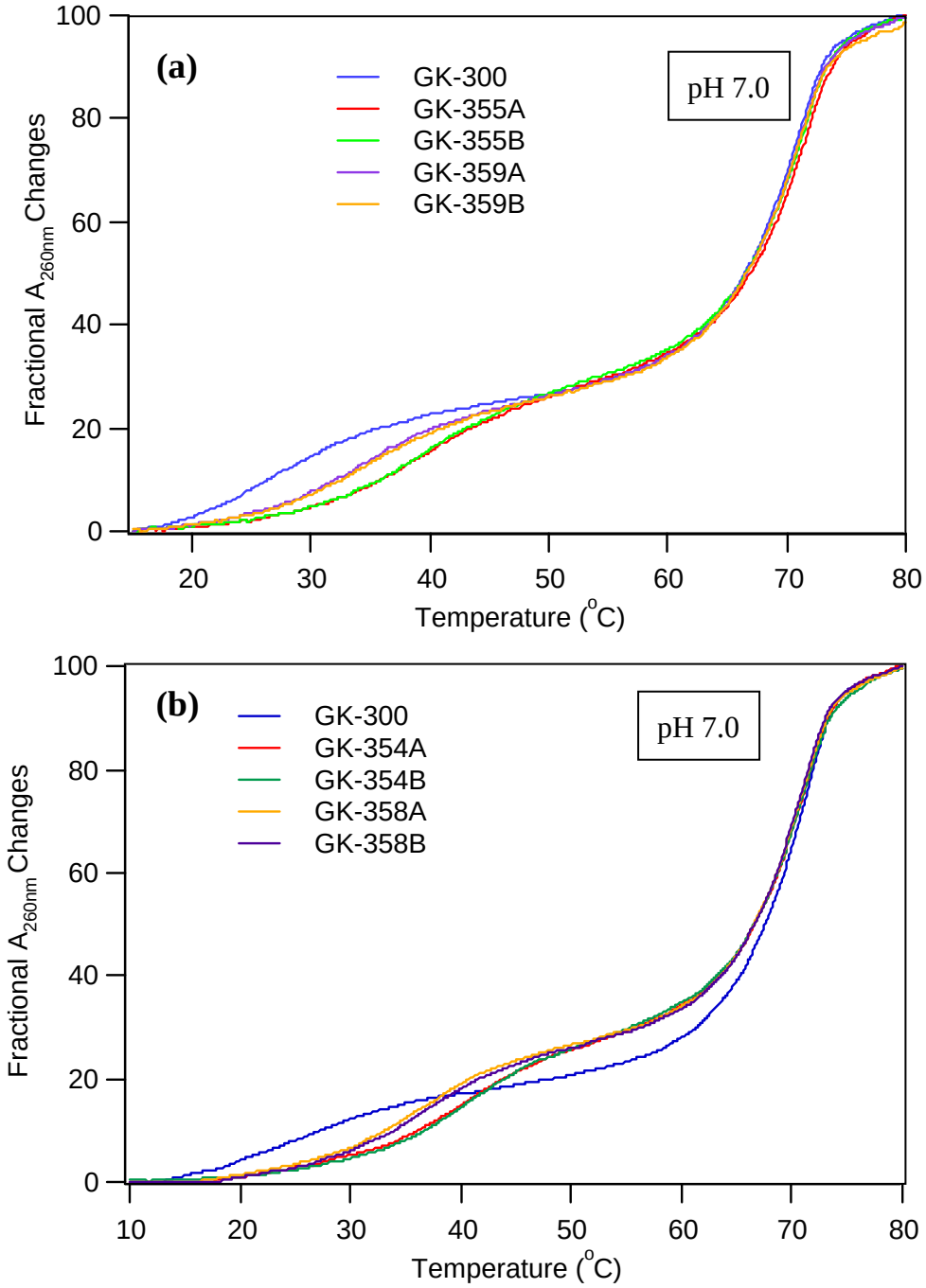


Figure S3. UV-melting profiles of the triple helicles at pH 7.0. The full-match duplex consisting of **ODN-2** and **ODN-3** (1.5 μM) was mixed with appropriate TFO (1.5 μM) in sodium cacodylate buffer (10 mM, pH 7.0) containing 100 mM NaCl, 1.0 mM spermine, and 10 mM $MgCl_2$. The temperature was raised at 0.1 °C/min and thermally induced transition of each mixture was monitored at 260nm. a) TFOs without polyamine moiety, b) TFOs with polyamine moiety on the anthraquinone ring.

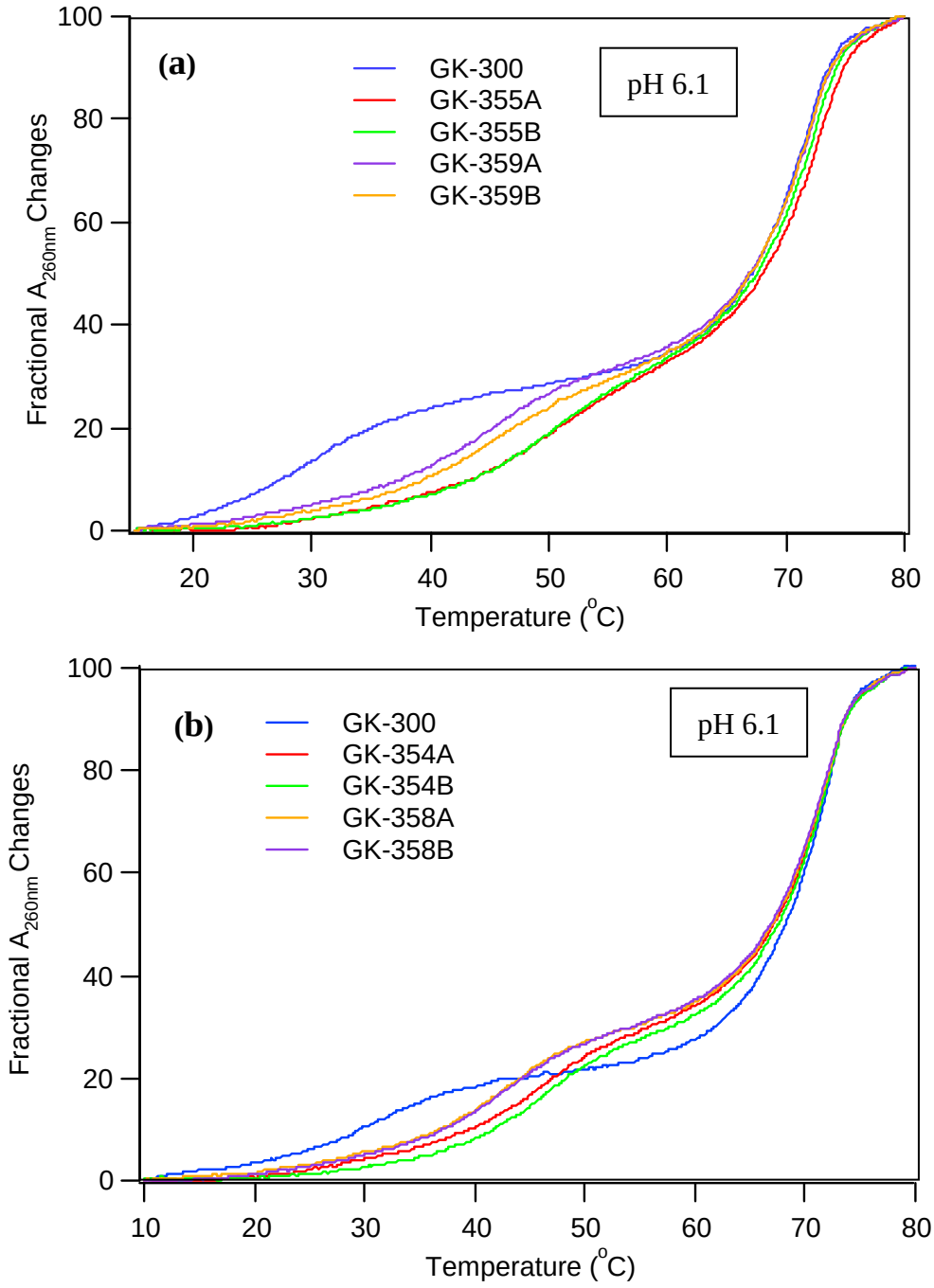


Figure S4. UV-melting profiles of the triple helicles at pH 6.1. The mismatch duplex consisting of **ODN-4** and **ODN-5** (1.5 μM) was mixed with appropriate TFO (1.5 μM) in sodium cacodylate buffer (10 mM, pH 6.1) containing 100 mM NaCl, 1.0 mM spermine, and 10 mM $MgCl_2$. The temperature was raised at 0.1 °C/min and thermally induced transition of each mixture was monitored at 260nm. a) TFOs without polyamine moiety, b) TFOs with polyamine moiety on the anthraquinone ring.

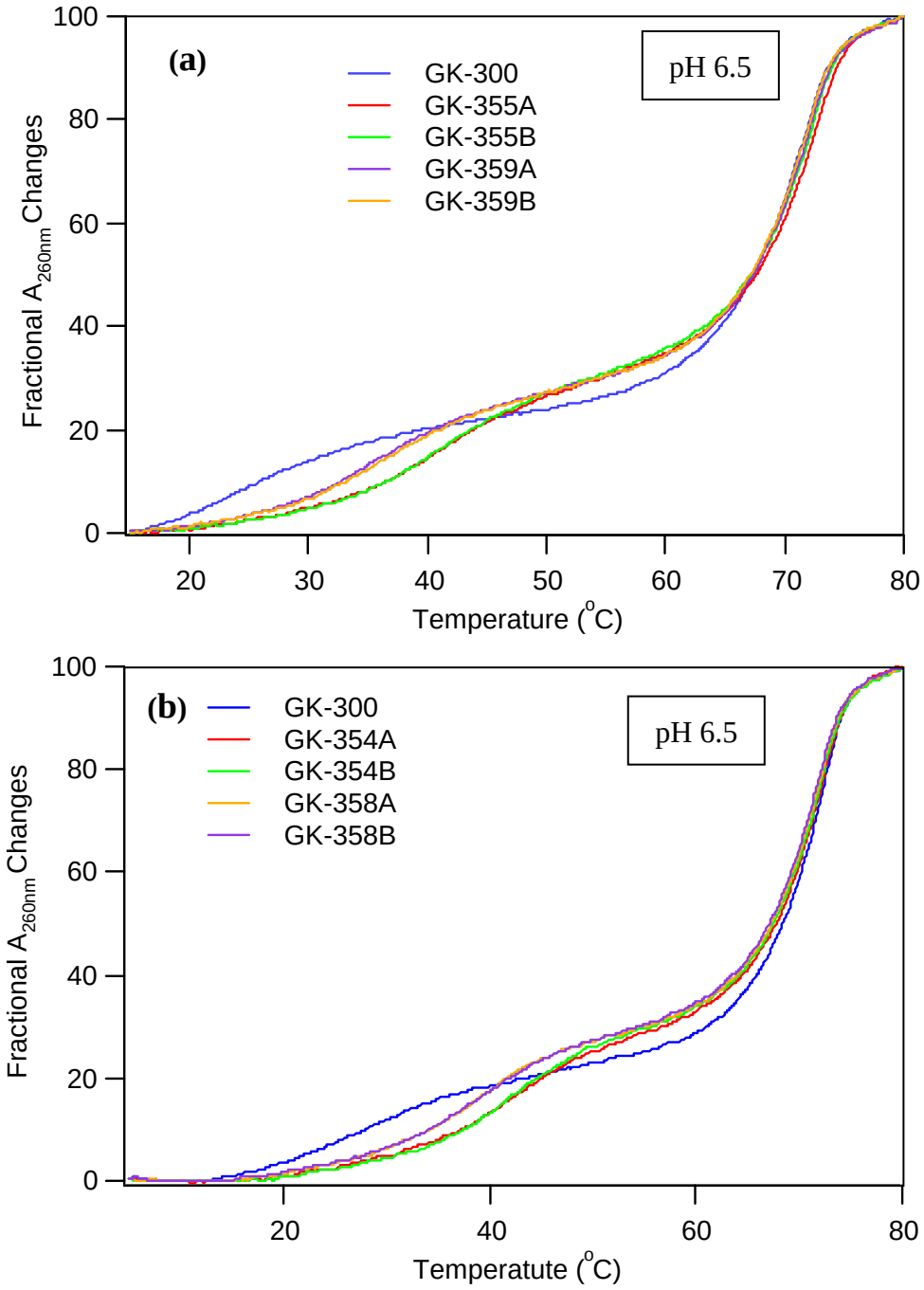


Figure S5. UV-melting profiles of the triple helicles at pH 6.5. The mismatch duplex consisting of **ODN-4** and **ODN-5** (1.5 μM) was mixed with appropriate TFO (1.5 μM) in sodium cacodylate buffer (10 mM, pH 6.5) containing 100 mM NaCl, 1.0 mM spermine, and 10 mM $MgCl_2$. The temperature was raised at 0.1 °C/min and thermally induced transition of each mixture was monitored at 260nm. a) TFOs without polyamine moiety, b) TFOs with polyamine moiety on the anthraquinone ring.

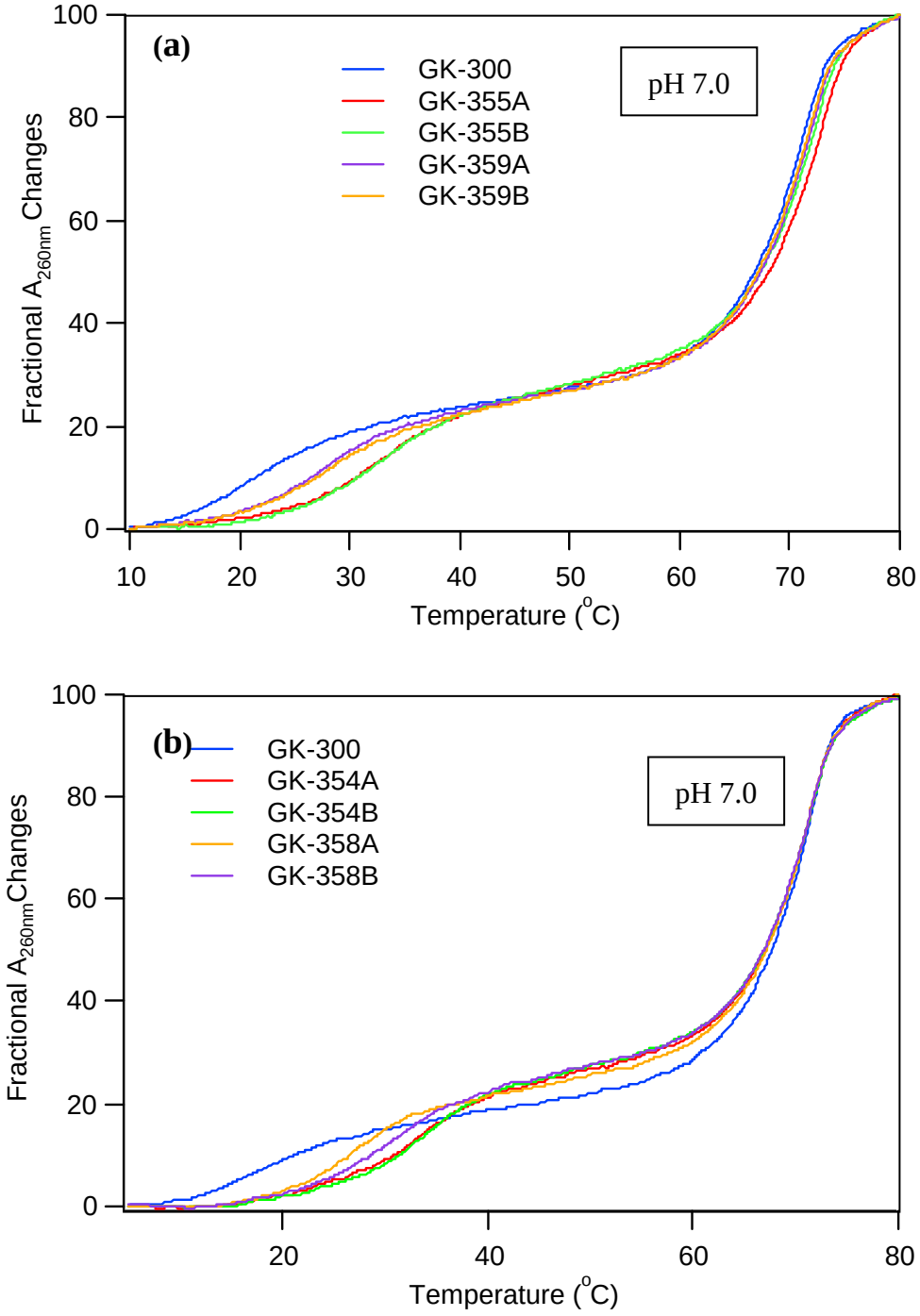


Figure S6. UV-melting profiles of the triple helicles at pH 7.0. The mismatch duplex consisting of **ODN-4** and **ODN-5** (1.5 μM) was mixed with appropriate TFO (1.5 μM) in sodium cacodylate buffer (10 mM, pH 7.0) containing 100 mM NaCl, 1.0 mM spermine, and 10 mM $MgCl_2$. The temperature was raised at 0.1 °C/min and thermally induced transition of each mixture was monitored at 260nm. a) TFOs without polyamine moiety, b) TFOs with polyamine moiety on the anthraquinone ring.

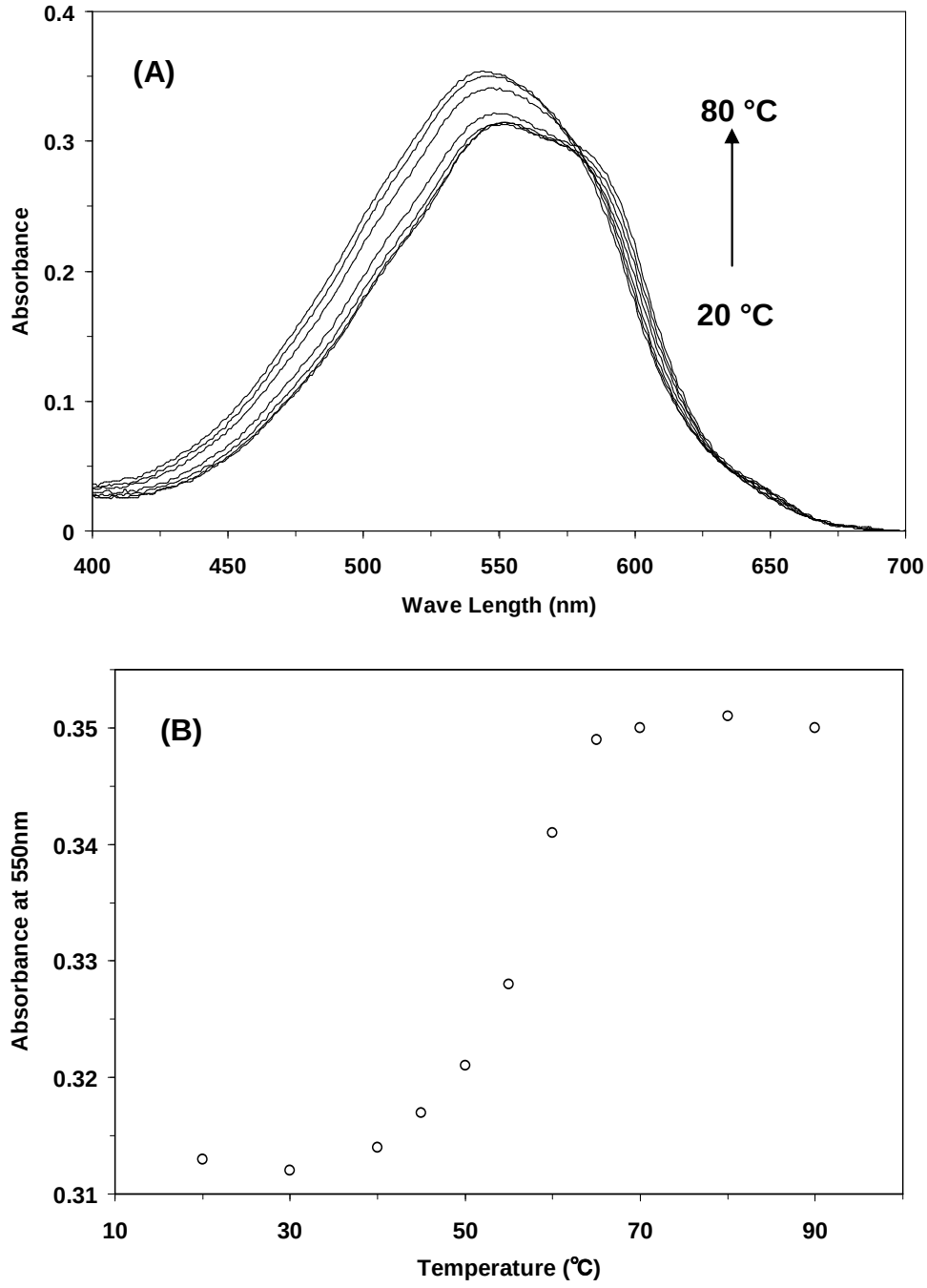


Figure S7. Temperature dependent UV-change of anthraquinone moiety in **GK-354A**. (A) Absorption spectra of anthraquinone moiety region in GK-354A. (B) Absorbance change of anthraquinone moiety in **GK-354A** at 550 nm. The experiment was carried out in the same condition as the UV-melting experiment at pH 6.1, although the concentration of the triplex was 28.0 μM.

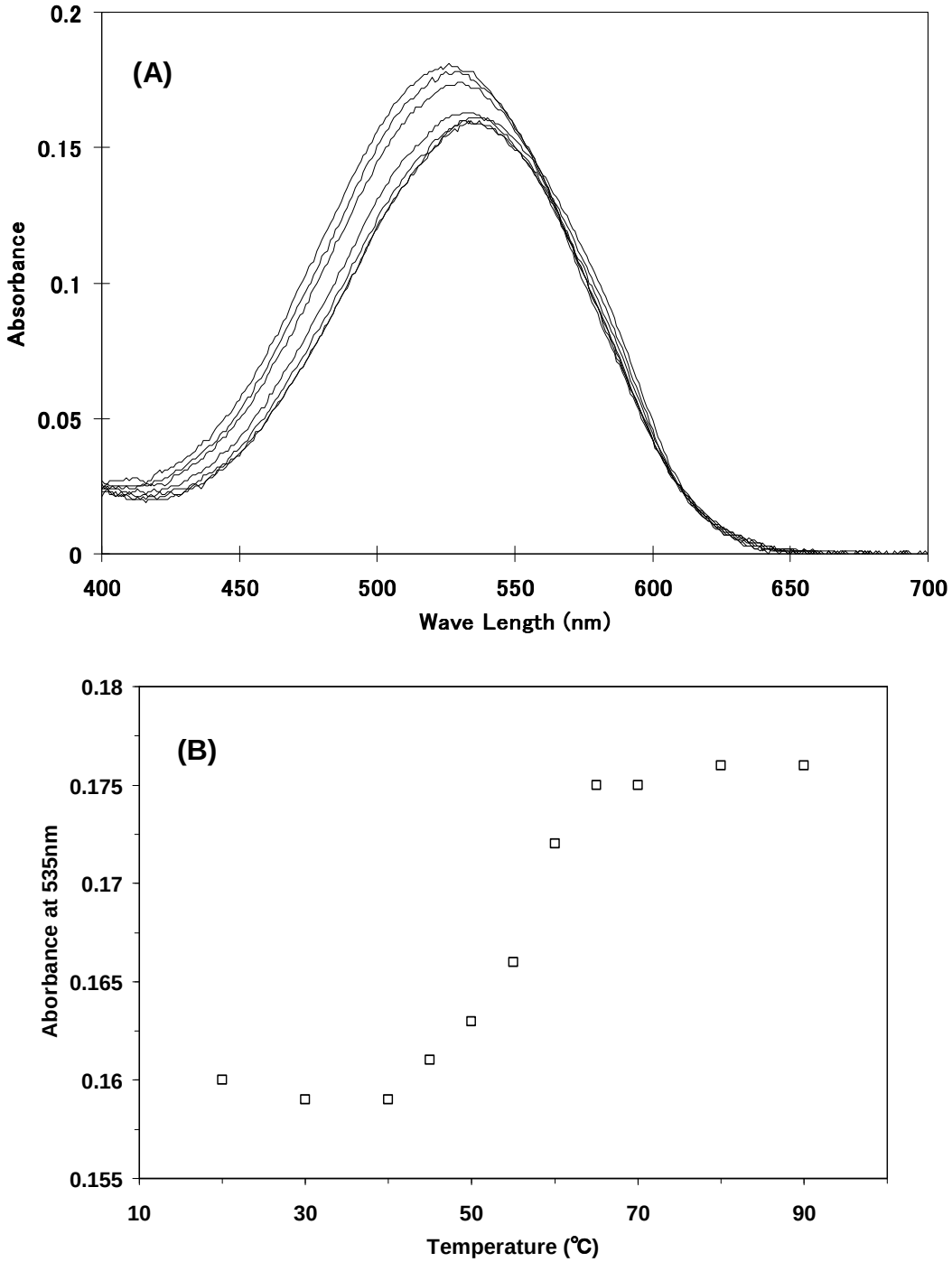


Figure S8. Temperature dependent UV-change of anthraquinone moiety in **GK-355A**. (A) Absorption spectra of anthraquinone moiety region in GK-354A. (B) Absorbance change of anthraquinone moiety in **GK-355A** at 535 nm. The experiment was carried out under the same condition as the UV-melting experiment at pH 6.1, although the concentration of the triplex was 28.0 μM.

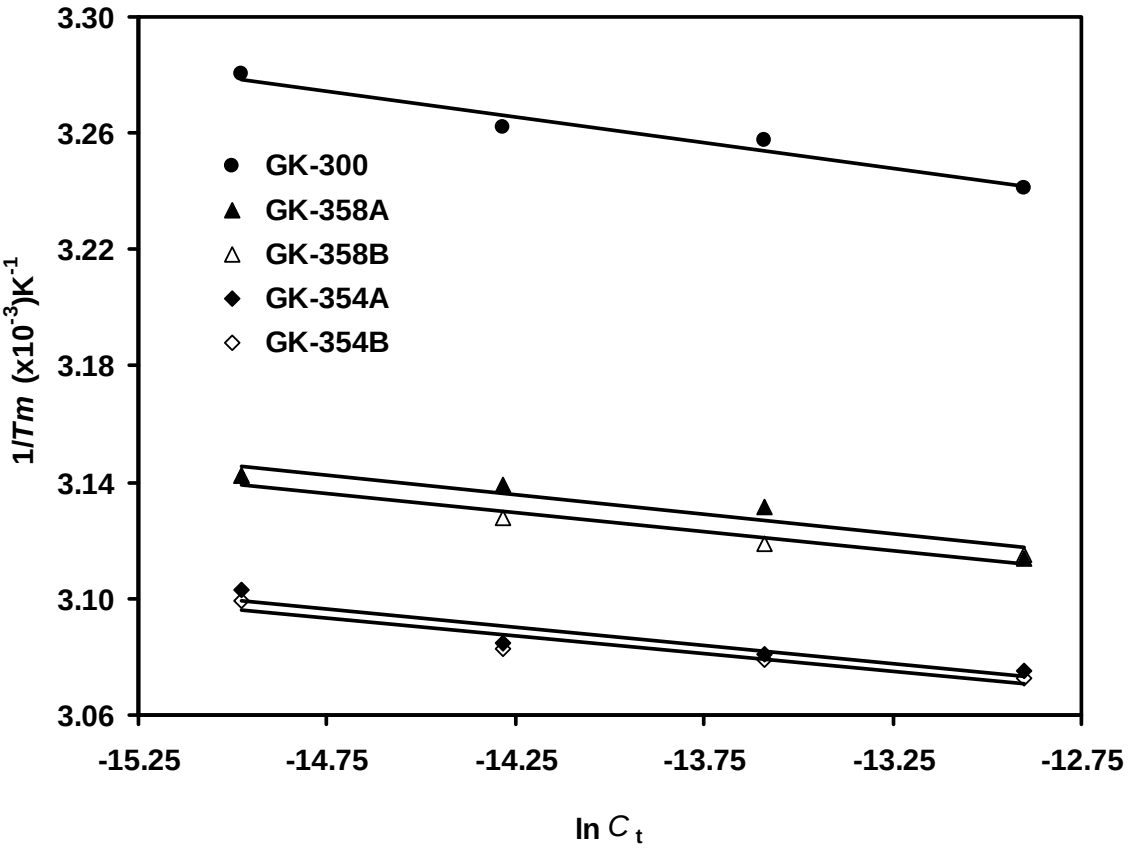


Figure S9. $1/T_m$ vs. ln C_t plot for melting of triplexes. Measurement were done in sodium cacodylate buffer (10 mM, pH 6.5) containing 100 mM NaCl, 1.0 mM spermine, and 10 mM $MgCl_2$ at different oligomer concentrations.

Table S1. Isolated yields and characterization data of the chimeric oligoDNA.

Oligomer	OD[a]	Isolated Yields (%)	ESI-mass Found	ESI-mass Calcd.
GK-368	43.4	42.2	7536.49	7536.21
GK-355A	11.6	28.0	7723.19	7723.32
GK-355B	9.9	24.0		
GK-359A	3.5	8.5	7666.95	7667.26
GK-359B	3.4	8.0		
GK-367A	16.7	40.5	7681.64	7681.27
GK-367B	18.2	44.5		
GK-354A	9.0	22.0	7868.55	7867.46
GK-354B	7.4	18.0		
GK-358A	3.4	8.0	7813.19	7811.40
GK-358B	3.5	8.5		
GK-366A	7.1	17.0	7827.28	7825.41
GK-366B	7.7	18.5		

[a]OD (optical density) is the absorbance of an oligomer at 260 nm per unit distance.

Bioconjugate Chemistry

ARTICLE

pubs.acs.org/bc

Synthesis of PAMAM Dendrimer Derivatives with Enhanced Buffering Capacity and Remarkable Gene Transfection Efficiency

Gwang Sig Yu,[†] Yun Mi Bae,[†] Hye Choi,[†] Bokyung Kong,[§] Insung S. Choi,[*,§] and Joon Sig Choi[*,†,‡]

[†]Department of Biochemistry

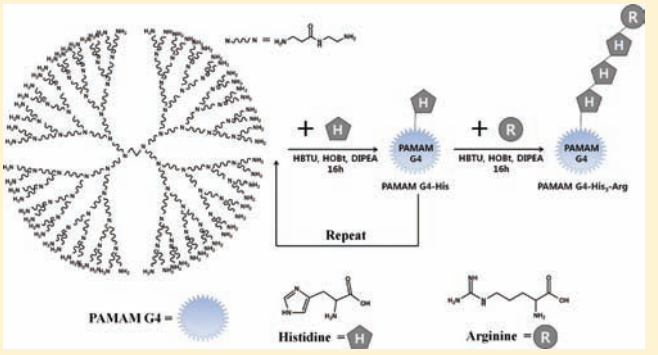
[‡]Graduate School of Analytical Science and Technology

Chungnam National University, Daejeon, 305-764, Korea

[§]Molecular-Level Interface Research Center, Department of Chemistry, KAIST, Daejeon, 305-764, Korea

Supporting Information

ABSTRACT: In this study, we introduced histidine residues into L-arginine grafted PAMAM G4 dendrimers to enhance proton buffering capacity and evaluated the physicochemical characteristics and transfection efficacies in vitro. The results showed that the synthesized PAMAM G4 derivatives effectively delivered pDNA inside cells and the transfection level improved considerably as the number of histidine residues increased. Grafting histidine residues into the established polymer vector PAMAM G4-arginine improved their proton buffering capacity. The cytotoxicity of PAMAM G4 derivatives was tested and it was confirmed that they displayed relatively lower cytotoxicity compared to PEI25KD in various cell lines. Also, confocal microscopy results revealed that PAMAM G4 derivatives effectively delivered pDNA into cells, particularly into the nucleus. These PAMAM dendrimer derivatives conjugated with histidines and arginines may provide a promising polymeric gene carrier system.



INTRODUCTION

The development of an effective and safe gene delivery carrier has become one of the most important factors enabling gene therapy. In the past decade, numerous studies have developed efficient transfection methods for delivering therapeutic genes into cells for human gene therapy. Viral and nonviral vector systems are the two major systems that transfer genetic material into cells. Currently, using adenoviruses and retroviruses to transfer genetic material (DNA or RNA) into cells is the general method in most ongoing gene therapy clinical trials. The viral vector system provides attractive advantages such as efficient transfection and high gene expression efficiency. However, there are some concerns such as immunogenicity, high toxicity, and the possibility of destructive integration into the human genome. Due to the disadvantages of viral vectors, the demands for alternatives to the viral vector system have increased.[1,2] Although they display lower transfection efficiency than viral vectors, using nonviral vectors to deliver therapeutic genes into cells has several advantages. Nonviral vectors can deliver a relatively larger size of DNA into cells, and they have lower cytotoxicity and greatly reduced immunogenicity.

Various methods are utilized to transfer genes into cells by nonviral approaches. Physical methods include a gene gun, electroporation, and hydrodynamic and ultrasound-mediated injection. These physical transfer techniques induce transient impacts on plasma membranes, so that genetic materials can be introduced. Compared with physical approaches, using chemical methods to transfer genes has also been investigated. Cationic lipids condense pDNA, which is negatively charged due to its phosphate backbone. Many cationic lipid-mediated gene delivery strategies have been studied since a report published by Felgner et al. in 1987.[3] Similar to cationic lipids, cationic polymers condense negatively charged pDNA through electrostatic interaction. Cationic polymers condense pDNA effectively and facilitate cellular uptake via endocytosis.[4−8] Cationic polymers include polyethyleneimine (PEI), polyamidoamine (PAMAM) dendrimer, chitosan, dextran, protamine, and cationic polypeptides such as poly(L-lysine).

PAMAM dendrimers are one of the most popular polymers used as a nonviral gene carrier because of their unique characteristics such as uniform size distribution, relatively higher transfection efficiency, and lower cytotoxicity compared to other traditional cationic polymers.[9,10] Many studies have investigated the enhanced transfection efficiency of modified PAMAM dendrimer derivatives. Grafting of specific ligands for certain receptors (e.g., RGD sequence for $\alpha_v\beta_3$ integrins) provides enhanced targeting effects to carriers.[11] Moreover, the acetylation of PAMAM dendrimers decreases cytotoxicity

Received: November 4, 2010
Revised: April 18, 2011
Published: May 02, 2011

ACS Publications © 2011 American Chemical Society

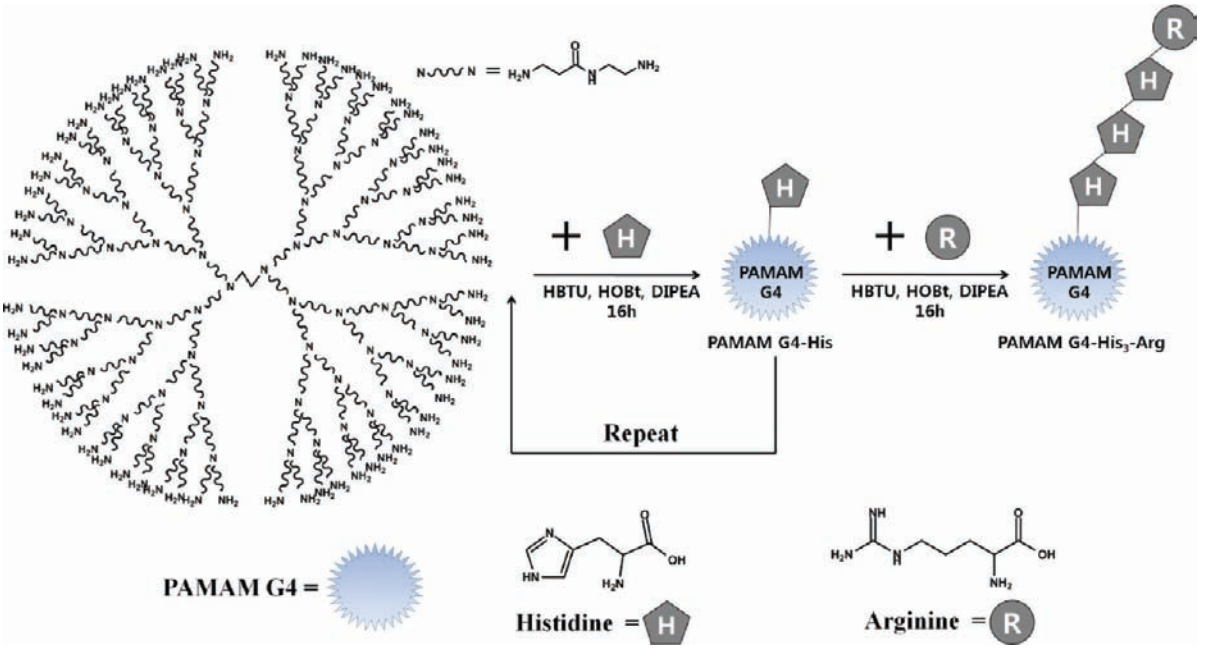


Figure 1. Overall synthesis scheme of PAMAM G4-His_n-Arg.

while maintaining membrane permeability.[12] In our previous study, we synthesized an arginine-conjugated PAMAM dendrimer, which shows enhanced transfection efficiency compared to the native PAMAM dendrimer. [13]

A PAMAM dendrimer has positively charged amine groups on the peripheral ends to allow interaction with the negatively charged pDNA phosphate backbone.[14,15] Therefore, it is essential that newly designed vectors have cationic functional groups in their structure. Moreover, several physiological barriers must be overcome to achieve effective transfection.[16] It is known that polyplexes could be internalized into cells by endocytosis forming endosomes.[17] These endosomes progress into a lysosome state, which has an acidic environment to digest external materials. Therefore, most of the complexes in lysosomes will collapse. Thus, the proton buffering ability of the carrier is needed to overcome this acidic environment of the lysosome. Although PAMAM dendrimers have proton buffering abilities (hypothesized proton sponge effect) in their tertiary amine, insertion of additional functional groups that act as proton sponges is required to enhance endosomal release.[18,19]

Durability against the acidic environment should increase the number of complexes escaping from endosomes to the cytosol. The histidine conjugation method could be helpful for increasing buffer capacity against acidic conditions due to the presence of imidazole ring groups that have pK_a of 6.0, which is a unique property that provides protonation ability in an acidic environment. Although native PAMAM dendrimers condense pDNA efficiently, additional conjugation with amino acids, such as histidine, arginine, and lysine, to the peripheral amine functional groups could contribute to their multifunctional properties. Particularly, histidine conjugation of a conventional polymer vector system has advantages not only in enhancing complexation ability but also in improving physicochemical strength against an acidic condition via the proton sponge effect. Some groups have reported applications of histidine as a proton buffering agent during liposomal delivery[20,21] and polyhistidine as a proton sponge unit.[22]

In this study, we conjugated histidine and arginine residues to PAMAM dendrimers to obtain higher proton buffering capacity with ionizable imidazole groups on histidine units together with the high gene expression ability of PAMAM G4-Arg. We investigated the physicochemical properties, polyplex formation, cytotoxicity, and transfection efficiency of PAMAM G4 derivatives. The intracellular distribution of synthesized PAMAM G4 derivatives was also confirmed using confocal microscopy.

MATERIALS AND METHODS

Materials. PAMAM generation 4, *N*,*N*-diisopropylethylamine (DIPEA), ammonium persulfate (APS), *N*,*N*,*N*′,*N*′-tetramethylethane-1,2-diamine (TEMED), and *N*,*N*-dimethylformamide (DMF) were purchased from Sigma-Aldrich (Seoul, South Korea). *N*-Hydroxybenzotriazole (HOBt), 2-(1*H*-benzotriazole-1-yl)-1,1,3,3-tetra-methyluronium (HBTU), and Fmoc-His(trt)-OH were purchased from Anaspec (San Jose, CA, USA), and Fmoc-Arg-(pbf)-OH was obtained from Novabiochem (San Diego, CA, USA). Fetal bovine serum (FBS), Dulbecco's modified Eagle's medium (DMEM), and 100× antibiotic−antimycotic agent were purchased from Gibco (Gaithersburg, MD, USA). The luciferase expression plasmid was prepared as reported previously.[23] The luciferase assay kit was purchased from Promega (Madison, WI, USA). The Micro BCA Protein Assay Kit was obtained from Pierce (Rockford, IL, USA).

Synthesis of PAMAM G4-$His_{(1,2,3)}$-Arg. Fourth-generation PAMAM was reacted with 4 equiv of Fmoc-His(trt)-OH, HBOt, and HBTU and 8 equiv of DIPEA in anhydrous DMF solution for 16 h at room temperature (R.T.). Then, the intermediate product was precipitated with an excess amount of cold ethyl ether. The precipitated intermediate was dissolved with 30% piperidine solution (v/v) and reacted for 1 h to deprotect the Fmoc group on the histidine unit. After the deprotection procedure, the intermediate product was precipitated with cold ethyl ether. Additional histidine elongation could be conducted by repeating the synthetic process described above. After elongation of the histidine unit, 4 equiv of

Fmoc-Arg(pbf)-OH, HOBt, and HBTU and 8 equiv of DIPEA were reacted with the intermediate product using the same method described above. After precipitation with cold ethyl ether, the intermediate product was reacted with 30% piperidine solution for 1 h to remove the Fmoc group on the arginine unit. Then, the product was washed and precipitated with cold ethyl ether. The precipitated product was dissolved with deprotection reagent (95:2.5:2.5, trifluoroacetic acid/triisopropylsilane/H_2O, v/v, respectively) and stirred for 6 h at R.T to deprotect the pbf and trt groups on each amino acid unit. The unrefined product was dialyzed with distilled water using dialysis membrane (MWCO 3,500, Spectra/por) for 24 h to purify the product from unreacted amino acids or coupling reagents. After dialysis, the final product was freeze−dried. Overall schemes for the synthesis of PAMAM conjugates are presented in Figure 1.

Agarose Gel Retardation Assay and Dynamic Light Scattering Analysis. A complex test was conducted to analyze the complex formation of PAMAM derivatives with plasmid DNA under various charge ratio conditions. Complexes were prepared containing polymers and plasmid DNA with different charge ratios by incubating them in HEPES buffer (25 mM, pH 7.4). A fixed volume of plasmid DNA and HEPES buffer with different polymer charge ratios was mixed at R.T. for 30 min. Each complex sample was analyzed on a 0.7% agarose gel containing ethidium bromide (0.5 μg/μL gel). Agarose gel electrophoresis typically required 30 min at 100 V. The size distribution and zeta potential of the polyplexes were measured using a Zetasizer Nano-Zs (Malvern Instruments, Worcestershire, U.K.).

PAGE Study. Native polyacrylamide gel electrophoresis study of PAMAM derivatives was performed on a Mini-Protean Tetra Cell System (Biorad, Hercules, CA, USA). Citrate buffer (pH 3.0, 0.1 M) was used as the buffer system, and 6% T gels (T = g acrylamide + g *N,N′*- methylenebisacrylamide/100 mL solution) were prepared with a 30% acrylamide mixture solution (Biorad) with a combination of APS, TEMED, and Tris-HCl buffer (pH 7.5). The 6% T gels were acidified (pH 2) before adding the APS and TEMED using 5 N HCl to protonate the polymers and produce a narrow band. Reverse polarity (with the cathode at the bottom of the gel) was used for analysis of the positively charged PAMAM derivatives. Native PAGE typically required 50 min at 100 V.

Polymer samples (1 μg) were prepared, and 1 μL of tracking dye (50% sucrose solution containing 1% methylene blue) was added to the samples for loading. Gels were stained overnight with 0.025% Coomassie Blue R-250 in 40% methanol and 7% acetic acid aqueous solution. After the staining process, the gels were destained with 10% (v/v) methanol and 10% acetic acid in water.

Acid−Base Titration Assay. The protonation ability of PAMAM derivatives was determined by the acid−base titration method. PEI25KD (2 mg, 8×10^{-8} mol) and the same equivalents of PAMAM G4, PAMAM G4-Arg, and PAMAM G4-$His_{(1,2,3)}$-Arg were titrated with 0.1 N HCl. NaCl (150 mM) and H_2O were titrated as a control group. The pH value was determined with a pH-meter (pH211 microprocessor pH meter, HANA Instruments, Seoul, South Korea).

Briefly, each titration sample was prepared by adding an equivalent amount of sample (8×10^{-8} mol) in 4 mL of 150 mM NaCl, and 100 μL of 1 N NaOH was added to the sample solution. Samples were titrated by adding aliquots (20 μL) of 0.1 N HCl until pH 3.0 was reached.

Cytotoxicity Assay. The cytotoxicity of the PAMAM derivatives was assessed using the EZ-Cytox Reagent (Daeil Lab Service, Seoul, South Korea) based on the WST-1 method. Briefly, HepG2, 293, and NIH 3T3 cells were seeded in 96-well plates at a density of 2×10^4 cells/well except for HeLa cells (1×10^4 cells/well) and incubated in 100 μL of DMEM containing 10% FBS. After a 1-day incubation, the cells were treated with various concentrations of PEI25KD, PAMAM G4, and PAMAM derivatives. After further incubation for 24 h, 10 μL of EZ-Cytox Reagent was added to each well and incubated for an additional 4 h. Absorbance was measured at 450 nm using a VESAmax microplate reader (VERSAmax, Molecular Devices, Sunnyvale, CA, USA).

Confocal Microscopy Study. HeLa cells (5×10^3 cell/well) were seeded on culture slides and incubated at 37 °C. After a 24 h incubation, the cells were treated with polyplexes composed of various polymers with Alexa Fluor 532 labeled pDNA. Alexa Fluor 532 labeled pDNA was prepared according to the manufacturer's protocol. After a further incubation for 24 h, old medium was removed, and the cells were washed with PBS. Cells were fixed in 4% paraformaldehyde for 10 min, and the nuclei were stained with 10 μg/mL bisbenzimide (Hoechst 33342) for 7 min and then washed with PBS several times. The plastic chamber on the glass slide was detached, and the cells were treated with mounting medium (Dako, Carpinteria, CA, USA) and covered with a coverslip. The fluorescent signal was analyzed using a Zeiss LSM 5 Live confocal laser microscope.

Cell Culture and Transfection Assay. Human hepatocellular liver carcinoma HepG2 cells, human embryonic kidney 293 cells, murine fibroblast NIH3T3 cells, and human epithelial carcinoma HeLa cells were maintained at 37 °C in an incubator (5% CO_2, 95% relative humidity). All cells were maintained in T25 flasks using DMEM supplemented with 10% FBS and 1% antibiotics. Cells were subcultured using a 0.25% trypsin/ethylenediaminetetraacetic acid solution when confluence reached 70−90%.

For the transfection study, cells were seeded in a 24-well plate at a density of 2×10^5 cells/well except for HeLa cells (1×10^5 cells/well) and incubated for 24 h to reach 70−80% confluency. The transfection complex was prepared by mixing 1 μg of plasmid DNA with various amounts of PAMAM derivatives containing 10% FBS for 30 min at R.T. To compare the transfection efficiency, PEI25KD/pDNA (polymer nitrogen(+)/pDNA phosphate(−) (N/P) ratio: 7/1, optimal condition) and PAMAM G4/pDNA (N/P ratio: 4/1, optimal condition) complexes were prepared as a control group. PAMAM G4 derivatives were prepared with N/P ratios of 4:1 to 8:1 to compare gene transfection efficiency in terms of charge ratios. Then, cells were treated with the complex solution and incubated for 24 h at 37 °C. Old medium was removed, and the cells were washed with DPBS and lysed for 30 min using reporter lysis buffer (Promega). Luciferase activity was measured using Lumat LB 9507 (Berthold Technology, Bad Wildbad, Germany), and protein content was measured using the Micro BCA Protein Assay Kit (Pierce).

Statistical Analysis. The statistical analysis was performed using the unpaired Student's *t*-test (*GraphPad Prism 5*). Differences between groups were considered statistically significant at $P < 0.05$ (*), $P < 0.01$ (**), and $P < 0.001$ (***).

RESULTS AND DISCUSSION

Synthesis of PAMAM G4-$His_{(1,2,3)}$-Arg. This study was based on our previous report in which we demonstrated that the transfection efficiency of the PAMAM G4 dendrimer is enhanced by surface modification with L-arginine. It was confirmed that introducing L-arginine to the surface of the PAMAM dendrimer enhanced transfection efficiency.[13] Some reports have indicated

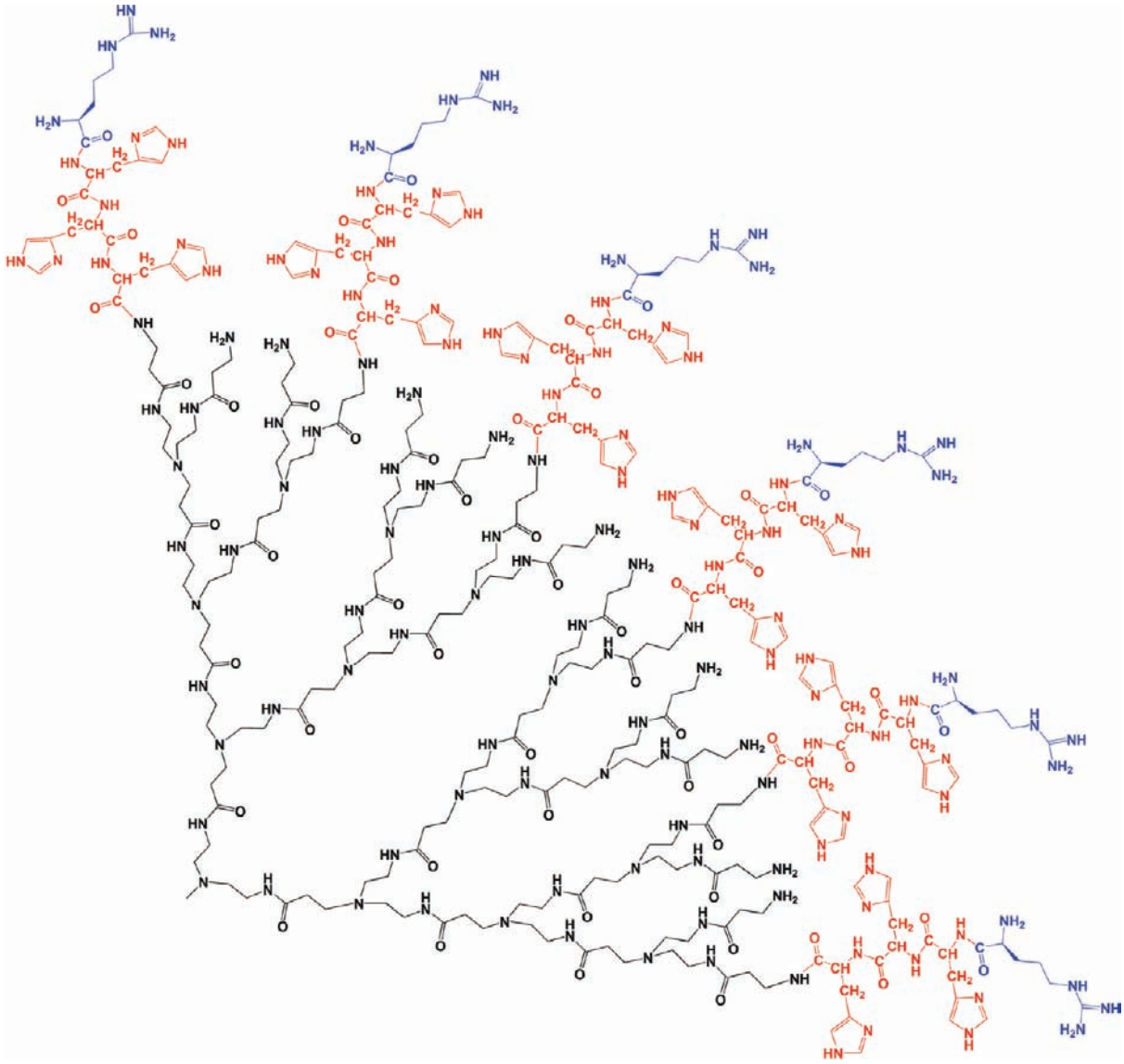


Figure 2. Chemical structure of PAMAM G4-His_3-Arg (quarter section). PAMAM G4 dendrimer core appears in black, histidines in red, and arginines in blue, respectively.

that arginine-rich peptides can deliver oligo DNAs and even proteins *in vivo*.[24,25] Furthermore, many groups have reported that oligo-arginine can serve as a membrane translocational signal.[26] Meanwhile, in 2008, Asayama et al. presented carboxymethyl poly(L-histidine) as a pH-sensitive polypeptide to enhance the transfection efficiency of polyplex gene delivery.[27] Recently, in 2009, Nakamura et al. reported that the conjugation of histidine with mannosylated cholesterol derivatives showed significantly higher cellular uptake in macrophages.[28] More recently, in 2010, Song et al. introduced histidine residues into the TAT peptide and applied them to a magnetofection system, and the transgene expression via ternary magnetofection complexes displayed a 4-fold improvement *in vitro*.[29] Many other groups have utilized polyhistidine to increase transfection efficiency.[30]

The histidine imidazole group has a pK_a value of 6.0 and plays a role as a proton sponge in a slightly acidic environment. Furthermore, the escape of pDNA from the endosome is one of the important steps for successful nonviral transfection methods, and the proton buffering ability of the gene carrier is necessary to increase transfection efficiency. Hence, in this study, we introduced histidine units into the L-arginine grafted PAMAM G4 dendrimer to enhance proton buffering capacity.

The synthesized PAMAM G4-$His_{(1,2,3)}$-Arg was confirmed by ^{1}H nuclear magnetic resonance (NMR) spectroscopy (Supporting Information, Figure S1). The number of histidine and arginine units conjugated to PAMAM G4 was calculated based on the ^{1}H NMR data. Arginine units had characteristic peaks at 1.5 ppm and 3.76 ppm, whereas the histidine units showed characteristic peaks at 4.5 ppm, 6.8 ppm, and 7.6 ppm. From the ^{1}H NMR results, it was confirmed that more than 60 histidine and arginine units were conjugated to the surface primary amines of PAMAM G4. This number of conjugated units means that more than 95% of the surface amines were covered with $histidine_{(1,2,3)}$-arginine peptide. The overall schematic synthesis process of PAMAM G4-$His_{(1,2,3)}$-Arg is presented in Figure 1, and the structural representation of the histidine-arginine peptide conjugated to PAMAM G4 (a quarter section) is shown in Figure 2.

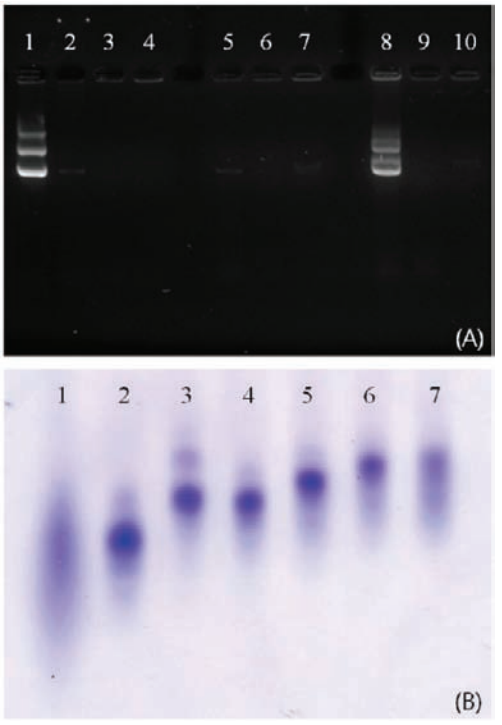


Figure 3. (A) Agarose gel electrophoresis retardation assay of pDNA by PAMAM G4 derivatives. pDNA only (lane 1); polymer/DNA charge ratio 1:1 (lanes 2, 5, and 8); 2:1 (lanes 3, 6, and 9); 4:1 (lanes 4, 7, and 10). Lanes 2−4, 5−7, and 8−10 represents PAMAM G4-His_1-Arg, PAMAM G4-His_2-Arg, and PAMAM G4-His_3-Arg with pDNA, respectively. (B) Native PAGE analysis of PAMAM G4 derivatives. PEI25KD, PAMAM G4, PAMAM G5, PAMAM G4-Arg, PAMAM G4-His_1-Arg, PAMAM G4-His_2-Arg, and PAMAM G4-His_3-Arg in lanes 1, 2, 3, 4, 5, 6, and 7, respectively.

Analysis of the Agarose Gel Retardation Assay. An agarose gel retardation assay was performed to confirm the complex formation of PAMAM derivatives with pDNA. Because the PAMAM derivatives have positively charged amine groups on their arginine units, they can interact with the negatively charged pDNA phosphate backbone. Each PAMAM derivative was complexed with a fixed amount of pDNA at an N/P ratio of 1:1 to 4:1. As shown in Figure 3A, PAMAM G4-His_1-Arg and PAMAM G4-His_2-Arg retarded pDNA at an N/P ratio of 1:1. However, PAMAM G4-His_3-Arg showed complete retardation at an N/P ratio of 2:1.

It is thought that the increased ratio of PAMAM G4-His_3-Arg compared to His_1 and His_2 is due to an increase in molecular weight and a decrease in charge density. Molecular weight and charge density of polycationic polymers are the most significant factors for forming mature polyplexes. It is generally accepted that polycationic vehicles, which have a high charge density, condense pDNA more effectively.[31] Furthermore, the distance between the DNA phosphate backbone and the polycation molecule is just as important to formation of polyplexes as the charge density.[32] The pK_a of the imidazole group on histidine is approximately 6.0; thus, these groups might remain poorly protonated in a physiological environment (pH 7.4). Hence, forming polyplexes with arginine residues on the peripheral end of a functional group occurs more often than that of histidine residues. It is thought that only a small portion of the protonated histidines participate in forming polyplexes, and that the surface arginines provide a main force for complexation with pDNA.

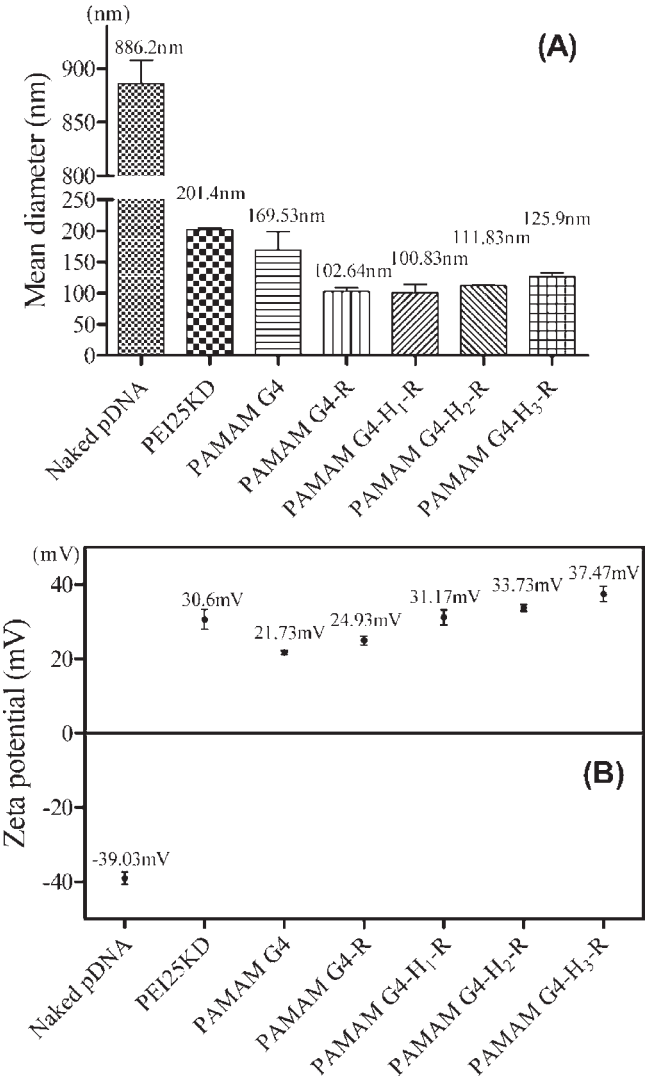


Figure 4. (A) Average diameter and (B) zeta potential values of pDNA and polymer/pDNA complexes. Data are expressed as mean ± standard deviation (n = 3).

Although grafting histidine units between the PAMAM G4 dendrimer and L-arginine may not play a major role in the formation of complexes, the results indicate that histidine-arginine peptide conjugated PAMAM derivatives could also effectively condense pDNA via electrostatic interactions at a relatively low N/P ratio.

Size Measurement and Zeta Potential Analysis of Polyplexes. Delivering the naked plasmid DNA into cells is very limited due to enzymatic degradation, the polyanionic character of pDNA, and its large size. Cationic proteins, such as serum proteins, can bind with pDNA in the bloodstream, and enzymes such as DNase may degrade the pDNA. Therefore, safe and efficient introduction of DNA into cytoplasm and translocation into the nucleus are essential steps for successful gene therapy.

In this study, the mean diameter and zeta potential values of each polyplex were examined at the optimum charge ratio. The charge ratio of PEI25KD was 7:1. PAMAM G4 and derivatives were examined at a charge ratio of 8:1. As shown in Figure 4A, the mean diameter of the naked pDNA was approximately 900 nm. The PEI25KD/pDNA complex showed a mean diameter of 201.4 ± 4.86 nm, and the native PAMAM G4 polyplex was

169.53 ± 49.92 nm. Interestingly, the arginine-grafted PAMAM G4 dendrimer revealed a size of 102.64 ± 11.12 nm compared to native PAMAM G4. The sizes of the PAMAM G4-His_1-Arg, PAMAM G4-His_2-Arg, and PAMAM G4-His_3-Arg polyplexes were 100.83 ± 22.81 nm, 111.83 ± 1.85 nm, and 125.9 ± 11.52 nm, respectively. From the results, the synthesized PAMAM derivatives, including PEI25KD and native PAMAM G4, formed nanometer-sized polyplexes effectively.

As shown in Figure 4B, the zeta potential values of the PAMAM derivatives increased along with the elongation of histidine units. PEI25KD showed a highly positively charged zeta potential value of 30.6 ± 4.60 mV and that of PAMAM G4 was 21.73 ± 0.93 mV. As expected, arginine- and histidine-coupled PAMAM derivatives showed increased zeta potential values compared to native PAMAM G4. The zeta potential value for PAMAM G4-Arg was 24.93 ± 2.03 mV, and this increased value seemed to come from the increased surface charge of polyplexes. Similar results were revealed for PAMAM G4-$His_{(1,2,3)}$-Arg with zeta potentials of 31.17 ± 3.46 mV, 33.73 ± 1.56 mV, and 37.47 ± 3.50 mV, respectively. As the guanidine group of arginine and the imidazole group of histidine have pK_a of 12.0 and 6.0, respectively, the $His_{(1,2,3)}$-Arg conjugated PAMAM derivatives displayed a positive charge under neutral conditions. Taken together, these results suggest that PAMAM derivatives can effectively condense pDNA into a nanometer size (around 100 nm) and possess zeta potential values of approximately 35 mV.

The actual size and shape of each polyplex were further obtained using atomic force microscopy (AFM) (Supporting Information, Figure S2). PEI25KD showed a mostly globular shape, and some large polyplexes were also observed. Particularly, PAMAM G4-Arg had a very compact particle size (<100 nm) and narrow size distribution compared to native PAMAM G4. PAMAM G4 and the His_3-Arg-conjugated PAMAM G4 displayed almost the same size distribution (100−200 nm), which is slightly larger than the DLS results. The difference in size distribution between the DLS and AFM images seems to have occurred because the AFM images are usually taken from dehydrated complexes that were prepared not in a buffer with salt but in deionized water, which is an unnatural condition compared with that of the DLS experiment.

Analysis of Native PAGE Assay. Figure 3B shows the relative size distribution of each synthesized PAMAM derivative. A reverse polarity system was applied because of the cationic nature of the PAMAM derivatives, including PEI25KD. A 0.1 M citrate solution was used as the buffer system because an acidic environment is essential for protonating samples and allows sample migration on a polyacrylamide gel. PEI25KD appeared as a broad band because of its high polydispersity nature (lane 1). Lanes 2, 3, and 4 represent PAMAM G4, PAMAM G5, and PAMAM G4-Arg, respectively. These groups are presented as control groups. Lanes 5, 6, and 7 are PAMAM G4-His_1-Arg, PAMAM G4-His_2-Arg, and PAMAM G4-His_3-Arg, respectively. The PAGE results showed that a different size distribution was observed as the histidine conjugation number increased. PAMAM G4-His_3-Arg showed less migration than other low molecular weight derivatives. Even though this method provides insufficient information about the molecular weights of the synthesized polymers, this PAGE result could be helpful for qualitative assessing and comparing the size distribution between the PAMAM derivatives.

Titration of PAMAM G4 Derivatives. The side group of histidine has a pK_a of 6.0, so it should be much less protonated at physiological pH than primary amine groups. Therefore, an increased number of histidine units on PAMAM derivatives

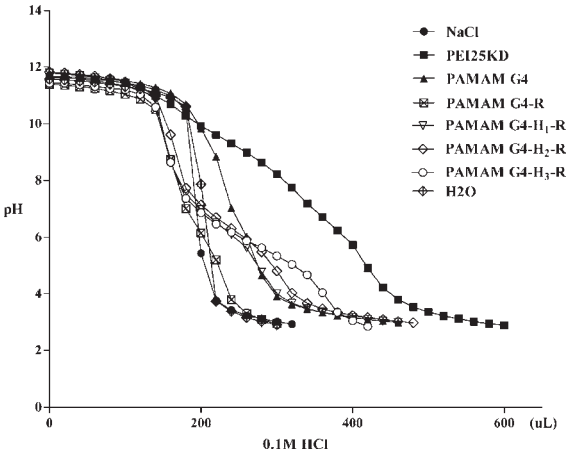


Figure 5. Acid−base titration profiles of the polymers.

may play an important role in increasing the buffer capacity at an acidic pH. This may also explain why $His_{(1,2,3)}$-Arg peptide-conjugated PAMAM G4 derivatives displayed much higher potency than PAMAM G4 and PAMAM G4-Arg in terms of the proton sponge effect. The acid−base titration profile of the $His_{(1,2,3)}$-Arg peptide conjugated to PAMAM G4 is presented in Figure 5. PEI25KD showed the strongest buffering ability, whereas native PAMAM G4 showed less buffering capacity. An overall decrease in buffering capacity was observed when only arginine was grafted to the PAMAM G4 dendrimer. Interestingly, restoration of the buffering effect in the pH range 6−7 was observed in the $His_{(1,2,3)}$-Arg conjugated PAMAM G4 dendrimer. More interestingly, an increase in buffering ability was observed in the pH range 3.5−6, as the number of histidines increased. Although the $His_{(1,2,3)}$-Arg peptide-conjugated PAMAM derivatives showed relatively low buffering ability compared to PEI25KD, they revealed increased buffering capacity in a slightly acidic pH range as the number of histidine residues increased. Moreover, the $His_{(1,2,3)}$-Arg peptide conjugation remarkably influenced the proton buffering ability compared with native PAMAM G4. This result could be strong evidence for the greatly increased proton buffering efficiency of the PAMAM G4-$His_{(1,2,3)}$-Arg derivatives through the protonation of imidazole rings in an acidic condition.

Cytotoxicity Study. The cytotoxicity of PAMAM G4 derivatives was confirmed using the EZ-Cytox Cell Viability Assay Kit based on the WST-1 assay. WST-1 (4-[3-(4-iodophenyl)-2-(4-nitrophenyl)-2*H*-5-tetrazolio]-1,3-benzene disulfonate) has been used to determine cytotoxic effects on mammalian cells.[33] Similar to the MTT assay, WST-1 reacts with mitochondrial succinate-tetrazolium reductase and forms a water-soluble formazan dye. MTT forms a water-insoluble formazan dye, so the use of WST-1 is convenient because the additional solubilization step can be omitted. To examine the cytotoxicity of polymer vectors, PEI25KD, native PAMAM G4, and PAMAM G4-Arg were compared with PAMAM derivatives at various concentrations in HepG2, 293, NIH3T3, and HeLa cells (Figure 6). Each cell line was incubated for 48 h with increasing amounts of polymers. The results showed that PEI25KD was highly toxic in every cell line, and that PAMAM derivatives were much less toxic. This is consistent with previous reports that the increased charge density of gene delivery carriers generally produces greater cytotoxicity.[5,34] Even though PAMAM G4-His_2-Arg showed a slight cytotoxic effect in 293 and HeLa cells as the polymer concentration increased, the $His_{(1,2,3)}$-Arg peptide

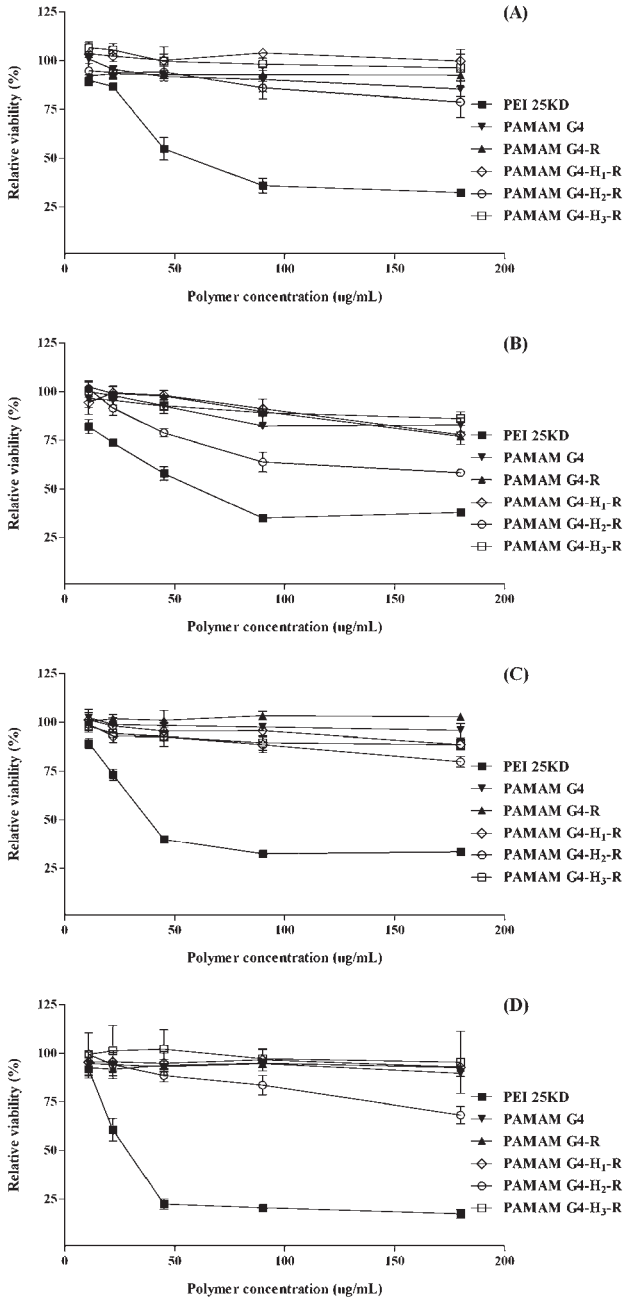


Figure 6. Cytotoxicity assay for (A) HepG2 cells, (B) 293 cells, (C) NIH3T3, and (D) HeLa cells. Each point indicates the average and standard deviation from triplicates.

conjugated PAMAM G4 derivatives displayed much lower and moderate cytotoxicity than PEI25KD at all concentration levels tested in this study.

Intracellular Distribution of Polyplexes. PAMAM G4 derivatives were complexed with Alexa Fluor 532-labeled pDNA at optimal charge ratios and transfected into HeLa cells to analyze the cellular distribution of polyplexes. After a 24 h incubation at 37 °C, the intracellular distribution of the polyplex was confirmed by confocal microscopy.

As shown in Figure 7, no signals were observed from the cell only (- pDNA/- polymer) sample group due to the lack of polymers delivering fluorescently labeled pDNA (A). Delivering

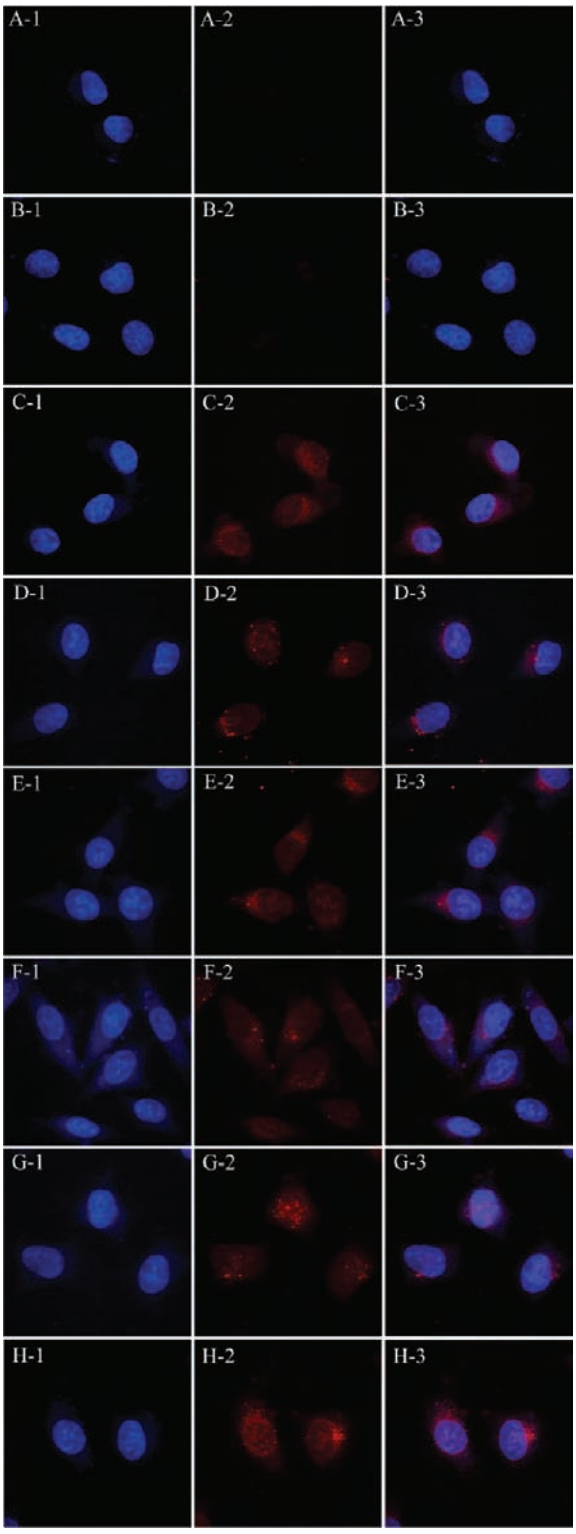


Figure 7. Confocal microscopy images. (A) HeLa cells only; (B) HeLa cells with pDNA; (C) PEI25KD/pDNA; (D) PAMAM G4/pDNA; (E) PAMAM G4-Arg/pDNA; (F) PAMAM G4-His_1-Arg/pDNA; (G) PAMAM G4-His_2-Arg/pDNA; and (H) PAMAM G4-His_3-Arg/pDNA polyplexes in HeLa cells. Bisbenzimide (Hoechst 33342) was used to stain the nucleus (blue, image 1) and Alexa 532-labeled pDNA was used to localize pDNA and polymer/pDNA complexes (red, image 2). The merged image of the respective image 1 and 2 is shown as image 3.

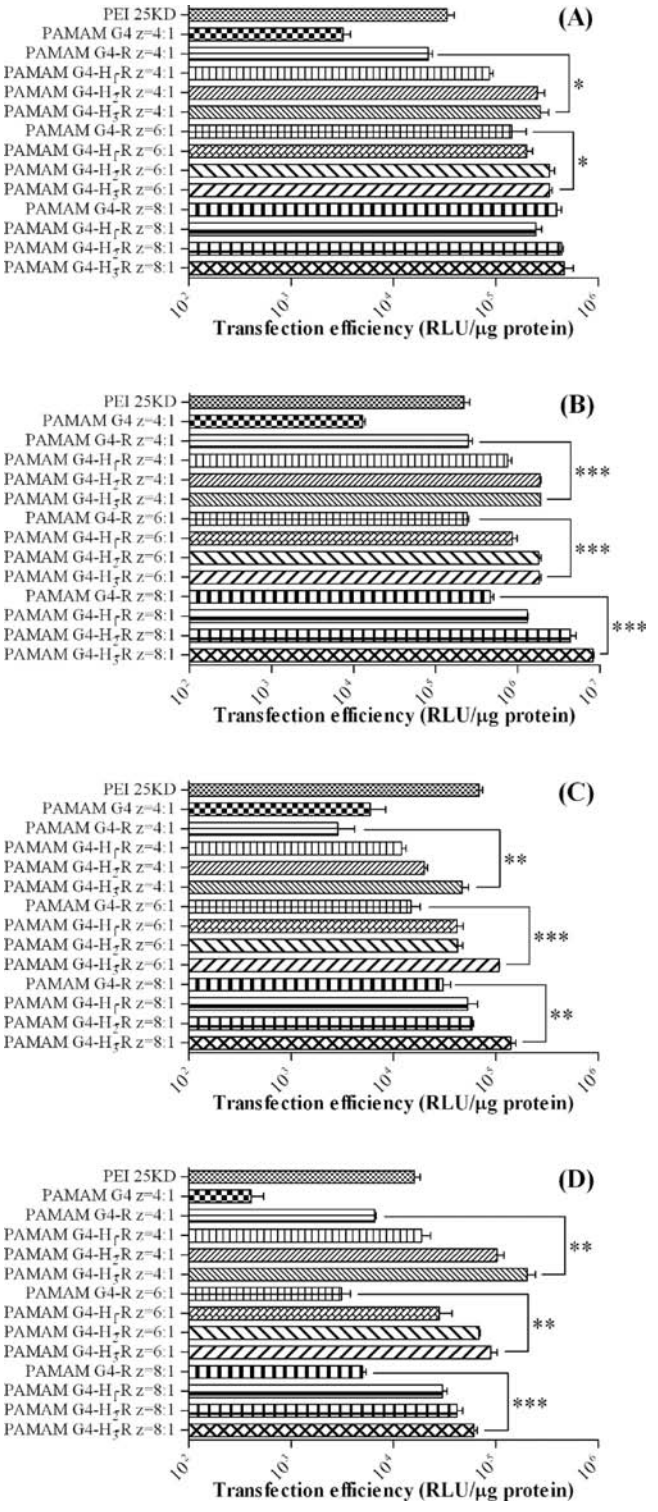


Figure 8. Transfection efficiencies of PAMAM G4 derivatives on (A) HepG2 cells, (B) 293 cells, (C) NIH3T3, and (D) HeLa cells. Data are shown as mean ± standard deviation ($n = 3$). *$p < 0.05$, **$p < 0.01$, and ***$p < 0.001$.

pDNA without polymer vectors also resulted in no pDNA signals in the cytoplasm or the nucleus (B). The PEI25KD polyplex showed a regular pattern of pDNA distribution, whereas PAMAM G4 and its derivatives showed a spot pDNA signal pattern (C, D). It was believed that PEI25KD had a high proton buffering ability, so that the polyplex could escape easily from endosome to the cytoplasm. However, PAMAM G4 and its derivatives showed much less proton buffering capacity than PEI25KD, so they localized in endosomes more than the PEI25KD polyplex. Because of these differences in proton buffering capacity, they were localized in different locations in the cells after the 24 h transfection. Interestingly, as shown in Figure 7 (F,G,H), the pDNA signal increased in both the cytoplasm and the nucleus as the histidine elongation number increased. The strongest pDNA signal was observed in three histidine units conjugated to the PAMAM G4 dendrimer (H). A more interesting point is that the pDNA signal increased inside the nucleus as the histidine elongation number increased. These results clearly indicate that inserting histidine units into PAMAM G4-Arg increased the cellular uptake and localization of polyplexes to the nucleus.

Transfection Efficiency of Different Cell Lines. HepG2, 293, NIH3T3, and HeLa cells were incubated with PAMAM G4 derivatives at various charge ratios to determine the transfection efficiency of the synthesized PAMAM G4 derivatives. Transfection efficiency was evaluated as the expressed luciferase activity divided by total cellular protein in the presence of 10% serum. PEI25KD, native PAMAM G4, and PAMAM G4-Arg were used as control reagents under optimal conditions. In general, an excess amount of polycationic polymers can condense oppositely charged DNA more compactly;[35] thus, excessive PAMAM G4 derivatives along with the polyplexes could have a positive effect on gene transfer, although the transfection efficiency may be saturated under optimum conditions. As shown in Figure 8, PAMAM G4 derivatives generally showed higher transfection efficiencies than the native PAMAM G4 dendrimer and even better than PEI25KD (N/P ratio of 7:1). Moreover, the transfection efficiency of the PAMAM G4 derivatives seemed to be dependent upon the number of histidines and the charge ratio. Interestingly, the highest transfection efficiency appeared at an N/P ratio of 4:1 in the case of HeLa cells. For HepG2, 293, and NIH3T3 cells, PAMAM G4 derivatives displayed higher gene expression levels as the number of conjugated histidines and the charge ratio increased. Interestingly, a significant increase in the gene expression level was observed in the $His_{(1,2,3)}$-Arg conjugated PAMAM G4 derivatives compared to PAMAM G4-Arg for the cell lines. The gene expression level increased up to 10-fold compared to PAMAM G4-Arg at a charge ratio of 8:1. This result indicates that the $His_{(1,2,3)}$-Arg conjugated PAMAM G4 dendrimer could improve gene transfection efficiency and suggests that the proton buffering effect of the imidazole group should improve complex durability and enhance the localization of complexes into the nucleus as well as the cytoplasm.

CONCLUSION

We synthesized PAMAM G4 derivatives with histidine and arginine residues and effectively transfected various cell lines through enhanced proton buffering capacity induced by histidine residue conjugation. Synthesized PAMAM G4 derivatives effectively condensed pDNA at a low charge ratio, and the transfection activity improved considerably when the number of histidine residues increased. Adding histidine units into the established PAMAM G4-Arg polymer vectors improved their proton buffering capacity in the pH range 3.5−6. The cytotoxicity of PAMAM derivatives was tested, and it was confirmed that they displayed relatively low cytotoxicity compared to PEI25KD in various cell lines. The confocal microscopy results revealed that PAMAM G4 derivatives effectively delivered pDNA into the cells, particularly into the nucleus.

In summary, PAMAM G4 derivatives showed remarkable transfection efficiency, low cytotoxicity, and improved proton buffering capacity and are highly promising as a new gene delivery vector system.

■ ASSOCIATED CONTENT

Supporting Information. ^{1}H nuclear magnetic resonance (NMR) spectra of the PAMAM G4 derivatives and atomic force microscopy images of polymer/pDNA complexes. This material is available free of charge via the Internet at http://pubs.acs.org.

■ AUTHOR INFORMATION

Corresponding Author

*E-mail addresses: ischoi@kaist.ac.kr, joonsig@cnu.ac.kr. Phone: +82-42-821-5489. Fax: +82-42-822-7548.

■ ACKNOWLEDGMENT

This work was supported by Basic Science Research Program through the National Research Foundation of Korea (NRF) funded by the Ministry of Education, Science and Technology (20100021647) and the "Human Resource Development Center for Economic Region Leading Industry" Project, supported by the Ministry of Education, Science & Technology (MEST) and the National Research Foundation of Korea (NRF).

■ REFERENCES

(1) Luo, D., and Saltzman, W. M. (2000) Synthetic DNA delivery systems. *Nat. Biotechnol. 18*, 33–37.

(2) Vijayanathan, V., Thomas, T., and Thomas, T. J. (2002) DNA nanoparticles and development of DNA delivery vehicles for gene therapy. *Biochemistry 41*, 14085–14094.

(3) Felgner, P. L., Gadek, T. R., Holm, M., Roman, R., Chan, H. W., Wenz, M., Northrop, J. P., Ringold, G. M., and Danielsen, M. (1987) Lipofection - a highly efficient, lipid-mediated DNA-transfection procedure. *Proc. Natl. Acad. Sci. U.S.A. 84*, 7413–7417.

(4) Chemin, I., Moradpour, D., Wieland, S., Offensperger, W. B., Walter, E., Behr, J. P., and Blum, H. E. (1998) Liver-directed gene transfer: a linear polyethylenimine derivative mediates highly efficient DNA delivery to primary hepatocytes in vitro and in vivo. *J. Viral Hepatitis 5*, 369–375.

(5) Haensler, J., and Szoka, F. C. (1993) Polyamidoamine cascade polymers mediate efficient transfection of cells in culture. *Bioconjugate Chem. 4*, 372–379.

(6) Hosseinkhani, H., Azzam, T., Tabata, Y., and Domb, A. J. (2004) Dextran-spermine polycation: an efficient nonviral vector for in vitro and in vivo gene transfection. *Gene Ther. 11*, 194–203.

(7) Erbacher, P., Zou, S. M., Bettinger, T., Steffan, A. M., and Remy, J. S. (1998) Chitosan-based vector/DNA complexes for gene delivery: Biophysical characteristics and transfection ability. *Pharm. Res. 15*, 1332–1339.

(8) Wu, G. Y., and Wu, C. H. (1988) Receptor-mediated gene delivery and expression invivo. *J. Biol. Chem. 263*, 14621–14624.

(9) Cloninger, M. J. (2002) Biological applications of dendrimers. *Curr. Opin. Chem. Biol. 6*, 742–748.

(10) Lee, C. C., MacKay, J. A., Frechet, J. M. J., and Szoka, F. C. (2005) Designing dendrimers for biological applications. *Nat. Biotechnol. 23*, 1517–1526.

(11) Shukla, R., Thomas, T. P., Peters, J., Kotlyar, A., Myc, A., and Baker, J. R. (2005) Tumor angiogenic vasculature targeting with PAMAM dendrimer-RGD conjugates. *Chem. Commun.* 5739–5741.

(12) Kolhatkar, R. B., Kitchens, K. M., Swaan, P. W., and Ghandehari, H. (2007) Surface acetylation of polyamidoamine (PAMAM) dendrimers decreases cytotoxicity while maintaining membrane permeability. *Bioconjugate Chem. 18*, 2054–2060.

(13) Choi, J. S., Nam, K., Park, J., Kim, J. B., Lee, J. K., and Park, J. (2004) Enhanced transfection efficiency of PAMAM dendrimer by surface modification with L-arginine. *J. Controlled Release 99*, 445–456.

(14) Boussif, O., Lezoualch, F., Zanta, M. A., Mergny, M. D., Scherman, D., Demeneix, B., and Behr, J. P. (1995) A versatile vector for gene and oligonucleotide transfer into cells in culture and in-vivo - polyethylenimine. *Proc. Natl. Acad. Sci. U.S.A. 92*, 7297–7301.

(15) Wu, G. Y., and Wu, C. H. (1987) Receptor-mediated in vitro gene transformation by a soluble DNA carrier system. *J. Biol. Chem. 262*, 4429–4432.

(16) Harashima, H., Shinohara, Y., and Kiwada, H. (2001) Intracellular control of gene trafficking using liposomes as drug carriers. *Eur. J. Pharm. Sci. 13*, 85–89.

(17) Conner, S. D., and Schmid, S. L. (2003) Regulated portals of entry into the cell. *Nature 422*, 37–44.

(18) Behr, J. P. (1997) The proton sponge: A trick to enter cells the viruses did not exploit. *Chimia 51*, 34–36.

(19) KukowskaLatallo, J. F., Bielinska, A. U., Johnson, J., Spindler, R., Tomalia, D. A., and Baker, J. R. (1996) Efficient transfer of genetic material into mammalian cells using Starburst polyamidoamine dendrimers. *Proc. Natl. Acad. Sci. U.S.A. 93*, 4897–4902.

(20) Shigeta, K., Kawakami, S., Higuchi, Y., Okuda, T., Yagi, H., Yamashita, F., and Hashida, M. (2007) Novel histidine-conjugated galactosylated cationic liposomes for efficient hepatocyte-selective gene transfer in human hepatoma HepG2 cells. *J. Controlled Release 118*, 262–270.

(21) Li, L., Nie, Y., Zhu, R., Shi, S. J., Luo, K., He, B., Yang, Y., Yang, J. X., and Gu, Z. W. (2008) Preparation and gene delivery of alkaline amino acids-based cationic liposomes. *Arch. Pharmacol. Res. 31*, 924–931.

(22) Putnam, D., Zelikin, A. N., Izumrudov, V. A., and Langer, R. (2003) Polyhistidine-PEG: DNA nanocomposites for gene delivery. *Biomaterials 24*, 4425–4433.

(23) Lee, M. J., Cho, S. S., You, J. R., Lee, Y., Kang, B. D., Choi, J. S., Park, J. W., Suh, Y. L., Kim, J. A., Kim, D. K., and Park, J. S. (2002) Intraperitoneal gene delivery mediated by a novel cationic liposome in a peritoneal disseminated ovarian cancer model. *Gene Ther. 9*, 859–866.

(24) Astriab-Fisher, A., Sergueev, D. S., Fisher, M., Shaw, B. R., and Juliano, R. L. (2000) Antisense inhibition of P-glycoprotein expression using peptide-oligonucleotide conjugates. *Biochem. Pharmacol. 60*, 83–90.

(25) Schwarze, S. R., Ho, A., Vocero-Akbani, A., and Dowdy, S. F. (1999) In vivo protein transduction: Delivery of a biologically active protein into the mouse. *Science 285*, 1569–1572.

(26) Vives, E., Brodin, P., and Lebleu, B. (1997) A truncated HIV-1 Tat protein basic domain rapidly translocates through the plasma membrane and accumulates in the cell nucleus. *J. Biol. Chem. 272*, 16010–16017.

(27) Asayama, S., Sudo, M., Nagaoka, S., and Kawakami, H. (2008) Carboxymethyl poly(L-histidine) as a new pH-sensitive polypeptide to enhance polyplex gene delivery. *Mol. Pharmaceut. 5*, 898–901.

(28) Nakamura, K., Kuramoto, Y., Mukai, H., Kawakami, S., Higuchi, Y., and Hashida, M. (2009) Enhanced gene transfection in macrophages by histidine-conjugated mannosylated cationic liposomes. *Biol. Pharm. Bull. 32*, 1628–1631.

(29) Song, H. P., Yang, J. Y., Lo, S. L., Wang, Y., Fan, W. M., Tang, X. S., Xue, J. M., and Wang, S. (2010) Gene transfer using self-assembled ternary complexes of cationic magnetic nanoparticles, plasmid DNA and cell-penetrating Tat peptide. *Biomaterials 31*, 769–778.

(30) Midoux, P., and Monsigny, M. (1999) Efficient gene transfer by histidylated polylysine pDNA complexes. *Bioconjugate Chem. 10*, 406–411.

(31) Fischer, D., Dautzenberg, H., Kunath, K., and Kissel, T. (2004) Poly(diallyldimethylammonium chlorides) and their N-methyl-N-vinylacetamide copolymer-based DNA-polyplexes: role of molecular weight and charge density in complex formation, stability, and in vitro activity. *Int. J. Pharmaceut. 280*, 253–269.

(32) Mita, K., Zama, M., and Ichimura, S. (1977) Effect of charge density of cationic polyelectrolytes on complex formation with DNA. *Biopolymers 16*, 1993–2004.

(33) Ishiyama, M., Tominaga, H., Shiga, M., Sasamoto, K., Ohkura, Y., and Ueno, K. (1996) A combined assay of cell viability and in vitro cytotoxicity with a highly water-soluble tetrazolium salt, neutral red and crystal violet. *Biol. Pharm. Bull. 19*, 1518–1520.

(34) Fischer, D., Bieber, T., Li, Y., Elsasser, H. P., and Kissel, T. (1999) A novel non-viral vector for DNA delivery based on low molecular weight, branched polyethylenimine: effect of molecular weight on transfection efficiency and cytotoxicity. *Pharm. Res. 16*, 1273–1279.

(35) Storkle, D., Duschner, S., Heimann, N., Maskos, M., and Schmidt, M. (2007) Complex formation of DNA with oppositely charged polyelectrolytes of different chain topology: Cylindrical brushes and, dendrimers. *Macromolecules 40*, 7998–8006.

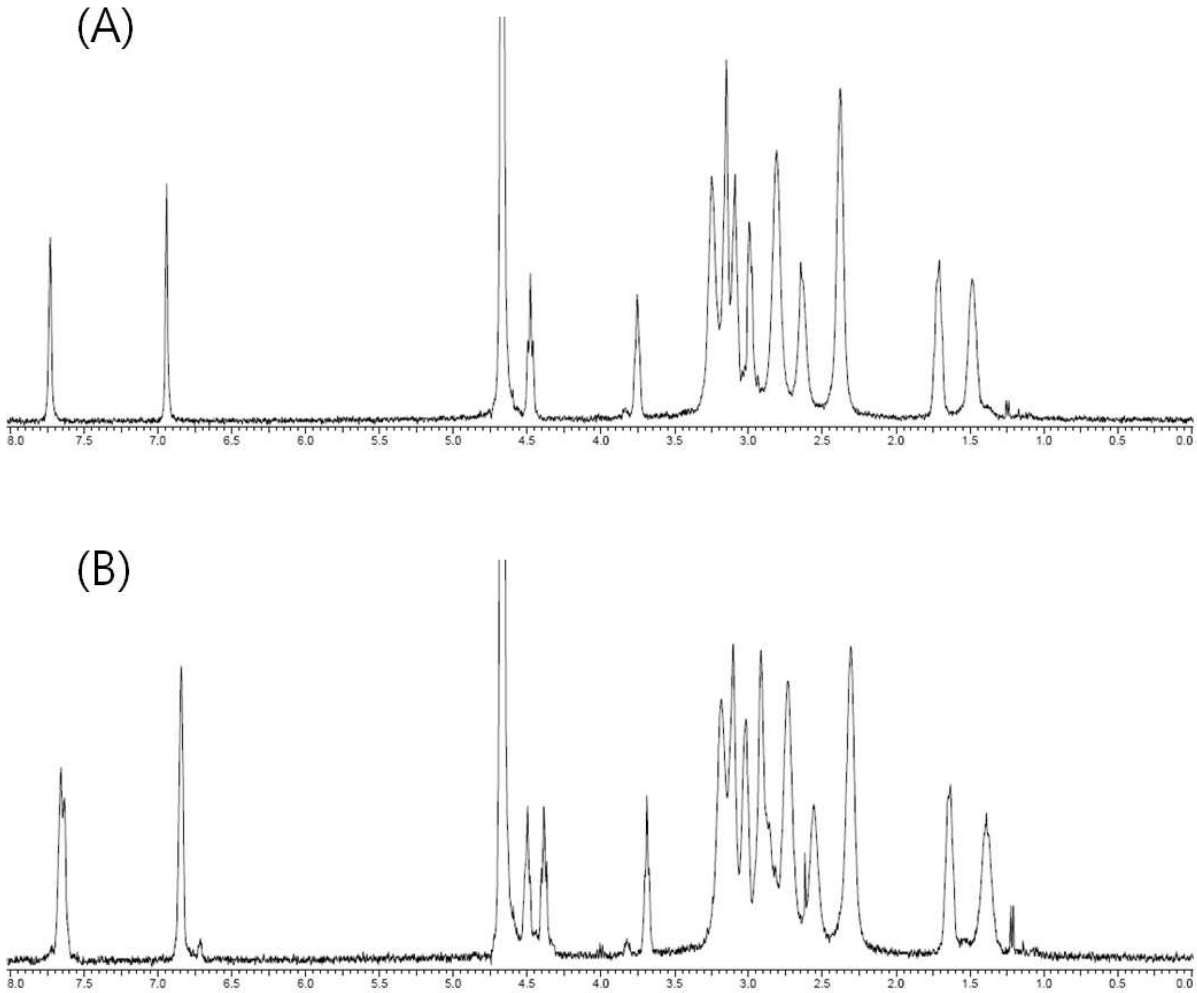
Synthesis of PAMAM dendrimer Derivatives with Enhanced Buffering Capacity and Remarkable Gene Transfection Efficiency

Gwang Sig Yu[1], Yun Mi Bae[1], Hye Choi[1], Bokyung Kong[2], Insung S. Choi[2,]*and Joon Sig Choi[1,3]*

[1]Department of Biochemistry, Chungnam National University, Daejeon, 305-764, Korea

[2]Molecular-Level Interface Research Center, Department of Chemistry, KAIST, Daejeon, 305-764, Korea

[3]Graduate School of Analytical Science and Technology, Chungnam National University, Daejeon, 305-764, Korea



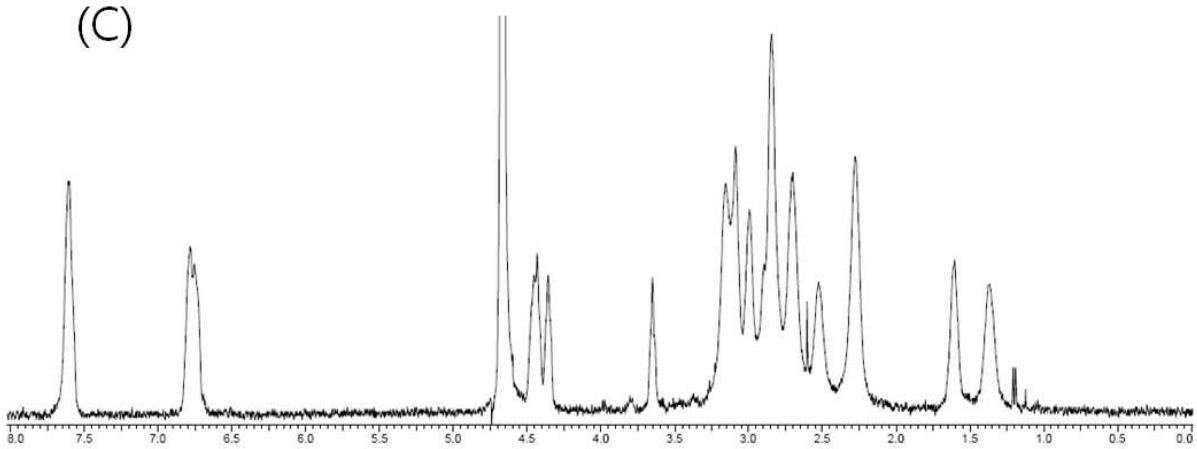


Figure. S1. ^{1}H nuclear magnetic resonance (NMR) spectra of the PAMAM G4 derivatives. PAMAM G4-His_1-Arg (A), PAMAM G4-His_2-Arg (B) and PAMAM G4-His_3-Arg (C).

As shown in Figure S1, the ^{1}H NMR spectra of the synthesized PAMAM G4 derivatives are like as followings, ^{1}H NMR (400MHz, D_2O) **PAMAM G4-His_1-Arg:** δ 1.49 (-$HCCH_2C\boldsymbol{H_2}CH_2NH$- of arginine, 120H), 1.71(-$HCC\boldsymbol{H_2}CH_2CH_2NH$- of arginine, 120H), 2.38(-$NCH_2C\boldsymbol{H_2}CO$- of PAMAM unit, 248H), 2.65 (-$CONHCH_2C\boldsymbol{H_2}N$- of PAMAM unit, and –$NC\boldsymbol{H_2}C\boldsymbol{H_2}N$- of PAMAM unit), 2.81 (-$CONHCH_2C\boldsymbol{H_2}NH_2$ of PAMAM unit and –$NC\boldsymbol{H_2}CH_2CO$- of PAMAM unit), 3.00 (-$HCCH_2CH_2C\boldsymbol{H_2}NH$- of arginine unit), 3.15 (-$CONHC\boldsymbol{H_2}CH_2N$- of PAMAM unit, -$CONHCH_2C\boldsymbol{H_2}NH_2$- of PAMAM unit and –$HCC\boldsymbol{H_2}C$- of histidine unit), 3.76 (-$\boldsymbol{H}CCH_2C$- of arginine unit, 60H), 4.48 (-(-$\boldsymbol{H}CCH_2CH_2CH_2NH$- of histidine unit, 60H), 6.94 (-$NHCHNC\boldsymbol{H}CCH_2CH$- of imidazole group of histidine), 7.73 (-$NHC\boldsymbol{H}NCHCCH_2CH$- of imidazole group of histidine). **PAMAM G4-His_2-Arg:** δ 1.39 (-$HCCH_2C\boldsymbol{H_2}CH_2NH$- of arginine unit, 128 H), 1.63 (-$HCC\boldsymbol{H_2}CH_2CH_2NH$- of arginine, 128 H), 2.31 (-$NCH_2C\boldsymbol{H_2}CO$- of PAMAM unit, 248H), 2.56 (-$CONHCH_2C\boldsymbol{H_2}N$- of PAMAM unit, and –$NC\boldsymbol{H_2}C\boldsymbol{H_2}N$- of PAMAM unit), 2.73 (-$CONHCH_2C\boldsymbol{H_2}NH_2$ of PAMAM unit and –$NC\boldsymbol{H_2}CH_2CO$- of PAMAM unit), 2.92 (-$HCCH_2CH_2C\boldsymbol{H_2}NH$- of arginine unit), 3.10 (-$CONHC\boldsymbol{H_2}CH_2N$- of PAMAM unit, -$CONHCH_2C\boldsymbol{H_2}NH_2$- of PAMAM unit and –$HCC\boldsymbol{H_2}C$- of histidine unit), 3.69 (-$\boldsymbol{H}CCH_2C$- of arginine unit, 63 H), 4.39 (-$\boldsymbol{H}CCH_2C$- of first histidine unit, 63 H), 4.50 (-$\boldsymbol{H}CCH_2CH_2CH_2NH$- of second histidine unit, 64 H), 6.84 (-$NHCHNC\boldsymbol{H}CCH_2CH$- of imidazole group of histidine), 7.66 (-$NHC\boldsymbol{H}NCHCCH_2CH$- of imidazole group of histidine). **PAMAM G4-His_3-Arg**: δ 1.37 (-$HCCH_2C\boldsymbol{H_2}CH_2NH$- of

arginine, 122 H), 1.61 (-HCC***H₂***CH_2CH_2NH- of arginine, 122 H), 2.28 (-NCH_2C***H₂***CO- of PAMAM unit, 248H), 2.53 (-$CONHCH_2$C***H₂***N- of PAMAM unit, and –NC***H₂***C***H₂***N- of PAMAM unit), 2.70 (-$CONHCH_2$C***H₂***NH_2 of PAMAM unit and –NC***H₂***CH_2CO- of PAMAM unit), 2.84 (-$HCCH_2CH_2$C***H₂***NH- of arginine unit), 3.09 (-CONHC***H₂***CH_2N- of PAMAM unit, -$CONHCH_2$C***H₂***NH_2- of PAMAM unit and –HCC***H₂***C- of histidine unit), 3.65 (-***H***CCH_2C- of arginine unit, 63 H), 4.36 (-***H***CCH_2C- of first histidine unit, 63 H), 4.43 (-***H***$CCH_2CH_2CH_2$NH- of second histidine unit, 61 H, and -***H***CCH_2C- of third histidine unit, 61 H), 6.78 (-NHCHNC***H***CCH_2CH- of imidazole group of histidine), 7.60 (-NHC***H***NCHCCH_2CH- of imidazole group of histidine). The number of histidine and arginine residues conjugated was calculated from ^{1}H NMR data. More than 61molecules of histidine and arginine were conjugated to a single PAMAM G4 dendrimer. According to ^{1}H NMR data, 61 histidine and arginine molecules were coupled to single PAMAM G4 dendrimer (PAMAM G4-His_1-Arg). In case of PAMAM G4-His_2-Arg, 63 histidine (first and second unit) and 64 arginine molecules were conjugated to the PAMAM G4 dendrimer. Also, the spectra of PAMAM G4-His_3-Arg showed each 63 histidine molecules (first and second histidine unit) and 61 histidine, arginine molecules (third histidine and arginine molecules) were coupled with PAMAM G4 dendrimer, respectively.

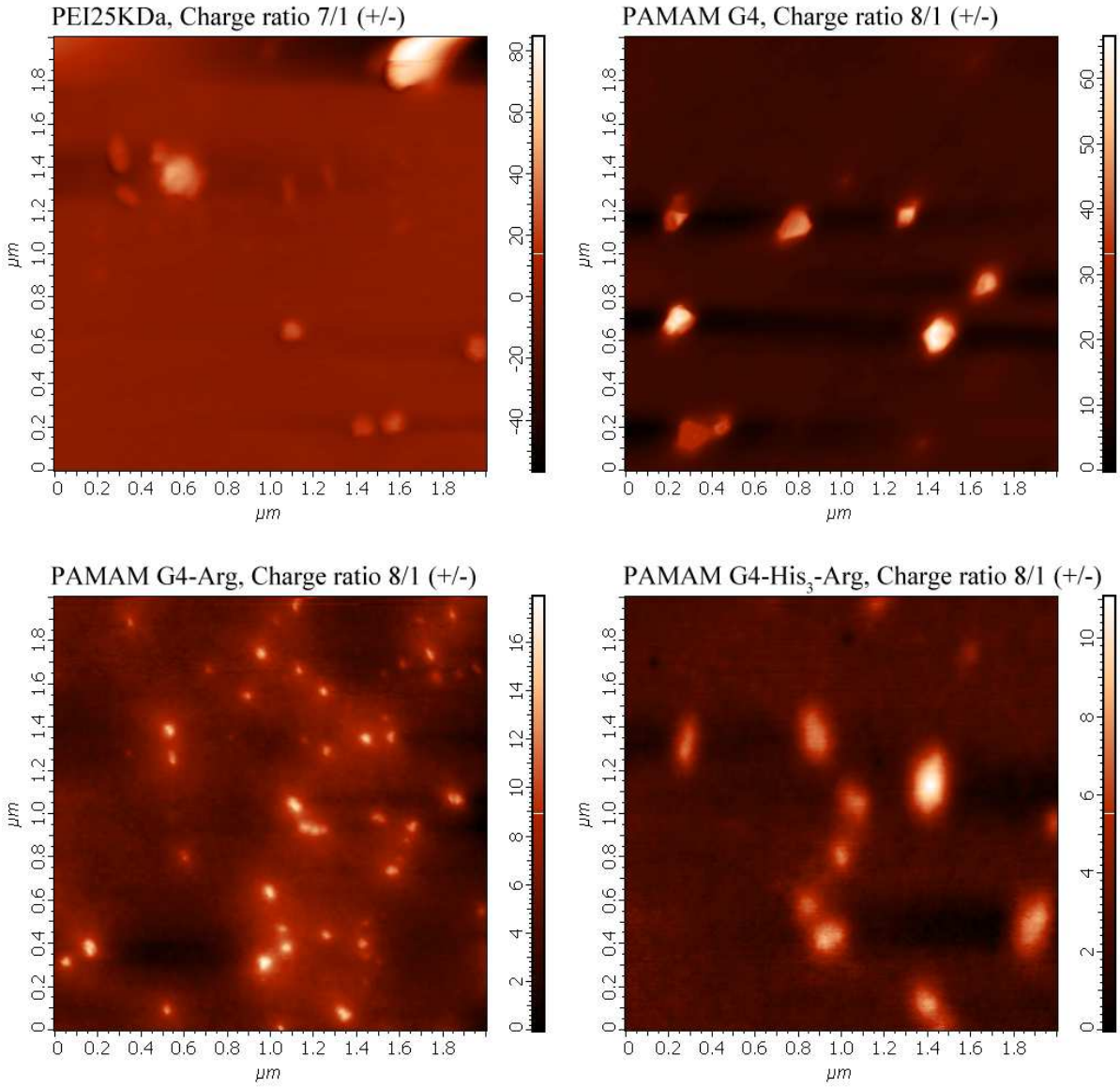


Figure. S2. Atomic force microscopy images of polymer/pDNA complexes.

Atomic force microscopy (AFM; NTEGRA-Spectra, NT-MDT, Moscow, Russia) was used to image the size and shape of the polyplex formation. Briefly, polymer/pDNA polyplexes at a charge ratio of 8:1 (except for PEI25KD, 7:1, optimal ratio) and a final pDNA concentration of 10 ng were prepared in deionized water. Polyplex solution (10 µl) was loaded onto the center of a silicon wafer, and the silicon wafer surface was dried at room temperature before taking images. AFM images were collected in tapping mode (semi-contact) at a scanning speed of 1 Hz. Images were analyzed using Nova software (Ver. 1.0.26).

Bioconjugate Chemistry

ARTICLE

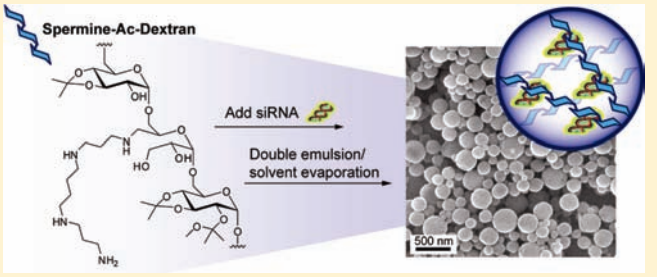
pubs.acs.org/bc

Acid-Degradable Cationic Dextran Particles for the Delivery of siRNA Therapeutics

Jessica L. Cohen, Stephanie Schubert,[†] Peter R. Wich, Lina Cui, Joel A. Cohen,[‡] Justin L. Mynar, and Jean M. J. Fréchet*

College of Chemistry, University of California, Berkeley, California 94720-1460, United States

ABSTRACT: We report a new acid-sensitive, biocompatible, and biodegradable microparticulate delivery system, spermine modified acetalated-dextran (Spermine-Ac-DEX), which can be used to efficiently encapsulate siRNA. These particles demonstrated efficient gene knockdown in HeLa-*luc* cells with minimal toxicity. This knockdown was comparable to that obtained using Lipofectamine, a commercially available transfection reagent generally limited to *in vitro* use due to its high toxicity.



INTRODUCTION

RNA interference (RNAi) has drawn much attention in the field of medicine due to its potential for treating chronic diseases and genetic disorders by harnessing the endogenous RNAi pathway.[1−3] RNAi is a biological mechanism wherein double-stranded RNAs can be used to reduce expression of target proteins.[4,5] Once the RNA is present in the cytoplasm of the cell, it is shortened and processed by the RNase III enzyme, Dicer,[6] and incorporated into a protein complex called the RNA-induced silencing complex (RISC).[7] One of the two strands of the short, double-stranded RNA is cleaved, and the activated RISC (which contains the guide strand of the RNA) binds to a complementary sequence of mRNA and results in its degradation.[8] The activated RISC is capable of multiple rounds of mRNA cleavage, which propagates gene silencing.[9] Due to its potential to silence genes in a sequence-specific manner, RNAi holds promise for treating many diseases that may not otherwise be accessed with current therapeutic technology.[1]

Various approaches have been developed that allow for exploitation of the RNAi process, principally through the use of exogenous synthetic small interfering RNA (siRNA), double-stranded RNAs that are typically 19−23 base pairs in length. Synthetic siRNA can be designed to target nearly any gene in the body, and is therefore attractive for a variety of medical applications. Previous reports have demonstrated that synthetic siRNAs are capable of knocking down targets in several diseases *in vivo*, including hepatitis B virus, human papillomavirus, and ovarian cancer.[10] Despite great therapeutic potential, the clinical application of siRNA is limited by delivery problems. siRNA does not cross cellular membranes efficiently due to its relatively large size, negative charge, and hydrophilicity. In addition, siRNA is unstable under *in vivo* conditions due to rapid degradation by serum nucleases.[11] Thus, the widespread use of RNAi therapeutics for disease prevention and treatment requires the development of clinically suitable, safe, and effective delivery vehicles.[10] In order to induce effective RNAi, these vehicles must overcome a variety of extracellular and intracellular obstacles; i.e., they should provide protection against nuclease activity and facilitate internalization and intracellular trafficking of the siRNA.[12] Even though significant advances have been made in the field, the development of vehicles that can efficiently deliver RNAi therapeutics both *in vitro* and *in vivo* remains a major challenge.

Both viral and non-viral carriers have been developed for the delivery of siRNA.[12−16] Although viral vectors are very efficient, they can cause immunogenic and inflammatory responses,[17,18] which raise concerns about their safety as delivery vectors. Non-viral vectors provide opportunities for improved safety, greater flexibility, and more facile manufacturing; however, most of the existing carriers suffer from low delivery efficiencies. The most common non-viral vectors involve complexes formed between cationic lipids[19,20] or polymers[21,22] and siRNA through electrostatic interactions between the negative phosphates along the nucleic acid backbone and the positive charges displayed on the vector. In addition to low transfection efficiencies, these systems also suffer from high toxicity due to their polycationic nature and limited stability *in vivo* due to non-specific interactions with serum proteins. The limitations associated with current delivery vehicles motivate the development of novel systems for siRNA delivery that may be able to overcome these obstacles.

Among many alternatives to cationic polymers and lipids commonly used to form polyplexes/lipoplexes with genetic material,[10,23,24] particles made from biodegradable and non-toxic materials such as slow-hydrolyzing poly(lactic-*co*-glycolic acid) (PLGA),[25,26] fast-degrading polyesters (such as DEAPA-PVA-PLGA),[27]

Received: December 2, 2010
Revised: April 10, 2011
Published: May 03, 2011

ACS Publications © 2011 American Chemical Society

and acid-sensitive poly(orthoesters) (POEs)[28] have been explored as *in vivo* gene delivery vectors. Another system based on acid-sensitive polyketals has also recently shown promise for delivery of siRNA both *in vitro* and *in vivo*.[29] These prior examples of particulate systems for siRNA and DNA delivery typically employ small quantities of cationic polymers[25,30] (i.e., poly(β-amino ester), PBAE, or polyethyleneimine, PEI), lipids such as DOTAP,[29] or small molecules such as spermine[26] blended with the carrier polymer to enhance loading of DNA/RNA and delivery efficiency. Formed by standard emulsion techniques, these particles combine physical entrapment of their payload with electrostatic complexation of genetic material while retaining biocompatible degradation mechanisms. However, some limitations of these systems relate to the synthetic flexibility, biocompatibility of the degradation products, and the paucity of chemical methods for the modification of the particle surface. For example, despite the promising transfection results obtained from PLGA microspheres, they still suffer from slow release rates[31] and the formation of DNA-damaging acidic by-products.[32,33]

Dextran, a homopolysaccharide of glucose, appears to be well poised for use as a polymeric carrier due to its biodegradability, wide availability, and ease of modification.[34] In addition, dextran already has a history of human use in clinical applications for plasma volume expansion and plasma substitution. The potential application of dextran for siRNA delivery has recently been demonstrated.[35−37] Previously, we described the development of a modular and tunable particle system based on acetal-modified dextran (Ac-DEX).[38,39] We have shown that Ac-DEX particles prepared by standard emulsion techniques—either water in oil (w/o) or water in oil in water (w/o/w)—have high encapsulation efficiencies for both hydrophobic small molecules[40] and high molecular weight hydrophilic cargoes,[38,39] such as proteins, and that the release rate of the encapsulated cargo was tunable.[39] These acid-degradable Ac-DEX particles were capable of delivering protein antigens to macrophages and dendritic cells. Besides their use as a successful vaccine carrier, microparticles prepared from Ac-DEX blended with a cationic polymer proved effective at delivering plasmid DNA to both phagocytic and non-phagocytic cells.[41] Although siRNA and plasmid can be applied to achieve similar functional outcomes, successful plasmid delivery carriers cannot necessarily achieve efficient siRNA delivery due to the major intrinsic structural differences and different location of action for siRNA and plasmid.[42−44] For example, reports from other groups have shown the difficulty of encapsulating the highly charged, hydrophilic, and rigid siRNA in particles by w/o/w emulsion, presumably due to leakage into the outer water phase.[45]

We now describe the preparation and preliminary evaluation of a new polymeric platform—spermine-modified Ac-DEX (spermine-Ac-DEX)—for the delivery of siRNA. The new system combines facile synthesis and biocompatibility with the additional benefit of controlled payload release sensitive to physiologically relevant acidic conditions. Acid-sensitive systems have particularly desirable characteristics, as cargo release can be triggered in response to endosomal acidification upon cellular uptake. Acid-catalyzed hydrolysis of spermine-Ac-DEX generates spermine-modified dextran, which may be able to be further metabolized by enzymes *in vivo*.[46−52]

The ability of spermine-Ac-DEX particles to overcome a variety of cellular obstacles and function as an efficient delivery vehicle for siRNA can be rationalized by its tailor-made design

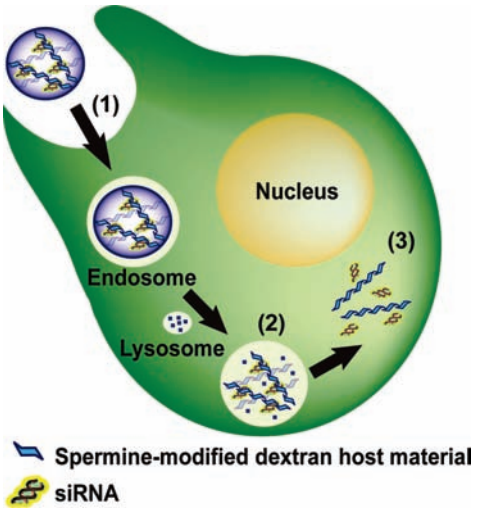


Figure 1. Particles are expected to efficiently transfect HeLa-*luc* cells due to their ability to overcome several obstacles to gene delivery. Ac-DEX particles should protect siRNA from degradation. (1) The particles are endocytosed by HeLa cells, and the vesicle is acidified upon fusion of the endosome with the lysosome. (2) Spermine Ac-DEX particles degrade in the acidic environment of the endolysosome and (3) the siRNA is released into the cytoplasm.

(Figure 1). We hypothesize that particulate formulation should provide protection of the encapsulated siRNA against chemical and enzymatic degradation. The cationic characteristics of spermine-Ac-DEX can facilitate the encapsulation of siRNA inside particles, and it may also favorably contribute to cellular uptake by enhancing interaction of the particles with negatively charged cell membranes. Once inside cells, hydrolysis of the polymer in the acidic endolysosomal compartment can allow the siRNA to be released from the particles. Endosomal escape may be achieved via the "proton sponge" effect of the amine moieties, as well as increased endosomal osmotic pressure by degradation of the spermine-Ac-DEX material. Overall, we speculate that it is the combination of protection and endolysosomal release that would be the most likely contributors to the successful delivery of siRNA using a spermine-Ac-DEX carrier.

EXPERIMENTAL PROCEDURES

General Materials and Methods. All chemicals were from Sigma-Aldrich (St. Louis, MO) unless otherwise noted. The antiluciferase siRNA (sense strand: 5′-CUU ACG CUG AGU ACU UCG A dTdT-3′) was obtained from Dharmacon (Lafayette, CO) and Silencer Negative Control #1 siRNA was purchased from Ambion (Austin, TX). Phosphate buffered saline (PBS, pH 7.4) was from Invitrogen (Carlsbad, CA). Reactions requiring anhydrous conditions were performed in flame-dried vessels and under a positive pressure of dry nitrogen. Water (dd-H_2O) for buffers and particle washing steps was purified to a resistance of 18 MΩ using a NANOpure purification system (Barnstead, USA). When used in the presence of acetal containing materials, dd-H_2O was rendered basic (pH 8) by the addition of triethylamine (TEA) (approximately 0.01%). ^{1}H NMR spectra were recorded at 400 or 500 MHz on a Bruker spectrometer. Elemental analyses were performed at the UC Berkeley Mass Spectrometry Facility. Fluorescence measurements were obtained using a Spectra Max Gemini XS plate-reading fluorimeter

(Molecular Devices, USA), usage courtesy of Prof. Carolyn Bertozzi. Absorbance measurements were obtained using a Spectra Max 190 microplate reader (Molecular Devices, USA), usage courtesy of Prof. Carolyn Bertozzi. Luminescence measurements were obtained using a GloMax 96 microplate luminometer (Promega, USA), usage courtesy of Prof. Eva Harris.

Synthesis of Spermine-Ac-DEX. *Partial Oxidation of Dextran.* Dextran (5.0 g, 30.9 mmol, M_w 9−11 000 g/mol, from *Leuconostoc mesenteroides*) was dissolved in 20 mL water. After adding sodium periodate (1.1 g, 51.4 mmol), the solution was stirred for 5 h at rt. The product was purified by dialysis of the solution against distilled water using a regenerated cellulose membrane with a MWCO of 3500 g/mol. The water was changed 5 times and the sample was lyophilized to obtain a white powder (4.2 g, 8.4 mol aldehyde functions/100 mol anhydroglucose unit, AGU). The degree of oxidation was determined colorimetrically (UV absorption at 562 nm) using a microplate reductometric bicinchoninic acid assay (Micro BCA Protein Assay Kit, Pierce, USA) according to the manufacturer's protocol and glucose monohydrate for calibration.

Synthesis of Partially Oxidized Acetalated Dextran. Acetalation of partially oxidized dextran was performed in a similar manner as described previously.[38] Briefly, 3.0 g partially oxidized dextran (18.5 mmol, 8.4 mol aldehyde functions/100 mol AGU) was modified with 2-methoxypropene (10.6 mL, 111 mmol) yielding partially oxidized acetalated dextran (4.3 g) containing 100 mol acyclic and 72.5 mol cyclic acetals/100 mol AGU. The degree of functionalization was determined by ^{1}H NMR spectroscopy in DCl/D_2O according to the method described by Broaders et al.[39] ^{1}H NMR (400 MHz, $CDCl_3$): δ 1.40 (s, br, acetal), 3.25 (br, acetal), 3.45, 3.50−4.10, 4.90, 5.10 (br, dextran).

Synthesis of Spermine-Ac-DEX. Partially oxidized Ac-DEX (2.0 g, 12.3 mmol) was stirred with spermine (4.0 g, 19.8 mmol) in 10 mL DMSO at 50 °C for 22 h. The reduction was performed for 18 h at room temperature by adding $NaBH_4$ (2.0 g, 52.9 mmol) to the DMSO solution. The spermine modified dextran was precipitated in dd-H_2O (40 mL). The product was isolated by centrifugation at 4000*g* for 5 min, and the resulting pellet was washed thoroughly with dd-H_2O (5 × 40 mL, pH 8) by resuspension followed by centrifugation and removal of the supernatant. Residual water was removed by lyophilization, yielding spermine functionalized acetalated dextran, spermine-Ac-DEX, (1.6 g) as a white powder containing 6.6 mol spermine/100 mol AGU. The degree of functionalization was determined by elemental analysis using the nitrogen content. Anal. (spermine-Ac-DEX) C, found 55.79; H, found 8.29; N, found, 1.24. ^{1}H NMR (400 MHz, $CDCl_3$): δ 1.40 (s, br, acetal), 1.60, 1.80, 2.60, 2.65, 2.75 (br, spermine), 3.25 (br, acetal), 3.45, 3.50−4.10, 4.90, 5.10 (br, dextran).

Synthesis of PBAE. PBAE, a white solid, was synthesized by the Michael-type addition of 4,4′-trimethylenedipiperidine to 1,4-butanediol diacrylate in THF as the solvent according to the method described by Lynn et al. (GPC: M_n = 42.6 kDa, PDI = 2.78).[53]

Preparation of Particles. *Particles Encapsulating siRNA.* Ac-DEX particles containing siRNA were prepared using a double emulsion water/oil/water (w/o/w) evaporation method similar to that described previously.[38,39] Stock siRNA solutions (2.66, 5.32, or 10.64 mg/mL depending on the desired initial siRNA feed) were prepared in nuclease-free distilled water. Spermine-Ac-DEX (25 mg) was dissolved in ice-cold CH_2Cl_2 (0.5 mL). The stock siRNA solution (25 μL) was added and the mixture was sonicated for 30 s on ice using a probe sonicator (Branson Sonifier 450) with a 1/2 in. flat tip, an output setting of 5, and a duty cycle of 80%. This primary emulsion was then added to an aqueous solution of poly(vinyl alcohol) (PVA, M_w = 13 000−23 000 g/mol, 87−89% hydrolyzed) (1 mL, 3% w/w in PBS) and sonicated for an additional 30 s on ice using the same settings. The resulting double emulsion was immediately poured into a second PVA solution (5 mL, 0.3% w/w in PBS) and stirred for 3 h at rt allowing the organic solvent to evaporate. The particles were isolated by centrifugation (10 250 rpm, 30 min) and washed with PBS (25 mL) and dd-H_2O (2 × 25 mL, pH 8) by vortexing and sonication followed by centrifugation and removal of the supernatant. The washed particles were resuspended in dd-H_2O (2 mL, pH 8) and lyophilized to yield a white, fluffy solid. Yields were typically between 50% and 85% per batch based on starting polymer and siRNA mass (12.5−21 mg of particles).

Ac-DEX/PBAE Particles. Particles consisting of Ac-DEX and PBAE were made in the same manner as described above, except that unmodified Ac-DEX and 10 wt % PBAE were used instead of spermine-Ac-DEX.

Empty Particles. Particles that did not contain siRNA were made in the same manner described above, except that the aqueous buffer in the primary emulsion consisted of dd-H_2O (25 μL) and no siRNA.

Quantification of Encapsulated siRNA. Particles containing siRNA were suspended at a concentration of 10 mg/mL in a 0.3 M acetate buffer (pH 5) and incubated at 37 °C under gentle agitation for 3 d using a Thermomixer R heating block (Eppendorf). After the particles had been fully degraded, aliquots were taken and analyzed for siRNA content using the Quant-iT Picogreen dsDNA assay (Molecular Probes) according to the manufacturer's instructions. Empty Ac-DEX particles were degraded in a similar fashion and used to determine background fluorescence. For this experiment, all solutions included heparin at 10 mg/mL to disrupt electrostatic interactions between blend polymers and siRNA to enable quantification. The results were compared to a standard curve and the mass of siRNA encapsulated was calculated. Fluorescence was measured using a SpectraMax Gemini XS microplate reader (Molecular Devices, Sunnyvale, CA, ex. 480 nm, em. 520 nm).

Zeta-Potential Analysis. Zeta-potentials of particles were measured using a Nano ZS ZetaSizer (Malvern Instruments, UK) at 25 °C after suspending particles in HEPES buffer (5 mM, pH 7.4) at 0.1 mg/mL. Data shown represent the average zeta-potential ± standard deviation of distributions of five sequential measurements.

Characterization of Particle Size by Scanning Electron Microscopy (SEM). Particles were suspended in dd-H_2O (pH 8) at a concentration of 0.3 mg/mL and the resulting dispersions were dripped onto silicon wafers. After 15 min, the water was wicked away using tissue paper and the samples were further dried under a stream of N_2 gas. The particles were then sputter-coated with a 2 nm layer of a palladium/gold alloy and imaged using a scanning electron microscope (S5000, Hitachi). The particle diameter and size distribution of the particles were determined by measuring 100 particles and analyzing the data using *Excel*. These micrographs were also used to assess particle morphology.

pH-Dependent Degradation of Ac-DEX Particles. Empty Ac-DEX particles were suspended in triplicate at a concentration of 1 mg/mL in either a 0.3 M acetate buffer (pH 5.0) or PBS (pH 7.4) and incubated at 37 °C under gentle agitation using a Thermomixer R heating block (Eppendorf). At various time

points, 50 μL aliquots were removed, centrifuged at 14 000*g* for 4 min to pellet out insoluble materials, and the supernatant was stored at −20 °C. The collected supernatant samples were analyzed for the presence of reducing polysaccharides using a microplate reductometric bicinchoninic acid based assay (UV absorption at 562 nm) according to the manufacturer's protocol (Micro BCA Protein Assay Kit, Pierce, USA). The curve was made by applying a Boltzmann fit.

pH-Dependent Release of siRNA from Ac-DEX Particles. This experiment was performed essentially in the same manner as above except siRNA-loaded particles were used instead of empty particles. The quantity of siRNA in the supernatant samples was determined by using the Quant-iT Picogreen dsDNA assay (Molecular Probes) according to the manufacturer's instructions. The amount of siRNA in each sample was calculated by fitting the emission to a calibration curve using the Quant-iT Picogreen dsDNA assay (Molecular Probes). For this experiment, all solutions included heparin at 12.5 mg/mL to disrupt electrostatic interactions between blend polymers and siRNA to enable quantification. The curve was made by applying a Boltzmann fit.

Cell Lines and Culture. HeLa cell lines stably expressing firefly luciferase (HeLa-*luc*) were maintained in Dulbecco's Modified Eagle's Medium (DMEM) supplemented with 10% (v/v) fetal bovine serum (FBS), 1% GlutaMAX, and 500 μg/mL Zeocin (all from Invitrogen except the serum, which was from Hyclone (Logan, UT)). Cell incubations were performed in a water-jacketed 37 °C/5% CO_2 incubator.

***In Vitro* siRNA Transfection Assay.** HeLa-*luc* cells were seeded (15 000 cells/well) into each well of a 96-well clear tissue culture plate (Costar, Corning, NY) and allowed to attach overnight in growth medium. Growth medium was composed of DMEM (with phenol red), 10% FBS, and 1% GlutaMAX. Particle samples (encapsulating either luciferase siRNA or control siRNA) were prepared in culture medium (without antibiotics) by alternately vortexing and sonicating in a Branson 2510 water bath for 20 s to generate homogeneous suspensions. The samples were then serially diluted in medium to give the indicated particle concentrations or equivalent siRNA doses. Existing medium was replaced with 100 μL of each particle dilution (2.19−35 pmol siRNA) in quadruple wells. The cells were allowed to grow for an additional 48 h before being analyzed for gene expression. Lipofectamine 2000 (Invitrogen, Carlsbad, CA) was used as a positive control for siRNA delivery and was prepared according to the manufacturer's instructions. Complexes containing equivalent doses of siRNA to particles were prepared by mixing Lipofectamine 2000 and siRNA (3:5:1 ratio). As negative controls, both equivalent doses of free siRNA in medium and medium alone were used.

After 48 h, the cells were washed with PBS (containing Mg^{2+} and Ca^{2+}, 3 × 100 μL), Glo Lysis Buffer (120 μL, Promega, Madison, WI) was added to each well, and the plate was vortexed at rt for 20 min. Samples from each well (100 μL) were transferred to the wells of a white 96-well tissue culture plate (Corning, Lowell, MA). Steady-Glo luciferase assay reagent (Promega) was reconstituted according to the manufacturer's instructions and injected into each well in series (100 μL/well) using a GloMax 96 microplate luminometer (Promega). After a 10 s post-injection delay, each well was read with a 2 s integration time.

Total Protein Assay. Cells treated identically and in parallel with transfection assays were tested on a second 96-well plate. After washing, the cells were lysed with M-PER Mammalian Protein Extraction Reagent (50 μL/well, Pierce, Rockford, IL) by incubating for 10 min at rt. PBS (50 μL/well) was then added, and the plate was briefly vortexed. Samples from each well (50 μL) were transferred to a black 96-well plate (Corning) already containing PBS (100 μL/well). A solution of 3 mg/mL fluorescamine in acetone (50 μL) was added to each well and mixed well using a multichannel pipet. After 5 min, fluorescence was measured using a SpectraMax Gemini XS reader (ex. 400 nm, em. 460 nm). Protein concentrations were determined using bovine serum albumin as a standard. Relative light units (RLU) from the luminometer were normalized to the total mass of cellular protein. The resulting data (RLU/mg of protein) are given as a mean ± standard deviation of four independent measurements. Percentage knockdown was calculated by comparison of treated cells to untreated cells. The data was compared to the knockdown of cells treated with particles loaded with control siRNA or control siRNA/Lipofectamine complexes.

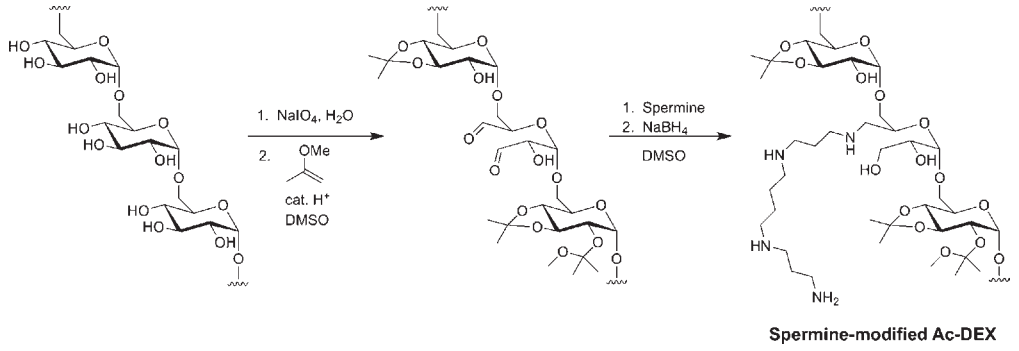
Viability Assay. Cells treated identically and in parallel with transfection assays were tested on a third 96-well plate. A 3.0 mg/mL solution of MTT (3-(4,5-dimethyl-2-thiazolyl)-2,5-diphenyl-2*H*-tetrazolium bromide) in medium (40 μL) was added directly to each well, and the plate was incubated for an additional 30 min. The medium was then replaced with DMSO (200 μL/well), 100 μL of which was transferred to another clear-bottom 96-well assay plate (Pro-Bind, Falcon) containing 100 μL DMSO and 25 μL of glycine buffer (0.1 M glycine, 0.1 M NaCl, pH 10.5) per well. The absorbances at 570 nm were measured using a SpectraMax 190 reader (Molecular Devices). Cell viability was normalized to the absorbance measured from untreated cells. Data are represented as a mean ± standard deviation of four measurements.

RESULTS AND DISCUSSION

Synthesis of Spermine-Modified Ac-DEX. Ac-DEX has several characteristics that make it well suited for the delivery of bioactive cargoes. Although this system has been used to successfully deliver protein antigens, adjuvants, and small molecule agents, the neutrally charged polymer cannot efficiently encapsulate siRNA. Taking advantage of the blend approach described above, we have recently reported the preparation of particles encapsulating plasmid DNA by formulating Ac-DEX with small amounts of the cationic polymer PBAE.[41] These particles were able to efficiently transfect both phagocytic and non-phagocytic cells *in vitro*. Inspired by this work, we tried to prepare Ac-DEX particles encapsulating siRNA by blending with either small polyamines or cationic polymers. While high loading and efficient delivery of plasmid DNA was achieved by blending Ac-DEX with PBAE, attempts to prepare siRNA-loaded particles by the same method only afforded particles with low loading and low encapsulation efficiency.

Domb and co-workers have reported the synthesis of various oligoamine polysaccharide conjugates for use in gene delivery.[54] They found that, of 300 different polycations prepared, only a few were active in transfecting cells. Dextran-spermine displayed especially high transfection efficiency, which they attributed to unique complexation properties between DNA and the grafted spermine moieties.[54] Dextran-spermine, and derivatives thereof, have shown high transfection of plasmid DNA both *in vitro* and *in vivo*.[55,56] Combining this pioneering work with the unique characteristics of our Ac-DEX, we have modified Ac-DEX with spermine for use in siRNA delivery.

Scheme 1. Schematic Illustration of the Synthesis of Spermine-Modified Ac-DEX



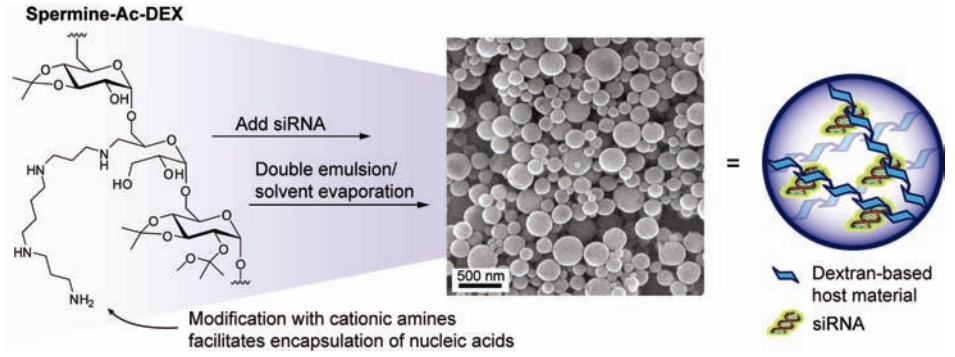


Figure 2. Preparation of spermine-modified Ac-DEX particles encapsulating siRNA showing a representative scanning electron micrograph of particles (scale bar = 500 nm) (center) and a cartoon illustration of siRNA-loaded particles (right).

Spermine-Ac-DEX was prepared by using reductive amination chemistry for the conjugation of spermine to Ac-DEX (Scheme 1). To increase the number of available aldehyde functionalization sites beyond the reducing chain ends of the polysaccharide, dextran was first lightly oxidized with sodium periodate, thus increasing significantly its aldehyde content[57] as evaluated by a reductometric bicinchoninic acid assay (BCA assay). Using this method, we settled on a loading of 8.4 aldehyde functions per 100 anhydroglucose units (AGU). Reaction of the remaining hydroxyl groups with 2-methoxypropene afforded partially oxidized Ac-DEX, an acid-sensitive, hydrophobic polymer that can be easily processed into microparticles. Finally, amine modification was performed between spermine and aldehyde-containing-Ac-DEX using sodium borohydride as the reducing agent. The amount of spermine conjugated to the dextran, calculated from the nitrogen content (%N) as determined by elemental analysis, averaged 6.6 spermine units per 100 AGU.

Preparation and Characterization of Spermine-Ac-DEX Particles. Spermine-Ac-DEX particles encapsulating siRNA were prepared via a standard double-emulsion technique (Figure 2). Particles prepared from unmodified Ac-DEX and Ac-DEX blended with 10 wt % PBAE, a formulation previously used for plasmid DNA, were also made for comparison purposes. The particles were visualized by scanning electron microscopy (SEM) to determine the average particle size and morphology. All particles were found to be spherical in shape with diameters in the range of 180 to 230 nm in the dry state, irrespective of particle formulation. The surface charge of the particles was determined by zeta-potential measurements. Unmodified Ac-DEX particles have a slightly negative zeta-potential due to the encapsulated siRNA. Blending the polymer with PBAE made the surface charge less negative owing to the cationic nature of the polymer, while the surface charge of spermine-Ac-DEX particles was positive. As expected, the surface charge decreased with increasing loadings of siRNA but remained positive for all particle formulations. Various particle characteristics are known to influence particle behavior *in vivo*, including particle size, shape, and surface charge.[58] When administered intravenously, positively charged particles are susceptible to opsonization by negatively charged serum proteins and clearance by cells of the reticuloendothelial system (RES). While a positive surface charge might be disadvantageous for delivery into the bloodstream, pulmonary delivery represents an attractive alternative delivery strategy for which there is precedent of success utilizing positively charged particles.[59,60] Indeed, we envision utilizing aerosolization for the delivery of our particles to the lungs.

The siRNA loading and loading efficiencies were determined by degrading a sample of particles under acidic conditions and analyzing the siRNA concentration using a Picogreen dsDNA assay (Table 1). The siRNA loading efficiency for unmodified Ac-DEX particles was low (5%), as expected based on previous reports with other particle systems, such as PLGA.[26] Blend particles formulated from Ac-DEX and a cationic polymer poly(β-amino ester) (PBAE) also showed low encapsulation efficiency for siRNA (7%), much lower than the plasmid encapsulation achieved with a similar particle formulation. This lower encapsulation efficiency for siRNA as compared to plasmid DNA may be due to the fact that siRNA has a lower molar mass than plasmid DNA (approximately 250× less) and, thus, may be

Table 1. Characterization of Particle Formulations

particle formulation (siRNA, feed)[a]	diameter[b,c] [nm]	zeta-potential[b] [mV]	siRNA loading[b,d] [μg mg^{-1}]	loading efficiency[b] (%)
Ac-DEX (Luc, 5)	230 ± 80	−5.5 ± 0.42	0.26	5
Ac-DEX/10% PBAE (Luc, 5)	N.D.	−3.4 ± 0.44	0.34	7
Spermine Ac-DEX (Luc, 10)	178 ± 76	9.2 ± 0.69	7.95	76[e]
Spermine Ac-DEX (Luc, 5)	229 ± 59	16.2 ± 0.58	4.70	91
Spermine Ac-DEX (Luc, 2.5)	185 ± 65	19.7 ± 0.63	2.28	95[f]
Spermine Ac-DEX (Control, 5)	195 ± 45	16.1 ± 0.71	5.11	98

[a] Luc − antiluciferase siRNA, Control − Silencer Negative Control #1 siRNA, Feed − amount of siRNA used in particle preparation, μg of siRNA per mg of polymer. [b] Characterized as described in the main text. [c] Some particle aggregation was observed upon resuspension following lyophilization. The mean particle diameter determined by light scattering for Spermine Ac-DEX (Luc, 5) and Spermine Ac-DEX (Control, 5) was 2.71 ± 1.54 μm and 6.45 ± 2.47 μm, respectively (Horiba Partica LA-950, Horiba Scientific). [d] siRNA loading in μg of siRNA per mg of particles (100% efficiency ≈ 5.0 μg of siRNA per mg of particles). A loading of 5 μg of siRNA per mg of particles corresponds to an N/P ratio of approximately 100. [e] 100% efficiency ≈ 10 μg of siRNA per mg of particles. [f] 100% efficiency ≈ 2.5 μg of siRNA per mg of particles. N.D. = not determined.

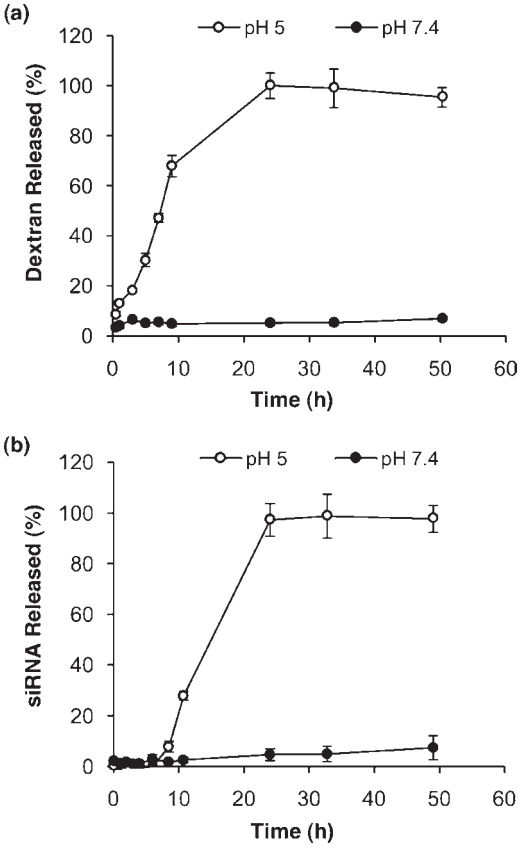


Figure 3. (a) Degradation of particles when incubated at pH 7.4 (black circles) and pH 5 (white circles), as determined by analysis of released soluble dextran. (b) Release of siRNA from spermine Ac-DEX particles when incubated at pH 7.4 (black circles) or pH 5 (white circles). Data represent the mean ± standard deviation of triplicate measurements.

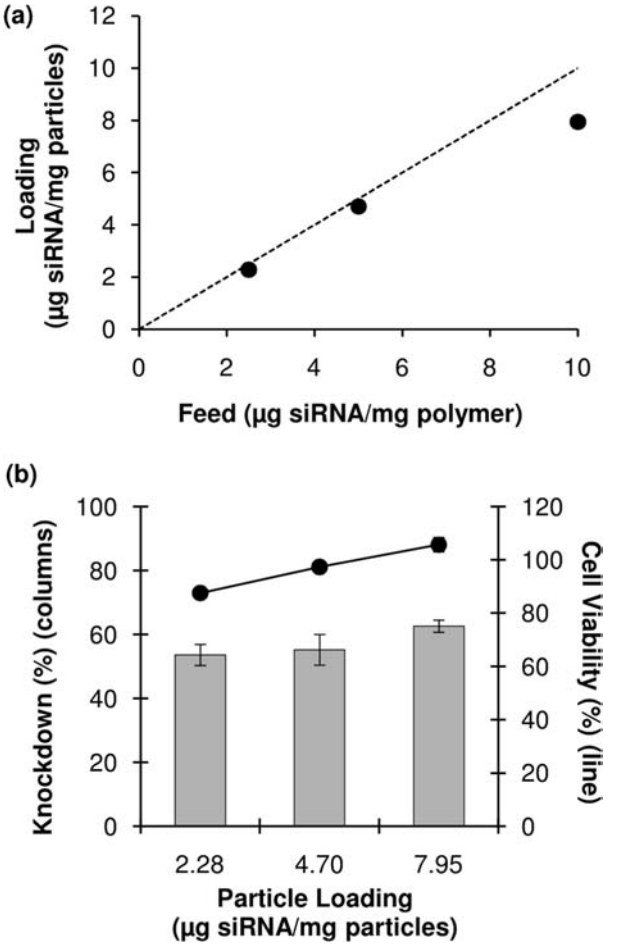


Figure 4. Optimized siRNA loading in particles and its effect on luciferase knockdown. (a) siRNA loading in particles compared with the feed amount of siRNA used in particle synthesis. Dashed diagonal line represents 100% loading efficiency. (b) Knockdown of luciferase activity with varying siRNA loadings. HeLa-*luc* cells were treated with particle doses equivalent to 17.2 pmol siRNA/well. Results were compared to untreated cells and the percentage knockdown of luciferase expression was calculated. Results (columns) are combined with results from a concurrently performed cytotoxicity assay (closed circles and line). Knockdown correlates with siRNA concentration, not particle loading.

more able to diffuse through the condensing polymer during the emulsion process, resulting in reduced loading efficiency.[61] Improved loading efficiencies (75−98%) were obtained for particles prepared from spermine-Ac-DEX. This loading compares favorably with other particle formulations, such as PLGA blended with spermidine for which 56% of the siRNA was encapsulated.[26] In contrast to previously reported particulate delivery systems, however, particles prepared using spermine-Ac-DEX did not require blending of a cationic material with the polymer due to the ability of the polymer to electrostatically interact with siRNA.

dx.doi.org/10.1021/bc100542r |*Bioconjugate Chem.* 2011, 22, 1056–1065

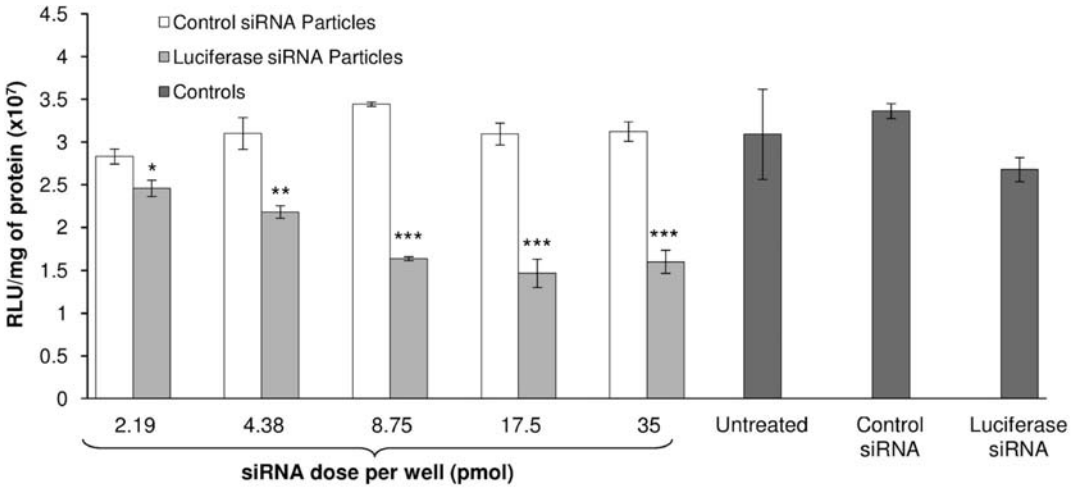


Figure 5. Spermine Ac-DEX particles can efficiently deliver siRNA to HeLa-*luc* cells. *In vitro* transfection of HeLa-*luc* cells with siRNA-loaded spermine Ac-DEX particles. HeLa-*luc* cells were treated with particles encapsulating either luciferase siRNA or control siRNA at various concentrations. Relative light units (RLU) from the luminometer were normalized to the total mass of cellular protein determined from a fluorescamine assay. Data represent the mean ± standard deviation of quadruplicate measurements. Statistical difference was performed with Student's *t*-test between untreated cells and each treatment group: $p < 0.05$ were marked with *, $p < 0.01$ with **, and $p < 0.001$ with ***.

A significant limitation of other commonly used particle delivery systems is their lack of ability to tune the release rate of the encapsulated cargo. Ac-DEX particles are designed to be relatively stable under physiological conditions (pH 7.4) but degrade under the mildly acidic conditions typically found in the lysosome (pH 5.0−5.5), thus allowing for the selective release of the therapeutic agent once inside the cell. We have shown that the rate of microparticle degradation can be easily varied by controlling the type of acetals (i.e., cyclic vs acyclic) formed on the dextran.[39] To determine the degradation rate of spermine-Ac-DEX particles, empty particles were incubated at 37 °C at either pH 5.0 or pH 7.4 and monitored for the release of soluble dextran (Figure 3a). No soluble dextran was detected after 48 h for the particles incubated at pH 7.4. In contrast, particles incubated in pH 5.0 buffer showed continuous release of dextran in the first 24 h at 37 °C, with a degradation half-life of 8 h. We also monitored the release of siRNA from the particles at pH 5.0 and pH 7.4 to determine if the release occurred in a pH-controlled manner (Figure 3b). Little or no release was observed at pH 7.4 after 48 h, while continuous release of siRNA was observed over 24 h at pH 5.0.

To study siRNA loading, three differently loaded batches of spermine-Ac-DEX particles encapsulating luciferase siRNA were prepared. The feed values for these particles were 2.5, 5.0, and 10 μg of siRNA per mg of polymer, respectively. Following preparation, the siRNA loading of the particles was quantified as described above (Figure 4a). Loadings of up to 8.0 μg of siRNA per mg of particle were achieved and the loading efficiency was above 75% for all particle batches. Efficient loading of siRNA into spermine-Ac-DEX particles is important because of the high cost of siRNA.

***In Vitro* Analysis of siRNA Delivery to HeLa Cells.** To test the transfection efficiency of spermine-Ac-DEX particles *in vitro*, we chose to knockdown a model reporter protein, firefly luciferase. HeLa cells that stably express firefly luciferase (HeLa-*luc* cells) were used as a model cell line. A more effective delivery system will lead to more cytosolic siRNA and luciferase mRNA cleavage, and thus a lower expression of luciferase protein. Firefly luciferase catalyzes the mono-oxygenation of luciferin, and during this process, a photon of light is produced. Thus, reduced expression of luciferase will result in the generation of fewer photons when the cells are incubated with the enzyme substrate.

We were interested in determining if particle loading or concentration influences the delivery efficiency of siRNA-loaded particles. Differentially loaded particles were prepared and HeLa-*luc* cells were incubated with particle doses equivalent to 17.2 pmol of siRNA per well. All of the particles could reduce luciferase expression of the cells (approximately 55−60% compared to untreated cells) with low toxicity (greater than 85% viability) (Figure 4b). The luciferase expression was comparable for all three batches of particles indicating that the particle loading and concentration within the tested range have a minimal impact on the overall performance, and the knockdown resulted from successful delivery of siRNA.

To determine if the knockdown was dose-dependent, HeLa-*luc* cells were incubated with varying siRNA doses for 48 h and analyzed for the expression of luciferase. As shown in Figure 5, spermine-Ac-DEX particles containing luciferase-specific siRNA efficiently knock down luciferase expression at all siRNA concentrations tested. Transfection with luciferase siRNA loaded spermine-Ac-DEX particles resulted in significant gene silencing (up to 60% knockdown compared with untreated cells). In comparison, treatment of cells with free siRNA did not affect the luciferase expression, indicating the importance of encapsulation of siRNA in particles. The extent of gene silencing depends on the amount of siRNA incubated with the cells (Figure 5). Treating cells with lower particle concentrations, and thus less siRNA, resulted in reduced knockdown. The optimal knockdown was obtained with the three highest siRNA dosages tested (8.75, 17.5, and 35 pmol of siRNA). This silencing effect was sequence specific as spermine-Ac-DEX particles loaded with a non-specific siRNA sequence (Silencer Negative control #1 siRNA) did not result in obvious reduction of luciferase expression. Importantly, there was no significant cytotoxicity associated with intracellular accumulation of spermine-Ac-DEX particles. MTT assay of cells incubated with particles showed greater than 80% cell viability for all particle concentrations tested (Figure 6).

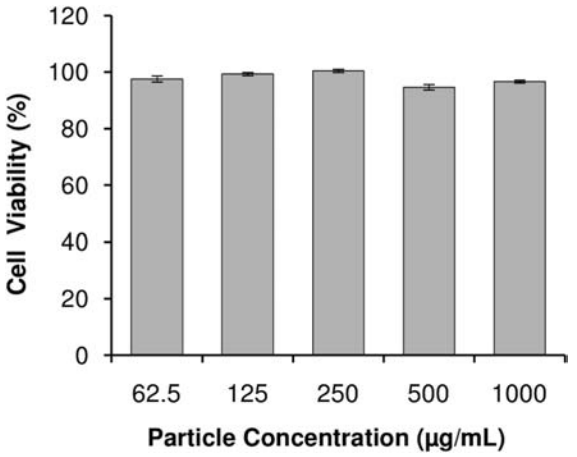


Figure 6. Spermine Ac-DEX particles are nontoxic at concentrations up to 1 mg/mL. MTT assay was used to measure cell viability compared with untreated cells. Data represent the mean ± standard deviation of quadruplicate measurements.

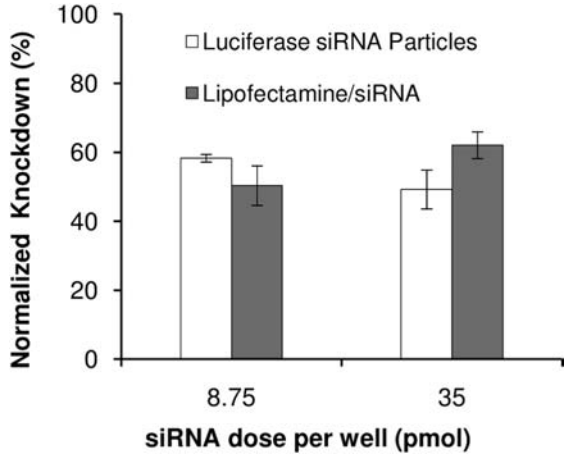


Figure 7. Spermine Ac-DEX particles show comparable activity compared with Lipofectamine 2000. Knockdown was normalized to the data from the cells treated with the control siRNA particles or complexes. Data represent the mean ± standard deviation.

Lipofectamine 2000, a commercially available cationic lipid-based reagent, was used as a positive control in the transfection experiment. This reagent is commonly used for *in vitro* transfection,[62] but it faces several obstacles for clinical translation.[63] Lipofectamine complexes with the luciferase-targeting siRNA as well as with the control siRNA were prepared so that the dose of siRNA would match that used with two of the particle concentrations tested (35 pmol siRNA per well and 8.75 pmol siRNA per well). We observed some non-specific reduction of luciferase expression using Lipofectamine 2000, most likely due to slight toxicity of the complexes. Thus, the knockdown was normalized to the data from the cells treated with the control siRNA complexes. The knockdown obtained with the spermine-Ac-DEX particles was comparable to that obtained with Lipofectamine 2000 at both siRNA doses tested (Figure 7). Due to their ability to provide efficient siRNA delivery with reduced cytotoxicity (97% cell viability for spermine-Ac-DEX particles compared to 75% for Lipofectamine), spermine-Ac-DEX particles represent an attractive delivery system that may offer several advantages over previously reported materials for siRNA delivery.

CONCLUSION

In summary, spermine-Ac-DEX particles represent a novel delivery vehicle which can efficiently deliver siRNA to cancer cells with minimal toxicity. Spermine-Ac-DEX combines the attractive properties of cationic polymers with those of polymeric particles affording a material that is safe and effective for gene delivery. Spermine modification of Ac-DEX facilitated the preparation of particles capable of encapsulating siRNA with high loading efficiency. *In vitro* evaluation demonstrated that the particles are capable of knocking down luciferase expression in HeLa-*luc* cells in a dose-dependent manner with low cytotoxicity. In comparison to previously reported gene delivery materials, spermine-Ac-DEX shows attractive new transfection and biodegradability features, and in addition can be easily modified[64] (for example, with peptide targeting ligands). Due to its acid-sensitivity, spermine-Ac-DEX allows for the selective release of siRNA after cellular internalization, with potential tunability of cargo release rate. Thus, spermine-Ac-DEX expands the potential application of Ac-DEX based particles and represents a promising vehicle for siRNA delivery. Future studies will explore the feasibility of using these particles to regulate protein expression *in vivo*.

AUTHOR INFORMATION

Corresponding Author

*Prof. Jean M. J. Fréchet, 718 Latimer Hall, College of Chemistry, University of California, Berkeley, Berkeley, CA 94720-1460. E-mail: frechet@berkeley.edu. Tel: (510) 643-3077. Fax: (510) 643-3079.

Present Addresses

†Institute of Pharmacy, Friedrich Schiller University of Jena, 07743 Jena, Germany.

‡Liquidia Technologies, Inc., Research Triangle Park, NC 27709, USA.

ACKNOWLEDGMENT

This project has been funded in part with Federal funds from the National Heart, Lung, and Blood Institute, National Institutes of Health, Department of Health and Human Services, under Contract No. HHSN268201000043C, and in part through the Fréchet "various gifts" fund for the support of research in new materials. We thank Ann Fischer and Michelle Yasukawa for help with cell culture, Dr. Peter Friebe and Dr. Eva Harris for assistance with and the use of their luminescence plate reader, and Dr. Chris Contag for kindly providing the HeLa-*luc* cell line. S. Schubert gratefully acknowledges the Deutsche Forschungsgemeinschaft (DFG) and P. R. Wich thanks the Alexander von Humboldt Foundation (AvH) for funding.

REFERENCES

(1) Fougerolles, A., Vornlocher, H.-P., Maraganore, J., and Lieberman, J. (2007) Interfering with disease: A progress report on siRNA-based therapeutics. *Nat. Rev. Drug Discovery 6*, 443–453.

(2) Bumcrot, D., Manoharan, M., Koteliansky, V., and Sah, D. W. Y. (2006) RNAi therapeutics: A potential new class of pharmaceutical drugs. *Nat. Chem. Biol. 2*, 711–719.

(3) Kurreck, J. (2009) RNA interference: From basic research to therapeutic applications. *Angew. Chem., Int. Ed. 48*, 1378–1398.
(4) Hammond, S. M., Caudy, A. A., and Hannon, G. J. (2001) Post-transcriptional gene silencing by double-stranded RNA. *Nat. Rev. Genet. 2*, 110–119.
(5) Tuschl, T. (2001) RNA interference and small interfering RNAs. *ChemBioChem 2*, 239–245.
(6) Bernstein, E., Caudy, A. A., Hammond, S. M., and Hannon, G. J. (2001) Role for a bidentate ribonuclease in the initiation step of RNA interference. *Nature 409*, 363–366.
(7) Rand, T. A., Ginalski, K., Grishin, N. V., and Wang, X. (2004) Biochemical identification of Argonaute 2 as the sole protein required for RNA-induced silencing complex activity. *Proc. Natl. Acad. Sci. U.S.A. 101*, 14385–14389.
(8) Ameres, S. L., Martinez, J., and Schroeder, R. (2007) Molecular basis for target RNA recognition and cleavage by human RISC. *Cell 130*, 101–112.
(9) Hutvágner, G., and Zamore, P. D. (2002) A microRNA in a multiple-turnover RNAi enzyme complex. *Science 297*, 2056–2060.
(10) Whitehead, K. A., Langer, R., and Anderson, D. G. (2009) Knocking down barriers: Advances in siRNA delivery. *Nat. Rev. Drug Discovery 8*, 129–138.
(11) Fröhlich, T., and Wagner, E. (2010) Peptide- and polymer-based delivery of therapeutic RNA. *Soft Matter 6*, 226–234.
(12) Pack, D. W., Hoffman, A. S., Pun, S., and Stayton, P. S. (2005) Design and development of polymers for gene delivery. *Nat. Rev. Drug Discovery 4*, 581–593.
(13) During, M. J. (1997) Adeno-associated virus as a gene delivery system. *Adv. Drug Delivery Rev. 27*, 83–94.
(14) Verma, I. M., and Somia, N. (1997) Gene therapy - Promises, problems, and prospects. *Nature 389*, 239–242.
(15) Schaffer, D. V., Koerber, J. T., and Lim, K. (2008) Molecular engineering of viral gene delivery vehicles. *Annu. Rev. Biomed. Eng. 10*, 169–194.
(16) Mintzer, M. A., and Simanek, E. E. (2009) Nonviral vectors for gene delivery. *Chem. Rev. 109*, 259–302.
(17) Thomas, C. E., Ehrhardt, A., and Kay, M. A. (2003) Progress and problems with the use of viral vectors for gene therapy. *Nat. Rev. Genet. 4*, 346–358.
(18) Zaiss, A. K., and Muruve, D. A. (2008) Immunity to adeno-associated virus vectors in animals and humans: A continued challenge. *Gene Ther. 15*, 808–816.
(19) Malone, R. W., Felgner, P. L., and Verma, I. M. (1989) Cationic liposome-mediated RNA transfection. *Proc. Natl. Acad. Sci. U.S.A. 86*, 6077–6081.
(20) Zimmerman, T. S., Lee, A. C. H., Akinc, A., Bramlage, B., Bumcrot, D., Fedoruk, M. N., Harborth, J., Heyes, J. A., Jeffs, L. B., John, M., Judge, A. D., Lam, K., McClintock, K., Nechev, L. V., Palmer, L. R., Racie, T., Röhl, I., Seiffert, S., Shanmugam, S., Sood, V., Soutschek, J., Toudjarska, I., Wheat, A. J., Yaworski, E., Zedalis, W., Koteliansky, V., Manoharan, M., Vornlocher, H.-P., and MacLachlan, I. (2006) RNAi-mediated gene silencing in non-human primates. *Nature 441*, 111–114.
(21) Neu, M., Fischer, D., and Kissel, T. (2005) Recent advances in rational gene transfer vector design based on poly(ethylene imine) and its derivatives. *J. Gene Med. 7*, 992–1009.
(22) Zhang, S., Zhao, B., Jiang, H., Wang, B., and Ma, B. (2007) Cationic lipids and polymers mediated vectors for delivery of siRNA. *J. Controlled Release 123*, 1–10.
(23) Lares, M. R., Rossi, J. J., and Ouellet, D. L. (2010) RNAi and small interfering RNAs in human disease therapeutic applications. *Trends Biotechnol. 28*, 570–579.
(24) Shim, M. S., and Kwon, Y. J. (2010) Efficient and targeted delivery of siRNA *in vivo*. *FEBS J. 277*, 4814–4827.
(25) Little, S. R., Lynn, D. M., Ge, Q., Anderson, D. G., Puram, S. V., Chen, J., Eisen, H. N., and Langer, R. (2004) Poly-B-amino ester-containing microparticles enhance the activity of nonviral genetic vaccines. *Proc. Natl. Acad. Sci. U.S.A. 101*, 9534–9539.
(26) Woodrow, K. A., Cu, Y., Booth, C. J., Saucier-Sawyer, J. K., Wood, M. J., and Saltzman, W. M. (2009) Intravaginal gene silencing using biodegradable polymer nanoparticles densely loaded with small-interfering RNA. *Nat. Mater. 8*, 526–533.
(27) Nguyen, J., Steele, T. W. J., Merkel, O., Reul, R., and Kissel, T. (2008) Fast degrading polyesters as siRNA nano-carriers for pulmonary gene therapy. *J. Controlled Release 132*, 243–251.
(28) Wang, C., Ge, Q., Ting, D., Nguyen, D., Shen, H.-R., Chen, J., Eisen, H. N., Heller, J., Langer, R., and Putnam, D. (2004) Molecularly engineered poly(ortho ester) microspheres for enhanced delivery of DNA vaccines. *Nat. Mater. 3*, 190–196.
(29) Lee, S., Yang, S. C., Kao, C.-Y., Pierce, R. H., and Murthy, N. (2009) Solid polymeric microparticles enhance the delivery of siRNA to macrophages *in vivo*. *Nucleic Acids Res. 37*, e145.
(30) Little, S. R., Lynn, D. M., Puram, S. V., and Langer, R. (2005) Formulation and characterization of poly (B amino ester) microparticles for genetic vaccine delivery. *J. Controlled Release 107*, 449–462.
(31) Pack, D. W. (2004) Timing is everything. *Nat. Mater. 3*, 133–134.
(32) Fu, K., Pack, D. W., Klibanov, A. M., and Langer, R. (2000) Visual evidence of acidic environment within degrading poly(lactic-co-glycolic acid) (PLGA) microspheres. *Pharm. Res. 17*, 100–106.
(33) Walter, E., Moelling, K., Pavlovic, J., and Merkle, H. P. (1999) Microencapsulation of DNA using poly(DL-lactide-co-glycolide): Stability issues and release characteristics. *J. Controlled Release 61*, 361–374.
(34) Heinze, T., Liebert, T., Heublein, B., and Hornig, S. (2006) Functional polymers based on dextran. *Adv. Polym. Sci. 205*, 199–291.
(35) Raemdonck, K., Naeye, B., Buyens, K., Vandenbroucke, R. E., Høgset, A., Demeester, J., and De Smedt, S. C. (2009) Biodegradable dextran nanogels for RNA interference: Focusing on endosomal escape and intracellular siRNA delivery. *Adv. Funct. Mater. 19*, 1406–1415.
(36) Raemdonck, K., Naeye, B., Høgset, A., Demeester, J., and De Smedt, S. C. (2010) Prolonged gene silencing by combining siRNA nanogels and photochemical internalization. *J. Controlled Release 145*, 281–288.
(37) Nagane, K., Jo, J.-I., and Tabata, Y. (2010) Promoted adipogenesis of rat mesenchymal stem cells by transfection of small interfering RNA complexed with a cationized dextran. *Tissue Eng., Part A 16*, 21–31.
(38) Bachelder, E. M., Beaudette, T. T., Broaders, K. E., Dashe, J., and Fréchet, J. M. J. (2008) Acetal-derivatized dextran: An acid-responsive biodegradable material for therapeutic applications. *J. Am. Chem. Soc. 130*, 10494–10495.
(39) Broaders, K. E., Cohen, J. A., Beaudette, T. T., Bachelder, E. M., and Fréchet, J. M. J. (2009) Acetalated dextran is a chemically and biologically tunable material for particulate immunotherapy. *Proc. Natl. Acad. Sci. U.S.A. 106*, 5497–5502.
(40) Bachelder, E. M., Beaudette, T. T., Broaders, K. E., Fréchet, J. M. J., Albrecht, M. T., Mateczun, A. J., Ainslie, K. M., Pesce, J. T., and Keane-Myers, A. M. (2010) *In vitro* analysis of acetalated dextran microparticles as a potent delivery platform for vaccine adjuvants. *Mol. Pharmaceutics 7*, 826–835.
(41) Cohen, J. A., Beaudette, T. T., Cohen, J. L., Broaders, K. E., Bachelder, E. M., and Fréchet, J. M. J. (2010) Acetal-modified dextran microparticles with controlled degradation kinetics and surface functionality for gene delivery in phagocytic and non-phagocytic cells. *Adv. Mater. 22*, 3593–3597.
(42) Rao, D. D., Vorhies, J. S., Senzer, N., and Nemunaitis, J. (2009) siRNA vs. shRNA: Similarities and differences. *Adv. Drug Delivery Rev. 61*, 746–759.
(43) Gary, D. J., Puri, N., and Won, Y.-Y. (2007) Polymer-based siRNA delivery: Perspectives on the fundamental and phenomenological distinctions from polymer-based DNA delivery. *J. Controlled Release 121*, 64–73.
(44) Takahashi, Y., Nishikawa, M., and Takakura, Y. (2009) Non-viral vector-mediated RNA interference: Its gene silencing characteristics and important factors to achieve RNAi-based gene therapy. *Adv. Drug Delivery Rev. 61*, 760–766.

(45) Murata, N., Takashima, Y., Toyoshima, K., Yamamoto, M., and Okada, H. (2008) Anti-tumor effects of anti-VEGF siRNA encapsulated with PLGA microspheres in mice. *J. Controlled Release 126*, 246–254.
(46) Vercauteren, R., Bruneel, D., Schacht, E., and Duncan, R. (1990) Effect of the chemical modification of dextran on the degradation by Dextranase. *J. Bioact. Compat. Polym. 5*, 4–15.
(47) Vercauteren, R., Schacht, E., and Duncan, R. (1992) Effect of the chemical modification of dextran on the degradation by rat liver lysosomal enzymes. *J. Bioact. Compat. Polym. 7*, 346–357.
(48) Crepon, B., Jozefonvicz, J., Chytry, V., Řihová, B., and Kopeček, J. (1991) Enzymatic degradation and immunogenic properties of derivatized dextrans. *Biomaterials 12*, 550–554.
(49) Gray, I. (1953) Metabolism of plasma expanders studied with carbon-14-labeled dextran. *Am. J. Physiol. 174*, 462–466.
(50) de Belder, A. N. (1996) Medical Applications of Dextran and Its Derivatives. *Polysaccharides in Medicinal Applications* (Dumitriu, S., Ed.) pp 505−524, Chapter 16, Marcel Dekker, New York.
(51) Rosenfeld, E. L., and Lukomskaya, I. S. (1957) The splitting of dextran and isomaltose by animal tissues. *Clin. Chim. Acta 2*, 105–114.
(52) Rosenfeld, E. L., and Saienko, A. S. (1964) Metabolism *in vivo* of clinical dextran. *Clin. Chim. Acta 10*, 223–228.
(53) Lynn, D. M., and Langer, R. (2000) Degradable poly(B-amino esters): Synthesis, characterization, and self-assembly with plasmid DNA. *J. Am. Chem. Soc. 122*, 10761–10768.
(54) Azzam, T., Eliyahu, H., Shapira, L., Linial, M., Barenholz, Y., and Domb, A. J. (2002) Polysaccharide-oligoamine based conjugates for gene delivery. *J. Med. Chem. 45*, 1817–1824.
(55) Azzam, T., Eliyahu, H., Makovitzki, A., Linial, M., and Domb, A. J. (2004) Hydrophobized dextran-spermine conjugate as potential vector for *in vitro* gene transfection. *J. Controlled Release 96*, 309–323.
(56) Hosseinkhani, H., Azzam, T., Tabata, Y., and Domb, A. J. (2004) Dextran−spermine polycation: An efficient nonviral vector for *in vitro* and *in vivo* gene transfection. *Gene Ther. 11*, 194–203.
(57) Bernstein, A., Hurwitz, E., Maron, R., Arnon, R., Sela, M., and Wilchek, M. (1978) Higher antitumor efficacy of daunomycin linked to dextran. *J. Natl. Cancer Inst. 60*, 379–383.
(58) Petros, R. A., and DeSimone, J. M. (2010) Strategies in the design of nanoparticles for therapeutic applications. *Nat. Rev. Drug Discovery 9*, 615–627.
(59) Gautam, A., Densmore, C. L., Golunski, E., Xu, B., and Waldrep, J. C. (2001) Transgene expression in mouse airway epithelium by aerosol gene therapy with PEI/DNA complexes. *Mol. Ther. 3*, 551–556.
(60) Jiang, H.-L., Xu, C.-X., Kim, Y.-K., Arote, R., Jere, D., Lim, H.-T., Cho, M.-H., and Cho, C.-S. (2009) The suppression of lung tumorigenesis by aerosol-delivered folate-chitosan-graft-polyethyleneimine/Akt1 shRNA complexes through the Akt signaling pathway. *Biomaterials 30*, 5844–5852.
(61) Fuller, J. E. (2008) in *Chemical Engineering*, Massachusetts Institute of Technology, Cambridge.
(62) Dalby, B., Cates, S., Harris, A., Ohki, E. C., Tilkins, M. L., Price, P. J., and Ciccarone, V. C. (2004) Advanced transfection with Lipofectamine 2000 reagent: Primary neurons, siRNA, and high-throughput applications. *Methods 33*, 95–103.
(63) Kongkaneramit, L., Sarisuta, N., Azad, N., Lu, Y., Iyer, A. K. V., Wang, L., and Rojanasakul, Y. (2008) Dependence of reactive oxygen species and FLICE inhibitory protein on Lipofectamine-induced apoptosis in human lung epithelial cells. *J. Pharmacol. Exp. Ther. 325*, 969–977.
(64) Beaudette, T. T., Cohen, J. A., Bachelder, E. M., Broaders, K. E., Cohen, J. L., Engleman, E. G., and Fréchet, J. M. J. (2009) Chemoselective ligation in the functionalization of polysaccharide-based particles. *J. Am. Chem. Soc. 131*, 10360–10361.

Bioconjugate Chemistry

ARTICLE

pubs.acs.org/bc

Targeting Tumor Cells through Chitosan-Folate Modified Microcapsules Loaded with Camptothecin

Alice Galbiati,[†] Claudio Tabolacci,[†] Blasco Morozzo Della Rocca,[†] Palma Mattioli,[†] Simone Beninati,[†] Gaio Paradossi,[‡] and Alessandro Desideri*[,†]

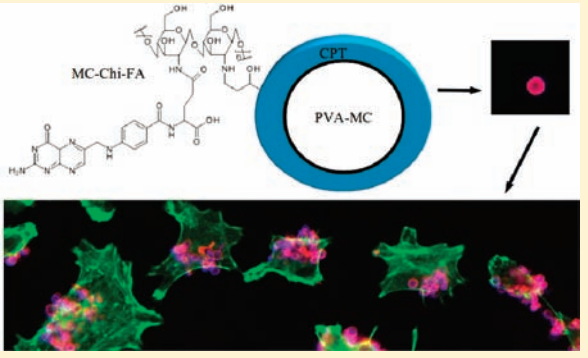
[†]Department of Biology

[‡]Department of Chemical Sciences and Technologies

University of Rome Tor Vergata, Via della Ricerca Scientifica, Rome 00133, Italy

Supporting Information

ABSTRACT: Poly(vinyl alcohol) microcapsules have been tailored as carriers to deliver camptothecin, an anticancer drug poorly soluble in water. The capsules have been reacted with a chitosan−folate complex in order to selectively target cancer cells overexpressing the folic acid receptor. Microcapsules decorated with the chitosan−folate complex have been characterized in their uptake and release of camptothecin, following the absorption band at λ = 370 nm diagnostic of the drug molecule. The selectivity of chitosan−folate microcapsules in targeting cancer cells has been demonstrated by fluorescence microscopy using HeLa cells, overexpressing the folate receptor and NIH3t3 fibroblasts as a negative control. The chitosan−folate microcapsules loaded with camptothecin significantly reduce the proliferation of HeLa tumor cells, while they have a negligible effect on fibroblasts. This work demonstrates that the chitosan−folate microcapsules represent a promising system to selectively target hydrophobic drugs, such as camptothecin, to tumor cells.



INTRODUCTION

Camptothecin (CPT) and its derivatives are chemical poisons that specifically target topoisomerase I, forming a stable ternary complex with the enzyme and DNA, inhibiting the unknotting process that is associated with replication and transcription.[1−3] These drugs are used in the treatment of ovarian carcinoma[4] (the fifth leading cause of cancer deaths in women) and in the treatment of small-cell lung cancer (SCLC) recurrent disease, which is among the most lethal malignancies.[5,6] Unfortunately, such chemical agents display a high degree of toxicity also against normal tissues that show enhanced proliferation rates, such as the bone marrow, gastrointestinal tract, and hair follicles.[7,8] Several systems have been devised to better deliver CPT, as those based on lipid nanoparticles,[9,10] dendrimers,[11] solid lipid nanoparticles,[12] and perfluorocarbon nanoemulsions,[13] but the main problem remains the selectivity toward tumor cells. Various approaches have been used to selectively target drugs against the tumor[14−16] such as the use of monoclonal antibodies,[17] or systems able to sense the changes in temperature and redox signals,[18] pH,[19] or membrane potential between normal cells and cancer cells, and similar strategies have been recently applied for the transport of CPT.[20,21] A promising strategy concerns the use of ligands specific for membrane receptors differentially expressed on pathological cells.[22,23]

Folate receptors (FR) are vastly overexpressed in a wide variety of human tumors, including ovarian, endometrial, colorectal, breast, lung, renal cell carcinomas, brain metastases derived from epithelial cancers, and neuroendocrine carcinomas, but rarely are found on normal cell surface . Folate (FA) has been conjugated to many polymers, such as polyethylenimine,[24] poly(L-lysine),[25] poly(ethylene glycol), and chitosan,[26] to give complexes that can be internalized by cells through a FR-mediated endocytic mechanism.[27] Among the various polymers, chitosan displays important useful properties being biodegradable and biocompatible since it can be degraded by lysozymes into *N*-acetyl-glucosamine, that is subsequently excreted as carbon dioxide via the glycoprotein synthetic pathway.[26] For this reason, chitosan has been widely used for different pharmaceutical and medical applications[28] and has also been used for gene complexation.[29−32] The delivery systems made by folate-conjugated polymers increase either the intracellular uptake of proteins or the transfection rate of DNA compared with unmodified polymer delivery systems.[33,34]

Poly(vinyl alcohol) (PVA) is a water-soluble and injectable polymer, which can be used as the basis for the construction of various structures. PVA has been recently used to produce microbubbles, air-filled biocompatible spherical structures that can be used as novel polymer based ultrasound contrast agents

Received: December 3, 2010
Revised: April 28, 2011
Published: May 06, 2011

ACS Publications © 2011 American Chemical Society

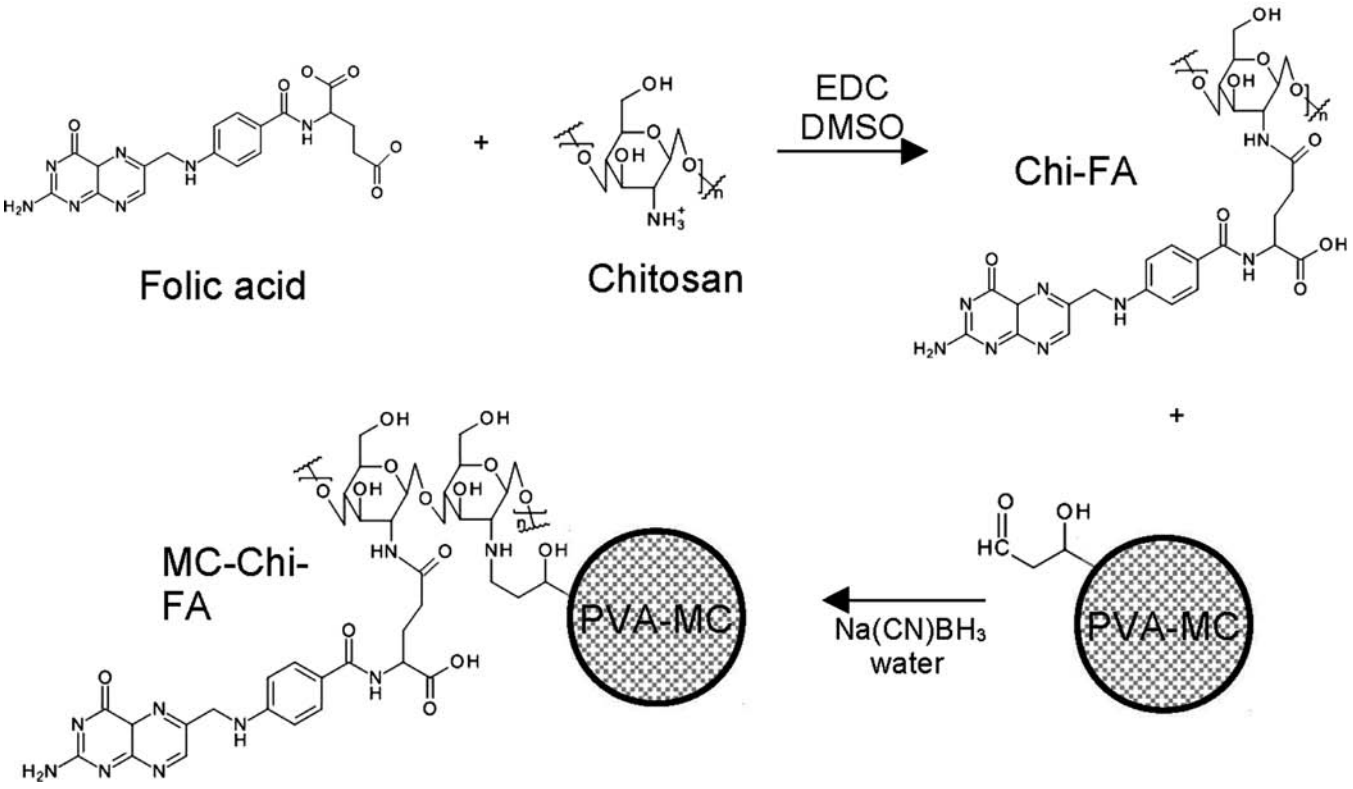


Figure 1. General scheme for the synthesis of chitosan−folate modified microcapsules (MC-Chi-FA). The chitosan−folate (Chi-FA) derivative is obtained by reacting chitosan and folate in DMSO using EDC to activate the COOH folate groups. Chi-FA is linked to MC using a reductive amination procedure.

(UCA),[35] as well as other already commercially available enhancers for echographic investigations.[36] In the presence of ethanol, the air present in PVA microbubbles is replaced by the solvent, giving rise to microcapsules (MC), that retain the spherical shape, with a mean diameter ranging from 3 to 5 μm depending on the preparations.[37] They are versatile and biocompatible microstructures whose surface has free OH groups and reactive aldehydes that can be used to functionalize them with different molecules.[37]

In this work, folic acid has been bound on a flexible arm of chitosan, which has then been conjugated to the PVA microcapsules (Figure 1), in order to be specifically directed against tumor cells of epithelial origin such as the HeLa cells. The loading and release of the antitumor drug CPT has been investigated, in both concentration and rate, for chitosan and chitosan-folate modified and unmodified microcapsules, and the specific interaction with tumor cells has been assayed by fluorescence microscopy. The results indicate that the chitosan−folate modified microcapsules specifically target tumor cells and strongly reduce their proliferation, while having a negligible effect on control cells, suggesting that they can represent an interesting system to be taken in consideration toward applications of targeted delivery.

MATERIALS AND METHODS

Materials. All solvents and reagents were of analytical grade and were used as received. Poly vinyl alcohol (PVA) was obtained from Sigma Aldrich. Number average molecular weight determined by membrane osmometry was 30 000 (5000 g/mol). Weight average molecular weight, determined by static light scattering, was 70 000 (10 000 g/mol). Low molecular weight (50 kDa) chitosan, 75−85% deacetylated, rhodamine-β-isothiocyanate, (*S*)-(+)-camptothecin, 95% HPLC, Triton X-100, folic acid, and dimethyl sulfoxide (DMSO) were Sigma products. Sodium periodate, and inorganic acids and bases, used for telechelic PVA preparation and microballoon synthesis and modifications, were RPE products from Carlo Erba. Cell culture media were obtained from Gibco. Alexa-488-conjugated phalloidin was obtained from Molecular Probes.

Instruments. High-resolution ^{1}H NMR spectra were recorded on a Digital NMR Spectrospin AVANCE 300, Bruker. Chitosan and chitosan−folate 3 mg/mL are dissolved in D_2O with 3% v/v CD_3COOD solution, using tetramethylsilane (TMS) as the internal standard. The release kinetics of the drug were performed using Perkin-Elmer Lambda 2 UV/vis double beam spectrophotometer. Fluorescence microscopy images were obtained with the DeltaVision system (Applied Precision, Washington, USA) equipped with an Olympus inverted microscope IX 70. The image workstation includes *SoftWoRx* software for digital image acquisition, deconvolution, and optical sectioning.

Synthesis of PVA-Coated Microbubbles and Conversion into Microcapsules. Synthesis of telechelic PVA was previously described.[38,39] Stable (air-filled) PVA-coated microbubbles were prepared by cross-linking telechelic PVA at the water/air interface. Vigorous stirring at room temperature for 2 h of 2% telechelic PVA aqueous solution (200 mL) by an Ultra-Turrax T-25 at 8000 rpm equipped with a Teflon coated tip generated a fine foam of telechelic PVA acting both as colloidal stabilizer and as air bubble coating agent. The cross-linking reaction was carried

out at room temperature. Floating microbubbles were separated from solid debris and extensively dialyzed against Milli-Q water. The aqueous suspensions of microbubbles were obtained and used for microcapsule preparation.

PVA microbubbles were converted into solvent-filled microcapsules by equilibrating an aqueous suspension in ethanol 70% solution. The microcapsule suspension was then extensively washed by a series of centrifugations at 1000*g* to remove excess ethanol.

Chemical Modifications. *Rhodamination of PVA-MC.* Suspensions of 1 mg/mL of MC were added with 10 μL of rhodamine-β-isothiocyanate[40] solution 2.3 mg/mL in DMSO and stirred for 1 h. The rhodamine excess was removed by at least 5 centrifugation steps at 1000*g* for 10 min, changing the external medium.

Synthesis of Chi-Rod. Chitosan 0.5% (w/v) was suspended in 100 mL of acetic acid 3% (v/v) solution. 50 mg of rhodamine-β-isothiocyanate was then added and stirring maintained for 48 h in the dark at 4 °C. The solution was adjusted to pH 9 with NaOH, and unreacted rhodamine-β-isothiocyanate was removed carrying out at least 5 centrifugation steps at 1000*g* for 10 min. The synthesized compound was extensively dialyzed against Milli-Q-water.

Synthesis of Chi-FA and Chi-FA-Rod. 1.2 mmol of EDC (*N*-(3-dimethylaminopropyl)-*N*′-ethylcarbodiimide hydrochloride) were added to 3 mmol of FA dissolved in 50 mL of DMSO, and left to react for 1 h in the dark at room temperature. Then, 50 mL of a 1% (w/w) chitosan or chitosan−rhodamine in 20 mM acetate buffer pH 4.7 was added to the reaction. After 16 h, the solution was brought to pH 9 with NaOH, and the compound purified by centrifugation followed by 3 days of dialysis against acetate buffer and extensive dialysis against Milli-Q water using a 12 kDa cutoff dialysis membrane. The compound was then freeze−dried.

Preparation of Chitosan Functionalized Microcapsules. Chitosan was conjugated to microcapsules by reductive amination. Chi or Chi-FA was dissolved in a sodium acetate 0.2 M, acetic acid 0.3 M buffer at pH 4.5 to a concentration of 0.15% (w/v). A 10 mL sample of 1 mg/mL microcapsule aqueous suspension was added with 4 μL of Chi or Chi-FA solution at room temperature. The pH was carefully adjusted to 5.0 with acetate buffer, following the addition of $Na(CN)BH_3$. The resulting suspension was stirred for 1 day at room temperature. The microcapsule suspension was then extensively dialyzed and washed to remove low molecular weight reaction products and unreacted chitosan.

Adsorption of the CPT on MC or MC-Chi-FA and Evaluation of Drug Release Kinetics. Suspensions of 1 mg/mL of MC or MC-Chi-FA were added with CPT in DMSO at a final concentration of 100 μM and stirred for 4 days in the dark. Then, three washes were performed by centrifugation at 1000*g* to remove the drug that was not adsorbed. The concentration of drug in the washing is calculated by spectrophotometer following the absorption at λ = 370 nm. The percentage of CPT adsorbed on microcapsules was indirectly estimated by subtracting the total concentration of drug present in the wash to the total drug used for the adsorption.

A suspension of MC o MC-Chi-FA 1 mg/mL (20 mL), previously adsorbed with CPT 100 μM, was resuspended in Dulbecco's modified Eagle's medium (D-MEM) without phenol red, with or without 10% fetal calf serum (FCS), and subdivided into 20 aliquots of 1 mL. The MC was kept in an incubator shaking at 140 rpm, 37 °C. At different times, the samples were centrifuged for 5 min at 2000*g* and the supernatant was read spectrophotometrically at λ = 370 nm. Absorption values were fitted with the equation $A = A_{max}[1 - \exp(Kt)]$ to estimate the time constant of the kinetics (K^{-1}) and maximum release A_{max}.

Cell Culture and Proliferation Assay. HeLa cells were cultured in RPMI-1640 and NIH3t3 cells were cultured in D-MEM, supplemented with 10% fetal calf serum (FCS), 200 mM glutamine, 100 U/mL penicillin, and 0.1 mg/mL streptomycin, and maintained in humidified atmosphere of 5% CO_2 at 37 °C. Cells were harvested twice a week and used at about 80% confluence.

For proliferation studies, cells were detached with trypsin/EDTA for 5 min and centrifuged. Cells were resuspended in RPMI-1640 medium without folate and seeded in 96-well culture dishes (2.5×10^3 cells per well) and cells were left to grow for 48 h. After this time, medium was refreshed and cells were incubated for additional 48 h with MC, MC-Chi, and MC-Chi-FA (either adsorbed with CPT or not). At the end of incubation, medium was refreshed again, and after 48 h, the percentage of cell proliferation was evaluated by the sulforhodamine assay,[41] calculating the values as a percentage of the control, considered to be 100%. Proliferation assays were also carried out by cell counting using a Neubauer modified chamber. In this case, cells are seeded in 12-well culture dishes at 7.5×10^3 cells per well. This protocol was established in order to discriminate between the antiproliferative effect due to the diffusion of CPT released from the microcaplules in the media and the one due to the direct cell−microcapsule interaction.

Microcapsule Localization. For fluorescence studies, cells were grown in Lab-Tek chamber slides (Nunc Inc.) in RPMI-1640 medium without folate and treated with MC as described previously. After 48 h of incubation, cells were washed, fixed with 3.8% paraformaldehyde solution in phosphate buffered saline, and permeated by using 0.1% Triton X-100. Actin filaments were labeled by using Alexa-488-conjugated phalloidin according to the manufacturer's instructions. Fluorescent signals were detected and photographed using a Delta Vision 3.0 microscope. To assess the direct involvement of folate mediated interaction, localization experiments have been carried out also in the presence of free folate. After 48 h of culture in folate-free medium, MC-Chi-FA were given to cells in either folate-free or folate-supplemented medium (final concentration 4 mg/L). Cells were fixed and stained after the 2 day treatment and localization assays were performed as described.

RESULTS AND DISCUSSION

Chitosan−Folate Complex Formation and Functionalization of Microcapsules. Chitosan−folate has been synthesized using published protocols[42] by reacting the NH_2 group of chitosan with the COOH groups of folate (Figure 1). The γ-carboxylate group is the most reactive one, although the α-carboxylate is also available for conjugation. The reaction has been verified through ^{1}H NMR spectroscopy that is not able to distinguish between the two contributions. The ^{1}H NMR spectrum of chitosan (Figure 2a) shows a series of peaks corresponding to protons linked to the C3, C4, and C2 carbon atoms of the sugar and to the methyl protons, falling at 3.90, 3.77, 3.18, and 2.07 ppm, respectively. The degree of chitosan deacetylation, obtained from the ratio of the integrals of the methyl peak over the C2 one, is found to be 85%. The NMR proton spectrum of chitosan−folate (Figure 2b), when

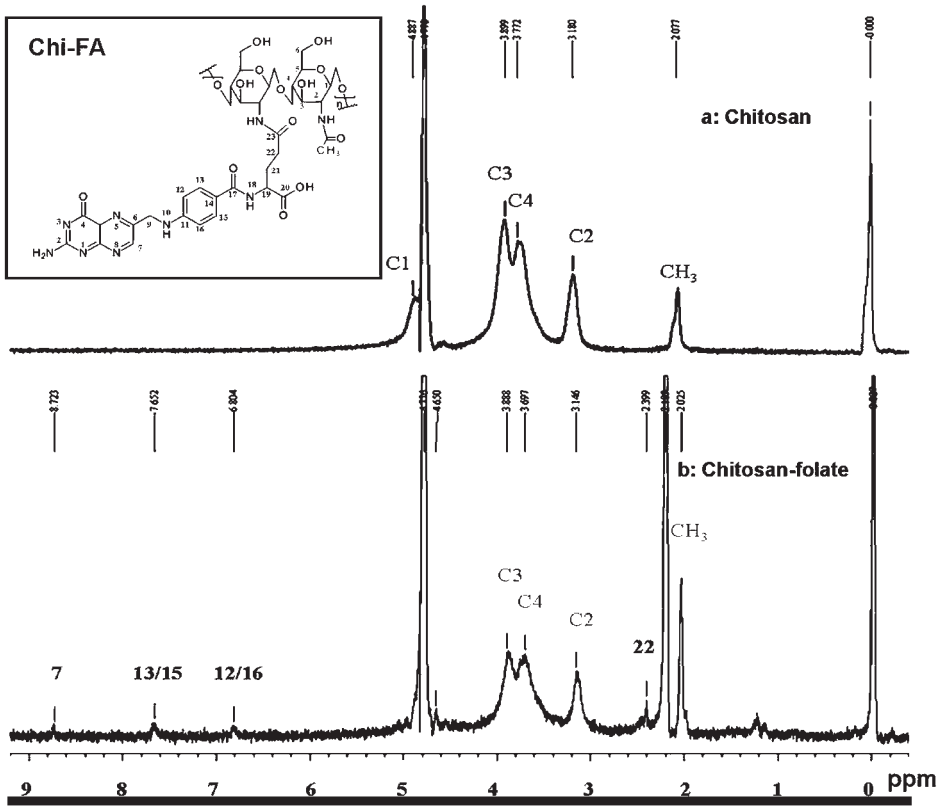


Figure 2. NMR spectra of chitosan and of the chitosan−folate derivative. (a) ^{1}H-NMR spectrum of chitosan solution in D_2O with 3% (v/v) CD_3COOD; (b) ^{1}H-NMR spectrum of 3 mg/mL of the chitosan−folate adduct in D_2O with 3% (v/v) CD_3COOD. Inset: Chemical structure of the chitosan−folate complex. In gray, the numbering of carbons of chitosan; and in black, the numbering of folate (see text for peak assignments).

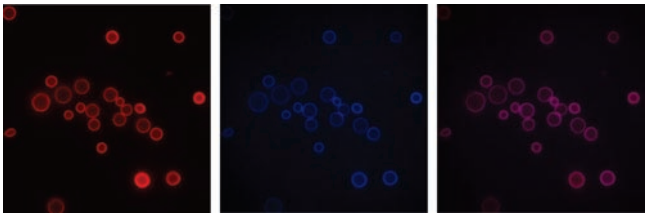


Figure 3. Fluorescence microscopy of decorated MC, adsorbed with CPT. Fluorescence microscope images of MC labeled with chitosan−rhodamine−folate, and absorbed with camptothecin. Left panel shows the rhodamine signal (red) on MC, the middle one the CPT signal (blue), and the right one the overlay of the two signals (violet).

compared to chitosan, shows additional peaks at 8.73, 7.66, and 6.83 ppm due to the folate aromatic rings and one at 2.40 ppm due to the protons linked to C22 (see inset of Figure 2 for the labeling of the different groups). The ratio between the integral of one of the folate aromatic peaks and the chitosan C2 peak at 3.14 ppm allows us to quantify the percentage of folate substitution on the chitosan NH_2 groups that is found to be 5%. On the basis of nominal molecular weight, this percentage corresponds to 15 folates per chitosan. Chitosan (Chi) and chitosan−folate (Chi-FA) have been also functionalized with rhodamine (Rod)[43] to give the Chi-Rod and Chi-FA-Rod complex. All the synthesized complexes have been then conjugated to microcapsules (MC) using the reductive amination procedure in the presence of $Na(CN)BH_3$,[35,37] to yield MC-Chi, MC-Chi-FA, and their rhodaminated counterparts MC-Chi-Rod and MC-Chi-FA-Rod.

The success of decoration and the ability of the modified MC's to incorporate CPT has been verified by incubating the microcapsules with 100 μM CPT for four days and observing their fluorescence microscopy images. Figure 3, representing the MC-Chi-FA-Rod system, shows that the red signal coming from rhodamine (λ_{ex} = 540 nm, λ_{em} = 625 nm, left panel) colocalizes with the blue signal originating from CPT (λ_{ex} = 370 nm, λ_{em} = 420 nm, middle panel), since they have an identical shape. The colocalization is confirmed by the overlay of the two images (right panel), that gives spheres characterized by a violet color. To our knowledge, this is the first time that CPT adsorbance on PVA MC is reported.

CPT Adsorption and Release. The adsorption of the drug has been carried out incubating the MC or MC-Chi-FA with camptothecin for 4 days with continuous stirring. The microcapsules have then been extensively washed in water and the concentration of drug bound on the MC's has been indirectly estimated quantifying the drug present in the washes by absorption spectroscopy measurements at λ = 370 nm, corresponding to the maximum in the camptothecin absorption spectrum. Considering an extinction coefficient ε = 17 670 $(M\ cm)^{-1}$ for CPT at λ = 370 nm, it has been evaluated that MC and MC-Chi-FA adsorb about 68% and 82% of the external drug concentration, respectively. When resuspended in D-MEM at 37 °C, the maximum of released drug, in the case of MC, is obtained after one hour, while in the case of MC-Chi and MC-Chi-FA, it is obtained after about 5 h. In detail, fitting the data, reported as percentage of release normalized to maximum released drug, gives rise to a rate of release of 2.4 ± 0.2 h^{-1} for MC, 0.68 ± 0.02

h^{-1} for MC-Chi, and $0.52 \pm 0.02\ h^{-1}$ for MC-Chi-FA (Figure S1). Figure 4 shows the release kinetics of CPT from MC, MC-Chi and MC-Chi-FA at 37 °C in the culture medium supplemented with 10% serum. The release properties of the microcapsules are influenced by the presence of serum in the medium; in fact, the release rates, obtained by fitting the data as described in the Methods section, correspond to $1.4 \pm 0.2\ h^{-1}$ for MC, $1.4 \pm 0.3\ h^{-1}$ for MC-Chi, and $2.7 \pm 0.8\ h^{-1}$ for MC-Chi-FA, values larger than those obtained in the absence of serum.

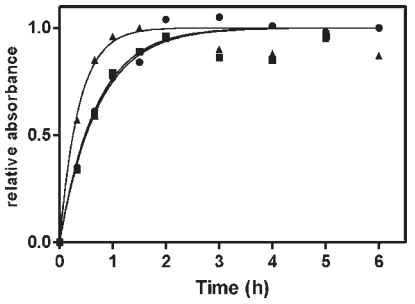


Figure 4. Drug release kinetics from MC. CPT release kinetics in D-MEM medium supplemented with 10% FCS at 37 °C, for nude microcapsules (MC, circles), chitosan microcapsules (MC-Chi, squares), and chitosan−folate microcapsules (MC-Chi-FA, triangles).

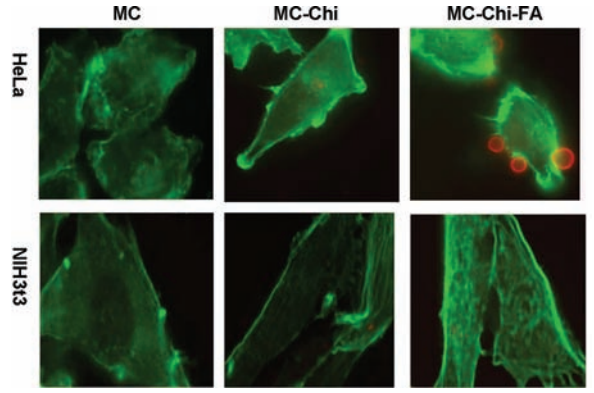


Figure 5. Localization of MC on the cells. Fluorescence microscopy image of HeLa tumor cells (up) and NIH3t3 fibroblast cells (down), treated for 48 h with MC (left), MC-chitosan (middle), and MC-chitosan-folate (right). The cells have been cultured in folate-free medium.

Interaction of MC with Different Cell Lines. The ability of MC and MC-Chi-FA to interact with cells has been tested incubating the capsules with two different cell types: HeLa cells, that overexpress the FR, and NIH3t3 fibroblasts, not expressing the receptor on their surface, as a negative control. The cells have been incubated for two days with 100 μg/mL of MC, MC-Chi, and MC-Chi-FA, all labeled with rhodamine-β-isothiocyanate on PVA, and then they have been extensively washed, stained, and imaged. Representative images from these experiments are shown in Figure 5. Control cells, fibroblasts, show no uptake of MC, independent of their functionalization, while HeLa cells exhibit a folate-dependent interaction. In our experiments, the unfunctionalized MC have never been found to interact with HeLa cells, while a small number of adhesions has been occasionally found for MC-Chi, likely due to a fusogenic activity of chitosan. In marked contrast, MC-Chi-FA frequently interact with the surface of HeLa cells and sometimes are also internalized, as reported in Figure S2 showing a large number of microcapsules bound to cells. The internalization of MC-Chi-FA by HeLa cells can be appreciated through a series of optical sections above and below the focal plane of the cell, such as the ones reported in Figure S3, where a representative sequence from outside to inside the cell is shown. A further hint to the nature of folate-mediated interaction is given by competition experiments, in which functionalized MC have been administered to cells together with folate in the medium. The effect of competition is striking, as in this case the uptake of MC-Chi-FA is substantially suppressed (Figure S2).

Effect of MC on Cell Proliferation. The impact of MCs on healthy and cancer cells has been followed, incubating cells in the presence of MC, MC-Chi, and MC-Chi-FA, either previously adsorbed with CPT or not. For drug adsorption, the microcapsules have been incubated with 100 μM CPT, and the amount of drug adsorbed was quantified. The quantity of MC used for the cell treatment is different and depends on the MC functionalization. For each experiment, we have taken care to have a concentration of adsorbed CPT equal to the IC_{50} of the specific cell line. In detail, a CPT concentration of 40 nM, corresponding to the IC_{50} value for the HeLa cells,[44] and one of 12 μM, corresponding to the IC_{50} for the NIH3t3,[45] have been used. The cells have been incubated with the microcapsules for 48 h and

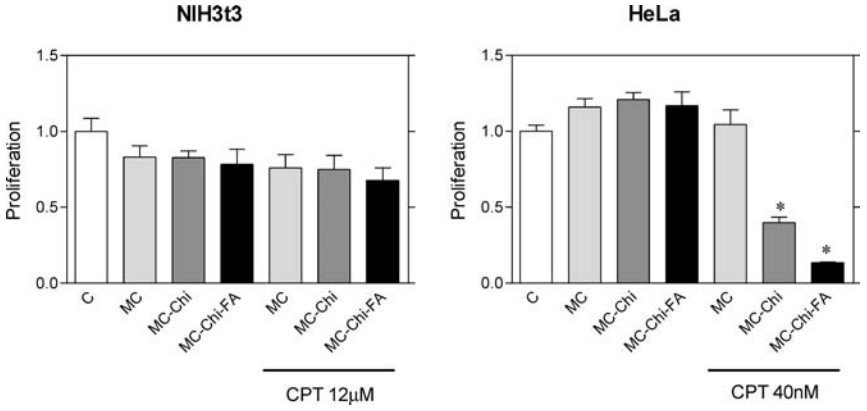


Figure 6. Effect of the decorated MC on cell lines. Proliferation of NIH3t3 fibroblast (left) and HeLa cells (right), treated for 48 h with MC, MC-chitosan (MC-Chi), and MC-chitosan-folate (MC-Chi-FA), with or without CPT adsorption. The treatment was removed and substituted with fresh medium, and then the proliferation was assayed after 48 h. Asterisks mark statistical significance ($p < 0.01$).

allowed to grow on fresh medium for additional 48 h before being assayed on their proliferation (Figure 6). This method has been established to allow the discrimination of the effect due to the diffusion of the drug lost from the capsules in the media from the one due to a direct capsules−cell interaction. Evaluation of cell proliferation after 48 h treatment indicates that the nude MC, previously incubated with CPT, has the same effect on HeLa viability as the chitosan−folate functionalized ones (Figure S4). Analysis of antiproliferative effect after media change and incubation for two additional days highlights the mortality due to a direct microcapsule−cell interaction (Figure 6). In the absence of CPT, a difference in proliferation no larger than 10% has been found on both cell lines for any kind of incubated MC. The antiproliferative effect of the microcapsules is slightly larger in the HeLa than in the control NIH3t3 cells for the MC-Chi system, a phenomenon that is not easy to interpret, although a more intense interaction of chitosan with HeLa cells could account for it. The most striking difference is observed upon incubation with the MC-Chi-FA. In this latter case, in fact less than 20% cells survive in the case of HeLa cells, while more than 80% of NIH3t3 cells are still active. The same results were obtained with the alternative method of cell counting, described in the Methods section, for which control cell numbers were approximately 2×10^5 and 3×10^5 per well, for HeLa and NIH3t3, respectively. This result confirms that the overexpression of the folate receptor permits a very efficient and selective targeting of HeLa cells from the MC-Chi-FA.

CONCLUSION

In this work, PVA microcapsules have been functionalized with chitosan or chitosan−folate and have been characterized for their ability to absorb and release CPT. The presence of chitosan or chitosan−folate on MC leads to greater absorption of the drug, likely because of an increased surface area of the functionalized microstructures, that can then accommodate a greater amount of drug.

Notably, MC-Chi-FA are able to bind and to be internalized by HeLa cells overexpressing the folate receptor, while no interaction is observed with NIH3t3 fibroblasts used as negative control (Figures 5 and S5). MC-Chi are found to occasionally adhere to both cell lines, likely because of the fusogenic properties of chitosan, due to the positive charges that allow electrostatic interactions with the negatively charged cell surface.[32,46] The results of cellular localization fully match proliferation experiments; in fact, MC-Chi-FA, interacting with HeLa cells, impact their proliferation while not perturbing the growth of NIH3t3 cells (Figure 6).

These results indicate that microcapsules modified with chitosan folate are a promising system to target camptothecin in tumors of epithelial origin since the presence of folate allows a selective recognition of HeLa tumor cells. Other studies will be performed on different cell lines also using functionalized microbubbles in the effort to design multivalent therapeutic agents that combine detectability (e.g., contrast agents for imaging techniques) with tissue specific drug delivery.

ASSOCIATED CONTENT

Supporting Information. Drug release kinetics in D-MEM, folate dependent localization, MC-Chi-Fa interaction, and uptake. This material is available free of charge via the Internet at http://pubs.acs.org.

AUTHOR INFORMATION

Corresponding Author

*Prof. Alessandro Desideri, Department of Biology, University of Rome Tor Vergata, Via della Ricerca Scientifica, Rome, Italy, Tel. +39 06 72594326, Fax +39 06 2022798. E-mail: desideri@uniroma2.it.

ACKNOWLEDGMENT

A.D. acknowledges support by the AIRC project number 10121

ABBREVIATIONS:

FA, folic acid; FR, folate receptor; PVA, poly(vinyl alcohol); MC, microcapsules; MC-Chi, chitosan conjugated MC; MC-Chi-FA, chitosan-folate conjugated MC; MC-Chi-Rod, chitosan-rhodamine conjugated MC; CPT, camptothecin

REFERENCES

(1) Hsiang, Y. H., and Liu, L. F. (1988) Identification of mammalian DNA topoisomerase I as an intracellular target of the anticancer drug camptothecin. *Cancer. Res. 48*, 1722–1726.

(2) Ulukan, H., and Swaan, P. W. (2002) Camptothecins: a review of their chemotherapeutic potential. *Drugs 62*, 2039–2057.

(3) Hede, M. S., Petersen, R. L., Frøhlich, R. F., Krüger, D., Andersen, F. F., Andersen, A. H., and Knudsen, B. R. (2007) Resolution of Holliday junction substrates by human topoisomerase I. *J. Mol. Biol. 365*, 1076–1092.

(4) Peng, L. H., Chen, X. Y., and Wu, T. X. (2008) Topotecan for ovarian cancer. *Cochrane Database Syst. Rev. 2*, CD005589.

(5) Sandler, A. B. (2001) Irinotecan in small-cell lung cancer: the US experience. *Oncology 15*, 11–12.

(6) Bruzzese, F., Rocco, M., Castelli, S., Di Gennaro, E., Desideri, A., and Budillon, A. (2009) Synergistic antitumor effect between vorinostat and topotecan in small cell lung cancer cells is mediated by generation of reactive oxygen species and DNA damage-induced apoptosis. *Mol. Cancer Ther. 8*, 3075–87.

(7) Mross, K., Richly, H., Schleucher, N., Korfee, S., Tewes, M., Scheulen, M. E., Seeber, S., Beinert, T., Schweigert, M., Sauer, U., Unger, C., Behringer, D., Brendel, E., Haase, C. G., Voliotis, D., and Strumberg, D. (2004) A phase I clinical and pharmacokinetic study of the camptothecin glycoconjugate, BAY 38−3441, as a daily infusion in patients with advanced solid tumors. *Ann. Oncol. 15*, 1284–1294.

(8) Pizzolato, J. F., and Saltz, L. B. (2003) The camptothecins. *Lancet 361*, 2235–2242.

(9) Huang, Z. R., Hua, S. C., Yang, Y. L., and Fang, J. Y. (2008) Development and evaluation of lipid nanoparticles for camptothecin delivery: a comparison of solid lipid nanoparticles, nanostructured lipid carriers, and lipid emulsion. *Pharmacol. Sin. 29*, 1094–1102.

(10) Koo, O. M., Rubinstein, I., and Onyuksel, H. (2005) Camptothecin in sterically stabilized phospholipid micelles: a novel nanomedicine. *Nanomedicine 1*, 77–84.

(11) Venditto, V. J., Allred, K., Allred, C. D., and Simanek, E. E. (2009) Intercepting the synthesis of triazine dendrimers with nucleophilic pharmacophores: a general strategy toward drug delivery vehicles. *Chem. Commun. (Camb.) 37*, 5541–5542.

(12) Yang, S., Zhu, J., Lu, Y., Liang, B., and Yang, C. (1999) Body distribution of camptothecin solid lipid nanoparticles after oral administration. *Pharm. Res. 16*, 751–757.

(13) Fang, J. Y., Hung, C. F., Hua, S. C., and Hwang, T. L. (2009) Acoustically active perfluorocarbon nanoemulsions as drug delivery

carriers for camptothecin: drug release and cytotoxicity against cancer cells. *Ultrasonics 49*, 39–46.

(14) Ferrari, M. (2005) Cancer nanotechnology: opportunities and challenges. *Nat. Rev. Cancer 5*, 161–171.

(15) Torchilin, V. P. (2007) Targeted pharmaceutical nanocarriers for cancer therapy and imaging. *AAPS J. 9*, 128–147.

(16) Caruthers, S. D., Wickline, S. A., and Lanza, G. M. (2007) Nanotechnological applications in medicine. *Curr. Opin. Biotechnol. 18*, 26–30.

(17) Rombi, G., Piu, G., Piro, S., and Anedda, V. (1993) Mab labelled liposomes as selective vehicles for drugs in H.I.V. infected cells. *Cytotechnology. 11*, 147–149.

(18) Howard, K. A., Dong, M., Oupicky, D., Bisht, H. S., Buss, C., Besenbacher, F., and Kjems, J. (2007) Nanocarrier stimuli-activated gene delivery. *Small 1*, 54–57.

(19) Dandagi, P. M., Mastiholimath, V. S., Gadad, A. P., Kulkarni, A. R., and Konnur, B. K. (2009) pH-Sensitive mebeverine microspheres for colon delivery. *Indian J. Pharm. Sci. 71*, 464–468.

(20) Chao, P., Deshmukh, M., Kutscher, H. L., Gao, D., Rajan, S. S., Hu, P., Laskin, D. L., Stein, S., and Sinko, P. J. (2010) Pulmonary targeting microparticulate camptothecin delivery system: anticancer evaluation in a rat orthotopic lung cancer model. *Anticancer Drugs 21*, 65–76.

(21) Dal Pozzo, A., Ni, M. H., Esposito, E., Dallavalle, S., Musso, L., Bargiotti, A., Pisano, C., Vesci, L., Bucci, F., Castorina, M., Foderà, R., Giannini, G., Aulicino, C., and Penco, S. (2010) Novel tumor-targeted RGD peptide-camptothecin conjugates: synthesis and biological evaluation. *Bioorg. Med. Chem. 18*, 64–72.

(22) Shpakov, A. O., Gur'ianov, I. A., Baianova, N. V., and Vlasov, G. P. (2008) The receptor of serpentine type and the heterotrimeric G protein as targets of action of the polylysine dendrimers. *Tsitologiia 50*, 1036–1043.

(23) Sudimack, J., and Lee, R. J. (2000) Targeted drug delivery via the folate receptor. *Adv. Drug Delivery Rev. 41*, 147–162.

(24) Liang, B., He, M. L., and Xiao, Z. P. (2008) Synthesis and characterization of folate-PEG-grafted-hyperbranched-PEI for tumor-targeted gene delivery. *Biochem. Biophys. Res. Commun. 367*, 874–880.

(25) Kim, S. H., Jeong, J. H., Joe, C. O., and Park, T. G. (2005) Folate receptor mediated intracellular protein delivery using PLL−PEG−FOL conjugate. *J. Controlled Release 103*, 625–634.

(26) Chan, P., Kurisawa, M., Chung, J. E., and Yang, Y. Y. (2007) Synthesis and characterization of chitosan-g-poly(ethylene glycol)-folate as a non viral carrier for tumor-targeted gene delivery. *Biomaterials 28*, 540–549.

(27) Lee, R. J., and Low, P. S. (1995) Folate-mediated tumor cell targeting of liposome-entrapped doxorubicin in vitro. *Biochim. Biophys. Acta 1233*, 134–144.

(28) Hejazi, R., and Amiji, M. (2003) Chitosan-based gastrointestinal delivery system. *J. Controlled Release 89*, 151–65.

(29) Azzam, T., Eliyahu, H., Shapira, L., Linial, M., Barenholz, Y., and Domb, A. J. (2002) Polysaccharide-oligoamine based conjugates for Gene Delivery. *J. Med. Chem. 45*, 1817–1824.

(30) Nimesh, S., Thibault, M. M., Lavertu, M., and Buschmann, M. D. (2010) Enhanced gene delivery mediated by low molecular weight chitosan/DNA complexes: effect of pH and serum. *Mol. Biotechnol. 46*, 182–196.

(31) Opanasopit, P., Techaarpornkul, S., Rojanarata, T., Ngawhirunpat, T., and Ruktanonchai., U. (2010) Nucleic acid delivery with chitosan hydroxybenzotriazole. *Oligonucleotides 20*, 127–136.

(32) Sun, X., and Zhang, N. (2010) Cationic polymer optimization for efficient gene delivery. *Mini. Rev. Med. Chem. 10*, 108–125.

(33) Zheng, Y., Song, X., Darby, M., Liang, Y., He, L., Cai, Z., Chen, Q., Bi, Y., Yang, X., Xu, J., Li, Y., Sun, Y., Lee, R. Y., and Hou, S. (2010) Preparation and characterization of folate-poly(ethylene glycol)-grafted-trimethylchitosan for intracellular transport of protein through folate receptor-mediated endocytosis. *J. Biotechnol. 145*, 47–53.

(34) Zheng, Y., Cai, Z., Song, X., Yu, B., Bi, Y., Chen, Q., Zhao, D., Xu, J., and Hou, S. (2009) Receptor mediated gene delivery by folate conjugated N-trimethyl chitosan in vitro. *Int. J. Pharm. 382*, 262–269.

(35) Cavalieri, F., El Hamassi, A., Chiessi, E., and Paradossi, G. (2006) Tethering functional ligands onto shell of ultrasound active polymeric microbubbles. *Biomacromolecules 2*, 604–611.

(36) Schutt, E. G., Klein, D. H., Mattrey, R. M., and Riess, J. G. (2003) Injectable microbubbles as contrast agents for diagnostic ultrasound imaging: the key role of perfluorochemicals. *Angew. Chem., Int. Ed. 42*, 3218–3235.

(37) Cavalieri, F., El Hamassi, A., Chiessi, E., and Paradossi, G. (2005) Stable polymeric microballoons as multifunctional device for biomedical uses: synthesis and characterization. *Langmuir 19*, 8758–8764.

(38) Paradossi, G., Cavalieri, F., Chiessi, E., Spagnoli, C., and Cowman, M. K. (2003) Poly(vinyl alcohol) as versatile biomaterial for potential biomedical applications. *J. Mater. Sci.: Mater. Med. 14*, 687–691.

(39) Paradossi, G., Cavalieri, F., Chiessi, E., Ponassi, V., and Martorana, V. (2002) Tailoring of physical and chemical properties of macro-and microhydrogels based on telechelic PVA. *Biomacromolecules 3*, 1255–1262.

(40) De Belder, A. N., and Granath, K. (1973) Preparation and properties of fluorescein labeled dextrans. *Carbohydr. Res. 30*, 375–378.

(41) Papazisis, K. T., Geromichalos, G. D., Dimitriadis, K. A., and Kortsaris, A. H. (1997) Optimization of the sulforhodamine B colorimetric assay. *J. Immunol. Methods. 208*, 151–158.

(42) Wan, A., Sun, Y., and Li, H. (2008) Characterization of folate-graft-chitosan as a scaffold for nitric oxide release. *Int. J. Biol. Macromol. 43*, 415–421.

(43) Qaqish, R. B., and Amiji, M. M. (1999) Synthesis of a fluorescent chitosan derivative and its application for the study of chitosan-mucin interactions. *Carbohydr. Polym. 38*, 99–107.

(44) Takara, K., Kitada, N., Yoshikawa, E., Yamamoto, K., Horibe, S., Sakaeda, T., Nishiguchi, K., Ohnishi, N., and Yokoyama, T. (2009) Molecular changes to HeLa cells on continuous exposure to SN-38 an active metabolite of irinotecan Hydrochloride. *Cancer Lett. 278*, 88–96.

(45) Suzuki, K., Doi, S., Yahara, S., and Uyeda, M. (2003) 2070-DTI, a Topoisomerase inhibitor produced by Streptomyces sp. Strain No. 2070. *J. Enzym. Inhib. 18*, 497–503.

(46) Pavinatto, F. J., Caseli, L., Pavinatto, A., dos Santos, D. S., Jr., Nobre, T. M., Zaniquelli, M. E., Silva, H. S., Miranda, P. B., and de Oliveira, O. N., Jr. (2007) Probing chitosan and phospholipid interactions using Langmuir and Langmuir-Blodgett films as cell membrane models. *Langmuir 23*, 7666–7671.

Supporting Information for "Targeting tumor cells through chitosan-folate modified microcapsules loaded with camptothecin"

Alice Galbiati, Claudio Tabolacci, Blasco Morozzo Della Rocca, Palma Mattioli, Simone Beninati, Gaio Paradossi and Alessandro Desideri

Contents: Five supplementary figures

Figure S1. Drug release kinetics from MC. CPT release kinetics in D-MEM medium at 37 °C, for nude microcapsules (MC, triangles), chitosan microcapsules (MC-Chi, circles), and chitosan-folate microcapsules (MC-Chi-FA, squares)

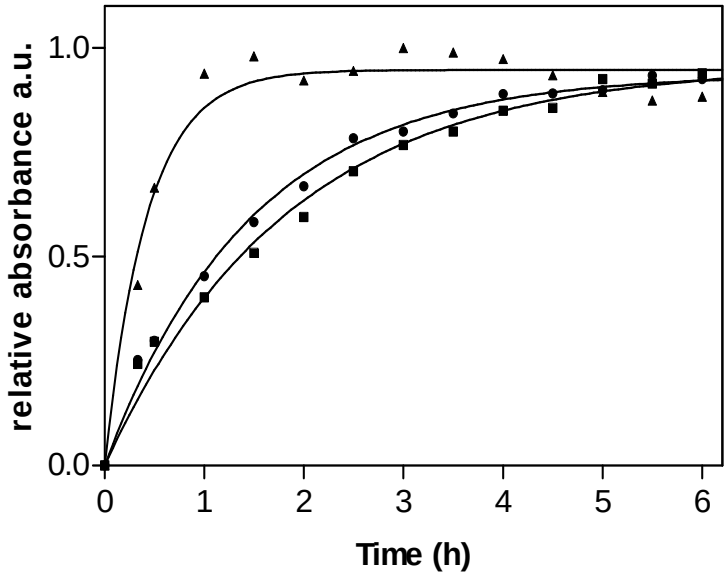


Figure S2. Lower magnification fluorescence microscope image of HeLa cells with MC-Chi-FA-Rod CPT. The capsule-cell interaction is a frequent event as shown by the large number of red spots in proximity of the cells.

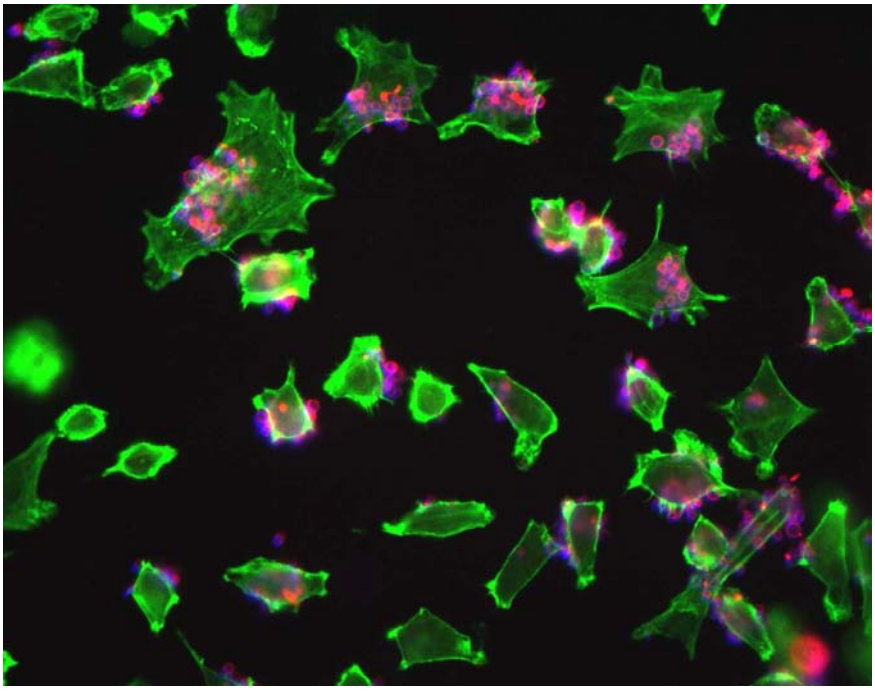


Figure S3. MC uptake. Representative Fluorescence microscopy images obtained at different focal planes of HeLa tumor cells treated with chitosan-folate microcapsules (MC-Chi-FA). MC were labeled with rhodamine on PVA. The numbering (I-IV) indicate the focal planes from the surface to the center of the cells.

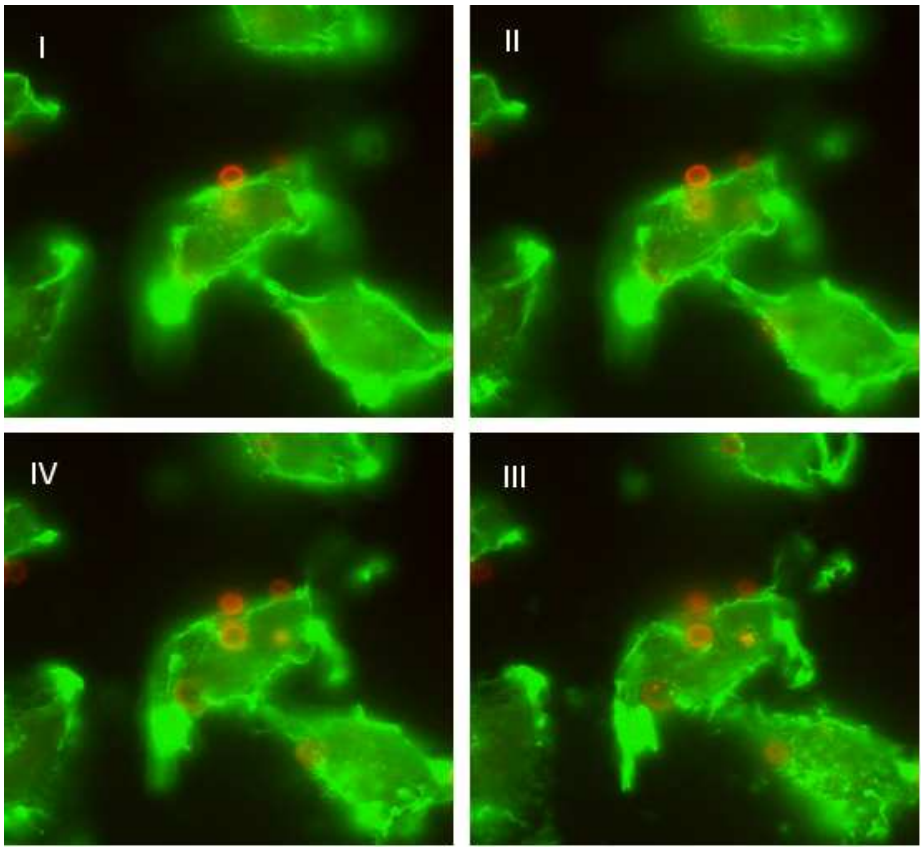


Figure S4. Effect of the nude and decorated MC on cell lines after 48 h of treatment. Proliferation of HeLa cells, treated for 48 hours with MC and MC-chitosan-folate (MC-Chi-FA), with or without CPT adsorption are shown. Cell numbers of controls are approximately 5×10^4.

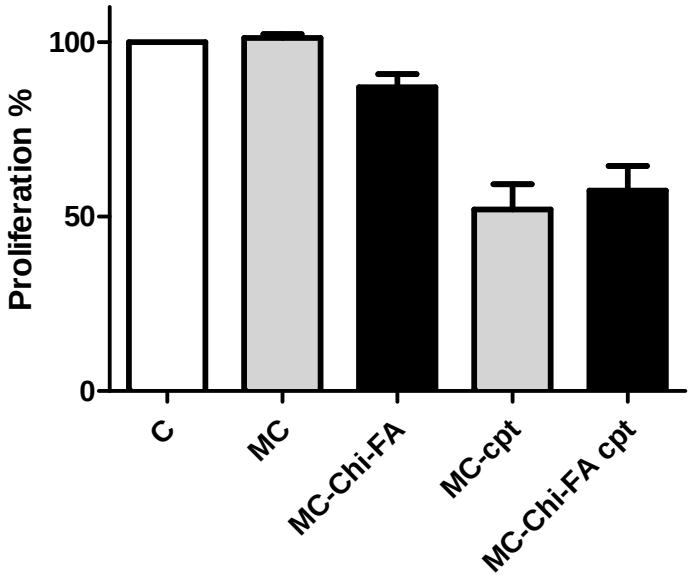
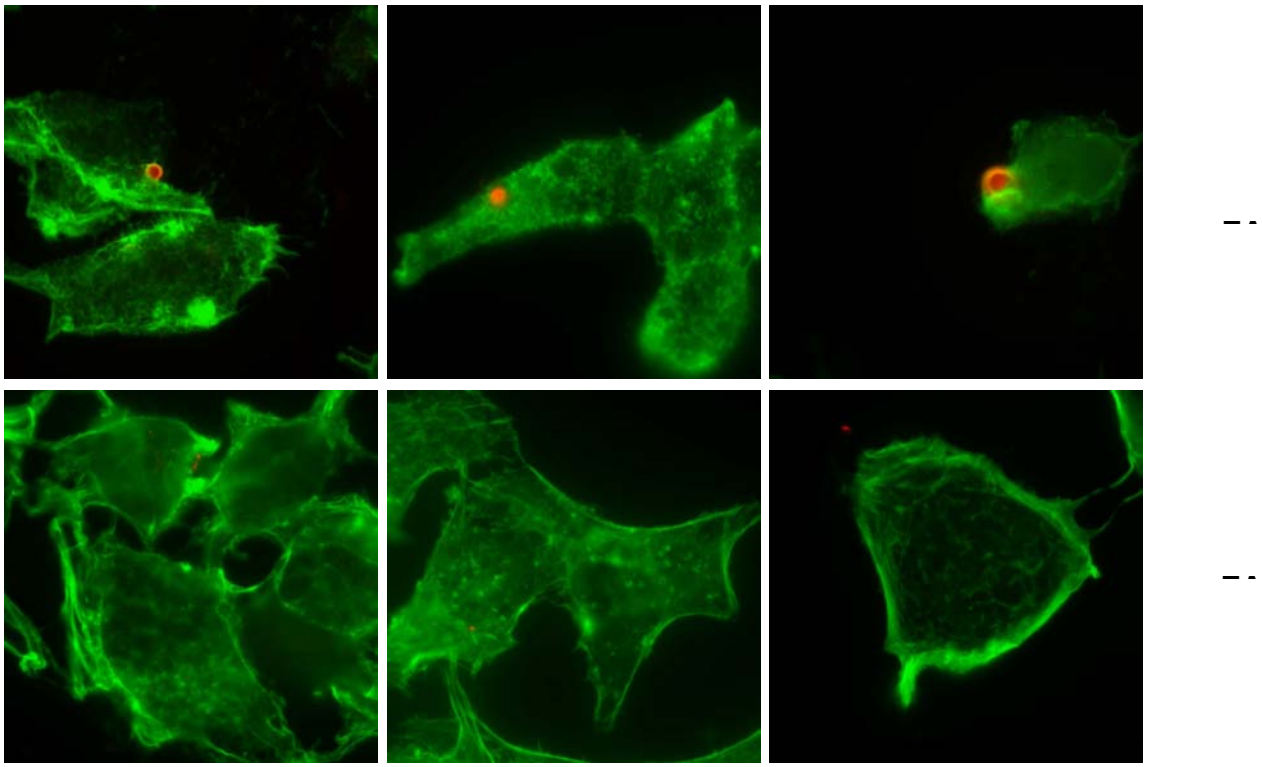


Figure S5. Experiments on folate dependent localization. Fluorescence microscope image of HeLa cells with MC-Chi-FA-Rod in the presence (lower panel) or absence (upper panel) of 4 mg/L of free folate for 48h.



Bioconjugate Chemistry

ARTICLE

pubs.acs.org/bc

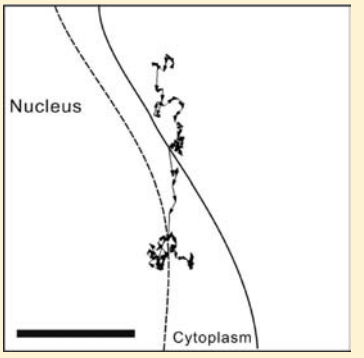
Targeted Nuclear Delivery using Peptide-Coated Quantum Dots

Chiung-Wen Kuo, Di-Yen Chueh, Narendra Singh, Fan-Ching Chien, and Peilin Chen*

Research Center for Applied Sciences, Academia Sinica, 128 Section 2, Academia Road, Nankang, Taipei 115, Taiwan

Supporting Information

ABSTRACT: Core/shell quantum dots (CdSe/Zns) conjugated with various nuclear localization signaling (NLS) peptides, which could facilitate the transportation of quantum dots across the plasma membrane into the nucleus, have been utilized to investigate the uptake mechanism of targeted delivery. Because of their brightness and photostability, it was possible to trace the trajectories of individual quantum dots in living cells using both confocal and total internal reflection microscopes. We found that, when the quantum dots were added to a cell culture, the peptide-coated quantum dots entered the cell nucleus while the uncoated quantum dots remained in the cytoplasm. At 8 nM, most of the peptide coated quantum dots were found in the cytoplasm due to aggregation. However, at a lower concentration (0.08 nM), approximately 25% of the NLS peptide-coated quantum dots entered the cell nucleus. We also found that some quantum dots without NLS coating could also enter the nucleus, suggesting that the size of the quantum dots may play an important role in such a process.



INTRODUCTION

There are increasing demands for the development of new materials and techniques to investigate the behavior of living cells where the cellular structures, biochemical activities, and interactions between cells and responses to exogenous reagents can be monitored as a function of time. To reveal the detailed mechanisms of the complicated intra- and intercellular events that occur in living cells, it is desirable to develop live-cell imaging techniques where the spatial and temporal information of the selected biomolecules or biological events can be recorded continuously during a biochemical process. Therefore, one of the most important issues in the development of live-cell imaging techniques is the ability to tag and track subcellular structures in living cells. Conventional approaches to investigate the spatiotemporal intracellular and intercellular events rely on fluorescently tagging the organelles or the biomolecules of interest using various organic fluorophores.[1] While plenty of dynamic and structural information has been obtained by organic fluorophores, their rapid photobleaching and broad, overlapping emission spectra sometimes limit this application in living-cell studies. Recent advances in the development of engineered fluorescent proteins provide an alternative approach to monitoring the dynamic behavior of living cells at the molecular level. However, fluorescent proteins also suffer in photostability when used in long-term observations.[2] To observe biochemical events in living cells for longer times, there is increasing interest in developing more robust inorganic nanomaterials such as metallic nanoparticles and semiconductor nanocrystals for live-cell imaging.[3−5] Whereas metallic nanoparticles, such as those including gold and silver, have been widely used for various analytical and therapeutic applications, it remains difficult to track individual metallic nanoparticles due to their inherent optical properties.[6] Semiconductor nanocrystals, also known as quantum dots, exhibit superior optical properties, allowing the tracking of individual cellular events with the advantages of a single excitation source, size-dependent emission spectra, a narrow spectral width, and excellent photostability. It has been demonstrated that the uptake of bioconjugated quantum dots can be tracked in living cells, and this has provided new insights into nanoparticle delivery mechanisms.[7−9]

When nanoparticles were used to study living cells, it was found that the uptake efficiency of the nanoparticles depended on their size and shape[10] and that most of the nanoparticles aggregated in the plasma membranes after entering the cells.[11,12] When investigating the behavior of living cells, it is always desirable to control the final destination of nanoparticles. One of the greatest challenges in targeted delivery is the delivery of nanoparticles into cell nuclei, but this is an important goal because the cell nucleus is the place where the genetic material is stored and the cell's function is regulated through the expression of genes. Understanding the targeted nuclear delivery process would advance our capabilities in the diagnosis of disease genotypes, also understanding biological processes in the nucleus.

To enhance the efficiency of targeted delivery, a common approach is to modify the surfaces of nanoparticles that carry probes or drugs with a wide range of biomolecules, followed by introducing the nanoparticles to cells by microinjection or transfection reagents.[9] However, if the nanoparticles are added directly into cell cultures, the nanoparticles aggregate near the cell membrane. Recently, some proteins or peptides with protein transduction domains have been shown to be capable of carrying proteins to penetrate the nuclear membrane. Several targeted delivery strategies have been developed using these biomolecules

Received: December 5, 2010
Revised: April 23, 2011
Published: May 02, 2011

ACS Publications © 2011 American Chemical Society

dx.doi.org/10.1021/bc100527m | *Bioconjugate Chem.* 2011, 22, 1073–1080

to decorate the surfaces of nanoparticles. For example, it has been reported that gold nanoparticles conjugated with nuclear localization signaling (NLS) peptides derived from adenoviral fiber proteins[13] are capable of penetrating the cell membrane of HepG2 cells, the membranes of which are known to be difficult to cross. However, no gold nanoparticles were found in the nucleus when the nanoparticles were modified only with NLS peptides. Only when the surfaces of these nanoparticles were modified with both NLS and the receptor-mediated endocytosis (RME) signaling peptide did the accumulation of gold nanoparticles in the cell nucleus become evident. NLS peptide-conjugated quantum dots have also been used to investigate the mechanism of nuclear targeting. Experimental evidence has shown that quantum dots with NLS coatings could be delivered into cell nuclei as long as the quantum dots are transfected into cells either through microinjection or incorporated with transfection reagents such as cationic liposomes.[14−17]

Here, we present studies of the trajectories of peptide-modified quantum dots without transfection reactions in living cells using both confocal and total internal reflection microscopy. Targeted nuclear delivery processes were investigated by quantum dots conjugated with NLS peptides derived from the adenoviral, SV40 virus, HIV-1 Tat protein, and adenoviral receptor mediated endocytosis (RME).

EXPERIMENTAL SECTION

Quantum Dot−Peptide Bioconjugates. In this experiment, cysteine-terminated nuclear localization signal (NLS) peptides derived from the adenovirus (CGGFSTSLRARKA), SV40 large T antigen (CGGGPKKKRKVGG), and HIV-1 Tat proteins (CGGRKKRRQRRRAP) and the peptides for receptor-mediated endocytosis (RME) (CKKKKKKSEDEYPYVPN) were purchased from MDBio Company (Taiwan) with purity of 77.72%, 80.77%, 95%, and 76.57%, respectively. These peptides were then conjugated to amine-derivatized, PEG-coated quantum dots (Qdot 545 Amino-PEG; Invitrogen). All peptides were first mixed with 10 mM dithiothreitol (DTT) for one hour and then purified using D-salt dextran desalting columns (Pierce) with phosphate-buffered saline buffer at pH 7.4. Sulfo-succinimidyl 4-(*N*-maleimidomethyl) cyclohexane-1-carboxylate (Sulfo-SMCC, Pierce) was used to couple the cysteine-terminated peptides to the amino-terminated quantum dots. A 2.5 mg/mL Sulfo-SMCC solution was mixed with the peptide solutions for two hours before adding to an 8 μM quantum dot solution. A NAP-10 column with PBS was equilibrated to remove excess reactants. The hydrodynamic diameters of the peptide-coated quantum dots were determined by gel filtration (Supporting Materials Figure S1). The hydrodynamic diameters of QDs-RME, QDs-HIV, QDs-NLS, and QDs-SV40 were measured to be 18 nm, 16.5 nm, 14.3 nm, and 14.1 nm, respectively.

Cell Culture. CHO-K1 cells were seeded in 30 mm plates on 90% Ham's F-12K medium, and supplemented with 10% (v/v) fetal bovine serum (FBS). NIH/3T3 fibroblast cells were grown in 90% Dulbecco's modified Eagle's medium, supplemented with 10% (v/v) calf serum that had been adjusted 4 mM L-glutamine, 1.5 g/L sodium bicarbonate, and 4.5 g/L glucose. CV-1 and HepG2 cells were grown in 90% minimum essential medium and Earle's BSS medium, supplemented with 10% (v/v) fetal bovine serum (FBS) that had been contained 2 mM L-glutamine, 1.5 g/L sodium bicarbonate, 0.1 mM nonessential amino acids, and 1.0 mM sodium pyruvate. All cell cultures were incubated at 37 °C and 5% CO_2.

Cytotoxicity of the Peptide-Conjugated QDs. To determine the cytotoxicity of the peptide-conjugated QDs, the cells were first seeded in 96-well plates at a density of 1×10^5 cells/mL. After 24 h of culture, the wells were refilled with fresh medium, and a serial dilution of peptide-conjugated QDs with QD concentrations ranging from 0.08 to 8 nM was added to each well. Control experiments were carried out with cells treated with an equivalent volume of medium without QDs. The cells were then incubated for 24 h at 37 °C. Cytotoxicity was measured using an MTT (3-(4,5-dimethylthiazol-2-yl) 2,5-diphenyltetrazolium bromide) assay. PBS solutions containing 10 μL of 5 mg/mL MTT stain (*in vitro* toxicology kit, Sigma) were added to each well, and the plates were incubated for four hours. After mixing, 90 μL of MTT solubilization solution was added to each well. The stain was aspirated, and the purple-colored crystals were dissolved with acidic isopropyl alcohol. After 15 min, the absorbance in each well was measured at 570 nm in a microplate reader (SpectraMax, Molecular Devices). Background absorbance was measured at 660 nm in PBS solution without the presence of cells and QDs. All experiments were repeated three times.

Imaging QDs in Living Cells. Approximately 1×10^5 cells/mL were seeded onto sterile 25 mm coverslips and cultured overnight at 37 °C. A total of 20 μL of peptide-coated QDs were mixed with 500 μL of serum-free medium. Subsequently, we added the mixture to the cell culture containing 1 mL of growth medium after observation. For the QD tracking experiment, we used 0.08 nM of the peptide-coated QDs. To visualize the cell nucleus, we stained the cells with DAPI (Molecular Probes). Uptake of the peptide-coated QDs was observed using a laser-scanning confocal microscope (Leica, SP5) and a total internal reflection microscope (Leica, AM TIRF MC) equipped with incubators. The trajectories of the QDs were identified and tracked using the Diatrack program (Semasopht, Chavannes, Switzerland). To track the trajectories of QDs in the cell nucleus, the locations of QDs were first identified by the confocal microscope. To ensure that each time only one quantum dot was monitored, the blinking phenomenon of single QDs was employed to identify the existence of single QDs using the criteria established in a previous experiment[18] where single QD displayed reproducible discrete "on" and "off" intensity.

RESULTS AND DISCUSSION

Cytotoxicity of Peptide-Conjugated QDs. Cytotoxicity is one of the major concerns when using semiconductor quantum dots in biomedical applications.[19,20] Many reports have focused on quantum dot toxicity for *in vitro* and *in vitro* studies. A wide range of results has been reported so far. However, it is now generally believed that well-capped quantum dots do not exhibit cytotoxicity for short times. The cytotoxicity of amino-PEG-modified quantum dots (Invitrogen) were measured at three different concentrations in CV-1 cell lines after 4 and 24 h of incubation. No sign of cytotoxicity was observed as shown in Figure S2 of the Supporting Information. We also used the MTT assay to evaluate the cytotoxicity of the peptide-conjugated quantum dots used in this experiment. Again, no significant cytotoxicity was observed as shown in Figure 1. For all evaluated concentrations, very little cytotoxicity was detected. No dependence on the concentration and incubation time was observed in the tested samples, indicating that the cytotoxicity of the quantum

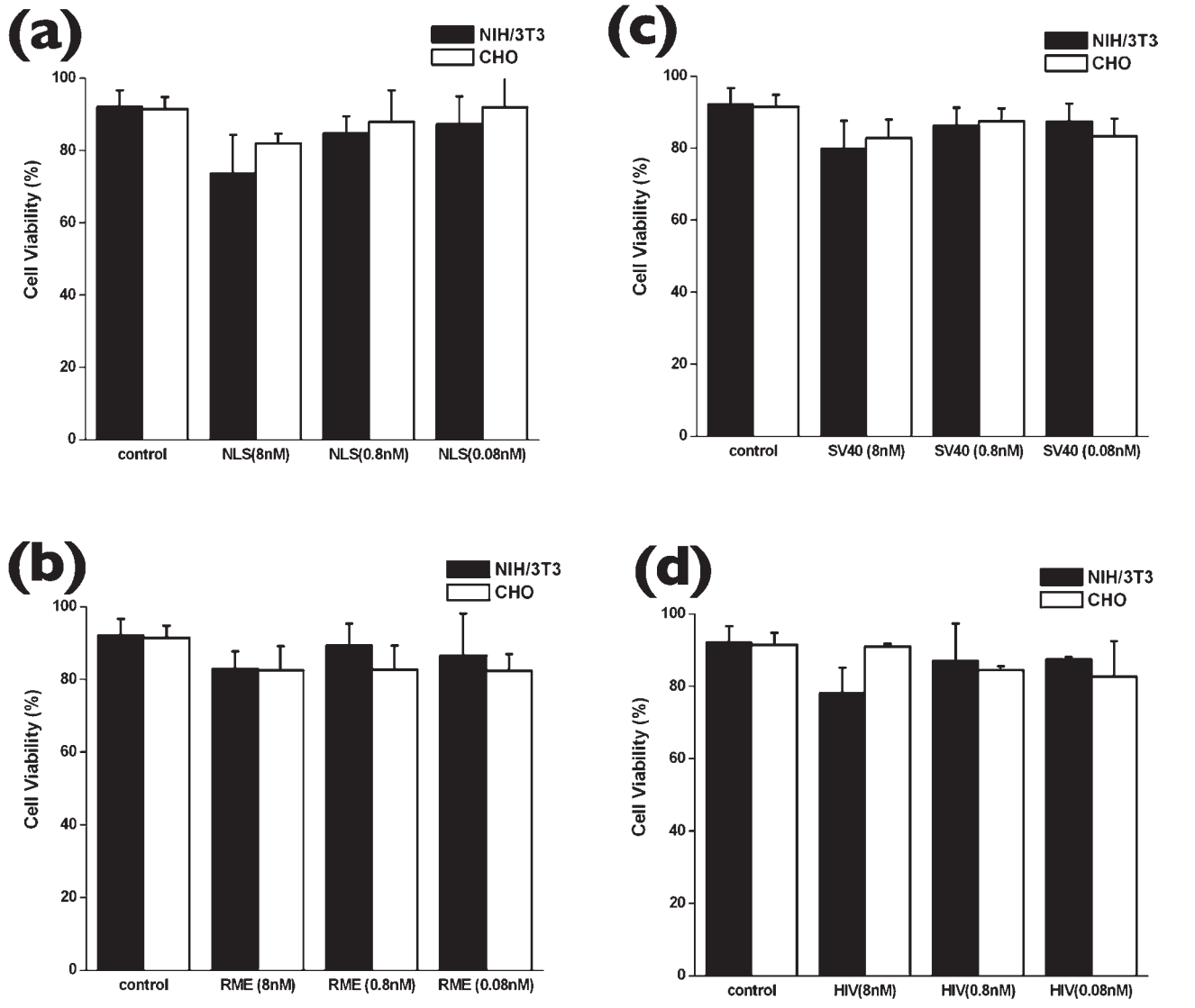


Figure 1. Cytotoxicity of peptide-coated quantum dots measured using the MTT assay in CHO and NIH/3T3 cells lines. (a) Cytotoxicity of Adenovirus-NLS peptide coated quantum dots. (b) Cytotoxicity of receptor-mediated endocytosis (RME) signaling peptide coated quantum dots. (c) Cytotoxicity of SV40 large T-antigen NLS (Tag-NLS) peptide coated quantum dots. (d) Cytotoxicity of HIV-1 Tat peptide-coated quantum dots.

dots used was negligible during the course of the experiment. Noted that prolonged UV−vis illumination of QDs may lead to the generation of toxic ion and oxidative radicals. However, such a phototoxicity effect was not significant under current experimental conditions.

Distribution of Peptide-Coated Quantum Dots in Cells. One of the advantages of using quantum dots for biomedical applications is their bright and robust emission, which allows the tracking of quantum dots for long times.[14,21,22] In this experiment, one of our goals was to investigate the translocation of nanoparticles through the cell membrane using quantum dots coated with NLS peptides derived from viruses. The peptide-coated quantum dots were added directly to the cell culture without transfection reagents, which may cause the aggregation of quantum dots. After one hour of incubation, the excess quantum dots in the culture medium were removed by washing the cells one time with a PBS solution, and fresh growth medium was added before observation. In this experiment, we first investigated the uptake of peptide-coated quantum dots in four different cell lines, including CHO, NIH 3T3, CV-1, and Hep G2 cells. For this experiment, we used two microscopic techniques: total internal reflection microscopy and confocal microscopy. At a higher concentration of QDs (8 nM), it was observed that most of the peptide-coated quantum dots could be internalized by all the cell lines tested in this experiment, as shown in Figure 2. The SV40 large T-antigen NLS (Tag-NLS) peptide-coated quantum dots were located in the cytoplasm of the HepG2 cells (Figure 2a). Similar behavior was also observed for the RME peptide-coated quantum dots inside the CV1 cells (Figure 2b). In contrast, the quantum dots without peptide coating were mostly found to stay outside of the cells as shown in Supporting Information Figure S3. The accumulation of quantum dots inside the cytoplasm can be attributed to the aggregation of quantum dots inside cells under such conditions. To avoid aggregation, we used a much lower concentration (0.08 nM). At this concentration, individual quantum dots were found to locate, not only in the cytoplasm, but also inside the cell nucleus. The behavior of HIV Tat NLS (Tat-NLS) peptide-coated quantum dots was

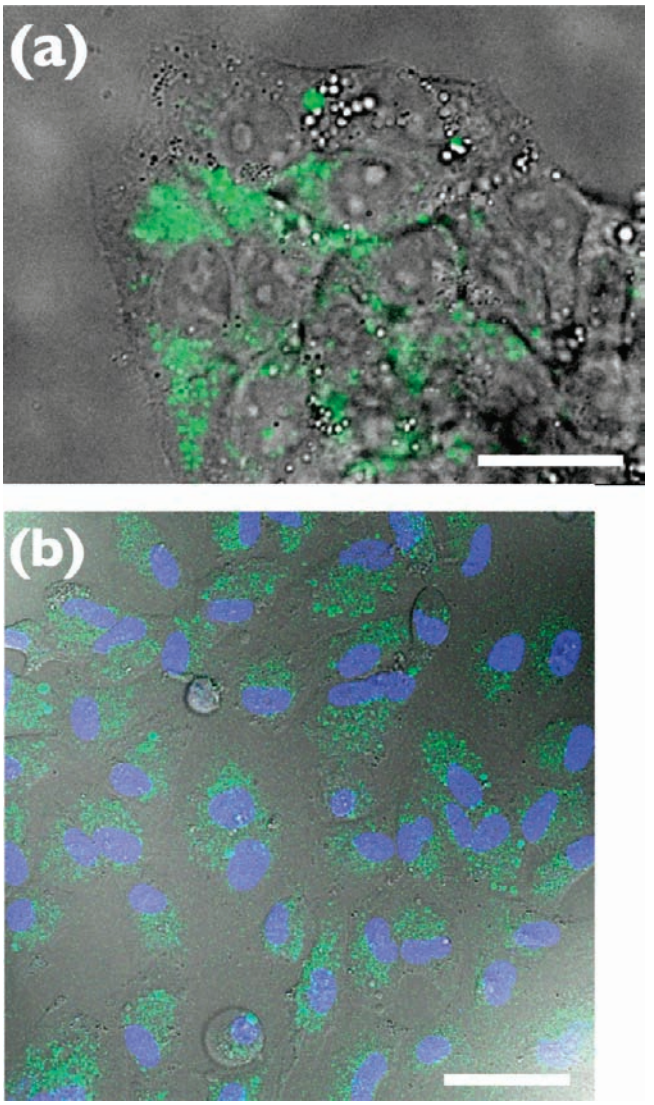


Figure 2. Confocal images of (a) 8 nM Tag-NLS peptide-coated quantum dots in HepG2 cells at 4 h. Bar: 20 μm. (b) 8 nM RME peptide-coated quantum dots in CV1 cells. Bar: 50 μm.

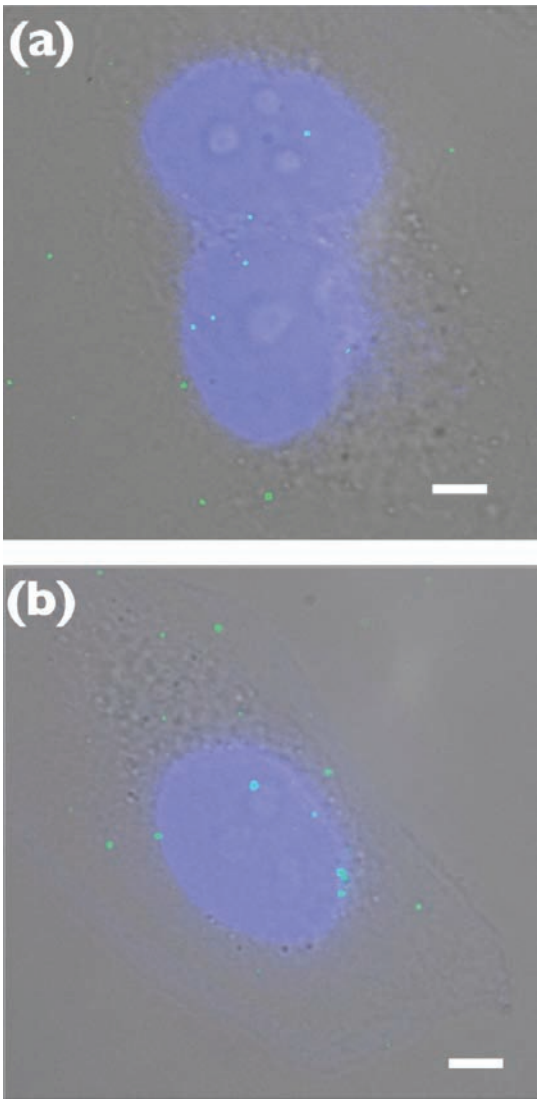


Figure 3. TIRFM images of (a) 0.08 nM Tat-NLS peptide-coated quantum dots in NIH/3T3 cells and (b) 0.08 nM Tag-NLS peptide-coated quantum dots in CV-1 cells. Bar: 5 μm.

observed in the living cells using a total internal reflection fluorescence microscope (TIRFM), which allows the visualization of a very thin (~200 nm) cross section of the cell near the glass−cell interface. Figure 3 shows TRIFM images of the NLS peptide-coated quantum dots in 3T3 and CV-1 cells. Because TRIF microscopy can be used to monitor the trajectories of NLS peptide-coated quantum dots during their uptake, it may provide a great opportunity to investigate the internalization pathway of peptide quantum dots. This may in turn help us to understand the pathway of virus internalization. To improve the cellular uptake efficiency and to visualize the endocytotic delivery processes within cells, quantum dots were coated with Tag-NLS peptides and Tat-NLS peptides and incubated with NIH 3T3 cells for two hours. Both types of peptide-coated quantum dots were found to enter cell nuclei; the cellular uptake and intracellular transport required approximately 30 min. Typical confocal images of single quantum dot inside the cell nucleus are shown in Figure 4, which shows 545 nm quantum dots coated with Tag-NLS peptides in the nucleus of NIH/3T3 cells.

Our results suggested that both Tag-NLS and Tat-NLS peptide-coated quantum dots could translocate across the cellular membrane barrier via a lipid raft-mediated endocytotic mechanism into the cell nucleus. It was reported previously that cell penetration peptides could enter the cell by hydrophilic macromolecules through the plasma membrane and into the nucleus, without the need for specific receptors.[9,23−28] To demonstrate the importance of the surface modification, we investigated the final locations of amino-PEG quantum dots without peptide coatings by confocal microscopy. We found that the quantum dots without targeting peptides did not enter the cell nuclei. However, they remained outside the cell nuclei, indicating that they are not capable of diffusing across the nuclear pore complex or within close proximity of the cell nuclei. When amino-PEG quantum dots were conjugated with targeting peptides, they could be used to penetrate or fuse with and thereby cross the plasma membrane without disruption or interference of the cell function. Therefore, it should be possible to use various targeting peptides to increase the permeability of drugs during

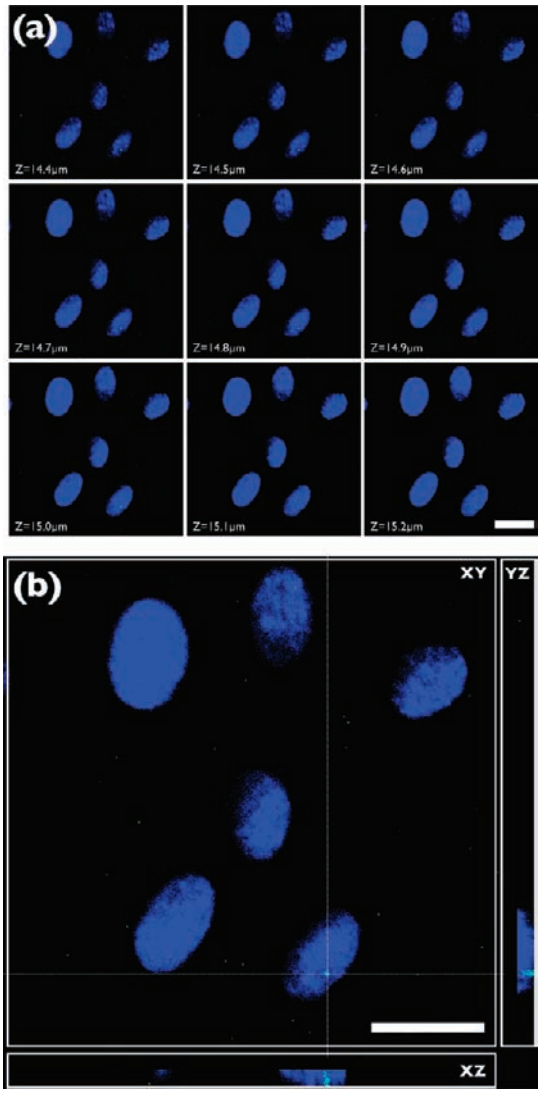


Figure 4. (a) *z*-Section confocal images and (b) a stacked image of Tag-NLS peptides quantum dot inside the NIH/3T3 cell nucleus. Bar: 20 μm.

drug delivery or to identify targeted molecules for the treatment of various diseases.

Diffusion Dynamics of Single Peptide-Coated Quantum Dots. The bright and robust emission from peptide-coated quantum dots allows us to track the trajectories of individual quantum dots during endocytosis and translocation events, as monitored using both total internal reflection microscopy and confocal microscopy.[2,29−35] To investigate the short-term diffusion behavior of quantum dots in the proximity of the nucleus, we used a total internal reflection microscope equipped with a CCD camera capable of recording the motion of quantum dots in the millisecond region. For visualization, we stained the cell nucleus with DAPI. During this experiment, we found that the trajectories of NLS-coated quantum dots were quite different. The trajectories can be classified into two types: "diffusive" and "trapped". The quantum dots in the "diffusive" state could travel more than one micrometer during the experiment, while the overall movement for quantum dots in the "trapped" state was less than one micrometer. To investigate the behavior of the peptide-coated quantum dots, we analyzed the mean square

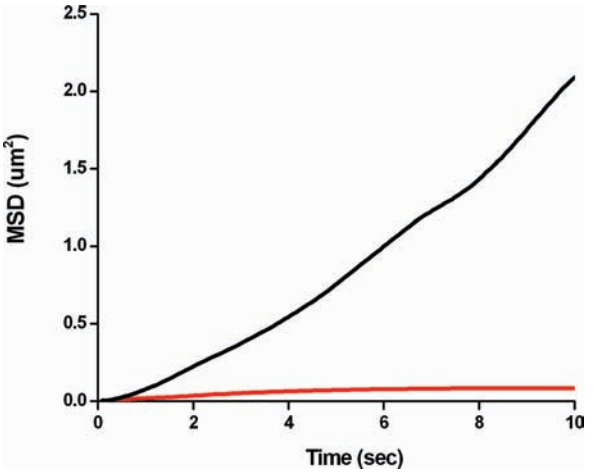


Figure 5. MSD as a function of time for Tat-NLS peptide coated quantum dots in the "diffusive" state (black line) and "trapped" state (red line).

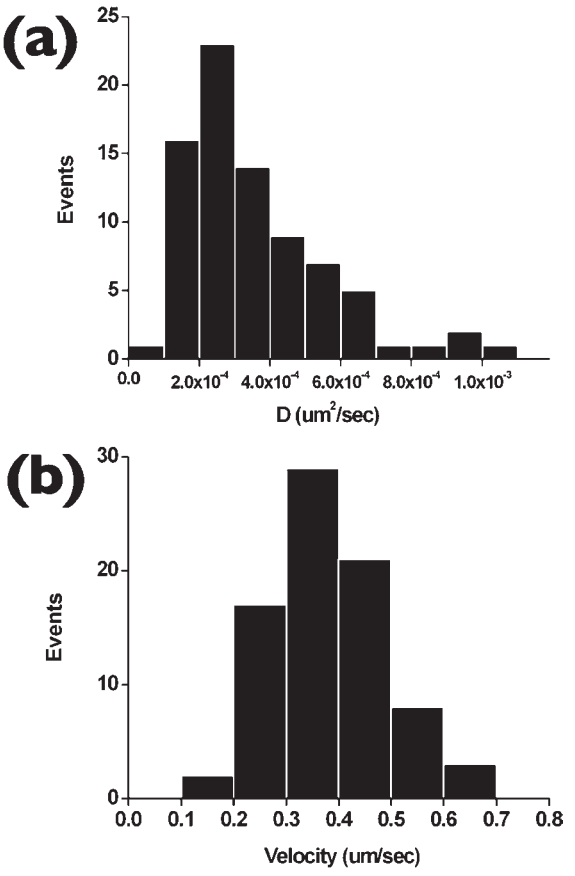


Figure 6. Histogram of the (a) diffusion coefficients and (b) average velocity of Tag-NLS peptide-coated quantum dots in CHO cells.

displacements of NLS peptide-coated quantum dots. The mean square displacements of the diffusive quantum dots in a few seconds were approximately a few micrometers squared.[36−38] However, for the trapped quantum dots, the mean square displacements in the same period of time were 1 to 2 orders of magnitude lower. Shown in Figure 5 is the MSD analysis of Tat-NLS peptide-coated quantum dots in the "diffusive" state

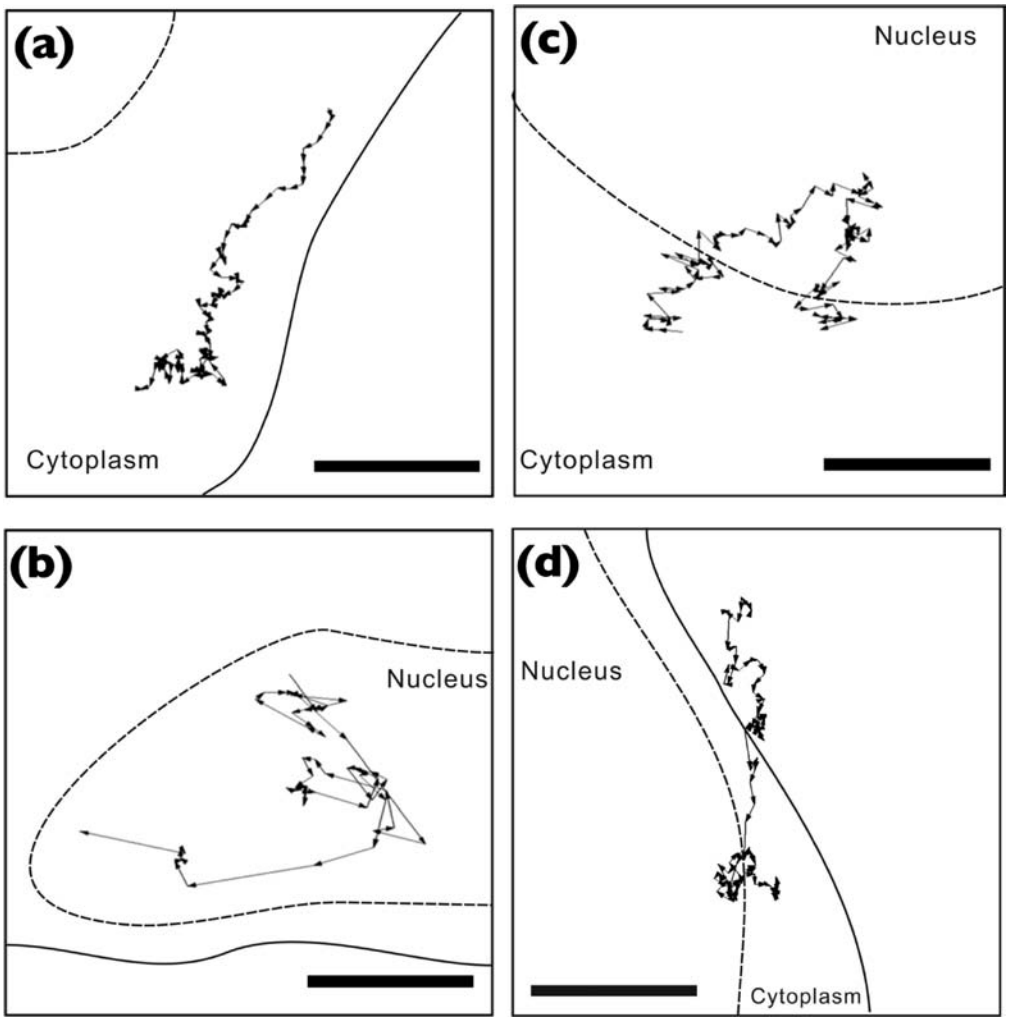


Figure 7. Four representative trajectories of RME peptide-coated quantum dots were cultured in CHO cells. (a) Staying in the cytoplasm. (b) Inside the nucleus. (c) Moving in out of the nuclear region. (d) From the nucleus to the cytoplasm. Scale bar: 5 μm.

(black line) and "trapped" state (red line). More MSD analysis can be found in the Supporting Information. We found that NLS peptide-coated quantum dots could easily access the perinuclear region. However, most of them became immobile after reaching this region. The velocity and diffusion coefficient distributions measured for 80 Tag-NLS peptide-coated quantum dots are plotted in Figure 6a and b. The average velocity measured for the "trapped" quantum dots in the cell nucleus was $0.38 \pm 0.1\ \mu$m/s; this immobile fraction of NLS peptides with particles could represent peptides trapped at the periphery of the cell nucleus, toward the cytoplasm. It was also observed that these particles clustered in within the nucleus. The average diffusion coefficient for the immobile fraction of Tag-NLS peptide-coated quantum dots was $(3.6 \pm 2.1) \times 10^{-4}\ \mu m^2/s$. For the "diffusive" quantum dots, the average velocity was also around 0.4 μm/s, however, the diffusion coefficient was about $6 \times 10^{-3} \mu m^2/s$. During this experiment, ~92% of the Tag-NLS peptide-coated quantum dots were in the "trapped" state.[39,40]

Overall, we analyzed the trajectories of 400 tracks of Tag-NLS peptide-coated quantum dots to determine their behavior. It was found that approximately 28% of these quantum dots could enter the cell nucleus, and approximately 92% of the quantum dots in the cell nucleus were in the "trapped" state, indicating a crowded environment inside the cell nucleus. A similar result was observed for Tat-NLS peptide-coated quantum dots, where approximately 25% of the quantum dots (34 out of 136) could enter the cell nucleus. However, only approximately 66% of them were in the "trapped" state. In other words, 8% of the Tag-NLS peptide-coated quantum dots were in the "diffusive" state whereas that for Tat-NLS peptide-coated quantum dots was measured to be 34%.

During long-term observation of the nuclear trafficking experiment, we used confocal microscopy to investigate quantum dots conjugated with receptor-mediated endocytosis (RME) signaling peptides, as these have been shown to directly access the cell nucleus through interaction with the nuclear pore complex. The RME peptide-coated quantum dots could undergo a receptor-mediated endocytotic pathway to enter the nuclei of CHO cells. The trajectories of RME-coated quantum dots can be classified into the following categories: inside the nucleus; from the nucleus to the cytoplasm; from the media to the cytoplasm, then into the nucleus; and staying in the cytoplasm. In this experiment, we monitored the trajectories of RME peptide-coated quantum dots in 60 cells. It was found that the majority of the trajectories (83%) reflected random motion inside the cytoplasm (Figure 7a). However, approximately 5% of the trajectories remained in the cell nucleus (Figure 7b), approximately 1.6%

of the trajectories moved in out of the nuclear region (Figure 7c) and 10% moved in out of cytoplasm to the nuclear region (Figure 7d). The trajectories are summarized in Figure 7.

CONCLUSIONS

We have synthesized various quantum dots conjugated with a range of nuclear localization signal peptides derived from viruses, which are known to associate with protein translocation into cell nuclei. At a high concentration, most of the peptide-coated quantum dots were internalized in the cytoplasmic region. However, they clustered near vesicles in the cytoplasm due to aggregation. At a lower concentration, we tracked the trajectories of individual quantum dots using both confocal microscopy and total internal reflection microscopy. It was found that approximately 28% of the Tag-NLS peptide-coated quantum dots and 25% of Tat-NLS peptide coated quantum dots could be delivered into the cell nucleus. Our results indicate that using specific NLS sequence of peptides for nuclear trafficking allowed us not only to understand the biological process pathway, but also to advance delivery technologies, such as gene therapies. We were able to use specific peptides coated quantum dots for carrier delivery in living cells, directly identifying the biofunctional interaction between the specific carriers and the cell nuclei of living cells. Single quantum dots are trafficked in and out of the nuclear periphery and toward the cytoplasmic region. These physical trajectories resolve the diffusion of molecules across the nuclear periphery and provide insight into the transport mechanisms and the dynamics of intracellular trafficking processes by peptides with diverse characteristics.

ASSOCIATED CONTENT

Supporting Information. Additional figures and table as described in the text. This material is available free of charge via the Internet at http://pubs.acs.org/.

AUTHOR INFORMATION

Corresponding Author

*Research Center for Applied Sciences, Academia Sinica, 128, Section 2, Academia Road, Nankang, Taipei 115, Taiwan. Phone: +886-2-27898000. Fax: +886-2-27896680. E-mail: peilin@gate.sinica.edu.tw.

ACKNOWLEDGMENT

This research was supported in part by the National Science Council, Taiwan under contract 97-2628-M-001-010-MY3 and by the Academia Sinica Research Project on Nano Science and Technology.

REFERENCES

(1) Betzig, E., Patterson, G. H., Sougrat, R., Lindwasser, O. W., Olenych, S., Bonifacino, J. S., Davidson, M. W., Lippincott-Schwartz, J., and Hess, H. F. (2006) Imaging Intracellular fluorescent proteins at nanometer resolution. *Science 313*, 1642–1645.

(2) Anthony, S., Zhang, L., and Granick, S. (2006) Methods to track single-molecule trajectories. *Langmuir 22*, 5266–5272.

(3) Medintz, I. L., Uyeda, H. T., Goldman, E. R., and Mattoussi, H. (2005) Quantum dot bioconjugates for imaging, labelling and sensing. *Nat. Mater. 4*, 435–446.

(4) Michalet, X., Pinaud, F. F., Bentolila, L. A., Tsay, J. M., Doose, S., Li, J. J., Sundaresan, G., Wu, A. M., Gambhir, S. S., and Weiss, S. (2005) Quantum dots for live cells, in vivo imaging, and diagnostics. *Science 307*, 538–544.

(5) Tkachenko, A. G., Xie, H., Liu, Y., Coleman, D., Ryan, J., Glomm, W. R., Shipton, M. K., Franzen, S., and Feldheim, D. L. (2004) Cellular trajectories of peptide-modified gold particle complexes: comparison of nuclear localization signals and peptide transduction domains. *Bioconjugate Chem. 15*, 482–490.

(6) De, M., Ghosh, P. S., and Rotello, V. M. (2008) Applications of nanoparticles in biology. *Adv. Mater. 20*, 4225–4241.

(7) Chan, W. C. W., and Nie, S. (1998) Quantum dot bioconjugates for ultrasensitive nonisotopic detection. *Science 281*, 2016–2018.

(8) Srinivasan, C., Lee, J., Papadimitrakopoulos, F., Silbart, L. K., Zhao, M., and Burgess, D. J. (2006) Labeling and intracellular tracking of functionally active plasmid DNA with semiconductor quantum dots. *Mol. Ther. 14*, 192–201.

(9) Derfus, A. M., Chan, W. C. W., and Bhatia, S. N. (2004) Intracellular delivery of quantum dots for live cell labeling and organelle tracking. *Adv. Mater. 16*, 961–966.

(10) Chithrani, B. D., Ghazani, A. A., and Chan, W. C. W. (2006) Determining the size and shape dependence of gold nanoparticle uptake into mammalian cells. *Nano Lett. 6*, 662–668.

(11) Nativo, P., Prior, I. A., and Brust, M. (2008) Uptake and intracellular fate of surface-modified gold nanoparticles. *ACS Nano 2*, 1639–1644.

(12) de la Fuente, J. M., and Berry, C. C. (2005) Tat peptide as an efficient molecule to translocate gold nanoparticles into the cell nucleus. *Bioconjugate Chem. 16*, 1176–1180.

(13) Tkachenko, A. G., Xie, H., Coleman, D., Glomm, W., Ryan, J., Anderson, M. F., Franzen, S., and Feldheim, D. L. (2003) Multifunctional gold nanoparticle−peptide complexes for nuclear targeting. *J. Am. Chem. Soc. 125*, 4700–4701.

(14) Hoshino, A., Fujioka, K., Oku, T., Nakamura, S., Suga, M., Yamaguchi, Y., Suzuki, K., Yasuhara, M., and Yamamoto, K. (2004) Quantum dots targeted to the assigned organelle in living cells. *Microbiol. Immunol. 48*, 985–994.

(15) Chen, F., and Gerion, D. (2004) Fluorescent CdSe/ZnS nanocrystal−peptide conjugates for long-term, nontoxic imaging and nuclear targeting in living cells. *Nano Lett. 4*, 1827–1832.

(16) Escriou, V., Carrière, M., Scherman, D., and Wils, P. (2003) NLS bioconjugates for targeting therapeutic genes to the nucleus. *Adv. Drug Delivery Rev. 55*, 295–306.

(17) Zhou, M., and Ghosh, I. (2007) Quantum dots and peptides: A bright future together. *Biopolymers 88*, 325–339.

(18) Chien, F. C., Kuo, C. W., and Chen, P. (2011) Localization imaging using blinking quantum dots. *Analyst 136*, 1608–1613.

(19) Derfus, A. M., Chan, W. C. W., and Bhatia, S. N. (2004) Probing the cytotoxicity of semiconductor quantum dots. *Nano Lett. 4*, 11–18.

(20) Kim, Y. S., Jiang, W., Oreopoulos, J., Yip, C. M., Rutka, J. T., and Chan, W. C. W. (2008) Biodegradable quantum dot nanocomposites enable live cell labeling and imaging of cytoplasmic targets. *Nano Lett. 8*, 3887–3892.

(21) Cho, S. J., Maysinger, D., Jain, M., Röder, B., Hackbarth, S., and Winnik, F. M. (2007) Long-term exposure to CdTe quantum dots causes functional impairments in live cells. *Langmuir 23*, 1974–1980.

(22) Jaiswal, J., Mattoussi, H., Mauro, J. M., and Simon, S. M. (2003) Long-term multiple color imaging of live cells using quantum dot bioconjugates. *Nat. Biotechnol. 21*, 47–51.

(23) Horton, K. L., Stewart, K. M., and Kelly, S. O. (2008) Cell-penetrating peptides as delivery vehicles for biology and medicine. *Org. Biomol. Chem. 6*, 2242–2255.

(24) Lindgren, M., Hällbrink, M., Prochiantz, A., and Langel, Ü. (2000) Cell-penetrating peptides. *Trends Pharmacol. Sci. 21*, 99–103.

(25) Duan, H., and Nei, S. (2007) Cell-penetrating quantum dots based on multivalent and endosome-disrupting surface coatings. *J. Am. Chem. Soc. 129*, 3333–3338.

(26) Takayama, K., Tadokoro, A., Pujals, S., Nakase, I., Giralt, E., and Futaki, S. (2009) Novel system to achieve one-pot modification of cargo molecules with oligoarginine vectors for intracellular delivery. *Bioconjugate Chem. 20*, 249–257.

(27) Medintz, I. L ., Pons, T., Delehanty, J. B., Susumu, K., Brunel, F. M., Dawson, P. E., and Mattoussi, H. (2008) Intracellular delivery of quantum dot−protein cargos mediated by cell penetrating peptides. *Bioconjugate Chem. 19*, 1785–1795.

(28) Delehanty, J. B., Medintz, I. L., Pons, T., Brunel, F. M., Dawson, P. E., and Mattoussi, H. (2006) Self-assembled quantum dot−peptide bioconjugates for selective intracellular delivery. *Bioconjugate Chem. 17*, 920–927.

(29) Saxton, M. J. (2008) Single-particle tracking: connecting the dots. *Nat. Methods 5*, 671–672.

(30) Jaiswal, J. K., and Simon, S. M. (2007) Imaging single events at the cell membrane. *Nat. Chem. Biol. 3*, 92–98.

(31) Kukura, P., Ewers, H., Muller, C., Renn, A., Helenius, A., and Sandoghdar, V. (2009) High-speed nanoscopic tracking of the position and orientation of a single virus. *Nat. Methods 6*, 923–927.

(32) Babcock, H. P., Chen, C., and Zhuang, X. (2004) Using single-particle tracking to study nuclear trafficking of viral genes. *Biophys. J. 87*, 2749–2758.

(33) Dahan, M., Lévi, S., Luccardini, C., Rostaing, P., Riveau, B., and Triller, A. (2003) Diffusion dynamics of glycine receptors revealed by single-quantum dot tracking. *Science 302*, 442–445.

(34) Pinaud, F., Michalet, X., Iyer, G., Margeat, E., Moore, H. P., and Weiss, S. (2009) Dynamic partitioning of a glycosyl-phosphatidylinositol-anchored protein in glycosphingolipid-rich microdomains imaged by single-quantum dot tracking. *Traffic 10*, 691–712.

(35) Jaqaman, K., Loerke, D., Mettlen, M., Kuwata, H., Grinstein, S., Schmid, S. L., and Danuser, G. (2008) Robust single-particle tracking in live-cell time-lapse sequences. *Nat. Methods 5*, 695–702.

(36) Courty, S., Luccardini, C., Bellaiche, Y., Cappello, G., and Dahan, M. (2006) Tracking individual kinesin motors in living cells using single quantum-dot imaging. *Nano Lett. 6*, 1491–1495.

(37) Manley, S., Gillette, J. M., Patterson, G. H., Shroff, H., Hess, H. F., Betzig, E., and Lippincott-Schwartz, J. (2008) High-density mapping of single-molecule trajectories with photoactivated localization microscopy. *Nat. Methods 5*, 155–157.

(38) Pinaud, F., Clarke, S., Sittner, A., and Dahan, M. (2010) Probing cellular events, one quantum dot at a time. *Nat. Methods 7*, 275–285.

(39) Sergé, A., Bertaux, N., Rigneault, H., and Marguet, D. (2008) Dynamic multiple-target tracing to probe spatiotemporal cartography of cell membranes. *Nat. Methods 5*, 687–694.

(40) Bannai, H., Levi, S., Schweizer, C., Dahan, M., and Triller, A. (2006) Imaging the lateral diffusion of membrane molecules with quantum dots. *Nat. Protoc. 1*, 2628–2634.

Supporting Materials

Targeted Nuclear Delivery using Peptide-Coated Quantum Dots**

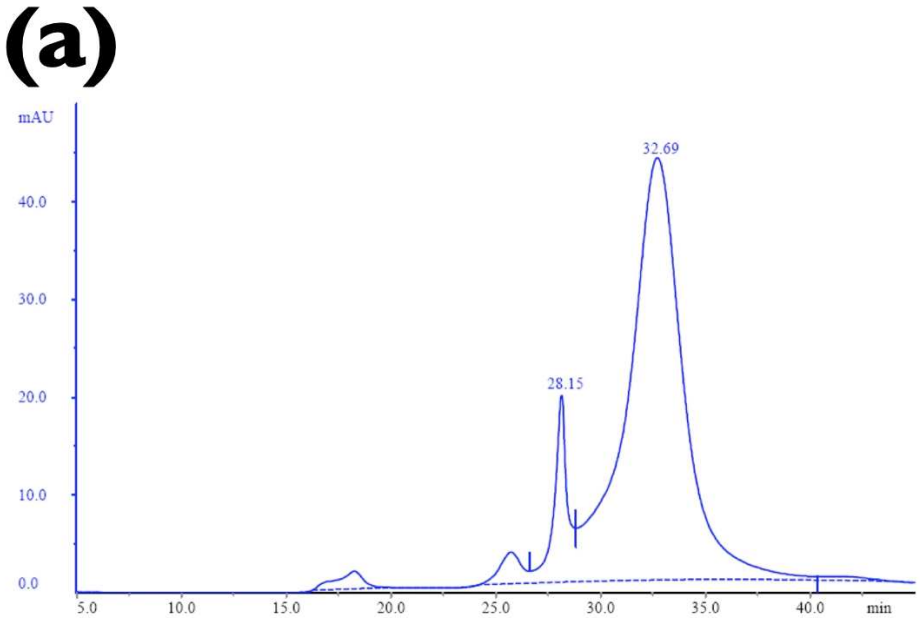
*By Chiung-Wen Kuo, Di-Yen Chueh, Narendra Singh, Fan-Ching Chien and Peilin Chen**

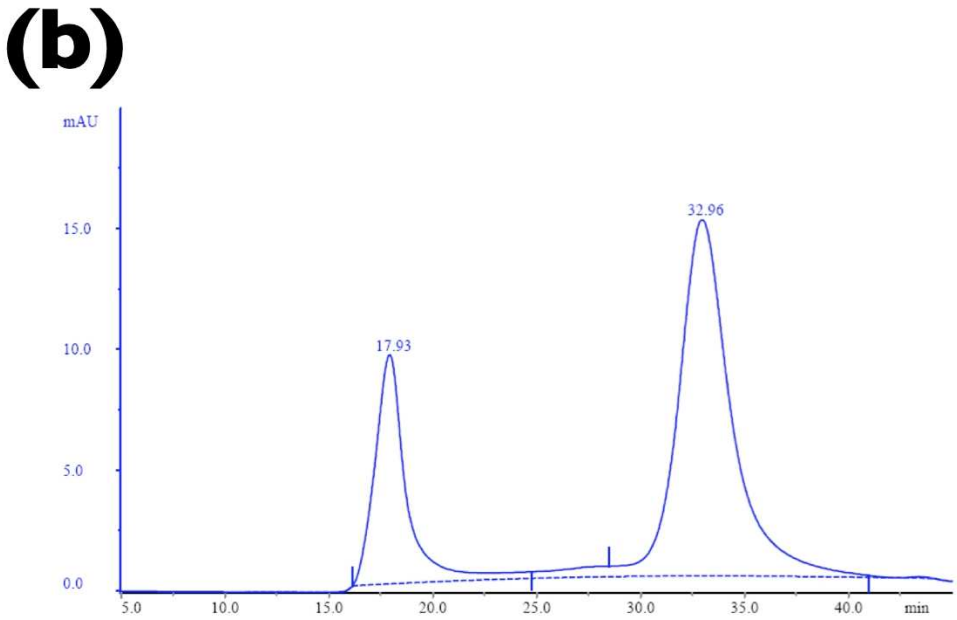
Peptide sequences	Origin of peptide
CGGFSTSLRARKA	Adenoviral NLS
CKKKKKKSEDEYPYVPN	Adenoviral RME
CGGGPKKKRKVGG	SV40 large T NLS
CGGRKKRRQRRRAP	HIV-1 Tat protein NLS

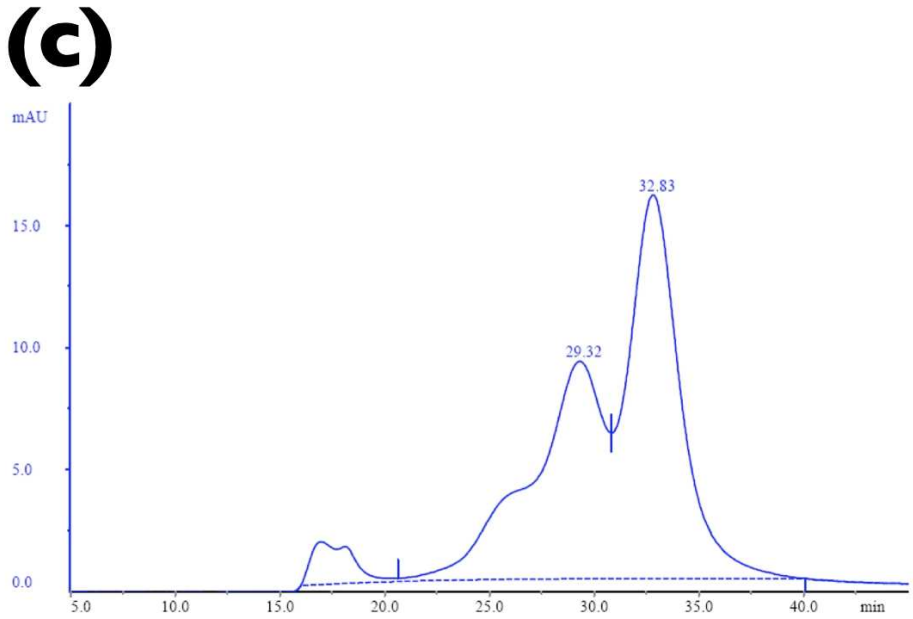
Table 1. Four different NLS peptides sequences are derived from the adenoviral, SV 40 large T, HIV-1 Tat protein, and adenoviral RME.

Gel Filtration

We analyzed QDs-RME, QDs-Tat-NLS, QDs-Tag-NLS and QDs-SV40 with hydrodynamic diameters of 18 nm, 16.5 nm, 14.3 nm and 14.1 nm. We calibrated the HD using 100 uL of a protein standard solution consisting of aprotinin (6.5 KDa, 2 nm HD), ribonuclease A (13.7 KDa, 3.3 nm HD), carbonic anhydrase (29 KDa, 4.1 nm HD), Ovalbumin (43 KDa, 6.1 nm HD), aldolase (150 KDa, 9.6 HD), ferritin (440 KDa, 12.2 nm HD), and thyroglobulin (669 KDa, 17 nm HD). The HD of all proteins were measured using three independent experiments.







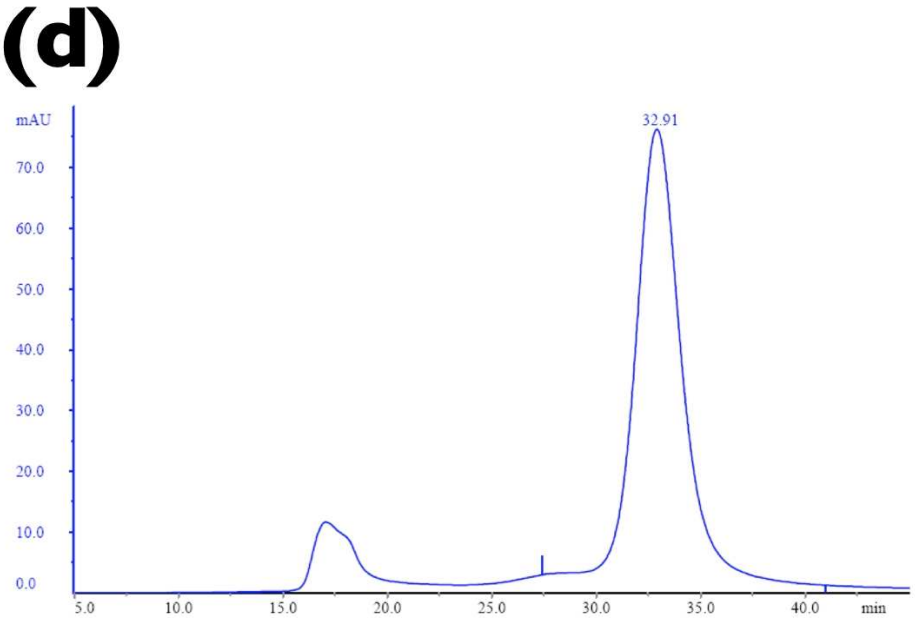


Figure S1. The hydrodynamic diameters measured using HPLC of (a) QDs-RME, (b) QDs-HIV, (c) QDs-NLS and (d) QDs-SV40 in a phosphate buffer at pH 7.4.

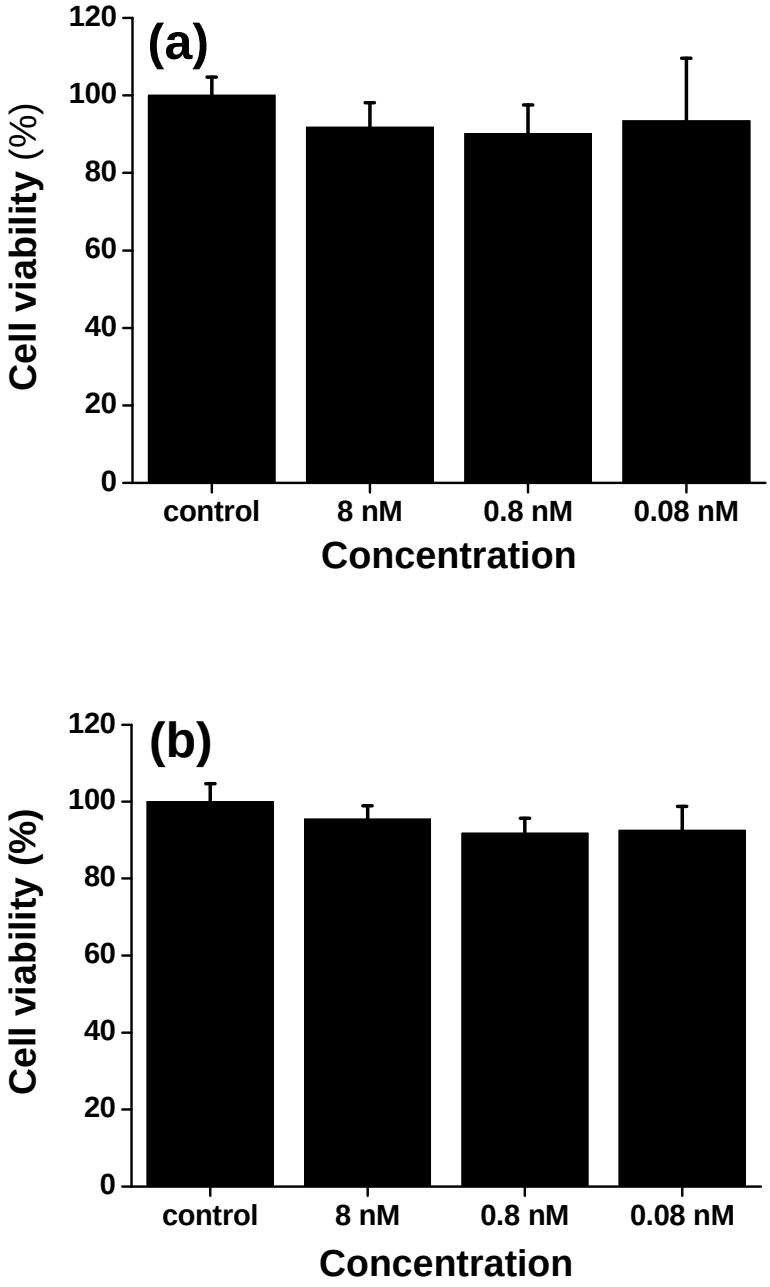


Figure s2. The cytotoxicity of amino-PEG-coated quantum dots measured using the MTT assay in CV1 cells. (a) 4 hours of incubation. (b) 24 hours of incubation.

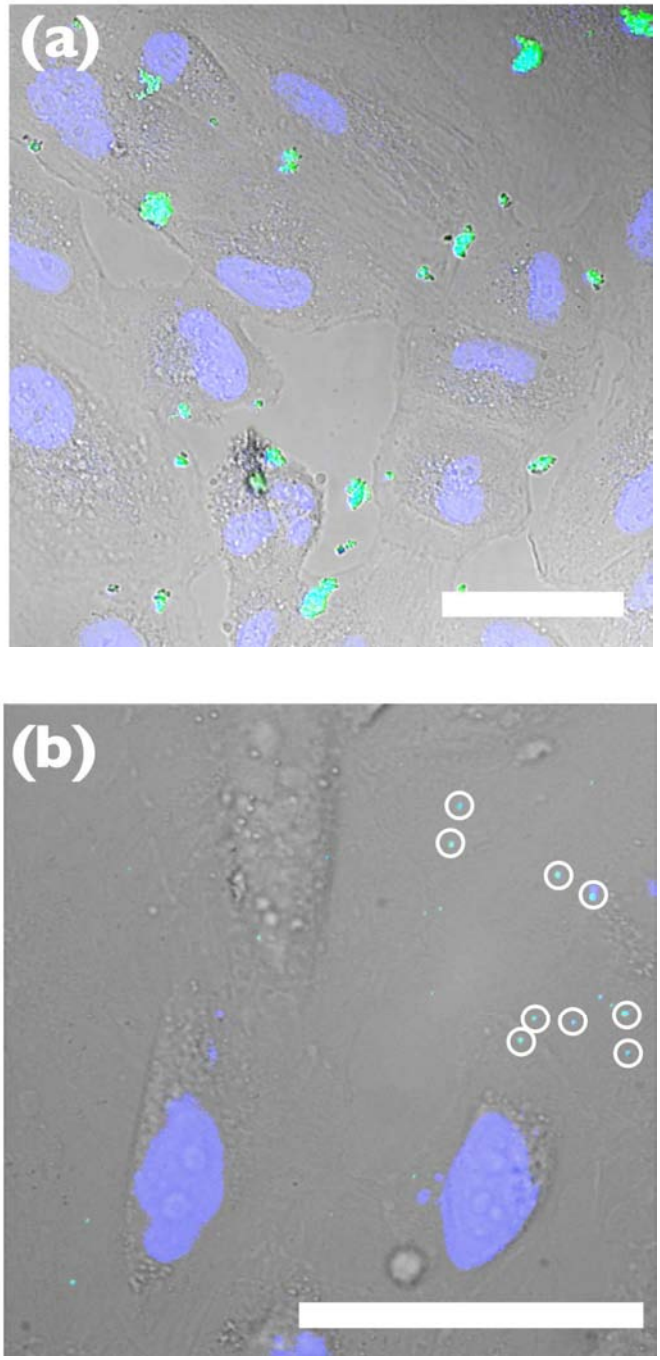


Figure S3. Confocal images of (a) 8 nM of amino-quantum dots in CV1 cells and (b) 0.08 nM concentration. Bar: 50 μm.

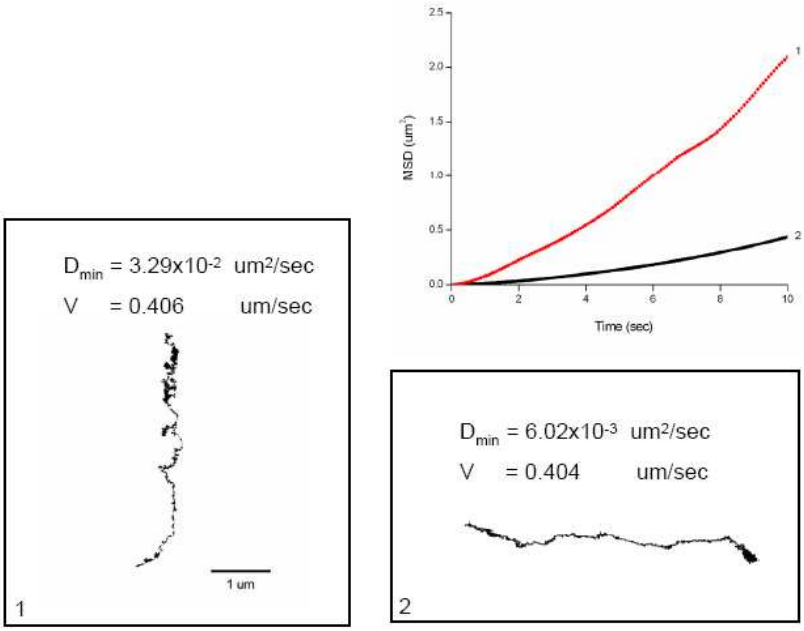


Figure S4 Two representative trajectories and MSD of Tat-NLS peptide coated quantum dots in the "diffusive" state.

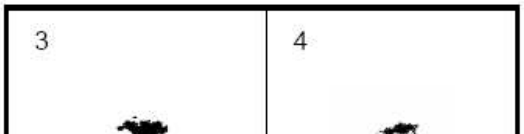


Figure S5 Four representative trajectories and MSD of Tat-NLS peptide coated quantum dots in the "trapped" state.

Bioconjugate Chemistry

ARTICLE

pubs.acs.org/bc

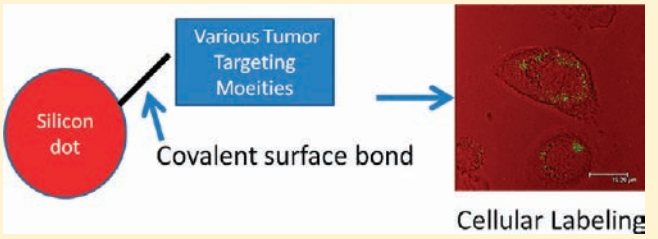
Bioconjugation of Luminescent Silicon Quantum Dots for Selective Uptake by Cancer Cells

Folarin Erogbogbo,[†,§] Chen-An, Tien,[†] Ching-Wen Chang,[†] Ken-Tye Yong,[§] Wing-Cheung Law,[§] Hong Ding,[§] Indrajit Roy,[†] Mark T. Swihart,[†,‡,*] and Paras N. Prasad[‡,§,*]

[†]Department of Chemical and Biological Engineering, [‡]Department of Chemistry and [§]Institute for Lasers, Photonics and Biophotonics, The University at Buffalo, State University of New York Buffalo, New York 14260-4200, United States

Supporting Information

ABSTRACT: Conventional quantum dots have great potential in cancer-related imaging and diagnostic applications; however, these applications are limited by concerns about the inherent toxicity of their core materials (e.g., cadmium, lead). Virtually all imaging applications require conjugation of the imaging agent to a biologically active molecule to achieve selective uptake or binding. Here, we report a study of biocompatible silicon quantum dots covalently attached to biomolecules including lysine, folate, antimesothelin, and transferrin. The particles possess desirable physical properties, surface chemistry, and optical properties. Folate- and antimesothelin-conjugated silicon quantum dots show selective uptake into Panc-1 cells. This study contributes to the preclinical evaluation of silicon quantum dots and further demonstrates their potential as an imaging agent for cancer applications.



INTRODUCTION

Quantum dots (QDs) are semiconductor nanocrystals, 1−10 nm in diameter, that typically consist of combinations of elements from groups II and VI (CdSe, CdTe, CdS, ZnS, and ZnSe), groups IV and VI (PbS and PbSe), or groups III and V (GaAs, GaN, InP, and InAs) of the periodic table.[1,2] They are attractive for optical imaging because of their size-tunable luminescence, high photostability, brightness, and broad excitation spectra that allow QDs with multiple emission wavelengths to be excited with a single source.[3−5] By adopting techniques from drug delivery and targeted imaging technologies, heavy metal based quantum dots have been rapidly developed and investigated for many biological applications including optical imaging,[6] sentinel lymph node mapping,[7] and multiplex imaging.[8] However, translation of these well-studied quantum dots to the clinic is inhibited by toxicity concerns that stem from their incorporation of toxic heavy metals such as cadmium.[9−12] This has led to encapsulations strategies that create complex nanostructures with different toxicity profiles.[13]

Even though extensive studies have been performed to monitor the safety of II−VI quantum dots, completely overcoming the toxicity concerns is not yet possible.[14−17] Thus, a re-evaluation of the fundamental materials at the core of the quantum dots is warranted. Silicon (Si) QDs may provide a breakthrough for quantum dot technology because they are based on a nontoxic element that is essential for human health, and the product of their degradation, silicic acid, can be readily excreted via the urine.[4,18,19] Even though Si QDs are attractive from a toxicity perspective, key challenges must be overcome to ensure that Si QDs can match the promise of better-studied quantum dots for biological applications. In particular, high quantum yield (QY) and long-term stability in water and biological media are essential.

The surface chemistry of Si QDs is of great interest, not only because this chemistry is much different from that of heavy metal based semiconductor nanostructures, but also because the Si QD's optical properties, which are the basis of their utility in bioimaging, strongly depend on the surface state of the particles. There have been a few reports on the synthesis and surface modification of Si QDs to improve their competitiveness with traditional quantum dots. Kortshagen's group has produced surface-modified Si QDs with QY above 70% at near-infrared wavelengths, for particles dispersed in organic solvents.[20] However, such high QY has not been achieved at shorter wavelengths or for Si QDs in aqueous dispersions. Sailor's group recently developed biodegradable porous silicon for imaging tumors via the enhanced permeation and retention (EPR) effect[21] and showed that clearance of the material was satisfactory. The free-standing Si QDs used here and Sailor's porous silicon particles are expected to have similar degradation routes and low toxicity from the core material. However, there are substantial differences in the chemistry, structure, and luminescence properties, to the extent that Si QDs may be considered a different nanostructure from porous silicon. To demonstrate the potential for multiphoton excitation of Si QDs, He et al. measured emission of Si QDs upon two and three photon excitation QDs,[22] while Kauzlaurich

Received: December 7, 2010
Revised: March 28, 2011
Published: April 07, 2011

ACS Publications © 2011 American Chemical Society

recently demonstrated two photon cellular imaging in macrophages.[23] Though promising, the luminescence from the Si QDs used for two photon cellular imaging was limited to the blue range of the spectrum. Tilley et al. showed nonspecific uptake of allylamine terminated blue-emitting Si QDs in HeLa cells.[24] Reipa's group[25] conjugated red emitting silicon nanoparticles to streptavidin, and demonstrated specific binding of the nanoparticles to biotinylated polystyrene beads. However, after bioconjugation, the particles emitted blue luminescence. Development of bioconjugation chemistry that maintains the size-tunable luminescence of Si QDs thus remains an important need for biological applications such as targeted imaging, where emission that does not compete with autofluorescence is desired. We previously fabricated micelle-encapsulated Si QDs with size-tunable emission wavelength for targeted imaging of cancer cells. This method takes advantage of the interaction between hydrophobic groups that allow Si QDs to be encapsulated into the hydrophobic core of the micelle. These were first demonstrated for *in vitro* imaging[4] and more recently for *in vivo* targeted tumor imaging in small animals.[26] However, those micelle-encapsulated constructs, in which each micelle typically contains many Si QDs, are not ideal for all purposes. Thus, bioconjugation of individual Si QDs remains of great interest, especially through the direct conjugation to surface carboxyl groups.[27]

Conventional QDs can be modified for targeting purposes via bioconjugation techniques that render them useful for multiple imaging applications. *In vivo*, long circulation times and clearance mechanisms that raise toxicity concerns may be overcome by using smaller particles that have short circulation times and can be excreted rapidly through the kidneys.[28] Though this is encouraging, it poses a different challenge because receptors for some biomolecules (such as folate) are present on renal cells.[29] Folate receptors (FR) are overexpressed on many types of cancer cells compared to normal cells, and they have some advantages compared to monoclonal antibodies, such as prolonged circulation times, low cost, and tumor to nontarget tissue ratios. FR's are also overexpressed in the kidneys. If heavy metal based quantum dots are used with folate-based targeting, toxicity concerns in the kidney would be increased just as they are for cancer therapeutic folate-toxin conjugates that undergo renal clearance. Even though there are no prior reports of Si-folate conjugates, renal toxicity from Si-folate conjugates is not an anticipated issue because no toxic components are included in the formulation. We recently observed low toxicity of folate-conjugated micelle-encapsulated silicon nanoparticle formations in MTS cytotoxicity assays.[4]

Here, we report the development of Si QD probes directly bound to biomolecules, including folate and antimesothelin, for targeted cancer cell imaging. As synthesized, carboxyl terminated Si QDs provide (i) stable luminescence; (ii) modifiable surface characteristics; and (iii) the potential to interface with biologically relevant molecules for an array of applications such as targeted cellular imaging. Undecylenic acid was the carboxylic acid of choice because of its demonstrated low toxicity (5000 mg/kg in mice), and it is one of the most effective ways of preventing the influences of oxidation of the silicon core.[27] Biologically relevant molecules conjugated via carbodiimide chemistry to the carboxylic acid group of the undecylenic acid included amino acids, vitamins, enzymes, proteins, and antibodies. Because folate has been demonstrated to be effective for targeting cancers in humans, folate terminated Si QDs were evaluated as imaging agents. A schematic of the conjugation process is shown in Figure 1.

EXPERIMENTAL METHODS

Materials. Silane (SiH_4, Voltaix, electronic grade, 99.999%), hydrofluoric acid (HF, Acros Organic, 48−51%), nitric acid (HNO_3, EMD, 68−70%), undecylenic acid (Acros Organic, 99%), lysine (Sigma-Aldrich, 95%), 1-ethyl-3-(3-dimethylaminopropyl)carbodiimide (EDC, Pierce Biotechnology, 98−100%), dimethyl sulfoxide (DMSO, Fisher Scientific, 99.9%), folic acid (Sigma-Aldrich, >98%), antimesothelin (clone 5B2, dilution 1:20; Novocastra, Newcastle Upon Tyne, United Kingdom), apo-transferrin (Sigma-Aldrich, ≥97%), and *N*-hydroxysulfosuccinimide (Sulfo-NHS, Fluka, ≥98.5%) were all used as received if not otherwise noted. The silicon nanoparticles were prepared by decomposing silane (SiH_4) via high-temperature CO_2 laser pyrolysis in an aerosol reactor based on the method developed by Li et al.[30,31] The raw product was a dark brown powder that was not photoluminescent. This product was collected without exposure to air and handled in a glovebox to prevent oxidation. The typical primary particle diameter in the aggregated raw silicon powder was approximately 10 nm.

Etching Procedure. To produce hydrogen-terminated photoluminescent Si QDs, the raw particles were dispersed in methanol, then etched in a mixture of hydrofluoric acid (48 wt %) and nitric acid (69 wt %) (10/1, v/v) for 2 to 4 min. Typically, 300 mg of silicon nanoparticles were dispersed in 30 mL of methanol by sonication. The silicon−methanol mixture was added to the acid mixture and stirred until the luminescence emission spectrum approached the desired color. At that point, 400 mL of methanol was added to quench the reaction. After washing the etched particles with a water−methanol mixture (3/1, v/v) three times (500 mL, 500 mL, 250 mL) to remove the adsorbed acid, we collected the particles on a poly(vinylidene fluoride) (PVDF) membrane filter (Millipore, hydrophilic Durapore, 0.1 μm pore size). Finally, the membrane was rinsed with pure methanol. The particles were finally sonicated from the membrane into vials containing undecylenic acid. All these steps were completed in the glovebox to prevent the oxidation of the Si QDs, which can reduce their photoluminescence quantum yield. The size of the particles after etching ranges from 5 nm down to 1 nm depending on the desired emission wavelength.

Si QD Functionalization. The hydrogen-terminated silicon QDs were dispersed in 20 mL of undecylenic acid to give a cloudy suspension. The reactant and the silicon particles were then transferred to a three-necked flask, and 20 mL of ethanol was added. Three freeze−pump−thaw cycles were used to remove dissolved oxygen from the mixture before reaction. The flask was then heated to 78.9 °C for 3 h, with stirring, under an argon atmosphere. The double bond on undecylenic acid reacts with the hydrogen-terminated silicon surface by hydrosilylation to give a covalent Si−C linkage on the surface of the Si QDs (Figure 1a). These surface-modified QDs can be dispersed in most nonpolar solvents such as chloroform, hexane, and toluene. After the reaction, the initially cloudy silicon dispersion became optically clear, confirming that reaction had occurred and the modified particles were dispersible in ethanol. To remove excess undecylenic acid, the silicon QDs were dialyzed against 3 L of ethanol three times with solvent change points of 30 min, 3 h, and 24 h in bags with MW cutoff of 7000. The purity of particles was verified by rotary evaporation, which produces a film

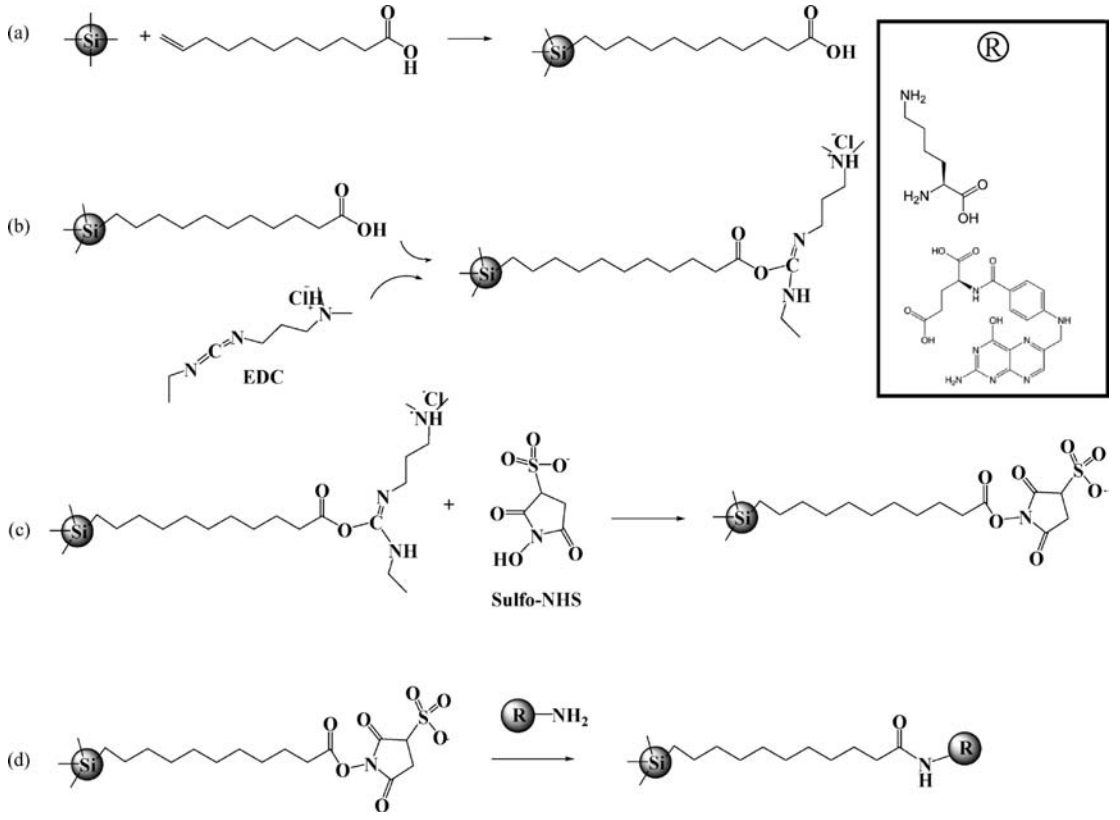


Figure 1. Schematic of surface functionalization and bioconjugation of silicon quantum dots: (a) hydrosilylation with undecylenic acid; (b) EDC coupling to form the o-acylisourea ester; (c) semistable amine reactive NHS-ester formation; (d) bioconjugation.

of undecylenic acid terminated Si QDs that can be readily dispersed in a variety of solvents and termination can be verified by FTIR.

Bioconjugation. In separate experiments, the Si QDs were conjugated to lysine, folic acid, antimesothelin, or apo-transferrin. An EDC-coupling reaction was used to form an amide bond between the carboxyl group on the Si QDs and a primary amine group on these reactants (Figure 1). Because the intermediate product of the EDC coupling was an unstable reactive o-acylisourea ester which could easily react with H_2O to regenerate the carboxyl group, we reacted sulfo-NHS with the o-acylisourea ester to produce a semistable amine-reactive NHS-ester. This amine-reactive NHS-ester consistently reacted with primary amines to yield a stable amide bond to the Si QDs. This implies that, ideally, we could conjugate any compound that has a primary amine group with Si QDs. To conjugate the Si QDs to folic acid, lysine, or transferrin, we started from 5 mL of the Si QD/ethanol sample and removed the ethanol by rotary evaporation. We next dissolved the Si QDs in 1 mL of DMSO. Eight milligrams of EDC and 8 mg of sulfo-NHS were each dissolved in 1 mL of LAL reagent water (LRW) or HPLC water, separately. These two compounds are unstable in water and must be freshly prepared for each experiment. The desired functional compound was also prepared in water (lysine or transferrin) or DMSO (folic acid) at 2 mg/mL. To start the EDC coupling reaction, 40 μL of EDC−water solution was added into the vial containing the Si QDs. After stirring for 1 min, 40 μL of sulfo-NHS was added, and stirring continued for 1 h to generate the semistable amine reactive NHS-ester. After forming the semistable intermediate, we separated the luminescent particles from the DMSO, EDC, and sulfo-NHS mixture by centrifugation. The particles then were introduced into the lysine or transferrin aqueous solution (0.8 mL containing 1.6 mg biomolecule) or folic acid DMSO solution (60 μL containing 0.12 mg folic acid). Initially, the mixture was cloudy, but after 15 min, the particles became well-dispersed. This reaction was carried out at room temperature for 1 h. Reaction products were separated by centrifugation at 10 000 *g* for 15 min after adding 1 mL of methanol to adjust the polarity of the solution to reduce the Si QD's dispersibility. The particles were washed by dispersing them in water, then collecting them by centrifugation thrice. For comparison, experiments were also performed using a one-step bioconjugation protocol, in which Si QDs were not separated from excess EDC and sulfo-NHS before adding the biomolecule to be conjugated to the particles. In the one-step protocol, the biomolecule was added to the reaction mixture ~5 min after adding the sulfo-NHS. The one-step method is more convenient and leads to fewer particle losses, but can also lead to cross-linking of biomolecules that have both amine and carboxyl functional groups, as discussed further below.

Cellular Imaging. Human pancreatic cancer cells (Panc-1) maintained in DMEM medium, with 10% fetal bovine serum (FBS) and appropriate antibiotic, were used for cellular imaging studies. As a standard, 8×10^5 cells are seeded for 100% confluency. One day before the treatment, an appropriate number of cells for 70−80% confluency were seeded in 35 mm cell culture dishes. On the day of treatment, the cells were incubated with bioconjugated Si QDs for 2 h at 37 °C at a confluency of 70−80%. After 2 h, cells were washed thrice with PBS, then imaged using a Leica laser scanning confocal microscope. The excitation wavelength used was 405 nm which was the shortest available wavelength on the microscope.

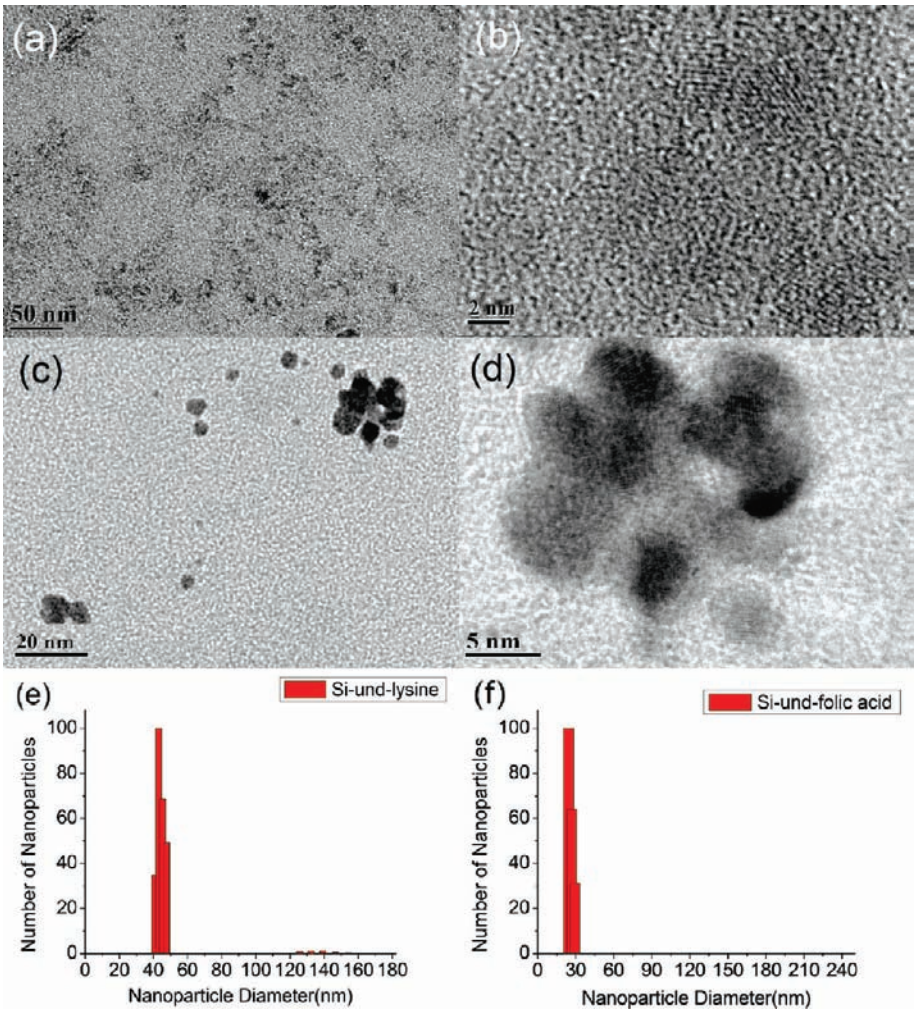


Figure 2. TEM images of (a,b) undecylenic acid terminated Si QDs and (c,d) Si QDs after bioconjugation to lysine. Hydrodynamic diameter distributions measured by DLS for (e) lysine-conjugated and (f) folic acid conjugated Si QDs. The mean diameter of Si-and-lysine particles is 46.7 nm, and the size of Si-and-folic acid particles is 26 nm.

Si QD Characterization. The silicon nanoparticles were characterized by transmission electron microscopy (TEM, JEOL 2010) before and after bioconjugation. Photoluminescence spectra (fluorescence spectra) were recorded with a Perkin-Elmer LS 50 fluorescence spectrometer with a 351 nm band-pass filter used to suppress any scattered light from the source. The excitation wavelength was set to 350 nm and the emission cutoff filter was set to 390 nm. Fluorescence quantum yield s (QYs) of the QD dispersions were determined by comparing the integrated emission from the QDs to rhodamine 6G dye solutions of matched absorbance. FTIR spectra were measured on a Bruker Vertex 70 spectrometer in attenuated total reflectance mode. The hydrodynamic diameter was measured by dynamic light scattering (BIC, 90 Plus). The uptake of bioconjugated Si QDs into pancreatic cancer cells was confirmed by laser confocal imaging (Leica Microsystems Semiconductor GmbH, Wetzlerm Germany, laser excitation at 405 nm).

RESULTS AND DISCUSSION

The size of the silicon nanoconstructs is shown in Figure 2. Figure 2a,b shows TEM images of the undecylenic acid-coated Si QDs at low and high magnification, respectively. Particles around 4−5 nm with lattice fringes are observed in Figure 2b. The average hydrodynamic diameter from DLS measurements was 23 nm. The large hydrodynamic diameter, relative to the crystalline core diameter, is attributed to the organic ligand on the surface of the silicon nanocrystals. These particles were conjugated with lysine using EDC and sulfo-NHS as depicted in Figure 1. After bioconjucation to lysine, some clusters are observed in the TEM images. The clusters are around 20 nm as seen in Figure 2d. The clusters consist of crystalline silicon QDs. Before the addition of lysine, the silicon content is estimated to be as high as 70% based on thermogravimetric analysis methods discussed previously,[32] and the QY is 15 ± 5% before bioconjugation and 5 ± 3% after bioconjugation. The DLS-measured hydrodynamic diameter increased from 23 to 46 nm after bioconjugation with lysine. These sizes are from the two-step reaction. This increase in size is attributed to possible aggregation and cross-linking between lysine molecules. The lysine molecules possess carboxyl groups that form semistable NHS-ester groups and readily react with available amine groups of other lysine molecules. When the particles were conjugated in a one-step process, in which EDC, sulfo-NHS, and lysine were added sequentially without intermediate separation steps, the

size of the particles was around 100 nm in TEM images (Supporting Information Figure S1) and the DLS-measured mean hydrodynamic diameter was 150 nm. Even though it is much larger than the initial particle, the size of around 100 nm is favorable for some biological applications. To reduce cross-linking, a protocol that involved centrifugation between steps C and D in Figure 1 was used, as described above. This resulted in NHS-terminated Si QDs that were directly reacted with the amine groups of the lysine particles. The overall diameter of the particles was smaller in the two-step process because the excess lysine did not react with itself as much as in the one-step protocol. Similarly, the folate-conjugated particles had a hydrodynamic diameter of 26 nm using the two-step protocol and 120 nm using the one-step protocol. These data indicate that the carboxyl group on lysine has a higher tendency to cross-link to form larger particles or that these particles are less hydrophilic and have some tendency to aggregate in water.

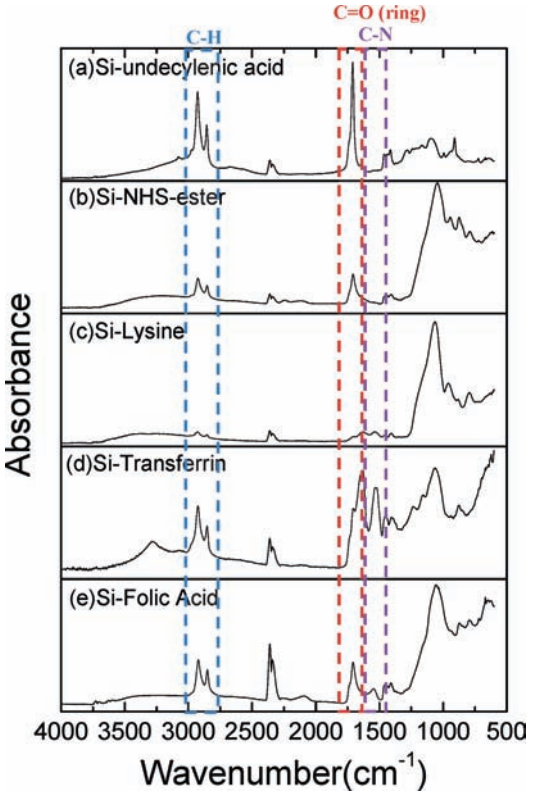


Figure 3. FTIR spectra of Si QDs after each step of the bioconjugation process.

Figure 3a displays the FTIR spectra of Si QDs after the hydrosilylation. The C−H stretch (2929, 2855 cm^{-1}), C−H bend (1461, 1438, 1416 cm^{-1}), and C═O stretch (1716 cm^{-1}) from the undecylenic acid are present in the spectrum. The absorbances at 3080, 2979, 2676, and 913−947 cm^{-1} are assigned to the deformation bend and stretch vibrations of O−H (COOH) bond. Growth of the Si−C peak at 1240 cm^{-1} and the absence of the Si−H peaks near 2100 cm^{-1} indicate the full removal of Si−H bonds in the hydrosilylated nanoparticles[32] (see Supporting Information Figure S2 for undecylenic acid FTIR spectrum). Figure 3b shows the FTIR spectrum of the semistable amine-reactive NHS-ester, in which the peak at 1707 cm^{-1} peak corresponds to the five-membered ring structure (see Supporting Information Figure S3 for the sulfo-NHS FTIR spectrum). Parts c, d, and e of Figure 3 show the IR spectra of the bioconjugated Si QDs. Figure 3d shows bands at 3270 cm^{-1} and 1635 cm^{-1} for amide A and amide I modes, respectively.[33] The amide III band is usually weak, but can be found at 1270 cm^{-1}. The absorbances at 1633 cm^{-1} and 1648 cm^{-1} in Figure 3d are assigned to α-helix and β-sheet structures. The peak at 1550 cm^{-1} is assigned to the C−N bond from the amide II group and the peak at 2252 cm^{-1} is from the

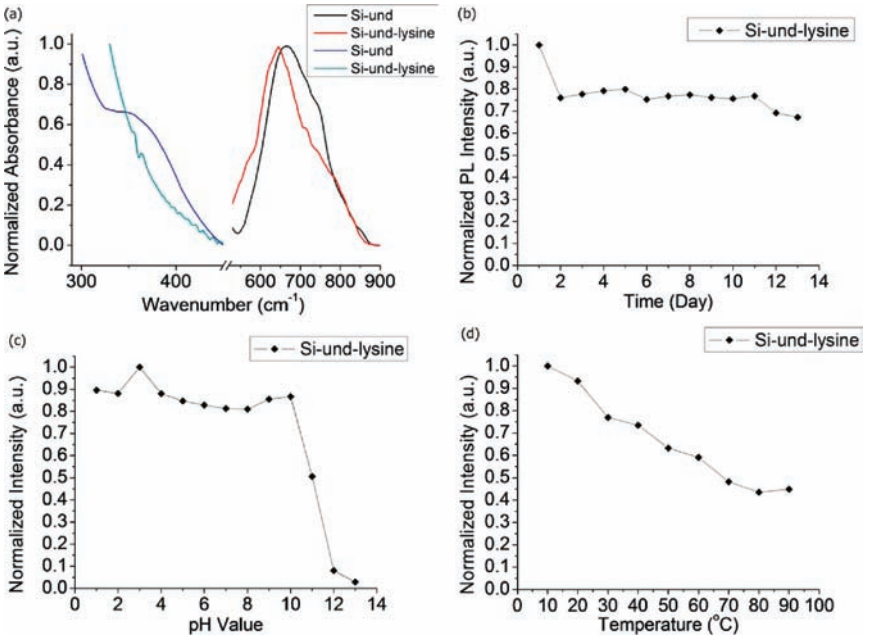


Figure 4. (a) Absorption and PL spectra undecylenic acid coated Si QDs (Si-und) and of lysine grafted Si QDs (Si-und-lysine) in a 50/50 (by volume) water/ethanol mixture. Stability of photoluminescence intensity from lysine grafted Si QDs in water, (b) over 13 days of storage at 4 °C, (c) at different pH levels in water, and (d) after heating to different temperatures in water. An average of three samples was used in the plots.

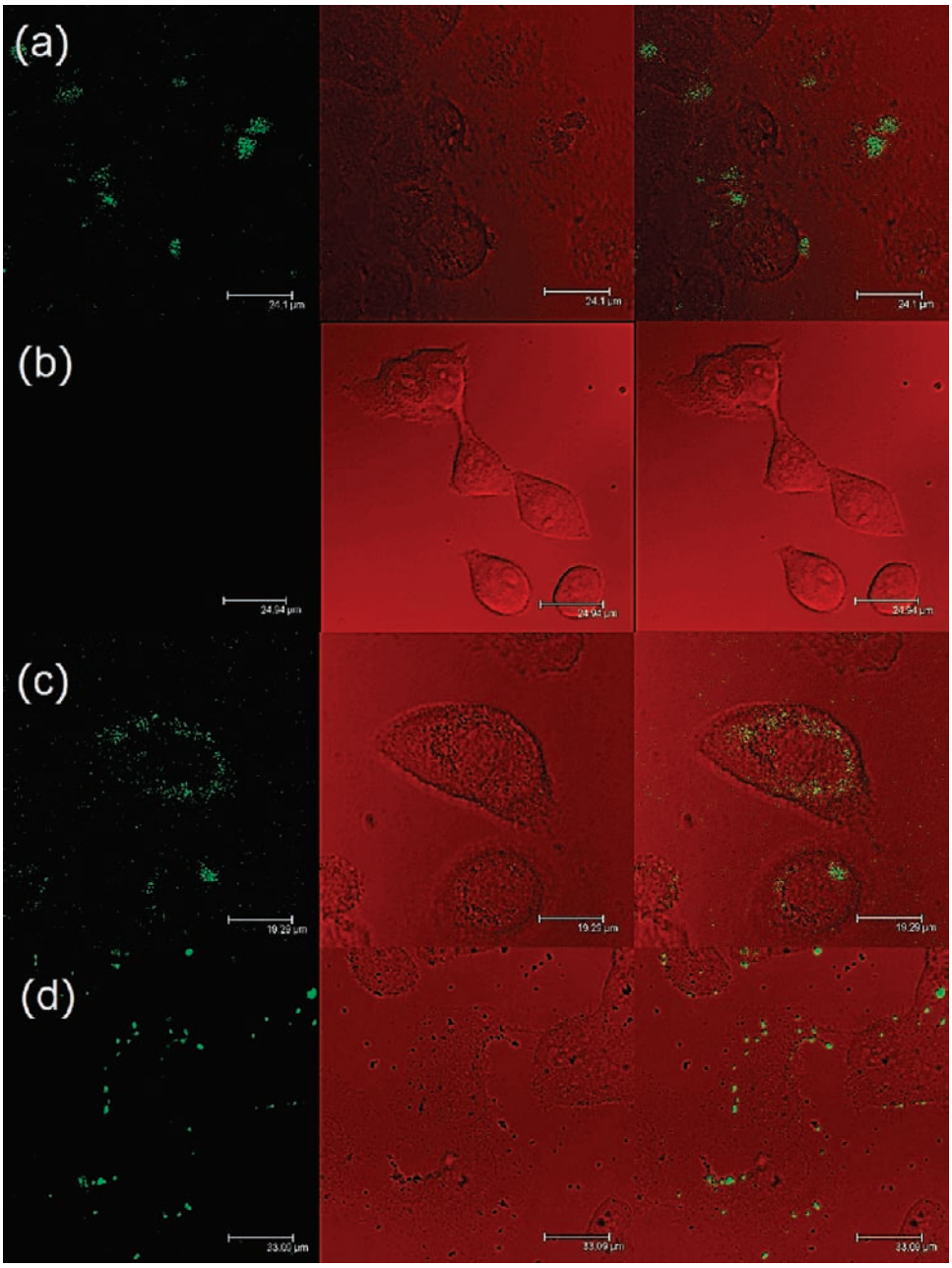


Figure 5. False-color confocal images of Panc-1 cells incubated with (a) lysine grafted Si QDs; (b) folic acid grafted Si QDs after incubation with excess folic acid; (c) folic acid grafted Si QDs; and (d) antimesothelin grafted Si QDs. From left to right, the panels show the luminescence images, the transmission images, and the overlay of the two. The scale bars are 24.1 μm, 24.94 μm, 19.29 μm, and 33.09 μm, respectively, in panels (a) through (d).

N−H bond on the silicon.[34] The six-membered ring structure has a very strong peak at 1710 cm^{-1} which confirmed the attachment of folic acid on Si QDs.

Figure 4a shows the absorption and PL emission spectra of undecylenic acid coated Si QDs and the PL of lysine-conjugated Si QDs. The emission peak shifts from 662 nm to 645 nm after the Si QDs are conjugated with lysine. Figure 4b shows the PL stability of the Si-lysine particles in water for 13 days. The first day after the bioconjugation, the Si QDs have the strongest photo luminescence intensity. Although the intensity dropped to 76% on the second day, the intensity remained stable for the next 11 days, until the 12th day when it dropped to 69%. This indicates that the undecylenic acid group was reasonably effective in protecting the Si QDs from oxidation. Even after the lysine conjugation and dispersion in water, the luminescence remained sufficiently stable for practical use over a period of at least two weeks. Figure 4c shows the PL intensity of lysine grafted Si QDs at different pH. From pH 1 to 10, it shows that Si QDs maintained a PL intensity that was at least 80% of the highest intensity at pH 3. Above pH 11, the PL intensity dropped drastically to 50.5% at pH 11, 8% at pH 12, and only 2% at pH 13. However, the PL is clearly stable over the entire range of biologically relevant conditions. Figure 4d displays the PL intensity of lysine-grafted Si QDs after heating to various temperatures. Although there is an obvious temperature dependence, the PL of the particles was higher than 40% of their initial

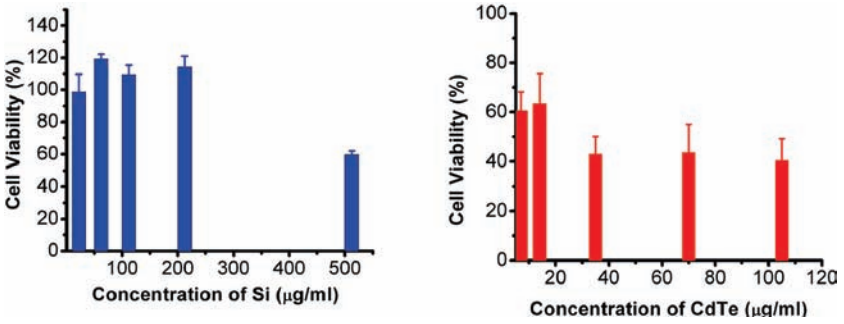


Figure 6. Cytotoxicity of (A) Si and (B) CdTe quantum dots toward Panc-1 cells. Error bars represent one standard deviation ($N = 3$). Note that the concentration range is much higher in (A) than in (B).

PL intensity at temperatures up to 90 °C. For in vivo application (30−40 °C), the PL intensity is more than 70% of the intensity at 10 °C.

To utilize Si QDs as an efficient targeted contrast agent for in vitro or in vivo imaging, the Si QDs must be conjugated with specific biorecognition molecules. Here, we present the conjugation of Si QDs with folate, antimesothelin, and transferrin. Panc-1 cells are an appropriate model to test cancer specific targeting by folate, transferrin, and antimesothelin because panc-1 cells have receptors for all three biomolecules.[35,36] Since folate, transferrin, and anti mesothelin receptors are minimally distributed in normal cells/tissues, they serve as excellent ligands for preferentially targeting cancerous cells and tissues in vitro and in vivo. The biomolecule-conjugated nanoprobes are transported into cells or localized on the membrane through the corresponding receptor. Figure 5 shows confocal microscopy images of panc-1 cells stained with the Si QD bioconjugates. Figure 5a shows the nonspecific targeting of lysine coated Si-QDs. As seen in the images, the Si bioconjugates are associated with the cells, but do not appear to have been internalized.

Figure 5b shows the cellular image obtained when Panc-1 cells were presaturated with excess folic acid for 2 h then incubated with folic acid-conjugated Si QDs (FA-Si QDs). There is no visible luminescence from the image indicating that FA-Si QDs are not taken up when the folate receptors are presaturated. Figure 5c shows the confocal image of Panc-1 cells incubated with FA-Si QDs for 2 h, without the folic acid pretreatment. The FA-Si QDs appear to be transported into cells through the corresponding receptor, demonstrating selective uptake via the folate receptors. Transferrin-grafted Si QDs also labeled the cancer cells, though less effectively than the FA-Si QDs (Supporting Information Figure S4). Figure 5d is shows Panc-1 cells incubated with antimesothelin grafted Si QDs (AM-Si QDs). The particles appear to be localized on the membrane of the cells indicating the efficacy of AM-Si QDs. The lack of any visible cell damage in all images is consistent with the expected biocompatibility of the Si QDs.

As cell morphology is not ideal for evaluating the toxicity of nanoparticle alone, MTS assays were used for comparative studies between toxicity profiles of hydrogen-terminated Si QDs with cysteine-capped CdTe QDs. The minimal encapsulation (cysteine is used in the CdTe QD synthesis) is intended to assess the inherent cytotoxicity of the core components. Figure 6 shows the in vitro cytotoxicity results for Si and CdTe QDs on a human pancreatic cancer (Panc-1) cell line at 24 h post-treatment. The inhibitory particle concentrations corresponding to 50% cell viability (IC_{50}) were ~40 μg/mL for CdTe compared to >500 μg/mL for the Si QDs. This demonstrates a significantly better toxicity profile for Si QDs when compared to Cd-based QDs.

DISCUSSION

Si QDs are beginning to become accepted as a nontoxic alternative to toxic quantum dots. The chemistry however has to be properly defined, and bioconjugation is one of the most important areas that must be investigated for the practical applications of SiQDs. The bioconjugation of SiQD can be challenging because standard protocols that are used for conventional quantum dots are not directly applicable to the functionalization of SiQDs. Short chain carboxyl groups like butenoic acid (results not shown) can produce bright orange luminescent particles; however, upon conjugation to lysine, the particles' emission becomes blue. This blue shifting also occurred when octane-terminated silicon nanoparticles were conjugated to DNA as luminescent labels.[37] It is important to maintain optical properties for imaging applications. Oxidation is normally responsible for the blue shift, and the method presented here prevents that complete blue shift from occurring. There is a very slight blue shift after conjugation; however, the particles are relatively stable as depicted in Figure 4. The particles are useful for labeling cancer cells with different targeting agents, which is of importance because targeted diagnosis and therapies are gaining traction in biomedical research.

CONCLUSION

A bioconjugation protocol for preparing smaller water-dispersible Si QDs has been developed and presented. A variety of appropriate functional groups for bioconjugation can be linked to the Si QDs for biological labeling. Antimesothelin and folic acid conjugated Si QDs were successfully applied for fluorescence imaging of pancreatic cancer cells. The excellent stability of the Si QDs in water provides longer observation time scale for targeting tumor cells without observable in vitro toxicity. Thus, the bioconjugated Si QDs presented here complement the larger micelle-encapsulated Si QD nanostructures we have previously developed, broadening the range of potential applications of Si QDs in biological imaging and diagnostics. This suggests that the Si QDs can be viable candidates for use in long-term and real-time cellular labeling and imaging.

ASSOCIATED CONTENT

Supporting Information. TEM images of the lysine-conjugated Si QDs prepared via the one-step protocol, FTIR

spectra of sulfo-NHS and undecylenic acid, and confocal images of transferrin-grafted Si QDs-targeted Panc-1 cells. This material is available free of charge via the Internet at http://pubs.acs.org.

AUTHOR INFORMATION

Corresponding Authors
*E-mail: pnprasad@buffalo.edu, swihart@buffalo.edu.

ACKNOWLEDGMENT

This study was supported by grants from the NCI RO1CA119397, and the John R. Oishei Foundation.

REFERENCES

(1) Prasad, P. N. (2003) *Biophotonics*, Wiley-Interscience, Hoboken, NJ.
(2) Prasad, P. N. (2004) *Nanophotonics*, Wiley-Interscience, Hoboken, NJ.
(3) Michalet, X., Pinaud, F. F., Bentolila, L. A., Tsay, J. M., Doose, S., Li, J. J., Sundaresan, G., Wu, A. M., Gambhir, S. S., and Weiss, S. (2005) Quantum dots for live cells, in vivo imaging, and diagnostics. *Science 307*, 538–544.
(4) Erogbogbo, F., Yong, K.-T., Roy, I., Xu, G., Prasad, P. N., and Swihart, M. T. (2008) Biocompatible luminescent silicon quantum dots for imaging of cancer cells. *ACS Nano 2*, 873–878.
(5) Alivisatos, A. P. (1996) Semiconductor clusters, nanocrystals, and quantum dots. *Science 271*, 933–937.
(6) Qian, X., Peng, X.-H., Ansari, D. O., Yin-Goen, Q., Chen, G. Z., Shin, D. M., Yang, L., Young, A. N., Wang, M. D., and Nie, S. (2008) In vivo tumor targeting and spectroscopic detection with surface-enhanced Raman nanoparticle tags. *Nat. Biotechnol. 26*, 83–90.
(7) Kim, S., Lim, Y. T., Soltesz, E. G., De Grand, A. M., Lee, J., Nakayama, A., Parker, J. A., Mihaljevic, T., Laurence, R. G., Dor, D. M., Cohn, L. H., Bawendi, M. G., and Frangioni, J. V. (2004) Near-infrared fluorescent type II quantum dots for sentinel lymph node mapping. *Nat. Biotechnol. 22*, 93–97.
(8) Stroh, M., Zimmer, J. P., Duda, D. G., Levchenko, T. S., Cohen, K. S., Brown, E. B., Scadden, D. T., Torchilin, V. P., Bawendi, M. G., Fukumura, D., and Jain, R. K. (2005) Quantum dots spectrally distinguish multiple species within the tumor milieu in vivo. *Nat. Med. 11*, 678–682.
(9) Hoshino, A., Fujioka, K., Oku, T., Suga, M., Sasaki, Y. F., Ohta, T., Yasuhara, M., Suzuki, K., and Yamamoto, K. (2004) Physicochemical properties and cellular toxicity of nanocrystal quantum dots depend on their surface modification. *Nano Lett. 4*, 2163–2169.
(10) Derfus, A. M., Chan, W. C. W., and Bhatia, S. N. (2003) Probing the cytotoxicity of semiconductor quantum dots. *Nano Lett. 4*, 11–18.
(11) Dubertret, B., Skourides, P., Norris, D. J., Noireaux, V., Brivanlou, A. H., and Libchaber, A. (2002) In vivo imaging of quantum dots encapsulated in phospholipid micelles. *Science 298*, 1759–1762.
(12) Lovric, J., Cho, S. J., Winnik, F. M., and Maysinger, D. (2005) Unmodified cadmium telluride quantum dots induce reactive oxygen species formation leading to multiple organelle damage and cell death. *Chem. Biol. 12*, 1227–1234.
(13) McNeil, S. E. (2009) Nanoparticle therapeutics: a personal perspective. *Wiley Interdisciplin. Rev.: Nanomed. Nanobiotechnol. 1*, 264–271.
(14) Hauck, T. S., Anderson, R. E., Fischer, H. C., Newbigging, S., and Chan, W. C. W. (2010) In vivo quantum-dot toxicity assessment. *Small 6*, 138–144.
(15) Fitzpatrick, J. A. J., Andreko, S. K., Ernst, L. A., Waggoner, A. S., Ballou, B., and Bruchez, M. P. (2009) Long-term persistence and spectral blue shifting of quantum dots in vivo. *Nano Lett. 9*, 2736–2741.
(16) Pons, T., Pic, E., Lequeux, N., Cassette, E., Bezdetnaya, L., Guillemin, F. o., Marchal, F. d. r., and Dubertret, B. (2010) Cadmium-free $CuInS_2$/ZnS quantum dots for sentinel lymph node imaging with reduced toxicity. *ACS Nano 4*, 2531–2538.
(17) Ron, H. (2006) A toxicologic review of quantum dots: toxicity depends on physicochemical and environmental factors. *Environ. Health Perspect. 114*, 165–172.
(18) Yong, K.-T., Qian, J., Roy, I., Lee, H. H., Bergey, E. J., Tramposch, K. M., He, S., Swihart, M. T., Maitra, A., and Prasad, P. N. (2007) Quantum rod bioconjugates as targeted probes for confocal and two-photon fluorescence imaging of cancer cells. *Nano Lett. 7*, 761–765.
(19) Fujioka, K., Hiruoka, M., Sato, K., Manabe, N., Miyasaka, R., Hanada, S., Hoshino, A., Tilley, R. D., Manome, Y., Hirakuri, K., and Yamamoto, K. (2008) Luminescent passive-oxidized silicon quantum dots as biological staining labels and their cytotoxicity effects at high concentration. *Nanotechnology 19*, 415102.
(20) Mangolini, L., Jurbergs, D., Rogojina, E., and Kortshagen, U. (2006) High efficiency photoluminescence from silicon nanocrystals prepared by plasma synthesis and organic surface passivation. *Phys. Status Solidi C 3*, 3975–3978.
(21) Park, J.-H., Gu, L., von Maltzahn, G., Ruoslahti, E., Bhatia, S. N., and Sailor, M. J. (2009) Biodegradable luminescent porous silicon nanoparticles for in vivo applications. *Nat. Mater. 8*, 331–336.
(22) He, G. S., Zheng, Q., Yong, K.-T., Erogbogbo, F., Swihart, M. T., and Prasad, P. N. (2008) Two- and three-photon absorption and frequency upconverted emission of silicon quantum dots. *Nano Lett. 8*, 2688–2692.
(23) Tu, C., Ma, X., Pantazis, P., Kauzlarich, S. M., and Louie, A. Y. (2010) Paramagnetic, silicon quantum dots for magnetic resonance and two-photon imaging of macrophages. *J. Am. Chem. Soc. 132*, 2016–2023.
(24) Warner, J. H., Hoshino, A., Yamamoto, K., and Tilley, R. D. (2005) Water-soluble photoluminescent silicon quantum dots. *Angew. Chem., Int. Ed. 44*, 4550–4554.
(25) Choi, J., Wang, N. S., and Reipa, V. (2008) Conjugation of the photoluminescent silicon nanoparticles to streptavidin. *Bioconjugate Chem. 19*, 680–685.
(26) Erogbogbo, F., Yong, K.-T., Roy, I., Hu, R., Law, W.-C., Zhao, W., Ding, H., Wu, F., Kumar, R., Swihart, M. T., and Prasad, P. N. (2010) In vivo targeted cancer imaging, sentinel lymph node mapping and multi-channel imaging with biocompatible silicon nanocrystals. *ACS Nano 5*, 413–423.
(27) Clark, R. J., Dang, M. K. M., and Veinot, J. G. C. (2010) Exploration of organic acid chain length on water-soluble silicon quantum dot surfaces. *Langmuir 26*, 15657–15664.
(28) Soo Choi, H., Liu, W., Misra, P., Tanaka, E., Zimmer, J. P., Itty Ipe, B., Bawendi, M. G., and Frangioni, J. V. (2007) Renal clearance of quantum dots. *Nat. Biotechnol. 25*, 1165–1170.
(29) Leamon, C. P., and Low, P. S. (2001) Folate-mediated targeting: from diagnostics to drug and gene delivery. *Drug Discovery Today 6*, 44–51.
(30) Li, X., He, Y., and Swihart, M. T. (2004) Surface functionalization of silicon nanoparticles produced by laser-driven pyrolysis of silane followed by $HF-HNO_3$ etching. *Langmuir 20*, 4720–4727.
(31) Swihart, M. T. (2003) Vapor-phase synthesis of nanoparticles. *Curr. Opin. Colloid Interface Sci. 8*, 127–133.
(32) Hua, F. J., Swihart, M. T., and Ruckenstein, E. (2005) Efficient surface grafting of luminescent silicon quantum dots by photoinitiated hydrosilylation. *Langmuir 21*, 6054–6062.
(33) Rozenberg, M., and Shoham, G. (2007) FTIR spectra of solid poly-l-lysine in the stretching NH mode range. *Biophysical Chemistry 125*, 166–171.
(34) Haris, P. I., and Severcan, F. (1999) FTIR spectroscopic characterization of protein structure in aqueous and non-aqueous media. *J. Mol. Catal., B 7*, 207–221.
(35) Ryschich, E., Huszty, G., Knaebel, H. P., Hartel, M., Büchler, M. W., and Schmidt, J. (2004) Transferrin receptor is a marker of malignant phenotype in human pancreatic cancer and in neuroendocrine carcinoma of the pancreas. *Eur. J. Cancer 40*, 1418–1422.
(36) Qian, J., Yong, K.-T., Roy, I., Ohulchanskyy, T. Y., Bergey, E. J., Lee, H. H., Tramposch, K. M., He, S., Maitra, A., and Prasad, P. N. (2007) Imaging pancreatic cancer using surface-functionalized quantum dots. *J. Phys. Chem. B 111*, 6969–6972.
(37) Wang, L., Reipa, V., and Blasic, J. (2004) Silicon nanoparticles as a luminescent label to DNA. *Bioconjugate Chem. 15*, 409–412.

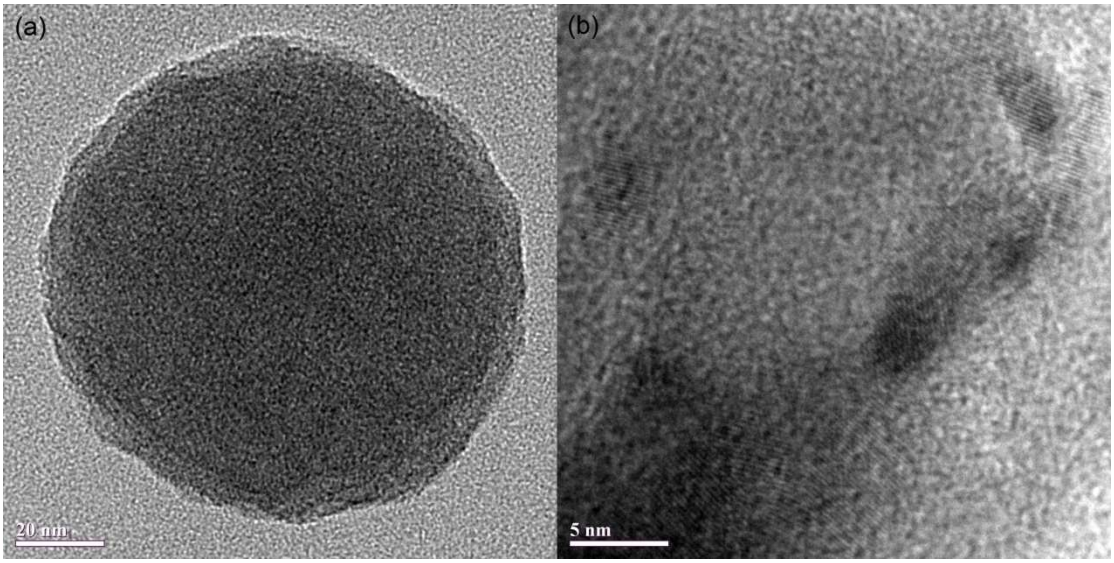
Supplementary Information:

Bioconjugation of Luminescent Silicon Quantum Dots for Selective Uptake by Cancer Cells

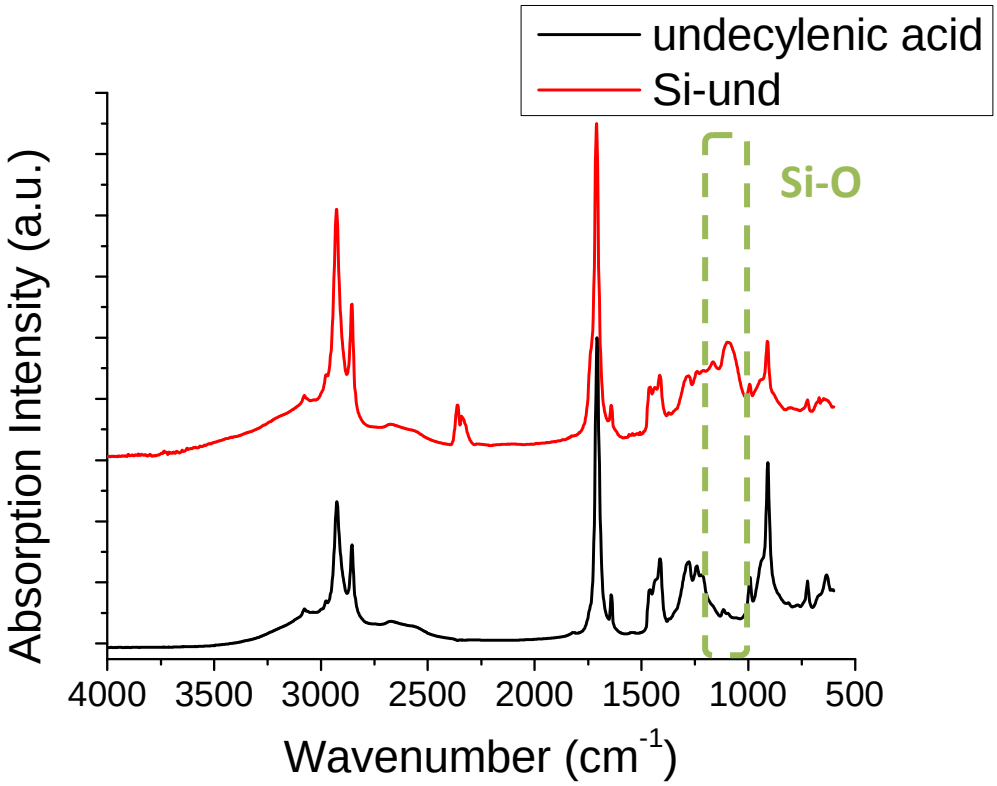
Chen-An Tien[a], Folarin Erogbogbo[a,c], Ching-Wen Chang[a,] Ken-Tye Yong[c], Wing-Cheung Law[c], Hong Ding[c], Indrajit Roy[a], Mark T. Swihart[a,b], Paras N. Prasad[b,c]**

Department of Chemical and Biological Engineering[a], Department of Chemistry[b] and Institute for Lasers, Photonics and Biophotonics[c], The University at Buffalo, State University of New York Buffalo, New York 14260-4200

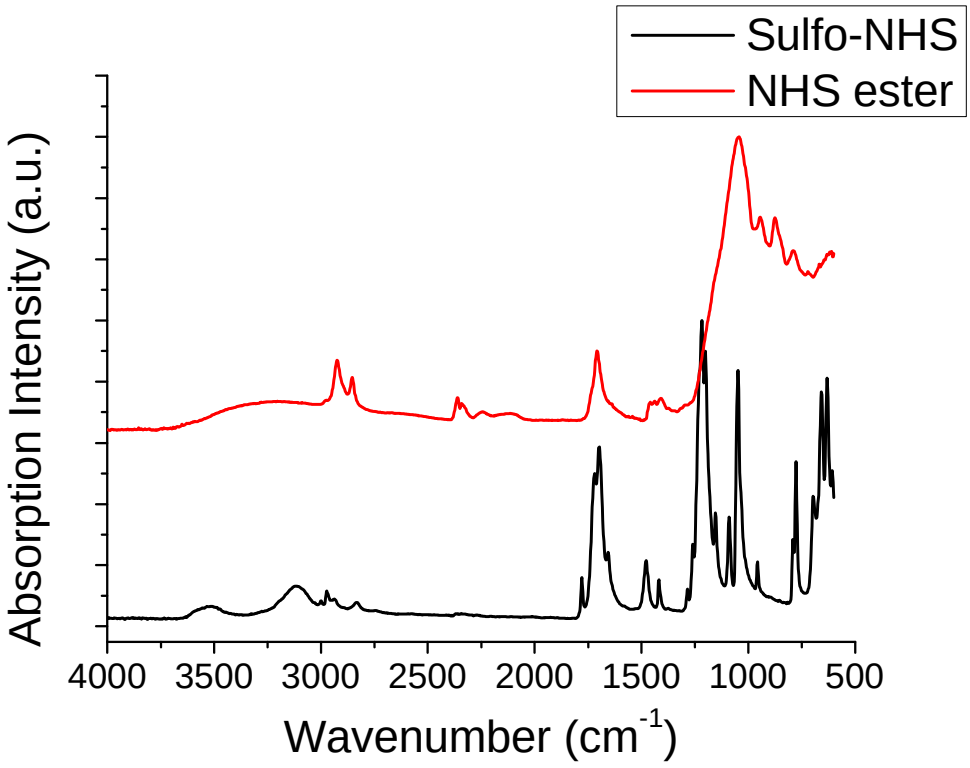
Email: pnprasad@buffalo.edu, swihart@buffalo.edu



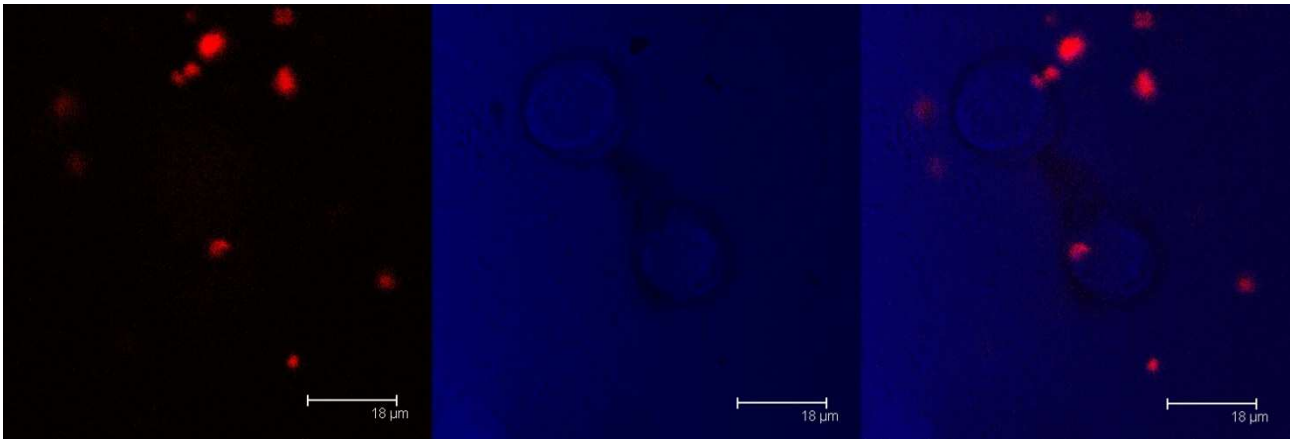
Supplementary Figure 1. The TEM images of Si-und-lysine particle made by protocol 1. The size is around 100nm in figure (a). The crystal structure can be seen in figure (b).



Supplementary Figure 2. This is the FTIR of undecylenic acid compared with Si-und.



Supplementary Figure 3. This shows the FTIR of sulfo-NHS compared with NHS-ester.



Supplementary Figure 4. The confocal image of apo-transferrin grafted Si QDs. The scale bar is 18 µm.

Bioconjugate Chemistry

ARTICLE

pubs.acs.org/bc

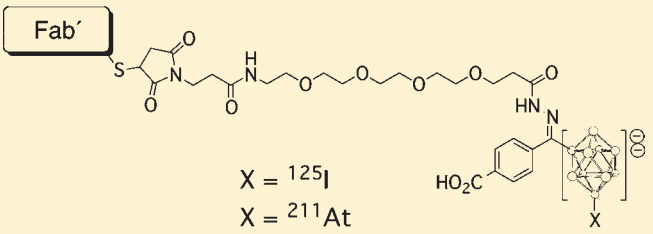
Reagents for Astatination of Biomolecules. 5. Evaluation of Hydrazone Linkers in ^{211}At- and ^{125}I-Labeled *closo*-Decaborate(2-) Conjugates of Fab′ as a Means of Decreasing Kidney Retention

D. Scott Wilbur,*[,†] Ming-Kuan Chyan,[†] Donald K. Hamlin,[†] Holly Nguyen,[‡] and Robert L. Vessella[‡]

[†]Department of Radiation Oncology and [‡]Department of Urology, University of Washington, Seattle, Washington 98195, United States

Supporting Information

ABSTRACT: Evaluation of monoclonal antibody (mAb) fragments (e.g., Fab′, Fab, or engineered fragments) as cancer-targeting reagents for therapy with the α-particle emitting radionuclide astatine-211 (^{211}At) has been hampered by low in vivo stability of the label and a propensity of these proteins localize to kidneys. Fortunately, our group has shown that the low stability of the ^{211}At label, generally a *meta*- or *para*--[^{211}At]astatobenzoyl conjugate, on mAb Fab′ fragments can be dramatically improved by the use of *closo*-decaborate(2-) conjugates. However, the higher stability of radiolabeled mAb Fab′ conjugates appears to result in retention of radioactivity in the kidneys. This investigation was conducted to evaluate whether the retention of radioactivity in kidney might be decreased by the use of an acid-cleavable hydrazone between the Fab′ and the radiolabeled *closo*-decaborate(2-) moiety. Five conjugation reagents containing sulfhydryl-reactive maleimide groups, a hydrazone functionality, and a *closo*-decaborate(2-) moiety were prepared. In four of the five conjugation reagents, a discrete poly(ethylene glycol) (PEG) linker was used, and one substituent adjacent to the hydrazone was varied (phenyl, benzoate, anisole, or methyl) to provide varying acid sensitivity. In the initial studies, the five maleimido-*closo*-decaborate(2-) conjugation reagents were radioiodinated (^{125}I or ^{131}I), then conjugated with an anti-PSMA Fab′ (107−1A4 Fab′). Biodistributions of the five radioiodinated Fab′ conjugates were obtained in nude mice at 1, 4, and 24 h post injection (pi). In contrast to *closo*-decaborate(2-) conjugated to 107−1A4 Fab′ through a noncleavable linker, two conjugates containing either a benzoate or a methyl substituent on the hydrazone functionality displayed clearance rates from kidney, liver, and spleen that were similar to those obtained with directly radioiodinated Fab′ (i.e., no conjugate). The maleimido-*closo*-decaborate(2-) conjugation reagent containing a benzoate substituent on the hydrazone was chosen for study with ^{211}At. That reagent was conjugated with 107−1A4 Fab′, then labeled (separately) with ^{125}I and ^{211}At. The radiolabeled Fab′ conjugates were coinjected into nude mice bearing LNCaP human tumor xenografts, and biodistribution data were obtained at 1, 4, and 24 h pi. Tumor targeting was achieved with both ^{125}I- and ^{211}At-labeled Fab′, but the ^{211}At-labeled Fab′ reached a higher concentration (25.56 ± 11.20 vs 11.97 ± 1.31%ID/g). Surprisingly, while the ^{125}I-labeled Fab′ was cleared from kidney similar to earlier studies, the ^{211}At-labeled Fab′was not (i.e., kidney conc. for ^{125}I vs ^{211}At; 4 h, 13.14 ± 2.03 ID/g vs 42.28 ± 16.38%D/g; 24 h, 4.23 ± 1.57 ID/g vs 39.52 ± 15.87%ID/g). Since the Fab′ conjugate is identical in both cases except for the radionuclide, it seems likely that the difference in tissue clearance seen is due to an effect that ^{211}At has on either the hydrazone cleavage or on the retention of a metabolite. Results from other studies in our laboratory suggest that the latter case is most likely. The hydrazone linkers tested do not provide the tissue clearance sought for ^{211}At, so additional hydrazones linkers will be evaluated. However, the results support the use of hydrazone linkers when Fab′ conjugated with *closo*-decaborate(2-) reagents are radioiodinated.



INTRODUCTION

The α-particle-emitting radionuclide astatine-211 (^{211}At), when combined with tumor-targeting agents, has great potential in the development of new radiopharmaceuticals for treatment of cancer,[1] particularly for blood-borne (e.g., lymphoma;[2] leukemia[3,4]), compartmentalized cancer (e.g., ovarian cancer[5−7]), minimal residual disease after surgical tumor resections,[8] and metastatic cancer.[9−11] Although most of the current investigations use intact monoclonal antibodies (mAb) or their F(ab′)$_2$ fragments for delivery of ^{211}At to cancer cells in vivo, some studies have shown that cancer-targeting agents with biological half-lives that are matched to the physical half-life of ^{211}At ($t_{1/2}$ = 7.21 h) can be effective therapeutic agents, even in solid tumors.[10] This later fact is of particular interest, as metastatic cancer can form tumors where barriers to penetration of intact MAbs have become present.[12,13] Therefore, we believe that the optimal cancer-targeting agents for carrying ^{211}At may be antibody Fab′ fragments, divalent genetically engineered mAb fragments such as

Received: December 11, 2010
Revised: March 25, 2011
Published: April 23, 2011

ACS Publications © 2011 American Chemical Society

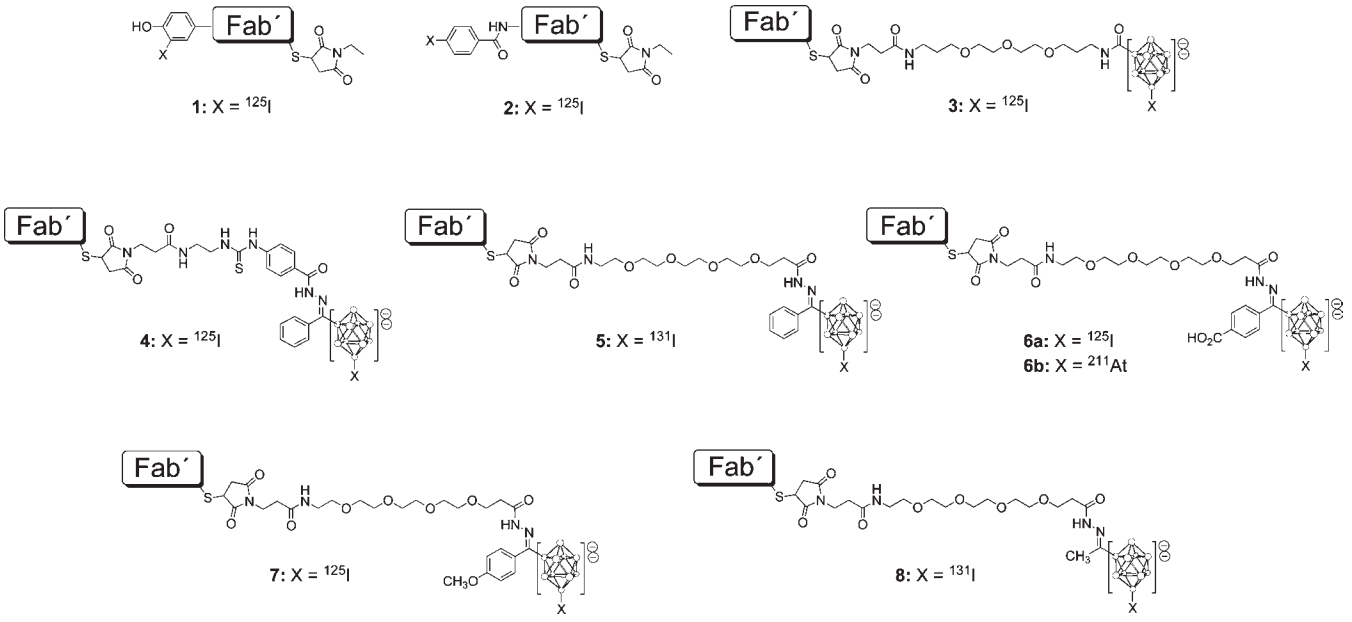


Figure 1. Depiction of radiolabeled 107−1A4 Fab′ conjugates showing chemical structures of directly radioiodinated Fab′, [^{125}I]**1**, versus Fab′ radiolabeled by conjugation with a lysine amine, [^{125}I]**2**, or conjugation with a free sulfydryl group, [^{125}I]**3**, [^{125}I]**4**, [^{131}I]**5**, [^{125}I]**6a**, [^{211}At]**6b**, [^{125}I]**7**, and [^{131}I]**8**. Note that Fab′ conjugates **4**−**8** contain acid-cleavable hydrazone functionalities.

diabodies,[14,15] or nanomolecular constructs that have biological half-lives closely matched to the half-life of ^{211}At.

Until recently, development of endoradiotherapy agents based on mAb Fab′ (or Fab) fragments or small genetically engineered mAb fragments has been problematic due to an inherent instability of ^{211}At label in vivo.[16] However, we have demonstrated that conjugates of ^{211}At-labeled mAb Fab′ fragments can be stabilized to deastatination by using nonahydro-*closo*-decaborate(2-) conjugates.[17] Despite this advancement, there is another major impediment to overcome before ^{211}At-labeled mAb Fab′ fragments can be effectively used in cancer therapy. That impediment is the inherent kidney localization of Fab′ and similar molecular weight engineered mAb fragments. Unlike intact MAbs or their F(ab′)$_2$ fragments, Fab′ fragments have a molecular size and shape that allows them to be filtered by the kidney glomerulus.[18,19] Like other proteins, once filtered Fab′ undergo reabsorption into the proximal tubule cells, presumably by binding megalin and cubulin receptors,[20−22] where they are ultimately degraded in the lysosomes.[23] There is evidence that complete degradation of the protein occurs by lysosomal peptidases; however, the radiolabeled metabolite, an amino acid adduct,[24,25] can have a slow release from the kidney. The retention of radiolabeled metabolites in kidneys is a critical issue when α-emitting radionuclides are used. Although therapy with ^{213}Bi-labeled Fab′[26] and ^{211}At-labeled diabodies[10] has been shown to be effective despite kidney localization, such reagents must be considered nonoptimal as therapeutic agents due to potential kidney toxicity. To address this issue, we have incorporated pH-sensitive hydrazone functionalities between the mAb Fab′ fragment and the *closo*-decaborate(2-) radiolabeling moiety as a potential means of obtaining a more rapid release of ^{211}At from kidneys. Although the hydrazone functionality has been used to release drugs within cells,[27] examples of its use in releasing radioactivity from kidneys were not readily found.

In this investigation, five hydrazone-containing *closo*-decaborate(2-) conjugates of anti-PSMA antibody, 107−1A4,[28] Fab′ (**4**−**8**) were prepared and evaluated in vivo to compare the release of ^{125}I or ^{211}At in kidney and other tissues. To better assess the effect of the hydrazone linker, biodistribution data previously reported for the same Fab′ directly radioiodinated, [^{125}I]**1**, radioiodinated with *N*-hydroxysuccinimidyl *para*-[^{125}I]iodobenzoate, **2**, and radioiodinated with a noncleavable *closo*-decaborate(2-) reagent, **3**,[17] were included in the comparison. Depictions of the radiohalogenated Fab′ conjugates are provided in Figure 1. The key feature of the Fab′ conjugates prepared in this study is that they contain hydrazone functionalities in molecular linkers between the Fab′ and the *closo*-decaborate(2-) moiety used for radiolabeling. Initial in vivo studies were conducted with ^{125}I- or ^{131}I-labeled Fab′ conjugates. In the studies, sulfhydryl-reactive, hydrazone-containing, *closo*-decaborate(2-) derivatives were radiolabeled prior to conjugation with Fab′-SH to ensure that the radioiodine was on the *closo*-decaborate(2-) cage moiety. In a later biodistribution study, Fab′-SH was conjugated prior to radiolabeling with the hydrazone-containing *closo*-decaborate(2-) derivative found in the first biodistribution studies to have the most favorable in vivo characteristics. That Fab′ conjugate was directly labeled with ^{211}At and (separately) ^{125}I, then the in vivo distribution of the coadministered ^{211}At and ^{125}I-labeled Fab′ was evaluated. The experiments conducted and results obtained in the investigation are reported herein.

EXPERIMENTAL PROCEDURES

General. Chemicals purchased from commercial sources were analytical grade or better and were used without further purification. Decaborane ($B_{10}H_{14}$) was obtained from Alfa Aesar (Ward Hill, MA). DL-Dithiothreitol (DTT), chloramine-T (ChT), and phosphate buffered saline (PBS) were obtained from Sigma-Aldrich (Sigma, St. Louis, MO). MPS-EDA.TFA (TFA salt of *N*-(2′-aminoethyl)-3-(maleimido)propionamide), **13**, and MAL-dPEG$_4$-*t*-boc-hydrazide, **16**, were obtained from Quanta

BioDesign (Powell, OH; quantabiodesign.com). *N*-Chlorosuccinimide (NCS), 4-aminobenzoic hydrazide, **10**, acetyl chloride, trifluoroacetic acid (TFA), and most other chemicals were obtained from Sigma-Aldrich (Milwaukee, WI). Solvents for HPLC analysis were obtained as HPLC grade and were filtered (0.2 μm) prior to use. Sephadex G-25 desalting columns (PD-10 and NAP-10) were obtained from Amersham Biosciences (Piscataway, NJ). Melting points were obtained in open capillary tubes on an EZ-Melt automated melting point apparatus (Stanford Research Systems, Sunnyvale, CA), and are uncorrected.

Radioactive Materials. All radioactive materials were handled according to approved protocols at the University of Washington. Standard methods for safely handling radioacative samples were employed.[29] Na[^{125}I]I was purchased from PerkinElmer Life Sciences (Billerica, MA) as high concentration/high specific activity radioiodide in 0.1 N NaOH. Measurement of ^{125}I and ^{211}At was conducted on a Capintec CRC-15R Radioisotope Calibrator using calibration numbers 319 and 44, respectively (designated by Capintec Technical Services). Tissue samples containing ^{211}At and ^{125}I were counted in a Wallac 1480 Wizard gamma counter (PerkinElmer Life and Analytical Services, Wellesley, MA). The tissue samples were initially counted to obtain both ^{211}At and ^{125}I counts, then were recounted after 3−5 days (0.1% or less ^{211}At remaining) to obtain ^{125}I counts. Radioactivity counts were imported into an *Excel* spreadsheet (Microsoft Corp., Redmond, WA) where calculations were made. The ^{211}At counts were obtained by subtracting ^{125}I counts from total counts. Individual tissue counts for ^{211}At were corrected for decay from the time of counting the first standard (at the beginning of the tissue counting process).

^{211}At was produced by irradiation of a thin layer (0.007 in.; 0.18 mm) of bismuth metal (99.999%, Aldrich) with 28.0 MeV α-particles on a Scandatronix MC-50 cyclotron using the conditions previously described.[30] All handling and processing of the irradiated target was done in a glovebox (Innovative Technologies, Inc., radioisotope glovebox) which was vented through a charcoal filter.

"Wet Chemistry" Isolation of Na[^{211}At]At. Briefly, an irradiated aluminum-backed bismuth target containing ~19.4 mCi of ^{211}At was placed in a 1 L polypropylene dissolution chamber and 10 mL of conc. HNO_3 was added (note: measurement of ^{211}At activity in the target must be considered an approximation due to attenuation and geometry). The HNO_3 solution was removed from the chamber using a pipet after 10 min, and was placed in a 50 mL round-bottom flask. An additional 5 mL of conc. HNO_3 was added to the dissolution chamber containing the irradiated target (as a rinse). After 5 min, the HNO_3 solution was removed and placed in the round-bottom flask with the other HNO_3 solution. The flask containing HNO_3 solution was connected to a distillation apparatus. A hotplate (preheated) at 260 °C was used to distill the HNO_3 leaving a white residue (~50 min). After cooling the flask containing the white residue, 8 mL of 8 M HCl was added with stirring to dissolve it. The resultant clear solution was removed and placed in a 20 mL scintillation vial. The flask was rinsed with an additional 2 mL 8 M HCl, and that was placed in the scintillation vial. An 8 mL quantity of diisopropyl ether (DIPE) was added to the scintillation vial, and that mixture was stirred at room temperature for 10 min. The 8 M HCl was removed by pipet to waste, and an additional 2 mL of 8 M HCl was added and stirred for 5 min. The 8 M HCl was removed to waste, and then 3 mL of 4 M NaOH was added. The NaOH solution was placed in a distillation apparatus and the H_2O was removed. The resulting residue was dissolved in 1 mL of H_2O and was adjusted to pH 9−10 by addition of 4 M HCl. A white gel was obtained, so an additional 1 mL of H_2O was added. That solution was filtered through a 0.2 mm Acrodisc to obtain a colorless solution (5.37 mCi), with 3.46 mCi remaining in the flask (did not rinse) and 8.6 mCi ^{211}At being retained on the filter. This was an early attempt at the wet chemistry approach to isolation of Na[^{211}At]At. Optimization was not done at that time, as the amount recovered was much more than required for the labeling experiment (note: the wet chemistry isolation procedure has been modified since the described experiments were conducted. The modified wet chemistry ^{211}At isolation procedure provides higher radiochemical yields (85 ± 11% decay corrected yields); a description of the modified ^{211}At isolation procedure will be published elsewhere). The Na[^{211}At]At vial was tightly sealed, placed in sealed (Ziploc) plastic bag, then transferred from the glovebox to a radiolabeling enclosure within a fume hood.

All radiohalogenation reactions were conducted in a charcoal-filtered Plexiglas enclosure (radioiodine fume hood, 20 × 24 × 36 in.^{3}, Biodex Medical Systems Inc., Shirley, NY) housed within a radiochemical fume hood. The radiohalogenation reactions were conducted in vials capped with Teflon-coated septa and were vented through a 10 mL charcoal filled syringe. Additions of reagents to, or removal of materials from, the radiohalogenation vessel were conducted by passing a syringe needle through the septa.

Spectral Analyses. ^{1}H NMR and ^{11}B NMR spectra were obtained on a Bruker AV 500 (500 MHz) instrument. Proton chemical shifts are expressed as ppm using tetramethylsilane as an internal standard (δ = 0.0 ppm). Boron chemical shifts used $BF_3.OEt_2$ as an external standard. High-resolution mass spectral (HRMS) data were obtained on a Bruker APEX III 47e Fourier transform mass spectrometer using electrospray ionization. For analysis, the samples were dissolved in 50/50 MeOH/H_2O and were introduced by an integral syringe infusion pump (Cole Parmer series 74900).

Chromatography. All synthetic reactions were monitored by HPLC. Analytical samples were assessed on a system that contained a Hewlett-Packard quaternary 1050 gradient pump, a variable wavelength UV detector (254 nm), and an Alltech ELSD 2000 evaporative light-scattering detector (Deerfield, IL). Analyses of HPLC data were conducted using Hewlett-Packard *HPLC ChemStation* software. Reversed-phase HPLC chromatography was carried out on an Alltech Altima C-18 column (5 μm, 250 × 4.5 mm) using a gradient solvent system at a flow rate of 1 mL/min. A gradient of MeOH and 0.05 M Et_3NHOAc was used. Starting with 0% MeOH, the initial solvent mixture was increased to 100% MeOH over the next 15 min, then held at 100% MeOH for 5 min. Retention times (t_R) obtained under these conditions are provided in the experimental procedures.

Preparative chromatography was conducted on most nonradioactive compounds for purification. Purification was accomplished using a Biotage SP Flash Purification System (Charlottesville, VA) on a reversed-phase C18 Flash 25+M or 40+M column, eluting with a mixture of MeOH and 0.05 M triethylammonium acetate (Et_3NHOAc) in water. A gradient was used which started with 100% Et_3NHOAc and was increased over 20 min to 100% MeOH. Fractions containing the desired product were combined and evaporated to dryness under vacuum on a rotary evaporator.

The product mixtures from radioiodination reactions of **14** and **17a**−**17d** were analyzed by, and radioactive peaks containing [^{125}I]**15**, [^{131}I]**18a**, [^{125}I]**18b**, [^{125}I]**18c**, and [^{131}I]**18d** were isolated from, a radio-HPLC using a C-18 column (Altima C-18, 5 mm, 250 × 4.5 mm; Alltech, Deerfield, IL) eluting at a flow rate of 1 mL/min using the same gradient conditions as described for nonradioactive iodination products. It should be noted that the pH of the Et_3NHOAc elution buffer was brought to 7.2 due to concerns for cleaving the hydrazone moiety during isolation. The HPLC equipment used in the analyses consisted of a Hewlett-Packard quaternary 1050 gradient pump, Waters 601 UV detector, and a Beckman model 170 radioisotope detector. Analysis of the HPLC data was conducted on Hewlett-Packard *HPLC ChemStation* software. The retention times (t_R) of the radioiodinated compounds are provided in the Experimental Procedures.

Size exclusion HPLC (SE-HPLC) separations of the conjugates of Fab′ were obtained on a Hewlett-Packard isocratic system consisting of a model 1050 pumping system and a model 1050 Multiple Wavelength Detector (280 nm). Proteins were evaluated on a Protein Pak 300 SW glass size exclusion column (10 mm, 8 mm × 30 cm, Waters Corporation, Milford, MA) run at 1.0 mL/min eluting with 50 mM sodium phosphate buffer (pH 6.8) which contained 300 mM NaCl, 1 mM EDTA, and 1 mM sodium azide. Analyses of the HPLC data were conducted using Hewlett-Packard *HPLC ChemStation* software. Retention times (t_R) for Fab′ and their conjugates were ∼11 min.

Compound Syntheses. Preparations of the following compounds were conducted as previously described: $[Et_3NH]_2B_{10}H_{10}$;[31] $[Et_3NH]_2B_{10}H_9$−CO−C_6H_5, **9a**;[32] $[Et_3NH]_2B_{10}H_9$−CO−$C_6H_4CO_2H$, **9b**,[32] $[Et_3NH]_2B10H_9$−CO−C_6H_4OMe, **9c**.[32]

$[Et_3NH]_2B_{10}H_9$−CO−CH_3, 9d. A solution of $[Et_3NH]_2B_{10}H_{10}$ (2 g; 6.2 mmol) and acetyl chloride (10 mL; 141 mmol) in anhydrous CH_3CN (25 mL) was stirred at room temperature for 4 min. After that time, the solution was triturated with diethyl ether (100 mL) and filtered. The crude product was dissolved in MeOH/H_2O (1:1) and purified via Biotage (C18 FLASH 40+M column) to yield 1.55 g (69%) of a red tacky solid. ^{1}H NMR (CD_3OD, 500 MHz): δ −0.20−1.06 (m, 9H), 1.31 (t, J = 7.5 Hz, 18H), 1.95 (s, 3H), 3.22 (q, J = 7.5 Hz, 12H). ^{11}B NMR (CD_3OD, 106.4 MHz): δ 5.10 (1B), 2.42 (1B), −19.30 (1B), −22.90 (1B), −25.38 (1B), −26.14 (1B), −26.98 (1B), −27.90 (1B), −29.14 (1B), −29.98 (1B). [Attempts to obtain HRMS data were unsuccessful.] HPLC: t_R = 7.1 min.

$[Et_3NH]_2B_{10}H_9$−C(C_6H_5)═NNH−CO−C_6H_4−NH_2, 11. A solution of $[Et_3NH]_2B_{10}H_9$−CO−C_6H_5, **9a** (200 mg, 0.469 mmol), 4-aminobenzoic hydrazide, **10** (85 mg, 0.562 mmol), and MeOH (8 mL) was stirred at room temperature for 16 h. The crude product solution was purified directly via Biotage (C18 FLASH 25+M column) to yield 242 mg (92%) of **11**. ^{1}H NMR (CD_3OD, 500 MHz): δ −0.08−1.13 (m, 9H), 1.23 (t, J = 7.4 Hz, 18H), 3.09 (q, J = 7.4 Hz, 12H), 6.65 (d, J = 8.8 Hz, 2H), 7.15−7.17 (m, 3H), 7.61−7.63 (m, 2H), 7.69 (d, J = 8.8 Hz, 2H). ^{11}B NMR (CD_3OD, 160.4 MHz): δ 0.69 (2B), −23.24 (1B), −26.65 (7B). HRMS (ES$^-$) $C_{14}H_{22}B_{10}N_3O$ $(M+H)^-$ calcd: 358.2693. Found: 358.2688. HPLC: t_R = 10.5 min.

$[Et_3NH]_2B_{10}H_9$−C(C_6H_5)═NNH−CO−C_6H_4−NCS, 12. A solution of **11** (100 mg, 0.18 mmol), TCDI (46.7 mg, 0.262 mmol) and anhydrous DMF (4 mL) was stirred at room temperature for 1 h. The solution was washed with 20% EtOAc/hexanes (5 × 15 mL), dried under vacuum for 2 h to yield 106 mg (99%) of a light-yellow tacky solid. ^{1}H NMR (CD_3OD, 500 MHz): δ −0.12−1.34 (m, 9H), 1.25 (t, J = 7.3 Hz, 18H), 3.14 (q, J = 7.3 Hz, 12H), 7.19−7.22 (m, 3H), 7.36 (d, J = 8.8 Hz, 2H), 7.60−7.62 (m, 2H), 7.98 (d, J = 8.8 Hz, 2H). ^{11}B NMR (CD_3OD, 160.4 MHz): δ 2.69 (1B), 1.78 (1B), −21.78 (1B), −25.80 (7B). HRMS (ES$^-$) $C_{15}H_{20}B_{10}N_3OS$ $(M+H)^-$ calcd: 400.2258. Found: 400.2250. HPLC: t_R = 13.7 min.

$[Et_3NH]_2B_{10}H_9$−C(C_6H_5)═NNH−CO−C_6H_4−EDA−MAL, 14. MPS-EDA.TFA, **13** (85 mg, 0.26 mmol) was added to a solution of **12** (100 mg, 0.17 mmol), NEt_3 (56 μL, 0.40 mmol) and anhydrous DMF (6 mL). The resultant solution was stirred at room temperature for 2 h, then volatile materials were removed under vacuum by rotary evaporation. The crude product was dissolved in MeOH/water (1/1) and purified via Biotage (C18 FLASH 25+M column) to provide 92 mg (68%) of a colorless solid. ^{1}H NMR (CD_3CN, 500 MHz): δ −0.08−0.93 (m, 9H), 1.16 (t, J = 7.4 Hz, 18H), 2.96 (q, J = 7.4 Hz, 12H), 3.29−3.33 (m, 2H), 3.41−3.45 (m, 2H), 3.50−3.53 (m, 2H), 3.54−3.65 (m, 2H), 6.72 (s, 2H), 7.16−7.21 (m, 3H), 7.46−7.50 (m, 2 H), 7.54−7.57 (m, 2H), 7.88 (d, J = 8.7 Hz, 2H). ^{11}B NMR (CD_3CN, 160.4 MHz): δ 2.65 (1B), 1.82 (1B), −21.73 (1B), −25.72 (7B). HRMS (ES$^-$) $C_{24}H_{32}B_{10}N_6O_4S$ $(M+H)^-$ calcd: 611.3215. Found: 611.3236. HPLC: t_R = 11.2 min.

$[Et_3NH]_2B_{10}H_9$−C(R)═NNH−CO−dPEG$_4$-MAL, 17a−17d. A solution of MAL-dPEG$_4$-CONHNH-BOC, **16** (1 g, 1.885 mmol), and neat TFA (4 mL) was stirred at room temperature for 3 min. After volatile materials were evaporated by a stream of argon, the acyl hydrazine derivative was washed with 10% EtOAc/hexanes (2 × 15 mL), and dried under vacuum overnight to provide a colorless oil. HPLC: t_R = 9.4 min. This material was used in the next step without further purification.

A methanol solution of MAL-dPEG$_4$-$CONHNH_2$, **16** (TFA salt; 100 mg, 0.184 mmol), and $[Et_3NH]_2B_{10}H_9$−CO−R (0.184 mmol) was stirred at room temperature for 1−4 h, then the volatile materials were removed on a rotoevaporator under vacuum. The crude products (**17a**−**17d**) were dissolved in MeOH/water (1/1) and purified via Biotage (C18 FLASH 25+M column). The gradient mixture was composed of MeOH and 0.05 M triethylammonium acetate. Starting with 100% 0.05 M triethylammonium acetate, increased to 100% MeOH over the next 20 min).

17a: R = C_6H_5; reaction time = 4 h; 118 mg (77%) yield. ^{1}H NMR (CD_3CN, 500 MHz): δ −0.22−0.99 (m, 9H), 1.22 (t, J = 7.2 Hz, 18H), 2.36−2.46 (m, 4H), 3.03 (q, J = 7.2 Hz, 12H), 3.27−3.35 (m, 2H), 3.47−3.52 (m, 2H), 3.54−3.64 (m, 16H), 3.66−3.81 (m, 7H), 6.79 (s, 2H), 7.11−7.22 (m, 3H), 7.50−7.63 (m, 2H). ^{11}B NMR (CD_3CN, 106.4 MHz): δ 1.44 (2B), −22.79 (1B), −26.27 (7B). HRMS (ES$^-$) $C_{25}H_{43}B_{10}N_4O_8$ $(M+H)^-$ calcd: 637.4017. Found: 637.4048. HPLC: t_R = 11.6 min.

17b: R = C_6H_4−CO_2H; reaction time = 1 h; 107 mg (66%) yield. ^{1}H NMR (CD_3CN, 500 MHz): δ −0.33−0.84 (m, 9H), 1.18 (t, J = 7.3 Hz, 18H), 2.31−2.44 (m, 4H), 2.51, 2.55 (2d, J = 3.8 Hz, 1H), 2.78, 2.81 (2d, J = 8.4 Hz, 1H), 3.13 (q, J = 7.3 Hz, 12H), 3.20−3.32 (m, 3H), 3.45 (q, J = 5.0 Hz, 3H), 3.52−3.59 (m, 9H), 3.63−3.67 (m, 4H), 3.69−3.73 (m, 1H), 3.93 (dd, J = 3.8, 8.4 Hz,1H), 5.21 (s, 1H), 6.75 (s, 2H), 6.92 (s, 1H), 7.54 (d, J = 8.7 Hz, 1H), 7.79 (d, J = 8.7 Hz, 1H), 8.22 (s, 1H). ^{11}B NMR (CD_3CN, 106.4 MHz): δ 1.60 (2B), −22.79 (1B), −26.01 (7B). HRMS (ES$^-$) $C_{26}H_{43}B_{10}N_4O_{10}$ $(M+H)^-$ calcd: 681.3915. Found: 681.3897. HPLC: t_R = 9.8 min.

17c: R = $C_6H_4-OCH_3$; reaction time = 1 h; 129 mg (81%) yield. ^{1}H NMR (CD_3CN, 500 MHz): δ −0.27−0.93 (m, 9H), 1.24 (t, J = 7.4 Hz, 18H), 2.37−2.49 (m, 4H), 3.13 (q, J = 7.4 Hz, 12H), 3.21−3.25 (m, 2H), 3.40−3.45 (m, 2H), 3.48−3.61 (m, 16H), 3.64−3.72 (m, 4H), 3.80−3.89 (m, 3H), 6.74 (s, 1H), 6.75 (s, 1H), 6.88 (d, J = 8.8 Hz, 1H), 6.94 (d, J = 8.8 Hz, 1H), 7.68 (d, J = 8.8 Hz, 1H), 7.78 (d, J = 8.8 Hz, 1H). ^{11}B NMR (CD_3CN, 106.4 MHz): δ 5.36 (1B), 3.03 (1B), −19.33 (1B), −21.51 (1B), −24.75 (2B), −25.48 (2B), −26.15 (2B). HRMS (ES^-) $C_{26}H_{45}B_{10}N_4O_9$ $(M+H)^-$ calcd: 667.4123. Found: 667.4128. HPLC: t_R = 11.8 min.

17d: R = CH_3; reaction time = 1 h; 72 mg (50%) yield. ^{1}H NMR (CD_3CN, 500 MHz): δ −0.34−0.97 (m, 9H), 1.21 (t, J = 7.4 Hz, 18H), 1.88 (s, 3H), 2.32−2.45 (m, 4H), 3.05 (q, J = 7.4 Hz, 12H), 3.21−3.31 (m, 2H), 3.41−3.46 (m, 2H), 3.48−3.59 (m, 16H), 3.61−3.69 (m, 4H), 6.74 (s, 1H), 6.75 (s, 1H). ^{11}B NMR (CD_3CN, 160.4 MHz): δ 4.30 (1B), 0.26 (1B), −20.08 (1B), −24.18 (1B), −26.64 (2B), −27.45 (2B), −28.18 (2B). HRMS (ES^-) $C_{20}H_{41}B_{10}N_4O_8$ $(M+H)^-$ calcd: 575.3860. Found: 575.3868. HPLC: t_R = 10.5 min.

General Procedure for Preparing Iodinated HPLC Standards; $[Et_3NH]_2B_{10}H_8I-C(R)=NNH-CO-dPEG_4-MAL$, 18a−18d. A 12 μmol quantity (159 μL; 10 mg/mL in MeOH) of *N*-chlorosuccinimide (NCS) was added to a solution containing 24 μmol of the *closo*-decaborate(2-) derivative (**17a**−**17d**), 12 μmol of NaI (17.9 μL; 100 mg/mL in deionized H_2O), and 5% HOAc/MeOH (0.5 mL). The reaction solution was stirred at room temperature for 1 min, then 12 μmol $Na_2S_2O_5$ (113 μL; 20 mg/mL in deionized H_2O) was added and the resultant solution was stirred at room temperature for 1 min. A small quantity of iodinated product was isolated from an analytical HPLC column for mass spectral analysis and to be used as a HPLC retention time standard for the radioiodination reactions. The identity of each standard was confirmed by high-resolution mass spectral data.

18a: R = C_6H_5; HRMS (ES^-) $C_{25}H_{42}IB_{10}N_4O_8$ $(M+H)^-$ calcd: 763.2978. Found: 763.3029 . HPLC: t_R = 12.5 min.

18b: R = $C_6H_5-CO_2H$; HRMS (ES^-) $C_{26}H_{42}IB_{10}N_4O_{10}$ $(M+H)^-$ calcd: 807.2876. Found: 807.2867. HPLC: t_R = 11.7 min.

18c: R = $C_6H_5-OCH_3$; HRMS (ES^-) $C_{26}H_{44}IB_{10}N_4O_9$ $(M+H)^-$ calcd: 793.3084. Found: 793.3100. HPLC: t_R = 12.3 min.

18d: R = CH_3; HRMS (ES^-) $C_{20}H_{40}IB_{10}N_4O_8$ $(M+H)^-$ calcd: 701.2821. Found: 701.2809. HPLC: t_R = 11.9 min.

General Procedure for Preparing [^{125}I]15, [^{131}I]18a, [^{125}I]18b, [^{125}I]18c, and [^{131}I]18d. To 50 μL of 1.0 mg/mL solution of the **14**, **17a**, **17b**, **17c**, or **17d** dissolved in a MeOH/2.5% HOAc mixture was added 1.1−1.4 mCi of Na[^{125}I]I or Na[^{131}I]I in 0.1 N NaOH. To this mixture was added 20 μL of 1 mg/mL *N*-chlorosuccinimide solution. The reaction was allowed to proceed at room temperature for 1 min, then 20 μL of 1 mg/mL sodium metabisulfite solution was added to quench. To this solution was added 50 μL of PBS and the volume was reduced to 50% under a stream of argon. The solutions containing radioiodinated derivatives ([^{125}I]**15**, [^{131}I]**18a**, [^{125}I]**18b**, [^{125}I]**18c**, or [^{131}I]**18d**) were used directly in the subsequent conjugation reactions.

Preparation of 107−1A4 and Its F(ab′)$_2$ Fragment. The monoclonal antibody 107−1A4, an IgG_1 mAb, which is reactive with the prostate-specific membrane antigen found in prostate tissue and upregulated in prostate cancer,[33] was obtained and purified as previously described.[28] The F(ab′)$_2$ fragment was prepared from intact mAb by digestion using pepsin (5.2 μg/mL in 80 mM NaOAc, pH 3.9) at 37 °C for 24 h. The F(ab′)$_2$ produced was purified on a Protein A column followed by a Fractogel TMAE column (EM Science, Gibbstown, NJ). The purified F(ab′)$_2$ was stored at refrigerator temperature. The 107−1A4 F(ab′)$_2$ was converted to Fab′-SH just prior to conjugation as described in the Experimental Procedures below.

Preparation of Fab′-SH Conjugate, 19. To 1.5 mL of 2.9 mg/mL F(ab′)$_2$ in PBS was added 60 μL of 100 mM DTT to make a final concentration of 4 mM DTT. This was gently mixed for 45 min at room temperature before passing through a PD-10 column eluting with PBS pH 6.5 with 1 mM EDTA. Protein containing fractions were combined to give 5 mL at 0.77 mg/mL Fab′-SH.

To 2.5 mL (1.9 mg; 0.038 μmol) of the Fab′-SH was added 30 μL of 11 mg/mL (0.33 mg; 0.48 μmol) **17b** in DMF. After 30 min at room temperature, a 10 μL aliquot of a 23.8 mg/mL *N*-ethylmaleimide (NEM) solution in DMF was added to react with the remaining sulfhydryl groups. After 10 min at room temperature, the mixture was split in half and each half was run over a PD-10 column. The protein fractions, containing **19**, were eluted in PBS and combined to yield 1.3 mg (64% protein recovery).

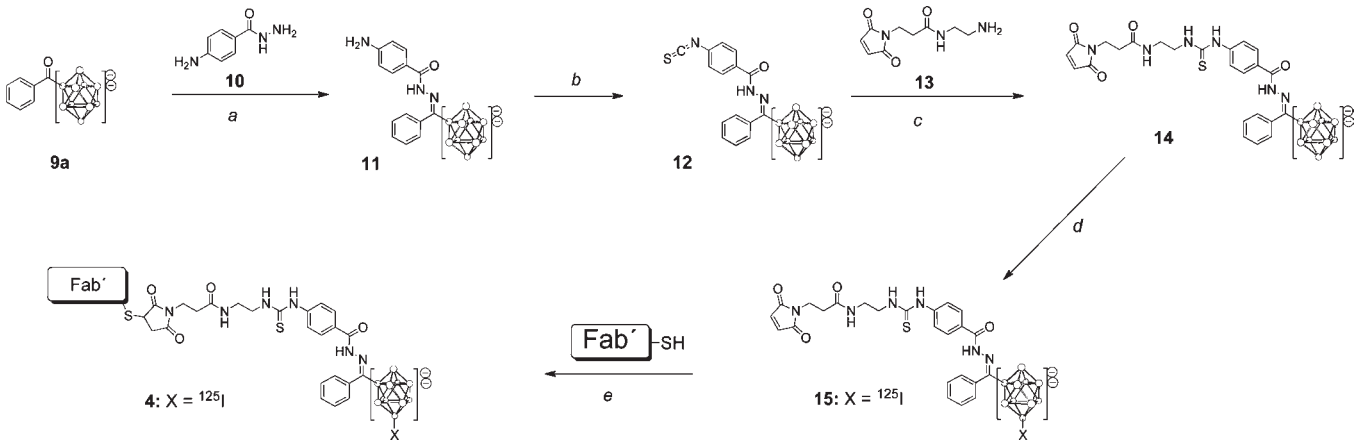
General Procedure for Conjugating [^{125}I]15, [^{131}I]18a, [^{125}I]18b, [^{125}I]18c, or [^{131}I]18d with 107−1A4 Fab′-SH. To 357 μL of 8.4 mg/mL 107−1A4 F(ab′)$_2$ in PBS was added 14.3 μL of 100 mM DTT to make a final concentration of 4 mM DTT. This was gently mixed for 45 min at room temperature before eluting over a PD-10 column (Sephadex G-25) with PBS pH 6.5 with 1 mM EDTA. Protein containing fractions were combined to give 2.5 mL at 1.25 mg/mL Fab′-SH.

A 0.5 mL aliquot of the Fab-SH solution was added to a PBS solution containing [^{125}I]**15**, [^{131}I]**18a**, [^{125}I]**18b**, [^{125}I]**18c**, or [^{131}I]**18d**. After 30 min at room temperature, 13 μL of 2 mg/mL *N*-ethylmaleimide in DMSO was added to cap the remaining sulfhydyl groups. After another 10 min at room temperature, the reaction mixture was passed over a PD-10 column by eluting with PBS. The protein-containing fractions were combined to give 85% recovery of protein with 30−40% radiochemical yields for [^{125}I]**15**, [^{131}I]**18a**, [^{125}I]**18b**, [^{125}I]**18c**, or [^{131}I]**18d**.

Assessment of Fab′-Hydrazone Cleavage with Acid. Fab′ conjugates [^{125}I]**3** and [^{125}I]**6a** were prepared by radioiodination of *N*-(15-(aminoacyldecaborate)-4,7,10-trioxatri-decanyl)-3-maleimidopriopionamide[17] and **17b**, respectively, followed by conjugation with Fab′ and purification as described above. Aliquots of the purified radioiodinated Fab′ conjugates (100 μL, 20 μg/2−6 μCi) were placed in three vials containing 200 μL of 50 mM sodium acetate solutions adjusted to pH 7, 4.5, and 2.0 using HCl. The radioiodinated Fab′ conjugate solutions were incubated at 37 °C for 26 h. Samples taken at 1, 4, and 26 h were placed in ultracentrifugation filters (Microcon YM-10), spun at 10 000 rpm for 10 min, then washed 3× with 200 μL PBS. The retentate and filtrate were counted in a gamma counter to provide the percent radioactivity bound to the protein.

Preparation of [^{125}I]6a by Direct Labeling. To 25 μL of 500 mM sodium phosphate pH 7.4 was added ~1 μL (157 μCi) Na[^{125}I]I in 0.1 N NaOH. To this, 22 μL of **19** (6.9 mg/mL) was added, followed by 10 μL of a solution containing 1 mg/mL chloramine-T in water. After 1 min at room temperature, the reaction was quenched with 10 μL of 1 mg/mL sodium metabisulfite in H_2O solution. The mixture was eluted on a NAP-10 column (Sephadex G-25) with PBS. The protein fractions were combined to give 149 μCi (95% radiochemical yield) of [^{125}I]**6a**.

Scheme 1[a]



[a] (a) MeOH, rt, 16 h, 92%; (b) TCDI, anhyd. DMF, rt 1 h, 99%; (c) **13**, Et_3N, anhyd. DMF, rt, 2 h, 68%; (d) MeOH, HOAc, Na[^{125}I]I, NCS, rt, 1 min; (e) Fab′-SH/PBS, 30 min, rt, NEM/DMSO, 10 min, rt.

Preparation of [^{211}At]6b. To 200 μL of 500 mM sodium phosphate pH 7.4 was added 300 μL (573 μCi) of Na[^{211}At]At solution, pH 9. To this, 22 μL of **19** (6.9 mg/mL) was added, followed by 50 μL of 1 mg/mL chloramine-T in H_2O. After 1 min at room temperature, the reaction was quenched with 50 μL of 1 mg/mL sodium metabisulfite in water. The mixture was run over a PD-10 column eluting with PBS. The protein fractions were combined to give 367 μCi (64% radiochemical yield) of [^{211}At]**6b**.

Biodistribution Studies. Biodistribution studies were conducted under a protocol approved by the Institutional Animal Care and Use Committee (IACUC) at the University of Washington. Male nude (nu/nu) and C.B.-17 SCID mice, obtained from Charles River Laboratories (Hollister, CA), were housed for 1 week in the isolator facility prior to beginning the study. The biodistribution experiments were conducted, when possible, by evaluation of two compounds (dual labeled; ^{125}I and ^{131}I, or ^{125}I and ^{211}At) in a single set of mice to decrease the number of mice required for the study. In the initial biodistribution studies, nude mice were injected with [^{125}I]**4**, an admixture containing [^{131}I]**5**/[^{125}I]**6** or an admixture containing [^{125}I]**7**/[^{131}I]**8**. The admixtures were prepared to provide a total of 30 μg of Fab′ conjugate having preset amounts of μCi of each radiolabeled compound. A later experiment evaluated an admixture of the directly labeled [^{125}I]**6a** and [^{211}At]**6b** in mice bearing the LNCaP tumor xenografts. The radioactive admixtures were diluted with phosphate buffered saline (PBS) to prepare an injection volume of ~100 μL and were injected into each of the nude mice via the lateral tail vein. The actual amount of injectate each animal received was determined by weighing the administering syringe before and after injection. Groups of 3−5 mice were sacrificed by cervical dislocation (under anesthesia) at 1 and 4 h post injection. The tissues were excised, blotted free of blood, weighed, and counted. Blood weight was estimated to be 6% of the total body weight.[34] Calculation of percent injected dose (%ID) and percent injected dose per gram (%ID/g) for the collected tissues was accomplished using internal standards for ^{125}I, ^{131}I, or ^{211}At counts. The full data obtained in each biodistribution study, including amounts injected, animal weights, and results of statistical significance (using Student's *t* test) are provided as Tables S1−S4 in the Supporting Information.

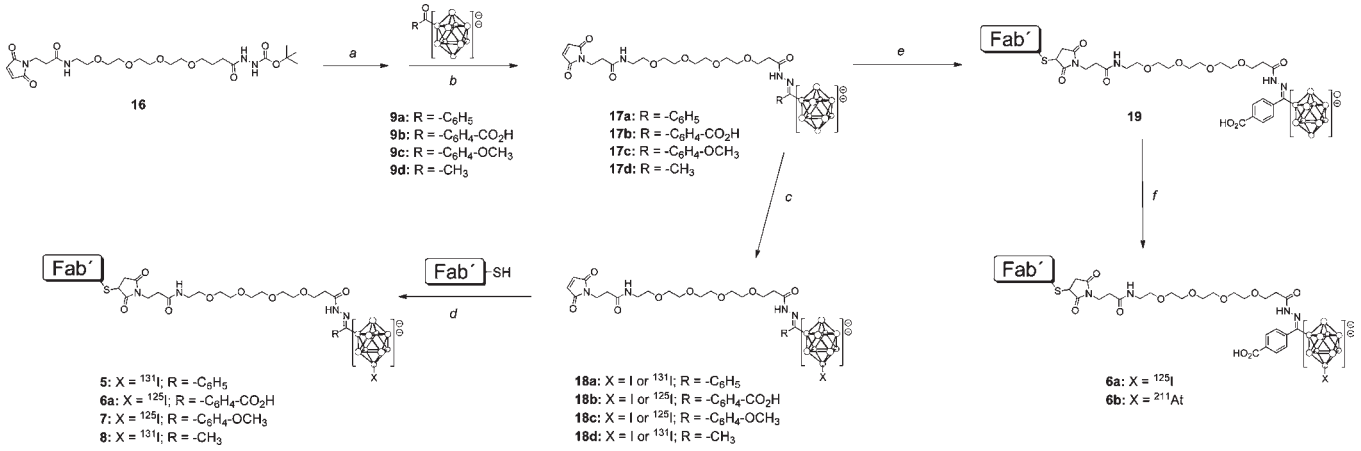
RESULTS

Syntheses of Maleimido-*closo*-decaborate(2-) Derivatives. Five *closo*-decaborate(2-) derivatives containing the maleimide functionality were targeted for conjugation with Fab′-SH. The synthetic pathways used to prepare the maleimido-*closo*-decaborate(2-) derivatives **14**, **17a**, **17b**, **17c**, and **17d** are shown in Schemes 1 and 2.

The initial synthesis was conducted to prepare the maleimide derivative **14**, as shown in Scheme 1. The first step to prepare **14** involved formation of the hydrazone functionality by reaction of *para*-aminobenzoic hydrazide, **10**, in MeOH at room temperature for 16 h with the readily prepared triethylammonium salt of the benzoyl adduct of *closo*-decaborate(2-) **9a**.[32] A 92% yield of the adduct **11** was obtained. Following that step, the aniline was converted to an isothiocyanate by reaction with thiocarbonyldiimidazole (TCDI) in anhydrous DMF. The crude isolated isothiocyanate derivative **12** was reacted with commercially available *N*-(2′-aminoethyl)-3-(maleimido)propionamide, **13**, to provide 68% of **14** after purification by reversed-phase flash chromatography.

In the structures of maleimido-*closo*-decaborate(2-) derivatives **17a**, **17b**, **17c**, and **17d**, the hydrazone functionality was changed from a phenacyl hydrazone (in **14**) to an alkyl acyl hydrazone to alter the sensitivity to acid cleavage. Within the group of compounds the nature of the functional group (R) bonded with the ketone carbon of the hydrazone was varied (i.e., phenyl, benzoate, anisole, and methyl) for the same purpose. A poly(ethylene glycol) (PEG) linker was incorporated to improve the aqueous solubility of the conjugation molecule. To simplify the syntheses, a commercially available PEG derivative (**16**) that contained both maleimide and acyl hydrazone functionalities was used. Thus, a one-pot, two-step synthesis could be used to prepare *closo*-decaborate(2-)-containing maleimide derivatives **17a**, **17b**, **17c**, and **17d**, as shown in Scheme 2. In those syntheses, the commercially available tBoc protected maleimido-dPEG$_4$-acylhydrazide, **16**, was deprotected in neat TFA, then that crude product was directly reacted with the readily prepared acyl derivatives of *closo*-decaborate(2-), **9a**−**9d**,[32] in MeOH at room temperature for 1−4 h to provide 50−81% yields of **17a**−**17d**.

Scheme 2[a]



[a] (a) TFA, rt, 3 min; (b) MeOH, **16** (TFA salt), **9a**, **9b**, **9c**, or **9d**, rt, 1−4 h, 50−81%; (c) NaI or Na[$^{125/131}$I]I, MeOH, HOAc, NCS, rt, 1 min; (d) Fab′-SH/PBS, 30 min, rt, NEM/DMSO, 10 min, rt, 30−40%; (e) Fab′-SH/PBS, **17b**/DMF, 30 min, rt, NEM/DMF, 10 min, rt, 64%; (f) sodium phosphate (0.5 M, pH 7.4), Na[^{125}I]I or Na[^{211}At]At, ChT, 1 min, $Na_2S_2O_5$, 95% and 64%, respectively.

Radioiodination of Maleimido-*closo*-decaborate(2-) Derivatives. Prior to incorporation of radioiodine, **14**, **17a**, **17b**, **17c**, and **17d** were iodinated by reaction of *N*-chlorosuccinimide (NCS) and NaI in 5% HOAc/MeOH solution. Small quantities of the iodinated product were obtained for use as HPLC retention time standards in the radioiodination studies. The nonradioactive iodinated derivatives were isolated using analytical reversed-phase HPLC. The identities of the isolated iodinated products were confirmed by high-resolution mass spectrometry.

Radioiodination reactions were conducted by reacting 50 μg quantities of the maleimido-*closo*-decaborate(2-) derivatives **14**, **17a**, **17b**, **17c**, and **17d** with 1−1.4 mCi of Na[^{125}I]I or Na[^{131}I]I in MeOH/2.5% HOAc and *N*-chlorosuccinimide to form [^{125}I]**15**, [^{131}I]**18a**, [^{125}I]**18b**, [^{125}I]**18c**, and [^{131}I]**18d**. After 1 min reaction time, sodium metabisulfite was used to quench the reaction. The MeOH solutions were diluted with phosphate buffered saline, and that solution was reduced to 50% volume under a stream of argon to remove organics. The crude isolated radioiodinated products were used directly in the Fab′ conjugation reactions.

Conjugation of Maleimido-*closo*-decaborate(2-) Derivatives. The protein used in the investigation was a Fab′ fragment of the anti-PSMA antibody, 107−1A4.[28] To prepare the Fab′ fragment, the intact antibody was digested following standard procedures employing pepsin at 37 °C for 24 h to form the F(ab′)$_2$ fragment. The F(ab′)$_2$ fragment was purified on a Fractogel column and was stored at refrigerator temperature until used. Just prior to running the conjugation reactions, the F(ab′)$_2$ was converted to the Fab′-SH fragment by reducing with 4 mM dithiothreitol (DTT) for 45 min at room temperature. After reduction, the Fab′ was purified over a size exclusion column (PD-10).

Radioiodinated maleimido-*closo*-decaborate(2-) derivatives [^{125}I]**15**, [^{131}I]**18a**, [^{125}I]**18b**, [^{125}I]**18c**, and [^{131}I]**18d** were reacted with Fab′-SH for 30 min at room temperature, then *N*-ethylmaleimide (NEM) was added to cap any unreacted thiol groups. The radioiodinated Fab′ conjugates were purified by elution on size exclusion columns. This overall radiolabeling procedure provided isolated radiochemical yields of 30−40% for [^{125}I]**4**, [^{131}I]**5**, [^{125}I]**6**, [^{125}I]**7**, and [^{131}I]**8**.

A nonradioactive Fab′ conjugate was prepared by reaction with the maleimido-*closo*-decaborate(2-) derivative **17b** with 107−1A4 Fab′-SH. The selection of Fab′ conjugated with maleimide derivative containing a benzoic acid moiety adjacent to the hydrazone, **17b**, was made based on the favorable biodistribution of its radioiodinated counterpart (see Figure 2). The conjugation reaction was conducted with a ratio of 1 Fab′-SH to 13 equiv of **17b**. The conjugation was allowed to run for 30 min at room temperature, then the remaining thiols were capped with NEM and the conjugate was purified by size-exclusion chromatography (PD-10). The isolated Fab′ conjugate was analyzed by size-exclusion HPLC to determine the peak shape, retention time, and number of species present.

Fab′-Hydrazone Cleavage with Acid. Fab′ conjugates [^{125}I]**3** and [^{125}I]**6a** were incubated at 37 °C in 50 mM sodium acetate solutions adjusted to pH 7, 4.5, and 2.0 for 26 h to assess the cleavage of the hydrazone functionality in [^{125}I]**6**. The control (noncleavable) Fab′ conjugate, [^{125}I]**3**, had no cleavage (97−98% protein-bound activity) after 26 h. However, acid-promoted cleavage (99% protein-bound at pH 7.0; 81% protein-bound at pH 4.5; 70% protein-bound at pH 2.0) was observed for the Fab′ conjugate, [^{125}I]**6a**, after 26 h of incubation time.

Radiohalogenation of Fab′-SH Conjugate 19. Direct radiohalogenation of Fab′ conjugate **19** was accomplished with ^{125}I and ^{211}At. Radioiodination of **19** was accomplished by reaction of Na[^{125}I]I and chloramine-T (ChT) for 1 min at room temperature. After quenching the reaction with sodium metabisulfite, elution of the labeled Fab′ conjugate over a size-exclusion column provided a 95% isolated radiochemical yields of [^{125}I]**6a**. Similarly, astatination of **19** was accomplished by reaction of Na[^{211}At]At with ChT for 1 min at room temperature to provide a 64% isolated radiochemical yield of [^{211}At]**6b** after quenching and purification.

Biodistributions of Radiolabeled Fab′-SH Derivatives. Three biodistribution studies were conducted using hydrazone-containing radioiodinated Fab′ conjugates to determine if the concentrations of radioiodine localized to kidney were effected by the inclusion of the hydrazone moiety. Dual-label biodistribution studies were conducted where possible to minimize the use of animals in the study. Thus, the initial three biodistribution

dx.doi.org/10.1021/bc1005625 |*Bioconjugate Chem.* 2011, 22, 1089–1102

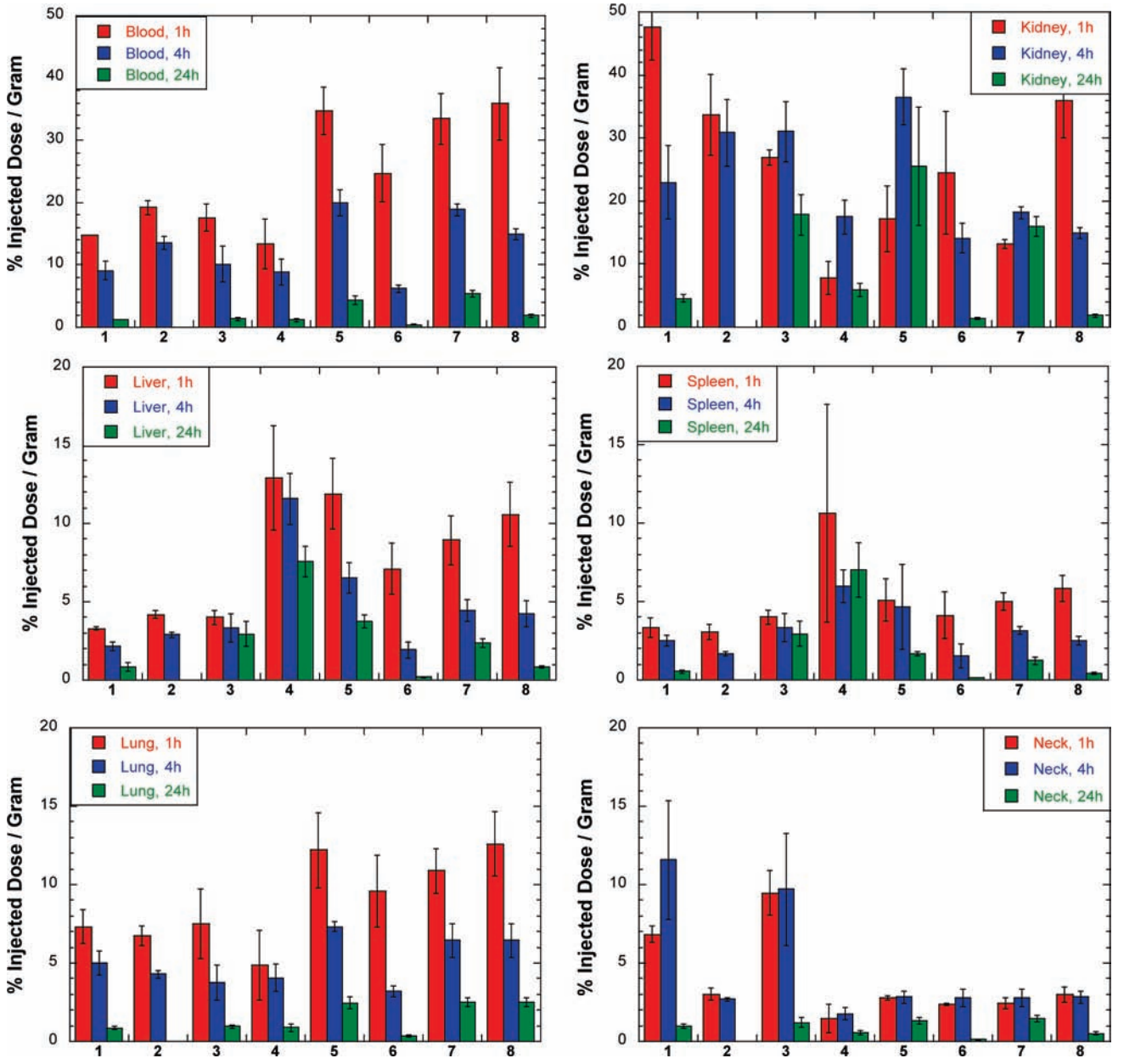


Figure 2. Bar graphs representing tissue concentrations (% ID/g) of radioiodinated 107−1A4 Fab′ and radioiodinated 107−1A4 Fab′ conjugates in selected tissues. The numbers on the *x*-axis represent the radioiodinated Fab′ derivatives depicted in Figure 1. Data plotted for directly labeled Fab′-NEM, [^{125}I]**1**, *para*-iodobenzoate-labeled Fab′-S-NEM, [^{125}I]**2**, and noncleavable radioiodinated Fab′-SH conjugate [^{125}I]**3** were obtained from the literature.[17] Data plotted for hydrazone-containing conjugates [^{125}I]**4**, [^{131}I]**5**, [^{125}I]**6a**, [^{125}I]**7**, and [^{131}I]**8** were obtained in this study. Identification of the tissue graphed is provided in the boxed legend within the graph. The percent injected dose/gram (%ID/g) values shown in each bar are average values in that tissue for 3−5 mice, and the error bars represent the standard deviation of those values. The first bar (red) represents values obtained at 1 h post injection (pi), the second bar (blue) represents values obtained at 4 h pi, and the third bar (green) represents values obtained at 24 h pi. Note that the range in %ID/g for the blood and kidney graphs (top) is 0−50%ID/g, whereas the range for the other 4 graphs is 0−20% ID/g. The data plotted in the bar graphs are provided as Tables S1, S2, and S3 in Supporting Information.

studies evaluated the following Fab′ conjugates: (1) [^{125}I]**4**; (2) [^{131}I]**5** and [^{125}I]**6a**; (3) [^{125}I]**7** and [^{131}I]**8**. The amount of protein injected into each mouse was kept constant throughout the groups (i.e., 30 μg/mouse). It was of high interest to compare the results obtained in this investigation with previous results obtained with a noncleavable maleimido-*closo*-decaborate(2-) Fab′ conjugate, [^{125}I]**3**. It was also of interest to compare the biodistribution results obtained in this study with results obtained from direct radioiodination, [^{125}I]**1**, and conjugation of a *para*-[^{125}I]iodobenzoate derivative, [^{125}I]**2** with the same Fab′. To highlight the comparison, the tissue concentrations (% injected dose/gram) of [^{125}I]**4**, [^{131}I]**5**, [^{125}I]**6a**, [^{125}I]**7**, and [^{131}I]**8** have been plotted along with published data for [^{125}I]**1**, [^{125}I]**2**, and [^{125}I]**3**. The comparison graphs for selected tissues are provided in Figure 2. The radioiodine concentrations obtained for selected tissues and blood in this study are provided as Tables S1, S2, and S3 in Supporting Information.

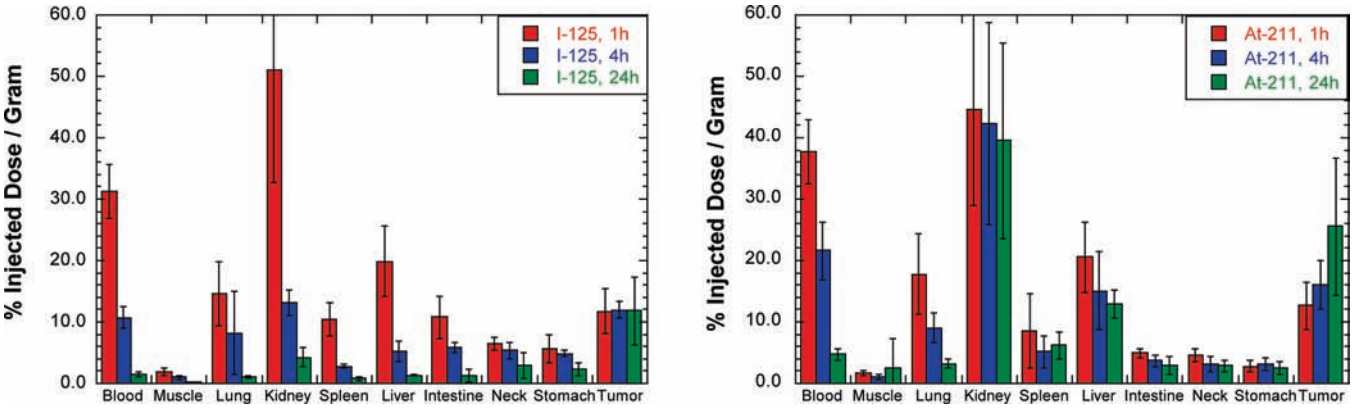


Figure 3. Bar graphs depicting the tissue concentrations (%ID/g) of [^{125}I]**6a** (left panel) and [^{211}At]**6b** (right panel). The Fab′-SH conjugates were prepared, then directly labeled with ^{125}I and (separately) ^{211}At. The labeled Fab′ conjugates were mixed and coadministered so that tissue comparisons could be made in the same animal. Each bar represents the average %ID/g obtained in a group of 5 mice for that radionuclide in a selected tissue, and the error bars represent the standard deviation of those values. The red bars are tissue concentrations at 1 h post injection (pi), blue bars at 4 h pi, and green bars at 24 h pi. The radionuclide being represented is shown in the boxed legend within the graph. The complete set of data for the values plotted are provided as Table S4 in the Supporting Information.

When examining the tissue concentrations in Figure 2, the values for tissue concentrations of Fab′ conjugates **1**, **2**, and **3** (from literature) should not be compared directly with those of Fab′ conjugates **4** through **8** evaluated in this study, as the studies were not conducted under exactly the same conditions. In general, it appears that the reported concentrations of radioiodinated Fab′ **1** through **3** are lower in most tissues than those obtained in this study for radioiodinated Fab′ conjugates **4** through **8**, except kidney and neck. The reasons for the differences are not known. While the relative concentrations are not evaluable, trends regarding clearance of radioiodine from tissues can be compared for all of the Fab′ conjugates. The tissue of highest interest in this study is kidney, as the high localization of radioactivity to that tissue is dose limiting for radiolabeled Fab′. In the mouse model, radioiodinated Fab′ [^{125}I]**1** produced by direct labeling of tyrosine residues was highly localized in kidney, but was cleared from that tissue within 24 h. In contrast to this, Fab′ conjugates [^{125}I]**2** and [^{125}I]**3** prepared by a two-step method using a *para*-[^{125}I]iodobenzoyl labeling reagent, or direct labeling after conjugation of a maleimido-*closo*-decaborate(2-) reagent, had little kidney clearance over a 24 h period.

It can be noted in Figure 2 that the kidney concentrations and clearance for Fab′ conjugates [^{125}I]**4**, [^{131}I]**5**, [^{125}I]**6a**, [^{125}I]**7**, and [^{131}I]**8** varied considerably. The concentration of [^{125}I]**4** in kidney was low, and appeared to clear over the 24 h period. With exception of the liver, there was a lower concentration of [^{125}I]**4** relative to [^{131}I]**5**, [^{125}I]**6a**, [^{125}I]**7**, and [^{131}I]**8** in the other tissues. The lower tissue concentrations may be an indication that the hydrazone in [^{125}I]**4** has a lower overall in vivo stability. The higher liver concentrations seen for [^{125}I]**4** may be due to a higher lipophilicity of the conjugate metabolites. The kidney concentrations of [^{131}I]**5** and [^{125}I]**7** did not decrease significantly over the 24 h period, indicating either that the hydrazone was not as readily cleaved or that the metabolites were retained. In contrast, kidney concentrations of [^{125}I]**6a** and [^{131}I]**8** decreased dramatically over the 24 h period. Indeed, the clearance from kidney of [^{125}I]**6a** and [^{131}I]**8** was similar to that seen with directly labeled Fab′ (i.e., [^{125}I]**1**).

A fourth biodistribution was conducted in nude mice bearing LNCaP human prostate cancer xenografts to compare the pharmacokinetics, tissue concentrations, and tumor localization of [^{125}I]**6a** and [^{211}At]**6b**. The results of that study are depicted in the bar graphs shown in Figure 3, and the data are provided as Table S4 in Supporting Information. In the coinjected, dual-labeled (^{125}I and ^{211}At) study, it was anticipated that the distribution of ^{125}I and ^{211}At would be very similar, as that had been the case in most prior studies using *closo*-decaborate(2-) protein conjugates and small molecules. It is apparent in Figure 3 that kidney (and liver) retention is much higher in the ^{211}At-labeled Fab′ conjugate. Interestingly, while the tumor concentration appeared to stay constant in the ^{125}I-labeled Fab′ conjugate, the concentration was higher and increased with time in the ^{211}At-labeled Fab′ conjugate.

DISCUSSION

An objective in our laboratory is to obtain a tumor-targeting agent for use with ^{211}At that has a blood half-life similar (e.g., 6−8 h) to the physical half-life of ^{211}At (7.21 h), so that tumor masses can be readily penetrated and an efficient delivery of that radionuclide to the tumor can be obtained. Intact MAbs have relatively long biological half-lives and do not penetrate tumors within a half-life of ^{211}At, making them unattractive as carriers of ^{211}At (for most cases). In contrast, small proteins (25 kDa or less) and peptides penetrate tumor masses readily, but are rapidly cleared from blood, so only a small fraction of the injected radioactivity gets to the tumor site(s). This latter point is important, as cost and availability of ^{211}At must be considered in developing a reagent that uses it. This makes mAb fragments, such as Fab′, of high interest as cancer targeting agents for ^{211}At, since they are small enough to penetrate tumors and have a long enough biological half-life (e.g., 6.8 h in mice[35]).

Our investigation of ^{211}At endoradiotherapy was hampered for a number of years by the fact that many ^{211}At-labeled tumor-targeting agents undergo deastatination in vivo, including Fab′ fragments.[16] However, more recently we demonstrated that switching from bonding of the ^{211}At with an aromatic carbon atom to bonding with a boron atom in an aromatic boron cage moiety provides high in vivo stability toward deastatination.[17,31,36] Of the boron cage moieties evaluated, the nonahydro-*closo*-decaborate

(2-) cage has become the ^{211}At-labeling moiety of choice, because it (a) is easily prepared, (b) is very reactive with electrophilic halogens, (c) is quite stable in vivo, and (d) appears to have minimal affect on the biodistribution of compounds studied. Although only small differences in biodistribution of radiohalogens are observed with *closo*-decaborate(2-) conjugates, it has been noted that the radiohalogens localized to kidney and/or liver can have slow clearance from those tissues.

In previous studies, we found that mAb Fab′ fragments conjugated with a noncleavable *closo*-decaborate(2-) moiety can have in vivo pharmacokinetics and tissue distributions that are quite different from the same protein directly labeled with radioiodine.[17] The difference is particularly noticeable in kidney. That difference can be readily seen in Figure 2 (top right panel), where the concentration of radioiodine-labeled Fab′, [^{125}I]**1**, decreases over a 24 h period, whereas in a radioiodinated Fab′ containing a noncleavable *closo*-decaborate(2-) conjugate, [^{125}I]**3**, the radioactivity is generally retained over that time period. It seems unlikely that the longer kidney retention is due to the dianionic *closo*-decaborate(2-) moiety, as similar kidney retention is observed when the same mAb Fab′ is radioiodinated using *N*-hydroxysuccinimidyl *para*-[^{125}I]iodobenzoate (to give [^{125}I]**2**). The retention of radiohalogens in kidney prompted us to survey literature approaches for diminishing the uptake of ^{211}At-labeled Fab′ or, alternatively, for releasing metabolites from kidneys.

Several different approaches have been studied to reduce renal localization and retention of radiolabeled proteins, their enzymatically produced fragments, and genetically engineered fragments.[23,37,38] An attractive approach is to decrease uptake of ^{211}At-labeled Fab′ without alteration of the Fab′ or labeling molecule. Such an approach, that of infusing basic amino acids, has been investigated for Fab′,[39−44] however, that approach can be difficult to control and the decrease in kidney concentration may not be enough to be useful for ^{211}At-labeled Fab′ (although it might be useful in combination with other approaches). Since it did not appear that infusion of basic amino acids would provide adequate clearance, approaches where the Fab′ was modified were considered. One possible modification would be to conjugate another molecule (e.g., large poly(ethylene glycol)) to the Fab′, such that its modified size/shape would block filtration by the glomerulus. Although attractive as an approach, based on literature reports we surmised that approach would likely lead to a loss of immunoreactivity of the Fab′ before complete blockage of filtration was achieved.[45] Likewise, alteration of the pI on the Fab′ by succinylation[46] or glycolation[47−49] also seemed likely to have a negative affect its antigen binding.

An alternate approach to blocking uptake in the kidney is to build functional groups into conjugation reagents that can be cleaved in the kidney to provide metabolites that are more readily cleared from kidneys. Several approaches have been described in the literature for decreasing the retention of radioactivity in the kidney after administration of radiolabeled antibodies or their fragments.[37,50] In one approach, investigators used enzymatically based methods to decrease the retention of radiolabeled molecules in the kidney. Those methods are based on the use of conjugation linkers containing esters susceptible to esterases[51−55] or specific peptide sequences that can be cleaved by pepidases.[56−61] While enzyme-mediated release of radioactive metabolites from kidneys functioned as designed, the results (kinetics and kidney concentrations) point to the need to explore additional methods. An alternate method is the use the low pH in lysosomes (pH 4.5−5.0[62,63]) for release of radioactivity from kidneys. That method was of particular interest, as the cleavage process is nonspecific and release kinetics can be optimized by chemical modification of the acid-cleavable chemical functionality. It has been shown that lysosomal pH can be used for release of drugs from antibodies.[27] While pH-sensitive *cis*-aconatyl[64] and acetal[65] linkages have been described, the use of readily prepared hydrazone-linked antibody−drug conjugates[66−70] appeared most promising.

Prior to this study, we evaluated the tissue distributions of a series of radioiodinated *closo*-decaborate(2-) compounds in mice to determine which structural features provided the lowest tissue concentrations.[32] In that study, compounds containing a hydrazone moiety had favorable pharmacokinetics and low tissue concentrations. While the study did not provide information that could be directly used to predict tissue distributions of metabolites of Fab′ radioiodinated on a *closo*-decaborate (2-) moiety, it did provide information on the distribution of radioiodinated hydrazone derivatives that were introduced into blood. The rapid clearance from blood and release of radioiodine from kidney encouraged us to prepare and evaluate radiolabeled Fab′ conjugated with sulfhydryl-reactive *closo*-decaborate(2-) derivatives containing a hydrazone functionality. In this study, mAb Fab′ fragments were used because they are of interest not only as a carrier molecule, but also as a model where differences in clearance rates between the radiohalogenated proteins could readily be observed.

Radioiodinated Fab′-hydrazone-*closo*-decaborate(2-) conjugates [^{125}I]**4**, [^{131}I]**5**, [^{125}I]**6a**, [^{125}I]**7**, and [^{131}I]**8** were prepared for the study using a two-step labeling approach. Radioiodinations of the maleimido-derivatives (**14**, **17a**, **17b**, **17c**, and **17d**) were conducted prior to conjugation with the Fab′ to ensure that all of the radioiodine was on the *closo*-decaborate(2-) moiety. By doing this, the interpretation of the tissue clearance was not confounded by having some of the radioactivity on protein tyrosine residues. In prior studies, thyroid and stomach concentrations of mAb fragments radioiodinated after conjugation with *closo*-decaborate(2-) indicated that some of the radioiodine reacted with protein tyrosine residues. Importantly, in those studies it appears that more than one *closo*-decaborate(2-) per antibody conjugate is required to ensure that the radioiodine only reacts with that moiety.

The data depicted in tissue bar graphs shown in Figure 2 show that the hydrazone-containing Fab′ conjugates, [^{125}I]**6a** and [^{131}I]**8**, have kidney clearance rates similar to that of directly (tyrosine) labeled Fab′, [^{125}I]**1**. Although the blood clearances are similar, Fab′ conjugates [^{125}I]**4**, [^{131}I]**5**, and [^{125}I]**7** have kidney localization and retention profiles that are very different from [^{125}I]**6a** and [^{131}I]**8**, or directly labeled [^{125}I]**1**. Tissue concentrations for [^{125}I]**4** are lower in general than for the other conjugates, with the exception of liver and spleen concentrations. Those concentrations are higher than for the other conjugates, perhaps indicating that some aggregation or serum protein binding occurred with the Fab′ conjugate or its metabolites. Release of ^{125}I from the liver also appears to be most efficient for [^{125}I]**6a** and [^{131}I]**8**. The only other major differences were seen in the neck (containing thyroid), where directly labeled [^{125}I]**1** was high at 1 and 4 h pi, as expected. As indicated previously, the high concentration of ^{125}I in neck for the noncleavable *closo*-decaborate(2-) conjugate [^{125}I]**3** may be attributable to some of the ^{125}I reacting with tyrosine residues on the Fab′ conjugate rather than the *closo*-decaborate(2-) cage. From these data, it was concluded that Fab′ conjugates [^{125}I]**6a** and [^{131}I]**8** have the most favorable in vivo characteristics for further study.

The ultimate goal in developing *closo*-decaborate(2-) conjugation reagents is to use them for direct labeling of the proteins with ^{211}At, as that is the simplest labeling procedure and provides the highest radiolabeling yields (up to 92% in our studies). Thus, conjugation of the maleimido-*closo*-decaborate(2-) reagent should be done prior to labeling. Although a two-step labeling procedure was used in the initial biodistribution studies to be certain that the radioiodine was bonded to the *closo*-decaborate(2-) moiety, ^{211}At does not stably bond to tyrosine residues, so direct labeling only occurs on the *closo*-decaborate(2-). An important issue that arose was to make a decision on which hydrazone-containing conjugation reagent to use. Although both of the labeling reagents, [^{125}I]**6a** and [^{131}I]**8**, were of interest, the choice of hydrazone derivative to use was limited to the conjugate containing a benzoic acid moiety, **17b**. This choice was made, as the acetyl-*closo*-decaborate(2-), **9d**, and its hydrazone-containing maleimido-*closo*-decaborate(2-) adduct, **17d**, were found to be somewhat unstable and difficult to purify.

It was of interest to determine if the Fab′ conjugate of choice, [^{125}I]**6a**, which contained a hydrazone functionality substituted with a *closo*-decaborate(2-) moiety and a *para*-benzoate moiety was cleaved under mild acid conditions. The use of hydrazone-containing linkers as a means of releasing radioactivity from kidney was based on previous literature reports that demonstrated antibody−drug conjugates containing hydrazone linkers released the drug under mild acid conditions (e.g., pH 4.5), but not at neutral pH.[66,67,71−74] The rate of acid cleavage can be dependent on the electronic nature of substituents on the hydrazine and aldehyde or ketone reacted that form the hydrazone,[75] making it possible to form hydrazone linkers that are too rapidly cleaved for in vivo use or, alternatively, very slowly cleaved under in vivo conditions.[76] Importantly, none of the previous hydrazone conjugates contained the dianionic *closo*-decaborate(2-) moiety. The results obtained from the in vitro acid-catalyzed cleavage analysis indicate that acid-catalyzed cleavage of the hydrazone functionality does occur for Fab′ conjugate [^{125}I]**6a**. The observed acid-catalyzed cleavage supports our hypothesis for the mechanism of in vivo release of radioactivity from the kidney and liver (Figure 2), but the kinetics of the cleavage under the in vitro conditions used appear much slower than the release of radioactivity from tissues. It seems likely that, at least in part, the biological mechanism for release of radioactivity from tissue is acid-catalyzed cleavage of the hydrazone functionality. However, to be certain of the actual mechanism of release from the kidneys, studies of metabolites in blood, urine, and feces would be required. Such metabolite studies are beyond the scope of this investigation.

All of the initial developmental studies were conducted with radioiodinated Fab′ conjugates, but the ultimate goal is to use them for targeting ^{211}At to cancer cells in vivo. In the final Fab′ study, **17b** was conjugated with 107−1A4 Fab′, then directly labeled with ^{125}I to prepare [^{125}I]**6a** and (separately) with ^{211}At to prepare [^{211}At]**6b**. An important difference in this biodistribution study was that the radiohalogenated Fab′ were evaluated in mice bearing LNCaP human prostate tumor xenografts. The 107−1A4 is an anti-PSMA antibody that binds with the prostate-specific membrane antigen (PSMA), which is highly expressed on the LNCaP cells.[28] This model was used to demonstrate that tumor targeting could be achieved, and to assess whether the cleavable hydrazone group caused a decrease in tumor concentration at the later time points. The biodistribution data are plotted in Figure 3. It had been presumed that the tissue distribution of the Fab′ conjugate [^{211}At]**6b** would be very similar to that of [^{125}I]**6a**. This presumption was based on many prior studies, where the two radionuclides had similar distributions when the carrier molecules were conjugated with a *closo*-decaborate(2-) moiety. The results show that the use of ^{211}At changes the retention of radioactivity in kidney, liver, and tumor from that obtained with the same Fab′ conjugate labeled with ^{125}I. The neck and stomach concentrations indicate that [^{211}At]astatide is not being released, so it seems likely that another metabolite is being retained. Although the nature of that metabolite is not known for certain, it should be noted that we have obtained similar differences in kidney retention for ^{125}I- and ^{211}At-labeled biotin derivatives that contain a ketone coupled to a *closo*-decaborate(2-) cage (unpublished results). Importantly, the kidney retention differences observed for that biotin derivative were alleviated by conversion of the ketone to an oxime derivative. That finding is suggestive that the nature of the conjugated ketone or other metabolite is changed when the *closo*-decaborate-(2-) is substituted with ^{211}At rather than ^{125}I. It also suggests that alternate hydrazone structures might provide the faster renal clearance being sought.

In conclusion, this study has demonstrated that chemical linkers containing hydrazone moieties can be used to increase the rate of clearance of radioactivity (radioiodine) from kidneys and other tissues. The differences in tissue clearance data indicate that changing the nature of the hydrazone and substituents attached to it can change the tissue clearance rates. The striking differences in tissue clearance observed between radioiodinated and astatinated Fab′ conjugate were surprising. That data indicate that additional studies must be conducted before effective hydrazone-containing linkers are found that function with ^{211}At. In contrast, the data obtained indicate that use of a hydrazone containing *closo*-decaborate(2-) labeling moiety might be highly beneficial for radioiodinated proteins or peptides that are localized to kidney.

■ ASSOCIATED CONTENT

Supporting Information. Four tables (Table S1−S4) containing biodistribution data for Fab′ conjugates [^{125}I]**4**, [^{131}I]**5**, [^{125}I]**6a**, [^{211}At]**6b**, [^{125}I]**7**, and [^{131}I]**8** are provided. This material is available free of charge via the Internet at http://pubs.acs.org/.

■ AUTHOR INFORMATION

Corresponding Author

*Address correspondence to: D. Scott Wilbur, Ph.D., Department of Radiation Oncology, University of Washington, Box 355016, 616 N.E. Northlake Place, Seattle, WA 98105. Phone: 206-616-9246. E-mail: dswilbur@u.washington.edu.

■ ACKNOWLEDGMENT

We thank Quanta BioDesign (Powell, Ohio) for the gift of MPS-EDA.TFA and MAL-dPEG$_4$-t-boc-hydrazide. We thank NIH (1 RO1 CA113431) for funding the studies.

■ ABBREVIATIONS:

ChT, chloramine-T; cpm, counts per minute; DTT, dithiothreitol; mAb, monoclonal antibody; MPS-EDA.TFA, trifluoroacetate salt of *N*-(2′-aminoethyl)-3-(maleimido)-propionamide; NCS, *N*-chlorosuccinimide; NEM, *N*-ethylmaleimide; %ID/g, percent

injected dose/gram; PBS, phosphate buffered saline; PEG, poly-(ethylene glycol); pi, post injection; rt, room temperature; tBoc, *tert*-butoxycarbonyl; TCDI, 1,1′-thiocarbonyldiimidazole; TFA, trifluoroacetic acid

REFERENCES

(1) Zalutsky, M. R., Reardon, D. A., Pozzi, O. R., Vaidyanathan, G., and Bigner, D. D. (2007) Targeted alpha-particle radiotherapy with ^{211}At-labeled monoclonal antibodies. *Nucl. Med. Biol. 34*, 779–85.

(2) Aurlien, E., Larsen, R. H., Kvalheim, G., and Bruland, O. S. (2000) Demonstration of highly specific toxicity of the α-emitting radioimmunoconjugate ^{211}At-rituximab against non-Hodgkin's lymphoma cells. *Br. J. Cancer 83*, 1375–1379.

(3) Zhang, M., Yao, Z., Zhang, Z., Garmestani, K., Talanov, V. S., Plascjak, P. S., Yu, S., Kim, H. S., Goldman, C. K., Paik, C. H., Brechbiel, M. W., Carrasquillo, J. A., and Waldmann, T. A. (2006) The Anti-CD25 monoclonal antibody 7G7/B6, armed with the α-emitter ^{211}At, provides effective radioimmunotherapy for a murine model of leukemia. *Cancer Res. 66*, 8227–8232.

(4) Zhang, Z., Zhang, M., Garmestani, K., Talanov, V. S., Plascjak, P. S., Beck, B., Goldman, C., Brechbiel, M. W., and Waldmann, T. A. (2006) Effective treatment of a murine model of adult T-cell leukemia using ^{211}At-7G7/B6 and its combination with unmodified anti-Tac (daclizumab) directed toward CD25. *Blood 108*, 1007–12.

(5) Elgqvist, J., Andersson, H., Back, T., Claesson, I., Hultborn, R., Jensen, H., Lindegren, S., Olsson, M., Palm, S., Warnhammar, E., and Jacobsson, L. (2006) Fractionated radioimmunotherapy of intraperitoneally growing ovarian cancer in nude mice with ^{211}At-MX35 F(ab′)$_2$: therapeutic efficacy and myelotoxicity. *Nucl. Med. Biol. 33*, 1065–72.

(6) Elgqvist, J., Andersson, H., Jensen, H., Kahu, H., Lindegren, S., Warnhammar, E., and Hultborn, R. (2010) Repeated intraperitoneal alpha-radioimmunotherapy of ovarian cancer in mice. *J. Oncol. 2010*, 394913.

(7) Andersson, H., Cederkrantz, E., Back, T., Divgi, C., Elgqvist, J., Himmelman, J., Horvath, G., Jacobsson, L., Jensen, H., Lindegren, S., Palm, S., and Hultborn, R. (2009) Intraperitoneal alpha-particle radioimmunotherapy of ovarian cancer patients: pharmacokinetics and dosimetry of ^{211}At-MX35 F(ab′)$_2$--a phase I study. *J. Nucl. Med. 50*, 1153–60.

(8) Zalutsky, M. R., Reardon, D. A., Akabani, G., Coleman, R. E., Friedman, A. H., Friedman, H. S., McLendon, R. E., Wong, T. Z., and Bigner, D. D. (2008) Clinical experience with alpha-particle emitting ^{211}At: treatment of recurrent brain tumor patients with ^{211}At-labeled chimeric antitenascin monoclonal antibody 81C6. *J. Nucl. Med. 49*, 30–8.

(9) Persson, M. I., Gedda, L., Jensen, H. J., Lundqvist, H., Malmstrom, P. U., and Tolmachev, V. (2006) Astatinated trastuzumab, a putative agent for radionuclide immunotherapy of ErbB2-expressing tumours. *Oncol. Rep. 15*, 673–80.

(10) Robinson, M. K., Shaller, C., Garmestani, K., Plascjak, P. S., Hodge, K. M., Yuan, Q. A., Marks, J. D., Waldmann, T. A., Brechbiel, M. W., and Adams, G. P. (2008) Effective treatment of established human breast tumor xenografts in immunodeficient mice with a single dose of the alpha-emitting radioisotope astatine-211 conjugated to anti-HER2/neu diabodies. *Clin. Cancer Res. 14*, 875–82.

(11) Boskovitz, A., McLendon, R. E., Okamura, T., Sampson, J. H., Bigner, D. D., and Zalutsky, M. R. (2009) Treatment of HER2-positive breast carcinomatous meningitis with intrathecal administration of alpha-particle-emitting ^{211}At-labeled trastuzumab. *Nucl. Med. Biol. 36*, 659–69.

(12) Jain, R. K., and Baxter, L. T. (1988) Mechanisms of heterogeneous distribution of monoclonal antibodies and other macromolecules in tumors: significance of elevated interstitial pressure. *Cancer Res. 48*, 7022–7032.

(13) Choi, J., Credit, K., Henderson, K., Deverkadra, R., He, Z., Wiig, H., Vanpelt, H., and Flessner, M. F. (2006) Intraperitoneal immunotherapy for metastatic ovarian carcinoma: Resistance of intratumoral collagen to antibody penetration. *Clin. Cancer Res. 12*, 1906–12.

(14) Holliger, P., and Hudson, P. J. (2005) Engineered antibody fragments and the rise of single domains. *Nat. Biotechnol. 23*, 1126–36.

(15) Wu, A. M., and Senter, P. D. (2005) Arming antibodies: prospects and challenges for immunoconjugates. *Nat. Biotechnol. 23*, 1137–46.

(16) Wilbur, D. S. (2008) [^{211}At]astatine-labeled compound stability: issues with released [^{211}At]astatide and development of labeling reagents to increase stability. *Curr. Radiopharm. 1*, 144–176.

(17) Wilbur, D. S., Chyan, M. K., Hamlin, D. K., Vessella, R. L., Wedge, T. J., and Hawthorne, M. F. (2007) Reagents for astatination of biomolecules. 2. Conjugation of anionic boron cage pendant groups to a protein provides a method for direct labeling that is stable to in vivo deastatination. *Bioconjugate Chem. 18*, 1226–40.

(18) Maack, T., Johnson, V., Kau, S. T., Figueiredo, J., and Sigulem, D. (1979) Renal filtration, transport, and metabolsim of low-molecular-weight proteins: a review. *Kidney Int. 16*, 251–270.

(19) Arend, W. P., and Silverblatt, F. J. (1975) Serum disappearance and catabolism of homologous immunoglobulin fragments in rats. *Clin. Exp. Immunol. 22*, 502–513.

(20) Verroust, P. J., and Christensen, E. I. (2002) Megalin and cubilin--the story of two multipurpose receptors unfolds. *Nephrol. Dial. Transplant 17*, 1867–71.

(21) Christensen, E. I., and Birn, H. (2002) Megalin and cubilin: multifunctional endocytic receptors. *Nat. Rev. Mol. Cell Biol. 3*, 256–266.

(22) Christensen, E. I., and Gburek, J. (2004) Protein reabsorption in renal proximal tubule-function and dysfunction in kidney pathophysiology. *Pediatr. Nephrol. 19*, 714–21.

(23) Trejtnar, F., and Laznicek, M. (2002) Analysis of renal handling of radiopharmaceuticals. *Q. J. Nucl. Med. 46*, 181–94.

(24) Wu, C., Jagoda, E., Brechbiel, M., Webber, K. O., Pastan, I., Gansow, O., and Eckelman, W. C. (1997) Biodistribution and catabolism of Ga-67-labeled anti-tac dsFv fragment. *Bioconjugate Chem. 8*, 365–369.

(25) Tsai, S. W., Li, L., Williams, L. E., Anderson, A. L., Raubitschek, A. A., and Shively, J. E. (2001) Metabolism and renal clearance of ^{111}In-labeled DOTA-conjugated antibody fragments. *Bioconjugate Chem. 12*, 264–270.

(26) Behr, T. M., Behe, M., Stabin, M. G., Wehrmann, E., Apostolidis, C., Molinet, R., Strutz, F., Fayyazi, A., Wieland, E., Gratz, S., Koch, L., Goldenberg, D. M., and Becker, W. (1999) High-linear energy transfer (LET) alpha versus low-LET beta emitters in radioimmunotherapy of solid tumors: therapeutic efficacy and dose- limiting toxicity of ^{213}Bi- versus ^{90}Y-labeled CO17−1A Fab′ fragments in a human colonic cancer model. *Cancer Res. 59*, 2635–43.

(27) Ducry, L., and Stump, B. (2010) Antibody-drug conjugates: linking cytotoxic payloads to monoclonal antibodies. *Bioconjugate Chem. 21*, 5–13.

(28) Brown, L., Wegner, S., Wang, H., Buhler, K., Arfman, E., Lange, P., and Vessella, R. (1998) A novel monoclonal antibody 107−1A4 with high prostate specificity: generation characterization of antigen expression, and targeting of human prostate cancer xenografts. *Prostate Cancer and Prostatic Diseases 1*, 208–215.

(29) Wilbur, D. S., Hamlin, D. K., Vessella, R. L., Stray, J. E., Buhler, K. R., Stayton, P. S., Klumb, L. A., Pathare, P. M., and Weerawarna, S. A. (1996) Antibody fragments in tumor pretargeting. Evaluation of biotinylated Fab′ colocalization with recombinant streptavidin and avidin. *Bioconjugate Chem. 7*, 689–702.

(30) Wilbur, D. S., Vessella, R. L., Stray, J. E., Goffe, D. K., Blouke, K. A., and Atcher, R. W. (1993) Preparation and evaluation of *para*--[^{211}At]astatobenzoyl labeled anti-renal cell carcinoma antibody A6H F(ab′)$_2$. In vivo distribution comparison with *para*-[^{125}I]iodobenzoyl labeled A6H F(ab′)$_2$. *Nucl. Med. Biol. 20*, 917–27.

(31) Wilbur, D. S., Chyan, M. K., Hamlin, D. K., and Perry, M. A. (2009) Reagents for astatination of biomolecules. 3. Comparison of *closo*-decaborate(2-) and *closo*-dodecaborate(2-) moieties as reactive groups for labeling with astatine-211. *Bioconjugate Chem. 20*, 591–602.

(32) Wilbur, D. S., Chyan, M. K., Hamlin, D. K., and Perry, M. A. (2010) Preparation and in vivo evaluation of radioiodinated *closo*-decaborate(2-)

derivatives to identify structural components that provide low retention in tissues. *Nucl. Med. Biol. 37*, 167–78.

(33) Silver, D. A., Pellicer, I., Fair, W. R., Heston, W. D., and Cordon-Cardo, C. (1997) Prostate-specific membrane antigen expression in normal and malignant human tissues. *Clin. Cancer Res. 3*, 81–5.

(34) Kaplan, H. M., Brewer, N. R., and Blair, W. H. (1983) Physiology, in *The Mouse in Biomedical Research* (Foster, H. L., Small, J. D., and Fox, J. G., Eds.) pp 248−292, Academic Press, New York.

(35) Fritzberg, A. R., Beaumier, P. L., Bottino, B. J., and Reno, J. M. (1994) Approaches to improved antibody- and peptide-mediated targeting for imaging and therapy of cancer. *J. Controlled Release 28*, 167–173.

(36) Wilbur, D. S., Thakar, M. S., Hamlin, D. K., Santos, E. B., Chyan, M. K., Nakamae, H., Pagel, J. M., Press, O. W., and Sandmaier, B. M. (2009) Reagents for astatination of biomolecules. 4. Comparison of maleimido-*closo*-decaborate(2-) and *meta*-[^{211}At]astatobenzoate conjugates for labeling anti-CD45 antibodies with [^{211}At]astatine. *Bioconjugate Chem. 20*, 1983–1991.

(37) Akizawa, H., Uehara, T., and Arano, Y. (2008) Renal uptake and metabolism of radiopharmaceuticals derived from peptides and proteins. *Adv. Drug Delivery Rev. 60*, 1319–28.

(38) Behr, T. M., Goldenberg, D. M., and Becker, W. (1998) Reducing the renal uptake of radiolabeled antibody fragments and peptides for diagnosis and therapy: present status, future prospects and limitations. *Eur. J. Nucl. Med. 25*, 201–212.

(39) Behr, T. M., Sharkey, R. M., Juweid, M. E., Blumenthal, R. D., Dunn, R. M., Griffiths, G. L., Bair, H.-J., Wolf, F. G., Becker, W. S., and Goldenberg, D. M. (1995) Reduction of the renal uptake of radiolabeled monoclonal antibody fragments by cationic amino acids and their derivatives. *Cancer Res. 55*, 3825–3834.

(40) Behr, T. M., Becker, W. S., Sharkey, R. M., Juweid, M. E., Dunn, R. M., Bair, H.-J., Wolf, F. G., and Goldenberg, D. M. (1996) Reduction of renal uptake of monoclonal antibody fragments by amino acid infusion. *J. Nucl. Med. 37*, 829–833.

(41) Behr, T. M., Sharkey, R. M., Sgouros, G., Blumenthal, R. D., Dunn, R. M., Kolbert, K., Griffiths, G. L., Siegel, J. A., Becker, W. S., and Goldenberg, D. M. (1997) Overcoming the nephrotoxicity of radiometal-labeled immunoconjugates: improved cancer therapy administered to a nude mouse model in relation to the internal radiation dosimetry. *Cancer 80* (Suppl.), 2591–2610.

(42) Kobayashi, H., Yoo, T. M., Kim, I. S., Kim, M.-K., Le, N., Webber, K. O., Pastan, I., Paik, C. H., Eckelman, W. C., and Carrasquillo, J. A. (1996) L-Lysine effectively blocks renal uptake of ^{125}I- or ^{99m}Tc-labeled anti-tac disulfide-stabilized Fv fragment. *Cancer Res. 56*, 3788–3795.

(43) Carrasquillo, J. A., Lang, L., Whatley, M., Herscovitch, P., Wang, Q.-c., Pastan, I., and Eckelman, W. C. (1998) Aminosyn II effectively blocks renal uptake of ^{18}F-labled anti-tac disulfide-stabilized Fv. *Cancer Res. 58*, 2612–2617.

(44) Hamilton, S., Odili, J., Wilson, G. D., and Kupsch, J. M. (2002) Reducing renal accumulation of single-chain Fv against melanoma-associated proteoglycan by coadministration of L-lysine. *Melanoma Res. 12*, 373–379.

(45) Li, L., Yazaki, P. J., Anderson, A. L., Crow, D., Colcher, D., Wu, A. M., Williams, L. E., Wong, J. Y., Raubitschek, A., and Shively, J. E. (2006) Improved biodistribution and radioimmunoimaging with poly-(ethylene glycol)-DOTA-conjugated anti-CEA diabody. *Bioconjugate Chem. 17*, 68–76.

(46) Kim, I., Kobayashi, H., Yoo, T. M., Kim, M.-k., Le, N., Han, E.-s., Wang, Q. C., Pastan, I., Carrasquillo, J. A., and Paik, C. H. (2002) Lowering of pI by acylation improves the renal uptake of ^{99m}Tc-labeled anti-Tac dsFv: effect of different acylating reagents. *Nucl. Med. Biol. 29*, 795–801.

(47) Kobayashi, H., Le, N., Kim, I. S., Kim, M. K., Pie, J. E., Drumm, D., Paik, D. S., Waldmann, T. A., Paik, C. H., and Carrasquillo, J. A. (1999) The pharmacokinetic characteristics of glycolated humanized anti-Tac Fabs are determined by their isoelectric points. *Cancer Res. 59*, 422–30.

(48) Kobayashi, H., Kim, I. S., Drumm, D., Kim, M. K., Paik, D. S., Le, N., Waldmann, T. A., Carrasquillo, J. A., and Paik, C. H. (1999) Favorable effects of glycolate conjugation on the biodistribution of humanized antiTac Fab fragment. *J. Nucl. Med. 40*, 837–45.

(49) Kim, M. K., Jeong, H. J., Kao, C. H., Yao, Z., Paik, D. S., Pie, Kobayashi, H., Waldmann, T. A., Carrasquillo, J. A., and Paik, C. H. (2002) Improved renal clearance and tumor targeting of ^{99m}Tc-labeled anti-Tac monoclonal antibody Fab by chemical modifications. *Nucl. Med. Biol. 29*, 139–46.

(50) Akizawa, H., and Arano, Y. (2002) Altering pharmacokinetics of radiolabeled antibodies by the interposition of metabolizable linkages. Metabolizable linkers and pharmacokinetics of monoclonal antibodies. *Q. J. Nucl. Med. 46*, 206–23.

(51) Haseman, M. K., Goodwin, D. A., Meares, C. F., Kaminski, M. S., Wensel, T. G., McCall, M. J., and Levy, R. (1986) Metabolizable ^{111}In chelate conjugated anti-idiotype monoclonal antibody for radioimmunodetection of lymphoma in mice. *Eur. J. Nucl. Med. 12*, 455–460.

(52) Weber, R. W., Boutin, R. H., Nedelman, M. A., Lister-James, J., and Dean, R. T. (1990) Enhanced kidney clearance with an ester-linked ^{99m}Tc-radiolabeled antibody Fab′-chelator conjugate. *Bioconjugate Chem. 1*, 431–437.

(53) Arano, Y., Wakisaka, K., Ohmono, Y., Uezono, T., Akizawa, H., Nakayama, M., Sakahara, H., Tanaka, C., Konishi, J., and Yokoyama, A. (1996) Assessment of radiochemical design of antibodies using an ester bond as the metabolizable linkage: evaluation of maleimidoethyl 3-(tri-*n*-butylstannyl)hippurate as a radioiodination reagent of antibodies for diagnostic and therapeutic applications. *Bioconjugate Chem. 7*, 628–637.

(54) Arano, Y., Wakisaka, K., Akizawa, H., Ono, M., Kawai, K., Nakayama, M., Sakahara, H., Konishi, J., and Saji, H. (1998) Assessment of the radiochemical design of antibodies with a metabolizable linkage for target-selective radioactivity delivery. *Bioconjugate Chem. 9*, 497–506.

(55) Quadri, S. M., Vriesendorp, H. M., Leichner, P. K., and Williams, J. R. (1993) Evaluation of indium-111- and yttrium-90-labeled linker-immunoconjugates in nude mice and dogs. *J. Nucl. Med. 34*, 938–945.

(56) Wakisaka, K., Arano, Y., Uezono, T., Akizawa, H., Ono, M., Kawai, K., Ohomomo, Y., Nakayama, M., and Saji, H. (1997) A novel radioiodination reagent for protein radiopharmaceuticals with L-lysine as a plasma-stable metabolizable linkage to liberate *m*-iodohippuric acid after lysosomal proteolysis. *J. Med. Chem. 40*, 2643–2652.

(57) Nakamoto, Y., Sakahara, H., Saga, T., Sato, N., Zhao, S., Arano, Y., Fujioka, Y., Saji, H., and Konishi, J. (1999) A novel immunoscintigraphy technique using metabolizable linker with angiotensin II treatment. *Br. J. Cancer 79*, 1794–9.

(58) Arano, Y., Fujioka, Y., Akizawa, H., Ono, M., Uehara, T., Wakisaka, K., Nakayama, M., Sakahara, H., Konishi, J., and Saji, H. (1999) Chemical design of radiolabeled antibody fragments for low renal radioactivity levels. *Cancer Res. 59*, 128–34.

(59) Li, L., Olafsen, T., Anderson, A. L., Wu, A., Raubitschek, A. A., and Shively, J. E. (2002) Reduction of kidney uptake in radiometal labeled peptide linkers conjugated to recombinant antibody fragments. Site-specific conjugation of DOTA-peptides to a Cys-diabody. *Bioconjugate Chem. 13*, 985–95.

(60) Fujioka, Y., Satake, S., Uehara, T., Mukai, T., Akizawa, H., Ogawa, K., Saji, H., Endo, K., and Arano, Y. (2005) In vitro system to estimate renal brush border enzyme-mediated cleavage of peptide linkages for designing radiolabeled antibody fragments of low renal radioactivity levels. *Bioconjugate Chem. 16*, 1610–6.

(61) Uehara, T., Koike, M., Nakata, H., Hanaoka, H., Iida, Y., Hashimoto, K., Akizawa, H., Endo, K., and Arano, Y. (2007) Design, synthesis, and evaluation of [^{188}Re]organorhenium-labeled antibody fragments with renal enzyme-cleavable linkage for low renal radioactivity levels. *Bioconjugate Chem. 18*, 190–8.

(62) De Duve, C., De Barsy, T., Polle, B., Trouet, A., Tulkens, P., and Van Hoof, F. (1974) Lysosomotropic agents. *Biochem. Pharmacol. 23*, 2495–2531.

(63) Mellman, I., Fuchs, R., and Helenius, A. (1986) Acidification of the endocytic and exocytic pathways. *Annu. Rev. Biochem. 55*, 663–700.

(64) Shen, W.-C., Persiani, S., and Srivastava, K. (1990) Chemical linkages in drug-antibody conjugation. *Biopharm.* 16–22.

(65) Gillies, E. R., Goodwin, A. P., and Frechet, J. M. (2004) Acetals as pH-sensitive linkages for drug delivery. *Bioconjugate Chem. 15*, 1254–63.

(66) Mueller, B. M., Wrasidlo, W. A., and Reisfeld, R. A. (1990) Antibody conjugates with morpholinodoxorubicin and acid-cleavable linkers. *Bioconjugate Chem. 1*, 325–30.

(67) Kaneko, T., Willner, D., Monkovic, I., Knipe, J. O., Braslawsky, G. R., Greenfield, R. S., and Vyas, D. M. (1991) New hydrazone derivatives of adriamycin and their immunoconjugates - a correlation between acid stability and cytotoxicity. *Bioconjugate Chem. 2*, 133–141.

(68) Schrappe, M., Bumol, T. F., Apelgren, L. D., Briggs, S. L., Koppel, G. A., Markowitz, D. D., Mueller, B. M., and Reisfeld, R. A. (1992) Long-term growth suppression of human glioma xenografts by chemoimmunoconjugates of 4-desacetylvinblastine-3-carboxyhydrazide and monoclonal antibody 9.2.27. *Cancer Res. 52*, 3838–3844.

(69) Hinman, L. M., Hamann, P. R., Wallace, R., Menendez, A. T., Durr, F. E., and Upeslacis, J. (1993) Preparation and characterization of monoclonal antibody conjugates of the calicheamicins: a novel and potent family of antitumor antibiotics. *Cancer Res. 53*, 3336–3342.

(70) Apelgren, L. D., Bailey, D. L., Briggs, S. L., Barton, R. L., Guttman-Carlisle, D., Koppel, G. A., Nichols, C. L., Scott, W. L., Lindstom, T. D., Baker, A. L., and Bumol, T. F. (1993) Chemoimmunoconjugate development for ovarian carcinoma therapy: preclinical studies with vinca alkaloid-monoclonal antibody constructs. *Bioconjugate Chem. 4*, 121–126.

(71) Braslawsky, G. R., Kadow, K., Knipe, J., McGoff, K., Edson, M., Kaneko, T., and Greenfield, R. S. (1991) Adriamycin(hydrazone)-antibody conjugates require internalization and intracellular acid hydrolysis for antitumor activity. *Cancer Immunol. Immunother. 33*, 367–374.

(72) Froesch, B. A., Stahel, R. A., and Zangemeister-Wittke, U. (1996) Preparation and functional evaluation of new doxorubicin immunoconjugates containing and acid-sensitive linker on small-cell lung cancer cells. *Cancer Immunol. Immunother. 42*, 55–63.

(73) King, T. P., Zhao, S. W., and Lam, T. (1986) Preparation of protein conjugates via intermolecular hydrazone linkage. *Biochemistry 25*, 5774–5779.

(74) Hollander, I., Kunz, A., and Hamann, P. R. (2008) Selection of reaction additives used in the preparation of monomeric antibody-calicheamicin conjugates. *Bioconjugate Chem. 19*, 358–61.

(75) Kalia, J., and Raines, R. T. (2008) Hydrolytic stability of hydrazones and oximes. *Angew. Chem., Int. Ed. Engl. 47*, 7523–6.

(76) Dirksen, A., and Dawson, P. E. (2008) Rapid oxime and hydrazone ligations with aromatic aldehydes for biomolecular labeling. *Bioconjugate Chem. 19*, 2543–8.

Supporting Information For:

Reagents for Astatination of Biomolecules. 5. Evaluation of hydrazone linkers in ^{211}At- and ^{125}I-labeled *closo*-decaborate(2-) conjugates of Fab´ as a means of decreasing kidney retention.

D. Scott Wilbur[*,†], Ming-Kuan Chyan[†], Donald K. Hamlin[†], Holly Nguyen[‡]

and Robert L. Vessella[‡]

Departments of [†]Radiation Oncology, and [‡]Urology,

University of Washington, Seattle, WA 98195

PAGES:

Table S1: Biodistribution data for Fab´ conjugate [^{125}I]**4** at 1, 4 & 24 h pi

Table S2: Biodistribution data for coinjected Fab´ conjugates [^{131}I]**5** & [^{125}I]**6a** at 1, 4 & 24 h pi

Table S3: Biodistribution data for coinjected Fab´ conjugates [^{125}I]**7** & [^{131}I]**8** at 1, 4 & 24 h pi

Table S4: Biodistribution data for coinjected [^{125}I]**6a** and [^{211}At]**6b** at 1, 4 and 24 h pi

Table S1: Tissue Distribution of Fab´ conjugate [^{125}I]4 in nude mice.[a]

Tissues	1h[b,c]	4h	24h
	[^{125}I]**4**	[^{125}I]**4**	[^{125}I]**4**
blood	13.00 ± 3.89	8.60 ± 1.98	1.11 ± 0.25
muscle	0.44 ± 0.14	0.49 ± 0.40	0.11 ± 0.16
lung	4.78 ± 2.19	3.95 ± 0.86	0.84 ± 0.21
kidney	7.71 ± 2.64	17.25 ± 2.65	5.43 ± 0.98
spleen	10.34 ± 6.71	5.82 ± 0.99	6.87 ± 1.72
liver	12.62 ± 3.23	11.29 ± 1.59	7.35 ± 0.95
intestine	2.78 ± 0.99	4.08 ± 2.21	0.80 ± 0.28
neck	1.45 ± 0.87	1.71 ± 0.34	0.52 ± 0.12
stomach	0.99 ± 0.37	1.28 ± 0.43	0.40 ± 0.06
urine[d]	5.99 ± 5.80	6.12 ± 2.54	1.20 ± 0.53

[a]Values shown are % injected dose / gram ± standard deviation. [b]Time of sacrifice from injection of radioactivity. [c]Data were obtained for *n* = 3 mice at 1 h, 5 mice at 4 h and 4 mice at 24 h; average animal weight for 1 h group, 26.32 ± 1.34 g, for 4 h group, 25.52 ± 1.36 g, and for 24 h group, 25.79 ± 1.00 g; Injectate for each animal had 3.7 μCi/30 μg of [^{125}I]**4** in approximately 100 μL of 0.9% sterile saline. [d]Urine was collected by syringe bladder tap after sacrifice.

Table S2: Tissue Distribution of Co-injected Fab´ conjugates [^{131}I]5 and [^{125}I]6 in nude mice.[a]

Tissues	1h[b,c]		4h		24h	
	[^{131}I]**5**	[^{125}I]**6**	[^{131}I]**5**	[^{125}I]**6**	[^{131}I]**5**	[^{125}I]**6**
blood	34.81 ± 3.82*	26.61 ± 4.96*	19.92 ± 2.11*	6.72 ± 0.65*	4.35 ± 0.68*	0.43 ± 0.11*
muscle	1.12 ± 0.21	1.11 ± 0.18	1.25 ± 0.18	0.99 ± 0.15	0.62 ± 0.07	0.07 ± 0.02
lung	12.20 ± 2.42	10.34 ± 2.45	7.33 ± 0.34*	3.49 ± 0.37*	2.45 ± 0.39*	0.36 ± 0.09*
kidney	17.24 ± 5.17	26.31 ± 10.40	36.52 ± 4.42*	15.29 ± 2.48*	25.58 ± 9.37*	1.47 ± 0.21*
spleen	5.10 ± 1.37	4.44 ± 1.58	4.67 ± 2.69	1.66 ± 0.84	1.67 ± 0.11	0.16 ± 0.03
liver	11.90 ± 2.25*	7.65 ± 1.76*	6.55 ± 0.97*	2.08 ± 0.56*	3.77 ± 0.41*	0.22 ± 0.04*
intestine	6.28 ± 3.20	5.88 ± 2.84	7.18 ± 2.14	7.71 ± 1.91	3.47 ± 0.98*	1.44 ± 0.77*
neck	2.81 ± 0.14*	2.54 ± 0.09*	2.58 ± 0.60*	1.68 ± 0.27*	1.32 ± 0.23*	0.13 ± 0.04*
stomach	12.26 ± 7.87	11.22 ± 7.87	2.37 ± 0.44	1.94 ± 0.41	1.25 ± 0.32*	0.38 ± 0.38*
urine[d]	14.36 ± 4.24*	23.27 ± 5.16*	20.02 ± 15.89	45.79 ± 53.85	13.57 ± 2.45*	2.47 ± 0.86*

[a]Values shown are % injected dose / gram ± standard deviation. [b]Time of sacrifice from injection of radioactivity [c]Data were obtained for *n* = 4 mice at 1 h, 4 mice at 4 h and 5 mice at 24 h; average animal weight for 1 h group, 26.02 ± 1.81 g, for 4 h group, 24.57 ± 0.50 g, and for 24 h group, 21.95 ± 1.56 g; Injectate for each animal had 5 μCi/15 μg of [^{131}I]**5** and 5 μCi/15 μg of [^{125}I]**6** in approximately 100 μL of 0.9% sterile saline. [d]Urine was collected by syringe bladder tap after sacrifice. *Denotes tissues/fluids that are statistically different based on paired Student-t test ($p>0.05$).

Table S3: Tissue distribution of coinjected Fab´ conjugates [^{125}I]7 and [^{131}I]8 in nude mice.[a]

Tissues	1h[b,c]		4h		24h	
	[^{125}I]**7**	[^{131}I]**8**	[^{125}I]**7**	[^{131}I]**8**	[^{125}I]**7**	[^{131}I]**8**
blood	37.18 ± 4.52	35.93 ± 5.81	20.98 ± 1.07*	14.96 ± 0.92*	5.94 ± 0.55*	1.90 ± 0.27*
muscle	0.77 ± 0.15	0.96 ± 0.11	1.30 ± 0.17	1.33 ± 0.13	0.73 ± 0.10*	0.28 ± 0.08*
lung	12.10 ± 1.57	12.60 ± 2.06	7.15 ± 1.19	6.01 ± 0.84	2.76 ± 0.31*	1.08 ± 0.17*
kidney	14.65 ± 0.79*	21.50 ± 1.67*	20.16 ± 1.03*	11.34 ± 0.90*	17.77 ± 1.72*	2.13 ± 0.33*
spleen	5.55 ± 0.60	5.85 ± 0.82	3.49 ± 0.27*	2.50 ± 0.25*	1.39 ± 0.18*	0.42 ± 0.09*
liver	9.93 ± 1.74	10.59 ± 2.04	4.96 ± 0.77	4.27 ± 0.83	2.61 ± 0.29*	0.84 ± 0.09*
intestine	8.15 ± 8.55	7.45 ± 7.16	6.92 ± 3.73	9.38 ± 4.38	1.17 ± 0.06*	0.57 ± 0.03*
neck	2.71 ± 0.39	2.99 ± 0.48	3.11 ± 0.61	2.82 ± 0.39	1.62 ± 0.26*	0.52 ± 0.10*
stomach	2.14 ± 0.64	2.28 ± 0.42	2.53 ± 0.38	2.47 ± 0.52	1.05 ± 0.16*	0.37 ± 0.06*
urine[d]	27.69 ± 14.66	46.97 ± 30.03	24.20 ± 8.56*	56.04 ± 19.70*	11.26 ± 1.14*	6.31 ± 0.63*

[a]Values shown are % injected dose / gram ± standard deviation. [b]Time of sacrifice from injection of radioactivity [c]Data were obtained for *n* = 3 mice at 1 h, 5 mice at 4 h and 3 mice at 24 h; average animal weight for 1 h group, 24.65 ± 1.28 g, for 4 h group, 23.86 ± 0.66 g, and for 24 h group, 19.75 ± 2.32 g; Injectate for each animal had 5 μCi/15 μg of [^{125}I]**7** and 5 μCi/15 μg of [^{131}I]**8** in approximately 100 μL of 0.9% sterile saline. [d]Urine was collected by syringe bladder tap after sacrifice. *Denotes tissues/fluids that are statistically different based on paired Student-t test ($p>0.05$).

Table S4: Tissue distribution of coinjected [^{125}I]6a and [^{211}At]6b in nude mice.[a]

Tissues	1h[b,c]		4h		24h	
	[^{125}I]**6a**	[^{211}At]**6b**	[^{125}I]**6a**	[^{211}At]**6b**	[^{125}I]**6a**	[^{211}At]**6b**
blood	41.65 ± 5.80	50.24 ± 6.98	10.70 ± 1.78*	21.64 ± 4.65*	1.45 ± 0.37*	4.74 ± 0.89*
muscle	1.89 ± 0.59	1.70 ± 0.48	0.96 ± 0.40	1.04 ± 0.38	0.14 ± 0.03	0.37 ± 0.08
lung	14.65 ± 5.22	17.78 ± 6.52	8.17 ± 6.79	9.01 ± 2.40	0.97 ± 0.21*	3.21 ± 0.69*
kidney	50.97 ± 18.28	44.50 ± 15.52	13.14 ± 2.03*	42.28 ± 16.38*	4.23 ± 1.57*	39.52 ± 15.87*
spleen	10.41 ± 2.70	8.56 ± 5.98	2.81 ± 0.24	5.15 ± 2.56	0.75 ± 0.22*	6.17 ± 2.22*
liver	19.90 ± 5.81	20.54 ± 5.72	5.24 ± 1.60*	15.08 ± 6.39*	1.36 ± 0.12*	12.89 ± 2.30*
intestine	10.77 ± 3.40*	4.94 ± 0.74*	5.88 ± 0.82*	3.70 ± 0.94*	1.27 ± 1.12	3.00 ± 1.43
neck	6.41 ± 1.07*	4.57 ± 0.98*	5.35 ± 1.31*	3.16 ± 1.18*	2.96 ± 2.14	2.85 ± 0.92
stomach	5.69 ± 2.33*	2.77 ± 0.91*	4.87 ± 0.54	3.11 ± 1.07	2.31 ± 1.13	2.48 ± 1.06
tumor	11.73 ± 3.61	12.69 ± 3.87	11.97 ± 1.31	16.01 ± 3.90	11.80 ± 5.59	25.56 ± 11.20
urine[d]	44.21 ± 6.17	18.98 ± 4.21	23.81 ± 48.05	5.00 ± 18.29	12.24 ± 11.37	18.03 ± 17.98

[a]Values shown are % injected dose / gram ± standard deviation. [b]Time of sacrifice from injection of radioactivity [c]Data were obtained for n = 5 mice at 1, 4 and 24 h; average animal weight for 1 h group, 21.19 ± 2.09 g, for 4 h group, 22.29 ± 1.67 g, and for 24 h group, 21.22 ± 3.13 g; Injectate for each animal had 3 μCi/15 μg of [^{125}I]**6a** and 5 μCi/15 μg of [^{211}At]**6b** in approximately 100 μL of 0.9% sterile saline. [d]Urine was collected by syringe bladder tap after sacrifice. *Denotes tissues/fluids that are statistically different based on paired Student-t test ($p>0.05$).

Bioconjugate Chemistry

ARTICLE

pubs.acs.org/bc

Efficient Orthogonal Bioconjugation of Dendrimers for Synthesis of Bioactive Nanoparticles

Hubert F. Gaertner,[†] Fabrice Cerini,[†] Arun Kamath,[‡] Anne-Françoise Rochat,[‡] Claire-Anne Siegrist,[‡] Laure Menin,[§] and Oliver Hartley*[,†]

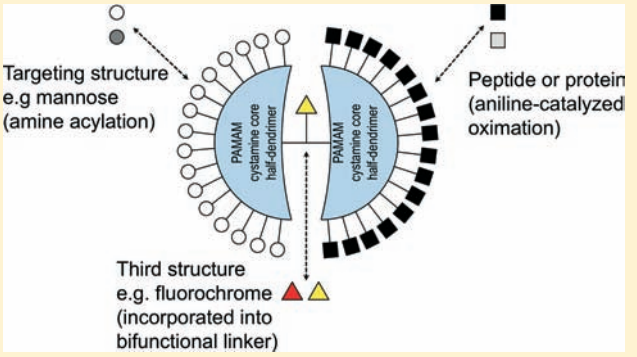
[†]Department of Structural Biology and Bioinformatics, Faculty of Medicine

[‡]Departments of Pathology-Immunology and Pediatrics, University of Geneva, 1 Rue Michel Servet, 1211 Geneva 4, Switzerland

[§]Service de Spectrométrie de Masse de l'ISIC (SSMI), EPFL, Bât. Chimie (BCH 1524), CH-1015 Lausanne, Switzerland

Supporting Information

ABSTRACT: Nanoparticles carrying biologically active functional sets (e.g., targeting moiety, payload, tracer) have potential use in a wide range of clinical applications. Though complex, such constructions should, as far as possible, have a defined molecular architecture and be monodisperse. However, the existing methods to achieve this goal are unsuitable for the incorporation of peptides and proteins, and those that provide for orthogonal introduction of two different types of functional element are incompatible with the use of commercially available materials. In this study, we have developed approaches for the production of nanoparticles based on commercially available polyamidoamine (PAMAM) dendrimers. First, we identified an optimized oxime conjugation strategy under which complex dendrimers can be fully decorated not only with model peptides, but also with recombinant proteins (insulin was taken as an example). Second, we developed a strategy based on a two-chain covalent heterodendrimer (a "diblock") based on cystamine core PAMAM dendrimers and used it to generate heterodendrimers, into which a peptide array and a mannose array were orthogonally introduced. Finally, by incorporating a functionalized linker into the diblock architecture we were able to site-specifically introduce a third functional element into the nanoparticle. We exemplified this approach using fluorescein, a mannose array, and a peptide array as the three functionalities. We showed that incorporation of a mannose array into a nanoparticle strongly and specifically enhances uptake by sentinel cells of the immune system, an important property for vaccine delivery applications. These PAMAM dendrimer-based approaches represent a robust and versatile platform for the development of bioactive nanoparticles.



INTRODUCTION

Dendrimers are branched polymers synthesized in a stepwise manner from a central core to generate particles that combine a precise, potentially monodisperse molecular architecture carrying a high density of surface functional groups. These properties make dendrimers attractive scaffolds for the generation of bioactive nanoparticles for clinical applications including drug and gene delivery, tumor targeting, bioimaging, tissue remodelling, generation of antiviral products, and vaccine delivery.[1−3]

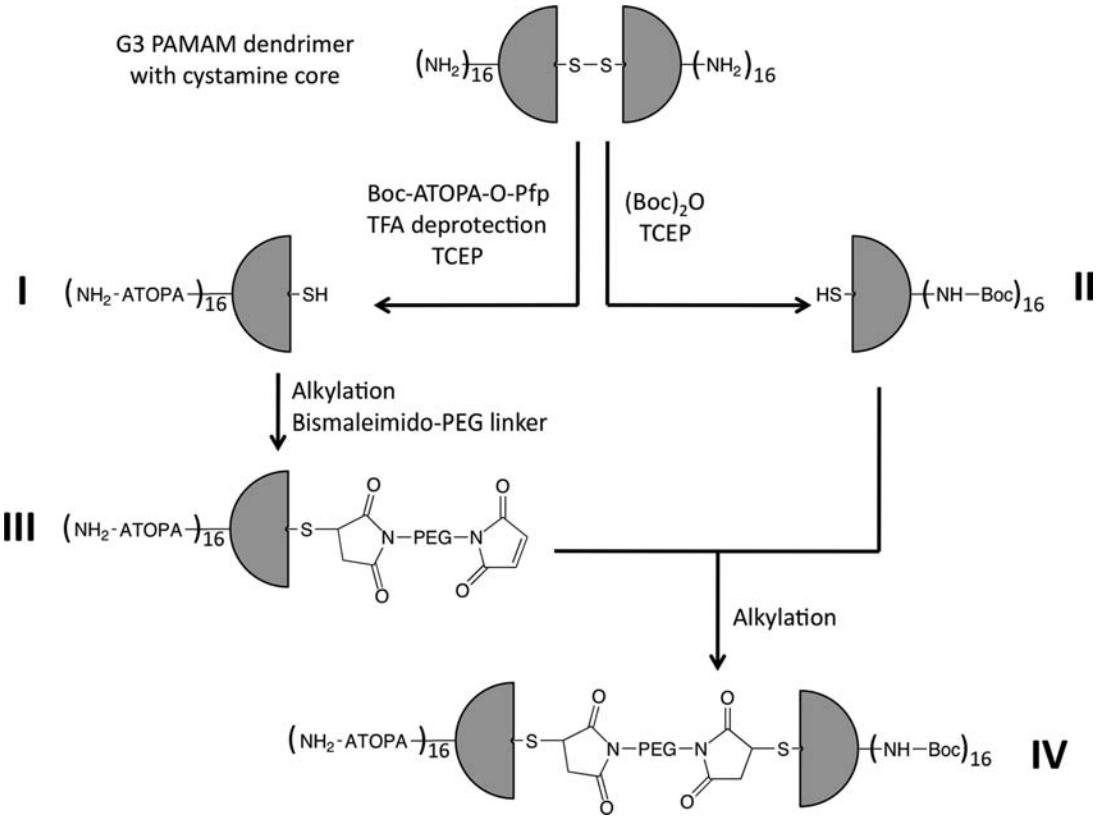
For these uses, it is highly desirable to obtain fully decorated scaffolds, thereby maximizing the possible benefits to biological activity of multivalent display,[4] as well as ensuring homogeneity and reproducibility from batch to batch and within each batch. While close to complete decoration of large, complex dendrimers has been achieved in the development of sugar arrays,[5,6] decoration with peptides and proteins has proven to be more challenging. None of the peptide/protein conjugation chemistry approaches explored so far, including hydrazone and oxime chemistry,[7,8] native chemical ligation,[9] click chemistry,[10,11] and noncovalent synthesis of protein dendrimers,[12] have proven powerful enough to fully decorate dendrimers more complex than tetramers and octamers.

A second challenge lies in developing the capacity to orthogonally introduce more than one active substituent into the nanoparticle architecture (e.g., a targeting moiety, a drug payload, a fluorescent tracer).[1,2] Approaches that enable multiple functional units to be independently attached to dendrimers via precision conjugation would be of significant value, enabling the copy numbers of different functional units to be optimized independently of one another. While several different strategies for the production of heterodendrimers carrying two different functional units have been presented,[8,13,14] none of these are

Received: December 13, 2010
Revised: May 13, 2011
Published: May 16, 2011

ACS Publications © 2011 American Chemical Society

Scheme 1. Diblock Approach Based on Cystamine Core PAMAM Dendrimers for the Preparation of Heterodendrimers Carrying Protein/Peptide Plus an Additional Functional Unit Set



compatible with the use of commercially available dendrimers as starting materials.

In this study, we present a robust strategy for conjugation of commercially available polyamidoamine (PAMAM) dendrimer scaffolds with peptides and proteins. This work is based on oxime chemistry, building on two recent discoveries in the field: first, that an alkoxyamine reacts much more readily with pyruvic acid than with N-terminal glyoxyl groups,[15] and second, that oxime ligation can be significantly accelerated and provide quantitative yields when aniline is used as a small-molecule organocatalyst.[16,17]

We have also developed an orthogonal diblock strategy for the generation of heterodendrimers from PAMAM dendrimers carrying a cystamine core. This approach is centered on the production of a key intermediate structure (Scheme 1) that is subsequently (i) acylated on the surface amines of one-half-dendrimer, those of the other half-dendrimer being temporarily protected and, following deprotection of the latter, (ii) decorated with an array of oxime-conjugated peptides on the other (Scheme 2). We exemplified this approach by producing G-3 heterodendrimers in which one half-dendrimer is decorated with mannose and the other with peptide.

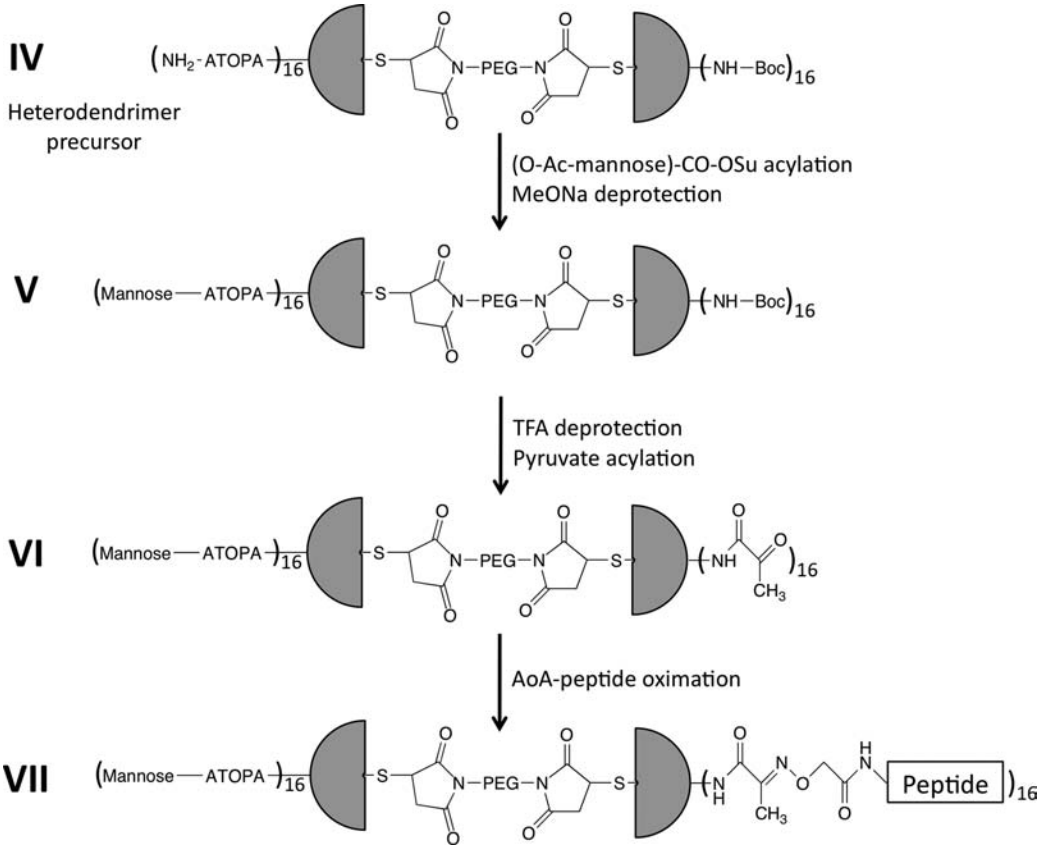
A potentially useful application of mannose−peptide/protein nanoparticles is in vaccine delivery: directly targeting a peptide or protein antigen to mannose-receptor-expressing sentinel cells of the immune system by incorporating it into a mannose-coated particle.[18−21] We produced such a heterodendrimer, further enhanced by the functionalization of the linkage between the two halves with fluorescein. This fluorescent mannose−peptide heterodendrimer was used to demonstrate the effect of incorporating a mannose array on the specific uptake of nanoparticles by dendritic cells and macrophages.

EXPERIMENTAL PROCEDURES

General Methods. Unless stated otherwise, all solvents and other chemicals were obtained from commercial sources and used as received. Amine-terminated PAMAM dendrimers were supplied by Sigma-Aldrich and Dendritic Nanotechnologies (Mount Pleasant, MI, USA). Analytical reverse-phase high-pressure liquid chromatography (HPLC) was performed on a Waters 2795 HPLC module coupled with 214 nm UV detection, using a Macherey Nagel 300A, 5 μm C8 column. Preparative HPLC was performed on a Delta 600 module coupled with a 2487 UV detector using a Vydac C8 column (250 × 22 mm i.d., 10 μm particle size) under previously described conditions.[17] Electrophoresis of peptide and protein constructs was performed on NuPage 12% Bis-Tris Gel from Invitrogen (MOPS buffer, 100 V). Matrix-assisted laser desorption/ionization time-of-flight mass spectrometry (MALDI-TOF-MS) spectra were obtained on a Perspective Biosystems Voyager SSTR or on a Shimadzu AXIMA CFR Plus mass spectrometer using sinapinic acid, 2,5 dihydroxybenzoic acid, or 2′,4′,6′-trihydroxyacetophenonemonohydrate as matrix. Electrospray ionization mass spectrometry (ESI-MS) spectra were measured on either a MicroMass Quattro Micro Mass Spectrometer or a Waters Q-TOF Ultima Mass Spectrometer, both used in positive ionization mode.

Generation of Pyruvate Dendrimers. *Succinimide Activated Pyruvate (pyruvate-OSu).* Pyruvate succinimide ester was prepared by activation of pyruvic acid (50 mg/mL) with 1 equiv dicyclohexylcarbodiimide and 1 equiv N-hydroxysuccinimide in CH_2Cl_2. The mixture was stirred overnight and filtered to remove the dicyclohexylurea precipitate. The solvent was evaporated

Scheme 2. Production of Mannose−Peptide Heterodendrimers



using reduced pressure, and the powder obtained was used without further purification.

PEG-Elongation of Dendrimer Arms. Where required, dendrimer arms were elongated with Boc-amino-PEG-COOH chains (either 2-[2-(Boc-amino)ethoxy]ethoxy}acetic acid (Boc-AEEA) or Boc-15-amino-4,7,10,13-tetraoxapentanedecanoic acid (Boc-ATOPA)), activated by esterification with pentafluorophenol (see Supporting Information for details of synthesis).

Dendrimer Functionalization. The dendrimer solution obtained from the supplier (20% w:v in MeOH) was diluted with 9 vol of CH_2Cl_2 containing 5 equiv of pyruvate-OSu per amino group. The solution was stirred overnight at room temperature and reaction completion was verified by the Kaiser test.[22] The solution was then concentrated under reduced pressure and the material resolubilized in CH_3CN/water (1:1 v/v) containing 0.1% w/v trifluoroacetic acid (TFA). The soluble fraction was further purified by preparative HPLC, using a 0−50% gradient elution system between 0.1% (w/v) TFA (solvent A) and acetonitrile/TFA/water, 900:1:100 (v:w:v) (solvent B) over 50 min, at 15 mL/min.

Conjugation of Pyruvate Dendrimers with Aminooxy-Functionalized Peptides and Insulin. The linear peptides LYRAG (Leu-Tyr-Arg-Ala-Gly) and the measles virus hemeagluttenin-derived peptide MVHA49−72 (Leu-Ile-Gly-Leu-Leu-Ala-Ile-Ala-Gly-Ile-Arg-Leu-His-Arg-Ala-Ala-Ile-Tyr-Thr-Ala-Glu-Ile-His-Lys) were synthesized according to standard automated techniques as previously described.[23] They were substituted at their α-amino groups with the aminoxyacetyl group (AoA), protected with the Boc function by reaction with Boc-aminooxyacetyl-OSu. AoA-Phe^{B1}-insulin was prepared according to standard techniques.[7] The derivatized products were single components on HPLC and had the expected mass spectra when analyzed by ESI-MS.

All conjugation experiments were performed in a 0.1 M acetate buffer containing 20% CH_3CN (v:v) or 8 M urea and 0.1 M anilinium acetate, pH 4.6. AoA-derivatized products (1.5−2.0 equiv) were mixed with 1 equiv of pyruvate dendrimer, and the reaction was allowed to proceed at room temperature for 20−40 h. The conjugation products were isolated by HPLC or, in the case of MVHA (49−72) conjugates, by dialysis.

Construction of Diblock Dendrimer Template. *G-3(ATOPA-NH_2)$_{16}$-S-PEG-maleimide (II in Scheme 1). Extension of Cystamine Core Dendrimer Arms with ATOPA Linker.* Boc-ATOPA-pentafluorophenyl ester (300 mg; for details of synthesis, see Supporting Information) was solubilized in 1 mL CH_2Cl_2 and added to 300 μL of a solution of G-3 cystamine core dendrimer (20% w/v in MeOH) at a 2-fold molar excess with respect to dendrimer surface amino groups. After overnight incubation at 20 °C, reaction completion was verified using a ninhydrin test. The reaction medium was then concentrated, solubilized in MeOH/CH_2Cl_2 (1:1 v/v), and purified on a LH-20 column equilibrated in the same solvent mixture.

Reduction of Cystamine Core to Produce Half-Dendrimers. The purified product (**I** in Scheme 1; 130 mg) was then deprotected in 4 mL TFA for 10 min at room temperature. TFA was removed under vacuum, and the remaining material was taken up in water and freeze−dried. This material was resuspended in 4 mL water, mixed with 1 mL of a 0.1 M tris(2-carboxyethyl)phosphine solution, and the pH adjusted to 5.0 with 1 M NaOH. After 2 h incubation at 20 °C, the material was purified by preparative

dx.doi.org/10.1021/bc1005653 |*Bioconjugate Chem.* 2011, 22, 1103–1114

HPLC on a C8 column using a 0−50% solvent B gradient over 50 min. The isolated material was characterized by ESI-MS (observed average mass 7456.9 ± 0.9 Da; calculated 7458.8 Da).

Attachment of Linker to Half-Dendrimer Sulfhydryl Group. 50 mg of the previous material was alkylated with a 2-fold molar excess of bismaleimido-4,7,10-trioxa-1,13-tridecanediamine linker (for linker synthesis, see Supporting Information) in a 0.1 M MES, 5 mM EDTA buffer pH 6.0 containing 50% CH_3CN. After 2 h incubation at 20 °C, the alkylated material (**III** in Scheme 1) was isolated by preparative HPLC and characterized by ESI-MS (observed average mass 8008.2 ± 0.4 Da; calculated 8008.4 Da). Material recovered: 44 mg.

*G-3(NH-Boc)$_{16}$-SH (**II** in Scheme 1).* A solution (300 μL) of a cystamine core G-3 dendrimer (20% (w:v) in MeOH) was added to $(Boc)_2O$ (5-fold molar excess over dendrimer surface amine groups) dissolved in 1 mL CH_2Cl_2. After overnight incubation at 20 °C, the material was purified on a LH20 column equilibrated in MeOH:CH_2Cl_2, 1:1 (v:v), and dried. The recovered material (65 mg) was solubilized in 3 mL MeOH:water 1:1 (v/v), TCEP was added to final concentration of 20 mM, and the pH was adjusted to 5.0 with 1 M NaOH. After 2 h incubation at 20 °C, the material was purified by preparative HPLC on a C4 column using a 20−60% B gradient over 40 min. Material recovered: 37 mg.

*G-3(ATOPA-NH$_2$)$_{16}$-S-PEG-S-G-3(NH-Boc)$_{16}$ (**IV** in Scheme 1).* Some 30 mg G-3(NH-Boc)$_{16}$-SH (**II** in Scheme 1) was reacted with a 1.5 molar excess of G-3(ATOPA-NH$_2$)$_{16}$-S-PEG-maleimide (**III** in Scheme 1) in 4 mL 50% MeOH containing 0.1 M MES, 5 mM EDTA, pH 6.0. After 3 h incubation at room temperature, the conjugation product (**IV** in Scheme 1) was purified by preparative HPLC on a C4 column and characterized by ESI-MS (observed average mass 13 112.9 ± 0.3 Da; calculated average mass 13108.9Da). Material recovered: 39 mg.

Production of Mannosylated Heterodendrimers. *Coupling Mannose to Unprotected Surface Amines.* Coupling of the succinimide ester of 3-(2,3,4,6-tetra-*O*-acetyl-α-D-mannopyranosylthio) propionic acid (see Supporting Information for details of synthesis) with G-3(ATOPA-NH$_2$)$_{16}$-S-PEG-S-G-3(Boc)$_{16}$ was carried out at 50 mg/mL in a MeOH/CH_2Cl_2 (1:1, v/v) at 20 °C for 15 h using a 2-fold molar excess of the activated ester with respect to the primary amino groups on the dendrimer, with a 3-fold excess of *N*-methylmorpholine. Complete acylation was verified using the ninhydrin test, and the carbohydrate dendrimer was isolated by chromatography on a LH20 column equilibrated in MeOH/CH_2Cl_2 (1:1 v/v). Material recovered: 37 mg. Deprotection of the acetylated mannose−dendrimer was achieved by treating the sample in MeOH/water (1:1 v/v) at 10 mg/mL at room temperature to which catalytic amounts of 0.3 M methanolic solution of MeONa (a total of 1 mol MeONa per mole of sugar 5−6 days) were added so that the pH was maintained at 8.5. The reaction was followed by analytical HPLC and considered to be complete after a total shift of the initial material into a more hydrophilic, symmetrical peak after 5−6 days of incubation.

Boc-Deprotection and Pyruvate Acylation. The resulting material was isolated by preparative HPLC on a C4 column, Boc-deprotected in neat TFA at 10 mg/mL for 5 min at room temperature, dried, and acylated with a 5-fold molar excess of Pyr-OSu under the same conditions used for homodendrimers (see pyruvate acylation) except that *N*-methylmorpholine was added to neutralize dendrimer solution in MeOH. The Boc-deprotected intermediate was characterized by MALDI-TOF-MS: observed envelope of 12 000−16 000 with an apex at 15000; calculated average mass: 15511.6 Da.

Peptide Oximation. Conjugation with AoA-LYRAG (AoA-Leu-Tyr-Arg-Ala-Gly) was carried out as for homodendrimers (see above) in 0.1 M sodium acetate buffer (pH 4.6) containing 20% CH_3CN (v:v) and 0.1 M anilinium acetate, using a 1.5−2.0 molar excess of peptide over dendrimer pyruvate groups. The conjugation product was isolated after 20 h incubation at room temperature by HPLC.

Construction of Fluorescein-Labeled Homo- and Heterodendrimers. *G-3(ATOPA-NH$_2$)$_{16}$-S-FAM.* G-3(ATOPA-NH$_2$)$_{16}$-SH (15 mg, **I** in Scheme 2) was alkylated with a 5-fold excess of 4-iodoacetamidofluorescein (4-iodoacetamido-FAM) in 1 mL of semiaqueous buffer of 50 mM NaH_2PO_4, 5 mM EDTA, containing 50% acetonitrile at pH 7.0. After 2 h incubation at room temperature, the conjugation product was isolated by preparative HPLC and characterized by ESI-MS (observed average mass 7845.6 ± 1.1 Da; calculated average mass 7847.1 Da). Material recovered: 12 mg.

G-3(ATOPA-Mannose)$_{16}$-S-FAM. G-3(ATOPA-NH$_2$)-S-FAM was acylated with a 2-fold molar excess of the succinimide ester of 3-(2,3,4,6-tetra-*O*-acetyl-α-D-mannopyranosylthio) propionic acid as described above. Material was purified after deprotection by gel filtration on a Phenomenex S2000 column equilibrated in 20% CH_3CN containing 0.1% TFA. Material recovered: 10 mg.

G-3(ATOPA-Pyr)$_{16}$-S-FAM. G-3(ATOPA-NH$_2$)-S-FAM (7 mg) was acylated with a 5-fold molar excess of Pyruvate-OSu in the presence of 3 equiv of *N*-methylmorpholine per free amino group in a MeOH/CH_2Cl_2 (1:1) mixture overnight at room temperature. The reaction medium was dried, purified by preparative HPLC, and characterized by ESI-MS (observed average mass 8966.3 ± 0.6 Da; calculated average mass 8968.1 Da. Material recovered: 8 mg.

G-3(ATOPA-Pyr=AoA-LYRAG)$_{16}$-S-FAM. AoA-LYRAG was conjugated to G-3(ATOPA-Pyr)$_{16}$-S-FAM by 48 h reaction at room temperature at a concentration of 0.2 mM using a 2-fold excess of peptide (with respect to the number of pyruvate functional groups on the dendrimer) in a buffer containing AcONa 0.1 M: CH_3CN (4:1 v/v) and 0.1 M anilinium acetate, pH 4.6. The conjugate was isolated by semipreparative HPLC on a C8 column and characterized by MALDI-TOF-MS (observed average mass for the highest substituted entity 19 143 Da (Na adduct); calculated mass 19 108).

G-3(ATOPA-Mannose)$_{16}$-S-AEEA-Lys(FAM)-ADOOA-S-G-3-(Pyruvate)$_{16}$ (bm). Construction of the heterodendrimer via a maleimido-AEEA-Lys(FAM)-ADOOA-maleimide linker (bm, see Supporting Information for details of synthesis) was carried out as with the nonlabeled PEG linker for the synthesis of G-3(ATOPA-NH$_2$)$_{16}$-S-PEG-S-G-3(NH-Boc)$_{16}$ (see above).

G-3(ATOPA-Mannose)$_{16}$-S-AEEA-Lys(FAM)-ADOOA-S-G-3-(Pyruvate)$_{16}$ (iac). The G-3(Boc)$_{16}$-SH half-dendrimer was alkylated with an iodoacetamide-AEEA-Lys(FAM)-ADOOA-iodoacetamide linker (iac, see Supporting Information for details of synthesis) by reacting a 2-fold molar excess of linker with the dendrimer in 0.1 M NaH_2PO_4 buffer containing 5 mM EDTA and 50% CH_3CN, pH 7.0. The conjugate was isolated by preparative HPLC on a C4 column, after overnight incubation, and characterized by ESI-MS (average observed mass 6091 ± 3 Da, calculated mass 6088 Da). The resulting material (2.1 μmol) was then reacted at room temperature with a 1.5-fold molar excess of G-3(ATOPA-NH$_2$)-SH in 0.1 M NaH_2PO_4 buffer containing 5 mM EDTA and 50% MeOH, pH 7.0, and the conjugate was isolated after 24 h incubation and characterized by ESI-MS (average observed mass 13 420.4 ± 2.9 Da, calculated mass 13 419.2 Da).

Table 1. Mass Spectrometric Characterization of Pyruvate-Conjugated Dendrimers

dendrimer	calculated average mass (Da)	observed mass (Da) ESI-MS
G-1$(Pyr)_8$	1990.4	1990.4 ± 0.4
G-2$(Pyr)_{16}$	4377.0	4376.7 ± 0.1[a]
G-3$(Pyr)_{32}$	9150.9	9170.1 ± 0.8[a]
G-1$(AEEA\text{-}Pyr)_8$	3151.8	3151.5 ± 0.1
G-2$(ATOPA\text{-}Pyr)_{16}$	8333.9	8333.4 ± 0.5

[a] ESI-MS spectra also identified contaminating products of 200 Da lower mass than the expected value (spectra are provided in Supporting Information).

Further functionalization with mannose and pyruvate was carried out as described for the nonfluorescent heterodendrimers.

Isolation of Lymph Node Dendritic Cells and Macrophages and Uptake Experiments. Balb/c mice (8−10 weeks old, Charles River Laboratories, L'Arbresle, France) were bred and kept according to requirements of the University of Geneva and Swiss and European guidelines. Single-cell suspensions of inguinal, axial, and brachial lymph nodes were prepared by enzymatic digestion as described.[24]

Cells (2×10^6 in 200 μL) were incubated with dendrimer preparations for 1 h at 37 or 4 °C. Cells were then preincubated with rat anti-CD16/32 mAb (2.4G2 clone) to block nonspecific antibody binding, and stained with conjugated antibodies against CD11c (HL3 clone), CD11b (M1/70 clone), and B220/CD45R (RA3−6B2 clone) (BD Pharmingen, San Diego, CA). Each sample was acquired on a FACS Canto cytometer and data were analyzed using *FlowJo* software (Tree Star, Ashland, OR). Total lymph-node cells were determined by forward/side scatter. Within this gate, $CD11c^+$ cells were taken to be dendritic cells, $CD11b^+$ $CD11c^-$ cells were taken to be macrophages, and $B220^+$ $CD11c^-$ $CD11b^-$ cells were taken to be B lymphocytes.

RESULTS

Pyruvate Conjugation of Dendrimers. Pyruvate dendrimers were successfully synthesized by acylation of the amine terminal groups of G-1, G-2, and G-3 PAMAM dendrimers with succinimide−activated pyruvate to yield G-1$(Pyr)_8$, G-2$(Pyr)_{16}$, and G-3$(Pyr)_{32}$ (see Scheme 1). Pyruvate acylation was also carried out on dendrimers of which the arms had been elongated through acylation with the amino-PEG-acids 2-[2-(Boc-amino) ethoxy]ethoxy}acetic acid (Boc-AEEA) and Boc-15-amino-4,7,-10,13-tetraoxapentanedecanoic acid (Boc-ATOPA) to yield G-1-$(AEEA\text{-}Pyr)_8$ and G-2$(ATOPA\text{-}Pyr)_{16}$.

All pyruvate conjugation reactions went to completion as determined by the ninhydrin test for remaining free amines. The resulting pyruvate dendrimers had the expected masses (Table 1) except the G-2$(Pyr)_{16}$ and G-3$(Pyr)_{32}$ pyruvate dendrimers, which gave ESI-MS data consistent with contaminating products of 200 Da lower mass than the expected value (spectra are provided in Supporting Information). These lower-mass products are most likely derived from lower-valency contaminants in the starting material. A loss of 200 Da corresponds not just to the lack of two pyruvate units but to the absence of two complete −$(NHCH_2CH_2NH\text{-pyruvate})$ units. Such contamination of higher-generation dendrimers with material lacking two terminal amine groups has been described.[6] The phenomenon is thought to be due to the formation of an intramolecular bis-amide instead of the addition of two ethylene diamines during manufacture.

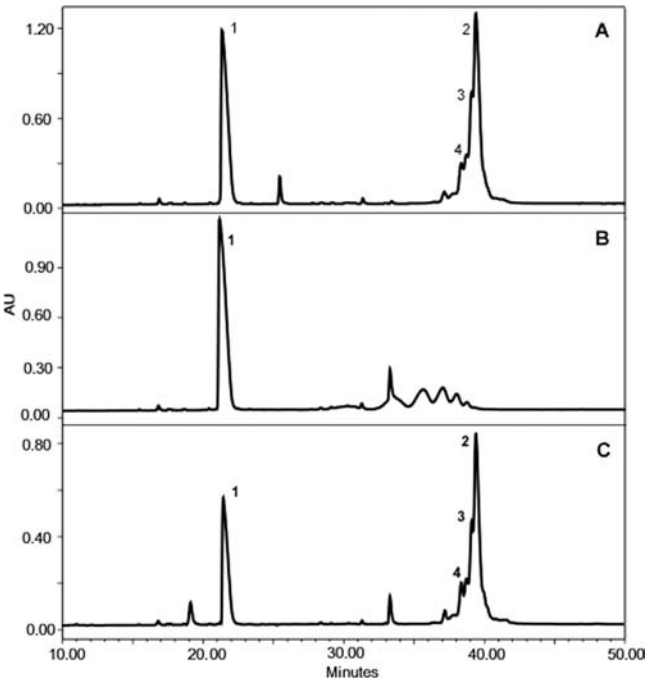


Figure 1. Importance of aniline catalysis for full decoration of pyruvate dendrimers by AoA-peptides and proteins. HPLC analyses of polyoxime formation after 15 h incubation at room temperature at various pH values, monitored at 214 nm. Reactions were carried out on 50 nmol G1-D$(Pyr)_8$ using 1.5 equiv AoA-LYRAG per dendrimer Pyr- group (excess elutes at 21.5 min). Peak 1 corresponds to the excess of AoA-peptide and peak 2 to the target octaoxime, while peaks 3 and 4 correspond to lower valency constructs (hexa- and pentaoxime). Trace A, reaction at pH 3.0 without anilinium acetate; trace B, reaction at pH 4.6; trace C, reaction at pH 4.6 in the presence of 0.1 M anilinium acetate.

Optimizing Conditions for Conjugation of Proteins and Peptides. The conditions for pyruvate−dendrimer conjugation with aminooxy-functionalized peptides and proteins were first optimized using the G-1$(Pyr)_8$ dendrimer and a small model peptide, AoA-LYRAG. Under previously established standard conditions for oxime ligation[7] but using pH values between 2 and 3 instead of the usual value of 4.6, the reaction goes essentially to completion (Figure 1A), with the hexa- and penta-oxime contaminants likely to have resulted from the decoration of lower-valency contaminants in the original dendrimer preparation (see above). Carrying out the reaction at pH 4.6 results in the formation of a mixture of conjugates containing mainly partially substituted intermediates and only traces of the fully substituted octamer (Figure 1B). When the reaction is carried out at pH 4.6 in the presence of 0.1 M aniline, however, the reaction goes essentially to completion (Figure 1C), yielding the fully substituted octamer together with the hexa- and penta-oxime contaminants seen in Figure 1A (these are also likely to have resulted from the decoration of lower valency contaminants in the original dendrimer preparation).

Evaluation of Mass Spectrometric Characterization Methods. Characterization of complex dendrimers with large peptide and protein substituents presents a methodological challenge, and we opted to evaluate ESI-TOF-MS (electrospray ionization time-of-flight mass spectrometry) and MALDI-TOF-MS as characterization tools. As reference materials, we used the octameric

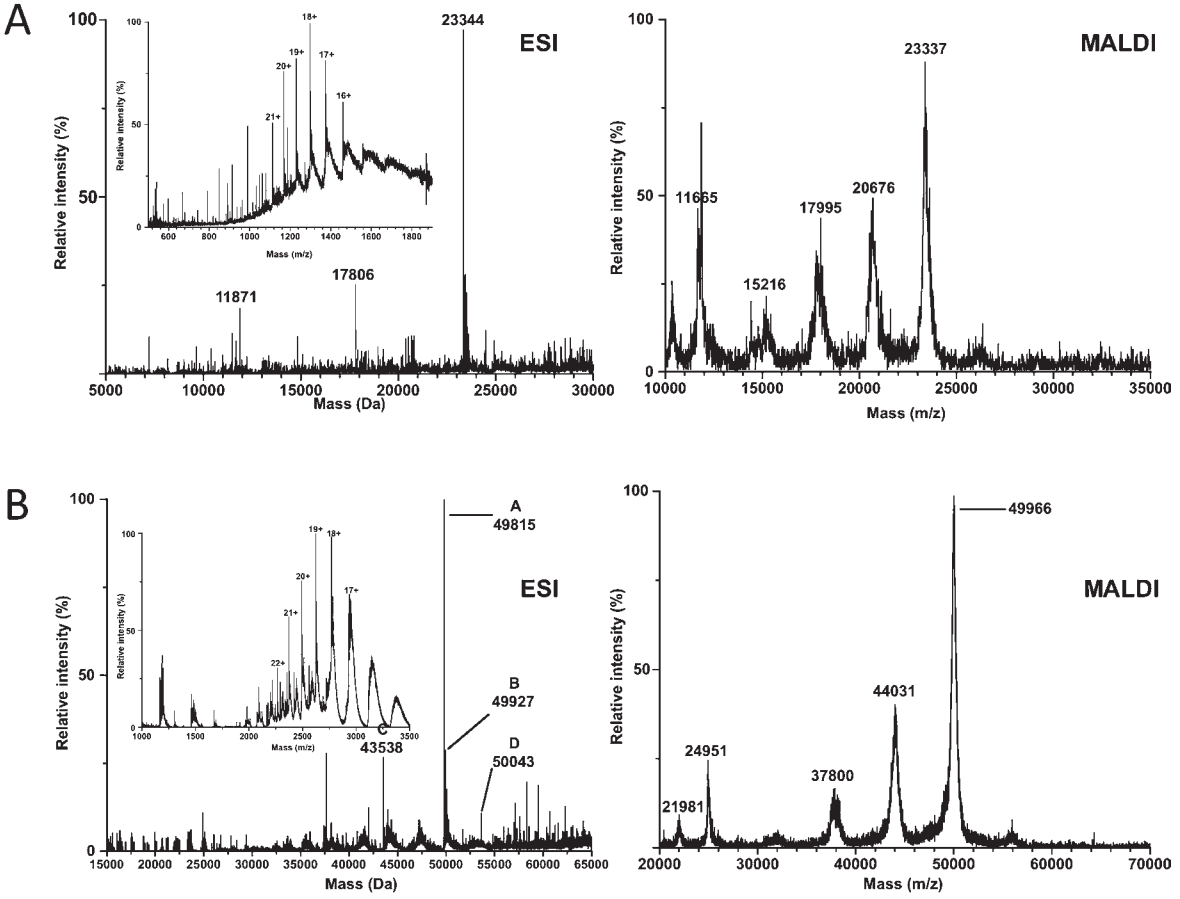


Figure 2. Experimental (inset) and deconvoluted ESI-TOF-MS of G-1(AEEA-Pyr=AoA-MVHA49−72)$_8$ (A) and G-1(AEEA-Pyr=AoA-Insulin)$_8$ (B) as compared with MALDI-TOF-MS. While ESI-TOF-MS analysis indicates that the samples predominantly contain fully decorated dendrimer with no traces of lower substituted contaminants, MALDI-TOF-MS analysis of the same samples reveals a mass component corresponding to the fully substituted dendrimer, plus mass components corresponding to the dendrimer lacking one, two, and three substituent moieties.

dendrimers resulting from the decoration of G-1(Pyr)$_8$ dendrimers with either AoA-MVHA49−72, yielding G-1(Pyr=AoA-MVHA49−72)$_8$, or AoA-insulin, yielding G-1(AEEA-Pyr=AoA-Insulin)$_8$. ESI-TOF-MS (Figure 2A) clearly indicated that in both cases the major component in the reaction mixture was indeed the fully decorated octamer (for AoA-MVHA49−72 observed average mass 23 343.8 ± 0.7 Da, calculated mass 23 344.5 Da; for AoA-insulin observed average mass 49 809 ± 5 Da, calculated mass 49 821.2 Da). The absence in the mixture of detectable levels of incompletely decorated material is indicative of the homogeneity of the reaction products. Analysis of the same material by MALDI-TOF-MS (Figure 2B) revealed peaks corresponding to the expected masses of the fully decorated octamers (observed average mass 23 401 Da for AoA-MVHA49−72; observed mass 48 862 Da for AoA insulin) plus a series of peaks corresponding to the expected masses minus multiples of the mass of the substituent moiety (i.e., approximately 2700 Da for MHVA(49−71) and 5800 Da for insulin). The absence of these lower mass species in the ESI-TOF mass spectra indicates that they do not correspond to incompletely decorated dendrimers but artifacts resulting from the destructive effect on the oxime bonds of the MALDI laser pulses, as described previously.[25] Hence, while ESI-TOF-MS has the advantage of being a non-destructive characterization method for the dendrimers in this study, it has the drawback of having, at least in our case, a ceiling size limit for detection at around 50 kDa. On the other hand, while MALDI-TOF-MS has the advantage of being able to detect dendrimers of higher mass, analysis of the results obtained should take account of the destructive effect of the laser pulses on oxime bonds.

Synthesis of Peptide and Protein-Conjugated Dendrimers. We next used the optimized oxime conjugation conditions to decorate a wider range of dendrimers (up to G-3), with or without arms extended by short PEG spacers, using the short LYRAG peptide, the longer measles virus hemeagluttenin (49−72) peptide, and recombinant insulin. The reaction products were characterized by mass spectrometry (Table 2).

These results indicate that the optimized oxime procedure yields fully decorated dendrimers from G-1 to G-3 either with or without PEG-extended arms and using three different aminooxy conjugated substituents. While the MALDI-TOF-MS spectra included signals corresponding to lower-substituted products, these would be expected to be due at least in part to the destructive effect of the laser desorption on oxime bonds (Figure 2).

Size exclusion chromatography of the reaction products revealed single symmetrical peaks for each product, with rank order of elution time (fastest to slowest) corresponding to rank order target size (largest to smallest; see Supporting Information, Figure S2).

Characterization of Insulin Dendrimers by SDS-PAGE. In order to further investigate the homogeneity of the dendrimer

Table 2. Peptide and Insulin Dendrimers Obtained by Aniline Catalyzed Oxime Bond Formation[a]

dendrimer	calculated average mass (Da)	observed average mass (Da) ESI-MS, ESI-TOF-MS MSMS	observed average mass (Da) MALDI-TOF-MS
G-1(Pyr=AoA-LYRAG)$_8$	7060.2	7060.1 ± 0.3	7061
G-2(Pyr=AoA-LYRAG)$_{16}$	14516.6	14517.4 ± 1.1	14520
G-3(Pyr=AoA-LYRAG)$_{32}$	29430.3	nd	envelope of 16000−29500
G-1(AEEA-Pyr=AoA-LYRAG)$_8$	8221.6	8221.5 ± 0.6	nd
G-2(ATOPA-Pyr=AoA-LYRAG)$_{16}$	18473.6	18472.6 ± 0.8	nd
G-1(Pyr=AoA-MVHA49−72)$_8$	23344.5	23344.4 ± 0.7	23450 ± 250
G-2(Pyr=AoA-MVHA49−72)$_{16}$	47113.3	nd	47200 ± 2003
G-3(Pyr=AoA- MVHA49−72)$_{32}$	94594.7	nd	envelope of 56000−95000
G-1(AEEA-Pyr=AoA-Insulin)$_8$	49821.2	49815.0 ± 1.0	49970 ± 500
G-2(ATOPA-Pyr=AoA-Insulin)$_{16}$	101672.8	nd	101500 ± 1000
G-1(Pyr=AoA-Insulin)$_8$	48659.8	nd	48700 ± 100
G-2(Pyr=AoA-Insulin)$_{16}$	97743.8	nd	98000 ± 1000
G-3(Pyr=AoA-Insulin)$_{32}$	195855.8	nd	envelope of 130000−190000

[a] All MALDI-TOF-MS mass determinations contain signals (probably artifactual, see text) attributable to lower substituted constructs (nd; not determined).

products, we used SDS-PAGE to analyze a series of insulin-decorated dendrimers of increasing complexity: G-1 (Pyr=AoA-Insulin)$_8$, G-1 (Pyr=AoA-Insulin)$_{16}$, and G-1 (Pyr=AoA-Insulin)$_{32}$ (Figure 3). Each sample appeared on the gel as a slower-migrating major component together with relatively few minor bands. On the basis of the mass spectrometric analysis of the same samples (Table 2), the major components most likely correspond to the fully decorated dendrimers. If this is the case, it would imply that size-dependent migration of the dendrimers on SDS-PAGE is not proportional to that of the globular protein markers, with the fully decorated G-1, G-2, and G-3 dendrimers, which have calculated masses of approximately 49, 98, and 196 kDa, respectively, migrating at positions corresponding to approximately 36, 50, and 100 kDa.

Comparison of the appearance of the G-1 (Pyr=AoA-Insulin)$_8$ sample on the gel with the corresponding ESI-TOF mass spectrum (Figure 2) indicates that sample treatment prior to gel loading is partially destructive. This is mostly likely because heating the samples in gel loading buffer led to brief exposure to basic pH levels at which oxime bonds are labile.[7] Despite this, the tight clustering bands close to the slowest migrating species, together with the absence of bands corresponding to unsubstituted material, provide further evidence of the high homogeneity of the decorated dendrimer samples.

Diblock Approach. The option of independently attaching multiple functional units to dendrimers via precision conjugation would be of significant value in the development of bioactive nanoparticles, and several different strategies have been employed to generate asymmetric bifunctional dendrimers.[8,13,14] With this aim in mind, we next worked on the development of a generic diblock heterodendrimer approach to be used as a scaffold for the display of an oxime-linked protein or peptide array together with an array corresponding to a second functional unit (Scheme 1).

A sample of G-3 PAMAM dendrimer with a cystamine core was divided into two batches, with one batch acylated with ATOPA and the other Boc-protected (**I** and **II** in Scheme 1). The modified dendrimer batches were then reduced, opening the cystamine core to yield sulfhydryl-bearing half-dendrimers. The ATOPA half-dendrimer (**I** in Scheme 1) was then alkylated with a moderate excess of bismaleimido-PEG linker, and the resulting monomaleidimido product (**III** in Scheme 1) was used to alkylate the Boc-protected half dendrimer (**II** in Scheme 1). This yields the heterodendrimer precursor, G-3(ATOPA-NH$_2$)$_{16}$-S-PEG-S-G-3(Boc)$_{16}$ (**IV** in Scheme 1).

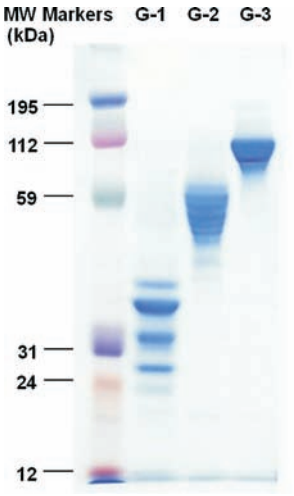


Figure 3. SDS-PAGE analysis of G-1 (Pyr=AoA-Insulin)$_8$, G-2 (Pyr=AoA-Insulin)$_{16}$, and G-1 (Pyr=AoA-Insulin)$_{32}$ (indicated as G-1, G-2, and G-3) indicating that dendrimer samples from each reaction show very limited dispersity.

This heterodendrimer precursor provides a versatile diblock platform for producing nanoparticles carrying two different sets of functional units. The first type of functional unit can be attached by acylation of the ATOPA amine groups on one-half of the heterodendrimer; then, a deprotection step can be used to reveal the amine groups on the other half of the heterodendrimer for attachment of the second type of functional unit.

Mannosylated Dendrimers. We chose to use the diblock approach to produce a heterodendrimer carrying a peptide on one side and a mannose array on the other (Scheme 2). Nanoparticles of this kind are of interest in the development of vaccine delivery vehicles, where the peptide or protein cargo would be an immunizing antigen and purpose of the mannose array is to

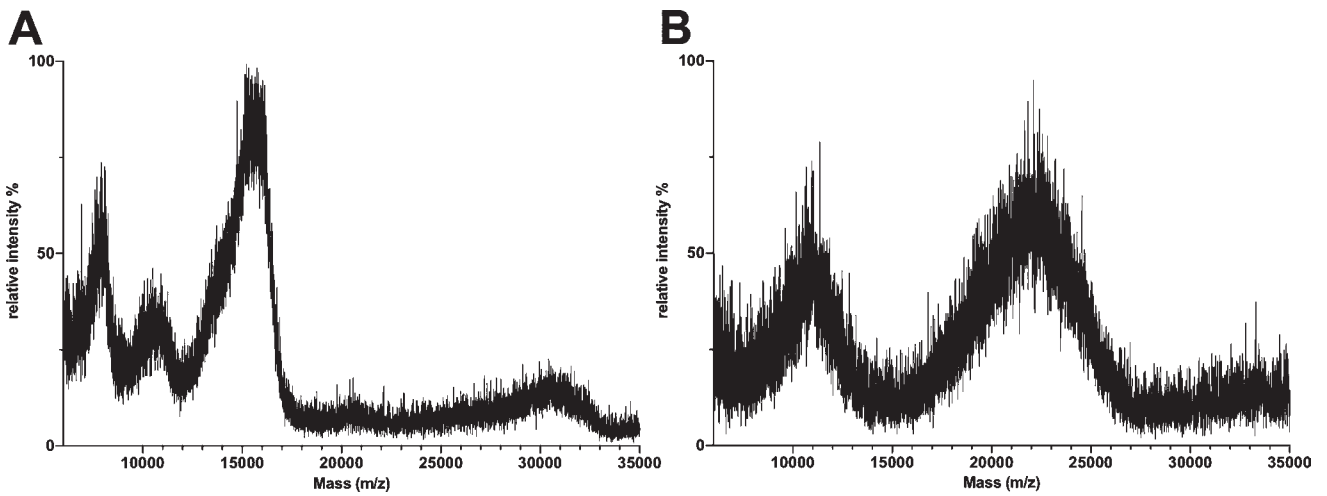


Figure 4. MALDI-TOF-MS characterization of G-3 (ATOPA-Mannose)$_{16}$-S-PEG-S-G-3(Pyruvate)$_{16}$ and the peptide-conjugated product. Respective theoretical average masses of fully substituted compounds are 16 633 and 26 772 Da.

specifically target the particle to macrophages and dendritic cells, whose efficient uptake of particulate antigens is crucial in the generation of strong immune responses.[19,20] While dendrimer conjugation with mannose has been achieved using both 4-isothiocyanatophenyl-α-D-mannopyranoside and 3-(2,3,4,6-tetra-*O*-acetyl-α-D-mannopyranosylthio)propionic acid,[5] the phenyl ring in the thiourea linker of the former reagent leads to a significantly hydrophobic product, and in the interest of hydrosolubility of the final product, we opted for the latter. The resulting mannosylated heterodendrimer (**V** in Scheme 2) was then Boc-deprotected and acylated with pyruvate, yielding a mannosylated pyruvate dendrimer (**VI** in Scheme 2) ready for oxime conjugation with aminooxy-peptides or proteins. For the purposes of this study, we used the model peptide AoA-LYRAG to produce the final product, a mannose−peptide heterodendrimer (**VII** in Scheme 2).

As expected, the heavily glycosylated mannose heterodendrimers migrated as diffuse bands on SDS-PAGE (data not shown), and as a consequence, this analytical method was not useful for their characterization. With regard to mass spectrometric analysis, while the starting heterodendrimer G-3 (ATOPA-NH_2)$_{16}$-S-PEG-S-G-3(Boc)$_{16}$ had a mass low enough to be characterized by ESI-MS (observed average mass 13 112.9 Da; calculated mass 13 108.9 Da), ESI-MS could not be used for analysis of the higher-molecular-weight glycodendrimers due to limitations of the technology, as noted previously.[26] According to MALDI-TOF-MS, mannose functionalization resulted in increased dispersity seen as a broadened peak with an envelope ranging between 6600 and 11 800 Da, apex at 9800 Da, for an expected value of 11 852 Da (Figure 4). The level of polydispersity introduced into our constructs at this stage is comparable with that seen in the work of others on carbohydrate conjugation of dendrimers,[6,26] including experiments in which dendrimers were directly modified with unprotected *p*-isothiocyanatophenyl α-D-mannopyranoside.[5]

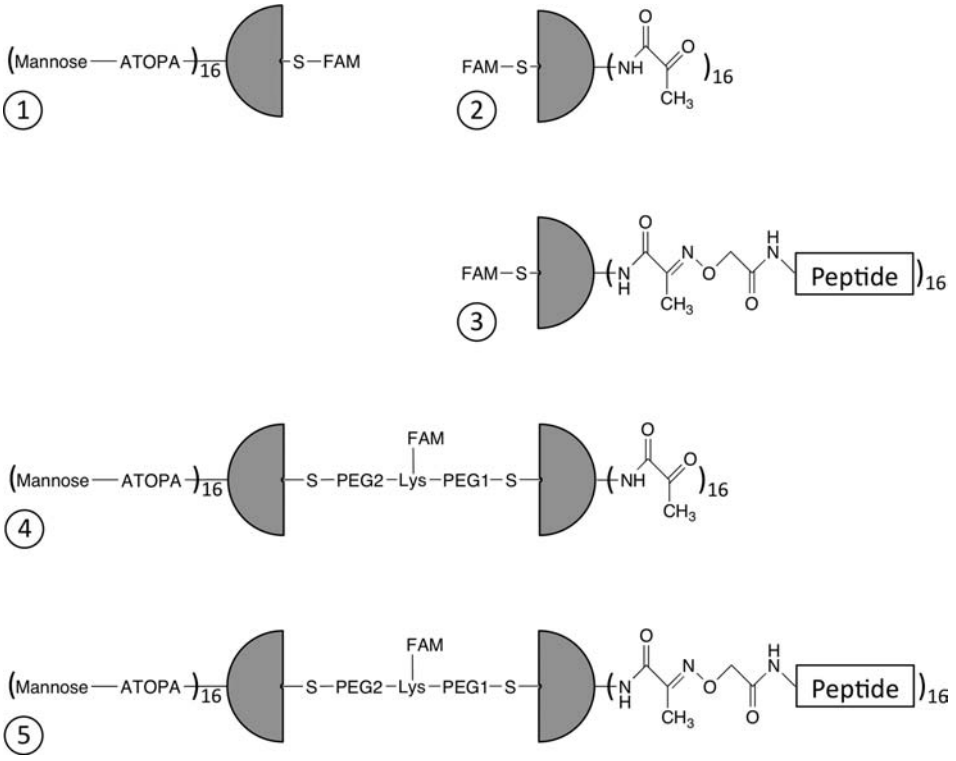
As expected, conjugating the mannosylated pyruvate heterodendrimer with AoA-LYRAG generated a mass shift (Figure 4), but while the theoretical shift is from 16 633 to 26 772 Da, the apexes of the observed peaks shifted from 15 500 to 22 100 Da, with the envelope of the product peak broadening further to span the range 16 000−26 000 Da. The lower apex mass value and further broadening of the product peak are most likely consequences of damage to oxime linkages during the MALDI process, as seen earlier with the insulin octamers (Figure 2). Hence, our results are consistent with complete peptide decoration of the mannosylated heterodendrimer.

Polymannose-Decorated Dendrimers Efficiently and Specifically Target Dendritic Cells and Macrophages. In order to investigate whether addition of a mannose array to dendrimers enhances uptake by sentinel cells, it was necessary to site-specifically incorporate a fluorescent label. We designed a panel of fluorescein-labeled constructs, three half-dendrimers labeled by alkylation of their core sulfhydryl group, and two diblock constructs labeled on the linker used to join the two half-dendrimers together (a G-3(ATOPA-NH_2)$_{16}$-S-PEG-S-G-3(Boc)$_{16}$ heterodendrimer in which N^{ε}-fluoresceinyl-lysine was introduced into the structure of the linker) (Scheme 3).

We had initially attempted to produce the labeled heterodendrimers by replacing the bismaleimidoPEG linker (see Scheme 2) with a maleimido-AEEA-Lys(FAM)-ADOOA-maleimide linker, but as previously seen for immunoconjugates,[27] these maleimide-linked structures showed limited stability at basic pH. Since mild basic conditions are required for the per-O-acetylmannose deprotection, we opted to make use of a diiodoacetyl analogue of the linker (see Supporting Information for further details) instead. Analysis by MALDI-TOF-MS confirmed that the fluorescent heterodendrimers made in this way were decorated with mannose and peptide to levels comparable with the nonfluorescent versions (see Supporting Information).

These fluorescent constructs (II through V in Scheme 3) were evaluated for specific *in vitro* uptake by sentinel cells using a flow cytometry technique on cell populations prepared from mouse lymph nodes (Figure 5). Lymphocytes predominate in this mixed population, which also contains dendritic cells and macrophages. While fluorescence uptake across the whole cell population was relatively low (Figure 5A), it was strongly and specifically enriched in the dendritic cell and macrophage groups (Figure 5B, C). Within these groups, mannose-functionalized half-dendrimers show a strongly increased uptake compared with the corresponding pyruvate functionalized dendrimers (Figure 5B,C). In the same way, uptake of the pyruvate-functionalized mannosylated heterodendrimer is strongly increased compared to the corresponding pyruvate-conjugated half-dendrimer. Importantly,

Scheme 3. Fluorescent Dendrimers Used in the Study of Mannose-Specific Uptake by Sentinel Cells[a]



[a] (1) Mannose G-3 half-dendrimer; (2) pyruvate G-3 half-dendrimer; (3) LYRAG peptide G-3 half-dendrimer; (4) mannose-pyruvate G-3 heterodendrimer; (5) mannose-LYRAG peptide G-3 heterodendrimer. Details of the structure and synthesis of the fluorescein linker (FAM) are provided in Supporting Information.

incorporation of mannose into dendrimers did not increase fluorescence incorporation into lymphocytes, which do not express mannose receptors (Figure 5D). Uptake of mannosylated dendrimer was blocked when incubation carried out at 4 °C (data not shown) and in the presence of mannan, a mannose receptor ligand (data not shown) suggesting an active uptake process by the macrophage and dendrimer cells groups mediated by mannose receptors.

Hence, in agreement with previous observations,[18,21] our results indicate that incorporation of a mannose array into nanoparticles strongly and specifically enhances uptake by macrophages and dendritic cells, most likely via surface lectin-mediated endocytosis. Enhanced uptake is not hindered by incorporation of a second half-dendrimer displaying a peptide array. Conjugating the pyruvate dendrimers with the LYRAG peptide also leads to a modest increase in incorporation, whether or not the particles carry mannose. The effect is nonspecific, i.e., nonsentinel cells showed similar levels of uptake as sentinel cells. LYRAG is a basic sequence, and this phenomenon is almost certainly a consequence of the polycation-mediated cell uptake a well-known and generalized phenomenon, exploited in gene delivery[28] and peptide transduction[29] strategies.

■ DISCUSSION

Dendrimers are readily synthesized, low-cost, monodisperse, high-valency molecular scaffolds, and as such represent promising building blocks for the generation of bioactive nanoparticles for use as both clinical and experimental tools.[1,2] However, a major obstacle in their use in these applications has been the absence of a conjugation chemistry powerful enough to fully decorate high-valency dendrimers with protein and peptide ligands.

In this study, we have made use of recent advances in oxime technology to develop an optimized conjugation strategy for decorating PAMAM dendrimers with peptides and proteins. The size range of the target products is close to or beyond the upper limit for the characterization methods typically used in protein chemistry, and although we opted to use different characterization methods, each one was subject to particular limitations: (i) the ESI-TOF-MS facilities that we used had an upper detection limit of 50 kDa for dendrimer-derived products; (ii) the MALDI-TOF-MS desorption process is partially destructive toward molecules containing oxime bonds [25] (Figure 2), as is (iii) heating samples in loading buffer prior to SDS-PAGE (Figure 3). Nonetheless, the combined evidence obtained from these three methods indicates that our conjugation strategy readily yielded highly homogeneous preparations of fully decorated dendrimers of up to 32 valency (G-3) obtained using both a synthetic 23mer virus-derived peptide and porcine insulin. This is an important breakthrough, since previous work on dendrimer conjugation has not yielded fully decorated dendrimers more complex than octamers. Because of the difficulties involved in the characterization of very large molecular products, we did not attempt to conjugate dendrimers of higher generation than G-3 in this study. Full decoration of larger, higher valency scaffolds should nonetheless be feasible, as long as the surface density of reactive groups does not reach a level where conjugation is limited by steric blockade. Should that occur, the problem could readily be addressed by

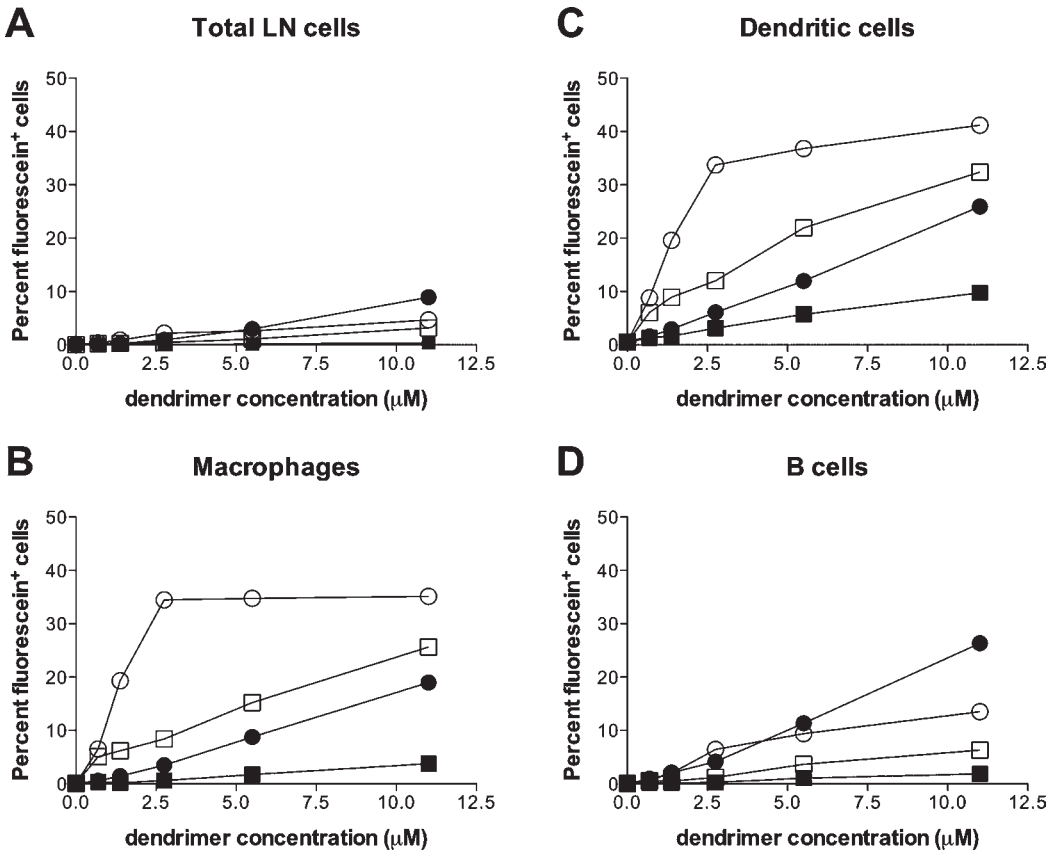


Figure 5. Specific mannose-dependent uptake of dendrimer nanoparticles by sentinel cells. Uptake of fluorescein-conjugated dendrimers (see Scheme 3) by cells prepared from mouse lymph nodes was detected by flow cytometry (FL-1 channel) on gated subpopulations (as indicated) after incubating the total cell population with dendrimers at different concentrations for 1 h at 37 °C. Filled squares, pyruvate G-3 half-dendrimer (16mer) (**2**); filled circles, LYRAG peptide G-3 half-dendrimer (16mer) (**3**); empty squares, mannose-pyruvate G-3 heterodendrimer (16mer + 16mer) (**4**); empty circles, mannose-LYRAG G-3 heterodendrimer (16mer + 16mer) (**5**).

elongation of the dendrimer arms through the attachment of flexible precision PEG chains such as AEEA or ATOPA (Table 2).

Importantly, the oxime conjugation strategy that we have developed is likely to be robust enough to be readily usable with a wide range of peptides and proteins, of both synthetic and recombinant origin. Use of recombinant proteins will generally require the introduction of an appropriate molecular hook for aminooxy modification. This could involve engineering either an extra surface cysteine residue to provide a free sulfhydryl group or an N-terminal serine or threonine residue, which could be quantitatively oxidized under extremely mild conditions to yield an aldehyde[30] for further functionalization.

Diblock Dendrimers: A Platform for Orthogonal Attachment of Two Functional Sets. Techniques that enable the specific incorporation of more than one functional unit (e.g., targeting ligand, payload, tracer) into the dendrimer architecture would be advantageous in the development of bioactive nanoparticles,[1,2] and a number of strategies for the generation of heterodendrimers have been proposed.[8,13,14] These approaches have the drawback of not being compatible with the use of commercially available starting materials, and in this context, it is significant that the orthogonal diblock strategy developed in this study centers on readily produced, commercially available cystamine core PAMAM dendrimers.

We chose to use mannose as the first functional unit, as there has been considerable interest in the development of carbohydrate-conjugated dendrimers,[5,6] and incorporation of a mannose array into a nanoparticle-based vaccine vehicle has the potential to increase immunogenicity by enhancing uptake processing and presentation by sentinel cells such as macrophages and dendritic cells.[19−21] An array of short synthetic peptide molecules attached via oxime conjugation was used as the second functional unit. Notwithstanding the additional challenge to characterization imposed by the incorporation of mannose residues into the dendrimers, we were able to confirm (Figure 4) that (i) the mannose-conjugated heterodendrimers could be fully decorated with a peptide array using the optimized oximation approach and (ii) mannose conjugation levels comparable to those reported in previous studies were obtainable. More efficient mannose conjugation might be achieved through the use of Cu(I) catalyzed azide−alkyne cycloaddition[10] because it is compatible with direct use of unprotected carbohydrate.

In order to visualize uptake of these particles by sentinel cells, it was necessary to devise a conjugation approach for site-specific conjugation of a third functional unit so that the particles could be derivatized with a fluorochrome. With the resulting trifunctionalized dendrimers, we were able to demonstrate that, in agreement with previously published work,[18−21] incorporation of a mannose array strongly and specifically enhances uptake of the dendrimers by sentinel cells. Mannose heterodendrimers may represent promising vaccine delivery vehicles for peptide and protein cargoes, and the conjugated linker could be used either to attach a fluorescent dye to aid the study of vehicle uptake *in vivo*[31]

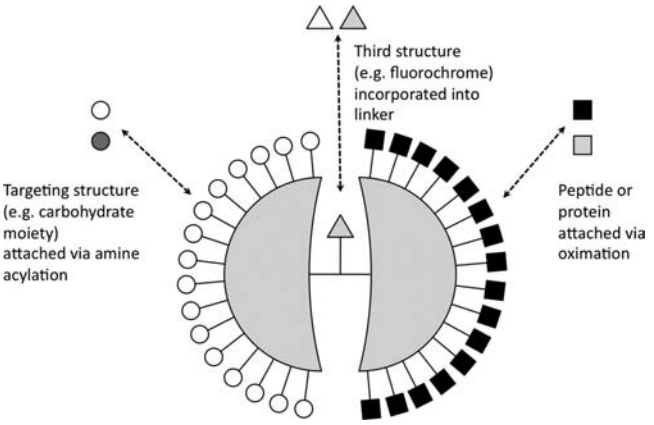


Figure 6. Versatile platform for synthesis of bioactive nanoparticles.

or to attach an immune modulator structure (e.g., a Toll-like receptor ligand) to enhance adjuvant activity.[32]

CONCLUSION

We believe that we have developed a robust new dendrimer conjugation strategy which can be used not only for the production of large multivalent dendrimers fully decorated with proteins and peptides, but also for the generation of specifically bi- and trifunctionalized dendrimers (Figure 6).

Given the mild conjugation conditions involved, the strategy should be applicable for dendrimer derivatization using a wide range of biologically relevant structures, providing a convenient platform for the production of bioactive nanoparticles for use in a wide range of clinical applications.

ASSOCIATED CONTENT

Supporting Information. Characterization of pyruvate-functionalized PAMAM dendrimers; size exclusion chromatography analysis of peptide-decorated dendrimers; synthesis of PEG linkers for dendrimer arm extension; synthesis and characterization of bifunctional linkers; synthesis and characterization of linker-conjugated mannose; mass spectrometry characterization of key intermediates IV (Scheme 1 in main text) and V (Scheme 2 in main text); characterization of fluorescein-labeled homo- and heterodendrimers. This material is available free of charge via the Internet at http://pubs.acs.org.

AUTHOR INFORMATION

Corresponding Author

*E-mail: oliver.hartley@unige.ch. Tel: +41 22 379 54 75. Fax +41 22 379 55 02.

ACKNOWLEDGMENT

We thank Robin Offord and Sylvie Tchertchian for critical discussion and the NMR group of Dr. Damien Jeannnerat at the University of Geneva for providing NMR spectra. We gratefully acknowledge support from Dormeur Investment Service Ltd.

REFERENCES

(1) Lee, C. C., MacKay, J. A., Frechet, J. M., and Szoka, F. C. (2005) Designing dendrimers for biological applications. *Nat. Biotechnol. 23*, 1517–26.

(2) Boas, U., and Heegaard, P. M. (2004) Dendrimers in drug research. *Chem. Soc. Rev. 33*, 43–63.

(3) Esfand, R., and Tomalia, D. A. (2001) Poly(amidoamine) (PAMAM) dendrimers: from biomimicry to drug delivery and biomedical applications. *Drug Discovery Today 6*, 427–436.

(4) Mammen, M., Choi, S.-K., and Whitesides, G. M. (1998) Polyvalent interactions in biological systems: implications for design and use of multivalent ligands and inhibitors. *Angew. Chem., Int. Ed. 37*, 2754–2794.

(5) Woller, E. K., and Cloninger, M. J. (2001) Mannose functionalization of a sixth generation dendrimer. *Biomacromolecules 2*, 1052–4.

(6) Woller, E. K., Walter, E. D., Morgan, J. R., Singel, D. J., and Cloninger, M. J. (2003) Altering the strength of lectin binding interactions and controlling the amount of lectin clustering using mannose/hydroxyl-functionalized dendrimers. *J. Am. Chem. Soc. 125*, 8820–6.

(7) Rose, K., Zeng, W., Regamey, P. O., Chernushevich, I. V., Standing, K. G., and Gaertner, H. F. (1996) Natural peptides as building blocks for the synthesis of large protein- like molecules with hydrazone and oxime linkages. *Bioconjugate Chem. 7*, 552–6.

(8) Mitchell, J. P., Roberts, K. D., Langley, J., Koentgen, F., and Lambert, J. N. (1999) A direct method for the formation of peptide and carbohydrate dendrimers. *Bioorg. Med. Chem. Lett. 9*, 2785–8.

(9) van Baal, I., Malda, H., Synowsky, S. A., van Dongen, J. L., Hackeng, T. M., Merkx, M., and Meijer, E. W. (2005) Multivalent peptide and protein dendrimers using native chemical ligation. *Angew. Chem., Int. Ed. Engl. 44*, 5052–7.

(10) Chun, C. K. Y., and Payne, R. J. (2009) Synthesis of MUC1 peptide and glycopeptide dendrimers. *Aust. J. Chem. 62*, 1339–1343.

(11) Yim, C. B., Boerman, O. C., de Visser, M., de Jong, M., Dechesne, A. C., Rijkers, D. T., and Liskamp, R. M. (2009) Versatile conjugation of octreotide to dendrimers by cycloaddition ("click") chemistry to yield high-affinity multivalent cyclic peptide dendrimers. *Bioconjugate Chem. 20*, 1323–31.

(12) Lempens, E. H., van Baal, I., van Dongen, J. L., Hackeng, T. M., Merkx, M., and Meijer, E. W. (2009) Noncovalent synthesis of protein dendrimers. *Chemistry 15*, 8760–7.

(13) Wu, P., Malkoch, M., Hunt, J. N., Vestberg, R., Kaltgrad, E., Finn, M. G., Fokin, V. V., Sharpless, K. B., and Hawker, C. J. (2005) Multivalent, bifunctional dendrimers prepared by click chemistry. *Chem. Commun. (Camb.)* 5775–7.

(14) Dirksen, A., Meijer, E. W., Adriaens, W., and Hackeng, T. M. (2006) Strategy for the synthesis of multivalent peptide-based nonsymmetric dendrimers by native chemical ligation. *Chem. Commun. (Camb.)* 1667–9.

(15) Kochendoerfer, G. G., Tack, J. M., and Cressman, S. (2002) Total chemical synthesis of a 27 kDa TASP protein derived from the MscL ion channel of M. tuberculosis by ketoxime-forming ligation. *Bioconjugate Chem. 13*, 474–80.

(16) Dirksen, A., Dirksen, S., Hackeng, T. M., and Dawson, P. E. (2006) Nucleophilic catalysis of hydrazone formation and transimination: implications for dynamic covalent chemistry. *J. Am. Chem. Soc. 128*, 15602–3.

(17) Dirksen, A., Hackeng, T. M., and Dawson, P. E. (2006) Nucleophilic catalysis of oxime ligation. *Angew. Chem., Int. Ed. Engl. 45*, 7581–4.

(18) Angyalosi, G., Grandjean, C., Lamirand, M., Auriault, C., Gras-Masse, H., and Melnyk, O. (2002) Synthesis and mannose receptor-mediated uptake of clustered glycomimetics by human dendritic cells: effect of charge. *Bioorg. Med. Chem. Lett. 12*, 2723–7.

(19) Geijtenbeek, T. B. H., and Gringhuis, S. I. (2009) Signalling through C-type lectin receptors: shaping immune responses. *Nat. Rev. Immunol. 9*, 465–479.

(20) Rieger, J., Freichels, H., Imberty, A., Putaux, J.-L., Delair, T., Jérôme, C., and Auzély-Velty, R. (2009) Polyester nanoparticles presenting

mannose residues: toward the development of new vaccine delivery systems combining biodegradability and targeting properties. *Biomacromolecules 10*, 651–657.

(21) Sheng, K. C., Kalkanidis, M., Pouniotis, D. S., Esparon, S., Tang, C. K., Apostolopoulos, V., and Pietersz, G. A. (2008) Delivery of antigen using a novel mannosylated dendrimer potentiates immunogenicity in vitro and in vivo. *Eur. J. Immunol. 38*, 424–36.

(22) Kaiser, E., Colescott, R. L., Bossinger, C. D., and Cook, P. I. (1970) Color test for detection of free terminal amino groups in the solid-phase synthesis of peptides. *Anal. Biochem. 34*, 595–598.

(23) Gaertner, H., Offord, R., Botti, P., Kuenzi, G., and Hartley, O. (2008) Semisynthetic analogues of PSC-RANTES, a potent anti-HIV protein. *Bioconjugate Chem. 19*, 480–9.

(24) Kamath, A. T., Valenti, M. P., Rochat, A. F., Agger, E. M., Lingnau, K., von Gabain, A., Andersen, P., Lambert, P. H., and Siegrist, C. A. (2008) Protective anti-mycobacterial T cell responses through exquisite in vivo activation of vaccine-targeted dendritic cells. *Eur. J. Immunol. 38*, 1247–56.

(25) Nardin, E. H., Calvo-Calle, J. M., Oliveira, G. A., Clavijo, P., Nussenzweig, R., Simon, R., Zeng, W., and Rose, K. (1998) Plasmodium falciparum polyoximes: highly immunogenic synthetic vaccines constructed by chemoselective ligation of repeat B-cell epitopes and a universal T-cell epitope of CS protein. *Vaccine 16*, 590–600.

(26) Ashton, P. R., Boyd, S. E., Brown, C. L., Nepogodiev, S. A., Meijer, E. W., Peerlings, H. W. I., and Stoddart, J. F. (1997) Synthesis of glycodendrimers by modification of poly(propylene imine) dendrimers. *Chem.—Eur. J. 3*, 974–984.

(27) Presentini, R., and Terrana, B. (1995) Influence of the antibody-peroxidase coupling methods on the conjugate stability and on the methodologies for the preservation of the activity in time. *J. Immunoassay 16*, 309–24.

(28) Pack, D. W., Hoffman, A. S., Pun, S., and Stayton, P. S. (2005) Design and development of polymers for gene delivery. *Nat. Rev. Drug Discovery 4*, 581–593.

(29) Wadia, J. S., and Dowdy, S. F. (2002) Protein transduction technology. *Curr. Opin. Biotechnol. 13*, 52–56.

(30) Gaertner, H. F., and Offord, R. E. (1996) Site-specific attachment of functionalized poly(ethylene glycol) to the amino terminus of proteins. *Bioconjugate Chem. 7*, 38–44.

(31) Misumi, S., Masuyama, M., Takamune, N., Nakayama, D., Mitsumata, R., Matsumoto, H., Urata, N., Takahashi, Y., Muneoka, A., Sukamoto, T., Fukuzaki, K., and Shoji, S. (2009) Targeted delivery of immunogen to primate M cells with tetragalloyl lysine dendrimer. *J. Immunol. 182*, 6061–6070.

(32) Pashine, A., Valiante, N. M., and Ulmer, J. B. (2005) Targeting the innate immune response with improved vaccine adjuvants. *Nat. Med. 11*, S63–8.

Supporting Information

1. Characterization of pyruvate–functionalized PAMAM dendrimers 2

2. Size exclusion chromatography analysis of peptide-decorated dendrimers 3

3. Synthesis of PEG linkers for dendrimer arm extension 4

4. Synthesis and characterization of bifunctional linkers 4

5. Synthesis and characterization of linker-conjugated mannose 7

6. Mass spectrometry characterization of key intermediates IV (scheme 1 in main text) and V (scheme 2 in main text). 10

7. Characterization of fluorescein-labeled homo- and heterodendrimers 11

1. Characterization of pyruvate–functionalized PAMAM dendrimers

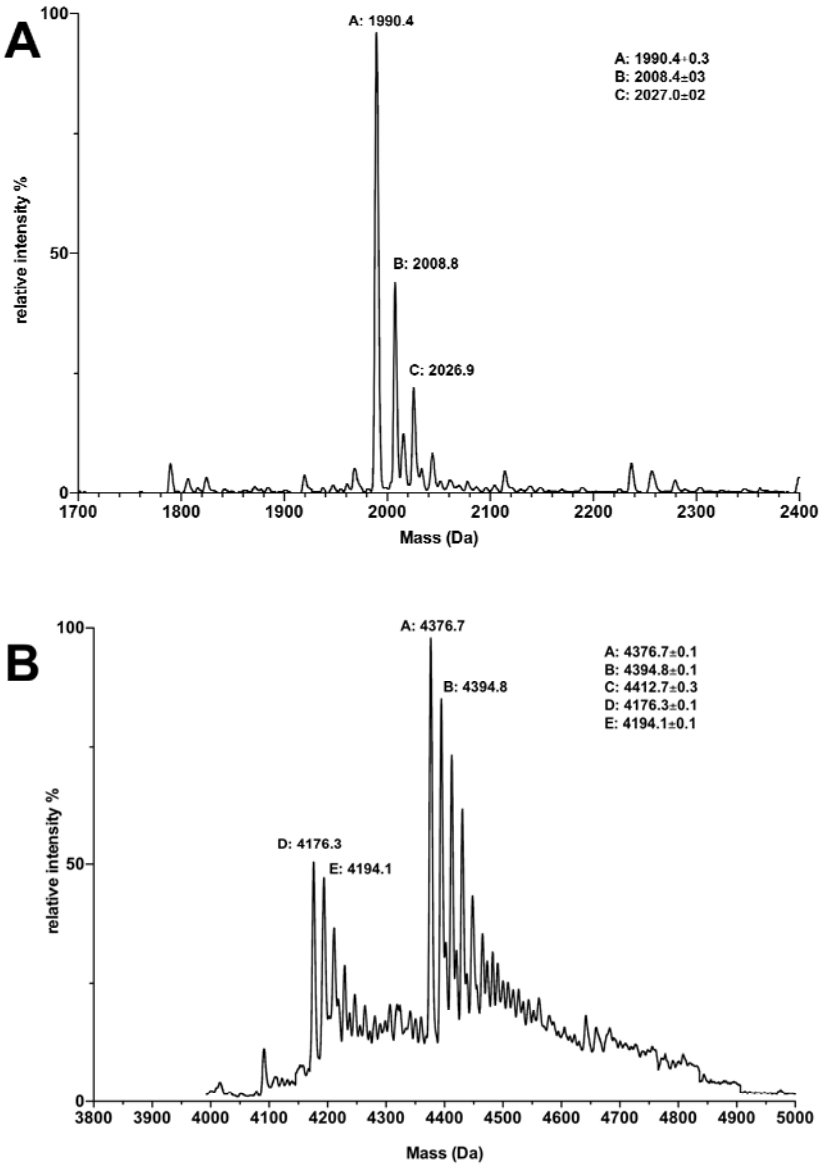


Figure S1. ESI-MS of G1-$(Pyr)_8$ (I) and G2-$(Pyr)_{16.}$ (II). **(A)** The spectrum of (I) is that of a major component of average mass 1990.4 in agreement with the calculated average value of 1990.4 Da. Minor signals are consistent with the presence of water adducts and a truncated parent compound of mass 1790 Da. **(B)** For G2-$(Pyr)_{16}$, the major component of average mass 4376.7 Da (calculated: 4377.0) is contaminated with a truncated parent compound of mass 4176.3 Da. Both components show water adducts.

NMR characterization of G2-(Pyr)16

^{1}H NMR (500 MHz, CD3OD) : δ = 2.52 (s, 48 H, CH3), 2.81-3.05 (m, CH2), 3.42-3.84 (m, CH2).

^{13}C NMR (125.76 MHz, CD3OD) : δ = 18.36, 24.91, 25.59, 29.52, 29.80, 35.57, 39.52, 39.79, 39.93, 40.26, 51.19, 51.46, 53.71, 58.31, 67.89, 71.33, 79.46, 97.85, 114.65, 116.98, 119.31, 121.64, 162.33, 162.88, 163.21, 172.69, 172.79, 172.87, 173.65, 174.51, 197.68.

2. Size exclusion chromatography analysis of peptide-decorated dendrimers

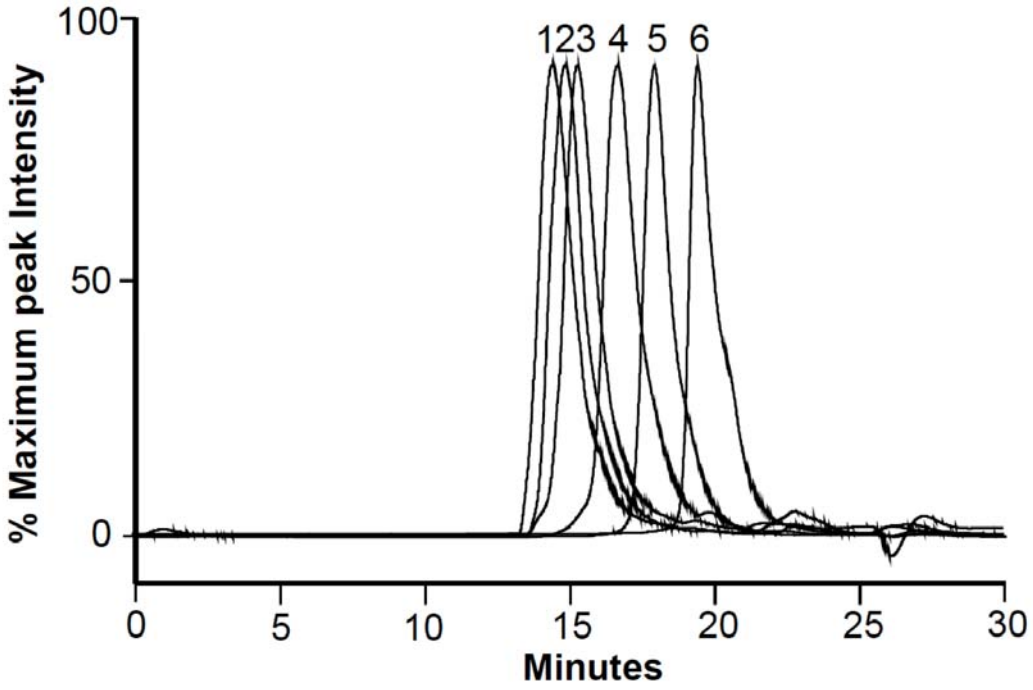


Figure S2. Size exclusion chromatography of peptide and insulin-dendrimers was performed on a Phenomenex BioSep-Sec-S2000 600 x 7.8mm column equilibrated in 0.1% TFA, 20% (v:v) CH_3CN, flow rate 1ml/min. Peaks eluted in the expected order with respect to target product size (largest to smallest): (1) G-3(Pyr=AoA-Insulin)$_{32}$, (2) G-2(ATOPA-Pyr=AoA-Insulin)$_{16}$ (3) G-2(Pyr=AoA-Insulin)$_{16}$, (4) G-1(Pyr=AoA-Insulin)$_{8}$, (5) G-2(Pyr=AoA-LYRAG)$_{16}$ and (6) G-1(Pyr=AoA-LYRAG)$_{8}$. For calculated average masses, see Table 2 in main text.

3. Synthesis of PEG linkers for dendrimer arm extension

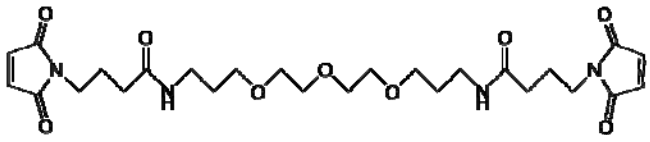
Boc-ATOPA-OPfp

The pentafluorophenol ester (-OPfp) was prepared by activation of Boc-15-amino-4,7,10,13-tetraoxapentanedecanoic acid (Boc-ATOPA) with 1 equivalent of DCC and 1 equivalent of N-hydroxysuccinimide (NHS) in ethyl acetate (EtOAc). The mixture was stirred overnight and filtered to remove the precipitate. The solvent was evaporated under reduced pressure and the oily product obtained was used without further purification. Boc-ATOPA-OPfp was preferred over the -OSu derivative because use of the latter compound resulted in significant formation of β-alanine adducts during coupling to the dendrimer, probably through Lossen rearrangement as previously described for PEG succinimide carbonates (*21*).

4. Synthesis and characterization of bifunctional linkers

Bismaleimido-4,7,10-trioxa-1,13-tridecanediamine

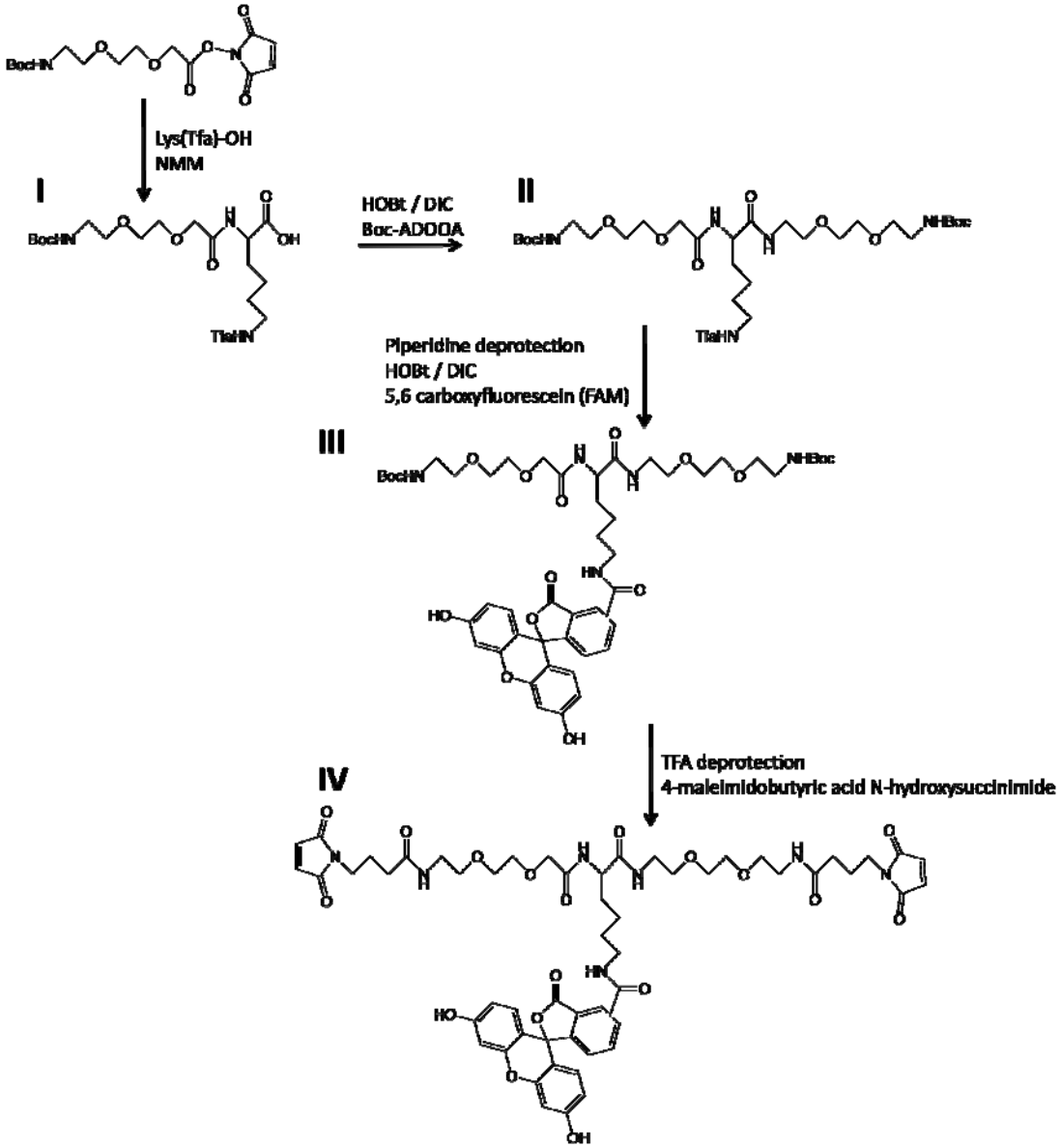
4-Maleimidobutyric acid N-hydroxysuccinimide ester was reacted in a 1.5-fold excess over amino groups of 4,7,10-trioxa-1,13-tridecanediamine (ATOTA) in DMF. After 3 h incubation, the bis-maleimido-ATOTA linker was isolated by preparative HPLC and characterized by ESI-MS ($[M+H]^+$ expected: 551.6; observed: 551.6).



Bismaleimido-4,7,10-trioxa-1,13-tridecanediamine linker

Maleimido-AEEA-Lys (FAM)-ADOOA-Maleimide

The fluorescein-labelled linker was prepared by incorporation of a side chain-protected lysine residue between {2-[2-(Boc-amino)ethoxy]ethoxy} acetic acid (Boc-AEEA) and 1-(Boc-amino)-3,6-dioxa-8-octaneamine (Boc-ADOOA), 5,6 carboxy-fluorescein (FAM) being attached on the lysine side chain. The separate steps involved in the synthesis are shown below.



Scheme S1. Synthesis of maleimido-AEEA-Lys (FAM)-ADOOA-Maleimide linker (**IV**)

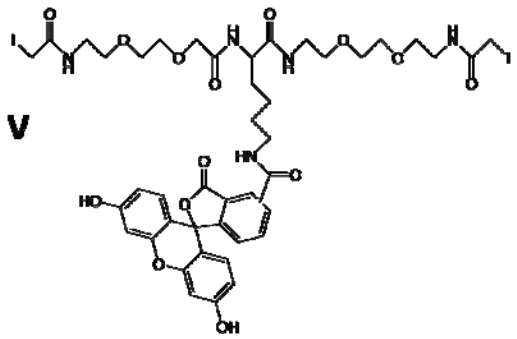
(i) Boc-AEEA-Lys-ADOOA-Boc. {2-[2-(Boc-amino)ethoxy]ethoxy} acetic acid N-hydroxysuccinimide (Boc-AEEA-OSu) was reacted with a 1.2 fold excess of Lys(TFA)-OH in DMSO in the presence of NMM. The resulting product, Boc-AEEA-Lys(TFA)-OH (**I** in Scheme S1) was isolated by preparative HPLC and characterized by ESI-MS ($[M+H]^+$ expected: 487.3; observed: 487.1). This material was activated with equimolar amounts of HOBt and DIC in DMF and added to a 2-fold molar excess of Boc-ADOOA. After overnight incubation, the product (**II** in Scheme S1) was isolated by preparative HPLC and characterized by ESI-MS ($[M+H]^+$ expected: 622.8; observed: 622.4). The dried material was solubilised in 50% MeOH and piperidine was added to a 1 M final concentration. After overnight incubation at 20°C, the mixture was adjusted to pH 3.0 and deprotected material was isolated by preparative HPLC using a 0-50% B gradient over 50 min at 15 mL/min.

(ii) AEEA-Lys(FAM)-ADOOA. FAM was activated for 5 min with equimolar amounts of HOBt and DIC in DMF then added in a 1.3-fold excess to Boc-AEEA-Lys-ADOOA-Boc that had previously been solubilised in DMF and neutralised with a 3 molar excess of NMM. After incubation for 15 h in the dark, the product (**III** in Scheme S1) was purified by preparative HPLC, dried and deprotected in neat TFA and freeze-dried after TFA evaporation; ESI-MS m/z $[M+H]^+$ expected: 781.1; observed: 780.4.

(iii) Maleimido-AEEA-Lys(FAM)-ADOOA-maleimide. 4-Maleimidobutyric acid N-hydroxysuccinimide ester was reacted in DMF with AEEA-Lys(FAM)-ADOOA at a 1.5-fold excess over amino groups of the linker for 3 h. The final product (**IV** in Scheme S1) was characterized by ESI-MS (m/z $[M+H]^+$ expected: 1115.7; observed: 1116.0).

Iodoacetamide-AEEA-Lys(FAM)-ADOOA-iodoacetamide

This analogue of the maleimido-AEEA-Lys(FAM)-ADOOA-maleimide linker was obtained by acylation of the bis-amino intermediate (**III** in Scheme S1) with iodoacetic acid N-hydroxysuccinimide ester instead of 4-Maleimidobutyric acid N-hydroxysuccinimide ester (reaction carried out under the same conditions). The final product was characterized by ESI-MS m/z $[M+H]^+$ (expected: 1111.4; observed: 1110.6).

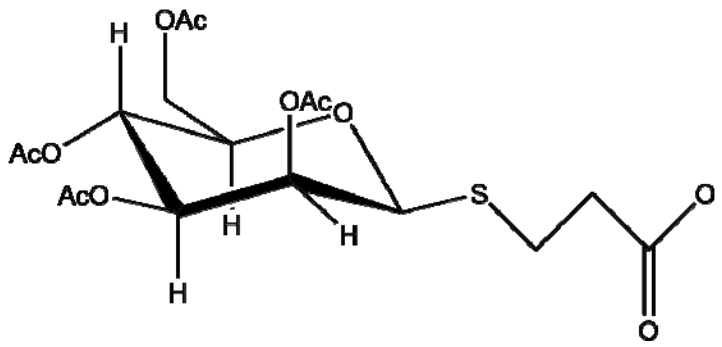


Iodoacetamide-AEEA-Lys(FAM)-ADOOA-iodoacetamide linker (V)

5. Synthesis and characterization of linker-conjugated mannose

3-(2,3,4,6-Tetra-O-acetyl-α-D-mannopyranosylthio)propionic acid

Preparation of per-O-acetylthioglycoside-propionate involved peracetylation with acetic anhydride (Ac_2O) followed by thioglycosydation with 3-thiopropionic acid in the presence of borontrifluoride diethyl etherate (BF_3OEt_2) as described previously (*20*), except that final material was purified by preparative HPLC using a 15-25 % solvent B gradient over 40 min.



3-(2,3,4,6-Tetra-O-acetyl-α-D-mannopyranosylthio)propionic acid

Succinimide activation was carried out with 1 equivalent dicyclohexylcarbodiimide (DCC) and 1 equivalent N-hydroxysuccinimide (NHS) in dimethoxyethane (DME). The mixture was stirred overnight and filtered to remove the precipitate. The solvent was evaporated using reduced pressure and the powder obtained was used without further purification.

The succinimide-activated product was characterized by using it in the synthesis of a mannose-coated dendrimer by direct acylation of G-2(ATOPA-NH_2)$_{16}$, followed by Zemplen deacylation. Both the protected intermediate and final compound were characterized by NMR.

NMR characterization of G-2(ATOPA-O-Ac-Mannose)$_{16}$

^{1}H NMR (500 MHz, CD_3OD) : δ = 2.11 (s, 48 H, CH_3), 2.20 (s, 48H, CH_3), 2.21 (s, 48H, CH_3), 2.30 (s, 48H, CH_3), 2.60-2.67 (m, CH_2), 2.70-2.73 (m, 32H, CH_2), 3.0-3.2 (m, CH_2), 3.03-3.10 (m, 32H, CH_2), 3.44-3.53 (m, CH_2), 3.68-3.70 (m, CH_2), 3.77-3.79 (m, CH_2), 3.87-3.89 (m, CH_2), 4.28 (dd, J = 2.2 and 14.2 Hz, 16H), 4.44 (dd, J = 5.0 and 11.9 Hz, 16H), 4.5-4.53 (m, 16H), 5.3 (dd, J = 3.2 and 13.2 Hz, 16H), 5.40-5.56 (m, 48H).

^{13}C NMR (125.76 MHz, CD_3OD): δ = 18.39, 20.62, 20.72, 20.78, 26.32, 27.87, 36.94, 37.78, 39.93, 40.23, 40.53, 49.87, 51.16, 58.33, 63.58, 67.41, 68.30, 70.40,

70.58, 71.08, 71.32, 71.48, 71.54, 71.57, 71.59, 72.04, 83.50, 171.44, 171.51, 171.53, 172.33, 173.60, 174.14.

NMR characterization of G-2(ATOPA-Mannose)$_{16}$

^{1}H NMR (500 MHz, CD_3OD) : δ = 2.58-2.67 (m, CH_2), 2.67-2.81 (m, CH_2), 2.87-2.93 (m, CH_2), 2.99-3.14 (m, CH_2), 3.44-3.58 (m, CH_2), 3.69-3.73 (m, CH_2), 3.75-3.79 (m, CH_2), 3.86-3.90 (m, CH_2), 4.03-4.09 (m, 80 H, CH).

^{13}C NMR (125.76 MHz, CD_3OD) : δ = 18.36, 28.80, 29.62, 35.66, 37.40, 37.73, 39.53, 40.48, 49.85, 51.45, 58.35, 62.95, 68.31, 69.03, 70.52, 71.22, 71.30, 71.45, 71.48, 71.54, 73.22, 73.71, 75.15, 87.46, 172.74, 174.23, 174.39.

6. Mass spectrometry characterization of key intermediates IV (scheme 1 in main text) and V (scheme 2 in main text).

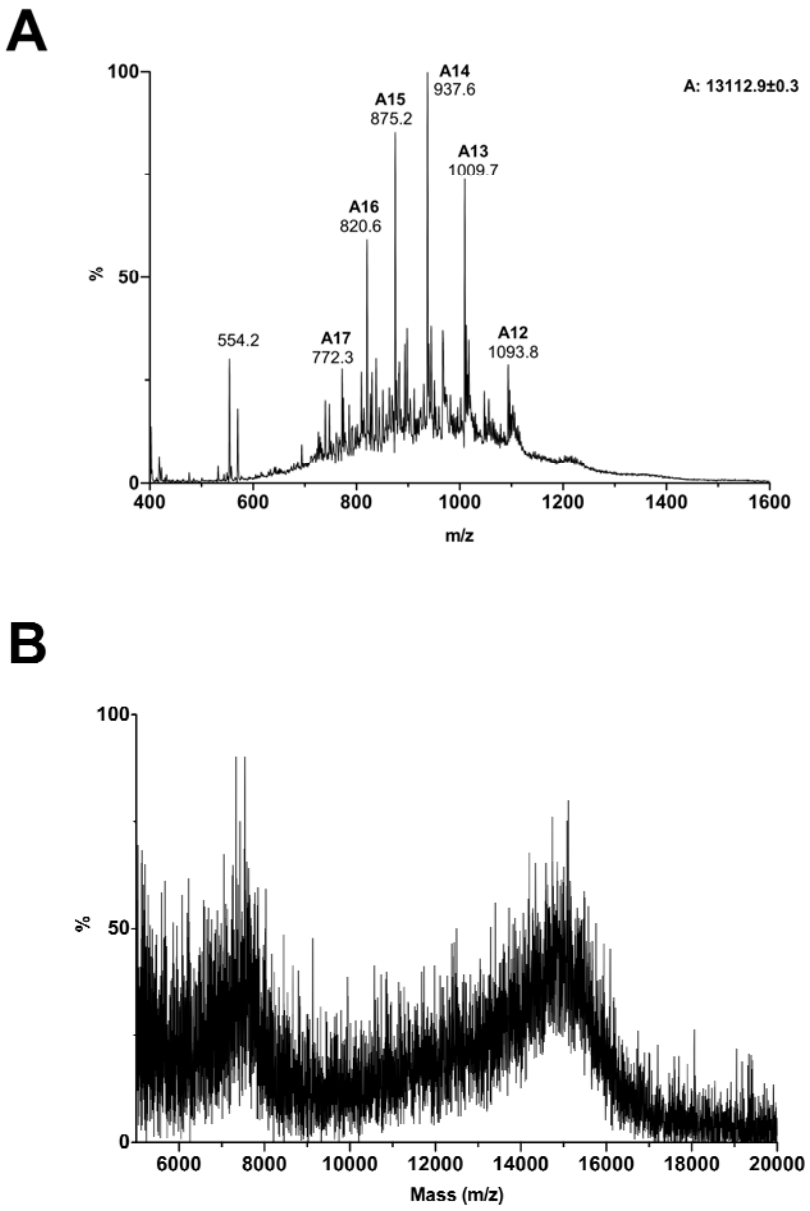


Figure S3: ESI-MS characterization of intermediate G-3(ATOPA-NH_2)$_{16}$-S-PEG-S-G-3(Boc)$_{16}$ (calculated average mass: 13108.9 Da) **(A)** and MALDI-TOF-MS characterization mannosylated derivative, G3-(ATOPA-Mannose)$_{16}$-S-PEG-S-G3-(NH_2)$_{16}$ (calculated average mass: 15511.6 Da) **(B)**.

7. Characterization of fluorescein-labeled homo- and heterodendrimers

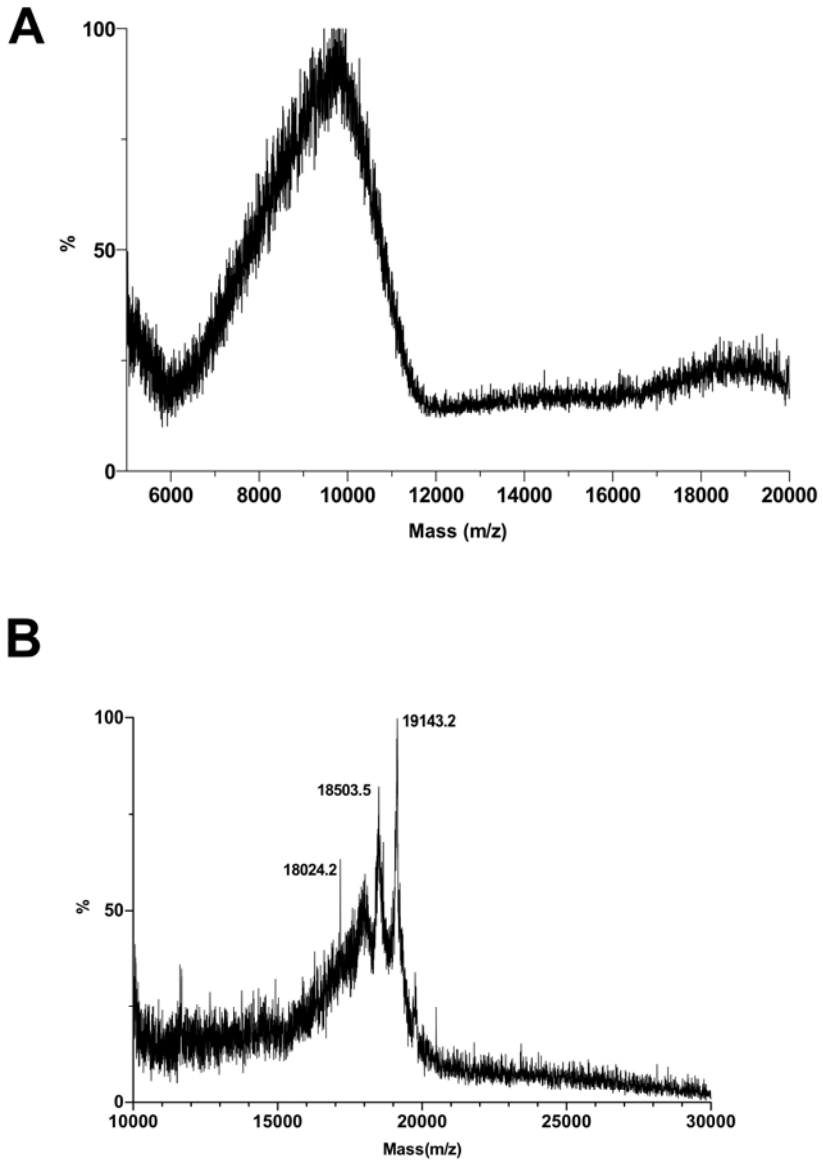


Figure S4: MALDI-TOF-MS characterization of G-3(ATOPA-Mannose)$_{16}$-S-FAM (calculated average mass: 11851.9 Da) **(A)** and G-3(ATOPA-Pyr=AoA-LYRAG)$_{16}$-S-FAM (calculated mass: 19107.8 Da) **(B)**.

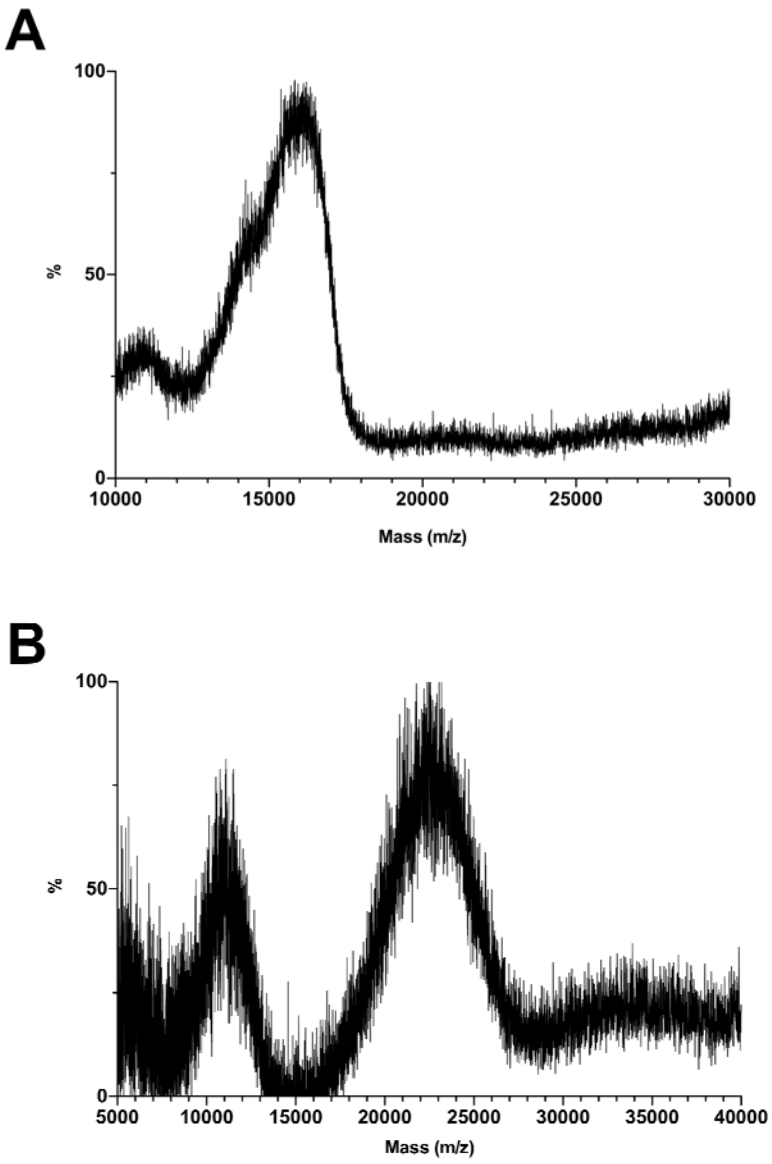


Figure S5. MALDI-TOF-MS characterization of G-3(ATOPA-Mannose)$_{16}$-S-PEG-K(FAM)-PEG-G-3(Pyr)$_{16}$ **(A)** and the corresponding AoA-LYRAG peptide-conjugated product **(B)**. Respective theoretical average masses of fully substituted compounds are 16942.9 Da and 27082.6 Da.

Bioconjugate Chemistry

ARTICLE

pubs.acs.org/bc

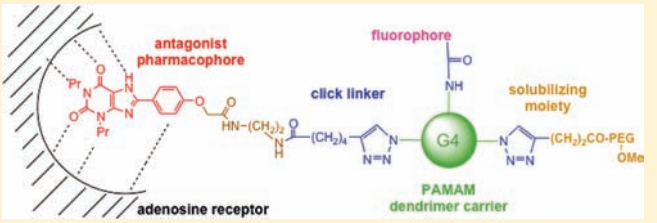
GPCR Ligand Dendrimer (GLiDe) Conjugates: Adenosine Receptor Interactions of a Series of Multivalent Xanthine Antagonists

Angela Kecskés,[†] Dilip K. Tosh,[†] Qiang Wei, Zhan-Guo Gao, and Kenneth A. Jacobson*

Molecular Recognition Section, Laboratory of Bioorganic Chemistry, National Institute of Diabetes and Digestive and Kidney Diseases, National Institutes of Health, Bethesda, Maryland 20892, United States

Supporting Information

ABSTRACT: Previously, G protein-coupled receptor (GPCR) agonists were tethered from polyamidoamine (PAMAM) dendrimers to provide high receptor affinity and selectivity. Here, we prepared GPCR ligand−dendrimer (GLiDe) conjugates from a potent adenosine receptor (AR) antagonist; such agents are of interest for treating Parkinson's disease, asthma, and other conditions. Xanthine amine congener (XAC) was appended with an alkyne group on an extended C8 substituent for coupling by Cu(I)-catalyzed click chemistry to azide-derivatized G4 (fourth-generation) PAMAM dendrimers to form triazoles. These conjugates also contained triazole-linked PEG groups (8 or 22 moieties per 64 terminal positions) for increasing water-solubility and optionally prosthetic groups for spectroscopic characterization and affinity labeling. Human AR binding affinity increased progressively with the degree of xanthine substitution to reach K_i values in the nanomolar range. The order of affinity of each conjugate was $hA_{2A}AR > hA_3AR > hA_1AR$, while the corresponding monomer was ranked $hA_{2A}AR > hA_1AR \geq hA_3AR$. The antagonist activity of the most potent conjugate **14** (34 xanthines per dendrimer) was examined at the G_i-coupled A_1AR. Conjugate **14** at 100 nM right-shifted the AR agonist concentration−response curve in a cyclic AMP functional assay in a parallel manner, but at 10 nM (lower than its K_i value), it significantly suppressed the maximal agonist effect in calcium mobilization. This is the first systematic probing of a potent AR antagonist tethered on a dendrimer and its activity as a function of variable loading.



INTRODUCTION

We have used poly(amidoamine) (PAMAM) dendrimers as polymeric nanocarriers for drugs that bind to G protein-coupled receptors (GPCRs) located on the cell surface.[1−3] These receptors are an important area of drug discovery. Agonists and antagonists of rhodopsin-like GPCRs constitute a large fraction (~30%) of the 324 molecular targets of FDA-approved drugs.[4] Multivalent GPCR ligand−dendrimer (GLiDe) conjugates, in which a strategically derivatized agonist or antagonist is covalently tethered from a high molecular weight PAMAM dendrimer, have displayed enhanced pharmacodynamic properties in comparison to those of the monomeric ligands.[2,3,5] One of the objectives of this approach is to favorably alter the pharmacokinetics of the drug in vivo when bound to the nanocarrier. It is also feasible to target the binding of a polymeric drug to aggregates of GPCRs, which have been shown to exist and have been postulated to be major participants in the varied biological effects of a given receptor.[6] GPCR dimers, including heterodimers of two different receptor classes, have already been established to have an altered pharmacology compared to that of homomeric GPCRs.[7] We have shown with molecular modeling that GLiDe conjugates of sufficient molecular size can adopt a suitable geometry to bridge multiple binding sites in such receptor aggregates.[8]

We initially reported the use of PAMAM dendrimers as scaffolds for the presentation of nucleosides and nucleotides that selectively activate adenosine receptors (ARs, particularly the A_{2A} and A_3 subtypes) or antagonize P2Y receptors (specifically the $P2Y_1$ subtype) to modulate intracellular signaling,[1,2,9] with both of these receptor families being GPCRs. These GLiDe conjugates are stable and biologically active without requiring the release of small molecules or cellular internalization, which are often an integral part of other polymeric drug delivery schemes.[10] Recently, we showed that a potent A_3AR agonist conjugate displayed cytoprotective effects in a cardiomyocyte culture heterologously expressing the A_3AR.[11] The present study extends the GLiDe conjugate approach for the first time from AR agonists to multivalent conjugates of AR antagonists. AR antagonists, the naturally occurring xanthines theophylline **1** and caffeine **2** being prototypical examples (Figure 1), are of therapeutic interest in the treatment of Parkinson's disease, diabetes, asthma, cancer, and other conditions.[4,12] The structure−activity relationship (SAR) of xanthine derivatives as AR antagonists has been exhaustively explored.[13,14] One of the earliest high affinity AR ligand probes was the 8-phenyl derivative xanthine amine congener (**3**, XAC), which is a moderately selective antagonist of the A_1AR subtype in the rat and is relatively nonselective in binding to human (h) ARs.[15] XAC contains an amine-terminal chain placed at an insensitive site on the pharmacophore and was designed as a functionalized

Received: December 17, 2010
Revised: May 2, 2011
Published: May 03, 2011

ACS Publications This article not subject to U.S. Copyright. Published 2011 by the American Chemical Society

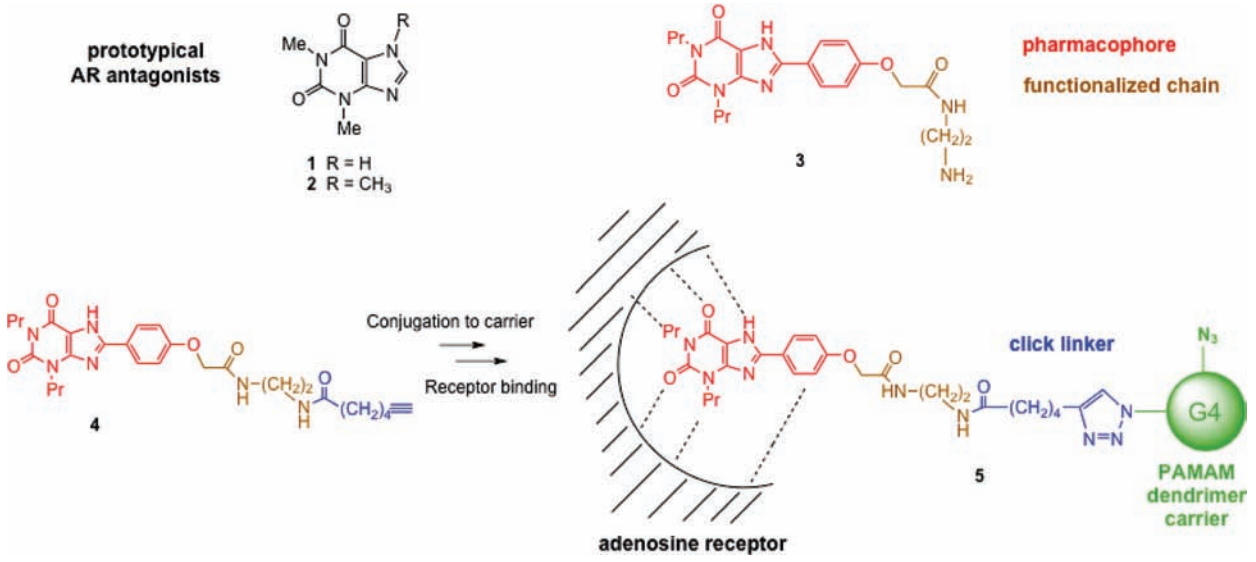


Figure 1. Structures of nonselective AR antagonists (**1**−**3**) and the design of a series of multivalent dendrimer conjugates of a potent xanthine, represented by the triazole derivative of unspecified stoichiometry in the general formula (**5**). Compound **3** is a functionalized XAC congener designed for attachment to carrier moieties with retention of the ability to bind potently to ARs. The conjugation of alkyne derivative **4** is performed using click chemistry, which forms a triazole linker on an insensitive site on the xanthine with respect to receptor recognition.

congener,[16] i.e., for attachment to larger carrier moieties and reporter groups with retention of the ability to bind potently to ARs.

In this study, we have identified a means of linking XAC to water-soluble PAMAM dendrimers by Cu(I)-catalyzed click chemistry between an alkyne and an azide,[17] which we found to preserve the high receptor affinity in this series. The degree of substitution by XAC and by polyethylene glycol (PEG) water-solubilizing chains was systematically varied and the effects on receptor affinity studied. This analysis suggests that each GLiDe conjugate molecule may bind to multiple AR binding sites in the vicinity on the cell surface. Furthermore, the ability to introduce prosthetic groups for receptor localization or characterization on the carrier without interfering with the high affinity in receptor binding was shown.

EXPERIMENTAL PROCEDURES

Chemical Synthesis. *Materials and Methods.* All reactions were carried out under a nitrogen atmosphere. We purchased *N*-ethyl-*N*′-dimethylaminopropylcarbodiimide hydrochloride (EDC.HCl) and the G4 PAMAM dendrimer (5 wt % solution in methanol) with an ethylenediamine core **6a** from Sigma-Aldrich (St. Louis, MO). All other reagents and solvents, except those indicated, came from Sigma-Aldrich. We purchased dialysis membranes (Spectra/Pore Membrane, MWCO 3500, flat width 18 mm) from Spectrum Laboratories (Rancho Dominguez, CA). Imidazole-1-sulfonyl azide hydrochloride was prepared.[18] Synthesis of XAC **3** is described elsewhere.[14] Active esters IRDye800CW **23** and IRDye700DX **24** were obtained from LI-COR Biosciences (Lincoln, NE). Amicon centrifugal ultrafilters (molecular weight cutoff 3000) were used.

Proton nuclear magnetic resonance (NMR) spectra were recorded on a Bruker DRX-400 spectrometer with d_6-DMSO as a solvent. The chemical shifts are reported in parts per million (ppm) relative to tetramethylsilane (δ 0.0 ppm) or in D_2O relative to HOD (4.80 ppm). ESI−high resolution mass spectroscopic (HRMS) measurements were performed on a proteomics optimized Q-TOF-2 (Micromass-Waters) using external calibration with polyalanine and matrix-assisted laser desorption ionization (MALDI) time-of-flight MS experiments on a Waters LCT Premier mass spectrometer at the Mass Spectrometry Facility, National Institute of Diabetes and Digestive and Kidney Diseases (NIDDK), NIH. Observed mass accuracies are those expected on the basis of known performance of the instrument as well as the trends in masses of standard compounds observed at intervals during the series of measurements. Reported masses are observed masses uncorrected for this time-dependent drift in mass accuracy. IR spectra were recorded using a PerkinElmer Spectrum One FT-IR spectrometer (applied as a DMSO solution).

*Azido-Derivatized G4 PAMAM dendrimer (**6b**).* The G4 PAMAM dendrimer containing an ethylene diamine core was obtained from Sigma-Aldrich and terminal amines reacted with imidazole-1-sulfonyl azide hydrochloride.[3] K_2CO_3 (3.48 g, 30.15 mmol), $CuSO_4 \cdot 5H_2O$ (34.6 mg, 0.163 mmol), and imidazole-1-sulfonyl azide hydrochloride (3.0 g, 1.04 mol) were added to a solution of G4 PAMAM dendrimer **6a**, (20 g, 10 w% in methanol, $[NH_2]$ = 16.3 mmol) in anhydrous methanol (11 mL), and the reaction mixture was stirred at room temperature overnight. The mixture was then dialyzed in deionized water for 7 days (changing water 4 times per day). Lyophilization after dialysis provided the azide-derivatized G4 dendrimer **6b** (3.2 g, 58%) as a solid. IR ν_{max} 2110 cm^{-1}. ESI-MS: calcd, 15,611; found, 15,545.

*G4 PAMAM, Conjugated with PEG [8] (**8**).* The azide-derivatized G4 PAMAM dendrimer **6b** (111 mg, 7.1 μmol) and a poly(ethylene glycol)methyl ether derivative of butynoic acid **7** (MW 2000, Aldrich Chemical Co., 114 mg, 57 μmol) were added to a mixture of DMSO (4 mL) and water (4 mL). The solution was treated with freshly prepared aqueous sodium ascorbate (1 M solution, 228 μL), followed by the addition of 7.5% aqueous cupric sulfate (380 μL, 113 μmol). The reaction mixture was stirred at room temperature (rt) overnight, and the product was purified by extensive dialysis in water (changing water 4 times per day for 2 days). The mixture was lyophilized to give compound **8**

(153 mg, 67%) containing ~8 equivalents of PEG per dendrimer molecule as a colorless foamy solid. ^{1}H NMR (DMSO-d_6, 400 MHz) δ 8.10 (br s), 4.35 (s), 4.13 (s), 3.5 (s), 3.41−3.44 (m), 3.33 (br s), 3.24 (s), 2.67−2.87 (m), 2.26 (br s). ESI-MS: calcd, 31,545; found, 32,077.

*G4 PAMAM, Conjugated with PEG [22] (**9**).* Compound **9** (74%) containing ~22 equivalents of PEG per dendrimer molecule was synthesized from dendrimer **6b** following the same method as that for compound **8**. ^{1}H NMR (DMSO-d_6, 400 MHz) δ 8.03 (br s), 4.35 (s), 4.25 (s), 3.59 (s), 3.39−3.44 (m), 3.32 (br s), 3.24 (s), 2.87 (br s), 2.66 (br s), 2.33 (s), 2.24 (br s). ESI-MS: calcd, 59,545; found, 59,855.

*N-(2-(2-(4-(2,6-Dioxo-1,3-dipropyl-2,3,6,7-tetrahydro-1H-purin-8-yl)phenoxy)-acetamido)ethyl)hept-6-ynamide (**4**).* 6-Heptynoic acid (33 μL, 0.27 mmol) and EDC (68.8 mg, 0.36 mmol) were added to a solution of compound **3** (77 mg, 0.18 mmol) in anhydrous DMF (3 mL) and stirred overnight at rt. Solvent was evaporated, and the residue was purified using flash silica gel column chromatography to give compound **4** (69 mg, 72%) as a colorless solid. ^{1}H NMR (CD_3OD, 400 MHz) δ 8.05 (d, J = 8.8 Hz, 2H), 7.14 (d, J = 8.8 Hz, 2H), 4.61−4.63 (m, 2H), 4.14 (t, J = 7.2 Hz, 2H), 4.01 (t, J = 7.6 Hz, 2H), 3.41−3.65 (m, 6H), 2.19−2.13 (m, 5H), 1.86−1.70 (m, 1H), 1.69−1.64 (m, 4H), 1.52−1.46 (m, 1H), 1.15 (d, J = 6.4 Hz, 1H), 1.17−0.95 (m, 6H). HRMS calculated for $C_{28}H_{37}N_6O_5$ (M + H)$^+$: 537.2825; found, 537.2823.

*G4 PAMAM, Conjugated with PEG [22] and the XAC [6] Derivative (**10**).* The azide-derivatized G4 PAMAM dendrimer **6b** (10.5 mg, 0.17 μmol) and a XAC alkyne derivative **4** (0.54 mg, 1.02 μmol) were added to a mixture of DMSO (0.4 mL) and water (0.4 mL). The solution was treated with freshly prepared aqueous sodium ascorbate (1 M solution, 3 μL), followed by the addition of 7.5% aqueous cupric sulfate (2.3 μL, 0.7 μmol). The reaction mixture was stirred at rt overnight, and the product was purified by extensive dialysis in water (changing water 4 times per day for 2 days). The mixture was lyophilized to give compound **10** (6.9 mg, 66%) containing ~22 equivalents of PEG and ~6 xanthine equivalents per dendrimer molecule as a foamy solid. ^{1}H NMR (DMSO-d_6, 400 MHz) δ 8.15 (br s), 8.09 (d, J = 8.8 Hz), 7.71−7.97 (m), 7.16 (d, J = 9.2 Hz), 4.54 (s), 4.24−4.36 (m), 4.12 (br s), 4.04 (t, J = 7.6 Hz), 3.81 (t, J = 7.6 Hz), 3.54−3.67 (m), 3.49 (br s), 3.14−3.47 (br m), 2.63−2.71 (br m), 2.07−2.33 (m), 1.42−1.81 (br m), 0.84−0.92 (br m). ESI-MS: calcd, 63,074; found, 63,069.

*G4 PAMAM, Conjugated with PEG [22] and the XAC [8] Derivative (**11**).* Compound **11** (70%) was synthesized from PEG conjugated dendrimer **9** following the same procedure as that for compound **10** using 8 equivalents of the XAC alkyne derivative **4**. ^{1}H NMR (DMSO-d_6, 400 MHz) δ 8.13 (br s), 8.10 (d, J = 8.8 Hz), 7.87−7.93 (m), 7.11 (d, J = 9.2 Hz), 4.55 (s), 4.32−4.36 (m), 4.12 (br s), 4.04 (t, J = 7.6 Hz), 3.85 (t, J = 7.6 Hz), 3.59−3.67 (m), 3.46 (br s), 3.14−3.42 (br m), 2.67−2.86 (br m), 2.05−2.33 (m), 1.51−1.75 (br m), 0.86−0.91 (br m). ESI-MS: calcd, 64,147; found, 64,251.

*G4 PAMAM, Conjugated with PEG [22] and the XAC [19] Derivative (**12**).* Compound **12** (75%) was synthesized from PEG conjugated dendrimer **9** following the same procedure as that for compound **10** using 19 equivalents of the XAC alkyne derivative **4**. ^{1}H NMR (DMSO-d_6, 400 MHz) δ 8.17 (br s), 8.07 (d, J = 8.8 Hz), 7.69−7.93 (m), 7.11 (d, J = 9.2 Hz), 4.54 (s), 4.30−4.35 (m), 4.13 (br s), 4.02 (t, J = 7.6 Hz), 3.84 (t, J = 7.6 Hz), 3.58−3.68 (m), 3.51 (br s), 3.13−3.48 (br m), 2.62−2.7 (br m), 2.05−2.33 (m), 1.39−1.81 (br m), 0.86−0.92 (br m). ESI-MS: calcd, 70,050; found, 70,074.

*G4 PAMAM, conjugated with PEG [22] and XAC [23] derivative (**13**).* Compound **13** (78%) was synthesized from PEG conjugated dendrimer **9** following the same procedure as that for compound **10** using 23 equivalents of the XAC alkyne derivative **4**. ^{1}H NMR (DMSO-d_6, 400 MHz) δ 8.13 (br s), 8.09 (d, J = 8.8 Hz), 7.91−7.86 (m), 7.11 (d, J = 9.2 Hz), 4.54 (s), 4.32−4.34 (m), 4.12 (br s), 4.04 (t, J = 7.6 Hz), 3.86 (t, J = 7.6 Hz), 3.58−3.68 (m), 3.44 (br s), 3.14−3.44 (br m), 2.67−2.87 (br m), 2.03−2.33 (m), 1.49−1.75 (br m), 0.86−0.92 (br m). ESI-MS: calcd, 72,197; found, 72,320.

*G4 PAMAM, Conjugated with PEG [22] and the XAC [34] Derivative (**14**).* Compound **14** (84%) was synthesized from PEG conjugated dendrimer **9** following the same method as that for compound **10** using 34 equivalents of the XAC alkyne derivative **4**. ^{1}H NMR (DMSO-d_6, 400 MHz) δ 8.11 (br s), 8.09 (d, J = 9.2 Hz), 7.90−7.85 (m), 7.11 (d, J = 9.2 Hz), 4.54 (s), 4.02 (t, J = 6.0 Hz), 3.87 (t, J = 7.6 Hz), 3.12−3.71 (br m), 2.67−2.74 (m), 2.30−2.38 (m), 2.10−2.14 (m), 2.05 (t, J = 7.2 Hz), 1.72−1.79 (m), 1.53−1.61 (m), 1.37−1.41 (m), 0.86−0.92 (br m). ESI-MS: calcd, 78,100; found, 77,999.

*G4 PAMAM, Conjugated with PEG [8] and the XAC [4] Derivative (**15**).* Compound **15** (67%) was synthesized from PEG conjugated dendrimer **8** following the same method as that for compound **10** using 4 equivalents of the XAC alkyne derivative **4**. ^{1}H NMR (DMSO-d_6, 400 MHz) δ 8.14 (br s), 8.08 (d, J = 8.8 Hz), 7.72−7.90 (m), 7.10 (d, J = 8.8 Hz), 4.54 (s), 4.34 (br s), 4.13 (br s), 4.02 (t, J = 7.6 Hz), 3.86 (t, J = 7.5 Hz), 3.60−3.67 (m), 3.49 (br s), 3.08−3.44 (br m), 2.67−2.87 (br m), 2.22−2.33 (br m), 1.48−1.68 (br m), 0.86−0.92 (br m). ESI-MS: calcd, 34,223; found, 34,377.

*G4 PAMAM, Conjugated with PEG [8] and the XAC [16] Derivative (**16**).* Compound **16** (72%) was synthesized from PEG conjugated dendrimer **8** following the same method as that for compound **10** using 17 equivalents of the XAC alkyne derivative **4**. ^{1}H NMR (DMSO-d_6, 400 MHz) δ 8.15 (br s), 8.09 (d, J = 8.8 Hz), 7.81−7.86 (m), 7.11 (d, J = 8.8 Hz), 4.54 (s), 4.34 (s), 4.19 (t, J = 7.5 Hz), 4.04 (t, J = 7.6 Hz), 3.52 (br s), 3.14−3.44 (br m), 2.62−2.74 (m), 2.03−2.33 (m), 1.39−1.75 (br m), 0.89−0.92 (br m). ESI-MS: calcd, 40,662; found, 40,461.

*G4 PAMAM, Conjugated with PEG [8] and the XAC [25] Derivative (**17**).* Compound **17** (80%) was synthesized from PEG conjugated dendrimer **8** following the same method as that for compound **10** using 26 equivalents of the XAC alkyne derivative **4**. ^{1}H NMR (DMSO-d_6, 400 MHz) δ 8.16 (br s), 8.09 (d, J = 8.8 Hz), 7.86−7.88 (m), 7.11 (d, J = 8.8 Hz), 4.54 (s), 4.02 (t, J = 6.8 Hz), 3.89 (t, J = 6.7 Hz), 3.51 (br s), 3.14−3.32 (m), 2.10−2.14 (m), 2.04 (t, J = 7.2 Hz), 1.72−1.77 (m), 1.51−1.61 (m), 1.35−1.43 (m), 0.81−0.92 (br m). ESI-MS: calcd, 45,492; found, 45,223.

*G4 PAMAM, Conjugated with PEG [8] and the XAC [37] Derivative (**18**).* Compound **18** (84%) was synthesized from PEG conjugated dendrimer **8** following the same method as that for compound **10** using 37 equivalents of the XAC alkyne derivative **4**. ^{1}H NMR (DMSO-d_6, 400 MHz) δ 8.18 (br s), 8.08 (d, J = 9.2 Hz), 7.86−7.88 (m), 7.11 (d, J = 8.8 Hz), 4.54 (s), 4.02 (t, J = 6.0 Hz), 3.87 (t, J = 6.8 Hz), 3.12−3.62 (br m), 2.67−2.74 (m), 2.33 (br s), 2.10−2.13 (m), 2.05 (t, J = 6.8 Hz), 1.72−1.77 (m), 1.53−1.61 (m), 1.37−1.43 (m), 0.88−0.92 (br m). ESI-MS: calcd, 51,931; found, 52,035.

*G4 PAMAM, Conjugated with PEG [8], XAC [37], and Alexa Fluor 488 (**20**).* A solution of Alexa Fluor 488 alkyne **19** (0.5 mg, 0.64 μmol) in water (0.5 mL) and freshly prepared sodium ascorbate (1 M, 5 μL) were added to a solution of the XAC-dendrimer conjugate **18** (8.2 mg, 0.16 μmol) in DMSO (0.5 mL). Then, 7.5% aqueous cupric sulfate (6 μL, 113 μmol) was added to the reaction mixture, which was stirred overnight at rt. The dendrimer derivative was purified by extensive dialysis in water, and lyophilization of the resulting solution gave compound **19** (5.9 mg, 66%) as an orange colored solid. ESI-MS: calcd, 57,065; found, 57,079.

*4-(2-Hept-6-ynamidoethyl)benzene-1-sulfonyl Fluoride (**21**).* 6-Heptynoic acid (11 μL, 0.09 mmol), HATU (31 mg, 0.08 mmol), and diisopropyl ethylamine (14 μL, 0.08 mmol) were added to a solution of 4-(2-aminoethyl)benzene-1-sulfonyl fluoride (Aldrich, 15 mg, 0.06 mmol) in anhydrous DMF (1 mL). The reaction mixture was stirred overnight at rt. The solvent was evaporated, and the residue was purified using flash silica gel column chromatography (hexane/ethyl acetate = 2:1) to give compound **21** (15.2 mg, 78%) as a colorless solid. ^{1}H NMR (CD_3OD, 400 MHz) δ 8.00 (d, J = 8.4 Hz, 2H), 7.60 (d, J = 8.0 Hz, 2H), 3.52−3.48 (m, 2H), 2.98 (t, J = 6.8 Hz, 2H), 2.32 (t, J = 7.2 Hz, 2H), 2.23−2.20 (m, 2H), 1.75−1.44 (m, 5H). HRMS calculated for $C_{15}H_{19}NO_3SF$ $(M + H)^+$: 312.1070; found, 312.1073.

*G4 PAMAM, Conjugated with PEG [8], XAC [37], Alexa Fluor 488, and the Benzene-sulfonyl Fluoride Derivative (**22**).* Benzene-sulfonyl fluoride alkyne derivative **21** (0.5 mg, 1.6 μmol) and freshly prepared sodium ascorbate (1 M, 3 μL) were added to a solution of XAC-dendrimer conjugate **20** (5.6 mg, 0.1 μmol) in DMSO (0.4 mL). Then, 7.5% aqueous cupric sulfate (4 μL, 0.9 μmol) was added to the reaction mixture, which was stirred overnight at rt. The dendrimer derivative was purified by extensive dialysis in water, and lyophilization of the resulting solution gave compound **22** (4.2 mg, 73%) as an orange colored solid. ESI-MS: calcd, 58,945; found, 59,155.

*G4 PAMAM, Conjugated with PEG [22], XAC [34], and the IR Dye 800 Derivative (**25**).* A solution of IR dye 800CW NHS ester **23** (0.5 mg, 0.42 μmol) in DMF (0.3 mL) was added to a solution of compound **14** (2.66 mg, 0.05 μmol) in DMF (1 mL) followed by triethylamine (10 μL, 0.42 μmol) and stirred overnight at rt. The dendrimer derivative was purified by extensive dialysis in water, and lyophilization of the resulting solution gave compound **25** (2.13 mg, 76%) as a green colored foamy solid. ESI-MS: calcd, 81,943; found, 82,258.

*G4 PAMAM, Conjugated with PEG [22], XAC [34], the IR Dye 700 Derivative (**26**).* A solution of IR dye 700DX NHS ester **24** (0.5 mg, 0.25 μmol) in DMF (0.3 mL) was added to a solution of compound **14** (2.32 mg, 0.03 μmol) in DMF (1 mL) followed by sodium tetraborate buffer (20 μL, 0.25 μmol), and the reaction mixture was stirred overnight at rt. The dendrimer derivative was purified by extensive dialysis in water, and lyophilization of the resulting solution gave compound **26** (2.19 mg, 83%) as a green colored foamy solid. ESI-MS: calcd, 88,511; found, 89,063.

Biological Methods. *Materials.* Penicillin−Streptomycin−Glutamine and Hygromycin B were purchased from Invitrogen (Carlsbad, CA). [^{3}H]*R*-*N*^{6}-(2-Phenylisopropyl)adenosine ([^{3}H]R-PIA, 42.6 Ci/mmol) was obtained from Moravek Biochemicals (Brea, CA). [^{125}I]4-Amino-3-iodobenzyl-5′-*N*-methylcarboxamidoadenosine ([^{125}I]I-AB-MECA, 2200 Ci/mmol) and [^{3}*H*]-2-[*p*-(2-carboxyethyl)phenylethylamino]-5′-*N*-ethylcarboxamidoadenosine ([^{3}H]CGS21680, 40.5 Ci/mmol) were purchased from PerkinElmer (Waltham, MA). DMEM/F12 medium, 1 M Tris-HCl (pH 7.5), and G418 Sulfate were purchased from Mediatech, Inc. (Herndon, VA). The calcium assay kit was from Molecular Devices (Sunnyvale, CA). All other reagents were from standard sources and are of analytical grade.

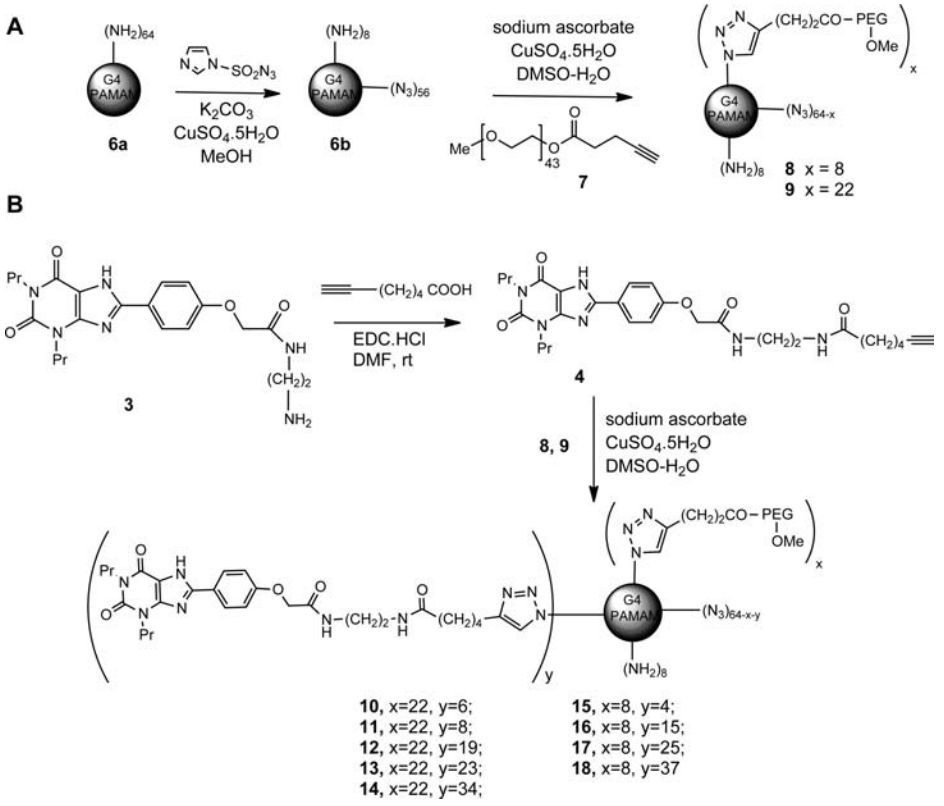
We prepared test compounds as 0.1 mM stock solutions in DMSO and stored them at 4 °C. Adenosine deaminase (25.3 U/mg) was purchased from Worthington Biochemical Corporation (Lakewood, NJ.)

Cell Culture and Membrane Preparation. We cultured Chinese hamster ovary (CHO) cells stably expressing the recombinant hA_1AR, $hA_{2B}AR$, and hA_3AR and human embryonic kidney (HEK) 293 cells stably expressing the $hA_{2A}AR$ in DMEM and F12 (1:1) supplemented with 10% fetal bovine serum (FBS), 50 U/mL penicillin, and 50 μg/mL streptomycin.[19] In addition, we added 800 μg/mL Geneticin to the $hA_{2A}AR$ media and 500 μg/mL Hygromycin B to the hA_1AR, $hA_{2B}AR$, and hA_3AR media. After harvesting the cells, we centrifuged them at 250*g* for 5 min at 4 °C. The pellet was resuspended in 50 mM Tris-HCL buffer (pH 7.5), containing 10 mM $MgCl_2$. The suspension was homogenized with an electric homogenizer for 10 s and was then recentrifuged at 20,000*g* for 30 min at 4 °C. The resultant pellet was homogenized again, resuspended in the buffer mentioned above in the presence of 3 U/mL adenosine deaminase, finally pipetted into 1 mL vials, and then stored at −80 °C until the binding experiments were conducted. We measured the protein concentration with BCA Protein Assay Kit from Pierce Biotechnology (Rockford, IL).[20]

Binding Assays. Binding assays using standard AR ligands were performed using the general methods reported.[21−23] Each tube in the binding assay contained 50 μL of increasing concentrations of the test ligand in Tris-HCl buffer (50 mM, pH 7.5) containing 10 mM $MgCl_2$, 50 μL of the appropriate agonist radioligand, and 100 μL of membrane suspension, added sequentially. For the hA_1AR (20 μg protein/tube), we used the radioligand [^{3}H]R-PIA (0.2 nM, precise final concentration is calculated for each experiment). For the $hA_{2A}AR$ (20 μg protein/tube), we used the radioligand [^{3}H]CGS21680 (10 nM). For the hA_3AR (20 μg protein/tube), we used the radioligand [^{125}I]I-AB-MECA (0.89 nM). We determined nonspecific binding with a final concentration of 10 μM unlabeled NECA diluted with the buffer. We incubated the mixtures at 25 °C for 60 min in a shaking water bath. We terminated binding reactions by filtration through Brandel GF/B filters under reduced pressure with an M-24 cell harvester (Brandel, Gaithersburg, MD). We washed filters three times with 3 mL of 50 mM ice-cold Tris-HCl buffer (pH 7.5). We then placed filters for hA_1AR and $hA_{2A}AR$ binding in scintillation vials containing 5 mL of Hydrofluor scintillation buffer and counted with a PerkinElmer Liquid Scintillation Analyzer (Tri-Carb 2810TR). We counted filters for hA_3AR binding with a Packard Cobra II γ-counter (PerkinElmer).

Cyclic AMP Accumulation Assay. CHO cells expressing the A_1AR or $A_{2B}AR$ were seeded in 24-well plates and incubated at 37 °C overnight. The following day, the medium was removed and replaced with DMEM containing 50 mM HEPES, 10 μM rolipram, 3 U/mL adenosine deaminase, and increasing concentrations of agonists. For measurements at the A_1AR, forskolin (10 μM) was added 30 min after the addition of agonists and incubated for another 15 min. Antagonists were added 20 min before the addition of agonists. The medium was removed, and the cells were lysed with 200 μL of 0.1 M HCl. One hundred microliters of the HCl solution was used in the Sigma Direct

Scheme 1. Use of Click Chemistry in Sequential Steps to Synthesize PAMAM Dendrimer Derivatives 9−18, Containing a Functionalized AR Antagonist (Average Structures Shown)[a]



[a] (A) PEG moieties were added as water-solubilizing groups, followed by conjugation of the xanthine alkyne derivative **4** (B). Compound **7** was calculated to contain approximately 43 PEG groups on the basis of its molecular weight (2000 D).

cAMP Enzyme Immunoassay following the instructions provided with the kit. The results were interpreted using a BioTek ELx808 Ultra Microplate reader (BioTek, Winooski, VT) at 405 nm.

Intracellular Calcium Mobilization. CHO cells expressing the A_1AR cells were grown overnight in 100 μL of media in 96-well flat bottom plates at 37 °C at 5% CO_2 or until 80−90% confluency. The calcium assay kit (Molecular Devices, Sunnyvale, CA) was used as directed without washing cells and with probenecid added to the loading dye at a final concentration of 2.5 mM to increase dye retention. Cells were loaded with 50 μL of dye with probenecid to each well and incubated for 60 min at rt. The compound plate was prepared using dilutions of various compounds in Hanks Buffer (pH 7.4). Samples were run on a FLIPR^{TETRA} (Molecular Devices) in duplicate at rt. Antagonists were added 20 min before the addition of agonists. Cell fluorescence was measured (excitation at 485 nm; emission at 525 nm) following exposure to agonists. Increases in intracellular calcium are reported as the maximum fluorescence value after exposure minus the basal fluorescence value before exposure.

Data Analysis. We initially measured the concentrations of the dendrimer−ligand complexes by the concentration of the dendrimer, not the attached ligand. We determined EC_{50} and apparent K_i values with Prism software (GraphPad, San Diego, CA); they are presented as the mean ± SE. The number of xanthine moieties on a given dendrimer that are accessible to receptors is uncertain; the data are therefore shown as apparent K_i values. Later, the same data were converted to the concentration of the xanthine moieties for graphic presentation. We repeated all experiments at least three times.

RESULTS

Chemical Synthesis. We prepared generation 4 (G4) PAMAM dendrimer conjugates of the potent, nonselective hAR antagonist XAC **3** (Scheme 1 and Table 1, **9**−**18**) to act as multivalent ligands of the receptors. The peripheral groups of the precursor dendrimer **6a** were modified to contain predominantly azido groups in place of the 64 terminal primary amines by reacting with imidazole-1-sulfonyl azide hydrochloride in methanol to give compound **6b**.[3,18] The same approach of preparing the PAMAM dendrimer for click chemistry by the substitution of amino groups with azides was taken in the synthesis of conjugates of AR agonists and $P2Y_1$ receptor antagonists.[3,9] Mass spectral data of **6b** indicated that 8 amino groups out of the 64 remained unreacted, and the presence of azido groups was confirmed by a strong IR peak at 2110 cm^{-1}. The presence of these residual amines was later used for synthetic advantage in the coupling of additional prosthetic groups. Prior to coupling of the pharmacophoric species, the dendrimer was appended with PEG moieties by a Cu(I)-catalyzed click cyclization using an alkyne-derivatized PEG **7** (end-capped by a methyl ether and a butynoyl ester) to yield the water-soluble and mainly uncharged PAMAM derivatives **8** and **9**, having 8 or 22 PEG moieties per dendrimer, respectively. Thus, two degrees of substitution with PEG of the 64-terminal groups of the G4 dendrimer were compared.

Table 1. Binding Affinity of a Series of XAC Dendrimer Conjugates (10−22), Dendrimer Precursors (9, $(PEG)_{22}$ series; 8, $(PEG)_8$ series), and Small Molecular Monomers (3 and 4) at Three Subtypes of Human ARs[a]

compound	# of XAC moieties/dendrimer	$K_{i,app}$ or *% inhibition*, A_1AR	$K_{i,app}$ or *% inhibition*, $A_{2A}AR$	$K_{i,app}$ or *% inhibition*, A_3AR
3[b]	(monomer)	8.3 ± 1.3 nM	5.8 ± 2.3 nM	13.8 ± 4.4 nM
4[b]	(monomer)	107 ± 13 nM	23.2 ± 11.2 nM	175 ± 15 nM
9[c]	0	*21.8 ± 17.8%*	*29.7 ± 4.1%*	*70.2 ± 3.7%*
10	6	*34.3 ± 14.2%*	*45.9 ± 2.3%*	*71.7 ± 6.7%*
11	8	*59.2 ± 3.5%*	61.5 ± 23.0 nM	219 ± 67 nM
12	19	91.0 ± 15.6 nM	11.4 ± 5.0 nM	30.6 ± 3.8 nM
13	23	47.1 ± 3.4 nM	4.2 ± 1.7 nM	18.1 ± 5.2 nM
14[b,c]	34	15.0 ± 4 nM	2.6 ± 0.6 nM	8.9 ± 3.3 nM
8[c]	0	*10.3 ± 5.2%*	*4.4 ± 5.8%*	*51.9 ± 3.6%*
15	4	193 ± 117 nM	32.7 ± 6.0 nM	99.7 ± 25.0 nM
16	15	95.4 ± 35.3 nM	15.1 ± 1.7 nM	48.7 ± 20.2 nM
17	25	54.3 ± 17.1 nM	4.6 ± 0.4 nM	25.2 ± 3.8 nM
18[b,c]	37	29.0 ± 7.1 nM	4.2 ± 0.3 nM	14.5 ± 4.4 nM
20	37	20.2 ± 6.5 nM	4.1 ± 0.2 nM	6.2 ± 0.9 nM
22	37	29.3 ± 8.2 nM	5.4 ± 1.8 nM	7.8 ± 1.2 nM
25[b]	34	ND	ND	6.8 ± 2.1 nM
26[b]	34	ND	3.7	20.3 ± 16.4 nM

[a] All experiments were done on CHO (A_1 and A_3AR) or HEK293 ($A_{2A}AR$) cells stably expressing one of four subtypes of human ARs. The binding affinity for A_1, A_{2A}, and A_3ARs was expressed as K_i values ($n = 3-5$) and was determined by using agonist radioligands ([^{3}H]R-PIA, [^{3}H]CGS21680, or [^{125}I]I-AB-MECA, respectively), unless noted. The percentage inhibition refers to the inhibition of radioligand binding at the concentration of 1 μM. The concentrations of the dendrimer−ligand complexes were measured by the concentration of the dendrimer, not the ligand. Therefore, all binding K_i values of dendrimers are expressed as K_{iapp} values. ND: not determined. [b] **3**, XAC; **4**, MRS5398; **14**, MRS5359; **18**, MRS5385; **25**, MRS5421; **26**, MRS5422. [c] PEGylated dendrimer **9** is the precursor of **10**−**14**; PEGylated dendrimer **8** is the precursor of **15**−**18**. Xanthine-derivatized **18** is the dendrimer precursor of **20** and **22**. Xanthine-derivatized **14** is the dendrimer precursor of **25** and **26**.

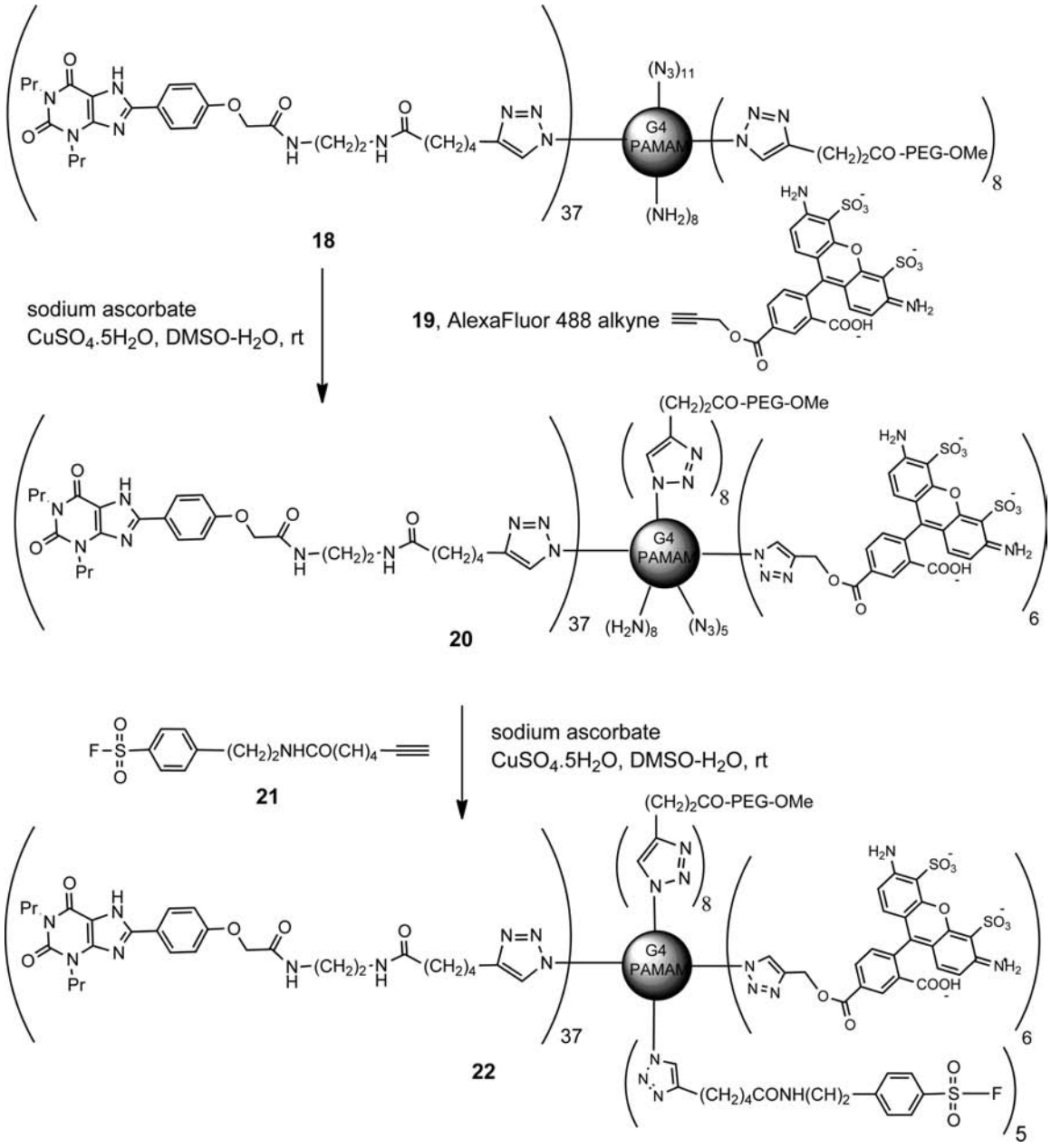
The synthetic method for cross-linking the receptor ligand to the nanocarriers **8** and **9** by click chemistry[3] required the introduction of an alkyne at an insensitive site on the xanthine moiety, and for this purpose, the hexynoyl amide derivative of XAC **4** was prepared. We have explored in detail the SAR at ARs at the distal region of the chain extended from the *para* position of the 8-phenylxanthines.[15,16] This is a site for unlimited chain derivatization, and thus, the alkyne-functionalized chain was used to provide click products with the azide-functionalized dendrimers.[3] We systematically varied the degree of substition of the dendrimer carrier with the GPCR ligand, i.e., the nonselective AR antagonist, ranging from substitution of an average of 4 to 37 of the terminal groups with the xanthine moiety. The efficiency of incorporation of the xanthine was nearly quantitative depending on the equivalents of **4** added to the click reaction, as indicated by mass spectroscopy. A fully XAC-substituted dendrimer was not prepared due to the limitation of aqueous solubility, which presented a concern in the absence of tethered PEG groups.

XAC conjugate **18**, which contained a random distribution of an average of 37 xanthine moieties and 8 PEG groups, was further derivatized with functional prosthetic groups that were coupled by click chemistry (Scheme 2). A fluorescent prosthetic group for spectroscopic characterization (Alexa Fluor 488) was included in conjugates **20** and **22**.[24] Alexa Fluor 488, which has emission and excitation maxima at 495 and 519 nm, respectively, has already been used as a fluorophore in small ligand probes of the $A_{2A}AR$.[25] Conjugate **22** also contained an aryl sulfonyl fluoride (an average of 5 moieties incorporated per PAMAM dendrimer) for affinity labeling of the receptor.[26] Aryl sulfonyl fluorides readily react irreversibly with proximal nucleophilic amino acids on a receptor yet are sufficiently stable to be applied in aqueous media. Two near-infrared (NIR) dyes[27] with absorption in the range of 800 nm (**25**) and 700 nm (**26**) were included in conjugates containing an average of 34 xanthine moieties per dendrimer. The NIR dyes were amide-linked to dendrimer **14** using the active ester precursors **23** and **24**, leading to an average degree of incorporation of 4 or 6 dye moieties incorporated per PAMAM dendrimer in **25** and **26**, respectively, as shown in Scheme 3.

Radioligand Binding. We tested the xanthine−dendrimer conjugates in binding assays at three hAR subtypes; we used standard radioligands[21−23] and membrane preparations from CHO cells (hA_1AR and hA_3AR) or HEK293 cells ($A_{2A}AR$) stably expressing a hAR subtype.[28,29] Binding affinity at the $A_{2B}AR$ was not determined because of the lack of a facile radioligand binding assay, but one representative conjugate was examined in a functional assay at this subtype.[19] Binding results shown in Table 1 indicated that receptor affinity was maintained in many of the conjugates. We used a previously reported monomeric antagonist of the ARs, XAC **3**,[16] and its hexynoyl derivative **4**, the synthetic precursor of the conjugates, for comparison in the binding assays. We included the parent dendrimers **8** and **9**, which contained a mixture of PEG, azido, and amino terminal groups, as controls; they were inactive or only weakly active in inhibiting the binding of hA_1AR and $hA_{2A}AR$ radioligands. The parent dendrimers **8** and **9** at 1 μM inhibited binding at the hA_3AR by 72% and 52%, respectively. However, we were not able to plot a full sigmoidal curve in the competition binding experiments to determine a K_i value. The relatively high displacement of radioligand at the hA_3AR by the parent dendrimers in high concentration may be related to the presence of aromatic triazolo rings on the surface of the dendrimer.

Inhibition of radioligand binding by dendrimer conjugates **14** and **18** in membranes of CHO cells expressing the hA_1 and A_3

Scheme 2. Synthesis of PAMAM Dendrimer Derivatives That Combined an Antagonist of the ARs and Functional Prosthetic Groups That Were Coupled by Click Chemistry (Average Structures Shown)[a]

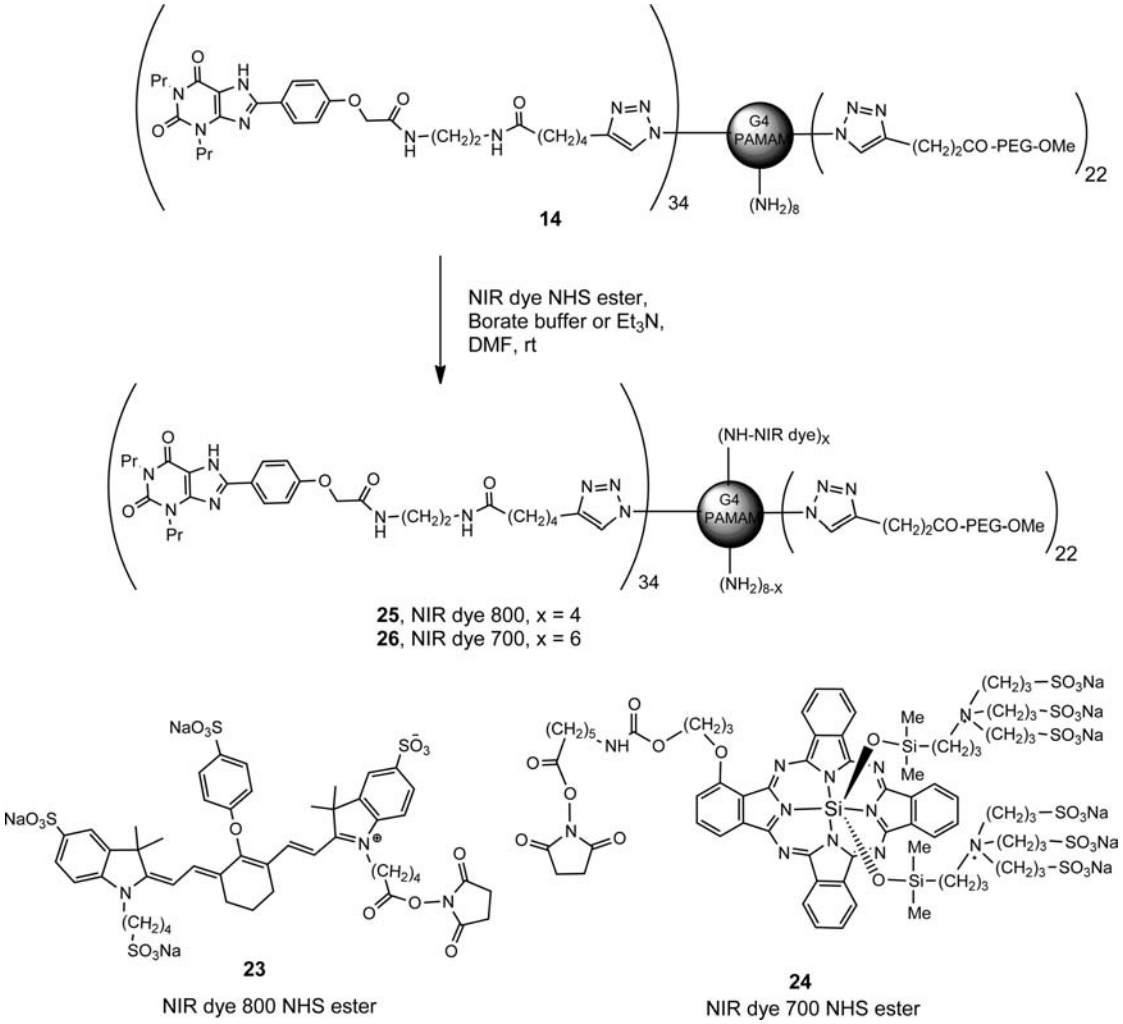


[a] These consisted of conjugates for fluorescent detection (**20**) and for irreversible binding to the receptors (**22**). The dendrimer precursor **18** contained a random distribution of 37 xanthine moieties.

ARs and HEK-293 cells expressing the $hA_{2A}AR$ is shown in Figure 2B,C. Inhibition of radioligand binding by the xanthine monomer **4** is shown for comparison in Figure 2A. The results were also plotted graphically to illustrate the dependence of the affinity on the degree of substitution (Figure 3). Two methods of calculating the data were used: initially according to the concentration of the dendrimer, which is a single multivalent molecule as was done in previous studies,[1,2,5,9] or according to the concentration of the pendant xanthine moieties. The latter method is a mathematical construct, not an authentic equilibrium constant, because the xanthine moieties could not all be available to compete for receptor binding sites, by virtue of spatial limitations.

There was a smooth dependence of the affinity on the degree of substitution of the XAC-derivatized click-linked dendrimers in both series containing 8 or 22 PEG groups out of a total of 64 terminal sites. The more highly substituted dendrimer derivatives were considerably more potent than lightly substituted conjugates in binding assays at the hA_1AR, $hA_{2A}AR$, and hA_3AR. Thus, there was a regular progression toward increased affinity at each of these AR subtypes for **10**−**14** (from 6 to 34 xanthine moieties) in the more heavily PEGylated series and for **15**−**18** (from 4 to 37 xanthine moieties) in the more lightly PEGylated series. The dendrimer conjugates having 8 PEG groups displayed K_i values at the $hA_{2A}AR$ that varied from 33 nM to 4 nM ($n = 3$), for **15** and

Scheme 3. Synthesis of PAMAM Dendrimer Conjugates That Combined an Antagonist of the ARs and Prosthetic Groups for NIR Detection That Were Coupled through Amide Linkage (Average Structures Shown)[a]



[a] The dendrimer precursor **14** contained a random distribution of 34 xanthine moieties.

18, respectively. The gain of affinity for the more highly PEGylated dendrimer series (Figure 3C and D) was steeper than the gain in the less highly PEGylated dendrimer series (Figure 3A and B). Thus, the affinity of the most highly substituted conjugate having 22 PEG groups (**14**) in binding to the ARs was particularly high, with K_i values of 15, 2.6, and 8.9 nM at hA_1AR, $hA_{2A}AR$, and hA_3AR, respectively. Therefore, the binding affinity at hAR subtypes (inversely related to apparent K_i) of these multivalent conjugates depended mainly on the degree of loading with the pharmacophore and secondarily on the degree of PEG substitution.

The order of affinity at AR subtypes for each conjugate was generally $hA_{2A}AR > hA_3AR > hA_1AR$. Therefore, a slight selectivity of these xanthine−dendrimer conjugates for the $hA_{2A}AR$ in comparison to that of the other ARs was demonstrated (3- to 6-fold for **14** and 4- to 7-fold for **18**). However, the corresponding monomers **3** and **4** displayed affinity in the order of $hA_{2A}AR > hA_1AR \geq hA_3AR$. Therefore, conjugation to the carrier altered the pharmacological profile of the xanthine by relatively increasing the A_3AR affinity. It is unknown whether this difference is due to the multivalency or to the chemical nature of the linker and its effect on interaction with the extracellular regions of the receptor.

The association of binding activity of the conjugate with a macromolecular species was confirmed by filtering a solution of compound **14** through a 3000 MW cutoff centrifugal filter. Both the UV absorption of the retained fraction and its binding activity were maintained following ultrafiltration. Thus, the observed activity was due to the intact conjugate, rather than a diffusable small molecular weight impurity.

High affinity in AR binding was maintained in the conjugates containing prosthetic groups for receptor characterization (**20**, **22**, **25**, and **26**). In fact, the K_i values of these conjugates were nearly the same as those of the precursors, i.e., XAC-conjugates **14** and **18**. This was a striking observation considering the structural diversity of the attached prosthetic groups. Compound **22** might have a component of nonequilibrium binding because of the chemically reactive sulfonyl fluoride group, but this was not evident from these binding results. The affinity of the 800 nm NIR dye in **25** was identical to precursor **14**, but the more sterically bulky NIR dye in **26** caused a slight (3-fold) loss of affinity at the A_3AR.

We further examined the A_1AR antagonist activity of compound **14**, one of the most potent conjugates for the AR subtypes

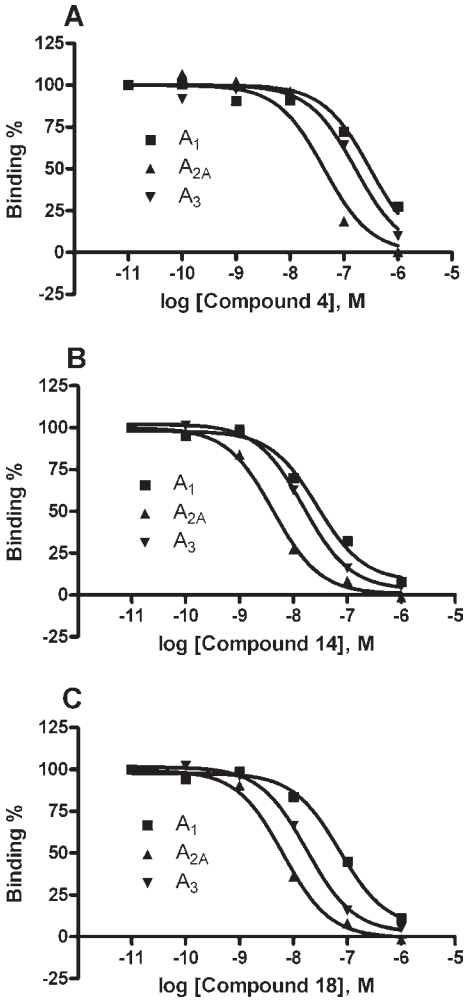


Figure 2. Inhibition of radioligand binding by xanthine monomer **4** (A) and dendrimer conjugates **14** (B) and **18** (C) (according to the concentration of the dendrimer) in membranes of CHO cells expressing the hA_1 and A_3 ARs and HEK-293 cells expressing the $hA_{2A}AR$.

in two types of functional assays in stably transfected CHO cells. We did not assay the functional effects at all the ARs; the G_i-coupled A_1AR is only representative of the full biological spectrum of the xanthines, and the behavior of the conjugate could be different at each of the AR subtypes. It was found that **14** at 100 nM right-shifted the concentration−response curve to the potent A_1AR agonist N^6-cyclopentyladenosine (CPA) in the cyclic AMP functional assay (inhibitory) in a parallel manner (Figure 4A). The EC_{50} values of CPA in the absence and presence of compound **14** at 100 nM were 1.5 ± 0.3 and 45 ± 17.2 nM, respectively. The activation of the A_1AR is also reported to stimulate mobilization of intracellular Ca^{2+} in various cells, which is likely dependent on $G\beta\gamma$ subunits.[30] CPA stimulated Ca^{2+} mobilization with an EC_{50} of 57.5 ± 16.8 nM (Figure 4B), and compound **14** at a concentration (10 nM) lower than its K_i value both right-shifted the CPA curve and suppressed the maximal effect, suggesting qualitative pharmacological differences between the conjugates and monomers. In contrast, the monomer XAC **3** at 10 nM or 100 nM (Figure 4C) inhibited CPA-induced calcium mobilization in A_1AR-expressing CHO cells in a competitive fashion. In the presence of 100 nM XAC, CPA displayed an EC_{50} of 346 ± 58 nM, corresponding to a 6-fold reduced potency.

A representative conjugate **14** was examined as an antagonist in a functional adenylate cyclase assay at the G_s-coupled $hA_{2B}AR$ expressed in CHO cells.[19] The multivalent xanthine at a concentration of 10 nM produced an 18-fold right-shift of the NECA response curve (Figure 5).

DISCUSSION

In this study, we used the Cu(I)-catalyzed alkyne−azide click reaction as a chemically and biologically effective means of linking a functionalized congener of a potent AR antagonist to PAMAM dendrimers. Click chemistry was previously used to link small molecular AR agonists to dendrimeric structures,[30] but this is the first systematic probing of PAMAM dendrimer conjugates of small-molecular AR antagonists. As with the agonist conjugates, high affinity of the GLiDe conjugates was achieved. The efficiency of the click reaction readily allowed a high degree of substitution in the dendrimer derivatives that could be varied by the proportion of PEG-alkyne or XAC-alkyne to dendrimer molecules that was added to the reaction.

The effectiveness of PEGylation of polymeric drug conjugtes to enhance polymer architecture, self-assembly, and bioavailability has been demonstrated.[31] In the present conjugates of a hydrophobic xanthine pharmacophore, water-solubility was increased, and the characteristic aggregation of PAMAM dendrimers was reduced by the presence of PEG groups. We compared different degrees of loading of the GPCR ligand and of PEG groups to the dendrimeric carrier. The ability to bind the ARs was not prevented by attached PEG groups (each approximately 43 oxoethylene units in length), similar to previous findings with AR agonist GLiDe conjugates.[32]

More highly XAC-substituted dendrimer derivatives prepared by click chemistry were particularly potent in binding to the ARs, with some selectivity for the $hA_{2A}AR$ subtype in comparison to that for hA_1 and hA_3ARs. There was also indication of high potency antagonist activity at the hA_{2B} for a representative derivative **14**. Nearly nanomolar affinities in binding to three AR subtypes were attained in the most highly XAC-substituted conjugates, with affinity enhancement for the conjugates versus monomer **4** being most pronounced for the A_3AR. The phenomenon of progressively increased affinity upon greater xanthine substitution was evident in both series of high and low PEG content. However, the function of the gain in AR affinity with increasing xanthine content did vary somewhat with different degrees of PEG substitution. The conjugates with an average of 22 PEG units, corresponding to a total of 44,000 D added to the molecular weight of the PAMAM, were initially weaker in binding to ARs than the 8 PEG series but gained more rapidly with increasing xanthine substitution. The molecular weights of the highly substituted conjugates **14** and **18** were ~78 and ~53 kD, respectively. Thus, the PEG content of these two conjugates amounted to approximately 56% and 30%, respectively, of the total mass.

Substitution with additional prosthetic groups of varied structure attached either by click or amide-forming reactions did not appreciably alter the binding affinity. For example, two sterically bulky NIR dyes with absorption in the range of 800 and 700 nm that are used in imaging in vivo[33] were incorporated in conjugates with retention of high receptor binding affinity. For example, conjugate **25** is identical in A_3AR affinity to its precursor and contains an average of 4 equivalents of IR dye 800CW, which is excited at 785 nm and fluorescence can be measured at 830 nm,

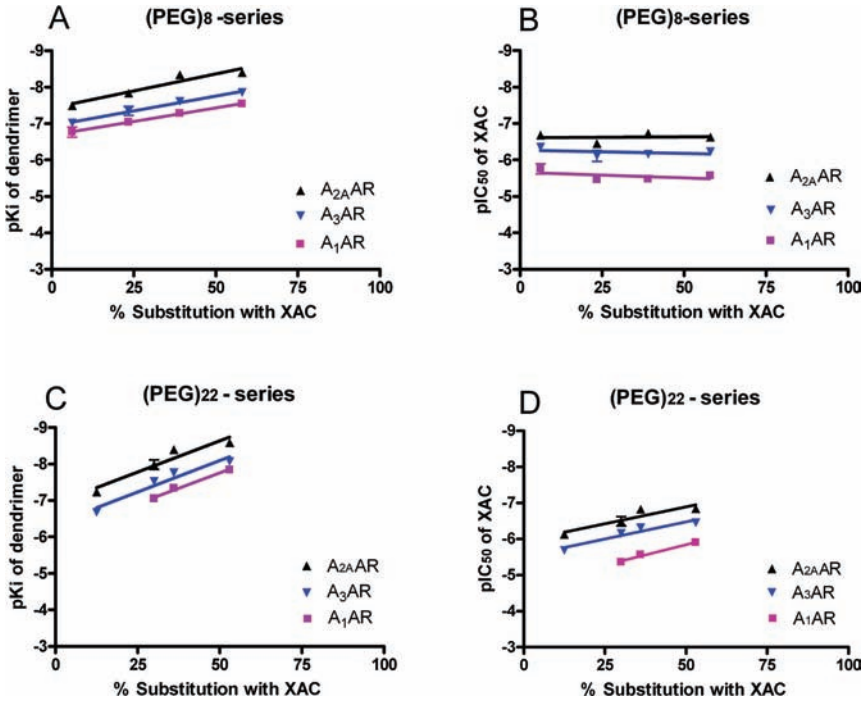


Figure 3. Inhibition of radioligand binding by dendrimer nucleoside conjugates in membranes of CHO cells expressing the hA_1 and A_3 ARs and HEK-293 cells expressing the $hA_{2A}AR$ showing dependence on the degree of substitution with the AR antagonist pharmacophore (XAC). Two methods of calculating the data were used on the basis of the definition of antagonist concentration: according to the concentration of the dendrimer (A,C) or according to the concentration of the pendant xanthine moieties (B,D). The conjugates were generally slightly selective for the $hA_{2A}AR$ in comparison to the hA_1 and hA_3ARs.

which is suitable for whole body imaging in small animals. Such GLiDe conjugates might eventually be useful for in vivo diagnostic imaging of tissue overexpressing ARs, such as occurs in disease states.[34] Thus, the ability to substitute the dendrimer with chemically diverse prosthetic groups in this series of AR conjugates allows for considerable structural breadth for probing and possibly targeting of the conjugates to the ARs or to cells having specific markers on the surface.

The advantages of nanocarriers for small molecular weight drugs include enhanced pharmacokinetic and pharmacodynamic properties. Our approach derivatizes a small molecular GPCR ligand for coupling to a carrier but allows it to remain active while covalently attached.[1,15] Internalization is not needed or desired because the binding sites of the receptors are accessible only from the extracellular medium. Molecular modeling indicated that flexible PAMAM dendrimers are able to spread over the cell surface, and purine conjugates of G3 dendrimers and higher generations can readily adopt a conformation that can bridge multiple GPCR binding sites.[8] In the theoretical model of a dendrimer conjugate of an $A_{2A}AR$ agonist bridging adjacent binding sites of an $A_{2A}AR$ homodimer, the distance between the two sites was ~35 Å, which was easily accommodated by two intermediate-spaced arms of the G3 dendrimer in a nonextended conformation. This roughly spherical G3 dendrimer conjugate had a diameter of ~67 Å, and the xanthine moieties of the present G4 conjugates in a non-extended conformation might be expected to achieve an estimated maximum separation of ~80 Å. This distance would be increased by stretching of the dendrimer over a surface.[35]

GPCRs tend not to be evenly or randomly distributed over the surface of a given cell; we demonstrated this for the hA_3AR expressed heterologously in CHO cells.[2] In general, GPCRs may exist as complexes with other receptors and associated proteins. The receptors to which a given GPCR pairs or forms a higher-order aggregate can dramatically affect its pharmacology, and the binding of an agonist to both protomers does not have equivalent pharmacological effects.[36] Thus, a multivalent GPCR ligand might display unanticipated, complex effects.[5] There is a lack of GPCR ligands that are designed specifically to interact with dimeric and oligomeric receptors. We do not have effective ligand tools for separating the effects of one receptor dimeric combination from another. The approach of mixing ligands for two different receptors[3,37,41] promises to be a means of achieving selectivity for receptors in a given tissue, on the basis of association or aggregation of GPCRs, in comparison to another tissue in which the same receptor may be alternatively paired. At this early stage, we do not know the topological requirements for selectively targeting these combinations of receptors because we are just beginning to detect their existence. Nevertheless, providing tools for studying these receptor aggregates is one of the objectives of this study. The multivalent binding to other types of cell surface receptors has been explored through sytematic structural modification of the carrier polymer.[42]

There is evidence here for multivalent binding of the same conjugate to more than one AR site. The fact that the AR affinity rose substantially with increased xanthine content, even when calculating IC_{50} values according to the concentration of the pharmacophore rather than the dendrimer as shown in Figure 3D, suggests that the same GLiDe conjugate molecule may bind to multiple AR binding sites. The interaction of the multivalent GLiDe conjugates can now be studied in cells expressing varying levels of a given AR or with other receptors coexpressed.

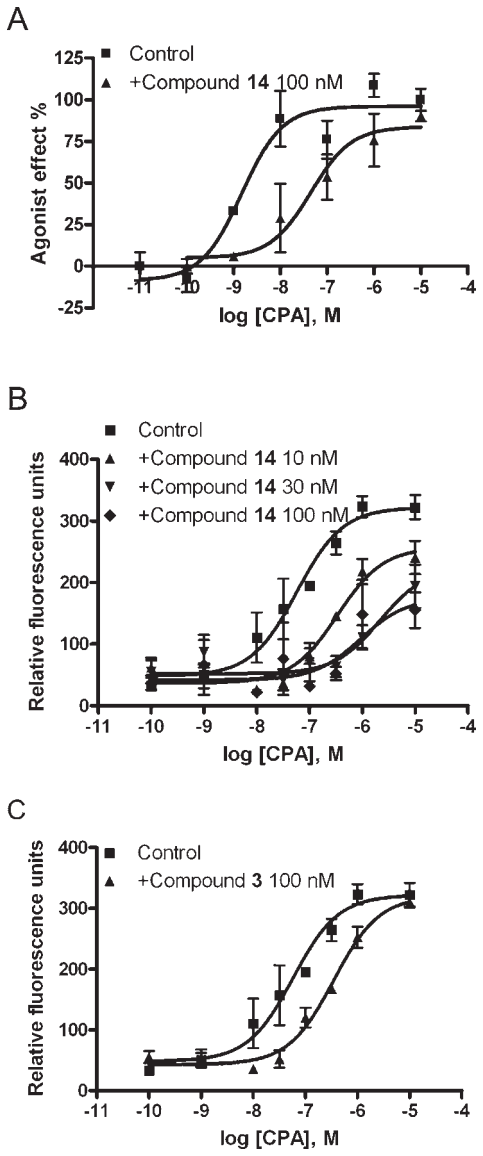


Figure 4. Antagonist activity of compound **14** in the inhibition of forskolin-stimulated cyclic AMP accumulation induced by agonist CPA (A) and the inhibition by **14** of CPA-induced calcium mobilization (B) in CHO cells stably expressing the hA_1AR. Part C shows the comparable inhibition by XAC **3** of CPA-induced calcium mobilization in hA_1AR-expressing CHO cells. Each curve is representative of three determinations. The EC_{50} values are listed in the text.

In previous studies, we have noted that the pharmacological profile of GLiDe conjugates can differ from that of the monomeric ligands both quantitatively and qualitatively.[5,11] For example, the dendrimer conjugates of AR agonists have displayed a shift in the AR subtype selectivity or in the correspondence between the binding and functional potencies.[2,11] Here, we have detected a qualitative difference in the A_1AR antagonistic response between a potent, multivalent xanthine conjugate and its corresponding monomer. Conjugate **14** acted as a competitive antagonist of the $G_{i\alpha}$-dependent effect of inhibition of adenylate cyclase, but at comparable concentrations acted as a noncompetitive inhibitor of calcium mobilization, which is likely independent of $G_{i\alpha}$. The functional effects at other AR subtypes were not determined here and will be the subject of further studies.

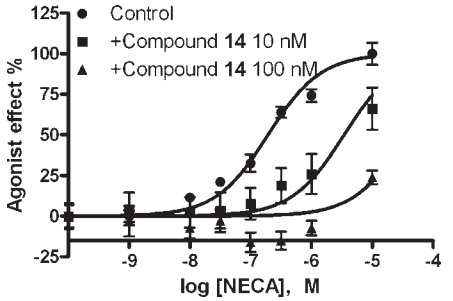


Figure 5. Antagonist activity of compound **14** in the stimulation of cyclic AMP accumulation induced by agonist NECA in CHO cells stably expressing the $hA_{2B}AR$. Each curve is representative of three determinations. The EC_{50} values for NECA in the absence and presence of 10 nM **14** are 194 nM and 3.46 μM, respectively.

In conclusion, we have synthesized and characterized pharmacologically a series of multivalent dendrimeric derivatives of a potent strategically functionalized AR antagonist. GLiDe conjugates provide different quantitative and qualitative pharmacological properties than do monomers. Prosthetic groups designed for therapeutic targeting or reporter groups for diagnostic purposes might be introduced. Various therapeutic applications[12] may be proposed for multivalent conjugates of AR antagonists. In vivo studies will be needed to fully characterize these potent ligands biologically and determine their advantage over monomeric drugs.

■ ASSOCIATED CONTENT

Supporting Information. ^{1}H NMR and mass spectra of representative compounds **14** and **18**. This material is available free of charge via the Internet at http://pubs.acs.org.

■ AUTHOR INFORMATION

Corresponding Author

*Bldg. 8A, Rm. B1A-19, NIH, National Institute of Diabetes and Digestive and Kidney Diseases, Bethesda, MD 20892-0810. Tel. 301-496-9024, Fax 301-480-8422. E-mail: kajacobs@helix.nih.gov.

Author Contributions

†Authors contributed equally to this study.

■ ACKNOWLEDGMENT

We thank Dr. John Lloyd and Dr. Noel Whittaker (NIDDK) for the mass spectral determinations, Dr. Martin Garraffo (NIDDK) for FT-IR measurements, and Khai Phan (NIDDK) for pharmacological measurements. We thank Dr. Francesca Deflorian (NIDDK), Dr. Michael Kilbey, III, and Dr. Kunlun Hong (Oak Ridge National Laboratory, Knoxville TN) for helpful discussions. This research was supported by the Intramural Research Program of the NIH, NIDDK.

■ ABBREVIATIONS

AR, adenosine receptor; cAMP, adenosine 3′,5′-cyclic phosphate; CGS21680, 2-[*p*-(2-carboxyethyl)phenylethylamino]-5′-*N*-ethylcarboxamidoadenosine; CHO, Chinese hamster ovary; CPA, N^6-cyclopentyladenosine; DIPEA, diisopropylethylamine;

DMEM, Dulbecco's modified Eagle's medium; DMF, *N*,*N*-dimethylformamide; DMSO, dimethylsulfoxide; EDC, *N*-ethyl-*N*′-dimethylaminopropylcarbodiimide; EDTA, ethylenediaminetetraacetic acid; GLiDe, GPCR ligand−dendrimer; GPCR, G protein-coupled receptor; HATU, 2-(1*H*-7-azabenzotriazol-1-yl)-1,1,3,3-tetramethyl uronium hexafluorophosphate methanaminium; HEK, human embryonic kidney; HEPES, 4-(2-hydroxyethyl)-1-piperazineethanesulfonic acid; I-AB-MECA, 2-[*p*-(2-carboxyethyl)phenyl-ethylamino]-5′-*N*-ethylcarboxamidoadenosine; IB-MECA, N^6-(3-iodobenzyl)-5′-*N*-methylcarboxamidoadenosine; MS, mass spectrometry; NECA, 5′-*N*-ethylcarboxamidoadenosine; NMR, nuclear magnetic resonance; NIR, near-infrared; PAMAM, polyamidoamine; PEG, polyethyleneglycol; R-PIA, *R*-N^6-(2-phenylisopropyl)adenosine.

REFERENCES

(1) Kim, Y., Hechler, B., Klutz, A., Gachet, C., and Jacobson, K. A. (2008) Toward multivalent signaling across G protein-coupled receptors from poly(amidoamine) dendrimers. *Bioconjugate Chem. 19*, 406–411.

(2) Klutz, A. M., Gao, Z. G., Lloyd, J., Shainberg, A., and Jacobson, K. A. (2008) Enhanced A_3 adenosine receptor selectivity of multivalent nucleoside-dendrimer conjugates. *J. Nanobiotechnol. 6*, 12.

(3) Tosh, D. K., Yoo, L. S., Chinn, M., Hong, K., Kilbey, S. M., Barrett, M. O., Fricks, I. P., Harden, T. K., Gao, Z. G., and Jacobson, K. A. (2010) Polyamidoamine (PAMAM) dendrimer conjugates of "clickable" agonists of the A_3 adenosine receptor and coactivation of the $P2Y_{14}$ receptor by a tethered nucleotide. *Bioconjugate Chem. 21*, 372–384.

(4) Overington, J. (2006) How many drug targets are there?. *Nat. Rev. Drug. Discovery 5*, 993–996.

(5) Jacobson, K. A. (2010) GPCR ligand-dendrimer (GLiDe) conjugates: future smart drugs?. *Trends Pharmacol. Sci. 31*, 575–579.

(6) Ferré, S., Baler, R., Bouvier, M., Caron, M. G., Devi, L. A., Durroux, T., Fuxe, K., George, S. R., Javitch, J. A., Lohse, M. J., Mackie, K., Milligan, G., Pfleger, K. D., Pin, J. P., Volkow, N. D., Waldhoer, M., Woods, A. S., and Franco, R. (2009) Building a new conceptual framework for receptor heteromers. *Nat. Chem. Biol. 5*, 131–134.

(7) Nakata, H., Suzuki, T., Namba, K., and Oyanagi, K. (2010) Dimerization of G protein-coupled purinergic receptors: increasing the diversity of purinergic receptor signal responses and receptor functions. *J. Recept. Signal Transduction 30*, 337–346.

(8) Ivanov, A. A., and Jacobson, K. A. (2008) Molecular modeling of a PAMAM-CGS21680 dendrimer bound to an A_{2A} adenosine receptor homodimer. *Bioorg. Med. Chem. Lett. 18*, 4312–4315.

(9) de Castro, S., Maruoka, H., Hong, K., Kilbey, S. M., Costanzi, S., Hechler, B., Gachet, C., Harden, T. K., and Jacobson, K. A. (2010) Functionalized congeners of $P2Y_1$ receptor antagonists: 2-Alkynyl (N)-methanocarba 2′-deoxyadenosine 3′,5′-bisphosphate analogues and conjugation to a polyamidoamine (PAMAM) dendrimer carrier. *Bioconjugate Chem. 21*, 1190–1205.

(10) Maeda, H., Bharate, G. Y., and Daruwalla, J. (2009) Polymeric drugs for efficient tumor-targeted drug delivery based on EPR-effect. *Eur. J. Pharm. Biopharm. 71*, 409–419.

(11) Keene, A. M., Balasubramanian, R., Lloyd, J., Shainberg, A., and Jacobson, K. A. (2010) Multivalent dendrimeric and monomeric adenosine agonists attenuate cell death in HL-1 mouse cardiomyocytes expressing the A_3 adenosine receptor. *Biochem. Pharmacol. 80*, 188–196.

(12) Jacobson, K. A., and Gao, Z. G. (2006) Adenosine receptors as therapeutic targets. *Nature Rev. Drug Discovery 5*, 247–264.

(13) Müller, C., and Jacobson, K. A. (2011) Xanthines as Adenosine Receptor Antagonists. In Methylxanthines. *In Handbook of Experimental Pharmacology* (Fredholm, B.B., Ed.) Vol. 200, pp 151−199, Springer, New York.

(14) Baraldi, P. G., Tabrizi, M. A., Gessi, S., and Borea, P. A. (2008) Adenosine receptor antagonists: translating medicinal chemistry and pharmacology into clinical utility. *Chem. Rev. 108*, 238–263.

(15) Jacobson, K. A., Kirk, K. L., Padgett, W. L., and Daly, J. W. (1985) Functionalized congeners of 1,3-dialkylxanthines: preparation of analogues with high affinity for adenosine receptors. *J. Med. Chem. 28*, 1334–1340.

(16) Jacobson, K. A. (2009) Functionalized congener approach to the design of ligands for G protein−coupled receptors (GPCRs). *Bioconjugate Chem. 20*, 1816–1835.

(17) van Dijk, M., Rijkers, D. T. S., Liskamp, R. M. J., van Nostrum, C. F., and Hennink, W. E. (2009) Synthesis and applications of biomedical and pharmaceutical polymers via click chemistry methodologies. *Bioconjugate Chem. 20*, 2001–2016.

(18) Goddard-Borger, E. D., and Stick, R. V. (2007) An efficient, inexpensive, and shelf-stable diazotransfer reagent: Imidazole-1-sulfonyl azide hydrochloride. *Org. Lett. 9*, 3797–3800.

(19) Adachi, H., Palaniappan, K. K., Ivanov, A. A., Bergman, N., Gao, Z. G., and Jacobson, K. A. (2007) Structure-activity relationships of 2, N^6,5′-substituted adenosine derivatives with potent activity at the A_{2B} adenosine receptor. *J. Med. Chem. 50*, 1810–1827.

(20) Bradford, M. M. (1976) A rapid and sensitive method for the quantitation of microgram quantities of protein utilizing the principle of protein-dye binding. *Anal. Biochem. 72*, 248–254.

(21) Klotz, K. N., Lohse, M. J., Schwabe, U., Cristalli, G., Vittori, S., and Grifantini, M. (1989) 2-Chloro-N^6-[^{3}H]cyclopentyladenosine ([^{3}H]CCPA)-a high affinity agonist radioligand for A_1 adenosine receptors. *Naunyn-Schmiedeberg's Arch. Pharmacol. 340*, 679–683.

(22) Jarvis, M. F., Schutz, R., Hutchison, A. J., Do, E., Sills, M. A., and Williams, M. (1989) [^{3}H]CGS 21680, an A_2 selective adenosine receptor agonist directly labels A_2 receptors in rat brain tissue. *J. Pharmacol. Exp. Ther. 251*, 888–893.

(23) Olah, M. E., Gallo-Rodriguez, C., Jacobson, K. A., and Stiles, G. L. (1994) ^{125}I-4-Aminobenzyl-5′-N-methylcarboxamidoadenosine, a high affinity radioligand for the rat A_3 adenosine receptor. *Mol. Pharmacol. 45*, 978–982.

(24) Middleton, R. J., and Kellam, B. (2005) Fluorophore-tagged GPCR ligands. *Curr. Opin. Chem. Biol. 9*, 517–525.

(25) Kumar, T. S., Mishra, S., Deflorian, F., Yoo, L. S., Phan, K., Kecskés, M., Szabo, A., Shinkre, B. A., Gao, Z. G., Trenkle, W. C., and Jacobson, K. A. (2011) Molecular probes for the A_{2A} adenosine receptor based on a pyrazolo[4,3-*e*][1,2,4]triazolo[1,5-c]pyrimidine scaffold. *Bioorg. Med. Chem. Lett. 21*, 2740–2745.

(26) Baraldi, P. G., Cacciari, B., Moro, S., Romagnoli, R., Ji, X.-d., Jacobson, K. A., Gessi, S., Borea, P. A., and Spalluto, G. (2001) Fluorosulfonyl- and bis-(b-chloroethyl)amino-phenylamino functionalized pyrazolo[4,3-e]1,2,4-triazolo[1,5-c]pyrimidine derivatives: Irreversible antagonists at the human A_3 adenosine receptor and molecular modeling studies. *J. Med. Chem. 44*, 2735–2742.

(27) Zwier, J. M., Roux, T., Cottet, M., Durroux, T., Douzon, S., Bdioui, S., Gregor, N., Bourrier, E., Oueslati, N., Nicolas, L., Tinel, N., Boisseau, C., Yverneau, P., Charrier-Savournin, F., Fink, M., and Trinquet, E. (2010) A fluorescent ligand-binding alternative using Tag-lite® technology. *J. Biomol. Screen. 15*, 1248–1260.

(28) Englert, M., Quitterer, U., and Klotz, K. N. (2002) Effector coupling of stably transfected human A_3 adenosine receptors in CHO cells. *Biochem. Pharmacol. 64*, 61–65.

(29) Jacobson, K. A., Park, K. S., Jiang, J. -l., Kim, Y. C., Olah, M. E., Stiles, G. L., and Ji, X. d. (1997) Pharmacological characterization of novel A_3 adenosine receptor-selective antagonists. *Neuropharmacology 36*, 1157–1165.

(30) Ethier, M. F., and Madison, J. M. (2006) Adenosine A_1 receptors mediate mobilization of calcium in human bronchial smooth muscle cells. *Am. J. Respir. Cell Mol. Biol. 35*, 496–502.

(31) Tosh, D. K., Chinn, M., Yoo, L. S., Kang, D. W., Luecke, H., Gao, Z. G., and Jacobson, K. A. (2010) 2-Dialkynyl derivatives of (N)-methanocarba nucleosides: 'Clickable' A_3 adenosine receptor-selective agonists. *Bioorg. Med. Chem. 18*, 508–517.

(32) Joralemon, M. J., McRae, S., and Emrick, T. (2010) PEGylated polymers for medicine: from conjugation to self-assembled systems. *Chem. Commun. (Cambridge, U.K.) 46*, 1377–1393.

(33) Kim, Y., Hechler, B., Gao, Z. G., Gachet, C., and Jacobson, K. A. (2009) PEGylated dendritic unimolecular micelles as versatile carriers for ligands of G protein-coupled receptors. *Bioconjugate Chem. 20*, 1888–1898.

(34) Adams, K. E., Ke, S., Kwon, S., Liang, F., Fan, Z., Lu, Y., Hirschi, K., Mawad, M. E., Barry, M. A., and Sevick-Muraca, E. M. (2007) Comparison of visible and near-infrared wavelength excitable fluorescent dyes for molecular imaging of cancer. *J. Biomed. Opt. 12*, 024017.

(35) Ochaion, A., Bar-Yehuda, S., Cohen, S., Barer, F., Patoka, R., Amital, H., Reitblat, T., Reitblat, A., Ophir, J., Konfino, I., Chowers, Y., Ben-Horin, S., and Fishman, P. (2009) The anti-inflammatory target A_3 adenosine receptor is overexpressed in rheumatoid arthritis, psoriasis and Crohn's disease. *Cell. Immunol. 258*, 115–122.

(36) Tomalia, D. A., Naylor, A. M, and Goddard, W. A. (1990) Starburst dendrimers: molecular level control of size, shape, surface chemistry, topology, and flexibility from atoms to macroscopic matter. *Angew. Chem., Int. Ed. 29*, 138–175.

(37) Han, Y., Moreira, I. S., Urizar, E., Weinstein, H., and Javitch, J. A. (2009) Allosteric communication between protomers of dopamine class A GPCR dimers modulates activation. *Nature Chem. Biol. 5*, 688–695.

(38) Portoghese, P. S., Ronsisvalle, G., Larson, D. L., Yim, C. B., Sayre, L. M., and Takemori, A. E. (1982) Opioid agonist and antagonist bivalent ligands as receptor probes. *Life Sci. 31*, 1283–1286.

(39) Morphy, R., and Rankovic, Z. (2005) Designed multiple ligands. An emerging drug discovery paradigm. *J. Med. Chem. 48*, 6523–6565.

(40) Soriano, A., Ventura, R., Molero, A., Hoen, R., Casadó, V., Cortés, A., Fanelli, F., Albericio, F., Lluís, C., Franco, R., and Royo, M. (2009) Adenosine A_{2A} receptor-antagonist/dopamine D_2 receptor-agonist bivalent ligands as pharmacological tools to detect A_{2A}-D2 receptor heteromers. *J. Med. Chem. 52*, 5590–5602.

(41) Jacobson, K. A., Xie, R., Young, L., Chang, L., and Liang, B. T. (2000) A novel pharmacological approach to treating cardiac ischemia: binary conjugates of A_1 and A_3 adenosine receptor agonists. *J. Biol. Chem. 275*, 30272–30279.

(42) Berque-Bestel, I., Lezoualc'h, F., and Jockers, R. (2008) Bivalent ligands as specific pharmacological tools for G protein-coupled receptor dimers. *Curr. Drug Discovery Technol. 5*, 312–318.

(43) Cairo, C. W., Gestwicki, J. E., Kanai, M., and Kiessling, L. L. (2002) Control of multivalent interactions by binding epitope density. *J. Am. Chem. Soc. 124*, 1615–1619.

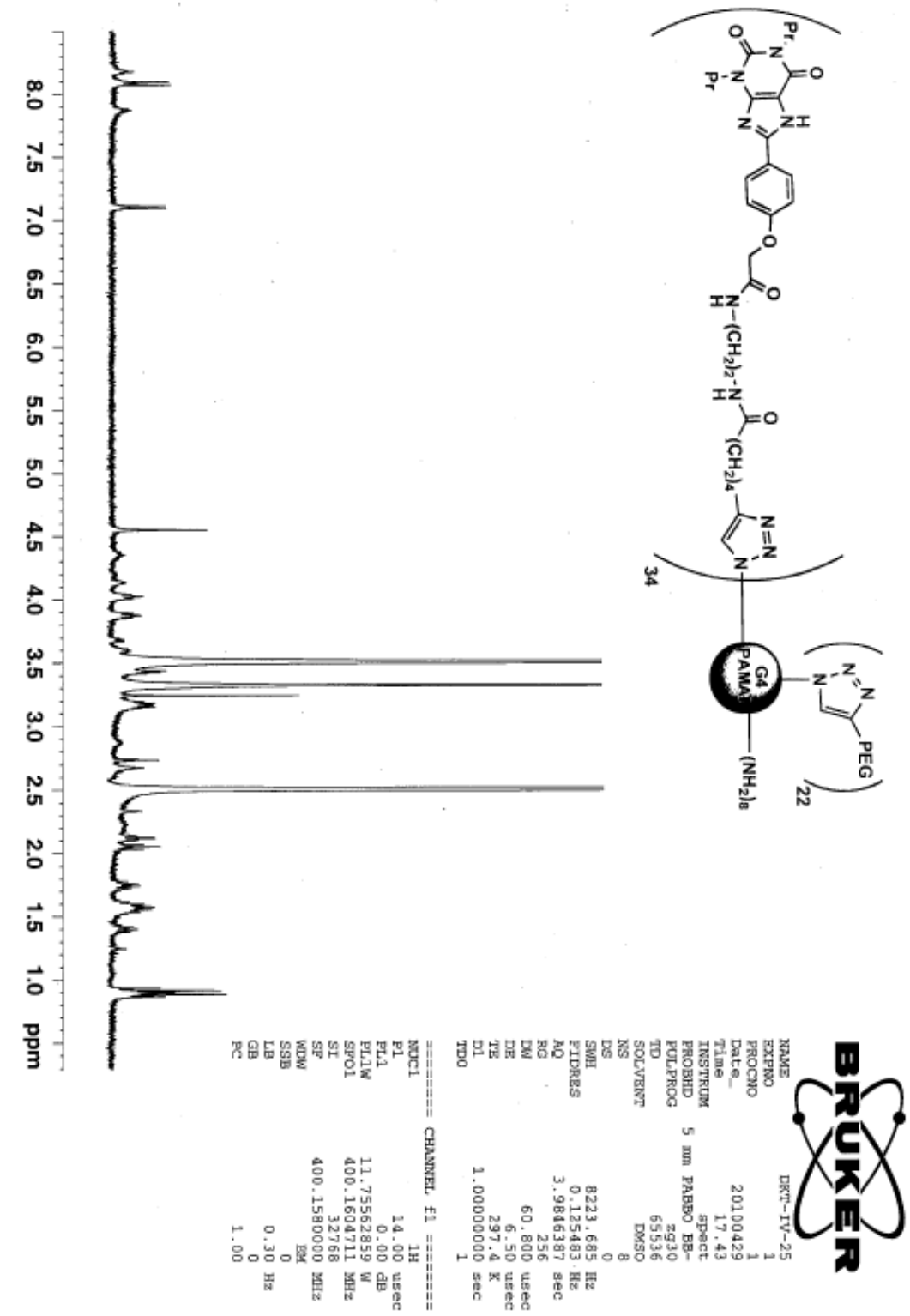
Supporting Information

GPCR Ligand Dendrimer (GLiDe) Conjugates:
Adenosine Receptor Interactions of a Series of Multivalent Xanthine Antagonists

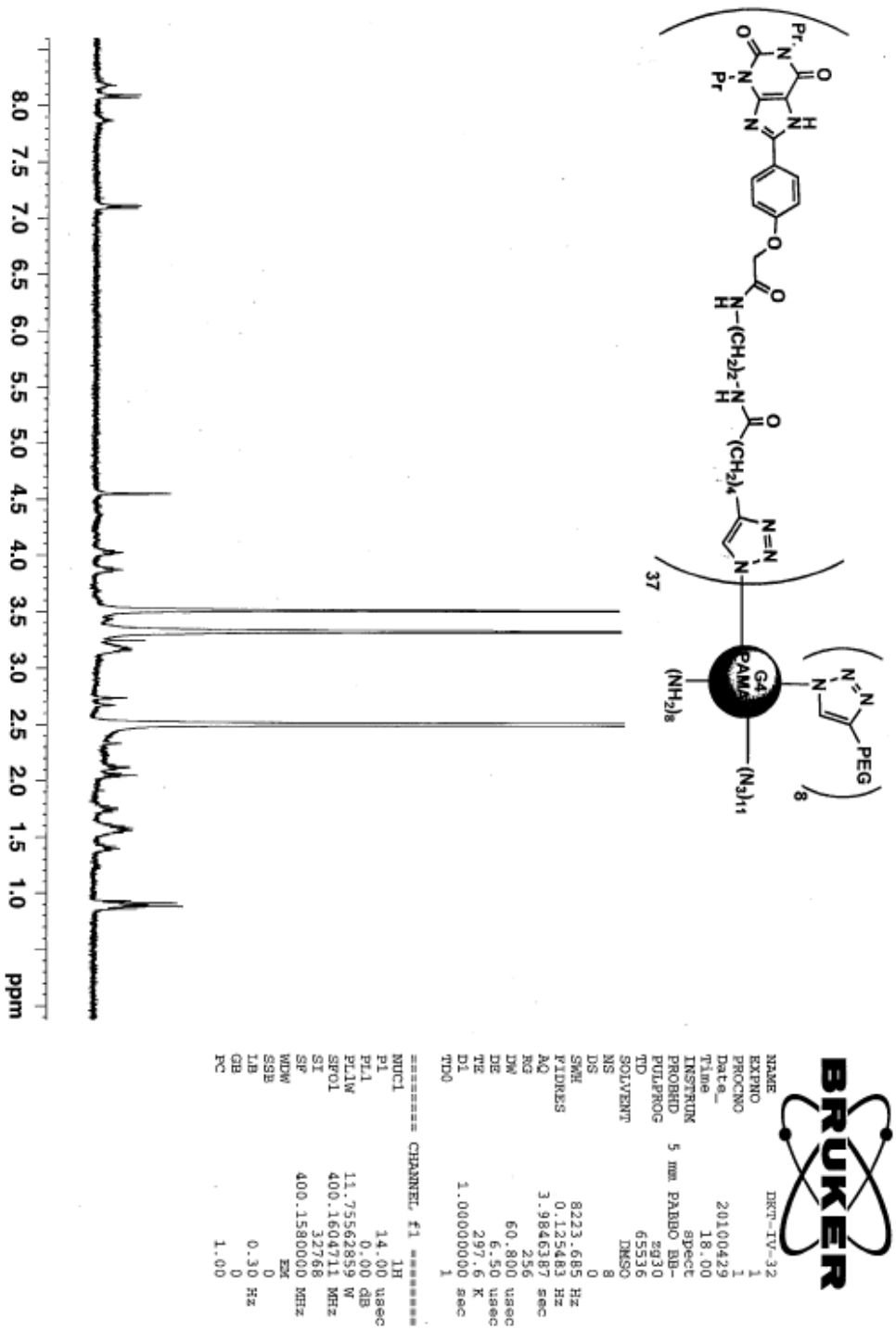
Angela Kecskés, Dilip K. Tosh, Qiang Wei, Zhan-Guo Gao, and Kenneth A. Jacobson

Contents: ^{1}H NMR and mass spectra of representative compounds **14** and **18**.

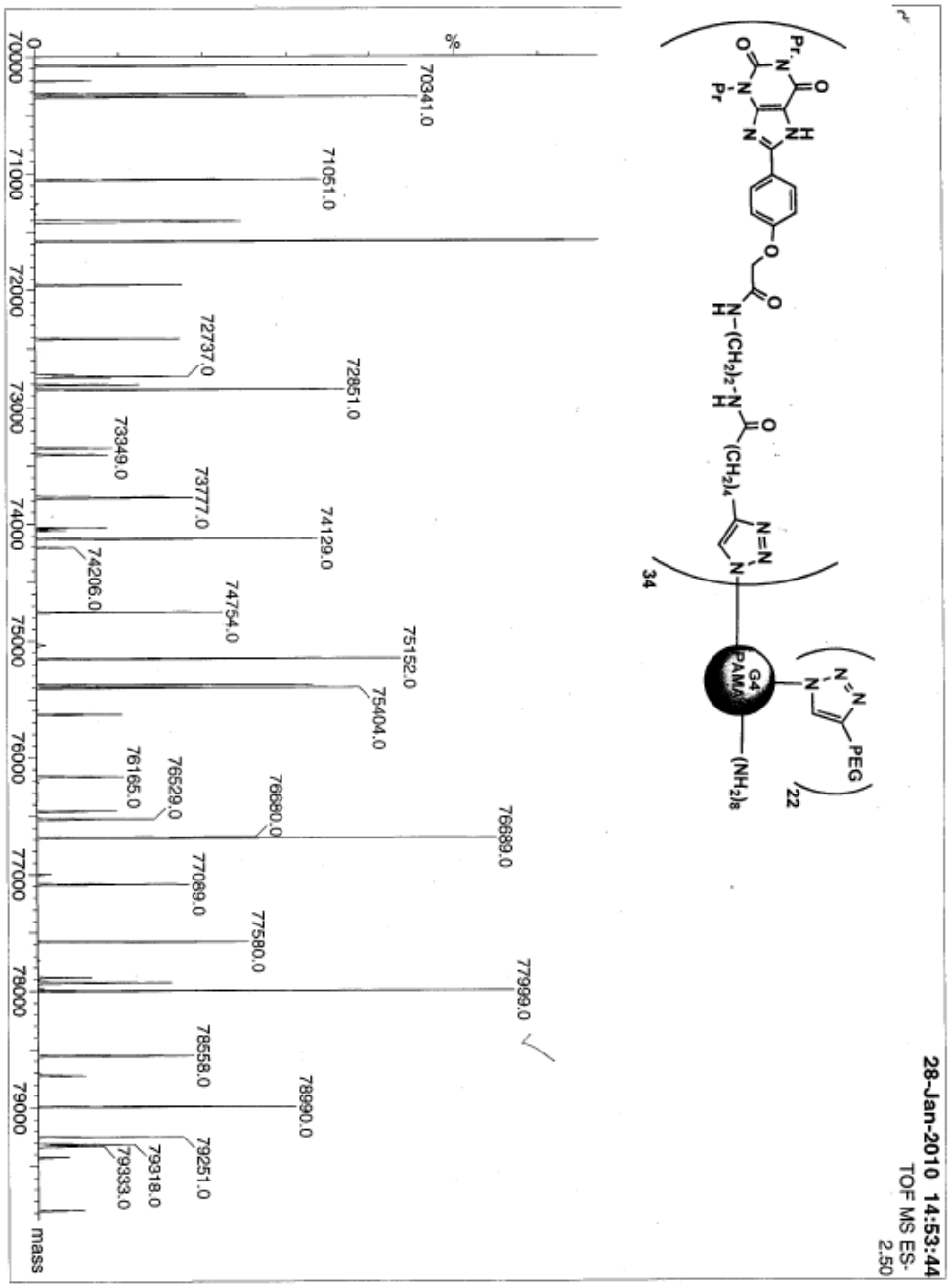
^{1}H NMR spectrum of compound **14**



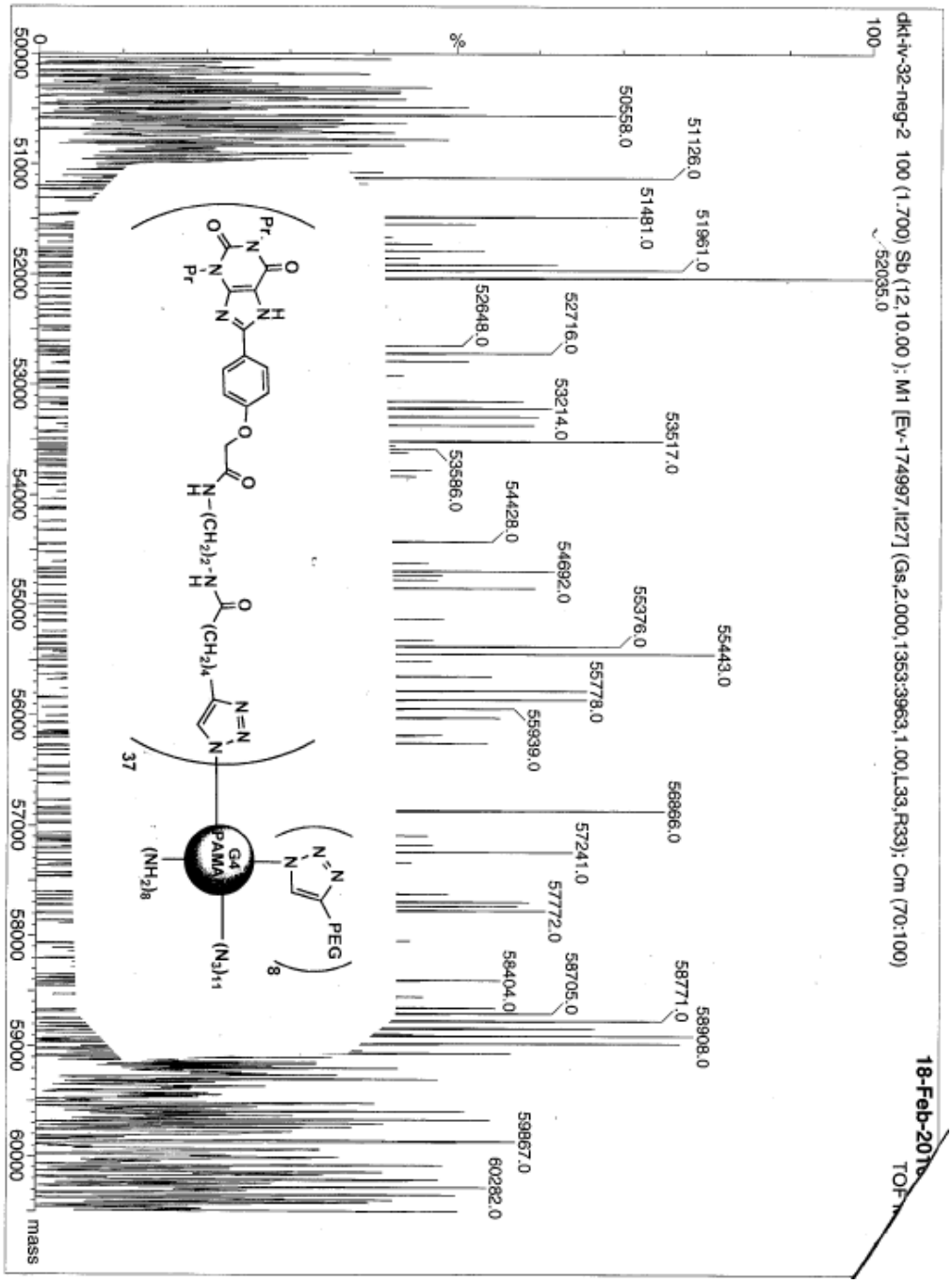
^{1}H NMR spectrum of compound **18**



Mass spectrum of compound **14**



Mass spectrum of compound **18**



Bioconjugate Chemistry

ARTICLE

pubs.acs.org/bc

Efficient Bifunctional Decadentate Ligand 3p-*C*-DEPA for Targeted α-Radioimmunotherapy Applications

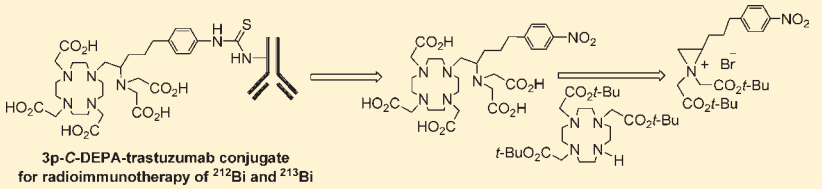
Hyun A Song,[†] Chi Soo Kang,[†] Kwamena E. Baidoo,[‡] Diane E. Milenic,[‡] Yunwei Chen,[†] Anzhi Dai,[†] M. W. Brechbiel,[‡] and Hyun-Soon Chong*[,†]

[†]Chemistry Division, Biological, Chemical, and Physical Sciences Department, Illinois Institute of Technology, Chicago, Illinois, United States

[‡]Radioimmune & Inorganic Chemistry Section, Radiation Oncology Branch, Center for Cancer Research, National Cancer Institute, NIH, Bethesda, Maryland, United States

S *Supporting Information*

ABSTRACT:



A new bifunctional ligand 3p-*C*-DEPA was synthesized and evaluated for use in targeted α-radioimmunotherapy. 3p-*C*-DEPA was efficiently prepared via regiospecific ring opening of an aziridinium ion and conjugated with trastuzumab. The 3p-*C*-DEPA-trastuzumab conjugate was extremely rapid in binding $^{205/6}$Bi, and the corresponding $^{205/6}$Bi-3p-*C*-DEPA-trastuzumab complex was stable in human serum. Biodistribution studies were performed to evaluate *in vivo* stability and tumor targeting of $^{205/6}$Bi-3p-*C*-DEPA-trastuzumab conjugate in tumor bearing athymic mice. $^{205/6}$Bi-3p-*C*-DEPA-trastuzumab conjugate displayed excellent *in vivo* stability and targeting as evidenced by low organ uptake and high tumor uptake. The results of the *in vitro* and *in vivo* studies indicate that 3p-*C*-DEPA is a promising chelator for radioimmunotherapy of ^{212}Bi and ^{213}Bi.

INTRODUCTION

The α-emitting radioisotopes, ^{212}Bi ($t_{1/2}$ = 60.6 m) and ^{213}Bi ($t_{1/2}$ = 45.6 m), have proven to be effective for radioimmunotherapy (RIT) of cancers.[1] The α-emitters with high α-energy (5−8 MeV) and a short emission path length (50−80 μm) can be closely deposited in the target tumor cells resulting in minimum damage to normal tissues.[2] The radionuclides, ^{212}Bi and ^{213}Bi, with very short half-lives decay ultimately to stable bismuth nuclides and are considered to be suitable for convenient outpatient RIT.[3] The therapeutic efficacy of ^{212}Bi and ^{213}Bi has been demonstrated in numerous preclinical and clinical trials involving cancer patients with leukemia, melanoma, and glioblastoma.[4−7]

Three optimal components, a bifunctional ligand, an antibody, and a radioisotope, are required for a successful RIT. An effective bifunctional ligand that can rapidly form a stable complex with the radionuclide should be employed to minimize toxic side effects related to biological deposition of the radionuclide if it becomes dissociated from the radiolabeled ligand−antibody conjugate during RIT.[8] Research efforts have been directed toward improving chelation chemistry for RIT. *C*-DOTA and *C*-DTPA (Figure 1) analogues are two bifunctional ligands that are frequently explored for RIT applications.[3] *C*-DOTA forms a kinetically inert and stable complex with Bi(III); however, the slow complex formation kinetics render this chelator unacceptable for use in RIT when employing short-lived radionuclides such as ^{213}Bi and ^{212}Bi.[9,10] The acyclic bifunctional ligand, *C*-DTPA, displayed rapid and high-yield radiolabeling with Bi(III) radioisotopes.[3] However, *C*-DTPA produced a less stable Bi(III)-*C*-DTPA complex than that of Bi(III)-*C*-DOTA,[3,11,12]

We recently reported the synthesis and evaluation of DEPA (Figure 1, 7-[2-(bis-carboxymethyl-amino)-ethyl]-4,10-bis-carboxymethyl-1,4,7,10-tetraaza-cyclododec-1-yl-acetic acid).[10] DEPA is a decadentate ligand in a hybridized form of the macrocyclic DOTA (1,4,7,10-tetraazacyclododecane-1,4,7,10-tetracarboxylic acid) and the acyclic DTPA (diethylenetriamine pentaacetic acid). This novel bimodal ligand DEPA was hypothesized to rapidly form a stable complex with a metal based on cooperative coordination of the macrocyclic and acyclic binding moieties. DEPA radiolabeled with $^{205/6}$Bi ($t_{1/2}$ = 15.3 d for ^{205}Bi; $t_{1/2}$ = 6.24 for ^{206}Bi), a γ-emitting surrogate of ^{212}Bi and ^{213}Bi was indeed found to be stable in human serum without any loss of the radioactivity for two weeks and displayed excellent *in vivo* stability in mice.[10]

With the promising complexation kinetics and stability data for DEPA, we sought preparation of an effective bifunctional

Received: December 20, 2010
Revised: May 4, 2011
Published: May 23, 2011

ACS Publications © 2011 American Chemical Society

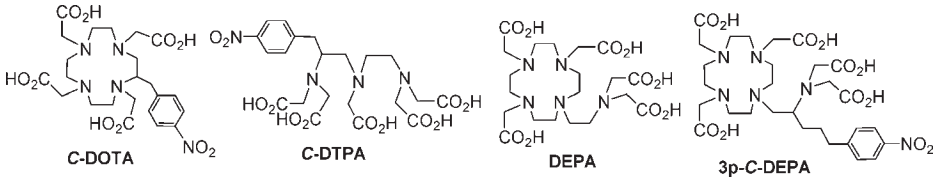


Figure 1. Ligands in clinical and preclinical use for RIT.

version of DEPA for RIT. In this paper, we report the synthesis and evaluation of a bifunctional DEPA analogue, 3p-*C*-DEPA (Figure 1, 2-[(carboxymethyl)][5-(4-nitrophenyl-1-[4,7,10-tris-(carboxymethyl)-1,4,7,10-tetraazacyclododecan-1-yl]pentan-2-yl)-amino]acetic acid), which contains the parent DEPA backbone and the isothiocyanate (NCS) group for conjugation to an antibody or a peptide. 3p-*C*-DEPA was synthesized, characterized, and conjugated to trastuzumab. Trastuzumab is a HER2 (human epidermal growth factor receptor 2) targeting antibody which has been reported to selectively target the HER2 protein overproduced in various tumors, including 90% of colorectal carcinomas.[13,14] The corresponding 3p-*C*-DEPA-trastuzumab conjugate was evaluated for its radiolabeling reaction kinetics with $^{205/6}$Bi. *In vitro* analysis of the 3p-*C*-DEPA-trastuzumab conjugate radiolabeled with $^{205/6}$Bi included assessment of its stability in human serum and retention of reactivity with HER2 using a radioimmunoassay. Finally, the *in vivo* biodistribution and tumor uptake of the $^{205/6}$Bi-labeled 3p-*C*-DEPA-trastuzumab was assessed in mice bearing s.c. tumor (LS-174T) xenografts. For comparison and as a reference standard, the *C*-DOTA-trastuzumab conjugate was evaluated in the same *in vitro* and *in vivo* studies.

EXPERIMENTAL PROCEDURE

Instruments and Methods. ^{1}H and ^{13}C NMR spectra were obtained using a Bruker 300 instrument and chemical shifts are reported in ppm on the δ scale relative to TMS or solvent. Electrospray iodization (ESI) high-resolution mass spectra (HRMS) were obtained on JEOL double sector JMS-AX505HA mass spectrometer (University of Notre Dame, IN). Analytical HPLC was performed on an Agilent 1200 instrument (Agilent, Santa Clara, CA) equipped with a diode array detector (λ = 254 and 280 nm), a thermostat set at 35 °C, and a Zorbax Eclipse XDB-C18 column (4.6 × 150 mm, 80 Å, Agilent, Santa Clara, CA). The mobile phase of a binary gradient (0−100% B/40 min; solvent A, 0.05 M AcOH/Et_3N, pH 6.0; solvent B, CH_3OH for method 1) at a flow rate of 1 mL/min was used for analytical HPLC. Semiprep HPLC was performed on an Agilent 1200 equipped with a diode array detector (λ = 254 and 280 nm), a thermostat set at 35 °C, and a Zorbax Eclipse XDB-C18 column (9.4 × 250 mm, 80 Å). The mobile phase of a binary gradient (0−100% B/160 min; solvent A = 0.05 M AcOH/Et_3N, pH 6.0; solvent B = MeOH for method 2) at a flow rate of 2 mL/min was used for semiprep HPLC. Size-exclusion HPLC (SE-HPLC) chromatograms were obtained on Agilent 1200 equipped with a diode array detector and an in-line IN/US γ-Ram model 2 radiodetector (Tampa, FL), fitted with Bio-Silect SEC 250−5 column (Biorad, Hercules, CA) or a TSKgel G3000PW column (Tosoh Biosep, Montgomeryville, PA).

Reagents. All reagents were purchased from Sigma-Aldrich (St. Louis, MO) and used as received unless otherwise noted. Trastuzumab (Herceptin; Genentech, South San Francisco, California) was obtained through the Veterinary Resources Program (National Institutes of Health, Bethesda, MD). ^{205,6}Bi was produced using a CS30 cyclotron (PET Dept, Clinical Center, NIH) and purified as described previously.[15] *C*-DOTA was purchased from Macrocyclics (Dallas, TX).

***tert*-Butyl-2,2′,2″-(10-(2-(bis(2-*tert*-butoxy-2-oxoethyl)-amino)-5-(4-nitrophenyl)-pentyl)-1,4,7,10-tetraazacyclododecane-1,4,7-triyl)triacetate (4).** To a solution of **1**[16] (547.7 mg, 1.06 mmol) and DIPEA (410.9 mg, 3.18 mmol) in CH_3CN (10 mL) was added trisubstituted cyclen **3** (546.6 mg, 1.06 mmol). The resulting mixture was stirred for 4 weeks at room temperature while monitoring the reaction progress using TLC. The reaction mixture containing the starting materials and the product **4** was concentrated to dryness. The residue was purified via column chromatography on silica gel (220−440 mesh) eluted with 3% CH_3OH in CH_2Cl_2. The fractions containing the product **4** along with the starting material **3** as impurity were combined. After evaporating the solvent, ether (20 mL) was added to the residue, and the starting material **3** formed a slurry which was removed by filtration. The filtrate containing the product **4** was washed with DI water (2 × 10 mL). The ether layer was dried over $MgSO_4$, filtered, and concentrated *in vacuo* to provide pure **4** (610 mg, 61%). ^{1}H NMR ($CDCl_3$, 300 MHz) δ 1.37−1.45 (m, 45 H), 1.60−1.78 (m, 2 H), 1.81−1.95 (m, 1 H), 2.02−2.19 (m, 1 H), 2.39−2.50 (m, 3H), 2.56−2.83 (m, 18 H), 3.21 (s, 4H), 3.26 (s, 2 H), 3.36 (dd, J = 16.9, 21.9 Hz, 4 H), 7.36 (d, J = 8.6 Hz, 2 H), 8.09 (d, J = 8.7 Hz, 2 H); ^{13}C NMR ($CDCl_3$, 300 MHz) δ 27.89 (t), 28.11 (q), 28.22 (q), 30.98 (t), 35.91 (t), 52.04 (t), 52.11 (t), 52.20 (t), 53.09 (t), 53.19 (t), 56.34 (t), 56.44 (t), 58.38 (t), 60.08 (d), 80.41 (s), 80.57 (s), 123.43 (d), 129.30 (d), 146.18 (s), 151.17 (s), 170.98 (s), 171.10 (s), 171.41 (s). HRMS (Positive ion FAB) Calcd for $C_{49}H_{85}N_6O_{12}$ $[M + H]^+$ m/z 949.6225. Found: $[M + H]^+$ m/z 949.6256. Analytical HPLC (t_R = 42 min, method 1).

Tri-*tert*-butyl-10-(2-(*tert*-butoxycarbonyl)-5-(4-nitrophenyl)-pentyl)-1,4,7,10-tetraazacyclo-dodecane-1,4,7-tricarboxylate (7). To a mixture of **5** (1.24 g, 3.85 mmol) and **6** (1.82 g, 3.85 mmol) in 1,2-dichloroethane (30 mL) was added portionwise sodium triacetoxyborohydride (1.14 g, 5.4 mmol). The mixture was stirred at room temperature for 14 h. The reaction mixture was quenched with saturated $NaHCO_3$ (40 mL), and the product was extracted while washing with CH_2Cl_2. The combined organic layers were dried over $MgSO_4$, filtered, and concentrated *in vacuo*. The residue was purified by silica gel (60−230 mesh) column chromatography eluted with 25% EtOAc in hexanes to provide **7** (1.90 g, 63%). ^{1}H NMR ($CDCl_3$, 300 MHz) δ 1.03−1.51 (m, 36 H), 1.51−2.01 (m, 4 H), 2.50−3.99 (m, 21 H), 7.30 (d, J = 8.5 Hz, 2 H), 8.08 (d, J = 8.4 Hz, 2H); ^{13}C NMR ($CDCl_3$, 300 MHz) 24.69 (t), 27.16 (t), 28.57 (q), 28.69 (q), 35.13 (t), 35.68, (t), 36.64 (t), 47.49 (t), 48.46 (d), 50.54 (t), 51.20 (t), 58.18 (t), 58.64 (t), 79.18 (s), 79.28 (s), 79.57 (s), 123.56 (d), 129.19 (d), 146.27 (s), 150.39 (s), 155.14 (s), 155.73 (s),

155.95 (s), 156.72 (s). HRMS (Positive ion ESI) Calcd for $C_{39}H_{67}N_6O_{10}$ $[M + H]^+$ m/z 779.4913, Found: $[M + H]^+$ m/z 779.4890.

5-(4-Nitrophenyl)-1-(1,4,7,10-tetraazacyclododecan-1-yl)-pentan-2-amine (8). Compound **7** (1.84 g, 2.36 mmol) at 0−5 °C was treated dropwise with 4 M HCl (g) in 1,4-dioxane (18 mL) over 20 min. The resulting mixture was warmed to room temperature and stirred for 22 h. Ether (100 mL) was added and stirred for 10 min. The resulting mixture was capped and placed in the freezer for 1 h. The slurry formed was filtered, washed with ether, and quickly dissolved in deionized (DI) water. The aqueous solution was concentrated *in vacuo* to provide **8** as an acidic salt (1.17 g, 89%). ^{1}H NMR (D_2O, 300 MHz) δ 1.50−1.71 (m, 4 H), 2.50−2.80 (m, 6 H), 2.82−3.40 (m, 15 H), 7.30 (d, J = 8.7 Hz, 2 H), 8.00 (d, J = 8.7 Hz, 2 H); ^{13}C NMR (D_2O, 300 MHz) δ 25.65 (t), 30.63 (t), 34.46 (t), 41.30 (t), 42.13 (t), 44.21 (t), 48.56 (t), 48.57 (d), 56.81 (t), 123.66 (d), 129.40 (d), 145.90 (s), 150.21 (s). HRMS (Positive ion ESI) Calcd for $C_{19}H_{35}N_6O_2$ $[M + H]^+$ m/z 379.2816. Found: $[M + H]^+$ m/z 379.2804.

A solution of the acidic salt **8** (670 mg, 1.7 mmol) in DI water (5 mL) was neutralized using 0.5 M NaOH. The aqueous layer was then extracted with $CHCl_3$ (2 × 25 mL). The aqueous layer was further adjusted to pH 10 and re-extracted with $CHCl_3$ (2 × 25 mL). The organic layers extracted from both neutral (pH 7) and basic (pH 10) solutions were combined, dried over $MgSO_4$, filtered, and concentrated *in vacuo* to provide free amine **8** (452 mg, 100%). ^{1}H NMR ($CDCl_3$, 300 MHz) δ 1.20−1.49 (m, 2 H), 1.60−1.89 (m, 2 H), 2.15−3.00 (m, 21 H), 7.33 (d, J = 8.6 Hz, 2 H), 8.14 (d, J = 8.6 Hz, 2 H); ^{13}C NMR ($CDCl_3$, 300 MHz) δ 27.26 (t), 35.00 (t), 35.64 (t), 45.16 (t), 46.01 (t), 46.95 (t), 48.71 (d), 52.10 (t), 62.56 (t), 123.27 (d), 129.00 (d), 145.94 (s), 150.24 (s).

Synthesis of 4 from Compound 8. To a solution of **8** (170.3 mg, 0.45 mmol) in CH_3CN (5 mL) was added *tert*-butyl bromoacetate (438.9 mg, 2.25 mmol) and K_2CO_3 (311.0 mg, 2.25 mmol). The resulting mixture was heated at 65 °C and stirred for 13 h while monitoring the reaction progress by analytical HPLC. The reaction mixture was cooled to room temperature, and the solvent was evaporated. The residue was purified by semi-prep HPLC (method 2, 138−143 min) to afford **4** (37 mg, 9%).

2-[(Carboxymethyl)][5-(4-nitrophenyl-1-[4,7,10-tris(carboxymethyl)-1,4,7,10-tetraazacyclo-dodecan-1-yl]pentan-2-yl)-amino]acetic Acid (9). Compound **4** (77.0 mg, 0.08 mmol) at 0−5 °C was treated dropwise with 4 M HCl (g) in 1,4-dioxane (15 mL) over 20 min. The resulting mixture was allowed to warm to room temperature for 22 h. Ether (∼20 mL) was added and continuously stirred for 10 min. The resulting mixture was capped and placed in the freezer for 1 h. The solid formed was filtered, washed with ether, and quickly dissolved in DI water. Evaporation of the aqueous solution gave **9** (68.0 mg, 97%) as an off-white solid. ^{1}H NMR (D_2O, 300 MHz) δ 1.26−1.40 (m, 1H), 1.48−1.70 (m, 3H), 2.52−2.78 (m, 2H), 2.90−3.70 (m, 27H), 3.75−3.98 (m, 2H), 7.35 (d, J = 8.3 Hz, 2H), 8.06 (d, J = 8.2 Hz, 2H); ^{13}C NMR (D_2O, 300 MHz) δ 27.08 (t), 34.64 (t), 48.45 (t), 48.82 (t), 50.22 (t), 51.09 (t), 52.40 (t), 53.58 (t), 54.28 (t), 55.46 (t), 59.43 (d), 123.55 (d), 129.40 (d), 145.71 (s), 150.54 (s), 169.54 (s), 172.97 (s), 173.93 (s); HRMS (Positive ion FAB) Calcd for $C_{29}H_{45}N_6O_{12}$ $[M + H]^+$ m/z 669.3095. Found: $[M + H]^+$ m/z 669.3086.

2,2′,2″-(10-(5-(4-Aminophenyl)-2-(bis(carboxymethyl)-amino)pentyl)-1,4,7,10-tetraaza-cyclododecane-1,4,7-triyl)-triacetic acid (10). To a solution of **9** (46.0 mg, 68.8 μmol) in DI H_2O (12 mL) was added dry 10% Pd/C (14.0 mg) under argon. The reaction mixture was subject to hydrogenation in a hydrogenation apparatus set at the constant pressure (15 psi) of H_2 (g) for 19 h. The resulting mixture was filtered over a Celite bed and washed thoroughly with DI H_2O. The filtrate was concentrated *in vacuo* to provide a light yellow solid **10** (44 mg, 100%). ^{1}H NMR (D_2O, 300 MHz) δ 1.22−1.38 (m, 1H), 1.43−1.68 (m, 3H), 2.45−2.63 (m, 2H), 2.81−3.70 (m, 27H), 3.80−3.98 (m, 2H), 7.17 (d, J = 8.5 Hz, 2H), 7.24 (d, J = 8.5 Hz, 2H); ^{13}C NMR (D_2O, 300 MHz) δ 27.04 (t), 27.46 (t), 34.18 (t), 48.50 (t), 48.98 (t), 50.28 (t), 51.12 (t), 52.50 (t), 53.69 (t), 54.50 (t), 55.49 (t), 59.40 (d), 123.01 (d), 127.55 (s), 130.10 (d), 143.28 (s), 169.50 (s), 173.13 (s), 174.22 (s); HRMS (positive ion ESI) Calcd for $C_{29}H_{47}N_6O_{10}$ $[M + H]^+$ m/z 639.3348. Found: $[M + H]^+$ m/z 639.3342.

2,2′,2″-(10-(2-(Bis(carboxymethyl)amino)-5-(4-isothiocyanatophenyl)pentyl)-1,4,7,10-tetraazacyclododecane-1,4,7-triyl)triacetic Acid (11). To a solution of **10** (7.0 mg, 8.2 μmol) in water (0.1 mL) was added $CSCl_2$ (7.0 μL, 7.0 μmol) in $CHCl_3$. The resulting mixture was stirred at room temperature for 2 h. The aqueous layer was isolated and concentrated *in vacuo* to give pure 3p-*C*-DEPA-NCS **11** as a solid (8.0 mg, 100%). ^{1}H NMR (D_2O, 300 MHz) δ 1.23−1.72 (m, 4H), 2.40−2.58 (m, 2H), 2.80−3.98 (m, 29H), 7.13 (s, 4H). HRMS (Positive ion FAB) Calcd for $C_{30}H_{43}N_6O_{12}S$ $[M + H]^+$ m/z 679.2761. Found: $[M + H]^+$ m/z 679.2747.

Conjugation of 3p-*C*-DEPA-NCS to Trastuzumab. All absorbance measurements were obtained on an Agilent 8453 diode array spectrophotometer equipped with a 8-cell transport system (designed for 1 cm cells). Metal-free stock solutions of all buffers were prepared using Chelex-100 resin (200−400 mesh, Bio-Rad Lab, Hercules, CA, Cat no 142−2842). Chelex resin (2.5 g) was added into the buffer solution (250 mL) and the mixture was shaken overnight in a shaker and filtered through a Corning filter system (Cat no 430513, pore size 0.2 μm). Disposable PD-10 Sephadex G-25 M columns (GE Healthcare, #17−0851−01) were rinsed with 25 mL of the appropriate buffer prior to addition of antibody or its ligand conjugates. Amicon centricon C-50 (50 000 MWCO) centrifugal filter devices (Millipore, Cat no UFC805008) were used for purification of trastuzumab conjugate (Bedford, MA). The initial concentration of trastuzumab was determined by the UV/vis spectroscopic method. Phosphate buffered saline (PBS, 1×, 11.9 mM Phosphates, 137 mM NaCl, and 2.7 mM KCl, pH 7.4) was purchased from Fisher and used as received. Conjugation buffer (50 mM HEPES, 150 mM NaCl, pH 8.6) were prepared as 1× solutions, chelexed, and filtered through the Corning filter. Trastuzumab (6.67 mg) was diluted to 1.6 mL using conjugation buffer (1:0.6), and the resulting solution was added to a PD-10 column. Conjugation buffer (10 mL) was added to the PD-10 column to exchange the buffer solution of the antibody and collected in a sterile test tube and checked for the presence of trastuzumab via analysis of the UV/vis spectrum at 280 nm. To a sterile test tube containing the recovered trastuzumab (6.14 mg) was added a 10-fold excess of 3p-*C*-DEPA-NCS (39.6 μL, 10 mM). The resulting solution was gently agitated for 16 h at room temperature and placed on a Centricon C-50 membrane and spun down to reduce volume. PBS (3 × 2 mL) was added to the remaining solution of the 3p-*C*-DEPA-trastuzumab conjugate, followed by centrifugation in order to remove unreacted ligand. The volume of purified conjugate antibody was brought to 1.0 mL with PBS. To measure [trastuzumab] in the 3p-*C*-DEPA-trastuzumab conjugate, a

UV/vis spectrometer was zeroed against a cuvette filled with 2.0 mL of PBS with a window open from 190 to 1100 nm. A 50 μL portion of PBS was removed and discarded, 50 μL of the 3p-*C*-DEPA-trastuzumab conjugate solution was added, and absorbance at 280 nm was noted. Beer's Law was used to calculate [trastuzumab] in the conjugate with molar absorptivity of 1.42. After centrifugation, 2.98 mg (2.02×10^{-5} M, 49.0%) of the trastuzumab remained.

Spectroscopic Determination of Ligand to Protein (L/P) Ratio. A stock solution of the Cu(II)-AAIII reagent was prepared in 0.15 M NH_4OAc, pH 7.0 by adding an aliquot of copper atomic absorption solution (1.55×10^{-2} M) into a 10 μM solution of AAIII to afford a 5 μM solution of Cu(II).[17] This solution was stored in the dark to avoid degradation over time. A UV/vis spectrometer was zeroed against eight well-dried blank cuvettes with a window open from 190 to 1100 nm. A cuvette was filled with AAIII solution (2 mL), and the other seven cuvettes with the Cu(II)-AAIII solution (2 mL). Cu(II)-AAIII solution (50 μL) in the seven cuvettes was removed and discarded. Milli-Q water (50 μL) was added to the second cuvette, and one to five 10 μL additions of 3p-*C*-DEPA (0.1 mM) were added to the five cuvettes to give a series of five different concentrations (2 mL total volume). The solutions in the third to the seventh cuvette were diluted to 2.0 mL by adding an aliquot of Milli-Q water. 3p-*C*-DEPA-trastuzumab conjugate (50 μL) was added to the eighth cuvette containing Cu(II)-AAIII reagent (1950 μL). After addition of 3p-*C*-DEPA-trastuzumab conjugate to the Cu(II)-AAIII solution, the resulting solution was equilibrated for 10 min. The absorbance of the resulting solution at 610 nm was monitored every 30 s over 6 min. The average of the absorbance of each solution was calculated, and the absorbance data from the Cu(II)-AAIII solutions containing six different concentrations were used to construct a calibration plot of A_{610} versus [3p-*C*-DEPA] by the equation, $Y = 0.0663 - (1.5284 \times 10^4)$[3p-*C*-DEPA] ($R^2 = 0.9969$), wherein $Y = A_{610\,nm}$. The concentration of 3p-*C*-DEPA in the 3p-*C*-DEPA-trastuzumab conjugate was calculated (3.98×10^{-5} M). The L/P ratio of the 3p-*C*-DEPA-trastuzumab conjugate ($[3.98 \times 10^{-5}\ M]/[2.02 \times 10^{-5}\ M]$) was measured to be 1.97.

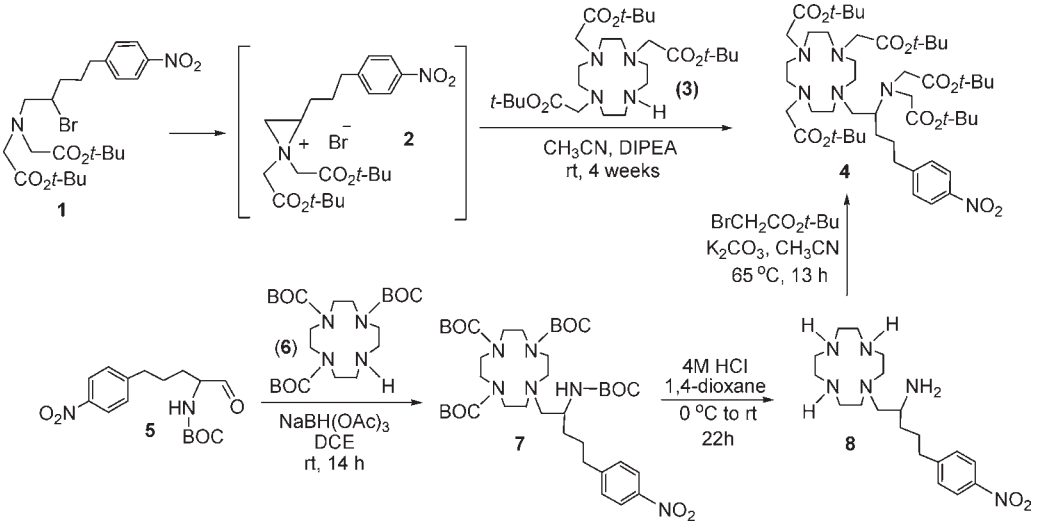
Radiolabeling of 3p-*C*-DEPA-trastuzumab or *C*-DOTA-Trastuzumab Conjugates with $^{205/6}$Bi. All HCl solutions were prepared from ultrapure HCl (Fisher, Cat no A466−500). For metal-free radiolabeling, plasticware including pipet tips, tubes, and caps was soaked in 0.1 M HCl overnight, washed thoroughly with Milli-Q (18.2 MΩ) water, and air-dried overnight. Ultrapure NH_4OAc (Aldrich, #372331) was purchased from Aldrich and used to prepare all NH_4OAc buffer solutions (0.1 M, pH 7). The buffer solutions were treated with Chelex-100 resin (Biorad, #142−2842, 1 g/100 mL buffer solution), shaken overnight at room temperature, and filtered through 0.22 μm filter (Corning, #430320) prior to use. To a buffer solution (120 μL, pH 7) in a capped microcentrifuge tube (1.5 mL, Fisher Scientific #05−408−129) was sequentially added a solution of *C*-DOTA-trastuzumab (30 μg) in PBS (13.5 μL) and $^{205/6}$Bi (0.1 M HI, 60.5 μCi, 12.7 μL) or 3p-*C*-DEPA-trastuzumab (30 μg) in PBS (9.6 μL) and $^{205/6}$Bi (0.1 M HI, 60.5 μCi, 12.7 μL). The final volume of the resulting solution was 146.2 and 142.3 μL for *C*-DOTA-trastuzumab and 3p-*C*-DEPA-trastuzumab, respectively, and the pH of the resulting reaction mixture was 5.5 for both conjugates. The reaction mixture was agitated on the thermomixer (Eppendorf, #022670549) set at 1000 rpm at room temperature for 1 h. The labeling efficiency was determined by SE-HPLC (Biorad, Bio-Silect SEC 250−5 column, 7.8 × 30 cm, eluent, PBS; flow rate, 1 mL/min). A solution of radiolabeled mixture (10 μL for *C*-DOTA-trastuzumab and 7 μL for 3p-*C*-DEPA-trastuzumab) was withdrawn at the designated time points (1 min, 5 min, 10 min, 20 min, 30 min, and 60 min), and DTPA solution (10 mM, 1 or 1.4 μL) was added to the mixture, and the resulting mixture was left for at least 20 min. HPLC samples were prepared and evaluated by SE-HPLC. Peaks for bound and unbound radioisotope appeared around 8.3 and 11 min, respectively.

***In Vitro* Stability of $^{205/6}$Bi-3p-*C*-DEPA-Trastuzumab Conjugate.** $^{205/6}$Bi-3p-*C*-DEPA-trastuzumab was prepared by reaction of 3p-*C*-DEPA-trastuzumab with $^{205/6}$Bi at either RT or 37 °C (5.0 M NH_4OAc, pH 5.5). The complex formed was purified from $^{205/6}$Bi by gel filtration chromatography using PD-10 column (Disposable PD-10 Sephadex G-25 M columns, GE Healthcare, Cat no 17−0851−01) eluted with PBS (pH 7.4, Fisher Scientific, Cat no BP2438−4). The fractions containing $^{205/6}$Bi-3p-*C*-DEPA-trastuzumab (700 μL, 22 μCi) were combined and added into human serum (700 μL, Gemini Bioproducts, #100110) in a microcentrifuge tube (Fisher Scientific, #05−408−129). The stability of the purified $^{205/6}$Bi-3p-*C*-DEPA-trastuzumab was evaluated for 4 days. The serum stability of the radiolabeled complexes was assessed by measuring the transfer of the radionuclide from each complex to serum proteins using SE-HPLC (TSKgel G3000PW column, 7.5 × 30 cm, eluent, PBS; flow rate, 1 mL/min). A solution of the radiolabeled complex in serum (20−80 μL) was withdrawn at the designated time point, treated with DTPA (5 mM, 1.0 μL), incubated at room temperature for 20 min, and then diluted with PBS (pH 7.4, 50−100 μL) prior to SE-HPLC.

Preparation of $^{205/6}$Bi-3p-*C*-DEPA-trastuzumab and $^{205/6}$Bi-*C*-DOTA-trastuzumab for Immunoreactivity and *In Vivo* Studies. For use in the *in vitro* binding and *in vivo* biodistribution and tumor targeting studies, $^{205/6}$Bi-3p-*C*-DEPA-trastuzumab and $^{205/6}$Bi-*C*-DOTA-trastuzumab with high specific activity were prepared. In this instance, two aliquots of $^{205/6}$Bi solution (100 μL in 0.1 M HI, 1.1 mCi each) were each neutralized to pH 5.5 with NH_4OAc solution (10 μL, 5 M, pH 7). An aliquot of each immunoconjugate containing 50 μg of protein in PBS was added to one or the other $^{205/6}$Bi solution. The mixtures were vortexed briefly and incubated at 37 °C. After 30 min, EDTA solution (5 μL, 0.1M) was added to each reaction, vortexed briefly, and further incubated for 5 min. The products were purified by gel filtration chromatography using disposable PD-10 columns. The labeling efficiencies were 85.8% and 67.3% for $^{205/6}$Bi-3p-*C*-DEPA-trastuzumab and $^{205/6}$Bi-*C*-DOTA-trastuzumab, respectively, as determined by the labeled products collected from the PD-10 columns. The purity of the labeled products as determined by SE-HPLC (TSKgel G3000PW column, PBS eluate at 0.5 mL/min) were >98% for each product. The specific activities were 16 mCi/mg and 13.6 mCi/mg for$^{205/6}$Bi-3p-*C*-DEPA-trastuzumab and $^{205/6}$Bi-*C*-DOTA-trastuzumab, respectively.

Radioimmunoassay. The immunoreactivity of the $^{205/6}$Bi-labeled trastuzumab conjugates was assessed in a radioimmunoassay using purified recombinant human Erb2/Fc chimera (rhErb2/Fc). Briefly, 50 ng aliquots of the rhErb2/Fc in PBS with Mg^{2+} and Ca^{2+} (50 μL) were added to each well of a 96-well plate and allowed to adsorb to the well at 4 °C. Following an overnight incubation, the solution was removed and 100 μL of 1% BSA in PBS (BSA/PBS) was added to each well and

Scheme 1. Synthesis of Precursor Molecule 4 to 3p-C-DEPA



incubated at room temperature for 30−60 min. Serial dilutions of $^{205/6}$Bi-trastuzumab conjugate (~300 000 to ~12 500 cpm in 50 μL of BSA/PBS) were added to the wells in duplicate, covered, and incubated at 37 °C for 4 h. The radiolabeled antibody was then removed and the wells were washed three times with PBS. The radioactivity was removed from the wells with a solution of 0.2 M NaOH with 1 mM EDTA (100 μL), adsorbing the solution to cotton filters, and transferring the filters to 12 × 75 mm polypropylene tubes. The radioactivity was measured in a γ-scintillation counter (WizardOne, Perkin-Elmer, Shelton, CT), and the percentage binding calculated for each dilution. The values presented are an average of the percent bound for the serial dilutions. The specificity of the radiolabeled trastuzumab was confirmed by incubating one set of wells with radiolabeled trastuzumab and 10 μg of unlabeled trastuzumab.

***In Vivo* Biodistribution and Tumor Targeting Studies.** *In vivo* studies were conducted using the human colon carcinoma cell line, LS-174T (kindly provided by Dr. J. Greiner, NCI). The LS-174T cell line was grown in Dulbecco's minimum essential medium (DMEM) supplemented with 10 mM glutamine along with 10% FetalPlex (Gemini Bio-Products, Woodland, CA) and 1 mM nonessential amino acids. Media and supplements were obtained from Lonza (Walkersville, MD). All *in vivo* studies were performed using 4−6 week old female athymic (nu/nu) mice (Charles River Laboratories, Wilmington, MA). All animal protocols were approved by the National Cancer Institute Animal Care and Use Committee. Mice were injected subcutaneously (s.c.) in the right rear leg with 2 × 10^6 LS-174T cells in media (200 μL) with 20% Matrigel (BD Biosciences, San Jose, CA). Mice were utilized in studies when the tumor xenografts maximal diameter measured 0.4−0.6 cm. Mice (n = 4 per time point) were injected intravenously (i.v.) with the $^{205/6}$Bi-labeled trastuzumab conjugates (~7.5 μCi on 0.6 μg) and sacrificed by exsanguination at 2, 6, and 24 h. The blood, tumor, and major organs were collected, wet-weighed, and counted in a γ-scintillation counter. The percent injected dose per gram (%ID/g) and standard deviation were calculated.

RESULTS AND DISCUSSION

The synthesis of the new bifunctional ligand 3p-C-DEPA is outlined in Scheme 1. An intramolecular substitution reaction of *N,N*-bisubstituted β-amino bromide **1** produced aziridinium ion **2** which was then reacted with trisubstituted cyclen **3** (1,4,7,10-tetraazacyclododecane). Regiospecific ring-opening of **2** by nucleophilic attack of bulky cyclen analogue **3**[10] occurred at the less hindered methylene carbon in **2** to provide **4** as the exclusive product (61%). The reaction was carried out at room temperature, although it proceeds extremely slowly at this mild condition (4 weeks). An intramolecular rearrangement product of **1** was obtained when the reaction was under reflux. The desired coupling product **4** was isolated via column chromatography and characterized by ^{1}H and ^{13}C NMR, analytical HPLC, and HRMS. To confirm the regiochemistry observed in the nucelophilic ring-opening of the aziridinium ion **2** at the methylene carbon, compound **4** was separately prepared via another synthetic route starting from **5** as shown in Scheme 1. Reductive amination of **5** with **6** using sodium triacetoxyborohydride provided **7** which was subsequently treated with HCl (g) in 1,4-dioxane to afford **8**. A base-promoted reaction of **8** with *tert*-butyl bromoacetate produced compound **4**, and comparison of the spectroscopic data of **4** that was separately produced via the two synthetic routes confirmed regiochemistry in the ring-opening of **2**. Synthesis of the bifunctional ligands 3p-*C*-DEPA (**9**) and 3p-*C*-DEPA-NCS (**11**) is shown in Scheme 2. The *tert*-butyl groups in **4** was removed by the reaction of **4** with 4 M HCl (g) in 1,4-dioxane to provide 3p-*C*-DEPA (**9**). The nitro group in **9** was transformed into the amino group by hydrogenolysis of **9** on Pd/C to provide **10** which was subsequently reacted with thiophosgene (g) in $CHCl_3$ to the desired bifunctional ligand 3p-*C*-DEPA-NCS (**11**) containing the isothiocyanate group for conjugation to an antibody.

3p-*C*-DEPA-NCS was conjugated to trastuzumab, and the concentration of trastuzumab in 3p-*C*-DEPA-trastuzumab conjugate was quantified by UV spectroscopic assay.[18] The Cu(II)-AAIII based UV−vis spectrophotometric assay was used for the determination of the number of 3p-*C*-DEPA ligand linked to trastuzumab (L/P ratio).[17] The ligand to protein (L/P) ratio for 3p-*C*-DEPA-trastuzumab conjugate was measured to be 1.97. For comparison, *C*-DOTA-NCS (Macrocyclics, TX) was conjugated to trastuzumab as reported previously.[19]

The purified 3p-*C*-DEPA trastuzumab conjugates (30−50 μg) in 0.25 M NH_4OAc buffer solution at pH 5.5 was radiolabeled

Scheme 2. Synthesis of 3p-C-DEPA (9) and 3p-C-DEPA-NCS (11)

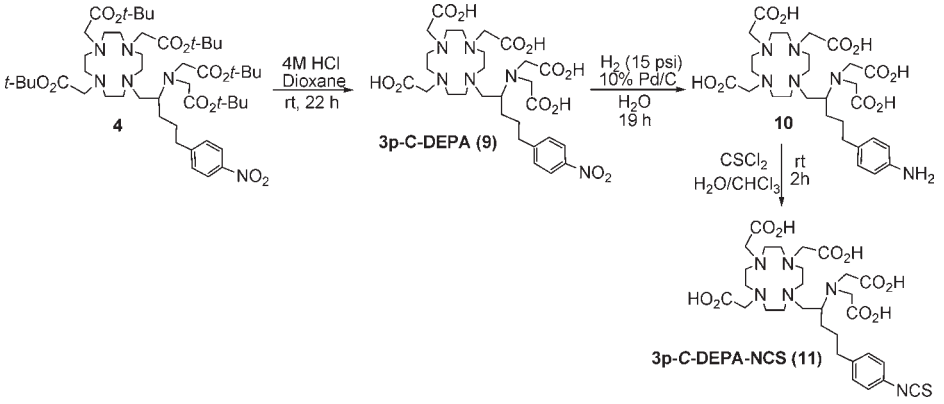


Table 1. Radiolabeling Efficiency (%) of Bifunctional Ligand-Trastuzumab Conjugates with $^{205/6}$Bi (0.25 M NH_4OAc, pH 5.5, RT)*

time (min)	3p-C-DEPA	C-DOTA
1	93.6 ± 0.4	8.4 ± 1.9
5	94.7 ± 0.9	17.2 ± 4.3
10	95.0 ± 0.4	28.7 ± 4.5
20	94.1 ± 0.6	38.0 ± 4.9
30	94.4 ± 1.6	49.7 ± 9.0
60	94.5 ± 0.5	60.2 ± 8.0

* Radiolabeling efficiency (mean ± standard deviation) was measured in triplicate.

with $^{205/6}$Bi (0.1 M HI) (60 μCi) at room temperature (RT). During the reaction time (1 h), the radiolabeling kinetics was determined by taking aliquots of the reaction mixture at 6 time points (1 min, 5 min, 10 min, 20 min, 30 min, and 60 min). The components were analyzed using SE-HPLC after challenging the reaction mixture with 10 mM DTPA, and the radiolabeling efficiency (%) was determined (Table 1 and the Supporting Information). The data indicate that $^{205/6}$Bi labeling of 3p-C-DEPA-trastuzumab conjugate were extremely rapid (1 min, >93%) at RT. As expected, radiolabeling of C-DOTA-trastuzumab conjugate with $^{205/6}$Bi was slow and incomplete at 24 h (60.2 ± 8.0%). The $^{205/6}$Bi-3p-C-DEPA conjugate was further evaluated for *in vitro* serum stability. The $^{205/6}$Bi-3p-C-DEPA conjugate was freshly prepared, purified, and incubated in human serum at 37 °C. At each time point (0 h, 1, 2, 3, 4 d), aliquots of the reaction mixture were analyzed using SE-HPLC after challenging the reaction mixture with 5 mM DTPA. $^{205/6}$Bi-3p-C-DEPA-trastuzumab was found to be stable in human serum without release of the radioactivity for at least 4 days (the Supporting Information).

The $^{205/6}$Bi-3p-C-DEPA-trastuzumab and $^{205/6}$Bi-C-DOTA-trastuzumab conjugates were independently prepared at 37 °C and pH 5.5 for specific activity and immunoreactivity evaluations prior to performing comparative *in vivo* biodistribution studies. The respective specific activities of 16.0 mCi/mg and 13.6 mCi/mg were measured for $^{205/6}$Bi-3p-C-DEPA and $^{205/6}$Bi-C-DOTA. The radiolabeling yields of 85.8% and 67.3% were determined for $^{205/6}$Bi-3p-C-DEPA and $^{205/6}$Bi-C-DOTA, respectively. Immunoreactivity of $^{205/6}$Bi-C-DOTA-trastuzumab and $^{205/6}$Bi-3p-C-DEPA-trastuzumab was assessed in a radioimmunoassay using recombinant human ErbB2/Fc Chimera (R&D Systems, Minneapolis, NM). The respective specific binding of 82.6% and 83.2% was measured for $^{205/6}$Bi-3p-C-DEPA-trastuzumab and $^{205/6}$Bi-C-DOTA-trastuzumab. In the presence of excess trastuzumab, $^{205/6}$Bi-3p-C-DEPA-trastuzumab and $^{205/6}$Bi-C-DOTA-trastuzumab exhibited the same nonspecific binding (7.6%).

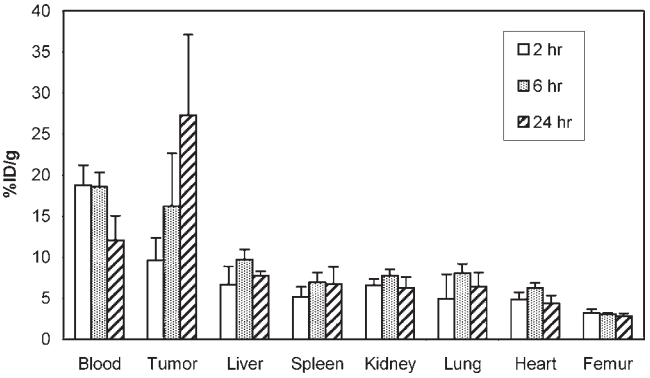


Figure 2. Biodistribution of $^{205/6}$Bi-3p-C-DEPA-trastuzumab conjugate in athymic mice bearing s.c. LS-174T tumors.

The *in vivo* stability and tumor targeting of $^{205/6}$Bi-3p-C-DEPA—trastuzumab was evaluated by performing biodistribution studies in LS174T-bearing athymic mice (i.v. injection, n = 4). $^{205/6}$Bi-C-DOTA-trastuzumab conjugate was evaluated for comparison. The mice were euthanized at 2 h, 6 h, and 24 h. Tumors, selected organs, and the blood were harvested, wet-weighed, and the radioactivity measured in a γ-counter (Figures 2 and 3). The highest tumor uptake was observed at 24 h for $^{205/6}$Bi-3p-C-DEPA-trastuzumab and $^{205/6}$Bi-C-DOTA-trastuzumab (27.3% and 25.8%, respectively). Among the organs, the highest accretion of radioactivity was observed in the liver: 7.73% for $^{205/6}$Bi-3p-C-DEPA-trastuzumab (6 h) and 8.02% for $^{205/6}$Bi-C-DOTA-trastuzumab (24 h). Both of the $^{205/6}$Bi-labeled conjugates exhibited the highest radioactivity level in the blood at 2 h which decreased over time. Renal and liver uptake of $^{205/6}$Bi-3p-C-DEPA-trastuzumab peaked at 6 h and decreased by 24 h. $^{205/6}$Bi-3p-C-DEPA-trastuzumab and $^{205/6}$Bi-C-DOTA-trastuzumab resulted in the respective radioactivity level of 6.27% and 5.52% in the kidney at 24 h. $^{205/6}$Bi-C-DOTA-trastuzumab exhibited an upward trend in the accumulation of radioactivity in the liver over the study period. Femur uptake of $^{205/6}$Bi-3p-C-DEPA-

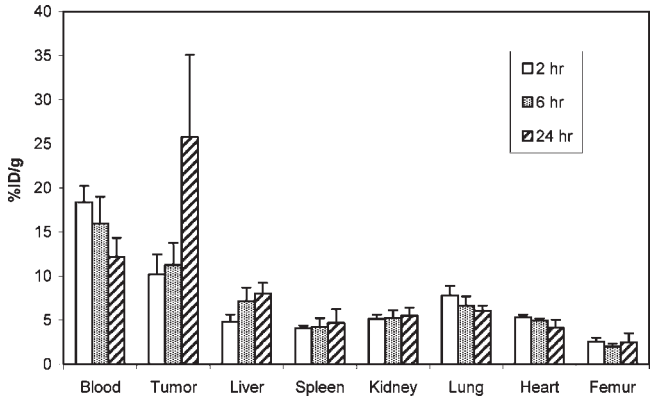


Figure 3. Biodistribution of $^{205/6}$Bi-*C*-DOTA-trastuzumab conjugate in athymic mice bearing s.c. LS-174T tumors.

trastuzumab peaked at 2 h (~3%) and decreased over the rest of the time points, while $^{205/6}$Bi-C-DOTA-trastuzumab displayed increased femur uptake from 2.00% at 6 h to 2.49% at 24 h. The respective tumor-to-blood ratio of $^{205/6}$Bi-3p-C-DEPA and $^{205/6}$Bi-*C*-DOTA at 24 h was 2.26 and 2.15. Both radioimmunoconjugates exhibited low blood to tissue ratios (<0.7) in all tissues and higher radioactivity level in tumor as compared to the normal organs over the time points.

In summary, the *in vitro* and *in vivo* experimental results indicate that the new ligand 3p-C-DEPA possesses great potential for RIT of ^{212}Bi and ^{213}Bi. Given complete and ongoing numerous preclinical and clinical studies of *C*-DOTA for alpha RIT, this new ligand deserves more extensive evaluations as a chelator of other potent α-emitters with a longer half-life including ^{212}Pb ($t_{1/2}$ = 10.64 h) and ^{225}Ac ($t_{1/2}$ = 10 d). ^{212}Pb is investigated as an *in vivo* generator of ^{212}Bi to abrogate the short half-life of the daughter isotope.[20] ^{225}Ac with the advantage of multiple α emissions is a potent α emitter and known to induce apoptosis even with a single particle traversal of the cell.[21] Although encouraging results on the therapeutic efficacy of *C*-DOTA-antibody conjugates radiolabeled with ^{212}Pb or ^{225}Ac as demonstrated in the preclinical studies using tumor-bearing mice was reported,[22−25] *C*-DOTA-antibody conjugates radiolabeled with ^{203}Pb or ^{225}Ac were less stable in serum.[21,26,27] The decadentate chelator 3p-C-DEPA possesses a larger macrocyclic backbone than *C*-DOTA and may be a suitable ligand for effectively sequestering ^{212}Pb and ^{225}Ac. 3p-C-DEPA will be further evaluated for various alpha RIT applications.

CONCLUSION

The new bifunctional ligand 3p-C-DEPA was efficiently prepared based on the synthetic route including the key reaction step, regiospecific ring-opening of aziridinium ion by nucleophilic trisubstituted cyclen. 3p-C-DEPA conjugated with trastuzumab was extremely rapid in binding $^{205/6}$Bi, and the corresponding $^{205/6}$Bi-3p-C-DEPA-trastuzumab complex was stable in human serum over a 4 day study period, well beyond any concerns of stability with ^{212}Bi and ^{213}Bi. *In vivo* biodistribution data indicate that 3p-C-DEPA-trastuzumab radiolabeled with $^{205/6}$Bi displayed excellent *in vivo* stability as evidenced by low organ uptake and excellent tumor targeting that was favorably compared to those of $^{205/6}$Bi-*C*-DOTA-trastuzumab. *In vitro* and *in vivo* data demonstrate that 3p-C-DEPA is a promising ligand for RIT applications of ^{212}Bi and ^{213}Bi.

ASSOCIATED CONTENT

Supporting Information. HPLC chromatograms for assessment of radiolabeling reaction kinetics and serum stability and *in vivo* biodistribution data. This material is available free of charge via the Internet at http://pubs.acs.org.

AUTHOR INFORMATION

Corresponding Author

*E-mail: Chong@iit.edu, Fax: 312-567-3494. Mailing address: 3101 S. Dearborn St, LS 182, Chemistry Division, Biological, Chemical, and Physical Science Department, Illinois Institute of Technology, Chicago, IL, 60616.

ACKNOWLEDGMENT

We acknowledge financial support from the National Institutes of Health (R01CA112503). This work was partly supported by intramural research program of NIH. Hyun A Song is the recipient of 2009 Illinois Institute of Technology Kilpatrick Fellowship.

REFERENCES

(1) Knox, S. J., and Meredith, R. F. (2000) Clinical radioimmunotherapy. *Sem. Radiat. Oncol. 10*, 73–93.

(2) Milenic, D. E., Brady, E. D., and Brechbiel, M. W. (2004) Antibody-targeted radiation cancer therapy. *Nat. Rev. 3*, 488–98.

(3) Hassfjell, S., and Brechbiel, M. W. (2001) The development of the α-particle emitting radionuclides ^{212}Bi and ^{213}Bi, and their decay chain related radionuclides for therapeutic applications. *Chem. Rev. 101*, 2019–36.

(4) Jurcic, J. G., Larson, S. M., Sgouros, G., McDevitt, M. R., Finn, R. D., Divgi, C. R., Ballangrud, Å. M., Klaus, K. A., Ma, D., Humm, J. L., Brechbiel, M. W., Molinet, R., and Scheinberg, D. A. (2002) Targeted alpha particle immunotherapy for myeloid leukemia. *Blood 100*, 1233–39.

(5) Mulford, D. A., Pandit-Taskar, N., McDevitt, M. R., Finn, R. D., Weiss, M. A., Apostolidis, C., Morgenstern, A., Divgi, C. R., Larson, S. M., Scheinberg, D. A., and Jurcic, J. G. (2004) Sequential therapy with cytarabine and bismuth-213 (Bi-213)-labeled-HuM195 (anti-CD33) for acute myeloid leukemia (AML). *Blood 104*, 496a.

(6) Allen, B. J., Raja, C., Rizvi, S., Li, Y., Tsui, W., Graham, P., Thompson, J. F., Reisfeld, R. A., Kearsley, J., Morgenstern, A., and Apostolidis, C. (2005) *Cancer Biol. Ther. 4*, 1318–24.

(7) Kneifel, S., Cordier, D., Good, S., Ionescu, M. C., Ghaffari, A., Hofer, S., Kretzschmar, M., Tolnay, M., Apostolidis, C., Waser, B., Arnold, M., Mueller-Brand, J., Maecke, H. R., Reubi, J. C., and Merlo, A. (2006) Local targeting of malignant gliomas by the diffusible peptidic vector 1,4,7,10-tetraazacyclododecane-1-glutaric acid-4,7,10-triacetic acid-substance P. *Clin. Cancer Res. 12*, 3843–50.

(8) Nikula, T. K., McDevitt, M. R., Finn, R. D., Wu, C., Kozak, R. W., Garmasteni, K., Brechbiel, M. W., Curcio, M. J., Pippin, C. G., Tiffany-Jones, L., Geerlings, M. W., Sr, Apostolidis, C., Molinet, R., Geerlings, M. W., Jr, Gansow, O. A., and Scheinberg, D. A. (1999) Alpha-emitting bismuth cyclohexylbenzyl DTPA constructs of recombinant humanized anti-CD33 antibodies: Pharmacokinetics, bioactivity, toxicity, and chemistry. *J. Nucl. Med. 40*, 166–76.

(9) Kumar, K., Magerstadt, M., and Gansow, O. A. (1989) Lead(II) and bismuth(III) complexes of the polyazacycloalkane-*N*-acetic Acids nota, dota, and teta. *J. Chem. Soc., Chem. Commun.* 145–6.

(10) Chong, H. S., Lim, S., Baidoo, K. E., Milenic, D. E., Ma, X., Jia, F., Song, H. A., Brechbiel, M. W., and Lewis, M. R. (2008) Synthesis and biological evaluation of a novel decadentate ligand DEPA. *Bioorg. Med. Chem. Lett. 18*, 5792–5.

(11) Brechbiel, M. W., and Gansow, O. A. (1992) Synthesis of *C*-functionalized trans-cyclohexyldiethylenetri-aminepenta-acetic acids for labeling of monoclonal antibodies with the bismuth-212-α particle emitter. *J. Chem. Soc., Perkin. Trans. 1* 1173–8.

(12) Milenic, D. E., Roselli, M., Mirzadeh, S., Pippin, C. G., Gansow, O. A., Colcher, D., Brechbiel, M. W., and Schlom, J. (2001) *In vivo* evaluation of bismuth-labeled monoclonal antibody comparing DTPA-derived bifunctional chelates. *Cancer Biother. Radiopharm. 16*, 133–54.

(13) Baselga, J. (2001) Phase I and II clinical trials of trastuzumab. *Ann. Oncol. 12*, S49–55.

(14) Agus, D. B., Bunn, P. A, Jr., Franklin, W., Garcia, M., and Ozols, R. F. (2000) HER-2/neu as a therapeutic target in non-small cell lung cancer, prostate cancer, and ovarian cancer. *Semin. Oncol. 27*, 53–63.

(15) Milenic, D. E., Garmestani, K., Brady, E. D., Albert, P. S., Ma, D., Abdulla, A., and Brechbiel, M. W. (2004) Targeting of HER2 antigen for the treatment of disseminated peritoneal disease. *Clin. Cancer Res. 10*, 7834–41.

(16) Chong, H. S., Song, H. A., Kang, C. S., Le, T., Sun, X., Dadwal, M., Lee, H. B., Lan, X., Chen, Y., and Dai, A. (2011) A highly effective bifunctional ligand for radioimmunotherapy of cancer. *Chem. Commun.*

(17) Brady, E. D., Chong, H. S., Milenic, D. E., and Brechbiel, M. W. (2004) Development of a spectroscopy assay for bifunctional ligand-protein conjugates based on copper. *Nucl. Med. Biol. 31*, 795–802.

(18) Lowry, O. H., Rosebrough, N. J., Farr, A. L., and Randall, R. J. (1951) Protein measurement with the folin phenol reagent. *J. Biol. Chem. 193*, 265–75.

(19) Chappell, L. L., Ma, D., Milenic, D. E., Garmestani, K., Venditto, V., Beitzel, M. P., and Brechbiel, M. W. (2003) Synthesis and evaluation of novel bifunctional chelating agents based on 1,4,7,10-Tetraazacyclododecane-*N*,*N*′,*N*″,*N*‴-Tetraacetic acid for radiolabeling proteins. *Nucl. Med. Biol. 30*, 581–95.

(20) Atcher, R. W., Friedman, A. M., and Hines, J. J. (1988) An improved generator for the production of ^{212}Pb and ^{212}Bi from ^{224}Ra. *Int. J. Appl. Instrum. Part A 39*, 283–6.

(21) McDevitt, M. R., Ma, D., Simon, J., Frank, R. K, and Scheinberg, D. A. (2002) Design and synthesis of ^{225}Ac radioimmunotherapeuticals. *Appl. Radiat. Isot. 57*, 841–7.

(22) Miao, Y, Hylarides, M, Fisher, D. R., Shelton, T., Moore, H., Wester, D. W., Fritzberg, A. R., Winkelmann, C. T., Hoffman, T., and Quinn, T. P. (2005) Melanoma therapy via peptide-targeted {alpha}-radiation. *Clin. Cancer Res. 11*, 5616–21.

(23) Milenic, D. E., Garmestani, K., Brady, E. D., Albert, P. S., Ma, D., Abdulla, A., and Brechbiel, M. W. (2005) Alpha-particle radioimmunotherapy of disseminated peritoneal disease using a 212Pb-labeled radioimmunoconjugate targeting HER2. *Cancer Biother. Radiopharm. 20*, 557–68.

(24) Miederer, M., Henriksen, G., Alke, A., Mossbrugger, I., Quintanilla-Martinez, L., Senekowitsch-Schmidtke, R., and Essler, M. (2008) Preclinical evaluation of the alpha-particle generator nuclide ^{225}Ac for somatostatin receptor radiotherapy of neuroendocrine tumors. *Clin. Cancer Res. 14*, 3555–61.

(25) Ballangrud, Å. M., Yang, W.-H., Palm, S., Enmon, R., Borchardt, P. E., Pellegrini, V. E., McDevitt, M. R., Scheinberg, D. A., and Sgouros, G. (2004) Alpha-particle emitting atomic generator (Actinium-225)-labeled trastuzumab (Herceptin) targeting of breast cancer spheroids: efficacy *versus* HER2/*neu* expression. *Clin. Cancer Res. 10*, 4489–97.

(26) Ruble, G., Wu, C., Squire, R. A., Gansow, O. A., and Strand, M. (1996) The use of ^{212}Pb-labeled monoclonal antibody in the treatment of murine erythroleukemia. *Int. J. Radiat. Oncol. Biol. Phys. 34*, 609–16.

(27) Mirzadeh, S., Kumar, K., and Gansow, O. A. (1993) The chemical fate of ^{212}Bi-DOTA formed by β- decay of ^{212}Pb-DOTA. *Radiochim. Acta. 60*, 1–10.

Supporting Information

An Efficient Bifunctional Decadentate Ligand 3p-*C*-DEPA for Targeted Alpha Radioimmunotherapy Applications

Hyun A Song,[1] Chi Soo Kang,[1] Kwamena E. Baidoo,[2] Diane E. Milenic,[2] Yunwei Chen[1], Anzhi Dai,[1] M. W. Brechbiel,[2] and Hyun-Soon Chong[1,*]

1. Radiolabeling reaction kinetics of *C*-DOTA-trastuzumab conjugate (SE-HPLC).

2. Radiolabeling reaction kinetics of 3p-*C*-DEPA-trastuzumab conjugate (SE-HPLC).

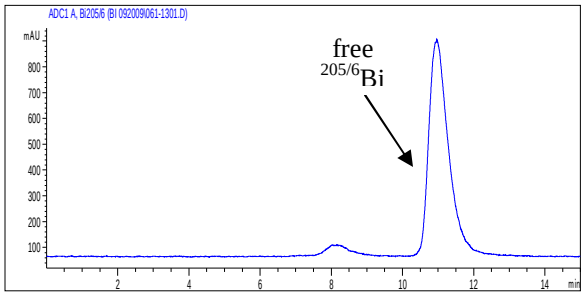
3. Serum stability of $^{205/6}$Bi-3p-*C*-DEPA-trastuzumab conjugate (SE-HPLC)

4. Biodistribution data for $^{205/6}$Bi-*C*-DOTA and $^{205/6}$Bi-3p-*C*-DEPA in athymic mice bearing s.c. LS-174T tumors (Table 1).

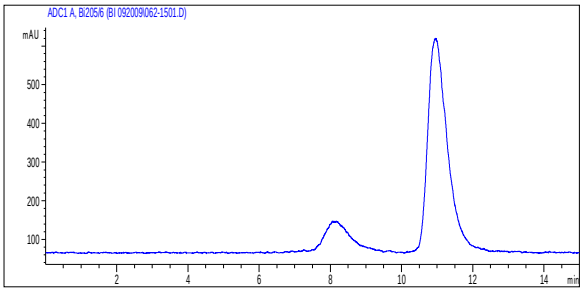
1. Radiolabeling reaction kinetics of *C*-DOTA-Trastuzumab conjugate with $^{205/6}$Bi (SE-HPLC).

Sample 1

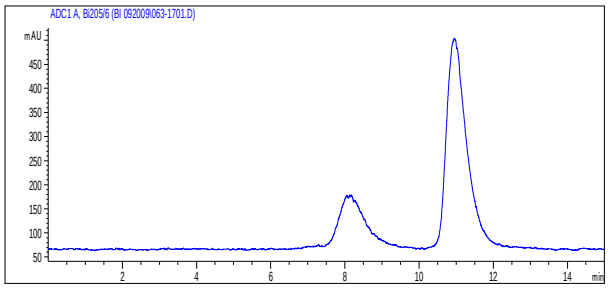
1 min (6.9%)



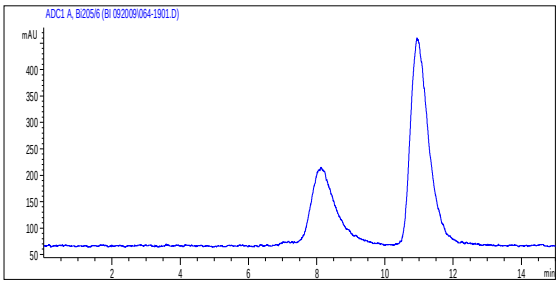
5 min (16.7%)



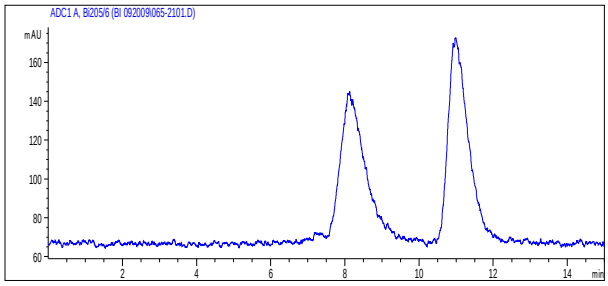
10 min (25.5%)



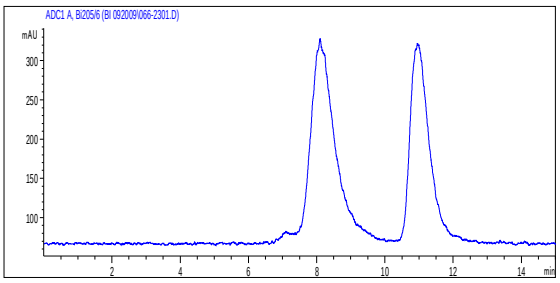
20 min (34.7%)



30 min (49.5%)

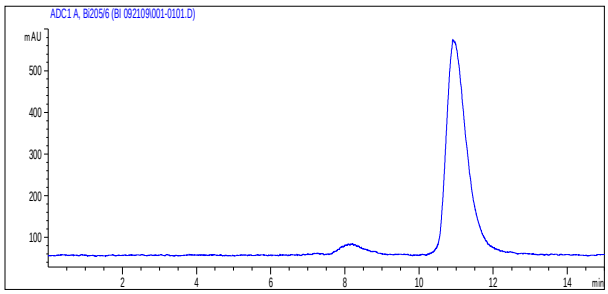


60 min (56.9%)

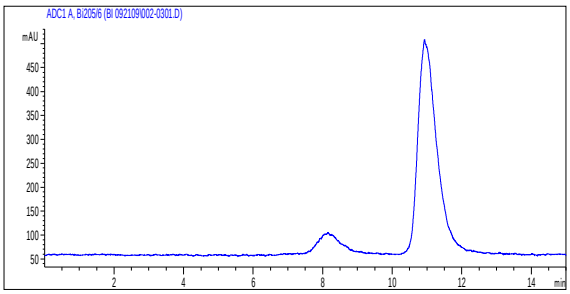


Sample 2

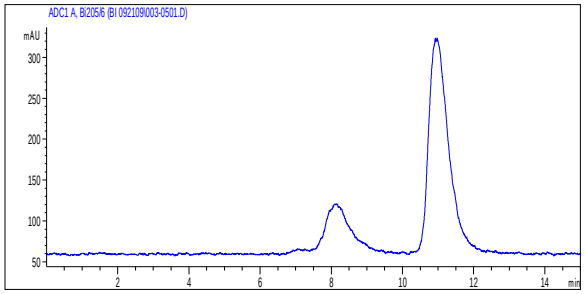
1 min (7.9%)



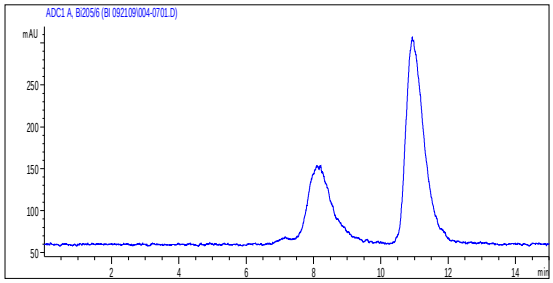
5 min (13.2%)



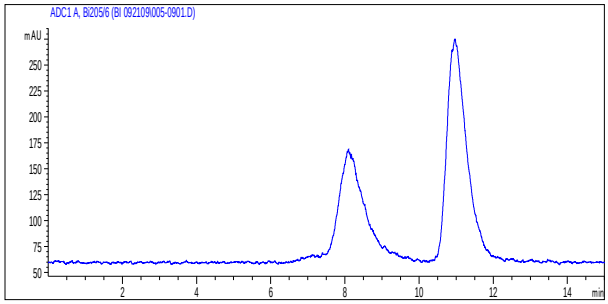
10 min (26.7%)



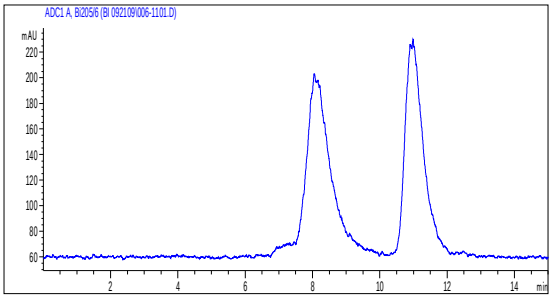
20 min (35.7%)



30 min (40.9%)

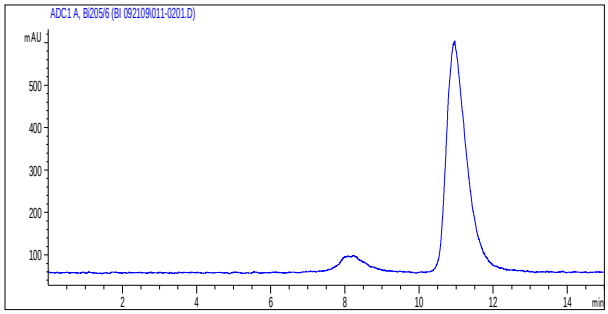


60 min (54.4%)

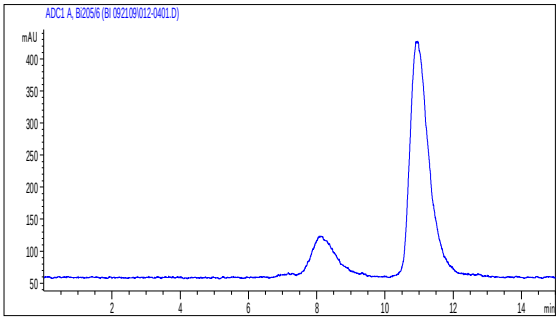


Sample 3

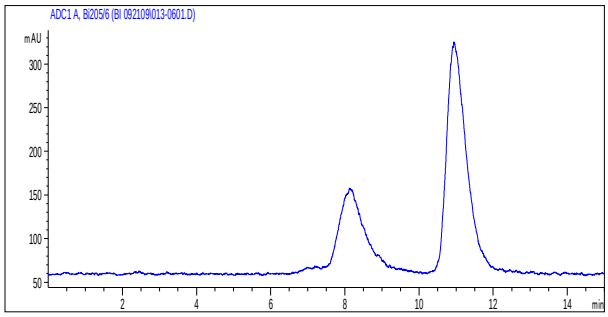
1 min (10.5%)



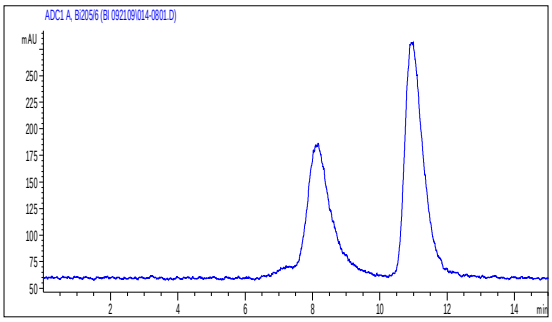
5 min (21.8%)



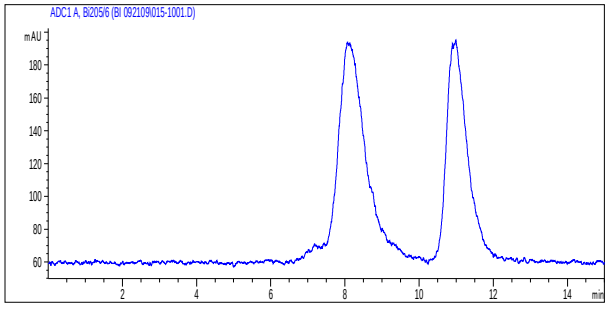
10 min (33.9%)



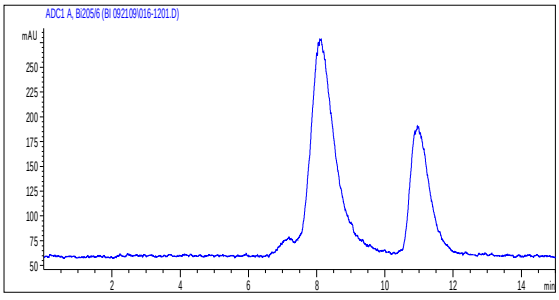
20 min (43.6%)



30 min (58.8%)



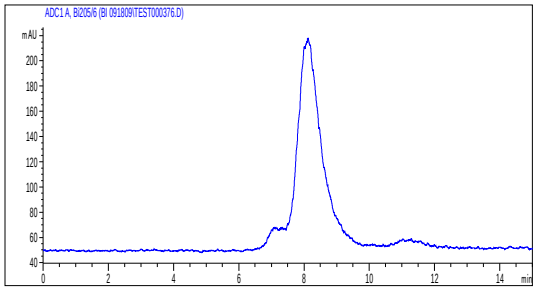
60 min (69.4%)



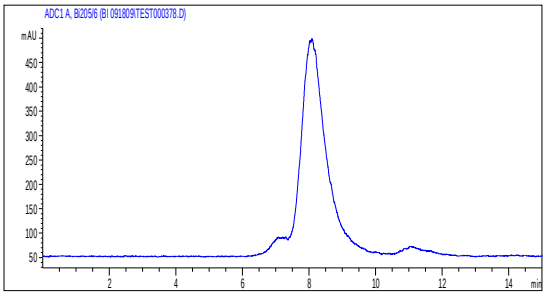
2. Radiolabeling reaction kinetics of 3p-*C*-DEPA-Trastuzumab conjugate with $^{205/6}$Bi (SE-HPLC).

Smaple 1

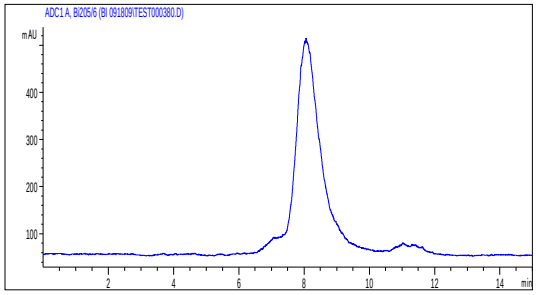
1 min (94.0%)



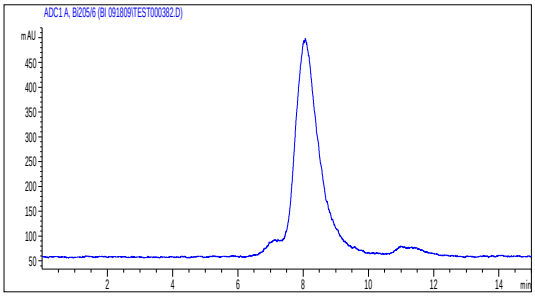
5 min (95.6%)



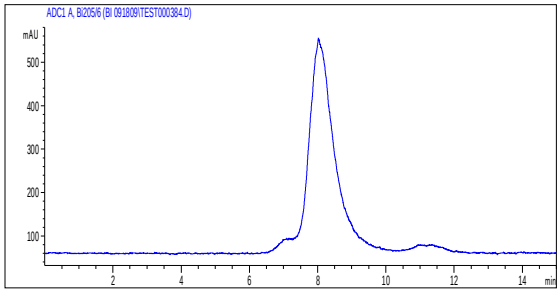
10 min (95.2 %)



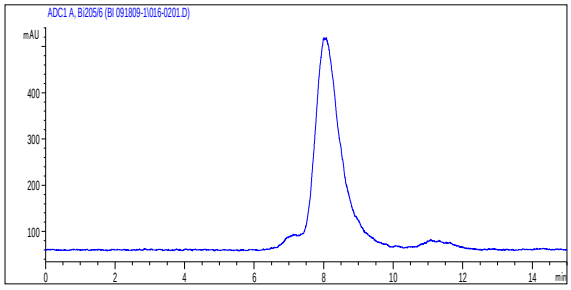
20 min (94.8%)



30 min (95.9%)

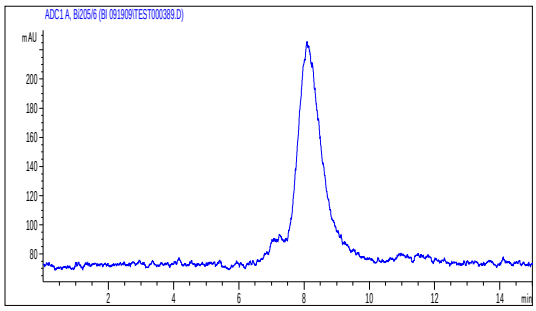


60 min (94.9%)

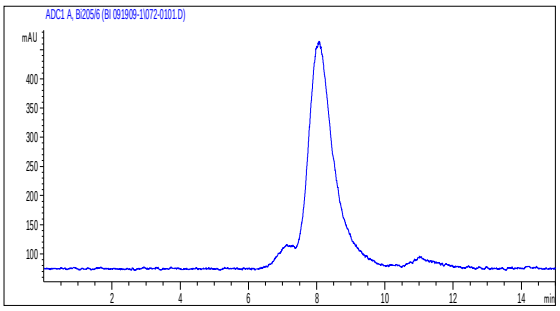


Sample 2

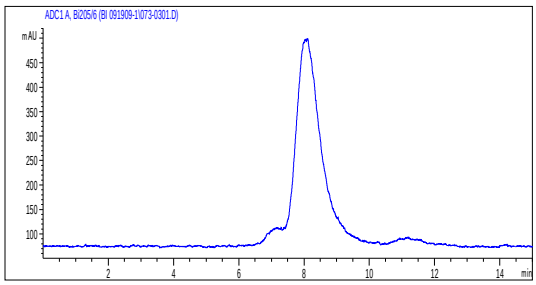
1 min (93.6%)



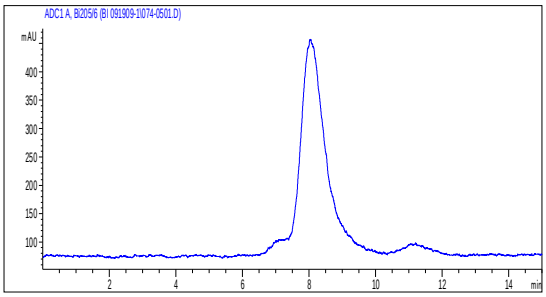
5 min (94.8%)



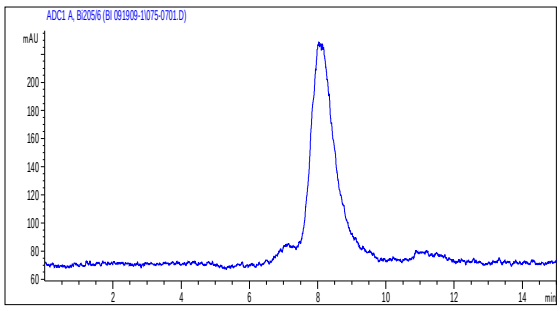
10 min (95.2%)



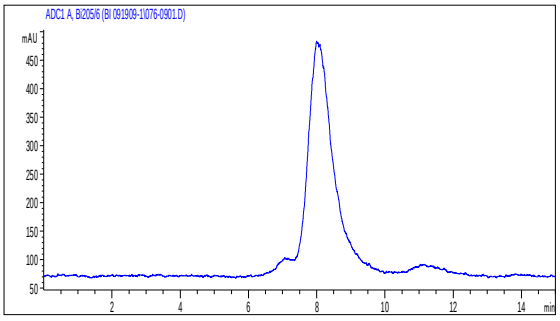
20 min (93.8%)



30 min (92.8%)

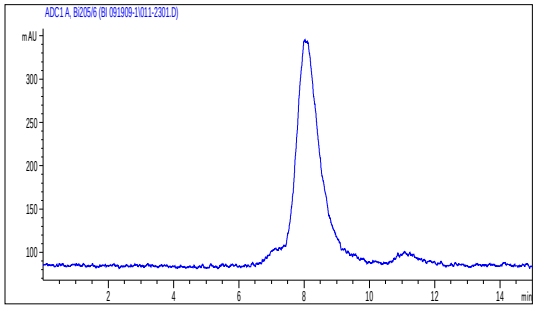


60 min (94.0%)

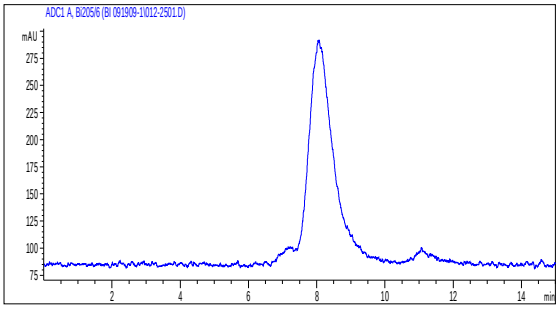


Sample 3

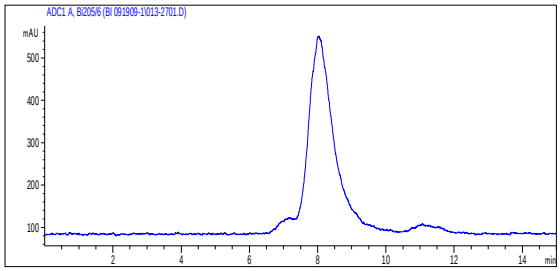
1 min (93.2%)



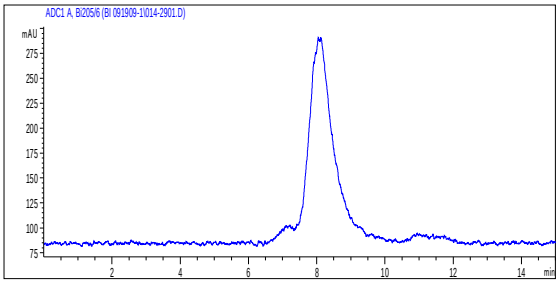
5 min (93.8%)



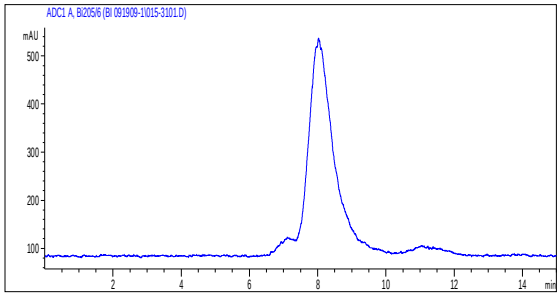
10 min (94.5%)



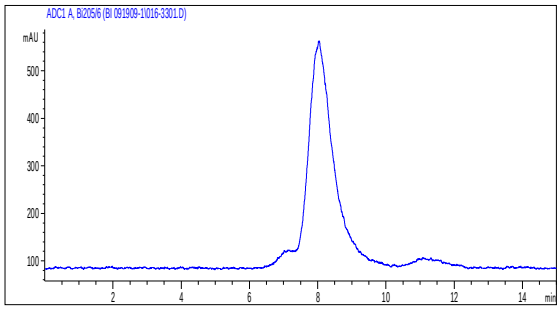
20 min (93.8%)



30 min (94.5%)

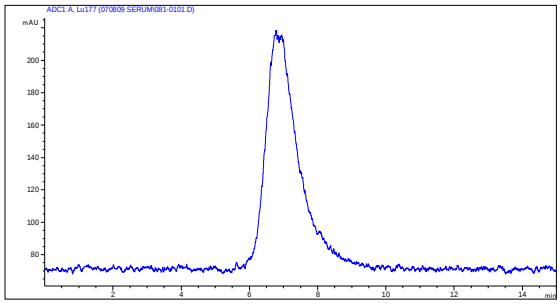


60 min (94.7%)

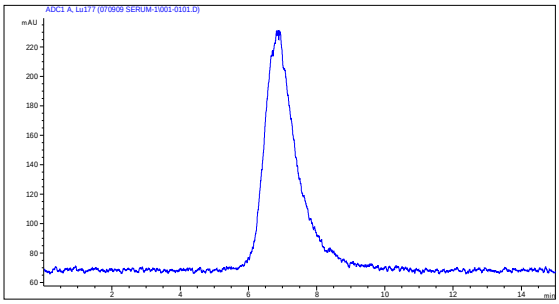


3. Serum stability of $^{205/6}$Bi-3p-*C*-DEPA-Trastuzumab conjugate (Size Exclusion-HPLC)

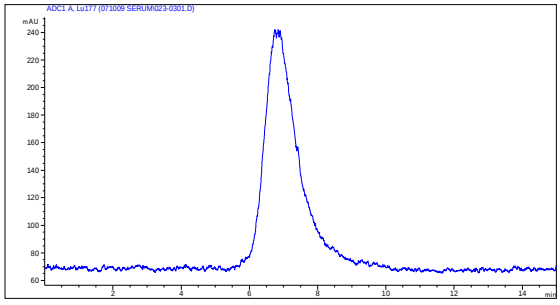
0 h (100%)



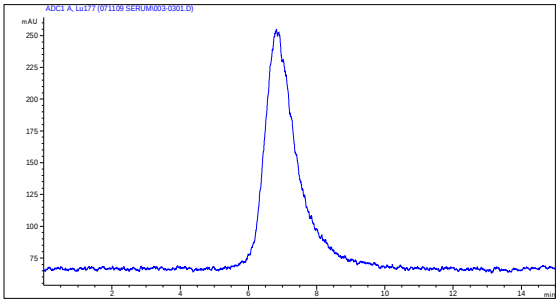
Day 1 (100%)



Day 2 (100%)



Day 3 (100%)



Day 4 (100%)

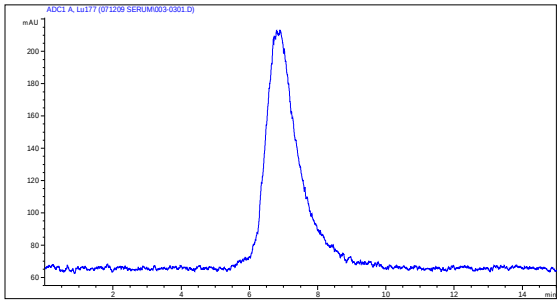


Table 1. Biodistribution of $^{205/6}$Bi-3p-*C*-DEPA-Trastuzumab conjugate and $^{205/6}$Bi-*C*-DOTA-Trastuzumab conjugate in athymic mice bearing s.c. LS-174T tumors.

Ligand	Tissue	Time points (h)								
		2h			6h			24h		
3p-*C*-DEPA	Blood	18.77	±	2.44	18.65	±	1.78	12.1	±	2.97
	Tumor	9.63	±	2.72	16.24	±	6.41	27.3	±	9.79
	Liver	6.64	±	2.24	9.70	±	1.23	7.73	±	0.56
	Spleen	5.19	±	1.2	6.96	±	1.19	6.75	±	2.08
	Kidney	6.60	±	0.78	7.77	±	0.74	6.27	±	1.31
	Lung	4.92	±	3.01	8.05	±	1.14	6.43	±	1.69
	Heart	4.88	±	0.85	6.26	±	0.6	4.35	±	0.96
	Femur	3.21	±	0.43	3.07	±	0.16	2.78	±	0.40
***C*-DOTA**	Blood	18.38	±	1.82	15.94	±	3.05	12.2	±	2.12
	Tumor	10.21	±	2.25	11.27	±	2.49	25.8	±	9.29
	Liver	4.84	±	0.81	7.19	±	1.51	8.02	±	1.23
	Spleen	4.09	±	0.31	4.26	±	0.96	4.70	±	1.57
	Kidney	5.17	±	0.44	5.26	±	0.88	5.52	±	0.89
	Lung	7.83	±	1.07	6.64	±	1.05	6.08	±	0.57
	Heart	5.34	±	0.29	4.94	±	0.23	4.12	±	0.92
	Femur	2.56	±	0.45	2.00	±	0.35	2.49	±	0.14

Bioconjugate Chemistry

ARTICLE

pubs.acs.org/bc

Real-Time Monitoring of Actin Polymerization in Living Cells Using Split Luciferase

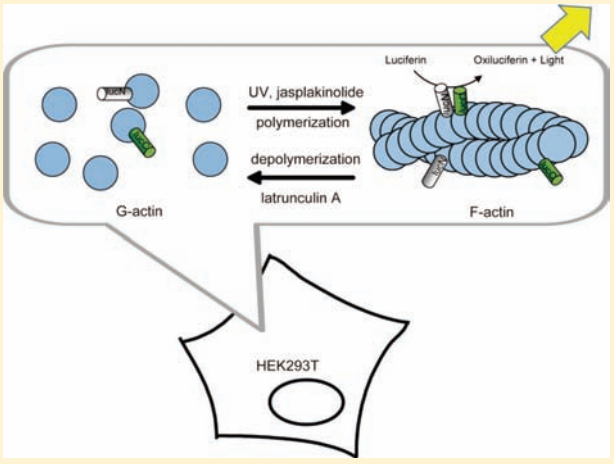
Tetsuya Ishimoto,[†] Takeaki Ozawa,[‡,§] and Hisashi Mori*[,†]

[†]Department of Molecular Neuroscience, Graduate School of Medicine and Pharmaceutical Sciences, University of Toyama, Toyama, Japan.

[‡]Department of Chemistry, Graduate School of Science, The University of Tokyo, Bunkyo-Ku, Tokyo, Japan.

[§]Precursory Research for Embryonic Science and Technology, Japan Science and Technology Agency, Tokyo, Japan.

ABSTRACT: Real-time monitoring of actin polymerization in living cells is beneficial for characterizing cellular activities such as migration, proliferation, and death. We developed new bioluminescence-based probe proteins that enable the monitoring of actin polymerization in living cells. Unlike other ordinary split luciferase probes, our probes were incorporated in endogenous actin filament that enabled it to measure the actin polymerization quantitatively. The probe proteins exhibited a dose-responsive decrease in photon emission intensity in response to the filamentous (F)-actin-disrupting agent latrunculin A. This technique has a high sensitivity with a high signal-to-noise ratio and is nontoxic compared with other methods of monitoring actin polymerization in living cells. Using this technique, we succeeded in monitoring the F-actin level in living cells during apoptosis progression induced by UV irradiation continuously for 12 h. F-actin was transiently upregulated after UV irradiation. Since UV-induced cell death was enhanced by treatment with latrunculin A during the period which F-actin is increased, transient upregulation of F-actin after UV is likely a protective reaction against UV-induced cell death. Our novel technique is an effective tool for investigating actin polymerization in living cells.



INTRODUCTION

Actin is a major cytoskeletal protein, the sequence of which is highly conserved among all eukaryotes, and is of two dynamic forms, globular (G) actin and its polymerized form, filamentous (F) actin. The organization of F-actin has been considered important for many cellular functions such as migration,[1,2] cancer cell invasion,[3] synaptic plasticity,[4,5] and cell death.[6,7] Measurement of the level of F-actin is important for analyzing cell activity. However, the conventional methods for analyzing F-actin have some limitations. Rhodamine-phalloidin (R-P) staining[8] cannot be used for the long-term and real-time monitoring of F-actin in living cells, since it requires cell fixation. Fluorescent probe proteins such as GFP-actin[9] and lifeact[10] are not suitable for the quantification of F-actin since their monomers can emit fluorescence. Recently, the fluorescence resonance energy transfer (FRET) technique has been used to monitor F-actin,[11] although the FRET signal intensity is not in proportion to the level of F-actin.[12] Furthermore, all the fluorescence-based methods have phototoxicity caused by excitation light. Thus, we tried to develop novel probe proteins to measure the F-actin level in living cells over a long period. The firefly split luciferase technique, which has been developed by several groups in the past decade,[13−15] was employed to develop probe proteins, since bioluminescence-based methods have some advantages in terms of the viability of cells and linearity of signal intensity. In this report, we describe the development of novel probe proteins for monitoring actin polymerization.

To validate the usefulness of our probe proteins, we focused on the regulation of actin polymerization in cell death. The disruption of F-actin induces apoptotic cell death in T cells and MCF10A cells, and enhances apoptosis by cytokine withdrawal in CTLL-20 cells.[16−18] These reports suggest that actin polymerization has a protective role against the cell death. However, few reports have described the detailed time course and quantification of the actin polymerization in cell death due to lack of appropriate method. Using our probe proteins, we attempt to elucidate the precise time course of actin polymerization after cell death stimulus and try to predict the critical period that F-actin works protectively.

EXPERIMENTAL PROCEDURES

Plasmid Construction. A MultiSite Gateway Three-Fragment Vector Construction kit (Invitrogen) was used for plasmid

Received: December 25, 2010
Revised: April 7, 2011
Published: May 18, 2011

ACS Publications © 2011 American Chemical Society

construction in accordance with the manual. This method is based on site-specific recombination of DNA fragments.[19,20] Briefly, PCR-fragments flanked by recombination sites were inserted to donor vectors to generate 5′, center, and 3′ entry clones by recombination called BP reaction. These three entry clones were reacted with destination vector to generate expression clones through site-specific recombination called LR reaction. This reaction allows construction of respective PCR-fragments in a definite order. However, after LR reaction, DNA sequences coding KGGRADPAFLYKVE, which originates from the sequence of recombination site, remain between center-clone-derived sequence and 3′-clone-derived sequence. All the expression clones are driven by an SV40 enhancer promoter sequence of the 5′ entry clone and have an SV40 poly A signal sequence at the 3′ region derived from pGL4.13 (Promega). The PCR-amplified amino (N)-terminal part, 1−1245 bases, of the luciferase (lucN) sequence (1 corresponding to A at the translational initiation site methionine codon ATG) and the carboxyl (C)-terminal part, 1246−1650 bases, of the luciferase (lucC) sequence derived from pGL4.13, and a β-actin protein coding sequence (Genbank: X03672) amplified from mouse cDNA were used for the construction of the split luciferase probe expression clones. The protein coding sequences of the expression clones nos. 1, 2, 3, and 4 are actin-KGGRADPAFLYKVE-lucN, actin-KGGRADPAFLYKVE-lucC, lucN-KGGRADPAFLYKVE-actin, and lucC-KGGRADPAFLYKVE-actin, respectively (Figure 1B). The linker sequence was further modified by the inverse PCR method[21] using a KOD plus mutagenesis kit (Toyobo). The protein coding sequences of the expression clones nos. 5, 6, 7, 8, 9, and 10 are lucN-GGGGSGGGGSKGGRADPAFLYKVE-actin, lucC-GGGGSGGGGSKGGRADPAFLYKVE-actin, lucN-actin, lucC-actin, lucN-GGGGSGGGGSGGGGS-actin, and lucC-GGGGSGGGGSGGGGS-actin, respectively (Figure 1B).

The MultiSite Gateway system was also used to generate a Cofilin-myc expression clone. A Cofilin (Genbank: BC058726) ORF and a Myc-Tag sequence (EQKLISEEDL) were amplified by PCR and inserted into the center and 3′ entry clones, respectively. Both clones were reacted with pDEST R4-R3, and the 5′ entry clone to obtain a Cofilin-KGGRADPAFLYKVE-Myc-expressing clone driven by an SV40 enhancer promoter.

For the GST fusion lucN-actin and lucC-actin protein expression in *Escherichia coli*, lucN-actin (No. 9) and lucC-actin (No. 10) were amplified by PCR using primers with a *Bam*HI site and a *Not*I site at each end. Amplified fragments were digested with *Bam*HI and *Not*I, then subcloned into the *Bam*HI and *Not*I sites of pGEX-6p-1 (GE Healthcare). All the constructs were confirmed by DNA sequencing using ABI3100 (Applied Biosystems).

Cell Culture and DNA Transfection. HEK293T (1.5×10^5 cells/dish or 0.5×10^5 cells/well) cells were cultured in DMEM supplemented with 10% FCS at 37 °C in 5% CO_2 on a 3-cm-diameter dish (Falcon) for UV irradiation and 3-(4,5-dimethyl-2-thizolyl)-2,5-diphenyl-2*H*-tetrazolium bromide (MTT) assay, and on a glass base dish (Iwaki) for R-P staining. HEK293T cells were transiently transfected using Lipofectamine 2000 (Invitrogen) in accordance with the manufacturer's instructions. Two microgram aliquots of each plasmid were used for cotransfection. When a 24-well culture plate was used for transfection, 4-fold smaller amounts of the reagent and DNA were used. Photon intensity emitted from cells was measured 48 h after transfection.

Cell Viability and Caspase-3 Assays. Cell viability was determined by MTT assay in accordance with the manual attached to the MTT cell viability assay kit (Biotium Inc.). After incubation with the tetrazolium salt MTT (1 mg/mL) for 2 h at room temperature, the harvested cells were solubilized with 1 mL of dimethyl sulfoxide. We measured the absorbance at wavelengths of 570 and 630 nm using a spectrophotometer (Gene Quant 1300, GE Healthcare). The sample signal intensity was obtained by subtraction of OD at 630 nm from OD at 570 nm and indicated as a percentage of the control value. To determine caspase-3 activity, we employed the Caspase 3&7 FLICA kit (ImmunoChemistry Technologies). The cellular substrate FAM-DEVD-FMK was added to the culture medium of the UV-irradiated cells. Fluorescence signals were detected by confocal microscopy (TCS-SP5, Leica).

Western Blotting. Cells were harvested and lysed using M-PER solution (Thermo Scientific). Proteins separated by SDS-PAGE were electrically transferred onto a PVDF membrane (GE Healthcare). The membrane was incubated with an anti-actin primary antibody (1:1000, Santa Cruz) or a polyclonal antiluciferase antibody (1:1000 Promega) in the Can Get Signal solution (Toyobo) at 4 °C overnight. The membrane was reacted with a secondary HRP-conjugated antibody (1:2000, Bio Rad) and visualized using an ECL plus Western blotting reagent (GE Healthcare). Chemiluminescence signals were detected using the LAS-1000 plus system (Fujifilm).

In Vitro Actin Polymerization Assay. Fifty micrograms of pyrene-conjugated actin[22] (Cytoskeleton) with or without probe proteins (1 μg each) was suspended in 2 mL of general actin buffer (5 mM Tris-HCl (pH 8.0), 0.2 mM $CaCl_2$, 0.2 mM ATP, 0.5 mM DTT) and centrifuged at 15 000 *g* for 30 min to remove residual F-actin. To polymerize actin, 1/10 vol of 10× polymerization buffer (500 mM KCl, 20 mM $MgCl_2$, 10 mM ATP) was added. Fluorescence signal intensity was measured every 5 min using a F-4500 spectrophotometer (Hitachi) at an excitation wavelength of 360 ± 10 nm and an emission wavelength of 405 ± 10 nm.

F/G Actin Separation of Cell Lysate by Ultracentrifugation. A G-actin/F-actin *in vivo* assay kit (Cytoskeleton) was used to separate F- and G-actin from the HEK293T lysate. HEK293T cells were lysed in the cell lysis and F-actin stabilization buffer that was provided in the kit. The cell lysate was centrifuged at 100 000 *g* for 1 h at room temperature. The pellet and supernatant were collected as the F-actin-and G-actin-containing fractions, respectively.

Expression of GST-Fusion Probe Proteins in *E. coli*. *E. coli* BL21 (DE3) was transformed by pGEX-6p-1-derived plasmids that encoded GST-lucN-actin and GST-lucC-actin. *E. coli* cells were homogenized by ultrasonication in 1% NP-40 in PBS (pH 7.4). Fusion proteins were purified by binding to glutathione-Sepharose 4B (GE Healthcare). Then, the bound fusion proteins were cleaved with PreScission Protease (GE Healthcare) to obtain lucN-actin and lucC-actin.

Immunoprecipitation Assay. Cofilin-myc and one of the probe proteins (lucN-actin or lucC-actin) were expressed in HEK293T cells. The cells were harvested in PBS, homogenized using a polytron homogenizer (Kinematica), and centrifuged at 2000 *g* for 5 min to remove debris. The protein solution was incubated with 1 μg of an antimyc antibody (Santa Cruz) or 5 μg of an antiluciferase antibody (Promega) bound to 25 μL of protein-G Sepharose (GE Healthcare) for 3 h at 4 °C. Then, the mixtures were washed 5 times, and the precipitates were analyzed by Western blotting using the antimyc (1:1000) and antiluciferase (1:1000) antibodies.

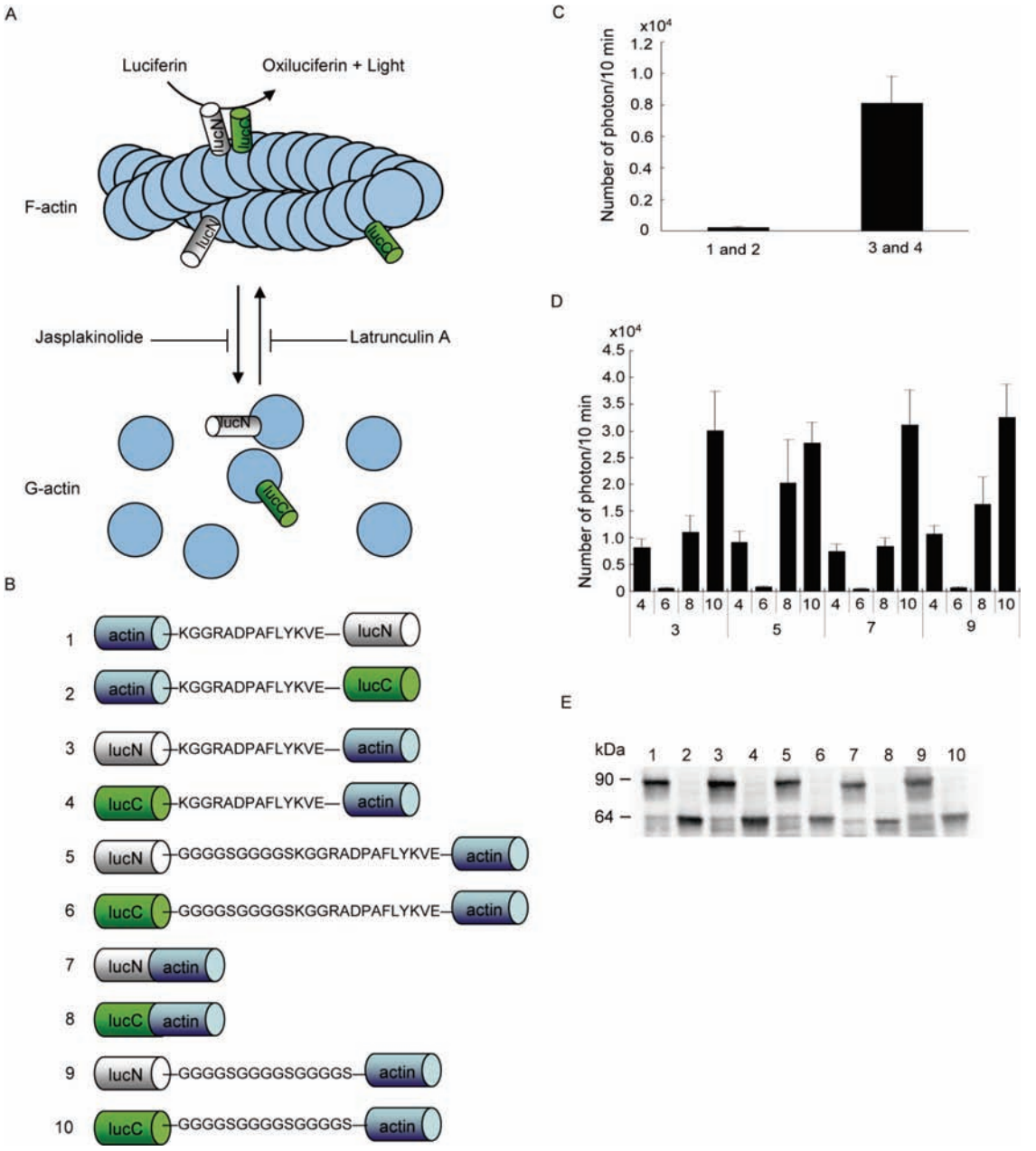


Figure 1. Development of probe proteins to measure actin polymerization. (A) Schema of measurement of level of F-actin based on bioluminescence intensity. LucN and lucC derived from firefly luciferase are fused with actin. Each probe protein is incorporated in the endogenous actin filament. When the lucN and lucC locate close to each other, they recover their luciferase activity and emit light. Jasplakinolide and latrunculin A are the agents that stabilize and inhibit actin polymerization, respectively. (B) Schematic structures of the actin probe proteins encoded by the expression clones nos. 1 to 10. LucN and lucC represent N-terminal and C-terminal split segments of the firefly luciferase, respectively. Amino acid sequences of the linker are indicated as single letters. (C) Combinations of expression clones nos. 1 and 2 and nos. 3 and 4 were expressed in HEK293T and the emitted photons were counted for 10 min using an image intensifier/CCD camera. (D) The numbers of photons emitted from all the combinations of odd and even numbers of clone shown in B except clones nos. 1 and 2 were measured. The numbers on the horizontal axis represent the combinations of probe proteins. All the data are presented as mean ± SEM $n = 4$. (E) The amount of each expressed probe protein was analyzed by Western blotting.

Measuring Photon Intensity Emitted from Cultured Cells. We used an Aequoria-2D/C8600 system (Hamamatsu Photonics) for photon counting. *Wasabi* software (U9304−02) was used for data acquisition and analysis. Cultured cells were taken out from a CO_2 incubator. The culture medium was changed to L15 medium containing 0.5 mM luciferin EF (Promega). The culture plate was placed in a dark box for 30 min. Then, the number of photons emitted from one culture dish well was measured using a charge coupled device (CCD) camera with an image intensifier attached to the top of the dark box. Photon intensity was measured every 5 min continuously for 12 h after UV irradiation or latrunculin A treatments and shown in Figure 4D,E. The numbers of emitted photon from wells were normalized to those from nontreated wells (control) and were plotted as relative intensity.

Cytochemical Staining and Image Acquisition. HEK293T cells were fixed with 4% paraformaldehyde in PBS. Cells were

incubated with 0.14 μM rhodamine-phalloidin (R-P)/PBS for 1 h at room temperature and washed with PBS. Hoechst staining was carried out in accordance with the manual of Caspase 3&7 FLICA kit (ImmunoChemistry Technologies). Fluorescence and bright field images were acquired using a laser confocal microscopy system (TCS-SP5, Leica) with a 63× Plan-Apochromat 1.4 NA lens (Leica) with immersion oil (Type F, Leica) at room temperature. Images were acquired using data acquisition/analysis software of the microscopy system (Leica application suite). No additional software adjustments were performed on images after acquisition. For the R-P signal quantification, the fluorescence intensity of eight randomly taken images using a 20× Plan-Apochromat 0.7 NA lens (Leica) was quantified using the Leica application suite. The intensity of the rhodamine signal was divided by that of the Hoechst staining signal of the same field. Calculated values are represented as a percentage of the control.

UV Irradiation. UV irradiation (at 254 nm, 9.6 kJ/m^2) was performed using a UV cross-linker (Spectrolinker XL-1000, Spectronics). HEK293T cells cultured in 3-cm-diameter dishes were taken out from a CO_2 incubator. The medium was changed to 2 mL of L15 medium (Invitrogen). The cells were irradiated with UV without removing the medium. After the irradiation, the cells were incubated at room temperature for 18 h.

Statistical Analysis. Data are presented as mean ± standard error of the mean (SEM). In the MTT assay, two-tailed Student's *t* test was used to determine statistical significance.

RESULTS

Development of Bioluminescence Probes for Long-Term Monitoring of Polymerization of Actin in Living Cells. We developed a novel method to measure the actin polymerization in living cells. The schema to measure the level of F-actin using split luciferase in living cells is shown in Figure 1A. The lucN-actin and lucC-actin fusion proteins are expressed in the cells and are incorporated in the actin filament randomly. When some of the lucN-actin and lucC-actin fusion proteins locate close to each other, they recover their enzymatic activity to emit light. Consequently, the intensity of photon emission is considered to depend on the level of F-actin. We screened the brightest pair of probe proteins. On the basis of the reported optimized cleavage site of firefly luciferase,[14,23] we constructed various luc-actin fusion probe proteins (Figure 1B). Combinations of expression clones nos. 1 and 2 and nos. 3 and 4 were expressed in HEK293T, and the emitted photons were counted for 10 min using the image intensifier/CCD camera. We found that the number of photons emitted from combination of nos. 3 and 4 was about 40 times larger than that of the combination of nos. 1 and 2 (Figure 1C). This result indicated that the N-terminal location of the luc fragment and the C-terminal location of actin are important for emission efficiency. Next, we tested all the combinations of odd and even numbers of expression clones nos. 3−10 (Figure 1B) to determine the brightest probe proteins. We found that the combination of the probe proteins nos. 9 and 10, which contained the flexible linker $(GGGGS)_3$,[24] showed the largest average photon count (Figure 1D) and decided to use this combination in the experiments reported here. To examine whether there were differences in expression level among probe proteins, lucN-actin (~87 kDa) and lucC-actin (~57 kDa) were analyzed by Western blotting using antiluciferase antibody. The difference in expression level of each probe protein was much smaller than the difference in light intensity seen in Figure 1C,D (Figure 1E). We used probes no. 9 (lucN-actin) and 10 (lucC-actin) in the following study.

Characterization of Developed Probe Proteins. To confirm the expression of probe proteins in living cells, lysates from HEK293T expressing probe proteins were analyzed by Western blotting using antiactin antibody. By comparing the intensities of the bands representing lucN-actin (87 kDa), lucC-actin (57 kDa), and endogenous actin (42 kDa), we found that the expression levels of probe ptoteins were less than 5% of endogenous actin (Figure 2A). Next, we determined whether incorporation of probe proteins in F-actin affected the kinetics of actin polymerization *in vitro*. Pyrene-conjugated actin and *E. coli* expressed probe proteins at a molar ratio of 25:1 were mixed in general actin buffer. Then, the polymerization buffer was added to start actin polymerization. The intensity of the fluorescence was measured for 90 min. We observed that the increasing ratio of fluorescence intensity was not changed by the existence of the probe proteins (Figure 2B). Subsequently, the samples used in the reaction were centrifuged to collect the F-actin fraction and analyzed by Western blotting. We detected bands corresponding to lucN-actin and lucC-actin for the sample that was treated with polymerization buffer (probes + P buffer) but not for the sample with general actin buffer alone (probes). This result indicates that incorporation of the probe proteins in F-actin did not affect the kinetics of actin polymerization in vitro (Figure 2C). Next, we confirmed whether the probe proteins were incorporated in F-actin in living cells. To separate F-actin and G-actin, HEK293T cells expressing probe proteins were harvested and ultracentrifuged.[25] The F-actin fraction in the pellet and the G-actin fraction in the supernatant were analyzed by Western blotting using the antiactin and antiluciferase antibodies, and we found that both lucN-actin and lucC-actin probe proteins were contained in each fraction. The ratio of probe proteins in the G-actin fraction to the F-actin fraction was similar to that of endogenous actin (Figure 2D). Then, we examined whether probe proteins could bind to one of the actin-binding proteins. Cofilin,[26] a well-defined actin-binding protein, was fused with the myc-tag sequence and expressed with probe proteins in HEK293T cells. The lysates from HEK293T cells were analyzed by co-immunoprecipitation using antimyc or antiluciferase antibodies. We found that probe proteins and cofilin-myc were contained in precipitated fractions with anti-myc and antiluciferase antibodies, respectively (Figure 2E). These results demonstrated that probe proteins associated with cofilin in the living cells. Finally, we tested whether the probes affect cell proliferation rate. HEK293T cells were transfected with probe proteins or wild-type luciferase (Luc). We did not find any difference in the intensity of MTT signals between the probe proteins- or Luc-expressing cells and the cells treated with lipofectamine alone (Figure 2F). Since light emission levels by luciferase−luciferin reaction and actin polymerization are both ATP-dependent, we tested whether luciferase activity affected the normal actin polymerization. HEK293T cells expressing probe proteins are treated with luciferin for 12 h, and then F- and G-actin fractions were separated. The ratio of F- and G-actin was similar to the control cells that were not treated with luciferin (Figure 2G). Thus, it is considered that normal actin polymerization is not affected by ATP consumption by probe proteins.

Developed Probe Proteins Can Measure the Level of F-Actin in Living Cells. Using the developed probe proteins, we examined whether the intensity of photons emitted by the

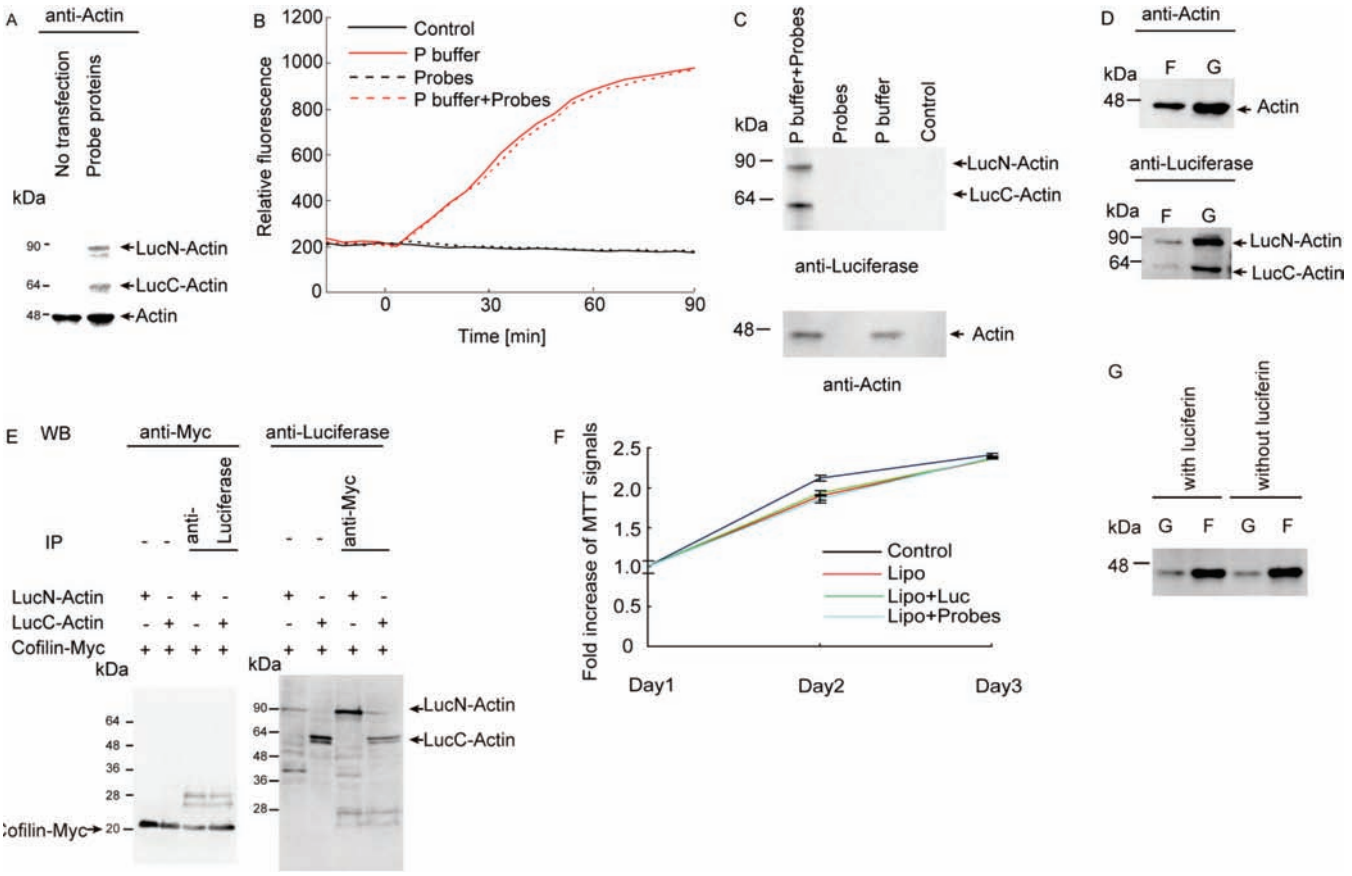


Figure 2. Characterization of probe proteins in vitro and in vivo. (A) Western blotting analysis of endogenous actin and probe proteins. HEK293T cells expressing probe proteins were analyzed by Western blotting using the antiactin antibody. The contrast of the image was adjusted to visualize the luc-actin fusion proteins. (B) Change in fluorescence intensity of pyrene-conjugated actin with probe proteins. Pyrene-actin with (dotted line) or without (solid line) probe proteins was treated with (red line) or without (black line) polymerization (P) buffer, then fluorescence intensity was measured every 5 min for 90 min. (C) Coprecipitation of probe proteins and pyrene-conjugated actin. After the fluorescence observation shown in B, each sample was centrifuged to precipitate F-actin. The pallet was analyzed by Western blotting using the antiluc antibody (upper panel). Then, antiluc antibody was stripped and the membrane was reacted with the antiactin antibody (lower panel). (D) Incorporation of probe proteins in F-actin in cells. HEK293T cells expressing probe proteins were harvested and ultracentrifuged to obtain F-actin in the pellet and G-actin in the supernatant fraction. The pellet was resuspended to the same volume as the supernatant fraction and analyzed by Western blotting. (E) Binding of probe proteins to an actin binding protein cofilin. Cofilin-myc and probe proteins were expressed in HEK293T cells and subjected to immunoprecipitation assay using the antimyc and antiluc antibodies. Total proteins from HEK293T cells expressing both cofilin-myc and one of the probe proteins were incubated with the antiluc (left panel) and antimyc (right panel) antibodies bound to protein-G Sepharose. The immunoprecipitates were analyzed by Western blotting (right two lanes of each panel). The lysate (1%) of transfected cells was directly analyzed by Western blotting as controls (left two lanes of each panel). (F) HEK293T cells were transfected with the plasmids that encoded wild-type luciferase (Luc) or probe proteins (Probes), the combination of nos. 9 and 10 (Figure 1B), using lipofectoamine 2000 (Lipo) on day 1. In the control, no plasmid or lipofectamine 2000 was added (Control). Cell viability was measured by the MTT method on days 1−3. Data are presented as mean ± SEM, $n = 4$. (G) F- and G-actin fractions from the cells expressing probe proteins in the presence (left) or absence (right) of luciferin were analyzed by Western blotting. In each Western blot, the locations of molecular weight markers (kDa) are shown on the left. Arrows indicate the locations of the bands corresponding to lucN-actin, lucC-actin, endogenous actin, and cofilin-myc.

probe proteins precisely reflected the level of F-actin in the cells. We added various concentrations of latrunculin A, which disrupts the actin filament by binding to G-actin,[27] to the culture medium of HEK293T expressing the probe proteins. After 3 h incubation with latrunculin A, luciferin was added and photon intensity was measured using the image intensifier/CCD camera in a dark box. We did not set any threshold to cut off the background noise. Depending on the latrunculin A concentration, photon intensity decreased (Figure 3A). At the highest concentration (50 μM) of latrunculin A, the photon emission was diminished almost completely. In the control experiment, Luc was expressed in the HEK293T cells and treated in the same manner as in Figure 3A. We observed no reduction in photon intensity following the treatment (Figure 3B). These results demonstrated that latrunculin A did not affect the activity of wild-type luciferase. Next, we evaluated the measurement of F-actin level in the cells using a conventional F-actin staining method. Cells were fixed after latrunculin A treatment and stained with R-P. Fluorescence microscopy analysis showed a dose-responsive decrease in fluorescence signal intensity, which represented the level of F-actin, accompanied with rounding of the cell shape (Figure 3C). The fluorescence signal intensity decreased with increasing concentration of latrunculin A (Figure 3D). However, at the highest concentration of latrunculin A (50 μM), the fluorescence intensity was about 30% of that of control cells and did not completely disappear (Figure 3D). Furthermore, the effect of an F-actin-

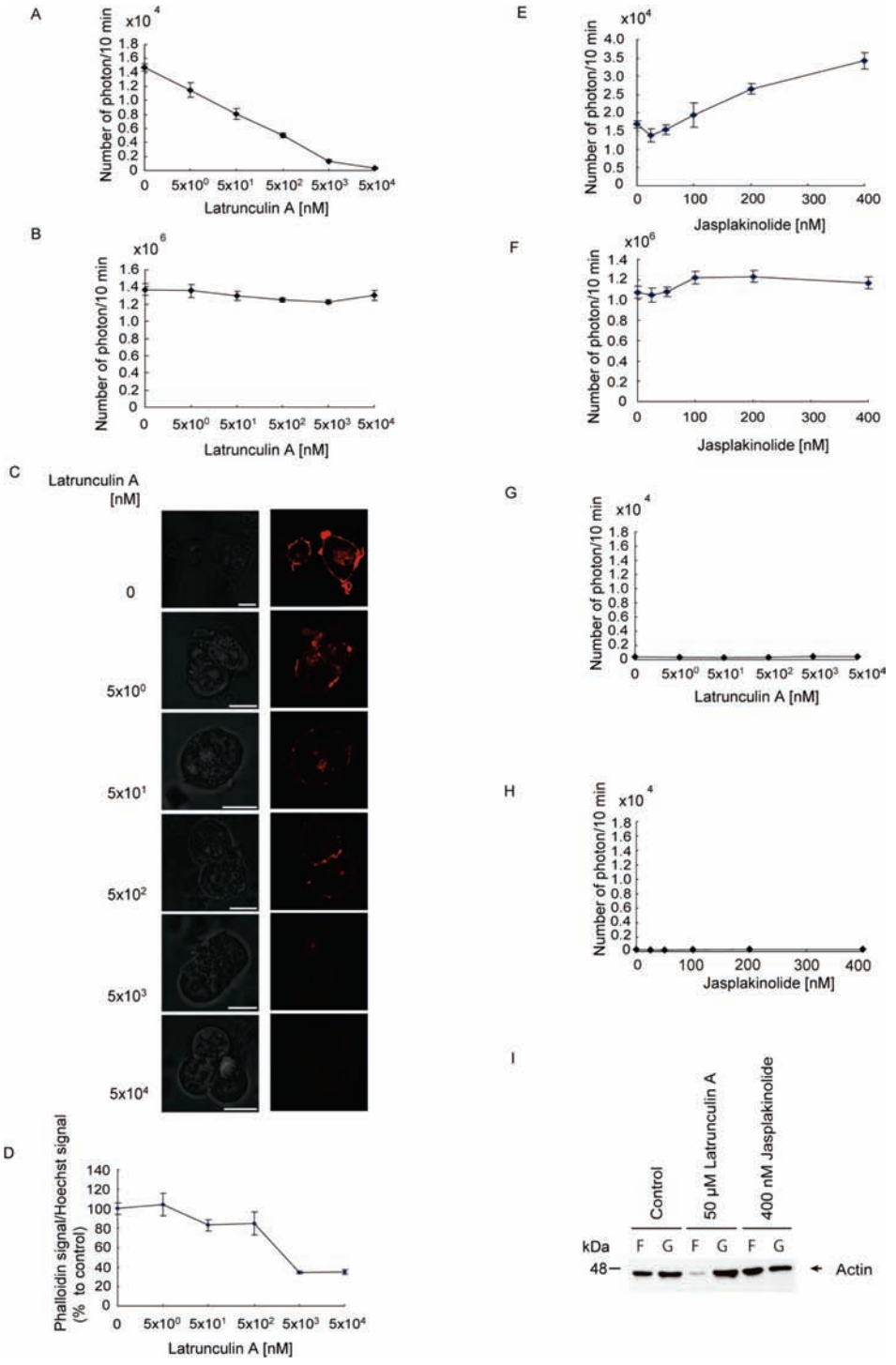


Figure 3. Effect of latrunculin A treatment on photon emission from F-actin probe proteins. (A) Concentration-dependent inhibition of photon emission from F-actin probe proteins by latrunculin A. The combination of probe proteins nos. 9 and 10 (Figure 1B) was expressed in HEK293T cells. Cells were treated with the indicated concentration of latrunculin A for 3 h. The intensity of photon emission in a period of 10 min from each culture well was measured. (B) Effect of latrunculin A on wild-type luciferase. The intensity of photon emission from the culture well expressing wild-type luciferase was measured as in (A). (C) Effects of latrunculin A on rhodamine-phalloidin (R-P) staining of HEK293T cells. Cells were treated with latrunculin A for 3 h and fixed. Red fluorescence represents F-actin. Fluorescence and bright field images were obtained by confocal microscopy. Bars indicate 10 μm. (D) Effects of latrunculin A on R-P staining of F-actin. R-P fluorescence signal intensity was normalized with Hoechst signal intensity. The values are expressed as a percentage of the control experiments without latrunculin A treatment. (E) Concentration-dependent increase in the intensity of photon emission from F-actin probe proteins after treatment with jasplakinolide. (F) Effect of jasplakinolide on wild-type luciferase. Photon emission was measured in the same manner as in (E). (G) Effects of latrunculin A on photon emissions from the cells expressing lucN and lucC. (H) Effects of jasplakinolide on photon emissions from the cells expressing lucN and lucC. (I) The amounts of F- and G- actin were analyzed by Western blotting after latrunculin A and jasplakinolide treatment. All the data are presented as mean ± SEM, n = 4 in (A, B, E, F, G, and H). n = 8 in (D).

dx.doi.org/10.1021/bc100595z |*Bioconjugate Chem.* 2011, 22, 1136–1144

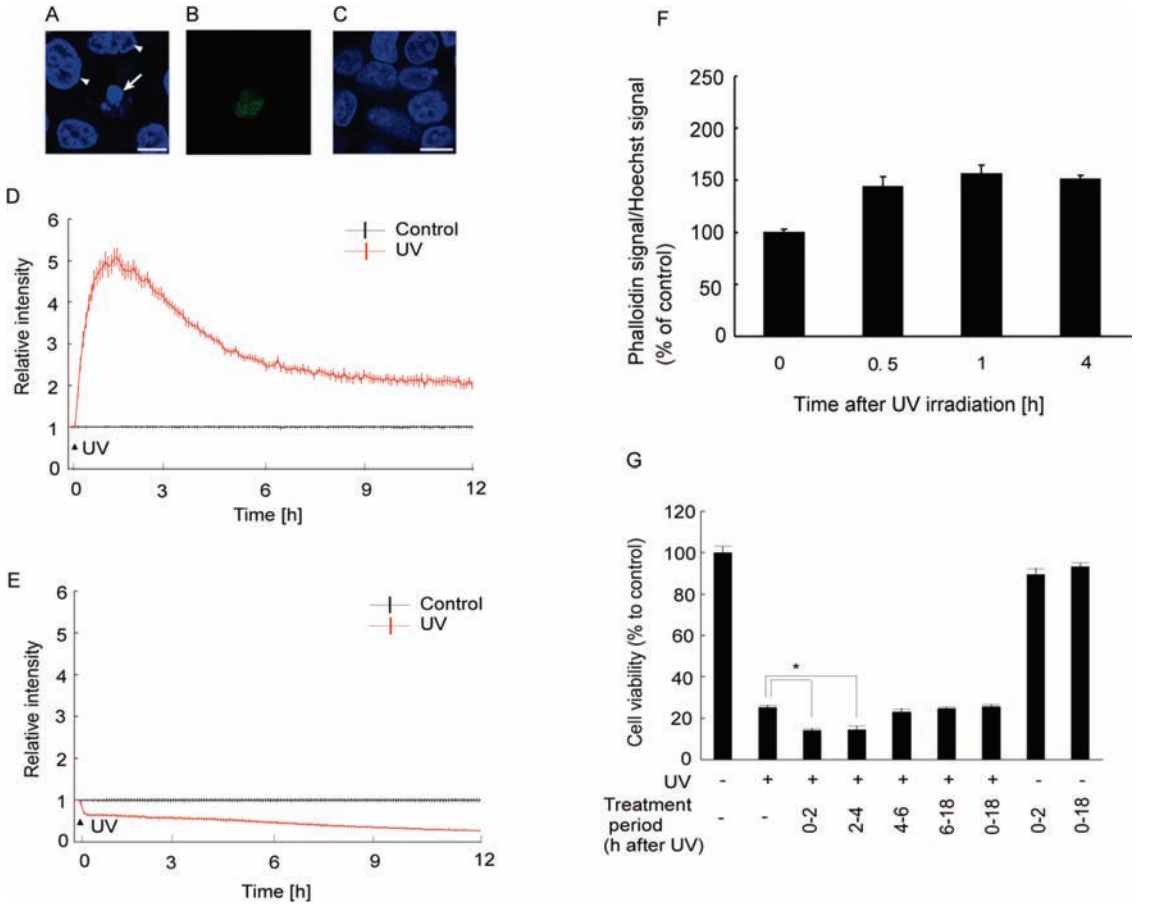


Figure 4. Effects of latrunculin A treatment on UV-induced apoptosis of HEK293T cells. (A) Cytochemistry of UV-irradiated cells stained with Hoechst (blue) 8 h after UV irradiation. The arrow indicates a cell with a condensed nucleus. Arrowheads indicate nuclear-membrane-localized chromatin stained with Hoechst. (B) Cells shown in A stained with caspase-3 activity indicator (green). (C) Non-UV-irradiated cells stained with Hoechst (blue). Bars indicate 10 μm in (A) and (C). (D) Time course of relative intensity of photon emission from F-actin probe proteins after UV irradiation (arrowhead). The red line represents the data from UV-irradiated cells. The black line represents that from the non-UV-irradiated control. (E) Time course of relative intensity of photon emission from cells expressing wild-type luciferase after UV irradiation. (F) Effects of UV on R-P staining of F-actin. The R-P fluorescence signals were normalized with Hoechst signals. The values are expressed as a percentage of the signal at time 0. (G) Effects of UV irradiation and latrunculin A treatment on cell viability assayed by the MTT method. Cells with and without UV irradiation were treated with or without 500 nM latrunculin A for indicated periods. Eighteen hours after UV irradiation, cell viability was measured. Cell viability is represented as a percentage of the viability of the control cells without UV irradiation and latrunculin A treatment. All the data are presented as mean ± SEM, $n = 4$, in (D,E,G). $n = 12$ in (F). * $p < 0.05$.

stabilizing reagent, jasplakinolide,[28] on photon emission from the probe proteins was tested. When jasplakinolide of more than 200 nM was added to the cells expressing the probe proteins, the cells emitted a significantly stronger light than when lower concentrations (<100 nM) were added (Figure 3E). We also tested a higher concentration (>400 nM) of jasplakinolide on the transfected cells and observed the tendency to emit a stronger light, but in those cases, the cells were often detached from the culture dishes (data not shown). We found that the photon emission of wild-type luciferase was not affected by jasplakinolide treatment (Figure 3F). The effects of jasplakinolide treatment on photon emission also support the idea that the photon intensity emitted from probe proteins quantitatively reflects the level of F-actin. Analysis of the effects of jasplakinolide on R-P staining of cells was not carried out because the binding sites of phalloidin and jasplakinolide are the same.[28] In order to confirm that lucN and lucC without actin fusing them do not interact each other, we measured the light intensity from the cells expressing lucN and lucC. The light intensity was much lower than the cells expressing lucN-actin and lucC-actin and did not react to latrunculin A and jasplakinolide (Figure 3G,H) as reported before.[29] To test whether latrunculin A and jasplakinolide change the amount of F-actin, HEK293T cells treated with the compounds were harvested, and F- and G- fractions were separated by centrifuge. The amount of F-actin was markedly reduced by latrunculin A and increased by jasplakinolide (Figure 3I). These changes of F-actin level are similar to the changes of light intensities seen in Figure 3A and E, supporting the functionality of the probe proteins.

Measurement of Actin Polymerization in HEK293T after UV Irradiation. We next applied these probe proteins to analyze the state of actin polymerization during apoptosis. First, we tried to characterize the HEK293T cell death induced by UV irradiation as a model. Fluorescence microscopy revealed that UV-irradiated cells exhibited nuclear condensation and chromatin localization at the nuclear membrane, as shown by Hoechst staining (Figure 4A), compared with the control cells (Figure 4C). In the cells that exhibited nuclear condensation, caspase-3 activation was observed (Figure 4B). These cells were

frequently detached from the culture dish (data not shown). Since these features were reported in lower-intensity UV- and cadmium-induced HEK293 apoptosis,[30,31] we assumed that the UV irradiation induced the apoptotic cell death. Then, we monitored the change in F-actin level after UV irradiation in real time and in living cells. Cells expressing the probe proteins were irradiated with UV, in the same manner as shown in Figure 4A, and photon emission intensity was measured continuously for 12 h after irradiation. We found that the relative photon intensity transiently increased after irradiation and gradually decreased after 2 h (Figure 4D). In the control experiment, Luc-expressing cells showed a decrease rather than an increase in photon emission intensity, which might be due to the toxic effect of UV irradiation (Figure 4E). Using conventional R-P staining, a transient increase of F-actin after UV irradiation was also detected, but the increase in signal was lower than that of our probes (Figure 4F). Considering the result of Figure 4D, we predicted that transient upregulation of F-actin in early phase (0−4 h) of apoptosis progression would be a protective reaction of the cell as reported in different cell lines.[16−18] To test this prediction, we determined the effects of latrunculin A on UV-induced HEK293T cell death. After the UV irradiation, 500 nM latrunculin A was added to the cells. Cell death was measured 18 h after irradiation by the MTT method. We found that the treatment with latrunculin A for 0−2 and 2−4 h after irradiation significantly enhanced UV-induced cell death (Figure 4G). In contrast, latrunculin A treatment 4 h after UV irradiation did not change the MTT signal intensity. Since latrunculin A treatment without UV did not induce significant cell death (Figure 4G), these results indicate that latrunculin A treatment accelerates UV-induced cell death only in the early period (0−4 h) after the irradiation. The period during which F-actin upregulation peaked (1−2 h after UV irradiation) (Figure 4D) overlapped with the period during which latrunculin A (500 nM) effectively enhanced the UV-induced cell death (0−2 h after UV irradiation) (Figure. 4G), suggesting a protective role of upregulated F-actin against apoptosis.

DISCUSSION

Characterization of the Probe Proteins We Developed. We successfully developed and improved the photon emission intensity of probe proteins to monitor actin polymerization (Figure 1). Expression of the probe proteins did not have any effect on HEK293T cell proliferation and actin polymerization ratio in vitro (Figure 2B,F). The probe proteins were incorporated in F-actin in vitro and in vivo (Figure 2C,D), and photon emission intensity decreased with increasing latrunculin A concentration (Figure 3A). The changes in photon emission of probe proteins induced by UV irradiation and latrunculin A treatments were consistent with those of R-P staining (Figure 3C,D). Above all, we conclude that our probe proteins can be used to precisely monitor actin polymerization in living cells. In previous studies, phalloidin has served as a useful tool to stain F-actin;[8] however, this reagent cannot be used in living cells because it requires cell fixation. The fluorescent GFP-actin protein[9] and lifeact[10] have been utilized to image the subcellular distribution of F-actin in living cells. However, these fusion proteins emit fluorescence even if they are monomers, and so are not suitable for quantification of the level of F-actin. Recently, the FRET technique has been employed to monitor F-actin,[11] although the FRET signal intensity is not in proportion to the level of F-actin.[12] These methods based on fluorescence observation have limits of autofluorescence noise and phototoxicity.[32] On the other hand, our probe proteins have little noise and no phototoxicity since no excitation light is required. These advantages enable us to carry out long-term quantitative measurement of F-actin in living cells (Figure 4). Since actin is a universal protein among all eukaryotic cells, and many cellular events are related to F-actin organization, our novel probe proteins can be applied to the analysis of a wide variety of phenomena involving actin polymerization in cells.

The increasing ratio of photon emission from probe proteins (Figure 4D) was higher than that of R-P signals (Figure 4F) in response to UV irradiation. Even if a high concentration of latrunculin A (50 μM) was added, we detected fluorescent signals from cells (Figure 3D), whereas the photon intensity from our probe proteins was diminished almost completely (Figure 3A). Thus, the main reason for this difference might be considered to be that the R-P signals contain about 40% of autofluorescence noise. In addition, another possibility that some F-actin was detected by R-P method and not by our method may explain the remained R-P fluorescence in Figure 3D. This point should be elucidated in the future.

The expression levels of our probe proteins are lower than that of GFP-actin.[33] Since GFP is known to have high stability,[34] it is possible that luc-actin fusion proteins are easier to be degraded than GFP-actin protein. This is a disadvantage because the degradation of probes reduces signal intensity. On the other hand, lower stability of our probe proteins may be an advantage, as they do not affect normal cell activities such as proliferation (Figure 2F).

Transient Increase in F-Actin Level Is Likely a Defensive Reaction of Cells. Some reports indicated F-actin disruption induced the apoptosis, and other reports showed enhancement of apoptosis by treatment with F-actin disruptive agent after apoptosis-inducing stimulation.[16−18] Thus, it is suggested F-actin has a protective role for the cells. However, the precise time course of actin polymerization during cell death has not been elucidated. Using our probe proteins, we succeeded in real-time monitoring of the actin polymerization in living cells after apoptosis induction and found that F-actin level was upregulated transiently after UV irradiation (Figure 4D). Furthermore, F-actin disruption with latrunculin A in the early period (0−2, 2−4 h after UV irradiation) enhanced the cell death, whereas later treatment (4−6, 6−18 h after UV irradiation) did not (Figure 4G). These results indicate that actin polymerization occurs in the early phase of apoptosis and support the hypothesis of protective role of actin polymerization against the cell death. In UV-induced apoptosis, several pathways are reported;[35] further study combined with pharmacological methods will reveal the mechanism of protective effect of actin polymerization on cell death.

AUTHOR INFORMATION

Corresponding Author

*Hisashi Mori, Ph.D., University of Toyama, 2630 Sugitani, Toyama 930-0194, Japan. Tel: +81-76-434-7230. Fax: +81-76-434-5015. E-mail: hmori@med.u-toyama.ac.jp.

ACKNOWLEDGMENT

This work was supported by PRESTO of the Japan Science and Technology Corporation (JST, No. 2602) and the Japan

Society for the Promotion of Science (JSPS, No. 2070331). The authors declare no competing financial interests.

REFERENCES

(1) Bailly, M., and Condeelis, J. (2002) Cell motility: insights from the backstage. *Nat. Cell Biol. 4*, E292–4.

(2) Mitchison, T. J., and Cramer, L. P. (1996) Actin-based cell motility and cell locomotion. *Cell 84*, 371–9.

(3) Sahai, E. (2005) Mechanisms of cancer cell invasion. *Curr. Opin. Genet. Dev. 15*, 87–96.

(4) Fukazawa, Y., Saitoh, Y., Ozawa, F., Ohta, Y., Mizuno, K., and Inokuchi, K. (2003) Hippocampal LTP is accompanied by enhanced F-actin content within the dendritic spine that is essential for late LTP maintenance in vivo. *Neuron 38*, 447–60.

(5) Matsuzaki, M., Honkura, N., Ellis-Davies, G. C., and Kasai, H. (2004) Structural basis of long-term potentiation in single dendritic spines. *Nature 429*, 761–6.

(6) Franklin-Tong, V. E., and Gourlay, C. W. (2008) A role for actin in regulating apoptosis/programmed cell death: evidence spanning yeast, plants and animals. *Biochem. J. 413*, 389–404.

(7) Ndozangue-Touriguine, O., Hamelin, J., and Breard, J. (2008) Cytoskeleton and apoptosis. *Biochem. Pharmacol. 76*, 11–8.

(8) Wulf, E., Deboben, A., Bautz, F. A., Faulstich, H., and Wieland, T. (1979) Fluorescent phallotoxin, a tool for the visualization of cellular actin. *Proc. Natl. Acad. Sci. U.S.A. 76*, 4498–502.

(9) Doyle, T., and Botstein, D. (1996) Movement of yeast cortical actin cytoskeleton visualized in vivo. *Proc. Natl. Acad. Sci. U.S.A. 93*, 3886–91.

(10) Riedl, J., Crevenna, A. H., Kessenbrock, K., Yu, J. H., Neukirchen, D., Bista, M., Bradke, F., Jenne, D., Holak, T. A., Werb, Z., Sixt, M., and Wedlich-Soldner, R. (2008) Lifeact: a versatile marker to visualize F-actin. *Nat. Methods 5*, 605–7.

(11) Okamoto, K., and Hayashi, Y. (2006) Visualization of F-actin and G-actin equilibrium using fluorescence resonance energy transfer (FRET) in cultured cells and neurons in slices. *Nat. Protoc. 1*, 911–9.

(12) Takanishi, C. L., Bykova, E. A., Cheng, W., and Zheng, J. (2006) GFP-based FRET analysis in live cells. *Brain Res. 1091*, 132–9.

(13) Ozawa, T., Kaihara, A., Sato, M., Tachihara, K., and Umezawa, Y. (2001) Split luciferase as an optical probe for detecting protein-protein interactions in mammalian cells based on protein splicing. *Anal. Chem. 73*, 2516–21.

(14) Luker, K. E., Smith, M. C., Luker, G. D., Gammon, S. T., Piwnica-Worms, H., and Piwnica-Worms, D. (2004) Kinetics of regulated protein-protein interactions revealed with firefly luciferase complementation imaging in cells and living animals. *Proc. Natl. Acad. Sci. U.S.A. 101*, 12288–93.

(15) Paulmurugan, R., Umezawa, Y., and Gambhir, S. S. (2002) Noninvasive imaging of protein-protein interactions in living subjects by using reporter protein complementation and reconstitution strategies. *Proc. Natl. Acad. Sci. U.S.A. 99*, 15608–13.

(16) Suria, H., Chau, L. A., Negrou, E., Kelvin, D. J., and Madrenas, J. (1999) Cytoskeletal disruption induces T cell apoptosis by a caspase-3 mediated mechanism. *Life Sci. 65*, 2697–707.

(17) Martin, S. S., and Leder, P. (2001) Human MCF10A mammary epithelial cells undergo apoptosis following actin depolymerization that is independent of attachment and rescued by Bcl-2. *Mol. Cell. Biol. 21*, 6529–36.

(18) Celeste Morley, S., Sun, G. P., and Bierer, B. E. (2003) Inhibition of actin polymerization enhances commitment to and execution of apoptosis induced by withdrawal of trophic support. *J. Cell Biochem. 88*, 1066–76.

(19) Hartley, J. L., Temple, G. F., and Brasch, M. A. (2000) DNA cloning using in vitro site-specific recombination. *Genome Res. 10*, 1788–95.

(20) Sasaki, Y., Sone, T., Yoshida, S., Yahata, K., Hotta, J., Chesnut, J. D., Honda, T., and Imamoto, F. (2004) Evidence for high specificity and efficiency of multiple recombination signals in mixed DNA cloning by the Multisite Gateway system. *J. Biotechnol. 107*, 233–43.

(21) Ochman, H., Gerber, A. S., and Hartl, D. L. (1988) Genetic applications of an inverse polymerase chain reaction. *Genetics 120*, 621–3.

(22) Cooper, J. A., Walker, S. B., and Pollard, T. D. (1983) Pyrene actin: documentation of the validity of a sensitive assay for actin polymerization. *J. Muscle Res. Cell Motil. 4*, 253–62.

(23) Kim, S. B., Kanno, A., Ozawa, T., Tao, H., and Umezawa, Y. (2007) Nongenomic activity of ligands in the association of androgen receptor with SRC. *ACS Chem. Biol. 2*, 484–92.

(24) Huston, J. S., Levinson, D., Mudgett-Hunter, M., Tai, M. S., Novotny, J., Margolies, M. N., Ridge, R. J., Bruccoleri, R. E., Haber, E., and Crea, R. et al. (1988) et al. Protein engineering of antibody binding sites: recovery of specific activity in an anti-digoxin single-chain Fv analogue produced in Escherichia coli. *Proc. Natl. Acad. Sci. U.S.A. 85*, 5879–83.

(25) Tu, Y., Wu, S., Shi, X., Chen, K., and Wu, C. (2003) Migfilin and Mig-2 link focal adhesions to filamin and the actin cytoskeleton and function in cell shape modulation. *Cell 113*, 37–47.

(26) Bernstein, B. W., and Bamburg, J. R. ADF/cofilin: a functional node in cell biology. *Trends Cell Biol. 20*, 187-95.

(27) Coue, M., Brenner, S. L., Spector, I., and Korn, E. D. (1987) Inhibition of Actin Polymerization by Latrunculin-A. *Febs Lett. 213*, 316–318.

(28) Bubb, M. R., Senderowicz, A. M., Sausville, E. A., Duncan, K. L., and Korn, E. D. (1994) Jasplakinolide, a cytotoxic natural product, induces actin polymerization and competitively inhibits the binding of phalloidin to F-actin. *J. Biol. Chem. 269*, 14869–71.

(29) Paulmurugan, R., and Gambhir, S. S. (2005) Firefly luciferase enzyme fragment complementation for imaging in cells and living animals. *Anal. Chem. 77*, 1295–302.

(30) Fan, Y., Wu, D., Jin, L., and Yin, Z. (2005) Human glutamyl-cysteine synthetase protects HEK293 cells against UV-induced cell death through inhibition of c-Jun NH2-terminal kinase. *Cell Biol. Int. 29*, 695–702.

(31) Mao, W. P., Ye, J. L., Guan, Z. B., Zhao, J. M., Zhang, C., Zhang, N. N., Jiang, P., and Tian, T. (2007) Cadmium induces apoptosis in human embryonic kidney (HEK) 293 cells by caspase-dependent and -independent pathways acting on mitochondria. *Toxicol. In Vitro 21*, 343–54.

(32) Dixit, R., and Cyr, R. (2003) Cell damage and reactive oxygen species production induced by fluorescence microscopy: effect on mitosis and guidelines for non-invasive fluorescence microscopy. *Plant J. 36*, 280–90.

(33) Westphal, M., Jungbluth, A., Heidecker, M., Muhlbauer, B., Heizer, C., Schwartz, J. M., Marriott, G., and Gerisch, G. (1997) Microfilament dynamics during cell movement and chemotaxis monitored using a GFP-actin fusion protein. *Curr. Biol. 7*, 176–83.

(34) Enoki, S., Saeki, K., Maki, K., and Kuwajima, K. (2004) Acid denaturation and refolding of green fluorescent protein. *Biochemistry 43*, 14238–48.

(35) Kulms, D., and Schwarz, T. (2000) Molecular mechanisms of UV-induced apoptosis. *Photodermatol. Photoimmunol. Photomed. 16*, 195–201.

Bioconjugate Chemistry

ARTICLE

pubs.acs.org/bc

Biodistribution Study of Nanometric Hybrid Gadolinium Oxide Particles as a Multimodal SPECT/MR/Optical Imaging and Theragnostic Agent

David Kryza,[*,⊥,†,‡] Jacqueline Taleb,[⊥,‡,§] Marc Janier,[†,‡] Laurence Marmuse,[§] Imen Miladi,[‡] Pauline Bonazza,[‡] Cédric Louis,[§] Pascal Perriat,[∥] Stéphane Roux,[‡] Olivier Tillement,[‡] and Claire Billotey[†,‡]

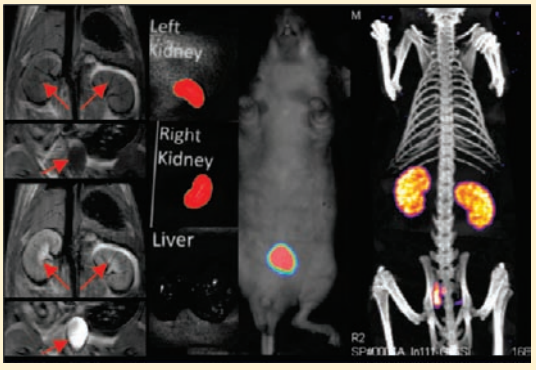
[†]Hospices Civils de Lyon, Lyon, France

[‡]LPCML UMR 5620 CNRS, Université Claude Bernard Lyon 1, Villeurbanne, France

[§]NanoH, Saint-Quentin Fallavier, France

[∥]UMR 5510 CNRS-INSA de Lyon, Villeurbanne, France

ABSTRACT: Nanometric hybrid gadolinium oxide particles (Gado-6Si-NP) for diagnostic and therapeutic applications (mean diameter 3−4 nm) were obtained by encapsulating Gd_2O_3 cores within a polysiloxane shell, which carries organic fluorophore (Cy 5) and is derivatized by a hydrophilic carboxylic layer. As residency time in the living body and methods of waste elimination are crucial to defining a good nanoparticle candidate and moving forward with steps for validation, this study was aimed at evaluating the biodistribution of these multimodal Gado-6Si-NP in rodents. Gado-6Si-NP were imaged following intravenous injection in control Wistar rats and mice using MRI (7 T), optical fluorescent imaging, and SPECT. A clear correlation was observed among MRI, optical imaging, and SPECT regarding the renal elimination. Quantitative biodistribution using gamma-counting of each sampled organ confirmed that these nanoparticles circulated freely in the blood pool and were rapidly cleared by renal excretion without accumulation in liver and RES uptake. These results demonstrate that Gado-6Si-NP display optimal biodistribution properties, enabling them to be developed as multimodal agents for *in vivo* imaging and theragnostics, especially in oncological applications.



INTRODUCTION

Explosive growth in the field of personalized medicine and nanotechnology has enabled advances in molecular imaging and therapies.[1,2] Numerous strategies are explored in order to apply nanoparticles with multiple functions to clinical use.[3] Some nanoparticles have multimodal properties that are interesting for medical imaging,[4−6] while others are developed for therapeutic purposes only[7−9] or for theragnostic use.[10−12] Whatever the nanoparticle's composition, the hydrodynamic diameter and the surface of the nanoparticle are important parameters that potentially modify the biodistribution of the nanoparticle within the body. Most available nanoparticles have a hydrodynamic diameter greater than 10 nm. According to several studies,[13−16] different types of nanoparticles with a hydrodynamic diameter between 3 and 7 nm demonstrate optimal circulation lifetime with efficient clearance and the ability to be filtered through the kidneys. Ideally, these compounds should behave as closely as possible to molecules already used as contrast agents or for therapeutic purposes. Because of surface differences, nanoparticles with a small hydrodynamic diameter behave differently once injected in a living organism. Therefore, it is mandatory that we accurately and quantitatively evaluate the biodistribution of the nanoparticle studied.

Our group has developed a unique nanoparticle platform which is able to be detected regardless of the imaging modality used in humans, and which can be used for therapy as a radiosensitizer, or with a specific labeling as a tool for internal radiotherapy. These nanoparticles are composed of a core of rare-earth atoms (gadolinium), surrounded by a silica shell which can be used to covalently label specific targeting molecules. Because of their composition, no rapid degradation is expected, and it is therefore crucial to understand their behavior in a living organism. On a first move, the biodistribution of the nanoparticle platform should be evaluated and optimized as necessary, prior to developing targeted nanoparticles. A previous study[17] has shown that these nanoparticles were filtered by the kidney, and that the nanoparticles were recovered without modification in the urine. Our study was aimed at assessing the exact repartition of the nanoparticles in control rats and mice over an 18-day period by labeling the nanoparticles with Indium 111.

Received: December 27, 2010
Revised: May 5, 2011
Published: May 06, 2011

ACS Publications © 2011 American Chemical Society

MATERIALS AND METHODS

Chemicals. Gadolinium chloride hexahydrate ($GdCl_3 \cdot 6H_2O$, 99.99%) was purchased from Metall Rare Earth Limited. Sodium hydroxide (NaOH, 99.99%), tetraethyl orthosilicate ($Si(OC_2H_5)_4$, TEOS, 98%), (3-aminopropyl)triethoxysilane ($H_2N(CH_2)_3$ $Si(OC_2H_5)_3$, APTES, 99%), Hepes solution (solution in water, pH 7.0−7.6), sodium chloride (NaCl), triethylamine (TEA, 99.5%), and nitric acid (HNO_3, 65%), dimethyl sulfoxide anhydrous ($(CH_3)_2SO$, DMSO >99.9%) diethyl ether ($(CH_3CH_2)_2O$ > 99%) were purchased from Aldrich Chemical (France). Cy5 mono-NHS-ester was purchased from Amersham Bioscience. Diethylenetriamine pentaacetic dianhydride ($C_{14}H_{19}N_3O_8$, DTPA-ba >98.0%) was purchased from TCI Europe. Ethanol, diethylene glycol (DEG, 99%), and other organic solvents (reagent grade) were purchased from SDS (France) and used as received. For the preparation of an aqueous nanoparticle solution, Milli-Q water (F > 18 MΩ) was used. Ultrafiltration was carried out using Vivaspin 5000 Da purchased from GE Healthcare.

Synthesis of NPs. The particles Gado-6Si-NP were provided from Nano-H SAS and prepared as previously described.[17] Briefly, gadolinium oxide (Gd_2O_3) nanoparticles embedded in a polysiloxane shell whose inner part is functionalized by Cy5 and outer part by carboxylic acid were synthesized as follows. In the first step, gadolinium oxide particles were obtained via precipitation at temperatures below 200 °C by applying a modified "polyol" synthesis.[18] In the second step, controlled polysiloxane shell growth was induced on the gadolinium nano-oxide cores (six silicium/one gadolinium) via hydrolysis/condensation of a mixture of TEOS and APTES. At this stage, Cy5 could be grafted inside the polysiloxane shell at the desired percentage by introducing the reaction product between Cy5 NHS ester with APTES in dry DMSO.[19] Finally, because of the presence of amine functions of APTES in the polysiloxane network, a postfunctionalization was carried out using DTPA-ba (via the formation of an amide linkage). Typically, a colloidal solution of hybrid nanoparticles in DEG (50 mL, [Gd] = 37 mM) was added into a suspension of DTPA-ba (4 equiv/Gd) in anhydrous DMSO (60 mL). The reaction mixture was stirred overnight at room temperature. Next, a mixture of acetone and diethyl ether (1:1, v:v) was poured into the reaction. A precipitate was formed, and a purification step was carried out via initial centrifugation at 6000 rpm for 5 min, and redispersion in ethanol and subsequent centrifugation (3-fold, 6000 rpm for 10 min). The nanoparticles were then redispersed in Milli-Q water at a high concentration. The colloidal solution was transferred into a Vivaspin 5000 Da, and ultrafiltration was performed. Finally, a freeze−drying protocol of Gado-6Si-NP was carried out.

NP Characterization. Direct measurements of particle size distribution were taken using the Zetasizer Nano S (Malvern Instruments, Malvern, U.K.). The hydrodynamic diameter of Gd_2O_3 core (in DEG) and Gado-6Si-NP (in water, pH = 7.4) was evaluated using photon correlation spectroscopy (PCS). Direct measurements of zeta potential of Gado-6Si-NP were performed using the Zetasizer Nano S (Malvern Instruments, Malvern, U.K.). Prior to the experiment, the solution was diluted in an aqueous solution containing 0.01 M NaCl and adjusted to the desired pH. Determination of the gadolinium content in a sample was performed using inductively coupled plasma-optical emission spectrometer (ICP-OES) analysis with a Varian 710-ES. Before measuring Gd concentration, samples of lyophilizat were redispersed in 10 mL Milli-Q water, and 1 mL of this colloidal solution was diluted in 14 M HNO_3 (1:1, v/v). After 30 min at 80 °C, the solution was diluted in HNO_3 (5%; 1:25, v/v). HRTEM was applied to obtain detailed structural and morphological information about the architecture of the core/shell. It was carried out using a JEOL 2010 microscope operating at 200 kV. Samples were prepared by diluting nanoparticle solution and depositing a drop on a copper grid coated by a thin film of amorphous carbon, allowing the liquid to dry in air at room temperature. Determination of the number of DTPA molecules per particle was calculated from the N/Gd ratio obtained by chemical analyses (ICP-OES and energy dispersive X-ray) taking into account the particle size.

Radiolabeling with Indium-111. For *in vivo* and quantitative biodistribution studies, hybrid gadolinium oxide nanoparticles were labeled using Indium-111 radionuclide (stability constant DTPA-In^{3+} close to 10^{29}).[29] Briefly, 370 MBq of high-purity ^{111}In-chloride (specific activity >185GBq/μg indium) in diluted hydrochloric acid (Covidien, Petten, The Netherlands) was added to 1 mL of a saline solution of hybrid nanoparticles ([Gd] = 100 mM]). Indium-111 links to the DTPA hydrophilic layer of the nanoparticles via coordination bonds.

The mixture was incubated for 30 min at room temperature. Gado-6Si-NP−^{111}In were separated from ^{111}In-chloride by PD-10 column (GE Healthcare Bio-Sciences AB, Uppsala, Sweden) as follows. The PD-10 column was first washed with 15 mL of 50 mM citrate buffer (pH = 5). The radiolabeling solution was then loaded on the PD-10 column, and fractions of 0.5 mL were eluted with 50 mM citrate buffer (pH = 5). Gado-6Si-NP−^{111}In were first eluted. The radioactivity of each fraction was counted using an ionization chamber (Capintec Radioisotope Calibrator CRC-15, Capintec Inc.). Finally, the four fractions with the highest radioactivity were pooled. The solution was then challenged with 200 μL of the complexing chelating agent diethylenetriaminepentaacetic acid (DTPA; 20 μmol) for 5 min to scavenge potential unbound ^{111}In. Another elution was performed on a PD-10 column using 50 mM citrate buffer (pH = 5) as eluent. The DTPA complex was eluted following Gado6Si-NP−^{111}In. Radiochemical purity was determined by instant thin layer chromatography (ITLC).

ITLC of the purified Gado-6Si-NP−^{111}In was performed using silica gel plates (Gelman Science Inc., Ann Arbor, MI, USA) in 50 mM citrate buffer (pH = 5) as the solvent, and a TLC scanner (MiniGita, Raytest, Isotopenmessgeräte, GmbH, Straubenhardt, Germany) in order to determine the percentage of free ^{111}In-chloride. Gado-6Si-NP−^{111}In remained at the origin, whereas residual ^{111}In-chloride migrated with an Rf of 0.8.

Stability of Gado-6Si-NP−^{111}In Nanoparticles. The purified Gado-6Si-NP−^{111}In were incubated in rat serum at 37 °C and 20 mM DTPA solution (pH = 7.4) for 4 h, 24 h, and 7 days. Radiochemical purity was determined as described previously.

Animals. All animal experiments were approved by the local animal ethics committee of University Claude Bernard Lyon 1, according to French legislation, and carried out in line with current guidelines. Adult male Wistar rats (200−250 g) and nude Swiss mice (20−25 g) were obtained from Charles River Laboratory (L'Arbresle, France). All animals were housed under standard environmental conditions (free access to food and water and a 12/12 h light/dark cycle), and acclimated for at least 48 h before experimentation.

For all experiments except scintigraphic and optical dynamic acquisition, a gaseous anesthesia protocol was applied using

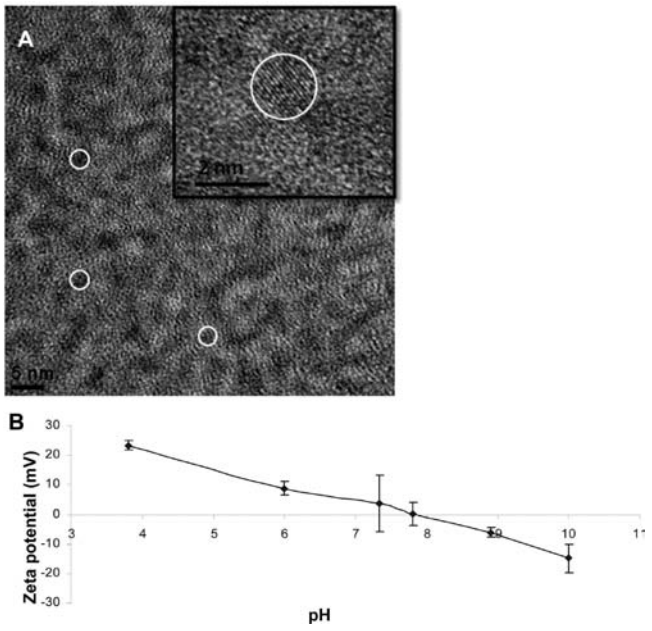


Figure 1. (A) HRTEM images of gadolinium oxide core nanoparticles representative of the whole sample. (B) Zeta potential of Gado-6Si-NP (n = 3).

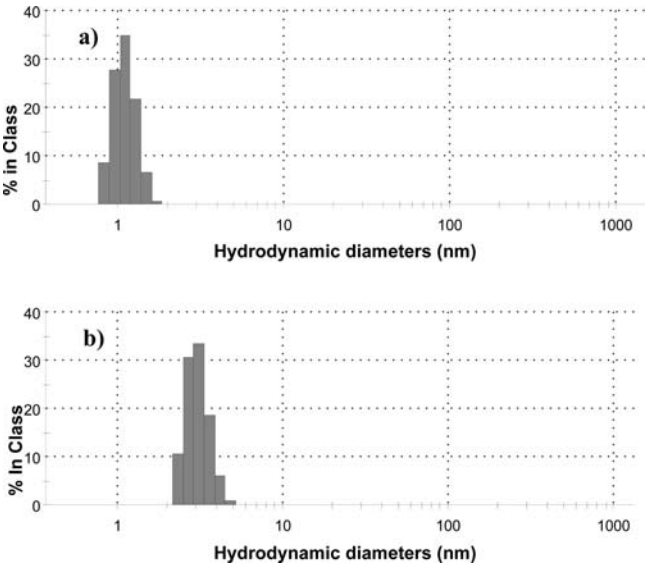


Figure 2. Size distribution determined by photon correlation spectroscopy (PCS) of gadolinium oxide core nanoparticles (a) and Gado-6Si-NP (b).

1−2% isoflurane (Laboratoire Bellamont, Boulogne Billancourt, France) in a mixture of O_2/N_2 (25/75%) at 0.8 L/min after an induction process. To avoid the absence of renal excretion by isoflurane gaseous anesthesia, scintigraphic and optical dynamic acquisition were performed immediately after chemical anesthesia (Ketamine1000, Virbac, Carros, France) at a dose of 0.15 mg per gram of body weight by IM injection, followed with medetomidine (Domitor, Orion Pharma, Espoo, Finland) at a dose of 0.5 (in rats) to 1 (in mice) μg per gram of body weight by IP. Anesthesia was monitored using a small animal respiratory monitoring system (Sa Instrument, Inc., NY, USA).

Biodistribution Study. Biodistribution of Gado-6Si-NP−^{111}In was studied in order to evaluate the potential of the multimodal nanohybrid agent. Radiolabeled nanoparticles in HEPES buffer containing 150 mM NaCl were injected intravenously through a caudal vein in rats after anesthesia had been administered. Rats were sacrificed at 2 h, 24 h, 72 h, 10 days, and 18 days postinjection, and organs of interest, such as the heart, lungs, spleen, liver, brain, kidneys, bones, muscles, skin, digestive tract, and cadaver were collected. Urine and feces were also collected each day and weighed and counted for 5 min in an automatic gamma scintillation counter (Wizard gamma counter, Perkin-Elmer, USA). Tissue distribution was expressed as the percentage injected dose per gram tissue (% ID/g) and as the percentage injected dose per organ (%ID/organ). The injected dose was calculated by adding activity of all organs, cadaver, and excretions (feces and urine). Renal and hepatobiliary eliminations were evaluated by measuring respectively urine and feces activities and expressed as cumulated radioactivity under total injected radioactivity.

Blood Circulation Half-Life of Radiolabeled Gado-6Si-NP. After IV injection of 10 MBq of Gado-6Si-NP−^{111}In in rats (n = 3), blood samples were removed at suitable time intervals (5 min, 10 min, 20 min, 30 min, 60 min, 120 min, and 240 min). Samples were weighed and counted for 5 min in an automatic gamma scintillation counter. Data points were fit to an exponential decay function to determine blood circulation half-life.

Imaging Studies. *Dynamic Scintigraphy and SPECT.* Acquisitions were obtained using a small animal Nano-SPECT/CT system (Bioscan, Washington, DC, USA). This system consists of four detectors (215 × 230 mm^2 NaI, 33 PMTs) equipped with interchangeable multipinhole apertures. Dynamic and SPECT/CT acquisitions were performed after IV injection of Gado-6Si-NP−^{111}In in 17 rats. Double phase (12 × 10 s images and 116 × 30 s images) dynamic acquisition was initiated immediately following the IV injection of Gado-6Si-NP−^{111}In in rats in supine position placed directly on the planar low-energy ultrahigh-resolution collimator set in order to verify the quality of the injection and analyze early organ nanoparticle uptake. X-ray CT (tube voltage of 55 kVp, exposure time of 500 ms, and 180 projections) and SPECT acquisitions were performed in rats in a supine position, placed in a temperature-controlled bed (Minerve, Esternay, France), in order to maintain body temperature (set to 37 °C). Afterward, the SPECT (20 000 cps per projection/20 projections) were acquired using a rat whole-body high-resolution aperture.

All image data was reconstructed and analyzed using InVivoScope (Bioscan, Washington, DC, USA).

In Vivo and Ex Vivo Optical Imaging. Fluorescence images as well as black and white pictures were acquired via a back-thinned CCD-cooled camera (ORCAIIBT-512G, Hamamatsu phonics, Massy, France) using a colored glass long-pass RG 665 filter (Melles Griot, Voisins les Bretonneaux, France), which cuts off all excitation light. Ventral, dorsal, and lateral views were acquired prior to Gado-6Si-NP injection in order to estimate the self-fluorescence level. Immediately after direct IV injection of 50 μL of Gado-6Si-NP in HEPES buffer containing 150 mM NaCl ([Gd] = 100 mM) in two nude Swiss mice under chemical anesthesia, a set of 2 s ventral (in one mouse) or dorsal (in the another mouse) images was acquired over 60 min. Ventral, dorsal, and lateral static views were then obtained using the parameters applied prior to injection. Euthanasia was performed 2 h after injection, and the liver, kidneys, brain, spleen, lungs, heart, skin, muscle, bone, and intestine were

Table 1. Biodistribution Data of Gado-6Si-NP—^{111}In in Wistar Rats[a]

	2 h (n = 3)	1 day (n = 3)	3 days (n = 4)	10 days (n = 3)	18 days (n = 4)
cadaver	21.67 ± 7.45	4.40 ± 1.08	3.68 ± 3.10	1.50 ± 0.54	1.18 ± 0.17
brain	0.01 ± 0.00	0.00 ± 0.00	0.05 ± 0.03	0.00 ± 0.00	0.00 ± 0.00
digestive tract	3.32 ± 0.79	1.58 ± 0.68	ND ± --	0.10 ± 0.04	0.09 ± 0.03
liver	2.97 ± 0.45	0.95 ± 0.33	1.14 0.41	0.33 ± 0.12	0.27 ± 0.03
heart	0.08 ± 0.01	0.01 ± 0.01	ND ± --	0.00 ± 0.00	0.00 ± 0.00
kidney	35.15 ± 7.77	17.73 ± 1.82	18.60 ± 1.12	6.77 ± 1.21	3.95 ± 0.41
lung	0.31 ± 0 0.04	0.03 ± 0.01	0.10 ± 0.09	0.02 ± 0.01	0.02 ± 0.01
muscles	0.12 ± 0.07	0.00 ± 0.00	ND ± --	0.00 ± 0.00	0.00 ± 0.00
bones	0.05 ± 0.03	0.01 ± 0.01	0.07 ± 0.04	0.00 ± 0.00	0.00 ± 0.00
skin	0.01 ± 0.01	0.00 ± 0.00	ND ± --	0.00 ± 0.00	0.00 ± 0.00
spleen	0.47 ± 0.23	0.28 ± 0.14	0.05 ± 0.02	0.09 ± 0.01	0.03 ± 0.01

[a] Data are expressed as percentage injected dose per gram of tissue (%ID/organ, mean ± standard deviation).

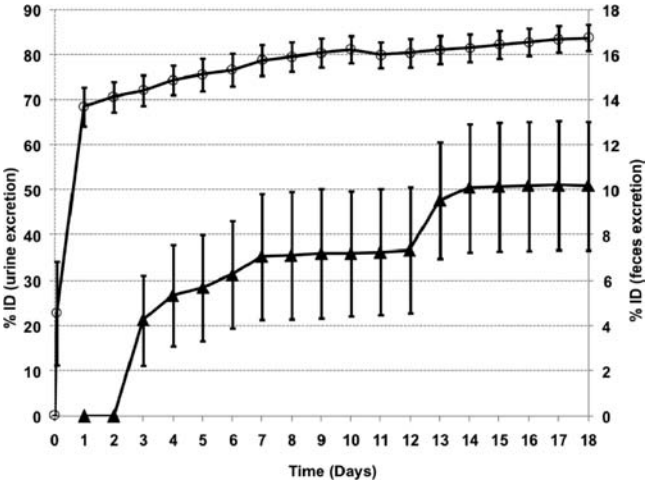


Figure 3. Elimination of Gado-6Si-NP—^{111}In after IV injection in Wistar rats. Values are expressed as percentage of cumulative activity measured in urine (circle) and feces (triangle) per injected dose (%ID). Data was expressed as mean ± standard deviation.

then collected in order to be imaged and compared with the same *ex vivo* organs of noninjected mice.

In Vivo MR Imaging. Two positioned supine Wistar rats were imaged using a 7-T system (Biospec; Bruker, Ettlingen, Germany) equipped with a 400 mT/m gradient under gaseous anesthesia. Three direction localizers were first used to localize kidneys, liver, and bladder. The imaging protocol consisted of a dynamic series of two coronal slices centered on the kidneys, bladder, and liver, and obtained using a T1-weighed MSME sequence (180° flip angle, 118/10.6 [repetition time ms/echo time msec], 3 mm section thickness, 100 mm field of view, 256−256 matrix, and 16.6kHz bandwidth) and respiratory triggered (Rapid Biomedical GmbH, Rimpor, Germany). Acquisition was initiated, and during the fourth repetition, bolus IV injection of 50 μL of Gado-6Si-NP in HEPES buffer containing 150 mM NaCl ([Gd] = 100 mM) was performed. Duration of each repetition was approximately 3 min. Rat body temperature was regulated at 37 °C. Positive enhancement of the signal (EHC) in each tissue was calculated as $(S_t - S_0)/S_0$, where S_t was the signal intensity value measured at each time after injection, and S_0 the signal value prior to injection.

RESULTS

NP Characterization. The nanoparticles used are core−shell particles with a core of gadolinium oxide. Gadolinium content was estimated to approximately 16% per particle. According to HRTEM (Figure 1), this core was well-crystallized with a bcc structure belonging to the *Ia*3 space group and with a size between 1.4 and 2 nm. This size is in line with the hydrodynamic diameter measured for the noncoated particles (Figure 2), of 1.2 ± 0.3 nm. After the hydrolysis−condensation, functionalization steps leading to the growth of a polysiloxane shell were evidenced by TEM and chemical analysis (EDX), and correlated with hydrodynamic diameter measured by DLS as 3.8 ± 0.1 nm (Figure 2). As previously stated, organic fluorophores conjugated to APTES were included during this coating step. This confers fluorescence properties to the hybrid gadolinium oxide nanoparticles.[20] Zeta potential measurements of Gado-6Si-NP in the pH range from 4 to 10 are shown in Figure 1. The iso-electric point was evaluated at pH 7−8.

Radiolabeling of Nanoparticles with ^{111}In. Gado-6Si-NP nanoparticles were labeled with $^{111}InCl_3$ in citrate buffer at pH 5. Nonspecifically bound ^{111}In was removed from Gado-6SiNP—^{111}In by adding excess DTPA, followed by a purification step using a PD-10 column. Nevertheless, a very small amount of radioactivity was separated from the nanoparticles by DTPA, indicating efficient and stable labeling. Following purification, radiochemical purity exceeded 99%. Radiochemical yield was 35 ± 3% (n = 10).

Solution Stability. Negligible radioactivity was lost from Gado-6Si-NP—^{111}In nanoparticles after 4 h incubation in both solutions. After 24 h and 7 days incubation, radiochemical purity was greater than 93% and 91%, respectively. This indicated that Gado-6Si-NP—^{111}In remained stable for at least 7 days in rat serum or aqueous 20 mM DTPA solutions.

Biodistribution Studies. When injecting a nontargeted nanoparticle using IV administration, optimal biodistribution should show dominant renal elimination, associated with the absence of reticulo-endothelial system uptake and the absence of significant uptake in other tissues.

Quantitative tissue distribution was performed over 18 days at 5 intervals (2 h, 24 h, 72 h, 10 days, and 18 days) following IV injection in order to evaluate the biodistribution of Gado-6Si-NP labeled with indium 111. Tissue distribution of Gado-6Si-NP expressed as the percentage injected dose per gram tissue as well as the percentage injected dose per organ are presented in

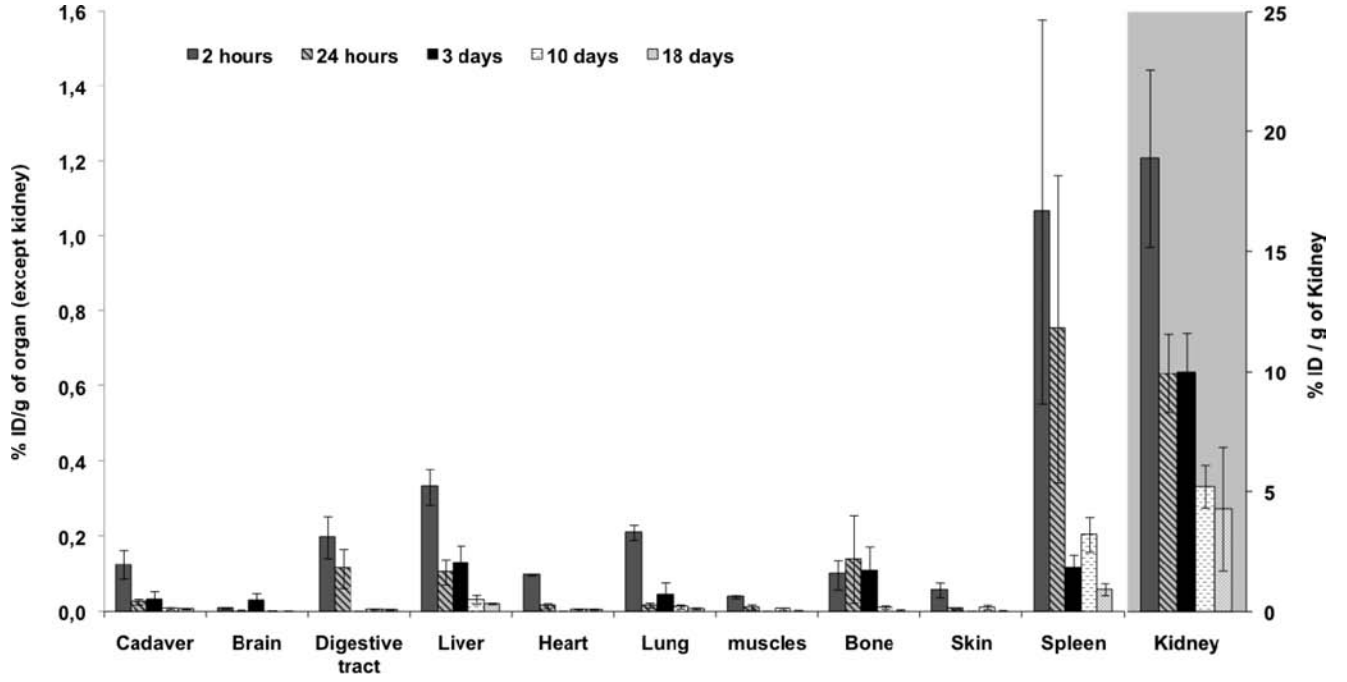


Figure 4. Biodistribution of Gado-6Si-NP—^{111}In in Wistar rats. Group of rats (n = 3 except at days 3 and 18, n = 4) were sacrificed at 2 h, 1 day, 3 days, 10 days, and 18 days after injection, and selected organs were sampled and measured for ^{111}In activity. Left axis: data is expressed as percent injected dose per gram of tissue (%ID/g). Right axis: data is expressed as percent injected dose per gram of kidney (shaded area).

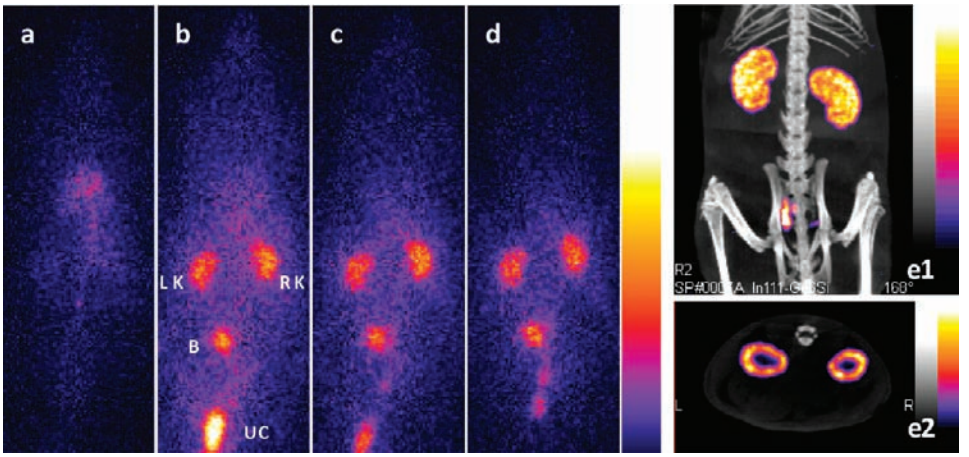


Figure 5. SPECT/CT *in vivo* imaging in Wistar rats. Planar sequential scintigraphic images acquired (a) during IV injection of 25 MBq of Gado-6Si-NP—^{111}In, (b) 15 min, (c) 30 min, and (d) 60 min after injection. Tomographic scintigraphy and X-ray CT of the whole body of the rat acquired at day 2, posterior projection (e1) and transversal slice (e2). LK: left kidney; RK: right kidney; B: bladder. UC: urine collector.

Figure 4 and Table 1. High levels of radioactivity were quickly observed in the kidneys after IV administration (35.2%ID/organ at 2 h), and were reduced from 18.6% at 3 days to 3.9% at 18 days. The blood circulation half-life of labeled Gado-6Si-NP was evaluated at 42 ± 3 min. Renal and liver excretion of Gado-6Si-NP were evaluated by measuring urine and feces activity, and expressed as cumulated radioactivity under total injected radioactivity (Figure 3). Gado-6Si-NP were dominantly and rapidly eliminated through renal excretion with 67 ± 4%ID and 84 ± 3% ID, compared to liver excretion with 4 ± 2%ID and 10 ± 3%ID after 1 day and 18 days, respectively, as demonstrated by the quantitative biodistribution study. Similar results were observed in scintigraphic imaging (Figure 5), MR imaging (Figure 6), and optical imaging (Figure 7), where injection signal increased rapidly in the kidneys, with initial increase in the cortex, followed by an increase in the pelvis and then the bladder. MRI dynamic acquisition (Figure 6) evidenced a moderately increased EHC signal (38% at 39 min) in the area of the liver, but this was not due to RES uptake, as no significant Gado-6Si-NP accumulation has been observed in the quantitative biodistribution analysis. This increase seems to be related to liver elimination of the Gado-6Si-NP, as radioactivity was found in the feces at later time points. The absence of Gado-6Si-NP accumulation in the liver, as well as in the spleen, lung, and bones (medulla) supported the absence of RES uptake (Table 1). This finding was confirmed using scintigraphic and optical imaging, where no significant signal was

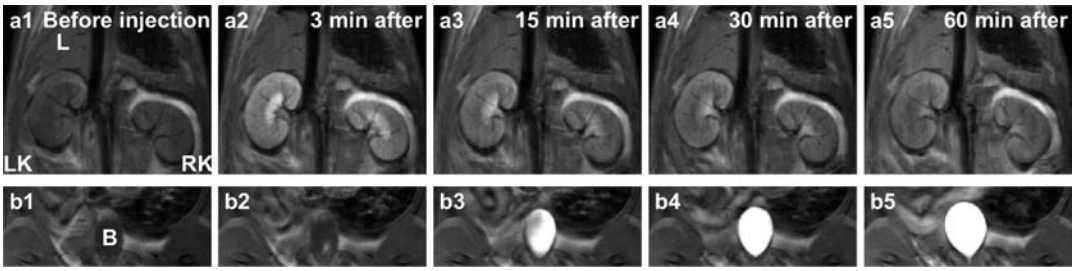


Figure 6. T1w.seq. coronal images acquired before and at 3, 15, 30, and 60 min after IV injection of 50 μL of Gado-6Si-NP, centered on kidneys (a) and bladder (b).

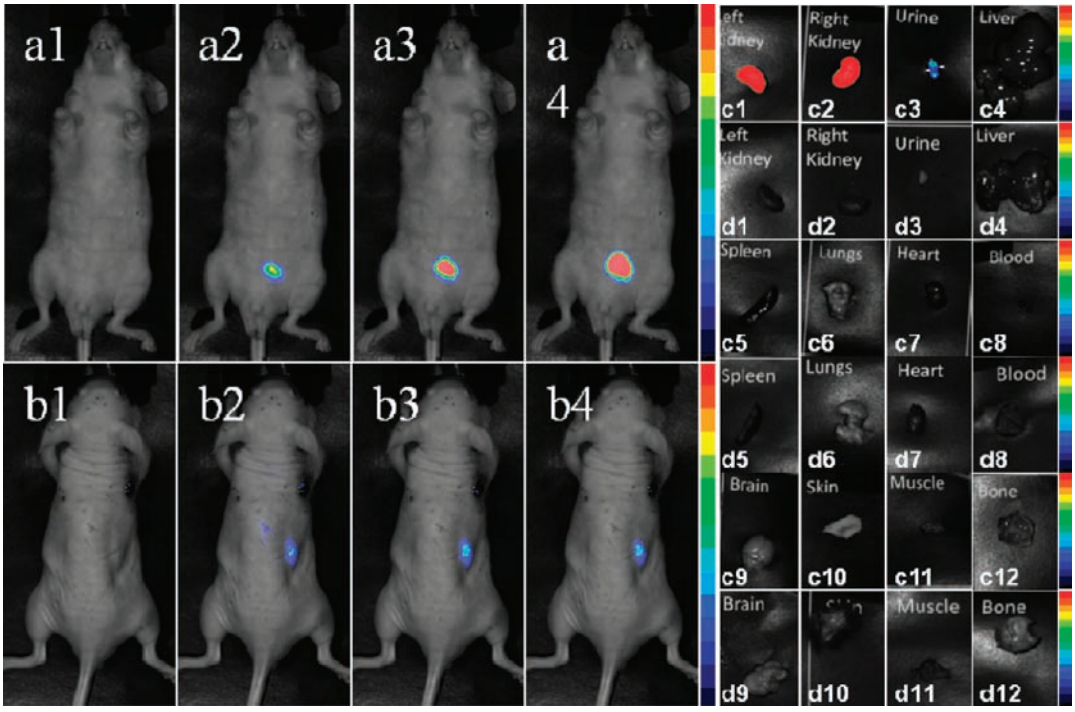


Figure 7. Ventral (a1,2,3,4) and dorsal (b1,2,3,4) planar fluorescence reflectance images acquired at the end of IV injection of Gado-6Si-NP (a1, b1), at 15 min (a2, b2), 30 min (a3, b3), and 60 min (a4, b4) postinjection. c 1 to 12: Fluorescence reflectance imaging of major organs after dissection of a nude mouse. Dissection was performed 2 h after IV injection of Gado-6Si-NP. d 1 to 12: Fluorescence reflectance imaging of some organs after dissection of a control nude mouse. Each image was acquired with an exposure time of 2 s.

seen in spleen, lung, and bones as shown in Figures 5 and 7. Finally, our study demonstrated the absence of brain uptake.

DISCUSSION

Quantitative *in vivo* biodistribution has shown that multimodal Gado-6Si-NP display excellent properties as contrast agents, with excellent renal filtration, and can be detected using different imaging modalities such as optical (fluorescence), MR, or isotopic (SPECT) imaging. This was an important step, as it is essential in determining the biodistribution and clearance of nanoparticles that may be used for imaging and theragnostic applications prior to their clinical use. Such a long-term quantitative distribution of silica nanoparticles has not yet been extensively reported.[21]

Overall, radiolabeling nanoparticles allows for whole-body imaging with high sensitivity and quantitative *ex vivo* biodistribution, which is considered to be a robust and reliable method for evaluating the *in vivo* behavior of a nanoprobe.[22] Nevertheless, the stability of the radiolabeling should be carefully controlled *in vitro* and *in vivo,* in order to ensure the accurate evaluation of *in vivo* biodistribution. No significant release of Indium 111 has been observed *in vivo,* as no significant bone uptake was measured, taking into account that trivalent radiometals such as indium are known to be taken up by bones[23] indicating an *in vivo* stability of the radiolabeling. Stability of the radiolabeling was also confirmed *in vitro*; due to their multimodal properties, it was possible to compare the biodistribution obtained using three different modalities in order to confirm the efficiency and stability of radiolabeling. In our study, indium 111 with a half-life of 2.8 days was used for this long-term biodistribution quantitative analysis over 18 days. Other radioisotopes could have been used to complex DTPA, such as technetium 99m (half-life: 6 h) or PET emitter gallium 68 (half-life: 1.13 h). However, due to their short half-lives, they were not suitable for long-term biodistribution assessment.

Biodistribution and clearance of nanoparticles depend on their chemical and biochemical properties such as size, surface functionality, and charge. In general, it is well-established that nanoparticles are taken up by the RES system following IV administration, leading to the clearance of nanoparticles from systemic circulation.[24]

In this study, a high rate of renal elimination of Gado-6Si-NP following IV injection was evidenced with more than 95% of Gado-6Si-NP eliminated 18 days after injection. Our γ-counting data revealed that Gado-6Si-NP showed minimal particle retention in major organs (especially RES tissue), and the major route of elimination was renal excretion (Table 1), which is consistent with results obtained from optical imaging, where the fluorescence signal could be observed in the urinary bladder and kidneys. This is attributed to the presence of hydrophilic molecules (DTPA), which functionalize these hybrid gadolinium oxide nanoparticles, as generally observed for other PEG-capped nanoparticles.[25−27] The derivatization of Gado-6Si-NP noticeably decreased liver retention and increased renal filtration into the bladder, whereas underivatized nanoparticles frequently accumulated in the liver and spleen.[17] This demonstrates that biodistribution and pharmacokinetics of Gado-6Si-NP were well-controlled. No significant Gado-6Si-NP accumulation was observed in lungs (Table 1). This result demonstrated that hydrophilic carboxylic DTPA coating prevents Gado-6Si-NP aggregation under *in vitro* and *in vivo* conditions, as usually observed with PEG coating.[28] Moreover, hydrodynamic particle size is known to be a key factor in the biodistribution of long-circulating nanoparticles,[16,29,30] and large nanoparticles tend to accumulate in the liver.[31] Burns et al.[15] have shown that the optimal probe size to obtain a reasonable circulation lifetime and efficient clearance is between 3 and 7 nm in hydrodynamic diameter, as the capillary pore diameter is estimated to be around 5 μm. The small size of these Gado-6Si-NP nanoparticles (mean diameter 3−4 nm) reduced plasma protein adsorption, opsonization, and hepatic filtration. Gado-6Si-NP can be effectively cleared out by renal excretion with more than 75%ID eliminated after 48 h, which is consistent with similar-sized probes.[13,14,32] Finally, another very interesting finding was the absence of significant uptake in any other tissues.

Since these nanoparticles are multimodal, they can be used with different imaging modalities, each modality having its own advantages and drawbacks.[33] MRI produces excellent spatial resolution, though sensitivity and specificity are critical issues. Optical imaging provides good sensitivity, but penetration of near-infrared light in tissues is limited to a few centimeters[34] with a high autofluorescence background, and with limited abilities to provide quantitative biodistribution *in vivo*. Isotopic imaging displays excellent sensitivity but low spatial resolution. Interests in multimodality imaging are numerous and offer many opportunities as multimodality imaging provides complementary information that cannot be discerned easily from one type of image modality alone, combining the benefits of each modality. The presence of gadolinium ions inside the organic shell, which is one the most efficient contrast agents for MRI, provides a strong positive contrast and allows for high-resolution soft tissue images *in vivo* (Figure 6), as predicted in a previous publication.[17]

In addition to imaging, the presence of gadolinium (atomic number $Z = 64$), which has a huge neutron capture cross section, provides opportunities for radiosensitization mainly based on the action of Auger electrons and γ-rays generated by ^{155,157}Gd after neutron capture.[35] Due to the high number of gadolinium ions per particle (about 40), irradiation of these hybrid gadolinium oxide nanoparticles has been shown to generate an *in vitro* cytotoxic effect.[36]

Finally, these nanoparticles exhibit multiple DTPA molecules (about 160 per particle) and can be functionalized with a large number of ligands, increasing the affinity to their biological target. The theragnostic approach of these nanoparticles, guided by multimodal imaging, allows us to envisage their application in oncology. Targeting these nanoparticles is currently being researched.

CONCLUSION

This study reports the *in vivo* biodistribution of hybrid gadolinium oxide nanoparticles using different imaging modalities and γ *ex vivo* counting. The biodistribution of these nanohybrid agents by MRI, optical and radionuclide, demonstrates that Gado-6Si-NP circulate freely in the blood pool, without RES uptake, and are eliminated by renal excretion. The understanding of the biodistribution and pharmacokinetics of nanoparticles is a key factor in the process of successfully developing new multimodal agents. Multimodal and quantitative biodistribution of this new category of nanoparticles shows promising properties that may enable us to develop them as targeted or nontargeted contrast media or therapeutic agents.

AUTHOR INFORMATION

Corresponding Author

*David KRYZA, Fédération Médecine Nucléaire - Radiopharmacie, Hôpital Edouard Herriot, 5 place d'Arsonval, 69437 Lyon cedex 03 - France. E-mail: david.kryza@chu-lyon.fr, Tel: +33 472 68 46 17, Fax: +33 472 11 69 57.

Author Contributions

⊥These authors contributed equally to this work.

ACKNOWLEDGMENT

This work was supported by the National Research Agency (ANR-PNANO).

REFERENCES

(1) Wagner, V., Dullaart, A., Bock, A. K., and Zweck, A. (2006) The emerging nanomedicine landscape. *Nat. Biotechnol. 24*, 1211–1217.

(2) Ferrari, M. (2005) Cancer nanotechnology: opportunities and challenges. *Nat. Rev. Cancer 5*, 161–171.

(3) Katz, E., and Willner, I. (2004) Integrated nanoparticle-biomolecule hybrid systems: synthesis, properties, and applications. *Angew. Chem., Int. Ed. 43*, 6042–6108.

(4) Chen, K., Li, Z. B., Wang, H., Cai, W., and Chen, X. (2008) Dual-modality optical and positron emission tomography imaging of vascular endothelial growth factor receptor on tumor vasculature using quantum dots. *Eur. J. Nucl. Med. Mol. Imaging 35*, 2235–2244.

(5) Jarrett, B. R., Gustafsson, B., Kukis, D. L., and Louie, A. Y. (2008) Synthesis of 64Cu-labeled magnetic nanoparticles for multimodal imaging. *Bioconjugate Chem. 19*, 1496–1504.

(6) Koole, R., van Schooneveld, M. M., Hilhorst, J., Castermans, K., Cormode, D. P., Strijkers, G. J., de Mello Donega, C., Vanmaekelbergh, D., Griffioen, A. W., Nicolay, K., Fayad, Z. A., Meijerink, A., and Mulder, W. J. (2008) Paramagnetic lipid-coated silica nanoparticles with a fluorescent quantum dot core: a new contrast agent platform for multimodality imaging. *Bioconjugate Chem. 19*, 2471–2479.

(7) Steiniger, S. C., Kreuter, J., Khalansky, A. S., Skidan, I. N., Bobruskin, A. I., Smirnova, Z. S., Severin, S. E., Uhl, R., Kock, M., Geiger, K. D., and Gelperina, S. E. (2004) Chemotherapy of glioblastoma in rats using doxorubicin-loaded nanoparticles. *Int. J. Cancer 109*, 759–767.

(8) Wang, B., Gou, M., Zheng, X., Wei, X., Gong, C., Wang, X., Zhao, Y., Luo, F., Chen, L., Qian, Z., and Yang, L. (2010) Co-delivery honokiol and doxorubicin in MPEG-PLA nanoparticles. *J. Nanosci. Nanotechnol. 10*, 4166–4172.

(9) Acharya, S., Sahoo, S. K. (2011) PLGA nanoparticles containing various anticancer agents and tumour delivery by EPR effect. *Adv. Drug. Deliv. Rev. 63*, 170−183.

(10) Lee, Y., Lee, H., Kim, Y. B., Kim, J., Hyeon, T., Park, H., Messersmith, P. B., and Park, T. G. (2008) Bioinspired surface immobilization of hyaluronic acid on monodisperse magnetite nanocrystals for targeted cancer imaging. *Adv. Mater. 20*, 4154–4157.

(11) Nehilla, B. J., Allen, P. G., and Desai, T. A. (2008) Surfactant-free, drug-quantum-dot coloaded poly(lactide-co-glycolide) nanoparticles: towards multifunctional nanoparticles. *ACS Nano 2*, 538–544.

(12) Sumer, B., and Gao, J. (2008) Theranostic nanomedicine for cancer. *Nanomedicine 3*, 137–140.

(13) Choi, H. S., Liu, W., Misra, P., Tanaka, E., Zimmer, J. P., Itty Ipe, B., Bawendi, M. G., and Frangioni, J. V. (2007) Renal clearance of quantum dots. *Nat. Biotechnol. 25*, 1165–1170.

(14) Kobayashi, H., and Brechbiel, M. W. (2005) Nano-sized MRI contrast agents with dendrimer cores. *Adv. Drug Delivery Rev. 57*, 2271–2286.

(15) Burns, A. A., Vider, J., Ow, H., Herz, E., Penate-Medina, O., Baumgart, M., Larson, S. M., Wiesner, U., and Bradbury, M. (2009) Fluorescent silica nanoparticles with efficient urinary excretion for nanomedicine. *Nano Lett. 9*, 442–448.

(16) Alexis, F., Pridgen, E., Molnar, L. K., and Farokhzad, O. C. (2008) Factors affecting the clearance and biodistribution of polymeric nanoparticles. *Mol. Pharm. 5*, 505–515.

(17) Bridot, J. L., Faure, A. C., Laurent, S., Riviere, C., Billotey, C., Hiba, B., Janier, M., Josserand, V., Coll, J. L., Elst, L. V., Muller, R., Roux, S., Perriat, P., and Tillement, O. (2007) Hybrid gadolinium oxide nanoparticles: multimodal contrast agents for in vivo imaging. *J. Am. Chem. Soc. 129*, 5076–5084.

(18) Bazzi, R., Flores, M. A., Louis, C., Lebbou, K., Zhang, W., Dujardin, C., Roux, S., Mercier, B., Ledoux, G., Bernstein, E., Perriat, P., and Tillement, O. (2004) Synthesis and properties of europium-based phosphors on the nanometer scale: Eu2O3, Gd2O3:Eu, and Y2O3:Eu. *J. Colloid Interface Sci. 273*, 191–197.

(19) Louis, C., Bazzi, R., Marquette, C. A., Bridot, J. L., Roux, S., Ledoux, G., Mercier, B., Blum, L., Perriat, P., and Tillement, O. (2005) Nanosized hybride particles with double luminescence for biological labeling. *Chem. Mater. 17*, 1673–1682.

(20) Fizet, J., Riviere, C., Bridot, J. L., Charvet, N., Louis, C., Billotey, C., Raccurt, M., Morel, G., Roux, S., Perriat, P., and Tillement, O. (2009) Multi-luminescent hybrid gadolinium oxide nanoparticles as potential cell labeling. *J. Nanosci. Nanotechnol. 9*, 5717–5725.

(21) Xie, G., Sun, J., Zhong, G., Shi, L., and Zhang, D. (2010) Biodistribution and toxicity of intravenously administered silica nanoparticles in mice. *Arch. Toxicol. 84*, 183–190.

(22) Schipper, M. L., Cheng, Z., Lee, S. W., Bentolila, L. A., Iyer, G., Rao, J., Chen, X., Wu, A. M., Weiss, S., and Gambhir, S. S. (2007) microPET-based biodistribution of quantum dots in living mice. *J. Nucl. Med. 48*, 1511–1518.

(23) Helbok, A., Decristoforo, C., Dobrozemsky, G., Rangger, C., Diederen, E., Stark, B., Prassl, R., and Von Guggenberg, E. (2010) Radiolabeling of lipid-based nanoparticles for diagnostics and therapeutic applications: a comparison using different radiometals. *J. Liposome Res. 20*, 219–227.

(24) Sadauskas, E., Wallin, H., Stoltenberg, M., Vogel, U., Doering, P., Larsen, A., and Danscher, G. (2007) Kupffer cells are central in the removal of nanoparticles from the organism. *Part Fibre Toxicol.* 4, doi:10.1186/1743-8977-4-10

(25) Moghimi, S. M., and Szebeni, J. (2003) Stealth liposomes and long circulating nanoparticles: critical issues in pharmacokinetics, opsonization and protein-binding properties. *Prog. Lipid Res. 42*, 463–478.

(26) Ballou, B., Lagerholm, B. C., Ernst, L. A., Bruchez, M. P., and Waggoner, A. S. (2004) Noninvasive imaging of quantum dots in mice. *Bioconjugate Chem. 15*, 79–86.

(27) Faure, A. C., Dufort, S., Josserand, V., Perriat, P., Coll, J. L., Roux, S., and Tillement, O. (2009) Control of the in vivo biodistribution of hybrid nanoparticles with different poly(ethylene glycol) coatings. *Small 5*, 2565–2575.

(28) Stelter, L., Pinkernelle, J. G., Michel, R., Schwartlander, R., Raschzok, N., Morgul, M. H., Koch, M., Denecke, T., Ruf, J., Baumler, H., Jordan, A., Hamm, B., Sauer, I. M., and Teichgraber, U. (2010) Modification of aminosilanized superparamagnetic nanoparticles: feasibility of multimodal detection using 3T MRI, small animal PET, and fluorescence imaging. *Mol. Imaging Biol. 12*, 25–34.

(29) Sun, X., Rossin, R., Turner, J. L., Becker, M. L., Joralemon, M. J., Welch, M. J., and Wooley, K. L. (2005) An assessment of the effects of shell cross-linked nanoparticle size, core composition, and surface PEGylation on in vivo biodistribution. *Biomacromolecules 6*, 2541–2554.

(30) Gupta, A. K., and Gupta, M. (2005) Synthesis and surface engineering of iron oxide nanoparticles for biomedical applications. *Biomaterials 26*, 3995–4021.

(31) Nagayama, S., Ogawara, K., Fukuoka, Y., Higaki, K., and Kimura, T. (2007) Time-dependent changes in opsonin amount associated on nanoparticles alter their hepatic uptake characteristics. *Int. J. Pharm. 342*, 215–221.

(32) Frangioni, J. V. (2003) In vivo near-infrared fluorescence imaging. *Curr. Opin. Chem. Biol. 7*, 626–634.

(33) Massoud, T. F., and Gambhir, S. S. (2003) Molecular imaging in living subjects: seeing fundamental biological processes in a new light. *Genes Dev. 17*, 545–580.

(34) Hwang, D. W., Ko, H. Y., Kim, S. K., Kim, D., Lee, D. S., and Kim, S. (2009) Development of a quadruple imaging modality by using nanoparticles. *Chemistry 15*, 9387–9393.

(35) Cerullo, N., Bufalino, D., and Daquino, G. (2009) Progress in the use of gadolinium for NCT. *Appl. Radiat. Isot. 67*, S157–160.

(36) Bridot, J. L., Dayde, D., Riviere, C., Mandon, C., Billotey, C., Lerondel, S., Sabattier, R., Cartron, G., Le Pape, A., Blondiaux, G., Janier, M., Perriat, P., Roux, S., and Tillement, O. (2009) Hybrid gadolinium oxide nanoparticles combining imaging and therapy. *J. Mater. Chem. 19*, 2328–2335.

Bioconjugate Chemistry

ARTICLE

pubs.acs.org/bc

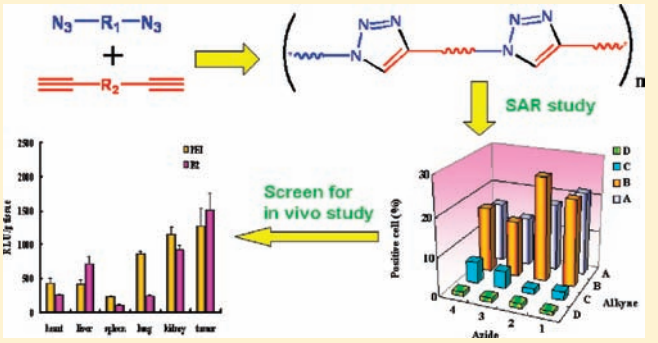
Linear Cationic Click Polymers/DNA Nanoparticles: In Vitro Structure−Activity Relationship and In Vivo Evaluation for Gene Delivery

Yu Gao, Qi Yin, Lingli Chen, Zhiwen Zhang, and Yaping Li*

Center of Pharmaceutics, Shanghai Institute of Materia Medica, Chinese Academy of Sciences, Shanghai 201203, China

Supporting Information

ABSTRACT: The aim of this work was to explore the structure−activity relationships (SAR) of a series of novel linear cationic click polymers with various structures for in vitro gene delivery and in vivo gene transfer. The experimental results revealed that the minimal structure variation could result in a crucial effect on DNA-binding ability, buffering capacity, and the cellular delivery capacity of polymer, all of which brought about the obvious effects on their transfection efficiencies. The polymer synthesized from diazide monomer containing bis-ethylenediamine unit and dialykene monomer containing bis-ethylene glycol unit (B_2) could effectively condense DNA into complex nanoparticles (B_2Ns), which showed the highest in vitro transfection efficiency. The biodistribution and transfection efficiency of B_2Ns in nude mice bearing tumor demonstrated the ability of effectively delivering DNA into tumor tissue. These results implied that this gene vector based on linear cationic click polymer could be a promising gene delivery system for tumor gene therapy.



INTRODUCTION

One of the hurdles to successful application of gene therapy is the development of a safe and efficient gene vector.[1,2] Nonviral vectors, in particular, cationic polymers, have received increasing attention due to easy manufacturing and low immunogenicity, which are commonly associated with the viral vectors.[3,4] However, nonviral vectors show less efficacy than viral vectors because of a lack of adequate function to overcome the intracellular barriers for efficient gene delivery.

Recently, many strategies have been undertaken in polymer science to realize the full potential of gene therapy. The modification of the existing polymers with functional groups such as imidazoles or targeting ligands to overcome the entry-based barriers is an effective tool to improve transfection efficiency.[5−7] Synthesis of biodegradable polycations containing a hydrolyzable ester bond or enzyme-degradable amide bond is one of the potential means to reduce the intrinsic toxicities of polymers.[8−10] The use of low molecular weight polymers, which can be eliminated via the kidney, is also a logical choice to increase safety.[11] However, there are still many problems in the existing cationic polymers, and the ideal polymers for gene transfer have not been found yet. Thus, the rational design of the biocompatible polymers that are well-defined and chemically tailored for clinical application of gene therapy remains a significant challenge.

Cationic polymers mediate gene transfer via condensing genes into nanometer-scale structure small enough to enter cells via endocytosis and intracellular trafficking of the genes.[12] Several recent reports have revealed that the related cationic polymers with small structural changes could result in a significant difference in transfection efficiency.[13−15] Polyplexes from poly(aspartamide) bearing two different side chains with one methylene variation showed completely different transfection and cytotoxicity profiles.[13] Altering the hydroxyl number and stereochemistry by the carbohydrate moieties in poly(glycoamidoamine)s resulted in dissimilar gene expression profiles.[14] Therefore, parallel synthesis and study on the structure−activity relationships (SAR) could be a powerful approach for the rapid identification of novel polymers for efficient gene delivery.[16,17]

The copper-catalyzed azide−alkyne cycloaddition has emerged as a unique ligation method combining selective reactivity and easy manufacturing,[18,19] and is used in a variety of polymer syntheses including the linear polymer, in which the azide- or alkyne-functionalized monomers could be easily tailored to form the different copolymers with different chemical and biological properties.[20,21] The amide−triazole moiety, which was formed during polymerization, could be an H-bond acceptor and increase the hydrophobic interactions of the polymer with DNA, thus improving the polymer−DNA binding stability.[22] Therefore, we

Received: January 5, 2011
Revised: March 17, 2011
Published: May 12, 2011

ACS Publications © 2011 American Chemical Society

could take advantage of the characteristics of click polymerization to develop a gene delivery system based on linear cationic click polymers (CPs). The amide−triazole moiety in the CP backbone could promote the strong polymer−DNA complexation and increase the serum stability of complexes. With the azide- or alkyne-functionalized monomers varied, the differences in efficacy between two polymers could be easily investigated to find out how the structural units affected the characteristics of the polymers or which structural unit played a key role during gene transfer. Consequently, the polymers that were designed to be nontoxic and effective could be found through the SAR study.

In our previous work, a series of novel linear CPs were designed and synthesized with various structural changes including the type of charge groups, the number of methylene or ethylene glycol groups, and the distance between charge groups, and the biocompatibility of CPs were evaluated.[23] From study based on the structure-biocompatibility relationships, we chose two CPs with good biocompatibility to preliminarily evaluate their in vitro transfection efficiency. The two CPs showed in vitro effective gene transfection, which indicated that CPs could be promising gene carriers and inspired us to investigate the behaviors of these CPs during gene transfer further. In this work, we aimed to explore the in vitro SAR of these click polymers and in vivo gene transfer. We examined the DNA-binding efficiency, buffering capacity, cellular uptake of DNA, and in vitro transfection efficiency of these polymers and tried to find out how the structural units affected the characteristics of the polymers, and which structural unit played a key role during gene transfer. Finally, a candidate polymer from the SAR was selected for the investigation of in vivo gene transfer.

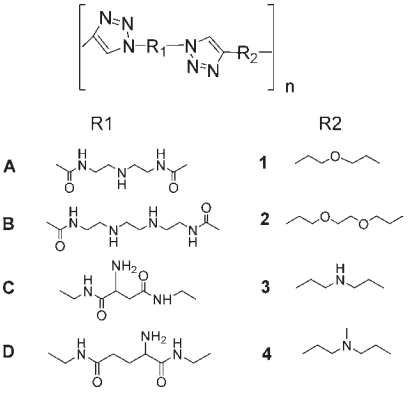
EXPERIMENTAL PROCEDURES

Materials. Trypsin-EDTA, phosphate buffered saline (PBS), and agarose were obtained from Gibco-BRL (Burlington, ON, Canada). The Dulbecco's modified Eagle medium (DMEM), RPMI 1640 medium, antibiotics, DNA loading buffer, and fetal bovine serum (FBS) were purchased from Invitrogen GmbH (Karlsruhe, Germany). YOYO-1 was purchased from Molecular Probes (Eugene, OR, USA). Ethidium bromide, trypan blue, and branched polyethylenimine (PEI, 25 kDa) were purchased from Sigma (St. Louis, MO, USA). Sixteen click polymers were synthesized using "click chemistry" and named $\mathbf{A_1}$−$\mathbf{A_4}$, $\mathbf{B_1}$−$\mathbf{B_4}$, $\mathbf{C_1}$−$\mathbf{C_4}$, and $\mathbf{D_1}$−$\mathbf{D_4}$ as described in our previous work (Scheme 1).[23] All other chemicals and solvents if not mentioned were of analytical grade and used as received without additional purification.

Plasmid EGFP-N1 (4.7 kb) encoding enhanced green fluorescent protein driven by immediate early promoter of CMV was purchased from Clontech (Palo Alto, CA, USA), and plasmid DNA containing random sequences was used as negative control (neg-DNA). pGL3-control vector was purchased from Promega (Madison, WI, USA). The plasmid DNA (pDNA) grown in DH5α strain of *E. coli* was isolated with the EndFree Plasmid Mega Kit (Qiagen GmbH, Hilden, Germany). The purity was confirmed by spectrophotometry (A260/A280), and DNA concentration was measured by UV absorption at 260 nm.

Cell Cultures. The cell lines HEK 293 (human embryonic kidney cell) and MDA-MB-468 (human breast cancer cell) cells were obtained from the American Type Culture Collection (ATCC, Manassas, VA, USA). HEK 293 cells were grown in DMEM containing 10% fetal bovine serum (FBS), 100 U/mL penicillin G sodium, and 100 μg/mL streptomycin sulfate. MDA-MB-468 cells were cultured in RPMI 1640 medium supplemented with 10% FBS and 1% antibiotics (100 U/mL penicillin G and 0.1 mg/mL streptomycin). Cells were maintained at 37 °C in a humidified and 5% CO_2 incubator.

Scheme 1. Cationic Click Polymers Used in This Study



Animals. BALB/c nude mice (18−20 g, 6 weeks old) were purchased from Shanghai Experimental Animal Center (Shanghai). All animal procedures were performed according to the protocol approved by the Institutional Animal Care and Use Committee at the Shanghai Institute of Materia Medica, Chinese Academy of Sciences.

Preparation and Characteristics of CP/DNA Complex Nanoparticles (CPNs). CPNs were prepared by the following procedures: briefly, pDNA (100 μg/mL) dissolved in sterile water was added to the CP solution diluted in sterile water with equal volume to obtain the desired polymer-amine to DNA-phosphate ratio (N/P ratio). Subsequently, solution was immediately vortexed for 30 s (XW-80A Votex mixer, Shanghai). The complex nanoparticles were allowed to sit at room temperature for 30 min. As positive control, PEI 25K/DNA complex nanoparticles (PEINs) were prepared with the same procedure as CPNs.

The particle size and zeta potential of CPNs were determined by the laser light scattering measurement using a Nicomp 380/ZLS zeta potential analyzer (Particle Sizing System, USA). The CPNs were prepared as described above, and the size measurement was performed at 25 °C at a 90° scattering angle and recorded for 300 s for each measurement.

The formation of CPNs was evaluated by agarose gel electrophoresis. After the DNA loading buffer was added to CPNs, CPNs containing 0.1 μg DNA at various N/P ratios were applied to a 1.0% agarose gel in Tris-acetate-EDTA (TAE) buffer containing 0.5 μg/mL ethidium bromide. Electrophoresis was carried out at 80 V for 45 min in TAE buffer. The resulting DNA migration pattern was revealed under UV irradiation.

Acid−Base Titration. The buffer capacity of CP was determined by acid−base titration assay over the pH values ranging from 10 to 2 as described previously.[24] Each CP was dissolved in 150 mM NaCl solution at an amino group concentration of 5 mM. The pH of the polymer solution was raised to 10 using 1 M NaOH. The resulting solution was then incrementally titrated with 0.1 M HCl. The pH of the solution was monitored with a Sartorius PB-10 pH meter. The experiment was performed at room temperature, each data point was collected at about 5 min after addition of the acid, and the time interval was the same

for all the samples. The pH profile was obtained for each polymer, and graphs of the data were generated accordingly.

Cellular Uptake Experiment. MDA-MB-468 cells were seeded in a 24-well plate with 0.5 mL growth medium and allowed to attach for 24 h. Nanoparticles were prepared at N/P ratio 32 for CPs with YOYO-1-labeled DNA concentration of 50 μg/mL. The DNA/YOYO-1 complex was prepared with 1 nM dye molecule/μg DNA and incubated 1 h at room temperature in the dark. The cells were then incubated with CPNs (DNA concentration 2.5 μg/well) in complete growth medium for 2 h at 37 °C followed by washing three times with PBS (pH 7.4), then trypsinized and resuspended in the medium. The residual fluorescence out of the cell membrane was quenched with 0.4% trypan blue for 2 min.[25] Then, cells were centrifuged and washed three times with PBS. The cell resuspension was finally subjected to flow cytometry (FACSCalibur, Becton Dickinson, USA) and analyzed with *CellQuest* software through fluorescence channel 1 (FL1).

Observation of Intracellular Distribution of CPNs. MDA-MB-468 cells were seeded on 35 mm glass-based dishes with 0.5 mL growth medium and allowed to attach for 24 h. After incubation with CPNs (N/P ratio 32, DNA concentration 2.5 μg/well) for 2 h at 37 °C, the medium was removed, and the cells were washed three times with PBS. The intracellular distribution of CPNs was observed by confocal laser scanning microscopy (CLSM) after staining lysosomes with LysoTracker Red (Molecular Probes, Eugene, OR, USA) and nuclei with Hoechst 33342 (Sigma, USA). The CLSM observation was performed using Leica TCS SP2 confocal spectral microscope (Leica Microsystems, Germany) with a 63× objective (Leica, Wetzlar, Germany) at excitation wavelengths of 633 nm (He−Ne laser), 488 nm (Ar laser), and 351 nm (UV laser) for LysoTracker Red (red), YOYO-1 (green), and Hoechst 33342 (blue), respectively.

In Vitro Transfection Experiment. Cells (HEK 293 and MDA-MB-468) were seeded in 24-well plates at a density of 1×10^5 cells per well in 500 μL of complete medium and incubated for 24 h prior to transfection. Then, the media were replaced with fresh complete growth medium containing CPNs with DNA concentration 2.5 μg/well at various N/P ratios. Media were replaced by fresh culture medium after 24 h, and cells were incubated for an additional 24 h. The expressed green protein could be observed under a fluorescence microscope. Finally, cells were collected and resuspended in PBS (pH 7.4). The transfection results were measured using a FACSCalibur through FL1 and the percentage of cells which expressed EGFP was counted (Supporting Information Figure S1). As control, naked DNA and click polymers/neg-DNA complex nanoparticles were used on cell cultures and examined as described above. As positive control, PEINs with mass ratio of 3 were prepared and transfected with media without FBS for 2 h before the medium was replaced with fresh complete growth medium.

In Vivo Biodistribution and Transfection Efficiency. For biodistribution study, female nude mice were inoculated with 100 μL of phosphate buffered saline (pH 7.4) containing 1×10^6 MDA-MB-468 cells by subcutaneous injection in the left flank. Tumors were allowed to grow to a volume of 200−300 mm^3. For qualitative evaluation, B_2/DNA nanoparticles (B_2Ns) with pDNA labeled by the cell-impermeable fluoresecnt dye YOYO-1 at N/P ratio 32 was injected into mice bearing breast tumor via the tail vein at a dose of 2 mg/kg. Mice were sacrificed at different time intervals after injection (n = 4 at each time point), and the principal organs were isolated. The extracted tissues were homogenized with lysis buffer (Promega, Madison, WI, USA), and the samples were centrifuged at 10 000 rpm for 5 min. The supernatant was measured using a microplate reader (Infinite F200, TECAN, Austria) with an excitation at 485 nm and exmission at 520 nm. The data were normalized to the tissue weight.

For in vivo transfection efficiency, female nude mice were inoculated with 100 μL of phosphate buffered saline (pH 7.4) containing 1×10^6 MDA-MB-468 cells by subcutaneous injection in the left flank. Experiments were performed at day 10 after inoculation when the tumor volume reached approximately 100 mm^3. For quantitative evaluation, B_2Ns formed with pGL3-contral vector at N/P ratio 32 were injected into the mice bearing breast tumor via the tail vein at a dose of 2 mg/kg in a 200 μL injection volume. For comparison, PEINs at mass ratio 1 were intravenously injected at the same DNA dosage. Animals were killed 48 h after i.v. injection, and the tissues were isolated. The organs were washed with cold saline and then homogenized with 1 mL lysis buffer using a tissue homogenizer. The homogenate was centrifuged at 15 000 × g for 15 min, and the luciferase activity was quantified by Luciferase Assay System using a chemiluminometer (NOVOSTAR, German). Relative light units (RLU) were measured for 5 s at room temperature, and the transfection efficiency was expressed as RLU/g tissue.

Statistical Analysis. Statistical analysis was performed using a Student's t-test. The differences were considered significant for p value < 0.05 and p < 0.01 indicative of a very significant difference.

RESULTS AND DISCUSSION

Buffering Capacity of CPs. It was assumed that the buffering capacity of cationic polymers like PEI could facilitate the endosomal escape of polyplexes by so-called "proton sponge effect". This capacity was a relevant physicochemical parameter in the transfection efficiency of the cationic polymer.[24,26] In order to understand the relationship between polymer buffering capacity and polymer structure, and how the buffering capacity affected the transfection efficiency of polymer, the acid−base titration experiment was performed to estimate the buffering capacity of CPs (Figure 1). The titration was monitored over the range of pH 10−2.0 in 150 mM NaCl solution to mimic the physiological condition.

It was expected that the presence of different amino groups with different pK_a would increase the buffer capacity of polymer. However, the titration curves did not show such trends. The flat slope in pH 5−7 which was relevant to the overall gene transfection process indicated the higher buffer capacity of CPs containing only one type of amine than that of CPs with two types of amine. $\mathbf{C_1}$, $\mathbf{C_2}$, $\mathbf{D_1}$, or $\mathbf{D_2}$ showed some buffering capacity in pH 5−7 (Figure 1C,D). When tertiary amine or secondary amine was added to CP, the buffering capacity of $\mathbf{C_3}$, $\mathbf{C_4}$, $\mathbf{D_3}$, or $\mathbf{D_4}$ decreased significantly, which was also found in polymers $\mathbf{A_4}$ and $\mathbf{B_4}$. $\mathbf{C_4}$ and $\mathbf{D_4}$ showed higher buffering capacity than $\mathbf{C_3}$ and $\mathbf{D_3}$, respectively, which demonstrated that CPs containing primary amine and tertiary amine had higher buffering capacity than polymers with primary amine and secondary amine (Figure 1C,D). $\mathbf{A_4}$ and $\mathbf{B_4}$ showed obviously low buffering capacity, which indicated that polymers containing both secondary amine and tertiary amine had weak ability in accepting hydrogen ions. From the above-mentioned, it was found that the different types

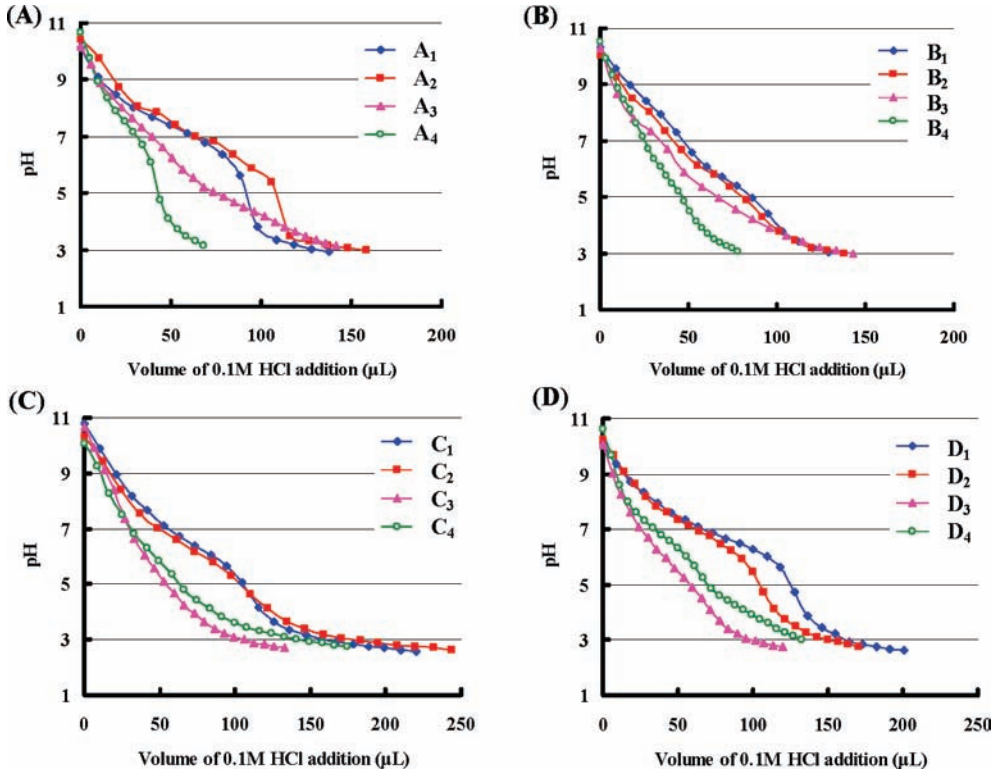


Figure 1. Titration curves of CPs at an amino group concentration of 5 mM.

of amines in CPs contributed differently to the buffering capacity of CPs.

The different polymers with the same secondary amine showed different buffering capacities. The buffering capacity of polymers in pH 5−7 decreased as the number of amines increased in the repeat unit ($\mathbf{A_1}$ > $\mathbf{B_1}$, $\mathbf{A_2}$ > $\mathbf{B_2}$), and also decreased as the number of amines increased in different monomers ($\mathbf{A_1}$ > $\mathbf{A_3}$, $\mathbf{B_1}$ > $\mathbf{B_3}$) (Figure 1A,B), which could be due to the protonation of an amine group electrostatically suppressed the protonation of the neighboring amines.[21] As a result, the correlation between the buffering capacity and polymer structure was not as direct as the correlation between the amount of the buffering groups and the structural variations.

Finally, the effects of methylene moiety and the ethylene glycol unit on the buffering capacity of CPs were evaluated. No obvious difference was found between polymers containing monomer **C** and **D** (Figure 1C,D), which indicated that the influence of the methylene moiety on the buffering capacity was negligible. The buffering capacities of polymers synthesized by monomers **A**, **B**, and **C**, but not monomer **D**, increased with ethylene glycol group in the polymer backbone increasing.

DNA Binding Ability. For efficient gene transfer and expression, the polymer should have the ability to condense DNA into nanoparticles and consequently mediated cell entry via endocytosis. CPs were examined for their ability to bind negative plasmid EGFP-N1 using a gel electrophoretic shift assay (Figure 2). Each polymer was combined with pDNA to form CPNs at various N/P ratios between 1 and 64. N/P ratios were calculated by the number of amine groups in the polymer repeat unit but not the amide nitrogens. All four CPs synthesized by monomer **A** or **B** could form complexes with DNA efficiently, it could be observed that the free DNA band completely disappeared at N/P ratio 2 for $\mathbf{A_1}$-$_4$ or $\mathbf{B_1}$-$_4$. $\mathbf{A_3}$ and $\mathbf{B_3}$ showed the strongest DNA binding ability with complete binding DNA at N/P ratio 1. However, CPs synthesized from monomer **C** or **D** could not bind DNA efficiently. $\mathbf{D_1}$ could not bind DNA completely even at N/P ratio 64. The differences in number and type of amines in the polymer backbone strongly affected its DNA binding ability. In the case of one type of amine in the polymer backbone, it was obvious that the secondary amine showed a stronger ability in DNA binding than primary amine in CP backbone by comparing $\mathbf{A_1}$-$_2$ with $\mathbf{C_1}$-$_2$. In the case of two types of amines in the polymer backbone, polymers with different combinations of amine types showed different DNA binding abilities. $\mathbf{C_4}$ showed greatly improved DNA binding ability compared with $\mathbf{C_1}$-$_2$ when tertiary amine was introduced into the backbone of the original polymer which only has a primary amine. However, no obvious difference was observed between $\mathbf{C_3}$ and $\mathbf{C_1}$-$_2$. By comparing $\mathbf{A_4}$ with $\mathbf{A_3}$ or $\mathbf{B_4}$ with $\mathbf{B_3}$, we could find that the DNA binding ability decreased a little by replacing the secondary amine with the tertiary amine. Comparing **C** series with **D** series, it was found that one more methylene group in the polymer backbone could greatly reduce the DNA binding ability no matter the types of amines on the polymer backbone. No obvious difference was observed between polymers containing **1** and **2**, which indicated that the influence of the ethylene glycol moiety on the DNA binding ability was neglectable. These results demonstrated that, besides the electronic interaction between polymer and DNA, other interactions such as hydrophobic interactions or $\pi-\pi$ interactions might also be very important.

Particle size is one of the important factors influencing the internalization of complexes. The size of particles less than 200 nm could be preferably internalized into most types of cells,[27] and a positive surface charge could lead to great interaction with the

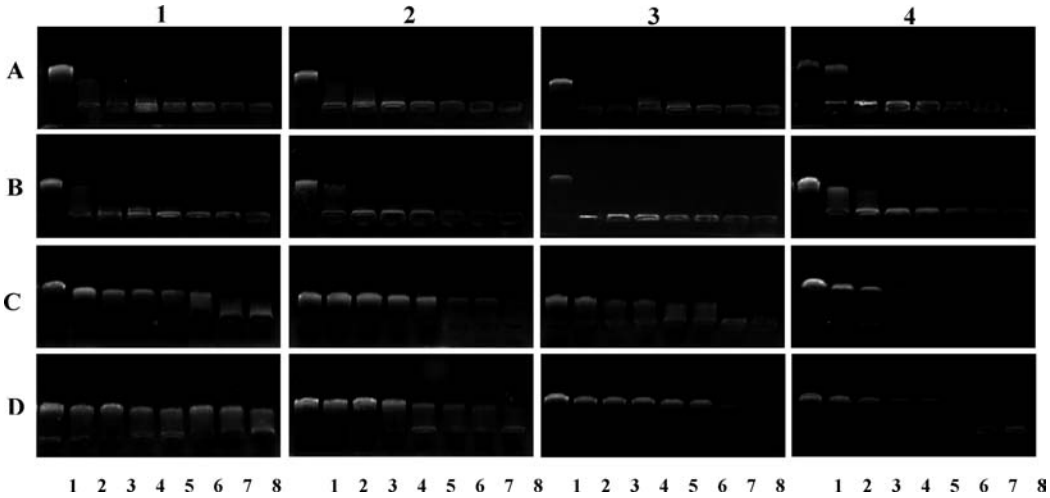


Figure 2. Agarose gel electrophoresis of CPNs at various N/P ratios. Lane 1: naked DNA control. Lanes 2 to 7: complexes prepared at N/P ratios of 1, 2, 4, 8, 16, 32, and 64 in water, respectively.

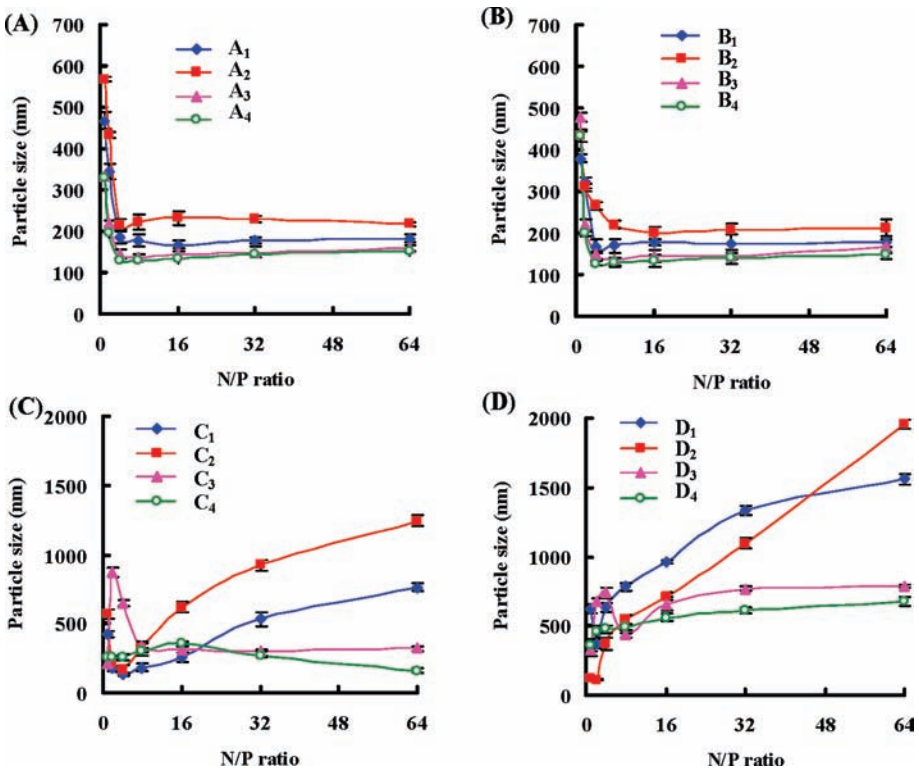


Figure 3. Average particle size of CPNs at different N/P ratios.

negative cell membrane.[28] In this study, all CPs could form nanoparticles with DNA in water. The average particle size of CPs as a function of N/P ratio was evaluated. Figure 3 showed some clear correlations between CP structure and the particle size. Polymer **A** series and **B** series formed smaller particles than polymer **C** series or **D** series, and showed constant particle sizes as N/P ratios increasing from 4 to 64. These results were in good agreement with the agarose gel electrophoresis assay that polymer **A** or **B** series showed stronger DNA binding ability with condensing DNA into smaller particles than polymer **C** or **D** series. Replacement of the azide-functionalized monomers containing ethylene glycol groups with monomers containing secondary amines or tertiary amines could significantly decrease the particle size of complex nanoparticles. The particle size of complex nanoparticles of **A**, **B**, or **C** series obviously increased with the ethylene glycol group in polymer backbone increasing. These results demonstrated that the polymers with higher amine density could yield stronger DNA condensation ability. Except C_4, the average sizes of polymer **C** series or **D** series increased with N/P ratio increasing, especially the polymers synthesized by azide-functionalized monomers containing the ethylene glycol groups. It was reported that the different polyplexes showed

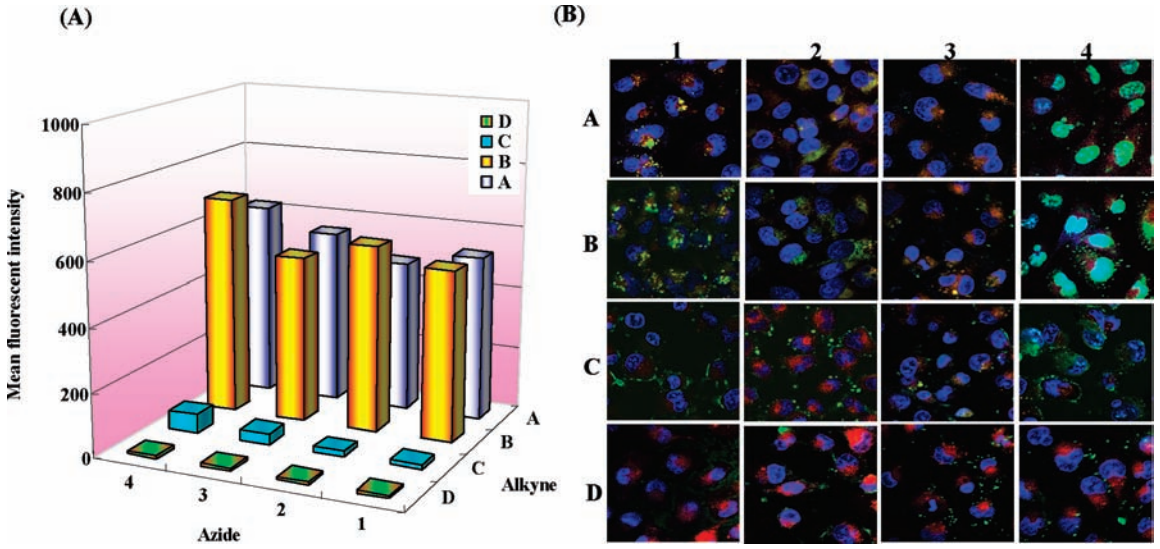


Figure 4. Cellular uptake (A) and intracellular distribution (B) of YOYO-1 labeled pDNA complexed with CPNs at N/P ratio 32 in MDA-MB-468 cells. Cells were incubated with CPNs with DNA concentration 5 μg/mL for 2 h. The nucleus and lysosome were stained by Hoechst 33342 (blue) and LysoTracker (red), respectively.

different structural property such as rods, toroids, aggregates, flower-like structures, and nanoparticles, and the molecular morphologies were strongly dependent on the charge ratios and polymer properties.[29] Polymer-DNA showed different condensate formation at different charge ratios. We assumed that complex nanoparticles formed by $\mathbf{C_1}$-$_2$ or $\mathbf{D_1}$-$_2$ could have more incompact structures at higher charge ratios.

Cellular Delivery of CPNs. The ability of different polymers to mediate the cellular uptake of DNA was measured in MDA-MB-468 cells by introducing a fluorescence based flow cytometry protocol. The pDNA was labeled with YOYO-1, an intercalating dye with a high affinity to DNA. The average fluorescence intensity per cell could be quantitatively assessed via flow cytometry. By this technique, the pDNA delivery efficiency could be directly determined as a function of polymer structure. Cells were incubated with complexes formed at the same N/P ratio of 32 for 2 h. There seems to be a positive correlation between DNA binding ability of CPs and cellular uptake of the corresponding CPNs. As shown in Figure 4A, the polymers synthesized by monomer **A** or **B** showed superior cellular uptake to monomer **C** or **D**. Due to the inefficiency in complexing DNA, nanoparticles formed by polymer **D** series showed negligible cellular uptake. In polymer **C** series, the cellular uptake of CPNs could increase by introducing a secondary amine or tertiary amine into the polymer backbone. The stronger DNA binding ability of $\mathbf{C_4}$ could be the main contribution to the cellular uptake. In polymers synthesized by monomers **A** and **B**, the replacement of the ethylene glycol unit with a tertiary amine in the polymer backbone could increase cellular uptake of CPNs, but not the secondary amine, which demonstrated that the polymer with a different amine would facilitate cellular DNA uptake. More ethylene glycol units in the polymer backbone synthesized using monomer **B** could increase cellular uptake, while the opposite result was acquired in polymers synthesized using monomer **A**.

The intracellular distribution of CPNs was further investigated with pDNA labeled by YOYO-1 (green), and nucleus and lysosome stained by Hoechst 33342 (blue) and LysoTracker (red), respectively. The intracellular distribution of different CPNs in MDA-MB-468 cells after 2 h incubation was significantly different (Figure 4B). The polymers synthesized using monomer **A** or **B** could facilitate the YOYO-1 labeled DNA into the whole cytoplasm. However, the green fluorescence was mostly around the cell membrane in cells treated with CPNs formed by polymers synthesized using monomer **C** or **D**, which were accordant with the result from flow cytometry. With the cellular uptake improved by introducing tertiary amine into the polymer backbone, the green fluorescence could be seen inside cells when incubated with complexes formed by $\mathbf{C_4}$. However, the colocalization of green and red fluorescence could not be easily observed, which demonstrated that the complexes formed by $\mathbf{C_4}$ endocytosed into cells were not sequestrated in lysosomes. In confocal images of cells treated with CPNs formed by $\mathbf{A_3}$ or $\mathbf{B_3}$, obvious yellow regions where YOYO-1 labeled DNA was localized in lysosomes could be observed, which suggested the segregation of YOYO-1 labeled DNA in lysosomal compartments without diffusing into cytoplasm. The confocal images of cells treated with CPNs formed by $\mathbf{A_1}$, $\mathbf{A_2}$, $\mathbf{B_1}$, or $\mathbf{B_2}$ displayed much more green regions in cytoplasm, which indicated that $\mathbf{A_1}$, $\mathbf{A_2}$, $\mathbf{B_1}$, or $\mathbf{B_2}$ complexes showed good endosomal escaping behavior which was consistent with the results of the buffering capacity. However, to our surprise, the green fluorescence was mostly in neclei when cells were incubated with complexes formed by $\mathbf{A_4}$ or $\mathbf{B_4}$, which had poor buffering capacity. Membrane destabilization of cationic polymers under different pH conditions was reported recently.[20] Membrane destabilization happened at either the acidic pH in the late endosomal compartment or the physiological pH at the cytoplasm, and would perturb either the membranes of cytoplasmic vesicles or organelles at physiological pH. In our previous study about the structure−biocompatibility relationship of these click polymers, polymers $\mathbf{A_4}$ and $\mathbf{B_4}$ demonstrated severe cytotoxicity and could disturb the erythrocyte membrane with high hemolysis ratio.[23] So, we inferred that these two polymers could have strong membrane destabilization effects, and the injury of the nuclear membrane would facilitate the nuclear delivery of DNA.

Transfection Efficiency of CPNs. In our pre-experiment, we found that most of the 16 CPNs showed the best transfection

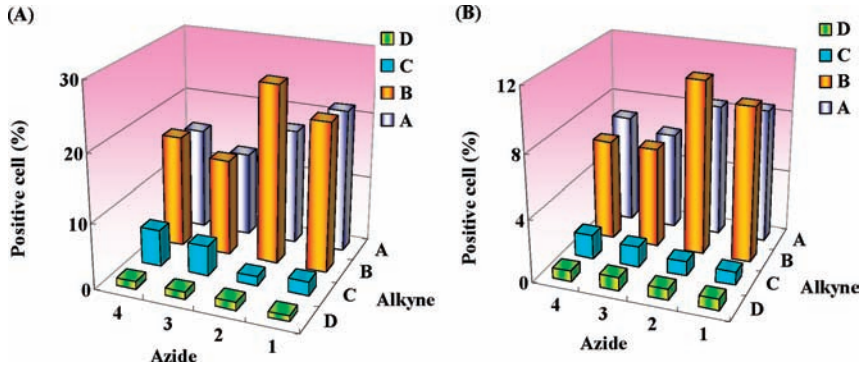


Figure 5. Transfection efficiency of CPNs at N/P ratio 32 with DNA concentration 5 μg/mL in HEK 293 cells (A) and MDA-MB-468 cells (B).

efficiency at N/P ratio 32, and considering that most CPs had good DNA binding ability and DNA condensing efficiency at N/P ratio 32, as a result, the transfection efficiency of 16 CPNs at N/P ratio 32 was compared to investigate the relationships of structure/transfection efficiency. Figure 5A,B showed the different transfection efficiency of 16 CPNs on the HEK293 and MDA-MB-468 cells. From the histograms, we could find that CPNs demonstrated the similar relationship of structure/transfection efficiency in the two cell lines. Complexes of **D** series could not transfect both of the cell lines. Complexes formed by $\mathbf{C_3}$ or $\mathbf{C_4}$ demonstrated the improved transfection efficiency compared with $\mathbf{C_1}$ and $\mathbf{C_2}$, which indicated that cellular uptake was a limiting factor with polymers of the **C** series. Among 16 CPNs, the complexes formed by $\mathbf{B_2}$ (B_2Ns) mediated the highest transgene expression in both cell lines, which was comparable to the PEINs group. Cells transfected with complexes formed with $\mathbf{A_1}$ or $\mathbf{B_1}$ also showed high gene expression. Complexes formed by polymers of **B** series displayed higher transfection efficency than that of **A** series, which indicated that the number of secondary amines in the polymer backbone could affect the gene expression. Complexes formed by polymer $\mathbf{A_3}$ or $\mathbf{B_3}$ demonstrated lower gene expression than B_2Ns, which indicated that endosomal escape of these polymers could be a limiting factor in promoting high gene expression. Cytotoxicity of polymers also is a very important parameter affecting transfeciton efficiency. From the results of cellular uptake, it could be found that the complexes formed by polymer $\mathbf{A_4}$ or $\mathbf{B_4}$ delivered a relatively high amount of DNA into each cell (Figure 4A), but they revealed a relatively low gene expression compared with B_2Ns (Figure 5). Among all 16 polymers, $\mathbf{A_4}$ and $\mathbf{B_4}$ showed the strongest cytotoxicity and induced the highest hemolysis rate.[23] The strong membrane destabilization effects of these two polymers could facilitate the nuclear delivery of DNA, but at the same time, destroy the normal function of cells, thus affected gene transfection and protein expression. The above results demonstrated that DNA-binding ability, buffering capacity, cytotoxicity, or the cellular delivery capacity of polymers could affect their complex transfection efficiencies.

In Vivo Biodistribution and Transfection Efficiency. According to the above structure−activity relationship, B_2Ns demonstrated high transfection efficiency with low toxicity. As a result, polymer $\mathbf{B_2}$ was chosen for further in vivo studies as follows.

The lethal toxicity was first investigated in MDA-MB-468 breast tumor-bearing mice. No lethal toxicity was observed for B_2Ns at N/P ratio 32 at 3 mg DNA/kg. Because the i.v. injection of B_2Ns in mice had a maximum volume, and the complex nanoparticles were apt to assemble under high concentration, the toxicity of B_2Ns at over 3 mg DNA/kg was difficult to determine, but it was easy to find that B_2Ns did not induce the obvious toxicity in mice under the experimental dose level (2 mg DNA/kg).

The biodistribution characteristics of nonviral vectors were among the most important factors affecting gene transfection efficiency. The difference in polymer structures and surface properties of nanoparticles leads to the difference in vivo biodistribution. It was reported that over half of the administered PEI/siRNA nanoparticles distributed to the liver in mice,[30] but the polyphosphazene/DNA nanoparticles mainly distributed into the lung in a short period of time.[31] As a result, it is necessary to investigate the biodistribution characteristics of newly synthesized click polymer/DNA complex nanoparticles.

To investigate the biodistribution of B_2Ns in tumor bearing mice, fluorescent dye YOYO-1 was chosen to label DNA. It is a cell-impermeant stain which shows over a thousandfold increase in its green fluorescence when bound to dsDNA. Tumor was allowed to grow to a volume of 200−300 mm^3 to facilitate qualitative observation of the fluorescence in each tissue under a real-time in vivo fluorescence imaging system. Then, the fluorescence was quantitatively evaluated. At the DNA concentration range 0−5 μg/mL, there is a perfect linear relationship between DNA concentration and fluorescence intensity.

The biodistribution profiles of B_2Ns in MDA-MB-468 solid tumor-bearing mice were shown in Figure 6A. B_2Ns could rapidly distribute into several principle tissues at 15 min after intravenous administration. A large amount of B_2Ns accumulated in the liver which could be due to the Kupffer cells scavenging charged particles.[30] At 15 min, some B_2Ns could be detected in tumor, and maximal accumulation of B_2Ns in tumor tissue was observed 1 h after administration. The distribution in tumor tissue was much higher than in heart, spleen, lung, and kidney, which could be attributed to the EPR effect.[32,33] The accumulation in each tissue decreased over time, and after 24 h, almost all B_2Ns was eliminated. These results demonstrated that the complex nanoparticles fromed by click polymers could not accumulate in the body.

The in vivo transfection efficiency of B_2Ns was compared with PEINs in MDA-MB-468 solid tumor-bearing mice. Due to the severe toxicity of PEI, the mass ratio of the administered complexes could not be over 1 under the experimental dose level (2 mg DNA/kg). The luciferase expression in heart, liver, spleen, lung, kidney, and tumor at 48 h after i.v. was shown in Figure 6B. The highest levels of luciferase expression were found in tumor, and much higher luciferase activity was detected in liver

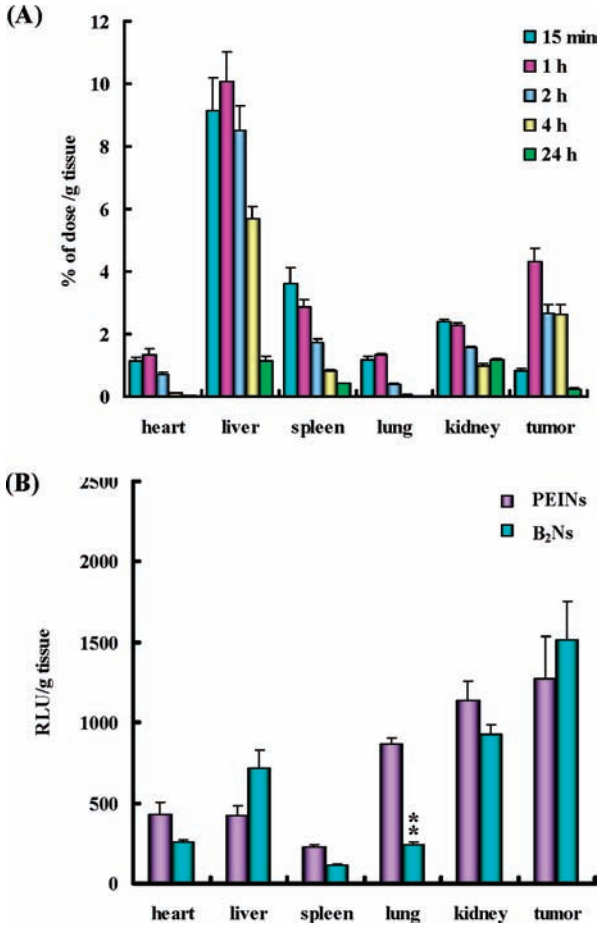


Figure 6. (A) Biodistribution of B_2Ns in nude mice bearing MDA-MB-468 tumor. Data were given as mean ± SD (n = 3). (B) Quantitative gene expression in vivo. Luciferase expression 48 h after intravenous administration of B_2Ns formed by polymer $\mathbf{B_2}$ into nude mice bearing MDA-MB-468 tumor at a dose of 2 mg DNA/kg. $^{**}p < 0.01$ compared with PEINs. Luciferase expression is plotted as RLU/g tissue. Data were given as mean ± SD (n = 3).

and kidney than other organs via injection of B_2Ns. The high tumor gene expression could be due to the targeting of nanoparticles to tumor via the EPR effect. In tumor, the gene expression of B_2Ns was a little higher than PEINs. In heart, spleen, and lung, the luciferase activity of PEINs was higher than that of B_2Ns, expecially in the lung. It was reported that PEI could induce severe aggregation of erythrocytes after intravenous injection, and the aggregation was apt to block pulmonary capillary, which provided enough time for gene expression in the lung.[34] However, in our previous work, $\mathbf{B_2}$ did not induce the obvious erythrocyte aggregation,[23] and the strong binding ability of triazole-amide to DNA could effectively overcome aggregation of nanoparticles in blood circulation. Therefore, the gene expression of B_2Ns in lung was significantly lower than that of PEINs ($p < 0.01$). The reduced distribution to lung tissue gave B_2Ns more opportunity to distribute to tumor and acquire more gene expression.

CONCLUSIONS

In vitro structure−activity relationship of 16 linear cationic click polymers and in vivo gene transfection of a candidate polymer selected from SAR study were evaluated in this work. Comparative analysis of 16 polymers revealed that the minimal structure variation had a crucial effect on buffering capacity, DNA-binding ability, or the cellular delivery capacity of polymer, all of which produced striking effects on their complex transfection efficiencies. The parallel screening led to the identification of a candidate polymer $\mathbf{B_2}$, which could effectively deliver DNA into tumor tissue. These results implied that gene vector based on this linear cationic click polymer could be a promising gene delivery system for tumor gene therapy.

ASSOCIATED CONTENT

Supporting Information. Representative FACS histograms of HEK 293 control cells, cells after transfected with naked DNA, $\mathbf{B_2}$/neg-DNA complex nanoparticles, or B_2Ns. This material is available free of charge via the Internet at http://pubs.acs.org.

AUTHOR INFORMATION

Corresponding Author

*Address: 501 Haike Road, Shanghai 201203, China. Tel.: +86-21-2023-1979. Fax: +86-21-2023-1979. E-mail address: ypli@mail.shcnc.ac.cn.

ACKNOWLEDGMENT

This work was supported by the National Basic Research Program of China (2010CB934000, 2007CB935800, and 2009CB930304), the National Natural Science Foundation of China (30925041, 30901866), National Science & Technology Major Project "Key New Drug Creation and Manufacturing Program" (nos. 2009ZX09501-024 and 2009ZX09301-001).

REFERENCES

(1) Edelstein, M. L., Abedi, M. R., Wixon, J., and Edelstein, R. M. (2004) Gene therapy clinical trials worldwide 1989−2004-an overview. *J. Gene Med. 6*, 597–602.

(2) Edelstein, M. L., Abedi, M. R., and Wixon, J. (2007) Gene therapy clinical trials worldwide to 2007-an update. *J. Gene Med. 9*, 833–842.

(3) Kootstra, N. A., and Verma, I. M. (2003) Gene therapy with viral vectors. *Annu. Rev. Pharmacol. Toxicol. 43*, 413–439.

(4) Li, S. D., and Huang, L. (2007) Non-viral is superior to viral gene delivery. *J. Controlled Release 123*, 181–183.

(5) Yang, Y., Xu, Z., Jiang, J., Gao, Y., Gu, W., Chen, L., Tang, X., and Li, Y. (2008) Poly(imidazole DMAEA)phosphazene DNA self-assembled nanoparticles for gene delivery: synthesis and in vitro transfection. *J. Controlled Release 127*, 273–279.

(6) Jiang, H. L., Kwon, J. T., Kim, E. M., Kim, Y. K., Arote, R., Jere, D., Jeong, H. J., Jang, M. K., Nah, J. W., Xu, C. X., Park, I. K., Cho, M. H., and Cho, C. S. (2008) Galactosylated poly(ethylene glycol)-chitosan-graft-polyethylenimine as a gene carrier for hepatocyte-targeting. *J. Controlled Release 131*, 150–157.

(7) Rudolph, C., Sieverling, N., Schillinger, U., Lesina, E., Plank, C., Thünemann, A. F., Schönberger, H., and Rosenecker, J. (2007) Thyroid hormone (T3)-modification of polyethyleneglycol (PEG)-polyethyleneimine (PEI) graft copolymers for improved gene delivery to hepatocytes. *Biomaterials 28*, 1900–1911.

(8) Russ, V., Günther, M., Halama, A., Ogris, M., and Wagner, E. (2008) Oligoethylenimine-grafted polypropylenimine dendrimers as degradable and biocompatible synthetic vectors for gene delivery. *J. Controlled Release 132*, 131–140.

(9) Piest, M., Lin, C., Mateos-Timoneda, M. A., Lok, M. C., Hennink, W. E., Feijen, J., and Engbersen, J. F. (2008) Novel poly(amido amine)s with bioreducible disulfide linkages in their diamino-units: structure effects and in vitro gene transfer properties. *J. Controlled Release 130*, 38–45.

(10) Yamanouchi, D., Wu, J., Lazar, A. N., Craig, K. K., Chu, C. C., and Liu, B. (2008) Biodegradable arginine-based poly(ester-amide)s as non-viral gene delivery reagents. *Biomaterials 29*, 3269–3277.

(11) Kunath, K., von Harpe, A., Fischer, D., Petersen, H., Bickel, U., Voigt, K., and Kissel, T. (2003) Low-molecular-weight polyethylenimine as a non-viral vector for DNA delivery: comparison of physicochemical properties, transfection efficiency and in vivo distribution with high-molecular-weight polyethylenimine. *J. Controlled Release 89*, 113–125.

(12) Pack, D. W., Hoffman, A. S., Pun, S., and Stayton, P. S. (2005) Design and development of polymers for gene delivery. *Nat. Rev. Drug Discovery 4*, 581–593.

(13) Miyata, K., Oba, M., Nakanishi, M., Fukushima, S., Yamasaki, Y., Koyama, H., Nishiyama, N., and Kataoka, K. (2008) Polyplexes from poly(aspartamide) bearing 1,2-diaminoethane side chains induce pH-selective, endosomal membrane destabilization with amplified transfection and negligible cytotoxicity. *J. Am. Chem. Soc. 130*, 16287–16294.

(14) Liu, Y., and Reineke, T. M. (2007) Poly(glycoamidoamine)s for gene delivery. Structural effects on cellular internalization, buffering capacity, and gene expression. *Bioconjugate Chem. 18*, 19–30.

(15) Wang, J., Gao, S. J., Zhang, P. C., Wang, S., Mao, H. Q., and Leong, K. W. (2004) Polyphosphoramidate gene carriers: effect of charge group on gene transfer efficiency. *Gene Ther. 11*, 1001–1010.

(16) Barua, S., Joshi, A., Banerjee, A., Matthews, D., Sharfstein, S. T., Cramer, S. M., Kane, R. S., and Rege, K. (2009) Parallel synthesis and screening of polymers for nonviral gene delivery. *Mol. Pharmaceutics 6*, 86–97.

(17) Akinc, A., Lynn, D. M., Anderson, D. G., and Langer, R. (2003) Parallel synthesis and biophysical characterization of a degradable polymer library for gene delivery. *J. Am. Chem. Soc. 125*, 5316–5323.

(18) Rostovtsev, V. V., Green, L. G., Fokin, V. V., and Sharpless, K. B. (2002) A stepwise huisgen cycloaddition process: copper(I)-catalyzed regioselective "ligation" of azides and terminal alkynes. *Angew. Chem., Int. Ed. Engl. 41*, 2596–2599.

(19) Lutz, J. F., and Zarafshani, Z. (2008) Efficient construction of therapeutics, bioconjugates, biomaterials and bioactive surfaces using azide-alkyne "click" chemistry. *Adv. Drug Delivery Rev. 60*, 958–970.

(20) Liu, Y., Díaz, D. D., Accurso, A. A., Sharpless, K. B., Fokin, V. V., and Finn, M. G. (2007) Click chemistry in materials synthesis. 3. Metal-adhesive polymers from Cu(I)-catalyzed azide-alkyne cycloaddition. *J. Polym. Sci., Part A: Polym. Chem. 45*, 5182–5189.

(21) van Dijk, M., Nollet, M. L., Weijers, P., Dechesne, A. C., van Nostrum, C. F., Hennink, W. E., Rijkers, D. T., and Liskamp, R. M. (2008) Synthesis and characterization of biodegradable peptide-based polymers prepared by microwave-assisted click chemistry. *Biomacromolecules 9*, 2834–2843.

(22) Srinivasachari, S., Liu, Y., Zhang, G., Prevette, L., and Reineke, T. M. (2006) Trehalose click polymers inhibit nanoparticle aggregation and promote pDNA delivery in serum. *J. Am. Chem. Soc. 128*, 8176–8184.

(23) Gao, Y., Chen, L. L., Zhang, Z. W., Gu, W. W., and Li, Y. P. (2010) Linear cationic click polymers for gene delivery: synthesis, biocompatibility and in vitro transfection. *Biomacromolecules 11*, 3102–3111.

(24) Sun, Y. X., Zeng, X, Meng, Q. F., Zhang, X. Z., Cheng, S. X., and Zhuo, R. X. (2008) The influence of RGD addition on the gene transfer characteristics of disulfide-containing polyethyleneimine/DNA complexes. *Biomaterials 29*, 4356–4365.

(25) Hashimoto, M., Morimoto, M., Saimoto, H., Shigemasa, Y., and Sato, T. (2006) Lactosylated chitosan for DNA delivery into hepatocytes: The effect of lactosylation on the physicochemical properties and intracellular trafficking of pDNA/chitosan complexes. *Bioconjugate Chem. 17*, 309–316.

(26) Tseng, W. C., Tang, C. H., and Fang, T. Y. (2004) The role of dextran conjugation in transfection mediated by dextran-grafted polyethylenimine. *J. Gene Med. 6*, 895–905.

(27) Zauner, W., Ogris, M., and Wagner, E. (1998) Polylysine-based transfection systems utilizing receptor-mediated delivery. *Adv. Drug Delivery Rev. 30*, 97–113.

(28) Akinc, A., Lynn, D. M., Anderson, D. G., and Langer, R. (2003) Parallel synthesis and biophysical characterization of a degradable polymer library for gene delivery. *J. Am. Chem. Soc. 125*, 5316–5123.

(29) Mann, A., Richa, R., and Ganguli, M. (2008) DNA condensation by poly-L-lysine at the single molecule level: Role of DNA concentration and polymer length. *J. Controlled Release 125*, 252–262.

(30) Malek, A., Merkel, O., Fink, L., Czubayko, F., Kissel, T., and Aigner, A. (2009) In vivo pharmacokinetics, tissue distribution and underlying mechanisms of various PEI(-PEG)/siRNA complexes. *Toxicol. Appl. Pharmacol. 236*, 97–108.

(31) Wolf, H. K., Luten, J., Snel, C. J., Oussoren, C., Hennink, W. E., and Storm, G. (2005) In vivo tumor transfection mediated by polyplexes based on biodegradable poly(DMAEA)-phosphazene. *J. Controlled Release 129*, 275–287.

(32) Tang, N., Du, G., Wang, N., Liu, C., Hang, H., and Liang, W. (2007) Improving penetration in tumors with nanoassemblies of phospholipids and doxorubicin. *J. Natl. Cancer Inst. 99*, 1004–1015.

(33) Maeda, H., Wu, J., Sawa, T., Matsumura, Y., and Hori, K. (2000) Tumor vascular permeability and the EPR effect in macromolecular therapeutics: a review. *J. Controlled Release 65*, 271–284.

(34) Verbaan, F. J., Oussoren, C., van Dam, I. M., Takakura, Y., Hashida, M., Crommelin, D. J., Hennink, W. E., and Storm, G. (2001) The fate of poly(2-dimethyl amino ethyl)methacrylate-based polyplexes after intravenous administration. *Int. J. Pharm. 214*, 99–101.

SUPPORTING INFORMATION FOR

The Linear Cationic Click Polymers/DNA Nanoparticles: In Vitro Structure-activity Relationship and In Vivo Evaluation for Gene Delivery

Yu Gao, Qi Yin, Lingli Chen, Zhiwen Zhang, Yaping Li*

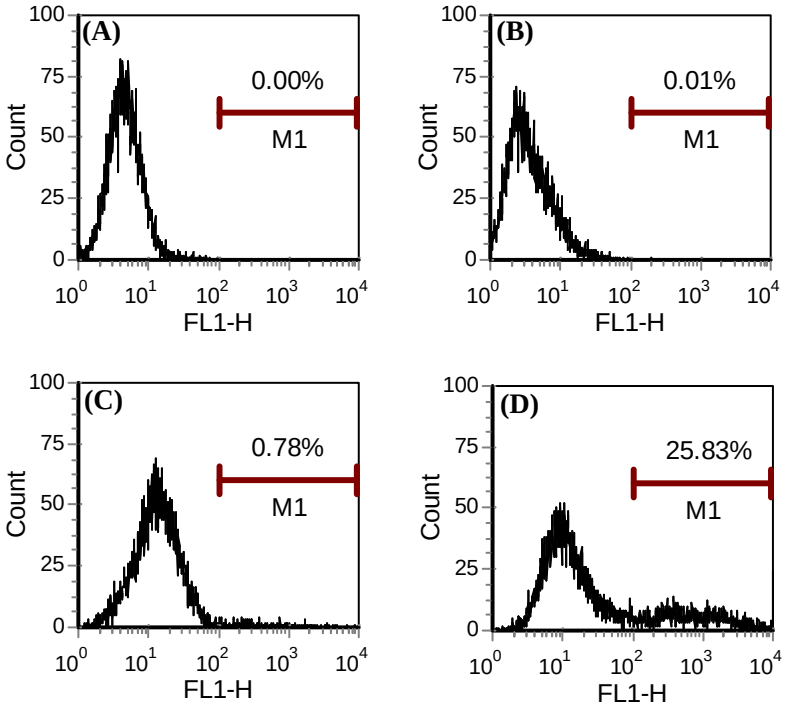


Figure S1. Representative FACS histograms of HEK 293 control cells (A), cells after transfected with naked DNA (B), **B_2**/neg-DNA complex nanoparticles (C) or B_2Ns (D).

Bioconjugate Chemistry

ARTICLE

pubs.acs.org/bc

Photoluminescent Hyperbranched Poly(amido amine) Containing β-Cyclodextrin as a Nonviral Gene Delivery Vector

Yan Chen,[†] Linzhu Zhou,[†] Yan Pang,[†] Wei Huang,[†] Feng Qiu,[†] Xulin Jiang,[‡] Xinyuan Zhu,[*,†] Deyue Yan,[†] and Qun Chen[*,§]

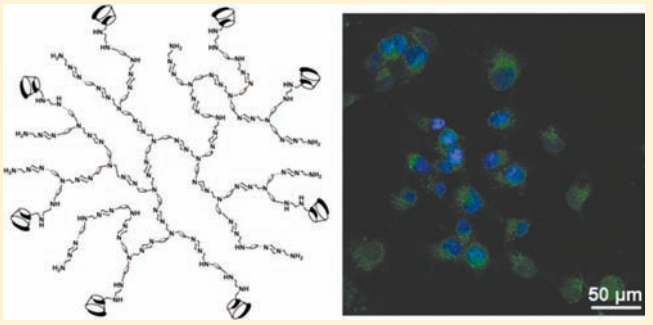
[†]School of Chemistry and Chemical Engineering, State Key Laboratory of Metal Matrix Composites, Shanghai Jiao Tong University, 800 Dongchuan Road, Shanghai 200240, People's Republic of China

[‡]Key Laboratory of Biomedical Polymers of Ministry of Education, Department of Chemistry, Wuhan University, Wuhan 430072, People's Republic of China

[§]Department of Physics & Shanghai Key Laboratory of Functional Magnetic Resonance Imaging, East China Normal University, North Zhongshan Road 3663, Shanghai 200062, People's Republic of China

Supporting Information

ABSTRACT: Hyperbranched poly(amido amine)s (HPAAs) containing different amounts of β-cyclodextrin (β-CD) (HPAA-CDs) were synthesized in one-pot by Michael addition copolymerization of *N,N′*-methylene bisacrylamide, 1-(2-aminoethyl)piperazine, and mono-6-deoxy-6-ethylenediamino-β-CD. In comparison to pure HPAA, the fluorescence intensity of HPAA-CDs was enhanced significantly while the cytotoxicity became lower. Ascribed to plenty of amino groups and strong photoluminescence, HPAA-CDs could be used as nonviral gene delivery vectors, and the corresponding gene transfection was evaluated. The experimental results indicated that HPAA-CDs condensed the plasmid DNA very well. By utilizing the fluorescent properties of HPAA-CDs, the cellular uptake and gene transfection processes were tracked by flow cytometry and confocal laser scanning microscopy without any fluorescent labeling. The transfection efficiencies of HPAA-CDs were similar to that of pure HPAA. In addition, the inner cavities of β-CDs in HPAA-CDs could be used to encapsulate drugs through host−guest interaction. Therefore, the HPAA-CDs may have potential application in the combination of gene therapy and chemotherapy.



INTRODUCTION

Nonviral gene delivery vectors especially cationic polymers are receiving more and more attention because of their easy manufacture, high compound stability, and low immunogenicity over viral vectors.[1−8] To achieve a safe and efficient DNA delivery, the exploration of polyplex formation between the polycations and the plasmid DNA (pDNA) and subsequent cellular uptake and trafficking of genetic materials in the cells is indispensable. By attaching the fluorescent probes onto polycations, the gene delivery process could be tracked.[9−12] However, the fluorescent labeling usually requires multiple complicated reactions. Even worse, the introduction of fluorescent probes might change the physical/chemical properties of gene vectors, resulting in a negative effect on the biocompatibility as well as on the transfection efficiency. Therefore, the preparation and application of photoluminescent polycationic vectors have become very attractive in the field of gene delivery.

In recent years, some polycations including poly(amido amine) and polyethylenimine were found to be photoluminescent polymers which could be used for fluorescence imaging.[13−20] However, comparing fluorescent materials with traditional fluorophores, the photoluminescence intensity of these polycations is still very weak.[20−22] We have noted that the photoluminescent property of polymers is closely related to their molecular conformations. By enhancement of the chain rigidity, the photoluminescence intensity of polymers can be improved.[19] For the traditional linear polycations, only limited end-groups are available for further modification. In contrast to the linear polymers, the highly branched polycations have a great number of various amine groups, which favors the following functionalization. At the same time, the highly branched polycations exhibit low cytotoxicity and high transfection efficiency because of their compact and globular structures.[23−27] In the present work, the biodegradable β-cyclodextrin (β-CD) with low cytotoxicity was incorporated into hyperbranched poly(amido amine) (HPAA) by a simple and efficient one-step Michael addition copolymerization. The introduction of big β-CD molecules enhanced the molecular rigidity of HPAA greatly, resulting in a dramatic improvement of

Received: January 7, 2011
Revised: April 28, 2011
Published: May 02, 2011

ACS Publications © 2011 American Chemical Society

photoluminescence. Using this fluorescent hyperbranched polycation as a nonviral gene vector, the cellular uptake and trafficking of genetic materials in the cells could be tracked. Furthermore, the inclusion capability of the β-CD cavities in this photoluminescent polycation provided a possible application in the combination of gene therapy and chemotherapy.

MATERIALS AND METHODS

Materials. 1-(2-Aminoethyl)piperazine (AP, 99%), poly(ethylenimine) (PEI, water free, M_w = 25 kDa, M_n = 10 kDa) and 3-(4,5-dimethyl-thiazol-2-yl)-2,5-diphenyl tetrazolium bromide (MTT) were purchased from Aldrich. *N,N′*-Methylenebis(acrylamide) (MBA, 96%), *p*-toluenesulfonyl chloride, 1,2-ethylenediamine (EDA), acetone, dimethyl sulfoxide (DMSO), sodium hydroxide (98%) were supplied by Shanghai Sinopharm Chemical Reagent Co., Ltd. Dulbecco's Modified Eagle's Medium (DMEM), fetal bovine serum (FBS), phosphate buffered solution (PBS), penicillin, and streptomycin were purchased from PAA Laboratories GmbH. All these chemicals were used as received without any further purification. Clear polystyrene tissue culture treated 6-well and 96-well plates were purchased from Corning Costar. β-CD was obtained from Shanghai Sinopharm Chemical Reagent Co., Ltd., and purified once by recrystallization from deionized water before use. Mono-6-deoxy-6-ethylenediamino-β-CD (EDA-β-CD) used here was synthesized according to the method reported in our previous work.[28]

Synthesis of HPAA and HPAA-CDs. Both HPAA and its β-CD derivatives (HPAA-CDs) were synthesized via the Michael addition polymerization in nitrogen atmosphere.[28] A typical procedure is as follows: MBA (3.0830 g, 20 mmol) was dissolved in 20 mL of ultrapure water under stirring. Then, AP (2.5190 g, 19.5 mmol) and EDA-β-CD (0.5885 g, 0.5 mmol) were dissolved in 10 mL of ultrapure water and also added into the above solution. The mixture was stirred vigorously at 60 °C in the dark for 60 h. At last, the mixture was precipitated in acetone, dried under vacuum at 50 °C, and a light yellow powder was obtained (4.64 g, yield: 75%). The β-CD content of the polymers (1.3% and 6.1% for the two samples) was determined by quantitative ^{13}C NMR. Thus, the two samples were named HPAA-CD1.3 and HPAA-CD6.1, respectively.

Complexation of HPAA-CDs and Rhodamine B. Rhodamine B (RB) was used as a model drug. Certain amounts of RB were added into HPAA-CD aqueous solutions. After stirring overnight, the RB-loaded polymer solutions were dialyzed against distilled water for 48 h to remove free RB, followed by lyophilization to give the HPAA-CD/RB complexes.

Characterization of Polymers. ^1H, ^{13}C, $^1H-^1H$ COSY, and $^{13}C-^1H$ HSQC NMR spectra were recorded on a Varian Mercuryplus-400 spectrometer with DMSO-d_6 as solvent. The resonance frequencies for ^1H and ^{13}C were 400 and 100 MHz, respectively. Quantitative ^{13}C NMR spectra were measured by the method of inverse gated ^1H decoupling. The molecular weights and their distributions of the synthesized samples were evaluated by GPC-MALLS (gel permeation chromatography - multiangle laser light scattering). The GPC-MALLS system consisted of a Waters 2690D separations module, a Waters 2414 refractive index detector (RI), and a Wyatt DAWN EOS MALLS detector. Two chromatographic columns (Shodex OH-pak SB-803 and SB-802.5, Showa Denko, Japan) with a precolumn (Shodex SB-G) were used in series. The sodium acetate (NaAc) solution was prepared by dissolving a calculated amount of sodium acetate in reverse osmosis water (0.3 M), and the pH was adjusted to 4.4 with acetic acid. The eluent was filtrated through a 0.22 μm HPLC filter and degassed prior to use by ultrasonic bath. The flow rate of the mobile phase was 0.6 mL/min. The data were processed with *Astra* software (Wyatt Technology). Fourier transform infrared (FTIR) measurements were performed on a Perkin-Elmer Spectrum 1000 FTIR spectrometer. The UV−vis spectra were recorded on a Perkin-Elmer Lambda 750s UV−vis spectrophotometer. The fluorescence spectra were measured on a QM/TM/RM fluorescence spectrophotometer (Photon Technology International, Inc.). Differential scanning calorimeter (DSC) measurements were conducted on a TA Instruments Q2000 under a nitrogen atmosphere. The heating rate was 20 °C/min.

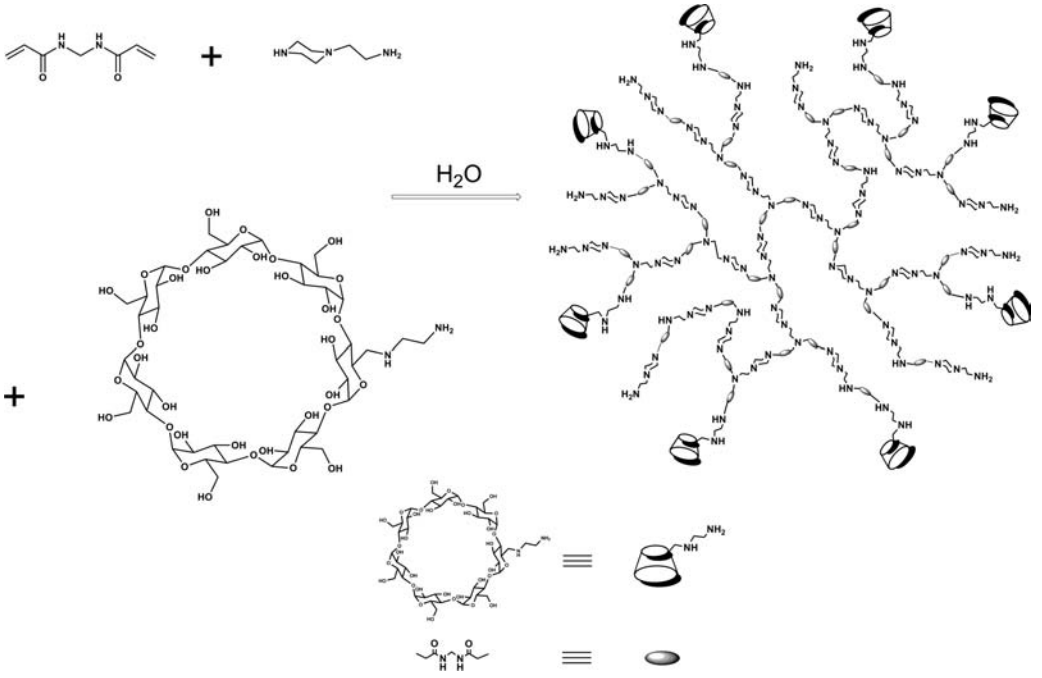
Agarose Gel Electrophoresis Experiments. Each polymer was examined for its ability to bind pDNA through gel electrophoresis experiments. All polymer stock solutions were prepared and mixed with pDNA solution at different N/P ratios (molar ratios of polymer nitrogen to pDNA phosphorus, N/P = 0, 5, 10, 20, 30, 40, 60, and 90) for 30 min at room temperature, and then analyzed on 1% agarose gel containing 0.5 μg/mL ethidium-bromide (EtBr). Then, gel electrophoresis was carried out in Tris-acetate-EDTA (TAE) running buffer with a current of 100 V for 60 min in a Sub-Cell system (Bio-Rad Laboratories, CA). DNA bands were visualized and photographed by a UV transilluminator and BioDoc-It imaging system.

Cell Cultures. COS-7 cells (a cell line derived from kidney cells of the African green monkey) were maintained in DMEM (4.5 g/L glucose) supplemented with 10% FBS, penicillin (100 units/mL), and streptomycin (100 units/mL) at 37 °C in a 5% CO_2 humidified atmosphere. Confluent cells were subcultured every 3 days using standard procedure.

Cell Viability Assay. For MTT assay, COS-7 cells were seeded into 96-well plates at a seeding density of 10 000 cells/well in 200 μL medium. After COS-7 cells were incubated for 24 h at 37 °C and 5% CO_2, the adherent cells reached approximately 60−70% confluence. Growth medium in the 96-well plates was then removed carefully by a transfer pipette and replaced with 200 μL medium containing serial dilutions of the polymers. The cells were grown for 24 h. Then, 20 μL of 5 mg/mL MTT assays stock solution in PBS was added to each well. After incubating the cells for 4 h, the medium containing unreacted dye was removed by a transfer pipette carefully. The obtained blue formazan crystals were dissolved in 200 μL/well DMSO and measured spectrophotometrically in a Perkin-Elmer 1420 Multilabel counter at a wavelength of 490 nm.

Cell Internalization. The cellular uptake experiments of HPAA-CD/pDNA complexes were characterized by flow cytometry and confocal laser scanning microscopy (CLSM). Flow cytometry was used to provide statistics on the uptake of HPAA-CD/pDNA into COS-7 cells. COS-7 cells (5.0×10^5 cells per well) were seeded in a 6-well tissue culture plate in 1 mL complete DMEM and cultured for 24 h until the adherent cells reached approximately 60−70% confluence, followed by removing the culture medium by a transfer pipette and replacing with fresh and prewarmed DMEM in the absence of 10% FBS. Then, the HPAA-CD/pDNA complexes in PBS (corresponding to 4 μg plasmid/well, N/P = 30) were added to different wells and the cells were incubated at 37 °C for predetermined time intervals. After the incubation, samples were prepared for flow cytometry analysis by removing the cell growth medium by a transfer pipette, rinsing with PBS buffer, and treating with trypsin.

Scheme 1. Synthetic Procedure of HPAA-CDs



Data for 1.0×10^4 gated events were collected and analysis was performed by means of a BD FACSCalibur flow cytometer and *CELLQuest* software.

For CLSM studies, COS-7 cells were seeded in 6-well plates at 2×10^5 cells/well in 1 mL complete DMEM and cultured for 24 h, followed by removing culture medium from the 6-well plates and washing with DMEM in the absence of 10% FBS. Then, the HPAA-CD/pDNA complexes (1 mL DMEM medium in the absence of 10% FBS) at the plasmid concentration of 4 μg/mL were added to each well. After incubation at 37 °C for predesignated time, culture medium was removed carefully by a transfer pipette and cells were washed with PBS three times. Then, the cells were fixed with 4% formaldehyde for 30 min at room temperature, and the slides were rinsed with PBS three times. Finally, the cells were stained with 2-(4-amidinophenyl)-6-indolecarbamidine dihydrochloride (DAPI) for 10 min and again the slides were rinsed with PBS three times. The slides were mounted and observed by a LSM 510META.

***In Vitro* Transfection Assay.** For transfection studies, cells were seeded at a density of 1×10^5 cells/well in 96-well plates and incubated for 16−24 h until 60−70% confluent at 37 °C and 5% CO_2. Immediately prior to transfection, the medium was removed by a transfer pipette. Then, cells were washed and replaced with fresh and prewarmed DMEM in the presence or absence of 10% FBS. The HPAA-CD/pDNA complexes (corresponding to 0.2 μg plasmid/well) were added to each well and the cells were incubated at 37 °C for 4 h. The medium was then replaced with fresh DMEM supplemented with 10% FBS and incubated for additional 48 h. The luciferase assay was carried out according to manufacturer's protocol (Promega). Relative light units (RLU) were measured with Varioskan Flash (Thermo Scientific, USA) GloMaxTM 96 microplate luminometer (Promega, USA). The obtained RLUs were normalized with respect to protein concentration in the cell extract determined using the BCA protein assay kit (Beyotime, China).

RESULTS AND DISCUSSION

Synthesis of HPAA-CDs. As mentioned in the introduction part, poly(amido amine) is a kind of cationic polymers with photoluminescence. Unfortunately, its photoluminescence is very weak. To improve its photoluminescence intensity, we introduced big β-CD molecules onto the surface of HPAA to enhance the molecular rigidness. The synthetic procedure of HPAA-CD is shown in Scheme 1. The monomers MBA, AP, and EDA-β-CD with an equal feeding molar ratio of MBA to AP/EDA-β-CD but different molar ratio of AP to EDA-β-CD (see Table 1) were mixed in water at 60 °C. After reaction for 60 h, HPAAs with different β-CD content (HPAA-CDs) were synthesized through Michael addition copolymerization. The experimental conditions and corresponding characterization data are summarized in Table 1, which confirms the formation of polymerized products. The actual β-CD content was calculated from quantitative ^{13}C NMR spectra. It is found that the β-CD contents of the polymers are 1.3% and 6.1%, named HPAA-CD1.3 and HPAA-CD6.1, respectively.

The resulting polymers were characterized by FTIR measurements. Figure 1 gives the FTIR spectra of pure HPAA, HPAA-CD1.3, and HPAA-CD6.1. For pure HPAA, the broad N−H stretching vibration around 3283 cm^{-1} indicates the existence of many amino groups. The bands at 2946 and 2820 cm^{-1} correspond to the antisymmetric and symmetric $-CH_2-$ stretching vibration, respectively. The absorption peaks of amide groups are clearly observed at 1647 and 1538 cm^{-1}, while the band at 1460 cm^{-1} results from the deformation vibration of the $-CH_2-$ groups. The FTIR spectral profile of HPAA-CD1.3 and HPAA-CD6.1 is quite similar to that of pure HPAA, suggesting that all polymers share the basic molecular structure. In the meantime, by comparison with pure HPAA, a new absorption at 1033 cm^{-1} appears in the curves of HPAA-CD1.3 and HPAA-CD6.1 and can be attributed to the C−O−C stretching vibrations of β-CDs.

Table 1. Reaction Conditions and Results of Michael Addition Copolymerization of MBA, AP, and EDA-β-CD

	monomer molar ratio								
entry	MBA (mmol)	AP (mmol)	EDA-β-CD (mmol)	actual CD content (%)[a]	M_n[b] (× 10^4)	M_w[b] (× 10^4)	M_w/M_n[b]	DB[a]	T_g[c] (°C)
HPAA	20	20	0	0	1.23	2.02	1.64	0.33	32.2
HPAA-CD1.3	20	19.5	0.5	1.3	0.95	1.72	1.81	0.34	38.1
HPAA-CD6.1	20	18	2	6.1	1.44	3.40	2.36	0.30	65.7

[a] Actual CD content in the resultant polymers and the degree of branching (DB) were calculated from quantitative ^{13}C NMR analysis. [b] Molecular weights and polydispersities were determined by GPC-MALLS. [c] T_g was measured by DSC.

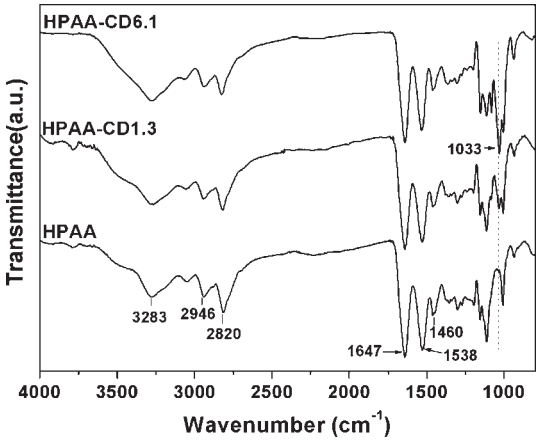


Figure 1. FTIR spectra of pure HPAA and HPAA-CDs.

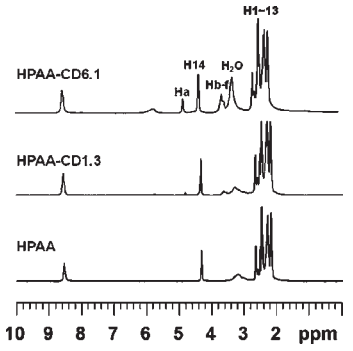


Figure 2. ^{1}H NMR spectra of pure HPAA and HPAA-CDs.

With the increase of β-CD content, the peak intensity of 1033 cm^{-1} band increases. The NMR studies further confirmed the formation of HPAA-CDs. In the ^{1}H NMR spectrum of pure HPAA (Figure 2), the signals at 2.1−2.7 ppm are attributed to the methylene groups in AP units, while the peak at 4.3 ppm comes from the protons of methylene groups between two amide groups in MBA units. After surface modification of HPAA by β-CDs, several new signals at 3.3−3.8, 4.8, and 5.7 ppm corresponding to the protons of β-CD appear. Figure 3 gives the quantitative ^{13}C NMR spectra of HPAA, HPAA-CD1.3, and HPAA-CD6.1. For pure HPAA, the carbonyl peak is located at 173 ppm while all methylene signals are found in the high field region between 32 and 62 ppm. In the ^{13}C NMR spectra of HPAA-CD1.3 and HPAA-CD6.1, the signals at 101, 81, 72, and 61 ppm are assigned to the methylene and methine groups of β-CD and become strong with the increase of β-CD content. Both FTIR

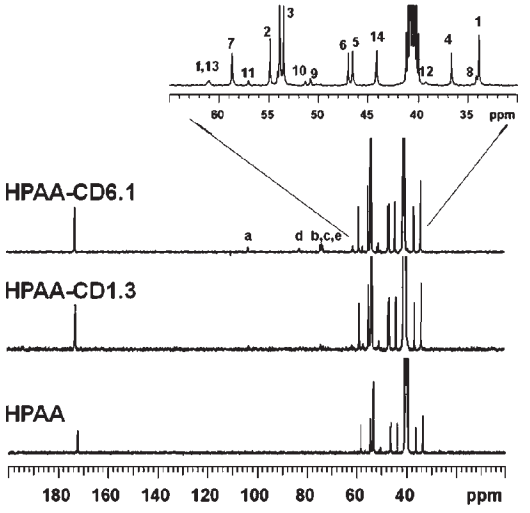
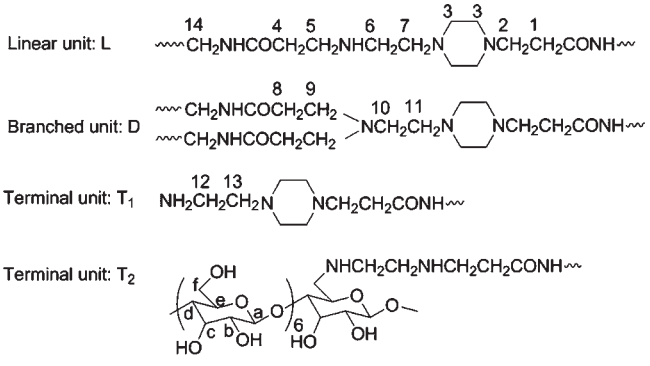


Figure 3. Quantitative ^{13}C NMR spectra of pure HPAA and HPAA-CDs.

Scheme 2. Schematic Illustration of the Molecular Structure of HPAA-CDs



and NMR studies demonstrate that different amounts of β-CDs have been successfully incorporated onto the surface of HPAA.

In order to calculate the degree of branching (DB) of pure HPAA and HPAA-CDs, all possible structure units including linear, branched, and terminal units are listed in Scheme 2. The two-dimensional NMR (2D-NMR) technique was used to assign the molecular structure.[29,30] As one example, Figure 4 gives the ^{1}H−^{1}H COSY and ^{13}C−^{1}H HSQC NMR spectra of HPAA-CD6.1. On the basis of the cross-peaks in the 2D-NMR spectra, the assignment of each structural unit for HPAA-CD6.1 is performed, and the corresponding details are given in Figure 4.

dx.doi.org/10.1021/bc200010w |Bioconjugate Chem. 2011, 22, 1162–1170

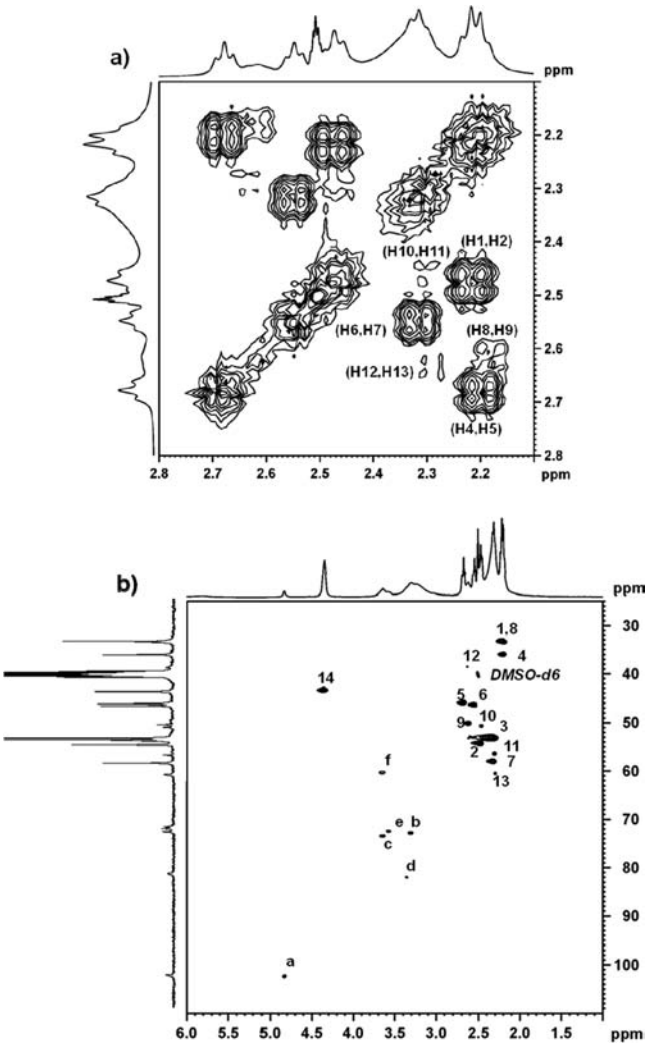


Figure 4. 2D NMR spectra of HPAA-CD6.1: (a) $^{1}H-^{1}H$ COSY spectrum, (b) $^{13}C-^{1}H$ HSQC spectrum.

Correspondingly, the DB values can be calculated according to the following equation:[31]

$$DB = (D + T)/(D + T + L)$$

where D, T, and L represent the fractions of the branched, terminal, and linear units, respectively. As listed in Table 1, the DB values of polymerized samples are higher than 0.30, suggesting the formation of hyperbranched polymers.

UV−vis and Fluorescent Properties of HPAA-CDs. Although without traditional fluorescent functional groups, both poly(amido amine) (PAMAM) dendrimer and hyperbranched poly(amido amine) (HPAA) are found to exhibit photoluminescence. It is believed that the key unit for the photoluminescence property of PAMAM dendrimer and HPAA is the tertiary amine with lone pair electrons inside the tight structure of highly branched polymers.[17,20] However, the photoluminescence of these polymers is weak. In the present work, different amounts of β-CD were incorporated onto HPAA to form HPAA-CDs, which limited the molecular mobility and then improved the photoluminescence. The optical properties of HPAA-CDs were studied by UV−vis and fluorescence spectroscopy. Figure 5a gives the UV−vis spectra of different polymer aqueous solutions with

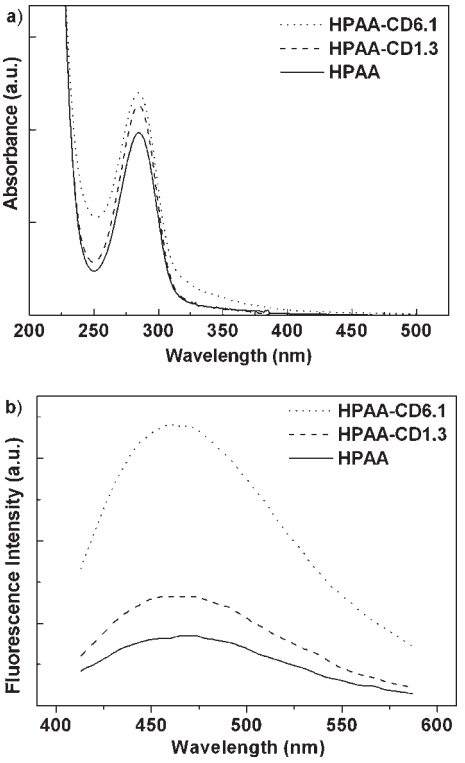


Figure 5. (a) UV−vis spectra and (b) fluorescence emission spectra of pure HPAA and HPAA-CDs in aqueous solutions (1 mg/mL) measured at room temperature, λ_{ex} = 375 nm.

a concentration of 1 mg/mL. An obvious absorption band at 295 nm related to the tertiary nitrogen can be observed. This UV−vis absorption increases with the β-CD content, because of the improved molecular rigidity of the HPAA backbone. Figure 5b shows the corresponding fluorescence emission spectra. It can be found that the HPAA-CD displays a broad fluorescent band at ~465 nm under excitation at 375 nm. With the increase of β-CD content from 0% to 6.1%, the fluorescence at 465 nm is enhanced significantly. The photoluminescence enhancement of HPAA-CDs may result from the restricted rotational motion of the terminal chains caused by the steric hindrance of big β-CD units, which decreases the collisional relaxation and fluorescence self-quenching.[19] The quantum yields of HPAA, HPAA-CD1.3, HPAA-CD6.1, and NH_2-terminated G4 PAMAM dendrimer were determined to be 0.59%, 0.68%, 0.73%, and 0.25%, respectively. Although the quantum yields of all the samples are not large, that of HPAA-CDs seem to be higher than that of G4 PAMAM dendrimer. The fluorescence emission spectra show that HPAA-CDs emit much stronger fluorescence than G4 PAMAM dendrimer with the same solution concentration. The experimental details are given in the Supporting Information. The strong fluorescence and cationic characteristics of HPAA-CD make it an excellent fluorescent nonviral gene delivery vector without fluorescent probes.

Cytotoxicity of HPAA-CDs. It is very important to evaluate the potential toxicity of polymeric materials for biomedical applications. Here, the *in vitro* cytotoxicity of the pure HPAA and two HPAA-CD samples was evaluated using the MTT assay against COS-7 cells with PEI (M_w = 25 kDa) as a control. The MTT assay is based on the ability of a mitochondrial dehydrogenation enzyme in viable cells to cleave the tetrazolium rings of

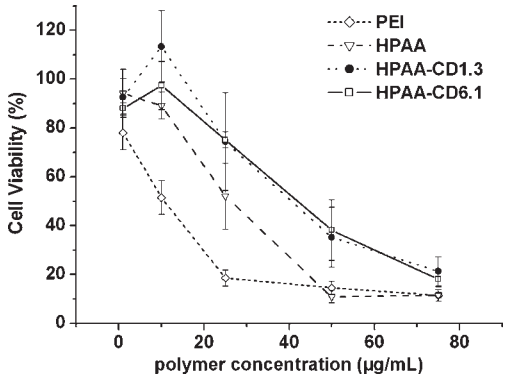


Figure 6. Cell viability of COS-7 against PEI, pure HPAA, and HPAA-CDs after culturing for 24 h. Results are presented as the mean ± SD (n = 6).

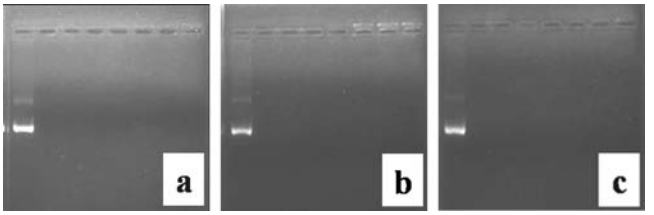


Figure 7. Agarose gel electrophoretic images. For each polymer, gel electrophoresis assays were performed at the N/P ratios of 0, 5, 10, 20, 30, 40, 60, and 90 from left to right in each image. The left lane (N/P = 0) contains DNA alone (no polymer) and is used as a control in each image. (a−c): Agarose gel electrophoresis data of DNA released from the complex with pure HPAA, HPAA-CD1.,3 and HPAA-CD6.1, respectively.

the pale-yellow MTT and form formazan crystals with dark-blue color. Therefore, the number of surviving cells is directly proportional to the level of formed formazan.[32,33] Figure 6 presents the cell viability after 24 h incubation with polymer samples at different concentrations. All the samples show cytotoxicity when the polymer concentration is above 50 μg/mL. It has been well reported that the strong positive charge of primary amino groups increases the cytotoxicity significantly.[34] Moreover, increasing molecular weight of polymers also induces enhanced cytotoxicity.[35] Thus, the relatively high cytotoxicity of HPAA and its CD-based derivatives may be attributed to the strong positive charges of primary amines and the high molecular weight. In comparison to the PEI control, both pure HPAA and HPAA-CD samples exhibit less toxicity in COS-7 cells and the cytotoxicity decreases with the incorporation of β-CDs. β-CD has been demonstrated to be biodegradable, which is of great importance in reducing toxicity by integrating it into polycations.[36] After the surface β-CD modification, a part of the primary amines of HPAA is replaced by the biodegradable and low cytotoxic β-CDs, resulting in the reduced cytotoxicity.

Polymer/pDNA Complexes. As one of the promising biodegradable polymers, poly(amido amine) was applied as an efficient nonviral gene vector. Considering the similar structure, the possibility of photoluminescent HPAA-CDs to be used as nonviral gene vectors was also evaluated. First, the ability of HPAA-CDs to form complexes with pDNA was examined by agarose gel electrophoresis at various molar ratios of polymer nitrogen to pDNA phosphorus (N/P ratios). Figure 7 shows the gel retardation results of the HPAA-CD/pDNA complexes.

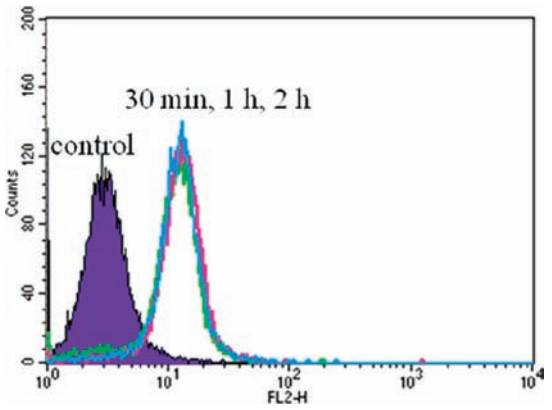


Figure 8. Flow cytometry histogram profiles of COS-7 cells incubated with the HPAA-CD6.1/pDNA complexes.

It indicates that, when the N/P ratio is higher than 5, the migration of pDNA is retarded completely for pure HPAA, HPAA-CD1.3, and HPAA-CD6.1. The agarose gel electrophoresis results clearly demonstrate that HPAA-CDs can condense pDNA very well.

Cell Internalization Studies. Benefiting from the strong photoluminescence of HPAA-CD, the cell internalization studies of HPAA-CD/pDNA complexes could be performed conveniently without fluorescent labeling. The cellular uptake of HPAA-CD6.1 which emitted the strongest fluorescence was determined by measuring the intracellular fluorescence intensity using flow cytometry. The HPAA-CD6.1/pDNA complexes (N/P = 30) were added to culture medium, and the COS-7 cells were incubated at 37 °C for the desired time. Here, COS-7 cells without any treatment were used as a blank control. Figure 8 gives the histograms of cell-associated HPAA-CD6.1 fluorescence. The relative geometrical mean fluorescence intensities of the HPAA-CD6.1/pDNA complex pretreated cells are much higher than that of non-pretreated cells. These prominent fluorescence signals are associated with the uptake of the HPAA-CD6.1/pDNA complexes into COS-7 cells. The mean fluorescence intensities almost do not change for incubation intervals longer than 30 min, indicating the rapid cellular internalization of the HPAA-CD6.1/pDNA complexes.

To further confirm the cell permeability of the HPAA-CD6.1/pDNA complexes, CLSM measurements were performed. In CLSM studies, the COS-7 cells were incubated with the HPAA-CD6.1/pDNA complexes for predesignated time (0.5 h, 2 h, 6 h, 10 h, and 24 h), and then the cell nucleus was stained with DAPI. The pretreated cells were observed under CLSM. Figure 9 shows that the HPAA-CD6.1 fluorescence appears in all cells but mainly in the cytoplasm. These results indicate that the HPAA-CD6.1/pDNA complexes are successfully internalized by COS-7 cells and mainly resided in cytoplasm. Actually, this is very important for intracellular applications of the polymer complexes, such as intracellular gene delivery.

***In Vitro* Transfection Assay.** Considering the high DNA condensation ability and low cytotoxicity, HPAA-CDs can be used as an efficient nonviral vector for gene delivery. *In vitro* transfection activity of HPAA-CD/pDNA complexes was evaluated in COS-7 cells in DMEM supplemented with or without 10% FBS in comparison with PEI by the luciferase assay. All transfection efficiencies were obtained in the absence of chloroquine, a reagent known to disrupt the endosomal membrane

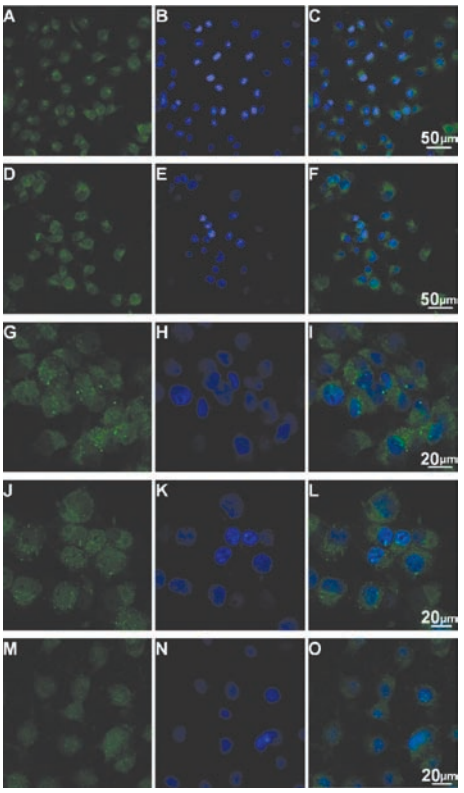


Figure 9. CLSM images of COS-7 cells incubated with HPAA-CD6.1/pDNA complexes for predesignated time (from top to bottom: 0.5 h, 2 h, 6 h, 10 h, 24 h). The green fluorescence is from HPAA-CD6.1 (A, D, G, J, M), and the blue is from the nuclei (cell nuclei were stained with DAPI) (B, E, H, K, N). The third column illustrates overlaid images (C, F, I, L, O).

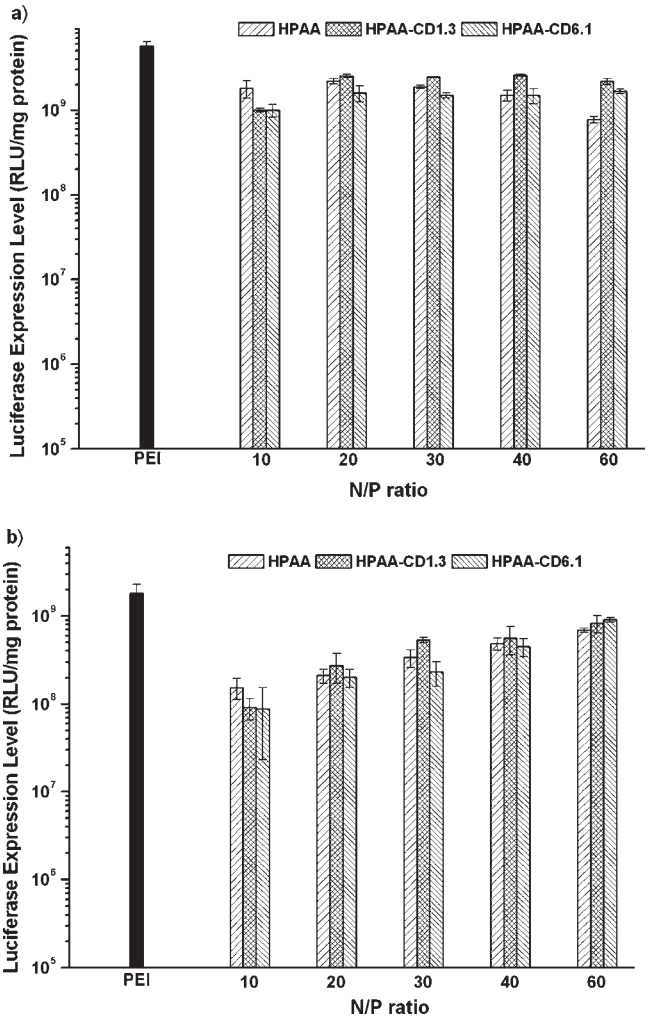


Figure 10. Transfection efficiency of pure HPAA and HPAA-CDs at various N/P ratios and branched PEI (25 kDa) at the optimal N/P ratio of 15 in COS-7 cells in different media: (a) serum free DMEM, (b) DMEM containing serum. Luciferase expression levels were measured 48 h later. Results are presented as the mean ± SD (n = 3).

and to enhance transfection of DNA complexes by trafficking through the endolysosomal pathway. Figure 10a shows that HPAA-CD/pDNA complexes in the serum-free medium have similar transfection efficiencies at different N/P ratios, which are slightly smaller than that of the PEI control. The β-CDs seem to have no remarkable effect on the transfection efficiency in the system. For potential *in vivo* applications, the evaluation of transfection activity in the presence of serum is indispensible. Because the formation and stability of vector/pDNA complexes can be easily changed by the medium, many cationic vectors used for gene transfer experiments are no longer effective in the systems containing serum.[37] In comparison to Figure 10a, Figure 10b shows that the transfection ability of HPAA-CD/pDNA complexes decreases at low N/P ratios in the presence of 10% FBS. With the increase of N/P ratios from 10 to 60, the transfection efficiencies of HPAA-CD complexes improve and finally become quite close to that of the PEI control, indicating the high stability of HPAA-CD/pDNA complexes in the presence of serum.

Complexation with Rhodamine B as Model Drug. It is well-known that β-CD has important applications in pharmaceutical fields due to its strong ability to selectively form inclusion complexes with a wide range of guest molecules.[38−44] For HPAA-CDs, the cavities of surface β-CDs can also be utilized to encapsulate drug molecules with proper size. Rhodamine B (RB) was chosen as a model drug. The obtained HPAA-CD/RB complexes were dissolved in water, and the fluorescent spectra

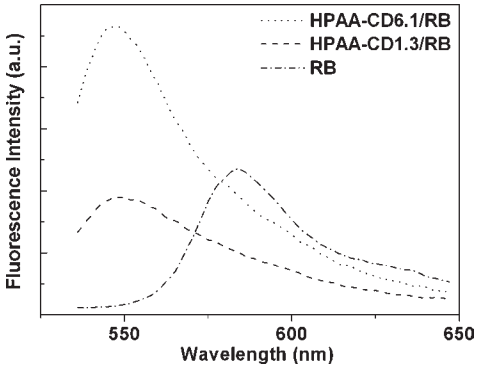


Figure 11. Fluorescence emission spectra of free RB in aqueous solution (0.005 mg/mL) and RB-loaded HPAA-CDs in aqueous solutions(0.5 mg/mL), λ_{ex} = 520 nm.

were acquired as shown in Figure 11. By comparison with the spectrum of free RB aqueous solution, the fluorescence of HPAA-CD/RB complexes shows an obvious blue shift from

585 to 545 nm. With the increase of β-CD content, the fluorescence intensity increases rapidly. These observations demonstrate that RB has been successfully included into the cavity of β-CD. Therefore, the introduction of CD onto the surface of HPAA provides a novel photoluminescent delivery material in the combination of gene therapy and chemotherapy.

CONCLUSIONS

Hyperbranched poly(amido amine)s (HPAAs) containing different amounts of β-CD (HPAA-CDs) have been synthesized by Michael addition copolymerization of MBA, AP, and EDA-β-CD. In comparison with pure HPAA, HPAA-CDs show lower cytotoxicity and significantly enhanced photoluminescence. HPAA-CDs can condense pDNA very efficiently. The cell internalization of the HPAA-CD/pDNA complexes has been studied through flow cytometry and CLSM by detecting the fluorescence of HPAA-CD itself, which avoids the fluorescent labeling process. It demonstrates that the cellular uptake of HPAA-CD/pDNA complexes is very fast and HPAA-CDs mainly locate in the cytoplasm of the cells during the gene transportation process. At the same time, the inner cavities of β-CDs in HPAA-CDs can be used as drug containers. Thus, HPAA-CDs may have potential applications as delivery materials in the combination of gene therapy and chemotherapy.

ASSOCIATED CONTENT

Supporting Information. Quantum yields and fluorescence emission spectra of pure HPAA, HPAA-CDs, and NH_2-terminated G4 PAMAM dendrimer in aqueous solutions. This material is available free of charge via the Internet at http://pubs.acs.org.

AUTHOR INFORMATION

Corresponding Author

*Tel.: +86-21-34205699; Fax: +86-21-34205722; E-mail: xyzhu@sjtu.edu.cn (X. Z.). Tel.: +86-21-62232274; Fax: +86-21-54344800; E-mail: qchen@ecnu.edu.cn (Q.C.).

ACKNOWLEDGMENT

This work is sponsored by the National Natural Science Foundation of China (20974062) and National Basic Research Program 2009CB930400, the Fok Ying Tung Education Foundation (111048), Shuguang Program (08SG14), Shanghai Leading Academic Discipline Project (Project Number: B202), and China National Funds for Distinguished Young Scientists (21025417).

REFERENCES

(1) Mintzer, M. A., and Simanek, E. E. (2009) Nonviral vectors for gene delivery. *Chem. Rev. 109*, 259–302.

(2) Park, T. G., Jeong, J. H., and Kim, S. W. (2006) Current status of polymeric gene delivery systems. *Adv. Drug Delivery Rev. 58*, 467–486.

(3) Li, S. D., and Huang, L. (2007) Non-viral is superior to viral gene delivery. *J. Controlled Release 23*, 181–183.

(4) De Smedt, S. C., Demeester, J., and Hennink, W. E. (2000) Cation polymer based gene delivery systems. *Pharm. Res. 17*, 113–126.

(5) Thomas, M., and Klibanov, A. M. (2003) Non-viral gene therapy: polycation-mediated DNA delivery. *Appl. Microbiol. Biotechnol. 62*, 27–34.

(6) Thomas, C. E., Ehrhardt, A., and Kay, M. A. (2003) Progress and problems with the use of viral vectors for gene therapy. *Nat. Rev. Genet. 4*, 346–358.

(7) Schaffert, D., and Wagner, E. (2008) Gene therapy progress and prospects: synthetic polymer-based systems. *Gene Ther. 15*, 1131–1138.

(8) Itaka, K., and Kataoka, K. (2009) Recent development of nonviral gene delivery systems with virus-like structures and mechanisms. *Eur. J. Pharm. Biopharm. 71*, 475–483.

(9) Hashimoto, M., Morimoto, M., Saimoto, H., Shigemasa, Y., and Sato, T. (2006) Lactosylated chitosan for DNA delivery into hepatocytes: the effect of lactosylation on the physicochemical properties and intracellular trafficking of pDNA/chitosan complexes. *Bioconjugate Chem. 17*, 309–316.

(10) Koh, C. G., Kang, X. H., Xie, Y. B., Fei, Z. Z., Guan, J. J., Yu, B., Zhang, X. L., and Lee, L. J. (2009) Delivery of polyethylenimine/DNA complexes assembled in a microfluidics device. *Mol. Pharmaceutics 6*, 1333–1342.

(11) Albertazzi, L., Serresi, M., Albanese, A., and Beltram, F. (2010) Dendrimer internalization and intracellular trafficking in living cells. *Mol. Pharmaceutics 7*, 680–688.

(12) Wang, C. F., Feng, M., Deng, J. J., Zhao, Y. F., Zeng, X., Hana, L., Pan, S. R., and Wu, C. B. (2010) Poly(α-glutamic acid) combined with polycation as serum-resistant carriers for gene delivery. *Int. J. Pharm. 398*, 237–245.

(13) Wang, D. J., and Imae, T. (2004) Fluorescence emission from dendrimers and its pH dependence. *J. Am. Chem. Soc. 126*, 13204–13205.

(14) Lee, W. I., Bae, Y., and Bard, A. J. (2004) Strong blue photoluminescence and ECL from OH-terminated PAMAM dendrimers in the absence of gold nanoparticles. *J. Am. Chem. Soc. 126*, 8358–8359.

(15) Pastor-Pérez, L., Chen, Y., Shen, Z., Lahoz, A., and Stiriba, S. (2007) Unprecedented blue intrinsic photoluminescence from hyperbranched and linear polyethylenimines: polymer architectures and pH-effects. *Macromol. Rapid Commun. 28*, 1404–1409.

(16) Wang, D. J., Imae, T., and Miki, M. (2007) Fluorescence emission from PAMAM and PPI dendrimers. *J. Colloid Interface Sci. 306*, 222–227.

(17) Imae, T., and Chu, C. C. (2009) Fluorescence investigations of oxygen-doped simple aminie compared with fluorescent PAMAM dendrimer. *Macromol. Rapid Commun. 30*, 89–93.

(18) Saravanan, G., Daigo, K., Imae, T., and Hamakubo, T. (2011) Visual observation of avidin-biotin affinity by fluorescent G4.5 poly(amidoamine) dendrimer. *Colloids Surf. B Biointerfaces 83*, 58–60.

(19) Yang, W., Pan, C. Y., Luo, M. D., and Zhang, H. B. (2010) Fluorescent mannose-functionalized hyperbranched poly(amido amine)s: synthesis and interaction with *E. coli*. *Biomacromolecules 11*, 1840–1846.

(20) Yang, W., and Pan, C. Y. (2009) Synthesis and fluorescent properties of biodegradable hyperbranched poly(amido amine)s. *Macromol. Rapid Commun. 30*, 2096–2101.

(21) Pistolis, G., Malliaris, A., Paleos, C. M., and Tsiourvas, D. (1997) Study of poly(amidoamine) starburst dendrimers by fluorescence probing. *Langmuir 13*, 5870–5875.

(22) Larson, C. L., and Tucker, S. A. (2001) Intrinsic fluorescence of carboxylate-terminated polyamido amine dendrimers. *Appl. Spectrosc. 55*, 679–683.

(23) Wu, D. C., Liu, Y., Jiang, X., He, C. B., Goh, S. H., and Leong, K. W. (2006) Hyperbranched poly(amino ester)s with different terminal amine groups for DNA delivery. *Biomacromolecules 7*, 1879–1883.

(24) Fischer, D., von Harpe, A., Kunath, K., Petersen, H., Li, Y. X., and Kissel, T. (2002) Copolymers of ethylene imine and *N*-(2-hydroxyethyl)-ethylene imine as tools to study effects of polymer structure on physicochemical and biological properties of DNA complexes. *Bioconjugate Chem. 13*, 1124–1133.

(25) Lim, Y. B., Kim, S. M., Lee, Y., Lee, W. K., Yang, T. G., Lee, M. J., Suh, H., and Park, J. S. (2001) Cationic hyperbranched poly(amino ester): a novel class of DNA condensing molecule with cationic surface,

biodegradable three-dimensional structure, and tertiary amine groups in the interior. *J. Am. Chem. Soc. 123*, 2460–2461.

(26) Lim, Y. B., Kim, S. M., Suh, H., and Park, J. S. (2002) Biodegradable, endosome disruptive, and cationic network-type polymer as a highly efficient and nontoxic gene delivery carrier. *Bioconjugate Chem. 13*, 952–957.

(27) Haensler, J., and Szoka, F. C. (1993) Polyamidoamine cascade polymers mediate efficient transfection of cells in culture. *Bioconjugate Chem. 4*, 372–379.

(28) Zhou, Y. Y., Guo, Z., Zhang, Y. W., Huang, W., Zhou, Y. F., and Yan, D. Y. (2009) Hyperbranched polyamidoamines containing β-cyclodextrin for controlled release of chlorambucil. *Macromol. Biosci. 9*, 1090–1097.

(29) Chen, L., Zhu, X. Y., Yan, D. Y., Chen, Y., Chen, Q., and Yao, Y. F. (2006) Controlling polymer architecture based on host-guest interactions. *Angew. Chem., Int. Ed. 45*, 87–90.

(30) Zhu, X. Y., Chen, L., Chen, Y., and Yan, D. Y. (2008) Using 2D NMR to determine the degree of branching of complicated hyperbranched polymers. *Sci. China Ser. B: Chem. 51*, 1057–1065.

(31) Hawker, C. J., Lee, R., and Fréchet, J. M. J. (1991) One-step synthesis of hyperbranched dendritic polyesters. *J. Am. Chem. Soc. 113*, 4583–4588.

(32) Mosmann, T. J. (1983) Rapid colorimetric assay for cellular growth and survival-application to porliferation and cyto-toxicity assays. *Immunol. Methods 65*, 55–63.

(33) Prabaharan, M., Grailer, J. J., Pilla, S., Steeber, D. A., and Gong, S. (2009) Amphiphilic multi-arm block copolymer based on hyperbranched polyester, poly(L-lactide) and poly(ethylene glycol) as a drug delivery carrier. *Macromol. Biosci. 9*, 515–524.

(34) Stasko, N. A., Johnson, C. B., Schoenfisch, M. H., Johnson, T., and Holmuhamedov, E. L. (2007) Cytotoxicity of polypropylenimine dendrimer conjugates on cultured endothelial cells. *Biomacromolecules 8*, 3853–3859.

(35) Zintchenko, A., Philipp, A., Dehshahri, A., and Wagner, E. (2008) Simple modifications of branched PEI lead to highly efficient siRNA carriers with low toxicity. *Bioconjugate Chem. 19*, 1448–1455.

(36) Pun, S. H., Bellocq, N. C., Liu, A., Jensen, G., Machemer, T., Quijano, E., Schluep, T., Wen, S., Engler, H., Heidel, J., and Davis, M. E. (2004) Cyclodextrin-modified polyethylenimine polymers for gene delivery. *Bioconjugate Chem. 15*, 831–840.

(37) Escriou, V., Ciolina, C., Lacroix, F., Byk, G., Scherman, D., and Wils, P. (1998) Cationic lipid-mediated gene transfer: effect of serum on cellular uptake and intracellular fate of lipopolyamine/DNA complexes. *Biochim. Biophys. Acta 1368*, 276–288.

(38) Harada, A., and Kamachi, M. (1990) Complex formation between poly(ethylene glycol) and α-cyclodextrin. *Macromolecules 23*, 2821–2813.

(39) Harada, A., Li, J., and Kamachi, M. (1992) The molecular necklace: a rotaxane containing many threaded α-cyclodextrins. *Nature 356*, 325–327.

(40) Koopmans, C., and Ritter, H. (2007) Color change of *N*-isopropylacrylamide copolymer bearing Reichardts dye as optical sensor for lower critical solution temperature and for host-guest interaction with beta-cyclodextrin. *J. Am. Chem. Soc. 129*, 3502–3503.

(41) Xue, J., Jia, Z. F., Jiang, X. L., Wang, Y. P., Chen, L., Zhou, L., He, P., Zhu, X. Y., and Yan, D. Y. (2006) Kinetic separation of polymers with different terminals through inclusion complexation with cyclodextrin. *Macromolecules 39*, 8905–8907.

(42) Zhu, X. Y., Chen, L., Yan, D. Y., Chen, Q., Yao, Y. F., Xiao, Y., Hou, J., and Li, J. (2004) Supramolecular self-assembly of inclusion complexes of a multiarm hyperbranched polyether with cyclodextrins. *Langmuir 20*, 484–490.

(43) Hwang, M. J., Bae, H. S., Kim, S. J., and Jeong, B. (2004) Polyrotaxane hexagonal microfiber. *Macromolecules 37*, 8820–8822.

(44) Chung, J. W., Kang, T. J., and Kwak, S. Y. (2007) Supramolecular self-assembly of architecturally variant alpha-cyclodextrin inclusion complexes as building blocks of hexagonally aligned microfibrils. *Macromolecules 40*, 4225–4234.

Supporting Information

Photoluminescent Hyperbranched Poly(amido amine) Containing β-Cyclodextrin as a Non-Viral Gene Delivery Vector

Yan Chen,[†] Linzhu Zhou,[†] Yan Pang,[†] Wei Huang,[†] Feng Qiu,[†] Xulin Jiang,[‡] Xinyuan Zhu,[*,†] Deyue Yan[†], Qun Chen[*,§]

[†] *School of Chemistry and Chemical Engineering, State Key Laboratory of Metal Matrix Composites, Shanghai Jiao Tong University, 800 Dongchuan Road, Shanghai 200240, People's Republic of China*

[‡] *Key Laboratory of Biomedical Polymers of Ministry of Education, Department of Chemistry, Wuhan University, Wuhan 430072, P. R. China*

[§] *Department of Physics & Shanghai Key Laboratory of Functional Magnetic Resonance Imaging, East China Normal University, North Zhongshan Road 3663, Shanghai 200062, People's Republic of China*

* *To whom correspondence should be addressed. Tel.: +86-21-34205699; Fax: +86-21-34205722; E-mail: xyzhu@sjtu.edu.cn (X. Z.). Tel.: +86-21-62232274; Fax: +86-21-54344800; E-mail: qchen@ecnu.edu.cn (Q.C.).*

The quantum yields of hyperbranched poly(amido amine) (HPAA), HPAAs containing different amount of β-cyclodextrin (HPAA-CDs) and NH_2-terminated G4 poly(amido amine) (PAMAM) dendrimer were measured using quinine sulfate in 0.05 M sulfuric acid (Φ_Q = 0.52 with excitation of 346.5 nm) as a reference standard[1] using the following equation:[2]

$$\Phi_S = \Phi_Q (F_S/F_Q) (A_Q/A_S) (n_s/n_Q)^2$$

Where F is the area under the fluorescence spectra, A is the absorbance. n is the refractive index of the solvent, and the subscript Q and S represent quinine sulfate and sample, respectively. The quantum yields of HPAA, HPAA-CD1.3, HPAA-CD6.1 and NH_2-terminated G4 PAMAM dendrimer are 0.59%, 0.68%, 0.73% and 0.25%, respectively. Although the quantum yields of all the samples are not large, HPAA-CDs seem to be higher than PAMAM dendrimer. The fluorescence emission spectra in Figure S1 show that HPAA-CDs emit much stronger fluorescence than G4 PAMAM dendrimer with the same solution concentration.

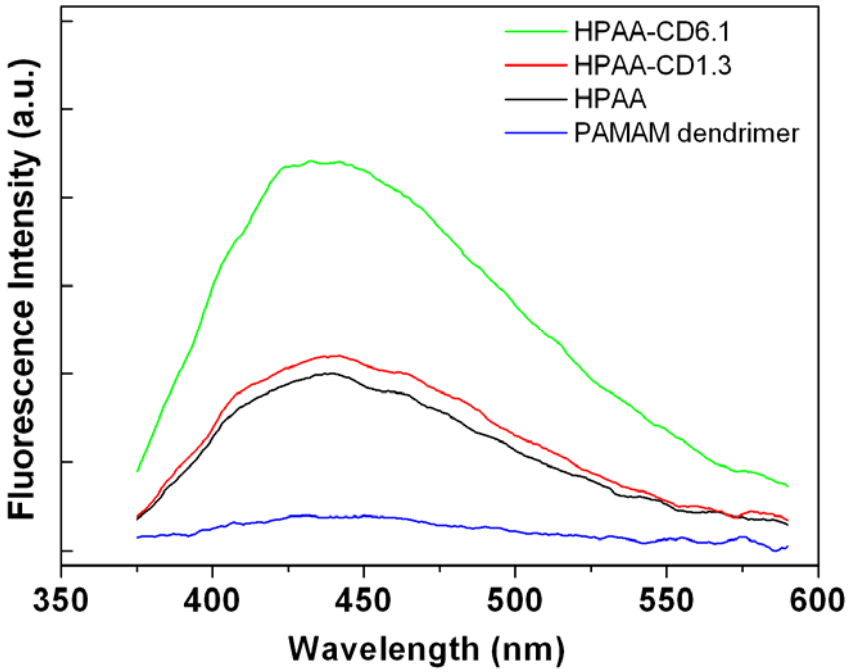


Figure S1. Fluorescence emission spectra of pure HPAA, HPAA-CDs and NH_2-terminated G4 PAMAM dendrimer in aqueous solutions (1 mg/mL), λ_{ex} = 350 nm.

LITERATURE CITED

(1) Heller, C. A., Henry, R. A., McLaughlin, B. A., and Bliss, D. E. (1974) Fluorescence spectra and quantum yields: quinine, uranine, 9,10-diphenylanthracene, and 9,10-bis(phenylethynyl) anthracenes. *J. Chem. Eng. Data*. *19*, 214-219.

(2) Onoda, M., Uchiyama, S., Santa, T., and Imai, K. (2002) A photoinduced electron-transfer reagent for peroxyacetic acid, 4-ethylthioacetylamino-7-phenylsulfony-2,1,3-benzoxadiazole, based on the method for predicting the fluorescence quantum yields. *Anal. Chem. 74*, 4089-4096.

Bioconjugate Chemistry

ARTICLE

pubs.acs.org/bc

Enhanced Intracellular Delivery and Chemotherapy for Glioma Rats by Transferrin-Conjugated Biodegradable Polymersomes Loaded with Doxorubicin

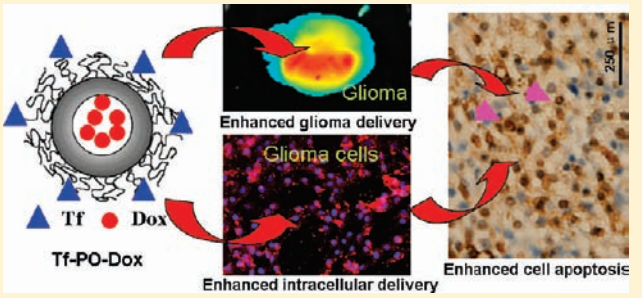
Zhiqing Pang,[†,‡] Huile Gao,[†,‡] Yuan Yu,[§] Liangran Guo,[†,‡] Jun Chen,[†,‡] Shuaiqi Pan,[†,‡] Jinfeng Ren,[†,‡] Ziyi Wen,[†,‡] and Xinguo Jiang[*,†,‡]

[†]Department of Pharmaceutics, School of Pharmacy, Fudan University, Shanghai, People's Republic of China, 201203

[‡]Key Laboratory of Smart Drug Delivery, Ministry of Education & PLA, People's Republic of China, 201203

[§]Department of Pharmaceutics, School of Pharmacy, The Second Military Medical University, Shanghai, People's Republic of China, 200433

ABSTRACT: A brain drug delivery system for glioma chemotherapy based on transferrin-conjugated biodegradable polymersomes, Tf-PO−DOX, was made and evaluated with doxorubicin (DOX) as a model drug. Biodegradable polymersomes (PO) loaded with doxorubicin (DOX) were prepared by the nanoprecipitation method (PO−DOX) and then conjugated with transferrin (Tf) to yield Tf-PO−DOX with an average diameter of 107 nm and surface Tf molecule number per polymersome of approximately 35. Compared with PO−DOX and free DOX, Tf-PO−DOX demonstrated the strongest cytotoxicity against C6 glioma cells and the greatest intracellular delivery. It was shown in pharmacokinetic and brain distribution experiments that Tf-PO significantly enhanced brain delivery of DOX, especially the delivery of DOX into brain tumor cells. Pharmacodynamics results revealed a significant reduction of tumor volume and a significant increase of median survival time in the group of Tf-PO−DOX compared with those in saline control animals, animals treated with PO−DOX, and free DOX solution. By terminal deoxynucleotidyl transferase-mediated dUTP nick-end-labeling, Tf-PO−DOX could extensively make tumor cell apoptosis. These results indicated that Tf-PO−DOX could significantly enhance the intracellular delivery of DOX in glioma and the chemotherapeutic effect of DOX for glioma rats.



INTRODUCTION

Treatment of malignant gliomas represents one of the most formidable challenges in oncology.[1] Despite combined therapies of surgery, radiotherapy, and chemotherapy, the prognosis for gliomas remains very poor, especially for glioblastoma, which has a median survival of 12 to 15 months.[2] Even with steady advances in drug discovery and targeted therapeutics that improve long-term control in systemic cancers, there has been little impact on the prognosis of patients with malignant gliomas.[1] The most notable obstacle underlying the disappointing results in glioma therapeutics is the presence of the blood-brain barrier (BBB), which serves to prevent delivery of potentially active therapeutic compounds.[3] Moreover, limited tumor cell drug uptake, intracellular drug metabolism, inherent tumor sensitivity to chemotherapy, and cellular mechanisms of resistance also contribute much to the poor effectiveness of treatment for glioma.[4] Therefore, a great deal of effort is presently focused on developing strategies to effectively deliver active drugs to brain tumor cells, improving therapeutic opportunities, efficiency, and patient survival, while decreasing side effects to normal cells. Magnetic resonance imaging (MRI)-guided focused ultrasound-induced BBB disruption and convection-enhanced delivery have emerged as leading investigational delivery techniques for the treatment of malignant gliomas.[2,5,6] However, expensive medical devices and potential hazards produced from repeated BBB opening or invasive neurosurgery greatly limit their application in glioma therapy. Thus, targeting drug delivery to glioma cells noninvasively using nanocarrier systems such as micelles, liposomes, nanoparticles (NPs), and dendrimers may be a better approach and has been widely investigated recently.[7−9]

As a new class of synthetic thin-shelled capsules based on block copolymer chemistry, polymersomes are self-assembled vesicles of amphiphilic block copolymers that currently attract great interest for their structural analogies with living organelles and potential applications as nanosized reactors or drug delivery systems.[10−13] Over the past decade, polymersomes were revealed to be promising alternatives to phospholipid-based vesicles regarding their remarkable, attractive, and feasible characteristics such as stealthiness, improved stability, and ease of functionalization.[13−15] Compared with liposomes (3−5 nm bilayer), polymersomes are extremely stable and robust with high membrane stability and low membrane permeability, which

Received: January 30, 2011
Revised: April 17, 2011
Published: May 02, 2011

ACS Publications © 2011 American Chemical Society

can overcome most of the stability problems (mainly drug leakage and disintegration of membrane) encountered in lipidic vesicles due to the high fluidity of their bilayers.[16,17] In addition, it has been evidenced that the physical and chemical properties of polymersomes including particles size, drug loading, surface modification, and even in vivo behavior may be broadly controlled and modulated through rich diversity of block copolymer chemistries (block fraction, block architecture).[13] Furthermore, desirable smart polymersomes can be designed to combine features required for drug delivery application, such as biodegradability,[18,19] targeting capability,[20,21] and responsiveness to biologically relevant stimuli [22] such as pH,[23] temperature,[24] light,[25] and reductive environment.[26] Therefore, polymersomes are good candidates for drug delivery carriers, which are currently being developed by many groups. However, the vast majority of present efforts are focused on the fabrication of novel functional polymersomes including biomimetic polymersomes for glioma cells treatment in vitro,[27] while in vivo exploitation of biodegradable polymersomes as brain drug delivery systems has rarely been reported.

The anthracycline doxorubicin, one of the most powerful anticancer agents, like most small-molecule anticancer agents, has a poor effect on glioma therapy for its inability to cross the BBB and achieve effective concentrations in the glioma cells. Although liposomal doxorubicin has been shown to be a safe treatment with moderate activity that might lead to long-term stabilization in recurrent high-grade glioma patients,[28] its poor blood-brain barrier penetration, limited intracellular delivery, and instability are still major limitations in the treatment of malignant glioma. By a secondary targeting strategy,[29] liposomes conjugated with two different targeting ligands might possess the ability to traverse the BBB and reach the secondary target (glioma cell), greatly improving gene therapy for glioma rats.[30] However, the preparation of two ligand-conjugated liposomes might be rather complicated and uncontrollable. Moreover, the high density of different surface ligands on liposomes might not only increase the possibility to opsonization and accelerate the blood clearance,[31] but also aggravate the instability of liposomes. As promising alternatives to liposomes, biodegradable poly(ethylene glycol)-poly(ε-caprolactone) (PEG-PCL) polymersomes functionalized with lactoferrin were proven to cross BBB and accumulate at the glioma site in our previous report.[32] However, the large vesicle size above 200 nm might accelerate the blood clearance and minimize the likelihood of crossing the BBB.[33] In addition, insufficient intracellular delivery also decreased the doxorubicin concentration in glioma cells. Thus, biodegradable polymersomes with better vesicle properties such as rational size and surface modification are still necessary for effective glioma targeting delivery.

In this study, doxorubicin, as a model small-molecule anticancer agent, was encapsulated into biodegradable PEG-PCL polymersomes with small vesicle size. As a classic both BBB targeting and tumor targeting ligand,[34] transferrin, was conjugated to the surfaces of polymersomes to prepare "Trojan horse" (Tf-PO−DOX) for glioma drug delivery. A single targeting ligand that could mediate both transport across the BBB and internalization into glioma cells represented the simplest approach for secondary targeting delivery. Enhanced intracellular delivery and glioma drug delivery were investigated in glioma bearing rats and then verified by pharmacodynamics tests including tumor volume, survival monitoring, and tumor cell apoptosis.

MATERIALS AND METHODS

Materials and Animals. The MPEG3k-PCL15.8k or Maleimide-PEG3.4k-PCL16k diblock copolymers were synthesized by ring-opening polymerization of ε-CL using MPEG (M_w 3000 Da, NOF Corporation, Japan) or Maleimide-PEG (M_w 3400 Da, NEKTAR, USA) as described elsewhere.[35] Doxorubicin (DOX) and daunorubicin was purchased from Beijing Huafeng United Technology (China) and National Institute for the Control of Pharmaceutical and Biological Products (China), respectively. Holo-transferrin, 2-iminothiolane (Traut's reagent), and phenylmethyl sulfonyl fluoride (PMSF) were ordered from Sigma and 5,5-dithiobis (2-nitrobenzoicacid) (Ellmann's reagent) was from Acros (Belgium). Human transferrin ELISA quantitation kit was obtained from Bethyl (Montgomery, TX, USA). Neuro-TACS II *In Situ* Apoptosis Detection Kit was purchased from R&D systems (Minneapolis, MN). C6 glioma cell line from rat was obtained from the American Type Culture Collection. Fetal bovine serum (FBS) and related cell culture medium were purchased from Invitrogen (Gibco, Carlsbad, CA). Plastic cell culture dishes, plates, and flasks were ordered from Corning Incorporation (Lowell, MA). Double distilled water was purified using a Millipore Simplicity System (Millipore, Bedford, MA, USA). All the other chemicals were analytical reagent grades and used without further purification. Wistar strain rats (weighing 200−230 g) were obtained from Shanghai SLAC Laboratory Animal Co. Ltd. (Shanghai, China). The animals involved in this study were treated according to protocols evaluated and approved by the ethical committee of Fudan University.

Preparation of Transferrin Conjugated Biodegradable Polymersomes. Biodegradable polymersomes were prepared with a blend of MPEG-PCL and Maleimide-PEG-PCL by the nanoprecipitation method.[12] Briefly, 20 mg of MPEG-PCL and 1 mg of Maleimide-PEG-PCL were dissolved in 1.0 mL of tetrahydrofuran (THF). The polymer solution was then injected slowly into 10 mL of 0.2 M citrate buffer (pH 4.0). Mild stirring was performed to induce self-assembly for 30 min. To remove THF and exchange the external buffer, the solution was dialyzed against 0.01 M PBS buffer (pH 7.4) for 12 h using dialysis membranes (MW cutoff, 14 000 Da) and the buffer solution is replaced by fresh PBS every 4 h. For DOX loading, 2 mg of DOX was added and the mixed solution was incubated in the dark at 40 °C for 24 h. By means of ultrafiltration, unencapsulated DOX was eluted and the vesicle dispersion was concentrated to yield DOX-loaded polymersome (PO−DOX).

Transferrin conjugation with DOX-loaded polymersomes was made as described previously.[35] In brief, transferrin was thiolated using 2-iminothiolane (Traut's reagent), then incubated with polymersomes for 6 h with a 1:3 molar ratio of thiolated transferrin to maleimide. By means of ultrafiltration again, unconjugated protein was removed and Tf-conjugated DOX-loaded polymersome (Tf-PO−DOX) solution was concentrated. All operations were conducted away from light.

Characterization of Tf-Conjugated DOX-Loaded Polymersome. The formation of blank polymersomes was visualized by cryo-transmission electron micrograph (Cryo-TEM, JEOL 2010, Japan).[35] The shape and size of unloaded polymersomes were observed by transmission electron microscope (TEM, JEM-1230, JEOL, Japan) following negative staining with 1% uranyl acetate solution. The mean diameters and zeta potential of Tf-PO−DOX were determined by dynamic light scattering (DLS) using a Zeta Potential/Particle Sizer NICOMP 380 ZLS (PSS.

NICOMP Particle Size System, Santa Barbara, CA, USA). Surface transferrin densities were determined by ELISA method combined with turbidimetry method as previously described.[35] Drug loading efficiency and in vitro release of DOX from Tf-PO−DOX was determined using fluorescence spectrometry (Ex: 480 nm and Em: 580 nm). In the latter, drug loaded polymersomes were suspended in a dialysis system which was monitored by periodic withdrawals of drug released into 0.01 M PBS (pH 4 and 7.4) or 10% rat plasma in PBS.[36]

Cell Uptake and Intracellular Drug Distribution of DOX-Loaded Polymersomes. A 24-well plate was seeded with C6 cells at a density of 10^5 per well, and the cells were allowed to attach for 24 h. Dispersions of PO−DOX and Tf-PO−DOX as well as free DOX solution were each added into the medium in triplicate to make a final DOX concentration at 4 μg/mL in each well. After 4 h incubation at 37 °C, the medium was removed and the cells were stained with 1 μg/mL of 4′,6-diamidino-2-phenylindole dihydrochloride (DAPI) for 10 min at room temperature. After PBS washing, the plate was subjected to observation under the fluorescence microscope (Olymus IX71, Japan).

Quantitative Determination of Cell Uptake of DOX-Loaded Polymersomes. Similarly to the above, C6 cells were seeded onto 24-well plates at a density of 10^5 per well, and the cells were allowed to attach for 24 h. Three groups of DOX preparations were respectively added into the medium to make a final DOX concentration at 4 μg/mL in each well (triplicate for each formulation). The plates were incubated for 1, 2, 4, 8, or 12 h at 37 °C. For each time point, cells in each well of the corresponding plate were washed three times with ice-cold PBS to remove surface-bound polymersomes and further incubated with 0.4 mL of 1% Triton X-100 at 4 °C overnight. Afterward, 25 μL of the cell lysate from each well was sampled to determine the total cell protein content using the BCA protein assay kit. The rest of the cell lysate was used for extraction and HPLC determination of DOX (Agilent 1200) with fluorescence detector at an excitation wavelength of 480 nm and an emission wavelength of 550 nm.[37] The uptake index (UI) was expressed as DOX (μg)/cellular protein (mg).

Intracellular Drug Distribution. Intracellular drug distribution studies were carried out as previously described with a little modification.[38] Briefly, C6 cells were seeded onto 6-well plates at 10^6 cells per well and allowed to attach for 12 h. Three groups of DOX preparations were respectively added into the medium to make a final DOX concentration at 4 μg/mL in each well (triplicate for each formulation). The plates were incubated for 1, 2, 4, 8, or 12 h at 37 °C. For each time point, cells in each well of the corresponding plate were washed three times with ice-cold PBS to remove surface-bound polymersomes and further collected by centrifugation at 3000 rpm for 5 min after cell dissociation. The resulting cell pellets were washed thrice with 3 mL ice-cold PBS, resuspended in 300 μL TM-2 buffer (0.01 M Tris−HCl, pH 7.4, 0.002 M $MgCl_2$, 0.0005 M PMSF), and incubated at room temperature for 1 min followed by ice water for 5 min. Triton X-100 was added to the suspension to a final concentration of 1% (v/v) and the suspension was incubated in ice water for an additional 5 min. After centrifugation at 1000 rpm at 4 °C for 10 min, the supernatant was transferred to determine the drug amount in cytoplasm and the isolated pellet was resuspended in 0.5 mL of TM-2 buffer for determination of the drug levels in nuclei. The drug levels of both cytoplasm and nuclei were determined by HPLC method as described above. The corresponding protein concentrations were measured using BCA protein assay kit. The uptake index (UI) was expressed as DOX (μg)/cellular protein (mg).

In Vitro Cytotoxicity of DOX-Loaded Polymersomes against C6 Cells. C6 cells were seeded onto a 96-well plate at a density of 10^4 per well and incubated for 24 h before exposure to different DOX formulations with a series of concentrations for a further 24 h at 37 °C. Eight wells for untreated cells were prepared as controls. After exposure, the cytotoxicity of these formulations was assayed by the MTT method. The experiments were performed in quadruplicate.

Tumor Implantation. Male rats were maintained at 22 ± 2 °C on a 12 h light−dark cycle with access to food and water ad libitum. For tumor implantation, animals were anesthetized with chloral hydrate (0.4 g/kg) intraperitoneally and then subjected to stereotaxic injection of approximately 3×10^5 of C6 cells (in 5 μL of RPMI-1640 medium) into the caudate nucleus region.[39] The injection location was 1 mm posterior and 2 mm right to the bregma, and 4.5 mm beneath the exposed dura mater. The burr hole in the skull was sealed with bone wax and the scalp incision was sutured.

Pharmacokinetics and Tissue Distribution of Tf-PO−DOX. Animal experiments were performed as previously described.[32] In brief, 12 days after tumor implantation, male rats were randomly divided into 3 groups for pharmacokinetics or tissue distribution studies and administrated intravenously with a dose of 5 mg/kg DOX in solution, PO and Tf-PO. For pharmacokinetics study, blood samples were collected from the retro-orbital plexus at 0.083, 0.25, 0.5, 1, 2, 4, 8, and 12 h following i.v. injection. At 24 h, the animals were decapitated and the brain tissues including cerebral cortex, left striatum, and right striatum (tumor tissue) were excised followed by quick washing with cold saline to remove surface blood. Blood sample and major organs including liver, spleen, kidney, lung, and heart were also collected. For tissue distribution at 4 h, the animals were decapitated and the brain tissues, blood sample, and other major organs were collected as described above.

Fluorescent imaging of brain and other major organs was investigated by a CRi in vivo fluorescent imaging system (CRI, Woburn, MA, USA) consisting of a highly sensitive Peltier cooled backlit CCD camera (2184 × 1472 pixels). In brief, the organs were placed in the light-tight chamber, the filter for emission was set at 550 nm, respectively, and the photon emission was integrated over a period of 5 s. After that, a grayscale reference image was collected under white light. For localization of the photon emission, grayscale and pseudocolor images were merged using *WinLight 32* software.

HPLC analysis was performed for determining levels of DOX in biological specimen.[37] In brief, the tissue samples were homogenized on ice with 3-fold volumes of deionized water followed by addition of 10 μL of daunorubicin (internal standard, 10 μg/mL). The samples were extracted with 2 mL of chloroform/methanol (4:1, v/v) following intense vortexing for 2 min. After centrifugation at 4000 *g* for 10 min, the subnatant was transferred and evaporated under a gentle stream of nitrogen at 40 °C. The residue was dissolved in 200 μL of methanol, and 20 μL was injected into the HPLC system. The blood plasma samples were extracted without the addition of water and reconstituted in the same manner. The chromatographic analysis was performed on the HPLC system (Shimadzu Scientific Instrument Inc., Japan) including a pump (model LC-10AT) and a fluorescence detector (model RF-10AXL; λ_{ex} = 480 nm, λ_{em} = 550 nm). Using potassium dihydrogen phosphate/

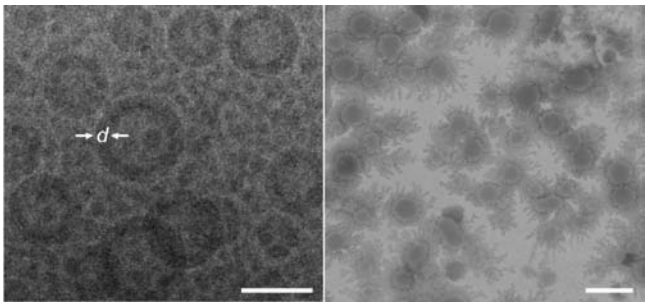


Figure 1. (A) Cryo-TEM images of polymersomes in water (bar 100 nm). The hydrophobic cores of polycaprolactone are the darker areas. (B) TEM images of polymersomes negatively stained with 1% uranyl acetate solution (bar 200 nm).

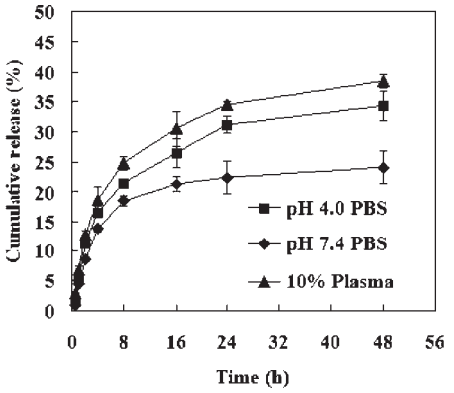


Figure 2. Cumulative releases (%) of doxorubicin from Tf-PO−DOX in different media.

acetonitrile/glacial acetic acid (70:30:0.3, v/v) with pH 3.0 as the mobile phase at a flow rate of 1.2 mL/min, chromatographic separations were achieved with a C_{18} analytical column (5 μm, 4.6 × 200 mm, Diamonsil, Dikma) equipped with a guard column (Nova-Pak, Waters) at 35 °C. The retention time of DOX and internal standard (daunomycin) was about 3.7 and 8.2 min, respectively.

For data analysis, the plasma data were fitted to a biexponential equation: $A(t) = A_1e^{-k1t} + A_1e^{-k2t}$, where $A(t)$ was %ID per mL of plasma (%ID, percentage of injected dose).[40] Pharmacokinetic parameters, such as plasma clearance (Cl) and steady-state volume of distribution (V_{ss}), were calculated from A_1, A_2, k_1, and k_2. Area under the blood concentration curve (AUC) was calculated by noncompartmental data analysis of blood concentrations. The brain permeability surface area (PS) product and brain uptake (expressed as %ID per g of tissue) were calculated as described elsewhere.[41]

Antitumor Efficacy in Rats Bearing Glioma. Tumor-bearing animals were equally and randomly divided into 4 groups, which received saline, DOX solution, PO−DOX, and Tf-PO−DOX, respectively. These preparations were i.v. injected at 2, 5, 8, and 11 days after glioma implantation, dosing at 1.5 mg/kg DOX.[32,42] On the 7th and 14th days, 6 rats per group were randomly sacrificed. Heart perfusion with 10% neutral buffered formalin was conducted after sacrifice, and the brain tissue sample was collected and fixed with 10% neutral buffered formalin for at least 48 h and then embedded in paraffin followed by routine hematoxylin and eosin (H&E) staining on 5-μm-thick sections using routine protocols.[43] The maximum diameter (a) and minimum diameter (b) of glioma tissue was measured under stereomicroscope, and the tumor volume (V) in each animal was calculated as $V = 0.5ab^2$. Paraffin-embedded brain tumor tissue sections (5 μm) were also prepared for apoptosis detection by Tdt-mediated dUTP nick-end labeling (TUNEL) according to the protocol of NeuroTACS II *In Situ* Apoptosis Detection Kit. Samples were counterstained with hematoxylin while positive signals were developed by diaminobenzidine (DAB).

Twelve tumor-bearing rats of each group were followed by survival monitoring. Survival data were analyzed with log-rank test in a Kaplan−Meier nonparametric analysis and summarized descriptively by means of median survival times with their respective 95% confidence intervals.

Statistical Analysis. Statistical differences in uptake index, pharmacokinetic parameters, and tumor volume were determined by one-way analysis of variance (ANOVA), followed by post hoc analysis of Bonferroni for multigroup comparison. $P < 0.05$ was considered significant.

RESULTS

Characterization of DOX-Loaded Polymersomes. Cryo-TEM results revealed that a blend of MPEG3k-PCL15.8k and Maleimide-PEG3.4k-PCL16k spontaneously assembled into polymersomes which were generally round with a diameter of approximately 100 nm. Moreover, the hydrophobic core of the membrane provided the contrast, and the membrane thickness was homogeneous with a measured width d of about 16 nm (Figure 1A), which is considerably greater than any previously studied lipid system. The self-assembled bilayers was also thicker than that we previously reported (10 nm)[35] due to the higher molecular weight of block polymer PCL, as this is clear and already has been demonstrated.[44] The TEM examination demonstrated that polymersomes were of vesicle-like shape with averaged diameters around 100 nm (Figure 1B), in good accordance with DLS results. A slight diameter increase was observed following DOX loading and Tf conjugation. The final average diameters of PO−DOX and Tf-PO−DOX were 101.8 ± 9.2 nm and 107.7 ± 11.3 nm, respectively. The zeta potential values of PO−DOX and Tf-PO−DOX in 0.001 M NaCl solution were −9.1 ± 0.6 mV and −9.3 ± 0.5 mV, respectively, indicating Tf conjugation had no influence on the zeta potential value of polymersomes. Drug loading capacity of DOX in the polymersomes was about 4.4% with entrapment efficiency above 96%. The mean Tf molecule numbers per polymersome on the surface of Tf-PO−DOX was 35.1 ± 6.2, which was a reasonable density for brain targeting justified in other studies.[41,45]

As shown in Figure 2, under three releasing conditions, the release profile of DOX from Tf-PO−DOX displayed a biphasic pattern that was characterized by a first rapid release (~17% of DOX was released within 4 h) followed by a slower and sustained release. After a 48 h incubation period, about 34.3%, 24.1%, and 38.4% of DOX were released from Tf-PO−DOX in pH 4.0, 7.4 PBS, and rat plasma, respectively. DOX was released much more rapidly in pH 4.0 than in pH 7.4 PBS, which might be attributed to acid-catalyzed hydrolysis of the PCL membrane[46] and increased hydrophilicity of DOX in acid condition.[47] The cumulative release of DOX from Tf-PO−DOX at 8 h in rat plasma was below 25% indicating that DOX entrapped in Tf-PO might be mostly preserved during the brain uptake process of Tf-PO−DOX.

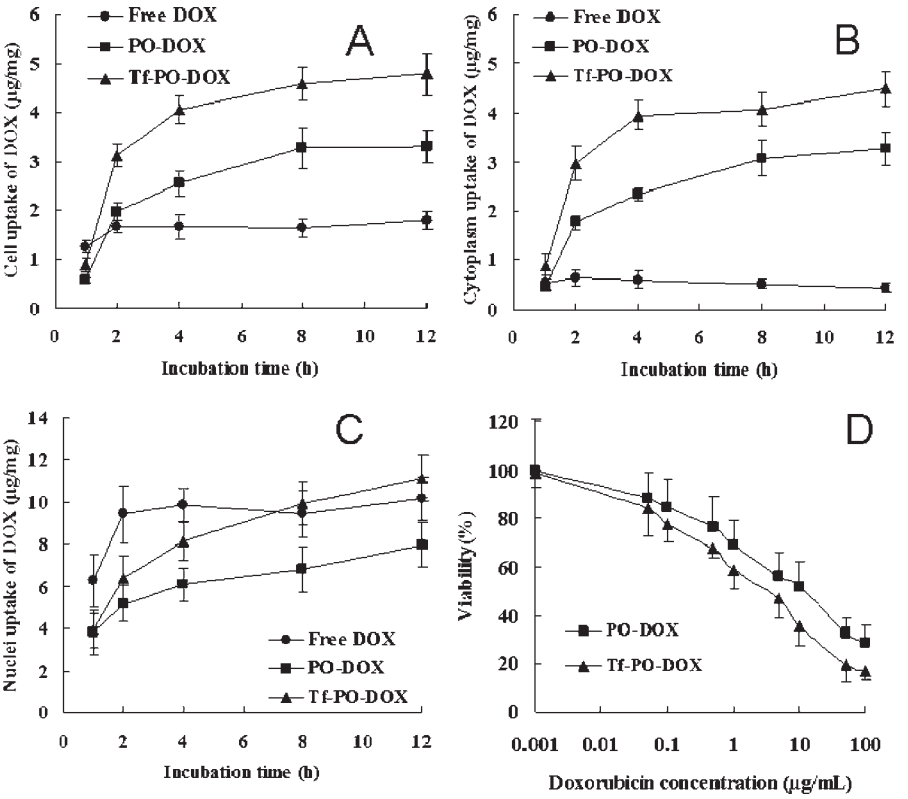


Figure 3. Cell uptake and intracellular distribution of free DOX, PO−DOX, and Tf-PO−DOX (4 μg/mL DOX) in C6 cell line from 1 to 12 h. Relative uptake in cell (A), cytoplasm (B), and nuclei (C). (D) C6 viability inhibition-logarithmic doxorubicin concentration curve of DOX loaded polymersomes.

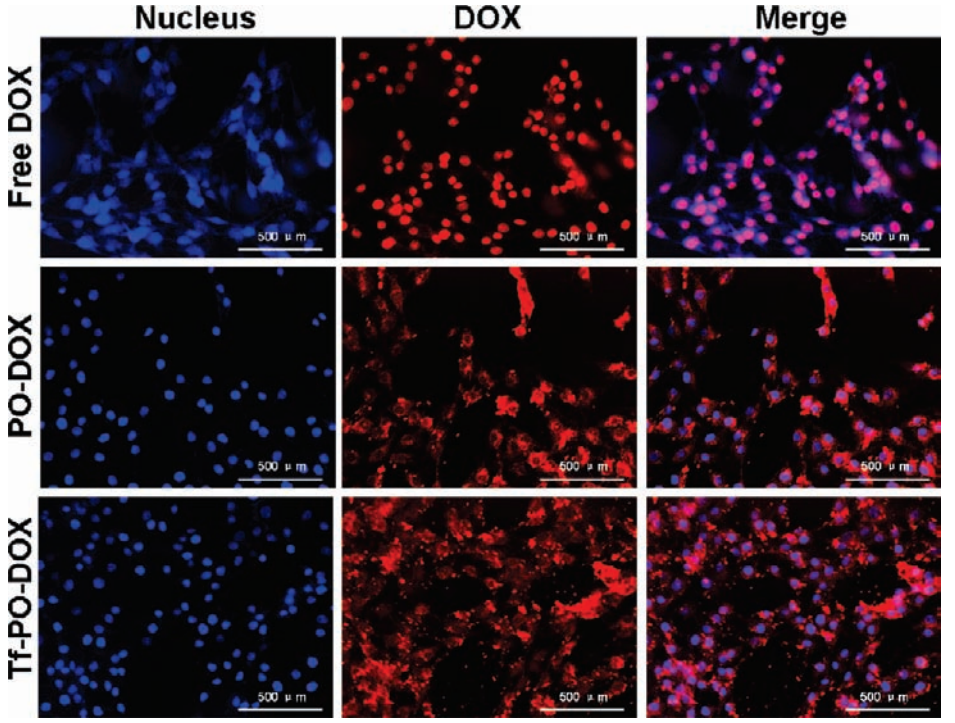


Figure 4. Fluorescence photographs of C6 cells after incubation for 4 h with free DOX, PO−DOX, and Tf-PO−DOX (4 μg/mL DOX).

Cell Uptake and Intracellular Distribution. Uptake of DOX-loaded polymersomes by C6 cells increased with time (Figure 3A). Tf-PO−DOX accumulated within the cells at a faster rate and to a larger extent than PO−DOX. After 12 h incubation, the UI for

dx.doi.org/10.1021/bc200062q |*Bioconjugate Chem.* 2011, 22, 1171–1180

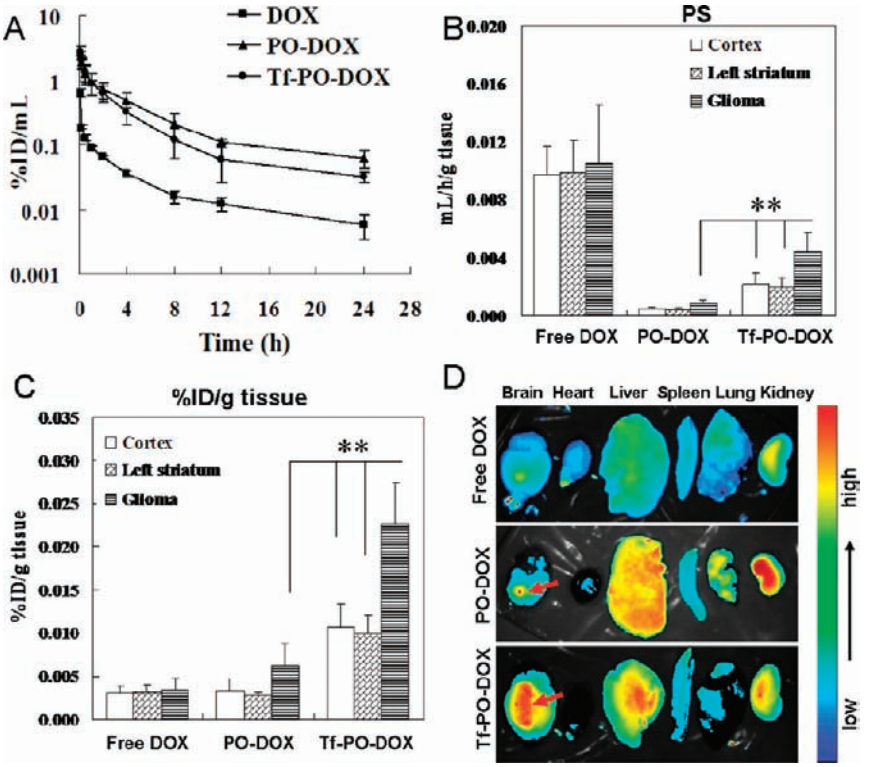


Figure 5. Pharmacokinetics and brain delivery of doxorubicin-loaded polymersomes. (A) %ID/mL of plasma of doxorubicin is plotted versus various times after i.v. injection of 5 mg/kg of doxorubicin solution, doxorubicin loaded Tf-PO, and PO in C6 glioma transplanted rats. (B) Permeability surface area (PS) product and (C) brain uptake of doxorubicin at 4 h after intravenous injection in C6 glioma transplanted rats. (D) Fluorescent imaging of main organs at 4 h after i.v. injection of 5 mg/kg of doxorubicin solution, PO−DOX, and Tf-PO−DOX in C6 glioma transplanted rats. Data represent means ± SD (n = 4). *P < 0.05, **P < 0.01 vs Tf-PO−DOX group. Data are means ± SD of n = 4 rats/point.

Tf-PO−DOX and PO−DOX were 4.8 and 3.3 μg/mg, respectively. The uptake of polymersomes in cytoplasm presented an initial rapid increase before 4 h (Figure 3B). After that, the uptake curve for polymersomes showed a slow decrease and tended to reach a plateau as the incubation time prolonged. A low cytoplasmic uptake of free DOX was obviously observed during the incubation period. In nuclei, the uptake for DOX-loaded polymersomes increased with time, while the uptake for free DOX rapidly reached the highest value at 4 h (Figure 3C). By 12 h, the uptake for Tf-PO−DOX into nuclei was significantly more than that for PO−DOX (P < 0.01), which might be attributed to higher cytoplasmic uptake for Tf-PO−DOX.

MTT assay on C6 cells viability showed that the cytotoxicity of Tf-PO−DOX and PO−DOX depended on their concentration. Viability−concentration curves (Figure 3D) demonstrated that the IC_{50} (DOX concentration of 50% inhibition) of these two formulations was 3.6 and 13.5 μg/mL, respectively, manifesting a 3.75× intensification of cell inhibition of Tf-PO−DOX compared to PO−DOX. The results indicated a significantly improved cytotoxicity mediated by Tf, which was in agreement with the higher intracellular delivery and higher nuclei uptake of Tf-PO−DOX than those of PO−DOX as presented above.

Intracellular distribution of polymersomes into C6 cells was also demonstrated by fluorescence microscopy photographs in which red fluorescence represented DOX and blue fluorescence referred to nuclei stained with DAPI (Figure 4). For free DOX, the red fluorescence nearly completely overlaid with the blue fluorescence, indicating that free DOX diffused into the cells and mainly concentrated at the nucleus, which agreed well with the results of quantitative determination. With Rregard to polymersomes, the same as the quantitative results, the red DOX fluorescence distributed mainly in the cytoplasm of cells except for partly in the nucleus, indicating that cell uptake of DOX-loaded polymersomes was not through the same diffusion mechanism as free DOX, but in a different way, possibly by endocytosis.

Pharmacokinetics and Tissue Distribution of Tf-PO−DOX. As shown in Figure 5 A, the blood clearance of DOX for free DOX, PO−DOX, and Tf-PO−DOX in rats occurred in a biexponential manner. In the group of free DOX, disappearance of DOX from the blood circulation was very rapid with the plasma concentration of only 0.19%ID/mL at 15 min. On the contrary, the plasma DOX concentration for PO−DOX and Tf-PO−DOX remained high for a long time. Even at 24 h after administration, the plasma DOX concentrations for PO−DOX and Tf-PO−DOX were 0.06%ID/mL and 0.03%ID/mL, which were 11.9-fold and 6.3-fold that for free DOX, respectively, exhibiting a remarkable prolonged plasma clearance. Pharmacokinetic parameters calculated from Figure 5 revealed that Tf-PO−DOX and PO−DOX significantly decreased the plasma clearance (Cl) of DOX from 1038 mL/h/kg to 101 and 76 mL/h/kg, respectively (P < 0.01). Meanwhile, AUC increased by 19.1- and 24.8-fold as compared to free DOX. However, there was no significant difference in Cl and AUC between Tf-PO−DOX and PO−DOX (P > 0.05), indicating that surface modification of Tf on polymersomes did not significantly change the blood clearance of polymersomes.

In order to investigate the brain delivery property of Tf-PO−DOX, brain uptake and PS product of brain tissue including

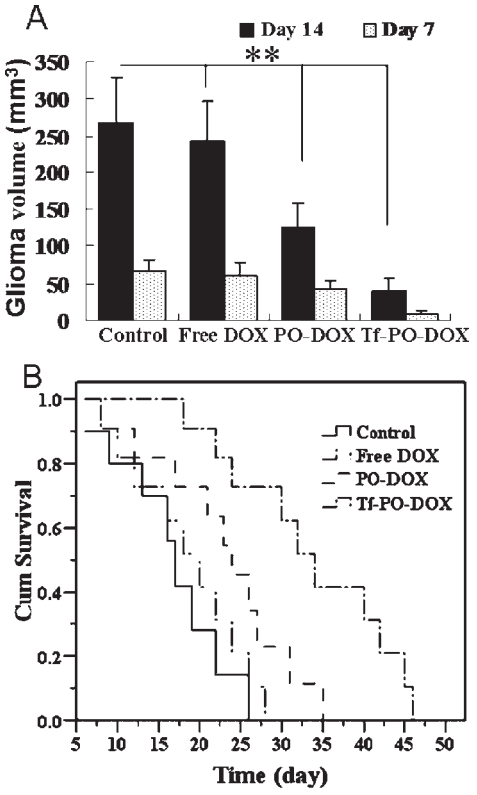


Figure 6. Antitumor effects of DOX-loaded polymersomes in glioma-bearing rats. (A) Glioma volume of different therapeutic groups at the 7th and 14th days (n = 4). ** P < 0.01 vs Tf-PO−DOX group. (B) Percentage of survival (Kaplan−Meier plot) of C6 glioma rat models.

cortex, left striatum, and glioma were quantitatively analyzed (Figure 5B,C). Although free DOX has the highest PS value of 0.040 mL/h/g (Figure 5B), the average brain uptake for free DOX was only around 0.007%ID/g (Figure 5C), which might be attributed to the rapid plasma clearance of free DOX. For free DOX, there was no significant difference of PS value and tissue uptake between cortex, left striatum, and glioma. For PO−DOX, despite the marked increase in plasma AUC, the BBB PS value was reduced to almost zero, resulting in poor uptake in brain cortex and left striatum. The glioma uptake of PO−DOX was as 2.4-fold that of free DOX, which might be due to the EPR effect of tumor tissue. Conversely, the use of Tf conjugated polymersomes significantly increased the PS value and brain uptake (P < 0.01). As compared to PO−DOX, the PS values of Tf-PO−DOX for cortex, left striatum, and glioma at 4 h were 3.7-fold, 3.8-fold, and 3.2-fold those of PO−DOX, respectively. The tissue uptake of Tf-PO−DOX for cortex, left striatum, and glioma at 4 h were 3.6-fold, 3.6-fold, and 3.0-fold those of PO−DOX, respectively. Although the PS value was only 37% that of free DOX, the average %ID/g glioma tissue for Tf-PO−DOX was 0.053%, which increased by 7.1-fold compared with free DOX, suggesting that Tf-PO might be a promising carrier for brain drug delivery, especially for glioma drug delivery.

Brain delivery and tissue distribution of DOX-loaded polymersomes were also determined by fluorescent imaging of main organs at 4 h after i.v. injection of 5 mg/kg of doxorubicin solution, PO−DOX, and Tf-PO−DOX in C6 glioma transplanted rats. As shown in Figure 5D, although PO−DOX showed intensified fluorescence intensity at the glioma site compared with free DOX, Tf-PO−DOX group demonstrated the highest brain fluorescence intensity especially at the glioma site among three groups, which agreed well with quantitative results presented above. DOX distribution in other tissues showed that polymersomes accumulated most in the liver but little in the heart, suggesting that polymersome DOX might have similar potential as Doxil (liposomal doxorubicin) to decrease heart toxicity of DOX.

Pharmacodynamics Experiments in Glioma Model Rats. The antitumor effects of DOX-loaded polymersomes in glioma-bearing rats were shown in Figure 6. The Tf-PO−DOX group presented the smallest glioma volume for rats sacrificed on the same day (Figure 6A), especially on the 14th day. On day 14, the tumor volume of the Tf-PO−DOX group was significantly lower than that of any other group (P < 0.01), indicating that Tf-PO−DOX treatment effectively inhibited the rapid growth of glioma. Life-span extension treated with a multidose of 1.5 mg/kg DOX on days 2, 5, 8, and 11 after glioma implantation was shown in Figure 6B. By log-rank test (Table 1), the median survival times of two polymersome groups were all significantly prolonged compared with that of saline control. However, the increase in survival times (IST) of the Tf-PO−DOX group was more considerable when compared with any other group (P < 0.05), which reached nearly 100% and 70% life-span extension compared with the saline control and free DOX group, respectively, indicating that Tf-PO−DOX possessed the most powerful antitumor activity.

The TUNEL assay further detected DNA fragmentation, a marker of late apoptosis, in nuclei of tumor cells on days 7 and 14 following chemotherapy with 4 different formulations (Figure 7). As shown in Figure 7D, for rats treated with Tf-PO−DOX, significant apoptotic responses of tumor cells in the periphery of tumor were obviously observed on day 7. However, little apoptosis was detected in any tumor tissues treated by free DOX and PO−DOX when compared with saline control (Figure 7B,C). Furthermore, much more apoptotic tumor cells in Tf-PO−DOX treated tumor tissues after 14 days (Figure 7H) were detected compared with any other treatment (Figure 7), although many were presented in PO−DOX treatment.

DISCUSSION

The thin film hydration method was commonly used to prepare biodegradable polymersomes; however, the hydration process needed a high temperature for a long time,[46] which might cause hydrolysis of polyesters block and unfavorable formation of polymersomes. The relative broad size distribution and large vesicle size[32,46] were also unfavorable defects for in vivo drug delivey.[48] Thus, in this study, the nanoprecipitation method was applied to prepare polymersomes, and small-sized polymersomes (107 nm) with a narrow size distribution (polydispersity index, PDI < 0.16 as determined from DLS) were formed, which agreed well with previous reports.[19] Compared with our previously reported large polymersomes (220 nm), small-sized polymersomes with the same zeta potential showed a higher cell uptake by C6 cells than that (1.5 μg/mg) for large polymersomes,[32] indicating that C6 cells favored the uptake of smaller polymersomes. Moreover, blood clearance of small-sized polymersomes was slower than that (156 mL/h/kg, unpublished data) for large polymersomes. These results agreed with previous research that particle size played a key role in cell uptake of stealth particles. For macrophage, large particle sizes were phagocytized more

Table 1. Median Survival Time for Glioma Implanted Rats of Different Therapeutic Groups (n = 12)

group[a]	median	standard error	95% confidence interval	Log-rank test	ISTc	ISTs
Control	17.0	1.3	14.5−19.5	-	-	-
Free DOX	20.0	3.0	14.1−25.9			-
PO−DOX	24.0	2.5	19.0−29.0	[b]	41.2	
Tf-PO−DOX	34.0	3.0	28.1−39.9	[c,d,e]	100.0	70.0

[a] Dosage of DOX is 4 × 1.5 mg/kg. [b] $P < 0.05$, [c] $P < 0.01$ vs control. [d] $P < 0.01$ vs DOX solution. [e] $P < 0.05$ vs PO−DOX. The increases in survival times (%) are compared to control (ISTC) or to DOX solution (ISTS).

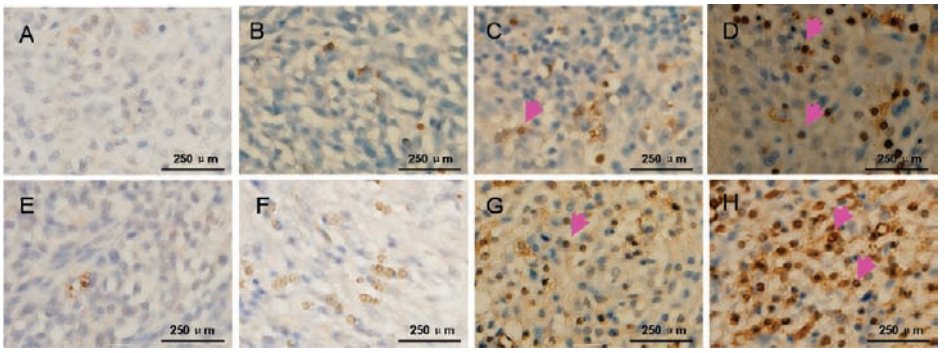


Figure 7. TUNEL staining of tumor tissue sections obtained from rat models 7 days (upper row) and 14 days (lower row) post C6 implantation, following i.v. injection of 1.5 mg/kg DOX on days 2, 5, 8, and 11. Saline control group, (A) and (E); Free DOX treatment, (B) and (F); PO−DOX treatment, (C) and (G); Tf-PO−DOX treatment, (D) and (H). Positive signals were developed by DAB. Cell nuclei were counterstained with hematoxylin.

efficiently while nonphagocytic uptake favored smaller particles.[49] Thus, small-sized polymersomes might have the advantages of both decreasing blood clearance and increasing intracellular delivery to glioma cells.

Considering that chemical and physical properties of the nanoparticles, including size, surface charge, and surface chemistry, are important factors that determine their pharmacokinetics (PK) and biodistribution, it was of significance to control vesicle size of polymersomes to around 100 nm, which is most optimal for improving the PK of polymersomes[48] and advantageous for endocytosis by brain capillary endothelial cells.[41,50] The zeta potential of drug-loaded polymersomes ranged from −10 to −9 mV, which agreed well with the optimal zeta potential within 10 mV, and might help to decrease MPS uptake and prolong blood circulation compared to the charged ones.[31,49] Moreover, the fully hydrophilic PEG (100%) content on the surface of polymersomes could confer good resistance to opsonization and extend vesicle circulation times.[13] Therefore, in this study, Tf-PO−DOX and PO−DOX greatly decreased the plasma clearance of DOX and increased AUC, which might be attributed to the optional particle size, surface charge, and surface chemistry of biodegradable polymersomes.

Inclusion of active targeting ligands in nanosized drug delivery systems was usually used to increase the rate of intracellular delivery and bioavailability of the drug.[31] In this study, Tf molecules with moderate density were conjugated to the polymersome surface to increase both the BBB permeability and intracellular delivery to glioma cells. In fact, despite the fact that PO−DOX could intensively increase the plasma AUC, the brain uptake was very low because of its poor BBB permeability. On the contrary, as compared to PO−DOX, Tf conjugated polymersomes significantly increased the BBB permeability and brain uptake by 3.7-fold and 3.6-fold, respectively, indicating that Tf modification with moderate density greatly facilitated the delivery of polymersomes across BBB. To create pharmacological efficacy, a major challenge was that the encapsulated drug must be delivered and released to the target cells. Although in vitro release of DOX from polymersomes was relatively slow, cell uptake and intracellular distribution results revealed that surface Tf conjugation to polymersomes significantly improved cell uptake and nuclei uptake of DOX, manifesting a significantly enhanced cytotoxicity against C6 cells. Moreover, the enhanced cytotoxicity was consistent with the in vivo efficacy of the Tf-PO−DOX in glioma rats. Compared with PO−DOX and free DOX, Tf-PO−DOX exhibited the most powerful antitumor activity by reducing the tumor volume, increasing median survival time of glioma rats, and extensively producing tumor cell apoptosis. The effect might be attributed to three factors as follows. First, optional chemical and physical properties of the polymersomes decreased the plasma clearance of DOX in the circulation and increased the possibility to cross BBB. Second, the Tf conjugation facilitated the BBB delivery of polymersomes and increased intracellular delivery of DOX in glioma cells, especially in nuclei, where its cytotoxicity was exerted. Finally, EPR effects at advanced stages of solid brain tumor also contributed much to accumulation of polymersomes in glioma.[51]

AUTHOR INFORMATION

Corresponding Author

*Tel.: +86-21-5198-0067; Fax: +86-21-5198-0069. E-mail address: xgjiang@shmu.edu.cn. Postal address: Department of Pharmaceutics, School of Pharmacy, Fudan University (Zhangjiang Campus). 826 Zhangheng Rd, Shanghai 201203, P.R. China.

■ ACKNOWLEDGMENT

This work was supported by National Basic Research Program of China (973 Program) 2007CB935800, National Science and Technology Major Project 2009ZX09310-006, National Natural Science Foundation of China (30762544), and the young teacher's initiative foundation of Fudan University. The authors acknowledge Dr. Kunpeng Li, School of Life Sciences, Zhongshan University, China, for his precious help on Cryo-TEM of polymersomes.

■ REFERENCES

(1) Orive, G., Ali, O. A., Anitua, E., Pedraz, J. L., and Emerich, D. F. (2010) Biomaterial-based technologies for brain anti-cancer therapeutics and imaging. *Biochim. Biophys. Acta 1806*, 96–107.

(2) Bidros, D. S., and Vogelbaum, M. A. (2009) Novel drug delivery strategies in neuro-oncology. *Neurotherapeutics 6*, 539–46.

(3) Juillerat-Jeanneret, L. (2008) The targeted delivery of cancer drugs across the blood-brain barrier: chemical modifications of drugs or drug-nanoparticles? *Drug Discovery Today 13*, 1099–106

(4) Bredel, M., and Zentner, J. (2002) Brain-tumour drug resistance: the bare essentials. *Lancet Oncol. 3*, 397–406.

(5) Hynynen, K. (2008) Ultrasound for drug and gene delivery to the brain. *Adv. Drug Delivery Rev. 60*, 1209–17.

(6) Liu, H. L., Hua, M. Y., Chen, P. Y., Chu, P. C., Pan, C. H., Yang, H. W., Huang, C. Y., Wang, J. J., Yen, T. C., and Wei, K. C. (2010) Blood-brain barrier disruption with focused ultrasound enhances delivery of chemotherapeutic drugs for glioblastoma treatment. *Radiology 255*, 415–25.

(7) Deeken, J. F., and Loscher, W. (2007) The blood-brain barrier and cancer: transporters, treatment, and Trojan horses. *Clin. Cancer Res. 13*, 1663–74.

(8) Caruso, G., Raudino, G., Caffo, M., Alafaci, C., Granata, F., Lucerna, S., Salpietro, F. M., and Tomasello, F. (2010) Nanotechnology platforms in diagnosis and treatment of primary brain tumors. *Recent Pat. Nanotechnol. 4*, 119–24.

(9) Ding, H., Inoue, S., Ljubimov, A. V., Patil, R., Portilla-Arias, J., Hu, J., Konda, B., Wawrowsky, K. A., Fujita, M., Karabalin, N., Sasaki, T., Black, K. L., Holler, E., and Ljubimova, J. Y. (2010) Inhibition of brain tumor growth by intravenous poly (beta-L-malic acid) nanobioconjugate with pH-dependent drug release [corrected]. *Proc. Natl. Acad. Sci. U.S.A. 107*, 18143–8.

(10) Chen, Q., Schonherr, H., and Vancso, G. J. (2009) Block-copolymer vesicles as nanoreactors for enzymatic reactions. *Small 5*, 1436–45.

(11) Christian, D. A., Cai, S., Bowen, D. M., Kim, Y., Pajerowski, J. D., and Discher, D. E. (2009) Polymersome carriers: from self-assembly to siRNA and protein therapeutics. *Eur. J. Pharm. Biopharm. 71*, 463–74.

(12) Meng, F., Engbers, G. H., and Feijen, J. (2005) Biodegradable polymersomes as a basis for artificial cells: encapsulation, release and targeting. *J. Controlled Release 101*, 187–98.

(13) Discher, D. E., Ortiz, V., Srinivas, G., Klein, M. L., Kim, Y., Christian, D., Cai, S., Photos, P., and Ahmed, F. (2007) Emerging applications of polymersomes in delivery: from molecular dynamics to shrinkage of tumors. *Prog. Polym. Sci. 32*, 838–857.

(14) Discher, D. E., and Eisenberg, A. (2002) polymer vesicles. *Science 297*, 967–973.

(15) Du, J., and O'Reilly, R. K. (2009) Advances and challenges in smart and functional polymer vesicles. *Soft Matter 5*, 3544–3561.

(16) Photos, P. J., Bacakova, L., Discher, B., Bates, F. S., and Discher, D. E. (2003) Polymer vesicles in vivo: correlations with PEG molecular weight. *J. Controlled Release 90*, 323–34.

(17) Upadhyay, K. K., Agrawal, H. G., Upadhyay, C., Schatz, C., Le Meins, J. F., Misra, A., and Lecommandoux, S. (2009) Role of block copolymer nanoconstructs in cancer therapy. *Crit. Rev. Ther. Drug 26* (2), 157–205.

(18) Liu, G., Ma, S., Li, S., Cheng, R., Meng, F., Liu, H., and Zhong, Z. (2010) The highly efficient delivery of exogenous proteins into cells mediated by biodegradable chimaeric polymersomes. *Biomaterials 31*, 7575–85.

(19) Meng, F., Hiemstra, C., Engbers, G. H. M., and Feijen, J. (2003) Biodegradable Polymersomes. *Macromolecules 36*, 3004–3006.

(20) Christian, N. A., Milone, M. C., Ranka, S. S., Li, G., Frail, P. R., Davis, K. P., Bates, F. S., Therien, M. J., Ghoroghchian, P. P., June, C. H., and Hammer, D. A. (2007) Tat-functionalized near-infrared emissive polymersomes for dendritic cell labeling. *Bioconjugate Chem. 18*, 31–40.

(21) Zhou, W., Meng, F., Engbers, G. H., and Feijen, J. (2006) Biodegradable polymersomes for targeted ultrasound imaging. *J. Controlled Release 116*, e62–4.

(22) Meng, F., Zhong, Z., and Feijen, J. (2009) Stimuli-responsive polymersomes for programmed drug delivery. *Biomacromolecules 10*, 197–209.

(23) Chen, W., Meng, F., Cheng, R., and Zhong, Z. (2010) pH-Sensitive degradable polymersomes for triggered release of anticancer drugs: a comparative study with micelles. *J. Controlled Release 142*, 40–6.

(24) Qin, S., Geng, Y., Discher, D. E., and Yang, S. (2006) Temperature-controlled assembly and release from polymer vesicles of poly(ethylene oxide)-block-poly(*N*-isopropylacrylamide). *Adv. Mater. 18*, 2905–2909.

(25) Mabrouk, E., Cuvelier, D., Brochard-Wyart, F., Nassoy, P., and Li, M. H. (2009) Bursting of sensitive polymersomes induced by curling. *Proc. Natl. Acad. Sci. U.S.A. 106*, 7294–8.

(26) Cerritelli, S., Velluto, D., and Hubbell, J. A. (2007) PEG-SS-PPS: reduction-sensitive disulfide block copolymer vesicles for intracellular drug delivery. *Biomacromolecules 8*, 1966–72.

(27) Upadhyay, K. K., Le Meins, J. F., Misra, A., Voisin, P., Bouchaud, V., Ibarboure, E., Schatz, C., and Lecommandoux, S. (2009) Biomimetic doxorubicin loaded polymersomes from hyaluronan-block-poly(gamma-benzyl glutamate) copolymers. *Biomacromolecules 10*, 2802–8.

(28) Fabel, K., Dietrich, J., Hau, P., Wismeth, C., Winner, B., Przywara, S., Steinbrecher, A., Ullrich, W., and Bogdahn, U. (2001) Long-term stabilization in patients with malignant glioma after treatment with liposomal doxorubicin. *Cancer 92*, 1936–42.

(29) Jones, A. R., and Shusta, E. V. (2007) Blood-brain barrier transport of therapeutics via receptor-mediation. *Pharm. Res. 24*, 1759–71.

(30) Zhang, Y., Zhang, Y. F., Bryant, J., Charles, A., Boado, R. J., and Pardridge, W. M. (2004) Intravenous RNA interference gene therapy targeting the human epidermal growth factor receptor prolongs survival in intracranial brain cancer. *Clin. Cancer Res. 10*, 3667–77.

(31) Li, S. D., and Huang, L. (2008) Pharmacokinetics and biodistribution of nanoparticles. *Mol. Pharm. 5*, 496–504.

(32) Pang, Z., Feng, L., Hua, R., Chen, J., Gao, H., Pan, S., Jiang, X., and Zhang, P. (2010) Lactoferrin-conjugated biodegradable polymersome holding doxorubicin and tetrandrine for chemotherapy of glioma rats. *Mol. Pharm. 7*, 1995–2005.

(33) Gao, K., and Jiang, X. (2006) Influence of particle size on transport of methotrexate across blood brain barrier by polysorbate 80-coated polybutylcyanoacrylate nanoparticles. *Int. J. Pharm. 310*, 213–9.

(34) Qian, Z., Li, H., Sun, H., and Ho, K. (2002) Targeted drug delivery via the transferrin receptor-mediated endocytosis pathway. *Pharmacol. Rev. 54*, 561–587.

(35) Pang, Z., Lu, W., Gao, H., Hu, K., Chen, J., Zhang, C., Gao, X., Jiang, X., and Zhu, C. (2008) Preparation and brain delivery property of biodegradable polymersomes conjugated with OX26. *J. Controlled Release 128*, 120–7.

(36) Lu, W., Tan, Y. Z., Hu, K. L., and Jiang, X. G. (2005) Cationic albumin conjugated pegylated nanoparticle with its transcytosis ability and little toxicity against blood-brain barrier. *Int. J. Pharm. 295*, 247–60.

(37) Pan, H., Han, L., Chen, W., Yao, M., and Lu, W. (2008) Targeting to tumor necrotic regions with biotinylated antibody and streptavidin modified liposomes. *J. Controlled Release 125*, 228–35.

(38) Hong, M., Zhu, S., Jiang, Y., Tang, G., and Pei, Y. (2009) Efficient tumor targeting of hydroxycamptothecin loaded PEGylated niosomes modified with transferrin. *J. Controlled Release 133*, 96–102.

(39) Lu, W., Wan, J., Zhang, Q., She, Z., and Jiang, X. (2007) Aclarubicin-loaded cationic albumin-conjugated pegylated nanoparticle for glioma chemotherapy in rats. *Int. J. Cancer 120*, 420–31.

(40) Kang, Y. S., Bickel, U., and Pardridge, W. M. (1994) Pharmacokinetics and saturable blood-brain barrier transport of biotin bound to a conjugate of avidin and a monoclonal antibody to the transferrin receptor. *Drug Metab. Dispos. 22*, 99–105.

(41) Huwyler, J., Wu, D., and Pardridge, W. M. (1996) Brain drug delivery of small molecules using immunoliposomes. *Proc. Natl. Acad. Sci. U.S.A. 93*, 14164–9.

(42) Hekmatara, T., Bernreuther, C., Khalansky, A. S., Theisen, A., Weissenberger, J., Matschke, J., Gelperina, S., Kreuter, J., and Glatzel, M. (2009) Efficient systemic therapy of rat glioblastoma by nanoparticle-bound doxorubicin is due to antiangiogenic effects. *Clin. Neuropathol. 28*, 153–64.

(43) Schoch, G., Seeger, H., Bogousslavsky, J., Tolnay, M., Janzer, R. C., Aguzzi, A., and Glatzel, M. (2006) Analysis of prion strains by PrPSc profiling in sporadic Creutzfeldt-Jakob disease. *PLoS Med. 3*, e14.

(44) Bermudez, H., Brannan, A. K., Hammer, D. A., Bates, F. S., and Discher, D. E. (2002) Molecular weight dependence of polymersome membrane structure, elasticity, and stability. *Macromolecules 35*, 8203–8208.

(45) Huang, R. Q., Qu, Y. H., Ke, W. L., Zhu, J. H., Pei, Y. Y., and Jiang, C. (2007) Efficient gene delivery targeted to the brain using a transferrin-conjugated polyethyleneglycol-modified polyamidoamine dendrimer. *FASEB J. 21*, 1117–25.

(46) Ghoroghchian, P. P., Li, G., Levine, D. H., Davis, K. P., Bates, F. S., Hammer, D. A., and Therien, M. J. (2006) Bioresorbable vesicles formed through spontaneous self-assembly of amphiphilic poly(ethylene oxide)-block-polycaprolactone. *Macromolecules 39*, 1673–1675.

(47) Sanson, C., Schatz, C., Le Meins, J. F., Soum, A., Thevenot, J., Garanger, E., and Lecommandoux, S. (2010) A simple method to achieve high doxorubicin loading in biodegradable polymersomes. *J. Controlled Release 147*, 428–435.

(48) Alexis, F., Pridgen, E., Molnar, L. K., and Farokhzad, O. C. (2008) Factors affecting the clearance and biodistribution of polymeric nanoparticles. *Mol. Pharm. 5*, 505–15.

(49) He, C., Hu, Y., Yin, L., Tang, C., and Yin, C. (2010) Effects of particle size and surface charge on cellular uptake and biodistribution of polymeric nanoparticles. *Biomaterials 31*, 3657–66.

(50) Massignani, M., LoPresti, C., Blanazs, A., Madsen, J., Armes, S. P., Lewis, A. L., and Battaglia, G. (2009) Controlling cellular uptake by surface chemistry, size, and surface topology at the nanoscale. *Small 5*, 2424–32.

(51) Fang, J., Nakamura, H., and Maeda, H. (2011) The EPR effect: Unique features of tumor blood vessels for drug delivery, factors involved, and limitations and augmentation of the effect. *Adv. Drug Delivery Rev. 63*, 136–151.

Bioconjugate Chemistry

ARTICLE

pubs.acs.org/bc

"Clickable", Trifunctional Magnetite Nanoparticles and Their Chemoselective Biofunctionalization

Manasmita Das,[*,†,‡] Debarati Bandyopadhyay,[†,§] Debasish Mishra,[∥] Satyajit Datir,[‡] Prasanta Dhak,[†] Sanyog Jain,[‡] Tapas Kumar Maiti,[§] Amit Basak,[†] and Panchanan Pramanik[†]

[†]Department of Chemistry

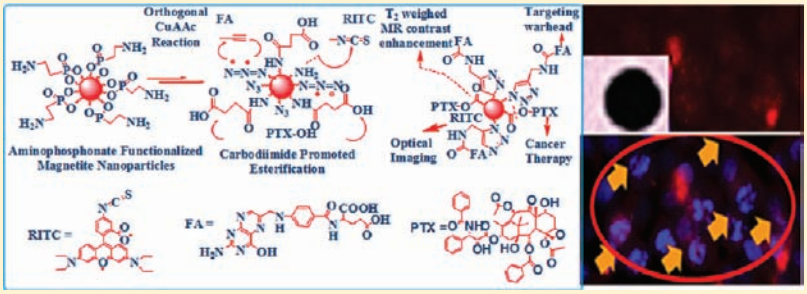
[∥]Department of Biotechnology

Indian Institute of Technology Kharagpur, Kharagpur 721302, India

[‡]Centre of Pharmaceutical Nanotechnology, Department of Pharmaceutics, National Institute of Pharmaceutical Education and Research (NIPER), Sector-67, SAS Nagar, Mohali 160062

[§]Molecular Biophysics Unit, Indian Institute of Science Bangalore, Bangalore 560012, India

ABSTRACT:



A multifunctional iron oxide based nanoformulation for combined cancer-targeted therapy and multimodal imaging has been meticulously designed and synthesized using a chemoselective ligation approach. Novel superparamagnetic magnetite nanoparticles simultaneously functionalized with amine, carboxyl, and azide groups were fabricated through a sequence of stoichiometrically controllable partial succinylation and Cu (II) catalyzed diazo transfer on the reactive amine termini of 2-aminoethylphosphonate grafted magnetite nanoparticles (MNPs). Functional moieties associated with MNP surface were chemoselectively conjugated with rhodamine B isothiocyanate (RITC), propargyl folate (FA), and paclitaxel (PTX) via tandem nucleophic addition of amine to isothithiocyanates, Cu (I) catalyzed azide−alkyne click chemistry and carbodiimide-promoted esterification. An extensive *in vitro* study established that the bioactives chemoselectively appended to the magnetite core bequeathed multifunctionality to the nanoparticles without any loss of activity of the functional molecules. Multifunctional nanoparticles, developed in the course of the study, could selectively target and induce apoptosis to folate-receptor (FR) overexpressing cancer cells with enhanced efficacy as compared to the free drug. In addition, the dual optical and magnetic properties of the synthesized nanoparticles aided in the real-time tracking of their intracellular pathways also as apoptotic events through dual fluorescence and MR-based imaging.

Superparamagnetic magnetite nanoparticles with tailored, biocompatible surfaces have elicited phenomenal interest among the scientific community with regard to their multifarious biomedical applicability including magnetic resonance imaging (MRI) contrast enhancement, magnetically modulated drug and gene delivery or hyperthermic treatment of malignant cells.[1−3] Surface engineering of superparamagnetic nanoparticles rely on two major approaches: (i) noncovalent approaches, such as the biotin-streptavidin technology or substrate passive adsorption,[4,5] and (ii) covalent approaches, based on the formation of relatively stable, covalent connections between hydroxyl groups on the nanoparticle surface and a suitable anchoring agent present in a specific position of the target molecule of interest.[6,7] Although the latter approach significantly improves the quality of hybrid nanoparticles (NPs), it suffers from the necessity to affect a great deal of complicated and hard-working chemical modifications, often involving nonaqueous solvents, harsh conditions, and tedious protection−deprotection sequences that is quite impracticable with complex biomolecules such as proteins, carbohydrates, or nucleic acids. Further, in many areas of pharmaceutical research, viz., drug delivery or nanomedicine, targeting molecules, chemotherapeutic drugs, or imaging agents need to be simultaneously integrated on the nanoscale delivery vehicles for the convenience of detection, evaluation, and treatment. However, controlled implementation of varied functions onto a single platform is difficult because all the functional groups

Received: February 1, 2011
Revised: May 4, 2011
Published: May 06, 2011

ACS Publications © 2011 American Chemical Society

present on the surface of nanoparticles have comparable reactivity. Simultaneously, an attempt to immobilize multiple functional entities on a symmetrically functionalized nanoplatform is fraught with the possibility of nonselective cross reactions. Magnetic nanoparticles (MNPs), bearing more than one type of surface functionality and different chemical reactivity, may be prospective precursors for such theragnostic systems, but their synthesis as well as precise characterization appears to be highly challenging. Ideally, a multifunctional surface should be designed in such a manner that all functional groups associated with a NP can react with its target bioactive at a site, complementary and chemoselective to its functional motif. An efficient method to produce such a multifunctional surface would be to grow a single-structured MNP based platform in bulk and then tune up its surface functionality as per the desired application. Such a strategy makes the initial part of the synthesis more amenable to large-scale production.

In recent years, "click chemistry" with its unique features such as high aqueous competency, chemical orthogonality, and applicability toward diverse substrates[8] has emerged as a burgeoning strategy for the development of surface-engineered polymers and nanoparticles with high selectivity and efficiency. Although a myriad of reactions fulfill the "click criteria", in view of their fast, complete transformability and 100% selectivity for the 1,4-disubstituted 1,2,3-triazole, the Cu (I) catalyzed Huisgen 1,3-dipolar cycloaddition of azides with terminal alkynes (CuAAc reaction) has emerged as the frontrunner under this category. We reasoned that an intelligent combination of "click chemistry" with conventional bioconjugation strategies will cut short the multistep reactions, commonly involved in the preparation of multifunctional nanobio hybrids with concomitant improvement in the selectivity of bioconjugation. In the present account, we describe a complete covalent approach towards the development of a multifunctional nanoplatform for combined cancer-targeted therapy and multimodal imaging using a unique collage of classical bioconjugation strategies with surface diazo transfer and "click chemistry". This multifunctional system comprises of four key components: (i) an iron-oxide based nanomagnetic core enveloped by a hydrophilic, biocompatible coating of 2-aminoethyl phosphonic acid to allow magnetic targeting, as well as T_2 weighted MR contrast enhancement, (ii) a fluorescent dye, viz., rhodamine B isothicyanate (RITC) to enable optical imaging, (iii) a cancer targeting molecule, viz., folic acid (FA) to target the folate-receptor (FR) overexpressed cancer cells, and (iv) a chemotherapeutic drug, viz., Paclitaxel (PTX) to induce cytotoxicity to cancer cells. Magnetite nanoparticles bearing three different functional moieties, viz., amine, azide, and carboxyl groups on a single-structured surface, were used as a synthon for the proposed nanomedical platform. Chemoselective conjugation of RITC and alkyne-functionalized FA and PTX was consummated via nucleophilic addition of amine to isothiocyanate, azide−alkyne click chemistry, and carbodiimide promoted esterification, respectively. Although combination of surface diazo transfer and click chemistry has been previously used by Polito et al. for the bioengineering of magnetic nanoparticles,[9] they used symmetrically functionalized nanoparticles that could accommodate only one ligand at a time. To the best of our knowledge, this is the first report on the systematic fabrication of amine-carboxyl-azide trifunctionalized magnetite nanoparticles and their chemoselective ligation with multiple diagnostic and therapeutic entities. Extensive physicochemical characterizations were undertaken to establish the feasibility of the proposed chemoselective trifunctionalization. Finally, in the course of extensive *in vitro* studies, we demonstrated that the synthesized nanoparticles could serve as a novel platform for "smart" cancer diagnosis and therapy.

MATERIAL AND METHODS

Materials. Anhydrous ferric chloride ($FeCl_3$) and ferrous chloride tetrahydrate ($FeCl_2 \cdot 4H_2O$) were obtained from Merck, Germany. Folic acid (FA), dicyclohexyl carbodiimide (DCC), *N*-hydroxysuccinimide (NHS), 1-[3-(dimethylamino) propyl]-3-ethylcarbodiimide hydrochloride (EDC), propargyl amine, triflic anhydride (Tf_2O), sodium azide (NaN_3), copper sulfate pentahydrate ($CuSO_4 \cdot 5H_2O$), sodium ascorbate, Rhodamine (B) isothiocyanate (RITC), Paclitaxel (PTX), MTT [3-(4,5-dimethylthiazol-2-yl)-2,5-diphenyltetrazolium], propidium iodide (PI), RNase A, Trypsin, 4′,6-diamidino-2-phenylindole dihydrochloride (DAPI), and agarose were purchased from Sigma Chemical Co. (St. Louis, MO, USA). 2-Aminoethyl phosphonic acid was prepared by refluxing *N*-2-(bromoethyl phthalimide) with triethyl phosphate under inert atmosphere. Commercially available dimethyl sulphoxide (DMSO) was dried over calcium hydride and purified via reduced pressure distillation. Pyridine (C_5H_5N) and triethyl amine (Et_3N) were dried over KOH and distilled prior to use. Dichloromethane (DCM) was dried over P_2O_5 and purified by normal distillation.

Synthesis Methodology. *Synthesis of Triflic Azide from Triflic Anhydride.* Triflic azide was synthesized from triflic anhydride following a reported protocol[10] with minor modifications. In brief, a mixure of DCM:MeOH:H_2O (3:10:3) was added to an aqueous solution (2 mL) of sodium azide (545 mg, 8.38 mmol) and the resultant mixture was cooled to 0 °C under vigorous stirring. Following the dropwise addition of triflic anhydride (896 μL, 4.19 mmol) and further vigorous stirring for 30 min at 0 °C, the temperature was raised to 10 °C and the biphasic mixture was stirred for 2 h. A saturated aqueous solution of sodium hydrogen carbonate was added dropwise until gas evolution had ceased. The two phases were separated and the aqueous layer was extracted with toluene (2 × 2 mL). The combined organic layers were used in the subsequent diazo transfer reactions.

Synthesis of Folic Acid Alkyne Derivative. Alkyne derivative of folic acid was prepared, following the previously reported literature procedures.[11] Briefly, folic acid (1 mmol) was reacted with DCC (1.5 mmol) in the presence of pyridine and DMSO under inert atmosphere. Following carbodiimide activation, propargyl amine (1.5 mmol) was added dropwise to the reaction mixture and left stirring overnight. The precipitated dicyclohexyl urea (DCU) was removed by filtration. The filtrate was added dropwise to ice-cold diethyl ether (Et_2O) at 0 °C to precipitate out the desired propargyl-folate derivative as a yellow−orange solid product (91% yield). ^{1}H NMR (DMSO-d_6, δ ppm) 8.62 (s, PtC_7 H, 1H), 8.2−8.35 (d, PtC6-CH_2NH-Ph 1H, J = 5.3 Hz), 7.95−8.1 (d,-CONHCHCOOH, 1H, J = 7.6 Hz), 7.6−7.65 (d, PhC_2H and Ph−C_6H, 2H, J = 8.2 Hz), 6.91 (br s, NH_2, 2H), 6.63−6.61 (d, Ph−C_3H and Ph−C_5H, 2H, J = 8.4 Hz), 4.49−4.48 (d, PtC_6−CH_2NH-Ph, 2H, J = 5.6 Hz), 4.32−4.45 (d, PtC_6−CH_2NH-Ph), 3.8 (m, -CONH−CH_2CCH, 2H), 3.8 (m, -CONH−CH_2CCH, 2H), 3.1 (t, −CONH−CH_2CCH, 1 Hz, J = 2.6 Hz), 2.5 (s, -CONH−CH_2CCH, 1H), 2.52 (br s, −OH,1H), 2.3 (m, −CH_2CO_2H, 2H), 2.07 (m, −$CHCH_2CH_2$, 1H), 1.7 (m, −$CHCH_2CH_2$, 1H). FTIR (KBr, cm^{-1}): 2369 (CC), 1718 (C═O), 1607 (CONH), 1508 (C═C), 1298, 1191

(C−O−C), 1127, 840, 626 (C−C). MS (ESI, m/z): $[M + H]^+$ calcd for $C_{22}H_{22}O_5N_8$ 479.

Synthesis of ***MNP 1***. Bare magnetite nanoparticles were synthesized by alkaline coprecipitation of Fe^{3+} and Fe^{2+} and subsequently modified with 2-aminoethyl phosphonic acid according to our previously published procedure.[12] Typically optimized for the generation of the hybrid surface proposed, 1 mmol of magnetite (Fe_3O_4) was reacted with 0.25 mmol of 2-aminoethyl phosphonic acid (APA). The suspension was ultrasonicated for 0.5 h, left to stirring at room temperature for 24 h, and finally, the modified nanoparticles (**MNP 1**) were recovered via magnetic decantation.

Synthesis of ***MNP 2***. The transformation of **MNP 1**-**MNP 2** was executed via desymmetrization of the primary amine functions on **MNP 1** to an amine-carboxyl-azide trifunctionalized surface through a sequence of (i) controlled, ring-opening linker elongation reaction with succinic anhydride and (ii) high-yielding Cu(II) catalyzed diazo transfer reactions with triflic azide. In brief, succinic anhydride (0.2 mmol) was added to an ultrasonicated suspension of **MNP 1** (200 mg) in anhydrous, distilled DMSO. The pH of the reaction mixture was adjusted to 8 by adding a few drops of triethylamine and left to stir for 24 h. Hybrid MNPs containing both amine and carboxyl groups were thoroughly washed with distilled water and finally isolated through magnetic decantation. An aqueous suspension (20 mL) of partially succinylated **MNP 1** (100 mg) was added to a freshly prepared solution of triflic azide, preactivated with $CuSO_4$ (0.05 mmol) and triethyl amine (0.5 mmol). Methanol (2 mL) was added to the reaction mixture and the suspension was left to stirring at room temperature. After 12 h, the reaction mixture was divided into two parts: one part was separated through magnetic concentration, washed thoroughly with deionized water, and freeze−dried for surface characterizations; while the other part was used in the subsequent steps without further isolation.

For preparing the magnetofluorescent analogue **MNP 2**, 1 mg of rhodamine isothiocyanate (RITC) was dissolved in 1 mL of DMSO−H_2O (1:1). The pH of the resultant mixture was adjusted to ∼8 with 1−2 drops of NaOH solution (0.1 N) and added dropwise to the suspension of **MNP 2** and stirred for 1 h in the dark. A small portion of the reaction mixture was separated through magnetic concentration, washed thoroughly, and freeze−dried for surface characterizations while the other part was kept undisturbed for the subsequent steps.

Synthesis of ***MNP 3***. The click reaction was performed in the same pot as the Cu(II) catalyzed diazo transfer. Cu(II), which was used as catalyst in the previous step, could effectively catalyze the click reaction through generation of Cu(I) in the presence of sodium ascorbate. In brief, sodium ascorbate (catalytic amount) was added to the suspension of **MNP 2**. Alkyne derivative of folic acid (0.25 mmol) was dissolved in DMSO−H_2O mixture (1:1) and the reaction mixture was stirred for 8 h. The "clicked" MNPs (**MNP 2**) were thoroughly washed with a 40% solution of ammonia, followed by repeated washing with distilled water to completely free the nanoparticles from Cu(II). The nanoparticles were finally washed with acetone, separated via magnetic decantation, freeze−dried, and used for subsequent conjugation with Paclitaxel (PTX).

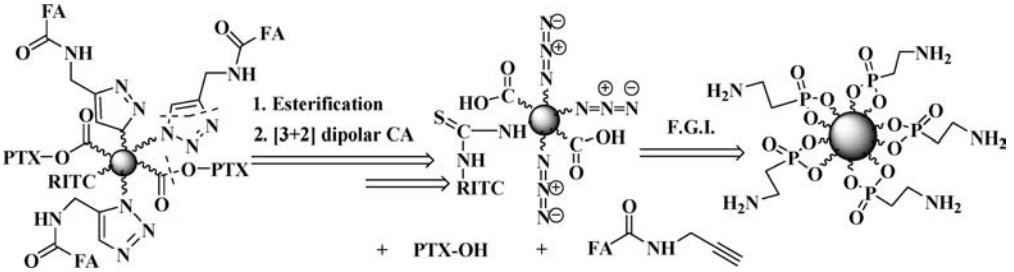
Synthesis of ***MNP 4***. Paclitaxel was conjugated with **MNP 3** via carbodiimide promoted esterification between the hydroxyl groups of PTX and surface-pendant carboxyl groups. In brief, an ultrasonicated suspension of **MNP 3** (5 mg) in DMSO (5 mL) was activated with EDC (0.0075 mmol). A few drops of Et_3N were added to maintain the solution pH at around 8. A solution of PTX (0.005 mmol) in DMSO (1 mL) was added to the resultant mixture and left stirring at room temperature for 48 h. The resulting conjugate (**MNP 4**) was thoroughly washed with distilled water, then acetone, and finally isolated using a rare earth magnet to afford the target nanoconstruct.

Characterizations. The phase analysis of the synthesized magnetite nanopowder was performed on an X'pert Pro Phillips X-ray diffractometer. High-resolution transmission electron microscopy (JEOL 3010, Japan) was employed to characterize the microstructure of the different nanoparticle preparations. The hydrodynamic (HD) size of the particle aggregates was measured by laser light scattering using a Brookhaven 90 Plus particle size analyzer. The surface charge of the nanoparticles was investigated through zeta potential measurements (Zetasizer 4, Malvern Instruments, U.K.) after dilution of the samples in 0.01 (M) phosphate buffer at pH 7.4. Surface chemistry of the nanoparticles was studied using a Thermo Nicolet Nexus FTIR model 870 spectrometer. The surface compositions of the different nanoparticle preparations were obtained by analyzing X-ray photoelectron spectroscopic (XPS) data using Al K_α excitation source in an ESCA-2000 Multilab apparatus (VG microtech). For a detailed structure-resolved analysis of the surface-bound ligands, high-resolution magic angle spinning (HR-MAS) nuclear magnetic resonance (NMR) experiments were pursued. Samples for MAS experiments were prepared by suspending 10 mg of each nanoparticle preparation in a 1:1 mixture of DMSO-d_6:D_2O (500 μL). HRMAS−NMR analysis was carried out with a 400 MHz FT-NMR spectrometer (Avance 400), equipped with a 5 mm HRMAS probe. For further authentication of PTX immobilization on the surface of **MNP 4**, the as-prepared conjugate (∼50 mg) was incubated with porcine liver esterase (PLE) at pH 8 for 72 h to ensure complete detachment of the drug molecules from NP surface. The hydrolysis solution was partitioned between chloroform and water, following which the organic layer was dried over sodium sulfate, concentrated in vacuum, and finally subjected to FTIR and NMR analysis. The data was authenticated by comparison against standard FTIR and NMR data for pure paclitaxel. All measurements unless otherwise specified were performed in triplicate ($n = 3$) and the results were averaged with percentage error determined through calculating the standard deviation from the mean.

Total Iron Determination and Quantification of Functional Molecules on NPs. Iron concentration in the various synthesized nanoparticles was determined spectrophotometrically as described in our previous reports.[13] The determination of amino groups on the surface of **MNP 1** was performed using the 2,4,6-trinitrobenzenesulfonic acid (TNBS) method as described earlier.[11] The transformation of **MNP 1** to **MNP 2** was tracked by monitoring the systematic reduction in amine density on the surface of nanoparticles, determined via the TNBS assy. The average number of RITC and FA molecules immobilized per particle was determined spectrophotometrically according to the protocol adopted in ref 13. For quantifying the amount of PTX immobilized on the surface of MNPs, **MNP 4** was suspended in a mixture of methanol:PBS (1:1) at pH 8 for 72 h to ensure complete detachment of the drug from the nanoparticle surface and analyzed by high-performance liquid chromatography (HPLC) at 227 nm.

Drug Release Studies. To obtain the PTX release profile from the drug-loaded nanoparticles, **MNP 4** (10 mg) was

Scheme 1. Retrosynthesis of the Target Multifunctional Nanohybrid



suspended in 10 mL of 1:1 (v/v) mixture of methanol and phosphate buffered saline (PBS) at 37 °C under constant stirring. The solution was divided into two sets, and pH of the individual sets was adjusted by titration with 0.1 (M) NaOH or 0.1 (M) HCl to achieve the pH values of 4 and 7.4, respectively. At different time intervals, 0.5 mL of the aliquot was withdrawn from the mixture and replaced with an equivalent amount of the release medium. The aliquot was centrifuged and the supernatant was analyzed for PTX content using HPLC analysis.

Cell Uptake Studies. The cells cultivated for *in vitro* experiments were human cervix adenocarcinoma, HeLa, and human osteosarcoma, MG-63 cell lines, obtained from the National Centre for Cell Sciences (NCCS) Pune, India. All cell lines were cultured on folate-free Dulbecco Modified Eagle's Medium (FFDMEM) and Minimal Essential Medium (MEM), respectively, with 10% fetal calf serum, 100 units mL^{-1} penicillin, and 100 $\mu g\ mL^{-1}$ streptomycin, 4 mmol L^{-1} glutamine at 37 °C in a 5% CO_2 and 95% air humidified atmosphere. Nanoparticle uptake by different cell lines was studied by magnetically activated cell sorting (MACS) and fluorescence microscopy.

The effect of surface-coating on the uptake of nanoparticles by HeLa cells was evaluated by culturing these cells with different nanoparticle preparations in the absence of folic acid in the culture medium. After 4 h of incubation, the cells were washed to remove free nanoparticles and cell sorting was performed with magnetically activated cell sorting (MACS). Three replicates were measured and the results were averaged with percentage error determined by calculating the standard deviation from the mean. To further evaluate the specificity of cellular targeting of the nanoparticle conjugates, the uptake of iron oxide folate conjugates by HeLa cells was also compared with the uptake by MG-63 cells that do not express the folate receptor as well as HeLa cells incubated with free folate.

***In Vitro* Cellular MR Imaging.** Samples for MR phantom imaging were prepared by suspending 10^6 cells in 50 μL low-melting 1% agarose gel. Cell suspensions cultured with different nanoparticle concentrations (0.01−0.1 mg/mL) were loaded into 1.5 mL eppendorf tubes and allowed to solidify at 4 °C. Samples were then sealed with additional agarose to avoid air susceptibility artifacts. MR imaging was performed with a 0.3 T clinical MRI scanner (Hitachi, Airis), using a prefabricated sample holder. A spin−echo multisection pulse sequence was selected from the Hitatchi Medical System (v 7.0) to acquire MR phantom images. Repetition time (TR) of 2100 ms and variable echo times (TE) of 95−150 ms were used. The spatial resolution parameters were set as follows: an acquisition matrix of 256 × 256, field of view of 240 × 240 mm^2, section thickness of 8 mm, and 2 averages. The MRI signal intensity (SI) was measured using the built-in software. T_2 values were obtained by plotting the SI of each sample over a range of TE values. T_2 relaxation times were then calculated by fitting a first-order exponential decay curve to the plot. The fitting equation can be expressed as $SI = A \times e^{(-TE/T_2)} + B$, where SI is the signal intensity, TE is the echo time, A is the amplitude, and B is the offset. The relaxivity, the R_2 value, was also calculated as the inverse of T_2.

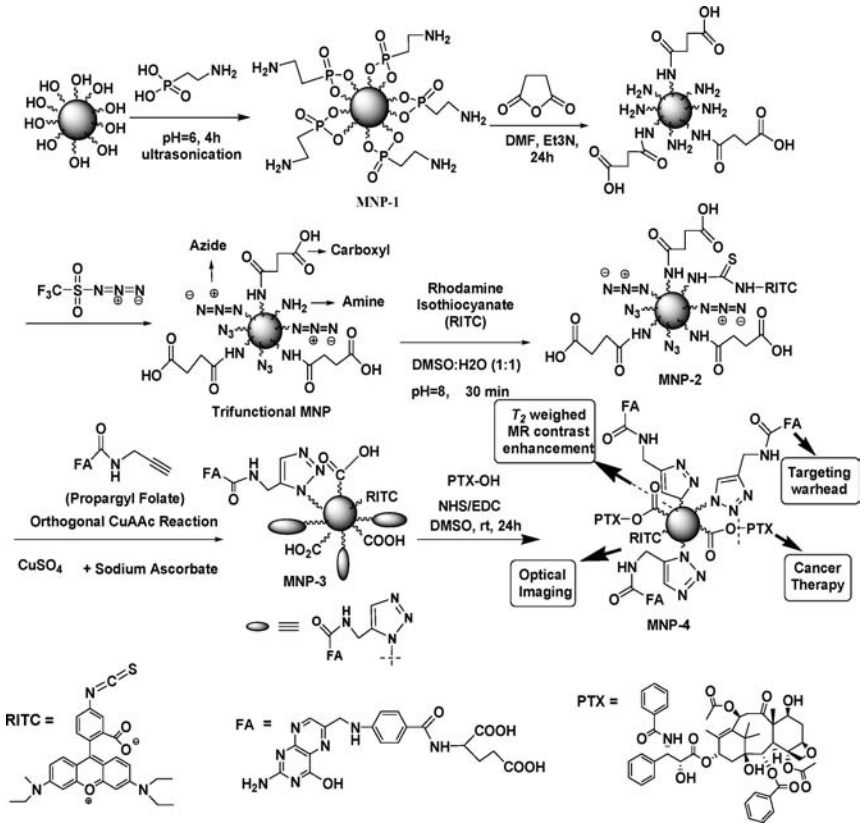
Nanoparticle Induced Cytotoxicity. HeLa cells (4×10^5) were seeded to 96 well tissue culture plates in a total volume of 180 μL of complete media and kept for 18 h, following which 20 μL of different nanoparticle preparations were added to the cells at different concentrations, incubated for 1 h at 37 °C in a humidified incubator (HERA cell) maintained at 5% CO_2. Thereafter, cells were washed thoroughly with PBS to remove the non-internalized particles and re-incubated for different time periods (1−48 h), MTT (4 mg/mL) was added to each well at the strength of 10% (v/v) and incubated for further 4 h at 37 °C. Subsequently, the media containing MTT was removed, and 200 μL of DMSO was added to dissolve the formazan crystals. The absorbance was measured using an ELISA plate reader (Biorad, USA) at 595 nm.

Nanoparticle Induced Apoptosis: Analysis of Cell-Cycle and Nuclear Morphology. For fluorescence microscopy, HeLa cells were treated with 200 μg/mL of different nanoparticle preparations for 0.5 h, washed thoroughly with PBS to remove the noninternalized particles, and incubated at 37 °C for 8, 12, and 24 h, respectively. Following incubation, the cells were smeared on a clean glass slide, fixed with 3.7% formaldehyde for 15 min, permeabilized with 0.1% Triton X-100, and stained with 1 μg/mL DAPI for 5 min at 37 °C. The cells were then washed with PBS and examined by fluorescence microscopy (Olympus IX 70). For cell-cycle analysis, HeLa cells were treated with 200 μg/mL of both **MNP 3** (used as control) and **MNP 4** for 0.5 h, washed thoroughly with PBS to remove the noninternalized particles, and incubated at 37 °C for 8, 12, and 24 h, respectively. Following incubation, the cells were washed with ice-cold PBS (10 mmol, pH 7.4) and resuspended in 200 μL of PBS followed by incubation with 20 μL DNase free RNase (10 mg/mL) and 20 μL of DNA intercalating dye propidium iodide (PI) (1 mg/mL) at 37 °C for 1 h in dark. Apoptotic cells were determined by their hypochromic subdiploid staining profiles. The distribution of cells in the different cell-cycle phases was analyzed from the DNA histogram using Becton-Dickinson FACS Caliber flow cytometer and *Modfit* software.

■ RESULTS AND DISCUSSION

The retrosynthesis of our target, presented in Scheme 1, shows two important reactions: formation of a pH-labile ester bond between hydroxyl groups of PTX and carboxyl functions on the

Scheme 2. Synthesis of the Target Nanoconstruct MNP 4 via a Chemoselective Protocol



nanoparticle surface and formation of a stable, biocompatible triazole linkage between alkyne functionalized folic acid and azide-terminated nanoparticles. While the former was executable through the classical carbodiimide promoted esterification reaction, the latter, in principle, could be achieved via orthogonal copper-catalyzed azide alkyne cycloaddition (CuAAc) reaction. Further retrosynthetic analysis suggested the involvement of a mixed amine-carboxyl-azide-terminated, trifunctional MNP intermediate, which, in principle, could be synthesized from an amine-functionalized nanomagnetite precursor through partial interchange of these amino functions with carboxyl functions, followed by a diazo transfer with the residual surface amino groups.[9] Notably, the ratio of different functional groups on the surface could be manipulated by playing with the stoichiometry of substrate/reactants involved in each functionalization step.

As a preliminary step toward the synthesis of our target, amine-functionalized magnetite nanoparticles (**MNP 1**) were prepared on a large scale by chemisorption of APA on magnetite nanoparticles.[12] The number of amine groups on the surface of **MNP 1** was determined by TNBS assay, as described in our earlier reports.[12] From this analysis, the numbers of amine groups on **MNP 1** was determined to be around 1.56 μmol/mg. Before proceeding for heterotrifunctionalization, model studies were conducted to check the feasibility and effectiveness of partial succinylation and Cu(II) catalyzed diazo transfer on single-structured aminated support. As evident from the loss of surface amine groups, **MNP1** was amenable to both succinylation and surface diazo transfer with conversion efficiencies of 75−80% and 90% (results not shown) respectively. On the basis of these preliminary observations, we sought to interchange only 50% of the surface amine groups with carboxyl groups while the remaining halves were left intact for diazo transfer. The primary amine functions on **MNP 1** were desymmetrized into the amine-carboxyl-azide trifunctionalized **MNP 2** through sequential ring-opening linker elongation reaction with succinic anhydride followed by a high-yielding Cu(II) catalyzed diazo transfer with triflic azide (Scheme 2). While surface amine density after succinylation was determined to be around 0.82 μmol/mg, following diazo transfer, the value declined to 0.09 μmol/mg, implying that there was no change in the efficiency of amine to azide transformation, even after heterobifunctionalization of the surface. The final amine/carboxyl/azide ratio of MNP 2 was 1:8:8. We chose to attach three types of functional molecules with **MNP 2**: (i) a fluorescent dye (viz. RITC); (ii) a targeting agent (viz. FA); and (iii) a chemotherapeutic drug (viz. PTX). Subsequently, a magnetofluorescent analogue of **MNP 2** was prepared by nucleophilic addition of surface-pendant amine functions with the isothiocyanate group of RITC. To check the orthogonality of bioconjugation, single-structured MNPs bearing either carboxyl or azide groups were synthesized and RITC conjugation was attempted maintaining exactly identical reaction conditions. However, as observed by UV and fluorescence spectroscopy, no detectable fluorescence was perceived with the resulting particles, implying that isothiocynate groups react selectively with amine groups. Starting from the magnetofluorescent analogue of **MNP 2**, we reached our target nanoconstruct **MNP 4** in just two steps, which involved simple Cu(I) catalyzed clicking of alkyne-terminated folate onto the surface azido

dx.doi.org/10.1021/bc2000484 |*Bioconjugate Chem.* 2011, 22, 1181–1193

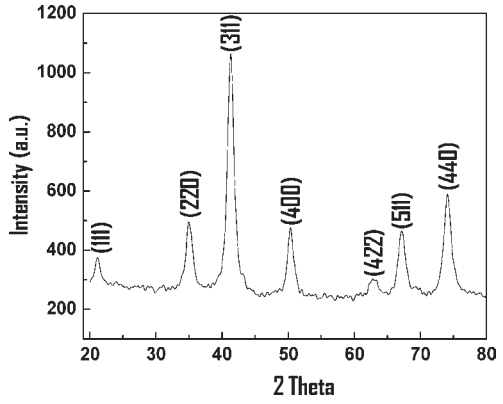


Figure 1. X-ray diffraction pattern of **MNP 1**.

groups, followed by carbodiimide-activated coupling between hydroxyl (−OH) groups of PTX and free carboxyl groups of **MNP 3**. To further testify whether the transformation of **MNP 2**-**MNP 3** was orthogonal, single-structured azide-terminated MNPs were reacted with both RITC and PTX under click conditions, and progress of the reaction was monitored through FTIR analysis. While almost complete disappearance of azide peaks (2041 cm^{-1}) was perceived in the case of reaction between azido-MNPs and propargyl folate only after 6 h (results not shown), FTIR spectra of MNPs reacted with RITC as well as PTX revealed no significant change in the intensity of the azide peak even after prolonged reaction (24 h), suggesting that neither isothiocyanate nor hydroxyl groups (the most reactive functional sites of RITC and PTX for complementary attachment) react under click conditions. In this regard, it should be mentioned that 2′- and 7-hydroxyl groups in PTX are the most suitable positions for its structural modification. Owing to the complexity of our system, it was not possible to determine the exact position of linkage between PTX and MNPs. However, as suggested by the earlier reports, it might be assumed that the 2′-hydroxyl position is less sterically hindered and more reactive than the 7-hydroxyl position reacted specifically with the free carboxyl groups of **MNP 3**.[14] By maintaining a very low fraction of surface reactive amino groups (only 5.8% of the total surface functional groups) on **MNP 2** and further blocking the same with excess of RITC, we eliminated the chance of interparticle cross-linking between the surface-pendant amine and carboxyl groups also as any nonspecific targeting within the biological system. It was further interesting to note that the Cu(I) species, required for the Hüisgen cycloaddition reaction, was generated *in situ*, deriving directly from Cu(II) salts used in the diazo transfer step. In fact, the addition of sodium ascorbate after the completion of diazo transfer initiates the reduction of Cu(II) to Cu(I), which, once formed, becomes immediately accessible to promote orthogonal coupling with the complementary alkyne, so that the transformation of **MNP 1**−**3** proceeded smoothly in a single pot, without necessitating the recovery of the intermediates.

The extent of RITC, FA, and PTX conjugation on **MNP 4** was quantified using UV spectrophotometry and HPLC analyses, respectively. From this analysis, the conjugation efficiency of RITC, FA, and PTX immobilized per unit mass (mg) of MNPs was calculated to be around 0.076, 0.574, and 0.362 μmol/mg, respectively. Since each particle contained magnetite (d = 5.214 g cm^{-3}) with an average radius of 4.5 nm, the average volume and mass of Fe_3O_4 particles are 3.8151 × 10^{-25} m^3 and 1.987 × 10^{-18} gm, respectively. Hence, 1 mg of Fe_3O_4 comprises 5.032 × 10^{14} particles. From these values, the average numbers of RITC, FA, and PTX immobilized per particle were determined to be around 88.89, 688.26, and 433.24, respectively. This concentration, however, was optimal for attaining a high targeting and chemotherapeutic efficiency *in vitro*.

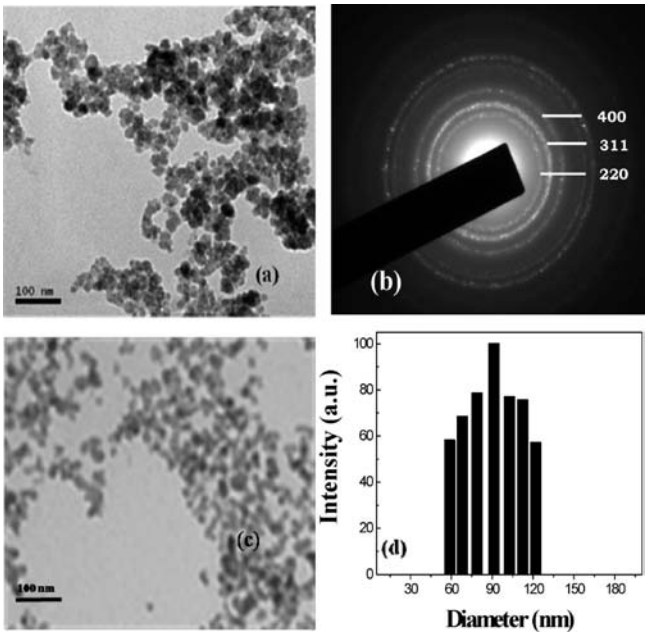


Figure 2. (a) Transmission micrograph of **MNP 1**; (b) SAED pattern of **MNP 1**; (c) TEM micrograph of **MNP 4**; and (d) particle size distribution (PSD) histogram of **MNP 4**, measured using DLS technique.

The high-resolution X-ray diffraction pattern of **MNP 1**, presented in Figure 1, corresponded to that of inverse spinel magnetite [Fe_3O_4] (JCPDS card no. 85−1436). The broadening of peaks indicated the nanocrystalline nature of **MNP 1**, which translated into an average core size of about 9.84 nm using the Debye−Scherrer formula for spherical particles. The selected-area diffraction (SAED) pattern (inset image) indicated the polycrystalline nature of the embedded magnetite particles. The individual planes identified from the SAED pattern correlated well with that of the X-ray diffraction pattern. Transmission electron microscopy (TEM) studies of **MNP 1** (Figure 2) revealed that the as-synthesized magnetite nanoparticles were close to spherical with an average diameter of 9 ± 0.5 nm. Representative TEM images of **MNP 4** indicated the presence of nearly spherical particles with average size in the range 10−15 nm. As evident from TEM, as well as dynamic light scattering (DLS) studies, the "clicked" nanoparticles, in particular, **MNP 4**, displayed much better dispersal and stability at physiological pH as compared to its amine-functionalized precursor (**MNP-1**), which is possibly due to the presence of a highly hydrophilic triazole moiety and the negative surface charge arising out of the free, deprotonated carboxyl and hydroxyl groups of FA and PTX, respectively. An aqueous suspension of **MNP 4** presented a mean HD of 91 ± 4 nm (PDI = 0.191 ± 0.009) with a surface charge of −41.4 ± 2 mV at neutral pH. These functional nanoaparticles were highly stable in aqueous medium as their HD, PDI, zeta potential, and T_2 relaxivity remained unaffected over a long period of time (Table 1).

Table 1. Stability Analysis of MNP 4

time (weeks)	1	2	3	4	6	8	12
HD (nm)	91.6 ± 4.6	89.7 ± −4.2	93.2 ± 5.1	92.9 ± 4.9	94.1 ± 3.7	93 ± 4.1	94.9 ± 5.4
PDI	0.197 ± 0.012	0.184 ± 0.009	0.193 ± 0.017	0.191 ± 0.014	0.204 ± 0.019	0.216 ± 0.022	0.198 ± 0.017
Zeta-potential (mV)	−43.4 ± 3.8	−43.8 ± 4.2	−41.9 ± 4.4	−40.7 ± 5.5	−38.6 ± 3.7	−39.3 ± 3.6	−37.6 ± 4.1
r_2 (s^{-1} mM^{-1})	70.8 ± 4.5	70.96 ± 5.19	69.7 ± 5.9	67.4 ± 5.6	65.7 ± 6.2	66.8 ± 6.3	65.8 ± 6.8

Exposure of **MNP 4** to various culture media (DMEM, RPMI, etc.) in the presence of serum revealed no significant alteration in hydrodynamic sizes and surface charge up to 72 h of incubation (results not shown), confering the suitability of these nanoparticles for biomedically relevant applications.

The FTIR spectrum of **MNP 1** (Figure 3) displays a strong band around 594 cm^{-1} attributed to the Fe−O vibration related to the magnetite core. A broad band, associated with the overlapping of Fe−O−P and P═O stretching, appears between 1160 and 928 cm^{-1}, which unambiguously suggests that a strong interaction between the phosphonate headgroup and the Fe_3O_4 surface is present. The band at 1633 cm^{-1}, associated with −NH bending (scissoring) vibration, however, testifies to the successful modification of magnetite surface by primary amine groups. Chemical treatment of these surface amine groups with succinic anhydride led to the partial interchange of these amine functions with carboxyl functions. The typical vibrations of $-CO_2H$ group (1704 cm^{-1}) and the amide linkage [1637 (amide I) and 1556 cm^{-1} (amide II)] appeared in the corresponding FTIR spectrum, which evidence the successful derivatization of the surface-amino group with succinic anhydride. It should, however, be noted that relative weakness in the intensity of the $-CO_2H$ vibration at 1710 cm^{-1} is possibly a consequence of intraparticle hydrogen bonding between the surface $-CO_2H$ groups. This, however, shifts the >C═O stretching bands of carboxylic acids to a much lower wavenumber (∼1625−1650 cm^{-1}) and superimposes with the amide I band. As a consequence of diazo transfer, an extra band appears in the FTIR spectrum of **MNP 2** at approximately 2041 cm^{-1} due to the asymmetric stretching of the N═N═N bond of the azide group. As already discussed, RITC comprised only 4−5% of the total surface functional groups and, therefore, could not be detected by FTIR analysis, albeit spectrophotometric studies clearly corroborated the successful labeling of MNPs with RITC. The successful immobilization of FA on **MNP 2** was clearly indicated by the disappearance of the 2041 cm^{-1} band and concomitant appearance of the characteristic bands of FA at 1603 and 1656 cm^{-1}. After PTX conjugation, the only distinguishable change in the spectrum was the appearance of a weak but fairly prominent band at approximately 1736 cm^{-1}, possibly associated with C═O stretching vibrations arising out of the covalent attachment of PTX to the carrier surface via an ester linkage. The relatively weak intensity of the ester stretching frequency might be a consequence of multiple ligand attachment on the nanoparticle surface. The surface of MNPs being shared by multiple functional molecules, relative fraction of individual functional entities associated with the nanoparticle surface, may be lower than the detection limit of the available spectroscopic techniques.[15]

The successful transformations of **MNP 1** to **MNP 3** via partial succinylation, surface diazo transfer, and CuAAc reactions were also studied using XPS analysis. The high-resolution N1s spectrum of **MNP 1** (Figure 4) reveals a broad shoulder at 398.6 eV corresponding to the free amino groups on the surface. At the ring-opening linker elongation step, the intensity of the -NH_2 peak gradually diminishes with concomitant appearance of a new peak at 400.6 eV, indicating the formation of amide (−NHCO) linkage between the amine groups of APA and succinic anhydride. A high-resolution spectrum of the nitrogen 1s binding energies of **MNP 2** reveals two distinct peaks, one centered at around 400 eV and another at 405 eV, with approximately 2:1 ratio of the peak areas. The relatively lower intensity, higher energy 405 eV peak is unusual for organic nitrogen, and this peak can be assigned to the central, electron-deficient nitrogen in the azide group. Reaction of **MNP 2** with the propargyl folate, linked via the click reaction, reduced the 405 eV peak to the level of noise. The nitrogen 1s signal at 400 eV broadens, indicating the presence of chemically distinct nitrogen atoms corresponding to the nitrogen atoms of the triazole linkage and amide bonding inside FA structure and partially succinylated surface amine functions as well. Assuming that the azide disappearance is correlated only to product formation, this provides additional evidence that the transformation is nearly quantitative.[16]

In general, ^{1}H NMR spectroscopy of ligands, bound to paramagnetic nanocrystals are difficult to perform because of large broadening effects, caused by paramagnetic features. Recently, Polito et al. have explored the possibility of using the high-resolution magic angle spinning (HRMAS) technique for the fine-structure-resolved characterization of even complex organic molecules bound to paramagnetic nanocrystals, such as nanosized iron oxides, while minimizing the effect of paramagnetic broadening. In line with Polito's approach, we tried to apply the HRMAS technique for further detailed structure-resolved analysis of the organic layer, associated with our multifunctional nanoconjugate. A comparison of the ^{1}H NMR of **MNP 2** and **MNP 3** unambiguously confirmed the presence of FA on **MNP 3**, as indicated by characteristic signals from pteridine ring proton (δ 9.2 ppm) and aromatic protons of the PABA moiety of FA (δ 8.1−7.9 ppm and 7.3−6.9 ppm), which, however, were absent in **MNP 2** (Figure 5). The presence of a prominent peak at 8.2 ppm in the NMR spectrum of **MNP 3** due to the triazole proton further testified to the successful end-functionalization of **MNP 2** via 1,3-dipolar cycloaddition. Careful inspection of these ^{1}H HRMAS NMR spectra, however, revealed that the spectral intensity of a proton was directly proportional to its distance from the nanoparticle surface, i.e., the longer the distance, the stronger the intensity. For example, the intensity of the triazole proton as well as aromatic protons of FA was disproportionally higher than the methylene protons of FA and phosphonic acid, lying in close proximity to the NP surface. The observation, however, is in close accordance with some of the earlier reports[17] and is attributed to (i) the restricted motion for protons closer to the MNP surface, (ii) heterogeneity caused by MNP surface features (terraces, edges, or vertices) of various sizes or facets, and (iii) spin−spin relaxation (T_2) broadening effect, which also depends on the size of NPs. In the case of **MNP 4**, overlap of aromatic protons of FA and PTX caused an inherent broadness in

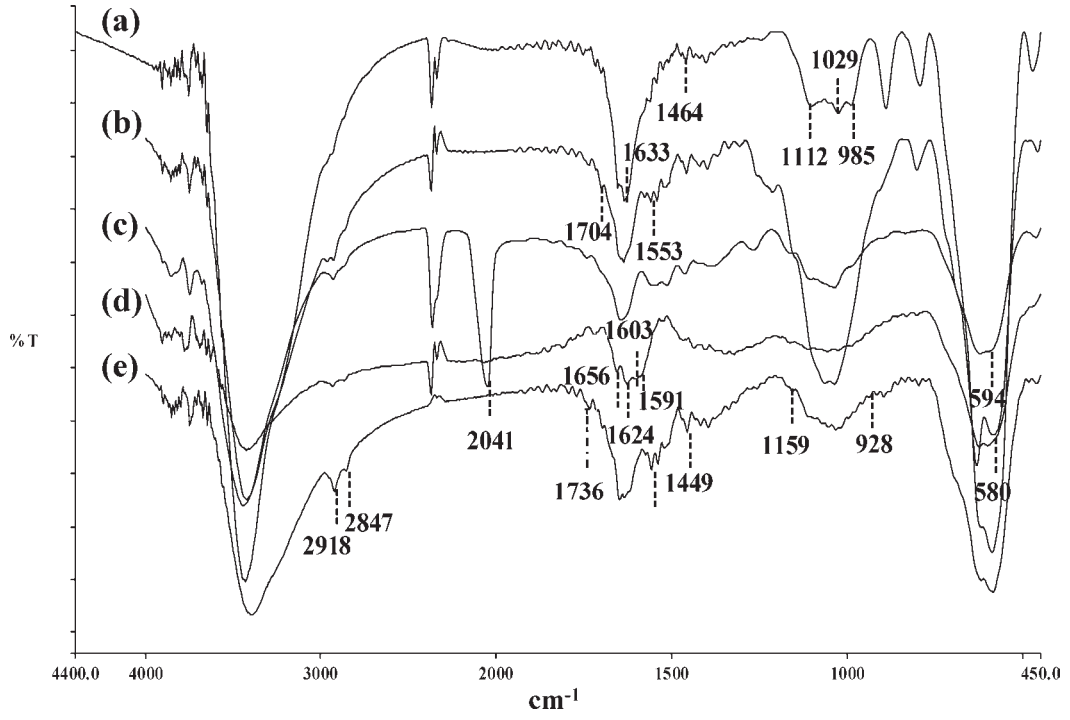


Figure 3. FTIR spectra of (a) **MNP 1**; (b) **MNP 1** (after succinylation); (c) **MNP 2**; (d) **MNP 3**; and (e) **MNP 4**.

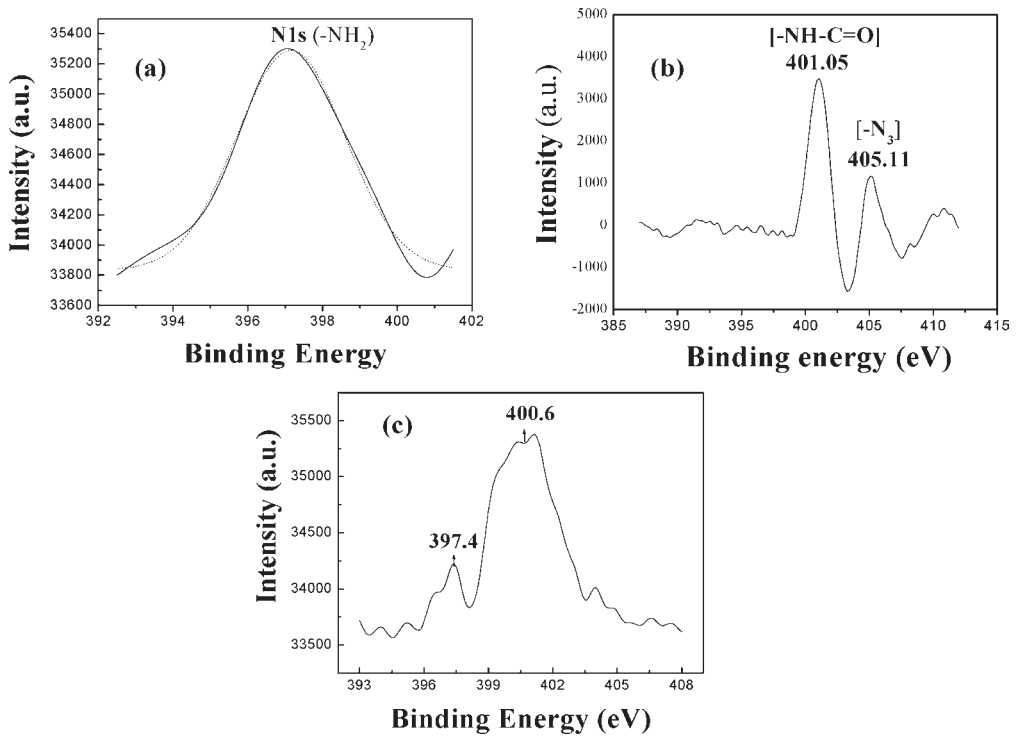


Figure 4. High-resolution N1s spectra of (a) **MNP 1**; (b) **MNP 2**; and (c) **MNP 3**.

the spectrum between δ 9.8 and 7.3 ppm and also in the lower aliphatic range (results not shown). Consistent with the findings of FTIR, spectral intensity of some of the key peaks of FA as well as PTX was too low to make a definitive structural assignment. To confirm the successful immobilization of PTX on MNP surface, we relied on an alternative strategy, which consisted of detachment of PTX from the surface of **MNP 4** through a base-catalyzed ester hydrolytic cleavage, followed by a mini-workup and subsequent characterization of the organic layer by FTIR and NMR analysis.

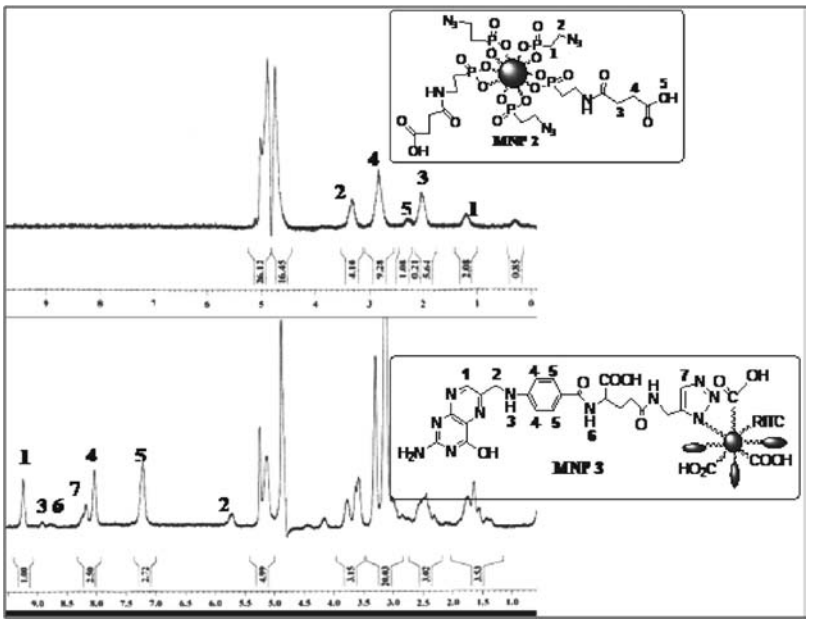


Figure 5. Structure-resolved analysis of "clicked" MNPs using HRMAS-NMR spectroscopy.

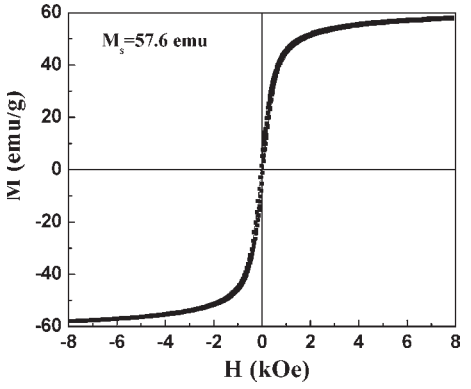


Figure 6. Magnetization (M-H) curve of **MNP 4**.

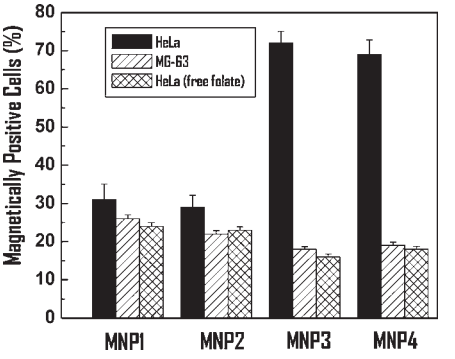


Figure 7. Quantification of **MNP** uptake by FR positive HeLa, FR negative MG-63 cell lines, and HeLa cells incubated with excess free folate via magnetically activated cell-sorting (MACS) analysis.

It should however be mentioned in this regard that surface modification had no detrimental effect on the intrinsic superparamagnetism of Fe_3O_4. Absence of hysteresis, coercivity, and remenance in the magnetization curve (Figure 6) corroborated the superparamagnetic nature of **MNP 4**. The saturation magnetization (57.3 emu/g) was, however, lower than that of bare Fe_3O_4 MNPs (~91 emu/g) ascribed to the organic coating associated with the nanomagnetite core. Proton relaxation measurements of **MNP 4** using a 0.3 T clinical MRI scanner further indicated the presence of superparamagnetic iron-oxide nanoparticles with appreciably high T_2 relaxation (70.794 s^{-1} mM^{-1}), ensuring their potential application as a MR contrast agent.

To further demonstrate the potential biomedical applications of the synthesized functional **MNP 4**, we evaluated the selective uptake of **MNP 1**−**4** against folate-receptor overexpressing human cervical carcinoma HeLa cells. Preliminary studies using magnetically activated cell sorting (MACS) indicated that cellular uptake of the conjugates containing FA as the targeting molecule was significantly enhanced in comparison to their nontargeted control (Figure 7). The observations demonstrated active targeting of magnetite nanoparticles through the interaction between the folate groups on nanoparticle surface and receptors of HeLa cells. With the aim to confirm the receptor specificity for the conjugate, the uptake of **MNP 1**−**4** by HeLa cells was compared with the uptake by (i) folate-receptor negative human osteosarcoma, MG-63 cell-line, and (ii) HeLa cells, preincubated with free folate. As internalization of the folate functionalized NPs was nominal in both cases, we corroborated the receptor-mediated internalization of our folate decorated MNPs.

To further evaluate the detectibility of **MNP** internalized cells by MRI and confirm their association with FR-overexpressing HeLa cells, MR phantom samples were prepared by suspending HeLa cells incubated with **MNP 1**−**4** for two hours in agarose. The T_2 weighed phantom image of cells, incubated with **MNP 3**−**4**, showed a significant negative contrast enhancement in comparison to their nontargeted control **MNP 1**, suggesting effective nanoparticle internalization inside the target cells (Figure 8). Slight losses in signal intensity were, however, observed for HeLa cells incubated with **MNP 1**, when compared to blank cells cultured without nanoparticles, attributed to some

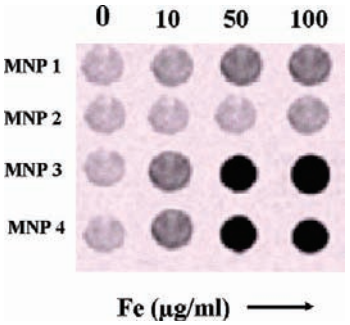


Figure 8. T_2-weighted spin−echo MR phantom images of HeLa cells incubated with 0−100 μg/mL of **MNP 1**−**4** for 2 h.

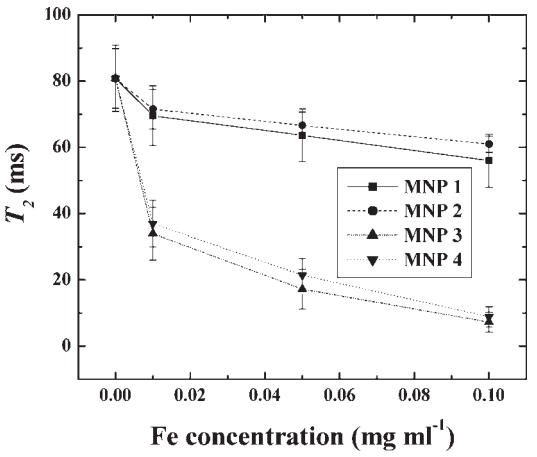


Figure 9. T_2 relaxation analysis of HeLa cell suspensions magnetically labeled with **MNP 1**−**4**.

nonspecific internalization of these nanometer-sized particles inside the target cells. The relative relaxation times of **MNP 1**−**4** were quantified through T_2 weighted spin−echo MR images. Figure 9 shows the T_2 relaxation time as a function of particle concentration in cell culture media. HeLa cells cultured with **MNP 3**−**4** had a shorter T_2 relaxation time (higher relaxivity) than **MNP 1**−**2** due to enhanced magnetism, which resulted from higher uptake of the former by HeLa cells in comparison to the latter. All these results unequivocally establish the potential of our as-prepared nanoformulation as a cancer-targeted, MR imaging probe.

In vitro stability or drug release studies, conducted with **MNP-4** at pH 4 and 7 using a 1:1 mixture of methanol and PBS (v/v) as the release medium showed a typical release profile, i.e., an initial burst release, followed by a sustained release pattern (Figure 10). The overall release rate was much higher at pH 4 and negligible drug release was observed at physiological pH (pH 7.2). Around 66.37% of the conjugated PTX was found to be released from **MNP 4** exposed to the release medium at pH 4 whereas only 35% release was observed at pH 7.5. This pH-dependent release behavior suggested that PTX will be released more in acidic tumor sites than in the normal tissues. Once the particles are internalized inside the cells through FR mediated endocytosis, the decreased pH values are supposed to induce further accelerated release inside the acidic endosomes of tumor cells through the rupture of acid as well as base-cleavable linkage between **MNP 4** and PTX.

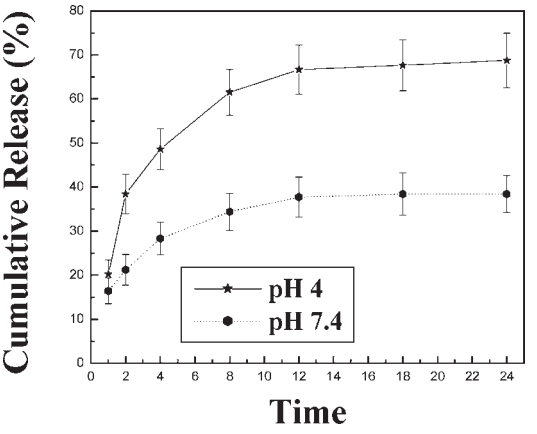


Figure 10. Drug release profile of **MNP 4** under different pH conditions.

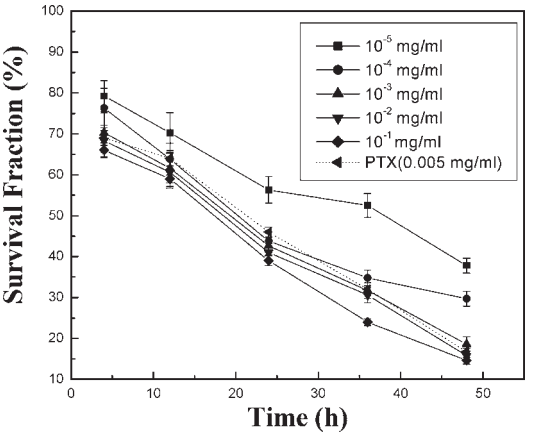


Figure 11. Reduction in viability of HeLa cells as a function of time and nanoparticle concentration in culture medium.

To further test the efficacy of PTX cleavage inside the target cells, HeLa cells were cultured with **MNP 1**−**4** and free PTX in a FA deficient medium. Nanoparticle-induced cytotoxicity was determined by the MTT assay. While nanoparticles deprived of PTX were shown to be noncytotoxic, both **MNP 4** and free PTX (dissolved in a 1:1 (v/v) mixture of MeOH and PBS) reduced the cellular viability in a time and dose-dependent fashion, establishing the ability of the cells to cleave PTX inside the acidic tumor endosomes (Figure 11). Cells exposed to PTX modified NPs demonstrated a notable downward trend in viability, following 24 h in culture. It was further observed that, for concentrations of PTX grafted nanoparticles at or higher than 10 μg/mL (equivalent PTX concentration of 4.792 μg/mL of PTX), the cells showed almost comparable reduction in cellular viability. Notably, cytotoxic activity of **MNP 4** was even higher than equivalent amount of the free drug under similar experimental conditions. The ability of these drug modified nanoparticles to induce significant cytotoxicity in such low concentrations promises the desired chemotherapeutic effect in the target site in very low dosages.

To verify whether **MNP-4** could induce cell death through the initiation of apoptosis, HeLa cells were exposed to 0.1 mg/mL of **MNP 1**, **3**, and **4** for 0.5 h, washed to remove the noninternalized nanoparticles, incubated at 37 °C for 24 h, and subsequently

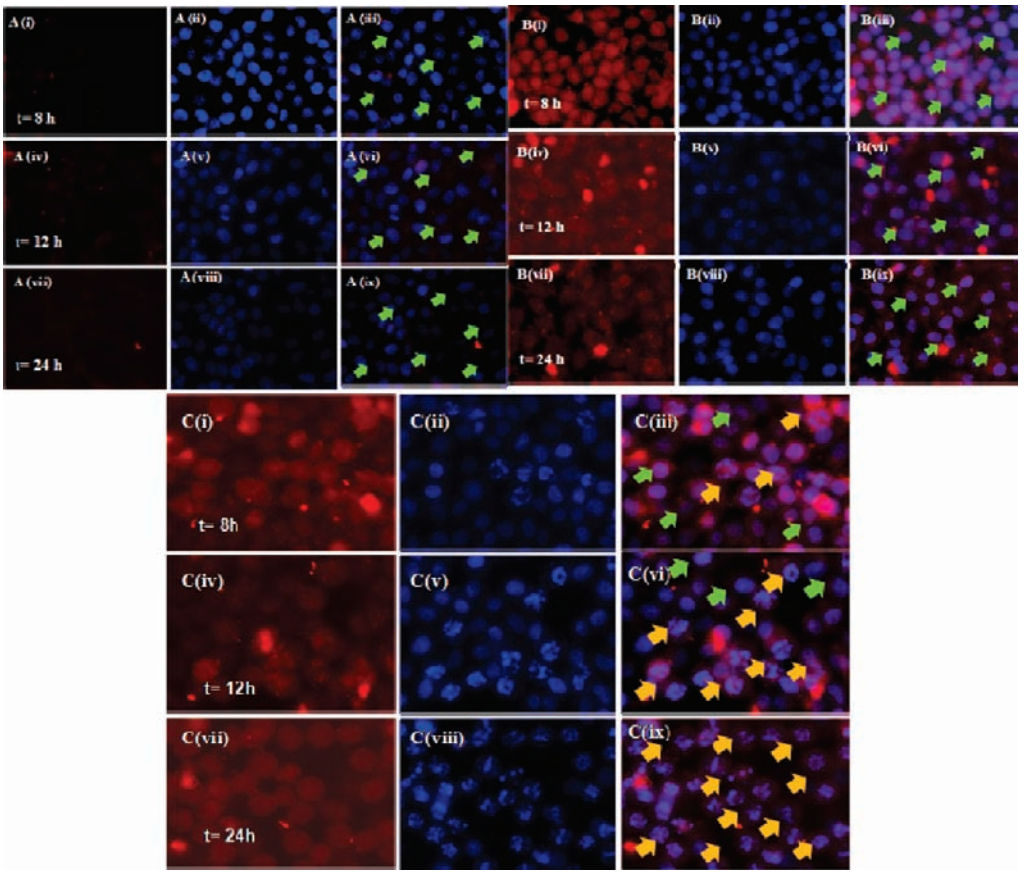


Figure 12. Fluorescence micrograph of [A(i−ix)] HeLa cells incubated with **MNP 1**, [B(i−ix)] **MNP 3**, and [C(i−ix)] **MNP 4** for 8, 12 and 24 h, respectively. The green and yellow arrows denote healthy and apoptotic nuclei, respectively. The left (i, iv, viii) and middle (ii, v, viii) panels of each incubation type represent RITC and DAPI fluorescence, respectively, while the right (iii, vi, ix) panel is the merged RITC and DAPI fluorescence images.

visualized using fluorescence microscopy. Results showed little or practically no internalization of the nontargeted controls **MNP 1**, as expected. On the contrary, intense red fluorescence was detected in the cytoplasm of cells treated with the folate targeted nanoparticles (**MNP 3**−**4**), demonstrating their cellular internalization through receptor-mediated endocytosis (Figure 12). With an aim to examine the nuclear morphology and identify cell death, cell nuclei were further stained with 4′,6-diamidino-2-phenylindole (DAPI), a nuclear staining dye known to exhibit strong blue fluorescence, when bound to DNA. As predicted from the cytotoxicity experiments, fluorescence images of HeLa cells, incubated with **MNP 1** and **MNP 3** for 8, 12, and even 24 h showed well-preserved nuclear structures without any detrimental effect on structural integrity. In contrast, typical features of nuclear apoptosis were prominent in cells incubated with **MNP 4** as early as 8 h. Cell nuclei segregated into segments accompanied by severe fragmentation, suggesting a major breakdown of the chromatin followed by DNA condensation in these nuclei. By the end of 24 h, massive fragmentation was observed leading to a huge population of apoptotic bodies.

To further quantify the extent of nanoparticle induced apoptosis, cell-cycle analysis was performed using the standard propidium iodide (PI) flow cytometric assay. Classification of HeLa cells into the various phases of the cell cycle following their incubation with **MNP 3** and **MNP 4** for different time spans (8−24 h) has been shown in Figure 13. Apoptosis, which is hallmarked by DNA fragmentation, was almost negligible in the case of both untreated cells and cells treated with control **MNP 3**, even after 24 h of incubation. On the contrary, significant DNA fragmentation could be envisaged in HeLa cells treated with **MNP 4** under similar experimental conditions, evidenced as a "sub-G1" peak in the DNA fluorescence histogram. Time-dependent cell cycle analysis of **MNP-4** incubated HeLa cells clearly indicated that the number of cells in the G_0/G_1 phase gradually decreased as a function of time with a concomitant elevation of both G_2/M and sub-G1 or apoptotic phases. While the ratio of cells present in G_0/G_1 to G_2/M phases after 8 h was 1.87, following 12 and 24 h of incubation the values decreased to 1.24 and 0.64, respectively, relative to 3.53 and 2.47 for untreated cells and cells incubated with **MNP 3** for 24 h. For **MNP 4**, massive cell death was observed at the end of 24 h as dead cells accounted for 92.59% of the total population, relative to only 53.69% for HeLa cells incubated with an equivalent amount of free PTX (cell cycle distribution not shown). The data not only are in good agreement with our fluorescence microscopic observations, but also correlate well with the cell cycle distribution profile of other PTX-based drug delivery systems based on biodegradable polymers like PLGA or chitosan.[18,19] In fact, the sub-G1 population for HeLa cells (92.59%) incubated with 0.2 mg/mL of **MNP 4** (equivalent paclitaxel concentration of 0.11 μmol) was appreciably higher than that for A549 cells (73.32%) incubated with wheat germ agglutinin (WGA) conjugated, PTX loaded PLGA nanoparticles (equivalent PTX concentration 20 μmol). The results unambiguously suggest that **MNP 4**

dx.doi.org/10.1021/bc2000484 |*Bioconjugate Chem.* 2011, 22, 1181–1193

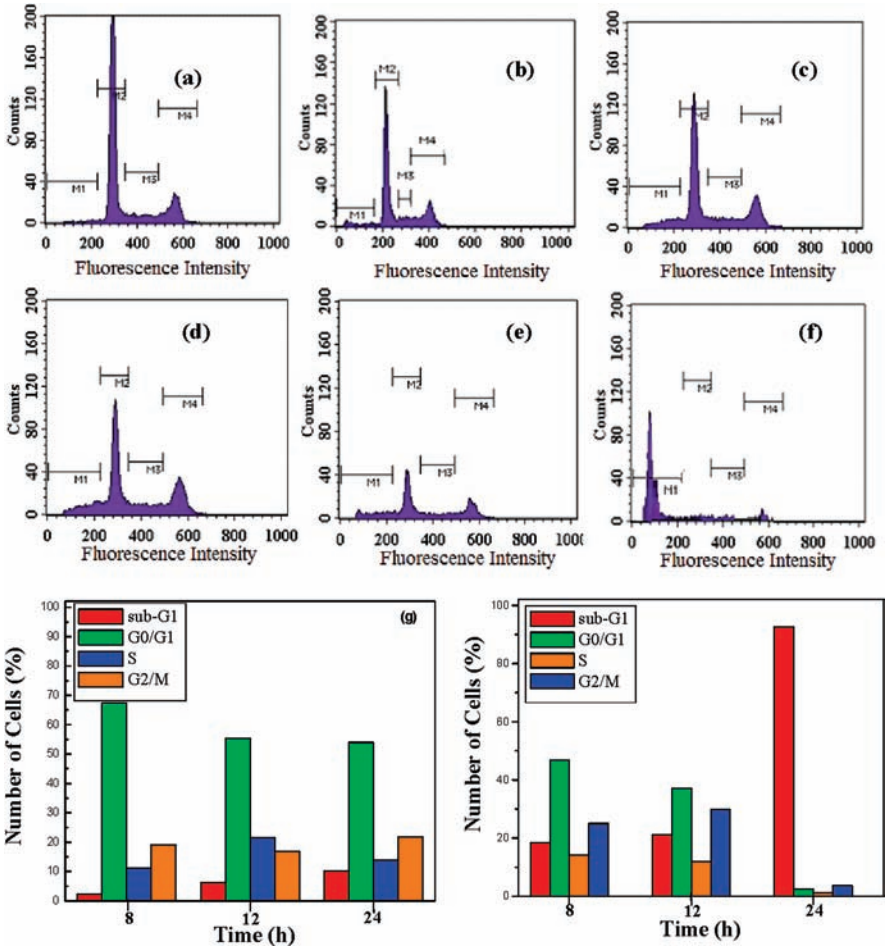


Figure 13. DNA fluorescence histogram of (a) untreated HeLa cells; (b,c) HeLa cells incubated with **MNP 3** for 12 and 24 h, respectively, (d−f) HeLa cells treated with PTX conjugated **MNP 4** for 8, 12, and 24 h, respectively, and (e) cell cycle analysis of HeLa cells treated with different MNP based formulations at different time points.

developed in the course of the present research can effectively arrest the cell cycle in the G_2/M phase, which was responsible for the morphological alterations visualized by fluorescence microscopy and ultimately causes cell death.

CONCLUSION

In conclusion, a biocompatible, theragnostic iron oxide nanoformulation for combined cancer-targeted therapy and multimodal imaging has been designed and successfully synthesized using a chemoselective protocol. Magnetite nanoparticles simultaneously bearing three types of functional groups, viz., amine, carboxyl, and azide groups, were used as the bioconjugating precursor. Such a trifunctional surface was executable through a sequence of highly controlled, partial succinylation, followed by Cu (II) catalyzed diazo transfer on APA functionalized magnetite nanoparticles. Chemoselective conjugation of cancer-targeting FA and chemotherapeutic PTX on the hybrid MNP surface was accomplished via CuAAc reactions and carbodiimide promoted esterification, respectively. The feasibility of chemoselective ligation on these bifunctional MNPs was demonstrated with extensive FTIR, XPS, and HRMAS-NMR analysis. *In vitro* cell uptake, MR imaging, and apoptosis studies established that that the bioactives chemoselectively appended to the nanomagnetite core allowed the nanoparticles to simultaneously target, image, and kill folate-receptor (FR) overexpressing cancer cells with enhanced efficacy as compared to the free drug. In a scientific panorama, in which the emergence of "smart", multifunctional nanoparticles appears to be one of the major breakthroughs in cancer theragnostics, the fabrication of these newly synthesized amine-carboxyl-azide trifunctionalized magnetite nanoparticles contributes a new toolbox for the non-polymer-based, chemoselective biofunctionalization of inorganic nanoparticles. Further, the positive attributes of *in vitro* study make these trifunctional nanoparticles a "smart" theragnostic platform for further *in vivo* evaluation.

AUTHOR INFORMATION

Corresponding Author

*E mail for correspondence: md_manasmita@yahoo.com.

ACKNOWLEDGMENT

The authors gratefully acknowledge the financial support provided by Council of Scientific and Industrial Research (CSIR, New Delhi), Department of Science and Technology (DST, New Delhi) and Department of Biotechnology (DBT, New Delhi) for this work. Thanks are due to Dr. K. R. Patil, National Chemical Laboratory (NCL) Pune and SAIF, Central

Drug Research institute (CDRI, Lucknow) for assistance with XPS and HRMAS analysis. Mr. Nirjhar Samanta, Midnapore Scan Center is duly acknowledged for his excellent assistance with MRI studies.

REFERENCES

(1) Sosnovik, D. E., and Weissleder, R. (2007) Emerging concepts in molecular MRI. *Curr. Opin. Biotechnol. 18*, 4–10.

(2) Mornet, S., Vasseur, S., Grasset, F., and Duguet, E. (2004) Magnetic nanoparticle design for medical diagnosis and therapy. *J. Mater. Chem. 14*, 2161–2175.

(3) Chorny, M., Polyak, B., Alferiev, I. S., Walsh, K., Friedman, G., and Levy, R. J. (2007) Magnetically driven plasmid DNA delivery with biodegradable polymeric nanoparticles. *FASEB J. 21*, 2510–2519.

(4) Gu, H., Xu, K., Xu, C., and Xu, B. (2006) Biofunctional magnetic nanoparticles for protein separation and pathogen detection. *Chem. Commun.* 941–949.

(5) Nishimura, K., Hasegawa, M., Ogura, Y., Nishi, T., Kataoka, K., Handa, H., and Abe, M. (2002) 4°C preparation of ferrite nanoparticles having protein molecules immobilized on their surfaces. *J. Appl. Phys. 91*, 8555–8556.

(6) Kell, J., and Simard, B. (2007) Vancomycin architecture dependence on the capture efficiency of antibody-modified microbeads by magnetic nanoparticles. *Chem. Commun.* 1227–1229.

(7) Carlesso, L. N., Tung, C. H., Tang, X. W., Cory, D., Scadden, D. T., and Weissleder, R. (2000) Tat peptide-derivatized magnetic nanoparticles allow in vivo tracking and recovery of progenitor cells. *Nat. Biotechnol. 18*, 410–414.

(8) (a) Yoo, E. J., Ahlquist, M., Kim, S. H., Bae, I., Fokin, V. V., Sharpless, K. B., and Chang, S. (2007) Copper-catalyzed synthesis of *N*-sulfonyl-1,2,3-triazoles: controlling selectivity. *Angew. Chem., Int. Ed. 46*, 1730–1733. (b) Rostovtsev, V. V., Green, L. G., Fokin, V. V., and Sharpless, K. B. (2002) A stepwise Huisgen cycloaddition process: copper(I)-catalyzed regioselective "ligation" of azides and terminal alkynes. *Angew. Chem., Int. Ed. 41*, 2596–2599.

(9) Polito, L., Monti, D., Canava, E., Delnevo, E., Russo, G., and Prosperi, D. (2008) One-step bioengineering of magnetic nanoparticles *via* a surface diazo transfer/azide−alkyne click reaction sequence. *Chem. Commun.* 621–623.

(10) Titz, A., Radic, Z., Schwardt, O., and Ernst, B. (2006) A safe and convenient method for the preparation of triflyl azide, and its use in diazo transfer reactions to primary amines. *Tetrahedron Lett. 47*, 2383–2385.

(11) Mishra, A. K., Chopra, M., and Jain, V. (2005) Convenient route for synthesis of bifunctional chelating agent: 1-(*p*-aminobenzyl) ethylenediaminetetramethylphosphonic acid−folate conjugate (Am-Bz-EDTMP−Folate). *Chem. Lett.* 1098–1099.

(12) Das, M., Mishra, D., Maiti, T. K., Basak, A., and Pramanik, P. (2008) Bio-functionalization of magnetite nanoparticles using an aminophosphonic acid coupling agent: new, ultradispersed, iron-oxide folate nanoconjugates for cancer-specific targeting. *Nanotechnology 19*, 415101.

(13) Das, M., Mishra, D., Dhak, P., Gupta, S., Maiti, T. K., Basak, A., and Pramanik, P. (2009) Biofunctionalized, phosphonate-grafted, ultrasmall iron oxide nanoparticles for combined targeted cancer therapy and multimodal imaging. *Small 5*, 2883–2893.

(14) Deutsch, H. M., Glinski, J. A., Hermandez, M., Haugwitz, R. D., Narayanan, L. V., Suffness, M., and Zalkow, L. H. (1989) Synthesis of congeners and prodrugs. 3. Water-soluble prodrugs of taxol with potent anti-tumor activity. *J. Med. Chem. 32*, 788–792.

(15) Zhou, H. Y., Du, F. F., Li, X., Zhang, B., Li., W., and Yan, B. (2008) Characterization of organic molecules attached to gold nanoparticle surface using high resolution magic angle spinning ^{1}H NMR. *J. Phys. Chem. C 112*, 19360–19366.

(16) Collman, J. P., Devaraj, N. K., Eberspacher, T. P. A., and Chidsey, C. E. D. (2006) Mixed azide-terminated monolayers: a platform for modifying electrode surfaces. *Langmuir 22*, 2457–2464.

(17) Polito, L., Colombo, M., Monti, D., Melato, S., Caneva, E., and Prosperi, D. (2008) Resolving the structure of ligands bound to the surface of superparamagnetic iron oxide nanoparticles by high-resolution magic-angle spinning NMR spectroscopy. *J. Am. Chem. Soc. 130*, 12712–24.

(18) Mo, Y., and Lim, L. Y. (2005) Preparation and in vitro anticancer activity of wheat germ agglutinin (WGA)-conjugated PLGA nanoparticles loaded with paclitaxel and isopropyl myristate. *J. Controlled Release 108*, 244–262.

(19) Li, F., Li, J., Wen, X., Zhou, S., Tong, X., Su, P., Li, H., and Shi, D. (2009) Anti-tumor activity of paclitaxel-loaded chitosan nanoparticles: An in vitro study. *Mater. Sci. Eng. 29*, 2392–2397.

Bioconjugate Chemistry

ARTICLE

pubs.acs.org/bc

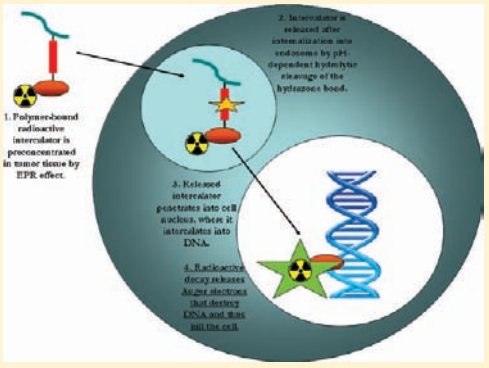
Ellipticine-Aimed Polymer-Conjugated Auger Electron Emitter: Multistage Organelle Targeting Approach

Ondrej Sedlacek,[†] Martin Hruby,[*,†] Martin Studenovsky,[†] Jan Kucka,[†] David Vetvicka,[‡] Lubomir Kovar,[‡] Blanka Rihova,[‡] and Karel Ulbrich[†]

[†]Institute of Macromolecular Chemistry AS CR, v.v.i., Heyrovsky Sq. 2, 162 06 Prague 6, Czech Republic

[‡]Institute of Microbiology AS CR, v.v.i., Videnska 1083, 142 20 Prague 4, Czech Republic

ABSTRACT: Radioactive decay of some radionuclides produces a shower of Auger electrons, potent ionizing radiation within a very short range in living tissue (typically ca. 100 nm). Therefore, they must be brought to DNA-containing cell compartments and preferentially directly to DNA to be fully biologically effective. They may be used for a triple-targeting approach (first targeting, polymer-based system targeting into tumor tissue due to EPR effect; second targeting, pH-controlled release of intercalator-bound Auger electron emitter in slightly acidic tumor tissue or endosome; third targeting, into DNA in cell nucleus by the intercalator) minimizing radiation burden of healthy tissues. We describe a first system of this type, an ellipticine derivative-bound iodine-125 attached to hydrazide moieties containing poly[*N*-(2-hydroxypropyl)methacrylamide]. The system is stable at pH 7.4 (0% intercalator released after 24 h incubation), while iodine-containing biologically active intercalator is released upon decrease of pH (25% intercalator released after 24 h incubation at pH 5.0—model of late endosomes). Both 2-*N*-(2-oxobutyl)-9-iodoellipticinium bromide and the noniodinated 2-*N*-(2-oxobutyl)ellipticinium bromide are potent intercalators, as proven by direct titration with DNA and ethidium displacement assay, and readily penetrate into cell nuclei, as proven by confocal microscopy. They retain chemotherapeutical antiproliferative properties of ellipticine against Raji, EL-4, and 4T1cells with IC_{50} in the range 0.27−8.8 μmol/L. Polymer conjugate of 2-*N*-(2-oxobutyl)-9-iodoellipticinium bromide is internalized into endosomes, releases active drug, possesses cytotoxic activity, and the drug accumulates in cell nuclei.



INTRODUCTION

Radiotherapy with radionuclides is common to treat various cancer types such as thyroid cancer.[1,2] For such radiotherapy, mostly β^- emitters are used.[1,3] Radioactive decay of many radionuclides (e.g., ^{111}In, ^{125}I, or ^{99m}Tc) is accompanied with emission of several so-called Auger electrons (AEs) with relatively low energy, which are emitted during reorganization of the electron shell of the atom after decay. Since a charged particle, like an electron, loses its energy in material most effectively (i.e., has the highest linear energy transfer, LET) just before it completely stops ("Bragg peak"[4]), AEs are biologically potent ionizing radiation within a very short range in living tissue (typically ca. 100 nm[2]). However, their very short range means that, if AE emitting radionuclides are intended to be used as radiotherapeuticals, they must be brought into cell nucleus and preferentially directly into DNA, as the main ionizing radiation biological target, to be effective by inducing double-strand breaks.[2,5,6] Especially advantageous in such cases are AE emitter-bearing antisense oligonucleotides,[7] nucleosides,[5,6] and intercalators,[8−11] e.g., ^{125}I-iodinated daunorubicin derivative,[8−10] which target and accumulate the radionuclide directly in DNA. Such isotopically labeled intercalators would be extra beneficial in connection with drug delivery system (see Figure 1), which would ensure selective targeted delivery of the radionuclide into tumor tissue (first targeting by enhanced permeation and retention - EPR - effect). Solid tumors spontaneously accumulate biocompatible polymers, polymer micelles, liposomes, and nanoparticles of the <200 nm size due to the leaky nature of the newly formed tumor neovasculature and poor or missing lymphatic drainage in the solid tumor tissue. Polymer size is thus the targeting mechanism here. This so-called EPR effect is quite universal for many solid tumors. In the tumor tissue, an intercalator bearing the radionuclide is released in its active form (second targeting by pH or enzyme-triggered release). The intercalator then brings the radionuclide into the cell nuclei (third targeting). This would decrease the main disadvantage of radionuclide delivery system—radiation burden of healthy tissues during transport into target tumor tissue—while keeping the advantage of the possibility to follow the biodistribution by real time γ-imaging from the primary γ-rays of the decay (which are far less biologically effective than AEs). To the best of our knowledge, the system described in this paper is the first one of this type in the literature to date.

In this paper, we describe a new polymeric system with AE emitter ^{125}I covalently bound in the form of DNA-intercalating ellipticine (5,11-dimethyl-6*H*-pyrido[4,3-*b*]carbazole) derivative 1-(9-iodo-5,11-dimethyl-6*H*-pyrido[4,3-*b*]carbazol-2-ium-2-yl)-2-butanone

Received: February 1, 2011
Revised: March 10, 2011
Published: April 23, 2011

ACS Publications © 2011 American Chemical Society

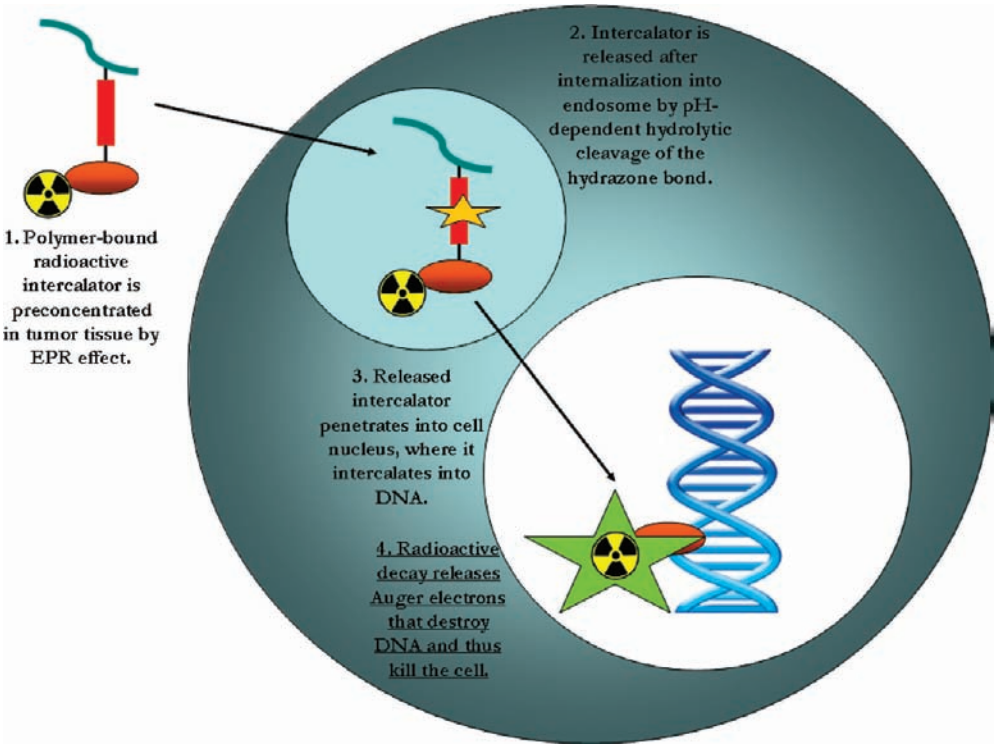


Figure 1. Scheme of triple targeting approach.

conjugated to biocompatible poly[*N*-(2-hydroxypropyl)methacrylamide-*co*-1-*N*-(6-hydrazino-6-oxohexyl)-2-methylacrylamide] (pHPMA-MAAcap hydrazide) via hydrolytically labile hydrazone bonds. To study biological and physicochemical properties of the system in detail and to compare the effect of iodination on chemotherapeutical cytostatic effectivity, intracellular distribution, intercalation ability, and so forth, we synthesized, as models, the system substituted with natural (stable) iodine and the system with the ellipticinium derivative without iodine.

EXPERIMENTAL PROCEDURES

Materials. No-carrier-added $Na^{125}I$ solution (24 GBq/mL) was purchased form Lacomed Ltd. (Czech Republic). All other chemicals were purchased from Sigma-Aldrich Ltd. (Prague, Czech Republic). The 9-iodoellipticine (**1b**) was synthesized by acetomercuration of ellipticine followed by the reaction with iodine according to ref 12.

Quaternization of Ellipticine and 9-Iodoellipticine (see Figure 2 for scheme). Ellipticine (**1a**, 10 mg, 0.041 mmol) or 9-iodoellipticine (**1b**, 15 mg, 0.041 mmol), respectively, and 1-bromo-2-butanone (25 μL, 0.245 mmol, 6 equiv) were added to methanol (1 mL) and the reaction mixture was stirred overnight at room temperature. Then, the reaction mixture was evaporated under reduced pressure and recrystallized from hexane-diethyl ether (2:1 v/v) to give **2a** or **2b**, respectively.

Melting point temperatures were determined on a Kofler' s block (VEB Analytik Dresden, Germany). NMR spectra were measured on a Bruker Avance MSL 300 MHz NMR spectrometer (Bruker Daltonik, Germany). UV/vis spectra were measured on a SPECORD 205 Spectrometer (Analytik Jena AG, Germany).

*2-N-(2-Oxobutyl)ellipticinium Bromide (**2a**).* Yield 11 mg (68%) of orange crystals, mp (hexane-diethyl ether 2:1 v/v) = 213−215 °C; R_f (ethanol−water 5:1 v/v) = 0.15; anal. ($C_{21}H_{21}N_2OBr$) C, H, N; ^{1}H NMR (300 MHz, CD_3OD) δ ppm 9.46 (s, 1H), 8.05−7.91 (m, 3H), 7.44 (t, J = 7.5, 1H), 7.33 (d, J = 8.1, 1H), 7.17 (t, J = 7.5, 1H), 5.69 (s, 2H), 2.87−2.79 (m, 5H), 2.46 (s, 3H)1.21 (t, J = 7.2, 3H); ^{13}C NMR (75 MHz, CD_3OD) δ ppm 203.94, 147.82, 145.79, 143.64, 134.30, 133.93, 132.56, 129.83, 127.34, 124.14, 123.25, 122.15, 121.26, 120.67, 112.44, 111.15, 68.12, 34.13, 15.29, 12.08, 7.53; MS (ESI+): m/z (relative intensity) 317.22 (100%, M^+ - Br^-), 260.60 (6%, M^+ - Br^- - CH_3CH_2CO); UV (CH_3OH) λ_{max}, nm (ε): 295 (30482).

*2-N-(2-Oxobutyl)-9-iodoellipticinium Bromide (**2b**).* Yield 16 mg (88%) of orange crystals, mp (hexane-diethyl ether 2:1 v/v) = 135−137 °C; R_f (ethanol−water 5:1 v/v) = 0.16; anal. ($C_{21}H_{20}N_2OBrI$) C, H, N; ^{1}H NMR (300 MHz, DMSO-d_6) δ ppm 12.29 (s, 1H, NH), 9.94 (s, 1H), 8.64 (s, 1H), 8.47 (d, J = 7.19 Hz, 1H), 8.27 (d, J = 7.27 Hz, 1H), 7.89 (d, J = 8.37 Hz, 1H), 7.47 (d, J = 8.42 Hz, 1H), 5.77 (s, 2H), 3.21 (s, 3H), 2.81 (s, 3H), 2.68 (q, J = 7.03 Hz, 2H), 1.03 (t, J = 7.19 Hz, 3H); ^{13}C NMR (75 MHz, DMSO-d_6) δ ppm (DEPT - 135) 202.87 (0), 148.41 (+), 146.16 (0), 143.30 (0), 138.37 (+), 135.37 (0), 134.65 (0), 133.76 (+), 130.36 (+), 128.40 (0), 125.97 (0), 121.81 (+), 114.81 (+), 114.58 (0), 112.11 (0), 66.64 (-), 32.70 (-), 15.31 (+), 12.25 (+), 7.29 (+); MS (ESI+): m/z (relative intensity) 442.99 (100%, M^+ - Br^-), 387.37 (8%, M^+ - Br^- - CH_3CH_2CO), 316.19 (10%, M^+ - Br^- -I); UV (CH_3OH) λ_{max}, nm (ε): 315 (27466).

Conjugation of 2a and 2b with pHPMA-MAAcap Hydrazide (see Figure 2 for scheme). The pHPMA-MAAcap hydrazide (weight average molecular weight M_w = 26.8 kDa, polydispersity $I = M_w/M_n$ = 1.87, where M_n is number-average molecular weight, 7.5 mol % hydrazide monomeric unit) was synthesized by radical

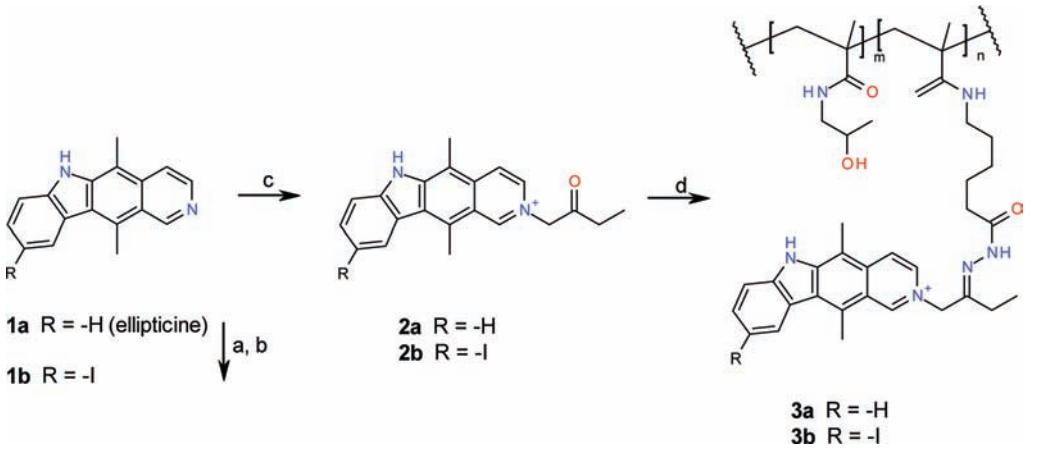


Figure 2. Synthesis of polymer-bound ellipticine and 9-iodoellipticine derivatives. Reagents and conditions: (a) $Hg(OAc)_2$, AcOH, 60 °C; (b) I_2; (c) 1-bromo-2-butanone, MeOH, RT; (d) pHPMA-MAAcap hydrazide, 9:1 MeOH/AcOH, RT.

copolymerization of 1-*N*-(2-hydroxypropyl)methacrylamide with 1-*N*-(6-hydrazino-6-oxohexyl)-2-methylacrylamide using azobis-(isobutyronitrile) as an initiator according to ref 13. The solution of pHPMA-MAAcap hydrazide (40 mg), ellipticinium derivative **2a** or **2b**, respectively (10 mg) and acetic acid (100 μL) in methanol (900 μL) was stirred at room temperature for 4 days. The polymer was then isolated by gel filtration on Sephadex LH-20 column (60 mL bed volume) using methanol as eluent, concentration of polymer-containing fractions under reduced pressure, precipitation into diethyl ether (5 mL), filtration, and drying. Yield 32 mg of **3a** and 38 mg of **3b**, respectively.

The drug content was assayed by UV−vis spectrophotometry in methanol using above-stated maximum wavelengths and molar absorbtivities. Molecular weights of the polymers were determined by gel permeation chromatography (GPC) in a mixture of acetate buffer (pH 6.5, 0.3 mol/L) and methanol (20:80 v/v) on a TSK 4000 column (Polymer Laboratories Ltd., U.K.) using a HPLC System Shimadzu (Shimadzu GmbH., Czech Republic) equipped with RI, UV, and multiangle light-scattering DAWN DSP-F detectors (Wyatt, U.S.A.).

Synthesis of [^{125}I]-2b and [^{125}I]-3b. The [^{125}I]-**2b** was synthesized by the same method as nonradiolabeled **2b** starting from 3.0 mg of ellipticine with additional $Na^{125}I$ stock solution (10 μL, 240 MBq) being added to nonradioactive iodine carrier. Yield 2.5 mg (39% chemical yield after two steps) of [^{125}I]-**2b** containing 20.4 MBq ^{125}I (8.5% radiochemical yield), i.e., specific radioactivity 8.2 MBq/mg.

Radioactivity of the product was measured on a ionization chamber Bqmetr 4 (Empos Ltd., Czech Republic). Purity was assayed by HPLC an a Shimadzu HPLC system (Shimadzu GmbH, Czech Republic) using a reverse-phase column (Chromolith Performance RP-18e 100 × 4.6 mm, Merck Ltd., Czech Republic) with UV−vis diode array detection. A mixture of water−acetonitrile was used as the eluent at a gradient 0−100 vol % and a flow rate of 2 mL/min. The product was homogeneous (single peak, R_t = 9.06 min) with all radioactivity in the **2b** peak (the particular fraction was collected and compared to radioactivity of the injected amount; nonradiolabeled **2b** was used as standard).

Conjugation to polymer was done in the same way as for the nonradiolabeled polymer, but using higher excess of polymer (15 mg) to *N*-2-oxobutyl-9-iodoellipticinium (2.0 mg). Yield 15 mg of the conjugate containing 1.95 wt % 9-iodoellipticine (UV−vis), 187 kBq/mg ^{125}I.

In Vitro Drug Release Study. Solutions of the drug conjugates (1 mg mL^{-1}, 1 mL) in phosphate buffered saline of pH 5.0, 6.5, and 7.4, respectively, were incubated in a water bath at 37 °C. At each time point, a sample (10 μL) was taken from each solution, diluted with dry methanol (990 μL), and filtered through a 0.22 μm syringe filter. Immediately after that, the amount of released ellipticinium derivative was determined by gel permeation chromatography in a mixture of acetate buffer (pH 6.5, 0.3 mol·L^{-1}) and methanol (20:80 v/v) on a TSK 3000 column (Polymer Laboratories Ltd., U.K.). UV−vis detection at absorbance maxima of the corresponding free drugs, i.e., 295 nm for **2a** and 315 nm for **2b**, were used for calculation of the drug release according to eq 1

$$r = S_f/(S_f + S_p) \times 100 \quad (1)$$

In eq 1, r is the released amount of drug in %, S_f is the peak area of free drug (low-molecular-weight fraction) and S_p is the peak area of polymer-bound drug (high-molecular-weight area). All experiments were carried out in duplicate.

In Vitro DNA Intercalation Studies. To evaluate the intercalating ability of synthesized compounds, both direct titration of DNA and ethidium bromide displacement assay by a modified procedure according to reported method[11] were used. In the direct titration method, the concentration dependence of fluorescence intensity of synthesized compounds with and without the presence of DNA was determined. So, the different volumes of the solution of measured compound in phosphate buffer saline (pH = 7.4) were added into two cuvettes with the 2 mL of phosphate buffer saline (pH = 7.4) with and without calf thymus DNA (100 μg.mL^{-1}). After 5 min incubation at room temperature, the fluorescence excitation and emission spectra of both samples were recorded in the particular emission/excitation maxima.

In the ethidium displacement method, the binding affinity of compounds to DNA was measured as the dependence of DNA−ethidium bromide complex fluorescence intensity decrease with ascendant concentration of the measured compound. Different volumes of measured compounds were added to the cuvette containing calf thymus DNA (100 μg.mL^{-1}) and ethidium bromide (50 μg.mL^{-1}). After 5 min of incubation, the intensity of emission at 583 nm was measured (excitation wavelength 546 nm, using this excitation, the fluorescence intensity of free ellipticine derivatives, as well as their complexes with DNA, was neglectable at this wavelength).

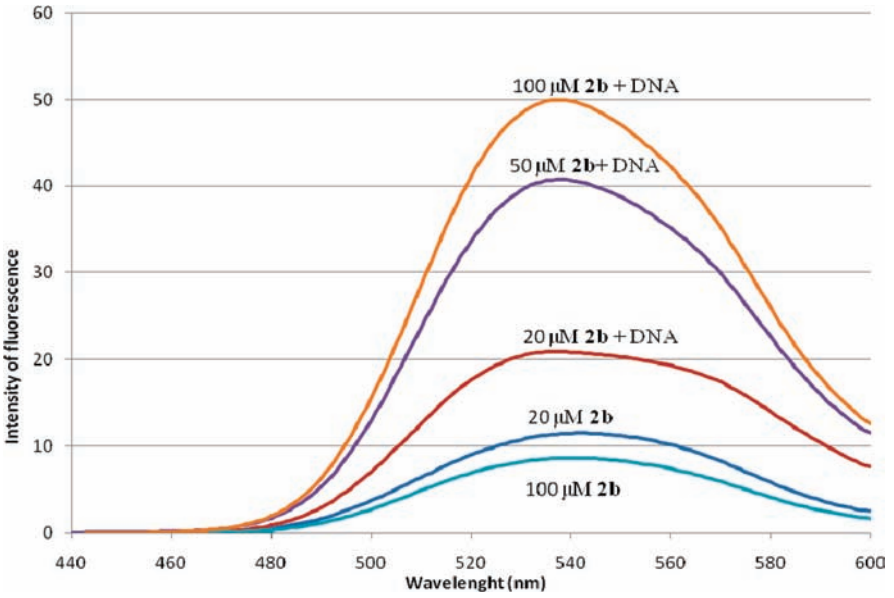


Figure 3. Fluorescence emission spectra of different **2b** concentrations with and without DNA (excitation wavelength at 310 nm).

In Vitro Cytotoxicity Assay and Internalization into the Cells. In vitro cytotoxicity of the micelles was assessed with either human or murine cancer cell lines. Ninety-six-well flat-bottomed microplates (NUNC, Roskilde, Denmark) were seeded with cancer cells: Raji, human B-cell lymphoma (1×10 cells per well); EL-4, murine T-cell lymphoma (5×10^3); 4T1, murine mammary tumor cell line (1×10^4 cells per well). The tested samples (in triplicates) were then added to the wells to obtain the desired drug concentration (0.1−2660 ng mL^{-1} free drug equivalent). The plates were incubated at 37 °C in humidified 5% CO_2 + 95% air atmosphere for 72 h. Cell viability was then evaluated by a standard MTT test according to ref 14. This assay is based on bioreduction of the yellow soluble 3-(4,5-dimethyldiazol-2-yl)-2,5 diphenyl tetrazolium bromide (MTT) to insoluble blue formazan by mitochondria. Formazan is then solubilized with detergent and measured spectrophotometrically at 540 nm. Cells cultivated in fresh medium were used as controls. The results are the means of four independent experiments; the standard deviation was lower than 5%.

Internalization of the ellipticine derivatives and conjugates into cells was assayed with 4T1 cells on confocal microscope using the intensive ellipticine-fluorophore caused fluorescence in analogy as described for doxorubicin conjugates.[15] Cell nuclei were visualized with the Hoechst 33342 nucleic acid dye.

RESULTS AND DISCUSSION

Ellipticine (**1a**) is natural alkaloid from plant *Ochrosia elliptica* with well-known anticancer properties; several of its derivatives have been introduced into clinical practice. We have chosen it as an ^{125}I carrier because of its potent DNA-intercalating activity and for its fluorescent properties (i.e., its intracellular fate may be easily followed by fluorescence microscopy without additional labeling). Furthermore, its electrophilic iodination via acetomercuro intermediate proceeds easily and leads to defined chemically stable 9-iodoellipticine (**1b**).[12] Although biological characterization of **1b** was not reported, 9-bromoellipticine was reported[16] to have similar IC_{50} values to ellipticine against selected cancer cell lines, so we expected the iododerivative to retain intercalating activity. We synthesized "cold" (stable natural iodine containing) **1b** in high yield (74%) by acetomercuration of ellipticine and subsequent one-pot exchange of the acetomercuro group with iodine to form the iododerivative **1b** (see Figure 2).

A hydrazone bond was chosen to connect ellipticine derivatives to polymer because of its susceptibility to hydrolysis under acidic conditions, as well as relative stability toward hydrolysis at neutral pH.[13,17−19] The conjugate would thus be relatively stable during transport in blood plasma at pH 7.4.[17,18] However, in more acidic tumor tissue (pH ca. 6.5[17,18]) or even after internalization into the tumor cell (pH in late endosomes is ca. 5.0[17,18]) the active intercalator would be rapidly released from the polymer carrier. Considering that ellipticine does not contain ketone, aldehyde, or hydrazide group, it has to be derivatized with a suitable linker. For this derivatization, we have chosen the tertiary isoquinoline-type nitrogen in position 2, which may be quaternized with suitable alkylating agent containing ketone moiety. Quaternization introduces permanent positive charge into the molecule, which increases solubility in water (this is important since both ellipticine and 9-iodoellipticine are only poorly soluble in water) and should contribute to the intercalation effectivity since DNA has negative charge due to phosphates. Quaternary ellipticine derivatives (as Celiptium) show similar or even higher activity than parent ellipticine while being readily water-soluble. For this purpose, commercially available 1-bromo-2-butanone was used. It readily reacts at room temperature with both ellipticine (**1a**) and 9-iodoellipticine (**1b**) to form the 2-*N*-(2-oxobutyl)ellipticinium derivatives **2a** and **2b**, respectively, in high yields (68% and 88%, respectively). These derivatives are readily soluble in both water and methanol in contrast to unquaternized compounds. When radiolabeled [^{125}I]-**2b** is synthesized, radioiodine should be introduced before quaternization since the positive charge decreases reactivity toward conventional electrophilic radioiodination and also bromide counteranion interferes by simultaneous electrophilic bromination.

All synthesized compounds retain strong fluorescent properties of ellipticine, makes following of intracellular fate of these derivatives easier (see below). The original ellipticine (**1a**) has emission maximum in acetic acid (i.e., in protonated form) at 517 nm with excitation maxima 277, 316, 356, and 413 nm

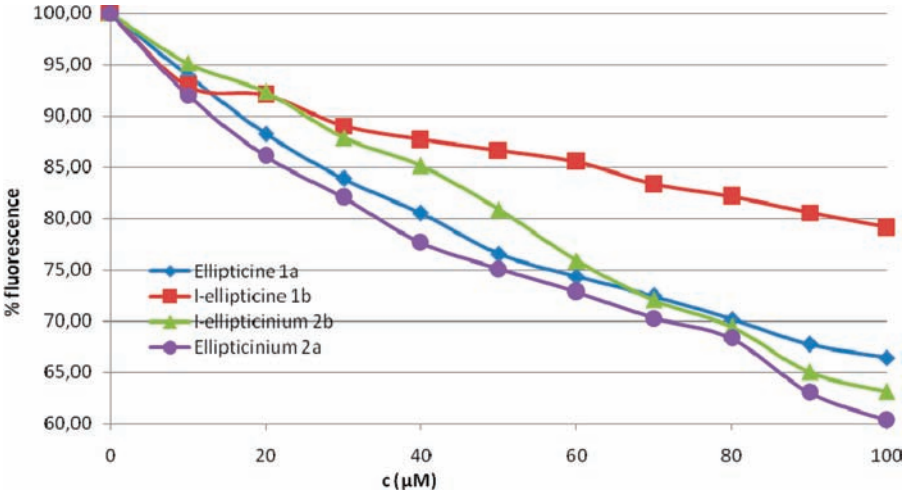


Figure 4. Decrease of ethidium bromide/DNA emission fluorescence intensity at 583 nm as a function of intercalator concentration (excitation wavelength 546 nm).

(relative intensities normalized to peak at 277 nm = 1.00 are 0.72 for 316 nm, 0.36 for 356 nm, and 0.27 for 413 nm), while **2a** has emission maximum shifted toward longer wavelengths at 540 nm. Also, the excitation spectrum of **2a** is shifted toward longer wavelengths (maxima at 283, 317, 363, and 425 nm; the relative intensities normalized to peak 283 nm = 1.00 are 0.65 for peak 317 nm, 0.31 for peak 363 nm, and 0.25 for peak 425 nm). The emission spectra of iodoellipticine **1b** has emission maximum at 451 nm, the excitation maxima were 283, 332, and 385 nm (relative intensity 1.00, 0.17, and 0.14, respectively), whereas the emission maximum of **2b** was at 532 nm and the excitation maxima at 310, 360, and 421 nm (relative intensities 1.00, 0.14, and 0.10, respectively).

Intercalation abilities of synthesized compounds were tested both directly on DNA (change in fluorescence intensity when added to DNA) and by ethidium bromide displacement assay. In direct intercalation titration, the fluorescence spectra at different concentration of **2b** in the presence of calf thymus DNA, as well as without it (blank sample), were measured. It was clearly observed that the intercalation of **2b** into the DNA caused enhancement of quantum fluorescence yield and therefore increase of fluorescence intensity in comparison with the blank sample (Figure 3). Self-quenching, high for free drug, was also suppressed by DNA-intercalation.

To determine the DNA-binding affinity of prepared compounds [which is the driving force of accumulation of the (radiolabeled) intercalator in DNA in cell nuclei due to shifting equilibrium toward intercalator binding to DNA], the decrease of ethidium bromide (50 μg.mL^{-1})−calf thymus DNA complex fluorescence intensity with rising concentration of all compounds was measured. All compounds showed similarly strong affinity to the DNA (Figure 4). For each compound, an attempt to measure EC_{50}, the concentration that caused the 50% decrease of ethidium bromide/DNA fluorescence intensity, has been done. The EC_{50} values of quaternized products **2a** and **2b** were 170 μM and 140 μM, respectively. However, the EC_{50} of ellipticine (**1a**) and 9-iodoellipticine (**1b**) could not be determined due to their poor solubility (which is also probably the main reason for lower apparent binding of **1b** compared to other ellipticine derivatives tested; however, since **1b** is only a synthetic intermediate in our case, we did not go into detailed study). The ellipticine derivatives thus proved to have sufficient DNA binding potential; however, for accumulation in cell nuclei, the ability to also penetrate into the cell nucleus is essential. This was tested in *in vitro* cell culture (see below). Mitochondrial DNA is generally considered as a less important target of DNA-damaging agents compared to nuclear DNA, mainly due to the overwhelming amount of DNA in cell nuclei compared to mitochondria, and also intercalators may easily pass through nuclear pore, but to reach mitochondrial DNA, they need to translocate across the mitochondrial membranes. This is why mitochondrial DNA was not considered in our study as a primary target.

Both ketones **2a** and **2b** were conjugated with polymer pHPMA-MAAcap hydrazide by acetic acid-catalyzed condensation in analogy to conjugation of anticancer anthracycline antibiotic doxorubicin,[13,17,18] also containing ketone moiety, forming derivatives **3a** and **3b**, respectively (the obtained drug loading was 10.0 wt % for **3a** and 8.5 wt % for **3b**). No significant change in molecular weights of the conjugates was observed, confirming no cross-linking or other side reactions.

Drug release in vitro was followed in phosphate buffered saline, pH 7.4 (pH of blood plasma), pH 6.5 (typical pH of tumor interstitial space due to partly hypoxic lactic acid metabolism), and pH 5.0 (typical pH of late endosomes after internalization of the system into cells). The drug release profiles for both **3a** and **3b** (see Figure 5) show similar trends—relatively fast release at pH 5.0 (22.8% released drug after 24 h for **3a** and 25.1% for **3b**)—while the conjugates are stable at both pH 6.5 and pH 7.4 (1.4% released drug after 24 h for **3a** and 1.5% for **3b** at pH 6.5 and 0.3% released drug after 24 h for **3a** and 0% for **3b** at pH 7.4). This means that the conjugate should be stable during transport in blood and the active intercalator should be released only after uptake by cells in their endosomes.

If we compare these release profiles with other hydrazones, one can see that the drug release rate as a function of pH highly depends on the chemical surrounding of hydrazone bond to be hydrolyzed, sterical aspects, eventual conjugation with adjacent double bonds, and electron density on the C=N carbon (on which hydrolysis takes place) play a role. In our case, as we hypothesize due to vicinity of the quaternary ammonium cation, the release rate is highly pH dependent. This is similar to the release rates of doxorubicin,[13,17,18] where vicinity of the hydroxyl groups plays the

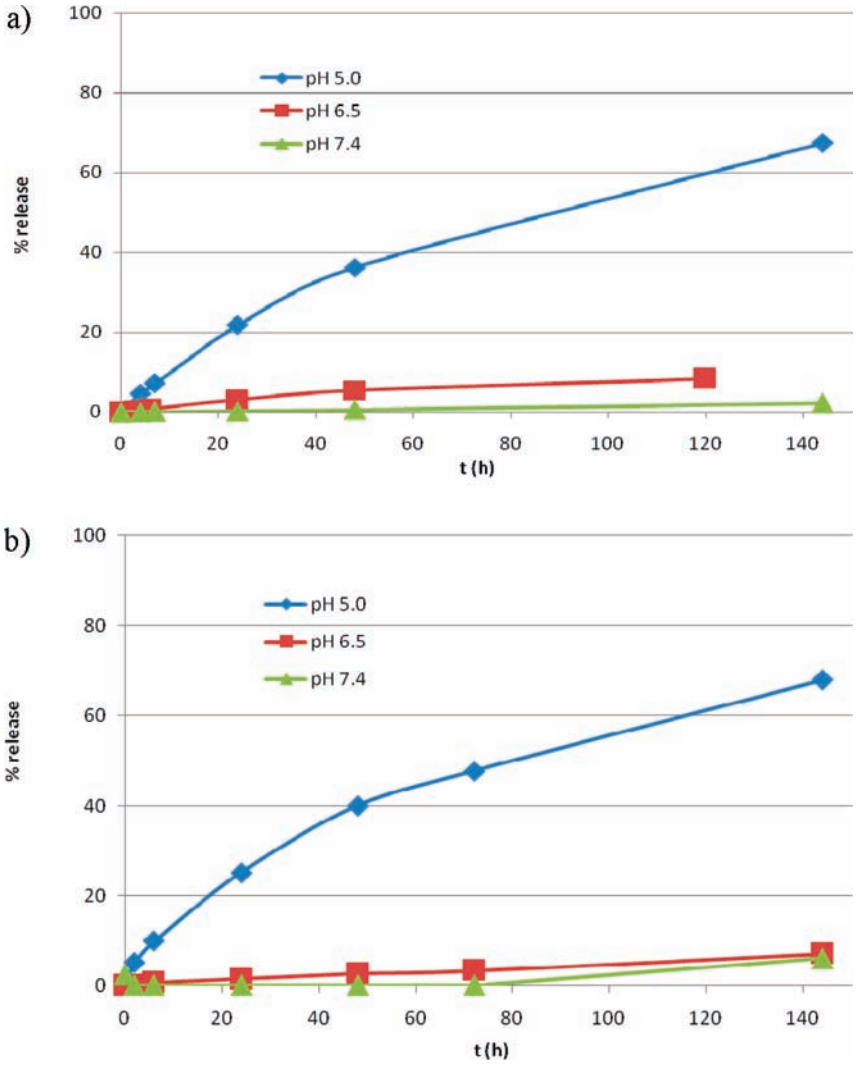


Figure 5. In vitro release of derivatives **3a** (above; a) and **3b** (below; b).

Table 1. Cytotoxicities of Ellipticine Derivatives on the Selected Cell Lines[a]

derivative	IC_{50} (Raji)	IC_{50} (EL4)	IC_{50} (4T1)
1a	8.8	0.27	6.7
1b	3.6	1.4	1.7
2a	2.0	1.3	6.9
2b	1.0	2.3	7.7
3b	7.6	11.5	16.5

[a] Raji, EL4, and 4T1; the IC_{50} values are stated in μmol/L.

critical role. However, the release rate in our case is considerably slower than that described for doxorubicin.[13,17,18] On the other hand, hydrazones with the same hydrazide part but with 2-hexanone or levulinic acid as ketone components are hydrolyzed much more rapidly and with lower relative pH dependence (fast hydrolysis of these compounds readily occurred even at neutral conditions)[20] than the (9-iodo)ellipticinium derivatives described in this paper or doxorubicin described in refs 13,17,18. However, fast hydrolysis of these compounds readily occurred even at pH-neutral conditions.

The radioiodinated derivatives were synthesized in analogy with the stable-iodine-containing derivatives. We first tested the no-carrier-added approach with direct radioiodination of ellipticine to **1b** using the chloramine method; however, high amounts of ellipticine-*N*-oxide and radioiodinated ellipticine-*N*-oxide were produced as byproducts. This is why we have chosen the analogy with the synthesis of nonradioactive **1b** (acetomercuration with subsequent reaction with iodine). This approach gave radiolabeled **1b**; although chromatographic purification is necessary, carrier-added iodine must be used and the yield is relatively low. The relatively low radiochemical yield may be mostly explained by the fact that one-half of the radioiodine is wasted as mercury-bound iodide during exchange reaction with the acetomercuro intermediate. The subsequent quaternization to **2b** and conjugation with polymer was than done in analogy with the nonradiolabeled conjugate.

We tested antiproliferative activity of the synthesized derivatives on selected cell lines (Raji, EL4, and 4T1, respectively; see Table 1 for the IC_{50} values). Antiproliferative activity is useful if the conjugates would be used as chemotherapeuticals and for the indirect demonstration of the ability of the ellipticine derivatives to achieve DNA in living cells, because intercalation activity is essential for the cytotoxicity of ellipticine derivatives. The MTT test was used to assay

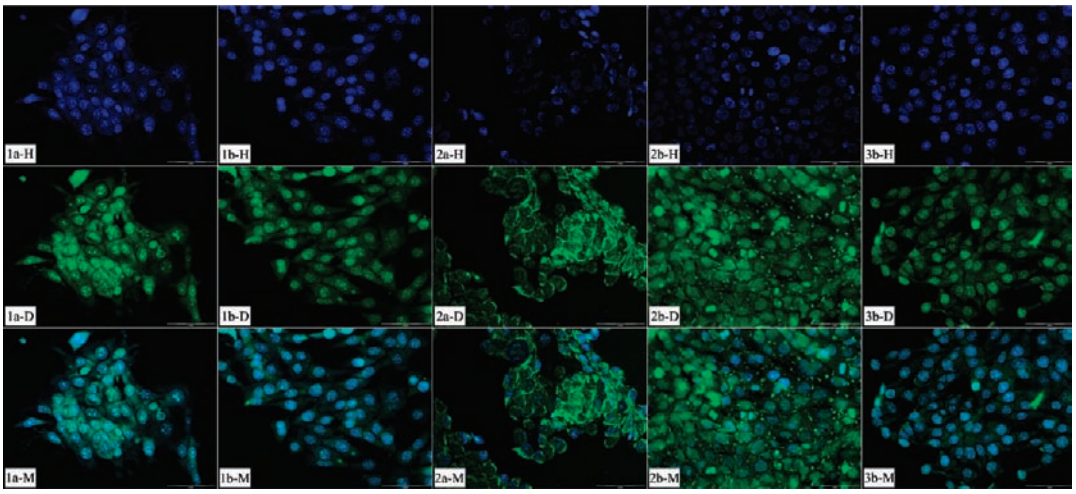


Figure 6. Internalization of ellipticine derivatives into cells. The images are marked as follows: substance tested stain; stains on the same particular cells: H, Hoechst 33342 dye; D, the particular drug or conjugate; M, merged channels H + D to confirm colocalization in cell nuclei.

cytotoxicity, since the standard [^{3}H]-thymidine assay would be useless for radioactive samples containing ^{125}I due to interference with radioactivity of tritium. Cytotoxicity of ellipticine and its low-molecular-weight derivatives was in the range 0.27−8.8 μmol/L. The cell lines differ in their sensitivity toward **1a**, **1b**, **2a**, and **2b** within ca. 1 order of magnitude, with EL-4 being more sensitive than the other lines for all the substances tested except **2b**. Iodination of ellipticine **1a** to 9-iodoellipticine **2b** increases its cytotoxic activity for the Raji and 4T1 cell lines but decreases the activity against the EL-4 cell line, but all effects were within 1 order of magnitude. Quaternization with 1-bromo-2-butanone also has effects only within 1 order of magnitude, for Raji cell line toxicity was increased by quaternization for both iodinated and noniodinated ellipticine and for EL4 and 4T1 cell lines quaternization somehow decreased cytotoxicity. One can thus conclude that the chemical modifications necessary to make ellipticine radioiodinable and conjugable with polymer (iodination and quaternization) did not compromise its biological effectivity. This is in agreement with expectations that 9-bromoellipticine does not differ in its cytotoxicity from ellipticine[16] and quaternary ellipticinium derivatives as Celiptium (N^2-methyl-9-hydroxyellipticinium) are effective anticancer agents.

We also studied cytotoxicity of polymer-bound **2b** (i.e., **3b**) to confirm that the effective **2b** may be released from the hydrazone conjugate **3b** in living cells. Polymer conjugates usually show lower cytotoxicity than free drugs, because the conjugate is ineffective in its polymer form unless free drug is released, so the main power of polymer conjugate is in selectivity of toxicity toward cancer cells. The polymer conjugate **3b**, a nonradioactive model of the AE emitter delivery system, was only 2−8-times (dependent on cell line) less effective than free drug **2b**. This means that the polymer **3b** is able to be internalized into the cells and to release free drug **2b** more effectively than similar hydrazone conjugates described in literature. For comparison, doxorubicin hydrazone conjugates are usually more than 10-times less biologically effective in vitro than the corresponding free drug.[13,17,18] This should be beneficial for the biological effectivity, because of low necessary dosage of the radiolabeled intercalator. Cytotoxicity also depends on the capacity of endocytosis of the cells, which is higher for tumor cells than for normal cells, which may further contribute to selectivity of the anticancer effect. Detailed study of the contribution of this factor in vitro and in vivo in the murine model will be a topic of further contributions.

The next step was direct proof that the ellipticine derivatives studied in this paper are effective intercalators not only on isolated DNA (see above the fluorescence studies), but also inside living cells. One can clearly see from the internalization study using fluorescence microscopy (Olympus, AX70-Provis) that ellipticinium derivative-related fluorescence is visible in cell nuclei for all **1a**, **1b**, **2a**, **2b**, and **3b** (see Figure 6). Localization in cell nuclei was confirmed by simultaneous staining of nuclear DNA by the Hoechst 33342 dye and overlay of the images.

Since only low specific activities (8.2 MBq/mg for [^{125}I]-**2b** and 187 kBq/mg for [^{125}I]-**3b**) compared to daunorubicin derivatives described in the literature[9] (ca. 100 GBq/mg) were obtained, only statistically insignificant differences between cytotoxicities of radiolabeled and nonradiolabeled **2b** and **3b** were obtained (data not shown). Improvement of both radiochemical yield and specific activity of the radiolabeled derivatives is thus still a challenge for future work.

CONCLUSIONS

The new type of polymer conjugates carrying Auger electron emitter-labeled intercalator was successfully synthesized and characterized. The system is designed for a triple-targeting approach (first targeting, polymer-based system targeting into tumor tissue; second targeting, pH-controlled intratumoral or intracellular release; third targeting, into cell nucleus by a DNA intercalator) minimizing the radiation burden of healthy tissues. The system is stable at the pH of blood plasma (pH 7.4) and releases active intercalator in acidic milieu with pH close to late endosome content (pH 5). It was confirmed that the studied ellipticine derivatives retain intercalation and cytotoxic properties of ellipticine and are accumulated in cell nuclei after exposure to cells in vitro. The system was synthesized in radiolabeled form; however, to achieve effective Auger electron cytotoxic effect specific radioactivity of the intercalator still has to be improved.

AUTHOR INFORMATION

Corresponding Author

*Martin Hruby, Heyrovsky Sq. 2, 162 06 Prague 6, Czech Republic. E-mail: mhruby@centrum.cz, Tel: +420 296 809 230, Fax: +420 296 809 410.

■ ACKNOWLEDGMENT

Financial support of the Grant Agency of the Czech Republic- (grants # P207/10/P054 and # P108/10/1560), of the Grant Agency of the Academy of Sciences of the Czech Republic (grant IAAX00500803) and of the Ministry of Education, Youth, and Sports of the Czech Republic (grant # IM4635608802) is gratefully acknowledged.

■ REFERENCES

(1) Dietlein, M., Luster, M., and Reiners, C. (2010) Nuclear medicine therapy of differentiated thyroid cancer: status quo. *Onkologe 16*, 678–689.

(2) Ting, G., Chang, C. H., Wang, H. E., and Lee, T. W. (2010) Nanotargeted radionuclides for cancer nuclear imaging and internal radiotherapy. *J. Biomed. Biotechnol.* Article ID 953537.

(3) Hong, H., Zhang, Y., Sun, J. T., and Cai, W. B. (2009) Molecular imaging and therapy of cancer with radiolabeled nanoparticles. *Nano Today 4*, 399–413.

(4) Usami, N., Kobayashi, K., Hirayama, R., Furusawa, Y., Porcel, E., Lacombe, S., and Le Sech, C. (2010) Comparison of DNA breaks at entrance channel and Bragg peak induced by fast C6+ ions-influence of the addition of platinum atoms on DNA. *J. Radiat. Res. 51*, 21–26.

(5) Dupertuis, Y. M., Xiao, W. H., De Tribolet, N., Pichard, C., Slosman, D. O., Delaloye, A. B., and Buchegger, F. (2002) Unlabelled iododeoxyuridine increases the rate of uptake of [I-125]iododeoxyuridine in human xenografted glioblastomas. *Eur. J. Nucl. Med. Mol. Imaging 29*, 499–505.

(6) Reske, S. N., Deisenhofer, S., Glatting, G., Zlatopolskiy, B. D., Morgenroth, A., Vogg, A. T. J., Buck, A. K., and Friesen, C. (2007) I-123-ITdU-mediated nanoirradiation of DNA efficiently induces cell kill in HL60 leukemia cells and in doxorubicin-, beta-, or gamma-radiation-resistant cell lines. *J. Nucl. Med. 48*, 1000–1007.

(7) Watanabe, N., Sawai, H., Ogihara-Umeda, I., Tanada, S., Kim, E., and Sasaki, Y. (2006) Molecular effect of auger electrons emitted by indium-111-labeled antisense oligonucleotide on n-myc in human neuroblastoma cells. *Eur. J. Nucl. Med. Mol. Imaging 33*, S184–S184.

(8) Murali, D., and DeJesus, O. T. (1998) Synthesis of 4′-epi-iodo-4′-deoxy-daunorubicin, a potential cancer radiotherapeutic agent. *Bioorg. Med. Chem. Lett. 8*, 3419–3422.

(9) Ickenstein, L. M., Edwards, K., Sjoberg, S., Carlsson, J., and Gedda, L. (2006) A novel I-125-labeled daunorubicin derivative for radionuclide-based cancer therapy. *Nucl. Med. Biol. 33*, 773–783.

(10) Ghirmai, S., Mume, E., Tolmachev, V., and Sjoberg, S. (2005) Synthesis and radioiodination of some daunorubicin and doxorubicin derivatives. *Carbohydr. Res. 340*, 15–24.

(11) Gardette, M., Papon, J., Bonnet, M., Desbois, N., Labarre, P., Wu, T. D., Miot-Noirault, E., Madelmont, J. C., Guerquin-Kern, J. L., Chezal, J. M., and Moins, N. Evaluation of new iodinated acridine derivatives for targeted radionuclide therapy of melanoma using (125)I, an Auger electron emitter. *Invest. New Drugs*, DOI 10.1007/s10637-010-9471-x.

(12) Devraj, R., Barrett, J. F., Fernandez, J. A., Katzenellenbogen, J. A., and Cushman, M. (1996) Design, synthesis, and biological evaluation of ellipticine-estradiol conjugates. *J. Med. Chem. 39*, 3367–3374.

(13) Etrych, T., Jelinkova, M., Rihova, B., and Ulbrich, K. (2001) New HPMA copolymers containing doxorubicin bound via pH-sensitive linkage: synthesis and preliminary in vitro and in vivo biological properties. *J. Controlled Release 73*, 89–102.

(14) Mosmann, T. (1983) Rapid colorimetric assay for cellular growth and survival - application to proliferation and cyto-toxicity assays. *J. Immunol. Methods 65*, 55–63.

(15) Hovorka, O., Etrych, T., Subr, V., Strohalm, J., Ulbrich, K., and Rihova, B. (2006) HPMA based macromolecular therapeutics: Internalization, intracellular pathway and cell death depend on the character of covalent bond between the drug and the peptidic spacer and also on spacer composition. *J. Drug Targeting 14*, 391–403.

(16) Vendome, J., Letard, S., Martin, F., Svinarchuk, F., Dubreuil, P., Auclair, C., and Le Bret, M. (2005) Molecular modeling of wild-type and D816V c-kit inhibition based on ATP-competitive binding of ellipticine derivatives to tyrosine kinases. *J. Med. Chem. 48*, 6194–6201.

(17) Etrych, T., Mrkvan, T., Chytil, P., Konak, C., Rihova, B., and Ulbrich, K. (2008) N-(2-hydroxypropyl)methacrylamide-based polymer conjugates with pH-controlled activation of doxorubicin. I. New synthesis, physicochemical characterization and preliminary biological evaluation. *J. Appl. Polym. Sci. 109*, 3050–3061.

(18) Ulbrich, K., and Subr, V. (2004) Polymeric anticancer drugs with pH-controlled activation. *Adv. Drug Delivery Rev. 56*, 1023–1050.

(19) Hruby, M., Etrych, T., Kucka, J., Forsterova, M., and Ulbrich, K. (2006) Hydroxybisphosphonate-containing polymeric drug-delivery systems designed for targeting into bone tissue. *J. Appl. Polym. Sci. 101*, 3192–3201.

(20) Hruby, M., Kucka, J., Lebeda, O., Mackova, H., Babic, M., Konak, C., Studenovsky, M., Sikora, A., Kozempel, J., and Ulbrich, K. (2007) New bioerodable thermoresponsive polymers for possible radiotherapeutic applications. *J. Controlled Release 119*, 25–33.

Bioconjugate Chemistry

ARTICLE

pubs.acs.org/bc

Engineering Bioactive Surfaces with Fischer Carbene Complex: Protein A on Self-Assembled Monolayer for Antibody Sensing

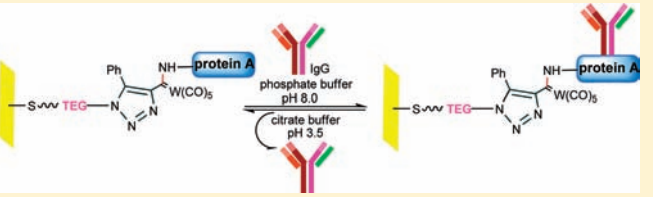
Piyali Dutta,[†] Sudeshna Sawoo,[†] Namrata Ray,[†] Othman Bouloussa,[‡] and Amitabha Sarkar*[,†]

[†]Department of Organic Chemistry, Indian Association for the Cultivation of Science, Kolkata-700032, India

[‡]Institut Curie, Laboratoire Physico-Chimie Curie (UMR CNRS 168), 26 rue d'Ulm, 75248 Paris cedex 05, France

Supporting Information

ABSTRACT: A Fischer carbene complex was grafted onto self-assembled monolayers (SAMs) on gold or glass by a copper-free "click" reaction. Pendant lysine residues of protein A obtained from *Staphylococcus aureus* rapidly reacted with the electrophilic metal complex on SAM effecting a covalent attachment of protein A with the surface. The protein A coated surface further led to bioaffinity immobilization of rabbit IgG in an oriented manner, a feature that also permits its purification from rabbit serum. Rabbit IgG could be removed from protein A coated surface by pH adjustment. The regenerated protein A surface was reused three times without loss of activity.



INTRODUCTION

Research in current years has revealed a huge potential of organometallic bioconjugates[1] in radiopharmaceuticals, novel drugs, and even organometallic bioanalysis. Coupling of an organometallic carboxylic acid to amino acids and peptides via amide formation is probably the most extensively studied conjugation reaction.[2,3] Biomolecules that have pendant primary amino or unhindered secondary amino groups react instantly and often quantitatively with electrophilic alkoxy Fischer carbene complexes of general formulas $(CO)_5W{=}C(OR^1)R^2$ to yield corresponding amino carbene complexes that are stable Fischer carbene bioconjugates.[4] Progress of this reaction can easily be monitored by the typical shift of W—CO stretch in the region 1900−2010 cm^{-1} which is transparent to most organic functional groups and water.[5] By adopting appropriate techniques, it is possible to place a Fischer carbene complex at the external terminus of a densely packed, stable, self-assembled monolayer (SAM) on a flat (e.g., glass slide) or a curved (e.g., colloidal gold) solid surface.[6−8] The exposed Fischer carbene complex on the molecular film can then be utilized to covalently graft a protein to the SAM on glass or gold as reported earlier.[6,8]

One of the most advanced applications of SAMs on solid surface is the design of biosensors.[9−14] Immobilization of proteins with retention of their activity on highly ordered monolayers is of paramount importance in diagnostic, affinity separation, and biomaterials technology.[15−17] The key factor behind the development of the immunosensor is the efficient immobilization of an antibody on the solid surface of assay device.[18,19]A number of techniques have been developed to immobilize antibodies on solid surfaces: physicochemical adsorption[20−26] on poly(L-lysine) coated glass, plastic, or nitro-cellulose membrane, Langmuir−Blodgett methods,[27,28] and covalent attachment.[29−36] Physical adsorption proves to be the easiest of procedures, but the method often suffers from relative instability, random orientation, and denaturation of attached antibodies, yielding poor reproducibility. Covalent attachment yields more stable, functional monolayers, but the orientation of proteins is often uncontrolled.

Bioaffinity interactions, being much more specific in structural recognition features, can guarantee a certain mode of orientation during binding of one protein with another. Protein A binds specifically to the Fc region of immunoglobulin molecules derived from various mammal species.[37−43] If protein A is covalently bound to a surface and its interaction with IgG is affinity controlled (hence potentially reversible by altering pH conditions), one can have a bioactive surface that can sense IgG protein and can be regenerated after each run. The present paper describes the results of such an approach.

We describe the following sequence: (a) formation of a highly ordered, densely packed monolayer on gold using C_{11}-chains with a triethylene glycol spacer and terminal Fischer carbene complex; (b) covalent immobilization of protein A by aminolysis reaction with the help of Fischer carbene termini on SAM; (c) bioaffinity immobilization of rabbit IgG and its detection on glass surface by fluorescence microscopy; and, finally, (d) recycling of the protein A slide for iterative purification. Atomic force microscopy (AFM) and ATR-IR were the two surface analytical techniques primarily used for following the chemistry and topology of SAM on gold surfaces.

Received: February 7, 2011
Revised: April 26, 2011
Published: May 17, 2011

ACS Publications © 2011 American Chemical Society

EXPERIMENTAL PROCEDURE

General Methods and Materials. Thin-layer chromatography was performed on TLC Silica gel 60 F_{254} purchased from Merck and visualized by UV and I_2 adsorption. Column chromatography was typically performed using 230−400 mesh silica gel. NMR spectra were recorded on Bruker Advance 200 or 300 MHz spectrometers at room temperature with $CDCl_3$ as solvent and TMS as internal reference. ATR-IR spectra were recorded on Nicolet 380 spectrometer. Contact angles were measured with a digidrop from GBX (Romans sur Isère, France). The thickness of self-assembled monolayers (SAMs) on gold slides was investigated by an ellipsometer (Sentech SE 500) operating at a 70° incidence angle. Fluorescence images were acquired using a Leica DM 3000 Upright Trinocular Research Microscope with Leica DFC 425 Scientific digital camera and LAS software. The topography of the protein coated surface was investigated by atomic force microscopy (diCP-II) with DI Company *SPMlab Analysis* software. Protein A from *Staphylococcus aureus* (MW 42 KDa),[44] IgG from rabbit serum (Reagent grade, > 95%, MW 150 KDa),[45,46] and gold coated slides (coated successively with a 20-Å-thick layer of titanium and a 100-Å-thick layer of gold) were purchased from Sigma-Aldrich. Gold chloride and BSA were obtained from SRL. Solvents like ethanol, DMF, and toluene were purchased from SRL and dried using standard procedure. Reagents were purchased from Sigma-Aldrich and were used as received.

***S*-11-(2-(2-(2-Bromoethoxy)ethoxy)ethoxy)undecylethanethioate (4).** Synthesis of 2--(2-(2-(undec-10-enyloxy)ethoxy)ethoxy)ethanol (**2**) and *S*-11-(2-(2-(2-hydroxyethoxy)ethoxy)ethoxy)undecylethanethioate (**3**) from 11-bromoundecene (**1**) was carried out following a procedure reported in literature.[7] To a solution of *S*-11-(2-(2-(2-hydroxyethoxy)ethoxy)ethoxy)undecylethanethioate (**3**) (2 g, 5.2 mmol) in dry DCM (16 mL) under argon atmosphere, carbon tetrabromide (2.1 g, 6.3 mmol) was added slowly. The reaction mixture was cooled to 0 °C and triphenyl phosphine (2 g, 7.6 mmol) in dry DCM (4 mL) was added dropwise to it. After stirring for 6 h, the solvent from the reaction mixture was evaporated out. The product was extracted with petroleum ether (3 × 15 mL), the combined organic layers were evaporated under vacuum, and the product was purified by flash column chromatography (30% ethyl acetate/petroleum ether). Product obtained was 2 g (86%). ^{1}H NMR ($CDCl_3$, 300 MHz): 1.21−1.26 (m, 14H), 1.49−1.56 (m, 4H), 2.30 (s, 3H), 2.84 (t, J = 6 Hz, 2H), 3.44 (q, J = 6 Hz, 4H), 3.55−3.67 (m, 8H), 3.80 (t, J = 6 Hz, 2H). ^{13}C NMR ($CDCl_3$, 75 MHz): 26.16, 27.14, 28.89, 29.18, 29.24, 29.53, 29.57, 29.63, 29.71, 30.36, 30.72, 70.15, 70.70, 70.80, 71.31, 71.64, 196.17. HRMS (ESI) m/z $[M+Na]^+$, calcd for $C_{19}H_{37}BrO_4SNa$ 463.1494; found 463.1498.

11-(2-(2-(2-Bromoethoxy)ethoxy)ethoxy)undecane-1-thiol (5). *S*-11-(2-(2-(2-Bromoethoxy)ethoxy)ethoxy)undecylethanethioate (**4**) (2 g, 4.5 mmol) was dissolved in dry methanol (15 mL) under argon atmosphere. To it 0.1 mL of concentrated HCl was added and the reaction mixture was heated under reflux for 5 h. Then, the crude reaction mixture was cooled and the solvent was concentrated under reduced pressure. Flash column chromatography (25% ethyl acetate/petroleum ether) afforded 1.6 g (89%) of compound (**5**). ^{1}H NMR ($CDCl_3$, 300 MHz): 1.23−1.31 (m, 14H), 1.51−1.61 (m, 4H), 2.48 (q, J = 6 Hz, 2H), 3.42 (q, J = 6 Hz, 4H), 3.54−3.63 (m, 8H), 3.78 (t, J = 6 Hz, 2H). ^{13}C NMR ($CDCl_3$, 75 MHz): 24.72, 26.17, 28.45, 29.14, 29.55, 29.57, 29.63, 29.72, 30.38, 34.13, 70.15, 70.65, 70.70, 70.80, 71.30, 71.62. HRMS (ESI) m/z $[M+Na]^+$, calcd for $C_{17}H_{35}BrO_3SNa$ 421.1388; found 421.1380.

Preparation of SAM with Compound 5. The gold surface (11 mm × 11 mm) was immersed in a mixture of concentrated H_2SO_4 and 30% aq. H_2O_2 (70:30 v/v) for 1 min, then washed with distilled water and dried under N_2. The cleaned gold surfaces were dipped in a freshly prepared 1 mM solution of compound **5** in dry ethanol for 36 h. The slides were then rinsed thoroughly with absolute ethanol in order to remove excess absorbate and dried under argon atmosphere.

Surface Modification by S_N2 Reaction from Bromide to Azide SAM. Nucleophilic displacement of bromide by azide was carried out in DMF with sodium azide. The bromo terminated gold substrate was incubated in a saturated solution of sodium azide in DMF and stirred for 48 h. The surface was then washed with water and dried under nitrogen.

Grafting of Fischer Carbene Complex (6) via Cu Free "Click" Cycloaddition Reaction. The alkynyl Fischer carbene complex **6** was synthesized using a reported procedure.[6] The gold slides covered with azido terminated monolayers were dipped in a 10 mM solution of Fischer carbene complex **6** in dry toluene under argon atmosphere at 50 °C for 4 h. It was then washed with dry toluene followed by absolute ethanol in order to ensure complete removal of excess Fischer carbene complex. Finally, the surface was dried under argon.

Covalent Immobilization of Protein A. Gold surfaces coated with Fischer carbene was immersed in a solution of protein A (10 mg/L) in phosphate buffer (pH 8.0) for 10 min at room temperature. The substrates were rinsed thoroughly with buffer solution (thrice), then with milli-Q water (thrice), and dried under argon atmosphere. The residual Fischer carbene complexes were blocked by treatment with 1 M ethanolamine (pH 9.0) for 30 min. Finally, the surfaces were treated with 1% (w/v) BSA in phosphate buffer (pH 8.0) for 2 h to block nonspecific binding. Then, the surfaces were extensively rinsed with milli-Q water and dried under argon.

Recognition of Rabbit IgG. The recognition experiment was carried out as following: protein A coated gold surfaces were incubated in a solution of rabbit IgG (50 μg/mL) in phosphate buffer (pH 8.0) for 1 h. The surfaces were extensively washed with phosphate buffer containing 0.05% Tween (v/v), followed by milli-Q water, and dried under argon atmosphere.

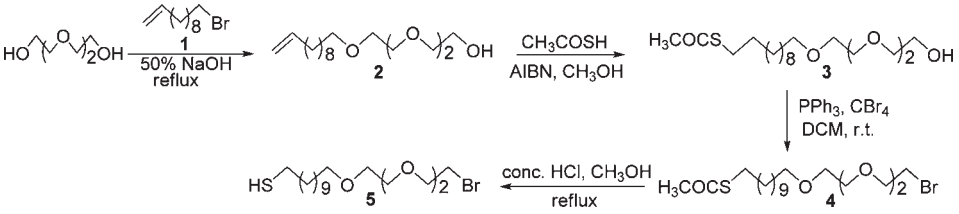
Regeneration of Protein A Coated Surface after Extraction of Rabbit IgG. The rabbit IgG coated surface was incubated in citrate buffer (pH 3.5) for 15 min. The slide was then immersed in phosphate buffer (pH 9.0) for 15 min to recover the protein A coated slide that was reused.

RESULTS AND DISCUSSION

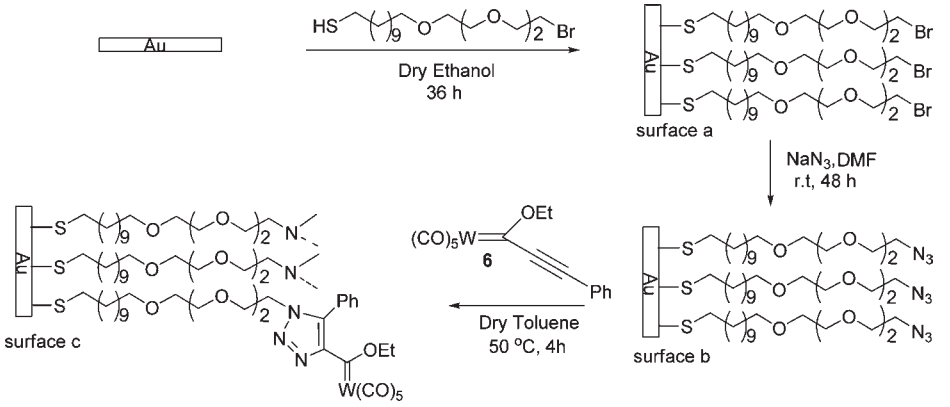
Synthesis of Bromo Terminated Long Chain Thiol with TEG Spacers. The bromo terminated long chain thiol was synthesized from triethylene glycol (TEG) according to the reaction sequence represented in Scheme 1.

The long chain thiol comprises four distinct parts: (i) thiol group for chemisorptions on Au surface, (ii) long hydrocarbon chain for creating a densely packed monolayer, (iii) a hydrophilic TEG spacer for maximum availability of the functional tether extending in water, and (iv) bromo group at the terminus of chain to be converted to the Fischer carbene moiety. TEG was first converted to monoalkene-TEG **2** by treatment with 11-bromoundecene in the presence of sodium hydroxide. Radical mediated addition of thiolacetic acid across the double bond in **2** followed by treatment with carbon tetrabromide and

Scheme 1. Synthesis of 11-(2-(2-(2-bromoethoxy)ethoxy)ethoxy)undecane-1-thiol (5)



Scheme 2. Grafting of Bromo Terminated Long Chain Thiol (5) and Sequential Chemical Modification of the Terminal Functional Group



triphenylphosphine afforded the brominated product **4**. The compound **4** was then hydrolyzed with catalytic amount of conc. HCl to obtain the desired thiol **5** in good yield. Each compound was purified by column chromatography and characterized by standard spectroscopic analyses.

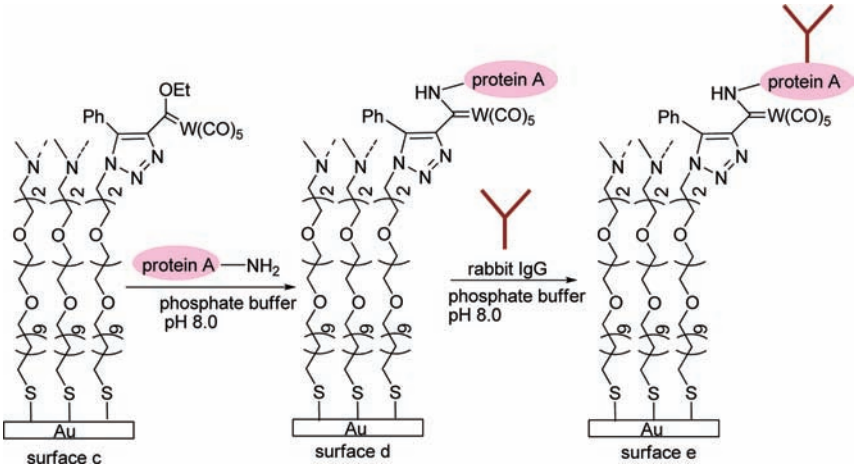
Formation of Fischer Carbene Terminated SAM on Gold Surface. A monolayer of bromo terminated thiol **5** was self-assembled on gold surface (surface a) following usual procedure. After thorough washing with ethanol, the gold surface was analyzed by ATR-IR spectroscopy. The presence of strong absorption bands at 2960.0 cm^{-1} and 2840.0 cm^{-1} (aliphatic C−H stretching) clearly indicated the presence of bromo terminated chains on the monolayer. The bromo terminated surface was then treated with saturated solution of sodium azide in DMF for 48 h at room temperature leading to surface b. The presence of a typical band at 2118.9 cm^{-1} established nucleophilic displacement of the bromine atom by azido group. The gold substrate was then treated with a solution of alkoxy Fischer carbene complex **6** in toluene at 50 °C for 4 h. Since the triple bond is highly activated due to the presence of strong electron withdrawing tungsten pentacarbonyl moiety, no Cu(I) salt is required as catalyst for the 1,3-dipolar cycloaddition reaction.[47] After thorough washing with toluene, it was analyzed by ATR-IR. The asymmetric stretch of the azido group at 2118.9 cm^{-1} was no longer visible. Instead, new absorption bands appeared at 2065.1 $cm^{-1}$and 1930.6 cm^{-1} for W—CO stretching. These clearly revealed that the Fischer carbene moiety was now covalently bound to the SAM (surface c).

Chemical modifications on the gold surface were also monitored by ellipsometry. Thickness of the initially formed bromo terminated monolayer was 2.87 nm. After nucleophilic substitution reaction with azido group, the thickness reduces to 2.74 nm, and after the "click" cycloaddition reaction with the activated triple bond in alkynyl Fischer carbene, the thickness of SAM increases to 3.43 nm reflecting the introduction of a much larger group on the SAM terminus. Contact angle measurements were also carried out on the gold-coated surfaces. While the contact angle of the bromo terminated SAM was found to be 99.8 ± 0.2°, it decreased to 85.6 ± 1.5° on displacement with azido group, which further decreased to 82.3 ± 1.1° on cycloaddition with Fischer carbene complex. These results are consistent with the changes brought about on the functionality of SAM on the gold surface.

Covalent Attachment of Protein A on SAM Leads to Bioaffinity Immobilization of Rabbit IgG. In immunoaffinity systems, one of the most important steps is immobilization of the antibody on the substrate surface, which can then be used for bioaffinity separation or biorecognition. Staphylococcal protein A is known to bind the Fc region of immunoglobulin molecules with high affinity; as a result, the Fab fragments point away from the surface, in order to allow for easy antigen−antibody binding.[48−50] This affinity between protein A and IgG is also extensively used for the development of an affinity system for antibody purification.[51] Accordingly, we sought to immobilize IgG molecules in an oriented fashion on surface-bound protein A.

Protein A consists of a single polypeptide chain of molecular weight 42 000. The three-dimensional structure of the protein A molecule is very stable to heat, denaturing agent, and a large pH interval (0.99−11.8) (see Supporting Information).[52] High frictional ratio of 2.1−2.2 and intrinsic viscosity of 29 mL/g suggest that protein A is not a typical globular protein but rather has a markedly extended shape having approximate dimensions of 2.5 × 25 nm.[44,53] At first, the Fischer carbene coated surface was treated with protein A solution in phosphate buffer (pH 8) at room temperature for 10 min (surface d, Scheme 3). The primary amino groups of the pendant lysine residues of protein A reacted

Scheme 3. Immobilization of Protein A and Rabbit IgG on Gold Surface



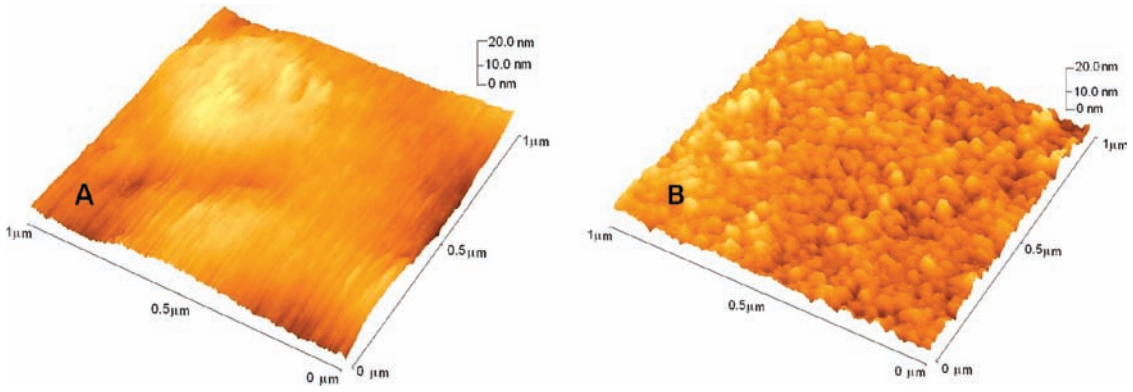


Figure 1. AFM topographic image of (A) Fischer carbene terminated SAM and (B) protein A immobilized by reaction with Fischer carbene complex.

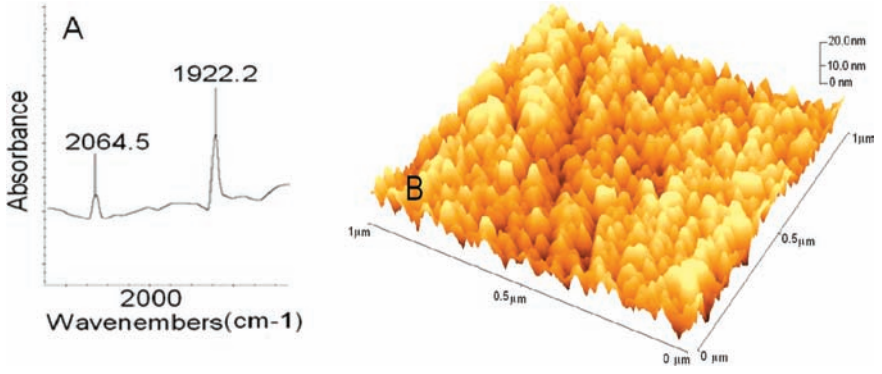


Figure 2. (A) ATR-IR spectrum and (B) AFM topographic image of rabbit IgG coated surface.

rapidly with the electrophilic carbene carbon resulting in the formation of new C—N bonds and thereby anchoring the protein covalently to the surface. This protocol was perceived as a mild, rapid, and reliable procedure for protein immobilization that would minimize multilayer formation. Physically adsorbed protein A molecules were then removed by repeated washing with the buffer solution and milli-Q water. The slides were then dried under a stream of argon.

The protein A coated surface was characterized by ATR-IR and AFM. After aminolysis, the absorption peaks for W—CO stretching show a decrease of 8 cm^{-1}. For AFM imaging, a noncontact mode was employed. Figure 1B represents the image of the surface after incubation in protein A solution for 10 min. A dense coverage was observed throughout the protein-coated surface, whereas the Fischer carbene terminated SAM did not show any significant undulation of the surface (Figure 1A). The

dx.doi.org/10.1021/bc200073r |*Bioconjugate Chem.* 2011, 22, 1202–1209

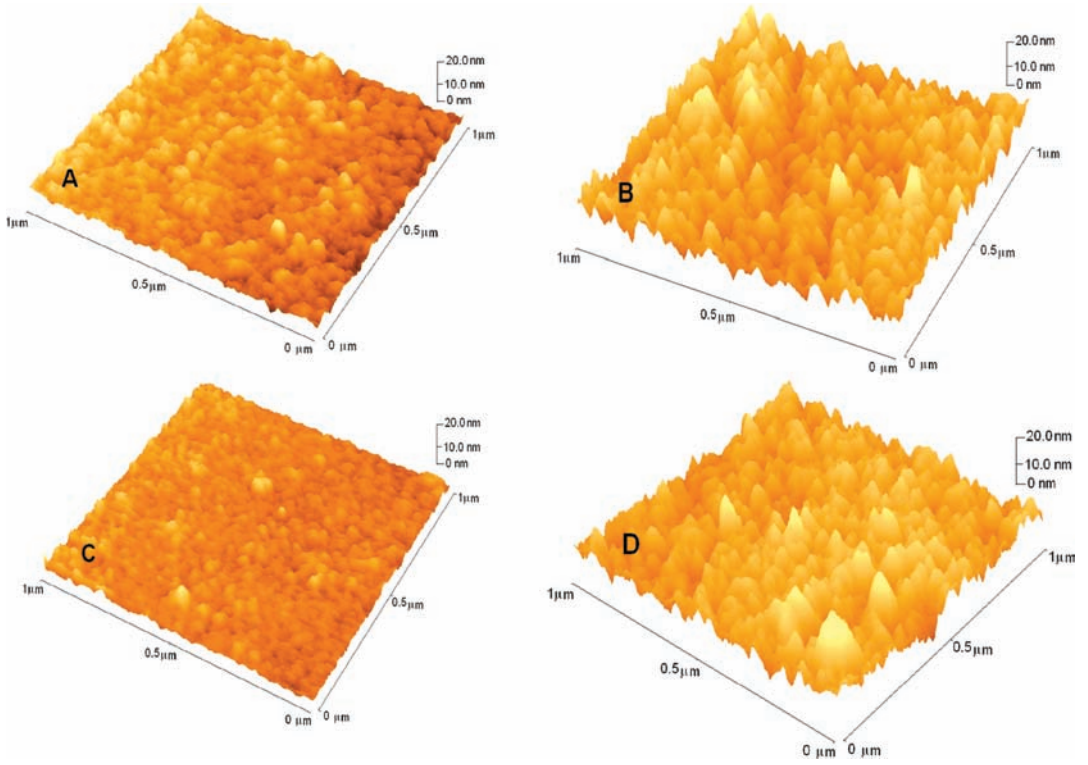


Figure 3. AFM topographic image of (A) protein A slide and (B) rabbit IgG after second cycle, (C) protein A slide, and (D) rabbit IgG coated slide after third cycle.

average height and the average roughness (Ra) of the Fischer carbene terminated gold surface were 4.23 and 0.61 nm, respectively. After protein A immobilization, the height and Ra increased to 7.13 and 0.95 nm, respectively (Figure 1B). The increase in height by 2.9 nm is consistent with the reported size of protein A molecule.

The protein A coated slide was then incubated in rabbit IgG solution in phosphate buffer (pH 8.0) for 1 h at room temperature.[54] Excess IgG was removed by washing with buffer and milli-Q water several times. Surface e in Scheme 3 represents the substrate surface carrying oriented IgG molecules on the self-assembled monolayer. ATR-IR spectrum of the IgG coated surface showed that the amino carbene band remained at the same position 2064.5 cm^{-1} and 1922.2 cm^{-1} which established that Fischer carbene complex did not undergo significant decomposition (Figure 2A). Figure 2B displays the AFM image of the IgG immobilized on protein A bonded surface. From AFM images, it was evident that the average height of the immobilized protein A (Figure 1B) increased from 7.13 to 15.78 nm and Ra changed to 1.59 nm after incubation in rabbit IgG. The change in height by 8.65 nm roughly corresponds to the height of IgG (8.5 nm).[55] The section analysis of the gold surfaces modified with Fischer carbene complex, protein A, and rabbit IgG are included in the Supporting Information.

Recycling of the Protein A Coated SAM on Flat Gold Surface. The interaction between protein A and rabbit IgG is affinity-driven. The immobilized IgG can be debased by changing the pH of the buffer medium. This ought to give rise to a free protein A surface which can be recycled. As described below, this expectation was indeed realized.

The initial average height of the protein A coated slide was found to be 7.13 nm by AFM (Figure 1B). After incubation with rabbit IgG, the height increased to 15.78 nm (Figure 2B). After removing the rabbit IgG, by treating the gold surface with a typical elution buffer like citrate buffer (pH 3.5) for 15 min the average height decreased to 7.11 nm (Figure 3A). After that, the slide was immersed in a neutralizing buffer like phosphate buffer (pH 9.0) for 15 min to restore original protein conformation. When it was incubated again in rabbit IgG solution, the average height increased to 15.81 nm (Figure 3B). On repeating the process for the third time, we observed that the height changed from 7.06 nm (Figure 3C) to 15.69 nm (Figure 3D). Thus, in all three cycles the change in height with immobilization of rabbit IgG is consistent with the height of IgG.

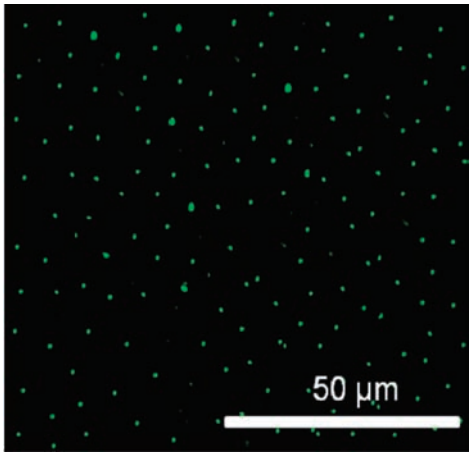


Figure 4. Fluorescence image of rabbit IgG coated slide, incubated in solution of FITC tagged goat antirabbit IgG in phosphate buffer.

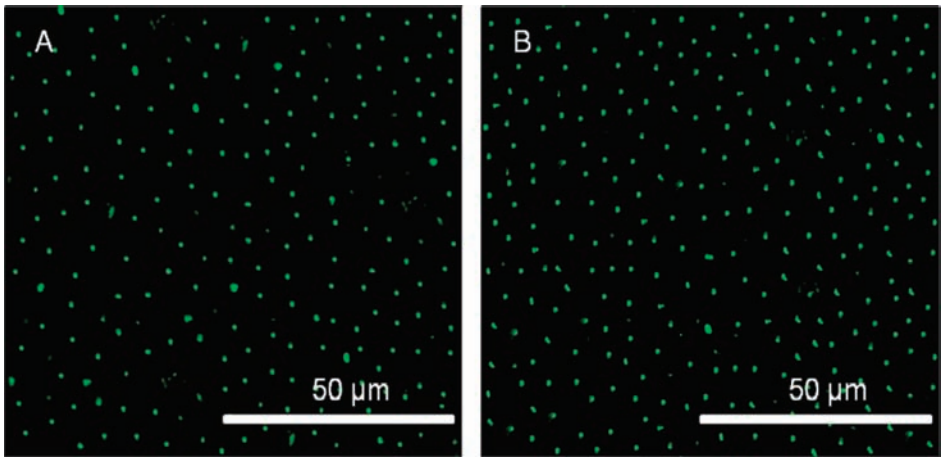


Figure 5. Fluorescence microscopy image of rabbit IgG coated slide after incubation in FITC tagged goat antirabbit IgG solution in phosphate buffer after (A) second cycle and (B) third cycle.

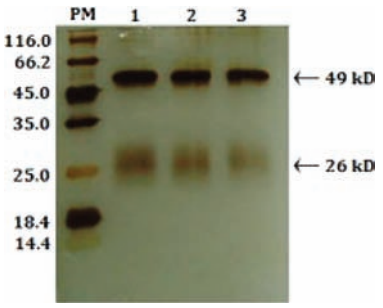


Figure 6. Picture of SDS-PAGE analysis of rabbit IgG fraction obtained by chemical reduction with 2-mercaptoethanol. Molecular weight standard is on lane (PM) and chemically reduced IgG after first cycle (lane 1), second cycle (lane 2), and third cycle (lane 3).

Detection of Rabbit IgG on Glass Using Fluorescence Microscope. The presence of rabbit IgG can also be proven visually by fluorescence microscopy techniques. These experiments were performed on glass slides using 11-bromoundecyltrichlorosilane as the primary chain. The bromo terminated surface was converted to the Fischer carbene terminated surface as depicted in Scheme 1. The Fischer carbene coated slide was subsequently treated with protein A solution and then with rabbit IgG solution as described before. After thorough washing by buffer, the IgG coated slide was immersed in a solution of FITC tagged goat anti rabbit IgG in phosphate buffer (pH 8). After careful washing with buffer and milli-Q water, the slide was observed under fluorescence microscope. Bright fluorescent spots were observed (Figure 4).

Fluorescence microscopy was also used to verify the regeneration of protein A after extraction of IgG on glass slides. The FITC tagged goat antirabbit IgG was used and fluorescence spots of nearly equal distribution of density were observed across several cross sections of the slide indicating high reproducibility (Figure 5).

Since protein A binds specifically with the Fc region of rabbit IgG, this property allows the use of surface-bound protein A for purification of rabbit IgG from rabbit serum. We used protein A coated microscopic glass slides and immersed it in a solution of rabbit serum (50 μg/mL) in phosphate buffer (pH 8.0) for 1 h. After thorough washing with buffer and milli-Q water, the slides were immersed into eluting buffer (citrate buffer pH 3.5) for 15 min. The citrate buffer containing the rabbit IgG was readily neutralized with Tris-HCl buffer (pH 9.0) and concentrated. The purified IgG was analyzed by SDS-PAGE gel after chemical reduction using 2-mercaptoethanol. IgG has a molecular mass of 150 kD and contains two heavy chains of 50 kD and two light chains of about 25 kD. By reduction with 2-mercaptoethanol, the heavy and the light chains were resolved. This is depicted in Figure 6. The spot at 49 kD represents the heavy chain and the spot at 26 kD represents the light chain. The cycle was repeated three times. No contaminants are visible in the purified IgG (Figure 6).

CONCLUSION

In conclusion, we have successfully applied a relatively mild protocol to modify Au/glass surface with Fischer carbene function that allows rapid immobilization of protein A on surface, which lead to oriented immobilization of rabbit IgG. The surfaces at different stages were characterized by ATR-IR and AFM. We also demonstrated that a protein A slide prepared by following our protocol can be used successively three times to purify rabbit IgG from rabbit serum. The work described above widens the scope of employing Fischer carbene complexes both in biological and biomedical studies.

ASSOCIATED CONTENT

Supporting Information. Synthesis of compound **2**, compound **3**, and Fischer carbene complexes, ATR-IR spectrum, procedure for functionalization of glass slides, ^{1}H and ^{13}C NMR spectra of **4** and **5**. This material is available free of charge via the Internet at http://pubs.acs.org.

AUTHOR INFORMATION

Corresponding Author

*E-mail: ocas@iacs.res.in. Tel: +91 33 2473 4971 ext. 407. Fax: +91-33-2473 2805.

ACKNOWLEDGMENT

The authors wish to thank Dr. Santiswarup Singha and Prof. Anjan Kr. Dasgupta at Department of Biochemistry, University

of Calcutta; R. Banik (AFM), P. P. Bhattacharya (IR) for technical supports at IACS; CSIR, New Delhi, for Research Fellowships (P.D. and N.R.); DST and IFCPAR, India, for financial support.

REFERENCES

(1) Jaouen, G. (2006) *Bioorganometallics: Biomolecules, labeling, Medicine*, Wiley-VCH Verlag GmbH & Co. KGaA, Weinheim.

(2) Moriuchi, T., and Hirao, T. (2010) Design of ferrocene-dipeptide bioorganometallic conjugates to induce chirality-organized structures. *Acc. Chem. Res. 43*, 1040–1051.

(3) van Staveren, D. R., and Metzler-Nolte, N. (2004) Bioorganometallic chemistry of ferrocene. *Chem. Rev. 104*, 5931–5985.

(4) Salmain, M., Licandro, E., Baldoli, C., Maiorana, S., Tran-Huy, H., and Jaouen, G. (2001) Transition metal ('Fischer-type') carbene complexes as protein labelling reagents. *J. Organomet. Chem. 617−618*, 376–382.

(5) Samanta, D., Sawoo, S., Patra, S., Ray, M., Salmain, M., and Sarkar, A. (2005) Synthesis of hydrophilic Fischer carbene complexes as organometallic marker and PEGylating agent for proteins. *J. Organomet. Chem. 690*, 5581–5590.

(6) Sawoo, S., Dutta, P., Chakraborty, A., Mukhopadhyay, R., Bouloussa, O., and Sarkar, A. (2008) A new bio-active surface for protein immobilization via copper-free 'click' between azido SAM and alkynyl Fischer carbene complex. *Chem. Commun.* 5957–5959.

(7) Samanta, D., Faure, N., Rondelez, F., and Sarkar, A. (2003) Towards "designer" surfaces: functionalisation of self-assembled monolayer (SAM) on colloidal gold by alkene metathesis. *Chem. Commun.* 1186–1187.

(8) Srivastava, P., Sarkar, A., Sawoo, S., Chakraborty, A., Dutta, P., Bouloussa, O., Méthivier, C., Pradier, C.−M., Boujday, S., and Salmain, M. (2011) A versatile approach for the immobilization of amines via copper-free "click" reaction between azido self-assembled monolayer and alkynyl Fischer carbene complex. Application to the detection of staphylococcal enterotoxin A antibody. *J. Organomet. Chem. 696*, 1102–1107.

(9) Samanta, D., and Sarkar, A. (2011) Immobilization of biomacromolecules on self-assembled monolayers: methods & sensor applications. *Chem. Soc. Rev. 40*, 2567–2592.

(10) Choi, M. M. F. (2004) Progress in enzyme-based biosensors using optical transducers. *Microchim. Acta 148*, 107–132.

(11) Sassolas, A., Leca-Bouvier, B. D., and Blum, L. J. (2008) DNA biosensors and microarrays. *Chem. Rev. 108*, 109–139.

(12) Jelinek, R., and Kolusheva, S. (2004) Carbohydrate biosensors. *Chem. Rev. 104*, 5987–6015.

(13) Campuzano, S., Gálvez, R., Pedrero, M., Manuel de Villena, F. J., and Pingarrón, J. M. (2003) An integrated electrochemical fructose biosensor based on tetrathiafulvalene-modified self-assembled monolayers on gold electrodes. *Anal. Bioanal. Chem. 377*, 600–607.

(14) Malhotra, B. D., and Chaubey, A. (2003) Biosensors for clinical diagnostics industry. *Sens. Actuators, B 91*, 117–127.

(15) Rusmini, F., Zhong, Z., and Feijen, J. (2007) Protein immobilization strategies for protein biochips. *Biomacromolecules 8*, 1775–1789.

(16) Jonkheijm, P., Weinrich, D., Schröder, H., Niemeyer, C. M., and Waldmann, H. (2008) Chemical strategies for generating protein biochips. *Angew. Chem., Int. Ed. 47*, 9618–9647.

(17) Wong, L. S., Khan, F., and Micklefield, J. (2009) Selective covalent protein immobilization: strategies and applications. *Chem. Rev. 109*, 4025–4053.

(18) Saerens, D., Huang, L., Bonroy, K., and Muyldermans, S. (2008) Antibody fragments as probe in biosensor development. *Sensors 8*, 4669–4686.

(19) Kurtinaitiene, B., Ambrozaite, D., Laurinavicius, V., Ramanaviciene, A., and Ramanavicius, A. (2008) Amperometric immunosensor for diagnosis of BLV infection. *Biosens. Bioelectron. 23*, 1547–1554.

(20) Ramanavicius, A., Kurilcik, N., Jursenas, S., Finkelsteinas, A., and Ramanaviciene, A. (2007) Conducting polymer based fluorescence quenching as a new approach to increase the selectivity of immunosensors. *Biosens. Bioelectron. 23*, 499–505.

(21) Ouerghi., O., Touhami., A., Othmane., A., Ouada, H. B., Martelet, C., Fretigny, C., and Jaffrezic-Renault, N. (2002) Investigating antibody-antigen binding with atomic force microscopy. *Sens. Actuators, B 84*, 167–175.

(22) Butler, J. E., Ni, L., Nessler, R., Joshi, K. S., Suter, M., Rosenberg, B., Chang, J., Brown, W. R., and Cantarero, L. A. (1992) The physical and functional behavior of capture antibodies adsorbed on polystyrene. *J. Immunol. Methods 150*, 77–90.

(23) Wu, Z., Yan, Y., Shen., G., and Yu, R. (2000) A novel approach of antibody immobilization based on *n*-butyl amine plasma-polymerized films for immunosensors. *Anal. Chim. Acta 412*, 29–35.

(24) Qian, W., Yao, D., Yu, F., Xu, B., Zhou, R., Bao, X., and Lu, Z. (2000) Immobilization of antibodies on ultraflat polystyrene surfaces. *Clin. Chem. 46*, 1456–1463.

(25) Caruso, F., Rodda, E., and Furlong, D. N. (1996) Orientational aspects of antibody immobilization and immunological activity on quartz crystal microbalance electrodes. *J. Colloid Interface Sci. 178*, 104–115.

(26) Chang, I. -N., Lin, J. -N., Andrade, J. D., and Herron, J. N. (1995) Adsorption mechanism of acid pretreated antibodies on dichlorodimethylsilane-treated silica surfaces. *J. Colloid Interface Sci. 174*, 10–23.

(27) Owaku, K., Goto, M., Ikariyama, Y., and Aizawa, M. (1995) Protein A Langmuir-Blodgett film for antibody immobilization and its use in optical immunosensing. *Anal. Chem. 67*, 1613–1616.

(28) Barraud, A., Perrot, H., Billard, V., Martelet, C., and Therasse, J. (1993) Study of immunoglobulin G thin layers obtained by the Langmuir-Blodgett method: application to immunosensors. *Biosens. Bioelectron. 8*, 39–48.

(29) Liu, X., Wang, H., Herron, J. N., and Prestwich, G. (2000) Photopatterning of antibodies on biosensors. *Bioconjugate Chem. 11*, 755–761.

(30) Jung, Y., Jeong, J. Y., and Chung, B. H. (2008) Recent advances in immobilization methods of antibodies on solid supports. *Analyst 133*, 697–701.

(31) Kausaite-Minkstimiene, A., Ramanaviciene, A., Kirlyte, J., and Ramanavicius, A. (2010) Comparative study of random and oriented antibody immobilization techniques on the binding capacity of immunosensor. *Anal. Chem. 82*, 6401–6408.

(32) Jain, S., Chattopadhyay, S., Jackeray, R., and Singh, H. (2009) Surface modification of polyacrylonitrile fiber for immobilization of antibodies and detection of analyte. *Anal. Chim. Acta 654*, 103–110.

(33) Susmel, S., Guilbault, G. G., and Ó Sullivan, C. K. (2003) Demonstration of labeless detection of food pathogens using electrochemical redox probe and screen printed gold electrodes. *Biosens. Bioelectron. 18*, 881–889.

(34) Pei, R., Cheng, Z., Wang, E., and Yang, X. (2001) Amplification of antigen−antibody interactions based on biotin labeled protein−-streptavidin network complex using impedance spectroscopy. *Biosens. Bioelectron. 16*, 355–361.

(35) Su, X. -L., and Li, Y. (2004) A self-assembled monolayer-based piezoelectric immunosensor for rapid detection of *Escherichia coli* O157:H7. *Biosens. Bioelectron. 19*, 563–574.

(36) Wadu-Mesthrige, K., Amro, N. A., and Liu, G. -Y. (2000) Immobilization of proteins on self-assembled monolayers. *Scanning 22*, 380–388.

(37) Bae, Y. M., Oh, B. -K., Lee, W., Lee, W. H., and Choi, J. -W. (2005) Study on orientation of immunoglobulin G on protein G layer. *Biosens. Bioelectron. 21*, 103–110.

(38) Kanno, S., Yanagida, Y., Haruyama, T., Kobatake, E., and Aizawa, M. (2000) Assembling of engineered IgG-binding protein on gold surface for highly oriented antibody immobilization. *J. Biotechnol. 76*, 207–214.

(39) Gao, D., McBean, N., Schultz, J. S., Yan, Y., Mulchandani, A., and Chen, W. (2006) Fabrication of antibody arrays using thermally responsive elastin fusion proteins. *J. Am. Chem. Soc. 128*, 676–677.

(40) Starodub, N. F., Pirogova, L. V., Demchenko, A., and Nabok, A. V. (2005) Antibody immobilisation on the metal and silicon surfaces. The use of self-assembled layers and specific receptors. *Bioelectrochemistry 66*, 111–115.

(41) Oh, B.−K., Kim, Y.−K., Lee, W., Bae, Y. M., Lee, W. H., and Choi, J.−W. (2003) Immunosensor for detection of *Legionella pneumophila* using surface plasmon resonance. *Biosens. Bioelectron. 18*, 605–611.

(42) Briand, E., Salmain, M., Compère, C., and Pradier, C. −M. (2006) Immobilization of Protein A on SAMs for the elaboration of immunosensors. *Colloids Surf., B 53*, 215–224.

(43) Demirel, G., Çağlayan, M. O., Garipcan, B., Duman, M., and Pişkin, E. (2007) Oriented immobilization of IgG on hydroxylated Si(001) surfaces via protein-A by a multiple-step process based on a self-assembly approach. *J. Mater. Sci. 42*, 9402–9408.

(44) Björk, I., Petersson, B.−Å., and Sjöquist, J. (1972) Some physicochemical properties of Protein A from *Staphylococcus aureus*. *Eur. J. Biochem. 29*, 579–584.

(45) Ito, W., Nakamura, H., and Arata, Y. (1989) Protein-protein interactions on the surface of immunoglobulin molecules. *J. Mol. Graphics 7*, 60–63.

(46) Strejan, G., and Campbell, D. H. (1971) Physicochemical, immunochemical and biologic properties of rabbit homocytotropic antibodies produced to crude extracts. *J. Immunol. 106*, 1363–1370.

(47) Chakraborty, A., Dey, S., Sawoo, S., Adarsh, N. N., and Sarkar, A. (2010) Regioselective 1, 3-dipolar cycloaddition reaction of azides with alkoxy alkynyl fischer carbene complexes. *Organometallics 29*, 6619–6622.

(48) Deisenhofer, J. (1981) Crystallographic refinement and atomic models of a human Fc fragment and its complex with fragment B of Protein A from *Staphylococcus aureus* at 2.9- and 2.8-A resolution. *Biochemistry 20*, 2361–2370.

(49) Hjelm, H., Sjödahl, J., and Sjöguist, J. (1975) Immunologically active and structurally similar fragments of Protein A from *Staphylococcus aureus*. *Eur. J. Biochem. 57*, 395–403.

(50) Lu, B., Smyth, M. R., and O'Kennedy, R. (1996) Oriented immobilization of antibodies and its applications in lmmunoassays and immunosensors. *Analyst 121*, 29R–32R.

(51) Hober, S., Nord, K., and Linhult, M. (2007) Protein A chromatography for antibody purification. *J. Chromatogr., B 848*, 40–47.

(52) Sjöholm, I. (1975) Protein **A** from *Staphylococcus aureus* spectropolarimetric and spectrophotometric studies. *Eur. J. Biochem. 51*, 55–61.

(53) Ohnishi, S., Murata, M., and Hato, M. (1998) Correlation between surface morphology and surface forces of Protein A adsorbed on mica. *Biophys. J. 74*, 455–465.

(54) Åkerström, B., and Björck, L. (1986) A physicochemical study of Protein G, a molecule with unique immunoglobulin G-binding properties. *J. Biol. Chem. 261*, 10240–10247.

(55) Coen, M. C., Lehmann, R., Gröning, P., Bielmann, M., Galli, C., and Schlapbach, L. (2001) Adsorption and bioactivity of Protein A on silicon surfaces studied by AFM and XPS. *J. Colloid Interface Sci. 233*, 180–189.

SUPPORTING INFORMATION

Engineering bio-active surfaces with Fischer carbene complex: Protein A on self assemble monolayer for antibody sensing

Piyali Dutta,[†] Sudeshna Sawoo,[†] Namrata Ray,[†] Othman Bouloussa,[‡] and Amitabha Sarkar *,[†]

[†]*Department of Organic Chemistry, Indian Association for the Cultivation of Science, Kolkata-700032, India; ocas@iacs.res.in*

Table of Contents

1. Synthesis of compound (2) and (3) ……S2

2. Synthesis of alkoxyalkynyl Fischer carbene complex (6)…….S3

3. Physicochemical properties of protein A……...S3

4. ATR-IR spectroscopy measurement of gold surface……S4

5. Procedure for functionalization of glass surface……...S6

6. ^{1}H and ^{13}C-NMR Spectrum of compound (4) and (5)……..S7

7. AFM characterization of gold surface ……...S10

8. References……...S11

1. Synthesis of 11-(2-(2-(2-bromoethoxy)ethoxy)ethoxy)undecane-1-thiol:[1]

(a) Synthesis of 2-(2-(2-(undec-10-enyloxy)ethoxy)ethoxy)ethanol (**2**):

A degassed solution 50% aqueous solution of NaOH (1.24 ml, 15.9 mmol) was added slowly with stirring to trigol (11.46 g, 76.3 mmol) under argon atmosphere. The resulting mixture was heated at 100 ^{o}C for 45 mins. After cooling it to room temperature, 11-bromoundecene (3.7 g, 15.9 mmol) was added dropwise. The mixture was heated under reflux for 24 h, cooled and then extracted with ethylacetate (3x10 ml). The collected ethylacetate layer was dried over sodium sulphate and concentrated under reduced pressure. Flash column chromatography (65% ethylacetate/petroleum ether) afforded 3.5g of pure product.

^{1}H NMR ($CDCl_3$): 1.21-1.26 (m, 12H), 1.53-1.57 (m, 2H), 1.97-2.04 (m, 2H), 2.77 (br, 1H), 3.42 (t, J=6Hz, 2H), 3.54-3.71 (m, 12H), 4.88-4.99 (m, 2H), 5.73-5.82 (m, 1H).

^{13}C NMR ($CDCl_3$): 26.11, 28.97, 29.14, 29.48, 29.49, 29.63, 33.87, 61.78, 70.08, 70.41, 70.65, 70.67, 71.64, 72.64, 114.20, 139.27.

(b) Synthesis of *S*-11-(2-(2-(2-hydroxyethoxy)ethoxy)ethoxy)undecylethanethioate (**3**):[1]

Thiolacetic acid (0.94g, 12.34 mmol) was added to a solution of compound **2** (1.5 g, 4.9 mmol) in dry methanol (20 ml) under argon atmosphere. AIBN (7 mg) was then added, after which the reaction mixture was irradiated by 450 W medium pressure mercury 1 amp for 7 h in a pyrex tube. The solvent was evaporated. Flash column chromatography (65% ethylacetate/pet ether) afforded 1.75g of pure product.

^{1}H NMR ($CDCl_3$): 1.18-1.21 (m, 14H), 1.46-1.53 (m, 4H), 2.27 (s, 3H), 2.81 (t, J=6 Hz, 2H), 3.40 (t, J=6Hz, 2H), 3.53-3.69 (m, 12H).

^{13}C NMR ($CDCl_3$): 26.11, 28.85, 29.15, 29.20, 29.49, 29.54, 29.59, 29.61, 30.68, 61.75, 70.06, 70.39, 70.64, 71.62, 72.66.

2. Synthesis of alkoxyalkynyl Fischer carbene (6):[2]

In a 100 ml two neck r. b. flask, 3.06 gm phenylacetylene (30 mmol) was taken in 30 ml dry ether under Argon. The stirred solution was cooled to -50 ºC and 19 ml of ^{n}BuLi in hexane (1.6 M, 30 mmol) was added drop wise. Stirring was continued for 1 h. In another 100 ml r. b. flask, 10.5 gm (30 mmol) of $W(CO)_6$ was taken in 30 ml dry ether under Ar and the suspension was cooled to -50 ºC. The phenylacetylide solution was then added to the tungsten hexacarbonyl suspension. The temperature was raised to 0 ºC and stirred for 1 h. The ether was evaporated and the salt dissolved in minimum amount of ice-cold water, to which 30 ml of Meerwin's salt solution (1 mM, 30 mmol) was added. The resulting dark red solution was extracted with petroleum ether (4 x 50 ml), concentrated and purified by flash column chromatography (pet ether: acetone 90:10) under N_2. Yield 76%, 10.9 gm.

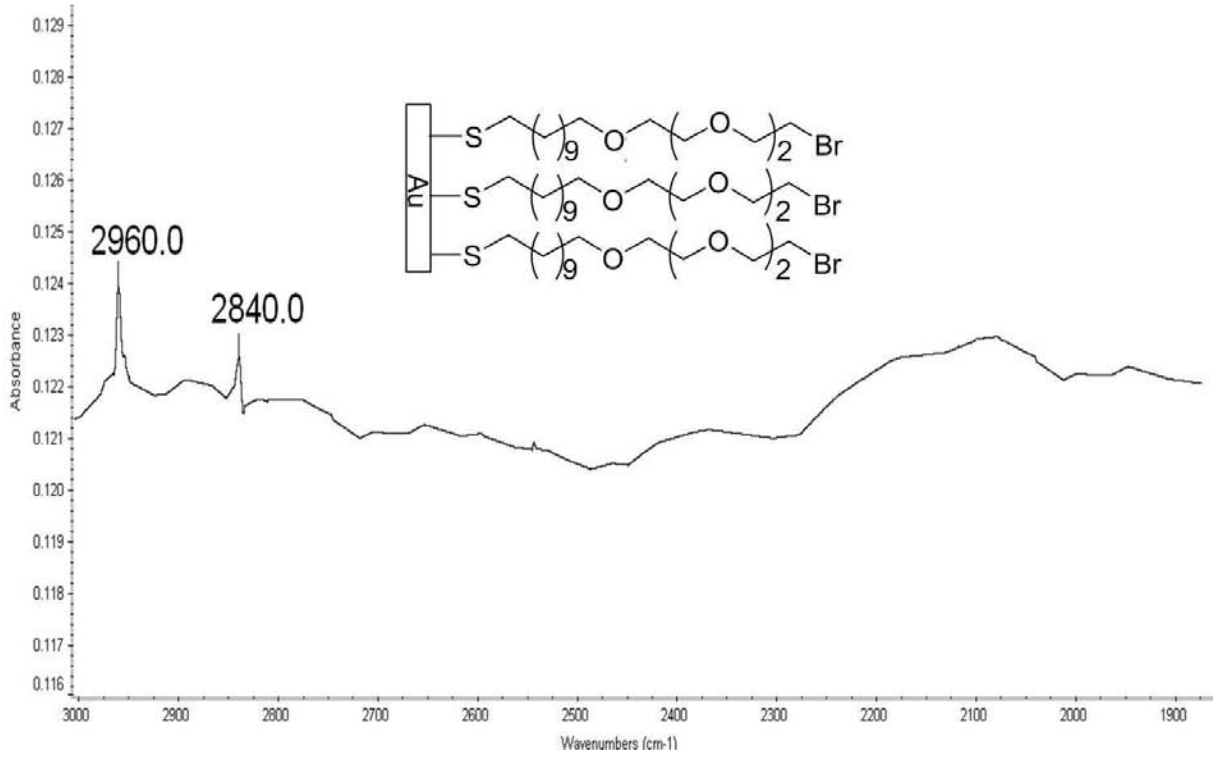
3. Physicochemical properties of protein A:[3,4]

Property	Value
$s^0_{20,w}$ (S)	2.1
Stokes radius (nm)	5.0
$D_{20,w}$ (cm^2/s)	4.3×10^{-7}
Huggins constant, K	0.66
$A^{1\%}_{280}$ (nm)	1.40
$A^{1\%}_{275}$ (nm)	1.65

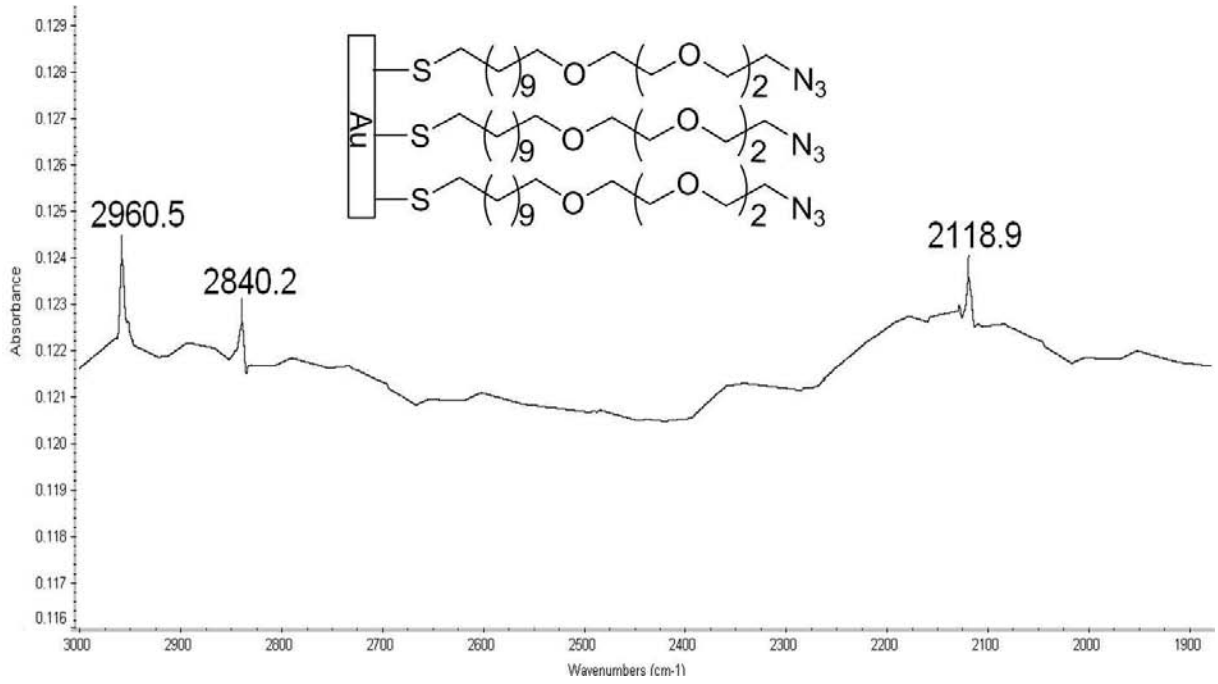
Its isoelectric point is 4.85 – 5.15. Protein A contains 50 % α-helical structure and 10 – 20 % β structures. It has four chemically equivalent tyrosine residues which are fully exposed on the surface. These tyrosine residues can be modified by tetranitromethane and acetylimidazole and are probably responsible for the protein's biological activity.

4. ATR-IR spectroscopy measurement of gold surface:

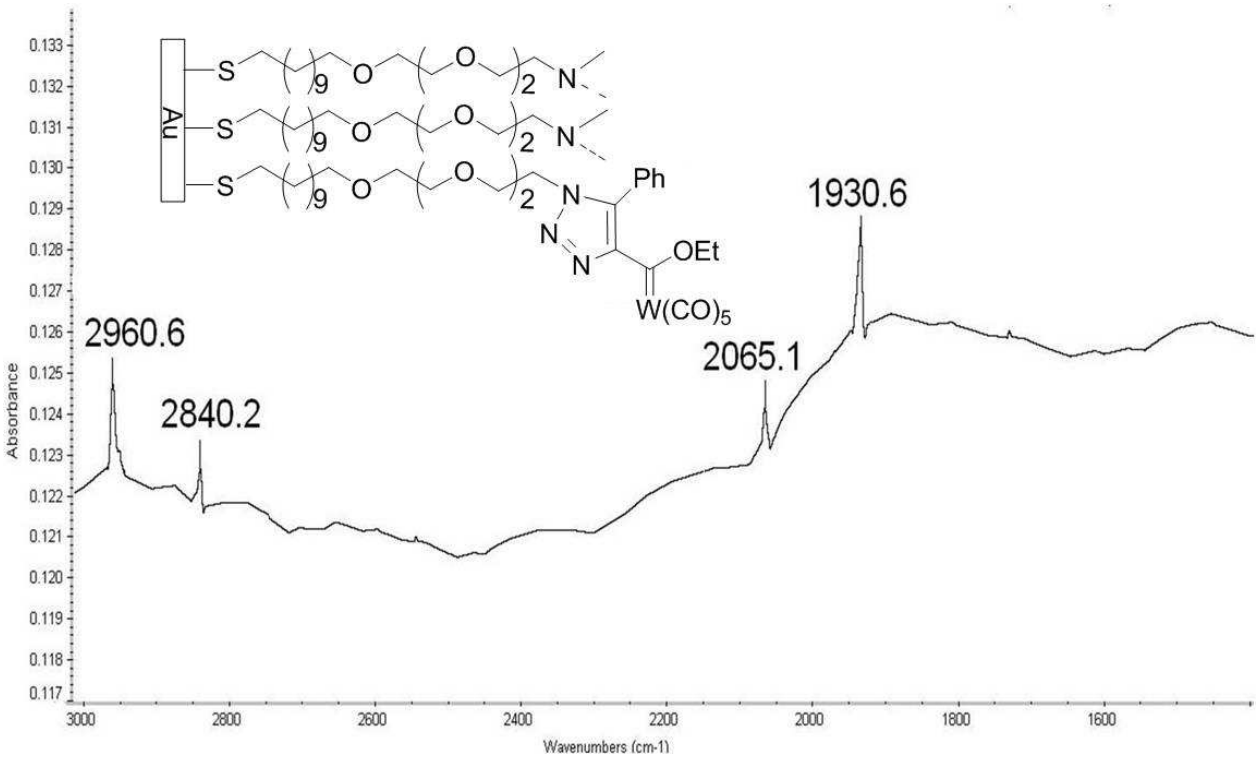
The bromo terminated SAM shows strong absorption band at 2960.0 $cm^{-1}$and 2840.0 cm^{-1}.



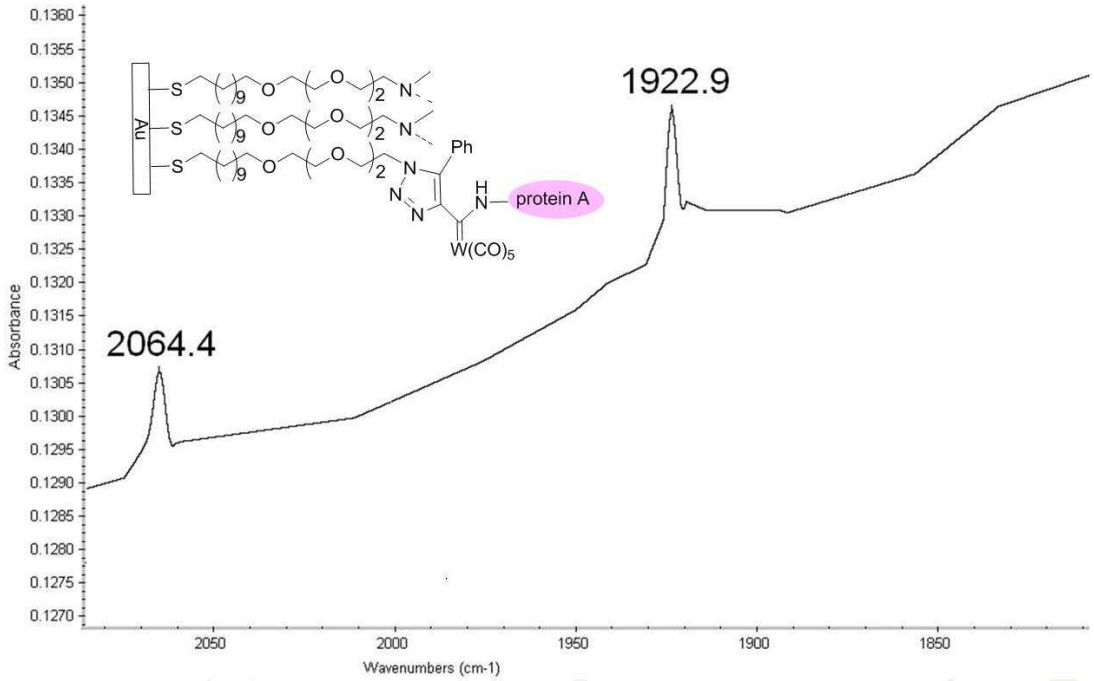
After nucleophilic displacement with sodium azide a new band originate at 2118.9 cm^{-1}.



After the ‘click’ cycloaddition reaction with alkynyl Fischer carbene the peak at 2118.9 cm^{-1} vanishes and two new band appeared at 2065.1 cm^{-1} and 1930.6 cm^{-1}.



After aminolysis with primary amine groups of pendant lysine residues of protein A the new W-CO stretching of amino carbene appeared at 2064.4 cm^{-1} and 1922.9 cm^{-1}.



5. Functionalization of glass surface:

i) Preparation of self assemble monolayer with 11-bromo-undecyl-trichlorosilane (BUTS):
The glass substrates were sequentially cleaned with piranha solution (a mixture of concentrated H_2SO_4 and 40% aq. H_2O_2) and water. Finally was dried under nitrogen. The cleaned glass surface was immersed in a 1% v/v solution of BUTS in dry toluene for 45 mins. After washing with dry toluene and ethanol the coated glass substrate was kept in oven at 100 ^oC for 10 mins.

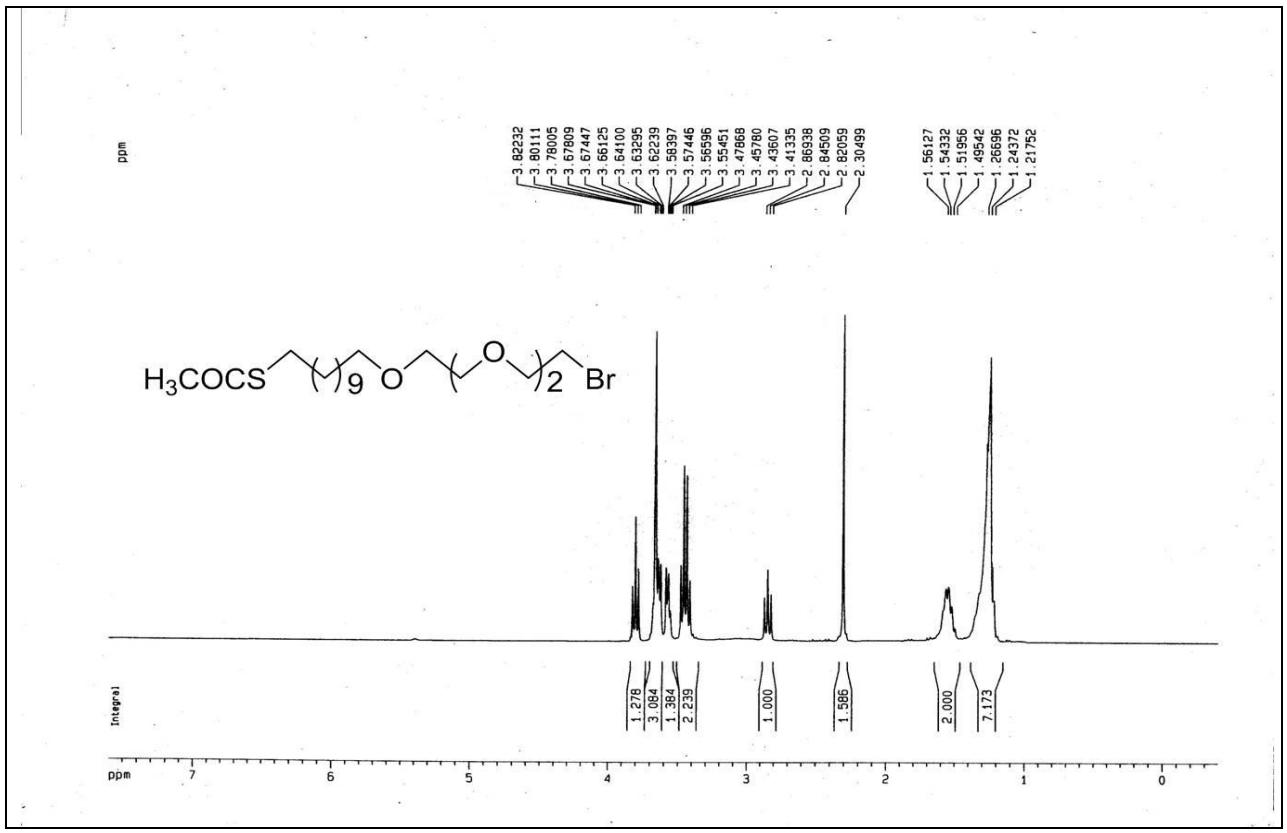
ii) Nucleophilic displacement with sodium azide:
The bromo coated glass slides was incubated in a saturated solution of NaN_3 in DMF and stirred for 48 h at room temperature. The slide was then extensively washed with distilled water and dried under nitrogen.

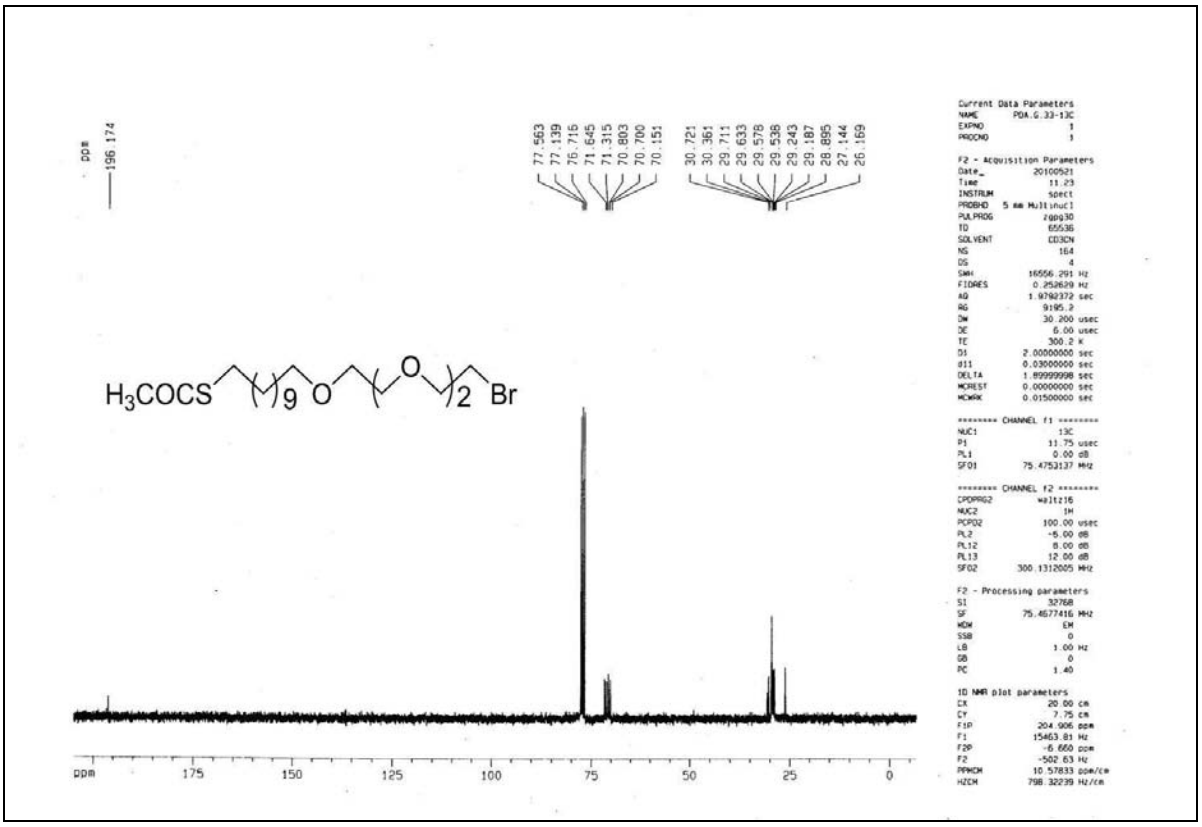
iii) Grafting of Fischer carbene complex (**6**) on glass surface via Cu free 'Click' cycloaddition reaction:
The azido coated glass slide was treated with 10 mM solution of Fischer carbene complex (**6**) in dry toluene at 50 ^oC for 4 h under argon. It was then washed with toluene followed by ethanol and dried under argon.

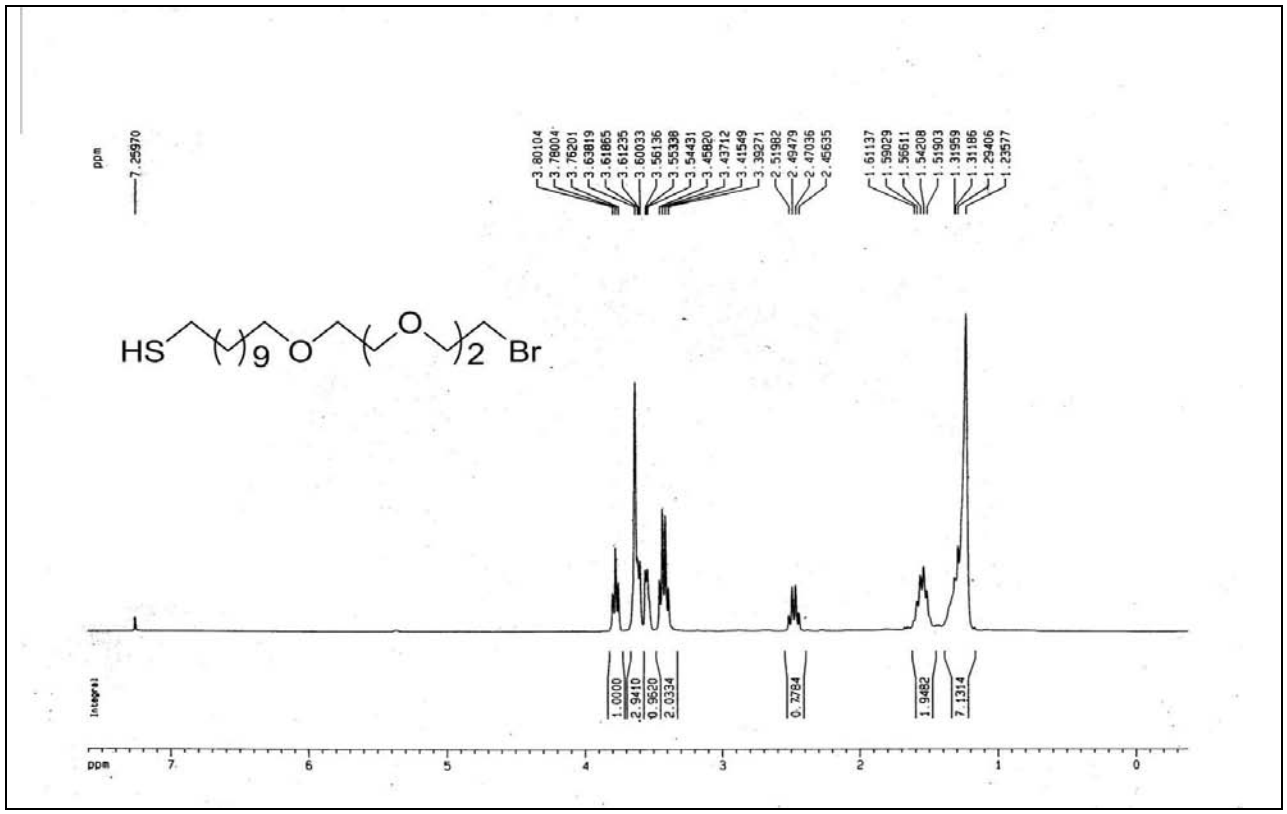
iv) Immobilization of protein A:
Glass surfaces coated with Fischer carbene was immersed in a solution of protein A (10 mg/L) in phosphate buffer (pH 8.0) for 10 min at room temperature. The substrates were rinsed thoroughly with buffer solution (thrice), then with milli-Q water (thrice) and dried under argon atmosphere. The remaining Fischer carbene complexes were blocked by treatment with 1M ethanolamine (pH 9.0) for 30 min. Finally, the surfaces were treated with 1 % (w/v) BSA in phosphate buffer pH 8.0 for 2 h to block non-specific binding. Then the surfaces were extensively rinsed with milli-Q water and dried under argon.

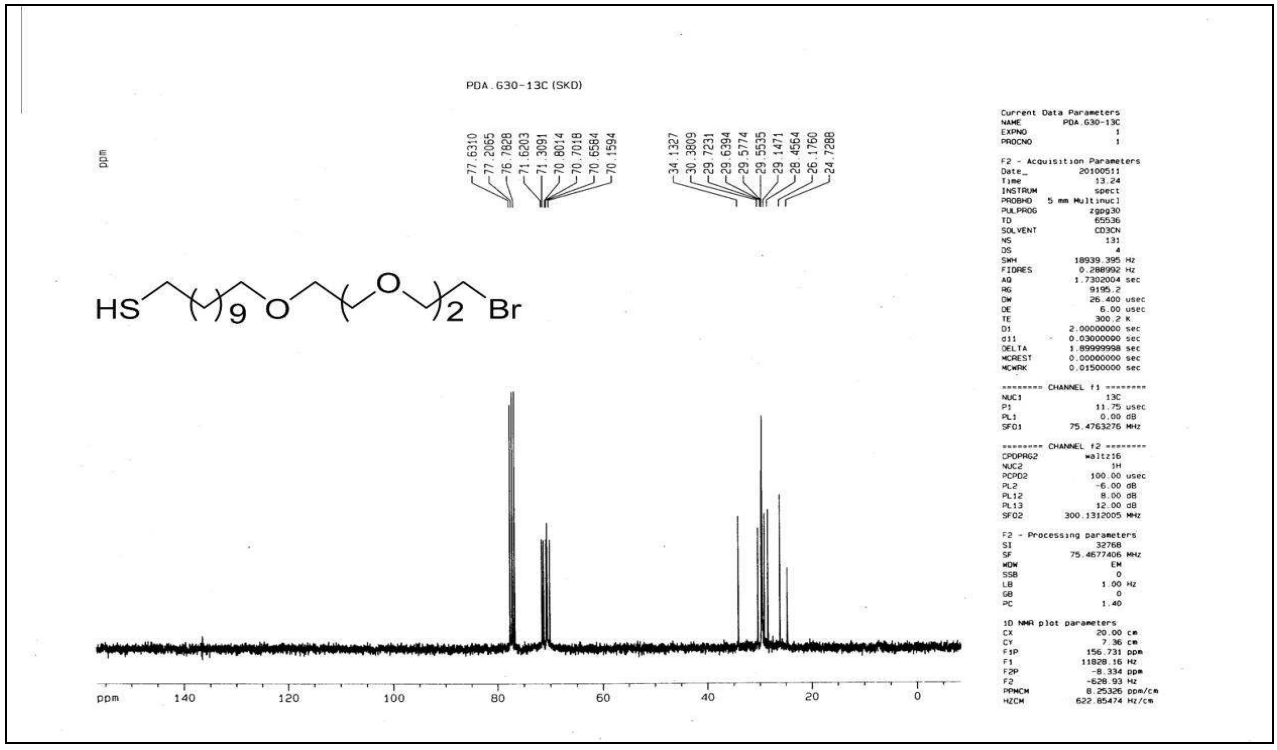
v) Successive binding of rabbit-IgG and FITC tagged goat anti-rabbit IgG:
Protein A coated glass surfaces were incubated in a solution of rabbit IgG (50 µg/ml) in phosphate buffer (pH 8.0) for 1 h. The surfaces were extensively washed with phosphate buffer containing 0.05 % Tween (v/v), followed by milli-Q water and dried under argon atmosphere. The IgG coated glass slide was further incubated in FITC tagged goat anti-rabbit IgG in phosphate buffer pH 8.0 for 1 h. Finally the surface was rinsed vigorously with phosphate buffer containing 0.05% Tween (v/v), followed by milli-Q water and dried under argon.

6.^{1}H NMR and ^{13}C NMR of compound (4) and (5).




ppm
196.174
77.563
77.139
76.716
71.645
71.315
70.803
70.700
70.151
30.721
30.361
29.711
29.633
29.578
29.538
29.243
29.187
28.895
27.144
26.169
H3COCS
9
O
O
2
Br
ppm
175
150
125
100
75
50
25
0
Current Data Parameters
NAME PDA.G.33-13C
EXPNO 1
PROCNO 1
F2 - Acquisition Parameters
Date_ 20100521
Time 11.23
INSTRUM spect
PROBHD 5 mm Multinucl
PULPROG zgpg30
TD 65536
SOLVENT CD3CN
NS 164
DS 4
SWH 16556.291 Hz
FIDRES 0.252629 Hz
AQ 1.9792372 sec
RG 9195.2
DW 30.200 usec
DE 6.00 usec
TE 300.2 K
D1 2.00000000 sec
d11 0.03000000 sec
DELTA 1.89999998 sec
MCREST 0.00000000 sec
MCWRK 0.01500000 sec
======== CHANNEL f1 ========
NUC1 13C
P1 11.75 usec
PL1 0.00 dB
SFO1 75.4753137 MHz
======== CHANNEL f2 ========
CPDPRG2 waltz16
NUC2 1H
PCPD2 100.00 usec
PL2 -6.00 dB
PL12 8.00 dB
PL13 12.00 dB
SFO2 300.1312005 MHz
F2 - Processing parameters
SI 32768
SF 75.4677416 MHz
WDW EM
SSB 0
LB 1.00 Hz
GB 0
PC 1.40
1D NMR plot parameters
CX 20.00 cm
CY 7.75 cm
F1P 204.906 ppm
F1 15463.81 Hz
F2P -6.660 ppm
F2 -502.63 Hz
PPMCM 10.57833 ppm/cm
HZCM 798.32239 Hz/cm


ppm
7.25970
3.80104
3.78004
3.76201
3.63819
3.61865
3.61235
3.60033
3.56136
3.55338
3.54431
3.45820
3.43712
3.41549
3.39271
2.51982
2.49479
2.47036
2.45635
1.61137
1.59029
1.56611
1.54208
1.51903
1.31959
1.31186
1.29406
1.23577
HS
9
O
O
2
Br
Integral
1.0000
2.9410
0.9620
2.0334
0.2784
1.9482
7.1314
ppm
7
6
5
4
3
2
1
0

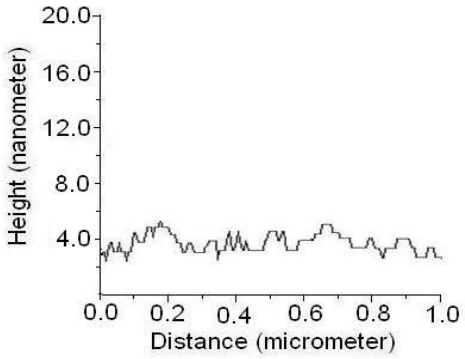

PDA.G30-13C (SKD)
ppm
77.6310
77.2065
76.7828
71.6203
71.3091
70.8014
70.7018
70.6584
70.1594
34.1327
30.3809
29.7231
29.6394
29.5774
29.5535
29.1471
28.4564
26.1760
24.7288
HS
9
O
O
2
Br
ppm
140
120
100
80
60
40
20
0
Current Data Parameters
NAME PDA.G30-13C
EXPNO 1
PROCNO 1
F2 - Acquisition Parameters
Date_ 20100511
Time 13.24
INSTRUM spect
PROBHD 5 mm Multinucl
PULPROG zgpg30
TD 65536
SOLVENT CD3CN
NS 131
DS 4
SWH 18939.395 Hz
FIDRES 0.288992 Hz
AQ 1.7302004 sec
RG 9195.2
DW 26.400 usec
DE 6.00 usec
TE 300.2 K
D1 2.00000000 sec
D11 0.03000000 sec
DELTA 1.89999998 sec
MCREST 0.00000000 sec
MCWRK 0.01500000 sec
======== CHANNEL f1 ========
NUC1 13C
P1 11.75 usec
PL1 0.00 dB
SFO1 75.4763276 MHz
======== CHANNEL f2 ========
CPDPRG2 waltz16
NUC2 1H
PCPD2 100.00 usec
PL2 -6.00 dB
PL12 8.00 dB
PL13 12.00 dB
SFO2 300.1312005 MHz
F2 - Processing parameters
SI 32768
SF 75.4677406 MHz
WDW EM
SSB 0
LB 1.00 Hz
GB 0
PC 1.40
1D NMR plot parameters
CX 20.00 cm
CY 7.36 cm
F1P 156.731 ppm
F1 11828.16 Hz
F2P -8.334 ppm
F2 -628.93 Hz
PPMCM 8.25326 ppm/cm
HZCM 622.85474 Hz/cm

.

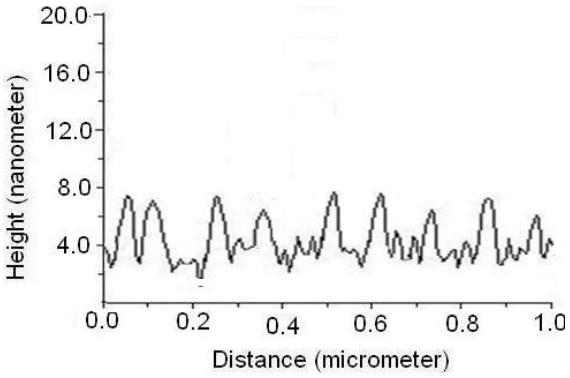
7. AFM characterization on gold surface:

The Ra of the bare gold surface is 0.243 nm.

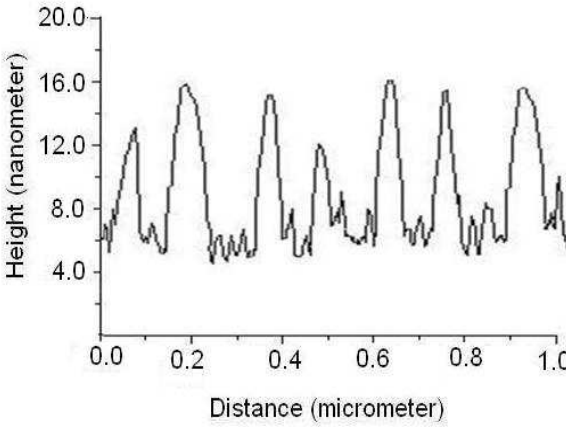
The section analysis of the gold surface modified with Fischer carbene complex:



The section analysis of the gold surface modified with protein A:



The section analysis of the gold surface modified with rabbit IgG:



Reference:

(1) Samanta, D., Faure, N., Rondelez, F., and Sarkar, A. (2003) Towards “designer” surfaces: functionalisation of self-assembled monolayer (SAM) on colloidal gold by alkene metathesis. *Chem. Commun.* 1186–1187.

(2) Sawoo, S., Dutta, P., Chakraborty, A., Mukhopadhyay, R., Bouloussa, O., and Sarkar, A. (2008) A new bio-active surface for protein immobilization via copper-free ‘click’ between azido SAM and alkynyl Fischer carbene complex. *Chem. Commun*. 5957–5959.

(3) Björk, I., Petersson, B. –Å., and Sjöquist, J. (1972) Some Physicochemical Properties of Protein A from *Staphylococcus aureus*. *Eur. J. Biochem.* 29, 579-584.

(4) Surolia, A., Pain, D., and Khan, M. I. (1982) Protein A: nature's universal anti-antibody. *TIBS*. 74 – 76.

Bioconjugate Chemistry

ARTICLE

pubs.acs.org/bc

Directed Covalent Immobilization of Fluorescently Labeled Cytokines

Tobias Recker,[†] Daniel Haamann,[‡] Anne Schmitt,[†] Andrea Küster,[†] Doris Klee,[‡] Stefan Barth,[§,∥] and Gerhard Müller-Newen*[,†]

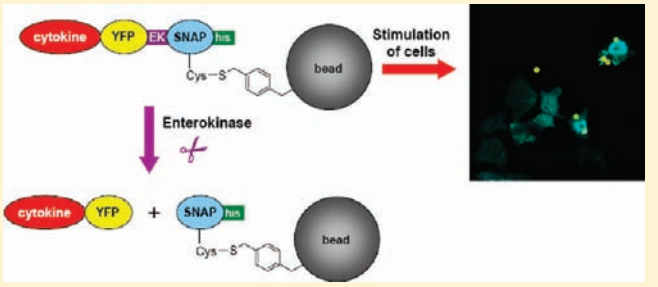
[†]Institute of Biochemistry and Molecular Biology, Medical School, RWTH Aachen University, Aachen, Germany

[‡]ITMC/DWI, RWTH Aachen University, Aachen, Germany

[§]Department of Experimental Medicine and Immunotherapy, Institute for Applied Medical Engineering, Aachen, Germany

[∥]Department of Pharmaceutical Product Development, Fraunhofer Institute for Molecular Biology and Applied Ecology, Aachen, Germany

ABSTRACT: Cytokines are important mediators coordinating inflammation and wound healing in response to tissue damage and infection. Therefore, immobilization of cytokines on the surface of biomaterials is a promising approach to improve biocompatibility. Soluble cytokines signal through receptors on the cell surface leading to cell differentiation, proliferation, or other effector functions. Random immobilization of cytokines on surfaces will result in a large fraction of inactive protein due to impaired cytokine−receptor interaction. We developed a strategy that combined (i) directed covalent coupling of cytokines, (ii) quantification of coupling efficiency through fluorescence detection, and (iii) a reliable protease cleavage assay to control orientation of coupling. For this purpose, fusion proteins of the SNAP-tag followed by an enterokinase recognition site, yellow fluorescent protein (YFP), and the cytokine of interest being either interleukin-6 (IL-6) or oncostatin M (OSM) were generated. The SNAP-tag is a derivative of O^6-alkylguanine-DNA alkyltransferase that couples itself covalently to benzylguanine. Bioactivities of the SNAP-YFP-cytokines were shown to be comparable with the nontagged cytokines. Efficient coupling of SNAP-YFP-cytokines to benzylguanine-modified beads was demonstrated by flow cytometry. The fact that enterokinase treatment released most of the fluorescence from the beads is indicative for directed coupling and only marginal adsorptive binding. Cellular responses to SNAP-YFP-cytokine beads were analyzed in cellular lysates and by confocal microscopy indicating that the directionally immobilized cytokines are fully signaling competent with respect to the activation of ERK and STAT3. The strategy presented here is generally applicable for the directed covalent immobilization of fluorescently labeled proteins including the convenient and reliable control of coupling efficiency and orientation.



1. INTRODUCTION

Cytokines are a large and heterogeneous group of proteins consisting of interleukins, interferons and growth factors.[1] These important and versatile mediators of intercellular communication are involved in virtually all physiological processes in the developing and adult organism. Depending on the individual cytokine and the cellular context, these proteins stimulate proliferation or differentiation of cells and may act in a pro- or anti-inflammatory manner on immune responses. Because of these properties, cytokines are promising molecules to modulate the response of the body to biomaterials. Therefore, immobilization of cytokines on the surface of biomaterials to direct the fate of adhered cells, augment wound healing, and control inflammatory responses is an active field of research.[2−4]

Cytokines bind specifically to cytokine receptors which consist of two or more subunits. These subunits can be different proteins (heterooligomeric receptors) or two or more copies of the same protein (homooligomeric receptors).[5] Shared subunits are known, which are used by different cytokines.[6] Gp130 is the shared receptor subunit of the IL-6 family of cytokines.[7] Two IL-6 molecules assemble two IL-6 receptor α-subunits (IL-6Rα) and two gp130 molecules leading to the formation of a hexameric receptor complex.[8] Other cytokines of this family such as oncostatin M (OSM) and leukemia inhibitory factor (LIF) bind to a heterodimer of gp130 with the OSM receptor (OSMR) or LIF receptor (LIFR), respectively, resulting in a heterotrimeric receptor complex.[9] In all cases, large surface areas of the cytokine must be accessible for the interaction with the receptor subunits to allow receptor complex formation. Therefore, random adsorptive or chemical immobilization of cytokines will lead to a large fraction of inactive protein. One could even imagine the generation of partial agonists by inadequate immobilization of cytokines leading to skewed signaling.

Signal transduction downstream of gp130 always involves the transcription factor STAT3 and the RAS/RAF/ERK cascade.[7] Depending on the cytokine, other pathways may also be activated. The hallmark of STAT3 activation is the phosphorylation of tyrosine residue 705 (Y705) by receptor associated Janus

Received: February 8, 2011
Revised: April 27, 2011
Published: May 02, 2011

ACS Publications © 2011 American Chemical Society

kinases (JAKs) and subsequent nuclear accumulation of the transcription factor.[10] ERK activation involves phosphorylation of the TEY-motif by the upstream kinase MEK. The kinetics of ERK activation determines the cellular response.[11] It is still a matter of debate as to what extent these key signaling events are initiated at the plasma membrane or after internalization of the receptor complex at signaling endosomes.[12] This issue is of considerable importance as soon as cytokines are immobilized on surfaces. Cytokines bound to surfaces cannot be internalized and therefore cannot signal from endosomes, raising the possibility that signaling from soluble and immobilized cytokines may differ.[13,14]

Furthermore, endocytosis of receptor complexes is a way to desensitize cells from further stimulation.[15] However, for gp130 it is known that the signaling cascade is downregulated by a classic feedback mechanism: activated STAT3 induces the suppressor of cytokine signaling 3 (SOCS3) protein expression.[16] Then, SOCS3 blocks further STAT3 activation at the gp130 receptor complex by mechanisms which are incompletely understood. Therefore, it will be interesting to see as to what extent immobilization of the cytokine interferes with the kinetics of the signaling events. Prerequisite for these investigations is a reliable technique to covalently immobilize cytokines on surfaces in a bioactive form.

We used cytokines of the IL-6-family to develop a new strategy for cytokine immobilization on surfaces that guarantees (i) site-directed covalent coupling through a tag that does not involve the cytokine itself, (ii) straightforward analysis of coupling efficiency by fluorescence detection, and (iii) proof of orientation of coupling by protease cleavage. Cytokines immobilized by this strategy are useful tools for basic research on cytokine signal transduction and the improvement of biomaterials.

2. EXPERIMENTAL PROCEDURES

2.1. Chemicals and Antibodies. PEGylated aminobenzylguanine (BG-PEG-NH_2) was provided by New England Biolabs (Ipswich, USA). Magnetic micromer-M PEG-COOH beads with a diameter of 3 μm were produced by Micromod (Rostock, Germany). Primary antibodies were purchased from the following companies: GFP, phosphorylated STAT3, and phosphorylated ERK1&2 (Rockland, Gilbertsville, USA), STAT3 and ERK1&2 (Santa Cruz, Santa Cruz, USA), IL-6, OSM, PE-conjugated IL-6 and PE-conjugated OSM (R&D, Minneapolis, USA), and SNAP (Open Biosystems, Huntsville, USA). Secondary antibodies were purchased from DAKO (Glostrup, Denmark). Enterokinase-kit was obtained from EMD Chemicals (Gibbstown, USA). Eukaryotic cell-culture media and antibiotics (Pen Strep) were purchased from Invitrogen (Carlsbad, USA).

2.2. Recombinant Plasmids and Proteins. The expression vector pET-17b from EMD Chemicals was used for the production of YFP-OSM and YFP-IL-6 in *E. coli*. The constructs consist of a hexahistidine (his)-tag, followed by a enterokinase recognition site (DDDDK), YFP, and the respective mature human cytokine. SNAP-YFP (fusion protein without cytokine) was also produced in *E. coli*. SNAP-YFP-cytokines were cleaved in *E. coli* and therefore produced in mammalian cells. The pcDNA5/FRT/TO vector of the Flp-In system (Invitrogen) was used for the expression of SNAP-YFP-OSM and SNAP-YFP-IL-6 in HEK293 cells. The constructs encode the signal sequence of IL-6 for secretion, followed by a his-tag, a SNAP-tag (New England Biolabs), the enterokinase recognition site, the enhanced yellow fluorescent protein (YFP), and finally the respective mature human cytokine. The YFP cDNA originated from the pEYFP-N1-vector (Clontech, Mountain View, USA).

2.3. Protein Expression. Flp-In T-Rex HEK293 were stably transfected with expression vectors encoding SNAP-YFP-cytokines using the T-Rex system (Invitrogen). For protein expression, cells were cultured in serum-free DMEM medium in a water-saturated atmosphere containing 5% CO_2 at 37 °C. Protein expression was induced by the addition of doxycycline (50 ng/mL). 72 hours after induction, the supernatant was collected and concentrated 20-fold by ultrafiltration using a Vivaspin 20 device (Sartorius Stedim biotech, Aubagne, France). For further characterization, SNAP-YFP-cytokines were purified using a Ni-NTA Spin-column according to the instructions of the manufacturer (Qiagen, Hilden, Germany). The different fractions were analyzed by SDS−PAGE, followed by Coomassie-staining or Western blotting. SNAP-YFP cytokines were quantified by ELISA using antibodies against the SNAP and YFP-moieties. SNAP-YFP served as a standard.

YFP-cytokines and SNAP-YFP were expressed in *E. coli* (strain BL-21 (DE3) pLysS) by the use of the pET-system.[17] Bacteria were grown at 37 °C in LB medium in the presence of 100 mM $ZnCl_2$ to an OD_{600} of 0.6−0.8. After the addition of IPTG (0.4 mM) and DTT (1 mM), the culture was incubated at 25 °C for 20 h. Bacteria were sedimented by centrifugation, the pellet shock-frozen and resuspended in lysis-buffer (20 mM phosphate buffer, pH 8.0, containing 500 mM NaCl). Lysozyme (1 mg/mL), benzonase (25 U/mL) and Triton-X100 (1%) were added to complete the lysis of bacteria. Lysates were shaken at 4 °C for 4 h and the recombinant proteins purified as described above. To determine the concentration of SNAP-YFP in the eluate, the absorbance at 514 nm was measured (NanoDrop, NanoDrop products, Wilmington, USA; extinction coefficient of YFP = 83,400 M^{-1} cm^{-1}).

2.4. Immobilization of SNAP-YFP-Cytokines. For immobilization, 50 μL of a suspension of micromer-M PEG-COOH beads (3.4×10^6 beads/μL) was functionalized with 50 μL of BG-PEG-NH_2 (2 mg/mL in 10% DMSO and 90% PBS pH 7.4) through EDC/NHS-chemistry:[18] At first, beads were shortly washed twice in MES-buffer (25 mM, pH 5.0) and then incubated (30 min, room temperature) in a freshly prepared mixture of 25 μL EDC solution (50 mg/mL) and 25 μL of NHS solution (50 mg/mL) in MES-buffer (25 mM, pH 5.0). After incubation, the supernatant was removed, and the beads were washed again with MES-buffer for 4 min. Then, 50 μL of BG solution was added, and the suspension was incubated for 16 h (4 °C) with slow tilt rotation. After washing four times with 100 μL of 0.05 mM Tris-HCl, pH 7.4, 10 μL of the bead suspension (1.6×10^6 beads/μL) was incubated for 16 h with 50 μL of purified SNAP-YFP-cytokine (1 μM) or concentrated supernatants of SNAP-YFP-cytokine producing cells. Incubation of beads with YFP-cytokine (no SNAP-tag) and incubation of unmodified beads (no benzylguanine on the surface) with SNAP-YFP-cytokine served as controls. Beads were washed with 100 μL of phosphate-buffer (0.1 M, pH 8.0) containing 2% BSA. After washing, beads were analyzed by flow cytometry or by confocal microscopy. SNAP-YFP-cytokine beads were stored at −80 °C in phosphate buffer (0.1 M, pH 8.0) containing 2% BSA. The concentrations of SNAP-YFP-IL-6 in the coupling buffer before and after coupling were determined with a previously described ELISA[19] using a biotinylated GFP antibody (Rockland).

2.5. Analysis of Beads by Flow Cytometry and Confocal Microscopy. Three microliters of a suspension of SNAP-YFP-cytokine beads (1.6×10^5 beads/μL) and the control beads were mixed with 100 μL of BD FACSFlow Sheath Fluid

(BD Bioscience, Franklin Lakes, USA). Beads were analyzed by flow cytometry (FACS Canto II, BD systems) using the appropriate adjustments for YFP detection. For cytokine detection, 7.5 μL of a suspension of SNAP-YFP-cytokine beads were incubated for 30 min in 25 μL of 0.1 M phosphate buffer (pH 8.0) containing 1 μL of a phycoerythrin (PE)-conjugated cytokine antibody (or without PE-antibody as a control). After incubation, 10 μL of bead suspension was mixed with 100 μL of BD FACSFlow Sheath Fluid and analyzed as described above detecting PE and YFP fluorescence.

For confocal microscopy, 2 μL of a suspension of SNAP-YFP-cytokine beads (1.6×10^5 beads/μL) was mixed with 5 μL of Shandon Immu-Mount (Thermo Fisher Scientific Inc., Waltham, USA) on a microscope slide and covered with a coverslip. After a short drying period, probes were analyzed using a Zeiss LSM 510 confocal microscope.

2.6. Stability of Coupling and Enterokinase Cleavage. Fifteen microliters of a suspension of SNAP-YFP-cytokine beads was incubated in 500 μL of serum free medium (DMEM-F:12 including Pen Strep) and incubated for different times at 37 °C. Then, the medium was removed by centrifugation, and beads were washed with 50 μL of 0.1 M phosphate buffer (pH 8.0). Detection of YFP and PE fluorescence by flow cytometry was performed as described above.

To 15 μL of a suspension of SNAP-YFP-cytokine beads (1.6×10^5 beads/μL), 50 μL of enterokinase solution was added. After incubation for 16 h at 4 °C, the beads were prepared for flow cytometry as described above.

2.7. Immobilization on NCO-sP(EO-*stat*-PO)-Coated Glass Coverslips. Glass coverslips (18 mm diameter, purchased from Menzel (Braunschweig, Germany)) were cleaned by sonication in water, acetone, and 2-propanol for 5 min each, followed by drying in a stream of nitrogen. Afterward, the substrates were transferred to a Unilab glovebox (MBraun, Garching, Germany) and treated with a solution of 0.3 mL of *N*-[3-(trimethoxysilyl)-propyl]ethylendiamine in 50 mL of dry toluene for 2 h, washed several times with dry toluene, and used without further storage. The spin coating solution was prepared by dissolving 10 mg/mL of the NCO-*s*P(EO-*stat*-PO) prepolymer (M_n = 12,000 g mol^{-1}; PDI = 1.15) in 1 mL of dry THF and adding 9 mL of deionized water. The solutions were used for layer preparation 5 min after mixing. For spin-coating, the samples were placed on the spin-coater, covered by the spin coating solution, and then accelerated within 5 s to 2500 rpm for 40 s.[20] Afterward, the samples were stored for 10 min and then used for immobilization of BG-PEG-NH_2 by dip-coating of the samples in a filtered solution of 0.5 mM BG-PEG-NH_2 in H_2O/DMSO 9:1 for 12 h. Then the samples were washed several times with H_2O and dried in a stream of nitrogen. A sticky μSLIDE-insert (IBIDI, Martinsried, Germany) with two chambers was fixed on the coverslip surface. The two chambers were incubated with SNAP-YFP-OSM or YFP-OSM (0.1 μM each) in phosphate buffer (0.1 M, pH 8.0) containing 2% BSA for 16 h at 4 °C. Chambers were washed as described in the immobilization section. Fluorescence was detected with a fluorescence scanner using 488 nm laser light for excitation and a 500−540 nm bandpass filter for detection. (Typhoon, GE Healthcare, Buckinghamshire, UK).

2.8. Stimulation of Cells. HepG2 cells were seeded on a 24-well plate and grown to 70% confluence. After starvation in serum free medium for 2 h, cells were incubated at 37 °C with varying concentrations of recombinant cytokines for different times as indicated in the figure legends. Cellular lysates were analyzed by SDS−PAGE and Western blotting using antibodies against phosphorylated STAT3, total STAT3, phosphorylated ERK and total ERK. For stimulation with immobilized cytokines cells were treated as described above but seeded on 24-well plates. Then 15 μL SNAP-YFP-cytokine beads (1.6×10^5 beads/μL) were added. Benzylguanine-modified beads were used as a control. Cells were incubated for different times. Cellular lysates were analyzed by SDS−PAGE and Western blotting as described above.

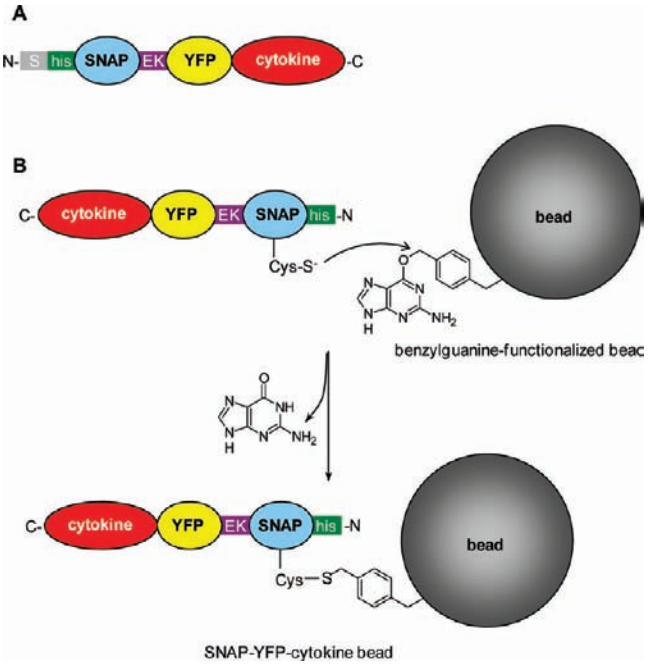


Figure 1. Scheme of a SNAP-YFP-cytokine and its surface coupling. (A) Schematic representation of the SNAP-YFP-cytokine construct encoded by the expression vector for the production of recombinant protein in mammalian cells. N, N-terminus; S, signal sequence (is cleaved-off during secretion); his, his-tag; SNAP, SNAP-tag; EK, enterokinase recognition site; YFP, yellow fluorescent protein; C, C-terminus. (B) Directed immobilization of a recombinant SNAP-YFP-cytokine through the SNAP-tag on a benzylguanine-functionalized bead surface. In this study, PEGylated aminobenzylguanine (BG-PEG-NH_2) was used. The three ethylene-glycol units that act as a spacer between benzylguanine and the bead are not shown.

2.9. Confocal Microscopy of Cells. HEK293 cells transiently transfected with gp130id-CFP[21] and OSMR were seeded on glass coverslips. SNAP-YFP-OSM (1 nM) or SNAP-YFP-OSM beads (1.6×10^5 beads/μL) were added. Cells were fixed with Shandon Immu-Mount and analyzed by confocal microscopy (Zeiss LSM 510) for CFP and YFP fluorescence. After induction with doxycycline (50 ng/mL) for 72 h, YFP fluorescence of HEK293 cells expressing SNAP-YFP-IL-6 was analyzed in a similar way.

Murine embryonic fibroblasts stably transfected with STAT3-CFP[22] were seeded on coverslips and grown to 40% confluence. Coverslips were transferred to a live-cell imaging chamber, and 15 μL of a suspension of SNAP-YFP-IL-6 beads (1.6×10^5 beads/μL) was added. After sedimentation of the beads, cells were stimulated by the addition of sIL-6Rα (final concentration 0.5 μg/mL). Images of CFP and YFP fluorescence were recorded every 20 min.

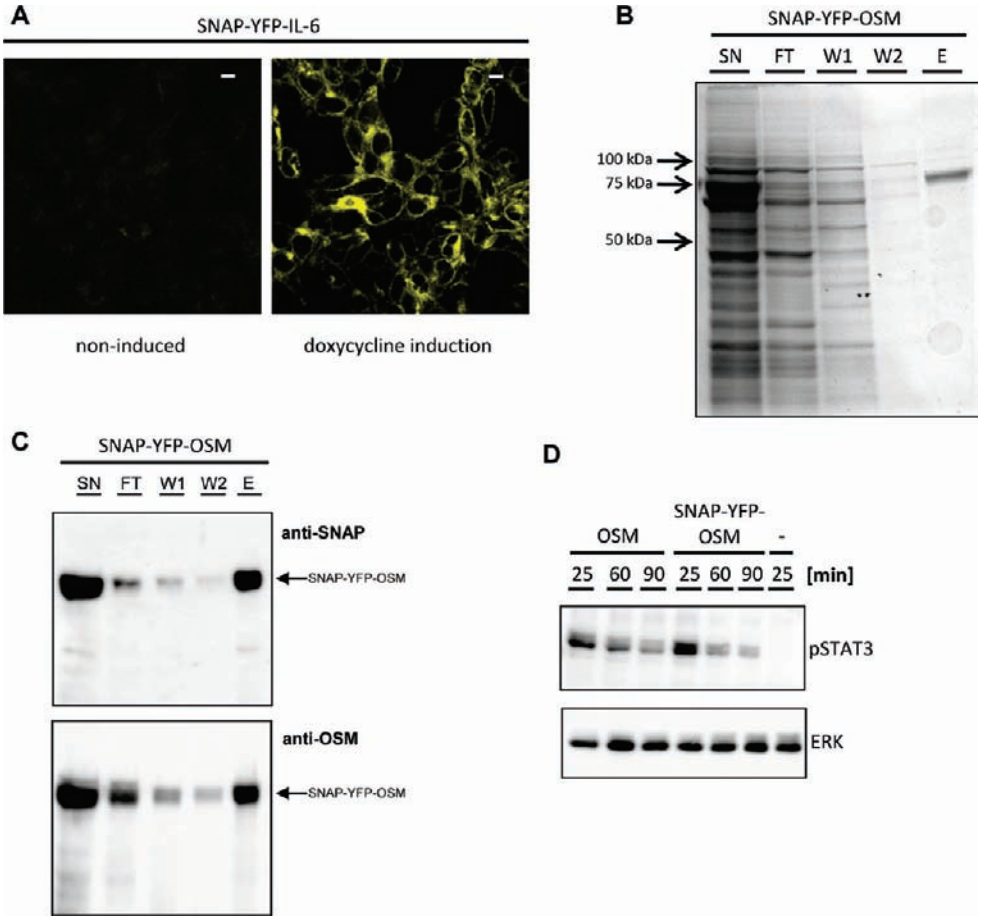


Figure 2. Inducible expression, purification, and activity of SNAP-YFP-cytokines. (A) HEK293 cells stably transfected with an expression vector encoding SNAP-YFP-IL-6 were seeded on coverslips. Protein expression was induced by the addition of doxycycline (50 ng/mL) for 72 h as indicated. Subsequently, cells were fixed and analyzed by confocal microscopy. Scale bars represent 5 μm. (B) Purification of SNAP-YFP-OSM by Ni-chelate affinity chromatography through the his-tag of the fusion protein. Fractions were analyzed by SDS−PAGE and subsequent Coomassie-staining of the gel. SN, supernatant from HEK293 cells stably expressing SNAP-YFP-OSM after induction with doxycycline (50 ng/mL) for 72 h; FT, flowthrough of the affinity column; W1 and W2, wash fractions; E, concentrated eluate. (C) Western blot analysis of the fractions described in B with SNAP and OSM antibodies. (D) HepG2 cells were stimulated with OSM (1 nM) or SNAP-YFP-OSM (1 nM) for different times. Cellular lysates were prepared and analyzed for OSM-induced phosphorylation of STAT3 by Western blotting. Detection of ERK served as a loading control. A representative example of three independent experiments is shown.

3. RESULTS

3.1. Expression, Purification, and Activity of SNAP-YFP-Cytokines. Cytokine constructs were designed that should permit (i) directed and specific coupling to a functionalized surface, (ii) straightforward detection and quantification of coupling efficiency, (iii) proof of directed coupling versus random coupling or unspecific adsorption, and (iv) purification of the recombinant protein. For this purpose, expression vectors were constructed encoding fusion proteins consisting of an N-terminal hexahistidine (his)-tag (aim iv), followed by a SNAP-tag (aim i), a recognition site for the protease enterokinase (aim iii), a yellow fluorescent protein (YFP, aims ii and iii), and finally the cytokine (Figure 1A). The SNAP-tag is derived from the human DNA repair protein O^6-alkylguanine-DNA alkyltransferase. The SNAP-tag couples itself autocatalytically to benzylguanine derivatives.[23] The chemistry of specific covalent coupling of the SNAP-tag to a benzylguanine-functionalized surface is shown in Figure 1B. YFP is a red-shifted variant of the green fluorescent protein (GFP) and can be detected separately from the cyan fluorescent protein (CFP), a blue-shifted variant of GFP.[24]

Flp-In T-Rex HEK293 cells were stably transfected with SNAP-YFP-OSM and SNAP-YFP-IL-6 using the Flp-In T-Rex expression system for targeted recombination and inducible expression of the transgene. Expression of the fluorescent cytokine upon induction with doxycycline is detectable by confocal microscopy (Figure 2A). The recombinant protein is mainly found within the membrane structures of the secretory pathway. The purification of SNAP-YFP-OSM from supernatants of stably transfected HEK293 cells by Ni-chelate affinity chromatography is shown in Figure 2B. SNAP-YFP-OSM elutes as a 75 kDa protein. The apparent molecular mass is in good agreement with the estimated molecular mass of the glycosylated fusion protein. In a Western blot, the protein is recognized by both a SNAP antibody and an OSM antibody documenting the integrity of the fusion protein (Figure 2C). SNAP-YFP-OSM and nontagged OSM induce equal STAT3 phosphorylation in HepG2 hepatoma cells (Figure 2D). SNAP-YFP-IL-6 was expressed, purified, and characterized in a similar way as a bioactive cytokine (data not shown).

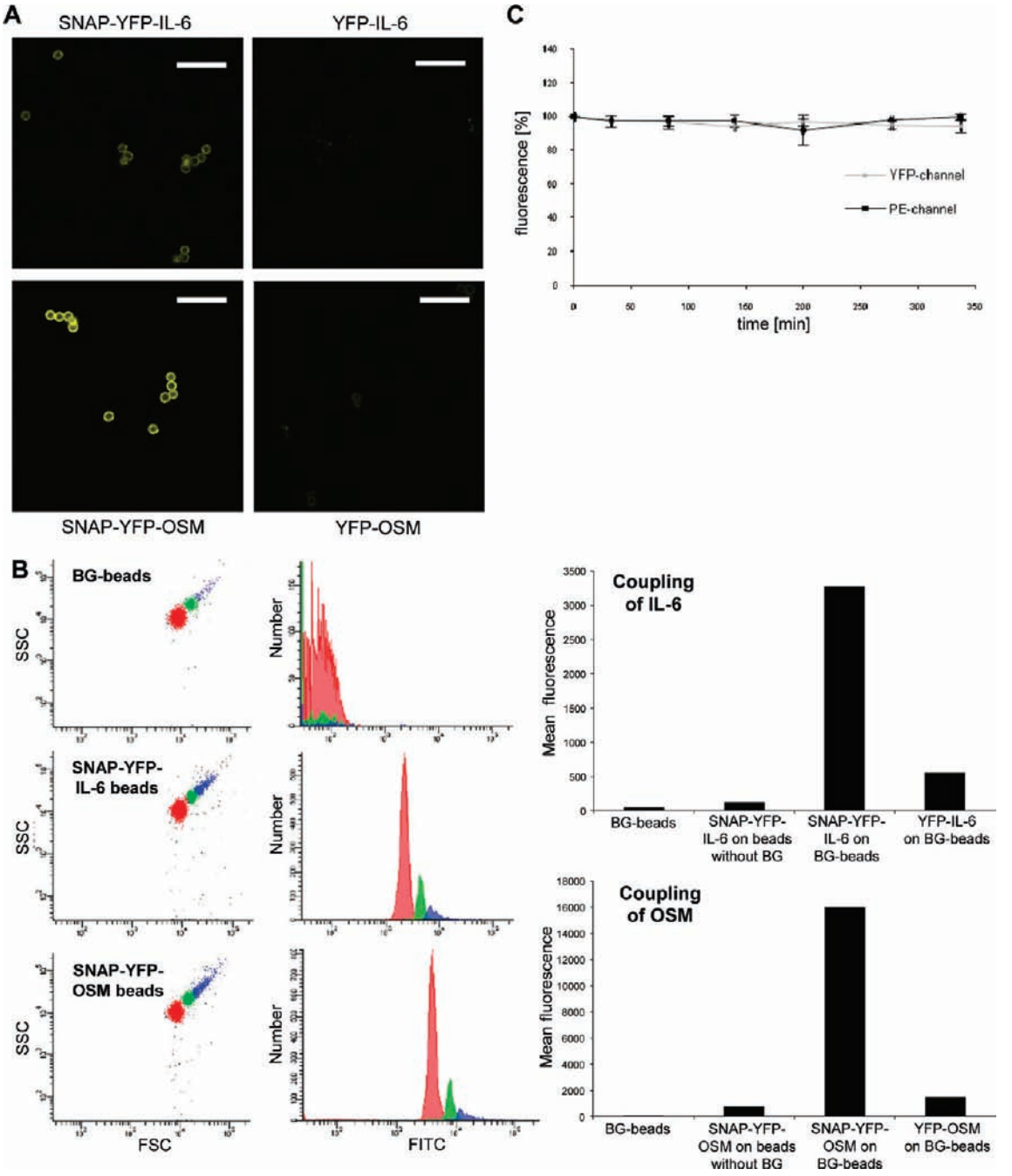


Figure 3. Immobilization of SNAP-YFP-cytokines on BG-modified beads. (A) BG-beads were treated for 16 h with SNAP-YFP-cytokines (1 μM) or YFP-cytokines (1 μM) as indicated. Subsequently, beads were analyzed by confocal microscopy using identical settings for laser intensity and detector gain. Scale bars represent 15 μm. (B) Unmodified beads or BG-beads were incubated for 16 h with YFP-IL-6, YFP-OSM, SNAP-YFP-IL-6, or SNAP-YFP-OSM (1 μM each). Fluorescence of the beads was analyzed by flow cytometry. Histograms of BG-beads, SNAP-YFP-IL-6 beads, and SNAP-YFP-OSM beads are shown with different bead populations in red (monomers), green (dimers), and blue (multimers). Mean fluorescence of the beads as measured by FACS is depicted as bar charts. A representative example of three independent experiments is shown. (C) SNAP-YFP-OSM beads were incubated for different times in cell culture medium at 37 °C. At the indicated time points, fluorescence of the beads was analyzed by flow cytometry. Besides YFP-fluorescence, phycoerythrin (PE) fluorescence of a PE-labeled hOSM antibody was detected to confirm the stability of the recombinant protein on the bead surface.

3.2. Coupling of SNAP-YFP-Cytokines to Benzylguanine-Modified Surfaces. We used beads as a substrate for surface immobilization of SNAP-YFP cytokines. We took advantage of the fact that beads can be analyzed by flow cytometry and added as a suspension to cell cultures. The surface of micromer-M-COOH beads (diameter, 3 μm) was functionalized with PEGylated aminobenzylguanine (BG-PEG-NH_2) using NHS/EDC coupling chemistry. The benzylguanine (BG) modified beads were incubated with SNAP-YFP-cytokines or YFP-cytokines and subsequently analyzed by confocal microscopy (Figure 3A). BG-beads treated with SNAP-YFP-cytokines show a strong ring-shaped fluorescence, whereas the fluorescence of the YFP-cytokine

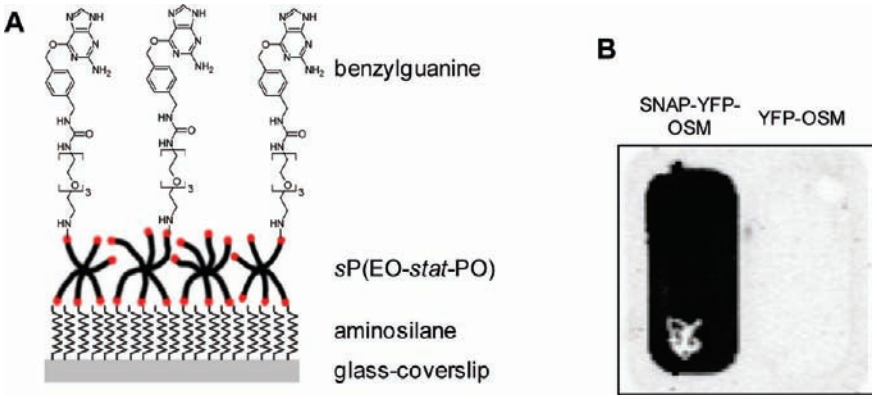


Figure 4. Immobilization of SNAP-YFP-cytokines on a BG-modified, star-PEG-coated surface. (A) Glass coverslips were first aminosilanized and then covered with *s*P(EO-*stat*-PO). BG-PEG-NH_2 was covalently attached through the reactive NCO-groups (red dots) of *s*P(EO-*stat*-PO). (B) The BG-modified *s*P(EO-*stat*-PO)-coated surface was incubated with SNAP-YFP-OSM (1 μM) or YFP-OSM (1 μM) for 16 h at 4 °C in two chambers on a glass slide. After washing, the fluorescence of the surface was analyzed by fluorescence scanning.

treated BG-beads is rather weak indicating a specific coupling of SNAP-YFP-cytokines to BG-modified beads. The weak fluorescence of YFP-cytokine treated BG-beads is most probably due to unspecific binding since micromer-M-COOH beads show almost no autofluorescence (not shown). Furthermore, the confocal images confirm that the micromer-M-COOH beads are monodisperse with a diameter of about 3 μm. The modified beads show a tendency to form aggregates.

Flow cytometry was used to analyze the relative amounts of immobilized SNAP-YFP-cytokines on BG-modified beads in a quantitative manner (Figure 3B). According to their sizes, three populations of BG-beads can be differentiated (depicted in red, green, and blue in Figure 3B). The red population most probably represents single beads. The green and blue populations represent aggregates of two (green) or three and more beads (blue). The BG-modified beads show almost no fluorescence. After incubation with SNAP-YFP-cytokine, the fluorescence of all populations of BG-beads strongly increases. The representation of several measurements as bar charts shows a strong increase of fluorescence when BG-modified beads were treated with SNAP-YFP-cytokines. A relatively weak fluorescence is measured when nonmodified beads were treated with SNAP-YFP-cytokines or when BG-modified beads were treated with YFP-cytokines lacking the SNAP-tag. These experiments strongly suggest a specific coupling of SNAP-YFP-cytokines to BG-modified beads through the SNAP-tag.

The concentrations of SNAP-YFP-IL-6 in the coupling buffer before and after coupling to a defined number of beads were determined by ELISA. From the difference of the concentrations, we calculated that about 550.000 molecules of SNAP-YFP-IL-6 are coupled to each bead. On the basis of the known dimensions of YFP, we estimated that a single SNAP-YFP-IL-6 molecule in an extended conformation would occupy 10 nm^2. If the beads are regarded as ideal spheres with a diameter of 3 μm, this would result in a surface occupancy of about 20%.

To test the stability of coupling, the SNAP-YFP-OSM beads were incubated under cell culture conditions for several hours at 37 °C (Figure 3C). At different times, beads were stained with an OSM specific PE-conjugated antibody. YFP and PE fluorescence was measured by flow cytometry. The almost constant fluorescence of the beads over time in both channels suggests that no SNAP-YFP-OSM is released from the SNAP-YFP-OSM beads and that no cleavage of OSM from the bead surface occurs.

To test the versatility of the approach, SNAP-YFP-OSM was immobilized on a flat glass surface. For this purpose, an aminosilanized glass coverslip was first covered with an isocyanate-terminated, star shaped copolymer containing poly(ethylene oxide) and poly(propylene oxide) (NCO-*s*P(EO-*stat*-PO) by spin-coating [20] (Figure 4A). The high reactivity of the hydrogel layer shortly after the coating procedure toward amines allowed the covalent attachment of BG-PEG-NH_2 by linkage of the amine group to the isocyanate group. The BG-modified surface of the glass slide was incubated with YFP-OSM or SNAP-YFP-OSM. Binding of the YFP-labeled cytokines was analyzed with a fluorescence scanner (Figure 4B). As a consequence of silanization and *s*P(EO-*stat*-PO) coating, no unspecific binding of YFP-OSM to the BG-modified surface was detected. The strong fluorescence of the surface area that was incubated with SNAP-YFP-OSM indicates a specific binding mediated by coupling of the SNAP-tag to benzylguanine.

3.3. Proof of Directed Coupling of SNAP-YFP Cytokines to BG-Modified Beads. The enterokinase cleavage site introduced between the SNAP-tag and YFP enabled us to unambiguously prove the directed coupling of SNAP-YFP cytokines to BG-modified beads (Figure 5A). BG-beads were incubated with SNAP-YFP-OSM or SNAP-YFP-IL-6. After the coupling reaction, a fraction of the beads was treated with the protease enterokinase. Subsequently, beads were incubated with PE-conjugated OSM or IL-6 antibodies, respectively. YFP and PE fluorescence of the beads were measured by flow cytometry. The results are summarized in Figure 5B. Enterokinase treatment reduces the YFP and PE fluorescence of the SNAP-YFP-cytokine beads by more than 80% indicating that the YFP-cytokine has been cleaved off from the bead surface by the protease. This result clearly shows that the SNAP-YFP-cytokines are bound to the bead surface by directed coupling via the SNAP-tag. Furthermore, the fact that the immobilized cytokines are accessible to the protease indicates that the immobilized cytokines are exposed on the bead surface. Remaining fluorescence of the beads after enterokinase treatment might reflect unspecifically bound protein, incomplete protease cleavage, or both.

3.4. Biological Activities of Immobilized SNAP-YFP-Cytokines. The activities of SNAP-YFP-cytokine beads were analyzed in cell culture. Beads were incubated with medium for 1 h under cell culture conditions. Subsequently, the activities of the supernatants of

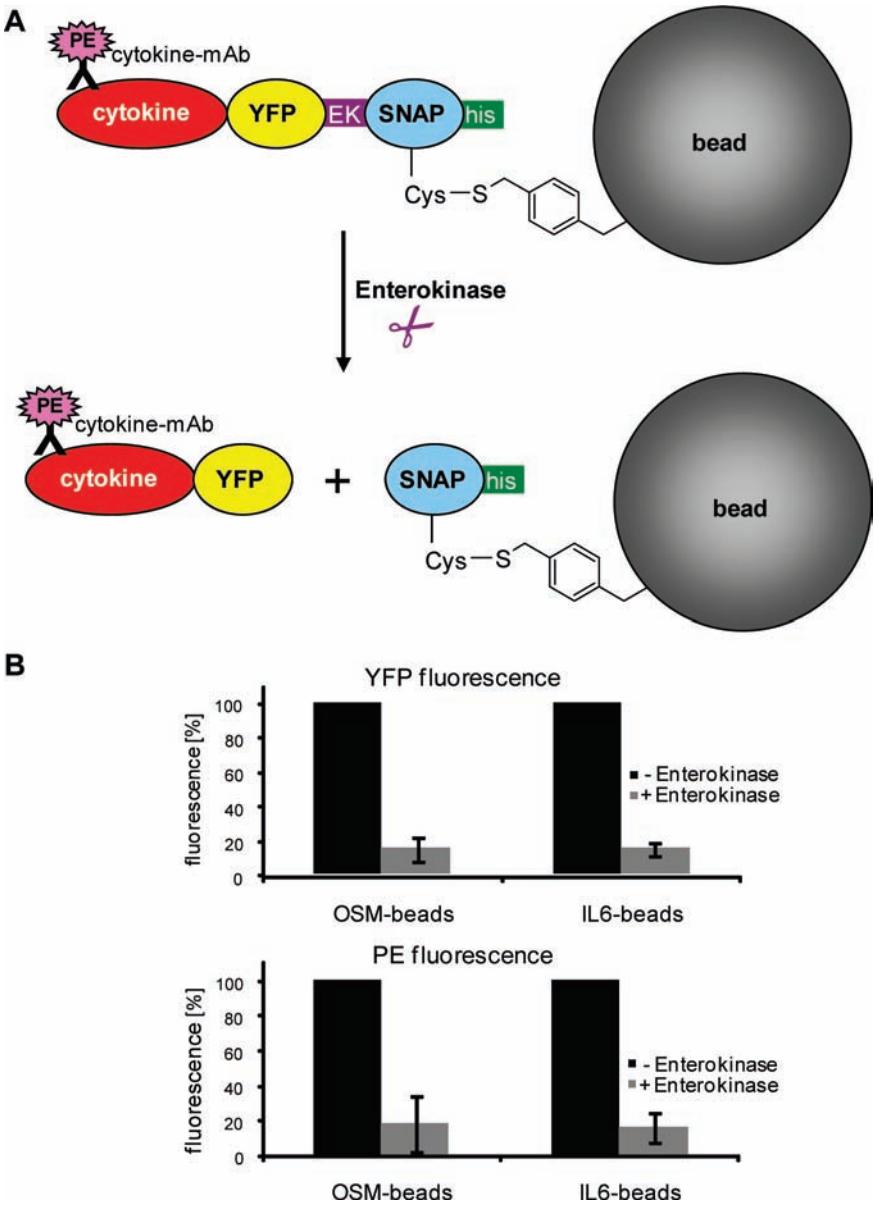


Figure 5. Proof of directed coupling of SNAP-YFP-cytokines. (A) Cleavage of the immobilized SNAP-YFP-cytokine by enterokinase releases the YFP-cytokine moiety. his, his-tag; SNAP, SNAP-tag; EK, enterokinase recognition site; YFP, yellow fluorescent protein. (B) SNAP-YFP-cytokine beads were incubated with enterokinase (0.02 U/μL) for 16 h at 4 °C. Beads were incubated with the respective PE-conjugated cytokine antibody and analyzed by flow cytometry f or PE and YFP fluorescence. Mean fluorescence of the beads is depicted in the bar chart. Fluorescence of beads without enterokinase was set to 100%.

the beads and the beads themselves were analyzed. The Western blot in Figure 6A shows that SNAP-YFP-IL-6 beads induce STAT3 phosphorylation in HepG2 cells, whereas the supernatant does not. This experiment shows that IL-6 immobilized through the SNAP-tag on BG-beads is biologically active. The observed response does not result from released cytokine because the supernatant of the preincubation of the beads is devoid of any activity. Empty beads show no activity. Interestingly, the time courses of phosphorylation induced by free IL-6 and immobilized IL-6 differ. A similar experiment was performed with free and immobilized SNAP-YFP-OSM (Figure 6B). In addition to STAT3, ERK phosphorylation was analyzed. Again the phosphorylation induced by the beads is delayed in comparison to the free cytokine. Supernatants of the SNAP-YFP-OSM beads show only very low activity indicating that the response mainly results from the immobilized cytokine and not from cytokine released from the beads.

3.5. Interaction of SNAP-YFP-OSM Beads with Cells Expressing gp130-CFP. OSM signals through the cytokine receptors gp130 and OSMR. HEK293 cell were transiently transfected with an expression vector encoding internalization-deficient (id) gp130 fused with the cyan fluorescent protein (gp130id-CFP). The lack of the internalization motif of gp130 increases the cell surface expression of the receptor. Nonlabeled OSMR was cotransfected. These cells were incubated with SNAP-YFP-OSM and after fixation analyzed by confocal microscopy (Figure 7A). Surface staining was observed after 30 min that increases during the following 60 min indicating the binding of SNAP-YFP-OSM to the cell surface receptors.

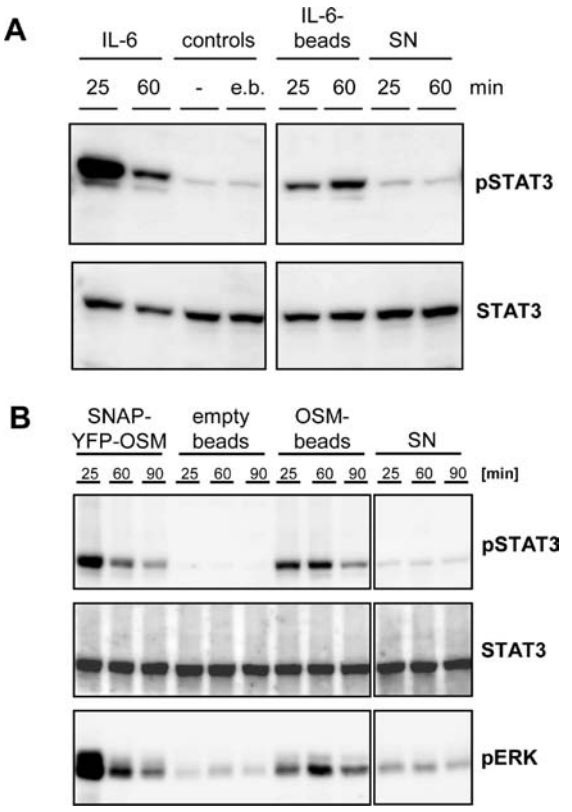


Figure 6. Biological activities of SNAP-YFP-cytokine beads. (A) SNAP-YFP-IL-6 beads were incubated with medium for 60 min at 37 °C. HepG2 cells were stimulated with the incubation supernatant (SN) or with the SNAP-YFP-IL-6 beads (IL-6-beads). In parallel, cells were stimulated with IL-6 (1 nM), incubated with medium alone (−) or empty beads (e.b.). Twenty-five minutes after stimulation, cells were lysed. STAT3 phosphorylation was analyzed by Western blotting (pSTAT3). Detection of total STAT3 served as a loading control. (B) In an experiment similar to that described in A, the activity of SNAP-YFP-OSM-beads was compared with free SNAP-YFP-OSM. ERK phosphorylation was also analyzed (pERK). Representative examples of three independent experiments are shown.

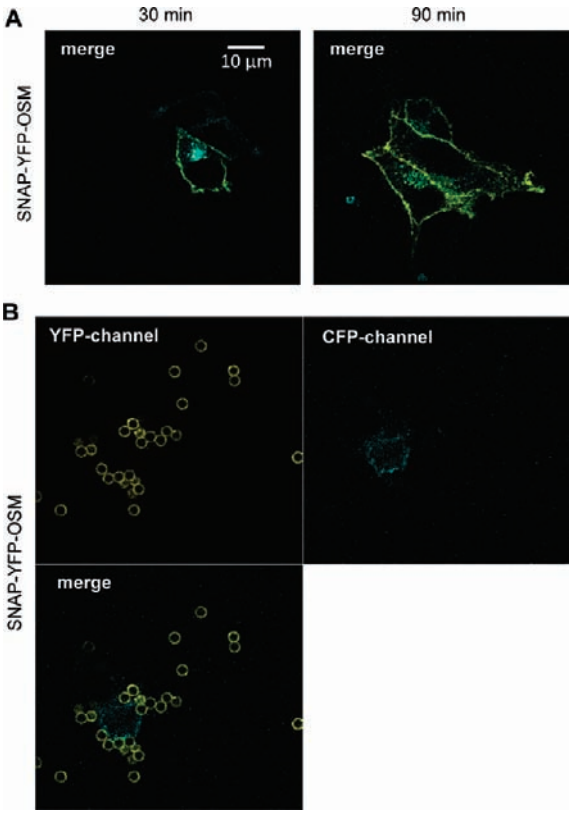


Figure 7. Confocal analysis of cell surface-binding of SNAP-YFP-OSM and SNAP-YFP-OSM beads. (A) HEK293 cells were transiently transfected with gp130id-CFP and OSMR. Cells were incubated with SNAP-YFP-OSM (1 nM) for the indicated times and subsequently fixed for microscopy. Images were taken by confocal laser-scanning microscopy. A merge of the YFP and CFP channels is shown. (B) The same experiment as that described in A was performed with SNAP-YFP-OSM beads. The cells were fixed after 60 min of incubation. Representative examples of three independent experiments are shown.

When the same cells were incubated with SNAP-YFP-OSM beads, enrichment of the beads around a transfected cell was observed (Figure 7B). The image of the CFP channel shows that the cell encompasses the beads to some extent, suggesting an interaction of the cell surface receptors with the SNAP-YFP-OSM beads.

3.6. Effect of SNAP-YFP-Cytokine Beads on the Subcellular Distribution of STAT3-CFP. Tyrosine phosphorylation of STAT3 in response to IL-6 and related cytokines leads to nuclear accumulation of the transcription factor. Murine embryonic fibroblasts (MEFs) lacking endogenous STAT3 ($MEF^{\Delta/\Delta}$) were stably transfected with STAT3 fused to the cyan fluorescent protein (STAT3-CFP). Since MEFs do not express the IL-6 receptor α-subunit (IL-6Rα), these cells respond to IL-6 only in the presence of soluble IL-6Rα (sIL-6Rα). Therefore, the time-point of stimulation is defined by the addition of sIL-6Rα.

$MEF^{\Delta/\Delta}$-STAT3-CFP cells were seeded on coverslips and analyzed under cell culture conditions at the confocal microscope. Upon stimulation with SNAP-YFP-IL-6 beads in the presence of sIL-6Rα, nuclear translocation of STAT3 during 60 min of observation is clearly visible (Figure 8A). After 60 min, a z-stack of sections was recorded and displayed as a three-dimensional (3D) image (Figure 8B). The image demonstrates that all cells showing nuclear accumulation of STAT3-CFP are in contact with SNAP-YFP-IL-6 beads. The confocal images shown in Figure 8C were made from fixed samples. Cells without contact to beads in the neighborhood of stimulated cells do not show any nuclear accumulation of STAT3-CFP. The right image shows that a bead close to cells but without contact does not stimulate the surrounding cells. These observations demonstrate that there is no significant release of free cytokine from the beads. Interestingly, a single bead−cell contact is sufficient for stimulation (left image).

In a similar experiment, HEK293-STAT3-CFP cells were incubated with SNAP-YFP-OSM beads. The 3D image after 90 min of stimulation shows nuclear accumulation of STAT3 (Figure 8D) and formation of nuclear bodies as described earlier.[10] In particular, after rotation of the image by 180° it is clearly visible that all stimulated cells are in close contact with SNAP-YFP-OSM beads.

On rare occasions, an accumulation of STAT3-CFP at the cell membrane engulfing a SNAP-YFP-IL-6 bead is visible (Figure 9, arrowhead). In this cell, nuclear accumulation of STAT3-CFP is to some extent inhibited.

4. DISCUSSION

In this study, we presented a versatile method for the directed covalent immobilization of proteins on surfaces which includes

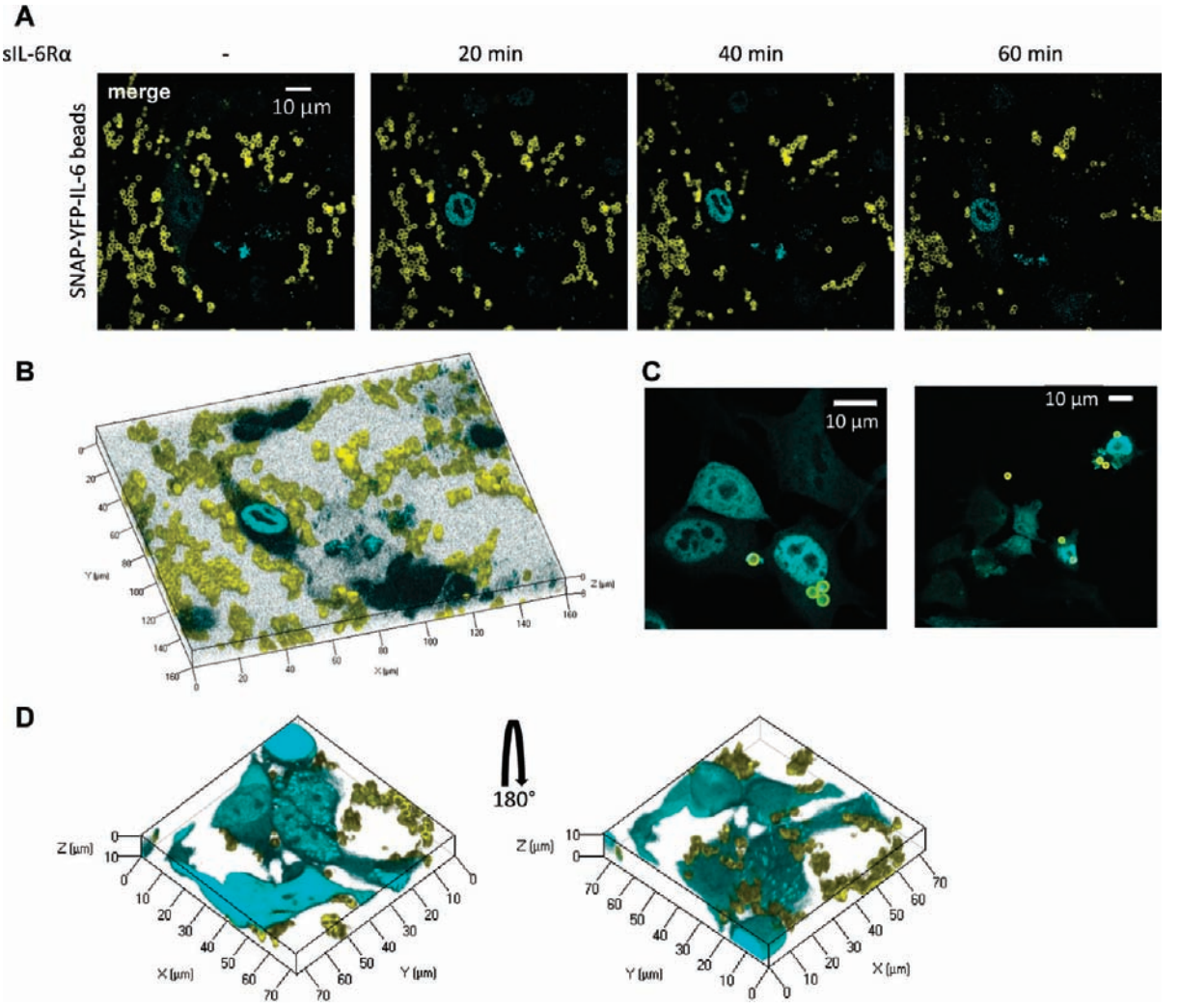


Figure 8. Analysis of SNAP-YFP-cytokine beads by confocal live-cell imaging. (A) MEF$^{\Delta/\Delta}$-STAT3-CFP cells were incubated with SNAP-YFP-IL-6 beads under cell culture conditions at the confocal microscope. Stimulation of the cells was initiated by the addition of sIL-6Rα (0.5 μg/mL), and images were taken at the indicated times. (B) A z-stack of images after 60 min of stimulation from the experiment shown in A is depicted as a 3D representation. (C) Another experiment, as described in A, was performed, and the samples were fixed after 30 min of stimulation. Only cells in contact with SNAPYFP-IL-6 beads show nuclear accumulation of STAT3-CFP (left and right image), and contact with a single bead is sufficient (left image). A bead close to cells but without contact is not sufficient for stimulation (right image). (D) HEK293-STAT3-CFP cells were incubated with SNAP-YFP-OSM beads for 90 min. A z-stack of images is depicted as 3D representations. All experiments have been repeated at least 3 times. Representative examples are shown.

the convenient and reliable control of efficiency and orientation of coupling. The method is based on the use of the SNAP-tag for immobilization on benzylguanine-modified surfaces.[25] The SNAP-tag is followed by a recognition site for the protease enterokinase, a YFP-tag, and finally the protein of interest. In addition, a his-tag was fused to the N-terminus for purification purposes. The enzyme-like activity of the SNAP-tag has the advantage of performing the coupling reaction under mild conditions without affecting protein structure and function.[23] The 1:1 stoichiometry of fluorescent label and protein of interest in the fusion protein allows quantification of the relative amount of immobilized protein even when different proteins of interest are analyzed such as SNAP-YFP-OSM and SNAP-YFP-IL-6 characterized in this study.

Directed coupling through a tag versus random chemical coupling of a protein of interest has the great advantage that the site of coupling on the protein is well-defined, and inactivation can be prevented. The tag used for coupling can be arranged in a way that protein function will not be affected. For the cytokines of the IL-6 family, it is known that the C-terminus is involved in receptor recognition.[26] Therefore, the tags were fused to the N-terminus of the protein. Indeed, characterization of the purified tagged fusion proteins revealed no difference in bioactivity compared to that of the nontagged cytokines. For proteins with a functionally important N-terminus, a C-terminal tag with YFP-EK-SNAP-his should be considered. The array of tags also serves as a spacer between surface and cytokine. The resulting exposition and flexibility of the cytokine facilitates receptor complex formation on the cell surface. This is of particular importance for IL-6 where two molecules of cytokine are needed to form a stable receptor complex.[8] Nevertheless, restriction of receptor movement can alter the cellular response.[27]

A general issue in directed protein immobilization on surfaces is the ratio of desired site-specific and covalent coupling versus unspecific adsorptive binding. The latter will lead to a large fraction of inactive or misbehaving proteins. To discriminate

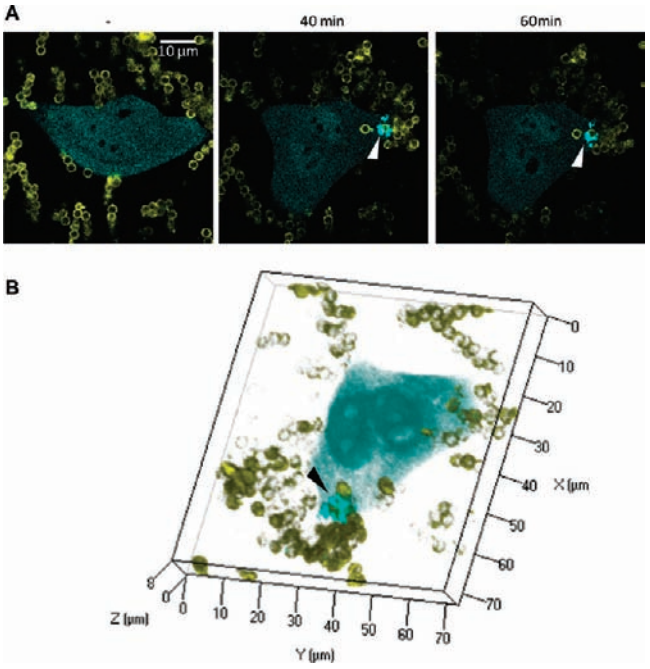


Figure 9. Unusual accumulation of STAT3-CFP around a SNAP-YFP-IL-6 bead. (A) MEF$^{\Delta/\Delta}$-STAT3-CFP cells were incubated with SNAP-YFP-IL-6 beads. Stimulation of the cells was initiated by the addition of sIL-6Rα (0.5 µg/mL), and confocal images were taken at the indicated times. (B) A z-stack of images after 60 min of stimulation from the experiment shown in A is depicted as a 3D representation. Arrowheads mark the site of STAT3-CFP accumulation.

between these two types of protein binding to surfaces, the enterokinase recognition site was introduced into the fusion protein. Treatment with enterokinase will in the case of directed coupling release the YFP-cytokine moiety of the fusion protein. Thus, a strong loss in fluorescence of the surface upon enterokinase treatment is indicative of directed, covalent coupling. In this study, materials with low protein adsorption were used. Therefore, a large fraction of fluorescence was released by enterokinase treatment clearly demonstrating oriented coupling. Depending on the application, materials with higher protein adsorption may be used. In such a situation, the cleavage assay will be of great value to quantify the amount of site-specifically immobilized protein. Moreover, one can envisage drug delivery systems, in which a protease can be used to release the protein of interest in a controlled manner.[28,29] In such a case, labeling with a fluorescent protein will be of great advantage to monitor the release process.

After establishing directed coupling, SNAP-YFP-cytokine beads were analyzed with respect to their bioactivity. Immobilized IL-6 and OSM activate STAT3 and ERK indicating that the immobilized cytokines are bioactive. Compared to the free cytokines, STAT3 and ERK phosphorylation in response to the immobilized cytokines is somewhat delayed and prolonged. After the stimulation of cells with beads, the immobilized cytokines may need more time to gain access to receptors than freely diffusing soluble cytokines. A similar delay of signaling was observed with cells seeded on growth-factor-modified surfaces.[3] ERK and STAT3 phosphorylation in response to stimulation with both free OSM and SNAP-YFP-OSM beads are transient indicating that feedback inhibition of the signaling pathway works for the free as well as the immobilized cytokine. Taken together, immobilization does not interfere with the basic signaling characteristics of the examined IL-6 family cytokines. Because covalently immobilized cytokines cannot be internalized, these findings indicate that internalization of the cytokine is neither necessary for activation of the signaling pathways nor for their attenuation. This conclusion is substantiated by earlier studies showing that feedback inhibition by SOCS3 rather than internalization is required for the transience of IL-6 signaling.[30] Thus, adequately immobilized cytokines of the IL-6 family can be used to functionalize surfaces of biomaterials and to investigate signal transduction. Accordingly, it has been shown that immobilized LIF is able to maintain the undifferentiated state of murine embryonic stem cells.[31,32] For growth factors that signal through receptor tyrosine kinases, endocytosis of the receptor complex seems to be more important for signaling and downregulation.[33] Therefore, immobilization of these kinds of mediators has a stronger impact on the kinetics of the signal.[34]

Fluorescently labeled and properly immobilized cytokines are a valuable tool to study localized signaling events by confocal microscopy and live cell imaging. In the case of the use of SNAP-YFP-cytokine beads for microscopic studies, the fluorescence label fits two purposes: (i) it allows localization of the beads and (ii) provides information of the cytokine load. The latter information is not directly accessible when nonfluorescent proteins are immobilized on fluorescent beads.[35] In a first approach, we studied the response of cells transfected with gp130-CFP or STAT3-CFP to stimulation with SNAP-YFP-cytokine beads. Accumulation of receptors was observed at the sites where beads contacted the cells. As a downstream response, nuclear accumulation of STAT3-CFP could be clearly detected. These experiments clearly show that STAT3 finds its way into the nucleus after activation at the plasma membrane and does not require directed transport through the endocytotic pathway. This does not exclude that STAT3 is also activated at signaling endosomes in response to stimulation with free cytokines,[36] but it seems that there is no strict requirement of signaling endosomes for STAT3-signaling in response to cytokines of the IL-6 family. However, concerning the high cytokine load of the beads some release of bioactive cytokine by, e.g., proteolytic cleavage after receptor binding cannot be entirely excluded.

Endocytosis of beads is restricted to nanoparticles with diameters in the submicrometer range because the vesicles formed during the process have a diameter of 100−500 nm.[37] Therefore, the 3 µm beads we used in this study can serve as a model system to mimic the activities of cytokines immobilized on larger surfaces, e.g., on biomaterials. However, occasionally we observed that the cell "tries" to engulf these particles (Figure 9) leading to mislocalization of signaling proteins such as STAT3. On the basis of these initial observations, it will be interesting to analyze signaling of cytokines immobilized to nanoparticles of different sizes by confocal microscopy.

AUTHOR INFORMATION

Corresponding Author

*Institut für Biochemie and Molekularbiologie, Universitätsklinikum RWTH Aachen, Pauwelsstrasse 30, 52074 Aachen, Germany. Phone: ++49 241 80 88860. Fax: ++49 241 80 82428. E-mail:mueller-newen@rwth-aachen.de.

ACKNOWLEDGMENT

This research project was supported by grants from the Deutsche Forschungsgemeinschaft (GRK 1035 "Biointerface"

and SFB 542, projects B12 and Z1). We thank Sabrina Korr for the generation of stable cell lines expressing SNAP-YFP-cytokines.

REFERENCES

(1) Nathan, C., and Sporn, M. (1991) Cytokines in context. *J. Cell Biol. 113*, 981–986.

(2) Chiu, L. L., and Radisic, M. (2010) Scaffolds with covalently immobilized VEGF and Angiopoietin-1 for vascularization of engineered tissues. *Biomaterials 31*, 226–241.

(3) Ito, Y. (2008) Covalently immobilized biosignal molecule materials for tissue engineering. *Soft Matter 4*, 46–56.

(4) Leclerc, C., Brose, C., Nouze, C., Leonard, F., Majlessi, L., Becker, S., von Briesen, H., and Lo-Man, R. (2008) Immobilized cytokines as biomaterials for manufacturing immune cell based vaccines. *J. Biomed. Mater. Res. A 86*, 1033–40.

(5) Wells, J. A., and de Vos, A. M. (1996) Hematopoietic receptor complexes. *Annu. Rev. Biochem. 65*, 609–34.

(6) Wang, X., Lupardus, P., Laporte, S. L., and Garcia, K. C. (2009) Structural biology of shared cytokine receptors. *Annu. Rev. Immunol. 27*, 29–60.

(7) Heinrich, P. C., Behrmann, I., Haan, S., Hermanns, H. M., Müller-Newen, G., and Schaper, F. (2003) Principles of interleukin (IL)-6-type cytokine signalling and its regulation. *Biochem. J. 374*, 1–20.

(8) Müller-Newen, G. (2003) The cytokine receptor gp130: faithfully promiscuous. *Sci. STKE 2003*, pe40.

(9) Skiniotis, G., Lupardus, P. J., Martick, M., Walz, T., and Garcia, K. C. (2008) Structural organization of a full-length gp130/LIF-R cytokine receptor transmembrane complex. *Mol. Cell 31*, 737–748.

(10) Herrmann, A., Sommer, U., Pranada, A. L., Giese, B., Küster, A., Haan, S., Becker, W., Heinrich, P. C., and Müller-Newen, G. (2004) STAT3 is enriched in nuclear bodies. *J. Cell Sci. 117*, 339–349.

(11) Kholodenko, B. N., Hancock, J. F., and Kolch, W. (2010) Signalling ballet in space and time. *Nat. Rev. Mol. Cell Biol. 11*, 414–426.

(12) McShane, M. P., and Zerial, M. (2008) Survival of the weakest: signaling aided by endosomes. *J. Cell Biol. 182*, 823–825.

(13) Chen, T. T., Luque, A., Lee, S., Anderson, S. M., Segura, T., and Iruela-Arispe, M. L. (2010) Anchorage of VEGF to the extracellular matrix conveys differential signaling responses to endothelial cells. *J. Cell Biol. 188*, 595–609.

(14) Kim, D. H., Smith, J. T., Chilkoti, A., and Reichert, W. M. (2007) The effect of covalently immobilized rhIL-1ra-ELP fusion protein on the inflammatory profile of LPS-stimulated human monocytes. *Biomaterials 28*, 3369–3377.

(15) Dittrich, E., Haft, C. R., Muys, L., Heinrich, P. C., and Graeve, L. (1996) A di-leucine motif and an upstream serine in the interleukin-6 (IL-6) signal transducer gp130 mediate ligand-induced endocytosis and down-regulation of the IL-6 receptor. *J. Biol. Chem. 271*, 5487–5494.

(16) Alexander, W. S., and Hilton, D. J. (2004) The role of suppressors of cytokine signaling (SOCS) proteins in regulation of the immune response. *Annu. Rev. Immunol. 22*, 503–529.

(17) Studier, F. W., Rosenberg, A. H., Dunn, J. J., and Dubendorff, J. W. (1990) Use of T7 RNA polymerase to direct expression of cloned genes. *Methods Enzymol. 185*, 60–89.

(18) Grabarek, Z., and Gergely, J. (1990) Zero-length crosslinking procedure with the use of active esters. *Anal. Biochem. 185*, 131–135.

(19) Helle, M., Boeije, L., de Groot, E., de Vos, A., and Aarden, L. (1991) Sensitive ELISA for interleukin-6. Detection of IL-6 in biological fluids: synovial fluids and sera. *J. Immunol. Methods 138*, 47–56.

(20) Groll, J., Ameringer, T., Spatz, J. P., and Moeller, M. (2005) Ultrathin coatings from isocyanate-terminated star PEG prepolymers: layer formation and characterization. *Langmuir 21*, 1991–1999.

(21) Giese, B., Roderburg, C., Sommerauer, M., Wortmann, S. B., Metz, S., Heinrich, P. C., and Müller-Newen, G. (2005) Dimerization of the cytokine receptors gp130 and LIFR analysed in single cells. *J. Cell Sci. 118*, 5129–5140.

(22) Herrmann, A., Vogt, M., Mönnigmann, M., Clahsen, T., Sommer, U., Haan, S., Poli, V., Heinrich, P. C., and Müller-Newen, G. (2007) Nucleocytoplasmic shuttling of persistently activated STAT3. *J. Cell Sci. 120*, 3249–3261.

(23) Keppler, A., Gendreizig, S., Gronemeyer, T., Pick, H., Vogel, H., and Johnsson, K. (2003) A general method for the covalent labeling of fusion proteins with small molecules in vivo. *Nat. Biotechnol. 21*, 86–89.

(24) Day, R. N., and Davidson, M. W. (2009) The fluorescent protein palette: tools for cellular imaging. *Chem. Soc. Rev. 38*, 2887–2921.

(25) Kindermann, M., George, N., Johnsson, N., and Johnsson, K. (2003) Covalent and selective immobilization of fusion proteins. *J. Am. Chem. Soc. 125*, 7810–7811.

(26) Krüttgen, A., Rose-John, S., Dufhues, G., Bender, S., Lütticken, C., Freyer, P., and Heinrich, P. C. (1990) The three carboxy-terminal amino acids of human interleukin-6 are essential for its biological activity. *FEBS Lett. 273*, 95–98.

(27) Salaita, K., Nair, P. M., Petit, R. S., Neve, R. M., Das, D., Gray, J. W., and Groves, J. T. (2010) Restriction of receptor movement alters cellular response: physical force sensing by EphA2. *Science 327*, 1380–1385.

(28) Hubbell, J. (2006) Matrix-bound growth factors in tissue repair. *Swiss Med. Wkly. 136*, 387–391.

(29) Sakiyama-Elbert, S. E., Panitch, A., and Hubbell, J. A. (2001) Development of growth factor fusion proteins for cell-triggered drug delivery. *FASEB J. 15*, 1300–1302.

(30) Thiel, S., Sommer, U., Kortylewski, M., Haan, C., Behrmann, I., Heinrich, P. C., and Graeve, L. (2000) Termination of IL-6-induced STAT activation is independent of receptor internalization but requires de novo protein synthesis. *FEBS Lett. 470*, 15–19.

(31) Alberti, K., Davey, R. E., Onishi, K., George, S., Salchert, K., Seib, F. P., Bornhauser, M., Pompe, T., Nagy, A., Werner, C., and Zandstra, P. W. (2008) Functional immobilization of signaling proteins enables control of stem cell fate. *Nat. Methods 5*, 645–650.

(32) Makino, H., Hasuda, H., and Ito, Y. (2004) Immobilization of leukemia inhibitory factor (LIF) to culture murine embryonic stem cells. *J. Biosci. Bioeng. 98*, 374–379.

(33) Kermorgant, S., and Parker, P. J. (2008) Receptor trafficking controls weak signal delivery: a strategy used by c-Met for STAT3 nuclear accumulation. *J. Cell Biol. 182*, 855–863.

(34) Ito, Y., Chen, G., Imanishi, Y., Morooka, T., Nishida, E., Okabayashi, Y., and Kasuga, M. (2001) Differential control of cellular gene expression by diffusible and non-diffusible EGF. *J. Biochem. 129*, 733–737.

(35) Kampmeier, F., Ribbert, M., Nachreiner, T., Dembski, S., Beaufils, F., Brecht, A., and Barth, S. (2009) Site-specific, covalent labeling of recombinant antibody fragments via fusion to an engineered version of 6-O-alkylguanine DNA alkyltransferase. *Bioconjugate Chem. 20*, 1010–1015.

(36) Xu, F., Mukhopadhyay, S., and Sehgal, P. B. (2007) Live cell imaging of interleukin-6-induced targeting of "transcription factor" STAT3 to sequestering endosomes in the cytoplasm. *Am. J. Physiol. Cell Physiol. 293*, C1374–C1382.

(37) Decuzzi, P., and Ferrari, M. (2008) The receptor-mediated endocytosis of nonspherical particles. *Biophys. J. 94*, 3790–3797.

Bioconjugate Chemistry

ARTICLE

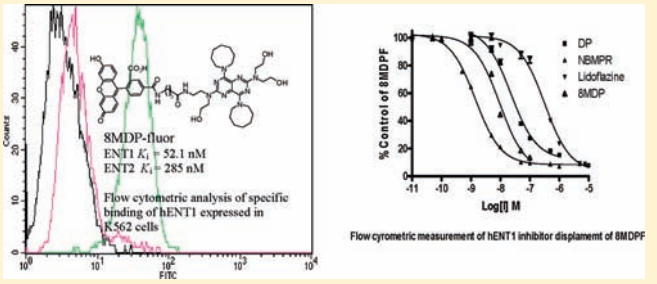
pubs.acs.org/bc

Design, Synthesis, and Evaluation of 2-Diethanolamino-4,8-diheptamethyleneimino-2-(*N*-aminoethyl-*N*-ethanolamino)-6-(*N*,*N*-diethanolamino)pyrimido[5,4-*d*]pyrimidine-fluorescein Conjugate (8MDP-fluor), As a Novel Equilibrative Nucleoside Transporter Probe

Wenwei Lin and John K. Buolamwini*

Department of Pharmaceutical Sciences, College of Pharmacy, 847 Monroe Avenue, Suite 327, University of Tennessee Health Sciences Center, Memphis, Tennessee 38163, United States

ABSTRACT: Nucleoside transporters are integral membrane glycoproteins that play critical roles in physiological nucleoside and nucleobase fluxes, and influence the efficacy of many nucleoside chemotherapy drugs. Fluorescent reporter ligands/substrates have been shown to be useful in the analysis of nucleoside transporter (NT) protein expression and discovery of new NT inhibitors. In this study, we have developed a novel dipyridamole (DP)-based equilibrative nucleoside transporter 1 (ENT1) fluorescent probe. The potent ENT1 and ENT2 inhibitor analogue of dipyridamole, 2,6-bis(diethanolamino)-4,8-diheptamethyleneiminopyrimido[5,4-*d*]pyrimidine (**4**, 8MDP), was modified to replace one β-hydroxyethyl group of the amino substituent at the 2-position with a β-aminoethyl group and then conjugated through the amino group to 6-(fluorescein-5-carboxamido)hexanoyl moiety to obtain a new fluorescent molecule, 2-diethanolamino-4,8-diheptamethyleneimino-2-(*N*-aminoethyl-*N*-ethanolamino)-6-(*N*,*N*-diethanolamino)pyrimido[5,4-d]pyrimidine-fluorescein conjugate, designated 8MDP-fluorescein (8MDP-fluor, **6**). The binding affinities of 8MDP-fluor at ENT1 and ENT2 are reflected by the uridine uptake inhibitory K_i values of 52.1 nM and 285 nM, respectively. 8MDP-fluor was successfully demonstrated to be a flow cytometric probe for ENT1 comparable to the nitrobenzylmercaptopurine riboside (NBMPR) analogue ENT1 fluorescent probe SAENTA-*X*8-fluorescein (SAENTA-fluor, **1**). This is the first reported dipyridamole-based ENT1 fluorescent probe, which adds a novel tool for probing ENT1, and possibly ENT2.



INTRODUCTION

Specialized integral membrane glycoproteins known as nucleoside transporters (NTs) are required for the influx and/or efflux of physiological nucleosides and many synthetic analogues.[1−3] Nucleoside transporters are classified into two families, namely, the equilibrative nucleoside transporter (ENT) and the concentrative nucleoside transporter (CNT) families, which are also known as the SLC29 and SLC28 gene families, respectively.[4,5] ENTs are the more widely distributed of the two NT families in mammalian tissues and possess broad substrate specificities for both purine and pyrimidine nucleosides, with ENT2 also efficiently transporting nucleobases.

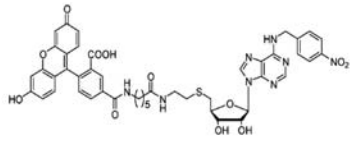
Nucleoside transporters play key roles in nucleoside and nucleobase uptake in salvage nucleotide synthesis and are also critical for the cellular uptake of several nucleoside analogues used in the treatment of cancers and viral infections, and serve as biomarkers of drug efficacy and drug resistance.[1,6,7] In addition, by regulating the concentration of adenosine available to cell surface adenosine receptors, they influence physiological processes such as cardiovascular activity, neurotransmission, and kidney function among others.[3,8−10] Distinct regional distributions of ENT1 and ENT2 have been observed in the human central nervous system.[11] It has also recently been shown that ENT1 and ENT2 play crucial roles in regulating the cystic fibrosis-related chloride transporter (CFTR) in human airway epithelia.[12] The inhibition of adenosine transport by NT inhibitors can potentially be exploited for site- and event-specific therapeutic approaches to treating ischemic heart disease and stroke.[13−18] Specific/selective inhibitors and ligands bound with high affinity are needed to track and quantify NT protein expression as well as to investigate their physiological roles and explore their therapeutic potential.

In the evaluation of nucleoside transporter inhibitors, radioligand uptake/displacement experiments have been widely used since nonradioactive methods are largely unavailable. Fluorescent probes are now available for ENT1,[19−21] but there are no such probes for other ENTs or CNTs. The fluorescent probes allow ligand−cell/protein interactions to be analyzed by flow cytometry, a facile technique that can eliminate problems associated with

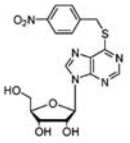
Received: February 9, 2011
Revised: April 11, 2011
Published: May 03, 2011

ACS Publications © 2011 American Chemical Society

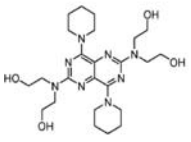
the use of radioactive materials. 5-(SAENTA)-*X*8-fluorescein (SAENTA-fluor, SF, **1**) is an example of an ENT1 fluorescent probe.[20] As an analogue of nitrobenzylmercaptopurine riboside (NBMPR, **2**), it has been used in several studies for nonradioactive assays of compounds' ENT1 inhibitory activities.[22−26]



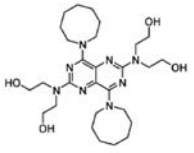
1 (SAENTA-*X*8-fluorescein, SF)



2 (NBMPR)



3 (Dipyridamole, DP)



4 (Heptamethyleneimine DP analog, 8MDP)

In our attempts to develop new ENT fluorescent probes, we have concentrated on the best compound we identified from a structure−activity relationship study of a series of dipyridamole (DP, **3**) analogues that we synthesized recently as ENT1 and ENT2 inhibitors.[23,27] This compound, the 8-membered ring dipyridamole analogue, compound **4** (8MDP) had K_i values of 0.97 nM and 90.8 nM against hENT1 and hENT2, respectively,[27] indicating much higher binding affinities than DP, which had K_i values of 14.5 nM and 308 nM against hENT1 and hENT2, respectively.[27] In the current study, we attached a fluorescent reporter group to a modified 8MDP to obtain a new fluorescent probe, which was successfully used in flow cytometric analysis of ENT1 protein expression as well as the measurement of relative affinities of ENT1 ligands.

EXPERIMENTAL PROCEDURES

Chemistry. Thin-layer chromatography (TLC) was conducted on silica gel plates (Analtech). Compounds were visualized by UV light (254 and 365 nm). 1D NMR spectra were recorded on a Varian Inova 500 MHz NMR instrument, using $CDCl_3$ or $(CD_3)_2SO$ as solvents and tetramethylsilane (TMS) as an internal standard. Flash column chromatography was performed on Fisher silica gel (170−400 mesh). Melting points were determined using a Fisher-Johns melting point apparatus and were reported uncorrected. Mass spectra were obtained on a Bruker-HP ESQUIRE Ion Trap LC/MS system. Elemental analyses were performed by Atlantic Microlab Inc., Norcross, GA. All solvents and reagents were purchased from Aldrich or other major chemical companies and used without further purification. All reactions were carried out under argon gas. Analytic high performance liquid chromatography (HPLC) was performed on a 150 mm × 2.00 mm Phenomenex Luna C_{18} column (3-μm particle size), protected by a Phenomenex SecurityGuard guard column (cartridge 4 mm × 2.00 mm internal diameter); and gradient CH_3CN/H_2O; 0 to 100 (15 min) with detection at 224 nm. The HPLC system consisted of an automated system with two Shimadzu LC-10AD VP liquid chromatography pumps, an SCL-10A VP system controller, a SIL-10AD VP auto injector, a sample cooler kept at 4 °C, and an SPD-M10A VP diode array detector. Chromatograms were acquired and analyzed with the Schimadzu Class-vp 7.3 SP1 software running on a Dell computer.

*2-Diethanolamino-4,8-diheptamethyleneimino-6-chloropyrimido[5,4-d]pyrimidine (**6**).* To a solution of 2,4,6,8-tetrachloropyrimido[5,4-*d*]pyrimidine (TCPP, **5**) (0.54 g, 2 mmol) in anhydrous THF (20 mL), heptamethyleneimine (1.06 mL, 8.4 mmol) was added. The reaction was stirred in an ice−water bath for 20 min, and then water (150 mL) was added to precipitate the reaction intermediate. After drying over a P_2O_5 desiccator, the intermediate was dissolved in dimethylsulfoxide (DMSO) (10 mL) with diethanolamine (3 mL, 30 mmol). The reaction was stirred at 120 °C for 3 days. The product, compound **6** (445 mg, 45% overall yield in 2 steps), was purified by flash silica gel chromatography (hexane/acetone = 5/1). Mp: 122−124 °C; MS (ESI) *m*/*z* 492 $(M + H)^+$, 514 $(M + Na)^+$. ^{1}H NMR (DMSO-d_6) δ 4.737 (t, 2H, exchanged with D_2O, 2 × OH, J = 5 Hz), 3.868 (m, 8H, 2 × $N(CH_2CH_2CH_2)_2CH_2$), 3.589 (t, 8H, $N(CH_2CH_2OH)_2$, J = 5 Hz), 1.796 (s, 8H, 2 × $N(CH_2CH_2CH_2)_2CH_2$), 1.534 (s, 8H, 2 × $N(CH_2CH_2CH_2)_2CH_2$), 1.495 (s, 4H, 2 × $N(CH_2CH_2CH_2)_2CH_2$). Anal. ($C_{24}H_{38}ClN_7O_2$) C, H, N.

*2-Diethanolamino-4,8-diheptamethyleneimino-6-[(N-dibenzylaminoethyl)-ethanolamino]-pyrimido[5,4-d]pyrimidine (**7**).* Compound **6** (370 mg, 0.75 mmol) was heated with 2-(2-dibenzylamino-ethylamino)-ethanol (3 g, 10 mmol) at 150 °C overnight. The product, compound **7** (130 mg, 23%), was purified by flash silica gel chromatography (hexane/acetone = 2/1) as a yellow sticky solid. MS (ESI) *m*/*z* 762 $(M + Na)^+$. ^{1}H NMR (DMSO-d_6) δ 7.306 - 7.251 (m, 10H, Ar), 7.181 (m, 4H, 2 × CH_2), 4.698 (s, 2H, disappeared after addition of D_2O, 2 × OH), 4.606 (s, 1H, disappeared after addition of D_2O, OH), 4.007−3.677 (*br* s, 8H, 2 × $N(CH_2CH_2CH_2)_2CH_2$), 3.575 (s, 12H, $N(CH_2CH_2OH)_2$, NCH_2CH_2OH), 3.520 (d, 4H, NCH_2CH_2ON, J = 6.5 Hz), 1.726 (*br* s, 8H, 2 × $N(CH_2CH_2CH_2)_2CH_2$), 1.496 (*br* d, 12H, 2 × $N(CH_2CH_2CH_2)_2CH_2$). LC retention time 5.804 min.

*2-Diethanolamino-4,8-diheptamethyleneimino-6-[(N-6-(fluorescein-6-carboxamido)-hexanoylaminoethyl)- ethanolamino]-pyrimido[5,4-d]pyrimidine (**8**).* The benzyl groups on compound **7** (100 mg, 0.13 mmol) were removed by hydrogenation in the presence of a catalytic amount of 10% Pd−C in methanol. After filtration and evaporation, the residue was reacted with commercially available 6-(fluorescein-5-carboxamido)hexanoic acid succinimidyl ester (10 mg, 17 μmol) in dimethylformamide (DMF) (3 mL) for 2 h. The solvent was removed under reduced pressure, and the residue was purified by sephadex LH-20 gel filtration with MeOH as the elution solvent to obtain the product **8** (7.2 mg, 41%) as a sticky gum. MS (ESI) *m*/*z* 1029 $(M - H)^-$. LC retention time 11.368 min.

Biological Testing. *[^{3}H]Uridine Uptake Experiments with K562 Cells Used to Determine ENT1 Inhibitory Activities of Test Compounds.* Human chronic myelogenous leukemia K562 cells (American Type Culture Collection (ATCC), Manassas, VA) were maintained in RPMI 1640 medium containing 10% fetal bovine serum and amikacin (60 mg/Liter), at 37 °C in 5% CO_2 and 95% air atmosphere. All experiments were done in sodium free uptake buffer (20 mM Tris/HCl, 3 mM K_2HPO_4, 1 mM $MgCl_2 \cdot 6H_2O$, 2 mM $CaCl_2$, 5 mM glucose, and 130 mM *N*-methyl-D-glucamine/HCl, pH 7.4). 5×10^5 K562 cells/sample were harvested and washed once with sodium free uptake buffer and resuspended in 50 μL of the same buffer. Uptake buffer

containing varying concentrations of compounds was then added, followed by 15 min of incubation, and then [^{3}H]uridine (37 mCi/mL) at a final concentration of 0.5 μM was added, followed by 2 min of incubation. Uptake was stopped by fast filtration to remove extracellular radioactive material, followed by 5 rapid washes with ice-cold uptake buffer. Cells were then solubilized overnight in 0.5 mL of 5% Triton X-100, and radioactivity was measured by β-scintillation counting.

[^{3}H]Uridine Uptake Experiments with PK15 Cells Stably Expressing Recombinant hENT2 Protein. The ENT2 cell line (porcine PK15 cells stably transfected with recombinant human ENT1 (hENT1)[28] was generously provided by Dr. Chung-Ming Tse, Johns Hopkins University. Cells were maintained in minimum essential (MEM) Alpha medium, with 5% fetal bovine serum, penicillin/streptomycin (50,000 units/L, 50 mg/L), and 0.1 mM nonessential amino acids, at 37 °C with 5% CO_2 and 95% air mixture. Cells were seeded at 40,000 cells/well in 48-well plates 24 h prior to uptake experiments. All experiments were performed at room temperature in sodium-free uptake buffer (140 mM *N*-methyl-D-glucamine, 5 mM HEPES, 5 mM KH_2PO_4, 1.0 mM $CaCl_2$, 1.0 mM $MgCl_2$, and 10 mM glucose, pH 7.4). Cells at 60−80% confluency were washed 3 times with uptake buffer, followed by 10 min of preincubation in the same buffer. Solutions containing varying concentrations of test compounds in uptake buffer were then added, followed by 15 min of incubation and addition of [^{3}H]uridine (0.2 μM, 37 mCi/mL specific activity). After 2 min of incubation with [^{3}H]uridine, cells were rapidly washed 3 times with ice-cold phosphate-buffered saline (pH 7.4) to stop uptake and remove extracellular [^{3}H]uridine. The cells were then solubilized overnight in 0.5 mL of 5% Triton X-100, and radioactivity was measured by a β-scintillation counter.

Uptake Inhibition Data Analysis. Percentage (%) inhibition was calculated for each sample by eq 1.

$$\%\ \text{inhibition} = 100\% - \frac{([^3\text{H}]\text{uridine}_s) \times 100\%}{([^3\text{H}]\text{uridine})} \quad (1)$$

where [^{3}H]uridine$_s$ is the amount of [^{3}H]uridine transported by hENT1 (or hENT2) in the presence of the test compound, and [^{3}H]uridine is the amount of [^{3}H]uridine transported in the absence of the test compound. The results were fed into the PRISM program (GraphPad, San Diego, CA) to derive concentration-inhibition curves. From these curves, the IC_{50} values were obtained and used to calculate the inhibition constant (K_i) value by eq 2.[29]

$$K_i = \text{IC}_{50}/(1 + [L]/K_L) \quad (2)$$

where [L] is the concentration of [^{3}H]uridine in individual tests (0.5 μM for hENT1; 0.2 μM for hENT2), and K_L is the K_m values for the uptake of [^{3}H]uridine by the corresponding transporter, 229 μM for hENT1 and 250 μM for hENT2.[28] The K_i values were used to compare the abilities of compounds to inhibit [^{3}H]uridine uptake and, for that matter, their inhibitory activity against hENT1 (or hENT2).

Flow Cytometry Assays. The compounds were tested to determine their ENT1 binding ability by a flow cytometric assay.[22] Briefly, K562 cells growing in RPMI 1640 medium were washed once, resuspended at 1.6×10^6 cells/mL in phosphate-buffered saline at pH 7.4, and incubated with SAENTA-fluorescein (30 nM) or 8MDP-fluor (40 nM) in the presence or absence of varying concentrations of test compounds at room temperature for 45 min. Flow cytometric measurements of cell-associated fluorescence were then performed with a FACSCalibur flow cytometer (Becton Dickinson, San Jose, CA) equipped with a 15 mW-argon laser (Molecular Resources Flow Cytometry Facility, University of Tennessee Health Sciences Center). In each assay, 5,000 cells were analyzed from suspensions of 4×10^5 cells/mL. The units of fluorescence were arbitrary channel numbers. Percentage (%) inhibition (i.e., ENT1-specific fluorescence in the presence of SAENTA-fluorescein or 8MDP-fluor) was calculated for each sample by eq 3.

$$\%\ \text{inhibition} = 100\% - \frac{(F_s) \times 100\%}{(F_f)} \quad (3)$$

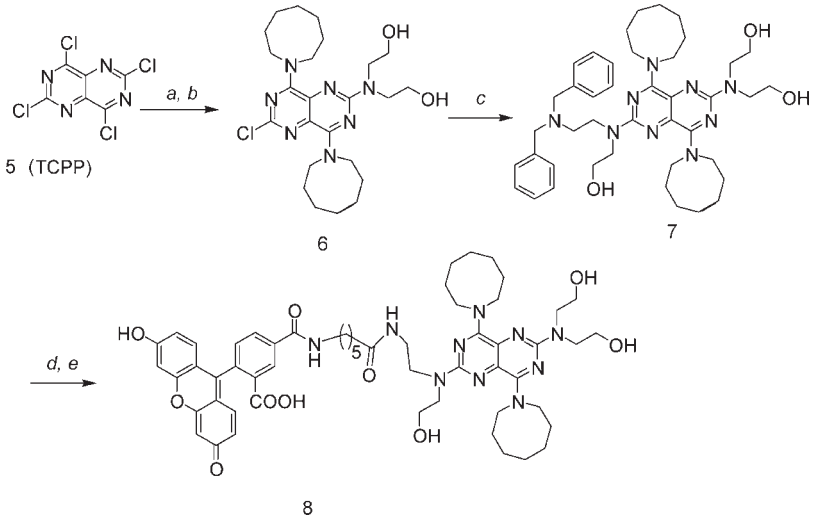
where F_s is the ENT1-specific fluorescence in the presence of test compounds, and F_f is the ENT1-specific fluorescence without the test compound, in mean channel numbers. The results were used to derive concentration-inhibition curves (Prism program) for IC_{50} values, which were used to calculate K_i values using eq 2, where [L] and K_L are the concentrations of the fluorescent probe (30 nM for SAENTA-fluor and 40 nM for 8MDP-fluor) and K_d values of the fluorescent probes (1.8 nM for SAENTA-fluor and 52.1 nM for 8MDP-fluor), respectively. The K_i values were used to compare the affinities of compounds for hENT1.

RESULTS

Chemistry. The synthetic route we followed, Scheme 1, resulted in the successful preparation of the new fluorescent probe. Starting with the reaction between 2,4,6,8-tetrachloropyrimido[5,4-*d*]pyrimidine (TCPP, **5**) with excess heptamethyleneimine (4.2-fold ratio) at 0 °C gave the 2,6-dichloro-4,8-diheptamethyleneimido intermediate. Reaction of the 2,6-dichloro intermediate with one equivalent of diethanolamine at 120 °C yielded the monochloro precursor compound **6** in overall yield of 45% for the two steps. Compound **6** was in turn reacted with 2-(2-dibenzylaminoethylamino)-ethanol at 150 °C to produce the protected amine compound, **7**. Removal of the benzyl groups of compound **7** was successfully effected by catalytic hydrogenation, which was followed by the reaction of the resulting primary amine with the activated fluorescein derivative, 6-(fluorescein-5-carboxamido)hexanoic acid succinimidyl ester to afford the target fluorescent probe, 8MDP-fluorescein conjugate, 8MDP-*X*8-fluorescein (8MDP-fluor, **8**) in 43% yield overall from the latter two steps.

Biology. *ENT1 and ENT2 Inhibitory Activities and 8MPD-Fluor.* For a probe to be useful, it must be bound by its intended molecular target(s) with high affinity, in this case ENT1 and ENT2. To assess this for the new fluorescent probe, we measured its ability to inhibit [^{3}H]uridine uptake by hENT1 expressed in K562 cells or recombinant hENT2 stably expressed in K15NTD cells. Dose−response experiments were carried out, and the IC_{50} values were used to derive inhibition constant (K_i) values according to eq 2, which are presented in Table 1 along with the K_i values of known equilibrative nucleoside transporter inhibitors that were also determined by the same methods, including dipyridamole and 8MDP (**4**, the most potent dipyridamole analogue ENT inhibitor reported to date). The results show that 8MDP-fluor (**8**) exhibited a reasonably high-affinity binding by hENT1 with a K_i value of 52.1 nM and a moderate-affinity binding by hENT2, with a K_i value of 285 nM, which is reasonable, considering that dipyridamole, the prototype ENT2 inhibitor, exhibited an ENT2 inhibitory K_i of 308 nM.

Scheme 1. Synthesis of 8MDP-Fluor (8)[a]



[a] Reagents: (a) heptamethyleneimine, anhydrous THF, ice−water bath; (b) diethanolamine, DMF, 120 °C; (c) 2-(2-dibenzylamino-ethylamino)-ethanol,[27] DMSO, 150 °C; (d) hydrogen, 10% Pd−C, MeOH; (e) 6-(fluorescein-5-carboxamido)hexanoic acid succinimidyl ester, DMF.

Table 1. hENT1 and hENT2 Inhibitory Activities of 8MPD, Its fluorescent Analogue 8MPD-F and Other Inhibitors

	hENT1 inhibitory activity		hENT2 inhibitory activity	
compound	% inhibition (at 10 μM)	K_i (nM)	% inhibition (at 10 μM)	K_i (nM)
DMSO	2.8 ± 0.1	NA[a]	0.0 ± 1.8	NA
9 (lidoflazine)	81.1 ± 0.1	573.8	43.2 ± 1.0	12,390
2 (NBMPR)	94.1 ± 0.1	0.65	90.1 ± 0.1	1,349
3 (dipyridamole)	97.4 ± 0.1	15.1	98.2 ± 0.2	308
4 (8MDP)	97.6 ± 0.1	0.97	98.9 ± 0.1	90.7
8 (8MDP-fluor)	99.6 ± 0.2	52.1	93.9 ± 0.1	285
1 (SAENTA-fluor)	92.6 ± 0.8	1.8	83.5 ± 0.4	4,436

[a] NA means not applicable.

8MDP-Fluor Exhibits Specific Staining of hENT1. To assess the effectiveness of 8MDP-fluor as a fluorescent probe, we compared it with SAENTA-fluorescein, which is used in flow cytometric analysis of ENT1 protein expression and testing of ENT1 ligands in our laboratory and by others.[22,26,30] Again, human CML K562 cells were used since they grow in suspension culture, which makes them highly suitable for use in flow cytometry experiments, unlike attached cells which have to be first detached and suspended for flow cytometry. As shown in Figure 1, the new 8DMP-fluor stained K562 cells in an ENT1-specific manner comparable to that by SAENTA-fluor. It took 40 nM concentration of 8DMP-fluor to obtain ENT1 staining comparable to that by 30 nM of SAENTA-fluor. This reflects the lower ENT1 binding affinity for 8MDP-F compared to that of SAENTA-fluor, as evident from Table 1. The interesting thing is that the higher concentration of 8DMP-fluor did not result in higher nonspecific staining as shown by staining in the presence of the standard ENT1 inhibitor NBMPR.

Comparison of 8MDP-Fluor and SAENTA-Fluor As Fluorescent Ligands for Use in Flow Cytometric Determination of the Relative Affinities of ENT1 Interacting Compounds. To test the potential utility of this new fluorescent molecule (8MDP-fluor) as a probe for assessing other molecules' ability to bind to ENT1, NBMPR, lidoflazine, dipyridamole, and 8MDP were used to displace 8MDP-fluor (8MDPF) from K562 cells in a concentration-dependent manner in flow cytometry experiments. For comparison, the same tests were performed with SAENTA-fluor (SF) as the fluorescent ligand. Radioligand binding studies have indicated that NBMPR, dipyridamole, and lidoflazine displace each other from ENT1.[31−33] Dipyridamole itself is fluorescent, with $Ex_{\lambda max}$ and $Em_{\lambda max}$ of 280 and 490 nm, respectively.[34] At the experimental dipyridamole concentrations and wavelengths used in the flow cytometric assay (Ex_{λ} = 488 nm and Em_{λ} = 533 nm), dipyridamole and 8MDP did not emit fluorescence that would interfere with the detection of bound 8MDP-fluor or SAENTA-fluor.

The dose-response displacement curves are shown in Figure 2, and the K_i values derived from them are presented in Table 2. Flow cytometric experiments using 8MDP-fluor as probe afforded K_i values of 0.81, 5.41, 12.9, and 181 nM for NBMPR, 8MDP, dipyridamole, and lidoflazine (**9**), respectively, whereas experiments that used SAENTA-fluor as the probe afforded K_i values of 0.43, 0.50, 8.18, and 279.9 nM, for NBMPR, 8MDP, dipyridamole and lidoflazine, respectively. Although the use of either the 8MDP-fluor or SAENTA-fluor as the probe indicated correctly the same relative order of ENT1 binding affinities for the inhibitors, it

dx.doi.org/10.1021/bc2000758 |*Bioconjugate Chem.* 2011, 22, 1221–1227

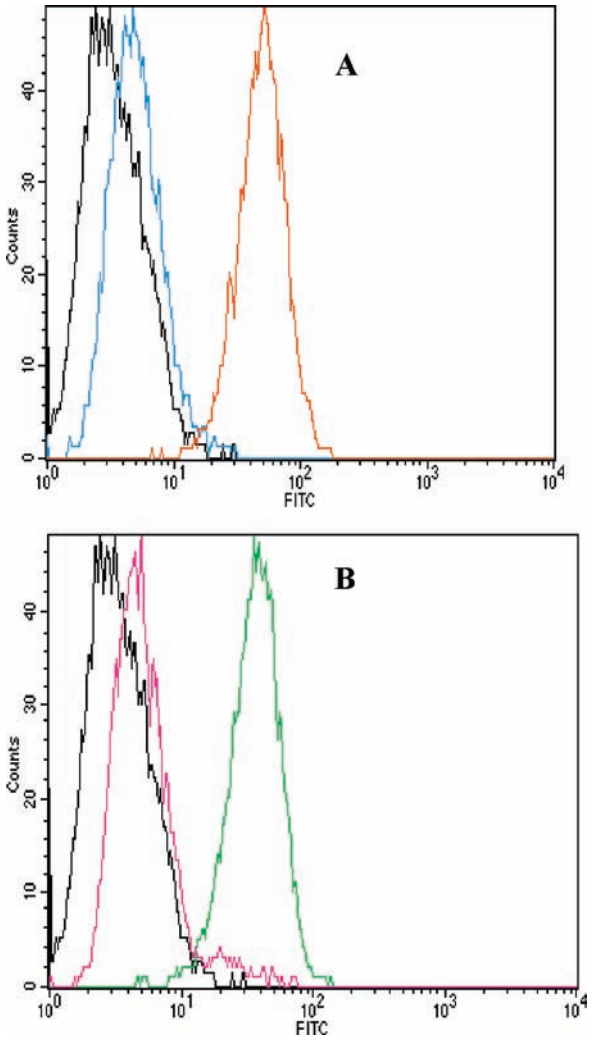
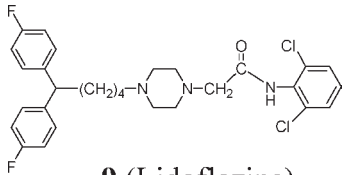


Figure 1. Flow cytometric histograms showing the ENT1 specific labeling in K562 leukemic cells by 8MDP-fluor (8MDPF, 40 nM; panel A) or SAENTA-fluorescein (SF, 30 nM; panel B). The binding of both fluorescent probes was effectively reversed by the presence of 10 μM NBMPR, the prototype ENT1 inhibitor, showing ENT1 affinity for the probes. Color-coding legend of histograms: black, K562 cells' autofluorescence; orange, K562 cells + 30 nM SF; blue, 30 nM SF + K562 cells +10 μM NBMPR; green line, K562 cells + 40 nM 8MDP-F; and red, K562 cells + 40 nM 8MDP-F + 10 μM NBMPR.

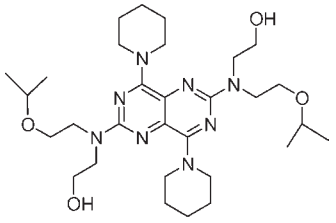
can be seen that the absolute K_i values differed depending on whether 8MDP-fluor or SAENTA-fluor was the fluorescent ligand.



9 (Lidoflazine)

DISCUSSION

Dipyridamole (DP, **3**) has displayed potent inhibitory activity against ENT1 (although not as good as NBMPR) and moderate inhibitory activity against ENT2.[35] It thus provides a good template for optimization to obtain more potent ENT1 and ENT2 inhibitors and probes since it is a clinically used drug. In the course of our structure−activity relationship (SAR) studies of DP analogues, we discovered that replacement of one each of the hydroxyl groups on each diethanolamine substituent at the 2- and 6-positions to give compound **6** had no detrimental effect on ENT1 binding activity but rather enhanced the binding affinity.[23] The high potency of compound **10** (ENT1 K_i = 4.3 nM; ENT2 K_i = 175 nM),[23,27] in which two of the hydroxyl groups of dipyridamole had been replaced by isopropoxy groups, suggested to us that the hydroxyl groups of dipyridamole provide possible attachment positions for reporter groups such as fluorophores. Thus, we took advantage of this opportunity to append a fluorescein group to the most potent dipyridamole analogue ENT1 and ENT2 inhibitor identified to date, compound **4** (8MPD).[23,27] To make the linkage resistant to hydrolysis, one of the hydroxyl groups of compound **4** was replaced by an amino group, which also provided an excellent nucleophilic handle (Scheme 1). The target probe, designated 8MDP-fluorescein conjugate (8MDP-fluor, **8**) was designed to attach the same fluorescent group used to synthesize SAENTA-fluorescein (**1**).[19,20]



10

In the synthesis, the key to achieving selective and sequential substitution of the different chlorines on the starting material, TCPP, was the control of reaction temperature, time, and reactant stoichiometries. The 4- or 8-position chlorine substituents are easier to substitute than the 2- and 6-position chlorines and were replaced at the low temperature of 0 °C, with the sparing of the 2- and 6-position chlorine substituents.

As might be expected, the attachment of a fluorescein moiety and replacement of O with NH in the new fluorescent probe (8MDP-fluor, **8**) significantly lowered inhibitory activities against hENT1 and hENT2, compared to that of the parent compound, 8MDP (**4**), but the fluorescent compound still retained enough potency to serve as an effective probe for ENT1. Interestingly, it still retained higher potency than dipyridamole as an ENT2 ligand and thus could potentially be developed as an ENT2 probe as well. This is not the case with SAENTA-fluor, which hENT2 binds with much lower affinity (K_i = 4,436 nM). Thus, unlike the 8MDP-fluor, SAENTA-fluor can serve as an effective hENT1 probe but not a probe for hENT2.

The results of the flow cytometric determination of the ability of other ENT1 inhibitors to displace 8MDP-fluor or SAENTA-fluor not only showed that the two fluorescent probes can both be used to correctly rank-order the relative affinities of ENT1 ligands but also showed interestingly that it was generally easier to displace SAENTA-fluor from hENT1 than it was to displace the new 8MDP-fluor. This could be due to the larger size of 8MDP-fluor relative to SAENTA-fluor. The only hENT1 inhibitor that deviated from this generalization was lidoflazine (**9**). The reason for this is not apparent, but might be related to possible different binding kinetics of the two fluorescent ligands and/or differences in their binding modes or sites relative to

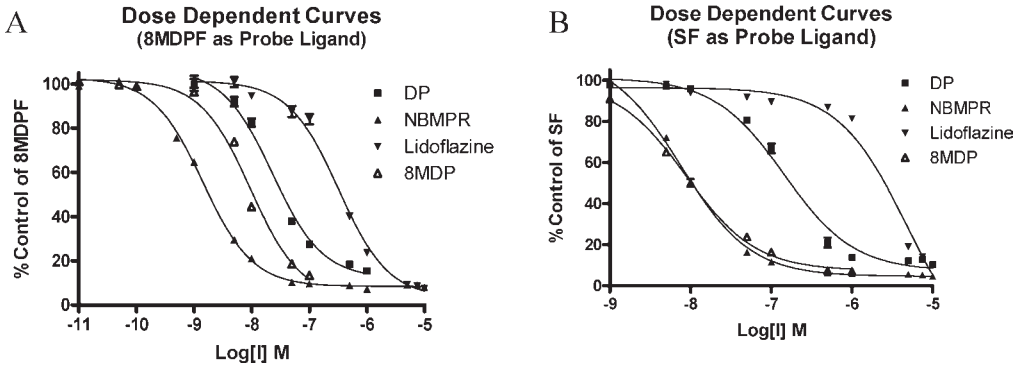


Figure 2. Dose-inhibition curves for the inhibition of 8MDP-fluor (A) or SAENTA-fluor (B) binding to hENT1 determined by a flow cytometric assay using K562 leukemic cells.

Table 2. Use of 8MDP-Fluor and SAENTA-Fluorescein As Ligands for Flow Cytometric Determination of Binding of Standard Inhibitors to hENT1 in K562 Cells

	8MDP-fluor as probe	SAENTA-fluor as probe
compound	K_i (nM)	K_i (nM)
9 (lidoflazine)	182	280
2 (NBMPR)	0.81	0.43
3 (dipyridamole, DP)	12.9	8.18
4 (8MDP)	5.41	0.50

lidoflazine binding. This observation might be worth a follow-up study.

In conclusion, we have synthesized and evaluated a new dipyridamole analogue-based fluorescent probe, which is a high-affinity ligand of both ENT1 and ENT2. We have demonstrated its ability to be an effective flow cytometry probe for the analysis of hENT1 protein expression and for the assessment of relative tightness of binding of compounds that interact with hENT1. Its significant binding to hENT2 suggests that it also has the potential to be used as an ENT2 fluorescent probe.

AUTHOR INFORMATION

Corresponding Author

*Phone: (901) 448-7533. Fax: (901) 448-6828. E-mail: jbuolamwini@uthsc.edu.

Notes

We have no conflicts of interest to report.

ACKNOWLEDGMENT

Financial support from the National Institutes of Health, grant number AI065372, is gratefully acknowledged. We are also grateful to Dr. C. M. Tse for kindly providing us with ENT2 cells.

REFERENCES

(1) Damaraju, V. L., Damaraju, S., Young, J. D., Baldwin, S. A., Mackey, J., Sawyer, M. B., and Cass, C. E. (2003) Nucleoside anticancer drugs: the role of nucleoside transporters in resistance to cancer chemotherapy. *Oncogene 22*, 7524–7536.

(2) Kong, W., Engel, K., and Wang, J. (2004) Mammalian nucleoside transporters. *Curr. Drug Metab. 5*, 63–84.

(3) King, A. E., Ackley, M. A., Cass, C. E., Young, J. D., and Baldwin, S. A. (2006) Nucleoside transporters: from scavengers to novel therapeutic targets. *Trends Pharmacol. Sci. 27*, 416–25.

(4) Young, J. D., Yao, S. Y., Sun, L., Cass, C. E., and Baldwin, S. A. (2008) Human equilibrative nucleoside transporter (ENT) family of nucleoside and nucleobase transporter proteins. *Xenobiotica 38*, 995–1021.

(5) Pastor-Anglada, M., Cano-Soldado, P., Errasti-Murugarren, E., and Casado, F. J. (2008) SLC28 genes and concentrative nucleoside transporter (CNT) proteins. *Xenobiotica 38*, 972–994.

(6) Pastor-Anglada, M., Felipe, A., and Casado, F. J. (1998) Transport and mode of action of nucleoside derivatives used in chemical and antiviral therapies. *Trends Pharmacol. Sci. 10*, 424–430.

(7) Zhang, J., Visser, F., King, K. M., Baldwin, S. A., Young, J. D., and Cass, C. E. (2007) The role of nucleoside transporters in cancer chemotherapy with nucleoside drugs. *Cancer Metastasis Rev. 26*, 85–110.

(8) Noji, T., Karasawa, A., and Kusaka, H. (2004) Adenosine uptake inhibitors. *Eur. J. Pharmacol. 495*, 1–16.

(9) Elwi, A. N., Damaraju, V. L., Baldwin, S. A., Young, J. D., Sawyer, M. B., and Cass, C. E. (2006) Renal nucleoside transporters: physiological and clinical implications. *Biochem. Cell Biol. 84*, 844–58.

(10) Loffler, M., Morote-Garcia, J. C., Eltzschig, S. A., Coe, I. R., and Eltzschig, H. K. (2007) Physiological roles of vascular nucleoside transporters. *Arterioscler., Thromb., Vasc. Biol. 27*, 1004–1013.

(11) Jennings, L. L., Hao, C., Cabrita, M. A., Vickers, M. F., Baldwin, S. A., Young, J. D., and Cass, C. E. (2001) Distinct regional distribution of human equilibrative nucleoside transporter proteins 1 and 2 (hENT1 and hENT2) in the central nervous system. *Neuropharmacology 40*, 722–731.

(12) Szkotak, A. J., Ng, A. M., Man, S. F., Baldwin, S. A., Cass, C. E., Young, J. D., and Duszyk, M. (2003) Coupling of CFTR-mediated anion secretion to nucleoside transporters and adenosine homeostasis in Calu-3 cells. *J. Membr. Biol. 192*, 169–179.

(13) Van Belle, H. (1995) Adenosine Uptake Blockers for Cardioprotection, in *Adenosine and Adenine Nucleotides: from Molecular Biology to Integrative Physiology* (Belardinelli, L., and Pelleg, A., Eds.) pp 373−378, Kluwer, Boston, MA.

(14) Abd-Elfattah, A.-S., Maddox, R. P., Jessen, M. E., Rebeyka, I. M., and Wechsler, A. S. (1998) Role of nucleoside transport and purine release in a rabbit model of myocardial stunning. *Mol. Cell. Biochem. 180*, 145–151.

(15) Zhu, Z., Hofmann, P. A., and Buolamwini, J. K. (2007) Cardioprotective effects of novel tetrahydroisoquinoline analogs of nitrobenzylmercaptopurine riboside in an isolated perfused rat heart model of acute myocardial infarction. *Am. J. Physiol. Heart. Circ. Physiol. 292*, H2921–H2926.

(16) Rudolphi, K. A., Schubert, P., Parkinson, F. E., and Fredholm, B. B. (1992) Neuroprotective role of adenosine in cerebral ischemia. *Trends Pharmacol. Sci. 13*, 439–445.

(17) Parkinson, F. E., Rudolphi, K. A., and Fredholm, B. B. (1994) Propentofylline: a nucleoside transport inhibitor with neuroprotective effects in cerebral ischemia. *Gen. Pharmacol. 25*, 1053–1058.

(18) Parkinson, F. E., Zhang, Y. W., Shepel, P. N., Greenway, S. C., Peeling, J., and Geiger, J. D. (2000) Effects of nitrobenzylthioinosine on neuronal injury, adenosine levels and adenosine receptor activity in rat forebrain ischemia. *J. Neurochem. 75*, 795–802.

(19) Jamieson, G. P., Brocklebank, A. M., Snook, M. B., Sawyer, W. H., Buolamwini, J. K., Paterson, A. R., and Wiley, J. S. (1993) Flow cytometric quantitation of nucleoside transporter sites on human leukemic cells. *Cytometry 14*, 32–38.

(20) Buolamwini, J. K., Wiley, J. S., Robins, M. J., Craik, J. D., Cass, C. E., Gati, W. P., and Paterson, A. R. P. (1994) Conjugates of fluorescein and SAENTA (5′-*S*-(2-aminoethyl)-N^6-(4-nitrobenzyl)-5′-thioadenosine): flow cytometry probes for the *Es* transporter elements of the plasma membrane. *Nucleosides Nucleotides 13*, 737–751.

(21) Robins, M. J., Peng, Y., Damaraju, V. L., Mowles, D., Barron, G., Tackaberry, T., Young, J. D., and Cass., C E. (2010) Improved syntheses of 5′-S-(2-aminoethyl)-6-N-(4-nitrobenzyl)-5′-thioadenosine (SAENTA), analogues, and fluorescent probe conjugates: analysis of cell-surface human equilibrative nucleoside transporter 1 (hENT1) levels for prediction of the antitumor efficacy of gemcitabine. *J. Med. Chem. 53*, 6040–6053.

(22) Zhu, Z., Furr, J., and Buolamwini, J. K. (2003) Synthesis and flow cytometric evaluation of novel 1,2,3,4-tetrahydroisoquinoline conformationally constrained analogues of nitrobenzylmercaptopurine riboside (NBMPR) designed for probing its conformation when bound to the *es* nucleoside transporter. *J. Med. Chem. 46*, 831–837.

(23) Lin, W., and Buolamwini, J. K. (2007) Synthesis, flow cytometric evaluation and identification of highly potent dipyridamole analogs as equilibrative nucleoside transporter 1 (ENT1) inhibitors. *J. Med. Chem. 50*, 3906–3920.

(24) Zhu, Z., and Buolamwini, J. K. (2008) Constrained NBMPR analogue synthesis, pharmacophore mapping and 3D-QSAR modeling of equilibrative nucleoside transporter 1 (ENT1) inhibitory activity. *Bioorg. Med. Chem. 16*, 3848–3865.

(25) Gupte, A., and Buolamwini, J. K. (2007) Novel C2-purine position analogs of nitrobenzylmercaptopurine riboside as human equilibrative nucleoside transporter 1 inhibitors. *Bioorg. Med. Chem. 15*, 7726–7737.

(26) Gupte, A., and Buolamwini, J. K. (2004) Novel halogenated nitrobenzylthioinosine analogs as es nucleoside transporter inhibitors. *Bioorg. Med. Chem. Lett. 14*, 2257–2260.

(27) Lin, W. (2006) Studies on Dipyridamole and Draflazine Analogs as Inhibitors of human Equilibrative Nucleoside Transporters hENT1 and hENT2, Ph.D. Dissertation, University of Tennessee Health Science Center, Memphis, TN.

(28) Ward, J. L., Sherali, A., Mo, Z. P., and Tse, C. M. (2000) Kinetic and pharmacological properties of cloned human equilibrative nucleoside transporters, ENT1 and ENT2, stably expressed in nucleoside transporter-deficient PK15 cells. ENT2 exhibits a low affinity for guanosine and cytidine but a high affinity for inosine. *J. Biol. Chem. 275*, 8375–8381.

(29) Cheng, Y., and Prusoff, W. H. (1973) Relationship between the inhibition constant (K_i) and the concentration of inhibitor which causes 50% inhibition (IC_{50}) of an enzymatic reaction. *Biochem. Pharmacol. 22*, 3099–3108.

(30) Addo, J. K., and Buolamwini, J. K. (2004) Design, synthesis, and evaluation of 5′-S-aminoethyl-N(6)- azidobenzyl-5′-thioadenosine biotin conjugate: a bifunctional photoaffinity probe for the es nucleoside transporter. *Bioconjugate Chem. 15*, 536–540.

(31) Hammond, J. R. (1991) Kinetic analysis of ligand binding to the Ehrlich cell nucleoside transporter: pharmacological characterization of allosteric interactions with the [3H]nitrobenzylthioinosine binding site. *Mol. Pharmacol. 39*, 771–779.

(32) Jones, K. W., and Hammond, J. R. (1992) Heterogeneity of [^{3}H]dipyridamole binding to CNS membranes: correlation with [^{3}H]nitrobenzylthioinosine binding and [3H]uridine influx studies. *J. Neurochem. 59*, 1363–1371.

(33) Deckert, J., Hennemann, A., Bereznai, B., Fritze, J., Vock, R., Marangos, P. J., and Riederer, P. (1994) [^{3}H]dipyridamole and [^{3}H]nitrobenzylthioinosine binding sites at the human parietal cortex and erythrocyte adenosine transporter: a comparison. *Life Sci. 55*, 1675–1682.

(34) Vargas, F., Rivas, C., Fuentes, A., Tse Cheng, A., and Velutini, G. G. (2002) The photochemistry of dipyridamole. *J. Photochem. Photobiol. 153*, 237–243.

(35) Buolamwini, J. K. (1997) Nucleoside transport inhibitors: structure-activity relationships and potential therapeutic applications. *Curr. Med. Chem. 4*, 35–66.

Bioconjugate Chemistry

ARTICLE

pubs.acs.org/bc

Well-Controlled Cationic Water-Soluble Phospholipid Polymer−DNA Nanocomplexes for Gene Delivery

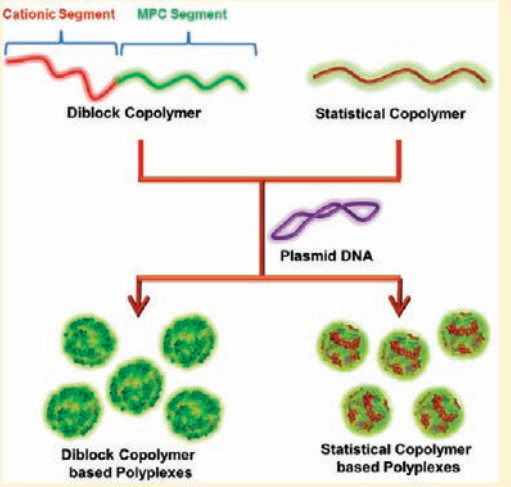
Marya Ahmed,[†] Neha Bhuchar,[†] Kazuhiko Ishihara,[‡] and Ravin Narain*[,†]

[†]Department of Chemical and Materials Engineering, Alberta Ingenuity Centre for Carbohydrate Science, University of Alberta, 116 Street and 85 Avenue, Edmonton, AB, T6G 2G6, Canada

[‡]Department of Materials Engineering, School of Engineering, The University of Tokyo, 7-3-1, Hongo, Bunkyo-ku, Tokyo 113-8656, Japan

Supporting Information

ABSTRACT: The facile synthesis of biocompatible and nontoxic gene delivery vectors has been the focus of research in recent years due to the high potential in treating genetic diseases. 2-Methacryloxyethyl phosphorylcholine (MPC) copolymers were recently studied for their ability to produce nontoxic and biocompatible materials. The synthesis of well-defined and water-soluble MPC polymer based cationic vectors for gene delivery purposes was therefore attractive, due to the potential excellent biocompatibility of the resulting copolymers. Herein, cationic MPC copolymers of varying architectures (block versus random) were produced by the reversible addition−fragmentation chain transfer (RAFT) polymerization technique. The copolymers produced were evaluated for their gene delivery efficacy in the presence and absence of serum. It was found that copolymer architectures and molecular weights do affect their gene delivery efficacy. The statistical copolymers produced larger particles, and showed poor gene transfection efficiency as compared to the diblock copolymers. The diblock copolymers served as efficient gene delivery vectors, in both the presence and absence of serum *in vitro*. To the best of our knowledge, this is the first report where the effect of architecture of MPC based copolymer on gene delivery efficacy has been studied.



INTRODUCTION

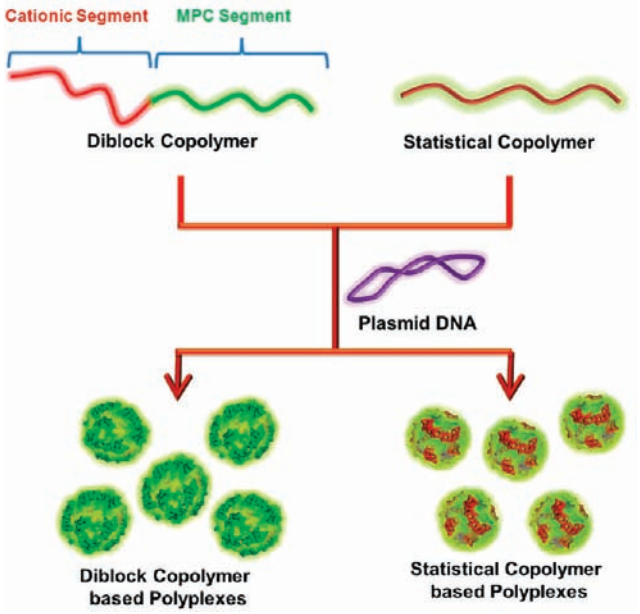
The successful treatment of genetic disorders by gene therapy is dependent on the facile synthesis of nonimmunogenic and nontoxic gene delivery vectors in reproducible manner.[1,2] A variety of nonviral gene delivery vectors have been produced and their transfection efficiencies are being evaluated, in an effort to determine the ideal gene delivery vector with enhanced gene expression and low toxicity.[2−11] Poly(ethylene glycol) (PEG) is one of the water-soluble and low-toxicity polymers that has been extensively explored in cationic gene delivery vectors to decrease the immunogenicity and toxicity of the later.[3,5,8,10,12] The drawbacks associated with PEGylated gene delivery systems are the low uptake of polyplexes and hence lower gene expression. Therefore, there is a need to develop alternative biocompatible polymers, which can be used as cationic gene delivery vehicles.[5]

The role of phospholipid polymers for biological functions is well-studied and it has been found that these polymers have the potential to produce bioinert surfaces for specific biological applications.[13,14] 2-Methacryloxyethyl phosphorylcholine (MPC) has a phosphorylcholine group in the molecule and shows very high water-solubility.[15] The MPC can be polymerized by a variety of radical polymerization techniques to yield the phospholipid polymers.[16] Hence, the production of the cationic MPC copolymer based vectors for gene delivery purposes is thought to be a useful technique to produce gene delivery agents of desired properties.[17−21] Lam et al. and others have produced block-type MPC copolymers by incorporation of tertiary amines with MPC polymer segments via the atom transfer radical polymerization technique (ATRP) and their role for gene and drug deliveries are investigated.[18] The incorporation of MPC units into tertiary amines is found to impact the DNA condensation ability and gene transfer efficiencies of cationic polymers.[17,21] Chim et al. further explored the role of DNA condensation abilities of cationic MPC block copolymers using atomic force microscopy (AFM) and transmission electron microscopy (TEM).[19] The increase in the MPC polymer segment in diblock copolymers is found to decrease the DNA condensation efficacies and hence the gene expression of the corresponding block copolymers.[17,20] It is shown that an approximately 3-fold increase in the tertiary amine component of copolymers is required to produce enhanced

Received: March 6, 2011
Revised: April 11, 2011
Published: May 03, 2011

ACS Publications © 2011 American Chemical Society

Scheme 1. Synthesis of Statistical and Diblock Copolymer Based Polyplexes Using β-Galactosidase Plasmid



gene expression *in vitro*.[20] However, an increase in cationic character also induces severe toxicity, and hence produces a major barrier toward the synthesis of biocompatible nonviral gene delivery vector.

We propose the synthesis of water-soluble and cationic polymers composed of the MPC and methacrylate with primary amine as block and random architectures by the reversible addition−fragmentation chain transfer (RAFT) method. The RAFT process is extensively studied for the synthesis of a range of polymeric materials for biomedical applications[22] and is chosen here due to the ease of synthesis of those hydrophilic polymers under aqueous conditions. The role of primary amines in gene delivery is well studied and is found to be superior to tertiary amines.[2] The synthesis of cationic polymers composed of the MPC and methacrylate with primary amine for gene delivery purposes is thought to improve the gene expression of the MPC copolymers, by promoting enhanced DNA condensation abilities. The predetermined ratio of MPC units to primary amine components is targeted to be 1. The determination of this ratio of monomers for copolymer synthesis is based on the previous work, which shows that polymers of this composition can deliver the gene of interest with higher efficacies and low toxicity and their gene expression is dependent on the architecture of the polymers.[23] The cationic polymers and MPC based copolymers of varying degree of polymerization were synthesized and their toxicity profiles were determined. These polymers were then tested for their DNA condensation ability and gene expression. To the best of our knowledge, this is the first approach where cationic MPC copolymers of similar compositions and of different architectures (block versus random; Scheme 1) are synthesized by RAFT method and their gene transfer abilities are explored in detail.

The polyplexes were synthesized at varying polymer to DNA ratios and their sizes and net charges were determined using transmission electron microscopy (TEM), dynamic light scattering (DLS), and zeta potential, respectively. The polyplexes synthesized were subjected to agarose gel electrophoresis to determine their stability in an electrophoretic environment. The gene expression of polyplexes synthesized using copolymers of block and random architectures in the presence and absence of serum was then compared and their toxicities after transfection were evaluated. Moreover, the uptake of polyplexes in Hep G2 cells was studied in detail using confocal microscopy and flow cytometry.

MATERIAL AND METHODS

Materials. *O*-Nitrophenyl β-D-galactopyranoside, (ONPG) (enzymatic), 37 wt % formalin, fluorescein isothiocyanate (FITC), β-mercaptoethanol, MTT assay kit to determine cell viability, phosphotungstic acid (PTA), and 3-[(3-cholamidopropyl)-dimethylammonio]-1-propanesulfonate (CHAPS) were purchased from Sigma Aldrich. Linear polyethyleneimine (PEI) (M_w = 25 kDa) was purchased from Polysciences Inc. Cell Culture media Dulbecco's Modified Eagle Medium (DMEM; low glucose with glutamine and sodium pyruvate), penicillin (10 000 U/mL), and streptomycin (10 mg/mL), 0.25% trypsin, Dulbecco's modified Phosphate Buffer Saline (DPBS), and fetal bovine serum (FBS) were obtained from Invitrogen. Micro BCA assay kit was obtained from Fisher Scientific. Gwiz β-galactosidase plasmid was purchased from Aldevron. MPC was obtained from NOF Co, Tokyo, Japan, which was produced by the previously reported method.[15,16] Cy5′ plasmid labeling kit was purchased from Bio Mirus. 4-Cyanopentanoic acid dithiobenzoate (CTP) was synthesized in the laboratory and 4,4′-azobis (4-cyanovaleric acid) (ACVA) was from Sigma Aldrich.

Synthesis of Monomers and Polymers. The cationic monomers and polymers of varying degree of polymerization and architecture were synthesized according to previously reported protocols.[21,23]

Synthesis of P(AEMA) macroCTA by RAFT Polymerization. MPC macroRAFT agent was synthesized using our previous protocol.[21] 2-Aminoethyl methacrylamide hydrochloride (AEMA) (1.0 g, 6.0×10^{-3} mol), 4-cyanopentanoic acid dithiobenzoate (CTP) (0.042 g, 1.5×10^{-4} mol), and 4,4′-azobis(4-cyanovaleric acid) (ACVA) (0.014 g, 5.0×10^{-5} mol) were dissolved in 2.0 mL water in a 10 mL reactor. The solution was purged with nitrogen for 30 min. After degassing, the solution was placed in an oil bath at a temperature of 60 °C. The reaction was stopped after 6 h by quenching in liquid nitrogen. Polymer was obtained by precipitating the mixture in acetone and washing 3−4 times to obtain a white powder. Any remaining traces of monomer were removed by washing the solution in water/acetone (1:7). The final powder was freeze−dried. The P(MPC_{18}) macroCTA molecular weight and PDI were found to be 2.5×10^3 g/mol and 1.2, respectively, by gel permeation chromatography.

Synthesis of P(AEMA-*b*-MPC) by RAFT Polymerization. Chain extension was carried out using MPC as the second block and AEMA/APMA macroRAFT agent. In a typical reaction procedure, MPC (0.40 g, 2.4×10^{-3} mol) and AEMA macroCTA (0.20 g, 8.0×10^{-5} mol) were dissolved in 2 mL water. Stock solution of ACVA (0.011 g, 4.0×10^{-5} mol) in 2-propanol was prepared and mixed with the reaction solution. The reactor was placed in an oil bath at 70 °C for 20 h. The diblock copolymer P($AEMA_{15}$-*b*-MPC_{17}) was obtained by precipitating the solution in acetone and washing the solution with methanol/acetone (1:7). The final powder was freeze−dried. The molecular weight of the resulting copolymer was found to be 7.6×10^3 g/mol and PDI 1.3.

dx.doi.org/10.1021/bc2001159 |*Bioconjugate Chem.* 2011, 22, 1228–1238

Synthesis of P(AEMA-*st*-MPC) by RAFT Polymerization. The random copolymers of MPC and AEMA were synthesized by adding the monomers in the required molar ratio. A typical polymerization procedure for the copolymerization of MPC and AEMA in ratio 4:3 is given as follows: MPC (0.48 g, 1.6×10^{-3} mol) and AEMA (0.20 g, 1.2×10^{-3} mol) were dissolved in 3 mL water. CTP (0.022 g, 8.1×10^{-5} mol) and ACVA (7.0 mg, 2.7×10^{-5} mol) were dissolved in 1.0 mL of 2-propanol and mixed with the aqueous solution of monomers. The reaction mixture was degassed and is kept at 70 °C in an oil bath for 20 h. The reaction was stopped by quenching in liquid nitrogen. The polymer was precipitated in acetone and washed repeatedly to obtain a powder. Any unreacted monomer was removed by washing the powder with water/acetone (1:7). The powder was freeze−dried to remove any traces of acetone. The molecular weight of the resultant copolymer P($AEMA_{15}$-*st*-MPC_{10}) was found to be 6.0×10^3 g/mol and the PDI was found to be 1.2 by aqueous GPC.

The molecular weight and molecular weight distributions of homo- and copolymers were determined using aqueous GPC (Viscotek GPC system). The sodium acetate/acetic acid (0.50 mol/L/0.50 mol/L) buffer was used as eluent at room temperature and at a flow rate of 1.0 mL/min and pullulan standards ($M_w = 5.0 \times 10^2 - 4.0 \times 10^6$ g/mol) were used for calibration. The compositions of statistical copolymers were analyzed using ^{1}H NMR.

Formation of Polyplexes. Polyplexes were made by mixing varying concentrations of polymers with 0.4.0 mg/mL of *gwiz-β*-galactosidase plasmid in OMEM. The complexes were vortexed and incubated for 30 min before their analysis. The particle sizes and surface charges were measured using Brookhaven Zeta Plus (zeta potential and particle size analyzer) instrument.

Cell Culture. Hela and Hep G2 cells were maintained in DMEM supplemented with 5.0 and 10% FBS, respectively, and 1.0% penicillin/streptomycin solution in a humidified atmosphere in the presence of 5% CO_2 at 37 °C. Upon 80% confluency, the cells were trypsinized with 0.25% trypsin and were seeded in tissue culture plates.

Determination of Lethal Dose50 (LD_{50}) Values. Hela cells were seeded in 96 well tissue culture plates at the density of 9.0×10^3 cells per well. The cells were incubated overnight and were treated with varying concentrations of polymers in the presence of serum containing media. The cells were further incubated for 12 h and 25 μL of MTT dye was added per well. After 2 h, 100 μL of lysis buffer was added and cells were allowed to lyse overnight. The absorbance was read at 570 nm using TECAN Genios pro microplate reader. The untreated cells and media alone were used as positive and negative controls, respectively. The percent cell viability was calculated (% cell viability = (treated cells − negative control)/(untreated cells − negative control). LD_{50} values for different polymers were determined using *Origin Pro* software and data were analyzed using Boltzman function to provide a sigmoidal fit.

Transfection. Hep G2 cells were seeded at the density of 1.0×10^5 cells per well in 24 well tissue culture plates and were incubated overnight. The media was removed and 150 μL of serum free OMEM or serum containing media was added followed by the addition of varying concentrations of polyplexes. The cells were incubated for four hours and polyplexes containing media were replaced with fresh serum containing media. The cells were allowed to grow for 48 h before their lysis (CHAPS in sodium phosphate lysis buffer) (pH = 7.5) followed by a freeze−thaw cycle. The activity of β-galactosidase was detected using β-galactosidase assay, as described before.[23]

Toxicity after Transfection. Hep G2 Cells were seeded in 24 well tissue culture plates as described above and were transfected with polyplexes in the manner identical to transfection conditions. 48 h post-transfection, 125 μL MTT dye was added per well followed by the addition of 500 μL of lysis buffer after two hours of incubation. The absorbance was read at 570 nm using TECAN plate reader. The untreated cells and media alone were used as positive and negative controls, respectively, and percent cell viability was determined as mentioned in the LD_{50} section.

Fluorescence Labeling of Copolymers. Fluorescein isothiocyanate (FITC) was dissolved in DMSO at 1.0 mg/mL concentration. P($AEMA_{26}$-*b*-MPC_{27}) and P($AEMA_{19}$-*st*-MPC_{21}) (57 mg/mL) were dissolved in 4.0% Na_2CO_3 (pH was adjusted to 8.5). Small aliquots of FITC (2.4 mg of FITC per 100 g of polymer) were slowly added to the polymer solutions in the dark while vortexing. The solution was incubated in the dark overnight. The solution was dialyzed in the dark (MWCO = 6000−8000 Da) against deionized water, and purified solution was stored in the dark at room temperature.

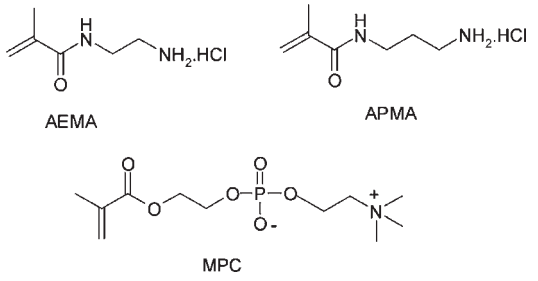
Fluorescent Labeling of Plasmid. *Gwiz-β*-galactosidae plasmid was labeled according to the manufacturer protocol. In brief, plasmid DNA (1.0 μg) was incubated with DNA labeling buffer and cy5′ fluorescent dye at 37 °C for 2 h. The cy5′-labeled plasmid was purified and labeling of plasmid was confirmed using confocal microscopy.

Uptake of Polymers and Polyplexes using Confocal Microscopy. Hep G2 cells were seeded in 6 well tissue culture plates containing glass coverslips. Upon 80% confluency, media was removed and cells were treated with FITC-labeled polymers alone, FITC-labeled polyplexes, or with cy5′-labeled polyplexes in the presence or absence of serum. The untreated cells were used as negative controls. The cells were incubated for 4 h, media was removed, and the cells were washed twice with DPBS before fixation using 3.7% formalin in DPBS. The cells were rehydrated with DPBS and fixed on microscope slides. The samples were analyzed using a Fluoview FV10i Olympus confocal microscope and samples were excited at 485 and 650 nm and detected at 535 and 670 nm, for FITC and Cy5′-labeled samples respectively, using 60× objective.

Flow Cytometry. Hep G2 cells were grown on 24 well tissue culture plate at the density of 1.0×10^5 cells per well and were allowed to adhere overnight. The media was then replaced with 150 μL of OMEM followed by the treatment with FITC-labeled polymers or polyplexes and cy5′-labeled polyplexes in the presence or absence of serum. The cells were further incubated for 3−4 h. The cells were rinsed with DPBS two times to remove the adherent polyplexes from the surface of cells, and were trypsinized and suspended in DPBS containing 3.7% formalin. The uptake of polymers and polyplexes was quantified using Beckman Coulter Quanta SC flow cytometer and FACS Quanta using FL1 channel for FITC and FL-4 channel for cy5′-labeled samples, respectively. The untreated cells were used as negative controls.

Agarose Gel Electrophoresis. The polyplexes were synthesized using conditions identical to transfection experiment and were loaded in 1.0% agarose gel containing 1.0 μg/mL ethidium bromide in 1× Tris acetate/EDTA buffer, and the gel was run at 140 V for 30 min and the DNA bands were visualized using UV transilluminator (Alpha Innotech; San Leandro, CA).

Scheme 2. Structures of Monomers, 2-Aminoethylmethacrylamide (AEMA), 3-Aminopropylmethacrylamide (APMA), and 2-Methacryloxyethyl Phosphorylcholine (MPC)



Stability of Polyplexes in the Presence of Serum Proteins. $P(AEMA_{26}$-*b*-$MPC_{27})$ and $P(AEMA_{19}$-*st*-$MPC_{21})$ polyplexes were prepared in OMEM as described above, and their size was determined using DLS. The polyplexes were then incubated with 10% fetal bovine serum, and the change in size and polydispersity of polyplexes as a function of time was monitored for four hours.

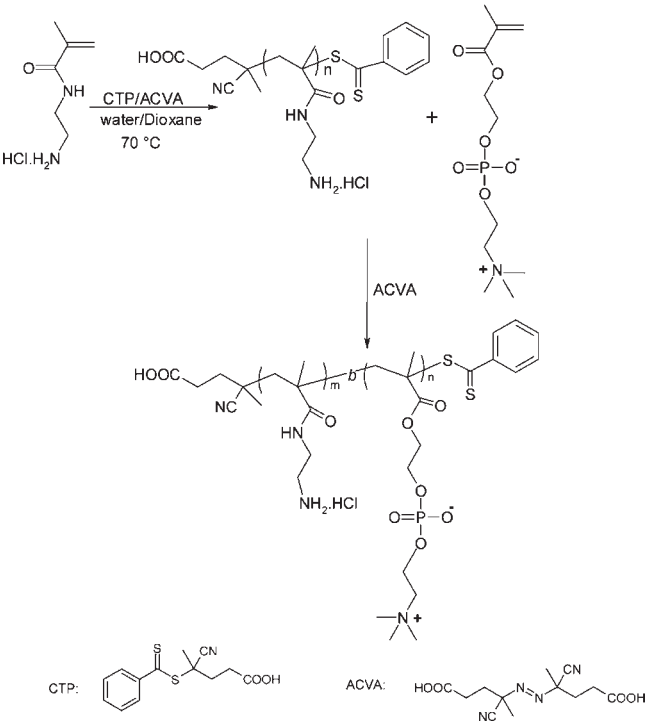
Determination of Protein Content on the Surface of Polyplexes. $P(AEMA_{26}$-*b*-$MPC_{27})$ and $P(AEMA_{19}$-*st*-$MPC_{21})$ polyplexes were prepared in deionized water under conditions used for transfection purposes. The polyplexes were incubated with 10% fetal bovine serum for 30 min. The polyplexes were centrifuged at 14 000 *g* for 60 min and supernatant was collected. The polyplexes were redispersed in deionized water and were washed two more times to ensure the removal of free proteins in solution. The supernatant and polyplexes were subjected to BCA assay to determine the amount of protein in the supernatant and on the surface of the polyplexes. The percent protein in solutions was determined by dividing the protein in solution by the total amount of protein added to the sample.

Transmission Electron Microscopy. Transmission electron microscope (TEM) images of polyplex samples stained with phosphotungstic acid (PTA) (synthesized using conditions identical to transfection experiments) were obtained using Philips transmission electron microscope equipped with a CCD camera.

RESULTS AND DISCUSSION

Phospholipid polymers, in particular, the phosphorylcholine groups bearing polymers, have high potential in the biomedical field due to the excellent biocompatibility of the resulting biomaterials.[24−27] Among them, the water-soluble MPC polymers are attractive for the development of gene delivery vectors that show biocompatible properties, including low toxicity and low protein activation ability. The copolymers composed of the MPC unit and methacrylates with primary amines (AEMA and APMA) units were prepared by the reversible addition−fragmentation chain transfer (RAFT) polymerization method, which allowed the production of a series of cationic copolymers of controlled dimensions and architecture in the absence of metal catalysts.[21,23] The chemical structures of MPC, APMA, and AEMA were shown (Scheme 2). The synthesis of statistical and diblock copolymers composed of the MPC polymer segment and AEMA polymer or APMA polymer segment was depicted in Schemes 3 and 4.

Scheme 3. RAFT Synthesis of Diblock Cationic MPC Polymers using CTP as Chain Transfer Agent and ACVA as Initiator at 70 °C



The cationic homopolymers and their corresponding MPC copolymers of varying degrees of polymerization and molecular weights were synthesized and their GPC data were shown in Table 1 (Supporting Information Figure S1 and S2). Subsequently, the copolymers were evaluated for their transfection efficiencies as a function of their molecular weight and architectures.

The copolymers (statistical and blocks) were designed in such a way that they have similar contents of cationic and phosphorylcholine groups. Such a composition was targeted to generate cationic vectors of low toxicity and improved DNA condensation ability and hence gene expression. Evaluation of a series of polymers for gene delivery is one way to select and understand the gene delivery efficacy of such materials.[29−32] Lam et al. synthesized a variety of MPC block copolymers with tertiary amine groups by ATRP, and their detailed study allowed the selection of copolymers with superior gene expression. However, the study revealed that a very high content of tertiary amine to the MPC unit is required to produce stable polyplexes for moderate gene expression.[18] In this work, we evaluated the transfection efficiencies of primary amine based cationic homopolymers and their corresponding MPC copolymers of varying architecture (block vs statistical) and chain length.

One of the important criteria that determines the biocompatibility of these copolymers was their cytotoxicity. The homopolymer and copolymers synthesized were subjected to cell viability assay, and their LD_{50} values were determined in Hela cells (Table 2). As expected, the cationic homopolymers P(AEMA) and P(APMA) showed high transfection efficacy and high toxicity as compared to the P(MPC) which were highly cell viable but with no gene expression.[2,17,18] The combination of these two systems was therefore expected to produce nontoxic

dx.doi.org/10.1021/bc2001159 |*Bioconjugate Chem.* 2011, 22, 1228–1238

Scheme 4. RAFT Synthesis of Statistical Cationic MPC Copolymers using CTP as Chain Transfer Agent and ACVA as Initiator at 70 °C

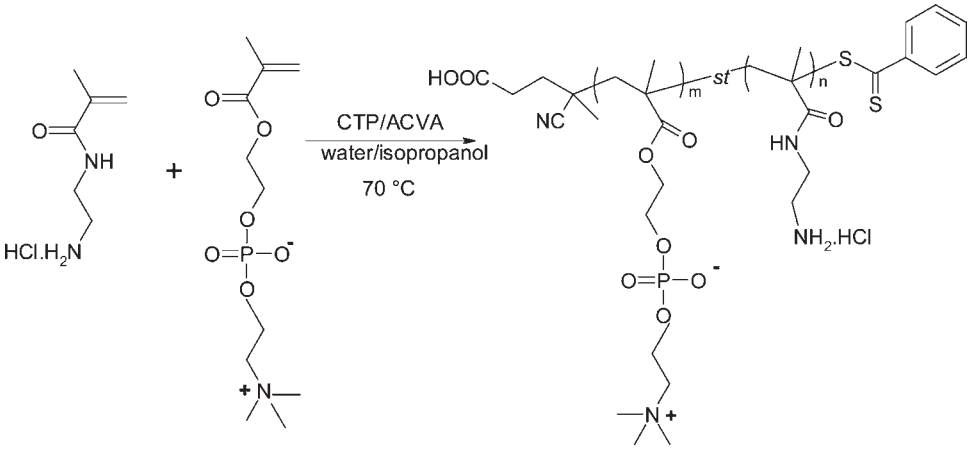


Table 1. GPC Data Showing the Molecular Weights and PDI of Cationic Homopolymers and Their Corresponding Copolymers Synthesized by RAFT Method

polymer samples	targeted M_n (kDa)	achieved M_n (kDa)	PDI
$P(AEMA)_{15}$	2.5	2.5	1.2
$P(PAEMA)_{36}$	6.6	6.0	1.2
$P(AEMA_{15}$-*b*-$MPC_{17})$	8.3	7.6	1.3
$P(AEMA_{26}$-*b*-$MPC_{27})$	1.9	12	1.3
$P(AEMA_{36}$-*b*-$MPC_{40})$	18.4	18	1.3
$P(AEMA_{10}$-*st*-$MPC_{15})$	8.3	6.0	1.2
$P(AEMA_{19}$-*st*-$MPC_{21})$	12.9	9.0	1.2
$P(AEMA_{40}$-*st*-$MPC_{36})$	18.3	17	1.2
$P(APMA)_{18}$	2.7	3.3	1.2
$P(APMA)_{37}$	7.1	6.7	1.1
$P(APMA_{18}$-*b*-$MPC_{16})$	8.6	8.2	1.1
$P(APMA_{22}$-*b*-$MPC_{37})$	13.3	15	1.3
$P(APMA_{37}$-*b*-$MPC_{40})$	20.4	18	1.3
$P(APMA_{7}$-*st*-$MPC_{14})$	8.6	5.4	1.2
$P(APMA_{14}$-*st*-$MPC_{22})$	13.3	9.0	1.2
$P(APMA_{32}$-*st*-$MPC_{32})$	20.4	15	1.2
$P(MPC)_{54}$	15.9	16	1.1

Table 2. Determination of Lethal Dose 50 (LD_{50}) Values of Cationic Homopolymers and Their Corresponding MPC Copolymers using MTT Assay

polymer samples	LD_{50} (μM)
$P(AEMA)_{15}$	141 ± 1.16
$P(AEMA)_{26}$	<12.4
$P(AEMA_{15}$-*st*-$MPC_{20})$	188 ± 1.33
$P(AEMA_{15}$-*b*-$MPC_{17})$	546 ± 1.42
$P(AEMA_{19}$-*st*-$MPC_{21})$	165 ± 1.97
$P(AEMA_{26}$-*b*-$MPC_{27})$	92.6 ± 1.1
$P(AEMA_{40}$-*st*-$MPC_{36})$	316 ± 1.23
$P(AEMA_{40}$-*b*-$MPC_{36})$	266 ± 1.06
$P(APMA)_{18}$	<12.4
$P(APMA)_{37}$	<12.4
$P(APMA_{18}$-*st*-$MPC_{16})$	520 ± 1.5
$P(APMA_{18}$-*b*-$MPC_{16})$	112 ± 1.43
$P(APMA_{14}$-*st*-$MPC_{22})$	>745
$P(APMA_{26}$-*b*-$MPC_{27})$	131 ± 1.04
$P(APMA_{32}$-*st*-$MPC_{32})$	271 ± 1.2
$P(APMA_{37}$-*b*-$MPC_{40})$	<12.4
$P(MPC)_{54}$	>745

and efficient gene delivery vectors, once the copolymers of specific architecture and compositions were identified. As expected, the presence of MPC polymer segment in cationic copolymers strongly enhanced the cell viability, regardless of the copolymer architecture (Table 2). The previous studies showed the synthesis of the MPC copolymers as gene delivery vectors; however, no toxicity data were provided.[20] In general, homopolymers of low molecular weights $P(AEMA)_{15}$ and $P(APMA)_{18}$ showed lower toxicity than their corresponding higher molecular weight counterparts. In contrast, P(MPC) showed no significant toxicity at the concentration of 750 μM. The statistical copolymers were found to be more cell viable than their corresponding block copolymers. For example, $P(AEMA_{19}$-*st*-$MPC_{21})$ showed higher cell viability, indicating LD_{50} of 165 μM as compared to $P(AEMA_{26}$-*b*-$MPC_{27})$, for which LD_{50} was 92.6 μM. Moreover, P(APMA) and their corresponding copolymers were found to be more toxic than P(AEMA). The LD_{50} value for $P(AEMA)_{15}$ was found to be 141 μM, as compared to $P(APMA)_{18}$ for which LD_{50} was 12.4 μM. The increased cell viability for AEMA based polymers compared to APMA based polymers was thought to be due to the greater distance between amine group and backbone of polymers in the case of APMA compared to AEMA, hence contributing to higher toxicity.[29] These results were consistent with previous study, where the effect of architecture of cationic glycopolymers on cell viability was studied.[29]

The MPC copolymers synthesized were then studied for their DNA complexation ability at various w/w ratios. The complexation of plasmid DNA with MPC copolymers was achieved by titrating the copolymers with fixed amount of DNA (1.2 μg), and the resulting polyplexes were studied by DLS for their sizes. At lower plasmid/polymers w/w ratios, aggregates ranging from 2

to 5 μm were observed. The increase in w/w ratio led to formation of stable polyplexes and the sizes of these polyplexes were measured using DLS and their charges were studied with zeta potential analyzer. The DLS data showed the presence of stable nanoplexes of in the range 50−200 nm in diameter in deionized water with strong net positive zeta values (Figure 1). These results were consistent with previous study, where polyplex formation using MPC block copolymers was studied.[19] In general, polyplexes synthesized using statistical copolymers were larger in diameter, as compared to the corresponding diblock copolymers. In contrast, P(MPC) did not allow the formation of stable polyplexes at any concentration of polymers to DNA ratios, as studied by DLS (data not shown).

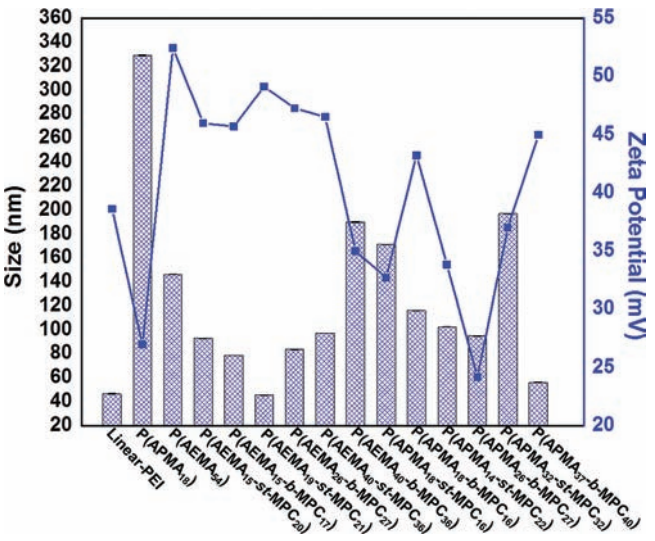


Figure 1. Dynamic light scattering (DLS) and zeta potential data for the MPC copolymers-DNA polyplexes. All samples were prepared in deionized water at fixed plasmid concentration, while polymer concentrations were varied to obtain stable particles.

The instability of MPC diblock copolymer based polyplexes in physiological conditions was found to be a major hurdle to their usage for gene delivery purposes.[16] Thus, only a few reports were available that showed the use of MPC diblock copolymers for gene or drug delivery purposes.[17−20] The conditions were optimized for the formation of polyplexes with net positive zeta values in OMEM media. The polyplexes were also subjected to agarose gel electrophoresis to determine their stability in the media (Supporting Information, Figure S3). The TEM images of polyplexes were then obtained to determine the role of polymer architecture on polyplex morphology (Figure 2).

Diblock copolymer based polyplexes such as P($AEMA_{26}$-*b*-MPC_{27}) and P($APMA_{26}$-*b*-MPC_{27}) showed the presence of spherical particles as compared to their statistical copolymer based polyplexes, such as P($AEMA_{19}$-*st*-MPC_{21}) and P-($APMA_{14}$-*st*-MPC_{22}) based polyplexes, which showed irregular shapes. Hence, in addition to the composition of copolymers, their architecture was found to play a dominant role in determining the shape of the polyplexes. These results were also in agreement with DLS data, where the net diameter of statistical copolymer based polyplexes was found to be greater than that of their corresponding diblock copolymers. The DNA condensation ability of MPC block copolymers was discussed by others with the help of TEM images.[18,19] It was shown that, for tertiary amine and MPC block copolymers, content of the MPC unit to amine ratios higher than 2 were required to produce spherical, well-condensed particles, and MPC unit to amine ratios lower than 2 produced irregular structures ranging from toroids to rods.[18,19] It should be noted that in our case the diblock copolymers with an equal amount of primary amine and MPC polymer segment produce spherical, well-condensed particles, as revealed by TEM images.

The stable polyplexes synthesized were tested for their gene delivery efficacy in Hep G2 cells using β-galactosidase assay. The

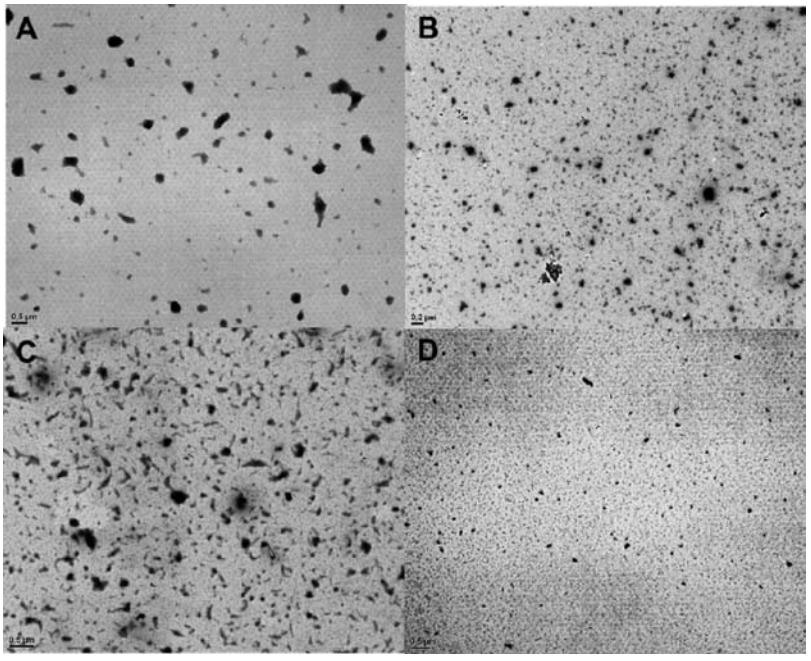


Figure 2. TEM images of polyplexes stained with PTA: (A) P($AEMA_{19}$-*st*-MPC_{21})-polyplexes, (B) P($AEMA_{26}$-*b*-MPC_{27})-polyplexes, (C) P($APMA_{14}$-*st*-MPC_{22})-polyplexes, (D) P($APMA_{26}$-*b*-MPC_{27})-polyplexes. The scale bar is 0.5 μm for images A, C, and D and 0.2 μm for B.

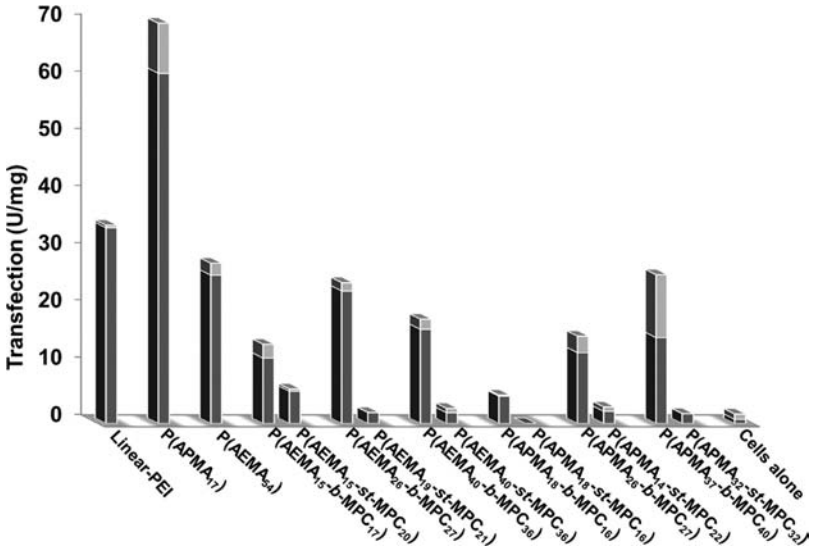


Figure 3. Gene expression as a function of copolymer architectures in the absence of serum proteins using Hep G2 cells. The transfection efficiencies are determined using β-galactosidase assay at DNA dose 0.6 μg. The standard deviations are shown by light color on the columns.

hydrolysis of substrate due to the production of β-galactosidase enzymes was detected by measuring the absorbance at λ = 420 nm. Figure 3 showed the gene transfection ability of MPC copolymers of varying degrees of polymerization. The gene expression of these copolymers was found to be dependent on the copolymer architectures and molecular weights of the copolymers. The copolymers of low molecular weights (6−7 kDa) showed lower gene expression, as compared to the copolymers of high molecular weights (10−12 kDa), for DNA dose of 0.6 μg, and the gene expression was comparable to that of linear PEI, which was used as a positive control. Further increase in molecular weights of copolymers (17−18 kDa) led to a decrease in gene expression most likely due the high toxicity of these copolymers.

Hence, the copolymers P($AEMA_{26}$-*b*-MPC_{27}) and P($APMA_{26}$-*b*-MPC_{27}) showed superior gene transfection as compared to the other copolymers of varying molecular weights. The gene expression of low molecular weight cationic homopolymer was higher than that of other homopolymers and copolymers; however, the toxicity of the homopolymers was a major issue for their use for gene delivery agents. Moreover, the statistical copolymers showed lower gene expression as compared to their corresponding block copolymers. For example, gene expression was found to be 23 ± 1 U/mg for P($AEMA_{26}$-*b*-MPC_{27}) and was 1.9 ± 0.1 U/mg for P($AEMA_{19}$-*st*-MPC_{21}). This significant difference in gene expression was attributed to the architecture of copolymers, which was also shown to affect the polyplex morphology. Sakaki et al. produced MPC copolymers having primary amino group of statistical architecture, which were shown to possess some gene delivery efficacy.[17] The block copolymers composed of the MPC polymer segment and polymer segments with tertiary amines have also been prepared and are shown to possess gene expression, and the optimum gene expression is obtained at tertiary amine to cationic ratio of 2 or higher.[18] However, to the best of our knowledge, there is no study where the effect of MPC copolymer architecture on gene expression has been studied. Herein, it is clearly shown that, in addition to the copolymer compositions, the architecture of copolymers plays a significant role in determining the gene expression. The effect of DNA dose on gene expression was further studied, in an effort to produce enhanced gene delivery using these copolymers (Figure 4). As shown in Figure 4, the AEMA copolymers showed improved gene transfection ability at higher DNA dose (1.2 μg) as compared to APMA-based copolymers. The gene expression was found to be highest (35 ± 4 U/mg) for P($AEMA_{26}$-*b*-MPC_{27}) based copolymers; although P($AEMA_{40}$-*b*-MPC_{36}) based polyplexes also showed enhanced gene expression (38 ± 8 U/mg), the toxicity of these copolymers was a major drawback at the higher DNA dose.

An important factor that determined the gene expression of polymeric vectors was their cellular uptake, which was dictated by a number of factors including the net charge of polyplexes, their morphology, and the content of serum proteins on the surface of polyplexes.[1,2] Although all MPC copolymer-based polyplexes showed strongly positive zeta potential values, as determined, the morphology of these polyplexes was found to vary as a function of copolymer architecture, as shown by TEM images. To determine if lower gene expression of statistical copolymer based polyplexes was related to their cellular uptake, β-galactosidase plasmid and copolymers individually were labeled to fluorescent dyes and their uptake by HepG2 cells was explored using confocal microscopy and flow cytometry. The FITC-labeled copolymers of P($AEMA_{26}$-*b*-MPC_{27}) and P($APMA_{26}$-*b*-MPC_{27}) and cy5′-labeled plasmid were used for this purpose. The polyplexes were formed by the incubation of cy5′-label-free plasmid with FITC-labeled polymers. These polyplexes and polymers alone were incubated with Hep G2 in the absence of serum, and uptake of polymers and polyplexes was studied using confocal microscopy and flow cytometry (Figure 5, Supporting Information Figure S5). These images showed that FITC-labeled polymers and polyplexes were well taken up by HepG2 cells, regardless of polymer architecture. The uptake of FITC-labeled copolymers and their corresponding polyplexes was further confirmed and quantified by flow cytometer analysis. It was shown that P($AEMA_{26}$-*b*-MPC_{27}) and P($AEMA_{19}$-*st*-MPC_{21}) and their polyplexes were taken up by Hep G2 cells, and lower transfection of statistical copolymer was not related to their lower uptake.

To further confirm that these results reflected the uptake of plasmid DNA and not the polymers alone (although these

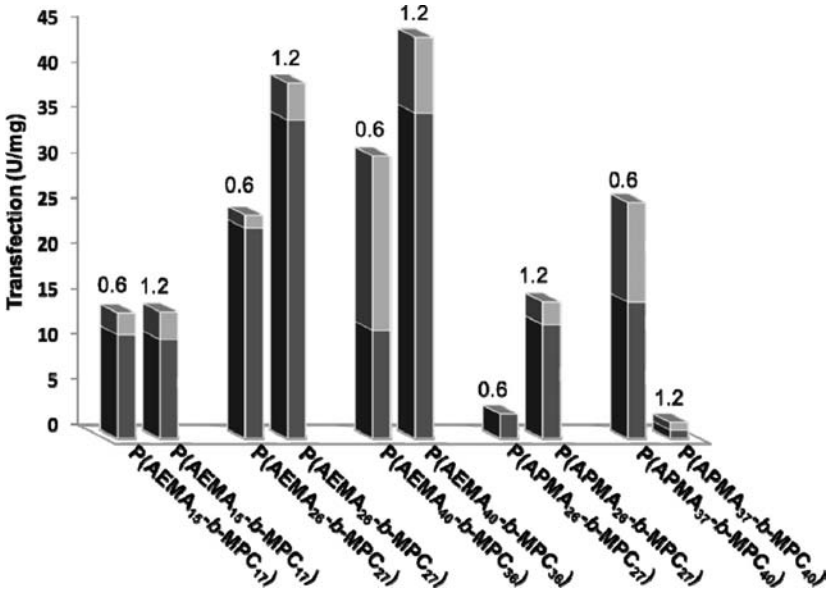


Figure 4. Gene expression of diblock copolymers in the absence of serum proteins using Hep G2 cells. The transfection efficiencies are determined using β-galactosidase assay at DNA doses 0.6 and 1.2 μg, as indicated on the graph. The standard deviations are indicated by light colors on the columns.

polyplexes were found to be stable as determined by agarose gel electrophoresis, the association of polyplexes with cell membrane proteins can lead to dissociation of plasmid from polyplexes, hence attributed toward lower uptake of polyplexes). β-Galactosidase plasmid was labeled with cy5′ fluorescent dye and cy5′-labeled polyplexes were then prepared by incubating label-free copolymers with labeled plasmid. The uptake of cy5′-labeled polyplexes was then studied using confocal microscopy and flow cytometry as before. (Figures 5 and 6).

The results obtained further supported the previous results that uptake of polyplexes by Hep G2 cells was independent of copolymer architecture and polyplexes produced as both block and statistical copolymers were well taken up. Hence, lower gene expression of statistical copolymers was not related to their lower uptake. The modification of living cells by exogenous DNA is a complex process, and successful uptake of foreign gene not always results in its expression. Layman et al. and others have also studied the relation between the cellular uptake of polyplexes and their gene expression, and it has been shown that successful uptake of polyplexes is not always related to the transfection.[33,34] It was thought that the mechanisms of uptake of block and statistical copolymer based polyplexes were different. The diblock copolymer based polyplexes were probably taken up by endocytosis owing to the smaller size of the particles and hence the facile release of DNA from the polyplexes, which contribute to their higher gene expression, as compared to the statistical copolymer-based polyplexes.

The main purpose for producing MPC copolymers for gene delivery purposes was to produce gene delivery vectors that showed minimum toxicity with enhanced gene expression, as well as minimal or no interactions with serum proteins.[2] The previous studies indicated that MPC polymers served as an excellent stealth layer and did not allow the adsorption of proteins on cationic or anionic surfaces modified with MPC polymer segments.[13] Although a handful of studies show the significance of synthesis of cationic MPC copolymers, no data have been shown so far that indicate the successful use of these copolymer based polyplexes in the presence of serum.[14−17] Chim et al. produced tertiary amine and MPC copolymers and it was shown that incorporation of an MPC polymer segment in the cationic segment greatly compromised the DNA protection ability of these copolymers from serum proteins and nucleases.[19] These data indicated that MPC copolymers were not ideal polymeric vectors to deliver the exogenous DNA in physiological conditions. The synthesis of MPC copolymers with primary amines was expected to change their physiological properties. The primary amine based polymers show better DNA condensation ability and DNA protection, and thus show better gene expression.[2] It was thought that synthesis of primary amine based copolymers would offer greater DNA protection from serum proteins and nucleases. However, a major concern in this approach was to determine if an MPC polymer segment was able to mask the cationic component of these copolymers. For this purpose, selected MPC copolymer based polyplexes, P($AEMA_{26}$-*b*-MPC_{27}) and P($AEMA_{19}$-*st*-MPC_{21}) based polyplexes, were prepared under conditions identical to those used for transfection purposes, and these polyplexes were incubated with 10% serum for four hours. The polyplexes were centrifuged to remove the excess of serum proteins and were washed three times with deionized water. The amount of serum proteins in the supernatant and on the surface of polyplexes was determined quantitatively using BCA assay (Supporting Information, Table S1). It was found that, regardless of polymer architecture, almost 89−90% of protein was present in supernatant 1 and a minimal amount of serum protein was detected in supernatant 2 and 3 and on polyplex surfaces. These results further confirmed the antifouling properties of MPC polymer based vectors, indicating that these copolymers had the potential to be used for gene delivery purposes site specifically. Moreover, the stability of these polyplexes in serum media as a function of time was determined using DLS. The polyplexes synthesized using MPC copolymers were found to be relatively stable in serum containing media; the slight aggregation of these polyplexes was reflected by higher polydispersity of the polyplexes upon the addition of serum proteins (Supporting Information, Table S2). This slight aggregation of polyplexes was also apparent by confocal microscope images

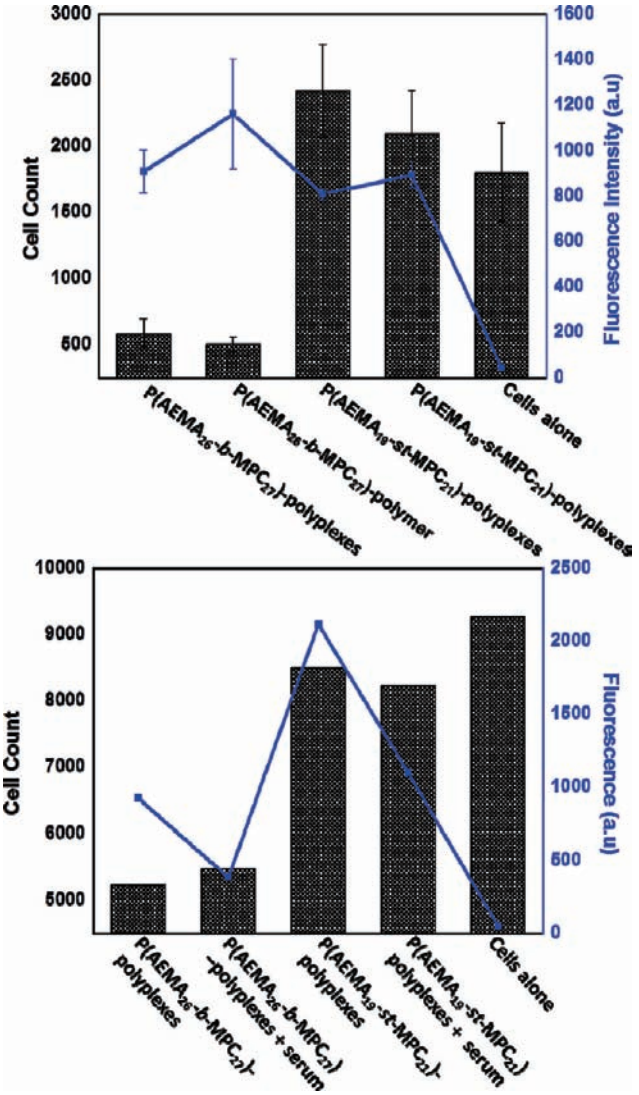


Figure 5. Polyplex uptake by Hep G2 cells after four hours of incubation by flowcytometer analysis. (A) FITC-labeled polymers and polyplexes in the absence of serum proteins. (B) Cy5′-labeled polyplexes in the presence and absence of serum proteins. The data indicate the amount of plasmid delivered to the cells (in line) and number of cells counted (in bars).

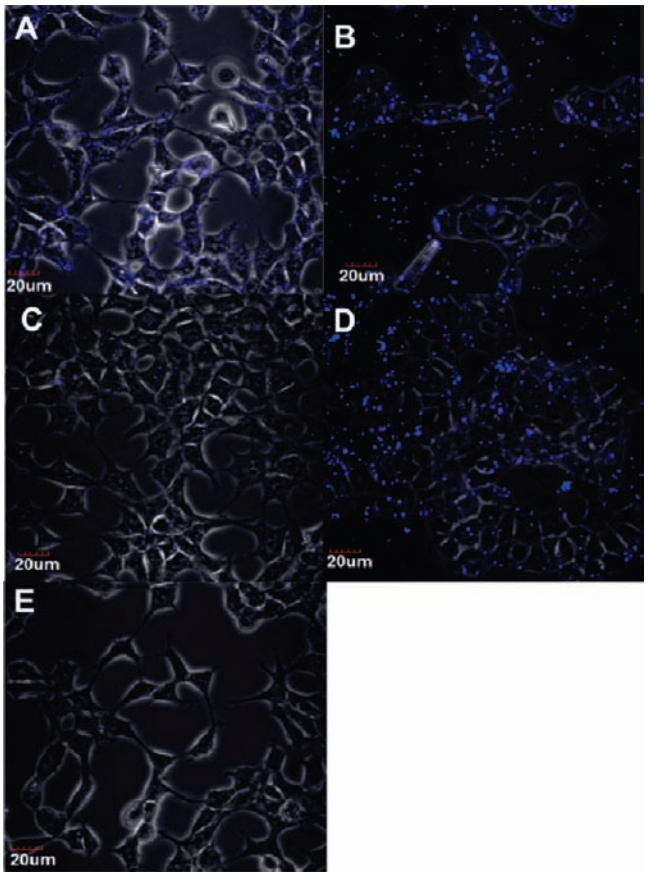


Figure 6. Confocal microscopy images of polyplex uptake by Hep G2 cells after four hours of incubation: (A) P(AEMA$_{26}$-*b*-MPC$_{27}$)-cy5′ labeled polyplexes in the absence of serum proteins, (B) P(AEMA$_{26}$-*b*-MPC$_{27}$)-cy5′ labeled polyplexes in the presence of serum proteins, (C) P(AEMA$_{19}$-*st*-MPC$_{21}$)-cy-5′ labeled polyplexes in the absence of serum proteins, (D) P(AEMA$_{19}$-*st*-MPC$_{21}$)-cy-5′ labeled polyplexes in the presence of serum proteins, (E) untreated cells.

(Figure 6B,D); the increase in polyplex size in these images, as compared to no serum treatments (Figure 6A,C) further supported the DLS data obtained. It should be noted that, after the addition of serum, polyplexes were strongly associated to the cell surface; however, their aggregation did not hinder the uptake of polyplexes by cells completely, which was further confirmed using flow cytometry analysis (Figure 6B,D,F). The data indicated that fluorescence intensity was reduced by almost half upon the addition of serum to the labeled polyplexes, possibly due to the aggregation of polyplexes. The results obtained showed that this trend of polyplex uptake and aggregation was independent of copolymer architecture. P(AEMA$_{26}$-*b*-MPC$_{27}$) and P(AEMA$_{19}$-*st*-MPC$_{21}$) based polyplexes were then subjected to transfection, and as expected, a slight decrease in gene expression was observed, possibly due to the lower uptake of these polyplexes in the presence of serum. However, it should be noted that the gene expression was still significantly comparable to serum-free treatments.

The toxicity after transfection of selected copolymer samples was then determined in Hep G2 cells (Figure 7, Supporting Information, Figure S6). These results further concluded that P(AEMA$_{26}$-*b*-MPC$_{27}$) based copolymers were excellent gene delivery agents and showed enhanced gene expression with minimum toxicity (~60% cell viability).

In short, the synthesis of a variety of MPC copolymers by RAFT allowed the careful selection of copolymers of specific architecture and molecular weight, which were found to show enhanced cell viability and gene expression. It was found that type of cationic monomer and molecular weight of copolymers and their architecture plays a significant role in determining the transfection efficacies of these copolymers. The low molecular weight copolymers of MPC (~7 KDa) were found to be less efficient in gene transfer, while in the case of high molecular weight copolymers (~18 KDa), the gene expression was compromised due to their high toxicity. In addition to molecular weight, the architecture of the copolymers was also found to be an important criterion in gene delivery. The statistical copolymers (regardless of their molecular weights) did not show any gene expression. P(AEMA$_{26}$-*b*-MPC$_{27}$) based polyplexes were found to be ideal MPC copolymers for gene delivery purposes, which retained antifouling properties of MPC units, in combination

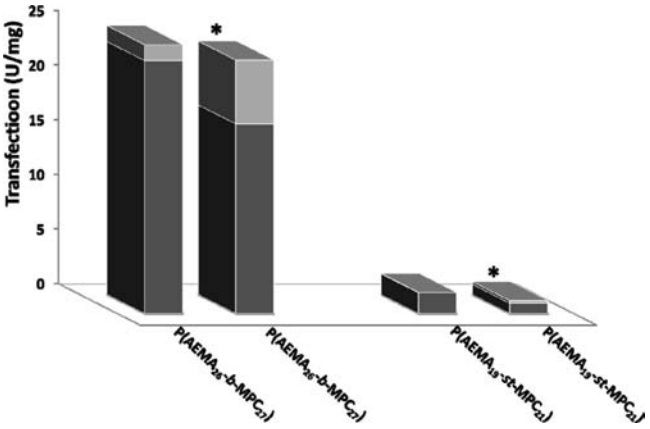


Figure 7. Gene expression of copolymers of varying architectures in the presence (*) and absence of serum proteins using Hep G2 cells. The transfection efficiencies are determined using β-galactosidase assay at DNA dose 0.6 μg.

with enhanced gene expression of amine component. These polymers were found to work well in the presence and absence of serum. These diblock copolymers and their corresponding polyplexes also showed high cellular uptake in the presence and absence of serum, which further supported their role as an ideal candidate for higher gene expression. Further studies will be performed to produce MPC copolymers for targeting purposes, and their role as a specific gene delivery agent *in vitro* and *in vivo* will be evaluated.

■ ASSOCIATED CONTENT

Supporting Information. GPC data for polymer synthesis, DLS data for serum polyplexes, agarose gel electrophoresis, and BCA assay for determination of serum proteins, confocal images, and cell viability studies. This material is available free of charge via the Internet at http://pubs.acs.org.

■ AUTHOR INFORMATION

Corresponding Author

*To whom correspondence should be addressed. E-mail: narain@ualberta.ca. Phone: (780) 492-1736. Fax: (780) 492-2881.

■ ACKNOWLEDGMENT

The authors acknowledge support from Natural Sciences and Engineering Research Council of Canada (NSERC) for the funding for this work.

■ REFERENCES

(1) Pathak, A., Patnaik, S., and Gupta, C. K. (2009) Recent trends in non-viral vector-mediated gene delivery. *Biotechnol. J. 4*, 1559–1572.

(2) Mintzer, A. M., and Simanek, E. E. (2009) Nonviral vectors for gene delivery. *Chem. Rev. 109*, 259–302.

(3) Blessing, T., Kursa, M., Holzhauser, R., Kircheis, R., and Wagner, E. (2001) Different strategies for formation of PEGylated EGF-conjugated PEI/DNA complexes for targeted gene delivery. *Bioconjugate Chem. 12*, 529–537.

(4) Boussif, O., Delair, T., Brua, C., Veron, L., Pavirani, A., and Kolbe, J. V. H. (1999) Synthesis of polyallylamine derivatives and their use as gene transfer vectors in vitro. *Bioconjugate Chem. 10*, 877–883.

(5) Le Bon, B., Van Craynest, N., Boussif, O., and Vierling, P. (2002) Polycationic diblock and random polyethylene glycol- or tris(hydroxymethyl)methyl-grafted (co)telomers for gene transfer: synthesis and evaluation of their in vitro transfection efficiency. *Bioconjugate Chem. 13*, 1292–1301.

(6) Zugates, T. G., Peng, W., Zumbuehl, A., Jhunjhunwala, S., Huang, Y.-H., Langer, R., Sawicki, A. J., and Anderson, G. D. (2007) Rapid optimization of gene delivery by parallel end-modification of poly(β-amino ester)s. *Mol. Ther. 15*, 1306–1312.

(7) Wolfert., A. M., Dash, R. P., Nazarova, O., Oupicky, D., Seymour, W. L., Smart, S., Strohalm, J., and Ulbrich, K. (1999) Polyelectrolyte vectors for gene delivery: influence of cationic polymer on biophysical properties of complexes formed with DNA. *Bioconjugate Chem. 10*, 993–1004.

(8) Sharma, R., Lee, S.-J., Bettencourt, C. R., Xiao, C., Konieczny, F. S., and Won, Y.-Y. (2008) Effects of the incorporation of a hydrophobic middle block into a PEG−polycation diblock copolymer on the physicochemical and cell interaction properties of the polymer−DNA complexes. *Biomacromolecules 9*, 3294–3307.

(9) Nakayama, Y., Kakei, C., Ishikawa, A., Zhou, M.-Y., Nemoto, Y., and Uchida, K. (2007) Synthesis and *in Vitro* evaluation of novel star-shaped block copolymers (blocked star vectors) for efficient gene delivery. *Bioconjugate Chem. 18*, 2037–2044.

(10) Shuai, X., Merdan, T., Unger, F., Wittmar, M., and Kissel, T. (2003) Novel biodegradable ternary copolymers *hy*-PEI-*g*-PCL-*b*-PEG: synthesis, characterization, and potential as efficient nonviral gene delivery vectors. *Macromolecules 36*, 5751–5759.

(11) Hsiue, H.-G., Chinag, Z.-H., Wang, H.-C., and Juang, M.-T. (2006) Nonviral gene carriers based on diblock copolymers of poly (2-ethyl-2-oxazoline) and linear polyethylenimine. *Bioconjugate Chem. 17*, 781–786.

(12) Lin, S., Du, F., Wang, Y., Ji, S., Liang, D., Yu, L., and Li, Z. (2008) An acid-labile block copolymer of PDMAEMA and PEG as potential carrier for intelligent gene delivery systems. *Biomacromolecules 9*, 109–115.

(13) Xu, Y., Takai, M., and Ishihara, K. (2009) Protein adsorption and cell adhesion on cationic, neutral, and anionic 2-methacryloyloxyethyl phosphorylcholine copolymer surfaces. *Biomaterials 30*, 4930–4938.

(14) Goda, T., Goto, Y., and Ishihara, K. (2010) Cell-penetrating macromolecules: Direct penetration of amphipathic phospholipid polymers across plasma membrane of living cells. *Biomaterials 31*, 2380–2387.

(15) Ishihara, K., Ueda, T., Nakabayashi, N., Ishihara, K, Ueda, T, and Nakabayashi, N. (1990) Preparation of phospholipid polymers and their properties as polymer hydrogel membrane. *Polym. J. 22*, 355–360.

(16) Ueda, T, Oshida, H, Kurita, K, Ishihara, K, and Nakabayashi, N. (1992) Preparation of 2-methacryloyloxyethyl phosphorylcholine copolymers with alkyl methacrylates and their blood compatibility. *Polym. J. 24*, 1259–69.

(17) Sakaki, S., Tsuchida, M., Iwasaki, Y., and Ishiara, K. (2004) A water-soluble phospholipid polymer as a new biocompatible synthetic DNA carrier. *Bull. Chem. Soc. Jpn. 77*, 2283–2288.

(18) Licciardi, M., Giammona, G., Du, J., Armes, P. S., Tang, Y., and Lewis, L. A. (2006) New folate-functionalized biocompatible block copolymer micelles as potential anti-cancer drug delivery systems. *Polymer 47*, 2946–2955.

(19) Chim, A. T. Y., Lam, W. K. J., Ma, Y., Armes, S. P., Lewis, L. A., Roberts, J. C., Stolnik, S., Tendler, B. J. S., and Davies, C. M. (2005) Structural study of DNA condensation induced by novel phosphorylcholine-based copolymers for gene delivery and relevance to DNA protection. *Langmuir 21*, 3591–3598.

(20) Lam, W. K. J., Ma, Y., Armes, S. P., Lewis, L. A., Baldwin, T., and Stolnik, S. (2004) Phosphorylcholine−polycation diblock copolymers as synthetic vectors for gene delivery. *J. Controlled Release 100*, 293–312.

(21) Bhuchar, N., Deng, Z., Ishihara, K., and Narain, R. (2011) Detailed study of the reversible addition−fragmentation chain transfer polymerization and co-polymerization of 2-methacryloyloxyethyl phosphorylcholine. *Polym. Chem. 2*, 632–639.

(22) Boyer, C., Bulmus, V., Davis, P. T., Ladmiral, V., Liu, J., and Perrier, S. (2009) Bioapplications of RAFT Polymerization. *Chem. Rev. 109*, 5402–5436.

(23) Ahmed, M., and Narain, R. (2011) Synthetic glycopolymer-based non-viral gene delivery systems: evaluation of polymer architectures, compositions and molecular weights on gene expression. *Biomaterials*.

(24) Ishihara, K., and Inoue, Y. (2010) Essential factors to make excellent biocompatibility of phospholipid polymer materials. *Adv. Sci. Technol. 76*, 1–9.

(25) Ishihara, K., Goto, Y., Matsuno, R., Inoue, Y., and Konno, T. (2011) Novel polymer biomaterials and interfaces inspired from cell membrane functions. *Biochim. Biophys. Acta 1810*, 268–275.

(26) Ishihara, K. (2000) Bioinspired phospholipid polymer biomaterials for making high performance artificial organs. *Sci. Technol. Adv. Mater. 1*, 131–138.

(27) Lewis, A. L. (2000) Phosphorylcholine-based polymers and their use in the prevention of biofouling. *Colloids Surf., B: Biointerf. 18*, 261–275.

(28) Deng, Z., Bouchekif, H., Babooram, K., Housni, A., Choytun, N., and Narain, R. (2008) Facile synthesis of controlled-structure primary amine-based methacrylamide polymers via the reversible addition-fragmentation chain transfer process. *J. Polym. Sci., Part A: Polym. Chem. 46*, 4984–4996.

(29) Reineke, M. T., and Davis, E. M. (2003) Structural effects of carbohydrate-containing polycations on gene delivery. 2. charge center type. *Bioconjugate Chem. 14*, 255–261.

(30) Green, J. J., Langer, R., and Anderson, G. D. (2008) A combinatorial polymer library approach yields insight into nonviral gene delivery. *Acc. Chem. Res. 41*, 749–759.

(31) Barua, S., Joshi, A., Banerjee, A., Matthews, D., Sharfstein, T. S., Cramer, M. S., Kane, S. R., and Rege, K. (2009) Parallel synthesis and screening of polymers for nonviral gene delivery. *Mol. Pharmaceutics 6*, 86–97.

(32) Lynn, M. D., Anderson, G. D., Putnam, D., and Langer, R. (2001) Accelerated discovery of synthetic transfection vectors: parallel synthesis and screening of a degradable polymer library. *J. Am. Chem. Soc. 123*, 8155–8156.

(33) Layman, M. J., Ramirez, M. S., Green, D. M., and Long, E. T. (2009) Influence of polycation molecular weight on poly(2-dimethylaminoethylmethacrylate)-mediated DNA deliver in vitro. *Biomacromolecules 10*, 1244–1252.

(34) Srinivasachari, S., Liu, Y., Prevette, L. E., and Reineke, T. M. (2007) Effects of trehalose click polymer length on pDNA complex stability and delivery efficacy. *Biomaterials 28*, 2885–2898.

Supporting Information

Well-Controlled Cationic Water-soluble Phospholipid Polymer-DNA Nano-complexes for Gene Delivery

Marya Ahmed[a], Neha Bhuchar[a], Kazuhiko Ishihara[b] and Ravin Narain[a*]

[a]Department of Chemical and Materials Engineering, Alberta Ingenuity Centre for Carbohydrate Science, University of Alberta, 116 St and 85 Ave, Edmonton, AB, T6G 2G6, Canada, [b]Department of Materials Engineering, School of Engineering, The University of Tokyo, 7-3-1, Hongo, Bunkyo-ku, Tokyo 113-8656, Japan

Table S1. Quantification of serum proteins present in the supernatant and on the surface of polyplexes.

Samples	**Relative amount of serum in solution (%)**	**samples**	**Relative amount of serum in solution (%)**
Supernatant-1	89	Supernatant-1	90
Supernatant-2	3.6	Supernatant-2	4.5
Supernatant-3	3.6	Supernatant-3	1.8
p($AEMA_{26}$-*b*-MPC_{27})polyplexes	3.6	p($AEMA_{19}$-*st*- MPC_{21})-polyplexes	4.5

Table S2. Change in size of polyplexes in the presence of serum proteins as a function of time.

Time (min)	**P($AEMA_{26}$-*B*MPC_{27}) polyplexes (nm)**	**P($AEMA_{19}$-*ST*-MPC_{21}) polyplexes (nm)**
0	78.4 ± 0.3	388 ± 0.25
5	35.6 ± 0.3	148 ± 0.3
30	56.4 ± 0.4	181 ± 0.35
60	75.6 ± 0.4	185 ± 0.3
150	86.1 ± 0.4	184 ± 0.4
240	104 ± 0	185 ± 0.4

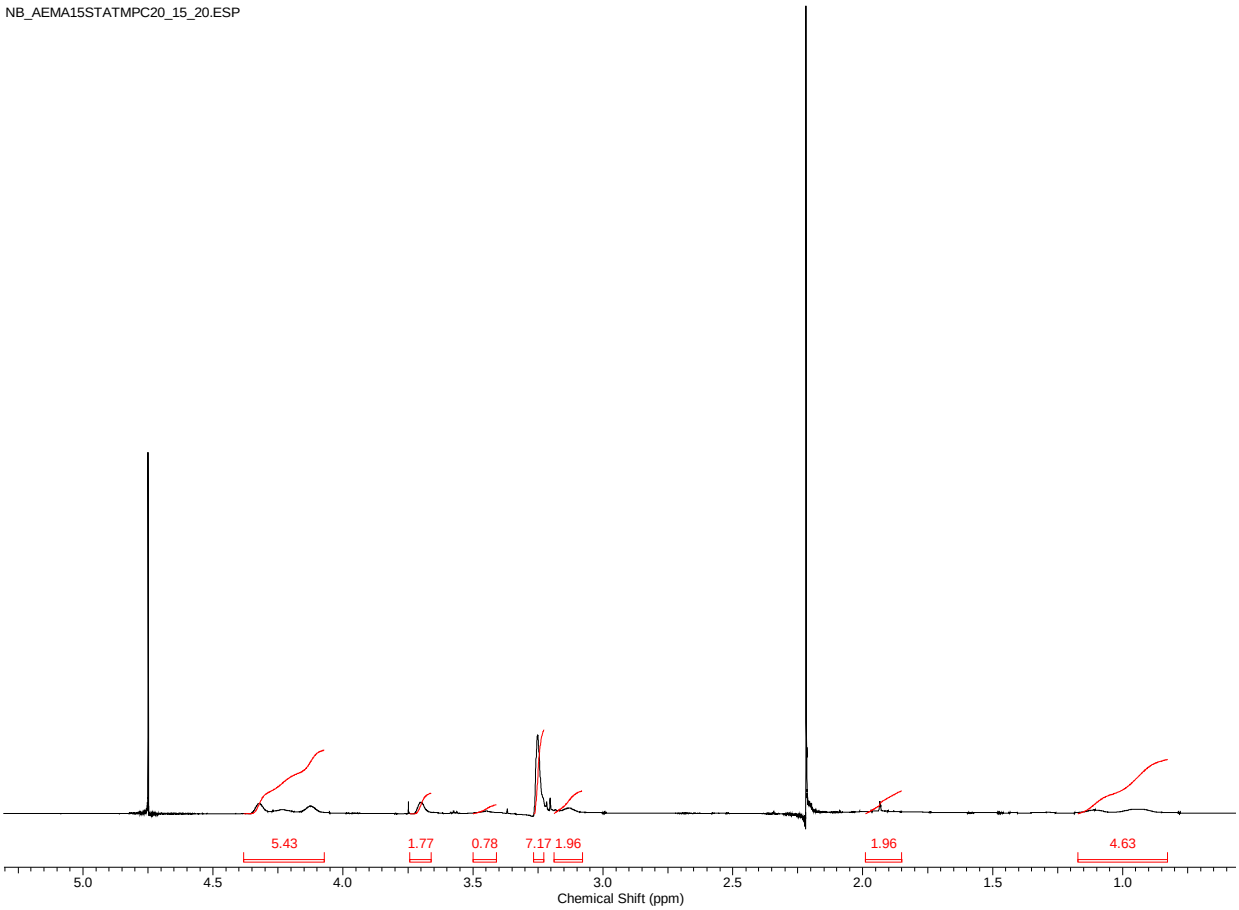


Figure S1: ^{1}H-NMR spectrum of random copolymer P($AEMA_{10}$-*st*-MPC_{10})

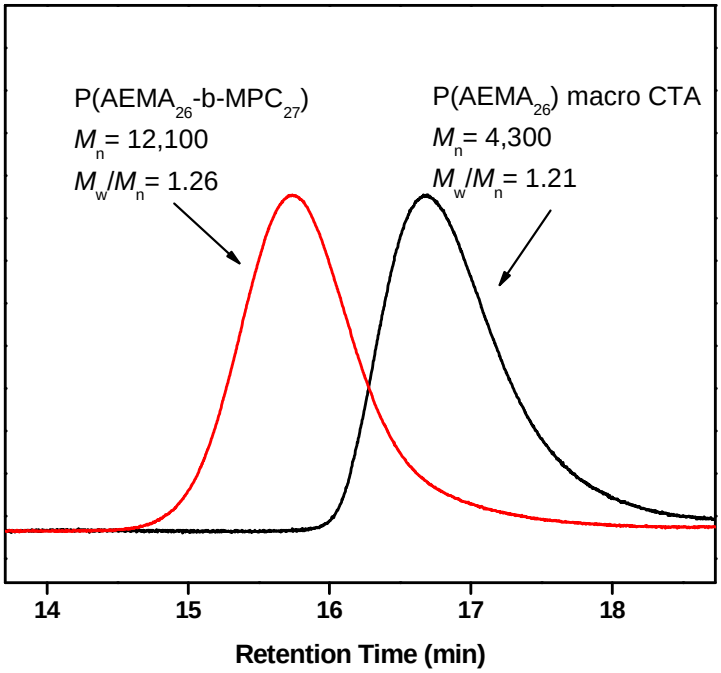


Figure S2. GPC traces showing the homopolymer $P(AEMA)_{26}$ and the resulting diblock polymer $P(AEMA_{26}$-*b*-$MPC_{27})$ by RAFT at 70 °C.

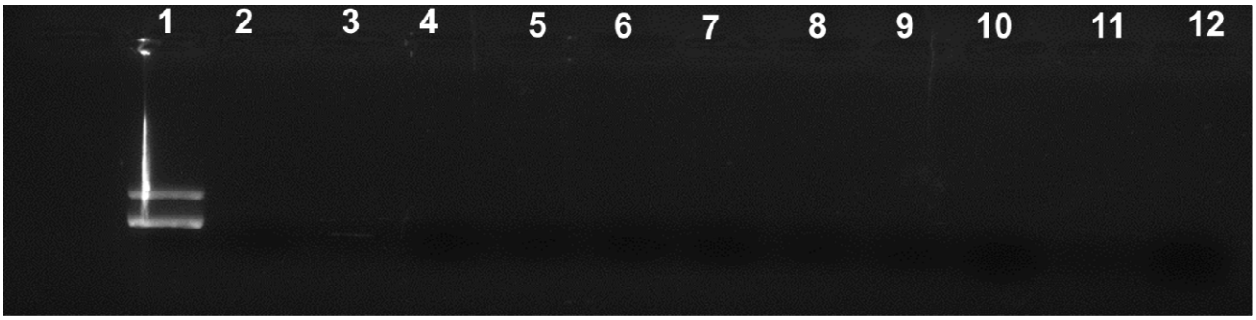


Figure S3. 1) DNA alone 2) $P(AEMA_{25}$-*st*-$MPC_{30})$ polyplexes 3) $P(AEMA_{25}$-*b*-$MPC_{30})$ polyplexes 4) $P(APMA_{15}$-*b*-$MPC_{20})$ polyplexes 5) $P(AEMA_{15}$-*b*-$MPC_{20})$ polyplexes 6)

P(APMA$_{25}$-*b*-MPC$_{30}$) polyplexes 7) P(APMA$_{25}$-*st*-MPC$_{30}$) polyplexes 8) P(APMA$_{40}$-*st*-MPC$_{40}$) polyplexes 9) P(AEMA$_{40}$-*st*-MPC$_{40}$) polyplexes 10) P(APMA$_{15}$-*st*-MPC$_{20}$) polyplexes 11) P(AEMA15-*st*-MPC$_{20}$) polyplexes 12) P(APMA$_{40}$-*b*-MPC$_{40}$) polyplexes.

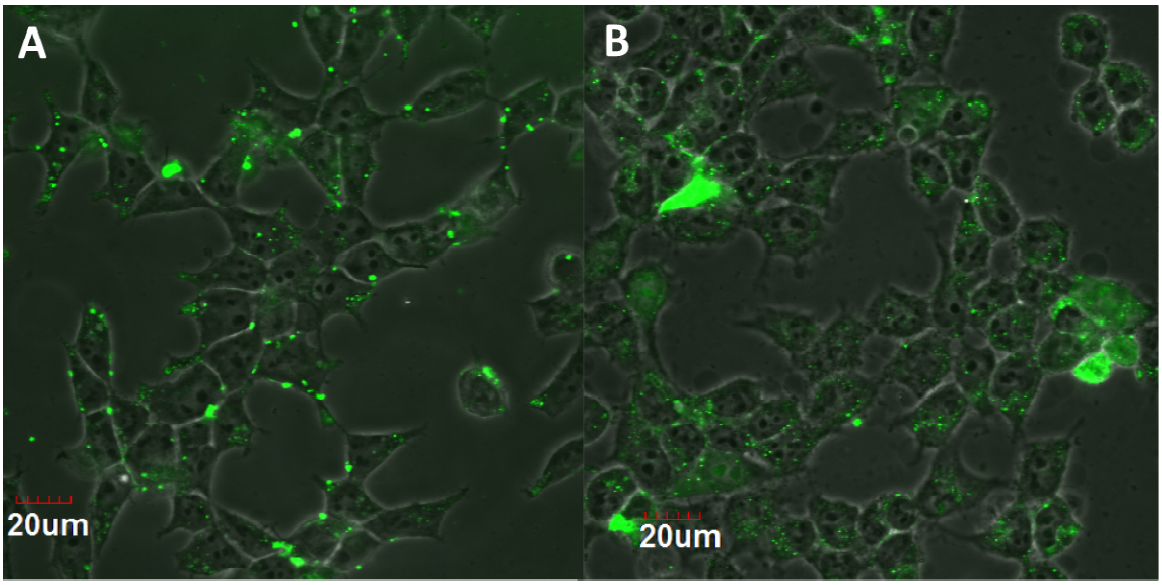


Figure S5. Confocal images showing the uptake of FITC-labelled polyplexes by Hep G2, A) FITC-labelled P(AEMA$_{26}$-*b*-APMA$_{27}$)-polyplexes, B) FITC-labelled P(AEMA$_{19}$-*st*-MPC$_{21}$) based polyplexes.

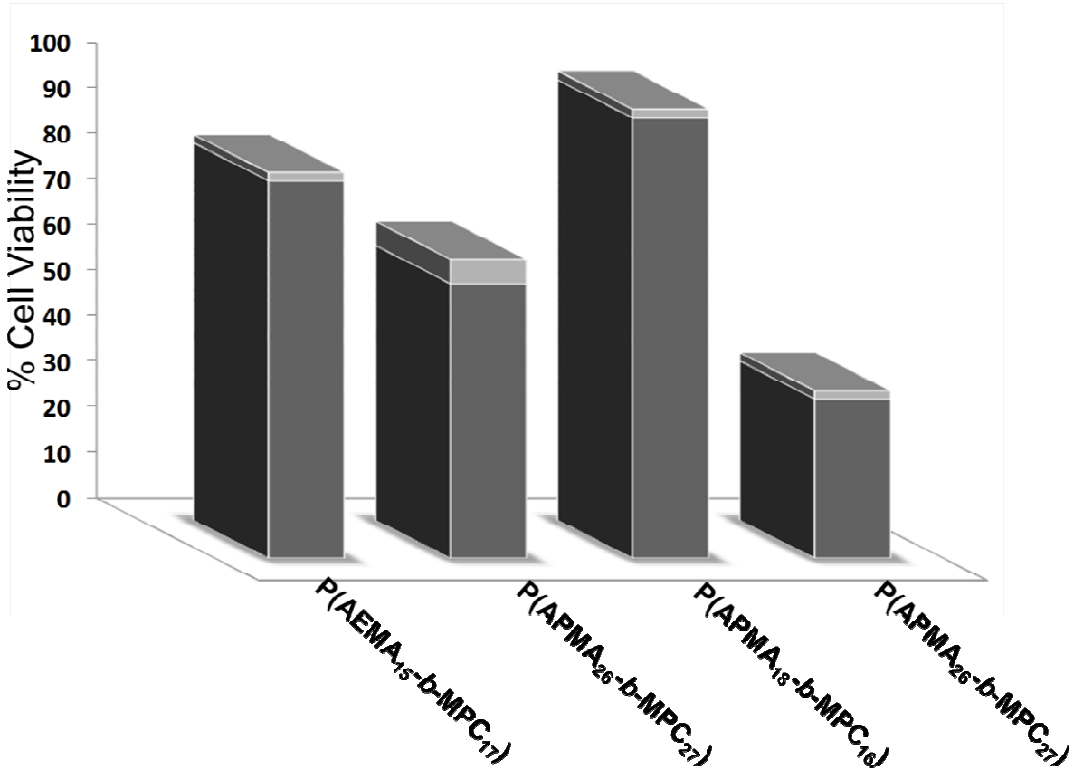


Figure S6. Cell Viability of Hep G2 cells studied post transfection.

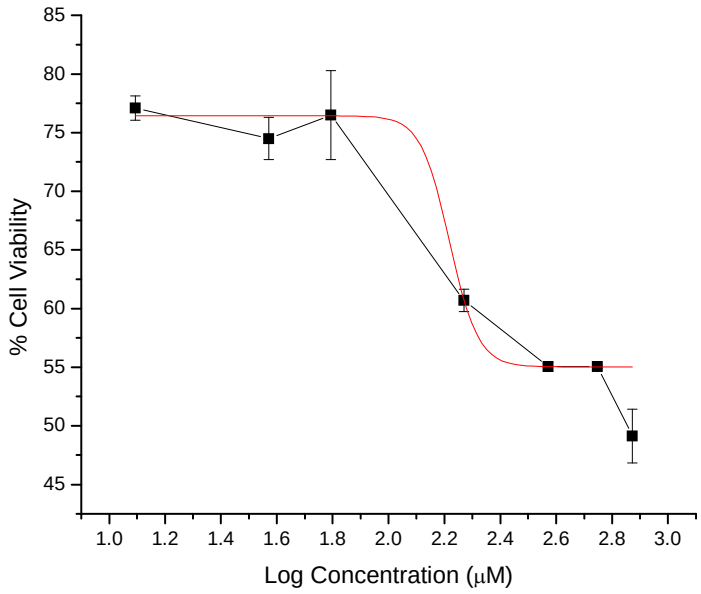


Figure S7. Determination of LD50 values for P($AEMA_{19}$-*st*-MPC_{21}).

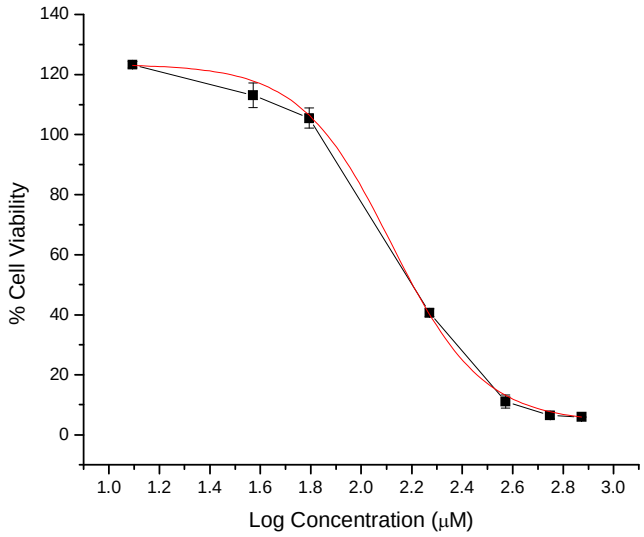


Figure S8. Determination of LD50 values for P($APMA_{26}$-*b*-MPC_{27}).

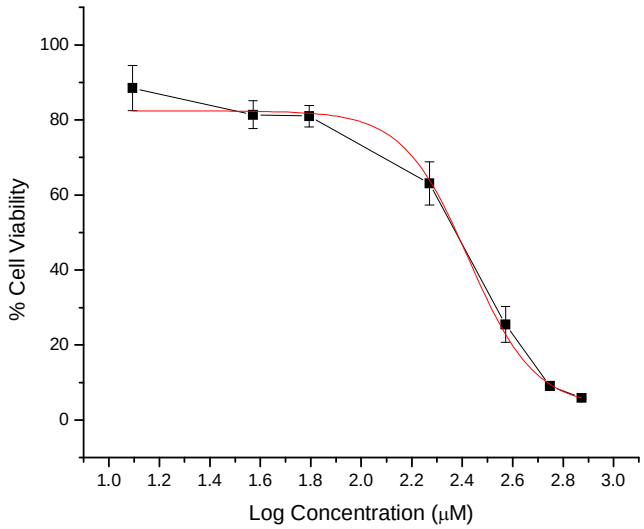


Figure S8. Determination of LD50 values for P($AEMA_{40}$-*b*-MPC_{36})

Bioconjugate Chemistry

TECHNICAL NOTE

pubs.acs.org/bc

Linking of Sensor Molecules with Amino Groups to Amino-Functionalized AFM Tips

Linda Wildling,[†] Barbara Unterauer,[‡] Rong Zhu,[†] Anne Rupprecht,[⊥] Thomas Haselgrübler,[§] Christian Rankl,[∥] Andreas Ebner,[†,‡] Doris Vater,[§] Philipp Pollheimer,[†] Elena E. Pohl,[⊥] Peter Hinterdorfer,[†,‡] and Hermann J. Gruber*[,†]

[†]Institute of Biophysics and [‡]Christian Doppler Laboratory for Nanoscopic Methods in Biophysics, J. Kepler University, Altenberger Str. 69, A-4040 Linz, Austria

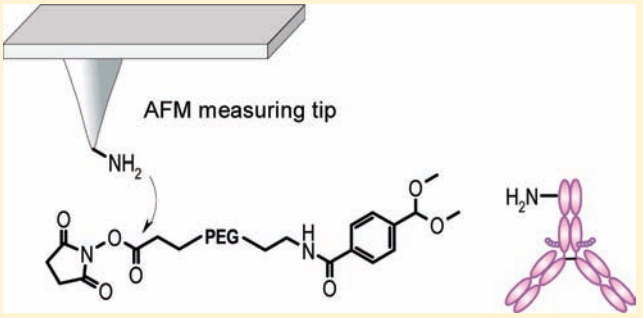
[§]Center for Advanced Bioanalysis, Scharitzer Str. 6-8, A-4020 Linz, Austria

[∥]Agilent Technologies Austria, Aubrunnerweg 11, A-4040 Linz, Austria

[⊥]Department of Biomedical Sciences, University of Veterinary Medicine, Veterinärplatz 1, A-1210 Vienna, Austria

Supporting Information

ABSTRACT: The measuring tip of an atomic force microscope (AFM) can be upgraded to a specific biosensor by attaching one or a few biomolecules to the apex of the tip. The biofunctionalized tip is then used to map cognate target molecules on a sample surface or to study biophysical parameters of interaction with the target molecules. The functionality of tip-bound sensor molecules is greatly enhanced if they are linked via a thin, flexible polymer chain. In a typical scheme of tip functionalization, reactive groups are first generated on the tip surface, a bifunctional cross-linker is then attached with one of its two reactive ends, and finally the probe molecule of interest is coupled to the free end of the cross-linker. Unfortunately, the most popular functional group generated on the tip surface is the amino group, while at the same time, the only useful coupling functions of many biomolecules (such as antibodies) are also NH_2 groups. In the past, various tricks or detours were applied to minimize the undesired bivalent reaction of bifunctional linkers with adjacent NH_2 groups on the tip surface. In the present study, an uncompromising solution to this problem was found with the help of a new cross-linker ("acetal-PEG-NHS") which possesses one activated carboxyl group and one acetal-protected benzaldehyde function. The activated carboxyl ensures rapid unilateral attachment to the amino-functionalized tip, and only then is the terminal acetal group converted into the amino-reactive benzaldehyde function by mild treatment (1% citric acid, 1−10 min) which does not harm the AFM tip. As an exception, AFM tips with magnetic coating become demagnetized in 1% citric acid. This problem was solved by deprotecting the acetal group before coupling the PEG linker to the AFM tip. Bivalent binding of the corresponding linker ("aldehyde-PEG-NHS") to adjacent NH_2 groups on the tip was largely suppressed by high linker concentrations. In this way, magnetic AFM tips could be functionalized with an ethylene diamine derivative of ATP which showed specific interaction with mitochondrial uncoupling protein 1 (UCP1) that had been purified and reconstituted in a mica-supported planar lipid bilayer.



INTRODUCTION

Atomic force microscopy (AFM) can operate in aqueous solution under physiological conditions[1] and reveal fine details not resolved by electron microscopy.[2] AFM is thus well-suited for the structural analysis of biomolecules and their assemblies.[1,3] In addition, an AFM tip can be functionalized with one or several probe molecules (e.g., antibodies) whereupon it can be used as a specific biosensor by which cognate target molecules (e.g., antigens) are detected when the tip is moved over the sample surface.[4−6] Binding is detected as a rupture event which is sensed by a vertically oscillated cantilever[7] preferably under simultaneous monitoring of sample topography.[8,9] Alternatively, the tip can be vertically oscillated at a fixed $X-Y$ position above a target molecule, in which case repeated binding−unbinding events are recorded as force−distance profiles. When repeating force−distance cycles at different force loading rates,[10] detailed biophysical parameters of the noncovalent bond can be calculated from the force data.[4,5,11−14]

Linear polymers, such as carboxymethylamylose,[15−18] poly(*N*-succinimidyl acrylate),[19] or poly(ethylene glycol) chains (PEG),[6,12,14,20−31] have regularly been used as flexible tethers

Received: February 23, 2011
Revised: April 13, 2011
Published: May 04, 2011

 © 2011 American Chemical Society

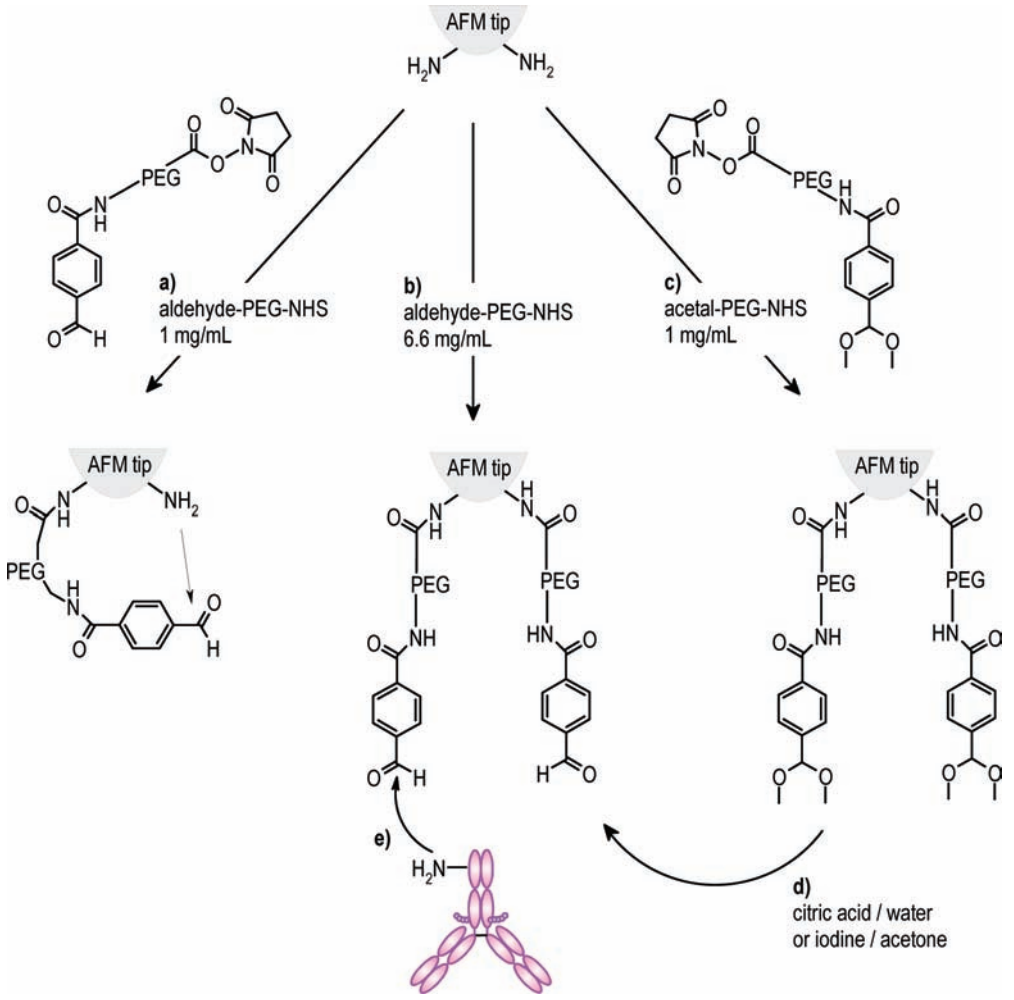


Figure 1. AFM tip functionalization with aldehyde-PEG-NHS as compared to acetal-PEG-NHS. Loop formation between adjacent amino groups can occur with aldehyde-PEG-NHS (a); it is largely suppressed at high concentrations of aldehyde-PEG-NHS (b). No loop formation occurs with acetal-PEG-NHS (c), since the acetal is converted into aldehyde only after derivatization of all NH_2 groups on the AFM tip (d). Lysine residues of proteins can be coupled to terminal benzaldehyde functions (e).

between the tip and the probe molecule, resulting in much higher probability for binding between the probe molecule on the tip and the target molecules on the sample surface. Tethering of probe molecules via linear polymers is usually performed in three stages. First, reactive sites are generated on the tip surface. Second, a linear polymer ("cross-linker") is attached with one reactive end while reserving the other end for the probe molecule. Third, the probe molecule is coupled to the free end of the polymer chain. The most straightforward scheme comprises (i) amino-functionalization of the tip, (ii) amide bond formation with a heterobifunctional cross-linker that has one amino- and one thiol-reactive end group, and (iii) attachment of a thiol-carrying probe molecule to the free end of the cross-linker.[6,8,9,25,28,32]

Unfortunately, antibodies and many other proteins possess no free thiols (cysteines) but lots of reactive amino functions (lysines, e.g., 80−90 per antibody).[33] At the same time, amino-functionalization is the predominant method of tip surface activation. This poses the problem of connecting tip-NH_2 with NH_2-protein with a bifunctional cross-linker, while preventing cross-linker loops between adjacent NH_2 groups on the tip surface. The nontrivial task has been solved by several strategies, each having its own advantages and drawbacks.

The simplest approach is to use a heterobifunctional cross-linker, as described above, and to pre-derivatize the protein with a reagent that introduces free thiol residues[20,24,25] or pentynoyl groups (for coupling to an azide on the linker via click chemistry).[22,34] These methods work well, yet ~0.2 mg of precious antibody is required per batch, and gel filtration is needed for rigorous removal of reagents. Consequently, the derivatized antibody is rather dilute which prevents refreezing of unused portions.

For minimization of antibody consumption, several methods have been developed in which the lysine residues of antibodies (or other proteins) are directly coupled to tip-bound cross-linker, without pretreatment of the protein. (i) Gold-coated tips were covered with a SAM containing exposed thiol groups to which a heterobifunctional linker (maleimide-PEG-NHS) was bound with its maleimide function.[12,14] In this way, the amino-reactive NHS ester group was spared for subsequent coupling of protein via lysine. (ii) Gold-coated tips were amino-functionalized with cystamine, and carboxymethylamylose was bound via some of its many NHS ester functions, leaving the other NHS ester groups for coupling of protein.[17,18] In both methods, the large radius of the gold-coated tips reduces their usefulness for high-resolution imaging. (iii) Silicon nitride tips were amino-silanized and

NHS-activated carboxymethylamylose was applied in the analogous way.[15,16] (iv) Silicon nitride tips were silanized with a mixture of aminosilane and a large excess of an inert silane, aiming at such a low surface density of NH_2 functions that homobifunctional NHS-PEG-NHS could react with one NHS ester function only, whereupon protein could react with the second NHS ester group.[30]

All NHS ester methods (i–iv) have in common that coupling of protein is fast and efficient, provided that the concentration of protein is high enough and the optimal pH value is chosen to outrun premature hydrolysis of the NHS ester functions.[35,36] In this respect, aldehyde functions are a promising alterative because they cannot hydrolyze. Under comparable conditions, coupling of amino groups to aldehydes is much slower than to NHS esters.[36,37] In a recent study, we took advantage of this kinetic difference by devising a new heterobifunctional cross-linker (aldehyde-PEG-NHS)[38] for AFM tip functionalization (Figure 1a,b). When applying the same concentration as with other cross-linkers (1 mg/mL), the tendency for loop formation between adjacent NH_2 groups was very pronounced (Figure 1a). At high concentration (6.6 mg/mL), however, the majority of NH_2 functions on the tip was rapidly consumed by reaction with NHS esters (Figure 1b); thus, most benzaldehyde functions were spared for coupling of protein.[38] This method was successfully used in a number of AFM studies.[21,23,38–49]

In the present study, the benzaldehyde function was kept in a protected form until all NH_2 groups on the tip surface had formed amide bonds with a new linker (acetal-PEG-NHS, Figure 1c). Subsequently, the acetal functions were converted into reactive aldehyde moieties. Dilute citric acid was found to cleave all acetal functions without harmful effects on the tip surface and on the gold mirror on the top side of the cantilever. This strategy affords effective tip functionalization at low cross-linker concentration, which adds to the advantage that synthesis of acetal-PEG-NHS is much simpler than of aldehyde-PEG-NHS.

EXPERIMENTAL PROCEDURES

Materials. Analytical-grade solvents and reagents were used as long as they were commercially available. Muscovite mica sheets were supplied by Christiane Gröpl (Austria). Si_3N_4 measuring tips were purchased from Veeco (Santa Barbara, CA) and Si_3N_4 chips from Wacker-Chemitronic GmbH (Germany). APTES was obtained from Aldrich. $NaCNBH_3$ was purchased from Fluka. Avidin, D-biotin, EAP, and ethanolamine hydrochloride were obtained from Sigma-Aldrich. EDA-ATP was obtained from BioLog (Bremen, Germany). NH_2-PEG-COOH was synthesized as described.[50] Acetal-PEG-NHS and aldehyde-PEG-NHS were synthesized as outlined in Figure 3 (see Supporting Information for details). Biotin-IgG was prepared by derivatization of goat IgG with biotin-cap-NHS as described.[25] Buffer A contained 100 mM NaCl, 50 mM NaH_2PO_4, and 1 mM EDTA (pH 7.5 adjusted with NaOH). Buffer B contained 300 mM NaH_2PO_4 and 1 mM EDTA (pH 7.5 adjusted with NaOH). PBS contained 150 mM NaCl and 5 mM NaH_2PO_4 (pH 7.4 adjusted with NaOH). Mitochondrial uncoupling protein 1 (UCP1) was purified and reconstituted into mica-supported bilayers as described in the Supporting Information.

Functionalization of AFM Tips with Acetal-PEG-NHS and Antibodies. AFM Tips (Si_3N_4) were amino-functionalized either with a solution of ethanolamine hydrochloride in DMSO ("room temperature method")[51] or with APTES from gas phase,[51,52] as specified. Attachment of acetal-PEG-NHS was performed by 2 h incubation of the tips in 0.5 mL of chloroform containing 1 mg/mL acetal-PEG-NHS and 0.5% (v/v) of TEA. Subsequently, the tips were rinsed in chloroform (3×). Two alternate methods were used for conversion of the acetal functions into aldehyde groups: (i) immersion in acetone containing 0.1% iodine for 5 min and rinsing in pure acetone (3 × 5 min), (ii) immersion in water containing 1% citric acid for 10 min and rinsing with water (3 × 5 min). For the coupling of the antibody, tips were transferred into a mixture of 50 μL biotin-IgG solution (0.2 mg/mL in buffer A) with 2 μL 1 M $NaCNBH_3$ stock solution (to reach a final concentration of 40 mM $NaCNBH_3$) for one hour. Subsequently, 5 μL of ethanolamine hydrochloride stock solution (1 M, preadjusted to pH 9.6 with 20% NaOH) was mixed into the biotin-IgG solution and incubation was continued for 10 more minutes. Finally, the tips were washed in PBS (3 × 5 min) and stored in PBS at 4 °C until use (up to 3 days). A detailed illustration of tip functionalization is found in the Supporting Information (Figure S5).

Monitoring of Single Unbinding Events between Tip-Bound Biotin-IgG and Mica-Bound Avidin by AFM. Avidin (1 mg/mL in PBS) was diluted with 1 mM NaCl to a final concentration of 0.5 μg/mL and absorbed to freshly cleaved mica. After 15 min, the substrate was rinsed with 1 mM NaCl (10×) and subsequently with PBS (10×). Force measurements with biotin-IgG-functionalized AFM tips were performed in a fluid cell of a commercial AFM (PicoSPM, Agilent, Tempe, AZ). Force–distance cycles were recorded at a 1 Hz vertical scan rate and 100–300 nm *z*-amplitude. The measurements were performed at a constant trace and retrace velocity. All measurements were done in PBS. For specific blocking of avidin–biotin interaction, the biotin residues on tip-bound IgG were masked by addition of free streptavidin (0.5 mg/mL final concentration) to the bath solution. The spring constants of the levers were determined by thermal noise method.[53,54]

Functionalization of Silicon Nitride Chips with Amino Groups, Acetal-PEG-NHS, and Biotin-IgG, with Quantitative Assay for Chip-Bound Biotin-IgG. Silicon nitride chips were precut, cleaned with chloroform (3×), dried with nitrogen, immersed in a piranha solution (70/30, H_2SO_4/H_2O_2, caution: piranha is extremely corrosive and can explode) for 30 min, extensively rinsed in water, dried with nitrogen, and heated to 160 °C for 5 min. The amino-functionalization was performed with the "room temperature method" as described before.[51] After washing in DMSO (3×) and ethanol (3×), the chips were dried in nitrogen and derivatized with acetal-PEG-NHS as described above for AFM tips. Cleavage of the acetal functions was always performed with citric acid (1%, in water, 1 or 15 min) and washing with water (3 × 5 min) or with iodine (0.1% in acetone, 5 min) and washing with acetone (3 × 5 min), as specified. Coupling of biotin-IgG was performed as described above for AFM tips, except that the concentration of biotin-IgG was varied as specified in the tables. Unused aldehyde functions were blocked with ethanolamine or with glycine, as specified. The surface density of biotin-IgG bound to the silicon nitride chips was determined by specific binding of ExtrAvidin-Peroxidase (EAP) as described before.[51] A detailed illustration of chip functionalization and estimation of its efficiency is found in the Supporting Information (Figure S6).

RESULTS AND DISCUSSION

Synthesis of Acetal-PEG-NHS and Aldehyde-PEG-NHS. The synthesis route for the new cross-linker acetal-PEG-NHS followed the typical scheme for long heterobifunctional

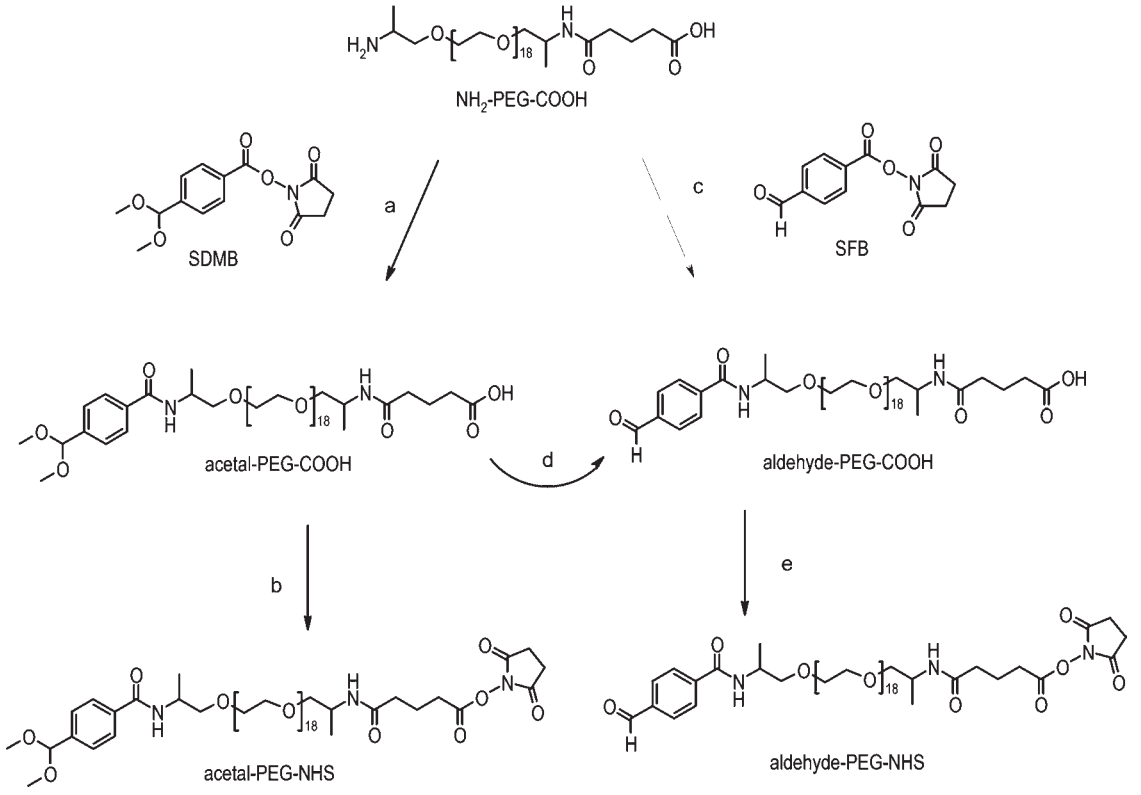


Figure 2. Synthesis of acetal-PEG-NHS and aldehyde-PEG-NHS. (a) NH_2-PEG-COOH was reacted with SDMB to give acetal-PEG-COOH. (b) The terminal carboxyl function was activated by conversion into an NHS ester (acetal-PEG-NHS). (c) Previously published method of preparing aldehyde-PEG-COOH by use of SFB.[38] (d) New synthesis of aldehyde-PEG-COOH by cleavage of the acetal function. (e) Conversion of the terminal COOH group into an aminoreactive NHS ester (aldehyde-PEG-NHS). Experimental details of the syntheses are found in the Supporting Information.

cross-linkers[25,38,50,51] in the sense that a short cross-linker (SDMB) was attached to the *N*-terminus of NH_2-PEG-COOH in the first step (Figure 2a). To our knowledge, the short cross-linker SDMB has been synthesized for the first time (see Figure S1 in the Supporting Information). After removal of all small molecules (excess of SDMB, free NHS, TEA), the carboxyl group of acetal-PEG-COOH was converted into an NHS ester, resulting in the heterobifunctional cross-linker acetal-PEG-NHS (Figure 2b).

As can be seen from Figure 2, the new module acetal-PEG-COOH served a second purpose also: cleavage of the acetal by iodine/acetone (0.1%, 10 min) or citric acid/water (1%, 10 min) afforded pure aldehyde-PEG-COOH (Figure 2d) which was easily converted into the previously published linker acetal-PEG-NHS (Figure 2e). In contrast to the new synthetic route (Figure 2a,d), the old method of reacting NH_2-PEG-COOH with SFB (Figure 2c)[38] had given a significant fraction of Schiff base adducts besides the desired amide product; thus, a cumbersome extraction scheme was required for purification of aldehyde-PEG-COOH from undesired PEG derivatives.[38] The new synthetic route for preparation of the old linker aldehyde-PEG-NHS (Figure 2, steps a, d, and e) is important because the new linker acetal-PEG-NHS can replace the old one in most but not all AFM applications (see Figure 5).

AFM Tip Functionalization, Using Iodine/Acetone for Cleavage of Tip-Linked Acetal Functions. As can be seen from Figure 1, the essential improvement of the new tip functionalization method rests on the use of a masked aldehyde (i.e., an acetal) which remains unreactive while amide bonds are formed between the linker and the amino groups on the tip surface. In the next step, the acetal function on the free end of the tip-bound linker was converted into an amino-reactive benzaldehyde function (step d). Hereby, it was critical to select the mildest available method in order to prevent damage to the tip surface and to the light-reflecting metal film on the top side of the cantilever. In a recent study, it had been found that dimethylacetals of aromatic aldehydes are cleaved within 5 min by 0.6% iodine in anhydrous acetone under neutral conditions.[55] In the present study, we further lowered the iodine concentration to 0.1% and found it fully sufficient to completely deprotect acetal-PEG-COOH within 5−10 min in bulk solution (Figure 2, step d). Consequently, acetone with 0.1% iodine was also applied to tip-linked acetal functions (Figure 1, step d).

After deprotection, the functionality of "tip-PEG-acetal" was examined by a established validation method:[25,38] Biotin-IgG was coupled to the tip-bound benzaldehyde functions (Figure 1, step e), using $NaCNBH_3$ for concomitant fixation of the initially formed Schiff base bonds (see Figure S5). The tip was then mounted in the AFM and the ligand function of the biotin residues was tested by repeated approach to, and retraction from, the test sample which consisted of a dense monolayer of avidin, bound to mica by electrostatic adsorption (Figure 3A).[51] A typical example of the resulting force curves is shown in Figure 3B. The *X*-axis corresponds to the vertical movement of the piezo which carries the cantilever, while the *Y*-axis mirrors the deflection of the cantilever (converted into force values by multiplying the deflection amplitude with the force constant of the particular cantilever). During the approach (gray line), the cantilever is in the resting position up to the point of contact.

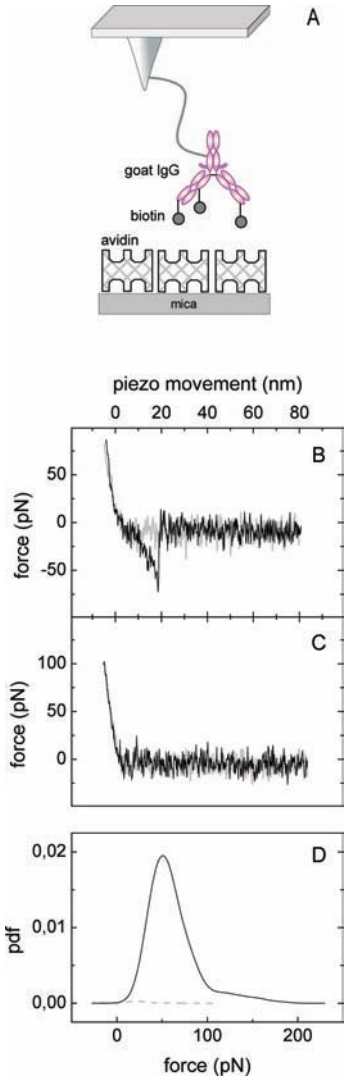


Figure 3. Force spectroscopy of single avidin−biotin interactions. (A) The AFM tip was functionalized with biotin-IgG, as outlined in Figure 1cd (or in greater detail in Figure S5, Supporting Information), using ethanolamine hydrochloride for tip amino-functionalization and iodine/acetone for cleavage of the acetal functions. In parallel, avidin was irreversibly adsorbed onto freshly cleaved mica. (B) Example of a force−distance cycle showing specific avidin−biotin unbinding. The piezo movement in the approach-and-retraction cycles was ±100 nm in 1 s, the force constant of the cantilever was 18 pN/nm, and the loading rate at unbinding was calculated as 1180 pN/s. Unbinding occurred at a rupture force of 51 pN and a tip−mica distance of 22 nm. (C) Example of a force−distance cycle performed in the presence of free streptavidin (0.5 mg/mL final concentration in PBS). (D) Probability density function (pdf) of the unbinding forces observed in 199 out of 948 force−distance cycles (solid line, 21% binding probability). In the presence of free streptavidin, only 3 out of 198 force−distance cycles showed apparent unbinding events (dashed gray trace, 1.5% binding probability).

Further approach causes upward bending of the cantilever. Retraction causes relaxation of cantilever bending, which does not stop at zero force but proceeds to negative values at further retraction. The reason is binding of a tip-tethered biotin residue to mica-bound avidin which causes progressive stretching of the PEG chain. At the critical force of 51 pN, the avidin−biotin bond is suddenly ruptured and the cantilever jumps to its resting position. The probability density function (pdf)[56] of 199 unbinding events (Figure 3D, solid line) shows the expected average avidin−biotin rupture force, as previously observed a the same force loading rate.[25,38,51]

The specificity of avidin−biotin interaction was demonstrated by blocking the biotin residues on the tip with free streptavidin from solution. As a consequence, most force−distance cycles showed only upward bending of the cantilever (Figure 3C) and only 1.5% of the force distance cycles showed downward deflection, in contrast to 21% before the addition of free streptavidin. This difference in binding probability is reflected by the much lower area of the unbinding force distribution function in the presence of streptavidin (dashed gray line in Figure 3D), as compared to the condition with no streptavidin (solid line).

For independent validation of the new tip functionalization method (Figure 1c,d,e), the procedure was applied to chips (5 mm × 5 mm) consisting of the same material as the AFM tips (Si_3N_4) and the area density of immobilized biotin-IgG was estimated from binding of EAP which is a conjugate between avidin and horse radish peroxidase.[25,38,51] Specific binding (Table 1, column 5) was calculated by subtracting nonspecific binding in the presence of free D-biotin (column 4) from total binding in the absence of free D-biotin (column 3). The results show that specific binding of EAP to immobilized biotin-IgG is far more pronounced than nonspecific adsorption. The actual numbers in columns 3−5 are similar as previously obtained with aldehyde-PEG-NHS,[38] except that aldehyde-PEG-NHS must be used at high concentrations (Figure 1b,e) in order to suppress loop formation on the surface (Figure 1a), whereas the new linker acetal-PEG-NHS can be used at the low concentration of 1 mg/mL (Table 1, column 1). From these findings, we conclude that all available amino groups on the tip surface fully react with the NHS ester function of acetal-PEG-NHS (1 mg/mL in chloroform with 0.5% TEA, 60 min), thereby eliminating the danger of loop formation on the tip surface when/after the acetal is converted into a benzaldehyde function in the next step (Figure 1d).

Table 1 also shows that there is no need to use antibody concentrations higher than 0.15 mg/mL (column 2). The same phenomenon has been observed when other PEG linkers were used for antibody linking to AFM tips.[25,38] It was conclusively explained by weak preadsorption of protein to the tip surface, with the effect that one protein molecule adsorbed within reach of a 6-nm-long PEG linker has an effective local concentration of 3 mM.[25] As a consequence, very low protein concentrations suffice to equip all PEG linkers on the AFM tip with a protein molecule. In practice, we have seen efficient tip functionalization with ≥0.03 mg/mL antibody concentration (data not shown).

AFM Tip Functionalization, using Dilute Citric Acid for Cleavage of Tip-Linked Acetal Functions. The above-described method of tip functionalization has successfully been applied in several AFM laboratories when suddenly the users complained that the gold mirror on the top side of the cantilever got destroyed during tip functionalization. Detailed analysis showed that this destruction occurred during acetal cleavage with iodine/acetone (Figure 1d) and that it only happened with cantilevers purchased after the producer had changed the production method. As a consequence, several publications could only be finished by switching back to tip functionalization with aldehyde-PEG-NHS (Figure 1b,e).[39,41,49]

In search for an alternative to iodine/acetone a study was found in which the diethylacetal of a PEG-linked benzaldehyde had completely been hydrolyzed within 5 h at pH 5, which had been adjusted with HCl.[57] This condition seemed promising in

Table 1. Tethering of Biotinylated IgG to Silicon Nitride Chips via Acetal-PEG-NHS (Iodine Method)[a]

[PEG linker] (mg/mL)	[biotin-IgG] (mg/mL)	total sites (μm^{-2}) [b]	nonspecific sites (μm^{-2}) [b]	specific sites (μm^{-2}) [b]
1	2	805 ± 124	27 ± 4	778 ± 143
10	2	742 ± 81	27 ± 4	715 ± 94
1	0.15	777 ± 136	151 ± 51	626 ± 153

[a] Silicon nitride chips were derivatized according to the scheme shown in Figure S6. Ethanolamine hydrochloride was used for amino-functionalization of silicon nitride (step a in Figure S6). Iodine (0.1%, in acetone, 5 min) was applied for cleavage of the acetal function (step c). [b] The number of biotin-IgG molecules per μm^2 (specific sites) was estimated from the difference EAP binding, measured in the absence (total sites, step f) and in the presence of free D-biotin (nonspecific sites, step e).

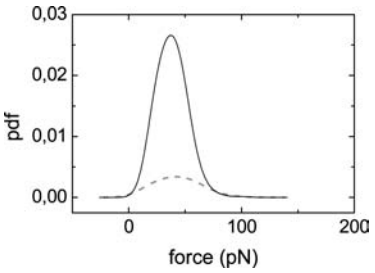


Figure 4. Force measurements of single avidin−biotin interactions. Tip functionalization and force spectroscopy were performed as in Figure 3, except that citric acid (1%, in water, 15 min) was used in place of iodine/acetone for conversion of acetal into aldehyde functions. The piezo movement in the approach-and-retraction cycles was ±150 nm in 1 s, the force constant of the cantilever was 37 pN/nm, and the loading rate at unbinding was calculated as 720 pN/s. The graph shows the probability density function (pdf) of the unbinding forces observed in 321 out of 985 force−distance cycles (solid line, 32.6% binding probability). In the presence of free streptavidin, only 41 out of 938 force−distance cycles showed apparent unbinding events (dashed gray line, 4.4% binding probability).

terms of mildness, but shorter reaction times and a more reliable way to adjust pH were required for practical purposes. For a first test, we treated acetal-PEG-COOH with 1% citric acid (pH 2.2, Figure S4) for 10 min and found that at least 99.6% (or more) of the acetal functions had been converted into benzaldehyde functions (see Supporting Information). Consequently, the AFM test experiment from Figure 3 was repeated, except that conversion of "tip-PEG-acetal" into "tip-PEG-aldehyde" was performed with 1% citric acid instead of iodine/acetone. The results are summarized in Figure 4. The unbinding force distribution shows the expected average unbinding force of ~50 pN, as well as high binding probability (32.6%, solid line) before and low binding probability (4.4%, dashed line) after specific block of avidin−biotin interaction with excess of streptavidin.

The modified tip functionalization protocol with 1% citric acid in place of iodine/acetone was again validated by imitation of tip functionalization on silicon nitride chips (Table 2). Columns 1 and 5 confirm the well-known trend that higher densities of amino groups are achieved with ethanolamine/DMSO as compared to gas-phase silanization with APTES.[51,52] In addition, the ethanolamine/DMSO method is less critical and easier to perform by newcomers. Nevertheless, the APTES method is to be preferred for high-quality AFM measurements.[58] When varying the incubation time with 1% citric acid (column 2), it was found that even the short time interval of 1 min was sufficient to deprotect 60−90% of the benzaldehyde functions on the chip (see column 5). From these data, it appears that 3−5 min of treatment with 1% citric acid is the best compromise between efficient acetal cleavage and minimal chemical stress on AFM tips.

Table 3 addresses the question regarding whether it is necessary to block potentially unused benzaldehyde functions on the AFM tip. Now, all chips were amino-functionalized with APTES in the gas phase, followed by reaction with acetal-PEG-NHS, cleavage of tip-bound acetal functions with 1% citric acid, and coupling of biotin-IgG to the resulting benzaldehyde functions on the chip. In case unused benzaldehyde functions are present on the chip surface, this should lead to covalent coupling of the ExtrAvidin-Peroxidase (EAP), which we use for "counting" of the biotin-IgG molecules on the chip surface. Such covalent coupling would contribute to nonspecific binding (column 4 in Table 3), in contrast to the specific interaction of EAP with biotin-IgG (column 5) which is blocked by excess of free D-biotin. Previously, it was shown that the terminal benzaldehyde is efficiently blocked by free ethanolamine in presence of $NaCNBH_3$.[38] Now, free ethanolamine was applied after coupling of biotin-IgG (lines 3 and 4) and compared to controls in which no attempt was made to block unused benzaldehyde functions (lines 1 and 2). However, no significant difference was found with respect to the extent of nonspecific binding. The same result was also obtained when glycine was used in place of ethanolamine (lines 5 and 6).

Lines 1, 3, and 5 in Table 3 differ from all chip functionalization assays in this and previous studies[25,38,51,52] by omission of Tween 20 in the incubation step with ExtrAvidin-Peroxidase (EAP). Absence of detergent was expected to enhance adsorption, and thereby also to accelerate covalent coupling of EAP to surface-bound benzaldehyde residues,[25] in case not all of them had reacted with biotin-IgG in the preceding step. The data in Table 3, however, do not show a significant difference in the extent of nonspecific binding of EAP to the chip surface, whether Tween 20 was present or not (columns 2 and 4). It is, therefore, concluded that nonspecific binding was merely caused by physical adsorption of ExtrAvidin-Peroxidase and not by covalent coupling to unused benzaldehyde functions. With respect to AFM tip functionalization, this means that all (or almost all) benzaldehyde groups on the tip surface appear to react with a protein molecule under the standardized reaction conditions and that blocking of putatively unused benzaldehyde groups is merely optional. In case blocking is desired, glycine is to be preferred over ethanolamine, because the lower pK_a of glycine allows for a more neutral pH during the blocking step (see legend to Table 3). An alternate method for blocking of potentially unused aldehyde functions at pH ~ 7.7 is described in the Supporting Information (part 4).

Rapid Imaging of Mitochondrial Uncoupling Protein with ATP-Functionalized AFM Tips. As describe above, citric acid (1%) allows for conversion of "tip-PEG-acetal" into "tip-PEG-aldehyde" without adverse effects on standard AFM cantilevers. Unfortunately, this is not true for MAC levers, the magnetic

Table 2. Tethering of Biotinylated IgG to Silicon Nitride Chips via Acetal-PEG-NHS (citric acid method).[a]

amino-functionalization	1% citric acid (min)	total sites (μm^{-2}) [b]	nonspecific sites (μm^{-2}) [b]	specific sites (μm^{-2}) [b]
ethanolamine	1	1389 ± 146	159 ± 49	1230 ± 169
	15	1486 ± 151	159 ± 49	1327 ± 185
APTES	1	645 ± 141	118 ± 27	527 ± 163
	15	1009 ± 95	118 ± 27	891 ± 117

[a] Silicon nitride chips were derivatized according to the scheme shown in Figure S6. The concentration of acetal-PEG-NHS was 1 mg/mL (step b in Figure S6). Citric acid (1%, in water, treatment time either 1 or 15 min) was applied for cleavage of the acetal function (step c). The concentration of biotin-IgG was 0.22 mg/mL (step d). [b] The number of biotin-IgG molecules per μm^2 (specific sites) was estimated from the difference in EAP binding, measured in the absence (total sites, step f) and in the presence of free D-biotin (nonspecific sites, step e).

Table 3. Comparison of Different Methods for Blocking of Unused Aldehyde Functions (citric acid method).[a]

blocking method	Tween 20[d]	total sites (μm^{-2}) [e]	nonspecific sites (μm^{-2}) [e]	specific sites (μm^{-2}) [e]
none	-	933 ± 133	142 ± 39	791 ± 92
	+	898 ± 344	96 ± 17	802 ± 344
ethanolamine [b]	-	775 ± 24	146 ± 28	629 ± 37
	+	715 ± 107	138 ± 26	577 ± 110
glycine [c]	-	1053 ± 345	81 ± 12	972 ± 345
	+	865 ± 146	90 ± 32	775 ± 149

[a] Silicon nitride chips were derivatized according to the scheme shown in Figure S6. APTES was used for amino-functionalization of the silicon nitride chips (step a in Figure S6). The concentration of acetal-PEG-NHS was 1 mg/mL (step b). Citric acid (1%, in water, 15 min) was used for cleavage of the acetal function (step c). The concentration of biotin-IgG was 0.15 mg/mL (step d). [b] Ethanolamine hydrochloride (0.05 volumes of a 1 M stock solution, adjusted to pH 9.6 with NaOH) or [c] glycine (0.05 volumes of a 1 M stock solution, adjusted to pH 8.3 with NaOH) was added to the biotin-IgG solution on the AFM tips after 1 h incubation and allowed to react for 10 min (step f in Figure S5). [d] The minus or plus signs indicate absence or presence of Tween 20 (0.1%) during incubation with EAP. In any case, Tween 20 was used in the subsequent washing steps. [e] The number of biotin-IgG molecules per μm^2 (specific sites) was estimated from the difference in EAP binding, measured in the absence (total sites, step f in Figure S6) and in the presence of free *d*-biotin (nonspecific sites, step e in Figure S6).

coating of which has been observed damaged to variable degrees by treatment with 1% citric acid (data not shown). MAC levers are indispensable for simultaneous "topography and recognition imaging" (TREC). In the so-called TREC mode, a biofunctionalized tip is magnetically oscillated near its resonance frequency while rapidly scanning the sample surface. Hereby, topographic features dampen the downward amplitudes of tip oscillation, while recognition of a target molecule on the sample surface by a tip-bound sensor molecule causes stretching of the PEG linker between the tip and the sensor molecule, which dampens the upward amplitudes of tip oscillation. Consequently, the envelope of the lower amplitudes yields the topographic image (Figure 5B), while the envelope of the upper amplitudes yields a map of recognition sites (Figure 5C). A more detailed explanation of the TREC imaging method can be found at the end of the Supporting Information.

Given the poor resistance of the magnetic coating of MAC levers to 1% citric acid, the new tip functionalization protocol with acetal-PEG-NHS cannot be applied to tips used for recognition imaging, and the older method with aldehyde-PEG-NHS must be used instead.[38] Nevertheless, the present study provides for a major improvement of the older method, albeit in an indirect way. Figure 2 depicts a new route for the synthesis of the old linker aldehyde-PEG-NHS (steps a, d, and e). Previously, the old linker was prepared by reaction of NH_2-PEG-COOH with succinimidyl formylbenzoate (SFB, step c). Unfortunately, SFB has two amino-reactive ends, thus several side products are formed in the reaction with NH_2-PEG-COOH which are difficult to remove and cause low yields of aldehyde-PEG-COOH. No such problem is encountered when reacting the new module SDMB with NH_2-PEG-COOH (step a) because it possesses only one amino-reactive group. Consequently, the yield of acetal-PEG-COOH is high and the intermediate is obtained in good yield. Cleavage of the acetal function (step d) and activation of the terminal carboxyl (step e) are also simple, thus the old linker aldehyde-PEG-NHS is obtained in high yield from the valuable starting material NH_2-PEG-COOH.

For the "proof of principle", the binding of ATP to the mitochondrial uncoupling protein, UCP1, was studied.[59] UCP1 is an anion transporter, which dissipates the mitochondrial inner membrane proton gradient and can be inhibited by di- or triphosphate nucleotides. Although some plausible models were proposed (for review, see Krauss et al.[60]), the exact mechanism of UCP1 inhibition remains unknown. In the absence of the protein crystallographic structure, the studies using tip-tethered ATP molecules are a powerful tool to elucidate different parameters of ATP-UCP interaction, such as location of the nucleotide binding site inside the membrane and a binding force of the nucleotide-protein interaction. The latter is a subject of our subsequent study.

The newly synthesized "old linker" acetal-PEG-NHS was used for flexible attachment of an ATP derivative to a MAC lever, as depicted in Figure 5A (for details, see Supporting Information). The functionalized tip was scanned over a mica-supported phospholipid bilayer which contained purified UCP1. The individual UCP1 molecules were nicely visible as round structures of defined size in the topographic image (Figure 5B). The specific recognition of the ATP-binding sites is mirrored in the recognition image (Figure 5C) of the TREC mode. For the competitive blocking of ATP-binding sites in the control experiment, 4.8 mM of free ATP was added to the buffer solution before scanning. Figure 5D shows that the protein spots in the

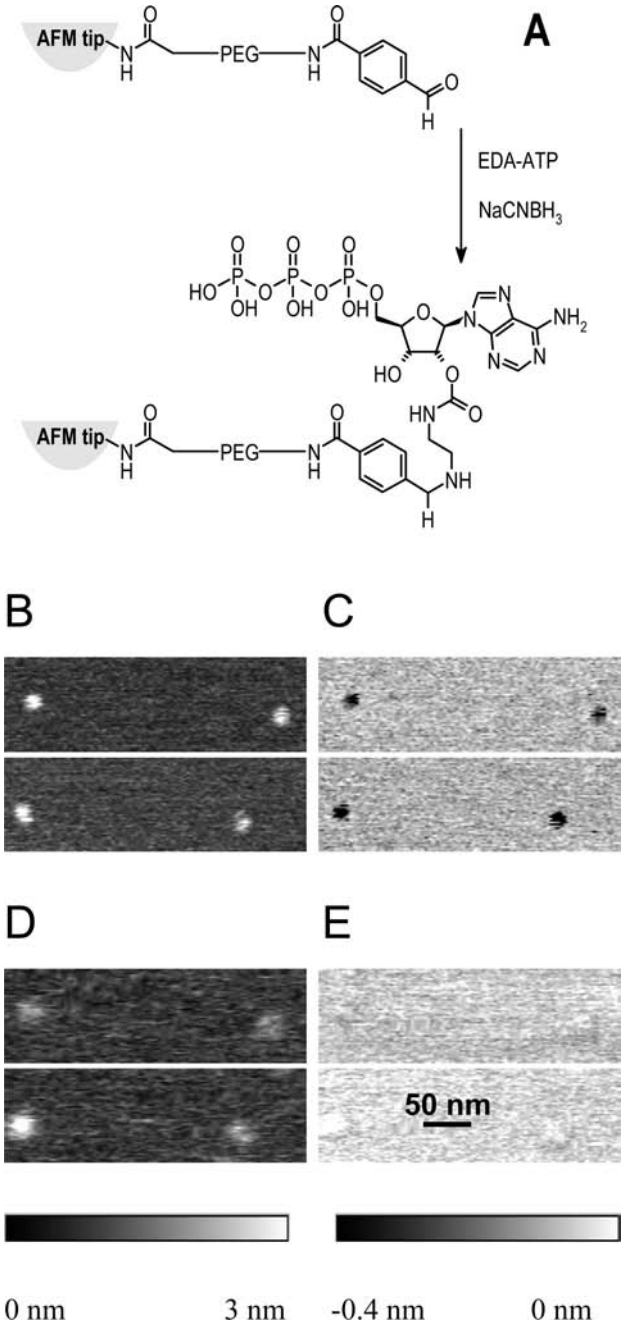


Figure 5. Topographic and recognition imaging of uncoupling protein 1 (UCP1) in planar supported bilayer with an ATP-functionalized AFM tip. (A) Reaction of tip-PEG-aldehyde with an ethylene diamine derivative of ATP (EDA-ATP) with concomitant reduction of the C═N bond by $NaCNBH_3$. Topographic images (B) and simultaneously acquired recognition images (C) of two different bilayer patches (top and bottom strip) in the absence of free ATP. Topographic images (D) and simultaneously acquired recognition images (E) of the same sample areas as in (B) and (C) after the addition of free ATP (final concentration 4.8 mM).

topographic image persisted, whereas only very dim shadows with the opposite amplitude were observed in the recognition image (Figure 5E), revealing the tiny amplitude of the spillover from the topographic image into the recognition image. The complete loss of the recognition after addition of free ATP (Figure 5E) clearly confirms that all recognition spots in Figure 5C were caused by specific binding of tip-linked ATP to UCP1 molecules in the planar lipid membrane.

CONCLUSIONS

The present study offers an uncompromised and simple solution to the nontrivial problem of linking the NH_2 groups of biomolecules to the NH_2 groups of amino-functionalized AFM tips. In contrast to previous methods, a bifunctional linker with a single amino-reactive end is used which is reacted with all available NH_2 groups on the tip surface. Subsequently, the free-tangling end of the PEG linker is converted into an amino-reactive aldehyde function which provides for coupling of sensor molecules via their NH_2 functions. In this way, the undesired cross-linking of adjacent NH_2 functions on the tip surface is perfectly avoided. The method is particularly suited for proteins, which are usually abundant in lysine residues. Other obvious applications are synthetic oligonucleotides with NH_2 groups on their 5′ or 3′ end, as well as small biomolecules or drugs with endogenous or artificially introduced amino functions.

The only weak point of the new tip functionalization protocol is the adverse effect of the acetal-to-aldehyde conversion step on the magnetic coating of cantilevers which are needed for fast imaging of recognition sites on the sample surface. Such cantilevers must be functionalized with the old linker aldehyde-PEG-NHS. Nevertheless, this older method has also profited from the present study because a simpler and more efficient synthesis route to aldehyde-PEG-NHS was found. The experiments with reconstituted UCP1 demonstrate a great application potential of recognition force microscopy for the functional studies of biomolecules which is not easily gained from other techniques.

ASSOCIATED CONTENT

Supporting Information. Syntheses of 4-(dimethoxymethyl)-benzoic acid, *N*-succinimidyl 4-(dimethoxymethyl)-benzoate, aldehyde-PEG-COOH, aldehyde-PEG-NHS, acetal-PEG-COOH, acetal-PEG-NHS. Kinetics of acetal cleavage at different pH values in aqueous solution. Detailed illustration of AFM tip functionalization via acetal-PEG-NHS. Illustration of silicon nitride chip functionalization and characterization with ExtrAvidin-Peroxidase. Method of AFM tip functionalization with EDA-ATP. Purification of UCP1 and reconstitution into mica-supported bilayer. This material is available free of charge via the Internet at http://pubs.acs.org.

AUTHOR INFORMATION

Corresponding Author

*To whom correspondence should be addressed at the Institute of Biophysics in Linz. Tel.: +43 (732) 2468-9271. Fax: +43 (732) 2468-9280, e-mail: hermann.gruber@jku.at.

ACKNOWLEDGMENT

We are indebted to Prof. Norbert Müller for use of NMR spectrometer facilities. This work was supported by the Austrian Science Foundation (FWF project SFB-F35, to P. H.), by the Austrian Research Promotion Agency (FFG, Austrian Nanoscience Initiative VO104-08-BI, project 819703 NSI-NABIOS, to H. J. G.), by the Christian Doppler Society, by EC grant SMW (grant number 213717, to P. H.), and by Deutsche Forschungsgemeinschaft (Po-524/3-1 and Po 524/5-1 to E. P.).

■ ABBREVIATIONS

AFM, atomic force microscope (or microscopy); acetal-PEG-COOH, see Figure 3; acetal-PEG-NHS, see Figure 2; acetal-PEG_{27}-NHS, see Figure 2; aldehyde-PEG-COOH, see Figure 2; aldehyde-PEG-NHS, see Figure 2; aldehyde-PEG_{27}-NHS, see Figure 2; ATP, adenosine-5′-*O*-triphosphate; biotin-cap-NHS, *N*-succinimidyl 6-(*N*-biotinoyl)-aminohexanoate; DMSO, dimethylsulfoxide; EAP, ExtrAvidin-Peroxidase; EDA-ATP, 2′-/3′-*O*-(2-aminoethylcarbamoyl)-adenosine-5′-*O*-triphosphate; EDTA, ethylene diamine *N,N,N′,N′*-tetraacetic acid; NH_2-PEG-NH_2, *O,O′-bis*-(2-aminopropyl)-poly(ethylene glycol) 800; NH_2-PEG-COOH, *N*-glutaryl derivative of NH_2-PEG-NH_2, see Figure 3; NHS, *N*-hydroxysuccinimide; pdf, probability density function; PBS, phosphate-buffered saline; PEG, poly(ethylene glycol); SDMB, *N*-succinimidyl 4-(dimethoxymethyl)-benzoate; SFB, *N*-succinimidyl 4-formylbenzoate; TEA, *N,N,N*-triethylamine; TREC mode, topography-and-recognition mode

■ REFERENCES

(1) Hörber, J. K., and Miles, M. J. (2003) Scanning probe evolution in biology. *Science 302*, 1002–1005.

(2) Scheuring, S., Müller, D. J., Ringler, P., Heymann, J. B., and Engel, A. (1999) Imaging streptavidin 2D crystals on biotinylated lipid monolayers at high resolution with the atomic force microscope. *J. Microsc. 193*, 28–35.

(3) P Parot, P., Dufrêne, Y. F., Hinterdorfer, P., Le Grimellec, C., Navajas, D., Pellequer, J. L., and Scheuring, S. (2007) Past, present and future of atomic force microscopy in life sciences and medicine. *J. Mol. Recognit. 20*, 418–431.

(4) Hinterdorfer, P., and Dufrêne, Y. F. (2006) Detection and localization of single molecular recognition events using atomic force microscopy. *Nat. Methods 3*, 347–355.

(5) Kienberger, F., Ebner, A., Gruber, H. J., and Hinterdorfer, P. (2006) Molecular recognition imaging and force spectroscopy of single biomolecules. *Acc. Chem. Res. 39*, 29–36.

(6) Raab, A., Han, W., Badt, D., Smith-Gill, S. J., Lindsay, S. M., Schindler, H., and Hinterdorfer, P. (1999) Antibody recognition imaging by force microscopy. *Nat. Biotechnol. 17*, 902–905.

(7) Radmacher, M., Cleveland, J. P., Fritz, M., Hansma, H. G., and Hansma, P. K. (1994) Mapping interactions forces with the atomic force microscope. *Biophys. J. 66*, 2159–2165.

(8) Stroh, C. M., Wang, H., Bash, R., Ashcroft, B., Nelson, J., Gruber, H., Lohr, D., Lindsay, S. M., and Hinterdorfer, P. (2004) Single-molecule recognition imaging microscopy. *Proc. Natl. Acad. Sci. U.S.A. 101*, 12503–12507.

(9) Stroh, C. M., Ebner, A., Geretschläger, M., Freudenthaler, G., Kienberger, F., Kamruzzahan, A. S. M., Smith-Gill, S. J., Gruber, H. J., and Hinterdorfer, P. (2004) Simultaneous topography and recognition imaging using force microscopy. *Biophys. J. 87*, 1981–1990.

(10) Evans, E., and Ritchie, K. (1997) Dynamic strength of molecular adhesion bonds. *Biophys. J. 72*, 1541–1555.

(11) Baumgartner, W., Hinterdorfer, P., Ness, W., Raab, A., Vestweber, D., Schindler, H., and Drenckhahn, D. (2000) Cadherin interaction probed by atomic force microscopy. *Proc. Natl. Acad. Sci. U.S.A. 97*, 4005–4010.

(12) Hukkanen, E., Wieland, J., Gewirth, A., Leckband, D., and Braatz, R. D. (2005) Multiple-bond kinetics from single-molecule pulling experiments: Evidence for multiple NCAM bonds. *Biophys. J. 89*, 3434–3445.

(13) Nevo, R., Stroh, C., Kienberger, F., Kaftan, D., Brumfeld, V., Elbaum, M., Reich, Z., and Hinterdorfer, P. (2003) A molecular switch between alternative conformational states in the complex of Ran and importin β1. *Nat. Struct. Biol. 10*, 553–557.

(14) Wieland, J. A., Gewirth, A. A., and Leckband, D. E. (2005) Single molecule adhesion measurements reveal two homophilic neural cell adhesion molecule bonds with mechanically distinct properties. *J. Biol. Chem. 280*, 41037–41046.

(15) Cross, B., Ronzon, F., Roux, B., and Rieu, J. P. (2005) Measurement of the anchorage force between GPI-anchored alkaline phosphatase and supported membranes by AFM force spectroscopy. *Langmuir 21*, 5149–5153.

(16) Desmeules, P., Grandbois, M., Bondarenko, V. A., Yamazaki, A., and Salesse, C. (2002) Measurement of membrane binding between recoverin, a calcium-myristoyl switch protein, and lipid bilayers by AFM-based force spectroscopy. *Biophys. J. 82*, 3343–3350.

(17) Touhami, A., Hoffmann, B., Vasella, A., Denis, F. A., and Dufrêne, Y. F. (2003) Probing specific lectin-carbohydrate interactions using atomic force microscopy imaging and force measurements. *Langmuir 19*, 1745–1751.

(18) Touhami, A., Jericho, M. H., and Beveridge, T. J. (2007) Molecular recognition forces between immunoglobulin G and a surface protein adhesin on living *staphylococcus aureus*. *Langmuir 23*, 2755–2760.

(19) Cecchet, F., Lussis, L., Jérôme, C., Gabriel, S., Silva-Goncalves, E., Jérôme, R., and Duwez, A.-S. (2008) A generic chemical platform for molecular recognition and stimuli-responsive probes based on scanning probe microscopy. *Small 4*, 1101–1104.

(20) Avci, R., Schweitzer, M., Boyd, R. D., Wittmeyer, J., Steele, A., Toporski, J., Beech, W., Arce, F. T., Spangler, B., Cole, K. M., and McKay, D. S. (2004) Comparison of antibody-antigen interactions on collagen measured by conventional immunological techniques and atomic force microscopy. *Langmuir 20*, 11053–11063.

(21) Bonanni, B., Kamruzzahan, A. S. M., Bizzarri, A. R., Rankl, C., Gruber, H. J., Hinterdorfer, P., and Cannistraro, S. (2005) Single molecule recognition between cytochrome C 551 and gold-immobilized azurin by force spectroscopy. *Biophys. J. 89*, 2783–2791.

(22) Chen, G., Ning, X., Park, B., Boons, G.-J., and Xu, B. (2009) Simple, clickable protocol for atomic force microscopy tip modification and its application for trace ricin detection by recognition imaging. *Langmuir 25*, 2860–2864.

(23) Francius, G., Alsteens, D., Dupres, V., Lebeer, S., De Keersmaecker, S., Vanderleyden, J., Gruber, H. J., and Dufrêne, Y. F. (2009) Stretching polysaccharides on live cells using single molecule force spectroscopy. *Nat. Protoc. 4*, 939–946.

(24) Hinterdorfer, P., Baumgartner, W., Gruber, H. J., Schilcher, K., and Schindler, H. (1996) Detection and localization of individual antibody-antigen recognition events by atomic force microscopy. *Proc. Natl. Acad. Sci. U.S.A. 93*, 3477–3481.

(25) Kamruzzahan, A. S. M., Ebner, A., Wildling, L., Kienberger, F., Riener, C. K., Hahn, C. D., Pollheimer, P. D., Winklehner, P., Hölzl, M., Lackner, B., Schörkl, D. M., Hinterdorfer, P., and Gruber, H. J. (2006) Antibody linking to atomic force microscope tips via disulfide bond formation. *Bioconjugate Chem. 17*, 1473–1481.

(26) Kienberger, F., Pastushenko, V. P., Kada, G., Gruber, H. J., Riener, C., Schindler, H., and Hinterdorfer, P. (2000) Static and dynamical properties of single poly(ethylene glycol) molecules investigated by force spectroscopy. *Single Mol. 1*, 123–128.

(27) Langry, K. C., Ratto, T. V., Rudd, R. E., and McElfresh, M. W. (2005) The AFM measured force required to rupture the dithiolate linkage of thioctic acid to gold is less than the rupture force of a simple gold-alkyl thiolate bond. *Langmuir 21*, 12064–12067.

(28) Lin, L., Wang, H., Liu, Y., Yan, H., and Lindsay, S. (2006) Recognition imaging with a DNA aptamer. *Biophys. J. 90*, 4236–4238.

(29) Lower, B. H., Yongsunthon, R., Shi, L., Wildling, L., Gruber, H. J., Wigginton, N. S., Reardon, C. L., Pinchuk, G. E., Droubay, T. C., Boily, J.-F., and Lower, S. K. (2009) Antibody-recognition force microscopy shows that outer membrane cytochromes OmcA and MtrC are expressed on the exterior surface of *Shewanella oneidensis* MR-1. *Appl. Environ. Microbiol. 75*, 2931–2935.

(30) Ratto, T. V., Langry, K. C., Rudd, R. E., Balhorn, R. L., Allen, M. J., and McElfresh, M. W. (2004) Force spectroscopy of the double-tethered concanavalin-A mannose bond. *Biophys. J. 86*, 2430–2437.

(31) Ros, R., Schwesinger, F., Anselmetti, D., Kubon, M., Schafer, R., Pluckthun, A., and Tiefenauer, L. (1998) Antigen binding forces of individually addressed single-chain Fv antibody molecules. *Proc. Natl. Acad. Sci. U.S.A. 95*, 7402–7405.

(32) Puntheeranurak, T., Wimmer, B., Castaneda, F., Gruber, H. J., Hinterdorfer, P., and Kinne, R. K. H. (2007) Substrate specificity of sugar transport by rabbit SGLT1: Single-molecule atomic force microscopy versus transport studies. *Biochemistry 46*, 2797–2804.

(33) Dorner, M. M., Bassett, E. W., Beiser, S. M., Kabat, E. A., and Tanenbaum, S. W. (1967) Studies on human antibodies: V. Amino acid composition of antidextrans of the same and of different specificities from several individuals. *J. Exp. Med. 125*, 823–831.

(34) Van Dongen, S. F. M., Teeuwen, R. L. M., Nallani, M., van Berkel, S. S., Cornelissen, J. J. L. M., Nolte, R. J. M., and van Hest, J. C. M. (2009) Single-step azide introduction in proteins via an aqueous diazo transfer. *Bioconjugate Chem. 20*, 20–23.

(35) Johnsson, B., Lofas, S., and Lindquist, G. (1991) Immobilization of proteins to a carboxymethyldextran-modified gold surface for biospecific interaction analysis in surface plasmon resonance sensors. *Anal. Biochem. 198*, 268–277.

(36) Lahiri, J., Isaacs, L., Tien, J., and Whitesides, G. M. (1999) A strategy for the generation of surfaces presenting ligands for studies of binding based on an active ester as a common reactive intermediate: A surface plasmon resonance study. *Anal. Chem. 71*, 777–790.

(37) Hölzl, M., Tinazli, A., Leitner, C., Hahn, C. D., Lackner, B., Tampe, R., and Gruber, H. J. (2007) Protein-resistant self-assembled monolayers on gold with latent aldehyde functions. *Langmuir 23*, 5571–5577.

(38) Ebner, A., Wildling, L., Kamruzzahan, A. S. M., Rankl, C., Wruss, J., Hahn, C. D., Hölzl, M., Kienberger, F., Blaas, D., Hinterdorfer, P., and Gruber, H. J. (2007) A new, simple method for linking of antibodies to atomic force microscopy tips. *Bioconjugate Chem. 18*, 1176–1184.

(39) Alsteens, D., Dupres, V., McEvoy, K., Wildling, L., Gruber, H. J., and Dufrêne, Y. F. (2008) Structure, cell wall elasticity and polysaccharide properties of living yeast cells, as probed by AFM. *Nanotechnology 18*, 384005.

(40) Chtcheglova, L. A., Waschke, J., Wildling, L., Drenckhahn, D., and Hinterdorfer, P. (2007) Nano-scale dynamic recognition imaging on vascular endothelial cells. *Biophys. J. 93*, L11–13.

(41) Francius, G., Lebeer, S., Alsteens, D., Wildling, L., Gruber, H. J., Hols, P., De Keersmaecker, S., Vanderleyden, J., and Dufrêne, Y. F. (2008) Detection, localization and conformational analysis of single polysaccharide molecules on live bacteria. *ACS Nano 2*, 1921–1929.

(42) Kloss, F. R., Gassner, R., Preiner, J., Ebner, A., Larsson, K., Hachl, O., Tuli, T., Rasse, M., Moser, D., Laimer, K., Nickel, E. A., Laschober, G., Brunauer, R., Klima, G., Hinterdorfer, P., Steinmuller-Nethl, D., and Lepperdinger, G. (2008) The role of oxygen termination of nanocrystalline diamond on immobilisation of BMP-2 and subsequent bone formation. *Biomaterials 29*, 2433–2442.

(43) Rankl, C., Kienberger, F., Wildling, L., Wruss, J., Gruber, H. J., Blaas, D., and Hinterdorfer, P. (2008) Multiple receptors involved in human rhinovirus attachment to live cells. *Proc. Natl. Acad. Sci. U.S.A. 105*, 17778–17783.

(44) Tang, J., Badelt-Lichtblau, H., Ebner, A., Preiner, J., Kraxberger, B., Gruber, H. J., Sleytr, U. B., Ilk, N., and Hinterdorfer, P. (2008) Fabrication of highly ordered gold nanoparticle arrays templated by crystalline lattices of bacterial S-layer protein. *ChemPhysChem 9*, 2317–2320.

(45) Tang, J., Ebner, A., Ilk, N., Lichtblau, H., Huber, C., Zhu, R., Pum, D., Leitner, M., Pastushenko, V., Gruber, H. J., Sleytr, U. B., and Hinterdorfer, P. (2008) High-affinity tags fused to S-layer proteins probed by atomic force microscopy. *Langmuir 24*, 1324–1329.

(46) Tang, J., Ebner, A., Kraxberger, B., Badelt-Lichtblau, H., Gruber, H. J., Sleytr, U. B., Ilk, N., and Hinterdorfer, P. (2001) Mapping short affinity tags on bacterial S-layer with an antibody. *ChemPhysChem 11*, 2323–2326.

(47) Zhu, R., Ebner, A., Kastner, M., Preiner, J., Howorka, S., and Hinterdorfer, P. (2009) Topography and recognition imaging of protein-patterned surfaces generated by AFM nanolithography. *ChemPhysChem 10*, 1478–1481.

(48) Zhu, R., Howorka, S., Proll, J., Kienberger, F., Preiner, J., Hesse, J., Ebner, A., Pastushenko, V. P., Gruber, H. J., and Hinterdorfer, P. (2010) Nanomechanical recognition measurements of individual DNA molecules reveal epigenetic methylation patterns. *Nat. Nanotechnol. 5*, 788–791.

(49) Tang, J., Krajcikova, D., Zhu, R., Ebner, A., Cutting, S., Gruber, H. J., Barak, I., and Hinterdorfer, P. (2007) Atomic force microscopy imaging and single molecule recognition force spectroscopy of coat proteins on the surface of *Bacillus subtilis* spore. *J. Mol. Recognit. 20*, 483–489.

(50) Riener, C. K., Kienberger, F., Hahn, C. D., Buchinger, G. M., Egwim, I. O. C., Haselgrübler, T., Ebner, A., Romanin, C., Klampfl, C., Lackner, B., Prinz, H., Blaas, D., Hinterdorfer, P., and Gruber, H. J. (2003) Heterobifunctional crosslinkers for tethering single ligand molecules to scanning probes. *Anal. Chim. Acta 497*, 101–114.

(51) Riener, C. K., Stroh, C. M., Ebner, A., Klampfl, C., Gall, A. A., Romanin, C., Lyubchenko, Y. L., Hinterdorfer, P., and Gruber, H. J. (2003) Simple test system for single molecule recognition force microscopy. *Anal. Chim. Acta 479*, 59–75.

(52) Ebner, A., Hinterdorfer, P., and Gruber, H. J. (2007) Comparison of different aminofunctionalization strategies for attachment of single antibodies to AFM cantilevers. *Ultramicroscopy 107*, 922–927.

(53) Butt, H.-J., and Jaschke, M. (1995) Calculation of thermal noise in atomic force microscopy. *Nanotechnology 6*, 1–7.

(54) Hutter, J. L., and Bechhoefer, J. (1993) Calibration of atomic-force microscope tips. *Rev. Sci. Instrum. 64*, 1868–1873.

(55) Sun, J., Dong, Y., Cao, L., Wang, X., Wang, S., and Hu, Y. (2004) Highly efficient chemoselective deprotection of *O,O*-acetals and *O,O*-ketals catalyzed by molecular iodine in acetone. *J. Org. Chem. 69*, 8932–8934.

(56) Baumgartner, W., Hinterdorfer, P., and Schindler, H. (2000) Data analysis of interaction forces measured with the atomic force microscope. *Ultramicroscopy 82*, 85–95.

(57) Akiyama, Y., Nagasaki, Y., and Kataoka, K. (2004) Synthesis of heterotelechelic poly(ethylene glycol) derivatives having α-benzaldehyde and ω-pyridyl disulfide groups by ring opening polymerization of ethylene oxide using 4-(diethoxymethyl)benzyl alkoxide as a novel initiator. *Bioconjugate Chem. 15*, 424–427.

(58) Ebner, A., Wildling, L., Zhu, R., Rankl, C., Haselgrübler, T., Hinterdorfer, P., and Gruber, H. J. (2008) Functionalization of probe tips and supports for single-molecule recognition force microscopy. *In: STM and AFM studies on (bio)molecular systems: Unraveling the nanoworld* (Samori, B., Ed.) pp 29−76, Vol XIV, Springer, Berlin.

(59) Urbankova, E., Voltchenko, A., Pohl, P., Jezek, P., and Pohl, E. E. (2003) Transport kinetics of uncoupling proteins. Analysis of UCP1 reconstituted in planar lipid bilayers. *J. Biol. Chem. 278*, 32497–32500.

(60) Krauss, S., Zhang, C. Y., and Lowell, B. B. (2005) The mitochondrial uncoupling-protein homologues. *Nat. Rev. Mol. Cell Biol. 6*, 248–261.

Supporting Information to:

Linking of Sensor Molecules with Amino Groups to Aminofunctionalized AFM Tips

Linda Wildling, Barbara Unterauer, Rong Zhu, Anne Rupprecht, Thomas Haselgrübler, Christian Rankl, Andreas Ebner, Doris Vater, Philipp Pollheimer, Elena E. Pohl, Peter Hinterdorfer, and Hermann J. Gruber*

*hermann.gruber@jku.at

Institute of Biophysics, J. Kepler University,
Altenberger Str. 69, A-4040 Linz, Austria;

Abbreviations Used in the Supporting Information Only. DCM, dichloromethane; DMB, 4-(dimethoxymethyl)-benzoic acid; DMF, *N*,*N*-dimethylformamide; PEG_{18} diamine, see Figure S3; RT, room temperature; SLS, sodium lauryl sulfate; TLC, thin layer chromatography; TSTU, *N*,*N*,*N'*,*N'*-tetramethyl-(*O*-succinimidyl)-uronium tetrafluoroborate.

Part 1: Syntheses of Crosslinkers p. 2

Part 2: Kinetics of Acetal Cleavage by Acid in Water p. 7

Part 3: Illustration of Tip/Chip Functionalization with Acetal-PEG-NHS p. 9

Part 4: Tip Functionalization with Aldehyde-PEG-NHS and EDA-ATP p. 12

Part 5: Reconstitution of UCP1 in Supported Planar Bilayer and Recognition Imaging with ATP-Functionalized Tips p. 13

Part 6: Explanation of simultaneous topography and recognition imaging with magnetically coated AFM cantilevers p. 14

Part 7: Literature Cited in the Supporting Information Only p. 16

PART 1

SYNTHESES OF CROSSLINKERS

Materials listed in the Supporting Information only. 4-Formylbenzoic acid and NHS were obtained from Aldrich. Ninhydrine was purchased from Merck. DCC and TSTU were obtained from Fluka. PEG_{18} diamine was purchased from Polypure (Norway).

Thin layer chromatography. Merck plastic sheets (silica gel 60) with fluorescent indicator were used for TLC. Eluents I, II, and III contained 70 parts of chloroform, 30 parts of methanol, and 4 parts of concentrated ammonia, or water, or acetic acid, respectively. Eluent IV contained 8 parts of chloroform and 2 parts of methanol. Acetal-protected and unprotected benzaldehyde residues were selectively detected as dark spots on plates with fluorescent indicator when illuminating at 254 nm. Amino groups were specifically stained with ninhydrine (0.1% ninhydrine and 2% acetic acid in 1-butanol) and heating to 120°C. All other components were visualized in iodine vapor.

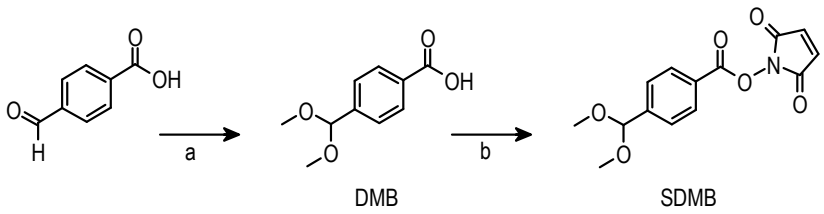


Figure S1. Synthesis of DMB (a, methanol/NH_4Cl) and SDMB (b, DCC/NHS).

Synthesis of 4-(Dimethoxymethyl)-benzoic Acid (DMB). The product was synthesized as described [Roberts et al., 2003], with slight modifications. 4-Formylbenzoic acid (2 g, 13.3 mmol) was dissolved in dry methanol (40 mL, pre-dried with 3 Å molecular sieves) and NH_4Cl (4 g, 74.8 mmol) was added. The reaction mixture was heated under reflux for 20 h. For maximization of the degree of acetalization, 3Å molecular sieves (~5 g) were added and the reaction mixture heated under reflux for an additional 2 h. The solid material was removed by filtration and the mixture was taken to dryness. The residue was dissolved in chloroform and the solution was filtered again. The solvent was removed and the product was recrystallized from n-hexane/chloroform (v/v, 3/1), filtered while still hot, and allowed to crystallize overnight (10 °C), yielding 1.83 g (9.33 mmol) product. According to TLC, the recrystallized product (R_f^{IV} = 0.4) appeared to contain a small fraction educt (R_f^{IV} = 0.2). However, no aldehyde signal was seen in the NMR spectrum. This finding suggests that the product was partially deprotected on the TLC plate. ^{1}H-NMR (200 MHz, $CDCl_3$) δ (ppm): 3.36 (6H, s, C***H***$_3$-O-) 5.48 (1H, s, -C***H***-(O-CH_3)$_2$) 7.26 (s, trace of C***H***Cl_3 in $CDCl_3$) 7.58 (2H, d, J = 8.4 Hz, H3 and H5 of aromatic ring, next to the acetal function) 8.14 (2H, d, J = 8.4 Hz, H2 and H6 of the aromatic ring, next to the COOH group).

Synthesis of *N*-Succinimidyl 4-(dimethoxymethyl)-benzoate (SDMB). DMB (1.33 g, 6.8 mmol) and hydroxysuccinimide (806 mg, 7 mmol) were dissolved in THF (25 mL, dried over basic Al_2O_3) and the solution was cooled using an ice bath. A solution of DCC (1.40 g, 6.8 mmol) in THF (10 mL) was added drop wise under argon while stirring. After 2 hours the ice-bath was removed and the reaction mixture was allowed to react overnight at RT. The supernatant was filtered and taken to dryness. The oily residue was dissolved in DCM, filtered, taken to dryness, and recrystallized from 2-propanol to yield 1.34 g (4.6 mmol) product which was pure by TLC (R_f^{IV} = 0.83), except for a trace of free acid (R_f^{IV} = 0.4). ^{1}H-NMR (200 MHz, $CDCl_3$) δ (ppm): 2.90 (4H, s, NHS) 3.32 (6H, s, C***H***$_3$-O-) 5.46 (1H, s, -C***H***=(O-CH_3)$_2$) 7.26 (s, trace of C***H***Cl_3 in $CDCl_3$) 7.60 (2H, d, J = 8.4 Hz, H3 and H5 of aromatic ring, next to the acetal function) 8.13 (2H, d, J = 8.4 Hz, H2 and H6 of the aromatic ring, next to the COOH group).

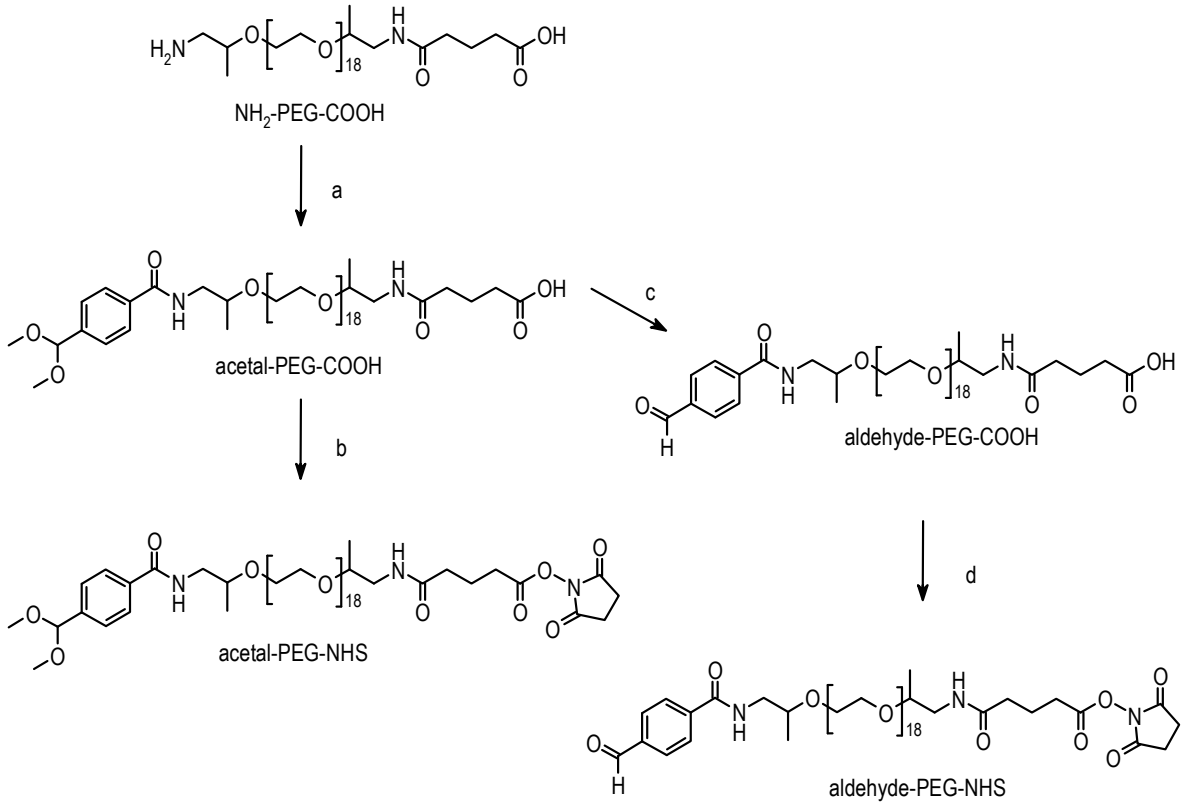


Figure S2. Synthesis of acetal-PEG-NHS and aldehyde-PEG-NHS. a: SDMB/chloroform/TEA, b: DMF/pyridine/TSTU, c: citric acid/water, d: DMF/pyridine/TSTU. According to the manufacturer of NH_2-PEG-NH_2, the molecular mass of the PEG chain was 800 g/mol. Mass spectrometry revealed the chain length distribution was n = 18 ± 4 [51].

Synthesis of α-{2-[4-(Dimethoxymethyl)-benzoyl]-aminopropyl}-ω-{2-[4-carboxy-butanoylamido]-propyl}-poly(oxyethylene)-800 (acetal-PEG-COOH). NH_2-PEG-COOH (503.10 mg, 471.38 µmol) was dissolved in chloroform (6.5 mL) and SDMB (247.80 mg, 845.36 µmol, dissolved in a minimal volume of chloroform) was added, followed by addition of TEA (232 µl, 1,68 mmol). The progress of the reaction was monitored by TLC in eluent III. When all ninhydrine-positive educt had been consumed, the solvent was removed and the residue was dissolved in methanol (5 mL). The solution was filtered and loaded on a size exclusion column (Sephadex^{TM} LH-20, 1.5 cm diameter, 97 cm bed height, solvent methanol, flow 0.4 mL/min). Fractions of 3.2 mL were collected and analyzed by TLC in Eluent II. Product fractions were combined, taken to dryness and dried under vacuum over night, yielding 570,3 mg (468.4 µmol, acetal-PEG-COOH) of viscous product which was pure by TLC (iodine: $R_f{}^{I'} = 0.56$, $R_f{}^{II} = 0.70$, $R_f{}^{III} = 0.74$, ninhydrine: $R_f{}^{II} = 0.70$, $R_f{}^{III} = 0.74$). ^{1}H NMR (200 MHz, $CDCl_3$) δ (ppm): 1.04-1.36 (10 H, m, NH_2-CH<(C***H***$_3$)-CH_2-O and NH_2-CH<(C***H***$_2$-C***H***$_3$)-CH_2-O of PEG_{800}) 1.92 (2 H, quin, J = 6.8 Hz, CO-CH_2-C***H***$_2$-CH_2-CO, position β' in glu) 2.28 (2 H, t, J = 7 Hz, NH-CO-C***H***$_2$-CH_2-CH_2-COOH, position γ' in glu) 2.38 (2 H, t, J = 6.7 Hz, NH-CO-CH_2-CH_2-C***H***$_2$-COOH, position α' in glu) 3.29 (6 H, s, (C***H*****$_3$**-O)$_2$-CH-)) 3.39-3.51 (6 H, m, N-C***H***<(CH_3)-C***H***$_2$-O and N-C***H***<(CH_2-CH_3)-C***H***$_2$-O of PEG_{800}) 3.63 (72 H, s, O-C***H***$_2$-C*H*$_2$-O, 18 ethylene glycol units) 5,41 (1 H, s, -C***H***=(O-CH_3)$_2$) 7.26 (s, trace of C***H***Cl_3 in $CDCl_3$) 7.50 (2°H, d, J = 8.2 Hz, ***H3*** and ***H5*** of aromatic ring) 7.80 (2 H, d, J = 8.2 Hz, ***H2*** and ***H6*** of aromatic ring).

Synthesis of α-{2-[4-(Dimethoxymethyl)-benzoyl]-aminopropyl}-ω-{2-[4-(*N*-succinimidyloxycarbonyl)-butanoylamido]-propyl}-poly(oxyethylene)-800 (acetal-PEG-NHS). Acetal-PEG-COOH (570.3 mg, 468 µmol) was dissolved in DMF (6 mL) and pyridine (3 mL) and TSTU (216 mg, 717 µmol) was added. After 2 h of stirring at RT, the mixture was taken to dryness. The residue was dissolved in a mixture of chloroform (50 ml) and methanol (10 mL), stirred for 20 min, the solid material was removed by filtration, and additional chloroform (40 mL) was added. The solution was swirled with cold buffer A (100 mM NaCl, 50 mM NaH_2PO_4, 1 mM EDTA, pH 7.5 adjusted with NaOH) for 2 min (2 × 100 mL). It was washed with water (3 × 40 mL), dried with as little Na_2SO_4 as was required to clarify the solution, and filtered through paper. The organic solvents were removed and the residue dried at 1-10 Pa overnight yielding 510.9 mg (393.6 µmol) of product which was pure by TLC (iodine: $R_f{}^{I} = 0.66$, $R_f{}^{II} = 0.68$, $R_f{}^{III} = 0.65$). ^{1}H NMR (200 MHz, $CDCl_3$) δ (ppm): 1.04-1.36 (10 H, m, NH_2-CH<(C***H***$_3$)-CH_2-O and NH_2-CH<(C***H***$_2$-C***H***$_3$)-CH_2-O of PEG_{800}) 2.08 (2 H, quin, J = 6.8 Hz, CO-CH_2-C***H***$_2$-CH_2-CO, position β' in glutaryl residue) 2.28 (2 H, t, J = 6.6 Hz, NH-CO-C***H***$_2$-CH_2-CH_2-COOH, position γ' in glutaryl residue) 2.68 (2 H, t, J = 6.8 Hz, NH-CO-CH_2-CH_2-C***H***$_2$-COOH, position α' in glutaryl residue) 2.85 (4 H, s, CO-C***H***$_2$-C***H***$_2$-CO of succinimidyl group) 3.32 (6 H, s, (C***H*****$_3$**-O)$_2$CH-)) 3.49-3.51 (6 H, m, N-C***H***<(CH_3)-C***H***$_2$-O and N-C***H***<(CH_2-CH_3)-C***H***$_2$-O of PEG_{800}) 3.63 (72 H, s, O-C***H***$_2$-C***H***$_2$-O, 18 ethylene glycol units) 5.41 (1 H, s, -C***H***=(O-CH_3)$_2$) 7.26 (s, trace of C***H***Cl_3 in $CDCl_3$) 7.50

(2°H, d, J = 8.2 Hz, ***H3*** and ***H5*** of aromatic ring) 7.80 (2 H, d, J = 8.2 Hz, ***H2*** and ***H6*** of aromatic ring).

Synthesis of α-{2-[4-Formylbenzoyl]-aminopropyl}-ω-{2-[4-carboxybutanoyl-amido]-propyl}-poly(oxyethylene)-800 (aldehyde-PEG-COOH). Acetal-PEG-COOH (736.4 mg, 591 µmol) was dissolved in acetone (30 mL) under argon, iodine (30 mg) was added and the solution was allowed to stir for 10 min. For removal of iodine the acetone fraction was mixed with water (50 mL) and washed with toluene (3 x 50 mL). The aqueous layer was taken to dryness and the residue dried at 1-10 Pa overnight yielding 679.4 mg (580 µmol) of product which was pure by TLC (iodine: R_f ^{II} = 0.59). ^{1}H NMR (200 MHz, $CDCl_3$) δ (ppm): 1.04-1.26 (10 H, m, NH_2-CH<(C***H***$_3$)-CH_2-O and NH_2-CH<(C***H***$_2$-C***H***$_3$)-CH_2-O of PEG_{800}) 1.96 (2 H, quin, *J* = 6.6 Hz, CO-CH_2-C***H***$_2$-CH_2-CO, position β' in glutaryl residue) 2.27 (2 H, t, J = 6.8 Hz, NH-CO-C***H***$_2$-CH_2-CH_2-CO-NH, position γ' in glutaryl residue) 2.40 (2 H, t, J = 6.7 Hz, NH-CO-CH_2-CH_2-C***H***$_2$-CO-NH, position α' in glutaryl residue) 3.33-3.52 (6 H, m, N-C***H***<(CH_3)-C***H***$_2$-O and N-C***H***<(CH2-CH_3)-C***H***$_2$-O of PEG_{800}) 3.66 (72 H, s, O-C***H***$_2$-C**H**$_2$-O, 18 ethylene glycol units) 4.04-4.44 (2 H, broad s, CO-N***H***-CH<(C)-CH_2-O of PEG_{800}) 7.26 (s, trace of C***H***Cl_3 in $CDCl_3$) 7.9-8.3 (4 H, m, aromatic ring) 10.09 (1 H, s, aldehyde). As a more convenient alternative to iodine/acetone, the acetal function was hydrolyzed with 1% citric acid (in water, 10 min, room temperature) in a parallel batch, whereupon the product was extracted into chloroform. The chloroform solution was washed with brine, dried with Na_2SO_4, filtered, and taken to dryness, yielding pure aldehyde-PEG-COOH, as well.

Synthesis of α-{2-[4-Formylbenzoyl]-aminopropyl}-ω-{2-[4-(*N*-succinimidyloxy-carbonyl)-butanoylamido]-propyl}-poly(oxyethylene)-800 (aldehyde-PEG-NHS). The synthesis of aldehyde-PEG-NHS followed the same protocol as the synthesis of acetal-PEG-NHS (see above) yielding a viscous product which was pure by TLC (iodine: R_f $^{I'}$ = 0.05, 0.68, R_f ^{II} = 0.70, R_f ^{III} = 0.66). ^{1}H NMR (200 MHz, $CDCl_3$) δ (ppm): 1.04-1.26 (10 H, m, NH_2-CH<(C***H***$_3$)-CH_2-O and NH_2-CH<(C***H***$_2$-C***H***$_3$)-CH_2-O of PEG_{800}) 2.08 (2 H, t, J = 6.6 Hz, CO-CH_2-C***H***$_2$-CH_2-CO, position β' in glutaryl residue) 2.26 (2 H, t, J = 6.8 Hz, CO-CH_2-C***H***$_2$-CH_2-CO, position γ' in glutaryl residue) 2.68 (2 H, t, J = 7.0 Hz, NH-CO-C***H***$_2$-CH_2-CH_2-CO-NH, position α' in glutaryl residue) 2.85 (4 H, s, CO-C***H***$_2$-C***H***$_2$-CO of succinimidyl) 3.33-3.58 (6 H, m, N-C***H***<(CH_3)-C***H***$_2$-O and N-C***H***<(CH_2-CH_3)-C***H***$_2$-O of PEG_{800}) 3.66 (72 H, s, O-C***H***$_2$-C*H*$_2$-O, 18 ethylene glycol units) 3.95-4.15 (2 H, broad s, CO-N***H***-CH<(C)-CH_2-O of PEG_{800}) 7.26 (s, trace of C***H***Cl_3 in $CDCl_3$) 7.9-8.3 (4 H, m, aromatic ring) 10.09 (1 H, s, aldehyde).

Synthesis of *α,ω-bis*-{2-[4-(Dimethoxymethyl)-benzoyl]-aminoethyl}-octadeca(oxyethylene) (acetal-PEG$_{18}$-acetal). PEG_{18} diamine (466 mg, 0.52 mmol) was dissolved in 6 mL chloroform and stirred under argon atmosphere. SDMB (245 mg, 0.84 mmol) and TEA (230 µL, 1.65 mmol) were added, and stirring was continued at room temperature under argon atmosphere. After 2 h the mixture was taken to dryness at the

rotavap, the residue was dissolved in methanol (5 mL) and subjected to chromatography on Sephadex LH-20 in methanol (column dimensions 1.5 cm × 95 cm, flow 0.4 mL/min, fraction size 3.2 mL). Elution of the product was detected by TLC in eluent II. The fractions containing pure product were combined and taken to dryness, yielding 570 mg (0.45 mmol). ^{1}H-NMR (200 MHz, $CDCl_3$) δ (ppm): 3.30 (12 H, s, C***H*****$_3$**-O-) 3.61 (80 H, broad s, PEG chain, including the two terminal O-C***H*****$_2$**-C***H*****$_2$**-NH- groups) 5.40 (2 H, s, -C***H***=(O-CH_3)$_2$) 6.98 (2 H, broad s, N***H***) 7.48 (2 H, dd, J_1 = 8.2 Hz, J_2 = 1.4 Hz, ***H3*** and ***H5*** of both aromatic residues) 7.26 (s, trace of C***H***Cl_3 in $CDCl_3$) 7.80 (2 H, dd, J_1 = 8.2 Hz, J_2 = 1.4 Hz, ***H2*** and ***H6*** of both aromatic residues).

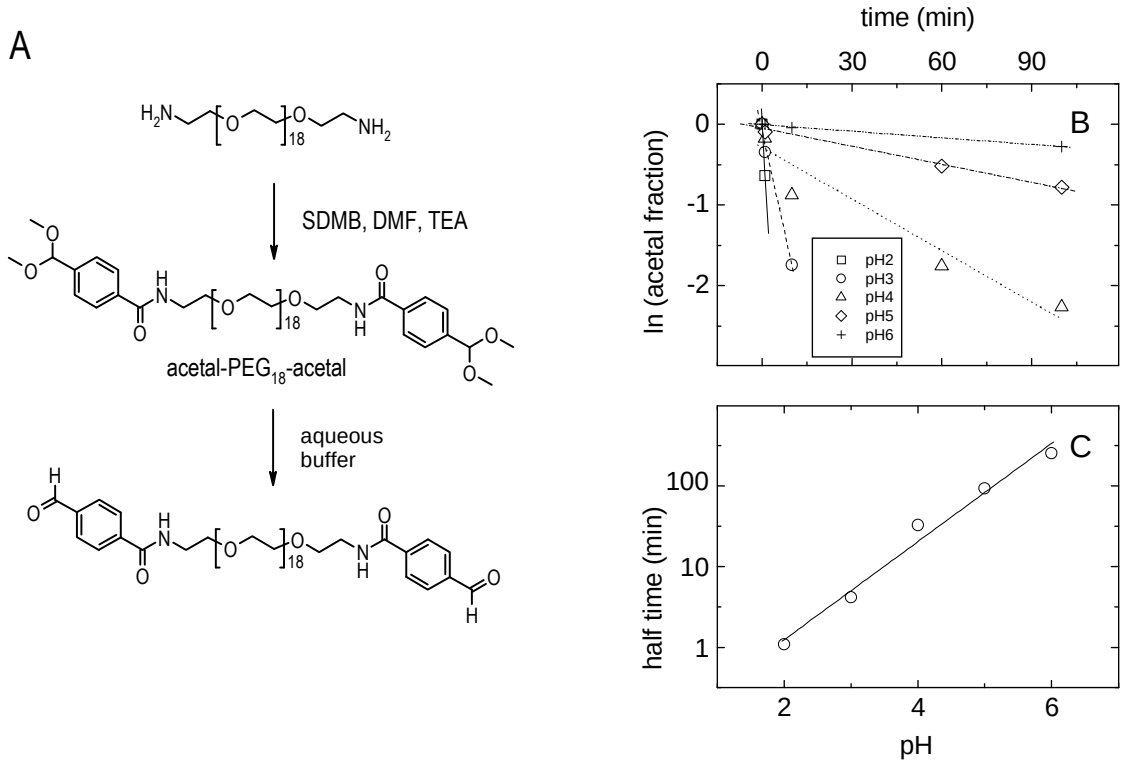


Figure S3. Synthesis of "acetal-PEG_{18}-acetal" and kinetics of acetal cleavage at different pH values. (A) PEG_{18} diamine was derivatized with SDMB on both amino functions (see above). (B) The time course of acetal cleavage at a given pH value was measured by dissolving 100 mg of acetal-PEG_{18}-acetal in 10 mL aqueous buffer (prepared by adjusting 5% citric acid to the specified pH with NaOH) and removing 1 mL aliquots at defined time intervals. The PEG components of the aliquot were extracted into chloroform. The chloroform solution was dried with Na_2SO_4, filtered, and taken to dryness and redissolved in $CDCl_3$. The change in the acetal content was calculated from the decrease of the methoxy signal (3.30 ppm) relative to the PEG signal (3.61 ppm) in the ^{1}H-NMR spectrum. The time courses were fit to monoexponential functions (lines in panel B) and the resulting half times are shown as a function of pH (panel C).

PART 2

KINETICS OF ACETAL CLEAVAGE BY ACID IN WATER

Figure S3 describes a series of experiments in which the pH dependence of acetal cleavage was studied under controlled conditions. The logic model compound for such a study would have been "acetal-PEG-COOH" (see Figure S2). Unfortunately, large amounts of this valuable compound would have been destroyed in the five time series at different pH values (Figure S3B), therefore "acetal-PEG_{18}-acetal" was prepared as a cheaper substitute (Figure S3A). Five different citric acid buffers were prepared by 5% citric acid (pH 1.9, see Figure S4) to pH 2, 3, 4, 5, or 6 with concentrated NaOH. For each time series, acetal-PEG-acetal was dissolved in the corresponding buffer to start the acetal cleavage process at the defined pH value. Aliquots were removed at different time intervals and the cleavage process was terminated by instantaneous partitioning of all PEG components into chloroform and the extent of acetal cleavage was calculated from the ^{1}H-NMR spectrum (see legend to Figure S3). The time series data were fit to monoexponential decay functions (shown in a linearized form in Figure S3B) and the corresponding half times were plotted as a function of pH (Figure S3C).

It is interesting to compare the results obtained with acetal-PEG-acetal (Figure S3) with the kinetics of acetal cleavage observed for free acetal-PEG-COOH (Figure S2) in 1% citric acid. According to Figure S4, an aqueous solution of citric acid (1%) has a pH value of 2.2. When synthesizing aldehyde-PEG-COOH from acetal-PEG-COOH (Figure S2), we regularly performed acetal cleavage by 10 min treatment in 1% citric acid. The ^{1}H-NMR spectrum of the resulting product was completely free from any trace of the methoxy signal (3.30) ppm, in spite of the fact that this 6-proton singlet is particularly sharp and intense. Consequently, we estimate that treatment with 1% citric acid cleave at least 99.6% of the acetal functions within 10 min. In a monoexponential time course, 99.6% turnover is reached after 8 half times. Consequently, a maximal half time of 10/8 = 1.25 min is calculated for the 10 min treatment of acetal-PEG-COOH. This estimate agrees reasonably well with the half time of 1.6 min interpolated in Figure S3C for cleavage of acetal-PEG_{18}-acetal in 5% citric acid (adjusted to pH 2.2 with NaOH). The minor discrepancy may relate to slight differences in the buffer systems and in the molecular structures.

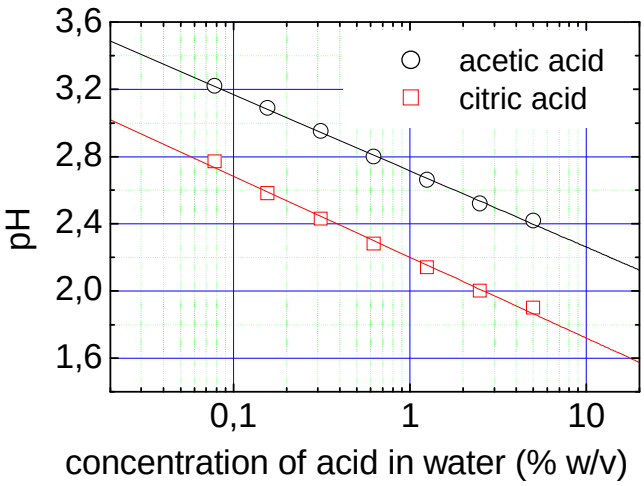


Figure S4. Dependence of pH on the concentration of unbuffered citric acid or acetic acid in pure water.

PART 3

ILLUSTRATIONS OF TIP / CHIP FUNCTIONALIZATION WITH ACETAL-PEG-NHS

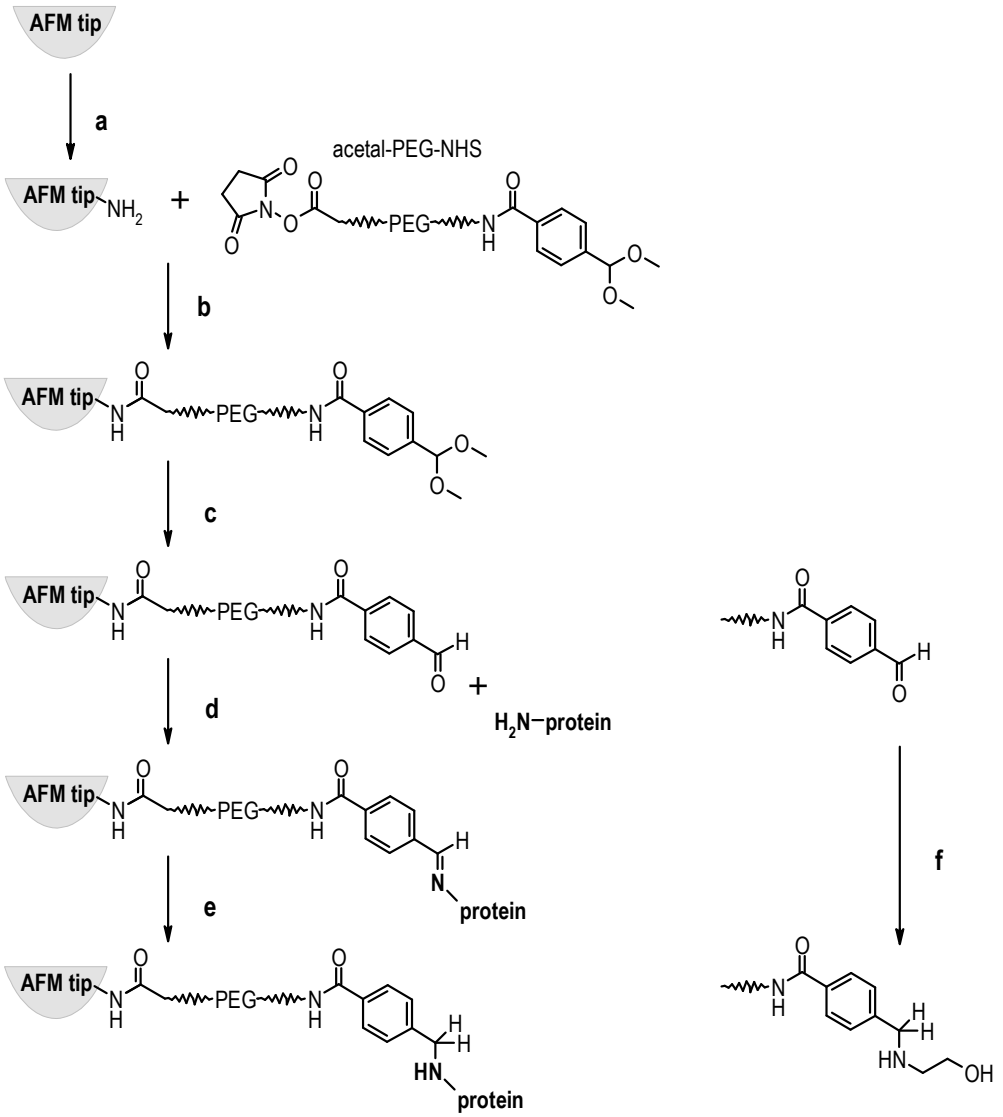


Figure S5. Scheme for tethering of proteins to AFM tips, using of acetal-PEG-NHS as heterobifunctional crosslinker. a) Aminofunctionalization of silicon nitride tip with ethanolamine hydrochloride in DMSO or with APTES in the gas phase. b) Amide bond formation in chloroform with TEA (0.5%). c) Deprotection with 0.1% iodine in acetone (5 min, iodine method) or with 1% citric acid in water (1-15 min, citric acid method). d) Schiff base formation with the lysine residue of a protein (e.g. 0.2 mg/mL antibody) in PBS (pH 7.4). e) Schiff base reduction with $NaCNBH_3$ (20 mM). In practice, step d and e are performed simultaneously since $NaCNBH_3$ is applied together with the antibody (1 h at RT). f) Blocking of unused benzaldehyde functions on the AFM tip by addition of 0.05 volumes of ethanolamine hydrochloride solution (1 M, pH 9.6 pre-adjusted with NaOH) or 0.05 volumes of glycine solution (1 M, pH 8.0 pre-adjusted with NaOH) and incubation for 5 min.

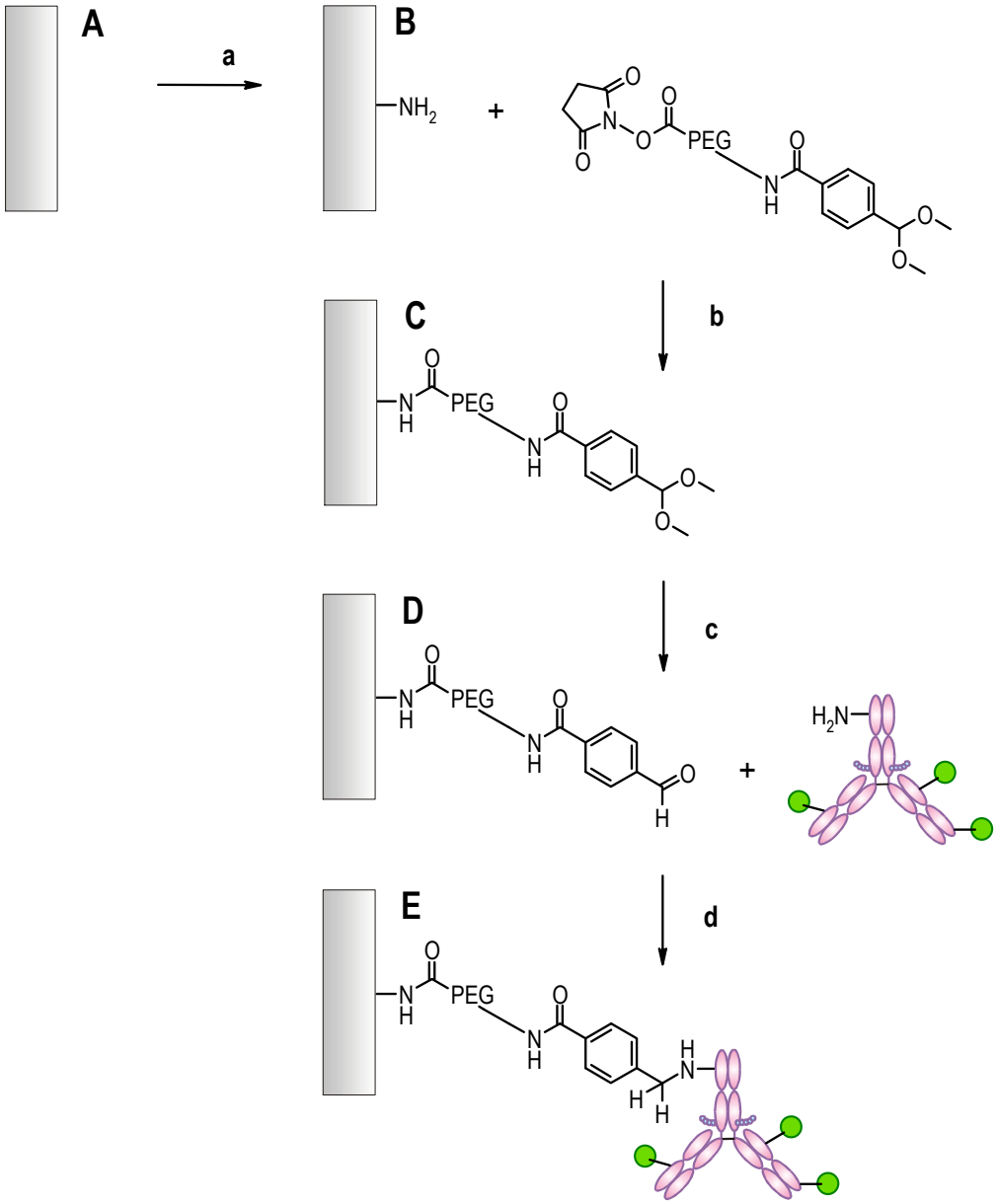


Figure S6. Schematic representation of chip functionalization and characterization. (a) Silicon nitride chips (A) were aminofunctionalized, either with ethanolamine hydrochloride in DMSO or with APTES in the gas phase (B). (b) Aminofunctionalized silicon nitride chips were reacted with acetal-PEG-NHS, resulting in amide-bond linked PEG chains with an acetal function (i.e., a protected aldehyde) on their free end (C). (c) Conversion of the acetal function into an aldehyde function (D) by use of iodine/acetone (0.1%, 5 min) or citric acid/water (1%, 15 min or 1 min, as specified), as stated for particular data. (d) Coupling of protein (biotin-IgG) by Schiff base formation with a lysine residue and concomitant fixation of the C=N double bond by reduction with $NaCNBH_3$ gives a stable C-N single bond (E). Continued on the next page.

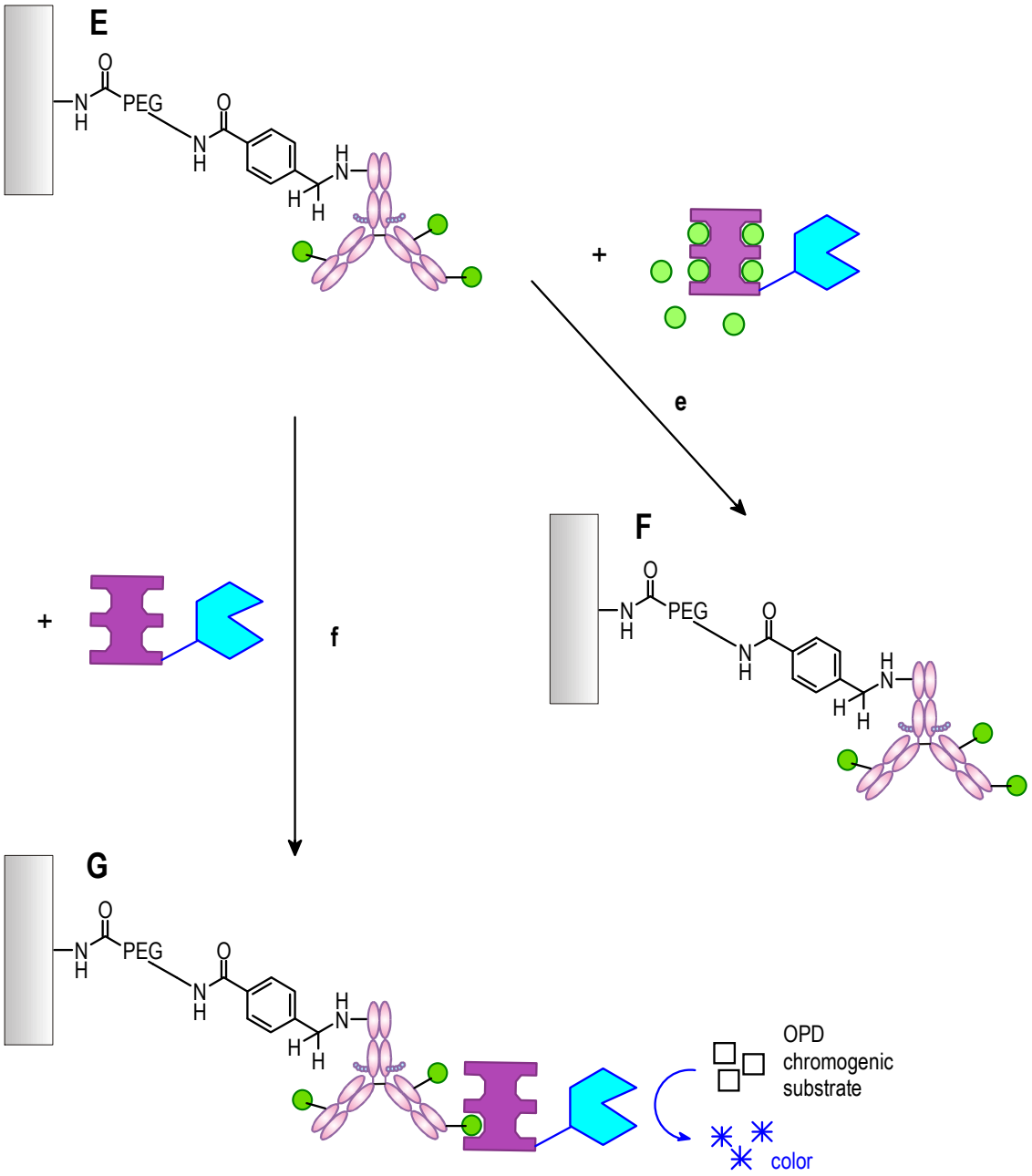


Figure S6 (continued from the previous page). (e) Control experiment for non-specific adsorption of ExtrAvidin®-peroxidase (EAP) to chips carrying biotin-IgG covalently bound via PEG linkers. The biotin-binding sites of EAP were pre-blocked by a large excess of free *d*-biotin, thus EAP cannot bind to immobilized biotin-IgG (F) and only nonspecific adsorption of EAP to the chip can occur. The amount of adsorbed EAP is estimated from the rate of color production, as explained below. (f) In the absence of free *d*-biotin, EAP is bound to the chip both by nonspecific adsorption (not shown) and by specific interaction (stage G). After removal of unbound EAP by washing, a chromogenic substrate is added and the amount of bound enzyme is calculated from the rate of color production [38, 51].

PART 4

TIP FUNCTIONALIZATION WITH ALDEHYDE-PEG-NHS AND EDA-ATP

Magnetically coated cantilevers (MAC levers, Agilent) were functionalized with the ethylene diamine-derivative of ATP (EDA-ATP, 2'-/3'-O-(2-aminoethylcarbamoyl)-adenosine-5'-O-triphosphate, BioLog) by a well established three-step procedure: (i) aminofunctionalization, (ii) attachment of the heterobifunctional polyethylene glycol linker (aldehyde-PEG-NHS, synthesized by the new synthesis route Figure S2acd), and (iii) reaction of "tip-PEG-aldehyde" with the amino group of EDA-ATP, using $NaCNBH_3$ for reduction (fixation) of the initially formed Schiff base conjugate (compare steps d and e in Figure S5).

Commercial MAC® levers were cleaned with chloroform and aminofunctionalized with APTES in the gas phase as described previously [51]. For attachment of aldehyde-PEG-NHS, the cantilevers were put in the solution of the crosslinker in chloroform at a concentration of 6.6 mg/ml. TEA at final concentration of 0.5% was added to deprotonate the amino functions on the tip and ensure amide bond formation. After about 1.5 hours of reaction, the cantilevers were washed in chloroform (3 ×) and dried in air.

Fifty µL aliquots of the commercial EDA-ATP solution (10 mM, in water, from BioLog) were pipetted into Eppendorf reaction vials, and frozen in liquid nitrogen. The vials were placed in a pre-cooled round-bottomed flask which was attached to a cold trap and evacuated at 1-10 Pa, in order to evaporate the water content in the frozen state. For coupling to "tip-PEG-aldehyde", one dried portion of EDA-ATP was redissolved in 9 µL of buffer B (1 mM EDTA and 300 mM NaH_2PO_4, pH adjusted to 7.5 with NaOH) and 1 µL of a 0.2 M solution of $NaCNBH_3$ (freshly prepared by dissolving 32 mg $NaCNBH_3$ in a mixture of 50 µL 100 mM NaOH plus 450 µL water, and diluting with 2 mL buffer B) was added. After mixing, this solution was transferred onto a sheet of clean Parafilm in a polystyrene Petri dish. Several cantilevers were immersed in the 10 µL droplet with their tips and incubated for 1 h. Subsequent deactivation of residual aldehyde functions on the tip was performed by addition of 0.5 µl 1 M ethanolamine hydrochloride solution (pre-adjusted to pH 9.6 with NaOH and stored in small aliquots at -25°C) and incubation for 10 min. The tips were washed 3 times and stored in buffer B treated with argon at 4°C.

The addition of 0.5 µL (0.05 vol) 1 M ethanolamine (pH 9.6) to 10 µL buffer B caused little change in pH. This was demonstrated by mixing 5 mL buffer B with 0.25 mL (0.05 vol) 1 M ethanolamine (pH 9.6) whereby the final pH rose from 7.5 to 7.7. The small extent of the pH change is due to the high phosphate concentration (300 mM) of buffer B. In contrast, regular buffer A does not have sufficient buffering capacity, as shown by mixing of 5 mL buffer A (50 mM phosphate only!) with 0.25 mL (0.05 vol) 1 M ethanolamine (pH 9.6) which gave a final pH of 9.2.

PART 5

RECONSTITUTION OF UCP1 IN PLANAR BILAYER AND RECOGNITION IMAGING WITH ATP-FUNCTIONALIZED TIPS

The coding region of murine Uncoupling protein 1 (UCP1) was amplified by PCR from a mouse EST clone and cloned into the expression vector pET-24a (Novagen, Germany), as described in [Rupprecht et al., 2010]. For protein expression E. coli strain Rosetta (DE3) (Novagen, Germany) was transformed. Inclusion body purification was performed according to the procedures, described previously [Smorodchenko et al., 2009; Rupprecht et al., 2010]. In brief, cells were disrupted by French press and centrifuged to eliminate cell debris. The inclusion bodies were obtained after supernatant centrifugation at 14000 g for 10 min. 2.5 mg protein from inclusion bodies per 100 mg lipid was used for the subsequent UCP1 purification. The inclusion bodies were washed in TRIS/glycerol buffer (100 mM Tris base, 5 mM EDTA, 10% glycerol, pH 7.5) with additional 2 % Triton X-100 first and then with 0.1 % sodium lauryl sulfate (SLS). For solubilization, the inclusion bodies were incubated at room temperature in TRIS/glycerol buffer with 2 % SLS and 1 mM DTT. After centrifugation the supernatant was incubated overnight with the mixture of 100 mg E. coli polar lipid (Avanti Polar Lipids, USA), 400 mg Triton X-114, 100 mg octyl-polyoxyethylene, 1 mM DTT and 1 mM ATP, then concentrated with Amicon Ultra-15 filters (Millipore, Germany) and dialyzed for two hours against TRIS/glycerol buffer supplemented with 1 mg/mL BSA and 1 mM DTT. Two further dialysis cycles were performed without DTT for a minimum of 12 h. Three final dialyses were completed with the assay buffer (see below).

Aggregated proteins were eliminated by centrifugation of the dialysate at 14000 g for 10 min. To eliminate incorrectly folded proteins, the supernatant was run over a column containing 1 g hydroxyapatite (Bio-Rad, Germany) [Lin & Klingenberg, 1980; Lin & Klingenberg, 1982]. For removal of non-ionic detergent, the sample was incubated with Bio-Beads SM-2 (Bio-Rad, Germany) [Rigaud et al., 1995]. The protein content of the obtained proteoliposomes was measured by Micro BCA Protein Assay (Perbio Science, Germany).

The AFM sample plate (Agilent Technologies, USA) with the coil for magnetic field application was covered with a small piece of aluminum foil, the centre of which was marked with a small dot to indicate the cantilever position for the charge-coupled device (CCD) camera. Freshly cleaved mica was placed on the aluminum film and mounted with a flow-through fluid cell. Ten µl stock solution of UCP1 proteoliposomes (with a lipid concentration of 4-5 mg/mL and a protein/lipid ratio of 0.02-0.03) was diluted with 240 µL of assay buffer (50 mM Na_2SO_4, 20 mM MES, 20 mM TRIS, 0.6 mM EDTA, pH 7.2). After short vortexing, the solution was injected into the fluid cell on the mica surface. After incubation for 8 min, the mica surface was thoroughly washed with buffer. Finally, 600 µL buffer was left in the fluid cell for measurements.

Mac-mode AFM imaging was performed using a PicoPlus 5500 AFM (Agilent). Recognition images [8, 9] were simultaneously recorded using the ATP-functionalized cantilever, which was driven by an alternating magnetic field at its resonant frequency. Images were recorded at an amplitude set-point of 2.3-8.4 nm, and with a ratio of 88-97 % to the amplitude observed before the cantilever touched the sample surface. The scanning speed for imaging was 2-4 µm/s. Experiments on the blocking of the recognition were conducted by injecting free ATP solution into the measurement solution at a final concentration of 4.8 mM. Both topography and recognition images were displayed after leveling by mean plane subtraction and scanning line correction (Gwyddion 2.9).

PART 6

EXPLANATION OF SIMULTANEOUS TOPOGRAPHY AND RECOGNITION IMAGING WITH MAGNETICALLY COATED AFM CANTILEVERS.

Topography and recognition imaging (TREC) is based on tapping mode AFM. A magnetic coil mounted either above or below the magnetically coated cantilever generates a sinusoidal oscillation of the cantilever when using a driving frequency which is adjusted to ~0.5 kHz below the resonance frequency of the cantilever. This allows for gentle and noninvasive scanning of the surface which is a prerequisite when using ligand-functionalized cantilevers for imaging purposes. In contrast to the conventional magnetical tapping mode (MAC®-Mode, Agilent), recognition imaging not only yields sample topography but also a simultaneously acquired map of recognition sites. For this purpose, the lower and the upper parts of the cantilever oscillation trace are separated by an electronic circuit which is termed the TREC box [8, 9] (see Figure S7A). The lower parts are only affected by the sample topography and used for the piezo feedback loop, resulting in the topographical image. In the case of a complex formation of a tip-bound ligand with a surface-embedded receptor, changes of the upper parts of the amplitude become observable. An important prerequisite is the stable tethering of the ligand to the tip with a distensible polymer linker. The chain length is typically chosen to be 3-9 nm and the working amplitude of cantilever oscillation is kept smaller than the sum of linker chain length plus the height of the receptor-ligand complex, thereby avoiding a forced rupture of the receptor-ligand complex while scanning above the receptor site [Preiner et al., 2009] A typical example is shown in Figure S7. [Ebner et al., 2005]. Individual avidin molecules were adsorbed to mica and the surface was scanned with a tip carrying a biotin residue via a 6 nm long PEG linker. The height of the avidin molecules resulted in a damping of the lower parts of the amplitude used for driving the piezo feedback loop (Figure S7A, blue trace). In parallel, the formation of an avidin-biotin complex while scanning over avidin hinders the upwards movement in the oscillation and results in a ~1nm lowered upper peak amplitude when using a peak-to-peak amplitude that is smaller than the length of the PEG chain (~6 nm) plus the height of avidin (~4 nm). Changes in the upper part

of the amplitude can directly be translated in recognition signals. As a result TREC allows for mapping of recognition sites simultaneously with gentle imaging of the sample surface, both at high resolution and a fast lateral scan rate.

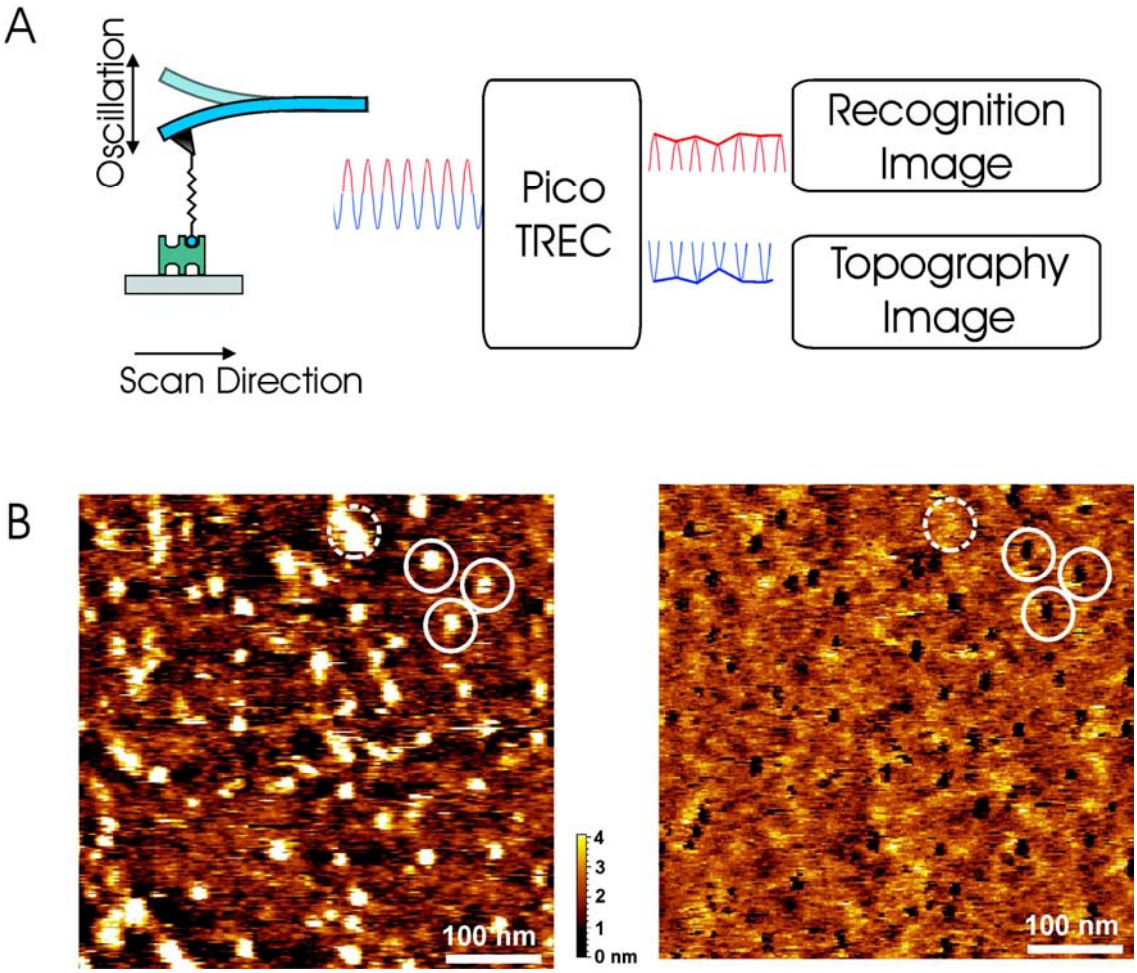


Figure S7. TREC imaging (Ebner et al. 2005). (A) Principle: The cantilever oscillation is split into lower and upper parts, resulting in simultaneously acquired topography and recognition images. (B) Avidin was electrostatically adsorbed to mica and imaged with a biotin-tethered tip. A good correlation between topography (left image, bright spots) and recognition (right image, dark spots) was found (exemplified by the three solid circles). Topographical spots without recognition indicate structures lacking specific interaction (dashed circle). The scan size was 500 nm × 500 nm. Reproduced with permission from [Ebner et al., 2005].

PART 7

LITERATURE CITED in the Supporting Information only

Ebner, A., Kienberger, F., Kada, G., Stroh, C. M., Geretschläger, M., Kamruzzahan, A. S. M., Wildling, L., Johnson, W. T., Ashcroft, B., Nelson, J., Lindsay, S. M., Gruber, H. J., and Hinterdorfer, P. (2005) Localization of single avidin-biotin interactions using simultaneous topography and molecular recognition imaging. *ChemPhysChem 6*, 897-900

Lin, C. S., and Klingenberg, M. (1980) Isolation of the uncoupling protein from brown adipose tissue mitochondria. *FEBS Lett. 113*, 2099-2303.

Lin, C. S., and Klingenberg, M. (1980) Characteristics of the isolated purine nucleotide binding protein from brown fat mitochondria. *Biochemistry 21*, 2950-2956.

Preiner, J., Ebner, A., Chtcheglova, L., Zhu, R., and Hinterdorfer, P. (2009) Simultaneous topography and recognition imaging: physical aspects and optimal imaging conditions. *Nanotechnology 20*, 215103.

Rigaud, J. L., Pitard, B., and Levy, D. (1995) Reconstitution of membrane proteins into liposomes: application to energy-transducing membrane proteins. Biochim. Biophys. Acta 1231, 223-246.

Roberts, S.L., Furlan, R.L.E., Otto, S., and Sanders, J.K.M. (2003) Metal-ion induced amplification of three receptors from dynamic combinatorial libraries of peptide-hydrazones. *Org. Biomol. Chem. 1*, 1625-1633.

Rupprecht, A., Sokolenko, E. A., Beck, V., Ninnemann, O., Jaburek, M., Trimbuch, T., Klishin, S. S., Jezek, P., Skulachev, V. P., and Pohl, E. E. (2010) Role of the transmembrane potential in the membrane proton leak. *Biophys. J. 98*, 1503-1511.

Bioconjugate Chemistry

TECHNICAL NOTE

pubs.acs.org/bc

Solid-Supported 2′-*O*-Glycoconjugation of Oligonucleotides by Azidation and Click Reactions

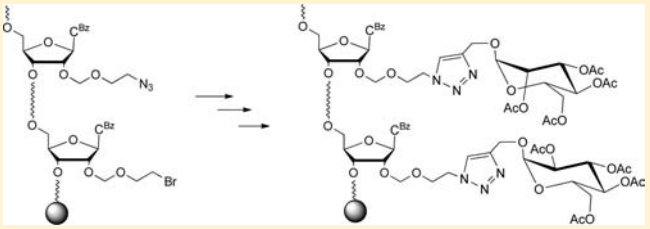
Anu Kiviniemi,*[,†] Pasi Virta,[†] Mikhail S. Drenichev,[‡] Sergey N. Mikhailov,*[,‡] and Harri Lönnberg[†]

[†]Department of Chemistry, University of Turku, FIN-20014 Turku, Finland

[‡]Engelhardt Institute of Molecular Biology, Russian Academy of Sciences, Vavilov Street 32, Moscow 119991, Russia

Supporting Information

ABSTRACT: 2′-*O*-[(2-Bromoethoxy)methyl]cytidine and 2′-*O*-[(2-azidoethoxy)methyl]cytidine have been prepared and introduced as appropriately protected 3′-phosphoramidite (**1**) and 3′-(*H*-phosphonate) (**2**) building blocks, respectively, into 2′-*O*-methyl oligoribonucleotides. The support-bound oligonucleotides were subjected to two consecutive conjugations with alkynyl-functionalized monosaccharides. The first saccharide was introduced by a Cu(I) promoted click reaction with **2** and the second by azidation of the 2-bromoethoxy group of **1** followed by the click reaction. The influence of the 2′-glycoconjugations on hybridization with DNA and 2′-*O*-methyl RNA targets was studied. Two saccharide units within a 15-mer oligonucleotide had a barely noticeable effect on the duplex stability, while introduction of a third one moderately decreased the melting temperature.



INTRODUCTION

Among various oligonucleotide conjugates, the 2′-conjugates have received special interest for the reason that upon formation of an A- or B-type duplex, the conjugate group is accommodated in the minor or major grooves, respectively, and hence, the duplex is not markedly destabilized.[1,2] Introduction of reactive functionalities in the 2′-position of nucleosides, incorporation of the resulting monomers into oligonucleotides, and their subsequent reactions with appropriately functionalized conjugate groups has been rather recently reviewed.[3] Somewhat surprisingly, such a stepwise protocol has only once been utilized for solid phase-synthesis of 2′-glycoconjugates, potentially useful for the delivery and targeting of therapeutic oligonucleotides,[4−8] although several procedures for the derivatization of other intrachain positions, including the C4′-position,[9,10] internucleosidic phosphoramidate linkage,[11,12] or intrachain non-nucleosidic units,[13−18] have been described. Very recently,[19] saccharide ligands have been conjugated by Cu(I) promoted click reaction[20,21] to 2′-*O*-(2-propynyl) groups on-support. Otherwise 2′-glycoconjugates have been obtained by converting prefabricated 2′-*O*-glycosyl nucleosides with all four natural heterocyclic bases[22] into phosphoramidite building blocks and introducing them into oligonucleotides on a solid-support.[23−26] The *cis* diol of the 2′-*O*-glycosyl group, when oxidized to dialdehyde with sodium periodate, has been shown to allow affinity labeling of different enzymes.[27−29]

We now report on a solid-supported conjugation method that enables the attachment of two different carbohydrate ligands to the 2′-position at desired sites within the chain. For this purpose, two building blocks, viz. 2′-*O*-[(2-bromoethoxy)methyl]-5′-*O*-(4,4′-dimethoxytrityl)cytidine 3′-(2-cyanoethyl-*N*,*N*-diisopropylphosphoramidite) (**1**) and 2′-*O*-[(2-azidoethoxy)methyl]-5′-*O*-(4,4′-dimethoxytrityl)cytidine 3′-(*H*-phosphonate) (**2**) monomers, were prepared and incorporated into 2′-*O*-methyl oligoribonucleotides. The azido group of the nucleoside units **2** was first subjected to a click reaction,[20,21] with a propynyl functionalized monosaccharide on-support. The bromo substituent of unit **1** was then displaced with azide ion on-support, as shown previously by Pourceau et al.,[14] and another click reaction was carried out. The hybridization efficiency of the conjugates with cDNA- and 2′-*O*-Me-RNA-oligonucleotides was assessed by UV-melting studies and compared to the hybridization of the corresponding unmodified sequence.

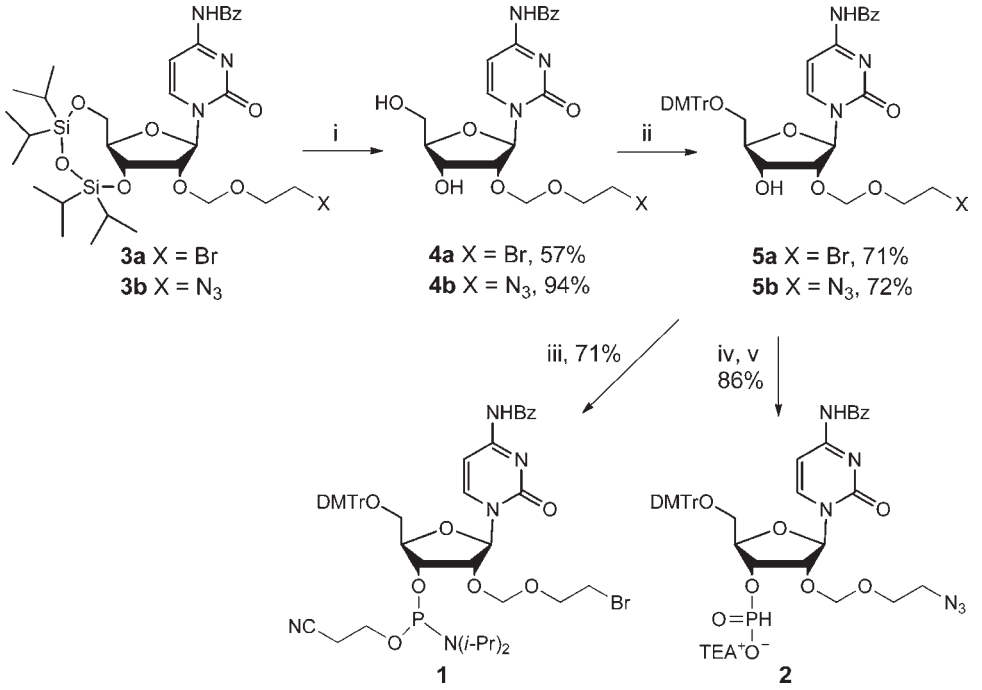
EXPERIMENTAL PROCEDURES

General Remarks. Synthetic reactions were monitored by TLC (Merck DC Kieselgel 60F_{254}), using UV light, iodine vapors, or heating with 10% H_2SO_4 (aq) for detection. Column chromatography was performed on Silica gel 60 (Fluka, 0.040−0.063 mm). The NMR spectra were recorded at 400 or 500 MHz. Chemical shifts are given in parts per million (ppm) and measured relative to the solvent signals (^{1}H and ^{13}C). Appropriate 2D NMR methods (COSY and HSQC) were used for peak assignment. Solvents were dried with 4 Å molecular sieves (DCM, pyridine and MeCN) or by distillation and storage over CaH_2 (Et_3N). The mass spectra were recorded using ESI ionization methods. RP HPLC analysis of the oligonucleotide conjugates was performed on a Thermo ODS Hypersil C18 (250 × 4.6 mm, 5 μm) analytical column, applying a gradient elution from 0 to 50% MeCN in

Received: February 25, 2011
Revised: April 11, 2011
Published: May 03, 2011

ACS Publications © 2011 American Chemical Society

Scheme 1[a]



[a] Reagents: (i) Bu_4NF, THF; (ii) DMTrCl, pyridine; (iii) 2-cyanoethyl *N,N*-diisopropylphosphoramidochloridite, Et_3N, DCM; (iv) diphenyl *H*-phosphonate, pyridine; (v) Et_3N, H_2O.

0.1 mol L^{-1} TEAA (aq, Et_3NHOAc) buffer over 60 min, at a flow rate of 1 mL min^{-1}, and detection at 260 nm.

2′-*O*-(2-Bromoethoxymethyl)-*N*^{4}-benzoylcytidine (4a). Nucleoside **3a** (1.30 g, 1.79 mmol), prepared as described earlier,[30] was dissolved in Bu_4NF trihydrate in THF (0.25 mol L^{-1}; 4.8 mL), kept for 10 min at 20 °C, evaporated to dryness, coevaporated with chloroform (2 × 10 mL), and applied onto a column with silica gel (25 g). The column was washed with DCM (100 mL), DCM-EtOH (97:3, v/v), and then eluted with DCM-EtOH (95:5) to obtain **4a** (490 mg, 57%) as a white amorphous foam (Scheme 1). ^{1}H NMR [400 MHz, $CDCl_3/CD_3OD$ (9:1)] δ_{ppm} 8.47 (d, 1H, J = 7.5 Hz, H-6), 7.98−7.40 (m, 6H, Bz, H-5), 5.88 (d, 1H, J = 2.2 Hz, H-1′), 5.02 (d, 1H, J = 6.5 Hz, OCHHO), 4.92 (d, 1H, J = 6.5 Hz, OCHHO), 4.33 (dd, 1H, $J_{2',3'}$ = 5.0 Hz, H-2′), 4.26 (dd, 1H, $J_{3',4'}$ = 7.5 Hz, H-3′), 4.07 (dt, 1H, $J_{4',5'a}$ = $J_{4',5'b}$ = 2.2 Hz, H-4′), 3.99 (dd, 1H, $J_{5'a,5'b}$ = 12.8 Hz, H-5′a), 3.89 (dd, 2H, J = 6.2 Hz, 5.9 Hz, OCH_2CH_2Br), 3.81 (dd, 1H, H-5′b), 3.44 (dd, 2H, OCH_2CH_2Br). ^{13}C NMR ($CDCl_3/CD_3OD$ (9:1)) δ_{ppm} 167.1 (C═O), 163.1 (C-4), 146.0 (C-6), 133.3, 129.0, 128.0 (Ph), 97.3 (C-5), 95.3 (OCH_2O), 90.9 (C-1′), 84.7 (C-4′), 79.9 (C-2′), 68.8 (C-3′), 68.0 (OCH_2CH_2Br), 60.1 (C-5′), 30.5 (OCH_2CH_2Br).

2′-*O*-(2-Azidoethoxymethyl)-*N*^{4}-benzoylcytidine (4b). Analogous to the preparation of **4a**, the desilylation of **3b** (1.12 mg, 1.63 mmol) yielded **4b** (683 mg, 94%) as a white amorphous foam. ^{1}H NMR (400 MHz, $CDCl_3$) δ_{ppm} 8.48 (d, 1H, J = 7.5 Hz, H-6), 8.00−7.40 (m, 6H, Bz, H-5), 5.88 (d, 1H, J = 2.5 Hz, H-1′), 5.03 (d, 1H, J = 6.5 Hz, OCHHO), 4.93 (d, 1H, OCHHO), 4.48 (dd, 1H, J = 5.3 Hz, H-2′), 4.41 (dd, 1H, J = 6.5 Hz, H-3′), 4.16 (ddd, 1H, $J_{4',5'a}$ = 1.9 Hz, $J_{4',5'b}$ = 1.5 Hz, H-4′), 4.08 (dd, 1H, $J_{5'a,5'b}$ = 12.5 Hz, H-5′a), 3.92 (dd, 1H, H-5′b), 3.82−3.71 (m, 2H, $OCH_2CH_2N_3$), 3.46−3.37 (m, 2H, $OCH_2CH_2N_3$). ^{13}C NMR (MHz, $CDCl_3$) δ_{ppm} 167.2 (C═O), 163.1 (C-4), 155.4 (C-2), 146.2 (C-6), 133.3, 129.0, 128.0 (Bz), 97.3 (C-5), 95.5 (OCH_2O), 91.2 (C-1′), 84.9 (C-4′), 79.9 (C-2′), 68.2 (C-3′), 67.4 ($OCH_2CH_2N_3$), 60.4 (C-5′), 50.9 ($OCH_2CH_2N_3$).

2′-*O*-(2-Bromoethoxymethyl)-5′-*O*-(4,4′-dimethoxytrityl)-*N*^{4}-benzoylcytidine (5a). Nucleoside **4a** (357 mg, 0.74 mmol) was dried by coevaporation with pyridine (2 × 20 mL). The residue was dissolved in dry pyridine (10 mL), 4,4′-dimethoxytrityl chloride (351 mg, 1.04 mmol) was added, and the resulted solution was kept in the dark for 16 h at 20 °C. MeOH (1 mL) was added and after 30 min, the mixture was concentrated in vacuo to near dryness. The residue was dissolved in DCM (50 mL) and washed with a 10% aqueous solution of sodium bicarbonate (20 mL) and water (2 × 20 mL). The organic layer was dried over anhydrous Na_2SO_4, the solvent was removed in vacuo, and the residue was coevaporated with toluene (2 × 10 mL) and purified by column chromatography on silica gel (20 g). The column was washed with a mixture of DCM, hexane, and Et_3N (75:23:2, v/v/v, 200 mL), followed by DCM, and the product was eluted with a mixture of DCM and Et_3N (98:2, v/v) to give **5a** (412 mg, 71%) as a foam. ^{1}H NMR (500 MHz, CD_3CN) δ_{ppm} 9.63 (br s, 1H, NH), 8.53 (d, 1H, J = 7.5 Hz, H-6), 8.00−7.94 (m, 2H, Bz), 7.60 (m, 1H, Bz), 7.52−7.46 (m, 4H, Bz, DMTr), 7.41−7.32 (m, 6H, DMTr), 7.29−7.22 (m, 2H, DMTr, H-5), 6.94−6.88 (m, 4H, DMTr), 5.92 (s, 1H, H-1′), 5.17 (d, 1H, J = 6.5 Hz, OCHHO), 4.95 (d, 1H, J = 6.5 Hz, OCHHO), 4.58 (m, 1H, H-3′), 4.38 (d, 1H, J = 5.0 Hz, H-2′), 4.15 (m, 1H, H-4′), 4.00−3.89 (m, 2H, OCH_2CH_2Br), 3.78 (s, 6H, DMTr-OMe), 3.56−3.46 (m, 4H, OCH_2CH_2Br, H-5′). ^{13}C NMR (125 MHz, CD_3CN) δ_{ppm} 167.2 (Bz-C═O), 163.0 (C-4), 158.8, 158.8 (DMTr), 154.9 (C-2), 144.9 (C-6), 144.5, 136.0, 135.6 (DMTr), 133.5, 132.9 (Bz), 130.2, 130.0 (DMTr), 128.7, 128.3, 128.1, 128.1 (DMTr, Bz), 127.1, 113.3 (DMTr), 96.5 (C-5),

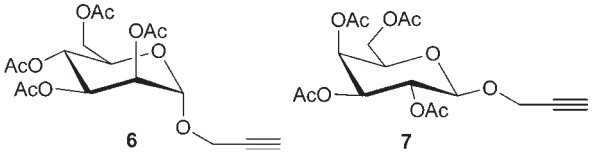
94.3 (OCH_2O), 89.8 (C-1′), 86.8 (DMTr-C_q), 82.6 (C-4′), 78.9 (C-2′), 68.3 (OCH_2CH_2Br), 68.0 (C-3′), 61.2 (C-5′), 55.0 (DMTr-OMe), 31.5 (OCH_2CH_2Br). HRMS(ESI): $[MH]^+$ $C_{40}H_{41}BrN_3O_9$ requires 786.2021, found 786.2019.

2′-*O*-(2-Azidoethoxymethyl)-5′-*O*-(4,4′-dimethoxytrityl)-β-D-*N*⁴-benzoylcytidine (5b). Analogous to the preparation of **5a**, the tritylation of nucleoside **4b** (778 mg, 1.74 mmol) yielded **5b** (940 mg, 72%) as a foam. ^{1}H NMR (500 MHz, CD_3CN) δ_{ppm} 9.29 (br s, 1H, NH), 8.48 (d, 1H, J = 7.5 Hz, H-6), 8.00−7.95 (m, 2H, Bz), 7.66 (m, 1H, Bz), 7.57−7.52 (m, 2H, Bz), 7.51−7.48 (m, 2H, DMTr), 7.41−7.35 (m, 6H, DMTr), 7.30 (m, 1H, DMTr), 7.18 (br d, 1H, J = 6.5 Hz, H-5), 6.96−6.91 (m, 4H, DMTr), 5.91 (d, 1H, J = 1.0 Hz, H-1′), 5.16 (d, 1H, J = 7.0 Hz, OCHHO), 4.94 (d, 1H, J = 6.5 Hz, OCHHO), 4.52 (m, 1H, H-3′), 4.32 (d, 1H, J = 5.0 Hz, H-2′), 4.11 (ddd, 1H, J = 9.0 Hz, 2.5 Hz, 2.5 Hz, H-4′), 3.88−3.76 (m, 8H, DMTr-OMe, $OCH_2CH_2N_3$), 3.53−3.37 (m, 5H, H-5′, $OCH_2CH_2N_3$, 3′−OH). ^{13}C NMR (125 MHz, CD_3CN) δ_{ppm} 167.2 (Bz-C=O), 162.9 (C-4), 158.8, 158.8 (DMTr), 154.8 (C-2), 144.9 (C-6), 144.5, 136.0, 135.6 (DMTr), 133.5, 132.9 (Bz), 130.2, 130.0 (DMTr), 128.7 (Bz), 128.2, 128.1, 128.1 (DMTr, Bz), 127.1, 113.3 (DMTr), 96.3 (C-5), 94.4 (OCH_2O), 89.8 (C-1′), 86.7 (DMTr-C_q), 82.6 (C-4′), 79.0 (C-2′), 68.0 (C-3′), 66.9 ($OCH_2CH_2N_3$), 61.2 (C-5′), 55.0 (DMTr-OMe), 50.7 ($OCH_2CH_2N_3$). HRMS(ESI): $[MH]^+$ $C_{40}H_{41}N_6O_9$ requires 749.2930; found, 749.2935.

2′-*O*-(2-Bromoethoxymethyl)-5′-*O*-(4,4′-dimethoxytrityl)-β-*N*⁴-benzoylcytidine 3′-(2-cyanoethyl-*N*,*N*-diisopropylphosphoramidite) (1). Compound **5a** (0.29 g, 0.37 mmol) was predried over P_2O_5 in a vacuum desiccator and dissolved in DCM (5 mL). Et_3N (260 μL, 1.85 mmol) and 2-cyanoethyl *N*,*N*-diisopropylphosphoramidochloridite (99 μL, 0.44 mmol) were added under nitrogen. After 2 h, the mixture was filtered through a short dried silica gel column (60−70% EtOAc in hexane and 0.1% Et_3N). The mixture of phosphoramidite **1** R_P- and S_P-diastereomers (0.26 g, 71%) was obtained as a colorless oil. ^{1}H NMR (500 MHz, CD_3CN) δ_{ppm} 9.22 (br, 1H, NH), 8.50 [d, 0.5H, J = 7.5 Hz, H-6 (*diast. I*)], 8.45 [d, 0.5H, J = 7.0 Hz, H-6 (*diast. II*)], 8.00−7.94 (m, 2H, Bz), 7.66 (m, 1H, Bz), 7.58−7.48 (m, 4H, Bz, DMTr), 7.43−7.34 (m, 6H, DMTr), 7.31 (m, 1H, DMTr), 7.11 [br, 0.5H, H-5 (*diast. I*)], 7.04 [br, 0.5H, H-5 (*diast. II*)], 6.96−6.90 (m, 4H, DMTr), 5.99 (br s, 1H, H-1′), 5.09 [d, 0.5H, J = 6.5 Hz, OCHHO (*diast. I*)], 5.06 [d, 0.5H, J = 6.5 Hz, OCHHO (*diast. II*)], 5.01 [d, 0.5H, J = 6.5 Hz, OCHHO (*diast. II*)], 4.96 [d, 0.5H, J = 6.5 Hz, OCHHO (*diast. I*)], 4.60 (m, 1H, H-3′), 4.47 [m, 0.5H, H-2′ (*diast. I*)], 4.41 [m, 0.5H, H-2′ (*diast. II*)], 4.28 [m, 0.5H, H-4′ (*diast. I*)], 4.23 [m, 0.5H, H-4′ (*diast. II*)], 4.05−3.85 [m, 2.5H, OCH_2CH_2Br, $OCHHCH_2CN$ (0.5H *diast. II*)], 3.84−3.46 [m, 13.5H, DMTr-OMe, OCH_2CH_2CN (2 × 0.5H *diast. I*), $OCHHCH_2CN$ (0.5H *diast. II*), $NCH(CH_3)_2$, OCH_2CH_2Br, H-5′], 2.71−2.67 [m, 2 × 0.5H, OCH_2CH_2CN (*diast. II*)], 2.58−2.53 [m, 2 × 0.5H, OCH_2CH_2CN (*diast. I*)], 1.21−1.12 [m, 12 × 0.5H (*diast. I*), 6 × 0.5H (*diast. II*), $NCH(CH_3)_2$], 1.06 [d, 6 × 0.5H, J = 7.0 Hz, $NCH(CH_3)_2$ (*diast. II*)]. ^{31}P NMR (200 MHz, CD_3CN) δ_{ppm} 148.6 (*diast. I*), 150.5 (*diast. II*). HRMS(ESI): $[MH]^+$ $C_{49}H_{58}BrN_5O_{10}P$ requires 986.3099; found, 986.3078.

2′-*O*-(2-Azidoethoxymethyl)-5′-*O*-(4,4′-dimethoxytrityl)-*N*⁴-benzoylcytidine 3′-(*H*-phosphonate) Triethylammonium Salt (2). Compound **5b** (0.37 g, 0.5 mmol) was dissolved in dry pyridine (2 mL), and diphenyl *H*-phosphonate (0.7 mL, 3.6 mmol) was added. After 45 min, water (0.6 mL) and Et_3N (0.6 mL) were added, and the reaction mixture was stirred for an additional 15 min. After evaporation, the residue was partitioned between DCM (20 mL) and 5% aq $NaHCO_3$ (20 mL). The organic layer was dried with Na_2SO_4, evaporated, and purified by silica gel chromatography (5−10% MeOH in DCM + 0.1% Et_3N), yielding product **2** (0.39 g, 86%) as a white foam. ^{1}H NMR (500 MHz, $CDCl_3/CD_3OD$ (1:1)) δ_{ppm} 8.53 (m, 1H, H-6), 7.99−7.94 (m, 2H, Bz), 7.61 (m, 1H, Bz), 7.55−7.49 (m, 2H, Bz), 7.47−7.40 (m, 2H, DMTr), 7.37−7.14 (m, 8.5H, DMTr, H-5, PH (0.5H)), 6.92−6.85 (m, 4H, DMTr), 6.19 (br, 0.5H, PH), 6.09 (s, 1H, H-1′), 5.05 (d, 1H, J = 7.0 Hz, OCHHO), 4.97 (d, 1H, J = 7.0 Hz, OCHHO), 4.92 (m, 1H, H-3′), 4.52 (m, 1H, H-2′), 4.35 (d, 1H, J = 7.0 Hz, H-4′), 3.87−3.76 (m, 8H, DMTr-OMe, $OCH_2CH_2N_3$), 3.64 (d, 1H, J = 11.0 Hz, H-5′a), 3.52 (d, 1H, J = 11.0 Hz, H-5′b), 3.43 (m, 2H, $OCH_2CH_2N_3$), 3.13 (br q, 6H, J = 6.5 Hz, CH_2 of Et_3N), 1.31 (t, 9H, J = 7.3 Hz, CH_3 of Et_3N). ^{13}C NMR (125 MHz, $CDCl_3/CD_3OD$, 1:1) δ_{ppm} 167.3 (Bz-C=O), 163.3 (C-4), 158.8 (DMTr), 156.2 (C-2), 144.8 (C-6), 143.9, 135.4, 135.1 (DMTr), 133.1, 133.0 (Bz), 130.2, 130.1 (DMTr), 128.7 (Bz), 128.3, 127.9, 127.9 (DMTr, Bz), 127.1, 113.2 (DMTr), 97.6 (C-5), 94.9 (OCH_2O), 89.4 (C-1′), 87.2 (DMTr-C_q), 82.0 (C-4′), 78.5 (C-2′), 70.1 (C-3′), 67.1 ($OCH_2CH_2N_3$), 60.9 (C-5′), 54.9 (DMTr-OMe), 50.7 ($OCH_2CH_2N_3$), 46.3 (CH_2 of Et_3N), 8.3 (CH_3 of Et_3N). ^{31}P NMR (200 MHz, $CDCl_3/CD_3OD$, 1:1) δ_{ppm} 2.53. HRMS(ESI): $[M]^-$ $C_{40}H_{40}N_6O_{11}P$ requires 811.2498; found, 811.2488.

Chart 1



Synthesis of 2′-*O*-Me-oligoribonucleotides. Oligonucleotides incorporating **1** and **2** were synthesized in a 1.0 μmol scale using commercial 500 Å CPG-succinyl-2′-*O*-Me-adenosine support. For the synthesizer, a protocol including both the phosphoramidite/tetrazole and *H*-phosphonate/pivaloyl chloride couplings was generated. For the coupling of phosphoramidite block **1** (0.13 mol L^{-1} solution in dry MeCN) and the commercial 2′-*O*-Me-nucleoside phosphoramidites, standard RNA phosphoramidite protocol was applied, with the exception of an extra detritylation step for monomer **1**. For the *H*-phosphonate monomer **2** [35 mmol L^{-1} solution in dry MeCN/pyrine (1:1, v/v)], a previously generated protocol was utilized.[9] Accordingly, the coupling time was 570 s on using pivaloyl chloride at a concentration of 100 mmol L^{-1} in dry MeCN/pyrine (1:1, v/v). An additional detritylation step was used also for monomer **2**. After the oligonucleotide assembly, the support-bound material was removed from the synthesizer, oxidized with iodine (0.1 mol L^{-1}) in wet pyridine (98:2, v/v) at rt for 1 h, washed with pyridine/MeCN/MeOH, and dried in vacuum. The oligonucleotides were released from the support and deprotected with concentrated ammonia (33% aqueous NH_3) at 55 °C overnight.

On-Support Click Conjugation. Alkynyl-functionalized ligands **6**[9] and **7**[31] (Chart 1) were conjugated to the azido groups of the support-bound oligonucleotides as follows. The ligands in MeOH (50 mmol L^{-1}, 15 equiv/azido group) were added onto the support. After that, $CuSO_4$ and tris[(1-benzyl-1,2,3-triazol-4-yl)methyl]amine (TBTA-ligand) were added as a 25 mmol L^{-1}

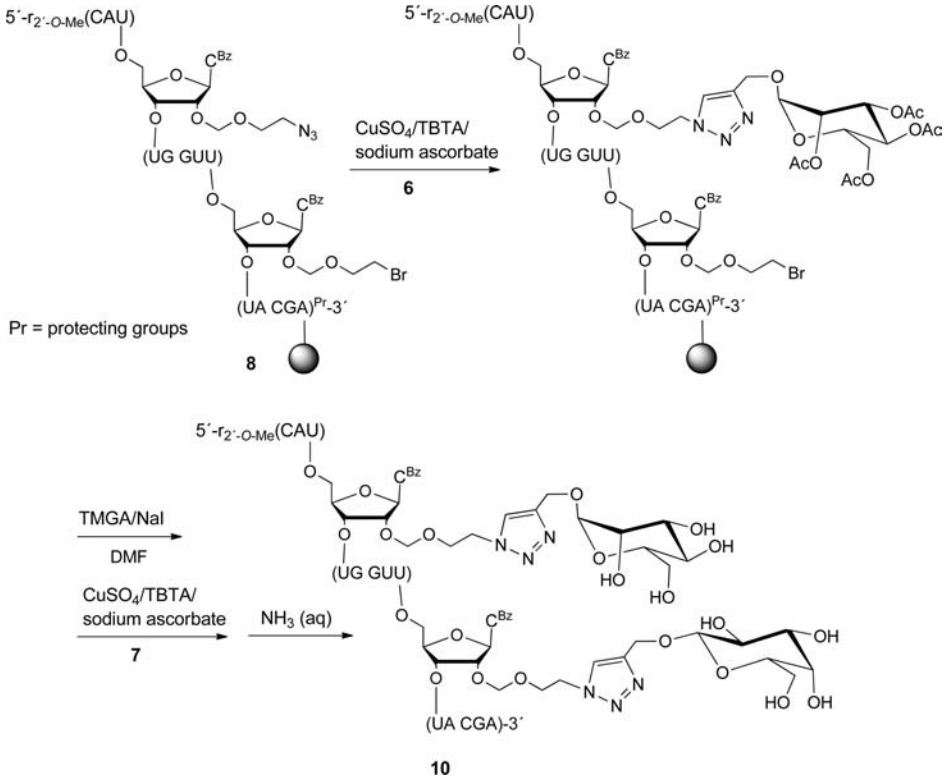


Figure 1. Solid-supported introduction of two different sugar ligands into 2′-positions within a 2′-*O*-Me-oligoribonucleotide (**10**).

solution in a 12:3:1 (v/v/v) mixture of water, DMSO, and 2-butanol (7.5 equiv/azido group). Finally, sodium ascorbate (15 equiv/azido group) as a 0.1 mol L^{-1} aqueous solution was added. The mixture was shaken at room temperature for 5 h. The support was collected by filtration and washed first with water, DMF, and MeOH. To remove the copper salt and TBTA ligand as quantitatively as possible, the support was then treated for 10 min with aqueous EDTA solution (0.1 mol L^{-1}), washed with water, and then for another 10 min with an aqueous solution of neomycin trisulfate (0.1 mol L^{-1}). Finally, the support was washed with water, DMF, DCM, MeOH, and MeCN.

On-Support Azidation. The support-bound oligonucleotides (0.5 μmol) were treated with a solution of tetramethylguanidinium azide (TMGA, 15.8 mg, 200 equiv) and NaI (15.0 mg, 200 equiv) in dry DMF (500 μL) for 1.5 h at 65 °C.[13] The support was collected by filtration and washed with DMF, DCM, water, and MeOH.

Characterization of the Conjugates. The identity of the sugar conjugates **10** and **11** was verified by ESI-MS. Observed masses are calculated from [(M-4H)/4]. ON**10** requires an isotopic mass of 5527.08; found, 5527.15. ON**11** requires an isotopic mass of 5830.19; found, 5830.18.

Melting Temperature Studies. The melting curves (absorbance versus temperature) were measured at 260 nm on a Perkin-Elmer Lambda 35 UV−vis spectrometer equipped with a multiple cell holder and a Peltier temperature controller. The temperature was changed at a rate of 0.5 °C/min (from 15 to 90 °C). The measurements were performed in 10 mmol L^{-1} potassium phosphate buffer (pH 7) containing 0.1 mol L^{-1} or 1.0 mol L^{-1} NaCl. The oligonucleotide conjugates and their cDNA or 2′-*O*-methyl RNA targets were used at a concentration of 2 μmol L^{-1}. T_m values were determined as the maximum of the first derivate of the melting curve.

RESULTS AND DISCUSSION

Synthesis of Monomeric Building Blocks. An *O*-glycosylation approach[30,32] was applied to the preparation of the 2′-*O*-(2-bromoethoxy)methyl (**3a**) and 2′-*O*-(2-azidoethoxy)methyl (**3b**) substituted cytidine monomers. Accordingly, 3′,5′-*O*-(1,1,3,3-tetraisopropyldisiloxane-1,3-diyl)-N^4-benzoylcytidine[33,34] was treated with (2-bromoethoxy)methyl acetate in the presence of tin tetrachloride at −12 °C.[30] Nucleoside **3a** was isolated in 88% yield, and conversion to the corresponding 2′-*O*-(2-azidoethoxy) methyl derivative (**3b**) by displacement of the bromo substituent with NaN_3 in DMF was virtually quantitative. The 3′,5′-cyclic silyl protecting group was removed from **3a** and **3b** with Bu_4NF in THF, and the 5′-OH of the deprotected nucleosides (**4a**,**b**) was protected with a 4,4′-dimethoxytrityl group to obtain **5a**,**b**. Finally, **5a** and **5b** were converted to 3′-(2-cyanoethyl-*N*,*N*-diisopropylphosphoramidite) (**1**) and 3′-(*H*-phosphonate) (**2**), respectively. Owing to the presence of the azido group, **5b** undergoes a Staudinger reaction upon phosphitylation, which prevents its conversion to a phosphoramidite reagent.[9,35]

The alkynyl-derivatized monosaccharide ligands, viz. propargyl 2,3,4,6-tetra-*O*-acetyl-α-D-mannopyranoside (**6**) and propargyl 2,3,4,6-tetra-*O*-acetyl-β-D-galactopyranose (**7**), used in the click conjugation were prepared from peracetylated α-D-mannopyranose and β-D-galactopyranose by boron trifluoride etherate promoted glycosidation with propargyl alcohol. The compounds exhibited ^1H and ^{13}C NMR chemical shifts identical to those reported earlier.[9,31]

Oligonucleotide Synthesis and Click Conjugation. The appropriately protected phosphoramidite (**1**) and *H*-phosphonate (**2**) building blocks were incorporated into 15-mer 2′-*O*-methyl oligoribonucleotides: 5′-(CAU $\mathbf{C^2}$UG GUU $\mathbf{C^1}$UA

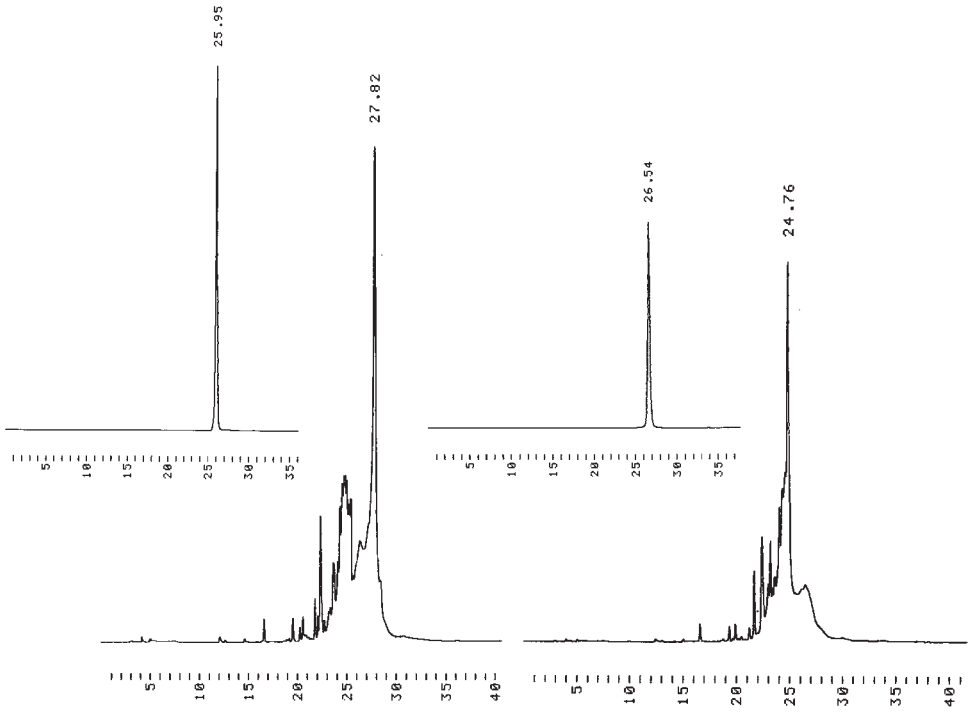


Figure 2. RP HPLC traces of the crude and purified oligonucleotide glycoconjugates **10** and **11**, respectively. For the chromatographic conditions, see the Experimental Procedures Section.

Table 1. Melting Temperatures for the Duplexes of Oligonucleotide Conjugates 10 and 11 with Their Complementary DNA and 2′-*O*-Methyl-RNA Sequences[a]

	compl. DNA T_m/°C and (ΔT_m/°C)		compl. 2′-*O*-methyl RNA T_m/°C and (ΔT_m/°C)
	0.1 mol L^{-1} NaCl	1.0 mol L^{-1} NaCl	0.1 mol L^{-1} NaCl
5′-CAU CUG GUU CUA CGA	50.1	61.7	72.0
5′-CAU *X*UG GUU *Y*UA CGA (**10**)	50.6 (+0.5)	60.6 (−1.1)	71.5 (−0.5)
5′-CAU *Y*UG GUU *X*UA *Y*GA (**11**)	47.0 (−3.1)	60.2 (−1.5)	68.2 (−3.8)

[a] ***X*** = monomer C^2 conjugated with **6**; ***Y*** = monomer C^1 conjugated with **7**.

CGA)-3′ (**8**) and 5′-(CAU $\mathbf{C^1}$UG GUU $\mathbf{C^2}$UA $\mathbf{C^1}$GA)-3′ (**9**) ($\mathbf{C^1}$ and $\mathbf{C^2}$ refer to nucleosidic units derived from **1** and **2**, respectively). The oligomers were assembled by phosphoramidite chemistry, with the exception of the insertion of **2**, which was carried out by pivaloyl chloride promoted *H*-phosphonate coupling. As also shown previously, the presence of an azido group in the growing solid-supported oligonucleotide chain does not disturb the phosphoramidite coupling of subsequent monomers.[9] The coupling yield of building block **1** was ∼99%, but the *H*-phosphonate block **2** was coupled in only 85% yield.

After completion of the chain assembly, oligonucleotides **8** and **9** were conjugated with the two alkynyl-functionalized monosaccharide ligands (**6** and **7**) (Figure 1). The azido group of monomeric unit **2** was first subjected to Cu(I) promoted click reaction with propargyl α-D-mannopyanoside tetraacetate (**6**), using a mixture of $CuSO_4$ and sodium arcorbate in the presense of tris[(1-benzyl-1,2,3-triazol-4-yl)methyl]amine (TBTA-ligand) as the source of Cu(I) ion (5 h, r.t.). The bromo substituent of monomeric unit **1** was then displaced with an azide ion, as reported previously by Pourceau et al.[13,14] Both tetramethylguanidinium azide[36] (TMGA/NaI/DMF, 65 °C) and less soluble NaN_3 (NaN_3/NaI/DMF, 65 °C) were used as a source of azide ions. The second click reaction was then performed using propargyl β-D-galactopyranoside tetraacetate (**7**) as the alkyne component. The oligonucleotide conjugates obtained (**10** and **11**) were deprotected and released from the support by standard ammonolysis (33% aq NH_3, 55 °C, overnight). The crude products were purified by RP-HPLC, and their identity was verified by ESI-MS. Figure 2 shows the HPLC traces of the crude conjugates and the homogeneity of the products after purification.

Melting Temperature Studies. It has been shown previously that oligonucleotides bearing a β-D-ribofuranosyl group at an intrachain 2′-O form stable complexes with RNA (ΔT_m = 0 °C) and maintain A-type helical geometry with the additional 2′-*O*-ribose moiety located in the minor groove.[2,24] Consistent with these findings, the sugar ligands attached in the present study to 2′-*O* via a [2-(4-hydroxymethyl-1*H*-1,2,3-triazol-1-yl)ethoxy]-methyl linker only slightly destabilize the duplex. Table 1 records the melting temperatures (T_m) for the duplexes of oligonucleotide conjugates **10** and **11** with the full cDNA and 2′-*O*-methyl RNA sequences at pH 7.

The saccharide ligands accommodated quite well in the duplex structure. Oligonucleotide **10** bearing two saccharide units in an

intrachain position exhibited even a slight stabilization of the duplex with the DNA target at a low ionic strength (ΔT_m = +0.5 °C) and a slight destabilization at a high ionic strength (ΔT_m = −1.1 °C). Addition of a third saccharide ligand to obtain conjugate **11** resulted in a moderate destabilization even at a low ionic strength (ΔT_m = −3.1). At high ionic strength, the destabilization was less prominent (ΔT_m = −1.5 °C). With the 2′-*O*-Me RNA target, two saccharide ligands within conjugate **10** were similarly well tolerated (ΔT_m = −0.5 °C), but with **11**, containing three saccharides, T_m again dropped significantly (ΔT_m = −3.8 °C). A tentative explanation for the marked destabilizing influence of the third saccharide, especially at low ionic strength, is that two of the sugars are rather close to each other within conjugate **11**, viz. in positions 10 and 13.

■ CONCLUSIONS

A convenient and reliable method for solid-phase introduction of two different types of saccharide ligands in desired positions of an oligonucleotide has been developed. The underlying principle is regiospecific introduction of azido- and bromo-functionalized building blocks into the oligonucleotide upon chain assembly and their subsequent derivatization on the support. A propynyl-functionalized saccharide is first attached to the azido groups by Cu(I) promoted 1,3-dipolar cycloaddition, and the same reaction is utilized to conjugate the second propynyl saccharide after conversion of the bromo substituents to azido groups by displacement with the azide ion. For the chain assembly, conventional phosphoramidite chemistry may be applied, except for the introduction of the azido functionalized building blocks that have to be coupled as *H*-phosphonates. The saccharide ligands are quite well accommodated to the duplexes formed with both DNA and 2′-*O*-Me RNA targets

■ ASSOCIATED CONTENT

Supporting Information. ESI-MS data and melting temperature curves for oligonucleotides **10** and **11**. This material is available free of charge via the Internet at http://pubs.acs.org.

■ AUTHOR INFORMATION

Corresponding Author

*(A.K.) Fax: +35823336700. E-mail: anu.kiviniemi@utu.fi. (S.N.M.) Fax: +074991359751. E-mail: smikh@eimb.ru.

■ ACKNOWLEDGMENT

Financial support from the Russian Foundation for Basic Research, Russian Academy of Sciences (Program "Molecular and Cell Biology"), and the Academy of Finland is gratefully acknowledged.

■ REFERENCES

(1) Manoharan, M. (1999) 2′-Carbohydrate modifications in antisense oligonucleotide therapy: importance of conformation, configuration and conjugation. *Biochim. Biophys. Acta 1489*, 117–130.

(2) Luyten, I., Esnouf, R. M., Mikhailov, S. N., Efimtseva, E. V., Michiels, P., Heus, H. A., Hilbers, C. W., and Herdewijn, P. (2000) Solution structure of a RNA decamer duplex, containing 9-[(2-*O*-(β-D-ribofuranosyl)-(β-D-ribofuranosyl]adenine, a special residue in lower eukaryotic initiator tRNAs. *Helv. Chim. Acta 83*, 1278–1289.

(3) Zatsepin, T. S., Romanova, E. A., and Oretskaya, T. S. (2004) Nucleosides and oligonucleotides containing 2′-reactive groups: synthesis and applications. *Russ. Chem. Rev. 73*, 701–733.

(4) Ugarte-Uribe, B., Pérez-Rentero, S., Lucas, R., Aviñó, A., Reina, J. J., Alkorta, I., Eritja, R., and Morales, J. C. (2010) Synthesis, cell-surface binding, and cellular uptake of fluorescently labeled glucose-DNA conjugates with different carbohydrate presentation. *Bioconjugate Chem. 21*, 1280–1287.

(5) Zhu, L., and Mahato, R. I. (2010) Targeted delivery of siRNA to hepatocytes and hepatic stellate cells by bioconjugation. *Bioconjugate Chem. 21*, 2119–2127.

(6) Lönnberg, H. (2009) Solid-phase synthesis of oligonucleotide conjugates useful for delivery and targeting of potential nucleic acid therapeutics. *Bioconjugate Chem. 20*, 1065–1094.

(7) Zatsepin, T. S., and Oretskaya, T. S. (2004) Synthesis and applications of oligonucleotide-carbohydrate conjugates. *Chem. Biodiversity 1*, 1401–1417.

(8) Yan, H., and Tram, K. (2007) Glycotargeting to improve cellular delivery efficiency of nucleic acids. *Glycoconjugate J. 24*, 107–123.

(9) Kiviniemi, A., Virta, P., and Lönnberg, H. (2008) Utilization of intrachain 4′-*C*-azidomethylthymidine for preparation of oligodeoxyribonucleotide conjugates by click chemistry in solution and on a solid support. *Bioconjugate Chem. 19*, 1726–1734.

(10) Kiviniemi, A., Virta, P., and Lönnberg, H. (2010) Solid-supported synthesis and click conjugation of 4′-*C*-alkyne functionalized oligodeoxyribonucleotides. *Bioconjugate Chem. 21*, 1890–1901.

(11) Chevolot, Y., Bouillon, C., Vidal, S., Morvan, F., Meyer, A., Cloarec, J.-P., Jochum, A., Praly, J.-P., Vasseur, J.-J., and Souteyrand, E. (2007) DNA-based carbohydrate biochips: a platform for surface glycol-engineering. *Angew. Chem., Int. Ed. 46*, 2398–2402.

(12) Bouillon, C., Meyer, A., Vidal, S., Jochum, A., Chevolot, Y., Cloarec, J.-P., Praly, J.-P., Vasseur, J.-J., and Morvan, F. (2006) Microwave assisted click chemistry for the synthesis of multiple labeled-carbohydrate oligonucleotides on solid support. *J. Org. Chem. 71*, 4700–4702.

(13) Pourceau, G., Meyer, A., Chevolot, Y., Souteyrand, E., Vasseur, J.-J., and Morvan, F. (2010) Oligonucleotide carbohydrate-centered galactosyl cluster conjugates synthesized by click and phosphoramidite chemistries. *Bioconjugate Chem. 21*, 1520–1529.

(14) Pourceau, G., Meyer, A., Vasseur, J.-J., and Morvan, F. (2009) Synthesis of mannose and galactose oligonucleotide conjugates by bi-click chemistry. *J. Org. Chem. 74*, 1218–1222.

(15) Ketomäki, K., and Virta, P. (2008) Synthesis of aminoglycoside conjugates of 2′-*O*-methyl oligoribonucleotides. *Bioconjugate Chem. 19*, 766–777.

(16) Morvan, F., Meyer, A., Jochum, A., Sabin, C., Chevolot, Y., Imberty, A., Praly, J.-P., Vasseur, J.-J., Souteyrand, E., and Vidal, S. (2007) Fucosylated pentaerythrityl phosphodiester oligomers (PePOs): automated synthesis of DNA-based glycoclusters and binding to *Pseudomonas aeruginosa* lectin (PA-IIL). *Bioconjugate Chem. 18*, 1637–1643.

(17) Karskela, M., Virta, P., Malinen, M., Urtti, A., and Lönnberg, H. (2008) Synthesis and cellular uptake of fluorescently labeled multivalent hyaluronan disaccharide conjugates of oligonucleotide phosphorothioates. *Bioconjugate Chem. 19*, 2549–2558.

(18) Katajisto, J., Virta, P., and Lönnberg, H. (2004) Solid-phase synthesis of multiantennary oligonucleotide glycoconjugates utilizing on-support oximation. *Bioconjugate Chem. 15*, 890–896.

(19) Yamada, T., Peng, C. G., Matsuda, S., Addepalli, H., Jayaprakash, K. N., Alam, M. R., Mills, K., Maier, M. A., Charisse, K., Sekine, M., Manoharan, M., and Rajeev, K. G. (2011) Versatile site-specific conjugation of small molecules to siRNA using click chemistry. *J. Org. Chem. 76*, 1198–1211.

(20) Rostovtsev, V. V., Green, L. G., Fokin, V. V., and Sharpless, K. B. (2002) A stepwise huisgen cycloaddition process: Copper(I)-catalyzed regioselective "ligation" of azides and terminal alkynes. *Angew. Chem., Int. Ed. 41*, 2596–2599.

(21) Tornoe, C. W., Christensen, C., and Meldal, M. (2002) Peptidotriazoles on solid phase: [1,2,3]-triazoles by regiospecific

copper(I)-catalyzed 1,3-dipolar cycloadditions of terminal alkynes to azides. *J. Org. Chem. 67*, 3057–3064.

(22) Mikhailov, S. N., Efimtseva, E. V., Gurskaya, G. V., Zavodnik, V. E., De Bruyn, A., Rozenski, J., and Herdewijn, P. (1997) An efficient synthesis and physico-chemical properties of 2′-*O*-*β*-D-ribofuranosyl-nucleosides, minor tRNA components. *J. Carbohydr. Chem. 16*, 75–92.

(23) Efimtseva, E. V., Kulikova, I. V., and Mikhailov, S. N. (2007) Disaccharide nucleosides and their incorporation into oligonucleotides. *Curr. Org. Chem. 11*, 337–354.

(24) Efimtseva, E. V., Bobkov, G. V., Mikhailov, S. N., Van Aerschot, A., Schepers, G., Busson, R., Rozenski, J., and Herdewijn, P. (2001) Oligonucleotides containing disaccharide nucleosides. *Helv. Chim. Acta 84*, 2387–2397.

(25) Mikhailov, S. N., Efimtseva, E. V., Rodionov, A. A., Shelkunova, A. A., Rozenski, J., Emmerechts, G., Schepers, G., Van Aerschot, A., and Herdewijn, P. (2005) Synthesis of RNA containing *O*-*β*-D-ribofuranosyl-(1′′-2′)-adenosine-5′′-phosphate and 1-methyladenosine, minor components of tRNA. *Chem. Biodiversity 2*, 1153–1163.

(26) Andreeva, O. I., Golubeva, A. S., Kochetkov, S. N., Van Aerschot A., Herdewijn, P., Efimtseva, E. V., Ermolinsky, B. S., and Mikhailov, S. N. (2002) An additional 2′-ribofuranose residue at a specific position of DNA primer prevents its elongation by HIV-1 reverse trancriptase. *Bioorg. Med. Chem. Lett. 12*, 681–684.

(27) Tunitskaya, V. L., Rusakova, E. E., Memelova, L. V., Kochetkov, S. N., Van Aerschot, A., Herdewijn, P., Efimtseva, E. V., Ermolinsky, B. S., and Mikhailov, S. N. (1999) The mapping of T7 RNA polymerase active site with novel reagents - oligonucleotides with reactive dialdehyde groups. *FEBS Lett. 442*, 20–24.

(28) Efimtseva, E. V., and Mikhailov, S. N. (2002) Disaccharide nucleosides and oligonucleotides on their bases. New tools for the study of enzymes of nucleic acid metabolism. *Rev. Biochem. (Moscow) 67*, 1136–1144.

(29) Gritsenko, O. M., Koudan, E. V., Mikhailov, S. N., Ermolinsky, B. S., Van Aerschot, A., Herdewijn, P., and Gromova, E. S. (2002) Affinity modification of *Eco*RII DNA methyltransferase by the dialdehyde-substituted DNA duplexes: mapping the enzyme region that interacts with DNA. *Nucleosides, Nucleotides Nucleic Acids 21*, 753–764.

(30) Bobkov, G. V., Mikhailov, S. N., Van Aerschot, A., and Herdewijn, P. (2008) Phosphoramidite building blocks for efficient incorporation of 2′-O-aminoethoxy(and propoxy)methyl nucleosides into oligonucleotides. *Tetrahedron 64*, 6238–6251.

(31) Mereyala, H. B., and Gurrala, S. R. (1998) A highly diastereoselective, practical synthesis of allyl, propargyl 2,3,4,6-tetra-*O*-acetyl-*β*-D-gluco, *β*-D-galactopyranosides and allyl, propargyl heptaacetyl-*β*-D-lactosides. *Carbohydr. Res. 307*, 351–354.

(32) Efimtseva, E. V., Kulikova, I. V., and Mikhailov, S. N. (2009) Disaccharide nucleosides as an important group of natural compounds. *Mol. Biol. (Russia) 43*, 301–312.

(33) Markiewicz, W. T. (1979) Tetraisopropyldisiloxane-1,3-diyl group for simultaneous protection of 3′- and 5′-hydroxy functions of nucleosides. *J. Chem. Res. (S)*, 24–25.

(34) Bobkov, G. V., Brilliantov, K. V., Mikhailov, S. N., Rozenski, J., Van Aerschot, A., and Herdewijn, P. (2006) Synthesis of oligoribonucleotides containing pyrimidine 2′-O-[(hydroxyalkoxy)methyl]-ribonucleosides. *Collect. Czech. Chem. Commun. 71*, 804–819.

(35) Coppola, C., Simeone, L., De Napoli, L., and Montesarchio, D. (2011) On the compatibility of azides in phosphoramidite-based couplings: synthesis of a novel, convertible azido-functionalized Cy-PLOS analogue. *Eur. J. Org. Chem. 6*, 1155–1165.

(36) Papa, A. J. (1966) Synthesis and azidolysis of 2-chlorotetramethylguanidine. Synthetic utility of hexa- and tetramethylguanidinium azide. *J. Org. Chem. 31*, 1426–1430.

Solid-supported 2´-*O*-glycoconjugation of oligonucleotides by azidation and click reactions

Anu Kiviniemi,[*,†] Pasi Virta,[†] Mikhail S. Drenichev,[‡] Sergey N. Mikhailov,[*,‡] and Harri Lönnberg[†]

[†] Department of Chemistry, University of Turku, FIN-20014 Turku, Finland (fax: +35823336700; email: anu.kiviniemi@utu.fi)

[‡] Engelhardt Institute of Molecular Biology, Russian Academy of Sciences, Vavilov Street 32, Moscow 119991, Russia (fax: +074991359751; e-mail: smikh@eimb.ru)

SUPPORTING INFORMATION

Table of Contents

General procedures S2
Figure S1. MS(ESI) spectrum of pure **10** S2
Figure S2. MS(ESI) spectrum of pure **11** S3
Figure S3. T_m curves of ON**10** and ON**11** with cDNA S3
Figure S4. T_m curve of ON**10** and ON**11** with 2´-*O*-methyl RNA S4

General procedures

The mass spectra of the oligonucleotides **10** and **11** were recorded by ESI ionization method. The melting curves (absorbance versus temperature) were measured at 260 nm on a Perkin-Elmer Lambda 35 UV-vis spectrometer equipped with a multiple cell holder and a Peltier temperature-controller. The temperature was changed at a rate of 0.5 ºC / min (from 15 to 90 ºC). The measurements were performed in 10 mmol L^{-1} potassium phosphate buffer (pH 7) containing 0.1 mol L^{-1} or 1.0 mol L^{-1} NaCl. The oligonucleotide conjugates and their complementary DNA or 2´-*O*-methyl RNA targets were used at a concentration of 2 μmol L^{-1}.

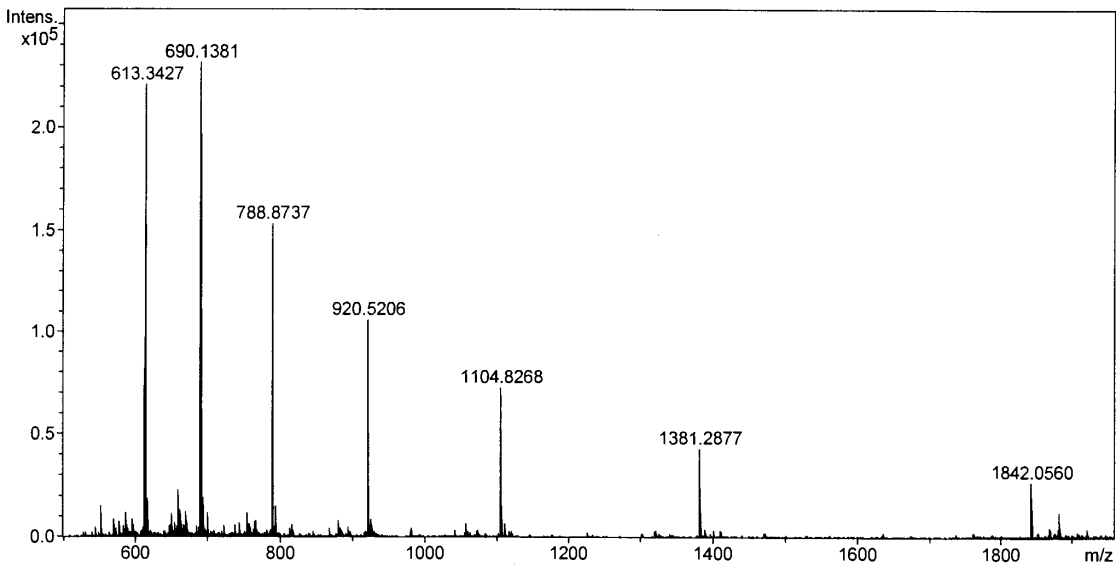


Figure S1. MS(ESI) spectrum of pure oligonucleotide **10**.

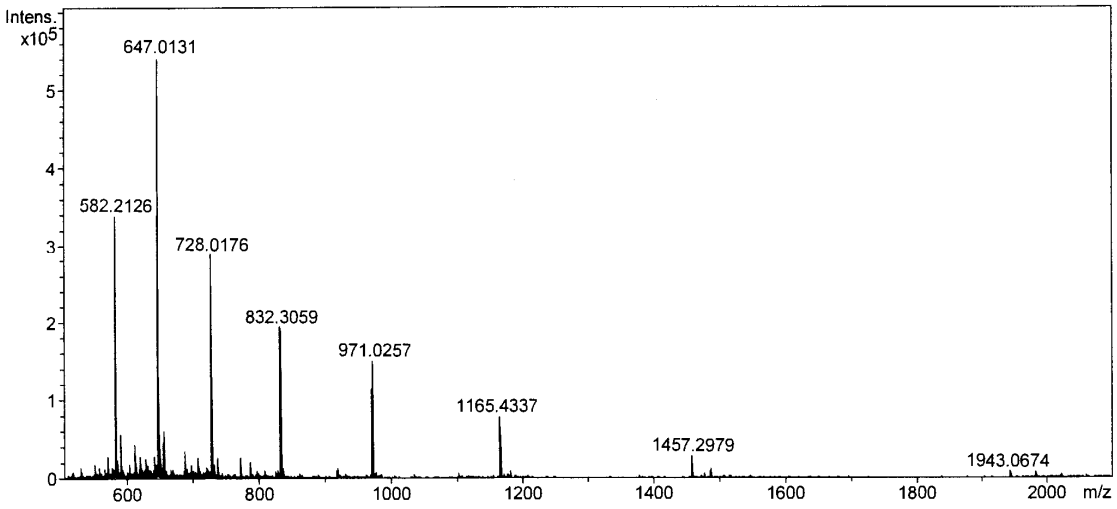


Figure S2. MS(ESI) spectrum of pure oligonucleotide **11**.

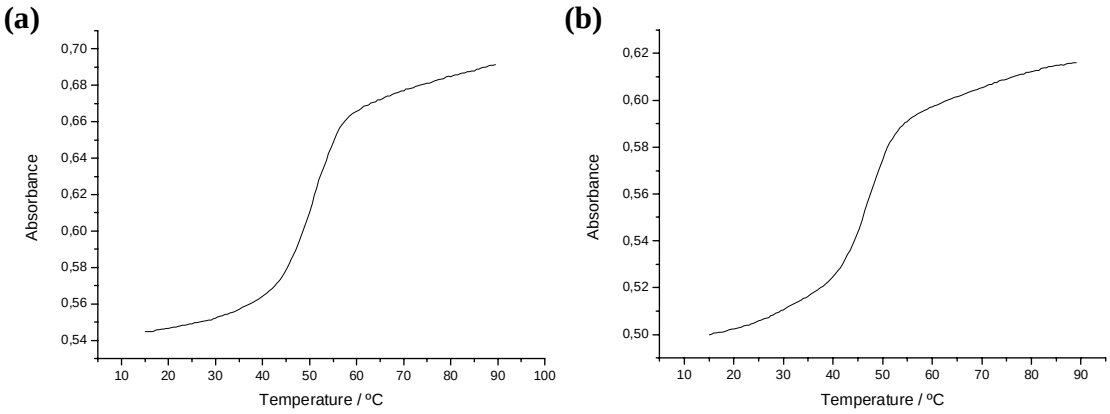


Figure S3. UV-melting profiles of duplexes formed by oligonucleotide conjugates **10** (a) and **11** (b) with the complementary DNA strand. (Salt concentration: 0.1 mol L^{-1} NaCl)

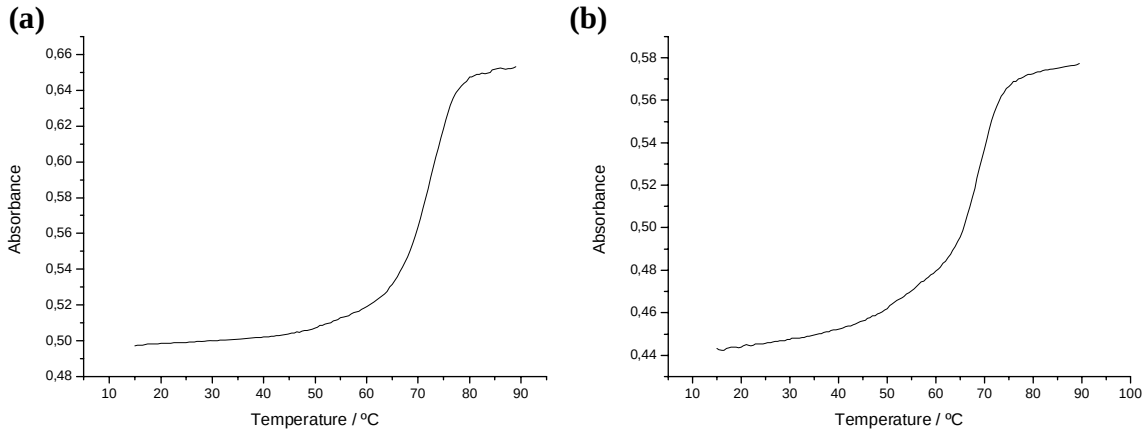


Figure S4. UV-melting profiles of duplexes formed by oligonucleotide conjugates **10** (a) and **11** (b) with the complementary 2´-*O*-methyl RNA strand. (Salt concentration: 0.1 mol L^{-1} NaCl)

Bioconjugate Chemistry

CORRECTION

pubs.acs.org/bc

Correction to "Site-Specific Conjugation of Monodispersed DOTA-PEGn to Thiolated Diabody Reveals Effect of Increasing Peg Size on Kidney Clearance and Tumor Uptake with Improved 64-Copper PET Imaging" Lin Li, Desiree Crow, Fabio Turatti, James R. Bading, Anne-Line Anderson, Erasmus Poku, Paul J. Yazaki, Jenny Carmichael, David Leong, David Wheatcroft, Andrew A. Raubitschek, Peter J. Hudson, David Colcher, and John E. Shively [*Bioconjugate Chemistry* **2011**, *22*, 709–716 DOI: 10.1021/bc100464e].

The article contained several errors at publication. The name of the author David Wheatcroft was listed incorrectly. Author footnote 2 should read Avipep PTY Ltd. and Victorian Cancer Biologics. Debra Tamvakis was left out of the Acknowledgments.

DOI: 10.1021/bc2002105
Published on Web 05/27/2011